MALAYSIAN JOURNAL OF ANALYTICAL SCIENCES

Published by The Malaysian Analytical Sciences Society

ISSN 1394 - 2506

Vol 23 No 1 (2019)

Vol 23 No 2 (2019)

Vol 23 No 3 (2019)

Vol 23 No 4 (2019)

Vol 23 No 5 (2019)

Vol 23 No 6 (2019)

2019

Malaysian Journal of Analytical Sciences Vol 23 No 1 2019

Articles 5 - 20 are selected papers from the "6th International Conference Fuel Cell and Hydrogen Technology 2017 (ICFCHT 2017), 11 - 13 April 2017, Kompleks Perbadanan Putrajaya, Putrajaya; organised by Fuel Cell Institute, Universiti Kebangsaan Malaysia and co-organised by Agency for the Assessment and Application of Technology, Indonesia

Guest Editor: Lorna Jeffery Minggu

Page

1. UNIQUE SIGNATURES OF HONEYS AS A MEANS TO ESTABLISH PROVENANCE 1
(Tanda Kenalan Unik Madu Sebagai Satu Cara Menentukan Provenans)
Syazwani Dzolin, Wan Aini Wan Ibrahim, Naji Arafat Mahat, Aemi Syazwani Abdul Keyon, Zuhaimy Ismail

2. A NEW ULTRA VIOLET-VISIBLE SPECTROPHOTOMETRIC METHOD FOR QUANTITATIVE DETERMINATION OF ACRYLAMIDE VIA HYDROLYSIS PROCESS 14
(Kaedah Spektrofotometrik Ultra Violet-Cahaya Nampak Baharu untuk Penentuan Akrilamida Secara Kuantitatif Melalui Proses Hidrolisis)
Yee-May Chong, Musa Ahmad, Lee Yook Heng

3. WATER EXTRACT OF ONION PEEL ASH: AN EFFICIENT GREEN CATALYTIC SYSTEM FOR THE SYNTHESIS OF ISOINDOLINE-1,3-DIONE DERIVATIVES 23
(Air Abu Kulit Bawang: Sistem Pemangkin Katalitik Hijau yang Effisien dalam Sintesis Terbitan Isoindolina-1,3-dion)
Poh Wai Chia, Poh Seng Chee, Mohd Haziq Aziz, Siti Aisha Mohd Radzi, Fu Siong Julius Yong, Su-Yin Kan

4. MITIGATION OF TOXIC *Alexandrium tamiyavanichii* USING CHITOSAN-SILICA COMPOSITE 31
(Mitigasi *Alexandrium tamiyavanichii* Bertoksik Menggunakan Komposit Kitosan-Silika)
Anwar Iqbal, Najwa Ahmad, Normawaty Mohammad Noor, Lee D. Wilson, Nur Hanisah Ibrahim

5. PRODUCTION OF TITANIUM DIOXIDE NANOFIBER (TNF): INFLUENCE OF ELECTROSPINNING PARAMETER ON CRYSTALLINE SIZE 40
(Penghasilan Nanogentian Titanium Dioksida (TNF): Pengaruh Parameter Elektroputaran Terhadap Saiz Habluran)
Norulsamani Abdullah, Siti Kartom Kamarudin, Loh Kee Shyuan

6. PRODUCTION OF ETHYL LEVULINATE VIA ESTERIFICATION REACTION OF LEVULINIC ACID IN THE PRESENCE OF ZrO_2 BASED CATALYST 45
(Penghasilan Etil Levulinat Melalui Pengesteran Asid Levulinik dengan Kehadiran Mangkin Berasaskan ZrO_2)
Dorairaaj Sivasubramaniam, Nor Aishah Saidina Amin, Khairuddin Ahmad, Nur

Aainaa Syahirah Ramli

7. EFFECT OF DEPOSITION TIME ON STRUCTURAL AND CATALYTIC PROPERTIES OF Pt FILMS ELECTRODEPOSITED ON Ti SUBSTRATE 52
(Kesan Masa Enapan Terhadap Sifat-sifat Struktur dan Katalitik bagi Filem Pt Dielektroenapan di atas Substrat Ti)
Siti Norsafurah Ab Malek and Yusairie Mohd

8. HYDROGEN SORPTION OF MAGNESIUM OXIDE CARBON NANOFIBRE COMPOSITE 60
(Serapan Hidrogen pada Komposit Magnesium Oksida Nano-gentian Karbon)
Nurul Zafirah Abd. Khalim Khafidz, Zahira Yaakob, Sharifah Najiha Timmiati, Kuen-Song Lin, Kean Long Lim

9. PdAu BIMETALLIC CATALYST FOR ELECTROOXIDATION OF GLYCEROL USING CYCLIC VOLTAMMETRY ANALYSIS 71
(PdAu Dwilogam Mangkin untuk Elektropengoksidaan Gliserol dengan Menggunakan Analisis Kitaran Voltametri)
Norilhamiah Yahya and Siti Kartom Kamaruddin

10. BIOHYDROGEN PURIFICATION FROM PALM OIL MILL EFFLUENT FERMENTATION FOR FUEL CELL APPLICATION 80
(Penulenan Gas Biohidrogen yang Terhasil dari Fermentasi Efluen Kilang Minyak Kelapa Sawit Untuk Aplikasi Sel Bahan Api)
Ying Tao Chung, Rosiah Rohani, Izzati Nadia Mohamad, Mohd Shahbudin Mastar@Masdar, Mohd Sobri Takriff

11. FACILE TECHNIQUE FOR THE IMMOBILISATION OF TIO_2 NANOPARTICLES ON GLASS SUBSTRATES FOR APPLICATIONS IN THE PHOTOCATALYTIC SELF-CLEANING OF INDOOR AIR POLLUTANTS 90
(Salutan nanopartikel TiO_2 ke atas Substrat Kaca Melalui Teknik Mudah untuk Penyingkiran Bahan Pencemar Udara dalaman Melalui Proses Fotokatalisis)
Kah Hon Leong, Jia Quan Lee, A. Ashok Kumar, Lan Ching Sim, Saravanan Pichiah

12. SYNTHESIS AND CHARACTERIZATION OF $SrSnO_3$ USING DIFFERENT SYNTHESIS METHODS 100
(Sintesis dan Pencirian $SrSnO_3$ yang Dihasilkan Melalui Kaedah Sintesis Berlainan)
Muhammad Arif Riza, Suhaila Sepeai, Norashikin Ahmad Ludin, Mohd Asri Mat Teridi, Mohd Adib Ibrahim

13. OPTIMISATION OF THE COMPOSITION AND PROCESS PARAMETER OF $CsH_2PO_4/NaH_2PO_4/SiO_2$ SOLID ACID COMPOSITE VIA THE TAGUCHI METHOD 109
(Pengoptimuman Komposisi dan Parameter Proses Bagi Komposit Asid Pepejal $CsH_2PO_4/NaH_2PO_4/SiO_2$ Melalui Kaedah Taguchi)
Norsyahida Mohammad, Abu Bakar Mohamad, Abdul Amir Hassan Kadhum, Kee Shyuan Loh

14. OPTIMIZATION OF HYDROGEN PRODUCTION FROM FRUIT WASTE THROUGH MESOPHILIC AND THERMOPHILIC DARK FERMENTATION: EFFECT OF SUBSTRATE-TO-INOCULUM RATIO 116
(Pengoptimuman Penghasilan Hidrogen dari Buangan Buah melalui Fermentasi Tanpa Cahaya pada Kondisi Mesofilik dan Termofilik: Pengaruh Nisbah Substrat-Inokulum)
Khamdan Cahyari, Muslikhin Hidayat, Siti Syamsiah, Sarto

15. DEHYDRATING ETHANOL USING A TERNARY SOLUTE AND EXTRACTIVE BATCH DISTILLATION 124
(Pengeringan Etanol Menggunakan Zat Larut Ternari dan Penyulingan Kelompok Hasil Ekstrak)
Tjukup Marnoto, I Gusti Suinarcana Budiaman, Chintya Rizki Hapsari, Risqi Angga Y. Prakosa, Khuzaimah Arifin

16. RESISTANCE OF NATIVE BACTERIA ISOLATED FROM ACTIVATED SLUDGE TOWARDS IRON AND MANGANESE 131
(Ketahanan Pencilan Bakteria Asli daripada Enapcemar Teraktif terhadap Ferum dan Mangan)
Nuratiqah Marsidi, Hassimi Abu Hasan, Mohd Izuan Effendi Halmi, Siti Rozaimah Sheikh Abdullah

17. PRODUCTION OF COMPOST FROM NON-SHREDDED EMPTY FRUIT BUNCHES MIXED WITH ACTIVATED LIQUID ORGANIC FERTILIZER IN TOWER COMPOSTER 138
(Penghasilan Kompos dari Tandan Kosong Kelapa Sawit Tanpa Cincang Dicampur dengan Baja Cair Aktif dalam Menara Komposter)
Irvan, Muhammad Rahman, Dedy Anwar, Bambang Trisakti, Hiroyuki Daimon

18. OXYGEN REDUCTION REACTION BEHAVIOURS OF CARBON NANOTUBES SUPPORTING Pt CATALYST FOR PROTON EXCHANGE MEMBRANE FUEL CELL 147
(Sifat Tindak Balas Penurunan Oksigen bagi Tiub Nanokarbon Disokong Mangkin Pt bagi Membran Penukaran Proton Sel Bahan Api)
Md Ahsanul Haque, Abu Bakar Sulong, Edy Herianto Majlan, Kee Shyuan Loh, Teuku Husaini, Rosemilia Rosli

19. EFFECT OF PULSED LASER ABLATION IN WATER ON THE CORROSION BEHAVIOUR AND SURFACE HARDNESS OF STAINLESS STEELS 155
(Kesan Ablasi Laser Gentian Denyut dalam Air terhadap Kakisan dan Kekerasan Permukaan Keluli Kalis Karat)
Sze Ney Chan, Wai Yin Wong, Walvekar Rashmi, Abdul Amir Hassan Kadhum, Mohammad Khalid, Kean Long Lim

20. EFFECT OF Cu-PUROLITE A400 RESIN ON ADSORPTION OF NITRATE AND NITRITE IN WASTEWATER TREATMENT 170
(Kesan Resin Purolit A400-Cu Terhadap Penjerapan Nitrat dan Nitrit dalam Rawatan Air Sisa)
Fatimah Batubara, Chairani Selviani, Muhammad Turmuzi, Edy Herianto Majlan

Malaysian Journal of Analytical Sciences, Vol 23 No 1 (2019): 1 - 13
DOI: https://doi.org/10.17576/mjas-2019-2301-01

MALAYSIAN JOURNAL OF ANALYTICAL SCIENCES
Published by The Malaysian Analytical Sciences Society
ISSN 1394 - 2506

UNIQUE SIGNATURES OF HONEYS AS A MEANS TO ESTABLISH PROVENANCE

(Tanda Kenalan Unik Madu Sebagai Satu Cara Menentukan Provenans)

Syazwani Dzolin[1], Wan Aini Wan Ibrahim[1, 2]*, Naji Arafat Mahat[1], Aemi Syazwani Abdul Keyon[1], Zuhaimy Ismail[3]

[1]*Department of Chemistry, Faculty of Science*
[2]*Centre for Sustainable Nanomaterials, Ibnu Sina Institute for Scientific and Industrial Research*
[3]*Department of Mathematical Sciences, Faculty of Science*
Universiti Teknologi Malaysia, 81310 UTM, Johor Bahru, Johor, Malaysia

**Corresponding author: waini@utm.my, wanaini@kimia.fs.utm.my*

Received: 8 August 2018; Accepted: 12 December 2018

Abstract

Global consumer demands for high quality genuine honey are increasing continuously. The ability to identify the geographical and botanical origins of honey would be of great importance to the improvement of quality control, as well as protection of reputation and confidence of the honey industry. The establishment of unique signatures of honey is one of the potential approaches for honey provenance. A great deal of literature has been published on honey authenticity and provenance. However, specific study focusing on the provenance of honey, especially those of the stingless bee species is lacking, especially in Malaysia. Consequently, this mini review is to highlight the presence of biomarkers in honeys for establishing their provenance *via* the application of spectroscopy and chemometric techniques.

Keywords: stingless bee, bee honey authenticity, provenance, spectroscopy, chemometric

Abstrak

Permintaan global pengguna terhadap madu tulen kualiti tinggi meningkat secara berterusan. Keupayaan untuk mengenal-pasti asal geografi dan botani madu akan menjadi amat penting kepada peningkatan kawalan kualiti, serta melindungi reputasi dan keyakinan industri madu. Kewujudan tanda kenalan unik madu adalah salah satu pendekatan yang berpotensi untuk asal madu. Banyak manuskrip telah diterbitkan untuk keaslian madu dan provenans. Walau bagaimanapun, kajian khusus yang memberi tumpuan kepada provenans madu, terutama bagi lebah tanpa sengat adalah sedikit terutamanya di Malaysia. Oleh itu, kajian tinjauan mini ini adalah untuk menyoroti kehadiran penanda bio dalam madu untuk menentukan provenansnya penggunaan teknik spektroskopi dan kemometrik.

Kata kunci: lebah tanpa sengat, keaslian madu lebah, provenans, spektroskopi, kemometrik

Introduction

Bee honey is appreciated worldwide by old folk and modern practitioners as a natural, nutritious product, mainly because of its therapeutic significance towards human health. Honey is produced by bees collecting nectar from flowers and converting it into a sweet natural product that is claimed to be healthier favourable nutritional option than plain sugar [1]. The properties of honey such as aroma, color, composition and flavour depend generally on the flowers, climate, geographical regions and honeybee species involved in its production [2, 3]. Honey is composed

mainly of fructose and glucose (65%), water (18%), minimal protein and lipid contents [4, 5]. It also consists of different quantities of minerals ranging between 0.02 g/100 g and 1.03 g/100 g, with potassium being the most abundant element comprising approximately one-third of the total mineral content [6-8]. Trace minerals such as potassium, calcium, sodium, iron, copper, zinc and manganese play a critical role in biological systems in which they maintain normal physiological systems and influence reproduction as catalyst for various biochemical reactions [9]. Because of the presence of various chemical compositions, honey has been found to significantly affect human nutrition, healing and preventing illness. In addition to its medicinal benefits, presence of contaminants such as pesticide residues and excessive amounts of minerals and heavy metals has been reported in honey, accentuating the needs for producing safe honey for human consumption [10].

Consumers have the rights to receive the truthfulness of information about the honey in market. The authenticity of honey is the major concern in order to prevent from the adulteration of honey and fraudulent practices during the manufacturing process. Depending on the common fraud, it also may represent a health risk to the consumers and therefore it is important to trace the authenticity of honey in the industry not only for economical but also for safety reasons. Generally, authenticity of honey means that correlation between declarations of honey label and the provenance of the honey itself. Over the past decade, honey is known to be the natural food product that possesses hundreds of benefits towards human health and becomes favourable by old folk and modern practitioners. Unfortunately, the authenticity of the honey decreases as the demand for it increases daily.

Normally, the composition of honey is closely related to its botanical origin and also the geographical area in which it originated. The characteristics of soil and climate will determine the floral that produce honey [11]. Contaminants are transferred from bees to ripened honey and alter its unique composition and the high quality [14]. The surrounding area of mines and steelworks, industrialized and urban areas or motorways with exhausts from vehicles has usually reflected in much higher concentrations of trace metals such as Al, Ba, Ca, Cd, Cr, Cu, Mg, Mn, Ni, Pb, Pd or Zn [12-16].

Provenance establishment of worldwide honey

In this day and age, the development of analytical approaches and advanced statistical techniques has gained interest for the determination of certain major and minor compounds in honey to serve as the biomarkers for its geographical or botanical origin. Thus far, several techniques have been used to analyze the compound composition of honeys. Generally, the most common methods are flame atomic absorption spectroscopy (FAAS) [17], electrothermal atomic absorption spectrometry (ETAAS) [18], high-performance ion chromatography (HPIC) [19], inductively coupled plasma-atomic emission spectroscopy (ICP-AES) [20, 21] and inductively coupled plasma-mass spectrometry (ICP-MS) [20, 22, 23].

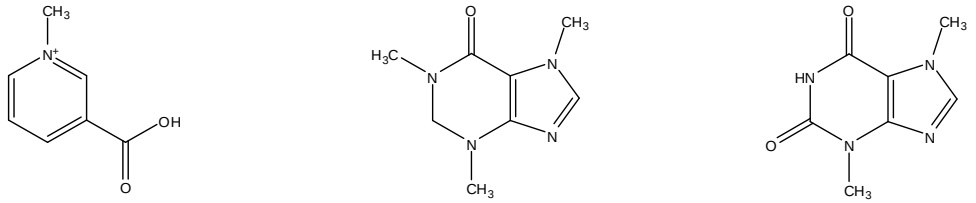
In recent years, authors have begun to apply chemometric techniques into spectroscopy methods in order to establish the provenance of honey. The chemometric evaluation is important to classify, categorize and discriminate the honey arising from different geographical areas [4, 24-26]. Chemometrics can be defined as a way to analyze complicated chemical raw data to more specific and precise data that can be seen and understand clearly. This process may take into account the extraction of information from raw data and ensuring the data selected consisted of maximum valuable information. Chemometrics can be grouped into three analyses such as exploratory analysis, classification or discriminant analysis and regression or prediction models [27]. Unsupervised approaches are usually used in exploratory analysis, which consist of algorithms that cluster metabolites into groups and visualize the data to show their similarities and differences. Principal component analysis (PCA) and hierarchical cluster analysis (HCA) are the commonly used of unsupervised methods. Other nested algorithmic techniques are soft independent modelling of class analogy (SIMCA) and k-nearest neighbours (kNN). For many years, few methods have been conducted in discriminant analysis such as linear discriminant analysis (LDA), partial least square discriminant analysis (PLS-DA), artificial neural networks (ANN), discriminant function analysis (DFA), canonical variant analysis (CVA) and support vector machine (SVM). In regression analysis, methods previously used were principle components regression (PCR), multiple linear regression (MLR), partial least square (PLS), orthogonal partial least square (OPLS), genetic programming/computing (GP/GC), genetic algorithm (GA), evolutionary programming (EP) and evolutionary algorithm (EA), classification and regression tree (CART) and multivariate adaptive regression splines (MARS).

This mini review focuses on the use of analytical approaches combined with chemometric techniques between year 2000 and 2017 for honey provenance (geographical and botanical origins) based on the presence of its biomarkers.

Nuclear magnetic resonance spectroscopy

Previously, many researches used nuclear magnetic resonance (NMR) to identify the origin of honeys as it possessed a powerful ability for compounds structures determination. This technique was frequently used as it provides broad understanding in complex structures especially in food like honey. Donarski et al. [28] studied on one hundred and eighty-two Corsican honey samples collected from five countries, namely Austria, France, Germany, Ireland and Italy that involved ten different regions. The results have demonstrated the viability of developing the accurate models to be used in identification of Corsican honey using proton nuclear magnetic resonance spectroscopy (^{1}H NMR). The produced NMR spectra were used as an input variable for PLS followed by LDA and GP. Overall, models were generated based on three methods; PLS-LDA, two-stage GP and combination of PLS-GP with classification rates for the discrimination of Corsican and non-Corsican honeys were 75.8, 94.5 and 96.2%, respectively. Venetian blind cross-validation was used to generate all models. The NMR spectroscopy was used to identify the molecular structural characteristics of present compounds that gave identity to variables that is most relevant to the classification of Corsican honey. Amazingly, for the first time, the alkaloid trigonelline have been reported to exist in Corsican honey (orange honey) which may prove to be an indicator of its geographical origin.

Schievano et al. [29] carried out a study using the ^{1}H NMR method. They identified and quantified trigonelline compound for the first time in Coffea honey from Colombia and Honduras with addition compounds, namely caffeine and theobromine which previously have not been reported by Donarski et al. [28]. Three marker compounds (Figure 1) with following range of amount have been proposed to be indicators of the botanical origin of the Coffea honeys; trigonelline (23 to 86 mg/kg), caffeine (15 to 98 mg/kg) and theobromine (25 to 160 mg/kg). The constraint in this study was the small number of samples because the Coffea honey is by no means a common product.



Trigonelline Caffeine Theobromine

Figure 1. Identified marker compounds in orange and *Coffea* honeys using NMR spectroscopy

In 2010, Donarski et al. [30] carried out another investigation to identify the botanical biomarkers from Corsican honey samples. The study was conducted for two years. In the first year, one hundred and eighty-two Corsican honey samples were collected from five countries; Austria, France, Germany, Ireland and Italy while in the second year, one hundred and ninety-two Corsican honey samples were collected from four countries namely Austria, France, Germany and Italy. Commercial chestnut honey, non-commercial honey and Corsican honey from the region Châtaigneraie were used as the outsource samples to compare and confirm the identity of the biomarkers present. Four biomarkers have been identified previously by Donarski et al. [28] during collection of the Corsican honey samples in the first year. The efficacy of GP was demonstrated during the determination of the biomarkers from the complexity of NMR spectroscopy data. They have elucidated the four biomarkers and claimed that the biomarkers were confirmed to be kynurenic acid and 2,5-dihydroxyphenylacetic acid. The kynurenic acid was found in sweet chestnut honey, whereas the 2, 5-dihydroxyphenylacetic acid was detected in strawberry-tree honey. Another two biomarkers have been characterized but unidentified. Therefore, they concluded that even honey

samples collected from similar geographical areas contained different compound composition basically according to their botanical origin.

Consonni and Cagliani [31] characterized geographically twenty-three polyflorals honey samples from Argentina, European Committee (EC) countries, Hungary and Italy and eighteen acacia honey from Italy and Hungary using NMR spectroscopy and chemometrics namely PCA and PLS-DA. The ^{1}H NMR spectra of the Acacia honey samples have similarity with the polyfloral honey samples. It means that, both showing the same water-soluble compounds content, even though they are different in concentrations. The compounds presence was grouped based on specific compound resonances comprised methyl amino acid region (0-2 ppm), sugars region (3-5.5 ppm) and aromatic region (6-10 ppm). Between the resonances, few compounds were readily identified, such as tyrosine, phenylalanine, formic acid, proline, alanine, threonine, acetate and lactic acid. The first two principal components (PCs) showed clear differentiation among samples based on different variety with 95.5% of the total variance. Corresponding to loading plot, acacia honey possessed high sugars content namely sucrose, turanose, α-glucose and β-glucose compared to the polyfloral honey. The PCA that was performed on a full spectrum did not provide a clear differentiation among the polyfloral honey samples according to the geographical origin. Following the unsuccessful separation of the polyfloral honey, hierarchical PLS-DA was conducted on thirteen polyfloral honey samples of certain origin and result showed a clear differentiation of samples based on their geographical origin with goodness fit, R^2 (91.9%) and prediction goodness parameter, Q^2 (72.7%). The unsupervised PCA technique demonstrated a clear geographical differentiation of the eighteen Acacia honey samples between Italian and Hungarian origins. Total six PCs exhibited 99.7% of total variance with $Q^2 = 98.1\%$.

Beretta et al. [32] conducted chemometric analysis to identify the botanical origin of commercial honey samples that were purchased from different locations in Milan, Italy in 2006 and 2007. Forty-four selected honey samples were from following floral sources; thyme, linden, orange, eucalyptus, multi-flora, honeydew, chestnut, almond, heather, rosa mosqueta, lavender, acacia, rosemary, rhododendron, cardoon, liquorice, sunflower, strawberry tree and French honeysuckle (*Hedysarum coronarium*). The 300 MHz ^{1}H NMR was used to construct the pattern of chemical compositions in honey samples and the results displayed the relationship between the compound composition and the botanical origin of honeys. Three botanical origin of honey samples, namely honeydew, chestnut and linden were chosen as suitable markers of origin based on their special characteristic that were not detectable in other honey origins. The honeydew honey showed the typical resonance of an aliphatic compound which claimed to derive from the plant phloem sap whereas in the chestnut honey, it displayed the typical signal of kynurenic acid. From the ^{1}H NMR profile in the linden honey, strong signals confirmed the presence of mono-terpene derivative cyclohexa-1,3-diene-1-carboxylic acid (CDCA) and 1-O-β-gentiobiosyl ester (CDCA-GBE). According to the specific markers obtained, the PCA multivariate technique had found different clusters of honeys. Therefore, this study strongly suggested that the proposed ^{1}H NMR method can distinguish the three honey botanical origins compared to other honey origins.

Lolli et al. [33] examined the data from seventy-one honey samples of five different floral origins, specifically chestnut, robinia, citrus, eucalyptus and polyfloral using high resolution nuclear magnetic resonance (HR-NMR). Both ^{1}H and ^{13}C NMR signals assigned the presence of α-glucopyranose, β-glucopyranose, α-fructofuranose, β-fructofuranose and β-fructopyranose as the marker compounds using deuterium oxide (D_2O) and (methyl sulfoxide)-$_{d6}$ solvents. Moreover, according to the overall data obtained, ^{1}H-^{13}C HMBC followed by chemometric analysis showed an effective technique to identify honey botanical origins. The chemometric techniques, PCA and general discriminant analysis (GDA) were used to analyze the spectral data. Between the two techniques, GDA showed higher efficiency compared to PCA in an effort to construct models in the prediction of honey origin.

Schievano and colleagues [34] carried out an investigation to identify the botanical origin of hundred and eighteen chloroform honey extracts obtained from Veneto beehives from four different botanical origins; acacia (Pseudo Acacia *robinia* L.), chestnut (*Castanea sativa*), linden (*Tilia* spp.) and polyfloral. A new simple and reproducible NMR approach combined with PCA and PLS-DA chemometric analysis was used to characterize the honey samples. Results through separate PCA modelling exhibited a specific characteristic (marker compounds) of each botanical origin based on the specific resonances obtained with 95% confidence intervals of the DmodX criterion and the critical value (D_{crit}). The identified marker compounds were 4-(1-hyfroxy-1-methylethyl)cyclohexa-1,3-

dienecarboxylic acid and 4-(1-methylethenyl)cyclohexa-1,3-dienecarboxylic acid from linden honey; chrysin from acacia honey; LACT-3-PKA from chestnut honey and hexanal from all botanical origin honeys. Data from PLS-DA found the coefficient of determination $R^2 = 0.67$ and validation correlation coefficient, $Q^2 = 0.77$.

Schievano et al. [35] performed a similar experiment as previously reported [33] to show that the botanical origin of three hundred and fifty-three chloroform extract of honey samples from seven different floral origins; six were monofloral (acacia, honeydew, orange, chestnut, eucalyptus, linden) and polyfloral. Specific markers of monofloral honeys have been identified using NMR-based metabolomic approach and associated with O2PLS-DA multivariate data analysis. The results exhibited high precision of classification that suggests the usefulness of this approach to discriminate the honey sample origin characteristic. Figure 2 displays the marker compounds detected from six monofloral honeys.The protons originated signals that extracted from the S-Plots were labeled in bold and marked with star.

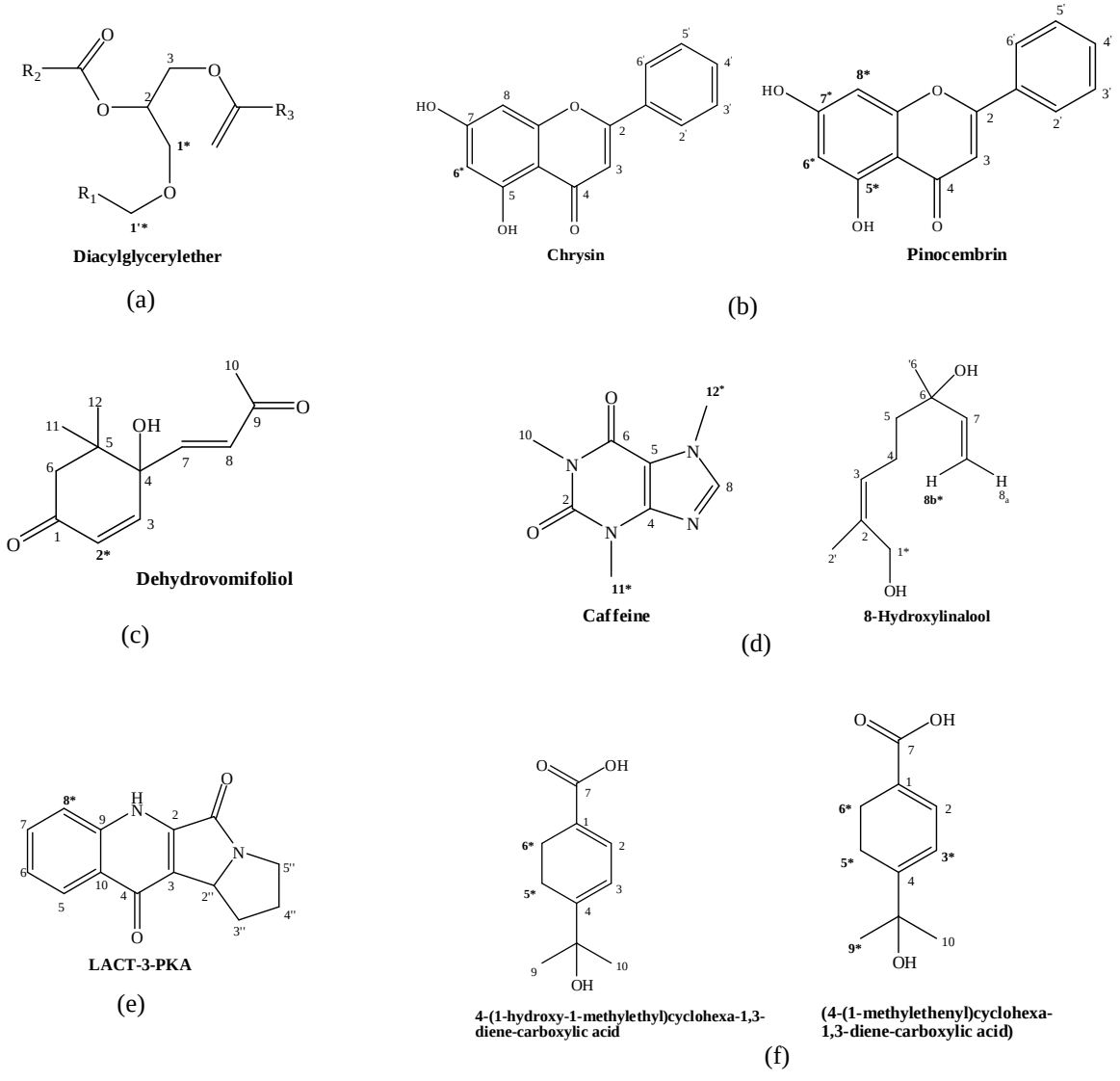


Figure 2. Identified marker compounds of monofloral honeys from (a) honeydew, (b) acacia, (c) eucalyptus, (d) orange, (e) chestnut and (f) linden

Ohmenhaeuser et al. [36] studied the qualitative and quantitative analysis of three hundred and twenty-eight honey samples to observe their botanical origin using ^{1}H and ^{13}C of 400 MHz NMR spectroscopy. Data analyzed by PCA showed clusters of honeys that came from the same botanical origin and the chemical shifts confirmed the presence of glucose and fructose to be one of the reasons of this differentiation and both compounds exhibited much higher peak intensity compared to other compounds using the NMR method. Additionally, the large number of overlapped signals caused other compounds to obscure. Further analysis showed 95-100% of accuracy has been determined using SIMCA and PLS-DA to classify spectra based on the honey botanical origins.

Gas chromatography-mass spectrometry

Gas chromatography (GC) has been widely used for classification of the geographical and botanical origins. When the technique was coupled with mass spectrometry (MS), this selective and sensitive detector allows structural elucidation of the analyzed compounds. A recent study by Azevedo et al. [45] conducted in Santa Catarina, Brazil demonstrated the geographical origin of honeydew honey. A total of twenty-one samples of bracatinga honeydew honey (Bhh) were collected from five mountainous regions namely Bocaino do Sul, Bom Retiro, Lages, Urubici and Urupema between February to June 2014. Free amino acids (FAA) have been identified to be marker compounds using GC-MS and from the data obtained, further classification by PCA technique have been demonstrated for these regions. In this study, PCA technique able to discriminate the honey samples based on their geographical origin with 82% of total variance (sum of two principal components). The authors claimed that FAA profile can be used in honey authenticity determination as it is a reliable analytical method.

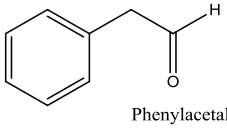
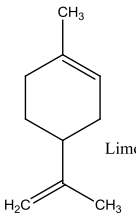
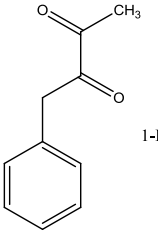
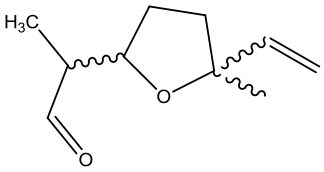
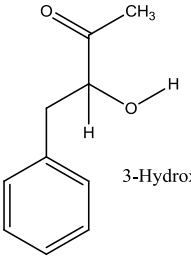
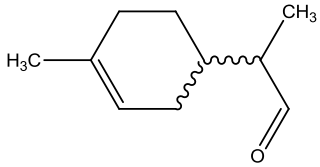
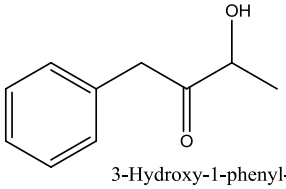
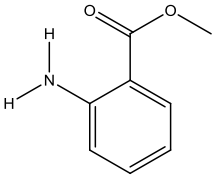
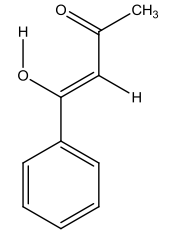
Castro-Vázquez [38] studied a total of forty-nine of Spanish monofloral honey sample from eucalyptus, citrus, thyme, rosemary, heather and lavender botanical origins to undergo analysis to isolate the marker volatile compounds using GC-MS and sensory analysis. HCA was first conducted and presented by the dendrogram to show the distribution of botanical origins of honey samples. The honey samples from the same botanical origins were assigned in the same cluster and this highlighted their similarity. Some similarities of different botanical origins have been detected by successively higher-level clusters, however in order to obtain more specific information, PCA analysis has been carried out. Therefore, several volatile compounds have been detected in higher composition such as in citrus honey contain linalool derivatives for examples sinensal isomers, limonyl alcohol α-4-dimethyl-3-cyclohexene-1-actaldehyde and citrus aroma; eucalyptus honey possessed hydroxyketones, (acetoin, 5-hydroxy-2,7-dimethyl-4-octanone), p-cymene derivatives, 3-caren-2-ol and spathulenol and cheese aroma; lavender honey profiled hexanal, nerolidol oxide, coumarin, hexanol, hotrienol and aromatic herb aromas; heather honey presented benzene, phenolic compounds, ripe fruit and spicy aromas. The compounds that were found in a specific honey sample can be used as markers of their botanical origins.

An isolated aroma compounds from a set of seventy-seven of unifloral honey samples from various botanical origins of Greece such as thyme (*Corydothymus capitatus*), pine (*Pinus* spp.), citrus (*Citrus* spp.), chestnut (*Castanea sativa*), fir (*Abies* spp.), cotton (*Gossypium hirsutum*) and heather (*Erica manipuliflora*) were obtained from headspace solid-phase micro-extraction (HS-SPME), followed by the analysis using GC-MS fingerprinting. For the discrimination of different types of honey, several biomarker groups have been detected, namely phenolics, aliphatics, aldehydes, terpenoids and alcohols. Specifically, for the thyme and citrus honeys, the compounds that act as biomarkers for their discrimination are shown in Table 1. According to the results from combined MS spectra of seven botanical origins, orthogonal partial least squares-discriminant analysis (OPLSTM-DA) exhibited a strong discriminant model. Moreover, the OPLSTM-hierarchical cluster analysis (OPLSTM-HCA) showed higher than 98% of percentage value of correct classification of honey samples. From the results obtained, it clearly demonstrated the potential of the use of combined HS-SPME-GC-MS and chemometric analysis (OPLSTM-HCA) in order to discriminate and classify honey samples based on their botanical origin [37].

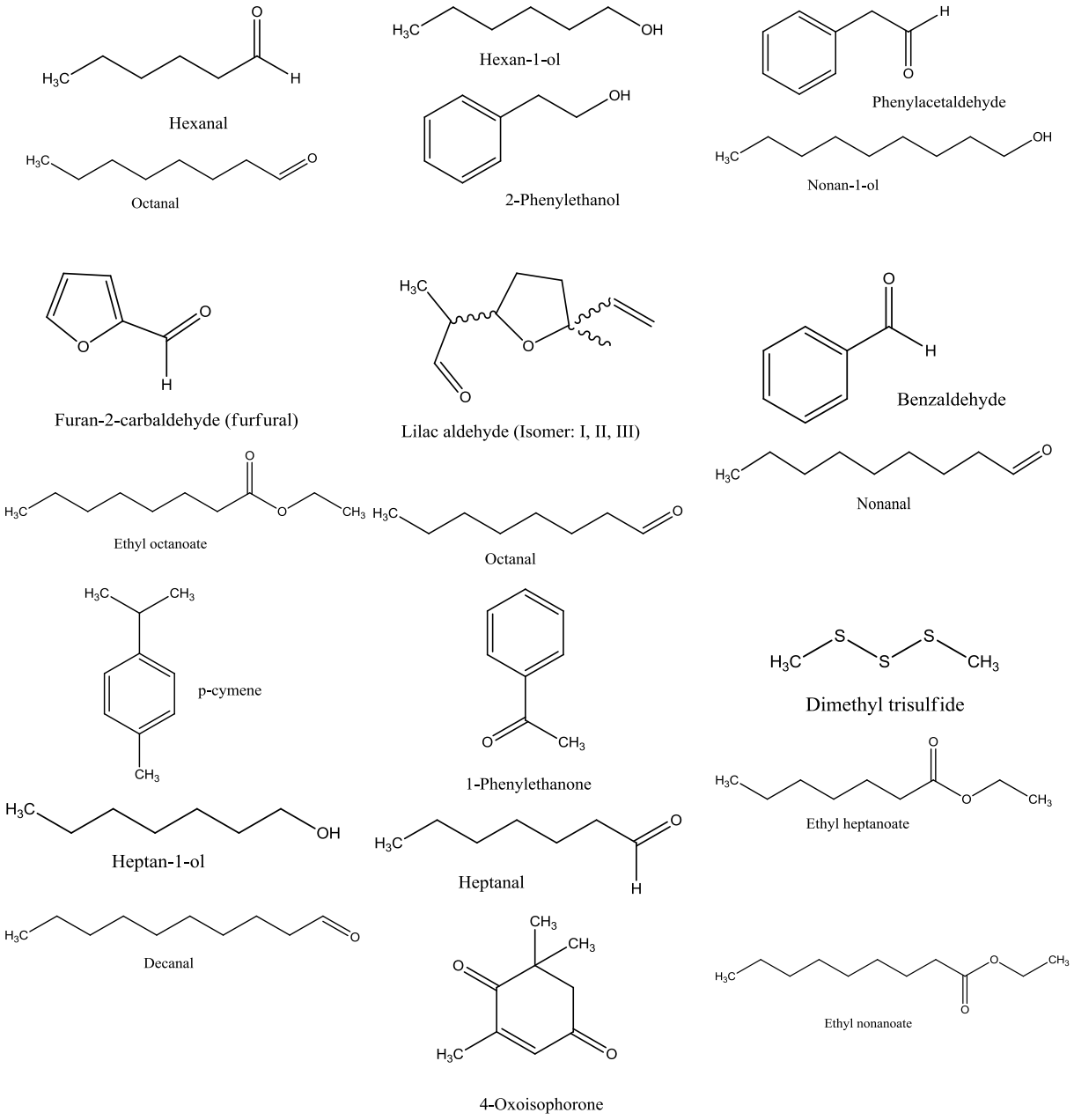
A study under Europe's largest research project on food traceability (EU TRACE) have been conducted by Cajka and coworkers [39] on three hundred and seventy-four honey samples consequently to trace honey origin based on volatile pattern processing using artificial neural network (ANN). The honey samples have been directly provided by producers and claimed their authenticity. The harvesting process took two years (2006 and 2007). In the first harvest period (2006), six types of honey samples were collected namely Corsican, non-Corsican-French, Italian, Austrian, Irish and German. For the second harvest process in 2007, only five types of honey samples were

collected; Corsican, non-Corsican-French, Italian, Austrian and German. In the preliminary data analysis, PCA analysis performed clustering among the samples and divided them into two groups, labelled as 'Corsica' and 'non-Corsica'. The honey samples from various geographical and floral origins have been analyzed using head-space solid-phase micro-extraction (HS-SPME) coupled with 2D-gas chromatography-time-of-flight mass spectrometry (GC-GC-TOF-MS). Twenty-six aroma compound markers (Figure 3) were selected based on the observed peaks that varied significantly in their intensities. The selected marker compounds were used to test the chemometric model, ANN with multilayer perceptron (MLP). The results obtained showed the best prediction (94.5%) and classification (96.5%) capabilities of ANN-MLP model to improve the model performance of total 2 years harvest compared to separate year harvests.

Table 1. Identified marker compounds of thyme and citrus honeys

Thyme honey	**Citrus honey**
 Phenylacetaldehyde	 Limonene
 1-Phenyl-2,3-butanedione	 Lilac aldehyde (Isomer: I, II, III)
 3-Hydroxy-4-phenyl-2-butanone	 1-p-menthen-9-al isomers
 3-Hydroxy-1-phenyl-2-butanone	 Methyl anthranilate
 3-Hydroxy-4-phenyl-3-buten-2-one	

A continuity from an earlier study on three hundred and seventy-four honey samples have been done by Stanimirova et al. [40] to trace the geographical origin of honeys based on volatile compound profiles using four pattern recognition techniques. In order to investigate the influence of the year of sampling on the discrimination, LDA, discriminant partial least squares (DPLS), SIMCA and SVM have been used to construct models for the discrimination of Corsican and non-Corsican-French honeys for both years using the selected marker aroma compounds as identified by Cajka et al. [39] (Figure 3). The results obtained from four chemometric models demonstrated that the SVM combined with Pearson VII universal kemel (PUK) gave the best performance (91.5%) even though the DPLS (87.4%) and the LDA (85.2%) showed high sensitivities and specificities. The combination of GC-GC-TOF-MS with LDA, DPLS and SVM models presented a successful application to detect mislabeling of Corsican honey.



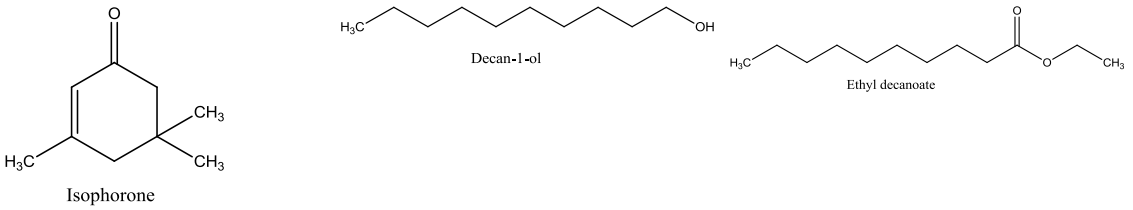


Figure 3. Identified marker aroma compounds of Corsican and non-Corsican-French honeys

Selected ion flow tube mass spectrometry

Selected ion flow tube mass spectrometry (SIFT-MS) has been used for trace gas analysis. The process involved the chemical ionization of volatile compounds in samples. Agila and Barringer [41] tested on unifloral American honeys from Ohio and Indiana, namely clover (*Trifolium* spp.), wildflower, star thistle (*Centaurea americana*), cranberry (*Vaccinium* spp.), blueberry (*Vaccinium* spp.) and unknown source to study the effect between the botanical origin and volatile compound profile of honey samples. These honey samples were analyzed using SIFT-MS coupled with SIMCA. Many volatile compounds were detected form all honey sample, however only several exhibited at high level in the samples such as 1-octen-3-ol, furfural, acetic acid, acetone, benzaldehyde and ethyl acetate. The honey samples from Ohio and Indiana with same botanical origins were totally having different volatile compound compositions. Indiana wildflower honey possessed the highest volatile compound composition, then Ohio wildflower honey. The same trend also can be observed in Indiana clover honey with higher volatile compounds concentration compared to Ohio clover honey. However, in this study, the highest concentration of most of the volatile compounds has been indicated in the unknown source of honey.

Near infrared spectroscopy

Near infrared (NIR) spectroscopy represents an emerging technique in the study of compounds containing O-H, N-H and C-H bonds but seldom been used by researchers. Woodcock and coworkers [42] investigated on the same number of honey samples as reported by Stanimirova et al. [40] and Cajka et al. [39] under a EU-funded TRACE project. In order to confirm the claimed by protected designation of origin (PDO) regions that is specified in European legislation, NIR spectroscopy have been used to construct a specific spectral fingerprinting for Corsican honey. In the preliminary screening, no separation was observed between the Corsican and non-Corsican honeys. Analysis using PCA gave some separation spectra between harvest 1 and harvest 2. However, there was a large amount of overlap between Corsican and non-Corsican honeys. By using cross-validation, a variable selection algorithm and a second derivative data pre-treatment, DPLS models have been developed. The results exhibited correct classification for Corsican (90.0%) and non-Corsican (90.3%) honey samples. Over again, using a variable selection procedure, highest correct classification percentage has been achieved, 90.4% and 86.3% for Corsican and non-Corsican honeys, respectively. This study is much on screening method, but in future it can be improved using advanced method to confirm the presence of honey biomarkers in order to identify its geographical origin.

Fourier transform-Raman spectroscopy

Fourier Transform (FT)-Raman Spectroscopy was not a popular technique to be used to profile honey compounds among honey researchers. However, Piernna and colleagues [43] investigated the geographical origin of a total of three hundred and seventy-four Corsican honey harvested in the year 2006 and 2007 from numerous countries in the Mediterranean region. The study focused on the discrimination of the honeys from different geographical origins namely France, Germany, Italy, Ireland and Austria in order to observe the potential of fingerprinting and profiling using FT-Raman spectroscopy. According to FT-Raman band assignments, the chemical information of honey may be due to the saccharides as shown in the region of 200 and 600 cm^{-1} of scattering bands associated the skeletal vibration motions with major contributions from the deformation of C-C-C, C-C-O, C-C and C-O groups of saccharides (Table 2). In addition, by the application of Raman spectroscopy, the minor contributions of other honey constituents such as proteins, unknown carbohydrates or organic acids can be observed in the region of specific wavenumbers (351; 424; 1,077; 1,126; 1,266 and 1,460 cm^{-1}). The date was further analyzed by PCA technique and result obtained did not show a clear pattern of discrimination or any outliers. Other exploratory methods used were PLS-DA and SVM where these models showed correct grouping between 85% and 90%. The

authors promised that the results from combination of Raman spectroscopy and chemometric techniques exhibited non-expensive discrimination of the honey origins. Unfortunately, in this study, they have not identified and characterized the actual compounds presence in the honey samples to be served as biomarker.

Table 2. Scattering bands of honey and their respective functional groups

Wavenumber (cm^{-1})	**Intensity**	**Type of Vibration**
3312-3334	medium	Stretching of O-H
2938-2944	very strong	Asymmetric stretching of CH_2
2900-2907	shoulder	Stretching of C-H
1636-1642	weak	Deformation of O-H of water
1458-1461	strong	Symmetric deformation in the plane of CH_2
1364-1369	medium	Asymmetric deformation in the plane of CH_2
1265-1267	strong	Deformation of C-C-H, O-C-H and C-O-H; vibration of peptide bond
1126-1127	strong	Deformation of C-O-H, vibration of C-N (protein or amino acid)
1077	strong	Stretching of C-O
1064-1069	strong	Stretching of C-O
979	very weak	Unknown
916-918	weak	Deformation of C-H and C-O-H
904	shoulder	Deformation of C-H
865-871, 822	weak	
777	very weak	Deformation of C-H
708-710	weak	
629-630	strong	Ring deformation
590-592	shoulder	Skeletal vibration
519-522	strong	Deformation of C-C-O and C-C-C
449-450	shoulder	Skeletal vibration
420-424	strong	Deformation of C-C-O and C-C-C
351	very weak	Unknown carbohydrates and proteins

Inductively coupled plasma

Inductively coupled plasma (ICP) technique is becoming widely accepted in food analysis for determination of major and trace elements. Chudzinska and Baralkiewicz [46] studied fifteen elements (Al, B, Ba, Ca, Cd, Cr, Cu, K, Mg, Mn, Na, Ni, Pb, Sr and Zn) in each of hundred and forty honey samples of three different types namely honeydew, buckwheat and rape honeys. These honey samples were collected in different areas of Poland between May to November in the years 2006-2007. The data obtained was subjected to LDA technique and revealed 100% discrimination between honey samples. Furthermore, the authors claimed that the values of K and Mn elements are important during the classification prediction and believed they could be markers for honey botanical origin.

A study by Chua et al. [20] constructed the elemental profiles of six honey from Malaysia, namely Tualang (*Koompassia excels*) from Tasik Pedu, Kedah, Gelam (*Malaleuca cajuputi*) from Gubir, Kedah, acacia from Kota Tinggi, Johor and other three forest honeys labeled as forest NS from Kampung Jerjak Seberang, Negeri Sembilan, forest M1 from Kampung Kemuning, Melaka and forest M2 from Kampung Tanjung Rimau Dalam, Melaka using the data obtained from both ICP-AES and ICP-MS. Results showed that the honeys possessed abundant of

potassium and sodium in the range of 69.3-78.6% and 14.1-28.7%, respectively. According to the PCA data obtained, these two elements were claimed to be mineral markers to distinguish the geographical origins of selected honeys. However, no explanation on provenance has been reported clearly as the results exhibited no correlation between the origin of honeys and the type of elements.

A recent study in Malaysia by Shadan et al. [44] exhibited the provenance of stingless bee honey collected from four different geographical regions of Johor, Malaysia (North, South, East and West) represented by five districts namely Segamat, Johor Bahru, Muar, Batu Pahat and Kota Tinggi. The collection period was during less rainy season in May, June and July. Multi-element distribution patterns were established using Inductively Coupled Plasma Optical Emission Spectrometry (ICP-OES) in combination with PCA and LDA techniques. The PCA results demonstrated 87.0% correct classification rate and improved to 96.2% with the use of LDA. The results indicated possible discrimination for the different geographical regions. Until now, this is the first documented data on the provenance establishment of stingless bee honey in Johor, Malaysia. Therefore, our aim is to further studies on the same aspect but in larger scale of the stingless bee honey geographical origins in Malaysia covering four regions namely Kedah, Johor, Selangor and Pahang which are represented by sixteen districts and covering different seasons within a year. Eighteen multi-trace metal ions (Pb, Cu, Mn, Zn, Ni, Cr, Cd, Al, Ba, Se, Ag, As, Co, Be, V, Tl, Th and U) were selected to construct their fingerprinting in identifying the authenticity with the assist of chemometric techniques (PCA and LDA).

Conclusion

Honey is well known as a complex matrix that is very difficult to analyze and characterize. Often the determination of their provenance is complicated because of the incomplete correlation between analytical parameters and honey provenance marker compounds. With globalization technologies, numerous studies have attempted to show the important used of the spectroscopy coupled with the chemometric techniques to exhibit the biomarkers of honeys according to their geographical and botanical origins. For now, it shows a great advantage to solve several problems in this field. Creation of honey databases can be much useful to help identify and quantify the upcoming data in order to monitor unexpected changes or fraud performers based on the established honey fingerprinting. However, issue dealing with the food policies, including legal requirements and standard need to be taken into consideration. Therefore, this field of study needs more time and efforts to improve the capability of technologies and develop databases for the determination of the honey authentication and the provenance according to its unique signatures. In addition, from the review, it can be concluded that the significant to highlight the type of bee species when studying about provenance in order to compare and compile the results from worldwide honey. To date, no comprehensive study in Malaysia has been conducted to establish provenance of bee honeys according to their marker compounds especially from stingless bee species. To the best of our knowledge, only a study by Shadan et al. [44] had documented the provenance establishment of stingless bee honey using multi-element analysis combined with chemometric techniques. Thus, our on-going study will further investigate the geographical origin of stingless bee honey samples specifically from *Heterotrigona itama* species collected from the four regions of Peninsular Malaysia. Concurrently, our study will classify honey samples and find markers of the honey authenticity according to their multi-trace metals concentrations.

Acknowledgment

We are thankful for the advice and assistance provided by Department of Chemistry, Malaysia. We are grateful for the financial support of the work by Universiti Teknologi Malaysia (UTM) (Research University Grant - Grant number QJ130000.2526.12H57).

References

1. Vanhanen, A. Emmertz, L. P. and Savage, P. (2011). Mineral analysis of mono-floral New Zealand honey. *Food Chemistry*, 128(1): 236–240.
2. Escuredo, O., Dobre, I., Fernández-González, M. and Seijo, M. C. (2014). Contribution of botanical origin and sugar composition of honeys on the crystallization phenomenon. *Food Chemistry*, (149): 84–90.
3. Tornuk, F., Karaman, S., Ozturk, I., Toker, O. S., Tastemur, B. and Sagdic, O. (2013). Quality characterization of artisanal and retail turkish blossom honeys: Determination of physicochemical, microbiological, bioactive properties and aroma profile. *Industrial Crops and Products*, (46):124–131.

4. Silva, L. R., Videira, R., Monteiro, A. P., Valentão, P. and Andrade, P. B. (2009). Honey from Luso region (Portugal): Physicochemical characteristics and mineral contents. *Microchemistry Journal*, (93): 73–77.
5. Khalil, M. I., Motallib, M. A., Anisuzzaman, A., Sathi, Z. S., Hye, M. and Shahjahan, M. (2001). Biochemical analysis of different brands of unifloral honey available at the northern region of Bangladesh. *Journal of Medical Science*, (1): 385–388.
6. Chakir, A., Romane, A., Barbagianni, N., Bartoli, D. and Ferrazzi, P. (2011). Major and trace elements in different types of Moroccan honeys. *Australian Journal of Basic and Applied Sciences*, 5(4):223–231.
7. Bogdanov, S., Haldimann, M., Luginbuhl, W. and Gallmann, P. (2007). Minerals in Honey: Environmental, geographical and botanical aspects. *Journal of Apicultural Research*, (46): 269–275.
8. de Ferrer, B. S. G., de Rodriguez, O., Pena, J., Martinez, J., and Moran, M. (2004). Mineral content of the honey produced in Zulia state, Venezuela. *Archivos Latinoamericanos de Nutricion*, 54(3): 346–348.
9. Staniškien, B., Matusevičius, P. and Budreckien, R. (2006). Honey as an indicator of environmental pollution. *Environmental Research, Engineering and Management*, 2(36): 53–58.
10. Mckee, B. (2003). Prevention of residues in honey: A future perspective. *Apiacta*, (38): 173–177.
11. Rashed, M. N. and Soltan, M. E. (2004). Major and trace elements in in different types of Egyptian mono-floral and non-floral bee honeys. *Journal of Food Composition and Analysis*, (17): 725-735.
12. Achudume, A. C. and Nwafor, B. N. (2010). The ecological assessment of metals in local brands of honey in Southwest Nigeria. *African Journal of Agricultural Research*, 5(18):2608-2610.
13. Stankovska, E. Stafilov, T. and Šajn, R. (2008). Monitoring of trace elements in honey from the Republic of Macedonia by atomic absorption spectrometry. *Environmental Monitoring Assessment*, (142): 117-126.
14. Tuzen, M. Silici, S. Mendil, D. and Soylak, M. (2007). Trace element levels in honeys from different regions of Turkey. *Food Chemistry*, 103(2): 325-330.
15. Floryszak-Wieczorek, F. Milczarek, G. Arasimowicz, M. and Ciszewski, A. (2006). Do nitric oxide donors mimic endogenous NO-related response in plants? *Planta*, (224): 1363-1372.
16. Bratu, I. and Georgescu, C. (2005). Chemical contamination of bee honey–identifying sensor of the environment pollution. *Journal of Central European Agriculture*, (6):95–98.
17. Yilmaz, H., and Yavuz, O. (1999). Content of some trace metals in honey from South-Eastern Anatolia. *Food Chemistry*, 4(65):475–476.
18. Przybylowski, P. and Wilczyńska, A. (2001). Honey as an environmental marker. *Food Chemistry*. (74): 3289–3291.
19. Buldini, P. L., Cavalli, S., Mevoli, A. and Sharma, J. L., (2001). Ion chromatographic and voltammetric determination of heavy and transition metals in honey. *Food Chemistry*, (73):487–495.
20. Chua, L. S., Abdul-Rahaman, N. L., Sarmidi, M. R. and Aziz, R. (2012). Multi-elemental composition and physical properties of honey samples from Malaysia. *Food Chemistry*, 135(3): 880–887.
21. Devillers, J., Dore, J., Marenco, M., Poirier-Duchene, F., Galand, N. and Viel, C. (2002). Chemometrical analysis of 18 metallic and non-metallic elements found in honeys sold in France. *Journal of Agricultural Food Chemistry*, (50): 5998–6007.
22. Chudzinska, M. and Barałkiewicz, D. (2011). Application of ICP-MS method of determination of 15 elements in honey with chemometric approach for the verification of their authenticity. *Food and Chemical Toxicology*, 49: 2741–2749.
23. Chudzinska, M., and Barałkiewicz, D. (2010). Estimation of honey authenticity by multi-element characteristics inductively coupled plasma-mass spectrometry (ICP-MS) combined with chemometrics. *Food and Chemical Toxicology*. 48: 284–290.
24. Latorre, M. J. Peña, R. Pita, C. Botana, A. García, S. and Herrero, C. (1999). Chemometric classification of honeys according to their type II. Metal content data. *Food Chemistry*, (66): 263–268.
25. González Paramás, A. M. Bárez, J. A. G. Garcia-Villanova, R. J. Palá, T. R. Albajar, R. A. and Sánchez, J. S. (2000). Geographical discrimination of honeys by using mineral composition and common chemical quality parameters. *Journal of the Science of Food and Agriculture*, (80): 157–165.
26. Baroni, M. V. Arrua, C. Nores, M. L. Fayé, P. del Pilar Díaz, M. Chiabrando, G. A. and Wunderlin, D. A. (2009). Composition of honey from Córdoba (Argentina): Assessment of North/South provenance by chemometrics. *Food Chemistry*, (114): 727–723.
27. Goodacre, R. Broadhurst, D. Smilde, A. Kristal, B. Baker, J. and Beger, R. (2007). Proposed minimum reporting standards for data analysis in metabolomics. *Metabolomics*. 3(3): 231–241.

28. Donarski, J. A., Jones, S. A., and Charlton, A. J. (2008). Application of cryoprobe ^{1}H nuclear magnetic resonance spectroscopy and multivariate analysis for the verification of corsican honey. *Journal of Agricultural and Food Chemistry*, 56(14): 5451–5456.
29. Schievano, E., Finotello, C., Mammi, S., Belci, A. I., Colomban, S. and Navarini, L. (2015). Preliminary characterization of monofloral *Coffea* spp. honey: Correlation between potential biomarkers and pollen content. *Journal of Agricultural and Food Chemistry*, (63): 5858–5863.
30. Donarski, J. A., Jones, S. A., Harrison, M., Driffield, M. and Charlton, A. J. (2010). Identification of botanical biomarkers found in corsican honey. *Food Chemistry*, 118(4):987–994.
31. Consonni, R. and Cagliani, L. R. (2008). Geographical characterization of polyfloral and acacia honeys by nuclear magnetic resonance and chemometrics. *Journal of Agricultural and Food Chemistry*, 56(16): 6873–6880.
32. Beretta, G., Caneva, E., Regazzoni, L., Bakhtyari, N. G. and Maffei F. R. (2008). A solid-phase extraction procedure coupled to ^{1}H NMR, with chemometric analysis, to seek reliable markers of the botanical origin of honey. *Analytica Chimica Acta*, 620(1–2): 176–182.
33. Lolli, M. Bertelli, D. Plessi, M. Sabatini, A.G. and Restani, C. (2008). Classification of Italian honeys by 2D HR-NMR. *Journal of Agricultural and Food Chemistry*, 56(4): 1298–1304.
34. Schievano, E., Peggion, E. and Mammi, S. (2010). ^{1}H Nuclear magnetic resonance spectra of chloroform extracts of honey for chemometric determination of its botanical origin. *Journal of Agricultural and Food Chemistry*, 58(1):57–65.
35. Schievano, E., Stocchero, M., Morelato, E., Facchin, C. and Mammi, S. (2012). An NMR-based metabolomic approach to identify the botanical origin of honey. *Metabolomics*, 8(4):679–690.
36. Ohmenhaeuser, M., Monakhova, Y. B., Kuballa, T. and Lachenmeier, D. W. (2013). Qualitative and quantitative control of honeys using NMR spectroscopy and chemometrics. *ISRN Analytical Chemistry*, 2013: 1-9.
37. Aliferis, K. A., Tarantilis, P. A., Harizanis, P. C. and Alissandrakis, E. (2010). Botanical discrimination and classification of honey samples applying gas chromatography/mass spectrometry fingerprinting of headspace volatile compounds. *Food Chemistry*, 121(3): 856–862.
38. Castro-Vázquez, L., Díaz-Maroto, M. C., González-Viñas, M. A. and Pérez-Coello, M. S. (2009). Differentiation of monofloral citrus, rosemary, eucalyptus, lavender, thyme and heather honeys based on volatile composition and sensory descriptive analysis. *Food Chemistry*, 112(4):1022–1030.
39. Cajka, T., Hajslova, J., Pudil, F. and Riddellova, K. (2009). Traceability of honey origin based on volatiles pattern processing by artificial neural networks. *Journal of Chromatography A*, 1216(9):1458–1462.
40. Stanimirova, I., Üstünb, B., Cajka, T., Riddelova, K., Hajslova, J., and Buydens, L. M. C. (2010). Tracing the geographical origin of honeys based on volatile compounds profiles assessment using pattern recognition techniques. *Food Chemistry*, 118(1):171–176.
41. Agila, A. and Barringer, S. (2012). Application of selected ion flow tube mass spectrometry coupled with chemometrics to study the effect of location and botanical origin on volatile profile of unifloral american honeys. *Journal of Food Science*, 77(10):1103–1108.
42. Woodcock, T., Downey, G. and O'Donnell, C. P. (2009). Near infrared spectral fingerprinting for confirmation of claimed PDO provenance of honey. *Food Chemistry*, 114(2): 742–746.
43. Piernna, J. A. Abbas, O. Dardenne, P. and Baeten, V. (2011). Discrimination of corsican honey by FT-raman spectroscopy and chemometrics. *Biotechnology, Agronomy, Society and Environment*, 15(1): 75–84.
44. Shadan, A. F. Mahat, N. A., Wan Ibrahim, W. A., Ariffin, Z. and Ismail, D. (2017). Provenance establishment of stingless bee honey using multi-element analysis in combination with chemometrics techniques. *Journal of Forensic Sciences*, 63(1): 80–85.
45. Azevedo, M. S., Seraglio, S. K. T., Rocha, G., Balders, C. B., Piovezan, M., Gonzaga, L. V., Falkenberg, D. B., Fett, R., and Costa, A. C. O. (2017). Free amino acid determination by GC-MS combined with a chemometric approach for geographical classification of bracatinga honeydew honey (*Mimosa scabrella* Bentham). *Food Control*, 78: 383–392.
46. Chudzinska, M. and Baralkiewicz, D. (2011). Application of ICP-MS method of determination of 15 elements in honey with chemometric approach for the verification of their authenticity. *Food and Chemical Toxicology*, 49(11): 2741–2749.

Malaysian Journal of Analytical Sciences, Vol 23 No 1 (2019): 14 - 22
DOI: https://doi.org/10.17576/mjas-2019-2301-02

MALAYSIAN JOURNAL OF ANALYTICAL SCIENCES
Published by The Malaysian Analytical Sciences Society
ISSN 1394 - 2506

A NEW ULTRA VIOLET-VISIBLE SPECTROPHOTOMETRIC METHOD FOR QUANTITATIVE DETERMINATION OF ACRYLAMIDE VIA HYDROLYSIS PROCESS

(Kaedah Spektrofotometrik Ultra Violet-Cahaya Nampak Baharu untuk Penentuan Akrilamida Secara Kuantitatif Melalui Proses Hidrolisis)

Yee-May Chong[1], Musa Ahmad[2]*, Lee Yook Heng[1]

[1]*School of Chemical Sciences and Food Technology, Faculty Sciences & Technology, Universiti Kebangsaan Malaysia, 43600 UKM Bangi, Malaysia*
[2]*Industrial Chemical Technology Programme, Faculty Sciences & Technology, Universiti Sains Islam Malaysia, 71800 Nilai, Malaysia*

**Corresponding author: andong@usim.edu.my*

Received: 5 August 2018; Accepted: 8 December 2018

Abstract

This paper reported the results for quantitative determination of acrylamide via hydrolysis process using ultra violet-visible (UV-Vis) spectrophotometric method. This quantitative determination started with hydrolysing acrylamide in a strong basic condition to yield ammonia and acid salt. The optimum conditions of hydrolysis (concentration of the base used and time for hydrolysis) were also determined. From this study, the optimum conditions to hydrolyse acrylamide were achieved using 6.0 M of sodium hydroxide (NaOH) for 10 minutes. The hydrolysis process was characterised by monitoring the ammonia produced using Nessler's reagent through the formation of yellow colouration in the presence of ammonia. After the optimisation of hydrolysis process, the characterisation of all parameters including concentration of Nessler's reagent used, reproducibility, dynamic range, and interference ions were studied. Linear dynamic ranges from 0-10 ppm acrylamide with limit of detection (LOD) of 0.074 ppm were obtained when 3.0 mM Nessler's reagent was used. The relative standard deviations (RSD) for reproducibility were 2.8-3.3%. No significant interference from cations such as Na^+, K^+, Ca^{2+} during quantitative analysis of acrylamide, but ions such as Fe^{3+} and NH_3 affected the analysis.

Keywords: acrylamide, hydrolysis, Nessler's reagent

Abstrak

Kajian ini melaporkan keputusan untuk penentuan kuantitatif akrilamida melalui proses hidrolisis dengan kaedah spektofotometrik UV-Nampak (UV-Vis). Penentuan kuantitatif ini dimulai dengan hidrolisis akrilamida dalam keadaan bes kuat dan menghasilkan ammonia dan garam asid sebagai hasil. Keadaan optimum hidrolisis seperti kepekatan bes yang digunakan serta masa hidrolisis optimum telah ditentukan. Daripada kajian, keadaan hidrolisis akrilamida yang optimum ialah menggunakan natrium hidroksida (NaOH) 6.0 M dan masa tindak balas selama 10 minit. Proses hidrolisis telah dicirikan dengan memantau ammonia yang terhasil menggunakan reagen Nessler yang akan menghasilkan warna kuning dengan kehadiran ammonia. Setelah mengoptimumkan proses hidrolisis, pencirian semua parameter termasuk kepekatan reagen Nessler yang digunakan, kebolehulangan, julat dinamik, dan ganguan ion telah dikaji. Julat dinamik linear daripada 0-10 ppm akrilamida dengan had pengesanan (LOD) 0.074 ppm telah diperolehi apabila reagen Nessler 3.0 mM digunakan. Sisihan piawai relatif (RSD) untuk kebolehulangan telah diperolehi pada julat 2.8-3.3%. Kation seperti Na^+, K^+, Ca^{2+} tidak memberikan gangguan yang ketara pada analisis kuantitatif akrilamida, tetapi ion seperti Fe^{3+} and NH_3 telah mengganggu analisis ini.

Kata kunci: akrilamida, hidrolisis, reagen Nessler

Introduction

In 2002, high levels of acrylamide were detected in heat-treated potato products and other baked products as reported by Swedish National Food Authority [1]. Formation of acrylamide in food occurs via reaction between reducing sugar such as glucose and amino acid asparagine at high temperature, known as Maillard reaction [2]. This toxic compound is also found in various carbohydrate-rich products such as French fries, potato crisps, cereals, bread and etc. The levels of acrylamide have been found up to 4 mg/ kg in potato crisps as reported by Erickson [3]. Research done by Dybing et al. revealed that the average consumption of acrylamide for adults were 0.3–0.6 µg/kg body weight while higher exposure for children and adolescents (0.4–0.6 µg/ kg body weight) [4]. This is due to the eating habits of children as they tend to consume more acrylamide-rich foods such as French fries and potato chips. The International Agency for Research on Cancer classified acrylamide as a neurotoxin (probable human carcinogen compound) due to its ability to form adducts with haemoglobin [5].

The conventional methods to determine acrylamide in foods are high-performance liquid chromatography (HPLC), gas chromatography-mass spectrometry (GC-MS) and other chromatographic methods. These chromatographic methods are time consuming, costly, and required high laboratory skills. Moreover, complicated sample preparation and derivatization of acrylamide e.g. bromination are laborious. Besides that, these techniques are not suitable for *in-situ* analysis due to the large size of the instruments.

Enzyme-linked immunosorbent assay (ELISA) technique has been developed for quantification of acrylamide. Specific antibody is required for detecting acrylamide due to its low molecular mass [6, 7]. The reported limits of detection (LODs) using ELISA techniques were very low apart from, complicated and time consuming procedures to produce antibodies which are among several issues for this technique.

Hu et al. developed a method for acrylamide detection based on the acrylamide-induced distance increase between quantum dots [8]. The principle of this detection method is distance-dependent fluorescence changes caused by acrylamide polymerization. Fluorescence intensity increases with the presence of acrylamide due to the increase in distance between quantum dots. However, the responded linear range (3.5×10^{-5} to 3.5 g/L) and LOD (3.5×10^{-5} g/L) were high.

There are some publications reported on voltametric determination of acrylamide [9-13]. Acrylamide forms adduct with haemoglobin and hence alter the electro-activity of haemoglobin. In spite of the low LOD (in nM), the sensors still need to undergo electrode clean-up process, and the modified electrodes must be stored at low temperature (4 °C). Besides that, the immobilized haemoglobin is not stable due to its short shelf life (only 14 days).

Some researchers reported on potentiometric biosensor of acrylamide degradation using microbial cells. Silva et al. hydrolysed acrylamide to acrylic acid and ammonia using *Pseudomonas aeruginosa*, prior detection using ammonium-ion selective electrode [14, 15]. Meanwhile, Ignatov et al. used oxygen electrode to test the respiration of *Brevibacterium* sp. cells in acrylamide solution [16, 17]. Although these sensors are selective towards acrylamide, but are able to detect acrylamide in most of the real food samples due to the high detection limits (in mM).

Some bio-molecules such as cells have been used for quantitative determination of acrylamide. Hasegawa et al. developed a sensor based on the ability of acrylamide to create stress onto the cells. The bacterial cells release fluorescence with the present of acrylamide [18]. Some electrochemical sensors based on deoxyribonucleic acid (DNA) have been developed to detect acrylamide [19, 20]. These sensors are based on the changes of guanine's current signal due to the formation of acrylamide adduct with DNA. Besides that, electrochemical characteristics of some living cells are used in the assessment of this cytotoxicity compound. PC-12 cell are immobilised on glassy carbon electrode (GCE) modified with graphene oxide and gold nanoparticles [21]. With the present of acrylamide, PC-12 cells are stimulated by acrylamide and reduced the peak current. However, the major reported disadvantages of this method were high linear range (in mM) and LOD.

To date, the optical acrylamide detection especially colorimetric is yet to be fully explored. Current fluorometric methods for detection of acrylamide still required the polymerization process and are not suitable for *in-situ* analysis. Therefore, there is a need to develop a new colorimetric method for acrylamide screening.

Optical determination is the easiest field screening on the presence of acrylamide compound in food samples due to obvious colour changes observed via naked eyes. Based on this reason, it is suitable for *in-situ* analysis. In this research, acrylamide was hydrolysed to its corresponding salt and ammonia. The level of ammonia produced was determined using Nessler's reagent to produce mercury (II) amido-iodine complex (yellow colouration) in basic condition. The overall reactions are shown in Equations 1 and 2, respectively.

$$CH_2CHC(O)NH_2 + NaOH \rightarrow CH_2CHC(O)ONa + NH_3 \quad (1)$$

$$2(HgI_4)^{2-} + NH_3 + 3OH^- \rightarrow HgO.Hg(NH_2)I + 7I^- + 3H_2O \quad (2)$$

The aim of this research is to explore a new optical method in quantifying the level of acrylamide in food sample.

Materials and Methods

Chemical and instrumentation

Acrylamide 99% and ammonium chloride (NH_4Cl) 99.5% were supplied by Sigma. Mercury (II) iodine 99% (HgI_2) was obtained from BDH. Potassium iodide (KI) 99.5%, sodium hydroxide (NaOH) 99%, and potassium chloride (KCl) 99% were purchased from Systerm. Calcium chloride ($CaCl_2$) 95% was supplied by HmbG Chemicals. Sodium chloride (NaCl) 99% and iron (II) chloride hexahydrate ($FeCl_2.6H_2O$) 99% were obtained from Acros. Varian Cary-50 was used for all absorbance measurements.

Characterisation of base hydrolysis process towards acrylamide

The condition for base hydrolysis process of acrylamide was optimised in terms of concentration of base used and time taken for hydrolysis. Acrylamide stock solution (100 ppm) was prepared by dissolving 0.01 g acrylamide powder in deionised water inside a volumetric flask and topped to 100 mL. Lower concentrations of acrylamide solutions were prepared by appropriate dilutions from stock solution.

The optimum molarity of base needed was tested by injecting 2 mL acrylamide solution (5 ppm) into various concentrations of NaOH (0-8 M), leaving the mixture for 15 minutes. Then, the Nessler's reagent was added into the hydrolysed acrylamide solution to form yellow complex called mercury (II) amido-iodine. In this study, 2 mL of hydrolysed acrylamide solution was added with 985 µL water and 40 µL of Nessler's reagent. The absorbance of the complex was obtained using UV-Vis spectrophotometer at the wavelength of 420 nm. As for the control, same protocols were repeated using water in substitution for acrylamide solution.

The hydrolysis of 2 mL acrylamide solution (5 ppm) injected with 6 M NaOH at different time were recorded. Next, the Nessler's reagent was added into hydrolysed acrylamide solution and the absorbance was measured.

Concentration optimisation of Nessler's reagent

The concentration of Nessler's reagent used in the solution was optimised. The formation of Nessler's complex was tested using various ratios of HgI_2 to KI. Sonication was applied to homogenise the solution during solution preparation. As the optimum ratio of HgI_2 and KI was obtained to form Nessler's complex, the optimum concentration of Nessler's reagent was determined by adding different concentrations of Nessler's reagent into the hydrolysed acrylamide solution. The absorbance of mercury(II) amido-iodine complex was measured using UV-Vis spectrophotometer.

Quantitative determination of acrylamide in solution

The reproducibility of this method was studied using eight different samples (same concentration of analyte and reagent). The absorbance value of mercury(II) amido-iodine complex was determined using UV-Vis spectrophotometer. The concentrations of acrylamide tested were 2 and 4 ppm.

The dynamic range was studied to determine the range of concentration for acrylamide which fulfil the Beer's law. Acrylamide solution was hydrolysed using 6.0 M NaOH for 10 minutes. The ammonia produced was determined using 3.0 mM Nessler's reagent and left for 5 minutes for the formation of mercury(II) amido-iodide complex. The absorbance of the complex was measured using UV-Vis spectrophotometer at the wavelength of 420 nm. The concentrations of acrylamide tested were 0–30 ppm.

The effects of some interference cations such as Na^+, K^+, Ca^{2+}, Fe^{2+}, and NH_3 present in acrylamide solution were also studied. The relative ratios of acrylamide solutions (without and with interference ions) were determined to study the effects and levels of interference. The effects of interference were determined based on the differences in absorbance values obtained from pure acrylamide solution and the acrylamide solution containing interference ions. If the difference is more than 10%, therefore the presence of interference ions is considered to affect the system.

Results and Discussion

Characterisation of base hydrolysis process towards acrylamide

In this study, NaOH serves two purposes, as the catalyst for base hydrolysis and to create a basic condition for the formation of mercury(II) amido-iodine complex as shown in Equations 1 and 2. Acrylamide, as a primer amide undergoes hydrolysis in basic condition. As shown in Figure 1, 6.0 M of NaOH is needed to hydrolyse acrylamide solution since acrylamide is a stable acid derivative group and requires stronger condition to hydrolyse. Figure 2 shows the completed base hydrolysis process of acrylamide in solution after 10 minutes.

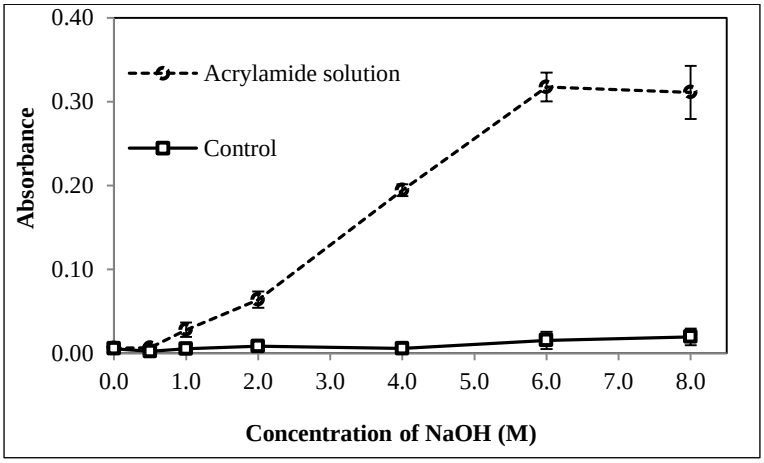


Figure 1. Absorbance of mercury(II) amido-iodine formed after acrylamide being hydrolysed by various concentration of NaOH

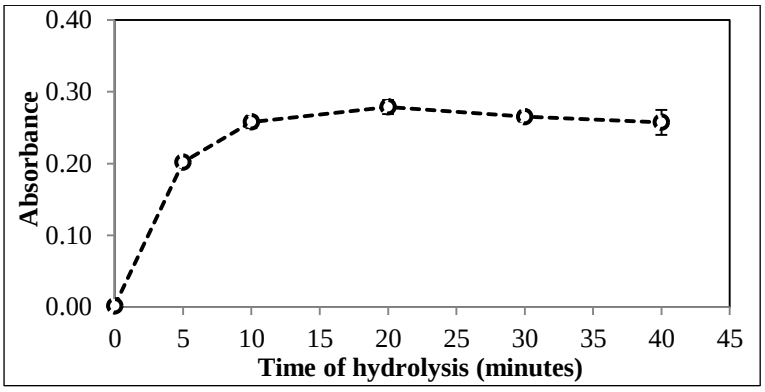


Figure 2. Absorbance of mercury(II) amido-iodine complex with acrylamide hydrolysed in various time measuring at wavelength of 420 nm

A study done by Paleologos and Kontominas reported that heating acrylamide at 70 °C in 5 M sulphuric acid for 6 hours or 4 M NaOH for 1 hour were able to completely convert acrylamide into its acid derivative [22].

Concentration optimisation of Nessler's Reagent

The Nessler's reagent is also known as potassium tetraiodomercurate(II) with yellow appearance and consists of two salts (HgI_2 and KI). From Equation 3, the optimum molar ratio (HgI_2:KI) in forming Nessler's reagent is 1:2. From Figure 3, the optimum concentrations of HgI_2 and KI are 0.075 M and 0.15 M, respectively. These results fulfilled the theoretical molar ratio of 1:2 to form Nessler's reagent. HgI_2 is hardly soluble in water and needs to be added into KI solution to form Nessler's reagent. When 0.075 M HgI_2 and less than 0.15 M KI used, some of the HgI_2 remain insoluble in the solution. Therefore, the formation of Nessler's reagent is not completed. This is the reason for not investigating the concentration of KI less than 0.15 M as shown in Figure 3b. The plateau result from Figure 3b shows that the concentration of KI is not affecting the formation of Nessler's reagent when the molar ratio with HgI_2 is equal or bigger than 2. Figure 4 shows that the optimum concentration of reagents used in this analysis as 3.0 mM.

$$HgI_2 + KI \rightarrow K_2[HgI_4] \quad (3)$$

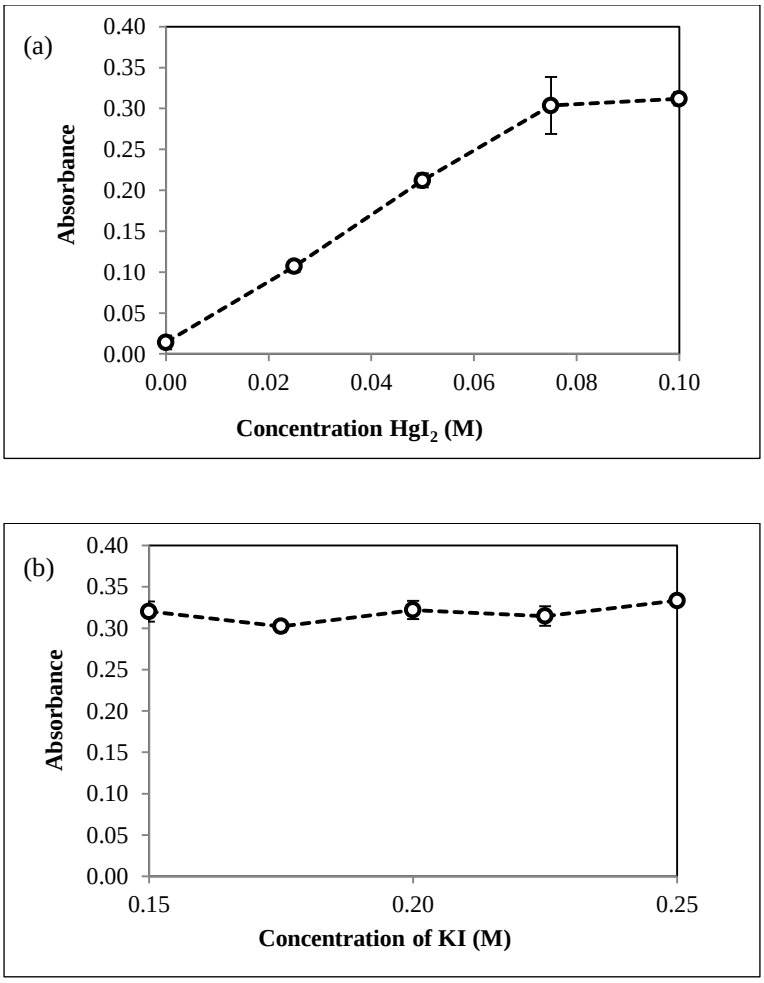


Figure 3. Absorbance of complex formed from hydrolysed acrylamide solution (5 ppm) with HgI_2 and KI in various concentrations

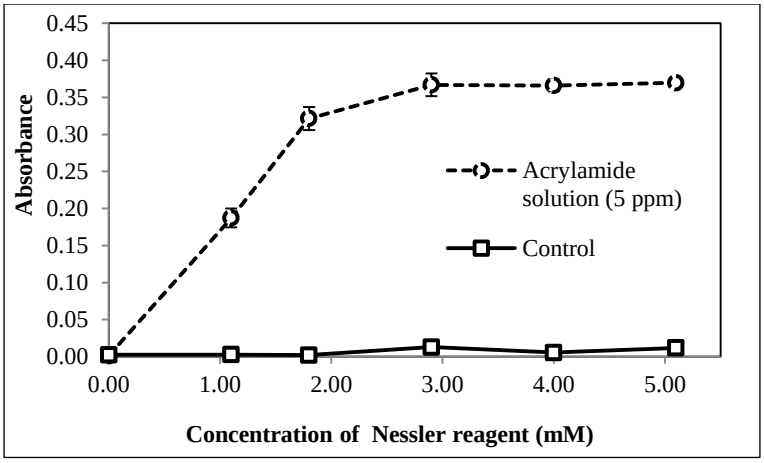


Figure 4. The effect of Nessler's reagent concentration in the detection of hydrolysed acrylamide solution. The absorbance was measured in at wavelength of 420 nm

Quantitative determination of acrylamide in solution

The reproducibility of this method enables the same experimental procedures being repeated. As shown in Figure 5, this method produced a good reproducibility where the RSD values were 2.8–3.3%. This result is as comparable to previous studies with reported RSD values of 3.17–6.15% [23].

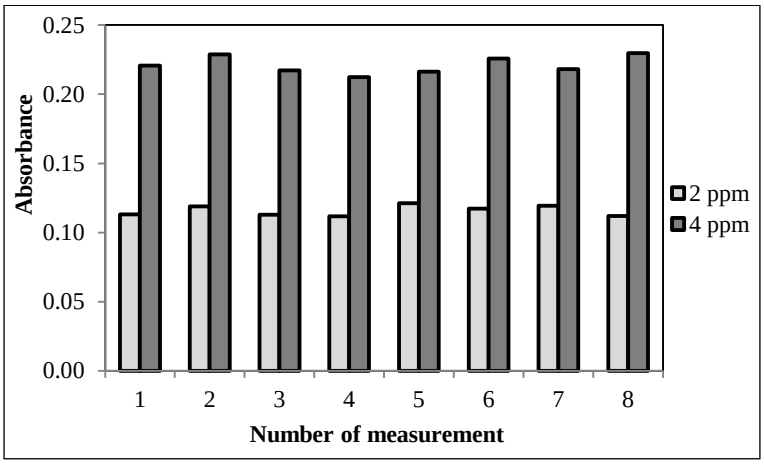


Figure 5. The reproducibility of mercury(II) amido-iodine complex formation at two different acrylamide concentrations after hydrolysis process

The absorbance of mercury(II) amido-iodide increased with the increasing concentration of acrylamide as shown in Figure 6. This is due to the increase in ammonia produced during hydrolysis, hence it is expected that more mercury(II) amido-iodine complex are formed as the absorbance increase. A linear dynamic range was obtained with the acrylamide range of 0–10 ppm. The calculated LOD for this method (the concentration of sample that yields a detector equal to three times the detector noise) was 0.074 ppm. This method performs better when compared with the work done by Silva et al. [14] where amidase was used to hydrolyse acrylamide and the generated ammonia was detected using ion selective electrode. The reported dynamic range was 7.1–284.3 ppm with the LOD of 3.2 ppm [14].

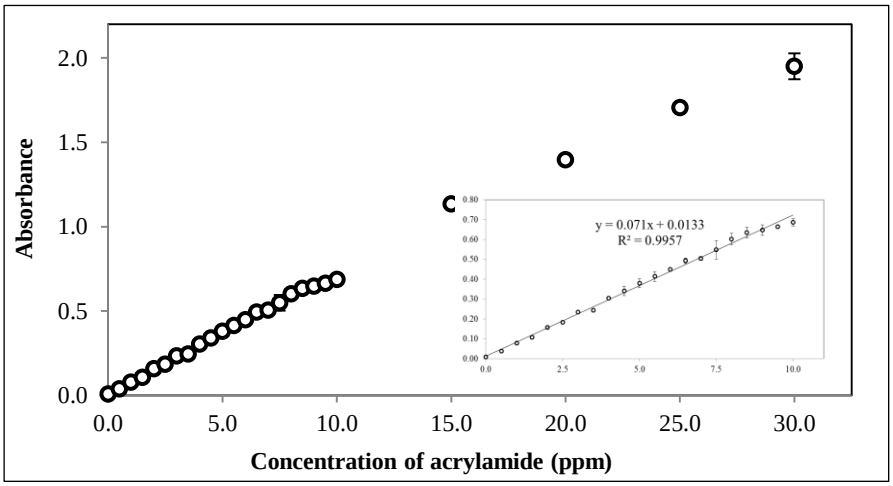


Figure 6. The response of hydrolysed acrylamide in the presence of Nessler's reagent. Absorbance measured in wavelength of 420 nm

Result for the studies of interference ions is shown in Table 1. Cations such as Na^+, K^+, and Ca^{2+} were not showing any significant interference. However, Fe^{3+} ion interfered when the ratio of acrylamide: interference ion greater than 1:10. This is because Fe^{3+} ion involved in two reactions system. First, the hydrolysis of Fe^{3+} ion in a base to form ferum(III) hydroxide will turns into darker colour. Second, the measured absorbance reveals that the presence of Fe^{3+} ion in the solution contributes to the same colour as the complex. This study also shows that Nessler's reagent is more sensitive towards NH_3 even at low concentration.

Table 1. Effect of interference ions in the detection of acrylamide

Concentration Ratio	**Relative Ratio (%)**				
	Na^+	**K^+**	**Ca^{2+}**	**Fe^{3+}**	**NH_3**
1:0.1	-2.17	-4.97	-4.70	-9.49	51.27
1:1	-2.58	-6.03	-2.98	4.04	437.89
1:10	-5.29	-2.50	-5.78	12.16	4051.35

Conclusion

Optical quantitative determination of acrylamide based on Nessler's reagent was studied. Acrylamide undergoes hydrolysis process to produce ammonia and corresponding acid salt. The concentration of base used and time for hydrolysis were determined and optimised. Nessler's reagent was chosen as it performs well in the formation of mercury(II) amido-iodine with ammonia. In this study, the generated ammonia after hydrolysis is directly proportional with acrylamide in the solution. Therefore, this base hydrolysis process for acrylamide explored in this study is considered to be a potential quantification of acrylamide. Thus, this study can be explored further to develop an optical sensor.

Acknowledgement

The authors gratefully acknowledge the financial support received from the Ministry of Education to Universiti Sains Islam Malaysia through research grant USIM/FRGS-FST-5-50311 and Universiti Kebangsaan Malaysia via grants DIP-2014-016 and DPP-2015-064. We would also like to acknowledge the Ministry of Higher Education for the MyBrain 15 scholarship to Yee-May Chong.

References

1. Tareke, E., Rydberg, P., Karlsson, P., Eriksson, S. and Törnqvist, M. (2002). Analysis of acrylamide, a carcinogen formed in heated foodstuffs. *Journal of Agricultural and Food Chemistry*, 50: 4998-5006.
2. Zyzak, D. V., Sanders, R. A., Stojanovic, M., Tallmadge, D. H., Eberhart, B. L., Ewald, D. K., Gruber, D. C., Morsch, T. R., Strothers, M. A., Rizzi, G. P. and Villagran, M. D. (2003). Acrylamide formation mechanism in heated foods. *Journal of Agricultural and Food Chemistry*, 51: 4782-4787.
3. Erickson, B. E. (2004). Finding acrylamide. *Analytical Chemistry*, 76: 247A-248A.
4. Dybing, E., Farmer, P. B., Andersen, M., Fennell, T. R., Lalljie, S. P. D., Müller, D. J. G., Olin, S., Petersen, B. J., Schlatter, J., Scholz, G., Scimeca, J. A., Slimani, N., Törnqvist, M., Tuijtelaars, S. and Verger, P. (2005). Human exposure and internal dose assessments of acrylamide in food. *Food and Chemical Toxicology*, 43: 365-410.
5. IARC (1994). International Agency for Research on Cancer, Lyon, France: pp. 389-433.
6. Preston, A., Fodey, T. and Elliott, C. (2008). Development of a high-throughput enzyme-linked immunosorbent assay for the routine detection of the carcinogen acrylamide in food, via rapid derivatisation pre-analysis. *Analytica Chimica Acta*, 608: 178-185.
7. Zhou, S., Zhang, C., Wang, D. and Zhao, M. (2008). Antigen synthetic strategy and immunoassay development for detection of acrylamide in foods. *Analyst*, 133: 903-909.
8. Hu, Q., Xu, X., Li, Z., Zhang, Y., Wang, J., Fu, Y. and Li, Y. (2014). Detection of acrylamide in potato chips using a fluorescent sensing method based on acrylamide polymerization-induced distance increase between quantum dots. *Biosensors and Bioelectronics*, 54: 64-71.
9. Stobiecka, A., Radecka, H. and Radecki, J. (2007). Novel voltammetric biosensor for determining acrylamide in food samples. *Biosensors and Bioelectronics*, 22: 2165-2170.
10. Krajewska, A., Radecki, J. and Radecka, H. (2008). A voltammetric biosensor based on glassy carbon electrodes modified with single-walled carbon nanotubes/hemoglobin for detection of acrylamide in water extracts from potato crisps. *Sensors*, 8: 5832-5844.
11. Garabagiu, S. and Mihailescu, G. (2011). Simple hemoglobin–gold nanoparticles modified electrode for the amperometric detection of acrylamide. *Journal of Electroanalytical Chemistry*, 659: 196-200.
12. Batra, B., Lata, S., Sharma, M. and Pundir, C. S. (2013). An acrylamide biosensor based on immobilization of hemoglobin onto multiwalled carbon nanotube/copper nanoparticles/polyaniline hybrid film. *Analytical Biochemistry*, 433: 210-217.
13. Batra, B., Lata, S. and Pundir, C. S. (2013). Construction of an improved amperometric acrylamide biosensor based on hemoglobin immobilized onto carboxylated multi-walled carbon nanotubes/iron oxide nanoparticles/chitosan composite film. *Bioprocess and Biosystems Engineering*, 36: 1591-1599.
14. Silva, N., Gil, D., Karmali, A. and Matos, M. (2009). Biosensor for acrylamide based on an ion-selective electrode using whole cells of *Pseudomonas aeruginosa* containing amidase activity. *Biocatalysis and Biotransformation*, 27: 143-151.
15. Silva, N. A. F., Matos, M. J., Karmali, A. and Racha, M. M. (2011). An electrochemical biosensor for acrylamide detection: Merits and limitations. *Portugaliae Electrochimica Acta*, 29: 361-373.
16. Ignatov, O. V., Rogatcheva, S. M., Vasil'eva, O. V. and Ignatov, V. V. (1996). Selective determination of acrylonitrile, acrylamide and acrylic acid in waste waters using microbial cells. *Resources, Conservation and Recycling*, 18: 69-78.
17. Ignatov, O. V., Rogatcheva, S. M., Kozulin, S. V. and Khorkina, N. A. (1997). Acrylamide and acrylic acid determination using respiratory activity of microbial cells. *Biosensors and Bioelectronics*, 12: 105-111.
18. Hasegawa, K., Miwa, S., Tajima, T., Tsutsumiuchi, K., Taniguchi, H. and Miwa, J. (2007). A rapid and inexpensive method to screen for common foods that reduce the action of acrylamide, a harmful substance in food. *Toxicology Letters*, 175: 82-88.
19. Qiu, Y., Qu, X., Dong, J., Ai, S. and Han, R. (2011). Electrochemical detection of DNA damage induced by acrylamide and its metabolite at the graphene-ionic liquid-Nafion modified pyrolytic graphite electrode. *Journal of Hazardous Materials*, 190: 480-485.
20. Li, D., Xu, Y., Zhang, L. and Tong, H. (2014). A label-free electrochemical bopsensor for acrylamide based on DNA immobilized on graphene oxide-modified glassy carbon electrode. *International Journal of Electrochemical Science*, 9: 7217-7227.

21. Sun, X., Ji, J., Jiang, D., Li, X., Zhang, Y., Li, Z. and Wu, Y. (2013). Development of a novel electrochemical sensor using pheochromocytoma cells and its assessment of acrylamide cytotoxicity. *Biosensors and Bioelectronics*, 44: 122-126.
22. Paleologos, E. K. and Kontominas, M. G. (2005). Determination of acrylamide and methacrylamide by normal phase high performance liquid chromatography and UV detection. *Journal of Chromatography A*, 1077: 128-135.
23. Chong, Y.-M., Ahmad, M., Heng, L. Y., Kusnin, N. and Shukor, M. Y. A. (2017). Acrylamide optical sensor based on hydrolysis using *Bacillus* sp. strain ZK34 containing amidase properties. *Sains Malaysiana*, 46: 1557-1563.

Malaysian Journal of Analytical Sciences, Vol 23 No 1 (2019): 23 - 30
DOI: https://doi.org/10.17576/mjas-2019-2301-03

MALAYSIAN JOURNAL OF ANALYTICAL SCIENCES
Published by The Malaysian Analytical Sciences Society
ISSN 1394 - 2506

WATER EXTRACT OF ONION PEEL ASH: AN EFFICIENT GREEN CATALYTIC SYSTEM FOR THE SYNTHESIS OF ISOINDOLINE-1,3-DIONE DERIVATIVES

(Air Abu Kulit Bawang: Sistem Pemangkin Katalitik Hijau yang Effisien dalam Sintesis Terbitan Isoindolina-1,3-dion)

Poh Wai Chia[1,2]*, Poh Seng Chee[1], Mohd Haziq Aziz[1], Siti Aisha Mohd Radzi[2], Fu Siong Julius Yong[2], Su-Yin Kan[3]

[1]School of Marine and Environmental Sciences
[2]Institute of Marine Biotechnology
Universiti Malaysia Terengganu, 21030 Kuala Nerus, Terengganu, Malaysia
[3]Faculty of Health Sciences,
Universiti Sultan Zainal Abidin, 21300 Kuala Nerus, Terengganu, Malaysia.

**Corresponding author: pohwai@umt.edu.my*

Received: 2 July 2018; Accepted: 27 November 2018

Abstract

Isoindoline-1,3-dione derivatives are important organic compounds associated with various interesting applications such as in the fields of material science, medicine, important building blocks and so on. Traditionally, the synthesis of isoindoline-1,3-dione derivatives are achieved using harmful and toxic catalysts, such as concentrated sulphuric acid, triphenylphosphine, ionic liquid [bmim][BF_4] or phthalimide-N-sulfonic acid. Thus, the development of a greener catalytic system for the synthesis of isoindoline-1,3-dione derivatives is highly sought after. In this work, an efficient synthesis of isoindoline-1,3-dione derivatives using the Water Extract of Onion Peel Ash (WEOPA) method is described. The new approach provides several advantages including the non-usage of external acids, recyclable catalytic system, cheap and the yield of the synthesized products were obtained in moderate to good yields by reacting various anilines with phthalic anhydride. The current improved method is scientifically important, due to it avoid the use of environmental harmful reagents and at the same time provides an alternative method for bio-waste management.

Keywords: water extract of onion peel ash, isoindoline-1,3-dione, recyclable catalytic system, anilines, phthalic anhydride

Abstrak

Terbitan isoindolina-1,3-dion adalah sebatian organik yang penting dan dikaitkan dengan pelbagai aplikasi yang menarik, seperti dalam bidang sains bahan, perubatan, blok bangunan penting dan sebagainya. Secara tradisinya, sintesis derivatif isoindolina-1,3-dion dicapai dengan menggunakan pemangkin berbahaya dan beracun, seperti asid sulfurik pekat, trifenilfosfin, cecair ionik [bmim] [BF_4] atau asid fitalimid-N-sulfonik. Oleh itu, pembangunan sistem pemangkin yang lebih hijau untuk sintesis derivatif isoindolina-1,3-dion sangat diperlukan. Dalam kerja ini, satu kaedah effisien dalam sintesis terbitan isoindolina-1,3-dion dengan menggunakan ekstrak air abu bawang dibincangkan disini. Kaedah baru ini memberikan pelbagai manfaat termasuk bebas daripada penggunaan asid luaran, sistem pemangkin kitar semula, murah dan hasil bagi produk sintesis yang didapati adalah sederhana hingga baik melalui tindak balas antara anilin-anilin dengan fitalik anhidrit. Kaedah yang ditambahbaik ini adalah penting secara saintifik, kerana ia mengelakkan penggunaan reagen berbahaya kepada alam sekitar dan pada masa yang sama menyediakan kaedah alternatif untuk pengurusan bio-sisa.

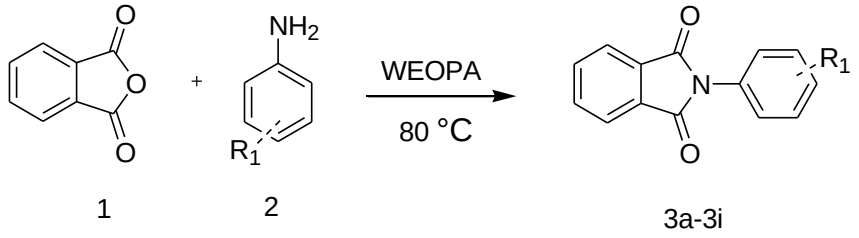
Kata kunci: ekstrak air abu bawang merah, isoindolina-1,3-dion, system pemangkin kitar semula, anilin, fitalik anhidrit

Introduction

Lately, there has been growing interest among chemists to develop simple and efficient green protocols for performing organic reactions due to the increase in environmental awareness worldwide [1-4]. The use of environmentally acceptable reagents, green solvents and biocatalysts are favorable, as it promote sustainable chemistry for synthesis processes conducted in both academic institutions and industries [5]. In particular, the use of aqueous media as green solvent has attracted the attention of the scientific community due to its environmental-friendly, cheap, benign solvent, non-flammability and readily available features, thus rendering its usefulness in the field of organic synthesis [6-8]. Furthermore, the use of water as a solvent in organic processes is promising and it is known to provide acceleration in the rate of chemical reactions as evidenced in a few recent literature [9-11].

At present, there has been growing awareness among synthetic chemists to utilize waste water, water extract of bio-wastes and vegetables juices to address and apply the concept of eco-friendly organic transformations. Among the main benefits identified from employing these green protocols include the biodegradable/recyclable nature and high catalytic activity of these green catalytic systems in organic transformations [12]. To date, numerous organic transformations have been carried out efficiently using these green and recyclable catalytic systems. Examples include the Suzuki-Miyaura reaction [13], synthesis of biaryls [14], Sonogashira reaction [15], Henry reaction [16], Dakin reaction [17] and so on. Based on a survey, the world generates approximately a million tons of bio-wastes monthly [18]. The rate of generation of bio-wastes is expected to escalate over time with the boom in world population [19]. From the perspective of green chemistry, unwanted wastes such as agricultural and food wastes are attractive resources as they are abundantly available and have the potential to become green catalytic systems in chemical processes.

Onions (*Allium cepa* L.) is one of the most important vegetable crops cultivated worldwide for culinary and other functional purposes [20]. In some developed countries, it is reported that more than 100,000 tons of onion waste are generated annually [21]. This bio-waste could adversely affect our environment and living organisms if it is sent directly to landfill without proper treatment [22]. As part of our continuous interest to develop green synthetic methodologies, we herein report on a simple, recyclable catalytic system and efficient protocol for the synthesis of isoindoline-1,3-dione derivatives using the Water Extract of Onion Peel Ash (WEOPA) (Scheme 1). Isoindoline-1,3-dione derivatives have found many attractive applications in material science [23], medicine [24], important building block [25] and so on. Traditionally, the synthesis of isoindoline-1,3-dione derivatives are achieved using harmful and toxic catalysts, such as the concentrated sulfuric acid [26] and triphenylphosphine [27]. Other methods are by using ionic liquid [bmim][BF_4] [28] and phthalimide-*N*-sulfonic acid [29], which entail the use of expensive reagents. The use of the WEOPA as a catalytic system to catalyze the synthesis of isoindoline-1,3-dione derivatives can reduce the environmental pressure exerted by bio-wastes. In addition, this work enables the development of a more sustainable synthesis that is of scientific significance and at the same time, overcome the aforementioned drawbacks.



Scheme 1. Synthetic route towards the preparation of isoindoline-1,3-dione derivatives in the presence of WEOPA

Materials and Methods

All chemicals and solvent were purchased from Sigma-Aldrich and Merck, were used without further purification. The ^{1}H and ^{13}C-NMR experiments were recorded using $CDCl_3$ as solvent on a Bruker Avance III 400 spectrometer and the chemical shifts were given in parts per million (ppm). The GC-MS analyses were recorded using a

Shimadzu QP2010SE, equipped with a Supelco fused silica capillary column (30 m × 0.25 mm i.d., 0.25 mm film thickness). The metal content was characterized using Varian Vista Pro Inductive Coupled Plasma Optical Emission Spectroscopy (ICP-OES).

Preparation of the water extract of onion peel ash

Onion waste was obtained from a nearby local waste disposal site at Kuala Nerus, Malaysia in March 2018. The outer layer and bulb of onion peel were separated, and the onion peel was washed with distilled water. The onion peels were then sliced into small pieces and air-dried for 2-3 days. The WEOPA catalytic system was prepared according to a previous method [12]. Initially, the dried peels (2.5 g) were burnt in the furnace at 500 °C for about 1 hour. The obtained ash was transferred into a 100 mL shake flask containing 25 mL of distilled water and the mixture was stirred for 1 hour. Subsequently, the mixture was filtered using Whatman filter paper No.1 and the resulting filtrate was termed as WEOPA.

General procedure for the synthesis of isoindoline-1,3-dione derivatives.

A 25 mL round bottom flask containing a mixture of phthalic anhydride (1.00 mmol) and aniline (1.00 mmol) was added with WEOPA (2 mL). The reaction mixture was stirred magnetically at 110 rpm and heated up to 80 °C. The progress of the reaction was monitored using Thin-Layer Chromatography (TLC). Upon the completion of the reaction, ethyl acetate (3 x 30 mL) was added into the mixture to extract the crude products. The organic layer was combined and dried with $MgSO_4$, before concentrated under reduced pressure. The crude product was purified over silica gel column chromatography with ethyl acetate/hexane (1:9) as its eluent. The aqueous recovered WEOPA was reused for the synthesis of other isoindoline-1,3-dione derivatives under identical condition.

Results and Discussion

Spectroscopic data of isoindoline-1,3-dione derivatives

2-phenyl isoindoline-1,3-dione **3a** ^{1}H-NMR (400 MHz, $CDCl_3$): δ 7.47-7.37 (m, 3H); 7.56-7.47 (m, 2H); 7.85-7.74 (m, 2H); 8.02-7.90 (m, 2H) ppm; ^{13}C NMR (100 MHz, $CDCl_3$) δ 123.76, 126.61, 128.07, 129.19, 131.67, 131.82, 134.38, 167.34 ppm; GC-MS: $C_{14}H_9NO_2$, m/z 223.06 $(M)^+$.

2-(*o*-tolyl) isoindoline-1,3-dione **3b** ^{1}H-NMR (400 MHz, $CDCl_3$): δ 2.21 (s, 3H); 7.20 (d, *J* = 7.5 Hz, 1H); 7.29-7.40 (m, 3H); 7.83.-7.76 (m, 2H); 7.72-8.00 (m, 2H) ppm; ^{13}C NMR (100 MHz, $CDCl_3$) δ 18.0, 123.82, 126.86, 128.83, 129.47, 130.60, 131.18, 132.11, 134.46, 136.59, 167.41 ppm; GC-MS: $C_{15}H_{11}NO_2$, m/z 237.08 $(M)^+$.

2-(*m*-tolyl) isoindoline-1,3-dione **3c** ^{1}H-NMR (400 MHz, $CDCl_3$): δ 2.42 (s, 3H); 7.24-7.18 (m, 3H); 7.42-7.36 (m, 1H); 7.83-7.74 (m, 2H); 7.79-7.91 (m, 2H) ppm; ^{13}C NMR (100 MHz, $CDCl_3$) δ 21.41, 123.66, 123.82, 127.31, 129.01, 129.13, 131.48, 131.82, 134.40, 139.21, 167.44 ppm; GC-MS: $C_{15}H_{11}NO_2$, m/z 237.08 $(M)^+$.

2-(m-tolyl) isoindoline-1,3-dione **3d** ^{1}H-NMR (400 MHz, $CDCl_3$): δ 2.40 (s, 3H); 7.30 (s, 4H); 7.82-7.76 (m, 2H); 7.98-7.92 (m, 2H) ppm; ^{13}C NMR (100 MHz, $CDCl_3$) δ 21.33, 123.65, 126.51, 129.02, 129.83, 131.88, 134.42, 138.20, 167.45 ppm; GC-MS: $C_{15}H_{11}NO_2$, m/z 237.08 $(M)^+$.

2-(4-methoxyphenyl) isoindoline-1,3-dione **3e** ^{1}H-NMR (400 MHz, $CDCl_3$): δ 3.85 (s, 3H); 7.02 (d, *J* = 8.7 Hz, 2H); 7.33 (d, *J* = 9.1 Hz, 2H); 7.83-7.73 (m, 2H); 8.00-7.90 (m, 2H) ppm; ^{13}C NMR (100 MHz, $CDCl_3$) δ 55.46, 114.46, 123.68, 124.31, 128.02, 131.83, 134.30, 159.29, 167.61 ppm; GC-MS: $C_{15}H_{11}NO_3$, m/z 253.07 $(M)^+$.

2-(4-isopropylphenyl) isoindoline-1,3-dione **3f** ^{1}H-NMR (400 MHz, $CDCl_3$): δ 1.31 (d, *J* = 7.1 Hz, 6H); 3.06-2.90 (m, 1H); 7.37 (d, *J* = 1.2 Hz, 4H); 7.85-7.74 (m, 2H); 8.03-7.70 (m, 2H) ppm; ^{13}C NMR (100 MHz, $CDCl_3$) δ 24.03, 34.01, 123.68, 126.67, 126.51, 127.27, 129.21, 131.91, 134.42, 148.94, 167.48 ppm; GC-MS: $C_{17}H_{15}NO_2$, m/z 265.11 $(M)^+$.

2-(4-fluorolphenyl) isoindoline-1,3-dione **3g** ^{1}H-NMR (400 MHz, $CDCl_3$): δ 7.20 (t, 2H); 7.83-7.36 (m, 2H); 7.80 (dd, *J* = 5.3 Hz, *J* = 3.0 Hz, 2H); 7.95 (dd, *J* = 5.3 Hz, *J* = 3.0 Hz, 2H) ppm; ^{13}C NMR (100 MHz, $CDCl_3$) δ 115.96,

116.31, 123.82, 127.63, 128.39, 128.43, 131.70, 134.54, 160.71, 163.23, 167.21 ppm; GC-MS: $C_{14}H_8FNO_2$, m/z 241.05 $(M)^+$.

2-(4-chlorophenyl) isoindoline-1,3-dione **3h** ^{1}H-NMR (400 MHz, $CDCl_3$): δ 7.40 (d, *J* = 8.7 Hz, 2H); 7.47 (d, *J* = 8.7 Hz, 2H); 7.85-7.74 (m, 2H); 8.01=7.88 (m, 2H) ppm; ^{13}C NMR (100 MHz, $CDCl_3$) δ 123.90, 127.74, 129.31, 130.23, 131.57, 133.79, 134.62, 167.02 ppm; GC-MS: $C_{14}H_8ClNO_2$, m/z 257.02 $(M)^+$.

2-(4-bromophenyl) isoindoline-1,3-dione **3i** ^{1}H-NMR (400 MHz, $CDCl_3$): δ 7.36 (d, *J* = 8.7 Hz, 2H); 7.63 (d, *J* = 8.7 Hz, 2H); 7.80 (dd, *J* = 5.5 Hz, *J* = 3.1 Hz, 2H); 7.94 (dd, *J* = 5.5 Hz, *J* = 3.1 Hz, 2H) ppm; ^{13}C NMR (100 MHz, $CDCl_3$) δ 121.78, 123.86, 128.04, 130.76, 131.64, 132.28, 134.67, 166.94 ppm; GC-MS: $C_{14}H_8BrNO_2$, m/z 300.97 $(M)^+$.

In the FT-IR analysis, the onion peels obtained from a local supermarket (Figure 1a) was compared to onion peels sampled from a local waste disposal site (Figure 1b). As shown in the FT-IR spectrum, the signals at 3393 cm^{-1} and 1637 cm^{-1} were attributed to the stretching vibration of hydroxyl groups and carbonyl groups, respectively. Also, all signals shown by the spectrum in Figure 1b (relative intensity, shapes and stretching frequencies) were well preserved compared to those shown by the FT-IR spectrum in Figure 1a. This indicates that there were no considerable changes observed in terms of the chemical structure (functional groups and hydrogen bonding network) of the onion peels recovered from a local waste disposal site compared to onion peels obtained from a local supermarket.

The metal content of the recovered onion peel (0.8 g) was analysed using ICP-OES and resulted in the following outputs: K (22927.00 ± 0.47 ppm), Na (14930.00 ± 0.21 ppm), Mg (7896.00 ± 6.26 ppm), S (2225.00 ± 1.44 ppm), P (2172.00 ± 2.13 ppm), Fe (1815.00 ± 1.03 ppm), Al (1366.00 ± 1.07 ppm), Sr (300.00 ± 2.52 ppm), Mn (216.00 ± 2.18 ppm), B (107.00 ± 0.09 ppm), Ba (53.00 ± 0.23 ppm), Zn (52.00 ± 0.11 ppm), Rb (35.00 ± 0.02 ppm), La (15.00 ± 0.31 ppm), Ga (15.00 ± 0.12 ppm), Cu (13.00 ± 0.17 ppm) and Pb (9.80 ± 0.23 ppm).

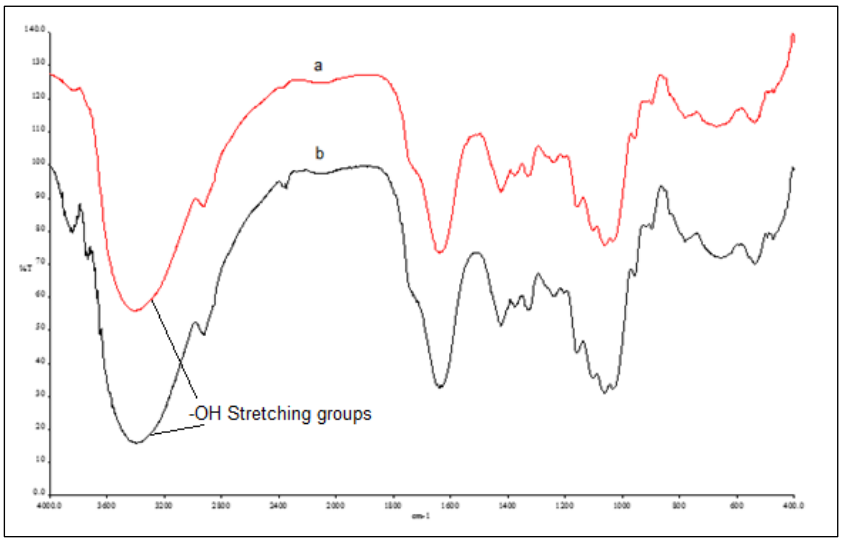


Figure 1. The FTIR spectra of (a) onion peels obtained from a local supermarket and (b) recovered onion peels from a local waste disposal site

For the optimisation of reaction condition, phthalic anhydride **1** and aniline **2** were chosen as the model starting materials. Initially, phthalic anhydride **1** (1.0 mmol) was reacted with aniline **2** (1.0 mmol) in the presence of 2.0 mL of H_2O at 50 °C to produce the corresponding product, **3a** (Table 1). After 3 hours, the yield of **3a** was found to be poor (Table 1, entry 1). It is worthy to note that when the H_2O was replaced with WEOPA under identical

reaction condition, **3a** was obtained at a moderate yield (54%) (Table 1, entry 2). The amount of WEOPA used was also studied. The usage of 2.0 mL of WEOPA as solvent has produced a good yield of **3a** (91%) (Table 1, entry 7). Interestingly, increases in the amount of WEOPA used did give rise to a better yield of **3a** (Table 1, entry 7). However, pro-longing the reaction time and increasing in the temperature used did not result in a better of yield of **3a** (Table 1, entries 9-10). Based on Table 1, the optimised condition was determined as 2.0 mL of WEOPA, 8 hours and 80 °C (Table 1, entry 7).

Table 1. The optimization of reaction condition for the synthesis of **3a**

Entry	Solvent (mL)	Time (hours)	Temperature (°C)	Yield (%)
1	H_2O (2.0)	3	50	30
2	WEOPA (0.5)	3	50	54
3	WEOPA (1.0)	3	50	60
4	WEOPA (2.0)	3	50	69
5	WEOPA (2.0)	3	80	78
6	WEOPA (2.0)	5	80	84
7	WEOPA (2.0)	8	80	91
8	WEOPA (3.0)	8	80	89
9	WEOPA (2.0)	8	100	90
10	WEOPA (2.0)	10	80	89

Next, the study on the general applicability of the WEOPA catalytic system was carried out using different anilines for the synthesis of isoindoline-1,3-dione derivatives under the optimised condition selected above**.** As shown in Table 2, the isoindoline-1,3-dione derivatives were obtained at moderate to good yields after silica gel column purification (64-91% yield). As indicated in Table 2, the anilines bearing the electron-donating groups (CH_3, OCH_3 and $(CH_3)_2CH$) afforded the corresponding isoindoline-1,3-dione derivatives **3b-3f** at moderate to good yields (Table 2, entries 2-6) compared to anilines bearing electron-withdrawing groups (F, Cl and Br) (Table 2, entries 7-9). In addition, the current protocol was considered as unprecedented compared to previous methods, because no solvents and additives were required for the synthesis of isoindoline-1,3-dione derivatives. Moreover, the isoindoline-1,3-dione derivatives were synthesized at a reasonable reaction time. The synthesized isoindoline-1,3-dione derivatives were characterised using spectroscopic techniques such as NMR (^1H and ^{13}C) and GC-MS analyses.

Table 2. Isolated yields and influence of the WEOPA catalytic system on the synthesis of isoindoline-1,3-dione derivatives

Entry	R_1	Product	Reaction Time (hours)	Isolated Yield (%)
1	H	3a	8	92
2	2-CH_3	3b	8	74
3	3-CH_3	3c	8	70
4	4-CH_3	3d	8	73
5	4-OCH_3	3e	8	88
6	4-$(CH_3)_2CH$	3f	8	75
7	4-F	3g	8	64
8	4-Cl	3h	8	66
9	4-Br	3i	8	68

In addition, we also examined the reusability of the WEOPA catalytic system using the model reaction. After the completion of reaction between phthalic anhydride **1** and aniline **2**, the recovered WEOPA was reused for at least 5 times without any significant loss in catalytic activity (Figure 2).

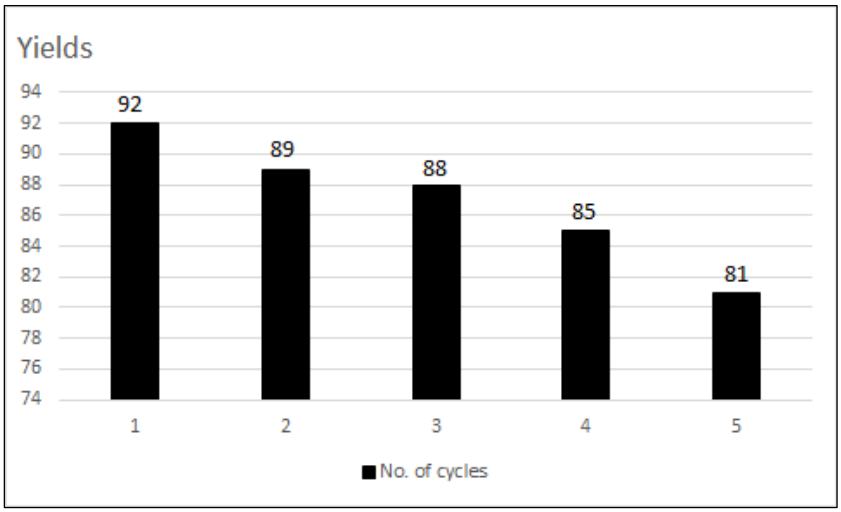


Figure 2. Reactivity of WEOPA based on five runs. Reaction conditions: 1.0 mmol of phthalic anhydride, 1.0 mmol of aniline, 2 mL of WEOP, 80 °C

At the moment, the mechanism of formation of isoindoline-1,3-dione derivatives catalysed by the WEOPA system is not well understood. However, metal content analysis showed that the onion peel ash consists of metal oxides including phosphorus, magnesium, zinc, manganese and sodium as major elements, accompanied by other minor constituents. We hypothesised that the metals in the WEOPA have facilitated the formation of isoindoline-1,3-dione derivatives and the proposed mechanism was shown in Figure 3.

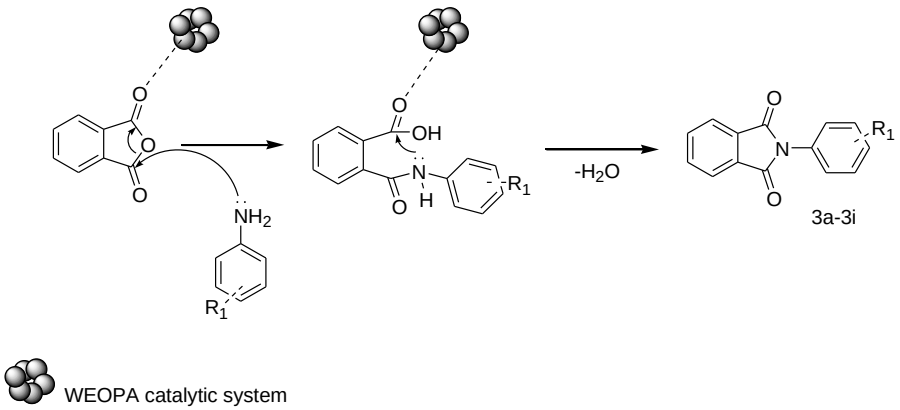


Figure 3. Proposed mechanism for the formation of isoindoline-1,3-dione derivatives catalyzed by the WEOPA

Conclusion

In this work, we have developed a simple, inexpensive and recyclable catalytic system for the synthesis of isoindoline-1,3-dione derivatives. Overall, the yields of the synthesized products were obtained in moderate to good yields (62-91%). In addition, the WEOPA could be recovered and reused for up to five times without any significant

loss in catalytic activity. It is worthy to note that the current protocol can be used to synthesize the isoindoline-1,3-dione derivatives without the presence of any additives, external acids or solvents. The results of this study might induce researchers to perform organic transformations using the WEOPA as a green solvent.

Acknowledgement

The authors would like to acknowledge Ministry of Education Malaysia (MOE) for its Fundamental Research Grant Scheme (FRGS 59499).

References

1. Chassaing, S. and Beneteau, V. (2017). Zeolite as green catalysts for organic synthesis: The cases of H-, Cu-& Sc-zeolites. *Current Organic Chemistry*, 21(9): 779-793.
2. Andersen, J. and Mack, J. (2018). Mechanochemistry and organic synthesis:from mystical to practical. *Green Chemistry*, 20(7): 1435-1443.
3. Kan, S.-Y., Yiong, W. S., Yong, F. S. J. and Chia, P.W. (2017). Synthesis of benzothiazole derivatives using ultrasound probe irradiation. *Malaysian Journal of Analytical Sciences*, 21(6): 1219-1225.
4. Asseri, S. N. A. R. M., Tan, S. H., Mohamad, W. N. K. W., Poh, S. C., Chia, P. W., Kan, S.-Y. and Chuah, T. S. (2017). $MgCl_2$ as efficient and inexpensive catalyst for the synthesis of 1,4-dihydropyridine derivatives. *Malaysian Journal of Analytical Sciences*, 21(1): 13-19.
5. Waseem, M. A., Srivasta, A., Srivasta, A. and Siddiqui, I. (2015). Water and ionic liquid synergy. A novel approach for the synthesis of benzothiazole-2 (3H)-one. *Journal of Saudi Chemical Society*, 35(1): 68-82.
6. Li, C.-J. and Chen, L. (2006). Organic chemistry in water. *Chemical Society Review*, 35(1): 68-82.
7. Kucherenjo, A., Kostenko, A., Zhdankina, G. M., Kuznetsova, O. Y. and Zlotin, S. G. (2018). Green asymmetric synthesis of Warfarin and Coumachlor in pure water catalyzed by quinoline-derived 1,2-diamines. *Green Chemistry*, 20(3): 754-759.
8. Han, M. Y., Lin, J., Li, W., Luan, W. Y., Mai, P. L. and Zhang, Y. (2018). Catalyst-free nucleophilic addition reactions of silyl glyoxylates in water. *Green Chemistry*, 20(6): 1228-1232.
9. Noshiranzadeh, N., Emami, M., Bikas, R. and Kozakiewicz, A. (2017). Green click synthesis of β-hydroxy-1, 2, 3-triazoles in water in the presence of a Cu (II)–azide catalyst: a new function for Cu (II)–azide complexes. *New Journal of Chemistry*, 41(7): 2658-2667.
10. Banerjee, B. (2017). Recent developments on ultrasound assisted catalyst-free organic synthesis. *Ultrasonics Sonochemistry*, 35: 1-14.
11. Miklós, F. and Fülöp, F. (2016). A simple green protocol for the condensation of anthranilic hydrazide with cyclohexanone and n-benzylpiperidinone in water. *Jornal of Heterocyclic Chemistry*, 53(1): 32-37.
12. Sarmah, M., Mondal, M. and Bora, U. (2017). Agro-waste extract based solvents: emergence of novel green solvent for the design of sustainable processes in catalysis and organic chemistry. *ChemistrySelect*, 2(18): 5180-5188.
13. Boruah, R. P., Abdul, A. A., Mitali, C., Bishwajit, S. and Diganta, S. (2015). $Pd(OAc)_2$ in WERSA: A novel green catalytic system for Suzuki–Miyaura cross-coupling reactions at room temperature. *Chemical Communications*, 51(57): 11489-11492.
14. Saikia, B., Boruah, P. R., Ali, A. A. and Sarma, D. (2015). 'On-water'organic synthesis: a green, highly efficient, low cost and reusable catalyst system for biaryl synthesis under aerobic conditions at room temperature. *RSC Advances*, 5(63): 50655-50659.
15. Dewan, A., Sarmah, M., Bora, U. and Thakur, A. J. (2016). A green protocol for ligand, copper and base free Sonogashira cross-coupling reaction. *Tetrahedron Letters*, 57(33): 3760-3763.
16. Surneni, N., Barua, N. C. and Saikia, B. (2016). Application of natural feedstock extract: The Henry reaction. *Tetrahedron Letters*, 57(25): 2814-2817.
17. Saikia, B. and Borah, P. (2015). A new avenue to the Dakin reaction in H_2O_2–WERSA. *RSC Advances*, 5(128): 105583-105586.
18. Choi, I. S., Cho, E. J., Moon, J.-H. and Bae, H.-J. (2015). Onion skin waste as a valorization resource for the by-products quercetin and biosugar. *Food Chemistry*, 188: 537-542.
19. Marshall, R. E. and Farahbakhsh, K. (2013). Systems approaches to integrated solid waste management in developing countries. *Waste Management*, 33(4): 988-1003.

20. Nile, S. H. and Park, S. W. (2013). Total phenolics, antioxidant and xanthine oxidase inhibitory activity of three colored onions (*Allium cepa* L.). *Frontier in Life Science*, 7(3-4): 224-228.
21. Sharma, K., Mahato, N., Nile, S. H., Lee, E. T. and Lee, Y. R. (2016). Economical and environmentally-friendly approaches for usage of onion (Allium cepa L.) waste. *Food Function*, 7(8): 3354-3369.
22. Gao, S., Li, L., Geng, K., Wei, X. and Zhang, S. (2015). Recycling the biowaste to produce nitrogen and sulfur self-doped porous carbon as an efficient catalyst for oxygen reduction reaction. *Nano Energy*, 16(2015): 408-418.
23. Pontrello, J. K., Allen, M. J., Underbakker, E. S. and Kiessling, L. L. (2005). Solid-phase synthesis of polymers using the ring-opening metathesis polymerization. *Journal of American Chemical Society*, 127(42): 14536-14537.
24. Sortino, M., Garibotto, F., Fihlo, V. C., Gupta, M., Enriz, R. and Zacchino, S. (2011). Antifungal cyctotoxic and SAR studies of a series of *N*-alkyl, *N*-aryl and *N*-alkylphenyl-1,4-pyrroledinones and related compounds. *Bioorganic Medicinal Chemistry*, 19(9): 2823-2834.
25. Bouissane, L., Sestelo, J. P. and Sarandeses, L. A. (2009). Synthesis of 3,4-disubstituted maleimides by selective cross-coupling reactions using indium organometallics. *Organic Letters*, 11(6): 1285-1288.
26. Hurd, C.D. and Prapas, A.G. (1959). Preparation of acylcic imides. *Journal of Organic Chemistry*, 24(3): 388-392.
27. Walker, M. A. (1995). A high yielding synthesis of N-alkyl maleimides using a novel modification of the Mitsunobu reaction. *Journal of Organic Chemistry*, 60(16): 5352-555.
28. Chen, D. C., Ye, H. Q. and Wu, H. (2007). A more efficient synthetic process of *N*-arylphthalimides in ionic liquid [bmim][BF_4]. *Catalysis Communications*, 8(10): 1527-1530.
29. Habibi, D. and Pordanjani, H. M. (2017). Phthalimide-N-sulfonic acid, an efficient catalyst for the synthesis of various isoindoline-1,3-dione derivatives. *Chemical Papers*, 71(11): 2293-2299.

Malaysian Journal of Analytical Sciences, Vol 23 No 1 (2019): 31 - 39
DOI: https://doi.org/10.17576/mjas-2019-2301-04

MALAYSIAN JOURNAL OF ANALYTICAL SCIENCES
Published by The Malaysian Analytical Sciences Society
ISSN 1394 - 2506

MITIGATION OF TOXIC *Alexandrium tamiyavanichii* USING CHITOSAN-SILICA COMPOSITE

(Mitigasi *Alexandrium tamiyavanichii* Bertoksik Menggunakan Komposit Kitosan-Silika)

Anwar Iqbal[1]*, Najwa Ahmad[2], Normawaty Mohammad Noor[2], Lee D. Wilson[3], Nur Hanisah Ibrahim[1]

[1]*School of Chemical Sciences,*
Universiti Sains Malaysia, 11800 USM Penang, Malaysia
[2] *Department of Marine Science, Kulliyyah of Science,*
International Islamic University Malaysia, Jalan Sultan Ahmad Shah, Bandar Indera Mahkota, 25200 Kuantan, Pahang, Malaysia
[3]*Department of Chemistry, 110 Science Place, Room 156 Thorvaldson Building,*
University of Saskatchewan, Saskatoon, S7N 5C9 Canada

**Corresponding author: anwariqbal@usm.my*

Received: 24 January 2018; Accepted: 13 September 2018

Abstract

The harmful algal bloom (HABs) phenomena affects human health, ecosystems, fishing, and tourism industries. In a single occasion, the loss due to HABs can reach thousands of Ringgit Malaysia. In this study, a chitosan-silica composite (RHA-CHi) was synthesized *via* sol-gel technique for the mitigation of *Alexandrium tamiyavanichii,* a toxic HAB species isolated from Malaysian waters. Rice husk ash silica was used as the silica precursor in the composite synthesis. The FT-IR spectroscopy suggests that the chitosan was covalently bonded with the surface silanol groups. Light microscope analysis showed that the algal cells were stuck on the surface of the composite and underwent lysis. The incorporation of chitosan decreased the surface negative charge of the silica, hence, increasing the electrostatic attraction between the cells and RHA-Chi. The removal efficiency of *A. tamiyavanichii* was 75% using 0.1 mg/mL of RHA-Chi in 2 hours, increasing to 85% after 24 hours. Reduced removal efficiency (16%) was observed using silica alone. The findings show that the chitosan-silica composite has high potential to be used in the mitigation of *A. tamiyavanichii*.

Keywords: toxic algae, flocculate, silica, chitosan, rice husk

Abstrak

Fenomena ledakan alga-bahaya mengancam kesihatan manusia, industri perikanan dan pelancongan. Dalam satu kejadian, kerugian boleh mencecah ribuan Ringgit Malaysia. Dalam kajian ini, komposit kitosan-silika (RHA-CHi) telah disintesis melalui kaedah sol-gel untuk mitigasi *Alexandrium tamiyavanichii,* spesis bertoksik HAB yang dipencilkan dari perairan Malaysia. Abu sekam padi telah digunakan sebagai pelopor silika dalam sintesis komposit. Spektroskopi FT-IR menunjukkan kitosan terikat secara kovalen dengan kumpulan silanol permukaan. Analisis mikroskopi cahaya menunjukkan sel alga melekat pada permukaan komposit dan mengalami lisis. Penggabungan kitosan telah mengurangkan cas negatif permukaan silika lalu meningkatkan tarikan elektrostatik antara sel dan RHA-Chi. Kecekapan penyingkiran *A. tamiyavanichii* dalam masa 2 jam apabila 0.1 mg/ml RHA-Chi digunakan adalah 75% dan meningkat ke 85% selepas 24 jam manakala pengurangan kecekapan penyingkiran (16%) diperhatikan bagi silika sahaja. Penemuan ini menunjukan komposit kitosan-silika mempunyai potensi yang tinggi untuk digunakan dalam mitigasi ledakan alga-bahaya terutamanya *A. tamiyavanichii*.

Kata kunci: alga beracun, mengumpal, silika, kitosan, sekam padi

Introduction

Climate change has an adverse effect on aquatic environment. Variation in water condition may cause transformation in phytoplankton community structure and composition, including a greater prevalence and geographical spread of harmful algal blooms (HABs) [1]. Under the right conditions (salinity, temperature, and nutrients) some algae tend to grow in a higher number to form a bloom. Most algal blooms are not harmful, but they do cause serious problems such as discoloration of water, produce a smelly odor or bad water taste. Besides, the algal bloom depletes the concentration of oxygen available in the water through respiration. As a result, many organisms particularly caged fishes (relevant to fish farms) will die. The problem does not stop there. At the end of the blooming season and as the algae begins to die, more oxygen will be used by the microbes to decompose the algae cells creating an oxygen-deprived zone known as hypoxic dead zones. In this zone, neither fish nor plants can survive.

Alexandrium tamiyavanichii is a toxic dinoflagellate that causes paralytic shellfish poisoning (PSP). The first case of PSP by this species was recorded in Sebatu, Malacca whereby mussels were banned from being consumed. This caused an economic problem for the breeders [2]. The second case was in Kuantan Port, Pahang where ten people were hospitalized [3]. The occurrence of this species and other HAB species indicate that HABs are a serious problem that require further attention, especially as it affects human and the ecosystem, as evidenced by the negative impact to fisheries and tourism industries.

Mitigation is a term used to describe the actions taken to deal with an existing or ongoing bloom by taking necessary precautions to reduce the negative impact of the bloom. To date, many physical [4-6], chemical [7,8] and biological approaches have been proposed for the mitigation of HABs [9-10].

Although these approaches may be effective, some methods have certain drawbacks. The chemical approach is not selective towards certain HAB species and may affect other parts of the aquatic ecosystem. The chemical compounds can eliminate or negatively impact organisms that are required to balance the aquatic ecosystem [11]. The biological approach is considered safe and often species selective [12], but its efficiency depends on many biotic and abiotic factors. In comparison to chemical and biological approaches, physical methods often pose fewer threats to aquatic environment.

The objective of this research is to mitigate toxin producing HAB species, *A. tamivanichii* using a physical approach based on the properties of a chitosan-silica composite. The chitosan-silica composite was prepared using a one-pot synthesis *via* a sol-gel method. This research will contribute towards new knowledge for mitigating HAB species and help to minimize the impact of HABs on human health, particularly in Malaysia.

Materials and Methods

Preparation of rice husk ash

The preparation of rice husk ash (RHA) was carried out according to the reported method by Adam et al. [13]. Dirt and other water-soluble impurities were removed from the rice husk (RH) by washing it with copious amount of water and dried in the oven at 70 °C overnight. The clean and dried RH was stirred for 24 hours in 1.0 M HNO_3 to remove metallic impurities. The acid treated RH was then filtered using 8" sieve with mesh size 125 mm - 20 µm and washed with distilled water until the pH of the filtrate became constant. The acid treated RH was dried in the oven at 70 °C overnight. The RH was then pyrolyzed in a furnace at 600 °C for 6 hours to produce RHA.

Preparation of silica from RHA

Sodium silicate solution was prepared by dissolving 3 g of RHA in 350 mL of 1.0 M NaOH for 24 hours. The sodium silicate solution was titrated with 3.5 M HCl with constant stirring until pH 3. As the solution reached pH 10, gel started to form. The gel was aged for 24 hours in the mother liquor in a closed plastic container. The gel was separated using centrifugation (HETTICH® Rotina 38) at 7000 rpm for 9 minutes. The recovered gel was dried at 70 °C for 24 hours. The dried xerogel was weighed before grinding with a mortar and pestle into a fine powder. The resulting white powder (RHA- SiO_2) was stored in a glass bottle for use in this study.

Synthesis of chitosan-silica composite

The composite was prepared similarly to the preparation method of sodium silicate with some modification. Chitosan (1 g) (Sigma-Aldrich, 75-85% deacetylated) was dissolved in 3.5 M HCl. The sodium silicate solution was titrated with the aqueous chitosan solution until pH 3. The yellow colored gel was aged for 24 hours before separation by centrifugation at 7000 rpm. The gel was dried at 70 °C for 24 hours. The yellow colored xerogel was ground to a fine powder and labeled as RHA-Chi.

Characterization

The FTIR spectra of the materials were obtained using a Perkin Elmer System 2000 spectrophotometer. Approximately 0.1 to 1.0 wt.% sample was mixed with 200-250 mg of fine potassium bromide powder by grinding in a mortar and pestle. The samples were prepared in pellet form and then analyzed in transmission mode over a wavelength range (400 - 4000 cm^{-1}) at a resolution of 4 cm^{-1}.

Culture of *Alexandrium tamiyavanichii*

The subculture of *A. tamiyavanichii* was prepared from the stock culture (f/2 medium) obtained from the Phycology Laboratory, Kulliyyah of Science, International Islamic University Malaysia. The culture was maintained in f/2 medium, at 12:12 light and dark cycle and temperature of ± 27 °C.

Algal mitigation and flocculation

For the algal mitigation and flocculation tests, three concentrations (0.01 mg/mL, 0.1 mg/mL and 1.0 mg/mL) of RHA-SiO_2 and RHA-Chi were used against 15 mL of *A. tamiyavanichii* culture containing ±1000 cells/mL. The control culture was conducted without any addition of RHA-SiO_2 or RHA-Chi. The experiments were carried out in triplicate in 60 ×10 mm petri dish. After the addition of RHA-SiO_2 or RHA-Chi, the pH of the medium was measured using a pH meter with a glass electrode. At variable intervals of 0, 1, 2, 6, 12 and 24 hours, after the addition of RHA-SiO_2 or RHA-Chi, 1.0 mL of sample aliquots were taken using micropipette. The cells were counted in a Sedgewick-Rafter cell after being fixed with Lugol's solution. The effectiveness of this method is determined by the value of Removal Efficiency (RE). Equation (1) was used to calculate the RE of the cells. The accumulated algae flocs were taken using a pipette and observed under a light microscope (Olympus CH30 Light microscope). Pictures were taken using Dino Capture 2.0 at a total magnification of 400×.

$$(RE) = \frac{\text{1-Number of live cells in test}}{\text{Number of live cells in control}} \text{ x } 100\% \quad (1)$$

Results and Discussion

Characterization of the composite

The FTIR spectrum of chitosan is shown in Figure 1(a). The stretching vibration of –OH groups of chitosan show a broad band at 3470 cm^{-1}, that may include contributions of N-H symmetrical stretching vibration of amine [14]. The –CH symmetric and asymmetric vibrations give rise to the transmission bands at 2919 and 2960 cm^{-1}, respectively. The band at 1598 cm^{-1} is due to the stretching vibration of amino groups. The weak bands at 1380 and 1421 cm^{-1} are due to the bending vibration of $–CH_2$ and symmetry deformation of $–CH_3$, respectively [15]. The FTIR band located at 1154 cm^{-1} is due to the asymmetric vibration of C-O in the oxygen bridge resulting from deacetylation of chitosan [16]. The bands within 1080–1025 cm^{-1} are attributed to the stretching vibration of C-O of the ring, COH, COC, and CH_2OH. The wagging of the saccharide structure of chitosan is characterized by the band around 890 cm^{-1} [17].

The FTIR spectrum of RHA-SiO_2 is shown in Figure 1(b). The stretching vibration of SiO–H bond and adsorbed water (HO-H) on the silica surface yields a broad peak with an envelope-like appearance around 3469 cm^{-1}[18]. The sharp band at 1639 cm^{-1} is attributed to the bending mode of absorbed water molecules on the silica, while the stretching vibration of Si-O-Si bond reveals a band observed at 1080 cm^{-1}[19]. The band at 968 cm^{-1} is due to the stretching vibration of the Si-OH bonds [20]. The symmetric stretching and bending modes of the bulk Si-O-Si bond is indicated by the bands at 801 and 467 cm^{-1}, respectively [21].

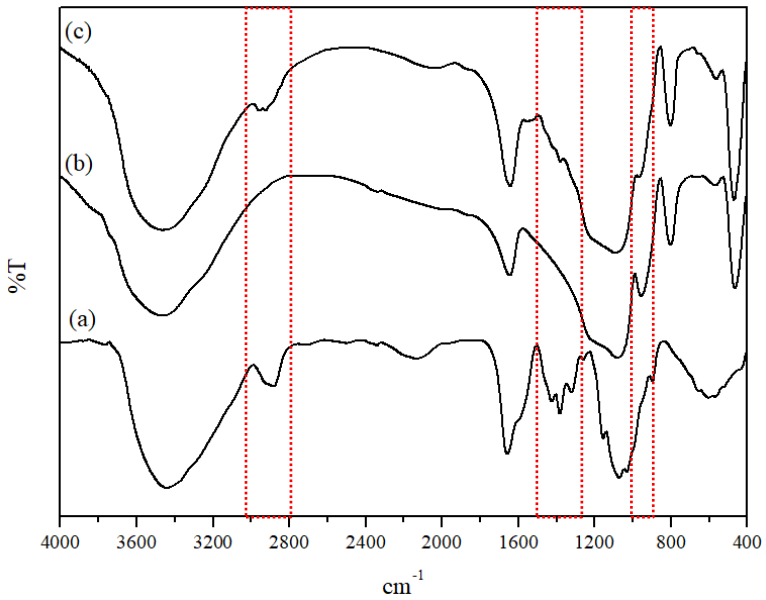


Figure 1. The FTIR spectra of (a) chitosan, (b) RHA-SiO_2 and (c) RHA-Chi

The FTIR spectrum of RHA-Chi is shown in Figure 1(c), where many of the bands related to the functional groups of silica and chitosan are extensively overlapped, and only a few prominent bands are resolved. The prominent bands are indicated using red boxes. The –CH symmetric and asymmetric vibrations of the chitosan can still be seen ~2900 and 1300 cm^{-1}. However these bands appears weaker compared to chitosan. Bands related to the stretching vibration of Si-OH, symmetric stretching and bending modes of bulk Si-O-Si bond can be seen at 968 cm^{-1} and 463 cm^{-1}, respectively. However, the intensity of the stretching vibration of Si-OH bond seems to be drastically reduced as compared to RHA-SiO_2 which indicates that bond formation occurs between the surface silanol groups of silica with the hydroxyl group of chitosan. The appearances of these bands indicated that chitosan had bonded onto silica forming a new composite.

The interaction between the hydroxyl groups of chitosan with the surface silanol groups of silica may have formed covalent bond *via* a condensation reaction shown by the reaction scheme in Figure 2 [22-24].

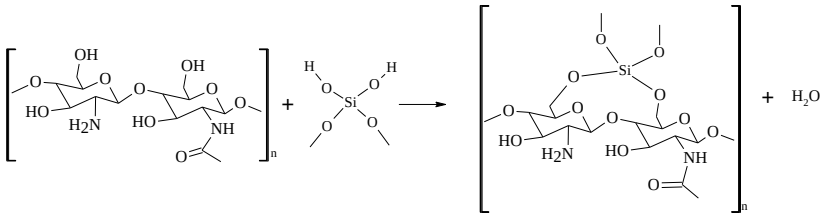


Figure 2. The condensation of the hydroxyl group of chitosan with the surface silanol groups of silica

In acidic condition, the amino groups of chitosan will be protonated, where the $–NH_3^+$ group has a high affinity for the negatively charged silicate species [25]. The $–NH_3^+$ group can form a more stable hydrogen bond with the silanol groups as compared to an uncharged NH_2 group. The electrostatic interaction between the protonated amino group of chitosan with the negatively charged dissociated hydroxyl silica is shown in Figure 3.

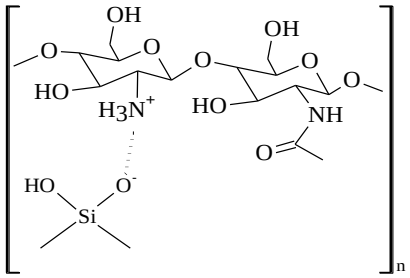


Figure 3. The interaction scheme between the protonated amine of chitosan with the negatively charged dissociated hydroxyl silica

The application of chitosan in seawater are limited due to the high alkalinity and ionic strength of seawater. The high alkalinity and ionic strength of seawater will prevent the polymer chitosan chain from unfolding. This will weaken the netting and the bridging properties of the chitosan [26]. The chitosan-silica linkages is expected to create a net-like structure that is flexible yet rigid. The macromolecular structure is expected to remain unfolded in seawater, resulting in more adsorption sites for the alga cells to be bound to the composite material.

Light microscopy analysis

The physical appearances of RHA-SiO_2 and RHA-Chi under a light microscope at a magnification of 400x are shown in Figures 4(a) and (b), respectively. Based on these optical images, RHA-SiO_2 has the appearance of transparent glass-like particles, while RHA- Chi is opaque and porous. The change in morphology and the physical appearance indicate the formation of a unique composite between chitosan and the silica matrix.

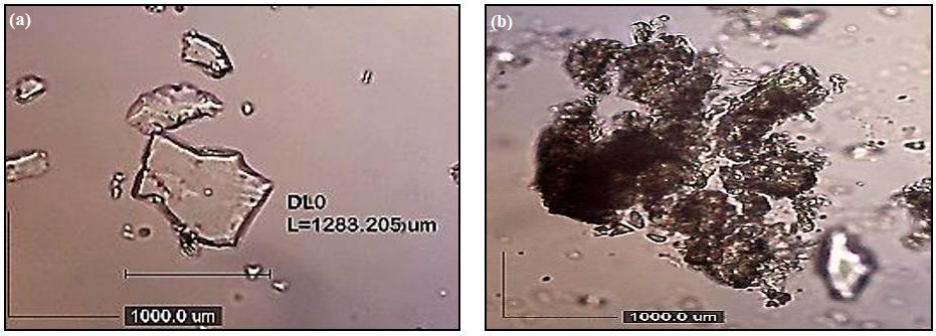


Figure 4. The micrographs of (a) transparent glass-like RHA-SiO_2 and (b) opaque and porous RHA-Chi composite material

Removal efficiency of *A. tamiyavanichii* using RHA-SiO_2

The HAB cells were observed to be immediately attracted to the RHA-SiO_2 when it was added. The RE values at different concentrations of RHA-SiO_2 is shown in Figure 5. The use of a concentration of 0.01 mg/mL and 0.1 mg/mL gave a RE value of 36% and 64%, respectively, in the first 2 hours. After 24 hours, the RE value dropped to 6% and 16%, respectively. This effect indicates that the RHA-SiO_2 is only able to temporarily trap the algal cell but did not kill them. The pH_{ZPC} of silica is around 2.0. Above the pH_{ZPC} value, the surface of the silica will be negatively charge and will repel the negatively charged algal cells. Throughout the experiment, the algal cells were not seen to be fully attached to the material as observed under the light microscope (Figure 6(a)). This finding is similar to that reported by Pan et al. [6], where the addition of unmodified beach sand was ineffective in removal of algal cells from the water column. The RE values were below 10% after 4 hours, indicating that sand alone did not have any flocculation ability. Instead, may act as a mass provider or ballast to carry flocs formed by modifiers to

the bottom of the water column [6]. The initial pH of the medium containing *A. tamiyavanichii* was pH 8.22 prior to the addition of RHA-SiO_2, where a decrease to pH 8.01 occurred in the presence of the composite (0.01 mg/mL) and to pH 7.44 at a higher composite dosage (0.1 mg/mL). Within 2 hours after the addition of 1.0 mg/mL of RHA-SiO_2, the calculated RE value was 70%. After 24 hours, the RE was at a favorable value of 84%. However, the medium became acidic (pH 6.18) at this condition. The mortality of *A. tamitayavanichii* may relate to the acidic pH conditions and not because of mitigation. Since the pH of the medium became acidic in the presence of excess RHA-SiO_2, the data suggest that it may not be safe to other aquatic environments. Most marine phytoplankton can only adapt to pH conditions near 7.8 [27]. Statistical analysis revealed that there were significant differences between each concentration tested ($p < 0.05$).

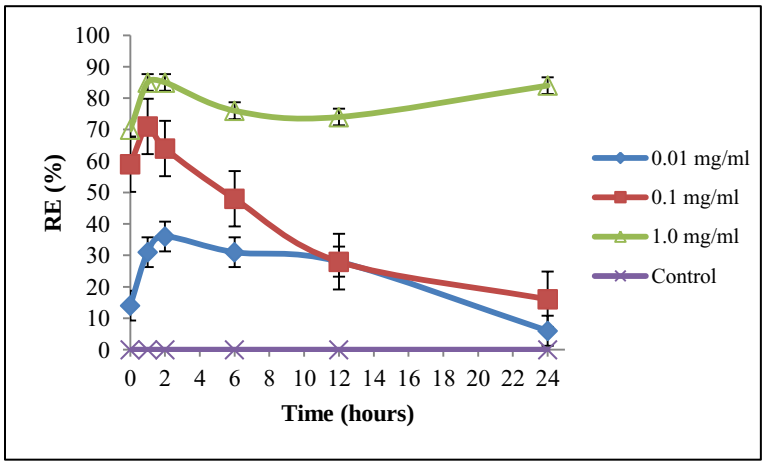


Figure 5. Time dependent Removal Efficiencies (REs) for variable dosage of the RHA-SiO_2 composite material

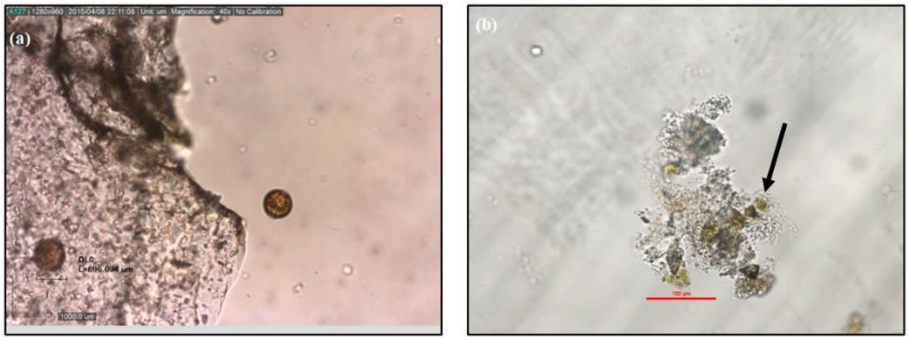


Figure 6. Micrographs showing the attachment of algae cells on (a) RHA-SiO_2 and (b) RHA-Chi

Removal efficiency of *A. tamiyavanichii* using RHA-Chi

The HAB cells immediately got attracted to the RHA-Chi as well when it was added. The RE values of *A. tamiyavanichii* using RHA-Chi are shown in Figure 7. Similar trends for all three dosages tested on *A. tamiyavanichii* with significant differences between these conditions ($p < 0.05$) were observed. The RE achieved when 1.0 mg/mL of RHA-Chi was used after 2 hours was 100%, however, the pH of the medium dropped to 5.42. Most of the algal cells were dead after 24 hours but not many were attached to RHA-CHi when viewed under a light microscope (image is not shown).

For the dosages of 0.01 and 0.1 mg/mL, the calculated RE values were 45% and 75% after 2 hours, respectively. By comparison, the RE values reached 85% at 24 hours for 0.1 mg/mL and 75 % for 0.01 mg/mL. The pH of the culture medium was 7.40 and 7.86 when 0.1 mg/mL and 0.01 mg/mL RHA-Chi composite was added. The pH is at

an acceptable range and deemed safe to other aquatic animals [27]. As seen in Figure 6(b), the algal cells are attached strongly to the surface of the composite. The interaction between the algal cells and chitosan is proposed to take place through electrostatic interactions between the composite and the algal cells. The incorporation of chitosan may have reduced the surface negative charge of the silica. As a result, the electrostatic attraction between the algal cells and the composite increased. The electrostatic interaction may cause internal osmotic imbalance leading to the lysis of the cell wall [28, 29]. As a result of cell wall lysis, leakage of intracellular content takes place as indicated by the arrow in Figure 6(b). The leaked intracellular content is still attached to the composite.

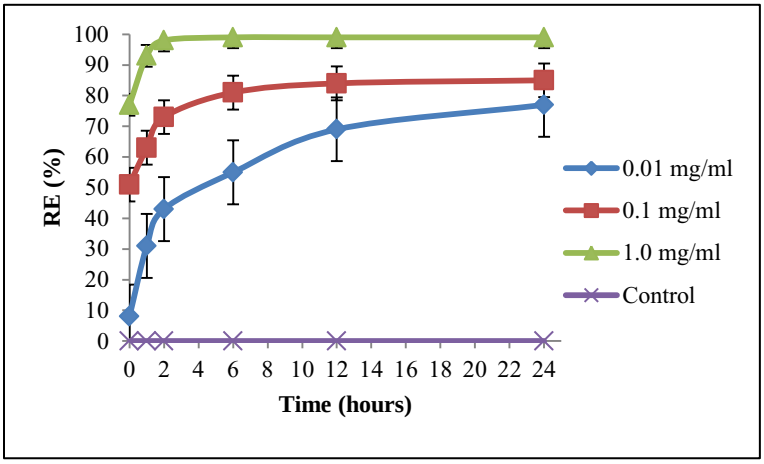


Figure 7. Time dependent Removal Efficiencies (REs) for different concentrations of RHA-Chi

The use of RHA-Chi for the mitigation of HABs offers a few advantages compared to several other current mitigation techniques. Firstly, this hybrid material displayed less environmental issues as both raw materials, i.e. rice husk ash (RHA) and chitosan are biocompatible and biodegradable. By comparison with the study by Pan et al. [6], PAC was used as a critical component in their mitigation of HAB, where this approach raised environmental concerns related to the balance of seawater. Secondly, the use of RHA-Chi is more cost effective since rice husk can be easily acquired free or at a low price from the rice milling industry and chitosan is a low-priced commercially available biomaterial.

Conclusion

RHA-Chi has been successfully deployed to capture, mitigate and flocculate the algal cells of *A. tamiyavanichii* as compared with RHA-SiO_2. The optimal concentration of RHA-Chi identified to mitigate *A. tamiyavanichii* was 0.1 mg/mL with an immediate effect of 50% RE in 2 hours, where the dosage does not cause significant change on the pH of the algal culture. The algal cells are proposed to be attached to the the composite *via* electrostatic attraction, whereas silica alone acted as a ballast to carry the formed flocks. RHA-Chi is suitable for application as a material for mitigation of *A. tamiyavanichii* because of its biocompatibility, biodegradability, and cost-effectiveness. The findings from this research can be used as a platform to further optimize and scale-up the study.

Acknowledgement

This study was supported by Universiti Sains Malaysia Short Term Grant (304/PKIMIA/6313215), Universiti Sains Malaysia Research University Grant (RUI) (1001/PKIMIA/8011083) and Fundamental Research Grant Scheme (FRGS-13-035-0276), Ministry of Higher Education (MOHE) Malaysia.

References

1. Wells, M. L., Trainer, V. L., Smayda, T. J., Karlson, B. S. O., Trick, C. G., Kudel, R. M., Ishikawa, A., Bernard, S., Wulfi, A., Anderson, D. M. and Cochlan, W. P. (2015). Harmful algal blooms and climate change: learning from the past and present to forecast the future. *Harmful Algae*, 49: 68-93.

2. Usup, G., Leaw, C. P., Asmat, A. and Lim, P. T. (2002). *Alexandrium* (Dinophyceae) species in Malaysian waters. *Harmful Algae,* 1: 265-75.
3. Mohammad-Noor, N., Aimimuliani A., Po T. L., Chui P. L. , Winnie L. S. L., G. R. Liow, Noraslinda M. B., Nurul A. H., Azlan M. N., Norazizah, K. and Devaraj, M. (2017). First report of paralytic shellfish poisoning (PSP) caused by *Alexandrium tamiyavanichii* in Kuantan Port, Pahang, East Coast of Malaysia. *Phycological Research*, 66:37-44.
4. Liu, Y., Cao, X., Yu, Z., Song, X. and Qiu, L. (2016). Controlling harmful algae blooms using aluminum-modified clay. *Marine Pollution Bulletin*, 103: 211-219.
5. Hao, H., Wu, M., Chen, Y., Tang, J. and Wu, Q. (2004). Cavitation mechanism in cyanobacterial growth inhibition by ultrasonic irradiation. *Colloids and Surfaces B: Biointerfaces*, 33: 151-156.
6. Pan, G., Jin, C. and Anderson, D. M. (2011). Modified local sands for the mitigation of harmful algal blooms. *Harmful Algae,* 10: 381-387.
7. Laue, P., Bährs, H., Chakrabarti, S. and Christian, S. E. W. (2014). Natural xenobiotics to prevent cyanobacterial and algal growth in freshwater: Contrasting efficacy of tannic acid, gallic acid, and gramine. *Chemosphere,* 104: 212-220.
8. Fan, J., Ho, L., Hobson, P. and Brookes, J. (2013). Evaluating the effectiveness of copper sulphate, chlorine, potassium permanganate, hydrogen peroxide and ozone on cyanobacterial cell integrity. *Water Research,* 47: 5153-5164.
9. Ying, Z. T., Yoonja K., Dianna B. and Christopher J. G. (2015). The ability of the red macroalga, *Porphyra purpurea* (Rhodophyceae) to inhibit the proliferation of seven common harmful microalgae. *Journal of Applied Phycol*ogy, 27:531–544.
10. Marcoval, M. A., Pan, J., Tang, Y. and Gobler, C. J. (2013). The ability of the branchiopod, *Artemia salina*, to graze upon harmful algal blooms caused by *Alexandrium fundyense*, *Aureococcus anophagefferens*, and *Cochlodinium polykrikoides*. *Estuarine*, *Coastal Shelf Science,* 131: 235-244.
11. Jančula, D. and Maršálek, B. (2011). Critical review of actually available chemical compounds for prevention and management of cyanobacterial blooms. *Chemosphere,* 85: 1415-1422.
12. Shao, J., Li, R., Lepo, J. E. and Gu, J. D. (2013). Potential for control of harmful cyanobacterial blooms using biologically derived substances: Problems and prospects. *Journal of Environmental Management,* 125: 149-155.
13. Adam, F., H. Osman, and Mohammed, H. K. (2009). The immobilization of 3-(chloropropyl)triethoxysilane onto silica by simple one pot synthesis. *Journal of Colloid and Interface Science,* 331:143-147.
14. Ramya, R., Sudha, P. N. and Mahalakshmi, J. (2012). Preparation and characterization of chitosan binary blend. *International Journal of Scientific and Research Publications,* 2(10): 1-9.
15. Mano, J. F., Koniarova, D. and Reis, R. L. (2003). Thermal properties of thermoplastic starch/synthetic polymer blends with potential biomedical applicability. *Journal of Materials Science: Materials in Medicine,* 14: 127-135.
16. Xu, Y., Kim, K., Hanna, M. and Nag, D. (2005). Chitosan-starch composite film: Preparation and characterization. *Industrial Crops and Products,* 21: 185-192.
17. Paluszkiewicz, C., Stodolak, E., Hasik, M. and Blazewicz, M. (2011). FT-IR study of montmorillonite–chitosan nanocomposite materials. *Spectrochimica Acta*, 79: 784-788.
18. Vetrieval, S. and Pandurangan, A. (2004). Vapour-phase oxidation of ethylbenzene with air over mn-containing MCM-41 mesoporous molecular sieves. *Applied Catalysis A: General*, 264: 243-252.
19. Adam, F. and Iqbal, A. (2011). The oxidation of styrene by chromium-heterogenous catalyst prepared from rice-husk. *Chemical Engineering Journal,* 160(2): 742-750.
20. Ibrahem, S. and Ibrahem, H. (2013). Preparation and study properties of silica using sol-gel method. *International Journal of Application or Innovation in Engineering & Management,* 12: 111-116.
21. Cruz, R. S. D., Silva, J. M. S. D., Arnold, U. and Schuchardt, U. (2001). Catalytic activity and stability of a chromium containing silicate in liquid phase cyclohexane oxidation. *Journal of Molecular Catalysis A: Chemical,* 171: 251-257.
22. Chassary P, Vincent, T. and Guibal, E. (2004). Metal anion sorption on chitosan and derivative materials: A strategy for polymer modification and optimum use. *Reactive and Functional Polymers,* 60:137-149.

23. Kavitha, K, Sutha, S., Prabhu, M., Rajendran, V. and Jayakumar, T. (2013). In situ synthesized novel biocompatible titania–chitosan nanocomposites with high surface area and antibacterial activity. *Carbohydrate Polymers,* 93: 731-9.
24. Budnyak , T. M., Pylypchuk, I.V., Tertykh, V. A., Yanovska, E. S. and Kolodynska, D. (2015). Synthesis and adsorption properties of chitosan-silica nanocomposite prepared by sol-gel method. *Nanoscale Research Letters,* 10: 87: 1-10.
25. Budnyak, T., Tertykh, V. and Yanovska, E. (2014). Chitosan immobilized on silica surface for wastewater treatment. *Materials Science (Medžiagotyra),* 20: 177-182.
26. Qun, G. and Ajun, W. (2006). Effects of molecular weight, degree of acetylation and ionic strength on surface tension of chitosan in dilute solution. *Carbohydrate Polymer,* 64(1): 29-36.
27. Berge, T., Daugbjerg, N., Andersen, B. B. and Hansen, P. J. (2010). Effect of lowered pH on marine phytoplankton growth rates. *Marine Ecology Progress Series,* 416: 79-91.
28. Rejane C. G., Douglas de, B. and Odilio, B. G. A. (2009). A review of the antimicrobial activity of chitosan. *Polímeros: Ciência e Tecnologia*, 19(3): 241-247.
29. Jiexia, L., Yi, Z., Yujun T., Yuanming Z., Li, A., Li, T., Ming, S. and Chengwu, Z. (2013). Freshwater microalgae harvested via flocculation induced by pH decrease. *Biotechnology for Biofuels,* 6(98): 1-11.

Malaysian Journal of Analytical Sciences, Vol 23 No 1 (2019): 40 - 44
DOI: https://doi.org/10.17576/mjas-2019-2301-05

MALAYSIAN JOURNAL OF ANALYTICAL SCIENCES
Published by The Malaysian Analytical Sciences Society
ISSN 1394 - 2506

PRODUCTION OF TITANIUM DIOXIDE NANOFIBER (TNF): INFLUENCE OF ELECTROSPINNING PARAMETER ON CRYSTALLINE SIZE

(Penghasilan Nanogentian Titanium Dioksida (TNF): Pengaruh Parameter Elektroputaran Terhadap Saiz Habluran)

Norulsamani Abdullah[1], Siti Kartom Kamarudin[1,2]*, Loh Kee Shyuan[1]

[1]*Fuel Cell Institute*
[2]*Department of Chemical and Process Engineering, Faculty of Engineering and Built Environment*
Universiti Kebangsaan Malaysia, 43600 UKM Bangi, Selangor, Malaysia

**Corresponding author: ctie@ukm.edu.my*

Received: 13 April 2017; Accepted: 17 April 2018

Abstract

This study aims to develop a small size of TNF using an electrospinning process. TNF is applied in direct methanol fuel cell (DMFC) as a catalyst, catalyst support and a filler in the membrane. This study involves determining the parameters that affect the electrospinning process, particularly in terms of the distance between the needle tip and collector towards the size of TNF crystalline. The production of TNF involves an electrospinning process, followed by a stabilization and calcination process. Fourier Transformation Infrared (FTIR) analysis was carried out to analyse the purity of the samples, while X-ray diffractometer (XRD) analysis was carried out to determine the size of crystalline. The result demonstrates that the longer the distance between the needle and collector, the smaller the size of the TNF produced. A smaller sized crystalline offers a significant impact on catalytic reaction and overall performance of DMFC.

Keywords: titanium dioxide, nanofiber, electrospinning, direct methanol fuel cell

Abstrak

Objektif utama kajian ini ialah membangunkan TNF bersaiz kecil untuk proses elektroputaran. Penggunaan TNF dalam sel bahan api metanol langsung (DMFC) adalah sebagai mangkin, sokongan mangkin dan pengisi di dalam membran. Kajian ini dijalankan untuk menentukan parameter yang dapat menjejaskan proses elektroputaran, iaitu jarak antara hujung jarum dan pengumpul, terhadap saiz habluran TNF. Penghasilan TNF melibatkan proses elektroputaran, diikuti dengan penstabilan dan kalsinasi. Analisis infra merah transformasi Fourier (FTIR) dijalankan untuk menganalisa ketulenan sampel, sementara analisis pembelauan sinar-X (XRD) untuk menentukan saiz habluran. Keputusan ujikaji menunjukkan semakin jauh jarak antara hujung jarum dan pengumpul, semakin kecil saiz TNF yang diperolehi. Pengurangan saiz habluran memberikan kesan yang besar kepada tindak balas pemangkinan dan prestasi keseluruhan DMFC.

Kata kunci: titanium dioksida, nanogentian, elektroputaran, sel fuel metanol langsung

Introduction

Titanium is a chemically-inert element, and the ninth-most common element found in the earth's crust [1]. Titanium dioxide (TiO_2) is among the metal oxide groups that have a wide range of applications, including cosmetics, paint, food, and catalysts and semiconductors. This study on TiO_2 focuses as catalyst support in direct methanol fuel cell (DMFC) application. TiO_2 consists of several types, including rutile, anatase and brookite. Each type of TiO_2 has a different application. For example, for catalysts, the most suitable is the rutile type.

The selection of a support for the nanostructures catalyst is an important factor for both catalytic activity and durability. Various combinations with different support setups have been developed by researchers, including TiO_2, cerium dioxide (CeO_2), tin dioxide (SnO_2), and tungsten(VI) oxide (WO_3). TiO_2 has especially received considerable attention, mainly because it is manufactured in small sizes, approximately in the range of 200 – 350 nm. Due to the smaller size of primary particles, TiO_2 allows for the manufacture of various catalysts of enhanced activity and has a higher surface area with optimal chemical stability. The addition of TiO_2 as a support catalyst can offer suitable thermal properties and dimensional stability, and the long-term life-cycle can also be improved [2]. It is a nanomaterial (ultrafine) that is used as a catalyst support in exhaust gas systems in cars, trucks and power plants, thus minimizing their overall environmental impact.

The production of TiO_2 nanofiber has already been discussed in many works in the literature before using several types of techniques. The most prominent technique for producing titania nanofiber is the electrospinning technique. The processing of this nanofiber is becoming more advanced and increasing the quality of the product in various applications. Research regarding TiO_2 nanofiber was initiated as early as 2003. Both Drew et al. and Li & Xia discussed the electrospinning techniques in their work, with successful products. Drew et al. investigated the metal oxide coated with polymer nanofibers, and the size of the fibers form is around 100 nm. Meanwhile, Li & Xia presented nanofibers diameter in the range of 20 to 200 nm, by varying several parameters in the electrospinning process [3, 4].

Madhugiri et al. applied another approach in producing TiO_2 nanofibers, which is electrostatic deposition. The rutile crystal is formed during the calcination with a temperature above 800 ^oC [5]. Another study by Ding et al. involves synthesizing the TiO_2 nanofibers, with 200 – 300 nm in diameter. The result showed that the pure titania nanofibers were obtained with high temperature calcinations [6]. The electrospinning techniques were also used by Watthanaarun et al. to produce PVP/TiO_2 composite nanofiber, and the diameter obtained was in the range of 120 – 350 nm. This study also investigated the effect of calcination temperature and time on size of fibers [7]. Suzuki et al. successfully produced the titania nanofibers with 20 – 50 nm in diameter by using a new technique called direct hydrothermal processing [8].

This study reported the fabrication of titanium dioxide nanofiber (TNF) *via* an electrospinning process. The main objective of the study is to determine the effect of electrospinning parameters, the distance between the needle tip and collector (DTC) towards the crystalline size of TNF. The TNF was prepared by the sol-gel method, followed by the electrospinning method, and a calcination process. The TNF sample was characterized by Fourier-transform infrared spectroscopy (FTIR) and X-ray diffraction (XRD) analysis. Based on the experimental results, the effect of the DTC parameter and the TNF crystalline size was discussed.

Materials and Methods

Materials

Poly(vinyl acetate), PVAc (Mw ~ 500,000), titanium isopropoxide, TiPP, N,N-dimethylformamide, DMF, and acetic acid were obtained from Sigma-Aldrich/USA. Ethanol (99.8%) was supplied by R&M Chemicals. All the chemicals were directly used in this study without any further purification. The main equipment used for producing the fiber is electrospinning, from the Nfiber Electrospinning Unit.

Methods

The nanofiber was produced by using the electrospinning technique. The electrospinning solution was prepared by the sol-gel method, whereby PVAc was used as the fiber base for this experiment. The PVAc (11.5 wt.%) was added to DMF, and stirred for 1 hour at 60 ^oC, for 12 hours. TiPP, 50 wt.%, and a few drops of acetic acid and ethanol were added to the polymer solution. The mixture was homogenized in a homogenizer for 2 minutes. The solution was then transferred to a syringe and the solution was injected in the electrospinning by applying a high voltage of 16 kV with 0.5 mL/h for the flowrate, and different distances between the tip of needle and the collector. The fiber was then stabilized in the oven for 8 hours, at 130 ^oC. The stabilized fiber underwent a calcination process in the furnace for 850 ^oC, and the powder size was normalized using a mortar and pestle. The purity of the TNF was analysed using FTIR analysis, while the structure and crystalline size of the sample underwent XRD analysis.

Results and Discussion

Figure 1 illustrates the existence of the functional group in the TNF sample from FTIR analysis. The sample is denoted by TNF (distance (cm)), TNF 12, TNF 13, TNF 14, TNF 15, TNF 16. The graph shows that all samples have functional group O-Ti-O, which appears in the wavenumber range of 450 cm^{-1} to 700 cm^{-1} [6]. The purity of the sample is proven from the FTIR analysis, where all other functional groups do not appear in the graph of the sample. Other solvents and chemical compounds were completely removed during the calcination process. The different parameters of electrospinning do not offer a significant impact on the functional group of the sample.

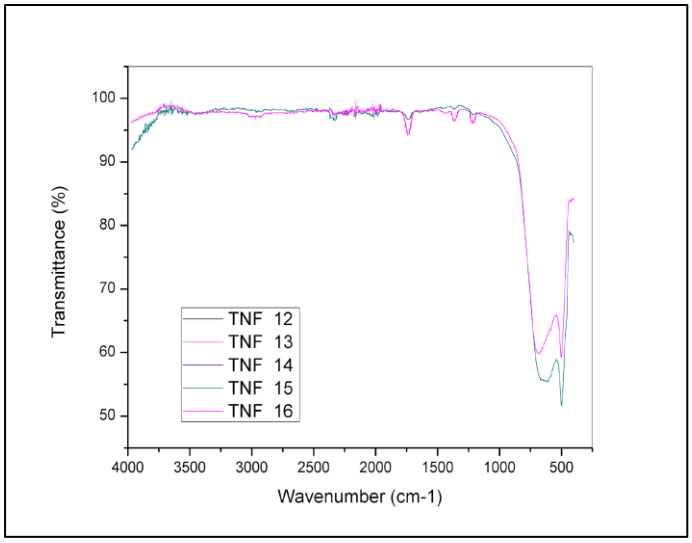


Figure 1. FTIR analysis of TNF sample after calcination process at 850 ^{o}C for 2 hours

Figure 2 presents the XRD pattern for the TNF sample with various distances between the needle tip and the collector. The result shows that the TNF structure exists in the rutile form, due to the high temperature used during the calcination process at 850 ^{o}C for 2 hours. There was almost no influence on the different distances during the preparation of nanofiber towards the crystal structure of TNF. XRD pattern for TNF sample shows the crystallographic tetragonal structure: related to the rutile structure form. The crystalline size was calculated using Debye-Scherrer equation (refer equation 1)[9], which needs data from the XRD analysis for the peak position of TiO_2 (110):

$$\text{Crystalline size} = 0.98\alpha / \beta\cos\theta \quad (1)$$

where α represents the wavelength of the X-ray, θ represents the angle at the peak, and β represents the width of the peak at half height. The crystalline size can also be determined from the XRD analysis using Eva software. It was calculated based on the Debye-Scherrer equation. The crystalline size for all samples is tabulated in Table 1.

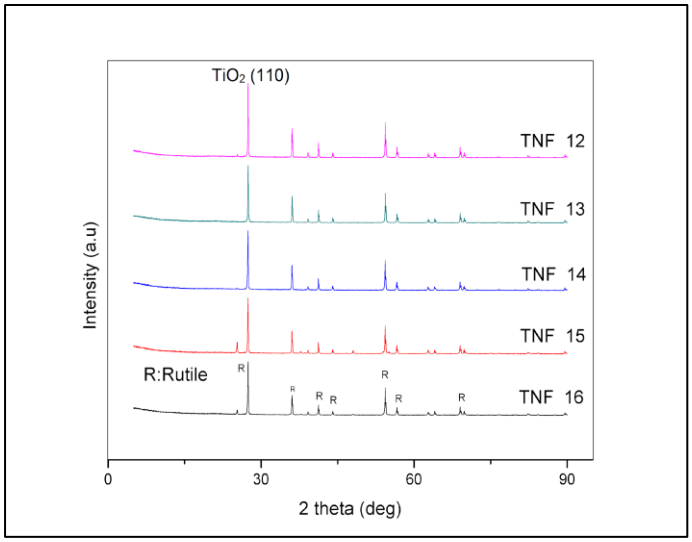


Figure 2. XRD patterns for TNF sample

Table 1. Calculated crystalline size from XRD analysis

Sample	FWHM (^{o})	Crystalline size (nm)
TNF 12	0.066	12.33
TNF 13	0.0704	11.55
TNF 14	0.0749	10.86
TNF 15	0.0799	10.18
TNF 16	0.0817	9.96

The smallest crystalline size of TNF, 9.96 nm, was calculated at the distance of 16 cm between the needle tip and the collector. The result also shows that, the higher the distance, the smaller the crystalline size produced. This is because of several technical and mechanical situations that occurred during the electrospinning process, namely, high voltage applied to the tip of the needle, and the electrical force makes the solution of TNF deformed from the shape caused by the surface tension alone, and forms Taylor cone. As the electrical field reaches critical values, the TNF solution overcomes its surface tension and viscoelastic force, resulting in the jet of solution in bending, winding and spiralling path towards the collector. This phenomenon is known as bending instability, which is the dominant thinning mechanism in electrospinning [10]. Figure 3 shows a detailed illustration of this phenomenon.

Next, the distances take place in process to produce the smallest size of TNF. The remote distance causes the bending instability phenomena to reoccur, increasing the loop circumference and producing thinner and smaller nanofibers on the collector. The distance also represents the area of the electric field involved in the electrospinning process. The changes in distance can change the morphological properties of the nanofiber, either for crystalline size, diameter, or bead density, and produce a variety shapes on the surface [11].

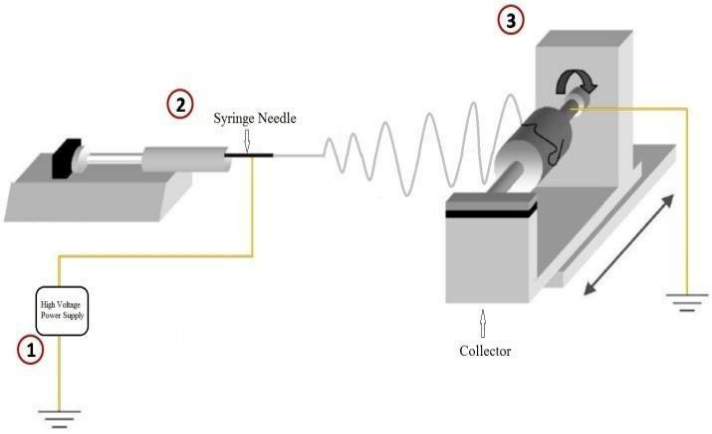


Figure 3. Illustration of dominant thinning mechanism

Conclusion

Finally, this study successfully produced TNF using electrospinning. The results show that the smaller crystalline size is an important factor to increase the active catalytic surface area. The electrospinning parameter has an effect on the size of the TNF, and one of the parameters involved is the distance between the needle tip and collector. The XRD result shows that the higher the distance, the smaller the crystalline size of TNF. The smallest crystalline size of 9.96 nm was obtained for the 16 cm distance between the needle tip and collector. This shows that the parameter of the electrospinning successfully produces a suitable size for the sample.

Acknowledgement

The authors gratefully acknowledge the financial support given for this work by Universiti Kebangsaan Malaysia (UKM) under DIP-2015-002.

References

1. Abdullah, N. and Kamarudin, S. (2015). Titanium dioxide in fuel cell technology: An overview. *Journal of Power Sources*, 278: 109 - 118.
2. Mallakpour, S., Zhiani, M., Barati, A. and Rostami, H. (2013). Improving the direct methanol fuel cell performance withpoly(vinyl alcohol)/titanium dioxide nanocomposites as a novel electrolyte additive. *International Journal of Hydrogen Energy*, 38(28): 12418 - 12426.
3. Drew, C., Liu, X., Ziegler, D., Wang, X., Bruno, F. F., Whitten, J. and Kumar, J. (2003). Metal oxide-coated polymer nanofibers. *Nano Letters*, 3(2): 143 - 147.
4. Li, D. and Xia, Y. (2003). Fabrication of titania nanofibers by electrospinning. *Nano Letters*, 3(4): 555 - 560.
5. Madhugiri, S., Sun, B., Smirniotis, P. G., Ferraris, J. P. and Balkus, K. J. (2004). Electrospun mesoporous titanium dioxide fibers. *Microporous and Mesoporous Materials*, 69(1): 77 - 83.
6. Ding, B., Kim, C. K., Kim, H. Y., Seo, M. K. and Park, S. J. (2004). Titanium dioxide nanofibers prepared by using electrospinning method. *Fibers and Polymers*, 5 (2): 105 - 109.
7. Watthanaarun, J., Pavarajarn, V. and Supaphol, P. (2005). Titanium(IV) oxide nanofibers by combined sol–gel and electrospinning techniques: preliminary report on effects of preparation conditions and secondary metal dopant. *Science and Technology of Advanced Materials*, 6(3): 240 - 245.
8. Suzuki, Y., Pavasupree, S., Yoshikawa, S. and Kawahata, R. (2005). Natural rutile-derived titanate nanofibers prepared by direct hydrothermal processing. *Journal of Materials Research*, 20(04): 1063 - 1070.
9. Ito, Y., Takeuchi, T., Tsujiguchi, T., Abdelkareem, M. A. and Nakagawa, N. (2013). Ultrahigh methanol electro-oxidation activity of PtRu nanoparticles prepared on TiO_2/-embedded carbon nanofiber support. *Journal of Power Sources*, 242: 280 - 288.
10. Zhang, L., Aboagye, A., Kelkar, A., Lai, C., and Fong, H. (2014). A review: Carbon nanofibers from electrospun polyacrylonitrile and their applications. *Journal of Materials Science*, 49(2): 463 - 480.
11. Chronakis, I. S. (2005). Novel nanocomposites and nanoceramics based on polymer nanofibers using electrospinning process - a review. *Journal of Materials Processing Technology*, 167(2): 283 - 293.

Malaysian Journal of Analytical Sciences, Vol 23 No 1 (2019): 45 - 51
DOI: https://doi.org/10.17576/mjas-2019-2301-06

MALAYSIAN JOURNAL OF ANALYTICAL SCIENCES
Published by The Malaysian Analytical Sciences Society
ISSN 1394 - 2506

PRODUCTION OF ETHYL LEVULINATE VIA ESTERIFICATION REACTION OF LEVULINIC ACID IN THE PRESENCE OF ZrO_2 BASED CATALYST

(Penghasilan Etil Levulinat Melalui Pengesteran Asid Levulinik dengan Kehadiran Mangkin Berasaskan ZrO_2)

Dorairaaj Sivasubramaniam[1], Nor Aishah Saidina Amin[1]*, Khairuddin Ahmad[1], Nur Aainaa Syahirah Ramli[2]

[1]*Chemical Reaction Engineering Group (CREG), Faculty of Chemical Engineering, Universiti Teknologi Malaysia, 81300 Skudai, Johor, Malaysia*
[2]*Advanced Oleochemical Technology Division, Malaysian Palm Oil Board (MPOB), 6, Persiaran Institusi, Bandar Baru Bangi, 43000 Kajang, Selangor, Malaysia*

**Corresponding author: noraishah@cheme.utm.my*

Received: 13 April 2017; Accepted: 17 April 2018

Abstract

Ethyl levulinate is widely used as a fuel additive, flavor or fragrance and as a component of fuel blending. This study focused on the production of ethyl levulinate from levulinic acid *via* esterification reaction in the presence of HPW/ZrO_2.The catalyst was prepared using the wet impregnation method, characterized by using FTIR, BET and NH_3-TPD and screened based on 20%, 40% and 60% HPW/ZrO_2. The 40% HPW/ZrO_2 catalyst exhibited the highest catalytic performance during the parameter screening stage which included catalyst loading (0.25–1.25g) and volume ratio of levulinic acid to ethanol (1:4 – 1:8). The highest ethyl levulinate yield of 99% corresponded to a catalyst loading of 0.5 g and volume ratio of levulinic acid to ethanol of 1:5 with reaction conditions at 150 °C for 3 hours. The esterification reaction of levulinic acid revealed that the catalytic performance was influenced by the acid sites and surface area of the catalyst. In addition, volume ratio was also a major factor in enhancing the ethyl levulinate yield.

Keywords: levulinic acid, ethyl levulinate, wet impregnation, esterification, phosphotungstic acid

Abstrak

Etil levulinat digunakan secara meluas sebagai komponen penting dalam bahan kosmetik, bahan tambahan dalam bahan api dan campuran bahan api. Kajian ini memberi tumpuan dengan penghasilan etil levulinat daripada asid levulinik melalui tindak balas pengesteran dengan kehadiran pemangkin HPW/ZrO_2. Pemangkin ini disediakan dengan menggunakan kaedah impregnasi basah dan dicirikan dengan menggunakan FTIR, BET dan NH_3-TPD, pemangkin ini ditapis berdasarkan 20%, 40%,dan 60% HPW/ZrO_2. Akhirnya, didapati 40% HPW/ZrO_2 menunjukkan mangkinan tinggi yang sesuai digunakan untuk pemeriksaan parameter melibatkan berat pemangkin (0.25–1.25g) dan nisbah isipadu LA kepada etanol (1:4 – 1:8). Penghasilan terbaik ditunjukkan dengan muatan pemangkin (0.5 g) dan nisbah isipadu asid levulinik kepada etanol (1:5) yang diperolehi hasil 99% EL pada 150 °C selama 3 jam. Penggunaan HPW/ZrO_2 sebagai pemangkin dalam tindak balas pengesteran LA mendedahkan bahawa reaktiviti pemangkin sangat dipengaruhi oleh bahagian asid dan luas permukaan pemangkin tersebut.

Kata kunci: asid levulinik, etil levulinate, impregnasi basah, pengesteran, asid fosfotungstik

Introduction

Biomass is required for the production of many bio-based chemicals, which are utilized as an alternative source to fossil fuels. One of the top ten platform chemicals that is in high demand is levulinic acid (LA). LA is produced *via* the acid hydrolysis reaction of lignocellulosic biomass [1-3]. The LA molecule contains two functional groups- a ketone and a carboxyl group. Therefore, LA can be used for the synthesis of organic chemicals such as levulinate ester, γ-valerolactone, α-agelica lactone, acrylic acid and 1,4-pentanediol [4]. Moreover, LA, known as one of the top twelve building blocks, is also widely used as chiral reagents, inks, coatings and chemical components in batteries. [5]. Many useful compounds are derived from LA, especially ethyl levulinate (EL), which is synthesized via esterification of LA with ethanol as shown in Figure 1. This highly promising chemical can act as an oxygenate additive in fuels [1].

EL is considered as one of the top biomass-derived chemical which can potentially replace fossil fuels in the synthesis of various industrial chemicals and blending components for transportation fuels. EL is also used as a flavoring agent, fuel oxygenate additive and feed to produce γ-valerolactone, which is another potential chemical that can be used as a fuel additive [6]. The production of EL from LA has attracted considerable attention because LA is one of the top biomass-derived platform molecules that is produced from C_6 carbohydrates derived from renewable ligno-cellulose [7].

EL is produced *via* the acid-catalyzed esterification of LA. Conventionally, mineral acids such as H_2SO_4 and H_3PO_4 have been utilized in the production of ethyl levulinate with high yields [8]. However, these catalysts are considered as not only harmful to the environment but also uneconomical and difficult to recycle. Hence, a heterogeneous catalyst was introduced as an alternative to eliminate the disadvantages of using a homogeneous catalyst.

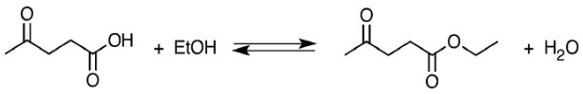


Figure 1. The reaction pathway to produce EL via esterification reaction of LA with ethanol [4].

Recently, Keggin-type heteropolyacids such as phophotungstic acid (HPW) has been widely used in acid- catalyzed reactions due to its strong Brønsted acidity site, high proton mobility and ability to accept electrons [8]. However, HPW had some characteristics that limited its application such as its low surface area and difficulty in separating from reaction mixtures. Many studies reported that a solution to the problem is by using metal oxide catalysts (e.g. SiO_2, SnO_2, TiO_2 and MgO) with HPW which makes it a heterogeneous acid catalyst. This paper investigates the production of EL via the esterification reaction of LA in the presence of HPW/ZrO_2 in different percentages of weight (wt.%), i.e. 20%, 40% and 60%. Parameter screening was conducted using a catalyst loading range of 0.25–1.25g and volume ratio of LA to ethanol (EtOH) in the range of 1:4 – 1:8.

Materials and Methods

Chemicals

All chemicals were obtained from Merck, Germany. The Keggin-type heteropolyacid used in the reaction was phosphotungstic acid (HPW) while zirconium oxide (ZrO_2) was used for the catalyst preparation. LA and ethanol were used as feedstock for the esterification reaction. The EL standard was used as a standard in GC analysis.

Catalyst preparation

The catalyst was prepared via wet impregnation method and employed the unit of percentage of weight (wt.%). Zirconium oxide (ZrO_2) was mixed with Keggin-type heteropolyacid (HPW). Zirconium oxide powder was weighed and added to 30 mL of water, following the stated amount of HPW. The mixture was then stirred at 80 ºC for 2 hours and dried in an oven for 12 hours at 100 ºC to remove excess water. Finally, the prepared catalyst was calcined at 500 ºC for 3 hours.

Catalyst characterization

FTIR spectra was used to identify the chemical bonds and functional groups in the sample. The FTIR spectra (KBr pellets) was recorded using Perkin Elmer in the range of 400-4000 cm^{-1}. The acidity properties of the catalysts were analyzed using NH_3-temperature program desorption (NH_3-TPD). The Brunauer-Emmet-Teller (BET) method was used to determine the surface area using Micrometrics ASAP2020 analyzer.

Catalytic activity

The conversion of LA to EL was carried out in the presence of 30 mL of ethanol as a solvent for the reaction. The solid acid catalyst and the reaction were carried out in a high pressure stirred autoclave reactor at 150 ºC. Finally, the product was analyzed using GC-FID to obtain the yield of products formed. The reactions were repeated at various temperatures and the reaction time was taken.

Product analysis

Samples were filtered with micropore filtrate to remove impurities and were analyzed by using Agilent 7820A as chromatography equipped with a flame ionization detector (FID) operating at 543 K. EL was separated using HP5 column (30m x 320 µm x 25 µm). N_2 was the carrier gas used in GC at a flow rate of 1.0 mL min^{-1}. The yield of EL was calculated using the following equation 1:

$$\text{EL yield (\%)} = \text{Mole of EL/ Initial mole of LA} \times 100\% \quad (1)$$

Results and Discussion

Catalyst characterization

To study the catalysis of HPW/ZrO_2 in the esterification reaction of LA, the characterization of different wt.% of HPW/ZrO_2 was carried out. Three characterization tests were conducted on the catalyst to determine its physical and chemical properties. Figure 2 represents Fourier transform-infrared spectroscopy (FTIR) spectra for parent ZrO_2, 20% HPW/ZrO_2, 40% HPW/ZrO_2 and 60% HPW/ZrO_2. The peak at 1076 and 977.91 cm^{-1} shows the bond between P-O and W=O in the structure after the wet impregnation of ZrO_2 as a support catalyst to HPW. In addition, when the loading of HPW increases, a weak peak appears at 729.09 cm^{-1} and becomes narrower, which confirms the content of HPW. The FTIR spectra of all the catalysts shows absorption peaks ranging from 500 cm^{-1} to 2000 cm^{-1}, which represents heteropolyacids anions of the Keggin structure.

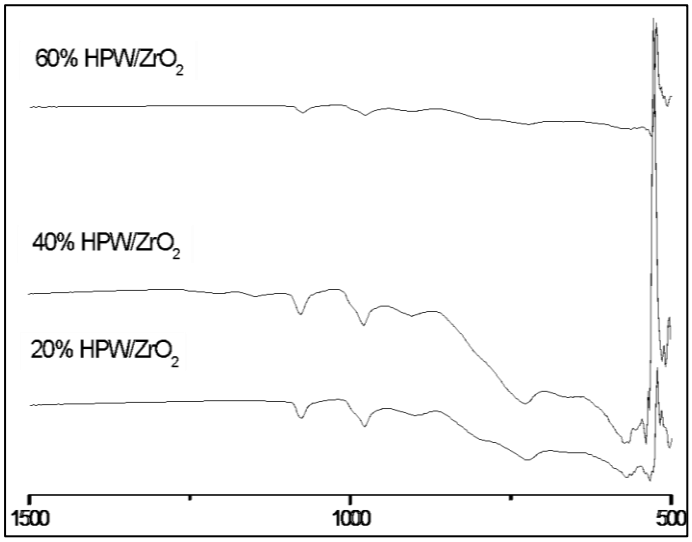


Figure 2. FTIR results for HPW/ ZrO_2 of 20%, 40% and 60% HPW/ZrO_2

BET was used to analyze the surface area of the catalyst when the loading of HPW was increased in the reaction that was supported by ZrO_2. Table 1 shows the total surface area of the solid catalyst. The surface area of the catalyst increases due to the porous characteristic of ZrO_2 that enables it to increase its own surface area when impregnated with other catalysts [9]. Based on the total surface area obtained, it has been concluded that the surface area influences the catalytic performance in the production of EL.

Table 1. BET analysis based on the total surface area of the parent and impregnated catalysts

Catalyst	**Total surface Area (m^2/g)**
HPW	4.55
ZrO_2	14.95
20% HPW/ ZrO_2	16.3
40% HPW/ ZrO_2	18.81
60% HPW/ ZrO_2	21.65

The acidity of the catalyst strongly affects the production of EL *via* the esterification reaction of LA. The total number of acidity sites of the HPW contributed to the Brønsted acidity site of the catalyst which enhances the esterification reaction to favour high selectivity of EL. Table 2 depicts the comparison of total acidity sites of both parent catalysts and impregnated ones. The acidity of ZrO_2 catalyst impregnated with HPW was higher because HPW is a super acid that increases the acidity of the catalyst.

Table 2. NH_3-TPD of the parent catalyst with impregnated catalyst

Catalyst	**NH_3-TPD (mmol/g)**
HPW	1.68
ZrO_2	0.27
20% HPW/ ZrO_2	0.93
40% HPW/ ZrO_2	0.64
60% HPW/ ZrO_2	0.79

Catalytic activity

The prepared HPW/ZrO_2 materials were tested for the production of EL from the esterification reaction of LA and ethanol at 150 °C for 3 hours. In this reaction scheme, the conversion of LA was tested using 20%, 40% and 60% of catalyst in the catalytic screening stage. This was followed by the parameter screening utilizing the catalyst that gave the highest yield of EL in the catalytic screening. 40% HPW/ZrO_2 gave the highest EL yield of 99%. Hence, 40% HPW/ZrO_2 was chosen for the parameter study which covered catalyst loading and volume ratio of LA to ethanol. Catalyst screening was conducted in the first stage to obtain the most-suitable catalyst for the next stage, known as parameter screening. Figure 3 shows a comparison of the effect of three different wt.% of HPW on EL yield.

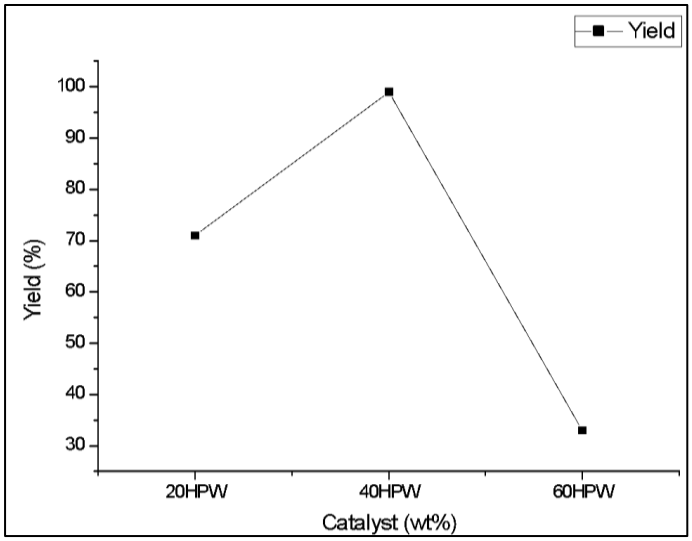


Figure 3. Effect of different HPW/ZrO_2 catalyst on EL yield

Based on the graph in Figure 3, 60% HPW/ZrO_2 only gave a yield of 33% of EL. This was due to the large amount of HPW impregnated in ZrO_2, which resulted in the catalyst becoming more active and converted to the other products. Moreover, high Brønsted acidity site is highly required by the catalyst for the conversion of LA to EL *via* esterification. Hence, HPW is highly favorable for the production of EL from LA [7]. Based on the catalyst screening, the effect of parameters was studied including the catalyst loading and volume ratio. This paper describes the application of heteropoly HPW in the direct conversion of LA with excess ethanol.

Effect of catalyst loading

Based on Figure 4, yield of EL increased when the catalyst loading was increased to the optimum point of 0.5 g, after which the yield decreased. The initial increase was due to the presence of the catalyst which increased the production of EL. However, excess loading might have caused leaching of the catalyst, thus causing the sharp fall in yield, Moreover, a high catalyst loading might have also caused formation of side-products and caused oxidation reactions to take place, thus reducing EL yield.

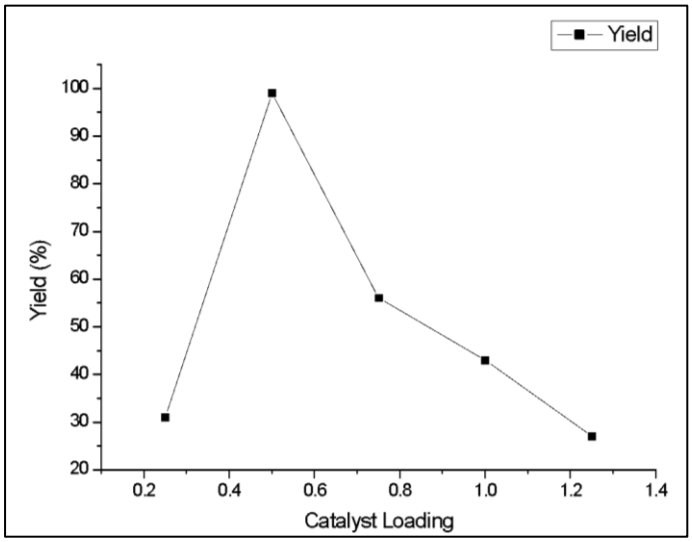


Figure 4. Effect of catalyst loading on yield of EL

0.5 g of catalyst gave the highest yield, which is 99%, thus making it the optimum loading for the reaction. The yield of EL decreased when a loading range of 0.75 to 1.25g was used. A decreasing trend of EL yield from 99% to 56% was observed when the catalyst loading increased from 0.5 to 0.75g. Moreover, HPW/ZrO_2 possesses strong Brønsted acid properties. There were many factors that influenced the catalytic activity of the esterification of LA but strong Brønsted acid properties of the catalyst played an important role in its catalytic activity. HPW/ZrO_2 has strong Brønsted acidity properties mainly due to the presence of both HPW.

Effect of volume ratio

The volume ratio parameter also affected the production of EL where a large quantity of ethanol diluted the LA and gave a low yield of EL [7]. Figure 5 shows that the yield decreased after the 1:5 volume ratio mark. The esterification reaction of LA with alcohol was a reversible reaction. High yield of the EL could be obtained when the reverse reaction was reduced [7]. The reduction of backward reaction occurred when the excess amount of ethanol was used in the reaction. Similarly, another study reported on the effect of large amount of ethanol that has been used in the reaction causing inhibition of the catalyst [10].

Continuous increase of the volume ratio from 1:5 to 1: 8 resulted in the yield to decrease from 99% to 42%, which is due to the fact that the esterification reaction is a reversible reaction and excessive ethanol favors ester production but too much ethanol may dilute the reactant, thereby resulting in lower ethyl levulinate yield. Additionally, excess ethanol in the reaction mixture may lead to side reactions such as ether formation and ethanol.

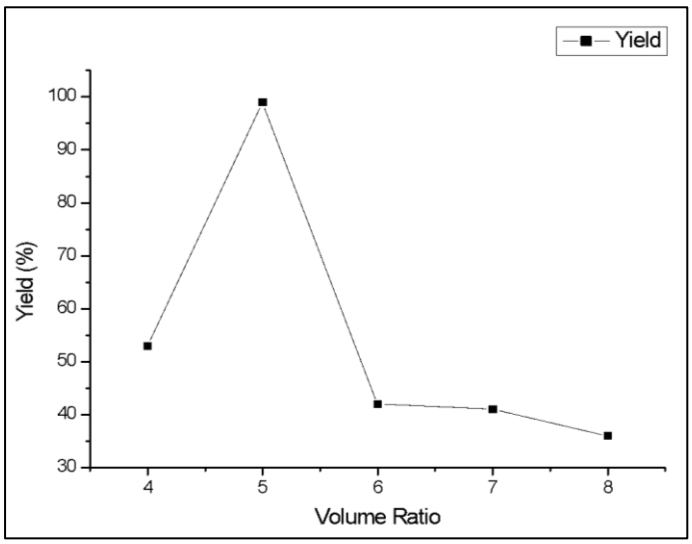


Figure 5. Effect of volume ratio of LA to ethanol on the production of EL

Conclusion

The esterification reaction of LA with ethanol to ethyl levulinate, a promising renewable biofuel, was systematically studied over super solid acid catalyst. The synthesis of EL from the esterification reaction of LA with ethanol at 150 °C for 3 hours using a loading of 0.5 g and volume ratio of LA to ethanol of 1:5 were the best conditions as it yielded 99% of EL. The catalyst exhibited best catalytic activity towards the esterification reaction of LA to produce EL. The unique performance of this catalyst, which is also known as a super solid acidity catalyst, was due to the combined characteristics of its strong Brønsted acidity and homogeneous dispersion of its active sites.

Acknowledgement

The authors would like to express their gratitude to Universiti Teknologi Malaysia and Ministry of Higher Education (MOHE), Malaysia for supporting the research under the Research University Grant (RUG), vote no 07H14.

References

1. Pasquale, G., Vázquez, P., Romanelli, G. and Baronetti G. (2012). Catalytic upgrading of levulinic acid to ethyl levulinate using reusable silica-included Wells-Dawson heteropolyacid as catalyst. *Catalysis Communications*, 18: 115-120.
2. Ya'aini, N., Amin, N. A. S. and Endud, S. (2013). Characterization and performance of hybrid catalysts for levulinic acid production from glucose. *Microporous and Mesoporous Materials*, 171: 14-23.
3. Ramli, N. A. S. and Amin, N. A. S. (2014). Catalytic hydrolysis of cellulose and oil palm biomass in ionic liquid to reducing sugar for levulinic acid production. *Fuel Processing Technology*, 128: 490-498.
4. Fernandes, D. R., Rocha, A. S., Mai, E. F., Claudio, J. A. and Mota, T. d. S. V. (2012). Levulinic acid esterification with ethanol to ethyl levulinate production over solid acid catalysts. *Applied Catalysis A: General*, 425–426: 199-204.
5. Serrano-Ruiz, J. C., Pineda, A., Balu, A. M., Luque, R., Campelo, J. M., Romero, A. A. and Ramos-Fernández J.M., 2012, Catalytic transformations of biomass-derived acids into advanced biofuels. *Catalysis Today*, 195 (1): 162-168.
6. Maldonado, G. M. G., Assary, R. S., Dumesic, J. A., Curtiss, L. A. (2012). Acid-catalyzed conversion of furfuryl alcohol to ethyl levulinate in liquid ethanol. *Energy & Environmental Science*, 5(10): 8990-8997.
7. Nandiwale, K. Y., Sonar, S. K., Niphadkar, P. S., Joshi, P. N., Deshpande, S. S., Patil, V. S. and Bokade, V.V. (2013). Catalytic upgrading of renewable levulinic acid to ethyl levulinate biodiesel using dodecatungstophosphoric acid supported on desilicated H-ZSM-5 as catalyst. *Applied Catalysis A: General*, 460–461: 90-98.
8. Zhao, G., Hu, L., Sun, Y., Zeng, X. and Lin, L. (2014). Conversion of biomass-derived furfuryl alcohol into ethyl levulinate catalyzed by solid acid in ethanol. *BioResources*, 9(2): 2634-2644.
9. Katryniok, B., Paul, S., Capron, M., Lancelot, C., Bellière-Baca, V., Rey, P. and Dumeignil F. (2010). A long-life catalyst for glycerol dehydration to acrolein. *Green Chemistry*, 12(11): 1922-1925.
10. Lee, A., Chaibakhsh, N., Rahman, M. B. A. and Tejo, B. A. (2010). Optimized enzymatic synthesis of levulinate ester in solvent-free system. *Industrial Crops and Products*, 32(3): 246-251.

Malaysian Journal of Analytical Sciences, Vol 23 No 1 (2019): 52 - 59
DOI: https://doi.org/10.17576/mjas-2019-2301-07

MALAYSIAN JOURNAL OF ANALYTICAL SCIENCES
Published by The Malaysian Analytical Sciences Society
ISSN 1394 - 2506

EFFECT OF DEPOSITION TIME ON STRUCTURAL AND CATALYTIC PROPERTIES OF Pt FILMS ELECTRODEPOSITED ON Ti SUBSTRATE

(Kesan Masa Enapan Terhadap Sifat-sifat Struktur dan Katalitik bagi Filem Pt Dielektroenapan di atas Substrat Ti)

Siti Norsafurah Ab Malek and Yusairie Mohd*

Faculty of Applied Sciences,
Universiti Teknologi MARA, 40450 Shah Alam, Selangor, Malaysia

**Corresponding author: yusairie@salam.uitm.edu.my*

Received: 13 April 2017; Accepted: 17 April 2018

Abstract

Platinum (Pt) films were prepared on Titanium (Ti) surface at various deposition times ranging from 30 to 90 minutes using the electrodeposition technique. The morphology of the Pt films was determined using field emission scanning electron microscope (FESEM). Furthermore, the electrocatalytic activity of the prepared Pt films towards methanol oxidation in alkaline medium was investigated using cyclic voltammetry. The surface morphology changed with different deposition times from less compact durian-like structure at shorter times (< 60 minutes) to more compact durian-like structure at longer times (> 60 minutes). The loading amount and surface coverage of Pt on the Ti surface were increased as the deposition time increased. The calculated values of electrochemically active surface area (ECSA) for the Pt films were increased with increasing deposition time as evident in 30 minutes (6.54 m^2 g^{-1}), 45 minutes (7.34 m^2 g^{-1}) and 60 minutes (8.08 m^2 g^{-1}). Nevertheless, the ECSA value dropped to 7.70 m^2 g^{-1} for longer deposition time (90 minutes). This may be caused by the coagulation of the Pt centres with the growth of neighbouring centres, which decreasing the available active surface area on the films. This film also demonstrated the highest stability for methanol oxidation reaction (MOR) in alkaline medium with the result of 5.18 mA cm^{-2} at 1 hour.

Keywords: Pt films, deposition time, methanol oxidation, alkaline medium

Abstrak

Filem Platinum (Pt) telah dienapkan ke atas titanium (Ti) untuk jangka masa yang berbeza dari 30 sehingga 90 minit menggunakan teknik elektroenapan. Morfologi filem Pt telah ditentukan menggunakan medan pancaran imbasan elektron mikroskop (FESEM). Tambahan lagi, aktiviti filem Pt terhadap pengoksidaan metanol dalam medium beralkali telah disiasat menggunakan voltammetri berkitar. Morfologi filem Pt telah berubah daripada kurang padat struktur durian (< 60 minit) kepada struktur durian yang lebih padat pada masa pengenapan Pt yang lebih lama (>60 minit). Jumlah muatan dan liputan permukaan filem Pt di atas permukaan Ti telah bertambah dengan penambahan masa enapan. Nilai-nilai kiraan kawasan permukaan aktif secara electrokimia (ECSA) untuk filem-filem Pt telah bertambah dengan pertambahan masa enapan seperti dibuktikan dalam 30 minit (6.54 m^2 g^{-1}), 45 minit (7.34 m^2 g^{-1}) dan 60 minit (8.08 m^2 g^{-1}). Walaubagaimanapun, nilai ECSA telah jatuh ke 7.70 m^2 g^{-1} bagi masa enapan yang lebih lama (90 minit). Ini mungkin disebabkan oleh pengumpalan pusat-pusat Pt dengan ketumbuhan pusat-pusat sekitaran di mana ini mengurangkan kawasan permukaan yang aktif sedia ada atas filem tersebut. Filem ini juga telah menunjukkan kestabilan tertinggi untuk tindak balas pengoksidaan metanol (MOR) dalam medium beralkali dengan keputusan 5.18 mA cm^{-2} pada 1 jam.

Kata kunci: filem Pt, masa enapan, pengoksidaan metanol, medium beralkali

Introduction

The study of methanol oxidation reaction (MOR) at Platinum (Pt) electrode has received great attentions from numerous researchers [1-6]. Generally, Pt is known to be a very stable and the most active metal for the oxidation of methanol [7-10]. Nevertheless, the usage of Pt catalyst in the practical application of direct methanol fuel cell (DMFC) is constrained mainly by the cost of Pt and its limited supply. In addition, Pt decays easily during methanol oxidation because its surface is poisoned by intermediate species like CO. This causes further methanol oxidation to be decayed over time.

Notably, Pt film may be deposited on a cheap substrate instead of using bulk or solid Pt because the electrooxidation of methanol occurs only on the surface of Pt. For this reason, Pt deposited on Titanium (Ti) substrate is ideal to minimise the cost of Pt-based electrodes. Ti has excellent properties as a substrate due to its high mechanical strength, reasonable cost, high corrosion resistance, wide electrochemical potential window, and good chemical stability [11].

Under comparable chemical and physical conditions, the catalytic activity of Pt film is shown to be highly dependent on its surface morphology [12]. The electrodeposition technique is one of the promising methods to produce the Pt film because of its low cost. The technique also provides better selections for the placement of the Pt particles onto the substrate. Furthermore, many parameters in the electrodeposition process such as deposition potential, deposition time, pH and electrolyte concentration can be manipulated in order to control the surface coverage, morphology, and particle size which can affect the electrocatalytic properties of the Pt films. For instance, Yin et al. [13] reported that the morphology of the Pt film is dependent on many factors such as deposition potential, deposition time, and concentration of electrolytes. Moreover, Ott et al. [14] claimed that an appropriate management of deposition time and current density during the galvanostatic process allows the morphology of the film produced on the substrate to be controlled accordingly.

The objective of this research is to investigate the effect of deposition time on the electrodeposition of Pt films on Ti substrate with high utilisation of Pt loadings, maximum performance in catalytic activity, and high stability towards methanol oxidation in alkaline medium. In this study, Pt films with different Pt loadings were deposited on the Ti substrate using the electrodeposition method at various deposition times (30, 45, 60, and 90 minutes) while the applied potential is kept at -0.20 V. Accordingly, this research is expected to provide better understanding on the effect of deposition time and Pt loadings on Ti substrate in the production of Pt electrocatalyst for DMFC.

Materials and Methods

Electrodeposition of Pt on Ti substrate

Firstly, the Ti substrate was etched in HCl at 80 °C for 15 minutes to remove the oxide layer on the Ti and to increase the roughness of the Ti surface to ensure better adhesion of the Pt films. Subsequently, the Pt films were deposited on the etched Ti substrate using the electrodeposition technique. A three-electrode Autolab Potentiostat (model Aut302 FRA2) controlled by a computer software (Nova 1.11) was used for this process. Notably, the three-electrode electrochemical cell consisted of the etched Ti substrate as the working electrode, Pt rod as the counter electrode, and the saturated calomel electrode (SCE) as the reference electrode. A bath solution containing 0.01 M hydrogen hexachloroplatinate(IV) hydrate in 0.3 M H_2SO_4 was used for the electrochemical deposition of Pt on the etched Ti substrate. Different deposition times (30, 45, 60, and 90 minutes) were implemented and the applied potential was kept constant at -0.20 V. After the electrodeposition process was completed, the Pt films were rinsed twice in water and then air-dried at room temperature for characterisation and further use.

Physical characterisation

The morphology of the Pt films was examined using field emission scanning electron microscope (FESEM, Carl Zeiss SMT Supra 40VP) in order to investigate the nucleation and growth of the Pt centres on the Ti substrate. FESEM images were recorded at an accelerating voltage of 5 kV with 5000x and 25 000x magnifications.

Electrochemical measurement

A three-electrode electrochemical cell - Pt rod as the counter electrode, the SCE as the reference electrode, and the Pt film-coated Ti with 1 cm^2 surface area prepared at different deposition times as the working electrode was used

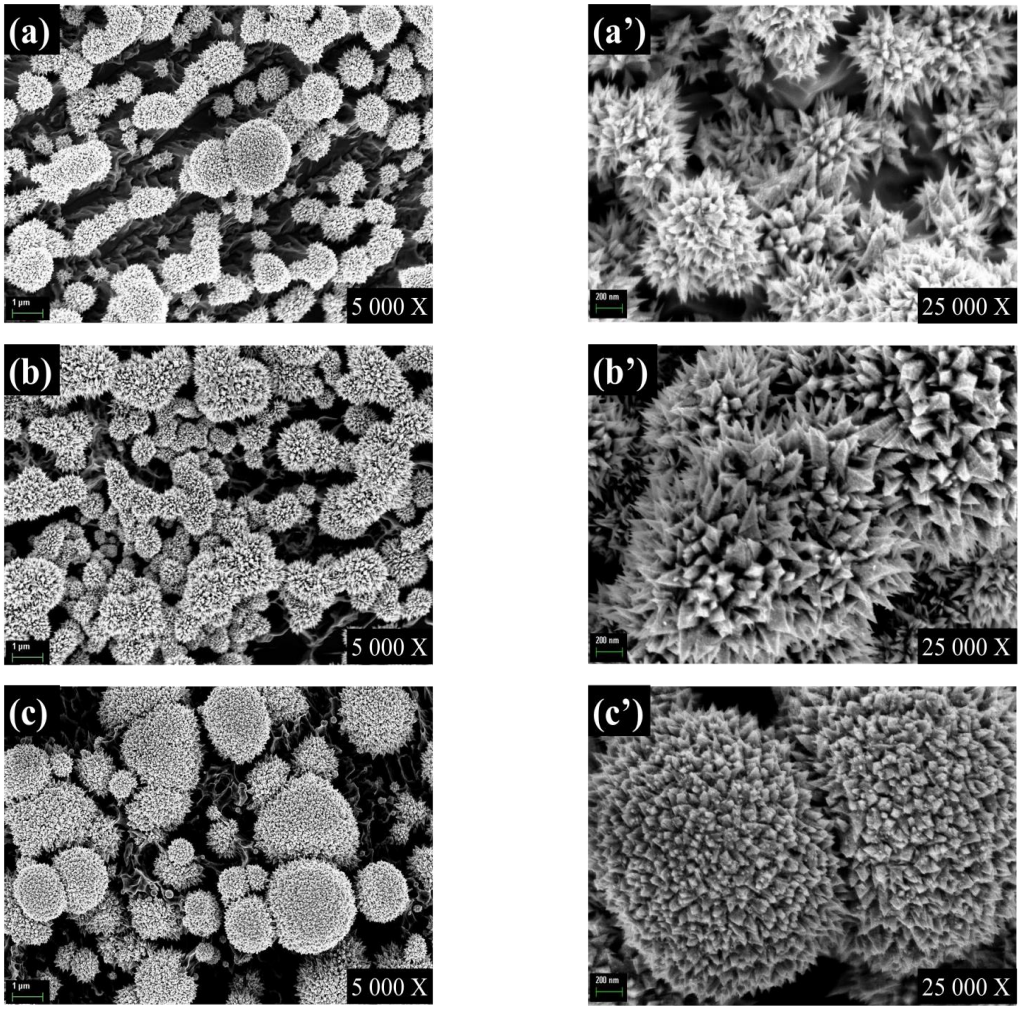
to perform the electrochemical analysis in alkaline medium. The alkaline medium of 0.5 M KOH contained 1.0 M CH_3OH solution. The stability of the prepared Pt films in the electrooxidation of methanol was investigated using chronoamperometry at a fixed potential of -0.50 V for 3600 s. Moreover, cyclic voltammetry technique was employed to study the catalytic activity of the Pt films with different deposition times for methanol oxidation reaction (MOR) at a scan rate of 50 mV s^{-1}. The specific electrochemically active surface area (ECSA) was calculated using the following equation:

$$ECSA = \frac{Q_H}{Q_{mono} \times L_{Pt}} \quad (1)$$

Accordingly, Q_H (µC cm^{-2}) is the charge corresponding to the area under hydrogen adsorption/desorption, Q_{mono} (210 µC cm^{-2}) is the charge required for adsorbing/desorbing a monolayer of hydrogen on a Pt surface, and L_{Pt} (µg cm^{-2}) is the Pt loading [15].

Results and Discussion

FESEM images of the Pt films deposited electrochemically at -0.20 V from 0.01 M $H_2PtCl_6.6H_2O$ + 0.3 M H_2SO_4 solution are shown in Figure 1. Images (a), (b), (c), and (d) illustrate 5000x magnification during the deposition times of 30, 45, 60, and 90 minutes, respectively. Conversely, images (a'), (b'), (c'), and (d') illustrate 25 000x magnification during the deposition times of 30, 45, 60, and 90 minutes, respectively.



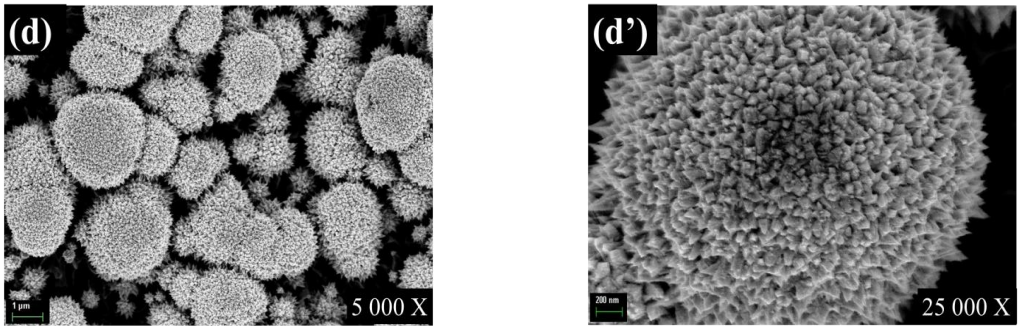


Figure 1. FESEM images of the Pt films at 5000x magnification deposited electrochemically at -0.20 V *vs* SCE for (a) 30 (b) 45 (c) 60 and (d) 90 minutes from 0.01 M $H_2PtCl_6.6H_2O$ + 0.3 M H_2SO_4 solution. Magnification at 25 000x for (a'), (b'), (c'), and (d').

As depicted in Figure 1(a) and (a'), highly scattered durian-like Pt centres were formed on Ti surface after deposition time of 30 minutes. The Ti surface was not completely covered by Pt films at this deposition time. As the deposition time was prolonged to 45 minutes, similar but denser and larger durian-like structure of Pt centres were formed on the Ti surface as displayed in Figure 1(b) and (b'). Increasing the deposition time to 60 minutes resulted in a gradual change in the structure of the deposited Pt films. The morphology of the Pt films prepared at 60 minutes was significantly different as compared to the Pt films prepared at shorter deposition times. As the result, a more compact durian-like with increasing surface coverage was formed as shown in Figure 1(c) and (c').

Subsequently, as the deposition time was increased to 90 minutes, the growth of cauliflower-like Pt centres can be clearly seen on the Ti surface as illustrated by Figure 1(d) and (d'). Moreover, the Pt centres agglomerated with each other like clusters. Notably, the FESEM images demonstrated that the Ti surface was almost covered by Pt centres and the amount of Pt loading increased with increasing deposition time. In conclusion, the deposition time significantly influenced the formation of surface morphology and the amount of Pt loading on the Ti substrate.

Figure 2 illustrates the cyclic voltammetry responses of electrodeposited Pt films (i.e. $Pt_{-0.20\ V,\ 30\ min}$, $Pt_{-0.20\ V,\ 45\ min}$, $Pt_{-0.20\ V,\ 60\ min}$ and $Pt_{-0.20\ V,\ 90\ min}$) in 0.5 M KOH solution. The cyclic voltammetry was scanned from -0.90 V to +0.20 V and back to -0.90 V at scan rate of 50 mV s^{-1}. From the cyclic voltammograms, it was found that the processes can be associated with: i) hydrogen adsorption/desorption region between -0.9 V and -0.56 V, ii) double layer region between -0.56 V and -0.4 V and iii) oxidation and reduction of PtO between -0.4 V and 0.2 V [16-18]. The hydrogen adsorption/desorption and Pt oxide reduction/oxidation peaks increased with increasing the deposition time during electrodeposition of Pt on Ti substrate. The ECSA of each prepared Pt films was calculated to identify the most optimum amount of Pt loadings that needs to be deposited on the substrate in order to achieve the optimum catalytic performance for electrochemical reaction in alkaline medium. Among these prepared Pt films, the lowest ECSA belongs to Pt film prepared at 30 minutes (i.e. $Pt_{-0.20\ V,\ 30\ min}$) was 6.54 $m^2\ g^{-1}$ due to the lowest amount of Pt loading on the Ti substrate. As the deposition time increased to 45 minutes, the ECSA was increased to 7.34 $m^2\ g^{-1}$. Then, the maximum ECSA of 8.08 $m^2\ g^{-1}$ was achieved as Pt films prepared at deposition time of 60 minutes (i.e. $Pt_{-0.20\ V,\ 60\ min}$).

Nevertheless, when the deposition time was increased to 90 minutes, the ECSA decreased to 7.70 $m^2\ g^{-1}$, indicating less Pt active surface area available for electrochemical reaction in alkaline medium. These findings agree well with the morphological observation by FESEM as in Figure 1(d), displaying more Pt centres are arranged closely to each other to form cluster. Thus, this leads to a decrease in the ECSA and limits its catalytic function. Based on the literature, it was found that higher ECSA values were reported by Tripkovic [19] and Doan [20] which were 10.8 $m^2\ g^{-1}$ and 8.2 $m^2\ g^{-1}$, respectively for hydrogen adsorption/desorption on Pt films coated on glassy carbon. Table 1 shows a summary for the deposition charge, Pt loading per geometrical area of the electrode, charge value of hydrogen desorption and corresponding ECSA for Pt films prepared at -0.20 V at different deposition times

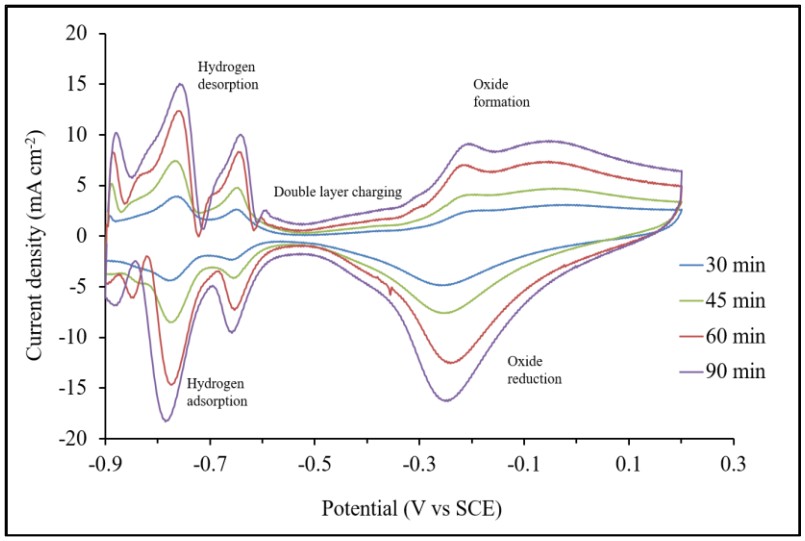


Figure 2. Cyclic voltammograms of Pt films deposited on Ti substrate at different deposition times (30, 45, 60, and 90 minutes) in 0.5 M KOH at scan rate of 50 mVs^{-1}.

Table 1. Deposition charge, Pt loading per geometrical area of the electrode, charge value of hydrogen desorption and corresponding ECSA for Pt films prepared at -0.20 V at different deposition times

Deposition Time (min)	**Deposition Charge ($C\ cm^{-2}$)**	**Pt Loading ($\mu g\ cm^{-2}$)**	**Charge Value of Hydrogen Desorption ($\mu C\ cm^{-1}$)**	**ECSA ($m^2\ g^{-1}$)**
30	2.2	1009	13800	6.54
45	3.9	1567	24200	7.34
60	5.3	2104	35600	8.08
90	7.7	2963	47800	7.70

Figure 3 shows the cyclic voltammograms of Pt films prepared at different deposition times ($Pt_{-0.20\ V,\ 30\ min}$, $Pt_{-0.20\ V,\ 45\ min}$, $Pt_{-0.20\ V,\ 60\ min}$, $Pt_{-0.20\ V,\ 90\ min}$) in 0.5 M KOH containing 1.0 M CH_3OH at scanning rate of 50 mV s^{-1}. The cyclic voltammetry was conducted to investigate the performance of the prepared Pt films towards methanol oxidation in alkaline medium. Two anodic peaks are observed in the forward and backward scan, which correspond to the oxidations of methanol and intermediate species, respectively. The findings indicate that the current densities peaks at forward scan for methanol oxidation reaction were 106.69 mA cm^{-2}, 125.76 mA cm^{-2}, 170.30 mA cm^{-2} and 158.78 mA cm^{-2} on $Pt_{-0.20\ V,\ 30\ min}$, $Pt_{-0.20\ V,\ 45\ min}$, $Pt_{-0.20\ V,\ 60\ min}$ and $Pt_{-0.20\ V,\ 90\ min}$, respectively. Interestingly, the current density peak at forward scan of methanol oxidation increased with increasing deposition time during electrodeposition process from 30 min to 60 min (i.e., $Pt_{-0.20\ V,\ 30\ min} < Pt_{-0.20\ V,\ 45\ min} < Pt_{-0.20\ V,\ 60\ min}$).

Nevertheless, the current density peak for methanol oxidation was decreased for Pt film prepared at 90 minutes deposition time ($Pt_{-0.20\ V,\ 90\ min}$). This could be attributed to the heavily aggregation of Pt centres on Ti substrate (refer Figure 2(d)), thus substantially reducing the available active catalytic sites of the resulting Pt film. Figure 4 illustrates the maximum current density at forward scan for methanol oxidation on different prepared Pt films for comparison. It can be concluded that a high amount of Pt loadings on substrate does not contribute to a maximum catalytic activity of the methanol oxidation but importantly the morphology and structure of the Pt itself ($Pt_{-0.20\ V,\ 30\ min}$ = 1009 µg cm^{-2}, $Pt_{-0.20\ V,\ 45\ min}$ =1567 µg cm^{-2}, $Pt_{-0.20\ V,\ 60\ min}$ = 2104 µg cm^{-2}, $Pt_{-0.20\ V,\ 90\ min}$ = 2963 µg cm^{-2}). Therefore, these results suggest that the Pt films prepared at 60 minutes had the largest active surface area for methanol oxidation as shown by the highest current density produced during methanol oxidation. This result is

consistent with the highest ECSA (8.08 $m^2 g^{-1}$) recorded for $Pt_{-0.20\ V,\ 60\ min}$ films than other Pt films as discussed earlier.

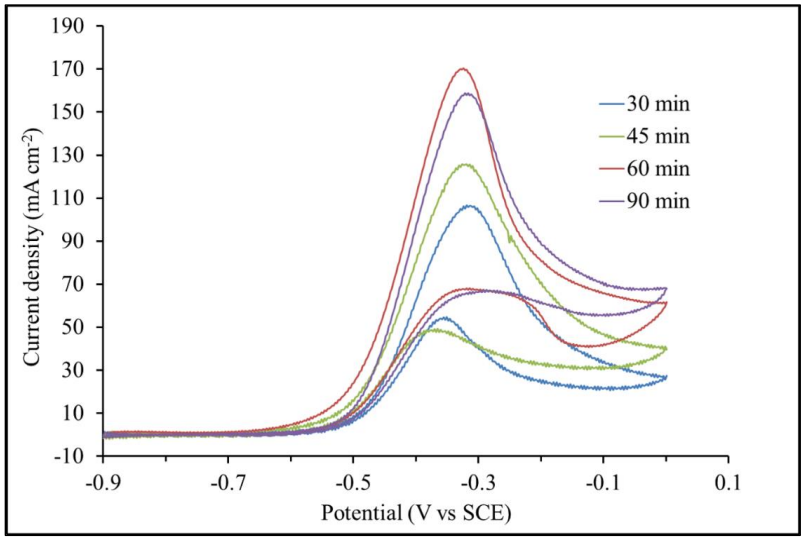


Figure 3. Cyclic voltammograms of methanol oxidation on Pt films deposited on Ti substrate at different deposition times (i.e. 30, 45, 60, and 90 minutes) in 0.5 M KOH containing 1.0 M CH_3OH, scan rate: 50 mV s^{-1}.

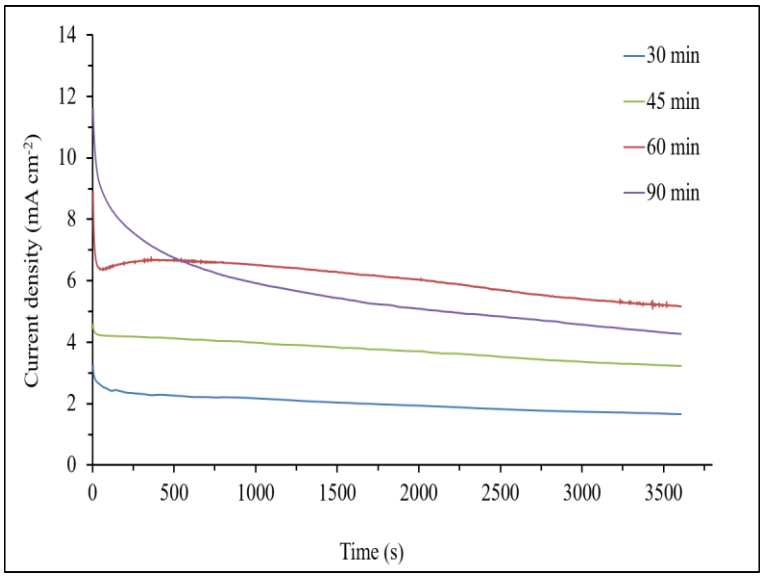


Figure 4. Chronoamperometric curves at -0.50 V of Pt films prepared at different deposition times (i.e. 30, 45, 60, and 90 minutes) in 0.5 M KOH containing 1.0 M CH_3OH

The ratio of I_f/I_b is used to evaluate the tolerance of the Pt film towards poisoning species (CO). The I_f/I_b value for $Pt_{-0.20\ V,\ 30\ min}$, $Pt_{-0.20\ V,\ 45\ min}$, $Pt_{-0.20\ V,\ 60\ min}$ and $Pt_{-0.20\ V,\ 90\ min}$ coatings were 1.95, 2.54, 2.63 and 2.36, respectively. These results demonstrate that the Pt film prepared at 60 minutes deposition time exhibits better resistance to the

poisoning species as compared to other the prepared Pt films. Table 2 shows the comparison of electrochemical performance of methanol oxidation on prepared Pt films.

Table 2. Comparison of electrochemical performance of methanol oxidation on Pt films deposited at different deposition times in 0.5 M KOH containing 1.0 M CH_3OH

Pt films	E_f (V)	I_f (mA cm^{-2})	E_b (V)	I_b (mA cm^{-2})	Onset potential (V)	Ratio I_f/I_b
$Pt_{-0.20\ V,\ 30\ min}$	-0.32	106.69	-0.35	54.75	-0.48	1.95
$Pt_{-0.20\ V,\ 45\ min}$	-0.32	125.76	-0.37	49.35	-0.50	2.54
$Pt_{-0.20\ V,\ 60\ min}$	-0.32	170.38	-0.34	64.67	-0.50	2.63
$Pt_{-0.20\ V,\ 90\ min}$	-0.32	158.78	-0.29	67.26	-0.50	2.36

E_f: potential peak for forward scan; I_f: current density peak for forward scan; E_b: potential peak for backward scan; I_b: current density for backward scan.

The stability of the prepared Pt films towards methanol oxidation in alkaline medium was investigated by chronoamperometry. Figure 4 illustrates the chronoamperograms of the prepared Pt films ($Pt_{-0.20\ V,\ 30\ min}$, $Pt_{-0.20\ V,\ 45\ min}$, $Pt_{-0.20\ V,\ 60\ min}$ and $Pt_{-0.20\ V,\ 90\ min}$) for methanol oxidation in 0.5 M KOH containing 1.0 M CH_3OH at a fixed potential of -0.50 V for a duration of 1 hour. Notably, Pt films prepared at 60 minutes demonstrated the highest stability compared to the other Pt films. At 3600 s, the oxidation current densities were 1.67 mA cm^{-2}, 3.23 mA cm^{-2}, 5.18 mA cm^{-2} and 4.28 mA cm^{-2} for $Pt_{-0.20\ V,\ 30\ min}$, $Pt_{-0.20\ V,\ 45\ min}$, $Pt_{-0.20\ V,\ 60\ min}$ and $Pt_{-0.20\ V,\ 90\ min}$ coatings, respectively. These results suggest that the Pt film prepared at 60 minutes deposition time exhibited high stability due to their tolerance with the poisoning species (CO) during methanol oxidation.

Conclusion

Pt films were successfully prepared on Ti substrate using the electrodeposition technique. The investigation on the effect of deposition time towards surface properties and catalytic activity of pure Pt coatings were studied. Based on the results, the best condition in producing pure Pt coating on Ti substrate was at -0.2 V for 60 minutes, at which this deposition condition has produced highest ECSA (8.08 $m^2\ g^{-1}$), the lowest onset potential, (-0.5 V), the highest current density peak (170.38 mA cm^{-2}) and I_f/I_b ratio (2.63) for methanol oxidation. The morphology and the loading amount of Pt on Ti substrate were significantly influenced by the deposition time. Furthermore, the experiments revealed that by varying deposition time (30, 45, 60 and 90 minutes) at a constant deposition potential of -0.20 V was an effective way to control the amount of Pt loadings on the Ti substrate. Notably, a good electrocatalyst should have at least two from these three features: (i) high current density for methanol oxidation, (ii) occurrence of methanol oxidation at low potential, and (iii) high stability of the electrode during methanol oxidation.

Acknowledgement

The authors wish to express their utmost gratitude to Universiti Teknologi MARA (UiTM), Malaysia for the financial support through Initiative Research Grant (600-IRMI/GIP 5/3 (0026/2016). Apart from that, the Faculty of Applied Sciences (UiTM) had also played a vital role by providing the necessary facilities.

References

1. Lima, A., Hahn, F. and Léger, J.-M. (2004). Oxidation of methanol on Pt, Pt–Ru, and Pt–Ru–Mo electrocatalysts dispersed in polyaniline: an in situ infrared reflectance spectroscopy study. *Russian Journal of Electrochemistry*, 40(3): 326-336.
2. Aramata, A., Kodera, T. and Masuda, M. (1988). Electrooxidation of methanol on platinum bonded to the solid polymer electrolyte, Nafion. *Journal of Applied Electrochemistry*, 18(4): 577-582.

3. Beden, B., Kadirgan, F., Lamy, C. and Leger, J. (1982). Oxidation of methanol on a platinum electrode in alkaline medium: Effect of metal ad-atoms on the electrocatalytic activity. *Journal of Electroanalytical Chemistry and Interfacial Electrochemistry,* 142(1-2): 171-190.
4. Prabhuram, J. and Manoharan, R. (1998). Investigation of methanol oxidation on unsupported platinum electrodes in strong alkali and strong acid. *Journal of Power Sources,* 74(1): 54-61.
5. Ordóñez, L., Roquero, P., Ramírez, J. and Sebastian, P. (2016). Methanol electro-oxidation on bimetallic PtMo/C catalysts and Pt/C-Mo/C mechanical mixtures. *International Journal of Electrochemical Science,* 11: 5364-5379.
6. Wang, H., Ji, S., Wang, W., Linkov, V., Pasupathi, S. and Wang, R. (2012). Pt decorated PdFe/C: extremely high electrocatalytic activity for methanol oxidation. *International Journal of Electrochemical Science,* 7: 3390-3398.
7. Antolini, E., Salgado, J. R. and Gonzalez, E. R. (2006). The methanol oxidation reaction on platinum alloys with the first-row transition metals: the case of Pt–Co and–Ni alloy electrocatalysts for DMFCs: A short review. *Applied Catalysis B: Environmental,* 63(1): 137-149.
8. Greeley, J. and Mavrikakis, M. (2004). Competitive paths for methanol decomposition on Pt(111). *Journal of the American Chemical Society,* 126(12): 3910-3919.
9. Greeley, J. and Mavrikakis, M. (2002). A first-principles study of methanol decomposition on Pt(111). *Journal of the American Chemical Society,* 124(24): 7193-7201.
10. Cao, D., Lu, G.-Q., Wieckowski, A., Wasileski, S. A. and Neurock, M. (2005). Mechanisms of methanol decomposition on platinum: A combined experimental and ab initio approach. *The Journal of Physical Chemistry B,* 109(23): 11622-11633.
11. Yi, Q., Huang, W., Zhang, J., Liu, X. and Li, L. (2008). Methanol oxidation on titanium-supported nano-scale Ni flakes. *Catalysis Communications,* 9(10): 2053-2058.
12. Kim, H. B., Ahn, S., Jang, H. J., Sim, S. B. and Kim, K. W. (2007). Evaluation of corrosion behaviors and surface profiles of platinum-coated electrodes by electrochemistry and complementary microscopy: Biomedical implications for anticancer therapy. *Micron,* 38(7): 747-753.
13. Yin, J., Jia, J. and Zhu, L. (2009). Double-template synthesis of platinum nanomaterials for oxygen reduction. *Microchimica Acta,* 166(1-2): 151-156.
14. Ott, A., Jones, L. A. and Bhargava, S. K. (2011). Direct electrodeposition of porous platinum honeycomb structures. *Electrochemistry communications,* 13(11): 1248-1251.
15. Pozio, A., De Francesco, M., Cemmi, A., Cardellini, F. and Giorgi, L. (2002). Comparison of high surface Pt/C catalysts by cyclic voltammetry. *Journal of Power Sources,* 105(1): 13-19.
16. Pletcher, D. (2009). A first course in electrode processes. Royal Society of Chemistry.
17. Solla-Gullón, J., Vidal-Iglesias, F., Herrero, E., Feliu, J. and Aldaz, A. (2006). CO monolayer oxidation on semi-spherical and preferentially oriented(100) and (111) platinum nanoparticles. *Electrochemistry communications,* 8(1): 189-194.
18. Attard, G., Gillies, J., Harris, C., Jenkins, D., Johnston, P., Price, M. and Wells, P. (2001). Electrochemical evaluation of the morphology and enantioselectivity of Pt/graphite. *Applied Catalysis A: General,* 222(1): 393-405.
19. Tripković, A. V., Popović, K. D., Lović, J., Jovanović, V. and Kowal, A. (2004). Methanol oxidation at platinum electrodes in alkaline solution: Comparison between supported catalysts and model systems. *Journal of Electroanalytical Chemistry,* 572(1): 119-128.
20. Doan, N., Sundqvist, T., Hiekkataipale, P., Korhonen, J., Kallio, T., Ruokolainen and Johans, C. (2015). Electrodeposited mesoporous Pt and Pt@ cb films as electrocatalysts for the oxygen reduction reactions and ethanol electrooxidation in both acid and alkaline media. *International Journal of Electrochemical Science,* 10: 2535-2553.

Malaysian Journal of Analytical Sciences, Vol 23 No 1 (2019): 60 - 70
DOI: https://doi.org/10.17576/mjas-2019-2301-08

MALAYSIAN JOURNAL OF ANALYTICAL SCIENCES
Published by The Malaysian Analytical Sciences Society
ISSN 1394 - 2506

HYDROGEN SORPTION OF MAGNESIUM OXIDE CARBON NANOFIBRE COMPOSITE

(Serapan Hidrogen pada Komposit Magnesium Oksida Nano-gentian Karbon)

Nurul Zafirah Abd. Khalim Khafidz[1], Zahira Yaakob[1,2], Sharifah Najiha Timmiati[1], Kuen-Song Lin[3], Kean Long Lim[1]*

[1]*Fuel Cell Institute*
[2]*Center for Sustainable Process Technology (CESPRO)*
Universiti Kebangsaan Malaysia, 43600 UKM Bangi, Selangor, Malaysia
[3]*Department of Chemical Engineering and Materials Science,*
Yuan Ze University, Chung-Li City 320, Taiwan

**Corresponding author: kllim@ukm.edu.my*

Received: 13 April 2017; Accepted: 17 April 2018

Abstract

Carbon nanofibres have high specific surface area to adsorb hydrogen on their surface and are widely investigated for hydrogen storage. Although carbon nanofibres can store a considerable amount of hydrogen, the adsorption of the latter must be conducted at cryogenic conditions. Here, MgO is proposed as a catalyst to improve the hydrogen storage performance of carbon nanofibres at room temperature because of the light weight MgO and its ability to dissociate hydrogen molecules. The magnesium oxide–carbon nanofibre (MgO–CNF) composite was prepared with polivinylpyrrolidone polymer and MgO via an electrospinner. The samples were characterised with field emission scanning electron microscopy, X-ray diffraction, Fourier transform infrared spectroscopy, thermogravimetric analysis, differential scanning calorimetry and microgravimetric analysis. The MgO particles were formed on the surface and embedded inside the MgO–CNFs, thereby increasing the specific surface area. The as-synthesised MgO–CNFs with a specific surface area of 547 m^2/g can store 2.54 wt.% of hydrogen at room temperature, showing more than 30% improvement as compared with that of CNFs.

Keywords: electrospinning, hydrogen storage, carbon nanofibre, metal oxide

Abstrak

Nano-gentian karbon mempunyai kelebihan dengan luas permukaan yang tinggi untuk menjerap hidrogen di atas permukaan nano-gentian karbon, berpotensi sebagai bahan penyimpanan hidrogen. Walaupun nano-gentian karbon mempunyai kebolehan untuk menyimpan hidrogen yang banyak, penjerapan hidrogen perlu dilakukan pada keadaan kriogenik. Di sini, magnesium oksida telah dicadangan sebagai pemangkin untuk meningkatkan prestasi nano-gentian karbon dalam penyimpanan hidrogen pada suhu bilik kerana ia adalah ringan dan berkebolehan untuk memisahkan molekul hidrogen. Komposit magnesium oksida nano-gentian karbon telah disediakan dengan polivinilpirolidon polimer dan magnesium oksida melalui kaedah elektroputaran. Sampel dicirikan dengan mikroskopi elektron pengimbasan pancaran medan, belauan sinar-X, spektroskopi inframerah transformasi Fourier, analisis termogravimetri, kalorimetri pengimbasan pembezaan dan mikrogravimetri. Zarah MgO terbentuk dipermukaan dan berada di dalam MgO–CNF telah meningkatkan spesifik luas permukaan. MgO–CNF dengan luas permukaan tentu 547 m^2/g, berkebolehan menyimpan hidrogen sebanyak 2.54 wt.% pada suhu bilik, yang mana peratus peningkatan kapasiti penyimpanan hidrogen melebihi 30% berbanding dengan menggunakan CNF sahaja.

Kata kunci: elektroputaran, penyimpanan hidrogen, nano-gentian karbon, oksida logam

Introduction

In addition to their excellent thermal and chemical stabilities and fast adsorption kinetics [1], carbon nanomaterials, such as carbon nanofibres (CNFs) with a large specific surface area of up to 700 m^2/g, can adsorb hydrogen gas on the surface or in the pores [2]. Nonetheless, a reasonable hydrogen adsorption capacity of > 2 wt.% H_2 [3] can only be achieved at cryogenic temperature or at high pressure. The recent study of Yang et al. [4] have shown that at 77 K and 1 bar, the hydrogen uptake of multiwalled carbon nanotube is only 0.21 wt.% H_2. Meanwhile, the maximum hydrogen storage of CNF obtained by Jaybhaye et al. [5] and Bai et al. [6] are 0.65 and 0.6 wt.% H_2 at 330 K and 9 MPa, respectively. Moreover, the amount of hydrogen absorption on all types of carbon materials at ambient temperature and pressure of up to 100 bars is less than 1.0 wt.% H_2 [7–9]. Hence, several attempts, such as the use of production techniques [10, 11], surface modification [12–14] and metal-doped materials [14–17] have been performed to enhance the hydrogen sorption of C-based materials. To exhibit a microstructure with a high surface area-to-volume ratio, CNFs can be produced using chemical vapour deposition (CVD), plasma-enhanced, arc discharge methods and pulsed laser deposition [10, 18, 19]. However, these methods are costly and difficult to produce in large scale [20]. One of the options to synthesise carbon nanofibre *via* electrospinning technique [21] because it is a versatile technique to produce micro- and nanoscale nanofibres. The CNFs produced from electrospinning have a small diameter in ranging from 5 nm to 500 nm [22], resulting in a large specific surface area.

Surface modifications *via* physical and chemical activations improve the hydrogen storage capacity [23]. Physical activation involves the gasification of carbon materials in the presence of oxidizing agents, such as CO_2 and steam. Meanwhile, chemical activation increases porosity *via* the chemical reactions between the reagents (KOH) and carbon materials. Chemical activation operates at a lower processing temperature and faster processing time, thereby producing higher porosity [23]. Activated carbon with a hydrogen storage capacity of 0.81 wt.% H_2 at 298 K and pressure of 100 bar was obtained by Kim et al. [24] after KOH activation. Nevertheless, a high specific surface area does not guarantee a high hydrogen storage capacity, especially at room temperature. Chen et al. [13] activated polyaniline-based carbon nanotubes with KOH and obtained a hydrogen storage capacity of 5.2 wt.% H_2 at a cryogenic temperature of 77 K and pressure of 50 bar. The chemical KOH activation of CNF was reported by Jiménez et al. [25], wherein the CNF adsorbed is 2.22 wt.% H_2 at 77 K and 10 bars. Nonetheless, storing hydrogen at cryogenic temperature is still less practical for an on-board hydrogen storage application. The presence of impurities, which reduces the hydrogen storage capacity [26], during the activation is also the main drawback of chemical activation.

Recently, researchers [27–30] have explored and investigated the use of metals on carbon nanomaterials to improve their ability to store more hydrogen at ambient temperature with low pressure. Metal and metal oxide such as NiO_2, TiO_2, CuO_2 and Pd have been commonly used as an additive in CNFs to explore their catalytic effect in improving the hydrogen adsorption capability of CNFs at room temperature. For instance, Im et al. [31] have achieved 2.8 wt.% H_2 at 100 bars and at room temperature by adding copper in activated CNFs. This result suggested that metallic compound can enhance the hydrogen adsorption via the spill-over phenomenon [3, 5, 8]. Furthermore, the surface modification with metal will create metal hydride formation. The hydrogen molecules adsorbed on the metal are dissociated, followed by migration of hydrogen atom migration on the carbon materials [14]. Some of the hydrogen atoms form stable bonds with surface, leading to irreversible adsorption. Lachawiec et al. [32] also stated that other hydrogen atoms can be reversibly released by migration back to the metal particles in the form of hydride. The favourable hydrogen uptake of metal-doped carbon nanofiber can achieve 2.81 wt.% H_2 at room temperature and at pressure of 70 bar [30].

In this work, magnesium-based material was chosen because of its light-weight characteristics, abundance and low cost as compared with NiO and CuO [33]. In addition, MgO has the catalytic ability to dissociate hydrogen molecules [34, 35], enabling it to possibly spill the hydrogen atom onto the carbon support. Hence, the combination of MgO and carbon nanofibre has a potential to improve the hydrogen storage capacity at room temperature with reduced pressure.

Materials and Methods

Materials

Both MgO (nano-powder size of < 50 nm) and polyvinylpyrrolidone (PVP) (M_W = 1,300,000 g/mol) were purchased from Sigma-Aldrich. Absolute ethanol (99%) was purchased from HmbG. All chemicals were used as received without further purification.

Preparation of the MgO–CNF composite

The precursor solution for electrospinning was prepared by mixing 7.50 g MgO and 2.50 g PVP in ethanol at 40 °C. The solution was stirred with a magnetic stirrer for 4 hours to obtain a homogeneous solution. Then, the homogeneous solution was electrospun through a 20 mL syringe with a capillary tip size with diameter of 0.45 mm, which was placed horizontally on an electrospinner (KSS Company), to produce the nanofibre composite mats. Electrospinning was performed at a voltage of 18 kV and at 15 cm between the tip and the rotating drum that was covered with an aluminium foil. A syringe pump was used to control the flow rate of the solution at 1.5 mL/hours. The nanofibre composite was stabilised at 80 °C for 2 hours before it was carbonised at 800 °C for 2 hours in nitrogen gas to form MgO–CNFs.

Characterization

The morphology and surface structure of the samples were studied with a Supra 55VP field emission scanning electron microscope (FE-SEM). The nanofibres were sputter coated with platinum to increase their electrical conductivity. Average diameters of nanofibres were estimated by averaging 60 diameter measurements in the FE-SEM images. Energy dispersive spectroscopy (EDS) was used to map and identify the element distribution in the nanofibres.

Bruker-D8 Advance X-ray Diffractometer with a Cu Kα radiation source (λ = 0.154 nm) was used to identify the phase compositions and the crystallinity of the samples. The X-ray diffraction (XRD) patterns were recorded in the scan range of 2θ from 10^o to 80^o. To characterise the chemical bonding between MgO and PVP, we obtained the FTIR spectra by using NICOLET-380. The measurements were obtained in the range of 4000 cm^{-1} to 400 cm^{-1}.

A STA 449 F3 Netzch Thermogravimetric Analyser (TGA) equipped with differential scanning calorimetry (DSC) was used to study the thermal stability and the different rates of energy in the endothermic (uptake heat) and exothermic (release heat) conditions. The samples were heated from room temperature to 700 °C at a heating rate of 10 °C/min under a continuous nitrogen flow.

The pressure–composition isotherm (PCI) hydrogen sorption was studied with a Cahn Thermax 500 microgravimetric balance with sensitivity of 1 μg at 298 K. A pressure sensor (0–6.9 MPa) was used to measure the hydrogen pressure in the chamber. All samples were tested for their hydrogen storage from 0.1 MPa to 5.0 MPa at room temperature. Before the measurement, the samples were outgassed overnight until they reach a constant mass. The whole system was purged with Ar gas, which flowed through a molecular sieve and a cold trap to remove moisture and any impure substances. Hydrogen was charged step-wise, and the data were recorded when the mass reaches equilibrium. Hydrogen uptake was calculated after the buoyancy correction of the experiment.

Results and Discussion

The surface morphologies of both the PVP–CNF and MgO–CNF composites are illustrated in Figure 1. The surface of PVP–CNFs (Figure 1a) was smooth and bead-free as compared with that of the MgO–CNF composite (Figure 1b). The morphology of the as-received MgO with irregular sphere particles is shown in Figure 1c. The incorporation of MgO in the precursor solution had a significant influence on the surface morphology of the CNF composite. The MgO–CNF composite was rough with particles forming on the surface and entrapping inside the nanofibres. The diameter of PVP–CNFs was 481 nm, with a specific surface area of 413 m^2/g. Meanwhile, the diameter of the MgO–CNF composite was irregular with an average of 459 nm and specific surface area of 547 m^2/g. As shown in Figure 1c, the as-received MgO particles with an average particle size of 27.4 ± 2.6 nm were agglomerated because of the high surface activity, as suggested by Ferari et al. [36]. The average particle size of the as-received MgO particles agrees with the average particle size of the MgO nanofibre composite of 25.3 ± 4.8 nm.

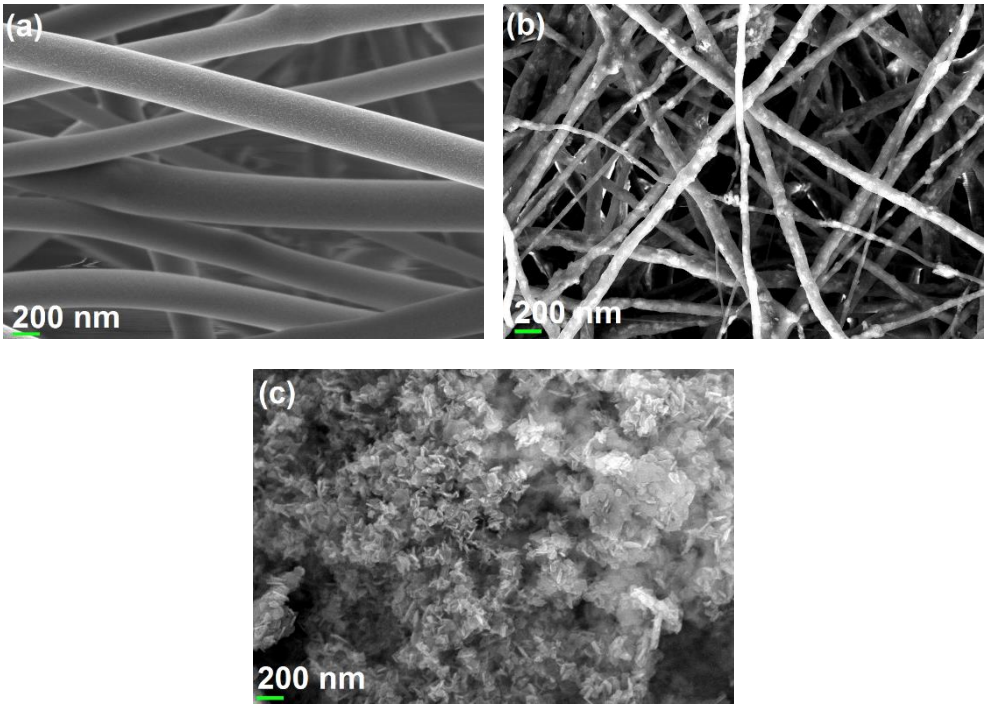
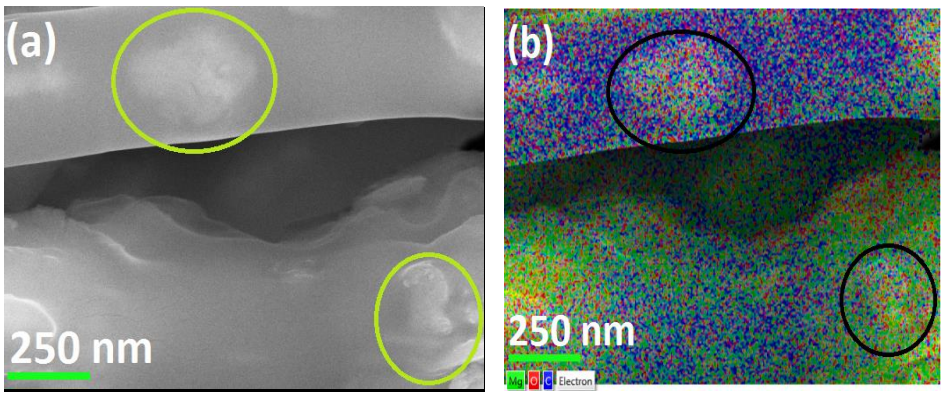


Figure 1. Field emission scanning electron microscope (FE-SEM) images of (a) the PVP–CNFs (b) MgO–CNF composite and (c) as-received MgO

EDS mapping was used to identify the elements in the CNF composite, as shown in Figure 2. The colour intensity of EDS mapping is associated with the concentration of elements in nanofibres; the higher the intensity, the higher the concentration and vice versa. The carbon element was uniformly distributed on the nanofibre, indicating that most of the other elements are embedded inside the CNFs. Meanwhile, high Mg concentration was detected at different areas of CNFs, corresponding to the particle-like bright spots (circle) in the SEM image. The results confirmed the presence of Mg compound in the CNFs.



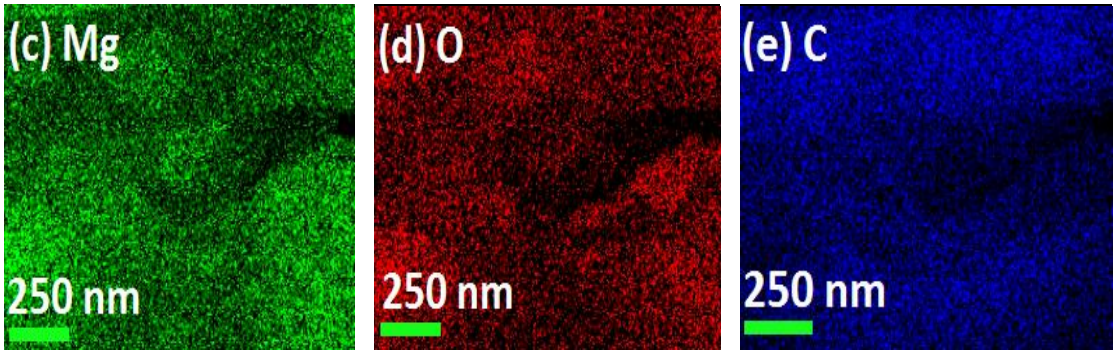


Figure 2. (a) Field emission scanning electron microscope (FE-SEM) image of the MgO–CNF composite. EDS mapping for (b) MgO–CNF composite, (c) Mg element, (d) O element and (e) C element

The XRD patterns of the PVP–CNFs, as-received MgO and MgO–CNF composite are presented in Figure 3. As shown in Figure 3a, two broad peaks are observed at 11º and 22º, which are induced by the PVP polymer. Both peak positions are similar with the results of Wang et al. [37] and Sivaiah et al. [38]. The broad peaks indicate that the CNFs have an amorphous phase. MgO peaks in Figure 3b were observed at the 2θ values of 37.1º, 43.1º, 62.5º, 74.6º and 78.6º, corresponding to the (111), (200), (202), (311) and (222) planes, respectively. All diffraction peaks were sharp, indicating that the MgO particles are crystalline [39, 40]. Additional peaks were observed at the 2θ values of 38.02º and 58.62º, belonging to the secondary $Mg(OH)_2$ phase. These peak positions at the 2θ values of 38.02º and 58.62º correspond to the crystal (101) and (110) planes, respectively [41]. The formation of $Mg(OH)_2$ was likely caused by the hydration of MgO upon exposure to humidity [42], where Mg^{2+} and OH^- were diffused into a layer of chemically and physically adsorbed water, forming and growing into a $Mg(OH)_2$ crystal.

The XRD pattern of the MgO–CNF composite nanofibre is presented in Figure 3c. The pattern of the composite was a combination of Figures 3a and b, with no detected additional peaks, indicating that the Mg compounds are stable with CNFs. However, peaks belonging to MgO in Figure 3c slightly shifted to the lower angle as compared with the MgO phase in Figure 3b, suggesting that MgO may experience tensile residue stress caused by the pulling effect during the formation of nanofibres in the electrospinning process.

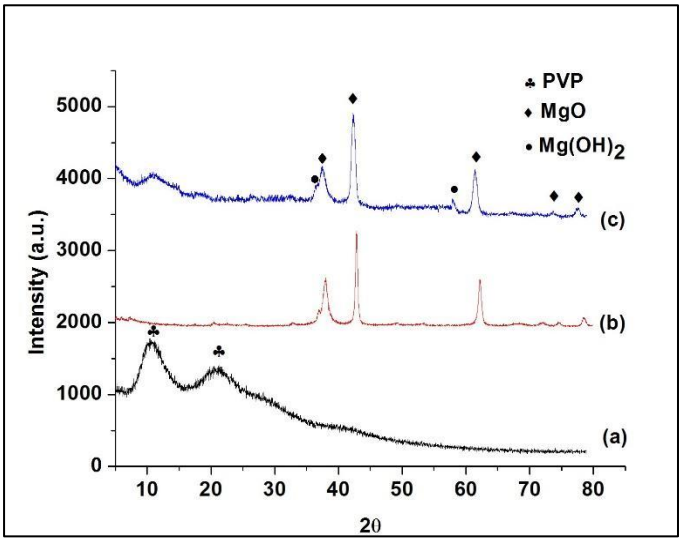


Figure 3. XRD patterns of (a) PVP–CNFs (b) as-received MgO and (c) MgO–CNF composite

FTIR was used to identify chemical bonding in the nanofibre composite. Figure 4 reveals the FTIR spectrum of the PVP nanofibre, PVP–CNFs, as-received MgO and MgO–CNF composite. Compared with the results of Baytak et al. [43], the PVP nanofibre spectrum had four main sharp peaks at 1659, 1463, 1421 and 1289 cm^{-1} in the present study. The peak at 1659 cm^{-1} is related to the stretching vibration of C=O. Meanwhile, the peak at 1463 and 1421 cm^{-1} are ascribed to the vibration bending and vibration deformation of methylene (CH_2) N-vinylpyrrolidone in the PVP chain, respectively. Another peak at 1289 cm^{-1} belongs to the stretching vibration of C–N. Other broad absorption peaks at 3420 and 2954 cm^{-1} are ascribed to the vibration bonding of O–H and the stretching vibration of C–H (methylene group), respectively [44]. All these peaks indicate the presence of PVP polymer in the nanofibre, which is consistent with the results of Dong et al. [45], Rafizah et al. [44] and Saravanan et al. [46]. After carbonization (Figure 4b), no significant characteristic peaks were observed, which confirms that only C atoms are present in the PVP–CNFs. These results are similar to the findings of Zhou et al. [47] and Guadagno et al. [48].

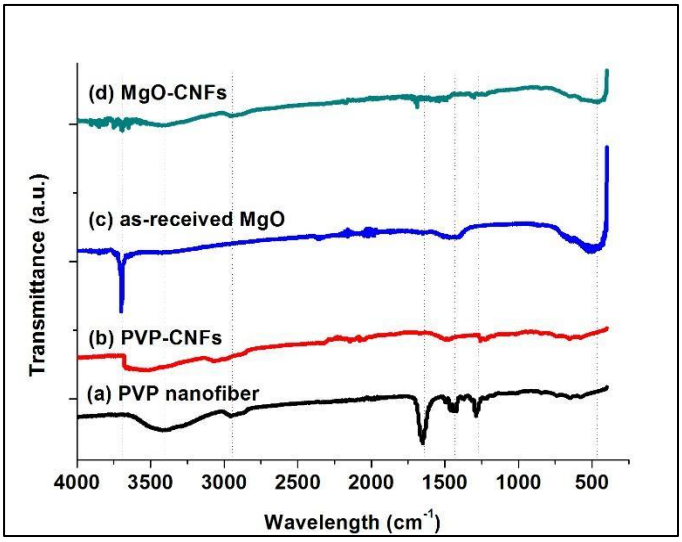


Figure 4. FTIR peak of (a) PVP nanofibre, (b) PVP–CNFs, (c) as-received MgO and (d) MgO–CNF composite

For as-received MgO, the MgO absorption peak was located at 490 cm^{-1}, which is similar with the results of Razaei et al. [25]. However, in the range of 4000–2500 cm^{-1}, a strong peak was detected at 3750 cm^{-1}. This peak was assigned to the isolated Mg–OH group. The presence of bending vibration of the O–H group is correlated to the exposure of the as-received MgO sample to humidity [51]. These results correspond to the observations in the XRD results. The FTIR spectra of MgO–CNFs were the superimposed FTIR spectra of both MgO and PVP–CNF. All functional groups and bonds corresponded well to their respective components, except that the transmittance signal of the Mg–OH group at 3750 cm^{-1} was less pronounced. This result indicates that the CNFs have changed the polarity of the Mg–OH bond.

The mass changes and thermal stability of the MgO–CNF composite are compared with those of the as-received MgO and PVP–CNFs, as shown in Figure 5. For TGA, a significant weight loss of the as-received MgO, PVP–CNFs and MgO–CNF composite can be observed at different temperatures as the temperature increases from room temperature to 700 °C. Meanwhile, the DSC graph shows multiple endothermic peaks (negative peak, releases heat). For PVP–CNFs, 5.2% weight loss was observed in the TGA curve between 25 °C to 166 °C, corresponding to a strong endothermic peak at 126 °C. The initial weight loss at temperature of less than 150 °C was due to the evaporation of solvent and any moisture from the nanofibre. This result is similar to the findings of Kim et al. [52] and Sales et al. [53]. At the temperature range from 373 °C to 466 °C, another significant weight loss of 71.5% was detected in the graph, which is associated with the thermal decomposition of the main chain PVP polymer [52]. Corresponding to the weight loss, an endothermic peak was also detected in the DSC graph at 449 °C. Beyond 500 °C, the PVP was decomposed completely, and a constant weight was obtained.

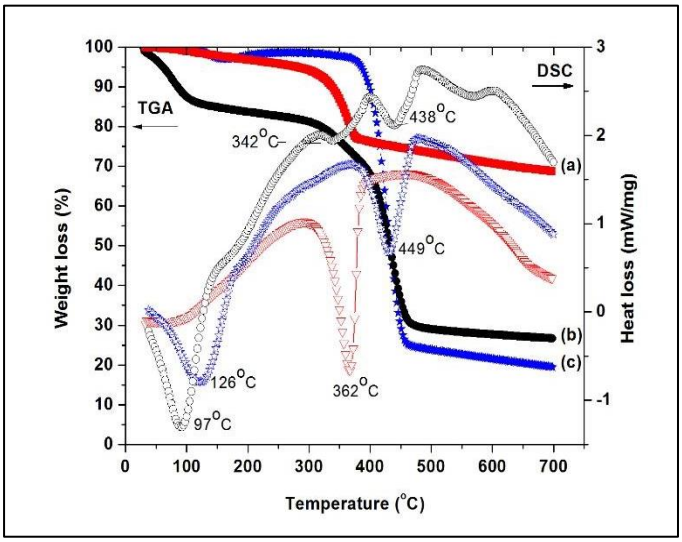


Figure 5. TGA–DSC graph of the (a) as-received MgO (▼) (b) MgO–CNF composite (□) and (c) PVP–CNFs (★). TGA: close symbol, DSC: open symbol

The as-received MgO showed a small weight loss of 0.98% between 52 °C to 311 °C. Similar to the results of PVP–CNFs, the first weight loss was related to evaporation of moisture that was trapped on the sample. A significant weight loss occurred at the temperature range from 326 °C to 374 °C, corresponding to an endothermic peak at 362 °C. This weight loss is associated to the decomposition of $Mg(OH)_2$ [54], which is an impure compound that was detected in the XRD results. As the temperature increased above 400 °C, the weight of the as-received MgO was continuously reduced. This result is associated with the transformation from the amorphous to crystalline phase of MgO [55].

The presence of MgO in the CNFs had affected the thermal stability of PVP. Similar to the two other samples, the first weight loss of 14.03% accompanied a strong endothermic peak at 92 °C was caused by the loss of solvent and moisture from the nanofibre composite. The second weight loss of 56.22% occurred between 278 °C and 488 °C was similar to the decomposition of PVP–CNFs and MgO, corresponding to two DSC peaks, that is, two broad endothermic peaks at 342 °C and 438 °C. Both peaks shifted to a lower temperature as compared with its respective components. This result suggests that the addition of MgO lowers the decomposition activation energy of the MgO–CNF composite, as shown in the Kissinger analysis below.

Kissinger's equation [56] was used to estimate the decomposition activation energy of the MgO–CNF composite. The logarithm of heating rates (β = 5 °C/min, 10 °C/min and 15 °C/min) has a linear inverse relationship with the maximum desorption temperature at each heating rate according to the equation 1below:

$$\ln [\beta/T_{max}^{2}] = -E_A/RT_{max} + A \quad (1)$$

where β is the heating rate, T_{max} is the maximum peak in the DSC curve, R is the gas constant and A is the linear constant. The activation energy was calculated from the slopes of $\ln [\beta/T_{max}^{2}]$ versus $1000/T_{max}$, as plotted in Figure 6. As shown in the figure, the incorporation of MgO into CNFs has lowered the decomposition activation energy of MgO from 191.53 kJ/mol to 182.68 kJ/mol.

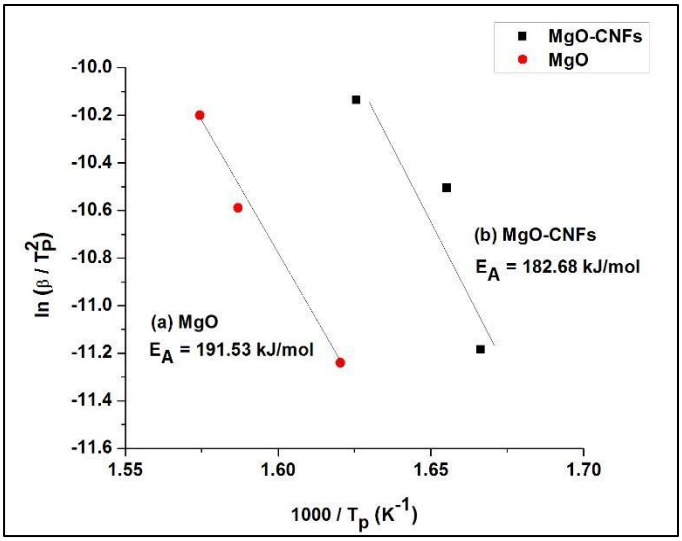


Figure 6. Kissinger's plot of the (a) as-received MgO and (b) MgO–CNFs

Figure 7 shows the hydrogen storage capacity of PVP–CNFs, as-received MgO and MgO–CNF composite at room temperature. PVP–CNFs, as-received MgO and MgO–CNFs adsorbed 1.90, 2.08 and 2.54 wt.% of hydrogen at 5.0 MPa and room temperature, respectively. With the addition of 75% of MgO in the CNFs, the hydrogen sorption capacity of CNFs was increased by approximately 30%, and the composite capacity was much higher than that of the as-received MgO. This improvement indicates that MgO has a synergetic effect in enhancing the sorption capacity because of a few possible reasons. Firstly, the rough surface morphology of the MgO–CNF composite increases the specific surface area, which provides more sites to adsorb the hydrogen. Secondly, MgO, which is distributed in the form of a single particle in CNFs homogenously in the composite, has effectively enhanced the hydrogen contact surface of MgO as compared with that of the as-received MgO, which tends to agglomerate. Lastly, the catalytic characteristics of metal oxide may reduce the adsorption activation energy and promote spill-over effect, as suggested by Yaakob et al. [30], who observed a similar improvement by using ZnO nanoparticles.

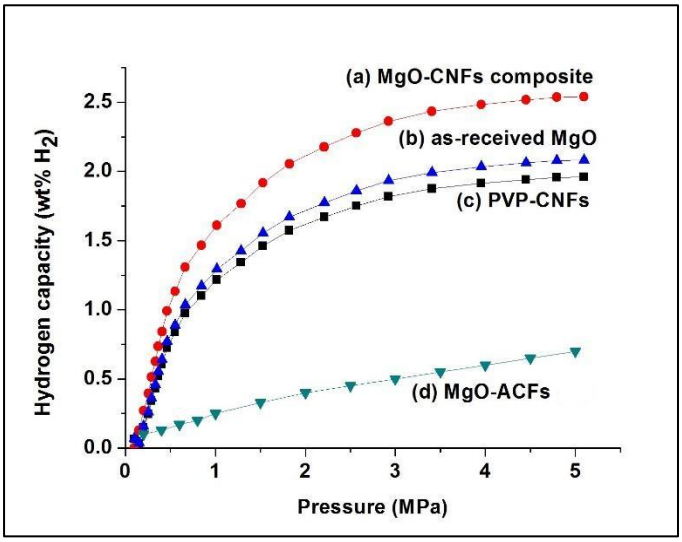


Figure 7. Pressure–composition isotherm of (a) MgO–CNF composite, (b) as-received MgO, (c) PVP–CNFs and (d) MgO-ACFs [31] at room temperature

The hydrogen sorption capacity of this work surpassed the findings of Im et al. [31], of which the MgO-activated polyacrylonitrile C fibres (MgO-ACFs) only adsorbed 0.7 wt.% H_2 at 5.0 MPa although the specific surface area of MgO-ACFs was up to twofold of that of this work. In this case, the role of MgO as a catalyst was suppressed probably because no MgO particles were exposed on the surface of ACFs, as indicated by the findings of Im et al. [3]. Presumably, the MgO particles on the surface have been removed during the chemical activation and washing process. Comparing the results, we can postulate that the position of MgO particles in the CNFs is of utmost importance to fully exploit the potential of metal oxide.

Conclusion

The MgO–CNF composite has been successfully synthesised using the electrospinning method. The addition of MgO in CNFs has increased the specific surface area of CNFs, which provides more hydrogen adsorption site and subsequently improves the hydrogen storage capacity. Nonetheless, the catalytic effect of MgO that promotes the spill-over mechanism has a larger role in enhancing the hydrogen storage capacity. Therefore, MgO must be located on the surface of CNFs to take advantage of its catalytic characteristics. This work has successfully improved the maximum hydrogen storage capacity of PVP–CNFs by more than 30% (2.54 wt%) at 5.0 MPa and at room temperature as compared with that of PVP–CNFs alone.

Acknowledgement

The authors would like to acknowledge the financial support given by the Universiti Kebangsaan Malaysia (DIP-2014-011, GGPM-2016-054) and Malaysian Ministry of Higher Education (FRGS/2/2014/ST05/UKM/03/1).

References

1. Raza, A., Wang, J., Yang, S., Si, Y. and Ding, B. (2014). Hierarchical porous carbon nanofibers via electrospinning. *Carbon Letters*, 15:1–14.
2. Ströbel, R., Garche, J., Moseley, P. T., Jörissen, L. and Wolf, G. (2006). Hydrogen storage by carbon materials. *Journal of Power Sources*, 159: 781 – 801.
3. Zubizarreta, L., Gome, E. I., Arenillas, Z., Ania, C. O., Parra, J. B. and Pis, J.J. (2008). H_2 storage in carbon materials. *Adsorption*, 14: 557 – 566.
4. Yang, S. J., Cho, J. H., Nahm, K. S. and Park, C. R. (2010). Enhanced hydrogen storage capacity of Pt-loaded CNT@MOF-5 hybrid composites. *International Journal of Hydrogen Energy*, 35: 13062 – 13067.
5. Jaybhaye, S., Sharon, M., Sharon, M., Sathiyamoorthy, D. and Dasgupta, K. (2006). Semiconducting carbon nanofibers and hydrogen storage. *Synthesis and Reactivity in Inorganic, Metal-Organic, and Nano-Metal Chemistry*, 37(6): 2007.
6. Bai, B. C, Kim, G. J., Naik, M. and Lee, Y.-S. (2011). The hydrogen storage capacity of metal-containing polyacrylonitrile-based electrospun carbon nanofibers. *Carbon Letters*, 12: 171 – 176.
7. Yurum, Y., Taralp, A. and Nejat Veziroglu, T. (2009). Storage of hydrogen in nanostructured carbon materials. *International Journal of Hydrogen Energy*, 34: 3784 – 3798.
8. Collin, D. J. and Zhou, H.-C. (2007). Hydrogen storage in metal-organic frameworks. *Journal of Materials Chemistry*, 17: 3154 - 3160.
9. Vasiliev, L. L., Kanonchik, L. E., Kulakov, A. G., and Babenko, V. A. (2007). Hydrogen storage system based on novel carbon materials and heat pipe heat exchanger. *International Journal of Thermal Sciences*, 46: 914 – 925.
10. Sami, A. and Hussein, A. (2015). Growth of carbon nanofibers synthesised from decomposition of liquid organic waste on a Ni/Al_2O_3 catalyst: Themodynamic and kinetic analyses. *Energy Procedia*, 74: 32 – 43.
11. Kvande, I., Chen, D., Yu, Z., Ronning, M. and Holmen, A. (2007). Optimization and scale-up of CNF prodcution based on intrinsic kinetic data obtained from TEOM. *Journal of Catalyst*, 256: 204 – 214.
12. Wang, J. and Kaskel, S. (2012). KOH activation of carbon-based materials for energy storage. *Journal of Materials Chemistry*, 22: 23710 – 23725.
13. Chen, Y., Zhu, H. and Liu, Y. (2011). Preparation of activated rectangular polyaniline-based carbon tubes and their application in hydogen adsorption. *International Journal of Hydrogen Energy*, 36: 11738 – 11745.
14. Kim, H., Lee, D. and Moon, J. (2011). Co-electrospun Pd-coated porous carbon nanofibers for hydrogen storage applications. *International Journal of Hydrogen Energy*, 36: 3566 – 3573.

15. Im, J. S., Kwon, O., Kim, Y. H., Park, S.-J. and Lee, Y.-S. (2008). The effect of embedded vanadium catalyst on activated electrospun CFs for hydrogen storage. *Microporous Mesoporous Materials*, 115: 514 – 521.
16. Froudakis, G.E. (2011). Hydrogen storage in nanotubes & nanostructures. *Materials Today*, 14: 324 - 328.
17. Konda, S. K. and Chen, A. (2016). Palladium based nanomaterials for enhanced hydrogen storage spillover and storage. *Materials Today*, 19: 100 – 108.
18. Manafi, S. A. and Badiee, S. H. (2008). Production of carbon nanofibers using a CVD method with lithium fluoride as a supported cobalt catalyst. *Research Letters in Materials Science*, 2008: 1 – 5.
19. Mitra, S., Sridharan, K., Unnam, J. and Ghosh, K. (2008). Synthesis of nanometal oxide and nanometals using hot-wire and thermal CVD. *Thin Solid Films*, 516: 798 – 802.
20. Rafique, M. M. A. and Iqbal, J. (2011). Production of carbon nanotubes by different routes - A review. *Journal of Encapsulation and Adsorption*, 1: 29 – 34.
21. Su, Z., Ding, J. and Wei, G. (2014). Electrospinning: A facile technique for fabricating polymeric nanofibers doped with carbon nanotubes and metallic nanoparticles for sensor applications. *Royal Society of Chemistry*, 4: 52598 – 52610.
22. Kunowsky, M., Marco-Lózar, J. P., Oya, A. and Linares-Solano, A. (2012). Hydrogen storage in CO_2-activated amoprhous nanofibers and their monoliths. *Carbon*, 50: 1407 – 1416.
23. Yang, S. J., Jung, H., Kim, T. and Park, C. R. (2012). Recent advances in hydrogen storage technologies based on nanoporous carbon materials. *Progress in Natural Science: Materials International*, 22: 631 – 638.
24. Kim, B. J., Lee, Y. S. and Park, S. J. (2008). Novel porous carbons synthesized from polymeric precursors for hydrogen storage. *International Journal of Hydrogen Energy*, 33: 2254 – 2259.
25. Jiménez, V., Ramírez-Lucas, A., Sanchéz, P., Valverde, J. L. and Romero, A. (2012). Hydrogen storage in different carbon materials: Influence of the porosity development by chemical activation. *Applied Surface Science*, 258: 2498 – 2509.
26. Sawai, N. U. and Harun, F. W. (2015). Hydrogen adsoprtion on agricultural-based activated carbons, zeolite templated-carbons and clay-based materials: A review. *Journal of Industrial & Engineering Chemistry Research*, 1: 1 – 7.
27. Jia, M. and Zhang, Y. (2009). Study on the synthesis of carbon fibers and CNF using potassium iodide catalyst. *Materials Letters*, 63: 2111 – 2114.
28. Sundaramurthy, J., Li, N., Kumar, P. S. and Ramakrishna, S. (2014). Perspective of electrospun nanofibers in energy and environment. *Biofuel Research Journal*, 2: 44 – 54.
29. Lim, K. L., Kazemian, H., Yaakob, Z. and Daud, W. R. W. (2010). Solid-state materials and methods for hydrogen storage: A critical review. *Chemical Engineering & Technology*, 33: 213 – 226.
30. Yaakob, Z., Khaadem, D. J., Shahgaldi, S., Daud, W. R. W. and Tasirin, S. M. (2012). The role of Al and Mg in the hydrogen storage of electrospun ZnO nanofibers. *International Journal of Hydrogen Energy*, 37: 8388 – 8394.
31. Im, J. S., Park, S. J., Kim, T. and Lee, Y. S. (2009). Hydrogen storage evaluation based on investigations of the catalytic properties of metal/metal oxides in electrospun carbon fibers. *International Journal of Hydrogen Energy*, 34: 3382 – 3388.
32. Lachawiec, A. J., Qi, J. G. and Yang, R. T. (2005). Hydrogen storage in nanostructured carbons by spillover: Bridge-building enhancement. *Langmuir*, 21: 11418 – 11424.
33. Campbell, F. C. (2012). Introduction and uses of lightweight materials. Lightweight materials - understanding the basics. *ASM International*, 1-31.
34. Ito, T., Sekino, T., Moriai, N. and Tokuda, T. (1981). Hydrogen adsorption on magnesium oxide powders. *Journal of the Chemical Society, Faraday Transactions*, 1(77): 2181 – 2192.
35. Wu, G., Zhang, J., Wu, Y., Li, Q., Chou, K. and Bao, X. (2009). Adsorption and dissociation of hydrogen on MgO surface: A first-principles study. *Journal of Alloys and Compounds*, 480: 788 – 793.
36. Ferrari, B., Moreno, R., Sarkar, P. and Nicholson, P. S. (200). Electrophoretic deposition of MgO from organic suspensions. *Journal of European Ceramic Society*, 20: 99 – 106.
37. Wang, C., Ma, C., Wu, Z., Liang, H., Yan, P., Song, J., Ma, N. and Zhao, Q. (2015). Enhanced bioavailability and anticancer effect of curcumin-loaded electrospun nanofiber: In vitro and in vivo study. *Nanoscale Research Letters*, 10: 439.
38. Sivaiah, K., Kumar, K. N., Naresh, V. and Buddhudu, S. (2011). Structural and optical properties of Li^+:PVP & Ag^+:PVP polymer films. *Materials Sciences and Applications*, 2: 1688 – 1696.

39. Tamilselvi, P., Yelilarasi, A., Hema, M. and Anbarasan, R. (2013). Synthesis of hierarchical structured MgO .by sol-gel method. *Nano Bulletin*, 2: 1301061 – 1301065.
40. Aykut, Y. (2013). Electrospun MgO-loaded carbon nanofibers: Enhanced field electron emission from the fibers in vacuum. *Journal of Physics and Chemistry Solids*, 74: 328 – 337.
41. Dhaouadi, H., Chaabane, H. and Touati, F. (2011). $Mg(OH)_2$ nanorods synthesized by a facile hydrothermal method in the presence of CTAB. *Nano-Micro Letters*, 3: 153 – 159.
42. Salamão, R. and Pandolfelli, V. C. (2008). Magnesia sinter hydration-dehydration behavior in refractory castables. *Ceramic International*, 34: 1829 – 1834.
43. Baytak, A. K., Duzmen, S., Teker, T. and Aslanoglu, M. (2017). Voltammetric determination of methylparaben and its DNA interaction using a novel platform based on carbon nanofibers and cobalt-nickel-palladium nanoparticles. *Sensors Actuators B*, 239: 330 – 337.
44. Rafizah, W. A. W. and Ismail, A. F. (2008). Effect of carbon molecular sieve sizing with poly(vinylpyrrolidone) K-15 on carbon molecular sieve-polysulfone mixed matrix membrane. *Journal of Membrane Science*, 307: 53 – 61.
45. Dong, G., Xiao, X., Liu, X., Qian B., Ma, Z., Ye, S., Chen, D. and Qiu, J. (2010). Preparation and characterization of Ag nanoparticle embedded polymer electrospun nanofibers. *Journal of Nanoparticle Research*, 12: 1319 – 1329.
46. Saravanan, L., Diwakar, S., Mohankumar, R., Pandurangan, A. and Jayavel, R. (2011). Synthesis, structural and optical properties of PVP encapsulated CdS nanoparticles. *Nanomaterials and Nanotechnology*, 1: 42 – 48.
47. Zhou, C., Liu, Z., Du, X., Mitchell, D. R. G., Mai, Y.-W., Yan, Y. and Ringer, S. (2012). Hollow nitrogen-containing core/shell fibrous carbon nanomaterials as support to platinum nanocatalysts and their TEM tomography study. *Nanoscale Reserach Letters*, 7(165): 1 - 11.
48. Guadagno, L., Raimondo, M., Vittoria, V., Vertuccio, L., Lafdi, K., Vivo, B. D., Lamberti, P., Spinelli, G. and Tucci, V. (2013). The role of carbon nanofiber defects on the electrical and mechanical properties of CNF-based resins. *Nanotechnology*, 24: 1 – 10.
49. Shao, C., Guan, H. and Liu, Y. (2006). MgO nanofibers via electrospinning technique. *Journal of Materials Science*, 41: 3821 – 3824.
50. Rezaei, M., Khajenoori, M. and Nematollahi, B. (2011). Synthesis of high surface area nanocrystalline MgO by pluronic P123 triblock copolymer surfactant. *Powder Technology*, 205: 112 – 116.
51. Sutcu, M., Akkrut, S. and Oku, S. (2010). Microstructural study of surface hydration on magnesia refractory. *Ceramics International*, 36: 1731 – 1735.
52. Kim, J.-H., Yoo, S.-J., Kwak, D.-H., Jung, H.-J., Kim, T.-Y., Park, K.-H., and Lee, J.-W. (2014). Characterization and application of electrospun alumina nanofibers. *Nanoscale Research Letters*, 9: 1 – 6.
53. Salles, T. H. C., Lombello, C. B and D'Ávila, M. A. (2015). Electrospinning of gelatin/poly(vinylpyrrolidone) blends from water/acetic acid solutions. *Materials Research*, 18: 509 – 518.
54. Behij, S., Hammi, H., Hamzaoui, A. H. and M'nif, A. (2013). Magnesium salts as compounds of the preparation of magnesium oxide from tunisian natural brines. *Chemical Industry and Chemical Engineering Quarterly*, 19: 263 – 271.
55. Mastuli, M. S., Ansari, N. S., Nawawi, M. A. and Mahat, A. M. (2012). Effects of cationic surfactant in sol-gel synthesis of nano sized magnesium oxide. *APCBEE Procedia*, 3: 93 – 98.
56. Kissinger, H. E. (1957). Reaction kinetics in differential thermal analysis. *Analytical Chemistry*, 29: 1702 – 1706.

Malaysian Journal of Analytical Sciences, Vol 23 No 1 (2019): 71 - 79
DOI: https://doi.org/10.17576/mjas-2019-2301-09

MALAYSIAN JOURNAL OF ANALYTICAL SCIENCES
Published by The Malaysian Analytical Sciences Society
ISSN 1394 - 2506

PdAu BIMETALLIC CATALYST FOR ELECTROOXIDATION OF GLYCEROL USING CYCLIC VOLTAMMETRY ANALYSIS

(PdAu Dwilogam Mangkin untuk Elektropengoksidaan Gliserol dengan Menggunakan Analisis Kitaran Voltametri)

Norilhamiah Yahya[1] and Siti Kartom Kamaruddin[2,3]*

[1]*Malaysian Institute of Chemical and Bioengineering Technology, Universiti Kuala Lumpur, 78000 Alor Gajah, Melaka, Malaysia.*
[2]*Fuel Cell Institute*
[3]*Department of Chemical and Process Engineering Universiti Kebangsaan Malaysia, 43600 UKM Bangi, Selangor, Malaysia.*

**Corresponding author: ctie@ukm.edu.my*

Received: 13 April 2017; Accepted: 17 April 2018

Abstract

This study was conducted to examine the performance of Palladium (Pd) based catalyst for glycerol oxidation in alkaline media by using half-cell in a cyclic voltammetry study. The sonication assisted reduction method by sodium citrate and sodium borohydride was employed to prepare a bimetallic PdAu catalyst. The crystallinity data of bimetallic Pd_2Au_1 and Pd_4Au_1 catalysts were characterised by powder X-ray powder diffraction (XRD). Meanwhile, morphology, rough composition and distribution of metallic elements from both catalysts were investigated by Field Emission Scanning Electron Microscope (FESEM) and Energy Dispersive X-ray (EDX), respectively. The performances of the synthesised catalysts were analysed for the electrooxidation of glycerol in alkaline media by cyclic voltammetry analysis and chronoamperometry analysis. It was found that Pd_2Au_1 showed higher performance in terms of peak current density (55.28 mA cm^{-2}), onset potential (-0.4152 V) and more stability towards glycerol oxidation compared to Pd_4Au_1. The cyclic voltammetry study yielded an electrochemically active surface area for Pd_2Au_1 catalyst at 14.12 m^2g^{-1}, compared to Pd_4Au_1 catalyst at only 12.7 m^2g^{-1}.

Keywords: PdAu, nanocatalyst, alkaline medium, glycerol oxidation, cyclic voltammetry

Abstrak

Kajian ini adalah untuk mengkaji prestasi mangkin berasaskan Palladium (Pd) untuk pengoksidaan gliserol dalam media alkali dengan menggunakan sel separuh dalam kajian voltammetri berkitar. Kaedah sonikasi dibantu kaedah penurunan oleh natrium sitrat dan natrium borohidrat telah digunakan untuk menyediakan mangkin dwilogam PdAu. Data penghabluran mangkin dwilogam Pd_2Au_1 dan Pd_4Au_1 telah dicirikan oleh pembelauan sinar-X (XRD). Sementara itu, morfologi, komposisi kasar dan taburan unsur logam daripada mangkin telah disiasat menggunakan mikroskopi elektron imbasan (FESEM) dan spektrometer serakan tenaga sinar-X (EDX). Prestasi mangkin yang disintesis dianalisa untuk melihat tindakbalas elektropengoksidaan gliserol dalam media beralkali oleh ujian kitaran voltammetri dan ujian kronoamperometri. Telah didapati bahawa Pd_2Au_1 menunjukkan prestasi yang lebih tinggi dari segi ketumpatan arus puncak (55.28 mA cm^{-2}), permulaan keupayaan potensi (-0.4152V) dan lebih kestabilan terhadap pengoksidaan gliserol dibandingkan dengan Pd_4Au_1. Kajian kitaran voltammetri menghasilkan kawasan permukaan elektrokimia aktif untuk mangkin Pd_2Au_1 sebanyak 14.12 m^2g^{-1}, di bandingkan dengan mangkin Pd_4Au_1 hanya sebanyak 12.7 m^2g^{-1}.

Kata kunci: PdAu, nanomangkin, media alkali, pengoksidaan gliserol, kitaran voltammetri

Introduction

Direct alcohol fuel cell has emerged as one of the alternative energies used to generate electricity without any combustion [1-3]. There are many types of fuel candidates used to replace fuel, one of which is methanol due to its high toxicity, high methanol crossover and slow electro-kinetic properties [4, 5]. This makes methanol unsuitable as a fuel for the commercialisation of fuel cell. One alternative being currently proposed is glycerol to replace methanol in fuel cell application. Glycerol can be obtained from various sources and one of them is from biodiesel production [6, 7]. Lately, research effort has been done to use glycerol as fuel in fuel cell application to convert glycerol as a value-added product [8]. Glycerol as fuel in fuel cell application has gained attention because of its attractive fuel components which are renewable from biomass production, less harmful, have high energy density, low vapour pressure, low cost, easy to store and low transportation needs [8]. On the other hand, theoretically, when glycerol is oxidised by inorganic catalysts, it is possible to obtain 10 electrons (when the reaction is not complete) against 14 electrons for a complete oxidation [9].

However, oxidation of glycerol is quite difficult and complicated due to the complex molecular structure in which partial oxidation will produce unwanted products such as glyceraldehyde, 1,3-dihydroxyacetone, glyceric acid, hydroxypyruvic acid, tartronic acid, mesoxalic acid, formic acid, ocilic acid and glycolic acid [10, 11]. All these partial oxidation products are not desirable as they will decrease the overall system efficiency. This becomes the primary challenge of glycerol oxidation. Due to this, selection of catalyst is the critical issue to increase the activity of glycerol oxidation in the anode side and at the same time minimise the cost of the fuel cell itself. Up until now, there are several catalysts used to study the oxidation of glycerol such as platinum and palladium (Pd). However, the use of platinum has brought another issue such as higher price and limited source [12]. In addition, platinum creates stability issues with another intermediate product of carbon monoxide poisoning of the platinum surface by adsorbing too strong on the platinum surface [13].

To overcome the problem, Palladium-Aurum (PdAu) bimetallic catalyst has been used in this study. Pd (111) and Au (111) planes are only 4% mismatched, making the combination Pd and Au perfect to be a miscible solution. Several previous studies showed that due to ensemble and ligand effect, this combination will enhance the electrocatalytic activity in terms of current density and tolerance to the carbon monoxide poisoning effect [14, 15]. To synthesise heterogeneous catalysts with small nanoparticles (less than 20 nm), highly dispersed and less agglomeration with high surface area are among the challenges. The physical-chemical concepts needed to understand the preparation of colloidal inorganic nanoparticles and the remarkable degree of control that has been achieved over their composition, size, shape and surface [16]. In this study, chemical reduction modified the classical "Turkevich" preparation method which has been used to synthesise PdAu nanoparticles in control temperature [17] as the catalyst in glycerol oxidation.

Materials and Methods

Materials

All precursor metal salts and chemical reagents such as Gold(III) chloride trihydrate ($HAuCl_4 \bullet 3H_2O$), Palladium chloride ($PdCl_2$), Trisodium citrate (Na_3Ct), Sodium borohydride ($NaBH_4$), vapour grown carbon nanofiber (VGCNF), Sodium hydroxide, glycerin, 2-propanol and 5 wt.% nafion solution were purchased from Sigma-Aldrich/USA**.**

Synthesis of PdAu catalysts via chemical reduction method

0.05 M $PdCl_2$ (Sigma-Aldrich/USA) and 0.01 M of $AuCl_3 \cdot HCl \cdot 4H_2O$ (Sigma-Aldrich/USA) were mixed (in 2:1 and 4:1 molar ratio) in a volumetric flask and sonicated for 2 hours to form a homogenous solution. A certain amount of trisodium citrate was added into the solution in a drop wise manner with constant stirring for another 2 hours [18]. The presence of a capping agent in this study is to inhibit the nanoparticles' over-growth and aggregation during the reduction process. Next, reduction of the metal precursors is carried out using an excess amount of freshly prepared ice-cold (0.3 M) sodium borohydride ($NaBH_4$) and the reduction was assisted by sonication for 3 hours. Since the stabilising and reducing agents are water soluble, the solvent can be removed by filtration and washing with DI water and dried at 80 ºC overnight.

Physical and electrochemical characterization of nanoparticles

XRD is a powerful method used for characterising crystalline materials of the metal synthesis. The samples of X-ray data were collected in the 2θ range of 20° to 90°. The FESEM analyses were performed using FESEM model Zeiss/SUPRA 55VP. FESEM analyses provide information about the morphology and topography of the catalyst samples. Meanwhile, EDX analysis normally determines the average surface elemental composition as well as elemental distribution mapping of the catalyst samples

The cyclic voltammetry and chronoamperometry analyses measurements were performed by using Autolab (PGSTAT101) electrochemical workstation under room temperature. The catalysts' ink solution was carefully transferred onto the glassy carbon electrode by using a micropipette and then left to dry in room temperature. The electrochemical characterisation of two types of catalysts was studied by a cyclic voltammetry (CV) test in the potential range of -0.7 to 0.4 V at a scan rate of 50 mVs^{-1} in 0.5 M glycerol/0.5 M NaOH solution. The electrolyte solution was de-oxygenated by bubbling it with N_2 at 200 mL min^{-1} for 30 minutes before taking any measurement of glycerol oxidation reaction**.**

Results and Discussion

XRD is a primary tool used to identify crystalline material structures. Figure 1 shows the XRD patterns which confirmed the presence of target metal in the catalyst samples of Pd_2Au_1 and Pd_4Au_1 that fit well with their characteristic of face-centred cubic (fcc) patterns. Table 1 shows the lattice parameter, crystallite size and atomic composition for each catalyst. The diffraction peaks in the catalyst sample Pd_2Au_1 exhibited the characteristic of face-centred cubic crystalline structure at 2θ values of 38.28°, 44.19°, 64.92°, and 77.40° which corresponded to the (111), (200), (220) and (311) planes. The diffraction peaks of Pd_4Au_1 are 39.15°, 44.64°, 65.12°, and 78.02° which corresponded to the (111), (200), (220) and (311) planes. The differences of diffraction peak positions for Pd_2Au_1 and Pd_4Au_1 indicate that Au has entered the Pd lattice and formed a homogeneous substitution of bimetallic nanoparticles [19]. The lattice parameter for Pd_2Au_1 and Pd_4Au_1 is exposed alloy with the dissolution of Au to Pd which made the lattice parameter increased from pure, which was Pd (0.3857 nm) [20] to 0.3991 nm and 0.3892 nm for Pd_2Au_1 and Pd_4Au_1, respectively. The average crystallite size for the synthesised catalysts was calculated based on the plane (111) diffraction peak using Scherrer's equation 1:

$$d_{XRD} = 0{:}9\ \lambda_{CuKa}/\beta 2\theta.\cos\theta max \quad (1)$$

where d is the average particle size (nm), λ is the wavelength of the X-ray used (1.54056 Å), θ is the angle at the maximum of the peak (rad), and β_{2A} is the width of the peak at half height in radians. The calculated average crystallite sizes obtained for both catalysts Pd_2Au_1 and Pd_4Au_1 are given in Table 1.

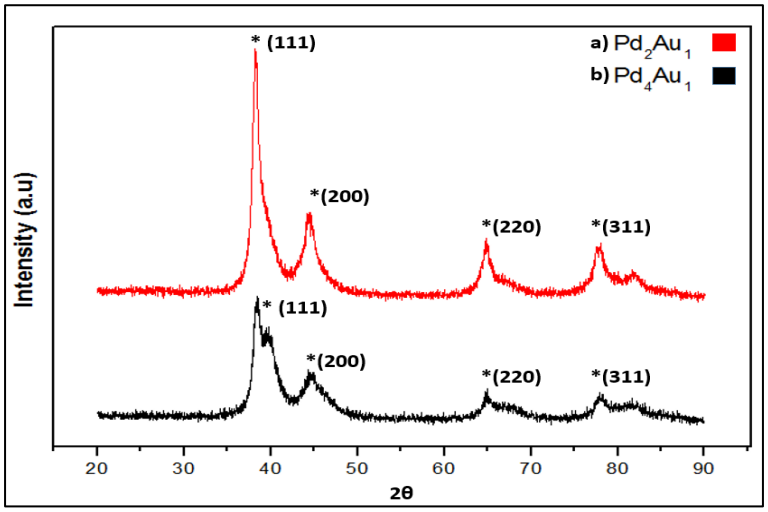


Figure 1. XRD patterns for a) Pd_2Au_1 and b) Pd_4Au_1 nanocatalysts

Table 1. Comparison between measured XRD and EDX results of samples a) Pd_2Au_1 and b) Pd_4Au_1

Sample	Catalyst Types	2θ	Lattice Parameter (nm)	Atomic Composition (XRD) Pd:Au	Atomic Ratio(EDX) Pd:Au	Crystallite Size (XRD)
a	Pd_2Au_1	38.28	0.3991	65.05:34.95	71.3:28.7	6.0
b	Pd_4Au_1	39.15	0.3892	79.4:20.6	80.2:19.8	4.2

The morphology of the synthesised Pd_2Au_1 and Pd_4Au_1 bimetallic catalysts was evaluated by using FESEM imaging as can be seen in Figure 2. The FESEM images illustrate homogenous nucleation and growth of bimetallic nanoparticles but with little agglomeration successfully generated by trisodium citrate and sodium borohydride reduction method [21]. Figure 3 shows EDX and mapping analysis which confirmed the presence of Pd and Au and the distribution of both metal catalysts. XRD results were correlated with EDX measurements to evaluate the bulk composition of both catalysts. Table 1 lists the bulk composition from EDX evaluation for both catalysts which was found to be so close to the nominal value. These results prove that the bulk composition of Pd and Au in the synthesis catalysts is in good agreement with the molar ratio of Pd to Au salt in the solution.

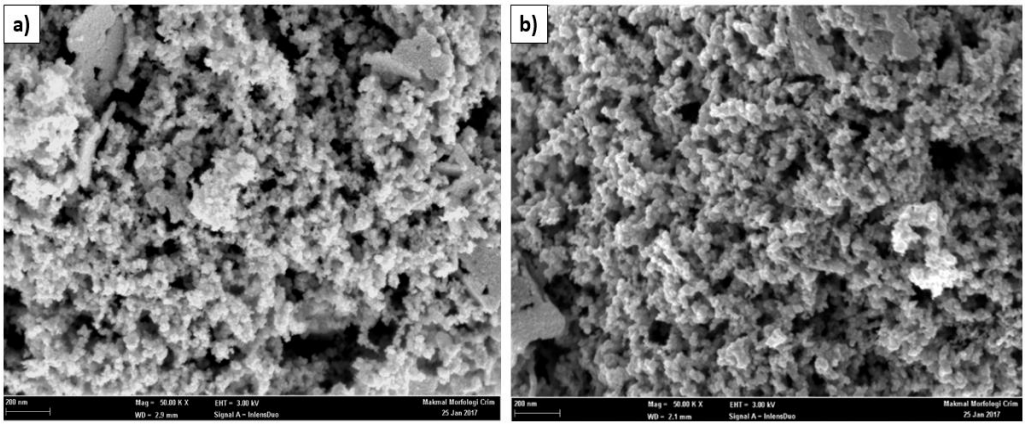
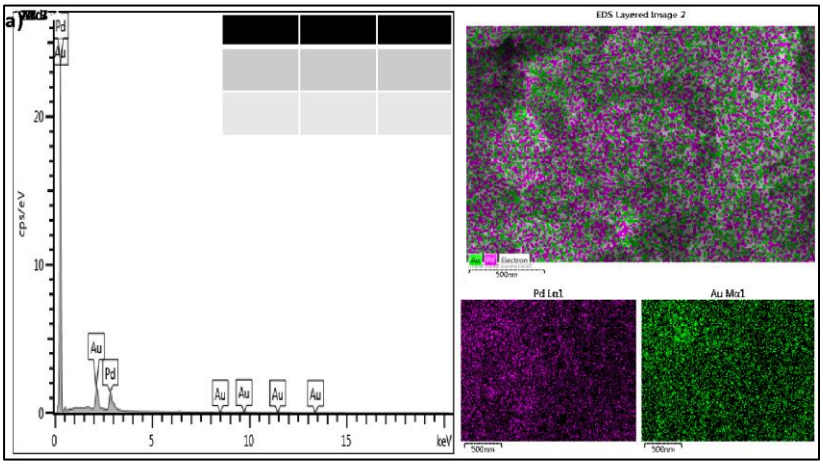


Figure 2. FESEM images of a)Pd_2Au_1 and b)Pd_4Au_1 nanocatalysts



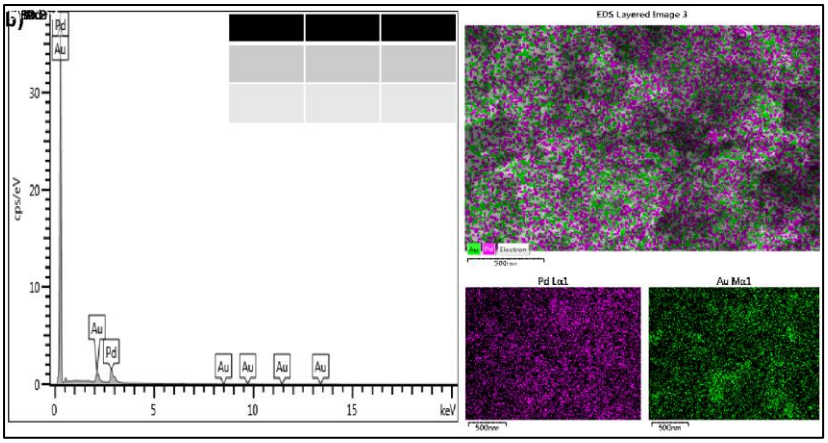


Figure 3. EDX analysis and element mapping on a) Pd_2Au_1 and b) Pd_4Au_1 nanocatalysts

Cyclic voltammetry study

The performances of catalysts in glycerol oxidation reaction (GOR) were evaluated in terms of two aspects: (1) onset potential (E_{on}); indicative of the catalytic activity over glycerol oxidation reactions, (2) forward anodic specific peak current density (I_f); showing the catalyst maximum performance. In order to acquire the qualitative information for catalysts activity in alkaline media, the typical CV behaviour of Pd_2Au_1 and Pd_4Au_1 catalysts were preliminarily investigated in 0.5 M NaOH without the presence of glycerol as shown in Figure 4. For comparison, the standard CV for Pd_2Au_1 and Pd_4Au_1 catalysts is also presented. The strong cathodic peak at E=-0.381 V and E=-0.378 V corresponding to the formation and reduction of palladium oxide in the CV was obtained from Pd_2Au_1 and Pd_4Au_1 catalysts, respectively. The electroactive surface area per gram of palladium was achieved by Pd_2Au_1/VGCNF at 14.12 m^2/g_{Pd} and Pd_4Au_1 at 12.7 m^2/g_{Pd}.

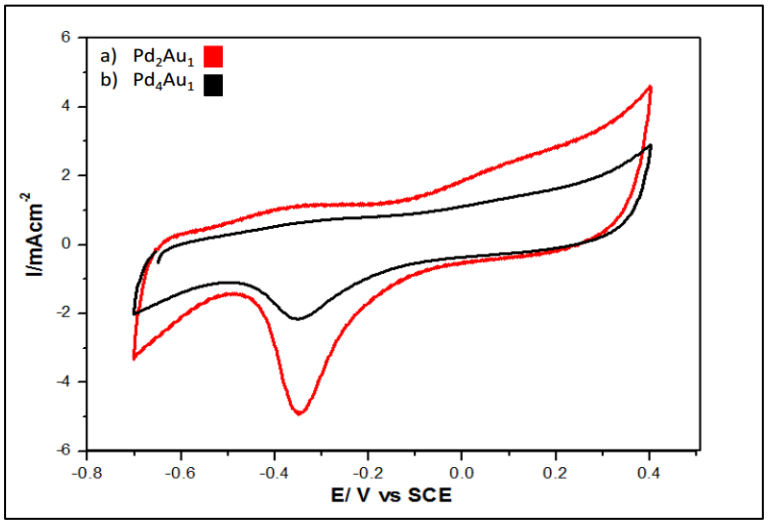


Figure 4. Cyclic voltammograms of a) Pd_2Au_1 and b) Pd_4Au_1 for the electrooxidation using 0.5M NaOH as an electrolyte scan rate of 50 mV/s.

Figure 5 shows the cyclic voltammetry study of glycerol oxidation in the electrolyte solution containing 0.5 M glycerol and 0.5 M NaOH on different catalysts at a scan rate of 50 mVs^{-1}. The electrooxidation of glycerol was characterised by two well-defined current peaks on the forward and reverse scans. In the forward scan, the peak

corresponded to the oxidation of freshly chemisorbed species coming from the glycerol adsorption and the anodic sweep grew systematically with the increasing values of potential (V). Meanwhile, reverse scan was associated with the removal of carbonaceous species formed during oxidation of glycerol [22]. The Pd_2Au_1 showed more negative onset potential for glycerol oxidation and higher anodic peak for current density (55.28 mA cm^{-2}) compared to Pd_4Au_1(41.31 mA cm^{-2}). This result shows that the metal compositions of the bimetallic cluster give the greatest effect towards glycerol oxidation. Since the reaction took place in an alkaline medium, the presence of OH ions will facilitate the active sites on catalyst. As can be seen in Figure 5, the steady-state oxidation forward current (I_f) can be detected at the potential above −0.4 V, which is above the starting potential of the adsorption of the hydroxyl ions (equation 2).

$$Pd + OH^- \leftrightharpoons Pd\text{-}OH_{ads} + e^- \quad (2)$$

$$C_3H_5(OH)_3 + 12\ OH^- \longrightarrow 2C_3O_5^{2-} + 10H_2O + 10e^- \quad (3)$$

$$C_3H_5(OH)_3 + 20\ OH^- \longrightarrow 3CO_3^{2-} + 14H_2O + 14e^- \quad (4)$$

The chemisorption of glycerol molecules on oxygen-containing species ($Pd\text{-}OH_{ads}$) indirectly assisted in getting rid of intermediate species that existed during the dissociative of glycerol molecules [23]. Thus, it allowed further reaction to occur without any difficulty. As a result, GOR will continue the current increase with the increase in potential. Moreover, partial oxidation of glycerol without C–C bond breaking and $C_3O_5^{2-}$ production leads to producing $10e^-$ (equation 3). Meanwhile, complete oxidation of glycerol produced $14e^-$ (equation 4) [24]. Furthermore, the addition of a second metal also provided more active sites for the electrooxidation of glycerol, while at the same time controlling the poisoning effect [25, 26]. The electrochemical active surface area (EASA) value for Pd_2Au_1 is higher compared to Pd_4Au_1 which is another reason attributed to the better performance of Pd_2Au_1 catalyst. The higher EASA refers to more active sites available to adsorb active oxygen atoms which will readily oxidise the intermediate products produced during the oxidation reaction on the catalyst surface. Ratio of current forward to current backward (If:Ib) that reflects the carbon monoxide tolerance shows that Pd_2Au_1 is higher compared to Pd_4Au_1. Bimetallic effect normally assists the mechanism of CO tolerance through modification of the electronic structure. Sticking probability of CO on Pd surface is reduced by the adjacent Au which improve the catalytic activity of the catalyst. This inhibits higher ratio of Au which will help to keep more active Pd sites available for glycerol oxidation, and hence provide the high CO tolerance of the Pd_2Au_1 bimetallic catalyst. Table 2 shows performance comparison between Pd_2Au_1 and Pd_4Au_1 catalysts.

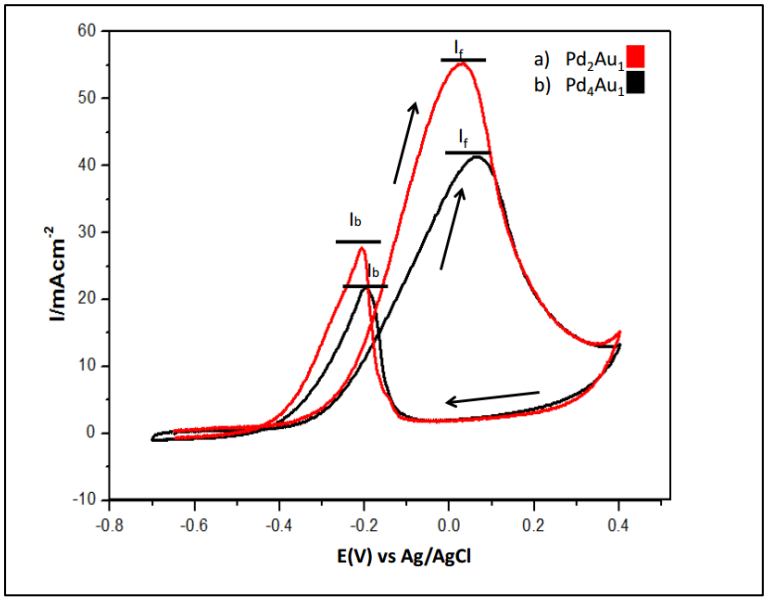


Figure 5. Cyclic voltammograms of a)Pd_2Au_1 and b)Pd_4Au_1 nanocatalysts for the electrooxidation of 0.5 M glycerol using 0.5M NaOH as an electrolyte scan rate of 50 mV/s.

Table 2. Performance of a) Pd_2Au_1 and b)Pd_4Au_1 nanoparticles for glycerol electrooxidation in alkaline media

Sample	Catalyst Types	Eon (V)	I_f ($mAcm^{-2}$)	I_B ($mAcm^{-2}$)	I_f/I_b	EASA (m^2g^{-1})
a	Pd_2Au_1	-0.4152	55.28	27.75	1.99	14.12
b	Pd_4Au_1	-0.4295	41.31	21.84	1.89	12.7

Chronoamperometry study

The durability of Pd_2Au_1 and Pd_4Au_1 bimetallic catalysts during long term operations was evaluated *via* chronoamperometry curves. Figure 6 illustrates the chronoamperometry measurements for 3600 seconds in electrolyte solution of 0.5 M NaOH and 0.5 M glycerol. As demonstrated in the chronoamperometry analysis, a decay of current value in the time interval indicates a considerable stability of the catalysts and a tolerance to poisoning by intermediates species. As in the cyclic voltammetry analysis, Pd_2Au_1 demonstrated better activity and stability compared to Pd_4Au_1. Noticeably, Pd_2Au_1 inhibited higher initial current density and limiting current density for a long time. It is shown that the presence of Au could improve the stability of the catalyst by giving a balanced adsorption between OH^- species from Au and species from glycerol adsorption on Pd [27]. Nevertheless, the current density reduction occurred too fast for both catalysts. Therefore, it is desirable to introduce a catalyst support to improve the stability of the catalysts.

.

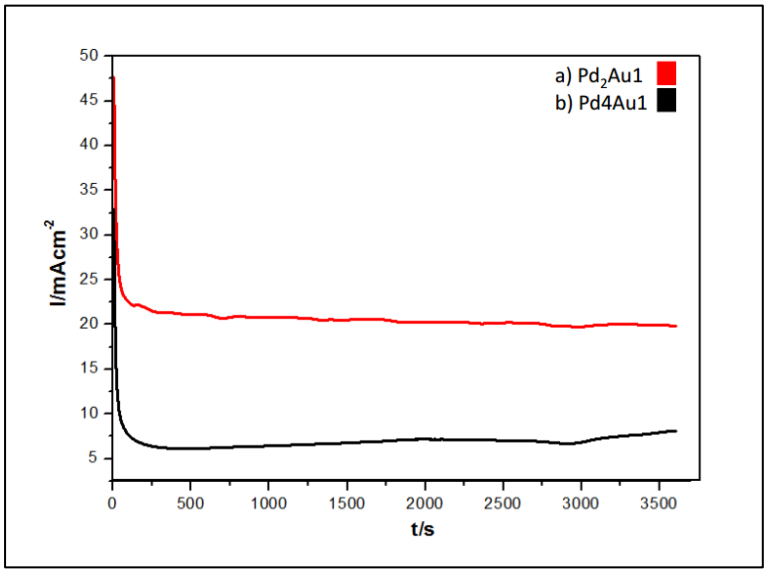


Figure 6. Chronoamperometry analysis of a)Pd_2Au_1 and b)Pd_4Au_1 for the electrooxidation of 0.5 M glycerol using 0.5M NaOH as an electrolyte scan rate of 50 mV/s

Conclusion

In summary, the two types of catalysts, namely Pd_2Au_1 and Pd_4Au_1 have been successfully synthesised by the reduction method. XRD data clearly showed the presence of bimetallic Pd_2Au_1 and Pd_4Au_1 catalysts. These two bimetallic catalysts were compared with each other for the electrooxidation of glycerol in alkaline media. The incorporation of a second metal which is Au modified the electronic configuration of the Pd catalyst which enhanced the activity towards glycerol oxidation. The CV results exhibited that Pd_2Au_1 catalyst showed excellent catalytic activity and high stability for glycerol oxidation compared to Pd_4Au_1 catalyst. Besides that, it could be observed that the onset potential for glycerol oxidation for Pd_2Au_1 was more negative than Pd_4Au_1 which was

attributed to the reaction that occurred faster. This means the improvement was strongly dependent on the composition (atomic Pd/Au ratio) of the catalysts. In addition, the I_f/I_b ratio which reflected poisoning species for the oxidation of glycerol showed that bimetallic Pd_2Au_1 again had higher ratio value which means bimetallic catalyst has a higher tolerance to the poisoning species. The obtained results confirmed the catalytic activity is affected by the presence of bimetallic active phase. The synthesis method for the development of Pd and Au bimetallic catalysts could be extended to other compositions in order to improve the catalytic activity of the catalysts and in the meantime minimise the utilisation of the noble metals.

.

Acknowledgements

The authors gratefully acknowledge the financial support given for this work by the Universiti Kebangsaan Malaysia (UKM) under DIP-2015-002 and Ministry of Education (MOE) under GSP/1/2015/TK01/UKM/01/1.

References

1. Kamarudin, M. Z. F., Kamarudin, S. K., Masdar, M. S. and Daud, W. R. W. (2013). Review: Direct ethanol fuel cells. *International Journal of Hydrogen Energy*, 38(22): 9438–9453.
2. Zainoodin, A. M., Kamarudin, S. K., Masdar, M. S., Daud, W. R. W., Mohamad, A. B. and Sahari, J. (2014). High power direct methanol fuel cell with a porous carbon nanofiber anode layer. *Applied Energy*, 113: 946–954.
3. Bambagioni, V., Bianchini, C., Marchionni, A., Filippi, J., Vizza, F., Teddy, J., Serp, P. and Zhiani, M. (2009). Pd and Pt-Ru anode electrocatalysts supported on multi-walled carbon nanotubes and their use in passive and active direct alcohol fuel cells with an anion-exchange membrane (alcohol = methanol, ethanol, glycerol). *Journal of Power Sources*, 190(2):241-251.
4. Thiam, H. S., Daud, W. R. W., Kamarudin, S. K., Mohammad, A. B., Kadhum, A. A. H., Loh, K. S., and Majlan, E. H. (2011). Overview on nanostructured membrane in fuel cell applications. *International Journal of Hydrogen Energy*, 36(4):3187–3205.
5. Basri, S., Kamarudin, S. K., Daud, W. R. W. and Yaakub, Z. (2010). Nanocatalyst for direct methanol fuel cell (DMFC). *International Journal of Hydrogen Energy*, 35(15): 7957–7970.
6. Zhiani, M., Rostami, H., Majidi, S., and Karami, K. (2013). Bis (dibenzylidene acetone) palladium (0) catalyst for glycerol oxidation in half cell and in alkaline direct glycerol fuel cell. *International Journal of Hydrogen Energy*, 38(13):5435–5441.
7. Habibi, E. and Razmi, H. (2012). Glycerol electrooxidation on Pd, Pt and Au nanoparticles supported on carbon ceramic electrode in alkaline media. *International Journal of Hydrogen Energy*, 37(22): 16800–16809.
8. Yang, F., Hanna, M. A. and Sun, R. (2014). Value-added uses for crude glycerol-a byproduct of biodiesel production. *Biotechnology for Biofuels*, 5: 13.
9. Li, S. S., Hu, Y. Y., Feng, J. J., Lv, Z. Y., Chen, J. R., and Wang, A. J. (2014). Rapid room-temperature synthesis of Pd nanodendrites on reduced graphene oxide for catalytic oxidation of ethylene glycol and glycerol. *International Journal of Hydrogen Energy*, 39(8): 3730–3738.
10. Bagheri, S., Julkapli, N. M. and Yehye, W. A. (2014). Catalytic conversion of biodiesel derived raw glycerol to value added products. *Renewable and Sustainable Energy Reviews*, 41: 113–127.
11. Pagliaro, M., Ciriminna, R., Kimura, H., Rossi, M. and Della, Pina C. (2007). From glycerol to value-added products. *Angewandte Chemie - International Edition*, 46(24): 4434–4440.
12. Liu, J. (2017). High performance platinum single atom electrocatalyst for oxygen reduction reaction. *Nature Communications*, 8: 15938.
13. Newton, M. A., Ferri, D., Smolentsev, G., Marchionni, V. and Nachtegaal, M. (2015). Room-temperature carbon monoxide oxidation by oxygen over Pt/Al_2O_3 mediated by reactive platinum carbonates. *Nature Communications*, 6: 1–7.
14. Ruvinsky, P. S., Pronkin, S. N., Zaikovskii, V. I., Bernhardt, P. and Savinova, E. R. (2008). On the enhanced electrocatalytic activity of Pd overlayers on carbon-supported gold particles in hydrogen electrooxidation. *Physical Chemistry Chemical Physics*, 10(44): 6665–6676.
15. Meng, H., Zeng, D. and Xie, F. (2015). Recent development of Pd-based electrocatalysts for proton exchange membrane fuel cells. *Catalysts*, 5(3): 1221–1274.
16. Niu, Z. and Li, Y. (2014). Removal and utilization of capping agents in nanocatalysis. *Chemistry of Materials*, 26(1): 72–83.

17. Qin, Y. H., Jia, Y. B., Jiang, Y., Niu, D. F., Zhang, X. S., Zhou, X. G., Niu, Li. and Yuan, W. K. (2012). Controllable synthesis of carbon nanofiber supported Pd catalyst for formic acid electrooxidation. *International Journal of Hydrogen Energy*, 37(9): 7373-7377.
18. Marshall, A. T., Golovko, V. and Padayachee, D. (2015). Influence of gold nanoparticle loading in Au/C on the activity towards electrocatalytic glycerol oxidation. *Electrochimica Acta*, 153: 370–378.
19. Yan, W., Tang, Z., Wang, L., Wang, Q., Yang, H. and Chen S. (2016). PdAu alloyed clusters supported by carbon nanosheets as efficient electrocatalysts for oxygen reduction. *International Journal of Hydrogen Energy*, 42(1): 218-227.
20. Wang, W., Kang, Y., Yang, Y., Liu, Y., Chai, D. and Lei Z. (2015). PdSn alloy supported on phenanthroline-functionalized carbon as highly active electrocatalysts for glycerol oxidation. *International Journal of Hydrogen Energy*, 41(2): 1272–1280.
21. Thottoli, A. K., Kaliani A. and Unni A. (2013). Effect of trisodium citrate concentration on the particle growth of ZnS nanoparticles. *Journal of Nanostructure Chemistry*, 3(1): 56.
22. Chen Z., Wang, S., Lian, C., Liu, Y., Wang, D., and Chen, C. (2016). Nano PdAu bimetallic alloy as an effective catalyst for the Buchwald – Hartwig reaction. *Asian Journal Communication*, 351–355.
23. Liang, Z. X., Zhao, T. S., Xu, J. B. and Zhu, L. D. (2009). Mechanism study of the ethanol oxidation reaction on palladium in alkaline media. *Electrochimica Acta*, 54(8): 2203–2208.
24. Simões, M., Baranton, S. and Coutanceau, C. (2010). Electro-oxidation of glycerol at Pd based nano-catalysts for an application in alkaline fuel cells for chemicals and energy cogeneration. *Applied Catalysis B: Environmental*, 93: 354–362.
25. Mahapatra, S. S. and Datta, J. (2011). Characterization of Pt-Pd/C electrocatalyst for methanol oxidation in alkaline medium. *International Journal of Electrochemistry*, 2011: 1–16.
26. Mao, H., Huang, T. and Yu A. (2016). Surface noble metal modified PdM/C (M ¼ Ru, Pt, Au) as anode catalysts for direct ethanol fuel cells. *Journal of Alloy and Compound*, 676: 390–396.
27. Thi, B., Lam, X., Chiku, M., Higuchi, E. and Inoue H. (2015). Preparation of PdAg and PdAu nanoparticle-loaded carbon black catalysts and their electrocatalytic activity for the glycerol oxidation reaction in alkaline medium. *Journal of Power Sources*, 297: 149–157.

Malaysian Journal of Analytical Sciences, Vol 23 No 1 (2019): 80 - 89
DOI: https://doi.org/10.17576/mjas-2019-2301-10

MALAYSIAN JOURNAL OF ANALYTICAL SCIENCES
Published by The Malaysian Analytical Sciences Society
ISSN 1394 - 2506

BIOHYDROGEN PURIFICATION FROM PALM OIL MILL EFFLUENT FERMENTATION FOR FUEL CELL APPLICATION

(Penulenan Gas Biohidrogen yang Terhasil dari Fermentasi Efluen Kilang Minyak Kelapa Sawit Untuk Aplikasi Sel Bahan Api)

Ying Tao Chung [1,2], Rosiah Rohani [1]*, Izzati Nadia Mohamad [1], Mohd Shahbudin Mastar@Masdar [1,2], Mohd Sobri Takriff [1]

[1]*Chemical Engineering Program & Research Centre for Sustainable Process Technology, Faculty of Engineering and Built Environment*
[2]*Fuel Cell Institute*
Universiti Kebangsaan Malaysia, 43600 UKM Bangi, Selangor, Malaysia

**Corresponding author: rosiah@ukm.edu.my*

Received: 13 April 2017; Accepted: 17 April 2018

Abstract

Palm Oil Mill Effluent (POME) is one of the major pollutants generated from palm oil mills. In Malaysia, POME is recognised as a promising source for producing biogas through a controlled fermentation process, which can be used as a source of renewable energy. Therefore, this research was conducted to upgrade the biohydrogen produced from POME fermentation *via* (i) absorption and (ii) membrane techniques. In this study, the current and power capacity of the purified biohydrogen was verified by using fuel cell. From the results, POME fermentation was found to consist of mainly H_2 and CO_2 of equal amounts. Therefore, biohydrogen purification using the absorption technique was next performed using three different solvents: methyl ethanol amine (MEA), ammonia (NH_3) and potassium hydroxide (KOH) solutions and compared with the membrane permeation method using polysulfone (PSF) membrane. The highest H_2 purity for MEA solutions was found to be 99%, at 1 M concentration and 5.0 mL/s feed mixed gas flow rate at 60 minutes absorption time. The purified biohydrogen using PSF membrane possessed the highest H_2 purity at nearly 77% at the pressure of 3 bar. The purified biohydrogen obtained from the two separation techniques were next tested in a proton exchange membrane (PEM) fuel cell and directly compared with the original biohydrogen mixture obtained from POME fermentation (50% H_2), where the gas ratios were represented using simulated gas composition. The findings in this study identified that the current and power produced at 100% H_2 (similar H_2 purity from the absorption technique) was 1.66 A and 9.31 W while at 75% H_2 (similar H_2 purity from the membrane technique) the current was 0.69 A and 3.01 W. Therefore, the results prove that both purification techniques demonstrate the significant potential for H_2 purification efficiency.

Keywords: absorption, alkaline solvent, biohydrogen, carbon dioxide, palm oil mill effluent, treatment

Abstrak

Efluen kilang minyak kelapa sawit (POME) merupakan salah satu daripada pencemar utama yang dihasilkan daripada kilang minyak sawit. Terkini, ianya telah dikenalpasti sebagai salah satu sumber yang berpotensi untuk menghasilkan biogas di Malaysia melalui kaedah fermentasi di dalam bioreaktor dalam keadaan terkawal, yang boleh dijadikan sebagai sumber tenaga diperbaharui. Oleh itu, kajian ini dijalankan bagi menambahbaik biohidrogen yang dihasilkan dari fermentasi POME menerusi (i) teknik penyerapan dan (ii) teknik membran. Kapasiti arus dan kuasa yang terhasil menerusi penulenan biohidrogen kemudiannya telah ditentukan menggunakan sel bahan api. Daripada keputusan yang diperoleh, fermentasi POME mengandungi gas H_2 dan CO_2 sahaja, dengan jumlah yang sama. Oleh itu, penulenan biohidrogen menggunakan teknik penyerapan telah dilakukan menggunakan tiga jenis pelarut iaitu larutan metil etanol amina (MEA), ammonia (NH_3) dan kalium hidroksida (KOH)

dan kaedah ini kemudiannya dibandingkan dengan teknik pemisahan membran, iaitu dengan menggunakan membran polisulfon (PSF). Peratusan tertinggi bagi H_2 yang telah ditulenkan menggunakan pelarut MEA adalah 99% pada kepekatan 1 M, kelajuan gas 5.0 mL/s dan masa penyerapan 60 minit. Sementara itu, penulenan biohidrogen menggunakan membran PSF mempunyai peratusan tertinggi penulenan H_2 hampir 77% pada tekanan 3 bar. Biohidrogen yang telah ditulenkan melalui kedua-dua teknik pemisahan telah diuji dalam sel bahan api PEM dan ianya telah dibandingkan secara langsung dengan campuran biohidrogen asal dari fermentasi POME (50% H_2), yang mana kesemua nisbah gas telah diwakili oleh komposisi gas tersimulasi. Arus dan kuasa yang telah dihasilkan pada 100% H_2 (ketulenan H_2 menyerupai peratusan dari teknik penyerapan) adalah 1.66 A dan 9.31 W manakala pada 75% H_2 (ketulenan H_2 menyerupai peratusan dari teknik membran) adalah 0.69 A dan 3.01 W. Keputusan ini telah membuktikan bahawa kedua-dua teknik penulenan biogas berpotensi tinggi bagi meninggikan kecekapan penulenan gas H_2.

Kata kunci: penyerapan, pelarut alkali, biohidrogen, karbon dioksida, efluen minyak kelapa sawit, rawatan

Introduction

The treatment of palm oil mill effluent (POME) has been an acceptable and widely used technique in the production of biogas as a potential source of renewable energy. The treatment process of POME is a method used to reduce its biochemical oxygen demand (BOD) and chemical oxygen demand (COD) before being discharged into the environment, releasing mixed gases comprising of CH4, H_2 and CO_2 [1]. The increasing concentrations of CO_2 into the atmosphere have raised concerns with respect to the environment. Notably, this prompted the need to consider new methods to control the emission of greenhouse gases (GHG). CO_2 is considered as the main anthropogenic contributor to the GHG effect, which is allegedly responsible for 60% of the increase in atmospheric temperature, commonly referred to as global warming [2]. Among the various sources of CO_2, fossil-fuel power plants are one of the major CO_2 contributors regarding this issue, generating approximately 30% of CO_2 from the production process into the earth's atmosphere [1]. Indeed, the POME treatment process under the anaerobic condition is believed to produce valuable biogases such as biohydrogen, which could be further upgraded to high value biohydrogen which could be utilised as alternative energy sources for the future sustainable development of energy [3]. The composition of biogas produced is highly dependent on the hydraulic retention time (HRT), in which HRT produced over 3 days would produce an equal amount of H_2 and CO_2 [4]. Thus, critical development of effective methods for the capture of CO_2 and biohydrogen purification has become a significant concern. The physical properties of CO_2 and H_2 (the major gases from POME treatment) are listed in Table 1.

Table 1. Physical properties of CO_2 and H_2 [5]

Gas	Molecular Weight (g mol^{-1})	Kinetic Diameter (Å)	Critical Pressure (kPa)	Critical Temperature (K)
CO_2	44.0	3.30	7386	304.2
H_2	2.0	2.89	1296	33.14

To date, numerous gas upgrading methods have been developed globally, including absorption, adsorption and membrane technology [6]. Gas absorption using alkanolamine has been used for CO_2 scrubbing on an industrial scale for decades. However, several drawbacks such as high energy consumption and severe corrosion problems are inherent in this process. Hence, the exploration of improved gas separation technology by researchers in this area is of great significant. Currently, the novel technology associated with membrane separation has emerged as one of the most feasible technologies for biohydrogen separation and purification processes [7]. Membrane technology in the development of biological systems can play multiple roles, including in fermentative biohydrogen technology. For example, a membrane bioreactor which employed submerged or externally connected porous-water filtration (microfiltration (MF), ultrafiltration (UF), nanofiltration (NF), and reverse osmosis (RO)) membranes could retain active biomass efficiently within the fermenter. Furthermore, it has been discovered that membrane technology could also assist in overcoming the issue of low reaction yields by allowing *in situ* and continuous removal of biohydrogen using membranes from the membrane bioreactor [7]. Gas upgrading for H_2 and CO_2 capture via absorption, membrane permeation and membrane contactor were reported as shown in Table 2.

Table 2. Summary of gas upgrading via absorption and membrane techniques

Technique	Gas Composition	Condition	Recovery	Reference
Absorption	10- 14 v/v% CO_2	Ammonia, sieve plate, 25 -55 ^oC	95-99% CO_2 capture	Diao et al. [8]
Absorption	8- 16 v/v% CO_2	MEA, 10-40 ^oC	>97% CO_2 capture	Ma et al. [9]
Membrane	Pure gases of H_2 and CO_2 were tested in sequence	Polybenzimidazole based asymmetric hollow fiber membrane, 400^oC	H_2 permeance 2.6 GPU CO_2 permeance 0.096 GPU Selectivity (H_2/ CO_2) 27.28	Kumbharkar et al. [10]
Membrane	79% CO_2, 21% H_2	Membrane Contactor, MEA as liquid carriers	92% H_2 purity	Modigell et al. [11]

Materials and Methods

The initial work on POME anaerobic fermentation to produce biogas was carried out by the Biohydrogen Research Group in Universiti Kebangsaan Malaysia (UKM) [4, 13]. The composition of the biogas mixture produced during the process mainly consisted of 39% H_2 and 49% CO_2 as reported by the literature and in previous work with no presence of H_2S [13, 14]. Since the capacity of biogas produced from fermentation in one day (24 hours) is limited to only 15 - 20 L/d and considered insufficient for continuous upgrading mode, a simulated model gas of H_2 and CO_2 was used with similar composition found in the literature. A mixed gas of H_2 and CO_2 at 50v%/50v% and single gases of H_2 gas (99.5%) and CO_2 gas (99.8%) were used and supplied by NIG Gas Sdn. Bhd. A mixed gas of H_2 and CO_2 (ratio 50:50) was also used in both absorption and membrane separation for H_2 purification evaluation.

Absorption

The absorption process was conducted using three types of alkaline solution, i.e. potassium hydroxide (KOH), mono-ethanolamine (MEA) and ammonia (NH_3). The absorption began by allowing the fixed feed mixture flow rate of gas comprising fixed gas of H_2/CO_2 with 50%/50% to enter the bubble glass reactor filled with an alkaline solution of different molarity (refer Figure 1). Next, the purified H_2 permeated at the outlet point was collected in a gas syringe to determine its final composition. For each experiment, data were averaged from two replicates for reproducibility. The parameters involved in the absorption process are listed in Table 3. The range of each parameter used was adapted from the study by Maceiras et al. where the solvent concentration, solvent temperature, gas mixture flow rate, and absorption time was in the range of 0 to 1 M, 25 to 70 ^oC, 2 to 7 mL/s and 0 to 100 min, respectively [15]. For the experiment, the solvent volume was kept constant at 1 L.

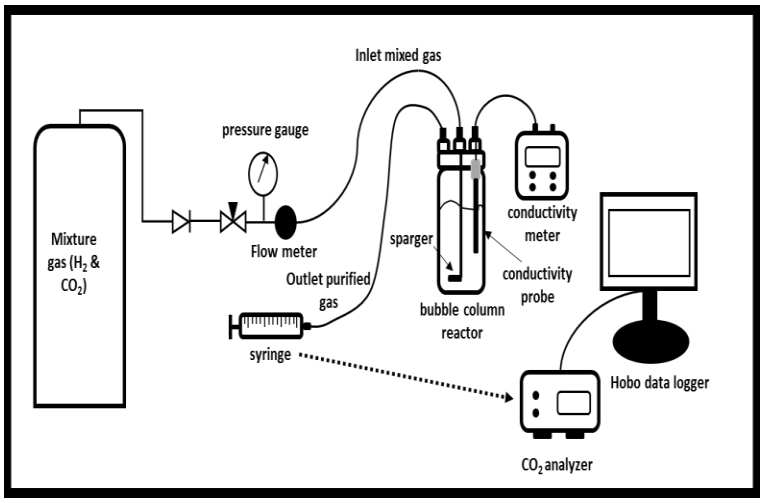


Figure 1. Schematic diagram of CO_2 absorption technique

Table 3. List of parameters for absorption technique

Parameter	**Range of Parameter**
Feed mixture gas flow rate (mL/s)	5.0
Feed mixture gas composition (H_2/CO_2)	50%/50%
Type of alkaline solution	KOH, NH_3, MEA
Concentration of solution (M)	1.0
Temperature of solution (^oC)	28
Time data recorded (min)	2,5,15,30 and 60
Diameter and height of reactor (cm)	8 and 22
Volume of solution (ml)	500

Membrane separation

Polysulfone (PSF) membranes were used in this study to determine the permeability and selectivity of H_2 and CO_2 during the gas separation and purification process (refer Figure 2). The PSF asymmetric membranes were supplied by the Advanced Membrane Research Centre (AMTEC), The University of Technology Malaysia (UTM), which was synthesised from PSF granules (Udel-P1700) in a solvent mixture of N,N dimethylacetamide, tetrahydrofuran and ethanol at an appropriate composition.

Gas permeation rate can be calculated by using pressure normalized flux in Eq. (1):

$$\frac{P}{l}i = \frac{Q_i}{(\Delta P)(A)} \quad (1)$$

where (P/l) is defined as pressure-normalized flux or permeability for gas i in GPU unit; Q_i is volumetric flow rate of gas i, ΔP is the pressure difference across membrane, A is the membrane effective surface area and l the membrane skin thickness.

Membrane selectivity (α) can be determined by dividing the permeability, p of H_2 over CO_2 as stated in Eq. (2):

$$\alpha = \frac{pH_2}{pCO_2} \quad (2)$$

The gas composition was determined by using Gas Chromatography (GC, model SRI 8600C, USA) to measure the composition of the mixed gases of H_2 and CO_2.

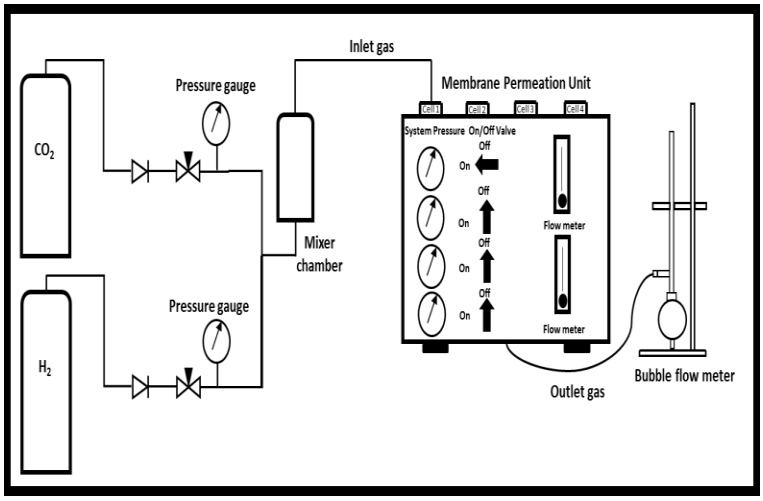


Figure 2. Schematic diagram of Membrane Permeation Unit

Fuel cell application

Finally, the purified H_2 mixture from the simulated model gas (using a similar composition obtained from the absorption and membrane separation technique) was tested in a fuel cell system supplied by the PEMFC stack from the Horizon Fuel Cell, model FCS-B20 with a maximum power capacity of 10 W. The effect of CO_2 the concentration on the PEMFC performance (voltage, current and power) was monitored to determine the optimum composition of H_2 with CO_2 existence for the fuel cell application. For each experiment, the power, current and voltage data were obtained from the average value of duplicate experiments. The data were presented in the plotted graph of power versus current, voltage versus time and power versus percentage of CO_2. The summary of the parameters involved in the H_2 PEMFC testing is listed in Table 4.

Table 4. List of parameters for PEMFC application

Parameters	**Range of parameters**
Composition mixture of H_2 and CO_2 (v%/v%)	50/50, 75/25, 90/10 and 100/0 of H_2 & CO_2
Feed mixture gas flow rate (cc/min)	55
Time of application (min)	30

Results and Discussion

The absorption and membrane separation techniques were employed to compare the H_2/CO_2 separation and purification efficiency in this work. The purified H_2 (simulated gas composition with the purity obtained *via* these methods) was then utilised in the fuel cell application for performance evaluation.

Absorption

In this study, the absorbents effects (KOH, NH_3, MEA) at 1 M concentration towards H_2 purification was performed

at the highest feed gas flow rate (5.0 mL/s) (refer Figure 3). The findings indicated a significant effect of 1 M solution concentration to the purification of H_2. The H_2 purity had reduced significantly at 1 M of KOH and MEA after 30 minutes of absorption, in which the reduction from 99% to 64% and 75% was observed for KOH and MEA solutions. While the purity for ammonia absorption was found relatively higher at 79% after 60 min of absorption. Also, the higher absorbent concentration could release more free ionic species which contributed to a greater CO_2 reaction in the absorption process. However, the decrement trend of gas purity indicated the presence of a CO_2 saturation stage during absorption [15]. Moreover, a higher feed flow rate was used to create turbulence effects for a rapid reaction between the gas and free ionic species contained in the solution [16].

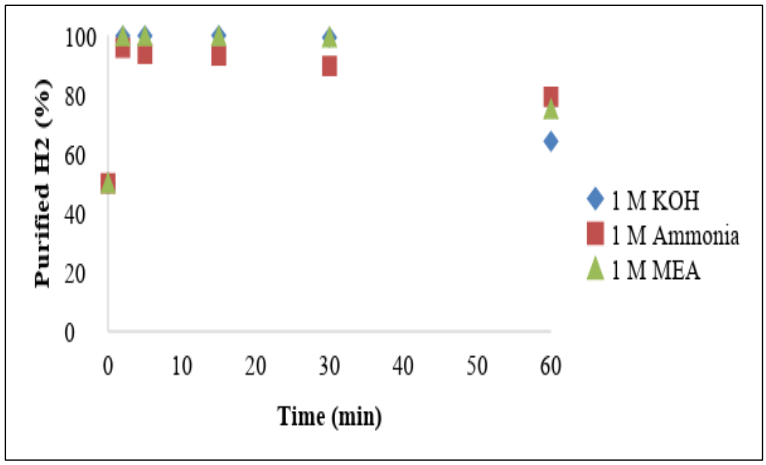


Figure 3. Purified H_2 composition *via* absorption technique with different alkaline solutions (KOH, NH_3, MEA) at 1 M concentration

Among these three solvents, MEA was preferred due to its excellent absorption performance in comparison to NH_3 and KOH solutions regarding its H_2 purification percentage. Although MEA exhibited similar absorption performance as KOH, MEA was more reliable and preferable in the market. Possibly due to its low cost and its ability to handle low CO_2 partial pressure gas stream during the absorption [2, 17]. Hence, MEA was concluded as a potential absorbent candidate for better absorption efficiency and to be further utilised instead of KOH.

Membrane separation

The separation performance of PSF membranes regarding CO_2 and H_2 permeance rate and selectivity at the pressure range of 1 to 8 bar was successfully measured. According to Figure 4, the highest permeance rate for H_2 for PSF membrane was indicated at 13.08 GPU (at 2 bar) while the highest permeability for CO_2 was recorded at 7.24 GPU (at 1 bar). Additionally, the selectivity for H_2/CO_2 was increasing proportionately concerning the pressure increment, in which the best selectivity was observed at 4.07 (tested at 4 bar). The PSF membrane was known as a glassy polymer and the permeant diffusion coefficient was more dominant than the solubility coefficient. Therefore, the smaller and non-condensable H_2 gas with a molecular diameter of 2.9 Å, was preferentially permeated through PSF polymer instead of CO_2 with a larger molecular diameter (3.3 Å) [18]. Hence, the permeance rate for H_2 was always higher than CO_2. In addition to the decrement trend of H_2 and CO_2 permeance against pressure, this could be explained based on the competitive solubility effects between the gas and polymer structures and the saturation of the polymer sorption site with gas molecules which resulted in membrane compaction [19, 20]. The plasticisation effect was not detected in this study due to the absence of CO_2 permeance increment with pressure.

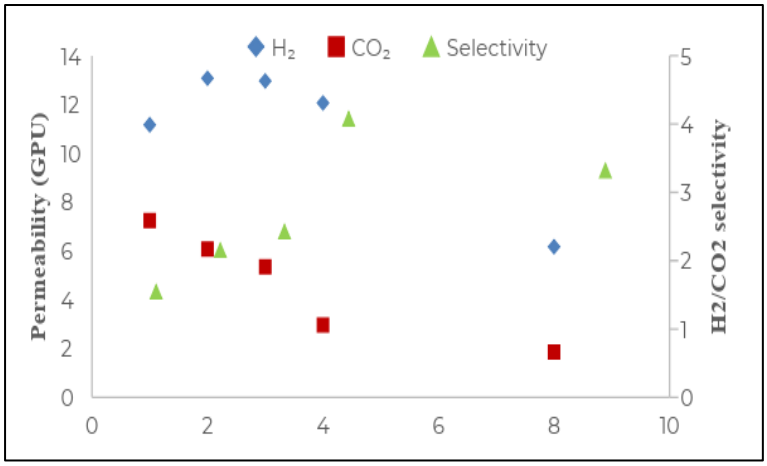


Figure 4. Gas permeation rate and selectivity for PSF Membrane

On the other hand, Figure 5 depicts the pressure effect on the H_2 and CO_2 gas composition in the permeate stream with different pressure using a fixed composition of 50%/ 50% of H_2/CO_2 feed gas mixture. The findings indicated that the H_2 purity increased significantly from 68 % to 77 % from the pressure of 1 to 3 bar. However, when the applied pressure increased from 4 to 8 bars, the H_2 purity began to gradually reduce with the lowest recorded at 52% (8 bar). This scenario was possibly due to the flux increment which enhanced the solubility and diffusion rates of H_2 [21]. Also, the optimum pressure for the satisfactory H_2 permeance rate was within the range of 1 to 3 bar. Thus, the integration between the membrane and bioreactor system was observed as being a practical approach since the internal pressure range was similar for both systems [22]. Therefore, this work has proven the separation efficiency of PSF membrane in the biohydrogen purification process with high permeability, the selectivity of H_2/CO_2 and high H_2 purity (77%).

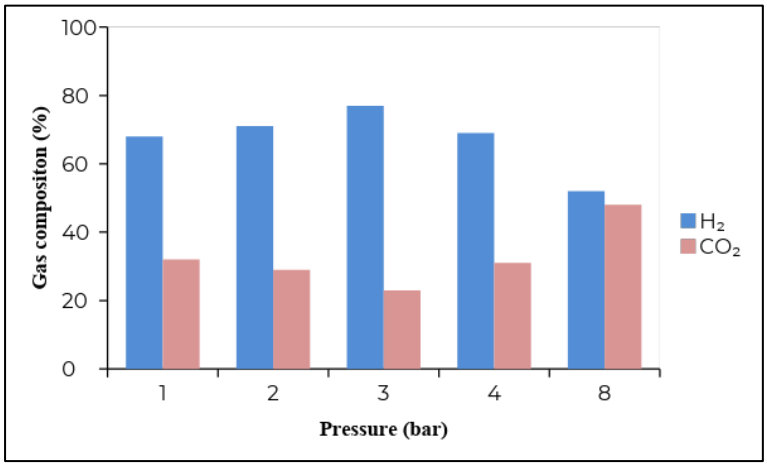


Figure 5. Gas composition in permeate stream after gas permeation test for PSF membrane

Fuel cell application

The purified biohydrogen from the two separation techniques was tested in the PEM fuel cell and compared with the original biohydrogen mixture from POME fermentation. Indeed, this composition was important to observe the fuel cell performance profile, when the fermented gas was used without further purification. Based on the results as shown in Figure 6, the profiles of stack power with current were found to be similar. At the beginning of the cell operation, the power increased steadily with the current, until a maximum power peak was achieved before the

power decreased with the current. The highest current recorded was in parallel with the H_2 composition, where the highest H_2 purity gave the highest current value and vice versa. The highest current recorded was 1.66 A for 100% H_2 purity while the lowest current was 0.32 A for 50% H_2 purity. Accordingly, this has proven that higher H_2 % supplied into PEMFC could generate a higher amount of current, which resulted in the higher amount of power. Hence, in a real fuel cell operation, the supply of high purity H_2 into the fuel cell is essential to ensure higher power generation.

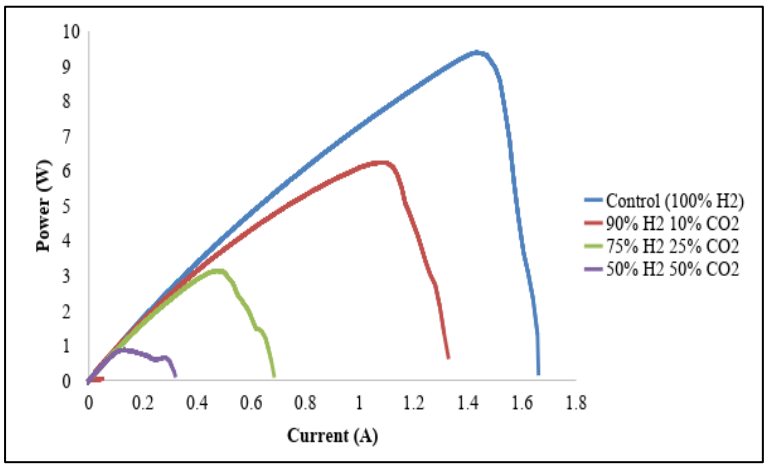


Figure 6. Power profile with current at different H_2 concentration

Meanwhile, Figure 6 also shows the average power produced by different CO_2 compositions. The power produced reached the highest value which was close to 9 W and conversely, the power recorded was less than 1 W for the lowest H_2 composition. The graph plotted showed a linear pattern of power produced with CO_2 composition present in the PEMFC. Therefore, it proved that the existence of CO_2 in the PEMFC gave a significant effect on PEMFC performance. Further, the CO_2 had obviously decreased the amount of power produced by PEMFC. The CO_2 presence in the PEMFC would affect the electrochemical catalytic rates, which interfere with proton transport across the polymer electrolyte or prevent the flow of reactants to or the reaction of products away from the anode or cathode charge transfer interfaces. Also, the presence of impurities may also decrease the operational lifetime of the fuel cell by increasing the component failure rate. Ahluwalia et al. suggested that any CO_2 impurity in the fuel adsorbs weakly on the platinum (Pt) catalyst [23]. According to Chew et al., at low CO_2 concentrations, the observed degradation in cell power can be explained based on CO produced from CO_2 on the active Pt surface and the subsequent adsorption of CO on the active Pt sites via the reverse water gas shift reaction (RWGSR) between CO_2 and the adsorbed H_2 [24]. Furthermore, at higher CO_2 concentrations, the decrease in cell potential due to the dilution of the H_2 also contributed to performance degradation. Therefore, it was essential to minimise the amount of CO_2 in the H_2 mixture to gain more power produced from the PEMFC.

Hence, this study has revealed that different H_2 concentrations supplied into the PEMFC would present different performances on the current and power produced. It was also proven that biohydrogen separation using the absorption technique could provide the best purification (close to 100% H_2 purity) and in turn, demonstrated the higher capacity of current and power (1.66 A and 9.31 W) in comparison to the membrane technique.

Conclusion

The absorption and membrane separation techniques were successfully investigated in H_2/CO_2 separation and the purification process where the highly-purified H_2 was further utilised in the fuel cell application. The observations and separation performance between the two separation techniques were satisfactory. Therefore, it could be concluded that MEA is the best alkaline solvent for absorption due to the high percentage of purified H_2 produced (99% for 1 M MEA). The PSF membranes possessed high H_2 permeance rate and H_2/CO_2 selectivity, which was

obtained at 13.08 GPU (at 2 bar) and 4.07 (tested at 4 bar), respectively. The absorption technique possessed better H_2 purity as the percentage of purified H_2 was close to 100% purity, while for membrane technique it was close to 80%. The highest current and power generated were 1.66 A and 9.31 W respectively from the feed mixture gas with 100%/0% of H_2/CO_2.

Acknowledgement

The authors gratefully acknowledge Kursi UKM-YSD for financial support of the project PKT 6/2012, Ministry of Education under FGRS/1/2018/TK02/UKM/02/2 and Universiti Kebangsaan Malaysia for research grant GUP-086-2016.

References

1. Sayari, A., Belmabkhout, Y. and Serna-Guerrero, R. (2011). Flue gas treatment via CO_2 adsorption. *Chemical Engineering Journal*, 171: 760–774.
2. Luis, P. (2016). Use of monoethanolamine (MEA) for CO_2 capture in a global scenario: Consequences and alternatives. *Desalination*, 380: 93–99.
3. Chin, M. J., Poh, P. E., Tey, B. T., Chan, E. S. and Chin, K. L. (2013). Biogas from palm oil mill effluent (POME): Opportunities and challenges from Malaysia's perspective. *Renewable Sustainable Energy Revision*, 26: 717–726.
4. Badiei, M., Jahim, J. M., Anuar, N. and Sheikh Abdullah, S. R. (2011). Effect of hydraulic retention time on biohydrogen production from palm oil mill effluent in anaerobic sequencing batch reactor. *International Journal of Hydrogen Energy*, 36: 5912–5919.
5. Kim, K., Ingole, P. G., Kim, J. and Lee, H. (2013). Separation performance of PEBAX/PEI hollow fiber composite membrane for $SO_2/CO_2/N_2$ mixed gas. *Chemical Engineering Journal*, 233: 242–250.
6. Rufford, T. E., Smart, S., Watson, G. C. Y., Graham, B. F., Boxall, J. , Diniz da Costa, J. C. and May, E. F. (2012). The removal of CO_2 and N_2 from natural gas: A review of conventional and emerging process technologies. *Journal of Petroleum Science and Engineering*, 94–95: 123–154.
7. Bakonyi, P., Nemestóthy, N. and Bélafi-Bakó, K. (2013). Biohydrogen purification by membranes: An overview on the operational conditions affecting the performance of non-porous, polymeric and ionic liquid-based gas separation membranes. *International Journal of Hydrogen Energy*, 38: 9673–9687.
8. Diao, Y.-F., Zheng, X.-Y., He, B.-S., Chen, C.-H. and Xu, X.-C. (2004). Experimental study on capturing CO_2 greenhouse gas by ammonia scrubbing. *Energy Conversion Management*, 45: 2283–2296.
9. Ma, S., Song, H., Wang, M., Yang, J. and Zang, B. (2013). Research on mechanism of ammonia escaping and control in the process of CO_2 capture using ammonia solution. *Chemical Engineering Research Design*. 91: 1327–1334.
10. Kumbharkar, S. C., Liu, Y. and Li, K. (2011). High performance polybenzimidazole based asymmetric hollow fibre membranes for H_2/CO_2 separation. *Journal of Membrane Science*, 375: 231–240.
11. Modigell, M., Schumacher, M., Teplyakov, V. V. and Zenkevich, V. B. (2008). A membrane contactor for efficient CO_2 removal in biohydrogen production. *Desalination*, 224: 186–190.
12. Mohamad, I. N., Rohani, R., Nor, M. T. M., Claassen, P., Muhammad, M. S., Masdar, M. S. and Rosli, M. I. (2017). An overview of gas-upgrading technologies for biohydrogen produced from treatment of palm oil mill effluent. *Journal Engineering Science and Technology*, 12: 725–755.
13. Chong, P. S., Jahim, J. M., Harun, S., Lim, S. S., Mutalib, S. A., Hassan, O. and Nor, M. T. M. (2013). Enhancement of batch biohydrogen production from prehydrolysate of acid treated oil palm empty fruit bunch. *International Journal of Hydrogen Energy*, 38: 9592–9599.
14. Mohamad, I. N., Rohani, R., Masdar, M. S. M., Nor, M. M. T. and Jahim, J. (2015). Permeation properties of polymeric membranes for biohydrogen purification. *International Journal of Hydrogen Energy*. 41: 4474–4488.
15. Maceiras, R., Alves, S. S., Cancela, M. Á. and Álvarez, E. (2008). Effect of bubble contamination on gas–liquid mass transfer coefficient on CO_2 absorption in amine solutions. *Chemical Engineering Journal.* 137: 422–427.
16. Zhao, B., Su, Y. and Peng, Y. (2013). Effect of reactor geometry on aqueous ammonia-based carbon dioxide capture in bubble column reactors. *International Journal of Greenhouse Gas Control*, 17: 481–487.

17. Spigarelli, B. P. and Kawatra, S. K. (2013). Opportunities and challenges in carbon dioxide capture. *Journal of CO_2 Utility*, 1: 69–87.
18. Choi, S., Lee, M., Oh, S. and Koo, J. (2003). Gas sorption and transport of ozone-treated polysulfone, *Journal of Membrane Science*, 221: 37–46.
19. Rezakazemi, M., Ebadi Amooghin, A., Montazer-Rahmati, M. M., Ismail, A. F. and Matsuura, T. (2014). State-of-the-art membrane-based CO_2 separation using mixed matrix membranes (MMMs): An overview on current status and future directions. *Progress in Polymer Science.* 39: 817–861.
20. David, O. C., Gorri, D., Urtiaga, A. and Ortiz, I. (2011). Mixed gas separation study for the hydrogen recovery from $H_2/CO/N_2/CO_2$ post combustion mixtures using a Matrimid membrane. *Journal of Membrane Science.* 378: 359–368.
21. Ebert, K., Fritsch, D., Koll, J. and Tjahjawiguna, C. (2004). Influence of inorganic fillers on the compaction behaviour of porous polymer based membranes, *Journal of Membrane Science*, 233: 71–78.
22. Bakonyi, P., Nemestóthy, N., Lankó, J., Rivera, I., Buitrón, G. and Bélafi-Bakó, K. (2015). Simultaneous biohydrogen production and purification in a double-membrane bioreactor system, *International Journal of Hydrogen Energy*, 40: 1690–1697.
23. Ahluwalia, R. K. and Wang, X. (2008). Effect of CO and CO_2 impurities on performance of direct hydrogen polymer-electrolyte fuel cells, *Journal of Power Sources*. 180: 122–131.
24. Chew, L. W., Masdar, M. S. and Kamarudin, S. K. (2015). Purification of bio-hydrogen using absorption techniques and the effect of CO_2 impurity on the PEMFC performance. *American Journal of Chemistry*, 5: 24–34.

Malaysian Journal of Analytical Sciences, Vol 23 No 1 (2019): 90 - 99
DOI: https://doi.org/10.17576/mjas-2019-2301-11

MALAYSIAN JOURNAL OF ANALYTICAL SCIENCES
Published by The Malaysian Analytical Sciences Society
ISSN 1394 - 2506

FACILE TECHNIQUE FOR THE IMMOBILISATION OF TIO_2 NANOPARTICLES ON GLASS SUBSTRATES FOR APPLICATIONS IN THE PHOTOCATALYTIC SELF-CLEANING OF INDOOR AIR POLLUTANTS

(Salutan nanopartikel TiO_2 ke atas Substrat Kaca Melalui Teknik Mudah untuk Penyingkiran Bahan Pencemar Udara dalaman Melalui Proses Fotokatalisis)

Kah Hon Leong[1]*, Jia Quan Lee[2], A. Ashok Kumar[3], Lan Ching Sim[1], Saravanan Pichiah[4]

[1]Department of Environmental Engineering, Faculty of Engineering and Green Technology, Universiti Tunku Abdul Rahman, Jalan Universiti, Bandar Barat, 31900 Kampar, Perak, Malaysia
[2]Environmental Engineering Laboratory, Department of Civil Engineering, Faculty of Engineering, University of Malaya, 50603 Kuala Lumpur, Malaysia
[3]Department of Chemical Engineering, School of Engineering and Technology, Periyar Maniammai University, Thanjavur - 613 403, India
[4]Department of Environmental Science and Engineering, Indian Institute of Technology (ISM) Dhanbad- 826004, Jharkhand, India

**Corresponding author: khleong@utar.edu.my*

Received: 13 April 2017; Accepted: 17 April 2018

Abstract

Self-cleaning technology employing titania (TiO_2) photocatalysts has major applications in the removal of indoor air pollutants. Pollutant removal efficiency significantly depends on the properties of the photocatalyst thin film, which is deposited on substrates. The present work developed a facile immobilisation technique that is based on simple sol–gel process. In this technique, TiO_2 nanoparticles are spray-coated onto a porous glass substrate. The uniformity of the TiO_2 coating on the glass surface was studied using a dynamic flowsense charge-coupled device camera. The influence of different TiO_2 nanoparticle concentrations in the ethanol phase was identified through rheological analysis, which showed that nanoparticle concentration is a crucial factor that affects the uniformity of the coating layer. The ability of the obtained material to catalyse formaldehyde photodegradation in presence of artificial UV light was investigated. Results demonstrated that >15.0 g/L TiO_2 is required to activate formaldehyde photodegradation and that uniform surface coatings with sufficient surface thickness can be obtained by spraying TiO_2 nanoparticles on glass substrates at concentrations of more than 15.0 g/L. This study demonstrated that uniformly coated photocatalysts for the efficient self-cleaning of indoor air pollutants can be fabricated through a facile technique.

Keywords: self-cleaning, TiO_2, sol-gel, formaldehyde, photocatalysis

Abstrak

Teknologi pembersihan menggunakan TiO_2 sebagai fotokatalis yang memainkan peranan penting terutamanya dalam menyingkirkan bahan pencemar udara dalaman. Pembersihan bahan pencemar ini sangat bergantung kepada ketebalan filem salutan terbentuk pada substrat. Dalam kajian ini teknik mudah dapat dicapai melalui proses sol-gel dan diikuti dengan salutan semburan TiO_2 berliang nanopartikel ke atas substrat kaca. Keseragaman pembentukan titania bersalut pada permukaan kaca dikaji menggunakan kamera "gabungan cas dinamik flowsense. Pengaruh kepekatan nanopartikle TiO_2 yang berbeza-beza dalam fasa etanol membawa kepada analisis reologi. Kajian reologi menunjukkan keberkesanan kepekatan nanopartikel bagi mendapatkan lapisan salutan yang seragam. Keberkesanan salutan dinilai dengan penyingkiran formaldehid dalam kehadiran

cahaya UV tiruan. Keputusan penyingkiran menunjukkan bahawa kepekatan TiO_2 yang tinggi dengan melebihi 15.0 g/L menunjukkan penyingkiran formaldehid pada tahap yang ketara disebabkan oleh keseragaman salutan pada permukaan kaca serta ketebalan permukaan yang mencukupi. Kajian ini menunjukkan prestasi yang baik dalam mengesahkan salutan fotokatalis yang seragam untuk meningkat keberkesanan penyingkiran bahan pencemar udara dalaman.

Kata kunci: penyingkiran, TiO_2, sol-gel, formaldehid, fotokatalisis

Introduction

Indoor air pollution is a growing concern and has emerged as a major health threat in numerous countries. Thus, indoor air pollution requires immediate resolution. On average, every human being spends approximately 90% of their daily life indoors. Therefore, humans are constantly exposed to indoor air pollutants. Exposure to indoor air pollutants can cause health issues, such as sick building syndrome. The most ubiquitous indoor air pollutants include CO_2, NO_2, formaldehyde and volatile organic compounds (VOCs) [1]. These pollutants can be found easily in any commercial or industrial building. Among these pollutants, formaldehyde is most common. The major sources of formaldehyde pollutants include formaldehyde-emitting building materials and consumer products, such as furniture and other wooden products. Combustion processes, such as smoking, cooking and incense burning, are also sources of formaldehyde emissions. The secondary formation of formaldehyde is triggered by the oxidation of VOCs and the reactions between ozone and terpenes. Researchers have only recently considered photocatalyst-based self-cleaning technology as a feasible solution to indoor air pollution [2].

Self-cleaning surface coatings that employ metal oxides are used as alternative approaches for the remediation of indoor air pollutants [3]. Self-cleaning coatings can be classified in two different categories, namely, superhydrophilic and superhydrophobic coatings [4–11]. Superhydrophilic coatings are progressive and are based on suitable metal oxides. They chemically degrade complex pollutants through a photon energy-assisted cleaning mechanism [4]. Superhydrophilic TiO_2-coated glass substrates provide a new way to clean indoor air pollutants. TiO_2 is a popular and widely studied semiconductor photocatalyst given its various superior advantages [12–14]. It exhibits excellent photocatalytic activity in the photodegradation of harmful and toxic organic aquatic pollutants [15–20]. Developed or modified TiO_2 composites have been used in water and energy-related applications, including the removal of toxic aquatic pollutants, the photoreduction of CO_2 and the production of hydrogen through hydrolysis.

Nevertheless, the application of TiO_2 to remediate air pollution, particularly indoor air pollution, has not been extensively studied. The use of TiO_2 as an immediate remedy for indoor air pollutants has attracted increased attention because of its superior photostability, photoactivity and superhydrophilicity compared with other photocatalysts [21, 22]. These unique qualities set a strong foundation for the effective removal of indoor air pollutants. However, the removal of air pollutants is a gas-phase reaction. Thus, the TiO_2 suspension technique used in water treatment is inappropriate for air pollution treatment because it will not facilitate the photocatalytic reaction in air. TiO_2 nanoparticles must be immobilised onto substrates, such as glass and walls, before they can be used to remove air pollutants. However, immobilising TiO_2 nanoparticles onto surfaces is difficult. Thus, an appropriate and cost-effective technique for the immobilisation of TiO_2 is needed. Coating has emerged as a facile approach for the immobilisation of TiO_2 nanoparticles on substrates.

Various coating techniques have been adopted by many researchers. These coating techniques include sputtering, chemical vapour deposition and thermal spraying [23–29]. However, all these methods have their own drawbacks, such as high temperature requirements that can change the TiO_2 microstructure. Moreover, all of these coating techniques are economically nonviable [23,30]. Hence, the present work demonstrates the deposition of a uniform, transparent, photocatalytic and superhydrophilic TiO_2 coating on a glass substrate through a simple spraying technique. The TiO_2-coated glass substrates have potential applications in the removal of indoor air pollutants, particularly formaldehyde.

Materials and Methods

Materials

Titania (TiO_2) powder (P25 Degussa), ethanol, acetone and isopropanol were purchased from R & M Chemicals. Deionised water was used in all experiments. All chemicals were of analytical grade and used without any further purification.

Spray coating

TiO_2 solutions with concentrations of 2.5, 5.0, 10.0, 15.0 and 20.0 g/L were prepared by mixing 0.5, 1, 2, 3 or 4 g of P-25 TiO_2 powder with 200 mL of ethanol, respectively. The solutions were stirred vigorously until homogenous and white in colour. Soda lime glass plates (20 mm × 20 mm × 2 mm) were first cleaned and washed several times with deionised water, then washed with acetone, ethanol and isopropanol in a sonicator. Then, the cleaned glass plates were dried in an oven at 80 °C to ensure that all surface contaminants were removed. Each prepared TiO_2 nanoparticle solution was loaded into a controlled pneumatic spray gun and carefully sprayed onto the cleaned soda lime glass for 10 s. Spraying was repeated five times to ensure that the coating solution was uniformly coated onto the glass surface. Then, the coated glass substrates were sintered.

Characterization

Film thickness was measured using a surface profilometer. Dynamics FlowSense Charge-coupled Device (CCD) camera (Dantech Dynamics, Denmark) was used to capture images of the TiO_2-coated glass substrates under cold light sources. Surroundings were kept dark to ensure that cold light passed through the glass surfaces coated with various TiO_2 concentrations at the same intensity. Image processing was performed for the analysis of surface properties. Images were converted to greyscale mode for surface plot and three-dimensional (3D) surface analysis. The intensity of images varied from 0 to 255 on the basis of the coated properties. Rheological experiments were performed with Anton Paar Physica MCR 302 with suitable geometry.

Photocatalytic experiment

The schematic of the experimental setup used in this study is shown in Figure 1. A compressor (MACO) with a capacity of 0 CFM to 6.3 CFM was used to provide steady-flow conditions. The air stream from the compressor was filtered using a filter regulator (SHAKO) and a 5 µm air filter (SMC) to filter out any dust particulates and excessive water vapour. The flow rate was manually adjusted by using a flowmeter (Dwyer, USA). Formaldehyde was aerosolised by forcing a stream of air through an aerating unit containing 37% formaldehyde solution (R & M Chemicals). UV-A light (HPMV 400V, NIKKON) was used as the radiation source for the photoreactor. Photocatalytic experiments were performed under a fume chamber with proper closure to prevent the dispersion of airborne formaldehyde and UV light radiation to the surroundings. Formaldehyde concentration was measured by using a Formaldemeter™ htV-m (PPM Technology, UK) every 15 minutes for 3 hours. Removal efficiency was calculated in accordance with the following equation 1:

$$\text{Removal} = \frac{(\text{Initial Concentration } (C_i) - \text{Final Concentration } (C_f) \times \text{Air flow rate } (Q)}{\text{Coating Surface Area } (A) \times \text{Removal Time } (t)} \quad (1)$$

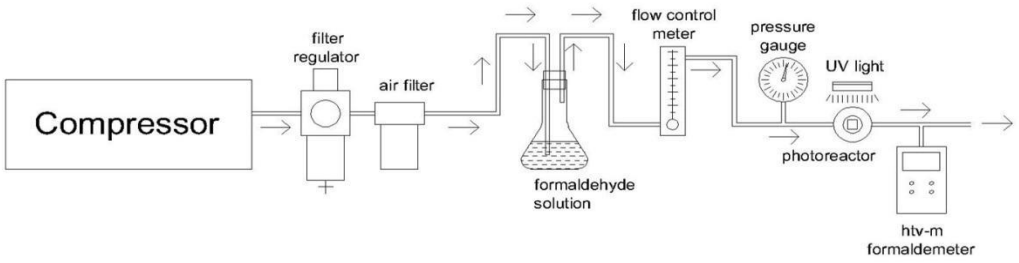


Figure 1. Photocatalysis experimental setup

Results and Discussion

Surface coating

Coating uniformity is an important criterion in the present study. The optimal TiO_2 concentration required to produce a uniform coating on the substrate was identified by depositing different concentrations of TiO_2 nanoparticles on glass substrates and by analysing the properties of the TiO_2-coated substrates. Analytical results indicated that the optimal TiO_2 concentration is >15.0 g/L. Figure 2 shows glass substrates coated with different TiO_2 concentrations, and Figure 3 shows the CCD camera images of these samples. As shown in these images, the surfaces of the substrates coated with less than 15.0 g/L TiO_2 appear rough and uneven. The substrate coated with 2.5 g/L TiO_2 exhibits a small pothole defect, as shown in Figure 3a. These defects decrease photocatalytic efficiency. The roughness of the coating surface decreases as TiO_2 concentration increases.

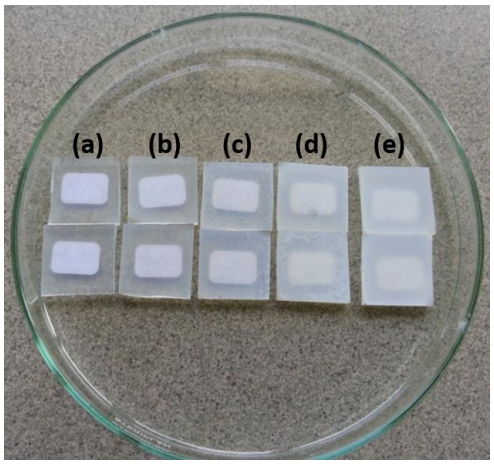


Figure 2. Images of glass surface coated with TiO_2 at different concentration (a) 2.5 g/L, (b) 5.0 g/L, (c) 10.0 g/L, (d) 15.0 g/L and (e) 20.0g/L

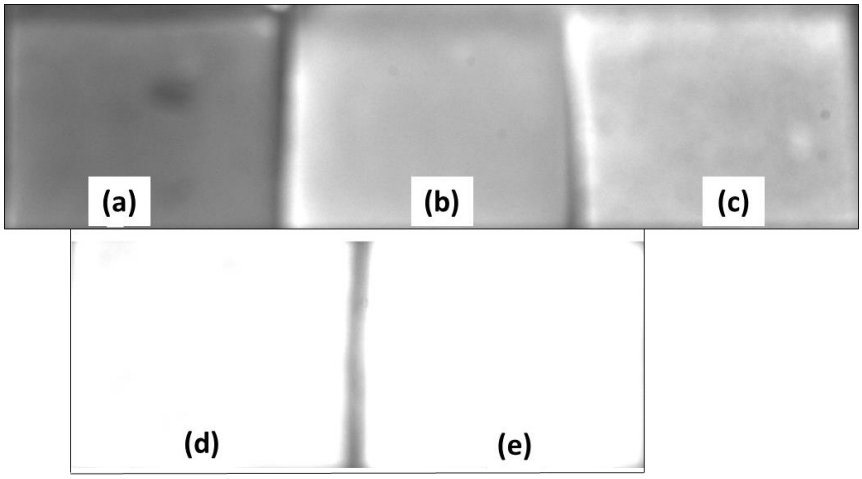


Figure 3. CCD images of different concentration coated on glass surface (a) 2.5 g/L, (b) 5.0 g/L, (c) 10.0 g/L, (d) 15.0 g/L and (e) 20.0 g/L

Figure 4 shows the two-dimensional (2D) perspective of coating thickness obtained by plotting the surfaces of substrates coated with different TiO_2 concentrations. The plot shows that surface coating intensity increases as TiO_2

concentration increases. In contrast to the surface of the glass substrate coated with <15.0 g/L TiO_2, that of the glass substrate coated with 15.0 g/L TiO_2 is highly uniform without any observable surface defects. The uniformity of the surface coatings is further verified by the 3D surface plot shown in Figure 5. Similar to the 2D plot, the 3D plot indicates that rough coatings are obtained when TiO_2 is deposited at low concentrations, whereas smooth, even coatings without defects are obtained when TiO_2 is deposited at concentrations greater than 15.0 g/L. These results prove the robustness of the simple spraying technique adopted in this study.

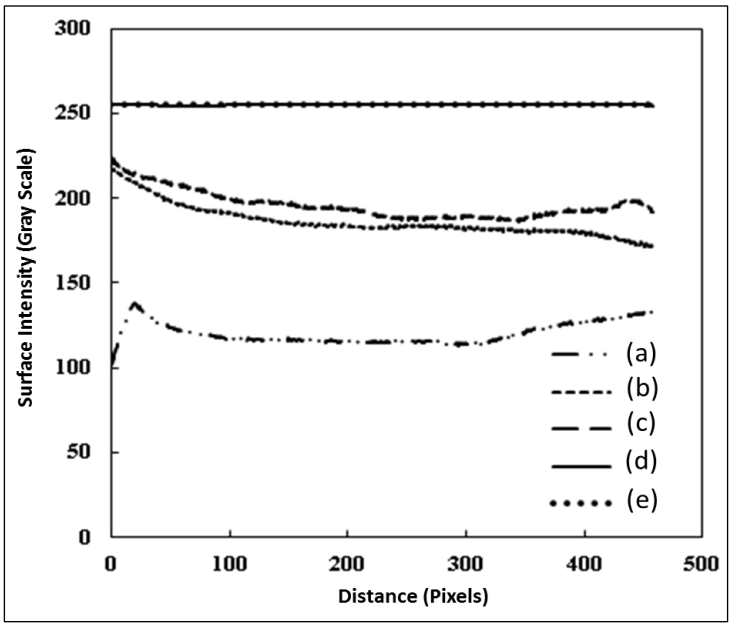


Figure 4. 2-D surface plotting for coating of different concentration (a) 2.5 g/L, (b) 5.0 g/L, (c) 10.0 g/L, (d) 15.0 g/L and (e) 20.0 g/L

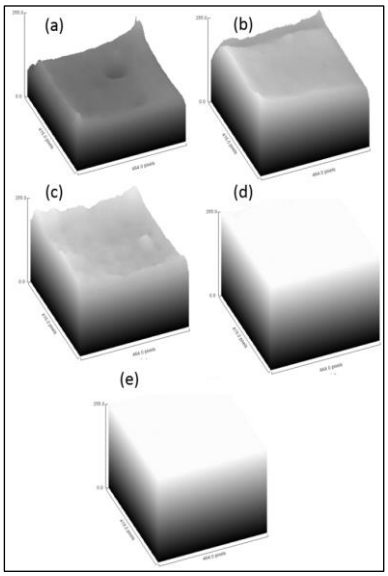


Figure 5. 3-D surface plotting for coating of different concentration (a) 2.5 g/L, (b) 5.0 g/L, (c) 10.0 g/L, (d) 15.0 g/L and (e) 20.0 g/L

The rheological behaviour of the suspension was inferred from the plot of shear stress versus shear rate shown in Figure 6a. As shown in the figure, all concentrations follow a linear trend, indicating Newtonian behaviour. Figure 6b shows the viscosity versus shear rate of different TiO_2 concentrations. Viscosity marginally increases as TiO_2 concentration increases, and the coating solution concentration of 20.0 g/L exhibits the highest viscosity. This phenomenon indicates that the increase in the degree of nanoparticle interaction in the colloidal suspension increases solvent immobilisation [31, 32]. Therefore, coating uniformity will be improved by increasing viscosity, as proven by the 2D and 3D surface plots.

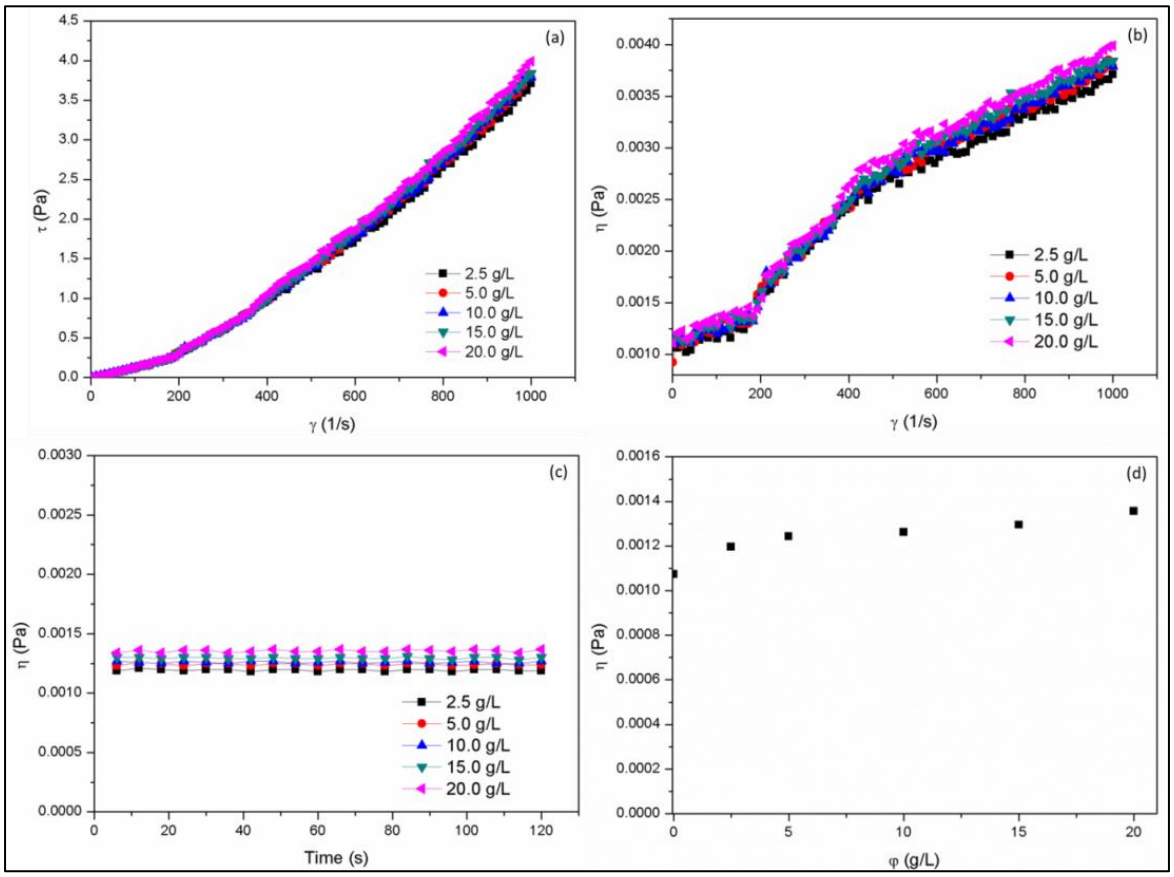


Figure 6. Rheological study (a) Shear stress versus shear rate, (b) Viscosity versus shear rate, (c) Viscosity versus time and (d) Viscosity versus TiO_2 concentration

Effect of Concentration on Formaldehyde Photocatalysis Efficiency

Figure 7 shows the photodegradation of formaldehyde over 3 hours of irradiation with artificial UV light. Formaldehyde concentration was recorded immediately once the airborne formaldehyde concentration had stabilised. As shown in the figure, coatings fabricated with TiO_2 concentrations of less than 15.0 g/L do not successfully remove formaldehyde and instead contribute to the overall level of airborne formaldehyde. Airborne formaldehyde levels have increased because nondegraded formaldehyde evaporates under heat emitted by UV light and becomes airborne once photon energy is activated. This phenomenon indicates that low amounts of TiO_2 cannot effectively photocatalyse formaldehyde degradation even after 3 hours of photodegradation and instead increases the levels of nondegraded formaldehyde in the chamber.

Meanwhile, coatings fabricated with TiO_2 concentrations of >15.0 g/L significantly decrease airborne formaldehyde levels after 3 h. On average, coatings prepared with 15.0 and 20.0 g/L TiO_2 decrease airborne formaldehyde levels to 0.15 and 0.30 ppm, respectively. This significant decrease may be attributed to photodegradation in the reaction chamber. Formaldehyde levels stabilise at the initial stage of photocatalysis induced by coatings containing 15.0 g/L TiO_2 because photodegradation capacity offsets the constant increase in airborne formaldehyde level attributed to evaporation. An overdosage of 20.0 g/L TiO_2 improves removal rate and overcomes the ongoing formaldehyde flow. The outperformance of formaldehyde increases the humidity level inside the reaction chamber. Humidity improves photodegradation. Sun et al. observed similar results [33]. The increase in humidity is attributed to water evaporation in the reaction chamber. The residual water that has not evaporated forms $^{\bullet}OH$ on the coated surfaces. The hydroxyl radical is a powerful oxidant given its high redox potential, and its presence increases the photodegradation rate. However, some of the residual water will evaporate because of the strong heat radiation from the light source, thus causing the degradation rate to fluctuate (Figure 7).

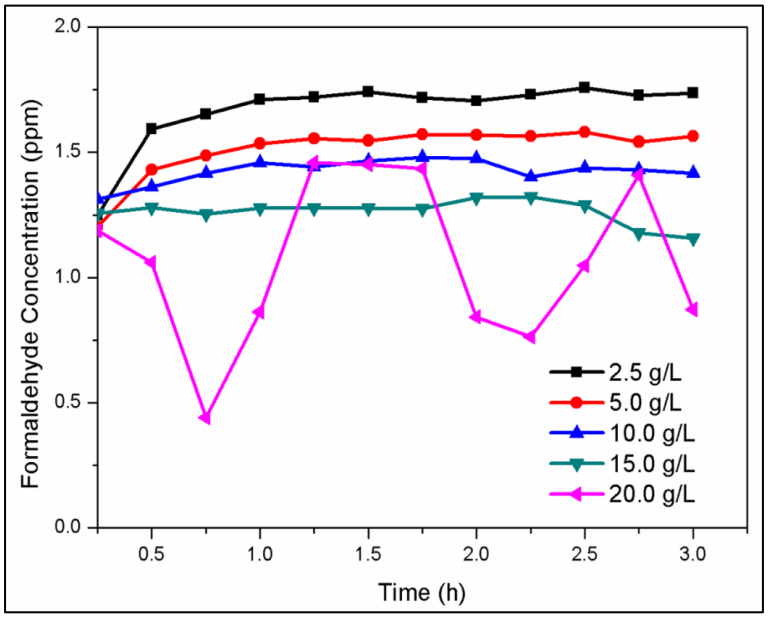


Figure 7. Photodegradation of formaldehyde airborne

Formaldehyde removal rate

As shown in Figure 7, the removal rate obtained with 15.0 g/L TiO_2 is 0.15 ppm, and 1 ppm of formaldehyde is equivalent to 1.23 mg/m^3 at room temperature. Therefore, the concentration of formaldehyde is 0.1845 mg/m^3. By taking airflow into account, where 50 mL/min = 3000 mL/h = 0.003 m^3/h, the amount of formaldehyde oxidised in 1 hour can be calculated as follows:

$$\begin{aligned} \text{Oxidised formaldehyde} &= 0.1845 \text{ mg/m}^3 \times 0.003 \text{ m}^3\text{/h} \\ &= 0.000554 \text{ mg/h} \\ &= 0.554 \text{ µg/h} \end{aligned}$$

Given that the area of the coated surface is 0.0004 m^2, the removal rate of the airborne formaldehyde in 1 hour will be as follows:

$$\begin{aligned} \text{Formaldehyde removal rate} &= (0.554 \text{ µg/h})/0.004 \text{ m}^2 \\ &= 138.5 \text{ µg m}^{-2} \text{ h}^{-1} \\ &= 1.385 \text{ mg m}^{-2} \text{ h}^{-1} \end{aligned}$$

Ichiura et al. reported that TiO_2 sheets fabricated by mixing pure TiO_2 with pulp obtained similar average removal rates of 10.0%–15.0% [34]. Yu et al. reported that TiO_2 nanoparticles deposited onto PTFE filters can catalyse formaldehyde photodegradation in the presence of UV light [35]. Liang et al. studied formaldehyde removal by TiO_2-coated thin films [36]. The present results indicate that the significant and rapid removal of formaldehyde will improve air and environmental quality.

Conclusion

Titania (TiO_2) nanoparticles were successfully immobilised on glass substrates through a simple spraying technique. Dynamic flow-sense images showed that highly uniform coatings can be obtained by spraying TiO_2 nanoparticles at concentrations exceeding 15.0 g/L. This result is further supported by 2D and 3D surface plots, wherein no surface defects were observed on coatings prepared with >15.0 g/L TiO_2. This result implies that the simple coating technique adopted in this study can yield TiO_2 coatings with high quality. Higher formaldehyde removal rates were obtained with coatings prepared with higher TiO_2 concentrations than those obtained with coatings prepared with lower TiO_2 concentrations.

Acknowledgement

This research work was supported by the Fundamental Research Grant (FP051-2013B), the Ministry of Education Malaysia and Universiti Tunku Abdul Rahman (UTAR) Research Fund (IPSR/RMC/UTARRF/2016-C2/L05).

References

1. George, C., Beeldens, A., Barmpas, F., Doussin, J-F., Manganelli, G., Herrmann, H., Kleffmann, J. and Mellouki, A. (2016). Impact of photocatalytic remediation of pollutants on urban air quality. *Frontiers of Environmental Science & Engineering*, 10(5): 2-11.
2. Chi, C., Chen, W., Guo, M., Weng, M., Yan, G. and Shen X. (2016). Law and features of TVOC and formaldehyde pollution in urban indoor air. *Atmospheric Environment*, 132: 85-90.
3. Romeas, V., Pichat, P., Guillard, C., Chopin, T. and Lehaut. C. (1999). Testing the efficacy and the potential effect on indoor air quality of a transparent self-cleaning TiO_2-coated glass through the degradation of a fluoranthene layer. *Industrial and Engineering Chemistry Research*, 38: 3878-3885.
4. Ganesh, V. A., Nair, A. S., Raut, H. K., Walsh, T. M. and Ramakrishna, S. (2012). Photocatalytic superhydrophilic TiO_2 coating on glass by electrospinning. *RSC Advances*, 2: 2067-2072.
5. Nishimoto, S., Kubo, A., Zhang, X., Liu, Z., Taneichi, N., Okui, T., Murakami, T., Komine, T. and Fujishima, A. (2008). Novel hydrophobic/hydrophilic patterning process by photocatalytic Ag nucleation on TiO_2 thin film and electroless Cu deposition. *Applied Surface Science*, 254: 5891-5894.
6. Nishimoto, S., Kubo, A., Nohara, K., Zhang, X., Taneichi, N., Okui, T., Liu, Z., Nakata, K., Sakai, H. and Murakami, T. (2009). TiO_2-based superhydrophobic–superhydrophilic patterns: Fabrication via an ink-jet technique and application in offset printing. *Applied Surface Science*, 255: 6221-6225.
7. Nakata, K., Udagawa, K., Ochiai, T., Sakai, H., Murakami, T., Abe, M. and Fujishima, A. (2011). Rapid erasing of wettability patterns based on TiO_2-PDMS composite films. *Materials Chemistry Physics*, 126: 484-487.
8. Fujishima, A., Rao, T. N. and Tryk, D. A. (2000). Titanium dioxide photocatalysis. *Journal of Photochemistry and Photobiology C: Photochemistry Reviews*, 1: 1-21.
9. Guo, Z., Liu, W. and Su, B.-L. (2011). Superhydrophobic surfaces: From natural to biomimetic to functional. *Journal of Colloid and Interface Science*, 353: 335-355.
10. Wang, X., Ding, B., Yu, J. and Wang, M. (2011). Engineering biomimetic superhydrophobic surfaces of electrospun nanomaterials. *Nano Today*, 6: 510-530.
11. Yu, J., Zhao, X., Yu, J. C., Zhong, G., Han, J. and Zhao, Q. (2001). The grain size and surface hydroxyl content of super-hydrophilic TiO_2/SiO_2 composite nanometer thin films. *Journal of Materials Science Letters*, 20: 1745-1748.
12. Leong, K. H., Monash, P., Ibrahim, S. and Saravanan, P. (2014). Solar photocatalytic activity of anatase TiO_2 nanocrystals synthesized by non-hydrolitic sol–gel method. *Solar Energy*, 101: 321-332.
13. Powell, M. J., Quesada-Cabrera, R., Taylor, A., Teixeira, D., Papakonstantinou, I. G., Palgrave, R., Sankar, G. and Parkin. I. (2016). Intelligent multifunctional $VO_2/SiO_2/TiO_2$ coatings for self-cleaning, energy-saving window panels. *Chemistry of Materials*, 28(5): 1369-1376.

14. Choi, Y., Kim, H-I., Moon, G-H., Jo, S. and Choi, W. (2016). Boosting up the low catalytic activity of silver for H_2 production on Ag/TiO_2 photocatalyst: Thiocyanate as a selective modifier. *ACS Catalysis,* 6(2): 821-828.
15. Leong, K. H., Gan, B. L., Ibrahim, S. and Saravanan, P. (2014). Synthesis of surface plasmon resonance (SPR) triggered Ag/TiO_2 photocatalyst for degradation of endocrine disturbing compounds. *Applied Surface Science,* 319: 128-135.
16. Han, D., Li, Y. and Jia, W. (2010). Preparation and characterization of molecularly imprinted SiO_2-TiO_2 and photo-catalysis for 2, 4-dichlorophenol. *Advanced Materials Letters,* 1: 188-192.
17. Weon, S. and Choi, W. (2016). TiO_2 nanotubes with open channels as deactivation-resistant photocatalyst for the degradation of volatile organic compounds. *Environmental Science & Technology,* 50(5): 2556-2563.
18. Singh, P., Vishnu, M. C., Sharma, K. K., Singh, R., Madhav, S., Tiwary, D. and Mishra, P. K. (2016). Comparative study of dye degradation using TiO_2-activated carbon nanocomposites as catalysts in photocatalytic, sonocatalytic, and photosonocatalytic reactor. *Journal of Desalination and Water Treatment,* 57(43): 20552-20564.
19. Sampaio, M., Silva, C. G., Silva, A. M. T. and Faria, J. L. (2016). Kinetic modelling for the photocatalytic degradation of phenol by using TiO_2-coated glass Raschig rings under simulated solar light. *Journal of Chemical Technology and Biotechnology,* 91(2): 346-352.
20. Paz, Y. and Heller, A. (1997). Photo-oxidatively self-cleaning transparent titanium dioxide films on soda lime glass: The deleterious effect of sodium contamination and its prevention. *Journal of Materials Research,* 12: 2759-2766.
21. Negishi, N., Matsuzawa, S., Takeuchi, K. and Pichat, P. (2007). Transparent micrometer-thick TiO_2 films on SiO_2-coated glass prepared by repeated dip-coating/calcination: characteristics and photocatalytic activities for removing acetaldehyde or toluene in air. *Chemistry of Materials,* 19: 3808-3814.
22. Thiruvenkatachari, R., Vigneswaran, S. and Moon, I. S. (2008). A review on UV/TiO_2 photocatalytic oxidation process. *Korean Journal of Chemical Engineering,* 25: 64-72.
23. Fan, S.-Q., Yang, G.-J., Li, C., Liu, G., Li, C. and Zhang, L.-Z. (2006). Characterization of microstructure of nano-TiO_2 coating deposited by vacuum cold spraying. *Journal of Thermal Spray Technology,* 15: 513-517.
24. Yu, J. and Zhao, X. (2001). Effect of surface treatment on the photocatalytic activity and hydrophilic property of the sol-gel derived TiO_2 thin films. *Materials Research Bulletin,* 36: 97-107.
25. O'Regan, B., Moser, J., Anderson, M. and Graetzel, M. (1990). Vectorial electron injection into transparent semiconductor membranes and electric field effects on the dynamics of light-induced charge separation. *Journal of Physical Chemistry,* 94: 8720-8726.
26. Takeda, S., Suzuki, S., Odaka, H. and Hosono, H. (2001). Photocatalytic TiO_2 thin film deposited onto glass by DC magnetron sputtering. *Thin Solid Film,* 392: 338-344.
27. Yang, G.-J., Li, C.-J., Han, F. and Ohmori, A. (2004). Microstructure and photocatalytic performance of high velocity oxy-fuel sprayed TiO_2 coatings. *Thin Solid Films,* 466: 81-85.
28. Seo, K.-L., Hyun, Y. and Lee, C.-S. (2014). Ultrasonochemical coating and characterization of TiO_2-coated zirconia fine particles. *Journal of Industrial and Engineering,* 20: 1819-1824.
29. Park, J. H., Kim, W.S., Jo, D.-H., Kim, J. S. and Park, J. M. (2014). Effect of Ce conversion underlayer coating on the photo-catalytic activity of TiO_2 sol–gel film deposited on hot-dip GI. *Journal of Industrial and Engineering,* 20: 1965-1972.
30. Zhang, X., Cooke, K., Carmichael, P. and Parkin, I. (2013). The deposition of crystallized TiO_2 coatings by closed field unbalanced magnetron sputter ion plating. *Surface Coatings Technology,* 236: 290-295.
31. Santillán, M. J., Membrives, F., Quaranta, N. and Boccaccini, A. R. (2008). Characterization of TiO_2 nanoparticle suspensions for electrophoretic deposition. *Journal of Nanoparticle Research,* 10: 787-793.
32. Barreto, P. L. M., Roeder, J., Crespo, J. S., Maciel, G. R., Terenzi, H., Pires, A. T. N. and Soldi, V. (2003). Effect of concentration, temperature and plasticizer content on rheological properties of sodium caseinate and sodium caseinate/sorbitol solutions and glass transition of their films. *Food Chemistry,* 82: 425-431.
33. Sun, S., Ding, J., Bao, J., Gao, C., Qi, Z. and Li, C. (2010). Photocatalytic oxidation of gaseous formaldehyde on TiO_2: An in situ DRIFTS study. *Catalysis Letters,* 137: 239-246.
34. Ichiura, H., Kitaoka, T. and Tanaka, H. (2003). Removal of indoor pollutants under UV irradiation by a composite TiO_2–zeolite sheet prepared using a papermaking technique. *Chemosphere,* 50: 79-83.

35. Yu, H., Zhang, K. and Rossi, C. (2007). Experimental study of the photocatalytic degradation of formaldehyde in indoor air using a nano-particulate titanium dioxide photocatalyst. *Indoor and Built Environment*, 16: 529-537.
36. Liang, W., Li, J. and Jin, Y. (2012). Photo-catalytic degradation of gaseous formaldehyde by TiO_2/UV, Ag/TiO_2/UV and Ce/TiO_2/UV. *Building and Environment*, 51: 345-350.

Malaysian Journal of Analytical Sciences, Vol 23 No 1 (2019): 100 - 108
DOI: https://doi.org/10.17576/mjas-2019-2301-12

MALAYSIAN JOURNAL OF ANALYTICAL SCIENCES
Published by The Malaysian Analytical Sciences Society
ISSN 1394 - 2506

SYNTHESIS AND CHARACTERIZATION OF $SrSnO_3$ USING DIFFERENT SYNTHESIS METHODS

(Sintesis dan Pencirian $SrSnO_3$ yang Dihasilkan Melalui Kaedah Sintesis Berlainan)

Muhammad Arif Riza, Suhaila Sepeai, Norasikin Ahmad Ludin, Mohd Asri Mat Teridi, Mohd Adib Ibrahim*

Solar Energy Research Institute (SERI)
Universiti Kebangsaan Malaysia, 43600 UKM Bangi, Selangor, Malaysia

**Corresponding author: mdadib@ukm.edu.my*

Received: 13 April 2017; Accepted: 17 April 2018

Abstract

Perovskites are materials that have many potential applications, such as humidity sensors, transparent conductive oxides, photocatalysts and capacitors. Strontium stannate ($SrSnO_3$) is a perovskite semi-conductor material with a wide band gap. Several synthesis methods are commonly used to form $SrSnO_3$, including solid-state reaction (SSR), sol-gel and hydrothermal. The SSR method requires high temperature calcination. On the other hand, sol-gel and hydrothermal methods merely need a lower calcination temperature to form perovskite materials. The sol-gel methods were done by adding a surfactant to $Sr(NO_3)_2$ and $SnCl_2$ solution in water before calcination. The autoclave approach was used in the hydrothermal method prior to calcination to form $SrSnO_3$. The objective of this study was to determine the morphological and optical properties of $SrSnO_3$ synthesized by sol-gel, hydrothermal and SSR. The band gap was calculated *via* Kubelka-Munk relations and were found to be 4.05 eV (hydrothermal), 5.50 eV (sol-gel) and 3.95 eV (SSR). Sol-gel methods showed the widest band gap for $SrSnO_3$. Optical results showed that there is a difference in terms of band gap for a perovskite synthesized by the different methods. Mass reduction analysis by TGA showed a sol-gel has mass loss of approximately 58% due to dehydration, which is more than for hydrothermally synthesized $SrSnO_3$. This reduction is higher than for $SrSnO_3$ synthesized by hydrothermal method. It was observed that different synthesis methods impact the optical properties and morphology of $SrSnO_3$ powders.

Keywords: perovskites, hydrothermal, sol-gel, band gap, solid-state reaction

Abstrak

Perovskit merupakan bahan yang mempunyai banyak potensi untuk digunakan sebagai penderia kelembapan, oksida konduktif lutsinar, fotomangkin dan kapasitor. Strontium stannat ($SrSnO_3$) adalah bahan separuh konduktif berstruktur perovskit dengan jurang jalur yang besar. Beberapa kaedah sintesis biasanya digunakan untuk membentuk $SrSnO_3$ termasuk tindak balas keadaan pepejal (SSR), sol-gel dan hidroterma. Kaedah SSR memerlukan penalaan suhu yang tinggi, manakala kaedah sol-gel dan hidroterma hanya memerlukan suhu pengkalsinan yang lebih rendah untuk membentuk bahan perovskit. Kaedah sol-gel dilakukan dengan menambah surfaktan pada larutan $Sr(NO_3)_2$ dan $SnCl_2$ dalam air sebelum pengkalsinan. Pendekatan autoklaf digunakan dalam kaedah hidroterma sebelum pengkalsinan untuk membentuk $SrSnO_3$. Objektif kajian ini adalah untuk menentukan morfologi dan ciri optik bagi bahan $SrSnO_3$ yang disintesis melalui kaedah sol-gel, hidroterma dan SSR. Jurang jalur telah dikira melalui hubungan Kubelka-Munk dan didapati nilainya adalah 4.05 eV (hidroterma), 5.50 eV (sol-gel) dan 3.95 eV (SSR). Kaedah sol-gel menunjukkan jurang jalur yang terbesar bagi $SrSnO_3$. Ciri optik menunjukkan wujudnya perbezaan antara jurang jalur bagi perovskit yang disintesis melalui kaedah yang berlainan. Analisa pengurangan jisim menggunakan TGA menunjukkan bahawa sol-gel mempunyai pengurangan jisim dianggarkan sebanyak 58% disebabkan penyahhidratan. Pengurangan ini adalah lebih tinggi berbanding dengan $SrSnO_3$ yang disintesis melalui kaedah hidroterma. Ia telah dilihat bahawa kaedah sintesis boleh memberi kesan pada ciri optik dan morfologi pada serbuk $SrSnO_3$.

Kata kunci: perovskit, hidroterma, sol-gel, julang jalur, tindak balas keadaan pepejal

Introduction

Strontium stannate ($SrSnO_3$) is a perovskite structured semi-conducting material with a wide band gap of 4.1 eV. It can also absorb light in the ultraviolet region [1, 2]. As such, it is a typical practice to introduce a dopant to the perovskite structure in order to allow the material to absorb a wider light spectrum and improve its conductivity. Besides having a wide band gap, perovskites possess many other interesting properties, such as superconductivity and colossal magnetoresistance. Perovskites like $MSnO_3$ (M = Sr, Ba, Ca) can be synthesized by several methods, and one of them is the solid-state reaction (SSR) method. This method involves mixing metal oxides in a mortar and then calcining at high temperatures. Liu et al. used this method to synthesize Sb doped $SrSnO_3$ by mixing tin oxide (SnO_2), strontium carbonate ($SrCO_3$) and antimony oxide (Sb_2O_3) into a mortar and calcining at ~1500 ˚C for 24 hours [3]. This method is relatively simple, but requires high calcination temperatures that consume a great deal of electricity [4].

Alternative methods with lower calcination temperatures include sol-gel and hydrothermal methods. The sol-gel method for synthesis of $SrSnO_3$ is a wet-chemical method that has been used to produce perovskite materials [5-7]. This method includes the use of metal nitrates, chlorides, acetates and other chemicals in a solution. The metal precursors are made into a solution and mixed with a surfactant to assist particle agglomeration and the perovskite formation reaction. The precursors and are surfactant stirred, heated and then dried before calcination. Kumar et al. synthesized Fe-doped $SrSnO_3$ by the sol-gel method and calcined at 650˚C for 2 hours [8]. This method requires a much lower calcination temperature for formation of $SrSnO_3$, but requires a more complicated synthesis [4].

Hydrothermal is another solution-oriented method. This method involves similar precursors used for sol-gel (metal salts, acetates, etc.), but also requires the use of an alkali and autoclave to form powders or nanorod perovskites [9, 10]. A study by Li et al. applied this method to synthesize $SrSnO_3$ nanorods by mixing SnCl, $Sr(NO_3)_2$ and cetyltrimethylammonium bromide (CTAB) in solution [11]. The solution was adjusted with NaOH drops until it reached a pH of 13. A suspension formed after reaching the said pH and it was transferred to an autoclave to be heated for several hours. The suspension was then calcined at 600 ˚C, or higher, for 3 hours until $SrSnO_3$ formed. This method was reported to have a low calcination temperature and result in fewer impurities in the product, but the use of autoclaves and long processing times make it less favourable for bulk production [12].

The purpose of the study is to synthesize $SrSnO_3$ using three different methods (SSR, sol-gel and hydrothermal) and characterize it in terms of morphology, optical properties and crystal quality. This study hopes to provide valuable insights into the three different methods of perovskite synthesis to aid in future studies of this material, as each method tends to give slightly different results to the final product.

Materials and Methods

No autoclave route (sol-gel)

The sol-gel method used for this study was based on Kumar et al. [8]. Reagent grade strontium nitrate with 99% purity ($Sr(NO_3)_2$), tin chloride with 98% purity ($SnCl_2$) and CTAB with >99% purity were obtained from Sigma Aldrich and added to 30 mL of deionized water. The solution was then stirred for 4 hours at 80˚C until the solution became a white gel. The gel was then dried at 100 ˚C on a hot plate in air until it transformed into a powder. The powder was washed with ethanol to reduce any remaining impurities and left to dry. The white powder, $SrSn(OH)_6$, was then calcined in the furnace at 650˚C for 2 hours until $SrSnO_3$ powder formed. The formation of $SrSnO_3$ can be described by the following equations 1 and 2:

$$Sr(NO_3)_2 + SnCl_2 + 4H_2O \rightarrow SrSn(OH)_6 + 2HCl + N_2 + 2O_2 \quad (1)$$

$$SrSn(OH)_6 \rightarrow SrSnO_3 + 3H_2O \quad (2)$$

Equation 1 describes the formation of $SrSn(OH)_6$ from the precursors and equation 2 shows the calcination of $SrSn(OH)_6$ to form the final product, $SrSnO_3$.

Autoclave route (hydrothermal)

A more detailed reaction route involving hydrothermal synthesis of $SrSnO_3$ can be found in Li et al. [11]. Strontium nitrate with 99% purity ($Sr(NO_3)_2$), tin chloride with 98% purity ($SnCl_2$) and CTAB with >99% purity were added to 30 mL deionized water and stirred. While stirring, NaOH 1 M was added, drop by drop, to the solution to maintain pH of 13 until a white suspension appeared. The suspension was placed in an autoclave and sealed for 16 hours at 160 ˚C. After the autoclave cooled to room temperature, the suspension turned into a white gel and was left to dry. When dried, the gel was a white coloured powder of $SrSn(OH)_6$. The powder was later calcined at 650 ˚C for 2 hours to form the $SrSnO_3$ powder.

Solid-state reaction route (SSR)

The SSR route used in this study was carried out based on James et al. [13]. Equimolar $SrCO_3$ and SnO_2 powders with 99% purity were obtained from Sigma Aldrich and mixed with a mortar and pestle. Acetone was added to the mixture to act as a binder for the powders. After mixing, the powder was transferred to a porcelain boat and calcined for 12 hours at 800˚C. The powder was then reground and calcined again at 850 ˚C for 18 hours. After the final grinding, the mixture was calcined once more at 900 ˚C for 24 hours. A white powder of $SrSnO_3$ was obtained after calcination. The simple solid-state reaction equation may be described by equation 3:

$$SrCO_3 + SnO_2 \rightarrow SrSnO_3 + CO_2 \quad (3)$$

Characterization

Thermogravimetric analysis (TGA) was done using a Perkin Elmer STA6000. The TGA-DSC testing was done under nitrogen with a heating rate of 10 ˚C/min at a temperature range of 30-1000 ˚C. X-ray diffraction (D8 Advance Bruker AXS Germany) with CuKα radiation was used to identify the crystal quality and crystal structure. UV-Vis spectroscopy data was obtained by diffuse reflectance at a wavelength range of 200-800 nm using a PerkinElmer UV/VIS/NIR Spectrometer Lambda 950. The morphology of the material was studied by using SEM Supra 55VP. X-ray Photoelectron Spectroscopy was done with Kratos/Axis Ultra delay-line detector (DLD).

Results and Discussion

Crystal structure

The XRD patterns for the $SrSn(OH)_6$ powders synthesized from the hydrothermal and sol-gel methods show the presence of hexagonal $SrSn(OH)_6$, as illustrated in Figure 1(a). These patterns were a match for a $SrSnOH_6$ precursor, according to database PDF00-009-0086. The peaks at 2θ values of 11˚, 20˚, 22˚, 28˚, 32˚, 36˚, and 41˚ corresponded to *hkl* numbers (Bragg reflection planes) of (110), (301), (004), (330), (512), (432) and (006), respectively. The lattice parameters, according to the PDF database, were $a = b = 16.35$ nm and $c = 12.34$ nm for the hydrothermal and sol-gel synthesized $SrSn(OH)_6$. The peaks were nearly identical to the peaks found in Li et al. [11], with minimal noise in the data. A similar peak for $SrSn(OH)_6$ was observed for both methods. However, there was an unknown peak at 5˚ for the sol-gel method. Meanwhile, there was an increased intensity for the (006) peak in hydrothermal route, which may correspond to deformity of the crystal structure.

The precursor powders from each route were calcined (with the exception of powders from SSR route) to produce the $SrSnO_3$ powders. The XRD spectra of the SSR, sol-gel and hydrothermal routes are shown in Figure 1(b). The XRD of powders via the hydrothermal route had a cubic crystal structure with lattice parameters of $a = b = c =$ 8.0682 according to PDF00-022-1442. The peaks are at 2θ values of 22˚, 25.2˚, 31.5˚, 44.5˚, 50.5˚, 55.5˚, 65.3˚, 70˚ and 74.3˚ and correspond to reflection planes of (200), (210), (220), (400), (420), (422), (440), (600) and (620), respectively. When compared to the patterns of the hydrothermally synthesized $SrSn(OH)_6$ precursors, it can be seen that the patterns have slight differences, due to the formation of the $SrSnO_3$ product from its precursors. The sol-gel synthesized $SrSnO_3$ powder also possesses similar notable peaks, but the presence of unknown peaks increased, and may indicate that more impurities were present that affected the crystal structure. The SSR synthesized $SrSnO_3$ has fewer unknown peaks at lower 2θ compared to the sol-gel method. Based on these spectra, all methods can produce $SrSnO_3$ with the correct perovskite crystal structure. The crystal quality, in terms of impurity presence in the $SrSnO_3$, was best for the hydrothermal method, followed by SSR. The sol-gel method was observed to have the highest impurities due to having multiple unknown diffraction peaks.

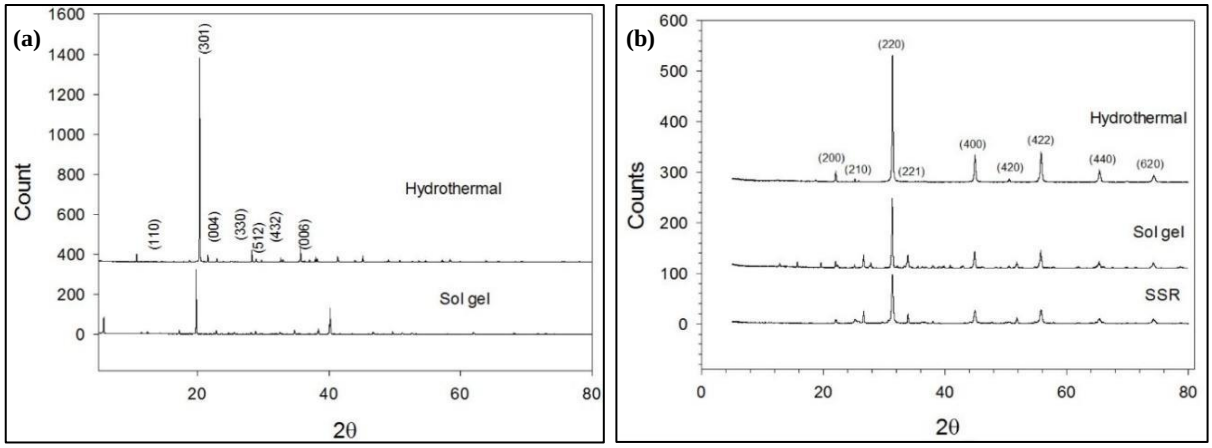


Figure 1. XRD spectra of (a) $SrSn(OH)_6$ and (b) $SrSnO_3$

Thermogravimetric analysis (TGA)

TGA analysis of $SrSn(OH)_6$ was done on the hydrothermal and sol-gel routes only. This analysis was done to determine whether the solutions formed correctly, if dehydration occurred and at what temperatures. This was not possible for the SSR route because the precursor oxides crystallized directly to $SrSnO_3$ instead of forming $SrSn(OH)_6$. The TGA for hydrothermal and sol-gel synthesized $SrSnO_3$ was done for the temperature range of 50 – 1000 ˚C, as shown in Figure 2.

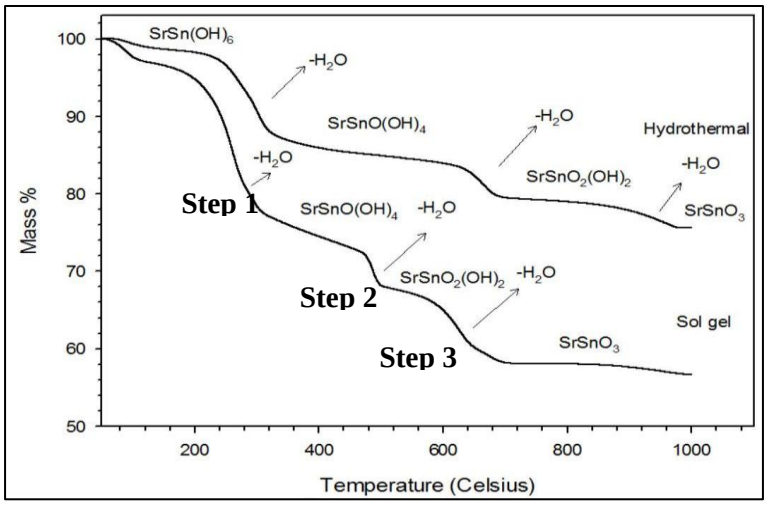


Figure 2. TGA analysis of $SrSn(OH)_6$ reduction into $SrSnO_3$

The $SrSn(OH)_6$ synthesized by the hydrothermal route also experienced mass reduction due to water evaporation. The minimum mass percent obtained after the analysis was ~78% of the original mass. The first 13% weight loss occurred at the temperature range of 230 – 350 ˚C. The second 3% mass reduction occurred at the temperature range of 630 – 690˚C of. The last ~2% weight loss due to evaporation occurred at 920 – 970˚C. The $SrSn(OH)_6$ powders synthesized by the sol-gel method experienced step-by-step weight loss to a minimum remaining mass percent of ~56%. A very small 3% weight loss occurred at ~88˚C and minor reductions occurred up to 190˚C. The 3% weight loss suggests that the water (H_2O) content was beginning to be removed from the material. There was a sudden mass drop of 17% at temperatures between 205 – 320˚C, which is where a large amount H_2O evaporated. The second notable H_2O evaporation occurred at 480 –500˚C and resulted in a weight loss of 5%. The last mass reduction of 6%

occurred at 610 ˚C and no more mass reduction occurred for temperatures greater than 700˚C. This suggests that at this temperature, $SrSn(OH)_6$ was dehydrated and 48% of its mass was reduced to finally form $SrSnO_3$. These three stages of weight loss due to hydration are in agreement with published literature [8]. Thus, the sol-gel method synthesized $SrSnO_3$ yielded less after exposure to high temperatures compared to hydrothermally synthesized $SrSnO_3$. The three steps of $SrSn(OH)_6$ dehydration maybe be represented by equations:

Step 1 - $SrSn(OH)_6 \rightarrow SrSnO(OH)_4 + H_2O$ (4)
Step 2 - $SrSnO(OH)_4 \rightarrow SrSnO_2(OH)_2 + H_2O$ (5)
Step 3 - $SrSnO_2(OH)_2 \rightarrow SrSnO_3 + H_2O$ (6)

Diffuse reflectance and band gap estimation

UV-Vis measurements were done on the $SrSnO_3$ powders synthesized by the different routes. The diffuse reflectance was obtained, as shown on Figure 3(a), and then converted into the Kubelka-Munk function for band gap determination [14]. Based on Figure 3(b), the band gap of hydrothermal, sol-gel and SSR synthesized $SrSnO_3$ was found to be 4.05 eV, 5.5 eV and 3.95 eV, respectively. The band gap of $SrSnO_3$ has been reported to be 4.1 eV in the literature [1, 8]. It can be seen that the band gap for hydrothermally prepared $SrSnO_3$ is closest to the value in the literature, followed by sol-gel and SSR. Sol-gel has the highest band gap and its value differs from the literature. This could mean that the $SrSnO_3$ powders made by sol-gel have more impurities (supported by XRD pattern), thus resulting in higher band gap.

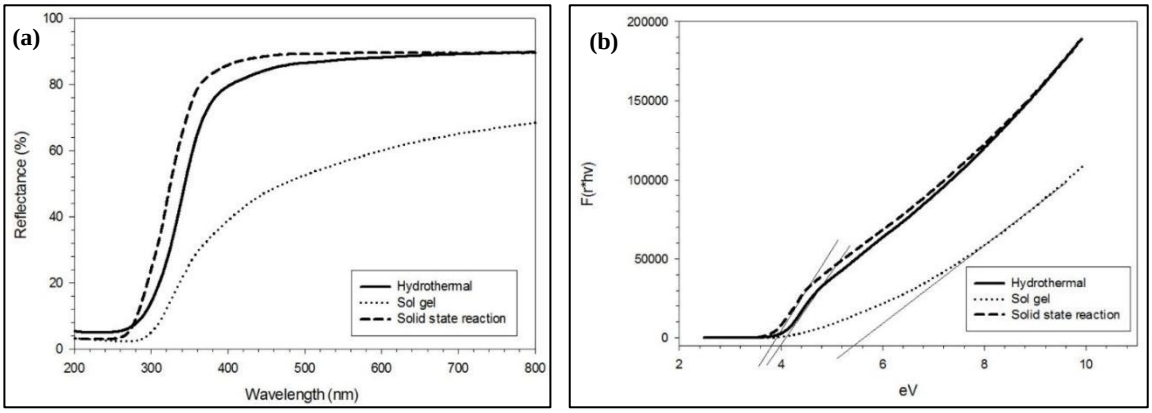


Figure 3. The optical analysis of $SrSnO_3$ (a) Reflectance spectra and (b) Diffuse reflectance transferred to Lubelka-Munk function for band gap determination [14]

Surface morphology

Figure 4(a) shows the SEM image for hydrothermally synthesized $SrSnO_3$. The $SrSnO_3$ was in the form of long cylinders, and a similar structure was also obtained by Li et al. [11]. This $SrSnO_3$ structure formation was due to NaOH reacting with $SnCl_4$ to form a $Sn(OH)_4$, which is able to dissolve in large amounts of NaOH and form $Sn(OH)_6^{2-}$ groups. This group reacts with cetyltrimethylammonium ion (CTA^+) from CTAB, forming CTA^+-$Sn(OH)_6^{2-}$ groups that allow crystals of $Sn(OH)_6^{2-}$ to grow along the orientation of the CTA^+ head group. Since the crystal has a direction to grow along the CTA^+ head group, this resulted in the crystals growing as rods, possibly long after the nucleation process in the autoclave [11]. Figure 4(b) shows the image of $SrSnO_3$ made by the SSR method. The powders have irregular sizes but are roughly similar in terms of shape. Sol-gel synthesized $SrSnO_3$, as shown in Figure 4(c), has larger powder clumps with a slightly irregular shape. The large powder clumps are due to the CTAB, which allows the growth of the crystals in all directions [13]. Based on these images, it would seem $SrSnO_3$ made by hydrothermal synthesis possesses a more uniform shape compared to the other methods that formed long shapes with varying sizes.

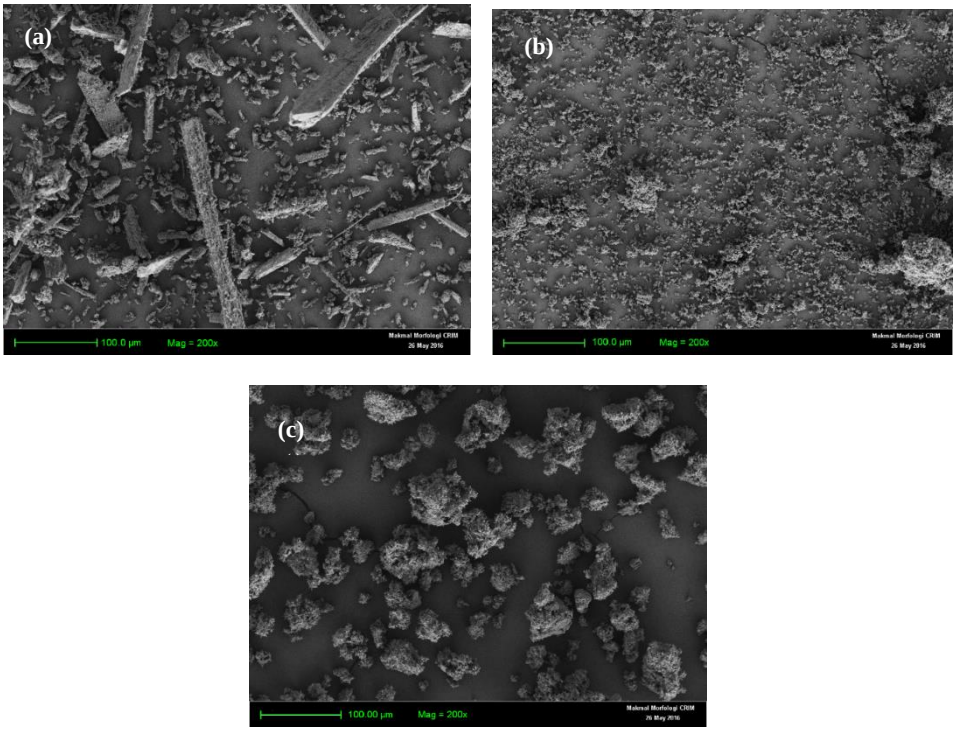


Figure 4. FESEM images at magnification of 200x of (a) hydrothermally synthesized $SrSnO_3$, (b) SSR synthesized $SrSnO_3$ and (c) sol-gel synthesized $SrSnO_3$

XPS spectra

Figure 5(a) shows the XPS spectra of O 1s in $SrSnO_3$ synthesized by the three methods. The hydrothermal method only has one peak present at 528 eV, where the O 1s is part of the main lattice of $SrSnO_3$ and the shoulder at 526.7 eV indicates the hydrated oxide species present in the sample, according to Kumar et al. [8]. The O 1s in the sol-gel has a vaguely visible peak at 528.7 eV. This small peak may indicate that only a small amount of O 1s was incorporated into the main lattice. The very small shoulder at 527.8 eV is the hydrated oxide species. The SSR $SrSnO_3$ has only one high peak for O 1s at 528.8 eV, and this indicates O 1s was well incorporated into the main $SrSnO_3$ lattice. Since the SSR method did not involve additional solutions or hydrates, there are no shoulders or peaks indicating that hydrated oxide species were present [8].

Figure 5(b) shows the Sn 3d peak for $SrSnO_3$. Two visible peaks are present for all $SrSnO_3$ synthesis methods. The first peaks at 483 – 484 eV for all methods indicate Sn $3d_{5/2}$. The second peak at ~492 eV for all methods corresponds to Sn $3d_{3/2}$. Both peaks are in accordance with the literature as Sn $3d_{5/2}$ and Sr $3d_{3/2}$ [15]. The peaks are highest for SSR followed by hydrothermal and sol-gel. The lowest peaks for the sol-gel method indicate that the Sn $3d_{5/2}$ and Sr $3d_{3/2}$ incorporation in the main lattice is less visible. Figure 5(c) shows the Sr $3d_{5/2}$ and Sr $3d_{3/2}$ peaks for $SrSnO_3$ produced by the three methods. Hydrothermal synthesized $SrSnO_3$ has peaks at 130.6 eV and 132 eV for Sr $3d_{5/2}$ and Sr $3d_{3/2}$, respectively. Sol-gel synthesized $SrSnO_3$ has Sr $3d_{5/2}$ and Sr $3d_{3/2}$ peaks at 132 and 133.5 eV, respectively. Finally, SSR has the highest peaks for Sr $3d_{5/2}$ and Sr $3d_{3/2}$ at 130.8 and 132.5 eV, respectively. According to these results, all have 2 peaks within 130 – 134 eV binding energy values, which corresponds to Sr^{2+} [15]. However, the variance in each spectrum of the three methods may suggest that the quality of Sr^{2+} bonding with main lattice is different, with SSR having the highest peak followed by sol-gel and hydrothermal. Overall, from the XPS spectra, SSR showed the most incorporation of each species (O 1s, Sr 3d and Sn 3d) into the main $SrSnO_3$ lattice, followed by hydrothermal and sol-gel.

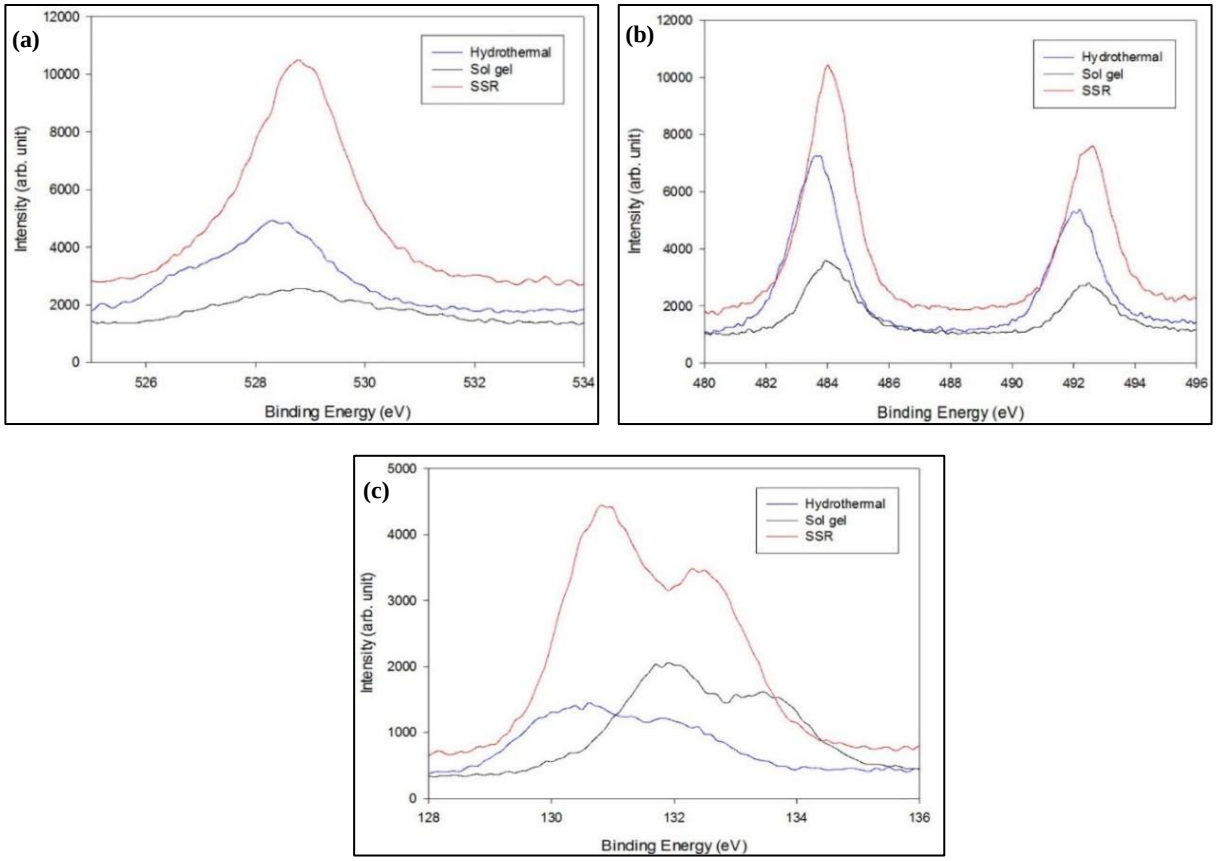


Figure 5. XPS spectra of $SrSnO_3$ synthesized via hydrothermal, sol-gel and SSR for (a) O 1s, (b) Sn 3d and (c) Sr 3d

Synthesis yield

Each synthesis method should produce different amounts of $SrSnO_3$ due to the different precursors used. All precursor solutions used had a basis of 10 mmol. Table 1 shows the yield percent of $SrSnO_3$ obtained after synthesis by the three different methods. Yield percentage is calculated by equation 7:

$$\text{Yield percent (\%)} = \frac{\text{Actual mass (g)}}{\text{Theoretical mass (g)}} \quad (7)$$

Table 1. Yield performance of $SrSnO_3$ obtained from three different synthesis methods

Synthesis Method	**$SrSnO_3$ Actual Yield Obtained (g)**	**Theoretical Yield**	**Yield%**
Hydrothermal	0.860	2.543	33.8%
Sol-gel	1.383	2.543	54.4%
Solid State Reaction (SSR)	2.176	2.543	85.6%

The SSR method yielded better by producing more $SrSnO_3$ powder, and this is why this method is still preferable in other studies [13, 16, 17]. Since this method uses powders only and not solvents, the yield is maximized. This

means that the weight of the total precursor oxides is close to the weight of the final product. Sol-gel produced the second highest yield. It produced more than the hydrothermal method because no filter or decanting was required since the solution was only heated and dried in same beaker. It was then only transferred once to the crucible for calcination.

Hydrothermally synthesized $SrSnO_3$ produced the least compared to SSR and sol-gel. The low yield was mainly due to the precursor solution being mixed with NaOH that mostly filled space in the autoclave container. Another factor would be loss of some main product $SrSn(OH)_6$ while filtering the solution from the autoclave. The difficulty of obtaining the product suspensions in the autoclave by scraping with a spatula also contributed to the loss of mass. Due to this difficulty, even though TGA analysis revealed that hydrothermal should yield more than sol-gel, the actual obtained yield was less.

Conclusion

The $SrSnO_3$ has been successfully synthesized *via* hydrothermal, sol-gel and SSR methods. The SEM showed that hydrothermal synthesized $SrSnO_3$ had the most regular and uniform particle shapes in the form of nanorods, followed by SSR and sol-gel. The TGA analysis showed both hydrothermal and sol-gel synthesized $SrSnO_3$ followed a 3-step dehydration process, with final minimum masses of 78% and 48% for hydrothermal and sol-gel, respectively. The hydrothermal and SSR methods had measured band gaps of 4.05 eV and 3.95 eV, respectively, which is close to the band gap value of 4.1 eV found in the literature. X-ray diffraction patterns and X-ray photoelectron spectra revealed the formation of orthorhombic phase $SrSnO_3$ nanoparticles through the three different synthesis methods. The XRD showed that $SrSnO_3$ with the least impurities was the hydrothermally synthesized $SrSnO_3$, followed by SSR and sol-gel. The XPS spectra of the $SrSnO_3$ produced by the SSR method showed a high binding energy intensity that indicated that each element was well incorporated into main lattice. The SSR method was followed by hydrothermal and sol-gel. In conclusion, $SrSnO_3$ can be produced using a low-cost method that results in some advantageous and disadvantageous material properties. With this option, the various dopants can be applied to the $SrSnO_3$ material to enhance some of its properties.

Acknowledgement

This work was supported by the Ministry of Higher Education, Malaysia and the research grant from Universiti Kebangsaan Malaysia (UKM) (Grant: GUP-2015-023).

References

1. Chen, H. and Umezawa, N. (2014). Sensitization of perovskite strontium stannate $SrSnO_3$ towards visible-light absorption by doping. *International Journal of Photoenergy*, 2014: 3–6.
2. Dohnalová, Ž., Gorodylova, N., Šulcová, P. and Vlček, M. (2014). Synthesis and characterization of terbium-doped $SrSnO_3$ pigments. *Ceramics International*, 40: 12637–12645.
3. Liu, Q., Dai, J., Zhang, X., Zhu, G., Liu, Z. and Ding, G. (2011). Perovskite-type transparent and conductive oxide films: Sb- and Nd-doped $SrSnO_3$. *Thin Solid Films*, 519(18): 6059–6063.
4. Ecija, A., Vidal, K., Larrañaga, A., Ortega-san-martín, L., Arriortua, M. I., Euskal, V. and Ehu, U. (2012). Synthetic methods for perovskite materials – structure and morphology. *Advances in Crystallization Processes*, 19: 485–505.
5. Para, T., Reshi, H. A. and Shelke, V. (2016). Synthesis of $ZnSnO_3$ nanostructure by sol gel method. *AIP Conference Proceedings*, 1731: 1–4.
6. Shan, C., Huang, T., Zhang, J., Han, M., Li, Y., Hu, Z., & Chu, J. (2014). Optical and electrical properties of sol − gel derived Ba−$LaSnO_3$ transparent conducting films for potential optoelectronic applications. *The Journal of Physical Chemistry C*, 118(13): 6994-7001.
7. Xu, K., Yao, M., Chen, J., Zou, P., Peng, Y., Li, F. and Yao, X. (2015). Effect of crystallization on the band structure and photoelectric property of $SrTiO_3$ sol–gel derived thin film. *Journal of Alloys and Compounds*, 653: 7–13.
8. Kumar, A., Quamara, J., Dillip, G., Joo, S. and Kumar, J. (2015). Fe(III) induced structural, optical, and dielectric behavior of cetyltrimethyl ammonium bromide stabilized strontium stannate nanoparticles synthesized by a facile wet chemistry route. *RSC Advance*, 5(22): 17202–17209.

9. Chen, C., Cheng, J., Yu, S., Che, L. and Meng, Z. (2006). Hydrothermal synthesis of perovskite bismuth ferrite crystallites. *Journal of Crystal Growth*, 291(1): 135–139.
10. Li-Jie, H., Dong, Z., Shou-hua, F., Bo, Z. and Gang, C. (2012). Hydrothermal synthesis and characterization of perovskite oxide $AgTaO_3$. *Chemical Research in Chinese Universities*, 28: 760–763.
11. Li, C., Zhu, Y., Fang, S., Wang, H., Gui, Y., Bi, L. and Chen, R. (2011). Preparation and characterization of $SrSnO_3$ nanorods. *Journal of Physics and Chemistry of Solids*, 72(7): 869–874.
12. Ahmadi, S., Asim, N., Alghoul, M., Hammadi, F., Saeedfar, K., Ludin, N. and Sopian, K. (2014). The role of physical techniques on the preparation of photoanodes for dye sensitized solar cells. *International Journal of Photoenergy*, 2014: 1-19.
13. James, K., Aravind, A. and Jayaraj, M. (2013). Structural, optical and magnetic properties of Fe-doped barium stannate thin films grown by PLD. *Applied Surface Science*, 282: 121–125.
14. Bellal, B., Hadjarab, B., Bouguelia, A. and Trari, M. (2009). Visible light photocatalytic reduction of water using $SrSnO_3$ sensitized by $CuFeO_2$. *Theoretical and Experimental Chemistry*, 45(3): 160–166.
15. Junploy, P., Thongtem, T., Thongtem, S. and Phuruangrat, A. (2014). Decolorization of methylene Blue by $Ag/SrSnO_3$ composites under ultraviolet radiation. *Journal of Nanomaterials*, 2014: 67.
16. Kotan, Z., Ayvacikli, M., Karabulut, Y., Garcia-Guinea, J., Tormo, L., Canimoglu, A. and Can, N. (2013). Solid state synthesis, characterization and optical properties of Tb doped $SrSnO_3$ phosphor. *Journal of Alloys and Compounds*, 581: 101–108.
17. Liu, Q., Wang, H., Chen, F. and Wu, W. (2008). Single-crystalline transparent and conductive oxide films with the perovskite structure: Sb-doped $SrSnO_3$. *Journal of Applied Physics*, 103(9): 93709.

Malaysian Journal of Analytical Sciences, Vol 23 No 1 (2019): 109 - 115
DOI: https://doi.org/10.17576/mjas-2019-2301-13

MALAYSIAN JOURNAL OF ANALYTICAL SCIENCES
Published by The Malaysian Analytical Sciences Society
ISSN 1394 - 2506

OPTIMISATION OF THE COMPOSITION AND PROCESS PARAMETER OF $CsH_2PO_4/NaH_2PO_4/SiO_2$ SOLID ACID COMPOSITE VIA THE TAGUCHI METHOD

(Pengoptimuman Komposisi dan Parameter Proses Bagi Komposit Asid Pepejal $CsH_2PO_4/NaH_2PO_4/SiO_2$ Melalui Kaedah Taguchi)

Norsyahida Mohammad[1], Abu Bakar Mohamad[1,2], Abdul Amir Hassan Kadhum[1,2], Kee Shyuan Loh[1]*

[1]*Fuel Cell Institute*
[2]*Department of Chemical and Process Engineering, Faculty of Engineering and Built Environment*
Universiti Kebangsaan Malaysia, 43600 UKM Bangi, Selangor, Malaysia

**Corresponding author: ksloh@ukm.edu.my*

Received: 13 April 2017; Accepted: 17 April 2018

Abstract

Solid acid composites of $CsH_2PO_4/NaH_2PO_4/SiO_2$ (CDP/SDP/SiO_2) were synthesised with varied SDP to CDP and SiO_2 to CDP mole fractions. The composites were arranged for optimisation *via* the Taguchi method with L9 orthogonal array, which manipulates four factors: the amount of SDP, amount of SiO_2, amount of pressure used for pellet production and operating temperature. Responses were recorded as the averaged conductivity value for each experimental set. The composite powders were uniaxially pressed to form pellets of 1 mm thickness for conductivity measurements. Conductivity value was averaged from three readings and used in the signal-to-noise (S/N) ratio formula. The S/N ratio was set such that larger is better and calculated to maximise the response required for the analysis. Operating temperature has the largest effect on the conductivity value of solid acid composites, whereas the amount of SiO_2 has the smallest effect. The amount of SDP in the composite has a larger effect than the pressure applied during pellet production prior to the conductivity measurements. The optimised composite consists of 0.2 mole fraction of SDP to CDP and 0.3 mole fraction of SiO_2 to CDP pressed at 3 tonnes cm^{-2} to produce pellets and tested at the temperature of 250 °C. The optimisation was validated by using analysis of variance from the Design-Expert® software.

Keywords: solid acid composite, caesium dihydrogen phosphate, Taguchi

Abstrak

Komposit asid pepejal $CsH_2PO_4/NaH_2PO_4/SiO_2$ (CDP/SDP/SiO_2) telah disintesis dengan pecahan mol SDP kepada CDP dan SiO_2 kepada CDP yang berbeza-beza. Komposit-komposit ini telah menjalani proses pengoptimuman melalui kaedah Taguchi, dengan susunan ortogonal L9 yang memanipulasi empat faktor iaitu kuantiti SDP, kuantiti SiO_2, kuantiti tekanan yang digunakan untuk penghasilan pelet dan suhu operasi. Output dicatatkan sebagai nilai kekonduksian purata bagi setiap set eksperimen. Serbuk komposit telah dimampatkan untuk membentuk pelet dengan ketebalan 1 mm untuk analisa kekonduksian. Nilai kekonduksian yang diperoleh dijadikan purata daripada tiga bacaan dan digunakan dalam formula nisbah isyarat kepada hingar (S/N). Nisbah S/N telah ditetapkan sebagai 'lebih besar adalah lebih baik' dan digunakan untuk memaksimakan tindak balas yang diperlukan untuk analisa. Suhu operasi mempunyai impak terbesar ke atas nilai kekonduksian komposit asid pepejal, manakala kuantiti SiO_2 mempunyai impak yang paling kecil ke atas nilai kekonduksian komposit asid pepejal. Kuantiti SDP dalam komposit mempunyai kesan yang lebih besar berbanding tekanan yang digunakan semasa penghasilan pelet sebelum analisa kekonduksian. Komposit yang telah dioptimumkan terdiri daripada 0.2 pecahan mol SDP kepada CDP dan 0.3 pecahan mol SiO_2 kepada CDP, memerlukan tekanan sebanyak 3 tan cm^{-2} untuk menghasilkan pelet dan diuji pada suhu 250 °C. Proses pengoptimuman ini disahkan oleh analisa varians dari perisian Design-Expert®.

Kata kunci: komposit asid pepejal, sesium dihidrogen fosfat, Taguchi

Introduction

The potential of solid acids as alternatives to membrane materials in the proton exchange membrane fuel cell (PEMFC) has been demonstrated [1–3]. Caesium dihydrogen phosphate, CsH_2PO_4 (CDP), is one of the most widely studied solid acids because of its high proton conductivity value of 2.2 x 10^{-2} S cm^{-1} at 240 °C [3, 4], its lack of decomposition or dehydration at intermediate temperatures and its non-production of catalyst poison in hydrogen-rich surroundings [5, 6]. The addition of hygroscopic oxides, such as SiO_2, ZrO_2, TiO_2 and Al_2O_3, generates strong surface interaction and enhances the stabilisation of the composite material, hence reducing the brittleness of solid acids [7, 8]. Sodium dihydrogen phosphate, NaH_2PO_4 (SDP), undergoes dehydration at lower temperatures compared with other solid acids and does not exhibit superprotonic conductivity [9]. Martsinkevich and Ponomareva [10] found that the conductivity of $Cs_{1-x}Na_xH_2PO_4$ composite for x values between 0 and 0.2 increases at about two orders of magnitude in the low temperature region in comparison to CDP.

This study identifies the effect of composition and process parameter on the conductivity value of the mixed-salt solid acid CDP/SDP/SiO_2 via the Taguchi method. This technique reduces the number of experiments required and minimises the variation in a process. Unlike other design of experiments (DOEs), such as factorial design, which requires testing of each possible combination, the Taguchi method tests pairs of combinations. This method produces the optimum combination of solid acid composition and process parameter for further testing and characterisation.

Materials and Methods

Solid acid CDP was synthesised by mixing stoichiometric amounts of caesium carbonate, Cs_2CO_3 (ReagentPlus®, ≥99% Sigma Aldrich) and phosphoric acid H_3PO_4 (≥85wt.% in H_2O, Sigma-Aldrich) according to the following reaction:

$$Cs_2CO_3 + 2H_3PO_4 \rightarrow 2CsH_2PO_4 + CO_2 + H_2O \quad (1)$$

In CDP synthesis, a measured amount of Cs_2CO_3 was dissolved in distilled water. A surfactant powder, cetyltrimethylammoniumbromide, CTAB (BioXtra®, ≥99% Sigma-Aldrich, MO, USA), was dissolved in ethanol separately and added to the Cs_2CO_3 solution to reduce water surface tension and assist in particle dispersion. The mixture was then stirred for 10 minutes until a clear solution was produced. Phosphoric acid was added dropwise into the mixture with continuous stirring for another 10 minutes. Acetone was added excessively to the mixture while stirring for another 30 minutes. The solution was vacuum filtered to produce CDP as a white precipitate. The synthesised CDP was dried at 130 °C for 24 hours and ground to produce white powder CDP.

Mixed-salt solid acid composites $CsNa_xH_2PO_4/ySiO_2$ (where x and y equals 0.1, 0.2 and 0.3) were synthesised by mechanical grinding of individual salts CDP, SDP (ReagentPlus®, ≥99% Sigma-Aldrich, MO, USA) and SiO_2 (purum p.a. powder, Sigma-Aldrich, MO, USA, 63 µm particle size). The composite powders were then pressed at 3, 4 and 5 tonnes cm^{-2} to form pellets of 1 mm thickness and 13 mm diameter followed by sintering at 230 °C for 1 hour. The pellets were painted with silver conductive paint to serve as the current collector and then connected to an impedance analyser (Metrohm Autolab B.V., The Netherlands).

Impedance readings were taken at several operating temperatures (210, 230 and 250 °C) with a frequency of 1.0×10^{-2} to 1.0×10^{6} Hz and a current of 0.01 A. The measured data were analysed using the Nova software packaged with the FRA2 module. The resistance value (*R*) was determined from the impedance data plotted on real and imaginary axes Z' and Z", respectively, known as the Nyquist plot. The curve is fitted using the equivalent circuit as in Figure 1. The proton conductivity value σ for each composite is calculated using *R* and is given by equation 2:

$$\text{Conductivity, } \sigma \text{ (Scm}^{-1}) = \frac{\frac{1}{R(\Omega)}}{\frac{A(cm^2)}{l(cm)}} \quad (2)$$

where *A* is the sectional area, and *l* is the thickness of the pellet.

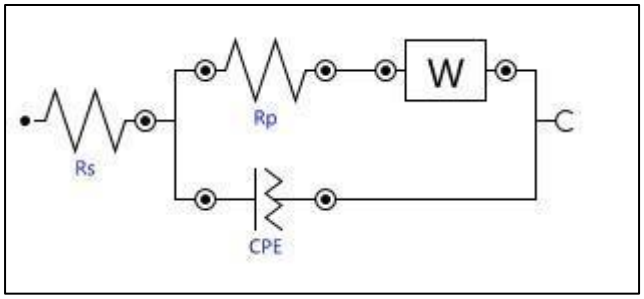


Figure 1. Equivalent circuit used to analyse the impedance data

The Taguchi method was applied to identify the effect of composition and process parameter on the conductivity of mixed-salt composite CDP/SDP/SiO_2. The selected DOE was Taguchi L9 orthogonal array, which manipulates four factors and three levels. DOE calculations were performed manually in an Excel spreadsheet and validated by a DOE software (Design-Expert® Version 6.0.10, Stat-Ease, Inc.).

The selected four factors are the amount of SDP, the amount of SiO_2, the pressure used for pellet production and the operating temperature. Table 1 presents the three levels selected for each of the factors. The amount of SDP in terms of mole fraction to CDP was limited between 0.1 and 0.3. Such limitation was applied because of the findings by Martsinkevich and Ponomareva that solid solutions exist between that range, whereas larger mole fractions resulted in individual SDP properties as measured by X-ray diffraction [10]. SiO_2 mole fraction lower than 0.3 caused higher conductivity for solid acid composites at temperatures higher than 180 °C [11]. Therefore, the SiO_2 range of 0.1 to 0.3 mole fractions was chosen for this study. The pressure applied during pellet production was fixed between 3 to 5 tonnes cm^{-2} due to the reproducibility of the pellets in this pressure range. Solid acid CDP is known for its high conductivity at temperatures above 230 °C. Hence, three levels between 210 and 250 °C were selected to observe the conductivity values of the composite around the optimum temperature.

Table 1. Factors, control parameters and levels of each parameter

Factor	**Control Parameter**	**Level**		
		1	**2**	**3**
A	Amount of SDP (mole fraction to CDP)	0.1	0.2	0.3
B	Amount of SiO_2 (mole fraction to CDP)	0.1	0.2	0.3
C	Pressure applied during pellet production (tonnes cm^{-2})	3	4	5
D	Operating temperature (°C)	210	230	250

Results and Discussion

The Taguchi L9 orthogonal array produced nine sets of level combinations (Table 2). Each set was run three times in randomised order to reduce error. Responses were recorded in Table 2 as the averaged conductivity value for each experimental set. The signal-to-noise (S/N) ratio was fixed to be *larger is better* and calculated to maximise the response according to the formula below:

$$\text{S/N ratio} = -10log_{10}\ \frac{1}{n}\sum_{i=1}^{n}\ \ \frac{1}{y_i^2} \quad (3)$$

where y_i is the observed response value, and n is the number of replications.

Table 2. Level combinations of designed experiments and results

Exp. No.	Factor				Conductivity (S cm^{-1})	S/N
	Amount of SDP (mole fraction to CDP)	Amount of SiO_2 (mole fraction to CDP)	Pressure Applied during Pellet Production (tonnes cm^{-2})	Operating Temperature (°C)		
1	0.1	0.1	3	210	4.5×10^{-5}	-90.0
2	0.1	0.2	4	230	1.3×10^{-4}	-78.9
3	0.1	0.3	5	250	3.4×10^{-3}	-50.0
4	0.2	0.1	4	250	7.6×10^{-3}	-43.3
5	0.2	0.2	5	210	1.1×10^{-4}	-85.5
6	0.2	0.3	3	230	3.4×10^{-3}	-59.9
7	0.3	0.1	5	230	4.0×10^{-4}	-77.9
8	0.3	0.2	3	250	7.2×10^{-3}	-43.1
9	0.3	0.3	4	210	3.8×10^{-4}	-90.5

The S/N values in Table 2 were used to obtain the averaged S/N values in Table 3. The difference between the highest averaged S/N value and the lowest averaged S/N value for each factor was then calculated (Table 3). The largest difference indicates the most significant factor. Operating temperature (°C) has the largest effect on the conductivity values of solid acid composites, followed by the amount of SDP, the pressure applied during pellet production and the amount of SiO_2. This finding supports the reported property of solid acids, namely, its high dependence on temperature, where the conductivity increases by two to three orders of magnitude at its superprotonic temperature. The amount of SiO_2 has the smallest effect on the conductivity values of solid acid composites. This characteristic enables the addition of SiO_2 to produce solid acid composites that are more robust and less brittle [9, 12] without significantly reducing the conductivity of the composite.

Table 3. Ranking of factors which affect the conductivity of the CDP/SDP/SiO_2 composite

Level	Averaged S/N Value for Each Factor			
	Amount of SDP (mole fraction to CDP)	Amount of SiO_2 (mole fraction to CDP)	Pressure Applied during Pellet Production (tonnes cm^{-2})	Operating Temperature (°C)
1	-72.97	-70.38	-64.31	-88.65
2	-62.90	-69.18	-70.90	-72.24
3	-70.49	-66.80	-71.14	-45.46
Difference	10.08	3.57	6.83	43.20
Rank	2	4	3	1

This DOE facilitates the identification of the optimum combination of factors to produce the highest conductivity value. For each factor, the optimum level was chosen from the highest averaged S/N value. For example, the optimum level of factor A (amount of SDP) was level 2, which was given by the highest averaged value of -62.90

(Table 3). Level 2 of the said factor also corresponds to 0.2 mole fraction of SDP to CDP, as defined in Table 1. Therefore, the output of this DOE indicates that the optimised composite should consist of 0.2 mole fraction of SDP to CDP and 0.3 mole fraction of SiO_2 to CDP pressed at 3 tonnes cm^{-2} during pellet production and tested at the temperature of 250 °C.

Similar results were obtained via Design-Expert® by limiting the factors to three, namely, the amount of SDP, the pressure used for pellet production and the operating temperature. We assume that the effect of SiO_2 is negligible and the factors are independent of each other prior to analysis of variance (ANOVA) in Design-Expert®. The ANOVA resulted in the model F-value of 163.58 and "Prob>F" value of 0.0061, indicating that this model is significant. The model given by Design-Expert® is adequate, as supported by the normality plot in Figure 2. The influence of factors on the conductivity of the composite is shown in Figures 3–5. The optimised solid acid composite (CDP23) was characterised via several methods, including differential scanning calorimetry, thermogravimetric analysis and X-ray diffraction. The findings have been published elsewhere [13].

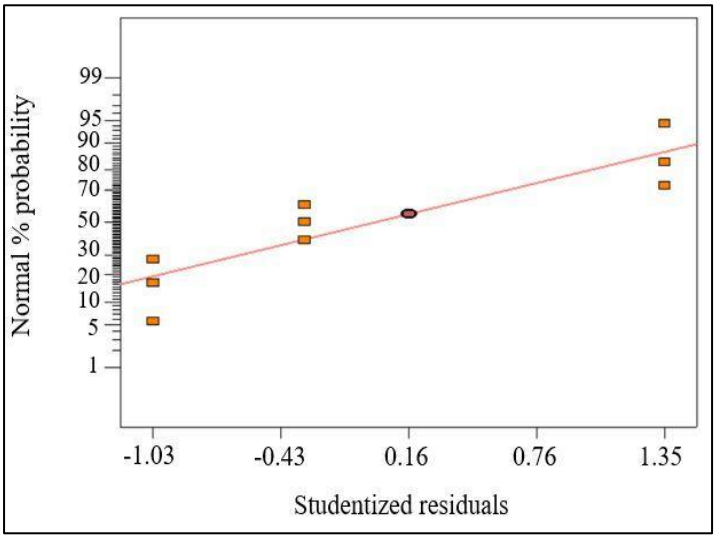


Figure 2. Normal probability plot of residuals for the measured conductivity values

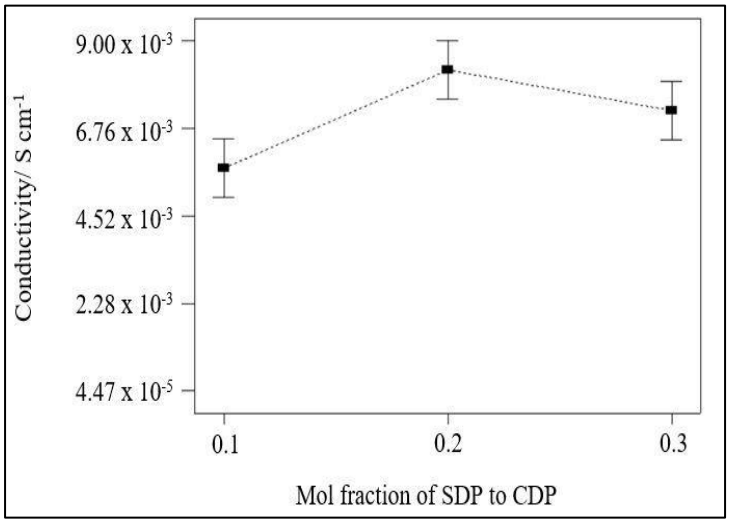


Figure 3. Influence of amount of SDP on the conductivity of the solid acid composite

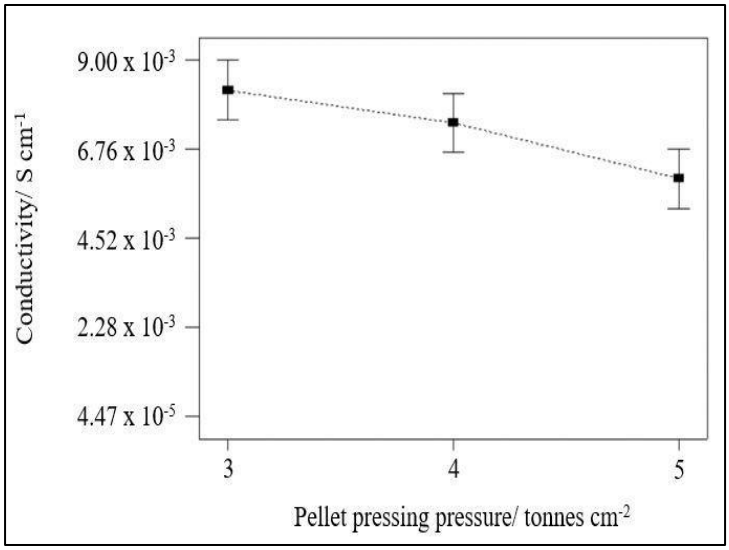


Figure 4. Influence of pellet pressing pressure on the conductivity of the solid acid composite

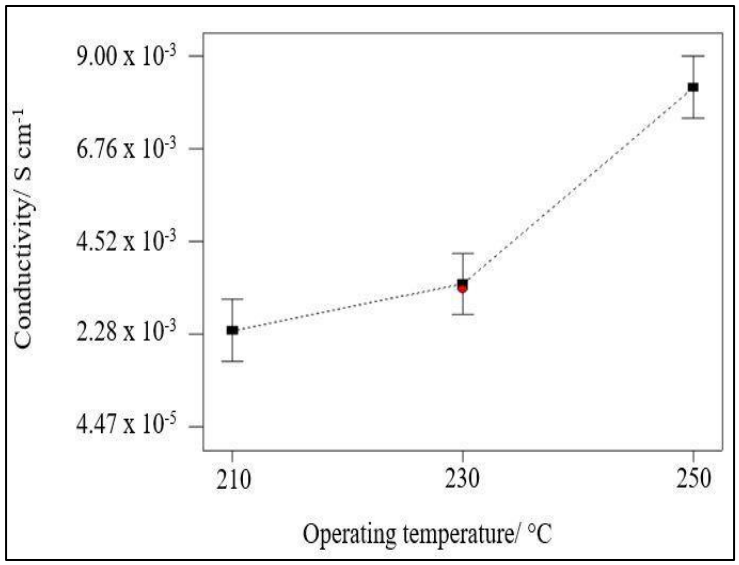


Figure 5. Influence of operating temperature on the conductivity of the solid acid composite

Conclusion

The Taguchi method enables the identification of trends in factors affecting the conductivity values of the solid acid composite CDP/SDP/SiO_2. The four factors selected for the analysis are the amount of SDP, the amount of SiO_2, the pressure used for pellet production and the operating temperature. The averaged conductivity values were recorded as responses and used to obtain the S/N ratio. Operating temperature has the highest influence on the conductivity value, followed by the amount of SDP. The amount of SiO_2 has the smallest effect on the conductivity values of solid acid composites. This characteristic allows for the addition of SiO_2 to enhance the robustness of the solid acid pellet. The calculations agreed with the results obtained by Design-Expert®. This study revealed that the optimised composite consists of 0.2 mole fraction of SDP to CDP and 0.3 mole fraction of SiO_2 to CDP pressed at 3 tonnes

cm^{-2} during pellet production and tested at a temperature of 250 °C. Future work should focus on the optimisation of membrane–electrode assembly fabrication parameters.

Acknowledgement

This work was financially supported by the Universiti Kebangsaan Malaysia through the University Research Grants (Grant Nos. GUP-2016-038 and DIP-2017-024).

References

1. Haile, S. M., Boysen, D. A., Chisholm, C. R. I. and Merle, R. B. (2001). Solid acids as fuel cell electrolytes. *Nature*, 410: 910-913.
2. Boysen, D. A., Uda, T., Chisholm, C. R. I. and Haile, S. M. (2004). High-performance solid acid fuel cells through humidity stabilization. *Science*, 303(5654): 68-70.
3. Haile, S. M., Chisholm, C. R. I., Sasaki, K., Boysen, D. A. and Uda, T. (2006). Solid acid proton conductors: From laboratory curiosities to fuel cell electrolytes. *Faraday Discussions*, 134: 17-39.
4. Taninouchi, Y.-K., Uda, T., Awakura, Y., Ikeda, A. and Haile, S. M. (2007). Dehydration behavior of the superprotonic conductor CsH_2PO_4 at moderate temperatures: 230 to 260 °C. *Journal of Materials Chemistry*, 17(30): 3182-3189.
5. Unnikrishnan, S. (2009). Micromachined dense palladium electrodes for thin-film solid acid fuel cells. (PhD Dissertation), University of Twente, Enschede.
6. Dupuis, A.-C. (2011). Proton exchange membranes for fuel cells operated at medium temperatures: Materials and experimental techniques. *Progress in Materials Science*, 56(3): 289-327.
7. Piao, J., Liao, S. and Liang, Z. (2009). A novel cesium hydrogen sulfate–zeolite inorganic composite electrolyte membrane for polymer electrolyte membrane fuel cell application. *Journal of Power Sources*, 193(2): 483-487.
8. Lavrova, G. V. and Ponomareva, V. G. (2008). Intermediate-temperature composite proton electrolyte $CsH_5(PO_4)_2/SiO_2$: Transport properties versus oxide characteristic. *Solid State Ionics*, 179(21–26): 1170-1173.
9. Boysen, D.A. (2004). Superprotonic solid acids: structure, properties, and applications (PhD Dissertation), California Institute of Technology.
10. Martsinkevich, V. V. and Ponomareva, V. G. (2012). Double salts $Cs_{1-x}M_xH_2PO_4$ (M = Na, K, Rb) as proton conductors. *Solid State Ionics*, 225: 236-240.
11. Ponomareva, V.G. and Shutova, E. S. (2007). High-temperature behavior of CsH_2PO_4 and CsH_2PO_4–SiO_2 composites. *Solid State Ionics*, 178(7–10): 729-734.
12. Baranov, A. I., Grebenev, V. V., Khodan, A. N., Dolbinina, V. V. and Efremova, E. P. (2005). Optimization of superprotonic acid salts for fuel cell applications. *Solid State Ionics*, 176(39–40): 2871-2874.
13. Mohammad, N., Mohamad, A. B., Kadhum, A. A. H. and Loh, K. S. (2017). Effect of silica on the thermal behaviour and ionic conductivity of mixed salt solid acid composites. *Journal of Alloys and Compounds*, 690: 896-902.

Malaysian Journal of Analytical Sciences, Vol 23 No 1 (2019): 116 - 123
DOI: https://doi.org/10.17576/mjas-2019-2301-14

MALAYSIAN JOURNAL OF ANALYTICAL SCIENCES
Published by The Malaysian Analytical Sciences Society
ISSN 1394 - 2506

OPTIMIZATION OF HYDROGEN PRODUCTION FROM FRUIT WASTE THROUGH MESOPHILIC AND THERMOPHILIC DARK FERMENTATION: EFFECT OF SUBSTRATE-TO-INOCULUM RATIO

(Pengoptimuman Penghasilan Hidrogen dari Buangan Buah melalui Fermentasi Tanpa Cahaya pada Kondisi Mesofilik dan Termofilik: Pengaruh Nisbah Substrat-Inokulum)

Khamdan Cahyari[1,2]*, Muslikhin Hidayat[1], Siti Syamsiah[1], Sarto[1]

[1]*Department of Chemical Engineering, Faculty of Engineering, Gadjah Mada University, Indonesia*
[2]*Dept. of Chemical Engineering, Faculty of Industrial Technology, Universitas Islam Indonesia, Indonesia*

**Corresponding author: khamdan.cahyari@uii.ac.id*

Received: 13 April 2017; Accepted: 17 April 2018

Abstract

This research was aimed to optimize hydrogen production from fruit waste, particularly on the effect of the substrate-to-inoculum ratio (SIR). Production of hydrogen was carried out through dark fermentation process both in mesophilic (30 °C, 1 atm) and thermophilic (55 °C, 1 atm) condition. Fermentation was conducted at SIR value ranging from 0.800 to 174 $VS_{substrate}$/g VS_{inoc}. In mesophilic fermentation, the highest cumulative total gas yield was achieved at SIR value of 19 corresponding total gas yield of 113 ml STP/g VS (5%v of H_2). In thermophilic condition, the highest H_2 yield was obtained at SIR value of 0.800 $VS_{substrate}$/g VS_{inoc} with H_2 yield of 294 mL STP/g VS (50 – 60%v of purity). It was noticed that the lower SIR value, the higher hydrogen yield. In summary, it is concluded that substrate-to-inoculum ratio (SIR) plays important role in dark fermentation process to produce renewable energy of hydrogen fuel.

Keywords: hydrogen, fermentation, substrate-to-inoculum ratio, fruit waste, renewable energy

Abstrak

Kajian ini merupakan langkah pengoptimuman penghasilan hidrogen dari bahan buangan buah, khususnya pada pengaruh nisbah substrat-inokulum (NSI). Penghasilan hidrogen dilakukan melalui proses fermentasi tanpa cahaya pada kondisi mesofilik (30 °C, 1 atm) dan termofilik (55 °C, 1 atm). Fermentasi dilakukan dengan variasi nilai NSI antara 0,800 dan 174 g $VS_{substrate}$/g VS_{inoc}. Pada fermentasi mesofilik, hasil gas total kumulatif tertinggi diperoleh pada nilai NSI 19 g $VS_{substrate}$/g VS_{inoc} dengan nilai penghasilan gas sebesar 113 ml STP/g VS (5%v/v gas H_2). Sedangkan proses fermentasi termofilik, hasil hidrogen kumulatif tertinggi dicapai pada nilai RSI 0,800 $VS_{substrate}$/g VS_{inoc} sebesar 294 ml STP H_2/g VS (ketulenan H_2 50-60%v/v). Hal ini menunjukkan bahawa semakin kecil nilai NSI, hasil gas hidrogen menjadi semakin besar. Sehingga dapat disimpulkan bahawa faktor nisbah substrat terhadap inokulum (NSI) memiliki peranan penting dalam proses fermentasi tanpa cahaya untuk menghasilkan sumber tenaga baharu hidrogen.

Kata kunci: hidrogen, fermentasi, nisbah substrat-inokulum, bahan buangan buah, tenaga baharu

Introduction

Indonesia is one of the developing countries with significant economic growth and social development in South East Asia (SEA) region nowadays. Consequently, the Indonesian Government need to secure its energy supply to

support this growth. For this purpose, the country relies mainly on fossil fuel in term of oil, coal, and gas accounting for approximately 96% of total primary energy consumption or equivalent to 1,358 million BOE in 2014 [1]. The high dependence on this fuel has led to many occurring environmental impacts during the last few decades such as depletion of natural resources (oil, coal and gas reserves), increases of CO_2 and particulate matter concentration in many cities, water contamination and climate changes [2]. To mitigate those impacts, the Indonesian Government has made some efforts to leverage the use of renewable energy sources for fulfilling energy demand in the future [3]. The Government Regulation No. 5/2006 states that the national energy share in the year 2025 is oil < 20%, gas 30%, coal 33%, renewable energy > 17% consisting of biofuel (5%), geothermal energy (5%), biomass, nuclear power, hydropower, solar energy (5%) and coal liquefaction (2%) [4]. The share of biofuel refers to biodiesel, bioethanol, biogas, and also biohydrogen which has a huge potential generation from renewable sources. Therefore, the government has made many efforts to implement strategies in developing renewable energy production efficiently.

Hydrogen fuel is one of the most promising fuels to mitigate major environmental impacts of fossil fuel. It is a clean energy carrier i.e. carbon free, emits only water vapor, has high energy density (142 kJ/g), has less emission of greenhouse gasses i.e.CO_2, and has better energy conversion in fuel cell up to 50% efficiency. Hydrogen production is conducted generally through water splitting when there is sufficient input of free excess energy, otherwise, it is uneconomically feasible to establish. Hydrogen production with the involvement of microbial activity to grow and generate hydrogen become more attractive to elaborate further due to its convenient process condition. For example, mesophilic dark fermentation of organic substrate is able to occur at ambient condition (35 °C, 1 atm, pH 5) with practical yield of 1-3 mol H_2/mol glucose [5]. In addition, utilization of organic waste as a substrate to generate this hydrogen provide simultaneous solution between mitigating waste problems and renewable energy production. One of these organic wastes available in abundant quantities from the agricultural sector in Indonesia is fruit waste.

The waste originates from a fragment of harvested fruits which turned into non-economically value products due to deterioration, market off-specs, and physical damages during agricultural production, post-harvesting handling and storage, processing, distribution, and consumption pattern. According to Central Bureau of Statistics of Indonesia, it was reported that there were more than 17.500 million tons of total edible fruits harvested throughout Indonesia in 2014. Apart from this quantity, the fruits turned into waste at particular percentages depending on cultivation, processing, and distribution technologies. For example, fruit and vegetable waste was estimated approximately 55% of total harvested in South and South East Asia region [6]. Global fresh fruit losses were estimated at least 6.800% of total harvested through region worldwide [7]. Local grocery fruit market in Yogyakarta Province, Indonesia threw away up to 10 tons/day i.e. 10% of incoming fruits due to deterioration during transportation [8]. The majority of these wastes were untreated prior to open dumping area which potentially causes severe environmental problems such as water and soil contamination, emission of methane, diseases, and other health-related problems.

Hydrogen production through dark fermentation is limited to low hydrogen yield and gas production rate due to non-optimized operational condition, of which is the substrate-to-inoculum ratio (SIR). When SIR is low, the fermentation occurs at the limited source of the substrate which potentially prevents the optimum growth of microorganisms. On the contrary, higher SIR indicates an overwhelming substrate which may cause inhibition of substrates, indigenous volatile compounds (e.g. limonene, eugenol, phloretin) and by-products (volatile fatty acids). Cappai et al. [9] reported that the optimum SIR was achieved at 0.140 g VS_{inoc}/g $VS_{substrate}$ (equivalent to SIR 7.140) with H_2 yield of 88.800 liters STP/kg VS of food waste). When peach pulp waste as a substrate, the optimum ratio was found at 0.009 VS_{inoc}/g $VS_{substrate}$ (SIR 111) [10]. This indicates that optimum SIR is affected by the type of substrate. Therefore, this research was meant to investigate the optimum condition of SIR on dark fermentation of fruit waste.

Materials and Methods

Source of inoculum and fruit waste

Source of mesophilic inoculum was originated from the residual sludge of cow dung-to-biogas plant. The thermophilic inoculum was collected from the residual sludge of organic fraction of municipal solid waste (OFMSW) to biogas plant. Both sludges passed through sub-sequential acid treatment (pH 5, 24 hours' exposure time) and heat-shock treatment (95 °C, 45 minutes).

Fruit waste i.e. Apple (*Malus pumila*), citrus (*Citrus* grandis (L.) Osbeck), and melon (*Cucumis melo*) was collected from the local grocery market. The waste was individually chopped and grounded using kitchen blender with the addition of tap water to ease the blending operation. It was then stored at cold room (5 °C, 1 atm) prior to being used in the experiment, thereafter called as feedstock.

Experimental set up

Dark fermentation of fruit waste was conducted using 120 mL serum vial injection bottles as a bioreactor for batch assays assessment. Each digester was filled out with 20 mL of inoculum seed, 15 mL of distilled water, 5 mL of macronutrients, and 2.500 mL of micronutrients and feedstock. The volume of feedstock added to bioreactor was adjusted to meet the substrate-to-inoculum ratio of each fruit waste within the range between 0.800 and 174 g $VS_{substrate}$/g VS_{inoc}. Each bioreactor was then closed and sealed using butyl rubber stopper and aluminum cap followed with flushing of N_2 gas for 3 minutes. The experimental run was performed in triplicate. A solution of macro- and micro-nutrients were also prepared by addition of 11.400 g $FeCl_2.4H_2O$, 4.681 g KH_2PO_4, 0.814 g NH_4Cl and 3 g $NaHCO_3$, 0.320 g $MgSO_4.7H_2O$, 32 mg $NiSO_4.6H_2O$, 50 mg $CaCl_2$, 7 mg $Na_2B_4O_7.10H_2O$, 14 mg $(NH_4)_6Mo_7O_{24}.4H_20$, 23 mg $ZnCl_2$, 21 mg $CoCl_6.H_2O$, 10 mg $CuCl_2.2H_2O$ into 1000 mL of DW respectively

Analysis

Total gas production during dark fermentation process was conducted through measurement of bioreactor's headspace pressure. Analysis of hydrogen content was performed using a gas chromatography unit (Auto System Perkin Elmer, Waltham, MA) equipped with Perkin Elmer packed column, 6'x 1.8" OD, 8-/100 mesh and thermal conductivity detector with oven, injection and detector temperatures as 75 °C, 150 °C, and 200 °C, respectively. Analysis of limonene concentration was performed using GC-MS (HP G1800C, Agilent, Palo Alto CA) with helium as a carrier gas with initial temperature of 50 °C and temperature increasing the rate of 15 °C/min up to 250 °C and it was maintained at this temperature for 3 minutes. Extraction of limonene in citrus was conducted using n-heptane (25 mL, 99% purity) to 14 mL of citrus juice and centrifugation at 3500 g (30 minutes). Nitrogen was used as carrier gas operating at 40 mL/min flow rate at 60 °C. Analysis of monosaccharide was carried out using HPLC-based on reference [11]. Analysis of moisture, total solid (TS), volatile solid (VS), and ash was carried out according to the standard method of water and wastewater analysis of American Public Health Association (APHA) procedures [12]. The degree of acidity (pH) was measured using digital pH meter (Jenway, UK).

Results and Discussion

Characteristics of selected fruit waste

Global fruit production was recorded nearly 400 million metric tons in 2014 [13]. It was comprised of bananas, watermelons, apples, grapes, citrus, mangoes, plantain, and melons as the top ten global fruit harvested as shown in Figure 1. Accordingly, most of the fruit waste consists of these sorts of fruits which may be found in any region. Valorization of these waste through fermentation to produce hydrogen is a promising method to mitigate environmental impacts and generating renewable energy sources on a global scale. Apple (*Malus pumila*), citrus (*Citrus grandis* (L.) Osbeck), and melon (*Cucumis melo*) waste was estimated to be the highest waste composition due to physical damage and deterioration during cultivation to transportation considering their soft peel structure compare to the other fruits. Global apple production was more than 84 million tons spread out throughout many regions, except for the small quantity in Southeast Asia (4.8 MMT). Therefore, this research was focused on the utilization of the three fruits as representative of global fruit waste and only citrus and melon as representative of SEA region.

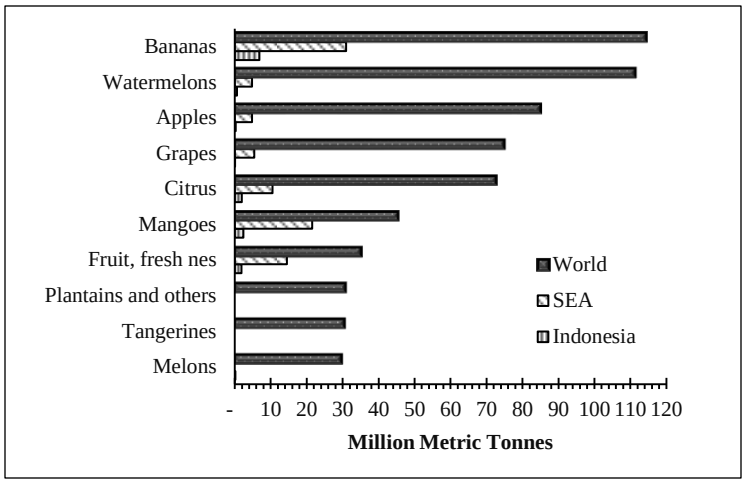


Figure 1. Fruit Production in Global region, Southeast Asia region (SEA), and Indonesia [13]

Apple (*Malus pumila*), citrus (*Citrus grandis* (L.) Osbeck), and melon (*Cucumis melo*) were characterized by their physicochemical properties as shown in Table 1. More than 90% of total fruit weight is composed of water and soluble sugars. Total and volatile solid of both citrus and apple are similar accounting for 5-6% and 97% respectively, except that of melon. The volatile solid content of melon is lower due to the higher content of ashes. It was reported that melon peels contain 69.770% of carbohydrate and 3.670% of Ashes [17]. Limonene was found in citrus fruit at 0.125 mg/L of whole citrus fruit juice. Phloretin was reported as a major component in apple seed at concentration 1,674 mg/kg. Although eugenol could be found in each of the fruit, the highest concentration was exhibited in melon fruit. These three volatile compounds are known as an antimicrobial agent. The previous experiments demonstrated that methane production was interrupted due to the presence of limonene with half maximum inhibitory concentration, IC_{50} was 669 mg/kg [20]. Phloretin in Apple was also reported to cause growth inhibition of some Gram positive and Gram-negative bacteria such as *Staphylococcus aureus* and *Salmonella typhimurium*, respectively with a MICs 125 μg/mL [21]. In addition, eugenol was shown to inhibit the activation and maturation of dendritic cells of microorganisms with IC_{50} approximately at 50 μM [22]. This indicates that optimization of hydrogen production from the fruit waste is also related to inhibition or retardation of these three volatile compounds. In addition, total soluble sugar was found higher in apple and melon compared to that in citrus indicating that the two fruits have higher readily available substrate for the fermentation process.

Table 1. Characteristics of fruit waste

Parameters	**Citrus (*Citrus grandis L.*)**	**Apple (*Malus pumila*)**	**Melon (*Cucumis melo*)**	**Refs.**
Total Solid (%)	6.020 (0.000)	5.040 (0.570)	6.720 (0.220)	
Volatile Solid (%)	96.810 (0.140)	97.690 (0.250)	90.630 (0.680)	
Ph	4.050 (0.040)	3.370 (0.010)	5.970 (0.060)	
Limonene (mg/L juices)	0.125 (0.010)	-	-	
Phloretin (mg/kg)	-	1,674	-	[14]
Total Dietary Fiber (g/100 g dried base)	63.240(1.430)	76.840(1.240)	41.690	[15 – 18]
Eugenol (μg/kg)	379	239	2302.400	[19]
Soluble Glucose (g/L)	5.110	7.180	6.960	
Soluble Fructose (g/L)	0.270	12.390	4.860	
Total Soluble Sugar (g/L)	5.380	19.570	11.820	

Mesophilic dark fermentation

Mesophilic fermentation of fruit waste was conducted at temperature of 30 °C, pressure 1 bar and pH 5.0. Five SIR values were investigated to evaluate its effect toward total gas yield of biohydrogen production. The previous reports state that optimum hydrogen production from ground waste paper was achieved at a substrate concentration of 18.58 ±2.45 g/L and biomass concentration of 0.5 g/L which is equivalent to SIR of 42. On the other hand, optimum SIR value of 111 and 7.140 was obtained from fermentation of peach pulp and food waste respectively. Since there is various optimum value for the particular type of substrate, this experiment investigated SIR value ranging from 19 – 174 g $VS_{substrate}$/g VS_{inoc}.

A time course of total gas yield and hydrogen percentages during fermentation of citrus and melon waste at the SIR values is illustrated in Figure 2. The highest total gas yield was obtained from citrus and melon fermentation at SIR value of 19 g $VS_{substrate}$/g VS_{inoc} corresponding to 113 and 98 ml STP/g VS respectively. Increasing SIR value to 174 g $VS_{substrate}$/g VS_{inoc} caused significant reduction of the yield up to 76%. A similar pattern of the yield was noticed for both citrus and melon.

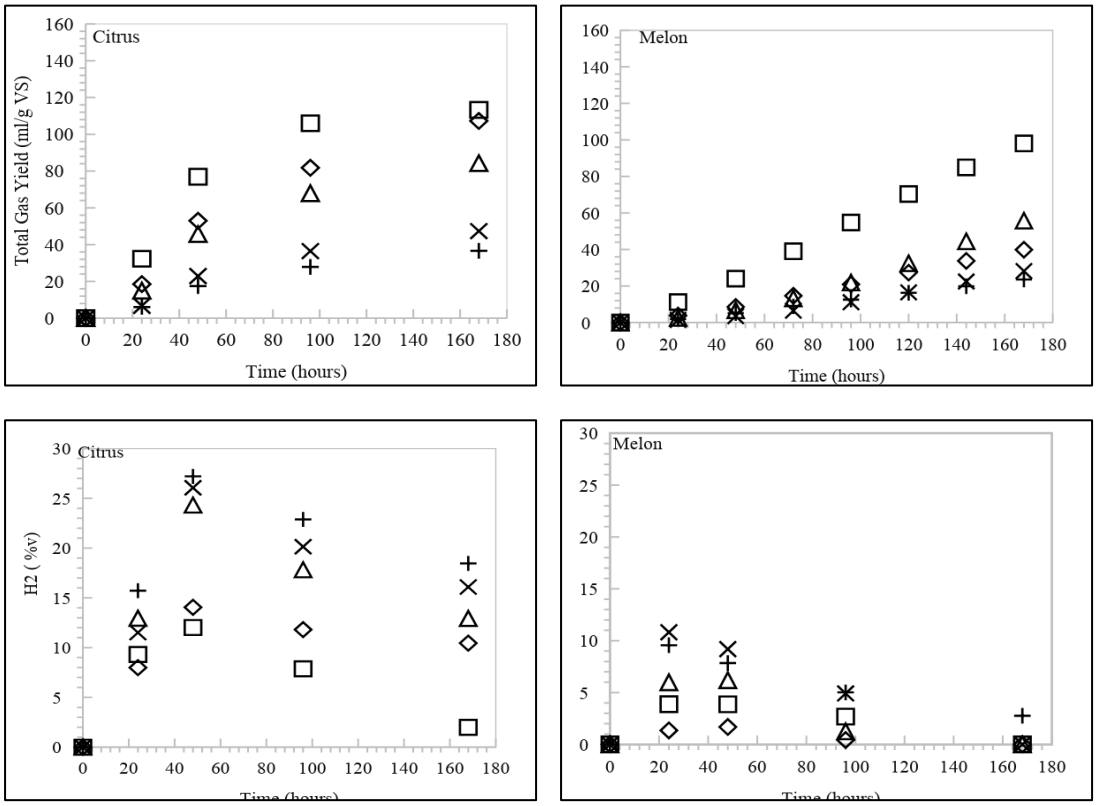


Figure 2. Total gas yield and percentages of hydrogen during mesophilic fermentation (30 °C, 1 atm) at various SIR values (□ SIR 19, ◊ SIR 29, Δ SIR 58,× SIR 116, +SIR 174)

The lower SIR value which implies an ideal ratio of carbon sources to the microorganism population, the higher total gas yield. High SIR may lead to the overwhelming food supply to the limited population of the microorganisms leading to substrate inhibition or by-products retardation such as volatile fatty acids accumulation (pH decrease) [5]. This result was in agreement with the previous report that higher substrate concentration (0.5 to 2 g/L) led to a reduction of hydrogen production from 105 to 50 ml STP H_2 (appx. 50% reduction) [23].

It was also exhibited that type of fruits does not affect the yield pattern towards SIR, except for its quantitative values. Citrus waste could generate higher total gas yield which might be due to high IC_{50} (669 mg/kg) and lower content of limonene (0.125 mg/L) compare to that of melon i.e. IC_{50} of 50 μM and eugenol content of 2302.400 μg/kg. Eugenol concentration at SIR of 174 was estimated to value of 41.760 mg/kg or 254 μM (5 times of IC_{50}). Meanwhile, limonene concentration at the same SIR was only 2.25 mg/kg (0.336% of IC_{50}). In addition, total dietary fiber (TDF) in citrus waste which mainly consists of cellulose, hemicellulose, pectin, lignin is higher (63.240%) compare to that of melon (41.690%). Higher TDF content provides more potential substrate to produce hydrogen at the same SIR, whereas it can decrease the gas yield at the increasing SIR due to recalcitrant properties of the fiber.

The highest hydrogen percentages of citrus and melon fermentation were achieved at the value of 27%v at 48 hours and 10.8%v at 24 hours, respectively. In Figure 1, it was noticed that this percentage declined after the 48 and 24 hours of citrus and melon fermentation respectively because of pH decreases thereby microbial activity to generate more hydrogen was retarded. The addition of buffer solution ($NaHCO_{3(aq)}$) could be the solution to improve the H_2 percentage by increasing the buffering capacity of the fermentation process. As a result, the hydrogen yield from the citrus and melon fermentation was approximately 14.333 and 4.900 mL H_2/g VS_{added} respectively. Although this result is considered low to the maximum achievable yield i.e. 4 mol H_2/mol glucose (497 mL H_2/g glucose), it is quite reasonable at mesophilic condition using fruit waste containing high TDF. As a comparison, hydrogen yield value of 0.02 mmol H_2/g cellulose (0.448 mL H_2/g cellulose) was obtained from fermentation of cellulose at 4.7 g/L and 26 °C. At higher temperature (37 °C), the yield increased to 3.66 mmol H_2/g cellulose (75 ml H_2/g cellulose) [24].

Thermophilic dark fermentation

Biohydrogen production from citrus, apple, and melon waste which was conducted in thermophilic condition is depicted in Figure 3. In this fermentation, Apple was also investigated as a substrate to accommodate the high global production of this fruit. Due to low H_2 yield during mesophilic fermentation, it was decided to conduct thermophilic one at 55 °C, 1 atm and pH 5.0. In addition, a lower SIR values of 0.800 and 1.500 g $VS_{substrate}$/g VS_{inoc} was also selected based on previous report that the optimum substrate (food waste) to inoculum ratio was 2 g $VS_{substrate}$/g VS_{inoc} [25]. The SIR value in this experiment was selected to even lower in order to authenticate whether or not similar pattern of gas yield will occur.

Hydrogen yield profile during fermentation of citrus, melon and apple is depicted in Figure 3. It was observed that a similar pattern of hydrogen gas yield occurred that the lower SIR of any fruit waste, the higher H_2 yield. The highest H_2 yield was obtained from apple waste at SIR 0.800 corresponding to H_2 yield of 294 mL STP/g VS (50-60%v of purity). This might be due to high content of TDF and total soluble sugars in apple waste compare to that of citrus and melon. It was also demonstrated that an increase in SIR value of 1.500 g $VS_{substrate}$/g VS_{inoc} could decrease H_2 yield up to 38%v. Whereas, the lower H_2 yield was attained from fermentation of melon waste at SIR of 1.500 corresponding to 133 mL STP H_2/g VS. This result is comparable to some previous report on thermophilic dark fermentation. As a comparison, a similar result was demonstrated from immobilized system of dark fermentation using glucose as substrate i.e. 1.9 mol H_2/mol glucose (244 mL H_2/g glucose) [26]. A lower yield was also reported when starch and cellulose was utilized as substrate with corresponding yield of 92 mL H_2/g starch and 102 mL H_2/g cellulose [5].

Effect of inhibition due to the presence of volatile compounds (limonene, eugenol and phloretin) was not observed significantly in comparison to that of mesophilic condition. Both lower SIR values and higher temperature provide concentration of these compounds significantly below inhibition concentration (IC_{50}). Low SIR implies less quantity of substrate addition to fermentation so that there is only limited concentration in the same population of microorganism. Whereas, higher temperature (55 °C) condition could induce evaporation of these compounds and decrease the solubility in water. The hydrogen yield is 20-fold in thermophilic fermentation compare to that of mesophilic one. Therefore, combination of these SIR and temperature results in optimum condition for improving H_2 yield in this fermentation.

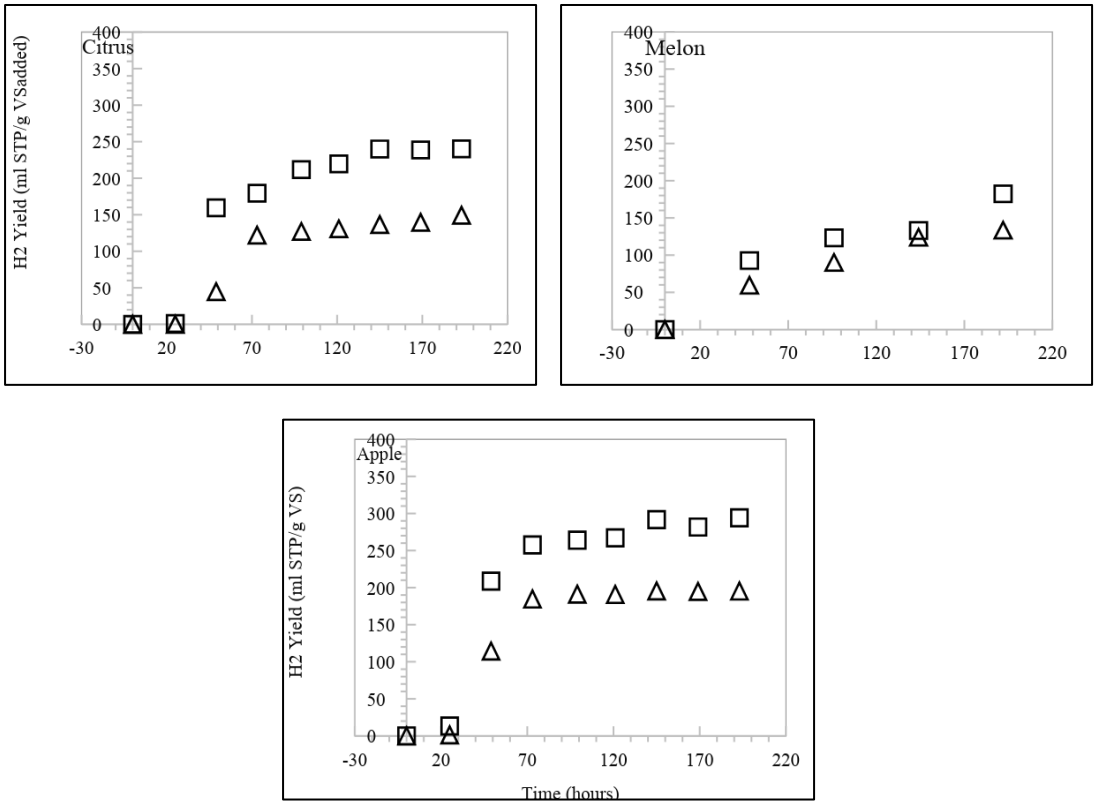


Figure 3. Profile of hydrogen yield during thermophilic fermentation (55 °C,1 atm) at various SIR values (□ SIR 0.800, Δ SIR 1.500)

Conclusion

Optimization of hydrogen production from fruit waste through dark fermentation was achieved through adjustment of the substrate-to-inoculum ratio (SIR). It was demonstrated that the lower SIR value, the higher total gas yield. The highest one was achieved from fermentation of apple waste at thermophilic condition (55℃) and SIR of 0.800 g $VS_{substrate}$/g VS_{inoc} corresponding to H_2 yield of 294 ml STP/g VS_{added} (50-60%v of H_2). It was noticed that there is the consistency of SIR effect toward hydrogen production regardless the type of fruit waste. This optimized condition may be implemented to improve the renewable energy of hydrogen production for better environment.

Acknowledgements

Authors extend their gratitude to Swedish International Development Cooperation Agency (SIDA), Sweden and Ministry of Research and Higher Education of Indonesia for financially supporting this research.

References

1. Sugiawan, Y. and Managi, S. (2016). The environmental Kuznets curve in Indonesia: Exploring the potential of renewable energy. *Energy Policy*, 98: 187–198.
2. Alam, M. S. and Paramati, S. R. (2015). Do oil consumption and economic growth intensify environmental degradation? Evidence from developing economies. *Applied Economics*, 47: 5186–5203.
3. Kumar, S. (2016). Assessment of renewables for energy security and carbon mitigation in Southeast Asia: The case of Indonesia and Thailand. *Applied Energy*, 163: 63–70.
4. Mujiyanto, S. and Tiess, G. (2013). Secure energy supply in 2025: Indonesia's need for an energy policy strategy. *Energy Policy*, 61: 31–41.
5. Elbeshbishy, E., Dhar, B. R., Nakhla, G. and Lee, H.-S. (2017). A critical review on inhibition of dark biohydrogen fermentation. *Renewable and Sustainable Energy Reviews*, 79: 656–668.

6. Gustavsson, J., Cederberg, C. and Sonesson, U. (2011). Global food losses and food waste. *Food Agricultural Organization of United Nation*. Access from http://www.fao.org/3/a-i2697e.pdf
7. Sanjaya, A., Cahyanto, M. and Millati, R. (2016). Mesophilic batch anaerobic digestion from fruit fragments. *Renewable Energy*, 98: 135–141.
8. Millati, R., Nurrihadini, O. D., Suroto, D. A. and Cahyari, K. (2009). Waste refinery program in Indonesia: Characterization of waste from "gemah ripah" fruit market as a feedstock for biogas production. *Department of Chemical Engineering*, Universitas Gadjah Mada, Indonesia.
9. Cappai, G., Gioannis, G. De and Muntoni, A. (2015). Effect of inoculum to substrate ratio (ISR) on hydrogen production through dark fermentation of food waste. In *Proceeding Sardinia, 15th International Waste Management and Landfill Symposium*. Cagliary, Italy: CISA Publisher.
10. Argun, H. and Dao, S. (2017). Bio-hydrogen production from waste peach pulp by dark fermentation: Effect of inoculum addition. *International Journal of Hydrogen Energy*, 42: 2569–2574.
11. Jeihanipour, A., Karimi, K. and Taherzadeh, M. J. (2010). Enhancement of ethanol and biogas production from high-crystalline cellulose by different modes of NMO pretreatment. *Biotechnology and Bioengineering*, 105: 469–476.
12. APHA (2012). Standard methods for the examination of water and wastewater. *American Public Health Association, DC*.
13. FAOUN. (2014). Data of Production Quantity of Crops. Access from http://www.fao.org/faostat/en/#data/QC [May 31, 2017].
14. Górnaś, P., Mišina, I., Olšteine, A., Krasnova, I., Pugajeva, I., Lācis, G., Siger, A., Michalak, M., Soliven, A. and Segliņa, D. (2015). Phenolic compounds in different fruit parts of crab apple: Dihydrochalcones as promising quality markers of industrial apple pomace by-products. *Industrial Crops and Products*, 74: 607–612.
15. Wang, L., Xu, H., Yuan, F., Pan, Q., Fan, R. and Gao, Y. (2015). Physicochemical characterization of five types of citrus dietary fibers. *Biocatalysis and Agricultural Biotechnology*, 4: 250–258.
16. Raji, Z., Khodaiyan, F., Rezaei, K., Kiani, H. and Hosseini, S. S. (2017). Extraction optimization and physicochemical properties of pectin from melon peel. *International Journal of Biological Macromolecules*, 98: 709–716.
17. Mallek-Ayadi, S., Bahloul, N. and Kechaou, N. (2017). Characterization, phenolic compounds and functional properties of Cucumis melo L. peels. *Food Chemistry*, 221: 1691–1697.
18. Macagnan, F. T., Santos, L. R. dos, Roberto, B. S., de Moura, F. A., Bizzani, M. and da Silva, L. P. (2015). Biological properties of apple pomace, orange bagasse and passion fruit peel as alternative sources of dietary fibre. *Bioactive Carbohydrates and Dietary Fibre*, 6: 1–6.
19. Atkinson, R. G. (2017). Phenylpropenes: Occurrence, distribution, and biosynthesis in fruit. *Journal of Agricultural and Food Chemistry*, 66(10): 2259-2272.
20. Ruiz, B. and Flotats, X. (2016). Effect of limonene on batch anaerobic digestion of citrus peel waste. *Biochemical Engineering Journal*, 109: 9-18.
21. Barreca, D., Bellocco, E., Laganà, G., Ginestra, G. and Bisignano, C. (2014). Biochemical and antimicrobial activity of phloretin and its glycosilated derivatives present in apple and kumquat. *Food Chemistry*, 160: 292–297.
22. Lin, C.-H., Lin, S. H., Lin, C.-C., Liu, Y.-C., Chen, C.-J., Chu, C.-L., Huang, H-C. and Lin, M.-K. (2016). Inhibitory effect of clove methanolic extract and eugenol on dendritic cell functions. *Journal of Functional Foods*, 27: 439–447.
23. Eker, S. and Sarp, M. (2017). Hydrogen gas production from waste paper by dark fermentation: Effects of initial substrate and biomass concentrations. *International Journal of Hydrogen Energy*, 42: 2562–2568.
24. Saratale, G. D., Chen, S.-D., Lo, Y.-C., Saratale, R. G. and Chang, J.-S. (2008). Outlook of biohydrogen production from lignocellulosic feedstock using dark fermentation - a review. *Journal of Scientific and Industrial Research*, 67: 962–979.
25. Laothanachareon, T., Kanchanasuta, S., Mhuanthong, W., Phalakornkule, C., Pisutpaisal, N. and Champreda, V. (2014). Analysis of microbial community adaptation in mesophilic hydrogen fermentation from food waste by tagged 16S rRNA gene pyrosequencing. *Journal of Environmental Management*, 144: 143–151.
26. Gokfiliz, P. and Karapinar, I. (2017). The effect of support particle type on thermophilic hydrogen production by immobilized batch dark fermentation. *International Journal of Hydrogen Energy*, 42: 2553–2561.

Malaysian Journal of Analytical Sciences, Vol 23 No 1 (2019): 124 - 130
DOI: https://doi.org/10.17576/mjas-2019-2301-15

MALAYSIAN JOURNAL OF ANALYTICAL SCIENCES
Published by The Malaysian Analytical Sciences Society
ISSN 1394 - 2506

DEHYDRATING ETHANOL USING A TERNARY SOLUTE AND EXTRACTIVE BATCH DISTILLATION

(Pengeringan Etanol Menggunakan Zat Larut Ternari dan Penyulingan Kelompok Hasil Ekstrak)

Tjukup Marnoto[1], I Gusti Suinarcana Budiaman[1], Chintya Rizki Hapsari[1], Risqi Angga Y. Prakosa[1], Khuzaimah Arifin[2]*

[1]*Chemical Engineering Department, Industrial Engineering Faculty*
Universitas Pembangunan Nasional "Veteran" Yogyakarta, Indonesia 55283
[2]*Fuel Cell Institute,*
Universiti Kebangsaan Malaysia, 43600 UKM Bangi, Selangor, Malaysia

**Corresponding author: khuzaim@ukm.edu.my*

Received: 13 April 2017; Accepted: 17 April 2018

Abstract

Anhydrous bioethanol is a material used in many applications including biofuel. Commonly, bioethanol is produced through sugar fermentation which results in a low concentration of ethanol. For utilization as biofuel, the lowest ethanol concentration should be 99.5%. Distillation is common technique to dry a mixture solution, however, the mixture of bioethanol and water is forming an azeotrope that limit the concentration of 96% ethanol. This paper discusses ethanol dehydration through extractive batch distillation by the addition of a ternary solute sodium hydroxide, citric acid, sulfuric acid, glycerol or ethylene glycol to ethanol. The initial concentration of ethanol used was 86% v/v, and the amount of ternary solute added was selected based on the colligative properties of the solution, which included a boiling point elevation (ΔT_B) that ranged from 5 to 25 °C. All the ternary solutes could break or shift the ethanol-water azeotrope. The highest concentration of ethanol was 99.91% v/v at ΔT_B = 25 °C with sulfuric acid as the ternary component. The resulted ethanol concentration exhibited a linear relationship with ΔT_B, which was also affected by the boiling point of the ternary solute. This study successfully produced anhydrous bioethanol by low cost and simple distillation process.

Keywords: bioethanol, azeotrope, colligative properties, ternary solute

Abstrak

Bioetanol anhidrat adalah bahan yang diperlukan dalam pelbagai aplikasi termasuk biofuel. Biasanya, bioetanol dihasilkan melalui penapaian gula, yang menghasilkan kepekatan etanol yang rendah. Supaya boleh digunakan dalam aplikasi biofuel, diperlukan kepekatan etanol sekurang-kurangnya 99.5%. Distilasi adalah kaedah yang umum digunakan untuk mengeringkan larutan, namun campuran bioetanol dan air membentuk azeotrop yang membatasi kepekatan 96% etanol. Kajian ini membincangkan pengeringan etanol dengan penambahan zat larut ternari: natrium hidroksida, asid sitrik, asid sulfurik, gliserol atau etilena glikol. Kepekatan awal etanol yang digunakan adalah 86% v/v. Jumlah zat larut yang ditambahkan dipilih berdasarkan sifat koligatif pelarut, termasuk ketinggian titik didih (ΔT_B) yang berkisar antara 5 hingga 25 °C. Semua bahan terner didapati boleh memecahkan atau mengalihkan azeotrop air etanol; kepekatan tertinggi etanol yang diperoleh ialah 99.91% pada ΔT_B = 25 °C dengan asid sulfurik sebagai komponen ternari. Kepekatan etanol yang dihasilkan memperlihatkan hubungan linear dengan ΔT_B, yang juga dipengaruhi oleh titik didih zat larut ternari. Kajian ini telah berjaya menghasilkan bioethanol kering melalui kaedah penyulingan yang murah dan sederhana.

Kata kunci: bioetanol, azeotrop, sifat koligatif, zat larut ternar

Introduction

Anhydrous ethanol is widely used in the chemical industry as a solvent, a raw material in the synthesis of esters and as an additive in detergents, paints, cosmetics, aerosols, perfumes, medicines, and organic food [1]. Anhydrous ethanol, with a purity exceeding 99.5%, is commonly called fuel-grade ethanol, and it is a biofuel material that can be used as a direct fuel replacement in vehicles and gasoline-powered machinery or can be mixed with conventional fuels. Fuel-grade ethanol with a higher-octane number (116-129) can be used as an octane booster for fuel with a lower octane number [2-6].

Bioethanol is often produced by fermenting sugar from a sugar source or starch with the help of *Saccharomyces cerevisiae* yeast, resulting in low-ethanol-concentration products that must then undergo purification. Molasses is a commonly used raw material or sugar source because processing molasses to bioethanol requires less time compared with the processing of other raw materials [7, 8]. The conventional method used to obtain pure ethanol is distillation. However, purification of ethanol by distillation is limited to a purity less than 96% ethanol, because the water-ethanol mixture under atmospheric pressure produces an azeotrope of 96% wt. ethanol and 4% wt. water at 78.1 °C [3, 9]. Dehydration is then carried out to obtain ethanol anhydrate or fuel-grade ethanol. The dehydration methods employed include the use of molecular sieves, membrane pervaporation separation, and extractive distillation using ternary solutes to break the azeotrope.

Research on ethanol dehydration and fuel-grade ethanol has been conducted by many researchers. Kusmiyati and Susanto [10] using a membrane pervaporation setup comprising an evaporator tank, a membrane pervaporation module (diameter × height = 20 × 120 cm), vacuum pump, and cooling column. They evaporated and then pumped bioethanol into the membrane module under 6 bars of permeate pressure, resulting in 99% v/v ethanol. Al-Asheh et al. [11] researched the potential of using bio-based adsorbents corn cop, stone palm, and oak tree, after activation through various zeolite molecular sieves (types 3A, 4A, and 5A) to separate the ethanol-water azeotrope. Type 3A molecular sieves possess the greatest surface area and exhibit the highest water absorption capacity among various bio-based adsorbents. Meanwhile, the process of ethanol dehydration using molecular sieves begins with the adsorption of water until the molecular sieves are saturated. A commercial NaA zeolite membrane showed a relatively high and efficient dehydration performance that was economical. The product obtained at pilot-plant scale was ethanol anhydrate with a purity >99.7%. [9, 12].

The total component splitting of the azeotrope solution requires the addition of a ternary solute, which changes the behavior of the liquid vapor in the distillation column. Several liquid and solid ternary solute materials can be used in ethanol dehydration, including benzene, pentane, furfural, ethylene glycol, diethyl ether, toluene, glycerol, salt, and ionic liquids (ILs) [13-18]. At the industrial scale, ILs offer the greatest potential in extractive distillation. The result of ethanol dehydration using sodium chloride, calcium chloride, potassium acetate, calcium nitrate, and a mixture of sodium and potassium acetates as the third component of the ternary system shows that with similar treatments, they can break the azeotrope and increase the ethanol concentration obtained by extractive distillation [1, 19]. Restrepo and Arias (2003) used an extractive distillation column to produce absolute ethanol with a $CaCl_2$ salt to break the water-ethanol azeotrope [20]. Ligero and Ravagnani studied the recovery of potassium acetate salt as a ternary substance in water-ethanol extractive distillation. They carried out the separation using a double evaporator and a single spray dryer. The single spray dryer is more attractive from an energy consumption viewpoint. One of the advantages of salt extractive distillation is the production of a distillate that is completely free from the substance used in the separation [21]. Gomis et al. performed ethanol dehydration in a pilot-plant-scale azeotropic distillation using four hydrocarbon entrainers—hexane, cyclohexane, isooctane and toluene, which represent the hydrocarbons in gasoline—in attempts to obtain a ready-to-use, ethanol-hydrocarbon fuel mixture [4]. Lie et al. studied two methods to separate a ternary azeotrope with a heterogeneous azeotrope using toluene that exists in that system as an entrainer and extractive distillation using glycerol as the solvent. They found that extractive distillation reduced the energy expended by as much as 27.7%. In addition, extractive distillation can reduce the energy used by as much as 18.8% compared with the energy consumed during conventional heterogenic azeotropic distillation [22].

The process of ethanol dehydration by various methods such as adsorption by molecular sieves, pervaporation membranes, azeotropic distillation and extractive distillation all require energy at substantial expense for

evaporation, regeneration, or distillation. Ethanol-water dehydration using extractive distillation ternary solutes will affect the expense of the process. Here, we explain how to determine the amounts of liquid and solid solute ternary components needed based on the colligative properties of the solutions. Colligative property is a property that is determined by concentration of the solute, and it does not depend on the kind of solute molecule, such as vapor pressure, osmosis, and boiling point. The presence of a ternary solute in the mixture can affect the arrangement of the liquid phase, which changes the composition of the vapor and liquid in equilibrium. This change in equilibrium composition can change the relative volatility of the solution, shifting or omitting the azeotrope and thus making the distillation separation system easier [1,12]. The selection of ternary solutes in this research is based on using colligative properties to determine the boiling point elevation of the solvent (i.e., water) shown by equations 1-6 below.

$$\Delta T_B = K_B . m \tag{1}$$

$$\Delta T_B = K_B . \frac{G_{sl}}{MW} . \frac{1000}{G_{sv}} \tag{2}$$

$$G_{sv} = (1 - X_e) . V_e . \rho_w \tag{3}$$

$$G_{sl} = \frac{\Delta T_B . MW . (1 - X_e) . V_e . \rho_w}{1000 . K_B} \tag{4}$$

For a liquid:

$$G_{sl} = V_{sl} . x_{sl} . \rho_{sl} \tag{5}$$

$$G_{sv} = (1 - X_e) . V_e . \rho_w + V_{sl} . (1 - x_{sl}) . \rho_{sl} \tag{6}$$

ΔT_B: boiling point elevation (°C), K_B: molal boiling point elevation constant (°C/m), m: molality of the solution (mol/kg), G_{sl}: mass of the solute (g), G_{sv}: mass of the solvent (g), MW: molecular weight (g/mol), X_e: percent by volume of ethanol (v/v), X_{sl}: percent by mass (g/g), ρ_w: density of water (g/mL) and ρ_{sl}: density of solute (g/mL).

Materials and Methods

The raw materials were ethanol (86% v/v) with 14% v/v water. The density (ρ) of water at 105 °C is 0.95106 g/ml, and the molal boiling-point elevation constant (K_B) of water is 0.51 °C/m. Various ternary solutes were investigated: 1). Sodium hydroxide (NaOH), molecular weight 40 gr/mol, density 1.5 g/ml, normal boiling point 318 °C; 2). Citric acid, molecular weight 192.13 g/mol, density 1.665 g/ml, normal boiling point 175°C; 3). Sulfuric acid (H_2SO_4), concentration 95%, molecular weight 98 g/mol, density 1.84 g/mL, normal boiling point 337 °C; 4). Glycerol, concentration 99%, molecular weight 92.0938 g/mol, density 1.26 g/mL, normal boiling point 290 °C; and 5). Ethylene glycol, concentration 99%, molecular weight 62.07 g/mol, density 1.1132 g/mL, normal boiling point 197.3 °C.

The extractive distillation apparatus used in the experiments is shown schematically in Figure 1. The various tools used in the process included a three-necked bottle, a heater, a distillation column filled to 55 cm with a filling material, a reverse cooler as a condenser, a collecting tube as a reflux regulator, a thermometer, and an Erlenmeyer flask to collect the product. Ethanol (86%) mixed with a ternary component was poured into the three-necked bottle for the distillation. First, a total reflux was conducted during the initial heating until the conditions were constant (1 h), as indicated by a constant high and low temperature. Then, the anhydrous ethanol was collected until a certain amount (25 ml) was obtained, and the reflux was kept steady; the anhydrous ethanol was then analyzed.

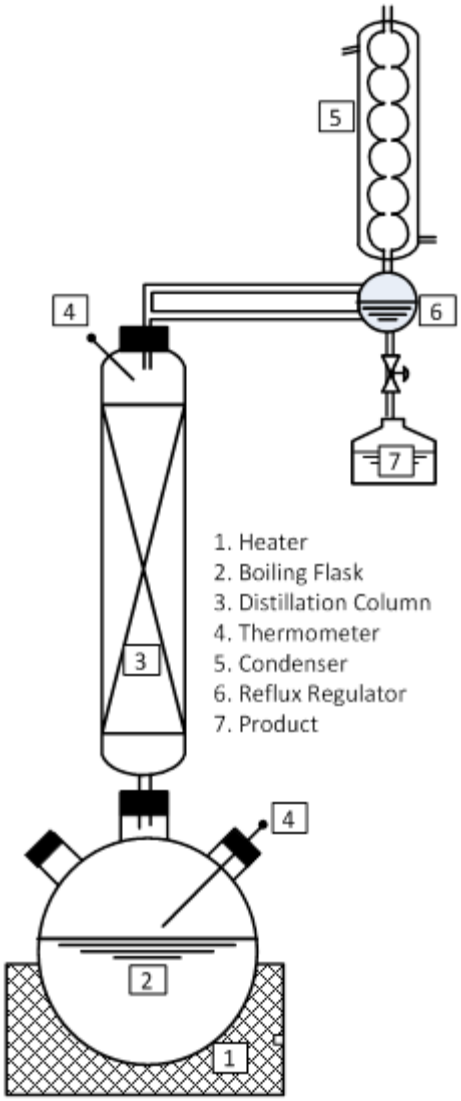


Figure 1. Scheme showing the batch extractive distillation apparatus

Results and Discussion

Before being distilled, the raw ethanol had a concentration of 86%. The raw material was then mixed with a ternary solute. The amount of ternary component necessary to achieve the desired boiling point elevation (ΔT_B) was calculated using the solution colligative property equation. The amount of ternary substance added to 100 ml of the raw ethanol (86%) was calculated using equations (4) and (5). These results are presented in Table 1.

The batch extractive distillation was performed under atmospheric pressure. The column temperature was constant at 62 °C, and the column below ranged from 74 to 76 °C. The addition of a solid ternary system component (sodium hydroxide or citric acid) or a liquid ternary system component (sulfuric acid, glycerol, or ethylene glycol) to 86% v/v ethanol with a water boiling point elevation of 5 °C to 25 °C resulted in anhydrous ethanol, surpassing the azeotrope concentration (>96%) ranging from 98.041 to 99.910% at a boiling point of 25 °C. The resulting anhydrous ethanol concentration arising from extractive batch distillation demonstrates that a ternary solute (either solid or liquid) can break or shift the azeotrope condition. The complete results are presented in Figure 2.

Table 1. Weight/volume of ternary substance on 100 mL ethanol (86%) for various boiling point elevations

ΔT_B (°C)	Weight/Volume of Ternary Solute/100 mL Ethanol 86% v/v				
	Sodium Hydroxide (g)	Citric Acid (g)	Sulfuric Acid (mL)	Glycerol (mL)	Ethylene Glycol (mL)
5	5.1413	24.6949	7.0171	9.4579	7.2035
10	10.2422	49.1957	14.3925	18.9686	14.4242
15	15.3009	73.494	22.1489	28.5284	21.6579
20	20.3156	97.5809	30.3113	38.1329	28.9028
25	25.2847	121.4489	38.9069	47.7784	36.1569

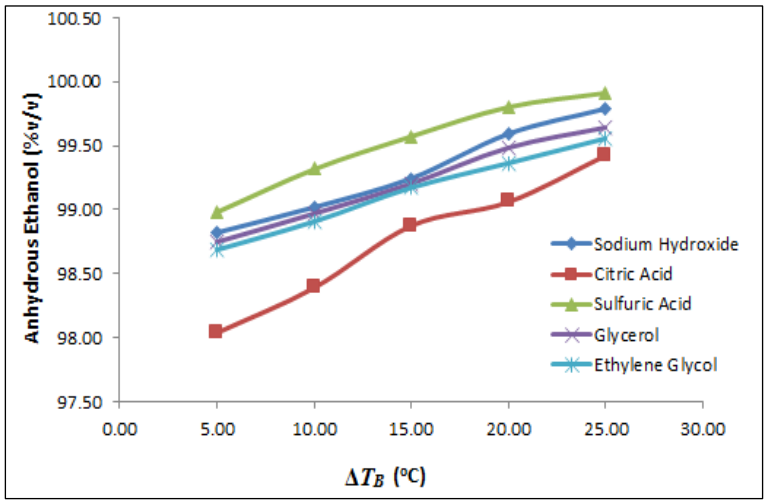


Figure 2. The anhydrous ethanol concentration as a function of the water boiling point elevation for different ternary systems

The increase in the anhydrous ethanol concentration because of extractive batch distillation exhibited a linear relationship with the boiling point elevation or the amount of solute ternary component added. The addition of sulfuric acid at a concentration of 22.148 mL to every 100 mL of 86% ethanol, corresponding to a ΔT_B of 15 °C, resulted in anhydrous ethanol with a concentration greater than 99.5%, which is equivalent to the ethanol concentration of standard fuel-grade ethanol, and achieved the desired ΔT_B. Meanwhile, sodium hydroxide was added at concentrations as low as 20.3156 g for every 100 mL of 86% ethanol (ΔT_B = 20 °C), and the addition of glycerol and ethylene glycol resulted in a ΔT_B = 25 °C. Thus, theoretically, if the separation achieved by extractive distillation continuously results in ethanol anhydrate with a concentration greater than 99.5% (standard fuel-grade ethanol) with an added ternary solute for higher boiling point elevation, then obtaining concentrations greater than 99.5% should be straightforward. However, the amount of ternary solute added should be optimized so that the ternary substance can be recovered and reused for efficient recycling. The highest anhydrous ethanol content was achieved using sulfuric acid as the ternary component, followed by those achieved using sodium hydroxide, glycerol, ethylene glycol and citric acid, with boiling point equivalents of 337, 318, 290, 197 and 175 °C, respectively. These results are clearly shown in Figure 3. These results show that the ternary solute phase, either solid or liquid, does not affect the concentration of the obtained anhydrous ethanol; rather, the ternary solute boiling point and its ternary solubility affect how it favors water/solvent. Result in this study is aligned with previous study reported [17, 23-24].

The relationship of ethanol concentration and boiling point elevation after adding each ternary solute can be determined by regression in equations 7-11 below:

$$C_{AE} = 0.0501\ \Delta T_B + 98.459 \text{ (sodium hydroxide)} \quad (7)$$

$$C_{AE} = 0.0687\ \Delta T_B + 97.725 \text{ (citric acid)} \quad (8)$$

$$C_{AE} = 0.0466\ \Delta T_B + 98.820 \text{ (sulfuric acid)} \quad (9)$$

$$C_{AE} = 0.0456\ \Delta T_B + 98.525 \text{ (glycerol)} \quad (10)$$

$$C_{AE} = 0.0436\ \Delta T_B + 98.482 \text{ (ethylene glycol)} \quad (11)$$

where C_{AE} is anhydrous ethanol concentration (% v/v).

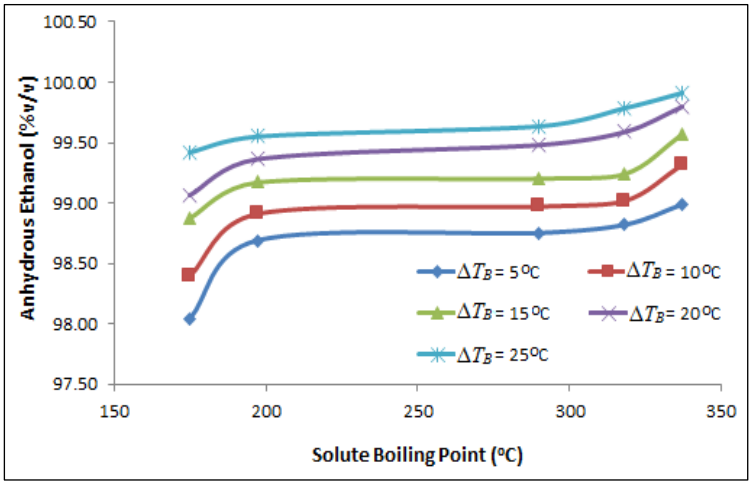


Figure 3. The effect of the anhydrous ethanol concentration on solute boiling point at ΔT_B values from 5 °C to 25 °C

Equations 7-11 are only valid for the addition of ternary solute. This shows that addition of ternary solute affects boiling point elevation and breaking of the azeotrope.

Conclusion

The colligative properties of a solution, particularly the boiling point elevation (ΔT_B), can be used to predict the amount of ternary substance that needs to be added. All the investigated ternary solutes (solid or liquid) could shift or break the ethanol-water azeotrope. The increase in the ethanol concentration from the extractive batch distillation was linear with the increase in the boiling point or the amount of ternary solute added as well as with the boiling point of the ternary solute. Meanwhile, the phase of the added ternary substance, either solid or liquid, had no effect. Therefore, anhydrous bioethanol can be produced by low cost and simple distillation process.

Acknowledgement

The authors would like to acknowledge the Universitas Pembangunan Nasional (UPN) "Veteran" Yogyakarta and The Directorate-General of New Renewable Energy and Energy Conservation (P3TKBTKE), Ministry of Energy and Mineral Resources of the Republic of Indonesia for sponsoring this project, and Universiti Kebangsaan Malaysia through GUP-2016-085 research grant.

References

1. Soares, R. B., Pessoa, F. L. P and Mendes, M. F. (2015). Dehydration of ethanol with different salts in a packed distillation column. *Process Safety and Environmental Protection*, 93:147-153.
2. Chen, W-C, Sheng, C-T, Liu, Y-C, Chen, W-J, Huang, W-L. and Chang S-H. (2014). Optimizing the efficiency of anhydrous ethanol purification via regenerable molecular sieve. *Applied Energy*, 135:483-489.

3. Dai, W., Word, D. P. and Hahn, J. (2014). Modeling and dynamic optimization of fuel-grade ethanol fermentation using fed-batch process. *Control Engineering Practice*, 22: 231-241.
4. Gomis, V, Pedraza, R, Saquete, M. D., Font, A. and García-Cano J. (2015). Ethanol dehydration via azeotropic distillation with gasoline fractions as entrainers: A pilot-scale study of the manufacture of an ethanol–hydrocarbon fuel blend. *Fuel*, 139:568-574.
5. Kalyani, D.C., Zamanzadeh, M., Müller, G. and Horn, S. J. (2017). Biofuel production from birch wood by combining high solid loading simultaneous saccharification and fermentation and anaerobic digestion. *Applied Energy*, 193:210-219.
6. Liu, H., Hu, B. and Jin, C. (2016). Effects of different alcohols additives on solubility of hydrous ethanol/diesel fuel blends. *Fuel*, 184: 440-448.
7. Romão, B. B, da Silva, F. B., de Resende, M. M. and Cardoso, V. L. (2012). Ethanol production from hydrolyzed soybean molasses. *Energy & Fuels*, 26(4): 2310-2316.
8. Sánchez, Ó. J. and Cardona, C. A. (2012). Conceptual design of cost-effective and environmentally-friendly configurations for fuel ethanol production from sugarcane by knowledge-based process synthesis. *Bioresource Technology*, 104: 305-314.
9. Sato, K., Aoki, K., Sugimoto, K., Izumi, K., Inoue, S. and Saito J. (2008). Dehydrating performance of commercial LTA zeolite membranes and application to fuel grade bio-ethanol production by hybrid distillation/vapor permeation process. *Microporous and Mesoporous Materials*, 115(1): 184-188.
10. Kusmiyati, S. H. (2015). Fuel grade bioethanol production from Iles-iles (*Amorphophaluscampanulatus*) tuber. *Procedia Environmental Sciences*, 23: 199-206.
11. Al-Asheh, S., Banat, F. and Al-Lagtah N. (2004). Separation of ethanol–water mixtures using molecular sieves and biobased adsorbents. *Chemical Engineering Research and Design*, 82(7): 855-864.
12. Kupiec, K., Rakoczy, J., Komorowicz, T. and Larwa, B. (2014). Heat and mass transfer in adsorption–desorption cyclic process for ethanol dehydration. *Chemical Engineering Journal.* 241: 485-494.
13. Pereiro, A.B., Araújo, J. M. M, Esperança, J. M. S. S, Marrucho, I. M. and Rebelo, L. P. N. (2012). Ionic liquids in separations of azeotropic systems – A review. *The Journal of Chemical Thermodynamics*, 46: 2-28.
14. Rodríguez, N. R., González, A. S. B., Tijssen, P. M. A. and Kroon, M. C. (2015). Low transition temperature mixtures (LTTMs) as novel entrainers in extractive distillation. *Fluid Phase Equilibria*, 385: 72-78.
15. Veiga, B.A., dos Santos, J. T. F, de Lima Luz Junior, L. F. and Corazza, M. L. (2017). Phase equilibrium measurements and thermodynamic modelling for the systems involving valeric acid, ethanol, ethyl valerate and water plus CO_2. *The Journal of Chemical Thermodynamics*, 112: 240-248.
16. Aouinti, L. and Belbachir, M. (2008). A maghnite-clay-H/polymer membrane for separation of ethanol–water azeotrope. *Applied Clay Science*, 39(1): 78-85.
17. Oliveira, F. S., Dohrn, R., Pereiro, A. B., Araújo, J. M. M, Rebelo, L. P. N. and Marrucho, I. M. (2016). Designing high ionicity ionic liquids based on 1-ethyl-3-methylimidazolium ethyl sulphate for effective azeotrope breaking. *Fluid Phase Equilibria*, 419: 57-66.
18. Wang, Y., Gong, C., Sun, J., Gao, H., Zheng, S. and Xu, S. (2010). Separation of ethanol/water azeotrope using compound starch-based adsorbents. *Bioresource Technology*, 101(15):6170-6176.
19. Mahdi, T., Ahmad, A., Nasef, M. M. and Ripin A. (2015). State-of-the-art technologies for separation of azeotropic mixtures. *Separation & Purification Reviews*, 44(4):308-330.
20. Llano-Restrepo, M. and Aguilar-Arias, J. (2003). Modeling and simulation of saline extractive distillation columns for the production of absolute ethanol. *Computers & Chemical Engineering*, 27(4): 527-549.
21. Ligero, E. L. and Ravagnani, T. M. K. (2003). Dehydration of ethanol with salt extractive distillation—a comparative analysis between processes with salt recovery. *Chemical Engineering and Processing: Process Intensification*, 42(7): 543-552.
22. Zhao, L., Lyu, X., Wang, W., Shan, J. and Qiu, T. (2017). Comparison of heterogeneous azeotropic distillation and extractive distillation methods for ternary azeotrope ethanol/toluene/water separation. *Computers & Chemical Engineering*, 100: 27-37.
23. Luyben, W. L. (2016). Control comparison of conventional and thermally coupled ternary extractive distillation processes. *Chemical Engineering Research and Design*, 106: 253-262.
24. You, X., Rodriguez-Donis, I. and Gerbaud, V. (2014). Extractive distillation process optimisation of the 1.0-1a class system, acetone - methanol with water. Klemeš, J. J., Varbanov, P. S. and Liew, P. Y. (Editors). *Computer Aided Chemical Engineering*, 33: pp. 1315-1320.

Malaysian Journal of Analytical Sciences, Vol 23 No 1 (2019): 131 - 137
DOI: https://doi.org/10.17576/mjas-2019-2301-16

MALAYSIAN JOURNAL OF ANALYTICAL SCIENCES
Published by The Malaysian Analytical Sciences Society
ISSN 1394 - 2506

RESISTANCE OF NATIVE BACTERIA ISOLATED FROM ACTIVATED SLUDGE TOWARDS IRON AND MANGANESE

(Ketahanan Pencilan Bakteria Asli daripada Enapcemar Teraktif terhadap Ferum dan Mangan)

Nuratiqah Marsidi[1], Hassimi Abu Hasan[1]*, Mohd Izuan Effendi Halmi[2], Siti Rozaimah Sheikh Abdullah[1]

[1]*Chemical Engineering Program, Research Centre for Sustainable Process Technology (CESPRO), Faculty of Engineering and Built Environment, Universiti Kebangsaan Malaysia, 43600 UKM Bangi, Selangor, Malaysia*
[2]*Department of Land Management, Faculty of Agriculture, Universiti Putra Malaysia, 43400 Serdang, Selangor. Malaysia*

**Corresponding author: hassimi@ukm.edu.my*

Received: 13 April 2017; Accepted: 17 April 2018

Abstract

A study was conducted to observe the resistance of native isolated bacteria towards selected heavy metals (iron; Fe and manganese; Mn) in a separate exposure. Isolated bacteria were evaluated by culturing them in nutrient broth medium that contained approximately 3 ×10^6 CFU/mL bacteria with different initial concentrations (0, 50, 100 and 200 mg/L). Result showed that a plate with bacterial growth indicated bacterial resistance, which was verified based on CFU/mL. At 0 mg/L, bacteria grew well on the plate with Fe and Mn. The bacterial number began to decrease at 50 and 100 mg/L for Fe and at 200 mg/L for Mn. Only a few colonies survived (isolate AM2) the toxicity of high Fe amount; the isolated bacteria almost showed no growth along the plate. AM2, AM3 and AM4 presented resistance to Mn until 200 mg/L, but not AM6. The bacteria showed no growth at 100 and 200 mg/L. Thus, the Fe and Mn concentrations that can be applied during acclimatisation ranged from 0 mg/L to 200 mg/L with isolated AM2 and AM4 for Fe and Mn removal.

Keywords: biosorption, drinking water resources, iron, manganese, resistance bacteria

Abstrak

Satu kajian telah dijalankan untuk melihat tahap ketahanan bakteria tempatan terhadap logam berat terpilih (ferum; Fe dan mangan; Mn) dalam pendedahan berasingan. Bakteria telah diuji dengan pengkulturan dalam medium kaldu nutrien mengandungi kira-kira 3x10^6 CFU/mL bakteria dengan kepekatan logam berat yang berbeza (0, 50, 100 and 200 mg/L). Sebagai keputusan, plat yang mempunyai pertumbuhan bakteria menunjukkan bahawa bakteria merintang kepada kepekatan masing-masing dan disahkan berasaskan unit pembentukan koloni per mL. Pada 0 mg/L, bakteria tumbuh di sepanjang plat yang mengandungi Fe dan Mn. Bilangan CFU/mL mula untuk berkurang pada 50 dan 100 mg/L bagi Fe manakala pada 200 mg/L, hanya beberapa koloni bertahan (pencilan AM2) disebabkan ketoksikan oleh Fe yang berkepekatan tinggi and hampir kesemua pencilan bakteria menunjukkan tiada pertumbuhan sepanjang plat. Bagi mangan, kesemua bakteria terpilih AM2, AM3 dan AM4 masih memberikan bilangan CFU/mL sehingga kepekatan 200 mg/L kecuali AM6, bakteria tidak menunjukkan pertumbuhan pada 100 dan 200 mg/L. Oleh itu, julat Fe dan Mn yang boleh diaplikasikan dalam penyesuaian bakteria ialah dari 0 hingga 200 mg/L dengan pencilan AM2 dan AM4 adalah untuk penyingkiran Fe dan Mn.

Kata kunci: biojerapan, besi, mangan, sumber air minuman, ketahanan bakteria

Introduction

Numerous treatment types are used in industries to remove heavy metals, such as cadmium, nickel, iron, plumbum, chromium and arsenic, from wastewater. Conventional treatment technologies for heavy metals include precipitation, electrocoagulation, filtration and sedimentation [1]. However, the use of these technologies is limited due to their time requirement, high cost and maintenance, as well as environmental toxicity caused by chemicals added into the process. Furthermore, Ahluwalia and Goyal [2] claimed that chemical technologies can generate large volumetric sludge and increase costs. Conventional methods are also either inefficient or expensive when heavy metals exist in low concentrations [3, 4]. Hence, researchers have introduced new methods using unlimited and easily available sources, such as microorganisms and wastes, to treat wastewater that contains heavy metals.

Microorganisms in natural environment, such as bacteria, fungi, algae and yeast, can be exploited for treating heavy metal that contains large amount of wastes. Indigenous community of microorganisms from a particularly polluted area commonly exhibits the ability to thrive in extreme and toxic conditions [5]. The heavy metal uptake of biomass can be divided into two common methods, namely, bioaccumulation (active metabolic mode) and biosorption (passive metabolic mode) [6-9]. Biosorption is a quick process and independent from specific nutrients, whereas bioaccumulation is a slow and nutrient-dependent process [10]. Non-living biomasses in biosorption are typically affected with physical and chemical factors, such as pH, temperature, biomass and heavy metal concentration in a solution.

The present study aims to determine the range of Fe and manganese concentrations that can affect the survival of native bacteria after exposure. In addition, possible potential of bacteria to uptake the metals were also investigated. The present result can be used for the isolation, identification, acclimatisation and treatment of bacteria in the future.

Materials and Methods

Source of activated sludge

Sample was collected from a domestic sewage in Bukit Puteri residence, Universiti Kebangsaan Malaysia. This waste was generated by more than 100 households whose toilets and kitchens were channelled into the sedimentation tank. The raw sewage, which was stored at 4 °C until usage, was a dark green sludge (pH 6.5) that consisted mainly of 95% water. Figure 1 shows the sequence of activated sludge collection, which was according to Nye method [11]. The activated sludge characteristics are listed in Table 1.



Figure 1. (a) Oxidation point at a residential area, (b) sampling bottle, (c) sampling point and (d) sample collection

Media preparation

Fe(III) chloride hexahydrate ($FeCl_3.6H_2O$) and Mn(II) chloride ($MnCl_2.4H_2O$) were the metal salts used to prepare the stock solution of metal ions in aqueous form. A stock solution was separately prepared for each of the metal ions by dissolving 1 g of the metal salts in 1000 mL of distilled water (1000 mg/L). The solutions were prepared using a volumetric flask. The concentration range used was prepared by serial dilution of the stock solution using deionised water [12]. The nutrient broth (NB) (Oxoid, Malaysia) that was used to enrich microbes consisted of yeast extract (2.0 g), peptone (5.0 g), sodium chloride (5.0 g) and agar (15.0 g) in 1 L of distilled water.

Screening, isolation and growth of native bacteria

Heavy metal-resistant bacterial species were isolated from the activated sludge by appropriate serial dilutions (10^{-1} – 10^{-4}) using 0.85% NaCl solution (Merck, Malaysia). A total of 0.1 mL of each dilution was spread onto a plate that contained nutrient agar (Oxoid, Malaysia) and incubated for 24 hours. These dilutions were characterised morphologically based on biochemical reactions. The isolates were maintained on a slant that contained nutrient agar. To determine the growth pattern of the isolates, one loop of a single colony was inoculated in 100 mL of NB medium grown in a shaker incubator at 37 °C with 150 rpm for 24 hours. Growth pattern was determined by using a spectrophotometer (HACH, USA) after a two-hour interval by measuring optical density (OD) at OD_{550}.

Biosorption studies of Fe and Mn

Bacteria were grown in an incubator shaker (Protech, Model SI-100D, Malaysia) at 150 rpm and 37 °C for 24 hours. The culture was centrifuged at 4000 rpm for 10 minutes (Eppendorf, Centrifuge 5810, Malaysia). The supernatant was discarded, and the bacterial pellet undergone cell washing using sterile saline water and dilution until the OD of 0.6 (550 nm). Approximately 10% of inoculum was inoculated using different concentrations (0–200 mg/L) of Fe and Mn salt in 250 mL Erlenmeyer flask following Fadel et al. method [13]. The observation was conducted within 24 hours with four-hour interval by measuring the OD. After 24 hours, the bacteria were spread onto the nutrient agar to determine the colony-forming unit per mL (CFU/mL) after exposure to Fe and Mn. The experiment set-up is presented in Table 1.

Table 1. (a, b) Iron at 0 and 24 hours; (c, d) manganese at 0 and 24 h in triplicate

Type of Heavy Metal	Physical Observation Before and After Exposure			
	Iron		Manganese	
0 h	a		c	
24 h	b		d	

Results and Discussion

Physicochemical parameters of the activated sludge

The activated sludge from oxidation pond was analysed in terms of water quality parameters, including pH, dissolved oxygen, total suspended solid, oxygen reduction potential and chemical oxygen demand. Table 2 shows the sample characteristics of activated sludge prior to its exposure to heavy metal.

Table 2. Characteristics of activated sludge from the oxidation pond effluent used for heavy metal exposure

Parameter	Value
pH	6.5
Total suspended solid (g/L)	18.83
Chemical oxygen demand (mg/L)	6000
Oxygen reduction potential (mV)	−67.5
Dissolved oxygen (mg/L)	1.86

Growth patterns of native bacteria

To screen the native bacteria obtained from the activated sludge, about 22 different bacteria were isolated through physical observation on plate agar. Gram staining was performed to determine the morphology of the respective bacteria. Among the 22 isolates, only seven isolates, namely, AM1, AM2, AM3, AM4, AM5, AM6 and AM7, showed different microscopic views. Most of the bacterial isolates were rod-shaped, chained and gram positive. Culturing of the isolated bacteria reduced the number of isolates to four, namely, AM2, AM3, AM4 and AM6 because the three other isolates experienced a slow growth, as shown in Figure 2. To illustrate the bacterial growth, the growth curve of each of the four isolates is displayed in Figure 3.

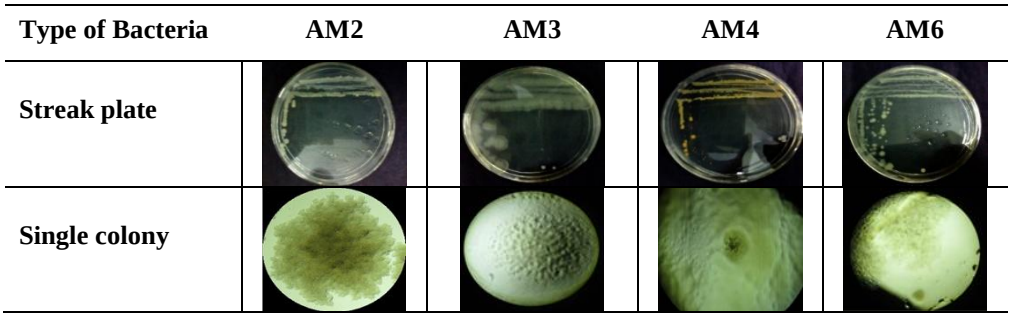


Figure 2. Four selected isolates, namely, AM2, AM3, AM4 and AM6

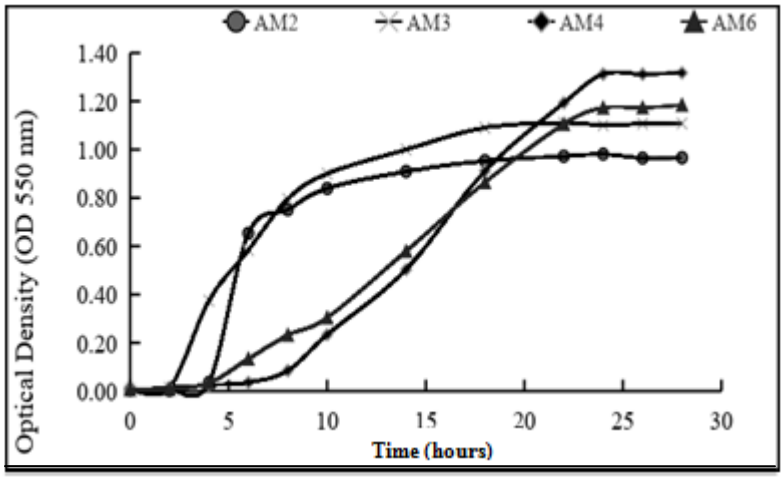


Figure 3. Growth curved of the four selected isolates (AM2, AM3, AM4 and AM6). AM2 and AM3 showed rapid growth, whereas AM4 and AM6 exhibited slow growth within 28 hours

Biosorption of Fe and Mn

The effects of Fe and Mn were determined based on CFU/mL. After 24 hours of exposure, samples were diluted to 10^{-1} and plated on nutrient agar for another 24 hours of incubation. The bacterial colonies were counted, and data are presented in Figure 4. Evaluation was performed using three different Fe concentrations, namely, 50, 100 and 200 mg/L. On average, AM2 showed increment in the number of bacterial colonies, with the highest number of bacterial colony of 2 x 10^3 CFU/mL at 200 mg/L plate. However, AM3 and AM6 only demonstrated bacterial growth at 50 mg/L Fe with only 9 x 10^2 and 1 x 10^2 CFU/mL, respectively. In addition, the CFU of AM4 was only 2.5 x 10^2 CFU/mL at 100 mg/L Fe. No bacterial growth was observed for AM3 and AM6 with 100 and 200 mg/L Fe and for AM4 with 50 and 200 mg/L Fe. This phenomenon occurred because these bacteria (AM3, AM4 and AM6) cannot resist Fe concentration at approximately 100 and 200 mg/L.

Among the four different types of bacteria, AM2 presented the highest resistance to Fe concentration to about 200 m/L. Theoretically, Fe is essential for growth, but it can be toxic to living cells at high concentration, as demonstrated by isolates AM3, AM4 and AM6. Fe is important for biological systems but only at definite low level [14]. Moreover, the addition of alone results in relatively unchanged bacterial growth, but the addition of glucose to Fe causes substantial increase in the rates of bacterial growth and biomass accumulation [15].

Different CFU/mL values among different bacteria may be due to the large surface area of biomass; consequently, the ability of bacteria to bind to the cell wall causes its high uptake of heavy metals [16, 17]. Nonetheless, bacteria that can survive well in high heavy metal concentrations, such as isolate AM2, are considerably important as bioremediation agents because they can achieve different transformations and immobilisation processes [18]. Figure 4 illustrates a bar graph of the CFU/mL values for the Mn biosorption of different types of selected isolates.

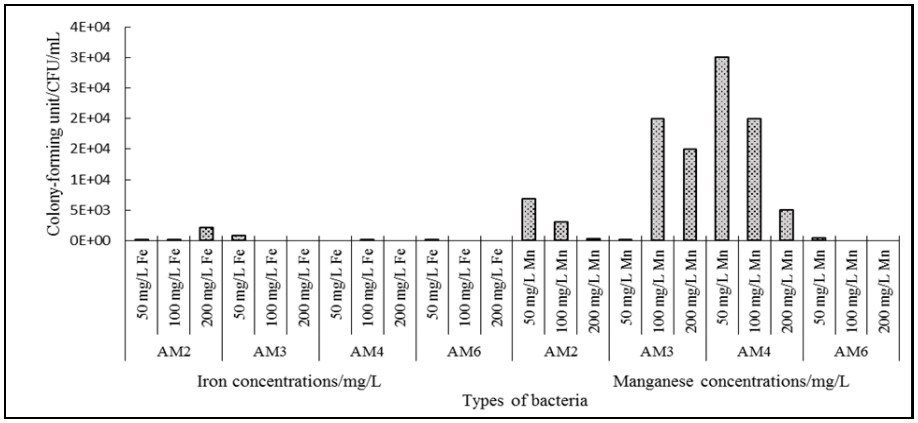


Figure 4. Colony-forming unit per mL (CFU/mL) of AM2, AM3, AM4 and AM6 towards different Fe and Mn concentration

Mn (50, 100 and 200 mg/L) biosorption showed different trends in the bar graph. The bacteria growth of AM2, (CFU/mL) steadily decreased along the experiment, with the highest bacterial growth of 6.9 x 10^3 CFU/mL. AM3 showed fluctuation at 50 mg/L because of minimal bacterial growth; however, at 100 and 200 mg/L, the CFU/mL began to increase and decrease (from 2 x 10^4 CFU/mL to 1.5 x 10^3 CFU/mL), respectively. During the first exposure of AM4, the bacterium resisted Mn at 50 mg/L with 3 x 10^4 CFU/mL. At 100 and 200 mg/L Mn, the bacterial colony count began to decrease to 2 x 10^4 and 5 x 10^3 CFU/mL, respectively. AM6 only demonstrated low growth at 50 mg/L and zero growth for 100 and 200 mg/L Mn. Overall, most of the bacteria presented a decreasing order of resistance with increased Mn concentration. This trend was attributed to that bacteria cannot resist high Mn concentration, and no growth eventually occurred at the end of the exposure period.

The microbial populations exhibited a wide spectrum of sensitivity to metal ions. Growth inhibition is a common response to heavy metal stress and an important indicator of heavy metal tolerance [19]. Growth was stimulated at low concentration. By contrast, at high metal concentration, the growth became gradually inhibited, toxic and finally terminated. These phenomena were observed in all the isolates, namely, AM2, AM3, AM4 and AM6.

Conclusion

Experimental study on resistance of native isolated bacteria from activated sludge towards Fe and Mn concluded that concentration of Fe and Mn suitable for the acclimatisation of bacteria are in the range of 0–200 mg/L. Isolate AM2 resists Fe until 200 mg/L. Isolate AM4 shows decreasing growth trend at Mn concentration ranging from 0 mg/L to 200 mg/L, indicating that it still grow but with decreasing value of number of CFU/mL compared to other three isolates (AM2, AM3 and AM6).

Acknowledgement

The author expresses gratitude to Universiti Kebangsaan Malaysia for funding this research under grant number GUP-2017-022.

References

1. Ahluwalia, S. S. and Goyal, D. (2007). Microbial and plant derived biomass for removal of heavy metals from wastewater. *Bioresource Technology*, 98: 2243–2257.
2. Tangahu, B. V., Abdullah, S. R. S., Basri, H., Idris, M., Anuar, N. and Mukhlisin, M. (2011). Review on heavy metals (As, Pb and Hg) uptake by plants through phytoremediation. *International Journal of Chemical Engineering*, 2011: 1–31.
3. Tsekova, K., Todorova, D., Dencheva, V. and Ganeva, S. (2010). Biosorption of copper(II) and cadmium(II) from aqueous solutions by free and immobilized biomass of *Aspergillus niger*. *Bioresource Technology*, 101(6): 1727–1731.
4. Ileri, O., Cay, S., Uyanik, A. and Erduran, N. (2014). Removal of common heavy metals from aqueous solutions by waste *Salvadora persica L*. Branches (Miswak). *International Journal of Environmental Research*, 8(4): 987–996.
5. Sannasi P., Kader J., Othman, O. and Salmijah, S. (2009). Physical growth and characterization of bacterial cells exposed to Cd(II), Cr(VI), Cu(II), Ni(II) and Pb(II). *Journal of Environment Research and Development*, 4(1): 8–18.
6. Hasan, H. A., Abdullah, S. R. S., Kofli, N. T. and Kamarudin, S. K. (2010). Biosorption of manganese in drinking water by isolated bacteria. *Journal of Applied Science*, 10(21): 2653–2657.
7. Hasan, H. A., Abdullah, S. R. S., Kofli, N. T. and Kamarudin, S. K. (2012). Isotherm equilibriums of Mn^{2+} biosorption in drinking water by locally isolated *Bacillus* species and sewage activated sludge. *Journal of Environmental Management*,111: 34–43.
8. Hasan, H. A., Abdullah, S. R. S., Kofli, N. T. and Jay, Y. S. (2016). Interaction of environmental factors on simultaneous biosorption of lead and manganese ions by locally isolated *Bacillus cereus*. *Journal of Industrial and Engineering Chemistry*, 37: 295–305.
9. Zainudin, F. M., Hasan, H. A. and Abdullah, S. R. S. (2016). Effect of initial concentrations on biosorption of manganese by locally isolated *Bacillus cereus*. *Jurnal Kejuruteraan*, 28: 73–78.
10. Kadukova, J. and Vircikova, E. (2005). Comparison of differences between copper bioaccumulation and biosorption. *Environment International*, 31(2): 227–232.
11. Nye, C. K. (2014). Phytoremediation of micropollutant through sub-surface constructed wetlands. Thesis of Bachelor Degree, Universiti Kebangsaan Malaysia.
12. Samarth, D. P., Chandekar, C. J. and Bhadekar, R. K. (2012). Biosorption of heavy metals from aqueous solution using *Bacillus licheniformis*. *International Journal of Pure & Applied Sciences & Technology*, 10(2): 12–19.
13. Fadel, M., Hassanein, N. M., Elshafei, M. M., Mostafa, A. H., Ahmed, M. A. and Khater, H. M. (2015). Biosorption of Manganese from Groundwater by Biomass of *Saccharomyces cerevisiae*. *HBRC Journal*, 13(1): 106–113.
14. Sorokina, E. V., Yudina, T. P., Bubnov, I. A. and Danilov, V. S. (2013). Assesment of iron toxicity using a luminescent bacterial test with an *Escherichia coli* recombinant strain. *Microbiology*, 82(4): 439–444.

15. Church, M. J., Hutchins, D. A. and Ducklow, H. W. (2000). Limitation of bacterial growth by dissolved organic matter and iron in the Southern Ocean. *Applied and Environmental Microbiology*, 66(2): 455–466.
16. Gadd, G. M (1994). The Genus Aspergillus. Springer Science, Business Media, New York: 361–374.
17. Iqbal, A., Zafar, S. and Ahmad, F. (2005). Heavy metal biosorption potential of *Aspergillus* and *Rhizopus* sp. isolated from wastewater treated soil. *Journal of Applied Science and Environmental Management*, 9(1): 123–126.
18. Ghane, M., Tabandeh, F. and Bandehpour, M. (2013). Isolation and characterization of a heavy metal resistant *Comamonas* sp. from industrial effluents. *Iranian Journal of Science and Technology*, 37(2): 173–179.
19. Malar, S., Vikram, S. S., Favas, P. J. C. and Perumal, V. (2014). Lead heavy metal toxicity induced changes on growth and antioxidative enzymes level in water hyacinths (*Eichhornia crassipes* (Mart.)). *Botanical Studies*, 55(54): 1–11.

Malaysian Journal of Analytical Sciences, Vol 23 No 1 (2019): 138 - 146
DOI: https://doi.org/10.17576/mjas-2019-2301-17

MALAYSIAN JOURNAL OF ANALYTICAL SCIENCES
Published by The Malaysian Analytical Sciences Society
ISSN 1394 - 2506

PRODUCTION OF COMPOST FROM NON-SHREDDED EMPTY FRUIT BUNCHES MIXED WITH ACTIVATED LIQUID ORGANIC FERTILIZER IN TOWER COMPOSTER

(Penghasilan Kompos dari Tandan Kosong Kelapa Sawit Tanpa Cincang Dicampur dengan Baja Cair Aktif dalam Menara Komposter)

Irvan[1,2]*, Muhammad Rahman[1], Dedy Anwar[1], Bambang Trisakti[1,2], Hiroyuki Daimon[3]

[1]*Chemical Engineering Department*
[2]*Sustainable Energy and Biomaterial Center of Excellence*
Universitas Sumatera Utara, Medan 20155, Indonesia
[3]*Department of Environmental and Life Sciences,*
Toyohashi University of Technology, Toyohashi, 441-8580, Japan

**Corresponding author: irvan@usu.ac.id*

Received: 13 April 2017; Accepted: 17 April 2018

Abstract

Empty fruit bunches (EFBs) with activated liquid organic fertiliser (ALOF) were composted in a tower composter. This study was conducted to evaluate the degradation of non-shredded EFB mixed with ALOF as an activator. The concrete tower composter with dimensions of 0.40 m x 0.40 m x 3.00 m was used to accelerate composting time by achieving thermophilic conditions. The moisture content (MC) of the compost was maintained at 55% - 65%. Compost quality, temperature, pH, MC, C/N ratio, bacterial count (BC) and electrical conductivity (EC) were recorded and evaluated. Composting was completed in 40 days, even though EFB turned to dark brown on day 10, indicating that the compost was mature. The quality of the final compost from day 10 to day 40 was slightly similar: pH of 7.6–8.4, MC of 41.16%–58.44%, C content of 20.27%–21.34%, N content of 1.02%–1.25%, C/N ratio of 19.94–20.24, BC of 17–41 x 10^6 CFU g^{-1} and EC of 3.74–4.90 dS m^{-1}. These results suggested that the quality of the obtained compost satisfied the Indonesian National Standard.

Keywords: activated liquid organic fertiliser, composting, empty fruit bunches, tower composter

Abstrak

Buah tandan kosong (EFB) dengan baja organik cecair teraktif (ALOF) telah dikompos di dalam menara komposter. Kajian ini dijalankan untuk menilai data degradasi EFB yang tidak diparut bercampur dengan ALOF sebagai pengaktif. Penggunaan menara komposter, yang diperbuat daripada konkrit dengan dimensi 0.40 m W x 0.40 m L x 3.00 m H, adalah untuk pecutan masa pengomposan bagi mencapai keadaan termofilik. Kandungan lembapan (MC) kompos dikekalkan dalam lingkungan 55 - 65%. Kualiti kompos, suhu, pH, kandungan lembapan, nisbah C/N, bilangan bakteria (BC), dan kekonduksian elektrik (EC) telah direkod dan dinilai. Proses pengomposan telah lengkap dalam masa yang singkat iaitu dalam 40 hari, dan pada hari yang ke-10, EFB telah bertukar warna menjadi coklat tua yang menunjukkan kematangan kompos. Kualiti kompos akhir dari hari 10 hingga ke hari 40 menunjukkan kualiti yang hampir sama iaitu pH antara 7.6 hingga 8.4; kandungan lembapan 41.16 - 58.44%; C 20.27 - 21.34%; N 1.02 - 1.25%; nisbah C/N 19.94 - 20.24; bilangan bakteria 17 - 41 x 106 CFU g^{-1}, dan kekonduksian elektrik 3.7 - 4.9 dS.m^{-1}. Kualiti kompos keluaran yang diperolehi telah mencapai Piawai Kebangsaan Indonesia (SNI).

Kata kunci: baja organik cecair teraktif, pengomposan, buah tandan kosong, menara komposter

Introduction

Indonesia is currently one of the countries with the largest production of crude palm oil (CPO); in 2012, this country produced 23.5 million tons of CPO [1]. In addition to CPO, liquid and solid wastes are generated by palm oil mills (POMs). Large amounts of solid wastes, such as empty fruit bunch (EFB; 23%), shell (5%) and mesocarp fibre (12%), are also obtained for every ton of EFB processed in POMs [2].

Composting is an alternative processing technology for solid and liquid wastes from POMs. Most EFBs are used as soil amendments in oil palm lands by placing EFBs around palm trees to provide a good environment for roots. However, this technique is costly in terms of labour and transportation [3]. EFB composting is usually time consuming because of environmental factors. The processing of EFB into compost has been extensively explored, and composting can be enhanced by introducing additional materials, such as animal waste [4, 5] and POME [6].

Activated liquid organic fertiliser (ALOF), which is used as a microbial source and moisture content (MC) buffer in composting, is obtained through the advanced fermentation of treated biogas effluent from an anaerobic digester. This effluent still possesses high nutrient and MC. Hence, ALOF addition to EFB may enrich composts with high nutrient and microbial sources. This research aimed to examine EFB composting in a tower composter and described the degradation of non-shredded EFB mixed with ALOF.

Materials and Methods

Materials

EFB (Sei Mangkei POM, Sumatera Utara, Indonesia) and ALOF (Biogas Pilot Plant, Universitas Sumatera Utara, Indonesia) were used as raw materials, and their characteristics are presented in Table 1.

Table 1. Characteristic of EFB and ALOF

No.	Parameters	EFB	ALOF
1	Moisture (%)	43.83	-
2	pH	7.80	8.09
3	C (%)	33.15	0.58
4	N (%)	0.99	0.10
5	C/N	33.48	5.80
6	Water Holding Capacity (%)	62.00	-
7	P_2O_5 (%)	-	0.016
8	K_2O (%)	-	0.167
9	COD (mg/l)	-	1.580

Equipment

The main equipment used in this study was a box-shaped composter tower constructed under a shade and a cement base at the Pusdiklat LPPM–Universitas Sumatera Utara, Indonesia. The composter tower measured 3 m in height and consisted of a 0.4 m x 0.4 m square pedestal. The composter was equipped with two 0.11 m x 0.11 m windows and a 0.40 m x 0.40 m manhole, which were used for sampling and product harvesting, respectively. Fifteen holes (1.905 cm) were made on each wall of the composter for oxygen intake (aeration) and inserted with a digital thermometer to measure the temperature of the composting material in the composter. A detailed sketch of the composter is presented in Figure 1.

Composting process

Composting was initiated by measuring the total weight of the non-shredded EFB. The EFB was poured with ALOF until the MC of the compost reached 55%–65%. No-turn composting operation was required during the process, but ALOF was poured again into the composter when the MC was too low to maintain the MC at 55% -65%.

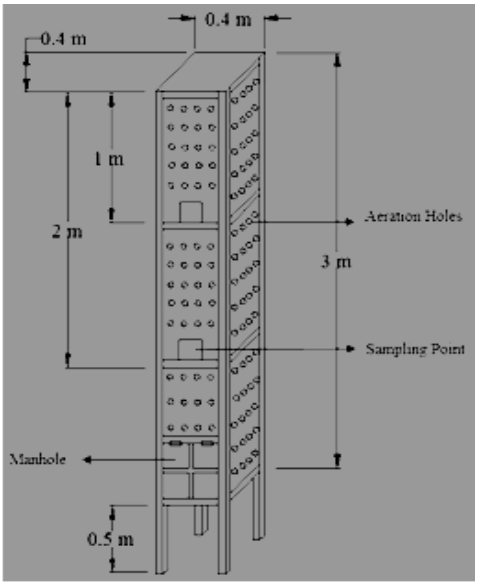


Figure 1. The tower composter

Sampling and Data Collection

Samples (20 g) were collected from the sampling window and stored at 4 °C. Temperature was measured by inserting a digital thermometer into the thermometer hole. The following data were obtained: temperature, MC, pH, C/N ratio and compost quality. Pile temperature was measured twice a day (morning and afternoon). Pile MC was also determined every 5 days *via* a drying oven method. pH was identified every 2 days. C and N contents were recorded on days 0, 10, 30 and 40 of the treatment through the Walkley–Black and Kjeldahl method, respectively. Bacterial growth and electrical conductivity (EC) were monitored on days 0, 10, 30 and 40 of the treatment by conducting bacterial count (BC) analysis and by using an EC meter, respectively.

Results and Discussion

Temperature profile

Temperature is the most important parameter to be measured during composting [7]. The average temperature profile in the morning and in the afternoon at heights of 0, 1 and 2 m of the compost pile from the bottom of the composter is presented in Figure 2. The initial temperature of the compost was 27 °C. Composting started once the compost was mixed with ALOF. After 24 days of operation, the average temperatures of the composting material at 0, 1 and 2 m increased to 51.5 ± 0.71 °C, 60.75 ± 0.35 °C and 52.5 ± 0.71 °C, respectively.

At the beginning of composting, the temperature increased from atmospheric temperature (27 °C) to thermophilic temperatures of 51.5 ± 0.71 °C, 60.75 ± 0.35 °C and 52.5 ± 0.71 °C at heights of 0, 1 and 2 m, respectively. The temperatures decreased and fluctuated from day 5 and finally remained almost constant after day 30 of the treatment. This result was consistent with those of Shen et al. [8] and Hock et al. [9], who reported that compost temperatures rapidly increase and then slowly decrease. This finding indicated that composting slowed down as nutrient availability became depleted.

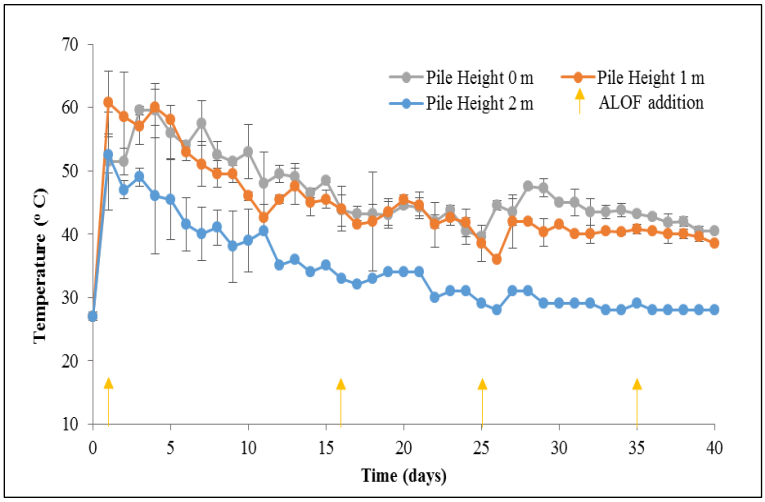


Figure 2. Temperature profiles during composting

MC profile

MC is one of the important factors that must be maintained during composting [10]. The MC profiles at heights of 0, 1 and 2 m of the compost pile from the composter bottom are presented in Figure 3. The initial MC of EFB was 43.83%. After EFB was mixed with ALOF, the MCs changed to 64.76%, 63.72% and 61.78% at 0, 1 and 2 m, respectively. MC also fluctuated during composting. To maintain MC at 55% - 65%, we added ALOF on days 1, 16, 25 and 35 of the treatment. MC evaluation at 2 m of compost was terminated on day 11 because shrinkage occurred in the composting material.

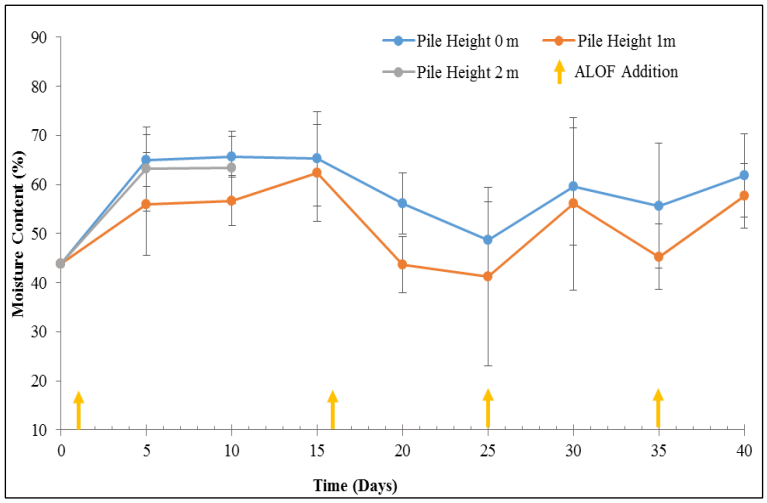


Figure 3. Moisture content profiles

The final MCs of the compost after 40 days at 1 and 2 m were 65.68% and 51.2% (average: 58.44%), respectively, and they were similar to those of Hock et al. [9] and Baharuddin et al. [10], who obtained final MCs of approximately 50% after 39 days and 52%, respectively. Tiquia et al. [11] demonstrated that the MC of a composting material must be maintained at 40% - 60% to favour microbial survival. An MC of >80% can kill aerobic microbes because of the lack of oxygen.

pH profile during composting process

The pH profile during composting is presented in Figure 4. The pH during 40 days of composting ranged from 7.8 to 8.4, indicating that the operational conditions were likely alkaline. The alkaline condition of a composting material is good for composting because this pH may inhibit the growth of pathogens, such as fungi, which can survive under acidic conditions [12].

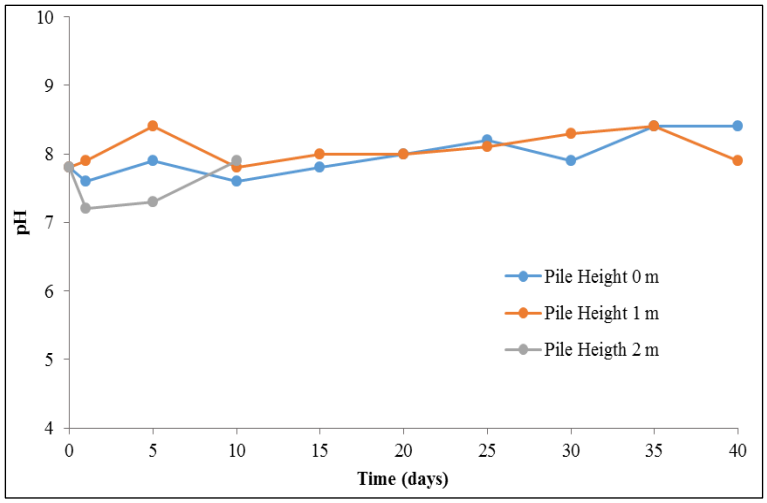


Figure 4. pH profiles

The pH of the pile at each height fluctuated slightly from day 0 to day 25 and became relatively constant until day 40. Changes in pH during composting are caused by microbial activity [13, 14]. In the first 5 days, pH increased from 7.8 to 8.6 because N is transformed into NH_3 or NH_4^+ *via* ammonification [13]. From day 5 to day 10, pH likely decreased to pH 7.6 because of the volatilisation of ammonium and the release of hydrogen ions as a result of nitrification [10]. The pH of the final mature compost was 8.4.

Profile of BC

Microbial growth during composting was observed by analysing BC. The number of microbial colonies and the average temperature of the composting material are presented in Figure 5.

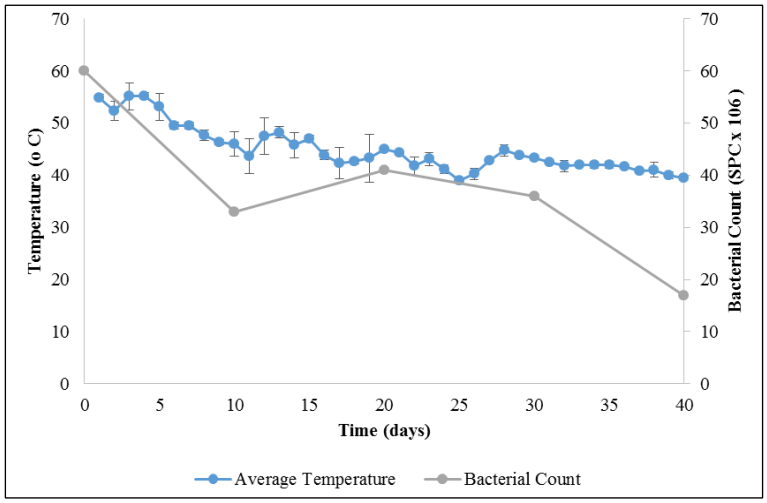


Figure 5. Profiles of bacterial count and temperature during composting

Two states of microbial growth during composting were observed on the basis of the average temperature of the composting material: thermophilic state (1^{st} to 15^{th}) and mesophilic state (day 16 to day 40). The initial BC was 60 x 10^6 CFU g^{-1}. After the thermophilic state was initiated on day 1, the BC drastically decreased because the total BC was initially dominated by mesophilic bacteria, and most of them died as the temperature increased and reached the thermophilic state. From day 10 to day 20, the BC increased because the thermophilic and mesophilic bacteria already survived in the thermophilic state and started to grow. From day 30 to day 40, the BC slowly decreased as nutrient availability decreased.

Compost analysis based on C/N ratio

To determine the quality of the compost produced during composting, we measured the C/N ratio in triplicate. The C/N ratio profile during composting is presented in Figure 6.

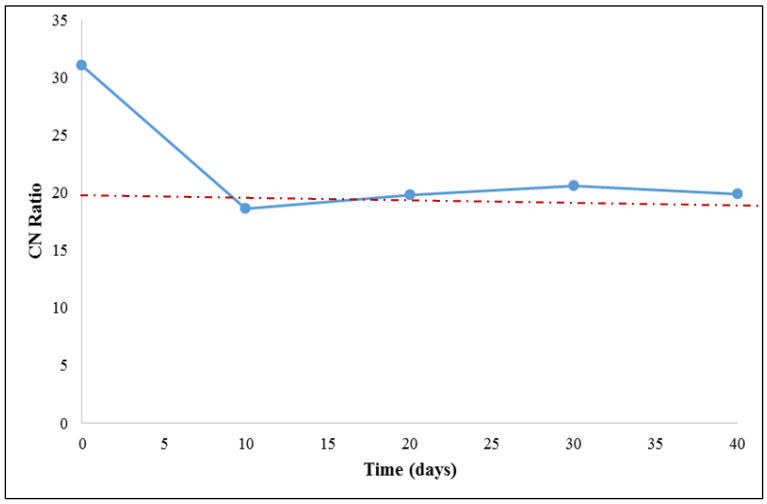


Figure 6. C/N ratio changes during composting

The C/N ratio is one of the important indicators that reflect the maturity of compost [6, 15]. In our study, this parameter was measured on days 0, 10, 20, 30 and 40 of the treatment. The initial C/N ratio of EFB was 33.48. After 10 days of composting, the C/N ratio significantly decreased to 18.64. From day 20 to day 40, the C/N ratio remained relatively constant at 19 – 20. At the end of composting, the C/N ratio was 19.94, indicating that the compost matured after 10 days because the C/N ratio of a standard matured compost is between 10 and 20 [6, 16]. The decrease in the C/N ratio was due to the decrease in C content or the increase in N content during composting. This phenomenon occurred because of the decomposition of organic materials during microbial activity [9, 17].

Compost analysis based on EC

EC reflects the level of salinity of a compost product and indicates possible phytotoxic or phyto-inhibitory effects [18]. The changes in EC during composting are presented in Figure 7. The initial EC of EFB was 6.72 dS m^{-1}, but this value decreased to 4.30 dS m^{-1} after 20 days of composting. On day 30, the EC increased to 4.42 dS m^{-1} and then decreased to 3.74 dS m^{-1} at the end of composting.

The decrease in EC during composting is a direct result of the increasing concentrations of nutrients, such as nitrate and nitrite [19]. The increase in EC may be due to the release of mineral salts, such as ammonium and phosphate ions, through the decomposition of organic substances [18]. The results of the complete analysis of compost quality are presented in Table 2.

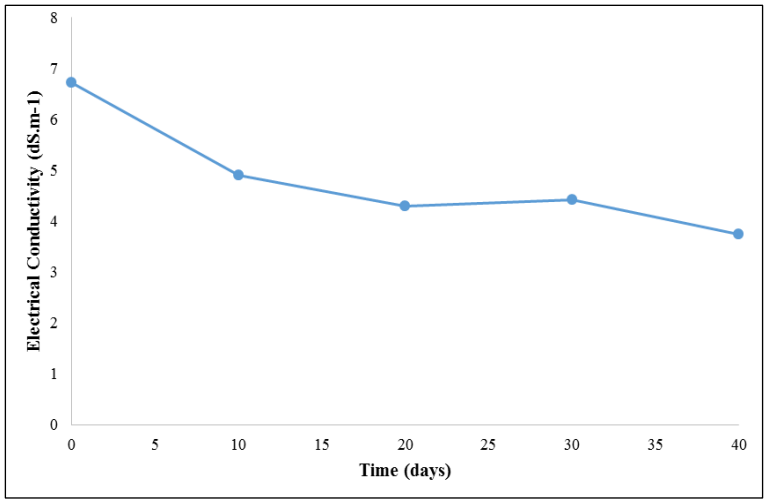


Figure 7. Changes in electrical conductivity

Table 2. Compost quality analysis

No	Parameters	Composting Material	
		Start up	Day 40
1	Moisture (%)	43.83	58.44
2	pH (%)	7.80	8.40
3	Water Holding Capacity (%)	62.00	64.00
4	C (%)	37.89	21.34
5	N (%)	1.22	1.07
6	C/N (%)	31.06	19.94
7	P (%)	0.201	0.091
8	K (%)	0.157	0.951
9	Na (ppm)	0.102	0.059
10	Ca (ppm)	1.759	2.043
11	Mg (ppm)	0.537	0.527
12	Cd (ppm)	0.894	0.437
13	Cu (ppm)	0.673	0.078
14	Fe (ppm)	1.073	0.051
15	Pb (ppm)	1.246	0.080
16	Zn (ppm)	2.370	0.052
17	Oil & Grease (%)	2.15	1.43

Conclusion

The composting of non-shredded EFB mixed with ALOF as microbial and nutrient sources and MC buffer in a box-shaped tower composter (0.4 m width x 0.40 m length x 3.00 m height) could produce mature compost for 10 days. The slight differences in the C/N ratio from 18.15 to 19.94 and the EC from 3.74 dS m^{-1} to 4.90 dS m^{-1} indicated that the quality of the compost on day 10 was similar to the quality of the compost on day 40.

Acknowledgement

This research was financially supported by Hibah BP-PTN Universitas Sumatera Utara, contract no: 6049/UN5.1.R/PPM/2016, date July19th, 2016.

References

1. Irvan, Trisakti, B., Sosanty, F. and Tomiuchi, Y. (2016). Effect of discontinuing sodium bicarbonate on fermentation process of palm oil mill effluent. *Asian Journal of Chemistry*, 28(2): 377 - 380.
2. Trisakti, B., Lubis, J., Husaini, T. and Irvan (2017). Effect of turning frequency on composting of empty fruit bunches mixed with activated liquid organic fertilizer. *IOP Conference Series: Materials Science and Engineering*, 180: 012150.
3. Kavitha, B., Jothimani, P. and Rajannan, G. (2013). Empty fruit bunch – a potential organic manure for agriculture. *International Journal of Science, Environment and Technology*, 2(5): 930 - 937.
4. Suhaimi, M. and Ong, H. K. (2001). Composting empty fruit bunches of oil palm. food and fertilizer technology centre. Retrieved from http://www.agnet.org/library/eb/505a/pdf. [Access online 11 December 2013].
5. Thambirajah, J. J., Zulkali, M. D. and Hashim, M. A. (1995). Microbiological and biochemical changes during the composting of oil palm empty fruit bunches – effect of nitrogen supplementation on the substrate. *Bioresource Technology*, 52(2): 133 - 144.
6. Baharuddin, A. S., Wakisaka, M., Shirai, Y., Abd-Aziz, S., Abdul Rahman, N. A. and Hassan, M. A. (2009). Co–composting of empty fruit bunches and partially treated palm oil mill effluents in pilot scale. *International Journal of Agricultural Research*, 4(2): 69 - 78.
7. Saiidi, S., Hasani, M., Hashemi, J. and Amini, M. (2012). Investigation of optimum conditions of co-composting process by using of sewage sludge and municipally waste. *The 1st International and the 4th national congress on recycling of organic waste in agricultural*, Isfahan, Iran. 26 - 27 April 2012.
8. Shen, Y., Rein, L., Li, G., Chen, T. and Guo, R. (2010). Influence of aeration on CH_4, N_2O and NH_3 emissions during aerobic composting of a chicken manure and high C/N waste mixture. *Waste Management*, 31(1): 33 - 38.
9. Hock, L. S., Baharuddin, A. S., Ahmad, M. N., Md Shah, U. K., Rahman, N. A. A., Abd-Aziz, S., Hassan, M. A. and Shirai, Y. (2009). Physicochemical changes in windrow co-composting process of oil palm mesocarp fiber and palm oil mill effluent anaerobic sludge. *Australian Journal of Basic and Applied Sciences*, 3(3): 2809 - 2816.
10. Baharuddin, A. S., Hook, L. S., Yusof, M. Z. M., Rahman, N. A. A., Shah, U. K. M., Hasan, M. A., Wakisaka, M., Sakai, K. and Shirai, Y. (2010). Effects of palm oil mill effluent (POME) anaerobic sludge from 50 cm^3 of closed anaerobic methane digested tank on pressed-shredded empty fruit bunch (EFB) composting process. *African Journal of Biotechnology*, 9(16): 2427 - 2436.
11. Tiquia, S. M., Tam, N. F. Y. and Hodgkiss, I. J. (1997). Effects of turning frequency on composting of spent pig-manure sawdust litter. *Bioresource Technology*, 62: 37 - 42.
12. Saidi, N., Chérif, M., Jedidi, N., Mahrouk, M., Fumio, M., Boudabous, A. and Hassen, A. (2008). Evolution of biochemical parameters during composting of various wastes compost. *American Journal of Environmental Sciences*, 4(4): 332 - 341.
13. Kananam, W., Suksaroj, T. T. and Suksaroj, C. (2011). Biochemical changes during oil palm (*Elaeis guineensis*) empty fruit bunches composting with decanter sludge and chicken manure. *Science Asia*, 37: 17 - 23.
14. Sundberg, C., Smars, S. and Jonsson, H. (2004). Low pH as an inhibiting factor in the transition from mesophilic phase in composting. *Bioresource Technology*, 95: 145 - 150.
15. Nutongkaew, T., Duangsuwan, W., Prasertsan, S. and Prasertsan, P. (2011). Production of compost from palm oil mill biogas sludge mixed with palm oil mill wastes and biogas effluent. *TIChE International Conference*, Hatyai, Songkhla, Thailand. 10 – 11 November 2011.
16. Zahrim, A. Y. and Asis, T. (2010). Production of non-shredded empty fruit bunch semi-compost. *Journal-The Institution of Engineers*, 71(4): 11 - 17.
17. Razali, W. A. W., Baharuddin, A. S., Talib, A. T., Sulaiman, A., Naim, M. N., Hassan, M. A. and Shirai, Y. (2012). Degradation of oil palm empty fruit bunches (OPEFB) fibre during composting process using in vessel composter. *BioResources*, 7(4): 4786 - 4805.

18. Gao, M., Liang, F., Yu, A., Li, B. and Yang, L. (2009). Evaluation of stability and maturity during forced-aeration composting of chicken manure and sawdust at different C/N ratios. *Chemosphere*, 78 (5): 614 - 619.
19. Pathak, A. K., Singh, M. M., Kumara, V., Arya, S. and Trivedi, A. K. (2012). Assessment of physico-chemical properties and microbial community during composting of municipal solid waste. *Recent Research in Science and Technology*, 4(4): 10 - 14.

Malaysian Journal of Analytical Sciences, Vol 23 No 1 (2019): 147 - 154
DOI: https://doi.org/10.17576/mjas-2019-2301-18

MALAYSIAN JOURNAL OF ANALYTICAL SCIENCES
Published by The Malaysian Analytical Sciences Society
ISSN 1394 - 2506

OXYGEN REDUCTION REACTION BEHAVIOURS OF CARBON NANOTUBES SUPPORTING Pt CATALYST FOR PROTON EXCHANGE MEMBRANE FUEL CELL

(Sifat Tindak Balas Penurunan Oksigen bagi Tiub Nanokarbon Disokong Mangkin Pt bagi Membran Penukaran Proton Sel Bahan Api)

Md Ahsanul Haque[1,2]*, Abu Bakar Sulong[1,3], Edy Herianto Majlan[1], Kee Shyuan Loh[1], Teuku Husaini[1], Rosemilia Rosli[1]

[1]*Fuel Cell Institute,*
Universiti Kebangsaan Malaysia, 43600 UKM Bangi, Selangor, Malaysia
[2]*Department of Applied Chemistry and Chemical Engineering,*
Islamic University, Kushtia-7003, Bangladesh
[3]*Department of Mechanical and Materials Engineering, Faculty of Engineering and Built Environment,*
Universiti Kebangsaan Malaysia, 43600 UKM Bangi, Selangor, Malaysia

**Corresponding author: ahsan.chem38@gmail.com*

Received: 13 April 2017; Accepted: 17 April 2018

Abstract

Sluggish oxygen reduction reaction (ORR) in cathode electrode is the most common problem in Proton Exchange Membrane (PEM) fuel cell systems. In this study, the ORR behaviours of a half-cell in the cathodic part were investigated which had an impact on its catalyst activity. The electrode was synthesized from multi-walled carbon nanotubes (MWCNT) supported platinum (Pt) catalyst, assigned as MWCNT/Pt, using an impregnation method. In this case, the hexachloroplatinic acid ($H_2PtCl_6.6H_2O$) acts as a Pt metal catalyst precursor. The PTFE (polytetrafloro-ethylene) was also used as sub-supporting material with MWCNT to produce MWCNT/PTFE composite. The Pt is deposited onto the surface of MWCNT/PTFE composite which forms MWCNT/PTFE/Pt electrode. Using CV and RRDE techniques, the electrochemical phenomena of MWCNT/Pt and MWCNT/PTFE/Pt electrodes in the 0.1 M KOH electrolyte solutions were analysed and compared. The electron transfer (n) from the K-L plot was recorded as 3.89 and 3.77 for MWCNT/Pt and MWCNT/PTFE/Pt electrode respectively. Based on the chronoamperometric analysis, the MWCNT/PTFE/Pt was found to be more stable than MWCNT/Pt. Therefore, the MWCNT/PTFE/Pt electrode may be recommended for PEM fuel cell application considering its electrochemical activity.

Keywords: oxygen reduction reaction, multi-walled carbon nanotube, cyclic voltammetry, chronoamperometric analysis

Abstrak

Kelembapan tindak balas penurunan oksigen (ORR) dalam katod elektrod adalah cabaran utama dalam sistem membran penukar proton (PEM) sel bahan api. Dalam kajian ini, tindak balas bagi ORR setengah-sel dikaji pada bahagian katod yang merupakan sebahagian daripada aktiviti pemangkin. Elektrod terhasil disintesis daripada tiub nanocarbon multi dinding (MWCNT) disokong pemangkin platinum (Pt) yang membentuk MWCNT/Pt dengan menggunakan kaedah pengisian. Dalam kes ini, asid heksakloroplatinik ($H_2PtCl_6.6H_2O$) bertindak sebagai pemangkin logam Pt pelopor. PTFE (politetrafloro-etilena) juga digunakan sebagai bahan sokongan tambahan dengan MWCNT untuk menghasilkan MWCNT/PTFE komposit. Kemudian, Pt telah ditambah ke atas permukaan MWCNT/PTFE komposit yang membawa kepada pembentukan MWCNT/PTFE/Pt elektrod. Berdasarkan kaedah CV dan RRDE telah dianalisis dan dibandingkan fenomena elektrokimia dengan menggunakan kandungan larutan elektrolit 0.1 M KOH bagi setiap bahan MWCNT/Pt dan MWCNT/PTFE/Pt elektrod. Pemindahan elektron (n) dari plot

K-L juga dikira dan direkodkan sebagai 3.89 bagi MWCNT/Pt dan 3.77 bagi MWCNT/PTFE/Pt elektrod. Berdasarkan analisis kronoamperometrik, MWCNT/PTFE/Pt adalah lebih stabil berbanding MWCNT/Pt. Oleh itu, elektrod MWCNT/PTFE/Pt adalah disyorkan untuk aplikasi PEM sel fuel dengan mengambilkira aktiviti elektrokimia.

Kata kunci: tindak balas penurunan oksigen, karbon nanotiub berbilang, kitaran volmetrik, analisis kronoamperometrik

Introduction

Green energy technology is fast developing due to the finite nature of fossil fuel reserves. There are also related concerns the CO_2 gas emission has boosted the popularity of green energy. Therefore, researchers are focusing on green energy generation especially solar cell and fuel cell technology. Proton exchange membrane fuel cell (PEMFC) is one of the prominent potential energy conversion devices in the fuel cell arena [1]. However, its commercial application has been limited due to a shortage of research on electrode catalysts. Electrode catalyst is the core of PEMFC and plays a vital role in electrochemical reactions. Therefore, the PEMFC's overall performance depends on electro-catalytic activity of cell.

Electrode catalyst is commonly synthesized from precise metals, such as platinum (Pt), and its alloys [nickel (Ni), ruthenium (Ru), rubidium (Rb), palladium (Pd)] are still widely used [2]. The Pt in particular is used for electrode catalyst fabrication. However, it is an expensive metal and therefore to reduce the Pt content in electrocatalyst, carbon supporting materials, such as carbon black, carbon powder, carbon cloth and carbon fiber among others have been used [3]. These are low cost materials with active surface area that enhances electrochemical reactions as well as provide the physical stability for electrodes.

At high operating temperature, the conventional supporting materials may face problems, such as Pt catalyst agglomeration, Pt migration and Pt detachment from the supporting materials [4]. When this happens, it reduces both cell durability and its performance, with respect to time, due to loss of active electrochemical surface area (ECSA) which shows catalyst degradation [5].

In recent years, carbon nanotube, such as single-walled carbon nanotube (SWCNT), multi-walled carbon nanotube (MWCNT) has caught the attention of researchers as catalyst alternative supporting materials due to their unique characteristics, high aspect ratio, high electron conductivity, and enhanced mass transport capability [6, 7]. The MWNT is effective against carbon corrosion when compared with SWCNT or Vulcan XC-72. Therefore, MWCNT shows better performance than the conventional carbon supporting materials [8].

The cathode reaction kinetics primarily represents oxygen reduction reactions (ORR) of PEMFC. The oxygen reduction reaction at cathode sites is more sluggish than the hydrogen oxidation reaction at anode site. Therefore, the excess or overpotential for ORR has been identified as a major problem for the cell performance [9, 10] as it consumes more than 80% of overall cell voltage [11, 12]. Reducing the over potential of ORR in cathode site is important to increase the PEMFC cell performance [13, 14, 15]. However, degradation is a challenge for PEM fuel cell as it may decrease the lifetime of cell. Catalyst maturation, loss or transfer of catalysts, corrosion of carbon, electrolyte and interface degradation [16], and decrease of the catalyst active surface area due to catalyst agglomeration occur primarily in the cathode [17]. Therefore, this study focuses on the ORR activity as well as the catalyst stability of synthesised MWCNT/Pt and MWCNT/PTFE/Pt electrodes.

Materials and Methods

Multi walled carbon nanotube (MWCNT), hexachloroplatinic acid ($H_2PtCl_6.6H_20$; 36%), ortho phosphoric acid (H_3PO_4; 85%), dimethyl acetamide (DMAc; 80%), polytetrafloro ethylene (PTFE; 60%), polybenzimadole (PBI), iso-propyl alcohol (IPA) and potassium hydroxide were purchased from the Sigma-Aldrich. The rotating ring-disk electrode (RRDE) consist of platinum ring and glass carbon (GC) electrode disk and is 5 mm in diameter, purchased from Pine Instrument Co. All chemicals were in analytical grade. Only deionized (DI) water was used throughout this experiment.

Pristine MWCNT has been oxidized using dual acid mixture of 2.0 M HNO_3/H_2SO_4 (v/v 1:3) [18]. The oxidised MWCNT (5.0 mg) and PTFE solution (50 μL) was later dissolved in DMAc (5.0 mL) and sonicated for 60 minutes

using a bath type sonicator. The mixture was filtered and washed using DMAc to remove excess PTFE. The obtained solid (MWCNT/PTFE) composite was dried in a vacuum drier.

The Pt nanoparticles were later deposited onto the surface of MWCNT/PTFE composite using hexachloro platinic acid ($H_2PtCl_6.6H_2O$) and aqueous ethylene glycol solvent. The MWCNT/PTFE mixture (10 mg) was then sonicated and the $H_2PtCl_6.6H_2O$ (1.4 mM) was added to the MWCNT/PTFE mixture solution and continuously stirred for 4 hours at ambient temperature. The followed mixture solution was refluxed at 140 °C temperature for 8 hours. After refluxing, the solid materials were accumulated by filtration solvent and the unwanted residue washed out using the DI water and dried in vacuum drier to obtain MWCNT/PTFE/Pt [19, 20].

Oxidised MWCNT (10 mg) was later dissolved in aqueous ethylene glycol adding $H_2PtCl_6.6H_2O$ (1.4 mM) for Pt precursor. This solution was stirred for 4 hours under room temperature and again refluxed under 140 °C temperature for 8 hours, before it was filtered and washed with DI water to remove any unwanted residue. Finally, the solid MWCNT/Pt was dried overnight in a vacuum drier. The synthesised MWCNT/Pt was later characterised and compared with MWCNT/PTFE/Pt.

The MWCNT/PTFE/Pt electrocatalyst films were prepared for electrochemical characterisation. The catalyst was later dissolved in IPA (80%) solvent and dispersed using ultrasound to attain a homogeneous solution. In this case, the MWCNT/PTFE/Pt catalyst loaded was 0.5 mg/mL and later 10 µL of catalyst solution was dropped onto the polished GC disk of an RRDE using micropipette. The electrode was dried in ambient conditions overnight. Again, 5 µL of Nafion (5 wt.%) ionomer was applied onto the MWCNT/PTFE/Pt electrode film and dried at room temperature. The same procedure was used to develop catalyst film of MWCNT/Pt.

An electrochemical analysis was carried out using Autolab potentiostat/galvanostat (AUT128N) in a three-electrode system under ambient temperature, whereas; glassy carbon, Ag/AgCl electrode and Pt wire were used as working electrode, reference electrode, and counter electrode respectively. The electro-catalytic activities of synthesised MWCNT/PTFE/Pt and MWCNT/Pt electrode toward the oxygen reduction reaction in a 0.1 M KOH electrolyte solution were analysed using CV and RRDE voltammetry in a negative potential range 0.0 V to -1.0 V with a scan rate of 10 mVs^{-1}. Prior to each experiment, the N_2 and O_2 gas was purged in the 0.1 M KOH electrolyte solution until saturation. From the third cycle, CV signal was recorded to be stable after few consecutive cycles. The linear sweep voltammetry (LSV) was also accomplished in an O_2 gas saturated medium of 0.1 M KOH electrolyte solution with various rotational speeds in the negative potential range 0.0 V to -1.0 V using the scan rate 10 mVs^{-1}. In this paper, all potentials are referred to as Ag/AgCl [21, 22].

Results and Discussion

The synthesised electrocatalyst MWCNT/PTFE/Pt and MWCNT/Pt were examined in oxygen and nitrogen gas saturated 0.1 M KOH electrolyte solution under the three-electrode system. The cyclic voltammetry (CV) curves of MWCNT/PTFE/Pt and MWCNT/Pt were performed at ambient temperature. From Figure 1, very little peak current was observed in case of nitrogen gas saturated of 0.1 M KOH electrolyte solution used for both synthesised electrodes that indicated almost inactive redox species with respect to Ag/AgCl electrode potential within the potential range at 0.0 V to -1.0 V. The cathodic peak current was exposed whenever oxygen gas saturated environment of 0.1 M KOH electrolyte was used. These observations suggest that MWCNT/PTFE/Pt and MWCNT/Pt electrodes successfully induced the ORR reactions in the alkaline media. Figure 1(a) and 1(b) showed that the highest peak current at -0.38 V and -0.22 V potentials for the MWCNT/Pt and MWCNT/PTFE/Pt electrodes, respectively. The oxygen reduction currents were recorded as 0.28 mA cm^{-2} and 0.22 mA cm^{-2} for the MWCNT/Pt and MWCNT/PTFE/Pt electrodes, respectively.

The RRDE (ring rotating disk electrode) was used to analyse the kinetics of oxygen reduction reaction of MWCNT/Pt and MWCNT/PTFE/Pt electrodes. The LSV (linear sweep voltammogram) curves were obtained based on the electrocatalyst loaded of RRDE using various rotation rates, 200 rpm, 400 rpm, 800 rpm, 1200 rpm and 1600 rpm respectively. The oxygen reduction current was increased corresponding with high rotation rate. Koutechy-Levich (K-L) equation suggests sluggish ORR, if reduction current density is constant [23]. From Figure 2, the diffusion limited current density increases corresponding with rotation rate which implies that the ORR is diffusion-

controlled reaction. The ORR polarization curve exhibited limiting current plateau corresponding with the diffusion-limited current density [21].

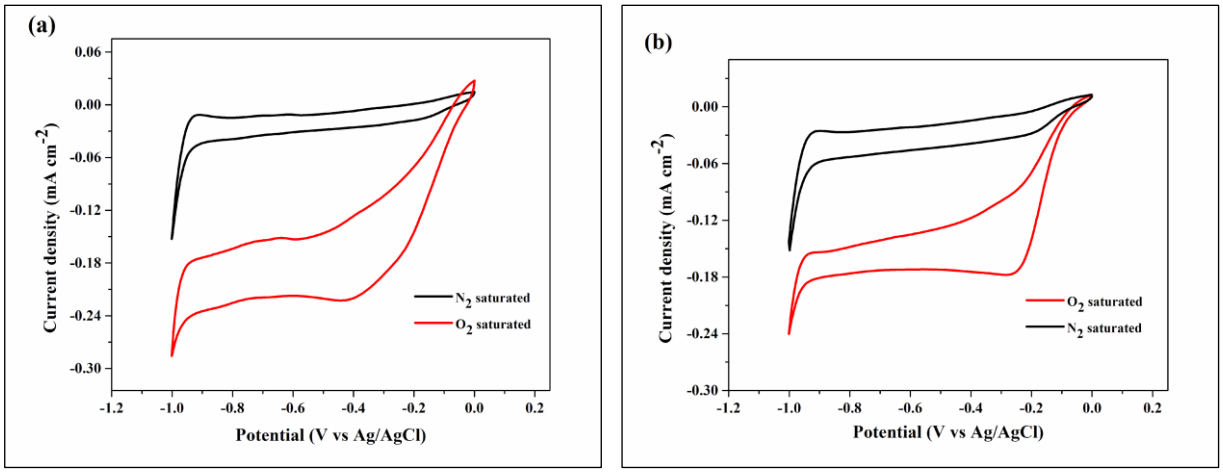


Figure 1. Cyclic voltammogram of (a) MWCNT/Pt and (b) MWCNT/PTFE/Pt electrodes in the O_2 and N_2 gas saturated of 0.1 M KOH electrolyte solution (scan rate: 10 mVs^{-1})

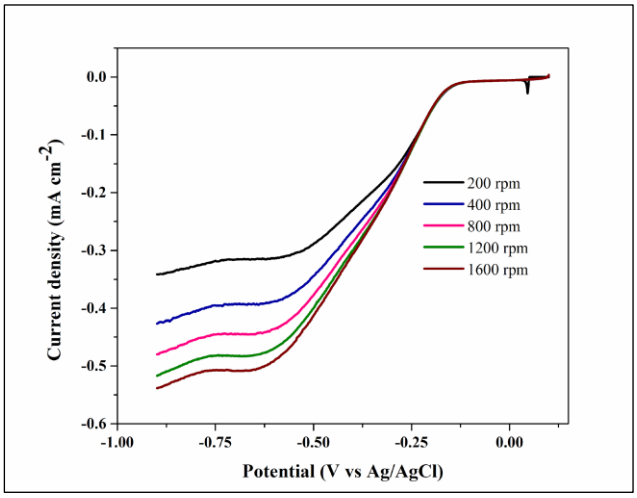


Figure 2. The ORR polarisation curves of MWCNT/PTFE/Pt electrodes in oxygen saturated environment of 0.1M KOH electrolyte with different rotation rate (scan rate: 10 mV s^{-1})

Generally, the ORR reaction may proceed using either two or four electrons transfer mechanism according to the following equation 1 and 2.

$$O_2 + 2H_2O + 4\bar{e} \rightarrow 4OH^- \quad (1)$$

$$O_2 + H_2O + 2\bar{e} \rightarrow HO_2^- + OH- \quad (2)$$

However, the peroxide (HO_2-) species is generated using first reduction process (equation 2) which may yield hydroxide ion (equation 3) [24]; or using a disproportionation reaction to generate hydroxide ions and oxygen gas (equation 4) [25].

$$HO_2^- + H_2O + 2\bar{e} \rightarrow 3OH^- \quad (3)$$

$$HO_2^- \rightarrow \tfrac{1}{2}O_2 + OH^- \quad (4)$$

Therefore, the overall catalytic activity depends on the ORR mechanism namely total number of electron transfer (n). The K-L plot was drawn according to following equation 5 which provides the value of n.

$$1/i = 1/i_k + 1/i_d \quad (5)$$

Whereas, i, i_k and i_d represent current density, kinetic current density, and diffusion limited current density respectively. The i_d can be determined using the Levich equation (equation 6) as follows:

$$i_d = 0.62\ n\ F\ C_{O2}\ D_{O2}^{2/3}\ \upsilon^{-1/6}\ w^{1/2} \quad (6)$$

where, n, F, C_{O2}, $D_{O2}^{2/3}$, $\upsilon^{-1/6}$ and $w^{1/2}$ represent the number of electrons consumed by O_2 molecule, Faraday constant (96485 C mol^{-1}), electrolyte oxygen conc. (1.2 x 10^{-6} mol cm^{-3}), oxygen diffusion coefficient (1.9 x 10^{-5} cm^2 s^{-1}), viscosity of 0.1 M KOH electrolyte solution (0.01 cm^2 s^{-1}) and rotation speed (rad s^{-1}) respectively [21].

Figure 3 shows two straight lines which represent the K-L plot of MWCNT/Pt and MWCNT/PTFE/Pt electrodes. This linear relationship indicates the 1st order reaction with respect to oxygen molecule. However, the values of n (total no. of electrons) are 3.89 and 3.77 for the MWCNT/Pt and MWCNT/PTFE/Pt respectively, calculated from the slop of K-L plot. Therefore, the four electron transfer mechanism was involved in the ORR reaction at the negative potential window. From Figure 4(a), it is clear the values of n, approximately 4 at the potential range -0.9 to -0.2 V. When the potential exceeds -0.2, then n abruptly decreases and gradually reaches zero under 0.0 V. It is significant that no appreciable ORR reaction takes place at zero potential. Figure 4(b), on the other hand shows that the yield % of HO_2^- species is almost at constant value within the same potential range, namely -0.9 to -0.2 V.

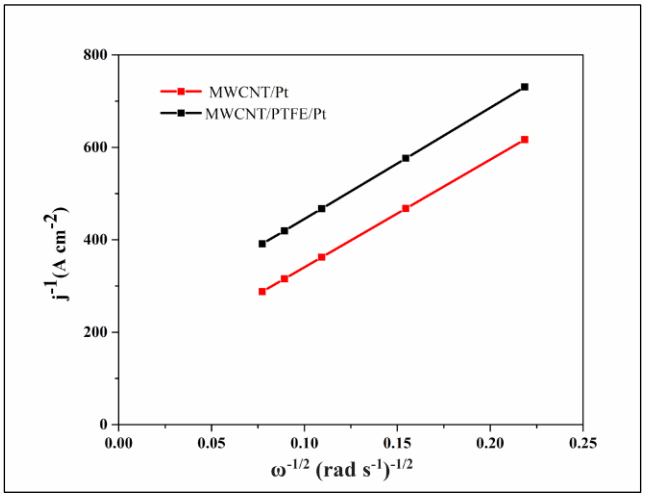


Figure 3. Koutecky-Levich (K-L) plots for MWCNT/Pt and MWCNT/PTFE/Pt electrodes

The performance of electrode stability was examined using the chronoamperometric (CA) analysis. Figure 5 shows the CA curves of the MWCNT/Pt and MWCNT/PTFE/Pt electrode at 0.3V for 7200 sec in 0.1 KOH electrolyte solution. The retention rate refers to the stability of electrode catalyst and is calculated by the ratio of final current density to the initial current density from the chronoamperometric curves [26]. The final current densities of MWCNT/Pt and MWCNT/PTFE/Pt are 0.0063 and 0.0075 mA/cm^2 and their initial current densities are 0.02987 and 0.01452 mA/cm^2, respectively. In addition, the retention rates are 0.211 and 0.517 for the MWCNT/Pt and MWCNT/PTFE/Pt catalyst respectively.These results therefore indicate MWCNT/PTFE/Pt electrode is more stable

owing to its high retention rate compared with the MWCNT/Pt, although it produced slightly less current densities. The PTFE acts as binder between the Pt catalyst and MWCNT supporting materials. This may be helpful for future research on catalyst stability.

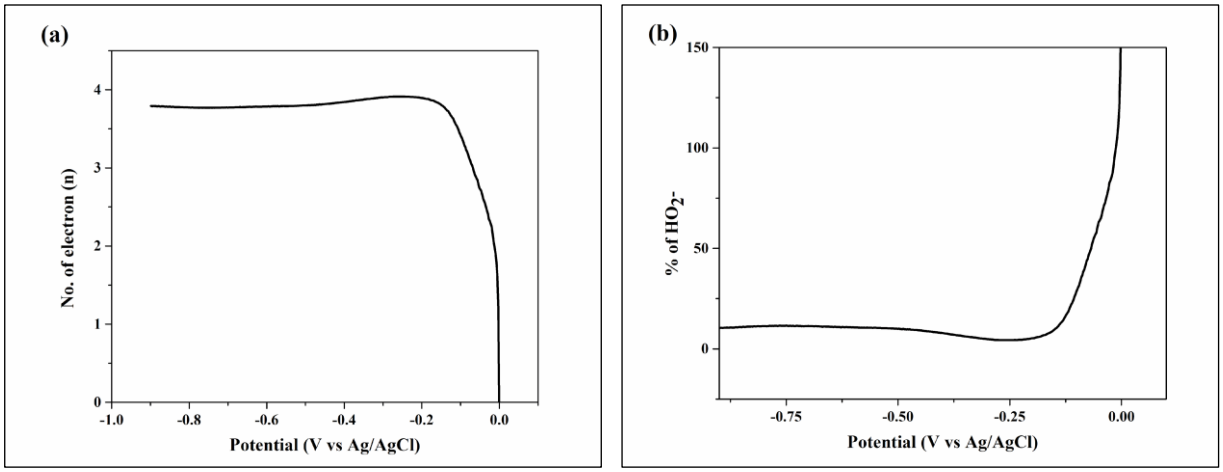


Figure 4. (a) Plot of electrons transfer number (n) *vs* potential and (b) % of HO_2^- vs potential for MWCNT/PTFE/Pt electrode.

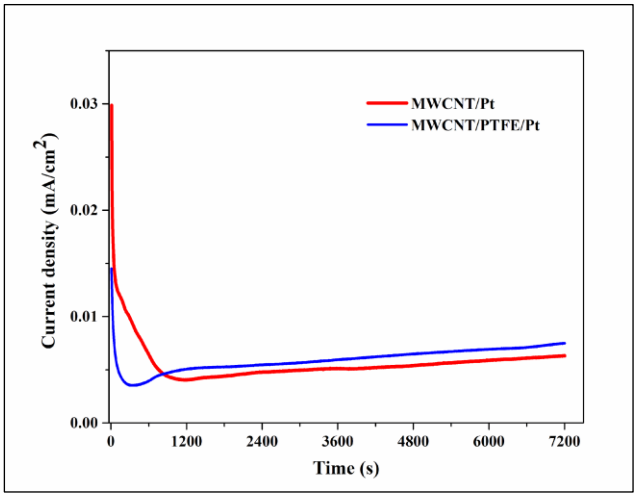


Figure 5. The chronoamperometric curves for synthesised catalyst in 0.1 KOH electrolyte solution at 0.3V

Conclusion

This study synthesised the MWCNT/PTFE/Pt and MWCNT/Pt electrocatalyst and showed promising electrocatalytic activity. It examined electrochemical phenomena at negative potential window (-0.9 V to 0.0 V). The oxygen reduction peak currents were recorded as 0.28 mA cm^{-2} and 0.22 mA cm^{-2} at the potential -0.38 V and -0.22 V respectively for MWCNT/Pt and MWCNT/PTFE/Pt electrode. Four electron transfer mechanism were involved in the ORR reaction. Based on the K-L plot, the values of n are calculated as 3.89 and 3.77 for MWCNT/Pt and MWCNT/PTFE/Pt electrode, respectively. Moreover, the ratios of current densities have recorded as 0.517 and 0.211 for MWCNT/PTFE/Pt and MWCNT/Pt electrode respectively.

Acknowledgement

The authors are indebted to Universiti Kebangsaan Malaysia for providing financial support to undertake this study under Grant AP-2013-010 and TRGS/2/3014/UKM/02/4/1.

References

1. Haque, M. A., Sulong, A. B., Loh, K. S., Majlan, E. H., Husaini, T. and Rosli, R. E. (2017). Acid doped polybenzimidazoles based membrane electrode assembly for high temperature proton exchange membrane fuel cell: A review. *International Journal of Hydrogen Energy*, 42(14): 9156-9179.
2. Paulus, U. A., Wokaun, A., Scherer, G. G., Schmidt, T. J., Stamenkovic, V., Radmilovic, V., Markovic, M. and Ross, P. N. (2002). Oxygen reduction on carbon-supported Pt− Ni and Pt− Co alloy catalysts. *The Journal of Physical Chemistry B*, 106(16): 4181-4191.
3. Kangasniemi, K. H., Condit, D. A. and Jarvi, T. D. (2004). Characterization of vulcan electrochemically oxidized under simulated PEM fuel cell conditions. *Journal of The Electrochemical Society*, 151(4): E125-E132.
4. Inaba, M. (2009). Durability of electrocatalysts in polymer electrolyte fuel cells. *ECS Transactions*, 25(1): 573-581.
5. Li, Q., Aili, D., Hjuler, H. A. and Jensen, J. O. (2016). High temperature polymer electrolyte membrane fuel cells. Springer, Switzerland.
6. Li, W., Liang, C., Qiu, J., Zhou, W., Han, H., Wei, Z., Gongquan, S. and Xin, Q. (2002). Carbon nanotubes as support for cathode catalyst of a direct methanol fuel cell. *Carbon*, 40(5): 787-790.
7. Wang, C., Waje, M., Wang, X., Tang, J. M., Haddon, R. C. and Yan, Y. (2004). Proton exchange membrane fuel cells with carbon nanotube based electrodes. *Nano Letters*, 4(2): 345-348.
8. Wang, X., Li, W., Chen, Z., Waje, M. and Yan, Y. (2006). Durability investigation of carbon nanotube as catalyst support for proton exchange membrane fuel cell. *Journal of Power Sources*, 158(1): 154-159.
9. Kinoshita, K. (1992). Electrochemical oxygen technology. John Wiley & Sons.
10. Kordesch, K. and Simader, G. (1996). Fuel cells and their applications. Weinheim: VCh.
11. Bernardi, D. M. and Verbrugge, M. W. (1992). A mathematical model of the solid- polymer- electrolyte fuel cell. *Journal of the Electrochemical Society*, 139(9): 2477-2491.
12. Toda, T., Igarashi, H., Uchida, H. and Watanabe, M. (1999). Enhancement of the electroreduction of oxygen on Pt alloys with Fe, Ni, and Co. *Journal of the Electrochemical Society*, 146(10): 3750-3756.
13. Hiesgen, R., Eberhardt, D., Aleksandrova, E. and Friedrich, K. A. (2006). Structure and local reactivity of supported catalyst/Nafion® layers studied by in- situ STM. *Fuel Cells*, 6(6): 425-431.
14. Ralph, T. R. and Hogarth, M. P. (2002). Catalysis for low temperature fuel cells. *Platinum Metals Review*, 46(3): 117-135.
15. Yu, X., & Ye, S. (2007). Recent advances in activity and durability enhancement of Pt/C catalytic cathode in PEMFC: Part I. Physico-chemical and electronic interaction between Pt and carbon support, and activity enhancement of Pt/C catalyst. *Journal of Power Sources*, 172(1): 133-144.
16. Zhang, S., Yuan, X. Z., Hin, J. N. C., Wang, H., Friedrich, K. A. and Schulze, M. (2009). A review of platinum-based catalyst layer degradation in proton exchange membrane fuel cells. *Journal of Power Sources*, 194(2): 588-600.
17. Silva, R. A., Hashimoto, T., Thompson, G. E. and Rangel, C. M. (2012). Characterization of MEA degradation for an open air cathode PEM fuel cell. *International Journal of Hydrogen Energy*, 37(8): 7299-7308.
18. Scheibe, B., Borowiak-Palen, E. and Kalenczuk, R. J. (2010). Oxidation and reduction of multiwalled carbon nanotubes—preparation and characterization. *Materials Characterization*, 61(2): 185-191.
19. Berber, M. R., Hafez, I. H., Fujigaya, T. and Nakashima, N. (2015). A highly durable fuel cell electrocatalyst based on double-polymer-coated carbon nanotubes. *Scientific Reports*, 5: 16711.
20. Okamoto, M., Fujigaya, T. and Nakashima, N. (2009). Design of an assembly of poly (benzimidazole), carbon nanotubes, and pt nanoparticles for a fuel- cell electrocatalyst with an ideal interfacial nanostructure. *Small*, 5(6): 735-740.
21. Toh, S. Y., Loh, K. S., Kamarudin, S. K. and Daud, W. R. W. (2016). The impact of electrochemical reduction potentials on the electrocatalytic activity of graphene oxide toward the oxygen reduction reaction in an alkaline medium. *Electrochimica Acta*, 199: 194-203.

22. Soo, L. T., Loh, K. S., Mohamad, A. B., Daud, W. R. W. and Wong, W. Y. (2016). Effect of nitrogen precursors on the electrochemical performance of nitrogen-doped reduced graphene oxide towards oxygen reduction reaction. *Journal of Alloys and Compounds*, 677: 112-120.
23. Wong, W. Y., Daud, W. R. W., Mohamad, A. B., Kadhum, A. A. H., Loh, K. S. and Majlan, E. H. (2013). Recent progress in nitrogen-doped carbon and its composites as electrocatalysts for fuel cell applications. *International Journal of Hydrogen Energy*, 38(22): 9370-9386.
24. Allen, J. B., Parsons, R. and Jordan, J. (1985). Standard potentials in aqueous solution. *Monographs in Electroanalytical Chemistry and Electrochemistry*, Dekker Marcel, Inc., New York–Basel.
25. Maldonado, S. and Stevenson, K. J. (2005). Influence of nitrogen doping on oxygen reduction electrocatalysis at carbon nanofiber electrodes. *The Journal of Physical Chemistry B*, 109(10): 4707-4716.
26. Abdullah, M., Kamarudin, S. K. and Shyuan, L. K. (2016). TiO_2 nanotube-carbon (TNT-C) as support for Pt-based catalyst for high methanol oxidation reaction in direct methanol fuel cell. *Nanoscale Research Letters,* 11(1): 553.

Malaysian Journal of Analytical Sciences, Vol 23 No 1 (2019): 155 - 169
DOI: https://doi.org/10.17576/mjas-2019-2301-19

MALAYSIAN JOURNAL OF ANALYTICAL SCIENCES
Published by The Malaysian Analytical Sciences Society
ISSN 1394 - 2506

EFFECT OF PULSED LASER ABLATION IN WATER ON THE CORROSION BEHAVIOUR AND SURFACE HARDNESS OF STAINLESS STEELS

(Kesan Ablasi Laser Gentian Denyut dalam Air terhadap Kakisan dan Kekerasan Permukaan Keluli Kalis Karat)

Sze Ney Chan[1], Wai Yin Wong[2]*, Walvekar Rashmi[1]*, Abdul Amir Hassan Kadhum[2,3], Mohammad Khalid[4], Kean Long Lim[2]

[1]*School of Engineering,*
Taylor's University Lakeside Campus, Jalan Taylor's, Subang Jaya, 47500, Selangor, Malaysia
[2]*Fuel Cell Institute*
[3]*Department of Chemical and Process Engineering, Faculty of Engineering and Built Environment*
Universiti Kebangsaan Malaysia, 43600 UKM Bangi, Selangor, Malaysia
[4]*Graphene & Advanced 2D Materials Research Group (GAMRG),*
Sunway University, No. 5, Jalan Universiti, Bandar Sunway, 47500 Subang Jaya, Selangor, Malaysia

Corresponding author: waiyin.wong@ukm.edu.my, RashmiGangasa.Walvekar@taylors.edu.my

Received: 13 April 2017; Accepted: 17 April 2018

Abstract

This work presents the use of pulsed fibre laser ablation in water (PLAW) to study the corrosion behaviour and surface hardness of stainless steels. A stainless-steel plate was ablated with a pulsed ytterbrium-doped fibre laser at a power of 4.2 W. The laser-ablated sample was subjected to corrosion testing using electrochemical impedance spectroscopy and potentiodynamic polarisation. The results correlated with surface morphology, X-ray diffraction profiles and Vicker's hardness values. PLAW can enhance the corrosion resistance of stainless steels in both neutral and acidic electrolytes. The corrosion potential of the laser-treated samples was more positive at −126 and −423 mV compared with that of the as-received samples at −209 and −439 mV in neutral and acidic electrolytes, respectively. The inhibition efficiencies of the laser-treated samples in neutral and acidic electrolytes were 98% and 52%, respectively. An improvement in the surface microhardness at a maximum of 8.7% was reported on the fibre laser-ablated stainless steels, thereby demonstrating the efficiency of fibre-laser-assisted PLAW in inhibiting corrosion and improving the hardness of stainless steel.

Keywords: stainless steel, corrosion inhibition, fibre laser, pulse laser ablation in water

Abstrak

Kajian ini bertujuan untuk mengkaji kesan penggunaan teknik ablasi laser gentian denyut dalam air terhadap kakisan dan kekerasan permukaan keluli kalis karat. Dalam kajian ini, plat keluli kalis karat telah diablasi dengan laser gentian denyutan terdop ytterbrium pada kuasa 4.2 W. Seterusnya, plat sampel ini dikaji terhadap kakisan dengan teknik spektroskopi impedans elektrokimia dan polarisasi potentiodinamik. Kajian terhadap morfologi permukaan, profil sinar-X dan kekerasan Viker juga dilakukan. Kajian menunjukkan bahawa teknik ini dapat mempertingkatkan rintangan kakisan keluli kalis karat dalam elektrolit neutral dan asid. Potensi kakisan yang lebih positif diperolehi pada sampel terablasi laser gentian, iaitu pada -126 mV dan -423 mV berbanding dengan sampel kawalan (-209 mV dan -439 mV), masing-masing dalam elektrolit neutral dan asid. Kecekapan perencatan kakisan pada sampel terablasi adalah 98% dalam elektrolit neutral dan 24% dalam elektrolit asid. Sebanyak 8.7% pembaikan dari segi kekerasan mikro pada permukaan sampel terablasi dicapai. Hasil kajian ini berjaya menunjukkan kelebihan penggunaan laser gentian dalam proses ablasi keluli kalis karat dalam meningkatkan ketahanan kakisan dan kekerasan permukaan.

Kata kunci: keluli kalis karat, kecekapan perencatan kakisan, laser gentian, ablasi laser denyut dalam air

Introduction

Metals are essential materials in manufacturing fields; they are used from heavy and small–medium industries to households. Stainless steels are widely used for different applications, such as kitchen utensils, structural beams, chemical vessels, outdoor usage and others, because of its outstanding mechanical and physical characteristic that can withstand harsh environment. Nonetheless, stainless steels, especially AISI 304 stainless steel, are still susceptible to corrosion, particularly due to pitting, crevice corrosion and stress corrosion cracking, when exposed to tensile stresses in a warm chloride environment. Therefore, enhancing the surface properties of the materials is highly required.

Numerous methods have been developed to prevent corrosion, such as protective coatings [1], cathodic protection [2] and corrosion inhibitor use [3]. However, these conventional methods are impractical because they require chemicals, high installation cost and maintenance and are not environmentally friendly [4]. Pulse laser ablation in liquid (PLAL) is a novel, clean and easy approach; it is marketed for its ability to modify the surface composition with high speed, low processing time and easy operation. Hence, PLAL can modify surface properties by enhancing the corrosion resistance, mechanical properties and biocompatibility of the uniform microstructures. Most studies that used this technique for surface modification have been performed using neodymium-doped yttrium aluminum garnet, Nd-YAG laser [5], excimer laser [6] or carbon dioxide, CO_2 laser [7]. Sun et al. [7] fabricated 304 stainless steel blades with chromium-chromium borides, Cr-CrB_2 powders by using CO_2 laser to enhance the microhardness and wear performance of 304 stainless steels; they revealed that the corrosion potentials of all alloyed layers were higher (-0.4306 V) compared with those of non-laser treated metal (-0.4493 V). Yue et al. [8] modified the surface of Ti-6Al-4V alloy using excimer laser to improve the corrosion behaviour for dental applications and demonstrated that the corrosion resistance of the alloys increased by seven times from the original. Laser surface modification can inhibit wear and enhance the fatigue resistance of machine components, because it can control surface morphology up to the submicron or even at a finer depth resolution than the submicron level. Fibre laser is environmentally safe, simple, low cost and practical for use in comparative studies [9, 10].

The current study mainly emphasises on the improvement of corrosion behaviour of ASTM 304/2B stainless steel by utilising the chemical-free technique, namely, PLAL with fibre laser. Surface morphology and hardness were determined using X-ray diffraction (XRD), scanning electron microscopy (SEM) and Vickers hardness test. Electrochemical corrosion testing was conducted to determine corrosion inhibition efficiency by using electrochemical impedance spectroscopy (EIS) techniques and potentiodynamic polarisation (PDP) to study the effect of metal surface modification through PLAL on corrosion resistance.

Materials and Methods

Materials

ASTM 304/2B stainless steel with a 6 cm x 4 cm dimension and a 1.2 mm thickness was the target metal that was used in this study. The composition of the metal steel is shown in Table 1 and is determined *via* arc-spark optical emission spectroscopy (WAS Foundry-Master, Oxford Instruments). Sodium chloride, NaCl (99% purity) was obtained from R&M Chemicals. Hydrochloric acid, HCl (ACS reagent, 37%) was obtained from Sigma-Aldrich. Ethanol, C_2H_5OH (95% purity) and acetone, CH_3COCH_3 (99.5% purity) were obtained from R&M Chemicals for sample cleaning purposes. Alumina suspension with a particle size of 0.05 µm was purchased from Buehler for metal polishing.

Table 1. Nominal chemical composition of metal used in the study (wt.%)

Type of Metal	C	Cr	Ni	Si	Mn	P	S	Fe
ASTM 304/2B stainless steel	0.03	19.2	8.11	0.38	1.12	0.02	<0.005	70.7

Sample preparation
Metal surfaces were initially polished with silicon carbide, SiC abrasive paper (grit size 500–2000 µm), followed by fine polishing using ASTM standard E3-11 0.05 µm alumina suspension. Acetone and ethanol were sequentially used to assist the ultrasonic cleaning on metal surfaces in a Crest 5 Gallon Heated Ultrasonic Cleaner (4HT-1014-6, Crest Ultrasonics Corp.) for 20 minutes at 50 °C. Finally, the metals were air dried prior to laser ablation.

Experimental set up
Laser ablation on stainless steel was performed using a pulsed ytterbrium-doped fibre laser (YLP-1-100-20-20-HC, IPG Photonics) with a wavelength of 1064 nm and a pulse width of ~100 ns. The metal target was fixed on a perspex block that is immersed in water at 5 mm depth from the metal surface using an 800 mL beaker. The experimental set up is shown in Figure 1. An impact diameter of 50 µm was used to ablate the metal targets. During laser ablation, an overlapping rate of 60%, a scanning speed of 2000 mm/s, a power irradiation of 4.2 W and laser pulse number of 100 000 were applied. At the end of the process, the metal surfaces were cleaned with wiper and air dried.

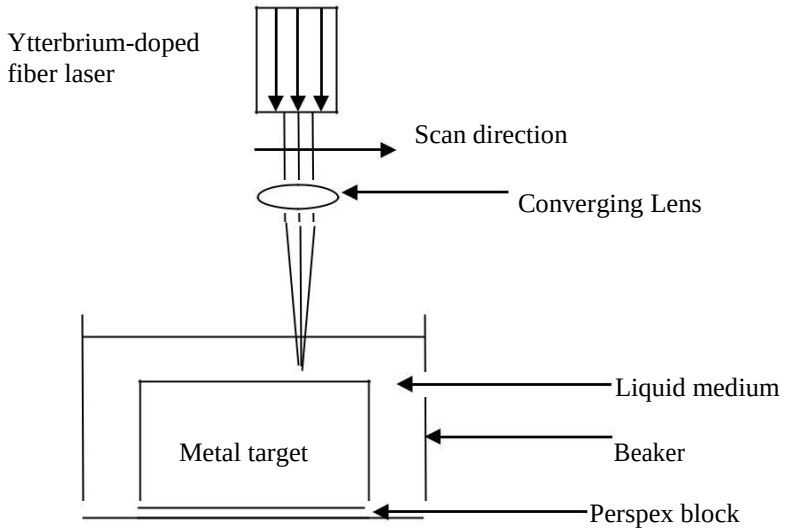


Figure 1. Schematic diagram of PLAL experiment set up

Electrochemical corrosion testing
The corrosion behaviour of the samples was studied using electrochemical testing on a potentiostat (Gamry Instrument Potentiostat/Galvanostat/ZRA model Ref. 600) that includes EIS and PDP. Two corrosion media were employed, including 3.5 wt.% NaCl [11] and 10% HCl [12] at room temperature. A three-electrode set up was used. The sample, as the working electrodewas mounted on the cell with an exposed area of 1.0 cm^2 to the electrolyte. Platinum wire and saturated calomel electrode (SCE) were used as the counter and reference electrodes, respectively. Prior to EIS measurement, the cell was switched to open-circuit-potential mode for 1 hour until potential stabilisation was achieved. EIS was performed at a frequency range of 10 –0.01 Hz that was applied at a signal amplitude perturbation of 10 mV. PDP measurement was conducted subsequently at a potential window of -500 –500 mV versus SCE and a scan rate of 0.5 mV/s.

Sample characterisation
The surface morphologies and elemental composition of the metal surfaces were studied using a field-emission SEM that is equipped with an energy dispersive spectrometer (EDX) (FEI Model, Quanta 400F) with a current beam of 1.1 nA and a beam voltage of 10 kV. A high-angle X-ray diffractometer (Bruker/D8 Advance) that is

equipped with Ni-filtered Cu Kα radiation with an accelerating voltage of 40 kV and a current of 40 mA was used to study the crystallographic structure on the sample surfaces. The grazing incidence technique was used. Microhardness tests were performed using a Vickers hardness tester (Mitutoyo, Model HM-210) to determine the microhardness in accordance with the ASTM B931-03 standard. The hardness of the as-received and laser-treated samples were determined by pressing an indenter onto the sample with a controlled test force *F* of 2 N and a dwell time of 10 s. The size of the indentation was optically determined by measuring two diagonals *d* of the square indentation with a microscope as an integral part of a Vickers tester. Five measurements were obtained for each sample, and the average value of the Vickers number (Hv) was calculated based on equation 1 [13], as follows:

$$\text{Vickers hardness} = 1.844\ F/d^2\ (\text{kgf/mm}^2) \quad (1)$$

Results and Discussion

Corrosion behaviour in NaCl and HCl solutions

Figure 2 presents the Nyquist plots for the samples immersed in 3.5 wt.% NaCl and 10% HCl, which represent neutral and acidic media, respectively. Both Figure 2 (a) and (b) illustrate capacitive loops even though Figure 2(a) shows an incomplete loop because of the high corrosion resistance of stainless steel towards a neutral medium. The presence of capacitive loop indicates that the corrosion of the stainless steel was mainly controlled by a charge transfer process, which is due to the dielectric nature of the metal oxide film on the surface [14]. In both media, laser-treated samples displayed larger capacitive loop compared with the as-received samples. Thus, the improved corrosion resistance is achieved upon laser treatment. Nonetheless, the Nyquist plot obtained in the neutral NaCl medium (Figure 2(a)) did not show perfect semicircles because stainless steel naturally shows higher resistance in the less corrosive neutral medium than in acidic medium. In the acidic medium, complete semicircles were obtained (Figure 2(b)) for both laser-treated and untreated samples. A good time constant (RC) behaviour was recorded at high frequency, which was attributed to the capacitive behaviour of stainless steel. This characteristic was accompanied by inductive behaviour at low frequency. This inductive loop is evident in other studies on metal corrosion in acid, mainly due to the slow changes in the surface microstructures of the samples because of the breakdown of passivation film upon corrosion. The different corrosion behaviours in neutral and acidic media were studied from the impedance and Bode plots (Figure 3). In neutral medium, two RCs were detected from the Bode plots, as shown by two continuous capacitive arcs, indicating the presence of layers of oxide film covering the sample surface. The interfacial processes in the NaCl electrolyte were modelled using the equivalent circuit fitting. The data are displayed in Table 2. The components in the equivalent circuit fitted in NaCl electrolyte include the film resistance (R_f), electrolyte resistance (R_s) and the constant phase element of the surface layer (CPE1). The parameter group (R_{ct}-CPE2) offers data on the mass transport during corrosion attack and charge transfer reaction through the oxide films, representing the capacitance of the double layer and charge transfer resistance, respectively. The increase in Rct values upon laser treatment indicates that the diffusion of ions into the micropores of the oxide film was reduced due to the large resistance to charge transfer, that is, Rf on the film surface.

In acidic medium, only one RC was displayed in the Bode plots, which may be attributed to the less significant effect of the oxide film. This film acts as a protective barrier for corrosion. Hence, the RC also correlated with the Nyquist plots, where much smaller capacitive loops were obtained in a harsh environment. The appearance of the inductive loop also indicated changes in the specimen properties during the corrosion process. The components in the equivalent circuit that was fitted for the HCl solution include the solution resistance (R_s), charge transfer resistance (R_{ct}), constant phase element of double layer (CPE_{dl}) and the inductance parallel with resistance (Figure 2(b)). Herein, we investigated corrosion resistance using the obtained charge transfer resistance. The R_{ct} values obtained on the laser sample showed insignificant improvement of corrosion resistance. In the circuit fitting, the CPE component was used because of the non-ideal capacitive behaviour of the system, in which the surface of the samples was expected to be non-uniform [15]. The impedance of CPE is shown in equation 2 [16], as follows:

$$ZCPE = Y_0^{-1}(jw)^{-n} \quad (2)$$

where Y_0 represents the magnitude of the CPE, and *n* is an exponential term between 0 and 1. The variation of *n* is dependent on the surface roughness of the surface. *n* varied between 0 and 1 for a corrosion system.

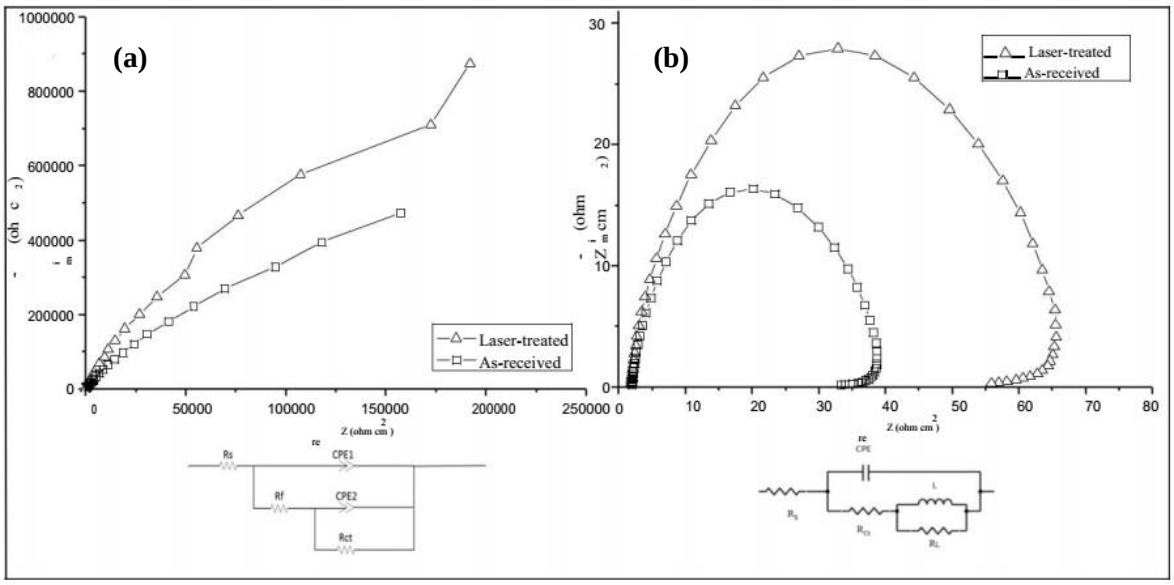


Figure 2. Nyquist plots from impedance spectroscopy for laser treated and as-received stainless steel in (a) 3.5 wt.% NaCl solution and (b) 10% HCl solution with equivalent circuit model

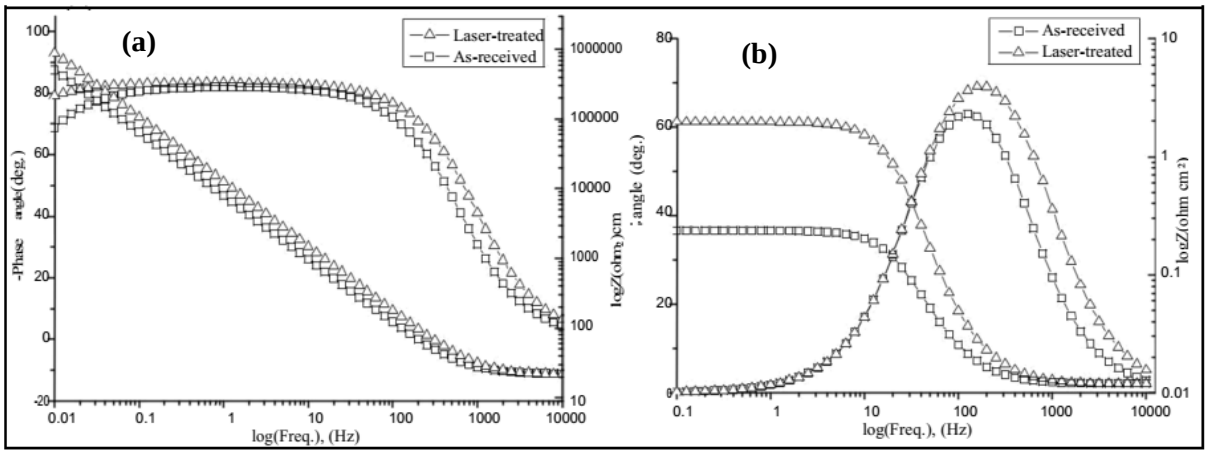


Figure 3. The experimental impedance and phase data in Bode format for stainless steel in (a) 3.5 wt.% NaCl solution and (b) 10% HCl solution and equivalent circuits to fit the impedance data

The inhibition efficiency (I.E.%) was calculated based on equation 3 [17].

$$I.E.\% = (R_{ct} - R^{o}_{ct}) / R_{ct} \times 100\ \% \quad (3)$$

where R_{ct} and R^{o}_{ct} are the charge-transfer resistance that were obtained from the circuit fitting with respect to laser-treated and as-received samples, respectively.

Table 2. Electrochemical impedance parameters and inhibition efficiency of stainless steel in 3.5 wt.% NaCl and 10% HCl solutions

Sample	R_f (Ωcm^1)	R_s (Ωcm^1)	CPE1/ CPE_{dl} /n $Y0(\Omega^{-1}cm^{-2})$	CPE2 /n $Y0(\Omega^{-1}cm^{-2})$	R_{ct} (Ωcm^1)	I.E.%
Stainless Steel in 3.5 wt.% NaCl Solution						
Laser treated	$1.18x10^7$	21.31	$1.45x10^{-5}$ / 0.93	$1.50x10^{-2}$/ 0.96	$1.58x10^6$	98.73
As-received	$2.13x10^6$	21.88	$2.33x10^{-5}$ / 0.92	$9.22x10^4$ / 0.27	$2.00x10^4$	-
Stainless Steel in 10% HCl Solution						
Laser treated	-	1.86	$1.59x10^{-4}$	-	61.96	51.88
As-received	-	1.96	$2.89x10^{-4}$	-	29.81	-

In both solutions, the value of R_{ct} of laser-treated sample appeared to be larger than the as-received sample, which contributed to the increase in the inhibition efficiency. The increased R_{ct} value that was observed on the laser-treated sample signified the improved resistance of the metal surface to electrochemical reaction. The surface-modified layer can restrict chemical reaction between metal surface and corrosive medium [16]. The improvement in corrosion resistance was shown to be more apparent in the less corrosive NaCl environment. Behpour et al. [18] reported that the maximum I.E.% of 304 stainless steel corrosion in 2 M HCl solution by a *Ferula gumosa* (galbanum) extract obtained from 90.7% at 1000 ppm of galbanum extract. In the current study, the highest I.E.% of laser-treated stainless steel in 3.5 wt.% NaCl was 98.7%, which displayed similar efficiency with the abovementioned study.

Figure 4 depicts the PDP of laser-treated and as-received samples in 3.5 wt.% NaCl and 10% HCl at 25 °C. Laser-treated samples showed slightly lower anodic and cathodic potential compared with the as-received sample, illustrating an enhancement in corrosion resistance. This finding may be associated with the presence of protective film, and previous studies have also shown that fine particles of chromium oxide (Cr_2O_3) can be formed when stainless steel is irradiated by laser [19]. Active–passive transitions were particularly observed from the appearance of shoulder at a potential that is exhibits increased positivity to the concerning corrosion potential values in neutral medium. This existence of shoulder indicated the occurrence of a passivation process due to the formation of the oxide layers. This phenomenon is not observed in the acidic medium, which is in good agreement with the obtained impedance results.

The corrosion potential (E_{corr}), corrosion current density (I_{corr}) and pitting potential (E_{pit}) extracted from the polarisation curves are tabulated and shown in Table 3. Notably. the laser-treated sample featured an improved corrosion behaviour compared with the as-received sample. The laser-treated sample exhibited a shift in Ecorr towards a noble direction, and the value of Icorr decreased conversely. Thus, the corrosion resistance of stainless steel is confirmed to be improved after pulse fibre laser ablation in water (PLAW) treatment. This finding correlate with the EIS results, in which laser-treated sample showed a more positive corrosion potential compared with the as-received samples in both corrosive media. Shadangi et al. [20] reported that laser-shock-peened interstitial free steel exhibited increased positive corrosion potential. This improvement in corrosion resistance after laser treatment may be attributed to the changes in microstructure and chemical composition. Furthermore, this laser treatment led to a solid solution strengthening effect, refined microstructure and increased Cr content that is found in stainless steel. Hence, an increasingly homogeneous distribution of Cr in stainless steel sample can be found because of laser treatment with overlapped pulse geometry, which offers an adequate barrier against corrosion. This finding will be discussed in the latter section.

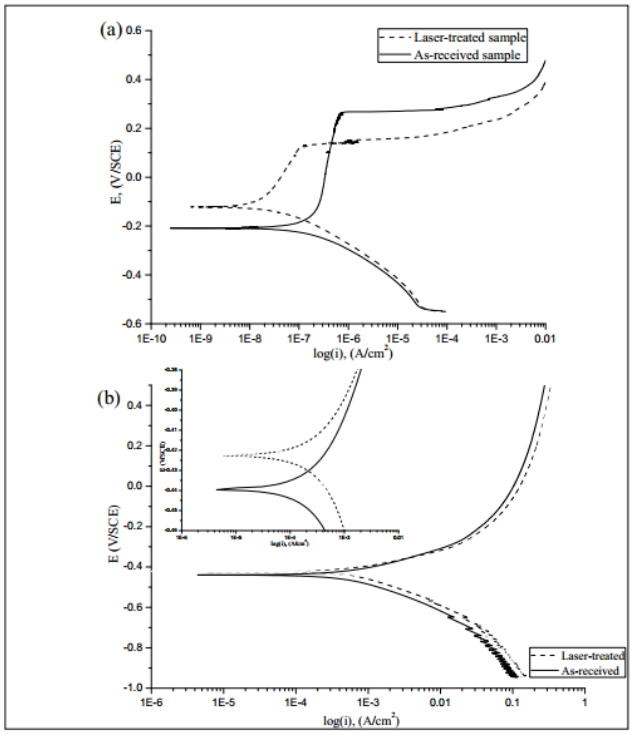


Figure 4. Polarisation curves of the samples immersed in (a) 3.5 wt.% NaCl solution and (b) 10% HCl solution with the blank and laser treated sample; and the inset shows the magnified Tafel region of the polarisation curve

Table 3. The results of potentiodynamic corrosion test of stainless steel in 3.5 wt.% NaCl and 10% HCl solution

Sample	**3.5 wt.% NaCl Solution**			**10% HCl Solution**	
	Corrosion Potential, E_{corr} (mV)	**Pitting Potential, E_{pit} (mV)**	**Corrosion Current Density, I_{corr} ($\mu A/cm^2$)**	**Corrosion Potential, E_{corr} (mV)**	**Corrosion Current Density, I_{corr} (mA/cm^2)**
Laser treated	-126	245.1	48.30	-423	1.47
As-received	-209	259.7	53.80	-439	2.52

A decreased corrosion current density implies a decreased corrosion rate. The laser-treated sample in NaCl solution exhibits a slightly lower I_{corr} than the as-received sample, thereby indicating that laser-treated samples are more unsusceptible to corrosion in neutral solution than untreated samples. The E_{corr} value of laser-treated sample was more positive at 83 mV higher than the as-received stainless steel in NaCl solution. Lu et al. [21] found that the E_{corr} of laser shot-peened stainless steel shifts to an increasingly noble direction from -790 mV to -656 mV in NaCl solution, which is in good agreement with our results. The E_{pit} of the as-received and laser-treated samples was 259.7 and 245.1 mV, as detected in the neutral medium. This finding was mainly attributed to the overlapping geometry that ablated on the sample surface, which altered the microstructure and chemical composition of the steel. An increased E_{pit} of the laser-treated sample indicates a decrease in sensitivity towards corrosion. Hence, the laser-treated sample poses increased corrosion resistance.

Similarly, the E_{corr} of laser treated sample shifted to a more noble value compared with the as-received sample in HCl solution at approximately 16 mV more positive than the original stainless steel. This finding indicated an improvement of stainless steel with passivation ability even in extreme corrosive condition, though the improvement is less apparent in HCl solution compared with that in neutral medium. As reported by Wang et al. [15], the E_{corr} that is obtained with laser-treated stainless steel substantially exceeds values of -504 mV. Nonetheless, the method of corrosion protection that was implemented in the study was cathodic protection, where 304 stainless steels were coupled with $CdTe/TiO_2$ electrode. Hence, this surface modification method can also offer comparative result with common corrosion protection methods, considering that the corrosion potential of laser-treated stainless steel in this work is almost at the same range (−480–402 mV) as that in previous reports on heptamolybdate ions as corrosion inhibitor on stainless steel under almost similar experimental conditions (−480 - 402 mV) [22].

XRD analysis

Figure 5 shows the XRD profiles of the as-received and PLAW-treated samples. The diffraction peaks show the presence of α-Fe (ferrite phase), as indicated by the peaks at 44.88°, 65.5° and 83.1°, the γ-Fe (austenite phase) at 92° and martensitic at 99° in the as-received sample.

Interestingly, the α-Fe peak at 44.88° in as-received sample disappeared after PLAW treatment. The peak from 44.88° to 44.08° slightly shifted after the laser treatment, indicating the formation of a γ-Fe peak upon laser treatment. γ-Fe is usually found as a result of rapid cooling during laser treatment, which is in good agreement with the results of Song et al. [23]. This occurrence is possibly attributed to the quenching effect on the metal surface immediately after laser ablation on the metal surface, thereby causing a change in the phase. Intensity at 67° also increased upon laser ablation, which is attributed to the increase in the surface metal oxide composition of Cr_2O_3 [24, 25]. Upon laser ablation, Cr may chemically react with O to form a passive film of hydrated Cr_2O_3, which is highly adherent and resistant to chemical attack [24]. Whenever the passive film is damaged, passivation immediately occurs [26]. The Cr_2O_3 that are present in laser-treated stainless steels isolate metal from the corrosive environment, thereby retarding corrosion. This process may be a possible reason for the enhanced corrosion resistance of stainless steel under potentiodynamic polarisation measurement. The ferrite network restricted the in-depth growth of pits because of the high Cr content in the austenite stainless steel and decreased the number of MnS inclusions, which are known to be the common sites for corrosion pit initiation.

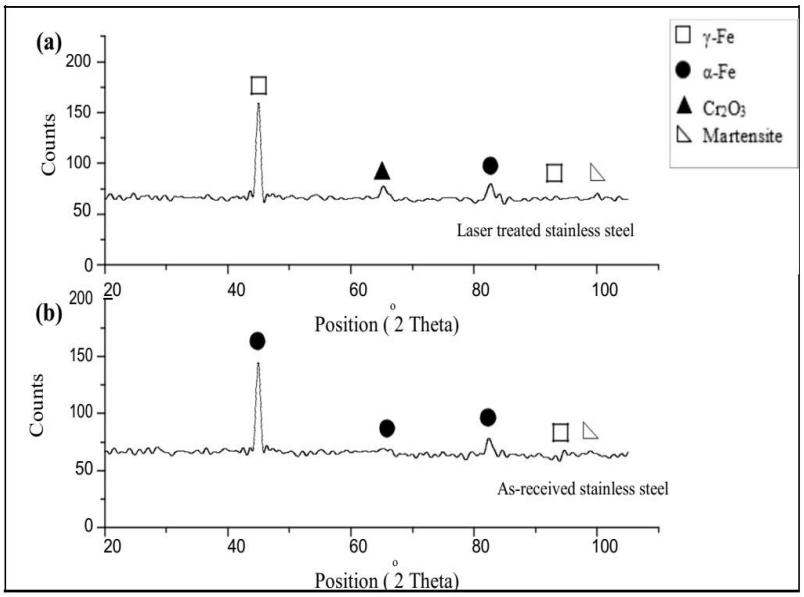


Figure 5. X-ray diffraction profiles of (a) laser treated stainless steel and (b) as-received sample

Surface morphology analysis

Figures 6 and 7 show the SEM images and distribution maps of the major elements of laser-treated and as-received stainless steels. The EDX analysis of laser treated and as-received sample before corrosion is presented in Table 5. The elemental mapping showed the homogeneous distribution of Fe, O, Cr and Mn. The image reveals that the microstructure patterns are consistent with the distribution of the major elements. Uniform chemical composition in the laser-treated area (Figure 6) proved that rapid solidification occurred due to high cooling rate during PLAW treatment. This high cooling rate refined the grain structures. The EDX mapping showed that the Cr and O particles that were evenly distributed over the surface on the laser-treated sample were slightly larger (Figure 8) than those in the as-received sample. Thus, the elemental composition on the surface comprised great amounts of Cr, possibly due to the laser treatment effect. This explanation was confirmed by the XRD results, which showed an increase in the intensity of the Cr_2O_3 peak on the laser-treated sample. This finding was also correlated with the EIS results, which revealed that laser-treated samples were less prone to corrosion.

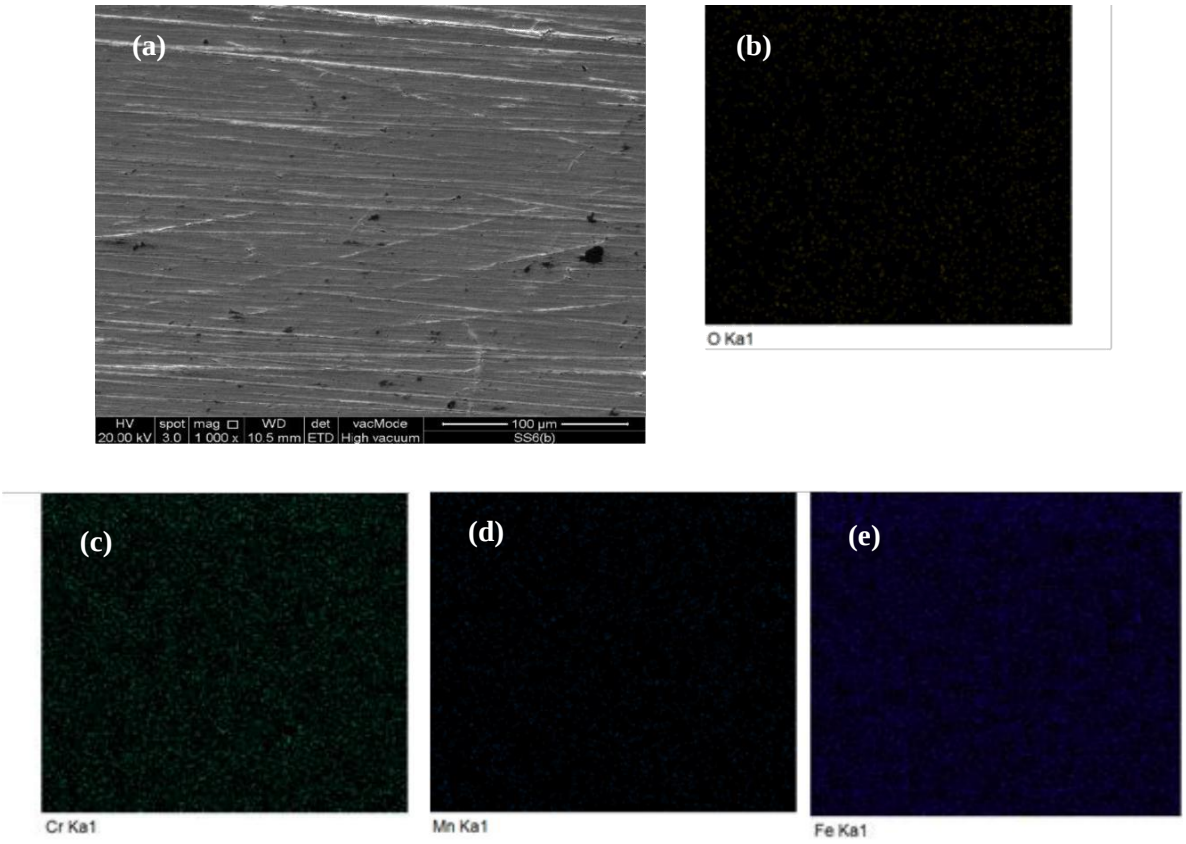


Figure 6. SEM image and distribution of major elements of laser treated sample before corrosion process: (a) SEM image; (b) the distribution map of O; (c) the distribution map of Cr; (d) the distribution map of Mn; (e) the distribution map of Mn and (f) the distribution map of Fe

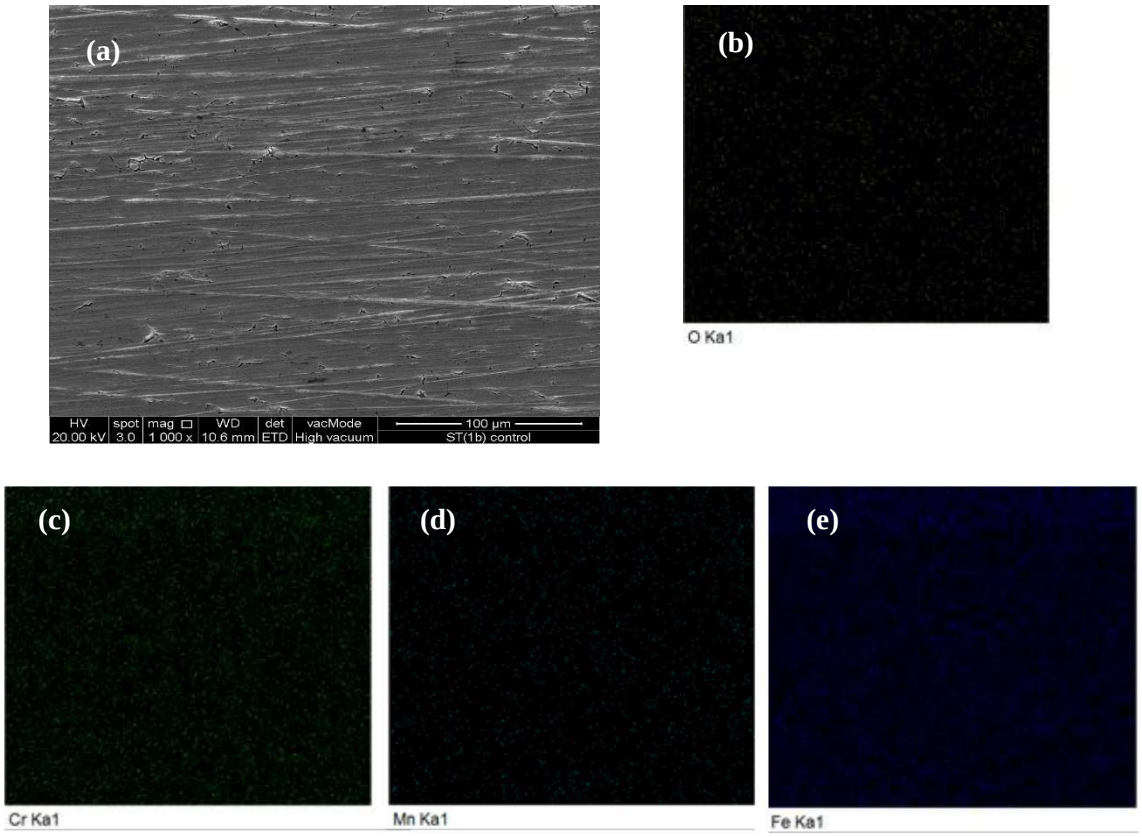


Figure 7. SEM image and distribution of major elements of as-received sample before corrosion process: (a) SEM image; (b) the distribution map of O; (c) the distribution map of Cr; (d) the distribution map of Mn; (e) the distribution map of Mn and (f) the distribution map of Fe

Figure 8 shows the surface morphologies and EDX spectrum of stainless steel samples that were immersed in NaCl solution after PDP measurement. Severe corrosive attack was observed on the as-received sample in NaCl solution, as shown by the strongly damaged surface due to pit formation and deformation (Figure 8(a)). Individual corroded pits clustered together and extended the area of corrosion attack. By contrast, the size of the pits on the laser-treated surface was relatively small. Moreover, the as-received sample showed high roughness and irregularity. Slight changes were observed in the surface morphology of the laser-treated sample, which has been subjected to only 4.2 W of power irradiation and allows less formation of refined grain structure in the laser-modified region.

EDX analysis in Figure 8 and Table 4 shows a little increment in oxide content on the laser-treated sample after corrosion compared with that of the untreated sample. EDX analysis showed that PLAW treatment seemed to result in the formation or thickening of the oxide film on the stainless steel, which increased the corrosion protective ability of stainless steel. Laser treatment on the stainless steel surface was suspected to lead to the refined microstructures through Cr content increase and solid solution strengthening. Hence, PLAW treatment is postulated to produce a homogeneous passive film of hydrated Cr_2O_3. Cr_2O_3 is commonly known as a protective metal oxide that is adherent and acts as a barrier against chemical attack [27]. The higher Cr content by 0.9 wt.% in the laser-treated sample (Figure 9(b)) relative to the as-received sample accounts for the less corroded morphology compared with the severely corroded morphology (Table 4). Figure 9 depicts the surface morphologies and EDX spectrum of samples immersed in HCl solution after PDP measurement. The EDX analysis shown in Figure 9 and Table 4 corresponds to the element distribution, which explains the appearance of few chromium and oxygen signals owing to the overlap geometry that ablated on the stainless steel surface. Thus, a continuous chromium-rich oxide layer

was internally formed. Upon laser treatment, chromium may react with oxygen to form a protective film, Cr_2O_3, which can hinder chemical attack. This behaviour reflects the effectiveness of PLAW treatment on the corrosion resistance of stainless steel in a corrosive environment. This finding is in good agreement with the electrochemical measurement results that were previously discussed.

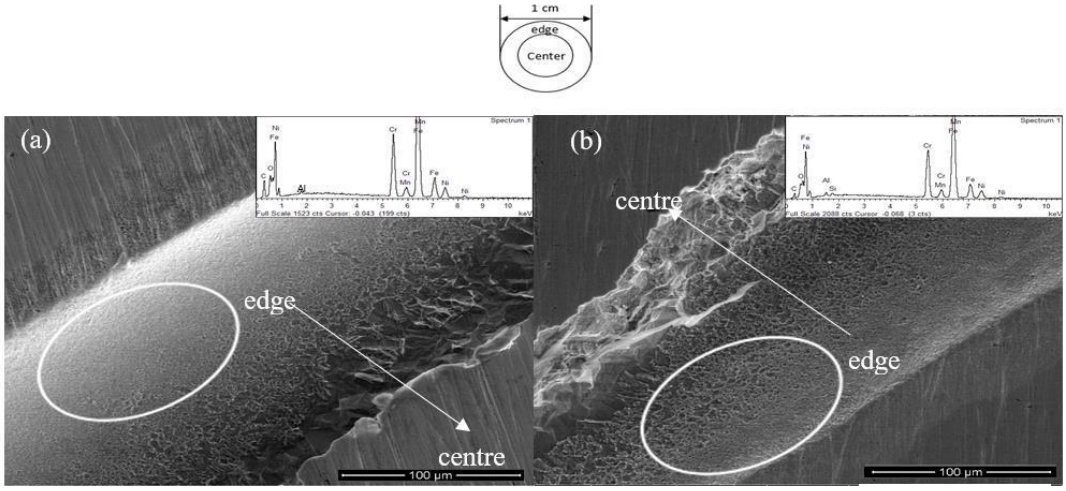


Figure 8. Corroded edge surface of the (a) laser treated and (b) as-received sample with relevant EDX result respectively after immersion in NaCl solution for 1 hour

Table 4. EDX analysis of laser treated and as-received samples before and after corrosion process with respective weight (wt.%)

Sample	**Weight (wt.%)**							
	C	**O**	**Cr**	**Mn**	**Fe**	**Ni**	**Al**	**Si**
Before corrosion process								
Laser treated sample	6.09	1.62	17.24	1.21	65.82	7.24	0.33	0.45
As-received stainless steel	6.02	2.12	17.18	1.19	65.70	6.88	0.46	0.44
After corrosion process (NaCl solution)								
Laser treated sample	14.03	4.04	18.17	1.19	55.26	6.67	0.64	-
As-received stainless steel	6.07	2.65	17.27	1.43	64.61	6.79	0.68	0.48
After corrosion process (HCl solution)								
Laser treated sample	9.75	1.59	19.12	1.50	60.44	7.10	-	0.50
As-received stainless steel	5.36	1.93	17.53	1.44	66.03	7.25	-	0.44

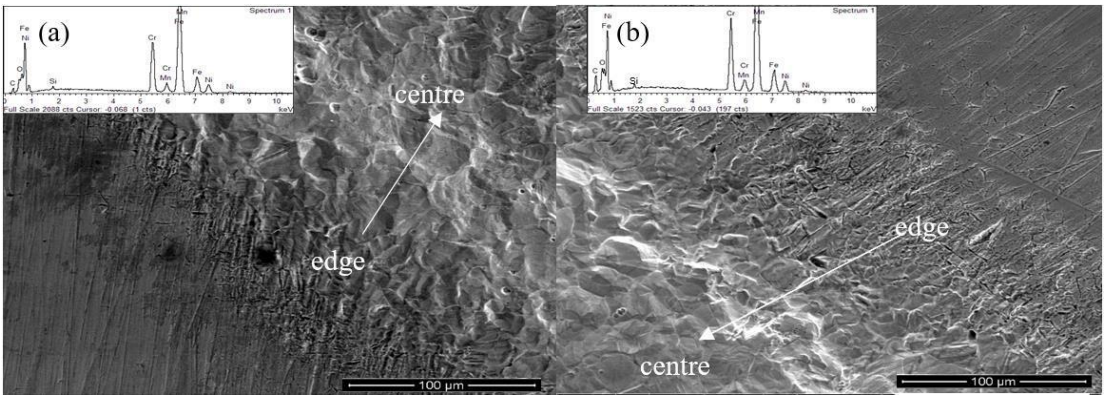


Figure 9. Corroded edge surface of the (a) laser treated and (b) as-received sample with relevant EDX result respectively after immersion in 10% HCl solution for 1 hour

The analyses demonstrated that laser treatment prominently improved the corrosion resistance of stainless steel without the use of coating or the addition of a corrosion inhibitor. This improvement is possibly associated with one major reason—a chemical reaction occurred on the metal surface, which resulted in metal oxide formation that passivated the corrosion and hardened the metal surface.

Vickers hardness test

Vickers hardness test was performed for the as-received and laser-treated stainless steel. Currently, limited works have reported on the relationship between metal corrosion resistance characteristics and metal hardness. Solid solution formation upon surface modification processes, such as laser treatment, strengthens the effect of mechanical strength can hence provide some insight on corrosion behaviour. The mean of microhardness of the stainless steel as a function of depth is illustrated in Figure 10. The microhardness of laser-treated sample increases and then continuously decline along the depth from the surface. The surface microhardness (196.94 Hv) of laser-treated sample was slightly improved by 8.7% from the as-received sample (181.2 Hv). This finding can be attributed to the martensite formation on the surface, and the hardness was significantly higher than the core original material due to the rapid cooling effect of the PLAL treatment [28]. This gradual enhancement was only apparent at <400 µm depth from the surface. The microhardness profile demonstrated that the hardness value reached its maximum only at a 100 µm depth from the surface. PLAW only induced slight work hardening due to low heating and high cooling rate on the surface. Hence, the microhardness only showed evident improvement at the upper layer of the stainless steel. This finding may also be due to the presence of coarse microstructure in the laser-treated sample because of the high cooling and low heating rate that were regulated from the PLAW treatment using ultra-pure water as a liquid medium. The microstructure of the laser-treated layer did not considerably change after subsequent laser ablation process in the PLAW treatment, and hence, the improvement in microhardness was not noteworthy. However, this slight improvement of microhardness can be attributed to the compressive residual stress that was induced by PLAW treatment, which increased the yield strength and surface microhardness in the near-surface layer of the stainless steel.

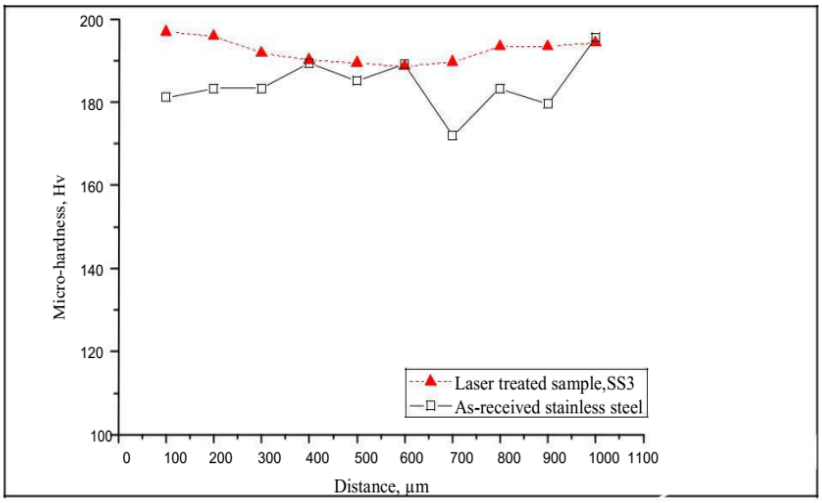


Figure 10. Microhardness profile as a function of depth from the surface on the cross-sectional plane of stainless steel sample

Conclusion

In this study, ASTM 304/2B stainless steel was subjected to PLAL treatment using fibre laser to study the effect of the treatment on corrosion resistance and surface and hardness properties of the steel. The influence of corrosion resistance on the surface modification revealed that stainless steel showed significant improvement, as evidenced by the 83 mV higher Ecorr value from that of the as-received sample and 98% inhibition efficiency in 3.5 wt.% NaCl solution. The improvement on the corrosion resistance was less remarkable in acidic medium. The microhardness of stainless steel slightly improved by 8.7% compared with that of the as-received metal due to the low laser ablation power applied. Hence, we conclude that fibre laser can be used for laser ablation to enhance the corrosion resistance and surface hardness of steel.

Acknowledgement

This work was substantially supported by the Universiti Kebangsaan Malaysia (GGPM-2016-054 & GGPM-2017-043). The authors are grateful to the Center for Research and Instrumentation, UKM for the support on the X-ray diffraction (XRD) characterisation of metal plate. The authors would like to thank Amrec Sirim Berhad for the support on the Vicker's Hardness Test.

References

1. Figueira, R., Silva, C. J. and Pereira, E. (2015). Organic–inorganic hybrid sol–gel coatings for metal corrosion protection: A review of recent progress. *Journal of Coatings Technology and Research*, 12(1): 1-35.
2. Chen, X., Li, X., Du, C. and Cheng, Y. (2009). Effect of cathodic protection on corrosion of pipeline steel under disbonded coating. *Corrosion Science*, 51(9): 2242-2245.
3. Musa, A. Y., Kadhum, A. A. H., Mohamad, A. B., Daud, A. R., Takriff, M. S., Kamarudin, S. K., and Muhamad, N. (2009). Stability of layer forming for corrosion inhibitor on mild steel surface under hydrodynamic conditions. *International Journal Electrochemical Science*, 4: 707-716.
4. Aparicio, M., Jitianu, A., Rodriguez, G. Degnah, A., Al-Marzoki, K., Mosa, J. and Klein, L.C. (2016). Corrosion protection of AISI 304 stainless steel with melting gel coatings. *Electrochimica Acta*, 202: 325-332.
5. Chong, P. H., Liu, Z., Wang, X. Y. and Skeldon, P. (2004). Pitting corrosion behaviour of large area laser surface treated 304L stainless–steel. *Thin Solid Films*, 453-454: 388-393.
6. Khalfaoui, W., Valerio, E., Masse, J. E. and Autric, M. (2010). Excimer laser treatment of ZE41 magnesium alloy for corrosion resistance and microhardness improvement. *Optics and Lasers in Engineering*, 48(9): 926-931.

7. Sun, G., Zhang, Y., Zhang, M., Zhou, R., Wang, K., Liu, C. and Luo, K. (2014). Microstructure and corrosion characteristics of 304 stainless steel laser-alloyed with Cr–CrB_2. *Applied Surface Science,* 295: 94-107.
8. Yue, T. M., Yu, J. K., Mei, Z. and Man, H. C. (2002). Excimer laser surface treatment of Ti–6Al–4V alloy for corrosion resistance enhancement. *Materials Letters,* 52(3): 206-212.
9. Boutinguiza, M., del Val, J., Riveiro, A., Lusquiños, F., Quintero, F., Comesaña, R. and Pou, J. (2013). Synthesis of titanium oxide nanoparticles by ytterbium fiber laser ablation. *Physics Procedia,* 41: 787-793.
10. Pacquentin, W., Caron, N. and Oltra, R. (2015). Effect of microstructure and chemical composition on localized corrosion resistance of a AISI 304L stainless steel after nanopulsed-laser surface melting. *Applied Surface Science,* 356: 561-573.
11. Lawrence, S. K., Adams, D. P., Bahr, D. F. and Moody, N. R. (2016). Environmental resistance of oxide tags fabricated on 304L stainless steel via nanosecond pulsed laser irradiation. *Surface and Coatings Technology,* 285: 87-97.
12. Ren, Y., Luo, Y., Zhang, K., Zhu, G. and Tan, X. 2008. Lignin terpolymer for corrosion inhibition of mild steel in 10% hydrochloric acid medium. *Corrosion Science*, 50: 3147-3153.
13. ASTM E92 Standard Test Method for Vickers Hardness of Metallic Materials. (2015). Access from http://www.wmtr.com/en.astme92.html.
14. El Maghraby, A. A. (2009). Corrosion inhibition of aluminum in hydrochloric acid solution using Potassium Iodate Inhibitor. *The Open Corrosion Journal,* 2:189-196.
15. Wang, Q.-Y., Wang, X.-Z., Luo, H. and Luo, J.-L. (2016). A study on corrosion behaviors of Ni–Cr–Mo laser coating, 316 stainless steel and X70 steel in simulated solutions with H2S and CO2. *Surface and Coatings Technology,* 291: 250-257.
16. Wang, X.-T., Wei, Q.-Y., Zhang, L., Sun, H.-F., Li, H. and Zhang, Q.-X. (2016). CdTe/TiO_2 nanocomposite material for photogenerated cathodic protection of 304 stainless steel. *Materials Science and Engineering: B,* 208: 22-28.
17. Musa, A. Y., Kadhum, A. A. H., Mohamad, A. B., Rahoma, A. A. B. and Mesmari, H. (2010). Electrochemical and quantum chemical calculations on 4,4-dimethyloxazolidine-2-thione as inhibitor for mild steel corrosion in hydrochloric acid. *Journal of Molecular Structure,* 969(1-3): 233-237.
18. Hanza, A. P., Naderi, R., Kowsari, E. and Sayebani, M. (2016). Corrosion behavior of mild steel in H2SO4 solution with 1, 4-di [1′-methylene-3′-methyl imidazolium bromide]-benzene as an ionic liquid. *Corrosion Science,* 107: 96-106.
19. Behpour, M., Ghoreishi, S., Kashani, M. K. and Soltani, N. (2009). Inhibition of 304 stainless steel corrosion in acidic solution by *Ferula gumosa* (galbanum) extract. *Materials and Corrosion,* 60(11): 895-898.
20. Shadangi, Y., Chattopadhyay, K., Rai, S. B. and Singh, V. (2015). Effect of LASER shock peening on microstructure, mechanical properties and corrosion behavior of interstitial free steel. *Surface and Coatings Technology,* 280: 216-224.
21. Lu, J. Z., Qi, H., Luo, K. Y., Luo, M. and Cheng, X. N. (2014). Corrosion behaviour of AISI 304 stainless steel subjected to massive laser shock peening impacts with different pulse energies. *Corrosion Science,* 80: 53-59.
22. Ait Albrimi, Y., Ait Addi, A., Douch, J., Souto, R. M. and Hamdani, M. (2015). Inhibition of the pitting corrosion of 304 stainless steel in 0.5M hydrochloric acid solution by heptamolybdate ions. *Corrosion Science,* 90: 522-528.
23. Song, B., Dong, S., Liu, Q., Liao, H. and Coddet, C. (2014). Vacuum heat treatment of iron parts produced by selective laser melting: Microstructure, residual stress and tensile behavior. *Materials & Design (1980-2015),* 54: 727-733.
24. Cui, C., Hu, J., Liu, Y., Gao, K. and Guo, Z. (2008). Morphological and structural characterizations of different oxides formed on the stainless steel by Nd:YAG pulsed laser irradiation. *Applied Surface Science,* 254(20): 6537-6542.
25. Cui, C., Hu, J., Liu, Y. and Guo, Z. (2008). Microstructure evolution on the surface of stainless steel by Nd:YAG pulsed laser irradiation. *Applied Surface Science,* 254(11): 3442-3448.
26. Llewellyn, D. and Hudd, R. (1998). Steels: metallurgy and applications: Butterworth-Heinemann.ASTM E92 Standard Test Method for Vickers Hardness of Metallic Materials. (2015). Access from http://www.wmtr.com/en.astme92.html.

27. Li, D., Feng, Y., Bai, Z., Zhu, J. and Zheng, M. (2007). Influence of temperature, chloride ions and chromium element on the electronic property of passive film formed on carbon steel in bicarbonate/carbonate buffer solution. *Electrochimica Acta,* 52(28): 7877-7884.
28. Marcuci, J. R. J., Souza, E. C. d., Camilo, C. C., Di Lorenzo, P. L. and Rollo, J. M. D. d. A. (2014). Corrosion and microstructural characterization of martensitic stainless steels submitted to industrial thermal processes for use in surgical tools. *Revista Brasileira de Engenharia Biomédica,* 30: 257-264.

Malaysian Journal of Analytical Sciences, Vol 23 No 1 (2019): 170 - 181
DOI: https://doi.org/10.17576/mjas-2019-2301-20

MALAYSIAN JOURNAL OF ANALYTICAL SCIENCES
Published by The Malaysian Analytical Sciences Society
ISSN 1394 - 2506

EFFECT OF Cu-PUROLITE A400 RESIN ON ADSORPTION OF NITRATE AND NITRITE IN WASTEWATER TREATMENT

(Kesan Resin Purolit A400-Cu Terhadap Penjerapan Nitrat dan Nitrit dalam Rawatan Air Sisa)

Fatimah Batubara[1], Chairani Selviani[1], Muhammad Turmuzi[1], Edy Herianto Majlan[2,3]*

[1]*Chemical Engineering Department, Faculty of Engineering,*
Universitas Sumatera Utara, Medan, 20155 Sumatera Utara, Indonesia
[2]*Fuel Cell Institute,*
Universiti Kebangsaan Malaysia, 43600 UKM Bangi, Selangor, Malaysia
[3]*Environmental Engineering Department,*
Faculty of Environmental Engineering,
Institut Teknologi Yogyakarta, D.I Yogyakarta, 55171, Indonesia

**Corresponding author: edyhm71@gmail.com*

Received: 13 April 2017; Accepted: 17 April 2018

Abstract

The exceedance of nitrate and nitrite concentrations over the water standard quality has caused potential human health dangers such as blue baby syndrome and the growth of aquatic plants (eutrophication). In this work, a Purolite A400 anion exchange resin impregnated by Cu (Purolite A400-Cu) is used to remove nitrate and nitrite in wastewater. High saturation capacities of 0.76 mg N/g and 0.88 mg N/g-nitrate and 0.10 mg N/g and 0.11 mg N/g-nitrite are obtained from Purolite A400 and Purolite A400-Cu. Scanning electron microscope measurement shows that the surface of Purolite A400-Cu is rough due to other deposited materials that originate from Cu deposition. Energy dispersive spectroscopy measurement indicates that the increase in adsorption is due to Cu impregnation with the addition of a positive surface charge on the resin by Cu. The adsorption capacities of nitrate and nitrite decrease with increases in sulphate, phosphate and chloride concentrations. Data are obtained from a fixed-bed column using the Thomas equation model. The breakthrough curve shows the C_t/C_0 ratio values in Purolite A400 and Purolite A400-Cu. Large C_t/C_0 values of 0.55 and 0.52-nitrate and 0.48 and 0.03-nitrite are obtained from Purolite A400 and Purolite A400-Cu.

Keywords: nitrite adsorption, nitrate adsorption, Purolite A400 resin, wastewater treatment, Cu impregnation

Abstrak

Kepekatan nitrat dan nitrit yang melebihi piawaian kualiti air akan berpotensi membahayakan kesihatan manusia, sindrom biru-bayi dan pertumbuhan tumbuhan akuatik (eutrofikasi). Purolit A400 resin pertukaran anion yang impregnasi Cu (Purolite-Cu) digunakan untuk mengurangkan kandungan nitrat dan nitrit dalam air sisa. Kapasiti ketepuan tertinggi diperolehi pada Purolit dan Purolit-Cu masing-masing 0.76 mg N/g; 0.88 mg N/g-nitrat dan 0.10 mg N/g; 0.11 mg N/g-nitrit. Pengukuran dengan menggunakan spektrometri serakan tenaga (EDS) membuktikan bahawa peningkatan penjerapan adalah disebabkan oleh impregnasi Cu dengan penambahan caj permukaan positif pada resin oleh logam Cu. Kapasiti penjerapan nitrat dan nitrit menurun apabila kepekatan sulfat, fosfat dan klorida bertambah. Data diperolehi daripada turus lapisan penjerap tetap menggunakan model persamaan Thomas. Lengkung bulus menunjukkan nilai nisbah C_t/C_0 dalam Purolit dan Purolit-Cu. Nilai Ct/C_0 terbesar diperoleh pada Purolit dan Purolit-Cu masing-masing 0.55 & 0.52-nitrat dan 0.48 & 0.03-nitrit.

Kata kunci: penjerapan nitrit, penjerapan nitrat, resin Purolit A400, rawatan air sisa, impregnasi Cu

Introduction

Nitrogen is an essential element for all living things and can be oxidised to nitrate and nitrite. The content of nitrates and nitrites in water bodies significantly affects water quality. Nitrates are stable and water-soluble ions that have a low tendency of adsorption or co-precipitation [1]. Nitrate concentrations that exceed the water quality standard are caused using nitrate-containing fertilisers and human and animal wastes that are not pre-treated [2]. The consequences of nitrate contamination are potential human health hazards such as methemoglobinemia in infants (called blue baby syndrome) and crop growth (eutrophication) [3]. Therefore, nitrate and nitrite should be removed to enable the produced pollutant load to meet the determined minimum concentration standard.

The processing methods for nitrates and nitrites can be physical, chemical or biological. Physical techniques include reverse osmosis [4], ion exchange [5], catalyst reduction [6], electro-dialysis [7] and carbon activation [8]. Chemical methods include chemical denitrification [9]. Biological techniques include thermophilic nitrification–denitrification [10], ion exchange membrane bioreactor [11] and microbial denitrification [12]. A simple, cost effective and easily implemented adsorption method should be selected to achieve significant efficiency in the uptake of ions and remove secondary pollutants [13]. Adsorption through ion exchange is an efficient method of removing several oxy-anions because adsorbents can be regenerated and reused [14]. The adsorbents, which are also natural resins, applied by the research institute, are modified zeolites with the addition of H_2SO_4 [15], amine group quarter-modified chitosan beads [14] and alloy Zr(IV) with sugar beet pulp [16]. Synthetic resins used in nitrate and nitrite removal are strong base anion exchange resins with considerable adsorption capacity, such as ion-exchange resin Dowex 21K XLT with modified ferrous metals [17], Purolite A100 [18], Purolite A520E [19-20], A-250 IXR [21], Purolite A300 [20] and Indion NSSR [22].

Complementary ions, such as chloride, sulphate and phosphate, that are present in influent solutions can reduce the efficiency of nitrate and nitrite removal. The effect of complementary ions on nitrate and nitrite removal depends on their amount of charge. One-charged chloride ions do not affect removal efficiency, whereas sulphate ions with more than one charge significantly reduce removal efficiency. In previous studies that analysed the effects of complementary ions [20], an increase in the concentration of sulphate complementary ions on Purolite A300 resins decreased the nitrate removal efficiency in modified and unmodified resin types. According to [17], a low concentration of complementary phosphate ions reduces nitrate adsorption capacity, and complementary chloride ions slightly decrease nitrate adsorption capacity with same charge amounts of nitrate ions. Reference [23] indicated that the sequence of anion exchange resin decreases in the sequences of $SO_4^{2-} > NO_3^- > Cl^- > HCO_3^-$.

A metal impregnation method is applied to increase the adsorption capacity of an anion exchange resin and enlarge the positive charge of the resin surface [24]. The impregnated resin increases the attraction between the positively charged metal ion and negatively charged nitrate and nitrite ions, thereby resulting in an increase in adsorption power. Reference [17] showed Fe impregnation in Dowex 21K XLT resin and obtained maximum nitrate adsorption capacities of 27.6 and 75.3 mg N/g in Dowex and Dowex-Fe. Metal impregnation has also been conducted on resins and natural adsorbents, such as Zr(IV) in sugar beet pulp [16], Fe(III) in limestone [25] and Mn(II) in zeolites [26].

In this study, nitrate and nitrite removal was performed using a Purolite A400 resin adsorbent modified with copper (Cu) metal. The nitrate and nitrite adsorption capacities were determined using Purolite A400 and Purolite A400-Cu in fixed-bed columns. The C_t/C_0 ratio values were determined on the effect of the initial concentration of nitrate + nitrite mixture and the concentration of complementary ions in the Thomas equation model.

Materials and Methods

Purolite A400 resin impregnation

Purolite A400 resin is a strong base anion exchange resin that takes the form of faded yellow spherical beads with a particle size of 300–1200 μm and a density of ± 1.08. The resin comprises a cross-linked polystyrene polymer structure with divinylbenzene and has a quaternary ammonium functional group of 1. Purolite A400 resin was obtained from Purolite Pt. Ltd., Singapore. In this resin, the chloride ion is exchanged with another anion [27].

Purolite A400 resin was impregnated with Cu to enlarge its adsorption capacity. Purolite A400 resin (10 g) was mixed into 1 L $CuCl_2.2H_2O$ solution and then stirred for 1 hour at 120 rpm. The pH was increased to 8.0 by adding a 1 M NaOH solution that was stirred for 1 hour at 30 rpm. The resin was filtered and washed with distilled water and then oven-dried for 24 hours at ± 45 °C [17].

Influent solution

Synthetic wastewater was obtained from the crystalline powders of EMSURE $NaNO_3$ and EMSURE $NaNO_2$ dissolved with distilled water with 50 and 5 mg/L concentrations, respectively. The concentrations were 60, 90 and 150 mg/l or 1:1 for the study of the effect of the complementary ions obtained from the crystal powder of EMSURE Na_2SO_4, EMSURE Na_3PO_4 and EMSURE NaCl with determined concentrations for each complementary ion of 45 and 75 mg/l and for the study of the effect of the initial concentration of $NaNO_3$ + $NaNO_2$ mixtures.

Nitrate and nitrite analysis

The final concentration (C_t) of nitrate was analysed by a UV analyser Secomam RS232 Pastel tool [28], and the nitrite content was analysed by Cary 50 Conc UV-visible spectrophotometry-variant at a wavelength of 543 nm [29, 30].

Fixed-bed column study

The fixed-bed column used a chromatograph column made of Pyrex tube with a diameter of ± 2.0 cm, height of ± 20 cm, anion resin height in a column of 15 cm and an influent rate to the column at 10 mL/min. The influent wastewater was pumped using a 12 V DC peristaltic pump with downflow through an infusion hose, I.V. needle 21 G x 11/2 and AC–DC adapter NAD-012 Namichi. The effluent wastewater samples were collected every 10 minutes, and the nitrate and nitrite contents were analysed using a UV analyser Secomam and a UV-visible spectrophotometer.

The adsorption capacities of removed nitrate and nitrite (mg N/g) from the influent solution that passed through the column is expressed in q, and q_{total} (total of adsorbed nitrate) in the fixed-bed column is the area under the absorbed nitrate concentration curve C_{ad} ($C_{ad} = C_o - C_t$) (mg/l) against the effluent time (t, min) and calculated by equation 1 [19, 31].

$$q_{total} = \frac{Q}{1.000}\int_{t=0}^{t=total} C_{ad}\,dt = \frac{Q}{1.000}\int_{t=0}^{t=total} (C_0 - C_t)dt \quad (1)$$

The equilibrium adsorption capacity (mg N/g) is calculated by equation 2.

$$q_{eq} = \frac{q_{total}}{w} \quad (2)$$

where w is the mass of the adsorbent (g) used in the fixed-bed column.

Adsorption model

The Thomas model used in the fixed-bed column is calculated by equation 3 as follows [32]:

$$\ln\left[\left(\frac{C_o}{C_t}\right) - 1\right] = \left(\frac{k_{Th} q_0 m}{Q}\right) - \left(\frac{k_{Th} q_0 V_{eff}}{Q}\right) \quad (3)$$

where V_{eff} = volume of effluent and V_{eff} = Q.t. Thus, equation 4 can be written as follows [19]:

$$\ln\left[\left(\frac{C_o}{C_t}\right) - 1\right] = \left(\frac{k_{Th} q_0 m}{Q}\right) - k_{Th} C_0 t \quad (4)$$

where k_{Th} = Thomas rate constant (mL / min mg), q_o = maximum solute concentration (nitrate) in solid phase (mg N/g), m = mass of adsorbent in column (g), Q = volumetric flow rate (mL/min), C_o = inlet nitrate concentration (mg

N/L), C_t = concentration of nitrate outlet at time t (mg N/L) and t = filtration time (min). k_T and q_o values are determined from the slope and intercept in the linear line plot, which is ln (C_0/C−1) against time t.

Results and Discussion

Characteristics of anion exchange resin

The morphology and elemental composition of Purolite A400 and Purolite A400-Cu resins were analysed using a scanning electron microscope (SEM)-Jeol 6510-LA and an energy dispersive spectroscopy (EDS)-Jeol 6510-LA. The test results are shown in Figures 1 and 2. The surface of Purolite A400 resin is smooth, as shown in Figure 1a, whereas the surface of Purolite A400-Cu resin is rough, as shown in Figure 1b. This finding is due to the presence of other deposited materials on the surface that originated from Cu deposition. Furthermore, the surface of Purolite A400 resin impregnated with Purolite A400-Cu contains Cu ion. The concentration value of impregnated Cu ion impregnated is presented in Table 1. As shown in Figure 2, the content of Cu in Purolite A400-Cu resin is 19.34%.

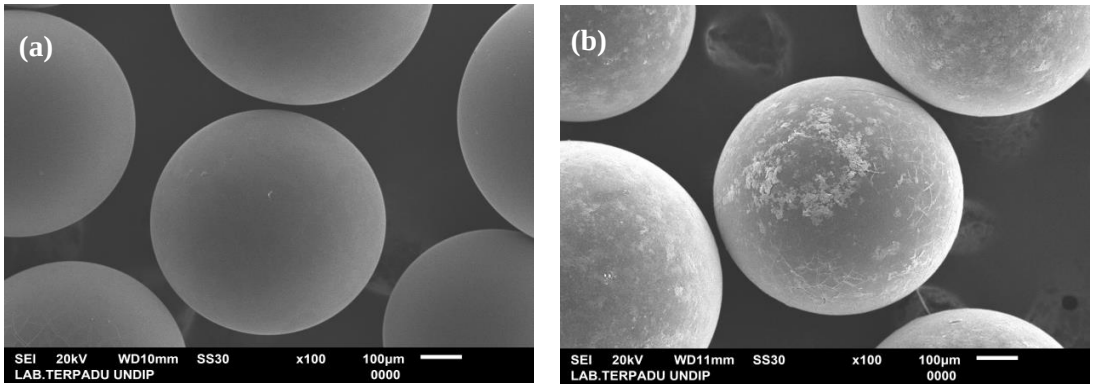


Figure 1. SEM test results (a) Purolite A400 resin and (b) Purolite A400-Cu resin (100x magnification)

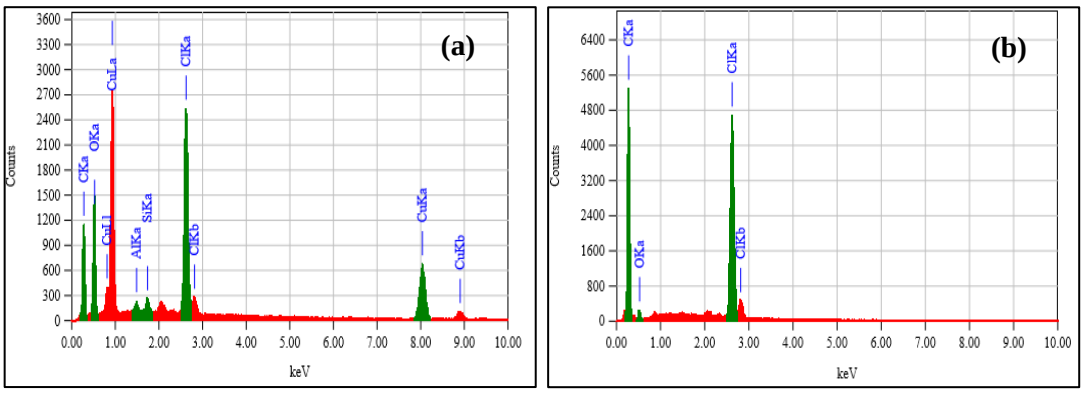


Figure 2. Results of EDS analysis (a) Purolite A400 Resin and (b) Purolite A400-Cu Resin

As shown in Table 1, Cl ion content in Purolite A400 resin also increases after impregnation from 7.98% to 9.67%. The chloride ion (Cl^-) in the resin is an interchangeable main anion [27].

Table 1. Composition of Purolite A400 and Purolite A400-Cu

Adsorbent	C (wt.%)	O (wt.%)	Cl (wt.%)	Cu (wt.%)	Al (wt.%)	Si (wt.%)
Purolite A400	86.64	5.38	7.98	-	-	-
Purolite A400-Cu	64.30	5.79	9.67	19.34	0.40	0.50

Adsorption capacity in fixed-bed columns

The adsorption capacities of Purolite A400 and Purolite A400-Cu resins in nitrate and nitrite removal are shown in Tables 2 and 3. The adsorption capacities of nitrate with Purolite A400 and Purolite A400-Cu resins at the 1st test column of Table 2 are 13.49 and 17.58 mg N/g, respectively. The equilibrium capacities of nitrate with Purolite A400 and Purolite A400-Cu are 0.67 and 0.88 mg N/g, respectively. Similarly, the adsorption capacities of Purolite A400 and Purolite A400-Cu against nitrite at the 1st test column in Table 3 are 1.99 and 2.05 mg N/g, respectively. The equilibrium capacities are 0.099 and 0.102 mg N/g. The difference between the nitrate and nitrite adsorption capacities using Purolite A400 and Purolite A400-Cu are 4.09 and 0.05 mg N/g, respectively.

Table 2. Adsorption capacity of nitrate removal using Purolite A400 and Purolite A400-Cu

No.	Test	Purolite A400			Purolite A400-Cu		
		C_t (mgL^{-1})	q_{total} (mg N/g)	q_{eq} (mg N/g)	C_t (mgL^{-1})	q_{total} (mg N/g)	q_{eq} (mg N/g)
1.	Nitrate + Nitrite (60 mg/L)	3.3	13.49	0.67	1.8	17.58	0.88
	Chloride (60 mg/L)	4.2			1.9		
	Sulphate (60 mg/L)	5.9			3.2		
	Phosphate (60 mg/L)	10.8			3.3		
2.	Nitrate + Nitrite (75 mg/L)	3.2	14.35	0.72	5.7	15.95	0.80
	Chloride (45 mg/l)	3.5			5.9		
	Sulphate (45 mg/l)	3.7			6.1		
	Phosphate (45 mg/l)	9.3			6.3		
3.	Nitrate + Nitrite (75 mg/L)	1.8	15.09	0.76	2.7	15.20	0.76
	Chloride (75 mg/L)	3.4			3.8		
	Sulphate (75 mg/L)	4.4			4.0		
	Phosphate (75 mg/L)	10.2			16.0		
4.	Nitrate + Nitrite (90 mg/L)	4.1	13.55	0.68	1.9	17.59	0.88
	Chloride (60 mg/L)	6.6			2.0		
	Sulphate (60 mg/L)	10.6			2.2		
	Phosphate (60 mg/L)	11.8			3.5		
5.	Nitrate + Nitrite (150 mg/L)	1.9	12.22	0.61	3.0	15.10	0.76
	Chloride (60 mg/L)	3.3			1.8		
	Sulphate (60 mg/L)	4.2			1.9		
	Phosphate (60 mg/L)	5.9			3.2		

The nitrate adsorption capacity using Purolite A400 is 13.49 mg N/g at the adsorption column volume (bed volume) of 9.24 BV. This finding is smaller than using Purolite A400-Cu, which is 17.58 mg N/g at the adsorption column volume (bed volume of) 10.19 BV. Similarly, the nitrite adsorption capacity using Purolite A400 resin with a bed column volume of 20.70 BV is 1.99 mg N/g. This finding is smaller than using Purolite A400-Cu, which is 2.05 mg N/g resin at a bed volume of 18.31 BV. The bed volume values between Purolite A400 and Purolite A400-Cu does not have significant difference. Thus, the bed volume value is the same on Purolite A400.

Table 3. Adsorption capacity of nitrite removal using Purolite A400 and Purolite A400-Cu

No.	Test	C_t (mgL^{-1})	q_{total} (mg N/g)	q_{eq} (mg N/g)	C_t (mgL^{-1})	q_{total} (mg N/g)	q_{eq} (mg N/g)
		Purolite A400			**Purolite A400-Cu**		
1.	Nitrate + Nitrite (60 mg/L)	0.040	1.99	0.10	0.006	2.05	0.10
	Chloride (60 mg/L)	0.043			0.006		
	Sulphate (60 mg/L)	0.049			0.459		
	Phosphate (60 mg/L)	0.057			0.865		
2.	Nitrate + Nitrite (75 mg/L)	0.042	1.99	0.10	0.041	2.18	0.11
	Chloride (45 mg/L)	0.056			0.047		
	Sulphate (45 mg/L)	0.066			0.049		
	Phosphate (45 mg/L)	0.126			0.055		
3.	Nitrate + Nitrite (75 mg/L)	0.030	2.03	0.10	0.006	2.22	0.11
	Chloride (75 mg/L)	0.031			0.023		
	Sulphate (75 mg/L)	0.036			0.064		
	Phosphate (75 mg/L)	0.054			0.097		
4.	Nitrate + Nitrite (90 mg/L)	0.150	1.27	0.06	0.091	1.57	0.08
	Chloride (60 mg/L)	0.784			0.396		
	Sulphate (60 mg/L)	2.288			0.723		
	Phosphate (60 mg/L)	3.226			3.214		
5.	Nitrate + Nitrite (150 mg/L)	0.036	1.08	0.05	0.052	1.47	0.07
	Chloride (60 mg/L)	2.235			0.615		
	Sulphate (60 mg/L)	2.869			1.581		
	Phosphate (60 mg/L)	3.248			3.396		

Breakthrough curve on nitrate removal

The nitrate adsorption breakthrough curve using Purolite A400 and Purolite A400-Cu resins with influent nitrate concentrations of 50 mg/L is shown in Figures 3 and 4, respectively. The effect of complementary ion concentration influences adsorption capacity (q_o) and Thomas (k_{Th}) constant. The Thomas model uses a linear regression equation where ln (C_o/C_t-1) is the ordinate (x-axis) and time (t) is the abscissa (x-axis). The ln (C_o/C_t1) value plot of t represents a straight line with a linear equation as y = a + bx, where a is the intercept that indicates the value of adsorption capacity (q_o) and b is the slope that indicates the value of Thomas' constant (k_{Th}).

The model parameters for the fixed-bed columns using equation 4 are shown in Table 4, where flow rate Q = 10 ml/min, influent nitrate concentration C_o = 50 mg/l and resin height t = 15 cm. As shown in Table 4, the value of k_{Th} increases with the increase of complementary ion concentration (chloride, sulphate and phosphate) and decreases when the initial concentration of nitrate + nitrite mixture increases in the nitrate removal using Purolite and Purolite-Cu. This finding shows the decrease in mass transfer rate due to the difference between the concentration of complementary ions in the resin and the concentrations of influent nitrate [33].

Table 4. Parameter of Thomas equation on nitrate removal

Test	**kT**	**q_0**	**k_T**	**q_0**
	Purolite		**Purolite-Cu**	
Nitrate + Nitrite (60 mg/L)	0.044	3.199	0.024	3.578
Chloride + Sulphate + Phosphate (45 mg/L)	0.036	3.238	0.004	2.087
Chloride + Sulphate + Phosphate (75 mg/L)	0.060	3.915	0.063	3.735
Nitrate + Nitrite (90 mg/L)	0.042	2.769	0.020	3.527
Nitrate + Nitrite (150 mg/L)	0.098	4.132	0.062	3.389

Each figure shows that the nitrate removal using Purolite A400 with an initial concentration of nitrate + nitrite mixture of 60 mg/L has a smaller C_t/C_o ratio of 0.536 compared with concentrations of 90 and 150 mg/L of 0.549 and 0.543 mg/L. For Purolite A400-Cu, C_t/C_o ratio of 0.52 was slightly smaller at the initial concentration of nitrate + nitrite mixture of 90 mg/L compared with the ration of 0.524 at 60 mg/L concentration. However, the value of C_t/C_o ratio obtained was 0.564 at the initial concentration of nitrate + nitrite mixture of 150 mg/L. For the effect of the concentration of chloride, sulphate and phosphate supplementation using Purolite A400, Ct/C_o ratio of 0.529 at 45 mg/L is smaller than the ratio of 0.536 at 75 mg/L concentration. Meanwhile, C_t/C_o ratio of 0.506 at 45 mg/L was significantly lower than C_t/C_o ratio of 0.556 at 75 mg/L concentration when using Purolite A400-Cu chloride, sulphate and phosphate. The value of C_t/C_o ratio affected final concentration (C_t) and filtration time when the resin surface absorbed nitrate ions in the column

Figures 3 and 4 shows that the C_t/C_o ratio of Purolite A400-Cu is smaller than that of Purolite A400 without impregnation. This condition is because the time to reach saturation is longer because the active side of Purolite A400-Cu is larger, and more nitrate ions are adsorbed. According to Kalaruban et al. [17], the time to reach saturation is faster using Purolite A400 than Purolite A400-Cu because the number of active sides on Purolite A400 resin surface is less than Purolite A400-Cu when complementary ions exist in the influent solution. The resin is rapidly saturated when the concentration of chloride ions is added to a solution that contains nitrate ions, and the saturation level is achieved when the ratio value of effluent concentration to influent concentration (C_t/C_o) in the column is large [20].

The breakthrough curve characteristic is sharply increased in Purolite A400 and Purolite A400-Cu. The faster the saturation is achieved, the higher the C_t/C_o ratio will be obtained. This condition occurs because the residence time in the column does not require considerable time to reach the adsorption equilibrium and the effluent nitrate solution leaves the column before the equilibrium is reached because the contact time between nitrate ions with Purolite A400 is short and the allowance efficiency decreases in saturation time [33].

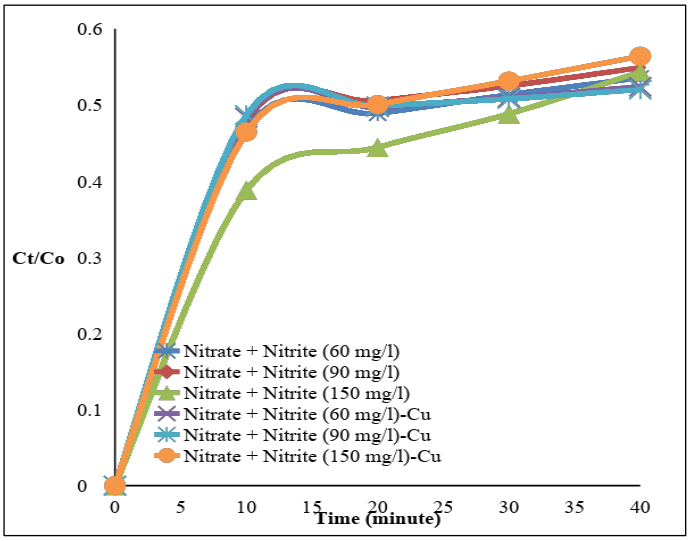


Figure 3. Breakthrough curve on nitrate removal based on the effect of initial concentration of nitrate and nitrite blends using Purolite A400 and Purolite A400-Cu

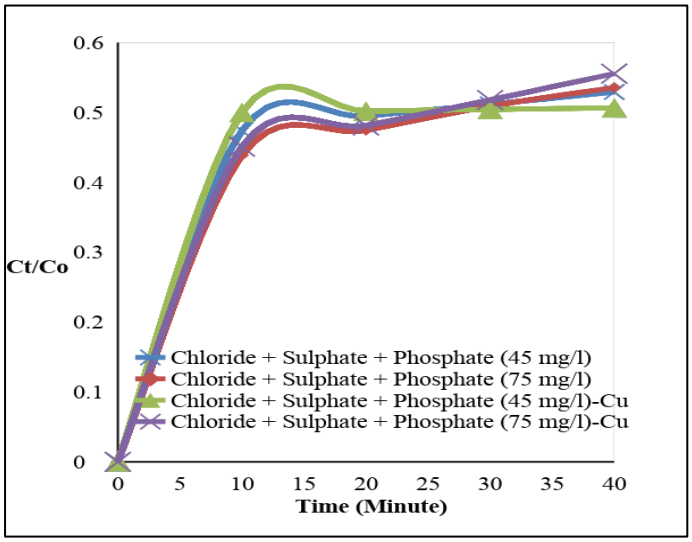


Figure 4. Breakthrough curve on nitrate removal based on the effect of compound ion concentration of chloride, sulphate and phosphate using Purolite A400 and Purolite A400-Cu

Breakthrough curve on nitrite allowance

Nitrite adsorption breakthrough curves using Purolite A400 and Purolite A400-Cu resins with influent nitrite concentrations of 5 mg/L are shown in Figures 5 and 6, respectively. The model parameters for the fixed-bed column shown in Table 5 are expressed in equation 4, where flow rate Q = 10 mL/min, influent nitrite concentration C_o = 5 mg/L and resin height t = 15 cm. As shown in Table 3, the value of k_{Th} increases with the increase of complementary ion concentration (chloride, sulphate and phosphate) and reduces when the initial concentration of nitrate + nitrite mixture increases at the nitrite removal using Purolite A400-Cu. This condition shows the decrease in mass transfer rate due to the difference between the concentration of complementary ions in the resin and the concentrations of influent nitrate [33].

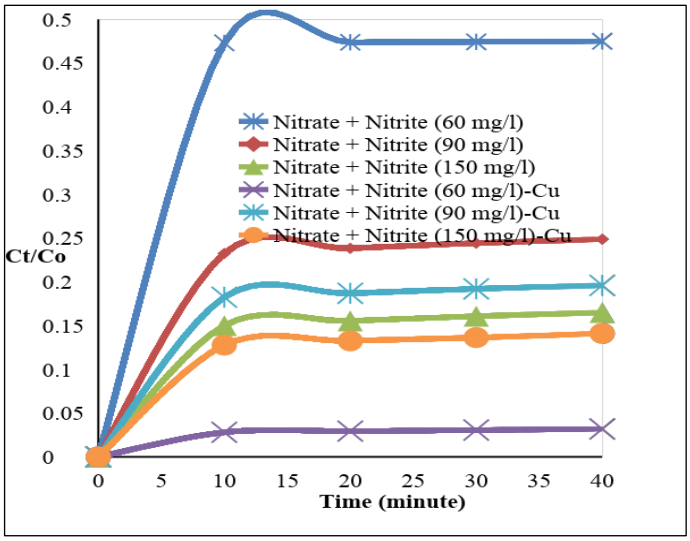


Figure 5. Breakthrough curve on nitrite removal based on the effect of initial concentration of nitric and nitrite blends using Purolite A400 and Purolite A400-Cu

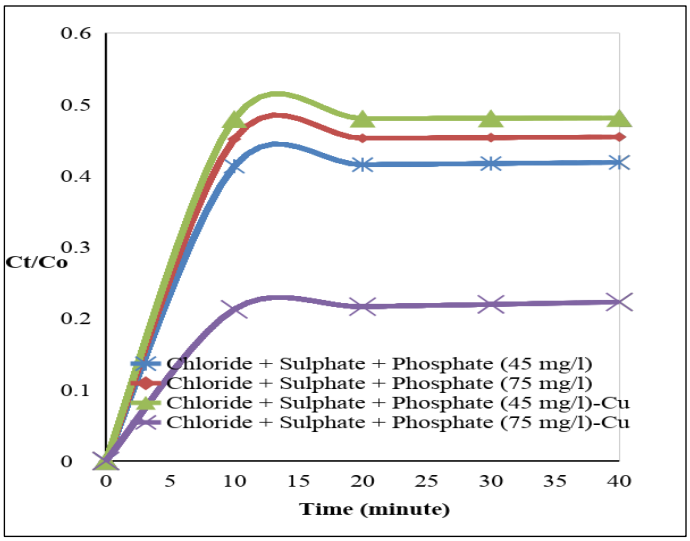


Figure 6. Breakthrough curve on nitrite removal based on the effect of compound ion concentration of chloride, sulphate and phosphate using Purolite A400 and Purolite A400-Cu

Each figure shows that nitrite removal using Purolite A400 with an initial concentration of nitrate + nitrite mixture of 60 mg/L has a greater C_t/C_o ratio of 0.48 compared with the ratios of 0.25 and 0.17 at 90 and 150 mg/L concentrations. For Purolite A400-Cu, the C_t/C_o ratio value at the initial concentration of nitrate + nitrite mixture 60 mg/L was significantly smaller than the C_t/C_o ratio of 0.03. The value of C_t/C_o ratio decreased to 0.20 at the initial concentration of nitrate + nitrite mixture of 90 mg/L. Meanwhile, the value of C_t/C_o ratio slightly decreased to 0.14 at the initial concentration of nitrate + nitrite mixture of 150 mg/L. For the effect of the concentration of chloride, sulphate and phosphate ions using Purolite A400, a smaller C_t/C_o ratio value was obtained at a concentration of 45 mg/L 0.42 compared with the ratio of 0.45 at 75 mg/L concentration. However, a large C_t/C_o ratio of 0.48 was obtained at 45 mg/mL concentration of chloride, sulphate and phosphate when using Purolite A400-Cu. Meanwhile, the value of C_t/C_o ratio was 0.22 at 75 mg/L concentration of chloride, sulphate and phosphate. The C_t/C_o ratio

value influenced final concentration (C_t) and filtration time when the resin surface absorbed nitrite ions in the column.

Table 5. Parameter of Thomas Equation on nitrite removal

Test	k_T	q_0	k_T	q_0
	Purolite		Purolite-Cu	
Nitrate + Nitrite (60 mg/L)	0.012	4.948	0.197	9.254
Chloride + Sulphate + Phosphate (45 mg/L)	0.035	5.195	0.009	4.866
Chloride + Sulphate + Phosphate (75 mg/L)	0.019	5.384	0.092	7.384
Nitrate + Nitrite (90 mg/L)	0.137	4.614	0.143	5.505
Nitrate + Nitrite (150 mg/L)	0.171	5.332	0.171	5.914

Figures 5 and 6 show that the C_t/C_o ratio using Purolite A400-Cu is significantly small and the time to reach saturation is long because the active side of Purolite A400-Cu resin has many pores and the adsorbed nitrite ions are greater than Purolite A400. However, the C_t/C_o ratio using Purolite A400 is smaller than Purolite A400-Cu for the influence of the 45 mg/L concentration of chloride, sulphate and phosphate 45. This finding is inconsistent with existing theory on the role of k_T and q_o values in C_t/C_o ratio. If the values of k_T and q_o using Purolite A400-Cu are relatively small, then the C_t/C_o ratio value is greater than Purolite A400. The breakthrough curve sharply increases due to the influence of the initial concentration of the mixture of nitrate + nitrite 60 mg/L and the effect of complementary ion concentration chloride, sulphate and phosphate of 75 mg/L. According to Li and Yang [23], breakthrough curves increased enormously because they dealt with complementary ion in the influent nitrite solution and mass transfer rate. A breakthrough point was achieved in a high influent concentration, and the increased concentration of influent adsorbate diminished the breakpoint time because the resin active site binding adsorbate rapidly saturated [32]. According to Babu and Gupta [33], the value of external mass transfer coefficient had a significant influence on the breakthrough curve. If the value of the external mass transfer coefficient is greater, the C_t/C_o ratio value is not close to 1 (close to few constant values, value <1 and asymptotically constant after a certain time). The value of C_t/C_o ratio asymptotically becomes constantly close to 1 when the value of external mass transfer coefficient is small.

Conclusion

Adsorption capacity was increased by modifying the adsorbent with metal impregnation that aimed at enlarging the surface positive charge. Cu content was obtained from Purolite A400 resin of 19.34%, and the adsorption capacities of nitrate and nitrite removal using Purolite A400 and Purolite A400-Cu resin were 13.49 (nitrate) and 17.58 mg N/g (nitrate) and 1.99 (nitrite) and 2.05 mg N/g (nitrite), respectively. The ratio of C_t/C_0 to nitrate and nitrate removal using Purolite A400-Cu resin was small, and the saturation time was achieved with a long time because the active side of Purolite A400-Cu was large, and many nitrate and nitrite ions were adsorbed. The value of C_t/C_0 in nitrate and nitrite removal was 0.506 at 45 mg/L concentration of chloride, sulphate and phosphate, and the value of C_t/C_0 was 0.03 at the initial concentration of nitrate + nitrite 60 mg/L mixture ratio.

Acknowledgement

This work was supported by University of Sumatera Utara under the talented program. We thank to Integrated Laboratory in Semarang, Indonesia for the resin test analysis result of the research.

References

1. Rajeswari, M., Rajakumar, S. and Ayyasamy, P. M. (2015). Evaluation of nitrate removal in aquatic system: A general view. *International Journal of Emerging Research in Management & Technology*, 9359 (12): 186 – 194.
2. Hanafi, H. A. and Azeema, S. M. A. (2016). Removal of nitrate and nitrite anions from wastewater using activated carbon derived from rice straw. *Journal of Environmental & Analytical Toxicology*, 6 (1): 1-6.

3. Chatterjee, S., Lee, D. S., Lee, M. W. and Woo, S. H. (2008). Nitrate removal from aqueous solutions by cross-linked chitosan beads conditioned with sodium bisulfate. *Journal of Hazardous Materials*, 166: 508 – 513.
4. Madaeni, S. S. and Koocheki, S. (2010). Influence of di-hydrogen phospate ion on performance of polyamide reverse osmosis membrane for nitrate and nitrite removal. *Journal Porous Material*, 17: 163 – 168.
5. Hekmatzadeh, A. A., Karimi-Jashani, A., Talebbeydokhti, N. and Klove, B. (2012). Modeling of nitrate removal for ion exchange resin in batch and fixed-bed experiments. *Desalination*, 284: 22 – 31.
6. Guy, K. A., Xu, H., Yang, J. C., Werth, C. J. and Shapley, J. R. (2009). Catalytic nitrate and nitrite reduction with Pd - Cu/PVP colloids in water: composition, structure, and reactivity correlations. *Journal Physical Chemistry*, 113, 8177 – 8185.
7. Bel, E. S., Hmida, H., Ouejhani, A., Lalleve, G., Fauvarque, J. F. and Dachraoui, M. (2013). A novel anionic electrodialysis membrane can be used to remove nitrate and nitrite from wastewater. *Desalination and Water Treatment* 23: 13 –19.
8. Khan, M. A., Ahn, Y. T., Kumar, M., Lee, W., Min, B., Kim, G., Cho, D. W., Park, W. B. and Jeon, B. H. (2011). Adsorption studies for the removal of nitrate using modified lignite granular activated carbon. *Separation Science and Technology*, 46: 2575 – 2584.
9. Sabzali, A., Gholami, M., Yazandbakhsh, A. R., Khodadadi, A., Musavi, B. and Mirzaee, R. (2006). Chemical denitrification of nitrate from groundwater via sulfamic acid and zinc metal. *Journal Environmental Health Science Engineering*, 3(3): 141 – 146.
10. Lopez-Vazquez, C. M., Kubare, M., Saroj, D. P., Chikamba, C., Schwarz, J., Daims, H. and Brdjanovic, D. (2013). Thermophilic biological nitrogen removal in industrial wastewater treatment. *Applied Microbiology Biotechnology*, 98(2): 945 – 956.
11. Matos, C. T., Velizarov, S., Crespo, J. G. and Reis, M. A. M. (2006). Simultaneous removal of perchlorate and nitrate from drinking water using the ion exchange membrane bioreactor concept. *Water Research*, 40(2): 231 – 240.
12. Zhang, Y. and Angelidaki, I. (2012). Bioelectrode-based approach for enhancing nitrate and nitrite removal and electricity generation from eutrophic lakes. *Water Research*, 46(19): 6445-6453.
13. Hannachi, C., Guesmi, F., Fatma, K., Missaoui and Hamrouni, B. (2014). Application of adsorption models for fluoride, nitrate and sulfate ion removal by AMX membrane. *International Journal of Technology*, 5(1): 60 – 69.
14. Sowmya, A and Meenakshi, S. (2013). An efficient and regenerable quartenary amine modified chitosan beads for the removal of nitrate and phosphate anions. *Journal of Environmental Chemical Engineering*, 1(4): 906-915.
15. Shaikh, I. I. and Chendake, Y. J. (2016). Removal of ammonium nitrate from aquaculture by sorption using zeolite. *International Journal of Scientific Research in Chemistry*, 1(1): 42 – 48.
16. Hassan, M. L., Kassem, N. F and El-Kader, H. A. A. (2010). Novel Zr (IV)/sugar beet pulp composite for removal of sulfate and nitrate anion. *Journal of Applied Polymer Science*, 117(4): 2205 – 2212.
17. Kalaruban, M., Loganathan, P., Shim, W. G., Kandasamy, J., Naidu, G., Tien, V. N. and Vigneswaran, S. (2016). Removing nitrate from water using iron-modified Dowex 21K XLT ion exchange resin: Batch and fluidised-bed adsorption studies. *Separation and Purification Technology*, 158: 62 – 70.
18. Bulgariu, L., Ceica, A., Lazar, L., Cretescu, I. and Balasanian, I. (2010). Equilibrium and kinetics study of nitrate removal from water by Purolite A100 resin. *Revista de Chimie*, 61(11): 1136 – 1141.
19. Nur, T., Shim, W. G., Loganathan, P., Vigneswaran S. and Kandasamy, J. (2014). Nitrate removal using Purolite A520E ion exchange resin: batch and fixed-bed column adsorption modelling. *International Journal of Environmental Science and Technology*, 12(4): 1311 – 1320.
20. Primo, O., Rivero, M. J., Urtiaga, A. M. and Ortiz, I. (2009). Nitrate removal from electro-oxidized landfill leachate by ion exchange. *Journal of Hazardous Materials*, 164(1): 389 – 393.
21. Li, W. B., Song, Y. B., Xu, H. K., Chen, L. Y., Dai, W. D. and Dong, M. (2015). Ion-exchange method in the collection of nitrate from freshwater ecosystem for nitrogen and oxygen isotope analysis: A review. *Environmental Science Pollution Research*, 22(13): 9575 – 9588.
22. Farajpourlar, M., Rao, S. R. M. and Rao, V. V. B. (2013). Studies on fixed and fluidized bed ion exchange column to treat wastewater. *IOSR Journal of Environmental Science, Toxicology and Food Technology*, 6(1): 1 – 6.

23. Li, H. and Yang, C. (2015). Nitrite removal using ion exchange resin: Batch vs. fixed bed performance. *Separation Science and Technology*, 50(11): 1721 – 1730.
24. Loganathan, P., Vigneswaran, S. and Kandasamy, J. (2013). Enhanced removal of nitrate from water using surface modification of adsorbents - A review. *Journal of Environmental Management*, 131: 363 – 374.
25. Swarna, A. (2014). Removal of arsenic using iron coated limestone. Master Theses & Specialist Projects. Western Kentucky University.
26. Zou, W., Han, R., Chen, Z., Jinghua, Z. and Shi, J. (2006). Kinetic study of adsorption of Cu(II) and Pb (II) from aqueous solutions using manganese oxide coated zeolite in batch mode. *Colloids and Surfaces A: Physicochemistry Engineering Aspects*, 279: 238 – 246.
27. Purolite (2017). Technical data ISO 9002. http://www.purolite.com. [Access online 7 September 2017].
28. Faiku, F and Haziri, A. (2016). Assesment of the water quality of Lumbardhi River, Prizren (Kosovo). *Bulgarian Chemical Communications*, 48(4): 646 – 658.
29. Zhang, J., Yang, C., Chen, C. and Yang, X. (2013). Determination of nitrite and glucose in water and human urine with light-up chromogenic response based on the expeditious oxidation of 3,3',5,5'-tetramethylbenzidine by peroxynitrous acid. *Analyst*, 138(8): 2398 – 2404.
30. Roohparvar, R., Shamspur, T. and Mostafavi, A. (2016). Application of modified silica coated magnetite nanoparticles to separation-preconcentration and determination of nitrite. *Chemical & Metallurgical Engineering Journal*, 4: 101 – 103.
31. Xu, X., Gao, B., Yue, Q., Li, Q. and Wang, Y. (2013). Nitrate adsorption by multiple biomaterial based resins: Application of pilot-scale and lab-scale products. *Chemical Engineering Journal*, 234: 397 – 405.
32. Chowdhury, Z. Z., Zain, S. M., Rashid, A. K., Rafique, R. F. and Khalid, K. (2013). Breakthrough curve analysis for column dynamics sorption of Mn(II) ions from wastewater by using *Mangostana garcinia* peel-based granular-activated carbon. *Journal of Chemistry*, 2013: 1 – 8.
33. Babu, B. V. and Gupta, S. (2005). Modeling and simulation for dynamics of packed bed adsorption. *Proceedings of International Symposium & 57th Annual Session of IIChE in association with AIChE (CHEMCON-2004)*, Mumbai.

Malaysian Journal of Analytical Sciences Vol 23 No 2 2019

Articles 18 - 20 are selected papers from the "The 6th International Conference on Fuel Cell & Hydrogen Technology 2017 (ICFCHT 2017); 11 - 13 April 2017 at Dewan Persidangan Kompleks Perbadanan Putrajaya, Putrajaya; organized by Fuel Cell Institute, Universiti Kebangsaan Malaysia and co-organized by Agency for the Assessment and Application of Technology, Indonesia

Guest Editor: Lorna Jeffery Minggu

		Page
1.	DETERMINATION OF BINDING CONSTANT OF MOLECULAR COMPLEX BETWEEN β-CYCLODEXTRIN AND BISPHENOL A BY USING ^{1}H NMR SPECTROSCOPY (Penentuan Malar Penambatan Kompleks Molekul di antara β-siklodekstrin dan Bisfenol A Menggunakan Spektroskopi 1H NMR) *Rosliana Rusli, Mohd Bakri Bakar, Salasiah Endud, Zainab Ramli*	182
2.	SYNTHESIS AND CHARACTERISATION OF N-ANALINEFERROCENYLAMIDE VIA CARBODIIMIDE COUPLING (Sintesis dan Pencirian N-Analineferosenilamida melalui Gandingan Silang Karbodiimida) *Ken Min Liew, Tei Tagg, Wan M. Khairul*	189
3.	ELECTROCHEMICAL PROPERTIES OF MESOPOROUS SILICA (SBA-15)-CARBON ELECTRODE (Ciri Electrokimia Karbon Silica Berliang Meso) *Noramira Saad, Mohammad Noor Jalil, Zainiharyati Mohd Zain, Hamizah Mohd Zaki*	197
4.	SOL-GEL/CHITOSAN HYBRID THIN FILM IMMOBILISED WITH CURCUMIN AS pH INDICATOR FOR pH SENSOR FABRICATION (Filem Nipis Hibrid Sol-gel/Kitosan Terpegun dengan Kurkumin sebagai Penunjuk pH bagi Fabrikasi Sensor pH) *Rosmawani Mohammad and Musa Ahmad*	204
5.	ELECTROSPUN POLY(VINYL ALCOHOL) NANOFIBERS DOPED WITH MESOPOROUS SILICA NANOPARTICLES FOR CONTROLLED RELEASE OF HYDROPHILIC MODEL DRUG (Elektrospun Poli(Vinil Alkohol) Nanofiber Didopkan Dengan Silika Nanopartikel Berliang Meso untuk Perlepasan Terkawal Model Dadah Hidrofilik) *Nur Izzah Md Fadilah, Haslina Ahmad, Mohd Firdaus Abd Rahman, Norizah Abdul Rahman*	212
6.	REMOVAL OF Pb(II) FROM AQUEOUS SOLUTION BY PINEAPPLE PLANT STEM (Penyingkiran Pb(II) dari Larutan Akueus Menggunakan Batang Tumbuhan Nanas) *Vivian Loh Zing Ting, Tan Yen Ping, Abdul Halim Abdullah*	219

7. COLOURIMETRIC BASED DETECTION OF GUNSHOT RESIDUE ON GLOVES WORN DURING SHOOTING 229
(Pengesanan Sisa Tembakan Berasaskan Kolorimetrik pada Sarung Tangan Semasa Menembak)
Azie Azyanti Mohd Rafae, Saiful Fazamil Mohd Ali, Ahmad Fahmi Lim Abdullah, Kah Haw Chang

8. SYNTHESIS AND MOLECULAR DOCKING OF 2,4,5-TRISUBSTITUTED-1,3-THIAZOLE DERIVATIVES AS ANTIBACTERIAL AGENTS 237
(Sintesis dan Penyatuan Molekul Terbitan 1,3-Tiazol Berpenggantian-2,4,5 Sebagai Agen Antibakteria)
Iswatun Hasanah Abdullah Ripain, Norashikin Roslan, Nurul Shazana Norshahimi, Siti Salwa Mohamed Salleh, Noraslinda Muhamad Bunnori, Nurziana Ngah

9. EFFECT OF TEMPERATURE ON THE CATALYTIC ACTIVITY OF NEW SYMMETRICAL TETRADENTATE PALLADIUM(II) SCHIFF BASE COMPLEXES IN COPPER-FREE SONOGASHIRA REACTION 247
(Kesan Suhu Terhadap Aktiviti Pemangkinan Kompleks Baru Paladium(II) Tetradentat Bes Schiff Bersimetri dalam Tindak Balas Sonogashira Tanpa Kuprum)
Shahrul Nizam Ahmad, Hadariah Bahron, Amalina Mohd Tajuddin

10. SYNTHESIS AND CHARACTERISATION OF NANOHYBRID ANTI-HYPERTENSIVE DRUG, CAPTOPRIL INTERCALATED INTO ZINC–ALUMINIUM LAYERED DOUBLE HYDROXIDE 255
(Sintesis dan Pencirian Nanohibrid Ubat Anti-Hipertensi, Captopril Tersisip ke dalam Zink-Aluminium Hidroksida Berlapis Ganda)
Zaemah Jubri, Siti Halimah Sarijo, Monica Limau Anak Jadam

11. SYNTHESIS AND CHARACTERIZATION OF BENZOHYDROXAMIC ACID AND METHYLBENZOHYDROXAMIC ACID METAL COMPLEXES AND THEIR CYTOTOXICTY STUDY 263
(Sintesis dan Pencirian Kompleks Logam Asid Benzohidroksamik dan Asid Metilbenzohidroksamik serta Kajian Sitotoksik)
Latifah Robbaniyyah Hassan, Hadariah Bahron, Kalavathy Ramasamy, Amalina Mohd Tajuddin

12. PYROLYTIC KEY INDICATORS OF BURNT PORCINE TISSUE IN THE PRESENCE OF PETROL UNDER OUTDOOR CONDITIONS 274
(Analisis Penunjuk Utama Pirolitik Tisu Khinzir Yang Dibakar Dengan Kehadiran Gangguan Petrol Dalam Keadaan Terbuka)
Gina Francesca Gabriel, Jennifer Shalini Jheyeaaseelan, Dheephikha Kumaraguru, Khairul Osman, Noor Hazfalinda Hamzah

13. SYNTHESIS AND CHARACTERIZATION OF SILICA-SILVER CORE-SHELL NANOPARTICLES 290
(Sintesis dan Pencirian Silika-Perak Nanopartikel Teras-Cengkerang)
Nur Kamilah Mohd, Wan Mohd Afiq Wan Mohd Khalik, Alyza A. Azmi

14. SEASONAL VARIATION AND ECOLOGICAL RISK ASSESSMENT OF HEAVY METAL CONTAMINATION IN SURFACE WATERS OF THE GANGES RIVER 300

(NORTHWESTERN BANGLADESH)
(Variasi Bermusim dan Penilaian Risiko Ekologi Terhadap Pencemaran Logam Berat di Permukaan Air Sungai Ganges (Barat Utara Bangladesh))
Md. Ayenuddin Haque, Md. Abu Sayed Jewel, Jakia Hasan, Md. Mazharul Islam, Sharif Ahmed, Lubna Alam

15. ULTRAFAST LIQUID CHROMATOGRAPHIC ESTIMATION OF SERTACONAZOLE NITRATE IN PHARMACEUTICALS USING ANALYTICAL QUALITY BY DESIGN 312
(Kromatografi Cecair Ultra-laju bagi Anggaran Sertaconazole Nitrat dalam Farmaseutikal Menggunakan Reka Bentuk Kualiti Analitikal)
Sagar Suman Panda, Venkata Varaha Ravi Kumar Bera, Rakeya Samanta

16. EFFECTS OF SILVER NANOWIRE-BASED POLYMER COMPOSITE MEMBRANE ON THE PHYSICAL AND ELECTROCHEMICAL PROPERTIES OF MALACHITE GREEN SENSOR 325
(Kesan Nanowayar Perak-Membran Komposit Polimer ke atas Sifat Fizikal dan Elektrokimia untuk Sensor Malakit Hijau)
Sharifah Nur Atikah Al Yahya, Sharina Abu Hanifah, Normazida Rozi, Nurul Huda Abd Karim, Lee Yook Heng

17. METHOD DEVELOPMENT AND VALIDATION FOR QUANTIFICATION OF CORTISOL AND CORTISONE USING ULTRA-HIGH PERFORMANCE LIQUID CHROMATOGRAPHY-TANDEM MASS SPECTROMETRY 336
(Pembangunan dan Pengesahan Kaedah untuk Kuantifikasi Kortisol dan Kortison Menggunakan Kromatografi Cecair Berprestasi Ultra Tinggi-Spektrometri Jisim Gabungan)
Hazirah Abd Azhar, Mohd Salleh Rofiee, Mohammad Zulfadhly Jan Jam, Muhammad Hisyam Jamari, Roziah Mohd Janor, Richard Johari James, Teh Lay Kek, Mohd Zaki Salleh

18. LASER-ASSISTED SILICON ETCHING FOR MICRO FUEL CELL ELECTRODE PLATE FABRICATION 345
(Fabrikasi Plat Elektrod Sel Bahan Api Mikro dengan Punaran Silikon Terbantu Laser)
Umi Azmah Hasran, Siti Kartom Kamarudin, Burhanuddin Yeop Majlis, Wan Ramli Wan Daud, Abdul Amir Hassan Kadhum, Gandi Sugandi

19. EFFECTS OF GRAPHITE/POLYPROPYLENE ON THE ELECTRICAL CONDUCTIVITY OF MANUFACTURED BIPOLAR PLATE 355
(Kesan Komposit Polimer Pengalir Grafit/Polipropilena Komposit Polimer Pengalir Ke atas Sifat Kekonduksian Elektrik bagi Pembuatan Plat Dwikutub)
Iswandi, Abu Bakar Sulong, Teuku Husaini

20. Nd:YAG LASER FABRICATION OF SILICON ELECTRODE PLATES FOR A COMBINED-MODE MICRO DIRECT METHANOL FUEL CELL 362
(Fabrikasi Plat Elektrod Silikon dengan Laser Nd:YAG untuk Sel Bahan Api Metanol Langsung Mikro Bermod Gabungan)
Umi Azmah Hasran, Siti Kartom Kamarudin, Burhanuddin Yeop Majlis, Wan Ramli Wan Daud, Abdul Amir Hassan Kadhum, Gandi Sugandi

Malaysian Journal of Analytical Sciences, Vol 23 No 2 (2019): 182 - 188
DOI: https://doi.org/10.17576/mjas-2019-2302-01

MALAYSIAN JOURNAL OF ANALYTICAL SCIENCES
Published by The Malaysian Analytical Sciences Society
ISSN 1394 - 2506

DETERMINATION OF BINDING CONSTANT OF MOLECULAR COMPLEX BETWEEN β-CYCLODEXTRIN AND BISPHENOL A BY USING ^{1}H NMR SPECTROSCOPY

(Penentuan Malar Penambatan Kompleks Molekul di antara β-siklodekstrin dan Bisfenol A Menggunakan Spektroskopi ^{1}H NMR)

Rosliana Rusli, Mohd Bakri Bakar*, Salasiah Endud, Zainab Ramli

Department of Chemistry, Faculty of Science,
Universiti Teknologi Malaysia, 81310 UTM Johor Bahru, Johor, Malaysia

**Corresponding author: bakribakar@utm.my*

Received: 4 July 2018; Accepted: 24 January 2019

Abstract

The inclusion complexation behaviour of bisphenol A (BPA) into hydrophobic cavity of β-cyclodextrin (β-CD) was investigated by using ^{1}H NMR spectroscopy in deuterium oxide by varying the molar ratios between β-CD and BPA from 1:0 to 1:2. The ideal molar ratio for the β-CD:BPA complex was determined as 1:1. In addition, the inclusion of BPA into β-CD produced significant changes in the chemical shifts of H5 and H3 protons, which were located inside the cavity of cyclodextrin. On the other hand, the H2, H4 and H6 protons that were located at the exterior surface of β-CD did not result in any significant changes in the chemical shift, and thus confirmed the formation of the β-CD:BPA inclusion complex. The observed chemical shifts of H5 and H3 protons, when BPA interacted with the β-CD cavity, were utilised to determine the binding association constant (K_a) and maximum chemical shift difference (Δ_{max}). From the nonlinear calculation, the K_a for H3 proton, i.e. 4.10 x 10^3 M^{-1}, was shown to be stronger than that of H5, i.e. 3.62 x 10^3 M^{-1}. However, the H5 proton gave a higher Δ_{max} than the H3 proton, which were 0.1412 ppm and 0.0573 ppm, respectively.

Keywords: cyclodextrin, bisphenol A, binding association constant

Abstrak

Kelakuan pengkompleksan rangkuman oleh bisfenol A (BPA) ke dalam rongga hidrofobik β-siklodekstrin (β-CD) diselidik melalui penggunaan spektroskopi ^{1}H NMR dalam deuterium oksida dengan mengubah nisbah molar antara β-CD dan BPA dari 1:0 hingga 1:2. Nisbah molar yang unggul untuk kompleks β-CD:BPA ditentukan sebagai 1:1. Tambahan pula, rangkuman BPA ke dalam β-CD menyebabkan perubahan ketara terhadap anjakan kimia pada proton H5 dan H3 siklodekstrin yang terletak di dalam rongga. Selain itu, proton H2, H4 dan H6 yang terletak di luar permukaan β-CD tidak mengalami perubahan pada anjakan kimia, dengan ini membuktikan bahawa pembentukan kompleks rangkuman β-CD:BPA. Perubahan anjakan kimia yang diperhatikan daripada proton H5 and H3 apabila BPA saling bertindak dengan rongga β-CD, digunakan untuk menentukan malar penyekutuan penambatan (K_a) dan perubahan anjakan kimia maksimum (Δ_{max}). Menggunakan hitungan tak-linear, malar K_a untuk proton H3 ialah 4.10 x 10^3 M^{-1} dilihat lebih kuat berbanding dengan proton H5, iaitu 3.62 x 10^3 M^{-1}. Walau bagaimanapun, proton H5 memberikan Δ_{max} yang ketara, iaitu 0.1412 ppm berbanding dengan proton H3, iaitu 0.0573 ppm.

Kata kunci: siklodekstrin, bisfenol A, **pe**malar penyekutuan penambatan

Introduction

Bisphenol A (BPA), 4,4'-(propane-2,2-diyl)diphenol (Figure 1), an organic compound that belongs to the group of Brominated Flame Retardants (BFRs), is in great demand for its use in polycarbonate plastics and epoxy resin production [1]. BPA is applied as plastic additives to protect against ignition and spread of flames in electrical appliances, building materials, furniture items, coating substances and others [2]. Nevertheless, disintegration, volatilisation and leaching of these products can cause the release of BPA into the environment and the chemical can pose a serious health threat to humans and wildlife. Based on previous animal studies, chemicals in the BFR group are associated with several health issues, including neuro behavioural toxicity, thyroid hormone disruption, and possibly cancer [3, 4]. In addition, BPA in nature has hydrophobic characteristics which can make its detection more difficult and complicated, consequently, many studies were published on the inclusion of BPA into beta-cyclodextrine (β-CD) cavity for its solubilisation [5], detection [6], degradation [7, 8], adsorption [9, 10] and removal [11] from the environment.

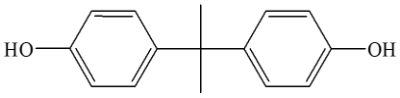


Figure 1. Structure of bisphenol A

The β-CD molecule is a cyclic oligosaccharide with seven glucopyranose units and can be represented as a truncated cone structure with hydroxy groups orientated at the rims of the cavity (Figure 2). Its hydroxy groups are divided into two types: the primary hydroxy groups at C6 and the secondary hydroxy groups at C2 as well as C3. At C6 position, the primary hydroxy groups of the glucose residues are arranged at the narrow rim, whilst the secondary hydroxy groups are located at the wider rim of the truncated cone. This structural characteristic of β -CD allows for the formation of a hydrogen bond between the hydroxyls, resulting in a molecule with an apolar cavity but at the same time, has a hydrophilic outside which is water soluble [12]. The key aspect of β-CD is its ability to form inclusion complexes with a variety of apolar guest molecules, such as phenol derivatives, in its cavity. This characteristic often results in modifications of their chemical and physical properties [13]. Therefore, valuable information on the stoichiometry, stability and mode of entry of a hydrophobic guest into the β-CD host could be obtained by the characterisation of the inclusion complexes in solution or solid state.

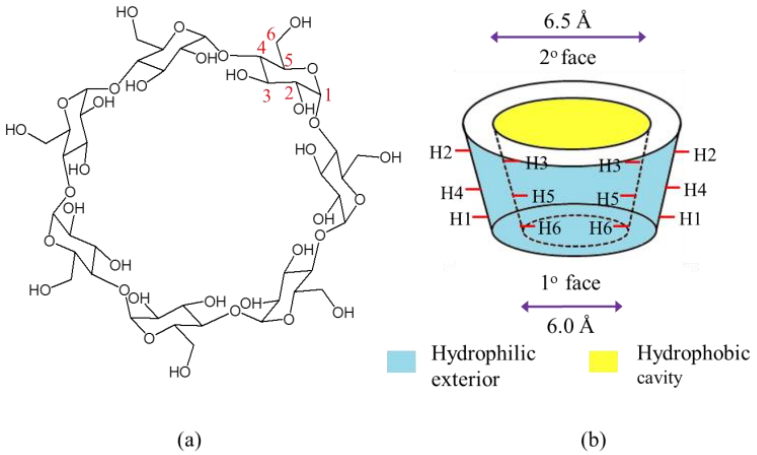


Figure 2. (a) Chemical structure of β-CD and (b) Truncated cone-shape of β-CD

In spite of the successful inclusion of BPA into β-CD cavity [5], there is no report on the binding association constant (K_a). Likewise, other research on BPA also did not include further determination of K_a [14-16]. K_a is usually calculated by using ultraviolet-visible or fluorescence spectroscopy. However, both BPA and β-CD are spectroscopically inactive, and thus did not show any changes upon the inclusion of complex formation. It is vital to compare K_a with materials that have more competence to form a complex with BPA and also methods that are more sensitive and accurate to detect and recognise a BPA molecule. Therefore, in the present work it is considered worthy of interest to determine the K_a of the inclusion complex between β-CD and BPA by using the ^{1}H NMR spectroscopy technique. Since the chemical shift of proton will change, depending on the molecular environment of the proton, this technique is expected to provide the value of K_a between BPA and β-CD.

Materials and Methods

Materials

All chemicals used were supplied by Sigma-Aldrich, Germany, and they were used without prior purification. Aqueous solutions of the BPA and β-CD precursors were prepared with distilled water. The FTIR spectra were recorded on a Perkin Elmer instrument. The ^{1}H NMR analysis of sample was performed on a Bruker 400 MHz spectrometer by using deuterium oxide as the solvent. K_a and Δ_{max} were simultaneously calculated by using Equation 1 and aided by Solver in Microsoft Excel.

Preparation of β-CD:BPA complex

β-CD (0.45 mmol, 0.50 g) and BPA (0.09 mmol, 0.02 g) were dissolved in an appropriate amount of boiling water to make a supersaturated solution. Then the solution was slowly cooled to room temperature, and the precipitate that formed was filtered to obtain the transparent complex crystal with a molar ratio of 1:0.2. The method was repeated by changing the BPA concentration to form the β-CD:BPA complex in the molar ratios of 1:0.4, 1:0.6, 1:0.8, 1:1.0, 1:1.2, 1:1.4, 1:1.6, 1:1.8 and 1:2.0.

Results and Discussion

Basically, many methods are used to prepare the β-cyclodextrin inclusion complexes, mainly in solid phase or solution. Even though complex formation in the solid phase is thermodynamically spontaneous, its stability is much weaker than in aqueous solution [17]. Generally, the process for complex formation in solid phase is slow and some solid-state reactions can take months, which is not practical. In this study, the complex was prepared by co-precipitation method in aqueous solutions by using β-CD and BPA as precursors. This method is commonly used for laboratory scale synthesis and importantly it yields highly pure and crystalline inclusion complex [18].

The inclusion of BPA into the β-CD cavity was studied by means of FTIR spectroscopy. The spectrum of β-CD:BPA (1:1) inclusion complex was compared with the β-CD and BPA standards, as shown in Figure 3. Both IR spectra of the inclusion complex of β-CD:BPA (1:1) and β-CD standard were practically the same. Also, the BPA molecules have distinct peaks at 1611.90 cm^{-1} and 1510.54 cm^{-1} (aromatic C=C stretch), 1247.00 – 1177.13 cm^{-1} (C-O stretch) and 827.51 cm^{-1} (aromatic *para* substituted, out of plane). However, all peaks in the spectrum of β-CD:BPA (1:1) complex were reduced in intensity. This is due to the restricted vibrational motion of the respective functional group when included within the β-CD cavity. On the other hand, the ether (C-O-C) peaks of β-CD at 1081.16 cm^{-1} and 1029.02 cm^{-1} still remained without any significant differences in the IR intensity. This effect can be attributed to the formation of an inclusion complex between the BPA and β-CD.

Investigation into the binding sites of the BPA on β-CD was carried out by means of ^{1}H NMR spectroscopy and the use of deuterium oxide (D_2O) as a solvent. Upon the inclusion of BPA into the β-CD cavity, there were two notable and quantitative chemical shifts of β-CD signals from the H3 and H5 protons inside the cavity, which was consistent with another study [5]. A comparison of the ^{1}H NMR peaks in Figure 4 showed that the H3 and H5 signals were shifted upfield, owing to the greater shielding from the BPA protons. Meanwhile, the other protons located at the exterior surfaces of β-CD, i.e. H2, H4 and H6, were not noticeably affected. A significant difference in the chemical shifts of H3 and H5 protons was seen, as H5 proton was considerably shifted from 3.72 ppm to 3.33 ppm. However, the H3 peak was shifted to some extent from 3.86 ppm to 3.69 ppm, as evident by the data of chemical shifts of the β-CD:BPA complexes with the molar ratios from 1:0 to 1:2.0. From this data, the K_a between β-CD and BPA molecules could be calculated. Typically, an ideal molar ratio between the host and guest molecule that forms the

inclusion complex is needed for the accurate determination of K_a. In this study, the ideal complex composition of β-CD:BPA, that led to an optimum chemical shift difference was determined by using the graph presented in Figure 4.

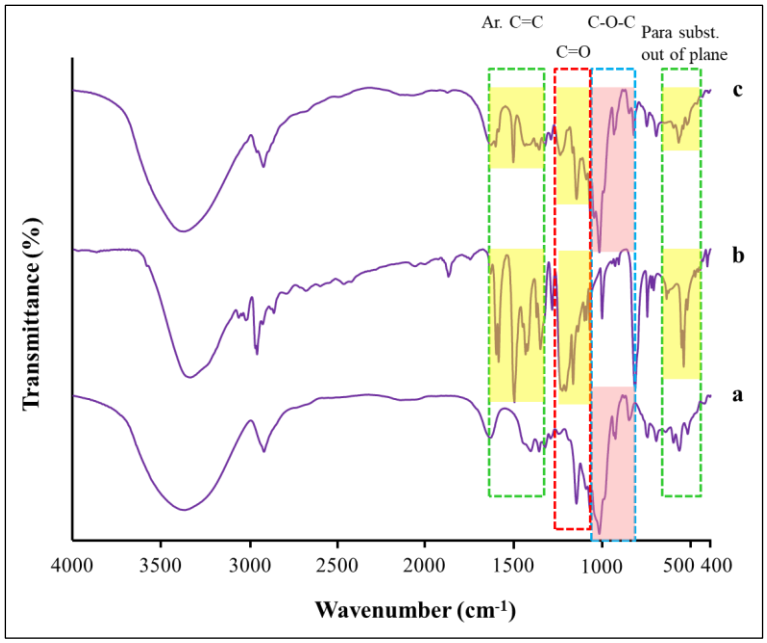


Figure 3. FTIR spectra of (a) β-CD standard (b) BPA standard and (c) β-CD:BPA (1:1) inclusion complex

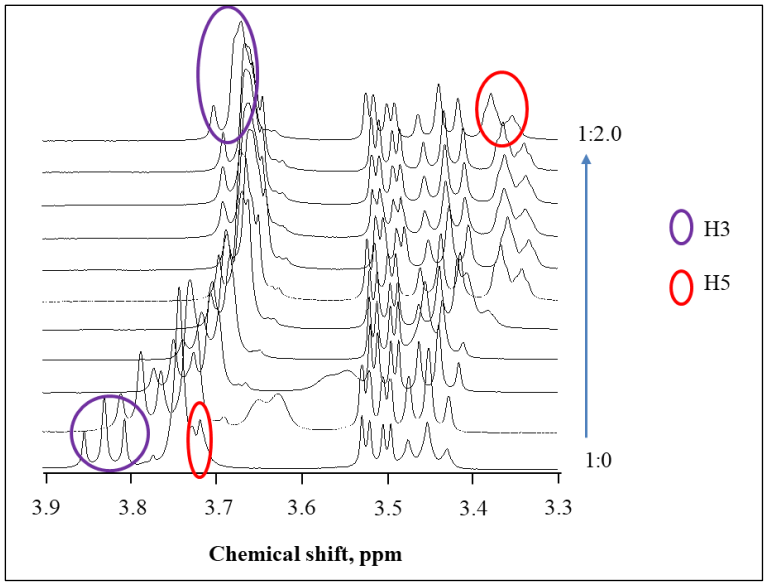


Figure 4. ^{1}H NMR spectra of β-CD:BPA complex with the molar ratios from 1:0 to 1:2.0 in D_2O at room temperature

Reportedly, the common molar ratios for inclusion complexation that involved β-CD are either 2:1, 1:2 or 1:1 and for β-CD:BPA inclusion complex the formation was only 1:1 [19]. From Figure 5, the synthesised molar ratio of

1:0.8 eventually formed the 1:1 inclusion complex of β-CD:BPA and further excess of BPA molecules will not form the 1:2 inclusion complex [5]. Therefore, an equation based on the 1:1 molar ratio complex was applied to determine the K_a:

$$\Delta = \frac{\Delta_{max} K_a [\text{BPA}]}{1 + K_a [\text{BPA}]} \quad (1)$$

Therefore, the binding curves for the H3 and H5 protons in β-CD were plotted by using the chemical shift difference calculated by means of Equation 1, and the ideal molar ratio was determined in Figure 5.

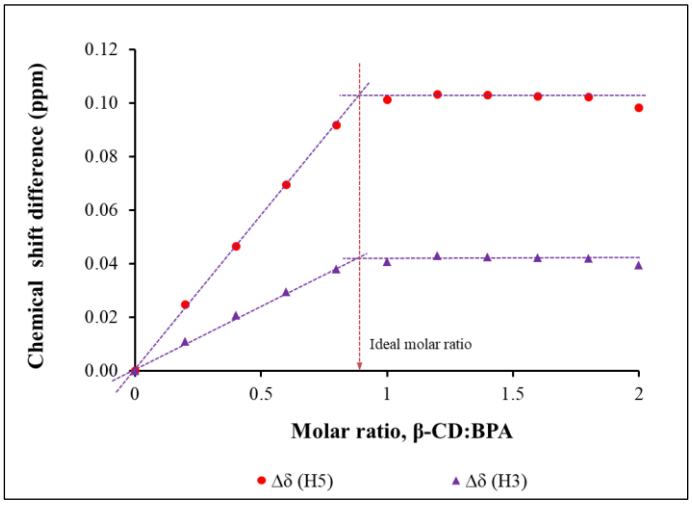


Figure 5. Determination of molar ratio system to synthesise 1:1 β-CD:BPA inclusion complex

As can be seen from Figure 6(a) and Table 1, H5 proton has higher chemical shift difference than H3, which was proven by the calculated Δ_{max} of 0.141 ppm for the H5 and 0.057 ppm for the H3 protons. From the results, it was apparent that the H3 curve was more closely fitted to the non-linear equation (Equation 1) as compared to H5. Besides, the calculated K_a for the H3 (4.10 x 10^3 M^{-1}) was much higher than the H5 (3.62 x 10^3 M^{-1}), confirming that the BPA molecules were included within the hydrophobic cavity of β-CD [5,20,21] through its secondary face (Figure 6 (b)). These values are essential in the selectivity coefficient calculation of materials that are developed to be used as a BPA sensor. Hence, a greater selectivity coefficient means the material is better to sense BPA.

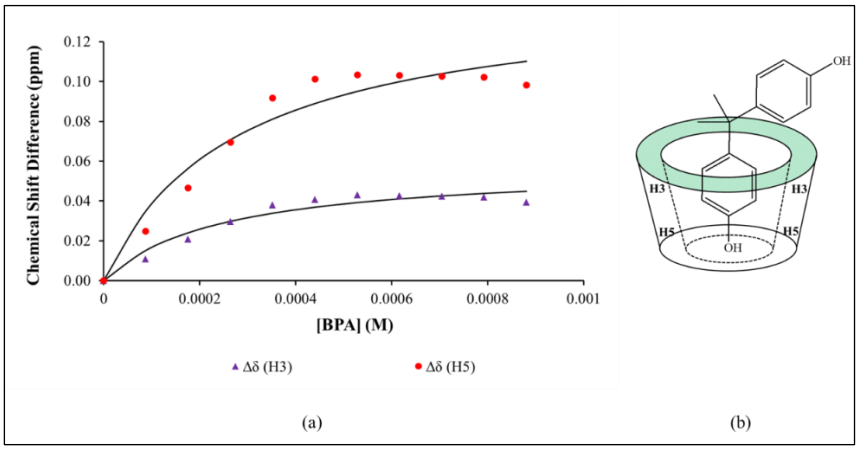


Figure 6. (a) Binding curves for H3 and H5 protons of β-CD and (b) structure of β-CD:BPA inclusion complex

Table 1. Binding association constant (K_a) and maximum chemical shift difference (Δ_{max}) for H3 and H5 protons

β-CD protons	Maximum Chemical Shift Difference, Δ_{max} (ppm)	Binding Association Constant, K_a (M^{-1})
H3	0.057	4.10×10^3
H5	0.141	3.62×10^3

Conclusion

K_a for the inclusion complex of BPA with β-CD was successfully determined by using ^{1}H NMR spectroscopy. Upfield shifts of the H5 and H3 protons located in the internal hydrophobic cavity of β-CD were observed with the calculated K_a of 3.62×10^3 M^{-1} and 4.10×10^3 M^{-1}, respectively. Based on the K_a value, the H3 proton located on the secondary faces of β-CD was suggested to play an important role in encapsulating the BPA molecules inside the β-CD cavity. In summary, these results revealed that the BPA molecules bind into the cavity *via* the β-CD secondary faces. The K_a can be further used by other researchers to study and compare the selectivity coefficient of BPA by various materials that were developed. Through this, researchers can distinguish materials that are better to be further developed as a BPA sensor.

Acknowledgement

The authors gratefully acknowledge the Nanotechnology Research Alliance, Faculty of Science, Universiti Teknologi Malaysia for the research facilities, and the Ministry of Higher Education (MOHE), Malaysia for their financial support through the Research University Grant (Q.J130000.2513.08H34) and Fundamental Research Grant Scheme (Q.J130000.2526.11H47).

References

1. Bittner, G., D. (2014). Chemicals having estrogenic activity can be released from some bisphenol A-free, hard and clear, thermoplastic resins. *Environmental Health*, 13: 103 – 120.
2. Jansssen, S. (2005). Brominated flame retardants: Rising levels of concern. health care without harm (HCWH), Arlington, VA, USA: pp. 10 - 11.
3. De Wit, C., A. (2002). An overview of brominated flame retardants in the environment. *Chemosphere*, 46: 583 – 624.
4. Eljarrat, E. and Barcelo, D. (2011). Brominated flame retardants. The handbook of environmental chemistry, Springer, Springer-Verlag Berlin Heidelberg, New York. 16: pp. 19 – 53.
5. Yang, Z.-X., Chen, Y. and Liu, Y. (2008). Inclusion complexes of bisphenol A with cyclomaltoheptaose (β-Cyclodextrin): Solubilization and structure. *Carbohydrate Research*, 343: 2439 – 2442.
6. Yu, X., Chen, Y., Chang, L., Zhou, L., Tang, F. and Wu, X. (2013). β-cyclodextrin non-covalently modified ionic liquid-based carbon paste electrode as a novel voltammetric sensor for specific detection of bisphenol A. *Sensor and Actuators B*, 186: 648 – 656.
7. Zhou, Y., Gu, X., Zhang, R. and Lu, J. (2015). Influences of various cyclodextrin on the photodegradation of phenol and bisphenol A under UV light. *Industrial & Engineering Chemistry Research*, 54: 426 – 433.
8. Wang, G., Wu, F., Zhang, X., Luo, M. and Deng, N. (2006). Enhanced photodegradation of Bisphenol A in the presence of β-cyclodextrin under UV light. *Journal of Chemical Technology and Biotechnology*, 8: 805 – 811.
9. Kono, H. and Nakamura, T. (2013). Polymerization of β-cyclodextrin with 1,2,3,4-butanetetracarboxylic dianhydride: Synthesis, structural characterization, and bisphenol A adsorption capacity. *Reactive & Functional Polymers*, 73: 1096 – 1102.
10. Aoki, N., Arai, R. and Hattori, K. (2004). Improved synthesis of chitosan-bearing β-cyclodextrin and its adsorption behavior towards bisphenol A and 4-nonylphenol. *Journal of Inclusion Phenomena and Macrocyclic Chemistry*, 50: 115 – 120.
11. Araki, M., Kawasaki, N., Nakamura, T. and Tanada, S. (2001). Removal of bisphenol A in soil by cyclodextrin derivatives. *Toxicological and Environmental Chemistry*, 79: 23 – 29.

12. Del Valle, E. M. M. (2004). Cyclodextrin and their uses: A review. *Process Biochemistry*, 39: 1033 – 1046.
13. Ezawa, T., Inoue, Y., Tunvichien, S., Suzuki, R. and Kanamoto, I. (2016). Changes in the physicochemical properties of piperine/β-cyclodextrin due to the formation of inclusion complexes. *International Journal of Medicinal Chemistry*, 2016: 1 – 9.
14. Shaikh, H., Sener, G., Memon, N., Bhanger, M., I., Nizamani, S.,M., Uzek, R. and Denizli, A. (2015). Molecularly imprinting surface plasmon resonance (SPR) based sensing of bisphenol a for its selective detection in aqueous systems. *Analytical Methods*, 7: 4661 – 4670.
15. Gao, Y., Cao, Y., Yang, D., Luo, X., Tang, Y. and Li, H. (2012). Sensitivity and selectivity determination of bisphenol A using SWCNT-CD conjugate modified glassy carbon electrode. *Journal of Hazardous Materials*, 199 – 200: 111 – 118.
16. Jo, M., Ahn, J.-Y., Lee, J., Lee, S., Hong, S., W., Yoo, J.-W., Kang, J., Dua, P., Lee, D.-K., Hong, S. and Kim, S. (2011). Development of single-stranded DNA aptamers for specific bisphenol A detection. *Oligonucleotides*, 21(2): 85 – 91.
17. Sjetli, J. (1988). Cyclodextrin technology. Topics in inclusion science. Kluwer Academic Publisher, Netherlands: pp. 85.
18. Miller, L. A., Carrier, R. L. and Ahmed, I. (2007). Practical consideration in development of solid dosage forms that contain cyclodextrin. *Journal of Pharmaceutical Sciences*, 96(7): 1691 – 1707.
19. Thodarson, P. (2011). Determining association constants from titration experiments in supramolecular chemistry. *Chemical Society Reviews*, 40: 1305 – 1323.
20. Chelli, S., Majdoub, M., Jouini, M., Aeiyach, S., Maurel, F., Chane-Ching, K., I. and Lacaze, P.-C. (2007). Host-guest complexes of phenol derivatives with β-cyclodextrin: An experimental and theoretical investigation. *Journal of Physical Organic Chemistry*, 20: 30 – 43.
21. Kitano, H., Endo, H., Gemmei-Ide, M. and Kyogoku, M. (2003). Inclusion of bisphenols by cyclodextrin derivatives. *Journal of Inclusion Phenomena and Macrocyclic Chemistry*, 47: 83 – 90.

Malaysian Journal of Analytical Sciences, Vol 23 No 2 (2019): 189 - 196
DOI: https://doi.org/10.17576/mjas-2019-2302-02

MALAYSIAN JOURNAL OF ANALYTICAL SCIENCES
Published by The Malaysian Analytical Sciences Society
ISSN 1394 - 2506

SYNTHESIS AND CHARACTERISATION OF *N*-ANALINEFERROCENYLAMIDE VIA CARBODIIMIDE COUPLING

(Sintesis dan Pencirian *N*-Analineferosenilamida melalui Gandingan Silang Karbodiimida)

Ken Min Liew[1], Tei Tagg[1], Wan M. Khairul[1,2]*

[1] *School of Fundamental Science*
[2]*Advanced Nano Materials (ANoMa) Research Group, School of Fundamental Science*
Universiti Malaysia Terengganu, 21030 Kuala Nerus, Terengganu, Malaysia

**Corresponding author: wmkhairul@umt.edu.my*

Received: 24 February 2019; Accepted: 24 March 2019

Abstract

Ferrocene is an orthodox organometallic complex. This "sandwich compound" was found to have great flexibility in chemical reactions. The use of ferrocenyl derivatives branches into various interesting fields especially for biological applications. Derivatives of ferrocenylamides are of great interest in the field of medicine and biology researches, due to their ability to bind with various biomolecules, i.e. DNA. Thus, a simple yet effective method in the formation of ferrocenylamide derivatives is desirable. Ferrocene is stable in both aqueous and aerobic media, it also has a certain degree of resistance to thermal degradation, and hence the synthesis of ferrocenyl derivatives via carbodiimide coupling is possible. In this work, *N*-analineferrocenylamide was synthesised from 3-(ethyliminomethyleneamino)-*N*,*N*-dimethylpropan-1-amine (EDC) coupling of ferrocenecarboxylic acid and *p*-phenylenediamine. This synthesis approach is a simple and easy one-pot reaction without the need of tedious conditions and has a good product yield.

Keywords: ferrocene, amide, EDC coupling

Abstrak

Ferosena merupakan kompleks organologam yang ortordoks. "Sebatian sandwich" ini didapati mempunyai pelbagai kebolehan di dalam tindakbalas kimia. Pengunaan terbitan-terbitan ferosena terjangkau di dalam pelbagai bidang yang menarik terutamanya dalam aplikasi biologi. Terbitan-terbitan ferosenilamida telah menarik minat yang mendalam dalam kajian bidang perubatan dan biologi, berdasarkan keupayaannya untuk terikat dengan pelbagai biomolekul seperti DNA. Justeru itu, kaedah yang ringkas dan efektif dalam pembentukan terbitan-terbitan ferosenilamida telah menjadi keutamaan. Ferosena adalah stabil di dalam kedua-dua media akues dan aerobik, ia juga mempunyai darjah keupayaan rintangan yang tertentu terhadap penguraian terma, yang telah memungkinkan sintesis terbitan-terbitan ferosena melalui gandingan silang karbodiimida. Di dalam kajian ini, *N*-analinaferosenilamida telah disintesiskan daripada gandingan silang 3-(etiliminometilenaamino)-*N*,*N*-dimetilpropan-1-amina (EDC) terhadap asid karboksilikferosena dan *p*-fenilenadiamina. Pendekatan sintesis adalah tindakbalas satu pot yang ringkas dan mudah tanpa memerlukan keadaan yang remeh dan berjaya menghasilkan hasilan yang baik.

Kata kunci: ferosena, amida, gantian silang EDC

Introduction

To date, the research on ferrocene and ferrocenyl derivatives are still advancing. Recent years, ferrocenyl derivatives are widely used in biological applications [1-10], material science [11] and catalysis [12-13]. Ferrocenyl amides were synthesised with various synthetic approaches in the previous occasions [14-19]. To the continuous

effort of creating simpler approach to ferrocenyl amide synthesis, this work involves a simple approach with carbodiimide coupling. The selected coupling method requires the use of only one reacting vessel, with minimal agitation and at room temperature.

This project uses ferrocenecarboxylic acid and *p*-phenylenediamine as starting materials, leading to the final product by a modification of the very successful Steglich esterification. Steglich esterification was reported as very successful for bimolecular esterification at rather high dilutions [20], with the use of 3~10% mol of 4-*N*,*N*-dimethylaminopyridine (DMAP) as homogenous organocatalyst. DMAP was used as "activator" for the coupling [21], to form a stable intermediate O-acylisourea [22] which resonates into a reactive species that significantly catalyse the coupling reaction.

Materials and Methods

All chemicals and solvents used in this study were obtained from standard commercial suppliers and used as received without further purification nor had treatment been carried out prior experimental works. Chemicals namely ethyl acetate (EA) and dichloromethane (DCM) were purchased from Fisher Scientific. In addition, chemicals namely *N*,*N*'-dicyclohexylcarbodiimide (DCC), 3-(ethyliminomethyleneamino)-*N*,*N*-dimethylpropan-1-amine (EDC), ferrocenecarboxylic acid, 4-(dimethylamino)pyridine and dimethyl sulfoxide-d_6 (DMSO-d_6) were supplied by Sigma-Aldrich. While, chemicals namely anhydrous magnesium sulphate, silica gel 60 and ethanol were obtained from Merck. The FT-IR spectra were recorded using Perkin Elmer Spectrum 100 FT-IR Spectrometer 100 in the range of 4000-400cm^{-1} using potassium bromide (KBr) pellets. ^{1}H NMR were recorded in DMSO-d_6 using Bruker Avance III 700 MHz at room temperature in the range between δ_H 0-15ppm. DFT calculations were performed with Gaussian 09 (version B.01) package [23].

Synthesis of *N*-analineferrocenylamide through DCC coupling

Synthesis approach for this compound was a modified method from an esterification reported by Srinivas et al. [24]. *N*-analineferrocenylamide was prepared by esterification between 4.35mmol of ferrocenecarboxylic acid and 6.53mmol of *p*-phenylenediamine (excess reagent), catalysed by 10% (0.44mmol) DMAP. *N*,*N*'-dicyclohexylcarbodiimide (DCC) of ratio 1:1 to the reagents was employed as the coupling agent. 1.0M DCC solution in methylene chloride was mixed in to a septum secured nitrogen purged round bottom flask, with the two solid reagents and a magnetic stir bar already mixed in. The DCC solution is kept as dry and clean as possible by transferring with a steel syringe needle. 50mL of anhydrous dichloromethane was then transferred into the flask by cannula transfer at 4^{o}C with the help of ice bath. The solution matrix was then immediately mixed using a magnetic stirrer for 6h at a temperature ideally kept below 10^{o}C, then another 72h at room temperature. Reaction mixture was filtered after the 72h, the crude deep orange filtrate was purified by silica gel (SiO_2) column (ethyl acetate: dichloromethane = 1:9), to yield a bright orange precipitate.

Synthesis of *N*-analineferrocenylamide through EDC coupling

The synthesis setup and steps were completely identical to that of DCC coupling described above, except for replacing the liquid DCC with solid EDC•HCl, the EDC•HCl crystals was directly mixed in together with 4.35mmol of ferrocenecarboxylic acid and 6.53mmol of *p*-phenylenediamine. The reaction matrix was directly fed into a silica gel (SiO_2) column (ethyl acetate: dichloromethane = 1:9), to yield a bright orange precipitate.

DFT optimisation and frequency calculation

The DFT calculation was performed by using B3LYP as hybrid functional. GEN was used as keyword to specify basis sets 6-31G(d,p) on the atoms C, H, O and N; DGaussDZVP [25] on the atom Fe.

Results and Discussion

Spectroscopic data of *N*-analineferrocenylamide

^{1}H NMR (700MHz, DMSO-d_6): δ 4.21(s, 5H, C_5H_5); 4.39 (t, $^3J_{HH}$ = 4Hz, 2H, β-C_5H_4); 4.88 (s, 2H, NH); 4.94 (t, $^3J_{HH}$ = 4Hz, 2H, α-C_5H_4); 6.54 (p-d, $^2J_{HH}$ = 8Hz, 2H, Ar); 7.27 (p-d, $^2J_{HH}$ = 8Hz, 2H, Ar), 9.10 (s, 1H, NH). IR (KBr): ν(N-H, secondary) 3422 cm^{-1}; ν(N-H, secondary) 3445 cm^{-1}; ν(N-H, primary) 3373 cm^{-1}; ν(C=C, Ar) 1647 cm^{-1}, 1544 cm^{-1}; ν(C=O, amide) 1606 cm^{-1}, 1544 cm^{-1}, ν(C-N, secondary) 1404 cm^{-1}, 1313 cm^{-1}. From the ^{1}H NMR of *N*-analineferrocenylamide, protons of the primary amine (H_7) appear as a singlet at δ_H 4.88 ppm, the deshielding

effect can be accounted to the diamagnetic anisotropy generated from circulating π-electrons of neighbouring phenyl ring [26]. The *para*-disubstituted benzene (H_5 and H_6) shows a typical AA'BB' pattern when expanded, due to the protons on the opposite sides of the ring are not magnetically equivalent, portraying a second order splitting. Both resonance and negativity effect of oxygen depletes the electron density on the proton H_4, leading to a deshielding effect, explains the very downfield H_4 compare to H_7 despite both being a proton attaching to a nitrogen atom. Furthermore, H_4 is highly possible to participate in hydrogen bonding, which further deshields the proton, much downfield compare to the typical 5.0-8.0ppm region of amides. H_4 appears as singlet at δ_H 9.10 ppm, a ferrocenylamide was reported previously to show a signal at δ_H 8.44 ppm, while phenylamide appeared at δ_H 9.07 ppm [27]. Meanwhile, Fc-H_α, Fc-H_β and Fc-C_5H_5 show a typical A_2B_2 splitting pattern in their NMR profiles, the cyclopentadienyl of some ferrocenyl amides also reported to have the same chemical shift region of 4.01 ppm to 4.70 ppm [29].

In the IR spectrum of *N*-analineferrocenylamide, the bands at 3422 cm^{-1}, 3445 cm^{-1} and 1544 cm^{-1} correspond to stretching and bending of N-H bonding present in the molecule. Some ferrocenyl derivatives have shown a NH bending at frequency of 3100 cm^{-1} to 3300 cm^{-1} [30]. Both secondary and primary amine stretching were observed in the spectrum in bands of medium intensity, in well agreement with the proposed structure. The typical bands for aromatic C=C is observed as a couple of 1605 cm^{-1} and 1544 cm^{-1}. A strong absorption at 1647 cm^{-1} shows the presence of C=O, highly possible from an amide. A few reported ferrocenyl amides had shown a C=O stretching at around 1600 cm^{-1} [15, 31-33]. At the fingerprint region, a couple of C-H and N-H out-of-plane (oop) bending is observed at 824 cm^{-1} and 747 cm^{-1} respectively, further supports the presence of *para*-substituted aromatic C-H [34,35] and NH groups [36] in the molecule.

DFT calculations

The DFT calculations do not involve any geometry constraint, no solvent optimisation, in gas phase. Table 1 shows the selected geometric parameters obtained. The data obtained are in good agreement compared to a published crystallography data of similarly structured ferrocenyl amide, namely (4-Ferrocenylphenyl)benzamide [37]. Bond lengths of the centre Fe atom to different carbon atoms from the substituted cyclopentadienyl ring are reported to be 2.034Å, 2.030Å, 2.028Å, 2.039Å and 2.059Å respectively, with the greatest bond length among the five being the one attached to a substituent group. However, in the DFT calculations, the C4 that attaches to a substituent group has a shortest bond length of 2.075Å to Fe. This might be due to the substituent group in the reported molecule is an electron donating benzene group, but the substituent of *N*-analineferrocenylamide at C4 is an electron withdrawing carbonyl group. The bond angles reported are in similar trend to the calculated bond angles, being 40.81°, 68.11° and 68.32° for one, two, three adjacent carbon spacing.

Table 1. Selected parameters from results obtained in DFT optimisation

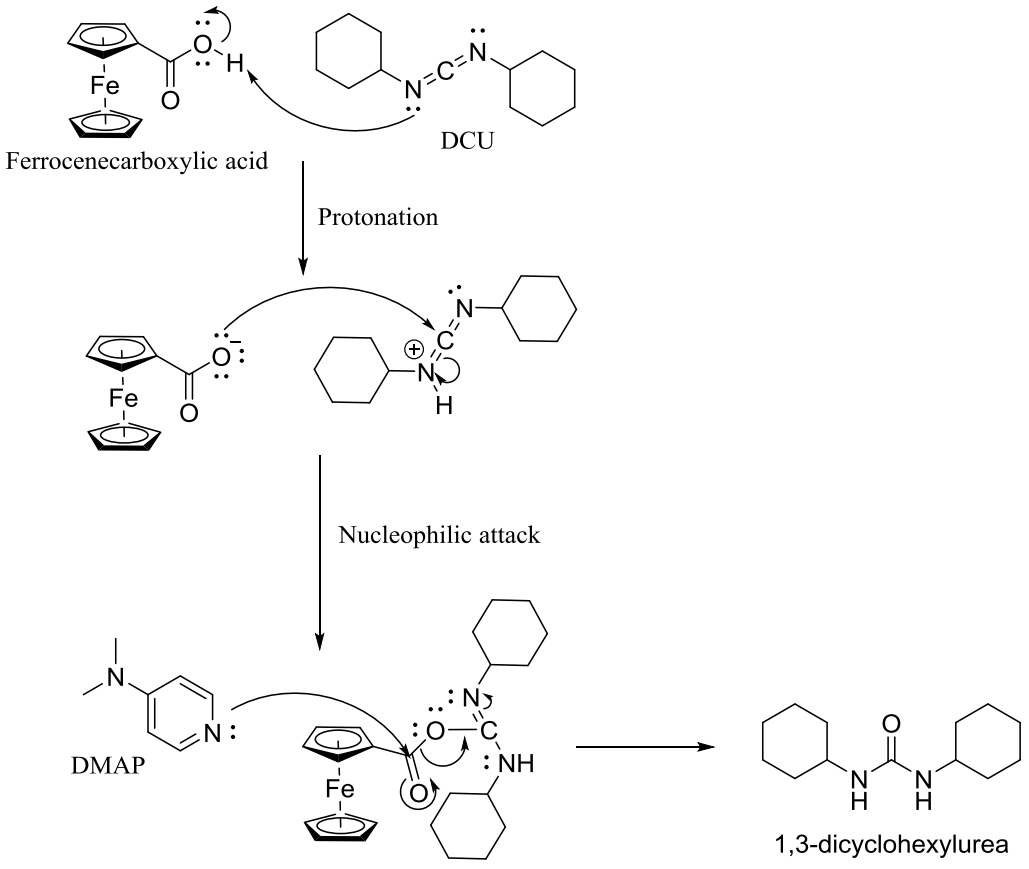
Corresponding Atoms	Bond Length (Å)	Bond Angle (°)
C1-Fe	2.086	-
C2-Fe	2.086	-
C3-Fe	2.076	-
C4-Fe	2.075	-
C5-Fe	2.078	-
C1-Fe-C2	-	40.11
C1-Fe-C3	-	67.44
C1-Fe-C4	-	67.47
C1-Fe-C13	-	112.8

Synthesis approach

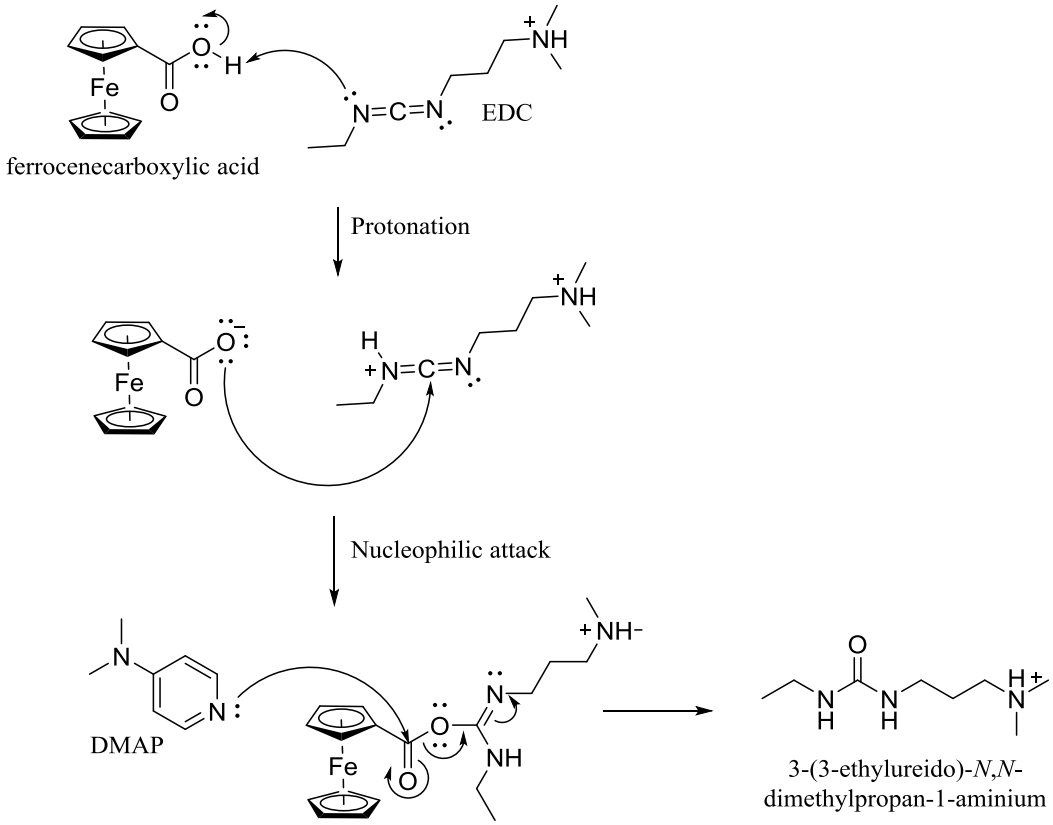
The yields from DCC and EDC coupling are 56% and 63% respectively. The primary difference of product matrix in the two different couplings are DCC coupling produces a large amount of precipitate, while EDC coupling produces little to no precipitate. The precipitate is a typical by-product of DMAP catalysed DCC coupling, *N,N'*-dicyclohexylurea (DCU) [38]. DCU is insoluble in most solvents including DCM and EA, which enables it to be separated through filtration.

On the other hand, EDC coupling produces a soluble urea, 3-(3-ethylureido)-*N.N*-dimethyl-1-propanaminium chloride as by-product. Separation of desired ferrocenyl amide from the two different coupling methods does not have much different, only filtering prior to column chromatography is required for DCC coupling. Thus, the slight difference in yield could be accounted to the multiple filtering attempt in removing DCU before the column chromatography. Furthermore, spikes of DCU were constantly observed in the NMR profile of *N*-analineferrocenylamide in the range of 1-2ppm. Ultimately, the synthesis was repeated by replacing DCC with EDC•HCl, which is known to be a water-soluble good alternative for carbodiimide coupling [39]. The product separation after EDC coupling is straight forward, effective and much lesser solvent consumption.

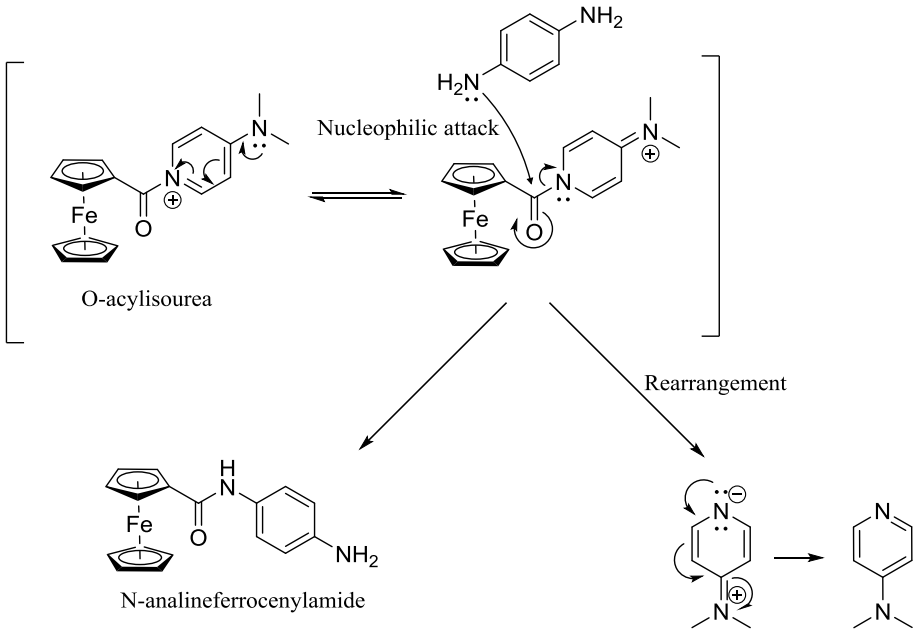
A mechanism was proposed for this synthesis referring to a few studies done previously [22,40,41]. After the nucleophilic attack from DMAP and expel of the urea leaving group shown in Scheme 1 and Scheme 2, a reactive intermediate O-acylisourea is formed. This intermediate is resonance stabilised, which enables it to exist for enough time to undergo nucleophilic attack, while reactive enough to be fully converted into end products [40, 43, 44]. The intermediate undergoes further nucleophilic attack from *p*-phenylenediamine to form the desired amide, as shown in Scheme 3.



Scheme 1. Proposed mechanism of by-product formation in DCC coupling



Scheme 2. Proposed mechanism of by-product formation in EDC coupling



Scheme 3. Formation of *N*-analineferrocenylamide from O-acylisourea

Overall, carbodiimide coupling is very effective, simple and adequate for the synthesis of ferrocenyl amide, i.e. *N*-analineferrocenylamide. A good yield of 63% was observed via EDC coupling.

Conclusion

At current stage of the study, we have demonstrated an efficient EDC coupling for the synthesis of ferrocenyl amide. Advantages of this synthesis are simple separation, one-pot reaction and relatively less tedious conditions. We anticipate that the same synthesis method could be used for the synthesis of other larger or more complex ferrocenyl amides.

Acknowledgement

The authors would like to acknowledge Ministry of Education Malaysia (MOE) for its Fundamental Research Grant Scheme (FRGS 59410), Institute of Genome Malaysia and Universiti Malaysia Terengganu for research facilities provided. We also would like to express our gratitude to MOE (Higher Education) for MyBrainSc Scholarship in supporting our postgraduate student's studies.

References

1. Singh, A., Saha, S. T., Perumal, S., Kaur, M. and Kumar, V. (2018). Azide−alkyne cycloaddition en route to 1H‑1,2,3-triazole-tethered isatin−ferrocene, ferrocenylmethoxy−isatin, and isatin−ferrocenylchalcone conjugates: synthesis and antiproliferative evaluation. *ACS Omega*, 3(1): 1263 – 1268.
2. Vashisht Gopal, Y. N., Jayaraju, D. and Kondapi, A. K. (2000). Topoisomerase II poisoning and antineoplastic action by DNA-nonbinding diacetyl and dicarboxaldoxime derivatives of ferrocene. *Archives of Biochemistry and Biophysics*, 376(1): 229 – 235.
3. Altaf, A. A., Lal, B., Badshah, A., Usman, M., Chatterjee, P. B., Huq, F., Ullah, S. and Crans, D. C. (2016). Synthesis, structural characterization, modal membrane interaction and anti-tumor cell line studies of nitrophenyl ferrocenes. *Journal of Molecular Structure*, 1113: 162 – 170.
4. Hodík, T., Lamač, M., Červenková Šťastná, L., Cuřínová, P., Karban, J., Skoupilová, H., Hrstka, R., Císařová, I., Gyepes, R. and Pinkas, J. (2017). Improving cytotoxic properties of ferrocenes by incorporation of saturated N-heterocycles. *Journal of Organometallic Chemistry*, 846: 141 – 151.
5. Lippert, R., Shubina, T. E., Vojnovic, S., Pavic, A., Veselinovic, J., Nikodinovic-Runic, J., Stankovic, N., and Ivanović-Burmazović, I. (2017). Redox behavior and biological properties of ferrocene bearing porphyrins. *Journal of Inorganic Biochemistry*, 171: 76 – 89.
6. Narváez-Pita, X., Rheingold, A. L., Meléndez, E. (2017). Ferrocene-steroid conjugates: Synthesis, structure and biological activity. *Journal of Organometallic Chemistry*, 846: 113 – 120.
7. Pérez, W. I., Soto, Y., Ortíz, C., Matta, J. and Meléndez, E. (2015). Ferrocenes as potential chemotherapeutic drugs: Synthesis, cytotoxic activity, reactive oxygen species production and micronucleus assay. *Bioorganic & Medicinal Chemistry*, 23(3): 471 – 479.
8. Sarkar, T., Banerjee, S., Mukherjee, S., Hussain, A. (2016). Mitochondrial selectivity and remarkable photocytotoxicity of a ferrocenyl neodymium(iii) complex of terpyridine and curcumin in cancer cells. *Dalton Transactions*, 45(15): 6424 – 6438.
9. Muenzner, J. K., Ahmad, A., Rothemund, M., Schrüfer, S., Padhye, S., Sarkar, F. H., Schobert, R., Biersack, B. (2016). Ferrocene-substituted 3,3′-diindolylmethanes with improved anticancer activity. *Applied Organometallic Chemistry*, 30(6): 441 – 445.
10. Takarada, J. E., Guedes, A. P. M., Correa, R. S., Silveira-Lacerda, E. de P., Castelli, S., Iacovelli, F., Deflon, V. M., Batista, A. A. and Desideri, A. (2017). Ru/Fe bimetallic complexes: Synthesis, characterization, cytotoxicity and study of their interactions with DNA/HSA and human topoisomerase IB. *Archives Biochemistry and Biophysics*, 636: 28 – 41.
11. Kulbaba, K. and Manners, I. (2001). Polyferrocenylsilanes: Metal-containing polymers for materials science, self-assembly and nanostructure applications. *Macromolecular rapid communications*, 22(10): 711 – 724.
12. Butsugan, Y., Araki, S. and Watanabe, M. (1995). Ferrocenes 3 enantioselective addition of dialkylzinc to aldehydes catalyzed by chiral ferrocenyl aminoalcohols. *Ferrocenes: Homogeneous Catalysis, Organic Synthesis, Materials Science*, 143 – 168.

13. Taei, M., Hasanpour, F. and Zahedi, G. (2015). Application of new ferrocene derivative for electrocatalytic determination of captopril using multiwall carbon nanotube modified carbon paste electrode. *Bulletin of Chemical Society Ethiopia*, 29(1): 149 – 156.
14. Ferreira, C. L., Ewart, C. B., Barta, C. A., Little, S., Yardley, V., Martins, C., Polishchuk, E., Smith, P. J., Moss, J. R., Merkel, M., Adam, M. J. and Orvig, C. (2006). Synthesis, structure, and biological activity of ferrocenyl carbohydrate conjugates. *Inorganic Chemistry*, 45(20): 8414 – 8422.
15. Zhao, M., Shao, G.-K., Huang, D.-D., Lv, X.-X. and Guo, D.-S. (2017). Synthesis, crystal structures and properties of ferrocenyl bis-amide derivatives yielded via the ugi four-component reaction. *Molecules*, 22 (5): 737.
16. Akbarzadeh, R., Mirzaei, P. and Bazgir, A. (2010). A simple synthesis of ferrocenyl bis-amides by a ugi four-component reaction. *Journal of Organometallic Chemistry*, 695(21):, 2320 – 2324.
17. Ekti, S. F. and Hür, D. (2008). Microwave assisted synthesis of ferrocene amides. *Inorganic Chemistry Communications*, 11(9): 1027 – 1029.
18. Huang, X.-F., Tang, J.-F., Ji, J.-L., Wang, X.-L. and Ruan, B.-F. (2012). Synthesis, characterization and antitumor activity of novel amide derivatives containing ferrocenyl pyrazol-moiety. *Journal of Organometallic Chemistry*, 706–707: 113 – 123.
19. Huang, X. F., Wang, L. Z., Tang, L., Lu, Y. X., Wang, F., Song, G. Q. and Ruan, B. F. (2014). Synthesis, characterization and antitumor activity of novel ferrocene derivatives containing pyrazolyl-moiety. *Journal of Organometallic Chemistry*, 749: 157 – 162.
20. Boden, E. P. and Keck, G. E. (1985). Proton-Transfer Steps in Steglich Esterification: A Very Practical New Method for Macrolactonization. *Journal of Organic Chemistry*, 50 (13): 2394 – 2395.
21. Pon, R. T. (1987). Enhanced coupling efficiency using 4-dimethylaminopyridine (DMAP) and either tetrazole, 5-(o-nitrophenyl) tetrazole, or 5-(p-nitrophenyl) tetrazole in the solid phase synthesis of oligoribonucleotides by the phosphoramidite procedure. *Tetrahedron Letters*, 28(32): 3643 – 3646.
22. Montalbetti, C. A. G. N. and Falque, V. (2005). Amide bond formation and peptide coupling. *Tetrahedron*, 61(46): 10827 – 10852.
23. Frisch, M. J., Trucks, G. W., Schlegel, H. B., Scuseria, G. E., Robb, M. A., Cheeseman, J. R., Scalmani, G., Barone, V., Petersson, G. A., Nakatsuji, H., Li, X., Caricato, M., Marenich, A. V., Bloino, J., Janesko, B. G., Gomperts, R., Mennucci, B., Hratchian, H. P., Ortiz, J. V., Izmaylov, A. F., Sonnenberg, J. L., Williams-Young, D., Ding, F., Lipparini, F., Egidi, F., Goings, J., Peng, B., Petrone, A., Henderson, T., Ranasinghe, D., Zakrzewski, V. G., Gao, J., Rega, N., Zheng, G., Liang, W., Hada, M., Ehara, M., Toyota, K., Fukuda, R., Hasegawa, J., Ishida, M., Nakajima, T., Honda, Y., Kitao, O., Nakai, H., Vreven, T., Throssell, K., Montgomery, J. A., Jr., Peralta, J. E., Ogliaro, F., Bearpark, M. J., Heyd, J. J., Brothers, E. N., Kudin, K. N., Staroverov, V. N., Keith, T. A., Kobayashi, R., Normand, J., Raghavachari, K., Rendell, A. P., Burant, J. C., Iyengar, S. S., Tomasi, J., Cossi, M., Millam, J. M., Klene, M., Adamo, C., Cammi, R., Ochterski, J. W., Martin, R. L., Morokuma, K., Farkas, O., Foresman, J. B., Fox, D. J. (2016) Gaussian 16 Revision B.01. Gaussian Inc.: Wallingford CT 2016.
24. Srinivas, P., Prabhakar, S., Chevallier, F., Nassar, E., Erb, W., Dorcet, V., Jouikov, V., Radha Krishna, P. and Mongin, F. (2016). Synthesis of ferrocene amides and esters from aminoferrocene and 2-substituted ferrocenecarboxylic acid and properties thereof. *New Journal of Chemistry*, 40(11): 9441 – 9447.
25. Sosa, C., Andzelm, J., Elkin, B. C., Wimmer, E., Dobbs, K. D. and Dixon, D. A. (1992). A local density functional study of the structure and vibrational frequencies of molecular transition-metal compounds. *The Journal of Physical Chemistry*, 96(16): 6630 – 6636.
26. Pavia, D. L., Lampman, G. M., Kriz, G. S. and Vyvyan, J. R. (2015). Introduction to Spectroscopy, Fifth Edition. Cengage Learning Asia, Singapore: pp. 390 – 397.
27. Kuo, L. J., Liao, J. H., Chen, C. T., Huang, C. H., Chen, C. S. and Fang, J. M. (2003). Two-arm ferrocene amide compounds: Synclinal conformations for selective sensing of dihydrogen phosphate ion. *Organic Letters*, 5(11): 1821 – 1824.
28. Kienz, T., Förster, C. and Heinze, K. (2014). Impact of O → S exchange in ferrocenyl amides on the structure and redox chemistry. *Organometallics*, 33(18), 4803 – 4812.
29. Carty, P., Grant, J. and Simpson, A. (1988) Synthesis of a novel ferrocene derivative having flame-retardant and smoke-suppressant properties. *Applied Organometallic Chemistry*, 2(3): 277 – 280.

30. N'Da David, D., Breytenbach Jaco, C., Smith Peter, J. and Lategan, C. (2010). Synthesis, cytotoxicity and antimalarial activity of ferrocenyl amides of 4-aminoquinolines. *Arzneimittelforschung*, 60(10), 627 – 635.
31. Javed, F., Altaf, A. A., Badshah, A., Tahir, M. N., Siddiq, M., Zia-Ur-Rehman, Shah, A., Ullah, S. and Lal, B. (2012). New supramolecular ferrocenyl amides: synthesis, characterization, and preliminary DNA-binding studies. *Journal of Coordination Chemistry*, 65(6): 969 – 979.
32. Siebler, D., Linseis, M., Gasi, T., Carrella, L. M., Winter, R. F., Förster, C. and Heinze, K. (2011). Oligonuclear ferrocene amides: Mixed-valent peptides and potential redox-switchable foldamers. *Chemistry - A European Journal*, 17(16): 4540 – 4551.
33. Heinze, K. and Schlenker, M. (2004) Main chain ferrocenyl amides from 1-aminoferrocene-1-carboxylic acid. *European Journal of Inorganic Chemistry*, 2004(14): 2974 – 2988.
34. Etter, M., Nigar, A., Ali, N. Z., Akhter, Z. and Dinnebier, R. E. (2016). Synthesis, spectroscopic and structural perspective of new ferrocenyl amides. *Solid State Science*, 55: 29 – 35.
35. Thomas, D. W. and Martell, A. E. (1956). Absorption Spectra of Para-Substituted Tetraphenylporphines1,2. *Journal of American Chemical Society*, 78(7): 1338–1343.
36. Sax, K. J., Saari, W. S., Mahoney, C. L. and Gordon, J. M. (1960). Preparation and infrared absorption spectra of some phenyl ethers. *Journal of Organic Chemistry*, 25(9): 1590 – 1595.
37. Dunkers, J. and Ishida, H. (1995). Vibrational assignments of 3-alkyl-3,4-dihydro-6-methyl-2h-1,3-benzoxazines in the fingerprint region. *Spectrochimica Acta Part A: Molecular and Biomolecular Spectroscopy*, 51(6): 1061–1074.
38. Altaf, A. A., Badshah, A., Khan, N., Tahir, M. N. (2010). (4-ferrocenylphenyl)benzamide. *Acta Crystallography Section E*, 66(7): 831.
39. Han, S.-Y. and Kim, Y.-A. (2004). Recent development of peptide coupling reagents in organic synthesis. *Tetrahedron*, 60(11): 2447 – 2467.
40. Valeur, E. and Bradley, M. (2009). Amide bond formation: Beyond the myth of coupling reagents. *Chemical Society Reviews*, 38(2): 606 – 631.
41. Williams, A. and Ibrahim, I. T. (1981). A new mechanism involving cyclic tautomers for the reaction with nucleophiles of the water-soluble peptide coupling reagent 1-ethyl-3-(3'-(dimethylamino) propyl) carbodiimide (EDC). *Journal of the American Chemical Society*, 103(24): 7090 – 7095.
42. Xu, S., Held, I., Kempf, B., Mayr, H., Steglich, W. and Zipse, H. (2005). The DMAP-catalyzed acetylation of alcohols - a mechanistic study (DMAP = 4-(Dimethylamino)Pyridine). *Chemistry - A European Journal*, 11(16): 4751 – 4757.
43. Vashist, S. K. (2012). Comparison of 1-ethyl-3-(3-dimethylaminopropyl) carbodiimide based strategies to crosslink antibodies on amine-functionalized platforms for immunodiagnostic applications. *Diagnostics*, 23 – 33.
44. Mojarradi, H. (2010). Coupling of substances containing a primary amine to hyaluronan via carbodiimide-mediated amidation. Independent Thesis Advanced Level of Professional Degree, Department of Biochemistry and Organic Chemistry, Chemistry, Disciplinary Domain of Science and Technology, Uppsala University.

Malaysian Journal of Analytical Sciences, Vol 23 No 2 (2019): 197 - 203
DOI: https://doi.org/10.17576/mjas-2019-2302-03

MALAYSIAN JOURNAL OF ANALYTICAL SCIENCES
Published by The Malaysian Analytical Sciences Society
ISSN 1394 - 2506

ELECTROCHEMICAL PROPERTIES OF MESOPOROUS SILICA (SBA-15)-CARBON ELECTRODE

(Ciri Electrokimia Karbon Silica Berliang Meso)

Noramira Saad, Mohammad Noor Jalil*, Zainiharyati Mohd Zain, Hamizah Mohd Zaki

Faculty of Applied Science,
Universiti Teknologi MARA, 40450 Shah Alam, Selangor, Malaysia

**Corresponding author: moham423@salam.uitm.edu.my*

Received: 19 August 2018; Accepted: 14 March 2019

Abstract

Mesoporous silica is material that possesses the pore sizes between 2 nm to 50 nm which had expanded their applications rapidly. In this study, mesostructured SBA-15 was synthesized and characterized then the electrochemical behaviour being analysed to determine the current signal and the impedance of mesoporous silica carbon electrode. The material with pore sizes 5.5 nm was successfully synthesized by surfactant templating technique, using triblock copolymer pluronic (P123) as directing agent and tetraethyl orthosilicate (TEOS) as silica sources. The synthesized SBA-15 was characterized using X-ray diffraction (XRD), scanning electron microscope (SEM), nitrogen adsorption-desorption and infra-red (IR). Two different electrodes were fabricated which carbon paste electrode (CPE) and hybrid SBA-15 with carbon paste electrode (SBA-15/MCPE) and analysed using cyclic voltammetry (CV) and electrochemical impedance spectroscopy (EIS). The SBA-15/MCPE results better adsorption and enhanced the response signal to 30% and lower resistance compared to CPE with 179Ω and 187Ω respectively due to addition of meso-sites which improved the electron pathway This study demonstrates that mesoporous silica (SBA-15) can be considered as promising material in development of high performance, lightweight and flexible devices in electrochemistry.

Keywords: mesoporous silica, SBA-15, electrochemical properties, mesoporous silica-carbon electrode

Abstrak

Bahan berliang meso ialah bahan yang mempunyai saiz liang antara 2 nm hingga 50 nm yang telah dikembangkan aplikasinya secara meluas. Dalam kajian ini, SBA-15 berliang meso telah disintesis dan dicirikan. Setelah itu, sifat elektrokimianya di analisis. Bahan dengan liang bersaiz 5.5 nm berjaya disintesis melalui teknik templat surfaktan menggunakan triblok ko-polimer pluronic (P123) sebagai agen pengarah dan tetraetil ortosilikat (TEOS) sebagai sumber silica. Bahan yang disintesis dicirikan menggunakan teknik pembelauan sinar-X, mikroskopi imbasan elektron, penyerapan penjerapan nitrogen dan infra merah. Dua elektrod berbeza telah difabrikasikan, iaitu elektrod pes carbon (CPE) dan elektrod yang dimodifikasi (SBA-15/MCPE). Kedua-dua elektrod yang difabrikasi di analisa dengan menggunakan alat voltametri berkitar dan spektroskopi impedans elektrokimia. SBA-15/MCPE menawarkan penjerapan yang baik dan meningkatkan signal respon sehingga 30% dan menghasilkan rintangan yang lebih rendah berbanding CPE iaitu masing-masing 179Ω dan 187Ω. Kajian ini menunjukkan bahawa SBA-15 boleh dianggap sebagai bahan yang berpotensi dalam menghasilkan alat yang berprestaai tinggi, ringan dan flexibel dalam electrokimia.

Kata kunci: silica berliang meso, SBA-15, pencirian elektrokimia, elektrod karbon-silika berliang meso

Introduction

The discovery of surfactant template silica such MCM-41, MCM-48 and SBA-15 were first reported in early 1990's which lead to whole new class of materials that offer high thermal and mechanical stability [1, 2]. Due to continuity

of mesoporous silica development, the studies regarding their properties are very active [3]. The unique properties of the mesoporous materials such uniform pore size, hexagonal array and large surface area [4] resulting excellent surface enhancement effect [5]. They are important for application in emergent areas such as energy storage in double layer supercapacitors [6], catalytic supports in fuel cell electrodes [7], adsorptions of bulky molecules in liquid phase [8] and improvements of selectivity in electro analysis [9].

Previous research had proved that mesoporous silica carbon paste enhanced the current signal compare to carbon paste electrode [10, 11, 12]. The materials were made from silica which SBA-15 provide 2D pore structure. Apparently, less research has been observed for SBA series compared to similar silica mesostructured, MCM series. The mechanism of electrode's surface during electrical charging is still under debate particularly regarding the effect of silica pore structure with the current signal obtained. In this study, the mesoporous silica (SBA-15) was synthesised than physically characterized. The electrochemical behaviours of the carbon electrode (CPE) and mixture of carbon with mesoporous silica electrode (SBA-15/MCPE) was than characterized using cyclic voltammetry (CV) and impedance spectroscopy (IS).

Materials and Methods

Chemicals and raw materials

The chemicals used were analytical grade and purchased from; Tri-block copolymer Pluronic P123, $EO_{20}PO_{70}EO_{106}$ (Sigma-Aldrich), tetraethyl orthosilicate, TEOS (98%, Aldrich), graphite powder (<20 μm, Aldrich), paraffin oil (Biobasic), hydrochloric acid, HCl (36%, Aldrich), Methanol, CH_4O, ethanol, C_2H_6O, deionized water, copper wire, glass tube, epoxy glue.

Instruments

Synthesized mesoporous silica was characterized by X-ray diffraction (Rigaku D/max-2500), FE-SEM from SUPRA 40 and for N_2 adsorption desorption (Micromeritics, ASAP 2060). The electrochemical measurements were carried out using an Auto-lab PGSTAT101 potentiostat which working electrode (CPE and SBA-15/MCPE), reference electrode (Ag/AgCl) and counter electrode (platinum).

Synthesis of SBA-15 silica

Mesoporous silica was prepared *via* surfactant templating technique as described by Sayari et al. [13]. Pluronic P123(4g) was dissolved in deionized water (30 mL) and HCl (2M, 120 mL) and stirred in closed container for 20 hours. The TEOS (8.5g) was added slowly to the mixture then being stirred vigorously for 15 minutes and kept under static condition for at temperature 35 °C for 20 hours. Thus, the substance was transferred to oven at 90 °C for 24 hours. The precipitate obtained was filtered, wash using deionized water and dried for 3 days at 45 °C. obtained silica then calcined at 500 °C in air for 6 hours.

Electrode fabrication

Two types of electrodes were prepared for cyclic voltammetry and electrochemical impedance properties as adapted from Hassan et al. [10]. The carbon paste electrode (CPE) was prepared by mixing graphite powder with paraffin oil. The SBA-15 was mixed with graphite powder and bind together using a few drops of paraffin oil to obtain modified carbon paste electrode (SBA-15/MCPE) paste. The pastes were packed tightly into the glass tube's cavity. Implementation of copper wire inside the tube provides electrical contact for the system. Then, bottom surface of the electrodes was polished using smooth paper and washed with deionized water.

Electrochemical measurement

The electrochemical measurements on electrodes were performed using cyclic voltammetry (CV) at scan rate 0.1 Vs^{-1} and recorded between -0.4V – 0.6V. The electrochemical impedance spectroscopy (EIS) measurements were performed using potentiostat at frequencies 1mHz to 10 MHz [12].

Results and Discussion

Mesoporous silica structural characterization

Powder X-ray diffractogram of synthesized mesoporous SBA-15 sample is shown in Figure 1. The diffractogram shows three resolved peaks at $2\theta \approx 0.9°$, 1.7° and 1.9°, corresponding index of (100), (110) and (200) respectively

which reflected as well-ordered mesoporous silica structured [14]. The presence of peaks can be assigned the diffractions from 2-d symmetry associated with the hexagonal structure [15].

Figure 2 shows FESEM micrographs of synthesized SBA-15 morphologies in 10k x of magnification. The micrographs show that the production of SBA-15 using P123 as directing agent possessing hexagonal-rod-like-shape to the material as reported [16].

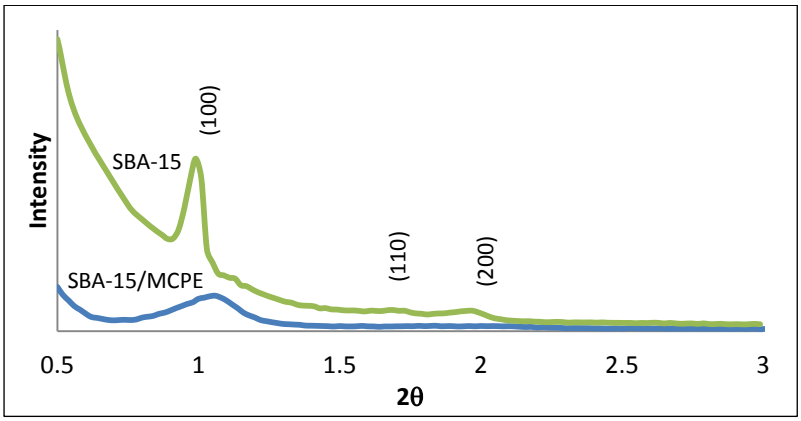


Figure 1. XRD diffraction pattern of calcined SBA-15 silica and mesoporous silica carbon paste (SBA-15/MCPE)

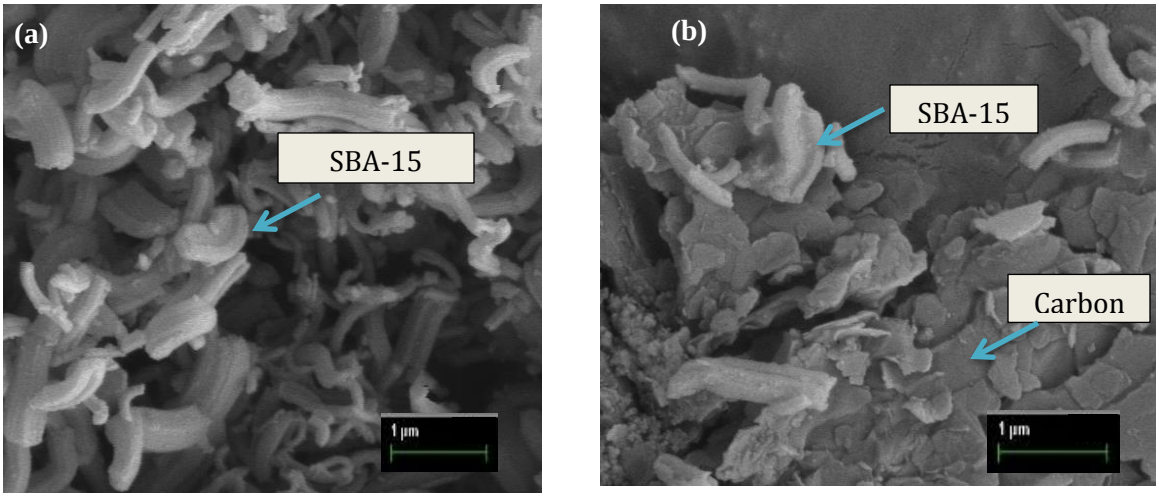


Figure 2. FESEM images of SBA-15 (A) calcined SBA-15 (B) SBA-15/MCPE

The pores structure of prepared mesoporous material was characterized by nitrogen adsorption measurements. The isotherm and pore size distributions of synthesized SBA-15 are shown in Figure 3 and 4. From the isotherm in Figure 3, calcined SBA-15 exhibits type-iv curves according to IUPAC classification [17] with hysteresis loop at relative pressure ($P/P_{\circ}$) at about 0.46 to 0.76, which indicate mesoporosity. Figure 4 shows the pore size distributions (PSD) curve as determined by BJH method. The PSD show well-defined peaks at pore diameter between 6.0 nm to 9 nm for SBA-15 sample. The presence of a low distributed peak between 4 nm to 6 nm could be the interconnected pore of SBA-15[18]. The BET surface area, pore volume and pore width of SBA-15 are summarized in Table 1.

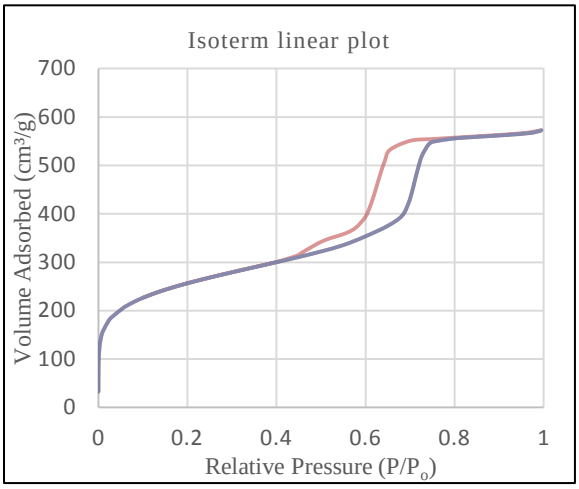


Figure 3. Nitrogen adsorption and desorption isotherms of SBA-15 (calcined at 550 °C)

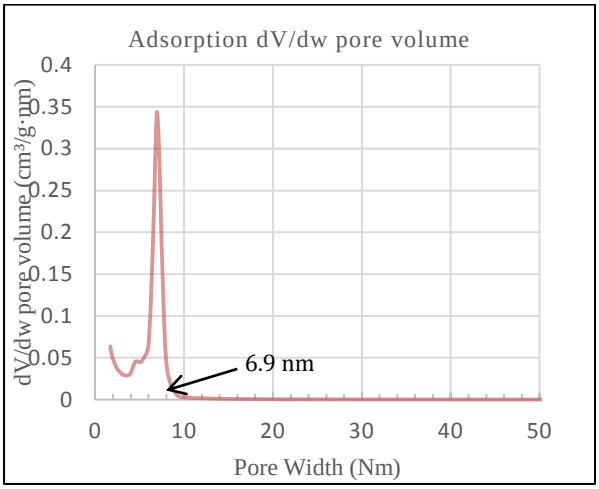


Figure 4. Nitrogen adsorption and desorption isotherms of SBA-15 (calcined at 550 °C)

Table 1. Pore properties of synthesised SBA-15 (calcined at 550 °C)

S_{BET}[(a)] (m^2/g)	Vp[(b)] (cm^3/g)	Dp[(c)] (nm)	Dp[(d)] (nm)
913.2626	0.8341	5.4271	4.9021

a Specific surface area determined by BET method,
b Total pore volume,
c Pores diameter (Dp) as determined by BJH from adsorption data
d Pores diameter (Dp) as determined by BJH from desorption data

Electrochemical behaviours study of mesoporous silica

The electrochemical behaviours were studied by cyclic voltammetry (CV) and electrochemical impedance spectroscopy (EIS). Figure 5 shows the cyclic voltammogram of $5.0x10^{-3}$ M of potassium ferrocyanide with two

different electrodes with the oxidation peaks positioned at 0.44V and 0.56V for SBA-15/MCPE and CPE respectively. As for reduction peaks of SBA-15/MCPE and CPE that positioned at -0.16V and -0.23V indicate the presence of redox process [12]. The voltammogram shows that the electrode with SBA-15 (MCPE) exhibits current enhancement with 0.00029 A compared to 0.00017 A of CPE. This enhanced the response by 30 % at oxidation peak. The same trend can be observed at the reduction peak.

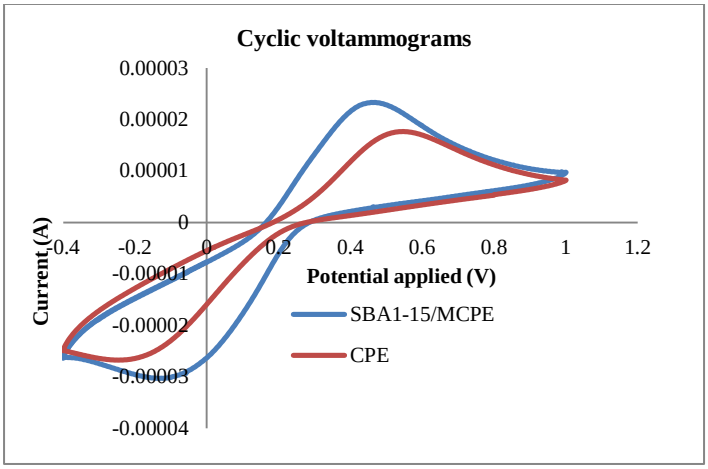


Figure 5. Cyclic voltammograms of 1mM of Fe(CN)3-4/-6 containing 0.1 M KCl as supporting electrolyte at CPE and MCPE

From Figure 6, the Nyquist plot indicates the frequency response of electrode. By fitting the data using Randles circuit (inset), R_{ct} of CPE and SBA-15/MCPE can be estimated to be 187Ω and 179Ω respectively. It is known that silica is non conducting material and suggests that the presence of silica with MCPE had modify surface morphology that attribute of conducting surface and nonconducting surface. This can be considered as self-assembled of micro electrode array as the silica surface contributes to varies spot of conducting and non-conducting site on the electrode surface. Thus, this suggests that SBA-15/MCPE surface promote good electron pathway between electrode and electrolyte. Results low electron-transfer resistance compared to CPE surface [19] as micro-electrode properties [20].

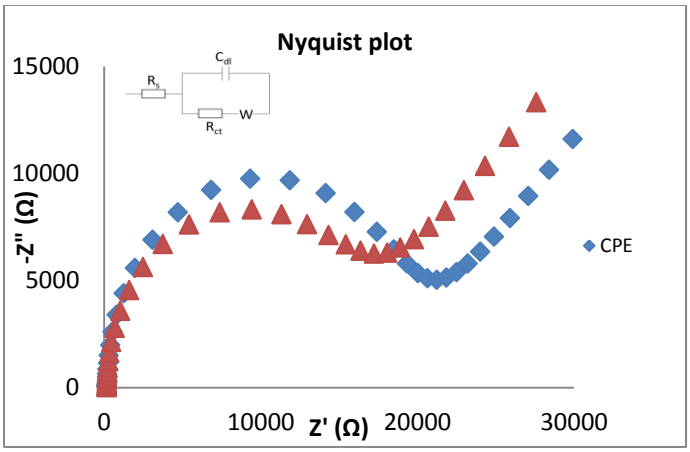


Figure 6. Nyquist plot at CPE and MCPE in of 1mM of Fe(CN)3-4/-6 containing 0.1 M KCl as supporting electrolyte

Conclusion

The mesoporous material was successfully synthesized with 5.5 nm pore size. Electrochemical study indicates that MCPE/SBA-15 result higher current by 30% and lower resistance compared to CPE with 187Ω and 179Ω respectively. From the results obtained, the SBA-15/MCPE which combined SBA-15 with carbon shows improvement in electrochemical behaviours due to unique characteristics of mesoporous silica material which prohibit uniform pore, large pores size and high pore volume. Higher fraction of mesopores in the carbon paste (MCPE) mixture promote higher current densities on the surface. This provides many favourable sites for electron transfer [21, 22] and shows a smaller resistance (179Ω) with respect to mainly carbons paste [23] as micro-electrodes properties. For further study, different pore structure silica as SBA-16 and the different composition of silica may be use to study the contribution towards the electrochemical behaviours.

Acknowledgement

The authors gratefully acknowledged the financial support from Research Management Centre (RMI), Universiti Teknologi MARA (UiTM) under the Supervision Intensive Grant (600-IRMI/MYRA 5/3/GIP(05/2017), Non-Destructive Biomedical and Pharmaceutical Research Centre of Faculty Farmacy, Universiti Teknologi MARA Puncak Alam and Institute of Science (Centre of Advanced Materials) Universiti Teknologi MARA Shah Alam for the facilities.

References

1. Prub, T., Macquarrie, D. J. and Clark, J. H. (2004). Cobalt–acetato complexes immobilised on PYPA-organomodified silica: A case study of different ways of immobilisation. *Journal of Molecular Catalysis A: Chemical*, 211(1-2): 209 – 217.
2. Guo, W., Luo, G. S. and Wang, Y. J. (2004). A new emulsion method to synthesize well-defined mesoporous particles. *Journal of Colloid and Interface Science*, 271(2): 400 – 406.
3. Cesarino, I., Marino, G., Matos, J. D. R. and Cavalheiro, É. T. (2007). Using the organofunctionalised SBA-15 nanostructured silica as a carbon paste electrode modifier: determination of cadmium ions by differential anodic pulse stripping voltammetry. *Journal of the Brazilian Chemical Society*, 18(4) 810 –817.
4. Hoffmann, F., Cornelius, M., Morell, J. and Fröba, M. (2006). Silica- based mesoporous organic–inorganic hybrid materials. *Angewandte Chemie International Edition*, 45(20): 3216 – 3251.
5. Sun, D., Xie, X. and Zhang, H. (2010). Surface effects of mesoporous silica modified electrode and application in electrochemical detection of dopamine. *Colloids and Surfaces B: Biointerfaces*, 75(1): 88 – 92.
6. Matos, J. R., Mercuri, L. P., Kruk, M. and Jaroniec, M. (2001). Toward the synthesis of extra-large-pore MCM-41 analogues. *Chemistry of Materials*, 13(5): 1726 – 1731.
7. Fuertes, A. B. (2004). Synthesis of ordered nanoporous carbons of tuneable mesopore size by templating SBA-15 silica materials. *Microporous and Mesoporous Materials*, 67(2-3): 273 – 281.
8. Shan, Y., & Gao, L. (2007). Formation and characterization of multi-walled carbon nanotubes/Co3O4 nanocomposites for supercapacitors. *Materials Chemistry and Physics*, 103(2-3): 206-210.
9. Marino, G., Bergamini, M. F., Teixeira, M. F. and Cavalheiro, E. T. (2003). Evaluation of a carbon paste electrode modified with organofunctionalized amorphous silica in the cadmium determination in a differential pulse anodic stripping voltammetric procedure. *Talanta*, 59(5): 1021 – 1028.
10. Hassan, H. M., Ab Rahman, N. B. and Jalil, M. N. (2016). Mesoporous silica electrochemical sensors for the detection of ascorbic acid and uric acid. *Malaysian Journal of Analytical Sciences*, 20(2): 351 – 357.
11. Ndamanisha, J. C. and Guo, L. P. (2012). Ordered mesoporous carbon for electrochemical sensing: A review. *Analytica Chimica Acta*, 747: 19 – 28.
12. Lufrano, F. and Staiti, P. (2010). Mesoporous carbon materials as electrodes for electrochemical supercapacitors. *International Journal Electrochemical Sciences*, 5: 903 – 916.
13. Sayari, A., Han, B. H. and Yang, Y. (2004). Simple synthesis route to monodispersed SBA-15 silica rods. *Journal of the American Chemical Society*, 126(44): 14348 – 14349.
14. Dos Santos, S. M. L., Nogueira, K. A. B., de Souza Gama, M., Lima, J. D. F., da Silva Júnior, I. J. and de Azevedo, D. C. S. (2013). Synthesis and characterization of ordered mesoporous silica (SBA-15 and SBA-16) for adsorption of biomolecules. *Microporous and Mesoporous Materials*, 180: 284 – 292.

15. Lin, C. L., Pang, Y. S., Chao, M. C., Chen, B. C., Lin, H. P., Tang, C. Y. and Lin, C. Y. (2008). Synthesis of SBA-16 and SBA-15 mesoporous silica crystals templated with neutral block copolymer surfactants. *Journal of Physics and Chemistry of Solids*, 69(2-3): 415 – 419.
16. Tadjarodi, A., Jalalat, V. and Zare-Dorabei, R. (2013). Synthesis and characterization of functionalized SBA-15 Mesoporous Silica by N, N-Bis (salicylidene) ethylenediamine Schiff-Base. *Journal of Nanostructures*, 3(4): 477 – 482.
17. Sing, K. S. W., Everett, D. H., Haul, R. A. W., Moscow, L., Pierotti, R. A., Rouquerol, J., and Siemienewska T. (1985). Reporting physisorption data for gas/solid systems with special reference to the determination of surface area and porosity. *Pure and Applied Chemistry*, 57(4): 603-619.
18. Tadjarodi, A., Jalalat, V. and Zare-Dorabei, R. (2013). Synthesis and characterization of functionalized SBA-15 mesoporous silica by N,N-bis (salicylidene) ethylenediamine Schiff-base. *Journal of Nanostructures*, 3(4): 477 – 482.
19. Ndamanisha, J. C., Bai, J., Qi, B. and Guo, L. (2009). Application of electrochemical properties of ordered mesoporous carbon to the determination of glutathione and cysteine. *Analytical Biochemistry*, 386(1): 79 – 84.
20. Daniele, S. and Bragato, C. (2014). From macroelectrodes to microelectrodes: Theory and electrode properties in environmental analysis by electrochemical sensors and biosensors. L. Moretto and K. Kalcher (Editors). Springer: New York.
21. Zhou, M., Guo, J., Guo, L. P. and Bai, J. (2008). Electrochemical sensing platform based on the highly ordered mesoporous carbon− fullerene system. *Analytical chemistry*, 80(12): 4642 – 4650.
22. Zhou, M., Ding, J., Guo, L. P. and Shang, Q. K. (2007). Electrochemical behavior of L-cysteine and its detection at ordered mesoporous carbon-modified glassy carbon electrode. *Analytical Chemistry*, 79(14): 5328 – 5335.
23. Yoon, S., Lee, J., Hyeon, T. and Oh, S. M. (2000). Electric double- layer capacitor performance of a new mesoporous carbon. *Journal of the Electrochemical Society*, 147(7): 2507 – 2512.

Malaysian Journal of Analytical Sciences, Vol 23 No 2 (2019): 204 - 211
DOI: https://doi.org/10.17576/mjas-2019-2302-04

MALAYSIAN JOURNAL OF ANALYTICAL SCIENCES
Published by The Malaysian Analytical Sciences Society
ISSN 1394 - 2506

SOL-GEL/CHITOSAN HYBRID THIN FILM IMMOBILISED WITH CURCUMIN AS pH INDICATOR FOR pH SENSOR FABRICATION

(Filem Nipis Hibrid Sol-gel/Kitosan Terpegun dengan Kurkumin sebagai Penunjuk pH bagi Fabrikasi Sensor pH)

Rosmawani Mohammad[1,2]* and Musa Ahmad[2,3]

[1]*Faculty of Bioengineering and Technology,*
Universiti Malaysia Kelantan, Jeli Campus, Locked Bag No. 100, 17600 Jeli, Kelantan, Malaysia
[2]*School of Chemical Sciences and Food Technology, Faculty of Sciences and Technology,*
Universiti Kebangsaan Malaysia, 43600 UKM Bangi, Selangor, Malaysia
[3]*Industrial Chemical Technology Program, Faculty of Science and Technology,*
Universiti Sains Islam Malaysia, Bandar Baru Nilai, 71800 Nilai, Negeri Sembilan, Malaysia

**Corresponding author: rosmawani@umk.edu.my*

Received: 10 October 2018; Accepted: 21 February 2019

Abstract

An optical pH sensor based on the immobilisation of curcumin in sol-gel/chitosan hybrid thin films was fabricated on a cellulose acetate sheet as solid support for preparing a thin film. The thin film was prepared using the dip coating method. This sensor gave a range of linear pH responses at pH 9-13 (R^2 = 0.9821). The relative standard deviation (RSD) values of repeatability of this sensor were 7.03% (pH 10) and 3.34% (pH 11), while the RSD values of reproducibility were 7.46% (pH 10) and 8.66% (pH 11). The photostability of immobilised curcumin gave an RSD value of 2.37% for a study period of 15 weeks. This sensor had a response time between 10-20 s, and no hysteresis effect was observed when the pH in a cycle of pH 2-12-2 was measured. This sensor was applied in the determination of pH in real samples, and the results were comparable to a conventional pH meter.

Keywords: optical pH sensor, hybrid sol-gel/chitosan, curcumin, thin film

Abstrak

Sensor optik pH berdasarkan pemegunan kurkumin dalam filem nipis hibrid sol-gel / kitosan difabrikasi di atas kepingan selulosa asetat sebagai penyokong untuk penyediaan filem nipis. Filem nipis telah disediakan menggunakan kaedah penyalutan celup. Sensor ini memberikan julat rangsangan linear pH pada pH 9-13 (R^2 = 0.9821). Nilai sisihan piawai relatif (RSD) bagi kebolehasilan sensor ini adalah 7.03% (pH 10) dan 3.34% (pH 11), manakala nilai RSD kebolehulangan ialah 7.46% (pH 10) dan 8.66% (pH 11). Kestabilanfoto reagen kurkumin terpegun memberikan nilai RSD 2.37% untuk tempoh kajian selama 15 minggu. Sensor ini mempunyai masa tindak balas antara 10-20 s dan tiada kesan histerisis diperhatikan apabila sensor digunakan untuk mengukur pH dalam kitaran pH 2-12-2. Sensor ini digunakan untuk penentuan pH dalam sampel sebenar dan hasilnya dapat dibandingkan dengan meter pH konvensional.

Kata kunci: sensor pH optik, sol-gel hibrid / kitosan, kurkumin, filem nipis

Introduction

Various synthetic reagents have been utilised as pH indicators. However, there are not many indicators in the pH range of 10-14 [1]. In this study, curcumin was chosen as a pH indicator and given a linear response at pH 8-12. Curcumin [1,7-bis (4-hydroxy-3-methoxyphenyl)-1,6-heptadiene-3,5-dione] is a natural yellow dye obtainable from

Curcuma longa (turmeric).

For the past decade, sol-gel has been used in various fields of chemical sensors and biosensors. This is due to its uniqueness due to several of its qualities such as chemical inertness, biodegradable, high photochemical, thermal stability and it does not swell in aqueous and organic solution [2]. However, the major disadvantage of sol-gel is the cracking problem. A considerable number of studies have been conducted to overcome the cracking problem by forming hybrid matrices including poly(ethylene oxide)–silica hybrid nanocomposites [3], silica–titania hybrid nanoparticles [4], silica matrix-poly(aniline boronic acid) hybrid [5], hybrid chitosan (CS)/calcium aluminosilicate nanocomposites thin films and membranes [6].

Meanwhile, chitosan has also been widely used in membrane application because it is chemically resistant, has good film-forming and hydrophilicity. However, the chitosan membrane tends to swell easily in water and alcohol solutions. Therefore, various research have been conducted to overcome this problem such as investigating the cross-linked structure of chitosan and hybridised chitosan with other polymers and inorganic substances [7].

In this work, the sol-gel/chitosan (SC) hybrid thin films were developed for the fabrication of an optical pH sensor. Hybridisation was used to overcome the weaknesses in both the sol-gel and chitosan as stated above. The hybridisation of sol-gel with chitosan is stabilised by strong hydrogen bonding, and the hybridization was able to overcome the brittleness of the sol-gel matrix [2, 8, 9]. The curcumin reagent was chosen as the pH indicator to be immobilised into the SC hybrid film in this work. In our previous work, sol-gel has been hybridised with chitosan melamine with different ratios [10]. To date, no study of curcumin reagent immobilised in sol-gel/pure chitosan hybrid thin film for optical pH sensor development has been reported.

Materials and Methods

Reagents

The curcumin (65-70%) was purchased from Sigma (St. Louis, MO, USA). Hydrochloric acid (37%) was obtained from Scharlau (Adelaide, Australia) and ethanol (95%) from Systerm (Shah Alam, Selangor, Malaysia). Tetraethyl orthosilicate (TEOS), Triton-x 100 and tris(hydroxymethyl)aminomethane were purchased from Fluka (Buchs, Switzerland). Sodium hydroxide and potassium chloride were acquired from Merck (Darmstadt, Germany). Potassium dihydrogen phosphate was purchased from Bendosen (Johor, Malaysia) and sodium hydrogen carbonate from BDH (London). Chitosan was supplied by Molbase (Shanghai, China).

Preparation of the stock solutions

The stock solutions of the sol-gel and chitosan were prepared according to the methods mentioned in our previous work [11], with some modifications. The SC hybrid solution was prepared by mixing the sol-gel solution and chitosan solution at a volume ratio of 9:1 (v/v) respectively. The mixture was stirred with a magnetic stirrer at 200 rpm for 2 hours in a sample bottle and prepared freshly for every fabrication of the optical thin film.

For immobilisation, the saturated curcumin reagent was prepared by dissolving this reagent in ethanol (95%) and stirred using a magnetic stirrer at 200 rpm for 1 hour. Then, this solution was left for a few hours until the undissolved reagent precipitated.

Construction of optical pH sensor

Initially, the mixture of the SC hybrid solution (9:1, v/v) and saturated curcumin reagent was prepared at a volume ratio of 2:1. This solution was stirred for 10-15 minutes using a magnetic stirrer bar. A thin film was prepared using the dip coating method, and cellulose acetate sheets were used as solid support with a measurement of 7.3 cm × 0.9 cm. The cellulose acetate sheets were dipped into the mixture of SC-curcumin using a dip coater. The cellulose acetate sheets containing hybrid SC-curcumin reagent were kept in a desiccator at room temperature overnight for drying purposes.

Evaluation of the optical pH sensor response

The absorbance readings were measured using an ultraviolet-visible spectrophotometer (model Varian Cary 50). Before use, the film was immersed in water to allow for the excess and unbound dyes to be removed. Then, the film

was immersed in buffer solutions of pH 1-13, and the absorbance spectra were measured at a wavelength of 300–700 nm. The response of the optical pH sensor was studied at a fixed wavelength of 502 nm as determined from the spectra.

Results and Discussion

The characterisation of the immobilised curcumin reagent was conducted for the development of an optical pH sensor including the optimisation of the volume ratio of the SC, pH effect, repeatability, reproducibility, hysteresis effect, stability, and real sample analysis. However, response time was not taken into consideration because of the difficulty in measuring the absorbance. This is because when the film was immersed in the buffer solutions pH 1-13, the colour changes that occurred were very fast (within 10–15 seconds). This was caused by the quick diffusion of H^+ ions through silica sol-gel hosts [12].

The effect of the SC ratio on the optical pH sensor response

The optimisation of the volume ratio of sol-gel and chitosan used was studied to get the optimum ratio that could overcome the cracking of the sol-gel film. As stated by Cajlakovic et al. [13], the addition of organic functional groups or organo-silane coupling agents containing epoxy, methacryl or amino functional groups can increase the gel's flexibility as well as reduce shrinkage, porosity, and density of the material. The volume ratios of sol-gel to chitosan studied were 9:1, 8:2, 7:3, 6:4, and 5:5, and the pure sol-gel film was also scrutinised as a control. Our observation showed that the films became opaque with the increasing volume of chitosan in the hybrid solution. The film at a ratio of sol-gel: chitosan 9:1 became transparent, while the films at other ratios became cloudy and opaque. A similar observation has been reported in our previous study when chitosan melamine was used in fabricating the hybrid thin film. However, only 1% of chitosan melamine was suitable to be added to the sol-gel solution due to the higher content of amino groups in chitosan melamine [10]. Meanwhile, in this study, almost 10% of chitosan was found to be optimum to be added in the sol-gel solution in order to fabricate the hybrid thin film.

As reported by Nivens et al. [14], 3-aminopropyltriethoxysilane (APTES), which is a compound that has an amino group as chitosan, was incorporated into the sol-gel. They stated that the concentrations of APTES and water must be quite low in preparing acid-catalysed multicomponent sol-gels; otherwise, the gels will form two layers and become cloudy due to the protonation of the amino groups. Furthermore, they stated that APTES is one of the organo-silane coupling agents that is commonly used for sensors and is used to bond organic probe molecules to glass and silica sol-gel surfaces. It is essential to overcome the leaching problems of the indicator molecules when they are immobilised into the sol-gel without covalent bonding.

As a comparison between the hybrid SC 9:1 film and pure sol-gel film, the absorbance spectra of the immobilised curcumin reagent in the hybrid film are higher than those found in the pure sol-gel film as shown in Figure 1. Therefore, the SC hybrid film at the ratio of 9:1 is chosen for further studies as an optimum ratio because it could give higher absorbance and could overcome the cracking problems of the sol-gel film, besides obtaining a transparent film. As reported by Gang et al. [8], Miao and Tan [2], and Wei and Collinson [9], the SC hybrids are able to overcome the cracking problems of the sol-gel films.

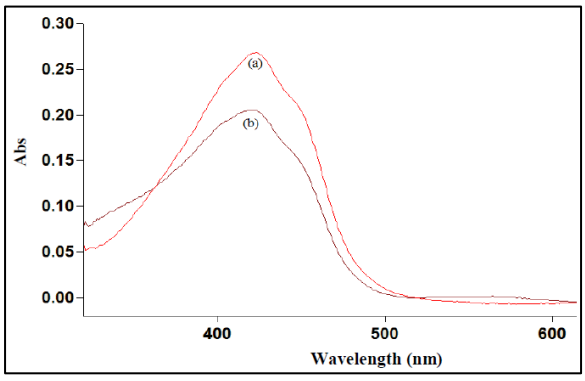


Figure 1. Absorbance spectra of curcumin immobilised in a) SC hybrid film at a ratio of 9:1 and b) sol-gel film

Analytical performance of the optical pH sensor

The spectral characteristics of the immobilised curcumin in pH 1-13 are shown in Figure 2. The initial colour of the film containing the immobilised curcumin was yellow. When the film was immersed in a buffer of pH 1-13, the film became yellow in the acidic and reddish-brown in the basic solutions. Figure 3 shows the graph of absorbance versus pH at the wavelengths of 423 nm and 502 nm, which are representative of the protonation and deprotonation regions, respectively. The sigmoid shape of the response curve is observed in Figure 3. The range of pH linear response for the curcumin reagent in the immobilised form is at pH 9-13 (R^2 = 0.9821), while the range of pH linear response for the curcumin reagent in the solution is at pH 8-12 (R^2 = 0.9854) [15]. Duong et al. [16] also reported the differences for the linear pH range in solution (pH 5-7) and the immobilised form (pH 6-9) for developing an optical pH sensor based on fluoresceinamine isomer II, covalently immobilised in a sol-gel matrix. Several differences had been reported by other researchers when the reagent is in a different form (in solution and immobilised forms) such as the differences in pKa values [12,17,18], absorbance spectra [17, 19], wavelengths [12, 19-21], and range of pH linear responses [16, 20]. As stated by Kessler and Wolfbeis [22], the dye may undergo a few changes such as spectral shifts, fluorescence quantum yield differences and molar absorptivity due to the interaction between the dye and its microenvironment [23].

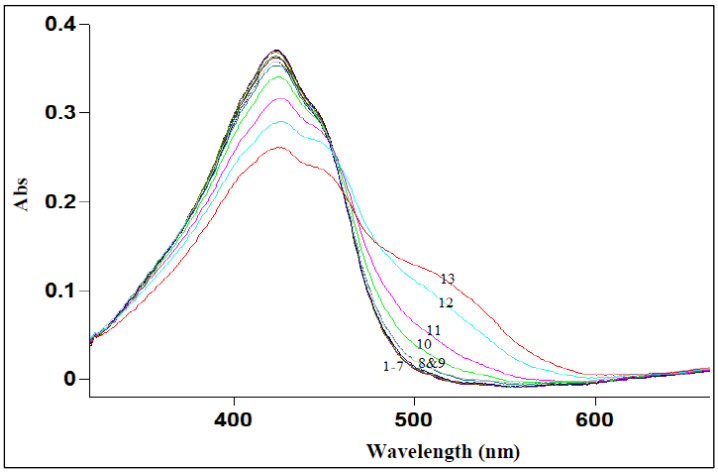


Figure 2. Absorbance spectra of curcumin immobilised in SC hybrid film (9:1) for pH 1-13

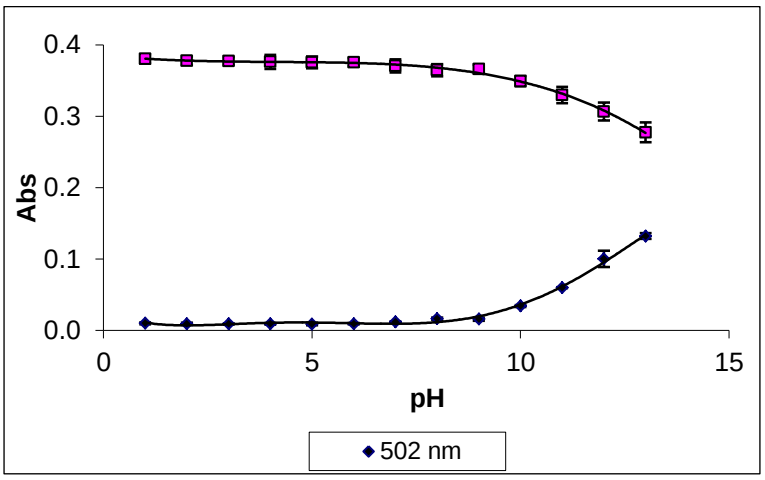


Figure 3. pH effect study of optical pH sensor towards pH 1-13

The reproducibility and repeatability of the SC hybrid film immobilised with curcumin reagent were conducted in pH 10 and pH 11. The RSD of the repeatability is found to be 7.03% (pH 10) and 3.34% (pH 11), while for reproducibility, the RSD values are 7.46% (pH 10) and 8.66% (pH 11) for the seven measurements taken. As expected, the repeatability of the hybrid film is better than its reproducibility since the variation in the absorbance is considerably greater for reproducibility compared to repeatability. The same observation has been reported in the literature [24, 25]. Therefore, a variation in absorbance was expected when measurements were taken at different points on different films. Meanwhile, the lower RSD obtained for repeatability was caused by using the same film and hence, the measurement could be taken at the same point on the same film. As a result, this could reduce the variation in absorbance when the absorbance reading was taken.

The reversibility of this optical sensor was studied by immersing the sensor in a buffer solution of pH 2-12 followed by a solution of pH 12-2. As shown in Figure 4, the response of the pH sensor displays no hysteresis when the sensor is used to measure different pH in the cycle of pH 2-12-2 (acid-base-acid). The t-test (confidence limit at 99%) shows no significant differences, and these results confirm the reversibility of the pH sensor.

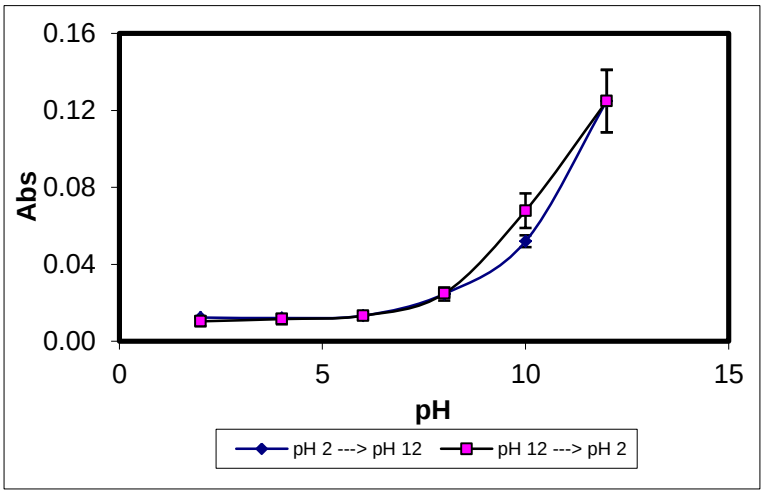


Figure 4. Hysteresis effect study on the response of the optical pH sensor

The absorbance reading (423 nm) on the first day is considered as 100% relative response. The SC hybrid film immobilised with curcumin reagent displays good storage stability for 15 weeks by maintaining >93% of the original response when stored dry at room temperature (Figure 5). However, it decreases up to 28% from the original response at week-20. Therefore, this indicates that the SC hybrid film immobilised with curcumin reagent is stable for a period of 15 weeks. Similar trend has been reported in our previous work based on curcumin reagent immobilized in sol-gel/chitosan melamine hybrid matrices [10].

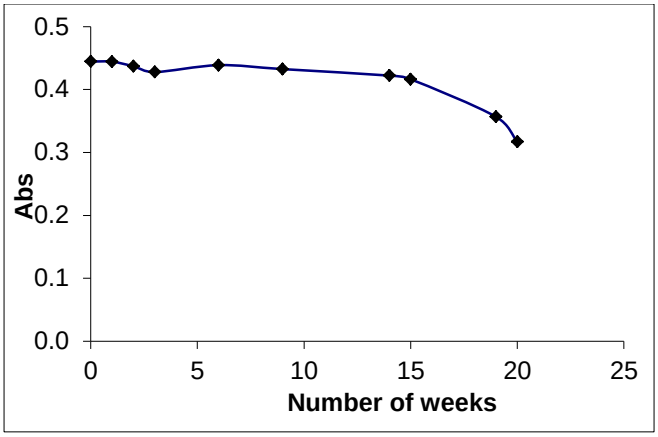


Figure 5. The shelf life of the SC hybrid film immobilised with curcumin reagent

Real sample study

This study was carried out using two samples, i.e., toothpaste and noodles. 6 g of toothpaste was dissolved in 60 mL of deionised water and filtered using filter paper. The filtrate was taken to measure the pH value using a pH meter. Meanwhile, the measurement of pH value based on pH sensor was carried out by immersing the hybrid film in the filtrate. Then, the absorbance readings of the hybrid film were measured using an ultraviolet-visible spectrophotometer at a wavelength of 502 nm. For the noodle samples, 140 g of noodles were put in 150 mL of deionised water and the same procedures were carried out for the determination of pH values using pH meter and pH sensor. The determination of pH values for both samples using this optical pH sensor show no significant differences (confidence limit = 99%) when compared with the results obtained by using a conventional pH meter (Tables 1 and 2).

Table 1. Determination of pH value for toothpaste using pH meter and pH sensor

Measurement	y=absorbance	x= pH sensor	pH meter
1	0.0154	9.23	9.16
2	0.0128	9.15	9.15
3	0.0078	8.98	9.13
4	0.0083	9.00	9.14
average		9.09	9.15
standard deviations		0.1218	0.0129

Table 2. Determination of pH value for noodles using pH meter and pH sensor

Measurement	y=absorbance	x= pH sensor	pH meter
1	0.0786	11.35	11.27
2	0.0831	11.50	11.27
3	0.0717	11.12	11.12
4	0.0840	11.53	11.28
average		11.37	11.24
standard deviations		0.1879	0.0768

Conclusion

An optical pH sensor based on curcumin reagent immobilised in SC hybrid film was successfully developed. The incorporation of chitosan into the sol-gel can overcome the cracking problem of the sol-gel film and reduces the porosity of the sol-gel film, thus reducing the leaching problem of the sol-gel film. This optical pH sensor demonstrated good repeatability and reproducibility with no hysteresis effect observed in the cycle of pH 2-12-2. In short, the advantageous features of this sensor include the ability to determine the wide range of alkaline medium and at high pH values since the range of pH linear response is from pH 9 to pH 13.

Acknowledgements

The authors are grateful for the facilities provided in the School of Chemical Sciences and Food Technology, Faculty of Sciences & Technology, Universiti Kebangsaan Malaysia and the financial support under IRPA Top-down 09-03-03-0006.

References

1. Nourmohammadian, F., Davoodzadeh, M. and Abdol-Ali, A. (2007). New cyclopentadiene derivatives as novel pH indicators. *Dyes and Pigments*, 74: 741 – 743.
2. Miao, Y. and Tan, S. N. (2001). Amperometric hydrogen peroxide biosensor with silica sol-gel/chitosan film as immobilization matrix. *Analytica Chimica Acta*, 437(1): 87 – 93.
3. Fabbri, P., Pilati, F., Rovati, L., Kenzie, R. and Mijovic, J. (2011). Poly(ethylene oxide)–silica hybrids entrapping sensitive dyes for biomedical optical pH sensors: Molecular dynamics and optical response. *Optical Materials* 33(8): 1362 – 1369.
4. Islam, S., Bidin, N., Riaz, S., Naseem, S. and Marsin, F. M. (2016). Correlation between structural and optical properties of surfactant assisted sol–gel based mesoporous SiO_2–TiO_2 hybrid nanoparticles for pH sensing/optochemical sensor. *Sensors and Actuators B*, 225: 66 – 73.
5. Li, J., Zhang, N., Sun, Q., Bai, Z. and Zheng, J. (2016). Electrochemical sensor for dopamine based on imprinted silica matrix-poly(aniline boronic acid) hybrid as recognition element. *Talanta*, 159: 379 –386.
6. Elnahrawy, A. M., Kim, Y. S. and Ali, A. I. (2016). Synthesis of hybrid chitosan/calcium aluminosilicate using a sol-gel method for optical applications. *Journal of Alloys and Compounds*, 676: 432 – 439.
7. Ying-Ling, L., Yu-Huei, S., Kuir-Rain, L. and Juin-Yih, L. (2005). Crosslinked organic-inorganic hybrid chitosan membranes for pervaporation dehydration of isopropanol-water mixtures with a long-term stability. *Journal of Membrane Science*, 251: 233 – 238.
8. Gang, W., Jing-Juan, X., Hong-Yuan, C. and Zu-Hong, L. (2003). Amperometric hydrogen peroxide biosensor with sol-gel/chitosan network-like film as immobilization matrix. *Biosensors and Bioelectrics*, 18(4): 335 – 343.
9. Wei, H. and Collinson, M. M. (1995). Functional-group effects on the ion-exchange properties of organically modified silicates. *Analytica Chimica Acta*, 397: 113-121.
10. Mohammad, R., Ahmad, M. and Jamaluddin, M. D. (2009). Pembangunan sensor optik pH berasaskan reagen kurkumin terpegun dalam matriks hibrid sol-gel/kitosan melamin. *Sains Malaysiana*, 38(3): 413-418.
11. Mohammad, R., Ahmad, M. and Heng, L. Y. (2014). Chilli hotness determination based on optical capsaicin biosensor using stacked immobilisation technique. *Sensors and Actuators B*, 190: 593 – 600.
12. Villegas, M. A. and Pascual, L. (1999). Sol-gel silica coatings doped with a pH-sensitive chromophore. *Thin Solid Film*, 351: 103 – 108.
13. Cajlakovic, M., Lobnik, A. and Werner, T. (2002). Stability of new optical pH sensing material based on cross-linked poly (vinyl alcohol) copolymer. *Analytical Chimica Acta*, 455: 207 – 213.
14. Nivens, D. A., Zhang, Y. and Angel, S. M. (1998). A fiber-optic pH sensor prepared using a base-catalyzed organo-silica sol-gel. *Analytical Chimica Acta*, 376: 235-245.
15. Mohammad, R., Ahmad, M. and Jamaluddin, M. D. (2007). Potensi kurkumin sebagai penunjuk pH semulajadi untuk pembangunan sensor optik pH. *Malaysian Journal of Analytical Sciences*, 11(2): 351-360.
16. Duong, H. D., Ok-Jae, S., Lam, H. T. and Rhee, J. I. (2006). An optical pH sensor with extended detection range based on fluoresceinamine covalently bound to sol-gel support. *Microchemical Journal*, 84(1-2): 50-55.
17. Lin, J. and Liu, D. (2000). An optical pH sensor with a linear response over a broad range. *Analytical Chimica*

Acta, 408: 49-55.
18. Malins, C., Glever, H. G., Keyes, T. E., Vos, J. G., Dressick, W. J. and MacCraith, B. D. (2000). Sol-gel immobilised ruthenium(II) polypyridyl complexes as chemical trandusers for optical pH sensing. *Sensors and Actuators B*, 67: 89 – 95.
19. Ensafi, A. A. and Kazemzadeh, A. (1999). Optical pH sensor based on chemical modification of polymer film. *Microchemical Journal*, 63: 381 – 388.
20. Liu, Z., Luo, F. and Chen, T. (2004). Polymeric pH indicators immobilized PVA membranes for optical sensors of high basicity based on a kinetic process. *Analytica Chimica Acta*, 519: 147-153.
21. Safavi, A. and Abdollahi, H. (1998). Optical sensor for high pH values. *Analytica Chimica Acta*, 367: 167 – 173.
22. Kessler, M. A. and Wolfbeis, O. S. (1991). New highly fluorescent ketocyanine polarity probes. *Spectrochim. Acta, Part A*, 47(2):187 – 192.
23. Ertekin, K., Karapire, C., Alp, S., Yenigul, B. and Icli, S. (2003). Photophysical and photochemical characteristics of an azlactone dye in sol-gel matrix; a new fluorescent pH indicator. *Dyes and Pigments*, 56: 125 – 133.
24. Ahmad, M. and Narayanaswamy, R. (1995). Development of an optical fibre Al(III) sensor based on immobilised chrome azurol S. *Talanta*, 42: 1337-1344.
25. Ahmad, M., Norezuny, M. and Jariah, A. (2001). Sensing material for oxygen gas prepared by doping sol-gel film with tris (2,2-bipyridyl) dichlororuthenium complex. *Journal of Non-Crystalline Solids*, 290: 86 – 91.

Malaysian Journal of Analytical Sciences, Vol 23 No 2 (2019): 212 - 218
DOI: https://doi.org/10.17576/mjas-2019-2302-05

MALAYSIAN JOURNAL OF ANALYTICAL SCIENCES
Published by The Malaysian Analytical Sciences Society
ISSN 1394 - 2506

ELECTROSPUN POLY (VINYL ALCOHOL) NANOFIBERS DOPED WITH MESOPOROUS SILICA NANOPARTICLES FOR CONTROLLED RELEASE OF HYDROPHILIC MODEL DRUG

(Elektrospun Poli(Vinil Alkohol) Nanofiber Didopkan Dengan Silika Nanopartikel Berliang Meso untuk Perlepasan Terkawal Model Dadah Hidrofilik)

Nur Izzah Md Fadilah[1], Haslina Ahmad[1,2]*, Mohd Firdaus Abd Rahman[3], Norizah Abdul Rahman[2]

[1]*Integrated Chemical Biophysics Research*
[2]*Department of Chemistry, Faculty of Science*
[3]*Institute of Advanced Technology*
Universiti Putra Malaysia, 43400 UPM Serdang, Selangor, Malaysia

**Corresponding author: haslina_ahmad@upm.edu.my*

Received: 19 August 2018; Accepted: 10 March 2019

Abstract

Nanofiber materials have often been reported as transporters for clinical drugs but face the limitation of burst releasing the drugs. Therefore, mesoporous silica nanoparticles (MSNs) have raised much interest to be used in drug delivery system because of their large pore volume and high surface area. In this study, nanofiber drug delivery system based on poly(vinyl alcohol) (PVA) loaded with novel ionic liquid templated MSNs were successfully prepared by the electrospinning method. The composite fiber mat was designed for the prolonged and sustained release of drug. MSNs were synthesized by co-condensation method with average particles size of ~70 nm and then loaded with hydrophilic model drug methylene blue (MB). The effect incorporation of MB-loaded MSNs into the polymer solution to form fibrous structure was investigated. Uniform PVA/MB nanofiber mat was also produced as controls. The morphologies of nanoparticles and composite nanofiber were characterized by field emission scanning electron microscope (FESEM). After electrospinning, electron microscope revealed that MSNs were randomly distributed in the regions of nanofiber. Drug release profiles of MB from MSNs and electrospun mats were evaluated. The results indicated that adsorption of model drug MB into MSNs and incorporation them into nanofiber are effective way of minimizing burst release of drug. Sustained delivery was achieved with controllable release during the 120h releasing period

Keywords: poly(vinyl alcohol), mesoporous silica nanoparticles, nanofiber, electrospinning, drug delivery

Abstrak

Bahan nanofiber sering dilaporkan sebagai penghantar untuk ubat-ubat klinikal tetapi ia menghadapi limit batasan dalam melepaskan ubat secara pecah. Oleh itu, silika nanopartikel berliang-meso (SMN) telah menimbulkan tarikan untuk digunakan dalam sistem penghantaran ubat-ubat kerana memiliki isipadu liang yang besar dan kawasan permukaan yang tinggi. Dalam kajian ini, sistem penghantaran ubat iaitu nanofiber yang berdasarkan poli(vinil alkohol) (PVA) dimuatkan bersama SMN cecair ionik baru telah berjaya disediakan melalui kaedah putaran elektro. Komposit tikar fiber telah direka untuk pembebasan ubat yang berpanjangan dan berterusan. SMN telah disintesis oleh kaedah pemeluwapan bersama dengan purata saiz partikel ~70 nm dan kemudian, dimuatkan dengan model hidrofilik ubat iaitu metilina biru (MB). Kesan penggabungan BM-SMN ke dalam polimer untuk membentuk struktur fiber telah dikaji. Nanofiber PVA/BM yang seragam juga dihasilkan sebagai kawalan. Morfologi nanopartikel dan komposit nanofiber telah dicirikan oleh mikroskop elektron pengimbasan pelepasan medan (MMEPP). Selepas putaran elektro, mikroskop elektron mendedahkan bahawa SMN berada secara rawak di dalam nanofiber. Profil pembebasan ubat BM dari SMN dan tikar putaran elektro telah dinilai. Keputusan menunjukkan bahawa penyerapan model ubat BM ke dalam SMN dan seterusnya memasukkannya ke nanofiber adalah cara yang berkesan untuk meminimumkan

pembebasan ubat secara pecah. Penghantaran yang berterusan telah dicapai dengan pembebasan yang dapat dikawal dalam tempoh 120 jam.

Kata kunci: poli(vinil alkohol), silika nanopartikel berliang-meso, nanofiber, elektrospining, penghantaran ubat

Introduction

In recent years, sustained and slow release of drugs has gained much attention towards the development of drug delivery systems (DDS). By designing DDS which can avoid burst release of drug as well as to protect normal tissue and healthy organs are becoming very crucial. The system includes minimizing the frequency of dosing, prolonging the period of the drug and providing a constant drug level. Hence, the therapeutic efficacies have been improved and could overcome the adverse side effects. Recently, a number of different carriers have been studied in order to control drug release such as micelles [1, 2], liposomes [3], biocompatible nanoparticles and electrospun nanofiber [4].

The nanofibers were widely produced by electrospinning method, in which fibers forming a matrix with interconnected pores through a polymer jet with the use of electric field [5]. Recently, drug is direct mixed to the polymer solution and blended before electrospinning. However, the electrospun mats for this approach could affect the burst release profile where the drugs were distributed throughout the volume of polymer solution. In order to overcome this problem, the encapsulating of the drugs in nanoparticles and incorporation of nanoparticles into random electrospun nanofiber has been employed. For instance, Jalvandi et al. [6] reported approximately 70% of levofloxacin (LVF) in the nanoparticles was release in burst fashion throughout the first 20 min compared to 45% of LVF released from core shell nanofiber in the first day. Song et al [7] were studied designed a co-delivery system based on poly(lactic-co-glycolic acid)(PLGA) and nanoparticles for drug delivery applications. Therefore, incorporation of nanoparticles into the polymer matrix has gained attention.

Mesoporous silica nanoparticles (MSNs) are one of the potential nanoparticles that have been used as a nanocarrier for drugs. MSNs have shown advantages and unique properties such as high specific surface area, large pore volumes and good biocompatibility with no cytotoxicity [8] therefore, it could provide an alternative method for encapsulation of drugs and thus incorporation into polymer nanofiber. Considering significant advantages of MSNs, we had successfully synthesized MSNs by using novel 1-hexadecylpyridinium bromide (C_{16}PyBr) IL as a template, then incorporated MSNs into poly(vinyl alcohol) (PVA) electrospun nanofiber produced by electrospinning technique. In this study, the key issue for preparing polymeric-inorganic nanoparticle fiber is the dispersion of MSNs in a polymer matrix uniformly while aggregation is avoided. Finally, the successfully fabricated electropun nanofiber/MSNs were investigated on release study by using methylene blue (MB) as a hydrophilic model drug.

Materials and Methods

Materials

Poly(vinyl alcohol) (PVA, MW~90000) was purchased from Nippon Gohsei Singapore Pte Ltd. All other chemicals used in the experiments were of analytical grade and used without further purification.

Synthesis of MSNs

Briefly, 0.5 g of ionic liquid template (C_{16}PyBr) was dissolved completely in 20 mL deionized water. The mixture was stirred at 750 rpm and maintained at 90 °C for 1 hour. Then, 2.0 mL TEOS and 60 µL TEA were added dropwise with the rate of 1mL/min to the above solution. The reaction was continuous stirring for another 1 hour. After the reaction completed, solution was cooled to room temperature. The synthesized nanoparticles were then centrifuged and further reflux in a mixture of 3 mL HCl and 60 mL ethanol under 90 °C for 24 hours to remove the template. The products were collected *via* centrifugation at 6000 rpm for 15 minutes and washed with ethanol several times to remove excess reactants. Finally, the obtained MSNs were dried in the oven at 60 °C for 24 hours.

Fabrication of MB-loaded MSNs

In order to prepare MB-loaded MSNs, 0.05 g of MSNs were soaked into 10 mL PBS that containing 0.1 mg/mL of MB. The solution was stirred in the dark place for 24 hours. The mixture was separated by centrifugation at 6000 rpm about 15 minutes. Finally, MB-loaded MSNs were dried at 60 °C for 24 hours to reach a constant weight. The

amount of MB loading into the MSNs was measured by determining their corresponding concentration difference in the medium before and after loading. The drug loading efficiency was calculated by using the following equation 1:

$$Drug\ loading\ efficiency(\%) = \frac{total\ amount\ MB - free\ amount\ MB}{total\ amount\ MB}\ x\ 100 \quad (1)$$

Fabrication of PVA/MB-loaded electrospun mat

An amount of MB-loaded MSNs which is 30 mg was first ultrasonically dispersed into the mixed solution of 4 mL deionized water and 1 mL acetone for 30 minutes. Then, 10 wt.% of PVA polymer was added and stirred at 80 °C to form a homogeneous solution. The electrospinning conditions were conducted as follows. Then, appropriate amount of citric acid as a crosslinking agent was added to the polymer solution. The electrospinning conditions were conducted as follows. The applied voltage on the needle of the syringe was controlled at 15kV, the rate of the polymer solution was fixed at 0.8 mL/h, and the distance between the tip of needle and the collector was 15 cm.

Characterization

TEM images were taken on a Tecnai G2 F20 electron microscope with an acceleration voltage of 200kV. BET surface area, average pore volume and average pore diameter of the nanoparticles were measured by physisorption of N_2 at 77 K over a Micromeritics ASAP 2020. Before measurement, the samples were degassed at 200 °C for 6 hours to remove moisture and adsorbed gas. The morphology observation was performed using FESEM (JEOL JSM-6700F, Japan). One hundred selected fibers randomly from the images were measured and analyzed using image analysis software to determine the fiber size distributions.

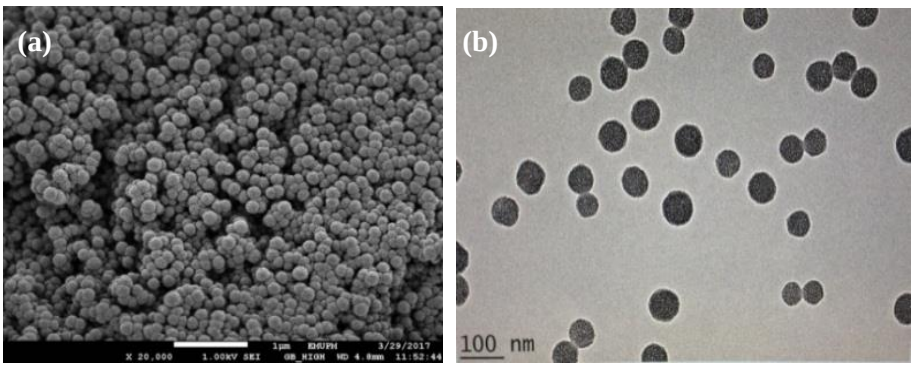
***In vitro* drug release**

The *in vitro* drug release studies were achieved in phosphate buffer saline (PBS, pH 7.4) at room temperature over 120 hours period of time. The 0.005 g MB-loaded MSNs and electrospun fiber were incubated and immersed in 10 mL PBS, separately. After that, 1 mL of the release buffer was taken out at determined time intervals for analysis and replaced with the same volume of fresh buffer. The electrospun nanofiber was taken out after immersion step and rinsed with abundant distilled water to remove the residual buffer. Then, it was freeze-dried for 2 days and the morphological change after drug release was observed by FESEM. The concentration of MB was determined by using UV-Vis spectrophotometer at 663.50 nm. The cumulative release was calculated based on the standard calibration curve.

Results and Discussion

The morphology and structure of MSNs and MB-loaded MSNs

Figure 1(a) and 1(b) showed FESEM and TEM images of the synthesized of bare MSNs, respectively. It can be seen that MSNs are approximately spherical in shape with uniform size of ~70 nm. Also, the nanoporous channels were clearly observed in the inner of MSNs. As shown in Figure 1(c), the N_2 adsorption-desorption isotherms confirmed the well-ordered mesoporous structure of MSNs and MB-loaded MSNs The properties of BET surface area, pore diameter, pore volume of the MSNs and MB-loaded MSNs also drug loading efficiency were shown in Table 1. The MSNs possessed average pore size about 5.5 nm, and the amount of MB loaded into MSNs was 91.9%. Therefore these MSNs have promising to be used as drug delivery agent.



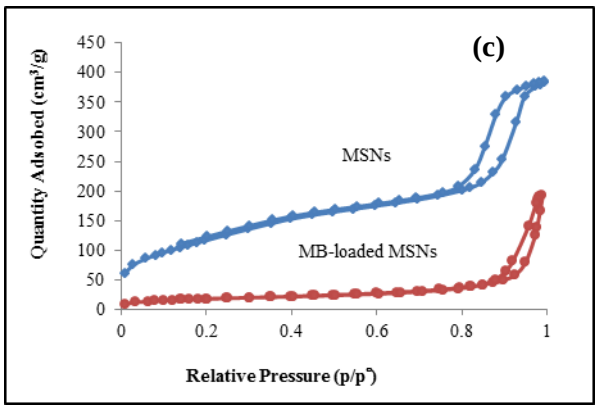


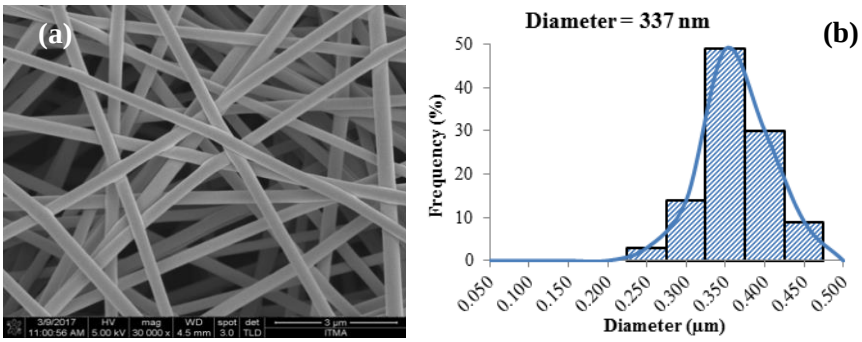
Figure 1. (a) FESEM image, (b) TEM image, and (c) nitrogen adsorption/desorption isotherms of MSNs and MB-loaded MSNs

Table 1. The properties of MSNs and MSN-loaded MB, and the drug loading efficiency

Samples	S_{BET} (m^2/g)	D_P (nm)	V_P (cm^3/g)	Drug-loading efficiency (%)
MSNs	429.14	5.5	0.63	-
MB-loaded MSNs	63.06	18.8	0.29	91.9

The morphology of electrospun composite mat

The FESEM images of PVA nanofiber before and after crosslinking are shown in Figure 2(a) and (c), respectively. The morphology of PVA nanofiber before cross-linked were uniform structure with no beads, fine and oriented fibers were formed as seen in Figure 2(a). Besides, the cross-linked PVA nanofiber were displayed stiffer and robust network with some interconnection at nanofiber junction [9]. It also was observed that the average diameter of cross-linked PVA nanofiber compared with non-crosslinked nanofiber were reduced from 337 nm to 250 nm, as shown in diameter distribution histograms below.



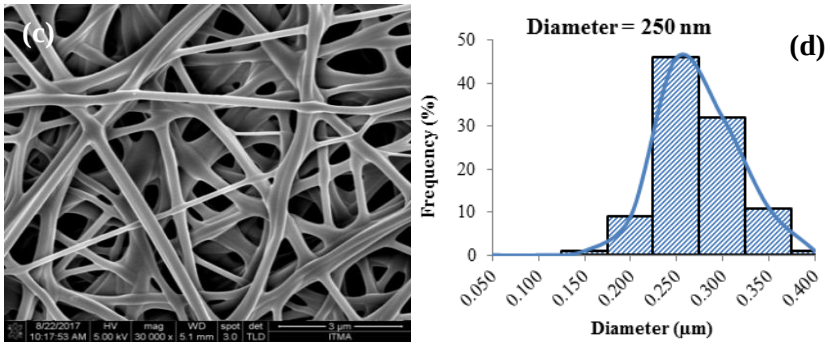


Figure 2. FESEM images of (a) non-crosslinked PVA, (c) cross-linked PVA nanofiber and (b, d) fibers diameter distribution histograms of resultant PVA nanofibers

The morphology of MSNs in electrospun mat

Figure 3 (a and b) showed FESEM images of PVA nanofiber loaded with MSNs. The figures depict that MSNs were well distributed in the PVA nanofiber. However, after addition of MSNs, the surface of electrospun PVA nanofiber seems to become rougher than electrospun without addition of MSNs. Furthermore, the average nanofiber diameter increased up to 529 nm in PVA-loaded MSNs electrospun mats as plotted through diameter distributions in Figure 3(c). This occurrence is due to the aggregation of MSNs in the polymer solution during electrospinning, rise in solution viscosity or incomplete dispersion during initial dispersion process into the polymer solution [6].

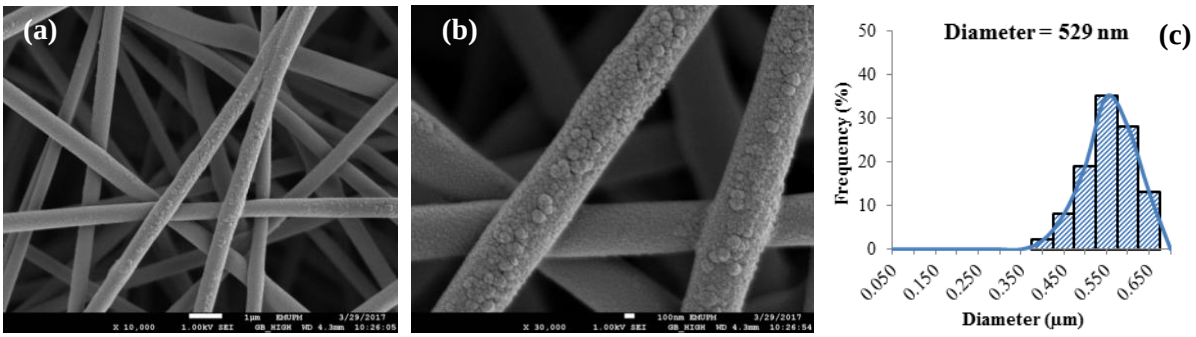


Figure 3. FESEM images of (a, b) PVA nanofiber loaded MSNs and (c) the corresponding diameter distribution histogram

The morphology of MB-loaded electrospun composite mats after releasing

The FESEM morphology of both PVA-loaded MB and the PVA-MB loaded MSNs electrospun mats after being immersed in PBS pH 7.4 for 120 hours are shown in Figure 4(a) and (c), respectively. By comparing with electrospun mats before immersing in PBS, the average fiber diameter increased because of the nanofibers were swollen in the PBS. There are several nanoparticles has been seen in the swollen nanofibers in Figure 4(c). As shown in the fiber diameter distributions in Figure 4(b) and (d), the average fiber diameter increased up to ~750 nm. This phenomenon occurred due to water molecules diffused into the polymer matrix and the interaction between the polymer chains decreased. Therefore, the polymer chains relaxed and the nanofibers swelled [10, 11].

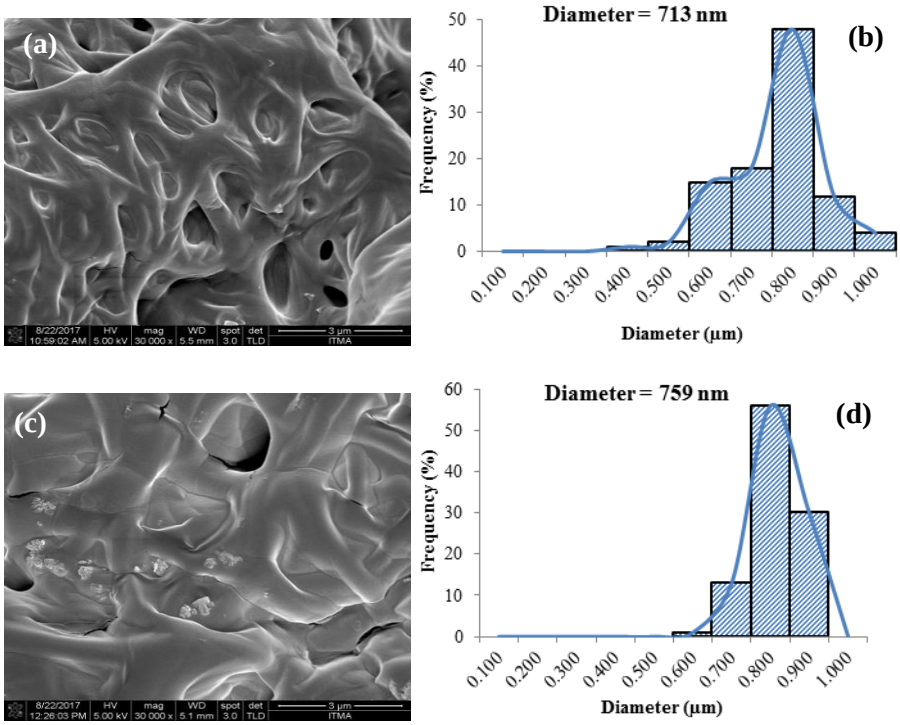


Figure 4. FESEM images of (a) PVA-loaded MB and (c) PVA-MB loaded MSNs electrospun mats after being incubated in PBS pH 7.4 for 120h, and (b,d) the corresponding fibers diameter distribution histograms

The cumulative release of MB from composite mats

The release of MB from MSNs alone and two different electrospun mats were measured by shaking in PBS solution (pH 7.4) at room temperature. The results as in Figure 5 showed that MB-loaded MSNs released speedily in the first 10 hours followed by fast manner with total amount of MB released nearly 90% up to 120 hours. The effect of incorporation MB-loaded MSNs in the nanofiber was investigated. The released rate of PVA-MB loaded MSNs was slowed down with 58% in the first 10 hours, followed by a sustained release up to total 76% till 120 hours. It revealed a long-term release compared to PVA-loaded MB which is without cooperation of MSNs. The presence of loaded MSNs give influences to reduce the burst release of drug [12].

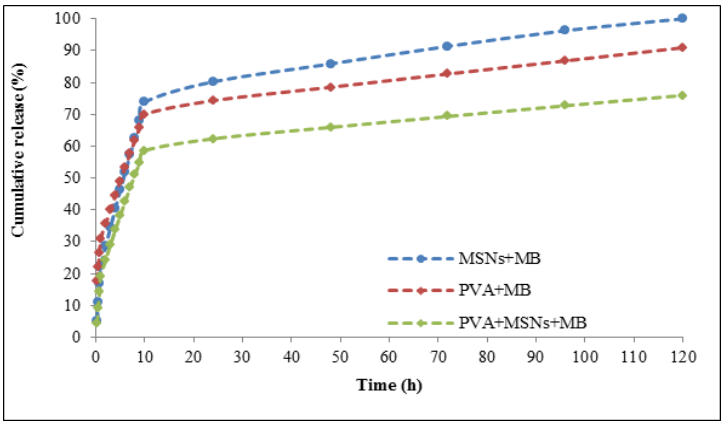


Figure 5. The cumulative MB release profile from MB-loaded MSNs, PVA/MB electrospun mats and PVA/MB loaded MSNs electrospun mats

Conclusion

MSNs were successfully synthesized by using 1-hexadecylpyridinium bromide (C_{16}PyBr) IL as template. The incorporation and confining of MSNs into the PVA nanofiber was successfully fabricated using the technique of electrospinning, while the release studies of MB were determined. The results showed that combination of MSNs-loaded MB into the nanofiber could prevent the burst release of drug as well as release in slow manner compared with the single MSNs-loaded MB. Thus, PVA/MSNs electrospun mats could be an excellent carrier for controllable delivery of drug. Therefore, it also may well be loaded with proper drugs to be applied for wound dressing. For further research, the tri-axial electrospinning technique which can fabricate up to three layers in one nanofiber and combination of different biodegradable polymers in each layer were suggested in order to achieve longer release profiles.

Acknowledgement

The authors gratefully acknowledge the Putra Grant IPS project GP-IPS/2017/9520100 from Universiti Putra Malaysia (UPM). We also would like to thank to MyBrain15 (Ministry of Higher Education) for educational scholarship scheme.

References

1. Aliabadi, H. M. and Lavasanifar, A. (2006). Polymeric micelles for drug delivery. *Expert opinion on drug delivery*, 3(1): 139 – 162.
2. Thipparaboina, R., Chavan, R. B., Kumar, D., Modugula, S. and Shastri, N. R. (2015). Micellar carriers for the delivery of multiple therapeutic agents. *Colloids and Surfaces B: Biointerfaces*, 135(1): 291 –308.
3. Vahed, S. Z., Salehi, R., Davaran, S. and Sharifi, S. (2017). Liposome-based drug co-delivery systems in cancer cells. *Materials Science and Engineering: C*, 71(1): 1327 – 1341.
4. Goyal, R., Macri, L. K., Kaplan, H. M. and Kohn, J. (2016). Nanoparticles and nanofibers for topical drug delivery. *Journal of Controlled Release*, 240(1): 77 – 92.
5. Khalf, A. and Madihally, S. V. (2017). Recent advances in multiaxial electrospinning for drug delivery. *European Journal of Pharmaceutics and Biopharmaceutics*, 112(1): 1 – 17.
6. Jalvandi, J., White, M., Truong, Y. B., Gao, Y., Padhye, R. and Kyratzis, I. L. (2015). Release and antimicrobial activity of levofloxacin from composite mats of poly (ε-caprolactone) and mesoporous silica nanoparticles fabricated by core–shell electrospinning. *Journal of Materials Science*, 50(24): 7967 – 7974.
7. Song, B., Wu, C. and Chang, J. (2012). Controllable delivery of hydrophilic and hydrophobic drugs from electrospun poly (lactic-co-glycolic acid)/mesoporous silica nanoparticles composite mats. *Journal of Biomedical Materials Research Part B: Applied Biomaterials*, 100(8): 2178 – 2186.
8. Mehrasa, M., Asadollahi, M. A., Nasri-Nasrabadi, B., Ghaedi, K., Salehi, H., Dolatshahi-Pirouz, A. and Arpanaei, A. (2016). Incorporation of mesoporous silica nanoparticles into random electrospun PLGA and PLGA/gelatin nanofibrous scaffolds enhances mechanical and cell proliferation properties. *Materials Science and Engineering: C*, 66(1): 25 – 32.
9. Vashisth, P. and Pruthi, V. (2016). Synthesis and characterization of crosslinked gellan/PVA nanofibers for tissue engineering application. *Materials Science and Engineering: C*, 67(1): 304 – 312.
10. Park, C. G., Kim, E., Park, M., Park, J. H. and Choy, Y. B. (2011). A nanofibrous sheet-based system for linear delivery of nifedipine. *Journal of Controlled Release*, 149(3): 250 – 257.
11. Liverani, L., Lacina, J., Roether, J. A., Boccardi, E., Killian, M. S., Schmuki, P., Schubert, D. W. and Boccaccini, A. R. (2017). Incorporation of bioactive glass nanoparticles in electrospun PCL/chitosan fibers by using benign solvents. *Bioactive Materials*, 3(1): 55 – 63.
12. Song, B., Wu, C. and Chang, J. (2012). Dual drug release from electrospun poly (lactic-co-glycolic acid)/mesoporous silica nanoparticles composite mats with distinct release profiles. *Acta Biomaterialia*, 8(5): 1901 – 1907.

Malaysian Journal of Analytical Sciences, Vol 23 No 2 (2019): 219 - 228
DOI: https://doi.org/10.17576/mjas-2019-2302-06

MALAYSIAN JOURNAL OF ANALYTICAL SCIENCES
Published by The Malaysian Analytical Sciences Society
ISSN 1394 - 2506

REMOVAL OF Pb(II) FROM AQUEOUS SOLUTION BY PINEAPPLE PLANT STEM

(Penyingkiran Pb(II) dari Larutan Akueus Menggunakan Batang Tumbuhan Nanas)

Vivian Loh Zing Ting, Tan Yen Ping*, Abdul Halim Abdullah

Department of Chemistry, Faculty of Science,
Universiti Putra Malaysia, 43400 UPM Serdang, Selangor, Malaysia

**Corresponding author: typ@upm.edu.my*

Received: 19 August 2018; Accepted: 25 February 2019

Abstract

The excessive release of lead (Pb) ions into water stream and large production of agricultural wastes cause water and land pollution. Adsorption is useful in eliminating Pb(II) from water environment. The potential use of agricultural waste, pineapple plant stem as adsorbent to reduce the amount of Pb(II) in aqueous solutions was investigated. The material was modified with oxalic acid (OA) to improve the adsorption efficiency of Pb(II). Adsorption isotherms and kinetics were determined for the adsorption of Pb(II) on natural pineapple plant stem (NPPS) and OA modified pineapple plant stem (OAPPS) from aqueous solution in batch studies. The adsorption capacity of Pb(II) on pineapple plant stem depends considerably on the solution pH, in which the amount of Pb(II) adsorbed increased with increasing solution pH, reached its maximal with 14.25 mg/g at pH 5 and 30.47 mg/g at pH 4 for NPPS and OAPPS, respectively. The adsorption performance of the adsorbents was also studied at different initial Pb(II) concentrations (50 – 150 mg/L), it was observed to be less affected at higher initial Pb(II) concentration. The adsorption isotherm was then investigated and the equilibrium data were well fitted with the Langmuir isotherm model with 13.30 and 27.70 mg/g as the calculated maximum capacities for NPPS and OAPPS, respectively. The adsorption of Pb(II) onto NPPS and OAPPS reached equilibrium after 60 minutes at all concentrations studied. The kinetics data were found to follow the pseudo-second order model.

Keywords: adsorption, lead, oxalic acid, pineapple plant stem

Abstrak

Pelepasan ion-ion plumbum (Pb) yang berlebihan ke dalam aliran air dan pengeluaran sisa pertanian yang banyak menyebabkan pencemaran air dan tanah. Penjerapan amat berguna untuk menyingkirkan Pb(II) dari air. Penyelidikan atas penggunaan sisa pertanian, iaitu batang nanas sebagai penjerap untuk mengurangkan Pb(II) dalam larutan akueus telah dijalankan. Tambahan pula, batang nanas telah dimodifikasi dengan asid oksalik untuk meningkatkan kecekapan penjerapan Pb(II). Penjerapan isotherma dan kinetik Pb(II) atas tumbuhan nanas semulajadi (NPPS) dan yang dimodifikasi (OAPPS) daripada larutan akueus dijelaskan melalui kajian kumpulan. Kapasiti penjerapan Pb(II) pada batang tumbuhan nanas sangat bergantung kepada pH, di mana kapasiti penjerapan meningkat dengan peningkatan larutan pH dari 1 hingga 4, mencapai maksimal dengan 14.25 mg/g pada pH 5 untuk NPPS dan 30.47 mg/g pada pH 4 untuk OAPPS. Prestasi jerapan batang nanas juga diuji dengan pelbagai kepekatan ion logam (50 – 150 mg/L), dan diperhatikan memberi kesan yang rendah dengan kepekatan yang lebih tinggi. Data keseimbangan penjerapan didapati bersesuaian dengan model isoterma Langmuir dengan 13.30 mg/g untuk NPPS dan 27.70 mg/g untuk OAPPS sebgai kapasiti maksima yang dikira oleh model. Penjerapan Pb(II) ke NPPS dan OAPPS mencapai keseimbangan selepas 60 minit pada semua kepekatan yang dikaji. Data kinetik didapati mengikuti model kinetik tertib pseudo-kedua.

Kata kunci: penjerapan, plumbum, asid oksalik, batang tumbuhan nanas

Introduction

Water is the most important resource for human being; however, water pollution becomes a serious worldwide environmental concern. Heavy metals, especially lead (Pb) is widely used for industrial purposes such as battery manufacturing, painting, metal plating and mining. The release of untreated industrial effluent to water environment affects large area of the water sources contaminated with heavy metals. Lead (Pb) is highly toxic and poses danger to living things [1, 2]. The Pb ions accumulate in living tissues damage the vital organs and systems, and eventually disrupt the normal metabolic functioning of body [3]. World Health Organization [4] has set the maximum Pb(II) concentration in drinking water at 0.01 mg/L. Therefore, it is essential to remove Pb(II) from water to minimize the lead poisoning through water drinking.

The common chemical treatment procedures for removal of heavy metal ions from aqueous solution such as ion exchange [5], flotation [6], membrane filtration [7] and electrochemical treatment [8] are efficient in reducing metal ions in water but are expensive to operate. Hence, these methods do not likely satisfy the requirement of industrial wastewater treatment industries which hope for inexpensive, cleaner and greener technology. Recently, researchers start to adopt adsorption with low cost materials as adsorbents to eliminate metal ions from aqueous solution. The adsorption with agricultural waste materials is considered suitable for the industries uses as it promotes the reuse of unwanted wastes, cost effective [9], possible to regenerate adsorbents and recover metals, as well as minimize the sludge generation.

The agricultural wastes consist of cellulose, hemicellulose and lignin which have various functional groups that can bind the metal cations from solution [10]. The properties are useful in the heavy metal ions adsorbing. Several adsorbents such as rice straw [11], coconut shell [12], ginkgo leaf, peanut shell [13], coffee husk [14], orange peel, lemon peel, banana peel and watermelon peel [15] have been used and tested for Pb(II) removal from aqueous solution. Pineapple is a common tropical fruit, used in food industry and consumed globally. After harvested from the farm, the stem was discarded as waste in municipal landfills or open burning. The plant stem represents about 60% of the total weight of the pineapple plant. The huge generation of pineapple waste and poor waste management lead to serious air and land pollutions. The disposal problem could be handled by reutilizing the pineapple plant stem (PPS) as an adsorbent in adsorption. This gives advantages to the society as value-added products will be produced from unused materials.

The usage of natural agricultural waste products poses drawbacks. Lignocellulosic plant materials may release organic matters to aquatic environment thus leaving secondary pollutants to the aqueous solution. The leaching of organic matter can be lowered by washing the adsorbents before using or modifying adsorbents in an appropriate manner. The pre-treatment and chemical modifications increase the surface area of adsorbent and add more surface functional groups on the adsorbent. Thus, the adsorbent capacity to adsorb metal ions might be improved. Oxalic acid (OA) is a simple acid and considered to be less toxic, frequently used in pharmaceutical industry. The carboxylic sites on OA are expected to add functional groups on the surface of adsorbent, thus give higher adsorption capacity of the modified adsorbent.

This study aims to assess the adsorption potential of the adsorbents prepared from the natural and OA modified pineapple plant stem for the removal of Pb(II) ions from aqueous solutions. The interactive effects of process parameters such as the pH of solution, initial Pb(II) concentrations and the contact time on the adsorption capacity of the adsorbent were studied. Furthermore, adsorption isotherms as well as kinetics models were discussed.

Materials and Methods

Preparation of adsorbents

The procedures to prepare the natural pineapple plant stem (NPPS) adsorbents were adopted from Chan et al. [16]. The stems were first cut into pieces, then grinded and sieved to particle size range 105 to 250 μm. Then, the particles were boiled with distilled water thrice before they were dried at 50 °C for 24 hours. The prepared NPPS were kept in air tight containers and ready to be used and undergo chemical modification.

The oxalic acid (OA) treatment of PPS was performed and modified according to previous method reported by Marshall et al. [17]. The dried PPS was added to 0.5 M OA at ratio of 1:20, agitated for 30 minutes at room temperature. The liquid mixture was then discarded and the residue was spread in tray. The wet PPS residue was activated at 120 °C in an oven for 90 minutes. The OA modified PPS (OAPPS) was then washed repeatedly with distilled water until neutral pH of filtrate was obtained. Finally, OAPPS was dried overnight in oven at 50 °C then it was kept in air tight container for further use.

Preparation of heavy metal stock solution

The heavy metal Pb(II) solution was prepared. A quantity of 1.5905 g $Pb(NO_3)_2$ crystal was dissolved in 1000 mL of distilled water to prepare the desired concentration of 1000 mg/L. The stock solution prepared was diluted to various concentrations ranged 50 to 150 mg/L for batch adsorption studies.

Batch adsorption studies

The batch experiment was carried out at room temperature to determine the adsorption capacity towards Pb(II) by mixing 25 mL of Pb(II) solution in centrifuge tube. An orbital shaker was set at 150 rpm, mixture was shaken at the agitation rate. A Pb(II) solution without adsorbents was served as control and to determine the initial concentration of the Pb(II) solutions prepared. The pH of the solutions was maintained and determined using pH meter. The analyte was collected and the final Pb(II) concentrations were analyzed using inductively coupled plasma optical emission spectroscopy (ICP-OES) instrument (Perkin Elmer, model Optima 2000DV). The steps mentioned were repeated under different conditions: solution pH, initial Pb(II) concentration and contact time. The experiments were conducted in triplicates. The initial and final concentration of Pb(II) were recorded and adsorption capacity was calculated using equation 1:

$$\text{Adsorption capacity } \left(\frac{\text{mg}}{\text{g}}\right) = \frac{\text{(Initial concentration - Final concentration) x volume of solution}}{\text{Weight of adsorbent}} \quad (1)$$

The effect of solution pH on the Pb(II) adsorption capacity by NPPS and OAPPS was studied. The prepared adsorbents with 0.05 g was added into a series of 100 mg/L Pb(II) solution and were shaken for 5 hours. The initial pHs of solution were varied from 1 to 7 by adjusting with 0.01 M HNO_3 and 0.1 M NaOH solution. After 5 hours, the residual solutions were analyzed using ICP-OES.

The effect of initial Pb(II) concentrations and contact time was investigated. The NPPS and OAPPS with dose of 0.05 g/25 mL were added into series of 50, 75, 100, 125 and 150 mg/L and were shaken at different time intervals: 5, 10, 15, 30, 60, 90, 120 and 180 minutes. The supernatants were collected at the mentioned time. The residual solutions were analyzed using ICP-OES. Later, the experimental data were fitted to Langmuir and Freundlich isotherm models, as well as pseudo-first and pseudo-second kinetics models to study the adsorption mechanism.

Results and Discussion

The study of the factors affecting the efficiency of heavy metal ions adsorption is important for the interest of industry. The performance of the Pb(II) adsorption is affected by solution pH, initial metal ion concentration and contact time. Studies on these factors were carried out to investigate the relationship between the adsorbate and adsorbents and propose the mechanism in the adsorption of Pb(II) by NPPS and OAPPS.

The effect of solution pH

The solution pH may influence the surface charge of adsorbent and the chemistry of metal [18]. The effect of solution pH on the Pb(II) removal was investigated with pH variation from 1 to 7 and are presented in Figure 1. The Pb(II) adsorption from aqueous solution may dependent on the pH value.

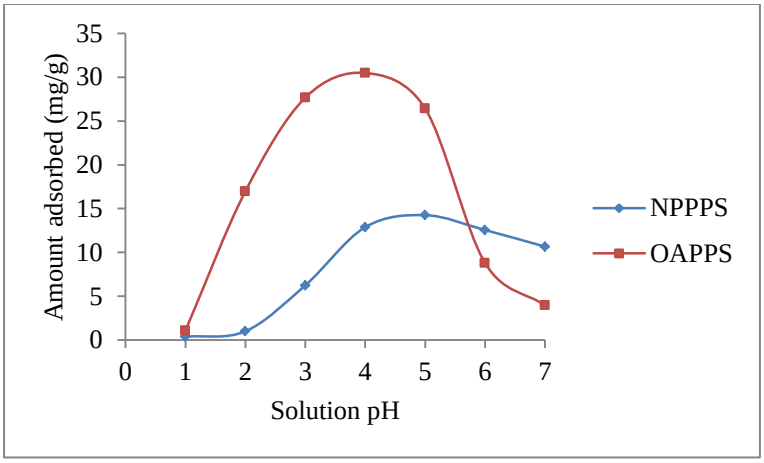


Figure 1. The effect of pH on Pb(II) adsorption by NPPS and OAPPS

The results portrayed that the Pb(II) adsorption increased with increasing pH till a maximum, then decreased afterwards. The maximum adsorption capacities were achieved at pH 5 with 14.25 mg/g and pH 4 with 30.47 mg/g of Pb(II) adsorption on NPPS and OAPPS, respectively at 25 °C.

The solution pH affects the surface characteristic of the adsorbents. This is due to the pH point of zero charge (pH_{pzc}) difference in each adsorbent. NPPS and OAPPS have neutral charges at pH 4 and pH 2.4, respectively. Adsorbents are negatively charged at solution pH higher than its pH_{pzc}. Hence, a lower pH_{pzc} means that the surface charge of adsorbent becomes negative at a lower pH, therefore the cationic Pb(II) ions at a wider range can be attracted.

In highly acidic solution (< pH 4), the functional groups, especially carboxyl groups on the adsorbents were protonated, gave a positive charge on the adsorbent surface. There might be a great electrostatic repulsion between the positive Pb(II) ions and the positive adsorbent species. Furthermore, the presence of hydrogen and hydronium ions creates a competitive environment for the available binding sites. This phenomenon lowers the adsorption capacity of both NPPS and OAPPS.

The carboxyl groups were less protonated when the solution pH was increased. When the pH values increased (pH 4 - 5), the adsorbent surface becomes less positive and the concentration of the competing positive ions (H^+ and H_3O^+) decreases, thus more electrostatic attraction occurred between Pb(II) and adsorbents surface. As a result, the adsorption capacity observed was found to be improved in slightly acidic solution.

The solution pH affects the metal speciation as well. At higher pH (> pH 5), the adsorption capacity was decreased. This is mainly due to the formation of hydroxyl metal complexes when Pb(II) started to precipitate. The basic environment facilitates the formation of precipitate complex with metallic ions attached to the hydroxide ions forming $Pb(OH)_2$ and negatively charged $Pb(OH)_3^-$ complex ions [19]. This again creates repulsion between the negative adsorbent species and negatively charged metal ions. In the effort to prevent precipitation, experiments were carried out at pH < 6 to make sure the Pb(II) were soluble and avoid the formation of metal hydroxides.

Effect of initial concentration and contact time

The initial Pb(II) concentrations were varied from 50 to 150 mg/L and batch studies were conducted at different time intervals to study the adsorption equilibrium and kinetics, while other factors were kept constant. The Pb(II) uptake was conducted over a period of 180 min at room temperature.

As shown in Figure 2(a), the Pb(II) adsorption by NPPS was less affected by the initial metal ion concentration. The maximum amount of Pb(II) adsorbed at different metal ion concentrations investigated was between 12.89 to 14.57

mg/g. There is less significance in Pb(II) uptake by NPPS at different initial Pb(II) concentrations. On the other hand, the Pb(II) adsorption by OAPPS was likely to be affected by the initial metal ion concentration as shown in Figure 2(b). The modified adsorbent adsorbed 15.29 mg/g Pb(II) at the lowest, 50 mg/L initial Pb(II) concentration. The adsorption performance was then sharply increased to 24.91 mg/g at 75 mg/L Pb(II) concentration and showed less difference in the adsorption capacity (25.98 mg/g - 27.53 mg/g) from 100 mg/L to 150 mg/L Pb(II) concentration.

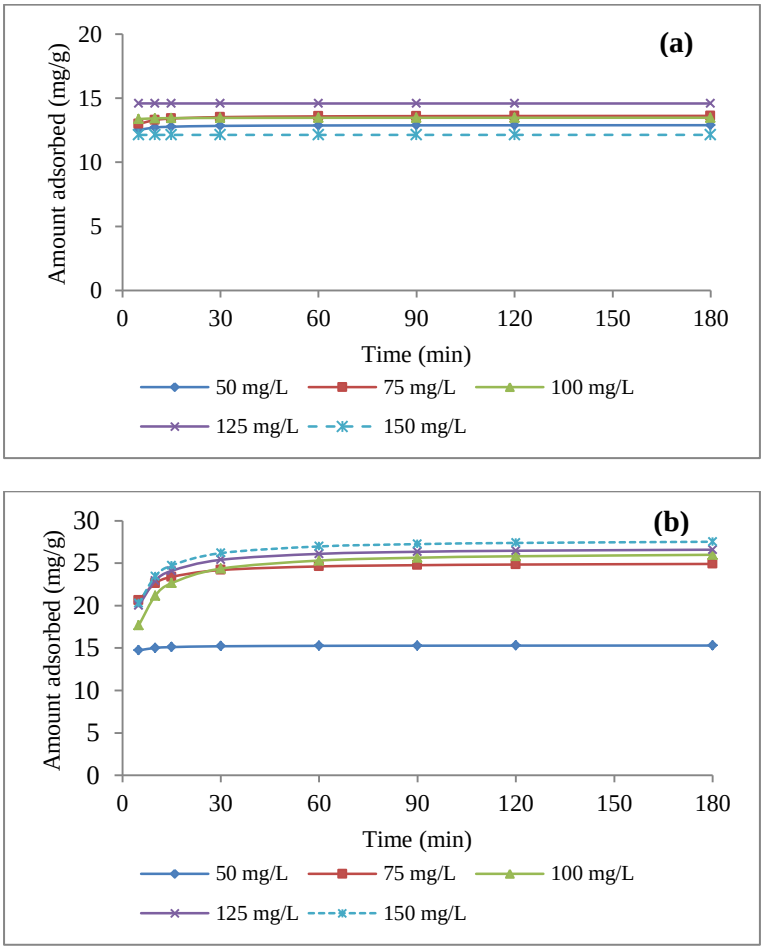


Figure 2. The effect of initial concentration and contact time onto (a) NPPS and (b) OAPPS

Mass transfer resistance of metal ions between the solution phase and the solid adsorbent phase occurred during adsorption and the initial adsorbate concentration serves as driving force to overcome it [20, 21]. At lower Pb(II) concentration, most Pb(II) ions could bind on the adsorbent surface as there is a large ratio of available adsorption site between the amount of Pb(II) present in the solution. As the initial Pb(II) concentration increased, the ratio of unoccupied binding site is getting smaller. The adsorption site was saturated with Pb(II) ions at constant mass of adsorbent, causing the more Pb(II) ions left unadsorbed in the solution. Maximum adsorption sites were occupied at high initial metal ion concentration; hence, there is less significance in the adsorption performance.

The adsorption capacity of NPPS and OAPPS increased with increasing contact time and reached the maximum and equilibrium after 60 minutes (Figure 2). At the initial phase or the time period from 0 to 30 minutes, a rapid adsorption was observed. This is mainly due to the unoccupied binding sites mostly available to interact with the Pb(II) ions [22]. As the adsorption time extended, the adsorption sites were majorly covered, thus reducing the

opportunity of Pb(II) ions to interact with the functional groups on the adsorbents. Upon reaching equilibrium, the saturated binding sites did not facilitate the Pb(II) adsorption giving an almost constant adsorption capacity. It was clearly observed that the equilibrium time was not dependent on the initial metal ion concentration. The results revealed that same equilibrium time can be achieved for all the initial Pb(II) concentrations investigated (50 – 150 mg/L).

The adsorption isotherm

The experimental data were fitted to two adsorption isotherm models: Langmuir and Freundlich models and studied. Langmuir [23] and Freundlich [24] isotherms are used to explain the mechanism of adsorption and the relationship between the amount of adsorbed metal ion and the concentration of metal ion remained in solution.

The Langmuir isotherm model proposes a monolayer adsorption of metal ion on the adsorbent surface. Besides, it also assumes that the number of adsorption sites are fixed, where there will be no adsorption occurred onto the adsorbent surface when the available binding sites are fully occupied. The linear form of the Langmuir isotherm is presented by equation 2:

$$\frac{C_e}{q_e} = \frac{1}{q_{max}} C_e + \frac{1}{q_{max} K_L} \tag{2}$$

where C_e refers to the equilibrium concentration of metal ions (mg/L); q_e is the amount of metal ions adsorbed at equilibrium (mg/g); q_{max} is the maximum amount or the amount of metal ions adsorbed; K_L is the Langmuir constant defining the adsorption capacity or the adsorption energy. A linear graph with C_e/q_e against C_e was plotted. The values of q_{max} and K_L can be calculated from the slope and the intercept of the isotherm.

The Freundlich isotherm model on the other contrary suggests multilayer metal ion adsorption. The amount of adsorbed metal ion on the surface of adsorbent is expected to be increased with the increasing adsorbate concentration. This model is linearized as shown in equation 3:

$$\log q_e = \frac{1}{n} \log C_e + \log K_F \tag{3}$$

where K_F refers to the Freundlich constant defining the capacity of the adsorption. The linear graph will yield an intercept of $\log K_F$ and a slope of $\frac{1}{n}$.

The parameter values for Langmuir and Freundlich isotherms are listed in Table 1. The R^2 values obtained from Langmuir models for Pb(II) adsorption by NPPS and OAPPS have correlation coefficient values, which are 0.9992 and 0.9997, respectively, whereas Freundlich models were 0.9228 and 0.9505 for NPPS and OAPPS, respectively. The correlation values obtained from the Langmuir models were relatively higher as compared to Freundlich's correlation values, suggesting that the Langmuir model is highly applicable to the adsorption system.

Table 1. Langmuir and Freundlich isotherm parameters

	Parameters	**NPPS**	**OAPPS**
Langmuir	q_{max} (mg/g)	13.30	27.70
	K_L (L/mg)	5.1130	8.6288
	R^2	0.9992	0.9997
Freundlich	K_F (L/mg)	8.7418	10.4304
	n	12.4688	4.9407
	R^2	0.9228	0.9505

This indicates that the monolayer adsorption of Pb(II) occurred on NPPS and OAPPS. The adsorbent, OAPPS have a higher Langmuir isotherm constant, K_L value. This indicates that Pb(II) ions have higher affinity to bind to the functional groups on OAPPS, resulted higher maximum adsorption capacity over OAPPS.

The adsorption kinetics

The contact time of adsorption determines the kinetics, then used to describe the rate of Pb(II) adsorption and the Pb(II) adsorption behavior onto NPPS and OAPPS.

The pseudo-first and pseudo-second order models are linearized as shown in equations 4 and 5, respectively.

$$\ln(q_e - q_t) = -k_1 t + \ln q_e \quad (4)$$

$$\frac{t}{q_t} = \frac{1}{q_e} t + \frac{1}{k_2 q_e^2} \quad (5)$$

where q_e is the amount of metal ions adsorbed at equilibrium (mg/g); q_t refers to the amount of metal ions adsorbed at time, t (mg/g) respectively; k_1 and k_2 refer to the rate constant of pseudo-first order and pseudo-second order, respectively.

Based on Table 2, the experimental data was best fitted with pseudo-second order model, suggesting that the adsorption might be a chemical process [25]. Chemical adsorption involved electron sharing or transfer limits the adsorption rate. The Pb(II) ions adsorption onto NPPS and OAPPS involved two phases. Initially, the adsorption is fast and equilibrium phase was attained. Afterwards, the Pb(II) adsorption was slow and proceed with less significance in the capacity with longer time.

Table 2. Comparison of experimental and theoretical adsorption capacities of pseudo-first order and pseudo-second order of adsorption at 150 mg/L Pb(II) solution

	Parameters	**NPPS**	**OAPPS**
Expeimental values	$q_{e,\,exp}$ (mg/g)	12.25	27.65
Pseudo-first order	$q_{e,\,cal}$ (mg/g)	0.63	3.68
	k_1 (1/min)	0.0102	0.0232
	R^2	0.4411	0.7079
Pseudo-second order	$q_{e,\,cal}$ (mg/g)	12.13	27.53
	k_2 (g/mg·min)	84.87	0.0197
	R^2	0.9994	0.9997

Adsorption mechanism and comparative adsorption study

The pineapple plant stem consists of intricate surface structure and composition, thus Pb(II) ions might interact in a number of possible ways on the surface of agro-waste adsorbent during adsorption. Based on this study, two main adsorption mechanisms were propsed, namely electrostatic attraction and monolayer chemisorption took place during the Pb(II) adsorbing by NPPS and OAPPS.

The capacities of Pb(II) ion adsorption onto NPPS and OAPPS were observed to depend on solution pH. The test results presumed that the adsorption mechanism involved the electrostatic interactions during the process. The optimum pH for Pb(II) adsorption by NPPS and OAPPS was 5 and 4, respectively. Thus, the batch adsorption studies were carried out in solution pH 4 - 5. In solution pH > 5, the dominant metal species in aqueous solution were lead hydroxide [$Pb(OH)_2$] and $Pb(OH)_3^-$ complex ions whereas Pb^{2+} and $Pb(OH)^+$ were the foremost metal

ions exist in solution pH < 5. The functional groups on NPPS and OAPPS were depronated at solution pH > 4. The adsorbents then act as negative species, attracted the dominant cationic Pb metal ions.

The adsorption isotherm and kinetics studies suggested that the Pb(II) adsorption onto NPPS and OAPPS to be a physicochemical reaction, involved both physical adsorption and monolayer chemisorption. The fast adsorption was observed at the initial phase of Pb(II) adsorption by NPPS and OAPPS, proposed the occurrence of physisorption and may be due to the macrospores of both adsorbents. Later, the adsorption process slowed down, chemical reaction, namely ion-exchange was anticipated. The abundant hydroxyl functional groups on NPPS might interact with the Pb(II) ions in the mechanisms shown in Equations 6 and 7.

$$C_n\text{-}OH + Pb^{2+} \rightarrow C_n\text{-}OPb^{+} + H_3O^{+} \quad (6)$$

$$(C_n\text{-}OH)_2 + Pb^{2+} \rightarrow (C_nO)_2Pb + 2H^{+} \quad (7)$$

After chemical modification with OA, more carboxyl functional groups present on the surface of OAPPS. Thus, ion exchange mainly occurred between the Pb(II) ions and electrons from carboxyl groups on the adsorbent and controlled the adsorption process. The possible mechanisms were shown below (equations 8 and 9):

$$C_n\text{-}COOH + Pb^{2+} \rightarrow C_n\text{-}COOPb^{+} + H_3O^{+} \quad (8)$$

$$(C_n\text{-}COOH)_2 + Pb^{2+} \rightarrow (C_n\text{-}COO)_2Pb + 2H^{+} \quad (9)$$

The capacities of the Pb(II) adsorbing by NPPS and OAPPS with the adsorbents reported in the text were compared and listed in Table 3.

Table 3. Comparison of Pb(II) adsorption capacities with different adsorbents

Agricultural wastes	**Maximum capacities (mg/g)**	**References**
Activated carbon	8.70	[13]
Peanut shell	11.26	
NPPS	12.13	This study
Citric acid modified rice straw	18.98	[11]
Orange peel	19.15	[15]
Banana peel	19.18	
Coffee husk	19.23	[14]
Lemon peel	19.32	[15]
Watermelon peel	19.39	
Ginkgo leaf	24.04	[13]
Coconut shell	26.14	[12]
OAPPS	27.53	This study

Table 3 shows that both NPPS and OAPPS are capable to uptake Pb(II) ions from aqueous solution. The adsorbent NPPS has a moderate adsorption capacity of 12.13 mg/g as it contains beneficial functional groups for adsorption. It was hypothesized that the carboxyl groups play a vital role in Pb(II) adsorption from aqueous solution by replacing the H^+ protons from the carboxyl groups with the Pb^{2+} ions and formed carboxylate groups. The adsorption capacity of Pb(II) on OAPPS was doubled to 27.53 mg/g after the chemical modification of PPS with OA. When heated, the

oxalic acid converted to oxalic acid anhydride and further reacted with the hydroxyl groups on PPS. Thus, carboxyl groups were added to the surface of PPS, led to increase in the adsorption of Pb(II) ions. Generally, NPPS and OAPPS showed great potentials to be used as adsorbents in wastewater treatment and industries for heavy metal ion removal from aqueous solution.

Conclusion

In this work, the agricultural waste, pineapple plant stem was successfully utilized as adsorbents for Pb(II) removal from aqueous solution. Furthermore, pineapple plant stem was undergone pre-treatment and chemical modification with oxalic acid. Overall, the oxalic acid modified pineapple plant stem (OAPPS) showed improved performance than the natural pineapple plant stem (NPPS) involved in the study. Batch studies were carried out under different conditions: solution pH, initial Pb(II) concentration and contact time to evaluate the adsorption efficiency of Pb(II) ions on NPPS and OAPPS. The Pb(II) adsorption was enhanced with increasing solution pH values and gave optimum pH at 5 with 14.25 mg/g and 4 with 30.47 mg/g Pb(II) adsorbed by NPPS and OAPPS, respectively. The Pb(II) adsorption capacity by both adsorbents improved with increasing initial Pb(II) concentration. Besides, it was observed that the adsorbents performances were less affected at higher initial metal ion concentration. The adsorption equilibrium data was well fitted with the Langmuir isotherm, proposing monolayer adsorption. Meanwhile, the Pb(II) ions adsorption onto NPPS and OAPPS reached equilibrium at 60 min and followed pseudo-second kinetics order model. The model suggests that the Pb(II) adsorption mechanism involved chemisorption. The results of this work suggest that pineapple plant stem can be an alternative adsorbent for the adsorption process in removing Pb(II) ions from wastewater.

Acknowledgement

This project was financially supported by Putra Grant Universiti Putra Malaysia. The authors acknowledge the Department of Chemistry, Faculty of Science, Universiti Putra Malaysia for the technical support.

References

1. United States Environmental Protection Agency (2017). Lead regulations. https://www.epa.gov/lead/lead-regulations#water [Access online 14 September 2017].
2. Salman, M., Athar, M. and Farooq, U. (2015). Biosorption of heavy metals from aqueous solutions using indigenous and modified lignocellulosic materials. *Reviews in Environmental Science and Bio/Technology*, 14(2): 211 – 228.
3. Lopes, A. C. B. A., Peixe, T. S., Mesas, A. E. and Paoliello, M. M. (2016). Lead exposure and oxidative stress: a systematic review. *Reviews of Environmental Contamination and Toxicology*, 236: 193 – 238.
4. World Health Organization (2017). Lead. http://www.who.int/ipcs/assessment/public_health/lead/en/ [Access online 14 September 2017].
5. An, F. Q., Wu, R. Y., Li, M., Hu, T. P., Gao, J. F. and Yuan, Z. G. (2017). Adsorption of heavy metal ions by iminodiacetic acid functionalized D301 resin: Kinetics, isotherms and thermodynamics. *Reactive and Functional Polymers*, 118: 42 – 50.
6. Peng, W., Han, G., Cao, Y., Sun, K. and Song, S. (2018). Efficiently removing Pb(II) from wastewater by graphene oxide using foam flotation. *Colloids and Surfaces A: Physicochemical and Engineering Aspects*, 556: 266 – 272.
7. Kalboussi, N., Rapaport, A., Bayen, T., Amar, N. B. and Ellouze, F. (2017). Optimal control of a membrane filtration system. IFAC Word Congress 2017, Jul 2017, Toulouse, France. Elsevier, 50(1): 8704 – 8709.
8. Un, U. T. and Ocal, S. E. (2015). Removal of heavy metals (Cd, Cu, Ni) by electrocoagulation. *International Journal of Environmental Science and Development*, 6(6): 425 – 429.
9. Mopoung, R. and Kengkhetkit, N. (2016). Lead and cadmium removal efficiency from aqueous solution by NaOH treated pineapple waste. *International Journal of Applied Chemistry*, 12(1): 23 – 35.
10. Ince, M. and Ince, O. K. (2017). An overview of adsorption technique for heavy metal removal from water/wastewater: A critical review. *International Journal of Pure and Applied Sciences*, 3(2): 10 – 19.
11. Guo, L., Liang, L.Y., Wang, Y. J. and Liu, M. D. (2015). Biosorption of Pb^{2+} from aqueous solution by rice straw modified with citric acid. *Environmental Progress & Sustainable Energy*, 35(2): 359 – 367.

12. El-Deen, G. E. S. and El-Deen, S. E. A. S. (2016). Kinetic and isotherm studies for adsorption of Pb(II) from aqueous solution onto coconut shell activated carbon. *Desalination and Water Treatment*, 57(59): 28910 – 28931.
13. Lee, M. E., Park, J. H. and Chung, J. W. (2019). Comparison of the lead and copper adsorption capacities of plant source materials and their biochars. *Journal of Environmental Management*, 236: 118 – 124.
14. Alhogbi, B. G. (2017). Potential of coffee husk biomass waste for the adsorption of Pb(II) ion from aqueous solutions. *Sustainable Chemistry and Pharmacy*, 6: 21 – 25.
15. Jena, S. and Sahoo, R. K. (2017). Removal of Pb(II) from aqueous solution using fruits peel as a low cost adsorbent. *International Journal of Science, Engineering and Technology*, 5(1): 5 – 13.
16. Chan, S. L., Tan, Y. P., Abdullah, A. H. and Ong, S. T. (2016). Equilibrium, kinetic and thermodynamic studies of a new potential biosorbent for the removal of Basic Blue 3 and Congo Red dyes: Pineapple (*Ananas comosus*) plant stem. *Journal of the Taiwan Institute of Chemical Engineers*, 61: 306 – 315.
17. Marshall, W. E., Wartelle, L. H., Boler, D. E., Johns, M. M. and Toles, C. A. (1999). Enhanced metal adsorption by soybean hulls modified with citric acid. *Bioresource Technology*, 69: 263 – 368.
18. Nameni, M., Alavi, M. M. and Arami, M. (2008). Adsorption of hexavalent chromium from aqueous solutions by wheat bran. *International Journal of Environmental Science & Technology*, 5(2): 161 –168.
19. Giraldo, L. and Moreno-Pirajan, J. C. (2008). Pb^{2+} adsorption from aqueous solutions on activated carbons obtained from lignocellulosic residues. *Brazil Journal of Chemical Engineering*, 25: 143 – 151.
20. Kariuki, Z., Kiptoo, J. and Onyancha, D. (2017). Biosorption studies of lead and copper using rogers mushroom biomass '*Lepiota hystrix*'. *South African Journal of Chemical Engineering*, 23: 62 – 70.
21. Elhafez, S. E. A., Hamad, H. A., Zaatout, A. A. and Malash, G. F. (2017). Management of agricultural waste for removal of heavy metals from aqueous solutions: adsorption behaviors, adsorption mechanisms, environmental protection, and techno-economic analysis. *Environmental Science and Pollution Research*, 24(2): 1397 – 1415.
22. Rafatullah, M. O., Sulaiman, R., Hashim and Ahmad, A. (2009). Adsorption of copper(II), chromium(III), nickel(II) and lead(II) ions from aqueous solutions by meranti sawdust. *Journal of Hazardous Materials*, 170: 969 – 977.
23. Langmuir, I. (1915). The constitution and fundamental properties of solids and liquids. *Part I. Solids, American Chemical Society*, 38: 2221 – 2295.
24. Freundlich, H. M. F. (1906). Uber die adsorption in lusungen. *Journal of Physic Chemistry*, 57: 385 –470.
25. Iqbal, M., Saeed, A. and Zafar, S. I. (2009). FTIR spectrophotometry, kinetics and adsorption isotherms modelling, ion exchange, and EDX analysis for understanding the mechanism of Cd^{2+} and Pb^{2+} removal by mango peel waste. *Journal of Hazardous Materials*, 164: 161 – 171.

Malaysian Journal of Analytical Sciences, Vol 23 No 2 (2019): 229 - 236
DOI: https://doi.org/10.17576/mjas-2019-2302-07

MALAYSIAN JOURNAL OF ANALYTICAL SCIENCES
Published by The Malaysian Analytical Sciences Society
ISSN 1394 - 2506

COLOURIMETRIC BASED DETECTION OF GUNSHOT RESIDUE ON GLOVES WORN DURING SHOOTING

(Pengesanan Sisa Tembakan Berasaskan Kolorimetrik pada Sarung Tangan Semasa Menembak)

Azie Azyanti Mohd Rafae[1], Saiful Fazamil Mohd Ali[2], Ahmad Fahmi Lim Abdullah[1], Kah Haw Chang[1]*

[1]*Forensic Science Programme,*
School of Health Sciences,
Universiti Sains Malaysia, 16150 Kubang Kerian, Kelantan, Malaysia
[2]*Criminalistic Section, Forensic Division,*
Department of Chemistry, Jalan Sultan, 46661 Petaling Jaya, Malaysia

**Corresponding author: changkh@usm.my*

Received: 5 February 2018; Accepted: 16 February 2019

Abstract

Determining the shooter is an important element during investigation of firearm related offences, particularly through the detection of gunshot residue (GSR) as forensic evidence on shooter's hand. However, such detection could be restrained if it is obstructed by the wearing of gloves by a shooter. Hence, it is worth investigating the presence of GSR on gloves, aiming to suggest an individual's contact with a weapon. In this study, Modified Griess Reagent (MGT) commonly available in forensic laboratory was utilised to screen GSR on individual gloves of different materials worn by a shooter during a shooting training session. The experimental results revealed that both the palm and back of gloves equally allows the detection of GSR by MGT (p = 0.083). No statistically significant association was evident between the types of gloves and positive indication of MGT (p = 0.122). The types of firearms, neither revolver nor semi-automatic pistol showed significant association with the detection of GSR on the gloves (p = 0.248). When two-hand shooting was performed, glove samples worn on left and right hands gave almost similar testing results (p = 0.626). Although the presence of GSR on a glove after a shooting could be relatively low, the study has demonstrated that applying MGT, a simple test could assist crime scene investigation in determining the presence of GSR, in cases when gloves were used.

Keywords: forensic science, gunshot residue, colourimetric test, Modified Griess Reagent, glove

Abstrak

Pengenalpastian seseorang penembak adalah unsur yang penting ketika penyiasatan kesalahan yang berkaitan dengan senjata api terutamanya melalui pengesanan sisa tembakan (GSR) sebagai bukti forensik pada tangan penembak. Walau bagaimanapun, pengesanan sedemikian boleh dihalang sekiranya bahan-bahan tersebut terhalang oleh pemakaian sarung tangan oleh seseorang penembak. Justeru, adalah bernilai untuk menyiasat kehadiran GSR pada sarung tangan yang bertujuan untuk mencadangkan perhubungan seseorang individu dengan suatu senjata api. Dalam kajian ini, reagen Griess terubahsuai (MGT) yang lazimnya boleh didapati di makmal forensik telah digunakan untuk menyaring GSR pada setiap sarung tangan yang diperbuat daripada pelbagai bahan yang berbeza dan dipakai oleh penembak ketika suatu sesi latihan tembakan. Keputusan eksperimen menunjukkan bahawa kedua-dua permukaan tapak and belakang sarung tangan sama-sama membenarkan pengesanan GSR oleh MGT (p = 0.083). Tiada perkiatan statistik bererti terbukti antara jenis sarung tangan dan penentuan positif MGT (p = 0.122). Jenis senjata sama ada revolver atau pistol separa automatik tidak menunjukkan perkaitan bererti dengan pengesanan GSR pada sarung tangan (p = 0.248). Apabila penembakan dua belah tangan dijalankan, sampel sarung tangan dipakai pada tangan kiri dan tangan kanan memberikan keputusan ujian yang hampir sama (p = 0.626). Walaupun kehadiran GSR pada suatu sarung tangan selepas suatu tembakan berkemungkinan agak rendah, kajian ini telah menunjukkan bahawa penggunaan MGT yang merupakan

suatu ujian yang mudah dapat membantu penyiasatan tempat jenayah dalam penentuan kehadiran GSR, terutamanya dalam kes-kes apabila sarung tangan telah digunakan.

Kata kunci: sains forensik, sisa tembakan, ujian kolorimetrik, reagen Griess terubahsuai, sarung tangan

Introduction

Determining the shooter is an important element during investigation of firearm related offences [1]. According to Locard's principle of exchange, traces originating from the discharge of a firearm should be deposited on any surface in the vicinity of the shooting event, especially on the hand of the shooter [2]. These traces, collectively known as gunshot residues (GSR), consist of discrete and characteristic combination of products originating from the primer, smokeless powder, projectile, casing and possibly also the firearm itself [1, 3]. In firearm related cases, successful detection of GSR on a suspect provides significant value aiding an investigation by offering scientific evidence which indicates the possibility of one's involvement in the use of a firearm [1].

In forensic analysis, the absence of GSR on an individual cannot be interpreted as that he/she was not involved in an alleged shooting incident. Severe depletion of such traces could occur when there is a time elapse between the incident and the time of sample recovery. A shooter could have washed his/her body and changed the clothes. Also, if a shooter's hands were protected such as by gloves, routine skin swab for GSR might turn out negative. Previous studies have suggested the transfer of epithelial cells from sweat and body oils of a shooter onto a firearm, leaving potential fingerprints [4, 5] and DNA [5-9] during shooting. Wearing of gloves by a shooter might restrict the deposition of these body fluids onto a firearm, and *vice versa*, GSR might not directly deposit onto the hands of the shooter due to the barrier of the gloves. In view of this, the recovery of GSR from gloves suspected to be worn by the suspect during a shooting would support the suggestion that he/she has held a weapon, thereby aiding the investigation of firearm related cases.

Currently, examination of GSR on the basis of their morphology and chemical composition using scanning electron microscope-energy dispersive X-ray (SEM-EDX) technique are routinely practiced in forensic laboratories [3]. A simplified system described in American Society for Testing and Materials (ASTM) standard guide remains widely accepted for the analysis and determination of GSR, including Malaysia [3, 10]. A drawback of the use of SEM-EDX is that the residues on a surface need to be transferred from that surface to a stub through a sampling procedure for the analysis. Tape lifting is a good procedure on surfaces such as skin and face of a suspected shooter, but less effective on fabric due to the buildup of debris on the stub and loss of stickiness with repeated dabs [3, 11]. Therefore, a colourimetric test is proposed to be directly applied on the glove surfaces without any procedure for transferring the residues. Colourimetric tests are widely used in casework examination, particularly for the estimation of shooting distance based on the particle distribution on a target, besides for screening for the presence of GSR and identification of a bullet hole [1, 3, 11-13]. Among colourimetric tests, Modified Griess Test (MGT) is commonly used as a presumptive test for nitrite-containing particles originating from burned smokeless powder, especially for the estimation of shooting distance [11-16]. Due to its availability in forensic laboratories, MGT was utilised in this study as a quick screening indicator for GSR, aiming to provide an initial empirical data that allow the investigative officer to determine the possible linkage between the gloves, the suspect and a shooting incident for forensic intelligence purpose.

Materials and Methods

Shooting and sampling

A semi-automatic pistol P-99 Walther® and a revolver Smith & Wesson® were used in firing the ammunitions (SME 9 mm and SME .38, SME Ordnance, Selangor, Malaysia) supplied by the Royal Malaysia Police in an open shooting range in Police Training Centre, Kuala Lumpur. Four types of gloves (two types of differently knitted cotton gloves, one polyurethane-type and one nylon-made gloves) commonly used at home or work and easily available in the market were selected. The gloves were worn by the shooter on both hands prior to shooting using both hands to hold the firearm. Positive control was prepared by spiking nitrate standard on the glove samples while clean glove samples were used as negative control.

GSR generation was achieved from ten consecutive shots with the respective firearm for more intense GSR traces for better characterisation of their distribution study. Immediately after the tenth shot, the individual gloves were separately collected from the hands, packed into separate paper bags and labeled accordingly. For each of firearm types, a total of two pairs of gloves of four different types were sampled, making a total of 32 glove samples in this study.

Reagent preparation

To prepare the fresh MGT reagent, 2.5 g of α-napthylamine hydrochloride (Merck, Kenilworth, NJ) was added into 7.5 g of sulphanilic acid (Merck, Kenilworth, NJ) to form reagent A. Then, 140 mL isopropyl alcohol (Merck, Kenilworth, NJ) was mixed with 60 mL distilled water to form Reagent B. Both reagents A and B were then mixed well and filtered into a 250 mL spray gun bottle. Filter paper Grade 1288 (Sartorius, Göttingen, Germany) was used to remove the undissolved particles from the MGT reagent.

Physical examination

Glove samples were examined visually and subsequently under stereomicroscope (Leica Microscope MZ 16, Leica Microsystems, Heerbrugg, Switzerland) equipped with a digital camera (Leica FC 290, Leica Microsystems, Heerbrugg, Switzerland). The magnification factors for image display ranged from 0.71x to 11.5x with the power of eyepiece at 10x. The microscopic system was supported by Leica Application Suite software (Leica Microsystems, Heerbrugg, Switzerland) for capturing photographs. The presence of any foreign particles on the gloves was carefully noted, comparing to the negative control glove samples which did not subjected to shooting exercise.

Colourimetric test

Gloves to be examined were laid on a sheet of A4 size paper. A cut piece of blotting paper (25 cm x 25 cm) was sprayed with the test reagent, and then carefully placed covering the entire glove. A cleaned glass plate was placed on top of the wet blotting paper and pressed gently for one minute. The blotting paper was then carefully removed and examined for the presence of red-to-pink-to-orange coloured spots [14-15]. The same procedure was carried out for the other side of a glove to ensure that the entire glove surface was screened. Since the two sides of a glove sample were tested with MGT, cautious must be considered to minimise cross contamination by utilising new pieces of A4 and blotting papers, as well as a thoroughly cleaned glass plate for the second surface testing. Note that the side in contact with the grip was labeled as "palm" whereas the side facing outward was labeled as "back". The test reagent was also tested on positive and negative controls.

Statistical analysis

A binary outcome for detection of GSR was determined as either "yes" or "no". Statistical analysis was conducted using Stata software version 12 (StataCorp, USA). Data cleaning and descriptive analyses were performed to ensure no error in the data. Chi Square test or Fisher Exact test was conducted to determine an association between the tested variable (*i.e.* sampling sites, types of gloves, left hand versus right hand, and types of firearms) and the detection of GSR using MGT. In this study, a *p*-value of <0.05 was considered as statistically significant.

Results and Discussion

Physical examination

Initial physical examination was focused on the presence of foreign particles on the surface of the gloves under the magnifications of 20× and 40×, and the observed flakes or particles were photographed. GSR particles of varying sizes of irregular shape were seen under the magnification of 20× (Figure 1a-b). Smaller particles in dust form were also observed at higher magnification (Figure 1c). The particles were black in colour that appeared similar to those observed when using smokeless powder as reported earlier [17]. On the contrary, control samples observed under microscope showed no evidence of such foreign particles. Therefore, visual observation indicated that these particles found on the glove surfaces could be the product of partial combustion of smokeless powder contained in the ammunition [11].

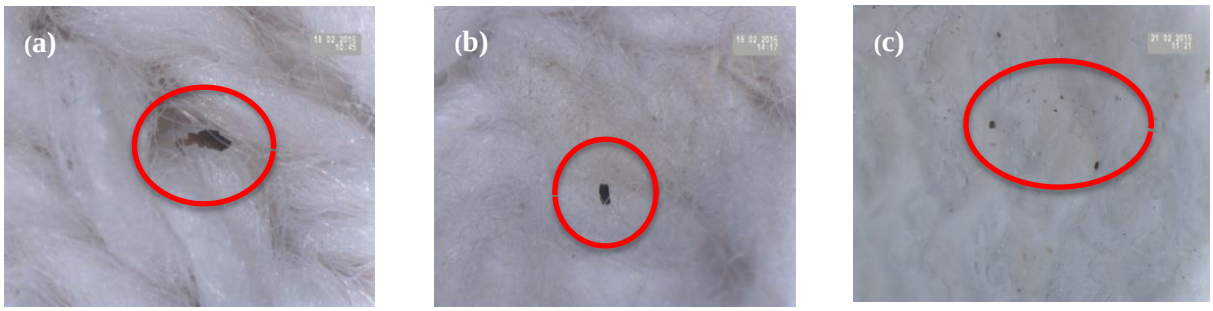


Figure 1. Illustration of (a) flakes, (b) particles and (c) smaller particles in dust form found on the glove surfaces after shooting

Colourimetric test

Determination of the presence of nitrate compounds arising from the combustion of ammunition using MGT has been routinely used to estimate shooting distance, particularly on a target such as clothing on victim's body. The study attempts to extend its utilisation on the gloves worn during firing. Prior to application of MGT on glove samples, negative control demonstrated that absence of colour reaction on clean glove surfaces, suggesting no interference from glove materials on the MGT test. The presence of GSR compounds on shooter's gloves was indicated by the appearance of red-to-pink colour spots similar to also observed from the positive control. Figure 2 illustrates photographs of blotting paper with GSR particles observed as light pink coloured spots after the application of MGT on the gloves used by the shooter during test firing.

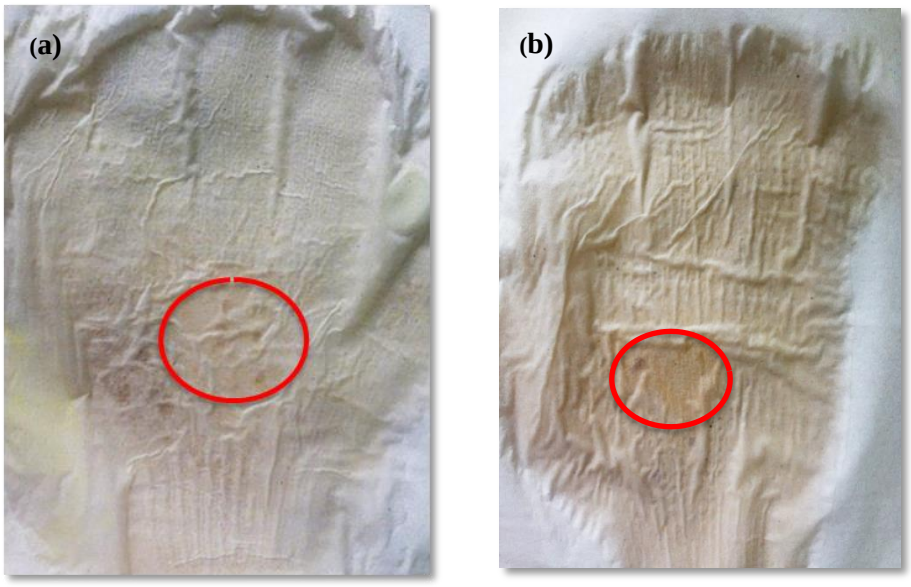


Figure 2. Light pink coloured spots appearing on blotting paper tested with (a) palm and (b) back of a knitted cotton glove

Positive determination by MGT is a consequence of chemical reaction between nitrate compounds originated from the smokeless powder with the reagent [1, 3, 11, 14-16]. Table 1 illustrates the frequency and percentage of colourimetric tests scored as "yes" or "no" after the application of MGT. In this study, 48 (75.0%) positive detection of GSR were recorded with 32 cases more than those negative detections. Note that the primary focus of this study was to qualitatively determine the presence of GSR on the gloves without considering the distribution pattern of the residues on the glove surfaces, in line with actual forensic investigation which aims to prove a shooting activity.

Table 1. Frequency and percentage of positive and negative determination

Detection of GSR	Frequency (%)
Yes	48 (75.0%)
No	16 (25.0%)
Total	64 (100.0%)

GSR detection on the "Back" versus "Palm" surfaces of the gloves

GSR tends to move outward and away from a firearm upon firing. A Chi Square test was used to determine association between the sampling sites and the positive detection of GSR, as showed in Table 2.

Table 2. Association between the sampling sites and the detection of GSR on gloves

Sampling Site	Detection		*p*-value
	Yes	No	
Back	27 (84.4%)	5 (15.6%)	0.083
Palm	21 (65.6%)	11 (34.4%)	

*Chi Square test was used

The Chi Square test showed that there is no statistically significant association between the sampling sites with the detection of GSR on gloves (p = 0.083) (Table 1). A total of 84.4% of the samples were reported with positive determination of GSR on the "back" of the gloves, regardless of the types of gloves and firearm used. On the other hand, the palm side of the gloves also recorded positive results of GSR in 65.6% of the glove samples, indicating that the GSR can also be deposited on the "palm" surface upon repeated firing. Literatures supported that GSR could be found on the firing hands, both on the "back" and "palm" sites [18, 19]. Generally, the dorsum of the hand holding the weapon would be exposed to deposition of GSR particles, thus giving positive results compared to the palm surface used to grab the pistol. Also, GSR can also be deposited on the "palm" surface upon repeated firing. The cleaning a firearm may also only partially eliminate the GSR [18]. It is also possible that the GSR found on the "palm" surface of a glove could be due to the transfer of previously deposited GSR on the grip of the pistol or revolver, which was termed as "memory effect" [18, 20]. By comparison, the "back" of a glove should certainly be the focus area in forensic examination due to the slightly higher possibility for the detection of GSR as demonstrated here.

Types of gloves

Among the four types of gloves used in this study, two were knitted typed cotton gloves and the other two were polyurethane- and nylon-made gloves, thus providing different surface texture for GSR deposition. Table 3 illustrates the association between the types of gloves worn during shooting and the positive detection of GSR.

Table 3. Association between the types of gloves worn during shooting and positive detection of GSR

Type of Gloves	Detection		*p*-value
	Yes	No	
A	12 (75.0%)	4 (25.0%)	0.122
B	15 (93.8%)	1 (6.3%)	
C	12 (75.0%)	4 (25.0%)	
D	9 (56.3%)	7 (43.8%)	

*Fisher Exact test was used

The former two were of coarser surface texture, where the weaves in between the yarn were relatively loose. Such cotton gloves could allow for the persistence of GSR falling onto and trapping within the yarn. This was supported in this experiment with 93.8% (type A) and 75.0% (type B) positive colourimetric results for the two respective types of cotton gloves. Polyurethane-made gloves (type C) also retain GSR allowing their detection in 75.0% of the glove samples. The polyurethane coating in this type of glove could have made the surface resistant to abrasion, and thus restrict the process of wearing away the GSR particles fallen onto it. On the contrary, the nylon-made gloves being the smoothest surface (type A), revealed relatively lower probability (56.3%) in detecting the presence of GSR on their surfaces, among all tested gloves. However, the statistical result shows no significant association between the types of gloves with the detection of GSR on gloves (p = 0.122), suggesting that the different types of gloves equally allow the detection of GSR. To the authors' knowledge, many researches have been conducted on the detection of GSR from various surfaces in the proximity of shooters, specifically on hands, face and the clothes they worn [1, 11, 19]. Testing on the presence of GSR on gloves which worn by a shooter to minimise the deposition of such residues onto his/her hands remain unexplored. This experimental outcome could be used to account for the witness or the suspect's statement about the shooting event, whether or not gloves have been worn during the shooting activity.

Left versus right worn gloves

As the shooting was performed using both hands, glove samples worn on left and right hands, as predicted, respectively revealed 81.3% and 87.5% probability of positive results. Statistical result (Table 4) shows that either left or right worn glove has no association with the positive detection of GSR (p= 0.626).

Table 4. Association between left or right worn gloves and positive detection of GSR

Sampling Hand	Detection		*p*-value
	Yes	No	
Right	14 (87.5%)	2 (12.5%)	0.626
Left	13 (81.3%)	3 (18.8%)	

*Fisher Exact test was used

GSR can be found on the firing hand when gloves were worn, regardless of left or right sides. It is noting that only the "back" sides of those glove samples were considered in this experiment. The experimental results also supported the finding by Jalanti et al. [18] and Ditrich [20], in which the abundance of GSR particles could be found in both hands if the other hand was used as support during a shooting event. In this case, the shooter was a right handed person. The left hand that was below the grip overlapped the right hand which was positioned above the grip while holding the grip. A relevant circumstance for slightly higher positive detection on right gloves that was more exposed to the chamber is possible. The finding is important for crime scene reconstruction or to verify the witness's or suspect's account that GSR could be present on both hands, when performing two-handed shooting.

Semi-automatic vs revolver

When comparing two different firearms, it was seen that a higher number of glove samples showed positive results when fired with a revolver (81.3%) as compared to a semi-automatic pistol (68.8%), although the Chi Square statistical test shows no association between the types of firearm and the detection of GSR on the glove samples (p = 0.248) (Table 5).

Literature reported that the firing mechanism of revolver allowed substantial amount of GSR to be escaped from the gap between the revolving drum and barrel, and subsequently contributed to the increased deposition of GSR [20]. The emitted plume from a revolver tends to surround the weapon including a shooter's hands [17], leading to possibility of positive indication on hands, in this case, the gloves worn during firing. On the contrary, a semi-automatic pistol ejects the spent cartridge from one side of the pistol and reloads a new round from the magazine. The smoke and particles are mainly emitted through the opening of ejection port, restricting the spread of GSR [20].

Although the plume of GSR released from these two weapons could be varied, it did not affect the detection of GSR that has been deposited on the gloves due to the firing activity.

Table 5. Association between the types of firearm used for shooting and positive detection of GSR on gloves worn during the shooting

Firearm	**Detection**		***p*-value**
	Yes	**No**	
Semi-automatic pistol	22 (68.8%)	10 (31.3%)	0.248
Revolver	26 (81.3%)	6 (18.8%)	

*Chi Square test was used

Conclusion

This study shows that the application of MGT colour test on any glove worn during a shooting provides useful results. Although the presence of GSR on a glove after a shooting could be relatively low, similar to the detection of such residues on hands, the positive indication of colourimetric test offers an investigative clue. The adherence of residues on the weaves of fabric making up a glove could persist longer than those retained on a shooter's hands which are lost due to washing and daily activities, or even with the time elapsed. With the application of colourimetric test, careful and proper handling of the evidence must be considered to avoid the loss of trace particles. To conclude, this study has demonstrated the utilisation of MGT as a quick and cost effective screening test to indicate the presence of GSR on gloves. It could serve as forensic intelligence lead, in order to relate a suspect during crime scene investigation. For future study, the factors such as the influence of the number shots, single-handed shooting as well as the duration of storage for the glove samples, which could affect the detection of GSR from such evidence, should be investigated.

Acknowledgement

Special thanks to the personnel in Royal Malaysia Police for the technical advice and supplying the ammunition samples. The authors thank Universiti Sains Malaysia for the financial support via the USM Short Term grant (304/PPSK/61313147). Special thanks to Associate Professor Lim Boon Huat and Associate Professor P.T. Jayaprakash for their editorial assistance.

References

1. Chang, K. H., Jayaprakash, P. T., Yew, C. H. and Abdullah, A. F. L. (2013). Gunshot residue analysis and its evidential values: A review. *Australian Journal of Forensic Sciences*, 45(1): 3 – 23.
2. Costa, R. A., Motta, L. C., Destefani, C. A., Rodrigues, R. R. T., do Espirito Santo, K. S., Aquije, G. M. F. V., Boldrini, R., Athayde, G. P. B., Carneiro, M. T. W. D. and Ramao, W. (2016). Gunshot residue (GSR) analysis of clean range ammunition using SEM/EDX, colorimetric test and ICP-MS: A comparative approach between the analytical techniques. *Microchemical Journal*, 129: 339 – 347.
3. Dalby, O., Butler, D. and Birkett, J. W. (2010). Analysis of gunshot residue and associated materials – A review. *Journal of Forensic Sciences*, 55(4): 924 – 943.
4. Barnum, C. A. and Klasey, D. R. (1997). Factors affecting the recovery of latent prints on firearms. *Journal of Forensic Identification*, 47(2): 141 – 149.
5. Amata, B., Aprea, G. M., Chiuri, A. and Zampa, F. (2015). Fingerprint on Trigger: A real case. *Forensic Science International*, 253: e25 – e27.
6. Polley, D., Mickiewicz, P., Vaughn, M., Miller, T., Warburton, R., Komonski, D., Kantautas, C., Reid, B., Frappier, R. and Newman, J. (2006). An investigation of DNA recovery from firearms and cartridge cases. *Canadian Society of Forensic Science Journal*, 39(4): 217 – 228.
7. Bille, T. W. (2007). Guns and the DNA left behind. Gun violence prosecution program. Virginia: National District Attorneys Association.
8. Richert, N. J. (2011). Swabbing firearm for handler's DNA. *Journal of Forensic Sciences*, 56(4): 972 – 975.

9. Nunn, S. (2013). Touch DNA collection versus firearm fingerprinting: Comparing evidence production and identification outcome. *Journal of Forensic Sciences*, 58 (3): 601 – 608.
10. ASTM (2008). Standard guide for gunshot residue analysis by scanning electron microscopy/energy dispersive X-ray spectrometry E1588-08. Pennsylvania: American Society for Testing and Materials International.
11. Goudsmits, E., Sharples, G. P. and Birkett, J. W. (2015). Recent trends in organic gunshot residues analysis. *Trends in Analytical Chemistry*, 74: 46 – 57.
12. Zeichner, A. and Glattstein, B. (1986). Improved reagents for firing distance determination. *Journal of Energetic Materials*, 4(1): 187 – 197.
13. Glattstein, B., Vinokurov, A., Levin, N. and Zeichner, A. (2000). Improved method for shooting distance estimation. Part 1. bullet holes in clothing items *Journal of Forensic Sciences*, 45(4): 80 – 806.
14. Dillon, J. H. (1990). A protocol for gunshot examination in muzzle to target distance determination. *AFTE Journal*, 22(3): 257 – 274.
15. Dillon, J. H. (1990). The modified Griess test: A chemically specific chromophoric test for nitrite compounds in gunshot residues. *AFTE Journal*, 22(3): 243 – 250.
16. Lau, L. (2007). Modified Griess test as part of the examination protocol in shooting range determination. *AFTE Journal*, 39(4): 281 – 287.
17. Chang, K. H. and Abdullah, A. F. L. (2012). Macroscopic examination of morphological features of propellant powders prevalence in Malaysia. *Malaysian Journal of Forensic Sciences*, 3(1): 46 – 51.
18. Jalanti, T., Henchoz, P., Gallusser, A. and Bonfanti, M. S. (1999). The persistence of gunshot residue on shooters' hands. *Science & Justice*, 39(1): 48 – 52.
19. Zeichner, A. and Levin, N. (1995). Casework experience of GSR detection in Israel, on samples from hands, hair, and clothing using an autosearch SEM-EDX System. *Journal of Forensic Sciences*, 22(2): 288 – 322.
20. Ditrich, H. (2012). Distribution of gunshot residue – the influence of weapon type. *Forensic Science International*, 220: 85 – 90.

Malaysian Journal of Analytical Sciences, Vol 23 No 2 (2019): 237 - 246
DOI: https://doi.org/10.17576/mjas-2019-2302-08

MALAYSIAN JOURNAL OF ANALYTICAL SCIENCES
Published by The Malaysian Analytical Sciences Society
ISSN 1394 - 2506

SYNTHESIS AND MOLECULAR DOCKING OF 2,4,5-TRISUBSTITUTED-1,3-THIAZOLE DERIVATIVES AS ANTIBACTERIAL AGENTS

(Sintesis dan Penyatuan Molekul Terbitan 1,3-Tiazol Berpenggantian-2,4,5 Sebagai Agen Antibakteria)

Iswatun Hasanah Abdullah Ripain[1], Norashikin Roslan[1], Nurul Shazana Norshahimi[1], Siti Salwa Mohamed Salleh[1], Noraslinda Muhamad Bunnori[2], Nurziana Ngah[1]*

[1]*Department of Chemistry, Kulliyyah of Science*
[2]*Department of Biotechnology, Kulliyyah of Science*
International Islamic University Malaysia, Kuantan Campus, Bandar Indera Mahkota, 25200 Kuantan, Pahang, Malaysia

**Corresponding author: nurziana@iium.edu.my*

Received: 19 August 2018; Accepted: 18 February 2019

Abstract

The emergence of antibiotic resistance against bacterial strains has attracted great interest in the discovery and development of new antibacterial agents. Thiazole derivatives have been widely used in the biological as well as pharmacological fields and their efficiency as pharmaceutical drugs are well established. In this study, a series of thiazole derivatives were synthesized in reaction between 3-chloroacetyl acetone and ammonium thiocyanate followed by incorporating selected amines in one-pot synthesis manner. The compounds were structurally characterized by Fourier Transform Infrared (FTIR), Proton Nuclear Magnetic Resonance (^{1}H NMR), Ultraviolet-Visible (UV-Vis) and Gas Chromatography-Mass Spectrometry (GC-MS). Their antibacterial properties were screened using disc diffusion technique against selected Gram-positive (*Bacillus cereus* and *Staphylococcus epidermidis*) as well as Gram-negative bacteria (*Escherichia coli* and *Pseudomonas aeruginosa*) with **T3** exhibited the most potent antibacterial activity. Molecular docking studies were also performed against Glucosamine-6-phosphate (GlcN-6-P) synthase which is known as the essential building block of most bacteria. The docking result displayed that **T3** exhibited the minimum binding energy of -7.09 kcal mol^{-1} as compared to **T1** and **T2** with -6.49 and -6.76 kcal mol^{-1}, respectively which is in agreement with antibacterial result. The output of this preliminary study will contribute in structural enhancement in drug discovery.

Keywords: thiazole derivatives, antibacterial, disc diffusion, molecular docking, GlcN-6-P synthase

Abstrak

Kewujudan rintangan terhadap bakteria telah menarik minat dalam penemuan dan perkembangan agen antibakteria yang terkini. Terbitan tiazol telah digunakan dengan meluas dalam bidang biologi dan farmakologi di mana keberkesanannya sebagai ubat farmaseutikal telah ditemui. Dalam kajian ini, terbitan tiazol telah disintesis dengan menindakbalaskan α-haloketon (3-kloroasetil aseton), ammonium tiosianat dan beberapa sebatian amina terpilih secara sintesis satu pot. Produk tindak balas yang terhasil telah dicirikan dengan Transformasi Fourier-Inframerah (FTIR), Proton Resonans Magnet Nukleus (^{1}H NMR), Ultralembayung-Sinar Nampak (UV-Vis) serta Kromatografi Gas-Spektrometer Jisim (GC-MS). Sifat antibakteria sebatian ini telah disaring menggunakan teknik serapan cakera terhadap bakteria Gram-positif (*Bacillus cereus* dan *Staphylococcus epidermidis*) dan Gram-negatif (*Escherichia coli* dan *Pseudomonas aeruginosa*) dengan **T3** menunjukkan aktiviti antibakteria yang paling berkesan. Penyatuan molekul telah dilakukan terhadap enzim Glukosamina-6-fosfat sintase (GlcN-6-P) yang merupakan unsur binaan penting bagi kebanyakan bakteria. Merujuk kepada keputusan penyatuan molekul, **T3** menunjukkan tenaga pengikatan yang paling minima iaitu -7.09 kcal mol^{-1} berbanding **T1** dan **T2** masing-masing pada -6.49 dan -6.76 kcal mol^{-1}, menunjukkan nilai-nilai ini bersetuju dengan keputusan saringan antibakteria. Keputusan kajian awal ini akan menyumbang kepada penambahbaikan struktur untuk penghasilan ubat.

Kata kunci: terbitan tiazol, antibakteria, resapan cakera, penyatuan molekul, GlcN-6-P sintase

Introduction

Bacteria are described as harmful tiny living things which can cause serious diseases such as diarrhea, infections to intravascular organ, nausea, inflammation and abdominal pain [1, 2]. Thus, there is a growing urge to develop treatment system to cure the diseases and one of the main options is in antibiotic field. Synthesized organic compound is turning into most suitable candidate as compared to other options such as inorganic and natural product extract because of its ease of structural design, high percentage yield and reduction of natural resources consumption [3-9]. A major challenge for this approach is to design a suitable compound which can surpass the increasing concern on antibiotic resistance.

In recent years, studies on structural and biological properties of thiazole have been the subject of considerable interest in the field of pharmacological among researchers. Thiazole derivatives were reported to exhibit excellent activities in biological fields such as anti-inflammatory, antifungal, anticancer, antibacterial, anticonvulsant, antiviral and antitumor [9]. Presence of nitrogen and sulphur atoms in thiazole structure has enhanced its physiochemical properties to be biologically active in most pharmacological areas [5]. Besides, incorporating different groups into the core structure of thiazole moiety at 2, 4 and 5- positions were reported to further enhance overall performance in term of efficiency of active site [10].

Furthermore, glucosamine-6-phosphate (GlcN-6-P) synthase represents an interesting protein target because it plays vital role in the protection of cell wall for most microorganisms as well as for human cell [11]. Inactivation of the enzyme in microbial cells significantly decreases population of bacteria without affecting the mammalian cells [12, 13]. Therefore there are a large number of studies on molecular docking for antibacterial agents focusing on GlcN-6-P synthase as their target enzyme [14, 15]. The potential inhibitor will form interaction with the active site of the enzyme and form a ligand-enzyme complex which is responsible in inhibition mechanism [16]. Thus, molecular docking studies are widely required in this field as the process will provide information on the interaction energy between ligand and target site of the enzyme.

In continuation to this effort, a series of 2, 4, 5-trisubstituted-1, 3-thiazole derivatives (Figure 1) of **T1**-**T3** were synthesized and their usability as antibacterial agents were screened against selected Gram-positive and Gram–negative bacterial strains. Next, in order to further understand the interaction between thiazole derivatives and the significant target enzyme in bacterial strains known as glucosamine-6-phosphate synthase (GlcN-6-P), molecular docking study was applied.

Materials and Methods

Reagents

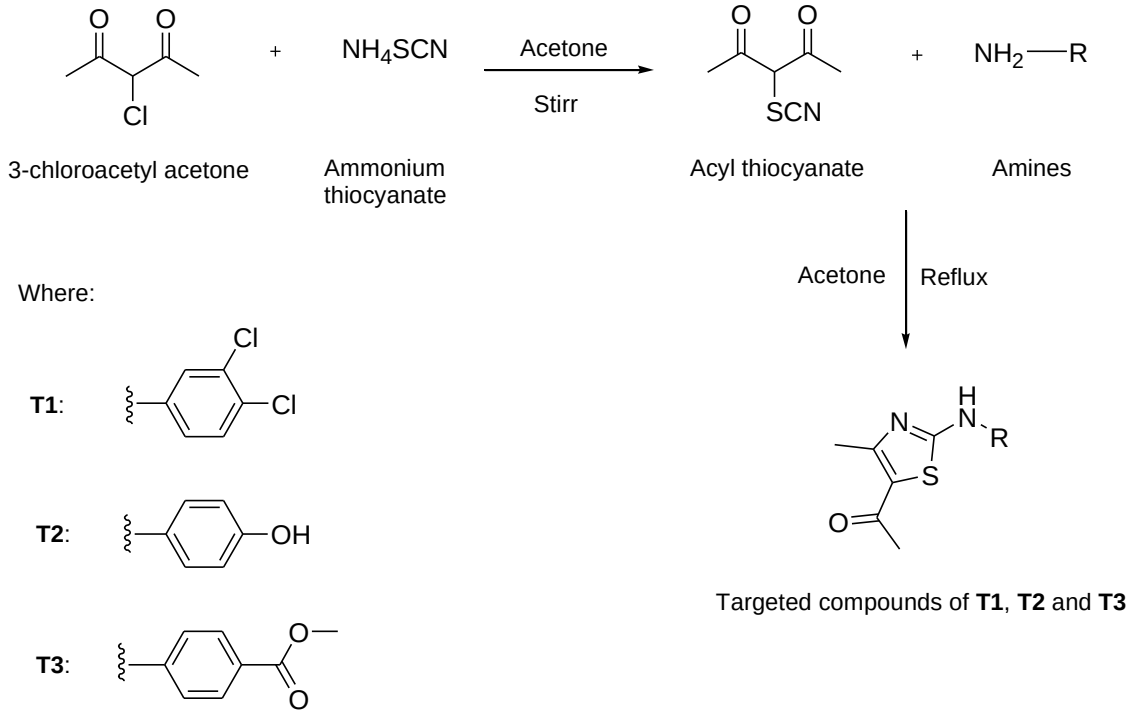
Ammonium thiocyanate, 3-chloroacetyl acetone, 3,4-dichloroaniline, 4-aminophenol, methyl-4-aminobenzoate, acetone, methanol, dichloromethane and dimethyl sulfoxide were purchased from standard commercial suppliers such as Sigma-Aldrich, Merck, Acrós Organics, Fisher Scientific and R & M Chemical. All chemicals and solvents used in this study were of reagent grade (AR) and used without further purification.

Materials and physical measurements

Melting points were measured on a Stuart Scientific Melting Point Apparatus SMP3 and were uncorrected. ^{1}H NMR spectra were recorded at 500 MHz on NMR machine Bruker Ultra Shield Plus 500 MHz spectrometer in deuterated dimethyl sulfoxide-d_6 (DMSO) using tetramethylsilane (TMS) as an internal standard. The chemical shifts were reported in ppm scale. IR spectra of the compounds were recorded from KBr pellets using Perkin Elmer FTIR GX spectrometer in the spectral range of 4000-400 cm^{-1}. UV-Vis were measured *via* Shimadzu UV-1601PC Spectrophotometer using methanol as solvent to generate absorption within 200-600 nm to study presence of electronic transition which the compounds might exhibit. The synthesized compounds were dissolved in dichloromethane (DCM) and analyzed using Perkin Elmer GC-MS (Clarus 500 Chromatography/Mass Spectrometry).

General experimental procedure

Ammonium thiocyanate (13 mmol) in acetone was added into a solution of 3-chloroacetyl acetone (13 mmol) in acetone and stirred for *ca*. 15 minutes at room temperature. After the formation of white precipitate, an equimolar amount of amine derivatives (13 mmol) in acetone was added drop wise and stirred at refluxed condition for *ca*. 2 hours. The reaction was carried out to give yellow solution with white precipitate of salt as by products. After completion, the reaction mixture was cooled to room temperature and filtered. The filtrate was allowed to be evaporated to form precipitate. The product formed was recrystallized from methanol to produce **T1**-**T3**. The synthetic route of the synthesized compounds is described in Scheme 1.



Scheme 1. The general synthetic work-up of thiazole derivatives

Determination of antibacterial activity

The antibacterial properties of the synthesized compounds (**T1**-**T3**) were screened for their antibacterial activity against Gram-positive bacterial strains (*Bacillus cereus* and *Staphylococcus epidermidis*) as well as Gram-negative bacterial strains (*Escherichia coli* and *Pseudomonas aeruginosa*) by disc diffusion technique [17]. Synthesized compounds were dissolved in DMSO at concentration of 50 mg/mL and impregnated on blank discs. The discs were placed on the agar surface pre-inoculated with suspension of bacteria (0.5 Mc Farland standards) and incubated for 24 hours at 37 ºC. Streptomycin served as antibiotic positive control and solvent blank (DMSO) as negative control respectively. After 18-24 hours of incubation at 37 ºC, the diameter of inhibition zone was observed and measured in mm.

Molecular docking

The synthesized molecules (**T1**-**T3**) were simulated for molecular docking using AutoDock 4.2 package software to investigate their affinity properties to the binding pocket of GlcN-6-P synthase. The enzyme as receptor was obtained from the RCSB Protein Data Bank (1MOQ) in pdb file format (https://www.rcsb.org/structure/1MOQ) and used as a rigid molecule [18]. Hydrogen atoms were added and water molecules were removed from amino acids. All the ligands were drawn using Chem Draw Ultra 7.0 and saved in mol file and the energies of compounds

were minimized before converted into pdb format *via* open Babel 2.4.1 software. During docking, the grid dimensions must surround the region of the active site in the macromolecules. The grid box was set at 46, 54 and 48Å for x, y and z axes respectively. The volume of the grid box was 31.98 Å by 16.58 Å by -2.57 Å with points separated by 0.375Å. The grid center was set to 5.472, -6.194 and -10.694 for x, y and z respectively which covered all the amino acid residues in the active pocket. Lamarckian Genetic Algorithm was applied as the docking algorithm with 100 runs, 150 population size, 27,000 maximum numbers of generations and 2,500,000 maximum numbers of energy evaluation.

Results and Discussion

Characterization study: 5-acetyl-4-methyl-2-(3, 4-dichloroaniline)-1,3-thiazole (T1)

Yellow solid (2.94 g, 75%), **T1** was prepared from ammonium thiocyanate (1 g, 13 mmol), 3-chloroacetylacetone (1.75 g, 13 mmol) and 3,4-dichloroaniline (2.10 g, 13 mmol) in the same manner as described in Scheme 1, m.p 184.1-185.3 ºC. ^{1}H NMR (500 MHz, DMSO-d_6): δ_H 2.43 (s, 3H, CH_3), 2.51 (s, 3H, CH_3), 7.53 (d, *J* 9 Hz, 1H, Ar-CH), 7.59 (d, *J* 9 Hz, 1H, Ar-CH), 8.03 (s, 1H, Ar-CH), 10.99 (s, 1H, NH of thiazole). IR (KBr pellet): ν(N-H) 3269 cm^{-1}, ν(C-H) 2924 cm^{-1}, ν(C=O) 1604 cm^{-1}, ν(C=N) 1545 cm^{-1}, ν(C-Cl) 714 cm^{-1}, ν(C-S) 652 cm^{-1}. UV-Vis (MeOH): λ_{abs} (n-π^*) 224 nm, 21600 M^{-1}cm^{-1}; λ_{abs} (π-π^*) 343 nm, 62200 M^{-1}cm^{-1}. M/S: Requires M$^+$ 299.99; Found M$^+$ 300.00, m/z: 285.00, 86.00 and 71.00.

5-acetyl-4-methyl-2-(4-aminophenol)-1,3-thiazole (T2)

Brown solid (2.26 g, 70%), **T2** was prepared from ammonium thiocyanate (1 g, 13 mmol), 3-chloroacetylacetone (1.75 g, 13 mmol) and 4-aminophenol (1.42 g, 13 mmol) in the same manner as described in Scheme 1, m.p. 192.3-193.4 ºC. ^{1}H NMR (500 MHz, DMSO-d_6): δ_H 2.38 (s, 3H, CH_3), 2.62 (s, 3H, CH_3), 6.78 (pseudo-d, *J* 9 Hz, 2H, Ar-CH), 7.35 (pseudo-d, *J* 9 Hz, 2H, Ar-CH), 9.38 (s, 1H, NH of thiazole), 10.47 (br s, 1H, OH). IR (KBr pellet): ν(N-H) 3242 cm^{-1}, ν(O-H) 3135 cm^{-1}, ν(C-H) 2962 cm^{-1}, ν(C=O) 1623 cm^{-1}, ν(C=N) 1596 cm^{-1}, ν(C-S) 723 cm^{-1}. UV-Vis (MeOH): λ_{abs} (n-π^*) 226 nm, 50300 M^{-1}cm^{-1}; λ_{abs} (π-π^*) 346 nm, 69200 M^{-1}cm^{-1}. M/S: Requires M$^+$ 248.06; Found M$^+$ 248.04, m/z: 233.00, 134.00 and 120.00.

5-acetyl-4-methyl-2-(methyl-4-aminobenzoate)-1,3-thiazole (T3)

Yellow solid (2.57 g, 68%), **T3** was prepared from ammonium thiocyanate (1 g, 13 mmol), 3-chloroacetylacetone (1.75 g, 13 mmol) and methyl-4-aminobenzoate (1.96 g, 13 mmol) in the same manner as described in Scheme 1, m.p. 210.7-211.7 ºC. ^{1}H NMR (500 MHz, DMSO-d_6): δ_H 2.45 (s, 3H, CH_3), 2.58 (s, 3H, CH_3), 3.83 (s, 3H, OCH_3), 7.76 (pseudo-d, *J* 9 Hz, 2H, Ar-CH), 7.96 (pseudo-d, *J* 9 Hz, 2H, Ar-CH), 11.13 (s, 1H, NH of thiazole). IR (KBr pellet): ν(N-H) 3280 cm^{-1}, ν(C-H) 3029 cm^{-1}, ν(C=O) 1711 cm^{-1}, ν(C=N) 1610 cm^{-1}, ν(C-S) 593 cm^{-1}. UV-Vis (MeOH): λ_{abs} (n-π^*) 229 nm, 21700 M^{-1}cm^{-1}; λ_{abs} (n-π^*) 284 nm, 14900 M^{-1}cm^{-1}; λ_{abs} (π-π^*) 352 nm, 82200 M^{-1}cm^{-1}. M/S: Requires M$^+$ 290.07; Found M$^+$ 290.08, m/z: 275.00, 247.00, 162.00 and 122.00. Structure of synthesized thiazole derivatives are shown in Figure 1.

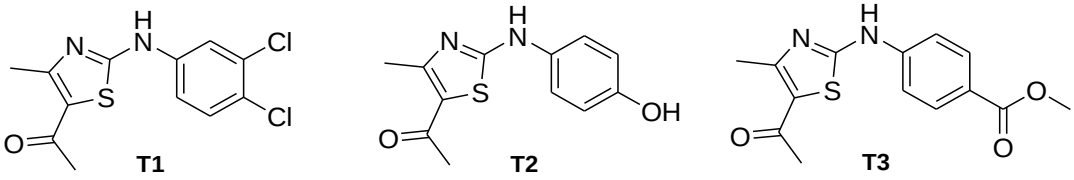


Figure 1. Structure of synthesized thiazole derivatives

A series of thiazole derivatives were successfully synthesized in moderately good yields according to previous literature with some modification [19]. The synthesis of the target compounds was straightforward, and the general synthetic pathway is illustrated in Scheme 1. Haloketone namely 3-chloroacetyl acetone was reacted with ammonium thiocyanate in acetone to give thiocyanato acetylacetone and ammonium salt as by-product. Next, the amines; 3, 4-dichloroaniline, 4-aminophenol and methyl-4-aminobenzoate were added to the reaction mixture to produce the titled compounds **T1**, **T2** and **T3** respectively. The chemical structure of compounds **T1**-**T3** was proved by spectroscopic and spectrometry data.

There are five important absorption bands of interest in all IR spectra of **T1**, **T2** and **T3** namely *v*(N-H), *v*(C-H), *v*(C=O), *v*(C=N) and *v*(C-S). The first band was assigned as N-H stretching and can be observed in the region of 3280-3242 cm^{-1} as previously reported [20]. C-H stretching can be observed at typical range between 3029 cm^{-1} and 2924 cm^{-1}. As reported in literature studies [21,22], C=O absorption band at 1711-1604 cm^{-1} appears as intense peak as a result of high dipole moment due to large partial negative charge of oxygen. Meanwhile, C=N and C-S stretching bands are observed at 1610-1545 cm^{-1} and 723-593 cm^{-1} respectively. Figure 2 shows the FTIR spectrum of 5-acetyl-4-methyl-2-(methyl-4-aminobenzoate)-1,3-thiazole (**T3**) as representative of this series.

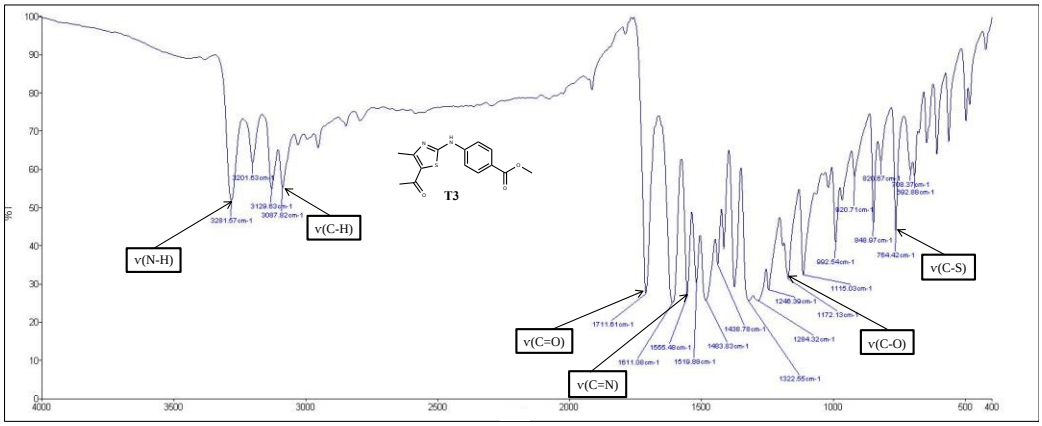


Figure 2. FTIR spectrum of 5-acetyl-4-methyl-2-(methyl-4-aminobenzoate)-1,3-thiazole (**T3**)

Meanwhile in ^{1}H NMR, two high intensity singlet resonances at δ_H 2.38-2.58 ppm represent two methyl moieties presented in all synthesized compounds (**T1**-**T3**). One of the observed resonances is found to be at higher chemical shift region due to deshielding effect of neighbouring C=O moiety [23]. In the range of δ_H 7.95-6.78 ppm, roofing effect due to para substituted phenyl group can be observed in **T2** and **T3** [24]. However, different pattern at δ_H 8.02-7.52 ppm is observed due to presence of tri-substituted phenyl in **T1**. The presence of NH resonance peaks as observed in all ^{1}H NMR spectra prove that the thiazole derivatives were successfully synthesized. NH resonance which appears as singlet is found to be at the most downfield region (δ_H 11.13-10.46 ppm) [25]. Figure 3 shows the ^{1}H spectrum of 5-acetyl-4-methyl-2-(methyl-4-aminobenzoate)-1,3-thiazole (**T3**) as representative of the group.

In addition to the compounds characterization, UV-Vis spectra of **T1**-**T3** were recorded below than 400 nm. All compounds exhibited similar UV band profile which comprised of two absorption bands with different intensity. The first band at 224-229 nm which is the lowest intensity absorption band (ε = 21600 - 50300 M^{-1} cm^{-1}) was assigned as n- π^* transition which attributed by lone pair of C=O, N-H and OH [26]. Besides that, second absorption band which can observed at 343-352 nm was attributed as higher intensity compared (ε =62200 – 82200 M^{-1} cm^{-1}) to the first absorption band. It is due to the electronic transition produced from excitation of unsaturated moiety in a molecular structure [27]. Plus, excitation of π electrons from lower to higher energy levels by several unsaturated chromophores such as aromatic and carbonyl moieties was responsible for the transition [28].

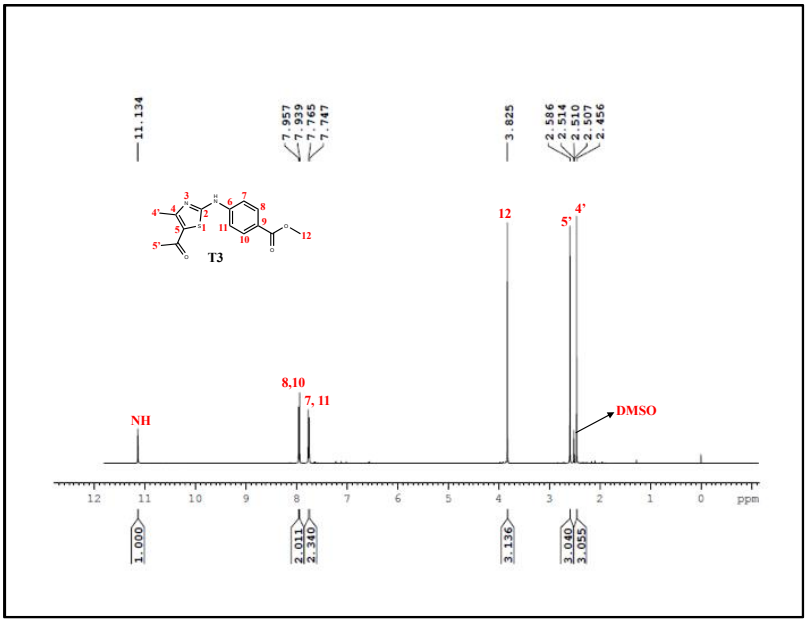


Figure 3. ^{1}H NMR spectrum of 5-acetyl-4-methyl-2-(methyl-4-aminobenzoate)-1,3-thiazole (**T3**)

Antibacterial activities

In this work, antibacterial screening test were used as preliminary evaluation. The screening was conducted by measuring the potential of these compounds to retard the growth of bacterial strains as show in Table 1. From the results obtained, it is shows that **T3** exhibited the excellent inhibitory growth against both Gram-positive (*S. cereus* and *S. epidermidis*) and Gram-negative (*E. coli* and *P. aeruginosa*) bacterial strains followed by **T2** and **T1**. The highest activity showed by **T3** might be due to the presence of electron donating group which is methoxy (OCH_3), which enhance its interaction towards the tested bacteria. Incorporation of methoxy group in the thiazole compound has boosted the antimicrobial activity in terms of increase in lipophilicity behavior that easily penetrated into the membrane of bacterial strains [29]. Besides, methoxy group also provides electron donating behaviour which enhanced the overall antibacterial activity of the synthesized compound [30]. Conversely, presence of electron withdrawing groups such as hydroxyl and chloro substituents in **T1** and **T2** weaken overall antibacterial performance.

Table 1. Diameter of clearing zone (mm) around the disc for bacterial strains

Compounds	**Zone of inhibition (mm)**			
	Gram-positive bacteria		**Gram-negative bacteria**	
	B. cereus	***S. epidermidis***	***E. coli***	***P. aeruginosa***
T1	8.7	9.0	8.0	7.0
T2	10.0	11.0	8.3	8.7
T3	12.0	11.0	8.5	10.0
DMSO	-	-	-	-
Streptomycin	20.0	21.0	18.0	19.0

Molecular docking

Considering the data obtained from the antibacterial screening result, it is worth to perform molecular docking study. Therefore, molecular docking studies were carried out to know the interaction of synthesized compounds

(**T1**-**T3**) against active site of glucosamine-6-phosphate synthase (GlcN-6-P) which is the target for antibacterial agents. GlcN-6-P synthase is considered as primary target because it is essential building block of bacteria which involves in biosynthesis of cell wall in most of bacteria and fungi [31, 32]. Inhibition of this enzyme will restrain the production cell membrane and significantly decrease population of bacteria [33].

In this experiment, orientation of inhibitors interaction in the active site of GlcN-6-P was determined by automated docking [34]. Figure 4 illustrates the best generated conformers for **T1**-**T3** and streptomycin molecules inside the binding pocket of GlcN-6-P synthase.

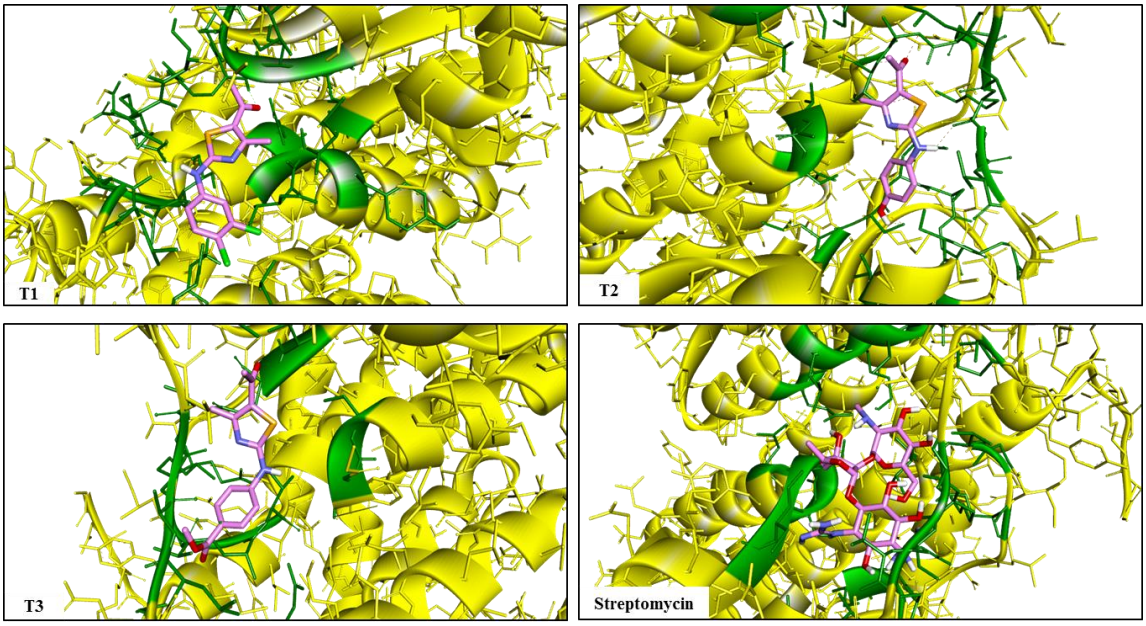


Figure 4. Docked conformations of thiazole derivatives (**T1**-**T3**) and standard drug (thick stick model) in the active site of GlcN-6-P synthase (thin stick and solid ribbon model)

The docking ligand molecules **T1**-**T3** with enzyme revealed that all the expected inhibitor compounds exhibiting the hydrogen bonding interactions with more than one amino acid residues in the active pockets of GlcN-6-P synthase which are showed in Figure 5. From the chemical structure of ligands, it can be observed that oxygen atom of carbonyl group at -5 position of thiazole moiety forms interaction with Ala400 (2.64 Å), Gln348 (1.71 Å) and Ser347 (2.07 Å). Besides that, the amine group in all thiazole derivatives form hydrogen bonding with amino acid residues namely Lys603 (2.17Å), Val399 (2.13 Å) and Ser401 (2.15 Å). The presence of different substituents in each phenyl moiety of thiazole derivatives which is chloro, hydroxyl and ester groups, respectively affects the interaction performance of ligands towards amino acid residues. For instance, hydroxyl atom that is attached to the phenyl group in **T2** tends to form hydrogen bonding with Thr355 (2.30 Å). Meanwhile, both oxygen atoms of ester group in **T3** form hydrogen bonding with Ala400 (1.45 Å) and Val399 (1.90 Å).

Furthermore, based on molecular docking prediction in Table 2 below, **T3** exhibited the best performance against the target enzyme as supported by its lowest binding energy (-7.09 kcal mol^{-1}) as compared to other ligands and as reported by other studies that state low binding energy is required for inhibition of enzyme [14, 35]. More negative binding energy is proportional to the activation energy for inhibition reaction which leads to tight binding of enzyme-inhibitor complex [16]. Meanwhile, **T1** and **T2** showed higher binding energy compared to **T3** which coincide with the antibacterial screening result. The result proved that higher binding energy of **T1** and **T2** towards enzyme is reflected in lower antibacterial activity in screening test. This computational prediction is in a very good agreement to antibacterial screening result which proves the significant impact of this molecular docking study.

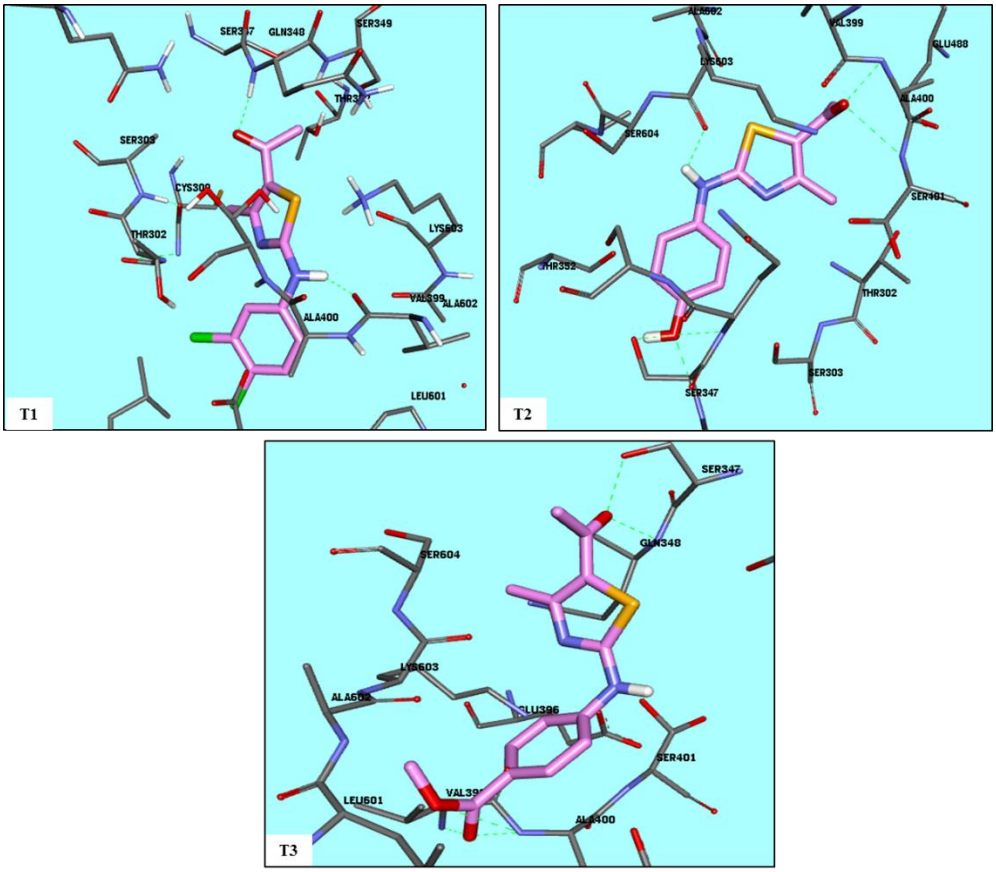


Figure 5. 3D view of all synthesized compounds (ligands) after molecular docking into the active site of GlcN-6-P synthase. Both ligands and amino acid residues of protein are presented in stick in size of 0.2 and 0.1 respectively. Bond length was found less than 3.0Å in all interactions

Table 2. Molecular docking parameters of **T1**-**T3** and standard drug towards GlcN-6-P synthase

Ligand	**Binding Energy (kcal mol^{-1})**	**Amino acid residues**
T1	-6.49	Gly348, Val399
T2	-6.76	Ala400, Lys603, Thr355, Ser347
T3	-7.09	Gln348, Ser347, Val399, Ala400, Ser401
Streptomycin (Std.)	-7.66	Val399, Ser401, Cys300, Ala602, Asn600, Thr302, Glu488

Conclusion

In conclusion, the present work has demonstrated that series of 2, 4, 5- trisubstituted-1,3-thiazole derivatives (**T1**-**T3**) were successfully synthesized in moderately good yield as well as characterized using different techniques and exhibited potential activity against the tested bacterial strains. Among the tested compounds, 5-acetyl-4-methyl-2-(methyl-4-aminobenzoate)-1, 3-thiazole (**T3**) has emerged as most active against tested bacterial strains. Molecular docking studies also revealed that **T3** has the lowest binding energy and may consider as a good inhibitor of GlcN-6-P synthase. For further investigation, complete antimicrobial procedure including *in vitro* assays should be

applied to evaluate the potential of thiazole derivatives against different types of bacteria and fungi with the support of molecular docking study.

Acknowledgement

We gratefully acknowledge grants from the Ministry of Education Malaysia FRGS14-15-0392, Department of Chemistry and Biotechnology, Kulliyyah of Science, International Islamic University Malaysia (IIUM) for providing the essential laboratory facilities. We also would like to thank the Central Laboratory, Universiti Malaysia Pahang for NMR services.

References

1. Tran, T., Nguyen, T., Do, T., Huynh, T., Tran, C. and Thai, K. (2012). Synthesis and antibacterial activity of some heterocyclic chalcone analogues alone and in combination with antibiotics. *Molecules*, 17(6): 6684 – 6696.
2. Kotb, E. R., Anwar, M. M., Abbas, H. S. and El-Moez, S. I. A. (2013). A concise synthesis and antimicrobial activity of a novel series of naphthylpyridine-3-carbonitrile compounds. *Acta Poloniae Pharmaceutica-Drug Research*, 70(4): 667 – 679.
3. Ejideke, I. P. and Ajibade, P. A. (2015). Synthesis, characterization, antioxidant and antibacterial studies of some metal (II) complexes of tetradentate Schiff base ligand: (4E)-4-[(2-{(E)-[1-(2,4-dihydroxyphenyl) ethylidene] amino}ethyl)imino]penta-2-one. *Bioinorganic Chemistry and Applications*, 9: 1 – 9.
4. Dayt, D. and Serra, G. (2010). Thiazole and oxazole alkaloids: Isolation and synthesis. *Marine Drugs*, 8: 2755 – 2780.
5. Kaur, K., Kaur, R. and Dhir, G. N. (2014). Synthesis and biological of amino acid and peptide conjugates of Rhein derivatives. *Journal of Advanced Pharmaceutical Education and Resource*, 4(3): 311 – 318.
6. Penta, S. and Vedula, R. R. (2012). A facile one-pot synthesis of thiazole-pyrazole derivatives *via* multicomponent approach. *Organic Communications*, 5(3): 143 – 149.
7. Bodireddy, M. R., Mohinuddin, P. M. K., Gundala, T. R. and Reddy, G. (2016). Lactic acid-mediated tandem one-pot synthesis of 2-aminothiazole derivatives: A rapid, scalable and sustainable process. *Organic Chemistry*, 2: 1 – 13.
8. Kołazcek, A., Fusiarz, I., Ławecka, J. and Braowska, D. (2014). Biological activity and synthesis of sulfonamide derivatives: A brief review. *Chemik Er Zeitung*, 68(7): 620 – 628.
9. Kushwara, N., Kushwara, S. K. S. and Rai, A. K. (2012). Biological activities of thiadiazole derivatives: A review. *International Research of Chemtech Research*, 4(2): 517 – 531.
10. Vijesh, A. M., Isloor, A. M., Telkar, S., Arulmoli, T. and Fun, H. K. (2013). Molecular docking studies of some new imidazole derivatives for antimicrobial properties. *Arabian Journal of Chemistry*, 6: 197– 204.
11. Pawlak, D., Stolarska, M., Wojciechowski, M. and Andruszkiewicz, R. (2015). Synthesis, anticandial activity of N^3-(4-methoxyfumaroyl) -(*S*)-2,3-diaminopropanoic amide derivatives–novel inhibitors of glucosamine-6-phosphate synthase. *European Journal of Medicinal Chemistry*, 90: 577 – 582.
12. Milewski, S. (2012). Glucosamine-6-phosphate synthase –the multi-facets enzyme. *Biochimica et Biophysica Acta-Protein Structure and Molecular Enzymology*, 1597(2): 173 –192.
13. Aouad, M. R., Mayaba, M. M., Naqvi, A., Bardaweel, S. K., Al-blewi, F. F., Messali, M. and Rezki, N. (2017). Design, synthesis, *in silico* and *in vitro* antimicrobial screenings of novel 1,2,4- triazoles carrying 1,2,3-triazole scaffold with lipophilic side chain tether. *Chemistry Central Journal*, 11(1): 1–13.
14. Krishna, B. G., Sarojini, B. K. and Darshanraj, C. G. (2010). Synthesis, characterization, molecular docking and evaluation of antibacterial, antiproliferative and anti-inflammatory properties of new pyridinyl substituted triazole derivatives. *Der Pharma Chemica*, 6(4): 345 – 361.
15. Rajasekaran, A., Sivakumar, K. K., Sureshkumar, K. and Manjushree, M. (2017). Design, synthesis, characterization and *in-vitro* antimicrobial activity of some hybridized triazole scaffolds. *Future Journal of Pharmaceutical Sciences*, 3(1): 1 – 10.
16. Tian, G. and Haffner, C. D. (2001). Linear relationships between binding energy of time-dependent inhibition of steroid 5α- reductase by Δ^1-4-azasteroids. *The Journal of Biological Chemistry*, 276(24): 21359 – 21364.
17. Koochak, H., Seyyednejad, S. M. and Motamedi, H. (2010). Preliminary study on the antibacterial activity of some medicinal plants of Khuzestan (Iran). *Asian Pacific Journal of Tropical Medicine*, 3(3): 180 – 184.

18. Mouilleron, S., Badet-Deisot, M. A. and Golielli-Pimpaneau, B. (2008). Ordering of C-terminal loop and glutaminase domains of glucosamine-6-phosphate synthase promotes sugar ring opening and formation of the ammonia channel. *Journal of Molecular Biology*, 377(4): 1174 – 1185.
19. Jumal, J., Latip, J. and Yamin, B. M. (2006). 2-(4-fluoroanilino)-4,5-dimethyl-1,3-thiazole. *Acta Crystallographica Section E Structure Report Online*, 62(4): 3305 – 3306.
20. Patel, D. D., Patel, M. S., Patel, V. S. and Patel, K. C. (2014). Synthesis and benzothiazole derivatives, their Schiff bases and its anti-infective biological activities. *International Journal of Advanced Research*, 2 (3): 1048 –1054.
21. Rawal, R. K., Tripathi, R., Katti, S. B., Pannecouque, C. and Clercq, E. D. (2008). Design and synthesis of 2-(2,6-dibromophenyl)-3-heteroaryl-1,3-thiazolidin-4-nes as anti-HIV agents. *European Journal of Medicinal Chemistry*, 43: 2800 – 2806.
22. Khattab, S. N. (2005). Synthesis and biological activity of novel amino acid-(*n*'-benzoyl) hydrazine and amino acid-(*n*'-nicotinoyl) hydrazine derivatives. *Molecules*, 10: 1218 – 1228.
23. Luzina, E. L. and Popov, A. V. (2009). Synthesis and anticancer activity of n-bis(trifluoromethyl)alkyl-n'-thiazolyl and *n*-bis(trifluoromethyl)alkyl-*n*'-benzothiazolyl ureas. *European Journal of Medicinal Chemistry*, 44 (2009): 4944 – 4953.
24. Upmanyu, N., Kumar, S., Shah, K. and Mishra, P. (2012). synthesis and antimicrobial studies of some 4-(substituted)-ethanoylamino-3-mercapto-5-(4-substituted) phenyl-1, 2, 4-triazoles. *Dhaka University Journal of Pharmaceutical Sciences*, 11(1): 7 – 18.
25. Anbazhagan, R. and Sankaran, K. R. (2013). Syntheses, spectral characterization, single crystal X-ray diffraction and DFT computational studies of novel derivatives. *Journal of Molecular Structure*, 1050: 73 – 80.
26. Nalwa, H. S., Hanack, M., Pawlowski, G. and Engel, M. K. (1999). Third-order nonlinear optical properties of porphyrazine, phthalocyanine and naphthalocyanine germanium derivatives: demonstrating the effect of π-conjugation length on third-order optical nonlinearity of two-dimensional molecules. *Chemical Physics*, 245: 17 – 26.
27. Qiao, L. and Hao, S. (2018). Novel trifluoromethylcoumarinyl urea derivatives: synthesis, characterization, fluoroscence, and bioactivity. *Molecules*, 23(600): 1 – 14.
28. Saylam, A., Seferoglu, Z. and Ertan, N. (2008). Synthesis of new hetarylazoindole dyes from some 2-aminothiazole derivatives. *Russian Journal of Organic Chemistry*, 44(4): 587 – 594.
29. Arora, P., Narang, R., Bhatia, S., Nayak, S. K., Singh, S., K. and Narasimhan, B. (2015). Synthesis, molecular docking and QSAR studies of 2, 4-disubsituted thiazoles as antimicrobial agents. *Journal of Applied Pharmaceutical Science*, 5(2): 28 – 42.
30. Majik, M. S., Rodrigues, C., Mascarenhas, S. and Souza, L. D. (2014). Bioorganic chemistry design and synthesis of marine natural product-based 1 *H*-indole-2, 3-dione scaffold as a new antifouling/ antibacterial agent against fouling bacteria. *Bioorganic Chemistry*, 54: 89 – 95.
31. Shia, J. S., Al-Bayati, R. I. H., Abdula, A. M. and Saour, K. Y. (2015). Docking study of some *N*-[4-(4-arylidene)-2-(4-substituted-phenyl)-5-oxo-4, 5-dihydro-imidazol-1-yl] benzenesulfonamide derivatives against glucosamine-6-phosphate synthase. *International Journal of Chemical Sciences*, 13(4): 1982 – 1990.
32. Venkatesh, T., Bodke, Y. D., Kenchappa, R. and Telkar, S. (2016). Synthesis, antimicrobial and antioxidant activity of chalcone derivatives containing thiobarbitone nucleus. *Medicinal Chemistry*, 6 (7): 440 – 448.
33. Fikrika, H., Ambarsari, L. and Sumaryada, T. (2009). Molecular docking studies of catechin and its derivatives as anti-bacterial inhibitor for glucosamine-6-phosphate synthase. *Earth and Environmental Science*, 31: 1 – 6.
34. Sarojini, B. K., Krishna, B. G., Darshanraj, C. G., Bharath, B. R. and Manjunatha, H. (2010). Synthesis, characterization, *in vitro* and molecular docking studies of new 2, 5-dichloro thienyl substituted thiazole derivatives for antimicrobial properties. *European Journal of Medicinal Chemistry*, 45(8): 3490 – 3496.
35. Venkatesh, T., Bodke, Y. D., Kenchappa, R. and Telkar, S. (2016). Synthesis, antimicrobial and antioxidant activity of chalcone derivatives containing thiobarbitone nucleus. *Medicinal Chemistry*, 6(7): 440 – 448.

Malaysian Journal of Analytical Sciences, Vol 23 No 2 (2019): 247 - 254
DOI: https://doi.org/10.17576/mjas-2019-2302-09

MALAYSIAN JOURNAL OF ANALYTICAL SCIENCES
Published by The Malaysian Analytical Sciences Society
ISSN 1394 - 2506

EFFECT OF TEMPERATURE ON THE CATALYTIC ACTIVITY OF NEW SYMMETRICAL TETRADENTATE PALLADIUM(II) SCHIFF BASE COMPLEXES IN COPPER-FREE SONOGASHIRA REACTION

(Kesan Suhu Terhadap Aktiviti Pemangkinan Kompleks Baru Paladium(II) Tetradentat Bes Schiff Bersimetri dalam Tindak Balas Sonogashira Tanpa Kuprum)

Shahrul Nizam Ahmad[1]*, Hadariah Bahron[1], Amalina Mohd Tajuddin[2]

[1]*Faculty of Applied Sciences,*
Universiti Teknologi MARA, 40450 Shah Alam, Selangor, Malaysia
[2]*Atta-ur-Rahman Institute for Natural Product Discovery,*
Level 9, Building FF3, UiTM Selangor, Kampus Puncak Alam, Bandar Puncak Alam, Selangor, Malaysia

**Corresponding author: shahrulnizam85@gmail.com*

Received: 29 August 2018; Accepted: 18 February 2019

Abstract

This paper reports the synthesis of two tetradentate Schiff bases namely 2,2'-(((2,2-dimethylpropane-1,3-diyl) bis(azanylylidene))bis(methanylylidene))bis(4-methoxylphenol), LM, and 2,2'-(((2,2-dimethylpropane-1,3-diyl)bis (azanylylidene))bis(methanylylidene))bis(4-nitrophenol), LN. The Schiff bases were reacted with palladium(II) acetate in 1:1 molar ratio yielding two palladium(II) complexes, PdLN and PdLM. The compounds were characterized through elemental analysis, infrared spectroscopy, ^{1}H and ^{13}C Nuclear Magnetic Resonance (NMR), magnetic susceptibility, molar conductivity and melting point. Complexation was indicated to have occurred by the shifting of the characteristic ν(C=N), ν(C-O) and δ(HC=N) peaks. This was supported by appearance of new peaks of ν(M-N) and ν(M-O) as well as disappearance of δ(O-H) peak on the IR and ^{1}H NMR spectra of the palladium(II) complexes. The diamagnetic and non-electrolytic nature of the complexes suggested square planar d^8 palladium(II) geometry and absence of counter ions, respectively. The catalytic activity of the palladium(II) complexes was investigated for copper-free Sonogashira reaction between iodobenzene and phenylacetylene in dimethylsulfoxide (DMSO) at 80 ^{o}C, 100 ^{o}C and 140 ^{o}C. The conversion of iodobenzene at 12 h reaction time was monitored by GC-FID. At 100 ^{o}C, the most active catalyst was PdLN, indicating that the electron withdrawing substituent $–NO_2$, has the ability to enhance catalytic properties of the complexes. At 140 ^{o}C, both palladium(II) complexes successfully converted 100% of iodobenzene.

Keywords: Schiff base, palladium(II) complexes, Sonogashira, temperature change

Abstrak

Kertas kajian ini melaporkan sintesis dua bes Schiff tetradentat iaitu 2,2'-(((2,2-dimetilpropana-1,3-diyl)bis(azanililidena))-bis(methanililidena))bis(4-metoksilfenol), LM dan 2,2'-(((2,2-dimetilpropana-1,3-diyl)bis(azanililidena))bis(methanili-lidena))bis(4-nitrofenol), LN. Bes Schiff tersebut telah ditindakbalaskan dengan palladium(II) asetat dengan nisbah mol 1:1, menghasilkan dua kompleks palladium(II), iaitu PdLN dan PdLM. Sebatian telah dicirikan melalui analisis unsur, spektroskopi inframerah (IM), Resonans Magnetik Nuklear (RMN) ^{1}H dan ^{13}C, kerentanan magnetik, kekonduksian molar dan takat lebur. Pengkompleksan ditunjukkan telah berlaku dengan penganjakan puncak ν(C=N), ν(C-O) dan δ(HC=N). Ia dikukuhkan lagi dengan munculnya puncak baru ν(M-N) dan ν(M-O) dan hilangnya puncak δ(O-H) pada spektrum IM dan ^{1}H RMN kompleks paladium(II). Sifat diamagnetik dan bukan elektrolit komplek mencadangkan geometri satah segiempat sama d^8 paladium(II) dan ketiadaan ion kaunter, masing-masing. Aktiviti pemangkinan komplek paladium(II) dikaji bagi tindakbalas Sonogashira tanpa kuprum antara iodobenzena dan fenilasetilena dalam dimetilsulfoksida (DMSO) pada 80 ^{o}C, 100 ^{o}C dan 140 ^{o}C. Peratusan

penukaran iodobenzena pada jam ke-12 tindak balas dipantau dengan GC-FID. Pada 100 ^{o}C, pemangkin yang paling aktif adalah PdLN, menandakan bahawa kumpulan tertukar ganti penarik elektron, $–NO_2$, boleh meningkatkan sifat pemangkinan kompleks. Pada 140 ^{o}C, kedua-dua kompleks paladium(II) berjaya menukarkan 100% iodobenzena.

Kata kunci: Bes Schiff, kompleks paladium(II), Sonogashira, perubahan suhu

Introduction

A Schiff base is typically formed through condensation reaction between a primary amine with an aldehyde or a ketone with removal of a water molecule [1]. It is also known as imine or azomethine and dubbed as a nitrogen analogue of an aldehyde or ketone, in which the carbonyl group (C=O) is replaced by an imine (C=N) [2]. Schiff bases and their transition metal complexes have been reported to have wide applications such as anticancer, antibacterial, antiviral [3], corrosion inhibition [4] and catalysis [5]. Schiff base metal complexes have been extensively investigated as homogeneous and heterogeneous catalysts in various chemical reactions including carbon-carbon coupling reactions [5]. They are reported to have outstanding catalytic activities and can withstand high temperatures of more than 100 °C, functioning effectively even in the presence of moisture [5].

Sonogashira reaction is an sp^2-sp carbon-carbon bond formation, usually between aryl or vinyl halide and terminal acetylene [6]. It has received enormous attention due to its wide application in synthesis of natural products, biologically active molecules, heterocycles, molecular electronics, dendrimers and conjugated polymers or nanostructures [6]. The original reaction has been modified since its discovery in 1975 by varying the palladium environment, base, catalyst loading, solvent, additive and temperature [7]. The movement towards copper-free Sonogashira reaction is increasing over the years as the application of copper salts as co-catalysts has experimentally proven to be the culprit of Glaser-type oxidative dimerization of the alkyne substrate [8] that caused contamination of the desired alkyne product.

The application of phosphine-based complexes as catalysts is common to enhance the performance of C-C formation reactions. However, these complexes have certain demerits in that they are sensitive towards air and moisture, relatively costly and environmentally harmful [9]. Nitrogen-based complexes like Schiff bases are believed to be good candidates to substitute phosphine-based complexes as the former are air- and moisture-stable, relatively cheaper and environmentally benign. Furthermore, Schiff bases are able to stabilize many different metals in various oxidation states, enhancing the performance of metals [10]. These advantages have popularised Schiff bases metal complexes in recent catalytic studies. Although the application of Schiff base complexes, for example, salen complexes in Heck and Suzuki coupling reaction is exhaustive, its application in copper-free Sonogashira reactions is still limited.

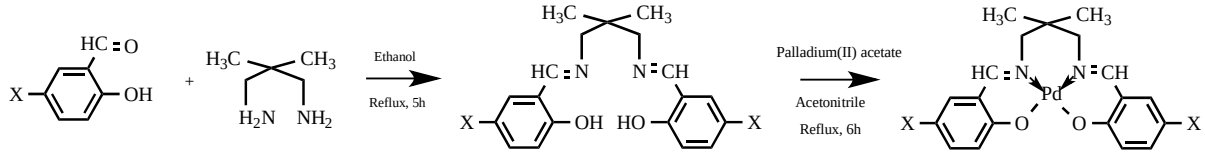
Much work has been devoted to optimize the reaction conditions for Sonogashira coupling reactions in which the optimum temperatures, catalyst loadings, solvents and bases were explored. Reaction conditions typically vary from one reaction to another depending on the types of substrates and catalysts used. An optimum temperature can be as low as room temperature [11, 12] as high as 140 °C [13]. The search for optimum reaction temperature is significant as inappropriate supply of heat to the reaction may inhibit the reaction and impede catalysts from performing effectively. Additionally, finding the optimum temperature is important for cost effectiveness. Optimization is essential particularly when palladium complexes are employed as catalysts because palladium black may occur if the reaction temperature is too high, causing deactivation of the catalytic sites. On the other hand, if the reaction temperature is too low, the percent conversion of reactants may be low.

This work reports the synthesis of two new complexes of palladium(II) with symmetrical tetradentate Schiff base ligands bearing ONNO donor atoms. The catalytic performance of the complexes was appraised on copper-free Sonogashira reaction between iodobenzene and phenylacetylene in dimethylsulfoxide (DMSO) for 12 hours at different temperatures. The findings reported herein are beneficial in understanding the catalytic performance of Schiff base complexes in homogenous Sonogashira reaction system with the absence of the conventional co-catalyst, copper(I) salt.

Materials and Methods

General

Ethanol, acetonitrile, 2,2-dimethyl-1,3-propanediamine, 5-methoxysalicyladehyde and 5-nitrosalicylaldehyde purchased from commercial suppliers were used without prior purification. The micro-analytical data (C, H, and N) of all ligands and complexes were obtained from Thermo Scientific Flash 2000 Elemental Analyser. Melting points were determined on Stuart SMP10. Perkin-Elmer Spectrum One FTIR spectrometer using KBr pellets was employed to record infrared (IR) spectra of ligands and complexes between 450–4000 cm^{-1}. ^{1}H and ^{13}C NMR spectra were recorded on a Bruker Varian-600MHz spectrometer as $CDCl_3$ solutions and expressed in parts per million (δ, ppm). The magnetic susceptibility of the palladium(II) complexes was measured using Sherwood Auto Magnetic Susceptibility Balance. The molar conductivity of the complexes was determined using Mettler Toledo Inlab 730 conductivity meter in 10^{-3} M of DMSO solution. The percent conversion of iodobenzene was monitored using Gas Chromatography-Flame Ionization Detection (GC-FID) model Agilent 6890N. The syntheses of ligands and complexes are presented in Scheme 1.



X= OCH_3, NO_2

Scheme 1. The synthesis of LM and LN and their palladium(II) complexes

Synthesis of LM and LN ligands

A hot solution of 2,2-dimethlyl-1,3-propanediamine $C_5H_{14}N_2$ (1 mmol, 0.1022 g) in absolute ethanol (10 mL) was added to a stirred solution of 5-methoxysalicylaldehyde $C_8H_8O_3$ (2 mmol, 0.3044 g) or 5-nitrosalicylaldehyde $C_7H_5NO_4$ (2 mmol, 0.3342 g) in absolute ethanol (5 mL) for LM and LN, respectively. The solution was refluxed for 5 hours, cooled and chilled overnight. The yellow solid obtained was filtered off, washed with cold ethanol and air dried.

Synthesis of PdLM and PdLN complexes

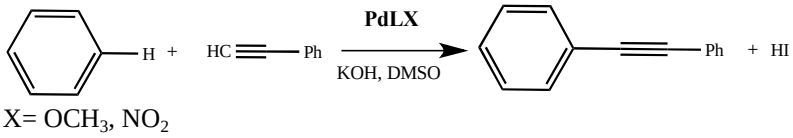
Palladium(II) acetate (1 mmol, 0.2248g) was dissolved in 10 mL of dry acetonitrile in a round-bottomed flask. The ligand LN (1 mmol, 0.4004 g) or LM $C_{21}H_{26}N_2O_4$ (1 mmol, 0.3705 g) was also dissolved separately in 10 mL of dry acetonitrile, then added dropwise into the metal solution. The mixture was refluxed for 6 hours. The orange (PdLM) or yellow (PdLN) solid obtained was washed with 5 mL of cold acetonitrile, filtered off and air-dried.

Copper–free Sonogashira reaction

A round-bottomed flask was charged with iodobenzene (1.0 mmol), phenylacetylene (1.5 mmol), palladium(II) Schiff base complex (0.02 mmol) and KOH (2.0 mmol), with stirring under aerobic condition in 7 mL of DMSO (Scheme 2). The mixture was heated at 80 °C, 100 °C and 140 °C for 12 hours and monitored every 3 hours by Gas Chromatography-Flame Ionization Detection (GC-FID) to determine the percentage conversion of iodobenzene, calculated using equation 1:

$$\% \text{ Conversion} = (A_{int} - A_{final})/A_{int} \quad (1)$$

where A_{int} is peak area of iodobenzene before reaction and A_{final} is peak area of iodobenzene after reaction.



Scheme 2. Copper-free Sonogashira reaction

Results and Discussion

Elemental analysis and melting point

The experimental percentages of elements C, H and N of the compounds are presented in Table 1 and are in close accord with the theoretical values. Based on the elemental analysis results, the structures of the ligands and palladium(II) complexes are as those predicted in Scheme 1. The temperature ranges for melting points listed in Table 1 represent the points at which the compounds started to melt and completely molten [14]. The melting points of the complexes are higher than their parent ligands, likely because of the increased molecular sizes and the presence of strong ionic and dative covalent bonds.

Table 1. Physicochemical properties of LM, LN and their respective palladium(II) complexes

Compound	Color	Percent Yield (%)	Chemical Formula	Melting Point (°C)	Elemental Analysis % (Calculated)		
					C	H	N
LM	Yellow	92.0	$C_{21}H_{26}N_2O_4$	101-105	68.09 (67.91)	7.07 (7.94)	7.56 (7.54)
LN	Yellow	91.0	$C_{19}H2_0N_4O_6$	210-212	57.00 (55.56)	5.04 (4.97)	13.99 (14.64)
PdLM	Orange	67.3	$C_{21}H_{24}N_2O_4Pd$	200-205	53.12 (51.63)	5.09 (5.47)	5.90 (6.19)
PdLN	Yellow	90.5	$C_{19}H_{18}N_4O_6Pd$	>300	45.21 (44.03)	3.59 (3.56)	11.10 (12.48)

Infrared spectroscopy

The IR spectra of LM, LN and their Pd(II) complexes are presented in Figure 1 and significant peaks listed in Table 2. The ν(C=N) peaks of ligands appeared in the range of 1611-1638 cm^{-1}, shifted by 10-31 cm^{-1} to lower frequencies of 1607-16201 cm^{-1} in the Pd(II) complexes, indicating that the C=N experienced a lowering in bond strength upon complexation through azomethine nitrogen. The lone pair of electrons on N was donated to the metal center in a Lewis acid-base interaction, resulting in the reduction of π-electron density on C=N, hence weakening it. The shifting of the C-O band from 1034 cm^{-1} in LM to 1041 cm^{-1} in PdLM, and from 1097 cm^{-1} in LN to 1100 cm^{-1} in PdLN, indicated coordination between ligands and palladium(II) through phenolic oxygen. A couple of new bands appeared in the range of 468-480 cm^{-1} and 540-571 cm^{-1} for palladium(II) complexes assignable to Pd-O and Pd-N, respectively, assenting with the values reported by Bahron et al. [16]. Other significant peaks that deserve some attention are the C=C stretch (1544-1592 cm^{-1}), and C-H sp^2 stretch (3008-3069 cm^{-1}), indicating the presence of benzene rings in the structure. The appearance of C-H sp^3 stretch in the range of 2943-2967 cm^{-1} are indicators that methyl (CH_3) groups are part of the chemical structures.

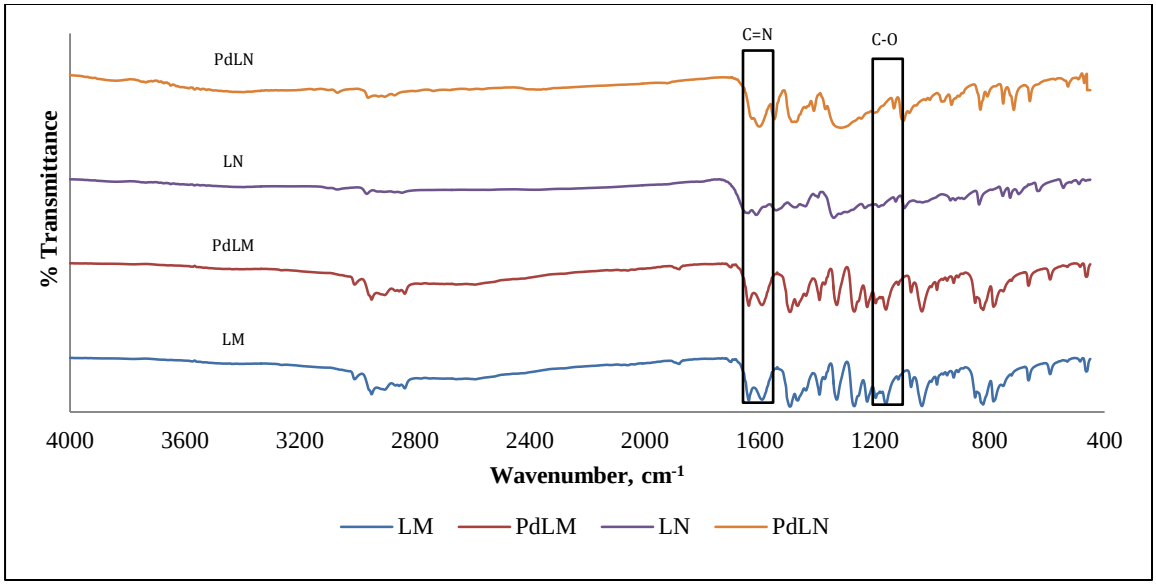


Figure 1. FTIR spectra of LM, LN and their Pd(II) complexes

Table 2. Selected infrared spectral data of LM, LN and their respective palladium(II) complexes

	Frequency, ν (cm^{-1})			
	LM	**PdLM**	**LN**	**PdLN**
C=N	1638(*s*)	1607(*s*)	1611(*s*)	1601(*s*)
C-O	1034(*s*)	1041(*w*)	1097(*m*)	1100(*m*)
Pd-N	-	571(*w*)	-	540(*w*)
Pd-O	-	468(*w*)	-	480(*w*)
C=C stretch	1592(*s*)	1541(*s*)	1544(*m*)	1550(*m*)
C-H sp^2 stretch	3008(*w*)	3014(*w*)	3069(*w*)	3068(*w*)
C-H sp^3 stretch	2951(*w*)	2943(*w*)	2967(*w*)	2963(*w*)
C-H sp^3 bend	1363(*s*)	1365(*w*)	1397(*w*)	1371(*w*)
CH_2 bend	1492(*s*)	1490(*w*)	1441(*w*)	1411(*w*)

br: broad, s: strong, m: medium, w: weak

Nuclear magnetic resonance spectroscopy

Table 3 presents ^{1}H NMR data of LM and PdLM. The spectra of LN and PdLN were not obtained due to their insolubility. The OH signals of LM appeared as a broad peak at the downfield region of 13.10 ppm in LM, indicating the existance of hydrogen bondings [15]. Due to the electronegative oxygen that withdrew electron density from the phenolic proton, the latter was highly deshielded from the magnetic field, causing the chemical shift to appear at the downfield region. The absence of the phenolic proton peak in the spectrum of PdLM shows that the coordination was established between phenolic oxygen and metal center through deprotonation of the hydroxyl group. The chemical shifts of aromatic hydrogen appeared as multiplets at 6.79-6.97 ppm. The values of coupling constants as tabulated in Table 3 are in the range of 1-3 Hz and 6-9 Hz, suggesting the existence of *meta* and *ortho* aromatic protons, respectively. This is in agreement with the chemical shifts reported by Amalina et al. [17]. These hydrogens were deshielded due to diamagnetic anisotropy contributed by circulating π electrons in the aromatic rings. The number of hydrogens was in concordance with the proposed structure. An evidence of

complexation can be seen through the shifting of δ(HC=N) singlet from 8.32 ppm in free LM to 7.56 ppm in PdLM, suggesting a shielding of the azomethine proton by the Pd(II) center. The presence of methyl group, CH_3, CH_2 and OCH_3 protons was detected as singlets at 1.10, 3.47 and 3.80 ppm in LM, respectively. These chemical shifts experienced very little or no shifting at all upon complexation, signifying their non-involvement.

Table 3. ^{1}H NMR spectral data of LM and PdLM

	Chemical Shift, δ (ppm)	
	LM	**PdLM**
OH	13.10 (s, 1H)	-
HC=N	8.32 (s, 1H)	7.52 (s, 1H)
CH_3	1.10 (s, 2H)	1.10 (s, 3H)
CH_2	3.47 (s, 2H)	3.50 (s, 2H)
OCH_3	3.80 (s, 3H)	3.80 (s, 3H)
Aromatic proton (Ar-H)	6.79-6.97 (m, *J*= 1-3, 6-9 Hz, 3H)	6.96-7.10 (m, *J*= 1-3, 6-9 Hz, 3H)

s: singlet, m: multiplet

Table 4 presents ^{13}C NMR data of LM. The peak of carbon bonded to oxygen of the phenolic group, δ(C-OH) appeared at 152.04 ppm, further upfield than the azomethine carbon which was detected at 165.45 ppm, demonstrating the bigger shielding effect of O than N. The signal for CH_3, OCH_3 and CH_2 were found at 24.44, 55.95 and 68.29 ppm, respectively. Aromatic carbons were detected in the range of 114.83-119.41 ppm. There are no ^{13}C NMR spectra obtained for PdLM, LN and PdLN owing to poor solubility of the compounds.

Table 4. ^{13}C NMR spectral data of LM

	Chemical shift, δ (ppm)
	LM
C-OH	152.04
C=N	165.45
CH_3	24.44
OCH_3	55.95
CH_2	68.29
Aromatic carbon (Ar-C)	114.83-119.41

Magnetic susceptibility and molar conductivity

All complexes revealed 0 effective magnetic moment, μ_{eff}, indicating the absence of unpaired electrons, corresponding to the diamagnetic square planar d^8 palladium(II) system. The complexes showed molar conductivity of 0 $\lambda_m/\Omega^{-1}cm^2\ mol^{-1}$ suggesting their non-electrolytic nature, with absence of any counter ions.

Catalytic activity of palladium(II) Schiff base complexes for copper-free Sonogashira reaction

PdLM and PdLN were screened as catalysts in copper-free Sonogahsira cross-coupling reaction of iodobenzene with phenylacetylene in the presence of potassium hydroxide (KOH) in dimethylsulfoxide (DMSO) at 80 °C, 100 °C, 140 °C with the catalyst loading of 2 mmol%. There was an increase in percent conversion of iodobenzene with temperature, and the percentage yield of the product of the coupling reaction was reported to be in direct proportion with temperature [18]. Table 5 shows that PdLN was a better catalyst than PdLM as the former reached 100% conversion of iodobenzene at 100 ^oC as opposed to 140 ^oC for the latter. PdLN had shown a better catalytic performance than the previously reported [13, 19] catalysed reaction which reached 100% conversion at 140 ^oC.

Table 5. Percentage of iodobenzene conversion

Catalyst	% Conversion of Iodobenzene		
	80 °C	100 °C	140 °C
PdLM	85	66	100
PdLN	85	100	100

The electron withdrawing group -NO_2, seemed to have enhanced the catalytic performance of PdLN more effectively than the electron donating group -OCH_3. Ahmad [20] reported the performance of an analogous unsubstituted palladium(II) complex as catalyst, showing 71% conversion of the iodobenzene, in between that of PdLM (66%) and PdLN (100%), at 100 ^{o}C. This clearly indicated the significance of the electronic environment of the Schiff base ligands on the catalytic activity of the central Pd(II). As there was no copper co-catalyst used, the undesired formation of the oxidative homocoupling product, a diyne, was not seen in the GC-FID chromatograms.

Conclusion

Two symmetrical tetradentate Schiff bases bearing *ONNO* donor atoms and their respective palladium(II) complexes namely PdLM and PdLN were successfully synthesized and characterized through elemental analysis, FTIR, ^{1}H and ^{13}C NMR, magnetic susceptibility and molar conductivity. The spectral data obtained showed that complexation between ligands with palladium(II) was achieved through azomethine nitrogen and phenolic oxygen. Reaction temperature was found to be in direct proportion with the percent conversion of iodobenzene. PdLN, bearing an electron withdrawing -NO_2 substituents, showed a higher catalytic activity than PdLM, bearing an electron donating -OCH_3 substituents. In future, lower temperature is planned to be applied for homogenous Sonogashira reaction system by having biphasic solvent system i.e. DMSO:H_2O

Acknowledgement

The authors would like to acknowledge the Ministry of Education, Malaysia and Universiti Teknologi MARA for the support through TPM scholarship, research grant (600-IRMI/PERDANA5/3 BESTARI(046/2018)) and research facilities.

References

1. Qin, W., Long, S., Panunzio, M. and Biondi, S. (2013). Schiff bases: A short survey on an evergreen chemistry tool. *Molecules*, 18(10): 12264 – 12289.
2. Abu-Dief, A. M. and Mohamed, I. M. A. (2015). A review on versatile applications of transition metal complexes incorporating Schiff bases. *Beni-Suef University Journal of Basic and Applied Sciences*, 4(2): 119 – 133.
3. Jarrahpour, A., Khalili, D., De Clercq, E., Salmi, C. and Brunel, J. M. (2007). Synthesis, antibacterial, antifungal and antiviral activity evaluation of some new bis-Schiff bases of isatin and their derivatives. *Molecules*, 12(8): 1720 - 1730.
4. Fateh, A., Aliofkhazraei, M. and Rezvanian, A. R. (2017). Review of corrosive environments for copper and its corrosion inhibitors. *Arabian Journal of Chemistry*. In Press.
5. Gupta, K. C. and Sutar, A. K. (2008). Catalytic activities of Schiff base transition metal complexes. *Coordination Chemistry Reviews*, 252: 1420 – 1450.
6. Chinchilla, R. and Najera, C. (2011). Recent advances in Sonogashira reactions. *Chemical Society Reviews*, 40(10): 5084 – 5121.
7. Prabhu, R. N. and Pal, S. (2015). Copper-free Sonogashira reactions catalyzed by a palladium(II) complex bearing pyrenealdehyde thiosemicarbazonate under ambient conditions. *Tetrahedron Letters*, 56(37): 5252–5256.
8. Siemsen, P., Livingston, R. C. and Diederich, F. (2000). Acetylenic coupling: A powerful tool in molecular construction. *Angewandte Chemie International Edition*, 39(15): 2632 - 2657.

9. Bakherad, M., Amin, A. H., Keivanloo, A., Bahramian, B. and Raeissi, M. (2010). Copper-and phosphine-free Sonogashira coupling reactions of aryl iodides catalyzed by an N,N-bis (naphthylideneimino) diethylenetriamine-functionalized polystyrene resin supported Pd(II) complex under aerobic conditions. *Tetrahedron Letters*, 51(43): 5653 - 5656.
10. Cozzi, P. G. (2004). Metal–Salen Schiff base complexes in catalysis: Practical aspects. *Chemical Society Reviews*, 33(7): 410-421.
11. Bakherad, M., Keivanloo, A., Bahramian, B. and Hashemi, M. (2009). Copper-free Sonogashira coupling reactions catalyzed by a water-soluble Pd–salen complex under aerobic conditions. *Tetrahedron Letters*, 50(14): 1557 - 1559.
12. Das, S. K., Sarmah, M. and Bora, U. (2017). An ambient temperature Sonogashira cross-coupling protocol using 4-aminobenzoic acid as promoter under copper and amine free conditions. *Tetrahedron Letters*, 58(22): 2094 - 2097.
13. He, Y. and Cai, C. (2011). Heterogeneous copper-free Sonogashira coupling reaction catalyzed by a reusable palladium Schiff base complex in water. *Journal of Organometallic Chemistry*, 696(13): 2689-2692.
14. Pavia, D. L., Lampman, G. M., Kriz, G. S. and Engel, R. G. (2005). Introduction to organic laboratory techniques: a small scale approach. Cengage Learning.
15. Aranha, P. E., dos Santos, M. P., Romera, S. and Dockal, E. R. (2007). Synthesis, characterization, and spectroscopic studies of tetradentate Schiff base chromium (III) complexes. *Polyhedron*, 26(7): 1373 -1382.
16. Bahron, H., Ahmad, S. N., Tajuddin, A. M. and Kadir, S. I. A. S. A. (2017). Substituent effect on catalytic activity of palladium(II) Schiff base complexes for Sonogashira reaction. *Pertanika Journal of Science and Technology*, 25: 115 – 124.
17. Amalina, M. T., Hadariah, B., Karimah, K., Wan, N. W. I. and Bohari, M. Y. (2012). Synthesis and characterisation of palladium(II) Schiff base complexes and their catalytic activities for Suzuki coupling reaction. *Malaysian Journal of Analytical Sciences*, 16(1): 79-87.
18. Rosa, D. S., Antelo, F., Lopes, T. J., Moura, N. F. D. and Rosa, G. R. (2015). Effects of solvent, base, and temperature in the optimisation of a new catalytic system for Sonogashira cross-coupling using NCP pincer palladacycle. *Quimica Nova*, 38(5): 605 - 608.
19. Guan, J. T., Yu, G. A., Chen, L., Qing Weng, T., Yuan, J. J. and Liu, S. H. (2009). CuI/PPh_3-catalyzed Sonogashira coupling reaction of aryl iodides with terminal alkynes in water in the absence of palladium. *Applied Organometallic Chemistry*, 23(2): 75-77.
20. Ahmad, S. N. (2018) Synthesis and characterization of palladium(II) and nickel(II) Schiff base complexes for homogenous catalytic and anticancer studies. Thesis of Doctor Philosophy, Universiti Teknologi MARA.

Malaysian Journal of Analytical Sciences, Vol 23 No 2 (2019): 255 - 262
DOI: https://doi.org/10.17576/mjas-2019-2302-10

MALAYSIAN JOURNAL OF ANALYTICAL SCIENCES
Published by The Malaysian Analytical Sciences Society
ISSN 1394 - 2506

SYNTHESIS AND CHARACTERISATION OF NANOHYBRID ANTI-HYPERTENSIVE DRUG, CAPTOPRIL INTERCALATED INTO ZINC–ALUMINIUM LAYERED DOUBLE HYDROXIDE

(Sintesis dan Pencirian Nanohibrid Ubat Anti-Hipertensi, Captopril Tersisip ke dalam Zink-Aluminium Hidroksida Berlapis Ganda)

Zaemah Jubri[1]*, Siti Halimah Sarijo[2], Monica Limau Anak Jadam[1]

[1]*Centre for Advanced Materials,*
Universiti Tenaga Nasional, 43000 Kajang, Selangor, Malaysia
[2]*Faculty of Applied Sciences,*
Universiti Teknologi MARA, 40450 Shah Alam, Selangor, Malaysia

**Corresponding author: zaemah@uniten.edu.my*

Received: 19 August 2018; Accepted: 10 March 2019

Abstract

Captopril (CPL), an anti-hypertensive drug was intercalated into the interlayer spaces of zinc–aluminium layered double hydroxide (ZLDH) for the formation of zinc–aluminium–captopril (ZCPL) hybrid nanocomposite material by self-assembly method. The concentration of CPL used was 0.08 M with pH 7.5 in a constant 3:1 molar ratio of zinc (Zn) to aluminium (Al) in the mother liquor. As a result of the successful intercalation of CPL, powder X-ray diffraction pattern (PXRD) shows the basal spacing increased from 8.90 Å in ZLDH to 9.69 Å in the ZCPL nanohybrid material. Fourier transform infrared (FTIR) spectroscopy study shows the intercalated compound of ZCPL resembled the spectra of ZLDH and CPL, thus indicating the presence of both functional groups in ZCPL spectra. CHNS analysis shows the ZCPL nanohybrid material contains 30.63% (w/w) of CPL which was calculated based on the percentage of carbon in the sample. It was also found that the BET surface area increased from 1.7 m^2/g in ZLDH to 10.9 m^2/g in ZCPL. The pore texture of the resulting material was also changed as the result of the intercalation and the expansion of the basal spacing during the formation of the layered intercalated ZCPL nanohybrid material.

Keywords: captopril, anti-hypertensive drug, intercalation, layered double hydroxide, nanocomposite

Abstrak

Captopril (CPL) iaitu ubat anti-hipertensi telah berjaya disisipkan ke dalam ruang antara lapis hidroksida berlapis ganda bagi pembentukan bahan hibrid ZCPL nanokomposit melalui kaedah pembentukan sendiri. Kepekatan CPL yang digunakan adalah 0.08M dan pH 7.5 dengan nisbah kepekatan tetap Zn : Al adalah 3 : 1 dalam larutan akueous. Penyisipan anion captopril dapat ditentukan dari pengembangan jarak basal PXRD daripada 8.90 Å bagi zink-aluminium hidroksida berlapis ganda (ZLDH) kepada 9.69Å bagi bahan nanohibrid ZCPL. Analisis inframerah transformasi Fourier (FTIR) menunjukkan kehadiran gabungan kumpulan berfungsi bagi ZLDH dan CPL kelihatan pada spektra ZCPL. Ini membuktikan CPL telah berjaya disisipkan di antara ruang hidroksida berlapis ganda bagi pembentukan bahan nanokomposit tersebut. Analisis CHNS menunjukkan bahan nanohibrid ZCPL mengandungi CPL dengan peratusan 30.63 % (w/w) yang ditentukan melalui pengiraan peratusan karbon di dalam sampel nanohibrid ZCPL. Luas permukaan BET telah meningkat daripada 1.7 m^2/g kepada 10.9 m^2/g masing-masing bagi ZLDH dan ZCPL. Struktur liang bahan nanohibrid yang terhasil juga telah berubah disebabkan penyisipan captopril telah mengembangkan jarak basal, begitu juga dengan pembentukan liang yang lebih besar berlaku hasil dari pembentukan bahan nanohibrid, ZCPL.

Kata kunci: captopril, ubat anti-hipertensi, sisipan, hidroksida berlapis ganda, nanokomposit

Introduction

Hydrotalcites like anionic clay mineral or layered double hydroxide (LDH), comprise two dimensional inorganic nanolayers emerged as materials with numerous medical applications including gene delivery [1] and drug delivery [2]. The design of effective drug delivery has become significant in modern pharmaceutics, aiming at minimising secondary effects, increasing drug bioavailability and stability, and better localisation of the pharmaceutical action [3]. The basic structure of LDH was derived by the substitution of divalent cations in a brucite lattice by trivalent cations in such way that the layers acquire a positive charge, which is balanced by the intercalation of anions and water between the layers [4].

LDHs generally represented by the general formula $[M^{II}_{1-x}\ M^{III}_{x}\ (OH)_2]^{x+}\ (A^{n-})_{x/n}\cdot yH_2O$, where M^{II} is the divalent metal cation (Mg^{2+}, Ca^{2+}, and Zn^{2+}), M^{III} is the trivalent metal cation (Al^{3+}, Cr^{3+}, Fe^{3+}, and Co^{3+}), and A^{n-} is the anion (Cl^-, CO_3^{2-}, and NO_3^-) [5]. Nowadays, LDHs are well-known materials due to its interesting properties such as excellent anion exchange capacity [6], good adsorptive removal of dye and phenol [7, 8], act as a controlled release formulation for nonsteroidal anti-inflammatory drugs (NSAIDs) [9] and has the potential to be used as drug delivery system [10]. It also has widespread application in the fields of catalysis [11], intumescent flame retardant [12], polymer [13], photocatalytic activity enhancement [14], ultrahigh energy density and stable supercapacitor [15], and good to be used as energy storage [16]. The layers of LDH possess positive charges which are counter-balanced by the anions present in the interlayer spacing and those anions are exchangeable with other suitable negatively charged species. The interlayer anion exchange capability of LDHs can be used to intercalate negatively charged functional biomolecules such as vitamins [17], DNA [18], and drugs within the LDH layer [19, 20]. Thus, LDH has the potential as a drug vehicle and could be used to regulate the release of drug from the drug intercalated LDH. Sustained drug release has the advantages as it could reduce the frequency of the drug intake and improve the patient's compliances [5].

In this study, captopril (CPL) drug which is a primary drug used for hypertension [14], was intercalated into the interlayer spaces of ZLDH by self-assembly method. The chemical structure of CPL is shown in Figure 1.

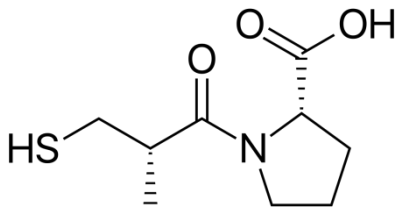


Figure 1. Chemical structure of CPL

The physicochemical properties of the zinc–aluminium–captopril (ZCPL) nanohybrid material will be discussed in this paper. The synthesised ZCPL nanohybrid material is expected to become a promising nanocarrier for CPL as a controlled release formulation for anti-hypertensive drugs.

Materials and Methods

All the chemicals used in the synthesis were obtained from various chemical suppliers and used without any further purification. All solution was prepared using deionised distilled water. Zinc nitrate hexahydrate $[Zn(NO_3)_2\cdot 6H_2O]$, aluminium nitrate ($AlNO_3\cdot 9H_2O$), sodium hydroxide (NaOH), CPL ($C_9H_{15}NO_3S$) were obtained from Sigma-Aldrich (USA), at 98% purity and used as received.

The synthesis of ZCPL was done by self-assembly method. A mother liquor containing zinc cation (Zn^{2+}) and aluminium cation (Al^{3+}) with Zn/Al initial ratio (R_i = 3) and CPL was prepared and the pH value that was adjusted to about 7.5. The concentration of CPL was 0.08 M and the reaction was carried out by stirring the solution under nitrogen atmosphere. The solution was aged for 18 hours in an oil bath shaker at 70 ^oC. The resulting precipitate was centrifuged, thoroughly washed, and dried in an oven at 70 ^oC for 3 days and kept in a sample bottle for further use and characterisations. A similar method was adopted for the preparation of ZLDH with nitrate anion (NO_3^-) as the intergallery anion by omitting the addition of CPL solution in the mother liquor.

Powder X-ray diffraction (PXRD) patterns of the samples were obtained by a Shimadzu diffractometer XRD-6000, using the filtered CuKα radiation. FTIR spectra were recorded by a Perkin-Elmer 1750 spectrophotometer. KBr pellet containing 1% sample was used to obtain the FTIR spectra. The surface morphology of the samples was observed by a scanning electron microscope (SEM), using JOEL JSM-6400. CHNS-O analyser, model EA 1108 of Finons Instruments was used for CHNS-O analysis. The surface characterisation of the materials was carried out by nitrogen gas adsorption desorption at 77 K using micromeritics ASAP 2000. Samples were degassed in an evacuated-heated chamber at 120 ^oC overnight.

Results and Discussion

Powder X-ray diffraction

Figure 2(a) shows PXRD patterns of ZLDH, CPL, and ZCPL. The PXRD patterns show a sharp, intense, and symmetry peak indicating a well-ordered nanolayered structure was formed in the resulting materials. As shown in the figure, CPL anion was successfully intercalated inside the interlayer of ZLDH with the increased of the basal spacing from 8.90 Å in ZLDH to 9.69 Å in the nanocomposite, ZCPL. The expansion of the basal is due to the inclusion of CPL anion into the ZLDH lamella, which is bigger than NO_3^-.

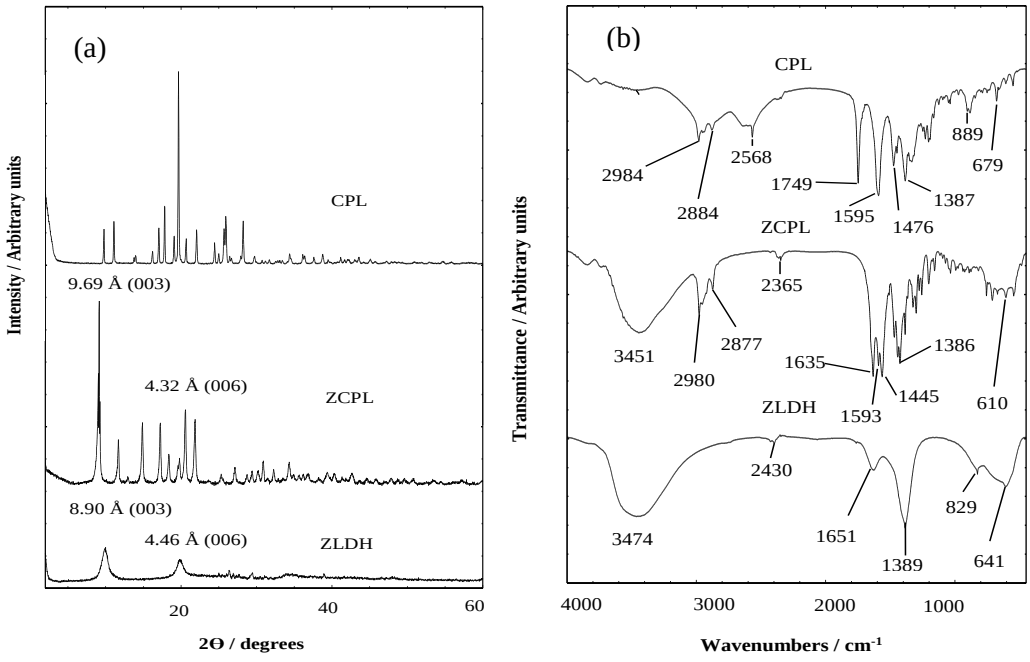


Figure 2. The PXRD patterns of (a) ZLDH, ZCPL, and CPL and (b) FTIR spectra for ZLDH, ZCPL, and CPL

Fourier transform infrared spectroscopy

Figure 2(b) shows the FTIR spectra for CPL, ZLDH, and ZCPL nanocomposites. The FTIR spectrum for ZLDH shows a broad absorption band at around 3474 cm^{-1} which is due to the presence of OH stretching modes of the

hydroxyl group in LDH. The band at 1642 cm^{-1} is due to the bending vibration of the interlayer water molecule. A sharp and intense peak located at approximately 1389 cm^{-1} is attributed to the stretching vibration of NO_3^- [22]. Another band at 829 and 641 cm^{-1} are due to the translation vibrations at Zn–OH and deformation vibration of OH–Zn–Al–OH, respectively [23].

The FTIR spectrum for CPL shows the characteristic frequencies at 889 cm^{-1} due to the –CN bending vibration, 1595 cm^{-1} due to the nitrogen ring, and 1749cm^{-1} indicating the carboxylate ion (COO^-) from COOH group. Characteristic peak at 2568 cm^{-1} indicates the presence of –SH group of CPL [24].

As expected, the FTIR spectrum of ZCPL resembles a mixture of both the spectra of CPL and ZLDH, indicating that both functional groups of CPL and ZLDH simultaneously present in ZCPL and confirms the intercalation of CPL in the interlamellar of ZCPL. The presence of the absorption band at 1386 cm^{-1} indicates the presence of CPL anion in ZCPL replacing NO_3^- in ZLDH. This shows that CPL has higher affinity than NO_3^- towards the inorganic interlamellar, thus occupies the interlamellar region between the inorganic layers and prevents further co-intercalation of NO_3^-. The most important feature in the FTIR spectra is the presence of new band at around 2980 and 610 cm^{-1} which indicates the presence of S–H and C–S stretching, respectively. This new band at 1593 cm^{-1} is due to the nitrogen ring of CPL, which confirms the presence of CPL in the interlayer spaces of the ZLDH.

Spatial orientation of captopril drug in Zn-Al-CPL nanocomposite

Based on the three dimensional molecular structure of CPL, the calculation obtained using Chem 3D Ultra 8.0 software is ilustrated in Figure 3(a). The length, height, and thickness of the CPL molecular structure were estimated to be 5.9, 5.0, and 3.2 Å, respectively. The ZLDH is composed of inorganic layers with octahedral coordinated Zn^{2+}. The CPL was suggested to be oriented in the interlayer gallery of ZLDH in a monolayer arrangement and was held in the orientation as shown in Figure 3(b) by the electrostatic attraction from the excess positive charge of ZLDH [21]. In the proposed spatial arrangement of CPL within the interlayer of ZLDH, the molecular structure of CPL is expected to be slightly slanted.

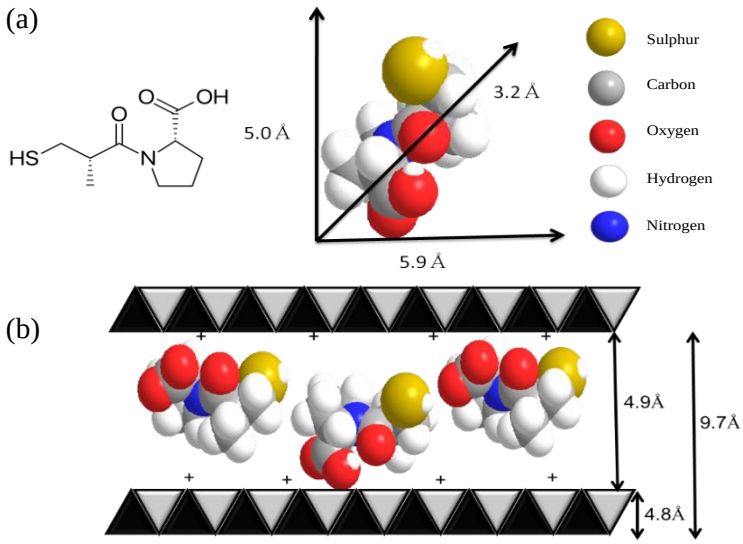


Figure 3. (a) Molecular structure of CPL and three–dimensional molecular size of CPL and (b) proposed spatial orientation of CPL in the interlayer of ZLDH

CHNS analysis

The CHNS analysis shows that ZCPL contained 30.63% of carbon, and 8.70% of sulfur which indicate that CPL was successfully intercalated into the lamellae of ZCPL. The percentage of nitrogen of 3.10% is due to the presence

of NO_3^- in ZLDH. And since the CPL also contains nitrogen atom, the 4.48% of nitrogen detected in CHNS analysis is due to the nitrogen atom of CPL.

Isotherm, surface area and pore size distribution

Figure 4(a) shows the adsorption–desorption isotherm for ZLDH and ZCPL nanocomposite material. As shown in the figure, the adsorption–desorption for ZCPL was Type IV, indicating a mesoporous-type material (20–500 Å) [25], with adsorption of a slow uptake of the adsorbent at a relative pressure of 0.05–0.8. Further increase of a relative pressure to >0.8 resulted in a rapid adsorption of the adsorbent, reaching an optimum at more than 45 cm^3/g at STP. A general shape of the isotherm for ZCPL did not differ very much from ZLDH; the Type IV isotherm remains. However, as shown in Figure 4(a), the adsorbate uptake was slow in the relative pressure range 0.05–0.9, after that rapid adsorption was observed. An optimum uptake of 5 cm^3/g at STP, indicates the slow uptake of the nitrogen gas. Desorption branch of the hysteresis loop for ZCPL was narrower compared to that of ZLDH, indicating different pore texture of the resulting material. This can be related to the different pore structure when NO_3^- was replaced by CPL during the formation of ZCPL with the formation of interstitial pores between the crystallite, different particle size, and morphology.

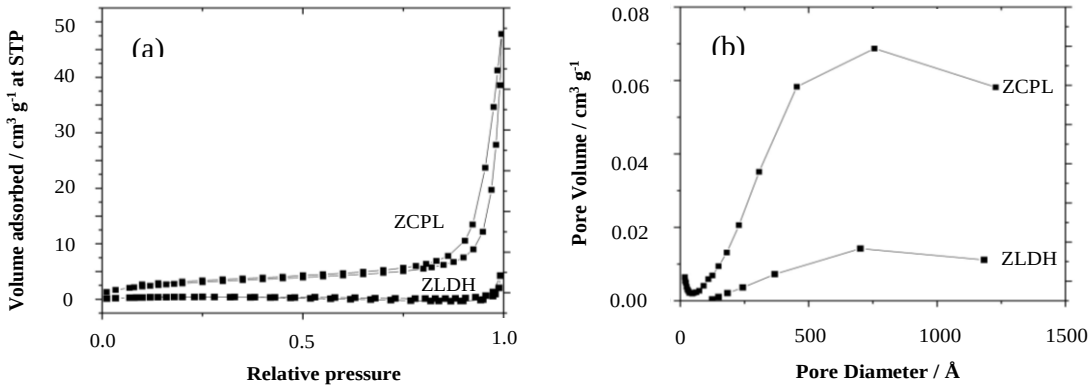


Figure 4. (a) Adsorption–desorption isotherms for nitrogen gas at 77 K for ZLDH and ZCPL and (b) BJH pore size distribution for ZLDH and ZCPL

The surface properties of ZLDH and ZCPL are summarised in Table 1. The intercalation of CPL has increased the BET specific surface area from 1.7 m^2/g in ZLDH to 10.9 m^2/g in ZCPL, which is due to the inclusion of bigger guest anion than the counter anion, NO_3^-. The intercalation of bigger anion of CPL resulting in the expansion of basal spacing of the resulting ZCPL nanocomposite and creates more pores in the crystallites, therefore the surface area increased significantly. Table 1 also shows that the BET average pore diameter for ZCPL was lower than that of ZLDH with 203 and 217 Å, respectively. On the other hand, the BJH desorption pore volume of ZCPL was higher than that of ZLDH.

Table 1. Elemental and surface properties of ZLDH and its intercalated compound, ZCPL

Material	Basal spacing (Å)	% C	% N	% S	BET Surface Area (m^2g^{-1})	BJH Desorption Pore Volume (cm^3g^{-1})	BET Average Pore Diameter (Å)	BJH Average Pore Diameter (Å)
ZLDH	8.90	0.0	3.10	0.0	1.7	0.010	217	161
ZCPL	9.69	30.63	4.48	8.70	10.9	0.282	203	199

The BJH pore size distribution for ZLDH and ZCPL are presented in Figure 4(b). Both materials show mesoporous type of material, with the adsorption isotherm Type IV. The BJH pore size distribution for ZLDH shows a broad peak at around 701 Å while for ZCPL an intense peak centered at around 756 Å indicating modification of pore texture in agreement with the formation of a new intercalated compound, ZCPL with basal spacing of 9.69 Å.

Surface morphology

Figures 5(a) and 5(b) show the field effect scanning electron microscopy (FESEM) morphology of ZLDH and ZCPL. ZLDH shows the typical morphology of LDH which shows agglomerates of compact and flake-like structure. The morphology of ZCPL shows a porous rod-like structure as the result of the intercalation of CPL into the layered structure of ZLDH. As shown in the figures, there was no significant difference in the morphology of the two samples. They were also very similar to the morphology of other intercalated compound of nanocomposites which has been reported earlier [22, 26].

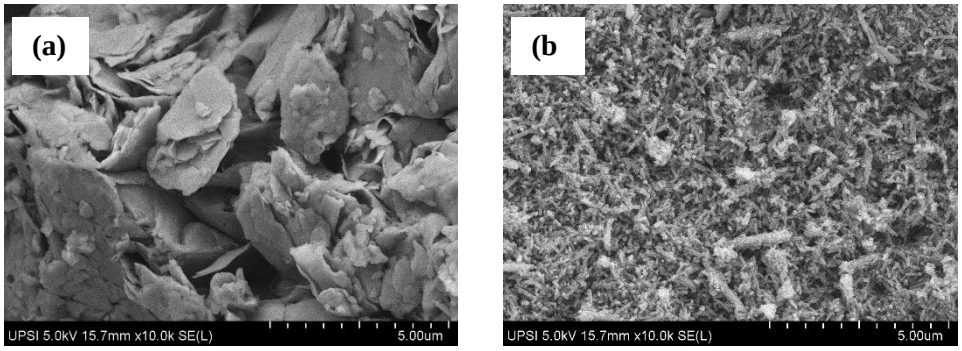


Figure 5. Scanning electron micrograph for ZLDH (a) and ZCPL (b) at 10, 000x magnification

Conclusion

The layered organic–inorganic nanohybrid was prepared using anti-hypertensive drug, CPL as an anionic guest and intercalated into the interspaces host of ZLDH by self-assembly method. The initial Zn: Al molar ratio of the mother liquor was 3:1 with pH 7.5 after the addition of NaOH. The PXRD pattern shows the basal spacing increased from 8.90 Å in ZLDH to 9.69 Å in ZCPL to accommodate the CPL anion to form hybrid nanocomposite of ZCPL. FTIR spectra of ZCPL resembles the functional groups of ZLDH and CPL and confirmed the CPL drug was successfully inserted into the interlayer structure of ZLDH. The BET surface area of the material increased from 1.7 m^2/g in ZLDH to 10.9 m^2/g in ZCPL if 0.08 M of CPL was used in the formation of nanohybrid. The pore texture of the resulting materials also changed as a result of the intercalation and the expansion of the basal spacing together with pore formation between the crystallite during the formation of the resulting intercalated ZCPL nanocomposite. The synthesised ZCPL nanohybrid material is expected to become a promising nano carrier for CPL as controlled release formulation for anti-hypertensive drugs.

Acknowledgement

The funds for the research were provided by Universiti Tenaga Nasional (UNITEN) and the Ministry of Higher Education of Malaysia (MOHE) under FRGS grant Vot No. 20160107FRGS.

References

1. Ladewig, K., Marcus, M., Zhi, P. X., Gray, P. P. and Gao, Q. (2010). Controlled preparation of layered double hydroxide nanoparticle and their application as gene delivery vehicles. *Applied Clay Science*, 48(12): 280 – 289.
2. Suman, S., Sayantan, R., Rituparna, A., Tapan, K. C. and Jui, C. (2017). Magnesium, zinc and calcium aluminium layered double hydroxide drug nanohybrids: A comprehensive study. *Applied Clay Science*, 135: 493 – 509.

3. Kuthati, Y., Kankala, R. K. and Lee, C. H. (2015). Layered double hydroxide nanoparticles or biomedical applications: Current status and recent prospects. *Applied Clay Science*, 112-113:100 – 116.
4. Duan, X. and Evans, D. G. (2006). Layered double hydroxides, structure and bonding. Springer, Berlin, pp. 1 – 234.
5. Sudipte, S., Ravi, T., Shiv, P., Shivali, D., Durga, P. M., Parimal, D., Shripathi, T., Mohan, K., Dipak, R. and Pralay, M. (2016). Layered double hydroxide as effective carrier for anticancer drug and tailoring of release rate through interlayer anions. *Journal of Controlled Release*, 224: 186 – 198.
6. Salak, A. N., Tedim, J., Alena, I. Kuznetsova, Mikhail, L. Maria, G. S. F. (2010). Anion exchange in Zn-Al layered double hydroxide: In-situ X-ray diffraction study. *Chemical Physics Letters*, 495: 73 – 76.
7. Chakrabarty, A. and Acharya, H. (2018). Facile synthesis of MgAl-layered double hydroxide supported metal organic framework nanocomposite for adsorptive removal of methyl orange dye. *Colloid and Interface Science Communications*, 24: 35 – 39.
8. Lupa, L., Cocheci, L., Pode, R. and Hulka, L. (2018). Phenol adsorption using aliquat 336 functionalized Zn-Al layered double hydroxide. *Separation and Purification Technology*, 196: 82 – 95.
9. Rives, V., Arco, M. D. and Martin, C. (2013). Layered double hydroxides as drug carriers and for controlled release of non-steroidal anti-inflammatory drugs (NSAIDs): A review. *Journal of Controlled Release*, 169: 28 – 39
10. Zhang, K., Xu, Z. P., Lu, J., Tang, Z. Y., Zhao, H. J., Good, D. A. and Wei, M. Q. (2014). Potential for layered double hydroxides-based innovative drug delivery systems. *International Journal of Molecular Sciences*, 15: 7409 – 7428.
11. Sipos, P. and Palinko, I. (2018). As-prepared and intercalated layered double hydroxides of the hydrocalumite type as efficient catalysts in various reactions. *Catalysis Today*, 306: 32 – 41.
12. Zhang, S., Yan, Y., Wang, W., Gu, X., Li, H., Li, J. and Sun, J. (2018). Intercalation of phosphotungstic acid into layered double hydroxide by reconstruction method and its application in intumescent flame-retardant poly(lactic acid) composites. *Polymer Degradation and Stability*, 147:142-150.
13. Sorrentino, A., Gorassi, M., Tortora, M., Vittoria, V., Constantino, U., Marmottini, F., Padella, F. (2005). Incorporation of Mg-Al hydrotalcite into a biodegradable poly(Ɛ-caprolactone) by high energy ball miling. *Polymer* 45: 1601 – 1608
14. Dutta, K., Das, S. and Pramanik, A. (2012). Concomitant synthesis of highly crystalline Zn-Al layered double hydroxide and ZnO: Phase interconversion and enhanced photocatalytic activity. *Journal of Colloid and Interface Science*, 366: 28 – 36.
15. Xiao, Y., Su, D., Wang, X., Wu, S., Zhou, L., Sun, Z., Wang, Z., Fang, S. and Li, F. (2017). Ultrahigh energy density and stable supercapacitor with 2D NiCoAl Layered double hydroxide. *Electrochimica Acta*, 253: 324 – 332.
16. Shao, M., Zhang, R., Li, Z., Wei, M. Evans, D. E. and Duan, X. (2015). Layered double hydroxide toward electrochemical energy storage and conversion: Design, synthesis and applications. *Chemical Communication*, 51: 15880 – 15893.
17. Gasser, M. S. (2009). Inorganic layered double hydroxides as ascorbic acid (vitamin C) delivery system – intercalation and their controlled release properties. *Colloids Surface B*, 73: 103 – 109
18. Li, Y., Bao, W., Wu, H., Wang, J., Zhang, Y., Wan, Y., Cao, D. and Wang, Q. (2017). Delaminated layered double hydroxide delivers DNA molecules as sandwich nanostructure into cells *via* a non-endocytic pathway. *Science Bulletin*, 62(10): 686 – 692.
19. Rojas, R., Linck, Y. G., Cuffini, S., Monti, G. and Giacomelli, C. E. (2015). Structural and physicochemical aspects of drugs release from layered double hydroxides and layered hydroxide salts. *Applied Clay Science*, 109-110: 119 – 126.
20. Rives, V., Arco, M. and Martin, C. (2014). Intercalation of drugs in layered double hydroxides and their controlled release: A review. *Applied Clay Science*, 88-89: 239 – 269.
21. Mohsin, S. M. N., Hussein, M. Z., Sarijo, S. H., Fakurazi, S., Arulselvan, P. and Yun Hin, T. Y. (2013). Synthesis of (cinnnamate-zinc layered hydroxide) intercalation compound for sunscreen application. *Chemistry Central Journal*, 26(7): 1 – 12.
22. Legrouri A., Badreddine, A., Barroug, A., Roy, J. P., Besse, P. (1999). Influence of pH on the synthesis of Zn-Al-nitrate layered double hydroxide and the exchange of nitrate by phosphate ions. *Journal of Material Science Letters*, 18: 1077 – 1079.

23. Hussein, M., Zainal, Z. and Hwa, T. K. (2000). Synthesis and properties of layered organic-inorganic hybrid material: Zn-Al layered double hydroxide-dioctyl sulfosuccinate nanocomposite. *Journal of Nanoparticle Research*, 2: 293 – 298.
24. Srivastava, A., Khare, B., Argal, R. and Patel, S. (2003). Microdetermination of anti-hypertensive drug captopril using 2,6-dichlorophenol indophenol. *Indian Journal of Chemistry*, 42: 3036 – 3040.
25. Jubri, Z., Mohd Yusuf, N. Z. A., Sarijo, S. H., Marsom, E. S. and Hussein, M. Z. (2017). Synthesis, characterization and controlled release properties of zinc-aluminium-beta-naphtoxyacetate nanocomposite. *Journal of Porous Materials*, 24(3): 573 – 582.
26. Xu, Z. P. and Braterman, P. S. (2010). Synthesis, structure and morphology of organic layered double hydroxide (LDH) hybrids: Comparison between aliphatic anions and their oxygenated analogs. *Applied Clay Science*, 48: 235 – 242.

Malaysian Journal of Analytical Sciences, Vol 23 No 2 (2019): 263 - 273
DOI: https://doi.org/10.17576/mjas-2019-2302-11

MALAYSIAN JOURNAL OF ANALYTICAL SCIENCES
Published by The Malaysian Analytical Sciences Society
ISSN 1394 - 2506

SYNTHESIS AND CHARACTERIZATION OF BENZOHYDROXAMIC ACID AND METHYLBENZOHYDROXAMIC ACID METAL COMPLEXES AND THEIR CYTOTOXICTY STUDY

(Sintesis dan Pencirian Kompleks Logam Asid Benzohidroksamik dan Asid Metilbenzohidroksamik serta Kajian Sitotoksik)

Latifah Robbaniyyah Hassan[1], Hadariah Bahron[1], Kalavathy Ramasamy[3], Amalina Mohd Tajuddin[1,2]*

[1]*Faculty of Applied Sciences,*
Universiti Teknologi MARA, 40450 Shah Alam, Selangor, Malaysia
[2]*Atta-ur-Rahman Institute for Natural Product Discovery*
[3]*Faculty of Pharmacy*
Universiti Teknologi MARA, 42300 Bandar Puncak Alam, Selangor, Malaysia

**Corresponding author: amalina9487@salam.uitm.edu.my*

Received: 29 August 2017; Accepted: 14 March 2019

Abstract

Hydroxamic acids, RCONHOH, are electronically flexible compounds for organic and inorganic analyses due to their more delicate structures compared to carboxylic acid. These acids are easy to deprotonate to produce hydroxamate ions. The syntheses, physico-chemical and characterization of benzohydroxamic acid (BHA) and methylbenzohydroxamic acid (CH_3-BHA) and their metal complexes VO(IV), Cr(III) and Ni(II) are reported herein. The metal complexes were synthesized by condensation reaction of BHA and CH_3-BHA with metal salts in 2:1 molar ratio. The compounds were characterized by elemental analysis, infrared spectroscopy (IR), ^{1}H and ^{13}C NMR, UV-Vis, TGA, magnetic susceptibility and molar conductance. From IR and magnetic susceptibility data, each complex is coordinated to the metal *via* oxygen and oxygen (*O,O*) in bidentate manner. The geometry of all metal complexes is octahedral except for $[VO(BHA)_2]$ that is square-pyramidal. The molar conductance values suggested that all complexes are non-electrolytic. A cytotoxicity study against human colorectal cancer, HCT116 cell lines, revealed that all the complexes are better anticancer agents than their parent ligands.

Keywords: hydroxamic acid, vanadium(IV), chromium(III), nickel(II), cytotoxicity

Abstrak

Asid hidroksamik, RCONHOH, adalah sebatian yang anjal elektronik untuk analisis organik and bukan organik kerana strukturnya yang lebih rapuh jika dibandingkan dengan asid karboksilat. Asid ini mudah untuk deprotonasi untuk menghasilkan ion hidrosamat. Sintesis, fizikokimia dan pencirian asid benzohidroksamik (BHA) dan asid metilbenzohidroksamik (CH_3-BHA) dan logam kompleksnya VO(IV), Cr(III) dan Ni(II) telah dilaporkan disini. Logam kompleks telah disintesis melalui kondensasi antara BHA dan CH_3-BHA dengan garam logam dalam nisbah molar 2:1. Semua sebatian yang dihasilkan telah dicirikan menggunakan analisis asas, spektroskopi inframerah (IR), ^{1}H dan ^{13}C NMR, UV-Vis, TGA, kerentanan magnet dan kekonduksian molar. Setiap kompleks logam berkoordinasi dengan logam melalui atom oksigen dan oksigen (*O,O*) dengan cara bidentat daripada data IR dan kerentanan magnet. Geometri untuk semua kompleks adalah geometri beroktahedron kecuali $[VO(BHA)_2]$ yang geometrinya adalah piramid segi empat sama. Semua kompleks logam adalah bukan elektrolit berdasarkan nilai kekonduksian molar. Kajian sitotoksik terhadap HCT116 menunjukkan bahawa semua kompleks logam adalah agen antikanser yang lebih baik daripada ligan induk mereka.

Kata kunci: asid hidroksamik, vanadium(IV), kromium(III), nikel(II), sitotoksik

Introduction

Hydroxamic acids have a potent functional group, -CONHOH, that plays an important role in forming therapeutic agents [1]. The ease of deprotonation of the CONHOH moiety to produce hydroxamate ion makes this acid more electronically flexible than its analogous carboxylic acid. As such, hydroxamic acids have received a lot of attention due to their importance in fulfilling a variety of roles in biology and medicine [2] such as being anticancer agents, inhibitors for sperm mobility and antiamoebic agents [3]. Ability to form stable metal chelates and possible NO-releasing properties also lead to their versatility in biological activity [2, 4].

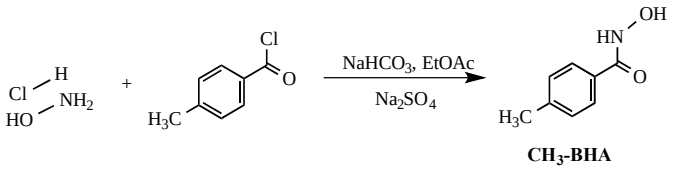
Vanadium, chromium and nickel complexes of BHA have been tested for their bioactivity and reported to possess anticancer properties; and its vanadium and chromium complexes have additional potential applications in treating diabetes [5]. However, studies on the effect of substituent groups in hydroxamic acid complexes on cytotoxicity are scarce. Thus, the anticancer properties of BHA as well as their methyl substituted counterparts' ligands and their metal complexes were investigated. This paper reports the synthesis, characterization and anticancer screening against HCT116 of BHA and CH_3-BHA as well as those of their VO(IV), Cr(III), Ni(II) complexes.

Materials and Methods

All chemicals and reagents were purchased from Sigma Aldrich and Merck and used without prior purification. Benzohydroxamic acid was purchased from Merck. The percentage composition of the elements C, H and N of the compounds were determined by using Thermo Scientific Flash 2000 Elemental Analyzer with methionine as a standard. Melting points were determined in capillaries using Stuart SMP10 and were uncorrected. The infrared spectra (IR) were recorded using a Perkin-Elmer Model 1750X FTIR spectrophotometer in the range of 4000□400 cm^{-1} as KBr discs. The ^{1}H and ^{13}C NMR spectra were recorded on a Bruker Varian-600MHz using TMS as an internal standard in DMSO. The UV-Vis spectra were obtained in absolute ethanol in the 200-900 nm range using Perkin Elmer UV-Vis Lambda 35 spectrophotometer at room temperature. The thermal decomposition behavior of the metal complexes was recorded using NETZSCH TG 209 F3 under nitrogen atmosphere at heating rate of 10 $^{o}C\ min^{-1}$ from room temperature to 900 $^{\circ}C$. Magnetic moments for the prepared complexes were characterized using the Guoy method with water as calibrant on Sherwood Auto Magnetic Susceptibility Balance. Molar conductivity measurements of BHA and CH_3-BHA series were determined in dimethylsulfoxide, DMSO and absolute ethanol (~10^{-3} M) at room temperature using a Mettler Toledo Inlab 730 conductivity meter.

Synthesis of methylbenzohydroxamic acid

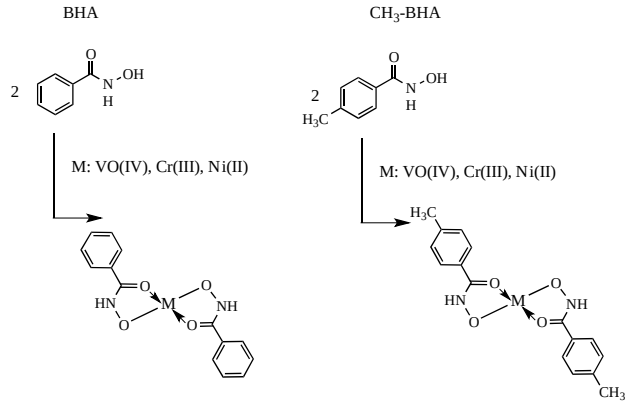
The synthesis of CH_3-BHA is presented in Scheme 1.



Scheme 1. Overall reaction of CH_3-BHA

Hydroxylamine hydrochloride (12 mmol, 0.9555 g) was added to a mixture solution of ethyl acetate and water containing sodium hydrogen carbonate ($NaHCO_3$). The mixture was stirred at room temperature. 4-methylbenzoyl chloride (10 mmol, 1.5640 g) was diluted with small amounts of ethyl acetate added dropwise to the mixture. The mixture was stirred for 5 minutes at room temperature. The organic layer was separated from aqueous layer, dried with anhydrous sodium sulphate. The solvent was removed in *vacuo* to afford pure product. Yield: 100%.

Synthesis of metal complexes
The reaction of metal salts with BHA and its derivative, CH_3-BHA in 1:2 molar ratio is presented in Scheme 2.



Scheme 2. General complexation reaction of BHA and CH_3-BHA

Synthesis of vanadyl benzohydroxamic acid [$VO(BHA)_2$]
BHA (10 mmol, 1.5314 g) was dissolved in deionized water and nitrogen gas (N_2) was bubbled through the solution for 10 minutes. Aqueous solution of vanadium(IV) oxide sulfate hydrate, $VOSO_4.xH_2O$ (5 mmol, 0.815 g) was added dropwise. The mixture was stirred for 30 minutes under N_2 at room temperature. A black-purplish precipitate was formed. The resulting precipitate was collected by filtration (pore size, 20 μm) and carefully washed with deionized water. The solid obtained was dried in vacuum at room temperature for 24 hours and then stored in a desiccator. Yield: 22.51%.

Synthesis of chromium benzohydroxamic acid [$Cr(BHA)_2(H_2O)_2$].H_2O
Chromium(III) chloride hexahydrate, $CrCl_2.6H_2O$ (1.63 mmol, 0.4343 g) was dissolved in a hot ethanolic solution (10 mL) of BHA (3.26 mmol, 0.4471 g). The pH of the resulting solution was adjusted to 5.5 using 0.1 M NaOH solution, where upon a greyish precipitate appeared. The solid obtained was filtered (pore size, 20 μm), washed with distilled water and dried over P_2O_5 in vacuum after being left standing at room temperature for 3 hours. Yield: 27.54%.

Synthesis of nickel benzohydroxamic acid [$Ni(BHA)_2(H_2O)(OAc)$]
Nickel(II) acetate tetrahydrate, $Ni(OAc)_2.4H_2O$ (5 mmol, 1.2443 g) was added to 10 mL of hot aqueous solution of BHA (5 mmol, 0.8941 g). 0.1 M NaOH solution was used to adjust the pH of the resulting solution to 5.5 until a light green precipitate appeared. The precipitate was collected through filtration (pore size, 20 μm) and washed with distilled water. The light green precipitate was left standing at room temperature before being dried over P_2O_5 in vacuum. Yield: 48.26%.

Synthesis of vanadium methylbenzohydroxamic acid [$VO(CH_3$-$BHA)_2$].H_2O
The solution of CH_3-BHA (5 mmol, 0.7657 g) in deionized water was bubbled with N_2 for 10 minutes before being added dropwise with an aqueous solution of $VOSO_4.xH_2O$ (2.5 mmol, 0.4075 g). The mixture was stirred under N_2 at room temperature for 30 minutes until a black-purplish precipitate appeared. The precipitate was collected by filtration (pore size, 20 μm) and washed with deionized water. The precipitate obtained was dried in vacuum at room temperature for 24 hours before being stored in a desiccator. Yield: 34.96%.

Synthesis of chromium methylbenzohydroxamic acid [$Cr(CH_3$-$BHA)_2(H_2O)_2$].$2H_2O$
10 mL of hot ethanolic solution was used to dissolve CH_3-BHA (10 mmol, 1.4356 g). $CrCl_3.6H_2O$ (5 mmol, 0.6661 g) was dissolved in a hot ultra-pure water (5 mL) and was mixed with the CH_3-BHA ethanolic solution. The greyish precipitate obtained was filtered off (pore size, 20 μm), washed with cold ethanol and dried over P_2O_5 in vacuum after being left standing at room temperature for 6 hours. Yield: 44.13%.

Synthesis of nickel methylbenzohydroxamic acid $[Ni(CH_3\text{-}BHA)_2(H_2O)_2].2H_2O$

CH_3-BHA (10 mmol, 1.657 g) was dissolved in hot ethanol (10 mL). 5 mL of hot ultra-pure water was added to $Ni(OAc)_2.4H_2O$ (5 mmol, 1.2443 g) before mixing with the ethanolic solution of CH_3-BHA. The mixture produced a light green precipitate. The precipitate was collected using filtration (pore size, 20 μm) and washed with cold ethanol before storing in desiccator. Yield: 7.96%.

Cytotoxicity study: Cell culture

The human colorectal carcinoma cell line, HCT116 (ATCC® CCL-247™), was cultured in the Roswell Park Memorial Institute RPMI 1640 Medium w/ 25mM HEPES & L-Glutamine, Biowest, supplemented with 10% heat inactivated fetal bovine serum (FBS) (PAA Laboratories) and 1% penicillin/streptomycin, Sigma Aldrich, (St Louis, US). Cultures were maintained in a humidified incubator at 37 °C in an atmosphere of 5% CO_2.

MTT assay

HCT116 cells were plated at 7,000 cells per well and allowed to incubate at 37 °C for 24 hours. BHA and CH_3-BHA ligand and their metal complexes were subjected to serial dilutions before being added to each well. The cells were treated with the compounds at concentrations ranging between 0.01–100 μM and incubated at 37 °C for 72 hours. The cytotoxicity of the compounds was assessed using the MTT method utilizing 3-(4,5-dimethylthiazol-2-yl)-2,5-diphenyl tetrazolium bromide (MTT or formazan) with minor modifications [6]. Briefly, 50 μL of 0.06 mol/L MTT solution was added to each well and plates were incubated at 37 °C for 4 hours. All solutions were removed and DMSO was added to dissolve the formazan crystals. The plates were read at 450 nm. Data generated were used to plot a dose-response curve from which the concentration of compounds required to kill 50% of cell population (IC_{50}) was determined.

Results and Discussion

Physical properties and elemental analysis

The physical characteristics and elemental analysis results of all compounds are shown in Table 1. BHA, CH_3-BHA and their VO(IV), Cr(III) and Ni(II) complexes are air-stable and relatively well soluble in polar organic solvents such as DMSO and DMF. The stoichiometry of all compounds was confirmed by elemental analysis (C,H,N). Bis-bidentate complexes were obtained upon reaction between the ligands, BHA and CH_3-BHA, with metal ions at 2:1 molar ratio. The analytical data are in good agreement with the calculated stoichiometry of the compounds.

Table 1. Physical data of BHA and CH_3-BHA and their metal complexes

Ligand/ Complex	Molecular Formula	Molecular Weight (g/mol)	Colour	Melting Point (°C)	Found (Calculated)%		
					C	H	N
$[VO(BHA)_2]$	$C_{14}H_{12}N_2O_5V$	339.20	Black-purplish	140-142	49.57 (49.77)	3.57 (3.65)	8.26 (9.47)
$[Cr(BHA)_2(H_2O)_2].H_2O$	$C_{14}H_{18}N_2O_7Cr$	378.30	Muddy green	Decomposed at 280	44.45 (44.27)	4.80 (4.10)	7.41 (7.96)
$[Ni(BHA)_2(H_2O)(OAc)]$	$C_{14}H_{12}N_2O_4Ni$	330.95	Light green	Decomposed at 240	50.81 (49.56)	3.65 (3.75)	8.46 (8.35)
CH_3-BHA	$C_8H_9NO_2$	151.20	Peach	152-154	62.64 (63.56)	5.86 (6.00)	9.72 (9.27)
$[VO(CH_3\text{-}BHA)_2].H_2O$	$C_{16}H_{16}N_2O_5V$	367.25	Black-purplish	153-156	50.12 (49.88)	4.44 (4.71)	7.37 (7.27)

Table 2 (cont'd). Physical data of BHA and CH_3-BHA and their metal complexes

Ligand/ Complex	Molecular Formula	Molecular Weight (g/mol)	Colour	Melting Point (°C)	Found (Calculated)%		
					C	H	N
$[Cr(CH_3\text{-}BHA)_2(H_2O)_2].2H_2O$	$C_{16}H_{16}N_2O_4Cr$	352.31	Grey	Decomposed at 250	45.52 (45.29)	5.31 (5.70)	6.23 (6.60)
$[Ni(CH_3\text{-}BHA)_2(H_2O)_2].2H_2O$	$C_{16}H_{16}N_2O_4Ni$	359.01	Light green	Decomposed at 250	44.68 (44.58)	5.23 (5.61)	6.50 (6.12)

Infrared spectroscopy

The coordination modes of ligands towards the metal ions can be determined from IR spectral studies. IR provides invaluable information on bonding and functional groups that exist in the compounds. The mode of coordination can be inferred through the shifting, disappearance and appearance of the new bands on the spectra of BHA, CH_3-BHA in their VO(IV), Cr(III) and Ni(II) complexes. The main infrared bands and their assignments are listed in Table 3. The IR spectra of BHA and CH_3-BHA with their metal complexes are shown in Figure 1 and Figure 2, respectively.

Table 3. Infrared spectral data for BHA and CH_3 BHA series complexes

Ligands/Complexes	Frequency (cm^{-1})					
	N-H	OH	C=O	N-O	V=O	M-O
BHA	3297 (*s*)	2749(*br*)	1647 (*s*)	899 (*s*)	-	-
$[VO(BHA)_2]$	-	-	1605 (*s*)	926 (*s*)	994 (*s*)	484 (*w*)
$[Cr(BHA)_2(H_2O)_2].H_2O$	-	-	1602 (*s*)	917 (*s*)	-	489 (*w*)
$[Ni(BHA)_2(H_2O)(OAc)]$	3226 (*s*)	-	1601 (*s*)	915 (*s*)	-	487 (*w*)
CH_3-BHA	3294 (*s*)	2759(*br*)	1651 (*s*)	903 (*s*)	-	-
$[VO(CH_3\text{-}BHA)_2(H_2O)_2].2H_2O$	-	-	1649 (*sh*)	917 (*s*)	968 (*s*)	487 (*w*)
$[Cr(CH_3\text{-}BHA)_2(H_2O)_2].2H_2O$	3216 (*b*)	-	1648 (*sh*)	917 (*m*)	-	478 (*w*)
$[Ni(CH_3\text{-}BHA)_2(H_2O)_2].2H_2O$	3232 (*m*)	-	1605 (*s*)	917 (*s*)	-	458 (*w*)

Note: *s*=strong, *m*=medium, *w*=weak, *b*=broad, *sh*=shoulder

The spectral investigation of BHA, CH_3-BHA spectra with their metal complexes indicated that the complexation had indeed occurred, in a bis-bidentate manner through the oxygen of the carbonyl (C=O) and hydroxyl (-OH) groups. Hence, the coordination mode suggested is the *O,O* mode. The N-H stretching vibrations were observed as strong bands at 3297 and 3294 cm^{-1} for BHA and CH_3-BHA, respectively. In their metal complexes, the N-H bands were absent for $[VO(BHA)_2]$, $[Cr(BHA)_2(H_2O)_2].H_2O$ and $[VO(CH_3\text{-}BHA)_2]$ and shifted to lower wavenumbers for $[Ni(BHA)_2]$, $[Cr(CH_3\text{-}BHA)_2]$ and $[Ni(CH_3\text{-}BHA)_2]$. The sharp bands ascribed to ν(N-O) at 899 and 903 cm^{-1} of BHA and CH_3-BHA, respectively, were shifted to higher wavenumbers and appeared at 915-926 cm^{-1} for the complexes, in concordance with the literature values [7].

The O-H bands that appeared in the regions of 2749 and 2759 cm^{-1} in BHA and CH_3-BHA spectra, respectively, are disappeared in all complexes suggesting deprotonation of OH and coordination of oxygen from the hydroxyl group to the metal ion. The shifting of ν(C=O) towards lower wavenumbers by 42-46 cm^{-1} in the BHA complexes indicating the involvement of carbonyl (C=O) group during complexation *via* oxygen atoms. This is further supported by the appearance of new weak bands of (M-O (M: VO, Cr, Ni) around 458-487 cm^{-1} in the spectra of complexes of BHA and CH_3-BHA, as similarly reported previously [8].

However, for $[VO(CH_3\text{-}BHA)_2]$ and $[Cr(CH_3\text{-}BHA)_2]$, there was no appreciable shifting of ν(C=O) observed in the spectra, but the intensity of the bands was reduced from strong to shoulder bands. This may be explained by the mixing with the $\nu_{C=C}$ aryl moiety. The stretching bands due to ν(C-N) of BHA and CH_3-BHA at 1437 and 1441 cm^{-1}, respectively, were observed to have shifted towards higher wavenumbers at 1491 and 1492 cm^{-1} in the complexes in concordance to Chauhan et al. [9]. $[VO(BHA)_2]$ and $[VO(CH_3\text{-}BHA)_2]$ displayed new bands at 994 and 968 cm^{-1}, respectively, assignable to the stretches of V=O [10,11].

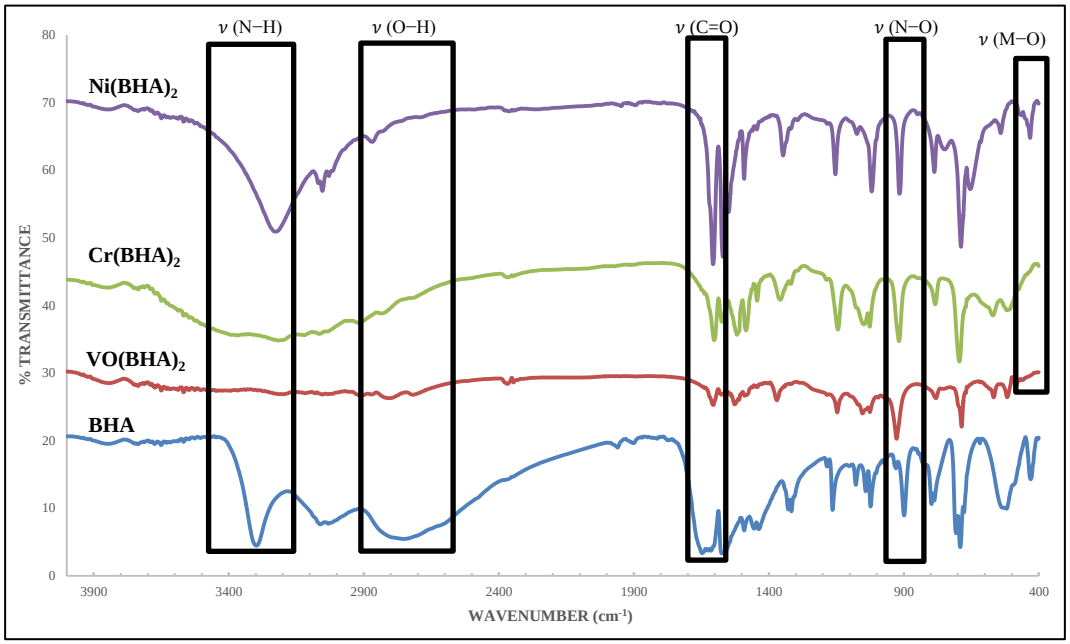


Figure 1. IR spectra for BHA series

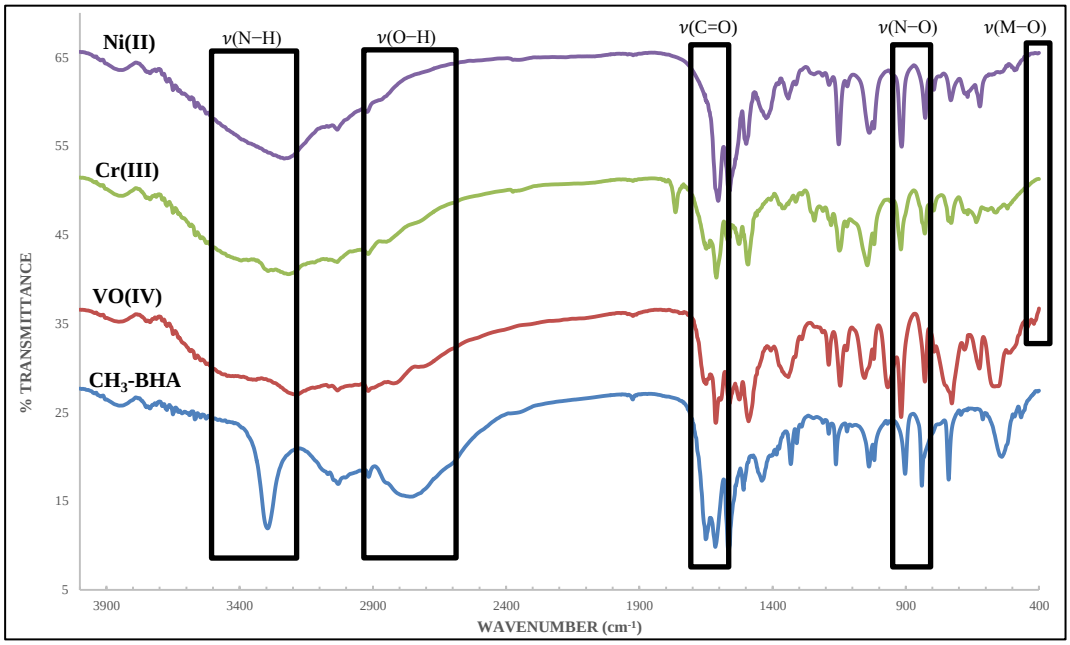


Figure 2. IR spectra for CH_3-BHA series

Nuclear magnetic spectroscopy

The ^{1}H and ^{13}C NMR spectra for the ligands were recorded in DMSO-d_6 using tetramethylsilane (TMS) as the internal standard. BHA shows two downfield singlets at 9.08 and 11.24 ppm due to NH and OH protons, respectively [12]. For CH_3-BHA, NH and OH protons were not observed due to the proton exchange with the deuterium that makes the peaks disappeared [13]. The ^{1}H NMR spectrum of BHA exhibits 3 resonances at 7.41–7.48, 7.50 and 7.76 ppm corresponding to the five protons of the benzene ring, while that of CH_3 BHA has 2 resonances at 7.23 and 7.62 ppm corresponding to four protons of the *para*-substituted derivative [12]. The methyl (CH_3) protons peaks appeared at 2.41 ppm.

^{13}C NMR was used on determining the number of nonequivalent carbons and types of carbons that exists in the ligands. Both information from ^{1}H NMR and IR are helping on determining the structure of the ligands together with ^{13}C NMR. There are 3 types of carbons exists in BHA and CH_3-BHA. They are carbonyl (C=O), aromatic carbon (Ar-C) and methyl carbon. The carbonyl (C=O) signals appeared at 164.79 and 164.03 ppm, respectively for BHA and CH_3-BHA [14]. The aromatic carbon for BHA appeared at 127.32 – 133.21 ppm, while for CH_3-BHA, these carbons appeared at 126.73 – 130.26 ppm. The methyl carbon appeared at 20.89 ppm. ^{1}H and ^{13}C NMR for all complexes could not be obtained due to paramagnetic behaviour of all complexes. Paramagnetic means there is an unpaired electron existing in the orbital that is slightly attracted to the magnetic fields thus making all the NMR signals vanished and difficult to assign [15].

Ultraviolet-visible spectroscopy

The geometry of the complexes can be predicted from UV-Vis study. The UV-Vis spectrum of BHA and CH_3-BHA and their VO(IV), Cr(III) and Ni(II) complexes were carried out as 10^{-3}x10^{-4} M in ethanol in the range of 900 – 200 nm. UV-Vis analysis of [Ni(CH_3-BHA)$_2$] cannot be performed due to the solubility problem. The absorption spectrum of BHA and CH_3-BHA consists of an intense band centered at 220 and 236 nm, respectively attributed to $\pi\rightarrow\pi^*$ transitions of aromatic rings. Another weak band observed was related to $n\rightarrow\pi^*$ transitions within C=O found at 336 nm for BHA but for CH_3-BHA, this transition was not observed. $\pi\rightarrow\pi^*$ transitions were found shifted to the lower regions in BHA and CH_3-BHA complexes. No $n\rightarrow\pi^*$ transition was observed in VO(CH_3-BHA)$_2$ spectrum. $n\rightarrow\pi^*$ transitions of [Cr(CH_3-BHA)$_2$] were found at 312 nm. Ligand-to-metal charge transfer (LMCT) bands were observable in the spectrum of [VO(BHA)$_2$] at 480 nm [16].

Thermogravimetric analysis

The presence and the bonding of water molecules in [Cr(BHA)$_2$].3H_2O were detected by using thermogravimetric analysis and the result is presented in Table 4. TGA graph for [Cr(BHA)$_2$].3H_2O is illustrated in Figure 3.

Table 4. Thermal behavior indicating the loss of H_2O molecules from [Cr(BHA)$_2$].3H_2O

Compound	Temperature Range (°C)	Weight Loss (%)		Lost Species
		Calculated	Found	
[Cr(BHA)$_2$(H_2O)$_2$].H_2O	154.5–250.64	14.27	14.00	3H_2O

Cr(BHA)$_2$(H_2O)$_2$].H_2O clearly indicates the loss of three molar equivalent of water molecules at the temperature of 154.5 - 250.64 °C supporting the results of elemental analysis. [Cr(BHA)$_2$(H_2O)$_2$].H_2O was in octahedral geometry by the presence of two molar equivalent of water molecules that coordinated to Cr(III). Another one molar equivalent of water molecule is lattice water that is present in the sphere of the complex [17]. The proposed structure of [Cr(BHA)$_2$(H_2O)$_2$].H_2O was illustrated in Figure 4.

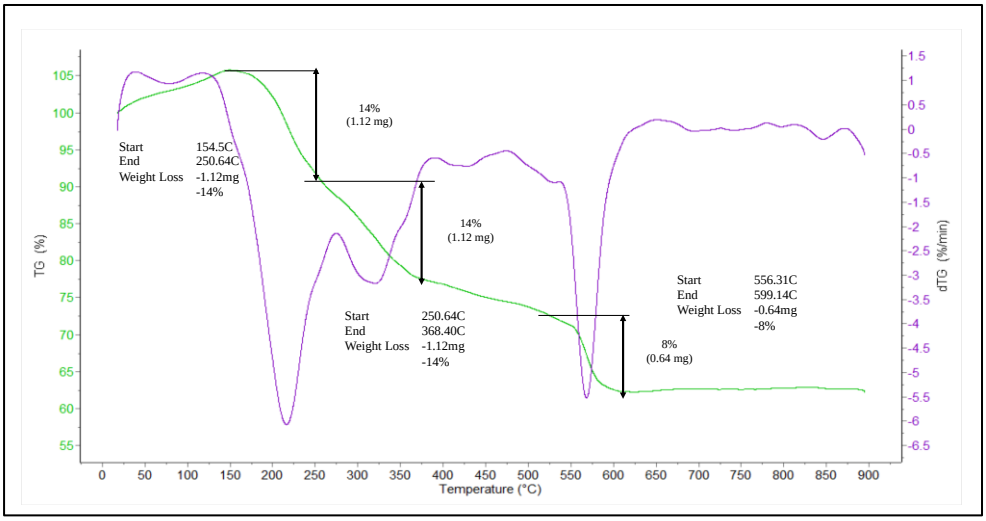


Figure 3. TGA graph of $Cr(BHA)_2(H_2O)_2].H_2O$

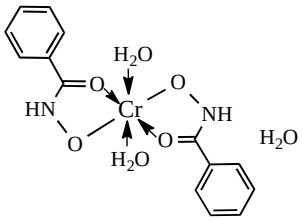


Figure 4. The proposed structure of $Cr(BHA)_2(H_2O)_2].H_2O$

Magnetic susceptibility and molar conductivity

The electrolytic nature and the geometries of all complexes were determined using magnetic susceptibility and molar conductance. Molar conductivities were recorded in 10^{-3} M DMSO at room temperature. Magnetic moments and molar conductivity data for all complexes were tabulated in Table 5.

Table 5. Molar conductance data for VO(IV), Cr(III) and Ni(II) complexes

Complexes	**μ_{eff} B.M**	**Molar conductance ($\Omega^{-1}cm^2$ mol^{-1})**
$[VO(BHA)_2]$	1.57	1.00
$[Cr(BHA)_2(H_2O)_2].H_2O$	3.05	3.37
$[Ni(BHA)_2(H_2O)(OAc)]$	3.24	6.82
$[VO(CH_3\text{-}BHA)_2].H_2O$	Diamagnetic	0
$[Cr(CH_3\text{-}BHA)_2(H_2O)_2].2H_2O$	3.18	0
$[Ni(CH_3\text{-}BHA)_2(H_2O)_2].2H_2O$	2.98	0

The proposed magnetic moments for $[Ni(BHA)_2]$, $Cr(BHA)_2(H_2O)_2].2H_2O$, $[Cr(BHA)_2(H_2O)_2].H_2O$, and $[Ni(CH_3\text{-}BHA)_2]$ are octahedral geometry [17, 18]. The magnetic moment for $[VO(BHA)_2]$ on the range of single electron of

the $3d^1$ system of square-pyramidal geometry [19]. [VO(CH_3-BHA)$_2$] has diamagnetic properties. It is suggested that the possible oxidation state of vanadium is V^{5+}. Thus, [VO(CH_3-BHA)$_2$] may exist in a dimeric nature [20].

Conductivity measurement is usually used on determining structural of metal chelates (mode of coordination) within the limits of their solubility. From Table 5, the molar conductivity (Λ_M) values for the complexes are in the range of 0 - 6.82 Ω^{-1} cm^2 mol^{-1} suggesting the non-electrolytic nature of the complexes in solutions. The molar conductivity values for the metal complexes indicate the non-existence of free ions acting as electrolytes in the solution [21].

Cytotoxicity study

All nine compounds, BHA and CH_3-BHA with their VO(IV), Cr(III) and Ni(II) complexes were evaluated for their biological activity, specifically cytotoxicity on colorectal carcinoma cell line (HCT116) as compared with standard, 5-fluorouracil. All tested compounds induced a concentration-dependent antiproliferative effect towards HCT116 cells upon treatment for 24 hours. All compounds are soluble in DMSO. IC_{50} values of BHA and CH_3-BHA series against HCT116 cells are shown in Table 6.

Table 6. IC_{50} values of BHA and CH_3BHA series on HCT116 cells

Ligands/Complexes	**IC_{50} ± SD values (μM)**
BHA	>100
[VO(BHA)$_2$]	42.00 ± 2.44
[Cr(BHA)$_2$(H_2O)$_2$].H_2O	>100
[Ni(BHA)$_{2(}$$H_2O$)(OAc)]	60.00 ± 4.03
CH_3-BHA	>100
[VO(CH_3-BHA)$_2$].H2O	49.00 ± 0.01
[Cr(CH_3-BHA)$_2$(H_2O)$_2$].2H_2O	>100
[Ni(CH_3-BHA)$_2$(H_2O)$_2$].2H_2O	40.00 ± 3.11
Standard (5-Fluorouracil)	13.07 ± 0.00

[Ni(CH_3-BHA)$_2$] display highest cytotoxicity activity among all tested compounds but considered as non-potent anticancer agents compared as 5-fluorouracil. BHA, CH_3-BHA, [Cr(BHA)$_2$].3H_2O and [Cr(CH_3-BHA)$_2$] display no inhibition towards HCT116. The ability of CH_3-BHA against cancer cells did not improve by the presence of electron donating group, -CH_3 but it gives significant effects on improving the inhibition of Ni(II) complexes towards the cancer cells.

VO(IV) and Ni(II) complexes of BHA and CH_3-BHA have better cytotoxicity compared to their free BHA and CH_3-BHA. This observation can be explained by Tweedy's chelation theory and cell permeability by Overtone. Tweedy stated that complexation will lower the polarity of metal ions due to their positive charge to be shared with donor groups. It will make an increase of the delocalization of π-electrons over the entire chelate ring. Thus, this will enhance the lipophilicity of the complexes. According to Overtone's concept of cell permeability, the entry of any molecule into a cell is controlled by its lipophilicity because the lipid membrane that surrounds the cell favours the passage of materials that are soluble in lipids. Consequently, the increase of lipophilicity upon complexation enhances the penetration of the complexes into cells and will block the metal binding sites of receptors [22]. This explains why the VO(IV) and Ni(II) complexes give a better cytotoxicity than their parent ligands, BHA and CH_3-BHA.

Conclusion

BHA and its derivative, CH_3-BHA, and their metal complexes VO(IV), Cr(III) and Ni(II) have been successfully synthesized and characterized by elemental analysis, infrared spectroscopy, ^{1}H and ^{13}C NMR spectroscopy,

UV Visible, TGA, magnetic susceptibility as well as molar conductivity. From the spectral study, the ligands were indicated to have coordinated through oxygen and oxygen (*O,O*) atoms to the metal center through bidentate manner. All complexes were paramagnetic except $[VO(BHA)_2]$. $[VO(BHA)_2]$ is diamagnetic suggesting the dimeric nature of this complex. All complexes were non-electrolyte. In concordance with the basic of chelation theory, metal complexes have shown higher toxicity against human colorectal cancer (HCT116) than their parent ligands, BHA and CH_3-BHA. $[Ni(CH_3\text{-}BHA)_2]$ shows the highest cytotoxicity of IC_{50} values, 40.00 μM.

Acknowledgement

The authors would like to acknowledge the Ministry of Education of Malaysia for the research fund (RAGS/1/2015/ST0/UITM/03/1), Faculty of Applied Sciences, UiTM for research facilities and Faculty of Pharmacy, UiTM for the facilities on cytotoxicity study.

References

1. Kakkar, R. (2013). Theoretical studies on hydroxamic acids. In S. P. Gupta (Ed.), *Hydroxamic Acids: A Unique Family of Chemicals with Multiple Biological Activities* (pp. 21–47). Springer.
2. Marmion, Celine, J., Griffith, D. and Nolan, K. B. (2004). Hydroxamic acids − an intriguing family of enzyme inhibitors and biomedical ligands. *European Journal of Inorganic Chemistry*, 2004(15): 3003 -3016.
3. Sharma, N., Kumari, M., Kumar, V., Chaudhry, S. C. and Kanwar, S. S. (2010). Synthesis, characterization, and antibacterial activity of vanadium(iv) complexes of hydroxamic acids. *Journal of Coordination Chemistry*, 63(1): 176 - 184.
4. Griffith, D., Krot, K., Comiskey, J., Nolan, K. B. and Marmion, C. J. (2008). Monohydroxamic acids and bridging dihydroxamic acids as chelators to ruthenium(III) and as nitric oxide donors: syntheses, speciation studies and nitric oxide releasing investigation. *Dalton Transactions*, (1): 137-147.
5. Farkas, E., Enyedy, É. A., Micera, G. and Garribba, E. (2000). Coordination modes of hydroxamic acids in copper(II), nickel(II) and zinc(II) mixed-ligand complexes in aqueous solution. *Polyhedron*, 19(14): 1727-1736.
6. Hazalin, N. A. M. N., Ramasamy, K., Lim, S. M., Wahab, I. A., Cole, A. L. J., Bakar, A., and Majeed, A. (2009). Cytotoxic and antibacterial activities of endophytic fungi isolated from plants at the National Park, Pahang, Malaysia. *BMC Complementary and Alternative Medicine*, 1–5.
7. Chauhan, D. S., Verma, K. K., and Garg, S. (2017). Synthesis, Characterization and antimicrobial studies on some pyridoxylidene - sulphamethoxazole Schiff base tellurium(IV) complexes. *Der Pharma Chemica*, 9(8): 59 – 64.
8. Srivastava, K. P., Singh, B., and Akbar, A. (2009). Synthesis and characterisation of Co(II) complexes of dibasic tetradentate (oo' no donor) ligand. *International Journal of ChemTech Research*, 1(1): 71 –79.
9. Chauhan, S., Deepak, Garg, S., and Verma, K. K. (2016). Study on 4-methoxybenzohydroxamate complexes of aryltellurium (IV) and diaryltellurium (IV). *International Journal of Chemical Sciences*, 14(1): 269 – 282.
10. Yadava, A. K., Yadav, H. S., Singh, S., Yadav, U. S. and Rao, D. P. (2013). Synthesis and characterization of some novel Schiff Base complexes of oxovanadium(IV) cation. *Journal of Chemistry*, 2013: 1 - 5.
11. Haratake, M., Fukunaga, M., Ono, M. and Nakayama, M. (2005). Synthesis of Vanadium (IV, V) hydroxamic acid complexes and in vivo assessment of their insulin-like activity. *Journal of Biological Inorganic Chemistry*, 10(3): 250-258.
12. Griffith, D., Bergamo, A., Pin, S., Vadori, M., Muller-Bunz, H., Sava, G., and Marmion, C. J. (2007). Novel platinum pyridinehydroxamic acid complexes: Synthesis, characterisation, X-ray crystallographic study and nitric oxide related properties. *Polyhedron*, 26: 4697 – 4706.
13. Pavia, D. L., Lampman, G. M., and Kriz, G. S. (2001). *Introduction to Spectroscopy* (Third ed.). United States of America: Brooks/Cole Thomson Learning: pp 310.
14. Naqeebullah, Farina, Y., Chan, K. M., Mun, L. K., Rajab, N. F., and Ooi, T. C. (2013). Diorganotin(IV) Derivatives of *n*-methyl *p*-fluorobenzo-hydroxamic acid: Preparation, spectral characterization, X-ray diffraction studies and antitumor activity. *Molecules*, 18(7): 8696 – 8711.
15. Miessler, G. L., Fischer, P. J., and Tarr, D. A. (2014). *Inorganic Chemistry* (Fifth ed.). United States of America: Pearson: pp 359-361.
16. Saif, M., El-shafiy, H. F., Mashaly, M. M., Eid, M. F., Nabeel, A. I., and Fouad, R. (2016). Synthesis, characterization, and antioxidant/cytotoxic activity of new chromone Schiff base nano-complexes of Zn(II), Cu(II), Ni(II) and Co(II). *Journal of Molecular Structure*: 1–42.

17. Abu Bakar, S. N., Bahron, H., and Kassim, K. (2010). Synthesis and characterization of a novel Schiff base derived from 2,4,6-trimethyl-m-phenylenediamine with o-vanillin and its metal complexes. *International Conference on Science and Social Research:* pp. 463 – 466.
18. Aranha, P. E., dos Santos, M. P., Romera, S., and Dockal, E. R. (2006). Synthesis, characterization , and spectroscopic studies of tetradentate Schiff base chromium(III) complexes. *Polyhedron*, 26(7): 1373 – 1382.
19. Ahmed, A. A., BenGuzzi, S. A., and Ahshad, O. M. (2009). Synthesis and characterization of some vanadyl Schiff bases complexes. *Rasayan Journal of Chemistry*, *2*(4), 781–785.
20. Mathew, N. (2011). Studies on metal complexes of some tridentate acylhydrazones. Dissertation of Doctor philosophy. Retrieved from http://hdl.handle.net/10603/6270.
21. Temel, H. (2014). Synthesis and spectroscopic studies of new Cu(II), Ni(II), VO(IV) and Zn(II) complexes with n,n′-bis(2-hydroxynaphthalin-1-carbaldehydene)-1,2-bis-(o-aminophenoxy)ethane. *Journal of Coordination Chemistry*, 57(9): 723 – 729.
22. Çıralıa, D. E., Uyar, Z., Koyuncu, İ., and Hacıoğlu, N. (2015). Synthesis, characterization and catalytic , cytotoxic and antimicrobial activities of two novel cyclotriphosphazene-based multisite ligands and their Ru(II) complexes. *Applied Organometallic Chemistry*, 29: 536 – 542.

Malaysian Journal of Analytical Sciences, Vol 23 No 2 (2019): 274 - 289
DOI: https://doi.org/10.17576/mjas-2019-2302-12

MALAYSIAN JOURNAL OF ANALYTICAL SCIENCES
Published by The Malaysian Analytical Sciences Society
ISSN 1394 - 2506

PYROLYTIC KEY INDICATORS OF BURNT PORCINE TISSUE IN THE PRESENCE OF PETROL UNDER OUTDOOR CONDITIONS

(Analisis Penunjuk Utama Pirolitik Tisu Khinzir Yang Dibakar Dengan Kehadiran Petrol Dalam Keadaan Terbuka)

Gina Francesca Gabriel, Jennifer Shalini Jheyeaaseelan, Dheephikha Kumaraguru, Khairul Osman, Noor Hazfalinda Hamzah*

Forensic Science Programme, Faculty of Health Sciences,
Universiti Kebangsaan Malaysia, Jalan Raja Muda Abdul Aziz, 50300 Kuala Lumpur, Malaysia

**Corresponding author: raviera@yahoo.com*

Received: 15 January 2018; Accepted: 31 January 2019

Abstract

This study was conducted to provide a chemical fingerprint of burnt porcine tissue (*Sus domesticus spp.*) in the presence of petrol using gas chromatography-mass spectrometry (GC-MS). The pyrolysis process was followed through using two methods; in the first method, the sample was allowed to continuously burn until auto-ignition was attained and the flames self-extinguished, and in the second method, upon auto-ignition of the sample, the flame was extinguished by placing an empty lid over the tin after the size of the flame reduced to burning within the tin. Six replicates of each method were burnt outdoors and underwent passive headspace extraction using activated carbon tablets. The activated carbon tablets together with the samples were then incubated in an oven for 16 hours at 80 °C. After the incubation process, the tablets were desorbed in 1 mL of pentane and were introduced into the GC-MS. Toluene was detected from the first method whereas 1,2,4-trimethylbenzene was detected from the second method. Pyrolytic key indicators of burnt porcine tissue in the presence of petrol were not detected under the specific environmental conditions implemented in this study. The volume of petrol together with the duration and temperature during the burning process, and the source of flame, played crucial roles in the generation and detection of pyrolytic products obtained during the fire.

Keywords: porcine bone, petrol, pyrolytic products, activated carbon tablet, gas chromatography-mass spectrometry

Abstrak

Kajian ini dijalankan untuk menjana data cap jari kimia bagi tisu khinzir (*Sus domesticus spp.*) yang dibakar dengan kehadiran petrol menggunakan kromatografi gas-spektrometri jisim (GC-MS). Proses pirolisis telah dijalankan mengikut dua kaedah; kaedah pertama dilakukan dengan membiarkan sampel terbakar dan apinya terpadam dengan sendiri, dan kaedah kedua, nyalaan api yang terbentuk daripada nyalaan auto pencucuhan telah dipadamkan dengan meletakkan penutup tin ke atas permukaan tin apabila saiz nyalaan api tersebut mengecil dan hanya tertumpu di dalam tin. Setiap sampel daripada kedua-dua kaedah telah dibakar secara terbuka dan menjalani proses penyerapan menggunakan penjerapan karbon teraktif dalam bentuk tablet. Proses pembakaran ini telah direplikasi sebanyak enam kali. Penjerapan karbon teraktif bersama sampel diinkubasi di dalam ketuhar selama 16 jam pada suhu 80 °C. Selepas proses inkubasi, tablet tersebut dinyaherap dalam 1 mL pentana dan dianalisa menggunakan GC-MS. Toluena dikesan daripada kaedah pertama manakala 1,2,4-trimetilbenzena dikesan daripada kaedah kedua. Petunjuk utama pirolitik tisu khinzir tidak dapat dikesan di bawah keadaan persekitaran spesifik yang diaplikasikan dalam kajian ini. Di samping itu, didapati bahawa isipadu petrol yang dibakar, tempoh pembakaran dan suhu yang dicapai semasa proses pembakaran serta sumber api memainkan peranan yang penting dalam menentukan kehadiran petunjuk utama produk pirolitik yang terhasil daripada sesuatu proses pembakaran.

Kata kunci: tulang khinzir, petrol, produk utama pirolitik, penjerapan karbon teraktif, kromatografi gas-spektrometri jisim

Introduction

Arson is a crime that occurs when a person deliberately or maliciously uses fire to destroy a property [1]. Though arson is an offense against property, it might include an offense against a person if someone is harmed, killed, or dies because of a feloniously set fire [2]. One of the common technique employed by arsonists is the use of ignitable liquids and fire accelerants to ignite and increase the rate and intensity of a fire. Ignitable liquid refers to any liquid that will readily ignite when exposed to heat whereas a fire accelerant is a substance that is used to increase the rate of burning for materials that do not promptly burn [3]. Hence, ignitable liquids can be also used as accelerants. Petrol is known to be the most dominant type of fire accelerant used and found in fire debris samples due to its ease in availability and rapid ignitability [3-5]. The use of petrol has also been associated with human intoxication and death whereby cases of it being ingested and injected with criminal intent either accidentally or intentionally had been reported [6].

Presently, the lack of knowledge pertaining to the pyrolytic key indicators of human remains in the presence of interferences, such as petrol, is alarming. Pyrolytic products refer to volatile compounds that are produced during the process of pyrolysis. Pyrolysis is a process, by which a solid or a liquid undergoes degradation of its chemicals into smaller volatile compounds under heat, without interacting with oxygen or any other oxidants, that is necessary for almost all solids or liquids to burn [7]. If human remains are present in a fire scene, the potential pyrolytic key indicators of human remains which are a homologous series of *n*-alkanes, *n*-alkenes, *n*-aldehydes, aromatics and nitrile compounds may be hidden due to the presence of interfering products [8-10]. Interfering products are a set of products detected in a sample that interferes with the proper identification of pyrolytic compounds of the target sample [7]. Petrol can be one of the potential interferences in the identification of human pyrolytic key indicators in a fire.

Although in depth work looking into the pyrolytic key indicators of human remains in the presence of petrol is still novice, previous studies focusing both on the pyrolytic key indicators of petrol and human tissues, individually, have been conducted, the former more detailed than the latter. Generally, pyrolytic data of human samples fall in the range of *n*-alkanes, *n*-alkenes, *n*-aldehydes, aromatics and nitrile compounds [8, 9, 11, 12]. A latest study conducted by DeHaan [13] proved that a homologous series of C_5-C_9 *n*-aldehydes serves as dominant pyrolytic key indicators of human samples because these compounds are not produced as major species in the pyrolysis of common household items such as carpet, wood products, and upholstery [13]. However, there are inconsistencies in the presence of *n*-aldehydes from the human pyrolytic model. Although DeHaan et al. [8, 13] and Gabriel et al. [12] detected these compounds in their studies, Purevsuren et al. [14], Agu [11] and Gabriel [9] did not detect any *n*-aldehydes in their pyrolytic work. The absence and presence of *n*-aldehydes were identified due to the differences in temperature, exposure durations and experimental methodology [9]. The inconsistencies in the literature should be addressed to validate the robustness of these pyrolytic key indicators of human tissue, particularly in the presence of interferences.

While the pyrolytic key indicators of human tissues are still being studied, those of petrol have been made known and are readily available across a range of studies [15-19]. A standard test method has also been made available *via* the American Society of Testing and Materials (ASTM) E1618-06, whom provided the pyrolytic key indicators of petrol to be of alkanes, aromatics such as C_3-C_5 alkyl benzenes, naphthalenes and indane together with distinctive chromatographic patterns expected when petrol is analysed [20].

This research is crucial for situations where human remains are not suspected to be present or have been devoured by the fire in the presence of petrol [9]. Bones can often be mistaken as sticks as they discolour to a yellowish-brownish-blackened hue due to environmental factors, including heat and exposure to chemicals [21]. The help of Deoxyribonucleic acid (DNA) fingerprinting that usually aids in the identification of individuals, fails in some cases because of the denaturation of DNA when exposed to high temperatures [22]. Unsuspected fire samples that resemble charred fragments collected from fire debris could potentially contain human tissues that have been burnt with petrol. This research was conducted to determine the pyrolytic key indicators of porcine tissue burnt in the

presence of petrol under outdoor conditions in order to address the former. Porcine tissue was chosen in this study because it has been proven to be a good representative of human tissue as suggested by various researchers [8, 9, 11-13] whom have determined clear similarities with no qualitative distinction between the pyrolytic products produced across these tissues in their respective work. Through this research, forensic scientists can be made aware of the chromatographic patterns that signifies the presence of human remains burned in the presence of petrol in fire debris samples [9].

Materials and Method

Standard test mixture

12 high purity compounds; benzene, ethylbenzene, butylbenzene, toluene, octane, *p*-xylene, propylbenzene, decane, tridecane, tetradecane, pentadecane and dodecane were prepared in 1 mg/mL standard solution (Sigma Aldrich, UK) and placed into six GC vials (2 mL, Fisher Scientific). The contents of all six GC vials (Fisher Scientific) were then injected into the GC-MS (Shimadzu, UK) and identified using the mass-to-charge ratio (*m/z)* values compared against the National Institute of Standards and Technology (NIST) (NIST/EPA/NIH Mass Spectral Library).

Standard of unleaded RON95 petrol

1.0 µL/mL of RON95 petrol in pentane was injected into the GC-MS. The identification of pyrolytic key indicators of petrol was executed as recommended by ASTM E1618-06 [20]. The total ion chromatogram (TIC) produced was analysed based on the retention times and *m/z* values. Each peak was identified by matching the data against the NIST (NIST/EPA/NIH Mass Spectral Library) and standard test mixture.

GC-MS parameters

1.0 µL of sample containing desorbed activated carbon tablet (ACT) in pentane was introduced through a split injector with a split ratio of 20:1 at injector temperature of 250 °C using an auto-sampler. A 128-0122 DB-1MS column (22 mm length × 0.2 mm inner diameter × 0.33 µm film thickness) (Crawford Scientific, UK) was used in this experiment. Helium carrier gas was maintained at a flow rate of 32.7 mL/min in the oven. The initial oven temperature was held at 40 °C for 5 minutes, then ramped to 280 °C at a rate of 15 °C/min and held for 2 minutes. The temperature of the detector was also maintained at 250 °C. Data collected from the GC-MS were analysed based on their retention times and *m/z* values matched against NIST library, standard test mixtures and standard petrol.

Preliminary study: Control sample

One aluminium tin can was sealed with a lid containing an ACT, which was hooked to a paper clip held by a magnet on the lid and was incubated in an oven for 16 hours at 80 °C according to guidelines from the American Society for Testing and Materials (ASTM) E1412-07 2012 [23]. After the incubation process, the ACT was removed and placed into a GC vial (Fisher Scientific) and desorbed with 1 mL of pentane. The GC vial containing the desorbed activated carbon in pentane was then introduced into the GC-MS. This process was repeated three times. An ACT was placed into a GC vial (Fisher Scientific) containing 1 mL of pentane and was introduced into GC-MS. The entire process was repeated three times. Both control samples were conducted to identify any interfering compounds that could rise from these two sources during the interpretation of GC-MS data of porcine bone burnt in the presence of petrol.

Optimization of volume and post-deprivation sampling times for petrol

Six replicates of 15 mL petrol samples were poured into individual 125 mL aluminium tin cans respectively. Each sample was allowed to burn for 1 minute. Ten seconds before the 1 minute mark, an empty lid was placed over the tin can to extinguish the flame *via* oxygen deprivation. Out of six replicates, three were allowed to cool for 3 minutes post-deprivation, whereas another three replicates were allowed to cool for 4 minutes post-deprivation. Post-deprivation sampling time refers to the time the sample was left to cool after extinguishment before being sealed by a lid containing ACT. Then, the empty lid was removed and sealed with another lid containing an ACT and was incubated in an oven for 16 hours at 80 °C. After the incubation process, the ACT was removed and placed into a GC vial (Fisher Scientific) containing 1 mL of pentane and was introduced into the GC-MS. The entire process was then repeated with six 30 mL of petrol samples that were burnt for 2 minutes and were allowed to cool

for 3 minutes and 4 minutes, post-deprivation. Both volume and post-deprivation sampling times were tested to observe the number of pyrolytic products generated and to determine the parameters that generated optimal chromatographic output.

Sample preparation

Fresh porcine femur bones were purchased from the Kajang Wet Market, Selangor, Malaysia. The bones were labelled according to the date acquired and stored in a laboratory freezer at -21°C. Before cutting, the bones were defrosted at room temperature for 30 - 40 minutes. The epiphyses of each bone were removed using a bench vice and a hacksaw. Scissors and tweezers were used to get rid of the remaining soft tissues on the bone. Then, the diaphysis was cut into 25 g ± 1.5 g, a recommended size, to be the best weight to generate optimum pyrolysis products [9]. Then, the bone fragment was placed into 125 mL aluminium tin can. 30 mL of unleaded RON95 petrol, purchased from the Shell Petroleum Company Ltd Malaysia was then added onto the bone. The entire process was repeated until twelve sets of 25 g ± 1.5 g of bone samples with 30 mL of petrol were obtained.

Pyrolysis process

The outdoor burning experiment was set up at the Forensic Science Simulation Site, Universiti Kebangsaan Malaysia (UKM), Selangor, Malaysia. A retort stand was placed on a flat ground and the tin can without the lid containing the sample was placed on a tripod stand during the burning process. The sample was heated using a Bunsen burner which was placed under the tin can and connected to a Liquefied Petroleum Gas (LPG) tank by using a 1.5 m length of gas hose and the flow of gas was controlled by a valve. A k-thermocouple connected to a digital thermometer model 51 II (Fluke) was used to monitor the temperature of the sample during pyrolysis. Six samples were allowed to continuously burn and self-extinguish and another six samples were not allowed to self-extinguish.

For the latter six samples, reaching the auto-ignition stage of the samples, the flames were extinguished using an empty lid when the size of the flames reduces to burning within the tin. These two methodologies were employed to compare and contrast the presence and type of pyrolysis products detected when the samples were purposely extinguished versus those that self-extinguished. The covered tin can contain the burnt sample was then left to cool for 4 minutes post-deprivation. The empty lid was then replaced with another lid containing an ACT, which was hooked to a paper clip held by a magnet on the lid. The tin was sealed shut and incubated in an oven for 16 hours at 80°C (ASTM E1412-07) [23]. After the incubation process, the ACT was removed and placed into a GC vial (Fisher Scientific) containing 0.5 mg/mL of tetrachloroethylene (internal standard) and desorbed with 1 mL of pentane. The GC vial containing the desorbed activated carbon in pentane was then introduced into the GC-MS.

Results and Discussion

Control sample for empty aluminium tin and ACT

The analysis of the aluminium tin can and ACT did not produce any volatile organic compounds, suggesting no possible interferences from these two sources during the analysis of the target compounds from burnt porcine bones in the presence of petrol.

Optimization of volume and post-deprivation sampling time for petrol

When 15 mL of petrol samples were burnt, the range of time the flames took to self-extinguish were between 1.33 minutes to 1.53 minutes. Hence, the burning time was shortened to 1 minute for the generation of detectable pyrolysis products. Post-deprivation sampling times of 3 minutes and 4 minutes were tested because the ranges of time taken for the headspace of the samples to cool to room temperature were between 3 minutes and 4.5 minutes.

The results of the repetitive analysis of 15 mL of burnt petrol that were cooled for 3 minutes post-deprivation are tabulated in Table 1 and a representative of total ion chromatogram (TIC) is labelled and illustrated in Figure 1. A range of C_2-alkylbenzenes and C_3-alkylbenzenes were detected. Toluene was also present. Indane and C_4-alkylbenzenes such as tetramethylbenzenes, which were the pyrolytic key indicators of petrol according to ASTM E1618-06 were not detected. In terms of consistently appearing products, toluene, *m*-xylene, *p*-xylene, 1,3,5-trimethylbenzene, 1,2,4-trimethylbenzene and 1,2,3-trimethylbenzene were relatively consistent in triplicate analysis. The maximum temperature attained during the heating process in the headspace above the samples were recorded to be in the range of 190°C to 314°C as illustrated in Figure 2.

Table 1. Eight compounds identified based on the *m/z* values and retention times for three 15 mL of burnt petrol samples at 3 minutes post-deprivation sampling time

No.	Retention Time(min)	Compound	Replicates		
			1	2	3
1.	3.385	toluene	√	√	√
2.	6.063	ethylbenzene	ND	ND	√
3.	6.296	*m*-xylene	√	√	√
4.	6.807	*p*-xylene	√	√	√
5.	8.192	1-ethyl-3-methylbenzene	ND	ND	√
6.	8.325	1,3,5-trimethylbenzene	√	√	√
7.	8.713	1,2,4-trimethylbenzene	√	√	√
8.	9.112	1,2,3-trimethylbenzene	√	√	√

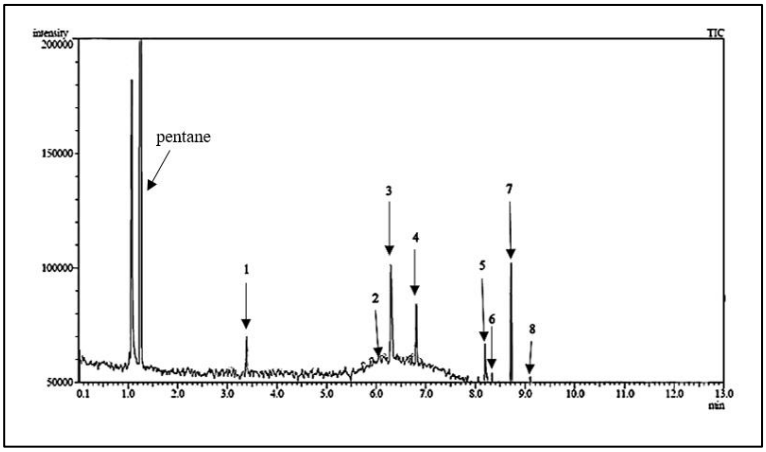


Figure 1. A representative of TIC of a 15 mL of burnt petrol sample at 3 minutes post-deprivation sampling time (replicate 3)

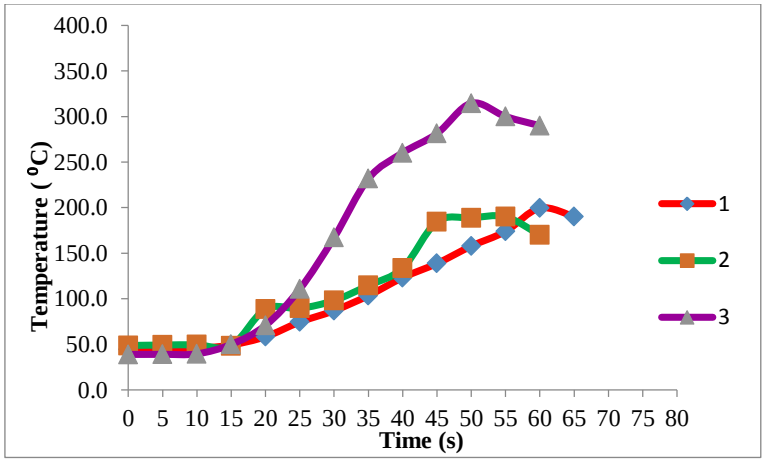


Figure 2. Overlay of three-time temperature profiles of 15 mL of burnt petrol samples at 3 minutes post-deprivation sampling time

The derived products for the 15 mL of burnt petrol samples, cooled for 4 minutes post-deprivation are tabulated in Table 2 and a representative of the total ion chromatogram (TIC) is labelled and illustrated in Figure 3. 15 mL of burnt petrol samples that were cooled for 4 minutes post-deprivation produced a range of C_2-alkylbenzenes, C_3-alkylbenzenes and C_4-alkylbenzenes. Toluene and indane were generated too. In terms of consistently appearing products, toluene, *m*-xylene, *p*-xylene, 1-ethyl-3-methylbenzene, 1,3,5- trimethylbenzene, 1,2,4-trimethylbenzene and 1,2,3-trimethylbenzene were relatively consistent across the three replicates. The maximum temperature attained during the heating process in the headspace above the samples were recorded to be in the range of 207°C to 374°C as illustrated in Figure 4.

Table 2. Thirteen compounds identified based on the *m/z* values and retention times for three 15 mL of burnt petrol samples at 4 minutes post-deprivation sampling time

No.	Retention Time (min)	Compound	Replicates		
			1	2	3
1.	3.385	toluene	√	√	√
2.	6.063	ethylbenzene	√	ND	√
3.	6.296	*m*-xylene	√	√	√
4.	6.807	*p*-xylene	√	√	√
5.	8.053	*n*-propylbenzene	ND	ND	√
6.	8.192	1-ethyl-3-methylbenzene	√	√	√
7.	8.325	1,3,5-trimethylbenzene	√	√	√
8.	8.469	1-ethyl-2-methylbenzene	√	ND	√
9.	8.713	1,2,4-trimethylbenzene	√	√	√
10.	9.112	1,2,3-trimethylbenzene	√	√	√
11.	9.259	indane	ND	ND	√
12.	10.395	1,2,4,5-tetramethylbenzene	√	ND	√
13.	10.435	1,2,3,5-tetramethylbenzene	√	ND	√

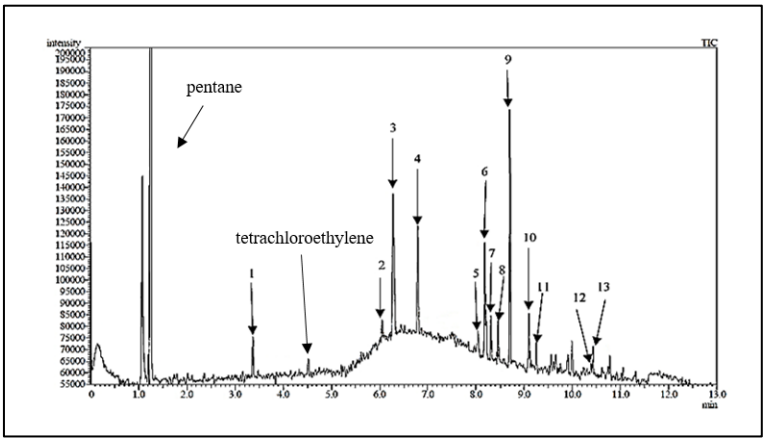


Figure 3. A representative of TIC of a 15 mL of burnt petrol sample cooled for 4 minutes post-deprivation sampling time (replicate 3)

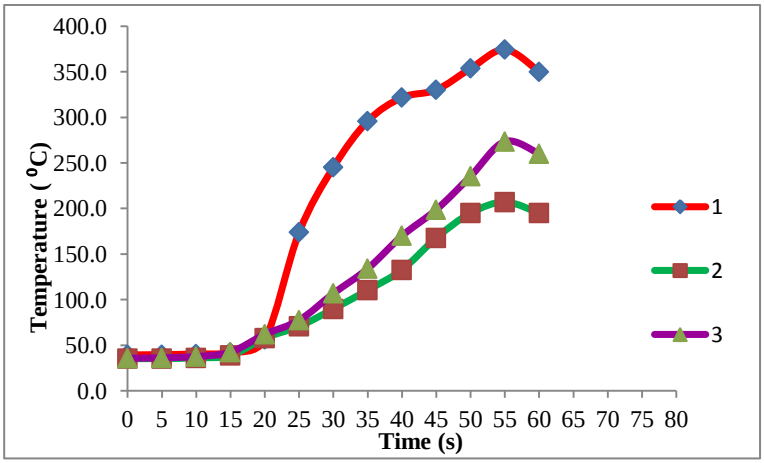


Figure 4. Overlay of three-time temperature profiles of 15 mL of burnt petrol samples at 4 minutes post-deprivation sampling time

When 30 mL of petrol samples were burned, the range of time it took to self-extinguish were between 2.08 minutes and 2.87 minutes. Hence, the burning time was shortened to 2 minute for the generation of detectable pyrolysis products. Post-deprivation sampling times of 3 minutes and 4 minutes were tested because the ranges of time taken for the headspace of the samples to cool to room temperature were between 3.8 minutes and 4.2 minutes.

The results of the repetitive analysis of 30 mL of burnt petrol samples cooled for 3 minutes post-deprivation are tabulated in Table 3 and a representative of total ion chromatogram (TIC) is labelled and illustrated in Figure 5. 30 mL of petrol samples cooled for 3 minutes post-deprivation produced a range of C_2-alkylbenzenes, C_3-alkylbenzenes and C_4-alkylbenzenes. Toluene and indane were also detected. In terms of consistently appearing products, C_2-alkylbenzenes, C_3-alkylbenzenes and C_4-alkylbenzenes were relatively consistent across the three replicates. The maximum temperature attained during the heating process in the headspace above the samples were recorded to be in the range of 224°C to 356°C as illustrated in Figure 6.

Table 3. Eighteen compounds identified based on the *m/z* values and retention times for three 30 mL of burnt petrol samples at 3 minutes post-deprivation sampling time

No.	Retention Time (min)	Compound	Replicates		
			1	2	3
1.	3.385	toluene	√	ND	√
2.	6.063	ethylbenzene	ND	ND	√
3.	6.296	*m*-xylene	√	√	√
4.	6.807	*p*-xylene	√	√	√
5.	8.053	*n*-propylbenzene	√	√	√
6.	8.192	1-ethyl-3-methylbenzene	√	√	√
7.	8.325	1,3,5-trimethylbenzene	√	√	√
8.	8.469	1-ethyl-2-methylbenzene	√	√	√
9.	8.713	1,2,4-trimethylbenzene	√	√	√
10.	9.112	1,2,3-trimethylbenzene	√	√	√
11.	9.259	indane	√	ND	√
12.	9.567	1-methyl-4-propylbenzene	√	√	√
13.	9.625	1-methyl-2-propylbenzene	√	ND	ND
14.	9.667	2-ethyl-1,4-dimethylbenzene	√	ND	ND
15.	9.908	1-methyl-4-(1-methylethyl)benzene	√	√	√
16.	10.000	1-methyl-2-(1-methylethyl)benzene	√	√	√
17.	10.400	1,2,4,5-tetramethylbenzene	ND	√	√
18.	10.435	1,2,3,5-tetramethylbenzene	ND	√	√

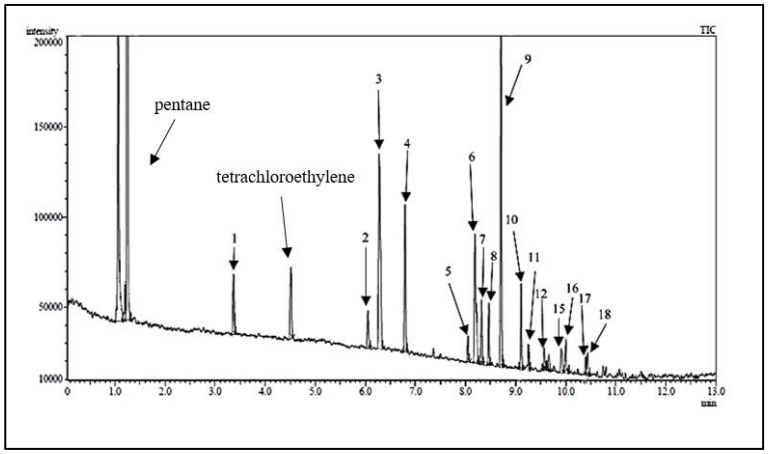


Figure 5. A representative of TIC of a 30 mL of burnt petrol sample at 3 minutes post-deprivation sampling time (replicate 3)

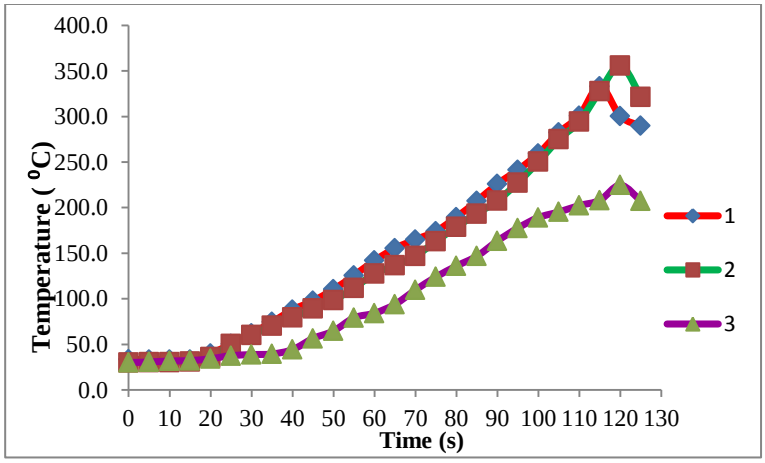


Figure 6. Overlay of three-time temperature profiles of 30 mL of burnt petrol samples at 3 minutes post-deprivation sampling time

The results of the derived products of 30 mL of burnt petrol samples cooled for 4 minutes post-deprivation are tabulated in Table 4 and a representative of total ion chromatogram (TIC) is labelled and illustrated in Figure 7. All the three samples generated consistent presence of toluene, indane and most of C_2-alkylbenzenes, C_3-alkylbenzenes and C_4-alkylbenzenes. Even though across the replicates, the rest of the products appeared with relatively good qualitative reproducibility, 2,3-dimethylhexane (replicate 2) and 1-ethyl-4-methylbenzene (replicate 3) were only detected once out of three replicates and these two compounds were only present in this analysis. This is most likely due to the fire dynamics experienced by the replicates during the burning process [7]. Replicate 3 experienced the lowest temperature ranges in comparison to the other two replicates. The lower temperatures could have shielded 1-ethyl-4-methylbenzene from being consumed by the higher levels of heat, and flames, as experienced by replicate 1 and replicate 2 as higher temperatures are known to cause further decomposition of smaller pyrolytic compounds [11, 12]. On the other hand, even though replicate 2 experienced higher temperature ranges in comparison to replicate 1 and replicate 3, 2,3-dimethylhexane was still detected. In this case, it could be down to the need of higher temperature ranges to volatilise 2,3-dimethylhexane from the petrol sample. Similar outcomes were noted in the literature whereby higher molecular weight compounds were found to require higher temperatures in order to resolve [7, 12, 24]. The maximum temperature attained during the heating process in the headspace above the samples were recorded to be in the range of 180 °C to 315 °C as illustrated in Figure 8.

Table 4. Twenty compounds identified based on the *m/z* values and retention times for three 30 mL of burnt petrol samples at 4 minutes post-deprivation sampling time

No.	Retention Time (min)	Compound	Replicates		
			1	2	3
1.	3.385	toluene	√	√	√
2.	3.875	2,3-dimethylhexane	ND	√	ND
3.	6.063	ethylbenzene	√	√	√
4.	6.296	*m*-xylene	√	√	√
5.	6.807	*p*-xylene	√	√	√
6.	8.053	*n*-propylbenzene	√	√	√
7.	8.192	1-ethyl-3-methylbenzene	√	√	√
8.	8.225	1-ethyl-4-methylbenzene	ND	ND	√

Table 4 (cont'd). Twenty compounds identified based on the *m/z* values and retention times for three 30 mL of burnt petrol samples at 4 minutes post-deprivation sampling time

No.	Retention Time (min)	Compound	Replicates		
			1	2	3
9.	8.325	1,3,5-trimethylbenzene	√	√	√
10.	8.469	1-ethyl-2-methylbenzene	√	√	√
11.	8.713	1,2,4-trimethylbenzene	√	√	√
12.	9.112	1,2,3-trimethylbenzene	√	√	√
13.	9.259	indane	√	√	√
14.	9.567	1-methyl-4-propylbenzene	√	√	√
15.	9.625	1-methyl-2-propylbenzene	ND	√	√
16.	9.667	2-ethyl-1,4-dimethylbenzene	√	√	√
17.	9.908	1-methyl-4-(1-methylethyl)benzene	√	√	√
18.	10.000	1-methyl-2-(1-methylethyl)benzene	√	√	ND
19.	10.400	1,2,4,5-tetramethylbenzene	√	ND	√
20.	10.435	1,2,3,5-tetramethylbenzene	√	ND	√

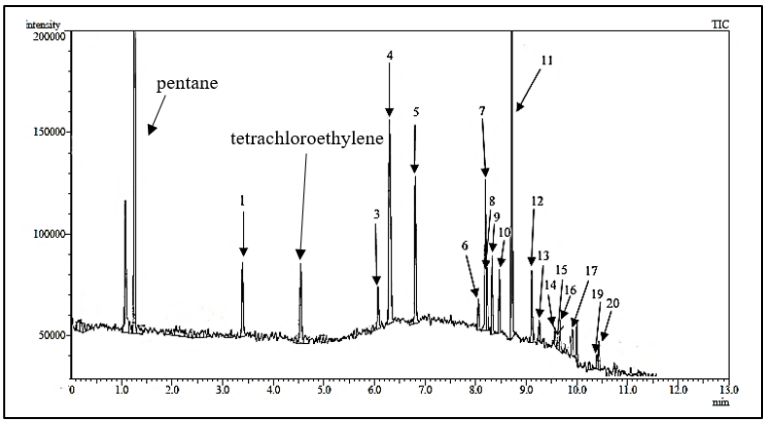


Figure 7. A representative of TIC of a 30 mL of burnt petrol sample at 4 minutes post-deprivation sampling time (replicate 3)

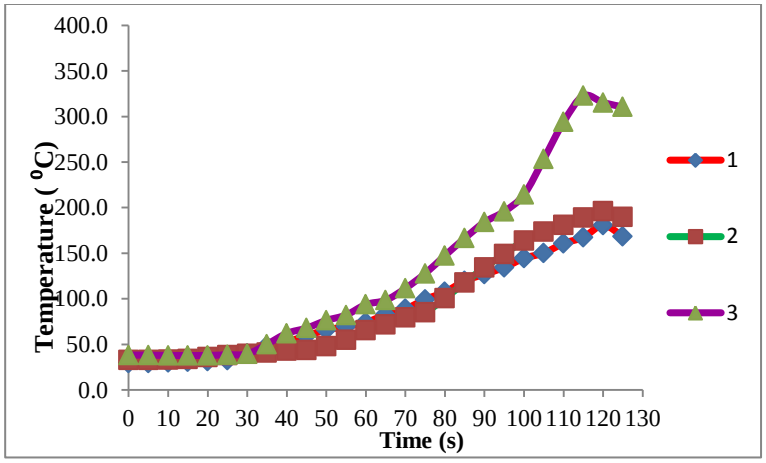


Figure 8. Overlay of three-time temperature profiles of 30 mL of burnt petrol samples at 4 minutes post-deprivation sampling time

30 mL of burnt petrol samples, as tabulated in Table 3 and Table 4 respectively produced a higher number of pyrolytic products (18 to 20 compounds) as compared to 15 mL of petrol samples (8 to 13 compounds) as tabulated in Table 1 and Table 2 respectively. This shows that larger volumes of petrol generated considerably more pyrolysis product in comparison to lesser volumes. The number of consistently detected products across the three replicates of sampling for 30 mL of burnt petrol samples cooled for 4 minutes post-deprivation as tabulated in Table 3 were 14 which is greater in comparison to 30 mL of burnt petrol samples cooled for 3 minutes post-deprivation as tabulated in Table 4 which were only 11. Thus, 30 mL of volume of petrol and 4 minutes post-deprivation sampling time were applied in the next stage of the experiment.

Porcine bone burnt in the presence of petrol

Pyrolysis processes have been applied by using two methods for this research. In the first method, the sample was allowed to continuously burn till it reached auto-ignition and the flames were allowed to self-extinguish. In the second method, upon auto-ignition, the flames were extinguished by placing an empty lid over the tin when the size of the flame reduces to burning within the tin. The results obtained across all the six replicates over both methods are tabulated across Table 5 and Table 6, respectively. A representative of total ion chromatogram (TIC) is labelled and illustrated in Figure 9 and Figure 10, respectively.

Across the six replicates for the first method, only toluene was detected as displayed in Table 5. Toluene only appeared in three of the six replicates. Maximum temperatures attained across the headspace above the six replicates varied and were between 315 °C to 547 °C with exposure to heat ranging from 2.35 minutes to 4 minutes, as illustrated in Figure 10.

Table 5. One compound identified based on the *m/z* values and retention time when six samples were allowed to continuously burn upon auto-ignition and self-extinguish

No.	Retention Time (min)	Compound	Replicates					
			1	2	3	4	5	6
1.	3.385	toluene	√	ND	ND	√	ND	√

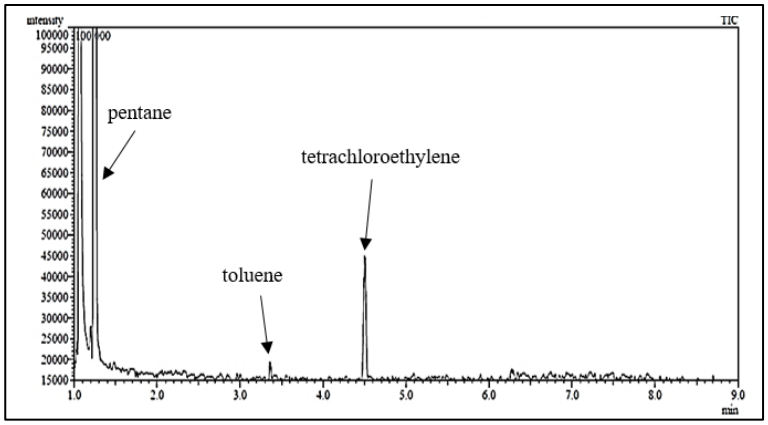


Figure 9. A representative of TIC when the sample was allowed to continuously burn upon auto-ignition and self-extinguish (replicate 4)

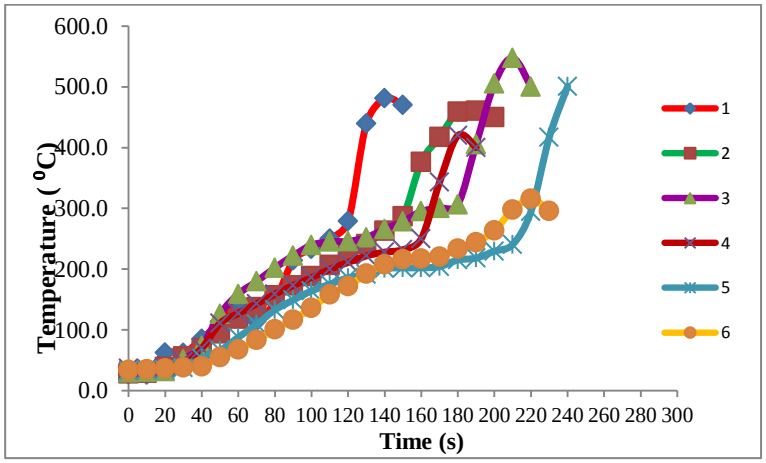


Figure 10. Overlay of six time temperature profiles when the samples were allowed to continuously burn upon auto-ignition and self-extinguish

Meanwhile, across the six replicates for the second method, only 1,2,4,-trimethylbenzene was detected, appearing in four of the six replicates, as displayed in Table 6. The maximum temperature attained during the heating process in the headspace above the samples were recorded to be in the range of 260°C to 580°C with the duration of exposure to heat ranging from 2.67 - 4.17 minutes as illustrated in Figure 11.

Table 6. One compound identified based on the *m/z* values and retention time when the flames upon auto-ignition were extinguished, when the size of the flames reduce to burning within the tin

No.	Retention Time (min)	Compound	Replicates					
			1	2	3	4	5	6
1.	8.713	1,2,4-trimethylbenzene	√	√	√	√	ND	ND

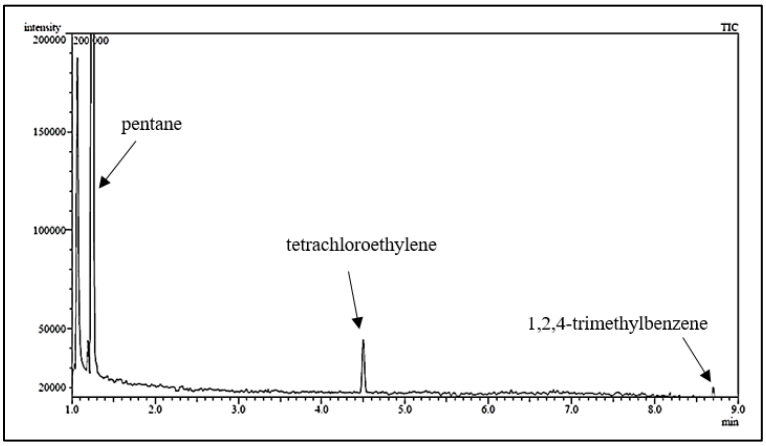


Figure 11. A representative of TIC when the flame auto-ignition was extinguished, when the size of the flame reduces to burning within the tin (replicate 3)

Good qualitative reproducibility across six replicates were not obtained for toluene and 1,2,4,-trimethylbenzene, respectively due to them being consumed or lost during the burning process [19]. Other petrol compounds as detailed in Table 4 were not detected. This could primarily be due to the extended burning duration of more than 2 minutes for 30 mL of petrol, in which most of the fuel could have been vaporized or consumed by auto-ignited flames [9]. Besides that, when 30 mL of petrol samples were burned during the preliminary study, maximum temperatures attained across the headspace of the six replicates were between 180 °C to 356 °C (Figure 6 and Figure 8), respectively. However, when petrol was burned together with porcine bones, temperatures exceeded 400 °C (Figure 10 and Figure 12) for most of the samples in both methods. These higher ranges of temperatures could have induced the thermal decomposition of pyrolysis products generated from petrol [11, 15]. In the absence of petrol, the maximum temperature attained in Gabriel et al.'s [12] work was 580 °C at approximately 13 minutes when porcine bones were burnt in an open flame under outdoor conditions. In this work, when petrol was used, the temperature raised to 580 °C within 3 - 4 minutes. This shows that petrol works as a good accelerant to increase the rate of burning of a material, in this case porcine tissue (in extension, human tissue).

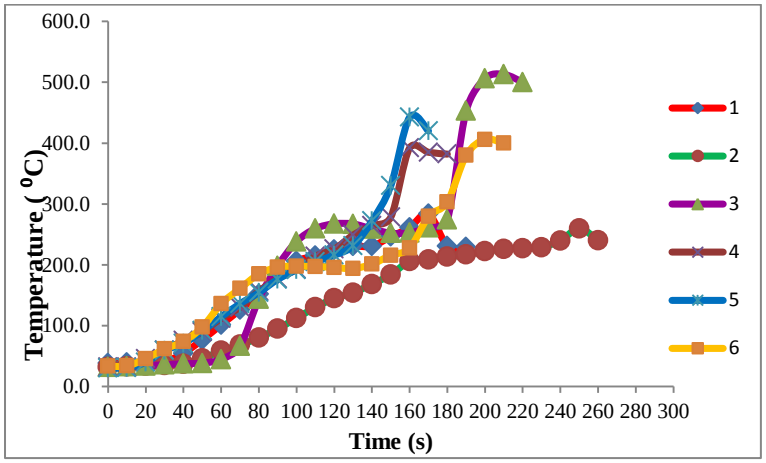


Figure 12. Overlay of six-time temperature profiles when the flames upon auto-ignition were extinguished, when the size of the flames reduce to burning within the tin

Toluene, detected in the first method, is a common compound that can be found from the pyrolysis of petrol as well as from the pyrolysis of porcine bones [12, 15]. It is not possible to distinguish the origin of toluene as coming from petrol or porcine bones. Moreover, toluene on its own cannot be used as a pyrolytic key indicator of human tissue burnt with petrol because toluene is a common interference product present in most household materials [15]. Whereas, 1,2,4-trimethylbenzene which was obtained from the second method, has been reported to be unique pyrolytic key indicator of petrol [20].

Nonetheless, the pyrolytic key indicators of porcine bone burnt with petrol were not detected across both methods, even though through visual observations, all the replicates of porcine bones burnt with petrol underwent auto-ignition during the burning process. Bone was noted to experience auto-ignition as the level of petrol within the tin was nearing the fully consumed stage and when the flames had changed focus to within the bone. The auto-ignition events were most likely due to ignition of petrol which could have raised the temperature in the tin, facilitating the auto-ignition of the porcine bones at an early stage [9]. However, the visualised auto-ignition of bones could have also been of petrol that had absorbed itself within the bone marrow and structures of the bone (bone functioning as a wick) [25, 26]. If this occurred, the visualised auto-ignition could be of petrol rather than the bone, explaining the absence of the pyrolytic products from bone.

From another point of view, the absence of pyrolytic products of porcine bones could be due to the short duration of burning. In Gabriel et al.'s [12] work, optimum pyrolysis products were detected when porcine bones were exposed to an open flame burnt under outdoor conditions for approximately 13 minutes. However, in this research, the burning time was only in the range of approximately 3 - 4 minutes, the short time duration would not have been sufficient enough for the bone to undergo optimum pyrolysis under outdoor conditions. Burning time was not lengthened to prevent petrol from being fully consumed by the fire. If the burning durations were lengthened, it would not depict a real fire scenario where petrol can still be found in fire debris because; i) the initial heat source would not be present throughout the fire, ii) petrol would have been absorbed into underlying materials such as clothing and wood that serve as a wick [25, 26] and iii) some parts of the body that were not exposed directly to the heat or protected from the heat, would contain remnants of petrol residue.

Even though temperatures rose to 580 °C within a short duration of time, the experimental methodology employed in a study also plays an important role in dictating the generation and detection of volatile compounds of bone. In previous work, DeHaan et al. [8] determined the presence of *n*-aldehydes from the burning of porcine fat in a contained micro furnace at 300 °C, 500 °C and 700 °C for 10 seconds. The use of a micro furnace in a contained environment facilitates more control on the combustion and pyrolysis process and also prevents any generated products from escaping [9] whereas in this research, porcine bones were burnt in an open flame under outdoor conditions in which many factors such as variation in the concentration of oxygen that is largely controlled by wind conditions, can alter the burning efficiency and prevent a steady supply of flames and heat [27, 28]. Hence, no *n*-aldehydes were detected. Similar outcomes were also suggested in Agu and Gabriel's work [9, 11]. In Gabriel et al.'s [12] work utilising similar environmental conditions as per this study minus the use of petrol, a homologous series of *n*-alkanes, *n*-alkenes, *n*-aldehydes, aromatics and nitrile were detected from auto-ignited bones, that were not present in this study. A plausible explanation here could be down to the source of flames used in both research. In Gabriel et al.'s [12] work, a portable gas canister was used, whereas in this study a LPG gas tank with an adjustable pressure valve was used. Variations in the experimental methodology particularly pressure and ratio of mixed gas supplied during the burning process could have altered the heat transfer rate and burning profiles of bones (auto-ignition versus no auto-ignition). This warrants further investigation as information degrading this is pertinent to the forensic community to understand the effects of different factors to the process of pyrolysis and combustion. Besides experimental methodology, other factors such as the presence of clothing and other materials around the human tissue, humidity and circumstances surrounding death have also been reported to impart a profound effect on the thermal decomposition of human tissues [29-31].

Conclusion

The pyrolytic key indicators of porcine bones were not detected when burnt together with petrol under the environmental conditions specific to this research. Toluene was detected when porcine bone samples in the

presence of petrol were allowed to continuously burn upon auto-ignition and self-extinguish. However, the presence of toluene was undistinguishable whether it was generated from the pyrolysis of petrol or porcine bones. Meanwhile, the only pyrolytic key indicator of petrol; 1,2,4-trimethylbenzene was detected when the flames were manually extinguished. This work highlighted the role of experimental parameters such as the volume of petrol, burning duration and temperatures attained during the burning process, in addition to experimental methodology, that has exerted influence on the generation and detection of key pyrolytic products and on the burning characteristics of both petrol and porcine tissue. In order to obtain a more robust output in the future, this study could be executed in a combustion fume hood that facilitates consistent air flow, limiting the effects of insufficient and excessive oxygen supply. Besides that, the results from this study could also be put to the test in a full scale outdoor burning with the use of the entire pig carcass and surplus of petrol, emulating real life fire scenarios.

References

1. Saferstein, R. (2017). Criminalistics: An introduction to forensic science. 12th edition. Pearson Education: pp. 524.
2. Adelson, L. (1955). Role of the pathologist in arson investigation. *Journal of Criminal Law, Criminology & Police Science*, 45(6): 760 – 768.
3. Hine, G. A. (2004). Fire scene investigation: An introduction for chemists, in analysis and interpretation of fire scene evidence, K. G. F. Jose R. Almirall, CRC Press LLC: pp. 46.
4. Pert, A. D., Baron, M. G. and Birkett, J. W. (2006). Review of analytical techniques for arson residues. *Journal of Forensic Sciences*, 51(5): 1033 - 1049.
5. Jackowski, J. (1997). The incidence of ignitable liquid residues in fire debris as determined by a sensitive and comprehensive analytical scheme. *Journal of Forensic Sciences*, 42(5): 828 - 832.
6. Rumiza, A. R., Khairul, O., Zuha, R. M. and Heo, C. C. (2010). An observation on the decomposition process of gasoline-ingested monkey carcasses in a secondary forest in malaysia. *Tropical Biomedicines*, 27(3): 373 - 383.
7. Stauffer, E. (2003). Concept of pyrolysis for fire debris analysts. *Science & Justice*, 43(1): 29 - 40.
8. Dehaan, J. D., Brien, D. J. and Large, R. (2004). Volatile organic compounds from the combustion of human and animal tissue. *Science and Justice*, 44(4): 223 - 236.
9. Gabriel, G. F. (2015). The analysis and discrimination of pyrolysis products from biological and non-biological sources. Thesis of Doctor Philosophy Degree, University of Strathclyde.
10. Mclellan, S. A. (1999). An investigation of the volatiles produced from pyrolysis of the body. Thesis of Master Degree, University of Strathclyde.
11. Agu, K. (2011). Investigation of the thermal degradation products of bon. Thesis of Doctor Philosophy Degree, University of Strathclyde.
12. Gabriel, G. F., Ismail, A., Abdul Ghani, A. A., Osman, K. and Noor Hazfalinda, H. (2017). The analysis of thermal decomposition products generated from porcine tissues exposed to outdoor burning conditions. *Malaysian Journal of Analytical Sciences*, 21(3): 585 - 596.
13. Dehaan, J. D., Taormina, E. I. and Brien, D. J. (2017). Detection and characterization of volatile organic compounds from burned human and animal remains in fire debris. *Science & Justice*, 57(2): 118 - 127.
14. Purevsuren, B., Avid, B., Gerelmaa, T., Davaajav, Y., Morgan, T. J., Herod, A. A. and Kandiyoti, R. (2004). The characterisation of tar from the pyrolysis of animal bones. *Fuel*, 83(7): 799 - 805.
15. Almirall, J. R. and Furton, K. G. (2004). Characterization of background and pyrolysis products that may interfere with the forensic analysis of fire debris. *Journal of Analytical and Applied Pyrolysis*, 71 (1): 51 - 67.
16. Cavanagh, K., Pasquier, E. D. and Lennard, C. (2002). Background interference from car carpets—the evidential value of petrol residues in cases of suspected vehicle arson. *Forensic Science International*, 125(1): 22 - 36.
17. Wineman, P. L. and Keto, R. O. (1994). Target-compound method for the analysis of accelerant residues in fire debris. *Analytica Chimica Acta*, 288(1): 97 - 110.
18. Lennard, C. J., Tristan Rochaix, V., Margot, P. and Huber, K. (1995). A GC–MS database of target compound chromatograms for the identification of arson accelerants. *Science & Justice*, 35(1): 19 - 30.
19. Sferopoulos, R. (2013). Test burning of carpet and foam and potential interferences in identifying petrol in arson investigation by gas chromatography/ mass spectrometry. Thesis of Doctor Philosophy Degree, Victoria University.

20. American Society of Testing and Materials E1618-06 (2006). ASTM E1618-06 standard test method for ignitable liquid residues in extracts from fire debris samples by Gas Chromatography-Mass Spectrometry. American Society of Testing and Materials. 11.
21. Rus Din, R. D., Zainal Ariffin, S. H., Senafi, S., Abdul Wahab, R. M. and Zainol Abidin, I. Z. (2014). Molecular mitochondrial DNA and radiographic approaches for human archaeology identification. *Sains Malaysiana*, 43(10): 1523 - 1535.
22. Arora, A., Gupta, P., Kapoor, S. and Mahajan, S. (2010). An analytic review of burnt bones in medicolegal sciences. *Journal of Punjab Academy of Forensic Medicine & Toxicology*, 10: 31 - 36.
23. American Society for Testing and Materials E1412-07 (2012). Astm E1412-07 standard practice for separation of ignitable liquid residues from fire debris samples by passive headspace concentration with activated charcoal. American Society for Testing and Materials.
24. Paczkowski, S. and Schütz, S. (2011). Post-mortem volatiles of vertebrate tissue. *Applied Microbiology and Biotechnology*, 91(4): 917 - 935.
25. Dehaan, J. D. and Nurbakhsh, S. (2001). Sustained combustion of an animal carcass and its implications for the consumption of human bodies in fires. *Journal of Forensic Sciences*, 46(5): 1076 -1081.
26. Dehaan, J. D. (2012). Sustained combustion of bodies: Some observations. *Journal of Forensic Sciences*, 57(6): 1578 - 1584.
27. The National Fire Protection Association (2017). NFPA 921: Guide for fire and explosion investigations. Massachusetts: The National Fire Protection Association.
28. Welker, J. R. and Sliepcevich, C. M. (1966). Burning rates and heat transfer from wind-blown flames. *Fire Technology*, 2(3): 211 - 218.
29. Chee Hau, T., Amir Hamzah, S. P. A., Khairul, O. and Noor Hazfalinda, H. (2013). Post mortem changes in relation to different types of clothing. *Malaysian Journal of Pathology*, 35(1): 77 - 85.
30. John D. Dehaan, D. J. I. (2011). Kirk's Fire Investigation. 8th edition. Pearson.
31. Osman, K., Noor Hazfalinda, H. and Gabriel, G. F. (2018). Penyiasatan forensik: Pengecaman identiti penjenayah. Penerbit Universiti Kebangsaan Malaysia: pp. 103.

Malaysian Journal of Analytical Sciences, Vol 23 No 2 (2019): 290 - 299
DOI: https://doi.org/10.17576/mjas-2019-2302-13

MALAYSIAN JOURNAL OF ANALYTICAL SCIENCES
Published by The Malaysian Analytical Sciences Society
ISSN 1394 - 2506

SYNTHESIS AND CHARACTERIZATION OF SILICA-SILVER CORE-SHELL NANOPARTICLES

(Sintesis dan Pencirian Silika-Perak Nanopartikel Teras-Cengkerang)

Nur Kamilah Mohd, Wan Mohd Afiq Wan Mohd Khalik, Alyza A. Azmi*

School of Marine and Environmental Sciences,
Universiti Malaysia Terengganu, 21030 Kuala Nerus, Terengganu, Malaysia

**Corresponding author: alyza.azzura@umt.edu.my*

Received: 10 February 2019; Accepted: 30 March 2019

Abstract

Silica-silver core-shell nanoparticles have received tremendous interests in various applications compared to the bare silver nanoparticles due to several important features such as exhibit higher surface area, the existence of a synergistic effect between the core and the shell, stabilize silver nanoparticles against aggregation, and easily control their properties by the changing shell structure and shell geometry. Due to this significance, this study was conducted to synthesis and characterization of silica-silver core-shell nanoparticles using the facile method without any surface modification needed. In the synthesis route, silica particles have been synthesis based on the Stöber method. The deposition of nanoscales silver layer on silica surface mainly involves the electrostatic attraction between $[Ag(NH_3)_2]^+$ions and silanol groups, and the addition of polyvinylpyrrolidone (PVP) has been acted as a reducing agent and stabilizing agent. UV-Vis spectroscopy evidenced the absorption of surface plasmon resonance (SPR) of silver nanoparticles in the range 380-450 nm. The crystallinity of silica-silver core-shell nanoparticles showed the face-centered cubic (fcc) structure by X-ray powder diffraction (XRD) analysis. The spherical shape of silica particles with an average 200-220 nm in size has been determined using scanning electron microscope (SEM). The high resolution-transmission electron microscope (HR-TEM) images visualized the successful formation of spherical silver nanoparticles on the silica surface with the average of size 10-40 nm. X-ray photoelectron spectroscopy analysis revealed the elemental compositions exist in the silica-silver core-shell nanoparticles. The synthesized silica-silver core-shell nanoparticles will be used as a potential catalyst in dye treatment application in the future work.

Keywords: core-shell, nanoparticles, silica-silver core-shell, deposited, Stöber method

Abstrak

Silika-perak nanopartikel teras-cengkerang telah menarik minat yang besar dalam pelbagai aplikasi berbanding dengan nanopartikel perak disebabkan oleh beberapa kelebihan seperti permukaan kawasannya lebih tinggi, kewujudan kesan sinergi di antara teras dan cengkerang, mengelakkan pengumpulan nanopartikel perak dan memudahkan untuk mengawal ciri-ciri yang dikendaki dalam nanopartikel teras-cengkerang dengan mengubah morfologi dan geometri partikel cengkerang. Sintesis dan pencirian silika-perak nanopartikel teras-cengkerang telah dilakukan tanpa sebarang pengubahsuaian terhadap permukaan partikel. Proses sintesis melibatkan penghasilan zarah silika menggunakan kaedah Stöber. Pemendapan lapisan perak nano pada permukaan silika melibatkan tarikan elektrostatik antara kumpulan ion $[Ag(NH_3)_2]^+$ dan kumpulan silanol, dan penambahan polivinilpirolidon (PVP) akan bertindak sebagai agen penurunan dan agen penstabilan. Pencirian silika-perak nanopartikel teras-cengkerang menggunakan spektroskopi ultra lembayung tampak (UV-Vis) telah menunjukkan penyerapan resonansi plasmon permukaan (SPR) nanopartikel perak dalam lingkungan 380 - 450 nm. Kehabluran silika-perak nanopartikel teras-cengkerang menunjukkan struktur berpusatkan kubik berpusat (fcc) dengan menggunakan pembelauan sinar-X (XRD). Zarah silika berbentuk sfera dengan saiz 200 nm ditentukan dengan menggunakan mikroskop imbasan elektron (SEM). Saiz perak yang telah didepositkan pada permukaan silika telah diukur menggunakan mikroskop transmisi elektron beresolusi tinggi (HR-TEM) dengan ukuran 10-40 nm. Analisis spektrometer fotoelektron sinar-X (XPS) telah mendedahkan komposisi unsur yang ada di

dalam silika-perak nanopartikel teras-cengkerang. Nanopartikel teras-petala silika-perak akan digunakan sebagai potensi rawatan pewarna pada masa akan datang.

Kata kunci: teras-cengkerang, nanopartikel, silika-perak nanopartikel teras-cengkerang, deposit, kaedah Stöber

Introduction

Metal core-shell nanoparticles have received tremendous interest in various fields because of the potential of combining the advantageous properties of two materials into a single constructional unit. It has been applied in such electronic, biomedical, and environmental field as an antimicrobial agent, drug carrier, or catalyst for pollutants removal. Comparing to the traditional nanoparticles, the combination of the two types of materials as a core and a shell into a single structure provides long term stability and flexibility in surface functionalization. Nischala and the co-workers stated that the core-shell nanoparticles offer several advantages such as high surface area, which increase their performance in any applied fields [1]. It also provides an advanced active interface and a potential synergistic effect between the core and shell to gain higher efficiency, especially in catalytic application [2].

The development of core-shell nanomaterials is expanding drastically driven by the demand in industry and society. Up to now, the construction and characterization of various core-shell nanomaterials have been published. For instance, the $BaTiO_3$-SiO_2 core-shell nanoparticles have been successfully enhancing the energy storage capacity [3], CdS-TiO_2 as a promising candidate for visible light active removal of dye pollutants in water [4], Fe_3O_4-Au as a nontoxic and biocompatible material for biomedical targeted drug delivery [5], Ag-TiO_2 as a gas sensing material [6], Fe-Ni as a catalyst for hydrogen generation [7] and CeO_2-TiO_2 as a catalyst for photoreduction of carbon dioxide under visible light irradiation [8]. Among these materials, the preparation of silica-based core-shell material has attracted our interest of study.

Silica (SiO_2) compound has been explored as a core material in the development of core-shell nanostructures. SiO_2 can be considered cheap and green materials, which can be found abundantly in plant husk and leaves. For example from the sugarcane bagasse [9], rice husk [10], sugar beet bagasse [11], sorghum leaves [12] and lotus flower leaves [13]. Thus, from an economic point of view, the utilization of SiO_2 as a core material may reduce the overall production cost of the metal-core-shell nanostructure. It also exhibits characteristics such as high chemical and thermal stabilities, chemical inertness, large surface areas, good compatibilities with other material and better stability against coagulation [14]. A large number of silanol (Si-OH) groups on the surface of SiO_2 consist of hydrophilic characteristics, which provides a strong interaction with any polar compound through hydrogen bonding interactions [15]. The SiO_2 compound can be synthesized following various methods such as flame synthesis [16], microemulsion modified technique [17] and extraction precipitation [18]. However, these methods suffer certain limitations including costly, produced non-uniform of the particle size and morphology, and the difficulty to remove the surfactant in the end product. Therefore, Stöber method has been adopted as it is easy to scale up the particle size and possibility effortless to transfer into the aqueous solution [19].

SiO_2 has been used as substrate materials for the immobilization of precious metal such as TiO_2 [20], Au [21], and Ni [22]. The bare metal nanoparticles are active and have a higher tendency to coalesce in solution form due to the van der Waals forces and high surface energy. In our study, the deposition of silver nanoparticles (Ag-Nps) on the SiO_2 core surfaces has been developed for the potential application in catalytic activities.

Herein, silica-silver, (SiO_2-Ag) core-shell nanoparticles were prepared with the addition of polyvinylpyrrolidone as a reducing and stabilizing agent. There were no linkers or metals such as tin(II) chloride, palladium, gold and organosilane added to activate SiO_2 particles prior to load Ag-Nps to the surface of the core. The addition of any linkers will be lead to the existence of impurities in the end product of SiO_2-Ag core-shell nanoparticles. Different concentration of ammoniacal silver nitrate solution which is a source of Ag ions was employed to control the coverage of Ag-Nps on the SiO_2 surface. The presences of surface plasmon resonance of Ag-Nps have been determined by UV-Vis spectroscopy. The crystalline natures were evidenced by X-ray powder diffraction (XRD), while the elemental compositions of SiO_2-Ag were evaluated by X-ray photoelectron spectroscopy (XPS). The size

and morphology of core-shell structure were visualized using scanning electron microscope (SEM) and high resolution-transmission electron microscope (HR-TEM).

Materials and Methods

Materials

Absolute ethanol (EMSURE, analytical grade), ethanol (R&M chemical, 95%, analytical grade), ammonium hydroxide (R&M Chemical, 25%, analytical grade), tetraethyl orthosilicate (Sigma-Aldrich, 98%, reagent grade), silver nitrate (Bendosen, analytical reagent), sodium hydroxide (R&M Chemical, analytical reagent), polyvinylpyrrolidone (Sigma Aldrich, average molecular weight 40,000). Deionized water from water purification system Milli-Q integral water system was used throughout the experiment (Merck, 18 ΩM).

Synthesis of silica particles

SiO_2 particles have been synthesized following the Stöber method. Absolute ethanol (30 mL), water (6 mL), ammonium hydroxide solution (1.5 mL) were mixed in a round-bottom flask at the room temperature under continuously stirring (1000 rpm) for 30 minutes. Next, 2.4 mL of tetraethyl orthosilicate was added and left for 3 hours and the resulting particles were centrifuged at 3600 rpm for 20 minutes. The products were washed for at least 3 times with deionized water and ethanol to separate the particles. The obtained SiO_2 then were dispersed in absolute ethanol for subsequently used.

Synthesis of silica-silver core-shell nanoparticles

Ammoniacal silver nitrate solution, $[Ag(NH_3)_2]^+$ was freshly prepared throughout the experiment. The silver nitrate solution was prepared by dissolving silver nitrate into 10 mL of deionized water. Next, 1 mL of sodium hydroxide (0.1 M) was added while slowly swirling. The formation of silver oxide, Ag_2O as the main product caused a color change from colorless to yellowish-brown. The chemical equation for the formation of Ag_2O shown in equation 1.

$$2AgNO_3 + 2NaOH \longrightarrow Ag_2O + 2NaNO_3 + H_2O \quad (1)$$

Next, 4 mL of aqueous ammonia was added slowly to the Ag_2O solution. The color of the solution turned clear indicates the formation of ammoniacal silver nitrate solution and the chemical equation is shown in Equation 2.

$$Ag_2O + 4NH_3 + 2NaNO_3 + H_2O \longrightarrow 2[Ag(NH_3)_2]NO_3 + 2NaOH \quad (2)$$

For the preparation of SiO_2-Ag core-shell nanoparticles, 5 g of the prepared SiO_2 dispersion was added into 10 mL of $[Ag(NH_3)_2]^+$ solution under continuous stirring for at a speed 700 rpm for 2 hours at the room temperature. This process allows an electrostatic attraction between $[Ag(NH_3)_2]^+$ ions with the hydroxyl groups on the surface of silica particles. After 2 hours, PVP (5×10^{-4} moL^{-1}) was added to the solution, followed by stir and reflux at 75˚C for 8 hours. The color of the solution changed darker, which indicates the growth of the outer silver nanoshell on the SiO_2 core surfaces. The solution was then centrifuged at 3600 rom for 20 minutes to remove excess Ag^+ ions, washed with ethanol and deionized water. The precipitate was redispersed in the deionized water prior to further characterization.

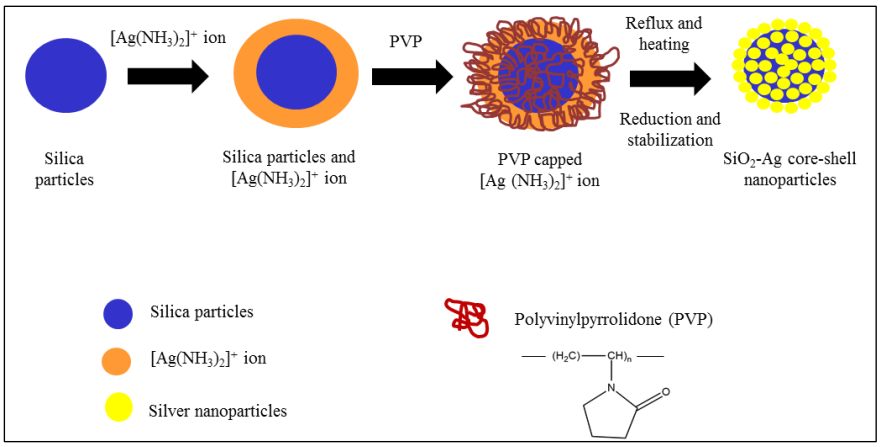
Characterization

SiO_2-Ag core-shell nanoparticles were characterized using standard spectroscopy and microscopy techniques. Spectroscopy study was carried out using UV-Vis spectrophotometer (UV-Shidmazu model 1800 with software UV Probe 2.43) in the wavenumber range from 200 to 800 nm. An amount of 0.01 g of the sample was added to 100 mL of deionized water and sonicated for 20 minutes to form a disperse solution. The samples were placed in a quartz cuvette, and the UV spectrum was recorded. The elemental composition of SiO_2-Ag core-shell nanoparticles was determined using X-ray photoelectron spectroscopy (XPS). It's were carried out with AXIS ULTRADLD (Shimadzu), equipped with Mg Kα ($h\upsilon$=1253.6 eV) X-ray source. The binding energies were referenced to the C1s peak energy at 284.6 eV.

The morphology of SiO_2 particles was observed using a scanning electron microscope (SEM, JEOL model 6360F). A drop of dispersion and also thin film was placed on a sample stub, dried, then sputter-coated with gold prior to examination in order to minimize charging effects. It was operated at an accelerating voltage of 10 and 15 kV with 15,000 magnifications. The morphologies and size of the SiO_2-Ag core-shell nanoparticles were observed using high transmission electron microscope (TECNAI G2 20 S-TWIN, with FEI), 200 kV. An amount of 0.001 g of samples was dispersed with 20 mL of water and ultra-sonicated for 20 minutes. Then, it was dried on the carbon-coated copper grids before measurement. The structural characterizations of prepared samples were carried out using X-ray powder diffraction (XRD) analyzer (X'Pert Pro). X-ray diffractometer with Cu Kα radiation (λ=1.54056 A) at a scanning rate of 0.301 degrees per second in the range 2Θ ranging from 10˚ to 80˚.

Results and Discussion

SiO_2-Ag core-shell nanoparticles were synthesized via the fabrication of Ag-Nps on the surface of SiO_2 particles with the addition of PVP as a reducing and stabilizing agent. The diagram for complete preparation of the SiO_2-Ag core-shell nanoparticles is shown in Scheme 1.



Scheme 1. Schematic representation of the reaction for the synthesis of SiO_2-Ag core-shell nanoparticles

SiO_2 particles were synthesized based on the Stöber method, with the reaction of TEOS in water-alcohol-ammonia solution. Two main reactions involved, which are the formation of the silanol group by hydrolysis process, followed by the formation of the siloxane bridges through a condensation polymerization reaction. The following reaction (equation 3-5) is proposed for the fabrication of Ag-Nps on the SiO_2 surface:

$$(RO)_3\text{-Si-OR} + H_2O \xrightarrow[-\ \text{R-OH}]{\text{Hydrolysis}} (RO)_3\text{-Si-OH} + \text{R-OH} \quad (3)$$

$$(RO_3)\text{-Si-OH} + (RO)_3\text{-Si-OH} \xrightarrow[-\ H_2O]{\text{Condensation}} (RO_3)\text{-Si-O-Si-}(RO_3) + H_2O \quad (4)$$

$$(RO)_3\ \text{Si-OH} + (RO_3)\text{-Si-OR} \xrightarrow[-\ \text{R-OH}]{\text{Condensation}} (RO_3)\text{-Si-O-Si-}(OR_3) + \text{R-OH} \quad (5)$$

The formation of $[Ag(NH_3)_2]^+$as a source of Ag^+ is based on the complexation of Ag ions by ammonia hydroxide solution. According to Strzałka and co-workers, the consumption of $[Ag(NH_3)_2]^+$ as a Ag ion source can be considered as a rapid and easy pathway in the synthesis of SiO_2-Ag core-shell nanostructure [23]. The deposition of Ag-Nps on the SiO_2 surface is formed based on the activation action of $[Ag(NH_3)_2]^+$ with SiO_2 core surfaces. The negatively charged ions of the silanol groups on the SiO_2 core surface will attract the $[Ag(NH_3)_2]^+$ ions due to the

electrostatic attractive interaction. The addition of PVP will reduce the oxidation state number of Ag^{+}, which is from +1 to 0. PVP also prevent aggregation in the dispersion due to the charge neutralization of the silanol group with $[Ag(NH_3)_2]^{+}$ ion [24]. The Ostwald ripening phenomenon where the particles in the reaction redissolve and their solvated species growth become larger particles can be avoided as PVP act as a stabilizer in the solution [25].

UV-Visible analysis

The formation of Ag-Nps loaded on the SiO_2 surface was monitored by UV-Vis spectrophotometer. The reduction of Ag ions (+1) to Ag (0) metal have been evaluated by recording the absorption spectrum of the SiO_2-Ag solution in the range of 200-800 nm. The UV-Visible spectra of SiO_2 particles and SiO_2-Ag core-shell nanoparticles at three different concentrations, which are 0.1 M, 0.2 M, and 0.3 M are depicted in Figure 1.

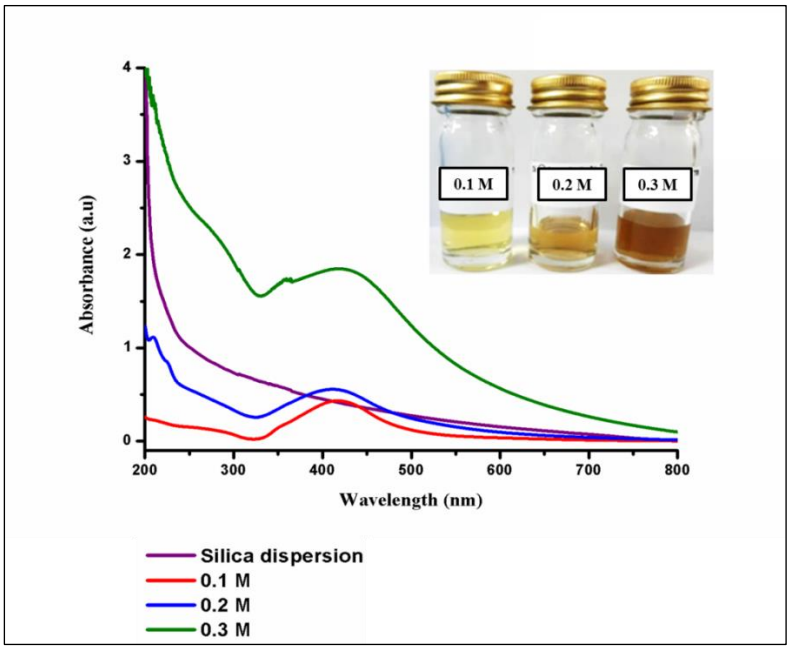


Figure 1. UV-Vis absorption spectra of SiO_2 dispersion, 0.1 M, 0.2 M and 0.3 M of SiO_2-Ag. (Inset shows the image of 0.1 M, 0.2 M and 0.3 M of SiO_2-Ag solution)

Optical absorption spectra of Ag loading show the presence of surface plasmon resonance (SPR) effect in the visible region. In this specific wavelength of 380 to 450 nm range, the incident light can induce a collective oscillation of the electron on the surface of Ag-Nps. This phenomenon is the main reason behind the color change of the Ag solution from light yellow to brownish as shown in the inset in Figure 1.

The Ag plasmonic properties are strongly correlated with their morphology, such as the size and coverage of the nanoparticles. In this case, the absorption band of SPR shows a red shift and broaden, which is an indication of larger coverage of Ag nanoparticles on the SiO_2 core surfaces as the concentration of $[Ag(NH_3)^{2+}]$ increases. The shift magnitude 1.839 is the highest in 0.3 M concentration, compared to 0.557 and 0.433 for 0.2 M and 0.1 M concentrations, respectively. The research conducted by Tzounis et al. demonstrated that the increase Ag-Nps decorated on the SiO_2 spheres enhances the increasing of the absorption peak intensity [26]. On the other hand, no absorbance peak is observed in UV-Vis spectra for bare SiO_2 particles, supporting that no attachment of Ag or any impurities on the SiO_2 surface.

Electron microscopy analysis

Figure 2(a) shows the representative SEM micrograph of the monodispersed SiO_2 particles. The image reveals the spherical shape of SiO_2 particles with a narrow size distribution. The average diameters of 200-220 nm were

measured. A smooth edges and bare surface of prepared SiO_2 particles has been observed, which is commonly detected in most SiO_2 particle preparation using the Stöber method. After Ag adsorption on the SiO_2 surface, the surface morphology of the SiO_2-Ag core-shell nanoparticles roughened (Figure 2b-d). The increase of the SiO_2-Ag surface roughness was due to the increase of Ag nanoparticles loaded on the SiO_2 core surfaces. This is consistent with the formation of a darker color solution when the concentration of $[Ag(NH_3)_2]^+$ is increased. A study conducted by Ghosh and Paria supporting our argument on the dependency of nanoshell thickness by the reaction concentration [27]. Another study by Postolache and co-workers [28] suggested that the increase of silver nitrate concentration effectively promotes the distribution of Ag-Nps onto the surface of SiO_2. In addition, there are no Ag-Nps residuals was observed, which indicates a stable Ag-Nps attachment to the SiO_2 spheres. Furthermore, it was found that the Ag-Nps were spherical in shape with the size ranges of 8-20 nm for 0.1 M and 0.2 M of SiO_2-Ag, while it ranges 10-40 nm for 0.3 M of SiO_2-Ag.

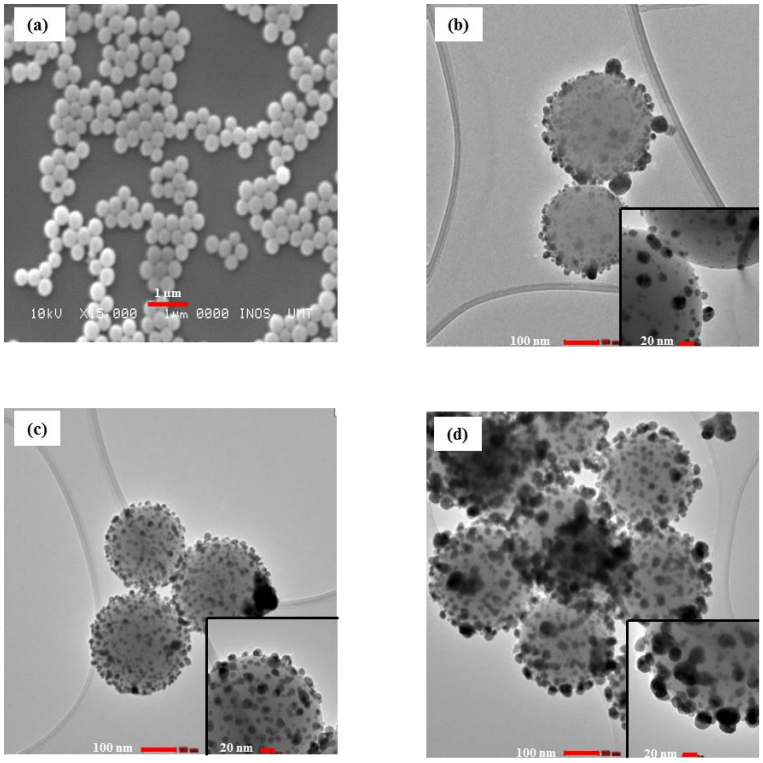


Figure 2. (a) SEM image of SiO_2 particles at 15,000 magnifications, HR-TEM images of (b) 0.1 M of SiO_2-Ag, (c) 0.2 M of SiO_2-Ag, (d) 0.3 M of SiO_2-Ag. Lower right sides images show the individual SiO_2-Ag core-shell HR-TEM images taken of 0.1 M, 0.2 M, and 0.3 M respectively

X-ray powder diffractometer analysis

Figure 3 illustrated the nature characteristic of the XRD pattern for the SiO_2 sphere and SiO_2-Ag core-shell in various concentrations. In the SiO_2 dispersion, broad diffraction peaks in the range of 15˚-30˚ centered at 22˚ correspond to their amorphous structure. A typical XRD pattern of the Ag-Nps was found to possess a face cubic centre (fcc) structure. The Bragg reflections at 2θ = 39.8°, 48.5°, 63.0° and 77.50° can be indexed to the (111), (200), (220) and (311) orientation, respectively. This confirms the deposition of the Ag nanoparticles on the SiO_2 core surfaces. These four peaks were detected which is corresponding to the fcc Ag phase. The fcc pattern of SiO_2-Ag core-shells fcc pattern is consistent with the previous research [29,30]. There are no major diffraction peaks as consequences of crystallographic impurities were found. The relative intensity of the (111) peak is higher compared to other peaks at each concentration indicates the plane orientation preferential to the surface of SiO_2 sphere.

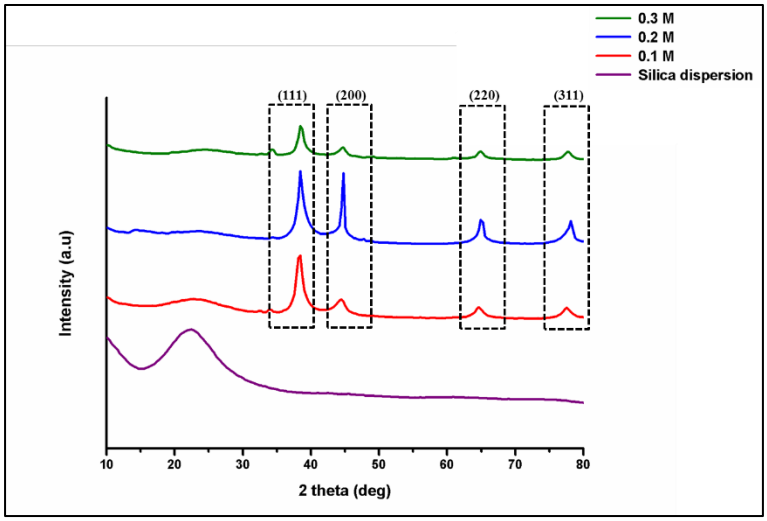
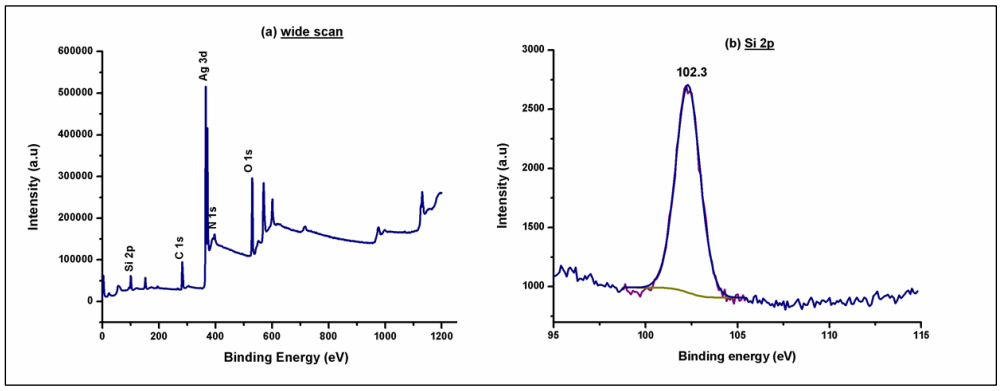


Figure 3. X-ray Powder diffraction patterns of SiO_2 particles, 0.1 M, 0.2 M and 0.3 M of SiO_2-Ag core-shell

X-ray photoelectron spectroscopy

X-ray photoelectron spectra for the SiO_2-Ag core-shell nanoparticles were acquired from binding energy regions containing peak arising from all elements that should be present in the sample, which are C 1s, Si 2p, Ag 3d, N 1s, and O 1s as shown in Figure 4. A survey scan in the region of 0 to 1200 eV indicates neither contribution from impurities nor contamination on the surface of the nanoparticles. The presence of carbon and nitrogen element on the surface of nanoparticles is contributing from PVP, which has been used as a reducing and stabilizing agent in the synthesis procedure. This is consistent with the fitting of three atomic species for C 1s (aromatic carbon, aliphatic and C-N/C=O species), and a single nitrogen species from PVP [31]. The Si 2p peak centered at 102.3 eV binding energy is attributed to Si-O_2 of the core spheres which correspond closely to the previous literature [32]. The Ag 3d peaks are found at 366.81 eV and 372.81 eV can be fitted to the typical spin-orbital-splitting pattern of Ag 3d5/2 and Ag 3d3/2, respectively. This confirms the reduction of Ag(+1) ion to Ag(0) metal, as appearance of the Ag 3d peak in XPS is the nature characteristic for zero-oxidation state. This finding was supported by Sakthisabarimoorthi and co-workers on the successful decoration of Ag element [33].



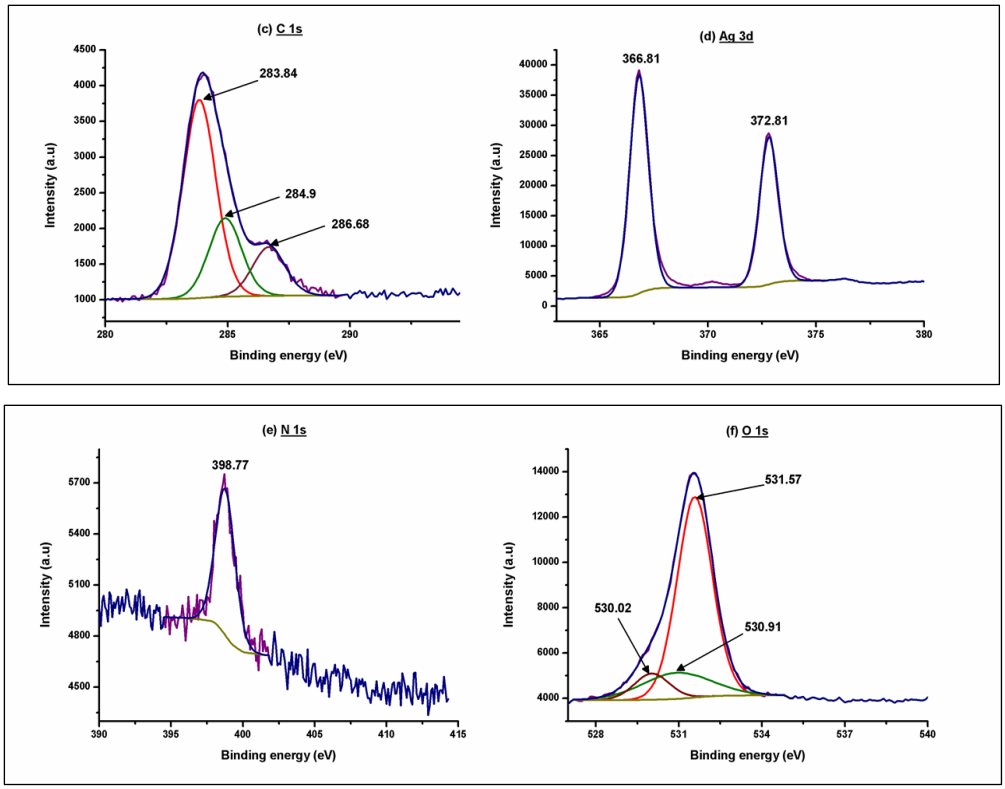


Figure 4. Representative of XPS spectra of (a) wide scan survey, (b) Si 2p, (c) C 1s, (d) Ag 3d, (e) N 1s, and (f) O 1s for SiO_2-Ag core-shell nanoparticles

Conclusion

SiO_2-Ag core-shell nanoparticles were successfully synthesized with the addition of PVP as a reducing and stabilizing agent without any surface modification needed. The increase of concentration ammoniacal silver nitrate solution leads to the increase in thickness of Ag-Nps loaded on the SiO_2 surface. The synthesized SiO_2-Ag core-shell nanoparticles exhibit the surface plasmon resonance wavelength of 380 to 450 nm range, which contributed to the existence of Ag-Nps. SEM images visualized the silica particles with 200-220 nm in size with a spherical shape while HR-TEM images show the Ag-Nps deposited to the surface of SiO_2 spheres with the average of size 10-50 nm. X-ray powder diffraction analysis revealed the crystalline nature of Ag-Nps. The elemental composition of SiO_2-Ag core-shell such as C 1s, Si 2p, Ag 3d, N 1s, and O 1s were established by X-ray photoelectron spectroscopy analysis. The SiO_2-Ag core-shell nanoparticles have been successfully synthesized and it is suggested that it can be used as a potential catalyst in the dye degradation process in future studies.

Acknowledgement

The authors gratefully acknowledge to Central Laboratory, Universiti Malaysia Terengganu for providing research facilities.

References

1. Nischala, K., Rao, T. N. and Hebalkar, N. (2011). Silica–silver core–shell particles for antibacterial textile application. *Colloids and Surfaces B: Biointerfaces*, 82(1): 203 – 208.
2. Wang, X., He, B., Hu, Z., Zeng, Z. and Han, S. (2014). Current advances in precious metal core–shell catalyst design. *Science and Technology of Advanced Materials*, 15(4): 043502.

3. Xu, C., Su, R., Wang, Z., Wang, Y., Zhang, D., Wang, J., J., Bian, J., Wu, C., Lou, X. and Yang, Y. (2019). Tuning the microstructure of $BaTiO_3$@SiO_2 core-shell nanoparticles for high energy storage composite ceramics. *Journal of Alloys and Compounds*, 784: 173 – 181.
4. Kamaruddin, S. and Stephan, D. (2011). The preparation of silica–titania core–shell particles and their impact as an alternative material to pure nano-titania photocatalysts. *Catalysis Today*, 161(1): 53 – 58.
5. Pati, S. S., Singh, L. H., Oliveira, A. C. and Garg, V. K. (2015). Chitosan functionalized Fe_3O_4@ Au core-shell nanomaterials for targeted drug delivery. *World Academy of Science, Engineering and Technology, International Journal of Chemical, Molecular, Nuclear, Materials and Metallurgical Engineering*, 9(6): 670 – 673.
6. Zhu, Z., Kao, C. T. and Wu, R. J. (2014). A highly sensitive ethanol sensor based on Ag@TiO_2 nanoparticles at room temperature. *Applied Surface Science*, 320: 348 – 355.
7. Azizi, M. A. H., Dzakaria, N., Isahak, W. N. R. W. and Yarmo, M. A. (2017). Effect of nickel on bimetallic nanoalloy catalyst for hydrogen generation. *Malaysian Journal of Analytical Sciences*, 21(4): 901 – 906.
8. Abdullah, H., Ismail, N. A., Yaakob, Z., Khan, M. R. and Rahim, S. A. (2017). CeO_2-TiO_2 for photoreduction of Co_2 to methanol under visible light: effect of ceria loading. *Malaysian Journal of Analytical Sciences*, 21(1): 166 – 172.
9. Mohd, N. K., Wee, N. N. A. N. and Azmi, A. A. (2017). Green synthesis of silica nanoparticles using sugarcane bagasse. In *AIP Conference Proceedings*, 1885(1): 020123.
10. Ghorbani, F., Sanati, A. M., and Maleki, M. (2015). Production of silica nanoparticles from rice husk as agricultural waste by environmental friendly technique. *Environmental Studies of Persian Gulf*, 2(1), 56 – 65.
11. San, N. O., Kurşungöz, C., Tümtaş, Y., Yaşa, Ö., Ortac, B. and Tekinay, T. (2014). Novel one-step synthesis of silica nanoparticles from sugarbeet bagasse by laser ablation and their effects on the growth of freshwater algae culture. *Particuology*, 17: 29 – 35.
12. Qadri, S. B., Gorzkowski, E. P., Imam, M. A., Fliflet, A., Goswami, R., Kim, H., Caldwell, J. D., Klemm, F. and Rath, B. B (2013). Production of nanoscale particles and nanorods of SiC from sorghum leaves. *Industrial Crops and Products*, 51: 158 – 162.
13. Landage, S. M., Kulkarni, S. G. and Ubarhande, D. P. (2012). Synthesis and application of silica nanoparticles on cotton to impart superhydrophobicity. *International Journal of Engineering Research and Technology*, 1(5): 1 – 7.
14. Kalele, S. A., Ashtaputre, S. S., Hebalkar, N. Y., Gosavi, S. W., Deobagkar, D. N., Deobagkar, D. D. and Kulkarni, S. K. (2005). Optical detection of antibody using silica–silver core–shell particles. *Chemical Physics Letters*, 404(1-3): 136 – 141.
15. Mansa, R. F., Sipaut, C. S., Rahman, I. A., Yusof, N. S. M. and Jafarzadeh, M. (2016). Preparation of glycine–modified silica nanoparticles for the adsorption of malachite green dye. *Journal of Porous Materials*, 23(1): 35 – 46.
16. Chang, H., Park, J. H. and Jang, H. D. (2008). Flame synthesis of silica nanoparticles by adopting two-fluid nozzle spray. *Colloids and Surfaces A: Physicochemical and Engineering Aspects*, 313: 140 –144.
17. Koźlecki, T., Polowczyk, I., Bastrzyk, A. and Sawiński, W. (2016). Improved synthesis of nanosized silica in water-in-oil microemulsions. *Journal of Nanoparticles*, 2016: 1 – 9.
18. Monshizadeh, M., Rajabi, M., Ahmadi, M. H. and Mohammadi, V. (2015). Synthesis and characterization of nano SiO_2 from rice husk ash by precipitation method. *3rd National Conference on Modern Researches in Chemistry and Chemical Engineering*: pp. 1 – 4.
19. Gholami, T., Salavati-Niasari, M., Bazarganipour, M. and Noori, E. (2013). Synthesis and characterization of spherical silica nanoparticles by modified Stöber process assisted by organic ligand. *Superlattices and Microstructures*, 61: 33 – 41.
20. Kitsou, I., Panagopoulos, P., Maggos, T., Arkas, M. and Tsetsekou, A. (2018). Development of SiO_2@ TiO_2 core-shell nanospheres for catalytic applications. *Applied Surface Science*, 441: 223 – 231.
21. Kandpal, D., Kalele, S. and Kulkarni, S. K. (2007). Synthesis and characterization of silica-gold core-shell (SiO_2@ Au) nanoparticles. *Pramana*, 69(2): 277 – 283.
22. Gac, W., Zawadzki, W., Słowik, G., Sienkiewicz, A. and Kierys, A. (2018). Nickel catalysts supported on silica microspheres for CO_2 methanation. *Microporous and Mesoporous Materials*, 272: 79 – 91.
23. Zienkiewicz-Strzałka, M., Pasieczna-Patkowska, S., Kozak, M. and Pikus, S. (2013). Silver nanoparticles incorporated onto ordered mesoporous silica from Tollen's reagent. *Applied Surface Science*, 266: 337 –343.

24. Jankiewicz, B. J., Jamiola, D., Choma, J. and Jaroniec, M. (2012). Silica–metal core–shell nanostructures. *Advances in Colloid and Interface Science*, 170(1-2): 28 – 47.
25. Atkins, P., Overton, T., Rourke, J., Weller, M. and Armstrong, F. (2010). Inorganic Chemistry. Oxford. New York : pp. 659.
26. Tzounis, L., Contreras-Caceres, R., Schellkopf, L., Jehnichen, D., Fischer, D., Cai, C., Uhlmann, P. and Stamm, M. (2014). Controlled growth of Ag nanoparticles decorated onto the surface of SiO_2 spheres: a nanohybrid system with combined SERS and catalytic properties. *RSC Advances*, 4(34): 17846 – 17855.
27. Ghosh, C. R. and Paria, S. (2011). Core/shell nanoparticles: Classes, properties, synthesis mechanisms, characterization, and applications. *Chemical Reviews*, 112(4): 2373 – 2433.
28. Postolache, P., Petrescu, V., Dumitrascu, D. D., Rimbu, C., Vrînceanu, N. and Cipaian, C. R. (2016). Research regarding a correlation core–shell morphology–thermal stability of silica–silver nanoparticles. *Chemical Engineering Communications*, 203(5): 649 – 659.
29. Din, L. B., Mie, R., Samsudin, M. W., Ahmad, A. and Ibrahim, N. (2015). Biomimetic synthesis of silver nanoparticles using the lichen Ramalina dumeticola and the antibacterial activity. *Malaysian Journal of Analytical Sciences*, 19(2): 369 – 376.
30. Chen, K. H., Pu, Y. C., Chang, K. D., Liang, Y. F., Liu, C. M., Yeh, J. W., Shih, H. C. and Hsu, Y. J. (2012). Ag-nanoparticle-decorated SiO_2 nanospheres exhibiting remarkable plasmon-mediated photocatalytic properties. *The Journal of Physical Chemistry* C, 116(35): 19039 – 19045.
31. Deng, Z., Chen, M. and Wu, L. (2007). Novel method to fabricate SiO_2/Ag composite spheres and their catalytic, surface-enhanced Raman scattering properties. *The Journal of Physical Chemistry C*, 111(31): 11692 – 11698.
32. Das, S. K., Khan, M. M. R., Parandhaman, T., Laffir, F., Guha, A. K., Sekaran, G. and Mandal, A. B. (2013). Nano-silica fabricated with silver nanoparticles: antifouling adsorbent for efficient dye removal, effective water disinfection and biofouling control. *Nanoscale*, 5(12): 5549 – 5560.
33. Sakthisabarimoorthi, A., Dhas, S. M. B. and Jose, M. (2017). Fabrication and nonlinear optical investigations of SiO_2@Ag core-shell nanoparticles. *Materials Science in Semiconductor Processing*, 71: 69 – 75.

Malaysian Journal of Analytical Sciences, Vol 23 No 2 (2019): 300 - 311
DOI: https://doi.org/10.17576/mjas-2019-2302-14

MALAYSIAN JOURNAL OF ANALYTICAL SCIENCES
Published by The Malaysian Analytical Sciences Society
ISSN 1394 - 2506

SEASONAL VARIATION AND ECOLOGICAL RISK ASSESSMENT OF HEAVY METAL CONTAMINATION IN SURFACE WATERS OF THE GANGES RIVER (NORTHWESTERN BANGLADESH)

(Variasi Bermusim dan Penilaian Risiko Ekologi Terhadap Pencemaran Logam Berat di Permukaan Air Sungai Ganges (Barat Utara Bangladesh))

Md. Ayenuddin Haque[1], Md. Abu Sayed Jewel[1], Jakia Hasan[2], Md. Mazharul Islam[3], Sharif Ahmed[3], Lubna Alam[4]*

[1]*Department of Fisheries, Faculty of Agriculture,*
University of Rajshahi, Rajshahi-6205, Bangladesh
[2]*Bangladesh Fisheries Research Institute,*
Marine Fisheries & Technology Station, Cox's Bazar-4700, Bangladesh
[3]*Marine Fisheries Academy,*
Fish Harbour, Isanagore, Chittagong-4000, Bangladesh
[4]*Institute for Environment and Development (LESTARI),*
Universiti Kebangsaan Malaysia, 43600 UKM Bangi, Selangor, Malaysia

**Corresponding author: lubna762120@gmail.com*

Received: 20 April 2018; Accepted: 11 February 2019

Abstract

The present work is evaluating the seasonal variation in metal pollution and the ecological risk indices of surface water of the Ganges River (Northwestern Bangladesh). Concentrations of Cr, Pb, Ni, Cd, As, Cu and Zn in surface water samples were determined by Flame Atomic Absorption Spectrophotometry. The level of heavy metals did not exceed the permissible limits of drinking water according to Department of Environment (DOE), Bangladesh and World Health Organization (WHO). Only Cr and Cd concentrations exceeded the permissible limits for aquatic life standards of the United States Environmental Protection Agency (USEPA) and Canadian Council of Ministers of the Environment (CCME). The heavy metal pollution index (HPI) showed that the seasonal contamination level followed the order: summer (136.13 (DoE), 220.72 (WHO) and 163.95 (USEPA, CCME)) > winter (57.38 (DoE), 91.36 (WHO) and 72.81 (USEPA, CCME)) > monsoon (16.49 (DoE), 25.36 (WHO) and 19.44 (USEPA, CCME)). Additionally, the HPI value crossed the critical index value (100) for drinking and aquatic life standard during summer season. The metal index (MI) value showed that the water was moderately (DoE), strongly (WHO) and seriously affected (USEPA, CCME) by heavy metals during summer season (3.15, 4.79 and 9.99 according to DoE, WHO and USEPA, CCME, respectively). While the ecology of the river is presently at low risk, this study suggests taking necessary measures to prevent the present pollution rate of contaminants from rising in the future.

Keywords: heavy metals, surface water, ecological risk indices, metal index

Abstrak

Kajian ini menilai variasi bermusim pencemaran logam dan indeks risiko ekologi bagi permukaan air di Sungai Ganges (Barat utara Bangladesh). Kepekatan Cr, Pb, Ni, Cd, As, Cu dan Zn dalam sampel permukaan air ditentukan oleh spektofotometri nyalaan serapan atom. Berdasarkan Jabatan Alam Sekitar (DoE) Bangladesh dan Pertubuhan Kesihatan Sedunia (WHO), tahap logam berat tidak melebihi paras yang dibenarkan bagi air minum. Hanya kepekatan Cr dan Cd melebihi had yang dibenarkan untuk piawaian akuatik badan Agensi Perlindungan Alam Sekitar Amerika Syarikat (USEPA) dan Majlis Menteri-Menteri Alam Sekitar Kanada (CCME). Indeks pencemaran logam berat (HPI) menunjukkan bahawa tahap pencemaran bermusim mengikuti susunan: musim panas (136.13 (DoE), 220.72 (WHO) dan 163.95 (USEPA, CCME))> musim sejuk (57.38 (DoE), 91.36 (WHO)

(USEPA, CCME)) > monsun (16.49 (DoE), 25.36 (WHO) dan 19.44 (USEPA, CCME)). Di samping itu, nilai HPI mencapai nilai indeks kritikal (100) untuk piawai air minuman dan hidupan akuatik semasa musim panas. Nilai indeks logam (MI) menunjukkan bahawa airnya sederhana (DoE), kuat (WHO) dan serius terjejas (USEPA, CCME) oleh logam berat pada musim panas (3.15, 4.79 dan 9.99 berdasarkan DOE, WHO dan USEPA). Walaupun ekologi sungai pada masa ini berisiko rendah, kajian ini bercadang untuk mengambil langkah-langkah yang perlu untuk mencegah kadar pencemaran semasa daripada meningkat pada masa akan datang.

Kata kunci: logam-logam berat, permukaan air, indeks risiko ekologi, indeks logam

Introduction

Environmental pollution is a worldwide concern and heavy metals are among the most impactful pollutants. Heavy metal contamination in aquatic ecosystems is a major concern due to the toxicity, persistence, non-biodegradable character and abundance of these metals in the environment, as well as their accumulation in aquatic habitats [1, 2]. Natural processes and activities related to urbanization and agriculture are basically the main contributors to heavy metal pollution in aquatic habitats [3]. While heavy metals in water exist only in trace concentrations, they are toxic to the human body. Therefore, water quality is a pressing issue in many countries. Currently, the vulnerability of water to contaminants from natural and anthropogenic sources has become a common global problem [4].

The Ganges River, which flows alongside Rajshahi city, is popularly known as Padma River in Bangladesh. It is very important for its multidimensional use as a fishery and for domestic (bathing and washing clothes) and recreational activities. However, in recent years, the continuous increase in demographic, the urbanized expansion and the increased weight for inhabitants in the city makes the aquatic ecosystem of this river the ultimate recipient of pollutants from various sources. These sources include industrial and municipal wastewater, urban surface water runoff, runoff from agricultural fields and other natural resources. Furthermore, with the construction of Farakka Barrage on the Ganges River in West Bengal of India, the flow of the river is decreasing daily. Therefore, water flow is comparatively slower today than during previous dry seasons. Slow water flow sometimes extends the standing time of pollutants; therefore, the pollutants easily subside into the water and sediment. Apart from these pollutants, during the dry season, agricultural activities are performed in waterless areas and fertilizer, pesticides and other wastes from these agricultural processes are typically discharged into the river.

Considering their biological and environmental threat, it is important to assess several heavy metals in the surface water of this river. Fully understanding the current heavy metal profile of this part of Ganges River is crucial for ecological safety. However, there is no such research that focuses on heavy metals in the surface water of the Ganges River in the Rajshahi region. Therefore, the current study was conducted to evaluate the concentration of heavy metals during different seasons in the surface water and the comprehensive assessment of ecological risk due to their contamination.

Materials and Methods

Study area

The study locations selected for the present study were T-dam (Site-1), Padma garden (Site-2), I-dam (Site-3) and Talaimari point (Site-4). All of these sites were situated between 24º21´42.41´´ N and 24º21´29.30´´ N and 88º34´31.18´´ E to 88º37´30.55´´ E (Figure 1) along the coast of Rajshahi city. Rajshahi falls within the western dry zone, which is one of the seven climatic zones that divides Bangladesh. As Rajshahi city does not possess any sewage system, the surface run-off essentially acts as a sewer, taking the overflow from septic tanks, domestic waste, wastes from commercial units, markets and small industries and ultimately discharging them all into the Ganges River.



Figure 1. Location of the study area. Modified from Google Earth-2017

Sample collection

A total of 12 water samples were collected from four study sites during the three study seasons (summer, monsoon and winter). Samples were collected from 10 cm below the water surface and stored in 100 mL polyethylene bottles at each site. Each bottle was washed more than three times in order to guarantee the monitoring accuracy. The sampling bottles were previously soaked and rinsed in 10% HNO_3 overnight. The collected water samples were acidified with concentrated HNO_3 at pH < 2 to avoid precipitation of heavy metals. Samples were kept on ice and brought to the laboratory, where they were stored in a refrigerator with a temperature below 4 ºC to prevent evaporation until analysis [5].

Digestion and analysis of heavy metals

Wet digestion of the samples was conducted in freshly prepared aqua regia (1:3 HNO_3: HCl) on a block digester to obtain 100 mL of aliquot. The heavy metal (Cr, Pb, Ni, Cd, Mn, As, Cu and Zn) concentrations in the water samples were measured with the Flame Atomic Absorption Spectrometer (Shimadzu, AA-6800) in the central lab of University of Rajshahi, Bangladesh.

Pollution evaluation indices: Heavy metal pollution index

The heavy metal pollution index (HPI) is a rating system that provides the aggregate influence of individual heavy metals on the total water quality. The rating system is an arbitrary value between 0 and 1. Its selection depends on the importance of individual quality considerations or it can be defined as inversely proportional to the standard permissible value (*Si*) for each parameter [6, 7]. The HPI is determined by using the formula equation 1 below [8]:

$$\text{HPI} = \frac{W_i \times Q_i}{1} \quad (1)$$

where *W*i and *Qi* are the unit weightage and sub-index of the i^{th} parameter, respectively; *Wi* is calculated by the weightage of i^{th} parameter and is given as equation 2 below:

$$Wi = \frac{K}{Si} \quad (2)$$

where *Wi* is the unit weightage and *Si* is the recommended standard for the i^{th} parameter, while *k* is the constant of proportionality. Individual quality rating, *Qi*, is given by the expression in equation 3 below:

$$Qi = \frac{100 \times Vi}{Si} \quad (3)$$

where *Qi* is the sub index of ith parameter, *Vi* is the monitored value of the ith parameter and *Si* is the standard or permissible limit for the ith parameter. The critical pollution index value is 100 [9]. For the present study, the *Si* value was obtained from the World Health Organization (WHO) standard [10, 11].

Metal index

According to Tamasi and Cini [12], the metal index (MI) was calculated using the following formula (equation 4):

$$\text{MI} = \sum_{i=1}^{n} \frac{C_i}{(MAC)_i} \quad (4)$$

where *Ci* is the concentration of each element and *MAC* is the maximum allowable concentration. An MI value >1 is a threshold of warning [13]. Classification of MI according to literature studies [14, 15] shown in Table 1.

Table 1. Evaluation standards for metal index (MI) and potential ecological risk indices (PERI)

Metal Index	**Potential Ecological Risk Indices**			
	C_f^i	*Cd*	E_r^i	**PERI**
< 0.3, Very pure				
0.3 – 1.0, Pure				
1.0 – 2.0, Slightly affected	< 1, non contaminated	<8, low	<40, low	<150, low
2.0 – 4.0, Moderately affected	≥ 1 < 2, light	≥ 8 < 16, moderate	≥40<80, moderate	≥150<300, moderate
4.0 – 6.0, Strongly affected	≥ 2, <3, moderate	≥ 16 < 32, relatively high	≥ 80 < 100, strong	≥300< 600, strong
> 6.0, Seriously affected	≥ 3, heavy	≥ 32, very high	≥ 320, extremely high	≥600, very strong

Potential ecological risk factor and risk index

The potential ecological risk index method was proposed by Hakanson [16] from a sedimentology perspective to assess the characteristics and environmental behaviour of heavy metal contaminants. The specific formulas are as follows:

The single contamination coefficient (equation 5):

$$C_f^i = \frac{C_{sl}^i}{C_n^i} \quad (5)$$

where C_f^i is the contamination coefficient of a particular heavy metal, C_{sl}^i is the measured data of heavy metals, and C_n^i is the reference value. In the present study, the reference value of heavy metals was taken from freshwater quality criteria for protection of aquatic life of United States Environmental Protection Agency (USEPA) [17] and the Canadian Council of Ministers of the Environment (CCME) [18]. The comprehensive contamination measure (*Cd*) as shown in equation 6:

$$C_d = \sum C_f^i \quad (6)$$

The potential ecological risk index (PERI) was calculated using equation 7:

$$\text{PERI} = \sum E_r^i \quad (7)$$

where PERI is risk index; E_r^i is the potential ecological risk index for the pollution of a single heavy metal and can be calculated using equation 8:

$$E_r^i = C_f^i \times T_f^i \quad (8)$$

where T_f^i and C_f^i are the response coefficient and contamination coefficient of single heavy metal, respectively. The value of T_f^i of each metal was taken from literature studies [16, 19]. The corresponding degrees of contamination and the evaluation standards for the levels of potential ecological risk are based on past results from relevant studies [20, 21] as tabulate in Table 1.

Statistical analysis

The calculation of risk indices was conducted in Microsoft Excel (Microsoft Office 2010). The correlation analysis was performed by SPSS software (version 20).

Results and Discussion

Distribution of metals in different seasons and sites

The results of heavy metal concentrations in surface water is shown in Table 2. The comparison of present findings with other national and international rivers is shown Table 3, where the present findings is compared with those from past research [22-28]. The average concentration of studied metals followed the decreasing order: Cr > Zn > Cu > Pb > Cd > Ni > As. The same distribution pattern of studied heavy metals was also shown in both summer and winter seasons. Therefore, Cr was the most abundant metal among metals. Its high value during the dry season notably may be due to high evaporation of surface water followed by elevated temperatures [29]. The higher concentration of Cr during the dry months was also reported in the Buriganga River, Bangladesh [30], in Cooum River, India [31] and in the Taizi River, China [32]. However, irregular patterns of these metals were observed during monsoon season (Table 2).

Table 2. Heavy metal concentrations (mg/L) at different seasons and sites of the Ganges River during the study period

Season	Sites	Cr	Pb	Ni	Cd	As	Cu	Zn
Summer	Site-1	0.018	0.009	0.005	0.006	0.002	0.012	0.011
	Site-2	0.102	0.022	0.006	0.014	0.003	0.045	0.110
	Site-3	0.092	0.023	0.005	0.009	0.006	0.011	0.027
	Site-4	0.010	0.005	0.001	0.004	0.002	0.006	0.007
Summer (Average ± SD)		0.056± 0.048	0.015± 0.009	0.004± 0.002	0.008± 0.004	0.003± 0.002	0.019± 0.018	0.039± 0.048
Monsoon	Site-1	0.002	0.002	ND	0.001	ND	ND	ND
	Site-2	0.006	0.001	ND	0.001	ND	0.003	ND
	Site-3	0.005	0.003	ND	ND	ND	0.001	ND
	Site-4	0.003	0.001	ND	ND	ND	ND	0.002
Monsoon (Average ± SD)		0.004± 0.002	0.002± 0.001	ND	0.001± 0.001	ND	0.002± 0.001	0.002± 0.000

Table 2(cont'd). Heavy metal concentrations (mg/L) at different seasons and sites of the Ganges River during the study period

Season	Sites	Cr	Pb	Ni	Cd	As	Cu	Zn
Winter	Site-1	0.020	0.005	0.001	0.001	0.001	0.003	0.040
	Site-2	0.100	0.025	0.003	0.004	0.004	0.022	0.078
	Site-3	0.087	0.014	0.006	0.006	0.003	0.016	0.019
	Site-4	0.008	0.002	0.001	0.002	0.001	0.002	0.010
Winter (Average ± SD)		0.054± 0.046	0.012± 0.010	0.003± 0.002	0.003± 0.002	0.002± 0.002	0.011± 0.010	0.037± 0.030
Total Average ± SD		0.038± 0.043	0.009± 0.009	0.004± 0.002	0.005± 0.004	0.003± 0.002	0.012± 0.013	0.030± 0.035
[a]DWSB		0.050	0.050	0.100	0.005	0.050	1.000	5.000
[b]WHO		0.050	0.070	0.010	0.003	0.010	2.000	0.500
[c]USEPA, [d]CCME		0.016	0.065	0.470	0.002	0.340	0.013	0.050

Note: SD, standard deviation, ND = Not detected.
[a]Drinking water standard for Bangladesh proposed through ECR (Department of Environment, Government of the People's Republic of Bangladesh, [40, 41].
[b]Drinking water standard of WHO [10, 11]
Aquatic life standard of water proposed by [c]USEPA [17] and [d]CCME [18].

The highest concentrations of Cr, Cd, Cu and Zn were recorded at Site-2 during summer season; at the same site, Pb showed its maxima during winter season. On the other hand, As showed its highest value at Site-3 during summer season. One possible reason for the higher value during the dry season may be due to the low water level and flow in the river; these entities were not substantial enough to dilute the disposal of sewage sludge and industrial effluents from septic tanks and metal industries. Therefore, during these low flow conditions, the accumulation of these metal concentration increases in river water. Such an effect was also previously noted by Yao et al. [33] and Dey et al. [34]. As such, the lower concentrations of heavy metals during the monsoon may be due to the dilution effect of pollutant [35, 36]. These temporal variations in the metal concentrations were generally consistent with seasonal variations in metal concentrations that have been reported in other rivers [37, 38, 39]. The possible reasons for higher concentration of metals at Site-2 followed by Site-3 might be due to presence of large drains at those sites that regularly empty their contents without treatment into the river. A similar observation was also made by [39], in the Nil river, where untreated discharged sewage and poultry waste were responsible for the elevated metal levels in the water.

During the study period, the average concentrations of all the metals were below the drinking water guidelines of both Department of Environment (DoE) [40, 41] and WHO [10, 11]. However, only the average concentration of Cr (0.038 mg/L) and Cd (0.005) exceeded the aquatic life guidelines of USEPA [17] and CCME [18]. The average concentration of the studied metals in the Padma River was also higher than the previous findings in the same river [22] as tabulate in Table 3.

The Pearson's correlation (PC) matrix for the analysed heavy metals is in Table 4. The metals showed a significant positive correlation with each other except for Cu-As, Zn-Ni and Zn-As. A significant correlation among most of the metals suggested similar sources of input (human or natural), similar levels of contamination and a mutual dependence in the river system for these metals [42, 43]. On the other hand, the negative associations in the matrix indicate that the increase in one of the parameters results in the decrease of the other and vice versa. Those variables with negative associations suggest that those metals do not have identical sources of pollution, as their sources of pollution differ [44].

Table 3. Comparison of heavy metal concentrations (mg/L) in water of Ganges River with national and international rivers

Rivers	Cr	Pb	Ni	Cd	As	Cu	Zn	References
Ganges River, Bangladesh	0.0378	0.0093	0.0035	0.0048	0.0028	0.0121	0.0304	Present study
Padma River, Bangladesh	0.0030	0.0015	0.0081	0.0020	0.0015	0.0200	0.0073	[22]
Meghna River, Bangladesh	0.0346	-	-	0.0030	-	-	0.0364	[23]
Buriganga River, Bangladesh	0.1140	0.1119	0.1500	0.0590	-	-	0.3320	[24]
Dhaleshwari River, Bangladesh	0.4413	0.0500	0.0072	0.0065	-	0.1547	-	[25]
Ganga river, India	-	0.1200	0.1400	0.0500	-	0.0100	0.0600	[26]
Mahrut River, Iraq	0.4961	0.2180	0.0860	0.0080	-	-	0.0028	[27]
Yangtz River, China	0.0210	0.0550	-	0.0047	-	0.0110	0.0094	[28]

Table 4. Correlation among the heavy metals in water of Ganges River, Bangladesh

	Cr	Pb	Ni	Cd	As	Cu	Zn
Cr	1						
Pb	0.964**	1					
Ni	0.817**	0.794**	1				
Cd	0.781**	0.786**	0.879**	1			
As	0.861**	0.910**	0.779**	0.737**	1		
Cu	0.812**	0.793**	0.770**	0.884**	0.574	1	
Zn	0.777**	0.781**	0.568	0.707*	0.534	0.901**	1

** Correlation is significant at the 0.01 level (2-tailed)
* Correlation (R^2) is significant at the 0.05 level (2-tailed)

Pollution evaluation indices: Heavy metal pollution index

The heavy metal pollution index (HPI) was in order the of: summer > winter > monsoon during the study period (Figure 2). The HPI value of summer season was far above the critical index value (100) for drinking water and aquatic life standards. This finding may be attributed to the disposal of domestic and municipal sewage and their lower dilution rate. During dry seasons, the river basin was available for agricultural activities, which also contributes to the increasing level of HPI during this season. Similarly, a previous study found agricultural activities as a major source of heavy meal in a tropical mountainous river in India [45]. Therefore, the HPI index suggested that better agricultural management practices need to be implemented during dry season for maintaining ecological integrity and protecting the lotic system from further degradation. However, the low computed value of HPI during monsoon season might be a result of the dilution of pollutants as was previously reported [6].

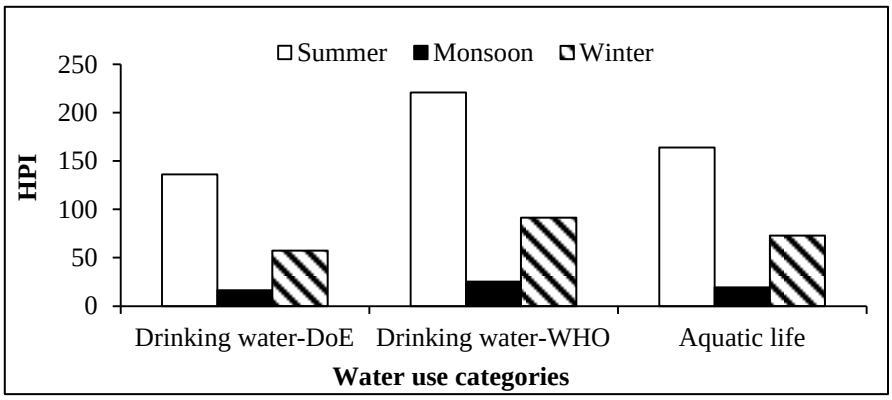


Figure 2. Heavy metal pollution index (HPI) in the Ganges River water according to the guideline levels of drinking and aquatic life water

Metal index

The metal index (MI), which was used for a better understanding of pollution status of Ganges River water during different seasons, is shown in Figure 3. The MI showed great variability among the seasons. According to the index value (9.99), during the summer season, the river water was seriously affected with heavy metals that can endanger the existence of the aquatic life. However, during the monsoon season, the dilution effect of flood water resulted in the reduction of the concentrations of the metals and thus the value of the MI. The effect of dilution on metal concentration have also been evident by Giri and Singh [46].

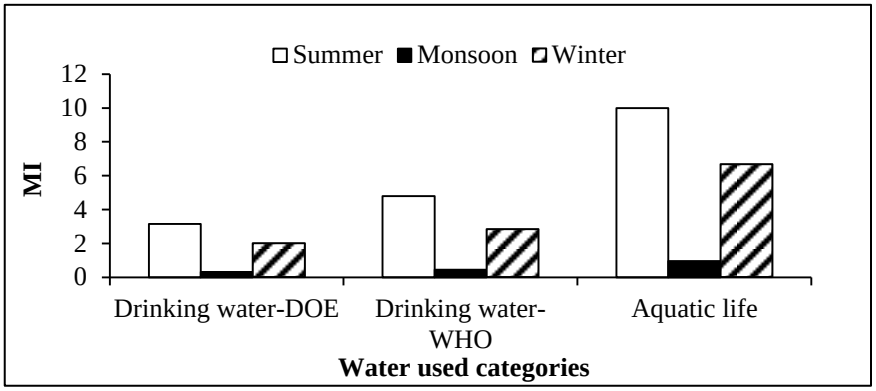


Figure 3. Metal index (MI) of surface water in the Ganges River according to the guideline levels of drinking and aquatic life water

Potential ecological risk index

The contamination factors of a single regulator (C_f^i) and the degree of contamination ($\sum C_f^i$) are shown in Table 5. The contamination factors of the seven heavy metals in this study decreased in the following order: Cr > Cd > Cu > Zn > Pb > Ni and As. Therefore, according to the contamination factor, the surface water of Ganges River was moderately contaminated with Cr and lightly contaminated with Cd and Cu. The surface water was not-contaminated with Pb, Ni, As and Zn. The degree of contamination indicates the moderate contamination of water during summer and low contamination during other two seasons.

Table 5. Contamination factor (C_f^i) and degree of contamination (*Cd*) of heavy metals of surface water in Ganges River, Bangladesh

Seasons	Contamination factor (C_f^i)							$Cd = \sum C_f^i$	Level
	Cr	Pb	Ni	Cd	As	Cu	Zn		
Summer	3.50	0.23	0.01	4.00	0.01	1.46	0.78	9.99	Moderate
Monsoon	0.25	0.03	0.00	0.50	0.00	0.15	0.04	0.97	Low
Winter	3.38	0.18	0.01	1.50	0.01	0.85	0.74	6.66	Low
Average	2.38	0.15	0.01	2.00	0.01	0.82	0.52	5.87	Low
Contamination level	Moderate	Non-Contaminaed	Non-contaminated	Light	Non-contaminated	Light	Non-contaminated		

The ecological risk factor (E_r^i) and potential ecological risk index (PERI) are shown in Table 6. The severity of the potential ecological risk for individual metals (E_r^i) decreased in the order of Cd > Cr > Cu > Pb > Zn > As > Ni. Cd is the most important metal and its risk factor indicates that the Ganges River was moderately contamination with this metal. Other heavy metals (Cr, Pb, Ni, As, Cu and Zn) showed low potential for ecological risk. A similar result also reported Cd as the most important of the metal pollutants, in terms of the risks it posed [33]. The PERI that accounted for the contamination caused by studied seven metals indicates the low potential ecological risk of the surface water of this river during the summer, monsoon and winter seasons. However, the level of risk that was evident during the study period should be reduced. Open municipal drain, household garbage and industrial pollutants should be checked with high priority so that they cannot enter into the river water. Furthermore, the local government should establish a treatment plant for these city wastes to protect the environment of the river.

Table 6. Ecological risk factor and Potential Ecological Risk Index (PERI) of heavy metals of surface water in Ganges River, Bangladesh

Seasons	Ecological Risk Factor (E_r^i)							$PERI = \sum E_r^i$	Contamination Level
	Cr	Pb	Ni	Cd	As	Cu	Zn		
Summer	7.00	1.15	0.04	120.00	0.09	7.31	0.78	136.37	Low
Monsoon	0.50	0.15	ND	15.00	ND	0.77	0.04	16.46	Low
Winter	6.75	0.92	0.03	45.00	0.06	4.23	0.74	57.73	Low
Average	4.75	0.74	0.04	60.00	0.08	4.10	0.52	70.19	Low
Contamination Level	Low	Low	Low	Moderate	Low	Low	Low		

Conclusion

The risk assessment on heavy metals using risk indices (HPI and MI) indicates that currently the analysed water sources from the Ganges River were unfit for drinking water and aquatic life standards. The risk was potentially high during the summer and winter seasons. Although the overall potential risk index showed a low contamination level, the increasing level of environmental pollution might make the ecosystem of the Ganges River (Northwestern Bangladesh) more alarming. Therefore, the present study recommends strict management actions to be taken in order to protect the ecological sustainability of this important river.

Acknowledgement

The authors are grateful to the Ministry of Higher Education Malaysia for providing funding (Grant no. TRGS/1/2015/UKM/02/5/2) and the Ministry of Science and Technology and the Government of the People's

Republic of Bangladesh for providing the National Science and Technology Fellowship (Grant no. 39.00.0000.012.20.004.16-439) for this research work.

References

1. Bastami, K. D., Bagheri, H., Kheirabadi, V., Zaferani, G. G., Teymori, M. B., Hamzehpoor, A., Soltani, F. and Ganji, S. (2014). Distribution and ecological risk assessment of heavy metals in surface sediments along southeast coast of the Caspian Sea. *Marine Pollution Bulletin*, 81(1): 262 – 267.
2. Fu, J., Zhao, C., Luo, Y., Liu, C., Kyzas, G. Z., Luo, Y., Zhao, D. and Zhu, H. (2014). Heavy metals in surface sediments of the Jialu River, China: Their relations to environmental factors. *Journal of Hazardous Materials*, 270: 102 – 109.
3. Krishna, A. K., Satyanarayanan, M. and Govil, P. K. (2009). Assessment of heavy metal pollution in water using multivariate statistical techniques in an industrial area: A case study from Patancheru, Medak District, Andhra Pradesh, India. *Journal of Hazardous Materials*, 167(1): 366 – 373.
4. Mohamed, A. A. J., Ibrahim, A. R., Lee, H. L., Hanna, M., Mohamed, M., Fadilah, T. and Nur, A. R. (2016). Assessment of groundwater quality parameters in northern region of Zanzibar Island. *Journal of Chemical Engineering and Bioanalytical Chemistry*, 1: 1 – 8.
5. Sehgal, M., Garg, A., Suresh, R. and Dagar, P. (2012). Heavy metal contamination in the Delhi segment of Yamuna basin. *Environmental Monitoring and Assessment*, 184: 1181 – 1196.
6. Reza, R. and Singh, G. (2010). Heavy metal contamination and its indexing approach for river water. *International Journal of Environmental Science and Technology*, 7: 785 – 792.
7. Prasad, B. and Sangita, K. (2008). Heavy metal pollution index of ground water of an abandoned open cast mine filled with fly ash: A case study. *Mine Water and the Environment*, 27: 265 – 267.
8. Ojekunle, O. Z., Ojekunle, O. V., Adeyemi, A. A., Taiwo, A. G., Sangowusi, O. R., Taiwo, A. M. and Adekitan, A. A. (2016). Evaluation of surface water quality indices and ecological risk assessment for heavy metals in scrap yard neighbourhood. *Springer Plus*, 5: 560.\
9. Prasad, B. and Kumari, S. (2008). Heavy metal pollution index of ground water of an abandoned open cast mine filled with fly ash: A case study. *Mine Water and the Environment*, 27(4): 265 – 267.
10. World Health Organization (2011). Guidelines for drinking-water quality. Word Health Organisation, Geneva.
11. World Health Organization (2008). Guidelines for drinking-water quality: incorporating 1st and 2nd addendum: Vol. 1 - recommendations, 3rd edition. World Health Organisation, Geneva.
12. Tamasi, G. and Cini, R. (2004). Heavy metals in drinking waters from Mount Amiata. Possible risks from arsenic for public health in the province of Siena. *Science of the Total Environment*, 327: 41 – 51.
13. Bakan, G., Bokeozkoc, H., Tulek, S. and Cuce, H. (2010). Integrated environmental quality assessment of Kızılırmak River and its coastal environment. *Turkish Journal of Fisheries and Aquatic Sciences*, 10: 453 – 462.
14. Lyulko, I., Ambalova, T. and Vasiljeva, T. (2001). To integrated water quality assessment in Latvia. In: MTM (Monitoring Tailor-Made) III, Proceedings of International Workshop on Information for Sustainable Water Management, Netherlands, pp. 449 – 452.
15. Caerio, S., Costa, M. H., Ramos T. B., Fernandes, F., Silveira, N., Coimbra, A., Mederios, G. and Painho, M. (2005). Assessing heavy metal contamination in Sado Estuary sediment: An index analysis approach. *Ecological Indicators*, 5: 151 – 169.
16. Hakanson, L. (1980). An ecological risk index for aquatic pollution control a sedimentological approaches. *Water Research*, 14**(**8): 975 – 1001.
17. United States Environmental Protection Agency (USEPA). Partition coefficient of metals in surface water, soil and waste, Office of the Research and Development, EPA/600/R-05/074, 2005, 2006.
18. Canadian Council of Ministers of the Environment (1999). For the protection of aquatic life. In: Canadian environmental quality guidelines. Canadian Council of Ministers of the Environment, Winnipeg.
19. Xu, Z. Q., Ni, S. J. and Tho, X. G. (2008). Calculation of heavy metals toxicity coefficient in the evaluation of potential ecological risk index. *Environmental Science & Technology*, 31: 112 – 115.
20. Dong, J., Bian, Z. and Wang, H. (2007). Comparison of heavy metal contents between different reclaimed soils and the control soil. *Journal of China University of Mining & Technology*, 36(4): 531 – 536.
21. Jiao, B., Xu, G., Li, D., Luo, J. and Yang, K. (2012). Hazards of heavy metals in coal. *Disaster Advances*, 5(4): 1812 – 1818.

22. Jolly, Y. N., Akter, J. S., Kabir, A. I. and Akbar, S. (2013). Trace elements contamination in the river padma. *Bangladesh Journal of Physics*, 13: 95 – 102.
23. Hassan, M., Mirza, A. T. M., Rahman, T., Saha, B. and Kamal, A. K. I. (2015). Status of heavy metals in water and sediment of the Meghna River, Bangladesh. *American Journal of Environmental Sciences*, 11: 427 – 439.
24. Bhuiyan, M. A. H., Dampare, S. B., Islam, M. A. and Suzuki, S. (2015). Source apportionment and pollution evaluation of heavy metals in water and sediments of Buriganga River, Bangladesh, using multivariate analysis and pollution evaluation indices. *Environmental Monitoring and Assessment*, 187: 4075.
25. Ahmed, M. K., Ahmed, S., Rahman, S., Haque, M. R. and Islam, M. M. (2008). Heavy metals concentration in water, sediment and their bioaccumulation in some freshwater fishes and mussel in Dhaleshwari River, Bangladesh. *Terrestrial and Aquatic Environment Toxicology*, 3(1): 33 – 41.
26. Aktar, M. W., Paramasivam, M., Ganguly, M., Purkait, S. and Sengupta, D. (2010). Assessment and occurrence of various heavy metals in surface water of Ganga river around Kolkata: a study for toxicity and ecological impact. *Environmental Monitoring and Assessment*, 160(1–4): 207 – 213.
27. Al-Obaidy, A. H. M. J., Al-Mashhady, A. A. M., Awad, E. S. and Kadhem, A. J. (2014). Heavy metals pollution in surface water of Mahrut River, Diyala, Iraq. *International Journal of Advanced Research*, 2 (10): 1039 – 1044.
28. Liu, H. and Li, W. (2011). Dissolved trace elements and heavy metals from the shallow lakes in the middle and lower reaches of the Yangtze River region, China. *Environmental Earth Sciences*, 62(7): 1503.
29. Majhi, A. and Biswal, S. K. (2016). Application of HPI (heavy metal pollution index) and correlation coefficient for the assessment of ground water quality near ash ponds of thermal power plants. *International Journal of Science Engineering and Advance Technology*, 4(8): 395 – 405.
30. Ahmad, M. K., Islam, S., Rahman, S., Haque, M. R. and Islam, M. M. (2010). Heavy metals in water, sediment and some fishes of Buriganga River, Bangladesh. *International Journal of Environmental Research*, 4(2): 321 – 332.
31. Kalaivani, T. R. and Dheenadayalan, M. S. (2013). Seasonal fluctuation of heavy metal pollution in surface water. *International Research Journal of Environment Science*, 2(12): 66 – 73.
32. Song, X., Hu, X., He, M., Liang, R., Li, X. and Sun, W. (2013). Spatial distribution and seasonal variations of heavy metals in surface water of the Taizi River. *Applied Mechanics and Materials*, 295-298: 1615 – 1618.
33. Yao, H., Qian, X., Gao, H., Wang, Y. and Xia, B. (2014). Seasonal and spatial variation of heavy metals in two typical Chinese Rivers: Concentrations, environmental risk, and possible sources. *International Journal of Environmental Research and Public Health*, 11: 11860 – 11878.
34. Dey, S., Das, J. and Manchur, M. A. (2015). Studies on heavy metal pollution of Karnafully River, Chittagong, Bangladesh. *Journal of Environmental Science, Toxicology and Food Technology*, 9: 79 – 83.
35. Mohiuddin, K. M., Otomo, K., Ogawa, Y. and Shikazono, N. (2012). Seasonal and spatial distribution of trace elements in the water and sediments of the Tsurumi river in Japan. *Environmental Monitoring and Assessment*, 184: 265 – 279.
36. Adamu, C. I., Nganje, T. N. and Edet, A. (2015). Heavy metal contamination and health risk assessment associated with abandoned barite mines in Cross River State: Southeastern Nigeria. *Environmental Nanotechnology, Monitoring and Management*, 3: 10 – 21.
37. Kumar, R. N., Solanki, R. and Kumar, J. I. N. (2013). Seasonal variation in heavy metal contamination in water and sediments of river Sabarmati and Kharicut canal at Ahmedabad, Gujarat. *Environmental Monitoring and Assessment*, 185: 359 – 368.
38. Li, S. Y. and Zhang, Q. F. (2010). Risk assessment and seasonal variations of dissolved trace elements and heavy metals in the Upper Han River, China. *Journal of Hazardous Materials*, 181: 1051 – 1058.
39. Krika, A. and Krika, F. (2017). Evaluation of the status of heavy metal pollution in surface water and sediments of the Nill River (North Eastern Aleria). *Pollution*, 3(2): 301 – 310.
40. Department of Environment, Government of the People's Republic of Bangladesh (2002). The general overview of pollution status of rivers of Bangladesh, Dhaka, Bangladesh.
41. Department of Environment (1997). The environment conservation rules. Poribesh Bhaban E-16, Agargaon, Shere Bangla Nagar Dhaka 1207, Bangladesh: pp. 179–226.
42. Suresh, G., Sutharsan, P., Ramasamy, V. and Venkatachalapathy, R. (2012). Assessment of spatial distribution and potential ecological risk of the heavy metals in relation to granulometric contents of Veeranam lake sediments, India. *Ecotoxicology and Environmental Safety*, 84: 117 – 124.

43. Li, F. Y., Fan, Z. P., Xiao, P. F., Oh, K., Ma, X. P. and Hou, W. (2009). Contamination, chemical speciation and vertical distribution of heavy metals in soils of an old and large industrial zone in Northeast China. *Environmental Geology*, 54: 1815 – 1823.
44. Ewa, E. E., Iwara, A. I., Offiong, V. E., Essoka, P. A. and Njar, G. N. (2013). Seasonal variation in heavy metal status of the Calabar River, Cross River State, Nigeria. *Journal of Natural Sciences Research*, 3(11): 78 – 83.
45. George, P., Joseph, S. and Moses, S.A. (2017). Heavy metal monitoring and health risk assessment of a tropical mountainous river in Kerala, India. *International Journal of River Basin Management*, 15(4): 475 – 484.
46. Giri, S. and Singh, A.K. (2014). Assessment of surface water quality using heavy metal pollution index in Subarnarekha River, India. *Water Quality Exposure and Health*, 5: 173 – 182.

Malaysian Journal of Analytical Sciences, Vol 23 No 2 (2019): 312 - 324
DOI: https://doi.org/10.17576/mjas-2019-2302-15

MALAYSIAN JOURNAL OF ANALYTICAL SCIENCES
Published by The Malaysian Analytical Sciences Society
ISSN 1394 - 2506

ULTRAFAST LIQUID CHROMATOGRAPHIC ESTIMATION OF SERTACONAZOLE NITRATE IN PHARMACEUTICALS USING ANALYTICAL QUALITY BY DESIGN

(Kromatografi Cecair Ultra-laju bagi Anggaran Sertaconazole Nitrat dalam Farmaseutikal Menggunakan Reka Bentuk Kualiti Analitikal**)**

Sagar Suman Panda*, Venkata Varaha Ravi Kumar Bera, Rakeya Samanta

Department of Pharmaceutical Analysis and Quality Assurance,
Roland Institute of Pharmaceutical Sciences (Affiliated to Biju Patnaik University of Technology, Odisha),
Khodasingi, Berhampur-760010, Odisha, India

**Corresponding author: sagarguddu2002@gmail.com*

Received: 24 May 2018; Accepted: 24 February 2019

Abstract

An analytical Quality by Design(AQbD) oriented ultra-fast liquid chromatography method was developed for quantification of sertaconazole nitrate in pharmaceutical dosage form. A central composite design (CCD) was employed to establish optimum chromatographic conditions ensuring method robustness by selecting methanol (%) and flow rate (mL/min) as the factors, to study their effect on the system suitability parameters such as retention time, plate number and tailing factor as the response variable. Further, the method was carried out with design of experiments (DoE) optimized chromatographic conditions. The intermediate precision of the method was studied using a full factorial design (FFD) considering the number of days and analysts as the variables. The chromatographic separation was achieved on a phenyl-hexyl column using methanol: water (92:8, %v/v) as the mobile phase at a flow rate of 1.3 mL/min and photo diode array detection at 260 nm. The values obtained for validation parameters were within the acceptance limit. The method was linear over 5-100 µg/mL of sertaconazole. Analysis of the system suitability suggested a high degree of method reproducibility and robustness. In a nutshell, the method was found to be highly suitable for its applicability in the determination of sertaconazole in bulk and tablet dosage form.

Keywords: sertaconazole, ultrafast liquid chromatography, quality by design, design of experiments, robustness

Abstrak

Reka bentuk kualiti analitikal berasaskan kaedah kromatografi cecair ultra-laju telah dibangunkan untuk pengkuantitian sertaconazole nitrat dalam bentuk dos farmaseutikal. Reka bentuk komposit berpusat (CCD) telah dibangunkan untuk mengoptimumkan keadaan kromatografi dalam memastikan keteguhan kaedahnya dengan memilih metanol (%) dan kadar aliran (mL/min) sebagai faktor, untuk menkaji kesannya terhadap sistem kesesuaian parameter seperti masa tahanan, nombor plat dan faktor pengekoran sebagai respons pembolehubah. Selanjutnya, kaedah diuji dengan reka bentuk eksperimen (DoE) yang telah dioptimumkan. Kepersisan pengantaraan kaedah telah dikaji dengan mengunakan reka bentuk berfaktor penuh (FFD) dengan bilangan hari dan ahli analisis diambil sebagai pembolehubah. Pemisahan kromatografi telah dicapai melalui turus fenil-heksi mengunakan metanol: air (92:8, %v/v) sebagai fasa bergerak pada kadar aliran 1.3 mL/min dan pengesanan susunan diod pada 260 nm. Nilai yang diperolehi untuk parameter validasi berada had yang dibenarkan. Kaedah adalah bersifat linear dari julat 5-100 µg/mL sertaconazole. Analisis kesesuaian sistem mencadangkan keteguhan dan kebolehulangan kaedah adalah tinggi. Oleh demikian, kaedah yang diperolehi adalah sesuai untuk aplikasi penentuan sertaconazole di dalam dos tablet dan pukal.

Kata kunci: sertaconazole, kromatografi cecair ultra-laju, kualiti reka bentuk, reka bentuk eksperimen, keteguhan

Introduction

Ultra-fast liquid chromatography (UFLC) is an economic and time-efficient alternative of high-performance liquid chromatography (HPLC) for fast analysis of drugs in pharmaceuticals [1-3]. This technique has diverse merits like lower mobile phase consumption, faster analysis, and high sensitivity that advocates for opting an UFLC method over HPLC for estimation of drugs in diverse samples. Sertaconazole nitrate i.e. (±)-1{2, 4-dihydro-β-[(7-chlorobenzo[b]thien-3-yl)-methoxy] phenethyl} imidazole nitrate (Figure 1) is an imidazole antifungal, used in treating candidiasis and seborrheic dermatitis [4, 5].

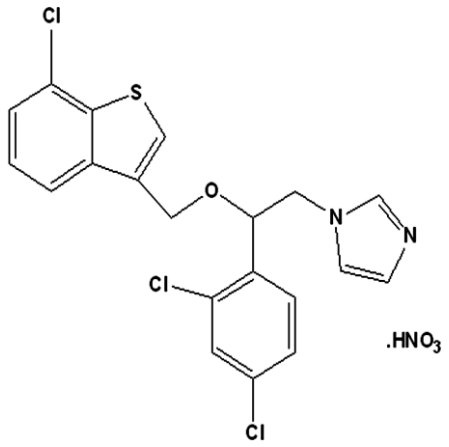


Figure 1. Chemical structure of sertaconazole nitrate

Literature reveals few chromatographic methods are reported for quantifying sertaconazole in pharmaceuticals and biological fluids, which include HPLC [6, 7] and LC-MS [8]. Lack of stability indicating nature, lower theoretical plate count, composite mobile phase, close supervisions of method parameters like mobile phase flow rate, injection volume, pH were the critical drawbacks found in the reported analytical methods. Moreover, there is no reported literature available describing a reliable analytical method for quantification of sertaconazole in diverse pharmaceutical samples. This calls for the development of an efficient and reliable UFLC method for estimation of sertaconazole in bulk API and pharmaceutical formulation.

Quality by Design (QbD) is a systematized holistic approach applicable to pharmaceutical development, which begins with predefined objectives and intent for accomplishing high quality in the end product and/or process [9]. Besides, it primarily facilitates rational understanding by establishing the cause-effect relationship between the quality attributes. Currently, QbD is extensively explored by analytical scientists for developing high-quality analytical methods [10-12]. QbD with respect to analytical methodology initiates with instituting the analytical target profile (ATP) and critical analytical attributes (CAAs), prioritizing followed by optimizing the critical method variables (CMVs) using an experimental design, followed by response surface analysis and desirability function to embark upon the optimal [13].

In the present research, a new UFLC method devoid of reported drawbacks was developed for quantifying sertaconazole in bulk drug and dosage form undertaking analytical QbD (AQbD) approach. A central composite design (CCD) design was adopted for systematic method optimization and establishing the optimum design space. The validation studies [14] were performed for the optimized chromatographic method. In addition, the precision of the method was ascertained by using a full factorial design (FFD). Further, the developed method was applied for the estimation of sertaconazole in tablets.

Materials and Methods

Reagents and standards

Sertaconazole nitrate (purity > 99.85%) was obtained from Glenmark Generics Ltd., India. Methanol (Merck Ltd., Mumbai, India) was of HPLC grade. The water for HPLC was obtained by using the TKA GenPure Ultra-Purification System, Germany. The commercial tablet formulation containing 500 mg of sertaconazole was procured from the local market and was analyzed by the developed method.

Instrumentation and chromatographic conditions

The UFLC system containing two Shimadzu Prominence UFLC LC-20AD pumps and SPD M20A photo diode array (PDA) detector with Shimadzu LC Solution Software was used for chromatography. Signal was recorded and integrated using Shimadzu LC Solution Software. Ultrasonicator (Enertech, India) was used during the mobile phase and sample preparation. Design of Experiments (DoE), optimization and data analysis were performed by using a trial version JMP software (SAS Institute, Inc., NC, USA) and Design Expert® 8.0.6 Software Full Version with Serial No. 1019-4550 (Stat-Ease, Inc., Minneapolis, MN, USA).

A Phenomenex phenyl-hexyl column, (250mm x 4.6 mm i.d., particle size 5 µm) was used for separation. Chromatography was performed at room temperature using the mobile phase methanol: water (92:8, v/v) at a flow rate of 1.3 mL/min. Both methanol and water were degassed using ultrasonication up to 20 minutes followed by filtration through a 0.22µm filter.

Defining ATP and CAAs

ATP and CAAs were established based on prior literature survey and study intent. In order to meet the ATP requirement of rapid and reliable estimation of sertaconazole in tablets a UFLC technique using reversed phase was selected with sorted CAAs such as retention time, plate number, and tailing factor.

Establishment of cause-effect relationship and risk management

A typical fish- bone diagram focusing multiple method variables as causes and their effects on the CAAs of the UFLC method was drawn. Inputs from the above diagram were subjected to a failure mode and effect analysis (FMEA) study. Risk priority number (RPN) was calculated to sort out the high-risk variables affecting the CAAs. Scores were assigned to each of them for severity(S), occurrence (O) and detectability (D). The RPN was calculated as per equation 1:

$$\text{Risk Priority Number (RPN)} = S \times O \times D \quad (1)$$

The method variables with scores more than 100 were considered as failure modes and were designated as critical method variables (CMVs) and were further subjected to systematic response surface optimization to create a robust analytical design space (DS)[15].

DoE guided method development and optimization

Two CMVs were identified, and their effect on method performance was evaluated by the DoE approach. A robust design space was established after selecting a CCD experimental domain, with the intent of obtaining fewer experiments and greater robustness. The CCD provided 10 experiments with 2 centres. In order to obtain bias-free responses, the experiments were randomized. A 10 µg/mL concentration of sertaconazole was tested for all the runs. The obtained data were fitted to an appropriate mathematical model by using the JMP software trial version (SAS Institute, Inc., NC, USA). Main and interaction effects among CMVs were studied using the developed model. Exhaustive data analysis based on multiple linear regression analysis (MLRA) was performed by evaluating the actual versus predicted plot, fit summary analysis, analysis of variance (ANOVA), lack of fit, the coefficient of correlation (R^2), adjusted and predicted R^2, predicted residual sum of squares (PRESS). Model aptness was decided by evaluating prediction expression, prediction profiler, interaction profiler; 2-D contour plot and 3-D response surface profiler.

Method control strategy

Method control strategies were defined based upon the results obtained for various system suitability parameters *viz.* retention time, plate number and tailing factor during the study days. $\bar{X} - S$ control chart was prepared for CMVs using Minitab® Software (Minitab Inc.) to monitor the instrument performance over a period of six days with three injections per day. The obtained observations were evaluated with respect to the mean ($\bar{X}$), mean of standard deviation ($\bar{S}$), LCL (lower control limit) and UCL (upper control limit). The information derived from control charts were used effectively to define the control strategy through the operable limits for CMVs.

Preparation of standard stock solution

Approximately 25 mg of sertaconazole was transferred into a 25 mL volumetric flask having 10 mL of methanol and ultrasonicated for 5 minutes. Finally, the volume was made up with methanol to produce 1000 µg/mL standard stock solution of sertaconazole. Calibration solutions were prepared from this solution at concentrations of 5-100 µg/mL of sertaconazole using mobile phase. Each calibration standard solution was injected in triplicates, chromatograms were obtained and mean peak areas were calculated. The linear calibration curve was drawn taking concentration (µg/mL) on the x-axis and the peak area on the y-axis. Regression analysis (including ANOVA) of calibration data was performed to detect the regression statistics.

Analysis of tablet dosage form

Tablet powder equivalent to 25 mg of sertaconazole was ultrasonicated for 20 minutes in a 25 mL volumetric flask, containing methanol. Volume was made up followed by filtration through a 0.45 µm filter. Further, the filtered solution was diluted for analysis, to obtain a test concentration within the linear range. These solutions were stored at 2-8 ºC for up to 6 days.

Validation studies: Accuracy

Recovery studies were performed in triplicate at 80% (16 µg/mL), 100% (20 µg/mL) and 120% (24 µg/mL) of the test concentration of sertaconazole. Drug present in the test solution was calculated using the calibration curve.

Precision

The precision study was performed in terms of system, inter- and intra-day. Six injections of a selected concentration of drug were carried out to determine the system precision. The intraday precision was found out using the peak area acquired by analyzing six solutions of a fixed amount of sertaconazole.

Inter-day precision of the method was studied using a full factorial design (FFD). Number of days (A) and analyst (B) were the two factors, and the peak area was the response chosen for the study. Total of 16 experimental runs was suggested by FFD using Design Expert® 8.0.6 Software Full Version with Serial No. 1019-4550 (Stat-Ease, Inc., Minneapolis, MN, USA). All the experimental runs were performed in randomized order to obtain results without any bias. Various effect tools, diagnostic plots, and model graphs were studied to find out critical method parameters affecting response. A solution of concentration 20 µg/mL of sertaconazole was analyzed by UFLC and percent relative standard deviations (%RSD) were calculated.

Limit of Detection (LOD) & Limit of Quantitation(LOQ)

Signal to Noise (S/N) ratio of 3:1 and 10:1 were considered vital for visual detection of LOD and LOQ, respectively.

Specificity and selectivity

Specificity was evaluated by inspecting the possible interference from the placebo. The commonly used additives (hydroxypropylmethyl cellulose, microcrystalline cellulose, magnesium stearate and talc) were incorporated into the standard solutions and were analyzed. Method selectivity was ensured by recovery and analysis of the analyte in presence of formulation components.

Results and Discussion

Method development studies

Based on prior knowledge and physicochemical properties of the analyte the initial chromatographic trials were conducted. Various chromatographic parameters, including mobile phase composition and ratio, stationary phase, mobile phase flow rates. were investigated to find the desired response. A Phenomenex phenyl-hexyl column was used for separation of the compound as it provides superior selectivity, high inertness with least tailing, resistance to extreme pH conditions, higher stability to aqueous mobile phases than compared to C_{18}. Various preliminary experimental trials were conducted at ambient temperature using different mobile phase compositions like methanol: water, methanol: buffer (pH 6.8), methanol: buffer pH 7.0 at varying ratios (i.e., 50:50, 60:40, 70:30, 80:20, 85:15, 90:10, 92:8, v/v) and flow rates (0.8, 1.0,1.2 and 1.3 mL/min). Methanol: water (92:8, v/v) at a flow rate of 1.3 mL/min produced a symmetrical peak at retention time of 6.2min with PDA detection at 260 nm. Further, to study the factors affecting the separation of sertaconazole and to optimize the method robustness, AQbD approach was implemented.

Cause-and-effect based risk assessment and its management

Evaluation of the Ishikawa fish-bone diagram (Figure 2) revealed the primary causes and secondary sub-causes, which are responsible for the variability and alteration in method performance.

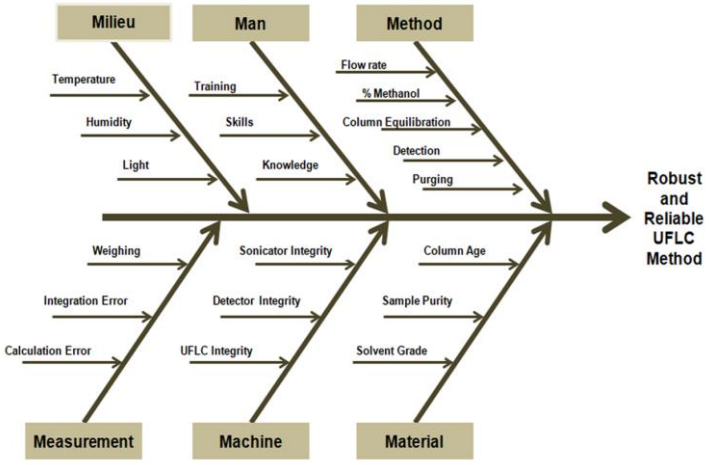


Figure 2. Typical fish-bone diagram depicting the cause and effect relationship between method variables and method performance

To carry out an effective risk assessment, for the present studies, the FMEA approach with RPN was utilized (Table 1). The CMVs were identified based on the final score followed by response surface optimization to create the DS for developing a robust and reliable UFLC method.

Table 1. Various failure modes studied during FMEA study

Mode of Failure	Effect	S	O	D	RPN Score
Solvent grade	Extra peaks	3	3	3	27
Flow rate	Multiple	5	5	7	175
Column age	Non-selectivity	4	3	2	24
Methanol %	Multiple	6	5	6	180
Sample purity	Extra peaks	2	3	2	12
Column equilibration	Extra peaks	3	3	3	27
Detection	Varying peak profile	2	2	2	8
Purging	Pressure variation	3	2	3	18

AQbD based chromatographic method optimization

Based on the risk assessment studies, two CMVs were identified with significant influence on the method performance. Percentage methanol and mobile phase flow rate were subjected to further studies to assess the method robustness. Ten experimental runs (Table 2) obtained as per CCD model were performed on a random basis using UFLC and responses were obtained to ensure method robustness for identifying optimized chromatographic conditions.

Table 2. Range of chromatographic variables studied as per experimental design

Run Number	Methanol %	Flow rate (mL/min)
1	90	1.4
2	92	1.4
3	92	1.3
4	92	1.2
5	90	1.2
6	90	1.3
7	94	1.3
8	92	1.3
9	94	1.2
10	94	1.4
Levels Studied	**Methanol %**	**Flow rate (mL/min)**
Low	90	1.2
Nominal	92	1.3
High	94	1.4

Optimization data analysis

The obtained data for each experimental run were fitted to a suitable mathematical model by MLRA using JMP software (SAS Institute, Inc., NC, USA). The developed model was allowed to study both the main effects and interaction effects among the CMVs studied.

After obtaining the responses suitable mathematical models were adopted. Prediction expression as polynomial equations (Eq.2-4) containing model terms for both main effects and interaction effects were generated for all the

three responses. It explains the relationship between the CMVs and CAAs and predicts the CAAs values within the levels of CMVs studied.

Retention Time = 6.2846429 + [-1.009667 × Methanol] + [-0.482667 × Flow rate] + [0.47825 × (Methanol × Flow rate)] + [0.1442143 × (Methanol × Methanol)] + [0.5112143 × (Flow rate × Flow rate) (2)

Plate Number = 7608.5357 + [117.18333 × Methanol] + [-1010.333 × Flow rate] + [624.025 × (Methanol × Flow rate)] + [-3328.671 × (Methanol × Flow rate)] + [83.278571 × (Flow rate × Flow rate) (3)

Tailing factor = 1.4722143 + [-0.028667 × Methanol] + [-0.077167 × Flow rate] + [-0.00125 × (Methanol × Flow rate)] + [-346929 × (Methanol × Methanol)] + [0.0205714 × (Flow rate × Flow rate) (4)

Evaluation of ANOVA was carried out for model fitness and significant difference ($p<0.05$) along with values of R^2 ($R^2>0.9$) were obtained. All these statistical parameters confirmed the suitability of the selected mathematical model for predicting the responses. Interaction effect analysis was carried out using interaction profilers. The plots (not shown in figures) for interaction suggested a non-linear pattern among the CMVs on the CAAs studied. High degree of interactions among both the CMVs was obtained for the CAA plate number, as the factor lines were intersecting each other. This intersection of factor lines indicated a potential cause for possible variability in plate count, which demands strict control measures to be undertaken.

Response surface analysis was carried out employing 2-D contour and 3-D plots (Figure 3- (a-d)). Figure 3(a) demonstrates the overall design space developed through 2-D contours. Figure 3(b) indicates maximal values of retention time at low levels of methanol % and flow rate. A typical "ridge" system was observed for both the CMVs for plate number and tailing factor. On the other hand, high plate number was observed at mid levels of methanol % and at low to mid levels of flow rate (Figure 3(c)). Optimum tailing values were obtained at mid levels of methanol % and at low to mid levels of flow rate (Figure 3(d)).

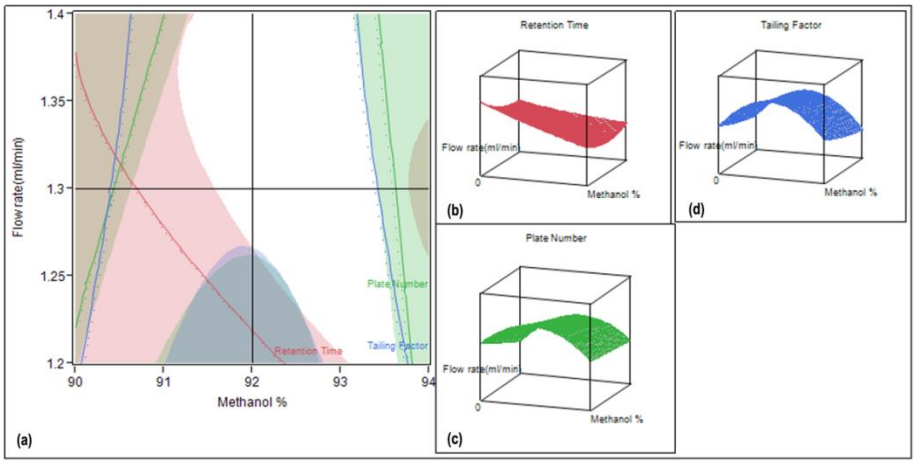


Figure 3. 2-D contour (a) and 3-D response surface (b, c, d) plots obtained for CAAs

The desirability plot along with prediction profiler (Figure 4) suggested optimum chromatographic conditions for the CAAs such as retention time, plate number and tailing factor. Further, the method was carried out with DoE optimized chromatographic conditions, which resulted in superior method robustness and efficient system suitability values compared to the reported HPLC method for sertaconazole [7]. The reported method proposed poor theoretical plate count of 1153 which is well below the standard minimum plate count by the USP (>2000) [16].

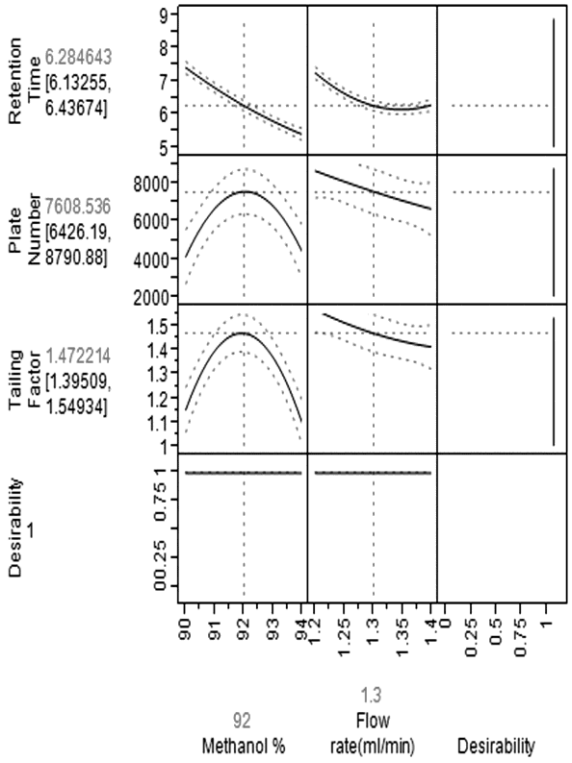


Figure 4. Prediction profiler along with desirability plot obtained for CAAs viz. retention time, plate number and tailing factor

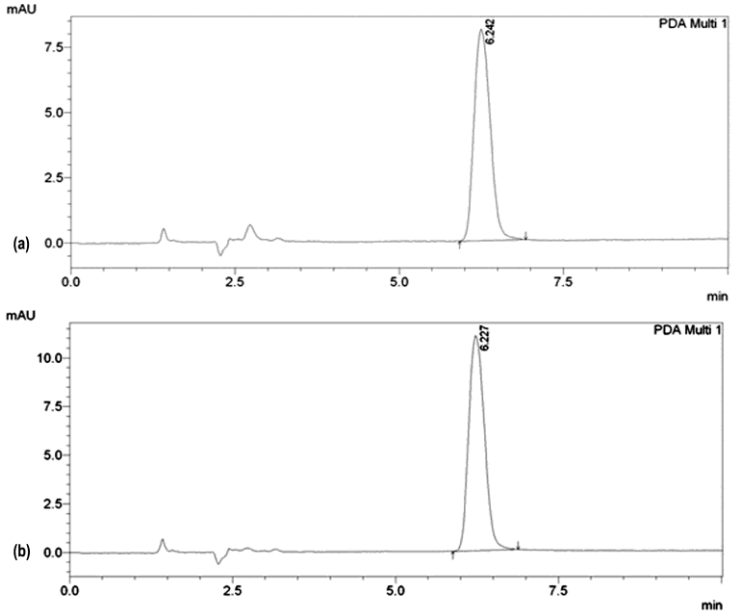


Figure 5. Typical representative chromatograms of sertaconazole in (a) standard drug and (b) tablet dosage form

Validation studies: Linearity

A linear calibration curve was obtained for sertaconazole within the concentrations of 5-100 µg/mL (R^2 = 0.999), which is much wider than the reported HPLC method [7]. The result of the regression analysis of linearity data suggested goodness of fit. The values obtained for statistical parameters such as multiple R, R^2, adjusted R^2 and standard error were 0.9995, 0.999, 0.9988 and 12756.45, respectively.

Accuracy

The results of recovery revealed (Table 3) a high degree of accuracy of the method. Average recoveries of drug ranging between 99.55 and 99.99%, for spiked concentrations, 16, 20 and 24 µg/mL, were obtained.

Table 3. Results of accuracy study

Level Studied (%)	Spiked Concentration (µg/mL)	Recovery* (%) ± S.D.
80	16	99.58 ±1.7
100	20	99.99 ± 1.0
120	24	99.55 ± 0.9

*Mean of three separate determinations

Precision

The % RSD for system and intraday precision was found to be 0.13 and 0.57, respectively. In the case of inter-day precision, the overall % RSD was found to be 0.45 using experimental design approaches.

Table 4. Experimental design matrix for inter-day precision

Run No.	Number of Day	Analysts
1	Day 1	2
2	Day 2	1
3	Day 2	2
4	Day 1	1
5	Day 2	1
6	Day 2	2
7	Day 2	1
8	Day 1	2
9	Day 2	1
10	Day 1	2
11	Day 2	2
12	Day 1	1
13	Day 1	1
14	Day 2	2
15	Day 1	2
16	Day 1	1

Application of an FFD (Table 4) ensured the screening of method factors, which can significantly affect the precision. An overall study of different effect tools, diagnostic plots, model graphs and response plots (Figure 6-a-d) revealed the number of days of the study was the most critical factor affecting the intermediate precision of the method.

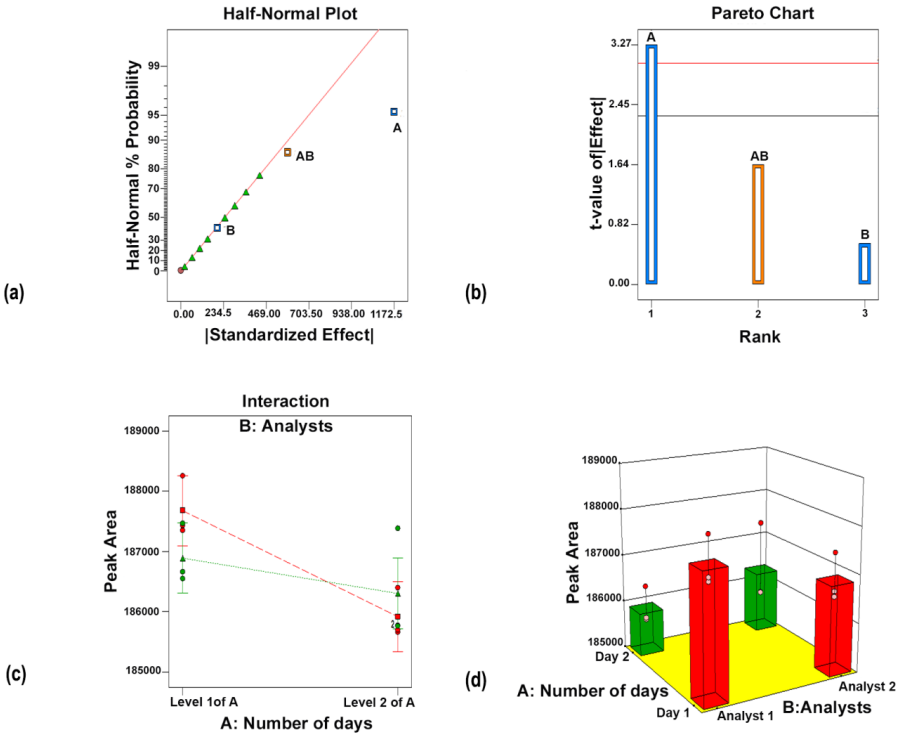


Figure 6. Effect tools, diagnostic plots and model graphs obtained for intermediate precision using experimental design; (a): Half-normal plot, (b): Pareto chart, (c): Interaction plot and (d):3-D surface plot

Further, the superior preciseness of the present method was confirmed by comparing the %RSD values obtained for the present method with that of the reported ones (Table 5).

Table 5. Comparison of % R.S.D. values obtained for the precision studies of the present method with the reported method

Precision Type	**%R.S.D.**			
	Reported Method for Cream [6]	Reported Method for Solution [7]	Reported Method for Powder [7]	Present Method for Tablet
Intra-day	1.72	0.9	0.6	0.57
Inter-day	2.17	0.6	0.5	0.45

Solution stability

The result of solution stability showed no significant degradation or change in sertaconazole content. The average (n = 3) recoveries were 99.22% (RSD = 0.2%) and 98.86% (RSD = 0.33%), for Days 1 and 2, respectively. The results suggest that drug solutions were stable up to two days under refrigeration.

Limit of detection (LOD) and limit of quantitation (LOQ)

The reported method [7] has a LOD and LOQ value of 1.24 and 3.78 µg/mL, respectively using a cyano column employing a complex mobile phase consisting of 0.1 M sodium dodecyl sulphate, 20% 1-propanol, and 0.3% triethylamine in 0.02 M ortho-phosphoric acid (pH 4). However, the present LOD and LOQ values were found to be 3.25 and 5.0 µg/mL, respectively using a phenyl-hexyl column employing methanol and water, and are well in accordance with the linearity concentrations studied.

Method control strategy

The system suitability results obtained during control runs indicated (Figure 7) a robust and optimum instrument performance within the DS for the most influential CMVs such as methanol proportion (±2%) and flow rate (±0.1mL/min).

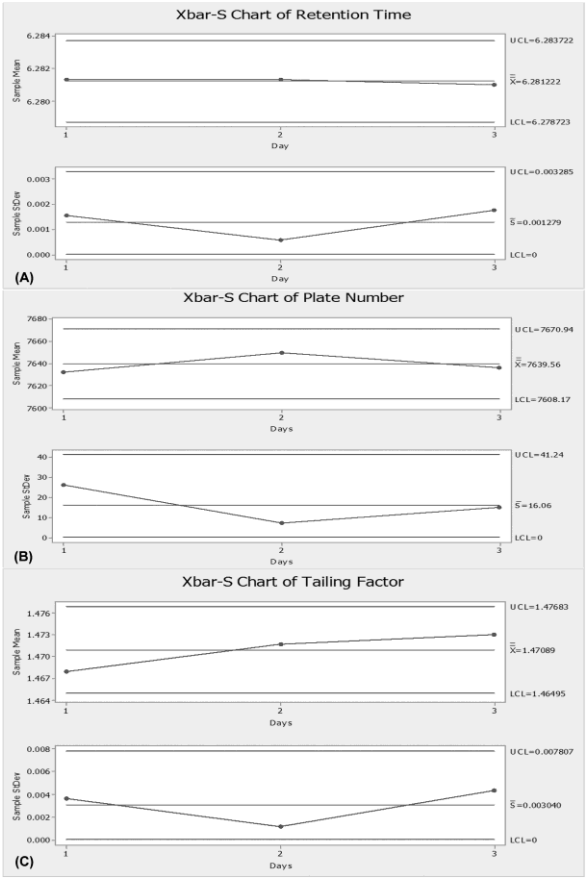


Figure 7. Control chart depicting method performance on different days of study

Specificity and selectivity

Study of a chromatogram obtained for placebo demonstrated no interference due to the commonly used excipients, which suggested method specificity. Further, method selectivity was ascertained by comparing the chromatograms of placebo (Figure 8) and drug in tablet dosage form (Figure 5 (b)).

Assay of tablet dosage form

The developed method was applied for the estimation of sertaconazole in the tablet dosage form. The result of the assay (n = 3) for the drug yielded 99.19% (SD = 0.75) of sertaconazole. Comparison of assay results (Table 6) with

that of the reported HPLC method using *t*-test indicated the aptness of the sample extraction procedure from the tablet dosage form. The comparison revealed that the calculated value of *t* was greater than tabulated one indicating a significant difference between the results of the reported and present method for quantifying sertaconazole in tablets and solution form. Contrary to the above observed the *t*-value was found well within the tabulated value indicating no significant difference among the results of the reported and present method for estimation of sertaconazole in powder and tablet dosage form, respectively. The higher percentage of recovery and noninterference of the formulation excipients in the estimation of the drug indicates the selectivity of the method. A typical chromatogram of the commonly used excipients and additives in the tablet dosage form depicted non-interference at analyte retention at 6.2min (Figure 8). Further, the results vowed the befitting nature of the AQbD approach for the present chromatographic studies.

Table 6. Comparison of results obtained for dosage form analysis by the reported method and the present method

Method	Formulation Type	Recovery* (%), S.D.	t-value (p = 0.05; df**= 4)	
			Tabulated	Observed
Reported [7]	Solution	97.0, 1.0	2.78	3.034
	Powder	98.4, 1.2	2.78	1.03
Present	Tablet	99.19, 0.75		

*Mean of three separate determinations, **df= Degrees of freedom

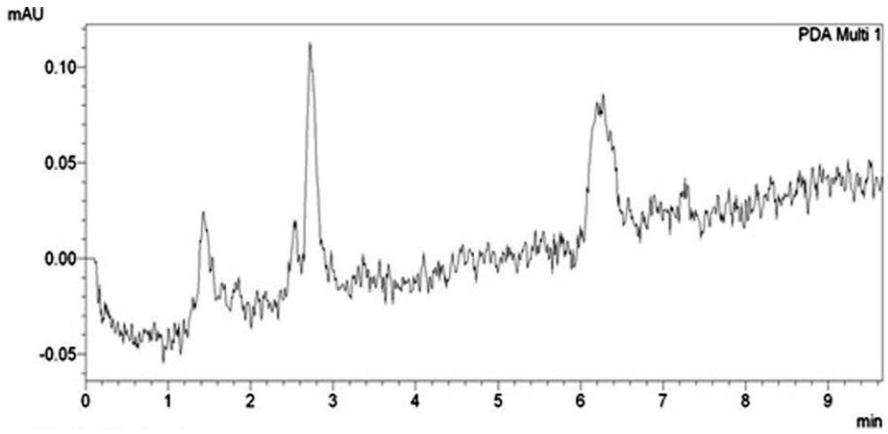


Figure 8. Typical chromatogram depicting non-interference of excipients and additives in analytes retention time

Conclusion

A reliable and robust reverse phase UFLC method was developed for the estimation of sertaconazole. Implementation of AQbD approach ensured that quality is built into the analytical method instead of testing. Use of methanol instead of acetonitrile as organic phase efficiently removed the toxicity issues related to the mobile phase. Validation studies according to ICH guidance presented satisfactory and acceptable results. Employing the DoE approach to an intermediate precision study revealed the effect of factors that may influence method preciseness over days of an experiment by a different analyst. The results obtained from the above studies indicate that this method is well suited for routine analysis of sertaconazole in bulk drug and pharmaceutical dosage forms. Further, this systematically optimized robust chromatographic method has the potential for future continuous improvement in method performance through strict monitoring of CAAs and may serve as a basis for optimizing the analytical method for sertaconazole present in biological samples for pharmacokinetics studies.

Acknowledgements

The authors are thankful to Glenmark Pharmaceuticals Ltd., India for providing the gift sample of sertaconazole nitrate standard drug and Roland Institute of Pharmaceutical Sciences, Berhampur-10, Odisha, India for providing the research facilities.

References

1. Panda, S. S., Bera, V. V. R. K., Mohanta, G. and Patel, P. K. (2012). New stability indicating RP-UFLC method for determination of trospium chloride in tablet dosage form. *Scientia Pharmaceutica*, 80: 955 – 964.
2. Panda, S. S., Bera, V. V. R. K., Mohanta, G. and Panda, J. (2013). Reverse phase ultrafast liquid chromatography method for simultaneous estimation of citicoline sodium and piracetam in tablets. *International Journal of Pharmaceutical Sceicnes and Nanotechnology*, 6(1): 1952 – 1957.
3. Panda, S. S., Bera, V. V. R. K., Mohanta, G. and Kumari, A. (2015). Ultrafast liquid chromatographic determination of naproxen sodium in pharmaceutical dosage form. *American Journal of Modern Chromatography*, 2(2): 16 – 25.
4. Carrillo-Munoz, A. J., Tur-Tur, C., Giusiano, G., Marcos-Arias, C., Eraso, E., Jauregizar, N. and Quindos, G. (2013). Sertaconazole: An antifungal agent for the topical treatment of superficial candidiasis. *Expert Review of Anti-Infective Therapy*, 11(4): 347 – 358.
5. Goldust, M., Rezaee, E. and Raghifar, R. (2013). Treatment of seborrheic dermatitis, comparison of sertaconazole 2% cream versus ketoconazole 2% cream. *Irish Journal of Medical Science*, 182(4): 703 – 706.
6. Albert, C., Fernandez, J. M., Rozman, E., Perez, J. A., Sacristan, A. and Ortiz, J. A. (1992). Determination of sertaconazole nitrate, a new imidazole antifungal, by high-performance liquid chromatography. *Journal of Pharmaceutical and Biomedical Analysis*, 10(2-3): 205 – 211.
7. Risk, M., Toubar, S. S., El-Alamin, M. M. A. and Azab, M. M. M. (2014). Micellar liquid chromatographic determination of sertaconazole and terconazole in bulk, pharmaceutical dosage forms and spiked human plasma. *Bulletin Faculty of Pharmacy, Cairo University*, 52(1): 155 – 164.
8. Wang, Y., Pang, L., Wu, M. and Ou, N. (2009) A validated LC-MS/MS method for determination of sertaconazole nitrate in human plasma. *Journal of Chromatography B*, 877(31): 4047 – 4050.
9. Pharmaceutical Development Q8. (2009), ICH Harmonized Tripartite Guideline: pp. 1 – 24.
10. Panda, S. S., Bera, V. V. R. K., Beg, S. and Sahu, S. K. (2015). Ultrafast liquid chromatographic method development and its validation for quantification of telaprevir in pharmaceutical dosage form by using quality by design approach. *Journal of Chromatographic Science*, 53(7): 1193 – 1202.
11. Panda, S. S., Beg, S., Bera, V. V. R. K. and Singh, P. (2015). Analytical quality-by-design compliant ultrafast liquid chromatographic method for determination of paliperidone in extended release tablet dosage form. *Journal of Bioanalysis & Biomedicine*, 7: 116 – 123.
12. Beg, S., Sharma, G., Katare, O. P., Lohan, S. and Singh, B. (2015). Development and validation of a stability-indicating liquid chromatographic method for estimating olmesartan medoxomil using quality by design. *Journal of Chromatographic Science* , 53(7): 1048 – 1059.
13. Lionberger, R. A., Lee, S. L., Lee, L. M., Raw, A. and Yu, L. W. (2008). Quality by design: concepts for ANDAs. *The AAPS Journal*, 10(2): 268 – 276.
14. Validation of analytical procedures: Text and methodology, ICH harmonized tripartite guideline, (2005). Access from https://www.ich.org/fileadmin/Public_Web_Site/ICH_Products/Guidelines/Quality/Q2_R1 /Step4/ Q2_R1_Guideline.pdf [Accessed online 11 February 2018].
15. McDermott, R. E., Mikulak, R. J. B. (2008) The basics of FMEA. CRC Press, Taylor & Francis Group, New York.
16. United States Pharmacopoeia 40th ed. (2017); The United States Pharmacopeia Convention, Rockville, MD.

Malaysian Journal of Analytical Sciences, Vol 23 No 2 (2019): 325 - 335
DOI: https://doi.org/10.17576/mjas-2019-2302-16

MALAYSIAN JOURNAL OF ANALYTICAL SCIENCES
Published by The Malaysian Analytical Sciences Society
ISSN 1394 - 2506

EFFECTS OF SILVER NANOWIRE-BASED POLYMER COMPOSITE MEMBRANE ON THE PHYSICAL AND ELECTROCHEMICAL PROPERTIES OF MALACHITE GREEN SENSOR

(Kesan Nanowayar Perak-Membran Komposit Polimer ke atas Sifat Fizikal dan Elektrokimia untuk Sensor Malakit Hijau)

Sharifah Nur Atikah Al Yahya[1], Sharina Abu Hanifah[1,2]*, Normazida Rozi[1], Nurul Huda Abd Karim[1], Lee Yook Heng[1]

[1]*Center for Advanced Materials and Renewable Resources, Faculty of Science and Technology*
[2]*Polymer Research Center (PORCE), Faculty of Science and Technology*
Universiti Kebangsaan Malaysia, 43600 UKM Bangi, Selangor, Malaysia

**Corresponding author: sharina@ukm.edu.my*

Received: 19 August 2018; Accepted: 18 March 2019

Abstract

Malachite green is widely used in the aquaculture, food, and textile industries. However, malachite green is carcinogenic, mutagenic, and teratogenic. Therefore, a chemical sensor was developed to detect malachite green in water samples. Screen-printed carbon electrode was coated with (p(AAm-*co*-EMA)/Ru(bpy)$_3^{2+}$/AgNWs to investigate its potential as a membrane for chemical sensor. The membrane was synthesized using the photopolymerization technique and characterized by fourier transform infrared (FTIR), ^{1}H nuclear magnetic resonance (^{1}H NMR), swelling test, field emission scanning electron microscopy/electron dispersive X-ray analysis (FESEM/EDX), thermogravimetric analysis (TGA), and cyclic voltammetry (CV). The peak of –CO in the FTIR spectra indicated that the copolymerization was successful. Furthermore, the NMR spectrum confirmed the FTIR result with the presence of peak at 4.2 ppm. Swelling test showed that p(AAm-*co*-EMA)/AgNWs had a lower swelling percentage than p(AAm-*co*-EMA) due to AgNWs filling the pores of the membrane, which can be seen in the cross section of the SEM micrograph. Thermal decomposition temperature of the membrane was around 400 °C. Cyclic voltammogram proved that the p(AAm-*co*-EMA)/Ru(bpy)$_3^{2+/}$AgNWs film coated on screen-printed carbon electrode which acted as a working electrode was able to detect malachite green by showing anodic peak around 0.25 V and cathodic peak around -1.0 V.

Keywords: malachite green, electrochemical sensor, photopolymerization, silver nanowires

Abstrak

Malakit hijau digunakan secara meluas dalam industri akuakultur, makanan dan tekstil. Walaubagaimanapun, malakit hijau bersifat karsinogenik, mutagenik dan teratogenik. Oleh itu, sensor kimia dibangunkan untuk mengesan malakit hijau dalam sampel air. Skrin bercetak elektrod karbon bersalut (p(AAm-*ko*-EMA)/Ru(bpy)$_3^{2+}$/AgNWs telah dibangunkan bagi mengkaji potensinya sebagai filem untuk sensor kimia. Membran tersebut disintesis dengan menggunakan teknik fotopempolimeran dan dianalisis menggunakan spektroskopi infra merah tranformasi fourier (FTIR), ^{1}H resonans magnetik nukleus (^{1}H RMN), mikroskopi imbasan elektron pancaran medan/penyebaran elektron sinar-X (FESEM/EDX), analisis termogravimetri (TGA) dan voltametri siklik (CV). Puncak -CO yang hadir dalam spektrum FTIR menunjukkan kopempolimeran telah berjaya. Spektrum NMR mengesahkan spektrum FTIR dengan kehadiran puncak pada 4.2 ppm. Ujian penyerapan air pula menunjukkan peratus serapan air p(AAm-*ko*-EMA)/AgNWs lebih rendah berbanding p(AAm-*ko*-EMA) kerana AgNWs memenuhi liang–liang yang terdapat dalam filem seperti yang ditunjukkan pada mikrograf keratan rentas SEM. Penguraian terma berlaku pada suhu 400 °C. Voltamogram siklik membuktikan filem p(AAm-*ko*-EMA)/Ru(bpy)$_3^{2+/}$AgNWs yang disalut atas skrin bercetak elektrod karbon

bertindak sebagai elektrod kerja berupaya mengesan malakit hijau dengan menunjukkan puncak anodik sekitar 0.25 V dan puncak katodik sekitar -1.0 V.

Kata kunci: malakit hijau, sensor elektrokimia, fotopempolimeran, wayar nano perak

Introduction

Malachite green or known as [4-[[4-(dimethylamino)phenyl]-phenylmethylidene]cyclohexa-2,5-dien-1-ylidene]-dimethylazanium (Figure 1) is a type of commercial triphenylmethane dye. Malachite green is widely used in the textile and food industries as dye while in the aquaculture industry, it is used as anti-bacteria, anti-fungi, and anti-protozoa for aquatic life. However, the Food and Drug Association (FDA) has banned its use in aquatic life because malachite green is carcinogenic, teratogenic, and mutagenic; causing cancer, disrupting the growth of embryos, and altering genetics [1]. Malachite green can adversely affect humans if they consume aquatic life that has been treated with malachite green. Due to these effects, several countries such as America, Canada, and China have banned its usage in the aquaculture industry. However, malachite green is widely used because the cost is cheap, it is effective, and easily available in the market. Therefore, the European Commission has determined that only 2 µg/kg of total residue of malachite green and leucomalachite green should be present in aquaculture products as the minimum required performance limits (MRPLs). MRPLs are the minimum analyte needed for any detection method. Various detection methods were introduced by many researchers like high performance liquid chromatography (HPLC), gas chromatography-mass spectrometry (GC-MS), and liquid chromatography-mass spectrometry/mass spectrometry (LC-MS/MS). However, the existing detection methods are time-consuming and have indirect measurements [2]. Therefore, many researchers have started focusing on sensors because they can be used as *in-situ* detection. Sensor is a device that transmits signals received from an input as the physical stimulus and converts them into data that can be processed [3]. There are many types of sensors that have caught the attention of researchers, for example biosensors, chemical sensors, and optical sensors. For the detection of malachite green, Fatma et al. [4] developed a dual detection sensor using polyvinyl chloride membrane, which showed a linear range at 10^{-5} to 10^{-3} M malachite green concentration. Meanwhile, Faridah et al. [5] introduced an electrochemical enzyme inhibition sensor by electro-polymerized butyryl-cholinesterase enzyme and polyprrole matrix on a sensor surface, which showed a limit of detection at 0.25 ppb malachite green concentration. Among all these types of sensors, electrochemical sensor has gained the most attention from researchers due to its simplicity and short analysis time.

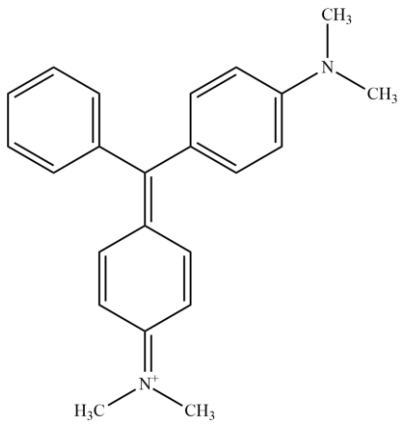


Figure 1. Chemical structure of malachite green

In this work, screen-printed carbon electrode coated with poly(acrylamide-*co*-ethyl methacrylate)/$Ru(bpy)_3^{2+}$/ silver nanowires (p(AAm-co-EMA)/$Ru(bpy)_3^{2+}$/AgNWs) was used as a working electrode for the detection of malachite green. Poly(acrylamide-*co*-ethyl methacrylate) in Figure 2 is a polymeric membrane acting as the immobilization matrix for $Ru(bpy)_3^{2+}$. Acrylamide (AAm) monomer is a colorless and odorless crystalline compound and soluble in water. The polymer form of AAm is usually used in the paper, textile, and water treatment industries. AAm monomer is used in polymer form in paper, textile and water treatment industries. AAm consists of the amide group

and carbonyl group. The presence of amide group causes the hydrophilicity of AAm, which forms a porous structure when undergoing polymerization [6] and it can provide better absorption capacity with a reduced polymer swelling [7]. The polymerization of AAm forming a porous structure can help in water absorption. Meanwhile, ethyl methacrylate (EMA) is a colorless liquid with a pungent smell that has hydrophobic and peel-able properties. The addition of a peelable property of EMA in copolymer can give an advantage to the non-disposable electrode and is used in the modification of electrode surface such as screen-printed electrode [8]. EMA consists of the carbonyl and ester groups. In this study, AAm acts as a host monomer while EMA acts as the comonomer to form poly(arylamide-*co*-ethyl methacrylate) (p(AAm-co-EMA)). In this study, only a small ratio of EMA monomer was added to alter the hydrophilicity of copolymer. This was due to the increasing mass percentage of EMA monomer, which can lead to hydrophilicity disruption of membrane, making it not suitable to use as membranes in sensors [9].

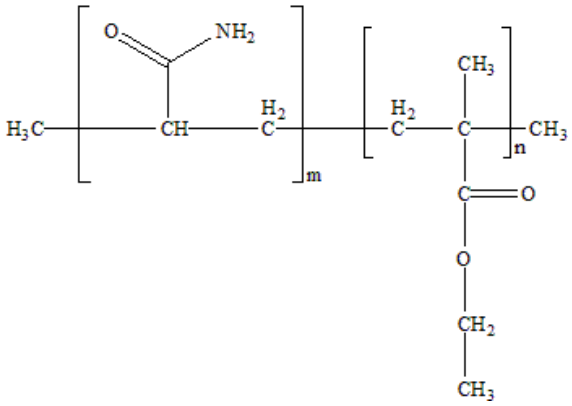


Figure 2. Chemical structure of poly(acrylamide-*co*-ethyl methacrylate)

Silver nanowires (AgNWs) are silver nanostructure with a diameter of nanometer that has electrical, optical, and thermal properties. AgNWs has the ability to increase the sensitivity of sensors three times compared to other film electrodes [10]. Furthermore, silver has s higher electric conductivity; 6.3 x 10^7 S/m than other metals [11]. Besides, AgNWs was proven to replace indium tin oxide (ITO) in solar cell applications. According to Lee et al. [12], sensors fabricated from AgNWs to detect hydrogen peroxide showed an acceptable detection limit of 46 µM with a fast response time of 2 s and high sensitivity of 749 µA mM^{-1} cm^{-2}. This is due to its nanostructure that assists the electron transfer and enhances the sensitivity of chemical sensor. On the other hand, $Ru(bpy)_3^{2+}$ is one of the ruthenium complexes that can be used to detect the presence of malachite green. $Ru(bpy)_3^{2+}$ has reversibility properties which allows it to develop a portable yet reusable sensor [13]. Besides, its usage with malachite green can form a redox reaction as proposed by Shao et al. [14]. Lan et al. [15] used the adsorption technique to immobilize $Ru(bpy)_3^{2+}$ on conducting polymer, while Liu et al. [16] and Shao et al. [14] used $Ru(bpy)_3^{2+}$ in free solution form to detect malachite green via the electrochemiluminescence technique. The presence of $Ru(bpy)_3^{2+}$ helps to produce z sensor with high sensitivity and low detection limit. Therefore, in this study, silver nanowires and $Ru(bpy)_3^{2+}$ were entrapped in the (p(AAm-*co*-EMA) to observe their ability to improve the sensitivity of sensors.

Materials and Methods

Chemicals

Chemicals used in this experiment were acrylamide (AAm), ethyl methacrylate (EMA), 2,2-dimethoxy-2-phenyl-acetophenone (DMPP) silver nanowires (AgNWs), and tris(2,2′-bipyridyl)dichloro-ruthenium(II) hexahydrate ($Ru(bpy)_3Cl_2.6H_2O$) purchased from Sigma Aldrich. Di-potassium hydrogen phosphates (K_2HPO_4) and potassium dihydrogen phosphate (KH_2PO_4) were bought from Nacalai Tesque and malachite green (MG) from R&M Chemical. Hydrochloric acid (HCl) and sodium hydroxide (NaOH) were freshly prepared in the laboratory for pH alteration of buffer. Deionized water was used in every experimental process.

Apparatus

The structural elucidations of samples were analyzed by Perkin Elmer 400 Fourier Transform Infrared Spectroscopy (FTIR) and Bruker 400 MHz Fourier Transform Nuclear Magnetic Resonance (NMR). The micrographs and energy dispersed spectrum were obtained using Zeiss Merlin Compact Field Emission Scanning Electron Microscope (FESEM). The thermal properties of samples were analyzed by Mettler Toledo STGA/SDTA851 Thermogravimetry Analysis (TGA). The cyclic voltammogram was performed by DropSens Portable Potensiostat, μStat400, Spain.

Preparation of polyacrylamide (pAAm), poly ethyl methacrylate (pEMA) and poly(acrylamide-co-ethyl methacrylate) (p(AAm-co-EMA))

Acrylamide solution was prepared by dissolving 1 g acrylamide, AAm and 0.016 g 2,2-dimethoxy-2-phenylacetophenone, (DMPP) in 885 μL of deionized water. Meanwhile, poly(acrylamide-*co*-ethyl methacrylate), p(AAm-*co*-EMA) was prepared with the ratio 9:1 by dissolving 0.9 g AAm and 0.016 g DMPP into 796 μL deionized water and 109 μL ethyl methacrylate (EMA). Poly ethyl methacrylate p(EMA) was also prepared by dissolving 0.016 g DMPP into 1091 μL EMA. All three solutions were placed into a sonicator at the temperature range from 30 to 35 °C for about 30 minutes. Membranes were formed after coating 50 μL of each solution on the plastic lids and exposed to ultraviolet in the presence of nitrogen for 10 minutes. These methods referred to Rozi et al. [9].

Swelling test

The p(AAm-*co*-EMA) and p(AAm-*co*-EMA)/AgNWs films were immersed in separated petri dishes that contained 10 mL distilled water at room temperature. For every 2 minutes, the membranes were taken out and dried with a tissue before the weight of the swollen membrane was recorded. The swelling percentages were calculated using Equation 1 below.

$$\text{Swelling percentage} = \frac{W_f - W_i}{W_i} \times 100\ \% \quad (1)$$

where, W_i is defined as initial weight of dry membranes and W_f is final weight of swollen membranes

Preparation of membranes and nanocomposite membranes

Acrylamide/ethyl methacrylate/silver nanowires, AAm/EMA/AgNWs solution was prepared by mixing it with different volume percentages of AgNWs, which were 0.02, 0.04, 0.06, 0.08, and 0.10 % v/v into AAm/EMA solution. Meanwhile, $Ru(bpy)_3^{2+}$ solution needed to be prepared first to produce poly(acrylamide-*co*-ethyl methacrylate)/ $Ru(bpy)_3^{2+}$, p(AAm-*co*-EMA)/$Ru(bpy)_3^{2+}$. The $Ru(bpy)_3^{2+}$ solution was prepared by dissolving 0.0374 g tris(2,2′-bipyridyl)dichlororuthenium(II) hexahydrate into 5 mL of deionized water. Different volume percentages of $Ru(bpy)_3^{2+}$ solution, which were 0.5, 1.0, 1.5, 2.0, and 2.5 %v/v, were mixed with AAm/EMA solution. Poly(acrylamide-*co*-ethyl methacrylate)/$Ru(bpy)_3^{2+}$/silver nanowires, p(AAm-*co*-EMA)/$Ru(bpy)_3^{2+}$/ AgNWs were prepared by mixing AAm/EMA solution with the optimized volume percentage of AgNWs and $Ru(bpy)_3^{2+}$. All the three solutions were placed on screen-printed electrodes at 5 μL each. Screen-printed carbon electrodes coated with the solutions were polymerized under nitrogen gas flow for 10 minutes and later used as working electrodes for the electrochemical analysis.

Preparation of electrochemical analysis

Firstly, 0.1 M pH 7 phosphate buffer solution and 1×10^{-5} M MG solution were prepared for electrochemical analysis. The buffer solution was prepared by mixing 49.9 mL dipotassium hydrogen phosphate solution (K_2HPO_4) and 0.1 mL potassium dihydrogen phosphate (KH_2PO_4) in 500 mL volumetric flask and the remaining volume was filled with deionized water. The pH of phosphate buffer solution was altered by using HCl and NaOH solutions until its pH reached pH 7. Meanwhile, 1×10^{-5} M MG solution was prepared by diluting 100 μL of 1×10^{-3} M MG in a 10 mL volumetric flask. Both solutions were fixed to be used as analyte solution. Then, a voltammetric cell was prepared by arranging three electrodes, which were working electrode, reference electrode, and auxiliary electrode, in a triangular form. The working electrode used was screen-printed carbon electrode coated with poly(acrylamide-*co*-ethyl methacrylate)/ $Ru(bpy)_3^{2+}$/silver nanowires, p(AAm-*co*-EMA)/$Ru(bpy)_3^{2+}$/AgNWs. The reference electrode

used was silver/silver chloride (Ag/AgCl) electrode and the auxiliary was glassy carbon electrode. The voltage range used was -1.5 V to 1.5 V with a scan rate of 0.1 V/s.

Results and Discussion

Fourier transform infra-red spectroscopy analysis

Figure 3 shows FTIR spectrum for polyacrylamide, pAAm, poly ethyl methacrylate, pEMA and poly(acrylamide-*co*-ethyl methacrylate), p(AAm-*co*-EMA).

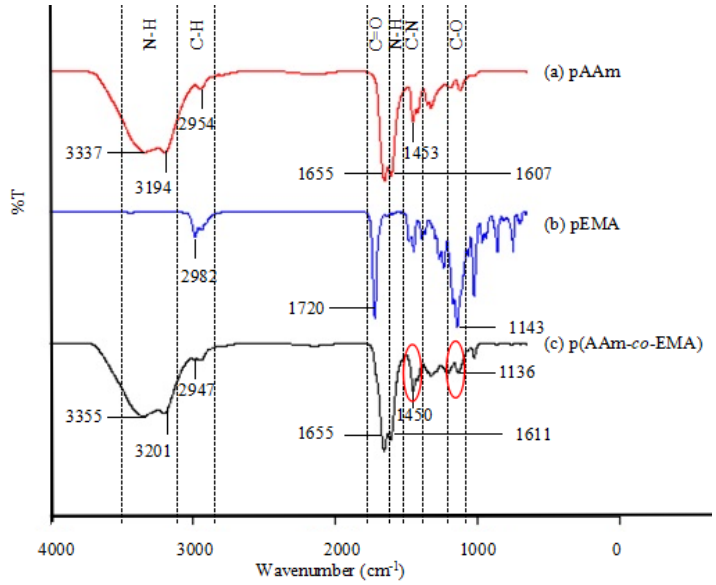


Figure 3. FTIR spectrum from (a) pAAm (b) pEMA and (c) p(AAm-*co*-EMA)

From Figure 3, pAAm showed strong bands at 3337 cm^{-1}, 3194 cm^{-1}, 1655 cm^{-1}, and 1607 cm^{-1}, due to N-H stretching, C=O stretching, and N-H bending, respectively. The N-H stretching showed two peaks because of the primary amide [17]. Meanwhile, pEMA displayed strong bands at wavenumbers 1720 cm^{-1} and 1143 cm^{-1}, due to C=O stretching and C-O stretching. The p(AAm-*co*-EMA) spectrum also revealed strong bands at wavenumbers 3355 cm^{-1}, 3201 cm^{-1}, 1655 cm^{-1}, and 1611 cm^{-1}, due to N-H stretching, C=O stretching, and N-H bending, respectively, which indicated the presence of AAm and EMA. Furthermore, the small peak at wavenumber 1136 cm^{-1} due to C-O stretching also indicated the presence of EMA. It was found that these spectra were comparable to the findings reported by Ain et al. [18]. These functional groups can be confirmed by NMR spectra.

^{1}H nuclear magnetic resonance spectroscopy

Figure 4 shows the ^{1}H NMR spectrum for polyacrylamide, pAAm and poly(acrylamide-*co*-ethyl methacrylate), p(AAm-*co*-EMA). NMR spectroscopy was used to analyze the content in the sample and its molecular structure by nuclear spin transition.

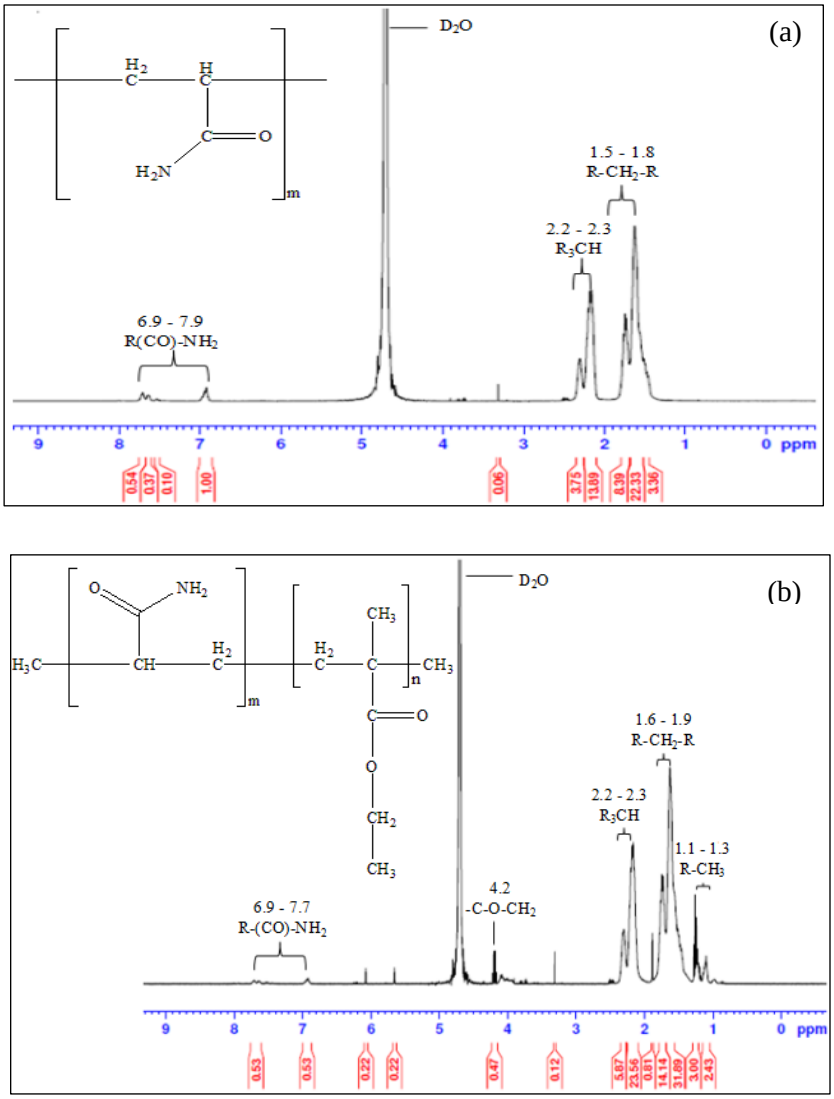


Figure 4. [1]H NMR spectrum of (a) pAAm and (b) p(AAm-*co*-EMA)

The presence of peaks at chemical shifts 6.9 ppm and 7.9 ppm in pAAm spectrum indicated that the primary amide group can also be seen in p(AAm-*co*-EMA) at chemical shifts 6.9 ppm and 7.7 ppm. The two peaks appeared in the spectrum because of the quadrupole broadening of amide group resonance. Furthermore, the nonequivalence of hydrogen on nitrogen happened due to restricted rotation [17]. Besides, the peaks at 2.2 ppm until 2.3 ppm and 1.6 ppm until 1.9 ppm indicated tertiary alkyl group and secondary alkyl group respectively, which represented AAm in p(AAm-*co*-EMA). Meanwhile, the peak at 4.2 ppm that indicated the ester group showed the presence of EMA in p(AAm-*co*-EMA). According to Pavia et al. [17], the desheilding effect occurred due to the electronegativity of oxygen atom attached to the carbon, while the peak split into a quartet because the ester group was part of a long polymer chain. The peaks for the primary alkyl group can be seen at chemical shift 1.1 ppm until 1.3 ppm because its hydrogens were a highly shielded type of proton and also showed the presence of EMA in p(AAm-*co*-EMA). These peaks corroborated the FTIR spectra and proved the photopolymerization of p(AAm-*co*-EMA).

Swelling test

Figure 5 shows the graph of swelling percentages of poly(acrylamide-*co*-ethyl methacrylate),p(AAm-*co*-EMA) and poly(acrylamide-*co*-ethyl methacrylate)/ silver nanowires, p(AAm-*co*-EMA)/AgNWs. From the figure below, it can be seen that the swelling ability for p(AAm-*co*-EMA) and p(AAm-*co*-EMA)/AgNWs had almost the same pattern for the first 6 minutes. However, after 8 minutes, p(AAm-*co*-EMA)/AgNWs showed a lower swelling percentage compared to p(AAm-*co*-EMA). The strong interaction between polymer matrix and AgNWs blocking the formation of pores caused the low diffusion [19]. The micrograph of cross section proved that the addition of AgNWs caused the low swelling percentage.

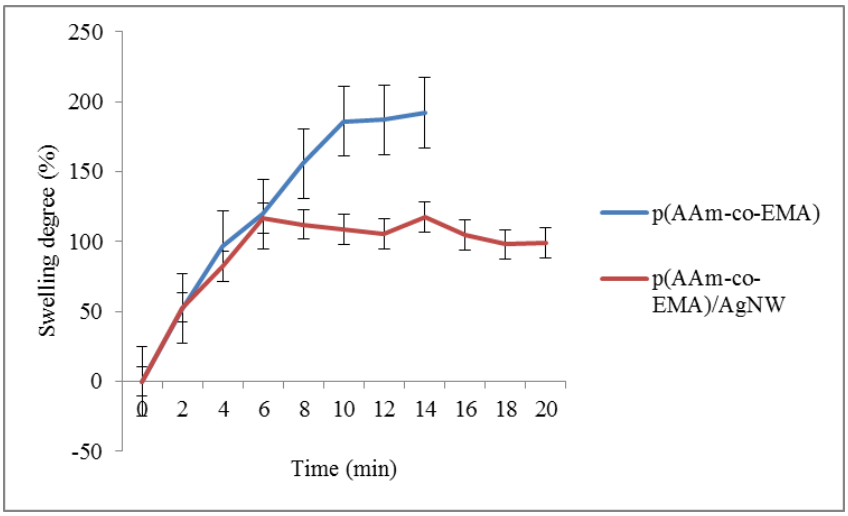


Figure 5. The swelling percentage as a function of time for p(AAm-*co*-EMA) and p(AAm-*co*-EMA)/AgNWs

Field emission scanning electron microscopy/electron dispersive X-ray

Figure 6 shows the micrograph of the cross section for poly(acrylamide-*co*-ethyl methacrylate), p(AAm-*co*-EMA) and poly(acrylamide-*co*-ethyl methacrylate)/silver nanowires, p(AAm-*co*-EMA)/AgNWs. From Figure 6(a), it shows the porous surface of p(AAm-*co*-EMA), while Figure 6(b) reveals the smooth surface of p(AAm-*co*-EMA)/AgNWs. This may be due to AgNWs acting as a filler, thus filling the pores on p(AAM-*co*-EMA). As a result, the swelling percentage of p(AAm-*co*-EMA)/AgNWs was lower than p(AAm-*co*-EMA).

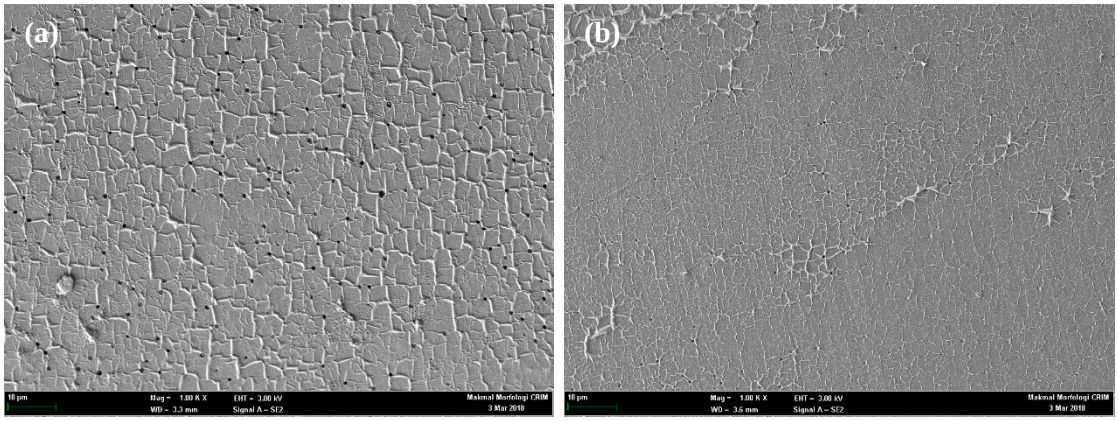


Figure 6. Cross-section micrograph at magnification 1000x (a) p(AAm-*co*-EMA) (b) p(AAm-*co*-EMA)/AgNW

Figure 7(a) shows the EDX spectrum for poly(acrylamide-*co*-ethyl methacrylate)/silver nanowires, p(AAm-*co*-EMA)/AgNWs. Meanwhile, Figure 7(b) shows the micrograph of dispersion of AgNW for p(AAm-*co*-EMA)/AgNWs. From the EDX spectrum, the presence of AgNWs can be seen with weight percentage 0.1%. The result was acceptable due to the presence of 0.06% v/v of AgNWs in p(AAm-*co*-EMA). The presence of other elements like carbon, C, oxygen, O, and nitrogen, N indicated the presence of p(AAm-*co*-EMA). From the mapping micrograph, AgNWs were not well distributed because of agglomeration. Therefore, Figure 7(b) shows an empty spot due to the inhomogeneity of AgNWs in p(AAm-*co*-EMA).

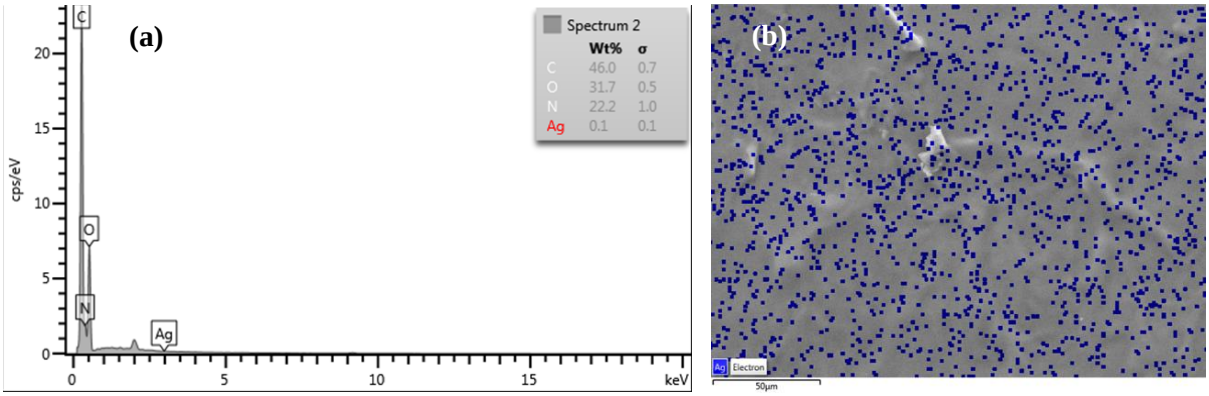


Figure 7. (a) EDX spectrum for p(AAm-*co*-EMA)/AgNWs (b) Mapping of AgNWs of p(AAm-*co*-EMA)/AgNWs

Thermogravimetry analysis

Figure 8 shows the thermogram of poly(acrylamide-*co*-ethyl methacrylate), p(AAm-*co*-EMA) and poly(acrylamide-*co*-ethyl methacrylate)/silver, p(AAm-*co*-EMA)/AgNWs. Both thermograms showed one step in the thermal degradation pattern. The degradation started at 322.84 °C and 499.82 °C. The presence of conductive materials like AgNWs was able to increase the heat resistance. Thus, it causes the maximum temperature of thermal degradation reading to increase. The increasing amount of silver nanoparticle showed the increase of maximum temperature of thermal degradation at range 2 °C to 11 °C [20]. However, the maximum thermal degradation temperature in both samples was about 400 °C. This was due to the very small amount of AgNWs present in p(AAm-*co*-EMA). The p(AAm-*co*-EMA) lost 69.53% of its weight and p(AAm-*co*-EMA)/AgNW lost 56.03% of its weight. According to Bihter et al. [20], the increasing amount of conductive material added should increase the loss of weight percentage. However, due to the different weights of samples used in this experiment, the loss of weight percentages differed.

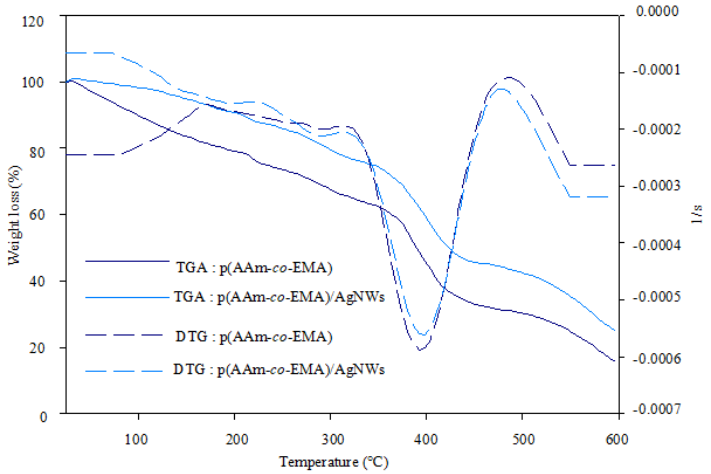


Figure 8. Thermogram for p(AAm-*co*-EMA) and p(AAm-*co*-EMA)/AgNWs

Electrochemical behaviors of malachite green

Figure 9 shows different electrochemical behaviors of 1 × 10^{-5} M MG solution by using different types of films coated on the screen-printed carbon electrode (SPE) that acted as the working electrode. The p(AAm-*co*-EMA)/SPE showed neither anodic nor cathodic peak in the cyclic voltammogram. Meanwhile, the p(AAm-*co*-EMA)/AgNWs/$Ru(bpy)_3^{2+/}$SPE showed that a small cathodic peak of malachite green can be seen at around -1.0 V and a small anodic peak can be seen at around 0.25 V [21]. The cathodic peak showed that one electron was oxidized to form malachite green cation radical, while the anodic indicated the deprotonated of malachite green cation radical to form malachite green free radical [15]. The schematic reaction for the detection of malachite green can be seen in Scheme 1. Malachite green radical formed with the help of redox reaction of $Ru(bpy)_3^{2+}$. Thus, the cyclic voltammogram showed the reversible reaction of malachite green. The p(AAm-*co*-EMA)/AgNWs/$Ru(bpy)_3^{2+/}$SPE showed the highest current values for both cathodic and anodic peaks. Thus, the presence of $Ru(bpy)_3^{2+}$ was able to help the detection of malachite green and AgNWs was able to increase the sensitivity of working electrodes. However, the lack of porosity of p(AAm-*co*-EMA) as shown in the cross section of SEM micrograph led to low current value.

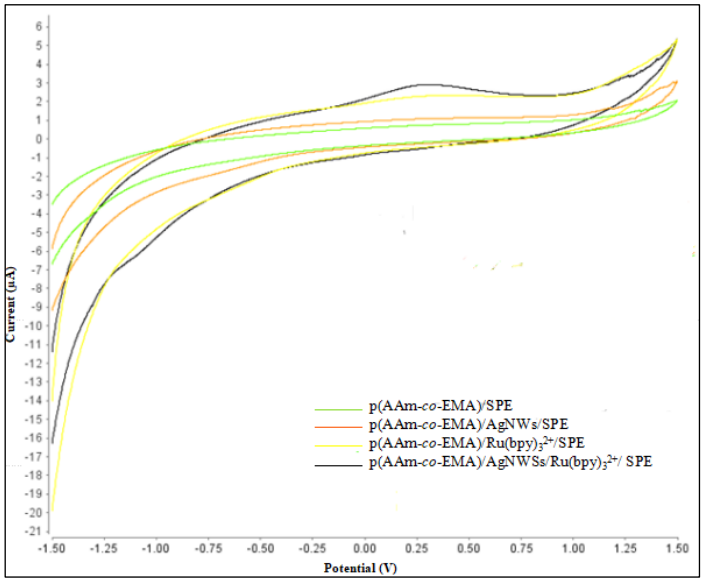


Figure 9. The cyclic voltammogram for different type of film coated on screen printed carbon electrode

$$Ru(bpy)_3^{2+} - e^- \rightarrow Ru(bpy)_3^{3+}$$

$$Ru(bpy)_3^{3+} + MG \rightarrow Ru(bpy)_3^{2+} + {}^{\bullet+}MG$$

$$MG - e^- \rightarrow {}^{\bullet+}MG$$

$${}^{\bullet+}MG \rightarrow {}^{\bullet}MG + H^+$$

$$Ru(bpy)_3^{3+} + {}^{\bullet}MG \rightarrow Ru(bpy)_3^{2+*} + {}^{+}MG$$

$$Ru(bpy)_3^{2+*} \rightarrow Ru(bpy)_3^{2+} + h\nu$$

Scheme 1. The proposed reaction for detection of malachite green [16]

Conclusion

The p(AAm-*co*-EMA)/AgNWs film that was characterized by ATR-FTIR showed peaks of –CN and –CO in the spectra, which confirmed that the copolymerization was successful. Besides, ^{1}H NMR spectrum proved the ATR-FTIR spectrum by showing the peak of carbonyl and amide groups. Meanwhile, the presence of silver nanowire (AgNWs) in poly(acrylamide-*co*-ethyl methacrylate) (p(AAm-*co*-EMA)) can be seen in the EDX spectrum and mapping micrograph. Based on the cyclic voltammogram, additions of AgNWs and $Ru(bpy)_3^{2+}$ in p(AAm-*co*-EMA) had improved the performance of malachite green detection. In conclusion, the p(AAm-*co*-EMA)/$Ru(bpy)_3^{2+/}$AgNWs film was suitable to use for developing a malachite green sensor with a need of porosity film modification.

Acknowledgement

The authors would like to extend their gratitude towards Faculty Sciences and Technology Universiti Kebangsaan Malaysia and Centre for Research and Innovation Management (CRIM), Universiti Kebangsaan Malaysia for providing research facilities that were used in this research. This work was supported by the FRGS/1/2016/TK07/UKM/02/2 and GUP-2016-061.

References

1. Srivastava, S., Sinha, R. and Roy, D. (2003). Toxological of malachite green. *Aquatic Toxological,* 66(3): 319 – 329.
2. Nurul, H. A. P, Faridah, S., Nur, A. M. S., Gayah, A. R., Othman, M. and Fatimah, A. B. (2013). Malachite green and leuco-malachite green detection in fish using modified enzyme biosensor. *Procedia Chemistry,* 20: 85 – 89.
3. Hahn, Y. B., Ahmad, R. and Tripathy, N. (2012). Chemical and biological sensors based on metal oxide nanostructures. *Chemical Communication,* 48: 10369 – 10385.
4. Fatma, I. K., Safa'a, M. R., Mamdouh, R. R., Mohamed K. A. E. and Hoda, M. M. (2013). A single novel PVC membrane for dual determination of sulphadimethoxine and malachite green in aquatic environment. *Arabian Journal of Chemistry*, 8: 787 – 792.
5. Faridah, S., Nurul, H. A. P., Gayah, A. R., Fatimah, A. B., Nur, A. M. S., Othman, M. and Zamri, I. (2013). Enzyme inhibition sensor for malachite green and leuco- malachite green detection in tilapia fish. *Malaysian Journal of Animal Science,* 16(1): 1 – 11.
6. Kadajji, V. G. and Betageri, G.V. (2011). Water soluble polymers for pharmaceutical applications. *Polymer,* 3: 1972 – 2009.
7. Gupta, I., Tomar, R. S., Nangpal, A. K. and Singhal, R. (2012). Synthesis and characterization of poly(AAm-co-BMA-co-AAc) hydrogels: Effect of acrylamide content on swelling behaviour. *Designed Monomers and Polymers,* 9(6): 589 – 605.
8. Yamashita, K., Matsuki, M., Matsuyama, N., Endo, T., Tojo, H. and Kurota, H. (2000). Composition for peelable coating. European Patent Office, Japan: EP 1 087 000 A1.
9. Rozi, N., Hanifah, S. A., Heng, L.Y. and Shyuan. L. H. (2016). Characterization of ultraviolet-photocured acrylamide based polymer. *American Institute of Physics,* 1784: 1 – 6.
10. Chen, S. and Guo, X. (2015). Improving the sensitivity of elastic capacitive pressure sensors using silver nanowire mesh electrodes. *IEEE Transactions on Nanotechnology,* 14(4): 619 – 623.
11. Liu, C. H. and Yu, X. (2011). Silver nano-wire based transparent, flexible, and conductive thin film. *Nanoscale Research Letters,* 6(1): 75.
12. Lee, J. H., Huynh-Nguyen, B. C., Ko, E., Kim, J. H. and Seong, G. H. (2015). Fabrication of flexible, transparent silver nanowire electrodes for amperometric detection of hydrogen peroxide. *Sensors and Actuators B: Chemical,* 224: 789 – 797.
13. Dong, L., Gari, R. R. S., Li, Z., Craig, M. M. and Hou, S. (2009). Graphene-supported platinum and platinum–ruthenium nanoparticles with high electrocatalytic activity for methanol and ethanol oxidation. *Carbon,* 48: 781 – 787.
14. Shao, J., Zhao, Y., Liu, Y. and Gao, Y. (2015). Detrermination of malachite green and leucomalachite green based on alectrochemiluminescence of $Ru(bpy)_3^{2+}$ at grapheme oxide modified glassy carbon electrode. *RSC Advances,* 5: 14547.

15. Lan, Q. F, Wang, W. C, Chen, X. H. and Chen, Z. D. (2017). A novel solid-state electrochemiluminescence sensor based on poly(3-amino-4 hydroxybenzenesulfonic acid) /$Ru(bpy)_3^{2+}$ modified electrode for determination of malachite green. *International Journal of Electrochemical Science*, 12: 6577 – 6587.
16. Liu, F., Yang, X., Zhao, Y. and Sun, S. (2013). Detection of malachite green and leucomalachite green based on electrochemiluminescence of mono- and bimetallic ruthenium tris-bipyridyl complexes at an Au electrode. *Analytical Methods*, 5(3): 660 – 665.
17. Pavia, D. L., Lampmam, G. M., Kriz G. S. and Vyvyan J. R. (2015) Introduction to spectroscopy. Cengage Learning, USA: pp. 252 – 269.
18. Ain, N. N. and Hanifah, S. A. (2017). Preparation and characterization of poly(acrylamide-*co*-ethyl methacrylate) nanocomposite membrane and its potential as chemical sensor. *Journal of Polymer Science and Technology*, 2(1): 56 – 61.
19. Hu, W., Niu, X., Li, L., Yun, S., Yu, Z. and Pei, Q. (2012). Intrinsically stretchable transparent electrodes based on silver-nanowire-crosslinked-polyacrylate composites. *Nanotechnology*, 23: 1 – 9.
20. Bihter, Z. and Mehmet, H. M. (2015). Fabrication and characterization of antibacterial polyurethane acrylate-based materials. *Materials Research*, 18(4): 867 – 872.
21. Kusuma, H. S., Sholihuddin, R. I., Harsini, M. and Darmokoesoemo, H. (2016). Electrochemical degradation of malachite green dye using carbon/TiO_2 electrodes. *Journal of Material Environmental Sciences*, 7(4): 1454 – 1460.

Malaysian Journal of Analytical Sciences, Vol 23 No 2 (2019): 336 - 344
DOI: https://doi.org/10.17576/mjas-2019-2302-17

MALAYSIAN JOURNAL OF ANALYTICAL SCIENCES
Published by The Malaysian Analytical Sciences Society
ISSN 1394 - 2506

METHOD DEVELOPMENT AND VALIDATION FOR QUANTIFICATION OF CORTISOL AND CORTISONE USING ULTRA-HIGH PERFORMANCE LIQUID CHROMATOGRAPHY-TANDEM MASS SPECTROMETRY

(Pembangunan dan Pengesahan Kaedah untuk Kuantifikasi Kortisol dan Kortison Menggunakan Kromatografi Cecair Berprestasi Ultra Tinggi-Spektrometri Jisim Gabungan)

Hazirah Abd Azhar[1,2], Mohd Salleh Rofiee[1], Mohammad Zulfadhly Jan Jam[1], Muhammad Hisyam Jamari[1], Roziah Mohd Janor[1,3], Richard Johari James[1,2]*, Teh Lay Kek[1,2], Mohd Zaki Salleh[1,2]

[1]*Integrative Pharmacogenomics Institute (iPROMISE)*
[2]*Faculty of Pharmacy*
Universiti Teknologi MARA Puncak Alam Campus, 42300 Bandar Puncak Alam, Selangor, Malaysia
[3]*Faculty of Computer & Mathematical Sciences,*
Universiti Teknologi MARA Shah Alam Campus, 40450 Shah Alam, Selangor, Malaysia

**Corresponding author: richard@uitm.edu.my*

Received: 30 May 2018; Accepted: 14 April 2019

Abstract

Cortisol and its metabolite cortisone have been used as a biological marker of stress in human psychobiological studies. Cortisol and cortisone quantitation may help to examine physiological responses towards stress. A highly sensitive and selective ultra-high performance liquid chromatography tandem mass spectrometry (UHPLC-MS/MS) method was developed for simultaneous quantitation of cortisol and cortisone in human serum. These two compounds were chromatographically separated using Agilent ZORBAX Eclipse Plus C_{18} Rapid Resolution HD column (2.1 mm × 50 mm, 1.8 µm) and were eluted with (A) 0.1% formic acid in water and (B) methanol mobile phase. The sample injection volume was 2 µL and the flow rate was set at 0.3 mL/min. The analytes were determined in positive ionization mode and quantitated by multiple-reaction monitoring (MRM) mode. The method was linear from 7.8 to 500 ng/mL for cortisol (r^2 = 0.986) and cortisone (r^2 = 0.990). The precision, accuracy, and recovery of the method for cortisol ranged from 1.98-10.46%, 90.68-91.94%, 90.38-93.88%, and cortisone ranged from 1.01-11.36%, 93.12-94.79% and 90.48-95.90%, respectively. The developed method has met the quality standards of European Medicines Agency (EMA).

Keywords: cortisol, cortisone, serum, ultra-high performance liquid chromatography-tandem mass spectrometry

Abstrak

Kortisol dan metabolitnya kortison telah digunakan sebagai penanda tekanan biologi untuk mengkaji psikobiologi manusia. Pengkuantitian kortisol dan kortison boleh membantu untuk menilai tindak balas fisologi terhadap tekanan. Kaedah kromatografi cecair berprestasi ultra tinggi -spektrometri jisim gabungan yang sangat sensitif dan selektif telah dibangunkan untuk pengkuantitian kortisol dan kortison secara serentak di dalam serum manusia. Kedua-dua sebatian ini telah dipisahkan secara kromatografi menggunakan turus Agilent ZORBAX Eclipse Plus C_{18} Resolusi Pantas HD (2.1 mm × 50 mm, 1.8 µm) dengan campuran fasa bergerak (A) 0.1% asid formik dalam air dan (B) metanol. Jumlah suntikan sampel adalah 2 µL dan kadar aliran ditetapkan pada 0.3 mL/min. Analisis ini telah ditentukan dalam mod pengionan positif dan dikira oleh mod pemantauan pelbagai tindak balas. Kaedah ini adalah linear dari 7.8 hingga 500 ng/mL untuk kortisol (r^2 = 0.986) dan kortison (r^2 = 0.990). Ketepatan, kejituan dan kadar pemulihan untuk kortisol adalah antara 1.98-10.46%, 90.68-91.94%, 90.38-93.88%, dan kortison terdiri daripada 1.01-11.36%, 93.12-94.79% dan 90.48-95.90%. Kaedah yang dibangunkan telah memenuhi piawaian kualiti agensi perubatan eropah (EMA).

Kata kunci: kortisol, kortison, serum, kromatografi cecair berprestasi ultra tinggi - spektrometri jisim gabungan

Introduction

Cortisol is the main glucocorticoid hormone produced by the adrenal cortex that regulates the metabolism of carbohydrates, proteins and lipids. Its synthesis is stimulated through a hypothalamic-adrenal-pituitary feedback system. Cortisol hormone in human body undergoes diurnal variation where the level is high early in the morning and reaches its lowest level at midnight [1, 2]. Cortisol is involved in the feedback mechanism of the immune system that suppresses immune activity, thus it is used to treat overactive immune diseases such as allergies, asthma, inflammatory disorder and autoimmune disease [3]. Cortisone is interconverted to the inactive metabolite of cortisol by enzymes 11β-hydroxysteroid dehydrogenase (11βHSD) [4-6].

Cortisol has been associated with physiological response towards depression, anxiety and stress [7-9]. Stress has been reported to increase the activity of the hypothalamus-pituitary-adrenal (HPA) axis with a subsequent rise in cortisol level [10, 11]. Thus, serum cortisol concentration may serve as a diagnostic tool for depressive disorder and stress. Low levels of cortisol are seen in patients with rare adrenal enzyme defects and after long-lasting stress. Uncontrolled stress has been associated with increased risk of several health complications such as heart disease, diabetes, immunosuppression and cognitive impairment [12]. Research by the Institute for Public Health reported that estimated 29.9% of adults in Malaysia are experiencing mental health problems such as depression and anxiety. The increasing trend of mental health problems from the prevalence of 10.7% estimated in 1996 demands close attention towards this issue [13]. Besides, a study by Armitage et al., stated that the prevalence of suicide in Malaysia was six to eight per 100000 population per year [14]. This figure indicates a high prevalence of psychiatric morbidity among Malaysian. Thus, proper intervention to monitor stress level in the Malaysian context is required.

Clinically, cortisol is measured directly from biological samples using immunoassays. However, this method has been known to have disadvantages such as sample matrix effect and cross-reactivity with endogenous steroid, lipids or metabolites which affect the method specificity [15-17]. Furthermore, low levels of serum cortisol and cortisone and similarity in their chemical structure, make this analysis a challenge [18]. Therefore, a highly specific and sensitive analytical tool is needed to quantitate the concentration of the two closely identical molecules such as cortisol and cortisone in biological samples. In this respect, quantitative analysis of low-concentration analytes is possible by using a highly reproducible, selective, and sensitive liquid chromatography-tandem mass spectrometry (LC/MS-MS) methods [19-21]. The validated method is useful for investigation of hormone status for the diagnosis and treatment of clinical disorders.

The charcoal-stripped serum has been widely used in biological and cellular studies. Charcoal-stripping of serum is intended to remove a variety of endogenous compounds, including hormones [22]. Since cortisol and cortisone are endogenous steroids, charcoal-stripped serum was used as a blank sample. Several factors contribute to the efficiency of removing hormones using activated charcoal which includes the amount of charcoal and temperature [23]. Pre-treated serum with charcoal powder may reduce matrix effect and increase method selectivity due to the removal of endogenous compounds that might interfere with the target compound [24-26].

The aim of this study was to develop and validate a method for simultaneous quantification of serum cortisol and cortisone using UHPLC-MS/MS according to the guideline outlined by European Medicines Agency (EMA) [27]. Evaluation of the performance of the method includes linearity, accuracy, precision, recovery, matrix effect and stability.

Materials and Methods

Materials and reagents

Standards of cortisol (98%) and cortisone (98%) were purchased from Sigma-Aldrich Co. (St. Louis, MO, USA). Fluconazole (98%) as an internal standard (IS) was purchased from Sigma-Aldrich Co. (St. Louis, MO, USA). All the liquid chromatography grade of methanol, acetonitrile and formic acid were purchased from Merck (Darmstadt,

Germany) and water used in the experiment was purified by using an ELGA PURELAB ultra purification system (Wycombe, Buckinghamshire, UK).

LC-MS/MS characteristics

Chromatographic separation was performed using Agilent ZORBAX Eclipse Plus C_{18} Rapid Resolution HD column (2.1 mm × 50 mm, 1.8 µm) and quantitation was performed on Agilent 6460 triple-quadrupole mass spectrometer equipped with auto-injector and quaternary pump. The injection volume was 2 µL and the column temperature was kept constant at 30 ºC. The mobile phases utilized used were: (A) distilled water with 0.1% formic acid and (B) methanol at a flow rate of 0.3 mL/min. The analytes were separated by a gradient of 0 to 6 minutes with increasing percentage of solvent B from 40 to 70%. Then the solvent ratio was maintained with 70% solvent B for 30 seconds and decrease gradually from 70 to 40% of solvent B over for 1.30 minutes. The LC condition was re-equilibrated to initial condition for 2.5 minutes. The analytes were determined in positive ionization mode and quantitated by multiple-reaction-monitoring (MRM) mode. Mass spectrometry was operated in Electrospray ionization (ESI) with Agilent jet stream technology with the optimum gas temperature at 280 ºC, gas flow at 12 L/min, nebulizer at 35 psi and capillary at 4000 V, respectively. Agilent Mass Hunter Qualitative Analysis (B.06.00) and Agilent Mass Hunter Quantitative Analysis (B.07.00) were used for the collection acquisition and analysis of the data.

Serum charcoal-stripping

Cortisol and cortisone are present in human serum at significant levels. A blank matrix which is free of the target analyte is needed for the preparation of calibration standards and quality control samples. Charcoal-stripping of serum was intended to remove a variety of endogenous compounds, including hormones. Serum samples were obtained from 6 healthy volunteers at Integrative Pharmacogenomics Institute (iPROMISE), Universiti Teknologi MARA. The serum was charcoal-stripped using 1g of activated charcoal powder added to 10 mL of pooled serum followed by incubation for 1 hour with agitation at 55 °C. After centrifugation at 14,000 g for 30 minutes, the supernatant was separated leaving the charcoal at the bottom and filtered using a 0.22 µm filter.

Sample extraction

Sample extraction was done using a simple protein precipitation in-house method. A 100 µL of serum sample was transferred into a tube, 20 ng/mL of fluconazole as an IS was added followed by 400 µL of ice-cold acetonitrile. The tube was vortexed to mix for 30 seconds and centrifuged at 4,100 rpm for 15 minutes at room temperature. The supernatant was transferred to a clean glass tube and evaporated to dryness using concentrator (5301, Eppendorf, Hamburg). The dried sample was reconstituted with 50 µL of methanol: water (1:1) followed by 30 seconds vortex mixing, which was then transferred to screw-capped injection vial.

Validation

The proposed method was validated in accordance with the European Medicines Agency (EMA). The linearity, accuracy, precision, recovery, matrix effect and stability of the method were evaluated. The calibration curves were prepared using charcoal-stripped blank serum spiked with both reference materials using 2-fold serial dilution from 500 ng/mL to 7.8 ng/mL. Each concentration point level was prepared and assayed in triplicates on 3 different days. The linearity was evaluated by analysing the slope, intercept and correlation coefficient, weight ($1/x^2$) linear least-squares regression. Intra-day and inter-day precision and accuracy were done by analysing three replicates samples spiked with both reference material at low, medium and high concentration level (20, 200 and 400 ng/mL) on the same day and on 3 different days for inter-day validation. The accuracy was evaluated by comparing the measured concentration with the true value and the precision was expressed as the relative standard deviation percentage (RSD%).

The extraction recovery was determined by comparing the peak areas from serum spiked before extraction with those spiked after extraction. The matrix effect was determined using the ratio of peak areas of the blank serum spiked after extraction with those of pure standard solution containing the same amount of the analyte. Then the coefficient variation of the IS-normalised matrix effect was assessed by dividing the matrix effect of the analyte by the matrix effect of the IS. The stability of the analytes in serum was assessed by analysing the spiked serum samples and kept at room temperature for 24 hours, in autosampler at 10 ºC for overnight and three times freeze-

thaw cycles at -80 ºC and compare to a freshly prepared QC sample. Three replicates were analysed for each storage condition at low, medium and high concentrations (20, 200 and 400 ng/mL).

Results and Discussion

An LC-MS/MS method for simultaneous quantitation of cortisol and cortisone concentration in human serum was developed and validated. Collision-induced dissociation was performed to produce two product ions that act as quantifier and qualifier. Quantifier and qualifier transitions used are described in Table 1.

Table 1. Quantifier and qualifier transition

Compound	Quantifier m/z	Qualifier m/z
Cortisol	363.2>121.1	363.2>91.1
Cortisone	361.2>163.1	361.2>121.1
Fluconazole (IS)	307.1>238.1	307.1>220.0

Gradient elution of mobile phase with 0.3 mL/min flow rate was suggested as a suitable method for complete and rapid separation of cortisol and cortisone. Figure 1 shows typical chromatograms for cortisol, cortisone and IS in serum. The retention times for cortisol, cortisone and IS were 5.46, 4.87 and 1.47 minute, respectively. The chromatograms show good separation with a sharp peak of target analytes, low background noise, and there are no significant interfering peaks from the sample matrix indicated that the method is highly selective to the target analytes. These results also indicated the rapid analytical time and high specificity should facilitate high throughput measurement of both cortisol and cortisone simultaneously in human serum.

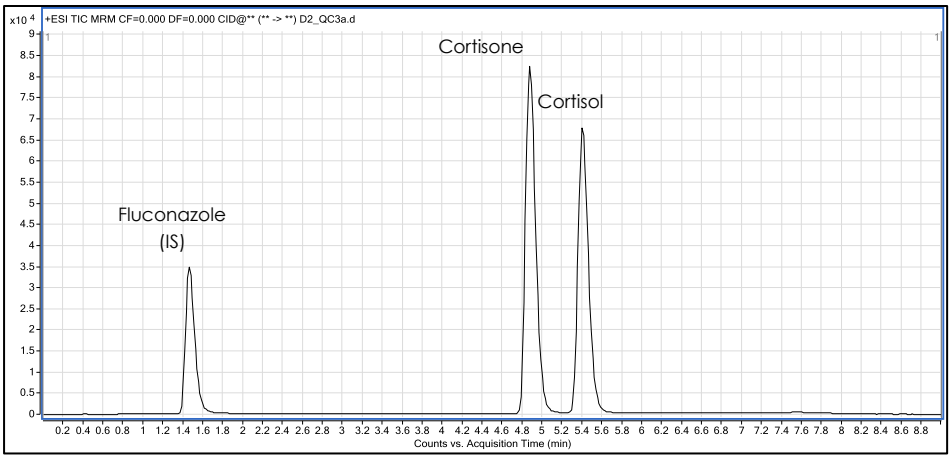


Figure 1. Chromatograms of cortisol, cortisone and fluconazole

The presence of endogenous cortisol and cortisone in the serum makes it difficult for method validation analysis. Several studies have used pooled human serum as a blank matrix [19, 28]. However, using pooled serum may cause variation in the baseline cortisol and cortisone concentration for different batches of pooled serum. Thus, the method used is neither consistent nor reproducible for long period or across laboratories. Another method adopted to overcome this problem is by using charcoal-stripped serum or plasma as a blank matrix to prepare calibration standard and quality control samples [3, 29, 30]. A study by Cao et al. revealed that charcoal treatment may completely or nearly completely extracted cortisol hormone present in fetal bovine serum and bovine calf serum [22]. In this study, activated charcoal powder was used to remove endogenous cortisol and cortisone from pooled human serum. The results demonstrate that activated charcoal powder efficiently removes endogenous cortisol and cortisol from human serum at the level lower than the detection limit, as shown in Figure 2. Both compounds were

removed from serum by 1 hours of incubation at 55 °C with 1 g/mL of activated charcoal powder. The high amount of charcoal powder attributed to the greater availability of surface area and increase the adsorption site and the high in temperature also contributed to the removal of the hormones where thermodynamic effect facilitates the sorption process [23]. The resultant cortisol and cortisone free serum is a suitable blank matrix for method validation analysis.

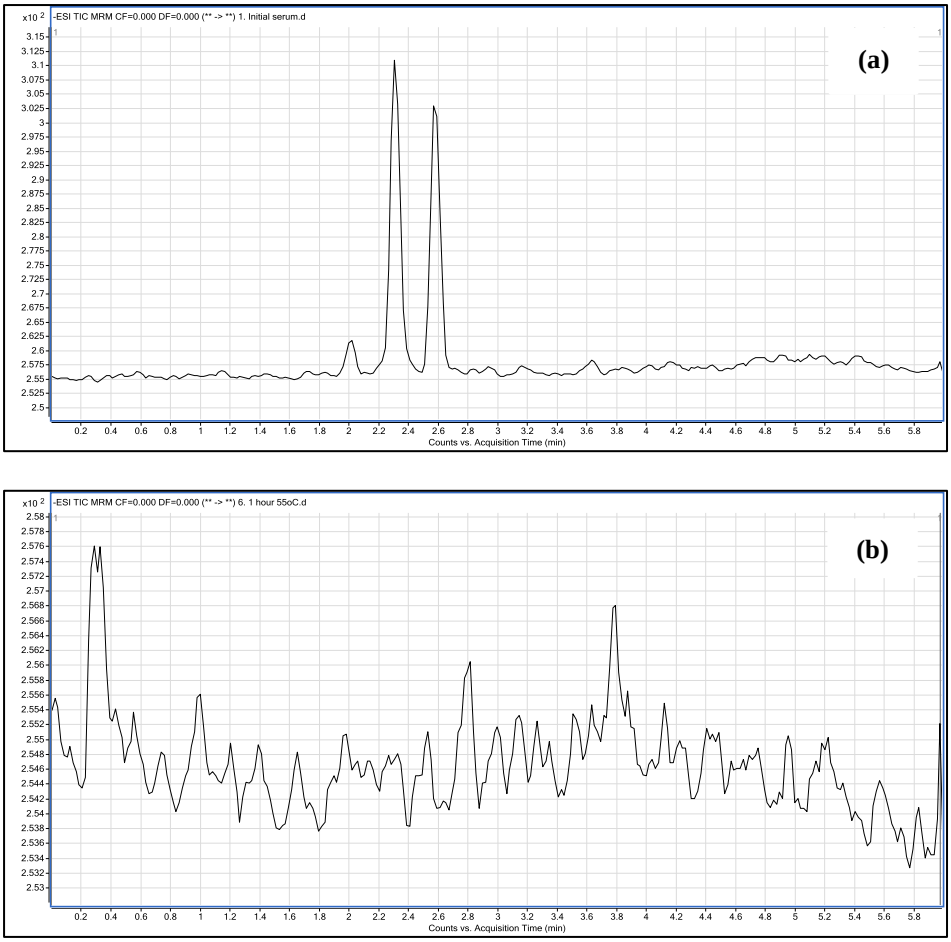


Figure 2. Chromatogram of pooled human serum samples (a) prior to and (b) after the removal of cortisol and cortisone by charcoal-stripping method

The correlation coefficients (r^2) of the calibration curves are 0.98 for cortisol and 0.99 for cortisone over the range of 7.8–500 ng/mL, indicating good linearity (Table 2). Accuracy and precision data are presented in Table 3. Intra-day accuracy ranges from 90.68 to 91.94% for cortisol and 93.12 to 94.79% for cortisone, while precision ranges from 1.98 to 10.46 for cortisol and 1.01 to 11.36 for cortisone. Inter-day accuracy ranges from 94.50% to 104.28% for cortisol and 100.70% to 104.28% for cortisone, while precision ranges from 7.18% to 11.00% for cortisol and 11.07% to 15.78% for cortisone. All the accuracy results are within the limit of ±15% and precision results are below 15% except for inter-day precision for cortisone where the result is slightly high. The results obtained using this method produced equivalent results from a previous study [3].

Table 2. The regression equation, correlation coefficients (r^2), linear range and lower limit of quantitation data

Compound	Regression Equation	Correlation Coefficients (r^2)	Linear Range (ng/mL)
Cortisol	0.112255X + 0.003791	0.98	7.8 - 500
Cortisone	0.166686X + 0.004023	0.99	7.8 - 500

Table 3. Precision and accuracy data

Compound	Spiked Concentration (ng/mL)	Intra-day			Inter-day		
		Mean Measured Concentration (ng/mL)	Precision (RSD%)	Accuracy (%)	Mean Measured Concentration (ng/mL)	Precision (RSD%)	Accuracy (%)
Cortisol	20	18.14	10.46	90.68	18.92	7.18	94.50
	200	183.89	2.20	91.94	208.56	10.37	104.28
	400	366.47	1.98	91.62	414.42	11.00	103.61
Cortisone	20	18.67	11.36	93.33	20.14	15.78	100.70
	200	186.23	1.01	93.12	207.21	11.07	103.61
	400	379.17	1.02	94.79	417.13	13.27	104.28

Extraction recovery and matrix effect data are shown in Table 4. The mean recoveries of serum samples spiked with standards at a low, medium and high concentration (20, 200 and 400 ng/mL) are 93.88%, 90.38% and 92.09% for cortisol and 95.90%, 90.48% and 92.54% for cortisone, respectively. This method managed to achieve high analyte recovery using a simple and cost-effective protein precipitation method as compared to the solid phase extraction (SPE) method [5]. The IS-normalized matrix effect of serum samples at all concentration levels are within the limit which is less than 15%.

Stability data are presented in Table 5. The stability test was done at three different conditions which were 24 hours room temperature, overnight in autosampler (10 ºC) and three times freeze-thaw cycles (-80 ºC). The stability value for both compounds in autosampler (10 ºC) overnight are within the limit which is ±15% of the nominal concentration. However, cortisol and cortisone compounds are not stable at medium and high concentration levels at 24-hour room temperature and both compounds are not stable at all concentration levels in three times freeze-thaw cycles (-80 ºC). The variation in analyte measurement that exceeded the acceptance limit could be due to the room temperature and evaporation effects [31]. Thus, to maintain the integrity of the results, samples should avoid these conditions that may cause instability of the compounds.

Table 4. Mean extraction recoveries and matrix effects of the cortisol and cortisone

Compound	Mean Extraction Recovery (%)			IS-Normalized Matrix Effect (%)		
	Low	Medium	High	Low	Medium	High
Cortisol	93.88	90.38	92.09	13.30	4.25	8.40
Cortisone	95.90	90.48	92.54	7.94	8.34	7.26

Table 5. Stability of the two analytes in 3 different conditions

Compound	Freshly Prepared Sample (ng/mL)	Overnight in Autosampler (10 ºC)		24 Hours at Room Temperature		Three Times Freeze-Thaw Cycles (-80 ºC)	
		Measured Concentration (ng/mL)	Stability (%)	Measured Concentration (ng/mL)	Stability (%)	Measured Concentration (ng/mL)	Stability (%)
Cortisol	18.70	21.18	113.52	20.64	110.73	15.73	84.24
	223.15	224.83	100.75	281.47	126.15	168.04	75.30
	417.20	431.48	103.05	503.74	121.01	342.17	82.13
Cortisone	19.40	21.22	109.62	19.74	101.96	16.40	84.6
	222.99	221.18	99.19	269.63	120.92	174.81	78.39
	418.18	424.88	101.30	493.80	118.27	352.33	84.32

Conclusion

Charcoal-stripped serum was used for method validation process and a highly selective, sensitive reliable and rapid quantitation method for cortisol and cortisone that fulfilled the criteria of European Medicines Agency (EMA) was developed and validated. The method developed may be useful to assess physiological response towards depression, anxiety and stress in future research work.

Acknowledgment

The authors fully acknowledged the Ministry of Education, Malaysia through the Fundamental Research Grant Scheme (FRGS, Sponsorship file number: FRGS/2/2014/SKK02/UITM/02/3) and Universiti Teknologi MARA through Bestari Perdana Grant (file number: 600-IRMI/DANA 5/3/BESTARI (P) 006/2018) and 241810/2016/RMJJ/15 for supporting this study. The authors wish to thank Professor Dr Azni Zain Ahmed of InQKA, Universiti Teknologi MARA, Malaysia for proofreading the article.

References

1. Knutson, U., Dahlgren, J., Marcus, C., Rosberg, S., Bronnegard, M., Stierna, P. and Albertsson-Wikland, K. (1997). Circadian cortisol rhythms in healthy boys and girls: Relationship with age, growth, body composition, and pubertal development. *Journal of Clinical Endocrinology and Metabolism*, 82(2): 536.
2. Aube, B. L. L., Curbow, B. A., Ostello, R. W. and Fitzgerald, S. T. (2002). A pilot study examining the relationship between stress and serum cortisol concentrations in women with asthma. *Respiratory Medicine*, 96: 823 – 828.
3. Lee, S., Lim, H. S., Shin, H. J., Kim, S. A., Park, J., Kim, H.C., Kim, H., Kim, H. J., Kim, Y.T., Lee, K. R. and Kim, Y. J. (2014). Simultaneous determination of cortisol and cortisone from human serum by liquid chromatography-tandem mass spectrometry. *Journal of Analytical Methods in Chemistry*, 2014: 787483.
4. De Palo, E. F., Antonelli, G., Benetazzo, A., Prearo, M. and Gatti, R. (2009). Human saliva cortisone and cortisol simultaneous analysis using reverse phase HPLC technique. *Clinica Chimica Acta*, 405: 60 – 65.
5. Ray, J. A., Kushnir, M. M., Rockwood, A. L. and Meikle, A. W. (2011). Analysis of cortisol, cortisone and dexamethasone in human serum using liquid chromatography-tandem mass spectrometry and assessment of cortisol: Cortisone ratios in patients with impaired kidney function. *Clinica Chimica Acta*, 412: 1221 – 1228.
6. Lee, S., Kwon, S., Shin, H. J., Lim, H. S., Singh, R. J., Lee, K. R. and Kim. Y. J. (2010). Simultaneous quantitative analysis of salivary cortisol and cortisone in Korean adults using LC-MS/MS. *BMB Reports*, 43(7): 506 – 511.
7. Zhai, X., Chen, F., Zhu, C. and Lu. Y. (2015). A simple LC-MS/MS method for the determination of cortisol, cortisone and tetrahydro-metabolites in human urine: Assay development, validation and application in depression patients. *Journal of Pharmaceutical and Biomedical Analysis*, 107: 450 – 455.

8. Levine, A., Zagoory-Sharon, O., Feldman, R., Lewis, J. G., and Weller. A. (2007). Measuring cortisol in human psychobiological studies. *Physiology and Behavior*, 90(1): 43 – 53.
9. Milam, J., Slaughter, R., Verma, G. and McConnell. R. (2014). Hair cortisol, perceived stress and dispositional optimism: a pilot study among adolescents. *Journal of Traumatic Stress Disorders & Treatment*, 3(3): 1 – 13.
10. Herane Vives, A., De Angel, V., Papadopoulos, A., Strawbridge, R., Wise, T., Young, A. H., Arnone, D. and Cleare. A. J. (2015). The relationship between cortisol, stress and psychiatric illness: New insights using hair analysis. *Journal of Psychiatric Research*, 70: 38 – 49.
11. Pani, S. C., Al Askar, A. M., Al Mohrij, S. I. and Al Ohali, T. A. (2011). Evaluation of stress in final-year Saudi dental students using salivary cortisol as a biomarker. *Journal of Dental Education*, 75(3): 377 – 384.
12. Lundberg, U. (2005). Stress hormones in health and illness: The roles of work and gender. *Psychoneuroendocrinology*, 30(10): 1017 – 1021.
13. Institute for Public Health (2015). National Health and Morbidity Survey 2015 (NHMS 2015): Non-Communicable Diseases, Vol. II. San Diego, California.
14. Armitage, C. J., Panagioti, M., Rahim, W. A., Rowe, R., O'Connor, R. C. (2015). Completed suicides and self-harm in Malaysia: A systematic review. *General Hospital Psychiatry*, 37(2): 153 – 165.
15. Singh, R., Goyal, M., Tiwari, S., Ghildiyal, A., Nattu, S. M. and Das, S. (2012). Effect of examination stress on mood, performance and cortisol levels in medical students. *Indian Journal of Physiology and Pharmacology*, 56(1): 48 – 55.
16. Owen, L. J., Adaway, J. E., Davies, S., Neale, S., El-Farhan, N., Ducroq, D., Evans, C., Rees, D. A., Mackenzie, F. and Keevil, B. G. (2013). Development of a rapid assay for the analysis of serum cortisol and its implementation into a routine service laboratory. *Annals of Clinical Biochemistry*, 50(4): 345 –352.
17. Turpeinen, U. and Hämäläinen, E. (2013). Determination of cortisol in serum, saliva and urine. *Best Practice and Research: Clinical Endocrinology and Metabolism*, 27(6): 795 – 801.
18. Monaghan, P. J., Keevil, B. G. and Trainer, P. J. (2013). The use of mass spectrometry to improve the diagnosis and the management of the HPA axis. *Reviews in Endocrine & Metabolic Disorder*, 14(2): 143 – 157.
19. Lopes Alves, A. N., Mendonca, B. B. and Valassi, H. P. L. (2015). Analytical performance of LC-MS/MS method for simultaneous determination of five steroids in serum. *Mass Spectrometry & Purification Techniques*, 1(2): 1 – 5.
20. Huang, W., Kalhorn, T. F., Baillie, M., Shen, D. D. and Thummel, K. E. (2007). Determination of free and total cortisol in plasma and urine by liquid chromatography-tandem mass spectrometry. *Therapeutic Drug Monitoring*, 29 (2): 215 – 224.
21. Kushnir, M. M., Rockwood, A. L., Roberts, W. L., Yue, B., Bergquist, J. and Meikle, A. W. (2011). Liquid chromatography-tandem mass spectrometry for analysis of steroids in clinical laboratories. *Clinical Biochemistry*, 44(1): 77 – 88.
22. Cao, Z., West, C., Norton-Wenzel, C. and Rej, R. (2009). Effects of resin or charcoal treatment on fetal bovine serum and bovine calf serum. *Endocrine Research*, 34(4): 101 – 108.
23. Ifelebuegu, A. O. (2012). Removal of steroid hormones by activated carbon adsorption—kinetic and thermodynamic studies. *Journal of Environmental Protection*, 3(6): 469 – 475.
24. Cooper, N., Khosravan, R., Erdmann, C., Fiene, J. and Lee, J. W. (2006). Quantification of uric acid, xanthine and hypoxanthine in human serum by HPLC for pharmacodynamic studies. *Journal of Chromatography B: Analytical Technologies in the Biomedical and Life Sciences*, 837: 1 – 10.
25. Ke, Y., Bertin, J., Gonthier, R., Simard, J. N. and Labrie, F. (2014). A sensitive, simple and robust LC-MS/MS method for the simultaneous quantification of seven androgen- and estrogen-related steroids in postmenopausal serum. *Journal of Steroid Biochemistry and Molecular Biology*, 144: 523 – 534.
26. Sánchez-Guijo, A., Oji, V., Hartmann, M. F., Traupe, H. and Wudy, S. A. (2015). Simultaneous quantification of cholesterol sulfate, androgen sulfates, and progestagen sulfates in human serum by LC-MS/MS. *Journal of Lipid Research*, 56(9): 1843 – 1851.
27. European Medicines Agency (2011). Guideline on bioanalytical method validation. Access from http://www.ema.europa.eu/docs/en_GB/document_library/Scientific_guideline/2011/08/WC500109686.pdf
28. Tai, S. S.-C. and Welch, M. J. (2004). Development and evaluation of a candidate reference method for the determination of total cortisol in human serum using isotope dilution liquid chromatography/mass spectrometry and liquid chromatography/tandem mass spectrometry. *Analytical Chemistry*, 76 (4): 1008 – 1014.

29. DiFrancesco, R., Frerichs, V., Donnelly, J., Hagler, C., Hochreiter, J. and Tornatore, K. M. (2007). Simultaneous determination of cortisol, dexamethasone, methylprednisolone, prednisone, prednisolone, mycophenolic acid and mycophenolic acid glucuronide in human plasma utilizing liquid chromatography-tandem mass spectrometry. *Journal of Chromatography B: Analytical Technologies in the Biomedical and Life Sciences*, 859(1): 42 – 51.
30. Ionita, I. A., Fast, D. M. and Akhlaghi, F. (2009). Development of a sensitive and selective method for the quantitative analysis of cortisol, cortisone, prednisolone and prednisone in human plasma. *Journal of Chromatography B: Analytical Technologies in the Biomedical and Life Sciences*, 877: 765 – 772.
31. Brinc, D., Chan, M. K., Venner, A. A., Pasic, M. D., Colantonio, D., Kyriakopolou, L. and Adeli, K. (2012). Long-term stability of biochemical markers in pediatric serum specimens stored at -80 °C: A CALIPER sub study. *Clinical Biochemistry*, 45: 816 – 826.

Malaysian Journal of Analytical Sciences, Vol 23 No 2 (2019): 345 - 354
DOI: https://doi.org/10.17576/mjas-2019-2302-18

MALAYSIAN JOURNAL OF ANALYTICAL SCIENCES
Published by The Malaysian Analytical Sciences Society
ISSN 1394 - 2506

LASER-ASSISTED SILICON ETCHING FOR MICRO FUEL CELL ELECTRODE PLATE FABRICATION

(Fabrikasi Plat Elektrod Sel Bahan Api Mikro dengan Punaran Silikon Terbantu Laser)

Umi Azmah Hasran[1]*, Siti Kartom Kamarudin[1,3], Burhanuddin Yeop Majlis[2], Wan Ramli Wan Daud[3], Abdul Amir Hassan Kadhum[3], Gandi Sugandi[4]

[1]*Fuel Cell Institute*
[2]*Institute of Microengineering and Nanoelectronics*
[3]*Department of Chemical and Process Engineering*
Universiti Kebangsaan Malaysia, 43600 UKM Bangi, Selangor, Malaysia
[4]*Research Center for Electronics and Telecommunication*
Lembaga Ilmu Pengetahuan Indonesia, Bandung, Indonesia

**Corresponding author: umi.h@ukm.edu.my*

Received: 13 April 2017; Accepted: 17 April 2018

Abstract

Silicon electrode plates for micro fuel cells were obtained using a microfabrication process based on the micro-electro-mechanical system (MEMS) technology. The dry etching process involved the laser ablation technique using the highly stable Nd:YAG. This technique is suitable for micromachining silicon substrates. The total size of the electrode plate was 2.5 cm x 2.5 cm and the active reaction area was 1 cm^2. An increase in laser scan numbers deepened the groove being etched on the silicon sample, but it showed a saturated behavior as the number of scans became higher. The time required to etch a complete electrode plate flow field with 14 square-shaped through-holes of 0.185 cm x 0.185 cm area using laser ablation was ~30 minutes, which was much shorter than the wet etching time of more than 10 hours with the potassium hydroxide solution (KOH) solution. The laser-etched flow field achieved vertical sidewalls as per the original design, whereas the wet-etched structure achieved a typical anisotropic hole structure with sidewalls that were approximately 54º to the electrode surface due to the <100> orientation of the silicon wafer. Therefore, the laser ablation technique was chosen to produce the electrode plates for the micro fuel cell as it can save time on the etching process and produce more precise flow field dimensions for the electrode plates with less process steps compared with the conventional wet etching processes using KOH solution.

Keywords: flow field design, MEMS technology, bulk micromachining, dry etching technique, laser ablation

Abstrak

Plat silikon untuk sel ahan api mikro dihasilkan menggunakan proses mikrofabrikasi yang berasaskan teknologi sistem mikro-elektro-mekanikal (MEMS) dengan proses punaran kering menggunakan teknik ablasi laser. Jenis laser yang digunakan untuk kerja punaran kering ini adalah Nd:YAG berkestabilan tinggi yang sesuai untuk pemesinan mikro bagi substrat silikon. Saiz keseluruhan plat elektrod yang dihasilkan adalah 2.5 cm x 2.5 cm, manakala kawasan aktif tindakbalas adalah 1 cm^2. Peningkatan bilangan imbasan menjadikan kawasan terablasi pada sampel lebih dalam tetapi punaran menjadi semakin tepu apabila bilangan imbasan semakin meningkat tinggi. Masa untuk memunar habis medan aliran plat elektrod yang mempunyai 14 lubang tembus berbentuk segi empat sama dengan keluasan 0.185 cm x 0.185 cm dengan menggunakan laser hanyalah kira-kira 30 minit, berbanding dengan proses punaran basah menggunakan kalium hidroksida (KOH) yang memakan masa lebih 10 jam. Proses yang lama ini juga memerlukan lapisan SiO_2 yang lebih tebal sebagai pelindung silikon semasa proses punaran dijalankan. Malah, punaran basah KOH ke atas wafer silikon dengan orientasi <100> memberi ciri lubang dengan dinding yang bersisi sendeng pada sudut ~ 54º dari permukaan plat dan mengakibatkan bukaan lubang mempunyai saiz yang lebih kecil daripada rekabentuk asal. Oleh itu, teknik ablasi laser dipilih untuk menghasilkan plat elektrod bagi mikro sel fuel kerana ia

dapat menjimatkan masa mikrofabrikasi dan menghasilkan dimensi medan aliran untuk plat elektrod yang lebih tepat dengan langkah aliran proses mikrofabrikasi yang kurang berbanding dengan proses punaran basah menggunakan larutan KOH.

Kata kunci: rekabentuk medan aliran, teknologi MEMS, pemesinan mikro pukal, proses punaran kering, teknik ablasi laser

Introduction

To design, characterize, and fabricate the electrode plate, electrode flow field is typically downscaled to the micro-size level on a silicon plate using the micro-electro-mechanical system (MEMS) micro-machining processes. Bulk micromachining is based on the dry etching method using laser ablation technique. Therefore, it does not have the limitations presented by the etching selectivity and the silicon crystal plane orientation; it also does not need the photolithography process for patterning the design onto the electrode plate. The same flow field design was used to produce the electrode plate structures using the wet etching method with potassium hydroxide solution (KOH) solution. This is the more established and conventional etching method typically used in MEMS fabrication.

Laser ablation is a simple micromachining technique that provides more simplified surface etching data and clear surface morphology [1]. The technique has been used to modify the physical structure of micro fuel cell components, such as gas diffusion layer (GDL), membrane electrode assembly (MEA), and bipolar plates. The transport property related to the two-phase air-liquid flow in ordinary GDL materials was improved by perforating the dual-layer diffusion media used with a laser beam to obtain a water transport channel. Large fixed-sized pores allow capillary diffusion for water transport to occur without the need for significant pressure gradients [2, 3]. The functional surface area of a membrane was reinforced by roughening up the surface using a modified femtosecond laser method, which resulted in compelling morphological effects without altering the membrane's local chemical properties. The coarse surface of the membrane was then coated with a thin layer of catalyst for the MEA, and subsequent performance tests showed that this modification increased catalyst utilization [4]. Meanwhile, selective laser sintering (SLS) is a technique for making additive materials for the graphite composite used in bipolar plates. A powder mixture containing graphite and binder material particles were sintered using laser scans, after which a liquid binder was then used to bind the powder mixture together to form a three-dimensional layer-by-layer structure. Using this approach, complex flow channels could be constructed in a shorter time, and the required cost was lower than the injection molding and compression molding process typically used in producing bipolar plates [5, 6].

Conventional microfabrication processes, such as isotropic, anisotropic, electrochemical, and ionic etching, provide limited design options; in comparison, laser ablation can produce almost any form or contour of the required silicon structures [7]. A very fast etching time can be obtained for high-intensity lasers in the gas environment when the appropriate local exposure dose is continuously released onto the silicon in the area to be etched. The operation of different types of gas lasers, such as the Argon-ion laser, Excimer laser, and CO_2 laser [8 – 12], depends on its emission wavelength and output power. Laser systems with different laser sources, such as the carbon dioxide (CO_2) laser [11], Excimer ultraviolet laser [8], Nd:YAG solid-state laser [13-15], Yb:YAG disc laser [9], and Yb fiber laser [1], are also suitable for silicon etching.

However, the energy absorbed by the laser beam can cause the local temperature of the silicon sample to rise, which may lead to the evaporation or melting of the silicon. This is accompanied by the local destruction of crystalline arrays in the area surrounding the melting zone [13]. Laser ablation may also produce undesirable damages, such as heat-affected zones, micro-cracks, and pulse breaks, which can then affect the micro fuel cell performance. The interaction between laser ablation and the surface being etched depends largely on the laser beam parameters, as well as the physical and chemical properties of the silicon. Therefore, proper methods of conducting laser source selection and laser parameter optimization are important to minimize sample damage [14, 16].

Materials and Methods

The laser system used in this work was the Nd: YAG laser, i.e., GSI Lumonics W670 Laser Trim system (General Scanning Inc., Somerville, US), which is more commonly utilized for applications other than silicon etching due to its high stability. Its photon energy (1.17 eV) exceeds the silicone band gap (1.12 eV) and makes it a suitable choice for micro-machining silicon substrates. Neodymium ($Nd:Y_3Al_5O_{12}$) is a crystal used as the laser ablation medium,

where the YAG housing is typically doped with about 1% (atomic) neodimium [17]. For this study, the laser machine was equipped with an optic pump for the krypton arc lamp that supplied energy to the laser medium, i.e. the YAG rod. It was used together with an optical Q-Switch unit for the laser beam in the x–y path direction.

The Nd:YAG laser was pumped using optical means with a flash tube or laser diode and it emitted infrared light with a regular wavelength of 1064 nm. During the laser ablation process, reflective mirrors forced the laser beam through the cavity towards one of the mirrors and then reflected it back to another mirror with further stimulation from the YAG rod. However, when the beam hit the front of the mirror, a small amount of beam was transmitted over the mirror while the rest was reflected into the cavity. This occurred in a continuous wave (CW) and the laser output was never interrupted. The steady energy production was stable and was generated over time, which could have caused an etching process to be irregular due to overheating.

The Q-switch solved this problem as it produced high peak power output that disturbed the optical cavity for a short period of time. When the optical cavity interference occurred, a continuous pumping resulted in the larger population inversion, which caused the pulse to become stronger and its duration to become shorter when the optical cavity was restored. Nonetheless, a YAG laser with a Q-switch could cause many particles to be formed around an etched groove.

Sample orientation has no significant effect on the etching result [18]. In the current work, the sample to be etched was attached to the target holder in a horizontal position. The laser beam angle was perpendicular to the sample surface and the laser's working distance was about 23 cm from the objective lens. The dimensions of the desired structures were obtained by controlling the specific parameters of the laser system, i.e. the q-rate, bite size, and power input. The scanned patterns on the sample surface was aligned by attaching the sample to the target holder at the same position throughout the ablation process.

The laser machine used a software program for the layout plan. The source files of the program were edited in C language and the GSI-laser language. Different designs had different work plans that were specific to the paths taken by the laser beam and the time required to carry out the ablation process until completion. Using mirrors, the laser scan speed could be controlled to be very fast for high throughput processing. The dry etching process with the laser ablation technique did not require additional chemicals during operation. The samples also did not need to be physically touched until the etching process was completed and this reduced the risk of contamination [16]. The finished electrode plate was then arranged on the cathode side of the micro fuel cell, as shown in Figure 1.

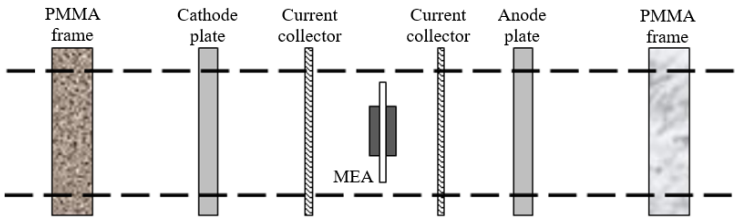


Figure 1. The schematic arrangement of the cathode electrode plate in a single cell assembly

Results and Discussion

The laser ablation technique did not require photolithography and photomask patterning processes for silicon etching. Figure 2 shows the result of a laser ablation process, in which a heat-affected zone occurred in the area surrounding the etched grooves and damaged the silicon surface. Typically, a silicon dioxide (SiO_2) layer is naturally formed on the silicon surface exposed to laser ablation in an airy environment. Therefore, it is the most suitable layer to be used for protecting the sample from experiencing severe damage from overheating [19]. A layer of SiO_2 was formed using a simple thermal oxidation technique [20] for the actual samples before the etching process was carried out.

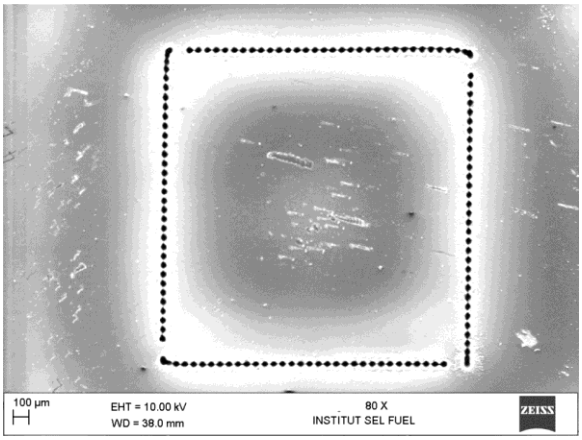


Figure 2. Laser ablation resulting in a heat-affected zone on the silicon surface

The Nd:YAG laser was scanned over the entire target surface according to the designed program to produce the required flow field for the electrode plates. The layout for each etching work design was "serialized", i.e., one scanning program should be completed before the next one began. The length of the sample processing time was dependent on each pattern in the overall design; hence, the patterns must be plotted in the correct order in the planned work sequence. Figure 3 shows a 4-inch diameter silicon wafer that was lightly scratched with a laser beam for mechanical breaking [21] to obtain blank samples of 2.5 cm × 2.5 cm size. The process flow to produce the required electrode flow field is given in Figure 4.

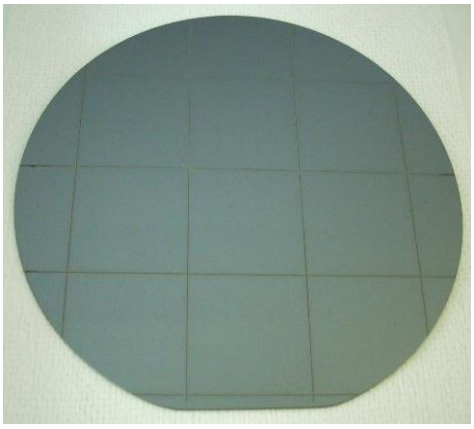


Figure 3. Scratch marks from the laser ablation technique on the oxidized 4-inch diameter wafer to produce 2.5 cm × 2.5 cm blank samples for the electrode plates

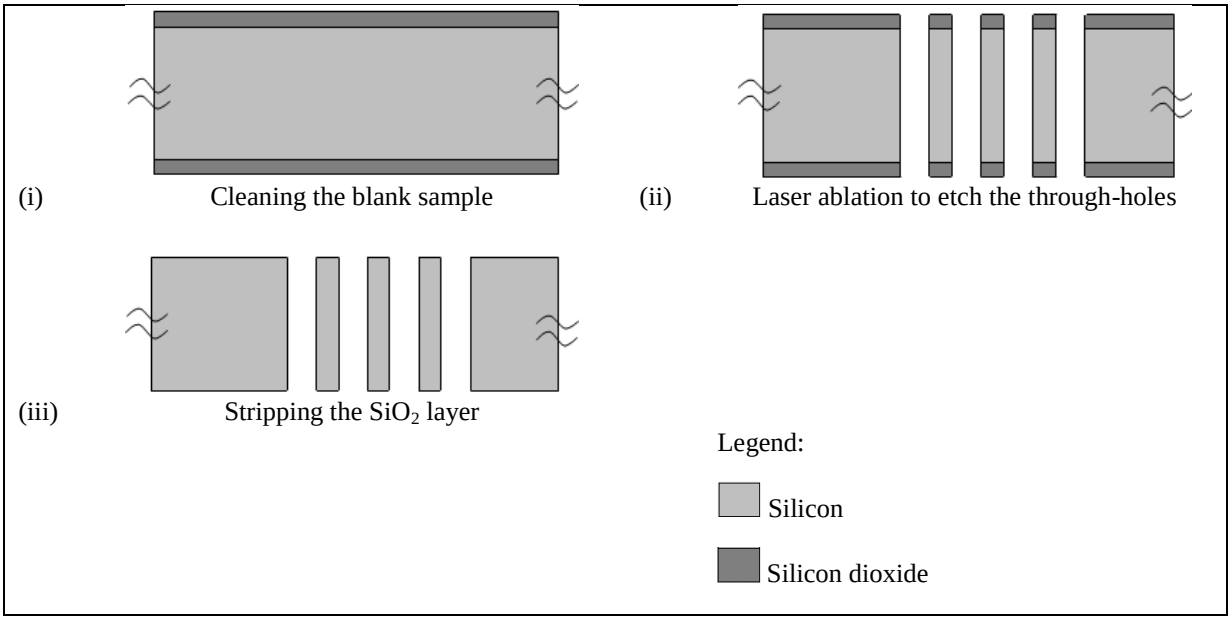


Figure 4. The laser ablation process flow for the electrode flow field microfabrication

Figure 5(a) shows that the bit size, i.e., the distance covered by the beam between the grooves, and the midpoint of the actual laser beam diameter, which controls the degree of the beam overlap, could be modified to adjust the distance between the pulse locations in the vertical (*v*) and horizontal (*w*) directions. The *q*-rate, i.e., the number of grooves etched per second, was set at a value of 1 kHz to produce the desired surface texture. The laser pulses could be separated to form the programmed flow field pattern by manipulating the number of scans at each pulse point. Hence, the coordinates of the pulse starting points and the directions of travel for the laser beam were programmed before the laser ablation process was carried out. The (0,0) coordinate was set on the bottom-left corner of the electrode plate. A 1 cm × 1 cm area was lightly etched to mark the active reaction site for the MEA. The coordinate details for each of the 14 starting points were specified in the laser program to produce the square-shaped through-holes flow field in the array shown in Figure 5(b) to give a 50% MEA active area utilization for the micro fuel cell.

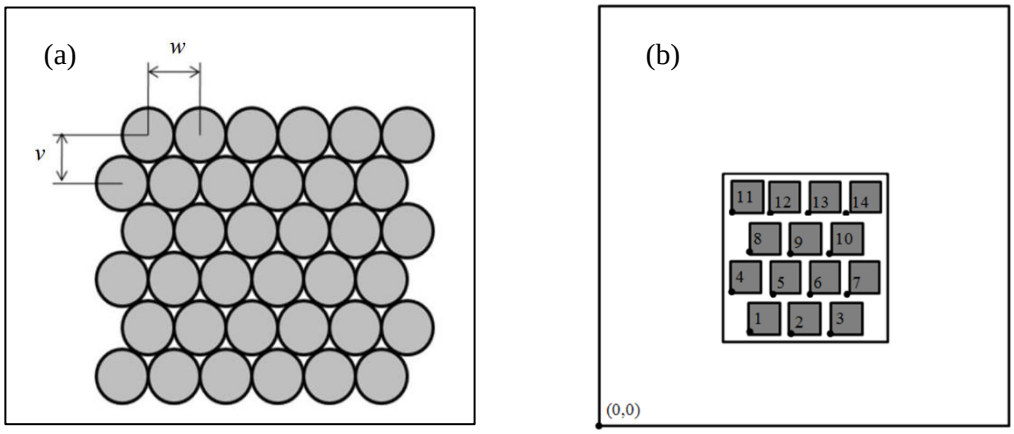


Figure 5. Laser ablation work plan to etch the electrode plate: (a) schematic of the planned beam path for the laser pulses and (b) the through-holes flow field array

The etched depth relationship was plotted as a function of laser ablation at 100% power, 2 kHz q-rate, and 2 mil bit size. All samples were taken from the same batch so that the silicon surface finish, clarity, reflection and refraction could be considered as being within the same range. The graph of the groove depth measurements over the number of laser scans, or ablation number, is shown in Figure 6. As can be seen, the increase in the number of laser scans caused the ablated groove to become even deeper. However, the curve of this inclination is not a straight line, indicating that the etching process becomes less effective at an even higher number of scans. This saturated behavior is in accordance with the laser ablation activity for silicon [1].

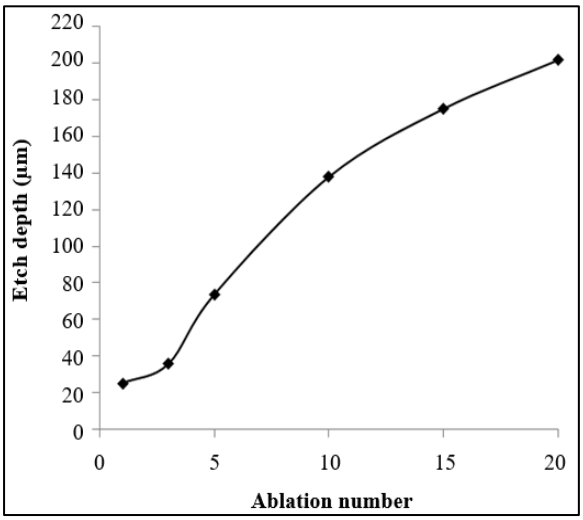


Figure 6. The relationship between the etched groove depth and the ablation number

This saturation behavior can be described as follows. The continuously etched groove caused the melted silicon material, which interacted with the laser beam, to gain mass. As the depth of the ablated area increased, the melted silicon was trapped in the form of ejecta mounds, which then absorbed and scattered most of the laser energy. As the mounds hardened and formed slags around the groove, further ablation was fended off. The movements of the ablated silicon material became more difficult, leading to the condensation of the material inside the groove. In fact, when the etched region moved further into the wafer, its lowest point gradually deviated from the laser beam focal plane. This reduced the effectiveness of the laser beam energy and the etching rate [1, 18]. The scanning electron micrograph (SEM) of the cross-section of the ablated region in Figure 7 shows a clear morphology of the etched structure, which indicates a non-uniform depth within the etched region that is possibly derived from the generally uneven laser energy distribution. This observation also shows that the flow field depth can be adjusted by controlling the number of laser scans carried out in the ablation process. A more serious microscopic erosion can be observed from the first laser beam that impacted the silicon surface compared with the subsequent ones.

The through-holes in the flow field shown in Figure 5(b) required about 55 laser scans to be completed. The silicon surface could be damaged by the formation of slags during the etching process, and this might reduce the electrical performance of the electrode plate when employed in a micro fuel cell. However, as the slags were deposited on top of the SiO_2 layer that was used as the etching mask, they could be easily cleaned after the ablation process was completed by immersing the sample in a buffered oxide etch (BOE) solution at room temperature without stirring or undergoing ultrasonic cleaning, followed by a DI water rinse. The cleaning time for the process shown in Figure 8 took 30 seconds and required at least a very thin 25 nm SiO_2 layer for protection.

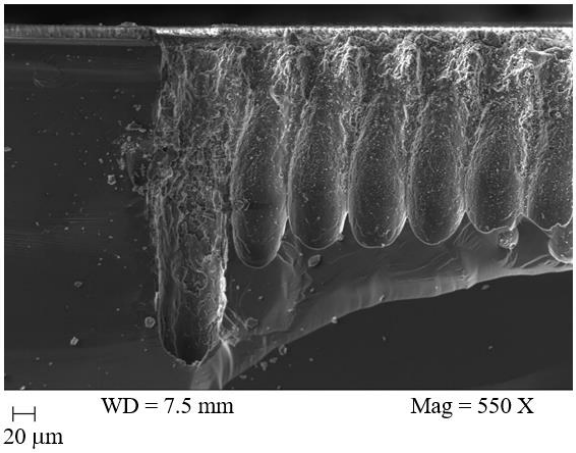


Figure 7. The ablated region cross-section after 20 laser scans

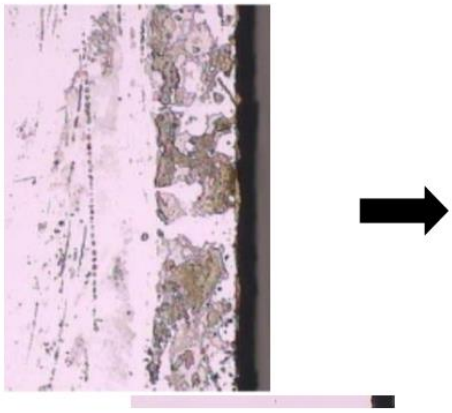
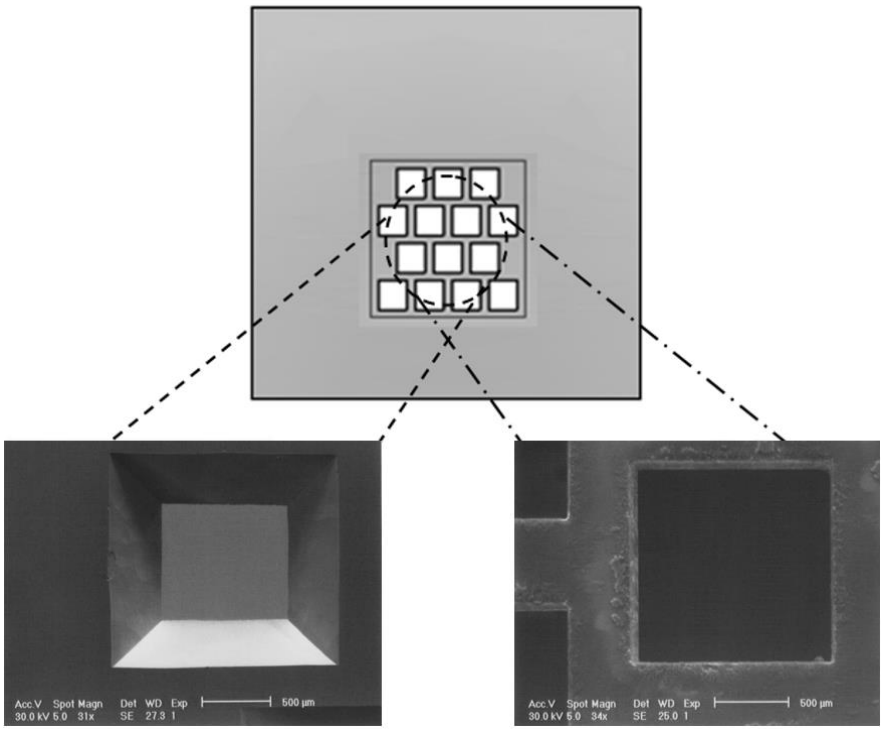


Figure 8. Slag cleaning on the surface of the oxidized sample surface that underwent laser ablation

In case of a serious slag formation, the ablated area should be briefly dipped in a KOH solution of 30% (w/w) concentration mixed with IPA 1% (v/v) at 80 °C to remove the laser slags and smoothen the sample surface. Figures 9(a) and (b) show a comparison between the flow field structure produced by a KOH wet etching process and by a dry etching process using laser ablation, respectively. The micromachined flow field in the cathode plate allows for the effective delivery of oxygen to the active area of the MEA. The SiO_2 layer was later stripped using a 10% (v/v) hydrofluoric acid (HF) solution to obtain the final sample. No micro cracks were observed on the surface of the sample. Nonetheless, micro cracks have an insignificant effect on the micro fuel cell performance in terms of electricity generation, if the electrical contact *via* a conductive layer for current collection was maintained on the overall sample surface.



(a) (b)

Figure 9. Comparison between the flow field patterns and structures produced by: (a) a KOH wet etching process and (b) a dry etching process using laser ablation

The time taken to complete the process of etching 14 through-holes of 0.185 cm × 0.185 cm area was more than 10 hours for the KOH wet etching process. The anisotropic KOH solution also displays characteristic V-sided sidewalls at an angle of ~54º from the <100> silicon plate surface, resulting in smaller-sized openings for reactant transport. The difference between the designed hole and the laser-etched hole is 28.6% (0.132 cm hole width and length), whereas the wet-etched hole yields a difference of 10.3% (i.e., 0.166 cm hole width and length for the larger opening) and 49.5% (i.e., 0.166 cm hole width and length for the smaller opening). Therefore, laser ablation is the preferred process because of two reasons: (1) the through-holes resemble the original flow field design and (2) the time taken to complete the dry etching process for the all the holes was only about 30 minutes. Further comparisons of the KOH etching and laser ablation processes in Table 1 show the weaknesses and advantages from the practical point of microfabrication and the planned design of the electrode flow field.

Table 1. Comparisons between the dry etching process with laser ablation and the wet etching process with KOH solution in terms of microfabrication and planned design of the electrode flow field

KOH etching	**Laser ablation**
● The etching time was very long and required a much thicker SiO_2 layer of about 6 µm to protect the silicon surface during the process. ● It required the complex and time-consuming photolithography process to effectively transfer the flow field pattern onto the silicon plate surface. There was also the risk of generating inaccurate patterns during the photo mask alignment step.	● A thin SiO_2 layer of about 25 nm was considered adequate to protect the silicon surface during the process. ● The photolithography process was not needed. The flow field pattern was precisely etched using the software program for the laser system.

- The etching time was used as the main technique to control the flow field structure and depth. Therefore, overetching might occur and result in incorrect structures being produced in the process.
- The etching process was low cost as it only required the widely available KOH solution and a common cleanroom facility.
- It was time-consuming, especially if the times required to complete the prior processes of thermal oxidation and photolithography were added to the total running time required.
- The anisotropic etching characteristics of KOH produced slanted sidewalls for the through-holes structure, which limited the process capability in following the design.
- The software program could be easily changed before and during the etching process to obtain the pattern and depth required for the flow field.
- The etching process was costly as it required a laser system that was suitable for silicon etching. This system may not be easily available in any cleanroom facility.
- The total time needed to complete the etching process for the electrode plate was short (i.e., ~30 min) and it also did not require the thermal oxidation and photolithography processes.
- The desired vertical sidewalls of the through-holes required by the design could be produced accordingly.

Conclusion

The dry etching process using laser ablation technique can be used to produce the desired flow field structure on the electrode plate for micro fuel cells. Compared with the conventional method of wet etching with the KOH solution, dry etching process using laser ablation technique was more successful in etching the required through-holes according to the planned design with shorter etching time. However, microfabrication using the KOH wet etching process in this work was deemed important because it is a typical low-cost, easy-to-run process for silicon fabrication that can be carried out in common cleanroom facilities.

Acknowledgments

The authors gratefully acknowledge the financial support for this work given by the Malaysian Research University Grant (GUP-2016-039) and the Ministry of Higher Education (Malaysia) Research Grant (FRGS/1/2016/TK09/UKM/03/1). The research was conducted with full technical support and assistance by the staff at the Fuel Cell Institute Laboratory (Universiti Kebangsaan Malaysia), IMEN-MEMS Fabrication Laboratory (Universiti Kebangsaan Malaysia), Microelectronic Fabrication Laboratory (Universiti Malaysia Perlis), and the LIPI Research Center for Electronics and Telecommunication Laboratory (Bandung, Indonesia).

References

1. O'Neill, W. and Li, K. (2009). High-quality micromachining of silicon at 1064 nm using a high-brightness MOPA-based 20-W Yb fiber laser. *IEEE Journal of Selected Topics in Quantum Electronics,* 15(2): 462 – 470.
2. Gerteisen, D. (2010). Transient and steady-state analysis of catalyst poisoning and mixed potential formation in direct methanol fuel cells. *Journal of Power Sources,* 195(19): 6719 – 6731.
3. Manahan, M. P., Hatzell, M. C., Kumbur, E. C. and Mench, M. M. (2011). Laser perforated fuel cell diffusion media. Part I: Related changes in performance and water content. *Journal of Power Sources,* 196(13): 5573 – 5582.
4. Whitacre, J. F., Murphy, R. D., Marrie, A. and Yalisove, S. M. (2009). Enhanced catalyst utilization in PEM fuel cells via ultrafast laser modification of the polymer exchange membrane surface. *Electrochemistry Communications,* 11(3): 655 – 659.
5. Bourell, D. L., Leu, M. C., Chakravarthy, K., Guo, N. and Alayavalli, K. (2011). Graphite-based indirect laser sintered fuel cell bipolar plates containing carbon fiber additions. *CIRP Annals - Manufacturing Technology,* 60(1): 275 – 278.
6. Guo, N. and Leu, M. C. (2012). Effect of different graphite materials on the electrical conductivity and flexural strength of bipolar plates fabricated using selective laser sintering. *International Journal of Hydrogen Energy,* 37(4): 3558 – 3566.
7. Petersen, K. E. (1982). Silicon as a mechanical material. *Proceedings IEEE,* 70(5): 420 – 457.

8. Long, Y., Xiong, L., Shil, T. and Tang, Z. (2007). Study of excimer laser electrochemical etching silicon. The 2nd IEEE International Conference on Nano/Micro Engineered and Molecular Systems, Bangkok, Thailand.
9. Trusheim, D., Schulz-Ruhtenberg, M., Baier, T., Krantz, S., Bauer, D. and Das, J. (2011). Investigation of the influence of pulse duration in laser processes for solar cells. *Physics Procedia*, 12, Part B: 278 –285.
10. Allard, M., Boughaba, S. and Meunier, M. (1997). Laser micromachining of free-standing structures in SiO_2-covered silicon. *Applied Surface Science*, 109–110(0): 189 – 193.
11. Chung, C. K., Wu, M. Y., Wu, J. C., Sung, Y. C. and Huang, G. R. (2006). *S*ilicon micromachining by CO_2 laser. The 1st IEEE International Conference on Nano/Micro Engineered and Molecular Systems, Zhuhai, China.
12. Chung, C. K., Wu, M. Y., Hsiao, E. J. and Sung, Y. C. (2007). Etching behavior of silicon using CO_2 laser. The 2nd IEEE International Conference on Nano/Micro Engineered and Molecular Systems, Bangkok, Thailand.
13. Alavi, M., Büttgenbach, S., Schumacher, A. and Wagner, H. J. (1991). Laser machining of silicon for fabrication of new microstructures. *Proceedings IEEE Transducers'91*: 512 – 515.
14. Minami, K., Wakabayashi, Y., Matsubara, T., Yoshimi, K., Yoshida, M., and Esashi, M. (1993). YAG laser assisted etching for releasing silicon micro structure. *Proceedings IEEE MEMS '93*: 53-58.
15. Lerner, B., Perez, M. S., Toro, C., Lasorsa, C., Rinaldi, C. A., Boselli, A. and Lamagna, A. (2012). Generation of cavities in silicon wafers by laser ablation using silicon nitride as sacrificial layer. *Applied Surface Science*, 258(7): 2914 – 2919.
16. Du, Z., Palina, N., Chen, J., Hong, M. and Hoex, B. (2012). Rear-side contact opening by laser ablation for industrial screen-printed aluminium local back surface field silicon wafer solar cells. *Energy Procedia*, 25: 19 – 27.
17. Koechner, W. (2006). *Solid-State Laser Engineering* (6 edition). London: Springer Ltd.
18. Yuan, W. and Ma, B. (2008). Micro-machinability of monocrystal silicon by direct etching using excimer laser. *Journal of Materials Processing Technology*, 200(1): 390 – 397.
19. Mizeikis, V., Juodkazis, S., Ye, J.-Y., Rode, A., Matsuo, S. and Misawa, H. (2003). Silicon surface processing techniques for micro-systems fabrication. *Thin Solid Films*, 438–439(0): 445 – 451.
20. Hasran, U. A., Kamarudin, S. K., Daud, W. R. W., Majlis, B. Y., Mohamad, A. B. and Kadhum, A. A. H. (2011). A simple thermal oxidation technique and KOH wet etching process for fuel cell flow field fabrication. *International Journal of Hydrogen Energy*, 36(8): 5136 – 5142.
21. Ogorodnikov, A. I. (2016). Finite-element simulation of scratching on a coated brittle plate. *AIP Conference Proceedings*, 1785(1): 030020.

Malaysian Journal of Analytical Sciences, Vol 23 No 2 (2019): 355 - 361
DOI: https://doi.org/10.17576/mjas-2019-2302-19

MALAYSIAN JOURNAL OF ANALYTICAL SCIENCES
Published by The Malaysian Analytical Sciences Society
ISSN 1394 - 2506

EFFECTS OF GRAPHITE/POLYPROPYLENE ON THE ELECTRICAL CONDUCTIVITY OF MANUFACTURED BIPOLAR PLATE

(Kesan Komposit Polimer Pengalir Grafit/Polipropilena Komposit Polimer Pengalir Ke atas Sifat Kekonduksian Elektrik bagi Pembuatan Plat Dwikutub)

Iswandi[1,2], Abu Bakar Sulong[1], Teuku Husaini[1,3]*

[1]*Fuel Cell Institute,*
Universiti Kebangsaan Malaysia, 43600 UKM Bangi, Selangor, Malaysia
[2]*Department of Mechanical Engineering,*
Institut Teknologi Medan, Medan 20152, Indonesia
[3]*Department of Chemical Engineering,*
Universitas Sumatera Utara, USU 20155, Indonesia

**Corresponding author: t.husaini.st@gmail.com*

Received: 13 April 2017; Accepted: 17 April 2018

Abstract

Conductive polymer composite (CPC) has been used on bipolar plates by compression and injection molding methods. The CPC material comprises 25% polypropylene and 75%graphite with size variation (40, 100, 150, and 200 µm) according to particle size dispersion test. The composite is mixed using an internal mixer to obtain a homogeneous mixture at a process temperature of 200 °C. Electrical conductivity tests are performed on each particle size composition. The highest electrical conductivity produced by compression and injection molding methods is 17 and 12 S/cm, respectively. These values are both obtained on a 40 µm graphite filler. Results show that the type of manufacturing process affects the value of electrical conductivity using the same material.

Keywords: injection molding, compression molding, bipolar plate

Abstrak

Komposit polimer pengalir (KPP) telah digunakan pada plat dwikutub dengan kaedah pengacuan mampatan dan pengacuan suntikan. Komposisi bahan KPP adalah polipropilena (PP) 25% dan grafit (G) 75% berat dengan variasi saiz 40 µm, 100 µm, 150 µm dan 200 µm dan dijalankan ujian serakan partikel saiz. Komposit dicampur menggunakan campuran dalaman untuk mendapatkan campuran yang sekata pada suhu proses 200 °C. Pengujian kekonduksian elektrik dijalankan pada masing-masing komposisi saiz partikel. Nilai kekonduksian elektrik tertinggi ditunjukkan pada pengisi grafit saiz 40 µm, pada masing-masing kaedah pembuatan. Kekonduksian elektrik tertinggi dihasilkan melalui kaedah pengacuan mampatan iaitu 17 S/cm dan proses pengacuan suntikan adalah 12 S/cm. Keputusan ujian menunjukkan bahawa proses pembuatan memberi kesan ke atas nilai kekonduksian elektrik menggunakan bahan yang sama.

Kata kunci: pengacuan suntikan, pengacuan mampatan, plat dwikutub

Introduction

The use of conductive polymer composite (CPC) in various applications related to renewable energy has increased in recent years. The manufacture of bipolar plates for polymer electrolyte membrane fuel cell technology (PEMFC) is a material application of CPC. Bipolar plates, the main components of PEMFC, are important in continuous

system. These plates contribute to the gas and water regulation, mechanical stability, and electrical conductivity of the fuel cell [1-3]. Hence, the bipolar plate manufacture requires filler material designs and manufacturing methods that can improve the electrical conductivity. Generally, a strong relationship between the materials used and the manufacturing process of the bipolar plate can produce the most excellent CPC. One of the filler materials commonly used is a carbon-based conductive filler material, which is an alternative to metals with electrical conductivity values ranging from 10^2S/cm to 10^5 S/cm [4].

Graphite, a carbon-based material, is proposed as a filler in the manufacture of bipolar plates. Selection of graphite as a filler material in the CPC application of bipolar plate presents advantages over metal-based materials. The carbon-based material is lighter with higher corrosion resistance and lower cost than that of metal, which is carbon malleable [5-8]. Carbon-based materials also display drawbacks, such as considerable brittleness and difficulty in machining to satisfy the specifications of the fuel cell stack. Robberg et al. [9] demonstrated that the ability filler (G) in the CPC indicates that the substantive polymer is an insulator, and graphite filler loading of more than 60% by weight in the composite can satisfy the minimum electrical conductivity.

Filler powder characterization is carried out through the filler particle size distribution analysis. Particle size distribution is generally displayed in the form of a normal distribution graph. Further statistical particle size distribution in the histogram shows three important values: the lowest value of the distribution (D_{10}), median (D_{50}), and the highest distribution (D_{90}) [10]. High S_W indicates a narrow size distribution. Conversely, low S_W suggests a wide particle size distribution. Generally, the powder is easily processed by injection molding when the S_W is smaller than2. The difficulty in feedstock injection increases when the S_W is more than4. Feedstock injection is considerably difficult when the S_W is more than 7.

Furthermore, the manufacturing process highly influences the easy processing of powder; it can increase the electrical conductivity and the CPC properties. Compression and injection molding processes are utilized in the production of various types of products used in the manufacture of plastic products and bipolar plates. The method used is determined based on the advantages of each manufacturing method [2, 11-12].

Materials and Methods

This study used SM240 polypropylene (PP) (Titan Petchem Sdn Bhd) as a binder, which presents the following properties: melting point, 160 °C–170 °C; processing temperature,190 °C–250 °C; melt flow rate,10 g/10 min; and density, 0.9g/cm^3. The electrically conductive material used in this study is a natural graphite from Asbury 3243 (Asbury Graphite Mills, Inc.). Graphite displays the following important properties: carbon content, 99%; normal powder size,≤60 m; surface area, 3 mm^2; electrical resistivity, 0.036 Ω; and density, 1.74 g/cm^3.The graphite particles are sorted into the following sizes: 40, 100, 150, and 200 μm. Particle size dispersion is carried out using a Malvern Mastersizer E version. Samples are manufactured using a compression molding method by hot compression with a capacity of 200 tons and injection molding of the plunger DSM Xplore (semiautomatic). Critical powder loading test determined that the compositions of PP binder and graphite (the highest filler material) are 25% and 75% by weight, respectively [13]. Particle size analysis and particle size distribution are conducted on each graphite size by using a Malvern Mastersizer E version. The electrical conductivity of the composite is evaluated using four-point probe tool window (Multi Height Four-Point Probe) with test unit RM3. Scanning electron microscopy (SEM) is used to observe graphite powder.

Results and Discussion

Figure 1 shows the graphite powder shape, which displays advantages and disadvantages for compression and injection molding processes. Graphite flake can produce high electrical conductivity of approximately 420 S/cm in the minus 320 mesh [14]. The flake shape causes difficulties in the flow injection molding. Mixing of particles with various sizes affects the particle arrangement in composites.

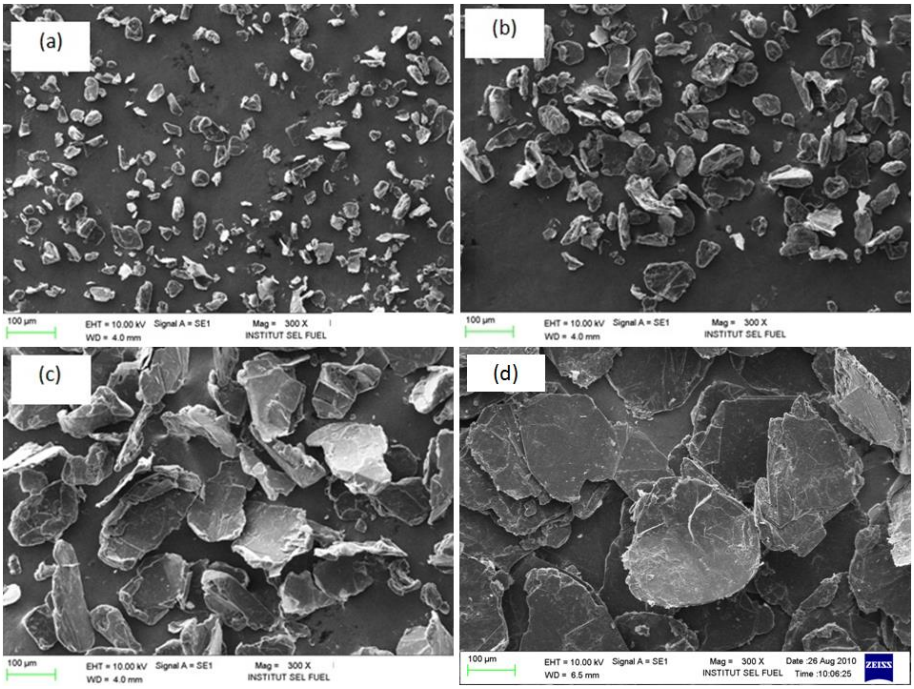


Figure 1. Scanning electron microscopy images of graphite type 3243 with the following particle sizes after sieving: (a) 40, (b) 100, (c) 150, and (d) 200 µm

Analysis results of the filler particle size distribution are shown in Table 1. The distribution percentage of particle size shows particle size distributions of 10%, 50%, and 90%, which are named as D_{10}, D_{50}, and D_{90}, respectively. The median size of the powder is a cumulative percentage of 50%, which is often named as the D_{50} size (Figure 2(a)) of the graphite particle with a size of 40 µm. The size distribution curve (S_W), which fills the space between large and small particles in the filler composition percentage of 75% by weight, shows large graphite particle sizes.

Table 1. Average particle size of the graphite powder filler

	Percentage Distribution of Particle Sizes			**Surface Area**	
(µm)	D_{10}	D_{50}	D_{90}	**(m^2/g)**	S_W
As received	18.8	56.4	127.8	0.161	2.12
40	18.1	34,8	62.3	0.204	4.76
100	26.5	104.3	212.3	0.125	2.83
150	27	151.7	291.9	0.095	2.47
200	39.8	201.4	364.8	0.075	2.66

The median particle size (D_{50}) and distribution curve (S_W) are key factors in the analysis of conductive powder. S_W, the cumulative distribution curve lognormal, is equivalent to multiplied or standard deviation of the particle size distribution. The distribution curve (S_W) affects the performance of the injection molding process. When the S_W value is high, the particle size distribution is narrow. By contrast, the low S_W value indicates a wide particle size distribution.

High S_W value indicates narrow particle size distribution. Low S_W value results in even distribution and easy injection process. The graphite filler powder presents a wide particle size distribution and low S_W value of 2, thereby

causing its easy injection. A graphite with 100 µm particle size (Figure 2. (b)) also shows S_W in wide particle size distribution, which indicates easy injection. The same trend is observed on graphite with particle sizes of 150 (Figure 2(c)) and 200 µm (Figure 2(d)). Generally, the CPC (G/PP, 75%/25%) exhibits a low S_W value, which suggests its mold ability.

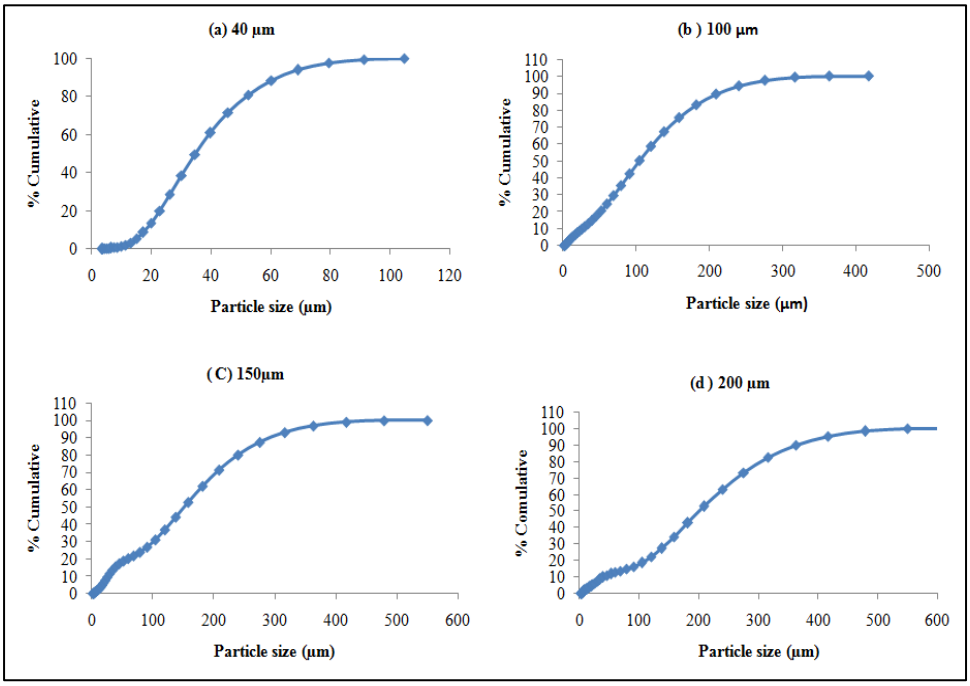


Figure 2. Cumulative percentage of the volume of graphite particle size distribution: (a) 40, (b) 100, (c) 150, and (d) 200µm

The electrical conductivity test results (Figure 3) show that the electric conductivity value decreases with increased particle size. This trend is observed in both CPC plate manufacturing methods. The electrical conductivity produced by compression molding method displays a higher value (17 S/cm) than that of the injection molding method (12 S/cm) in the 40 µm particle size. Consequently, the filler particle dispersion produced by compression molding is higher than that by injection molding method. Particle shape influences the particle dispersion of fillers. The flake particle shape is more suitable for compression molding method in producing high electrical conductivity value than those of other forms, such as sphere [14]. This condition is attributed to the flake shape, which can easily form the dispersion of compression molding due to the large pressure area on the compression. The electrical conductivity devaluation and subsequent increase in particle size are also shown in Figure 3.

This phenomenon is due to the formation of empty spaces between large particles. The free space formation for electrical conductivity hinders the establishment of electricity networks because PP, as binder, will fill the empty space formed between particles. This observation is supported by the SEM image in Figures 4 and 5 for the injection and compression molding processes, respectively. Large particle size will increase the pore size and electrical resistance of the composite material. Figure 3 displays that the electrical conductivity produced by injection molding approaches the values of compression molding method. This trend is due to the particle form, which increases the electrical conductivity value produced by the former method. In general, the particle shape also affects the electrical conductivity value. The graphite flake used as filler in this research can improve the electrical conductivity value. However, the flake shape of the filler material for injection molding can constrain the feedstock flow due to the rotation of particles at the injection proses of feedstock, which results in irregular formation of a mutable block in the flake structure [15]. Increasing the injection pressure can reduce the effects of constraints

caused by agglomeration. This finding is supported by the microstructure observation using SEM, as shown in Figures 4 and 5 for injection and compression molding methods, respectively.

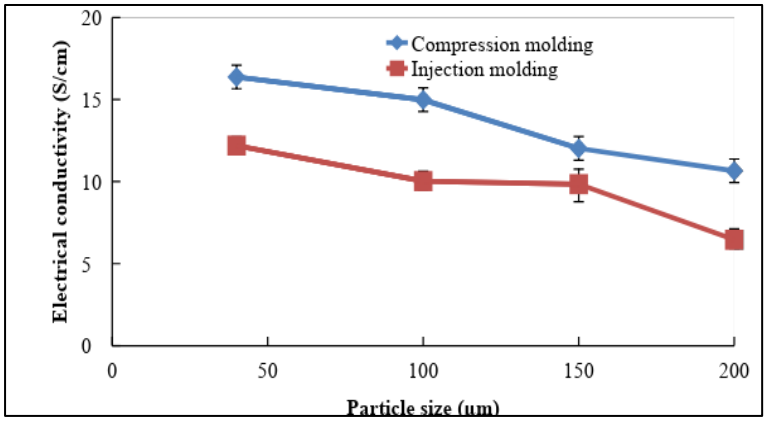


Figure 3. Electrical conductivity by compression and injection molding methods

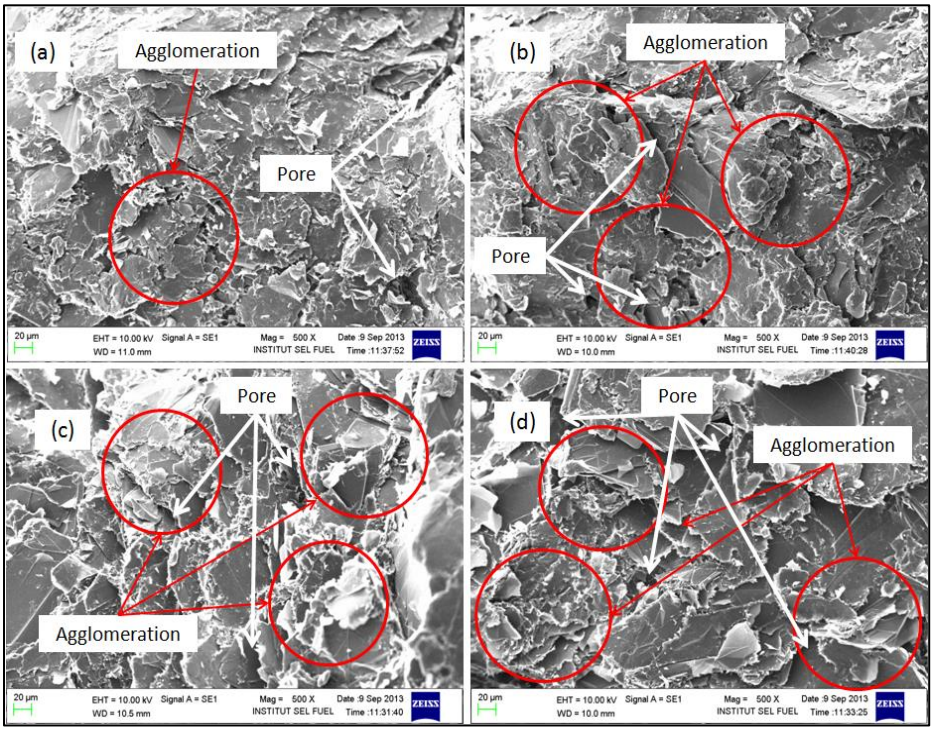


Figure 4. SEM images for the injection molding method:(a) 40, (b) 100, (c) 150, and (d) 200 µm

The SEM image in Figure 4. demonstrates the uniform particle dispersion and the particle agglomeration, which can also result in networking between particles. Consequently, the electrical conductivity increases, and the graphite filler content is higher than 60% by weight [3]. Figure 4(a) shows the particle size agglomeration of 40 µm on several fronts, and the solid bond between particles is shown in red circle. Thus, the electrical conductivity increases, which can affect the flow ability of the feedstock in the injection molding process. The small pores of the composite, which are indicated by an arrow at a composite size of 40 µm, increase the electrical conductivity. By

contrast, Figures5 (a), 5(b), 5(c), and 5(d) present an increase in agglomeration, as indicated by the red circle. This increase also influences the increase in pore volume in composites indicated by the arrow. Such result is similar to Mahyoedin [16] who found that particle size affects the flow ability of feedstock during the injection molding process. Increased pore size will reduce the networking between particles, as shown in the compositions of particles with sizes of 100, 150, and 200 µm (indicated by the arrow), and decrease the electrical conductivity.

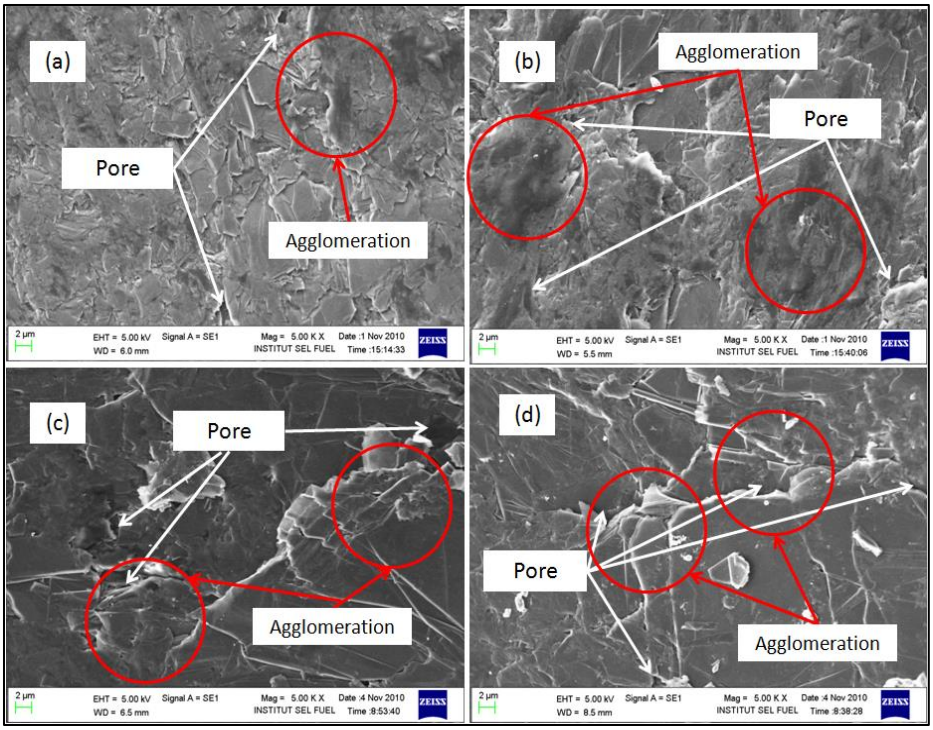


Figure 5. SEM images for the compression molding method: (a) 40, (b) 100, (c) 150, and (d) 200 µm

SEM images in Figure 5 show a compact binding between particles by compression molding. Nonetheless, the pores that can affect electrical conductivity still exist. The composite microstructure displays compact particle arrangement. Thus, the electrical network increases the electrical conductivity. Figures 5(a-d) generally indicate a more compact surface in the composite formation by compression molding than that with the injection molding method. The composite microstructure analysis results for the compression and injection molding processes are in accordance with the electrical conductivity test results presented in Figure 3.

The electrical conductivity produced by compression molding is higher than that by injection molding. The filler particles comprising a close composite by the compression process can develop better electrical networks than those by injection molding. The SEM image analysis on compression molding (Figure 5) demonstrates that the number of pores marked with arrows and the agglomeration indicated with red circle are lower than those of the injection molding process.

Conclusion

Injection and compression molding methods are often used in the manufacture of bipolar plates with PP and G. The particle size variation in the composite (25% PP and75% G by weight) with different manufacturing processes affects the electrical conductivity. The highest electrical conductivity produced by both manufacturing methods is observed in 40 µm particle size; the highest value of 17 S/cm is produced by compression molding. The use of small particle sizes in the compression molding process affects the particle compaction by reducing the number of pores and agglomeration and increasing the electrical network between particles.

Acknowledgment

The authors gratefully acknowledge the financial support provided by the Malaysian Ministry of Higher Education FRGS/1/2017/TK10/UKM/02/6 and GUP-2016-084.The authors also want to express their gratitude to Prof. Dr. Hj. Jaafar Sahari.

References

1. Antunes, R. A., De Oliveira, M. C., Ett, G. and Ett, V. (2011). Carbon materials in composite bipolar plates for polymer electrolyte membrane fuel cells: A review of the main challenges to improve electrical performance. *Journal of Power Sources*, 196(6): 2945-2961.
2. Hermann, A., Chaudhuri, T. and Spagnol, P. (2005). Bipolar plates for PEM fuel cells: A review. *International Journal of Hydrogen Energy*, 30(12): 1297-1302.
3. Hsiao, M. C., Liao, S. H., Yen, M. Y., Ma, C. C. M., Lee, S. J., Lin, Y. F. and Hung, C. H. (2009). Electrical and thermal conductivities of novel metal mesh hybrid polymer composite bipolar plates for proton exchange membrane fuel cells. In ASME 2009 *7th International Conference on Fuel Cell Science, Engineering and Technology*: pp. 871-878.
4. Clingerman, M. L., Weber, E. H., King, J. A. and Schulz, K. H. (2002). Synergistic effect of carbon fillers in electrically conductive nylon 6, 6 and polycarbonate based resins. *Polymer Composites*, 23(5): 911-924.
5. Blunk, R., Elhamid, M. H. A., Lisi, D. and Mikhail, Y. (2006). Polymeric composite bipolar plates for vehicle applications. *Journal of Power Sources*, 156(2): 151-157.
6. Heinzel, A., Mahlendorf, F., Niemzig, O. and Kreuz, C. (2004). Injection moulded low cost bipolar plates for PEM fuel cells. *Journal of Power Sources*, 131(1-2): 35-40.
7. Taherian, R. (2014). A review of composite and metallic bipolar plates in proton exchange membrane fuel cell: Materials, fabrication, and material selection. *Journal of Power Sources*, 265: 370-390.
8. Taherian, R., Hadianfard, M. J. and Golikand, A. N. (2013). Manufacture of a polymer-based carbon nanocomposite as bipolar plate of proton exchange membrane fuel cells. *Materials & Design*, 49: 242-251.
9. Robberg, K. (2003). Handbook of fuel cells-fundamentals, technology and application. Fuel cell technology and application. Wiley & Sons: New York: pp. 308-314.
10. German, R. M. and Bose, A. (1997). Injection molding of metals and ceramics. Princeton, New Jersey: Metal Powder Industries Federation.
11. Mighri, F., Huneault, M. A. and Champagne, M. F. (2004). Electrically conductive thermoplastic blends for injection and compression molding of bipolar plates in the fuel cell application. *Polymer Engineering & Science*, 44(9): 1755-1765.
12. Pozio, A., Zaza, F., Masci, A. and Silva, R. F. (2008). Bipolar plate materials for PEMFCs: A conductivity and stability study. *Journal of Power Sources*, 179(2): 631-639.
13. Iswandi, S., J., Sulong, A. B. and Husaini, T. (2016). Critical powder loading and rheological properties of polypropylene/graphite composite feedstock for bipolar plate application. *Malaysian Journal of Analytical Sciences*, 20(3): 687-696.
14. Zhang, J., Zou, Y. and He, J. (2005). Influence of graphite particle size and its shape on performance of carbon composite bipolar plate. *Journal of Zhejiang University Science*, 6(10): 1080-1083.
15. Mannschatz, A., Muller, A. and Moritz, T. (2011). Influence of powder morphology on properties of ceramic injection molding feedstocks. *Journal of the European Ceramic Society*, 31(14): 2551-2558.
16. Mahyoedin, Y. (2013). Injection molding process of material composite polypropylene filler graphite and carbon black, in mechanical and material engineering. Universiti Kebangsaan Malaysia: Bangi: pp. 156.

Malaysian Journal of Analytical Sciences, Vol 23 No 2 (2019): 362 - 375
DOI: https://doi.org/10.17576/mjas-2019-2302-20

MALAYSIAN JOURNAL OF ANALYTICAL SCIENCES
Published by The Malaysian Analytical Sciences Society
ISSN 1394 - 2506

Nd:YAG LASER FABRICATION OF SILICON ELECTRODE PLATES FOR A COMBINED-MODE MICRO DIRECT METHANOL FUEL CELL

(Fabrikasi Plat Elektrod Silikon dengan Laser Nd:YAG untuk Sel Bahan Api Metanol Langsung Mikro Bermod Gabungan)

Umi Azmah Hasran[1]*, Siti Kartom Kamarudin[1,3], Burhanuddin Yeop Majlis[2], Wan Ramli Wan Daud[3], Abdul Amir Hassan Kadhum[3], Gandi Sugandi[4]

[1]*Fuel Cell Institute*
[2]*Institute of Microengineering and Nanoelectronics*
[3]*Department of Chemical and Process Engineering*
Universiti Kebangsaan Malaysia, 43600 UKM Bangi, Selangor, Malaysia
[4]*Research Center for Electronics and Telecommunication*
Lembaga Ilmu Pengetahuan Indonesia, Bandung, Indonesia

**Corresponding author: umi.h@ukm.edu.my*

Received: 13 April 2017; Accepted: 17 April 2018

Abstract

A silicon wafer was microfabricated to produce a new combined-mode flow field for the purpose of distributing methanol fuel throughout the anode side of a micro direct methanol fuel cell (DMFC). Active mode of operation, which generally produces more power, is more suited to higher power requirements compared with the passive mode. Different power outputs using different modes may be required during cell operation by devices that can potentially use the micro DMFC. The new flow field design in the electrode structure of the micro DMFC must manage the methanol fuel transport in either active or passive mode. The flow field area was designed to obtain 50% of the 1 cm^2 active reaction area of the membrane electrode assembly. The proposed design was simulated using COMSOL multi-physics software and microfabricated by incorporating two flow field designs on the anode plate, namely, the grid flow field for the active mode and the porous flow field for the passive mode. The silicon wafer used to produce the electrode plate was a <100> p-type single-sided polished substrate and the MEMS-based microfabrication process to form the required electrode structures was dry etching with laser ablation. The current collector layers used were titanium/copper with a thickness of 1.1 µm and gold with a thickness of 0.18 µm. The completed single-cell micro DMFC obtained a maximum performance of 1.86 mW/cm^2 at a voltage of 138.7 mV.

Keywords: anode flow field, MEMS technology, active mode, passive mode, dry etching technique

Abstrak

Wafer silikon telah dimikrofabrikasi untuk menghasilkan medan aliran baru berbentuk mod gabungan bagi pengedaran bahan api metanol ke seluruh bahagian anod di dalam DMFC mikro. Mod operasi aktif, yang umumnya menghasilkan lebih banyak kuasa, adalah lebih sesuai dengan keperluan kuasa yang lebih tinggi berbanding mod operasi pasif. Output kuasa yang berbeza menggunakan mod yang berbeza dijangka diperlukan semasa operasi sel oleh peranti yang berpotensi menggunakan DMFC mikro. Reka bentuk medan aliran baru dalam struktur elektro DMFC mikro ini mesti menguruskan pengangkutan bahan api metanol sama ada dalam mod aktif atau pasif semasa operasi. Kawasan medan aliran direka untuk mendapatkan ~ 50% daripada kawasan reaksi aktif 1 cm^2 himpunan elektrod membran. Reka bentuk baru ini disimulasikan menggunakan perisian multifizik COMSOL dan dimikrofabrikasi dengan menggabungkan dua reka bentuk medan aliran pada sekeping plat anod, iaitu medan aliran grid untuk mod aktif dan medan aliran poros untuk mod pasif. Wafer silikon yang digunakan untuk menghasilkan plat elektrod adalah substrat <100> tergilap sebelah jenis-p dan proses mikrofabrikasi yang berasaskan MEMS untuk membentuk

struktur elektrod yang diperlukan adalah punaran kering dengan ablasi laser. Lapisan pengumpul arus adalah titanium/tembaga dengan ketebalan 1.1 μm dan emas dengan ketebalan 0.18 μm. Sel tunggal DMFC mikro yang telah disiapkan dapat memberikan prestasi maksimum 1.86 mW/cm^2 pada voltan 138.7 mV.

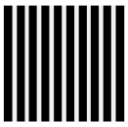
Kata kunci: medan aliran anod, teknologi MEMS, mod aktif, mod pasif, proses punaran kering

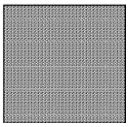
Introduction

In this work, a silicon wafer was oxidized and micromachined with the required design to produce a flow channel for the purpose of distributing fuel and oxidant throughout anode and cathode areas, respectively. The reactants and by-products in a micro direct methanol fuel cell (DMFC) are typically moved throughout the active reaction site by using one of these transfer methods or operating modes at a time, that is, either active or passive modes. The flow channel is known as a flow field, and the flow plate is generally known as electrode plate or plate separator. The uniform distribution of reactants (i.e. diluted methanol as fuel and oxygen from the surrounding air as oxidant) and the effective removal of by-products (i.e., carbon dioxide and water) from the fuel cell is an important function of the flow field to reduce the polarization of methanol concentration and obtain an efficient fuel cell operation [1]. The functional components of a micro fuel cell are mainly the flow field (or electrode) plate, membrane electrode assembly (MEA), proton exchange membrane, catalytic layer, gas diffusion layer, and current collector [2].

In general, a fuel cell that operates in active mode generates more power than the ones operating in passive mode. The electrode plate design is typically developed by considering only one operating mode, which results in the usage of that mode during the entire operation. However, the power supply requirement may vary for the same application based on the operation of a device, e.g., electronic devices require more power during "talk mode" and can utilize the active design, whereas the "standby mode" is less power consuming and can utilize the passive design. The objective of this work was to create a new structure that manages the transport of fuel inside the cell by microfabricating a flow field design that incorporates active and passive mode features at the unit cell level on the anode plate. Therefore, the electrode plate design concept to be studied can give the resulting micro DMFC the ability to operate in both modes during operation. Focus was given on the anode flow field design because methanol fuel transportation has a major effect on the micro DMFC performance. Meanwhile, the cathode plate flow field design was micromachined with passive-mode features. Table 1 shows the types and characteristics of common electrode plate designs for an anode used in micro DMFC to select the most suitable combination of active and passive channels for the anode plate based on the advantages and disadvantages demonstrated by each design.

Table 1. Types and characteristics of common anode plate designs in micro DMFC

	Type	Schematic	Advantages	Disadvantages	References
(a)	Parallel		▪ A uniform distribution is made but only in ideal conditions.	▪ Water droplets formed during the reactions may block the channels, and fuel velocity from the active mode operation may not be enough to remove them. ▪ A low and unstable cell voltage is produced.	[3]
(b)	Single Serpentine		▪ For a small-sized flow field, this channel design typically covers its entire active area. ▪ Water droplets formed in the channel are pushed out of the cell by high-speed carbon dioxide gas bubble.	▪ Fluid friction at the wall and channel corner increases the pressure drop and reduces fuel concentration.	[4]

				▪ Fluid may bypass parts of the channel due to pressure difference between the neighboring channels.	
(e)	Column, spot, grid, pin, or dot		▪ This allows fluid to flow across the channel network to avoid problematic areas in the flow field.	▪ This has low flow velocity and uneven flow distribution due to the inlet and exit positions.	[4]
(f)	Porous		▪ This is similar to a mesh design, except for the size of the pores and fabrication method, and it allows capillary action for fuel transport into the active area for reaction.	▪ This is suitable only for small-sized micro fuel cells due to high pressure drop.	[5]

Materials and Methods

Electrode plate design

The new electrode structure highlights the concept of a combined-mode micro DMFC by incorporating two flow field designs on the anode plate, namely, the grid flow field (active mode) and the porous flow field (passive mode). The design of the electrode plate was determined based on the micro-electromechanical systems (MEMS) technology used to microfabricate the silicon substrate with the Miller index as a reference. During the planning stage, the limitations in the microfabrication process and the operation requirements of the micro DMFC were taken into account to ensure good distribution of reactants and removal of by-products in the anode and cathode channels. Table 2 summarizes the new design features that were selected for the anode and cathode plates.

Table 2. Design features of the new electrode plate

Plate	**Mode**	**Flow Field Design**	
Cathode	Passive	Square through-hole	
Anode	Combined	Design 1: Active	Grid
		Design 2: Passive	Porous

The process flow using laser ablation for flow field etching of the new anode plate design is shown in Figure 1, and it can be used for a combined active–passive micro DMFC mode. The grid flow field was a series of square-shaped platforms arranged in the middle of a shallow rectangular groove or channel that carries the fuel and by-products from the inlet to the outlet by using a liquid pump. The porous flow field was located within each grid platform and consists of a capillary array, where the capillary number on the platform was limited by the grid size and the capillary action drove the fuel in the reservoir etched on the other side of the electrode plate toward the active reaction site. The directions of the fuel inlet and outlet were opposite each other. The flow field design was determined to obtain an active reaction site, which was ~50% of the 1 cm^2 MEA area. Figure 2 shows the flow field configuration of the combined-mode design.

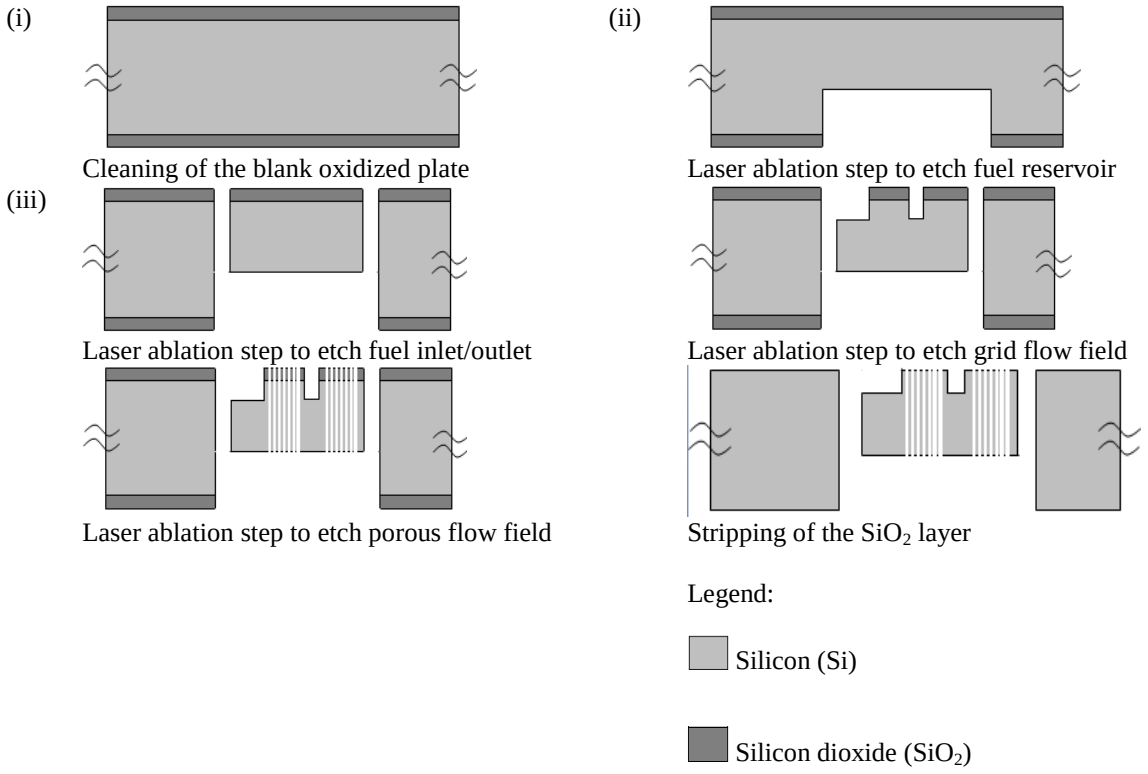


Figure 1. Process flow using laser ablation for flow field etching of the anode plate.

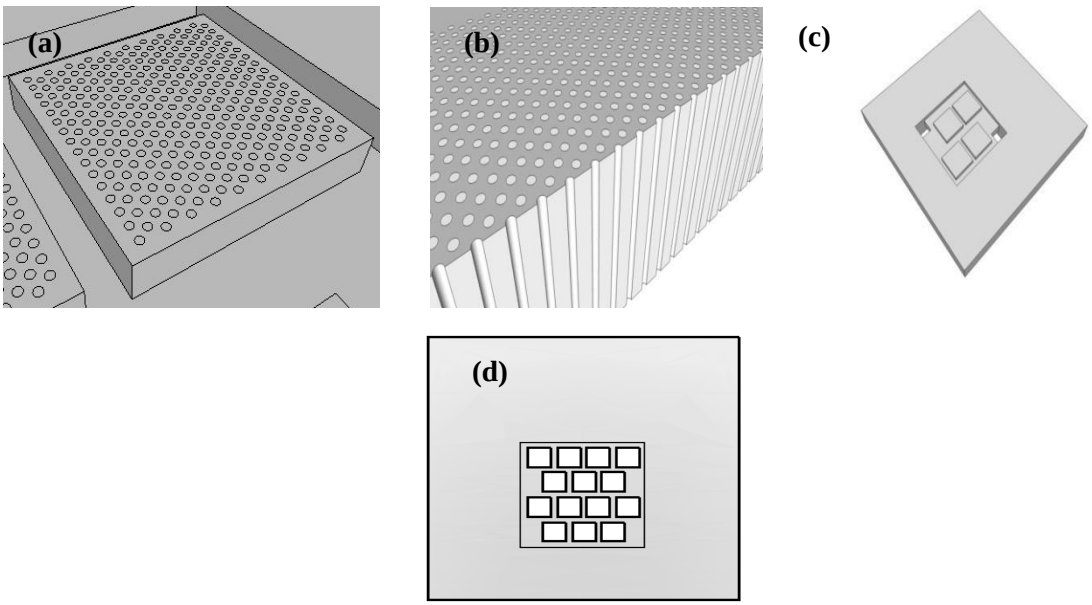


Figure 2. Electrode plate design: (a) the grid-porous anode flow field design, (b) the capillary structure on the grid platform, (c) the fuel inlet and outlet in the opposite position of the anode plate, as well as an overview of the grid design with its channel arrangement, and (d) the square through-hole cathode flow field design

Dry etching with laser ablation

The silicon wafer that was used to produce the electrode plate was a <100> p-type single-sided polished substrate with a diameter of 4 inches, a thickness of 500 ± 20 μm, and a resistance of 0–20 Ωcm. The MEMS-based microfabrication process that was used to form the required electrode structures was dry etching with laser ablation using the GSI Lumonics W670 Laser Trim System (General Scanning Inc., Somerville, USA). Table 3 provides the details of the laser system settings for dry etching processes in normal operating conditions. This type of laser machine is typically used to trim and test the thickness of the deposition layer and circuit board components such as printed circuit boards and surface-mount technology, but it is also suitable for etching silicon substrate. Its high-speed scanner has an objective lens with an 80% optical efficiency that focuses the laser beam onto the work surface of the silicon wafer, and the beam can move in the x–y direction using the toggle action. The focus distance for the short focus objective was set at 13.5 cm when the laser was at 100% power. The laser machine used a software developed and edited in C language and GSI-laser program to carry out the etching process and produce the flow field design required in this work.

Table 3. Laser system for the dry etching process in normal operating conditions

Operating details	**Technical specifications**
Power requirements	115 Vac @ 50–60 Hz
Optical efficiency	> 80%
Field size scan	10 cm x 10 cm (with s spot size of 30–50 μm at cutting surface)
Spot coverage	≥ 90% (i.e. minimum diameter/maximum diameter)
Beam diameter	0.12 cm at $1/e^2$ power point
Beam divergence	2.0 mrad ±5%
Wavelength transmission	1.06 μm (near-infrared area)
Pulse-to-pulse instability	±5% RMS of 500 Hz to 10 kHz
Q-switch pulse width	100–350 ns
Spectrum sensitivity	300 nm–0 μm
Rate of pulse repetition	Modified to fit 30 kHz using acousto-optic Q-switch

Current collector fabrication

The etching protective layer was the oxidation layer, SiO_2 and the characterization step was carried out after the layer was formed [6]. Silicon wafer is a semiconductor material. Hence, current collectors were needed for electricity conduction, and these were deposited by sputtering conductive metals onto the wafer surface to reduce ohmic resistance in the micro fuel cell. Titanium (Ti), i.e. the adhesive metal film used, was deposited on top of the SiO_2 layer followed by the current collector layers from copper (Cu) and gold (Au) materials. Figure 3 shows a schematic of this process, in which the metal target atoms were deposited onto the plate after it was bombarded by argon (Ar) ion in the sputtering chamber.

The Ti layer with a thickness of less than 1 μm was deposited to promote the adhesion of the current collector layers onto the plate surface because titanium has good adhesion on a clean surface of silicon, or SiO_2, and is often used as an adhesion layer for less sticky metals, such as Cu and Au. Another metal that is commonly used as an adhesive material for silicon-based plates is chromium [7]. The current collector deposition process consists of two stages: (1) deposition of an electrical conduction layer, i.e., Cu, and (2) deposition of a corrosion resistance layer, i.e. Au. Cu is much less expensive than Au and used as the main conductive layer for the current collector because its conductivity is four times higher than that of aluminum and the performance of a micro DMFC increased with the thickness of the Cu layer [8]. The Au layer is much thinner compared with Cu and mainly acts as a corrosion resistance layer that covers and protects the Cu layer from being oxidized in air to a reddish-colored cupric oxide (Cu_2O) because it is an undesirable semi-conductive material. Furthermore, the chemical properties of Au are less reactive than those of Cu in its normal state. Thus, the Au layer can also protect the Cu layer from direct contact

with the methanol fuel during operation because Cu can be eroded by methanol at ambient temperatures, and this corrosion may worsen at high temperatures.

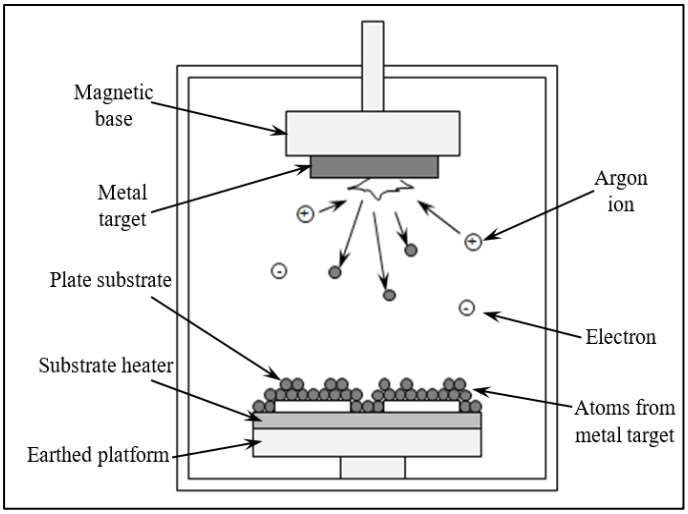


Figure 3. Schematic of the sputtering chamber for Ti and Cu targets

Micro fuel cell assembly

Cell assembly was performed to integrate the electrode plates fabricated in this work and the MEA optimized by means of statistical response surface method (RSM) used in a previous work [9]. The silicon-based electrode plates provided the mechanical support needed and ensured that the mass transport process inside the cell worked as planned. The MEA's active area, which was an area of 1 cm × 1 cm where the reaction occurred, became the limiting value in determining the total area of the entire electrode plate set at 2.5 cm × 2.5 cm. The remaining area surrounding the active area was required as an electrical contact surface for current collection and a placement area for the sealing gasket during cell assembly. Figure 4 shows the arrangement of the anode and cathode plate areas in conjunction with the MEA from the cell assembly perspective.

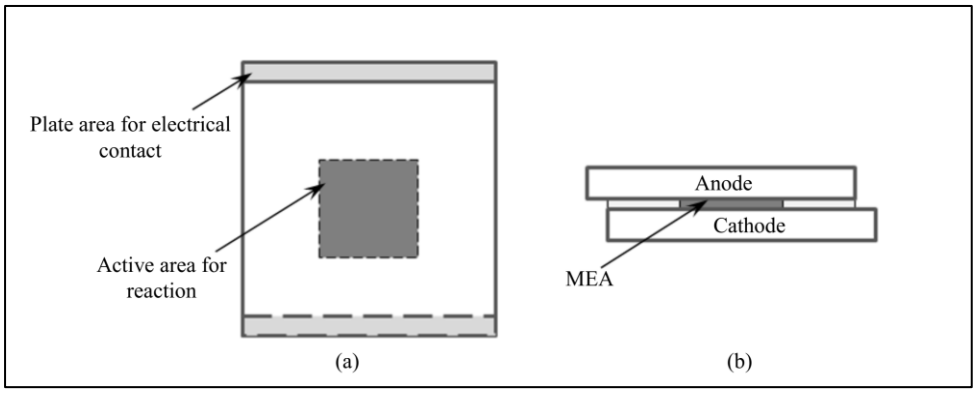


Figure 4. Illustration of the anode and cathode plate arrangement in conjunction with the MEA: (a) top view and (b) side view

The MEA went through a reprotonation step and was then placed between the electrode plates. A gasket with a thickness of about 50 μm was inserted between the plates, and a bonding adhesive was applied to seal the cell to avoid fuel leakage or short circuit between the anode and cathode surfaces. The new micro DMFC was then

mounted with a PMMA frame, and teflon tubes formed the fuel inlet and outlet. The finished electrode plates were assembled together with the optimized MEA to complete a single-cell micro DMFC and prepare it for performance testing, as shown in Figure 5.

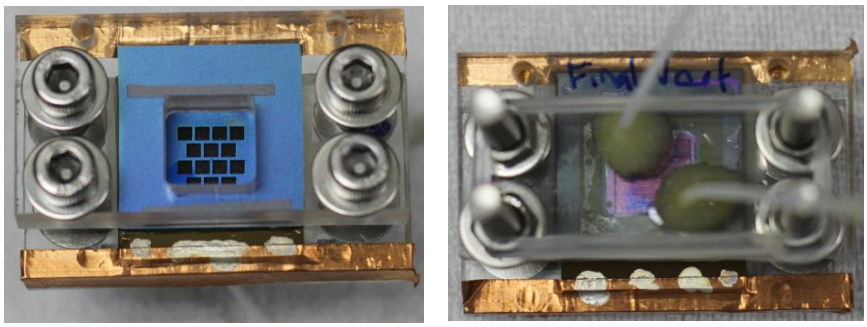


Figure 5. View of the new micro DMFC after assembly for the (a) cathode side and the (b) anode side

Performance test of micro DMFC

Fuel cell testing was conducted using a WMPG1000 multichannel potentiostat–galvanostat model (WonATech, Korea) to study the performance of the new electrode plate design for different cell orientations. The schematic of the experimental setup is shown in Figure 6. Methanol fuel was pumped into the cell after it passed through the pulse dampener, thereby stabilizing the fuel flow by filling the chamber with air that would be compressed when the liquid pressure increased, given that this condition resulted in a dampening of the flow pulsation. Oxygen was supplied into the cathode side from the surrounding air.

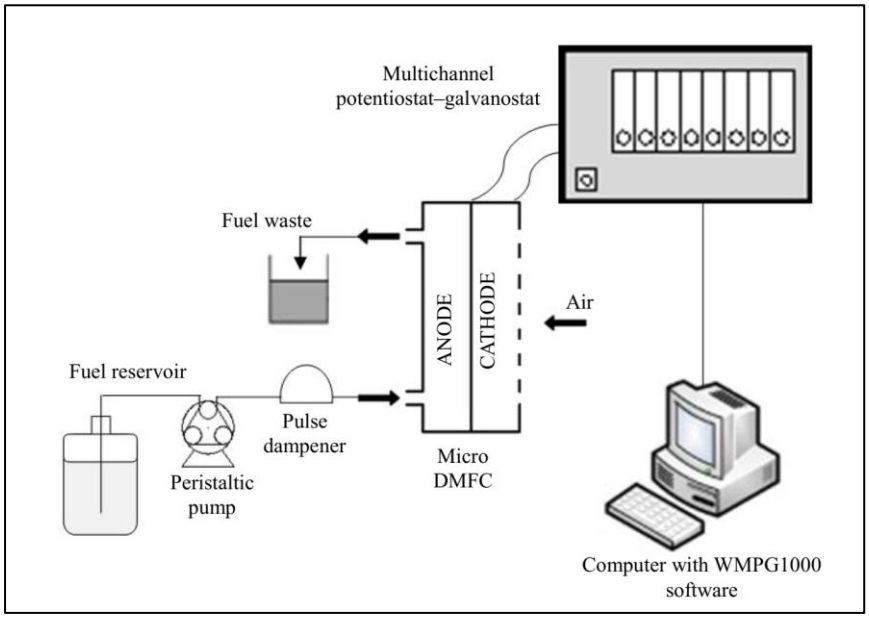


Figure 6. Schematic of cell performance test

Results and Discussion

The flow field is a new combined grid-porous design where the grid structure, which is the active-mode flow field design, acts as a platform for the capillaries in the porous structure, which is the passive-mode flow field design.

Figure 7 shows that a laser beam with a diameter of ~60 μm was obtained when the plate surface was exposed to a single laser pulse. Removal of laser ejecta was dominated by explosive vaporization and slag areas comprising micrometer-sized and submicrometer-sized ejecta materials. This situation occurred when the laser beam pulsed with enough energy to reach the melting latent heat of silicon; at this point, its crystals started melting to form a groove. The temperature continued to rise from the melting point to the evaporation point, and the local silicon material was removed when the latent heat of vaporization was reached. Just as the process completed, the evaporation process stopped and the liquid silicon gradually recrystallized when the latent heat was insufficient to maintain its liquidity. A similar phenomenon was observed by Yuan and Ma [10] and O'Neill and Li [11]; this phenomenon resulted in the restrengthening of the Si surface and high shear strength at the groove wall. The influence of q-rate on the laser ablation diameter was less obvious. Figure 7(a) shows a shallow ripple because the laser pulse energy decreased with the increase in frequency and resulted in the decrease in the overall pit size because only the middle part of the laser beam could reach the melting point. By contrast, Figure 7(b) shows that the pit appears to be more pronounced at lower frequencies, but a much larger amount of undesirable recrystallized molten silicon was formed at the edges.

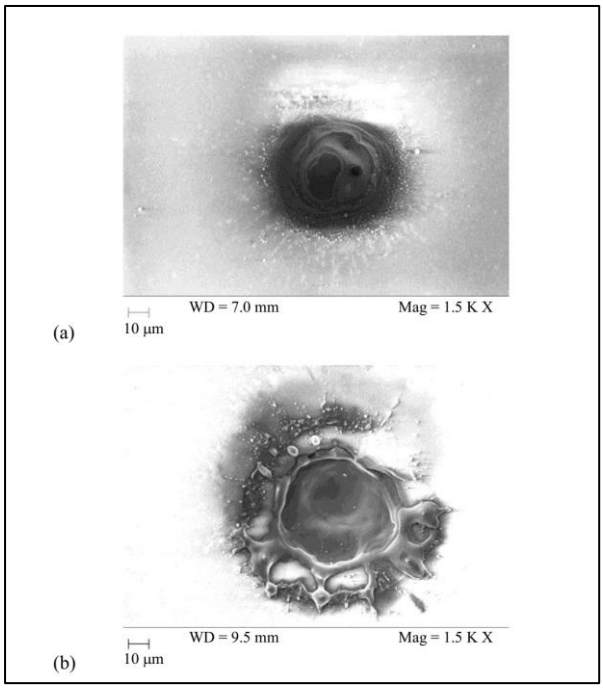


Figure 7. Pit formed by a focused beam point at q-rates: (a) 1 kHz and (b) 3 kHz

Figure 8 shows that the laser pulse separation can be influenced by the laser-bit size, i.e., the distance between the pulses increased as the bit size was increased. A comparison shows that if the pulse separation is too small, then the distance between the grooves decreases until the thin walls between adjacent grooves are destroyed and the laser ablation lines overlap with each other, as shown in Figure 8(a). This technique was used to remove a complete Si layer from the wafer to form the channel and reservoir structures, as well as the fuel inlet and outlet holes required by the flow field design.

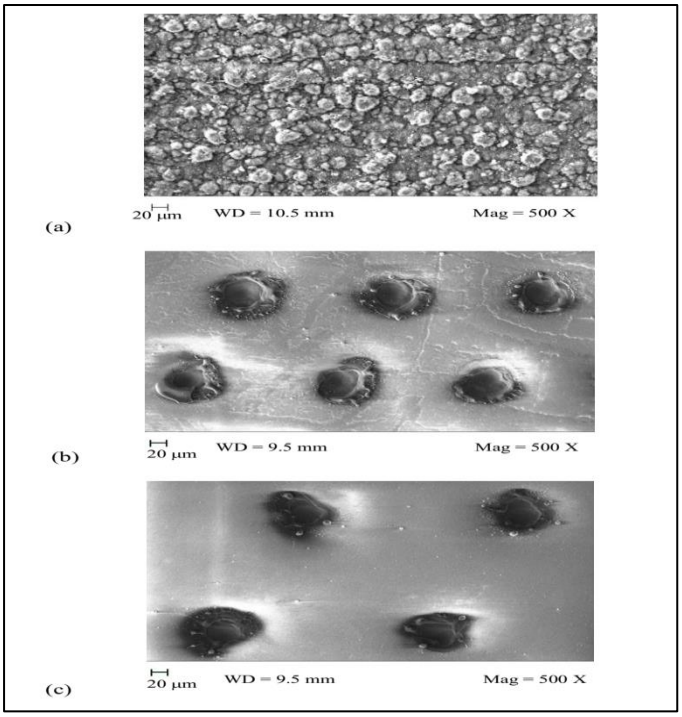


Figure 8. SEM micrographs for the local morphology of capillary structures formed using the bit size (a) 1 mil, (b) 7 mil, and (c) 10 mil.

A 30% (w/w) potassium hydroxide (KOH) solution containing 1% (v/v) isopropanol (IPA) at 80 °C was used in the wet etching process to remove the slag surrounding the ablated area. The images of etched holes in Figure 9 were taken by using an Olympus STM6 microscope (Olympus Corporation, Japan) with magnification capabilities of 5/10/20/50×. The desired capillary structure for the porous flow field was determined by monitoring the etching time, which was performed to clean the lasered plate, as shown in Figure 9(a). To maintain the round shape of the capillary structure, the etching process was divided into 5 slots of 1 minute each, and the plate was rinsed with deionized (DI) water at the end of each slot to stop the etching process before proceeding to the next slot, as shown in Figure 9(b). When the plate was continuously etched for more than 2 minutes, the crystal orientation of the <100> p-type Si wafer used as the electrode plate turned the original round shape of the capillary into a rhombus-shaped structure, as shown in Figure 9(c). This slag removal technique resulted in a less-round shape for the capillary structure when the total etching time exceeded 5 minutes.

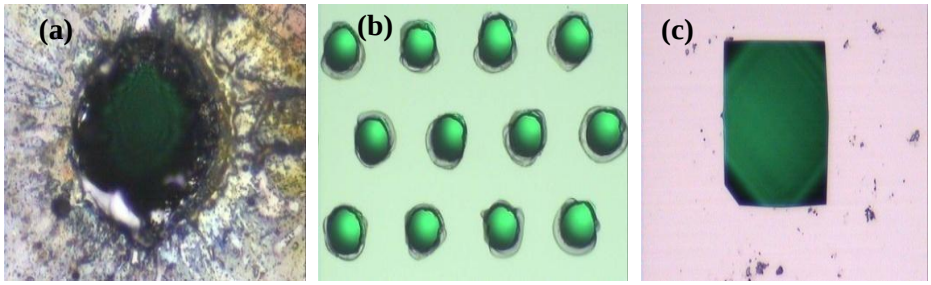


Figure 9. Porous flow field with capillary structure after (a) the laser ablation process, (b) 5 consecutive times of the 1 minute etching slot, and (c) continuous etching for more than 2 minutes

The channel structure for the grid flow field was formed with laser ablation, as shown in Figure 8(a), and cleaned with the KOH solution, as shown in Figure 10. The number of laser scans required to obtain the desired depth of the fuel reservoir and grid channels was 10 and 5 times, respectively. Figures 10(a–e) show a minute-by-minute wet etching process up to the fifth minute, which was the limiting time set by the cleaning process for the capillary structure. Figure 11 shows a magnification of the three important structures in the grid flow field: the grid platforms, the fuel inlet/outlet holes, and the fuel flow channel. The size of the square grid platforms was limited by the desired 50% open ratio of the anode active area [12].

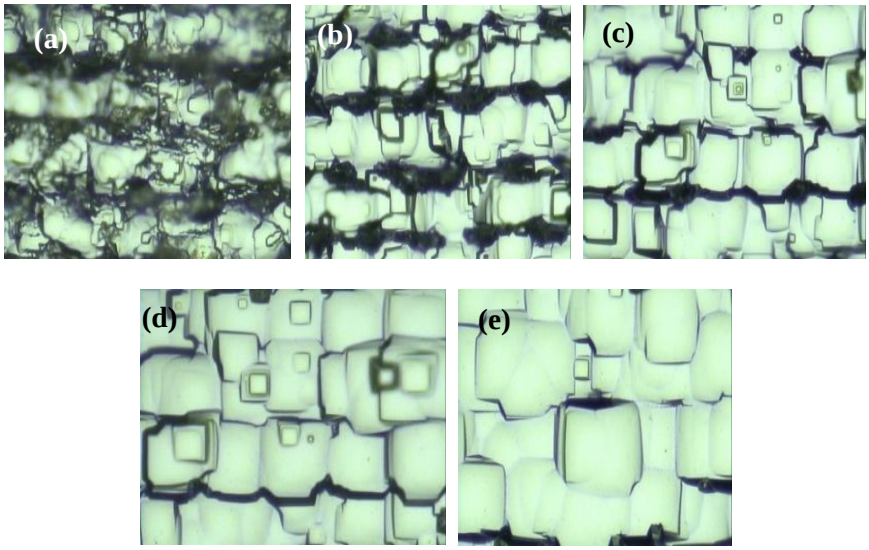


Figure 10. Laser-ablated surface for the channel structure observed using a microscope with 50× magnification after slag removal with KOH solution for the (a) 1st minute, (b) 2nd minutes, (c) 3rd minutes, (d) 4th minutes, and (e) 5th minutes

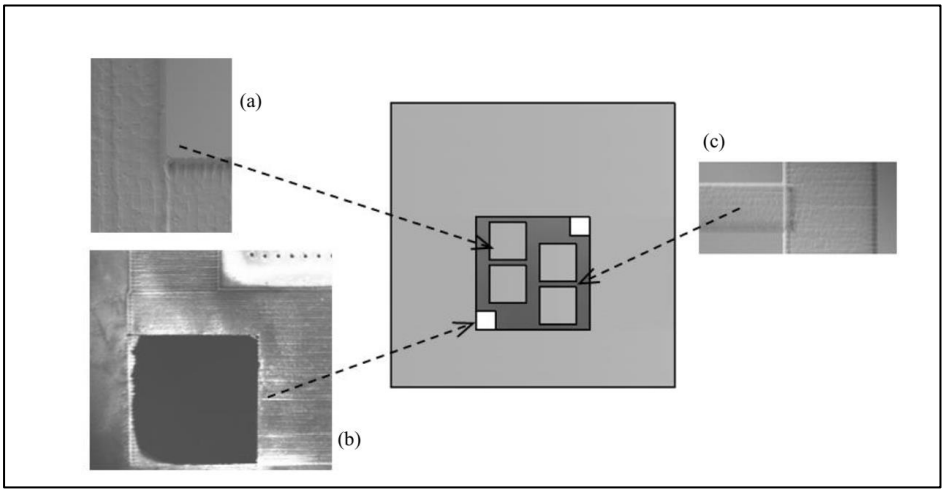


Figure 11. Three important structures in the grid flow field: (a) the grid platforms, (b) the fuel inlet/outlet holes, and (c) the fuel flow channel

Aside from providing the anode with the MEA contact surface, the grid platforms were also used as the porous flow field site. The inlet/outlet hole diameter was determined by the diameter size of the rigid teflon tube used to conduct the methanol fuel being pumped in and out of the cell, whereas the flow channel dimensions were important to ensure good transport of the reactants and by-products going in and out of the cell, respectively. The height of the grid platforms is also the depth of the fuel flow channel, and this feature became the limiting dimension in the etching process.

After the cleaning process was completed, the plate was rinsed with DI water and the remaining SiO_2 protective layer was stripped by soaking the plate in a 10% (w/w) hydrofluoric acid solution. Finally, the plate was rinsed with DI water and blow-dried with nitrogen gas. A film thickness measurement mapping instrument, i.e. Filmetrics F50, was used to ensure that the SiO_2 layer was completely removed before proceeding to the next step in the process. The scanning electron microscope (SEM) image in Figure 12 shows the height of the grid platform after 5 laser scans, and a value of 113.6 μm was obtained, which is satisfactorily comparable to the design value of 100 μm.

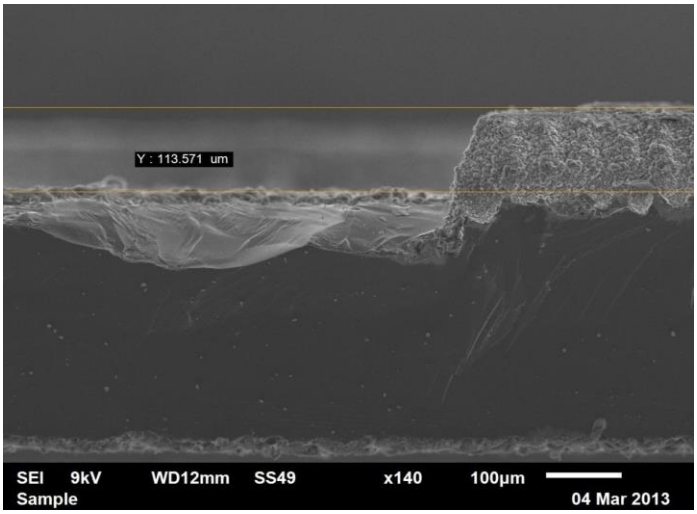


Figure 12. Grid platform structure formed by laser ablation

After the completion of the etching processes, the plate had a blank Si surface. Before the current collectors were deposited onto the plate, the silicon plate underwent a dry oxidation process that lasted for ~5 hours. The plates were arranged in close proximity to each other in the quartz tube of the mini furnace to promote good oxygen flow in the furnace, thereby resulting in optimum quality and thickness of the desired oxide layer. A thin SiO_2 layer with a thickness of about 500 nm was grown on the silicon surface to give hydrophilic properties to the surfaces of the capillary walls to 'pull' the fuel from the fuel reservoir to the MEA reaction area by increasing the angle of contact between the wall and the fuel and reducing the capillary pressure drop. This non-conductive SiO_2 layer also acted as an electrical insulating layer between the current collector layers and the Si substrate.

Ti and Cu metal targets of 99.99% purity were used, and sputtering was performed in an environment with a 1.2×10^{-2} Torr operating pressure and a flow rate of 7–14 s/cm with the radio frequency sputtering power set at 80 W. The layer thickness depended on the plasma power and the overall gas pressure used for the sputtering process [13]. As these parameters were set before the process, the desired metal thickness was controlled by the sputtering time. The desired thickness of the current collectors was 0.8 μm for Ti/Cu layers [14] and the sputtering rates were used as the initial estimates, which were 1.0 and 7.8 nm/min for Ti and Cu, respectively.

Au metal targets of 99.99% purity were used, and the sputtering was performed by using a BAL-TEC SCD 005 sputter coater (BalTec Inc, Switzerland) with a 0.3–0.6 Torr operating pressure. At 30 mA current, an Au layer of 25 nm was expected to be deposited at a sputtering time of 120 s. Therefore, the sputtering process was performed for 16 minutes to obtain the required thickness of 0.2 μm. Given the sputter coater conditions, the plate was sputtered twice at 480 s each before the process was completed [14]. The SEM micrographs in Figure 13 show the cross section of the current collectors after the deposition process. The Ti/Au layers in Figure 13(a) display a column structure, whereas the Cu layer in the Ti/Cu/Au deposition shows a grain structure. The Au layer thickness in Figure 13(a) was ~0.18 μm, which gave an average thickness value of Ti/Cu layer of about 1.1 μm. Both values are close to the targeted Ti/Cu/Au layer thickness.

The performance test that was performed for the cell produced a maximum performance of 1.86 mW/cm^2 at a voltage of 138.7 mV. A performance comparison study was conducted between the results of this work and a previous work by Onoe et al. [15], as shown in Table 4. This study was performed is because their work used an anode electrode structure that incorporated a porous design (passive) and serpentine design (active). Unfortunately, their Pt-Ru loading was not stated. Table 4 shows that despite requiring a lower Pt catalyst loading on the cathode side, their micro fuel cell yielded a much lower power output. However, a separate work by Halim et al. [16] proved that the cathode catalyst loading is an insignificant parameter in a micro DMFC. Therefore, a lower Pt loading can be used by the MEA for this new structure in future studies.

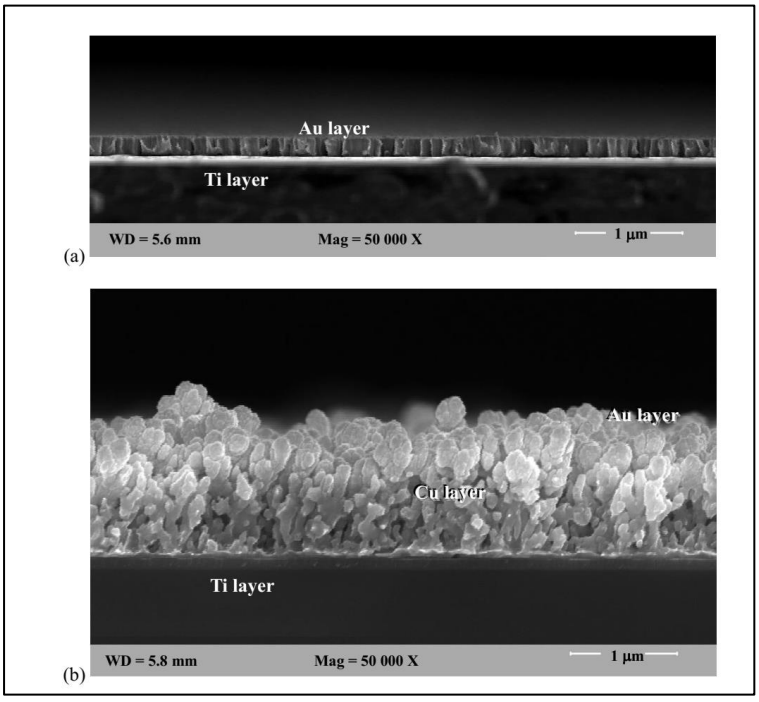


Figure 13. SEM micrographs for the deposited (a) Ti/Au layers and (b) Ti/Cu/Au layers

Table 4. Performance comparison between the new micro DMFC with a similar combined-mode design

Ref.	Active area (cm^2)	Methanol Concentration (M)	Flow Field Design	MEA Materials	System Type and Flow Rate	Maximum Power (mW/cm^2)	Fabrication based on the MEMS Technique
[15]	0.64	1	Serpentine-porous	Membrane: Nafion 115; anode and cathode: Pt (loading: 2.5 mg/cm^2)	Active-passive	0.016	The micro channel (250 μm depth) and the capillary structure inside the 30 μm channel with a 7 μm diameter is etched by using the deep reactive-ion etching process; current collector: Au (0.1 μm)
This work	1	5	Grid-porous	Membrane: Nafion 117; anode: Pt-Ru; cathode: Pt (loading: 8.0 mg/cm^2)	Active-passive (2 mL/min)	1.86	A micro channel with a depth of ~100 μm and inlet/outlet holes were micromachined using laser ablation; current collectors: Ti/Cu (1.1 μm)/Au (0.18 μm)

Conclusion

In addition to functioning as an etching mask and protecting the silicon surface from severe damage during the laser ablation process, the SiO_2 layer can also provide hydrophilic properties to the capillary wall to reduce the capillary pressure drop and act as an electrical insulating layer between the metallic coating of the current collectors and the Si substrate. Laser ablation was used in a dry etching process to microfabricate an electrode plate that could be used as an anode plate in a micro DMFC. The anode plate flow field was successfully structured to create a new combined-mode design that comprises the grid flow field and porous flow field on a single-plate substrate, which worked well in a micro DMFC. The micro DMFC with the new anode structure produced a maximum performance of 1.86 mW/cm^2 at a voltage of 138.7 mV. The silicon-based conductive plate from this work serves as a proof of concept in the field of micro fuel cell research in Malaysia.

Acknowledgment

The authors gratefully acknowledge the financial support given for this work by the Malaysia Research University Grant (GUP-2016-039) and the Ministry of Higher Education (Malaysia) research grant FRGS/1/2016/TK09/UKM/03/1. The research was conducted with full technical support and assistance at the Fuel Cell Institute Laboratory (Universiti Kebangsaan Malaysia), the IMEN-MEMS Fabrication Laboratory (Universiti Kebangsaan Malaysia), the Microelectronic Fabrication Laboratory (Universiti Malaysia Perlis), and the LIPI Research Center for Electronics and Telecommunication Laboratory (Bandung, Indonesia).

References

1. Xu, C. and Zhao, T. S. (2007). In situ measurements of water crossover through the membrane for direct methanol fuel cells. *Journal of Power Sources*, 168(1): 143-153.
2. Chen, X., Li, T., Shen, J. and Hu, Z. (2017). From structures, packaging to application: A system-level review for micro direct methanol fuel cell. *Renewable and Sustainable Energy Reviews*, 80: 669-678
3. Chen, W., Yuan, W., Ye, G., Han, F. and Tang, Y. (2017). Utilization and positive effects of produced CO_2 on the performance of a passive direct methanol fuel cell with a composite anode structure. *International Journal of Hydrogen Energy*, 42(23): 15613-15622.

4. Deng, H., Sang, S., Zhang, Y., Li, Z. and Liu, X. (2013). Investigations of silicon-based air-breathing micro direct methanol fuel cells with different anode flow fields. *Microelectronic Engineering,* 111: 180-184.
5. Yuan, W., Wang, A., Yan, Z., Tan, Z., Tang, Y. and Xia, H. (2016). Visualization of two-phase flow and temperature characteristics of an active liquid-feed direct methanol fuel cell with diverse flow fields. *Applied Energy*, 179: 85-98.
6. Hasran, U. A., Kamarudin, S. K., Daud, W. R. W., Majlis, B. Y., Mohamad, A. B. and Kadhum, A. A. H. (2011). A simple thermal oxidation technique and KOH wet etching process for fuel cell flow field fabrication. *International Journal of Hydrogen Energy,* 36(8): 5136-5142.
7. Williams, K. R., Gupta, K. and Wasilik, M. (2003). Etch rates for micromachining processing - Part II. *Journal of Microelectromechanical Systems*, 12(6): 761-768.
8. Sung, M.-F., Kuan, Y.-D., Chen, B.-X. and Lee, S.-M. (2011). Design and fabrication of light weight current collectors for direct methanol fuel cells using the micro-electro mechanical system technique. *Journal of Power Sources*, 196(14): 5897-5902.
9. Hasran, U. A., Kamarudin, S. K., Daud, W. R. W., Majlis, B. Y., Mohamad, A. B., Kadhum, A. A. H. and Ahmad, M. M. (2013). Optimization of hot pressing parameters in membrane electrode assembly fabrication by response surface method. *International Journal of Hydrogen Energy,* 38(22): 9484-9493.
10. Yuan, W. and Ma, B. (2008). Micro-machinability of monocrystal silicon by direct etching using excimer laser. *Journal of Materials Processing Technology,* 200(1): 390-397.
11. O'Neill, W. and Li, K. (2009). High-quality micromachining of silicon at 1064 nm using a high-brightness MOPA-based 20-W Yb fiber laser. *IEEE Journal of Selected Topics in Quantum Electronics,* 15(2): 462-470.
12. Yang, H. and Zhao, T. S. (2005). Effect of anode flow field design on the performance of liquid feed direct methanol fuel cells. *Electrochimica Acta,* 50(16-17): 3243-3252.
13. Husna, J., Aliyu, M. M., Islam, M. A., Chelvanathan, P., Hamzah, N. R., Hossain, M. S. and Amin, N. (2012). Influence of annealing temperature on the properties of ZnO thin films grown by sputtering. *Energy Procedia*, 25(0): 55-61.
14. Agilent Technologies (2008). A silicon-based air-breathing micro direct methanol fuel cell using MEMS technology. *Semiconductor Manufacturing Technology – Elite Development.* Retrieved from http://www.paper.edu.cn/download_feature_paper.php?serial_number=AgilentF-02
15. Onoe, S., Tanaka, H., Hoshino, K., Matsumoto, K. and Shimoyama, I. (2005). Miniature fuel cell with conductive silicon electrodes. Paper presented at the 13th International Conference on Solid-State Sensors, Actuators and Microsystems, Seoul, Korea.
16. Halim, F. A. L., Hasran, U. A., Masdar, M. S. and Kamarudin, S. K. (2017). Design of experiment approach for characterization and development of membrane electrode assembly in a passive vapor-feed direct methanol fuel cell. Paper presented at the 6th International Conference on Fuel Cell & Hydrogen Technology 2017, Putrajaya, Malaysia.

Malaysian Journal of Analytical Sciences Vol 23 No 3 2019

Articles 11 - 19 are selected papers from the "The Malaysia Separation Science Conference 2017 (MySSC 2017), 23 - 25 October 2017 at Pulai Spring Resort, Johor, Malaysia; organized by Universiti Teknologi Malaysia, Johor, Malaysia.

Guest Editor: Wan Aini Wan Ibrahim

		Page
1.	*Candida rugosa* LIPASE IMMOBILIZED ON DIETHYLAMINOETHYL-CELLULOSE (DEAE) FOR ESTERIFICATION OF BUTYL OLEATE (Lipase daripada *Candida rugosa* Tersekatgerak pada Dietilaminoetil-Selulosa (DEAE) untuk Penghasilan Ester Butil Oleat) *Mohd Basyaruddin Abdul Rahman, Ruhil Naznin Azaman, Emmy Maryati Omar, Muhammad Alif Mohammad Latif, Emilia Abdulmalek*	376
2.	SALICYLATE-BASED PROTIC IONIC LIQUIDS AS A POTENTIAL ANTIOXIDANT (Cecair Ionik Protik Berasaskan Salisilat Berpotensi Sebagai Antioksida) *Nur Afiqah Ahmad, Khairulazhar Jumbri, Anita Ramli, Noraini Ghani, Haslina Ahmad*	383
3.	HIDROGEL BERSIFAT PEKA TERHADAP RANGSANGAN SUHU UNTUK PENJERAPAN DAN PEMBEBASAN DADAH (Hydrogel with Thermo-Responsive Behavior for Drug Adsorption and Release) *Teow Yeit Haan and Kushalini Rames*	390
4.	CHEMICAL COMPONENTS OF POLYMERASE CHAIN REACTION IN 18S rRNA FOR DETECTION OF *Cryptosporidium* FROM RIVER WATER SAMPLES (Komponen Kimia Tindak Balas Berantai Polimerase di dalam 18S rRNA untuk Pengesanan *Cryptosporidium* dari Sampel Air Sungai) *Mohd Aiman Barudin, Mohammad Lokman Md Isa, Afzan Mat Yusof*	401
5.	MAGNETITE GRAPHENE FOR ELECTROCHEMICAL DETERMINATION OF URIC ACID (Magnetit Grafin untuk Penentuan Elektrokimia Asid Urik) *Yee Kin Weng, Azleen Rashidah Mohd Rosli, Farhanini Yusoff*	407
6.	VALIDATION ON CARBON DIOXIDE HYDRATE FORMATION THROUGH ANALYSIS ON THE SOLUBILITY OF CO_2 IN WATER USING HENRY'S LAW AND THE EXPERIMENTAL PRESSURE-TIME CURVE (Mengesahkan Pembentukan Hidrat Karbon Dioksida Melalui Kajian Terhadap Kadar Keterlarutan CO_2 di dalam Air Menggunakan Hukum Henry dan Graf Tekanan-Masa)	423

Mohd Hafiz Abu Hassan, Colin Edwards Snape, Lee Stevens

7. NUTRIENT DISTRIBUTION IN THE BESUT RIVER BASIN, TERENGGANU, MALAYSIA (SOUTH CHINA SEA) 436
(Taburan Nutrien di Lembangan Sungai Besut, Terengganu, Malaysia (Laut China Selatan))
Suhaimi Suratman, Azyyati Abdul Aziz, Tan Hock Seng, Hee Yet Yin, Fatin Adlina Md Nasir, Dung Quang Le, Norhayati Mohd Tahir

8. RARE EARTH ELEMENTS IN SEDIMENT CORES OBTAINED FROM THE PORTS OF TANJUNG PELEPAS AND SEDILI, JOHOR AS POLLUTION INDICATORS 444
(Unsur Nadir Bumi dalam Teras Sedimen Diperolehi dari Pelabuhan Tanjung Pelepas dan Sedili, Johor Sebagai Penunjuk Pencemaran)
Wai Seong Koh and Che Abd Rahim Mohamed

9. POTENTIAL OF CABBAGE EXTRACT (*Brassica oleracea*) AS ANTI-FOULING AGENT IN ALKYD UNDERCOAT FOR MILD STEEL IN SEAWATER 451
(Potensi Ekstrak Kubis (*Brassica oleracea*) Sebagai Ejen Anti-Kotoran bagi Cat Asas Alkid untuk Keluli Lembut di dalam Air Laut)
Mohammad Fakhratul Ridwan Zulkifli, Norasidayu Mohd Radzi, Suriani Mat Jusoh1,Jasnizat Saidin, Wan Mohd Norsani Wan Nik

10. SYNTHESIS OF MESOPOROUS NANOPARTICLES VIA MICROWAVE-ASSISTED METHOD FOR PHOTOCATALYTIC DEGRADATION OF PHENOL DERIVATIVES 462
(Sintesis Nanopartikel Bermesoliang Melalui Kaedah Bantuan-Gelombang Mikro untuk Degradasi Fotomangkin daripada Terbitan Fenol)
Nur Farhana Jaafar, Nor Amira Marfur, Nurfatehah Wahyuny Che Jusoh, Yuki Nagao, Nur Hidayahtul Nazirah Kamarudin, Rohayu Jusoh, Mohammad Anwar Mohamed Iqbal

11. THE USE OF LOW GRADE LIMESTONE IN ACID MINE DRAINAGE TREATMENT 472
(Penggunaan Batu Kapur Bergred Rendah dalam Rawatan Saliran Lombong Berasid)
Anuar Othman, Azli Sulaiman, Ismail Ibrahim

12. PREPARATION AND CHARACTERIZATION OF IMPROVED HYDROPHILIC POLYETHERSULFONE/REDUCED GRAPHENE OXIDE MEMBRANE 479
(Penyediaan dan Pencirian Penambahkaikan Hidrofilik Membran Polietersulfon/Grafin Oksida Terturun)
Madzlan Aziz, Nur Fatihah Tajul Arifin, Woei-Jye Lau

13. GREEN MICROWAVE-ASSISTED AQUEOUS ENZYMATIC EXTRACTION OF *Elateriospermum tapos* SEED OILS 488
(Pengekstrakan Hijau Minyak Bijian *Elateriospermum tapos* Menggunakan Kaedah Enzim Berakues Berbantu Gelombang Mikro)
Nuraimi Azlan Hadi Tan and Ida Idayu Muhamad

14. OPTIMIZATION OF HERBAL HEALTH TEA FLAVORED WITH ROASTED RICE GERM (KHAO DAWK MALI 105) USING RESPONSE SURFACE METHODOLOGY 495

(Pengoptimuman Teh Kesihatan Herba yang Bercampur dengan Germa Beras Panggang (Khao Dawk Mali 105) Menggunakan Kaedah Gerak Balas Permukaan)
Sriwiang Rittisak, Ratchanee Charoen, Ratchagon Pongsri, Pattraporn Tearyakul, Wanticha Savedboworn, Wiboon Riansa-ngawong

15. RAPID SPECTROPHOTOMETRIC METHOD FOR HISTAMINE DETERMINATION IN FISH USING ALIZARIN RED S AND METAL 505
(Kaedah Spektrofotometri Pantas untuk Penentuan Histamin dalam Ikan Menggunakan Alizarin Merah S dan Logam)
Miftakhul Jannatin, Ayu Nabila Izazi Latjuba, Sri Wahyuni, Ganden Supriyanto, Wan Aini Wan Ibrahim

16. KINETIC DEGRADATION OF TOTAL PHENOLIC CONTENT, DPPH RADICAL SCAVENGING AND XANTHINE OXIDASE INHIBITORY ACTIVITIES IN YANANG (*Tiliacora triandra*) LEAF EXTRACT DURING PREPARATION PROCESS 516
(Degradasi Kinetik Kandungan Jumlah Fenolik, Aktiviti Pemerangkapan Radikal DPPH dan Xantin Oksidase dalam Ekstrak Daun Yanang (*Tiliacora triandra*) Semasa Proses Penyediaan)
Sunee Eadmusik, Chanthima Phungamngoen, Natthaya Choosuk

17. ESTERIFICATION OF ACETIC ACID AND BENZYL ALCOHOL OVER ZEOLITE HX PRODUCED FROM BANGKA BELITUNG KAOLIN 524
(Pengesteran Asid Asetik dan Benzil Alkohol ke atas Zeolit HX Dihasilkan daripada Kaolin Bangka Belitung)
Vita Nur Iftitahiyah, Didik Prasetyoko, Hartati2, Yatim Lailun Ni'mah, Hasliza Bahruji, Hadi Nur

18. FRACTIONATION OF AQUEOUS EXTRACT OF *Ficus deltoidea* VAR. *Kunstleri*'s LEAVES USING SOLID PHASE EXTRACTION METHOD FOR ANTICANCER ACTIVITY ON DU145 CELL LINE 534
(Pemeringkatan Ekstrak Akueus dari Daun *Ficus deltoidea* var. *Kunstleri* Menggunakan Kaedah Pengestrakan Fasa Pepejal untuk Aktiviti Antikanser Pada Titisan Sel DU145)
Husnul Hanani Soib, Harisun Yaakob, Mohamad Roji Sarmidi Mohamad Norisham Mohamad Rosdi

19. CUTICULAR HYDROCARBONS OF PUPAL CASES OF *Chrysomya megacephala* (FABRICIUS) AND ITS POSSIBLE USE FOR ESTIMATING POSTMORTEM INTERVAL 548
(Hidrokarbon Kutikel Kepompong *Chrysomya megacephala* dan Kegunaannya untuk Menganggar Sela Masa Kematian)
Nurul Nadhirah Nasir, Mohamad Afiq Mohamed Huri, Reena Abd. Rashid, Jaafariah Jaafar, Naji Arafat Mahat

Malaysian Journal of Analytical Sciences, Vol 23 No 3 (2019): 376 - 382
DOI: https://doi.org/10.17576/mjas-2019-2303-01

MALAYSIAN JOURNAL OF ANALYTICAL SCIENCES
Published by The Malaysian Analytical Sciences Society
ISSN 1394 - 2506

Candida rugosa LIPASE IMMOBILIZED ON DIETHYLAMINOETHYL-CELLULOSE (DEAE) FOR ESTERIFICATION OF BUTYL OLEATE

(Lipase daripada *Candida rugosa* Tersekatgerak pada Dietilaminoetil-Selulosa (DEAE) untuk Penghasilan Ester Butil Oleat)

Mohd Basyaruddin Abdul Rahman[1,2]*, Ruhil Naznin Azaman[2], Emmy Maryati Omar[1,2], Muhammad Alif Mohammad Latif[1,2], Emilia Abdulmalek[1,2]

[1]*Integrated Chemical BioPhysics Research, Faculty of Science*
[2]*Department of Chemistry, Faculty of Science*
Universiti Putra Malaysia, 43400 UPM Serdang, Selangor, Malaysia

**Corresponding author: basya@upm.edu.my*

Received: 19 August 2018; Accepted: 14 May 2019

Abstract

Lipase from *Candida rugosa* was immobilized onto diethylaminoethyl-cellulose (DEAE) through physical adsorption method with high percentage of protein absorption obtained at 84%. The lipase-DEAE was used to catalyze the enzymatic esterification of butyl oleate by reacting oleic acid and butanol in hexane. Butyl oleate, an alkylic ester of long-chain fatty acid is now in high demand to produce biodiesel. The effect of reaction temperature, thermostability of the immobilization lipase, stability in organic solvent, leaching with hexane and storage studies under various conditions of immobilized lipase were investigated. The optimum esterification was found to be up to 90% yield. Only a slight of lipase leached out after being washed by 20 mL of hexane. This showed that lipases were strongly attached to the DEAE support *via* physical adsorption method, and it could be used as industrial biocatalyst.

Keywords: immobilized enzyme, lipase, cellulose, esterification, biodiesel

Abstrak

Lipase dari *Candida rugosa* tersekatgerak pada dietilaminoetil-selulosa (DEAE) melalui kaedah penjerapan fizikal menunjukkan peratusan penyerapan protein tertinggi pada kadar 83.4%. Lipase-DEAE digunakan sebagai mangkin untuk sintesis berenzim butil oleat melalui tindak balas asid oleik dan butanol di dalam heksana. Butil oleat, satu ester alkilik dari asid lemak rantai panjang kini mempunyai permintaan tinggi untuk penghasilan biodiesel. Kesan suhu tindak balas, kestabilan terma lipase tersekatgerak, kestabilan pelarut organik, pelunturan dengan heksana dan kajian penyimpanan pada pelbagai kondisi lipase tersekatgerak telah diselidiki. Hasil tindak balas pada keadaan optima didapati menghampiri 90%. Hanya sedikit kuantiti lipase yang hilang selepas proses pelunturan setelah dicuci oleh pelarut heksana 20 mL. Ini menunjukkan bahawa lipase telah tersekatgerak dengan kuat pada bahan DEAE melalui kaedah penjerapan fizikal, dan ianya boleh digunakan sebagai biomangkin industri.

Kata kunci: enzim tersekatgerak, lipase, selulosa, esterifikasi, biodiesel

Introduction

Immobilization of enzymes and proteins onto insoluble materials forms the basis of many biotechnological processes and analytical devices. The main reason of immobilization is to ease enzyme-product separation and to allow enzyme recyclability, persistency of functional activity rather than to stabilize enzymes and proteins.

Previously many materials have been used to immobilize enzymes such as layered double hydroxides, [1] mica [2] and metal organic frameworks (MOFs) [3]. Several properties are desirable for the continuous operation of the apparatus setup for the bioconversion using an immobilized enzyme reactor. Immobilization is bound to lead the changes in the environment of the enzyme, and hence cause changes in the observed properties [4]. The most commonly used support for enzyme immobilization is the ion-exchange resins as these readily adsorb most protein.

Diethylaminoethyl-cellulose or DEAE-cellulose is the most widely used of all the cellulosic ion exchangers and most variable in quality. In addition to provide a low density of charge and easy penetration by large molecule, this cellulose adsorbent offers a supporting matrix that is hydrophilic and consequently minimizes the hydrophobic interactions that complicate the adsorption of protein to ion exchange resins. Because of the ready penetration of substantial portion of the cellulose structure by protein molecules, the capacity of adsorbents such as DEAE-cellulose for the adsorption of protein is not strongly affected by particle size [5]. One of the earliest studies found out that immobilized amyloglucosidase on DEAE-cellulose showed greater stability at 50 ^{o}C than the free amyloglucosidase [6]. DEAE-cellulose was also reported shifting the pH optimum of amyloglucosidase to a lower value. In another work, immobilization of a bacterial nitrile-hydratase on DEAE-cellulose had slightly decreased the activity's optimum pH and increased the optimum temperature and thermal stability of the system [7].

Major advantages of adsorption as a general method of insolubilizing enzymes are that usually no reagents and only a minimum of activation steps is required. This method offers cheaper alternative as it can be carried out easily and less disruptive to the enzyme compared to other methods that focus on chemical interaction such as covalent bonding and cross linking. *Candida rugosa* lipase is a well-known microbial lipase, which hydrolyses all ester bonds of natural or synthetic triacylglycerols. Lipase from *Candida rugosa* has also been widely used for several stereoselective esterification and transesterification reactions in organic medium [8]. Esterification of oleyl alcohol and bioalcohol (e.g. ethanol and butanol) give a fatty acid ester (e.g. ethyl oleate and butyl oleate) that is useful for pharmaceuticals and cosmeceuticals. It can also be used for biodiesel production as the main components of biodiesel are alkylic esters of long-chain fatty acids. Other than the alkali-catalyzed transesterification of a vegetable oil with alcohol, enzymatic reactions could also be used to produce these esters in the biodiesel industry.

The use of lipases to catalyze the esterification step is attractive, because they can be used under mild reaction conditions. However, several challenges must be overcome in order for the enzymatic route to be economical as current commercial immobilized enzymes are expensive which costs approximately 1,000USD per/kg [9]. This has stimulated a search for cheaper immobilized lipases that have high activity and stability. Therefore, the aims of the current work were to study the immobilization of *Candida rugosa* lipase onto DEAE-cellulose and to optimize the synthesis of butyl oleate, a model system for biodiesel synthesis by enzymatic esterification.

Materials and Methods

Materials

Lipase from *Candida rugosa* (E.C.3.1.1.3, Type VII) and DEAE-cellulose were purchased from Sigma Chemical Co. (St. Louis, MO). All other chemicals (butanol, oleic acid, sodium hydroxide) and solvents (hexane, ethanol, acetone) used in this study were of analytical grade.

Water extraction of lipase

Commercial lipase from *Candida rugosa* was partially purified by dissolving lipase (1.5 g) in distilled water (15 mL) with continuous stirred for 30 minutes in the lowest stirring manner. This mixture was then centrifuge at 10,000 rpm for 15 minutes. The supernatant was used as partially purified lipase or stored at 4 ^{o}C prior to use.

Immobilization of lipase

The partially purified lipase (15.0 mL) was added to DEAE-cellulose (2.0 g). The mixture was shaken at 100 rpm in a water bath at room temperature for 1 hour. The immobilized lipase was separated by filtration through Whatman no. 1 filter paper (pore size 11µm). The volume of supernatant after filtration was recorded and kept for protein assay. The immobilized enzyme was lyophilized at –40 ^{o}C in a freeze drier.

Protein assay
The amount of protein content before and after immobilization was determined by using the method of Bradford Coomassie brilliant blue assay procedure using bovine serum albumin as standard [10].

Esterification assay
Enzymatic esterification tested consisting of native lipase (0.3 g) or DEAE-cellulose-immobilized lipase (0.3 g), butanol (4.00 mmol), oleic acid (2.00 mmol) in hexane (2.0 mL). The mixture was incubated at 30 ^{o}C for 5 hours with continuous shaking at 150 rpm in a horizontal water-bath shaker. The reaction was terminated by dilution with 3.50 mL ethanol:acetone (1:1 v/v) and the remaining free fatty acid in the reaction mixture was determined by titration with 0.15M NaOH using an automatic titrator ABU91 to an end point of pH of 10. The activity was expressed as μmol/min/mg protein.

Biocatalytic properties of the immobilized lipase:
Effect of reaction temperature
The reaction mixtures containing native or DEAE-cellulose-immobilized lipase were incubated at different temperature ranging from 30 ^{o}C to 70 ^{o}C for 5 hours with continuous shaking at 150 rpm. The relative activities were expressed as percentage of the activities at different temperature compared to reaction temperature of 40 ^{o}C. All experiments were carried out in triplicate.

Effect of thermostability
Enzymes were incubated at various temperatures ranging from 30 ^{o}C to 70 ^{o}C in sealed vials for one hour. The enzymes were left to cool at room temperature before the esterification activity. The relative activities were expressed as percentages of the relative activities at different temperature compared to the activity of the untreated enzyme. All experiments were carried out in triplicate.

Effect of leaching
The leaching procedure was done by washing the DEAE-cellulose-immobilized lipase (0.30 g) with hexane of 4, 8, 12, 16 and 20 mL with additional 4 mL at each washing. The activities of DEAE-cellulose-immobilized lipase at each volume of hexane were determined by esterification reaction. The activity of the lipases was expressed as percentages of the relative activities at different wash cycle compared to the activity of the unwashed enzyme. All experiments were carried out in triplicate.

Effect of stability in organic solvent
The stability of the immobilized enzyme in organic solvent was compared to native lipase. The DEAE-cellulose-immobilized lipase and native lipase were incubated in hexane without shaking at room temperature starting from day one to day ten. After the incubation, the activity was determined at 30 ^{o}C. The relative activities were expressed as percentages of their activities to the different time intervals compared to the activity at day one. All experiments were carried out in triplicate.

Effect of storage stability
This study was conducted to investigate the stability of native lipase compare to immobilized lipase at different storage temperature (-20 ^{o}C, 0 ^{o}C and room temperature). Both lipases were kept for 60 days. The relative activities were expressed as percentages of esterification activities at 60 days compared to the initial activity at day one. All experiments were carried out in triplicate.

Results and Discussion

Enzyme stability can be improved by immobilization of enzymes on insoluble supports. DEAE-cellulose showed significantly high amount of protein loading up to 84% thus making it a suitable matrix for enzyme immobilization. Generally, enzyme immobilized on the support was assumed to be distributed within the support and localized at the surfaces [11]. When adsorption of enzyme was done, large protein molecule of lipase from *Candida rugosa* were distributed randomly in its interlayers, replacing the smaller molecules of water. Immobilization method effectiveness was determined through activities of the immobilized lipase at different conditions. High protein loading of enzyme on the support will lead to higher enzymatic activity. The enzymatic conversion of biodiesel

butyl oleate in hexane was higher for the DEAE-cellulose immobilized lipase (89%) compared to native lipase (45%). Enzyme shows high chemoselectivity and mild conditions compared to harsh alkaline or acid catalysis system. This biodiesel synthesis by enzymatic esterification reactions of long fatty acids can also be expanded to other aliphatic bioalcohols (methanol, ethanol, n-propanol).

Effect of reaction temperature

Figure 1 shows the activities of the immobilized and native lipase increased at temperatures between 30 ^{o}C and 40 ^{o}C. However, drastic decrease in activities occurs after 50 ^{o}C. Activity of lipase was low at 30 ^{o}C may be due to the diffusion limitation of the reactant cause by the increase in reactant viscosity at lower temperature. The optimum temperature for both the enzymes was at 40 ^{o}C. Lipase immobilized onto DEAE-cellulose seemed to protect the enzyme against denaturation by heat as their activities were higher compared to native lipase at temperatures higher than 50 ^{o}C. Lipases are easily denatured at higher temperature where the peptide bonds and amino acid chains are reactive and can participate in deleterious reactions at high temperature. This will lead to weak stabilizing interaction that built up a conformational stability in an enzyme to be destroyed by heat. This problem can be solved by ample conformational mobility, which it can achieve through attachment on solid support [12].

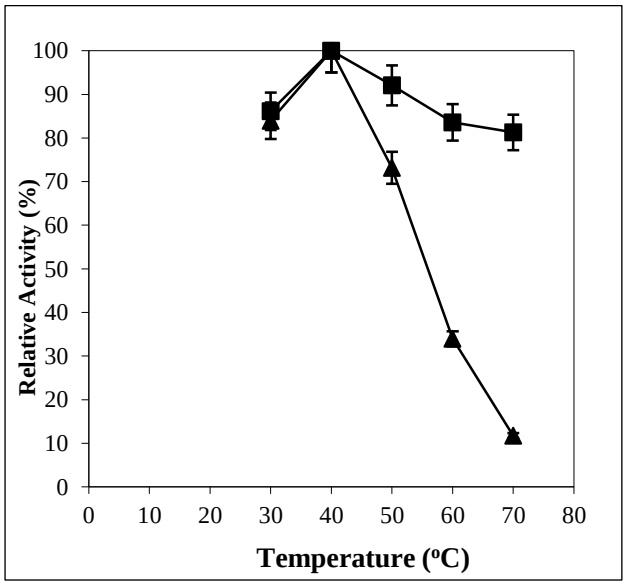


Figure 1. Effect of temperature on the relative esterification activity of DEAE-cellulose immobilized lipase and native lipase. Reactions were performed in hexane with 1:1 mole ratio of 1-butanol and oleic acid. Bars indicate standard deviation. (▲ Native Lipase; ■ Immobilized Lipase on DEAE-cellulose)

Effect of thermostability

Stability of lipase immobilized on DEAE-cellulose is shown in Figure 2. The immobilized lipase preparations were significantly more thermo-stable than the native lipase after 1 hour of incubation at temperatures ranging from 40 ^{o}C to 70 ^{o}C. The immobilized lipase had higher activity than native lipase because the immobilization can perform its vibrational and more complex movement required for efficient catalyst activity. At temperatures above 30 ^{o}C, enzyme resistance to adverse heat influences and persistency of its molecular integrity to face denaturants were deteriorated. This denaturation is due to a fully functional monomeric enzyme loses its biological activity *in vitro* by unfolding of its tertiary structure to a disordered polypeptide. Nevertheless, finding has shown that besides temperature and pH, presence of chaotropic agents also influences denaturation of these enzymes. Denaturation of these enzymes occurs in an equivalent way, encouraging unfolding of the three-dimensional protein structure [13]. In most models of thermal deactivation, an active lipase undergoes a reversible or irreversible structural change (*i.e.* a temperature-induced conformational transition) to produce a catalytically inactive form because such process is essentially unimolecular, it is frequently characterized by first-order kinetics.

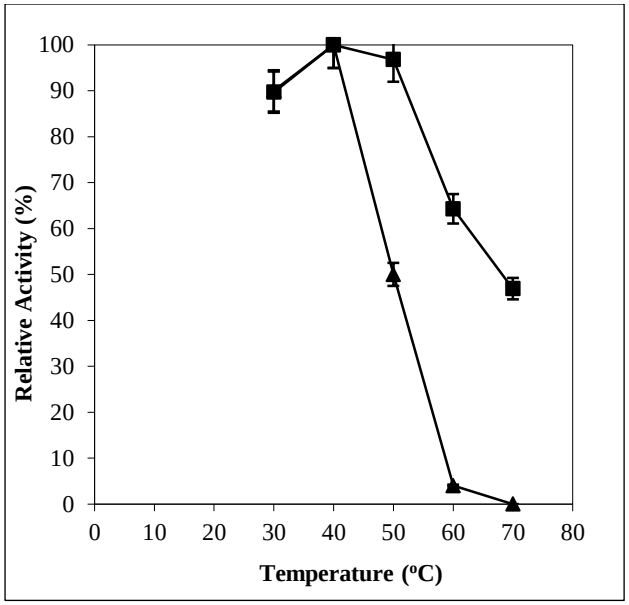


Figure 2. Percent relative activity of native lipase and DEAE-cellulose immobilized lipase after 1 hour incubation at various temperatures. Reactions were performed in hexane with 1:1 mole ratio of 1-butanol and oleic acid at 30ºC. Bars indicate standard deviation. (▲ Native Lipase; ■ Immobilized Lipase on DEAE-cellulose)

Stability in hexane

The stability evaluation of enzyme preparations in hexane is shown in Figure 3.

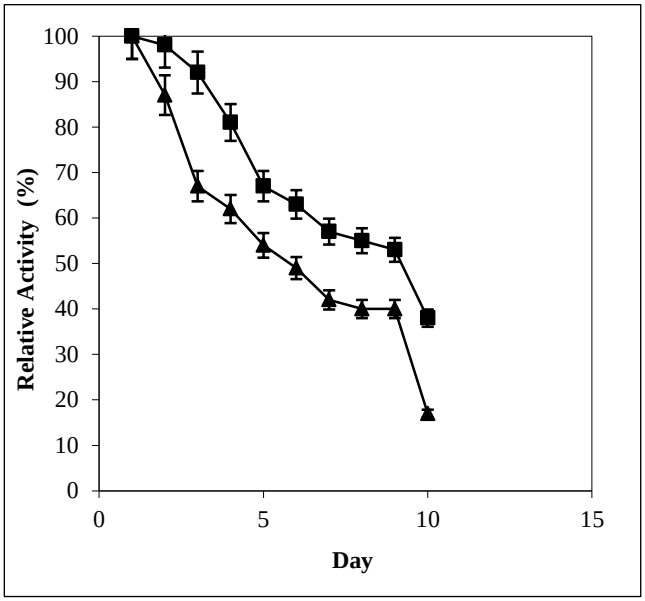


Figure 3. Percent relative activity of native lipase and DEAE-cellulose immobilized lipase as affected by incubation in hexane at room temperature (25 ºC) from day 1 to day 10. Reactions were performed in hexane with 1:1 mole ratio of 1-butanol and oleic acid at 30 ºC. Bars indicate standard deviation. (▲ Native Lipase; ■ Immobilized Lipase on DEAE-cellulose)

Stability of the lipase immobilized onto DEAE-cellulose remained stable at 50% of its relative activities compared to native lipase (40%) when incubated in hexane at room temperature up to 9 days. Immobilization seemed to protect the enzyme from denaturation caused by the presence of organic solvent. Supports may induce water molecules surrounding lipase, which was necessary for its catalytic activities from being stripped away by organic solvent [14]. The essential water layer around the enzyme must be preserved to maintain the active conformation of enzyme. A large amount of water may result to the undesirable side reaction such as hydrolysis of acid anhydrides and halogenates. The thermodynamic equilibrium of most processes is unfavorable in water. Therefore, enzyme may be stable in organic solvents than they are in water and this is the reason why they are used as reaction medium in enzymatic activities. Although the polar solvent tends to strip water from enzyme molecule, the supports may trap and prevent disruption of the enzyme bound water essential to maintain the three-dimensional structure of the enzyme for catalysis [15].

Leaching study on immobilized lipase

Figure 4 shows that all the derivatized lipase preparations retained their catalytic activities at 100% even after 4 washing cycles. The fifth cycle showed only a slight leached not more than 1% for all the immobilized lipase. This might reflect the loss of some enzyme during washing and be an inherent consequence of its immobilization on each support surface [16]. This finding is an indication that lipase remained immobilized on the support even after washing with 20 mL of hexane. With this, DEAE-cellulose is proven to be suitable support for enzyme immobilization as it prevents enzyme from being washed away. This also proved that the method of adsorption used in this study is a suitable method of immobilization and had been successfully done [17].

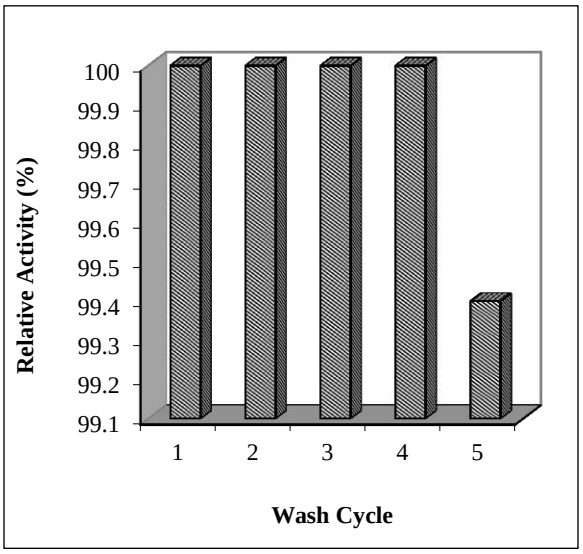


Figure 4. Effect of leaching on the relative esterification activity of DEAE-cellulose immobilized lipase. Reactions were performed in hexane with 1:1 mole ratio of 1-butanol and oleic acid at 30 ºC

Storage stability

The residual activities of various lipase preparations were determined after storing for 60 days under various conditions. All lipases exhibited full catalytic activity after storing them at –20 ^{o}C. Immobilized lipase also retained their catalytic activity at 100% when stored at 0 ^{o}C but decreased to 65% for the storage at room temperature. The native lipase was able to retain 70% of activity for 0 ^{o}C storage but decreased abruptly to 25% of activity when stored at room temperature. At very low temperatures, lipase is probably locked in its native, catalytically active conformation. Immobilized lipase showed increase in storage stability compared to native lipase, when stored at higher temperatures. At these temperatures, the stabilization may be owed to the multipoint attachment of the enzymes to the supports, creating a more rigid enzyme molecule. Hence disruption of the active centre becomes less likely to occur [18].

Conclusion

Lipase from *Candida rugosa* has been successfully immobilized on DEAE-cellulose using physical adsorption method. The method employed was a success referring to the increase in activity and stability of lipase after immobilization. Immobilized lipase was found to be more stable compared to the native lipase under higher temperature, in solvent and under different storage conditions. DEAE-cellulose had satisfied a number of criteria as it allows easy lipase immobilization without having to lose its catalytic activity and it can be obtained through simple and inexpensive method. This environmental friendly and mild reaction conditions of butyl oleate production for biodiesel could be a better choice for industrial application.

Acknowledgement

This project was supported by the Ministry of Science, Technology and Innovation, Malaysia research grant (Vot. No. 5450618).

References

1. Abdul Rahman, M. B., Basri, M., Hussein, M. Z., Rahman, R. N. Z. A., Zainol, D. H. and Salleh, A. B. (2004). Immobilization of lipase from *Candida Rugosa* on layered double hydroxides for esterification reaction. *Applied Biochemistry and Biotechnology - Part A Enzyme Engineering and Biotechnology*, 118: 313-320.
2. Zaidan, U. H., Rahman, M. B. A., Basri, M., Othman, S. S., Rahman, R. N. Z. R. A. and Salleh, A. B. (2010). Silylation of mica for lipase immobilization as biocatalysts in esterification. *Applied Clay Science*, 47: 276-282.
3. Lian, X., Fang, Y., Joseph, E., Wang, Q., Li, J., Banerjee, S., Lollar, C., Wang, X. and Zhou, H. C. (2017). Enzyme-MOF (Metal-Organic Framework) composites. *Chemical Society Reviews*, 46: 3386 – 3401.
4. Liu, D., Chen, J. and Shi, Y. (2018). Advances on methods and easy separated support materials for enzymes immobilization. *Trends in Analytical Chemistry*, 102: 332-342.
5. Sirisha, V. L., Ankita, J. and Amita, J., (2016). Enzyme immobilization: An overview on methods, support material, and applications of immobilized enzymes. *Advances in Food and Nutrition Research*, 79: 179-211.
6. O'Neill, S. P., Dunnill, P. and Lilly, M. D. (1971). A comparative study of immobilized amyglucosidase in a packed bed reactor and a continuous stirred tank reactor. *Biotechnology and Bioengineering*, 13: 337-352.
7. Fradet, H., Arnaud, A., Rios, G. and Galzy, P. (1985). Hydration of nitriles using a bacterial nitrile-hydratase using DEAE-cellulose. *Biotechnology and Bioengineering*, 27: 1581-1585.
8. Othman, S. S., Basri, M., Hussein, M. Z., Abdul Rahman, M. B., Rahman, R. N. Z. A., Salleh, A. B., and Jasmani, H. (2008). Production of highly enantioselective (-)-methyl butyrate using *Candida Rugosa* lipase immobilized on epoxy-activated supports. *Food Chemistry*, 106(2): 437-443.
9. Stoytcheva, M. and Montero, G. (2011). Biodiesel: Feedstocks and processing technologies, In. Tech, Croatia: pp. 397-410.
10. Bradford, M. M. (1976). A rapid and sensitive method for the quantitation of microgram quantities of protein utilizing the principle of protein-dye binding. *Analytical Biochemistry*, 72: 248-254.
11. Abdul Rahman, M. B., Md. Yunus, N. M., Othman, S. S., Basri, M., Salleh, A. B. and Rahman, R. N. Z. A. (2006). New lipases and proteases, Nova Science Publishers, Inc. New York: pp. 111-125.
12. Paiva, A. L., Balcão, V. M. and Malcata, F. X. (2000). Kinetics and mechanisms of reactions catalyzed by immobilized lipases. *Enzyme and Microbial Technology*, 27(3–5): 187-204.
13. Becktell, W. J. and Schellman, J. A. (1987). Protein stability curves. *Biopolymers*, 26: 1859-1877.
14. Klibanov, A. M. (1986). Enzymes that work in organic solvents. *Chemtec*h: 54-359.
15. Gorman, L. A. and Dordick, J. S. (1992). Organic solvents strip water off enzymes. *Biotechnology and Bioengineering*, 39: 392-397.
16. Abdul Rahman, M. B., Md Yunus, N. M., Hussein, M. Z., Rahman, R. N. Z. A., Salleh, A. B. and Basri, M. (2005). Application of advanced materials as support for immobilisation of lipase from *Candida rugosa*. *Biocatalysis and Biotransformation*, 23: 233-239.
17. Zaidan, U. H., Abdul Rahman, M. B., Othman, S. S., Basri, M., Abdulmalek, E., Abdul Rahman, R. N. Z. R. and Salleh, A. B. (2012). Biocatalytic production of lactose ester catalysed by mica-based immobilised lipase. *Food Chemistry*, 131(1): 199-205.
18. Bosley, J. (1997). Turning lipases into industrial biocatalysts. *Biochemical Society Transactions*, 25: 174-178.

Malaysian Journal of Analytical Sciences, Vol 23 No 3 (2019): 383 - 389
DOI: https://doi.org/10.17576/mjas-2019-2303-02

MALAYSIAN JOURNAL OF ANALYTICAL SCIENCES
Published by The Malaysian Analytical Sciences Society
ISSN 1394 - 2506

SALICYLATE-BASED PROTIC IONIC LIQUIDS AS A POTENTIAL ANTIOXIDANT

(Cecair Ionik Protik Berasaskan Salisilat Berpotensi Sebagai Antioksida)

Nur Afiqah Ahmad[1], Khairulazhar Jumbri[1,2]*, Anita Ramli[1], Noraini Ghani[1,2], Haslina Ahmad[3]

[1]*Department of Fundamental and Applied Science*
[2]*Centre of Research in Ionic Liquids (CORIL)*
Universiti Teknologi PETRONAS, 32610 Seri Iskandar, Perak, Malaysia
[3]*Department of Chemistry, Faculty of Science,*
Universiti Putra Malaysia, 43400 UPM Serdang, Selangor, Malaysia

**Corresponding author: khairulazhar.jumbri@utp.edu.my*

Received: 19 August 2018; Accepted: 20 May 2019

Abstract

Salicylate-based protic ionic liquids (PILs) were synthesised, characterised and assessed in this study for potential antioxidant in drug design. The synthesised PILs were known as 3-dimethylamino-1-propanol salicylate (3DMAPS) and 3-diethylamino-1-propanol salicylate (3DEAPS). Proton nuclear magnetic resonance (^{1}HNMR), Fourier transformation infrared spectroscopy (FTIR) and thermogravimetric analysis (TGA) were used to characterise the synthesised PILs. Furthermore, the antioxidant activity of the synthesised PILs was determined using the 2,2-diphenyl-1-picrylhydrazyl (DPPH) free radical assay. Both 3DMAPS and 3DEAPS showed a good antioxidant activity compared to parent acid (salicylic acid) as these two compounds could scavenge 20% of DPPH free radical at a concentration of 66.76 ± 0.09 µM and 27.27 ± 0.10 µM, respectively.

Keywords: protic ionic liquids, salicylic acid, radical scavenging, free radical, DPPH assays

Abstrak

Cecair ionik protik (PILs) berasaskan salisilat disintesis, dicirikan dan dinilai untuk potensi antioksidan dalam reka bentuk dadah. Dua PILs iaitu 3-dimetilamino-1-propanol salisilat (3DMAPS) dan 3-diethilamino-1-propanol salisilat (3DEAPS) telah berjaya disintesis. Proton resonans magnetik nuklear (^{1}HNMR), spektroskopi transformasi inframerah (FTIR) dan analisis termogravimetrik (TGA) digunakan untuk pencirian PIL yang di sintesis. Tambahan pula, aktiviti antioksidan PIL ditentukan dengan menggunakan ujian radikal bebas 2,2-difenil-1-pikrilhidrazil (DPPH). Kedua-dua 3DMAPS dan 3DEAPS menunjukkan aktiviti antioksidan yang baik berbanding dengan asid induk (asid salisilat) kerana kedua-dua sebatian ini boleh membakar 20% radikal bebas DPPH masing-masing pada kepekatan 66.76 ± 0.09 µM dan 27.27 ± 0.10 µM.

Kata kunci: cecair ionic protik, asid salisilik, perangkap radikal, radikal bebas, ujian DPPH

Introduction

Ionic liquid (IL) is a molten salt with a melting point below 100 °C. This compound can exist as a liquid or solid form at room temperature [1]. Furthermore, IL is also known as 'green solvent' due to negligible vapour pressure [2]. A growing trend has been seen in the development of IL in various applications such as organic synthesis, biocatalysis [3], electrochemistry [4], extraction [5] and in pharmaceutical [6]. IL can be classified into two classes; aprotic and protic ionic liquids. Protic ionic liquids (PILs) are a new family member of IL with available polar proton attached on the cation structure, which could lead to hydrogen bonding interaction [7]. Besides, these

compounds can be easily synthesised by mixing an equimolar solution of Brønsted acid and Brønsted base [8]. The formation of PILs is highly depending on the transfer of proton from the Brønsted acid to Brønsted base [7].

Over the past few years, PILs have attracted increasing attention and have been considered for plethora of applications such as electrochemistry [9], fuel cell [10] and drug delivery [11]. In drug delivery, PILs are used in membrane transport due to the tuneable degree of ionicity. However, to the best of our knowledge, only a few studies have been dedicated to synthesise PILs with specific biological applications [11–13]. In this study, salicylic acid was used as the anion based PILs for potential antioxidant. Salicylic acid is one of the phenolic acid derivatives reported to display multiple biological applications such as antioxidant activity, antimicrobial and anti-inflammatory [14]. In addition, low solubility of this acid in water can cause insufficient performance of the salicylic acid. Therefore, the modification of salicylic acid in the form of IL is one of the alternative ways to enhance the performance of this drug compound.

Materials and Methods

Materials

3-dimethylamino-1-propanol (purity 99%), methanol and salicylic acid were kindly supplied by Merck Sdn. Bhd company (Darmstadt, Germany). 3-diethylamino-1-propanol was purchased from Acros (Shah Alam, Malaysia). All of these chemicals were used as received without further purification.

Synthesis and characterization of PILs

Protic ionic liquids (PILs) were synthesised by neutralisation reaction. An equimolar of salicylic acid (0.05 mol, 6.9 g) was added to equimolar amount of different base namely 3-dimethylamino-1-propanol and 3-diethylamino-1-propanol (5.9 mL and 7.4 mL, respectively). The base was placed into two-neck round bottom flask immersed in ice bath and equipped with a reflux condenser. Since the reaction is exothermic, the temperature was maintained around 0-5 °C while an acid was added drop wise. Then, the solvent (methanol) was removed by heating the mixture at 50 °C under vacuum using rotary evaporator for 3 hours. Afterwards, the structure and purity of PILs were characterised using Bruker Avance 500 MHz ^{1}HNMR spectrometer. The structure of PILs was further characterised via Shimadzu FTIR at wavenumber of 4000 cm^{-1} to 400 cm^{-1} to determine amine and carbonyl functional groups. The thermal stability of PILs was determined using PerkinElmer, Pyris V-3.81 thermogravimetric analyser.

Antioxidant activity

The methods for antioxidant activity was obtained from Brand-Williams [15] using 2,2-diphenyl-1-picrylhydrazyl (DPPH) free radical assay with slight modifications. PILs with various final concentrations (10 -100 µM) in methanol were added into DPPH solution in methanol (60 µM, 3.9 mL). After that, the mixture was incubated in dark condition for 30 min at room temperature. The decrease in absorbance was monitored using UV-Vis at wavelength of 517 nm. The antioxidant activity was calculated using equation 1 as shown below:

$$AA\ (\%) = (A_0 - A_1)/A_0 \times 100\ \% \quad (1)$$

where A_0 is the absorbance of the DPHH without PILs and A_1 is the absorbance of the sample (PILs and DPPH) at 517 nm.

Results and Discussion

^{1}HNMR

The ^{1}HNMR was used to determine the structure and purity of the synthesised PILs. Figure 1 shows the ^{1}HNMR spectrum of 3DMAPS and 3DEAPS PILs, respectively.

3-Dimetylamino propanol salicylate (3DMAPS)

Pale yellow liquid (Yield: 94.5%) ^{1}H NMR ($CDCl_3$) δ(ppm): 1.94 (m, 2H), 2.79 (s, 6H), 3.26 (t, 2H), 3.83 (t, 2H), 6.82 (t, 1H), 6.99 (d,1H), 7.37 (t, 1H), 7.85 (d, 1H).

3-Diethylamino propanol salicylate (3DEAPS)
Pale yellow liquid (Yield: 99.5%) ^{1}H NMR ($CDCl_3$) δ(ppm): 1.25 (t, 6H), 1.73 (m, 2H), 3.09 (m, 6H), 3.71 (t, 2H), 6.82 (dd, 2H), 7.29 (d, 1H), 7.85 (d, 1H).

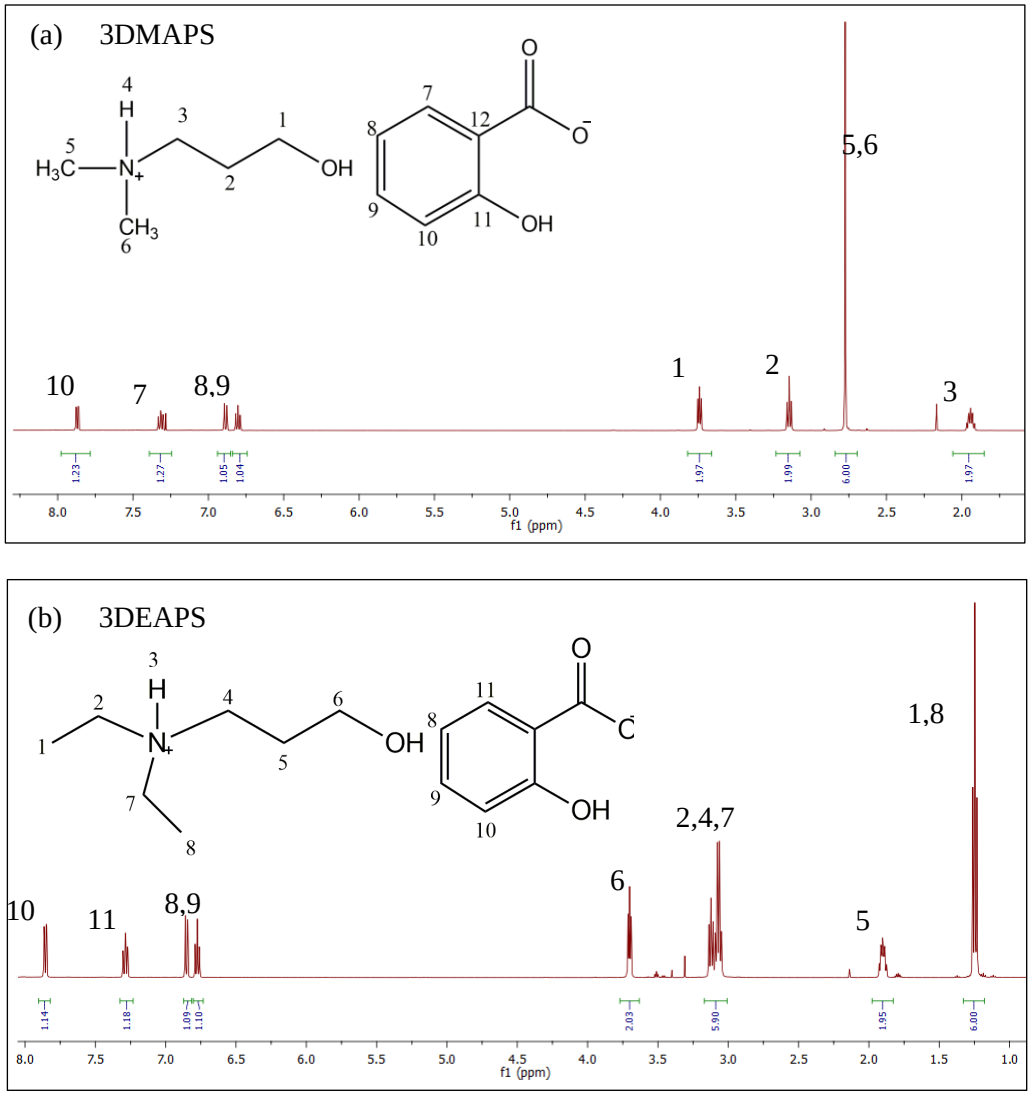


Figure 1. ^{1}H NMR of synthesized PILs (a) 3DMAPS, (b) 3DEAPS

FTIR spectroscopy
The synthesised PILs were further characterised using Fourier transform infrared spectroscopy (FTIR). From the FTIR spectra, the vibration peak of the amine and carbonyl functional group was studied to determine the formation of the PILs. Figure 2 (a and b) shows the FTIR spectra of synthesised PILs with neat alkanolamine and phenolic acid. It can be seen that neat phenolic acid (salicylic acid, SA) spectrum has a sharp peak at wavenumber of 1650.77 cm^{-1}. This indicated the vibration frequency of the carbonyl group (C=O) of carboxylic acid [16].

Meanwhile, there was no –NH bending vibration detected in the neat 3DMAP and 3DEAP due to the absence of –NH bond in the tertiary alkanolamine (3DMAP and 3DEAP). However, in the 3DMAPS spectrum, a new weak peak was observed at 1625.70 cm^{-1} and at 1626.18 cm^{-1} in 3DEAPS, which denotes the vibration peaks of

protonated tertiary amine –NH^+ [17, 18]. On top of that, the carboxylate anion (–COO^-) was detected at 1377.408 and 1379.818 cm^{-1} in the spectrum of the 3DMAPS and 3DEAPS, respectively. Thus, it could be deduced that the resonance effect of the carboxylate anion had caused the shift of the peak as the hydrogen atom from hydroxyl group of the SA was transferred to the nitrogen atom of the tertiary alkanolamine [19]. The findings are in agreement with the results reported by other researchers [20,21].

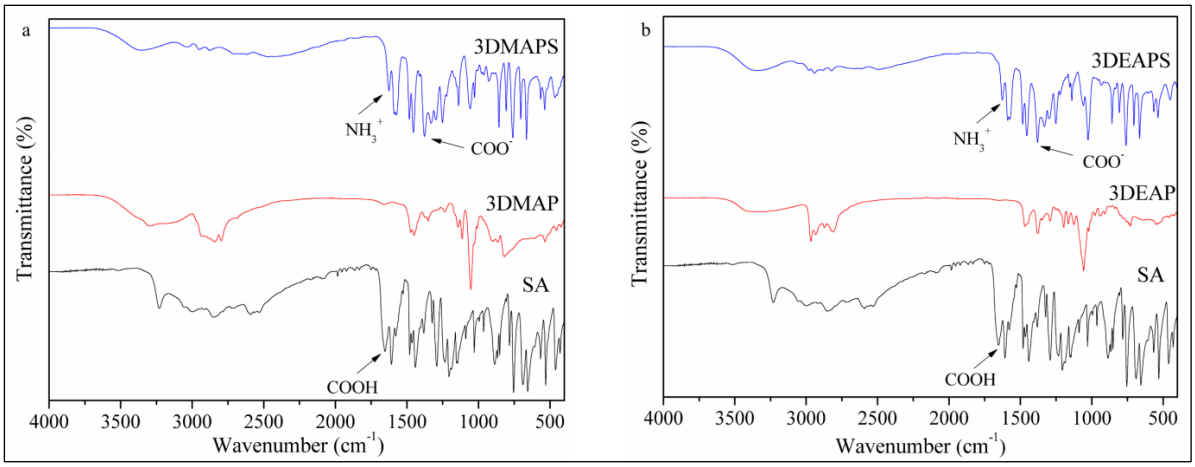


Figure 2. IR spectrum for 3DMAPS and 3DEAPS of synthesized PILs.

Thermal stability

Thermal decomposition temperature of the synthesised PILs was recorded ranging from 50 °C until 350 °C. Figure 3 shows the thermograms of 3DMAPS and 3DEAPS PILs. As can been seen, the 3DMAPS has slightly higher thermal decomposition temperature (T_d) than 3DEAPS (190.70 °C and 188.80 °C, respectively). It could be concluded that the alkyl chain length only gave a small effect towards the thermal stability of PILs. This was because as the alkyl chain length increases from methyl to ethyl, the intermolecular Van der Waals force interaction also increased [22]. Hence, this led to the reduction of strength in intramolecular bonding [23]. Moreover, increasing alkyl chain length can form a more stable carbocation that helps the 3DEAPS to be easily decomposed [24]. Similar findings have been observed in other studies [23].

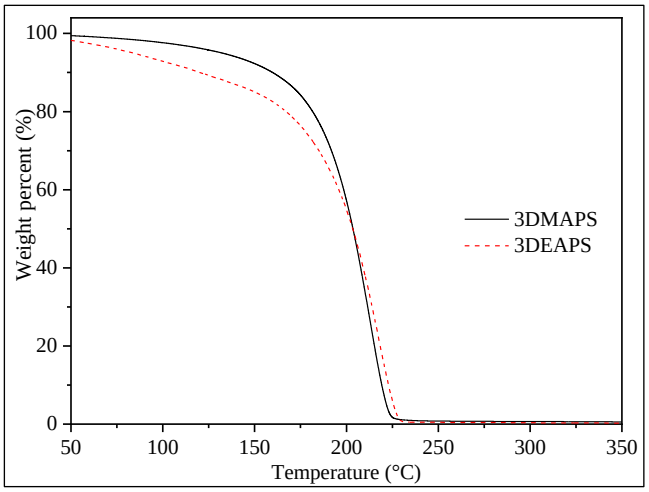


Figure3. Thermogravimetric trace PILs

Antioxidant activity

The results of antioxidant activity were expressed in terms of IC_{20} value, which represent the effective concentration required to scavenge 20% of DPPH free radical. Low IC_{20} value indicates more effective antioxidant activity. The IC_{20} was calculated from the difference concentration of PILs and SA ranging from 10 to 100 µM. Table 1 shows the summarised IC_{20} value of synthesised PILs and parent acid (SA). From the results obtained, it can be seen that the IC_{20} of parent acid (SA) was not detected at the selected range of concentration. This was due to low effectiveness of SA towards the DPPH free radical. However, both PILs (3DMAPS and 3DEAPS) were able to scavenge 20% of free radical at concentration of 66.76 ± 0.09 µM and 27.27 ± 0.10 µM, respectively, due to the huge number of active group (OH and NH group) present in the compound. The –OH and –NH transfer the hydrogen atom *via* hydrogen abstraction to stabilise DPPH free radical [25], hence increasing the antioxidant activity. Furthermore, by comparing these two PILs, 3DEAPS (27.27 ± 0.10 µM) was found to be a more effective antioxidant than 3DMAPS (66.76 ± 0.09 µM). This was because $[3DEAP]^+$ exhibited a more bulky structure than $[3DMAP]^+$ (Figure 4), which could reduce the hinder of the radical scavenging by increasing the tendency of hydrogen abstraction at –NH group of the cation structure [26].

Table 1. IC_{20} value of PILs

Sample	**IC_{20} (µM)**
Salicylic Acid (SA)	ND
3DMAPS	66.76 ± 0.09
3DEAPS	27.27 ± 0.10

ND = not detected

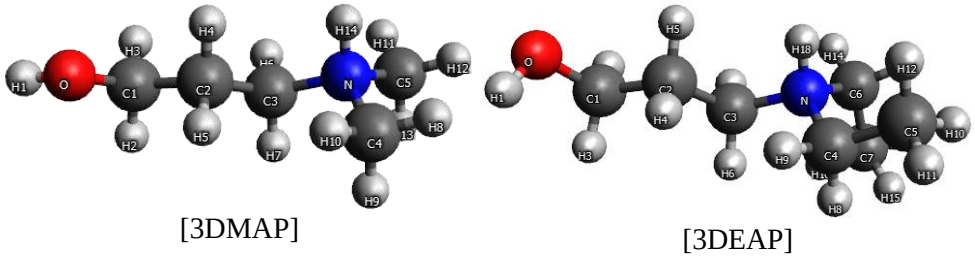


Figure 4. Structure of $[3DMAP]^+$ and $[3DEAP]^+$

Conclusion

The 3DMAPS and 3DEAPS PILs have been successfully synthesised and characterised and their application as a potential antioxidant was determined. The synthesised PILs showed a remarkable antioxidant activity compared to that of parent acid (SA) due to the extra number of active group present (–OH and –NH) in the structure. The presence of extra active group led to a high DPPH scavenging, thus increasing antioxidant activity. For future works, kinetics study and other antioxidant assays are suggested to be considered to further confirm the antioxidant activity of the synthesised compound. Besides, increasing in concentration could be carried out to determine the half maximal inhibition concentration (IC_{50}) value of the samples.

Acknowledgement

This research was funded by Short Term Internal Research Fund (STIRF 0153AA-F21), Universiti Teknologi PETRONAS. Nur Afiqah Ahmad acknowledges the UTP Graduate Assistantship (GA) scheme, Universiti Teknologi PETRONAS.

References

1. Freemantle, M. (2010). An introduction to ionic liquids. Royal Society of Chemistry: pp. 1-2.
2. Stoimenovski, J., Dean, P. M., Izgorodina, E. I. and MacFarlane, D. R. (2012). Protic pharmaceutical ionic liquids and solids: Aspects of protonics. *Faraday Discussions*, 154(1): 335-352.
3. Yang, Z. and Pan, W. (2005). Ionic liquids: Green solvents for nonaqueous biocatalysis. *Enzyme and Microbial Technology*, 37(1): 19-28.
4. Hayouni, S., Robert, A., Ferlin, N., Amri, H. and Bouquillon, S. (2016). New biobased tetrabutylphosphonium ionic liquids: Synthesis, characterisation and use as a solvent or co-solvent for mild and greener Pd-catalyzed hydrogenation processes. *RSC Advances*, 6(114): 113583-113595.
5. Visser, A. E., Swatloski, R. P., Reichert, W. M., Mayton, R., Sheff, S., Wierzbicki, A. and Rogers, R. D. (2002). Task-specific ionic liquids incorporating novel cations for the coordination and extraction of Hg^{2+} and Cd^{2+}: Synthesis, characterisation, and extraction studies. *Environmental Science and Technology*, 36(11): 2523-2529.
6. Siodmiak, T., Piotr Marszall, M. and Proszowska, A. (2012). Ionic liquids: A new strategy in pharmaceutical synthesis. *Mini-Reviews in Organic Chemistry*, 9(2): 203-208.
7. Greaves, T. L. and Drummond, C. J. (2008). Protic ionic liquids: Properties and applications. *Chemistry Reviews*, 108(1): 206-237.
8. Kennedy, D. F. and Drummondt, C. J. (2009). Large aggregated ions found in some protic ionic liquids. *Journal of Physical Chemistry B*, 113(17): 5690-5693.
9. Gung, S. T., Sun, I. W., Ou-Yang, W. C., Su, S. G., Lin, M. W., Lai, C. A. and Lin, Y. C. (2012). Synthesis and characterisation of protic ionic liquids containing cyclic amine cations and tetrafluoroborate anion. *Journal of the Iranian Chemical Society*, 8(1): 149-165.
10. Yasuda, T. and Watanabe, M. (2013). Protic ionic liquids: Fuel cell applications. *MRS Bulletin*, 38(7): 560-566.
11. Stoimenovski, J. and MacFarlane, D. R. (2011). Enhanced membrane transport of pharmaceutically active protic ionic liquids. *Chemical Communications*, 47(41): 11429-11431.
12. Mirskova, A. N., Adamovich, S. N., Mirskov, R. G. and Voronkov, M. G. (2014). Pharmacologically active salts and ionic liquids based on 2-hydroxyethylamines, arylchalcogenylacetic acids, and essential metals. *Russian Chemical Bulletin*, 63(9): 1869-1883.
13. Pernak, J., Goc, I. and Mirska, I. (2004). Anti-microbial activities of protic ionic liquids with lactate anion. *Green Chemistry*, 6(7): 323-329.
14. Randjelović, D., Stojiljković, N., Laketić, D., Ilić, I., Randjelović, N., Veljković, S. and Sokolović, D. (2016). The beneficial biological properties of salicylic acid. *Acta Facultatis Medicae Naissensis*, 32(4): 259-265.
15. Brand-Williams, W., Cuvelier, M. E. and Berset, C. L. W. T. (1995). Use of free radical method to evaluate antioxidant activity. *LWT - Food Science and Technology*, 28(1): 25-30.
16. Jadrijević-Mladar Takac, M. and Vikić Topić D. (2004). FT-IR and NMR spectroscopic studies of salicylic acid derivatives . II . Comparison of 2-hydroxy- and 2 , 4- and 2,5-dihydroxy derivatives. *Acta Pharmaceutica*, 54(3): 177-191.
17. Sinsheimer, J. E. and Keuhnelian, A. M. (1966). Near-infrared spectroscopy of amine salts. *Journal of Pharmaceutical Sciences*, 55(11): 1240-1244.
18. Cook, D. (1964). Protonation site in organic bases from Infrared X—H deformation modes. *Canadian Journal of Chemistry*, 42(10): 2292-2299.
19. Pavia, D. L., Lampman, G. M. and Kriz, G. S. (2010). Introduction to spectroscopy. Cengage Learning: pp. 370-372.
20. Puttipipatkhachorn, S., Nunthanid, J., Yamamoto, K. and Peck, G. E. (2001). Drug physical state and drug-polymer interaction on drug release from chitosan matrix films. *Journal of Controlled Release*, 75(1–2): 143-153.
21. Kung, K.-H. (2006). Coordination complexes of p-Hydroxybenzoate on Fe oxides. *Clays and Clay Minerals*, 37(4): 333-340.
22. Arellano, I. H. J., Guarino, J. G., Paredes, F. U. and Arco, S. D. (2011). Thermal stability and moisture uptake of 1-alkyl-3-methylimidazolium bromide. *Journal of Thermal Analysis and Calorimetry*, 103(2): 725-730.
23. Song, Y., Xia, Y. and Liu, Z. (2012). Influence of cation structure on physicochemical and antiwear properties of hydroxyl-functionalized imidazolium bis(trifluoromethylsulfonyl)imide ionic liquids. *Tribology Transactions*, 55(6): 738-746.

24. Montanino, M., Carewska, M., Alessandrini, F., Passerini, S. and Appetecchi, G. B. (2011). The role of the cation aliphatic side chain length in piperidinium bis(trifluoromethansulfonyl)imide ionic liquids. *Electrochimica Acta*, 57(1): 153-159.
25. Oyeyemi, V. B., Keith, J. A. and Carter, E. A. (2014). Trends in bond dissociation energies of alcohols and aldehydes computed with multireference averaged coupled-pair functional theory. *Journal of Physical Chemistry A*, 118(17): 3039-3050.
26. Gordon, M. H., Paiva-Martins, F. and Almeida, M. (2001). Antioxidant activity of hydroxytyrosol acetate compared with that of other olive oil polyphenols. *Journal of Agricultural and Food Chemistry*, 49(5): 2480-2485.

Malaysian Journal of Analytical Sciences, Vol 23 No 3 (2019): 390 - 400
DOI: https://doi.org/10.17576/mjas-2019-2303-03

MALAYSIAN JOURNAL OF ANALYTICAL SCIENCES
Published by The Malaysian Analytical Sciences Society
ISSN 1394 - 2506

HIDROGEL BERSIFAT PEKA TERHADAP RANGSANGAN SUHU UNTUK PENJERAPAN DAN PEMBEBASAN DADAH

(Hydrogel with Thermo-Responsive Behavior for Drug Adsorption and Release)

Teow Yeit Haan[1,2]* and Kushalini Rames[2]

[1]*Research Centre for Sustainable Process Technology (CESPRO), Faculty of Engineering and Built Environment*
[2]*Chemical Engineering Programme, Faculty of Engineering and Built Environment*
Universiti Kebangsaan Malaysia, 43600 UKM Bangi, Selangor, Malaysia

**Corresponding author: yh_teow@ukm.edu.my*

Received: 22 April 2019; Accepted: 12 May 2019

Abstrak

Dalam kajian ini, hidrogel bersifat peka terhadap rangsangan suhu disintesis sebagai media penyampaian dadah. Prestasi hidrogel yang disintesis dikaji dengan menggunakan peratusan asid sitrik yang berbeza iaitu 5%, 10%, dan 15%. Penggunaan asid sitrik yang banyak membawa kepada ikatan yang kuat sesama polimer, seterusnya meningkatkan peratus transmisi kumpulan berfungsi O-H dan kehidrofilikan hidrogel. Maka, molekul aspirin yang mempunyai kumpulan berfungsi asid karboksilik bersifat polar akan lebih cenderung dijerap pada permukaan hidrogel yang disintesis dengan menggunakan 15% asid sitrik melalui ikatan hidrogen. Di samping itu, rangkaian polimer yang padat lebih peka terhadap rangsangan suhu. Oleh itu, hidrogel yang disintesis dengan menggunakan 15% asid sitrik adalah lebih berkesan untuk membebaskan molekul aspirin yang dijerap padanya. Dalam kajian penjerapan dan pembebasan dadah yang dijalankan, keputusan yang tercapai didapati lebih menepati model Langmuir dan model Kinetik Pseudo pertama. Model Langmuir menyatakan bahawa penjerapan aspirin hanya melibatkan satu lapisan di permukaan hidrogel. Setelah penjerapan berlaku pada sesuatu tempat di permukaaan hidrogel, tiada lagi penjerapan berterusan yang akan berlaku. Manakala model Kinetik Pseudo pertama menerangkan bahawa penjerapan yang berlaku adalah melalui mekanisme fizikal, molekul aspirin akan dijerap atas permukaan hidrogel tanpa berlakunya tindak balas dengan permukaan hidrogel.

Kata kunci: hidrogel, rangsangan suhu, penjerapan dadah, pembebasan dadah, suhu badan

Abstract

In this study, hydrogel with thermo-responsive behavior was synthesized as a medium for drug delivery. Performance of synthesized hydrogel was studied using a different percentage of citric acid at 5%, 10%, and 15%. The use of a large amount of citric acid leads to a strong polymer bond, thus increasing the percentage of O-H functional group subsenquently hydrophilicity of hydrogel. Therefore, polar aspirin molecules with functional group of carboxylic acid are more likely to be adsorbed on the surface of the hydrogel synthesized using 15% citric acid *via* hydrogen bonding. In addition, dense polymer chain is more responsive to temperature change. Hence, hydrogel synthesized using 15% citric acid is more effective to release the adsorbed aspirin molecules. In the drug adsorption and release study, the results achieved were fitted closely with the Langmuir model and the Pseudo first kinetic model. Langmuir model implied that aspirin adsorption involves only one layer on the surface of the hydrogel. After adsorption occurs on the hydrogel surface, no further assorption will occur. While the Pseudo first kinetic model supported that the adsorption occurs through physical mechanisms where aspirin molecules will be adsorbed on the surface of the hydrogel without the occurrence of reaction.

Keywords: hydrogel, thermo-responsive, drug adsorption, drug release, body temperature

Pengenalan

Hidrogel merupakan polimer yang mempunyai struktur jaringan tiga dimensi silang yang dibentuk oleh kumpulan hidrofilik [1]. Hidrogel wujud sejak 1960-an, ia diguna secara meluas berdasarkan sifat-sifat istimewanya yang mampu memberi tindak balas yang serta-merta terhadap rangsangan yang dikenakan ke atasnya seperti suhu, pH, daya ionik, daya elektrik, daya tarikan magnetik, serta kehadiran enzim [2]. Selain itu, hidrogel menpunyai jangka hayat yang agak panjang dimana ia dapat digunakan dalam tempoh masa yang panjang dengan menunjukkan prestasi yang stabil [3]. Di samping itu, hidrogel berupaya mengembung, menyerap 4000 kali ganda air daripada berat keringnya tanpa terlarut dalam air, dan menakung air menjadikannya amat berguna untuk diaplikasi dalam pelbagai bidang seperti pertanian, perubatan, process rawatan air, dan juga kosmetik [4].

Peristiwa letupan Tianjin, China yang berlaku pada 12 Ogos 2015 telah membunuh sebanyak 170 orang dan mencederakan ratusan orang yang bertempat di sekitar tempat kejadian. Antara kecederaan yang paling banyak dilaporkan ialah kes kulit terbakar. Perubatan analgesik diberi kepada mangsa letupan melalui kaedah menelan ataupun dengan suntikan untuk mengurangkan kesakitan. Namun, kedua-dua kaedah penyampaian dadah tersebut mengambil masa yang agak lama untuk bertindak balas dan mencapai sel-sel kulit yang cedera. Selain daripada mencapai sel sasaran, dadah yang diberi melalui kedua-dua kaedah tersebut turut bertindak balas dengan sel-sel yang tidak disasarkan. Hal ini akan mengurangkan keberkesanan dadah dalam perubatan dan meningkat risiko ketoksikan dadah terhadap badan manusia [5].

Kelemahan kaedah perubatan dalam tragedi letupan Tianjin, China mencetus idea mengguna hidrogel sebagai medium penyampaian dadah. Kebolehan hidrogel untuk menyerap, menakung, dan membebas berdasarkan rangsanagan tertentu menjadikannya medium yang sesuai digunakan untuk penyampaian dadah secara luaran terutamanya dalam kes kecemasan dimana dadah dapat disasarkan pada bahagian tercedera dan bertindak balas dengan serta merta.

Objektif kajian ini adalah menghasilkan hidrogel bersifat peka terhadap rangsangan suhu dimana hidrogel yang dihasilkan boleh diguna untuk penjerapan dan pembebasan dadah. Prestasi penjerapan dan pembebesan dadah hidrogel yang dihasil dalam kajian ini diuji dengan menggunakan aspirin, sejenis dadah penahan sakit yang diguna secara meluas. Manakala isoterma penjerapan keseimbangan dan isoterma penjerapan kinetik diguna untuk menerangkan kelakuan hidrogel dalam proses penjerapan.

Bahan dan Kaedah

Bahan kimia

Karboksimetil selulosa (CMC), hidroksietil selulosa (HEC), dan asid sitrik yang digunakan untuk sintesis hidrogel dibekal oleh Sigma-Aldrich, Jerman. Manakala aspirin yang dibeli daripada Sigma-Aldrich, USA diguna untuk penyediaan larutan dadah.

Proses sintesis hidrogel

Hidrogel disintesis dengan menggunakan CMC dan HEC sebagai polimer dan asid sitrik sebagai penghubung silang. 2 g HEC dilarutkan dalam 400 mL air suling dan dikacau sehingga sebati. Apabila larutan yang jernih diperolehi, 6 g CMC dicampurkan ke dalam larutan tersebut. Nisbah CMC kepada HEC yang digunakan dalam kajian ini ialah 3:1 dimana jumlah kepekatan larutan HEC-CMC adalah 2%. Larutan HEC-CMC dikacau berterusan selama 24 jam untuk menghasilkan larutan jernih yang likat. Seterusnya, 5% asid sitrik ditambahkan ke dalam larutan HEC-CMC dan diteruskan dengan proses pengacauan pada 250 rpm. Larutan hidrogel yang terhasil dituang ke dalam piring petri dan dikeringkan dalam ketuhar semalaman pada suhu 80 ºC. Sampel hidrogel yang berbeza dihasilkan dengan menggunakan 10% dan 15% asid sitrik.

Analisis inframerah transformasi fourier (FTIR)

Analisis FTIR (Nicolet-6700, USA) dijalankan untuk mengenalpasti kumpulan berfungsi yang wujud pada hidrogel. Semasa analisis FTIR, infra-merah dengan panjang gelombang antara 500 hingga 4000 cm^{-1} dipancar ke atas sampel hidrogel. Spektra FTIR yang terhasil kemudiannya dicatat dalam komputer.

Analisis mikroskop imbasan elektron (SEM)
Analisis SEM (Carl Zeiss Inc, Jerman) dijalankan untuk mengkaji struktur permukaan hidrogel. Sampel hidrogel disalut dengan satu lapisan emas yang nipis sebelum analisis SEM dijalankan. Mikrograf SEM yang menunjukkan struktur permukaan hidrogel diperolehi pada voltan 10 kV dan pembesaran sebanyak 10.00 kx.

Analisis sudut sentuh
Sifat hidrofilik hidrogel dikenalpasti dengan ujian sudut sentuh. Sampel hidrogel dilekat pada slaid kaca. Slaid kaca bersama dengan sampel hidrogel dikepit pada tempat pemegang sampel di instrumen analisis bentuk jatuhan, DSA (Kruss, Jerman) yang selaras dengan kanta mikroskop. Seterusnya, setitis air suling (~13 µL) dititis ke atas sampel hidrogel tersebut. Imej titisan air suling pada permukaan hidrogel ditangkap dengan mikroskop dan sudut sentuh antara permukaan hidrogel dengan air suling dan udara diukur oleh perisian DSA.

Ujian pembengkakan
Berat hidrogel pada keadaan kering ditimbang. Hidrogel yang ditimbang kemudiannya direndam dalam air suling selama 30 minit. Hidrogel yang telah membengkak selepas 30 minit rendaman dikeluarkan dari air suling dan beratnya ditimbang semula. Peratus pembengkakan hidrogel diukur dengan menggunakan persamaan 1:

$$\text{Peratus pembengkakan} = \frac{W_t - W_o}{W_o} \times 100\% \quad (1)$$

dimana W_t ialah berat hidrogel setelah 30 minit rendaman dan W_o ialah berat hidrogel pada keadaan kering.

Kajian pemuatan dan pembebasan dadah
Larutan aspirin dengan kepekatan 500 mg/L, 1000 mg/L, 1500 mg/L, dan 2000 mg/L disediakan dengan melarutkan serbuk aspirin ke dalam air suling. Larutan aspirin yang disediakan kemudiannya disejukkan kepada 4 °C. Sampel hidrogel yang disintesis dimasukkan ke dalam larutan aspirin yang bersuhu 4 °C. Kepekatan larutan aspirin diambil setiap 2 minit sehingga bacaan kepekatan larutan aspirin menjadi malar. Langkah yang sama diulang dengan menggunakan larutan aspirin yang berlain kepekatan dan hidrogel yang disintesis dengan peratusan asid sitirk yang berbeza. Kapasiti penjerapan aspirin pada masa t dikira dengan menggunakan persamaan 2:

$$q_t = \frac{(C_O - C_t)V}{W} \quad (2)$$

dimana q_t ialah kapasiti penjerapan pada masa t (mg/g), C_O ialah kepekatan awal larutan yang dijerap (mg/L), C_t ialah kepekatan larutan yang dijerap pada masa t (mg/L), V ialah isipadu larutan yang dijerap, dan W ialah berat penjerap (g).

Untuk kajian pembebasan dadah, suhu larutan yang dijerap bersama hidrogel dipanaskan sehingga mencapai 37 °C. Kepekatan larutan aspirin diambil setelah 45 minit. Langkah yang sama diulang dengan menggunakan larutan aspirin yang berlain kepekatan dan hidrogel yang disintesis dengan peratusan asid sitirk yang berbeza.

Isoterma penjerapan keseimbangan
Isoterma penjerapan keseimbangan menerangkan jenis ikatan yang terbentuk antara molekul bahan terlarut dan permukaan penjerap serta sifat lapisan bahan terjerap pada keadaan seimbang [6]. Dalam kajian ini, model Langmuir dan model Freundlich digunakan untuk mengkaji isoterma penjerapan keseimbangan. Model Langmuir menerangkan bahawa penjerapan berlaku dengan hanya melibatkan satu lapisan bahan dijerap yang terbentuk pada permukaan penjerap dimana tenaga penjerapan adalah malar. Semua bahagian di permukaan penjerap mempunyai kecenderungan yang sama untuk dijerap oleh bahan terlarut. Setelah bahagian tersebut dijerap oleh bahan terlarut, maka tiada lagi proses penjerapan akan berlaku pada bahagian berkenaan [7]. Model Langmuir dapat diwakili dengan persamaan 3:

$$q_e = \frac{q_m K_L C_e}{1 + K_L C_e} \quad (3)$$

dimana q_e ialah kapasiti penjerapan pada keseimbangan (mg/g), C_e ialah kepekatan larutan yang dijerap pada keseimbangan (mg/L), q_m ialah kapasiti penjerapan yang maksimum (mg/g), dan K_L ialah pemalar Langmuir yang digunakan untuk mengukur tenaga penjerapan (L/mg).

Manakala model Freundlich menyatakan bahawa penjerapan melibatkan beberapa lapisan dimana bahagian yang dijerap akan melanjutkan proses penjerapan dengan melibatkan tenaga penjerapan yang berbeza [7]. Model Freundlich dapat diwakili dengan persamaan 4:

$$q_e = K_f C_e^{1/n} \tag{4}$$

dimana q_e ialah kapasiti penjerapan pada keseimbangan (mg/g), C_e ialah kepekatan larutan yang dijerap pada keseimbangan (mg/L), K_f ialah kapasiti penjerapan yang maksimum (mg/g), dan n ialah pemalar Freundlich yang digunakan untuk mengukur tenaga penjerapan.

Isoterma Penjerapan Kinetik

Isoterma penjerapan kinetik menerangkan kadar proses penjerapan. Dua model isoterma penjerapan kinetik yang digunakan dalam kajian ini, iaitu, model Kinetik Pseudo pertama dan model Kinetik Pseudo kedua. Model Kinetik Pseudo pertama yang diwakili oleh persamaan 5 menerangkan bahawa penjerapan yang berlaku adalah bersifat fizikal dimana bahan terlarut akan membentuk ikatan yang lemah pada permukaan penjerap. Manakala, model Kinetik Pseudo kedua yang diwakili oleh persamaan 6 menyatakan bahawa berlakunya tindak balas kimia antara permukaan penjerap dengan bahan terlarut sepanjang proses penjerapan. Ikatan kimia akan terbentuk di antara permukaan penjerap dan bahan terlarut dalam masa yang singkat [8].

$$\log(q_e - q_t) = \log q_e - \frac{K_{ad}}{2.303} t \tag{5}$$

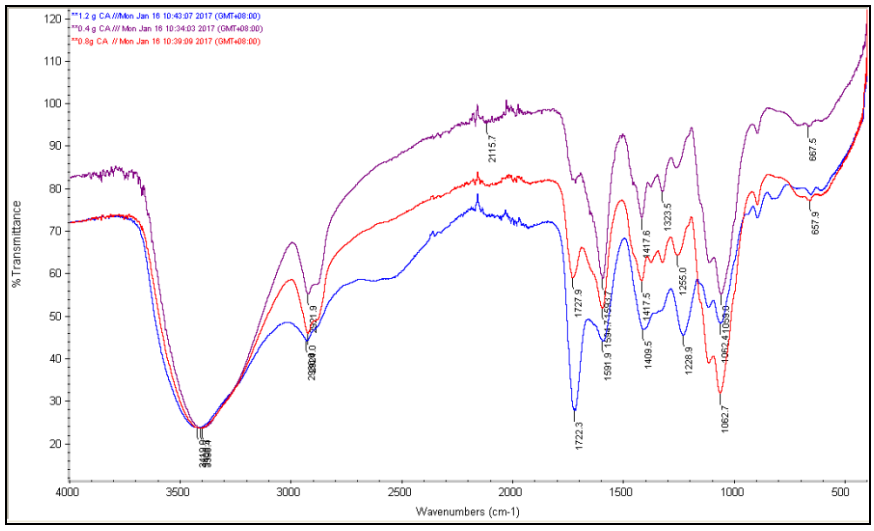
$$\frac{t}{q_t} = \frac{1}{h} + \frac{t}{q_t} \tag{6}$$

dimana q_e ialah kapasiti penjerapan pada keseimbangan (mg/g), q_t ialah kapasiti penjerapan pada masa t (mg/g), K_{ad} ialah pemalar untuk model Kinetik Pseudo pertama, dan h ialah pemalar model Kinetik Pseudo kedua.

Keputusan dan Perbincangan

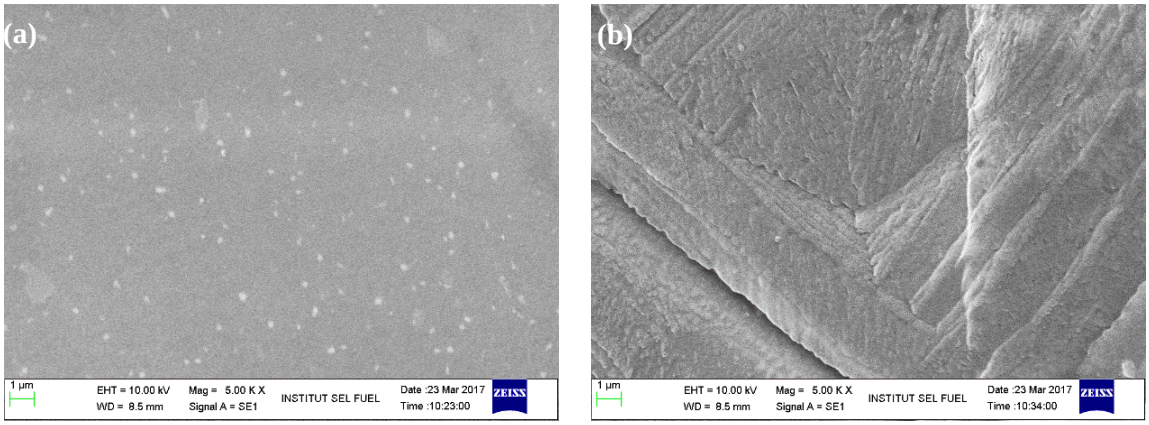
Pencirian hidrogel

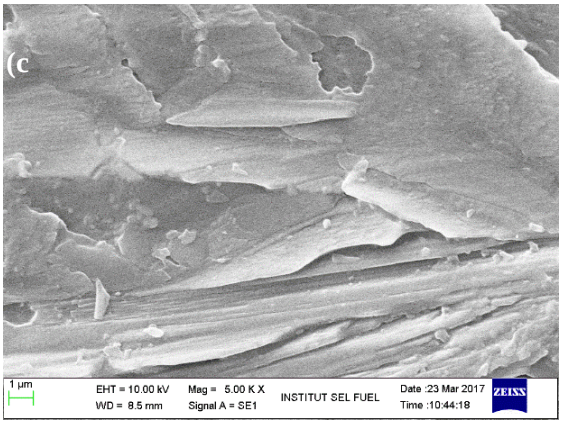
Rajah 1 menunjukkan spektra FTIR untuk hidrogel yang disintesis. Kewujudan kumpulan berfungsi hidroksil (O-H) pada kesemua hidrogel yang disintesis dikenalpasti dengan ketampilan puncak di sekitar panjang gelombang 3200-3600 cm^{-1} seperti yang ditunjukkan dalam spektra FTIR [9]. Kesemua spektra FTIR dalam Rajah 1 menunjukkan corak yang seiras dengan kewujudan puncak di sekitar panjang gelombang 3200-3600 cm^{-1} yang disebabkan oleh kumpulan berfungsi O-H, puncak di sekitar panjang gelombang 1780-1710 cm^{-1} yang disumbang oleh kumpulan berfungsi karboksil (COOH), dan puncak di sekitar panjang gelombang 1050-1150 cm^{-1} yang ditunjukkan oleh ikatan antara karbon dan oksigen. Perbandingan sesama tiga jenis hidrogel yang disintesis menunjukkan bahawa peratus transmisi adalah paling tinggi untuk hidrogel yang disintesis dengan menggunakan 15% asid sitrik, diikuti dengan hidrogel yang disintesis dengan menggunakan 10% asid sitrik, dan seterusnya hidrogel yang disintesis dengan menggunakan 5% asid sitrik. Hal ini kerana penggunaan asid sitirk yang banyak mendorong kepada ikatan yang kuat sesama polimer (CMC dan HEC). Menurut Awada et al. [10], ikatan sesama polimer terhasil melalui interaksi antara kumpulan berfungsi COOH dan kumpulan berfungsi OH dalam proses pengesterifikasi. Tindak balas ini melibatkan kumpulan berfungsi COOH yang banyak dimana ianya boleh didapati daripada asid sitrik. Maka, penggunaan asid sitrik yang banyak akan membawa kepada ikatan yang kuat sesama polimer [9]. Kedua-dua CMC dan HEC mempunyai kumpulan berfungsi O-H. Ikatan yang kuat antara CMC dan HEC seterusnya meningkatkan peratus transmisi kumpulan berfungsi O-H.



Rajah 1. Spektra FTIR untuk hidrogel yang disintesis

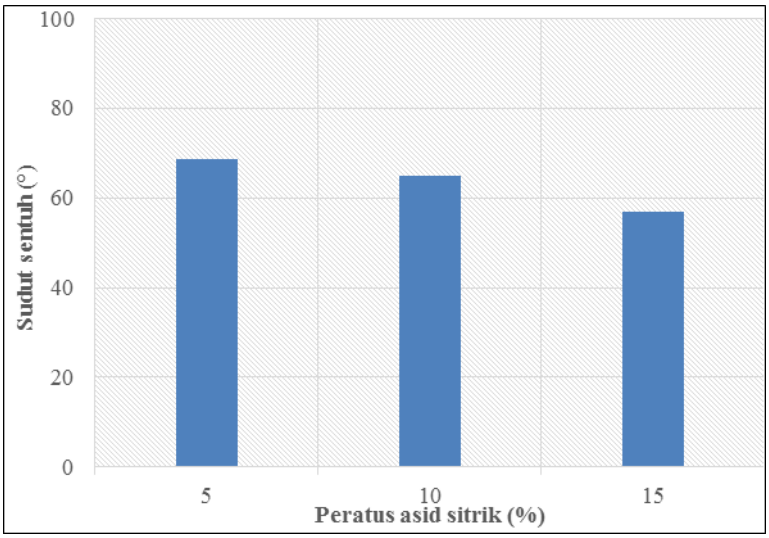
Rajah 2 menunjukkan mikrograf SEM untuk permukaan hidrogel yang disintesis. Seperti yang ditunjukkan dalam Rajah 2, kekasaran permukaan hidrogel meningkat dengan peningkatan peratusan asid sitrik. Peratusan aisd sitrik yang tinggi akan memberi ikatan rangkaian polimer yang lebih kuat seperti yang diterangkan sebelum ini. Hal ini juga akan menghasilkan struktur rangkaian polimer yang lebih padat, tegar, dan kasar [12]. Keputusan kajian yang seiras juga didapati oleh Saputra et al. [13] dimana kumpulan penyelidikan mendapati bahawa hidrogel yang disintesis dengan menggunakan peratusan asid sitirk yang lebih tinggi akan menghasilkan permukaan yang lebih kasar [13].





Rajah 2. Mikrograf SEM untuk permukaan hidrogel (a) 5% asid sitrik (b) 10% asid sitrik (c) 15% asid sitrik

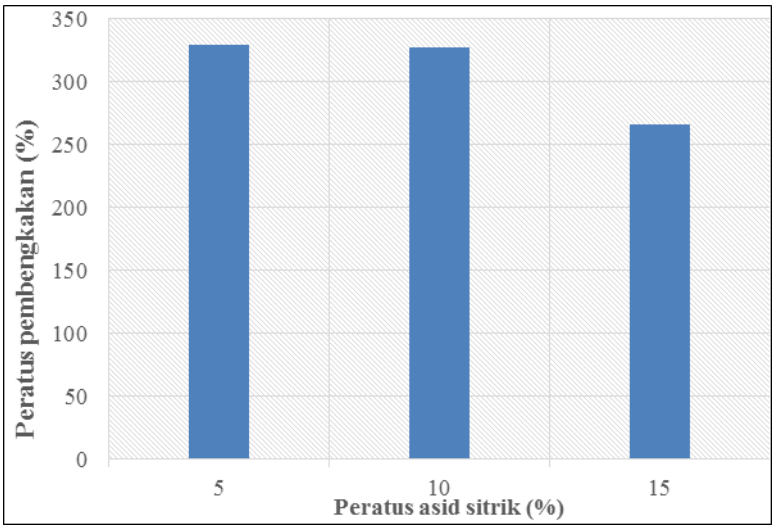
Rajah 3 menunjukkan nilai sudut sentuh untuk hidrogel yang disintesis. Secara keseluruhannya, kesemua hidrogel yang disintesis mendapat nilai sudut sentuh yang kurang daripada 90 darjah. Menurut Yuan dan Lee [14], permukaan pepejal yang menunjukkan nilai sudut sentuh yang kurang daripada 90 darjah tergolong sebagai permukaan yang bersifat hidrofilik. Sifat hidrofilik hidrogel disebabkan oleh kewejudan kumpulan berfungsi OH pada struktur hidrogel seperti yang dibincangkan dalam analisis FTIR. Selain daripada itu, nilai sudut sentuh untuk hidrogel yang disintesis menurun dengan peningkatan peratusan asid sitirk. Ini adalah disebabkan oleh penambahan peratus transmisi kumpulan berfungsi OH yang disumbang oleh ikatan hidroksil yang kuat sesama polimer. Secara teori, permukaan pepejal yang mempunyai nilai sudut sentuh yang lebih rendah adalah lebih hidrofilik. Jadi, sifat hidrofilik hidrogel yang disintesis adalah lebih tinggi dengan peningkatan peratusan asid sitirk [15].



Rajah 3. Imej dan nilai sudut sentuh untuk hidrogel yang disintesis

Rajah 4 menunjukkan peratus pembengkakan untuk hidrogel yang disintesis. Dalam ujian pembengkakan, hidrogel yang direndam dalam air suling akan mengembang melalui penyerapan air suling. Hal ini akan menambah berat hidrogel setelah 30 minit ujian pembengkakan. Seperti yang ditunjukkan dalam Rajah 4, peratus pembengkakan hidrogel menurun dengan peningkatan peratusan asid sitirk. Walaupun analisis FTIR menunjukkan bahawa hidrogel yang disintesis dengan menggunakan peratusan asid sitrik yang lebih tinggi mempunyai peratus transmisi kumpulan berfungsi OH yang lebih tinggi dan nilai sudut sentuh yang lebih rendah dengan penanda sifat hidrofilik yang lebih

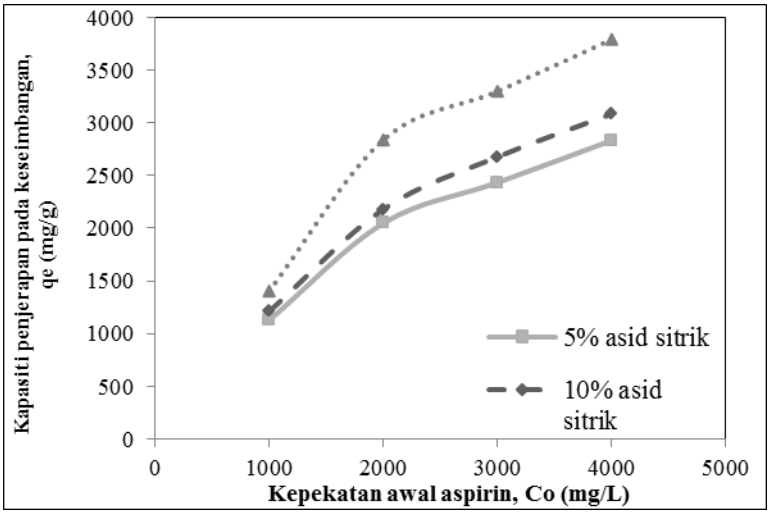
tinggi berbanding dengan hidrogel yang lain, rangkaian polimernya yang lebih padat, tegar, dan kasar merupakan faktor utama yang mengurang peratus pembengkakan dan penyerapan air oleh hidrogel tersebut [16]. Oleh itu, hidrogel dengan kandungan peratus asid sitirk sebanyak 15% mempunyai peratus pembengkakan yang paling rendah antara hidrogel yang disintesis dalm kajian ini.



Rajah 4. Peratus pembengkakan untuk hidrogel yang disintesis

Pemuatan dadah

Rajah 5 menunjukkan kapasiti penjerapan hidrogel pada keseimbangan berdasarkan kepekatan awal larutan aspirin yang berlainan. Seperti yang ditunjukkan pada Rajah 5, kapasiti penjerapan hidrogel pada keseimbangan semakin meningkat dengan peningkatan kepekatan awal larutan aspirin. Dengan peningkatan kepekatan awal larutan aspirin, lebih banyak molekul aspirin yang dapat menjerap pada permukaan hidrogel, seterusnya membawa kepada kapasiti penjerapan keseimbangan yang lebih tinggi [17].



Rajah 5. Kapasiti penjerapan hidrogel pada keseimbangan berdasarkan kepekatan awal larutan aspirin yang berlainan

Selain daripada itu, Rajah 5 menunjukkan bahawa hidrogel yang disintesis dengan menggunakan peratusan asid sitrik yang tinggi menyumbang kepada potensi penjerapan yang lebih mendadak. Analisis FTIR yang ditunjukkan pada Rajah 1 membukti bahawa hidrogel yang disintesis dengan menggunakan peratusan asid sitrik yang lebih tinggi mempunyai peratus transmisi kumpulan berfungsi OH dan COOH yang lebih tinggi. Maka molekul aspirin yang mempunyai kumpulan berfungsi asid karboksilik bersifat polar akan lebih cenderung dijerap pada permukaan hidrogel yang disintesis dengan menggunakan 15% asid sitrik melalui ikatan hidrogen dimana ia mempunyai lebih banyak kumpulan berfungsi OH dan COOH [18].

Keputusan yang didapati daripada kajian pemuatan dadah seterusnya dikaji untuk menentukan isoterma penjerapan keseimbangan. Jadual 1 menunjukkan nilai-nilai pemalar dan nilai R^2 untuk isoterma penjerapan keseimbangan yang dikaji dalam kajian ini, iaitu model Langmuir dan model Freundlich. Nilai R^2 yang ditunjukkan oleh model Langmuir dalam Jadual 1 mempunyai nilai bacaaan yang lebih tinggi berbanding dengan model Freundlich. Maka, terjelas keputusan yang didapati daripada kajian pemuatan dadah lebih menepati model Langmuir. Model Langmuir menyatakan bahawa molekul bahan terlarut (aspirin dalam kajian ini) menjerap ke atas permukaan penjerap (hidrogel dalam kajian ini) dan meliputi penjerap dengan satu lapisan molekul bahan terlarut. Setelah penjerapan berlaku pada sesuatu tempat di permukaaan hidrogel, tiada lagi penjerapan berterusan yang akan berlaku [19].

Jadual 1. Nilai-nilai pemalar dan nilai R^2 untuk model Langmuir dan model Freundlich

Peratusan Asid Sitrik (%)	**Model Langmuir**			**Model Freundlich**		
	q_m (mg/g)	**K_L (L/mg)**	**R^2**	**K_f (mg/g)**	**n**	**R^2**
5	3333.33	16228.50	0.998	72.03	2.10	0.994
10	5000.00	14594.28	0.985	32.54	1.70	0.948
15	5000.00	36205.65	0.999	86.74	1.98	0.981

Analisis isoterma penjerapan kinetik untuk kajian pemuatan dadah dilakukan berdasarkan model Pseudo Kinetik pertama dan model Pseudo Kinetik kedua. Model Pseudo Kinetik pertama menerangkan bahawa mekanisme penjerapan bahan terlarut adalah melalui penjerapan secara fizikal dimana tenaga interaksi antara molekul bahan terlarut dan permukaan penjerap mempunyai magnitud yang sama [20]. Manakala model Pseudo Kinetik kedua menjelaskan bahawa mekanisme penjerapan bahan terlarut adalah berdasarkan penjerapan sceara kimia. Dalam penjerapan jenis ini, berlakunya tindak balas sesama molekul bahan terlarut dan permukaan penjerap. Molekul bahan terlarut akan terikat pada permukaan penjerap melalui ikatan valen [21].

Jadual 2 dan Jadual 3 adalah nilai-nilai pemalar, nilai R^2, dan peratusan ralat untuk model Pseudo Kinetik pertama dan model Pseudo Kinetik kedua. Seperti yang ditunjukkan dalam Jadual 2 dan Jadual 3, data yang didapati daripada kajian pemuatan dadah lebih menepati model Pseudo Kinetik pertama dengan pemberian nilai R^2 yang lebih tinggi dan peratusan ralat (Ɛ) yang lebih rendah berbanding dengan model Pseudo Kinetik kedua. Maka terjelas bahawa molekul aspirin akan dijerap atas permukaan hidrogel tanpa berlakunya tindak balas dengan permukaan hidrogel.

Jadual 2. Nilai-nilai pemalar, nilai R^2, dan peratusan ralat untuk model Pseudo Kinetik pertama

Peratusan Asid Sitrik (%)	**Kepekatan Awal Aspirin (mg/L)**	**K_{ad} (min^{-1})**	**q_e (mg/g)**	**$q_{e,\ exp}$ (mg/g)**	**ε (%)**	**R^2**
5	500	0.23	1757.92	1127.74	35.85	0.978
	1000	0.14	2619.99	2048.32	21.82	0.926
	1500	0.24	4523.76	2434.38	46.19	0.932
	2000	0.29	6131.97	2832.81	53.80	0.940
10	500	0.08	1205.04	1210.07	0.42	0.992
	1000	0.18	3497.04	2180.07	37.66	0.902
	1500	0.12	3438.75	2677.02	22.15	0.972
	2000	0.14	4105.82	3084.41	24.88	0.931
20	500	0.06	1163.59	1403.40	17.09	0.965
	1000	0.14	3449.05	2838.23	21.52	0.918
	1500	0.15	4240.33	3298.86	28.54	0.905
	2000	0.18	5623.41	3791.39	48.32	0.903

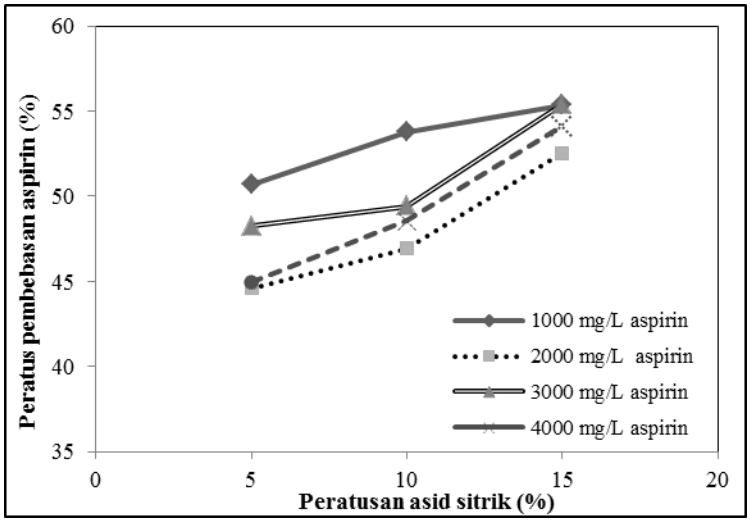
Jadual 3. Nilai-nilai pemalar, nilai R^2, dan peratusan ralat untuk model Pseudo Kinetik kedua

Peratusan asid sitrik (%)	**Kepekatan awal aspirin (mg/L)**	**k (g/mg min)**	**h (mg/g min)**	**$q_{e,\ exp}$ (mg/g)**	**ε (%)**	**R^2**
5	500	$2.11e^{-5}$	131.58	1127.74	54.89	0.866
	1000	$7.41e^{-6}$	185.19	2048.32	59.03	0.812
	1500	$1.08e^{-5}$	270.27	2434.38	51.31	0.935
	2000	$7.76e^{-6}$	344.83	2832.81	57.51	0.938
10	500	$4.49e^{-1}$	3333.33	1210.07	92.88	0.443
	1000	$4.44e^{-6}$	111.11	2180.07	129.35	0.377
	1500	$1.32e^{-6}$	131.58	2677.02	273.55	0.384
	2000	$1.92e^{-8}$	192.31	3084.41	3142.11	0.064
20	500	$2.35e^{-5}$	147.06	1403.40	78.14	0.659
	1000	$2.63e^{-6}$	263.16	2838.23	252.33	0.859
	1500	$3.13e^{-6}$	312.50	3298.86	203.14	0.697
	2000	$8.06e^{-7}$	322.58	3791.39	427.51	0.732

Pembebasan dadah

Rajah 6 menunjukkan peratus pembebasan aspirin berdasarkan peratusan asid sitrik yang digunakan untuk sintesis hidrogel. Berdasarkan keputusan yang didapati daripada kajian pembebasan dadah, pelepasan aspirin dari hidrogel ke dalam larutan pada suhu badan dibuktikan. Ini menyakinkan bahawa hidrogel yang dihasilkan dalam kajian ini adalah peka terhadap suhu dimana ia dapat menyerap dan membebaskan aspirin berdasarkan rangsangan suhu. Seperti yang ditunjuk dalam Rajah 6, peratus pembebasan aspirin meningkat dengan pertambahan peratusan asid sitrik yang digunakan untuk sintesis hidrogel. Ini adalah disebabkan oleh rangkaian polimer yang lebih padat terbentuk dengan menggunkan peratusan asid sitirk yang lebih tinggi. Berdasarkan pernyataan yang diterangkan

oleh Mitra dan Dey [16], rangkaian polimer yang lebih padat akan lebih peka terhadap rangsangan suhu maka ia adalah lebih berkesan untuk membebaskan molekul aspirin yang dijerap padanya.



Rajah 6. Peratus pembebasan aspirin berdasarkan peratusan asid sitrik yang digunakan untuk sintesis hidrogel

Kesimpulan

Hidrogel yang bersifat peka terhadap rangsangan suhu telah berjaya disintesis dalam kajian ini dengan menggunakan CMC dan HEC sebagai polimer dan asid sitrik sebagai penghubung silang. Dari segi pencapaian, kesemua jenis hidrogel yang disintesis dalam kajian ini terbukti mempunyai sifat unggul untuk mengembung, menyerap dadah (aspirin dalam kajian ini), dan membebas dadah pada suhu badan. Hal ini ternyata hidrogel yang disintesis dalam kajian ini dapat diaplikasi dalam bidang perubatan untuk merawat kecederaan luaran terutamanya pada masa kecemasan. Antara hidrogel yang disintesis dalam kajian ini, hidrogel yang disintesis dengan 15% asid sitrik menunjuk prestasi yang paling cemerlang dengan kapasiti penjerapan pada keseimbangan dan peratus pembebasan aspirin yang paling tinggi. Kandungan asid sitrik yang tinggi menjadikan hidrogel lebih bersifat hidrofilik, seterusnya mencetus penjerapan yang pantas.

Dalam kajian penjerapan dan pembebasan dadah yang dijalankan, keputusan yang tercapai didapati lebih menepati model Langmuir dan model Kinetik Pseudo pertama. Model Langmuir menyatakan bahawa penjerapan aspirin hanya melibatkan satu lapisan di permukaan hidrogel. Setelah penjerapan berlaku pada sesuatu tempat di permukaaan hidrogel, tiada lagi penjerapan berterusan yang akan berlaku. Manakala model Kinetik Pseudo pertama menerangkan bahawa penjerapan yang berlaku adalah melalui mekanisme fizikal, molekul aspirin akan dijerap atas permukaan hidrogel tanpa berlakunya tindak balas dengan permukaan hidrogel. Sedangkan idea utama kajian ini adalah untuk menghasilkan media penyampaian dadah yang diguna secara luaran pada bahagian kulit yang mengalami kecedaran, adalah wajar mencadangkan bahawa hidrogel yang dihasilkan diteruskan dengan ujikaji kepekaan dan kesan ke atas kulit buatan.

Penghargaan

Pengarang ingin mengucapkan terima kasih kepada Geran Universiti Penyelidikan (GUP-2017-098) atas sokongan kewangan ke atas kajian ini.

Rujukan

1. Rosiak, J. M., and Yoshii, F. (1999). Hydrogels and their medical applications. *Nuclear Instruments and Methods in Physics Research, Section B: Beam Interactions with Materials and Atoms*, 151(1–4): 56–64.
2. Yahia, L. H. (2017). History and applications of hydrogels. *Journal of Biomedical Sciencies*, 4(2): 13.

3. Ahmed, E. (2015). Hydrogel: Preparation, characterization, and applications: A review. *Journal of Advanced Research*, 6(2): 105-121.
4. Biondi, M., Borzacchiello, A., Mayol, L. and Ambrosio, L. (2015). Nanoparticle-integrated hydrogels as multifunctional composite materials for biomedical applications. *Gels*, 1(2): 162-178.
5. Heng, P. W. S. (2018). Controlled release drug delivery systems. *Pharmaceutical Development and Technology*, 23(9): 833-833.
6. Fan, H. T., Shi, L. Q., Shen, H., Chen, X. and Xie, K. P. (2016). Equilibrium, isotherm, kinetic and thermodynamic studies for removal of tetracycline antibiotics by adsorption onto hazelnut shell derived activated carbons from aqueous media. *RSC Advances*, 6(111): 109983-109991.
7. Syakirin, M., Mohd, F. and Nurjaliah, S. (2015). Adsorption of manganese in aqueous solution by steel slag. *Procedia Environmental Sciences*, 30: 145-150.
8. Dada, A. O., Olalekan, A. P., Olatunya, A. M. and Dada, O. (2012). Langmuir, Freundlich, Temkin and Dubinin–Radushkevich Isotherms Studies of Equilibrium Sorption of Zn^{2+} Unto Phosphoric Acid Modified Rice Husk. IOSR *Journal of Applied Chemistry*, 3(1): 38-45.
9. Demitri, C., Del Sole, R., Scalera, F., Sannino, A., Vasapollo, G., Maffezzoli, A. and Nicolais, L. (2008). Novel superabsorbent cellulose-based hydrogels crosslinked with citric acid. *Journal of Applied Polymer Science*, 110(4): 2453-2460.
10. Awada, H., Bouatmane, M. and Daneault, C. (2015). High strength paper production based on esterification of thermomechanical pulp fibers in the presence of poly(vinyl alcohol). *Heliyon*, 1(3): e00038.
11. Tahmasebpoor, M., De Martín, L., Talebi, M., Mostoufi, N. and Van Ommen, J. R. (2013). The role of the hydrogen bond in dense nanoparticle-gas suspensions. *Physical Chemistry*, 15(16): 5788-5793.
12. Bukhari, S. M. H., Khan, S., Rehanullah, M., and Ranjha, N. M. (2015). Synthesis and characterization of chemically cross-linked acrylic acid/gelatin hydrogels: Effect of pH and composition on swelling and drug release. *International Journal of Polymer Science*, 20(15): 1-15.
13. Saputra, A. H., Hapsari, M., Pitaloka, A. B. and Wulan, P. P. D. K. (2015). Synthesis and characterization of hydrogel from cellulose derivatives of water hyacinth (*Eichhornia crassipes*) through chemical cross-linking method by using citric acid. *Journal of Engineering Science and Technology*, 10: 75-86.
14. Yuan, Y. and Lee, T. R. (2013). Contact angle and wetting properties. *Springer Series in Surface Sciences*, 51(1): 3–34.
15. Du, J., Wu, Q., Zhong, S., Gu, X., Liu, J., Guo, H. and Zou, J. (2015). Effect of hydroxyl groups on hydrophilic and photocatalytic activities of rare earth doped titanium dioxide thin films. *Journal of Rare Earths*, 33(2): 148-153.
16. Mitra, A. and Dey, B. (2011). Chitosan microspheres in novel drug delivery systems. *Indian Journal of Pharmaceutical Sciences*,73(4): 355-366.
17. Chen, J. J., Ahmad, A. L. and Ooi, B. S. (2013). Poly(N-isopropylacrylamide-co-acrylic acid) hydrogels for copper ion adsorption: Equilibrium isotherms, kinetic and thermodynamic studies. *Journal of Environmental Chemical Engineering*, 1(3): 339-348.
18. Deruiter, J. (2005). Carboxylic acid structure and chemistry : Part 1. *Springer*, pp. 1–11.
19. Ibrahim, M. B. and Sani, S. (2014). Comparative isotherms studies on adsorptive removal of congo red from wastewater by watermelon rinds and neem-tree leaves. *Open Journal of Physical Chemistry*, 04(04): 139-146.
20. Simonin, J. P. (2016). On the comparison of pseudo-first order and pseudo-second order rate laws in the modeling of adsorption kinetics. *Chemical Engineering Journal*, 300: 254-263.
21. Plazinski, W., Dziuba, J. and Rudzinski, W. (2013). Modeling of sorption kinetics: The pseudo-second order equation and the sorbate intraparticle diffusivity. *Adsorption*, 19(5): 1055-1064.

Malaysian Journal of Analytical Sciences, Vol 23 No 3 (2019): 401 - 406
DOI: https://doi.org/10.17576/mjas-2019-2303-04

MALAYSIAN JOURNAL OF ANALYTICAL SCIENCES
Published by The Malaysian Analytical Sciences Society
ISSN 1394 - 2506

CHEMICAL COMPONENTS OF POLYMERASE CHAIN REACTION IN 18S rRNA FOR DETECTION OF *Cryptosporidium* FROM RIVER WATER SAMPLES

(Komponen Kimia Tindak Balas Berantai Polimerase di dalam 18S rRNA untuk Pengesanan *Cryptosporidium* dari Sampel Air Sungai)

Mohd Aiman Barudin[1], Mohammad Lokman Md Isa[2,3], Afzan Mat Yusof[2,3]*

[1]*Department of Biomedical Science, Kulliyyah of Allied Health Sciences*
[2]*Department of Basic Medical Sciences, Kulliyyah of Nursing*
[3]*Integrated Cellular and Molecular Biology Cluster (iMolec)*
International Islamic University Malaysia, Jalan Sultan Ahmad Shah, Bandar Indera Mahkota, 25200 Kuantan, Pahang, Malaysia.

**Corresponding author: afzan@iium.edu.my*

Received: 19 August 2018; Accepted: 18 May 2019

Abstract

The gene of 18S ribosomal RNA or 18S rRNA is the universal gene function as a general genetic marker for species identification of microorganisms including parasites. *Cryptosporidium* has distinct 18S rRNA genes along different species within the same genus. In this study, polymerase chain reaction or PCR was used to study chemical components of PCR setup in amplification of 18S rRNA gene of this parasite. *Cryptosporidium* was collected from river water samples and its presence was confirmed using specific immunofluorescence detection of this parasite. Isolated water containing *Cryptosporidium* was then subjected to genomic DNA extraction before PCR step. The chemical components of PCR consisting of $MgCI_2$, deoxynucleotide triphosphate (DNTPs), Polymerases, free DNase-water, universal primers and PCR buffer were studied in different volume and concentration. Each chemical component of PCR was optimized differently in yielding the same final volume of 20 µL per each reaction. The value range of chemical components of PCR consisted of $MgCI_2$ (0.1 µM-0.5 µM), dNTPs (50-250 mM), free DNase water (5-10 µL), polymerases (0.2-0.5 U) and universal primers (2-20 µM). The result indicated that 0.2 µM of $MgCI_2$, 100 mM of dNTPs, less than 10 µL of free DNase water, 0.5 U of polymerases and 10 mM of universal primers were the best combination to get better result for molecular identification of 18S rRNA *Cryptosporidium*. As a conclusion, accurate and proper concentration or volume of each PCR chemical components is essential for molecular identification of 18S rRNA *Cryptosporidium* gene. In future studies, study on gradient temperature parameters of PCR run can be included to study the chemical nature of amplified genes either in denaturation, annealing or extension steps.

Keywords: chemical, *Cryptosporidium*, polymerase chain reaction, 18S ribosomal RNA gene

Abstrak

Gen 18S ribosomal RNA adalah gen universal yang berfungsi sebagai penanda genetik umum untuk pengenalpastian spesies mikroorganisma termasuk parasit. *Cryptosporidium* mempunyai gen 18S rRNA yang berlainan daripada spesies berbeza dalam genus yang sama. Dalam kajian ini, tindak balas berantai polymerase atau PCR digunakan untuk mengkaji komponen kimia susun atur PCR dalam amplifikasi gen 18S rRNA bagi parasit ini. *Cryptosporidium* telah diambil dari sampel air sungai dan disahkan kehadirannya menggunakan pengesanan immunopendaflour terhadap parasit ini. Sampel air yang diambil mengandungi *Cryptosporidium* yang kemudiannya diteruskan untuk pengekstrakan genomik DNA sebelum peringkat PCR. Komponen kimia PCR yang terdiri daripada $MgCI_2$, deoksinukleotida trifosfat (dNTPs), polimerase, air yang bebas DNase, primer umum dan larutan penimbal PCR telah dikaji dalam isipadu dan kepekatan yang berbeza. Setiap komponen kimia PCR dioptimakan secara

berbeza dalam menghasilkan isipadu akhir 20 uL bagi setiap tindak balas. Nilai julat komponen kimia PCR terdiri daripada $MgCI_2$ (0.1 µM-0.5 µM), dNTPs (50-250 mM), air bebas DNase (5-10 µL), polimerase (0.2-0.5 U) dan primer primer umum (2-20 µM). Keputusan menunjukkan bahawa 0.2 µM $MgCI_2$, 100 mM dNTPs, air bebas DNase yang kurang daripada 10 µL, 0.5 U polimerase dan 10 mM primer umum adalah kombinasi terbaik untuk mendapatkan dapatan yang lebih baik bagi pengenalpastian molekul *Cryptosporidium* 18S rRNA. Kesimpulannya, kepekatan atau isipadu yang tepat dan sesuai bagi setiap komponen kimia PCR adalah penting untuk pengenalpastian molekul gen *Cryptosporidium* 18S rRNA. Bagi kajian masa depan, kajian ke atas kecerunan parameter suhu untuk menjalani PCR boleh dimasukkan untuk mengkaji sifat semulajadi kimia pada gen yang diamplifikasi untuk peringkat-peringkat penyahaslian, pelekatan atau penyambungan.

Kata kunci: kimia, *Cryptosporidium*, tindak balas rantai polimerase, gen 18S ribosomal RNA

Introduction

Cryptosporidiosis is prevalent in developing countries, perhaps because the high contamination from environmental and hygiene conditions [1]. In contrast, the cryptosporidiosis transmission in developed countries is possibly not similar as compared to developing countries. *Cryptosporidium* oocysts are frequently found in contaminating surface waters because of anthroponotic activity, agricultural practices, sewage effluent, native animal or livestock fecal contamination as well as extremely resistant to chlorine and monochloramine for water disinfection [2]. In addition to being resistant to commonly used disinfectant chemicals, it is commonly considered that oocysts can persist for several months or more in the aquatic environment [3]. Other than that, the relatively low infectious dose of *Cryptosporidium* at least 10 oocysts can pose a challenge to water utilities for provision of purified drinking water [4]. To date, this parasitic occurrence has been reported in different geographical location of river [5]. In fact, 11.5% of Malaysian river water samples were reported to get contaminated with *Cryptosporidium* oocysts [6]. Recently, two cases have been reported on *Cryptosporidium* occurrence in Kuantan, Pahang [7,8].

Meanwhile, amplification of 18S rRNA gene loci is been the most widely accepted method to provide information on species identification [9]. An optimized method of PCR for *Cryptosporidium* oocysts is essential in detection of single loci with specific primers. DNA extraction for this parasite turns to be effective once disruption of the robust oocyst wall takes place for releasing sporozoite nuclei. Meanwhile detachment of DNA and histone protein is important for primer to have accessibility to anneal and thus, facilitating the amplification of specific DNA sequence using PCR [10]. It is a challenge for diagnosing *Cryptosporidium* to the species/genotype level due to the lower occurrence and the rich presence of PCR inhibitors from environmental water samples. It is essential for the public and environmental health assessment for identifying the contamination sources of *Cryptosporidium* oocysts [11]. In addition, optimization of chemical constituents of PCR reagents is also important to get correct amplicon of PCR upon the completion of PCR with the specific primer on annealing specific gene sequences [12]. All chemical reagents like dNTPs, $MgCI_2$, primers, polymerases and water have their own limitation either low or high proportion could lead to successfulness of PCR [13]. Manipulation of chemical nature of those chemical reagents can be useful to set up a better reaction mix of PCR prior to run the reaction [14]. Thus, in this study, chemical reagent constituents of PCR are optimized accordingly to result in successfulness of PCR on amplification of *Cryptosporidium* 18S rRNA gene.

Materials and Methods

Collection of river water samples

This study was carried out in Kuantan and Balok, Pahang. The upstream, midstream and downstream area in both Kuantan River and Balok River were selected as the sampling sites. Kuantan River runs from Lembing River through Kuantan City where this city is located near the mouth of Kuantan River before this river flows out to the South China Sea. Meanwhile, Balok River is located close to industrial area and residential area in Gebeng area and Balok city, respectively.

Water processing

United States Environmental Protection Agency 1623.1 method was used to detect *Cryptosporidium* from river water samples [15]. River water samples were processed to be concentrated using continuous flow centrifuge (CFC Express System) (Scientific Methods Inc, Granger, Indiana, USA) prior to immunomagnetic separation using Dynabeads® GC-Combo (Dynal, Cat. no. 730.02, Oslo, Norway).

Fluorescein isothiocyanate staining
Purified oocysts of river water samples were stained using a fluorescein isothiocyanate labelled monoclonal antibody kit specific to *Cryptosporidium* oocysts (Cellabs Pty Ltd., cat. no. KR2111A6, Brookvale, Australia) and then were examined using fluorescence microscope under 400x magnification.

DNA extraction from water samples
DNA of *Cryptosporidium* oocysts from river water sample was extracted by using QIAamp DNA Mini Kit (QIAGEN, Germany) with minor modifications.

Optimization of chemical components in PCR reaction mixture
Each chemical component of PCR was optimized differently in yielding the same final volume of 20 µL per each reaction. The value range of chemical components of PCR consists of $MgCI_2$ (0.1 µM-0.5 µM), dNTPs (50-250 mM), free DNase water (5-10 µL), polymerases (0.2-0.5 U) and universal primers (2-20 µM). The results of several PCR reactions in different volume of PCR chemical components were run based on nested PCR.

Identification of 18S rRNA sequence
Nested PCR of 18S rRNA was carried out for *Cryptosporidium* genotyping [16]. Purified commercially genomic DNA of *C. parvum* was set to be a positive control. Distilled water was used as a negative control for nested PCR. Agarose solution (1.2%) was prepared with 1 µL GelRed. The gel was electrophoresed at 100 V for 40 min and then visualized using GelDoc Ez System (Bio-Rad).

Results and Discussion

Out of six river water samples, five were detected with *Cryptosporidium*. The findings were confirmed by using 18S rRNA-based PCR method. The result of secondary PCR products of 18S rRNA gene showed that only one sample from upstream point of Kuantan River did not appear a single band on the 1.2% agarose gel. In this study, the positive results of genotyping approach showed that only five water samples out of six samples from two rivers contained DNA of *Cryptosporidium* oocysts. A previous study had revealed distribution of *Cryptosporidium* species in river water samples of Kuantan River and Balok River, especially at downstream point [7, 8]. Each chemical component of PCR was optimized differently in yielding the same final volume of 20 µL per each reaction. The value range of chemical components of PCR consisted of $MgCI_2$ (0.1-0.5 µM), dNTPs (50-250 mM), free DNase water (5-10 µL), polymerases (0.2-0.5 U) and universal primers (0.1-0.5 µM). The result indicated that 2 mM of $MgCI_2$, 100 mM of DNTPs, less than 10 µL of free DNase water, 0.5 U of polymerases and 10 mM of universal primers were the best combination to get acceptable results for molecular identification of 18S rRNA *Cryptosporidium*. To understand the function of chemical reagents used in this study, it is critical to optimize and troubleshoot the optimal PCR conditions at a time in obtaining the desired PCR product of *Cryptosporidium* 18S rRNA gene (Table 1). However, unbalanced composition of PCR chemical reagents may cause non-specific amplicons and reduce PCR specificity [17].

Table 1. Different volumes of PCR chemical components in nested PCR

$MgCI_2$ (µM)	dNTPs (mM)	Free-DNaseWater (µL)	DNA Polymerases (U)	Universal Primers (µM)
0.1	50	5	0.2	2
0.2	100	6	0.3	8
0.3	150	7	0.4	12
0.4	200	8	0.45	16
0.5	250	9	0.5	20

In this study, Taq DNA polymerase was used as it is suitable for obtaining desired amplicon products and more efficient as a hot start PCR [18]. Normally, the molar concentration of polymerase is comparatively low as compared to other chemical reaction components as recommended volume supplied is 1-2.5 Units per 100 µL reaction volume. Reduced concentration of polymerases ensure specificity while higher counterpart causing nonspecific amplicons [19]. DNA polymerases are favored in PCR process with a cofactor like magnesium ion [20]. They are easily manipulated resulting in the stringency of PCR as its ionic concentration is critical. In fact, it is also determined by EDTA in PCR buffer and deoxynucleotide 5'-triphosphates (dNTPs). In principle of PCR chemistry, dNTP-Mg^{2+} soluble complexes tend to interact with the DNA template backbone thereby activating DNA polymerase function (Figure 1). Soluble complexes are recognized as a substrate for DNA polymerase to act on [21]. However, increased magnesium ion can reduce polymerase specificity, stabilize the duplex strand of DNA template or fidelity of Taq DNA polymerase, stabilize the duplex strand of DNA template and spurious incorrect primer annealing thereby resulting in undesired or non-specific amplicons [22]. In contrast, insufficient concentration of Mg^{2+} can cause no amplicons or yields are likely to be poor [23]. $MgCI_2$ was optimized in this study because the reaction cannot proceed without the sufficient concentration of Mg^{2+} ion. The optimized concentration is additional option from the recommended protocol because the nature of DNA template can be affected by PCR inhibitors from environmental factors [24]. In such case, it is crucial to increase the concentration of magnesium ion for PCR stringency and specificity.

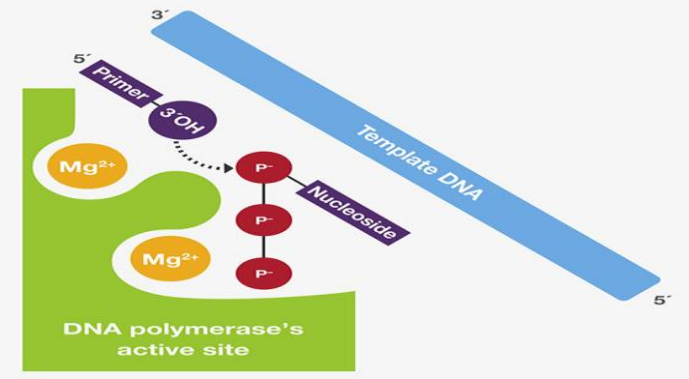


Figure 1. Illustration of polymerase chain reaction on DNA molecules along with other PCR chemical components involved in the PCR reaction

On the other hand, four dNTPs should be at the appropriate equivalent concentrations of 50 µM even though the reaction commonly can compromise between 20 and 200 µM [25]. In our study, dNTPs were optimized accordingly from the lowest to highest concentration to find an optimal concentration that is suitable for PCR reaction. Reduced dNTPs concentrations can increase PCR specificity while higher one can work oppositely [26]. The desired length of PCR products is not long, below 500 bp and thus, higher dNTP concentration is not required. In our practice, optimization of each dNTP is essential for working dNTPs solution to reach the optimal balance in final reaction coupled with other PCR reagents. It is important that four dNTP's concentrations should be used equivalently for minimizing misincorporation errors [27]. One of the main components to be discussed is universal primers. Its concentration should be optimal at 0.1-0.5 µM. In our study, primer was optimized for both concentrations and final volume in 20 µL PCR reaction mix. Higher concentration of universal primers can result in template mis priming at non-specific sites and thus, leading to accumulated non-specific products formation [28]. However, the primers should be prepared at slightly higher concentration than optimal to avoid of its exhaustion that possibly compromise the desired amplicon yield upon PCR completion [29]. Finally, free-DNase water is generally the easiest component for optimization since it is essentially important to be included in PCR reaction mix for avoiding any residual enzymatic activity such as DNase that can degrade DNA template during PCR reaction until its completion [30]. However, the volume of water should not higher than half of PCR mix volume. In our study, the volume of PCR mix was set to be at 20 µl per reaction only. Thus, it is only tolerated for manipulation below than 10 µL to avoid diluting other essential chemical components of PCR such as DNA polymerase, dNTPs, MgCI2 and universal

primers as primers were already diluted from its working concentration of primer stock. Equal concentration of dNTPs with the excessive volume of water in PCR reaction mix indirectly can affect the formation of desired amplicon upon PCR completion [31].

Conclusion

Accurate and proper concentration or volume to each PCR chemical components is essential for molecular identification of 18S rRNA *Cryptosporidium* gene. These optimized PCR chemical components can be applied to other water samples infected with *Cryptosporidium* for species identification. In future studies, study on gradient of temperature parameters of PCR run can be included to study the chemical nature of amplified genes either in denaturation, annealing or extension steps.

Acknowledgement

The authors acknowledge to International Islamic University Malaysia (IIUM) for financial support through P-RIGS18-037-0037.

References

1. Shrivastava, A. K., Kumar, S., Smith, W. A. and Sahu, P. S. (2017). Revisiting the global problem of cryptosporidiosis and recommendations. *Tropical Parasitology*, 7(1): 8.
2. Huang, C., Hu, Y., Wang, L., Wang, Y., Li, N., Guo, Y., Feng, Y. and Xiao, L. (2017). Environmental transport of emerging human-pathogenic *Cryptosporidium* species and subtypes through combined sewer overflow and wastewater. *Applied and Environmental Microbiology*, 83(16): AEM-00682.
3. Sales-Ortells, H., Agostini, G. and Medema, G. (2015). Quantification of waterborne pathogens and associated health risks in urban water. *Environmental Science & Technology*, 49(11): 6943-6952.
4. Adamska, M., Sawczuk, M., Kolodziejczyk, L. and Skotarczak, B. (2015). Assessment of molecular methods as a tool for detecting pathogenic protozoa isolated from water bodies. *Journal of Water and Health*, 13(4): 953-959.
5. Zahedi, A., Paparini, A., Jian, F., Robertson, I. and Ryan, U. (2016). Public health significance of zoonotic *Cryptosporidium* species in wildlife: critical insights into better drinking water management. *International Journal for Parasitology: Parasites and Wildlife*, 5(1): 88-109.
6. Triviño-Valencia, J., Lora, F., Zuluaga, J. D. and Gomez-Marin, J. E. (2016). Detection by PCR of pathogenic protozoa in raw and drinkable water samples in Colombia. *Parasitology Research*, 115(5): 1789-1797.
7. Afzan, M. Y., Mardhiah, M., Muhammad Razman, A. R., Qamarul Iqmal, A., Sharmeen Nellisa, S., Nur Hazirah, H., Najat, H. and Ridhwan, A. W. (2015). The occurrence *Cryptosporidium* oocysts in selected rivers and its physical assessments in Kuantan, Pahang. *Journal of Applied Science Research*, 11(17): 19-25.
8. Mohd Aiman, B., Muhammad Lokman, M. I. and Afzan, M. Y. (2017). First molecular characterization of *Cryptosporidium* from three different points of two main rivers in Kuantan, Malaysia using 18S rRNA gene nested PCR. *Asian Pacific Journal of Tropical Disease*, 7(9): 930-934.
9. Thompson, R. C. A. and Ash, A. (2016). Molecular epidemiology of *Giardia* and *Cryptosporidium* infections. *Infection, Genetics and Evolution*, 40: 315-323.
10. Richard, R. L., Ithoi, I., Abd Majid, M. A., Wan Sulaiman, W. Y., Tan, T. C., Nissapatorn, V. and Lim, Y. A. L. (2016). Monitoring of waterborne parasites in two drinking water treatment plants: A study in Sarawak, Malaysia. *International Journal of Environmental Research and Public Health*, 13(7): 641.
11. Lim, Y. A., Mahdy, M. A. and Surin, J. (2013). Unravelling *Cryptosporidium* and *Giardia* in Southeast Asia. In Parasites and their vectors. Springer, Vienna: pp. 77-102.
12. Al-Delaimy, A. K., Al-Mekhlafi, H. M., Nasr, N. A., Sady, H., Atroosh, W. M., Nashiry, M., Anuar, T. S., Moktar, N., Lim, Y. A. and Mahmud, R. (2014). Epidemiology of intestinal polyparasitism among Orang Asli school children in rural Malaysia. *PLoS Neglected Tropical Diseases*, 8(8): e3074.
13. Kumar, T., Onichandran, S., Lim, Y. A., Sawangjaroen, N., Ithoi, I., Andiappan, H., Salibay, C. C., Dungca, J. Z., Chye, T. T., Sulaiman, W. Y. and Lau, Y. L. (2014). Comparative study on waterborne parasites between Malaysia and Thailand: A new insight. *The American Journal of Tropical Medicine and Hygiene*, 90(4): 682-689.
14. Lim, Y. A. L. and Vythilingam, I. (Eds.). (2014). Parasites and their vectors: A special focus on Southeast Asia. Springer Science & Business Media.

15. United States Environmental Protection Agency (2012). Method 1623.1: *Cryptosporidium* and *Giardia* in water by filtration/IMS/FA. Cincinnati: United States Environmental Protection Agency. http://www.doc88.com/p-0416866100459.html [Access online 3 July 2018].
16. Mahmoudi, M. R., Nazemalhosseini-Mojarad, E., Kazemi, B., Haghighi, A., Mirzaei, A., Mohammadiha, A., Jahantab, S., Xiao, L. and Karanis, P. (2015). *Cryptosporidium* genotypes and subtypes distribution in river water in Iran. *Journal of Water and Health*, 13(2): 600-606.
17. Lee, S. C., Ngui, R., Tan, T. K., Roslan, M. A., Ithoi, I. and Lim, Y. A. (2014). Aquatic biomonitoring of *Giardia* cysts and *Cryptosporidium* oocysts in peninsular Malaysia. *Environmental Science and Pollution Research*, 21(1): 445-453.
18. Hall, T. (2011). BioEdit: An important software for molecular biology. *GERF Bulletin Bioscience*, 2(1): 60-61.
19. Kumar, S., Stecher, G. and Tamura, K. (2016). MEGA7: Molecular evolutionary genetics analysis version 7.0 for bigger datasets. *Molecular Biology and Evolution*, 33(7): 1870-1874.
20. Zainal Abidin, Z. A., Abdul Malek, N., Zainuddin, Z. and Chowdhury, A. J. K. (2016). Selective isolation and antagonistic activity of actinomycetes from mangrove forest of Pahang, Malaysia. *Frontiers in Life Science*, 9(1): 24-31.
21. Ghani, N. A. A. A., Othman, N. and Baharudin, M. K. H. (2013). Study on characteristics of sediment and sedimentation rate at Sungai Lembing, Kuantan, Pahang. *Procedia Engineering*, 53: 81-92.
22. Ghani, N. A. A., Mohamad, N. A. and Hui, T. W. (2016). Rainfall analysis to determine the potential of rainwater harvesting site in Kuantan, Pahang. *ARPN Journal of Engineering Applied Science*, 11(11): 7264-7268.
23. Alshaebi, F. Y., Yaacob, W. Z. W., Samsudin, A. R. and Alsabahi, E. (2009). Risk assessment at abandoned tin mine in Sungai Lembing, Pahang, Malaysia. *Electronic Journal of Geotechnical Engineering*, 14: 1-9.
24. Le Blancq, S. M., Khramtsov, N. V., Zamani, F., Upton, S. J. and Wu, T. W. (1997). Ribosomal RNA gene organization in *Cryptosporidium parvum*. *Molecular and Biochemical Parasitology*, 90(2): 463-478.
25. Xiao, L., Escalante, L., Yang, C., Sulaiman, I., Escalante, A. A., Montali, R. J., Fayer, R. and Lal, A. A. (1999). Phylogenetic analysis of *Cryptosporidium* parasites based on the small-subunit rRNA gene locus. *Applied and Environmental Microbiology*, 65(4): 1578-1583.
26. Stenger, B. L., Clark, M. E., Kváč, M., Khan, E., Giddings, C. W., Dyer, N. W., Schultz, J. L. and McEvoy, J. M. (2015). Highly divergent 18S rRNA gene paralogs in a *Cryptosporidium* genotype from eastern chipmunks (*Tamias striatus*). *Infection, Genetics and Evolution*, 32: 113-123.
27. Ikarashi, M., Fukuda, Y., Honma, H., Kasai, K., Kaneta, Y. and Nakai, Y. (2013). First description of heterogeneity in 18S rRNA genes in the haploid genome of *Cryptosporidium andersoni* Kawatabi type. *Veterinary Parasitology*, 196 (1-2): 220-224.
28. Jellison, K. L., Distel, D. L., Hemond, H. F. and Schauer, D. B. (2004). Phylogenetic analysis of the hypervariable region of the 18S rRNA gene of *Cryptosporidium* oocysts in feces of Canada geese (*Branta canadensis*): evidence for five novel genotypes. *Applied and Environmental Microbiology*, 70 (1): 452-458.
29. Ruecker, N. J., Matsune, J. C., Wilkes, G., Lapen, D. R., Topp, E., Edge, T. A., Sensen, C. W., Xiao, L. and Neumann, N. F. (2012). Molecular and phylogenetic approaches for assessing sources of *Cryptosporidium* contamination in water. *Water Research*, 46(16): 5135-5150.
30. Yang, B., Wang, Y. and Qian, P. Y. (2016). Sensitivity and correlation of hypervariable regions in 16S rRNA genes in phylogenetic analysis. *BMC Bioinformatics*, 17(1): 135.
31. Xiao, L., Limor, J. R., Li, L., Morgan, U., Thompson, R. C. and Lal, A. A. (1999). Presence of heterogeneous copies of the small subunit rRNA gene in *Cryptosporidium parvum* human and marsupial genotypes and *Cryptosporidium felis*. *The Journal of Eukaryotic Microbiology*, 46(5): 44S.

Malaysian Journal of Analytical Sciences, Vol 23 No 3 (2019): 407 - 422
DOI: https://doi.org/10.17576/mjas-2019-2303-05

MALAYSIAN JOURNAL OF ANALYTICAL SCIENCES
Published by The Malaysian Analytical Sciences Society
ISSN 1394 - 2506

MAGNETITE GRAPHENE FOR ELECTROCHEMICAL DETERMINATION OF URIC ACID

(Magnetit Grafin untuk Penentuan Elektrokimia Asid Urik)

Yee Kin Weng, Azleen Rashidah Mohd Rosli, Farhanini Yusoff*

School of Marine and Environmental Sciences,
Universiti Malaysia Terengganu, 21030 Kuala Nerus, Terengganu, Malaysia

**Corresponding author: farhanini@umt.edu.my*

Received: 17 February 2019; Accepted: 22 May 2019

Abstract

In this work, the magnetite-reduced graphene oxide (Fe_3O_4/rGO) was fabricated for a selective voltammetric detection of uric acid. The magnetite-reduced graphene oxide is biocompatible sensing material that was synthesized through one-step reaction mechanism. The attachment of spherical like Fe_3O_4 particle on the rGO sheet was characterized by Fourier Transform Infrared (FTIR), Ultraviolet-Visible Spectroscopy (UV-Vis) and Scanning Electron Microscopy (SEM). The electrochemical performance of the Fe_3O_4/rGO/GCE electrode were studied by Cyclic Voltammetry (CV) and Differential Pulse Voltammetry (DPV). The superparamagtism property of the Fe_3O_4 anchoring on the rGO sheet provides a conduction pathway for the analyte diffusion meanwhile promote the electron transfer kinetic between the electroactive species and electrode surface. The enhanced current response signal produced from the reduction-oxidation process by the electroactive species were optimized further in parameters of scan rate, concentration of uric acid and pH value of the supporting electrolyte. The observed DPV response displays a linearity relationship on uric acid concentration ranging from 4 µM to 100 µM with correlation coefficient 0.989 and a sensitivity of 0.08478 µA/µM. The detection limit and limit of quantitation were found to be 3.04 µM and 10.14 µM respectively.

Keywords: magnetite, reduced graphene oxide, uric acid, electrochemical sensor

Abstrak

Dalam hasil kerja ini, magnetit-grafin oksida terturun (Fe_3O_4/rGO) telah difabrikasikan untuk tujuan pengesanan voltametrik terpilih bagi asid urik. Magnetit-grafin oksida terturun merupakan bahan sensor bioserasi yang telah disintesis melalui mekanisma tindak balas satu langkah. Pelekatan zarah sfera Fe_3O_4 pada lembaran rGO telah dicirikan menggunakan Inframerah Transformasi Fourier (FTIR), Spektroskopi Sinar Ultra Lembayung Terlihat (UV-Vis), dan Mikroskop Imbasan Elektron (SEM). Prestasi elektrokimia elektrod Fe_3O_4/rGO/GCE telah dikaji menggunakan kaedah Voltametri Berkitar (CV) dan Voltammetri Pembezaan Denyutan (DPV). Ciri-ciri superparamagnetisma Fe_3O_4 yang terlekat di atas lembaran rGO menyediakan laluan konduktif untuk penyerapan analit dan juga meningkatkan kinetik pemindahan elektron di antara spesies elektroaktif dan permukaan elektrod. Peningkatan isyarat tindakbalas arus yang dihasilkan dari proses pengoksidaan dan pengurangan oleh spesies elektroaktif telah dioptimumkan lebih lanjut didalam pengoptimuman kadar imbasan, kepekatan asid urik dan nilai pH elektrolit sokongan. DPV yang telah diperhatikan menunjukkan hubungan linear di antara kepekatan asid urik antara 4 µM sehingga 100 µM berserta pekali kolerasi 0.989 dan sensitivity 0.08478 µA/µM. Had pengesanan dan had kuantifikasi masing-masing adalah 3.04 µM dan 10.14 µM.

Kata kunci: magnetit, grafin oksida terturun, asid urik, sensor elektrokimia

Introduction

Uric acid (UA) is a biomolecule compound that plays significant role in regulate the homeostasis and metabolism system of the human body. The relative concentration of the UA varies dependently on tissue sites, which may accumulate temporarily or localized for extended period [1]. The UA that is sparingly water-soluble biochemical compound can be determined in the blood serum and excretion waste of the mammalian in the forms of urine. The clinical screening assessment for the uric acid serve as the fundamental tool in understanding various clinical conflicts that link to the uric acid level in human body. The abnormal amount of uric acid may potentially associated with diseases in term of chronic and acute that hold the risk of fatality [2]. The type of diseases that show close relationship to the abnormal amount of uric acid in body fluid including gout, hyperuricemia, rheumatoid and arthritis. Abnormal elevation in the level of uric acid in the body fluid will probably results several recognized clinical problem, which uric acid probably serve as the etiological agent. At high concentration, the uric acid can converted into oxidative radical and its derivatives, which has high cellular permeability and ability to interrupt during the DNA transcription and translation [3].

Quantitative and qualitative determination of the uric acid are significantly useful to provide related information especially in field of pharmaceutical, nursery, pathology, and medical field. There are varieties of techniques have been proposed with promising sensitivity and consistency in term of detection limit and the amount of uric acid quantified [4, 5]. Recently, electrochemical sensing has been highlighting as sophisticate alternative in identification of disease diagnosis molecules including UA [6]. Meanwhile, due to unique electronic properties and stiffness of the nano-sized graphene carbon allotrope, it has been widely adopted in material development and research activities was intensified on exploitation of graphene in photocatalysis, environmental remediation, and energy storage [1,7]. Graphene is a newly carbon material with nanoscale-dispersed phase at two dimensions other than zero-dimensional fullerene, one-dimensional carbon nanotube, and three-dimensional graphite [8]. The distinctive properties of graphene which are electrochemical beneficial have drawn noticeable attentions among the researchers to uncover its unique structure and properties. The graphene has 2D honeycomb lattice structure favored by the sp^2 hybridization of each carbon atom in the domain. The covalent reinforcement of the domain rendering graphene has strong mechanical strength and making it an ideal material for sustaining the engineering application as well as industrial manufacturing process.

Aside from its excellent physically strength, it has been found that graphene poses large surface–to-volume ratio, high thermal conductivity (3000 W $m^{-1}K^{-1}$), and extremely high electron mobility at room temperature (2.0×10^5 cm^2 V^{-1} s^{-1}) [8]. Such intriguing special of the graphene highly promoted as new potential electrode material for the application in electrochemically determination analyte of interest. A water-dispersible nanocomposite consisting of both magnetite and reduced graphene oxide was designed to address the issue associated with removal of arsenic in typical water treatment process [9]. By coupling both beneficial factors from the graphene and magnetite, the electronic and mechanical performance of the resulting compound may be enhanced. The combinations of excellent electrocatalytic activity of magnetite and good electronic properties of graphene serve as a promising hybrid material on measuring the UA content in biological sample. The UA monitoring examination is clinical diagnostic important as excessive amount of uric acid accumulated may potentially associated with disease of either chronic or acute as well as fatality.

The development of graphene-based hybrid material has been explore through its intended application in electronic industry, microprocessor chipset, and battery manufacture [10]. In order to resolve the difficulties coped in determination of uric acid in real sample, the fabrication of magnetite (Fe_3O_4) supported on the reduced graphene oxide (rGO) nanocomposite coated on glassy carbon electrode (GCE) is proposed in this paper. The Fe_3O_4/rGO/GCE has demonstrated better biocompatibility as compare to bare glassy carbon electrode. Its noticeable electron transfer kinetic enhances the overall performance of the electrochemical instrumental about the desirable sensitivity and selectivity of electrode react with.

Materials and Methods

Reagent and apparatus

The concentrated sulfuric acid (H_2SO_4, 98%), hydrochloric acid (HCl), ammonia (NH_3), potassium permanganate ($KMnO_4$), hydrogen peroxide (H_2O_2, 30%) sodium nitrate and uric acid were purchased from the Merck, Germany.

The natural graphite powder, hydrazine hydrate, iron(II) chloride tetrahydrate ($FeCl_2 \cdot 4H_2O$), and iron(III) chloride hexahydrate ($FeCl_3.6H_2O$) were obtained from Merck, Germany. The electrocatalytic performance of the magnetic nanocomposite decorated glassy electrode will be electrochemically analyzed by using 3-electrode system consists of counter electrode made of a platinum wire, silver/silver chloride electrode (Methrom AUTOLAB, Netherlands), with 3 M of KCl) as reference electrode, and magnetite-reduced graphene oxide modified glassy electrode (BASi MF-2012 3.0mm diameter) as the working electrode, with the use of Potentiostat/Galvanostat module PGSTAT (Metrohm AUTOLAB, Nertherlands).

Synthesis of rGO

Firstly, GO was prepared by modified Hummer's method as reported by Yusoff et al. [11]. The graphene oxide solid sample obtained from the modified Hummers' method was grounded with mortar and pester. The 0.5g of fine powder GO first dispersed in deionized water and sonicate for 30 minutes at 60 ^oC. Later, 5g of ascorbic acid added into the homogenized GO solution and stirred with magnetic bar for 30 minutes at 60 ^oC. The mixture underwent a color changes from yellowish brown to black precipitate, indicative of reduction of GO. The reduction product was treated with centrifugation and remove the supernatant. The black paste of rGO was added with excess 30% hydrogen peroxide to eliminate the unreacted AA by sonicating for 30 minutes at 60 ^oC. After sonication, the resulted black solid was obtained by centrifugation and wash with ethanol, deionized water 3 times respectively, and dried in the oven at 100 ^oC.

Co-precipitation of magnetite

The ferric (10.4 g) and ferrous chloride (4.0 g) can be prepared in a 2:1 mole ratio in 200 mL of degassed deionized water. The solution containing both ferric and ferrous species was heated up to 50 ^oC for 10 minutes. After the heating process completed, 2 mL of 25% ammonium hydroxide was added dropwise into the mixture solution under constant stirring rate at 50 ^oC. The pH of the mixture was adjusted using the relatively small amount of sodium hydroxide solution to maintain the solution within the pH range of 9-10. The solution stirred continuously at the same condition for one hour. The black solid magnetite was separated from the solution using a strong magnet, washed with 1:1 composition mixture of ethanol and deionized water. The solid mass was dried in the oven at 70 ^oC for 6 hours.

Preparation of magnetic nanocomposite (Fe_3O_4/rGO) through co-precipitation

The obtained graphite oxide powder (0.5 g) was homogenized in 300 mL deionized water through ultra-sonication for 35 minutes. The solutions of ferrous chloride (0.1584 g/25 mL) and ferric chloride (0.4055 g/2 5mL) will be prepared according to 1:2 molar ratio, which is the elemental stoichiometric need for the exact composition of the magnetite required. The resulting monodispersed solution was added with the as prepared iron (II/III) solutions slowly at room temperature and stirred at low speed power. Next, alkalization of the mixture solution by adding 30% ammonia solution. The pH of the mixture was adjusted to a magnitude of 10-11. Later on, the stirring mixture was gradually heated up to 90 ^oC and meanwhile promoting a reducing atmosphere by introduction of suitable amount of hydrazine hydrate (10 mL). The solution heated up for 4 hours at constant stirring condition. The resulting black solution cooled under room atmosphere and filtered with mixture of ethanol and water (1:1). The black powder obtained after drying in the oven at 70 ^oC for 2 hours.

Fabrication of the magnetite-graphene composite film

Prior to the surface modification of the bare glassy carbon electrode (3 mm in diameter), the surface was polished with fine alumina slurry (0.05 μm) and rinse thoroughly with deionized water. The GCE will then ultra-sonicate in the acetone and deionized water successively and dry under ambient condition. The Fe_3O_4/rGO (1.0 mg) was added into 1 mL of deionized water and produced a homogeneous suspension after completion of one-hour sonication. Finally, 5 μL of the Fe_3O_4/rGO homogenized solution was drop-casted on the pretreated GCE and allowed to dry in a vacuum desiccator for 2 hours.

Electrochemical Measurement

The Fe_3O_4/rGO/ GCE-modified electrode was used to determine uric acid by electrochemical means. The potential applied varies from -0.2 to 0.8 in order to study the redox behavior of the uric acid under cyclic voltammetry. The unmodified glassy carbon electrode was used to replace the Fe_3O_4/rGO/ GCE-modified electrode in comparison of

their thermal stability, electron kinetic transfer, electrode performance and efficiency. Other than this, the stability of the electrode designed will investigate at different external condition in the experiment. Parameters such as pH, concentrations and scan rate were used to study the optimum performance of the overall electrochemical system built.

Results and Discussion

Physical characterization of Fe_3O_4/rGO

The distinction in the functionalities and moieties of each constituents can be determined using the substrate nature and characteristic peaks demonstrated in the IR spectrum. The pure graphite in Figure 1(a) displays a smooth line passes through the region of 4000 to 1500 cm^{-1} with no single peak appear. The layer intercalation and surface modification of graphite using the modified Hummers method was indicated successfully by the changes in the shape of the spectrum obtained for GO. The FTIR spectrum of GO shown a broad peak at the region around 2950-3699 cm^{-1}, which designated to the stretching vibration of OH groups of water molecules adsorbed on graphene oxide. The oxygen functionalities of the graphene oxide described by the peak value of 1730 cm^{-1}, 1400 cm^{-1}, 1210 $cm^{-1,}$ and 1020 cm^{-1} corresponding to the carbonyl C=O, carboxyl COO-, epoxy C-O, and alkoxy C-OH stretching vibration [12, 13]. The absorption band value of 1612 cm^{-1} being assigned to the aromatic C=C stretching vibration of the carbon domain. Upon successful chemical reduction of GO with AA, the characteristic absorption peaks responsible for the oxygen moieties present in the GO no longer observed in the rGO spectrum [14–16]. A significant peak at 580 cm^{-1} was determined in the spectra of synthesized Fe_3O_4 nanocomposite, where it defines the stretching vibrational mode of Fe-O intrinsically at the tetrahedral void [17]. The stretching vibrations of –OH at low-frequency region of 3400 cm^{-1} and the band 1612 cm^{-1} was ascribed to the bending mode of the water molecules absorbed on magnetite surfaces [18]. In the view of spectrum obtained for Fe_3O_4/rGO, the absorption bands being assigned to oxygenated group was greatly reduced in intensity and the transmittance band around 584 cm^{-1} is attributed to the Fe-O bonding vibration, indicated the existence of magnetite [19]. There are additional symmetric and antisymmetric stretching mode of carboxylic group, COO- with corresponding absorption peak value at 1585 cm^{-1} and 1414 cm^{-1}.

The optical properties of each constituent materials was measured and the progressive changes on the optical behavior were studied based on exposure upon the ultraviolet-visible light wavelength region. In Figure 1(b), the pure graphite exhibits no significant absorption peak in the range of 200 nm to 800 nm. This is mainly due to the non-functionalized surface and inertness nature of the pure graphite in response toward the radiation. The dramatic changes to the surface morphology and functioning group attached to the graphitic surface layer will promote the absorption of radiation that brought about excitation of outermost electrons into higher energy state. The GO displayed an optical π-π^* aromatic C-C bond absorption band at 231 nm and a shoulder peak at 300 nm which responsible to n-π^* transition of the carbonyl C=O bond [20]. Upon subjected to the AA green reduction, the as-prepared rGO revealed a bathochromic shift absorption at wavelength of 259 nm indicated the successful restoration of electronic conjugation structure and removal of oxygenated group covalently bonded to the graphene oxide surface [10, 21]. The Fe_3O_4 nanoparticle shows continuous absorption throughout the ultraviolet-visible range of 200 nm to 80 0nm without any identifiable strong absorption peak. Similarly, the resultant Fe_3O_4/rGO demonstrated a sharp increment in the optical absorption particularly at near band edge followed by a steady state absorbance approximately at 268nm [18]. The redshifted absorption pattern suggested the incorporation of Fe_3O_4 onto the surface of graphitic sp^2 domain of rGO which underlying an enhanced photocatalytic performance.

The surface morphology and structural feature of each type of constituents and nanohybrids materials were elucidated through SEM imaging. In Figure 2, GO and rGO demonstrated units of random aggregates with corrugation nature extending over the carbon domain. This unique surface changes was attributed to the chemical destruction and restoration of graphitic sp^2 hybridized network happened during intercalation stage and functionalization of graphitic surface [22]. The spontaneous graphitic sheet scrolling is thermodynamically favored, at which the irreversible wrinkle nature of rGO sustains a beneficial high ratio of total surface area to volume [23]. The existences of extra hole defects and vacancies spreading throughout the rGO sheets in comparison to GO is because of the introduction of sp^3 oxygenated carbon population and discontinuation of the interplanar C-C bonding. This supported that GO was successfully reduced to rGO. The SEM image was obtained for magnetite nanoparticle as shown in Figure 2(d). The magnetite synthesized from co-precipitation appears as sphere-like

discrete particle with mean size differences in dimension of nanoparticle [24]. The resultant Fe_3O_4/rGO nanocomposite was shown in Figure 2 (e) with visible discrete outline of both different rGO and MnP nanoparticles. The rGO film was densely anchored with spherical magnetite nanoparticle of uniform size. The crystal growth suppressive effect due interaction of GO sheet and Fe_3O_4 has restrained the extent of Fe_3O_4 agglomeration that could facilitate the electron transfer from Fe_3O_4 through the rGO sheet producing an enhanced electrochemical response.

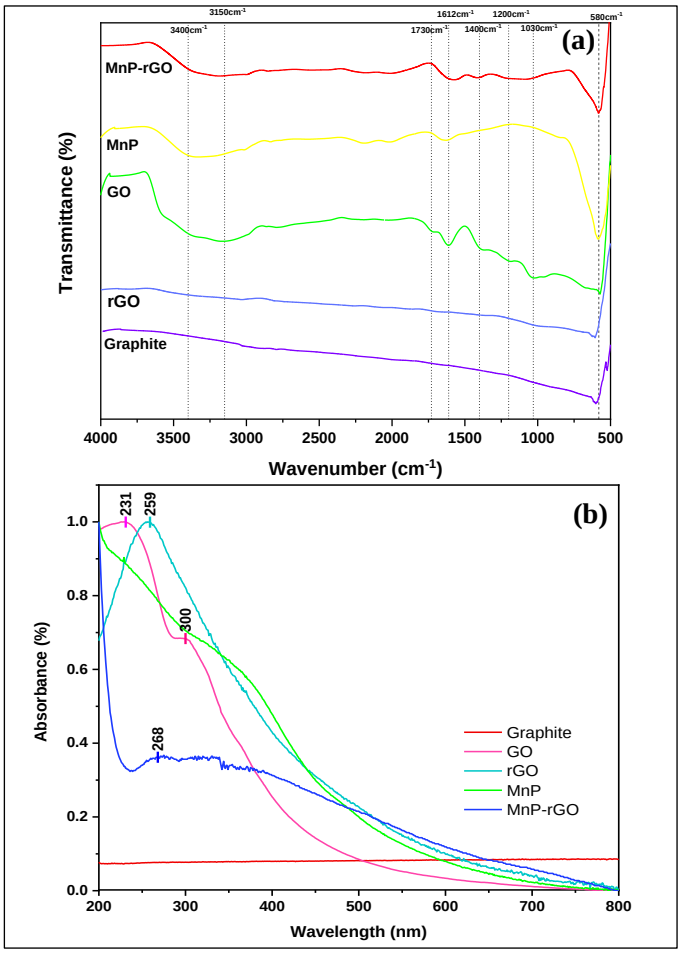


Figure 1. (a) FTIR spectrum and (b) UV-vis spectra of graphite, GO, rGO, Fe_3O_4 and Fe_3O_4/rGO nanocomposite

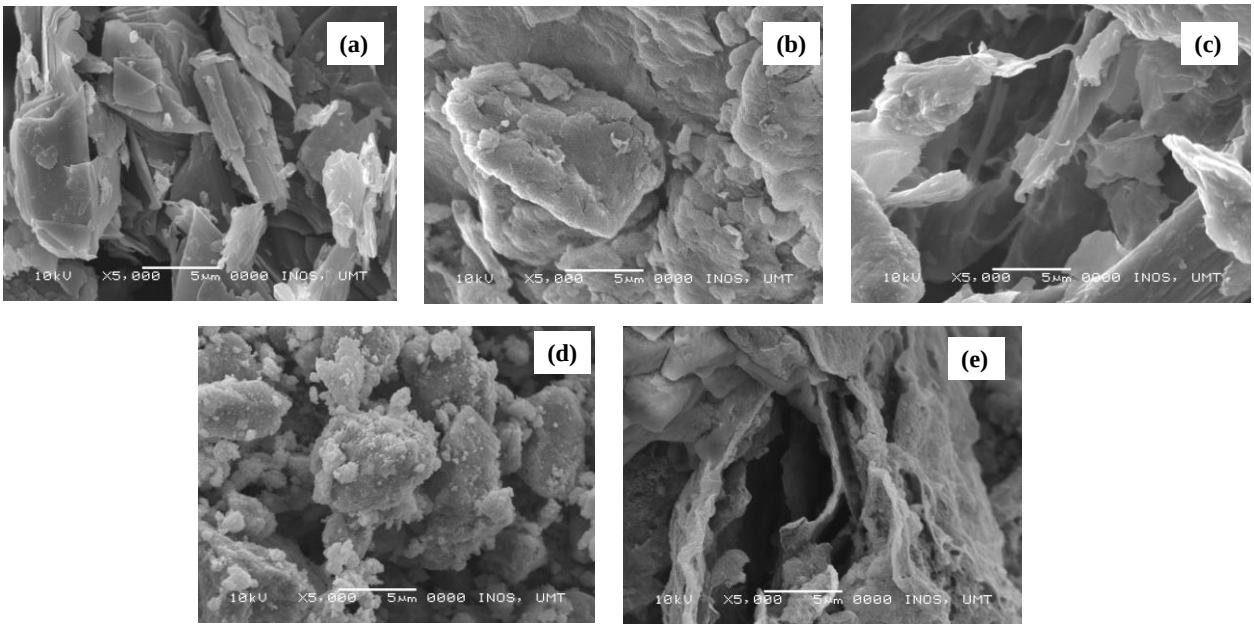


Figure 2. SEM micrographs of (a) graphite, (b) GO, (c) rGO, (d) Fe_3O_4, and (e) Fe_3O_4/rGO with magnification of x5000 and the operational voltage of 10 kV

Electrochemical characterization of Fe_3O_4/rGO

The electrochemical performance of Fe_3O_4/rGO was studied using cyclic voltammetry as Fe_3O_4/rGO/GCE modified electrode. For comparison purpose, bare GCE, rGO/GCE and Fe_3O_4/GCE were also studied. Each individual contribution to the observed electrochemical responses were compared in the presence of supporting electrolyte, 1.0 M KCl and 5 mM of redox probe agent, $K_4[Fe(CN)_6]$. The peak potential separation (ΔE_p) and the quasi-reversible behavior of the one-electron redox behavior of $[Fe(CN)_4]^{3-/4-}$ used as indicative measurement in determination of electrode surface improvement. From Figure 3(a), CV measurement on the bare GCE electrode in the presence of $[Fe(CN)_4]^{3-/4-}$ couple resulted both anodic I_{pa} and cathodic peak current I_{pc} at 391.4 mA and -384.4 mA , respectively. The ΔE_p measured for the bare GCE is 237.6mV. After surface modification of GCE with rGO and Fe_3O_4, the voltammetric response generated from both single Fe_3O_4 (I_{pa} = 455.3 mA, I_{pc} = -433.3 mA) and rGO (I_{pa} 524.2 mA, I_{pc} = -531.2 mA) coating material which show remarkable peak current increment with a lower ΔE_p profile as 219.8 mV and 184.8 mV respectively. The rGO supported Fe_3O_4 hybrid composite further enhanced the electrochemical activity, where the anodic and cathodic peak current increase to 629.6 mA and -627.4 mA, almost two folds increase compare to bare GCE. This integrated hybrid material dedicated as promising platform of superior conductivity and electrocatalytic performance in sharpening the electrochemical measurement response for electroactive species which describes the Fe_3O_4/rGO nanocomposites has the narrowest of ΔE_p (157.4 mV) among the other materials. The deviation from ideal ΔE_p value, 57 mV can be devoted to the incomplete chemical reversibility of redox couple, stability of analyte upon subjected to oxidation and subsequently reduced back to origin state, electron transfer kinetic rate, and existence of interfacial barrier [25]. On the basis of the slope measurement from Randles-Sevcik plot for ferrocyanide oxidation, the linear dependence of peak current, I_{pa} on the square root of scan rate can offer quantitative information about the effective surface area (EASA) and diffusion coefficient of the electroactive species. The proportional of Randles-Sevcik slope to the EASA was observed in the order of GCE > Fe_3O_4/GCE > rGO/GCE > Fe_3O_4/rGO/GCE as shown in Figure 3 (b). The improved electroactive surface areas of Fe_3O_4/rGO composite greatly highlights the excellent nature of surface layer deposited on GCE electrode overcome the performance achieved through rGO and Fe_3O_4, individually. Data obtained from CV information is simplified in Table 1.

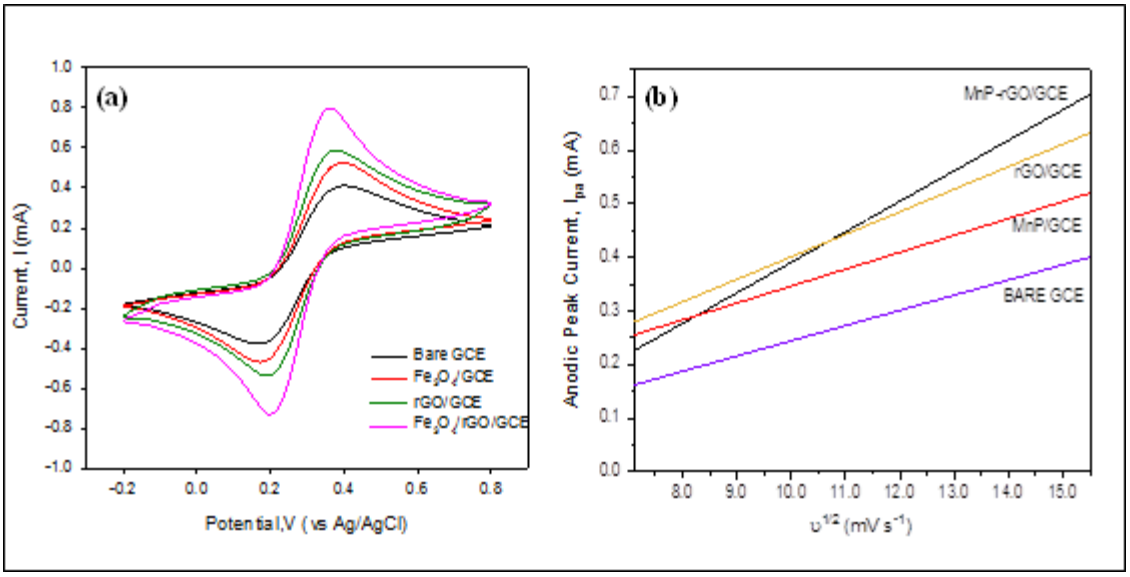


Figure 3. (a) Cyclic voltammogram of bare GCE, GO/GCE, rGO/GCE, Fe_3O_4/GCE, and Fe_3O_4/rGO/GCE (b) Randles-Sevcik Plot of different modified electrodes for EASA determination

Table 1. Peak potential separation for bare GCE and modified electrode in the presence of 1.0 M KCl and 5 mM redox probe solution

Electrodes	**I_{pa}, µA**	**I_{pc}, µA**	**E_{pa}, mV**	**E_{pc}, mV**	**ΔE_p, mV**	**Slope (10^{-5})**	**EASA, cm^{-2} (10^{-6})**
GCE	391.4	-384.4	409.9	172.3	237.6	2.84	8.48
Fe_3O_4/GCE	455.3	-433.3	394.8	175.0	219.8	3.16	9.42
rGO/GCE	524.2	-531.2	379.7	194.9	184.8	4.20	12.5
Fe_3O_4/rGO/GCE	629.6	-627.4	359.8	202.3	157.4	5.69	17.0

Electrochemical performance of Fe_3O_4/rGO/GCE in the presence of UA

The voltammetric responses of the Fe_3O_4/rGO/GCE toward UA detection and its application in different sensing environment was studied in the 0.1M PBS buffer solution of pH 7 containing 400 µM UA analyte. The electron transfer behavior through different sensing interface of electrode was studied using the same instrument configuration and parameter setups. The cyclic voltammograms of various modified electrodes in Figure 4 revealed the electrocatalytic performance of Fe_3O_4/rGO nanocomposite coated GCE outstands the other surface-modifed electrode. There was a minor difference in the anodic peak potential for the UA oxidation on various surface modified electrode. However, the rGO/GCE shows a higher current background baseline at the end of forward scan. This baseline signals was refined on the proposed Fe_3O_4/rGO/GCE, which assumed due to the depleted electrical double layer (EDL), and capacitance current accumulated at the charged electrode. The anodic peak current has been improved as much as 1.65 µA (81.28%) compared to bare GCE under the same 50 mVs^{-1} scan rate. The increment in the anodic peak current, I_{pa} was parallel to the calculated diffusion coefficient using the Randles-Sevcik equation shown in equation 1.

$$I_P = (2.69 \text{ X } 10^5)\, n^{3/2}\, A\, D^{1/2}\, C\, v \quad (1)$$

where n is the number of electron taking part in the redox reaction (n=2), A is the electroactive surface area, cm^2 (A = 0.08cm^2 respect to GCE), D as the diffusion coefficient, c is the bulk concentration, mol cm^{-3} (c = 4 X 10^{-4} mol cm^{-1}) and scan rate, V s^{-1} (v = 0.05 V s^{-1}) is denoted by v.

The Fe_3O_4/rGO/GCE modified electrode stands a better diffusivity (D = 4.57 x 10^{-13} cm^2 s^{-1}) compared to another modified electrode. Thus, it do allows faster rate of mass transport for UA molecules diffuses across the concentration gradient and bulk solution molecules near the surface of electrode in a voltammetric detection. The cyclic voltammogram of UA in 0.1 M PBS buffer solution show a typical observation, where only one anodic peak was recognized. It expressing that the undergoing reaction is of irreversible for UA reduction. This can be attributed to the characteristic of UA and its possible alternative oxidation pathway of the electrode process demonstrated in the Figure 4 (inset) [26]. The primary partially oxidized UA product is composed of 4,5-dihydroxyluric acid, which is liable to oxidative degradation in favor the formation of chemically stable allantoin molecules. The diffusion coefficient results from bare GCE and different surface-modified electrodes summarized in Table 2.

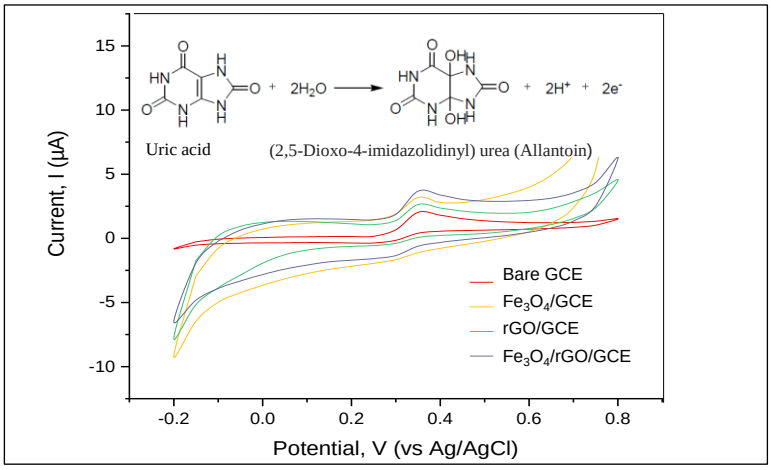


Figure 4. Cyclic voltammetric response of different surface-modified electrode in 400uM UA containing 0.1M PBS buffer solution (pH 7)

Table 2. The diffusion coefficient results from bare GCE and different surface-modified electrodes in 0.1M PBS solution (pH = 7) containing 400μM UA

Material (s)	**Anodic Peak Potential, E_{pa} (V)**	**Anodic Peak current, I_{pa} (μA)**	**Diffusion Coefficient, D (cm^2 s^{-1})/(10^{-13})**
Bare GCE	0.35	2.03	1.39
rGO	0.35	3.18	3.42
Fe_3O_4	0.35	2.64	2.35
Fe_3O_4-rGO	0.35	3.68	4.57

The optimum condition used to investigate the electrochemical behavior of UA was then performed based on the three parameters chosen for voltammetric detection purpose. The effect of scan rate, analyte concentration and pH of the supporting electrolyte were focused for any enhancement effect in the UA oxidation signal. The improved signal to noise ratio can be helpful in defining the UA content in the urine sample, which can be said equally important in recovery, precision and accuracy study that accounts for the repeatability as well as reproducibility. The conventional 3-electrode system was applied in parameter optimization with modified electrode Fe_3O_4/rGO/GCE as the working electrode and a 2 mm diameter platinum rod dedicated as counter electrode in complement to silver/silver chloride, Ag/AgCl (KCl=3.0M).

The scan rate selected for cyclic voltammetry detection of UA ranging from 50 $mVs^{-1`}$ to 250 mVs^{-1} with a 50 mVs^{1} as the increment constant at each running cycles (n = 6). The instrument calibration factor and diagnostic test was

performed before running the experiment. The electroanalysis profile selected in procedure and configuration was fixed with 5 mV step potential and starting potential of 0.15 V. The cyclic voltammogram displayed in Figure 5(a) revealed the effect of scan rate variation on the peak current recorded for the UA oxidation process. Table 3 depicted that increasing the scan rate from 50 mVs^{-1} to 250 mVs^{-1} positively shifts the peak potential from 0.356 V to 0.367 V. Correspondingly, the scan rate variation increases linearly with the diffusion coefficient, D calculated that facilitated the flux movement and diminishing of diffusion layer grow in an electrode process. This gradually shift in peak potential ascribed to UA oxidation implying the consequence of kinetic limitation happened between the active edges of the Fe_3O_4/rGO decorated on the GCE surface and UA molecules [24]. The linearity relationship between the peak current value recorded and variation of scan rate defined the characteristic of a surface adsorption-limiting process [27].

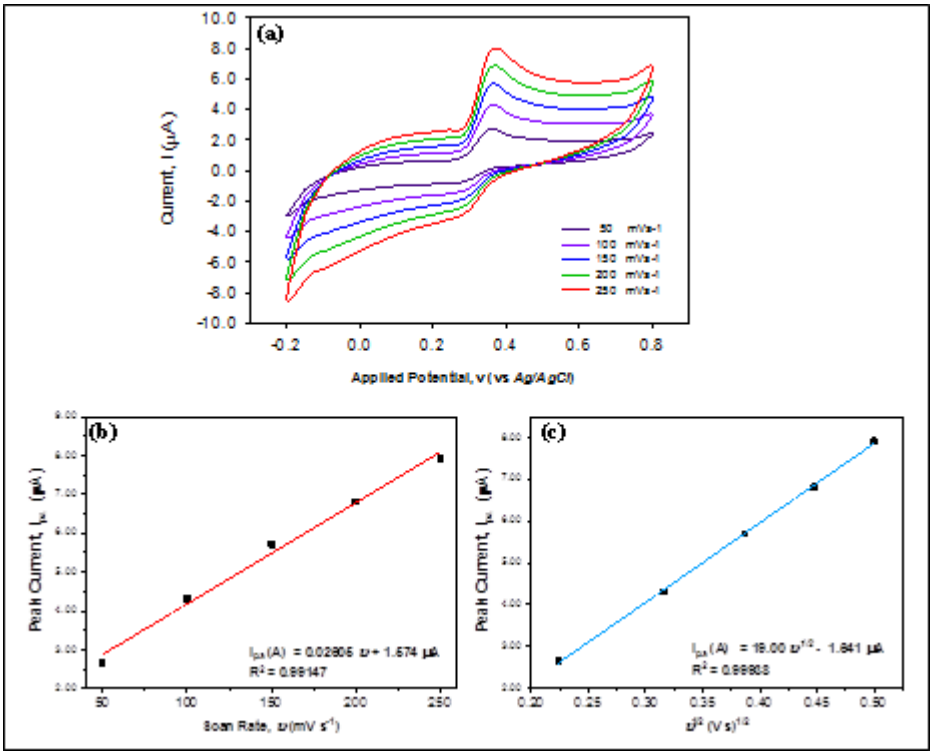


Figure 5. (a) Cyclic voltammogram of 400μM UA standard measured at different scan rate (50- 250mVs^{-1}) and (b) Plot of peak current against scan rate and (c) Randles-Sevcik plot for diffusion coeffient determination

Table 3. Scan rate variations and its related properties measurement result

Scan Rate ($mV\ s^{-1}$)	**Anodic Peak Potential, E_{pa} (v)**	**Anodic Peak Current, I_{pa} (A)/(10^{-6})**	**Square Root of Scan Rate ($V^{1/2}\ s^{-1/2}$)**	**Diffusion Coefficient ($cm^2\ s^{-1}$)/(10^{-13})**
50	0.356	2.65	0.224	2.378
100	0.359	4.32	0.316	6.290
150	0.362	5.70	0.387	10.97
200	0.364	6.81	0.447	15.66
250	0.367	7.92	0.500	21.17

The Figure 5(b) displayed the peak current is directly proportional to the scan rate with a linear regression equation of I_{pa} (A) = 2.605 x10^{-8} v + 1.574 x10^{-6} , R^2= 0.99147. Meanwhile, another identical relationship was illustrated in Figure 5 (c) which is a Randles-Revcik plot useful in effective surface area (EASA) and diffusion coefficient, D of a substrate molecule. A higher proportional linearity (R^2=0.99938) relationship was identified in the plots of anodic peak current (I_{pa}) against square root of scan rate variation ($v^{1/2}$) under the studied range of scan rate. The obtained regression equation I_{pa} (A) = 1.9 x10^{-5} $v^{1/2}$ – 1.641 x10^{-6} with correlation coefficient nearly to unity suggested the UA oxidation over the Fe_3O_4/rGO/GCE surface was diffusion-limiting dominated over the adsorption-controlled mechanism [28]. These results provided that the mass transfer or absorption controlled process of UA oxidation take place at the low scan rate instead of diffusion-limiting dominated at high scan rate [29]. The scan rate 50 mVs^{-1} was selected for the further part of the optimization where its peak potential was nearly to the zero. In view of the current response of UA is being diffusion controlled, a slower scan rate will allow the UA molecules diffuses through the bulk electrolyte toward the electrode surface. Even though there will be growth in the diffusion layer, it provides certain degrees of sensitivity and stability about the variation in peak current and peak-to-peak separation especially in the study of pH parameter optimization.

A series of UA standard concentration was selected within range from 100 µM to 800 µM. The experiment was designed to run 6 cycles simultaneously at 50 mVs^{-1} scan rate with a magnitude of 0.05 V step potential sweeping from initial potential -0.2 V to end potential 0.8 V. The reagent and standard preparations were kept constant as described previously. The step up current responses obtained from the increasing concentration of UA show a corresponding contribution of faradaic current from higher electroactive species in an electrode process. The respectively current response and peak potential variation according to the amount of UA introduced was tabulated in Table 4.

Table 4. Result of anodic peak potentials and peak currents at various UA concentrations (100-800 µM)

Concentration (s)	**Anodic Peak Potential, I_{pa} (V)**	**Anodic Peak Current, I_{pc} (µA)**
100	0.35	1.23
200	0.35	1.65
400	0.35	2.69
600	0.35	3.47
800	0.35	4.59

Based on the cyclic voltammogram result in Figure 6(a), the peak potential being unchanged for five successive different UA standard measurements at constant scan rate and experimental condition. This reflects good stability and accountability in measuring the current responses originated from various UA standard concentrations in suggested cyclic voltammetry technique. The calibration curve was plotted against the concentration of UA ranging from 100 µM to 800 µM provided a good fitting of data with correlation coefficient equal to 0.99711. The linearity behavior of UA concentration and anodic peak currents can be expressed as I_{pa} (A) = 4.757 x10^{-9} *c* + 7.270 x10^{-7}, as shown in the Figure 6 (b). The highest current achieved was 4.59 µA correspondingly to the highest upper limit of UA concentration, which is 80 0µM and the trend then followed in descending order of 600 µM (3.47 µA) < 400 µM (2.69µA) < 200 µM (1.65 µA) < 100 µM (1.23 µA). The result obtained implies that the Fe_3O_4/rGO nanocomposite manage to electrocatalyze the UA oxidation meanwhile current transport at the electrode surface facilitated by gapless conducting material of rGO due excellent electron conductivity [1, 7]. The preferential concentration for the following research purpose was chosen 400µM, which is the intermediate value at full concentration range of UA studied. It gives sharp and well-defined oxidative current peak of considerable good sensitivity and peak resolution.

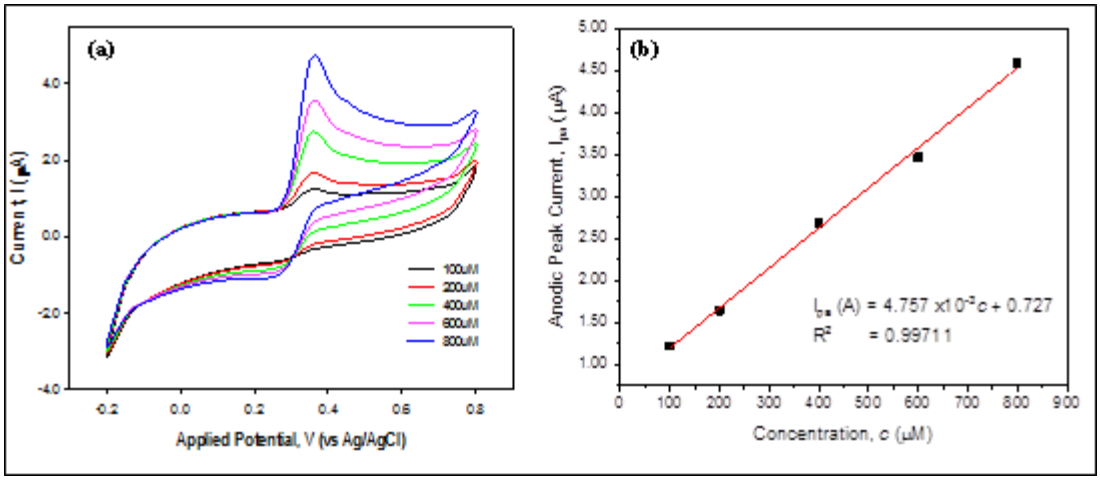


Figure 6. (a) Cyclic voltammetry measurements at various concentrations ranging from 100 μM to 500 μM of UA standard solution and (b) Calibration curve of anodic peak current against UA concentration (100-800 μM)

The effect of supporting electrolyte (PBS buffer solution) pH on the CV and DPV response of 400 μM UA were conducted by varying the pH from 4.0 to 9.0. The changes to the chemical environment surrounding the UA molecules in reaction of electrochemical oxidation was investigated in term of peak current and potential as well as the charging effect due electrolyte properties. Refers to Figure 7(a) and (b), the anodic peak potential shifts negatively as pH varying from 4.0 to 9.0 in both CV and DPV measurement. The DPV displays even higher sensitivity and selectivity as compared to typical CV technique due slow decay rate of capacitance current and non-faradaic current corresponds to the background current. These profound negative shifts suggested that the redox reaction of UA involved proton transferred at the Fe_3O_4-rGO modified electrode. The pH changes will affects the adsorption performance of Fe_3O_4/rGO, which can be rationalized based on the charge accumulation on the electroactive surface sites, degree of ionization of analyte, electrostatic repulsion or attraction between analyte and functionalized electrode surface [14, 30].

The uric acid solubilized in alkalizing solution presented majorly as deprotonated urate bearing an overall negative charged surface was repelled from redox site dominated by hydroxyl groups. Similarly, changes the pH from alkaline to acidic will neutralized the negative charged urate as non-ionized uric acid and the electrostatic attraction between the UA and Fe_3O_4-rGO/GCE surface was strengthen [31]. Figure 7(c), the pH selected was 7.0, which is neutral and assembles to normal urine pH of 6.0 to 7.5. The peak current measured in both CV and DPV techniques revealed that the pH selected is stable and high sensitivity in view of high peak currents and negligible interference. The results obtained was summarized in Table 5. The plot of anodic peak potential versus pH in Figure 7(d) expressed linearity (R^2 = 0.99509) in the pH range of 4 to 9 with a slope of -56 mV pH^{-1}, which closely approximate to the theoretical Nernst equation value (-59mV pH^{-1}). This again implies that the electrochemical oxidation of UA involves an equivalent number (n=2) of electron and proton [24, 31].

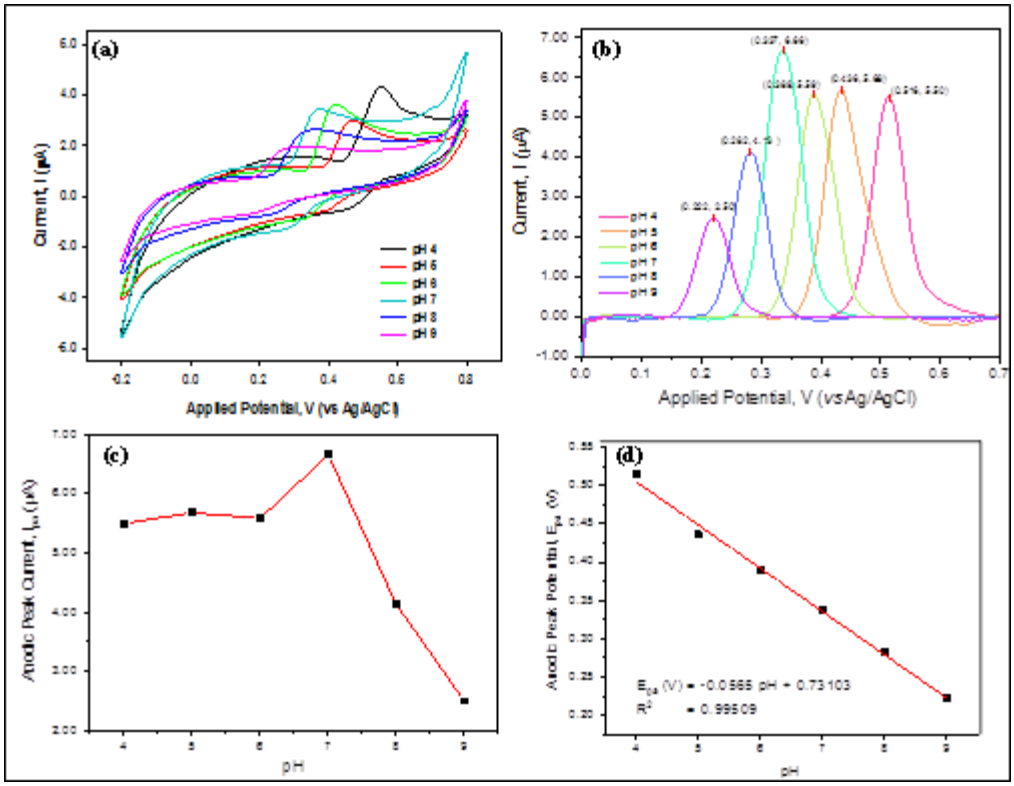


Figure 7. (a) Influences of electrolyte pH on the oxidative peak current of UA in cyclic voltammogram, (b) DPV response toward UA determination according to pH changes from 4.0 to 9.0, (c) Plot of peak current against pH value of the supporting electrolyte (0.1M PBS solution) and (d) Plot of anodic peak potential against pH value of the supporting electrolyte (0.1M PBS solution)

Table 5. Peak current and potential values correspond to the pH variation

pH	Cycic voltmammetric Response(s)		Differential Pulse Voltammetric Response(s)	
	Peak Potential, E_p (V)	Peak Current, I_p (μA)	Peak Potential, E_p (V)	Peak Current, I_p (μA)
4	0.553	4.34	0.515	5.50
5	0.470	3.03	0.436	5.68
6	0.424	3.64	0.389	5.59
7	0.373	3.48	0.337	6.66
8	0.337	2.57	0.282	4.13
9	0.262	1.79	0.222	2.50

Limit of detection (LOD) and Limit of Quantification (LOQ)

The LOD and LOQ calculated are 3.04 μM and 10.14 μM, respectively, which is comparable, excellent and suitable for UA content determination compared to the previous study tabulated in Table 6.

Table 6. Comparison of current work with the previous study of uric acid determination

Electrode	Detection Method	Detection Limit (μM)	References
Pani/AuNPs	DPV	20.0	[32]
ZnO/rGO	DPV	8.5	[33]
AgNPs/rGO	DPV	8.2	[34]
Modified GCE (0.5M NaOH solution)	DPV	4.7	[35]
Fe_3O_4/rGO	DPV	3.04	Current work

Additionally, the current response proportional increases with the UA concentration added into the phosphate buffer solution of pH 7. In the lower range of concentration, the linear regression equation obtained was $I_{pa}(A) = 8.477 \times 10^{-8} c + 8.43743 \times 10^{-6}$ with a correlation coefficient of 0.989 and sensitivity of 0.08478 μA/μM. In the second linear dynamic segment, the linearity was expressed as $I_{pa}(A) = 6.631 \times 10^{-9} c + 1.65937 \times 10^{-5}$ with a $R^2 = 0.953$ correspond to higher UA concentration ranging from 100 μM to 800 μM (Figure 8b). The declination in sensitivity (slope) at higher magnitude of concentration was described by the kinetic limitation of electroactive species toward the Fe_3O_4/rGO/GCE surface in a transport mechanism [7, 36]. A surge amount of oxidation products inhibits the adsorption site for electrocatalytic oxidation of UA, thereby resulting lower down the electrode response sensitivity to 0.00663 μA/μM.

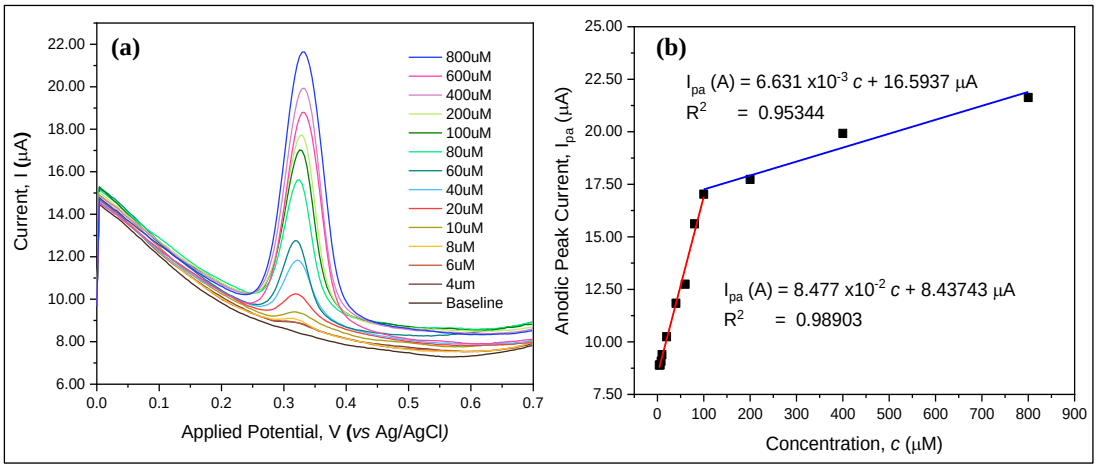


Figure 8. (a) DPV response measured over a range of UA concentration from 0 μM to 800 μM and (b) The relationship between the oxidation peaks current against UA concentration (4-800 μM)

Conclusion

The Fe_3O_4/rGO hybrid material had successfully synthesized through one facile reduction of GO and co-precipitation of Fe_3O_4 which accounts for high percentage yield of product, cost effectiveness and being environmental green catalytic composite. The enhanced electrocatalytic performance of the Fe_3O_4/rGO/GCE electrode provides a comprising potential in voltammetry determination of physiologically related molecules such as ascorbic acid and dopamine. The Cyclic Voltammetry (CV) result in the previous part has revealed the improved electronic properties of the resultant nanocomposite in term of the low resistivity, rapid electron transfer, and well defined peak resolution as well as peak separation. In additional, the physical properties of as-synthesized Fe_3O_4/rGO nanocomposite was successfully investigated by various characterization techniques, including Fourier Transform Infrared Spectroscopy (FTIR), Ultraviolet-visible Spectroscopy (UV-Vis), Scanning Electron

Microscopy (SEM). The Differential Pulse Voltammetry (DPV) was used in complementary to the application CV and EIS in electrochemically characterization of Fe_3O_4/rGO nanocomposite. The Fe_3O_4-rGO/GCE sensing electrode exhibits high selectivity and sensitivity in UA oxidation with low detection limit of 3.04 μM. The results suggested the great potential use of Fe_3O_4/rGO/GCE in selectively non-enzymatic sensing of UA as compared to conventional UA determination such as chromogen-dependent colorimetric method and enzymatic technique by uricase.

Acknowledgement

The authors are grateful to Fundamental Research Grant Scheme (FRGS) FRGS/1/2017/STG01/UMT/02/2 for financial support as well as Universiti Malaysia Terengganu for providing facilities for undertaking this research.

References

1. Wang, H., Ren, F., Wang, C., Yang, B., Bin, D., Zhang, and Du, Y. (2014). Simultaneous determination of dopamine, uric acid and ascorbic acid using a glassy carbon electrode modified with reduced graphene oxide. *RSC Advances*, 4(51): 26895–26901.
2. So, A. and Thorens, B. (2010). Science in medicine uric acid transport and disease. *The Journal of Clinical Investigation*, 120(6): 1791–1799.
3. Muraoka, S. and Miura, T. (2003). Inhibition by uric acid of free radicals that damage biological molecules. *Pharmacology and Toxicology*. 93 (6): 284–289.
4. Lavanya, N., Fazio, E., Neri, F., Bonavita, A., Leonardi, S.G., Neri, G. and Sekar, C. (2015). Simultaneous electrochemical determination of epinephrine and uric acid in the presence of ascorbic acid using SnO_2 graphene nanocomposite modified glassy carbon electrode. *Sensors and Actuators B: Chemical*, 221: 1412–1422.
5. Jiang, J. and Du, X. (2014). Sensitive electrochemical sensors for simultaneous determination of ascorbic acid, dopamine, and uric acid based on Au@Pd-reduced graphene oxide nanocomposites. *Nanoscale*, 6 (19): 11303–11309.
6. Teymourian, H., Salimi, A. and Khezrian, S. (2013). Fe_3O_4 Magnetic nanoparticles/reduced graphene oxide nanosheets as a novel electrochemical and bioeletrochemical sensing platform. *Biosensors and Bioelectronics*, 49: 1–8.
7. Peik-See, T., Pandikumar, A., Nay-Ming, H., Hong-Ngee, L. and Sulaiman, Y. (2014). Simultaneous electrochemical detection of dopamine and ascorbic acid using an iron oxide/reduced graphene oxide modified glassy carbon electrode. *Sensors*, 14(8): 15227–15243.
8. Zheng, D., Hu, H., Liu, X. and Hu, S. (2015). Application of graphene in elctrochemical sensing. *Current Opinion in Colloid and Interface Science*, 20 (5–6): 383–405.
9. Chandra, V., Park, J., Chun, Y., Lee, J. W., Hwang, I. C. and Kim, K. S. (2010). Water-dispersible magnetite-reduced graphene oxide composites for arsenic removal. *ACS Nano*, 4(7): 3979–3986.
10. Farghali, M., Material, A., Salah, T. and Al-enizi, A. M. (2014). Graphene/magnetite nanocomposite for potential environmental application. *International Journal of Electrochemical Sciences*, 10: 529–537.
11. Yusoff, F., Ngai, T. Z., Chai, C. H. and Lee, P. S. (2018). The electrochemical behavior of zinc oxide/ reduced graphene oxide composite electrode in dopamine. *Malaysian Journal of Analytical Sciences*, 22 (2): 227–237.
12. Andrijanto, E., Shoelarta, S., Subiyanto, G. and Rifki, S. (2016). Facile synthesis of graphene from graphite using ascorbic acid as reducing agent. *AIP Conference Proceedings*. 1725: 020003.
13. Yusoff, F. and Mohamed, N. B. (2018). The physical and electrochemical characteristic of gold nanoparticles supported pedot/graphene composite as potential cathode material in fuel cells. *Malaysian Journal of Analytical Sciences*, 22(6): 921–930.
14. Thi, N., Hoan, V., Thu, A., Duc, H. Van, Cuong, N. D., Khieu, D. Q.,Vo, V., Vuong, N. T. and Vn, H. (2016). Fe_3O_4/reduced graphene oxide nanocomposite: Synthesis and its application for toxic metal ion removal. *Journal of Chemistry*, 2016: 1–10.
15. Mahmood, H., Habib, A., Mujahid, M., Tanveer, M., Javed, S. and Jamil, A. (2014). Band gap reduction of titania thin films using graphene nanosheets. *Materials Science in Semiconductor Processing*, 24(1): 193–199.
16. Wang, A., Yu, W., Huang, Z., Zhou, F., Song, J., Song, Y., Long, L., Cifuentes, M. P., Humphrey, M. G., Zhang, L., Shao, J. and Zhang, C. (2016). Covalent functionalization of reduced graphene oxide with porphyrin by means of diazonium chemistry for nonlinear optical performance. *Scientific Reports*, 6: 1–12.

17. Li, Q., Kartikowati, C. W., Horie, S., Ogi, T., Iwaki, T. and Okuyama, K. (2017). Correlation between particle size/domain structure and magnetic properties of highly crystalline Fe_3O_4 nanoparticles. *Scientific Reports*, 7(1): 1–4.
18. Rajput, S., Pittman, C. U., and Mohan, D. (2016). Magnetic magnetite (Fe_3O_4) nanoparticle synthesis and applications for lead (Pb^{2+}) and chromium (Cr^{6+}) removal from water. *Journal of Colloid and Interface Science*, 468: 334–346.
19. Kamakshi, T., Sundari, G. S., Erothu, H. and Rao, T. P. (2018). Synthesis and characterization of graphene based iron oxide (Fe_3O_4) nanocomposites. *Rasayan Journal of Chemistry*, 11(3): 1113–1119.
20. Yang, S., Yue, W., Huang, D., Chen, C., Lin, H. and Yang, X. (2012). A facile green strategy for rapid reduction of graphene oxide by metallic zinc. *RSC Advances*, 2(23): 8827-8832.
21. Xue, Y., Chen, H., Yu, D., Wang, S., Yardeni, M., Dai, Q., Guo, M., Liu Y., Lu, F., Qu, J. and Dai, L. (2011). Oxidizing metal ions with graphene oxide: the in situ formation of magnetic nanoparticles on self-reduced graphene sheets for multifunctional applications. *Chemical Communications*, 47(42): 11689–11691.
22. Dimiev, A. M. and Tour, J. M. (2014). Mechanism of graphene oxide formation. *ACS Nano*, 8 (3): 3060–3068.
23. Aneesh, P. K., Nambiar, S. R., Rao, T. P. and Ajayaghosh, A. (2014). Electrochemically synthesized partially reduced graphene oxide modified glassy carbon electrode for individual and simultaneous voltammetric determination of ascorbic acid, dopamine and uric acid. *Analytical Methods*, 6(14): 5322–5330.
24. Hariani, P.L., Faizal, M., Ridwan, R., Marsi, M., and Setiabudidaya, D. (2013). Synthesis and Properties of Fe_3O_4 Nanoparticles by Co-precipitation Method to Removal Procion Dye. *International Journal of Environmental Science and Development*. 4 (3): 336–340.
25. Elgrishi, N., Rountree, K. J., McCarthy, B. D., Rountree, E. S., Eisenhart, T. T., and Dempsey, J. L. (2018). A practical beginner's guide to cyclic voltammetry. *Journal of Chemical Education*, 95(2): 197–206.
26. Chao, M., Ma, X. and Li, X. (2012). Graphene-modified electrode for the selective determination of uric acid under coexistence of dopamine and ascorbic acid. *International Journal of Electrochemical Science*, 7(3): 2201–2213.
27. Yusoff, F., Aziz, A., Mohamed, N., and Ab Ghani, S. (2013). Synthesis and characterizations of BSCF at different pH as future cathode materials for fuel cell. *International Journal of Electrochemical Science*. 8 (8): 10672–10687.
28. Yusoff, F., Mohamed, N., Azizan, A. and Ab Ghani, S. (2016). The perovskite $Ba_{0.5}Sr_{0.5}Co_{0.2}Fe_{0.8}O_{3-}$MWCNT modified glassy carbon electrode - its characterization and capacity in oxygen reduction reaction. *International Journal of Electrochemical Science*, 11(7): 5766–5780.
29. Tukimin, N., Abdullah, J. and Sulaiman, Y. (2017). Development of a PrGo-modified electrode for uric acid determination in the presence of ascorbic acid by an electrochemical technique. *Sensors (Switzerland)*. 17 (7): 1539.
30. Sun, H., Cao, L. and Lu, L. (2011). Magnetite/reduced graphene oxide nanocomposites: one step solvothermal synthesis and use as a novel platform for removal of dye pollutants. *Nano Research*, 4(6): 550–562.
31. Zhang, W., Chen, J., Li, Y., Yang, W., Zhang, Y. and Zhang, Y. (2017). Novel UIO-66-NO2@XC-72 nanohybrid as an electrode material for simultaneous detection of ascorbic acid, dopamine and uric acid. *RSC Advances*, 7(10): 5628–5635.
32. Stoyanova, A., Ivanov, S., Tsakova, V. and Bund, A. (2011). Au nanoparticle-polyaniline nanocomposite layers obtained through layer-by-layer adsorption for the simultaneous determination of dopamine and uric acid. *Electrochimica Acta*, 56(10): 3693–3699.
33. Yusoff, F., Lee, P.S, and Noorashikin, M.S. (2018). The electroxidation of uric acid at zinc oxide/reduced graphene oxide composites modified electrode. *AIP Conference Proceeding.* 2031:1-6. Kaur, B., Pandiyan, T., Satpati, B. and Srivastava, R. (2013).
34. Simultaneous and sensitive determination of ascorbic acid, dopamine, uric acid, and tryptophan with silver nanoparticles-decorated reduced graphene oxide modified electrode. *Colloids and Surfaces B: Biointerfaces*, 111: 97–106.
35. Wang, Y. and Tong, L. L. (2010). Electrochemical sensor for simultaneous determination of uric acid, xanthine and hypoxanthine based on poly (bromocresol purple) modified glassy carbon electrode. *Sensors and Actuators, B: Chemical*, 150(1): 43-49.

36. Khamlichi, R. El, Bouchta, D., Anouar, E. H., Atia, M. Ben, Attar, A., Choukairi, M., Tazi, S., Ihssane, R., Faiza, C., Khalid, D. and Khalid, R. T. (2017). A novel l-leucine modified sol-gel-carbon electrode for simultaneous electrochemical detection of homovanillic acid, dopamine and uric acid in neuroblastoma diagnosis. *Materials Science and Engineering C*, 71: 870–878.

Malaysian Journal of Analytical Sciences, Vol 23 No 3 (2019): 423 - 435
DOI: https://doi.org/10.17576/mjas-2019-2303-06

MALAYSIAN JOURNAL OF ANALYTICAL SCIENCES
Published by The Malaysian Analytical Sciences Society
ISSN 1394 - 2506

VALIDATION ON CARBON DIOXIDE HYDRATE FORMATION THROUGH ANALYSIS ON THE SOLUBILITY OF CO_2 IN WATER USING HENRY'S LAW AND THE EXPERIMENTAL PRESSURE-TIME CURVE

(Mengesahkan Pembentukan Hidrat Karbon Dioksida Melalui Kajian Terhadap Kadar Keterlarutan CO_2 di dalam Air Menggunakan Hukum Henry dan Graf Tekanan-Masa)

Mohd Hafiz Abu Hassan[1]*, Colin Edwards Snape[2], Lee Stevens[2]

[1]*Faculty of Science and Technology,*
Islamic Science University of Malaysia, Bandar Baru Nilai, 71800 Nilai, Negeri Sembilan, Malaysia
[2]*Cleaner Fossil Energy and Carbon Capture Technologies Research Group, Faculty of Engineering,*
University of Nottingham, NG7 2TU Nottingham, United Kingdom

**Corresponding author: mhafiz.a.h@usim.edu.my*

Received: 21 September 2017; Accepted: 3 May 2019

Abstract

A rise of 2 ^oC in the Earth's temperature is likely to occur when the concentration of carbon dioxide (CO_2) in the atmosphere reaches approximately 450 ppm. CO_2 emissions are closely related to the continual use of fossil fuels. In order to make fossil fuels sustainable, carbon capture and storage (CCS) is required to reduce CO_2 emissions. CO_2 hydrate (CO_2:$6H_2O$) formation has been investigated as a way to capture CO_2. The formation of hydrate in this work was experimentally investigated in batch mode inside a vertical fixed-bed reactor (FBR), also known as high-pressure volumetric analyser (HPVA). Standard silica gel with an average particle size of 200–500 µm, mean pore size of 5.14 nm, a pore volume of 0.64 cm^3/g, and a surface area of 499 m^2/g was used as a porous medium. The presence of hydrate in FBR was justified by using graphic methods. The solubility of CO_2 in water using Henry's law and the experimental pressure–time (P-t) curve were analysed to determine the formation of hydrate. Hydrate formation was confirmed when the mole fraction of CO_2 dissolved in water exceeded the Henry's law value as well as a two-stage pressure drop in the experimental P-t curve.

Keywords: greenhouse effect, carbon dioxide hydrate, silica gel, Henry's law, pressure-time curve

Abstrak

Kenaikan suhu bumi sebanyak 2 ^oC berkemungkinan terjadi apabila kandungan karbon dioksida di persekitaran mencapai lebih kurang 450 ppm. Pembebasan CO_2 berkait rapat dengan penggunaan bahan api fosil yang berterusan. Bagi menghasilkan bahan api fosil yang mampan, simpanan dan perangkap karbon (CCS) diperlukan untuk mengurangi pelepasan CO_2. Formasi CO_2 hidrat telah dikaji untuk memerangkap CO_2. Pembentukan hidrat telah dikaji untuk memerangkap karbon dioksida melalui eksperimen yang dijalankan menggunakan reaktor (FBR), juga dikenali sebagai penganalisa volumetrik tekanan tinggi (HPVA). Gel silika dengan purata saiz 200–500 µm, purata diameter liang 5.14 nm, isipadu liang 0.64 cm^3/g, dan luas permukaan 499 m^2/g telah digunakan sebagai medium untuk pembentukan hidrat. Pembentukan hidrat di dalam reaktor disahkan melalui kaedah analisis graf. Kadar keterlarutan CO_2 di dalam air dan graf tekanan-masa dikaji untuk menentukan pembentukan hidrat. Pembentukan hidrat disahkan apabila bilangan mol CO_2 yang larut di dalam air melebihi nilai hukum Henry dan juga dua peringkat penurunan tekanan dapat dilihat dalam lengkung experimen P-t.

Kata kunci: kesan rumah hijau, hidrat karbon dioksida, gel silica, hukum Henry, graf tekanan-masa

Introduction

Human activities since the Industrial Revolution, such as burning coal, natural gas, and oil, to power machines for manufacturing and transportation have now increased the concentration of CO_2 (type of greenhouse gases) in the atmosphere, intensifying the natural warming caused by the greenhouse effect [1]. Biello reported that CO_2 levels in the atmosphere have reached 400 ppm for the first time in at least 800,000 years [2], which is far above the value recorded before the Industrial Revolution: 280 ppm [1]. Biello also stated that global temperatures are estimated to rise by 2 ^{o}C if the concentration of CO_2 in the atmosphere reaches 450 ppm [2].

With the persistent use of fossil fuels, the capture of CO_2 needs to be considered [3] where International Energy Agency (IEA) highlighted that carbon capture and storage (CCS) has been a favorable mitigation against climate change by 2050 [4]. There are three leading technologies for CO_2 capture, namely post-combustion capture, pre-combustion capture at IGCC plants, and oxy-fuel combustion. Post-combustion capture can be attained in the flue gas stream emitted from conventional steam power plants, entailing the separation of CO_2 from the flue gas mixture. Oxy-fuel combustion is a process where a fuel is combusted with oxygen (O_2) in a nitrogen (N_2)-free environment to produce a flue/exhaust gas consisting of CO_2 and water (H_2O). While the main concept of pre-combustion is to produce fuel gas containing mostly CO_2 and H_2 (an attractive future clean energy source) emitted in the range between 283–290 K at a pressure range of 20–70 bar [5].

D'Alessandro et al. [6] highlighted several promising new materials for CO_2 capture methods such as physical or chemical absorbents, adsorption of solids, cryogenic systems, membranes, hydrate-based gas separation (HBGS), and chemical looping combustion by metal oxides. HBGS is one of the most promising approaches in CO_2 capture field [7–10]. This CO_2 capture method involves clathrate or gas hydrate crystallization and can be applied to both post- (from flue gas) and pre-combustion (from fuel gas) capture, respectively. However, the HBGS process is more suitable for pre-combustion CO_2 capture from a fuel gas mixture than a flue gas mixture because the partial pressure of the shifted fuel gas (40% CO_2 and 60% H_2) is up to 1,000 times higher than that of the flue gas (17% CO_2 and 83% N_2) in post-combustion capture [11]. Thus, HBGS has been chosen in this study because the CO_2 hydrate formation is a continuous operation, thus making it possible to treat a large amount of gaseous stream, recovering more than 99 mol% of CO_2 from the fuel gas [12].

The HBGS process relies on the ability of water to form non-stoichiometric crystalline compounds in the presence of CO_2, N_2, O_2, and H_2, as well as natural gas components at high pressures (10–70 bar) and low temperatures (near 273 K) [6]. Mainly, there are three conditions necessary for hydrate formation to occur: (i) low temperature and high pressure are needed for these solid compounds to form from pure water, depending on the physical and chemical properties of the guest molecule; (ii) guest molecules must be present such as methane, ethane, or carbon dioxide; (iii) a sufficient amount of water, not too much and not too little [13]. Carrol [13] also stated that the CO_2 hydrate formation conditions are in the range of 273.15–283 K at the pressure range of 12.7–45 bar, wherein this is the case for a pure CO_2 system. A number of techniques have been investigated by researchers to capture CO_2 with gas hydrate formation by implementing the most traditional way (bulk water), solid adsorbent (porous medium), and promoters (oxygenated solvents, surfactants, semi-clathrate hydrate, and hydrophobic former). However, the focus of this study was to justify the formation of hydrate inside fixed-bed reactor (FBR) or HPVA, wherein silica gel was used as a solid adsorbent (porous medium) to omit the need of stirring process inside the reactor.

Most of the experiments that used silica saturated with water inside FBR have shown greater CO_2 uptake as compared to bulk water in a stirred tank reactor (STR). Adeyemo et al. [14] investigated clathrate crystallization in a silica gel column from fuel gas mixture at the operating conditions of 272.15 K and 70 bars, respectively. Three different silica gels were used (gel 1 with a pore size of 30 nm and particle size of 40–75 μm; gel 2 with a pore size of 100 nm and particle size of 40–75 μm; gel 3 with a pore size of 100 nm and particle size of 75–200 μm) and the highest CO_2 composition in hydrate was observed for gel 3 around 92 mol% (CO_2 uptake of 2 mmol of CO_2 per g of H_2O). Kumar et al. [15] employed three types of silica gel (mesh size of 60–120 (type A), 100–200 (type B), and 230–400 (type C)), which had almost similar pore diameters and different surface areas with type C having the highest surface area and type A the lowest. The CO_2 uptake obtained at 274 K and 36 bars in pure CO_2 indicated silica gel with larger surface area (type C) led to the higher gas consumption as well as reduced the induction time.

The conversion of water to hydrate for type C was 50 mol%, which was 20% higher than type B and almost 50% higher than type A.

Park et al. [16] studied the hydrate phase equilibria for the fuel gas and water mixtures inside various sizes of silica gel pores and concluded that silica gel with the highest pore diameter exhibited the best driving force for hydrate formation that was close to the bulk water. They mentioned that the capillary effect due to the presence of geometrical constraints caused the equilibrium lines to be shifted to the inhibition region, which was to the left side of the bulk water system. They added that this effect was more significant at smaller pore sizes (6.0 nm) due to the decreased activity of water caused by the partial ordering and bonding of water molecules with hydrophilic surfaces of pores. Kang et al. [17] conducted an investigation on three different silica gel pores (25 nm, 100 nm, and 250 nm) at the operating conditions of 274.15 K and 60 bar, and the observed phase equilibria justified the statement made by Park et al. [16] in which silica gel with pore size of 25 nm demonstrated the highest inhibition effect.

Babu et al. [12] employed silica sand (average pore diameter of 329 µm and pore volume of 0.22 cm^3/g) and silica gel (average pore diameter of 100 nm and pore volume of 0.83 cm^3/g) as the solid beds in the reactor to explore the formation of hydrate from fuel gas mixture at the operating temperature of 274.15 K and three different pressures (75 bar, 85 bar, 90 bar). Silica sand demonstrated better CO_2 capture capability with a 36 mol% conversion of water to hydrate which was almost two-thirds higher than silica gel. Further work on silica sand was performed by Mekala et al. [18] at different particle sizes (0.16 mm, 0.46 mm, and 0.92 mm), wherein 0.46 mm silica sand was found to have the optimum CO_2 uptake and rate of hydrate formation. Other than silicas, there are two more solid adsorbents being investigated by the researchers in the HBGS field, which are zeolites [18–21] and glass beads [22]. Xiaoya et al. [19] proved that the formation of CH_4 hydrate inside zeolite A-type pores is possible. Zhong et al. [20] conducted an investigation using zeolite 13X in FBR for the HBGS process from a CO_2/CH_4 gas mixture (40 mol% CO_2 and 60 mol% CH_4) at 277.15 K and in the pressure range of between 52–67 bar. They found that hydrate growth in the fixed-bed zeolite 13X was improved as the driving force increased from 25 bar to 40 bar. However, the comparison with STRs showed that the selectivity towards hydrate formation was lower for the fixed bed of zeolite 13X due to the massive moisture content available inside the pores, which increased the geometrical constraint or capillary effect [17]. Hence, they concluded that zeolite 13X can be used to enhance hydrate formation, but may not be a proper candidate for CO_2 capture from the CO_2/CH_4 gas mixture.

Recently, a number of parameters have been investigated to improve the gas uptake of hydrate formation inside the FBR, such as altering porous medium parameters used inside the reactor, varying the concentration of promoters, and employing different types of reactor orientations. Also, a majority of the researchers has used batch mode [23] to investigate hydrate formation in fuel gas mixture as an alternative to semi-batch mode. Additionally, Babu et al. [24] said that for the commercialization of HBGS, the use of FBR in batch mode was proposed by Babu et al. [25] which is similar to an industrial process namely Skarstrom cycle [26]. Also, they said this HBGS cycle can be conducted in a four step batch process namely, pressurization, hydrate formation, depressurization or thermal stimulation (H_2 rich), and hydrate decomposition (CO_2 rich). Moreover, Babu et al. [25] said the proposed cycle involves two fixed-bed columns and enables a continuous operation similar to how a pressure swing adsorption cycle would operate [27].

Additionally, Babu et al. [8] managed to observe hydrate formation by employing 5.53 mol% THF and 0.3 mol% TBAB in batch mode (1.5 cm bed height of silica sand), respectively, at 279 K and 60 bars. Then, Zheng et al. [7] managed to obtain CO_2 uptake of 2.4 mmol of CO_2 per g of H_2O at 283 K and 60 bars by employing 5.56 mol% THF inside a horizontal batch FBR (100 nm silica sand was used as porous media). They also discovered that this horizontal orientation had 1.5 times higher gas uptake as compared to the common (vertical) orientation. This new finding demonstrates the continuous interest by researchers to ensure that CO_2 hydrate can be used as a promising method for CCS by exploiting the advantages of porous medium in FBR such as those examined in this work by employing the HPVA. However, because of its limitation in which the formation of hydrate could not be seen directly by the eyes, there was no hydrate formation investigation being performed by using the HPVA previously. Thus, two approaches were used to justify the formation of hydrate in this work: analysis of P-t curves [28] and study of CO_2 dissolution in water suggested by Servio et al. [29].

Theoretically, the mechanism of hydrate formation can be described through a P-t curve, as explained by Tang et al. [28] with three phases: dissolution, nucleation, and hydrate growth. The decrease in the initial pressure of the system indicates the dissolution phase of hydrate formation, wherein labile cluster will form immediately. Later, the pressure becomes constant, indicating the nucleation phase of hydrate formation where labile clusters will agglomerate to form dodecahedral, tetrakaidecahedral, or hexakaidecahedral clusters. Finally, when the size reaches a critical value, growth begins. The hydrate growth phase is represented by subsequent curve/s that can be observed after the nucleation phase on the P-t curve. Thus, this will be a basic guideline to determine the formation of CO_2 hydrate in this work together with the study on CO_2 dissolution in water, wherein Servio et al. [29] plotted the equilibrium mole fraction of CO_2 in water in the presence of hydrate at various operating temperatures and pressures. This study will help validate the formation of hydrate inside any reactor where visuality is the main issue, as experienced in this work through the HPVA.

Materials and Methods

Materials and apparatus

Standard silica gel [21, 23, 31] was purchased from Fisher Scientific. CO_2 gas with a purity of 99.99% (maximum 103 bar), He gas with purity of 99.99% (34.4 bar) for venting or cleaning purposes, and N_2 gas/compressed air (5.2–5.5 bar) to control the pneumatic valves of the HPVA were supplied by BOC (a member of the Linde Group). All the materials were used without further purification.

The high-pressure volumetric analyser (model HPVA-100) that consists of constant temperature bath or water bath, vacuum pump, and degassing unit was manufactured by Micromeritics. The oven used (Model AX30) was manufactured by Carbolite and has a maximum temperature of 250 ^oC and a minimum temperature of 40 ^oC. The weighing balance (Model: AEA – 220A) used was manufactured by AE Adam and it can measure a maximum mass up to 220 g and a minimum mass of 10 mg. The high-speed blender was used to vigorously mixed silica gel with water [21, 23, 31].

Sample preparation method

Silica gel was initially dried inside the oven for one night at 200 ^oC. Dry silica gel (0.5 g) was placed inside blender and water was added in excess (19 times the mass of dry silica gel) so that the total mass of the mixture was 50 g. The silica gel and water mixture were vigorously stirred at the speed of 37000 rpm [30, 31] for 90 seconds using a high-speed blender. Then, the mixture was left at atmospheric condition until the final mass reached equilibrium. Finally, the amount of equilibrium moisture content inside silica gel pores was measured by using a degassing unit. The amount of water content was necessary to calculate the final conversion of water to CO_2 hydrate.

CO_2 hydrate formation

The system was manually purged with He gas three times to clean the line from any impurities. Next, the operating conditions, such as experiment time (in minute), analysis gas port, operating pressure (in bar), and temperature (in K), were pre-defined. After that, the sample cell was charged with wet silica gel and was placed inside water bath. The mixture of 70 vol% water + 30 vol% antifreeze was used to avoid the formation of ice inside water bath and to make sure that the water mixture was consistently circulated throughout the process. The cell's valve was initially closed.

Before the commencement of each experiment, the cell was pressurized to required pressure through a supply vessel containing CO_2 gas with a purity of 99.99%, and at the same time the desired operating temperature was established through constant temperature bath. After the operating conditions were achieved, the cell's valve was fully opened. Subsequently, the experiment for hydrate formation was left running for 1,200 minutes.

After the completion of each experiment, the pressure was reduced to atmospheric pressure at the same operating temperature for hydrate decomposition. Then, the system was automatically vented with He gas several times to clean the line for the next experiment. Subsequently, the cell's valve was fully closed and the sample cell was removed from the HPVA. Finally, the pressure–time (P-t) curve obtained after completion of the experiment was analysed to calculate the conversion of water to hydrate, CO_2 uptake, and rate of hydrate formation [31].

Results and Discussion

The formation of hydrate in the HPVA was examined by studying the P-t curves obtained together with the study of CO_2 dissolution in water according to Henry's law [29, 32], and then followed by analysis of CO_2 uptake and rate of hydrate formation. Three sets of experiments were performed for each sample and some control experiments were performed to distinguish between hydrate formation and physical adsorption by using the HPVA. The study on various driving forces towards hydrate formation was also presented.

Validation on CO_2 hydrate formation: P-t curve

All prepared samples were used to investigate hydrate formation in the HPVA at 275 K and 35 bars by using pure CO_2 gas (99.99% purity). As seen in Figure 1, the two-stage pressure drop trend was observed during the hydrate formation experiment where the total pressure drops achieved after 1,200 minutes was around 2 bar.

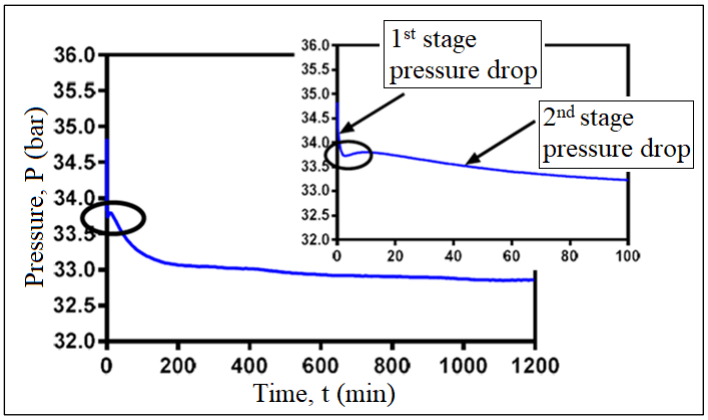


Figure 1. P-t curves that show two-stage pressure drop in 1,200 minutes and the first 100 minutes at the experimental conditions of 35 bar and 275 K

The complete dissolution of CO_2 in water inside silica gel pores was observed after the pressure dropped approximately from 35 bar to 33.8 bar as indicated by point **a–c** (the first stage of pressure drops). Initially, point **a-b** indicates that the dissolution of CO_2 in water happened at around five minutes in which Sloan et al. [33] stated that upon dissolution of gas in water, labile clusters form immediately. Concurrently, labile clusters started to agglomerate by sharing faces, thus increasing disorder, which explained no pressure drop from point **b–c**. This process continued until the size of the cluster agglomerate reached a critical value at point **c** wherein Sloan et al. [33] said this was the point where primary nucleation happens. Also, Tang et al. [28] described the time from point **a–c** as an induction time for hydrate formation. Moreover, the fast induction time observed in this work, which was around 10 minutes, by employing FBR agreed with the one reported in the literature [7-9, 11]. Then, the second stage of pressure drop was observed immediately after point **c** and this significant pressure drop is known as the hydrate growth stage until no more drop-in pressure was observed in batch FBR as indicated by point **d**. Finally, several stages of pressure drop were observed after 100 minutes (point **d**) before it reached a plateau approximately at 1,000 minutes.

CO_2 solubility in water

Since the experiments were conducted in batch mode or isochoric condition, the total number of moles of CO_2 consumed can easily be calculated by using the Ideal Gas law equation. Then, the mole fraction of CO_2 dissolved in water was calculated to be 0.0438 where the value of Henry's constant at 275 K was obtained from Carrol et al. [32]. This value was not considered for the justification of hydrate formation because the value of Henry's constant in their work was calculated at atmospheric pressure that was not the same with the operating pressures employed in this work. However, this value was presented in the figure for the comparison purpose. Thus, the equilibrium mole fraction of CO_2 in water at various operating temperatures and pressures plotted by Servio et al. [29] was used as a guideline to determine the formation of hydrate in the system. The formation of hydrate was confirmed when the

total experimental mole fraction was higher than the equilibrium mole fraction at the experimental conditions (275 K and 35 bar). Based on the data given by Servio et al. [29], the equilibrium mole fraction was found to be 0.0165 at these experimental conditions.

Figure 2(a) illustrates the total mole fraction of CO_2 consumed in water for all samples throughout the experiments, while Figure 2(b) illustrates the mole fraction of CO_2 consumed during hydrate growth. The red-dashed line in Figure 2(a) shows the total CO_2 dissolved in water at the experimental conditions in which further CO_2 consumed after that is known as the growth of hydrate. The total mole fraction of CO_2 involved in hydrate formation was 0.060 as shown in Figure 2(b). Since the formation of hydrate was justified, the study on final water to hydrate conversion, CO_2 uptake, and rate of hydrate formation are presented in the next section.

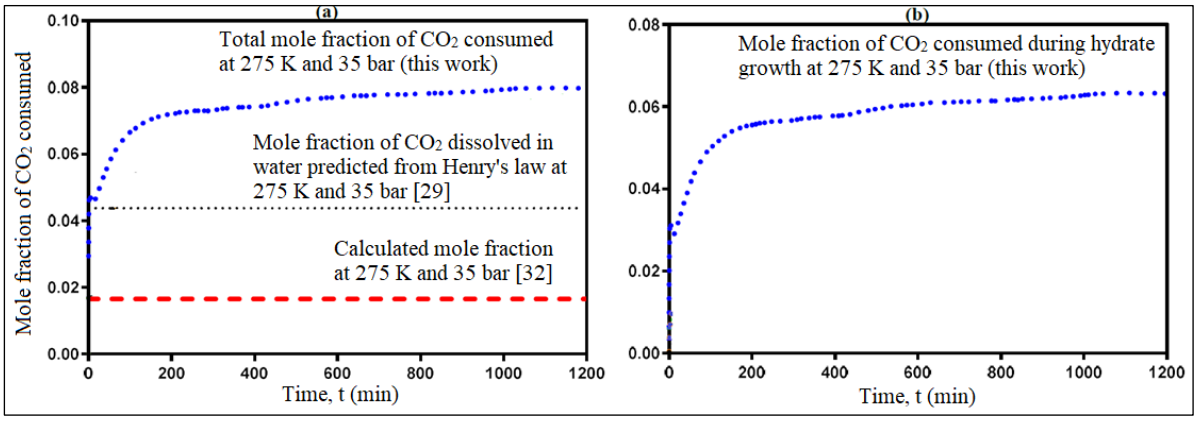


Figure 2. Mole fraction of CO_2 in water inside silica gel pores in 1,200 minutes; (a) total mole fraction of CO_2 and (b) mole fraction of CO_2 during hydrate growth

Control experiments

Six control experiments were performed by using silica contacted with water at various operating conditions. Initially, several experiments using wet (two experiments) and dry (two controlled experiments) silica gels, respectively, were performed to distinguish the formation of hydrate and physical adsorption in the HPVA. Then, the experiments at various operating pressures and temperatures (four controlled experiments; outside hydrate forming region) were performed to further investigate the formation of hydrate in the HPVA.

CO_2 adsorption profile for dry and wet silica gel

Dry silica gel was prepared by using a degassing unit. The sample was dried at 100 ^oC for one night before the commencement of the experiment. The experiments on wet and dry silica gels were performed at the same operating pressure (36 bar) and different operating temperatures (275 K and 298 K, respectively). Figure 3 illustrates the P-t curves for wet and dry silica gels in 600 minutes. The rapid one-stage pressure drops obtained for dry silica gel at both operating temperatures was expected due to normal physical adsorption. The experiment conducted at 298 K on wet silica gel gave slight one-stage pressure drop and was expected due to the normal solubility of CO_2 in water. Further investigation of mole fraction of CO_2 dissolved in water at this operating temperature is presented in the next section. Two-stage pressure drop was observed for the experiment using wet silica gel executed at 275 K due to the formation of hydrate as previously explained. The nucleation stage started after almost 10 minutes and this is known as the induction time for CO_2 hydrate formation. Next, the hydrate growth stage was seen in which the pressure drops of 1 bar occurred after almost 550 minutes. Then, the constant pressure until 600 minutes indicated the end of hydrate formation. Thus, the formation of hydrate in the HPVA was confirmed.

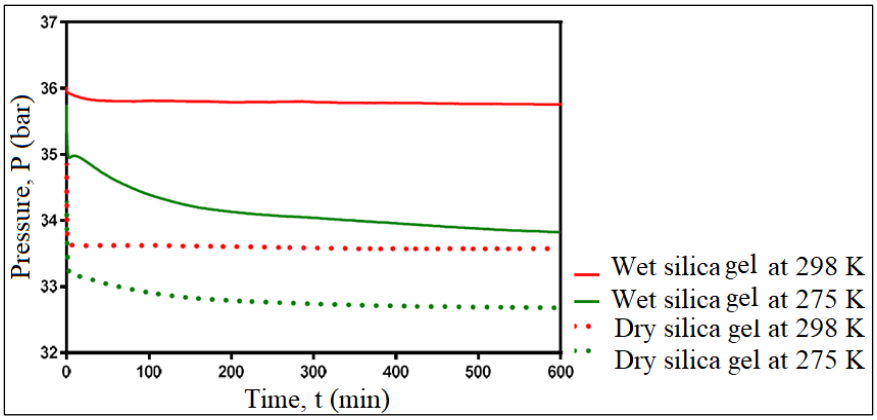


Figure 3. P-t curves for dry and wet silica gels at the operating pressure of 36 bar and temperatures of 275 K and 298 K in 600 minutes

Various operating conditions

More hydrate formation experiments were investigated within and outside of hydrate forming conditions. Table 1 summarizes the operating conditions together with their calculated driving force (ΔP) in which the equilibrium pressure at each operating temperature was obtained from the experimental data plotted by Yang et al. [22].

Table 1. Experimental operating conditions with their respective calculated driving force

Exp.	Operating temperature (K)	Operating pressure (bar)	Equilibrium pressure (bar)	Driving force, ΔP (bar)	Hydrate forming region
1	275	36	17	19	Yes
2	275	30	17	13	Yes
3	275	22	17	5	Yes
4	280	36	30	6	Yes
5	280	26	30	-	No
6	288	36	-	-	No
7	293	36	-	-	No
8	298	36	-	-	No

The study on CO_2 solubility in water at these various operating conditions was performed to justify the formation of hydrate. However, only one P-t curve (experimental conditions of 22 bar and 275 K) was presented, as illustrated in Figure 4 due to the same trend (either two or several stages of pressure drop) observed for all experiments that exhibited hydrate formation. Then, further study on CO_2 uptake was executed for the experiments that exhibited hydrate formation.

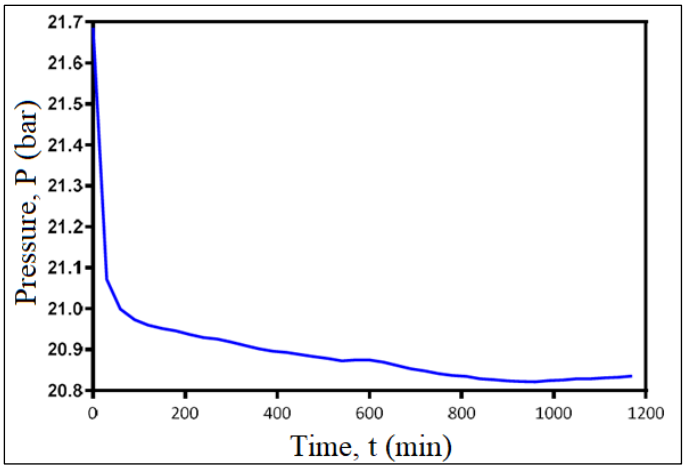


Figure 4. P-t curves that show several stages of pressure drop in 1200 minutes at the experimental conditions of 22 bar and 275 K

CO_2 solubility in water

The analysis of solubility of CO_2 in water was done according to Servio et al. [29] for experiments executed within hydrate forming conditions and Diamond et al. [34] for experiments performed outside hydrate forming regions. Based on the data plotted by Servio et al. [29], the solubility of CO_2 in water in the presence of hydrate at 36 bars was 0.0165 mole fraction of CO_2 at 275 K and 0.021 mole fraction of CO_2 at 280 K. The plotted data also showed that at 275 K, the solubility of CO_2 was the same at pressure ranges from 20 bar to 60 bar. Thus, the value of 0.0165 was also chosen for the operating pressure of 22 bar and 30 bar, at the operating temperature of 275 K. According to data plotted by Diamond et al. [34], the solubility of CO_2 in water at 280 K and 26 bars was 0.023 mole fraction of CO_2. The value observed at 36 bars was 0.022 mole fraction of CO_2 at 288 K, 0.021 mole fraction of CO_2 at 293 K, and 0.018 mol fraction of CO_2 at 298 K. Figures 5 & 6 illustrate the mole fraction of CO_2 dissolved in water at hydrate forming conditions in 600 minutes.

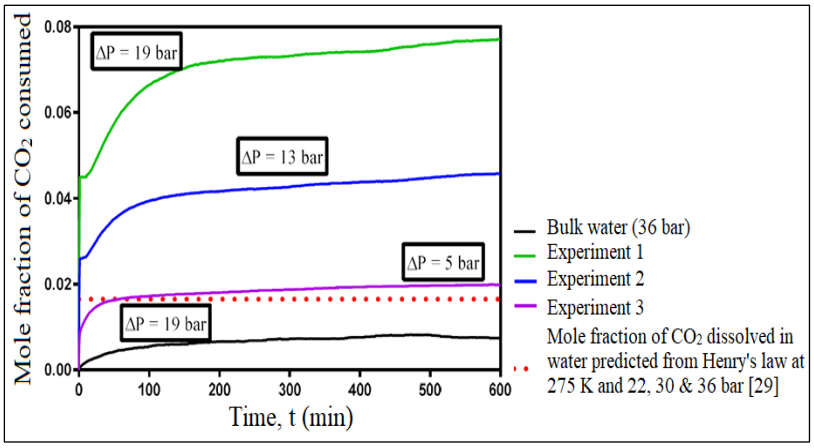


Figure 5. Mole fraction of CO_2 consumed at the operating temperature of 275 K and various driving forces (ΔP) in 600 minutes

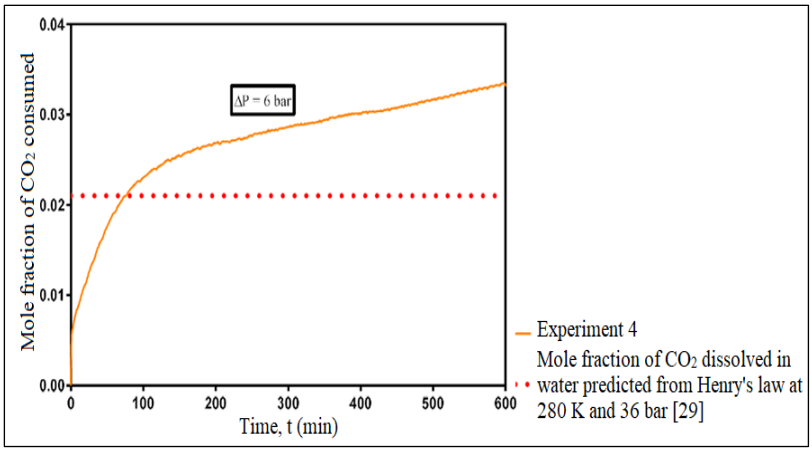


Figure 6. Mole fraction of CO_2 consumed at the operating conditions of 280 K and 36 bars in 600 minutes

It was observed that the total mole fraction of CO_2 soluble in water for Experiments 1 (275 K and 36 bar), 2 (275 K and 30 bar), 3 (275 K and 22 bar), and 4 (280 K and 36 bar) was higher than the value recorded by Servio et al. [29]. The CO_2 consumption obtained before it reached the red-dashed line was assumed to have been caused by the formation of labile clusters. Hence, further CO_2 consumption observed after that was due to the formation of CO_2 hydrate. The total mole fraction of CO_2 dissolved in water increased drastically as the driving force increased, which also justified the formation of CO_2 hydrate. The highest value observed was from Experiment 1 with the driving force of 19 bar, followed by Experiment 2 (driving force of 13 bar), Experiment 4 (driving force of 6 bar), and Experiment 3 (driving force of 5 bar). Even though the driving force for Experiments 3 and 4 was almost the same, only minimal hydrate growth was observed for Experiment 3 due to the low pressure in the system. This indicates that in hydrate forming regions, hydrate formation is easily enhanced by increasing the pressure rather than lowering the temperature. In contrast, the experiment by employing bulk water did not show any hydrate formation at all after 600 minutes, as shown in Figure 6, which explained the importance of a porous medium replacing the stirring process in bulk water system.

Figure 7 illustrates the mole fraction of CO_2 dissolved in water at non-hydrate forming conditions in 600 minutes. It was observed that the total mole fraction of CO_2 soluble in water for Experiments 5 (280 K and 26 bar), 7 (293 K and 36 bar), and 8 (298 K and 36 bar) was lower than the equilibrium mole fraction of CO_2 in water presented by Diamond et al. [34]. However, a small amount of CO_2 dissolved in water was observed which was higher than the equilibrium mole fraction of CO_2 for Experiment 6 (288 K and 36 bar). In summary, in the hydrate forming region, the equilibrium mole fraction of CO_2 in water was reduced as the temperature decreased [29]. Thus, the highest solubility of CO_2 observed in water at the lowest temperature in this study was due to the existence of CO_2 hydrate. In contrast, the solubility of CO_2 in water reduced as the temperature increased in the non-hydrate forming region. This trend was comparable to the equilibrium mole fraction of CO_2 in water as shown in the literature [34], which explains the non-existence of hydrate at these conditions.

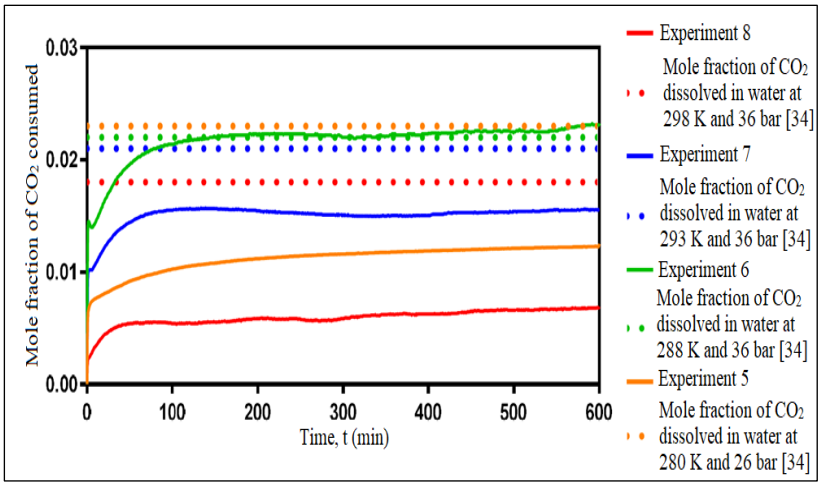


Figure 7. Mole fraction of CO_2 consumed at the non-hydrate forming conditions (Experiments 5– 8) in 600 minutes

High driving force enhanced water conversion to hydrate and gas uptake

The study on CO_2 uptake was performed for Experiments 1–4 where CO2 hydrate was previously found to exist at these experimental operating conditions. The average weight of wet silica gel used was 0.5 g, which led to a total of 0.004 moles of water. All experiments were analysed for a 600-minute period as this was the average time for the hydrate formation to be completed. Table 2 shows that Experiment 1 had the highest CO_2 uptake with a value of 3.75 ± 0.01mmol of CO_2 per g of H_2O, followed by Experiment 2 (1.65 ± 0.18mmol of CO_2 per g of H_2O), Experiment 4 (0.56 ± 0.03mmol of CO_2 per g of H_2O), and finally Experiment 3 (0.26 ± 0.02mmol of CO_2 per g of H_2O). All experiments had relatively low CI, which showed good reproducibility of the experiments at these various operating conditions.

Table 2. Summary of results for hydrate formation experiments perfo**rmed at various hydrate forming** conditions in 600 minutes (Experiments 1–4)

Exp.	Operating conditions	Driving force, ΔP (bar)	Replication	CO_2 uptake (mmol of CO_2/g of H_2O)	Mean CO_2 uptake (mmol of CO_2/g of H_2O)
1	275 K & 36 bars	19	1 2	3.74 3.75	3.75±0.01
2	275 K & 30 bars	13	1 2	1.77 1.52	1.65±0.21
3	275 K & 22 bars	5	1 2	0.23 0.27	0.26±0.02
4	280 K & 36 bars	6	1 2	0.54 0.58	0.56±0.03

The conversion of water to hydrate and gas uptake for Experiments 1–4 with their respective error bars are presented in Figure 8. The highest driving force experiment (Experiment 1 with the driving force of 19 bar) converted the highest water to hydrate with 40 mol% in 600 minutes, which was 50% higher than Experiment 2. This was followed by Experiment 2, almost 16 mol% higher than Experiment 3. These three experiments were executed at 275 K with Experiment 3 having the lowest driving force (5 bar). Furthermore, Experiment 4, which

was performed at higher temperature (280 K) but with ΔP of 6 bar, exhibited 50% greater result as compared to Experiment 3. This indicated that the increased driving force enhanced the formation of CO_2 hydrate.

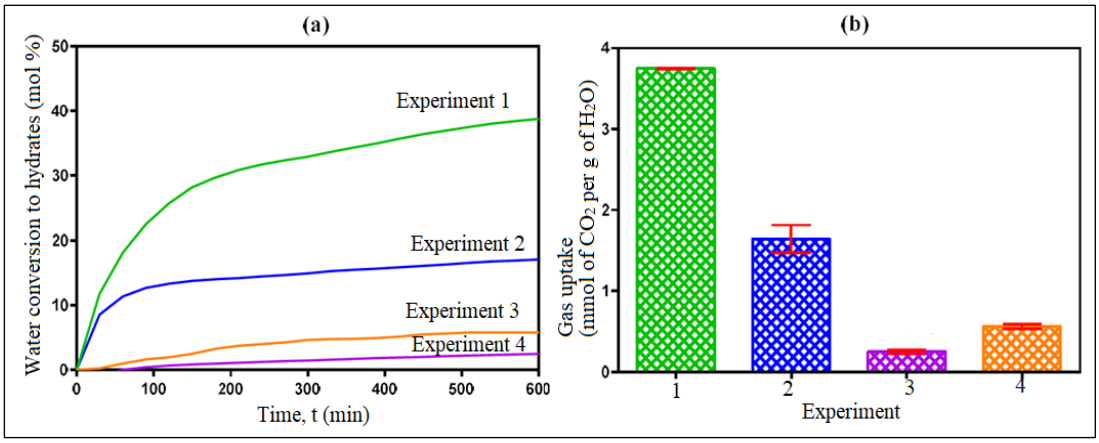


Figure 8. Comparison of (a) water conversion to hydrate and (b) CO_2 uptake at the hydrate forming conditions in 600 minutes

Conclusion

The solubility of CO_2 in water using Henry's law and the experimental pressure–time (P-t) curve were analysed to determine the formation of hydrate. Hydrate formation was confirmed when the mole fraction of CO_2 dissolved in water exceeded the Henry's law value as well as a two-stage pressure drop in the experimental P-t curve. Several experiments that were investigated in the HPVA at various operating conditions justified that hydrate formation only occurred at hydrate forming conditions with the lowest CO_2 uptake of 0.26±0.02 mmol of CO_2 per g of H_2O at 22 bars and 275 K and the highest CO_2 uptake of 3.75±0.01 mmol of CO_2 per g of H_2O at 36 bars and 275 K. In the hydrate forming region, the equilibrium mole fraction of CO_2 in water was reduced as the temperature decreased. Thus, the highest solubility of CO_2 observed in water at the lowest temperature in this study was due to the existence of CO_2 hydrate. In contrast, the solubility of CO_2 in water reduced as the temperature increased in the non-hydrate forming region, which explains the non-existence of hydrate.

Acknowledgement

The authors gratefully acknowledge the Ministry of Higher Education and Islamic Science University of Malaysia (USIM) for their financial support in this work (Grant number: PPPI/FST/0217/051000/12118).

References

1. Caitlyn, K. (2014). Climate change: Atmospheric carbon dioxide. https://www.climate.gov/news-features/understanding-climate/climate-change-atmospheric-carbon-dioxide. [Access online 20 January 2015].
2. Biello, D. (2013). 400 ppm: Carbon dioxide in the atmosphere reaches prehistoric levels. http://blogs.scientificamerican.com/observations/2013/05/09. [Access online 20 January 2015].
3. Kunze, C. and Spliethoff, H. (2012). Assessment of oxy-fuel, pre- and post-combustion-based carbon capture for future IGCC plants. *Applied Energy*, 94: 109-116.
4. IEA (2008). Energy technology perspectives. OECD/IEA Publications 9, Paris: pp. 55-57.
5. Metz, B., Davidson, O., Coninck, H. D., Loos, M. and Meyer, L. (2005). IPCC special report on carbon dioxide capture and storage. Intergovernmental Panel on Climate Change, New York pp. 109-110.
6. D'Alessandro, D. M., Smit, B and Long, J. R. (2010). Carbon dioxide capture: Prospects for new materials. *Angewandte Chemie International Edition*, 49: 6058-6082.
7. Zheng, J., Lee, Y. K., Babu, P., Zhang, P. and Linga, P. (2016). Impact of fixed bed reactor orientation, liquid saturation, bed volume and temperature on the clathrate hydrate process for pre-combustion capture. *Journal of Natural Gas Science and Engineering*, 35:1499-1510.

8. Babu, P., Ho, C.Y., Kumar, R. and Linga, P. (2014). Enhanced kinetics for the clathrate process in a fixed bed reactor in the presence of liquid promoters for pre-combustion carbon dioxide capture. *Energy*, 70: 664-673.
9. Linga, P., Kumar, R. and Englezos, P. (2007). Gas hydrate formation from hydrogen/carbon dioxide and nitrogen/carbon dioxide gas mixtures. *Chemical Engineering Science*, 62: 4268-4276.
10. McCallum, S. D., Riestenberg, D. E., Zatsepina, O. Y. and Phelps, T. J. (2005). Effect of pressure vessel size on the formation of gas hydrates. *Journal of Petroleum Science & Engineering*, 56: 54-64.
11. IEA Clean Coal Centre (2011). Pre-combustion capture of CO_2 in IGCC plants No 11/14, London: pp.11-14.
12. Babu, P., Kumar, R. and Linga, P. (2013). Pre-combustion capture of CO_2 in a fixed bed reactor using the Clathrate hydrate process. *Energy*, 50: 364-373.
13. Carroll, J. (2009). Natural gas hydrates (a guide for engineers). Elsevier Inc., Burlington: pp. 1-15.
14. Adeyemo, A., Kumar, R., Linga, P., Ripmeester., J. and Englezos, P. (2010). Capture of CO_2 from flue or fuel gas mixtures by clathrate crystallization in a silica gel column. *International Journal of Greenhouse Gas Control*, 4: 478-485.
15. Kumar, A., Sakpal, T., Linga, P. and Kumar, R. (2013). Influence of contact medium and surfactants on carbon dioxide Clathrate hydrate kinetics. *Fuel*, 105: 664-671.
16. Park, S., Lee, S., Lee, Y., Lee, Y. and Seo, Y. (2013). Hydrate-based pre-combustion capture of carbon dioxide in the presence of a thermodynamic promoter and porous silica gels. *International Journal of Greenhouse Gas Control*, 14: 193-199.
17. Kang, S. P., Lee, J. and Seo, Y. (2013). Pre-combustion capture of CO_2 by gas hydrate formation in silica gel pore structure. *Chemical Engineering Journal*, 218: 126-132.
18. Mekala, P., Busch, M., Mech, D. and Patel, R. S. (2014). Effect of silica sand size on the formation kinetics of CO_2 hydrate in porous media in the presence of pure water and seawater relevant for CO_2 sequestration. *Journal of Petroleum Science & Engineering*, 122: 1-9.
19. Xiaoya, Z., Jianwei, D.U., Deqing, L., Shuanshi, F. and Cuiping, T. (2009). Influence of A-type zeolite on methane hydrate formation. *Chinese Journal of Chemical Engineering*, 17: 854-859.
20. Zhong, D. L., Li, Z., Lu, Y. Y., Wang, J. L., Yan, J. and Qing, S. L. (2016). Investigation of CO_2 capture from a CO_2 + CH_4 gas mixture by gas hydrate formation in the fixed bed of a molecular sieve. *Industrial & Engineering Chemistry Research*, 55(29): 7973-7980.
21. Mohd Hafiz, A. H., Snape, C. E. and Stevens, L. (2018). Bed height of zeolite affected CO_2 hydrate formation using high pressure volumetric analyser. *Asian Journal of Chemistry*, 30(10): 2269-2272.
22. Yang, M., Song, Y., Liu, W., Zhao, J., Ruan, X., Jiang, L. and Li, Q. (2013). Effects of additive mixtures (THF/SDS) on carbon dioxide hydrate formation and dissociation in porous media. *Chemical Engineering Science*, 90: 69-76.
23. Mohd Hafiz, A.H., Snape, C.E. and Stevens, L. (2018b). The effect of silica particle sizes and promoters to equilibrium moisture content for CO_2 hydrate formation in HPVA. *AIP Conference Proceedings*, 1972: 030019.
24. Babu, P., Linga, P., Kumar, R. and Englezos, P., (2015). A review of the hydrate-based gas separation (HBGS) process for carbon dioxide pre-combustion capture. *Energy*, 85: 261-279.
25. Babu, P., Kumar, R. and Linga, P. (2013b). A new porous material to enhance the kinetics of clathrate process: Application to precombustion carbon dioxide capture. *Environmental Science Technology*, 47: 13191-13198.
26. Skarstrom, C. W. (1960). Method and apparatus for fractionating gaseous mixtures by adsorption. US Patent, No: 2944627.
27. Grande, C. A. (2012). Advances in pressure swing adsorption for gas separation. *ISRN Chemical Engineering Science*, 2012: 1-13.
28. Tang, J., Zeng, D., Wang, C., Chen, Y., He, L. and Cai, N. (2013). Study on the influence of SDS and THF on hydrate-based gas separation performance. *Chemical Engineering Research and Design*, 91: 1777-1782.
29. Servio, P. and Englezos, P. (2001). Effect of temperature and pressure on the solubility of carbon dioxide in water in the presence of gas hydrate. *Fluid Phase Equilibria*, 190: 127-134.
30. Dawson, R., Stevens, L. A., Williams, O. S. A., Wang, W., Carter, B. O., Sutton, S., Drage, T. C., Blanc, F., Adams, D. J. and Cooper, A. I. (2014). Dry bases: carbon dioxide capture using alkaline dry water. *Energy & Environmental Science*, 7: 1786-1791.

31. Mohd Hafiz, A. H., Snape, C. E. and Stevens, L. (2017). Enhance CO_2 hydrate formation inside the HPVA by vigorous stirring during sample preparation. *Proceeding of Postgraduate Seminar on Science and Technology*, 7th November 2016, Nilai, Malaysia.
32. Carrol, J., Slupsky, J. and Mather, E. (1991). The solubility of CO_2 in water at low pressure. *Journal of Physic and Chemistry*, 20: 1201-1209.
33. Sloan, E. D. and Koh, C. A. (2008). Clathrate hydrates of natural gases. Taylor & Francis Group, Boca Raton: pp. 130-138.
34. Diamond, L. W. and Akinfiev, N. N. (2003). Solubility of CO_2 in water from -1.5 to 100 ^oC and from 0.1 to 100 MPa: Evaluation of literature data and thermodynamic modelling. *Fluid Phase Equilibria*, 208: 265-290.
35. Babu, P., Ong, H. W. N. and Linga, P. (2016). A systematic kinetic study to evaluate the effect of tetrahydrofuran on the clathrate process for pre-combustion capture of carbon dioxide. *Energy*, 94: 431-442.

Malaysian Journal of Analytical Sciences, Vol 23 No 3 (2019): 436 - 443
DOI: https://doi.org/10.17576/mjas-2019-2303-07

MALAYSIAN JOURNAL OF ANALYTICAL SCIENCES
Published by The Malaysian Analytical Sciences Society
ISSN 1394 - 2506

NUTRIENT DISTRIBUTION IN THE BESUT RIVER BASIN, TERENGGANU, MALAYSIA (SOUTH CHINA SEA)

(Taburan Nutrien di Lembangan Sungai Besut, Terengganu, Malaysia (Laut China Selatan))

Suhaimi Suratman[1,2]*, Azyyati Abdul Aziz[1], Tan Hock Seng[1], Hee Yet Yin[1], Fatin Adlina Md Nasir[1], Dung Quang Le[3], Norhayati Mohd Tahir[1]

[1]Institute of Oceanography and Environment
[2]Institute of Tropical Biodiversity and Sustainable Development
Universiti Malaysia Terengganu, 21030 Kuala Nerus, Terengganu, Malaysia
[3]PETRONAS Twin Towers,
Kuala Lumpur City Centre, 50088 Kuala Lumpur, Malaysia

**Corresponding author: miman@umt.edu.my*

Received: 19 August 2018; Accepted: 11 May 2019

Abstract

The aim of this study was to determine the distribution of nitrogen (N)- and phosphorus (P)-based nutrients in the Besut River basin, Malaysia (South China Sea). The mean concentrations of ammonia, nitrate, total dissolved N and total particulate N were 43 µg/L N, 195 µg/L N, 485 µg/L N, 431 µg/L N, respectively. In contrast to N, lower mean concentrations of P were recorded with values of 2.30 µg/L P (dissolved inorganic P), 4.84 µg/L P (total dissolved P) and 8.35 µg/L P (total particulate P). In general, higher concentrations of nutrients were recorded in the middle and lower reaches of the river basin due to human activities. Elevated levels of both forms of nutrients were present during the wet season due to terrestrial run-off to the water column. The molar ratio of dissolved inorganic N:P (nitrate + ammonia: inorganic P) was extremely high (72:1), much higher than the Redfield ratio (16:1), suggesting the nutrient-limiting factor for phytoplankton growth in this river basin was P. The results from this study can be used as a baseline comparison for future monitoring of this river basin.

Keywords: surface water, nutrients, N:P ratio, Besut River basin

Abstrak

Tujuan kajian ini adalah untuk menentukan taburan nutrien berasaskan nitrogen (N) dan fosforus (P) di lembangan Sungai Besut, Malaysia (Laut China Selatan). Purata kepekatan ammonia, nitrat, jumlah N terlarut dan jumlah N partikulat masing-masing adalah 43 µg/L N, 195 µg/L N, 485 µg/L N, 431 µg/L N. Jika dibandingkan dengan N, purata kepekatan P yang direkodkan adalah rendah dengan nilai 2.30 µg/L P (tak organik P terlarut), 4.84 µg/L P (jumlah terlarut P) and 8.35 µg/L P (jumlah partikulat P). Umumnya, kepekatan nutrien adalah tinggi di kawasan pertengahan dan hilir lembangan sungai yang disebabkan oleh aktiviti manusia. Aras kepekatan adalah bertambah untuk kedua-dua jenis nutrien di musim basah hasil daripada larut lesap dari daratan ke kolum air. Nisbah molar takorganik terlarut N:P (nitrat + ammonia: tak organik P) adalah sangat tinggi (72:1) berbanding nisbah Redfield (16:1) yang mencadangkan faktor penghad nutrien untuk pertumbuhan fitoplankton di sungai ini adalah P. Hasil daripada kajian ini boleh digunakan sebagai perbandingan dasar pemantauan seterusnya untuk lembangan sungai ini.

Kata kunci: air permukaan, nutrien, nisbah N:P, lembangan Sungai Besut

Introduction

Nutrient input to surface water has increased dramatically in recent decades and anthropogenic activities are the major sources [1]. These anthropogenic sources include both domestic and industrial wastewater discharge, agricultural practices, mining and atmospheric deposition. Nitrogen (N)- and phosphorus (P)-based nutrients are important for primary productivity and also the most threatening pollutants for most aquatic systems [2, 3]. Excessive levels of both nutrients in the surface water contribute to the deterioration of water quality through processes such as eutrophication, and hence contribute to hypoxic events [4, 5]. Besides light, nutrients are the major factor controlling the growth of phytoplankton and most studies have shown that N and P are the limiting nutrients for marine and freshwater systems, respectively [6, 7].

The Besut River basin is situated on the east coast of Peninsular Malaysia. The Besut River is the largest river in the district of Besut, Terengganu, is approximately 40 km in length and flows from Besut to the mouth of the river at Kuala Besut and discharges into the southern part of the South China Sea. The Besut River basin comprises the Besut River and its main tributaries such as the Pelagat, Jertih, Tenang, Angga, Peda, La and Keruak Rivers. This area experiences a tropical climate and is strongly influenced by the Northeast (NE) monsoon from November to February and Southwest (SW) monsoon from March to September. The NE monsoon season brings heavy rains to this area and is known as the wet season, while the SW monsoon is referred to as the dry season [8]. The main anthropogenic activities in this basin are agriculture and residential. The residential areas are concentrated in three major towns, namely Jertih, Kampung Raja and Kuala Besut. There are no major industrial activities in this basin. This river basin is important since it provides water for irrigation as well as water supplies for the surrounding areas and also provides waste water dilution [9].

This study focused on the distribution of N-based nutrients (nitrate, ammonia, total dissolved N (TDN) and total particulate N (TPN)) and P-based nutrients (dissolved inorganic P (DIP), total dissolved P (TDP) and total particulate P (TPP)) during the dry and wet seasons. The concentration of chlorophyll-a (chl-a) as an indicator of phytoplankton biomass was also determined. The molar ratio of dissolved inorganic N:P was calculated in order to know the limiting nutrient in this basin.

Materials and Methods

Sampling was carried out during dry pre-monsoon (2/6/2002, 4/8/2002 and 26/10/2002) and wet monsoon (23/11/2002) periods at eight sampling stations (B1, B2, B3, B4, B5, B6, B7 and B8) as shown in Figure 1. All stations were located in the freshwater area. Only one sampling was performed during the wet monsoon period due to rough weather conditions which most of the stations were flooded and could not be accessed. Due to the water shallow (<2 m), water samples were only collected by hand-dipping the bottles beneath the water surface and stored in acid-washed polyethylene bottles. The samples were temporarily placed in an ice cooler and transported to the laboratory. At the laboratory, 500 mL samples were vacuum-filtered through 0.45 µm cellulose membrane filters and the dissolved samples were stored frozen at -20 ^{o}C until analysis. The dissolved and particulate forms of the nutrients were analysed based on the standard colourimetric method [10]. The chl-a was determined spectrophotometrically [11]. The data obtained were then tested by two-way analysis of variance (ANOVA) at the 95% significance level to show differences between sampling dates and sampling stations.

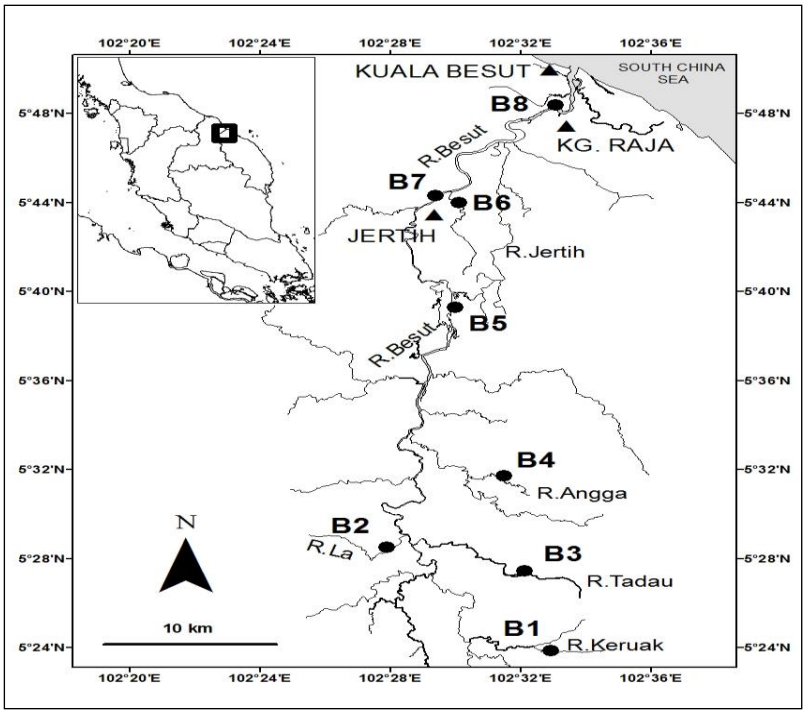
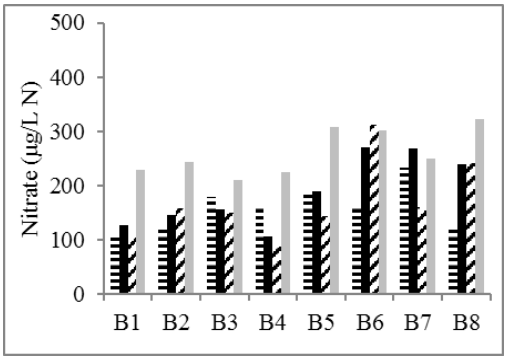


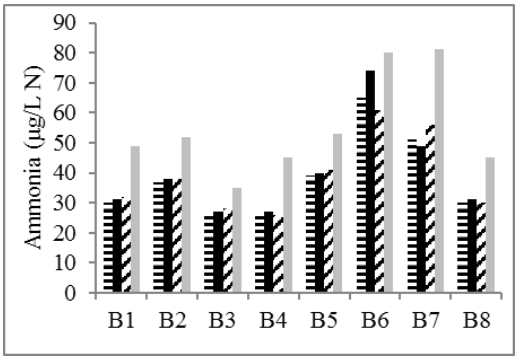
Figure 1. Location of sampling stations in the Besut River basin

Results and Discussion

Nutrients and chl-a distribution

Figures 2 and 3 show the distribution of N- and P-based nutrients in the Besut River basin. Based on the ANOVA test, in general all nutrients showed no significant difference ($p > 0.05$) between sampling stations, but did show significantly differences ($p < 0.05$) between sampling dates. Among the N-based nutrients, TDN recorded higher concentrations ranging from 130 to 1099 (mean 485±230) µg/L. This was followed by TPN, nitrate and ammonia with the values of 50–1033 (mean 431±288) µg/L, 88–323 (mean 195±68) µg/L and 26–81 (mean 43±16) µg/L, respectively. For the P-based nutrients, higher ranges of concentrations were observed for TPP: 2.28–19.32 (mean 8.35±4.32) µg/L. The concentrations of TDP and DIP varied from 1.54 to 12.21 (mean 4.84±2.67) µg/L and from 0.28 to 7.28 (mean 2.30±1.83) µg/L, respectively.





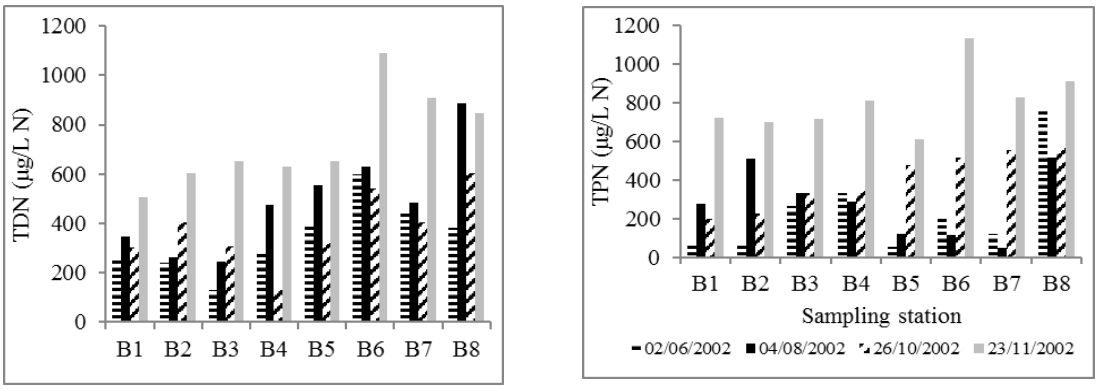


Figure 2. Variation of N-based nutrient concentrations in the Besut River basin

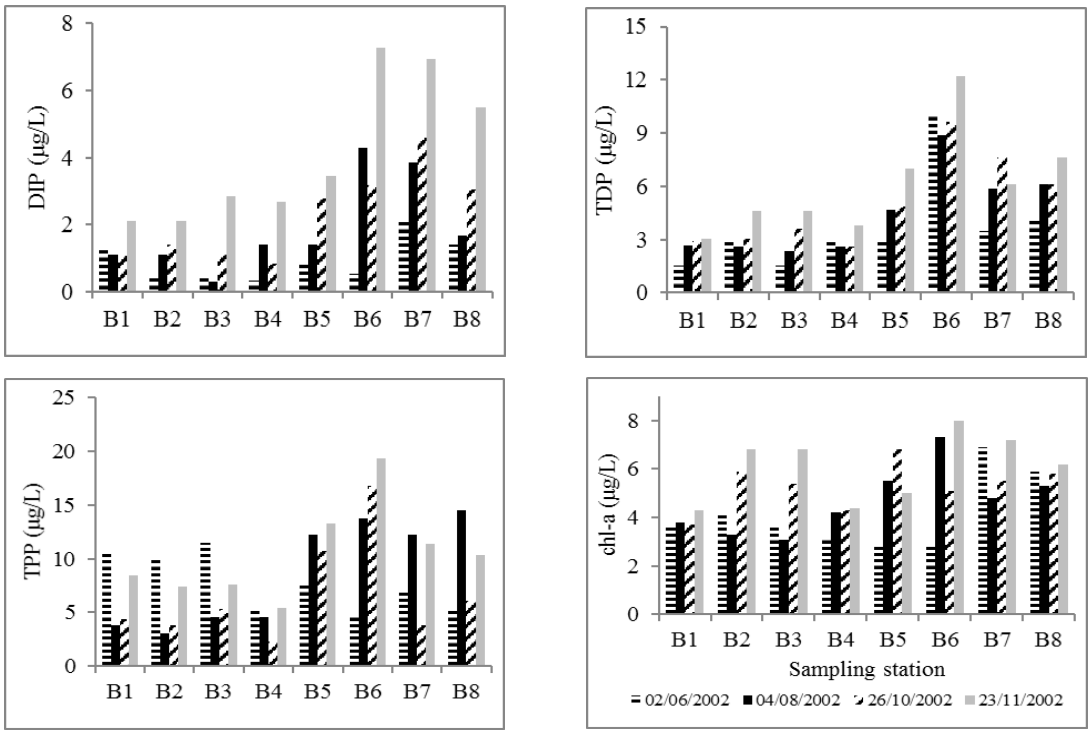


Figure 3. Variation of P-based nutrient concentrations in the Besut River basin

An increasing trend of nutrient concentrations was found going from the upstream to the downstream stations, especially at stations B6, B7 and B8 at which recorded among the highest concentrations. As mentioned earlier, the main activities in this river basin are agriculture and residential areas, which concentrated in the three towns Jertih, Kampung Raja and Kuala Besut. These towns are located in the middle and downstream areas of this river basin. It is believed that there is no proper waste management in these towns as most of the sewage effluent flows straight into the river. These effluent sources include domestic sewage and municipal waste water. Numerous studies have revealed domestic and municipal effluents as an important source of nutrients to river systems [12-14]. Run-off from agricultural activities can also contribute to enhanced nutrient contents through the diffusion process, especially when excessive fertilizers are used [15, 16]. Even though agricultural activities (palm oil plantation) are practised at the upper reaches of this river, the nutrient concentrations here were relatively low compared to downstream stations which implies that agricultural activities have a minimal influence on nutrient concentrations in this river basin.

In general, the nutrient distributions were high during the wet monsoon period compared to the dry pre-monsoon period. Many studies also recorded the same observation in their study area [17-19]. An observed increase in the nutrients measured during the wet monsoon period was associated with heavy rainfall that leads to peak river discharge and high terrestrial run-off. The run-off component from the land includes agricultural and municipal wastes from the surrounding area and is responsible for high concentrations of nutrients along the surface of the Besut River basin. Conversely, during the dry season period, lower nutrient concentrations were recorded. This is possibly due to little rainfall causing weakened river flow and diminished the flushing from upstream during the dry season, therefore the waste water drainage and nutrient inputs to the water column were also low.

The chl-a concentrations were in the range 2.9–8.0 (mean 5.1±1.4) µg/L. The distribution of chl-a showed no significant difference ($p > 0.05$) between sampling stations, but again significant differences ($p < 0.05$) between sampling dates based on the ANOVA test. In general, higher chl-a concentrations were recorded at the middle and upstream stations which may be due to high nutrient input in these particular areas.

A comparison of data obtained from the present study has been made with selected previous data from river basins in Malaysia (Table 1). In general, the Besut River basin recorded lower concentrations of nutrients. This is probably due to the fact that there are no major anthropogenic activities within the basin; most activities are related to agriculture and residential areas. The Marang, Kemaman and Nerus River basins recorded relatively higher values of nutrients in Terengganu due to large scale agriculture and plantation activities in these areas. In addition, a few big towns are located in these three river basins such as Marang, Chukai and Kuala Terengganu. The Selangor River basin recorded higher concentrations for most of the nutrients which could be attributed to input from municipal waste, aquaculture farms and ex-mining ponds. As reported for the Bertam River, discharge of waste and use of fertilizers in farming areas were the main sources of nutrients. Sand mining in the river can also increase the nutrient concentrations as this activity could result in the resuspension of sediment, which could release a significant amount of nutrients attached to the sediment into the river water as observed in the Kelantan River.

Table 1. Comparison of nurients within selected area in Malaysia river basin

River	Nitrogen (µg/L N)				Phosphorus (µg/L P)			Ref.
	Ammonia	Nitrate	TDN	TPN	DIP	TDP	TPP	
Besut, Terengganu	26 - 81	88 - 323	130 - 1,099	50 - 1,033	0.28 - 7.28	1.54 - 12.21	2.28 - 19.32	This study
Marang, Terengganu	16 - 161	65 - 426	-	-	27 - 62	-	-	[12]
Kemaman,Terengganu	-	31- 496	-	143 - 1652	1.28 - 26.12	-	4.89 - 468.30	[20]
Nerus, Terengganu	1 - 35	174 -743	-	-	4 - 29	-	-	[21]
Selangor, Selangor	10 - 980	50 -4300	510 - 13,400	-	1 - 123	4 - 370	-	[22]
Sarawak, Sarawak	30 - 670	30 - 140	-	-	30 - 740	-	-	[23]
Kelantan, Kelantan	260 - 410	13,300 - 21,700		-	-	-	-	[24]
Liwagu, Sabah	50 - 300	700 - 3,500	-	-	60 - 480	-	-	[25]
Merbok, Kedah	10 - 3,410	10 - 410	-	-	20 - 160	-	-	[26]
Bertam, Pahang	70 - 190	720 - 3,410	-	-	800 - 1,350	-	-	[27]

- = not analysed

N:P ratio

The relationship between two parameters can be obtained via plot regressions of one parameter against another. This technique requires sufficient variability in the various parameters for the slope of the line to be determined. By using the whole data, the regressions between the concentrations of chl-a versus DIN (nitrate + ammonia) and chl-a versus DIP were determined as shown in Figure 4 (note that the concentrations of DIN and DIP have been changed from µg/L to µM). It appears that the chl-a concentrations of all samples were highly correlated with DIN (R^2=0.31; R=0.56) and DIP (R^2=0.53; R=0.73). This means that the distribution patterns of chl-a (as an indicator for phytoplankton) were influenced by the inorganic nutrients. This result is consistent with other studies and further supports the argument that inorganic nutrients are the major nutrients for phytoplankton growth [6, 28, 29].

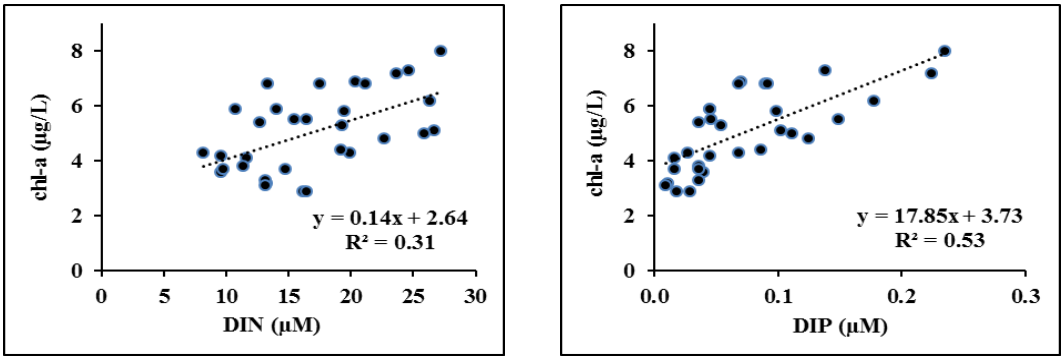


Figure 4. Molar concentrations of DIN and DIP versus chl-a

The regression graph of DIN versus DIP was plotted in order to determine the molar ratio of N:P in the Besut River basin (Figure 5). Although some studies have used the total concentrations of N and P in order to calculate the N:P molar ratio [16, 29], the inorganic forms of N- and P-based nutrients are the major nutrients used for phytoplankton growth [28, 29, 31], hence DIN and DIP were used here. The slope of the graph indicated that the N:P mean molar ratios of all samples was about 72:1 (R^2=0.57; R=0.76). This value is much higher than the value proposed by Redfield ratio (16:1), which is probably due to high DIN input from agriculture and residential areas in the Besut River basin. The calculated N:P molar ratio showed that DIP is the limiting nutrient in the Besut River basin, i.e. the primary production of phytoplankton is controlled by the availability of DIP. Many studies of surface freshwater systems have also observed the same trends of P-limiting nutrients in their area such as Colorado Lakes, U.S [29], Setiu River, Malaysia [32], Lake Michigan, U.S. [33] and Lake Baringo, Kenya [34]. For the freshwater system, the main input of nutrients is from point and non-point sources which are mainly from agriculture, industrial and domestic wastes. In going from the terrestrial to the aquatic system (e.g. run-off from land), the movement of P is more limited compared to the N due to the process of P binding to the soils [7]. As a result, N is more likely to flow to the freshwater, making P relatively very low in concentration and more limiting than N.

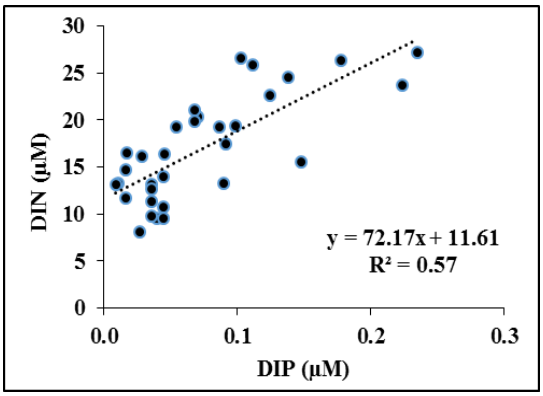


Figure 5. The molar ratio of DIN versus DIP

Conclusion

The present study shows that nutrients in both dissolved and particulate forms were higher downstream compared to upstream of the Besut River basin. This situation revealed the influence of continuous input from domestic and municipal discharges from three major towns in the Besut River basin. The high concentrations of the nutrients observed during the wet monsoon period were possibly due to the run-off process from the land into the river. Comparisons with other study areas showed that nutrient concentrations in the Besut River basin were still low. Based on the calculated N:P molar ratio, the limiting nutrient in this study area was DIP. The results obtained were based on the short term sampling. It is suggested to prolong the sampling in order to get more data of nutrients input, their loading and model it. This further assessment should provide a better understanding of nutrients distribution and related process for future prediction and comparison study.

Acknowledgements

The authors appreciated the Department of Chemical Sciences, Universiti Malaysia Terengganu for the financial support. This work was partly supported by the Higher Institution Centre of Excellence (HICoE) research grant (Vote no. 66928) awarded to the Institute of Oceanography and Environment, Universiti Malaysia Terengganu. The assistance of Norsuria Yahaya and Siti Rahayu A. Rashid in the sampling and analysis is kindly acknowledged. We are grateful for the helpful comments on the manuscript from anonymous reviewer. Thanks to Dr. Rose Norman for assistance with proof reading of the manuscript.

References

1. Jickells, T. D., Andrews, J. E., Parkes, D. J., Suratman, S., Aziz, A. A. and Hee, Y. Y. (2014). Nutrient transport through estuaries: The importance of the estuarine geography. *Estuarine, Coastal and Shelf Science*, 150: 215–229.
2. Drolc, A., and Zagorc, K. J. (2008). Diffuse sources of nitrogen compounds in the Sava River basin, Slovenia. *Desalination*, 226(1–3): 256–261.
3. Gao, W., Howarth, R. W., Swaney, D. P., Hong, B., and Guo, H. C. (2015). Enhanced N input to Lake Dianchi basin from 1980 to 2010: drivers and consequences. *Science of the Total Environment*, 505: 376–384.
4. Ling, T. Y., Michelle, C. M., Nyanti, L., Norhadi, I. and Justin, J. J. E. (2010). Impacts of aquaculture and domestic wastewater on the water quality of Santubong River, Malaysia. *Journal of Environmental Science and Engineering*, 4 (4): 11-16.
5. Hee, Y. Y. and Suratman, S. (2016). Physico-chemical parameter profile during dry and wet seasons in southern South China Sea. *Asian Journal of Chemistry*, 28(10): 2146-2152.
6. Smith, V. H. (2003). Eutrophication of freshwater and coastal marine ecosystems. A global problem. *Environmental Science and Pollution Research*, 10(2): 126-139.
7. Statham, P. J. (2012). Nutrients in estuaries-an overview and the potential impacts of climate change. *Science of the Total Environment*, 434: 213-227.
8. Malaysia Meteorological Department, MMD (2008). Access from http://www.met.gov.my/english/ education/climate/climate01.html). Access online 15 May 2018.
9. Suratman, S., Hang, H. C., Shazili, N. A. M. and Mohd Tahir, N. (2009). A preliminary study of the distribution of selected trace metals in the Besut River basin, Terengganu, Malaysia. *Bulletin of Environmental Contamination and Toxicology*, 82: 16-19.
10. Grasshoff, K., Ehrhardt, M. and Kremling, K. (1983). Determination of nutrients. In: Methods of seawater analysis 2nd edition. Florida: Verlag Chemie: pp. 419.
11. Parsons, T. R., Maita, T. and Lalli, C. M. (1984). Plant pigment. In: A manual of chemical and biological method for seawater analysis. Oxford: Pergamon Press: pp. 173.
12. Suratman, S. and Mohd Tahir, N. (2013). Kesan antropogenik terhadap kualiti air di lembangan Sungai Marang, perairan selatan Laut China Selatan. *Sains Malaysiana*, 42(6): 743-751.
13. Shiddamaiilayya, N. and Pratima, M. (2008). Impact of domestic sewage on freshwater body. *Journal of Environmental Biology*, 29(3): 303-308.
14. Badr, E. S. A. (2016). Spatio-temporal variability of dissolved organic nitrogen (DON), carbon (DOC), and nutrients in the Nile River, Egypt. *Environmental Monitoring and Assessment*, 188(10): 580.

15. Kim, G., Chung, S. and Lee, C. (2007). Water quality of runoff from agricultural-forestry watersheds in the Guem River basin, Korea. *Environmental Monitoring and Assessment*, 134: 441-452.
16. Shen, Z-.L. and Liu, Q. (2009). Nutrients in th Changjiang River. *Environmental Monitoring and Assessment*, 153: 27-44.
17. Rahaman, S. M., Sarder, L., Rahaman, M., Ghosh, A., Biswas, S., Siraj, S. and Islam, S. (2013). Nutrient dynamics in the Sundarbans mangrove estuarine system of Bangladesh under different weather and tidal cycles. *Ecological Processes*, 2(1): 29.
18. Anand, S. S., Sardessai, S., Muthukumar, C., Mangalaa, K. R., Sundar, D., Parab, S. G. and Kumar, M. D. (2014). Intra and inter seasonal variability of nutrients in a tropical monsoonal estuary (Zuari, India). *Continental Shelf Research*, 82: 9-30.
19. Kawasaki, N., Nagao, N., Yusoff, F., Imai, A. and Kohzu, A. (2016). Seasonal changes of nutrient distributions along Selangor River, Malaysia. *International Journal of Advances in Chemical Engineering and Biological Sciences*, 3(1): 113-116.
20. Suratman, S, Hee, Y. Y. and Mohd Tahir, N. (2014). Nutrient status of the Kemaman River basin in the southern South China Sea (Malaysia). *Asian Journal of Chemistry*, 26(7): 2047-2052.
21. Mohd Tahir, N., Suratman, S., Jusoh, S. R., Yahaya, S. N., Mohd Yusoff , N. and Law A. T. (2005). Penentuan indeks kualiti air dan nutrien terlarut di Sungai Nerus, Terengganu. *Malaysian Journal of Analytical Sciences*, 9(1): 193-197.
22. Kawasaki, N., Kushari, M. R. M., Nagao, N., Yusoff, F., Imai, A. and Kohzu, A. (2016). Seasonal changes of nutrient distributions along Selangor River, Malaysia. *International Journal of Advances in Chemical Enggering and Biological Sciences*, 3(1): 113-116.
23. Heng, L. Y., Madhan, M., Sumok, P. and Chukong, L. N. (2007). Pemonitoran intensif beberapa nutrien dalam Sungai Sarawak di Kuching, Sarawak, Malaysia. *Sains Malaysiana*, 36(2): 133-137.
24. Yen, T. P. and Rohasliney, H. (2013). Status of water quality subject to sand mining in the Kelantan River, Kelantan. *Tropical Life Sciences Research*, 24(1): 19-34.
25. Cleophas, F., Isidore, F., Han, L. K. and Bidin, K. (2013). Water quality status of Liwagu River, Tambunan, Sabah, Malaysia. *Journal of Tropical Biology and Conservation*, 10: 67-73.
26. Fatema, K., Wan Maznah, W. O. and Mat Isa, M. (2014). Spatil and tmporal variation of physico-chemical parameters in the Merbok estuary, Kedah, Malaysia. *Tropical Life Sciences Research*, 25(2): 1-19.
27. Khalik, W. M. A. W. M., Abdullah, M. P., Padli, N. and Amerudin, N. A. (2013). Assessment on nutrient status in water and sediment quality of Bertam River, Cameron Highlands. *International Journal of Chemical Sciences*, 11(2): 709-720.
28. Jordan, M. M. and Joint, I. (1998). Seasonal variation in nitrate:phosphate ratios in the English Channel 1923-1987. *Estuarine, Coastal and Shelf Science*, 46: 157-164.
29. Morris, D. P. and Lewis, W. M. (1988). Phytoplankton nutrient limitation in Colorado mountain lakes. *Freshwater Biology*, 20: 315-327.
30. Tamminee, T. (1982). Effects of ammonium effluents on planktonic primary production and decomposition in a coastal brackish water environment 1. Nutrient balance of the water body and effluent test. *Netherland Journal of Sea Research*, 16:455-464.
31. Luo, G., Bu, F., Xu, X., Cao, J. and Shu, W. (2011). Seasonal variations of dissolved inorganic nutrients transported to the Linjiang Bay of the Three Gorges Reservoir, China. *Environmental Monitoring and Assessment*, 173: 55-64.
32. Suhaimi, S., Mohd Tahir, N. and Suryati, S. (2004). Dissolved nutrients and chlorophyll a status of the Setiu River, Terengganu, Malaysia. *Bulletin of Environmental Contamination and Toxicology*, 73(6): 1094-1100.
33. Schelske, C. L. and Stoemer, E. F. (1972). Phosphorus, silica, and eutrophication of Lake Michigan. Pages 157–171. In: Nutrients and Eutrophication. G. E. Likens (editor) American Society Limnology Oceanography, Allen Press, Lawrence.
34. Okech, E.O., Kitaka, N., Oduor, S.O. and Verschuren, D. (2018). Tropic state and nutrient limitation in Lake Baringo, Kenya. *African Journal of Aquatic Science*, 43(2):169-173.

Malaysian Journal of Analytical Sciences, Vol 23 No 3 (2019): 444 - 450
DOI: https://doi.org/10.17576/mjas-2019-2303-08

MALAYSIAN JOURNAL OF ANALYTICAL SCIENCES
Published by The Malaysian Analytical Sciences Society
ISSN 1394 - 2506

RARE EARTH ELEMENTS IN SEDIMENT CORES OBTAINED FROM THE PORTS OF TANJUNG PELEPAS AND SEDILI, JOHOR AS POLLUTION INDICATORS

(Unsur Nadir Bumi dalam Teras Sedimen Diperolehi dari Pelabuhan Tanjung Pelepas dan Sedili, Johor Sebagai Penunjuk Pencemaran)

Wai Seong Koh and Che Abd Rahim Mohamed*

Faculty of Science and Technology,
Universiti Kebangsaan Malaysia, 43600 UKM Bangi, Selangor, Malaysia

**Corresponding author: carmohd@ukm.edu.my*

Received: 23 February 2019; Accepted: 12 May 2019

Abstract

Sediment core samples obtained from the Port of Sedili and Tanjung Pelepas, Johor were slice into layers with intervals of 3 cm to estimate the contamination levels of rare earth elements at harbour areas. An analysis of rare earth elements (REEs) including La, Ce, Pr, Nd, Sm, Eu, Gd, Tb, Dy, Ho, Er, Tm, Yb and Lu were conducted using the Inductively Couple Plasma Mass Spectrometry. The measured concentration of REEs normalized with Fe as an enrichment factors signal. A positive value ratio of Ce/Ce* anomalies (1.10 - 1.18) was shown at the Port of Sedili whereas at the Port of Tanjung Pelepas showed negative Ce/Ce* anomaly values (0.87 - 0.96). However, both stations showed weak positive Eu/Eu* anomaly values of 0.76 - 0.84 (Port of Sedili) and 0.96 - 1.0 (Port of Tanjung Pelepas). Fractionation index was also using to define the relative behaviour of LREEs to HREEs by the ratio of La/Yb_n. The results of this study support the proposition to use REEs as an indicator of pollution.

Keywords: rare earth elements, core sediment, harbour, pollution indicator, value ratio

Abstrak

Sampel diperolehi di pelabuhan Sedili dan Tanjung Pelepas, Johor dipotong setiap lapisan 3 cm untuk anggaran tahap pencemaran unsur nadir bumi di kawasan pelabuhan. Analisis unsur nadir bumi (REEs) iaitu La, Ce, Pr, Nd, Sm, Eu, Gd, Tb, Dy, Ho, Er, Tm, Yb dan Lu dilakukan dengan Induktif Pasangan Plasma Mass Spektrometri. Kepekatan REEs yang diperolehi akan dinormalkan dengan Fe sebagai faktor penunjuk perkayaan. Nilai nisbah Ce/Ce* anamoli (1.10 - 1.18) adalah positif diperolehi di Pelabuhan Sedili manakala negatif Ce/Ce* anamoli (0.87 - 0.96) di Pelabuhan Tanjung Pelepas. Walaubagaimanapun, kedua-dua stesen menunjukkan nilai positif lemah Eu/Eu* anamoli iaitu 0.76 - 0.84 (Perlabuhan Sedili) dan 0.96 - 1.0 (Perlabuhan Tanjung Pelepas). Indek pecahan juga digunakan untuk mengenalpasti tingkahlaku LREEs hingga HREEs melalui nisbah La/Ybn dan keputusan mendapati menyokong penggunaan REEs sebagai penunjuk pencemaran.

Kata kunci: unsur nadir bumi, teras sedimen, pelabuhan, penunjuk pencemaran, nilai nisbah

Introduction

REEs are unique metal elements that have similar chemical and physical properties. REEs have low solubility and are not easily transferred during geological processes such as weathering, erosion and transportation due to similarities in electron configurations [1-3]. Hence, REEs have been used extensively to trace the natural processes that happen in the marine environment and are also used as indicators to trace anthropogenic disturbances in marine

environments [4-9]. The accumulation of light rare earth elements (LREE), enriched by industrial processes such as petroleum catalytic cracking can yield anomaly REE concentrations in river and marine sediments [9].

Concentration levels of REEs in Malaysian habour sediments are not well published by national or international scientists. In order to establish information on Malaysian harbour sediments, we chose two habours at Tanjung Pelepas and Sedili, with the objective of studying the distribution of REE concentrations in sediment cores.

Materials and Methods

Sediment core samples of about 70 cm in length from Tanjung Pelepas (Station 1) and Sedili (Station 2) ports were collected with a gravity corer and sliced at 3 cm intervals. The coordinates of the sampling location (Figure 1) for the Ports of Sedili and Tanjung Pelepas are (N 01˚ 55' 54.3'', E 104˚ 06' 39.8'') and (N 01˚20' 17.5'', E 103˚ 32' 46.4''), respectively. Sediment samples were dried in an oven at 60^{o}C until constant weight before being crushed into homogenized powder using a mortar and pestle, and then sieve through 63 µm diameter. About 0.5 g of dried sample was digested in a mixture of $HClO_4$: HNO_3 (1:5 v/v) for 2 hours. An amount 10 mL of hydrofluoric acid and 2 ml of hydrogen peroxide were then added and further digested to get a paste. The digested samples were dissolved in 2% HNO_3 up to 30 mL [10]. Similarly, blank and standard reference material (SRM) samples were prepared following the same procedures to verify our analyses. Concentration levels of REE in the samples were determined using calibrated ICP-MS (Model Perkin-Elmer Elan 9000).



Figure 1. Sampling stations in the east and west coast Peninsular of Malaysia

Results and Discussion

Post-Archean Australian Shale (PAAS) composition was used to normalize REEs in the study area. PAAS normalized REE patterns in this study can be classified into 2 types. Figure 2a shows relatively flat PAAS normalized REEs whereas Figure 2b shows the enrichment of LREE. The enrichment of LREE reflects the intense silicate weathering of crustal materials and a resultant increase in LREEs in the detrital. This also suggests that its source is from the landmass [11,12]. Generally, REE concentrations at the Port of Sedili is higher than that at the Port of Tanjung Pelepas (Figure 3). Based on the results listed in Table 1, both stations show that LREE is more abundant than HREE. The REEs uptake sequence is LREE > HREE, and REE concentrations show a decreasing

trend with the increase of depth. Organism behaviors such as bioturbation might increase the concentration of metals in the surface sediment [6,13,14].

Anthropogenic activity is a factor that raises the loading of metals into the environment [15]. Lanthanum (La) and ytterbium (Yb) were chosen as representatives for LREE and HREE. The enrichment factor (EF) > 2.0 suggest that there are anthropogenic sources, whereas EF < 2.0 is of natural origin. The EF values for both stations are less than 1 and there is no significant enrichment of REEs (Fig. 4).

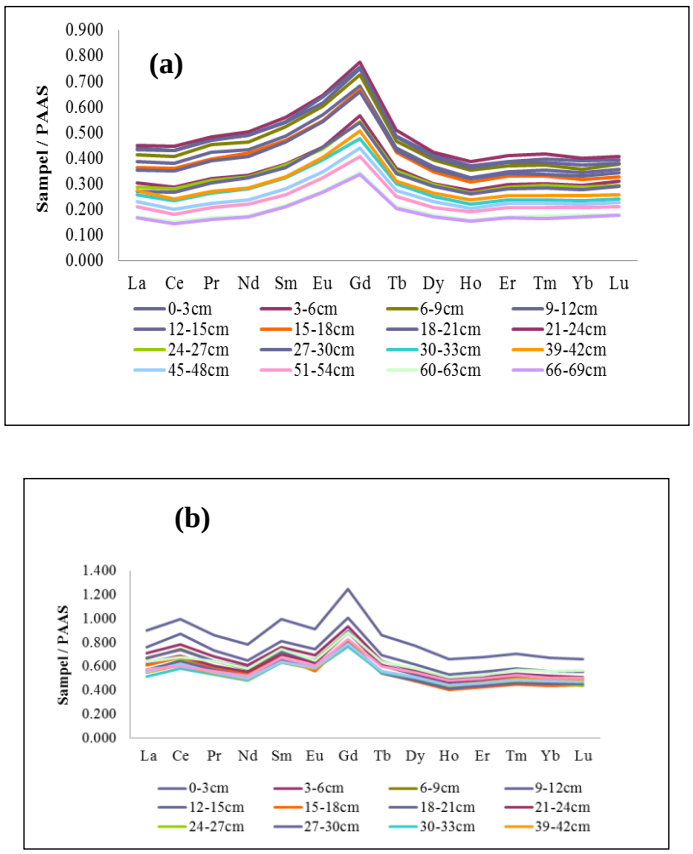


Figure 2. The PAAS normalized REE Distribution Pattern at study station (a) Tanjung Pelepas Port and (b) Selidi Port

Table 1. The Distribution of ∑LREE, ∑HREE, ∑(LREE/HREE), $(La/Yb)_n$, Ce* and Eu* at the Ports of Tanjung Pelepas and Sedili

Depth (cm)	Location	∑LREE	∑HREE	∑(LREE/HERE)	$(La/Yb)_n$	Ce*	Eu*
0-3	TPP	74.98	9.45	7.93	1.13	0.94	0.97
	SDL	131.41	13.15	9.99	1.36	1.17	0.83
3-6	TPP	77.30	9.78	7.91	1.13	0.96	0.98
	SDL	120.46	12.16	9.91	1.37	1.13	0.82
6-9	TPP	70.89	9.04	7.84	1.16	0.94	0.98
	SDL	113.77	11.60	9.81	1.35	1.14	0.82
9-12	TPP	74.81	9.37	7.98	1.16	0.95	1.00
	SDL	113.67	11.49	9.89	1.36	1.12	0.78
12-15	TPP	66.45	8.50	7.82	1.13	0.94	0.99
	SDL	103.63	10.40	9.86	1.38	1.13	0.80
15-18	TPP	62.91	8.15	7.72	1.15	0.94	0.98
	SDL	104.39	10.35	10.09	1.40	1.12	0.76
18-21	TPP	61.45	8.23	7.46	1.07	0.94	0.99
	SDL	152.96	16.20	9.44	1.34	1.13	0.82
21-24	TPP	50.89	7.06	7.21	1.04	0.92	0.96
	SDL	106.85	11.53	9.26	1.31	1.11	0.80
24-27	TPP	49.29	6.86	7.18	1.00	0.93	0.97
	SDL	98.73	10.43	9.46	1.21	1.18	0.84
27-30	TPP	47.44	6.77	7.01	0.98	0.93	1.00
	SDL	99.41	10.37	9.59	1.26	1.13	0.81
30-33	TPP	42.01	5.86	7.17	1.09	0.90	1.00
	SDL	90.59	10.60	8.55	1.06	1.11	0.83
39-42	TPP	43.64	6.21	7.02	1.09	0.88	0.99
	SDL	94.40	10.73	8.80	1.12	1.12	0.82
45-48	TPP	36.50	5.42	6.74	1.05	0.89	0.99
	SDL	95.67	10.67	8.96	1.16	1.13	0.83
51-54	TPP	33.40	4.98	6.70	1.02	0.87	0.99
	SDL	95.81	11.35	8.44	1.14	1.05	0.81
60-63	TPP	27.29	4.22	6.47	0.97	0.90	1.00
	SDL	107.84	12.18	8.86	1.14	1.06	0.80
66-69	TPP	26.28	4.12	6.38	0.98	0.87	1.00
	SDL	-	-	-	-	-	-
Average					TPP	0.92	0.99
					SDL	1.12	0.81

(*) normalized with the Post Achaean Australian Shale (PAAS)

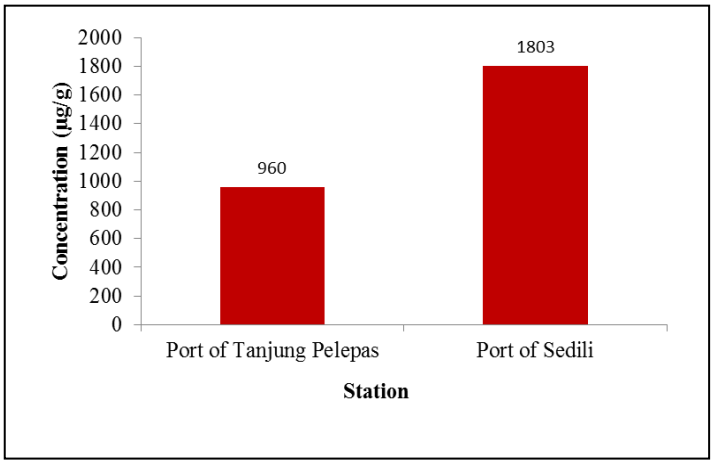


Figure 3. Total concentration of REE for Port of Tanjung Pelepas and Port of Sedili

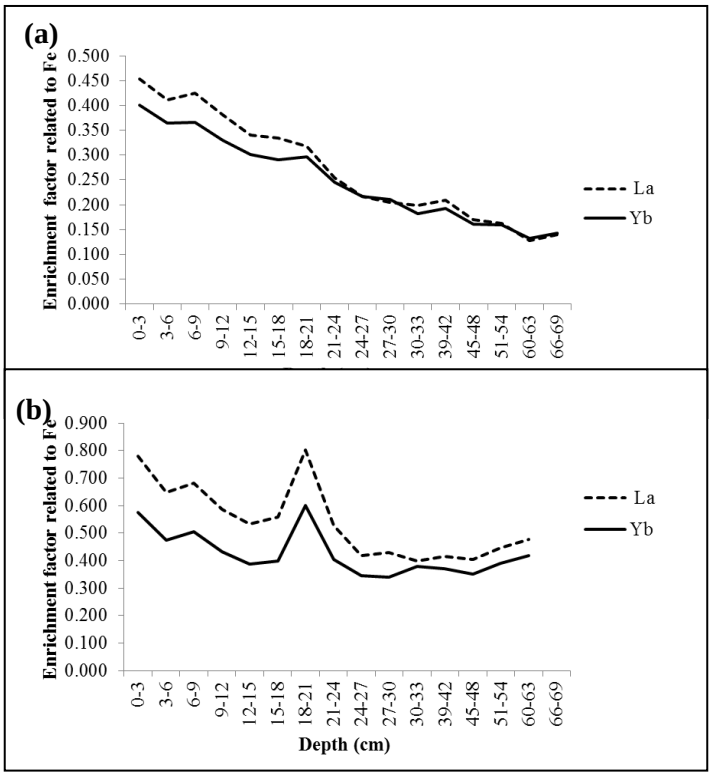


Figure 4. Iron normalized enrichment factor for La as a function of depth at each sampling station (a) Tanjung Pelepas Port and (b) Selidi Port

The Ce element occurs more abundant in oceanic ferromanganese compared to seawater. Marine manganese nodules have positive Ce* anomalies due to Cerium easy hydrolyses and co-precipitates with manganese [3]. A negative Ce* anomaly (<1) shows that the environment is oxic, the reduction process has occurred and the dissolution of insoluble Ce (IV) is reduced to soluble Ce (III) [16]. Liu and Cao [17] suggests that high biogenic and

chemical depositions will have a negative Ce* anomaly. Positive Ce/Ce* anomalies (1.10 - 1.18) result in Port of Sedili whereas Tanjung Pelepas showed negative Ce/Ce* anomalies (0.87 - 0.96). Negative Ce* anomalies in the Port of Tanjung Pelepas suggest high biological activity occurs in the study area. Both stations showed weak positive Eu/Eu* anomaly values; 0.76 - 0.84 at the Port of Sedili and 0.96 - 1.0 at the Port of Tanjung Pelepas. Rudnick [18] suggested that positive Eu* anomalies may be due to the input of hydrothermal vents, aeolian or lithogenic sources. Hydrothermal vents are absent in Malaysian waters, thus the positive Eu* anomalies at both stations may have resulted from aeolian or lithogenic sources. A high ratio of La/Ybn indicates a high erosion rate [19]. The ratio of La/Ybn at the Ports of Tanjung Pelepas and Sedili varied from 0.97 to 1.16 and 1.06 to 1.40 respectively, thus the erosion rate is higher at Port of Sedili compared to the Port of Tanjung Pelepas.

Conclusion

REEs elements are suitable for use as pollution indicators due to its unique characteristics. The concentration of REEs at the Port of Sedili was higher compared to that at the Port of Tanjung Pelepas. There is no significant enrichment of REEs at both stations. The negative Ce/Ce* anomaly value shows that the Port of Tanjung Pelepas had an oxic environment.

Acknowledgement

The authors would like to thanks the laboratory and individuals for their help during this research and we are grateful for the financial support from the Science Fund Grant No 04-01-02-SF0801 and KPT P(5) 400-7/2/29-4(65)UPM/700-3/1/JSPS. Finally, many thanks to the laboratory staff of the School of Environmental and Natural Resource Sciences for their technical supports.

References

1. Kimoto, A., Nearing, M. A., Zhang, X. C. and Powell D. M. (2006). Applicability of rare earth elemenoxides as a sediment tracer for coarse-textured soils. *Catena*, 65(3): 214-221.
2. Shynu, R., Rao, V. P., Kessarkar, P. M. and Rao, T. G. (2011). Rare earth elements in suspended and bottom sediments of the Mandovi estuary, central west coast of India: Influence of mining. *Estuarine, Coastal and Shelf Science*, 94(4): 355-368.
3. Zhihua, C., Aiguo, G., Yanguang, L., Haiqing, S., Xuefa, S. and Zuosheng, Y. (2001). REE geochemistry of surface sediments in the Chukchi Sea. *Science in China Series D: Earth Sciences*, 46(6): 603-611.
4. Åström, M. (2001). Abundance and fractionation patterns of rare earth elements in streams affected by acid sulphate soils. *Chemical Geology*, 175(3): 249-258.
5. Borrego, J., López-González, N., Carro, B. and Lozano-Soria, O. (2004). Origin of the anomalies in light and middle REE in sediments of an estuary affected by phosphogypsum wastes (south-western Spain). *Marine Pollution Bulletin*, 49(11): 1045-1053.
6. Davranche, M., Pourret, O., Gruau, G., Dia, A. and Le Coz-Bouhnik, M. (2005). Adsorption of REE(III)-humate complexes onto MnO_2: Experimental evidence for cerium anomaly and lanthanide tetrad effect suppression. *Geochimica et Cosmochimica Acta*, 69(20): 4825-4835.
7. Elderfield, H. and Sholkovitz, E. T. (1987), Rare earth elements in the pore waters of reducing nearshore sediments. *Earth and Planetary Science Letters*, 82(3): 280-288.
8. Haley, B. A., Klinkhammer, G. P. and Mcmanus, J. (2004). Rare earth elements in pore waters of marine sediments. *Geochimica et Cosmochimica Acta*, 68(6): 1265-1279.
9. Olmez, I., Sholkovitz, E. R., Hermann, D. and Eganhouse, R. P. (1991). Rare earth elements in sediments of southern California: A new anthropogenic indicator. *Environmental Science Techonology*, 25(2): 310-316.
10. Mohamed, C. A. R, Narita, H., Harada, K. and Tsunogai, S. (1996). Sedimentation of natural radionuclides on the seabed across the northern Japan Trench. *Geochemical Journal*, 30: 217-229.
11. Ramesh, R., Ramanathan, A. L., Ramesh, S. and Purvaja, V. R. (2000). Distribution of rare earth elements and heavy metals in the surficial sediments of the Himalayan river system. *Geochemical Journal*, 34(4): 295-319.
12. Yang, W. L., Mao, X. Y. and Dai, X. X. (2001). REE characteristics and environmental significance in core 96-7-1 in Elson Lagoon in the region of Barrow in the Arctic. *Chinese Journal of Polar Research*, 13(2): 91-106.

13. Peterson, G. S., Ankley, G. T. and Leonard, E. N. (1996). Effect of bioturbation on metal-sulfide oxidation in surficial freshwater sediments. *Environmental Toxicology and Chemistry*, 15(12): 2147-2155.
14. Bat, L., Sezgin, M. and Sahin, F. (2018). Heavy metal contamination of aquatic resources from Turkish Black Sea waters. *Journal of Environmental Protection and Ecology*, 19(2): 558–563.
15. Sadiku, M., Baruti, B. and Kelmendi, M. (2017). Presence of heavy metals in water and sediment of rivers Trepca and Sitnica. *Journal of Environmental Protection and Ecology*, 18(1): 10–21.
16. Liu, Y. G., Miah, M. and Schmitt, R. (1988). Cerium: A chemical tracer for paleo-oceanic redox conditions. *Geochimica et Cosmochimica Acta*, 52(6): 1361-1371.
17. Liu, Y. and Cao, L. M. (1987). Introduction of elemental geochemistry (in Chinese), Beijing. Geological Publishing House: pp. 81-97.
18. Rudnick, R. L.(1992). Eu anomalies and the lower continental crust. *Geochimica et Cosmochimica Acta*, 56(3): 963-970.
19. Anawar, H. and Freitas, M. C. (2010) Analysis of major and trace elements by INAA to predict the thousands year old sediment deposition environment in the Meghna river delta. *Journal of Radioanalytical and Nuclear Chemistry*, 283(2): 347-352.

Malaysian Journal of Analytical Sciences, Vol 23 No 3 (2019): 451 - 461
DOI: https://doi.org/10.17576/mjas-2019-2303-09

MALAYSIAN JOURNAL OF ANALYTICAL SCIENCES
Published by The Malaysian Analytical Sciences Society
ISSN 1394 - 2506

POTENTIAL OF CABBAGE EXTRACT (*Brassica oleracea*) AS ANTI-FOULING AGENT IN ALKYD UNDERCOAT FOR MILD STEEL IN SEAWATER

(Potensi Ekstrak Kubis (*Brassica oleracea*) Sebagai Ejen Anti-Kotoran bagi Cat Asas Alkid untuk Keluli Lembut di dalam Air Laut)

Mohammad Fakhratul Ridwan Zulkifli[1], Norasidayu Mohd Radzi[1], Suriani Mat Jusoh[1],Jasnizat Saidin[2], Wan Mohd Norsani Wan Nik[1]*

[1]*School of Ocean Engineering*
[2]*Institute of Marine Biotechnology*
Universiti Malaysia Terengganu, 21030 Kuala Nerus, Terengganu, Malaysia

**Corresponding author: niksani@umt.edu.my*

Received: 1 January 2019; Accepted: 22 May 2019

Abstract

An investigation was conducted on cabbage extract *(Brassica oleracea)* to observe its function as green antifouling agent in alkyd undercoat for mild steel in seawater. Cabbage extract shows 43.6% of inhibition efficiency towards *Pseudomonas aeruginosa* bacteria at 15.525 g/mL cabbage concentration. FTIR analysis shows the complexation between alkyd paint and cabbage extract where the peak in OH, C-H and C=O have shifted indicating the chain scission of the alkyd resin polymer backbone with cabbage extract. Weight gained analysis reveals that coated mild steel incorporated with cabbage extract had reduced the fouling attachment. However, weight gained value increases as the immersion period increases for all coated samples. Morphological profile of coated mild steel shows an attachment of fouling where prominent attachment can be observed on coated mild steel without cabbage extract.

Keywords: anti-fouling, alkyd undercoat, *Brassica oleracea*, *Pseudomonas aeruginosa*, mild steel

Abstrak

Kajian telah dilaksanakan terhadap ekstrak kubis untuk melihat fungsinya sebagai ejen anti-kotoran hijau di dalam cat asas alkid untuk keluli lembut di dalam air laut. Ekstrak kubis menunjukkan sebanyak 43.6% kecekapan perencatan terhadap bakteria *Pseudomonas aeruginosa* pada ekstrak kubis berkepekatan 15.525 g/mL. Analisis FTIR menunjukkan pengkompleksan antara pelitup cat asas alkid dan ekstrak kubis di mana puncak OH, C-H dan C=O telah berubah menandakan berlaku tindakbalas guntingan pada rantai utama polimer resin alkid yang mengandungi ekstrak kubis. Analisis pertambahan berat menunjukkan keluli lembut bersadur yang mengandungi ekstrak kubis telah mengurangkan kelekatan kotoran. Walaubagaimanapun, nilai pertambahan berat telah meningkat apabila tempoh rendaman meningkat untuk kesemua sampel bersadur. Profil morfologi keluli lembut bersadur menunjukkan perlekatan kotoran di mana perlekatan ini lebih jelas kelihatan pada keluli lembut bersadur tanpa gabungan ekstrak kubis.

Kata kunci: anti-kotoran, cat asas alkid, *Brassica oleracea*, *Pseudomonas aeruginosa*, keluli lembut

Introduction

Mild steel is vastly used in industrial application to build bridges, building and other structures including different types of machine parts [1]. Mild steel is low in cost and therefore it is relatively high in demand for this steel especially in maritime industry. Mild steel possesses enough strength despite its low carbon content. Besides, mild steel can be molded into any required shape and was known as one of the most versatile materials as it can be formed into various shapes.

However, growth of marine organism like barnacle, seaweed and bio-fouling is one of the paramount problems resulting in poor performance of the materials. One of the methods to avoid biofouling is by using antifouling coating based on organotin compounds such as tributyltin (TBT) and triphenyltin. However, organotin are not environmental-friendly as it is not readily degradable and are toxic to the environment. Hence, Internal Maritime Organization (IMO) prohibits the application of TBT in ships, effective on 17 September 2008 [2].

Therefore, development of environmentally antifoul coating to protect mild steel against marine organism attachment and fouling is utmost important. The potential of cabbage *(brassica oleracea)* as an eco-friendly antifouling for mild steel in seawater was then investigated. To achieve the objective, few methods were used in this study including crystal violet anti biofilm assay, weight measurements and scanning by electron microscope.

Materials and Methods

Surface preparation of mild steel

Mild steel grade JR235 (25mm x 25mm x 4mm) was cut into square shape and polished using copper brush to remove any loose rust or loose mill scales. Then the samples were soaked in thinner and wiped with a wet cloth to free its surface from any oil or dirt. Then it was rinsed with distilled water in accordance to ASTM D 2651 – 01 standard. The specimens were then stored in a desiccator prior to use.

Extraction of cabbage

Cabbages were purchased from the local supermarkets and cut into small pieces. Moisture in cabbages was removed through refrigeration at -80 ^{o}C for 24 hours. Then, it was transferred to a vacuum refrigerator with a temperature set at -40 ^{o}C in order to evaporate any frozen water in the plastic. Once the cabbage was dried, it was crushed into powder form. Then, the cabbage powder was immersed in 500 mL of methanol and soaked in a sonicator to accelerate the extraction. Finally, the rotary evaporator (rotavapor) was used to remove the solvents from samples.

Preparation of coating

MCI Paint Blue-I Undercoat (White) was used as an undercoating and it is suitable to be used under several conditions [3]. Four different weights of cabbage that are 2g, 4g, 6g, and 8g were incorporated in the coating. The modified coating was stirred for several hours. The specimens were coated using dip coating method. The thickness of the coating allowed for this paint is in the range of 80 to 120 microns which was measured by using PosiTector 6000 thickness gauge.

Antifouling crystal violet anti-biofilm assay

Pseudomonas aeruginosa used in this study is a type of marine bacteria that can grow in seawater as it has a very simple nutritional requirement. Muller Himpton Brooth and Muller Himpton Agar were prepared. The prepared bacteria, nutrient broth, sample of cabbage extract were then pipetted inside the 96 wells of microtiter plate and transferred into an incubator for 24 hours to allow the biofilms to grow. The optical density (OD) of bacteria liquid culture was determined and the reading must be less than 0.2 OD. After 24 hours of incubation at 37 ºC, the medium was gently removed and placed in the oven at 60 ºC for it to dry. The microtiter plate well was stained with 200 µL of 1% of crystal violet for 20 minutes at room temperature. The unbound crystal violet stain was removed and the well was gently washed three times with 200 µL distilled water without touching the well's wall. The wells then were air-dried for 15 minutes and the crystal violet in each well was solubilized by adding 200 µL of 75% alcohol and incubated at room temperature for 10 minutes in the shaker. The motion plate was read at 492 nm by using ELISA reader. The data was analysed using equation 1.

$$\text{Inhibition efficiency}(\%) = \frac{(\text{OD Negative control} - \text{OD Sample})}{\text{OD Negative control}} \times 100 \quad (1)$$

Immersion test

The immersion test was conducted at Merang Jetty, Terengganu. The samples were hung in a cage and sunk into the seabed below the jetty for 75 days as shown in Figure 1. The results were taken every 15 days and the weight changes were observed.

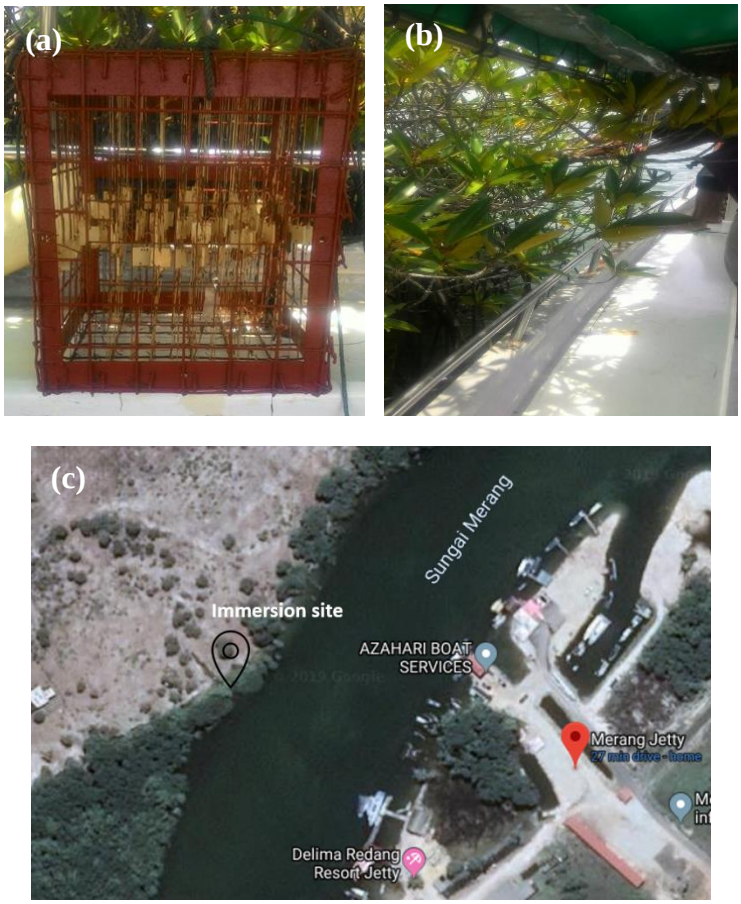


Figure 1. (a) Cage used as the sample holder, (b) Immersion took place at mangrove area and (c) Location of the immersion area

Fourier transform infrared

Fourier transform infrared (FTIR) was carried out using Thermo Nicolet 380 FTIR Spectrometer. The sample was placed on germanium crystal and passed through infrared light with the frequency ranging from 3960 - 660 cm^{-1} with spectral resolution of 4 cm^{-1} [4]. FTIR data were recorded in transmittance mode. The spectral pattern was analysed and matched according to IR absorption table.

Weight loss method

The process started by recording the initial weight of the mild steel specimen after it was coated with alkyd paints with and without cabbage extract. The plates were weighed every 15 days and the data were recorded. As part of the analysis procedure, the weight of these plates were re-measured after each immersion time interval. Equation 2 was used to calculate the percentage of the weight gained while Equation 3 was used to determine anti-fouling efficiencies.

$$\text{Weight gain (\%)} = \frac{\text{final weight} - \text{initial weight}}{\text{total weight}} \times 100 \quad (2)$$

$$\text{Anti fouling efficiency (\%)} = \frac{\text{weight gained}_0 - \text{weight gained}_1}{\text{weight gained}_0} \times 100 \quad (3)$$

where weight gained$_0$ is the weight gained percentage of coated samples without cabbage extract and weight gained$_1$ is the weight gained percentage of coated samples with cabbage extract.

Scanning electron microscopy

Scanning electron microscope (SEM) model JEOL JSM-6360LA was used in this study to observe and analyses the morphology of coated mild steel. The samples were subjected to coating process with an ultrathin gold particle layer using JFC-1600 Auto Fine Coater (JEOL Ltd., Tokyo, Japan). The gold coated samples being electrically conductive allows for scanning process on the sample surface at an accelerated voltage of 15 kV and a working distance of 10 mm.

Results and Discussion

Optical density

Pseudomonas aeruginosa was pipetted in 96 well plates. The percentage reading of inhibition efficiency for dilution test of antifouling crystal violet anti-biofilm assay was calculated using equation 1. From Table 1, the reading of OD negative control is greater than the value of OD sample.

Table 1. Inhibition efficiency of cabbage extract at various concentrations

Concentration of Cabbage (g/ml)	Optical Density of Cabbage Sample	Inhibition Efficiency (%)
15.525	1.737	43.6
7.763	1.864	39.5
3.881	2.067	32.9
1.941	2.212	28.2
0.970	2.334	24.2
0.485	2.449	20.5
0.243	2.928	4.9
OD negative	3.080	

Figure 2 shows the dilution test plot of the cabbage extracts towards the target bacteria of *Pseudomonas aeruginosa*. As the concentration of cabbage extract increases, the ability to inhibit the formation of biofilm also increases. Generally, plants are known to have natural fouling inhibition effect against Gram-negative and Gram-positive bacteria [5]. The bacteria used in this test were *Pseudomonas aeruginosa*, a type of Gram-negative bacteria. The activity against this type of bacteria indicated the presence of broad-spectrum antibiotic compounds or simply any general metabolic toxins. The antimicrobial efficiency of components in plants depends on the chemical structure of active components and the concentration used. Some of the chemical components present in plants giving antimicrobial characteristics that include thiosulfinates, saponin, flavonoids, phenolic, organic acids, and glucosinolates [6]. The phenolic compound such as terpenes, aliphatic alcohol, aldehydes, ketones, acids and isoflavonoids are the main components in plants that have antimicrobial activity [7].

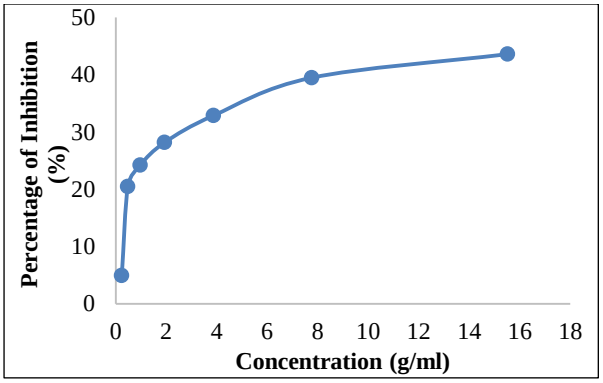


Figure 2. Percentage of inhibition efficiency of cabbage extract towards targeted bacteria (*Pseudomonas aeruginosa*)

Fouling inhibition effect of cabbage is strongly influenced by its active ingredient known as phenolic compounds. This compound is well known as anti-microbial agent that either kills microorganisms or suppresses their growth. The antimicrobial activity of phenolic compounds is to alter microbial cell permeability, hence enable the loss of macromolecules from the cell interior [6, 8]. The cabbage showed anti-microbial activity against *Pseudomonas aeruginosa* due to the presence of the phenolic compound.

Fourier transform infrared

FTIR spectrum was used to identify the functional groups of the active components present in cabbage extract, alkyd paint and the modified alkyd paint based on the peak values in the recorded spectrum. The FTIR spectrum of cabbage extract is shown in Figure 3. The absorption band at 3368.06cm^{-1} can be attributed to the O-H stretching in alcohol group while another peak at 2937.04 cm^{-1} can be assigned to C-H stretching for alkenes. The peak obtained at 2106.99 cm^{-1} showed the presence of C≡C stretching representing the alkynes compound. Broad absorption at 1638.01 cm^{-1} indicates the presence of N-H bending while at 1412.11 cm^{-1} revealed the presence of C-C stretching (aromatic ring). The functional group of alcohol, carboxylic acid, ester, and ethers were found at peak value of 1059.80 cm^{-1} (C-O stretching). Cabbage showed infrared absorbance characteristics of carboxylic acid (O-H) at the peak of 919.93 cm^{-1}. The functional alkenes group (=C-H) was also found in the cabbage at the peak of 866.76 cm^{-1}. Other functional group found were C-CL stretching, alkyl halides at the peak of 818.67 cm^{-1}. The phenolic compound was characterised as having at least one aromatic ring with one or more hydroxyl groups attached to it [9].

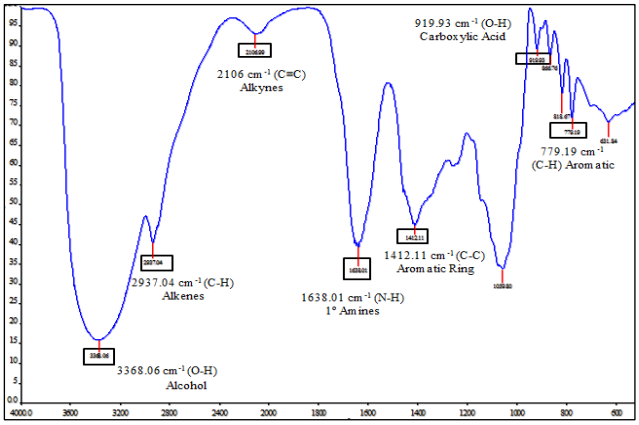


Figure 3. FTIR spectrum for cabbage extract

FTIR spectrum of alkyd undercoat is shown in Figure 4. C-H stretching alkenes is found at 2926.63 cm^{-1}, 1735.12 cm^{-1} indicating the presence of stretching C=O while C-C and C-H aromatics were found at 1417.05 cm^{-1} and 743.49 cm^{-1}.

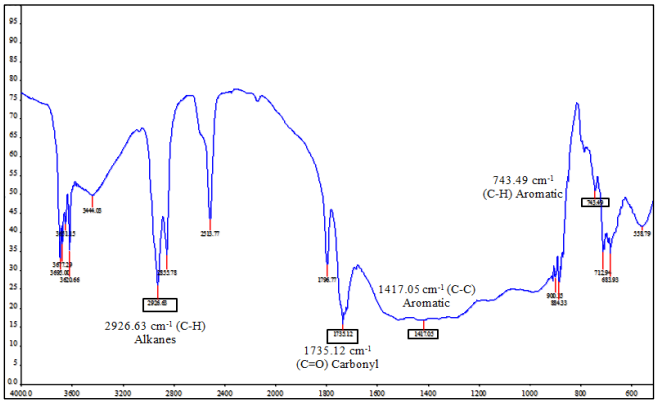


Figure 4. FTIR spectrum for alkyd undercoat

Figure 5 shows the spectrum profile of alkyd undercoat with the incorporation of cabbage extract. A broad band of stretching OH shifted from 3368.06 to 3319.93 cm^{-1} due to alkyd resin polymer backbone dissociate while cabbage extract has been associated in the polymer to form a complexation. C-H stretching in medium intensity was shifted from 2937.04 to 2927.33 cm^{-1} while a strong intensity band of carbonyl shifted from 1727.25 to 1735.12 cm^{-1} due to chain scission of alkyd undercoat polymer that allows reaction with other molecules.

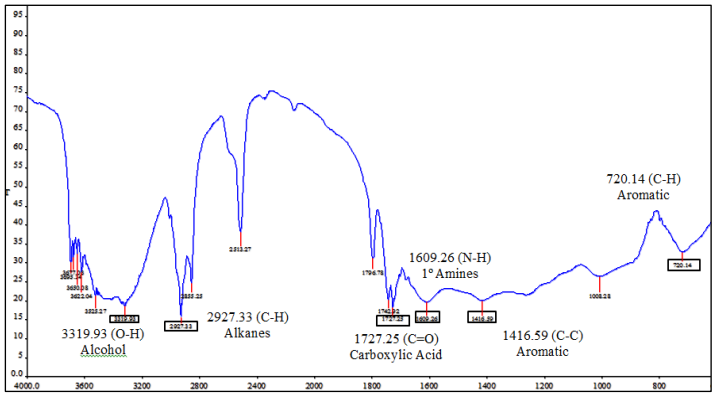


Figure 5. FTIR spectrum graph for alkyd undercoat incorporated with cabbage extract

Weight measurement

Table 2 shows the percentage data of additional weight for all tested samples. The coated samples without any cabbage loading show the highest percentage in weight gain. Sample with the highest concentration of cabbage (0.20 g/mL) shows the least percentage in additional weight for the entire period of immersion. Figure 6 shows the percentage of additional weight for each sample with different cabbage concentration relative to its immersion period. Upon addition of cabbage extract in alkyd undercoat, the weight gain of the coated samples was reduced and the efficiency increases. As the concentration of cabbage extract increases, the value of weight gain was found to decrease and the efficiency increases. However, as the immersion period increases, weight gains were also increased for all coated samples which consequently reduce its anti-fouling efficiency.

Table 2. Weight measurement data for different concentration of cabbage

Sample concentration (g/ml)	Days	Initial weight (g)	Final weight (g)	Total weight (g)	Additional weight (%)	Anti-fouling efficiency (%)
0.00	15	14.85	14.878	29.756	0.094	-
	30	14.409	14.611	29.222	0.691	-
	45	14.148	14.475	28.95	1.13	-
	60	14.698	15.173	30.346	1.565	-
	75	14.543	15.057	30.114	1.707	-
0.05	15	14.978	15.001	30.002	0.077	18
	30	14.694	14.859	29.718	0.555	20
	45	14.686	15.001	30.002	1.05	7
	60	14.783	15.216	30.432	1.424	9
	75	14.682	15.15	30.3	1.543	10
0.10	15	14.712	14.729	29.458	0.058	38
	30	14.617	14.742	29.484	0.424	39
	45	14.577	14.817	29.634	0.81	28
	60	14.73	15.076	30.151	1.148	27
	75	14.513	14.912	29.823	1.336	22
0.15	15	14.848	14.856	29.712	0.027	71
	30	14.782	14.865	29.73	0.279	60
	45	14.47	14.634	29.268	0.56	50
	60	14.836	15.078	30.157	0.803	49
	75	14.634	14.942	29.884	1.03	40
0.20	15	15.098	15.1	30.2	0.007	93
	30	14.813	14.855	29.71	0.142	79
	45	14.755	14.84	29.68	0.285	75
	60	14.998	15.167	30.333	0.555	65
	75	14.872	15.076	30.152	0.675	60

The fouling process involves three main stages known as the formation of conditioning film, micro-fouling and macro-fouling [10]. During conditioning film phase, organic molecules in the water attached to the surface of the immersed object and within minutes intensify their activity for further attachment. During the second phase (micro-fouling), the combination of conditioning film and dead bacteria cells generates the first stage of micro fouling. Then the macro-algae, diatoms colonies and protozoa spore's attachment increase the micro-fouling extent within the first two to three weeks, generating the second film layer. Lastly, the final stage is when the micro-fouling encourages the attachment of algae, animal larvae and spores, and followed by the settlement of a mature marine organism, the process which is called macro-fouling [10].

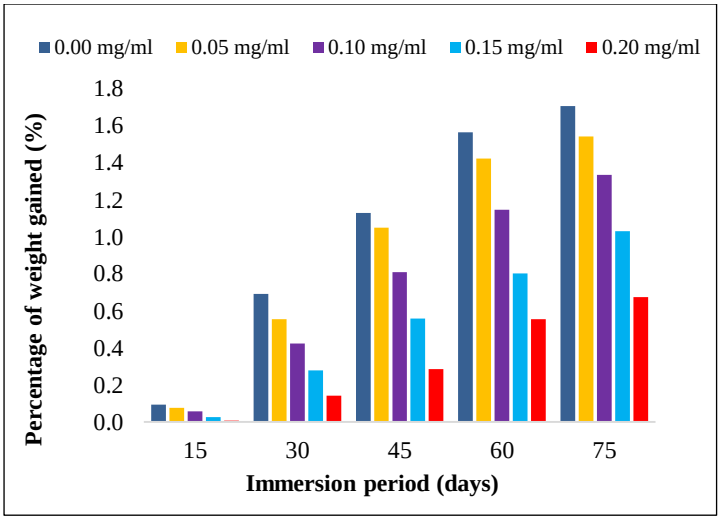


Figure 6. Percentage of weight gain by different concentration of cabbage extract

Cabbage extract contains a compound known as phenolic compound. Phenolic compound was usually derived from natural sources such as plants foods such as fruits, cereal grain, and vegetables that have antifungal properties. The most common phenolic compounds are phenolic acids, flavonoids, and lignin [11]. Phenolic acids affect the cell membrane of Gram-positive and Gram-negative bacteria and lead to a change in cell surface hydrophobicity and charge which ultimately cause leakage of cytoplasmic content [12]. Figure 7 shows how the phenolic compound in the cabbage extract reacted to the organism in the water by inhibiting the microorganism from attaching at the mild steel surface. The hydroxyl group attached to the benzene ring (phenolic compound) interrupts the formation of conditioning film (the first step of fouling process) on the metal surface and repels the attachment of organism in seawater with the present of OH^- in the modified paint.

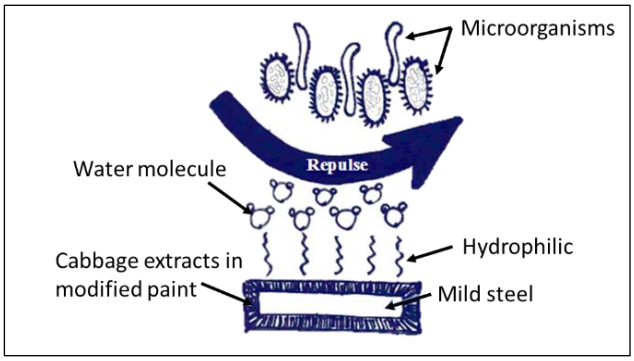
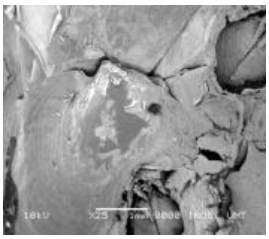
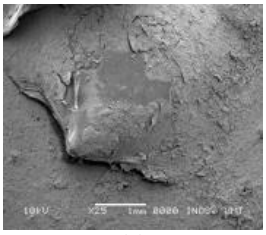
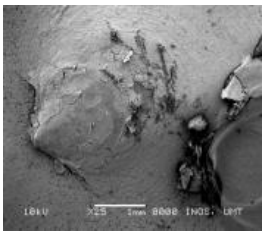
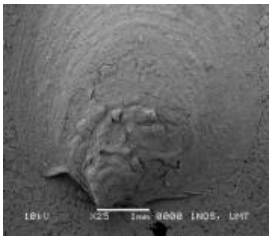
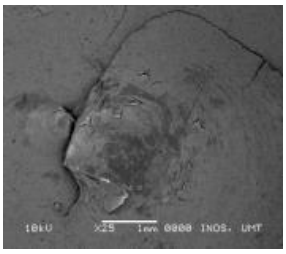


Figure 7. The mechanism of antimicrobial function in cabbage

Scanning electron microscope

The morphology profile of coated samples is shown in Table 3. The attachment and formation of the fouling organism on the surface of mild steel can be observed. The cabbage which acts as an inhibitor was chemically absorbed on the surface of the metal and formed a protective thin film with inhibitor effect [13]. Based on the camera image in Figure 8, there are many fouling organisms formed at the surface of coated mild steel without incorporation of cabbage extract. Figure 9 shows an image of coated mild steel with the highest concentration of cabbage extract (0.20 mg/mL). At this stage, the least amount of fouling attachment can be seen.

Table 3. SEM and camera image after 75 days of immersion test at Merang Jetty

Sample Concentration (g/mL)	**SEM Image (x 25 magnification)**	**Camera Image**
0.00	 (a)	 (b)
0.05	 (c)	 (d)
0.10	 (e)	 (f)
0.15	 (g)	 (h)
0.20	 (i)	 (j)

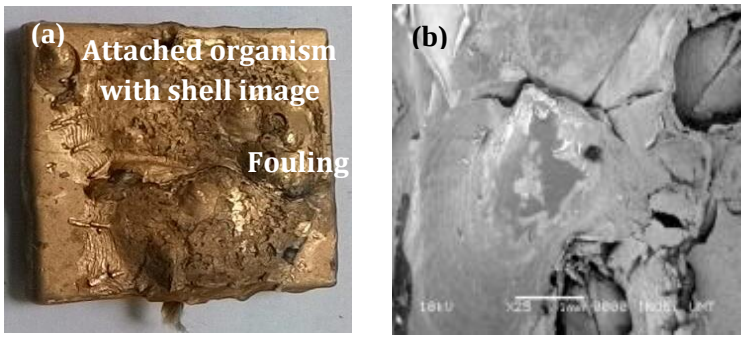


Figure 8. (a) Camera image and (b) SEM image of 25 times magnification after immersion test for 0.00 mg/mL concentration

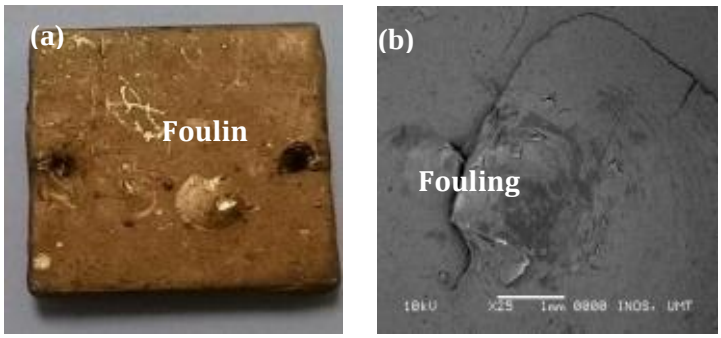


Figure 9. (a) Camera image and b) SEM image of 25 times magnification after immersion test for 0.20 mg/mL concentration

The amount of fouling attached on the surface of mild steel for all coated samples is tabulated in Table 3. Visual observation shows that the fouling attachment is decreasing as the concentration of cabbage extract increases. It can be inferred that the incorporation of cabbage extract increases the anti-fouling properties of the alkyd undercoat. According to the suggested mechanism previously discussed, cabbage extract has the potential to be an anti-fouling agent in alkyd paint.

Conclusion

Crystal violet anti-biofilm assay and weight measurement prove that cabbage has a good antifouling properties and performance. Anti-fouling efficiency increases as the cabbage extract concentration is increased but decreases in longer immersion period. FTIR analysis shows that there is complexation reaction between alkyd undercoat and cabbage extract that contributes to the anti-fouling performance of the modified alkyd undercoat. The results show that cabbage extract has the ability to inhibit the growth of fouling for immersed metal surface even with low concentration of the extract. Therefore, it is inferred that cabbage extract as a natural product has a potential as an additive in paint to reduce fouling settlement on the coated mild steel.

Acknowledgement

The author would like to thank laboratory staff of Maritime Technology, School of Ocean Engineering and Institute of Marine Biotechnology for their assistance and Ministry of Higher Education for the look east policy grant (53168).

References

1. Finšgar, M. and Jackson, J. (2014). Application of corrosion inhibitors for steels in acidic media for the oil and gas industry: A review. *Corrosion Science*, 86: 17-41.

2. Qian, P. Y., Xu, Y. and Fusetani, N. (2009). Natural products as antifouling compounds: recent progress and future perspectives. *Biofouling*, 26(2): 223-234.
3. Abdullah, S. H. (2012). Antifouling potential of mangrove bark condensed tannins (*Rhizophora apiculata*) as antifouling for mild steel in seawater. Thesis of Bachelor Degree, Universiti Malaysia Terengganu.
4. Samsudin, A. S., Khairul, W. M., and Isa, M. I. N. (2012). Characterization on the potential of carboxy methylcellulose for application as proton conducting biopolymer electrolytes. *Journal of Non-Crystalline Solids*, 358: 1104-1112.
5. Yayan, J., Ghebremedhin, B. and Rasche, K. (2015). Antibiotic resistance of *Pseudomonas aeruginosa* in pneumonia at a single university hospital center in Germany over a 10-year period. *PLOS one*, 10(10): 1-20.
6. Hayek, S. A. and Ibrahim, S. A. (2013). Current limitations and challenges with lactic acid bacteria: A review. *Food and Nutrition Sciences*, 4(11): 73-87.
7. Tiwari, B. K., Valdramidis, V. P., O'Donnell, C. P., Muthukumarappan, K., Bourke, P. and Cullen, P. J. (2009). Application of natural antimicrobials for food preservation. *Journal of Agricultural and Food Chemistry*, 57(14): 5987-6000.
8. Bajpai, V. K., Rahman, A., Dung, N. T., Huh, M. K., and Kang, S. C. (2008). In vitro inhibition of food spoilage and foodborne pathogenic bacteria by essential oil and leaf extracts of *Magnolia liliflora* Desr. *Journal of Food Science*, 73(6): 314-320.
9. Balasundram, N., Sundram, K. and Samman, S. (2006). Phenolic compounds in plants and agri-industrial by-products: Antioxidant activity, occurrence, and potential uses. *Food Chemistry*, 99(1): 191-203.
10. Nurioglu, A. G., and Esteves, A. C. C. (2015). Non-toxic, non-biocide-release antifouling coatings based on molecular structure design for marine applications. *Journal of Materials Chemistry B*, 3(32): 6547- 6570.
11. Teodoro, G. R., Ellepola, K., Seneviratne, C. J. and Koga-Ito, C. Y. (2015). Potential use of phenolic acids as anti-Candida agents: a review. *Frontiers in Microbiology*, 6: 1420.
12. Cho, J. Y., Kwon, E. H., Choi, J. S., Hong, S. Y., Shin, H. W. and Hong, Y. K. (2001). Antifouling activity of seaweed extracts on the green alga *Enteromorpha prolifera* and the mussel *Mytilus edulis. Journal of Applied Phycology*, 13(2): 117-125.
13. Dariva, C. G. and Galio, A. F. (2014). Corrosion inhibitors–principles, mechanisms and applications. In developments in corrosion protection. InTech Open Publisher.

Malaysian Journal of Analytical Sciences, Vol 23 No 3 (2019): 462 - 471
DOI: https://doi.org/10.17576/mjas-2019-2303-10

MALAYSIAN JOURNAL OF ANALYTICAL SCIENCES
Published by The Malaysian Analytical Sciences Society
ISSN 1394 - 2506

SYNTHESIS OF MESOPOROUS NANOPARTICLES VIA MICROWAVE-ASSISTED METHOD FOR PHOTOCATALYTIC DEGRADATION OF PHENOL DERIVATIVES

(Sintesis Nanopartikel Bermesoliang Melalui Kaedah Bantuan-Gelombang Mikro untuk Degradasi Fotomangkin daripada Terbitan Fenol)

Nur Farhana Jaafar[1]*, Nor Amira Marfur[1], Nurfatehah Wahyuny Che Jusoh[2], Yuki Nagao[3], Nur Hidayahtul Nazirah Kamarudin[4,5], Rohayu Jusoh[6], Mohammad Anwar Mohamed Iqbal[1]

[1]*School of Chemical Sciences, Universiti Sains Malaysia, 11800 USM Penang, Malaysia*
[2]*Department of Chemical Process Engineering, Malaysia-Japan International Institute of Technology (MJIIT), Universiti Teknologi Malaysia Kuala Lumpur, Jalan Sultan Yahya Petra, 54100 Kuala Lumpur, Malaysia*
[3]*School of Materials Science, Japan Advanced Institute of Science and Technology, 1-1 Asahidai, Nomi, Ishikawa 923-1292, Japan*
[4]*Research Center for Sustainable Process Technology (CESPRO),*
[5]*Chemical Engineering Programme, Faculty of Engineering and Built Environment, Universiti Kebangsaan Malaysia, 43600 UKM Bangi, Selangor, Malaysia*
[6]*Faculty of Chemical and Natural Resources Engineering, Universiti Malaysia Pahang, Lebuhraya Tun Razak, 26300 Gambang, Kuantan, Pahang, Malaysia*

**Corresponding author: nurfarhana@usm.my*

Received: 14 January 2019; Accepted: 26 April 2019

Abstract

Mesoporous transition metal oxides have gained attention widely since they possess both optical and electronic properties of transition metal oxides especially for photocatalytic degradation application. In this research work, mesoporous titania nanoparticles (MTN) and mesoporous zinc oxide nanoparticles (MZN) were successfully synthesized using microwave (MW)-assisted method to degrade phenol derivatives under visible light irradiation. The microwave sintering effect on the surface of these modified structures was studied to relate with their photocatalytic performance. The characterization results indicated that MW-assisted method was mainly contributed in generating Ti^{3+} site defects (TSD) and oxygen vacancies (OV) in MTN while for MZN contained only OV as one of the strategies in light-absorption modification for TiO_2 and ZnO to enhance their photoactivity. MTN also showed the degradation of 2-chlorophenol was up to 97% while degradation of phenol by MZN was up to 87%.

Keywords: mesoporous nanoparticles, titanium dioxide, zinc oxide, microwave-assisted, photocatalytic

Abstrak

Logam oksida peralihan bermesoliang telah mendapat perhatian secara meluas kerana mereka mempunyai kedua-dua sifat optik dan elektronik bagi oksida logam peralihan terutamanya untuk aplikasi degradasi fotomangkin. Dalam kajian ini, nanopartikel titania bermesoliang (MTN) dan nanopartikel zink oksida bermesoliang (MZN) telah berjaya disintesis menggunakan kaedah bantuan-gelombang mikro (MW) untuk mendegradasi terbitan fenol di bawah sinaran cahaya nampak. Kesan pensinteran gelombang mikro pada permukaan struktur yang diubahsuai telah dikaji untuk dikaitkan dengan prestasi fotomangkin mereka. Keputusan pencirian menunjukkan bahawa kaedah bantuan-MW merupakan penyumbang utama dalam pembentukan tapak Ti^{3+} cacat (TSD) dan kekosongan oksigen permukaan (OV) dalam MTN manakala bagi MZN hanya mengandungi OV sebagai salah

satu strategi untuk pengubahsuaian penyerapan-cahaya bagi TiO_2 and ZnO untuk meningkatkan fotoaktiviti mereka. MTN juga menunjukkan degradasi 2-klorofenol sehingga 97% manakala degradasi fenol oleh MZN sehingga 87%.

Kata kunci: nanopartikel bermesoliang, titanium dioksida, zink oksida, bantuan-gelombang mikro, fotomangkin

Introduction

Among various semiconductors, TiO_2 and ZnO are the most promising photocatalysts since they possess good photosensitivity and chemical stability besides non-toxic and low cost. TiO_2 is generally used in production of sunscreen, dye sensitized solar cells, orthopedic and pharmaceutical field [1-3]. On the other hand, ZnO is frequently used in the production of biodiesel, supercapacitor, water purification and biomedical industries [4-7]. However, they are affected by some limitations related to optical and electronic properties [8, 9]. TiO_2 and ZnO have a large band gap which is 3.20 eV and 3.37 eV, respectively [10, 11]. Their wide band gap can reduce their photocatalytic performance in the UV wavelength region which contributes around 3 to 5% of the total solar spectrum. Hence, these photocatalysts are highly active under UV light illumination rather than visible light irradiation. Besides that, fast recombination of photo-induced holes and electrons may restrict their photodegradation efficiency. Therefore, major energy loss and very low photocatalytic reaction occur resulting from significant absence of electron donors or acceptors [12, 13].

Nowadays, mesoporous transition metal oxides have been studied widely since they are well known for having both optical and electronic properties of transition metal oxides. These properties give many advantages for different applications since it can have various morphologies and compositions including fibers, nanoparticles, monoliths and thin films besides possess large and uniform pore size which increase high surface area and long range of ordering structure also tunable pore diameter [14].

Through (MW)-assisted process, the efficiency of these photocatalysts can be enhanced since this method to increase their porosity and generate numerous site defects which are TSD and OV for MTN and OV for MZN [15-19]. Microwave is an essential appliance practically in most kitchens. This appliance is beneficial in term of time's consumption and energy savings compared to traditional food preparation methods [20]. Different methods have been investigated to synthesize mesoporous nanoparticles including e-beam irradiation, high-temperature hydrogenation, plasma treatment, sol-gel and vacuum activation [21-24]. However, these synthesis methods involve uneven temperature distribution, long reaction time and reduction conditions. (MW)-assisted process has been successfully demonstrated as being fast and effective in the preparation of mesoporous materials [25-27].

Generally, the microwave radiation will heat the reactants but not the reaction container itself as the radiation passes through the walls of the container. Process of microwave heating involve the transferring of electromagnetic energy to thermal energy. Heat also can be supplied throughout the sample since microwaves capable in penetrating the materials and storing energy [28]. Particularly, energy transfer has the potential to reach a uniform and heat the thick materials in the short time since it does not depend on the heat dispersion from the surfaces. Hence, the heating can be uniform throughout the material and may lead to less formation of by-products and/or decomposition products, if the machine is well-designed. In addition, the microwave energy is capable to increase the heating rate, decrease the kinetics of crystallization and potentially form new metastable phases [29]. This method also provides a uniform and speedy reaction environment to produce materials with homogenous and dispersed morphology [30]. Nevertheless, the popularity of using (MW)-assisted process in synthesizing mesoporous nanomaterial keep increasing due to its various benefits such as shorter the reaction times, heating of selective material, transferring of energy instead of heat, volumetric heating ability, obtaining high purity materials and heating starts from interior of material body and in many cases smaller particle sizes [31].

Use of MTN and MZN as photocatalyst usually applies in Advanced oxidation process (AOP). AOP is a set of chemical treatment methods to degrade the organic and inorganic material in wastewater thru oxidation. Photocatalytic degradation is one of AOPs procedures that promote the generation of electron-hole pairs once the photon excited from the valance band (VB) to the conduction band (CB) when the catalyst irradiated by light. Besides that, this process has demonstrated a great potential for wastewater treatment method to degrade organic pollutant and mainly suitable for the removal of non-biodegradable materials such as aromatics, petroleum

constituent, pesticides and volatile organic in wastewater. Through this process, the pollutant materials are converted into stable inorganic compounds such as carbon dioxide and water which are less hazardous [32-35].

Chlorophenol is a common pollutant released from industrial parks into aqueous environmental system which has gained a great concern due to their high toxicity, stability and potentially carcinogenic. Therefore, there are many studies conducted regarding the appropriate methods to eliminate these compounds to decrease the adverse effect toward the environment and humans. Based on the Environmental Quality Act 1979 (Sewage and Industrial Effluent), Department of Environment (DOE) in Malaysia has gazette allowable limit that this pollutant should be treated not more than 1 mg L^{-1} before being released to the environment as they can affect the odor and taste of drinking water with concentrations as low as a few μgL^{-1}.

In this study, (MW)-assisted process was used to synthesized MTN and MZN to degrade 2-chlorophenol and phenol, respectively under visible light irradiation. The effect of microwave sintering on the surface of these modified structures regarding to generation of site defects which were TSD and OV in MTN while for MZN contained only OV were studied as one of the strategies in light-absorption modification for TiO_2 and ZnO to enhance their photocatalytic performance.

Materials and Methods

Reagents and material

Titanium (IV) isopropoxide (TTIP), zinc acetate and sodium dodecyl sulfate (SDS) surfactant were bought from Sigma-Aldrich. 2-propanol, phenol and hydrochloric acid (HCl) were purchased from MERCK, Malaysia. Acetone and methanol were purchased from RPE Reagent pure Erba. Sodium hydroxide (NaOH) and ammonium hydroxide (NH_4OH) were purchased from QREC^{TM} and 2-chlorophenol (2-CP) from Alfa Aesar, Germany with 99% purity.

Synthesis of mesoporous nanoparticles

The mesoporous titania nanoparticles (MTN) was synthesized by the microwave (MW)-assisted process. SDS surfactant was dissolved in distilled water, 2-propanol and ammonia solution. The mixture was stirred continuously for 30 minutes at 50 °C in water bath. Then, titanium (IV) isopropoxide (TTIP) was added into the mixture and continued stirring for 2 hours at 80 °C before placing in the MW. MW heating was conducted in a domestic MW oven (Samsung ME711K), which can be operated with power ranging from 100-800 W and frequency of 2.45 GHz. The power density of MW was adjusted with 0.56 Wg^{-1} and the heating of the mixture was continued for 2 hours to allow the formation of sol-gel. The obtained product was collected and dried overnight in an oven before calcined at 600 °C for 3 hours. This procedure was applied in the synthesis of mesoporous zinc oxide nanoparticles (MZN) except the TTIP was replaced with zinc acetate and the obtained product was calcined at 550 °C for 3 hours.

Material characterization

The chemical oxidation of the catalysts was determined using X-ray photoelectron spectroscopy (XPS) conducted on a Kratos Ultra spectrometer equipped with an Mg Kα radiation source (10 mA, 15 kV). The crystalline structures of the catalysts were carried out using a Bruker Advance D8 X-ray powder diffractometer (XRD). The band gap of the catalysts was measured using UV-Vis diffuse reflectance spectra (UV-Vis DRS) using Perkin-Elmer Lambda 900 UV/VIS/NIR spectrometer with an integrating sphere. Nitrogen adsorption-desorption isotherms were used to determine the textural properties at liquid nitrogen temperatures using a SA 3100 Surface Analyzer (Beckman Coulter). The Brunnauer-Emmett-Teller (BET) was used to calculate surface area of the catalyst.

Photodegradation of phenol derivatives

The photoactivity of the MTN and MZN was tested on degradation of 2-CP and phenol, respectively. The photocatalytic experiments were performed in a batch reactor with connected to 48 W fluorescence lamp as a visible light source. For photoactivity process, 0.075 g of catalyst was added to the solution with the desired concentration (200 mL) and stirred for 1 h in the dark condition to achieve adsorption-desorption equilibrium before continued for another 6 h under light irradiation. During the reaction, aliquots of 2 mL were taken out at intervals of 30 min and centrifuged in a Hettich Zentrifugen Micro 120 at 15000 rpm for 15 minutes before being analyzed by UV-Vis spectrophotometry (Shimadzu UV-Vis Spectrometer, UV-2600) for determination of residual concentration of

solution. Each set of experiments was performed triplicates. The adsorption band of 2-CP and phenol was taken at 274 and 270 nm, respectively. The percentage degradation was calculated using the following equation 1:

$$\text{Degradation (\%)} = \frac{C_i - C_t}{C_i} \times 100 \quad (1)$$

where C_i and C_t are the initial concentration 2-CP and the concentration at time t, respectively.

Results and Discussion

Characterization of the catalysts

Fig. 1 shows the XRD diffractogram of MTN (Figure 1a) and MZN (Figure1b). Figure 1a demonstrated a series of XRD peaks for the TiO_2 anatase phase was observed at 25.3° (101), 37° (004), 38° (112), 48° (200), 53° (105) and 55° (211). Other than anatase phase, TiO_2 rutile phase was detected at 28° (110) and 54° (211) as well as brookite phase at 32° (121). The MZN (Figure 1b) demonstrated all the peaks are fits with the hexagonal wurtzite structure of ZnO (JCPDS No. 01-072-2743). A series of XRD peaks for the ZnO at 31°, 34.4°, 36°, 47.3°, 57°, 63°, 67.9° and 69.5° were corresponding to (100), (002), (101), (102), (110), (103), (112) and (201) planes, respectively. It can be observed that both catalysts illustrated a good crystallinity, degree of orderliness and mesoporous uniformity where indicated that MW-assisted method efficaciously provide a good heat distribution during synthesis by heating the entire reaction solution with proper temperature to improve the structural arrangement [36].

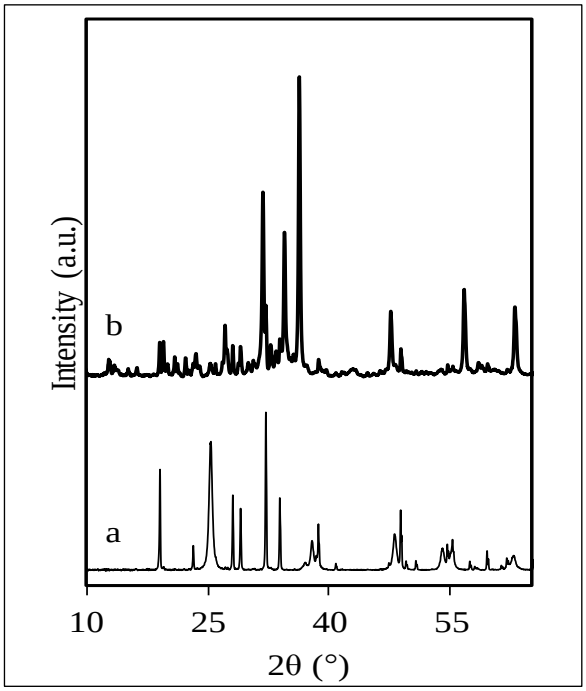


Figure 1. XRD diffractograms of (a) MTN and (b) MZN

The chemical states of MTN and MZN were determined using XPS as showed in Figure 2. Figure 2a shows the Ti2p spectrum of MTN in the region of 454-470 eV. The Ti2p can be fixed into five peaks which are at 458.2 ($Ti2p_{3/2}$), 459 ($Ti2p_{3/2}$) and 462.5 ($Ti2p_{1/2}$) eV were assigned to Ti^{3+}, while the peaks at 455.6 ($Ti2p_{3/2}$) and 465.2 ($Ti2p_{1/2}$) eV were attributed to Ti^{4+} [37]. The O1s spectrum of MTN (Figure 2b) illustrated the presence of Ti^{4+}-O peaks at 529.8 and 533.5 eV, whereas peaks at 530.2 and 532.6 eV is attributed to Ti^{3+}-O and hydroxide or hydroxyl group (OH^-), respectively [38]. According to Naeem et al. the development of OH^- peak indicated the presence of OV in the catalyst [39]. The oxidation state of Zn in MZN (Figure 2c) was illustrated by Zn2p doublet peaks at 1018

eV ($Zn2p_{3/2}$) and 1041 eV ($Zn2p_{1/2}$) indicated the oxidation state of Zn is 2+ where the different in binding energy for both peaks are 23 eV which further confirmed the characteristic of a Zn^{2+} oxidation state in ZnO wurtzite structure [40]. Figure 2d shows the O1s spectrum of MZN can be fixed into three peaks at 528.35, 530 and 533 eV. The peak at 528.35 eV was attributed to O^{2-} ions in ZnO wurtzite structure of hexagonal Zn^{2+} which can be illustrated as Zn-O bonds [41]. The presence of OV in the MZN can be detected at peak 530 eV where this peak illustrated the O^{2-} in the oxygen deficient regions with the matrix of ZnO [42], while the highest peak at 533 eV was assigned to the presence of loosely bound of oxygen on the surface of ZnO [43]. These results confirmed the presence of TSD and OV in the MTN as well as OV in MZN where it is a good prospective because the photocatalyst depends mainly on the OV and TSD especially for application under visible light irradiation.

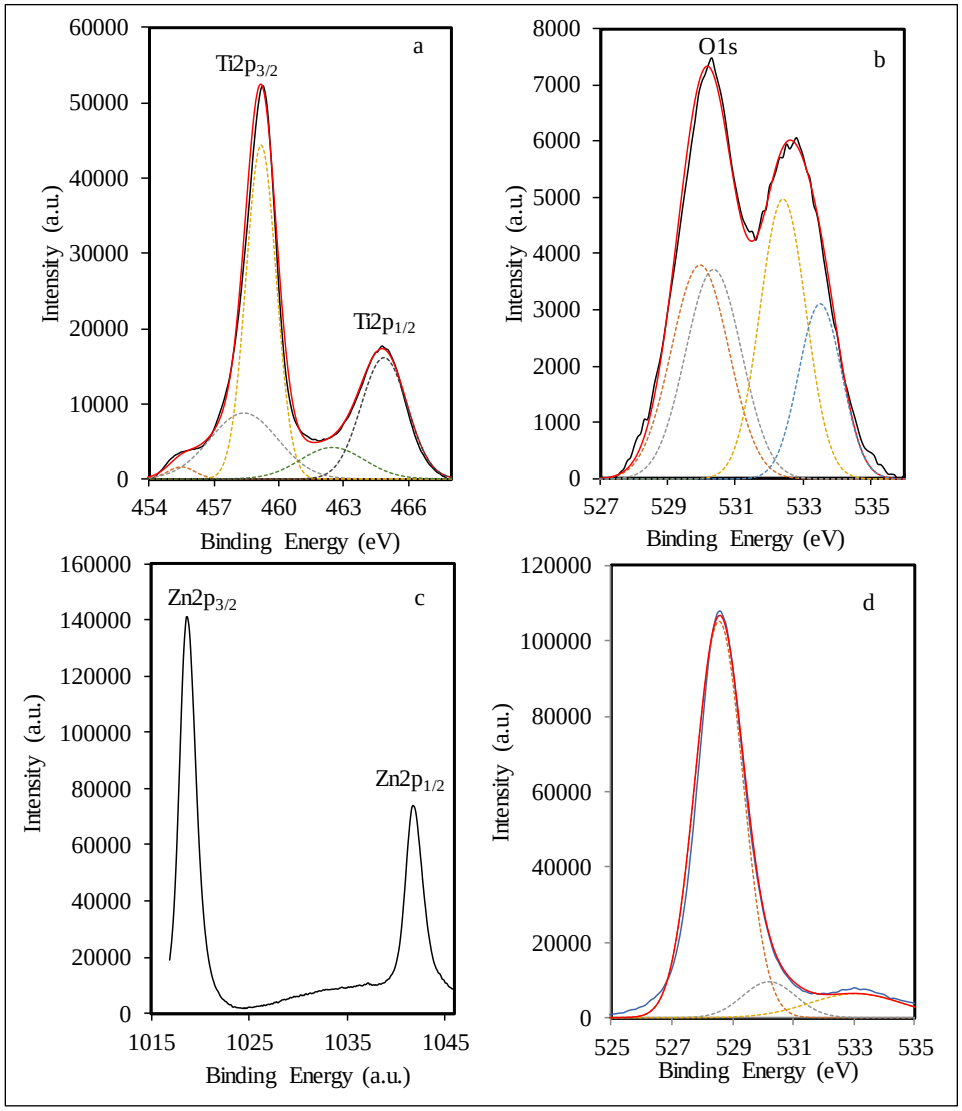


Figure 2. XPS spectra of (a) Ti2p and (b) O1s of MTN, (c) Zn2p and (d) O1s of MZN

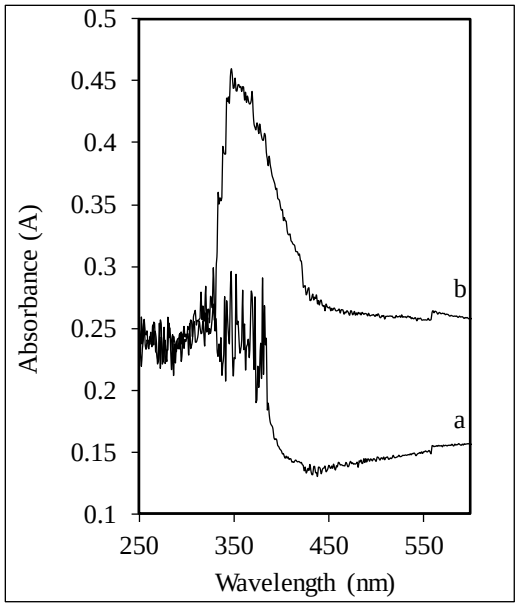


Figure 3. UV-Vis diffuse reflectance spectra at range 250-600 nm of (a) MTN and (b) MZN

Based on the characterization results, it's revealed that MW-assisted method was successfully synthesized MTN and MZN. This method shows potential for self-modified MTN containing TSD and OV, while and MZN containing OV as one of the strategies in light-absorption modification for TiO_2 and ZnO to enhance their photoactivity. This method promising limit time required in synthesis of catalyst compared with other conventional chemical synthesis method where it's allowed the hydrolysis and condensation processes occurred during the microwave electromagnetic radiation (red arrow) after the precursor formed at the template created by SDS. In addition, it also demonstrated as being effective in the preparation of mesoporous materials since can provide a uniform and fast reaction environment to produce materials with homogenous and dispersed morphology [40]. The microwave energy is capable to increase the heating rate, reduce the kinetics of crystallization and potentially form new metastable phases [29]. This method affects the nucleation without having direct contact between the reacting chemicals and energy sources which demonstrates that the volumetric heating is not involving the heat diffusion or the wall [26]. Furthermore, the microwave energy is directly applied to the solution over molecular interaction with the electromagnetic field. The heat generated in this method pass throughout the material uniformly resulting good in the sintering by inhibits the particle growth. Figure 4 shows the schematic diagram of MW-assisted process. The particle growth may also reduce during the heat treatment which leading to a higher surface area and improve the catalyst efficiency. Electromagnetic wave in microwave caused the water dipole rotation and ion oscillation on crystallization mechanism which may differ from conventional heating.

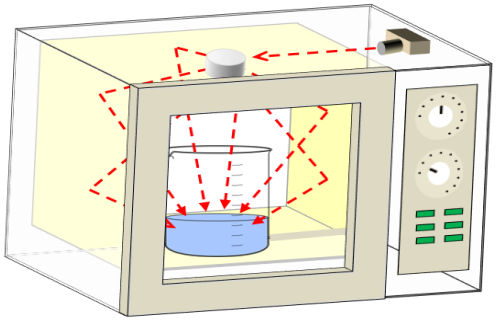


Figure 4. Schematic diagram of microwave-assisted process

Catalytic testing on photodegradation of phenol derivatives

The photocatalytic activity of MTN and MZN was tested on the degradation of phenol derivatives under visible light irradiation as showed in Figure 5. It was after 6h irradiation clearly observed that both catalysts successfully degrade 97% and 88% of 2-CP (MTN) and phenol (MZN), respectively. The 2-CP was almost successfull degraded by MTN probably due to the presence of TSD and OV which may acted as electron acceptors to lesson electron hole recombination and improves the photoactivity although the band gap in the UV range. Generally, the MTN required energy larger or equal than 387.5 nm to excite the electron from the valance band (VB) to the conduction band (CB). However, the presence of TSD and OV allowed the electrons to excite from VB to TSD and OV as well as from TSD and OV to CB [19]. Their presence not only facilitates the electrons excitation but also allowed the photoactivity undergoes under visible light irradiation since the electrons can be excited from VB, TSD and OV. In contrast, the band gap of MZN has been allowed to be applied under visible light but the presence of OV in MZN may inhibit the electron-hole recombination to enhance the photoactivity. The stability and reusability of the catalysts were further studied by repeating a series of experiments in degrading 2-CP and phenol for MTN and MZN, respectively as demonstrated in Figure 6. In each new cycle, the catalyst was collected, washed and calcined according to synthesis procedure before being used for degradation of a fresh 2-CP or phenol solution. Figure 6 illustrated that both catalysts were still active with the slight decrease after five repeatation of experiment. The MTN shows the degradation of 2-CP was decreased from 97% to 86%, while degradation of phenol by MZN decrease from 87% to 79%. These results reveal that both catalysts have a good stability and potentially to use repeatly under visible light irradiation.

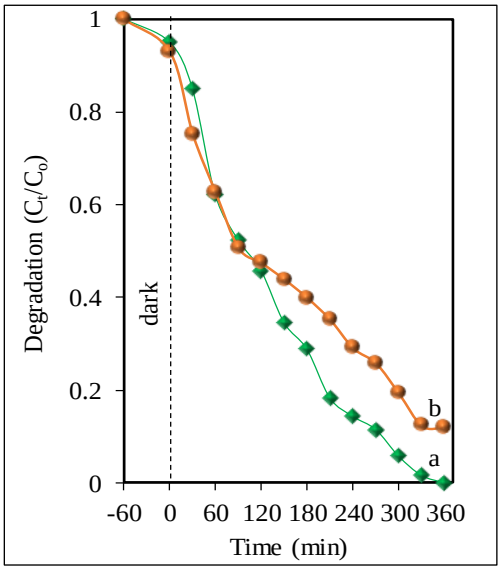


Figure 5. Photocatalytic performance of (a) MTN and (b) MZN for degradation of 2-CP and phenol, respectively [$C_{2\text{-CP/phenol}}$: 10 ppm, pH: 5, $W_{catalyst}$: 0.075 g, t: 360 min]

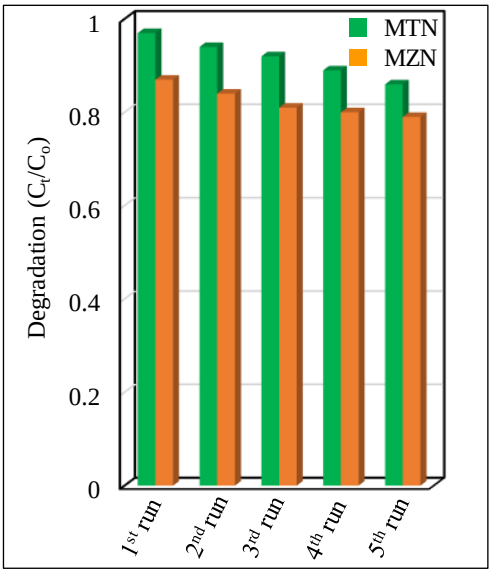


Figure 6. Regeneration study of MTN and MZN for degradation of 2-CP and phenol, respectively [$C_{2\text{-CP/phenol}}$: 10 ppm, pH: 5, $W_{catalyst}$: 0.075 g, t: 360 min]

Conclusion

We successfully synthesized MTN and MZN *via* MW-assisted process using different precursors to degrade different chlorophenols under visible light radiation. Based on the XPS results, the microwave sintering effect on the surface of these modified structures has generated TSD and OV in MTN while MZN contained only OV which have significantly enhanced their photocatalytic performance. XRD results indicated that both catalysts demonstrated a good crystallinity, degree of orderliness and mesoporous uniformity where indicated that MW-assisted method efficaciously provides a good heat distribution during synthesis by heating the entire reaction solution with proper temperature to improve the structural arrangement. Therefore, this method has high potential to be used in synthesizing mesoporous materials due to its sintering effects. MTN also had degraded about 97% of 2-CP while MZN had degraded around 87% of phenol.

Acknowledgement

The authors are grateful for the financial support by Ministry of Education Malaysia for Fundamental Research Grant Scheme (203.PKIMIA.6711607) and Universiti Sains Malaysia (USM) for Short Term Grant (304/PKIMIA/6315055).

References

1. Aba-Guevara, C. G., Medina-Ramírez, I. E., Hernández-Ramírez, A., Jáuregui-Rincón, J., Lozano-Álvarez, J. A. and Rodríguez-López, J. L. (2017). Comparison of two synthesis methods on the preparation of Fe, N-Co-doped TiO_2 materials for degradation of pharmaceutical compounds under visible light. *Ceramics International*, 43(6): 5068-5079.
2. Reinosa, J. J., Docio, C. M. Á., Ramírez, V. Z. and Lozano, J. F. F. (2018). Hierarchical nano ZnO-micro TiO_2 composites: High UV protection yield lowering photodegradation in sunscreens. *Ceramics International*, 44(3): 2827-2834.
3. Zhu, M., Chen, L., Gong, H., Zi, M. and Cao, B. (2014). A novel TiO_2 nanorod/nanoparticle composite architecture to improve the performance of dye-sensitized solar cells. *Ceramics International*, 40(1): 2337-2342.
4. Baskar, G. and Soumiya, S. (2016). Production of biodiesel from castor oil using iron(II) doped zinc oxide nanocatalyst. *Renewable Energy*, 98: 101-107.

5. Khatami, M., Alijani, H. Q., Heli, H. and Sharifi, I. (2018). Rectangular shaped zinc oxide nanoparticles: Green synthesis by Stevia and its biomedical efficiency. *Ceramics International*, 44: 15596-15602.
6. Prasankumar, T., Aazem, V.I., Raghavan, P., Ananth, K.P., Biradar, S., Ilangovan, R. and Jose, S. (2017). Microwave assisted synthesis of 3D network of Mn/Zn bimetallic oxide-high performance electrodes for supercapacitors. *Journal of Alloys and Compounds*, 695: 2835-2843.
7. Mirzaei, A., Yerushalmi, L., Chen, Z., Haghighat, F. and Guo, J. (2018). Enhanced photocatalytic degradation of sulfamethoxazole by zinc oxide photocatalyst in the presence of fluoride ions: Optimization of parameters and toxicological evaluation. *Water Research*, 132: 241-251.
8. Li, F. B. and Li, X. Z. (2002). The enhancement of photodegradation efficiency using Pt–TiO_2 catalyst. *Chemosphere*, 48(10): 1103-1111.
9. Houshmand, A., Daud, W. M. A. W. and Shafeeyan, M. S. (2011). Tailoring the surface chemistry of activated carbon by nitric acid: study using response surface method. *Bulletin of the Chemical Society of Japan*, 84(11): 1251-1260.
10. Khan, M. M., Lee, J. and Cho, M. H. (2014). Au@TiO_2 nanocomposites for the catalytic degradation of methyl orange and methylene blue: An electron relay effect. *Journal of Industrial and Engineering Chemistry*, 20(4): 1584-1590.
11. Ahmad, M., Ahmed, E., Hong, Z. L., Jiao, X. L., Abbas, T. and Khalid, N. R. (2013). Enhancement in visible light-responsive photocatalytic activity by embedding Cu-doped ZnO nanoparticles on multi-walled carbon nanotubes. *Applied Surface Science*, 285: 702-712.
12. Pouran, S. R., Bayrami, A., Aziz, A. A., Daud, W. M. A. W. and Shafeeyan, M. S. (2016). Ultrasound and UV assisted Fenton treatment of recalcitrant wastewaters using transition metal-substituted-magnetite nanoparticles. *Journal of Molecular Liquids*, 222: 1076-1084.
13. Zheng, X., Li, D., Li, X., Chen, J., Cao, C., Fang, J., Wang, J., He, Y. and Zheng, Y. (2015). Construction of ZnO/TiO_2 photonic crystal heterostructures for enhanced photocatalytic properties. *Applied Catalysis B: Environmental*, 168: 408-415.
14. Faisal, M., Bouzid, H., Harraz, F. A., Ismail, A. A., Al-Sayari, S. A. and Al-Assiri, M. S. (2015). Mesoporous Ag/ZnO multilayer films prepared by repeated spin-coating for enhancing its photonic efficiencies. *Surface and Coatings Technology*, 263: 44-53.
15. Anas, S., Rahul, S., Babitha, K. B., Mangalaraja, R. V. and Ananthakumar, S. (2015). Microwave accelerated synthesis of zinc oxide nanoplates and their enhanced photocatalytic activity under UV and solar illuminations. *Applied Surface Science*, 355: 98-103.
16. Jaafar, N. F. and Jalil, A. A. (2018). Photocatalytic degradation of phenol derivatives over silver supported on mesoporous titania nanoparticles. *Malaysian Journal of Analytical Sciences*, 22(5): 807-816.
17. Kajbafvala, A., Zanganeh, S., Kajbafvala, E., Zargar, H. R., Bayati, M. R. and Sadrnezhaad, S. K. (2010). Microwave-assisted synthesis of narcis-like zinc oxide nanostructures. *Journal of Alloys and Compounds*, 497 (1-2): 325-329.
18. Tripathy, N., Ahmad, R., Kuk, H., Hahn, Y. B. and Khang, G. (2016). Mesoporous ZnO nanoclusters as an ultra-active photocatalyst. *Ceramics International*, 42(8): 9519-9526.
19. Jaafar, N. F., Jalil, A. A., Triwahyono, S. and Shamsuddin, N. (2015). New insights into self-modification of mesoporous titania nanoparticles for enhanced photoactivity: Effect of microwave power density on formation of oxygen vacancies and Ti^{3+} defects. *RSC Advances*, 5(110): 90991-91000.
20. Thostenson, E. T. and Chou, T. W. (1999). Microwave processing: fundamentals and applications. *Composites Part A: Applied Science and Manufacturing*, 30(9): 1055-1071.
21. Hoang, S., Berglund, S. P., Hahn, N. T., Bard, A. J. and Mullins, C. B. (2012). Enhancing visible light photo-oxidation of water with TiO_2 nanowire arrays via cotreatment with H_2 and NH_3: Synergistic effects between Ti^{3+} and N. *Journal of the American Chemical Society*, 134(8): 3659-3662.
22. Zhang, Z. K., Bai, M. L., Guo, D. Z., Hou, S. M. and Zhang, G. M. (2011). Plasma-electrolysis synthesis of TiO_2 nano/microspheres with optical absorption extended into the infra-red region. *Chemical Communications*, 47(29): 8439-8441.
23. Yuan, Z., Xiao-Xuan, W., Lv, H. and Wen-Chen, Z. (2007). EPR parameters and defect structures of the off-center Ti^{3+} ion on the Sr^{2+} site in neutron-irradiated $SrTiO_3$ crystal. *Journal of Physics and Chemistry of Solids*, 68(9): 1652-1655.

24. Bromiley, G. D. and Shiryaev, A. A. (2006). Neutron irradiation and post-irradiation annealing of rutile (TiO_{2-x}): effect on hydrogen incorporation and optical absorption. *Physics and Chemistry of Minerals*, 33(6): 426-434.
25. Suwarnkar, M. B., Dhabbe, R. S., Kadam, A. N. and Garadkar, K. M. (2014). Enhanced photocatalytic activity of Ag doped TiO_2 nanoparticles synthesized by a microwave assisted method. *Ceramics International*, 40(4): 5489-5496.
26. Zhou, H., Tan, X., Huang, J. and Chen, X. (2017). Sintering behavior, phase evolution and microwave dielectric properties of thermally stable Li_2O-3MgO-mTiO_2 ceramics ($1 \leq m \leq 6$). *Ceramics International*, 43(4): 3688-3692.
27. Wang, W., Bai, W., Shen, B. and Zhai, J. (2015). Microwave dielectric properties of low temperature sintered $ZnWO_4$-TiO_2 composite ceramics. *Ceramics International*, 41: S435-S440.
28. Kamarudin, N. H. N., Jalil, A. A., Triwahyono, S., Artika, V., Salleh, N. F. M., Karim, A. H., Jaafar, N. F., Sazegar, M. R., Mukti, R. R., Hameed, B. H. and Johari, A. (2014). Variation of the crystal growth of mesoporous silica nanoparticles and the evaluation to ibuprofen loading and release. *Journal of Colloid and Interface Science*, 421: 6-13.
29. Komarneni, S., Rajha, R. K. and Katsuki, H. (1999). Microwave-hydrothermal processing of titanium dioxide. *Materials Chemistry and Physics*, 61(1): 50-54.
30. Shi, M., Kang, L. and Jiang, Y. (2014). Microwave-assisted synthesis of mesoporous tungsten carbide/carbon for fuel cell applications. *Catalysis Letters*, 144(2): 278-284.
31. Clark, D. E., Folz, D. C. and West, J. K. (2000). Processing materials with microwave energy. *Materials Science and Engineering: A*, 287(2): 153-158.
32. Khaki, M. R. D., Shafeeyan, M. S., Raman, A. A. A. and Daud, W. M. A. W. (2017). Application of doped photocatalysts for organic pollutant degradation-A review. *Journal of Environmental Management*, 198: 78-94.
33. Antonopoulou, M., Evgenidou, E., Lambropoulou, D. and Konstantinou, I. (2014). A review on advanced oxidation processes for the removal of taste and odor compounds from aqueous media. *Water Research*, 53: 215-234.
34. Oturan, M. A. and Aaron, J. J. (2014). Advanced oxidation processes in water/wastewater treatment: principles and applications. A review. *Critical Reviews in Environmental Science and Technology*, 44(23): 2577-2641.
35. Bokare, A. D. and Choi, W. (2014). Review of iron-free Fenton-like systems for activating H_2O_2 in advanced oxidation processes. *Journal of Hazardous Materials*, 275: 121-135.
36. Yuan, S., Sheng, Q., Zhang, J., Yamashita, H. and He, D. (2008). Synthesis of thermally stable mesoporous TiO_2 and investigation of its photocatalytic activity. *Microporous and Mesoporous Materials*, 110(2-3): 501-507.
37. Khan, M. M., Ansari, S. A., Pradhan, D., Ansari, M. O., Lee, J. and Cho, M. H. (2014). Band gap engineered TiO_2 nanoparticles for visible light induced photoelectrochemical and photocatalytic studies. *Journal of Materials Chemistry A*, 2(3): 637-644.
38. Huang, C.N., Bow, J.S., Zheng, Y., Chen, S.Y., Ho, N. and Shen, P. (2010). Nonstoichiometric titanium oxides via pulsed laser ablation in water. *Nanoscale research letters*, 5(6): 972-785.
39. Naeem, M., Hasanain, S. K., Kobayashi, M., Ishida, Y., Fujimori, A., Buzby, S. and Shah, S. I. (2006). Effect of reducing atmosphere on the magnetism of $Zn_{1-x}Co_xO$ ($0 \leq x \leq 0.10$) nanoparticles. *Nanotechnology*, 17(10): 2675-2680.
40. Bazant, P., Kuritka, I., Munster, L. and Kalina, L. (2015). Microwave solvothermal decoration of the cellulose surface by nanostructured hybrid Ag/ZnO particles: A joint XPS, XRD and SEM study. *Cellulose*, 22(2): 1275-1293.
41. Hsieh, P. T., Chen, Y. C., Kao, K. S. and Wang, C. M. (2008). Luminescence mechanism of ZnO thin film investigated by XPS measurement. *Applied Physics A*, 90(2): 317-321.
42. Katoch, A., Choi, S.W., Kim, H. W. and Kim, S. S. (2015). Highly sensitive and selective H_2 sensing by ZnO nanofibers and the underlying sensing mechanism. *Journal of Hazardous Materials*, 286: 229-235.
43. Wang, J., Wang, Z., Huang, B., Ma, Y., Liu, Y., Qin, X., Zhang, X. and Dai, Y. (2012). Oxygen vacancy induced band-gap narrowing and enhanced visible light photocatalytic activity of ZnO. *ACS Applied Materials & Interfaces*, 4(8): 4024-4030.

Malaysian Journal of Analytical Sciences, Vol 23 No 3 (2019): 472 - 478
DOI: https://doi.org/10.17576/mjas-2019-2303-11

MALAYSIAN JOURNAL OF ANALYTICAL SCIENCES
Published by The Malaysian Analytical Sciences Society
ISSN 1394 - 2506

THE USE OF LOW GRADE LIMESTONE IN ACID MINE DRAINAGE TREATMENT

(Penggunaan Batu Kapur Bergred Rendah dalam Rawatan Saliran Lombong Berasid)

Anuar Othman[1,2], Azli Sulaiman[1]*, Ismail Ibrahim[2]

[1]*Department of Chemistry, Faculty of Science*
Universiti Teknologi Malaysia, 81310 Johor Bahru, Johor, Malaysia
[2]*Mineral Research Centre,*
Department of Mineral and Geoscience Malaysia, 31400 Ipoh, Perak, Malaysia

**Corresponding author: azli@kimia.fs.utm.my*

Received: 25 October 2017; Accepted: 22 January 2019

Abstract

In this study, low grade limestone (LGL) was used in treating acid mine drainage (AMD). Based on X-ray fluorescence (XRF) result, the content of calcium carbonate mineral in limestone used was around 80% that can be considered as LGL. The pH of AMD samples increased after treated with all parameter weights of LGL at every five minutes of interval times. The parameters weights of LGL used in the experiments were 1.0, 2.0, 3.0, 4.0, 5.0 and 6.0 g. For every parameter weight of LGL, the interval times used were 0, 5, 15, 20, 25 and 30 minutes. The highest of pH value obtained was 6.44 ± 0.00 by using 6.0 g of LGL at interval time 30 minutes. The suitable pH value chosen was 6.11 ± 0.00 by using 5.0 g of LGL at interval time 20 minutes because the parameter had complied with Standards A and B of Environmental Quality Act 1974 with less cost compared to other parameters. Heavy metals content such as arsenic, cadmium, chromium, iron, manganese and zinc had decreased after reaction with all LGL weights. The content of arsenic in AMD samples after reaction with all LGL weights had complied with both standards' requirement except with 1.0 g of LGL. The percentage of removal heavy metals by using all parameter weights of LGL such as arsenic, cadmium, chromium, iron, manganese and zinc were around 98.8 to 99.8%, 53.8 to 88.5%, 94.7 to 96.5%, 99.6 to 100%, 34.6 to 38.9% and 27.0 to 90.1%, respectively.

Keywords: limestone, acid mine drainage, heavy metal

Abstrak

Dalam kajian ini, batu kapur bergred rendah (LGL) telah digunakan dalam rawatan saliran lombong berasid (AMD). Berdasarkan keputusan pendaflour sinar-X (XRF), kandungan mineral kalsium karbonat di dalam batu kapur yang digunakan adalah sekitar 80% yang boleh dianggap sebagai LGL. pH sampel AMD telah bertambah selepas bertindakbalas dengan semua parameter berat LGL pada setiap lima minit selang masa. Parameter berat LGL yang digunakan dalam eksperimen adalah 1.0, 2.0, 3.0, 4.0, 5.0 dan 6.0 g. Untuk setiap parameter berat LGL, selang masa yang digunakan adalah 0, 5, 10, 15, 20, 25 dan 30 minit. Nilai pH yang paling tinggi diperolehi adalah 6.44 ± 0.00 dengan menggunakan 6.0 g LGL pada selang masa 30 minit. Nilai pH yang paling sesuai telah dipilih adalah 6.11 ± 0.00 dengan menggunakan 5.0 g LGL pada selang masa 20 minit kerana parameter ini adalah kurang kos untuk mematuhi Piawai A dan B berbanding parameter yang lain. Kandungan logam berat seperti arsenik, kadmium, kromium, besi, mangan dan zink telah berkurangan selepas bertindakbalas dengan semua berat LGL. Kandungan arsenik dalam sampel-sampel AMD selepas bertindakbalas dengan semua berat LGL telah dipatuhi dengan kehendak kedua-dua standard kecuali dengan menggunakan 1.0 g LGL. Peratusan penyingkiran logam berat dengan menggunakan semua parameter berat LGL seperti arsenik, kadmium, besi, mangan dan zink masing-masing adalah sekitar 98.8 hingga 99.8%, 53.8 hingga 88.5%, 94.7 hingga 96.5%, 99.6 hingga 100%, 34.6 hingga 38.9% and 27.0 hingga 90.1%.

Kata kunci: batu kapur, saliran lombong berasid, logam berat

Introduction

Limestone is a versatile material that can be used in many industries such as paper making, glass, food, plastics, paint, rubber, etc. [1, 2]. Limestone is a sedimentary rock with chemical formula $CaCO_3$ [3] and 4% of the earth crust contains carbonate mineral that consists limestone, chalk and biominerals [4]. Limestone also can be used as a neutralization agent in treating acidic water especially in treating AMD [5]. Other materials that can be used to treat AMD are organic material [6], carbide lime [7], hydrated lime [8], quicklime [9], etc. In this study, low grade limestone was used in treating AMD. Limestone with the content of calcium carbonate mineral less than 94% can be classified as LGL [10]. The objective of this study is to show that LGL can be used as a material in treating AMD.

AMD is a global environmental problem caused by oxidation of sulphide minerals [11] such as pyrite, marcasite, arsenopyrite, sphalerite, chalcocite, etc. with the presence of water and sulphate oxidizing bacteria (SOB). AMD occurs can be shown in equations 1 to 3 [12].

$$FeS_2 + 7O_2 + 2H_2O \longrightarrow 2FeSO_4 + 2H_2SO_4 \quad (1)$$

$$4FeSO_4 + O_2 + 2H_2SO_4 \longrightarrow 2Fe_2(SO_4)_3 + 2H_2O \quad (2)$$

$$7Fe_2(SO_4)_3 + FeS_2 + 8H_2O \longrightarrow 15FeSO_4 + 8H_2SO_4 \quad (3)$$

AMD can be defined as acidic water in which its pH is less than 5, contains high concentration of sulphate and heavy metals such as arsenic, copper, lead, nickel, zinc, etc.

Materials and Methods

Study area

The study is focussed on the AMD problem that occurred in a tin tailing pond. The tin tailing pond is in a tin mine located in northern Perak. The tin tailing pond is a recycled pond which involves the activities related to tin ores.

Materials

In this study, LGL was used as neutralization agent and obtained from Pengkalan Hulu, Perak. AMD sample was collected from tin tailing pond also located in Pengkalan Hulu, Perak.

Instrumentation

Elemental analyses for LGL sample were determined by X-ray fluorescence using Shimadzu XRF-1700 sequential X-ray fluorescence spectrometer. The pH were measured using a Mettler Toledo Ross FE 20 pH meter. The metal ions concentrations of the AMD samples were analysed by Perkin Elmer Optima DV 5300 ICP-OES.

Methods

Six experiments were carried out with different weights of low grade limestone used 1, 2, 3, 4, 5 and 6 g, respectively. The different weights of limestone were added into individual 1 L beakers that contained 500 mL AMD samples. The AMD samples with different limestone weights were stirred at 500 rpm by using overhead mechanical stirrer. During the stirring process, pH values of the solutions were recorded at interval times of 0, 5, 15, 20, 25 and 30 minutes. The AMD samples were analysed by using ICP-OES for heavy metals content before and after reaction. Figure 1 shows the jar test of LGL reacted with AMD and Figure 2 shows the LGL samples before and after reaction with AMD.

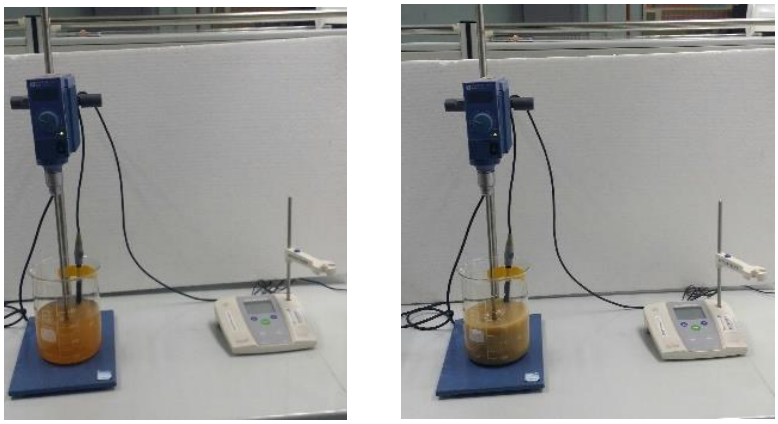


Figure 1. Jar test of AMD reacted with LGL



Figure 2. LGL before and after reaction with AMD sample

Results and Discussion

XRF result in Table 1 shows that the limestone used in this study was low grade because the content of calcium oxide obtained was 44 % as shown in Table 1. The percentage of calcium carbonate calculated was around 80% which indicates that it is a low grade limestone [3].

Table 1. X-ray fluorescent analysis result

Element Oxide	Result (%)
Fe_2O_3	0.48
MnO	0.11
TiO_2	0.20
CaO	44.15
K_2O	1.08
SiO_2	19.24
Al_2O_3	3.28
MgO	0.89
Na_2O	0.08

Table 2 shows the pH values of AMD samples before and after reaction with LGL as neutralisation agent. The initial pH of AMD samples was ~2.47. The highest pH obtained was 6.44 ± 0.00 by using 6.0 g of LGL at interval time 30 minutes. However, the optimal parameters selected was 5.0 g of LGL with retention time of 20 minutes which resulted in pH value of 6.11 ± 0.00. These parameters were chosen because it complied with Standards A and B of Environmental Quality Act 1974 which stated that the pH value for Standards A and B are 6.0 and 5.5 [13], respectively. Standard A refers to the discharge of effluent is upstream from catchment area and Standard B refers to the discharge of effluent is downstream from catchment area. Furthermore, the selected parameters will cost less in order to reach pH 6 compared to the other parameters. The reaction between LGL and AMD sample is shown in equation 4. pH value increase with the increasing of time caused to a lot of calcite ($CaCO_3$) dissolved in AMD sample. The reaction between LGL with AMD produced calcium ion (Ca^{2+}) and carbonic acid (HCO_3^-). Carbonic acid further reacted with hydrogen ion (H^+) to produce water and carbon dioxide gas. As a result, the use of H^+ can increase pH in AMD sample after the reaction [14].

$$CaCO_3 + H^+ \longrightarrow Ca^{2+} + HCO_3^- \quad (4)$$

Table 2. pH of AMD sample before and after reaction with six different weights of LGL

Weight of LGL (g)	Interval Time (minutes)	pH	
		Before Reaction	After Reaction
1.0	5	2.47 ± 0.00	3.84 ± 0.00
	10	2.47 ± 0.00	4.00 ± 0.00
	15	2.47 ± 0.00	4.07 ± 0.00
	20	2.47 ± 0.01	4.12 ± 0.00
	25	2.47 ± 0.01	4.15 ± 0.00
	30	2.47 ± 0.01	4.18 ± 0.01
2.0	5	2.47 ± 0.00	4.35 ± 0.01
	10	2.47 ± 0.00	4.72 ± 0.01
	15	2.47 ± 0.00	4.98 ± 0.00
	20	2.47 ± 0.01	5.16 ± 0.00
	25	2.47 ± 0.01	5.43 ± 0.01
	30	2.47 ± 0.01	5.50 ± 0.00
3.0	5	2.47 ± 0.00	4.90 ± 0.01
	10	2.47 ± 0.00	5.27 ± 0.01
	15	2.47 ± 0.00	5.54 ± 0.00
	20	2.47 ± 0.01	5.75 ± 0.00
	25	2.47 ± 0.01	5.92 ± 0.01
	30	2.47 ± 0.01	6.04 ± 0.01
4.0	5	2.47 ± 0.00	5.09 ± 0.00
	10	2.47 ± 0.00	5.52 ± 0.01
	15	2.47 ± 0.00	5.79 ± 0.01
	20	2.47 ± 0.01	5.99 ± 0.00
	25	2.47 ± 0.01	6.13 ± 0.01
	30	2.47 ± 0.01	6.24 ± 0.01

Table 2 (cont'd). pH of AMD sample before and after reaction with six different weights of LGL

Weight of LGL (g)	Interval Time (minutes)	pH	
		Before Reaction	After Reaction
5.0	5	2.47 ± 0.00	5.27 ± 0.00
	10	2.47 ± 0.00	5.65 ± 0.01
	15	2.47 ± 0.00	5.92 ± 0.01
	20	2.47 ± 0.01	6.11 ± 0.00
	25	2.47 ± 0.01	6.23 ± 0.01
	30	2.47 ± 0.01	6.33 ± 0.01
6.0	5	2.47 ± 0.00	5.36 ± 0.00
	10	2.47 ± 0.00	5.75 ± 0.01
	15	2.47 ± 0.00	6.04 ± 0.01
	20	2.47 ± 0.01	6.23 ± 0.00
	25	2.47 ± 0.01	6.34 ± 0.00
	30	2.47 ± 0.01	6.44 ± 0.00

Table 3 shows the heavy metals content in AMD samples before and after reaction with LGL. The results show that the content of heavy metals in AMD samples such as arsenic, cadmium, iron, chromium, manganese and zinc decreased after treated with LGL. Iron and chromium can be effectively treated by using LGL because the result show that in all AMD samples, the percentage of iron and chromium removal were more than 95%. Their final concentrations complied with Standards A and B, iron are 1.0 mg/L and 5.0 mg/L, whereas for chromium (III) are 0.20 mg/L and 1.0 mg/L, respectively. For chromium (VI), Standards A and B is 0.05 mg/L. The concentration of arsenic obtained after reaction complied with both standards except with 1.0 g of LGL that did not reach pH value 5. The optimum of pH for arsenic removal is around 5 [15]. Standards A and B for arsenic are 0.05 mg/L and 0.10 mg/L, respectively. For zinc, its concentration complied with both standards after reaction with 4.0, 5.0 and 6.0 g of LGL, respectively. Standards A and B for zinc is 2.0 mg/L. The concentrations of manganese and cadmium obtained after reaction in all parameters did not comply with both standards because manganese and cadmium can only be precipitated at pH around 10 and 11, respectively. Other techniques such as adsorption and oxidation are suitable to be used in treating manganese and cadmium. The reaction between AMD samples and LGL produced precipitation. Precipitation is one of the separation techniques to reduce heavy metals content in AMD samples. Heavy metals such as iron or zinc can be precipitated as carbonate or hydroxide metals as shown in Equations 5 and 6, respectively [14].

$$Fe^{2+} + HCO_3^- \longrightarrow FeCO_3 + H^+ \quad (5)$$

$$Zn^{2+} + 2H_2O \longrightarrow Zn(OH)_2 + 2H^+ \quad (6)$$

Table 3. Heavy metals content in AMD samples before and after reaction with LGL

LGL Weight (g)	Element	Before Reaction (mg/L)	After Reaction (mg/L)	Percentage Removal of Heavy Metals
1.0	As	6.44 ± 0.34	0.08 ± 0.00	98.8
	Cd	0.26 ± 0.01	0.12 ± 0.00	53.8
	Fe	317.27 ± 13.41	1.41 ± 0.02	99.6
	Cr	0.57 ± 0.02	0.03 ± 0.00	94.7
	Mn	61.63 ± 2.65	40.29 ± 0.22	34.6
	Zn	11.49 ± 0.45	8.39 ± 0.05	27.0

Table 3 (cont'd). Heavy metals content in AMD samples before and after reaction with LGL

LGL Weight (g)	Element	Before Reaction (mg/L)	After Reaction (mg/L)	Percentage Removal of Heavy Metals
2.0	As	6.44 ± 0.34	0.03 ± 0.00	99.5
	Cd	0.26 ± 0.01	0.11 ± 0.00	57.9
	Fe	317.27 ± 13.41	0.32 ± 0.00	99.9
	Cr	0.57 ± 0.02	0.02 ± 0.00	96.5
	Mn	61.63 ± 2.65	40.16 ± 0.30	34.8
	Zn	11.49 ± 0.45	6.30 ± 0.05	45.2
3.0	As	6.44 ± 0.34	0.01 ± 0.00	99.8
	Cd	0.26 ± 0.01	0.07 ± 0.00	73.1
	Fe	317.27 ± 13.41	0	100
	Cr	0.57 ± 0.02	0.02 ± 0.01	96.5
	Mn	61.63 ± 2.65	39.07 ± 0.18	36.6
	Zn	11.49 ± 0.45	2.43 ± 0.01	78.6
4.0	As	6.44 ± 0.34	0.01 ± 0.00	99.8
	Cd	0.26 ± 0.01	0.07 ± 0.03	73.1
	Fe	317.27 ± 13.41	0	100
	Cr	0.57 ± 0.02	0.02 ± 0.00	96.5
	Mn	61.63 ± 2.65	38.26 ± 0.34	37.9
	Zn	11.49 ± 0.45	1.69 ± 0.03	85.3
5.0	As	6.44 ± 0.34	0.01 ± 0.00	99.8
	Cd	0.26 ± 0.01	0.03 ± 0.00	88.5
	Fe	317.27 ± 13.41	0	100
	Cr	0.57 ± 0.02	0.02 ± 0.00	96.5
	Mn	61.63 ± 2.65	37.48 ± 0.16	39.2
	Zn	11.49 ± 0.45	1.14 ± 0.01	90.1
6.0	As	6.44 ± 0.34	0.01 ± 0.00	99.8
	Cd	0.26 ± 0.01	0.03 ± 0.00	88.5
	Fe	317.27 ± 13.41	0	100
	Cr	0.57 ± 0.02	0.02 ± 0.00	96.5
	Mn	61.63 ± 2.65	37.64 ± 0.07	38.9
	Zn	11.49 ± 0.45	1.14 ± 0.01	90.1

Conclusion

LGL is capable to treat AMD by increasing the pH that complies with Standards A and B. The best pH value chosen was 6.11 ± 0.00 by using 5.0 g of LGL at interval time 20 min. LGL is also suitable to be used in reducing heavy metals content in AMD such as arsenic, chromium and zinc by precipitation process. LGL is not suitable to be used for reducing manganese and cadmium content in AMD. More alkaline materials such as hydrated lime, quicklime,

sodium hydroxide and so on are suitable to treat these heavy metals. Manganese and cadmium can be precipitated as hydroxide metals at pH 10 [16] and pH range 10.5 to 11 [17], respectively.

Acknowledgement

The authors acknowledge the support of the Mineral Research Centre and the Chemistry Department, Faculty of Science, Universiti Teknologi Malaysia. Appreciation goes to the Director of Mineral Research Centre, Md Muzayin Alimon, Head of Rock Based Technology Section, Dr. Rohaya Othman, Head of Mineral Processing, Dr. Nazwin Ahmad and to Ex-Head of Rock Based Technology Section, Nasharuddin Isa, Mineral Research Centre staff especially to staff of Rock Based Technology Section, staff of Mining and Quarry Section and staff of Mineral Processing Technology Section.

References

1. Kirboga, S. and Oner, M. (2013). Application of experimental design for the precipitation of calcium carbonate in the presence of biopolymer. *Powder Technology*, 249: 95-104.
2. Othman, A., Isa, N. and Othman, R. (2015). Preparation of precipitated calcium carbonate using additive and without additive. *Jurnal Teknologi*, 77(3): 49-53.
3. Erdogan, N. and Eken, H.A. (2015). Precipitated calcium carbonate production, synthesis and properties. *Physicochemical Problems of Mineral Processing*, 2: 79-84.
4. Shirsath, S. R., Sonawane, S. H., Saini, D. R. and Pandit, A. B. (2015). Continuous precipitation of calcium carbonate using sonochemical reactor. *Ultrasonics Sonochemistry*, 24: 132-139.
5. Muhammad, S. N., Mohd Kusin, F., Md Zahar, M. S., Halimoon, N. and Mohamat Yusuf, F. (2015). Passive treatment of acid mine drainage using mixed substrates: Batch experiments. *Procedia Environmental Sciences*, 30: 157-161.
6. Othman, A., Sulaiman, A. and Sulaiman, S. K. (2015). The study on the effectiveness of organic material in acid mine drainage treatment. *Jurnal Teknologi*, 77(2): 79-84.
7. Othman, A., Sulaiman, A. and Sulaiman, S.K. (2017). Carbide lime in acid mine drainage treatment. *Journal of Water Process Engineering*, 15: 31-36.
8. Othman, A., Sulaiman, A. and Sulaiman, S. K. (2017). The use of hydrated lime in acid mine drainage treatment. *AIP Proceeding*, 1847: 1-6.
9. Othman, A., Sulaiman, A. and Sulaiman, S. K. (2017). The use of quicklime in acid mine drainage treatment. *Chemical Engineering Transaction*, 56: 1585-1590.
10. Harrison, D. J. (1993). Industrial minerals laboratory manual; Limestone. *Minerology and Petrology Group*, *British Geological Survey*. Technical Report, WG/92/29: pp. 1-45.
11. Teng, W., Kuang, J., Luo, Z. and Shu, W. (2017). Microbial diversity and community assembly across environmental gradients in acid mine drainage. *Minerals*, 7(106): 1-10.
12. Ekolu, S. O., Diop, S., Azene, F. and Mkhize, N. (2016). Disintegration of concrete construction induced by acid mine drainage attack. *Journal of the South African Institution of a Civil Engineering*, 58(1): 34-42.
13. Environmental Quality Act 1974 (Act 127), Regulations, Rules & Orders. (2015). International Law Book Services, Selangor.
14. Chowdhury, A. R., Sarkar, D. and Datta, R. (2015). Remediation of acid mine drainage-impacted water. *Current Pollution Reports*, 1: 131-141.
15. Nenov, V., Dimitrova, N., Dobrevsky, I. and Rands, D. G. (1992). Effective precipitation of arsenic from aqueous solution by iron(iii) sulfate. *Clean – Soil Air Water*, 20(1): 14-17.
16. Kursunoglu, S. and Kaya, M. (2014). Dissolution and precipitation of zinc and manganese obtained from spent zinc-carbon and alkaline battery powder. *Physicochemical Problems of Mineral Processing*, 50(1): 41-45.
17. Aube, B. and Zinck, J. (2003). Lime treatment of acid mine drainage in Canada. *Brazil-Canada Seminar on Mine Rehabilitation*, 1 – 3 December, Florianopolis, Brazil.

Malaysian Journal of Analytical Sciences, Vol 23 No 3 (2019): 479 - 487
DOI: https://doi.org/10.17576/mjas-2019-2303-12

MALAYSIAN JOURNAL OF ANALYTICAL SCIENCES
Published by The Malaysian Analytical Sciences Society
ISSN 1394 - 2506

PREPARATION AND CHARACTERIZATION OF IMPROVED HYDROPHILIC POLYETHERSULFONE/REDUCED GRAPHENE OXIDE MEMBRANE

(Penyediaan dan Pencirian Penambahkaikan Hidrofilik Membran Polietersulfon/Grafin Oksida Terturun)

Madzlan Aziz[1]*, Nur Fatihah Tajul Arifin[2], Woei-Jye Lau[1]

[1]Advanced Membrane Technology Centre,
[2]Department of Chemistry,
Faculty of Science, Universiti Teknologi Malaysia,
81310 Johor Bahru, Johor, Malaysia

**Corresponding author: madzlan@utm.my*

Received: 25 October 2017; Accepted: 22 January 2019

Abstract

Polyethersulfone (PES)/reduced graphene oxide (rGO) membrane was prepared by phase inversion method for water treatment. Graphene oxide (GO) was obtained *via* modified Hummer's method and reduced to rGO where $NaBH_4$ was chosen as a reducing agent. FTIR was used to investigate functional groups left on rGO after reduction process. The FTIR peak at 1718 cm^{-1}, attributed to the carbonyl (C=O) group, was absent after GO was reduced. Interlayer spacing of GO and rGO were obtained using XRD. It was found that the interlayer spacing of GO was reduced from 7.87 to 3.68 Å after reduction process due to the removal of some of the functional groups from the material. The membrane cross section showed that addition rGO increase the length of finger-like pores as compared to neat PES when it is observed under SEM. It was observed that the membrane hydrophilicity is enhanced as the contact angle of PES reduced from 69.70^o to 32.99^o when rGO 24 hours was introduced into the polymer matrix. The highest pure water flux obtained was 174.29 L/m^2h. The membranes showed significant enhancement when rGO was used in the polymer matrix.

Keyword: polyethersulfone, phase inversion method, modified Hummer's method, reduced graphene oxide

Abstrak

Membran polietersufon (PES)/grafin oksida terturun (rGO) telah dihasilkan melalui kaedah fasa terbalik untuk rawatan air. Grafin oksida (GO) dihasilkan menerusi kaedah Hummer terubahsuai dan diturunkan kepada rGO menggunakan $NaBH_4$ sebagai ejen penurunan. FTIR digunakan untuk menyiasat kumpulan berfungsi yang hadir pada rGO selepas proses penurunan. Puncak FTIR pada 1718 cm^{-1} yang menunjukkan kumpulan karbonil (C=O) tidak hadir selepas GO terturun. Jarak antara lapisan GO dan rGO telah dikaji menggunakan XRD. Didapati jarak antara lapisan GO berkurang daripada 7.87 Å ke 3.68 Å selepas proses penurunan kerana sebilangan kumpulan berfungsi telah terkeluar dari bahan. Keratan rentas membran menunjukkan bahawa penambahan rGO meningkatkan panjang liang seperti jejari berbanding PES asli apabila dilihat menggunakan SEM. Didapati bahawa sifat hidrofilik membran telah dipertingkatkan kerana sudut sentuh air PES telah berkurang dari 69.70^o kepada 32.99^o apabila rGO 24 jam ditambah ke dalam matriks polimer. Bacaan fluks air tulen tertinggi ialah 174.29 L/m^2h. Membran menunjukkan perubahan ketara apabila rGO digunakan di dalam matriks polimer.

Kata kunci: polietersulfon, kaedah fasa terbalik, kaedah Hummer terubahsuai, grafin oksida terturun

Introduction

Recently, study has claimed that polyethersulfone (PES) has great membrane-forming and excellent physicochemical properties which lead it to be used widely as a membrane in water treatment [1] such as in microfiltration, ultrafiltration and nanofiltration [2]. PES is a thermally stable and has excellent mechanical and chemical properties [3]. However, PES suffers from fouling due to its' hydrophobic characteristics [3] that will affect the performance of the membrane [4]. Thus, it is suggested that PES to undergo several modification to overcome the fouling problem such as blending with amphiphilic polymer [1], blending with hydrophilic polymers [5], grafting with hydrophilic monomer or blending with inorganic nanoparticles [4]. However, study stated that blending with hydrophilic material is one of the most promising method to enhance the properties of PES [6].

Graphene and its' derivatives received a lot of attentions in many fields which includes electronics, mechanics and water treatment [7]. This is because of its high surface area [4], excellent electrical and thermal conductivity as well as outstanding mechanical properties [8]. By forming interfacial bonding with polymer matrix, graphene promises that it can improve the physicochemical properties of polymers [9]. Nevertheless, pristine graphene is found to agglomerate during the formation process of homogeneous composites. Therefore, it is suggested that graphene need to undergo several modifications to overcome this problem [10]. For instance, graphene oxide (GO) which can be formed via modified Hummer's method is the most favorable material to be added into the polymer matrix as it can improve the membrane performance [4]. Besides that, GO/polymer composites able to improve the mechanical strength of the polymer [11].

For instance, study conducted by Lee and colleague [12] shows that addition of GO in polysulfone (PSf) able to improve the mechanical strength and hydrophilicity of the membrane. Besides that, Jin and coworkers [13] claimed that addition of GO increased the porosity of the membrane because large pores were observed. In addition, the mechanical strength and thermal stability become better. GO also able to form a good miscibility with PES and enhanced the hydrophilicity as the contact angle reduced from 70.8° (neat PES) to 58.4° (GO/PES). Based on the literature review, there are many studies that have been conducted using GO. However, reports on reduced graphene oxide (rGO) in polymer membrane is still very few. Through reduction process, some of the functional groups will be eliminated [14]. rGO (Figure 1) can form interaction with polymer and improve the performance of the membrane as there are still oxygen functional group left after reduction process [15]. Therefore, the objective in study is to prepare rGO/PES composite membrane and to analyze the effect of addition of rGO towards the membrane hydrophilicity.

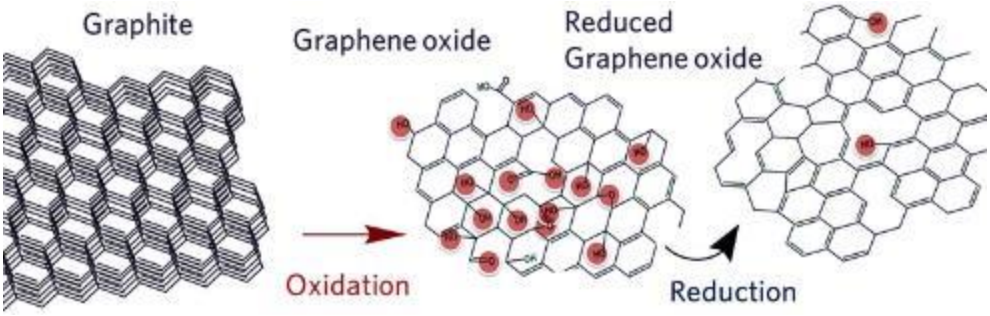


Figure 1. Chemical reaction of graphite to rGO [16]

Study area

PES was chosen as a polymer host because it is used extensively in water treatment [17]. To reduce GO, $NaBH_4$ was chosen as a reductant because it is a strong reducing agent [18] and environmental friendly [19]. This research will include the effect of reduction time towards GO and its compatibility with polymer composites. Firstly, the GO was obtained by oxidation of graphite *via* modified Hummer's method. Then, it was reduced through chemical reduction method. The reduction time was in the range of 8 – 32 hours to elucidate the effect of reduction time on GO. Then, it was mixed with PES to study the compatibility with polymer composites. ATR-FTIR was used to study the

functional groups that exist on the surface of rGO. The morphology of the GO and rGO were characterized using FESEM. Interlayer spacing of GO and rGO were studied using XRD. Meanwhile, contact angle was used to investigate the hydrophilicity of the membrane. On the other hand, SEM was chosen to observe the membrane cross-section and a cross-flow filtration system was used to evaluate the water flux.

Materials and Methods

GO was produced via modified Hummer's method. An amount of 4 g graphite powder was added into 100 mL of concentrated H_2SO_4 and followed by the slowly addition of 4 g of $NaNO_3$. This was then followed by a slow addition of 12 g of $KMnO_4$ under stirring condition and the temperature of the mixture was maintained below 10 $^{\circ}$C in ice bath. The mixture was stirred at 35 $^{\circ}$C for 30 minutes before 100 mL of deionized water was added to the mixture and a yellowish brown solution was formed. The mixture was stirred again for 30 minutes at 95 $^{\circ}$C. Lastly, 600 mL of distilled water, 20 mL of 30 % H_2O_2 aqueous solution and 100 mL of 10 wt.% HCl were added after bright yellow color with bubbles appeared in the solution. The mixture was centrifuged and washed with deionized water to expel metal ion and acid until neutral pH was obtained. GO film that produced was dried in an oven for 12 hours at 60 $^{\circ}$C [20]. To obtain rGO, GO was reduced using sodium borohydride ($NaBH_4$) *via* chemical reduction. Firstly, 0.8 g of GO was sonicated in 50 mL of water for 30 minutes. $NaBH_4$ solution was prepared and the pH value was adjusted with NaOH to pH 12 to prevent any occurring hydrolysis. After half an hour, $NaBH_4$ solution was added drop-wise into GO solution and the solution was heated at 80 °C for 8 hours with continuous stirring. After finishing hours, the mixture was filtered out *via* vacuum filtration and washed with EtOH and distilled water for several times. The product was dried in an oven at 70 $^{\circ}$C for 24 hours to obtain reduced graphene oxide. The procedure was repeated with different reduction time (8, 16, 24 and 32 hours) [21].

Membrane was casted by using phase inversion method. PES (20 wt.%) and PVP (1%) were dispersed in NMP at 60 $^{\circ}$C for 24 hours to obtain homogeneous solution. rGO-8h (0.5 wt.%) was dispersed and sonicated in NMP for 30 minutes. Then, with the aid of continuous stirring the solution was mixed together for 24 hours at 60 $^{\circ}$C. After that, the mixture was casted on a clean glass plate. The glass plate was immersed into non-solvent (water) bath [11]. It was left until the phase inversion method is completed which is after the membrane get separated from glass plate. Finally, the membrane was peeled and washed. The membrane was dried at room temperature for 24 hours [4]. The method was repeated with GO, rGO-16h, rGO-24h, and rGO-32h.

Results and Discussion

Figure 2 shows the FT-IR spectrum of GO and rGO. Figure 2(a) shows that there are peaks around 3195 cm^{-1} and 1718 cm^{-1} which indicates that hydroxyl (-OH) and carbonyl (C=O) groups exist on the surface of GO respectively. Intense peak at 1620 cm^{-1} shows bending mode of water molecules. Epoxy group exist on GO as there is peak at 1224 cm^{-1} and vanishes during the reduction process [22]. Besides that, some of the oxygenated functional groups have been removed from the surface of GO through the reduction process [23]. When GO is reduced, it is clearly shown that there are no peaks can be found at 1718 cm^{-1} which indicates the C=O groups have been eliminated. Figure 2(e) indicates that there is C-H asymmetric stretching vibration mode (2919 cm^{-1}) when GO is reduced for 8 hours [24]. Supposedly, as GO is being reduced many of –OH groups have been reduced. However, the –OH peak became more intense and this might be due to the fact that $NaBH_4$ reduction would form residual hydroxyl functional groups when GO is reduced for 32 hours (Figure 2(b)) [25]. Overall, peak in the range of 1300 – 1450 cm^{-1} indicates tertiary alcohol bending [22]. Meanwhile, peak around 1636 – 2655 cm^{-1} shows the deformation vibration of –OH groups [24].

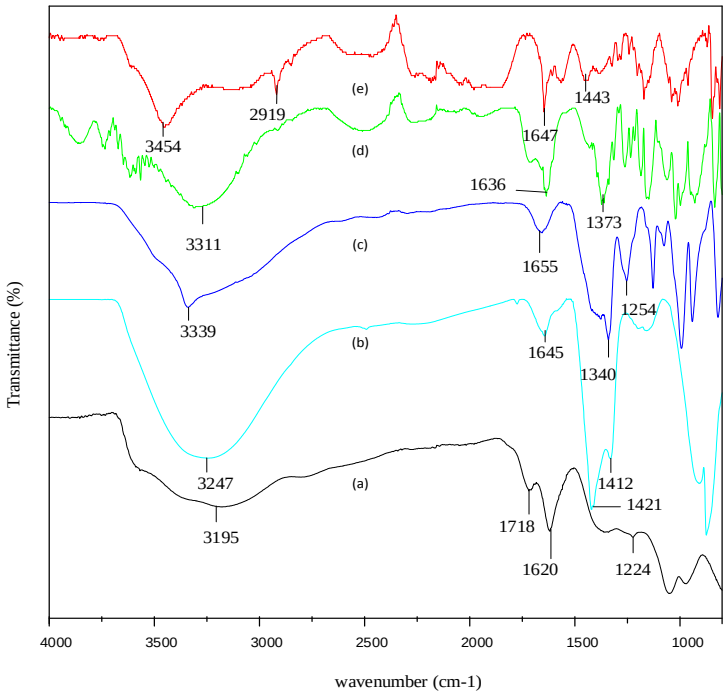


Figure 2. FT-IR spectrum of (a) GO (b) rGO-32h (c) rGO-24 h (d) rGO-16 h (e) rGO-8h

Figure 3 shows the XRD spectrum of (a) graphene oxide and (b) reduced graphene oxide. Based on Figure 3(a) it shows that there is an intense peak on $2\theta = 11.23^{O}$ which corresponds to the diffraction of GO plane (002). On the other hand, rGO (b) with index number of (002) indicates a broad spectrum at $2\theta = 24.16^{O}$. From this result, the interlayer spacing of GO and rGO are calculated by using Bragg's Law, $\lambda = 2d \sin\theta$ where λ is the wavelength of the X-ray beam, d is the interlayer spacing, and θ is the diffraction angle. It is found that the interlayer spacing of GO is 7.87 Å. This result may be explained by the fact that, expansion on graphene oxide occurred as oxygen functional groups attached on the surface of the material [15, 26]. Besides that, the oxidation process has broken the π-π van der Waals bond between the lamella thus increasing the interlayer spacing [27]. Meanwhile, the interlayer spacing of rGO is 3.68 Å because most of the functional groups are removed during the reduction process [25].

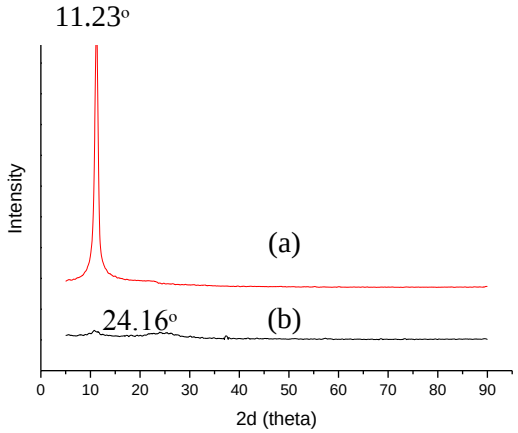


Figure 3. XRD spectrum of (a) graphene oxide (b) reduced graphene oxide

Figure 4 shows the morphology of GO and rGO. Based on Figure 4 (a), GO exhibits wrinkles on its surface of [27,28]. The wrinkles will contribute to the conducting characteristics. Furthermore, the formation of the wrinkles and crumples like structure might be due to the existence of H_2O molecules and hydroxyl or carboxyl groups [30]. In addition, the formation of wrinkles on the surface of GO means that the sp^2-hybridized structure of the stacked graphene sheets has broken up [8]. Figure 4 (b – e) shows that the surface of rGO are rougher and aggregated in disordered solid than GO. These results are likely to be related to the aggregation of rGO due to the strong van der Waals forces [29].

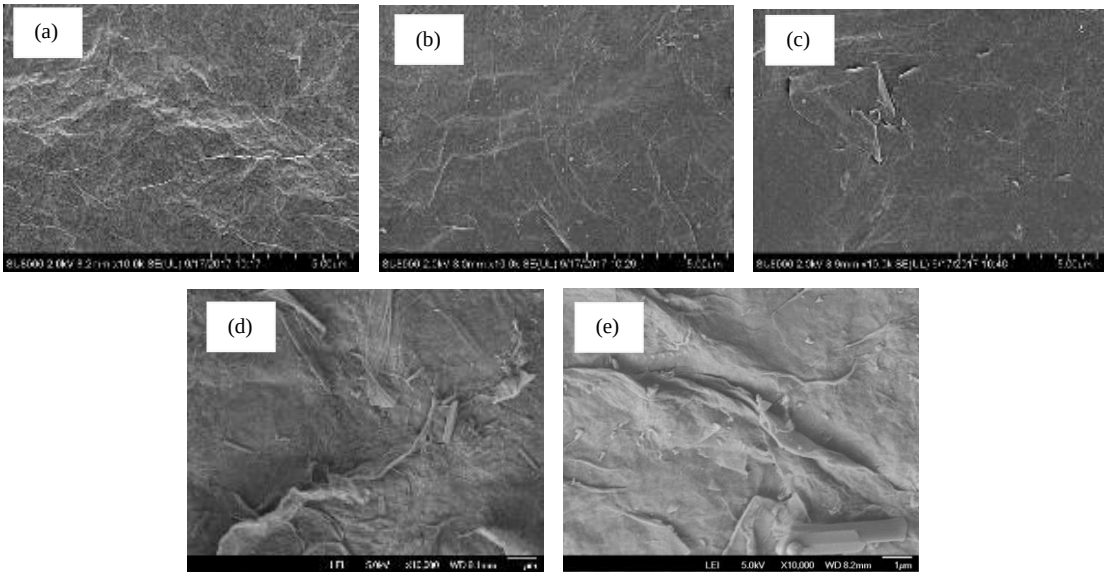
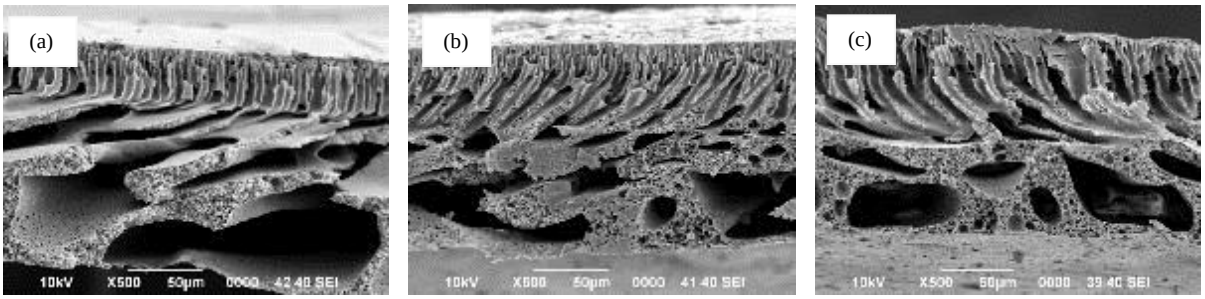


Figure 4. Morphology of (a) GO (b) rGO-8h (c) rGO-16h (d) rGO-24h (e) rGO-32h under 10000x magnification

The membrane cross section (Figure 5) shows a typical structure where it contain asymmetric porous structure with a dense skin top-layer followed by a finger-like porous sub-layer [4]. The cross section shows that the finger-like pore does not contain any trace of GO inside the membrane. Even as this happened, it does not mean that the nanomaterials are absent in the polymer matrix. This is because, the size of the nanomaterial is small and is not visible when it is observed using SEM [31]. The finger-like porous sub-layer increased when 0.5% GO (Figure 5(b)) was added into the membrane. This is because, the hydrophilic characteristic of GO leads to fast exchange of solvent and non-solvent during the phase inversion process which leads to extended porosity. GO is also able to induce pores on the skin top layer. After the addition of 0.5 % rGO, denser pore can be observed. Interestingly, as the reduction time of GO increased the pore density increased. However, the finger-like pores of the membranes are connected continuously with the finger-like sublayer [11].



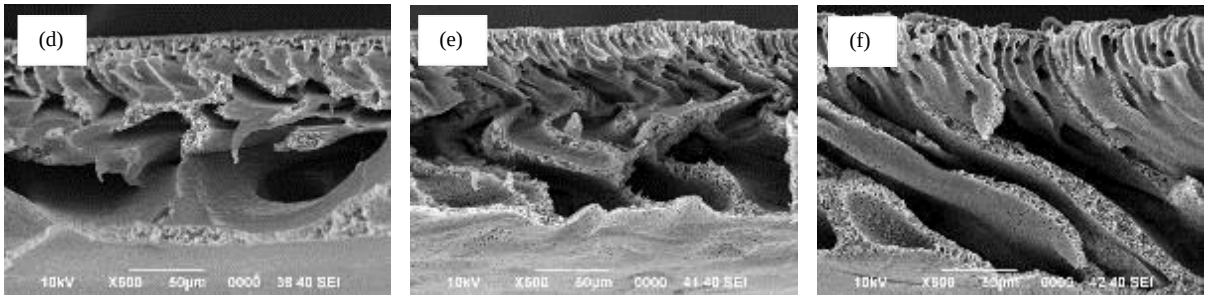


Figure 5. The cross section of (a) PES (b) PES/GO (C) PES/rGO-8h (d) PES/rGO-16h (e) PES/rGO 24h and (f) PES/rGO-32h membrane

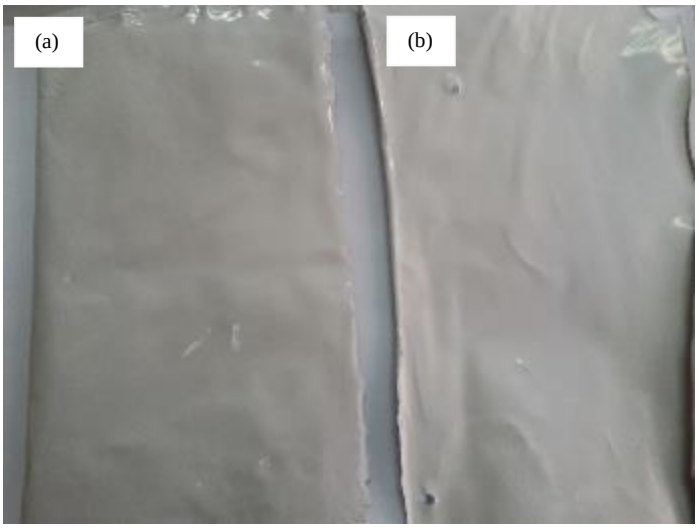


Figure 6. Comparison of (a) top (b) bottom surface of PES/GO membrane

The membrane contact angle reveals that the hydrophilicity greatly improves when rGO is used. The hydrophobic nature of rGO can interact well with hydrophobic PES. It can therefore be assumed that the addition of rGO improved the hydrophilicity of the membrane [32]. During the phase inversion process rGO migrates to the surface of the mixed matrix membranes in order to decrease the interfacial energy [4, 33]. However, when rGO is reduced for 32 h there is no significant decrease in the contact angle, it increases instead. This can be explained by the fact that significant amount of oxygen functional groups have been eliminated during the reduction process [34]. Therefore, the contact angle increases from 32.99^{o} to 55.05^{o} (Table 1).

Table 1. Contact angle of the membrane

Membrane	**PES**	**PES/GO**	**PES/rGO 8 h**	**PES/rGO 16 h**	**PES/rGO 24 h**	**PES/rGO 32 h**
Contact angle (°C)	69.70	64.45	34.84	34.20	32.99	55.05

Nevertheless, in this study the pure water flux does not rely on the membrane contact angle. As illustrated in Table 1, even though the membrane contact angle of PES/GO is 64.45^{o} but it shows the highest flux, 174.29 L/m^{2}h

(Figure 7). With the addition of GO, the material gathered on the surface of the membrane due to hydrophilic functional groups, like hydroxyl (Figure 6) [13]. These results are in line with previous study conducted by Chai and colleague where they stated that the value of flux increases because of bigger pore size, enhancement of porosity as well as improvement in hydrophilicity [31]. Meanwhile, 40.71 L/m^{2}h is the lowest flux achieved as the rGO was reduced at 32 h. This may be due to blocking effect by the rGO particles. As the reduction time increased, a large amount of oxygen functional groups was eliminated which caused the rGO to be difficult to be dispersed in the polymer solution. This is because, GO and rGO possessed contrast characteristics especially in terms of dispersion. GO has a well dispersion in many solvents which includes water and alcohol due to the strong electrostatic repulsion between single layers. In contrast, because of $\pi - \pi$ stacking rGO is likely to agglomerate in solution which greatly limits the concentration of single layer solutions [34]. Thus, it blocked the membrane's surface and decreased the pure water flux as well as hydrophilicity.

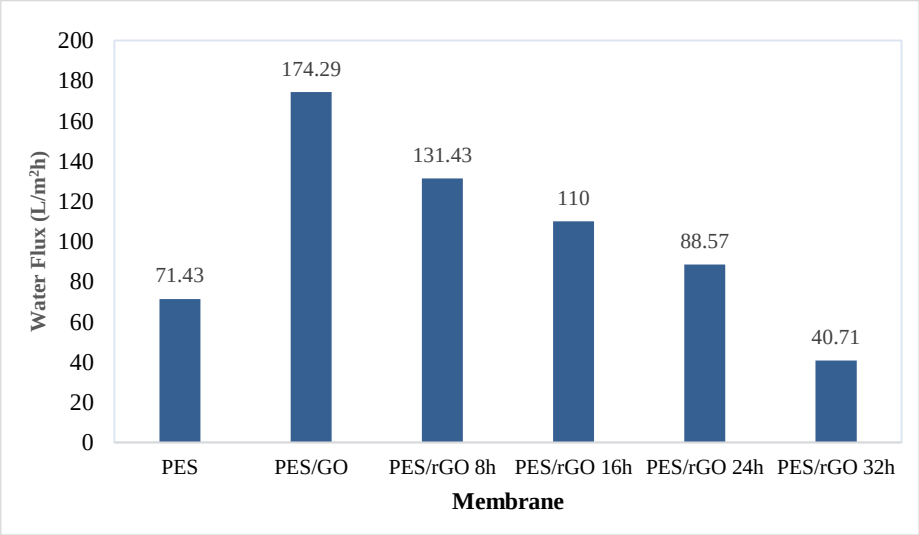


Figure 7. Pure water flux at 1 bar

Conclusion

The GO and rGO were prepared by using modified Hummer's method and chemical reduction respectively. The result showed that the carbonyl functional groups were removed after reduction process. The removal of functional groups on rGO was further confirmed using XRD as the result showed that the interlayer spacing decreased. The morphology of GO revealed that wrinkles were formed on the surface while rGO have a rougher surface due to the aggregation. The cross section of the membrane showed that all the membranes have porous structure. The contact angle of showed great improvement when rGO were introduced into the polymer matrix. Hence, due to more porous structure and increase in hydrophilicity PES/GO membrane exhibit a higher pure water flux.

Acknowledgement

We would like to express our gratitude to Faculty of Science Universiti Teknologi Malaysia for all the facilities and HiCOE research grant (4J199) from the Ministry of Higher Education of Malaysia for the financial support.

References

1. Forati, T., Atai, M., Rashidi, A. M., Imani, M. and Behnamghader, A. (2014). Physical and mechanical properties of graphene oxide/polyethersulfone nanocomposites. *Polymer Advance Technology*, 25:322–328.
2. Razmjou, A., Resosudarmo, A., Holmes, R. L. and Li, H. (2012). The effect of modified TiO_2 nanoparticles on the polyethersulfone ultrafiltration hollow fiber membranes. *Desalination*, 287: 271–280.

3. Mehrparvar, A. and Rahimpour, A. (2015) Surface modification of novel polyether sulfone amide (PESA) ultrafiltration membranes by grafting hydrophilic monomers. *Journal Industry and Engineering Chemistry*, 28: 359–368.
4. Zinadini, S., Zinatizadeh, A. A., Rahimi, M., Vatanpour, V., and Zangeneh, H. (2014) Preparation of a novel antifouling mixed matrix PES membrane by embedding graphene oxide nanoplates. *Journal Membrane Science*, 453: 292–301.
5. Peyravi, M., Rahimpour, A., Jahanshahi, M., Javadi, A. and Shockravi, A. (2012). Tailoring the surface properties of PES ultrafiltration membranes to reduce the fouling resistance using synthesized hydrophilic copolymer. *Microporous Mesoporous Materials*, 160:114–125.
6. Qu, P., Tang, H., Gao, Y., Zhang, L. P. and Wang, S. (2010) Polyethersulfone composite membrane blended With cellulose fibrils. *BioResources*, 5: 2323–2336.
7. Xiang, Q., Yu, J. and Jaroniec, M. (2012). Graphene-based semiconductor photocatalysts. *Chemistry Society Reviews*, 41: 782.
8. Compton, O. C. and Nguyen, S. T. (2010). Graphene oxide, highly reduced graphene oxide, and graphene : Versatile building blocks for carbon-based materials. *Small*, 6:711–723.
9. Kuilla, T., Bhadra, S., Yao, D. and Kim, N. H. (2010). Recent advances in graphene based polymer composites. *Progress Polymer Science*, 35: 1350–1375.
10. Shah, R., Kausar, A., Muhammad, B. and Shah, S. (2015). Progression from graphene and graphene oxide to high performance polymer-based nanocomposite: A review. *Polymer Plastic Technology Engineering*, 54:173–183.
11. Ganesh, B. M., Isloor, A. M. and Ismail, A. F. (2013). Enhanced hydrophilicity and salt rejection study of graphene oxide-polysulfone mixed matrix membrane. *Desalination*, 313: 199–207.
12. Lee, J., Chae, H. R., Won, Y. J. and Lee, K. (2013) Graphene oxide nanoplatelets composite membrane with hydrophilic and antifouling properties for wastewater treatment. *Journal Membrance Science*, 448: 223–230.
13. Jin, F., Lv, W., Zhang, C. and Li, Z. (2013). High-performance ultrafiltration membranes based on polyethersulfone–graphene oxide composites. *RSC Advances*, 3: 21394.
14. Johnson, D.W., Dobson, B. P. and Coleman, K. S. (2015). A manufacturing perspective on graphene dispersions. *Current Opinion Colloid Interface Science*, 20: 367–382.
15. Mishra, S. K., Tripathi, S. N., Choudhary, V. and Gupta, B. D. (2014) SPR based fibre optic ammonia gas sensor utilizing nanocomposite film of PMMA/reduced graphene oxide prepared by in situ polymerization. *Sensors Actuators, B Chemical*, 199: 190–200.
16. Dahlberg, T. (2016). The first order Raman spectrum of isotope labelled nitrogen-doped reduced graphene oxide. Retrieved from http://www.diva-portal.org/smash/get/diva2:905266/FULLTEXT01 .pdf.
17. Ahmad, A. L., Abdulkarim, A. A., Ooi, B. S. and Ismail, S. (2013). Recent development in additives modifications of polyethersulfone membrane for flux enhancement. *Chemical Engineering Journal*, 223: 246–267.
18. Pei, S. and Cheng, H. M. (2012). The reduction of graphene oxide. *Carbon*, 50: 3210–3228.
19. Yang, Z., Zheng, Q., Qiu, H., Li, J. and Yang, J. (2015). A simple method for the reduction of graphene oxide by sodium borohydride with $CaCl_2$ as a catalyst. *New Carbon Materials*, 30: 41–47.
20. Lee, D. C., Yang, H. N., Park, S. H. and Kim, W. J. (2014). Nafion/graphene oxide composite membranes for low humidifying polymer electrolyte membrane fuel cell. *Journa Membrance Science*, 452: 20–28.
21. Liang, Y., Wu, D., Feng, X. and Müllen, K. (2009). Dispersion of graphene sheets in organic solvent supported by ionic interactions. *Advance Materials*, 21: 1679–1683.
22. Mathkar, A., Tozier, D., Cox, P. and Ong, P. (2012). Controlled, stepwise reduction and band gap manipulation of graphene oxide. *Journal of Physical Chemistry Letters*, 3: 986-991.
23. Deka, M. J., Baruah, U. and Chowdhury, D. (2015). Insight into electrical conductivity of graphene and functionalized graphene: Role of lateral dimension of graphene sheet. *Materials Chemistry Physics*, 163: 236–244.
24. Silwana, B., Van der Horst, C., Iwuoha, E. and Somerset, V. (2015). Synthesis, characterisation and electrochemical evaluation of reduced graphene oxide modified antimony nanoparticles. *Thin Solid Films*, 592:124–134.
25. Shin, H. J., Kim, K. K., Benayad, A. and Yoon, S. M. (2009). Efficient reduction of graphite oxide by sodium borohydride and its effect on electrical conductance. *Advances Functional Materials*, 19: 1987–1992.

26. Naebe, M., Wang, J., Amini, A. and Khayyam, H. (2014). Mechanical property and structure of covalent functionalised graphene/epoxy nanocomposites. *Scientific Reports*, 4: 1–7.
27. Hu, Y., Song, S. and Lopez-Valdivieso, A. (2015). Effects of oxidation on the defect of reduced graphene oxides in graphene preparation. *Journal of Colloid Interface Sciences*, 450: 68–73.
28. Kellici, S., Acord, J., Ball, J. and Reehal, H. S. (2014). A single rapid route for the synthesis of reduced graphene oxide with antibacterial activities. *RSC Advances*, 4: 14858.
29. Liu, S., Zeng, T. H., Hofmann, M. and Burcombe, E. (2011). Antibacterial activity of graphite, graphite oxide, graphene oxide, and reduced graphene oxide : Membrane and oxidative stress. *ACS Nano*, 9: 6971–6980.
30. Han, J. W. and Kim, J. (2015). Reduction of graphene oxide by resveratrol : a novel and simple biological method for the synthesis of an effective anticancer nanotherapeutic molecule. *International Journal of Nanomedicine*, 10: 2951–2969.
31. Chai, P. V., Mahmoudi, E., Teow, Y. H. and Mohammad, A.W. (2017). Preparation of novel polysulfone-Fe_3O_4/GO mixed-matrix membrane for humic acid rejection. *Journal of Water Process Engineering*, 15: 83–88.
32. Ganesh, B. M., Isloor, A. M. and Ismail, A. F. (2013). Enhanced hydrophilicity and salt rejection study of graphene oxide-polysulfone mixed matrix membrane. *Desalination*, 313: 199–207.
33. Celik, E., Park, H., Choi, H. and Choi, H. (2011). Carbon nanotube blended polyethersulfone membranes for fouling control in water treatment. *Water Research*, 45: 274–282.
34. Cote, L. J., Cruz-silva, R. and Huang, J. (2009). Flash reduction and patterning of graphite oxide and its polymer composite. *Journal of American Chemical Society*, 131(17): 11027–11032.

Malaysian Journal of Analytical Sciences, Vol 23 No 3 (2019): 488 - 494
DOI: https://doi.org/10.17576/mjas-2019-2303-13

MALAYSIAN JOURNAL OF ANALYTICAL SCIENCES
Published by The Malaysian Analytical Sciences Society
ISSN 1394 - 2506

GREEN MICROWAVE-ASSISTED AQUEOUS ENZYMATIC EXTRACTION OF *Elateriospermum tapos* SEED OILS

(Pengekstrakan Hijau Minyak Bijian *Elateriospermum tapos* Menggunakan Kaedah Enzim Berakues Berbantu Gelombang Mikro)

Nuraimi Azlan Hadi Tan[1] and Ida Idayu Muhamad[1,2]*

[1]*Department of Bioprocess and Polymer Engineering, Faculty of Chemical and Energy Engineering*
[2] *IJN-UTM Cardiovascular Engineering Centre*
Universiti Teknologi Malaysia, 81310 Johor Bahru, Johor, Malaysia

**Corresponding author: idaidayu@utm.my*

Received: 25 October 2017; Accepted: 22 January 2019

Abstract

Microwave-assisted aqueous enzymatic extraction (MAAEE) is a promising green technology that is fast, efficient and energy saving. The physicochemical parameters and fatty acids composition of the MAAEE-extracted oil were reportedly quite comparable with those of solvent-extracted oil and control oil, showing no significant differences ($p > 0.05$) among the extraction methods. However, the oxidative stability of the MAAEE obtained oil was found to be considerably improved in the comparison as evident by the determinations of chemical profile values. Moreover, the microwave-enzymatic adjuvant improved the oil extraction yield as well as the oxidation properties of the oil produced without altering its other quality attributes. The present work compared the quality characteristics of microwave-assisted aqueous enzymatic extracted *Elateriospermum tapos* seed oil with those of hexane-extracted oil and control oil. Interestingly, MAAEE process has achieved 12% and 16% higher extraction efficiency and concentrated omega-3 fatty acid, respectively compared to non-enzymatic microwave-assisted extraction (MAE). Although resulted in lower yield than hexane-extraction (Soxhlet), MAAEE extracted 24% higher concentrated omega-3 fatty acid with almost 99% removal of anti-nutrient amygdalin within 75 seconds. Hence the study on the interaction of extraction parameters as well as the MAAEE optimization process is sustainably feasible.

Keyword: microwave assisted aqueous enzymatic extraction, seed oils, *Elateriospermum tapos*, amygdalin

Abstrak

Pengekstrakan enzim berakues yang dibantu dengan gelombang mikro (MAAEE) adalah teknologi hijau yang menjanjikan proses yang pantas, cekap dan penjimatan tenaga. Parameter fizikokimia dan komposisi asid lemak daripada minyak yang diekstrak MAAEE dilaporkan setara berbanding dengan minyak ekstrak-pelarut dan minyak kawalan serta tidak menunjukkan perbezaan ketara ($p > 0.05$) di antara kaedah pengekstrakan. Walau bagaimanapun, kestabilan oksidatif minyak MAAEE didapati lebih baik dalam perbandingan seperti yang ditunjukkan oleh penentuan nilai-nilai profil kimia. Tambahan pula, adjuvan gelombang mikro-berenzim meningkatkan hasil pengeluaran minyak serta ciri pengoksidaan minyak yang dihasilkan tanpa mengubah sifat-sifat kualiti yang lain. Kajian ini membandingkan ciri-ciri kualiti minyak biji *Elateriospermum tapos* secara kaedah pengekstrakan enzim berakues-berbantu gelombang mikro dengan minyak ekstrak-pelarut heksana dan minyak kawalan. Menariknya, proses MAAEE telah masing-masing mencapai kecekapan pengekstrakan 12% dan kepekatan asid lemak omega-3 16% lebih tinggi berbanding pengekstrakan berbantu gelombang mikro tanpa berenzim (MAE). Walaupun hasilan lebih rendah daripada pengekstrakan heksana (Soxhlet), MAAEE memperoleh asid lemak omega-3 berkepekatan 24% lebih tinggi dengan hampir 99% penyingkiran amigdalin anti-nutrien dalam 75 saat. Oleh itu, kajian mengenai interaksi parameter pengekstrakan serta proses pengoptimuman MAAEE menunjukkan kewajaran secara lestari.

Kata kunci: pengekstrakan enzim berakues dibantu gelombang mikro, minyak bijian, *Elateriospermum tapos*, amigdalin

Introduction

Microwave uses electromagnetic wave which penetrates certain materials to provide volumetric heating through ionic conduction and dipole rotation [1]. Water and aqueous based solvent system offer an increasingly crucial choice for the replacement of conventional organic solvent [2]. Therefore, the microwave assisted aqueous enzymatic extraction (MAAEE) method is a highly potential, green, fast, efficient and energy saving method which eliminates the disadvantages of conventional solvent extraction method with undesirable effect on oil quality. Moreover, the treatment of seeds with enzymes enhances the extraction of oil yield due to its hydrolyzed structural polysaccharide of the cell walls and proteins associated with the lipid bodies [3]. MAAEE had been applied for oil extraction from seed crops such as pumpkin seed [3] and Forsythia suspense seed [2]. Omega-3 fatty acid is an essential fatty acid that need to be consumed through supplements or food products due to the incapability of human body to generate the compound naturally by itself [4]. Perah or scientifically known as *Elateriospermum tapos* seed (ETS) is an underutilized Malaysia local plant seed that had been reported to be rich of omega-3 fatty acid (Figure 1). A research by Yong and Salimon [5] claimed that ETS contains 17.4% of alpha linolenic acid (ALA) (PubChem CID: 5280934). The current work applies MAAEE for extraction of ETS oil, quantification of the specific amount of omega-3 fatty acid concentration and its anti-nutrient, amygdalin.

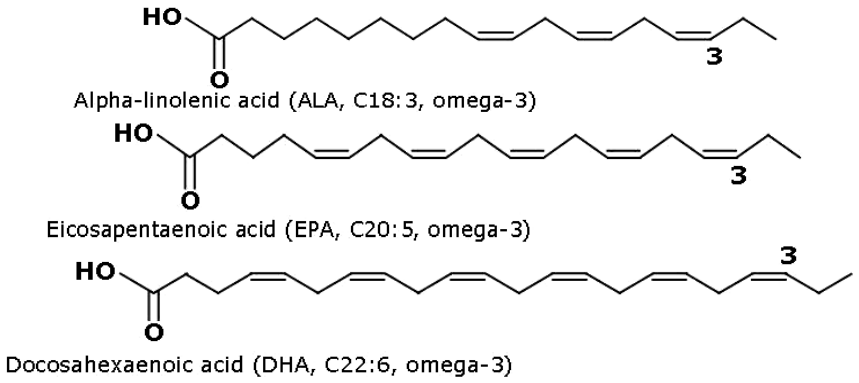


Figure 1. Properties and molecular structure of omega-3 fatty acid [6].

Materials and Methods

Plant materials

Elateriospermum tapos seed (ETS) was obtained at a local farm in Kuala Lipis, Pahang, Malaysia and was botanically identified by Biodiversity Unit, Institute of Bioscience, University Putra Malaysia (specimen voucher number SK2782/15). The seeds were manually cleaned and flooded with tap water to separate the extraneous matters (dust, vain seeds and straw from threshed seeds). The shells were removed; cleaned seeds were grinded using a laboratory grinder (MX-898M Panasonic, Malaysia) and sieved (Retsch siever, Germany) to a desired particle size and then stored at -20 °C in airtight bags until further use. The moisture content of the seeds, which were 6-7%, was determined using the infrared moisture analyser (FD-620 Kett, Japan).

Reagents

Cellulase from *Aspergillus niger* (Tokyo Chemical Industry), pectinase from *Aspergillus niger* (1.02U/mg) and proteinase from *Aspergillus melleus* (≥3 units/mg solid) from Sigma Aldrich, hexane analytical and GC grade from Qrec and Merck, Malaysia.

Extraction process

For Soxhlet extraction (SE) process, 5 g of ETS (0.5 mm particle sizes) were placed into each thimble and 150 mL hexane was used as a solvent. This process was carried out by refluxing each sample for 6 hours on a heating mantle. After the elapsed time, a rotary evaporator was used to evaporate the solvents. The SE extraction produced

48.99±0.79% of oil, which was set at 100% oil recovery in the comparison with the MAAEE in this study. Next, the samples were collected and preserved at -20 °C in sealed bottles for further analysis.

For MAAEE method, a domestic microwave oven system was used (Sharp Model R-397J, Malaysia) equipped with digital control system for irradiation time and irradiation microwave power (110 W, 330W, 550 W, 770 W and 1100 W) and operates at 2.4 GHz. A mode stirring table was also included in microwave system to dissipate the microwave energy during microwave heating which is facilitate the extraction sample to heat up homogeneously. Subsequently, 5 g of grinded ETS and enzyme cocktail (cellulose: pectinase: proteinase) ratios of 1.4:1.7:1.4 were accurately weighed and placed into a 250 mL flask with 1:5 solid to solvent ratio (based on preliminary experiment). Subsequently, the MAAEE extraction was conducted according to the design of experiment (DOE) at the following conditions; 110-1100 W irradiation power, 30-120 s extraction time, 1-5% enzyme cocktail concentration and 0.5-1.5 mm particle size with a total of 30 experiment runs.

After extraction, the solution obtained from MAAEE was then centrifuged at 10000 rpm speed for 15 minutes, and oil phase was withdrawn using a micropipette. The oil was then weighed, and the extraction yield was expressed as the mass percentage ratio (oil extracted /total oil obtained by SE method, %) which result an optimal oil extraction yield of 46.12±1.48% at 110 W microwave power, 30 s extraction time, 1% enzyme cocktail concentration and 0.5 mm particle size (based on previous study). Next, the samples were collected and preserved at -20 °C in sealed bottles for further analysis.

Identification and quantification of omega-3 fatty acid concentration

The extracted ETS oil was converted to fatty acids methyl ester (FAMEs) prior to injection. About 1 µL of the sample was injected into GC (model Perkin Elmer Auto System XL) to analyze the omega-3 fatty acid. It was equipped with flame ionization detector and BPX 90 capillary column (60 m x 0.25 mm x 0.55 µm). The detector temperature and injector temperature were programmed at 250 °C. The oven temperature program was set at the initial 100 °C followed by ramp 1 at 20.0 °C /min to 170 °C, hold for 0.00 min, ramp 2 at 10.0 °C/min to 230 °C , hold for 7 minutes and ramp 3 at 30 °C/min to 250 °C, hold for 2 minutes. Nitrogen was used as the carrier gas. Subsequently, the peaks detected by the retention time were identified by comparing the result produced with standards under the same condition. Different concentrations (100, 200, 300, 400, 500, 600, 700, 800, 900 and 1000 ppm) had been prepared from omega-3 fatty acid (alpha linolenic acid) standard (Sigma Aldrich, Germany). The standards were injected in GC using the same condition of fatty acids analysis. The calibration curve of absorbance versus concentration graph was plotted. The concentration of extracted omega-3 was determined in mg of ω-3/g of oil using equation 1.

$$C_{\omega-3} = \frac{[C \times V]}{W_{oil}} \quad (1)$$

$C_{\omega-3}$ indicates the concentration of the extracted omega-3, mg of ω-3/g of oil; C indicates the concentration of omega-3 obtained from calibration curve, mg/mL; V indicates the volume of omega-3 fatty acid solution, mL and W_{oil} is the weight of the extracted oil, g.

FTIR analysis

The chemical structure of ETS oil extracted by MAAEE, MAE and SE were determined by FTIR spectrometer (Perkin-Elmer Spectrum One) equipped with a deuterated triglycine sulphate (DTGS) as a detector and a KBr/ Germanium as a beam splitter. A few drops of ETS oil were put onto the ATR multibounce plate of crystal at controlled ambient temperature (25 °C). For each analysis of sample, the ATR plate was carefully cleaned with methanol and dried with spot light to efficiently remove the traces of oil as well as to avoid any interference of the results. All spectra were scanned over the wave number interval of 4000 to 400 cm^{-1} with an average of 16 scans at resolution of 4 cm^{-1}.

Results and Discussion

In Table 1, MAAEE method extracted omega-3 fatty acid at 3.3 fold greater which is about 24.2% (w/w) higher compared to SE, and almost 2 fold greater when compared to MAE. The result shows highly significant differences

by all method at $p < 0.05$. This shows the ability of MAAEE method to extract large concentration of omega-3 fatty acid.

Table 1. Omega-3 concentration obtained by SE, MAE and MAAEE

Extraction Method	Retention Time (minutes)	Concentration mg ω-3/g oil
SE	12.674	106.57±4.32[a]
MAE	12.687	184.92±10.60[b]
MAAEE	12.696	348.96±24.88[c]

[a, b, c] different letters show significantly different ($p< 0.05$)

The improved extractability of omega-3 fatty acid concentration might be due to the polar properties of the solvent used in the extraction method. Soxhlet extraction used hexane (non-polar solvent) as solvent whereas MAAEE and MAE methods used aqueous based solvent. The presence of polar compound such as water, ethanol, and methanol tend to increase the yield of omega-3 fatty acid during the extraction. According to the report by Sánchez-Camargo [7], who extracted omega-3 using supercritical fluid extraction which involved co-solvent of ethanol, the yield of omega-3 compositions was increased with increase of ethanol composition. This could be due to the omega-3 fatty acid is bonded better to more polar molecules [7]. In addition, assistance by microwave heating shows a good increment of omega-3 fatty acid concentrations as can be observed in Table 1.

Microwave energy rapidly heats up the sample directly which encourage the dipole rotation of the molecules and the migration of the ion that enhances the penetration of the solvent in matrix, disrupt the cell wall and released the intracellular product into the surrounding solvent [8]. Nevertheless, MAAEE method produced omega-3 fatty acid concentrations that is 16.4% higher compared to the MAE method. Enzyme cocktail together with the aqueous based solution in MAAEE lead to more effective solubilization and hydrolysis of the proteins through protein network breakdown of the cotyledon cells, and in the protein (olesin) based membranes surrounding lipid bodies indicating more oil being released into the solvent [9]. Therefore, it is verified that the addition of enzyme cocktail in microwave assisted extraction improve the extraction of omega-3 fatty acid compound. Fatty acids profiles of ETS oil extracted by difference techniques extraction were also compared to evaluate the performance of MAAEE technique (Table 2).

From the result exhibited in Table 2, nine main components comprised of four saturated fatty acids (SAFA), three monounsaturated fatty acids (MUFA) and two polyunsaturated fatty acids (PUFA) were identified. Palmitic acid C16.0 (13.10-13.51%) and stearic 18:0 (3.8-5.45%) were the most predominant SAFA; oleic acid C18:1 (34.00-34.64%) was the principle MUFA; linoleic acid C18:2 (32.61-34.65%) and linolenic acid C18:3 (11.23-14.99%) were two main compounds of PUFA. These values are like those reported by Yong and Salimon [5], with difference about 0 to 4%. The comparison of SE, MAAEE and MAE techniques for ETS oil shows that the values of fatty acids had no significant difference $p> 0.05$ except palmitic acid, linoleic acid (omega 6 fatty acid) and linolenic acid (omega-3 fatty acid) $p< 0.05$. Microwave irradiation could break cell walls through the internal heating and enhance the volume swelling of the cells in the seed kernels. Combination with enzyme cocktail would adequately destruct the oil bodies and cell walls to expedite oil release though the breakdown of the protein network of cotyledon cells and olesin based membranes surrounding the lipid bodies [2, 9].

Table 2. Fatty acid profile of ETS oil

Fatty Acid	**Composition (%)**			
	SE	**MAE**	**MAAEE**	**Lipid extraction [5]**
Myristic acid (14:0)	0.06±0.04[a]	0.11±0.04[a]	0.04±0.05[a]	0.06±0.01
Palmitic acid (16:0)	13.44±0.11[b]	13.51±0.15[b]	13.10±0.05[a]	13.40±0.07
Palmitoleic acid (16:1)	0.37±0.17[a]	0.16±0.01[a]	0.11±0.01[a]	0.11±0.01
Stearic acid (18:0)	3.68±1.09[a]	5.44±0.04[a]	5.45±0.15[a]	3.59 ± 0.02
Oleic acid (18:1)	34.59±0.70[a]	34.68±0.06[a]	34.00±0.37[a]	32.53±0.17
Linoleic acid (18:2)	32.81±0.28[a]	34.65±0.25[b]	32.61±0.24[a]	31.81±0.10
Linolenic (18:3)	14.99±0.54[b]	11.23±0.35[a]	14.41±0.31[b]	17.14±0.21
Arachidic Acid (20:0)	0.06±0.11[a]	0.18±0.00[a]	0.23±0.02[a]	0.22±0.01
Gadoleic Acid (20:1)	0.03±0.02[ab]	ND	0.03±0.01[b]	ND
Total saturated fatty acid	17.24±1.34[a]	19.23±0.23[a]	18.83±0.27[a]	17.66±0.50
Total monounsaturated fatty acid	34.96±0.89[a]	34.84±0.06[a]	34.15±0.38[a]	32.50±0.36
Polyunsaturated fatty acid	47.80±0.82[b]	45.88±0.61[a]	47.02±0.55[ab]	49.08±0.29

[a, b] different letters show significantly different ($p < 0.05$), ND: not detected

Meanwhile, comparison of extraction techniques on the content of omega-3 fatty acid concentration shows that Soxhlet extraction obtained the lowest result (10.66 ± 0.43%) compared to MAAEE (34.90 ± 2.49%) and MAE (18.49 ± 1.06%). Moreover, the amount of amygdalin content could be minimized by the MAAEE technique as it gave the lowest amount as shown in Figure 2.

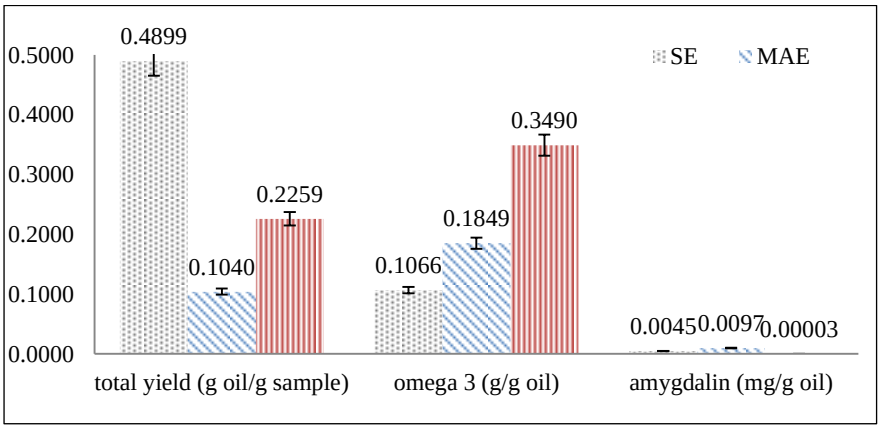


Figure 2. Comparison of the total yield, omega-3 fatty acid concentration and amygdalin concentration by SE, MAAEE, MAE techniques

The FTIR spectra of oil extracted by these techniques are very similar and the spectra feature can be related to those of triacyglycerols (90-95%) along with the di and monoacylglycerols (5%) and other trace levels of some components (Figure 3).

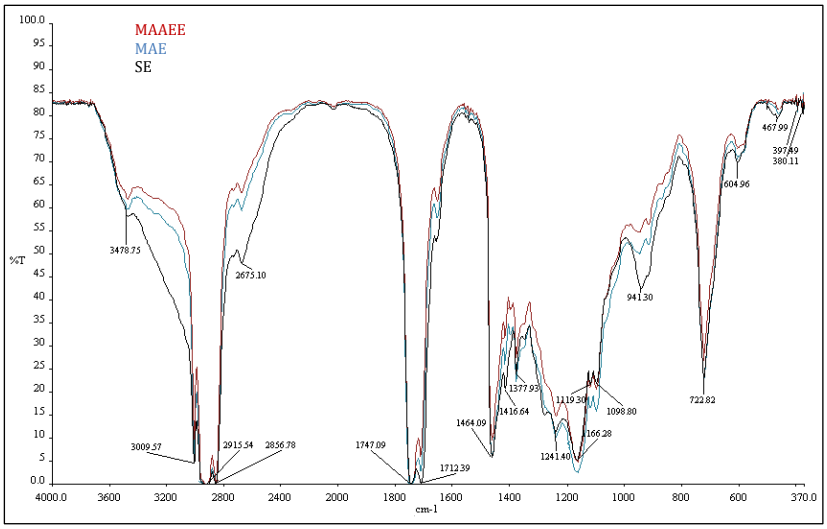


Figure 3. FTIR spectra of ETS oil by MAAEE, MAE and SE

However, minor dissimilarity on the ETS oil extracted by these techniques can be identified in terms of small band shifts and small changes in the relative peak intensity (absorbencies). The exact position of the band and peak shift is affected by the oil composition due to the changes of fatty acid proportion [10]. According to these results it can be concluded that the microwave heating and incorporation with enzyme cocktail do not change the chemical properties of the ETS oil.

Conclusion

Microwave assisted aqueous enzymatic extraction (MAAEE) technique has proven to provide the best alternative for effective and green extraction of Elateriospremum tapos seed (ETS) oil compared to microwave assisted extraction (MAE) and Soxhlet extraction (SE). MAAEE uses aqueous solution that does not involve organic solvents for extraction. MAAEE was found to improve the efficiency of extraction about 12% higher compared to MAE, but 26% lower compared to SE. The extracted ETS oil is a potential source of essential polyunsaturated fatty acids as it contains significant amount of omega-3 fatty acids (alpha linolenic acid). Using MAAEE technique, extracted omega-3 fatty acid concentration improved to 16% and 24% higher compared to using MAE (18.49 ± 1.06%) and SE (10.66 ± 0.43%) techniques respectively which was identified at the retention time range of 12.674-12.696 minutes. The extracted ETS oil shows good quality oil via MAAEE due to the significantly reduced amygdalin content with almost 99% was removed from 0.0097 mg/g oil (MAE), 0.0045 mg/g oil (SE) to 0.00003 mg/g oil (MAAEE). Therefore, MAAEE is preferred as an extraction technique due to its fast extraction time (30 s) compared to SE which requires 6 hour extraction time resulting to MAAEE technique ability to provide high composition of linolenic acid compared to MAE.

Acknowledgement

The authors would like to thank the Ministry of Science and Innovation (MOSTI) Malaysia, the Ministry of Higher Education (MOHE) and Research Management Centre UTM for their funding support of this study.

References

1. Chan, C., Yusoff, R., and Ngoh, G. (2013). Modeling and kinetics study of conventional and assisted batch solvent extraction. *Chemical Engineering Research and Design*. 92(6): 1169–1186
2. Gai, Q.-Y., Jiao, J., Wei, F.-Y., Luo, M., Wang, W., Zu, Y.-G. and Fu, Y.-J. (2013). Enzyme-assisted aqueous extraction of oil from *forsythia suspense* seed and its physicochemical property and antioxidant activity. *Industrial Crops and Products*, 51: 274–278.

3. Jiao, J., Li, Z., Gai, Q., Li, X., Wei, F., Fu, Y. and Ma, W. (2014). Microwave-assisted aqueous enzymatic extraction of oil from pumpkin seeds and evaluation of its physicochemical properties, fatty acid compositions and antioxidant activities. *Food Chemistry*, 147: 17–24.
4. Kapoor, R. and Patil, U. K. (2011). Importance and production of omega-3 fatty acids from natural sources. *International Food Research Journal*, 18: 493–499.
5. Yong, O. Y., and Salimon, J. (2006). Characteristics of *Elateriospermum tapos* seed oil as a new source of oilseed. *Industrial Crops and Products*, 24(2): 146 – 151
6. Temelli, F., Saldaña, M. D. A., Moquin, P. H. L. and Sun, M. (2008). Supercritical fluid extraction of specialty oils. Martínez, J. L. (Ed). Supercritical fluid extraction of nutraceuticals and bioactive compounds. London: CRC Press/Taylor & Francis: pp. 52 – 99.
7. Sánchez-Camargo, A. P., Meireles, M. Â. A., Ferreira, A. L. K., Saito, E. and Cabral, F. A. (2012). Extraction of ω-3 fatty acids and astaxanthin from brazilian rrdspotted shrimp waste using supercritical CO_2 + ethanol mixtures. *Journal of Supercritical Fluids*, 61: 71 – 77.
8. Li, J., Zu, Y.-G., Luo, M., Gu, C.-B., Zhao, C.-J., Efferth, T. and Fu, Y.-J. (2013). Aqueous enzymatic process assisted by microwave extraction of oil from yellow horn (*Xanthoceras sorbifolia* Bunge.) seed kernels and its quality evaluation. *Food Chemistry*, 138(4): 2152 – 2158.
9. Latif, S. and Anwar, F. (2011). Aqueous enzymatic sesame oil and protein extraction. *Food Chemistry*, 125(2): 679 – 684.
10. Vlachos, N., Skopelitis, Y., Psaroudaki, M., Konstantinidou, V., Chatzilazarou, A, and Tegou, E. (2006). Applications of Fourier transform-infrared spectroscopy to edible oils. *Analytica Chimica Acta*, 573-574: 459–465.

Malaysian Journal of Analytical Sciences, Vol 23 No 3 (2019): 495 - 504
DOI: https://doi.org/10.17576/mjas-2019-2303-14

MALAYSIAN JOURNAL OF ANALYTICAL SCIENCES
Published by The Malaysian Analytical Sciences Society
ISSN 1394 - 2506

OPTIMIZATION OF HERBAL HEALTH TEA FLAVORED WITH ROASTED RICE GERM (KHAO DAWK MALI 105) USING RESPONSE SURFACE METHODOLOGY

(Pengoptimuman Teh Kesihatan Herba yang Bercampur dengan Germa Beras Panggang (Khao Dawk Mali 105) Menggunakan Kaedah Gerak Balas Permukaan)

Sriwiang Rittisak[1]*, Ratchanee Charoen[1], Ratchagon Pongsri[1], Pattraporn Tearyakul[1], Wanticha Savedboworn[2], Wiboon Riansa-ngawong[2]

[1]*Department of Innovation and Product Development Technology, Faculty of Agro-Industry*
[2]*Department of Agro-industry Technology and Management, Faculty of Agro-Industry*
King Mongkut's University of Technology North Bangkok, 25230 Prachinburi, Thailand.

**Corresponding author: sriwiang.t@agro.kmutnb.ac.th*

Received: 25 October 2017; Accepted: 22 January 2019

Abstract

Herbal health tea flavored with roasted rice germ was formulated using mixture design and response surface methodology (RSM). The ranges for dried bael fruit powder (*Aegle marmelos* (L.) Correa), dried pandan (*Pandanus amaryllifolius*) leaf powder and roasted rice germ were 20 – 50%, 20 – 50% and 30 – 70%, respectively. At optimum condition, the herbal tea flavored with roasted rice germ consisted of 45.25% of dried bael fruit powder, 21.68% of dried pandan leaf powder and 33.07% of roasted rice germ. The product contained 4.22% moisture and 3.18% total ash. For antioxidant activity, it was found that herbal health tea had 69.03% DPPH scavenging activity and 75.16 mg GAE/g total phenolic content. Water activity of the product was 0.374. The aerobic plate count was less than 1×10^2 CFU/g as well as yeast and mold were not found. Color with L*, a*, b* values and transmittance of brewed herbal tea were 60.11, -1.43, 14.10 and 75.87%, respectively with almost clear greenish-yellow appearance. Consumer acceptability test on 150 consumers indicated that the product was liked very much (Overall liking score = 7.6) with 99.3% of them accepted the product.

Keywords: herbal health tea, rice germ, mixture design, response surface methodology, antioxidant activity

Abstrak

Teh kesihatan herba yang ditanam dengan germa beras panggang di formulasi dengan menggunakan kaedah gerak balas permukaan (RSM). Julat untuk serbuk buah bael kering (*Aegle marmelos* (L.) Correa), serbuk daun pandan (*Pandanus amaryllifolius*) dan germa beras panggang, masing -masing adalah 20 - 50%, 20 - 50% dan 30 - 70%. Pada keadaan optimum, teh herba yang dibekalkan dengan germa beras panggang terdiri daripada 45.25% serbuk buah bael kering, 21.68% serbuk daun pandan kering dan 33.07% germa beras panggang. Produk ini mengandungi kelembapan 4.22% dan abu sebanyak 3.18%. Bagi aktiviti antioksidan, didapati teh kesihatan herba mempunyai aktiviti skaveng DPPH sebanyak 69.03% dan kandungan fenolik sebanyak 75.16 mg GAE/g. Aktiviti air produk ialah 0.374. Perkiraan plat aerobikkurang daripada 1 × 102 CFU/g serta ragi dan acuan tidak dijumpai. Warna dengan nilai L*, a*, b* dan kepancaran teh herba yang di bru masing-masing adalah 60.11, -1.43, 14.10 dan 75.87%, dengan penampilan kuning kehijauan yang jelas. Ujian penerimaan pelanggan pada 150 pengguna menunjukkan bahawa produk itu sangat disukai (Keseluruhan skor suka = 7.6) dengan 99.3% daripada mereka menerima produk tersebut.

Kata kunci: teh kesihatan herba, germa beras, rekaan campuran, kaedah gerak balas permukaan, aktiviti antioksidan

Introduction

Herbs have been used for centuries to treat a variety of medical illnesses. They are usually consumed in the form of tea, i.e. an infusion of dried plant part (leaves, flowers, seeds, roots and bark) steeped in boiling water [1, 2]. Herbal teas are widely sold in health food store. Available as pure or blended samples, herbal teas are popular because of their fragrance, antioxidant properties and therapeutic application [3, 4].

Many people believed that herbal teas are natural and safe because they consist of bioactive substance that can promote health and mitigate illness [1, 5]. Herbal teas are good source of bioactive substance like vitamin, carotenoids, flavonoids, and some organic acids in addition to fruits and vegetables [6]. They are believed to have certain health effects in treating various types of illness (cancer, cardiovascular, cerebro-vascular and neuro-degenerative diseases) and are commonly classified base on their therapeutic actions such as anti-inflammatory, antispasmodic, carminative, antidepressant, diuretic, and laxative herbs. [7, 8].

Rice germ is a by-product of the rice milling process which is included in rice bran. Rice germ provides as rich source of protein, fat, dietary fiber and nutrient essential for life such as phenolic compound, vitamin E and gamma-amino-butyric acid, etc. which are useful for human [9, 10]. The roasted rice adds a nutty flavor and aroma that combines perfectly with green tea. This green tea is popular in Japan, where it has a long tradition. Due to the health benefit and flavored of the roasted rice germ, there is increasing interest in its consumption.

Response surface methodology (RSM) is a powerful mathematical technique based on regression analysis used to develop and improve (optimize) products and processed that have two or more factors that influence the response. RSM have been wildly used by food companies to develop food products as well as to analyze, model and optimize product formulations and processes [11, 12]. In this study, herbal health tea flavored with roasted rice germ was formulated using the mixture design and RSM. This study aimed at optimizing the formulation to obtain a herbal health tea flavored with roasted rice germ that contained high total phenolic compounds, free-radical scavenging activity as well as tastefully favorable among consumers.

Materials and Methods

Materials

The ingredients from 15 herbs were screened by pass-fail screening and scoring screening method. Two herbs were selected (bael fruit and pandan leaf) for this study. Dried bael fruit (*Aegle marmelos* (L.) Correa) and dried pandan (*Pandanus amaryllifolius*) leaf purchased from Dongbang herb shop, Prachinburi Province, Thailand. Germ from Thai rice variety (cv. Khao Dawk Mali 105) was obtained from Jibtong Surin Rice Mill, Surin Province, Thailand. Rice germ was roasted in a pan for 2 minutes. The dried raw material was ground to a powdery form by electric grinder and sieved through 35 mesh.

Extraction process

In order to prepare each sample, the mixed three components of herb powder 2.0 grams was then packed into tea bags. The herbal health tea (in tea bags) was extracted with 100 mL of hot water at 90 °C for 3 minutes. The extract was filtered through Whatman No.4 filter paper and then centrifuged to clarify. The herbal tea solution was prepared directly before the analysis.

Experimental design

In this study, the mixture design was used to formulate herbal health tea flavored with roasted rice germ. The range of its components were 20 – 50% dried bael fruit powder (*Aegle marmelos* (L.) Correa), 20 – 50% dried pandan (*Pandanus amaryllifolius*) leaf powder and 30 – 70% roasted rice germ, bringing to a total of 100%. The experimental design of variable is shown in both Figure 1 and Table 1. The experimental design was run to three points (replications) at the centroid of the design (formulation 7 – 9), in order to provide accurate prediction in the center of design or perhaps at pure blend, to enable better estimated of model coefficient. The responses measured three properties of herbal health tea; total phenolic content, DPPH free radical scavenging activity and sensory evaluation.

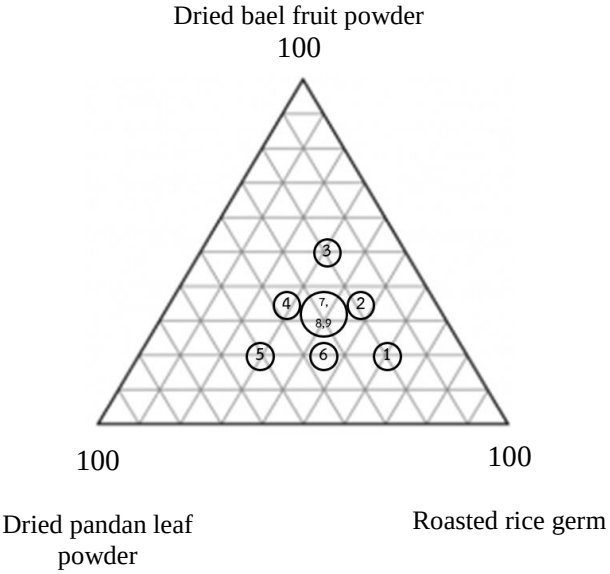


Figure 1. Herbal health tea flavored with roasted rice germ formula from mixture design

Table 1. The experimental design of herbal health tea flavored with roasted rice germ formulation

Formulation	Dried Bael Fruit Powder (%)	Dried Pandan Leaf Powder (%)	Roasted Rice Germ (%)
1	20	20	60
2	35	20	45
3	50	20	30
4	35	35	30
5	20	50	30
6	20	35	45
7	30	30	40
8	30	30	40
9	30	30	40

Determination of total phenolic content

Total phenolic content of herbal health tea flavored with roasted rice germ extract was determined according to the method of [13]. An amount 150 µL of herbal health tea extract, 2400 µL of nanopure water and 150 µL of 0.25 N Folin-Ciocalteu reagent were combined and then mixed well by vortex. The mixture was allowed to react for 3 minutes then 300 µL of 1 N Na_2CO_3 solution was added and mixed well again by shaking. The solution was incubated at room temperature in the dark for 2 hours. The absorbance was measured at 725 nm using a spectrophotometer and the result were expressed as milligram of Gallic acid equivalent (GAE) per 1 gram of extract using standard curve prepared from Gallic acid solution.

1,1-diphenyl-2-picrylhydrazyl (DPPH) free radical scavenging activity assay

The antioxidant activity of herbal health tea flavored with roasted rice germ extract was determined according to the method of Matthus [14]. The DPPH radical scavenging assay is regularly used for the relatively rapid evaluation of the antioxidant activity. DPPH is a stable free radical, even at room temperature, and shows strong absorbance at

515 nm. The DPPH radical accepts and electron or hydrogen radical to become a stable diamagnetic molecule with a different color. Thus, the degree of its discoloration from purple to yellow is attributed to the hydrogen donating ability of the added compound, which is indicative of its radical scavenging potential.

Briefly, 80 µL of sample was mixed with 200 µL of 0.05% DPPH in a total volume of 4 mL methanol and allowed to react in the dark for 30 minutes. The results were expressed as percent inhibition using the equation 1.

$$\% \text{ inhibition} = (\text{Absorbance of control} - \text{Absorbance of samples})/\text{Absorbance of control} \times 100 \quad (1)$$

Sensory evaluation

The 72 untrained panels evaluate the overall liking score of herbal health tea flavored with roasted rice germ by using 9-point hedonic scale, with 1 being dislike extremely and 9 being like extremely [15]. The sample of herbal health tea infusion was placed 30 ml in a 1 oz. plastic cup with cover cap. The 4 samples of herbal health tea coded with three-digit random number and served monadically according to experimental design (Balance in complete block design: BIB) (Table 2) to each panelist was randomized to minimize bias. Temperature of the herbal health tea served was controlled at 65 – 75 °C [16].

Table 2. Experimental design (Balance in complete block design: BIB) of herbal health tea flavored with roasted rice germ infusion serving for panels

No. of Panel				No. of Formulation			
1	19	37	55	1	4	6	7
2	20	38	56	2	6	8	9
3	21	39	57	1	3	8	9
4	22	40	58	1	2	3	4
5	23	41	59	1	5	7	8
6	24	42	60	4	5	6	9
7	25	43	61	2	3	6	7
8	26	44	62	2	4	5	8
9	27	45	63	3	5	7	9
10	28	46	64	1	2	5	7
11	29	47	65	2	3	5	6
12	30	48	66	3	4	7	9
13	31	49	67	1	2	4	9
14	32	50	68	1	5	6	9
15	33	51	69	1	3	6	8
16	34	52	70	4	6	7	8
17	35	53	71	3	4	5	8
18	36	54	72	2	7	8	9

Statistical analysis

Mixture design was used to examine the effects of the three variables: dried bael fruit powder (X_1), dried pandan leaf powder (X_2) and roasted rice germ (X_3). The experimental design (Mixture design) used in the RSM are listed in Table 1. A total 9 experimental runs were completed and the total phenolic content (mg GAE/g), antioxidant activity (% inhibition) and overall liking score (9 point hedonic scale) expressed as the dependent variables, was determined. These variable was expressed individually as function of the independent variables. A Scheffe second

degree polynomial was used to express total phenolic content (Y_1), antioxidant activity (Y_2) and overall liking score (Y_3) of herbal health tea as a function of the independent variables as follows (equation 2):

$$Y = \beta_1X_1 + \beta_2X_2 + \beta_3X_3 + \beta_{12}X_1X_2 + \beta_{13}X_1X_3 + \beta_{23}X_2X_3 \quad (2)$$

where Y represents the response variable, β_1, β_2, β_3, β_{12}, β_{13}, β_{23} is parameter estimates for each linear, cross product term produced from prediction model, X_1, X_2, X_3 = linear terms of dried bael fruit powder, dried pandan leaf powder and roasted rice germ, X_1X_2, X_1X_3, X_2X_3 cross product terms of (dried bael fruit powder x dried pandan leaf powder), (dried bael fruit powder x roasted rice germ) and (dried pandan leaf powder x roasted rice germ). The response surface graphs from the Scheffe quadratic canonical polynomial model were generated by a statistical program (Minitab version 13.2, Minitab Inc., PA). Finally, all graphs were optimized by using the criteria: (1) maximum total polyphenol content, (2) maximum antioxidant activity and (3) overall liking score > 6.0 [16 ,17].

Verification of model

Optimization of herbal health tea flavored with roasted rice germ formulation, including percentage of dried bael fruit powder, percentage of dried pandan leaf powder and percentage of roasted rice germ to a total of 100% for maximize of total phenolic content and overall liking score were calculated by using the predictive equation from RSM. The actual determination of total phenolic content, antioxidant activity and overall liking score were carried out at the optimal formulation and the result (observed value) was compared to the predicted value.

Quality measurement of the developed herbal health tea flavored with roasted rice germ

Total phenolic content and antioxidant activity were carried out according to the method of Thaipong et al. and Matthus, respectively [13, 14]. Moisture, and ash content were also determined according to AOAC methods [18]. Color analysis was carried out on brewed herbal health tea using a colorimeter (Hunter Lab Model Colorflex) to obtain the color values (CIE, L* a* b* values and transmittance). Water activity of product was determined by using AQUA LAB Model series 3TE. Product quality was evaluated by microbial aerobic total plate count and yeast and mold following the Bacteriological Analytical Manual methods [19].

Consumer acceptance test of the developed herbal health tea flavored with roasted rice germ

One hundred and fifty consumers who were member of the elder circle of Chaophraya Abhaibhubejhr hospital and the retired circle of government officer, Prachinburi province, Thailand, were selected by the following criteria: they have to be over 55 years old, health conscious and regularly exercise. They answered questionnaires about product acceptability and purchase intent of herbal health tea flavored with roasted rice germ. They were asked to rate herbal health tea samples. The sample was placed in a 2 oz. plastic cup covered serving to each consumers. Consumers rated sample using a 9-point hedonic scale for the overall liking, color, odor, taste and aftertaste of the herbal health tea using a ballot in questionnaires.

Results and Discussion

Model fitting for response surface methodology

The total phenolic content (expressed as mg GAE/g), the antioxidant activity (expressed as % inhibition) and overall liking score (expressed as 9-point hedonic scale) of herbal health teas flavored with roasted rice germ obtained from the 9 experiments are listed in Table 3. The mean total phenolic content, antioxidant activity and overall liking score of 9 formulations of the independent variables, varied from 70.94 – 77.20 mg GAE/g, 63.94 – 69.20% and 5.5 – 6.3, respectively (Table 3). The experimental data were used to calculate the coefficients of the Scheffe second degree polynomial equation (Table 4). The coefficient of multiple determination (R^2) for the response of total phenolic content, antioxidant activity and overall liking score being 0.993, 0.629 and 0.839, respectively. This mean that the calculated model was able to explain 99.3%, 62.9% and 83.9% of the results in the case of total phenolic content, antioxidant activity and overall liking score, respectively. Joglekar and May [20] suggested that for a good fit of a model, R^2 should be at least 0.80. It means that the model can be used for predicting the response. Therefore, the model of total phenolic content (R^2 = 0.993) and overall liking score (R^2 = 0.839) can predict the total phenolic content and overall liking score in herbal health tea flavored with roasted rice germ. While, the coefficient (R^2) for the response of the antioxidant activity being low R^2 (0.629). In this study, the antioxidant activity of herbal health

tea was assessed by the DPPH assay. Some authors have shown significant differences in free radical scavenging activity according to the assay method use [21] and have reported that the DPPH assay is simpler, and faster than FRAP and ORAC assay [22], but may give and underestimate of the antioxidant capacity. Thus, the different tests should be used in further study for a good fit model. The development of functional beverages with high content of phenolic and antioxidant activity has been widely studied [23, 24] and the industry could benefit from these studies, that is new functional food products, especially bioactive beverages, could be developed.

Table 3. The total phenolic content, antioxidant activity and overall liking score of herbal health tea flavored with roasted rice germ

Formulation	Independent Variables (X)			Dependent Variables (Response: Y)		
	Dried Bael Fruit Powder (X_1) (%)	Dried Pandan Leaf Powder (X_2) (%)	Roasted Rice Germ (X_3) (%)	Total Phenolic Content (Y_1) (mg GAE/g)	Antioxidant Activity (Y_2) (%)	Overall Liking Score (Y_3)
1	20	20	60	72.02±0.04	65.94±0.44	5.6±1.8
2	35	20	45	77.20±0.52	68.76±0.28	6.0±1.8
3	50	20	30	76.73±0.10	69.00±0.16	6.1±1.3
4	35	35	30	74.59±0.10	67.47±0.06	6.3±1.6
5	20	50	30	72.19±0.08	66.06±0.12	5.5±1.6
6	20	35	45	70.94±0.16	63.94±0.14	5.7±1.7
7	30	30	40	74.23±0.14	69.20±0.08	5.6±1.8
8	30	30	40	74.78±0.06	66.32±0.08	6.0±1.4
9	30	30	40	74.81±0.06	68.27±0.22	5.6±1.6

Table 4. The predictive regression model of total phenolic content, antioxidant activity and overall liking score in mixture design experiment

Dependent Variable: Y	Predictive Model	R^2
Y_1: Total phenolic (mg GAE/g)	$0.488X_1+0.869X_2+0.576X_3+0.001X_1X_2+0.013X_1X_3-0.005X_2X_3$	0.993
Y_2: Antioxidant activity (%)	$0.385X_1+0.774X_2+0.632X_3+0.001X_1X_2+0.011X_1X_3-0.008X_2X_3$	0.629
Y_3: Overall liking score	$-0.168X_1-0.186X_2-0.068X_3+0.014X_1X_2+0.009X_1X_3+0.009X_2X_3$	0.839

Effect of three components on total phenolic content and overall liking score

The empirical model is plotted as a two dimension surface representing the response (total phenolic content and overall liking score) (Figure 2). Contour plot illustrates the effect of three components (dried bael fruit powder, dried pandan leaf powder and roasted rice germ) on total phenolic content (a) and overall liking score (b). The decrement of total phenolic content with the mixture of ingredients (dried bael fruit powder, dried pandan leaf powder, roasted rice germ) in formulations up to a critical point can be observed from the Figure 2. Meanwhile, as the dried bael fruit powder increased, the total phenolic content was increased (Figure 2a) due to the total phenolic content of ingredients (dried bael fruit powder, dried pandan leaf powder and roasted rice germ were total phenolic content 89.09, 69.80 and 65.02 mg GAE/g, respectively). The maximum yields were in the experimental region.

From the graph, the maximum total phenolic content (≥ 76 mg GAE/g) was obtained with dried bael fruit powder locating between 29.57% and 50.00%, dried pandan leaf powder locating between 20.00% and 27.22% and roasted rice germ locating between 20.00% and 40.22%. In addition, as the dried bael fruit powder increased, the overall liking was increased. On the other hand, as the roasted rice germ increase, the overall liking was decreased (Figure

2b). The maximum score were located in the experimental region. From the graph, the maximum overall liking score (≥ 6.1) was obtained with dried bael fruit powder locating between 33.88% and 50.00%, dried pandan leaf powder locating between 20.00% and 36.31% and roasted rice germ locating between 30.00% and 33.75%. It means the herbal health tea flavored with roasted rice germ formula from three components in this region had a good taste.

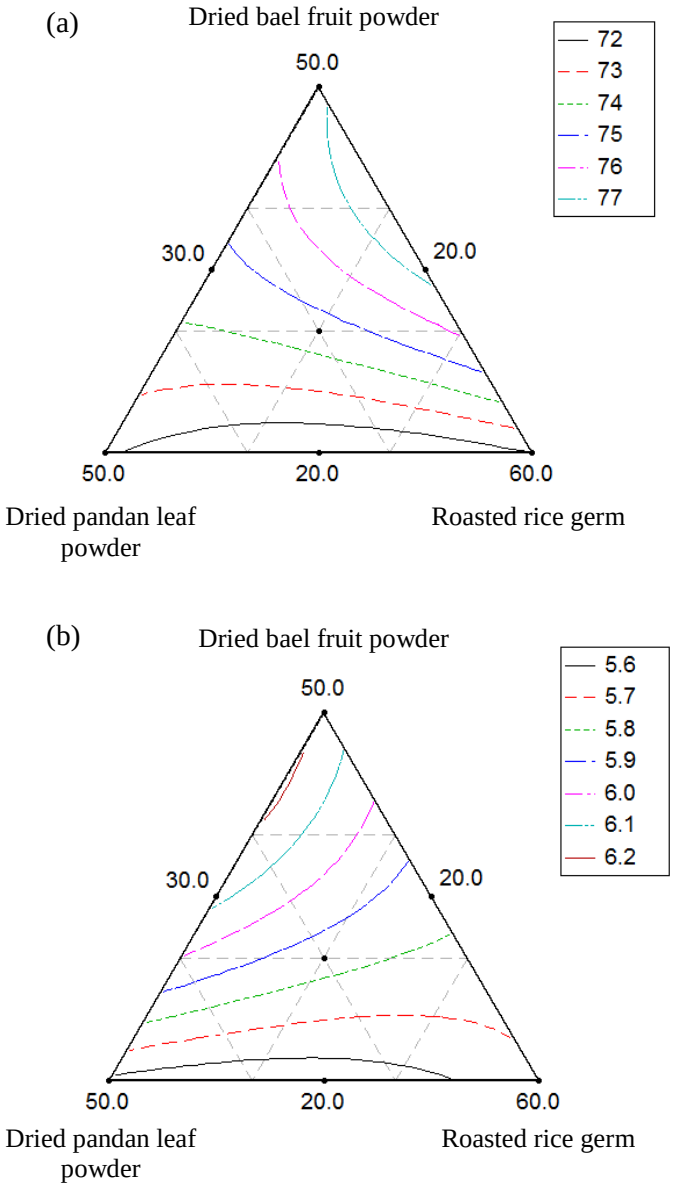


Figure 2. Effects of three components (dried bael fruit powder, dried pandan leaf powder and roasted rice germ) on total phenolic content (a) and overall liking score (b)

Verification of predictive model

Response surface methodology (RSM) was employed to attain an optimal formulation that would yield maximal total phenolic content and overall liking score. According to Figure 3, the optimal formulation consisted of dried bael fruit powder in the range of 39.38 – 50.00%, dried pandan leaf powder of in the range of 20.00 – 27.22% and roasted rice germ in the range of 30.00 – 33.75%, respectively, with the predicted maximal total phenolic content

of ≥ 76 mg GAE/g, and overall liking score of ≥ 6.1. The optimum contour map for hedonic rating should over 6.0 [16, 17]. Furthermore, the verification studies have been carried out to validate the optimization result obtained by the response surface analysis. Five points (A, B, C, D and E) in the optimal region were used to model verification (Figure 3). It was suggested that the errors between predicted and verification were to be considered small as the observed values were less than 5% (ranged from 0.10% to 4.35%) level of significance, means that the model is acceptable for optimization (Table 5).

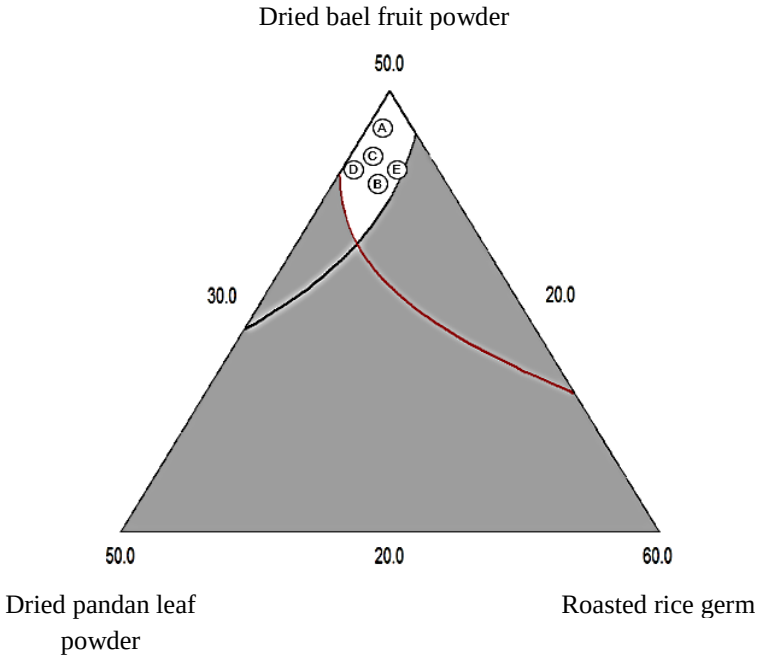


Figure 3. The optimal overlapping (white area) of herbal health tea flavored with roasted rice germ formulation

Table 5. Results of verification tests for the fitted model

Formulation	Dried Bael Fruit Powder (%)	Dried Pandan Leaf Powder (%)	Roasted Rice Germ (%)	Predicted Value	Observed Value	Error (%)
				Total Phenolic Content (mg GAE/g)		
A	48.72	20.77	30.51	76.57	75.84±0.12	0.95
B	43.58	24.01	32.41	76.32	76.40±0.10	0.10
C	47.33	21.68	30.99	76.52	75.87±0.08	0.85
D	45.75	23.74	30.51	76.14	76.80±0.08	0.87
E	45.25	21.68	33.07	76.82	76.48±0.06	0.44
Formulation				**Overall Liking Score**		
A	48.72	20.77	30.51	6.8	6.9±1.2	1.47
B	43.58	24.01	32.41	6.8	6.7±1.3	1.47
C	47.33	21.68	30.99	6.8	6.6±1.2	2.94
D	45.75	23.74	30.51	6.9	6.6±1.3	4.35
E	45.25	21.68	33.07	6.8	7.0±1.1	2.94

In many cases, the determination of proportions is important to obtaining the desired output mixture design, a special type of RSM, is a very effective method of determining the proportions of ingredients of a blend [25]. In this study, the formulation of herbal health tea flavored with roasted rice germ was optimized to obtain the highest concentration of total phenolic content. The response surface analysis denoted that the maximum predicted value of total phenolic content was 76.82 mg GAE/g under the following formulations: 45.25% of dried bael fruit powder, 21.68% of dried pandan leaf powder and 33.07% of roasted rice germ. Base on the regression analysis, the model had a satisfactory coefficient of R^2 = 0.993. Furthermore, this tea components could be the optimum of bioactive compound that consumer would accept in term of its sensory properties.

The developed herbal health tea flavored with roasted rice germ qualities

The developed herbal health tea flavored roasted rice germ contained 4.22% moisture and 3.18% total ash. For antioxidant activity, it was found that herbal health tea had 69.03% DPPH scavenging activity and 75.16 mg GAE/g total phenolic content. Water activity of the product was 0.374. The aerobic plate count was less than 1×10^2 CFU/g and yeast and mold were not found. Color with L*, a*, b* values and transmittance of brewed herbal tea were 60.11, -1.43, 14.10 and 75.87%, respectively with almost clear greenish-yellow appearance.

Consumer acceptability using central location test

One hundred and fifty consumers participated in the performance test. Consumer population predominantly consisted of females who made up 51% of the total population. The participants were 55 years of age and over, which was expected since the target consumers were pre-recruited. Thirty six percent of consumers were employed and 34% participants were unemployed. Fifty two percent of the consumers had completed their bachelor's degree and 26% had post graduate degrees (above bachelor degree). Income data revealed that 46% earned 10,000 baht/month and below.

Consumer rating for overall liking, color, odor, taste and aftertaste of herbal health tea flavored roasted rice germ (mean value = 7.6, 7.7, 7.5, 7.2 and 7.2, respectively) indicated that product was very much liked. 99.3% of consumers accepted the product which received the highest percentage of positive response for purchase intent (99.3%). When consumer were asked if they would purchase the product after knowing the health benefit information, the purchase intent slightly change (100%). The positive purchase intent for product cost (2.0 grams for 20 tea bags) at 51 - 100 baht and 101 – 150 baht were 54% and 46%, respectively.

Conclusion

Based on the mixture design experiments, RSM was used to optimize the formulation of herbal health tea flavored with roasted rice germ. The Scheffe second quadratic polynomial model developed for the yield of total phenolic content and overall liking score from mixture ingredients (dried bael fruit powder, dried pandan leaf powder and roasted rice germ). The optimal formula of the herbal health tea flavored with roasted rice germ consisted of 45.25% of dried bael fruit powder, 21.68% of dried pandan leaf powder and 33.07% of roasted rice germ. In addition, The RSM was successful in identifying the optimum herbal health tea formula for the maximum total phenolic content and overall liking score. This study provides a basis for herbal health tea production.

Acknowledgement

This research was funded by King Mongkut's University of Technology North Bangkok. Contact no. KMUTNB-60-GOV-047.4.

References

1. Craig, W. J. (1999). Health-promoting properties of common herbs. *American Journal of Clinical Nutrition*, 70 (suppl): 491S – 499S.
2. Lazar, M. A. (2004). East meets West: and herbal tea finds a receptor. *Journal of Clinical Investigation*, 113(1): 23 – 25.
3. Naithani, V., Nair, S. and Kakkar, P. (2006). Decline in antioxidant capacity of Indian herbal teas during storage and its relation to phenolic content. *Food Research International*, 39(2): 176 – 181.
4. Aoshima, H., Hirata, S. and Ayabe, S. (2007). Antioxidative and anti-hydrogen peroxide activities of various herbal teas. *Food Chemistry*, 103(2): 617 – 622.

5. Thomson, C. and Lutz, R. B. (2001). Herbs and botanical supplements: Principles and concepts, In: Nutrition in the prevention and treatment of disease. Academic press: pp. 261 – 275.
6. Speiky, H., Rocco, C., Carrasco, C., Lissi, E. A. and Lopez-Alarcon, C. (2006). Antioxidant screening of medicinal herbal teas. *Phytotherapy Research*, 20(6): 462 – 467.
7. Romm, A., Ganora, L., Hoffmann, D., Yarnell, E., Abascal, K. and Coven, M. (2010). Fundamental principles of herbal medicine. In: Romm, A., Hardy, M.L. and Mills, S. (Eds.) Botanical Medicine for Women's health, Churchill Livingstone/Elsevier: pp. 24 – 74.
8. Wachtel-Galor, S. and Benzie, I. F. F. (2011). Herbal medicine: An introduction to its history, usage, regulation, current trends, and research needs. In: Benzie, I.F.F. and Wachtel-Galor, S. (Eds.) Herbal Medicine: Biomolecular and Clinical Aspect, CRC Press: pp. 1 – 10.
9. Kim, I. H., Kim, C. J., You, J. M., Lee, K.W., Kim, C. T., Chung, S. H. and Tae, B.-S. (2002). Effect of roasting temperature and time on the chemical composition of rice germ Oil. *Journal of the American Oil Chemists' Society*, 79(5): 413 – 8.
10. Mori, H., Kawabata, K., Yoshimi, N., Tanaka, T., Murakami, T., Okada, T. and Murai, H. (1999). Chemopreventive effects of ferulic acid on oral and rice germ on large bowel carcinogenesis. *Anticancer Research*, 19(5A): 3775 – 3778.
11. Granato, D., Calado, V. M. A. and Jarvis, B. (2014). Observations on the use of statistical methods in food science and technology. *Food Research International*, 55: 137 – 149.
12. Liu, C., Yu, J., Wang, J., Liu, Z. and Wang, Q. (2012). Application of response surface methodology to optimize supercritical carbon dioxide extraction of oil from rapeseed (*Brassica napus* L.). *International Journal of Food Science & Technology*, 47(6): 1115 – 1121.
13. Thaipong, K., Boonprokob, U., Crosby, K., Zevallos, L. C. and Byme, H. D. (2006). Comparison of ABTS, DPPH, FRAP and ORAC assays for estimating antioxidant activity from guava extracts. *Journal of Food Composition and Analysis*, 19(6-7): 669 – 675.
14. Matthus, B. (2002). Antioxidant activity of extracts obtained from residues of different oilseeds. *Journal of Agricultural of Food Chemistry*, 5(12): 3444 – 3452.
15. Peryam, D. R. and Pilgrim, F. J. (1957). Hedonic scale method of measuring food preferences. *Journal of Food Science*, 11(9): 9 – 14.
16. Resurrecction, A. V. A. (1998). Consumer sensory testing for product development. Aspen Publishers, Inc., Maryland.
17. Grosso, N. R. and Resurrecction, A. V. A. (2002). Prediction consumer acceptance rating of cracker-coated and roasted peanuts from descriptive analysis and hexanal measurements. *Journal of Food Science*, 67(4): 1530 – 1537.
18. AOAC (2000). Official method of analysis. 17th edition. The Association of Official Analytical Chemistry, Arlington, Virginia.
19. Bacteriological Analytical Manual (2001). Available Source from https://www.fda.gov/Food/FoodScienceResearch/LaboratoryMethods/ucm2006949.htm. Access date October 12, 2017].
20. Joglekar, A. M. and May, A. T. (1987). Product excellence through design of experiments. *Cereal Food World*, 32: 857 – 868.
21. Sara P., Michael H. G., Monica B., Francisca P. L. Francisco S. and Maria P. A. (2014). Modelling extraction of white tea polyphenols: the influence of temperature and ethanol concentration. *Antioxidants*, 3(3): 684 – 699.
22. Pooja S. and Modi H. A. (2015). Comparative study of DPPH, ABTS and FRAP assays for determination of antioxidant activity. *International Journal of Research in Applied Science and Engineering Technology*, 3(6): 636 – 641.
23. Owczarek L., Jasinska U., Osinska M. and Skapska S. (2004). Juices and beverages with a controlled phenolic content and antioxidant capacity. *Polish Journal of Food and Nutrition Sciences*, 13(3): 261 – 268.
24. Soccol C. R., Lima I. F. P., Lindner J. D., Parada J. L. and Soccol V. T. (2012). Development of and innovative nutraceutical fermented beverage from herbal mate (*Ilex paraguariensis* A. St.-Hil.) extract. *International Journal of Molecular Sciences*, 13(1): 788 – 800.
25. Yeliz B. S., Ezgi A. D. and Nimetullah B. (2016). Mixture design: A review of recent applications in the food industry. *Pamukkale University Journal of Engineering Sciences*, 22(4): 297 – 304.

Malaysian Journal of Analytical Sciences, Vol 23 No 3 (2019): 505 - 515
DOI: https://doi.org/10.17576/mjas-2019-2303-15

MALAYSIAN JOURNAL OF ANALYTICAL SCIENCES
Published by The Malaysian Analytical Sciences Society
ISSN 1394 - 2506

RAPID SPECTROPHOTOMETRIC METHOD FOR HISTAMINE DETERMINATION IN FISH USING ALIZARIN RED S AND METAL

(Kaedah Spektrofotometri Pantas untuk Penentuan Histamin dalam Ikan Menggunakan Alizarin Merah S dan Logam)

Miftakhul Jannatin[1], Ayu Nabila Izazi Latjuba[1], Sri Wahyuni[1], Ganden Supriyanto[1,2]*, Wan Aini Wan Ibrahim[3]

[1]*Department of Chemistry, Faculty of Science and Technology*
[2]*Laboratory of Sensor and Biosensor, Institute of Tropical Disease*
Universitas Airlangga, Jl. Mulyorejo Kampus C UNAIR Surabaya 60115, Indonesia
[3]*Department of Chemistry, Faculty of Science,*
Universiti Teknologi Malaysia, 81310 UTM Johor Bahru, Johor, Malaysia

**Corresponding author: ganden-s@fst.unair.ac.id*

Received: 25 October 2017; Accepted: 22 January 2019

Abstract

An analytical method for the determination of histamine using metals and alizarin red S (ARS) reagents by UV-Visible spectrophotometry was developed. Cu(II), Co(II) and ARS were used to form colored complex with histamine. The developed method was used to detect qualitatively and quantitatively the presence of histamine. Absorbance of Cu(II) and Co(II) complex were measured at a maximum wavelength of 505.5 and 567 nm, respectively. Optimization of analytical parameters such as concentration of metals, concentration of ARS, sample solution pH, and optimum time for complex formation were performed. Experimental results showed that the optimum concentration of Cu(II) was 50 ppm, 75 ppm ARS, sample solution pH 6, and 15 minutes optimum time, while the optimum concentration of Co(II) was 125 ppm, ARS was 75 and 50 ppm, sample solution pH 5 and 10 minutes optimum time. Method validation indicated that the coefficient of variation, limit of detection (LOD) (S/N =3), and limit of quantitation (LOQ = 10S/N) of Cu(II) were 0.65%, 8.94 ppm, and 29.82 ppm respectively with a sensitivity of 0.0054 ppm and linearity of 0.9959. Accuracy of histamine determination through Cu-ARS-histamine complex at a concentration of 50, 100, and 150 ppm were 105.7% (RSD = 0.777%, n = 3), 105.06% (RSD = 0.606%, n = 3), and 94.12% (RSD = 0.767%, n = 3), respectively. Meanwhile, the CV, LOD, and LOQ of Co(II) were 0.28%; 2.58 ppm; and 8.6 ppm respectively with a sensitivity of 0.0006 ppm and linearity of 0.9965. Accuracy of histamine determination through Co-ARS-histamine complex at a concentration of 50, 75, and 125 ppm were 98.33%, 95.83%, 93.88%, respectively. The proposed method was successfully applied to the determination of histamine in a fish sample with quantitative recovery; for Cu(II) complex (99.23%) and Co(II) complex (102.62%).

Keywords: histamine, metals, Cu(II), Co(II), ARS, UV-visible spectrophotometry

Abstrak

Kaedah analisis untuk penentuan histamin menggunakan logam dan reagen alizarin merah S (ARS) telah dibangunkan menggunakan spektrofotometri ultralembayung-nampak. Cu(II), Co(II), dan ARS digunakan untuk membentuk kompleks berwarna dengan histamin. Kaedah yang telah dibangunkan digunakan untuk mengesan histamin secara kualitatif dan kuantitatif. Serapan kompleks Cu(II) dan Co(II) diukur pada panjang gelombang maksimum masing-masing 505.5 dan 567 nm. Pengoptimuman parameter analisis seperti kepekatan logam, kepekatan ARS, pH larutan sampel, dan masa optimum bagi pembentukan kompleks telah dilakukan. Keputusan eksperimen menunjukkan bahawa kepekatan optimum Cu(II) ialah 50 ppm, 75 ppm ARS, pH 6 larutan sampel, dan masa optimum 15 minit, manakala kepekatan optimum Co(II) ialah 125 ppm, ARS ialah 75 dan 50 ppm, pH larutan sampel 5 dan 10 minit masa optimum. Pengesahan kaedah menunjukkan bahawa pekali variasi (CV),

had pengesanan (LOD) (S/N = 3) dan had kuantititatif (LOQ = 10 S/N) Cu(II) masing-masing adalah 0.65%, 8.94 ppm dan 29.82 ppm dengan sensitiviti 0.0054 ppm dan kelinearan 0.9959. Ketepatan penentuan histamin melalui kompleks Cu-ARS-histamin pada kepekatan 50, 100, dan 150 ppm ialah 105.7% (RSD = 0.777%, n = 3), 105.06% (RSD = 0.606%, n = 3), dan 94.12% (RSD = 0.767%, n = 3), sementara itu,CV, LOD, dan LOQ Co(II) masing-masing adalah 0.28%; 2.58 ppm dan 8.6 ppm dengan kepekaan 0.0006 ppm dan kelinearan 0.9965. Ketepatan penentuan histamin melalui kompleks Co-ARS-histamin pada kepekatan 50, 75, dan 125 ppm masing-masing adalah 98.33%, 95.83%, dan 93.88%. Kaedah yang dicadangkan berjaya digunakan untuk menentukan histamin dalam sampel ikan dengan pengembalian kuantitatif untuk kompleks Cu(II) (99.23%) dan kompleks Co(II) (102.62%).

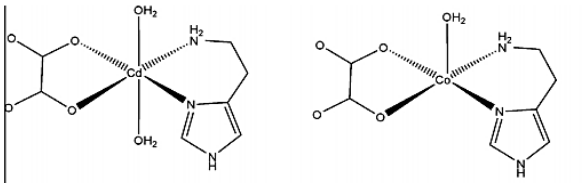
Kata kunci: histamin, logam, Cu(II), Co(II), alizarin merah S, spektrofotometri ultralembayung-nampak

Introduction

Histamine with chemical formula $C_5H_9N_3$ is a is a small-molecule hormone present in essentially all mammalian tissues which acts at the central nervous system level and in the regulation of sleep [1]. Histamine is produced in species of the *Scombroidae* family such as tuna and mackerel, mahi-mahi, blue fish, and sardine [2]. Histamine is one of the most toxic and most commonly found in foods and its concentration is frequently regarded as one of the biomarkers for quality control during the food production, transportation and marketing [3, 4]. Nowadays, an increased consumption of fish has been recommended due to its health promoting properties. However, some fish can cause histamine poisoning if its quality is not assured [5].

As a result, there were some regulations about histamine level in food. Based on Standard Nasional Indonesia (SNI) 01-2360 year 2008, histamine maximum limit in Indonesian fish is 100 mg kg^{-1}. The European Commission has made a regulation of safety requirements on the histamine presence in seafood with amounts lower than 10 mg/kg of histamine which indicate that fish has good quality, a level of 30 mg/kg suggests significant deterioration, and a content of 50 mg/kg or higher is an evidence of definite decomposition [6]. While the United States Food and Drug Administration (FDA) has established 50 ppm of histamine as the chemical index for fish spoilage [7]. Based on the assessment of poisoning cases, the guidance levels suggested for histamine content in seafood are: <50 ppm for safe consumption; 200–1000 ppm as probably toxic; and >1000 ppm as toxic and unsafe for human consumption [8, 9].

Several analytical methods have been developed for the analysis and determination of histamine levels such as ultrasensitive flow injection electrochemical [10], lignin modified glassy carbon electrode [11], thin layer chromatography (TLC) [12], high performance liquid chromatography (HPLC) [13], ^{1}H NMR [14], electrochemiluminescence [15], liquid chromatography tandem mass spectrometry [16], polymerase chain reaction/denaturing gradient gel electrophoresis (PCR-DGGE) [3] and spectrophotometry [17]. Complex reaction between histamine, Co(II) and oxalate has been reported [18] with the complex structure shown (Figure 1), but it has not given a significant change of wavelength and solution color. On the other hand, alizarin red S (ARS) with chemical structure shown (Figure 2) is well known to form colored complex with metallic and organic compounds such as Al(III) [19], Cu [20], Co and Ni [21], Cu, Co, Ni and cysteine [22], and Ni-histamine [23] with a wide range of ARS solvents.



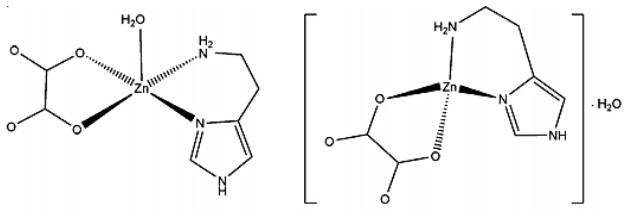


Figure 1. Complex structure of histamine-metal-oxalate [19]

The presence of a quinoid oxygen, with two hydroxyl groups at the α- and β-positions in ARS makes it very suitable for chelation, and its derivatives are well known colorimetric reagents with several applications. Furthermore, the presence of sulphonate groups in the molecule improves its reactivity [25]. ARS dye can exist in different forms depending on the type of media used, so this study used ARS as a complexing and coloring agent in the determination of histamine.

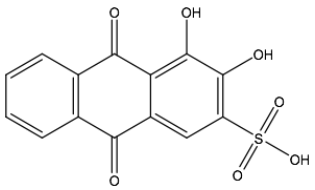


Figure 2. Chemical structure of ARS

In this study, a novel spectrophotometric method for determination of histamine has been developed based on histamine-metal-ARS complex formation. Analytical procedure for the determination of histamine is based on the complex's reaction, which can form a colored compound and then the absorbance was measured using UV-visible spectrophotometer. Optimization of metal concentration, ARS concentration, solution pH and time for formation of complexes have been investigated as well. The analytical validation parameters namely LOD, LOQ, sensitivity, coefficient of variation (CV), linearity, and accuracy were performed. The validated method was then applied to the determination of histamine in fish sample.

Materials and Methods

Materials

Histamine reference standard was purchased from Sigma Aldrich (Science Park Drive, Singapore). Copper sulphate hexahydrate, cobalt(II) nitrate hexahydrate, and ARS were purchased from Merck (Darmstadt, Germany). Methanol, sodium acetate, sodium hydrogen phosphate, sodium dihydrogen phosphate, acetic acid, trichloroacetic acid, and sodium hydroxide were pure analytical grade. Whatman filter paper 42 from Merck (Darmstadt, Germany) was used to filtering the sample extract.

Instrumentation

A Shimadzu-1800 UV-Visible spectrophotometer (Kyoto, Japan) was used to measure the wavelength and absorbance of the complexes formed. ThermoFisher Scientific Eutech 700 pH meter from (Massachusetts, USA) was used to measure the pH of the buffer solution prepared and standard solution for analytical optimization of solution pH.

Preparation of reagent

Histamine (0.1000 g) was weighed and dissolved in methanol, then transferred to a 100 mL volumetric flask and made up to the mark with the same solvent. $CuSO_4.6H_2O$ (0.3929 g) was weighed and dissolved in distilled water. The solution was transferred to a 100 mL volumetric flask and made up to mark with distilled water. $Co(NO_3)_2.6H_2O$ (0.4940 g) was weighed and dissolved in distilled water. The solution was transferred to a 100 mL volumetric flask and made up to mark with distilled water. All solutions were shaken to homogenize. The same procedure was performed for ARS with a weight of 0.1 gram. Buffer solutions used to make an acidic and alkaline

medium were phosphate buffer solution and acetic buffer solution. Phosphate buffer solution for pH 6, 7, and 8 was made from 1 M sodium hydrogenphosphate and sodium dihydrogen phosphate solution. While acetic buffer solution for pH 4 and 5 was made from 1 M acetic acid and trichloroacetic acid solution.

Preparation of ARS-metal complex solution

A 0.25 mL ARS stock solution 1000 ppm and 1.0 mL pH 7 buffer solution were transferred quantitatively into a 10 mL volumetric flask and added with 1.0 mL Cu(II) stock solution 1000 ppm, respectively. It was made up to the mark with methanol, and shaken until homogeneous and left for 10 min. The wavelength of complex solution formed was scanned from 300-800 nm and maximum absorbance was noted. The same procedure was repeated for Co(II) solution.

Preparation of histamine-ARS-metal complex solution

A 0.25 mL ARS stock solution 1000 ppm, 1.25 mL of histamine stock solution 1000 ppm, 1 mL buffer solution of pH 7 buffer solution were transferred into a 10 mL volumetric flask and added with 1.0 mL Co(II) stock solution 1000 ppm, left at room temperature for 10 min. It was made up to mark with methanol. The wavelength of complex solution formed was scanned from 300 - 800 nm and maximum absorbance was noted. The same procedure was repeated for Cu(II) solution.

Optimization of metal concentration

4 sets of 10 mL volumetric flask were prepared, and each volumetric flask was added with 1.25 mL histamine stock solution. In each volumetric flask, then added with Cu(II) stock solution with variation volume of 0.25; 0.50; 0.75; and 1.00 mL 1000 ppm, hence the concentration of metal was 25, 50, 75, and 100 ppm; then added with 1.00 mL pH 7 buffer solution; and 0.25 mL ARS stock solution 1000 ppm. Another 4 pieces of 10 mL volumetric flask was added with 1.25 mL histamine stock solution; then added with 1.00 mL buffer solution pH 7; 0.25 mL alizarin red S and 1.00; 1,25 and 1,50 mL of Co(II) stock solution. Then in each volumetric flask, the solution was diluted with methanol to mark and homogenized. The solution was allowed to stand for 10 minutes and its absorbance was measured at the maximum wavelength. A plot of the relationship between the concentration of alizarin red S and absorbance was made. The optimum concentration of the metal was obtained from the concentration value of the solution having the greatest absorbance value.

Optimization of ARS concentration

8 sets of 10 mL volumetric flask were prepared, and each volumetric flask was added with 1.25 mL histamine stock solution. In each volumetric flask was added with metal aqueous solution according to the optimum concentration and then added with 1.00 mL buffer solution pH 7; and 0.25, 0.50, 0.75, and 1.00 mL of ARS stock solution 1000 ppm, hence the concentration of ARS was 25, 50, 50, 75, and 100 ppm. The solution was diluted with methanol to the mark and homogenized. The solution was allowed to stand for 10 minutes and its absorbance was measured at the maximum wavelength. A curve of the relationship between the concentration of red alizarin S and absorbance was made. The optimum concentration of the metal was obtained from the concentration value of the solution having the greatest absorbance value.

Optimization of pH solution

10 sets of 10 mL volumetric flask were prepared. Each volumetric flask was added 1.25 mL of histamine stock solution and metal aqueous solution according to the optimum concentration, ARS with optimum concentration, and then added with 1.00 mL buffer pH solution of 4, 5 , 6, 7, and 8 in each flask. The solution was diluted with methanol to the mark and homogenized. The solution was allowed to stand for 10 minutes and its absorbance measured at the maximum wavelength. A curve of the relationship between the concentration of red alizarin S and absorbance was made. The optimum pH was obtained from the pH value of the solution having the greatest absorbance value.

Optimization of time

10 sets of 10 mL volumetric flask were prepared, and each volumetric flask was added 1.25 mL of histamine stock solution. In each volumetric flask was added a solution of metal in accordance with the optimum concentration, ARS with optimum concentration, and then added with 1.00 mL of optimum buffer pH solution. The solution was

allowed to stand for 10 minutes and its absorbance measured at the maximum wavelength. A curve of the relationship between the concentration of red alizarin S and absorbance was made. The optimum time was obtained from the time value of the solution having the greatest absorbance value.

Determination of histamine in fish

A sample preparation as follows was tried to detect and determine the histamine in fish fillets according to the previous method [25]. Briefly, 10 g fish muscle was minced with 10 mL of 10% trichloroacetic acid in water using a homogenizer. The homogenate was spiked with histamine standard, resulting in artificial contamination at 50, 100, and 150 mg/kg. The homogenate neutralized by 0.1 mL 0.1 M NaOH solution was centrifuged at 3000 r/min for 5 minutes. Then2 mL of the supernatant was then filtered through a Whatman filter paper 42. The supernatant then used to determination of histamine in fish sample with the optimum condition for each metal.

Results and Discussion

A spectrophotometric method for the determination of histamine is based on the complex reaction between histamine, ARS, and metal using an UV-visible spectrophotometer with a concentration of histamine 125 ppm, ARS 25 ppm, and metal(II) 100 ppm has been done. From Figure 3, it can be seen that the complex compounds of ARS and Cu(II) and Co(II) produce maximum wavelength at 544 nm and 543 nm, respectively. Structure of ARS-metal in various media which has been found before by the simple Hückel method [26] indicates that alizarin complexation occurs at the peri-hydroxy carbonyl group and results in the formation of the C=O → M–O coordination bond as shown in Figure 4(a). In acidic media, O-M bond remains covalent and the electronic absorption spectra of alizarinates are identical to the spectrum of nonionized alizarin as shown in Figure 4(b) in which H atom is replaced with metal atom. In alkali solution, alizarin reacted with metal ions as the *ortho*-diphenol compound as shown in Figure 4(c).

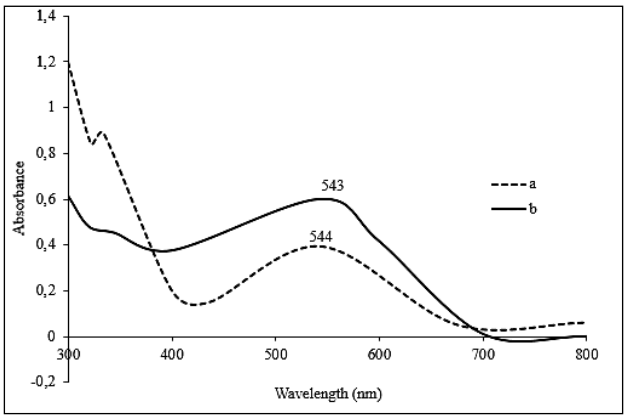
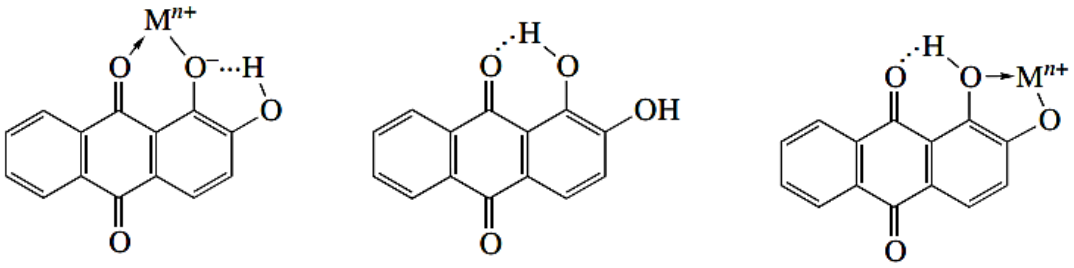


Figure 3. (a) UV-visible spectra of ARS-Cu(II) complex (b) ARS-Co(II) complex



(a) (b) (c)

Figure 4. Structure of ARS complex in various medium (a) neutral medium (b) acidic medium (c) alkaline medium [26]

This complex compound will then react with histamine forming a new pink complex compound with a maximum wavelength for Cu(II) and Co(II) at 505.5 nm; and 567 nm, respectively. These results indicate that a shift in the wavelength of maximum absorption into lower wavelength due to hypsochromic effect for Cu(II) and greater due to bathochromic effect for Co(II) and electron configuration of Co and Cu as shown in Figure 5. The metals bind the existing amine group on histamine and carbonyl group of ARS. This compound is predicted that it has an octahedral shaped molecular. Based on crystal field theory, octahedral shape has an energy splitting as shown in Figure 6 when stabilizing energy of metal-ligand complex due to the amount of electrons in t_{2g} meanwhile unstabilizing energy of metal-ligand complex is due to the amount of electrons e.g. Cu and Co have the same amount of electrons in t_{2g} but it has different amount of electrons e.g. Cu has three electrons while Co has an electron there. It means that Cu is more unstable than Co, so Cu needed more energy to form the complex than Co. Furthermore, it would give a greater wavelength. In the molecular structure of the complex as shown in Figure 7, histamine acts as a bidentate ligand by chelating the metal ion. The metal is in a square pyramidal geometry defined by two N atoms of aqua ligand at apex of pyramid. Histamine along with neighboring carbonyl ion participates in weak hydrogen bonds of N–H-O in the crystal packing of [Metal(His)(ARS)$(H_2O)_2$] complex.

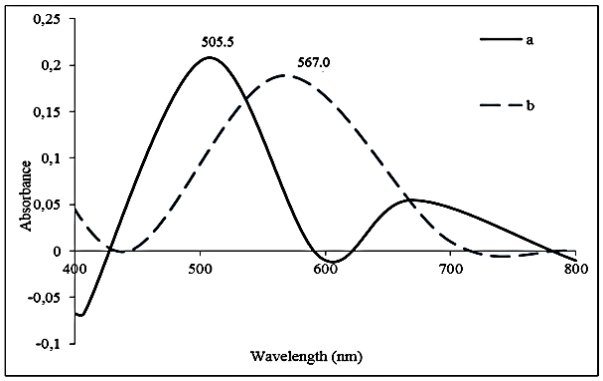


Figure 5. (a) UV-visible spectra of ARS-histamine-Cu(II) complex (b) ARS-histamine-Co(II) complex

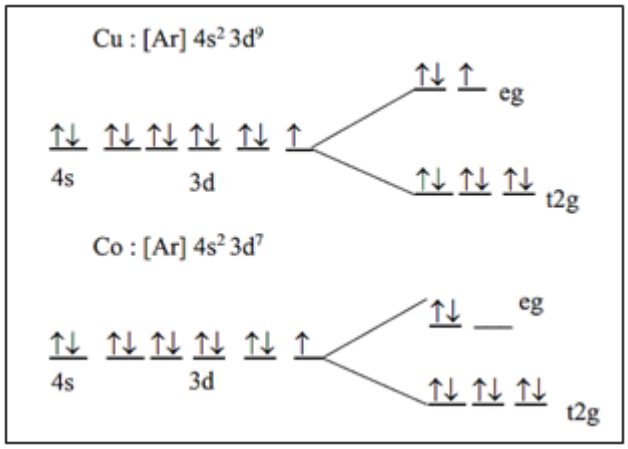


Figure 6. Splitting energy of Cu and Co due to crystal field theory

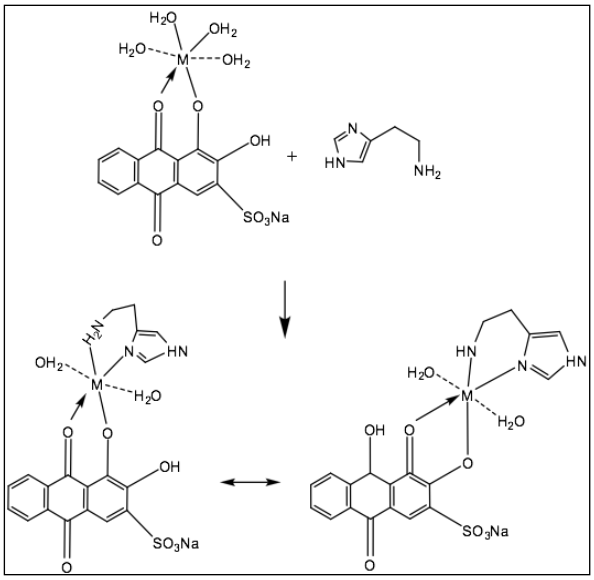
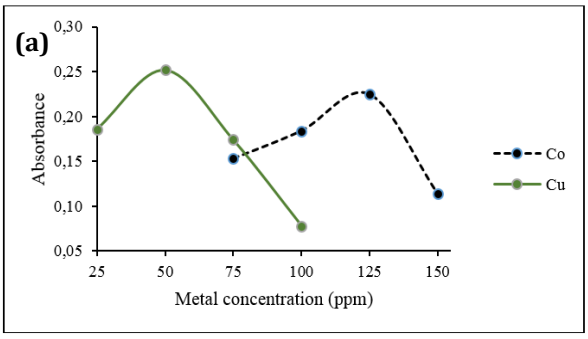
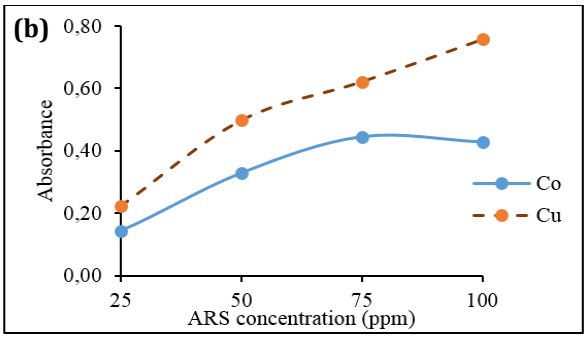


Figure 7. The prediction reaction of metal(II), histamine and ARS

The wavelength of the histamine - ARS - metal complex compound is used as the wavelength for the entire analytical parameter optimization. Optimization of metal and ARS concentration is obtained from the increase in absorbance due to higher concentration. The optimum results of Cu(II) and Co(II) concentration are 50 and 125 ppm as shown in Figure 8(a) and (b), respectively. Optimization of ARS for Cu(II) and Co(II) complex is 75 ppm as shown in Figure 8(b).





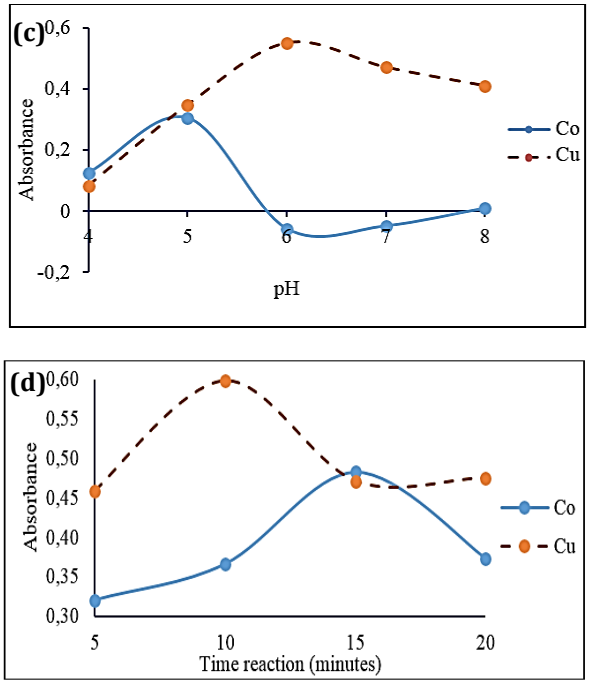


Figure 8. Optimization of (a) metal concentration (b) ARS concentration (c) pH solution (d) time due to the higher absorbance

The optimum pH for complex formation was determined. In Figure 8(c), it is obtained that pH optimum is at pH 6 and 5 for Cu(II) and Co(II), respectively. The reaction of Cu(II) and Co(II) complex formation took place in acidic conditions because in pH > 7 histamine - ARS - Cu(II) and pH > 6 Co(II) solution lead the precipitation of $M(OH)_2$ and starts to form colloidal solution. It is because in this condition, Ksp $M(OH)_2$ has been reached [27]. Time of Cu(II) and Co(II) complex are 10 and 15 minutes, respectively, as shown in Figure 8(d).

From the results of the optimization (concentration of ARS and metal(II), pH and time), linear calibration curves are obtained at the range of 25 - 150 ppm of histamine as shown in Figure 9. The linear regression for Cu(II) and Co(II) is $y = 0.0054x - 0.1944$ and $R^2 = 0.9959$; $y = 0.0006x + 0.3136$ and $R^2 = 0.9965$, respectively. Validation parameters for each metal are shown in Table 1. Based on linear regression and Table 1, linearity is closed to 1 so it is quite good. Two directions ANOVA shows $t_{table} < t_{calculation}$, so H_0 is rejected and there is a correlation between the concentration with absorbance. The accuracy of the method range of 101.63% and 96.01% for Cu(II) and Co(II) complex is shown in the Table 2 so it is indicated that this method of approaching the actual state of histamine concentration. Variation coefficient of histamine by 0.650% and 0.275% is shown in Table 3 for each metal. Furthermore, Cu(II) complex has higher sensitivity than Co(II) with a sensitivity of 0.0054; while sensitivity of Co(II) complex is 0.0006 obtained from the slope of histamine standard curve.

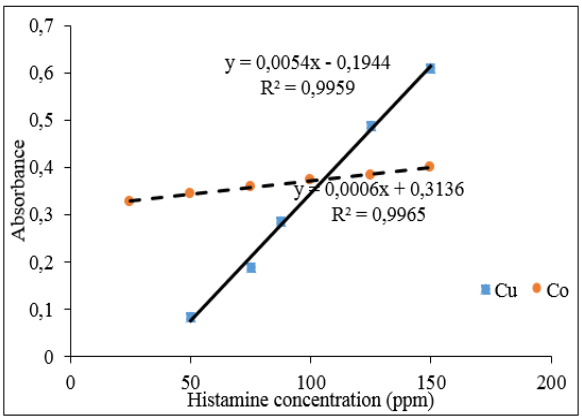


Figure 9. Calibration curve of histamine

Table 1. Validation parameters of method

Validation Parameter	**Result**	
Metal	Cu(II)	Co(II)
LOD	8.94 ppm	2.58 ppm
LOQ	29.82 ppm	8.6 ppm
Linearity	0.99	0.99
Sensitivity	0.0054/ppm (slope)	0.0006/ppm (slope)

Table 2. Accuracy of method for Cu(II) and Co(II) complex

Actual Concentration (ppm)	**Cu(II)**		**Co(II)**	
	Found Concentration (ppm)	**Recovery (%)**	**Found Concentration (ppm)**	**Recovery (%)**
50	52.935	105.70	49.167	98.33
100	105.060	105.06	95.830	95.83
150	121.513	91.12	140.830	93.88
	Mean	101.63	Mean	96.01

Table 3. Variation coefficient (precision) of histamine standard for Cu(II) and Co(II) complex

Histamine (ppm)	**Cu(II) Absorbance**				**Precision (%)**	**Co(II) Absorbance**				**Precision (%)**
	x_1	**x_2**	**x_3**			**x_1**	**x_2**	**x_3**		
50	0.090	0.091	0.091	0.091	0.777	0.344	0.343	0.342	0.343	0.291
100	0.303	0.303	0.301	0.303	0.406	0.371	0.373	0.369	0.371	0.539
150	0.566	0.565	0.573	0.568	0.767	0.398	0.398	0.398	0.398	0.000
			Mean		0.650			Mean		0.275

The optimum result of method has been used for histamine determination in fish. The sample which known previously of histamine levels was spiked using histamine standard solutions at concentrations of 50, 100, and 150 mg/kg. Then the mixed solution was determined using the developed spectrophotometric method as shown in Table 4. Recovery results obtained was close to 100%, it means that both of these metals complexes have a good recovery to be applied to fish samples.

Table 4. Sample application of Cu(II) and Co(II) complex

	Cu(II)		Co(II)	
Real Concentration (ppm)	**Found Concentration (ppm)**	**Recovery (%) (*n* = 3)**	**Found Concentration (ppm)**	**Recovery (%) (*n* = 3)**
Fish	52	-	52	-
Fish + 50	100	97.72	105	102.71
Fish + 100	149	98.26	157	103.03
Fish + 150	202	101.71	206	102.12
	Mean	99.23	Mean	102.62

Conclusion

The spectrophotometric method for the determination of histamine based on complex reaction using metals and ARS as reagent has been developed which has simple methodology, easy work-up, applicable, and accurate.

Acknowledgement

The authors are grateful to Analytical Laboratory of Chemistry Department of Universitas Airlangga, Surabaya, Indonesia for providing the facilities to carry out this research work.

References

1. Kaştaş, G., Paşaoğlu, H., Karabulut, B. and Bulut, İ. (2010). Structural and spectroscopic studies on cadmium complex of a biogenic amine, histamine. *Chemical Physics Letters*, 488 (4-6): 162–167.
2. Bulushi, I. A., Poole, S., Deeth, H. C. and Dykes, G. A. (2009). Biogenic amines in fish: Roles in intoxication, spoilage, and nitrosamine formation—a review. *Critical Reviews in Food Science and Nutrition*, 49(4): 369–377.
3. Diaz, M., Ladero, V., Redruello, B., Sanchez-Llana, E., Rio, B., Fernandez, M., Martin, M. C. and Alvarez, M. A. (2016). A PCR-DGGE method for the identification of histamine-producing bacteria in cheese. *Food Control*, 63: 216-223.
4. Altieri, I., Semeraro, A., Scalise, F., Calderari, I. and Stacchini, P. (2016). European official control of food: Determination of histamine in fish products by a HPLC–UV-DAD Method. *Food Chemistry*. 211: 694–699.
5. Evangelista, W. P., Silva, T. M., Guidi, L. R., Tette, P. A. S., Byrro, R. M. D., Silva, P. S., Fernandes, C. and Gloria, M. B. A. (2016). Quality assurance of histamine analysis in fresh and canned fish. *Food Chemistry*, 211: 100-106.
6. Veseli, A., Vasjari, M., Arbneshi, T., Hajrizi, A., Svorc, L., Samphao, A. and Kalcher, K. (2016). Electrochemical determination of histamine in fish sauce using heterogeneous carbon electrodes modified with rhenium(iv) oxide. *Sensors and Actuators B*. 228: 774–781.
7. Department of Health and Human Services, Public Health Service, Food and Drug Administration, Center for Food Safety and Nutrition (2011). Fish and fishery products hazards and controls guidance, 4th edition 2011, April.
8. Lehane, L. and Olley, J. (2000). Review histamine fish poisoning revisited. *International Journal of Food Microbiology*, 58 (1-2): 1–37.

9. Keow, C. M., Bakar, F. A., Salleh, A. B., Heng, L. Y., Wagiran, R., Bean, L. S. (2007). An amperometric biosensor for the rapid assessment of histamine level in tiger prawn (*Penaeus monodon*) spoilage, *Food Chemistry*, 105(4): 1636–1641.
10. Akbari-adergani, B., Norouzi, P., Ganjali, M. R., and Dinarvand, R. (2010). Ultrasensitive flow-injection electrochemical method for determination of histamine in tuna fish sample. *Food Research International Journal*, 43(4): 1116-1122.
11. Degefu, H., Amare, M., Tessema, M. and Admassie, S. (2014), Lignin modified glassy carbon electrode for the electrochemical determination of histamine in human urine and wine samples. *Electrochimica Acta Journal*, 121: 307-314.
12. Tao, Z., Sato, M., Han, Y., Tan, Z., Yamaguchi, T. and Nakano, T. (2011). A simply and rapid method for histamine analysis in fish and fishery products by TLC determination. *Food Control*, 22(8): 1154-1577.
13. Wang, Z., Wu, J., Wu, S. and Bao, A. (2013). High performance liquid chromatographic determination of histamine in biological samples: the cerebrospinal fluid challenge–a review. *Analytica Chimica Acta*, 24(774): 1-10.
14. Henry, B., Gizzi, P. and Delpuech, J. (2015), Magnetic Non-equivalence and dynamic NMR of N-methylene protons in a histamine-containing pseudopeptide: Alanyl-glycyl-histamine. *Tetrahedron*, 71(36): 6227-6244.
15. An, D., Chen, Z., Zheng, J., Chen, S., Wang, L. and Su, W. (2016). Polyoxometalate functionalized tris(2,2-bipyridyl)dichlororuthenium(II) as the probe for electrochemiluminescence sensing of histamine, *Food Chemistry*, 194: 966–971.
16. Chimalakonda, K. C., Pang, E., Weaver, J. L., Howard, K. E., Patel, V. and Boyne II, M. T. (2015). Development and validation of a liquid-chromatography tandem mass spectrometry method to determine in vitro and in vivo histamine release, *Journal of Pharmaceutical and Biomedical Analysis*, 102: 494–499.
17. Jancsó, A., Selmeczi, K., Gizzi, P., Nagyc, N. V., Gajda, T. and Henry, B. (2011). The role of terminal amino group and histidine at the fourth position in the metal ion binding of oligopeptides revisited copper(II) and nickel(II) complexes of glycyl-glycyl-glycyl-histamine and its n-boc protected derivative. *Journal of Inorganic Biochemistry*, 105(1): 92-101.
18. Kaştaş, G., Pasaoglu, H. and Karabulut, B. (2011). Magnetic, structural and computational studies on transition metal complexes of a neurotransmitter, histamine. *Journal of Molecular Structure*, 1000(1-3): 39–48.
19. Sathish, R. S., Kumar, M. R., Rao, G. N., Kumar, K. A. and Janardhana, C. (2007). A water-soluble fluorescent fluoride ion probe based on ARS–Al(III) complex. *Spectrochimica Acta Part A*, 66: 457–461.
20. Panahi, H. A., Karimi, M., Moniri, E. and Soudi, H. (2008). Development of a sensitive spectrophotometeric method for determination of copper. *African Journal of Pure and Applied Chemistry*, 2(10): 96–99.
21. Rohilla, R. and Gupta, U. (2012) Simultaneous determination of cobalt(ii) and nickel(ii) by first order derivative spectrophotometry in micellar media. *E-Journal of Chemistry*, 9(3): 1357-1363.
22. Gahlan, A. A., El-Mottaleb, M.A., Badawy, N. A., Kamale, F. H. and Ali, S. H. (2014). spectrophotometeric studies on binary and ternary complexes of some metal ions with ARS and cysteine. *International Journal of Advanced Research*, 2(10): 570–584.
23. Jannatin, M., Supriyanto, G., Pudjiastuti, P. (2017). A novel spectrophotometric method for the determination of histamine based on its complex reaction with Ni(II) and ARS. *Indonesian Journal of Chem*istry, 17(1): 139-143.
24. Ali, N. M., Amaniampong, P. N. and Karam, A. (2016). Determination of optimal conditions for eelectrodeposition of tin(II) in the presence of ARS. *Heliyon*, 2(12): 1-26.
25. Xie, Z., Wang, Y., Chen, Y., Xu, X., Jin, Z. and Ding, Y, (2017). Tuneable surface enhanced raman spectroscopy hyphenated to chemically derivatized thin-layer chromatography plates for screening histamine in fish. *Food Chemistry*, 230: 547–552.
26. Fain, V. Y., Zaitsev, B. E. and Ryabov, M. A. (2004). Metal complexes with alizarin and ARS: Electronic absorption spectra and structure of ligands. *Russian Journal of Coordination Chemistry*, 30(5): 365–370.
27. Day, R. A. and Underwood, A. L. (2002). Analisis kimia kuantitatif. Edisi keenam. Penerbit Erlangga, Jakarta, Indonesia.

Malaysian Journal of Analytical Sciences, Vol 23 No 3 (2019): 516 - 523
DOI: https://doi.org/10.17576/mjas-2019-2303-16

MALAYSIAN JOURNAL OF ANALYTICAL SCIENCES
Published by The Malaysian Analytical Sciences Society
ISSN 1394 - 2506

KINETIC DEGRADATION OF TOTAL PHENOLIC CONTENT, DPPH RADICAL SCAVENGING AND XANTHINE OXIDASE INHIBITORY ACTIVITIES IN YANANG (*Tiliacora triandra*) LEAF EXTRACT DURING PREPARATION PROCESS

(Degradasi Kinetik Kandungan Jumlah Fenolik, Aktiviti Pemerangkapan Radikal DPPH dan Xantin Oksidase dalam Ekstrak Daun Yanang (*Tiliacora triandra*) Semasa Proses Penyediaan)

Sunee Eadmusik[1]*, Chanthima Phungamngoen[1], Natthaya Choosuk[2]

[1]*Department of Agro-industry Technology and Management, Faculty of Agro-industry*
[2]*Department of Innovation and Product Development Technology, Faculty of Agro-industry*
King Mongkut's University of Technology North Bangkok, 25230 Prachinburi, Thailand

**Corresponding author: sunee.e@agro.kmutnb.ac.th*

Received: 25 October 2017; Accepted: 22 January 2019

Abstract

Presently, canned bamboo shoots in Yanang (*Tiliacora triandra* (Colebr.) Diels) leaf extract is produced in order to expand shelf-life and ease to prepare food. The objectives of this research were to investigate the effect of different thermal processing during Yanang leaf extract preparation on total phenolic content, DPPH radical scavenging and xanthine oxidase inhibitory activities and to determine kinetics of the extract's quality alterations. The preparation included 1:12 (w/v) leaves to water ratio, 32,000 rpm blending speed and different heating temperature at 60, 70 or 80 ^{o}C for 15 minutes. Data were collected at 0, 1, 3, 6, 9, 12 and 15 minutes of heating time. The results showed that fresh Yanang leaf extract had total phenolic content of 680.16 ± 19.57 mg GAE/100 mg db. and it possessed DPPH radical scavenging and xanthine oxidase inhibitory activities at 163.53 ± 0.87 µg BHT/mL and 78.58 ± 0.17%, respectively. The results revealed that an increase in heating temperature and time decreased total phenolic content and the DPPH radical scavenging and xanthine oxidase inhibitory activities of Yanang leaf extract. During 15 minutes heating, the total phenolic content of Yanang leaf extract ranged from 526.33 ± 28.79 to 638.93 ± 29.69 mg GAE/100 mg db., DPPH radical scavenging activity ranged from 92.86 ± 1.66 to 136.41 ± 5.70 µg BHT/mL and xanthine oxidase inhibitory activity ranged from 72.64 ± 0.34 to 76.65 ± 0.50%. The change of total phenolic content (R^2 = 0.809-0.959) followed zero-order kinetic model and that of DPPH radical scavenging activity (R^2=0.783-0.920) while xanthine oxidase inhibitory activity (R^2 = 0.864-0.922) followed second-order kinetic model.

Keywords: Yanang, *Tiliacora triandra*, total phenolic content, xanthine oxidase, kinetic model

Abstrak

Pada masa ini, pucuk buluh dalam ekstrak daun Yanang (*Tiliacora triandra* (Colebr.) Diels) yang ditinkan dihasilkan untuk meningkatkan hayat simpanan dan kemudahan untuk menyediakan makanan. Objektif penyelidikan ini adalah untuk mengkaji kesan pemprosesan terma yang berbeza semasa penyediaan ekstrak daun Yanang terhadap kandungan jumlah fenolik, aktiviti pemerangkapan radikal DPPH dan xantin oksidase dan untuk menentukan kinetik perubahan kualiti ekstrak. Penyediaan melibatkan nisbah daun kepada air, 1:12 (w/v) 32,000 rpm halaju adunan dan suhu pemanasan yang berbeza pada 60, 70 atau 80 ^{o}C selama 15 minit. Data dikumpulkan pada masa pemanasan 0, 1, 3, 6, 9, 12 dan 15 minit. Keputusan menunjukkan bahawa ekstrak daun Yanang segar mempunyai kandungan jumlah fenolik sebanyak 680.16 ± 19.57 mg GAE/100 mg berat kering dan aktiviti pemerangkapan radikal DPPH dan xantin oksidase ialah 163.53 ± 0.87 µg BHT/mL dan 78.58 ± 0.17%. Keputusan menunjukkan bahawa peningkatan suhu pemanasan dan masa menurunkan kandungan jumlah fenolik dan aktiviti ekstrak daun

Yanang. Selepas 15 minit pemanasan, kandungan fenolik jumlah ekstrak daun Yanang ialah dari 526.33 ± 28.79 hingga 638.93 ± 29.69 mg GAE/100 mg berat kering, aktiviti perencatan radikal DPPH adalah daripada 92.86 ± 1.66 hingga 136.41 ± 5.70 µg BHT/mL dan aktiviti perencatan xantin oksidase dalam julat 72.64 ± 0.34 hingga 76.65 ± 0.50%. Perubahan kandungan fenolik jumlah (R^2 = 0.809-0.959) adalah mengikut model kinetik tertib sifar dan aktiviti pemerangkapan radikal DPPH (R^2 = 0.783-0.920) sementara aktiviti penghambatan xantin oksidase (R^2 = 0.864-0.922) adalah mengikut modeltertib kedua.

Kata kunci: Yanang, *Tiliacora triandra*, kandungan jumlah fenolik, xantin oksidase, model kinetik

Introduction

Tiliacora triandra (Colebr.) Diels belongs to the family of *Menispermaceae.* It is known in Thai as Yanang. Its leaf and root are widely used in the Southeast Asia countries due to its health benefits [1]. Traditionally, Yanang root has been used as antipyretic and antimalarial agents [2] while Yanang leaf has been used for anticancer and immune modulator [3]. Previous studies reveal that tiliacorinine, tiliacorine and nor-tiliacorinine are bisbenzylisoquinoline alkaloids found in Yanang [4, 5] and gum from Yanang has a similar structure to xylan according to their FTIR spectra [2]. Several studies also show that Yanang contains bioactive compounds, such as phenolic compounds, which possess significant antioxidant properties [6]. Ferulic acid, *p*-coumaric acid, sinapic acid and syringic acid are specific phenolic compounds presented in Yanang leaf extract. The ability to stabilize free radicals and break the oxidation chain of these phenolic compounds has been reported [7]. Yanang leaves are usually extracted with water to be cooked especially with bamboo shoots because of its remedy for gout (gouty arthritis). The treatment for gout involves the use of therapeutic agent such as xanthine oxidase inhibitors [8]. The enzyme, xanthine oxidase, converts hypoxanthine into xanthine and sequent into uric acid which can accumulate in human body and cause gout. However, the stability of bioactive compounds is unstable depending on the pH, light, oxygen, temperature and enzymatic activities [9].

Several studies reported the degradation of phenolic compounds and antioxidant activity in fruits and vegetables during thermal processing [10, 11, 12]. Tian et al. [10] revealed that up to 72% of total phenolic content and 61% of 2,2-diphyneyl-2-picryl-hydrazyl (DPPH) radical scavenging activity in purple-fleshed potatoes decreased during cooking. Recently, Méndez Lagunas et al. [12] reported losses of 78% total phenolic content and 74% DPPH radical scavenging in strawberry during convective drying. Nevertheless, no information related with alteration of xanthine oxidase during thermal processing.

Presently, canned bamboo shoots in Yanang leaf extract is produced in order to expand shelf-life and ease to prepare food. The preparation process of Yanang leaf extract could impair the stabilities of bioactive compounds and properties. Therefore, the aims of this study were to investigate the effect of different thermal processing during Yanang leaf extract preparation on total phenolic content, DPPH radical scavenging and xanthine oxidase inhibitory (XOI) activities and to determine kinetics of the extract's property degradations.

Materials and Methods

Chemicals and reagents

All chemicals and reagent were analytical grade. Folin-Ciocalteu reagent was purchased from Loba Chemie Pvt Ltd. (Mumbai, India) while Na_2CO_3 was purchased from Ajax Finechem Pty Ltd. (Auckland, New Zealand). Tablets of sodium phosphate buffer were obtained from Amresco LLC (Ohio, USA). Xanthine and xanthine oxidase were obtained from Himedia Laboratories Pvt. Ltd. (Mumbai, India). Dimethyl sulfoxide (DMSO) was obtained from Sigma-Aldrich (Missouri, USA).

Plant material and extraction

Yanang (*Tiliacora triandra*) leaves, obtained from the local market in Prachinburi province of Thailand, were washed with excess water to remove dust and the infected leaves were discarded. Only consistent green-colored leaves with more than 3 cm width x 5 cm length were collected. The collected leaves were then naturally dried and kept at 6 ^oC until used within 7 days. Fifty grams of Yanang leaves were mixed with 600 mL water (leaves to water ratio is 1:12) and blended using a Buono-17778P blender (Taiwan, ROC) at 32,000 rpm for 1 minute. The Yanang leaf extract was obtained by filtering through 2 layer-muslin cloth and adjusted to 600 mL with water. The Yanang leaf extract was freshly prepared before each experiment.

In order to determine the kinetic degradation of chemical properties of Yanang leaf extract, the extract was heated at 60, 70 and 80 ^{o}C. The samples were collected at 0, 1, 3, 6, 9, 12 and 15 minutes after heating and total phenolic content, DPPH radical scavenging activity and XOI activity were determined.

Determination of total phenolic content

Total phenolic content determination was performed following the method described by Singthong et al. [6]. Briefly, 20 µL of Yanang leaf extract were mixed with 1.58 mL of water and 100 µL of Folin-Ciocalteu reagent. After 5 minutes incubation at room temperature, the mixture was added with 300 µL of 2% (w/v) Na_2CO_3 and then placed in the dark at room temperature for 2 hours. Absorbance of the mixture was measured at 765 nm using an Optima SP-300 spectrophotometer from Optima Inc. (Tokyo, Japan). Gallic acid (0-200 mg/L) was used as a standard for the calibration curve. Total phenolic content of Yanang leaf extract was expressed as mg Gallic acid equivalent/100 mg dry basis (mg GAE/ 100 mg db.).

Determination of DPPH radical scavenging activity

DPPH radical scavenging activity was measured following the method described by De Ancos et al. [13]. Ten µL of Yanang leaf extract were diluted with 90 µL of water, mixed with 3.9 mL of 25 mM DPPH and placed in the dark for 30 minutes. Absorbance of the mixture was measured at 515 nm. Butylhydroxytoluene (BHT) was used as a standard. DPPH radical scavenging activity of Yanang leaf extract was expressed as µg BHT/mL.

XOI activity assay

XOI activity with xanthine as the substrate was measured with the method described by Azmi et al. [8]. The assay mixture consisted of 300 µL of 50 mM sodium phosphate buffer pH 7.5, 100 µL of Yanang leaf extract sample, 100 µL of 0.2 U/mL freshly prepared xanthine oxidase in phosphate buffer and 100 µL of distilled water. After pre-incubation at 37 °C for 15 minutes, 200 µL of 0.15 mM xanthine was added into the mixture. The mixture was then incubated at 37 °C for 30 minutes. The reaction was stopped with the addition of 200 µL of 0.5 M HCl. The absorbance was measured spectrophotometrically at 295 nm against a blank which was prepared in the same way but the enzyme solution was replaced with phosphate buffer. An assay of control sample prepared by using 100 µL DMSO instead of Yanang leaf extract sample was also performed in order to have a maximum uric acid formation. Allopurinol, a well-known xanthine oxidase inhibitor, was used as a positive control at a concentration of 100 µg/mL. Percentage of XOI activity was calculated as following (equation 1):

$$\%\text{XOI} = \left(\frac{Abs_{control} - Abs_{extract\ sample}}{Abs_{control}} \right) \times 100 \quad (1)$$

where $Abs_{control}$ is absorbance of control sample when DMSO was used. Abs_{sample} is absorbance of Yanang leaf extract sample.

Statistical analysis and development of kinetic model

Experiments were carried out in triplicate. The data were expressed as mean ± standard deviation. The means of all parameters were examined using analysis of variance (One-way ANOVA). Duncan's New Multiple Range Test (DMRT) was used to determine the multiple comparison of mean values at a level of $P < 0.05$. Correlations were established by regression analysis. A SPSS statistical program version 16 was used to perform the calculation.

The data of degradation (quality-time curve) were fitted to three different kinetic models according to the following equations (2-4):

The zero order reaction; $C = C_0 - kt$ (2)

The first order reaction; $\ln C = \ln C_0 - kt$ (3)

The second order reaction; $\frac{1}{C} = \frac{1}{C_0} + kt$ (4)

where *C is* quality (total phenolic content, DPPH radical scavenging activity or XOI activity) of Yanang leaf extract at time *t*. C_0 is initial quality (total phenolic content, DPPH radical scavenging activity or XOI activity) of Yanang leaf extract at time 0. *k is* reaction rate constant and *t* is time (minutes)

The effect of temperature on the degradation rate constant was assumed to follow the Arrhenius equation 5;

$$k = k_0 \exp [-E_a/RT] \quad (5)$$

where as *k* is rate constant, k_0 is pre-exponential factor, E_a is activation energy for the degradation (J/mol), R is gas constant (8.314 J/mol.K), and T is absolute temperature (K).

Results and Discussion

Total phenolic content

The total phenolic content of Yanang leaf extract is shown in Figure 1(a). It varied from 526.33 ± 28.79 to 733.74 ± 21.63 mg GAE/100 mg db. depending on the heating temperature and time. The preparation process at 80 ^{o}C for 15 minutes gave the least total phenolic content, 526.33 ± 28.79 mg GAE/100 mg db. During 15 minutes heating at 60 ^{o}C, the total phenolic content of Yanang leaf extract ranged from 594.85 ± 28.32 to 623.74 ± 17.62 mg GAE/100 mg db. It ranged from 638.93 ± 29.69 to 680.78 ± 43.54 mg GAE/100 mg db. and from 526.33 ± 28.79 to 733.74 ± 21.63 mg GAE/ 100 mg db. for heating at 70 ^{o}C and 80 ^{o}C, respectively. The results showed that an increase in heating temperature and time decreases the total phenolic content in Yanang leaf extract due to the fact that phenolic compounds are heat labile [14]. Compared with fresh Yanang leaf extract, a reduction of 2.03-22.62% in total phenolic content was observed in Yanang leaf extract after 15 minutes heating.

A previous study reported that the total phenolic content of 1:10 (w/v) ethanolic Yanang leaf extract incubated at 70 ^{o}C for 15 minutes was 8.60 mg GAE/g db. [15]. Other study determined total phenolic content and antioxidant activities of 100 mg Yanang leaf powder extracted separately with 12 mL water, ethanol or acetone in a shaking water bath at 25 ^{o}C for 15 minutes. It was found that, among the three solvents, the water extraction gave a great amount of phenolic compounds and high antioxidant activities [6]. The total phenolic content of the water extract was the highest (97.90 mg GAE/g) compared with the ethanol and acetone extracts which was 26.70 and 16.46 mg GAE/g, respectively.

The difference in total phenolic content was a result of different extraction methods including sample preparation, type of solvent used, extraction temperature and extraction time. Based on the same solvent used and same basis (mg GAE/100 mg db.), the total phenolic content of Yanang leaf extract reported in the present study was much higher than that reported by Singthong et al. [6] (526.33-733.74 compared to 9.79 mg GAE/100 mg db.). This finding might due to a different extraction method. According to Singthong et al. [6], Yanang leaves were dried at 60 ^{o}C for 3 hours and ground into powder before the extraction using a shaking water bath at 25 ^{o}C for 15 minutes whereas this present study extracted fresh Yanang leaves using a high speed blender at 32,000 rpm for 1 minute.

DPPH radical scavenging activity

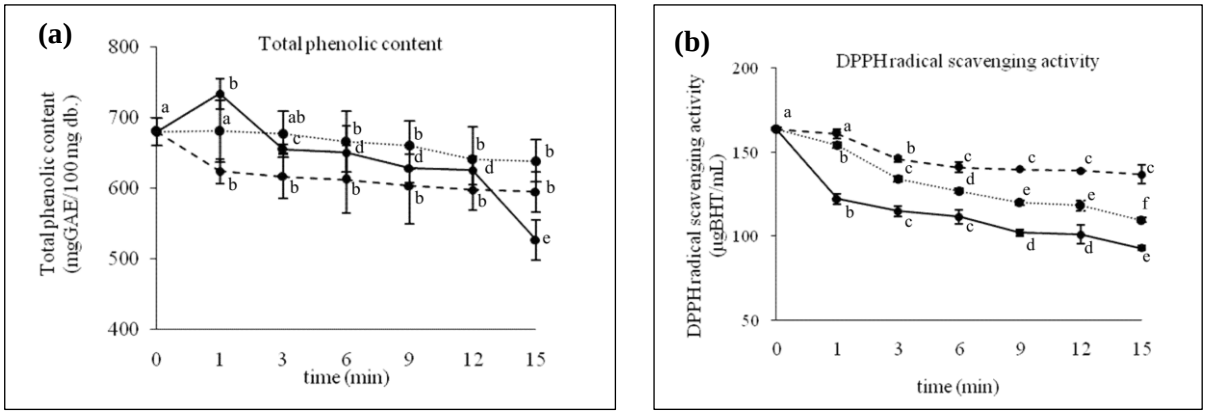
The DPPH radical scavenging assay was performed to determine an antioxidant potential of Yanang leaf extract by donating a hydrogen atom to DPPH radical. The DPPH radical scavenging activity of Yanang leaf extract ranged from 92.86 ± 1.66 to 163.53 ± 0.87 µg BHT/mL as shown in Figure 1(b). The preparation process at 80 ^{o}C for 15 minutes gave the least DPPH radical scavenging activity, 92.86 ± 1.66 µg BHT/mL. During 15 minutes heating at 60 ^{o}C, the DPPH radical scavenging activity of Yanang leaf extract ranged from 136.41 ± 5.70 to 160.49 ± 2.60 µg BHT/mL. The DPPH radical scavenging activity ranged from 109.54 ± 1.41 to 154.01 ± 1.72 µg BHT/mL and from 92.86 ± 1.66 to 121.99 ± 3.07 µg BHT/mL for heating at 70 ^{o}C and 80 ^{o}C, respectively. Compared with fresh Yanang leaf extract, a reduction of 1.86 - 43.22% in DPPH radical scavenging activity was observed in Yanang leaf extract after 15 minutes heating.

Considering the results, an increasing in heating temperature and time led to a decrease in the DPPH radical scavenging activity of Yanang leaf extract along with its total phenolic content (Figure 1a-b). This could be due to the fact that phenolic compounds possess an antioxidant activity. Thus, a reduction of total phenolic content subsequently resulted in a decrease in the DPPH radical scavenging activity. A rise in heating temperature and time not only diminished phenolic compounds but also accelerated a radical formation through the oxidation reaction [14].

Previous researches have studied on DPPH radical scavenging activity in Yanang leaf extract. Singthong et al. [6] investigated the DPPH radical scavenging activity of Yanang leaf powder extracted separately with water, ethanol or acetone and revealed that IC_{50} value of the extract was 0.197, 0.333 and 0.419 mg/g, respectively. Other study reported the IC_{50} value of 16.19 ppm in Yanang leaf extracted with water compared to that of 9.63 ppm in Yanang leaf extracted with methanol [3]. However, Taejarerniriyakul et al. indicated that Yanang leaf extracted with methanol has an IC_{50} value of 68.83 µg/mL [16].

XOI activity

The XOI activity is associated with gout incident. XOI inhibits the biosynthesis of uric acid from purine in the body and it has been assumed that either by increasing the excretion of uric acid or reducing the uric acid production helps to reduce the risk of gout [8]. The XOI activity of Yanang leaf extract is shown in Figure 1(c). The XOI activity varied from 72.64 ± 0.34 to 79.95 ± 0.35% depending on heating temperature and time. The preparation process at 80 ^{o}C for 15 minutes gave the lowest activity at 72.64 ± 0.34%. During 15 minutes heating at 60 ^{o}C, the XOI activity of Yanang leaf extract ranged from 76.65 ± 0.50 to 79.95 ± 0.35%. It ranged from 74.87 ± 0.27 to 77.31 ± 0.37% and from 72.64 ± 0.34 to 76.92 ± 0.44% for heating at 70 ^{o}C and 80 ^{o}C, respectively. The results showed that an increase in heating temperature and time decreases the XOI activity of Yanang leaf extract. Compared with fresh Yanang leaf extract, a reduction of 1.25-7.90% in XOI activity was observed in Yanang leaf extract after 15 minutes heating. No research has studied the XOI activity in Yanang leaf extracted with water. However, none XOI activity of methanolic and ethanolic Yanang leaf extracts was reported [16, 17]. According to the results, heating temperature and time considerably gave huge effect on the chemical properties of Yanang leaf extract. An increase in heating temperature and time decreased total phenolic content, DPPH radical scavenging and XOI activities of Yanang leaf extract.



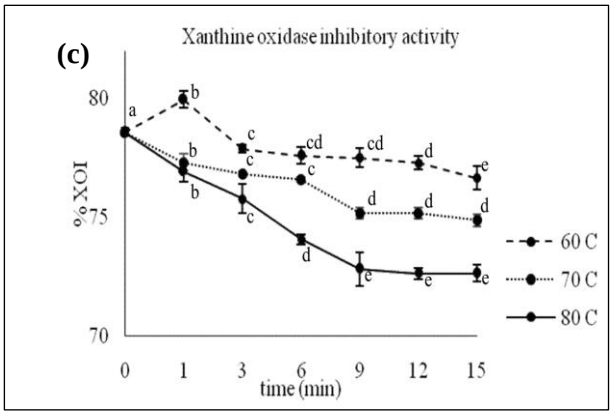


Figure 1. (a) Total phenolic content (b) DPPH radical scavenging activity and (c) XOI activity of Yanang leaf extract during heating at 60 ^{o}C, 70 ^{o}C and 80 ^{o}C for 15 minutes.

Kinetic degradation of Yanang leaf extract's properties

Kinetic degradations of total phenolic content, DPPH radical scavenging activity and XOI activity in Yanang leaf extract were determined by performing a regression analysis. The data of degradation were then fitted to three different kinetic models as previous mentioned in equation 2-4. The results revealed that the degradation of total phenolic content at all heating temperatures was described as a zero-order reaction with coefficient of determination between 0.809 and 0.959 (Table 1). The degradations of DPPH radical scavenging and XOI activities were second-order reactions with coefficient of determination between 0.783 and 0.920 and between 0.864 and 0.922, respectively.

Table 1. Reaction rate constant (k) and coefficient of determination (R^2) of total phenolic content, DPPH radical scavenging activity and XOI activity in Yanang leaf extract during preparation process

Temperature	Zero-Order		Second-Order			
	Total Phenolic Content		DPPH Scavenging Activity		XOI Activity	
	k (mg GAE/100 mg.min)	R^2	k (mL/µg BHT.min)	R^2	k(1/%.min)	R^2
60 ^{o}C	2.354	0.945	8×10^{-5}	0.783	2×10^{-5}	0.922
70 ^{o}C	3.035	0.959	2×10^{-4}	0.920	4×10^{-5}	0.886
80 ^{o}C	12.770	0.809	2×10^{-4}	0.810	7×10^{-5}	0.864

Temperature dependence of the degradations was determined by using Arrhenius equation as described in equation 5. A ln k - 1/T graph was plotted in order to express an effect of temperature on reaction rate constant. As shown in Figure 2, the temperature dependence of rate constants followed Arrhenius relationship as indicated by high correlation coefficient which was 0.848, 0.764 and 0.998 for total phenolic content, DPPH radical scavenging activity and XOI activity, respectively. The Arrhenius equations for Yanang leaf extract's properties are shown in Table 2.

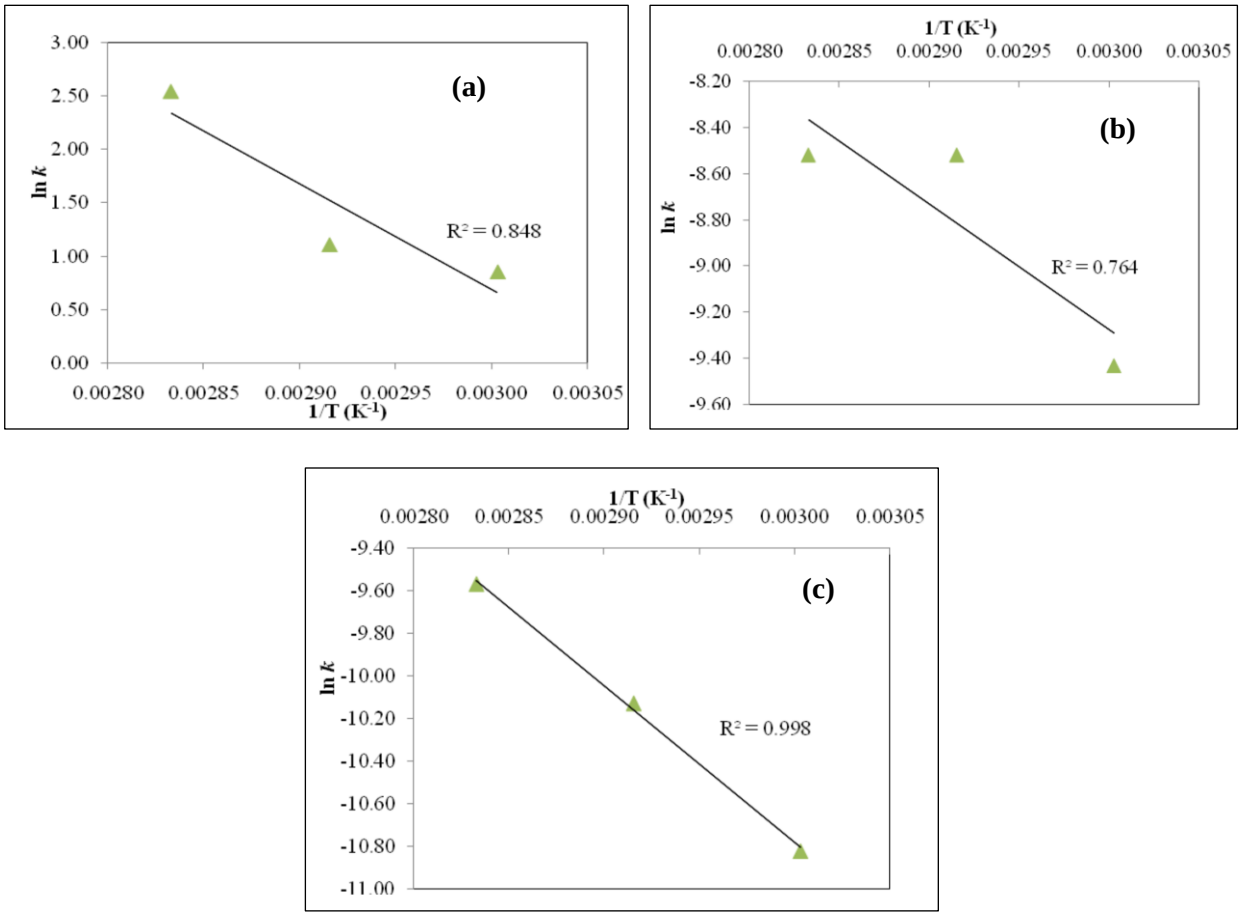


Figure 2. Arrhenius plots of (a) total phenolic content (b) DPPH radical scavenging activity and (c) XOI activity in Yanang leaf extract

Table 2. Arrhenius equation of total phenolic content, DPPH radical scavenging activity and XOI activity degradations in Yanang leaf extract

Property	**R^2**	**Arrhenius Equation**
Total phenolic content	0.848	k = exp [(-1186.91/T) + 30.291]
DPPH scavenging activity	0.764	k = exp [(-653.86/T) + 7.0355]
XOI activity	0.998	k = exp [(-886.29/T) + 11.324]

Conclusion

The preparation process of Yanang leaf extract for canned bamboo shoots production degraded its chemical properties. An increase in heating temperature and time decreased the total phenolic content, DPPH radical scavenging activity and XOI activity of the extract. The results showed that Yanang leaf extract contained total phenolic content at 526.33-638.93 mg GAE/100 mg db., DPPH radical scavenging activity at 92.86-136.41 µg BHT/mL and XOI activity at 72.64-76.65%. After 15 minutes heating, the total phenolic content, DPPH radical scavenging activity and XOI activity decreased 2.03-22.62%, 1.86-43.22% and 2.80-7.90%, respectively. The degradation of total phenolic content was a zero-order reaction (R^2=0.809-0.959) while that of DPPH radical scavenging activity (R^2=0.783-0.920) and XOI activity (R^2=.0864-0.922) were second-order reactions. Arrhenius

plots exhibited high coefficient of determination which were 0.848, 0.764 and 0.998 for total phenolic content, DPPH radical scavenging activity and XOI activity, respectively.

Acknowledgement

This research was funded by King Mongkut's University of Technology North Bangkok (KMUTNB), Thailand. Contract no. KMUTNB-GOV-58-42.1. Authors also would like to thank the Faculty of Agro-industry, KMUTNB Prachinburi campus for the facilities and support.

References

1. Rattana, S., Cushine, B., Taepongsorat, L. and Phadungkit, M. (2016). Chemical constituents and *in vitro* anticancer activity of *Tiliacora triandra* leaves. *Pharmacognosy Journal*, 8(1): 1-3.
2. Singthong, J., Ningsanond, S. and Cui, S.W. (2009). Extraction and physicochemical characterisation of polysaccharide gum from Yanang (*Tiliacora triandra*) leaves. *Food Chemistry*, 114(4): 1301-1307.
3. Rattana, S., Padungkit, M. and Cushnie, B. (2010). Phytochemical screening, flavonoid content, and antioxidant activity of *Tiliacora triandra* leaf extracts. *Proceedings of the 2nd Annual International Conference of Northeast Pharmacy Research*: pp. 60-63.
4. Mahidol, C., Sahakitpichan, P. and Ruchirawat, S. (1994). Bioactive natural products from thai plants. *Pure and Applied Chemistry*, 66(10-11): 2353-2356.
5. Saiin, C. and Markmee, S. (2003). Isolation of anti-malarial active compound from Yanang (*Tiliacora triandra* Diels). *Kasetsart Journal (Natural Science)*, 37(1): 47-51.
6. Singthong, J., Oonsivilai, R., Oonmetta-aree, J. and Ningsanond, S. (2014). Bioactive compounds and encapsulation of Yanang (*Tiliacora triandra*) leaves. *African Journal of Traditional, Complementary and Alternative Medicine*, 11(3): 76-84.
7. Sriket, P. (2014). Chemical components and antioxidant activities of Thai local vegetables. *KMITL Science and Technology Journal Part B*, 14(1): 18-24.
8. Azmi, S. M. N., Jamal, P. and Amid, A. (2012). Xanthine oxidase inhibitory activity from potential malaysian medicinal plant as remedies for gout. *International Food Research Journal*, 19(1): 159-165.
9. Saénz, C., Tapia, S., Chávez, J. and Robert, P. (2009). Microencapsulation by spray drying of bioactive compounds from cactus pear (*Opuntia ficus-indica*). *Food Chemistry*, 114(2): 616-622.
10. Tian, J., Chen, J., Lv, F., Chen, S., Chen, J., Liu, D. and Ye, X. (2016). Domestic cooking methods affect the phytochemical composition and antioxidant activity of purple-fleshed potatoes. *Food Chemistry*, 197(Part B): 1264-1270.
11. Turturică, M., Stănciuc, N., Bahrim, G. and Râpeanu, G. (2016). Effect of thermal treatment on phenolic compounds from plum (*prunus domestica*) extracts – A kinetic study. *Journal of Food Engineering*, 171: 200-207.
12. Méndez-Lagunas, L., Rodríguez-Ramírez, J., Cruz-Gracida, M., Sandoval-Torres, S. and Barriada-Bernal, G. (2017). Convective drying kinetics of strawberry (*Fragaria ananassa*): Effects on antioxidant activity, anthocyanins and total phenolic content. *Food Chemistry*, 230: 174-181.
13. De Ancos, B., Sgroppo, S., Plaza, L. and Cano, M.P. (2002). Possible nutritional and health-related value promotion in orange juice preserved by high-pressure treatment. *Journal of the Science of Food and Agriculture*, 82(8): 790-796.
14. Kalt, W. (2005). Effects of production and processing factors on major fruit and vegetable antioxidants. *Journal of Food Sciences*, 70(1): R11-R19.
15. Phomkaivon, N. and Areekul, V. (2009). Screening for antioxidant activity in selected thai wild plants. *Asian Journal of Food and Agro-Industry*, 2(4): 433-440.
16. Taejarernwiriyakul, O., Buasai, M., Rattanatranurak, I., Sriyod, P. and Chanluang, S. (2011). Xanthine oxidase inhibitory activity of medicinal plants. *Thai Pharmaceutical and Health Science Journal*, 6(1): 1-6.
17. Jiwajinda, S., Santisopasri, V., Murakami, A., Kim, O-K., Kim, H.W. and Ohigashi, H. (2002). Suppressive effects of edible thai plants on superoxide and nitric oxide generation. *Asian Pacific Journal of Cancer Prevention*, 3(3): 215-223.

Malaysian Journal of Analytical Sciences, Vol 23 No 3 (2019): 524 - 533
DOI: https://doi.org/10.17576/mjas-2019-2303-17

MALAYSIAN JOURNAL OF ANALYTICAL SCIENCES
Published by The Malaysian Analytical Sciences Society
ISSN 1394 - 2506

ESTERIFICATION OF ACETIC ACID AND BENZYL ALCOHOL OVER ZEOLITE HX PRODUCED FROM BANGKA BELITUNG KAOLIN

(Pengesteran Asid Asetik dan Benzil Alkohol ke atas Zeolit HX Dihasilkan daripada Kaolin Bangka Belitung)

Vita Nur Iftitahiyah[1], Didik Prasetyoko[1]*, Hartati[2], Yatim Lailun Ni'mah[1], Hasliza Bahruji[3], Hadi Nur[4]

[1]*Department of Chemistry, Faculty of Science,*
Institut Teknologi Sepuluh Nopember (ITS), Kampus ITS Sukolilo, Surabaya 60111, Indonesia
[2]*Department of Chemistry, Faculty of Science and Technology,*
Universitas Airlangga (UNAIR), Kampus C UNAIR, Mulyorejo Surabaya 60115, Indonesia
[3]*Centre of Advanced Material and Energy Sciences,*
University Brunei Darussalam, Jalan Tungku Link, BE 1410, Brunei Darussalam
[4]*Ibnu Sina Institute for Scientific and Industrial Research,*
Universiti Teknologi Malaysia, 81310 UTM Skudai, Johor, Malaysia

**Corresponding author: didikp@chem.its.ac.id*

Received: 25 October 2017; Accepted: 22 January 2019

Abstract

The activity of zeolite HX acid catalyst synthesized from kaolin was investigated for esterification of acetic acid with benzyl alcohol. Zeolite HX was synthesized using kaolin minerals obtained from Bangka Belitung Sumatra, Indonesia *via* hydrothermal method and followed by cation exchange treatment. The conversion of acetic acid was driven by the presence of Brønsted acidity with the porosity plays a crucial role in determining product selectivity. The influence of reactants concentration, the effect of reaction time and the amount of catalyst loading were investigated to obtain optimum condition of the reaction. Zeolite HX catalyzed esterification of acetic acid to achieve 58.78% of conversion with increasing the concentrations of benzyl alcohol enhanced the conversion. The acetic acid esterification follows the Eley-Rideal mechanism with the conversion improved by prolonging the reaction time and increasing the amount of catalyst used in the system.

Keywords: zeolite HX, kaolin, esterification, benzyl alcohol, fragrance

Abstrak

Aktiviti mangkin zeolit HX di sintesis daripada kaolin telah dikaji untuk pengesteran asid asetik dan benzil alkohol. Zeolit HX telah di sintesis menggunakan mineral kaolin daripada Bangka Belitung (Sumatra, Indonesia) melalui kaedah hidrotermal dan diikuti rawatan penukaran kation. Aktiviti zeolit ditentukan oleh keasidan intrinsik Brønsted dengan keliangan zeolit HX memainkan peranan penting dalam pemilihan bentuknya. Pengoptimuman terperinci parameter proses seperti nisbah molar, tindak balas masa dan pemangkin ke atas HX juga dijalankan untuk menilai kesan optimum pada aktiviti pemangkin dan pemilihan. Zeolit HX didapati menjadi pemangkin untuk pengesteran dengan penukaran asid asetik sehingga 58.78% diperolehi dengan peningkatan kepekatan benzil alkohol. Pengesteran asid asetik mengikut mekanisma Eley-Rideal menghasilkan penukaran lebih baik dengan peningkatan dalam masa tindak balas dan jumlah makin yang digunakan di dalam sistem.

Kata kunci: zeolit HX, kaolin, pengesteran, benzil alkohol, bau-bauan

Introduction

Ester compounds derived from carboxylic acid is an important commodity, which often used in perfumery, plasticizer, solvent and precursor for synthesis of fine chemicals. The synthesis of ester compound involved a direct reaction between carboxylic acid and alcohol, however the approach often limited by equilibrium thus limiting the resulting yield. In order to ensure the completion of the reaction, the presence of acid catalyst and the use of an excess amount of reactants are necessary. Solid acid catalyst has become an ideal choice of catalyst due to better separation between catalyst and the resulting product at the end of the reaction. Zeolite has been extensively studied as acid catalyst for esterification of acetic acid and benzyl alcohol, with HZSM-5 [1], Zeolite HY [2], and H-Beta [3] were among the most investigated catalysts for such reaction. The activity of zeolite was determined based on the intrinsic acidity and the presence of impregnated metal. The porosity of zeolite also contributed to the activity in which the shape and the size of the pores affecting product selectivity. The diffusional limitation caused by the size of the pore often lead to low product selectivity and catalyst deactivation caused by poor accessibility of the reactant to reach the active site of the catalyst and the pore blockage caused by the resulting products that trapped inside the pores [4].

Zeolite NaX from faujasite is composed of sodalite cage with 6-rings (D6R) hexagonal structure with average radius of 1.3942 nm [5]. The presence of three-dimensional pore structure and the acidity properties of zeolite X have been key aspects that determined its potential as catalyst. In general, zeolite NaX was prepared using commercial silica and alumina precursors. However, recent work showed that the use of alternative silica and alumina precursor directly obtained from naturally occurring materials such as kaolin produced zeolite with high acidity and porosity. Kaolin is a naturally occurring mineral that abundantly available in Indonesia particularly in south Sumatra, Bangka Belitung and Java Island. Kaolin from Bangka Belitung has low iron and titanium content but rich in silica (54.9 wt.%) and alumina (36 wt.%), which is an ideal precursor for synthesizing zeolite NaX.

In this study, the performance of zeolite HX synthesized from kaolin was investigated as acid catalyst in esterification reaction. The activity was also compared to kaolin in order to obtain the effect of porosity and acidity towards the conversion of acetic acid. Optimization of the parameter such as molar ratio of the reactant, the amount of catalyst used, and the reaction time were investigated to enhance the acetic acid conversion and selectivity towards benzyl acetate.

Materials and Methods

Materials

Materials used for the synthesis of zeolite HX were kaolin, sodium hydroxide (99 wt.% NaOH Merck), sodium aluminate (53 wt.% $NaAlO_2$ Merck), colloidal silica (LUDOX) (30 wt.% SiO_2 and 70 wt.% H_2O Merck), ammonium acetate (Merck) for cation exchange. Kaolin was obtained from Bangka Belitung contained 36 wt.% Al_2O_3, 54.9 wt.% SiO_2, 3.34 wt.% Fe_2O_3 and 1.88 wt.% K_2O. Pyridine was used as probe molecule for acidity testing to determine the amount of Lewis and Brønsted acid sites of the samples.

Synthesis of zeolite HX as catalyst

The zeolite NaX was synthesized by hydrothermal method at 110 °C for 12 hours according to our previous study [7]. The synthesized gel procedure can be divided into three steps, i.e. (1) the synthesis of seed gel (SG), (2) the synthesis of feedstock gel (FG), and (3) the combination of SG and FG to become overall gel (OV).

The SG (Al_2O_3:$4SiO_2$) was prepared by vigorous stirring of NaOH pellet and demineralized water mixture. Then, the sodium aluminate and colloidal silica were added into NaOH solution under constant stirring for about 20 minutes until homogeneous mixture were formed. The mixture was then left to age for 24 hours at room temperature. In the second step of the synthesis, the feedstock gel (Al_2O_3:$4.3SiO_2$) was prepared by mixing colloidal silica and Bangka Belitung kaolin which was used directly without prior treatment. The mixture was dissolved in NaOH solution. The OV was obtained by combination of the first and second resulting mixture to follow 18 to 1 ratio of FG to SG. The mixture was continuously stirred for another 30 minutes, then left to age for 24 hours at room temperature. The OV was transferred to polypropylene bottle and heated at 110 °C. The solid produced after hydrothermal treatment was filtered and thoroughly washed with distilled water until the pH of the supernatant is neutral. The resulting powder was dried and calcined in air at 500 °C with the heating rate of 2°/min for 1 hour.

The cation exchange was carried out using 1N of ammonium acetate solution by mixing with 1g of zeolite NaX. The mixture was refluxed at 60 °C for 3 hours. The solids were filtered and dried at 105 °C for 24 hours to obtain the NH_4X. The cation exchange process was summarized in equation 1 and 2. The NH_4X was calcined at 550 °C under air flow for 5 hours to decompose NH_4 to NH_3, thus forming the HX catalyst for esterification [9].

$$NaX_{(s)} + CH_3COONH_{4\,(l)} \rightarrow NH_4X_{(s)} + CH_3COONa_{(l)} \quad (1)$$

$$NH_4X_{(s)} \rightarrow HX_{(s)} + NH_{3(g)} \quad (2)$$

Characterization

The crystalline phase of zeolite was investigated using X-ray diffraction, XRD. XRD pattern was obtained by Philips X'pert XRD instrument with Cu Kα radiation with a step size of 0.04° and counting time of 10s. The data were recorded in the 2θ range of 5−40°. The morphology of sample was monitored by the micrograph of Scanning Electron Microscopy (SEM) ZEIS EVO MA 10 and coated by Pd/Au. Surface area of the catalyst was measured using nitrogen as adsorbent at P/P_0 – 0.99 by the BET method. The BJH and SF method were used to determine the size of mesopore and micropore, respectively. TEM HT-7700 micrograph shows the pore types of synthesized material.

Surface acidity was estimated by pyridine FT-IR. About 12 mg of zeolite HX pellet was dehydrated at 400 °C (heating rate 1°C/min) for 4 hours with the N_2 flow. The temperature was cooled down to room temperature (30 °C) under the flow of N_2 and the sample was exposed to pyridine vapor until saturation. The evacuation of excess pyridine was conducted by heating the sample at 150 °C for 3 hours. The amount of Brønsted and Lewis acid sites was determined by evaluating the amount of remaining adsorbed pyridine detected using infrared spectroscopy at wavenumbers of 1700-1400 cm^{-1} [9]. The amount Brønsted (B) and Lewis (L) acid sites were observed from the peaks area of adsorbed pyridine at around 1540 and 1450 cm^{-1}, then followed by calculation of acid sites concentration using B and L extinction coefficients (k) of 1.88 and 1.42 $cm.mmol^{-1}$ [10].

Catalytic activities

The zeolite catalytic activity was performed in a three-neck flask equipped with a water-cooled condenser. This assembly was heated using thermo stated hotplate. The desired amount of catalyst was dried before reacting at 110 °C for 12 hours. Acetic acid was added to benzyl alcohol with a molar ratio of 1:2, 1:4 and 1:6 with each reaction time variation from 0, 60, 240, 360, 480, 600 and 720 minutes. Esterification was carried out over a range of catalyst loading (2.5, 5 and 10 wt.%). The supernatant was analyzed by titration with 0.1 N KOH, using phenolphthalein indicator to get acetic acid conversion [11]. The resulting products were analyzed by gas chromatography- mass spectrometry (GC-MS).

Results and Discussion

Catalyst characterization

XRD analysis was used to determine the structure and crystalline phase of the synthesized NaX. The measurement was carried out at diffraction angel between 5-40° as can be seen in Figure 1(a). The XRD pattern of zeolite X following calcination in air indicates the presence of high crystalline structure with the pattern was identical to the standard of zeolite X [12]. The peaks appeared at 2θ = 6.15; 10.02; 23.28; 26,64; 31.95° showed high diffraction intensity which also identical to the XRD pattern of FAU type as reported by the *International Zeolite Association* (IZA) [13]. This confirmed that NaX was successfully formed from kaolin *via* hydrothermal synthesis. Figure 1(b) showed the SEM images of resulting powder that revealed the morphology of NaX crystallite as hexagonal structure with average crystallite size of ~ 1 µm. The zeolite also consisted of agglomerates to form zeolite cluster.

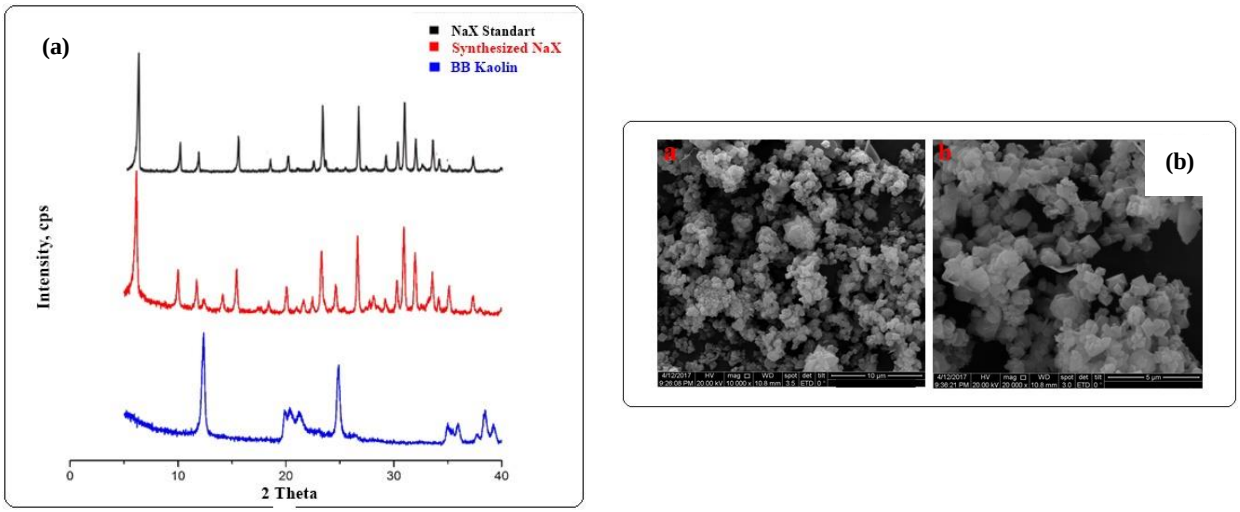


Figure 1. (a) XRD pattern of NaX standard, synthesized NaX and kaolin (b) SEM micrograph of NaX standard (left) and synthesized NaX (right)

Surface area and pore size distribution of the samples were characterized using nitrogen adsorption-desorption analysis. Specific surface area of kaolin and zeolite HX were analyzed using BET method, with the nitrogen adsorption-desorption profile provides the information of the type of pore of the samples (Figure 2(b)). The isotherm of Zeolite HX showed the adsorption of nitrogen at low relative pressure with hysteresis at P/P_0 of ~ 0.4, which were characteristic for isotherm type I and IV. This feature indicated the presence of both microporous and mesoporous structures in the synthesized zeolite. The zeolite HX isotherm showed a high adsorption of nitrogen at relative pressure, P/P_0 within 0-0.3 which indicates a monolayer formation of adsorbed N_2 on the surface. Increasing the relative pressure, P/P_0 the amount of adsorbed nitrogen showed a drastic increment of adsorbed nitrogen volume (P/P_0 >0.4). The hysteresis loop was also occurred at P/P_0 of 0.4 as shown in Figure 2(a).

Analysis of kaolin showed almost no adsorption of nitrogen at a relative pressure, P/P_0 of 0.01-0.3 which indicated the kaolin has a type II isotherm. This type II isotherm corresponded to the presence of nonporous structure in the powder. The surface area and pore analysis data calculated from N_2 adsorption studies were tabulated in Table 1.

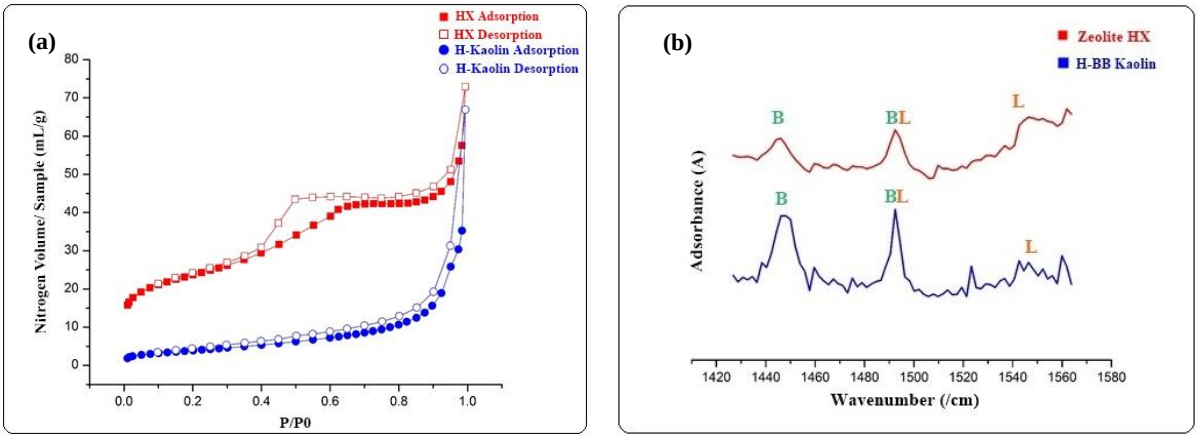


Figure 2. (a) Nitrogen adsorption-desorption isotherm of zeolite HX and kaolin, (b) FTIR spectra of pyridine-adsorption on zeolite HX and kaolin

Table 1. Surface and Pore Analysis of the zeolite HX and kaolin

Sample	S_{BET} [a] (m^2/g)	S_{meso} [d] (m^2/g)	S_{mikro} (m^2/g)	V_{meso} [b] (cm^3g^{-1})	V_{mikro} [b] (cm^3g^{-1})	$V_{total\ pori}$ [c] (cm^3g^{-1})	D_{meso} (nm)[d]	D_{mikro} (nm)[e]
Kaolin	14.51	16.182	-	0.130	0.006	1.348	3.06; 3.84	0.35; 0.90
Zeolite HX	80.24	57.169	23.071	0.096	0.027	2.256	3.41	1.47

Figure 3 shows pore size distribution analyzed by BJH and SF method. The pore size analysis of the synthesized zeolite HX indicated the presence of mesopores structure with average diameter of 3.41 nm (Figure 3(a) and micropores structure with average size of 1.47 nm (Figure 3(b)). The mesoporous structure was generated from the formation of skeletal framework during the rearrangement and condensation of tetrahedral silica.

Surface acidity of zeolite HX was analyzed using FTIR spectroscopy in the 1700-1400 cm^{-1} of wavelength region (Figure 2(a)) with using pyridine as probe molecule. The pyridine molecules formed a protonated pyridium ($C_5H_5NH^+$) ion upon interaction with Brønsted acidity to give adsorption at wavenumber of 1540-1545 cm^{-1}. The interaction between adsorbed pyridine with Lewis acidity formed *via* coordinated bonding complex between free electron pairs of pyridine molecules with empty orbitals of the Al. This characteristic feature of the coordinated bond occurred at ~ 1440-1452 cm^{-1}. The band appeared at 1490 cm^{-1} was assigned to a coordinated site of Brønsted and Lewis acid sites. The amount of Brønsted and Lewis acidity of zeolite HX were calculated as 0.1817 and 0.05314 mmol/g, respectively.

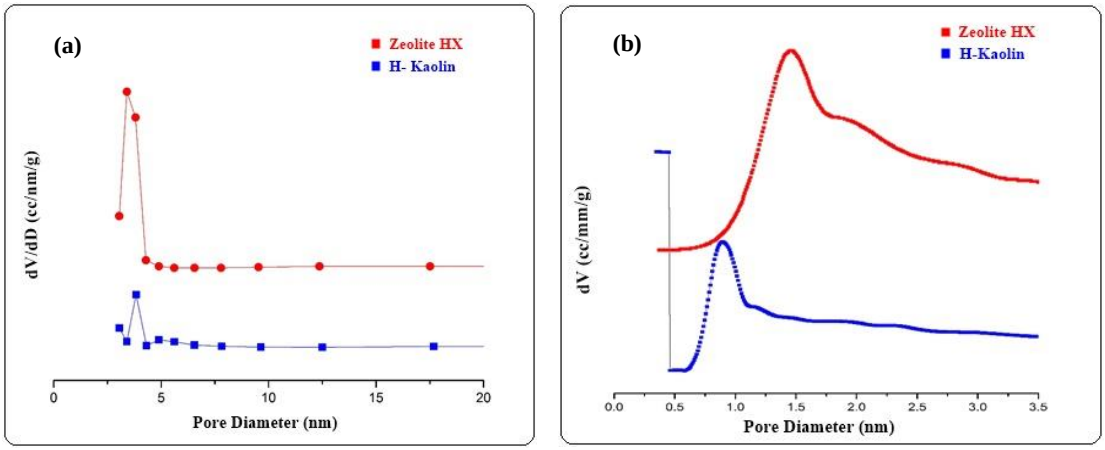


Figure 3. (a) Mesopore distribution (BJH) and (b) micropore distribution (SF) of the samples

Figure 4 shows the TEM images of the synthesized zeolite obtained following calcination in air at 500 ^oC. The TEM analysis showed a low transmission of electron beam images indicating the zeolite HX was formed of solid packed material without the presence of hollow structure. This indicates that the mesopore structure of the zeolite analyzed by N_2 adsorption method was formed due to the intra-cystalline interaction between the particulate zeolite [14].

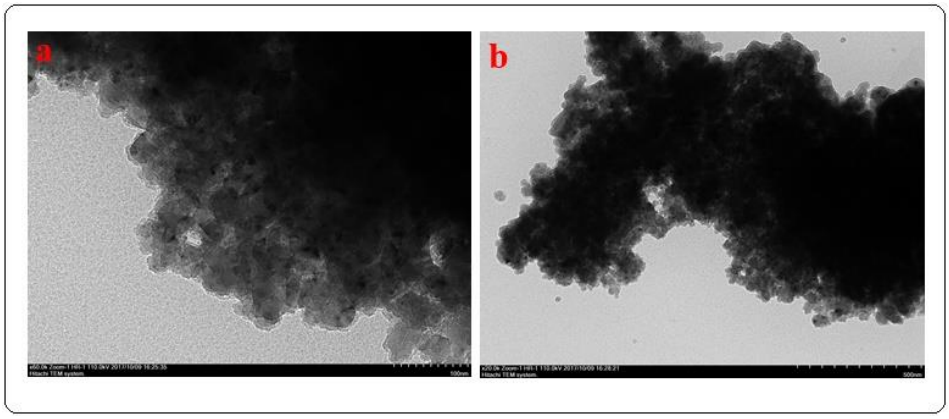


Figure 4. TEM image of zeolite HX

Esterification of acetic acid and benzyl alcohol on zeolite HX and kaolin

The activity of the catalyst was evaluated on the esterification of carboxylic acids with alcohol. Acetic acid was chosen as an ideal molecule for esterification reaction on zeolite HX due to the simplicity of the structure to undergo complete esterification without producing coke deposition on the catalysts surface. This is very important to prevent catalyst deactivation, particularly when long reaction was carried out. The catalyst was activated at 105 °C for 12 hours in air prior to catalytic reaction in order to remove physically adsorbed water molecules and activate the acid sites of the catalyst.

Catalytic performance of zeolite HX and the amount of acid sites were compared to kaolin and the results were illustrated in Figure 5. The esterification reaction was carried out for 4 hours, with molar ratio of acetic acid and benzyl alcohol was kept at 1: 4 ratios (AA: BA) with 2.5% wt. of catalyst was used in the reaction. Figure 5 shows the conversion of acetic acid for kaolin and zeolite HX. It was found that the catalytic activity of zeolite HX was higher than kaolin to give ~ 45.41% of acetic acid conversion. Kaolin surprisingly also showed significant activity with ~ 20.14% of acetic acid conversion within 4 hours of reaction. It is apparent that the catalytic activity of zeolite HX and kaolin were strongly dictated by the amount of acid sites presence on the catalysts surface. The amount of acid sites calculated using the peak area of adsorbed pyridine in infrared spectra showed that H-kaolin has lower Brønsted acidity but higher Lewis acidity in comparison to the zeolite HX. This suggests that the esterification of acetic acid with benzyl alcohol favors Brønsted acidity which according to the literature, it follows Eley-Rideal mechanism (Figure 9). We also suggest that the pore size of zeolite HX may also contribute to the activity of the catalyst. N_2 adsorption analysis revealed the micro-sized diameters of kaolin was smaller than zeolite HX, leading to difficulty of reactant to diffuse and interact with the acid sites within the pore. Furthermore, the mesopore surface area of H-kaolin was lower than zeolite HX, which has detrimental effect on the activity of the catalyst.

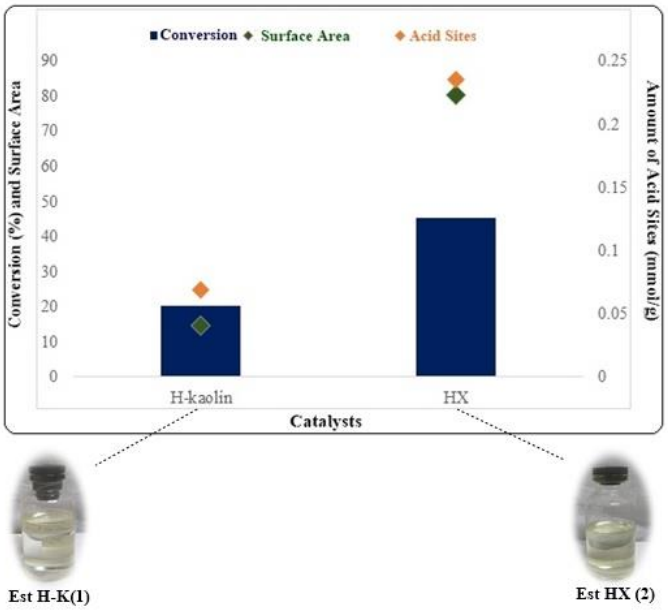


Figure 5. The conversion of acetic acid in esterification with benzyl alcohol on zeolite HX and kaolin as acid catalyst

Effect of acetic acid and benzyl alcohol ratio

The conversion of acetic acid was investigated by increasing the amount of benzyl alcohol in the reaction. The molar ratio of acetic acid to benzyl alcohol were varied from 1:2, 1:4 to 1: 6 while using zeolite HX as catalyst. The reaction was carried out at 110 °C for 720 minutes with the product sampling and analysis were measured at 120 minutes interval. The plot of acetic acid conversion with reaction time were shown in Figure 6. The percentage of acetic acid conversion increased at 1:4 acetic acid to benzyl alcohol molar ratio to give ~58.47% conversion within 720 minutes. This is significantly higher in comparison to the 1:2 acetic acid to benzyl alcohol ratio which gives ~48.03% of acetic acid conversion. Further increasing the ratio to 1:6, the catalytic activity was decreased to give ~ 39.00% of acetic acid conversion. Although increasing the amount of benzyl alcohol improved catalytic conversion of acetic acid, the presence of excess benzyl alcohol also contributed to deactivation of the catalyst. We attributed this deactivation to the poisoning of acid sites on zeolite HX with benzyl alcohol that consequently inhibited the esterification reaction [15].

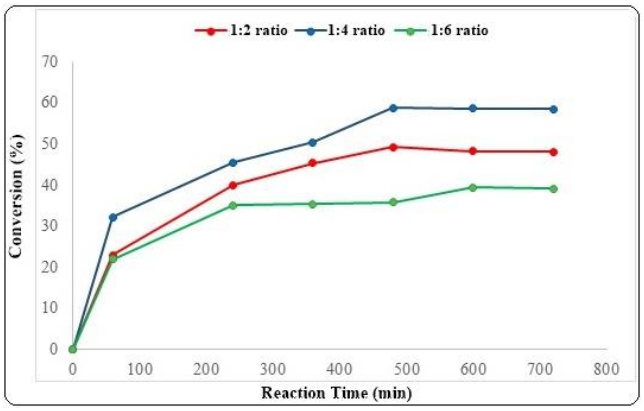


Figure 6. The influence of acetic acid to benzyl alcohol molar ratios on the conversion of acetic acid using zeolite HX as catalyst

Effect of reaction time

Table 2 summarized detail analysis of acetic acid conversion at different reaction time while using zeolite HX as catalyst. The conversion of acetic acid within 60 mins into the reaction showed that the 1:4 ratio was higher than 1:2 and 1:6. It is interesting to see that when the ratio of acetic acid to benzyl alcohol were varied, the reaction reached steady state at different reaction time. At 1:6 molar ratio, the reaction reached steady state at 240 minutes, with extended reaction time showed negligible changes on the conversion. This further consolidate the suggestion that in the presence of excess of benzyl alcohol in the reaction, it is prone to deactivate the active sites of the catalyst, presumably by occupying the acid sites. At 1:4 molar ratio of acetic acid to benzyl alcohol, the reaction achieved steady state at 500 minutes to give maximum acetic acid conversion of 58%.

Table 2. Conversion of acetic acid (%) with varying molar ratio and reaction time on zeolite HX

Molar Ratio (AA:BA)	Time (minutes)						
	0	**60**	**240**	**360**	**480**	**600**	**720**
1 : 2	0	22.89	39.93	45.32	49.18	48.21	48.03
1 : 4	0	32.15	45.41	50.31	58.78	58.58	58.47
1 : 6	0	21.71	35.06	35.36	35.68	39.31	39.00

Influence of the amount of acid catalyst

The influence of the amount of catalyst used during the reaction on the conversion of acetic acid were carried out by increasing the catalyst loading from 2.5%, 5% and 10% wt. Figure 7 shows the percentage of acetic acid conversion for every reaction. It is clear that the reaction was affected by the amount of acid catalyst with the conversion increased from 45.41% to 48.04%.

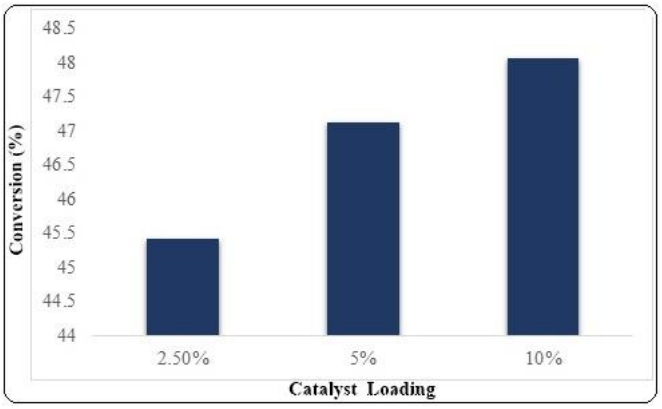


Figure 7. The influence of catalyst loading on acetic acid conversion (%)

The product of esterification reaction over zeolite HX was analyzed using GC-MS as shown in Figure 8. Only one product was detected, and it was identified as benzyl acetate. This indicate the selectivity of the reaction towards esterification product, benzyl acetate was 100%. The presence of benzyl alcohol (peak 1) and benzyl acetate (peak 2) were shown at retention time of 9.74 and 10.47 minutes (Figure 8). The catalytic mechanisms of benzyl acetate formation were proposed in Figure 9. We suggest that the reaction followed the Eley-Riedel mechanism previously proposed by Kirumaki et al. [5]. The reaction involved several mechanistic steps i.e. the adsorption of acetic acid on Brønsted acid sites that increased the electrophilicity of the carbon carbonyl; the nucleophile on benzyl alcohol interacted with the carbonyl to form an oxonium ion; proton transfer lead to water removal, and finally deprotonation to form the benzyl acetate [16].

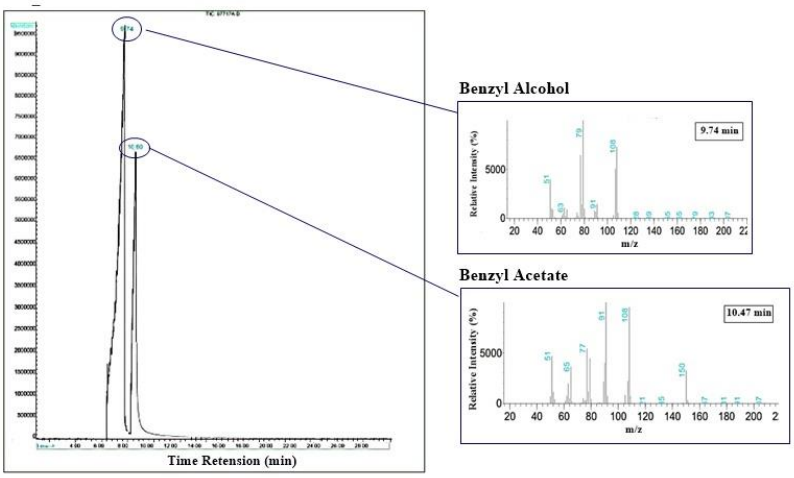


Figure 8. The GC-MS of esterification product

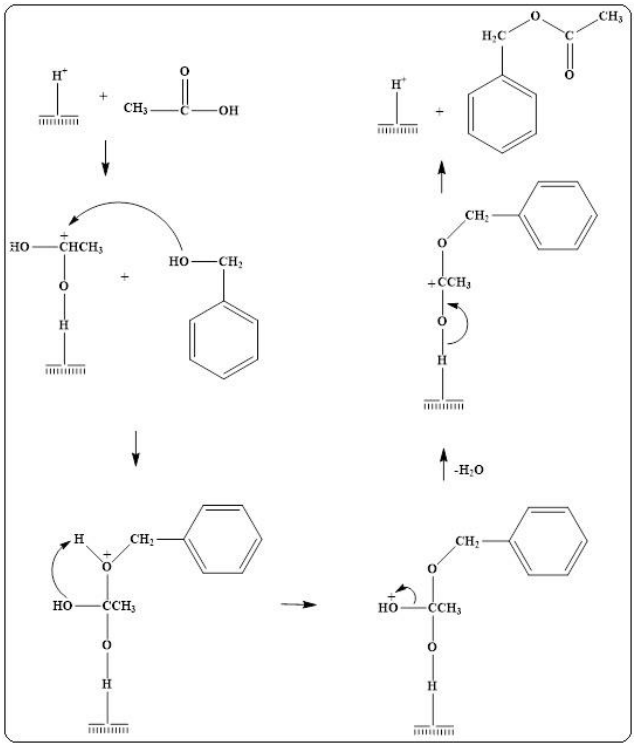


Figure 9. Proposed mechanism for esterification of acetic acid and benzyl alcohol

Conclusion

The activity of the synthesized zeolite HX catalyst from kaolin was investigated in esterification reaction of acetic acid with benzyl alcohol. The high activity of zeolite HX catalyst in the esterification reaction of acetic acid was due to the presence of Brønsted acidity (0.1817 mmol/gram) with high surface area (80.24 m^2/gram) and mesopore structure (3.41 nm). Optimization studies of the reaction revealed that varying the molar ratios of acetic acid to

benzyl alcohol increased the conversion to 58.78% with 100 % selectivity towards benzyl acetate. The conversion of acetic acid was also improved when the reaction time was increased to 720 minutes. The amount of catalyst used during the reaction was also affected the catalytic conversion of benzyl alcohol to benzyl acetate.

Acknowledgement

Authors would like to acknowledge the Ministry of Research and Higher Education, Indonesia, under "PBK" research grant 2017-2019.

References

1. Kirumakki S. R., Nagaraju N. and Narayanan S. (2003). Kinetics of esterification of aromatic carboxylic acid over zeolites Hβ aand HZSM5 using dimethyl carbonate. *Applied Catalysis A: General*, 248: 161-167.
2. Kirumakki S. R., Vijayashree, S. and Nagaraju, N. (2001). Catalytic esterification of benzyl alcohol with acetic acid by zeolites and their modified forms. *Indian Journal of Chemical Technology*, 8: 362-367.
3. Kirumakki S. R., Nagaraju N. and Chary K. V. R. (2006). Esterification of alcohols with acetic acid over zeolites Hβ, HY and HZSM5. *Applied Catalysis A: General*, 299: 185-192.
4. Gokulakrishnan, N., Pandurangan, A. and Sinha, P. K. (2007). Esterification of acetic acid with propanol isomers under autogeneous pressure: A catalytic study of Al-MCM-41 molecular sieves. *Journal of Molecular Catalysis A: Chemical*, 263: 55-61.
5. Kirumakki S. R., Nagaraju N. and Narayanan S. (2004). A comparative esterification of benzyl alcohol with acetic acid over zeolites Hβ, HY and HZSM5. *Applied Catalysis A: General*, 273: 1–9.
6. Mozgawa, W., Krol M. dan Barczyk. (2011). FT-IR of zeolites from different structural groups.*Chemik*, 65(7): 667-674.
7. Iftitahiyah. V. N. (2016). Synthesis of zeolite NaX from Bangka Belitung Kaolin as renewable source and its characterization. *Thesis*. Institut Teknologi Sepiluh November, Indonesia (ITS)
8. Jermy, B. R. dan Pandurangan, A. (2005). Catalytic application of Al-MCM-41 in the esterification of acetic acid with various alcohols. *Applied Catalysis A: General*, 288(1–2): 25–33.
9. Hartati, Prasetyoko, D., Santoso, M., Bahruji, H. and Triwahyono, S. (2014). Highly active aluminosilicates with a hierarchical porous structure for acetalization of 3,4- dimethoxybenzaldehyde. *Jurnal Teknologi (Sciences & Engineering)* 69(5): 25-30.
10. Emeis, C. A. (1993). Determination of integrated molar extinction coefficients for infrared absorption bands of pyridine adsorbed on solid acid catalysts. *Journal of Catalysis*, 141: 347-354.
11. Kusumaningtyas, D., Prasetyoko, D., Suprapto., Sugeng, T., Jalil A. A. and Rosyidah, A. (2017). Esterification of benzyl alcohol with acetic acid over H-ZSM-5 mesoporous. *Bulletin of Chemical Reaction Engineering and Catalysis*, 12(2): 243-250.
12. Purnomo, C. W., Salim, C. dan Hinode, H. (2012). Synthesis of pure Na–X and Na–A zeolite from bagasse fly ash. *Microporous and Mesoporous Materials*, 162: 6–13.
13. Khoshbin, R. and Karimzadeh, R. (2017). Synthesis of mesoporous ZSM-5 from rice husk ash with ultrasound assisted alkali-treatment method used in catalytic cracking of light naphtha. *Advanced Powder Technology*, 28(8): 1888-1897.
14. Schmidt, F., Lohe, M. R., Buchner, B., Giordanino, F., Bonino, F. and Kaskel, S. (2013). Improved catalytic performance of hierarchical ZSM-5 synthesized by desilication with surfactants. *Micropore Mesopore Materials.* 165: 148–157.
15. Induri, S., Sengupta, S., dan Basu, J. K. (2010). A kinetic approach to the esterification of maleic anhydride with methanol on H-Y zeolite. *Journal of Industrial and Engineering Chemistry*, 16(3): 467-73.
16. Nandiwale K. Y., Galande N. D., Raut S. A. and Bokade V. V. (2015). Benzylation of acetic acid to benzyl acetate over highly active and reusable micro/meso HZSM5. *Chemical Engineering Research and Design*, 93: 584-590.

Malaysian Journal of Analytical Sciences, Vol 23 No 3 (2019): 534 - 547
DOI: https://doi.org/10.17576/mjas-2019-2303-18

MALAYSIAN JOURNAL OF ANALYTICAL SCIENCES
Published by The Malaysian Analytical Sciences Society
ISSN 1394 - 2506

FRACTIONATION OF AQUEOUS EXTRACT OF *Ficus deltoidea* VAR. *Kunstleri*'s LEAVES USING SOLID PHASE EXTRACTION METHOD FOR ANTICANCER ACTIVITY ON DU145 CELL LINE

(Pemeringkatan Ekstrak Akueus dari Daun *Ficus deltoidea* var. *Kunstleri* Menggunakan Kaedah Pengestrakan Fasa Pepejal untuk Aktiviti Antikanser Pada Titisan Sel DU145)

Husnul Hanani Soib[1], Harisun Yaakob[1,2]*, Mohamad Roji Sarmidi[2,3], Mohamad Norisham Mohamad Rosdi[1]

[1]*Department of Bioprocess Engineering, Faculty of Chemical and Energy Engineering*
[2]*Institute of Bioproduct Development*
[3]*Innovation Centre in Agritechnology for Advanced Bioprocessing (ICA)*
Universiti Teknologi Malaysia, 81310 UTM Skudai, Johor, Malaysia

**Corresponding author: harisun@ibd.utm.my*

Received: 25 October 2017; Accepted: 22 January 2019

Abstract

Ficus deltoidea var. *kunstleri* or also known as 'Mas Cotek' belongs to the Moraceae family. It is widely used for postnatal treatment, anti-diabetic, anti-breast cancer, anti-nociceptive and anti-hypertension. In this study, the anticancer effects of flavonoid compounds from aqueous ethanolic fractions of *F. deltoidea* var. *kunstleri* leaves against prostate cancer cell lines, DU145 were investigated. The aqueous extract of *F. deltoidea* var. *kunstleri* was subjected for fractionation by solid phase extraction method by using various concentration of aqueous - ethanol ranging 20-99.8%. The fractions (fraction **I-IV**) were screened to obtain the most active fraction through total phenolic and flavonoid contents and MTT assays. The induction of apoptosis was evaluated using Annexin V-FITC/PI while the morphological changes of DU145 cells was assessed using acridine orange/propidium iodide (AO/PI) staining method. HPLC, FTIR-ATR and LC-MS/MS analysis were conducted for identification and confirmation of bioactive compounds. Fraction **I** which was fractionated using 20% of ethanol exhibited the highest polyphenol contents and highest inhibition against DU145 at 100 µg/mL (45.45%). Furthermore, cell viability of DU145 cells treated with crude extract of *F. deltoidea* var. *kunstleri* and its active fraction (**I**) were also compared using MTT assay. It was revealed that the crude and its active fraction **I** caused cell reduction through apoptotic machinery which was evidenced by the formation of apoptotic bodies, fragmentation, cell blebbing and cell shrinkage. These findings were confirmed by AO/PI staining method and Annexin V-FITC/PI. The presence of bioactive compounds of vitexin and isovitexin were identified by HPLC, FTIR-ATR and LC-MS/MS analysis. Positive correlations had been established between total phenolic and flavonoid content and anti prostate cancer activities. Therefore, these results suggest that flavonoids content of *F. deltoidea* var. *kunstleri* and its fraction **I** could potentially can be developed as an anti-cancer agent for prostate cancer.

Keyword: anti-cancer, antioxidant, *F. deltoidea* var. *kunstleri*, prostate cancer, vitexin

Abstrak

Ficus deltoidea var. *kunstleri* atau juga dikenali sebagai 'Mas Cotek' tergolong dalam keluarga Moraceae. Ia digunakan secara meluas untuk rawatan selepas bersalin, anti diabetes, anti kanser payudara, anti nosiseptif dan anti hipertensi. Dalam kajian ini, kesan antikanser oleh sebatian flavonoid daripada pemeringkatakan akueus etanol daun *F. deltoidea* var. *kunstleri* terhadap titisan sel kanser prostat, DU145 telah dikaji. Ekstrak akueus daripada *F. deltoidea* var. *kunstleri* telah dipilih untuk pemeringkatan oleh pengestrakan fasa pepejal menggunakan pelbagai kepekatan akueus - etanol berkadaran 20-99.8%. Semua pemeringkatan (pecahan **I-IV**) telah disaring untuk mendapatkan pecahan yang paling aktif melalui jumlah kandungan fenol dan flavonoid serta ujian MTT. Induksi melalui apoptosis dinilai menggunakan Annexin V-FITC/PI manakala perubahan morfologi

pada sel DU145 juga telah dinilai menggunakan kaedah pewarnaan acridin oren/propidium iodida (AO/PI). HPLC, FTIR-ATR dan LC-MS/MS analisis telah digunakan untuk mengenalpasti dan pengesahan sebatian bioaktif. Pecahan **I** yang terpecah menggunakan 20% etanol mempamerkan kandungan polifenol tertinggi dan perencatan paling tinggi terhadap DU145 pada 100 µg/mL (45.45%). Tambahan pula, sel hidup DU145 yang telah dirawat oleh ekstrak mentah *F. deltoidea* var. *kunstleri* dan pecahan aktifnya (**I**) juga telah dibandingkan menggunakan ujian MTT. Ia telah membuktikan bahawa ekstrak mentah dan pecahan aktifnya **I** menyebabkan pengurangan sel melalui mesin apoptosis dimana telah dibuktikan melalui pembentukan badan-badan apoptosis, pemecahan, sel kembung dan pengecutan sel yang disahkan oleh kaedah pewarnaan AO/PI dan Anexin V-FITC/PI. Kehadiran sebatian bioaktif vitexin dan isovitoksin telah dikenal pasti oleh analisis HPLC, FTIR-ATR and LC-MS/MS. Hubungan positif telah wujud di antara jumlah kandungan fenol dan flavonoid dan aktiviti anti-kanser prostat. Oleh itu, keputusan ini mencadangkan bahawa kandungan flavonoid *F. deltoidea* var. *kunstleri* dan pecahannya boleh dibangunkan sebagai agen anti-kanser untuk kanser prostat.

Kata kunci: anti-kanser, antioksida, *F. deltoidea* var. *kunstleri*, kanser prostat, vitexin

Introduction

Throughout the years, many studies have given attention to antioxidant activity along with phenolic and flavonoid content of plants [1-3]. Based on the findings, these bioactive constituents can inhibit the initiation, progression and spread of the cancer. As the cancer can be caused by a process of angiogenesis, it is believed to inhibit development of blood vessels for the growth of tumours [4]. Study has proved that plant containing higher amounts of phenolic and flavonoid may indicate the medicinal properties [5] which may act as anti-cancer [6] and anti-tumor [7]. Flavonoids are polyphenol compounds that have various pharmacological effects. They have the ability to induce certain enzyme like glucuronosyl transferase which can detoxify carcinogens in the body [8]. Besides, by alterating the gene expression, it enhanced the apoptosis and decreased the growth of neoplastic cells without harming healthy tissue.

Prostate cancer or typically known as a prostate adenocarcinoma is a prostatic malignancy which occurs at prostate gland of epithelial cells. It commonly develops at the posterior of the gland contrasting with benign enlargement where it occurs at the centre of prostate [9]. Globally, prostate cancer has become the most common non-skin cancer which attacks mostly of older men especially in western countries [10]. The progress of prostate cancer is slow as it takes longer time for invasion and metastasis. A normal cell can turn to cancer cell due to several factors such as mutation in its DNA either inherited or acquired by chemicals, viruses, radiations, diet intake, family history, environment and age. As DNA is mutated, it causes alteration in gene expression and consequently leads to activation of proto-oncogenes to oncogenes as wells as inactivation of tumors suppressor genes [11]. However, to date, the causes of the development of the prostate cancer still remain unknown and unclear.

Ficus deltoidea or locally knows as Mas Cotek is well distributed throughout the Southeast Asia and also can be found in Africa [12]. It comes from the family of Moraceae, genus Ficus and species of *deltoidea*. According to Corner [13], there are about 13 varieties of *F. deltoidea* which are differentiated based on morphological of leaves and figs. Studies revealed that *F. deltoidea* possessed antimicrobial effects [14], antinociceptive [15], antioxidant [14, 16, 17] as well as anti-inflammatory [18, 19]. Moreover, based on the studies conducted by Zunoliza et al. [18], it proved that *F. deltoidea* contained high levels of vitexin and isovitexin. Vitexin is a class of lignan compounds and flavonoid glycoside found in certain plants [20]. Vitexin induced anti-tumor [3] and exerted cytotoxicity activity by proapoptotic process which mediated by a decreased Bcl-2/Bax ratio together with activation of caspases and prevent cells from undergoing angiogenesis and metastasis [21].

Solid phase extraction (SPE) is one of the famous techniques used for fractionation especially for antioxidant compounds [22-25]. It is a simple and low cost method as compare to other liquid-liquid extraction method while it can reduce the usage of the sample and solvent [26, 27]. SPE have the ability to retain compound of interest on the sorbent while matrix interferences will be eluted from the cartridge via washing step; and later, the compounds of interest will be eluted with stronger solvent [25]. Basically, there are three main principles in SPE comprising of loading the sample, washing away undesired compounds and eluting desired compounds. The sample must be in liquid state so that the analytes in the sample will bind to the solid sorbent before the elution step. To wash off and collect the compounds of interest, most studies have used different types of solvents like ethyl acetate, hexane or

dichloromethane [28, 29] or using the same type of solvent with different polarity [23]. Besides, Patelinc et al. [23] have developed different types of eluent solvent ranging from 30% ethanol to 70% ethanol in order to determine the activity of phenolic compounds from different fractions of Propolis on antioxidant and cellular metabolic effects in yeast. Theoretically, increasing polarity of the eluent will extract more polar compounds. Indeed, the selection of the solvent used for elution highly affects the group of compounds to be extracted [30, 31].

This study was conducted to explore the fractionation process of *F. deltoidea* var. *kunstleri* crude extract using solid phase extraction method and the relationship between antioxidant and anticancer activities in view of prostate cancer cell line, DU145.

Materials and Methods

Materials and chemicals

Vitexin, isovitexin, 2,2-diphenyl-1picrylhydrazyl (DPPH), thiazolyl blue tetrazolium bromide (MTT) was purchased from Sigma-Aldrich®, USA. HPLC-grade methanol, formic acid, ethanol, Folin–Ciocalteu reagent was purchased from Merck®, Germany. *Penicillin streptomycin*, Dulbecco's modified eagle medium (DMEM), trypsin EDTA, phosphate buffered saline (PBS), fetal bovine serum (FBS) were obtained from GIBCO®, USA.

Plant material

The leaves of variety of *F. deltoidea* var. *kuntleri* were purchased from Moro Seri Utama Enterprise, Batu Pahat, Johor, Malaysia. It was authenticated by a botanist, Dr Shamsul Khamis from Institute of Bioscience, Universiti Putra Malaysia (UPM). A voucher specimen (SK 2312/13) of plant was deposited in Institute of Bioproduct Development, Universiti Teknologi Malaysia for further reference.

Plant extraction

The ground leaves of variety (7 g) were boiled with 300 mL of distilled water at 90 °C for about 1 hour and 50 minutes. The extract was filtered using filtration paper Whatman (No.1) and concentrated under a reduced temperature at 40 °C using rotary evaporator. Then, the sample was freeze-dried (Brand: Labconco) and stored at -20 °C until further use.

Fractionation by solid phase extraction method

The method implied was based on method developed by Patelinc et al. [23] with slightly modification in which the eluting solvents from 20, 40, 60 and 99.8% of ethanol (EtOH) were used to collect different fractions of polarity which assigned as fraction **I-IV**. Previously, this variety was chosen based on *in vitro* screening results consisted of total phenolic and flavonoid content, DPPH analysis as well as MTT assay as mentioned in previous study [32]. An amount 10 mg of standardized aqueous extract of *F. deltoidea* var. *kuntleri* was dissolved in 1 mL of distilled water and vortex thoroughly. The bonded silicas C_{18} of SPE cartridge (Phenomenex®, USA) was pre-conditioned with 5 mL of methanol followed by 5 mL of distilled water. The fractions **I-IV** were collected using eluent co-solvent of 20, 40, 60 and 99.8% of EtOH (Figure 2). All collected fractions were dried at 40 °C in centrifugal evaporator and stored at -20 °C until further use.

Determination of total phenolic content

A total phenolic content (TPC) was carried out using Folin-Ciocalteu assay as explained by Singleton et al. [33]. Gallic acid was used as standard ranging from 0.02-0.10 mg/mL. An amount of 5 mL of 10% of Folin-Ciocalteu reagent was added into 1 mL of the fractions or standard. Then, they were mixed for five minutes. After that, 4 mL of 7.5% sodium carbonate, $NaCO_3$ solution was added and left for 60 minutes. The absorbance was read at 760 nm by using UV-Vis spectrophotometer. A gram of garlic acid equivalents (GAE) per gram of extract was used as results of total phenolic content.

Determination of total flavonoid content

A total flavonoid content (TFC) was performed based on the method determined by Atanassova et al. [34] with some modification. An amount of 1 mg/mL of sample or standard stock solution was mixed up with 0.3 mL of sodium nitrate, $NaNO_2$. After five minutes, 0.3 mL of aluminium chloride, $AlCl_3$ was added and the mixture was left for six minutes. Next, 2 mL of sodium hydroxide, NaOH was added into mixture. The analyses are then

performed in triplicate and the standard curve with serial catechin solutions 0.05, 0.10, 0.25 and 0.50 mg/mL was used for calibration. The absorbance was read at 510 nm and the results are expressly as a gram of catechin equivalents (CE) per gram of extract.

Cell culture: *In vitro* screening of different fractions

The prostate cancer cell line (DU145) was obtained from American Type Culture Collection (Maryland, USA). The cells were cultured with media supplemented with DMEM, 1% of streptomycin and 10% (v/v) of fetal bovine serum. The cells were incubated at 37 °C in humidified atmosphere of 5% CO_2.

Cell viability using MTT (3-[4, 5-dimethylthiazol-2-yl]-2, 5 diphenyl tetrazolium bromide) assay

MTT assay is a routine method for screening the toxicity effects of extract or certain compound on cells. The method is based on the reduction of certain enzyme called dehydrogenase enzymes of viable cells through mitochondrial activity [35]. The cells at 70-80% of confluence were trypsinized and seeded into 96-well plate with density of 1 x 10^5 cells/mL. Cells were incubated for 48 hours for treatments. Afterwards, cells were resuspended with medium (without serum) for starvation and reincubated for 3-4 hours. Next, 90 µL fresh medium and 10 µL MTT solution (5 mg/mL) were added and incubated for another 4 hours. After that, the media was removed and 200 µL of DMSO was added to allow dissolution of purple MTT. The optical density of solution was measured at 570 nm using ELISA reader.

$$\text{Percentage of viable cell (\%)} = \frac{\text{Optical density of sample}}{\text{Optical density of control}} \times 100 \quad (1)$$

Acridine orange and propidium iodode (AO/PI) staining assay by florescence microscope

Cells of DU145 were seeded and treated with 100 µg/mL of fraction **I** and 93.11 µg/mL of standardized aqueous of *F. deltoidea* var. *kuntleri* (IC_{50} value - data not shown). After 48 hours incubated with the treatments, the growth medium was discarded. The cells were then stained with the dye mixture containing 10 µL of 1 mg/mL AO and 10 µL of 1 mg/mL of PI. The stained cells were examined and observed using inverted florescence microscope.

Annexin V-FITC/PI by flow cytometry

The cells were washed with cold PBS before resuspended in 1x binding buffer at a concentration of 1 x 10^5 cells/mL. Then, 100 µL (1 x 10^5 cells/mL) of cells were transferred into a 5 mL culture tube followed by 5 µL of FITC annexin V and 5 µL PI. Next, the tubes were vortex and incubated for 15 minutes at room temperature in the dark. After that, 400 µL of 1 x binding buffer were added to each tube and the cells were analyzed by flow-cytometry within 1 hour.

Quantitative analysis of most active fraction by HPLC

HPLC analysis was performed based on the previous study conducted by Elham et al. [36] with slightly modification. In this method, two types of solvent system used which were HPLC-grade methanol (absolute) and formic acid (1%) as well as two standards which were vitexin and isovitexin. A reversed-phase Nucleosil C_{18} column was maintained at 25 °C while mobile phase at flow rate of 1 mL/min. The wavelength used was 330 nm and the separation time estimated was 30 minutes.

Detection of compounds by Fourier transform infrared spectroscopy- attenuated total reflectance

FTIR spectra were obtained using Perkin Elmer Spectrum 400 Infrared spectroscope coupled with an air-cooled deuterated triglycine sulphate (DTGS) detector. Attenuated total reflectance (ATR) scan technique was used on all of the samples. The infrared measurements were taken at resolution 4 cm^{-1} with 16 inferograms co-added before Fourier transformation. The data were recorded at mid-IR range of 650-4000 cm^{-1}. The samples used for the analysis in a dried form.

Identification of active compound of most active fraction by LC-MS/MS

Detection of compounds presence in the active fraction was identified using ultra performance liquid chromatography (UPLC), Waters Acquity (Milford, MA), coupled with triple quadrupole-linear ion trap tandem

mass spectrometer (Applied Biosystems 4000 Q TRAP; Life Technologies Corporation, Carlsbad, CA) with an electrospray ionisation (ESI) source. A column of C_{18} reserved phase Acquity column (150 4.6 mm, 1.7 lm).

Statistical analysis

Analysis of variance (ANOVA one-way) was used to analyze the data from the experiments. The data was compared with the identified control specific to negative control and the experiments were carried out triplicate. Pearson's correlation coefficient test was used to assess correlations between means and p <0.05 was set as the limits of significance.

Results and Discussion

Total phenolic and flavonoid content

Fraction **I** demonstrated the highest contents of phenolic (53.284 ± 0.023 mg GAE/g) and flavonoid (506.291 ± 0.003 mg CE/g) followed by fraction **II** > **III** > **IV**.

Table 1. Total phenolic and flavonoid contents of the fractions of *F. deltoidea* var. *kunstleri* extracts expressed in terms of gallic acid equivalent (mg of GAE/g of extract)

Fractions	TPC (mg GAE/g)	TFC (mg CE/g)
I	53.284 ± 0.023	506.291 ± 0.003
II	33.644 ± 0.001	363.834 ± 0.001
III	32.223 ± 0.011	333.032 ± 0.003
IV	27.954 ± 0.034	322.099 ± 0.003

MTT (3-[4, 5-dimethylthiazol-2-yl]-2, 5 diphenyl tetrazolium bromide) assay

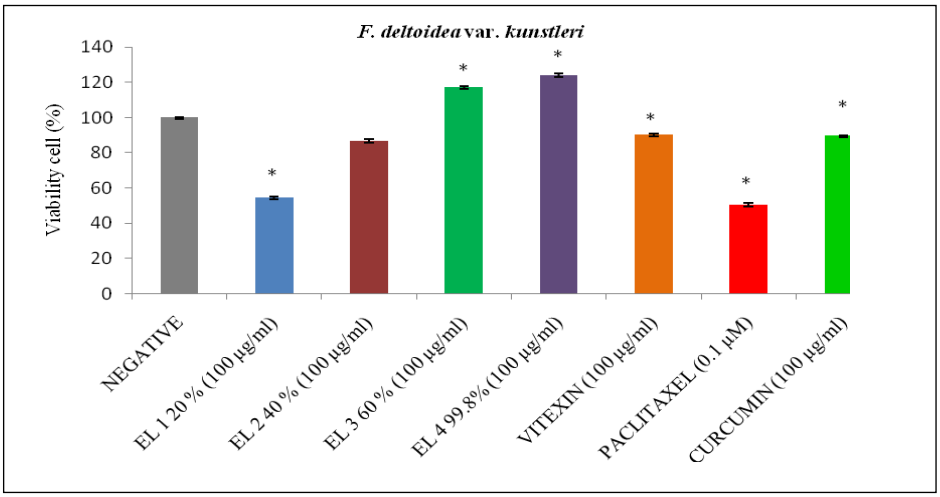
The viability of cells treated with four fractions eluted from different polarities of EtOH/water as eluents was examined in Table 2 and Figure 1. The highest inhibition of prostate cancer was established at fraction **I** which was eluted by 20% of EtOH. The inhibition of DU145 cells decreased as the polarity of eluent used increased (20% - 99.8% of EtOH). The results were significant differences as compared to several controls (p <0.05). Unfortunately, the effect of cytotoxicity of vitexin and curcumin were similar (p >0.05). The result suggested that the higher polarity of eluent trapped many polar compounds such as flavonoids, phenols and tannins which are believed to enhance the effect of cytotoxicity on cancer cells. The trend of the cell viability also increases as less polar eluents was used. It was aligned with the method used for fractionation as it was widely influenced the compounds extracted from the fractions. Three types of standards used which were vitexin, paclitaxel-synthetic drug and curcumin (contained 95% curcuminoids) and the results showed that paclitaxel possessed the highest inhibition as compared to the natural compound unlike vitexin and curcumin. In addition, the inhibition of DU145 by fraction **I** was significantly higher as compared to vitexin and curcumin alone.

Table 2. The effects of ethanolic fractions after 48 hours of treatments on DU 145 cell lines

Treatments	**Mean No. of Viability Cells (%) ± S.E.M** *
Fraction **I** – 20%	54.55 ± 0.36 ^{a,b,c}
Fraction **II** – 40%	86.68 ± 0.35 ^{a,b,c}
Fraction **III** – 60%	117.15 ± 0.44 ^{a,b,c}
Fraction **IV** – 99.8%	123.99 ± 0.67 ^{a,b,c}
^{a} Paclitaxel (0.1 µM)	50.91 ± 0.17 ^{a,c}
^{b} Vitexin (100 µg/mL)	90.29 ± 0.35 ^{a}
^{c} Curcumin (100 µg/mL)	89.63± 0.09 ^{a}

The *p* – value (< 0.05) of the treatments were compared with control groups.

Different letter explained the significantly the effects of the fractions compared to control (mean, n=3).



'*' indicate that the results were significantly different for both controls (p< 0.05). The data is presented as mean (n = 3) from triplicate analysis and the error bar indicate standard deviation. EL 1 = fraction **I** of 20% EtOH, EL 2 = fraction **II** of 40% EtOH, EL 3 = fraction **III** of 60% EtOH, EL 4 = fraction **IV** of 99.8% EtOH.

Figure 1. The effects of various treatments on the viability of DU145 cell after 48 hours treatment. The fractionated extract of *F. deltoidea* var. *kunstleri* and active compounds (vitexin and curcumin) were compared to the negative control (untreated cell) as well as positive control (paclitaxel).

Solid phase extraction

The importance of SPE method to enhance the concentration of polyphenol derived from crude extract was analyzed in this study. The method was considered as cost effective as it could reduce the usage of the solvent and the sample compared to other liquid-liquid chromatography technique. SPE method cleaned up the crude extract by removing unnecessary components while retaining the respective compounds [37]. As proven, the total phenolic and flavonoid contents from the *F. deltoidea* var. *kunstleri*'s fractions were higher as compared to the crude (data not shown). Moreover, the used of reverse phase of C_{18} cartridge was eluted more phenolic and flavonoid compounds. Increase

polarity of the eluent, the more polar compounds will be eluted and collected [30, 31]. A study done by Sultana et al. [38] had reported that the antioxidants compounds like phenolic and flavonoids are well extracted using aqueous organic solvents rather than absolute organic solvent. It was proved when 99.8% of EtOH had extracts lowest polyphenols compounds while the mixture of EtOH/water had extracts highest respective compounds. As for comparisons, the total polyphenolic content of the fractions was higher compared to the crude previously. It is due to different compositional mixtures of the solvent eluents (EtOH/water) facilitate in breaking the cell membranes of the compounds to be eluted [39]. Moreover, it also denoted that solid phase extraction method is effective method for intensify, separation and collection more polyphenol compounds which can enhance the isolation process if involved [40, 41].

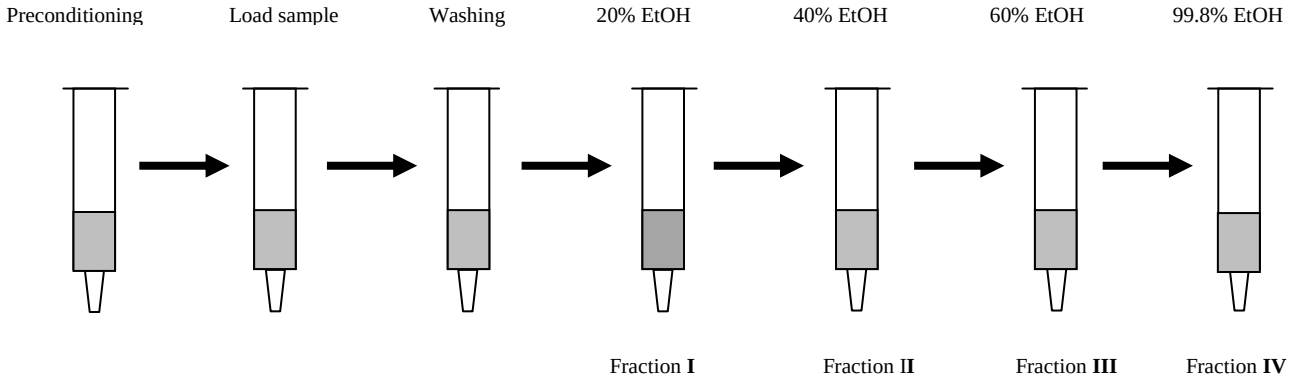


Figure 2. Preparation of fractions (**I** – **IV**) extracted from different polarity of eluents of EtOH/water by solid phase extraction

Correlation between anti cancer activity and total phenolic and flavonoid content

Table 3 showed the correlation among antioxidant and anti-cancer activities against DU145. The correlation coefficient number was between -1 to 1. As the number of correlation coefficient obtained from linear relationship nears to 1, it indicates the stronger relationship between two variables. Meanwhile, positive (+) indicate the positive direction of relationship. It showed that, the total phenolic content was positively correlated to total flavonoid content ($y = 7.509 + 105.18$, $r^2 = 0.993$) whereas negative correlation was observed in total phenolic ($y = -2.619x + 191.87$, $r^2 = -0.928$) and flavonoid ($y = -0.353x + 230.33$, $r^2 = -0.946$) content corresponding to toxicity activity in view of MTT assay.

Table 3. The Pearson correlation coefficients (*r*) among antioxidant and anti-cancer activities against DU145 cell line

Relationship	**Correlation coefficients (r)**	***p* (2-tailed)**
Total phenolic and flavonoid content	0.993	0.007
Total phenolic content and toxicity activity	-0.928	0.072
Total flavonoid content and toxicity activity	-0.946	0.054

It was proven by mean high percentage of radical scavenging activities could retard and inhibit the growth of cancer. Studies have confirmed that the occurrence of cancer is due to the presence of unstable molecules in the body known as reactive oxygen species (ROS) [42]. ROS comprises of singlet oxygen, superoxide anion radical and the peroxide anion. When the body contains high free radical, it will give harm and cause damage to the cellular or genomic in the prostate cell and later lead to the development of cancer. At this point, the role of antioxidant is to stabilize the free radical. Based on the findings, the phenolic compounds can inhibit the initiation, progression and deter the spread of the cancer. Other than that, it also had been stated by Yizhong et al. [43] in their article that

antioxidant activities of phenolic compounds had been proved to have a connection on anti-cancer activities. It can be proved when the consumption of traditional Chinese medicinal plants could lower the incidence of cancer. Besides, they also added that the stronger antioxidant activities of plants contain higher total phenolic content leading to a stronger correlation to the anticancer activities.

Morphology evaluation by acridine orange and propidium iodode (AO/PI) staining assay

Nuclear morphology changes on the DU145 cells were further examined using AO/PI double staining method whereby apoptotic, viable and necrotic features were determined (Figure 3a-3d). The study revealed that crude extract of *F. deltoidea* var. *kunstleri* and its active fraction **I** posses' cytotoxicity effect related to apoptosis compared to control (Figure 3a). A normal appearance of cells was observed at untreated cells while morphologies of the cell treated with *F. deltoidea* var. *kunstleri* and its active fraction **I** undergoes certain changes which indicated the event of apoptosis. It included formation of apoptotic bodies, fragmentation, cell blebbing and chromatin condensation.

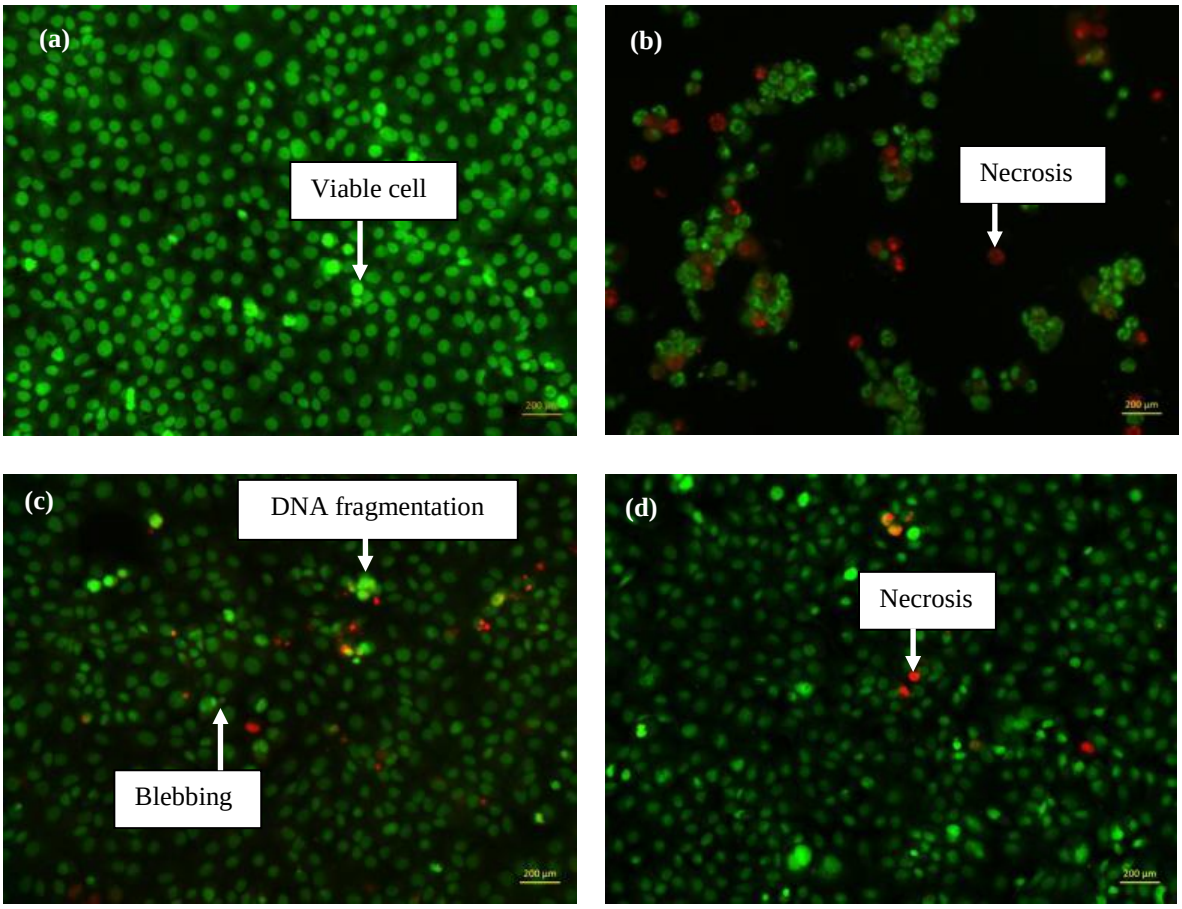
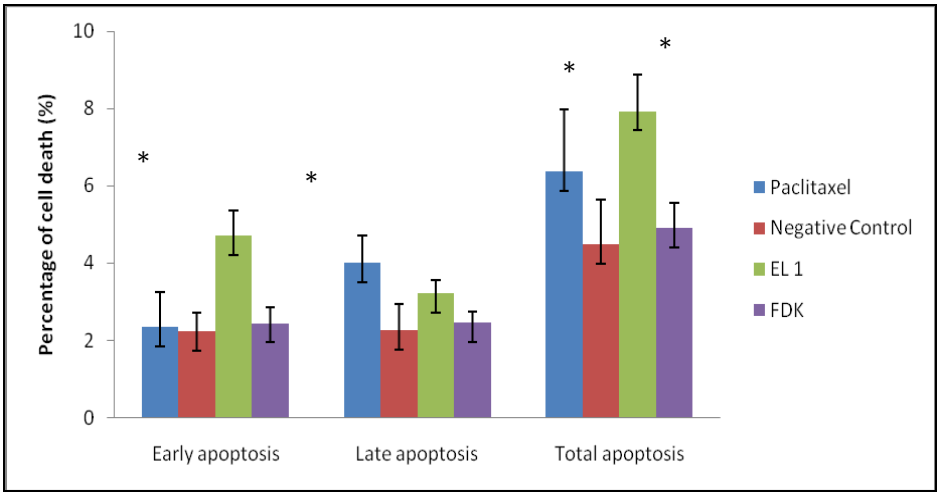


Figure 3. Morphological changes of DU145 cells with apoptotic feature were observed. The cells were treated with crude extract of *F. deltoidea* var. *kusntleri* and its active fraction, fraction **I** for 48 hours. The stained cells were viewed using a fluorescent microscope (x200). (a) untreated DU145 cells, (b) positive control Paclitaxel (c), crude extract of *F. deltoidea* var. *kunstleri* and (d) active fraction **I**

Annexin V-FITC/PI by flowcytometry

In this study, a quantitative analysis of cells undergoing apoptosis was performed by using Annexin V-FITC/PI assay. Annexin–V FITC/PI assay is a method based on the principle of translocation of phosphatidylserine (PS) during apoptosis in which this assay uses fluorescent dyes (annexin and propidium iodide) to detect type of early apoptosis before morphological cells changes. Apoptosis is a physiological process of cell death by which it helps body to maintain the number of proliferative cells. Thus, the numbers of cells are equals to the number of cell death. At a normal condition, the cells which were embeded with the asymmetrical membrane are maintained by ATP-dependant named flippases and floppases [44]. However, when there is an apoptosis event, the enzyme called flippase caused translocation of phosphatidylserine (PS) – types of phospholipid from inner layer of cytosol to the outer layer of membrane. The exposure of PS on outer layer caused the annexin (high affinity) to bind with it.



'*' indicate that the treatment was significant to negative control of untreated cell ($p < 0.05$). EL 1 = fraction **I** of 20% EtOH, FDK = *F. deltoidea* var. *kunstleri*

Figure 4. Assessment of apoptosis by annexin-V/FITC on prostate cancer cell line DU145 after 48 hours of incubation. The percentage of total number of cell death was calculated based on summed up of the number of early stage of apoptotic cells (annexin V+/PI-) and late stage of apoptotic cells (annexin V+/PI+).

As shown in Figure 4, early stage apoptotic cells (annexin V+/PI-) induced by fraction **I** was statistically higher than the control while in late stage apoptotic cell (annexin V+/PI+), paclitaxel was statistically higher than control (p <0.05). As a whole, paclitaxel and fraction **I** showed significant difference compared to negative control in view of total percentage of early and late apoptosis. Despite the significant effect of fraction, **I** to induce apoptosis, the numbers of viable cells found were quite high (80-90%). It was presumed that the cell death of DU145 induced by fraction **I** and *F. deltoidea* var. *kunstleri* does not occurred via the apoptosis pathway. It was aligned with other study which suggested that the aqueous extract of *F. deltoidea* promoted cell detachment rather than causing cell death. To some extent, the aqueous extract could cause apoptosis at higher concentration 1000 µg/mL. In other related studies, Fattahi et al. [45] had obtained the IC_{50} of 2 mg/mL when using aqueous extract. It was suggested that, most probably the compound which exhibited anti-cancer properties originated from non-polar compounds compared to polar compounds. Other than that, study has revealed that the annexin-V FITC/PI may not be an absolute method to show apoptosis events as it also can determine the pathological effects [46, 47].

FTIR-ATR analysis of active fraction I

It was suggested that the anti-cancer effect of fraction **I** towards DU145 was due to the presence of polyphenolic compounds which were confirmed by FTIR-ATR analysis (Figure 5). FTIR-ATR analysis was done to support the presence of compounds where the analysis will observe the presence of functional group found in the fractions of

20% EtOH (Figure 4.12). The functional group of phenolic -OH was observed at peak of 3259 cm^{-1}, alkene C=C at peak 1602 cm^{-1}, an asymmetric stretch nitro compound N-O at peak 1517 $cm^{-1,}$ an asymmetrical bending vibration of C-H at 1393 cm^{-1} (CH_3). In addition, symmetrical C-O-C stretching vibration also found at peak of 1050 cm^{-1} and C-H bonded at peak 900-675cm^{-1}.

HPLC analysis

The quantifications of dry weights were calculated based on the linearity of calibration curves of vitexin and isovitexin (1 μg/mL – 100 μg/mL) in which x is the concentration of the compound while y is a peak area. Vitexin was showed good linearity with regression equation (y = 22955x + 48627, r^2 = 0.995) as well as isovitexin with regression equation (y = 33932 x + 46459, r^2 = 0.996). It has been recognized that the active fraction **I** contained of vitexin and isovitexin (Figure 6). The dry weight of compounds obtained were 5.05 ± 0.13 mg/g and 0.42 ±0.01 mg/g. In respect to vitexin, the result was higher compared to the study done by Farsi et al. [12] where they found 4.27 mg/g of aqueous extracts of *F. deltoidea* (not mentioned variety). It was promoted that the used of homogenous mixture of 20% EtOH/water as eluents extracted high percentage of vitexin. Likewise, with the mixture of eluents, it can preserve the composition of vitexin extracted initially by the crude (data not shown). It may due to the closeness of polarity in which the mixture contains high polarity attributed from 80% water. Nevertheless, after fractionation occurred at 20% EtOH, it had higher competency to elute more isovitexin (0.42 mg/g) from the sample and cause it to increase twice compared to the crude (0.24 mg/g).

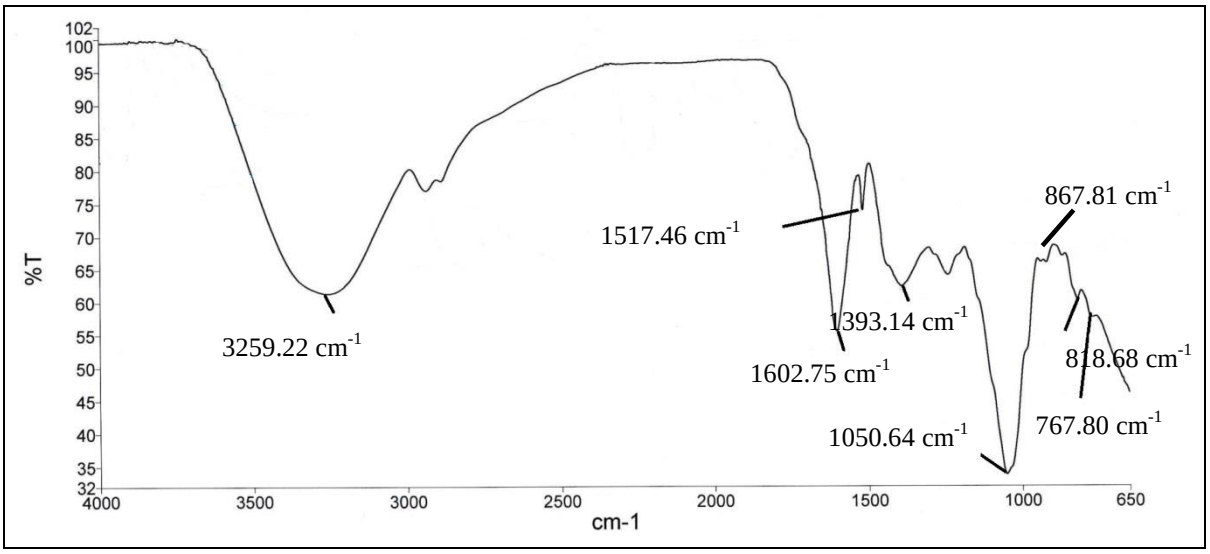
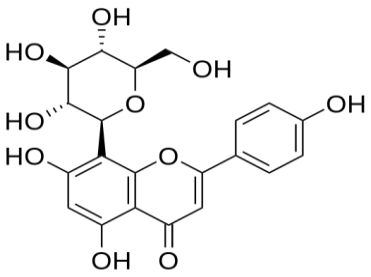
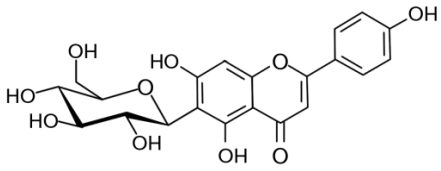


Figure 5. FTIR-ATR Spectrum of active fraction **I** (20% EtOH)



(1)



(2)

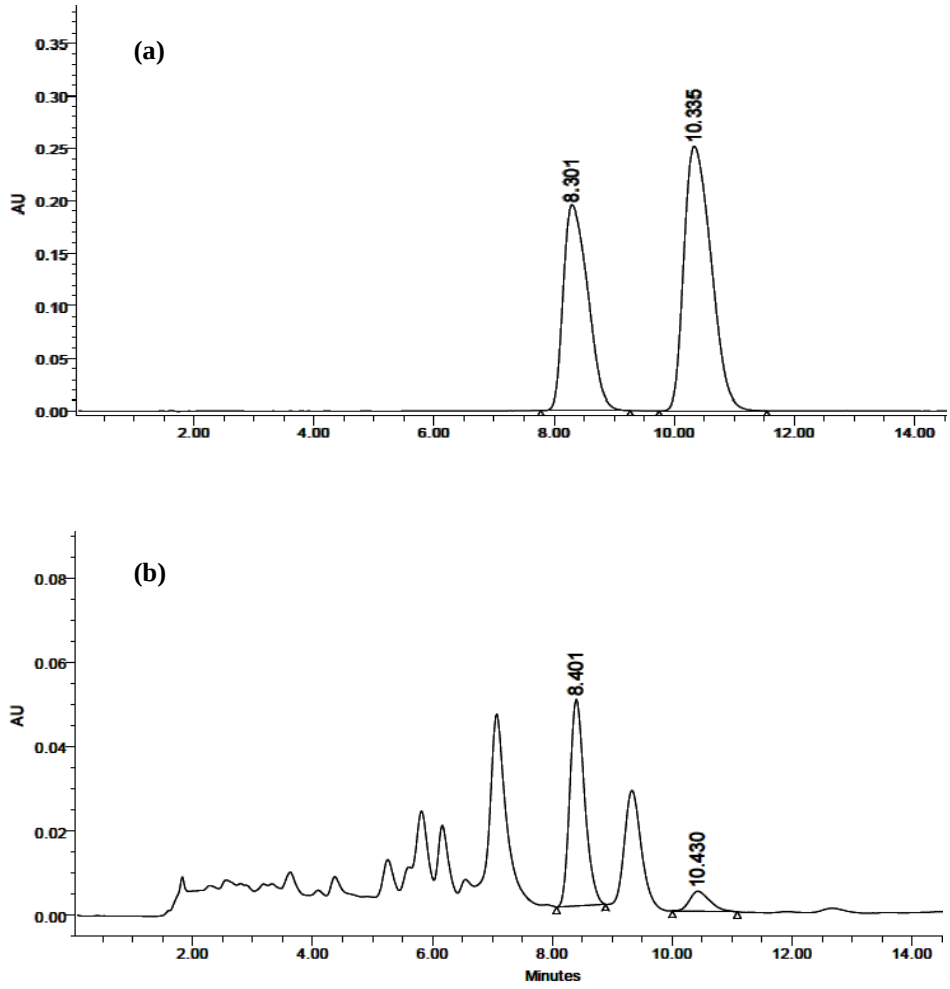


Figure 6. Chromatograms of vitexin (1) and isovitexin (2) found in fraction **I** monitored at wavelength of 330 nm. A, standard; B, Active fraction **I**

LC-MS/MS

In this study, identification of active compound Apigenin-8-*C*-glucoside flavones (vitexin) was identified in active fraction **I** (Figure 7). It was characterized by $[M - H]^-$ based on the MS fragment at m/z 431, 341, 311, 269.

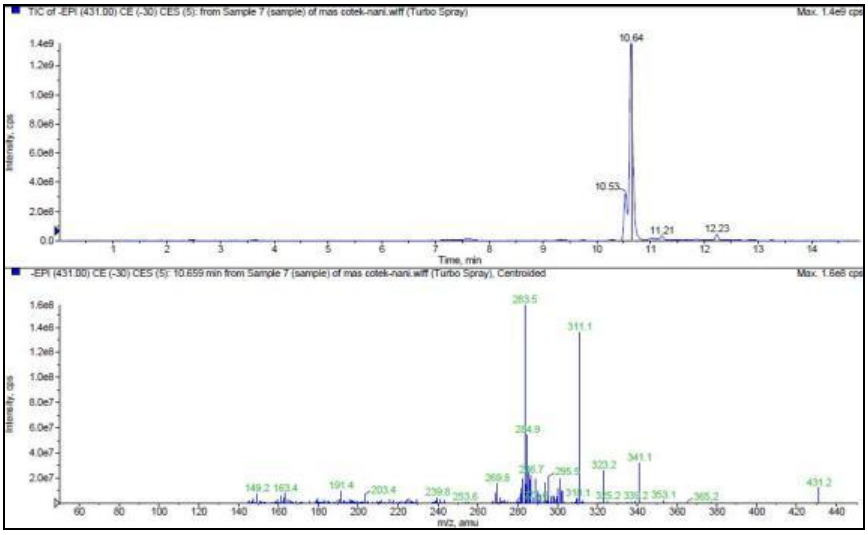


Figure 7. The EPI mass spectra of the vitexin following solid phase extraction from m/z 431

Conclusion

The relationship between antioxidant properties and total phenolic and flavonoid contents as well as toxicity activity of *F. deltoidea* var. *kunstleri'*s fractions towards the inhibition of prostate cancer was successfully identified. Besides, it was established that SPE method extracted high concentration of antioxidant compounds as compared to the crude extract. Moreover, it also denoted that the extracts of *F. deltoidea* var. *kunstleri* and its fraction **I** induced apoptosis activity towards prostate cancer cell line DU145. It was proved as the cells undergo certain morphological changes which indicated the event of apoptosis like DNA blebbing, DNA fragmentation and cell shrinkage. Other than that, study showed that there was a highly correlation of antioxidant activity against prostate cancer. High content of polyphenols including bioactive marker like vitexin play a major role towards prostate cancer inhibition. This study suggested that the fraction **I** of *F. deltoidea* var. *kunstleri* could inhibit the prostate cancer cell line DU145 as same as the crude extracts could by its structure function relationship mechanism revealed by HPLC, FTIR-ATR and LCMS/MS methods. For future studies, it is recommended to use non polar solvent during the extraction method as well as the fractionation using SPE. It is important to discover the effects of non-polar compounds despite the currents study had established cytotoxicity of mostly polar compounds. Besides, due to the presence of polyphenols compounds extracted from the fractions, it is advised to further isolate and purify the fraction to obtain specific compounds.

Acknowledgement

The corresponding author wishes to thank the Ministry of Education and Universiti Teknologi Malaysia (UTM) under Fundamental Research Grant Scheme (FRGS-R.J130000.7809.4F204) for financing this research project.

References

1. Li, Y., Ma, D., Sun, D., Wang, C., Zhang, J., Xie, Y. and Guo, T. (2015). Total phenolic, flavonoid content, and antioxidant activity of flour, noodles, and steamed bread made from different colored wheat grains by three milling methods. *The Crop Journal*, 3(4): 328 - 334.
2. Settharaksa, S., Jongjareonrak, A., Hmadhlu, P., Chansuwan, W. and Siripongvutikorn, S. (2012). Flavonoid, phenolic contents and antioxidant properties of Thai hot curry paste extract and its ingredients as affected of pH, solvent types and high temperature. *International Food Research Journal*, 19(4): 1581 - 1587.
3. Kefayati, Z., Motamed, S., Shojaii, A., Noori, M. and Ghods, R. (2017). Antioxidant activity and phenolic and flavonoid contents of the extract and subfractions of *Euphorbia splendida* Mobayen. *Pharmacognosy Research*, 9(4): 362 - 365.

4. Wahle, K. J., Brown, I., Rotondo, D. and Heys, S. (2010). Plant phenolics in the prevention and treatment of cancer. In M. Giardi, G. Rea and B. Berra (Eds.). *Bio-Farms for Nutraceuticals.* United State: Springer: pp. 36 - 51.
5. Adefegha, S. A. and Oboh. G. (2011). Cooking enhances the antioxidant properties of some tropical green leafy vegetables. *African Journal of Biotechnology*, 10(4): 632 - 639.
6. Sahreen, S., Khan, M. R. and Khan, R. A. (2014). Effects of *Carissa opaca* fruits extracts on oxidative pulmonary damages and fibrosis in rats. *BMC Complementary and Alternative Medicine*, 14(1): 1 - 9.
7. Islam, S., Akhtar, M., Parvez, S., Alam, J. and Alam, F. M. (2013). Antitumor and antibacterial activity of a crude methanol leaf extract of *Vitex negundo* L. *Archives of Biological Sciences*, 65(1): 229 - 238.
8. Jain, N. K., Siddiqi, M. A. and Weisburger J. H. (2006). Protective effects of tea on human health. United Kingdom: Cromwell Press.
9. McConnel, T. H. (2007). The nature of disease: Pathology for the health professions. United States: Lippincott Wiliams & Wilkin.
10. Henry, R.Y. and O'mahony, D. (1999). Treatment of prostate cancer. *Journal of Clinical Pharmacy and Therapeutics*, 24: 93 - 102.
11. Rang, H. P., Dale, M. M., Ritter, J. M. and Flower, R. J. (2008). Pharmacology. United States: Churchill Livingstone.
12. Farsi, E., Mariam, A. Sook, Y. H., Mohamed B. K. A., Mun, F. Y. and Mohd, Z. A. (2014). Standardized extract of *Ficus deltoidea* stimulates insulin secretion and blocks hepatic glucose production by regulating the expression of glucose-metabolic genes in streptozitocin induced diabetic rats. *BMC Complementary and Alternative Medicine*, 14: 220.
13. Corner, E. J. H. (1969). The complex of *Ficus deltoidea*; a recent invasion of the Sunda Shelf. *Philosophical Transactions of the Royal Society of London*, 256: 281 - 317.
14. Lee, S. W., Wendy, W., Julius, Y. F. S. and Desy, F. S. (2011). Characterization of antioxidant, antimicrobial, anti cancer property and chemical composition of *Ficus deltoidea* Jack. Leaf extract. *Journal of Biologically Active Products from Nature*, 2011: 2231 - 1874.
15. Sulaiman, M. R., Hussain, M. K., Zakaria, Z. A., Somchit, M. N., Moin, S., Mohamad, A. S. and Israf, D. A. (2008). Evaluation of the antinociceptive activity of *Ficus deltoidea* aqueous extract. *Fitoterapia*, 79: 557 - 561.
16. Wahid, S. Mahmud, T. M. M., Maziah, M., Yahya, A. and Rahim, M. A. (2010). Total phenolics content and antioxidant activity of hot water extracts from dried *Ficus deltoidea* leaves. *Journal of Tropical Agriculture and Food Science*, 38 (1): 115 - 122.
17. Norra I. (2011). Free radical scavenging activity and phenolic content of *Ficus deltoidea* accessions MFD4 and MFD6 leaves. *Journal of Tropical Agriculture and Food Science*, 39(1): 000 -000.
18. Zunoliza, A., Khalid, H., Zhari, I. and Rasadah, M. A. (2009). Anti-inflammatory activity of standardised extracts of leaves of three varieties of *Ficus deltoidea. International Journal of Pharmaceutical and Clinical Research*, 1(3): 100 - 105.
19. Zakaria, Z. A., Hussain, M. K., Mohamad, A. S., Abdullah, F. C. and Sulaiman, M. R. (2011). Anti-inflammatory activity of the aqueous extract of *Ficus deltoidea*. *Biological Research for Nursing*, 14(1): 90 - 97.
20. Sahreen, S., Khan, M. R. and Khan, R. A. (2013). Estimation of flavoniods, antimicrobial, antitumor and anticancer activity of carissa opaca fruits. *BMC Complementary and Alternative Medicine*, 13(1): 372.
21. Hwa, J. C., Jae, S. E., Bang, G. K., Sun, Y. K., Hoon, J. and Yunjo, S. (2006). Vitexin, a HIF-1α inhibitor, has anti-metastatic potential in PC12 cells. *Molecules and Cells*, 22(3): 291 - 299.
22. Hock, E. K., Azrina, A., Amin, I. and Faridah Abas. (2012). Antioxidative properties of defatted dabai pulp and peel prepared by solid phase extraction. *Molecules*, 17: 9754 - 9773.
23. Petelinc, T., Polak, T., Demšar, L. and Jamnik, P. (2013). Fractionation of phenolic compounds extracted from propolis and their activity in the yeast saccharomyces cerevisiae. *PLoS ONE*, 8(2): e56104.
24. Vesna, T. T., Sonja, M. D., Jasna, M. C., Gordana, S. C. and Sladana, M. S. (2007). Solid phase extraction of antioxidant compounds from commercial cranberry extract and its antiradical activity. *Acta Periodica Technologica*, 38: 157 - 164.
25. Theodoridis, G., Lasakova, M., Sherikova, V., Tegou, A., Giannntsiou, N. and Jandera, P. (2006). Molecular imprinting of natural flavonoid antioxidants: Application in solid-phase extraction for the sample pre-treatment of natural products prior to HPLC analysis. *Journal of Separation Science*, 29: 2310 - 2321.

26. Sanagi, M. M., Sulaiman, A. and Ibrahim, W. A. W. (2007). Principles of chemical analysis. (2nd edition). Department of Chemistry, Faculty of Science, Universiti Teknologi Malaysia.
27. Ku, Y. R., Liu, Y. C. and Lin, J. H. (2001). Solid-phase extraction and high-performance liquid chromatographic analysis of prednisone adultered in a foreign herbal medicine. *Journal of Food and Drug Analysis*, 9(3): 150 - 152.
28. Misbah, H., Abdul Aziz, A. and Aminudin, N. (2013). Antidiabetic and antioxidant properties of *Ficus deltoidea* fruit extracts and fractions. *BMC Complementary and Alternative Medicine*, 118(13): 1 - 12.
29. Farsi, E., Shafaei, A., Hor, S. Y., Khadeer Ahamed, M. B., Yam, M. F., Attitalla, I. H., Asmawi. M. Z. and Ismail, Z. (2011). Correlation between enzymes inhibitory effects and antioxidant activities of standardized fractions of methanolic extract obtained from *Ficus deltoidea* leaves. *African Journal of Biotechnology*, 67(10): 15184 - 15194.
30. Anwar, F. and Przybylski, R. (2012). Effect of solvents extraction on total phenolics and antioxidant activity of extracts from flaxseed (*Linum usitatissimum* L.). *Acta Scientiarum Polonorum Technology Aliment*, 11(3): 293 - 301.
31. Stankovic, M. S. (2011). Total phenolic content, flavonoid concentration and antioxidant activity of *Marrubium peregrinum* L. extracts. *Kragujevac Journal Science*, 33: 63-72.
32. Soib, H. H., Ware, I., Yaakob, H., Mukrish, H. and Sarmidi. M. R. (2015). Antioxidant and anticancer activity of standardized extracts of three varieties of *Ficus deltoidea'* s leaves. *Jurnal Teknologi*, 77(3): 19 - 25.
33. Singleton, V. L., Orthofer, R. and Lamuela-Raventos, R. M. (1999). Analysis of total phenols and other oxidation substrates and antioxidants by means of Folin Ciocalteau reagent. *Method Enzymology*, 299: 152 - 178.
34. Atanassova, M., Marinova, D. and Ribarova, F. (2005). Total phenolics and total flavonoids in Bulgarian fruits and vegetables. *Journal of the University of Chemical Technology Metallurgy*, 40: 255 - 260.
35. Patel, H. D., Zaveri, A. D., Zaveri, D. N., Shah, S. and Solanki, A. (2013). Comparison of the MTT and alamar blue assay for in vitro anti-cancer activity by testing of various chalcone and thiosemicarbazone derivatives. *International Journal of Pharmaceutical and Biological Sciences*, 4 (2): 707 - 716.
36. Elham, F., Shafie, A., Hor, S. Y., Khadeer Ahamed, M. B., Yam, M. F., Asmawi. M. Z. and Ismail, Z. (2013). Genotoxicity and acute and subchronic toxicity studies of a standardized methanolic extract of *Ficus deltoidea* leaves. *Clinics*, 68(6): 865 - 875.
37. Zwir-Ferenc, A. and Biziuk, M. (2006). Solid phase extraction technique–trends, opportunities and applications. *Polish Journal of Environmental Studies*, 15(5): 677 - 690.
38. Sultana, B., Anwar, F. and Ashraf, M. (2009). Effect of extraction solvent/technique on the antioxidant activity of selected medicinal plant extracts. *Molecules*, 14: 2167 – 2180.
39. Dai, J. and Mumper, R. J. (2010). Plant phenolics: Extraction, analysis and their antioxidant and anticancer properties. *Molecule*s, 15: 7313 - 7352.
40. Khoo, He., Azlan, A., Ismail, A. and Abas F. (2012). Antioxidative properties of defatted dabai pulp and peel prepared by solid phase extraction. *Molecules*, 17(8): 9754 - 0773.
41. Camel, C. (2003). Solid phase extraction of elements. *Spectrochimica Acta*, 58(7): 1177 - 1233.
42. Himmat, S. C. (2011). Prospective study of antioxidants, its mechanism and potential role in cancer. *International Journal of Research in Pharmaceutical and Biomedical Science*, 2(3): 888 - 894.
43. Yizhong, Cai., Qiong, L., Mei, S. and Harold, C. (2003). Antioxidant activity and phenolic compounds of 112 traditional Chinese medicinal plants associated with anticancer. *Life Sciences*, 74: 2157 - 2184.
44. Mariño, G. and Kroemer, G. (2013). Mechanisms of apoptotic phosphatidylserine exposure. *Cell Research*, 23(11): 1247 - 1248.
45. Fattahi, S., Ardekani, A. M., Zabihi, E., Abedian, Z., Mostafazadeh, A., Pourbagher, R. and Niaki, A. A. (2013). Antioxidant and apoptotic effects of an aqueous extract of *Utica dioica* on the MCF-7 human breast cancer cell line. *Asian Pacific Journal of Cancer Prevention*, 14(9): 5317 - 5323.
46. Demchenko, A. P. (2012). The change of cellular membranes on apoptosis: Fluorescence detection. *Experimental Oncology*, 34(3): 263 - 268
47. Heerde, W. L. V., Robert-Offerman, S., Dumot, E. A. W. J., Hofstra, L., Doevendans, P. A. and Smits, J. (2000). Markers of apoptosis in cardiovascular tissues: Focus on Annexin V. *Cardiovascular Research*, 45(3): 549 - 559.

Malaysian Journal of Analytical Sciences, Vol 23 No 3 (2019): 548 - 560
DOI: https://doi.org/10.17576/mjas-2019-2303-19

MALAYSIAN JOURNAL OF ANALYTICAL SCIENCES
Published by The Malaysian Analytical Sciences Society
ISSN 1394 - 2506

CUTICULAR HYDROCARBONS OF PUPAL CASES OF *Chrysomya megacephala* (FABRICIUS) AND ITS POSSIBLE USE FOR ESTIMATING POSTMORTEM INTERVAL

(Hidrokarbon Kutikel Kepompong *Chrysomya megacephala* dan Kegunaannya untuk Menganggar Sela Masa Kematian)

Nurul Nadhirah Nasir[1], Mohamad Afiq Mohamed Huri[1], Reena Abd. Rashid[2], Jaafariah Jaafar[1], Naji Arafat Mahat[1]*

[1]*Department of Chemistry, Faculty of Science, Universiti Teknologi Malaysia, 81310 UTM Johor Bahru, Johor, Malaysia*
[2]*Chemistry (Forensic Analysis) Programme, Faculty of Applied Sciences, Universiti Teknologi MARA, 40450 Shah Alam, Selangor, Malaysia*

**Corresponding author: naji@kimia.fs.utm.my*

Received: 25 October 2017; Accepted: 22 January 2019

Abstract

Pupal cases of *Chrysomya megacephala* are commonly found at death scenes; however, its utilization for forensic investigation remains nascent. Although the use of cuticular hydrocarbons (CHCs) for estimating the age of pupal cases has been reported, they were either laboratory-controlled experiments or in environmental conditions peculiar to Malaysia. Hence, this present research examined the CHCs in the pupal cases of *C. megacephala* exposed to the natural weathering in Malaysia provides empirical evidence for its age estimation. While confirmation of the identity of CHCs was done using gas chromatography-mass spectrometry, gas chromatography-flame ionization detector was used for quantifying the concentrations. The hexane extract of the pupal cases of *C. megacephala* contained a mixture of odd-numbered high molecular weight aliphatic (heptacosane (*n*-C27) and nonacosane (*n*-C29)), and branched alkanes (tetradecane, 2,6,20-trimethyl- and octadecane, 3-ethyl-5-(2-ethylbutyl)). Significant decrease (p <0.05) in the concentrations of n-C27 and n-C29 was observed, with the pattern being highly correlated (r > -0.926) with that of subsequent weathering intervals. Such findings had enabled formulation of credible mathematical algorithms for relating the concentrations of *n*-C27 and *n*-C29 in the pupal cases of *C. megacephala* versus the natural weathering intervals for its age estimation in Malaysia.

Keywords: forensic science, cuticular hydrocarbon, *Chrysomya megacephala*, postmorterm interval, Malaysia

Abstrak

Kepompong *Chrysomya megacephala* biasa dijumpai di tempat penemuan kematian; namun, penggunaanya dalam penyiasatan forensik masih baharu. Meskipun penggunaan kutikel hidrokarbon (CHC) dalam menganggar umur kepompong telah dilaporkan, ia sama ada dijalankan dalam ujikaji makmal terkawal ataupun dalam keadaan persekitaran yang janggal untuk Malaysia. Justeru, kajian ini yang menyelidik CHC dalam kepompong *C. megacephala* terdedah kepada proses luluhawa semulajadi di Malaysia memberikan bukti empirikal dalam menganggar usianya. Pengesahan identiti CHC dilakukan dengan menggunakan kromatografi gas-spektrometer jisim, manakala kromatografi gas-pengesan nyalaan pengionan digunakan untuk menentukan kepekatannya. Ekstrak heksana kepompong *C. megacephala* mengandungi campuran alifatik molekul berat yang bernombor ganjil (heptakosana (*n*-C27) dan nonakosana (*n*-C29)) dan alkana bercabang (tetradekana, 2,6,20-trimetil- dan oktadekana, 3-etil-5-(2-etilbutil)). Penurunan signifikan (p <0.05) dalam kepekatan *n*-C27 dan *n*-C29 dapat diperhatikan, dengan corak penurunan berkorelasi tinggi (r> -0.926) dengan sela masa luluhawa. Penemuan tersebut membolehkan perumusan algoritma matematik yang mapan bagi mengaitkan kepekatan *n*-C27 dan *n*-C29 dalam kepompong C. *megacephala* dengan sela masa luluhawa semula jadi untuk menganggar usianya di Malaysia.

Kata kunci: sains forensik, hidrokarbon kutikel, *Chrysomya megacephala*, sela masa kematian, Malaysia

Introduction

Forensic entomology deals with utilization of insect evidence for providing accurate estimation of minimum postmortem interval (mPMI) from the developmental patterns of necrophagous insects [1, 2]. In Peninsular Malaysia, *Chrysomya megacephala* (Fabricius) (Diptera: Calliphoridae) has been reported as the first and dominant necrophagus species infesting dead bodies and/or animal models followed by *Chrysomya rufifacies* (Macquart) (Diptera: Calliphoridae) [3, 4]. Being the first infesting necrophagous species in Malaysia, estimation of mPMI using the developmental pattern of *C. megacephala* may prove as the most appropriate. Studies have indicated that the duration for completing the life cycle for *C. megacephala* ranges between 7.25 to 8 days [4-6] beyond which estimation of PMI has to rely on the developmental patterns of the subsequent necrophagous insects such as *C. rufifacies*. It is pertinent to indicate here that upon completion of the life cycle, pupal cases of *C. megacephala* are commonly found at crime scenes [1]. However, its evidential value for estimating PMI remains scarcely reported in the body of literature. In this context, developing a means for assessing the age of those pupal cases may be useful for estimating the mPMI, considering the fact that *C. megacephala* being the first necrophagous insect to oviposit in corpses in many countries including Malaysia. Although the application of cuticular hydrocarbon (CHC) analysis for estimating the age of pupal cases of *C. megacephala* [7, 8] and larvae of *C. rufifacies* [9] has been suggested, these studies pertained to either laboratory setting or without adequate indication on the ambient conditions where the field experiments were conducted.

Zhu et al. [8], while reporting on the regular changes of CHC composition in the pupal cases of *C. megacephala* in China, indicated that the range of means of daily ambient temperature, relative humidity and the overall total rainfall for the 90 days of sampling period as 9.4-22.8 °C, 35–91% and 72.9 mm, respectively. However, they did not report the actual daily ambient data and the total daily rainfall in the field experiment that they conducted. In contrast to the description of the general conditions that they described [8], the ambient temperature in the low land areas of Malaysia has been reported to range between 21.5°C to 36.3°C, with rain being a commonplace occurrence [10]. Considering the migratory behavior of the post-feeding larvae of *C. megacephala* and their tendency to bury themselves into the surrounding soil for pupating [11], findings reported by Zhu et al. [8] by which the pupal cases 'was placed on the grass land with sandy soil and some shrubs' may not reflect the natural condition in Malaysia. In addition, different habitats may have different composition of soil types that may potentially influence the CHC compositions of pupal cases of necrophagous insects, an avenue for further research.

Therefore, this present research aiming at providing the first ever empirical data for exploring the possible use of CHC compositions in the pupal cases of *C. megacephala* exposed to natural weathering conditions prevailing in Malaysia for forensic use at estimating the minimum PMI, acquires significance.

Materials and Methods

Chemicals and reagents

The chemicals used in this present research were: *n*-C21 to *n*-C40 (50 mg/L) alkane standard (Fluka, USA) and analytical grade n-hexane (QRec, New Zealand). The ultrapure water produced by Biopak Polisher (Merck, Germany) was used without further purification. Stock solution that contained 20 alkane standards (n-C21 to n-C40) (50 mg/L) was used. From the standard stock solution, six working solutions were prepared using hexane *via* serial dilution; 5, 10, 20, 30, 40 and 50 µg/mL.

Experimental design

A total of 24 pupal cases of *C. megacephala* were collected from decomposing beef substrates in a sunlit habitat within the UTM Skudai Campus (1°33′45.6″ N, 103°39′09.2″ E) (Figure 1(a)), located at about 41.47 m above the sea level, and the soil type was loam. Physical characterization of the soil was made following the description provided by previous researchers [12]. For studying the temporal variations of CHC profiles, the pupal cases (Figure 1(b)) were exposed to the weathering process at day-0, day-7 and day-14. During each

weathering interval, three samples (each sample consisted of eight pupal cases) were analysed.

For enabling easier sampling while mimicking the natural behavior, pupal cases were buried at about 3 cm below the soil surface, approximately 1 m radius surrounding the decomposing substrates. Such a radius and depth were chosen due to the dispersal behavior of the post feeding larvae of *C. megacephala* as indicated by the previous researchers [11]. The daily ambient temperature and relative humidity were recorded *in situ* using a digital data logger, while a calibrated rain gauge was utilized for recording the total daily rainfall during observation period.

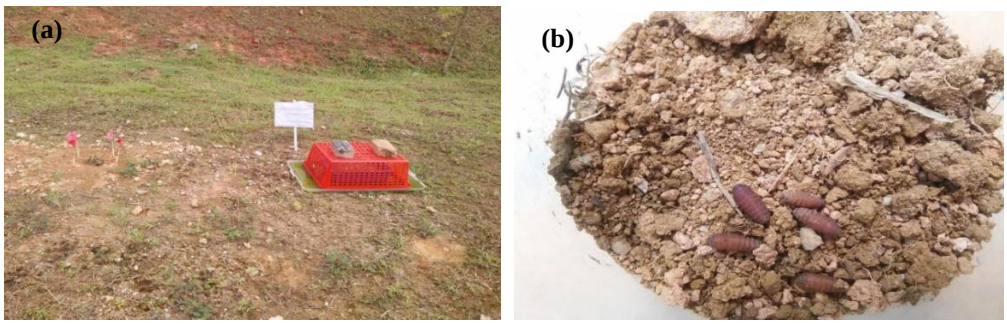


Figure 1. Photographs of (a) decomposition and burial site, as well as (b) sample of pupal cases of *C. megacephala* collected from soil surrounding a representative beef substrate decomposing in UTM Skudai Campus exposed to the weathering process at day-7

Sample pre-treatment

In this study, the pre-treatment step was conducted with minor modification from the methods described in past literature [8]. A sample (eight pupal cases each) collected for a particular interval of observation was cleaned using ultrapure water with the aid of a small tip drawing brush for removing the attached soil, dried using a clean filter paper and weighed. To extract the CHC, sample was immersed in n-hexane (800 µL) and vortexed for 10 mins. Extracted sample was concentrated under a stream of nitrogen gas and dissolved in n-hexane (50 µL) for quantitative and qualitative analyses using gas chromatography-flame ionization detector (GC-FID) and gas chromatography-mass spectrometry (GC-MS), respectively. Using the commercial alkane standard (n-C21 to n-C40), a daily chromatographic run was performed for evaluating the linearity of the analytical response, as well as ascertaining the identity of CHC that may be present in the extracted sample.

Analytical instrumentations

The analytical conditions for analyzing CHCs using GC-MS and GC-FID were optimized *in situ* and the conditions are tabulated in Table 1.

Table 1. The analytical conditions used for GC-FID and GC-MS.

Parameter	**Conditions**	
Instrument	GC-FID	GC-MS
	(7890B GC Agilent, Australia)	(7890B GC coupled with 7010 MS, Agilent, Australia)
Carrier Gas	Helium	Helium
Capillary Column	HP-5 capillary column	HP-5MS capillary column
	(30 m x 0.320 mm i.d., 0.25 µm film)	(60 m x 0.250 mm i.d., 0.25 µm film)
Injection Mode	Splitless	

Table 1 (cont'd). The analytical conditions used for GC-FID and GC-MS.

Parameter	Conditions	
Injection Volume	1 µL	
Injector Temperature	280°C	300°C
Detector Temperature	330°C	
Oven Temperature	Initial temperature of 200°C (held for 1 min); ramped to 230°C at 15°C/min; ramped to 310°C at 5°C/min (held for 20 mins)	
Analytical Software	-	Mass Hunter
Major and Confirmatory Ions (m/z)	-	n-C27 (major: 85, confirmatory: 380) n-C29 (major: 85, confirmatory: 408)

Statistical analyses

Data analyses were performed using the IBM-SPSS version 20.0 software and the normality of data for statistical inference was tested using Shapiro-Wilks. All the data were normally distributed with the *p* values for Shapiro-Wilks exceeding 0.05. For comparing the concentrations of *n*-C27 and *n*-C29 in pupal cases of *C. megacephala* at three different weathering intervals (day-0, 7 and 14), one-way analysis of variance (ANOVA) with Tukey-Kramer post hoc test was used. For associating the concentrations of *n*-C27 and *n*-C29 with that of weathering intervals, Pearson correlation coefficient analysis was utilized. Level of significance of 0.05 was considered for assigning the significance among groups [13].

Results and Discussion

Calibration curve, LOD and LLOQ

While confirmation of the identity for Heptacosane (*n*-C27) and nonacosane (*n*-C29) was done using GC-MS (7890B GC coupled with 7010 MS, Agilent, Australia), quantitation of such compounds was made using GC-FID (7890B GC Agilent, Australia). The representative chromatograms generated from GC-MS and GC-FID for *n*-C21 to *n*-C40 standard mixture are presented in Figures 2(a)-(b), respectively. All the hydrocarbon standards were well separated with total separation times for the 20 hydrocarbons using GC-MS and GC-FID being about 31 and 30 mins, respectively. Using GC-MS, *n*-C27 and *n*-C29 from the pupal cases (day-0) eluted at 10.956 and 13.316 mins, respectively (Figure 3(a)); the same eluted at 10.963 and 13.276 mins from GC-FID (Figure 3(b)). The mass spectra for *n*-C27 and *n*-C29 from the NIST library, as well as those obtained from representative samples are presented in Figures 4-5. Following the recommendation made by Miuc et al. [14], ions (m/z) 85 and 380 were used for confirming the identity of *n*-C27; the same were 85 and 408 for *n*-C29.

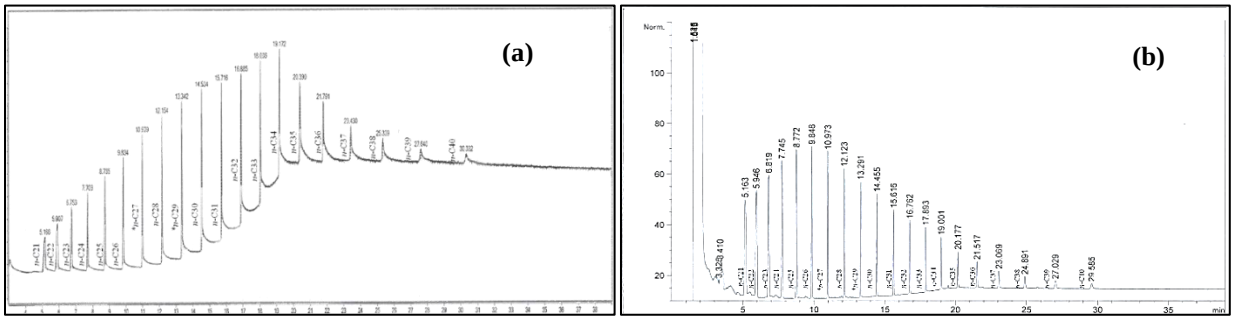


Figure 2. GC-MS (a) and GC FID (b) chromatograms obtained for *n*-C21- *n*-C40 standard mixture. Heptacosane (*n*-C27) and nonacosane (*n*-C29) were used for comparison and regression studies

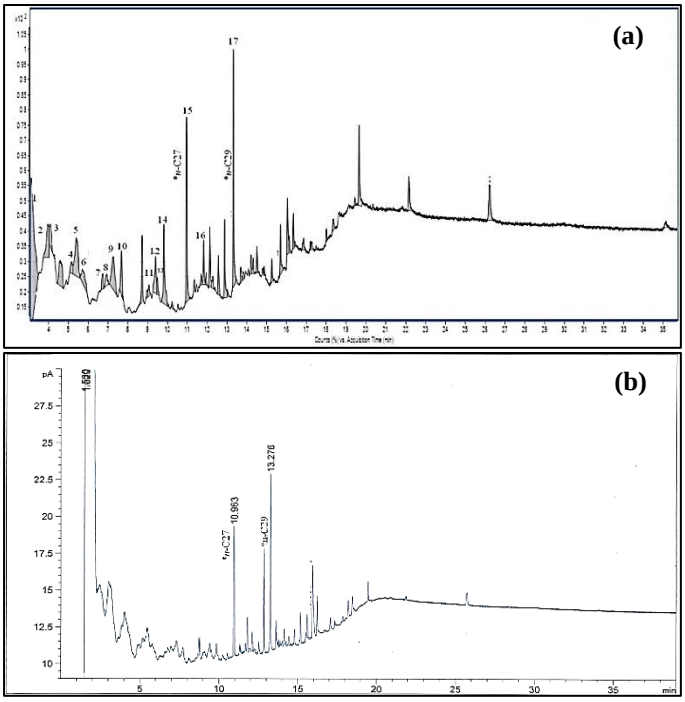


Figure 3. GC-MS (a) and GC-FID (b) representative chromatograms of CHC for *C. megacephala* pupal case at Day-0. Heptacosane (*n*-C27) and nonacosane (*n*-C29) were used for comparison and regression studies.

Table 2. Analytical figures of merit for hydrocarbons analysed.

Two Prevailing Hydrocarbons	**Range of Calibration Curve (µg/mL)**	**Coefficient of Determination (R^2)**	**Equation**	**LOD (µg/mL)**	**LLOQ (µg/mL)**
Heptacosane (*n*-C27)	0-50	0.9978	y=2.2712x + 2.1462	3.68	5.58
Nonacosane (*n*-C29)	0-50	0.9974	y=1.7094x + 8.8207	4.77	7.22

The guideline prescribed by the USFDA [15] was used for accepting the calibration curves, as well as LODs and LLOQs. The calibration curve was accepted when $R^2 \geq 0.995$. The LOD and LLOQ were mathematically calculated using signal-to-noise ratios of 3:1 and 5:1, respectively.

Analysis of CHC compositions in pupal cases of *C. megacephala*

It is pertinent to indicate here that in Malaysia, upon reaching the fully grown stage of third instar larvae, *C. megacephala* would start to wander away from the decomposing corpses/carcasses and pupate by burying themselves in the surrounding soil until the emergence of tenerals [11]. Hence, it is expected that, in forensic investigation, the pupal cases of this necrophagous species can largely be found at about 1-3 cm underneath the soil surface [4]. Such a condition does not only lead to the abiotic (weathering) degradation of CHC in the pupal cases, but also leaving them fully exposed to biodegradation by soil-microbiota [17, 18]. Despite its unique post-feeding behavior and the possible influence of soil microbiota on CHC biodegradation of pupae and pupal cases of *C. megacephala*, specific discussion on this aspect, in view of its forensic application, remains unreported so far.

Review of literature reveals no specific study focusing on CHC compositions in pupae and pupal cases of necrophagous insects exposed to weathering conditions in tropical countries like Malaysia. Except for only one reported field study [8] (daily ambient temperature: 9.4-22.8 °C, daily relative humidity: 35-91%, total rainfall: 72.9 mm) with the ambient conditions peculiar for tropical countries like Malaysia, the remaining studies were conducted in laboratory-controlled conditions detailed below. While Ye et al. [19] conducted their pupae weathering experiment at constant 24 °C and 75% relative humidity using sawdust as the rearing medium, Zhu et al. [7] did the same at 25 ± 1°C with photoperiod of 14:10 h (light: dark). In another laboratory study, Frere et al. [20] compared the CHC compositions in the new (year 2012) and old (year 1997) pupal cases of *Hydrotaea aenescens* (Diptera: Muscidae) although the weathering conditions were not indicated. Generalization of the findings from other biogeoclimatic regions [7, 19, 20] for interpreting the CHC data in pupae and pupal cases of necrophagous insects found in tropical countries may prove to be erroneous. Therefore, the specific attempt made in this present research at examining CHC compositions in the pupal cases of *C. megacephala* buried at about 3cm underneath the surrounding soil at three different weathering intervals (day-0, day-7 and day-14) in Malaysia acquires forensic significance. Recognizing the possibility of using CHC compositions in the pupal cases of *C. megacephala* for estimating mPMI, and because climatological factors [21-24] can potentially influence its composition, the data *viz.* ambient temperature, relative humidity and total rainfall were recorded here too.

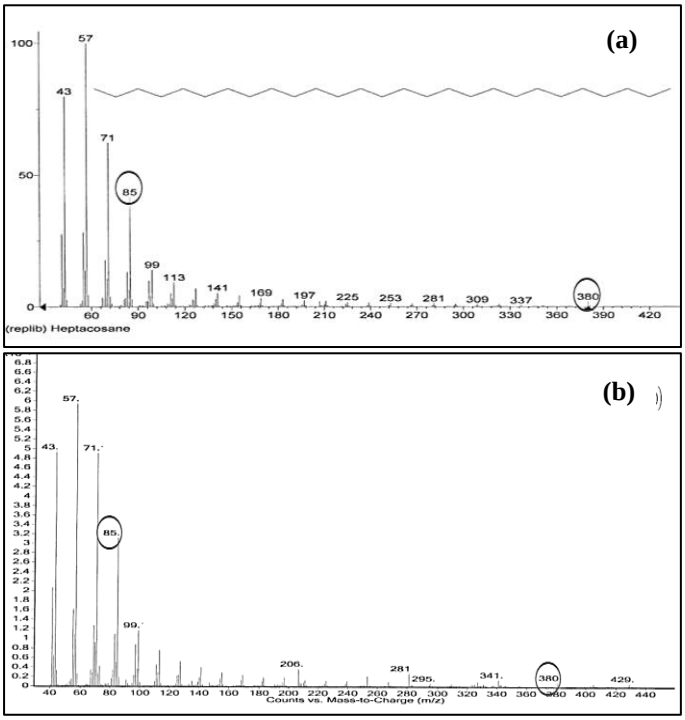


Figure 4. Mass spectrum for heptacosane (*n*-C27) from (a) the NIST library and (b) a sample. As suggested by Miuc et al. [14], m/z 85 and 380 were used as the major and confirmatory ions, respectively

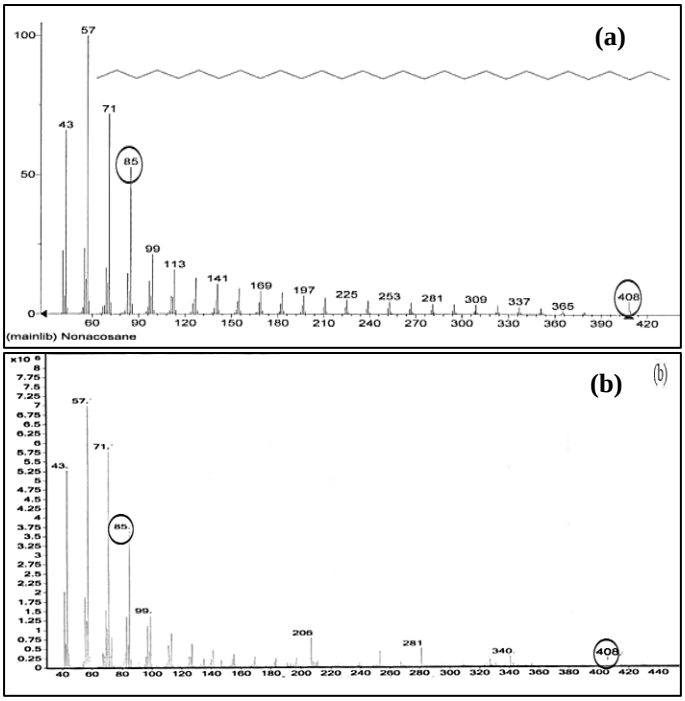


Figure 5. Mass spectrum for nonacosane (*n*-C29) from (a) the NIST library and (b) a sample. As suggested by Miuc et al. [14], m/z 85 and 408 were used as the major and confirmatory ions, respectively.

Climatological conditions

The data on daily ambient temperature and relative humidity, as well as the daily total rainfall at the decomposition site are tabulated in Table 3. It was observed that the daily ambient temperature during the span of observation period (day-0 until day-14) ranged between 28.2-30.1°C with the overall means during day-7 and day-14 being 29.5 ± 0.5 and 29.3 ± 0.7, respectively. Such a low variation in the ambient temperature recorded here was consistent with indication made by Trewin [25] that the differences in ambient temperature between the warmest and coldest months in the tropics only ranged between 1-4 °C. In addition, the daily relative humidity recorded here ranged between 75.7-95% (mean ± SD: 84.8 ± 4.2%) with the highest and lowest humidity recorded on day-2 and day-8, respectively. The highest relative humidity observed on day-2 (95.2%) may be attributable to the presence of heavy rain (12.6 mm) during that day. As for the daily total rainfall during the span of observation period, the amounts ranged between 0.0-12.6 mm.

Table 3. Daily ambient temperature, relative humidity and daily total rainfall recorded during the observation period (16^{th}-30^{th} November 2016).

Days	Temperature (°C)		Humidity (%)		Daily Total Rainfall (mm) and Its Duration (symbol)
	Mean ± SD	Ranges	Mean ± SD	Ranges	
0*	28.6	28.6	86.2	86.2	0.4 (□)
1	28.6±0.9	25.7-29.7	83.1±4.2	78.9-87.3	0.0 (☼)
2	29.3±0.5	27.9-30.0	90.7±4.5	86.2-95.2	12.6 (□)
3	29.2±0.6	28.4-30.0	85.3±4.3	81.0-89.6	0.8 (☘)
4	29.5±0.5	28.8-30.4	83.1±4.1	78.9-87.3	0.2 (☘)
5	29.8±0.7	28.9-30.9	86.4±4.3	82.1-90.7	2.4 (□)
6	30.0±0.3	29.5-30.5	83.3±4.2	79.1-87.5	0.4 (☘)
7	29.8±0.5	29.1-30.6	82.5±4.1	78.1-86.6	0.0 (☼)
Overall mean and (range) of day-7	**29.5±0.5**	**(28.6-30.0)**	**84.9±4.2**	**(78.9-95.2)**	**(0.0-2.6)**
8	30.1±0.5	29.2-31.0	82.3±4.1	75.7-86.4	0.0 (☼)
9	29.8±0.8	28.1-31.0	88.7±4.4	81.6-93.1	6.4 (□)
10	29.7±0.4	29.1-30.5	87.5±4.4	83.1-91.9	4.6 (□)
11	29.3±0.3	28.5-29.8	82.7±4.1	78.6-86.8	0.0 (☼)
12	29.4±0.3	28.9-30.1	82.9±4.1	76.3-87.0	0.0 (☼)
13	28.2±0.8	26.2-29.4	82.6±4.1	78.5-86.7	0.0 (☼)
14	28.4±0.7	27.4-29.3	84.6±4.2	77.8-88.8	0.8 (☘)
Overall mean and (range) of day-14	**29.3±0.7**	**(28.2-30.1)**	**84.5±4.2**	**(75.7-93.1)**	**(0.0-6.4)**
Overall mean and (range) of observation period	**29.3±0.6**	**28.2-30.1**	**84.8±4.2**	**75.7-95.2**	**(0.0-12.6)**

Day-0 refers to the day tenerals emerged from the pupae. While the ambient temperature and relative humidity were recorded at every two-hour interval *in-situ* using a data logger, the daily total rainfall was recorded using a rain gauge.
Legend: no rain (☼); rain during the day (□), rain during the night (☘).

It is paramount to mention that ambient temperature plays pivotal roles at influencing the composition of CHC [23, 26]. High temperature (35-40°C) has been associated with larger amount of long chain n-alkanes (*n*-C21 to *n*-C36) than that of at lower temperature [21-24, 27]. Similarly, insects that are exposed to low relative humidity (10-3%) have been reported to contain larger amount of long chain n-alkanes when compared with that of higher ones (95-100%). Since the climatological condition reported here was largely different from a field work reported by Zhu et al. [8], the need for conducting this present research in Malaysia for forensic application appears imperative.

Despite the possibility of ambient temperature, humidity and rainfall being factors affecting CHC compositions in necrophagous insects, laboratory experiments conducted by others [20, 26] also did not provide such information. Since in real forensic applications 'Calliphoridae collected from the field experience constant fluctuation in both temperature and humidity' [26], this present research that evaluated the CHC compositions in pupal cases of *C. megacephala* buried in soil under field conditions in a tropical country like Malaysia where rain is commonplace, deserves specific forensic consideration.

Changes of CHC profiles in the pupal cases over the stipulated weathering intervals

Analysis of the hexane extract of the pupal cases of *C. megacephala* (Table 4) revealed a mixture of mostly odd-numbered high molecular weight (≥ 18 carbons [28]) aliphatic (i.e. *n*-C27 and *n*-C29) and branched alkanes (i.e. tetradecane,2,6,20-trimethyl- and octadecane,3-ethyl-5-(2-ethylbutyl)-). Only four peaks that represented tetradecane (*n*-C17) can be classified as low molecular weight hydrocarbons. This was consistent with the findings of the previous researchers, indicating the great mass abundance of odd-numbered high molecular weight aliphatic hydrocarbons in the pupal cases of *C. megacephala* exposed to the field weathering process in Guangdong, China [8].

Table 4. Mean (± SD) relative abundance of CHCs in pupal cases of *C. megacephala* exposed to three natural weathering intervals using GCMS

Peaks	Retention Time	CHC	Classification	Chemical Name	Mean ± SD relative abundance		
					Day-0	Day-7	Day-14
1	3.082	$C_{17}H_{36}$	Branched alkane	Tetradecane, 2,6,10-	25.98±1.30	27.00±1.35	40.4±2.02
2	3.965	$C_{17}H_{36}$	Branched alkane	Tetradecane, 2,6,10-	3.08±0.15	22.91±1.14	0.76±0.04
3	4.084	$C_{17}H_{36}$	Branched alkane	Tetradecane, 2,6,10-	1.91±0.10	undetected	undetected
4	5.160	$C_{27}H_{56}$	N-alkane	Heptacosane	6.32±0.32	0.92±0.05	0.67±0.03
5	5.389	$C_{17}H_{36}$	Branched alkane	Tetradecane, 2,6,10-	4.84±0.24	4.13±0.21	undetected
6	5.711	$C_{27}H_{56}$	N-alkane	Heptacosane	2.15±0.11	1.97±0.10	undetected
7	6.743	$C_{27}H_{56}$	N-alkane	Heptacosane	0.90±0.45	undetected	undetected
8	6.919	$C_{27}H_{56}$	N-alkane	Heptacosane	0.94±0.05	undetected	undetected
9	7.261	$C_{27}H_{56}$	N-alkane	Heptacosane	4.93±0.25	3.94±0.20	3.19±0.16
10	7.673	$C_{27}H_{56}$	N-alkane	Heptacosane	3.13±0.16	2.58±0.13	2.37±0.12
11	9.057	$C_{27}H_{56}$	N-alkane	Heptacosane	2.62±0.13	1.66±0.08	0.63±0.03
12	9.389	$C_{27}H_{56}$	N-alkane	Heptacosane	3.40±0.17	2.63±0.13	2.37±0.12
13	9.475	$C_{26}H_{54}$	Branched alkane	Octadecane, 3-ethyl-	0.69±0.03	1.28±0.06	0.70±0.05
14	9.811	$C_{27}H_{56}$	N-alkane	Heptacosane	4.58±0.22	3.05±0.15	2.59±0.13
15*	10.956	$C_{27}H_{56}$	N-alkane	Heptacosane	6.23±0.31	1.57±0.08	1.09±0.05
16	11.812	$C_{26}H_{54}$	Branched alkane	Octadecane, 3-ethyl-	1.54±0.08	undetected	undetected
17*	13.316	$C_{29}H_{60}$	N-alkane	Nonacosane	12.28±0.61	7.19±0.36	1.49±0.07
Overall percentage composition for:				N-alkane	47.48%	25.51%	14.40%
				Branched alkane	38.04%	55.32%	41.86%

*The prevailing CHCs used for quantitation and correlation studies

The mean relative abundance for aliphatic alkanes (*n*-C27 and *n*-C29) reduced progressively over the three different intervals of exposure i.e. 47.48% (day-0), 25.51% (day-7) and 14.40% (day-14). In contrast, variations in the mean relative abundance of branched alkanes i.e. 38.04% (day-0), 55.32% (day-7) and 41.86% (day-14) were observed. Although the mean ± SD relative abundance for tetradecane (*n*-C17, peak 1) had increased progressively from day-0 (25.98 ± 1.30%) to day-14 (40.40 ± 2.02%), the same pattern of progressive increase was not observed for the remaining peaks for branched alkanes (peaks 2, 3, 5, 13 and 16).

Considering the high similarity in the chromatographic profiles obtained from the three different weathering intervals, representative GC-MS chromatogram for the pupal cases of *C. megacephala* at day-0 alone is presented here (Figure 3(a)). Unlike the significant changes in the chromatographic profile of the CHC in the pupal cases during the 30, 60 and 90 days weathering intervals reported by previous researchers [8], specific changes in the obtained chromatographic profiles during the three weathering intervals analyzed here were not found. The high similarity in the chromatographic profiles of CHCs observed in this present research may be attributable to the fact that the pupal cases were only subjected to relatively shorter durations of weathering interval (up to 14 days) than that of 90-day interval studied by Zhu et al.[8]. Weathering interval apart, the high similarity in the

chromatographic profiles may also be due to relatively small variations in the weathering conditions observed in this present research, an avenue for further study. Since Zhu et al. [8] did not provide the detailed daily ambient conditions by which the weathering process took place, suitable comparison with the findings reported here could not be made. Because *n*-C27 and *n*-C29 were consistently observed in all the samples, and their relative abundances progressively reduced over time, formulating credible mathematical algorithms for associating such concentrations with that of durations of weathering process may provide a useful means for estimating the age of the pupal cases recovered at the crime scene.

Concentrations of two prevailing hydrocarbons in the CHC compositions of *C. megacephala* pupal cases and its association with weathering intervals

In this present research, the prevailing CHCs (i.e. *n*-C27 and *n*-C29) in the pupal cases of *C. megacephala* buried in soil surrounding a decomposing beef meat substrate exposed to the three weathering intervals (day-0, day-7 and day-14) were quantitated and the data are tabulated in Table 5. Such a finding was consistent with the indication made by Zhu et al. [8] that the relative mass abundance of aliphatic CHCs i.e. *n*-C27, *n*-C29, *n*-C31 and *n*-C33 'was expected to be a better indicator for the weathering time' in field experiments. Although Zhu et al. [7] reported a great abundance of odd numbered CHCs (*n*-C29, *n*-C27, *n*-C31 and *n*- C25) in the pupal cases of *C. megacephala* within the laboratory setting, the abundance of even numbered CHCs was evidently increased with longer duration of weathering, observable from their tabulated data.

In a separate laboratory experiment, Ye et al. [19] reported that the *n*-C27 and *n*-C29 being the most abundant compounds found in the pupal cases of *C. megacephala* with *n*-C31 and *n*-C33 being undetected, similar to the observation reported in this present research. In this context, differences in climatic conditions [21-24], as well as soil microbiota at the decomposition site can be the determinant factors for variations observed in CHCs compositions. Therefore, in view of applying CHC analysis of *C. megacephala* pupal cases for estimating PMI in Malaysia, the relative mass abundance for the aliphatic CHCs of *n*-C27 and *n*-C29 may provide the better indicators for the weathering time exposure.

Table 5. Concentrations of heptacosane (*n*-C27) and nonacosane (*n*-C29) at three different weathering intervals

	Descriptive Statistic			**Comparison Among Weeks of Exposure**		
Two prevailing Hydrocarbons	**Day-0 (µg/mL)**	**Day-7 (µg/mL)**	**Day-14 (µg/mL)**	**Day-0 versus Day-7**	**Day-0 versus Day-14**	**Day-7 versus Day-14**
Heptacosane (*n*-C27)	23.96 ± 1.51	9.07 ± 0.11	6.29 ± 0.18	$P < 0.05$	$P < 0.05$	$P < 0.05$
Nonacosane (*n*-C29)	43.76 ± 0.83	17.96 ± 0.59	7.72 ± 0.23	$P < 0.05$	$P < 0.05$	$P < 0.05$

Concentrations (µg/mL) of heptacosane (*n*-C27) and nonacosane (*n*-C29) are presented as mean ± standard deviation. One-way ANOVA with Tukey-Kramer post hoc test was used for comparing the concentrations of heptacosane (*n*-C27) and nonacosane (*n*-C29) among the three durations of exposure.

In general, the concentration of *n*-C29 (43.76-7.72 µg/mL) was observably higher than that of *n*-C27 (23.96-6.29 µg/mL), with both the *n*-C27 and *n*-C29 concentrations showed decreasing pattern over the different weathering intervals. The highest concentrations of *n*-C27 and *n*-C29 were observed in pupal cases analysed on day-0, while the lowest being on day-14. Comparison using the One-way ANOVA with Tukey-Kramer post hoc test revealed significant decrease ($p < 0.05$) in the concentrations of both the *n*-C27 and *n*-C29 across the three different weathering intervals analysed in this present research.

The significant decrease ($p < 0.05$) in the concentrations of aliphatic CHCs *n*-C27 and *n*-C29 observed in this present research was consistent with observation made in a field work reported by Zhu et al. [8]. The decrease can be attributable to degradation by abiotic factors such as the prevailing climatic conditions [17, 29] (e.g. ambient temperature, relative humidity and rainfall), as well as soil physicochemical parameters (temperature, pH, water

content, oxygen and inorganic nutrients) [30]. Such conditions would cause evaporation, dissolution, dispersion, emulsification, adsorption on suspended materials, as well as photooxidation of the aliphatic CHCs (n-C27 and n-C29), hence reducing their concentrations [31].

Abiotic factor apart, degradation of the hydrocarbons by the soil microbiota such as *Pseudomonas aeruginosa* has also been reported in the literature [30]. Besides, many other microorganisms have been reported to exhibit the ability to use complex pathways for degrading n-alkanes into carbon dioxide and water as their growth substrates [32]. In this context, Berthe-Corti and Fetzner [33] indicated that spontaneous oxidation of n-alkane as the pivotal player in its degradation into fatty acids.

The associations between the concentrations of aliphatic CHC *n*-C27 and *n*-C29 in the pupal cases of *C. megacephala* with that of the weathering intervals are presented in Table 6. The Pearson correlation coefficients for *n*-C27 and *n*-C29 were -0.926 and -0.970, respectively; the regression values being 0.857 and 0.941, correspondingly. Considering the categorical definition of the strength of correlation coefficient prescribed by Munro [13], the concentrations observed for these two aliphatic CHCs can be construed as 'very high'. The 'very high' strength of correlation coefficient observed here statistically supports the usefulness of the association for decision making. Therefore, it is possible to suggest formulation of credible mathematical algorithm for relating the concentrations of *n*-C27 and *n*-C29 in the pupal cases of *C. megacephala* with that of the three weathering intervals evaluated here.

Table 6. Association between the concentrations of *n*-C27 and *n*-C29 in the pupal cases of *C. megacephala* with that of weathering intervals

Two Prevailing Hydrocarbons	**Pearson Correlation Coefficients (r) and Regressions (r2) between the Concentrations of n-C27 and n-C29 in the Pupal Cases of *C. megacephala* and Weathering Intervals**			
	r values	***p* values**	**r^2 values**	**Regression Equation**
Heptacosane (*n*-C27)	-0.926	P < 0.05	0.857	y=21.942-8.837x
Nonacosane (*n*-C29)	-0.970	P < 0.05	0.941	y=41.167-18.020x

Munro [13] prescribed the strength of association as follows: 0.00- 0.025 (little if any); 0.26-0.49 (low); 0.50-0.69 (moderate); 0.70-0.89 (high); 0.90-1.00 (very high).

Conclusion

The results of this present research further accentuate the proposition made by Zhu et al. that the decomposition of CHC 'is theoretically predictable in fresh puparia and changes regularly over time' [8]. Thus, analyzing CHC compositions in the pupal cases of *C. megacephala* for estimating the weathering time that they were exposed to the environment, for providing suitable information for estimating late PMI in Malaysia perspective, appears forensically feasible. This finding throws light at appreciating the currently-neglected pupal cases that are commonly found at crime scenes as an important piece of physical evidence.

Acknowledgement

We are thankful to Universiti Teknologi Malaysia for providing Research University Grants (Q.J130000.2526.16H92 and Q.J130000.2626.09J64) for conducting this research project.

References

1. Gennard, D. (2012). Forensic entomology: An introduction. Wiley Press.
2. Mahat, N. A., Yin, C. L., and Jayaprakash, P. T. (2014). Influence of paraquat on *Chrysomya megacephala* (Fabricius) (Diptera: Calliphoridae) infesting minced-beef substrates in Kelantan, Malaysia. *Journal of Forensic Sciences*, 59(2): 529-532.

3. Kavitha, R., Nazni, W. A., Tan, T. C., Lee, H. L., and Azirun, M. S. (2013). Review of forensically important entomological specimens collected from human cadavers in Malaysia (2005-2010). *Journal of Forensic and Legal Medicine*, 20(5): 480-482.
4. Mahat, N. A. and Jayaprakash, P. T. (2013). Forensic entomology in Malaysia: A review. *Malaysian Journal of Forensic Sciences*, 4(1): 1-6.
5. Lee, H. L. (1989). Recovery of forensically important entomological specimens from human cadavers in Malaysia-an update. *Malaysian Journal of Pathology*, 11: 33-36.
6. Mahat, N. A., Zafarina, Z., and Jayaprakash, P. T. (2009). Influence of rain and malathion on the oviposition and development of blowflies (Diptera: Calliphoridae) infesting rabbit carcasses in Kelantan, Malaysia. *Forensic Science International*, 192(1-3): 19-28.
7. Zhu, G. H., Xu, X. H., Yu, X. J., Zhang, Y., and Wang, J. F. (2007). Puparial case hydrocarbons of *Chrysomya megacephala* as an indicator of the postmortem interval. *Forensic Sci International*, 169(1): 1-5.
8. Zhu, G.-H., Yu, X.-J., Xie, L.-X., Luo, H., Wang, D., Lv, J.-Y. and Xu, X.-H. (2013). Time of death revealed by hydrocarbons of empty puparia of *Chrysomya megacephala* (Fabricius) (Diptera: Calliphoridae): A field experiment. *PLoS ONE*, 8(9): e73043.
9. Zhu, G. H., Ye, G. Y., Hu, C., Xu, X. H. and Li, K. (2006). Development changes of cuticular hydrocarbons in *Chrysomya rufifacies* larvae: potential for determining larval age. *Medical and Veterinary Entomology*, 20(4): 438-44.
10. Malaysian Meteorological Department (2015). Retrieved from the Malaysia Meteorological Department website: http://www.met.gov.my [Date access 20 June 2015].
11. Omar, B., Marwi, M., Oothuman, P., and Othman, H. (1994). Observations on the behaviour of immatures and adults of some Malaysian sarcosaprophagous flies. *Tropical Biomedicine*, 11: 149-149.
12. Chau, J. F., Bagtzoglou, A. C., and Willig, M. R. (2011). The effect of soil texture on richness and diversity of bacterial communities. *Environmental Forensics*, 12(4): 333-341.
13. Munro, B. H. (2005). Statistical methods for health care research. Lippincott Williams & Wilkins.
14. Miuc, A., Voncina, E. and Lecnik, U. (2015). Composition of organic compounds adsorbed on PM_{10} in the air above maribor. *Acta Chimica Slovenia*, 62(4): 834-848.
15. USFDA (2001). Guidance for industry: Bioanalytical method validation. U.S. Department of Health and Human Services Food and Drug Administration- Center for Drug Evaluation and Research (CDER)-Center for Veterinary Medicine (CVM).
16. Tiwari, G. and Tiwari, R. (2010). Bioanalytical method validation: An updated review. *Pharmaceutical Methods*, 1(1): 25-38.
17. Serrano, A., Gallego, M., González, J. L., and Tejada, M. (2008). Natural attenuation of diesel aliphatic hydrocarbons in contaminated agricultural soil. *Environmental Pollution*, 151(3): 494-502.
18. Sharma, R., Kumar Garg, R., and Gaur, J. R. (2015). Various methods for the estimation of the post mortem interval from Calliphoridae: A review. *Egyptian Journal of Forensic Sciences*, 5(1): 1-12.
19. Ye, G., Li, K., Zhu, J., Zhu, G., and Hu, C. (2007). Cuticular hydrocarbon composition in pupal exuviae for taxonomic differentiation of six necrophagous flies. J Med Entomol. 44(3): p. 450-456.
20. Frere, B., Suchaud, F., Bernier, G., Cottin, F., Vincent, B., Dourel, L., Lelong, A. and Arpino, P. (2014). GC-MS analysis of cuticular lipids in recent and older scavenger insect puparia. An approach to estimate the postmortem interval (PMI). *Anal Bioanalytical Chemistry*, 406(4): 1081-1088.
21. Wagner, D., Tissot, M. and Gordon, D. (2001). Task-related environment alters the cuticular hydrocarbon composition of harvester ants. *Journal Chemical Ecology*, 27(9): 1805-1819.
22. Savarit, F. and Ferveur, J. F. (2002). Temperature affects the ontogeny of sexually dimorphic cuticular hydrocarbons in Drosophila melanogaster. *Journal Expimental Biology*, 205(20): 3241-3249.
23. Ingleby, F. C. (2015). Insect cuticular hydrocarbons as dynamic traits in sexual communication. *Insects*, 6(3): 732-742.
24. Ingleby, F. C., Hosken, D. J., Flowers, K., Hawkes, M. F., Lane, S. M., Rapkin, J., House, C. M., Sharma, M. D. and and Hunt, J. (2014). Environmental heterogeneity, multivariate sexual selection and genetic constraints on cuticular hydrocarbons in Drosophila simulans. *Journal of Evolution Biology*, 27(4): 700-713.
25. Trewin (2014). The climates of the tropics and how they are changing. In Harding, S., McComiskie, R., Wolff, M., Trewin, D., and Hunter, S. (Eds.). State of the Tropics 2014 Report (pp. 39-51). Australia, James Cook University.

26. Pechal, J. L., Moore, H., Drijfhout, F. and Benbow, M. E. (2014). Hydrocarbon profiles throughout adult Calliphoridae aging: A promising tool for forensic entomology. *Forensic Sci International*, 245: 65-71.
27. Sarkar, N., Mukherjee, A. and Barik, A. (2013). Long-chain alkanes: Allelochemicals for host location by the insect pest, *Epilachna dodecastigma* (Coleoptera: Coccinellidae). *Applied Entomology and Zoology*, 48(2): 171-179.
28. Bettelheim, F. A., Brown, W. H., Campbell, M. K. and Farrell, S. O. (2009). Introduction to general, organic and biochemistry. Cengage Learning Publication.
29. Hejazi, R. F. and Husain, T. (2004). Landfarm performance under arid conditions. 2. Evaluation of parameters. *Environmental Science Technology*, 38(8): 2457-2469.
30. Sharma, A., Kumar, P. and Rehman, M. B. (2014). Biodegradation of diesel hydrocarbon in soil by bioaugmentation of *Pseudomonas aeruginosa*: A laboratory scale study. *International Journal of Environmental Bioremediation & Biodegradation*, 2(4): 202-212.
31. Wang, Z., Fingas, M., Lambert, P., Zeng, G., Yang, C. and Hollebone, B. (2004). Characterization and identification of the Detroit River mystery oil spill. *Journal of Chromatography A*, 1038(1-2): 201-214.
32. Dibble, J. T. and Bartha, R. (1979). Effect of environmental parameters on the biodegradation of oil sludge. *Applied and Environmental Microbiology*, 37(4): 729-739.
33. Berthe-Corti, L. and Fetzner, S. (2002). Bacterial metabolism of n-alkanes and ammonia under oxic, suboxic and anoxic conditions. *Acta Biotechnologica*, 22(3-4): 299-336.

Malaysian Journal of Analytical Sciences Vol 23 No 4 2019

Articles 10 - 21 are selected papers from the "Joint Seminar of UKM-Gifu University, 27 - 31 March 2018 at Gifu University, Japan; organized by Gifu University, Japan.

Guest Editor: Siti Fairus Mohd Yusoff and Nurul Izzaty Hassan

Page

1. FACILE ORGANIC-INORGANIC HYBRID SORBENTS FOR EXTRACTION OF POLLUTANTS FROM AQUEOUS SAMPLES – A REVIEW 561
(Pengerap Hibrid Organik-Tak Organik Mudah bagi Pengekstrakan Pencemar dari Sampel Akueus – Sebuah Ulasan)
Mohd Marsin Sanagi, Nyuk-Ting Ng, Faridah Mohd Marsin, Mohamad Raizul Zinalibdin, Zetty Azalea Sutirman, Aemi Syazwani Abdul Keyon, Wan Aini Wan Ibrahim

2. AN OPTICAL SENSOR BASED ON GRAPHENE QUANTUM DOTS FOR HYDROGEN PEROXIDE DETECTION 572
(Sensor Optik berasaskan Titik Kuantum Grafin untuk Pengesanan Hidrogen Peroksida)
Amiruddin Ashil Mastar, Jaafar Abdullah, Nor Azah Yusof, Yap Wing Fen

3. ROLE OF L-GLUTAMINE IN THE IN-VITRO GROWTH OF HCT-8 AND HT-29 CELL LINES 580
(Peranan L-Glutamin dalam Pertumbuhan Sel HCT-8 dan HT-29 In-Vitro)
Afzan Mat Yusof and Mohammed Abdullah Jainul

4. COMPARISON OF EXTRACTION TECHNIQUES FOR THREE *Calophyllum* SPECIES AND THEIR ANTIOXIDANT ACTIVITY 586
(Perbandingan Teknik Pengekstrakan untuk Tiga Spesies *Calophyllum* dan Aktiviti Antioksidan)
Siti Nurhafizah Ramli, Nurul Iman Aminudin, Farediah Ahmad, Deny Susanti

5. A GREEN COLORIMETRIC METHOD USING GUAVA LEAVES EXTRACT FOR QUALITY CONTROL OF IRON CONTENT IN PHARMACEUTICAL FORMULATIONS 595
(Kaedah Kalorimetrik Hijau Mengunakan Ekstrak Daun Jambu Bagi Kawalan Kualiti Kandungan Besi di dalam Formulasi Farmaseutikal)
Watsaka Siriangkhawut, Kraingkrai Ponhong, Kate Grudpan

6. REMOVAL OF PARAQUAT HERBICIDE BY CETYLTRIMETHYL AMMONIUM BROMIDE MODIFIED PINEAPPLE LEAVES 604
(Penyingkiran Herbisid Parakuat oleh Daun Nanas yang Diubahsuai dengan Setiltrimetil Ammonium Bromida)
Nik Ahmad Nizam Nik Malek, Muhd Hafiz Jusoh, Auni Afiqah Kamaru

7. INTERACTION STUDIES OF PUTATIVE CHEMICAL LIGANDS IN BINDING SITES OF THERMOSTABLE LIPASE FROM *Geobacillus zalihae* STRAIN T1 613
(Kajian Interaksi Ligan Kimia pada Tapak Pengikatan Lipase Termostabil daripada *Geobacillus zalihae* Stren T1)
Mohd Basyaruddin Abdul Rahman and Muhammad Alif Mohammad Latif

8. ADSORPTION OF MALACHITE GREEN ONTO MODIFIED CHITOSAN–SULFURIC ACID BEADS: A PRELIMINARY STUDY 625
(Penjerapan Malakit Hijau ke atas Manik Kitosan-Asid Sulfurik Terubahsuai: Satu Kajian Awal)
Suhaila Mohd Yusoff, Wan Saime Wan Ngah, Faizatul Shimal Mehamod, Faiz Bukhari Mohd Suah

9. ANTIBACTERIAL AND ANTIOXIDANT ACTIVITIES OF EXTRACTS FROM *Calophyllum ferrugineum* AND *Calophyllum incrassatum* 637
(Aktiviti Antibakteria dan Antioksidan Terhadap Ekstrak daripada *Calophyllum ferrugineum* dan *Calophyllum incrassatum*)
Nurul Iman Aminudin, Farediah Ahmad, Muhammad Taher

10. HYDROSILYLATION OF ALDEHYDES CATALYZED BY DIETHYL 2-PYRIDYLPHOSPHONATE 648
(Hidrosililasi Aldehida Bermangkin Dietil 2-Piridilfosfonat)
Natsuhisa Oka, Kousuke Ito, Kaori Ando

11. THE INTERACTION BETWEEN FIREFLY LUCIFERIN WITH G-QUADRUPLEX DNA AND CT-DNA 654
(Interaksi antara Lusiferin Kunang-Kunang bersama DNA G-Kuadrupleks dan CT-DNA)
Nurul Huda Abd Karim, Roshatiara Shamsuddin, Aida Mastura Mohd Yussof, Nur Amirah Harunar Rashid

12. RARE EARTH METAL DOPED CaO AS CATALYST FOR THE TRANSESTERIFICATION REACTION OF COOKING OIL 660
(Logam Nadir Bumi Dop CaO sebagai Mangkin untuk Tindak Balas Transesterifikasi Minyak Masak)
Wan Nur Aini Wan Mokhtar, Mohd Rushashraaf Ramli, Muhammad 'Azim Jamaluddin, Suria Ramli

13. UTILIZATION OF DEEP EUTECTIC SOLVENT (DES) AS POROGEN IN THE FABRICATION OF POLYMERIC MONOLITHIC CAPILLARY COLUMN 667
(Penggunaan Pelarut Eutektik Dalam (DES) Sebagai Porogen Dalam Fabrikasi Turus Kapilari Monolitik Polimerik)
Nabilah Suhaili, Lee Wah Lim, Takeuchi Toyohide, Rizafizah Othaman

14. ISOLATION OF NEW ROTUNDONE FROM THE ROOTS OF *Croton hirtus* (EUPHORBIACEAE) 677
(Pemencilan Komponen Rotundona Terbaharu daripada Akar *Croton hirtus* (Euphorbiaceae))
Andi Rifki Rosandy , Anis Asmi Azman, Rozida Khalid, Rizafizah Othaman, Azwan Mat Lazim, Iqbal M. Choudary, Yana Maulana Syah, Jalifah Latip, Ikram M. Said, Muntaz Abu Bakar

15. PRELIMINARY INVESTIGATION OF LOW CURRENT FLASH SINTERING IN ZIRCONIA NANOPARTICLE COMPACT 682
(Kajian Awal Persinteran Kilat Arus Rendah dalam Nanopartikal Zirkonia Kompak)
Michiyuki Yoshida, Mitsuki Hada, Yutaka Shinoda, Osamu Sakurada, Fumihiro Wakai

16. SYNTHESIS AND BINDING PROPERTIES OF TERT-BUTYL AMIDE MACROCYCLES FOR PSEUDOROTAXANES FORMATION 690
(Sintesis dan Sifat Pengikatan Makrosiklik Tetrabutil-Amida bagi Penghasilan Pseudorotazen)
Nurul Izzaty Hassan and Douglas Philp

17. EFFECT OF PLASTICIZERS AND LITHIUM PERCHLORATE ON POLY(L-LACTIC ACID)-POLY(PROPYLENE GLYCOL) SOLID POLYMER ELECTROLYTE 703
(Kesan Pemplastik dan Litium Perklorat terhadap Elektrolit Polimer Pepejal Poli(L-Asid Laktik)-Poli(Propilena Glikol))
Siti Munirah Manap, Azizan Ahmad, Mohd Sani Sarjadi, Farah Hannan Anuar

18. QUANTITATIVE ANALYSIS OF PHENOLICS CONTENT IN TWO ROSELLE VARIETIES (*Hibiscus sabdariffa*) BY HIGH PERFORMANCE LIQUID CHROMATOGRAPHY 715
(Analisis Kuantitatif bagi Sebatian Fenolik dalam Dua Varieti Roselle (*Hibiscus sabdariffa*) menggunakan Kromatografi Cecair Berprestasi Tinggi)
Siti Aishah Mohd Ali, Satirah Zainalabidin, Jalifah Latip

19. SOLUTION CASTING EPOXIDIZED NATURAL RUBBER/POLY(VINYLIDINE FLUORIDE) MEMBRANE FOR PALM OIL EFFLUENT TREATMENT 725
(Pengacuanan Larutan Membran Getah Asli Terepoksida/Poli(Vinilidina Fluorida) untuk Rawatan Efluen Kilang Minyak Sawit)
Norliyana Mod, Farah Hannan Anuar, Rizafizah Othaman

20. ANALYSIS OF HEAVY METAL CONCENTRATIONS IN BALLAST WATER AND SEAWATER AT TANJUNG PELEPAS PORT 736
(Analisis Kandungan Kepekatan Logam Berat dalam Air Balast dan Air Laut di Pelabuhan Tanjung Pelepas)
Jacqueline Chong Kar Xin, Sharina Abu Hanifah, Nor Aishah Salleh, Normazida Rozi, Norfaizan Padli

21. PSYCHROTOLERANT ACTINOBACTERIA *Barrientosiimonas humi* 39T AS A SOURCE OF DIKETOPIPERAZINE 748
(Aktinobakteria Psikrotoleran *Barrientosiimonas humi* 39T Sebagai Sumber Sebatian Diketopiperazin)
Andi Rifki Rosandy, Yeoh Chiann Ying, Cheah Yoke Kqueen, Muntaz Abu Bakar, Azira Muhamad, Rozida Mohd Khalid

Malaysian Journal of Analytical Sciences, Vol 23 No 4 (2019): 561 - 571
DOI: https://doi.org/10.17576/mjas-2019-2304-01

MALAYSIAN JOURNAL OF ANALYTICAL SCIENCES
Published by The Malaysian Analytical Sciences Society
ISSN 1394 - 2506

FACILE ORGANIC-INORGANIC HYBRID SORBENTS FOR EXTRACTION OF POLLUTANTS FROM AQUEOUS SAMPLES – A REVIEW

(Pengerap Hibrid Organik-Tak Organik Mudah bagi Pengekstrakan Pencemar dari Sampel Akueus - Sebuah Ulasan)

Mohd Marsin Sanagi[1,2*], Nyuk-Ting Ng[1], Faridah Mohd Marsin[1], Mohamad Raizul Zinalibdin[1], Zetty Azalea Sutirman[1], Aemi Syazwani Abdul Keyon[1], Wan Aini Wan Ibrahim[1,2]

[1]*Department of Chemistry, Faculty of Science*
[2]*Centre for Sustainable Nanomaterials, Ibnu Sina Institute for Scientific and Industrial Research*
Universiti Teknologi Malaysia, 81310 Skudai, Johor, Malaysia

**Corresponding author: marsin@kimia.fs.utm.my*

Received: 19 August 2018; Accepted: 22 June 2019

Abstract

Rapid and efficiency extraction of pollutants from aqueous samples has been an important issue in analytical sciences. Solid phase extraction using sorbents is a well-known separation method and recognized as an efficient and economical method for removal of pollutants from water. In the past few years, there has been growing interest on extractions using organic-inorganic hybrid materials. Formed by incorporating inorganic species into organic matrix, these materials offer some advantages such as high selectivity, permeability, and mechanical and chemical stabilities. This present article discusses recent significant advances in analytical solid-phase extraction employing organic-inorganic composite and nanocomposite sorbents for the extraction of organic and inorganic pollutants from aqueous samples. Classifications and synthesis methods of organic-inorganic hybrid sorbents are described. The physicochemical characteristics, extraction properties and analytical performances of selected sorbents are discussed, including morphology and surface characteristics, types of functional groups, interaction mechanism, selectivity and sensitivity, accuracy, and regeneration abilities. Organic-inorganic hybrid sorbents in combination with extraction techniques are highly promising as an emerging research field for sample preparation of complex samples such as food, biomedical and environmental matrices with analytes at trace levels.

Keywords: organic-inorganic hybrid sorbents, extraction methods, environmental pollutants, aqueous samples

Abstrak

Pengekstrakan pencemar dari sampel akueus dengan cepat dan cekap merupakan isu penting dalam sains analisis. Pengekstrakan fasa pepejal menggunakan pengerap adalah kaedah pemisahan yang diketahui ramai dan dikenali sebagai satu kaedah yang cekap dan ekonomi bagi penyingkiran pencemar dari air. Dalam beberapa tahun kebelakangan, minat terhadap pengekstrakan menggunakan bahan hibrid organik-tak organik telah berkembang. Terbentuk melalui gabungan spesis tak organik ke dalam matrik organik, bahan ini menawarkan beberapa kelebihan misalnya mempunyai kepilihan tinggi, kebolehtelapan, serta kestabilan mekanikal dan kimia. Artikel ulasan ini membincangkan kemajuan penting dalam analisis pengekstrakan fasa pepejal menggunakan pengerap komposit dan nanokomposit organik-tak organik bagi pengekstrakan pencemar organik dan tak organik dari sampel akueus. Klasifikasi dan kaedah sintesis pengerap hibrid organik-tak organik diterangkan. Pencirian fizikokimia, sifat pengekstrakan dan prestasi analisis pengerap terpilih dibincangkan, termasuk pencirian morfologi dan permukaan, jenis kumpulan berfungsi, mekanisma interaksi, pemilihan dan kepekaan, ketepatan dan kebolehan guna semula. Pengerap hibrid organik-tak organik digabung dengan teknik pengekstrakan merupakan bidang penyelidikan yang sangat menjanjikan bagi penyediaan sampel kompleks misalnya matrik makanan, bioperubatan dan alam sekitar dengan analit pada tahap surih.

Kata kunci: pengerap hibrid organik-tak organik, kaedah pengekstrakan, pencemar alam sekitar, sampel akueus

Introduction

Water pollution may be defined as the presence of excessive amounts of hazard (pollutants) in water, in such a way that it is no longer suitable for drinking, bathing, cooking or other uses. The pollution is generally induced by humans. Rapid development of industrialization, agricultural activities and exploitation of natural resources together with the growth of human population over the past few decades have inevitably resulted in raising water pollution. Substances such as leached pesticides, herbicides, heavy metals and other types of environmental pollutants are known to be toxic or carcinogenic. They are often discharged as effluent or wastewaters into water bodies; thus detrimental to human health and ecosystem stability. Halder and Islam [1] and Khatun [2] reported that skin diseases, diarrhea, cholera, and respiratory illnesses (common cold, asthma) are the most common health problems caused by water contamination. Furthermore, about 13 million people die in the world annually, mainly attributed to water, indoor and outdoor air pollutions [3].

In order to ensure the wellbeing of the society, each substance presence in drinking water must below their maximum contaminant limit as set by US Environmental Protection Agency. For instance, the allowable concentration for polychlorinated biphenyls, simazine, atrazine, and benzene are 0.5, 4.0, 3.0, and 5.0 μg/L, respectively whereas, heavy metal such as lead (Pb), copper (Cu), mercury (Hg), cadmium (Cd), selenium (Se), chromium (Cr), and arsenic (As) are 15, 1300, 2, 5, 50, 100 and 100 μg/L, respectively [4].

Several treatment methods have been proposed for removal of such pollutants from industrial and natural water such as ion-exchange, evaporation, chemical precipitation, adsorption, reverse osmosis and membrane separation. Among them, adsorption is a promising method in most applications, considering the favorable features including cost, energy consumption, convenience and reusability [5].

The development of organic–inorganic hybrid materials is trendy especially in the last decade. By definition, organic-inorganic hybrid material refers to composite materials formed by the combination of inorganic materials and organic polymers into a single-phase system, which has molecular interaction in between the molecules (Figure 1) [6]. In addition, they demonstrate better properties compared to their individual counterparts while eliminating or reducing their particular limitations. These new materials, considered as innovative advanced materials, open a land of promising applications in many areas especially in environmental fields. Organic compounds have the advantages of functional variation, synthetic versatility and reactivity whereas inorganic compounds have generally high thermal stability and robustness, resulting in high selectivity toward a target analyte and increased adsorption capacity [4, 7].

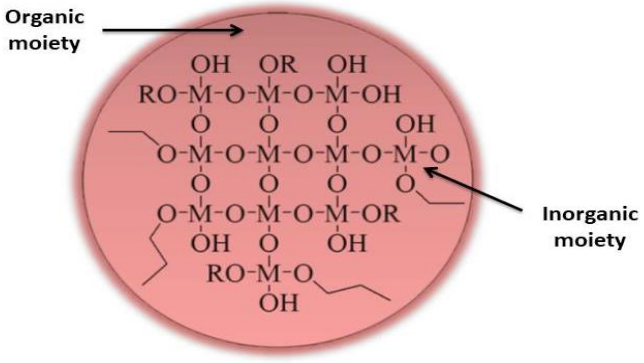


Figure 1. Schematic concept of organic-inorganic hybrid material

This review outlines the information on the use of organic-inorganic hybrid materials for adsorption of different types of pollutants from aqueous solutions. Recent findings are critically reviewed in order to reveal the efficiency of organic-inorganic hybrid materials as adsorbents for water treatment applications. This review consists of three

aspects. Firstly, a highlight on classification and synthesis routes of organic-inorganic hybrid sorbents is described. Secondly, the physiochemical properties such as chemical stability, morphology surface characteristic and interaction mechanism of the synthesized organic-inorganic hybrid materials are described. Finally, the review discusses the application of the hybrid materials as sorbents for the analysis and removal of environmental pollutants from aqueous matrices. Here, the adsorption characteristics and analytical performances of the sorbents are listed, compared and described.

Classification of organic-inorganic hybrid materials: Classification based on type of interaction

Organic-inorganic hybrid materials are not simply physical mixtures. Indeed, they are either a homogenous mixture consisting of monomers and miscible organic/inorganic components, or heterogeneous mixture, where at least one of the components has a characteristic length in the order of nanometer (a few Å to several tens of nanometers) [8, 9]. The properties of these materials are not only the sum of the individual contributions from both components, but the strong synergy created by a hybrid interface can be predominant. Hence, organic-inorganic hybrid materials are grossly classified on the basis of the nature of the interface; class I and class II (Figure 2). In class I, organic and inorganic compounds are interacted by weak bonds such as hydrogen, van der Waals, π-π interaction or ionic bonds. Class II is associated with the hybrid materials in which the components are linked together through strong chemical bonds (covalent or ionic-covalent bonds). Nevertheless, many hybrid materials of class II can also have the same kind of weak bonds that define the class I hybrids.

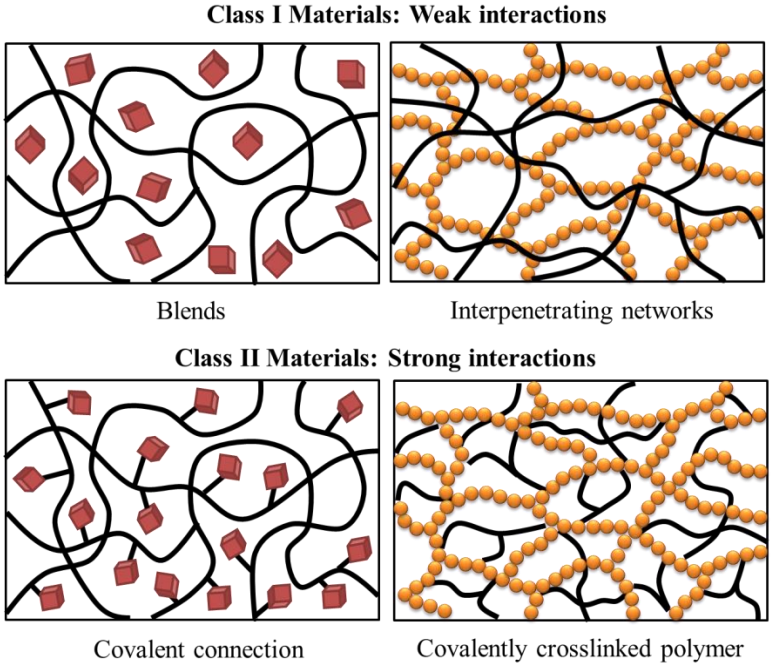


Figure 2. Types of inorganic-organic hybrid materials

General preparation of hybrid materials

Irrespective of types of interface between organic and inorganic components, there are a number of chemical pathways that can be performed to synthesize a given organic-inorganic hybrid material using different experimental conditions or molecular precursors. The fundamental synthetic strategies for all types of hybrids are illustrated in Figure 3.

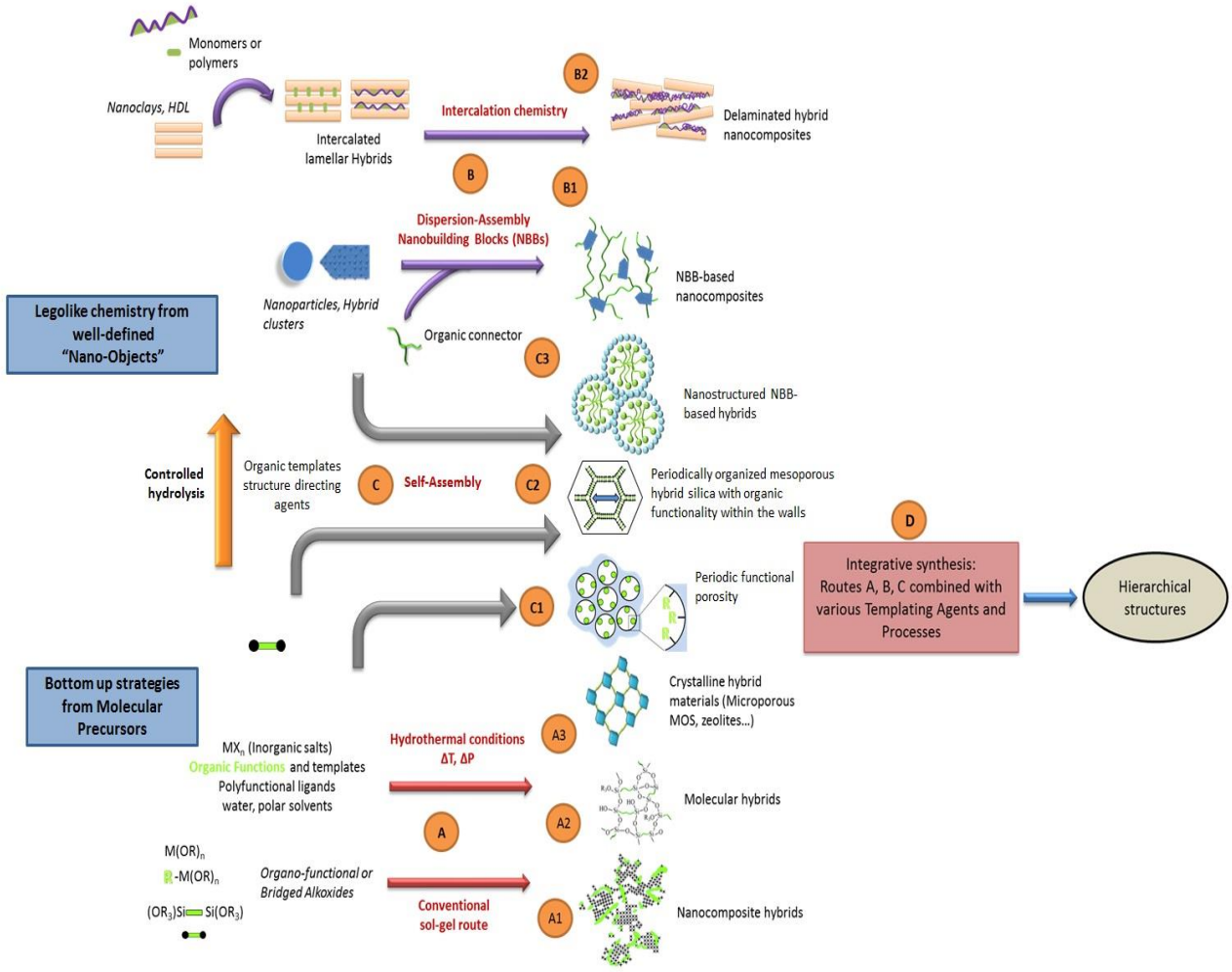


Figure 3. Main chemical routes for the synthesis of organic–inorganic hybrids

Path A corresponds to the soft chemistry-based approaches including conventional sol-gel method (by using specific bridge and polyfunctional precursors) and hydrothermal synthesis. In conventional sol-gel pathways (route A1) amorphous hybrid networks are obtained through hydrolysis and condensation reactions from alkoxyorganosilanes or alkoxyorganostannanes ($R'Si(OR)_3$, $R'-Sn(OR)_3$ where R' is an organic functionality) of alkoxides or metal halides ($M'(OR)_n$,MX_n with M = Sn, Ce, Zr, Nb, Al etc.) and mixtures thereof. It can take into account that the solvent used may contain diverse organic or biological components (chromophores, polyfunctional macromonomers, biopolymers, viruses, enzymes, etc.) that can interact or trapped within the inorganic component via H-bonding, π-π and van der Waals interactions. The procedures are simple, inexpensive and able to produce amorphous nanocomposite hybrid materials which can be easily shaped into films or bulks. However, these materials are also polydisperse in size and locally heterogeneous in chemical composition, making it difficult to understand their structure-properties relationships [9, 10].

In route A2, sol−gel method has been carried out using specific bridged and poly functionalized precursors such as silsesquioxanes $X_3Si-R'-SiX_3$ (R′ is an organic spacer, X = Cl, Br, −OR) to prepare homogeneous organic-inorganic hybrid materials with better degree of local organization. In particular, the organic spacer is complemented by using

two terminal functional groups of urea. The combination of aromatic bridges framed or alkyl groups and urea groups allows better self-assembly through the capability of the organic components to establish both strong hydrogen bond networks and efficient packing via π-π or hydrophobic interactions.

Another synthetic methodology for hybrid materials in path A is hydrothermal synthesis (route A3) performed in polar solvents (water, formamide, etc.) in the presence of organic templates. This method has been used to develop numerous microporous hybrid materials such as zeolites with wide range of applications in the domain of adsorbents or catalysts. Also, metal organic frameworks (MOFs) with a high and tunable porosity and a crystalline architecture have been prepared via this method.

Path B illustrates strategies based on the assembling (route B1) or the dispersion (route B2) of well-defined nanobuilding blocks (NBB) which provide nanostructured hybrid networks with better structural definition [11]. These NBB are often inorganic moieties such as clusters or nanoparticles (metal oxides, metals and alloys, chalcogenides), nanoparticle composite type core/shell, or nano-sheets of lamellar compounds (clays, double hydroxides, phosphates, oxides and lamellar chalcogenides) that able to intercalate organic compounds. The NBB are capped with polymerizable ligands or connected by organic spacers of telechelic molecules, polymers, or functional dendrimers. This approach of NBB presents two major advantages; 1) Prefabricated NBB often show a lower reactivity compared to that of molecular precursors; 2) The nanobuilding components that are nanometric, monodispersed, and have well-defined structures and shapes facilitate characterization and control over the quality of the final material.

Depending on the nature, structure and functionality of the nanobuilding blocks, various organic-inorganic hybrid materials with tunable electrical and optical properties can be prepared, associated with different assembling methods. Furthermore, the step by-step preparation of these materials allows for a better control over their structure on the semi-local scale.

Path C represents self-assembling procedures [9, 11]. Self-assembling has gained interests as it involves the organization or the texturation of growing inorganic or hybrid networks, templated growth by organic surfactants (route C1). The success of this approach is related to the ability to control and tune hybrid interfaces. It also allows the construction of a continuous ensemble of nanocomposites from ordered dispersions of inorganic bricks in a hybrid matrix to highly controlled nanosegregation of organic polymers within inorganic matrices. One of the striking examples is the synthesis of mesostructured hybrid networks. Recently, the template growth of mesoporous hybrids has been proposed by using bridged silsesquioxanes as precursors in presence of surfactants (route C2). The approach yields a new class of periodically organized mesoporous hybrid silicas with organic functionality within the walls. These nanoporous materials show a high degree of order and their mesoporosity is added advantage for further organic functionalization via grafting reactions.

Meanwhile, route C3 explores the combination of self-assembly and NBB methods. The procedures shows the combination of NBB approach with the use of organic template that self-assemble allow one to control the assembling step. Moreover, they yield a large variety of interfaces between the organic and the inorganic components such as covalent bondings, complexations, electrostatic interactions, and many more. These NBB with tunable functionalities can, through molecular recognition processes, permit the development of a new field in chemistry.

The final pathway in tailoring hybrid materials (path D) is an integrative synthesis [9, 11]. The approaches mentioned above mainly offer the controlled design and assembling of hybrid materials in the 1 to 500 Å range. However, the development of micro-molding methods, in which the use of controlled phase separation phenomena, emulsion droplets, latex beads, bacterial threads, colloidal minerals or organo-gelifiers lead to controlling the shapes of complex objects in the micron scale. This path describes the combination of these methods and those above described along paths A, B, and C to produce hierarchically organized materials in terms of structure and functions.

Application of organic-inorganic hybrid sorbents for environmental pollutants in aqueous matrices

Environmental pollution issues have existed for many years. It was caused by the discharge of hazardous species into surrounding environment in excess of permitted limits. This phenomenon is of concern as the discharge of these materials is high in toxicity and a serious threat to public health. Examples of environmental pollutants include heavy metals, dyes, triazine herbicides, polycyclic aromatic hydrocarbons (PAHs), polychlorinated biphenyls (PCBs), organophosphorus pesticides (OPPs), tricyclic antidepressants (TCA), organochlorine pesticides (OCPs), endocrine disrupting chemicals, phenolic compounds, etc. Analysis of these leached contaminants into environmental water is challenging since they usually exist at trace levels (mg/L – μg/L) thus demanding more elaborate analytical procedures [4]. Tedious sample preparation is usually necessary for the preconcentration of targeted species to meet the sensitivity of a particular analytical instrument for getting reliable experimental data.

Organic-inorganic hybrid sorbents employed in solid phase extraction or water treatment are highly advantageous as the sorbent chemistry tailored to a particular analyte can be controlled well by manipulating both the organic and inorganic units of the resulting hybrid materials [7]. This is important for the promotion of good homogeneity and alteration of chemical or physical properties of an organic-inorganic hybrid sorbent to share the common properties (polarity, porosity, hydrophobicity, etc.) and suit for the adsorption of certain groups of analytes. With this in mind, investigation of such hybrid materials has gained considerable attention from analytical chemists for the fabrication of sorbents employed in different types of solid phase extraction methods such as micro-solid phase extraction, dispersive-solid phase extraction, magnetic-solid phase extraction, stir bar sorption extraction, rotating disk sorption extraction, etc. The developed organic-inorganic hybrid sorbents have proved to be a new powerful tool to improve sensitivity, accuracy, selectivity, recoveries, precision and linearity of an analytical procedure. For this reason, a variety of organic-inorganic hybrid sorbents have been developed and applied in the analysis of a wide range of environmental pollutants include pharmaceutical compounds, agricultural products, heavy metals and many other organic compounds present in environmental water samples (Table 1).

Table 1. Recent organic-inorganic hybrids sorbents for the extraction of several common environmental pollutants

Sorbent	**Analyte**	**Real Sample**	**LOD**	**q_{max}**	**Method of Extraction/ Water Treatment**	**Reference**
Palmitic acid coated magnetic nanoparticles	38 pesticides	Tap water, bottled drinking water and pool water	20 - 30 ng/L	-	M-SPE	[12]
Poly(methacrylic acid)/SiO_2/Al_2O_3	imazethapyr herbicide	-	-	4.5 mg/g	Batch adsorption	[13]
Graphene-based tetraethoxysilane-methyltrimethoxysilane sol-gel hybrid magnetic nanocomposite	polar and non-polar OPPs	Tap water, river water, lake water and seawater	1.40 - 23.7 pg/mL	37.18 - 76.30 mg/g	M-SPE	[14]
Chrysin-functionalized silica-core shell magnetic nanoparticles	Copper(II)	River water, lake water and tap water	0.3 ng/mL	114.25 mg/g	M-SPE	[15]

Table 1 (cont'd). Recent organic-inorganic hybrids sorbents for the extraction of several common environmental pollutants

Sorbent	**Analyte**	**Real Sample**	**LOD**	**q_{max}**	**Method of Extraction/ Water Treatment**	**Reference**
Ion-imprinted iodole-functionalized silica-supported sorbent	Antimony(III)	Tap water, river water and lake water	40 ng/L	39.6 mg/g	SPE	[16]
Mercapto-functionalized hybrid sorbent	Antimony(III)	Tap water, river water, mineral wastewater and seawater	2.5 ng/L	-	SPE	[17]
Hybrid organic-inorganic nafion intercalated layered double hydroxide	Mercury(II)	Drinking water	0.004 µg/L	302.14 mg/g	SPE	[18]
Surface Cr(VI)-imprinted magnetic nanoparticles	Chromium(VI)	Tap water, river water and lake water	0.29 µg/L	2.50 mg/g	M-SPE	[19]
Piperazine functionalized magnetic sporopollenin	Lead(II) and arsenic(III)	-	-	13.36 mg/g (lead ion) and 69.86 mg/g (arsenic ion)	Batch adsorption	[20]
Magnetite–Polypyrrole Composite	Naproxen, diclofenac sodium, and mefenamic acid	Tap water, river water and wastewater	0.9 - 3.5 µg/L	-	M-SPE	[21]
Magnetic sporopollenin-cyanopropyltriethoxys-ilane	Ketoprofen, ibuprofen, diclofenac and mefenamic acid	Tap water, lake water, river water and wastewater	0.21 - 0.51 µg/L	-	M-SPE	[22]
Ionic liquids intercalated in montmorillonite	Polychlorinated biphenyls	Wastewater	3 - 43 ng/L	-	RDSE	[23]

SPE: Solid phase extraction; M-SPE: Magnetic solid phase extraction; RDSE: Rotating disk sorption extraction

Environmental monitoring is performed to monitor the quality of surrounding water matrices and fully understand its level of water contamination by harmful pesticide and herbicide compounds. Many organic-inorganic hybrid

sorbents are made up of magnetite and organic units. Other than providing simple sorbent separation by applying magnetic force, functionalization of organic part on magnetite also provides magnetite protection for the prevention of leaching of magnetite. Tavakoli et al. [12] had successfully synthesized palmitic acid coated magnetic nanoparticles for the extraction, preconcentration and analysis of 38 pesticides with gas chromatographic detection. The limits of detection (LOD) were found to be as low as 20-30 ng/L and excellent preconcentration factor (PF) was as high as 1000. Good linearity with coefficient of determination, $R^2 > 0.98$, and satisfactory relative recoveries (%RR) in the range of 63-110% with low relative standard deviation (%RSD) in between 3.67-6.57% were achieved in the investigation. The developed sorbent was applied in the analysis of real samples, namely tap water, bottled drinking water and pool water. For real sample analysis, no pesticide residues were detected in tap water and bottled drinking water as the quantity of targeted pesticides compounds could be lower than the LOD of the developed method. On the other hand, diazinon and permethrin I, II were found in pool water at concentrations of 81 ng/L and 159 ng/L, respectively. In Iran, the maximum residual limit (MRL) of entire pesticides is 100 ng/kg except for methoxychlor at 20 000 ng/kg and permethrin I, II total value at 300 000 ng/L.

Outstanding analytical performance of the developed fatty acid coated magnetite sorbent towards selected pesticides was achieved, this could be due to the changes in the overall hydrophobicity of the developed sorbents resulted from the interaction of highly lypophilic surfactant surface and highly hydrophilic magnetite surface during the synthesis steps. The method was compared to classical solid phase extraction (SPE) employed C_{18} cartridge. Indeed, in some cases, SPE could be more efficient than the developed method in terms of analytical performances. However, the developed method showed advantages as being faster, cheaper and easier to perform than the classical SPE method and only little amount of organic solvents was used. Accordingly, the presence of diazinon and permethrin I, II in pool water is worrisome. There was possibility that the water contamination was due to the pest-repellent or personal care product wore by the pool users or leaking of nearby farmland effluent water into the pool. The issue should be paid significant attention as some pesticides are very toxic to aquatic life and nearby beneficial insects to avoid the imbalance of affected ecosystem. Human beings could be poisoned by absorbing toxic pesticide compounds through the skin and respiration.

Another organic-inorganic composite was synthesized *via* template magnetite on sorbent or vice versa. Omastová and Mičušík [24] reported combination of polypyrrole (PPy) and magnetite could increase the processability and mechanical properties of resulted polymer. The anions from oxides of metal bounded to PPy structure and acted as a co-dopant, similar to anion of the oxidizing agent. The presence of metal oxides in PPy minimized the surface energy of the PPy particles, thus increasing the conductivity and thermo-oxidative stability than samples without additive. In a recent study by Faridah and co-workers [21] showed that the magnetic separation and dispersibility of magnetite combined with the electrostatic interaction by PPy have been applied for successful extraction of selected non-steroidal anti-inflammatory drugs (NSAIDs) with high sensitivity and precision (LOD of 0.9-3.5 μg/L; %RSD of <7.16%), good accuracy (%RR of 97.87-100.42%) and good linearity (R^2 of 0.88–0.94). The developed magnetized PPy sorbent was successfully applied to the determination of NSAIDs naproxen, diclofenac sodium and mefenamic acid in tap water, river water, and wastewater samples. NSAIDs are among the highly produced and globally well-known pharmaceutical product due to their good analgesic, antipyretic and other good properties to reduce pain and anti-inflammation. Although NSAIDs are not classified as hazardous contaminant yet, their potential toxicity remains as an arising concern regarding their continuous leaching into the surrounding environments derived from human usage, improper disposal or excretion.

Another type of well-known environmental pollutants is the heavy metals. These are elements that have high atomic weight and five times greater density compared to water. They have high toxicity at low concentration and are naturally found on earth and can be leaching out to surrounding via human activities in the form of industrial or mining wastes. Due to their high stability, these pollutants are highly persistent in environment and cannot be degraded easily [25]. Thus, investigation of economical and efficient analytical procedures or water remediation steps tailored on heavy metals is always a joint attention and shared goal for scientists worldwide. It has been shown that adsorption is one of the most efficient ways for the uptake of heavy metals in marine environment in both laboratory-scaled sample preparation step and industrial-scaled water treatment system [26]. Therefore, sorbents with outstanding adsorption characteristics, mechanical and physical properties are of high demand for monitoring purposes. A surface Cr(VI)-imprinted magnetic nanoparticles sorbent was developed by Qi et al. [19] for

preconcentration and determination of toxic Cr(VI) in tap water, lake water and river water samples. The prepared sorbent was synthesised by combining both surface ion-imprinted and sol-gel techniques. Under optimized environment, the preconcentration factor, linearity, LOD, %RR and %RSD of the developed extraction method were found to be 98, R^2=0.994, 0.29 µg/L, 96.1-99.2% and 2.1-3.4%, respectively. Non-imprinted polymers and the developed sorbent were studied to compare their selectivity towards Cr(VI). In the presence of seven interference ions, the developed sorbent showed excellent selectivity toward Cr(VI) with %RR in the range of 96.5%-99.8% while non-imprinted polymer offered only 24.4%0-39.8% for the recovery of Cr(VI). For real sample analysis, Cr(VI) was found in both lake water and river water samples at concentrations of 19.32 µg/L and 8.36 µg/L, respectively.

Conclusion and Outlooks

In this review, classification of organic-inorganic hybrids and their major synthesis routes, namely sol-gel, self-assembly, assembling of nanobuilding blocks and interpenetrating networks were discussed. A broad range of organic-inorganic hybrids materials are highly potential for applications in different aspects such as analytical, medical, mechanics, electronics and etc. This is due to easy handling of their physico-chemical properties, mechanical and chemical stabilities, morphological and surface characteristics, type of functional groups and bondings by manipulating their synthesis conditions, quantity and type of organic and inorganic materials used for their synthesis process. These properties should be studied carefully to ensure the compatibility of the developed sorbents with the corresponding sorbate and to fully understand the physical or chemical interactions of the sorbent-sorbate pairs. Under proper fabrication condition, the adsorption or extraction performance of the resulted hybrid material would be largely improved and served as an excellent sorbent in real environmental samples with high matrix effect. As discussed in this article, organic-inorganic hybrid sorbents are highly capable to be employed in the analysis of real environmental waters without significant matrix effects.

In brief, organic-inorganic hybrid sorbents will be an important and fascinating research aspect in analytical field. Under proper development, organic-inorganic hybrid sorbents with advantages of eco-friendly and low cost could be fulfilled. Therefore, these sorbents are expected to be mass-produced and marketed for the use of researchers for environmental monitoring purpose and wastewater treatment industry. Stability of the resulted sorbent should be highlighted to avoid any leaching substances forming secondary pollutants enter into the surrounding environment. Certainly, the use of natural organic polymer (biopolymers such as cellulose, sodium alginate, chitosan etc.) and inorganic substances (clay) are highly encouraged. Overall, such materials should be studied extensively because of their easy, fast, low cost and flexible production system as well as their unique features formed.

Acknowledgement

The authors would like to thank Universiti Teknologi Malaysia for facilitations and the Ministry of Higher Education Malaysia for financial support through vote number Q.J130000.2509.09H84. The authors declared no conflict of interest.

References

1. Halder, J. N. and Islam, M. N. (2015). Water pollution and its impact on the human health. *Journal of Environment and Human*, 2(1): 36-46.
2. Khatun, R. (2017). Water pollution: Causes, consequences, prevention method and role of wbphed with special reference from Murshidabad district. *International Journal of Scientific and Research Publications*, 7(8): 269-277.
3. Prüss-Üstün, A., Bonjour, S. and Corvalán, C. (2008). The impact of the environment on health by country: A meta-synthesis. *Environmental Health*, 7(1): 7.
4. Ng, N. T., Kamaruddin, A. F., Wan Ibrahim, W. A., Sanagi, M. M. and Abdul Keyon, A. S. (2018). Advances in organic–inorganic hybrid sorbents for the extraction of organic and inorganic pollutants in different types of food and environmental samples. *Journal of Separation Science*, 41(1): 195-208.
5. Xu, L. and Wang, J. (2017). The application of graphene-based materials for the removal of heavy metals and radionuclides from water and wastewater. *Critical Reviews in Environmental Science and Technology*, 47(12): 1042-1105.

6. Zvonkina, I. and Soucek, M. (2016). Inorganic–organic hybrid coatings: Common and new approaches. *Current Opinion in Chemical Engineering*, 11: 123-127.
7. Samiey, B., Cheng, C.-H. and Wu, J. (2014). Organic-inorganic hybrid polymers as adsorbents for removal of heavy metal ions from solutions: A review. *Materials*, 7(2): 673-726.
8. Judeinstein, P. and Sanchez, C. (1996). Hybrid organic–inorganic materials: A land of multidisciplinarity. *Journal of Materials Chemistry*, 6(4): 511-525.
9. Sanchez, C., Julián, B., Belleville, P. and Popall, M. (2005). Applications of hybrid organic–inorganic nanocomposites. *Journal of Materials Chemistry*, 15(35-36): 3559-3592.
10. Kaushik, A., Kumar, R., Arya, S. K., Nair, M., Malhotra, B. and Bhansali, S. (2015). Organic–inorganic hybrid nanocomposite-based gas sensors for environmental monitoring. *Chemical Reviews*, 115(11): 4571-4606.
11. Mir, S. H., Nagahara, L. A., Thundat, T., Mokarian-Tabari, P., Furukawa, H. and Khosla, A. (2018). Organic-inorganic hybrid functional materials: An integrated platform for applied technologies. *Journal of The Electrochemical Society*, 165(8): B3137-B3156.
12. Tavakoli, M., Hajimahmoodi, M. and Shemirani, F. (2014). Trace level monitoring of pesticides in water samples using fatty acid coated magnetic nanoparticles prior to GC-MS. *Analytical Methods*, 6 (9): 2988-2997.
13. Casarin, J., Gonçalves, A. C., Segatelli, M. G. and Tarley, C. R. T. (2017). Poly(methacrylic acid)/SiO_2/Al_2O_3 based organic-inorganic hybrid adsorbent for adsorption of imazethapyr herbicide from aqueous medium. *Reactive and Functional Polymers*, 121: 101-109.
14. Nodeh, H. R., Ibrahim, W. A. W., Kamboh, M. A. and Sanagi, M. M. (2017). New magnetic graphene-based inorganic–organic sol-gel hybrid nanocomposite for simultaneous analysis of polar and non-polar organophosphorus pesticides from water samples using solid-phase extraction. *Chemosphere*, 166: 21-30.
15. Ali, L. I. A., Ibrahim, W. A. W., Sulaiman, A., Kamboh, M. A. and Sanagi, M. M. (2016). New chrysin-functionalized silica-core shell magnetic nanoparticles for the magnetic solid phase extraction of copper ions from water samples. *Talanta*, 148: 191-199.
16. Zhang, D., Zhao, Y. and Xu, H.-B. (2017). Hydrothermal-assisted derived ion-imprinted sorbent for preconcentration of antimony(III) in water samples. *Separation Science and Technology*, 52(12): 1938-1945.
17. You, N., Liu, T.-H., Fan, H.-T. and Shen, H. (2018). An efficient mercapto-functionalized organic–inorganic hybrid sorbent for selective separation and preconcentration of antimony(III) in water samples. *RSC Advances*, 8(10): 5106-5113.
18. Shamsayei, M., Yamini, Y. and Asiabi, H. (2018). Evaluation of reusable organic-inorganic nafion/layered double hydroxide nanohybrids for highly efficient uptake of mercury ions from aqueous solution. *Applied Clay Science*, 162: 534-542.
19. Qi, X., Gao, S., Ding, G. and Tang, A.-N. (2017). Synthesis of surface Cr (VI)-imprinted magnetic nanoparticles for selective dispersive solid-phase extraction and determination of Cr(VI) in water samples. *Talanta*, 162: 345-353.
20. Ahmad, N. F., Kamboh, M. A., Nodeh, H. R., Halim, S. N. B. A. and Mohamad, S. (2017). Synthesis of piperazine functionalized magnetic sporopollenin: a new organic-inorganic hybrid material for the removal of lead (II) and arsenic (III) from aqueous solution. *Environmental Science and Pollution Research*, 24(27): 21846-21858.
21. Mohd Marsin, F., Wan Ibrahim, W. A., Abdul Keyon, A. S. and Sanagi, M. M. (2018). box–behnken experimental design for the synthesis of magnetite–polypyrrole composite for the magnetic solid phase extraction of non-steroidal anti-inflammatory drug residues. *Analytical Letters*, 51(14): 2221-2239.
22. Wahib, S. M. A., Ibrahim, W. A. W., Sanagi, M. M., Kamboh, M. A. and Keyon, A. S. A. (2018). Magnetic sporopollenin-cyanopropyltriethoxysilane-dispersive micro-solid phase extraction coupled with high performance liquid chromatography for the determination of selected non-steroidal anti-inflammatory drugs in water samples. *Journal of Chromatography A*, 1532: 50-57.
23. Fiscal-Ladino, J. A., Obando-Ceballos, M., Rosero-Moreano, M., Montaño, D. F., Cardona, W., Giraldo, L. F. and Richter, P. (2017). Ionic liquids intercalated in montmorillonite as the sorptive phase for the extraction of low-polarity organic compounds from water by rotating-disk sorptive extraction. *Analytica Chimica Acta*, 953: 23-31.
24. Omastová, M. and Mičušík, M. (2012). Polypyrrole coating of inorganic and organic materials by chemical oxidative polymerisation. *Chemical Papers*, 66(5): 392-414.

25. Tchounwou, P. B., Yedjou, C. G., Patlolla, A. K. and Sutton, D. J. (2012). Heavy metal toxicity and the environment. Springer Basel, Basel: pp. 133-164.
26. Fu, F. and Wang, Q. (2011). Removal of heavy metal ions from wastewaters: A review. *Journal of Environmental Management*, 92(3): 407-418.

Malaysian Journal of Analytical Sciences, Vol 23 No 4 (2019): 572 - 579
DOI: https://doi.org/10.17576/mjas-2019-2304-02

MALAYSIAN JOURNAL OF ANALYTICAL SCIENCES
Published by The Malaysian Analytical Sciences Society
ISSN 1394 - 2506

AN OPTICAL SENSOR BASED ON GRAPHENE QUANTUM DOTS FOR HYDROGEN PEROXIDE DETECTION

(Sensor Optik berasaskan Titik Kuantum Grafin untuk Pengesanan Hidrogen Peroksida)

Amiruddin Ashil Mastar[1], Jaafar Abdullah[1,2]*, Nor Azah Yusof[1,2], Yap Wing Fen[1,3]

[1]*Department of Chemistry*
[2]*Institute of Advanced Technology*
[3]*Department of Physic, Faculty of Science*
Universiti Putra Malaysia, 43400 UPM Serdang, Selangor, Malaysia

**Corresponding author: jafar@upm.edu.my*

Received: 19 August 2018; Accepted: 8 July 2019

Abstract

Graphene quantum dots (GQDs) is a zero-dimensional material of the carbon family and considered as a small cutting fragment from graphene sheet. It has unique electronic and optical properties due to electron confinement in the finite size of graphene cluster that leads to the opening of energy gap and quantization of electronic energy. In this study, biosensing based on GQDs in combination with enzyme (horseradish peroxidase, HRP) for the determination of hydrogen peroxide (H_2O_2) has been presented. The GQDs was used as an indicator reveals the fluorescence property of the system based on fluorescence quenching of GQDs which is induced from the enzymatic reaction. The presence of H_2O_2 quenches the fluorescence intensity of GQDs system which is proportional to the concentration of H_2O_2. Parameters optimization such as response time, enzyme concentrations, pH of buffer have been investigated. For linear calibration graph, it showed a linear dependence on the H_2O_2 concentration ranging from 1.0 to 100.0 μM with the detection limit of 1.0 μM.

Keywords: quantum dots, fluorescence, hydrogen peroxide, quenching, sensor

Abstrak

Titik kuantum grafin (GQDs) adalah bahan dimensi-sifar keluarga karbon dan dianggap sebagai serpihan kecil dari lembaran grafin. Ia mempunyai ciri-ciri elektronik dan optik yang unik disebabkan oleh pengasingan elektron dalam saiz finit kelas grafin yang membawa kepada pembukaan jurang tenaga dan pengkuantuman tenaga elektronik. Dalam kajian ini, biopenderiaan berasaskan GQDs digabungkan dengan enzim (peroksidase *horseradish*, HRP) untuk penentuan hidrogen peroksida (H_2O_2) telah dibentangkan. GQDs digunakan sebagai penunjuk mempamerkan sifat pendarfluor sistem berasaskan pendarfluor pelindapkejutan GQD yang diaruhkan dari tindak balas enzim. Kehadiran H_2O_2 mengurangkan keamatan pendarfluor sistem GQD yang berkadaran dengan kepekatan H_2O_2. Pengoptimuman parameter seperti masa tindak balas, kepekatan enzim, pH penimbal telah dikaji. Bagi graf penentukuran linear, ia menunjukkan kebergantungan kelinearan terhadap kepekatan H_2O_2 di antara 1.0 hingga 100.0 μM dengan had pengesanan 1.0 μM.

Katakunci: titik kuantum, pendarfluor, hidrogen peroksida, pelindapkejutan, sensor

Introduction

As a new member of the graphene family, graphene quantum dots (GQDs), which combine the excellent properties of graphene and quantum dots, have attracted considerable attention from scientists in the fields of chemistry, physics, materials, biology and etc [1]. GQDs represent single-layer to tens of layers of graphene of a size less than

30 nm. Its exceptional properties such as low toxicity, stable photoluminescence, chemical stability and better resistance to photo bleaching making them promising in biocompatibility and applied in many applications such as bio-imaging, optoelectronics, photovoltaics, controlled drug delivery, energy conversion storage devices and sensor [2].

GQD exhibiting fluorescence has recently aroused increasing interest in their optical and electronic properties [3, 4]. Quantum confinement, edge effects, oxygen-containing groups, structural defects, and doping elements contribute considerably to the luminescent properties of the GQD [5, 6]. With excellent characteristics like large surface area and diameter, fine surface grafting using the π-π conjugated network, and other special physical properties. In addition, the carboxyl and hydroxyl groups at their edge enable them to display excellent water solubility and render them suitable for successive functionalization with various organic, inorganic, polymeric, or biological species [7]. GQD are increasingly considered to be a promising material to replace the commonly used semiconductor for biosensing and bioimaging related applications, detection of glucose and sensing for metal ions [8, 9].

Hydrogen peroxide (H_2O_2) plays a vital role in many different fields like biological, clinical, environmental, pharmaceutical and food industries. Moreover, it is also a very important species in biology and biochemical reactions. For example, a higher concentration of H_2O_2 contributes to the oxidative damage of many different enzymes and proteins leading to atrocious effects in human health, and in some cases, it may even lead to cancer. In the context of chemistry, it is a main by-product in catalytic reactions of oxidase enzymes. So, it is very important not only to sense and detect H_2O_2 but also to determine its exact concentration. Basically, there are several methods such as spectrophotometry, titration methods, luminescent techniques and electrochemical methods for the detection and quantification of H_2O_2 that have been reported in literature. Among these methods, optical techniques offer simplicity, selectivity, a fast response time, less laborious work and involve no reference electrode. Usually, these methods employ enzymes for the detection because of its specificity and effective binding towards particular functional group.

In this work, we explore the use of GQDs for the determination of H_2O_2 and its role in advanced sensing applications. We demonstrated the fluorescence quenching of GQDs induced by H_2O_2 with the presence of HRP. The idea of the system is to utilize the GQDs as a fluorescence indicator, which can provide sensitive biological analysis. Another advantage of the system is its high resistance to photo-bleaching and intense light emission by high quantum efficiency [6].

Materials and Methods

Reagents

Graphene quantum dots was purchased from ACS material (USA). Peroxidase from horseradish was bought from Sigma-Aldrich (USA). Hydrogen peroxide solution was acquired from Sigma-Aldrich (Germany). Phosphate buffer was prepared by mixing monosodium phosphate (Na_2HPO_4) and disodium phosphate (NaH_2PO_4) (Schmidt) solutions. Deionize water for preparation of aqueous solution was purified using Thermo Scientific water purification system (18.2 MΩ cm).

Instrument

The fluorescence intensity was recorded using SYNERGY H1 Hybrid Multi-Mode Reader. UV-Vis spectrometer PerkinElmer Lambda 35 was used to analyse the sample. The FTIR spectra of the samples were obtained at ambient temperature using the KBr disc method. The disk containing 1 mg of the sample was recorded in the wavelength range of 500 - 4000 cm^{-1} using a series 100 Perkin Elmer FTIR 1650 spectrophotometer.

Procedure of hydrogen peroxide determination

For preparation of 1000 U/mL of peroxidase from horseradish (HRP) (EC 1.11.1.7, 146 U/mg), 0.8 mg of HRP was dissolved in 116.8 μL of phosphate buffer solution (PBS) pH 7.0. Stock solution of H_2O_2 in the concentration of 1.0 - 100 μM was prepared daily. GQD was sonicated for 10 min every time before mixing with the enzyme and H_2O_2.

For the assay procedure, 20 µL of HRP (20 unit) and 30 µL H_2O_2 was mixed in 96-well microplate. The mixture was incubated for 2 minutes and then 50 µL of GQD (0.5 mg/mL) was added. The fluorescence intensity of the mixture was recorded in the wavelength of 400 - 800 nm. The excitation was fixed at 400 nm and the fluorescence intensity of the mixture was measured at wavelength of 524 nm. The quenching effect was calculated based on the following equation 1:

$$\text{Net fluorescence intensity (at 524 nm)} = T_0 - T_{20} \quad (1)$$

where T_0 = intensity at 0 min and T_{20} = intensity after 20 min reaction.

Parameter optimization study

For reaction time optimization, the reaction of the GQD/HRP towards H_2O_2 (100 µM) was recorded at specific wavelength (524 nm) every 5 minutes for 25 minutes reaction time. The graph of net fluorescence intensity versus time was plotted to obtain optimize reaction time for the system. Effect of pH buffer on the GQDs/HRP system was also studied in this work. The intensity of GQDs-HRP towards H_2O_2 (100 µM) was recorded by varying the pH in the range of 6 to 8. In order to achieve maximum response of the GQDs/HRP system, the effect of HRP concentration was investigated in the range of 5 to 50 units.

Results and Discussion

Characterization GQD

Figure 1 shows GQDs was characterized using UV-Vis absorption spectroscopy and spectrofluorometry. As shown, the absorption of GQDs was observed at wavelength of 380 nm, while maximum fluorescence emission peak was obtained at wavelength of 524 nm. The surface morphology of GQDs was also studied by using transmission electron microscopy (TEM). The TEM image of GQDs shows well-dispersed spherical shape with diameter ranging from 10 - 15 nm (Figure 2). To further understand functional group attached on the surface of GQDs, Fourier Transform Infrared Spectroscopy (FTIR) was investigated. As shown in Figure 3, the FTIR spectrum of GQDs shows a broad band of O-H at 2495 cm^{-1}, C-H (3023 cm^{-1}), C=O (1580 cm^{-1}), C=C (1427 cm^{-1}). Functional groups presence in the spectrum shows the GQDs have carbonyl group. Similar observation was also report by Shen [9] and Tetsuka [11] where the presence of these groups makes the GQDs well soluble in water, improve adsorbing ability to biomolecules and has potential application for biosensing.

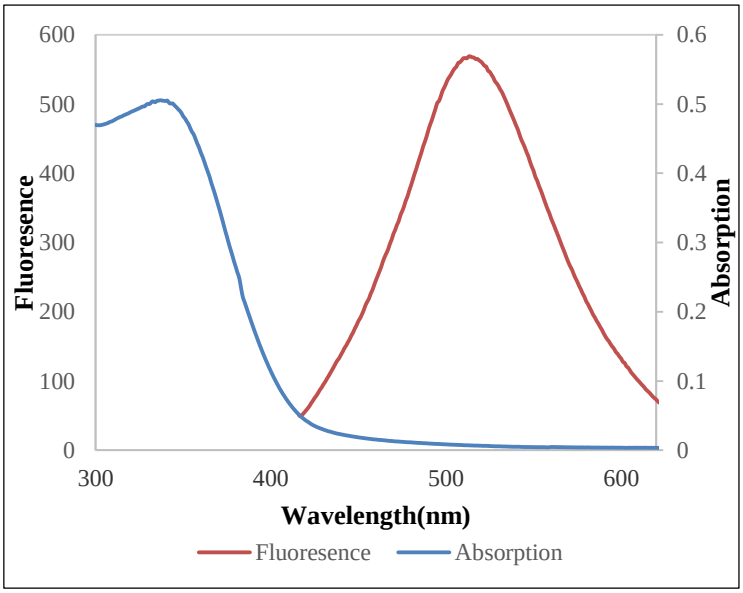


Figure 1. The absorption and fluorescence spectra of GQDs

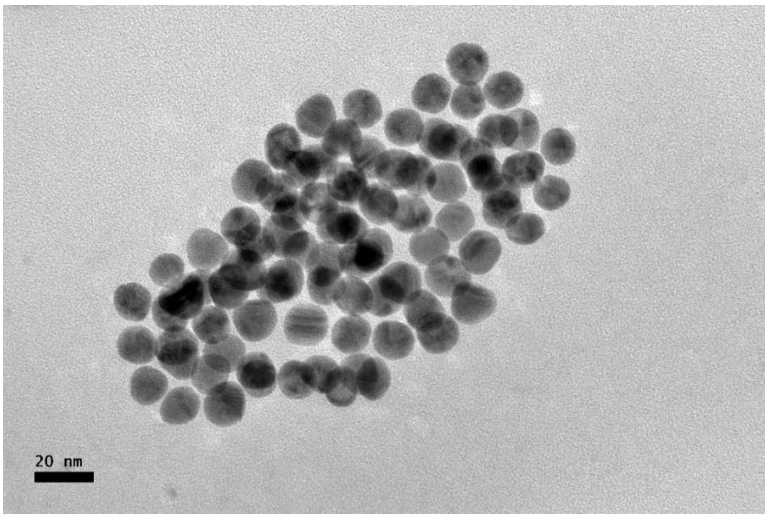


Figure 2. The TEM image of GQDs (100,000x magnification)

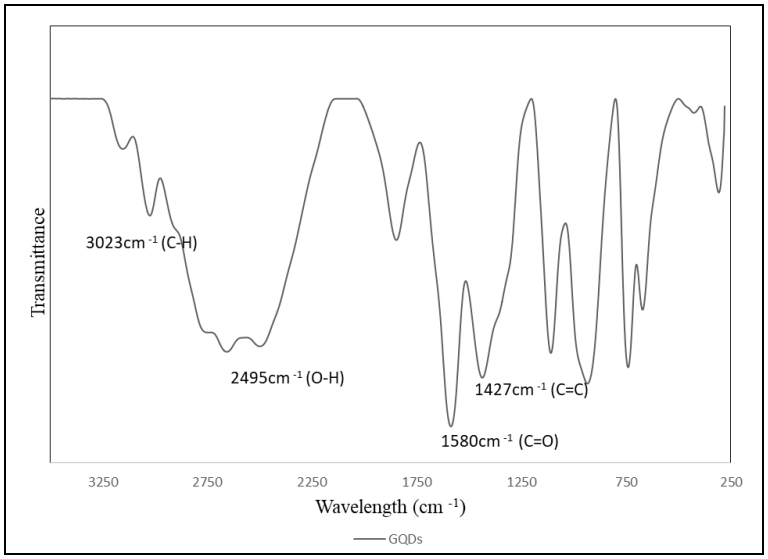


Figure 3. FTIR spectra of GQDs

The basic principle of detection

The basic principle of the reaction of GQD-HRP in the presence of H_2O_2 is illustrated in Figure 4. In the presence of the HRP, H_2O_2 will be oxidized to form H_2O and O_2. At the same time the GQDs is quenched and the fluorescence emission produced is decreased. Usually, the quenching of fluorescence emission of GQDs occurs due to either energy transfer [10], charge diverting [11], and surface absorption [12], which could change the surface state of GQDs. In this study, the possible mechanism for GQD/HRP quenching is related to H_2O_2 existence as the quencher. When there is an interaction between the GQDs and H_2O_2, it is assumed to undergo collisional quenching causing fluorescence intensity to decrease. Collisional quenching occurs when the excited state of GQDs is neutralized by the H_2O_2 molecules, prompting to the reduction of the GQDs fluorescence intensity [13]. The quenching effect in the absence of HRP was also evaluated and it shows no significant quenching (data not shown). When the HRP enzyme was added into the reaction system, significant reduction of fluorescence intensity was obtained (quenching effect). Thus, this observation shows that the HRP enzyme is important in the quenching effect of the system.

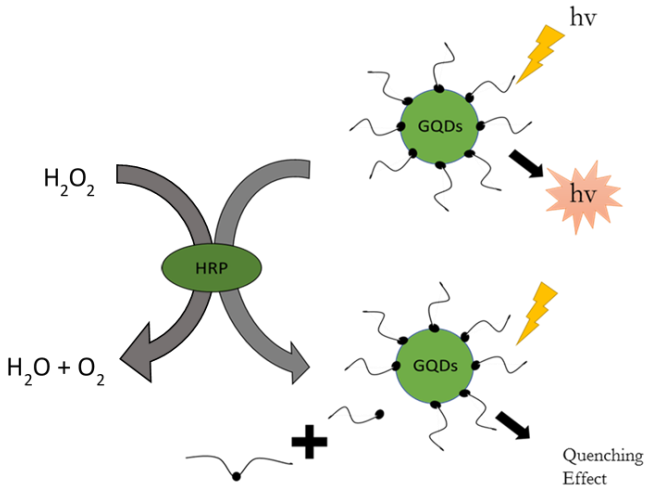


Figure 4. Possible mechanism of the GQDs/HRP system in the presence of H_2O_2, where H_2O_2 quenched the GQDs and leading to reduction of the fluorescence intensity of the system

Parameter optimization

The experimental parameter was optimized in order to improve the performance of the prepared GQDs/HRP system for the determination of H_2O_2. Figure 5 depicts the effect of reaction time towards the fluorescence intensity of the GQDs. It can be noted that as the time increase the fluorescence intensity was gradually increased until reaction time of 20 minutes. Above 20 minutes, the response of the system approaching saturation point. Therefore, response time of 20 minutes was chosen for further experiment.

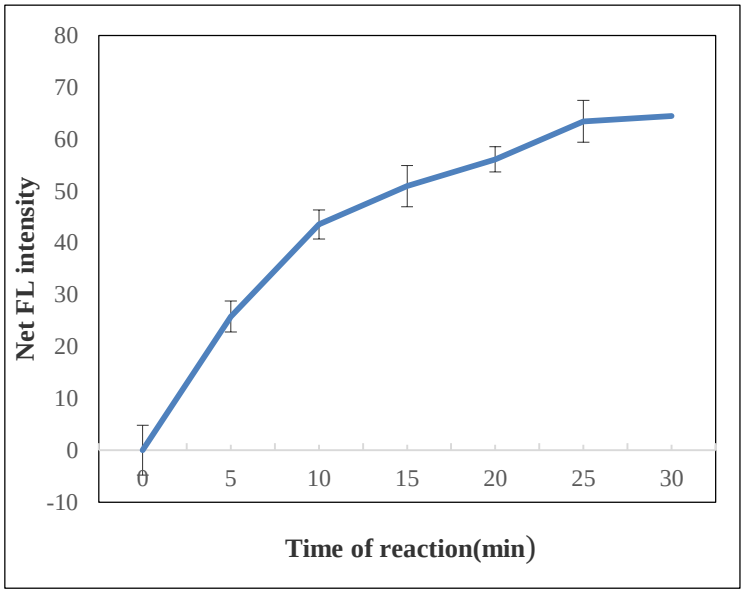


Figure 5. Effect of response time

The effect of pH on the GQDs/HRP response is very important because the enzyme activity of HRP and GQDs are dependent on the pH condition. The experiment was carried out in the range of pH 6.0 to 8.0 as illustrated in

Figure 6. The pH of the reaction solution shows a significant influence on the response of GQDs/HRP assay system. The optimum pH value was observed at pH 7 which is agreed with work reported previously [14], which explored QDs-HRP/uricase hybrid system for uric acid detection.

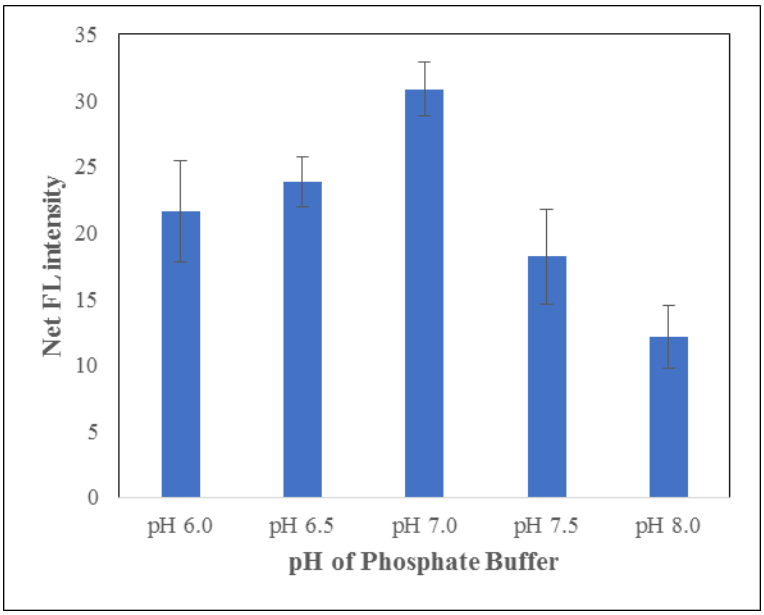


Figure 6. Effect of pH on the response of GQDs/HRP system

To further increase the sensitivity of the prepared hybrid system, the effect of concentration of HRP was investigated. From Figure 7, the intensity of the system increases as the concentration of HRP increases. From this study, we decided to choose concentration of HRP of 20 units for the assay because the amount used is sufficient for the reaction system to produce significant quenching effect for determination of H_2O_2.

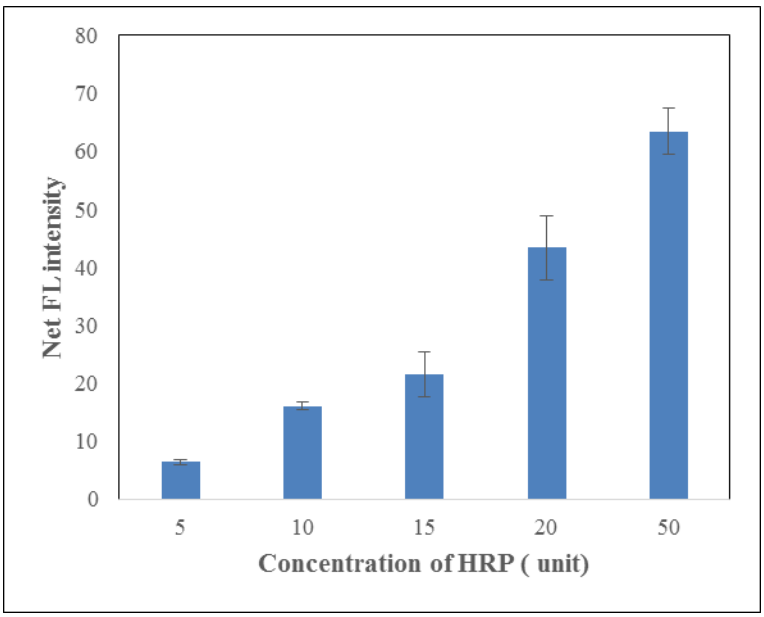


Figure 7. Effect of HRP concentration on the GQDs/HRP system towards H_2O_2 (100.0 μM)

Analytical performance of the GQDs/HRP towards H_2O_2

The performance of the prepared GQDs/HRP system towards different concentration of H_2O_2 in the dynamic range of 1.0 to 500.0 µM was evaluated. As shown in Figure 8, the linearity of the GQDs/HRP system towards H_2O_2 was in the concentration range of 1.0-100.0 µM with linear regression equation of y = 11.18x -2.11 (R^2 =0.9939). Limit of detection (LOD) was calculated according to $3S_b/b$, where S_b is the standard deviation of the blank measurements (n=3), b is the slope of the calibration curve [5] and the calculated LOD was found to be at 1.0 µM. Reproducibility study of the GQDs/HRP was evaluated at H_2O_2 concentration of 10 µM in phosphate buffer solution (pH 7.0) and the relative standard deviation (RSD) of 9.75% (n=5) was obtained.

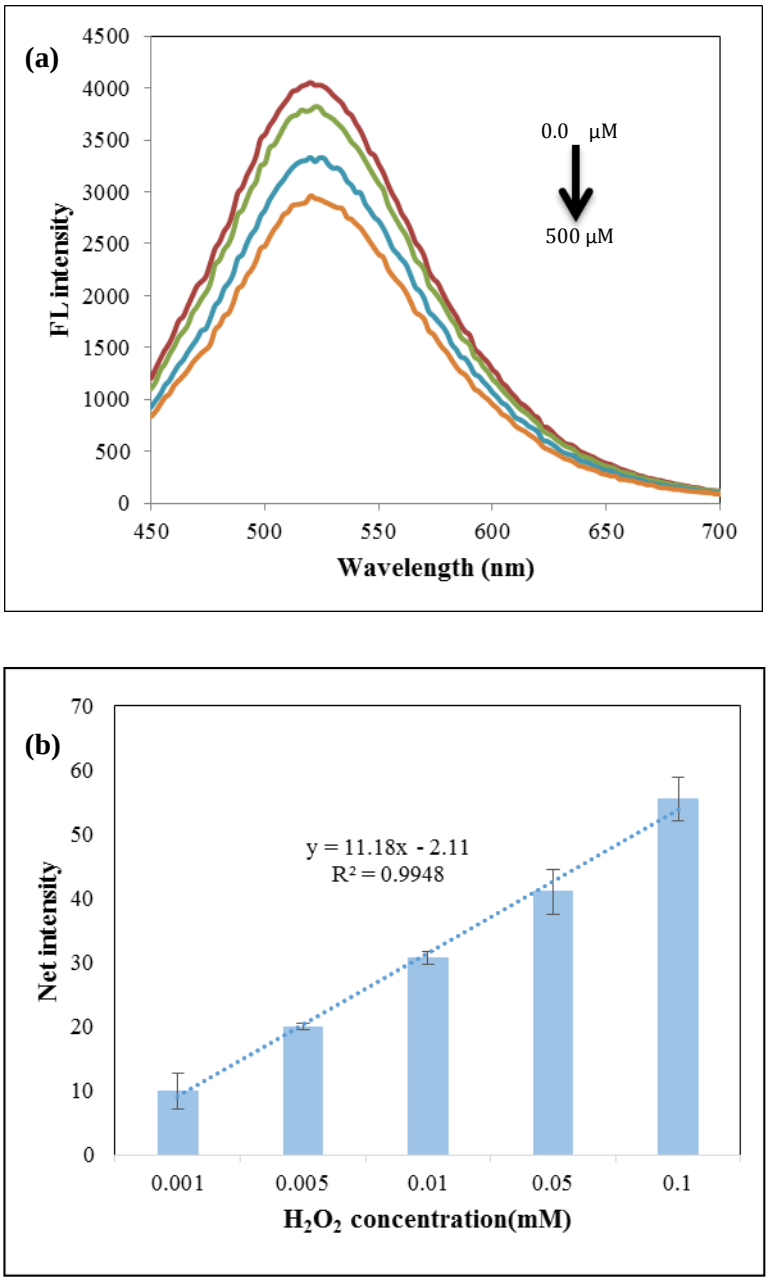


Figure 8. (a) Quenching effects of QDs towards different concentrations of H_2O_2, (b) Calibration curve of the developed GQDs/HRP system towards different concentration of H_2O_2 (1.0 - 100.0 µM)

Conclusion

A simple and convenient technique for H_2O_2 determination based on quenching of the fluorescence of GQDs has been developed. Under the optimum conditions, the GQDs/HRP system achieved a good linear relationship between the net fluorescence intensity of the system and the concentration of H_2O_2 in the range of 1.0 to 100 μM with LOD of 1.0 μM. The developed method has shown its potential to determining the concentration of hydrogen peroxide.

Acknowledgements

The authors are gratefully acknowledged the financial support provided by Universiti Putra Malaysia under Putra Grant (GP-IPB/2016/9515403).

References

1. Azmi, N. E., Ramli, N. I., Abdullah, J., Abdul Hamid, M. A., Sidek, H., Abd Rahman, S. and Yusof, N. A. (2015). A simple and sensitive fluorescence based biosensor for the determination of uric acid using H_2O_2-sensitive quantum dots/dual enzymes. *Biosensors and Bioelectronics*, 67: 129-133.
2. Dong, C., Qian, H., Fang, N. and Ren, J. (2006). Study of fluorescence quenching and dialysis process of CdTe quantum dots, using ensemble techniques and fluorescence correlation spectroscopy. *Journal of Physical Chemistry B*, 110(23):11069-11075.
3. He, S., Song, B., Li, D., Zhu, C., Qi, W., Wen, Y. and Fan, C. (2010). A graphene nanoprobe for rapid, sensitive, and multicolor fluorescent DNA analysis. *Advanced Functional Materials*, 20(3): 453-459.
4. Ji, X., Zheng, J., Xu, J., Rastogi, V. K., Cheng, T. C., DeFrank, J. J. and Leblanc, R. M. (2005). (CdSe)ZnS quantum dots and organophosphorus hydrolase bioconjugate as biosensors for detection of paraoxon. *Journal of Physical Chemistry B*, 109(9): 3793-3799.
5. Kim, K. E., Kim, T. G. and Sung, Y. M. (2012). Fluorescent cholesterol sensing using enzyme-modified CdSe/ZnS quantum dots. *Journal of Nanoparticle Research*, 14(1179): 1-9.
6. Lu, C.-H., Yang, H.-H., Zhu, C.-L., Chen, X. and Chen, G.-N. (2009). A graphene platform for sensing biomolecules. *Angewandte Chemie*, 48(26): 4785-4787
7. Ponomarenko, L. A., Schedin, F., Katsnelson, M. I., Yang, R., Hill, E. W., Novoselov, K. S. and Geim, A. K. (2008). Chaotic dirac billiard in graphene quantum dots. *Science*, 320(5874): 356-358.
8. Razmi, H. and Mohammad-Rezaei, R. (2013). Graphene quantum dots as a new substrate for immobilization and direct electrochemistry of glucose oxidase: Application to sensitive glucose determination. *Biosensors and Bioelectronics* 41: 498-504.
9. Shen, J., Zhu, Y., Yang, X., Zong, J., Zhang, J. and Li, C. (2012). One-pot hydrothermal synthesis of graphene quantum dots surface-passivated by polyethylene glycol and their photoelectric conversion under near-infrared light. *New Journal of Chemistry* 36: 97-101.
10. Tang, J. and Marcus, R. A. (2006). Determination of energetics and kinetics from single-particle intermittency and ensemble-averaged fluorescence intensity decay of quantum dots. *The Journal of Chemical Physics*, 125 (044703): 1-8.
11. Tetsuka, H., Asahi, R., Nagoya, A., Okamoto, K., Tajima, I., Ohta, R. and Okamoto, A. (2012). Optically tunable amino-functionalized graphene quantum dots. *Advanced Materials*, 24(39): 5333-5338.
12. Wang, D., Wang, L., Dong, X., Shi, Z. and Jin, J. (2012). Chemically tailoring graphene oxides into fluorescent nanosheets for Fe^{3+}ion detection. *Carbon*, 50(6): 2147-2154.
13. Xie, R., Wang, Z., Zhou, W., Liu, Y., Fan, L., Li, Y. and Li, X. (2016). Graphene quantum dots as smart probes for biosensing. *Analytical Methods*, 8(20): 4001–4016.
14. Zhuo, S., Shao, M. and Lee, S. T. (2012). Upconversion and downconversion fluorescent graphene quantum dots. *Ultrasonic preparation and photocatalysis. ACS Nano*, 6(2): 1059-1064.

Malaysian Journal of Analytical Sciences, Vol 23 No 4 (2019): 580 - 585
DOI: https://doi.org/10.17576/mjas-2019-2304-03

MALAYSIAN JOURNAL OF ANALYTICAL SCIENCES
Published by The Malaysian Analytical Sciences Society
ISSN 1394 - 2506

ROLE OF L-GLUTAMINE IN THE *IN-VITRO* GROWTH OF HCT-8 AND HT-29 CELL LINES

(Peranan L-Glutamin dalam Pertumbuhan Sel HCT-8 dan HT-29 *In-Vitro*)

Afzan Mat Yusof[1]* and Mohammed Abdullah Jainul[2]

[1]*Department of Basic Medical Sciences, Kulliyyah of Nursing*
[2]*Department of Biomedical Science, Kulliyyah of Allied Health Sciences*
International Islamic University Malaysia, Bandar Indera Mahkota, Jalan Sultan Ahmad Shah, 25200 Kuantan, Pahang, Malaysia

**Corresponding author: afzan@iium.edu.my*

Received: 19 August 2018; Accepted: 3 July 2019

Abstract

L-glutamine is one of the essential supplements of *in-vitro* growth medium for cancer cells. The amino acid L-glutamine is well known as the vital source of nutrition in cancer cell growth for its ability to provide carbon and nitrogen. A common phenomenon of cancer cell is the rapid production of lactic acid through aerobic glycolysis. Apart from nutritional value, the released ammonia from L-glutamine may neutralize the acidic environment to ensure continuous cell growth. The current study is to observe the effect of L-glutamine concentration in culture media for cancer cell lines. Detection of L-glutamine consumption by the cells was carried out after 8 hours of incubation period. Numerous culture media were prepared adding L-glutamine concentration of 0 mM, 5 mM and 10 mM with different pH range. The cell density was calculated after 8 hours of incubation using trypan blue staining method. UV-Vis spectrophotometer was used to detect the concentration of L-glutamine consumption. The result shows that the cell density did not increase significantly in the media without L-glutamine supplement whereas, a rapid increase was observed in L-glutamine supplemented growth media in HCT-8 and HT-29 cell lines. The L-glutamine consumption was found higher in the media with low pH, but a relatively low L-glutamine consumption was observed in media with higher pH condition. The result confirms the necessity of L-glutamine in cancer cell growth. In addition, higher L-glutamine uptake in acidic condition supports the role of L-glutamine in acid resistance activity in cancer cell growth.

Keywords: L-glutamine, cancer cell growth, aerobic glycolysis, acid resistance

Abstrak

L-glutamin adalah salah satu tambahan penting dalam pertumbuhan medium *in-vitro* untuk sel-sel kanser. Asid amino L-glutamin terkenal sebagai sumber pemakanan penting dalam pertumbuhan sel kanser kerana keupayaannya menyediakan karbon dan nitrogen. Fenomena sel kanser yang biasa adalah pengeluaran asid laktik melalui glikolisis aerobik. Selain daripada nilai pemakanan, ammonia yang dikeluarkan dari L-glutamin dapat meneutralkan persekitaran asid untuk memastikan pertumbuhan sel berterusan. Kajian semasa adalah untuk melihat kesan kepekatan L-glutamin dalam media kultur untuk sel-sel kanser. Pengesanan penggunaan L-glutamin oleh sel-sel telah dilakukan selepas 8 jam tempoh inkubasi. Sejumlah media kultur telah disediakan dengan menambah kepekatan L-glutamin sebanyak 0 mM, 5 mM dan 10 mM dengan pelbagai pH yang berlainan. Ketumpatan sel dikira selepas 8 jam inkubasi menggunakan kaedah pewarnaan trypan biru. UV-Vis spektrofotometer digunakan untuk mengesan kepekatan penggunaan L-glutamin. Hasilnya menunjukkan bahawa ketumpatan sel tidak meningkat dengan ketara dalam media tanpa tambahan L-glutamin sedangkan, peningkatan pesat diperhatikan dalam media pertumbuhan L-glutamin ditambah dalam sel-sel HCT-8 dan HT-29. Penggunaan L-glutamin didapati lebih tinggi dalam media dengan pH rendah, tetapi penggunaan L-glutamin yang agak rendah diperhatikan dalam media dengan keadaan pH yang lebih tinggi. Hasilnya mengesahkan keperluan L-glutamin dalam pertumbuhan sel kanser. Di samping itu, penyerapan L-glutamin yang lebih tinggi dalam keadaan berasid menyokong peranan L-glutamin dalam aktiviti rintangan asid dalam pertumbuhan sel kanser.

Kata kunci: L-glutamin, pertumbuhan sel kanser, glikolisis aerobik, rintangan asid

Introduction

Glutamine is a non-essential amino acid which is produced abundantly in the human body. It is considered as one of the essential nutrients in different physiological functions and especially in the cell growth [1]. Glutamine supplies high energy to the cells in the process of cell proliferation which involve in vast protein and nucleic acid synthesis [2].

Glutamine directly involves in numerous regulatory processes of the cancer cell growth. Nitrogen is one of the essential atoms required in amino acids, nucleotides, amino sugars and in case of rapidly dividing cancer cells the nitrogen demand is very high. Glutamine supplies nitrogen atom by breaking down into glutamate and ammonia [3]. The glutamate produced due to the dissociation of glutamine is assumed to participate actively in tricarboxylic acid (TCA) Cycle in cancer cell [4]. However, apart from the energy supply glutamine possess a function of acid resistance [5, 6, 7].

Warburg effect describes the phenomenon of energy production by cancer cells where the cells undergo aerobic glycolysis that results accumulation of huge amount of lactic acid [8]. The excess production of lactic acid decreases the extracellular pH value [5]. According to Griffiths, the biological reactions linked to cancer cell growth are mostly pH dependant and cell growth is greatly affected if the extracellular pH value is below 5.6. Hence, it is detrimental to maintain a continuous acid resistance in order to sustain cancer cell growth [9]. Huang et al. proposed that glutamine plays a key role in extracellular acid resistance [5]. In all cell culture media glutamine is an essential component to supply energy [10]. It was also observed that the glutamine uptake is higher in cancer cells than in normal cells [11].

Therefore, the study was performed to prevail the role of glutamine in extracellular acid neutralization in *in-vitro* cancer cell culture. The quantitative detection of ammonia in the cell culture media and the cell growth quantification is essential in order to understand the role of ammonia in acid resistance.

Materials and Methods

Experimental cell lines

Two colorectal cancer cell lines namely HCT8 and HT29 were used as the experimental cell lines. HCT-8 cells was purchased from AddexBio Technologies, Inc., San Diego, United States and HT29 from American Type Culture Collection, Virginia, United States.

Preparation of culture media

A set of four different Dulbecco's Modified Eagle's Medium (DMEM) cell culture media with varying concentration of L-glutamine was prepared where the L-glutamine concentrations were 0, 5 and 10 mM. All the culture media were supplemented with 10% fatal bovine serum (FBS, heat inactivated) and 1% Antibiotics-Antimycotic mixed stock solution (Sigma Aldrich) consisting of penicillin, streptomycin and amphotericin. The composition of the supplemented DMEM medium is shown in Table 1.

Table 1. Composition of 100 mL of supplemented DMEM culture medium

Ingredient	Percentage (%)	Volume (mL)
DMEM	89	89
Fetal bovine serum (FBS, heat activated)	10	10
Antibiotics-antimycotic mixed stock solution	1	1
Total	100	100

Cell growth assay

HCT-8 and HT-29 cell lines were seeded into t_{25} cell culture flask containing media supplemented with 0, 5 and 10 mM of L-glutamine, respectively. In each flask approximately 1×10^5 cells were seeded. After seeding the cell lines, the flasks were incubated at 37 °C and 5% CO_2 in air. After 8 hours of incubation, the cells were counted staining with 0.4% trypan blue solution. The cells were diluted with 0.4% trypan blue solution and loaded onto the haemocytometer. The number of cells in each of the five red outlined squares (Figure 1) were counted, and the total number of cells were determined using following equation [12].

$$\begin{aligned}\text{Total Cells} &= \text{Mean cell count in 5 squares} \times \text{dilution factor} \times 10^4 \times \text{volume of the cells} \\ &= \text{Mean cell count} \times \text{dilution factor} \times 10^4 \times \text{volume of the cells}\end{aligned} \quad (1)$$

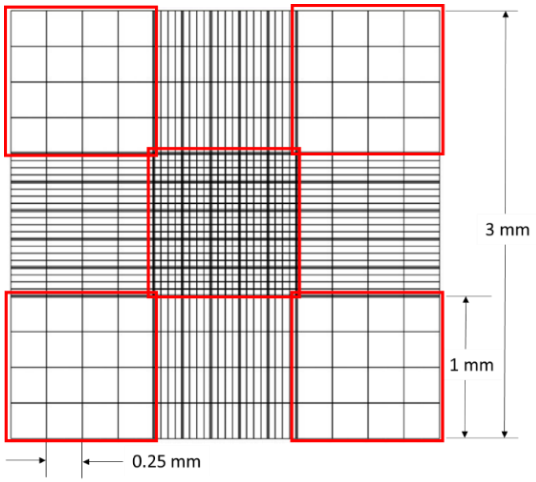


Figure 1. Grid pattern of the haemocytometer chamber. The number of the cells in red outlined squares to be calculated

UV-Vis spectrophotometric observation

Approximately 1×10^5 cell of both HCT-8 and HT-29 cell lines were seeded into t_{25} cell culture flask separately with complete DMEM media supplemented with 5 mM of L-glutamine. The cell culture flasks were incubated at 37 °C and 5% CO_2 in air. After 8 hours of incubation the media were collected into previously labelled 10 mL falcon tubes. The cells were counted in haemocytometer with 0.4% trypan blue staining. The L-glutamine and glutamate concentration were determined in UV-Vis spectroscopy using glutamine/glutamate determination kit (GLN-1; Sigma-Aldrich). Each of the samples was divided into two parts, first part of was subjected to measure glutamate directly and the second part was to measure glutamine plus glutamate as directed by the glutamine/glutamate determination kit protocol. The L-glutamine concentration in the media was calculated by subtracting the value of part one from the value of part two. The glutamine was transferred to glutamate by the addition of glutaminase, and the glutamate was dehydrogenized to α-ketoglutarate where NAD^+ reduces to NADH. The glutamate amount is directly proportional to the amount of NADH and hence NADH concentration was taken into consideration. The NADH concentration was measured in UV-Vis spectrophotometer at 340 nm. A standard curve was prepared following the protocol described in glutamine/glutamate determination kit to calculate the concentration of glutamate in the experimental samples.

Data analysis

Data collected was analysed into graph by using Microsoft Excel 2013. The glutamate concentration was determined by plotting a concentration vs absorbance standard curve. The L-glutamine consumption data was normalized with the cell numbers.

Results and Discussion

The L-glutamine concentration is very crucial in the growth of cancer cell. The study observed that higher glutamine concentration promotes the growth dramatically. Beside L-glutamine concentration, the pH condition is also important especially in cancer cell growth. HCT-8 and HT-29 cells maintained their growth even with no L-glutamine supplement in the media with higher pH range (pH 7.3) (Figure 2). But in non-glutamine supplemented media with pH 6.5, there was no notable growth in both HT-29 and HCT-8 cell lines. However, L-glutamine supplement stimulates cell growth in both pH condition but the growth is relatively higher in pH 7.3.

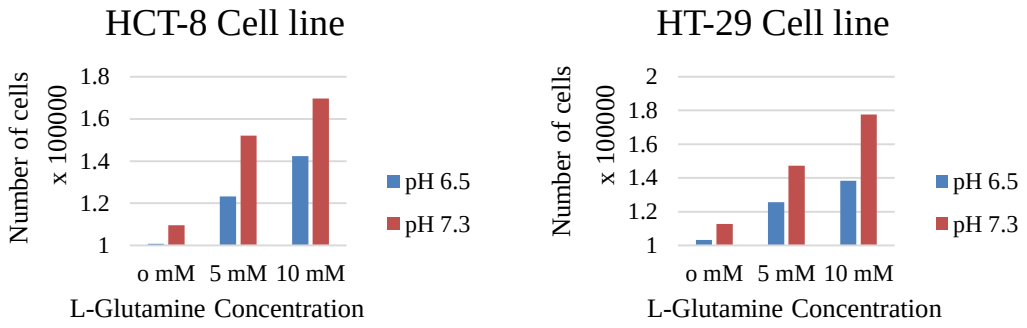


Figure 2. Cell growth after 8h of incubation. The media were supplemented with 0, 5 and 10 mM of L-glutamine in pH 6.5 and pH 7.3

The study evaluated the comparative growth of two different cancer cells in different pH condition and well as with various concentration of L-glutamine in growth media. The result shows that in pH 7.3, the HCT-8 cell growth had been increased up to 1.7-fold with 10 mM L-glutamine supplement in the culture media. HCT-8 cells grow moderately in pH 7.3 with 5 mM L-glutamine supplement to reach 1.52×10^5 cells where the initial number of cells was 1×10^5. The HT-29 cell line also follows the similar trend with the increase of L-glutamine concentration in the media with pH 7.3. After 8 hours of inoculation, the number of cells were obtained 1.13×10^5, 1.47×10^5 and 1.78×10^5 in the media supplemented with 0 mM, 5mM and 10 mM L-glutamine respectively. The result also shows that HT-29 cell line growth rate is comparatively higher than that of HCT-8 cell lines at pH 7.3. At pH 6.5, the number of HCT-8 cells reached as high as 1.42×10^5 with 10 mM of L-glutamine while HT-29 cell growth was comparatively lower with same concentration of L-glutamine. These observations showed cancer cell proliferation is influenced by the glutamine [11]. Other study by Huang et al. [5] have stated the same condition in which HeLa (cervical cancer cells) and MCF-7 cells (breast cancer cells) growth are reduced due to glutaminase activity is inhibited under acidic environment. HeLa and MCF-7 cells growth increased at pH 7.3 compared at pH 6.3 even in the glutamine absence. In such case, alkaline pH has been recognized as an important role increasing cell proliferation [13].

To investigate the L-glutamine consumption from the media a UV-Vis spectroscopy assay was carried out using glutamine/glutamate determination kit. HCT-8 and HT-29 cells were supplemented with 5 mM L-glutamine, incubated for 8 hours and then L-glutamine consumption was determined. Figure 3 shows that both HCT-8 and HT-29 cells exhibited higher L-glutamine uptake in pH 6.5 than in pH 7.3, although the trend is opposite in case of cell growth (Figure 2). The glutamine consumption normalized for cell density was relatively lower in media with pH 7.3 than in in media pH 6.5. Glutamine consumption was 55% and 52% more in HCT-8 and HT-29 cells at pH 6.5 compared to pH 7.3.

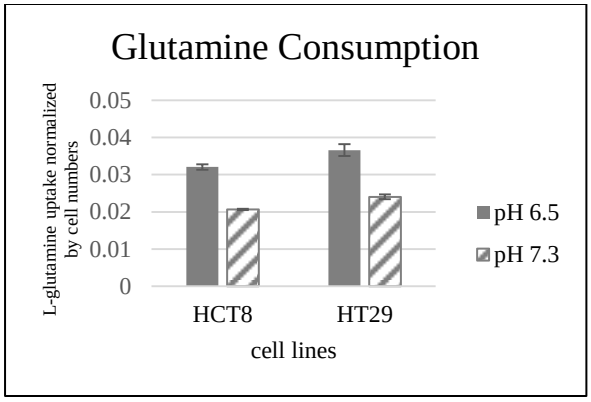


Figure 3. Normalized glutamine consumption from the media after 8 hours of incubation at pH 6.5 and pH 7.3. Bars represents the mean ±SD (Standard Deviation).

It is well known that glutamine metabolism promotes cancer cell proliferation by fuelling TCA cycle [4]. Due to the rapid cell growth cancer cells go through a distinctive metabolism characteristic that requires extensive biosynthesis and elevated energy to maintain rapid proliferation [14]. Two primary components, glucose and glutamine are the major energy provider as well as mediators of macromolecular synthesis in cell proliferation. In normal cells, proliferation takes place in lower energy environment which may be carried out by glucose metabolism, and hence the glutamine consumption is lower [15].

Apart from elevated energy requirement, cancer cell growth is also dependent on intracellular pH condition [5]. The increased aerobic glycolysis in cancer cells results decrease in extracellular pH as low as 5.6 [9, 16]. But several biological processes involved in cancer cell proliferation sternly depend on pH. And hence it is essential to continuously maintain a higher extracellular pH in order to promote proliferation. The findings of the study recommend the role of glutamine in extracellular acid resistance. Higher pH contributes in neutralizing abundant lactic acid produced by aerobic glycolysis and maintain the pH higher. Whereas, at pH 6.5, lactic acid lowers the pH of the media and slow down the cell growth. Overall, acid resistance is a must in cancer cell proliferation.

Higher concentration of L-glutamine and high pH confirms the optimum environment for cancer cell proliferation, thus there was robust growth of both of the cell lines. On the other hand, at higher pH state the glutamine consumption is lower compared to lower pH state. This could be due to the less need of acid resistance activity in higher pH state. In the media glutamine is reduced to glutamate and ammonia. The basic ammonia neutralizes lactic acid and maintain a constant extracellular pH. In the same way, lower pH state requires more acid to be eliminated and thus glutamine uptake in higher. Overall, the obtained data suggests that besides providing nutrients, glutamine conversion is essential to resist continuous acidic stress in extracellular environment of the cancer cells.

Conclusion

The study was performed to support the hypotheses that the highly glutamine dependency of cancer cells is not only because of nutrition but also to fight against acid stress. The experimental findings of higher glutamine consumption in lower pH supports the assumption of the possible acid resistance activity. Elevated cancer cell growth at higher pH state also recommends the importance of acid resistance in cancer cell proliferation. Further studies related to glutamine and acid resistance would help to understand homeostasis and anticancer therapeutic design.

Acknowledgement

This study is mainly supported by International Islamic University Malaysia, Publication Research Grant Scheme; P-RIGS18-037-0037.

References

1. Moyer, M. P., Armstrong, A., Aust, J. B., Levine, B. A. and Sirinek, K. R. (1986). Effects of gastrin, glutamine, and somatostatin on the in vitro growth of normal and malignant human gastric mucosal cells. *Archives of Surgery*, 121(3): 285-288.
2. Vander Heiden, M. G., Cantley, L. C. and Thompson, C. B. (2009). Understanding the Warburg effect: the metabolic requirements of cell proliferation. *Science*, 324(5930): 1029-1033.
3. Hensley, C. T., Wasti, A. T. and DeBerardinis, R. J. (2013). Glutamine and cancer: cell biology, physiology, and clinical opportunities. *The Journal of Clinical Investigation*, 123(9): 3678-3684.
4. Corbet, C. and Feron, O. (2015). Metabolic and mind shifts: from glucose to glutamine and acetate addictions in cancer. *Current Opinion in Clinical Nutrition & Metabolic Care*, 18(4): 346-353.
5. Huang, W., Choi, W., Chen, Y., Zhang, Q., Deng, H., He, W. and Shi, Y. (2013). A proposed role for glutamine in cancer cell growth through acid resistance. *Cell Research*, 23(5): 724.
6. Bayley, J. P. and Devilee, P. (2012). The Warburg effect in 2012. *Current Opinion in Oncology*, 24(1): 62-67.
7. Kee, H. J. and Cheong, J. H. (2014). Tumor bioenergetics: an emerging avenue for cancer metabolism targeted therapy. *BMB reports*, 47(3): 158.
8. Warburg, O. (1956). On the origin of cancer cells. *Science*, 123(3191): 309-314.
9. Griffiths, J. R. (1991). Are cancer cells acidic? *British journal of cancer*, 64(3): 425.
10. Eagle, H. (1955). Nutrition needs of mammalian cells in tissue culture. *Science*, 122(3168): 501-504.
11. Medina, M. A., Sánchez-Jiménez, F., Márquez, J., Quesada, A. R. and de Castro Núñez, I. (1992). Relevance of glutamine metabolism to tumor cell growth. *Molecular and Cellular Biochemistry*, 113(1): 1-15.
12. Sambrook, J. and Russell, D. W. (2006). Estimation of cell number by hemocytometry counting. *Cold Spring Harbor Protocols*, *2006*(1), pdb-prot4454.
13. White, K. A., Grillo-Hill, B. K. and Barber, D. L. (2017). Cancer cell behaviors mediated by dysregulated pH dynamics at a glance. *Journal of Cell Science*, 130(4): 663-669.
14. Vander Heiden, M. G., Cantley, L. C. and Thompson, C. B. (2009). Understanding the Warburg effect: the metabolic requirements of cell proliferation. *Science*, 324(5930): 1029-1033.
15. Helmlinger, G., Sckell, A., Dellian, M., Forbes, N. S. and Jain, R. K. (2002). Acid production in glycolysis-impaired tumors provides new insights into tumor metabolism. *Clinical Cancer Research*, 8(4): 1284-1291.
16. Tannock, I. F. and Rotin, D. (1989). Acid pH in tumors and its potential for therapeutic exploitation. *Cancer Research*, 49(16): 4373-4384.

Malaysian Journal of Analytical Sciences, Vol 23 No 4 (2019): 586 - 594
DOI: https://doi.org/10.17576/mjas-2019-2304-04

MALAYSIAN JOURNAL OF ANALYTICAL SCIENCES
Published by The Malaysian Analytical Sciences Society
ISSN 1394 - 2506

COMPARISON OF EXTRACTION TECHNIQUES FOR THREE *Calophyllum* SPECIES AND THEIR ANTIOXIDANT ACTIVITY

(Perbandingan Teknik Pengekstrakan untuk Tiga Spesies *Calophyllum* dan Aktiviti Antioksidan)

Siti Nurhafizah Ramli[1], Nurul Iman Aminudin[1]*, Farediah Ahmad[2], Deny Susanti[1]

[1]*Department of Chemistry, Kulliyyah of Science,*
International Islamic University Malaysia, 25200 Kuantan, Pahang, Malaysia
[2]*Department of Chemistry, Faculty of Science,*
Universiti Teknologi Malaysia, 81310 Skudai, Johor, Malaysia

**Corresponding author: nuruliman@iium.edu.my*

Received: 19 August 2018; Accepted: 23 June 2019

Abstract

Calophyllum is a pan-tropical genus belonging to the Guttiferae family and is known in Malaysia as '*bintangor*'. There has been continual interest to further investigate the phytochemistry of *Calophyllum* species since this genus is a rich source of active secondary metabolites, which show anti-HIV, cytotoxicity, and antimicrobial properties. This study was conducted to investigate the effect of extraction techniques on the phytochemicals content and antioxidant activity of the barks, leaves, and heartwood extracts of three *Calophyllum* species, namely *C. incrassatum*, *C. rubiginosum*, and *C. canum*. Soxhlet and maceration extraction techniques by using methanol as solvent were chosen in this study. The maceration extraction technique produced higher percentage yield as compared to Soxhlet extraction for leaves and barks of the three *Calophyllum* species. The highest percentage yield was obtained from the bark extract of *C. canum* (21.76%), followed by the bark extract of *C. rubiginosum* (20.24%) and leaves extract of *C. rubiginosum* (19.34%). Meanwhile, the Soxhlet extraction technique gave higher percentage yield as compared to the maceration technique for heartwood extracts of all samples. The phytochemical screening test revealed that all extracts contained tannin, phenol, flavonoid, terpenes, cardiac glycoside, coumarin, and phytosterol. The highest total phenolic content was obtained from Soxhlet extraction technique. The bark extract of *C. canum* displayed the highest phenolic content (461.90 mg GAE/g), followed by the bark extract of *C. incrassatum* (394.52 mg GAE/g) and leaves extract of *C. incrassatum* (227.89 mg GAE/g). The bark extract of *C. canum* showed the lowest IC_{50} value (3.07 µg/mL), followed by the bark extract of *C. incrassatum* (5.12 µg/mL) and leaves extract of *C. incrassatum* (5.93 µg/mL). Pearson's correlation test showed a positive correlation between total phenolic content and DPPH radical scavenging activity.

Keywords: *Calophyllum, C. incrassatum, C. rubiginosum, C. canum,* antioxidant

Abstrak

Calophyllum ialah sejenis genus pan-tropika milik keluarga Guttiferae dan dikenali di Malaysia sebagai *'bintangor'*. Terdapat minat yang berterusan untuk mengkaji fitokimia *Calophyllum* spesies memandangkan genus ini merupakan sumber yang kaya dengan metabolit sekunder aktif yang menunjukkan ciri-ciri anti-HIV, sitotoksisiti dan antimikrob. Kajian ini dijalankan untuk mengkaji kesan teknik pengekstrakan terhadap kandungan fitokimia dan aktiviti antioksidan daripada ekstrak kulit, daun dan batang daripada tiga spesies *Calophyllum*, *C. incrassatum*, *C. rubiginosum* dan *C. canum*. Teknik pengekstrakan Soxhlet dan rendaman dengan menggunakan metanol sebagai pelarut telah dipilih dalam kajian ini. Teknik pengekstrakan rendaman menghasilkan hasil peratusan yang lebih tinggi berbanding dengan pengekstrakan Soxhlet untuk daun dan kulit ketiga-tiga spesies *Calophyllum*. Hasil peratusan paling tinggi diperoleh daripada ekstrak kulit *C. canum* (21.76%) diikuti oleh ekstrak kulit *C. rubiginosum* (20.24%) dan ekstrak daun *C. rubiginosum* (19.34%). Sementara itu, teknik pengekstrakan Soxhlet memberikan hasil peratusan yang lebih tinggi berbanding dengan teknik rendaman untuk ekstrak batang dari semua sampel. Ujian saringan fitokimia menunjukkan semua ekstrak mengandungi tanin, fenol, flavonoid, terpena, kardiak glikosida, komarin dan fitosterol.

Jumlah kandungan fenolik tertinggi diperolehi daripada teknik pengekstrakan Soxhlet. Ekstrak kulit *C. canum* menunjukkan kandungan fenolik tertinggi (461.90 mg GAE/g) diikuti oleh ekstrak kulit *C. incrassatum* (394.52 mg GAE/g) dan ekstrak daun *C. incrassatum* (227.89 mg GAE/g). Ekstrak kulit *C. canum* menunjukkan nilai IC_{50} terendah (3.07 μg/mL) diikuti oleh ekstrak kulit *C. incrassatum* (5.12 μg/mL) dan ekstrak daun *C. incrassatum* (5.93 μg/mL). Ujian korelasi Pearson menunjukkan korelasi positif antara jumlah kandungan fenolik dan aktiviti pemerangkapan radikal DPPH.

Kata kunci: *Calophyllum, C. incrassatum, C. rubiginosum, C. canum,* antioksidan

Introduction

Calophyllum, or locally known as '*bintangor*' is one of the genera in the Guttiferae family. It had been used traditionally to treat a variety of health conditions, such as malaria, bronchitis, inflammation, diabetes, and other health problems [1]. Researchers have developed interest to investigate this species due to the isolation of coumarins known as '*the calanolides*' from *C. lanigerum* against HIV-1 replication [2]. In addition, phytochemical studies reporting on other *Calophyllum* species revealed that they are rich with bioactive compounds such as xanthones, flavonoids, and triterpenoids [1]. These compounds display a broad spectrum of bioactivity, e.g. antioxidant, anti-HIV, anti-fungal, anti-malarial, and cytotoxicity [3].

Plant extraction is the most important step in a phytochemical study since the quality and quantity of the extracts are the key factors that influence the type of isolated compounds and bioactivity results. There are limited numbers of phytochemical studies reported on these three *Calophyllum* species, i.e. *C. incrassatum*, *C. rubiginosum, and C. canum*. Hence, the best extraction technique suitable for these three species is unknown. The commonly used extraction technique reported for other *Calophyllum* species is maceration [4-5]. However, there are also several reports on the *Calophyllum* species that employed Soxhlet extraction [6-7]. Hence, this study was designed to compare the best extraction technique between maceration and Soxhlet techniques for *C. incrassatum*, *C. rubiginosum*, and *C. canum* since the best techniques for these species are yet to be determined. In this study, the extracts from both extraction techniques were evaluated qualitatively through phytochemical screening, and quantitatively through antioxidant assay. The reliability and correlation of the data obtained through antioxidant assay was determined by performing statistical analyses, namely *t*-test and Pearson's correlation.

Materials and Methods

Chemicals and reagents

Ferric (III) chloride, sodium hydroxide, chloroform, sulphuric acid, glacial acetic acid, acetic anhydride and sodium carbonate were obtained from R&M Chemicals. Meanwhile, gallic acid, 2,2 diphenyl-1-picrylhydrazyl (DPPH), ascorbic acid, butylated hydroxyl toluene (BHT) and Folin-Ciocalteu's reagent were obtained from Sigma Aldrich.

Extraction of *Calophyllum* species

The samples of leaves, barks and heartwoods of all *Calophyllum* species were dried and ground before subjected into extraction process. Soxhlet and maceration extractions were performed employing methanol as the solvent. For Soxhlet, dried samples (100 g) were extracted with methanol (900 mL) for 16 hours and 30 minutes. For maceration, dried samples (50 g) were soaked with methanol (450 mL) in closed beaker for 72 hours. The maceration process was repeated for three times. The extracts were filtered by using filter paper and concentrated under reduced pressure by using rotary evaporator to yield the crude extracts. The crude extracts were kept in vials at 4 ^{o}C before subjected to phytochemical screening and antioxidant assay.

Phytochemical screening of *Calophyllum* species

Test for tannin

A small quantity of extracts was dissolved in a test tube containing methanol (1 mL) followed by the addition of distilled water (2 mL) and ferric (III) chloride solution (10% w/v, 4 drops). The presence of tannin was indicated by formation of greenish brown precipitate [8].

Test for phenol
A small quantity of extract was dissolved in a test tube containing methanol (2 mL) followed by the addition of distilled water (2 mL) and ferric (III) chloride solution (10% w/v, 10 drops). The presence of phenol was indicated by change in colour of extract solution to yellowish green [9].

Test for flavonoid
A small quantity of extract was dissolved in a test tube containing methanol (3 mL) followed by the addition of distilled water (10 mL). The test tube was gently shaken before the addition of sodium hydroxide solution (10% w/v, 1 mL). The presence of flavonoid was indicated by change in colour of extract solution to yellow [10].

Test for terpene
A small quantity of extract was dissolved in a test tube containing methanol (1 mL) followed by the addition of chloroform (2 mL). Then, concentrated sulphuric acid (1 mL) was added carefully along the side of test tube. The presence of terpene was indicated by formation of reddish brown ring [11].

Test for cardiac glycoside
Phytochemical screening for cardiac glycoside was performed according to Killer-Killiani's test. A small quantity of extract was dissolved in a test tube containing methanol (1 mL). Glacial acetic acid containing ferric (III) chloride solution (10% w/v, 1 mL) was added into the test tube followed by addition of concentrated sulphuric acid (1 mL). The presence of cardiac glycoside was indicated by formation of brown ring at the interface [12].

Test for coumarin
A small quantity of extracts was dissolved in a test tube containing methanol (2 mL) followed by the addition of sodium hydroxide solution (10% w/v, 3 mL). The presence of coumarin was indicated by change in colour of extract solution to yellow [13].

Test for phytosterol
Phytochemical screening for phytosterol was performed according to Libermann-Burchard's test. The extract (2 mg) was dissolved in acetic anhydride (1 mL) and heated to boiling. The hot extract solution was immediately cooled in ice bath. Concentrated sulphuric acid (1 mL) was carefully added along the side of test tube. The presence of phytosterol was indicated by formation of brown coloured ring at the interface of two layers [14].

Test for saponin
A small quantity of extracts was dissolved in a test tube containing methanol (3 mL) followed by addition of distilled water (2 mL). The tube was vigorously shaken. The presence of saponin was indicated by formation of frothing layer [10].

Antioxidant assay
Total phenolic content
The total phenolic content of all extracts was assessed by using Folin-Ciocalteau's assay [15]. Samples (40 µL) with concentrations ranging from 1000 until 7.81 µg/mL were mixed with Folin-Ciocalteau's reagent (20 µL) in 96-well microplate. The mixture was allowed to incubate for 5 minutes at room temperature. Upon incubation, sodium carbonate solution (6% w/v, 80 µL) followed by distilled water (60 µL) was added to the reaction mixture and kept in the dark for 90 minutes. The absorbance was recorded at 760 nm. A calibration graph of standard gallic acid was constructed and the total phenolic content of the extracts was expressed as mg Gallic acid equivalent (GAE) per gram of extract.

DPPH radical scavenging activity

DPPH radical scavenging activity of all extracts were evaluated following the method described by Kassim et al. [15] with minor modifications. DPPH reagent (2000 µM, 15 µL) was added to the samples (85 µL) with concentration ranging from 1000 to 7.81 µg/mL in methanol obtained from two-fold serial dilution in 96-well microplate. The reaction mixture was allowed to incubate in dark conditions at room temperature for 30 minutes.

The colour conversion from purple to yellow illustrates the samples are active as antioxidant agents. The absorbance of DPPH radical scavenging activity was measured at 517 nm. The radical scavenging activity were analyzed and compared with ascorbic acid and butylated hydroxytoluene (BHT) as the positive controls. The percentage of DPPH scavenging inhibition was calculated by using the following formula [15]:

$$\text{Scavenging concentration (\%)} = \frac{A_{\text{DPPH blank}} - (A_{\text{sample}} - A_{\text{blank sample}})}{A_{\text{DPPH blank}}} \times 100 \quad (1)$$

where, $A_{\text{DPPH blank}}$ is the absorbance of DPPH solution, A_{sample} is the absorbance of tested sample and DPPH solution and $A_{\text{blank sample}}$ is the absorbance of tested sample without DPPH solution.

Statistical analysis

Triplicates data of each sample were used for statistical analysis with values reported as mean ± standard deviation. Standard curves were generated and calculation of the 50% inhibitory concentration values was performed using GraphPad Prism software. The statistical analysis was performed by using SPSS for Windows (version 22). A *t*-test was performed to determine the significant difference between treatment of samples and control. Pearson's correlation coefficient test was used to determine the correlation between the two antioxidant assays.

Results and Discussion

Extraction yield of *Calophyllum* species

This study proposed two types of extraction method, namely Soxhlet extraction and maceration extraction techniques, to obtain the crude extracts from different parts of *C. incrassatum*, *C. rubiginosum*, and *C. canum*. The percentage yield of extract is shown in Table 1. The maceration technique was identified to provide better extraction yield for the leaves and barks of the three *Calophyllu*m species. The highest yield was obtained from the bark extract of *C. canum* (21.76%), followed by the bark extract of *C. rubiginosum* (20.24%) and leaves extract of *C. rubiginosum* (19.34%). In contrast, the heartwood of the three species gave the highest percentage yield of extract by the Soxhlet extraction technique. The heartwood extract of *C. canum* (9.62%) gave the highest yield, followed by *C. rubiginosum* (6.40%) and *C. incrassatum* (4.39%).

Table 1. Percentage yield of extracts from *Calophyllum* species

Sample	Crude Extract	Percentage Yield (%)
C. incrassatum	CILS	14.38
	CILM	19.34
	CIBS	12.30
	CIBM	18.00
	CIHS	4.39
	CIHM	3.66
*C. rubigi**n**osum*	CRLS	9.18
	CRLM	14.28
	CRBS	14.67
	CRBM	20.24
	CRHS	6.40
	CRHM	3.84

Table 1(cont'd). Percentage yield of extracts from *Calophyllum* species

Sample	Crude Extract	Percentage Yield (%)
C. canum	CCLS	13.46
	CCLM	13.82
	CCBS	20.90
	CCBM	21.76
	CCHS	9.62
	CCHM	3.46

CILS: *C. incrassatum* leaves Soxhlet; CILM; *C. incrassatum* leaves maceration; CIBS: *C. incrassatum* barks Soxhlet; *C. incrassatum* barks maceration; CIHS; *C. incrassatum* heartwoods Soxhlet; CIHM: *C. incrassatum* heartwoods maceration; CRLS; *C. rubiginosum* leaves Soxhlet; CRLM; *C. rubiginosum* leaves maceration; CRBS: *C. rubiginosum* barks Soxhlet; CRBM: *C. rubiginosum* barks maceration; CRHS; *C. rubiginosum* heartwoods Soxhlet; CRHM: *C. rubiginosum* heartwoods maceration; CCLS; *C. canum* leaves Soxhlet; CCLM; *C. canum* leaves maceration; CCBS: *C. canum* barks Soxhlet; CCBM: *C. canum* barks maceration; CCHS; *C. canum* heartwoods Soxhlet; CCHM: *C. canum* heartwoods maceration.

Herein, different extraction techniques had different efficiency and percentage yields due to the degree of availability of extractable compounds. The result indicated that the maceration extraction technique was more effective to produce high percentage yield for the leaves and barks of all *Calophyllum* species. This occurrence was mainly due to the introduction of heat from the Soxhlet extraction technique. Prolonged heating may cause heat sensitive compounds to degrade [16]. Unlike Soxhlet, the maceration technique was able to preserve the heat sensitive compounds. Furthermore, the crudes were extracted thrice in the maceration technique instead of once in Soxhlet. These factors may affect the results and give higher percentage yield from the sample.

Phytochemical screening

Phytochemical analysis of all extracts revealed the presence of tannin, phenol, flavonoid, terpene, cardiac glycoside, coumarin and phytosterol. Meanwhile, saponin was only detected in the bark extract of *C. canum* yielded from Soxhlet extraction technique. The results of the screening were summarized in Table 2.

Table 2. Phytochemical screening of extracts from *calophyllum* species

Sample	Crude	Tannin	Phenol	Flavonoid	Terpene	Cardiac Glycoside	Coumarin	Phytosterol	Saponin
C. incrassatum	CILS	+++	+++	+++	+++	+++	+	+++	-
	CILM	++	+++	++	++	++	+++	+	-
	CIBS	+++	+++	+++	++	++	++	+++	-
	CIBM	+++	++	++	+++	+++	+	+++	-
	CIHS	+	+++	++	++	++	++	++	-
	CIHM	++	++	+	++	++	+	+++	-
C. rubiginosum	CRLS	++	++	+++	+	+	++	++	-
	CRLM	+	++	+++	+	+	++	+	-
	CRBS	+++	+++	++	++	+++	+	++	-
	CRBM	+++	++	+++	+++	+++	++	+++	-
	CRHS	++	++	++	+++	+++	++	++	-
	CRHM	++	+	+	+++	++	+	+	-

Table 2 (cont'd). Phytochemical screening of extracts from *calophyllum* species

Sample	Crude	Tannin	Phenol	Flavonoid	Terpene	Cardiac Glycoside	Coumarin	Phytosterol	Saponin
C. canum	CCLS	+++	+++	++	++	++	+++	+++	+
	CCLM	++	++	++	++	++	++	+	-
	CCBS	+++	+++	++	+++	+++	+++	+++	-
	CCBM	+++	++	+	+++	++	++	++	-
	CCHS	+	++	++	++	++	+	+++	-
	CCHM	+	+	+	+++	++	+	++	-

CILS: *C. incrassatum* leaves Soxhlet; CILM; *C. incrassatum* leaves maceration; CIBS: *C. incrassatum* barks Soxhlet; *C. incrassatum* barks maceration; CIHS; *C. incrassatum* heartwoods Soxhlet; CIHM: *C. incrassatum* heartwoods maceration; CRLS; *C. rubiginosum* leaves Soxhlet; CRLM; *C. rubiginosum* leaves maceration; CRBS: *C. rubiginosum* barks Soxhlet; CRBM: *C. rubiginosum* barks maceration; CRHS; *C. rubiginosum* heartwoods Soxhlet; CRHM: *C. rubiginosum* heartwoods maceration; CCLS; *C. canum* leaves Soxhlet; CCLM; *C. canum* leaves maceration; CCBS: *C. canum* barks Soxhlet; CCBM: *C. canum* barks maceration; CCHS; *C. canum* heartwoods Soxhlet; CCHM: *C. canum* heartwoods maceration; +++ = Highly presence; ++ =Moderately presence; + = Slightly presence; - = Absence

The phytochemical screening test showed the presence of tannin in all extracts from both extraction techniques. From the observation, tannin was observed to be present in a significant amount in all leaves and barks extracts of the three *Calophyllum* species, except the heartwood extracts. The analysis suggested tannin was highly present in the leaves extracts of all *Calophyllum* species obtained through the Soxhlet extraction technique. In contrast, the extraction techniques did not express differences in terms of tannin content for all barks and some heartwood extracts of the *Calophyllum* species. The extracts from leaves, barks, and heartwood of *C. incrassatum*, barks of *C. rubiginosum*, and leaves and barks of *C. canum* obtained from the Soxhlet extraction technique demonstrated the highest phenol content. Meanwhile, for the maceration technique, only the leaves of *C. incrassatum* showed the highest phenol content. Hence, the Soxhlet extraction technique affected the phenol content where most of the extracts displayed higher phenol content as compared to the maceration technique.

The presence of flavonoid was observed in all extracts from both extraction techniques. The extracts from leaves and barks of *C. incrassatum* and leaves of *C. rubiginosum* obtained by the Soxhlet extraction technique expressed higher flavonoid content, which signified that these parts contained the highest amount of flavonoid. Meanwhile for the maceration technique, high content of flavonoid could only be observed in the leaves and barks of *C. rubiginosum*. As a conclusion, the Soxhlet extraction technique demonstrated higher availability of flavonoid content as compared to the maceration technique in most parts of the *Calophyllum* species. In contradiction, the maceration technique yielded better terpene content in most parts of extracts, especially for *C. rubiginosum* and *C. canum*. Terpenes were distributed largely in the extracts from the bark and heartwood of *C. rubiginosum* and bark and heartwood of *C. canum*, respectively.

In general, the qualitative analysis of cardiac glycoside, coumarin, and phytosterol revealed positive presence in all extracts. High content of cardiac glycoside was found in the leaves extract of *C. incrassatum*, bark and heartwood extracts of *C. rubiginosum*, and bark extract of *C. canum* obtained from Soxhlet extraction. Meanwhile, only the leaves and bark extracts of *C. canum* obtained by Soxhlet extraction displayed the highest intensity of coumarin as compared to the other species. Negative presence of saponin was observed in majority parts of extracts from the three *Calophyllum* species. However, saponin was detected from the leaves extract of *C. canum* yielded from the Soxhlet extraction technique in minimum amount.

Antioxidant activity of *Calophyllum* species

The total phenolic content (TPC) of the samples was expressed as mg GAE per gram of extract. The evaluation of TPC was performed by using the calibration curve of standard gallic acid ($y = 0.0021x + 1.7678$, $R^2 = 0.9926$). The TPC of each *Calophyllum* species at the concentration of 1000 µg/mL was calculated and tabulated as displayed in Table 3. The leaves and bark extract of all species from the Soxhlet extraction technique showed higher TPC value as compared to maceration. The highest TPC value was depicted from the bark extract of *C. canum* (461.90 mg

GAE/g), followed by bark extract of *C. incrassatum* (394.52 mg GAE/g), and leaves extract of *C. incrassatum* (227.89 mg GAE/g). Nevertheless, the heartwood extract of *C. incrassatum* displayed the lowest TPC value (2.70 mg GAE/g) as compared to the heartwood of other *Calophyllum* species obtained from the Soxhlet extraction technique.

Table 3. TPC, DPPH SC_{50} and Pearson correlation coefficient values

Sample	Crude	Total Phenolic Content[a] (mg GAE/g of Extract at 1000 µg/mL)	DPPH IC_{50} (µg/mL)[a]	*r* coefficient
C. incrassatum	CILS	227.89 ± 2.14***	5.93 ± 0.22 $^{*b, ***c}$	0.816*
	CILM	67.10 ± 0.18***	26.57 ± 0.60 $^{***b, ***c}$	0.678
	CIBS	394.52 ± 37.86*	5.12 ± 0.10$^{***b, ***c}$	0.572
	CIBM	84.70 ± 15.60***	11.54 ± 1.30$^{**b, c}$	0.924**
	CIHS	2.70 ± 2.55***	39.39 ± 0.58$^{**b, ***c}$	0.905**
	CIHM	65.19 ± 0.74***	27.45 ± 0.35$^{***b, ***c}$	0.813*
C. rubiginosum	CRLS	126.19 ± 4.51**	11.1 ± 0.17$^{***b, ***c}$	0.665
	CRLM	59.71 ± 1.86***	28.43 ± 1.18$^{***b, ***c}$	0.747*
	CRBS	198.00 ± 35.74***	8.56 ± 0.61$^{*b, ***c}$	0.873**
	CRBM	104.14 ± 2.59***	9.22 ± 0.71$^{*b, **c}$	0.918**
	CRHS	64.33 ± 0.76***	27.68 ± 0.20$^{***b, ***c}$	0.892**
	CRHM	42.35 ± 11.80*	31.02± 0.76$^{***b,*** c}$	0.892**
C. canum	CCLS	181.44 ± 3.82*	17.76 ± 0.40$^{***b, ***c}$	0.684
	CCLM	83.62 ± 4.18***	20.31 ± 0.55$^{**b, **c}$	0.746*
	CCBS	461.90 ± 10.97*	3.07 ± 0.43$^{***b, ***c}$	0.713*
	CCBM	77.11 ± 2.78***	11.89 ± 0.74$^{***b, *c}$	0.858**
	CCHS	69.10 ± 3.98***	24.71 ± 0.75$^{**b, ***c}$	0.809*
	CCHM	21.84 ± 0.93	35.50 ± 0.90$^{***b, ***c}$	0.960**
AA[d]			6.92 ± 0.039	
BHT[d]			13.40 ± 0.12	

[a]: Data represents mean ± standard deviation of three replicate experiments; [b]: Significant different value *P* compared to ascorbic acid; [c]: Significant different value *P* compared to BHT; [d]: Positive control; CILS: *C. incrassatum* leaves Soxhlet; CILS: *C. incrassatum* leaves Soxhlet; CILM; *C. incrassatum* leaves maceration; CIBS: *C. incrassatum* barks Soxhlet; *C. incrassatum* barks maceration; CIHS; *C. incrassatum* heartwoods Soxhlet; CIHM: *C. incrassatum* heartwoods maceration; CRLS; *C. rubiginosum* leaves Soxhlet; CRLM; *C. rubiginosum* leaves maceration; CRBS: *C. rubiginosum* barks Soxhlet; CRBM: *C. rubiginosum* barks maceration; CRHS; *C. rubiginosum* heartwoods Soxhlet; CRHM: *C. rubiginosum* heartwoods maceration; CCLS; *C. canum* leaves Soxhlet; CCLM; *C. canum* leaves maceration; CCBS: *C. canum* barks Soxhlet; CCBM: *C. canum* barks maceration; CCHS; *C. canum* heartwoods Soxhlet; CCHM: *C. canum* heartwoods maceration; *: $P < 0.05$; **: $P < 0.01$; ***: $P < 0.001$

All extracts were subjected to TPC determination by using Folin-Ciocalteu's reagent. Generally, this spectrophotometric method allows possible evaluation of all phenolic compounds, such as flavonoids, polyphenols and others [17]. Folin-Ciocalteu's reagent consists of the mixture of phosphomolybdic ($H_3PMo_{12}O_{40}$) and phosphotungstic ($H_3PW_{12}O_{40}$) acid complexes [18]. The detection of phenolic compounds in the extract by using Folin-Ciocalteu assay is dependent on the reaction of phenolic compounds in alkaline medium provided by sodium carbonate solution to the metal acid mixtures. This reaction results in the formation of blue complexes of molybdene (Mo_8O_{23}) and tungsten (W_8O_{23}). The degree of the blue complexes represents the amount of phenolic compounds, which can be measured spectrophotometrically at the wavelength of 760 nm [19].

Conventional solvent extraction methods such as Soxhlet and maceration extraction techniques are frequently used in extracting polyphenolic compounds from plants. The chosen extraction technique plays a significant role in determining the quantity of phenolic constituents in extracts. This study suggested the Soxhlet extraction technique was better to extract phenolic constituents from *C. incrassatum*, *C. rubiginosum*, and *C. canum* as compared to maceration based on their higher TPC values. High content of phenolic compounds might be influenced by the introduction of heat from the Soxhlet technique. An increase in temperature would allow cell structures, such as cell wall, membrane layer and organelles, to disintegrate. Thus, the mass transfer between the soluble phenolic constituents into the solvents was improved [20]. As a result, more phenolic constituents will be available in the extract.

The antioxidant activities of all extracts were also evaluated based on the IC_{50} values in comparison to ascorbic acid (IC_{50} 6.92 µg/mL) and butylated hydroxytoluene (IC_{50} 13.40 µg/mL) as the positive controls. The calculated IC_{50} for all extracts is presented in Table 3. All tested samples that showed ($p < 0.05$) were considered as statistically and significantly different as compared to ascorbic acid and BHT as positive controls. The leaves and barks extracts of all species from the Soxhlet extraction technique gave lower IC_{50} values as compared to maceration. The bark extract of *C. canum* (IC_{50} 3.07 µg/mL), followed by the bark extract of *C. incrassatum* (IC_{50} 5.12 µg/mL) and leaves extract of *C. incrassatum* (IC_{50} 5.93 µg/mL) displayed low IC_{50} values comparable to both positive controls. This result indicated that the three extracts were superior in terms of antioxidant activity as compared to the positive controls. The heartwood extracts of *C. incrassatum* displayed the highest IC_{50} values among all heartwood extracts at IC_{50} 39.39 µg/mL.

The Pearson's correlation analysis was performed to establish a relationship between TPC and DPPH radical scavenging activity using different concentrations ranging from 1000 – 7.81 µg/mL. The correlation coefficient, *r*, was evaluated as depicted in Table 3. Most of the extracts demonstrated positive correlation with *r* coefficient value in the range of 0.573 to 0.960 between the two parameters. This statistical data suggested that high TPC would contribute to high antioxidant activity of the extracts. It could be deduced that the phenolic compounds are the major contributor to the antioxidant activity by the DPPH method.

Conclusion

The maceration technique gave better yield of extracts from the leaves and barks of all *Calophyllum* species. On the other hand, the Soxhlet extraction technique produced higher percentage yield of heartwood extracts. Phytochemical screening of all extracts depicted the presence of tannin, phenol, flavonoid, terpene, cardiac glycoside, coumarin, and phytosterol. However, Soxhlet extraction provided the best phytochemicals content as compared to maceration extraction. This preliminary screening will provide beneficial reference for future research in determining the suitable extraction technique to isolate certain desired classes of compounds, since each method has its own advantages. Most of the extracts also showed potent antioxidant activity, suggesting that natural antioxidant compound can be isolated in the future.

References

1. Alkhamaiseh, S. I., Taher, M., Ahmad, F., Qaralleh, H., Althunibat, O. Y., Susanti, D. and Ichwan, S. J. A. (2012). The phytochemical content and antimicrobial activities of Malaysian *Calophyllum canum* (stem bark). *Pakistan Journal of Pharmaceutical Sciences*, *25*(3): 555–563.
2. Aminudin, N. I., Ahmad, F., Taher, M. and Zulkifli, R. M. (2016). Cytotoxic and antibacterial activities of constituents from *Calophyllum ferrugineum* ridley. *Records of Natural Products*, 10(5): 649–653.
3. Ee, G. C. L., Teh, S. S., Mah, S. H., Jamaluddin, N. A., Muhamad Sahimi, M. S. and Ahmad, Z. (2015). Acetyl-cholinesterase enzyme inhibition effects of *Calophyllum* species. *Tropical Journal of Pharmacautical Research*, 14(11): 2005–2008.
4. Lim, C. K., Hemaroopini, S., Gan, S. Y., Loo, S. M., Low, J. R., Jong, V. Y. M., Soo, H. S., Leong, C. O., Mai, C. W. and Chee, C. F. (2016). *In vitro* cytotoxic activity of isolated compounds from Malaysian *Calophyllum* species. *Medicinal Chemistry Research*, 25(8): 1686–1694.

5. Rea, A., Tempone, A. G., Pinto, E. G., Mesquita, J. T., Rodrigues, E., Silva, L. G. M., Sartorelli, P. and Lago, J. H. G. (2013). Soulamarin isolated from *Calophyllum brasiliense* (Clusiaceae) induces plasma membrane permeabilization of trypanosoma cruzi and mytochondrial dysfunction. *PLoS Neglected Tropical Diseases*, 7(12): 1–8.
6. Attoumani, N., Susanti, D. and Taher, M. (2013). Antioxidant, antimicrobial and total phenolic contents of *Calophyllum symingtonianum*. *Journal of Coastal Life Medicine*, 1(1): 49–53.
7. Cheng Lian Ee, G., Mah, S. H., Teh, S. S., Rahmani, M., Go, R. and Taufiq-Yap, Y. H. (2011). Soulamarin, a new coumarin from stem bark of *Calophyllum soulattri*. *Molecules*, 16(11): 9721–9727.
8. Zohra, S. F., Meriem, B., Samira, S. and Alsayadi Muneer, M. S. (2012). Phytochemical screening and identification of some compounds from mallow. *Journal of Natural Product Plant Research*, 2(4): 512–516.
9. Ojiako, E. N. (2014). Phytochemical analysis and antimicrobial screening of *Moringa oleifera* leaves extract. *The International Journal of Engineering and Sciences*, 3(3): 32–35.
10. Belay, K. and Sisay, M. (2014). Phytochemical constituents and physicochemical properties of medicinal plant (*Moringa oleifera*) around bule hora. *Chemistry and Materials Research Online)*, 6(7): 2225–956.
11. Khanum, R., Jahangir, M., Aziz-Ur-Rehman, Abbasi, M. A., Mazhar, F., Kausar, S., Riaz, T. and Ajaib, M. (2013). Phytochemical screening and antioxidant evaluations of different fractions of *Argyrolobium roseum*. *Asian Journal of Chemistry*, 25(13): 7485–7489.
12. Solihah, M., Wan Rosli, W. and Nurhanan, A. (2012). Phytochemical screening and total phenolic content of Malaysian *Zea Mays* hair extracts.19(4): 1533–1538.
13. Fowoyo, P. T. and Oladoja E. O. (2015). Phytochemical screening, nutritional composition and antimicrobial activity of *Moringa oleifera* seed and leaf extract against selected gastrointestinal pathogens. *IOSR Journal of Pharmacy and Biological Sciences*,10(6): 2319–7676.
14. Joshi, A., Bhobe, M. and Sattarkar, A. (2013). Phytochemical investigation of the roots of *Grewia microcos* linn. *Journal of Chemical and Pharmaceutical Research*, 5(7): 80–87.
15. Kassim, N. K., Rahmani, M., Ismail, A., Sukari, M. A., Ee, G. C. L., Nasir, N. M. and Awang, K. (2013). Antioxidant activity-guided separation of coumarins and lignan from *Melicope glabra* (Rutaceae). *Food Chemistry*, 139: 8792.
16. Abd Hamid, N. H., Latip, J. and Markom, M. (2018). the effect of different conventional methods of extraction on *Marantodes pumila var. pumila* leaves in relation to free radical scavenging activity. In *The 2017 UKM FST Postgraduate Colloqium*. AIP Publising.
17. Benvenuti, S., Pellati, F., Melegari, M. and Bertelli, D. (2004). Polyphenols, anthocyanins, ascorbic acid, and radical scavenging activity of *Rubus*, *Ribes*, and *Aronia*. *Journal of Food Science*, 69(3): 164–169.
18. Ainsworth, E. A. and Gillespie, K. M. (2007). Estimation of total phenolic content and other oxidation substrates in plant tissues using Folin-Ciocalteu reagent. *Nature Protocols*, 2(4): 875–877.
19. Azlim-Almey, A. A., Ahmed J. K. C., Syed Zahir, I., Mustapha, S. K., Aisyah, M. R. and Kamarul R. K. (2010). Total phenolic content and primary antioxidant activity of methanolic and ethanolic extracts of aromatic plant leaves. *International Food Research Journal*, 17: 1077–1083.
20. Javier, D. V. A., Hector, R.-E., Juan Jose, L.-G., Maria L, L.-G., Paola, H.-C., Raúl, Á.-S. and Carlos Enrique, O.-V. (2017). Effect of solvents and extraction methods on total anthocyanins, phenolic compounds and antioxidant capacity of *Renealmia alpinia* (Rottb.) maas peel. *Czech Journal of Food Sciences*, 2017: 456–465.

Malaysian Journal of Analytical Sciences, Vol 23 No 4 (2019): 595 - 603
DOI: https://doi.org/10.17576/mjas-2019-2304-05

MALAYSIAN JOURNAL OF ANALYTICAL SCIENCES
Published by The Malaysian Analytical Sciences Society
ISSN 1394 - 2506

A GREEN COLORIMETRIC METHOD USING GUAVA LEAVES EXTRACT FOR QUALITY CONTROL OF IRON CONTENT IN PHARMACEUTICAL FORMULATIONS

(Kaedah Kalorimetrik Hijau Mengunakan Ekstrak Daun Jambu Bagi Kawalan Kualiti Kandungan Besi di dalam Formulasi Farmaseutikal)

Watsaka Siriangkhawut[1]*, Kraingkrai Ponhong[1], Kate Grudpan[2]

[1]*Creative Chemistry and Innovation Research Unit,*
Department of Chemistry and Center of Excellence for Innovation in Chemistry, Faculty of Science,
Mahasarakham University, Maha Sarakham 44150, Thailand
[2]*Department of Chemistry, Faculty of Science,*
Center of Excellence for Innovation in Analytical Science and Technology,
Chiang Mai University, Chiang Mai 50200, Thailand

**Corresponding author: watsaka@hotmail.com*

Received: 17 April 2019; Accepted: 22 June 2019

Abstract

A cost-effective and environmentally friendly approach using a simple micro-volume colorimetric method with non-synthetic reagent from plant extracts has been proposed. The crude aqueous extracts from dried guava leaves were utilized as an alternative natural reagent for quantification of iron. The method was based on the measurement of a dark brown complex formed by the reaction between Fe(III) and the crude aqueous extracts in acetate buffer pH 4.5 at 562 nm. The optimum conditions for the extraction parameters such as type of solvent, extraction time and mass of dried plant were investigated. Under the optimum conditions, a linear calibration graph in the range of 1.0 - 10.0 mg L^{-1} Fe(III) was obtained with limits of detection and quantification of 0.30 and 1.0 mg L^{-1} Fe(III), respectively. Relative standard deviations of 2.6 and 2.1% were achieved for 2.0 and 4.0 mg L^{-1} Fe(III) (n=7), respectively. The developed method was successfully applied to quality control of iron in antianemic drug samples. The results are in good agreement with those obtained by the FAAS method at the 95% confidence level. High percentage recoveries between 93 and 99% were obtained.

Keywords: guava leaf, natural reagent, colorimetry, iron, pharmaceutical formulations

Abstrak

Pendekatan yang mesra alam dan kos efektif mengunakan kaedah kalorimetrik isipadu-mikro yang mudah dikemukakan dalam kajian ini. Ekstrak akues dari daun jambu yang dikeringkan telah digunapakai sebagai alternatif reagen semulajadi bagi pengkuantitian kandungan besi. Kaedah berasaskan pengukuran kompleks coklat gelap yang terhasil melalui tindak balas Fe(III) dan bahan mentah ekstrak di dalam larutan penimbal asetat pH 4.5 pada 562 nm. Keadaan optimum untuk parameter pengekstrakan seperti jenis pelarut, masa pengekstrakan dan jisim daun yang dikeringkan telah dikaji. Pada keadaan optimum, graf kalibrasi linear diperolehi pada julat 1.0 - 10.0 mg L^{-1} Fe(III) dengan had pengesanan dan pengkuantitian masing-masing ialah 0.30 and 1.0 mg L^{-1} Fe(III). Sisihan piawai relative dicapai pada 2.6 dan 2.1% masing-masing bagi 2.0 and 4.0 mg L^{-1} Fe(III) (n=7). Kaedah yand dibangunkan telah Berjaya digunapakai bagi tujuan kawalan kualiti besi di dalam sampel dadah antianemik. Keputusan yang diperolehi adalah standing dengan hasil yang diperolehi mengunakan kaedah FAAS pada aras keyakinan 95%. Peratus perolehan semula yang tinggi antara 93 dan 99% telah diperolehi.

Keywords: daun jambu, reagen semulajadi, kalorimetri, besi, formulasi farmaseutikal

Introduction

Iron (Fe) is an essential mineral. Iron-deficiency anemia [1] is a serious health problem affecting a large proportion of the world's population especially high prevalence in women and children. Most iron-deficiency anemias respond well to treatment with oral or parenteral iron which contains iron (II) or iron(III) compounds to increase the number of red blood cells [2]. However, pharmaceuticals often cause side effects: nausea, anorexia, diarrhea and metal taste in the mouth [3]. Therefore, it is important to develop a simple, fast and inexpensive method for quality control of antianemic drugs and determination of iron content in pharmaceutical formulations, especially when a lot of samples have to be analyzed in the minimum of time.

Analytical techniques commonly used for iron determination in pharmaceutical formulations include flame atomic absorption spectrometry (FAAS) [4], inductively coupled plasma-optical emission spectrometry (ICP-OES) [5], and spectrophotometry using various complexing agents such as 4-(2-pyridylazo) resorcinol [6], pyrocatechol [7], ferrozine [8], Ferene S [8], 1,10-phenanthroline [8,9] and Tiron [10, 11].

Nowadays, green analytical technique or procedure which concerns the use of environmentally friendly chemicals and small-volume process is of much interest [12]. The extracts of plant or animal tissues with little purification or modification, natural reagents, have been used instead of high purity chemical reagents when a reagent is only required in excess, or a crude extract contains the necessary active compound [13]. The crude plant extracts including guava (*Psidium guajava* Linn.) leaves extract [14], green tea (*Camellia sinesis*) extract [15,16], *Phyllanthus emblica* Linn. [17] and *Smilax china* L. root extract [18] were reported as chromogenic agent for analysis of iron in combination with flow-based analytical techniques.

Guava (*Psidium guajava* L.) is widely cultivated and its fruit is popular in Asia. Literature studies considered these leaves as a promising source of phenolic compounds such as gallic acid, ferulic acid, catechin, quercetin and kaemferol [19-21]. Phenolic compounds contain a hydroxyl group are responsible for binding to or chelating with metal ions and phenolic groups in the presence of a third adjacent hydroxyl (pyrogallols) show increased stability with the Fe(III) ion [22].

In 2005, fresh guava leaves extract has been published as a model natural reagent for iron(III) analysis in spiked water samples using flow injection analysis system [14]. However, the low sensitivity was obtained and the reproducibility for extraction of fresh guava leaves extracts is low depending on the batch of fresh guava leaves and also on the season. Until now, the application of guava leaves extract for iron determination in real samples was not published elsewhere. Therefore, this work was aim to develop a simple and reliable method using natural reagent extracted from dried guava leaves as chromogenic reagent for iron determination in pharmaceutical samples. The microplate reader with visible detection was used to minimize the reagent/chemical usage, reduce the waste production during analysis, and provide fast measurement.

Materials and Methods

Chemicals and reagents

All chemicals used were of analytical reagent grade. Deionized water from a Simplicity 185 (Millipore, Billerica, MA, USA) with resistivity of 18.2 MΩ cm was used throughout the experiments. A 1000 mg L^{-1} Fe(III) standard solution for FAAS (Merck, Darmstadt, Germany) was used for all experimental study. Working standard solutions of iron with different concentrations were prepared by appropriately diluting the stock solution. Acetate buffer solutions at different pH were prepared from sodium acetate (Carlo Erba, Milano, Italy) and acetic acid (Carlo Erba, Milano, Italy). Methanol (Merck, Darmstadt, Germany), ethanol (Merck, Darmstadt, Germany), and acetone (Carlo Erba, Milano, Italy) were used as extracting solvent. Hydrochloric acid (HCl, 37%) (Univar, Ingleburn, New South Wales, Australia) was used for dissolution of the samples. Tannic acid (Carlo Erba, Milano, Italy), Folin-Ciocalteu reagent (Merck, Darmstadt, Germany), and sodium bicarbonate (Carlo Erba, Milano, Italy) were used for analysis of total phenolic contents.

Instrumentation
A visible spectrophotometer, Genesys^{TM} 20 (Thermo Fisher Scientific, USA) with Thermo Scientific VISION*lite 5* software was used for scanning the absorbance at selected wavelengths. A microplate reader, EZ Read 800 (Biochrom, UK) was used for micro-volume colorimetric determination using 96 well microplate. All pH measurements were conducted using a pH meter (Model 713, Metrohm, Switzerland). The FAAS measurements were performed with an Agilent 280FS AA atomic absorption spectrometer (Agilent Technologies, CA, USA) equipped with a deuterium background corrector. Detection wavelength for Fe was 248.3 nm and all instrumental conditions were followed according to the manufacturer's recommendation using an air/acetylene flame.

Preparation of natural reagent
Guava leaves (> 5 kg) were collected in August 2017 and then cut into small pieces, cleaned, washed with deionized water and air dried. The dried leaves were ground to fine powder form using a blender machine (La Moulinette DPA 130, Tefal, France) and then homogeneously mixed and stored in a dry place until required for use.

Plant powder (5.0 g) and deionized water or other solvents (100 mL) were stirred in an extraction flask for 30 minutes. The extract was filtered through a filter paper (Whatman® No.4, UK) and made up to a volume of 100 mL with deionized water.

Total phenolic contents
Total phenolic contents, in terms of tannic acid equivalents of the guava leaf extracts, were determined using the Folin-Ciocalteu reagent assay (method 952.03) [23]. An aliquot of guava leaves extract or standard tannic acid solution was pipetted into a 100 mL volumetric flask containing 75 mL of water. Then, 5 mL of Folin-Ciocalteu reagent and 10 mL of sodium carbonate saturated solution were added and the volume was adjusted with deionized water. The solutions were mixed and allowed to stand for 30 minutes at room temperature. Finally, absorbance was measured at 760 nm.

Sample preparation
Ten commercially available pharmaceutical samples of two different forms of ferrous fumarate (F1-F7) and ferrous sulfate (S1-S3) were selected and bought directly from drug stores in Maha Sarakham Province, Thailand. Prior to analysis, a set of 20 tablets was weighed and manually ground to fine powder with an agate mortar and pestle.

Samples were prepared following the Association of Official Analytical Chemists (AOAC) method 977.30 [24]. Briefly, a portion of fine powder containing about 60 mg Fe, was accurately weighed and mixed with 100 mL of water and 4 mL of concentrated HCl. The mixture was boiled in a steam bath for 30 minutes and then allowed to cool to room temperature before dilution with water to a volume of 200 mL, placed in a volumetric flask and filtrated through a filter paper (Whatman® No.1, UK). Iron content was analyzed by FAAS. For analysis by the proposed colorimetric method, hydrogen peroxide was added to ensure the complete oxidation of Fe(II) to Fe(III).

Micro-volume colorimetric assay
This assay was performed in 96 well microplate and reactive solutions were measured by a micro-volume colorimeter. For the construction of standard curves, 50 µL of natural reagent and 50 µL of acetate buffer pH 4.5 were added to each well of microplate. Then, aliquots comprising seven different concentrations (0, 1, 2, 4, 6, 8, and 10 mg L^{-1}) of iron standard solutions or sample solutions were added. Deionized water was then used to make up the volume to 250 µL per well. The microplate was shaken to mix the contents, followed by reading at 562 nm using a microplate reader.

Results and Discussion

Extraction of natural reagent from guava leaves
The main components in guava leaf are phenolic compounds [19-21]. Type of solvent has a strong impact on the yield of extraction. In this study, different polar solvents such as methanol, ethanol, acetone and water were investigated. Total phenolic contents (as tannic acid) of each extract were evaluated. The methanol extract gave the highest tannic acid (3.19 g/100g). The total phenolic contents (as tannic acid) for ethanol, acetone and water were 1.98, 0.37 and 2.85 g/100g, respectively. However, it would be more beneficial if the extraction could be carried out

in the aqueous phase and used directly without purification [13]. Therefore, water was selected as the suitable extraction solvent for its simplicity and the reduced of amounts of chemicals used.

One interesting property of polyphenolic compounds is their ability to influence iron absorption. For the preliminary study, a simple extraction method for guava leaves was performed by stirring with water. Crude aqueous extract from guava leaf was used as natural reagent without purification. Complexation of crude extract with iron and other metal ions was subjected to preliminary investigation by the batchwise method. As shown in Figure 1, the mixture of crude aqueous extracts with a buffer solution at 4.5 had a yellow color. After mixing the extracts with other metal ions such as copper, aluminium and iron, marked changes in color were observed only for iron which turned from yellow to dark brown. Obvious differences in absorption spectra of natural reagent and natural reagent with iron were observed with maximum absorption wavelength of 570 nm. This result indicated the possibility of iron complexation with crude extract from guava leaves.

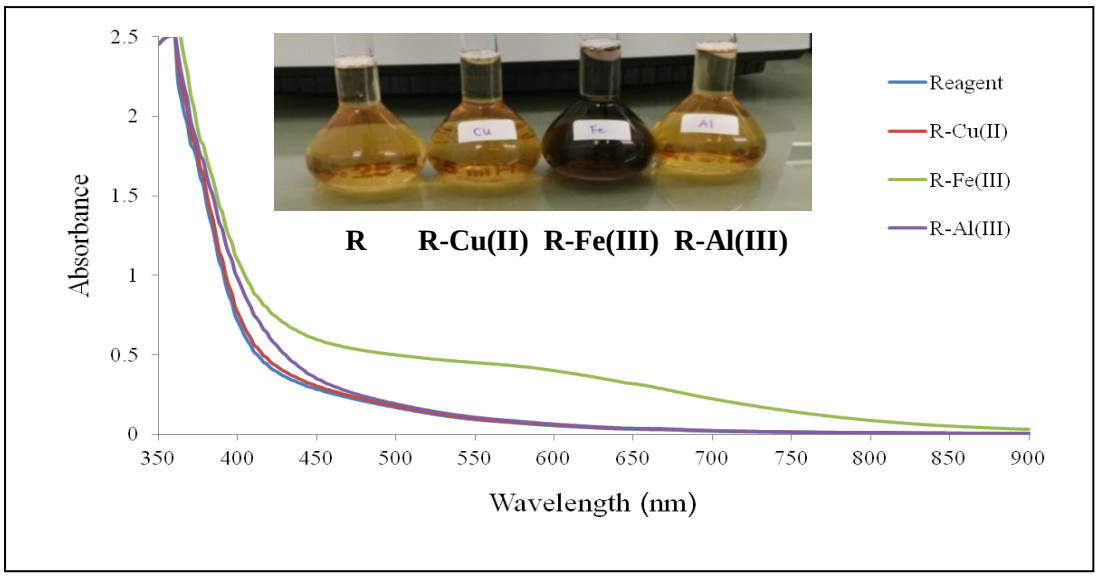


Figure 1. Visual detection and visible spectra of natural reagent (R) with Cu(II), Fe(III) and Al(III) at pH 4.5

Effect of pH on the complexation of natural reagent with iron was investigated over the range of 3.5 – 6.0 using 1 M acetate buffer (n=3). As shown in Figure 2, absorbance of iron-reagent complex increased with pH from 3.5 to 4.5. At pH 5.0 – 6.0, the turbid solutions were observed, thus, the absorbance cannot be measured. This result indicated that the iron-reagent complex forms efficiently in the range of pH 4.5. Therefore, the acetate buffer pH 4.5 was chosen.

Interaction of Fe(II)/Fe(III) with natural reagent extract was also investigated and compared for sensitivity. Both Fe(II) and Fe(III) formed color complexes with guava leaves extract and Fe(III)-natural reagent complex had higher molar absorptivity. Therefore, to obtain the best sensitivity, Fe(III) was chosen as the standard to form complexes with natural reagents for construction of calibration/standard addition graphs.

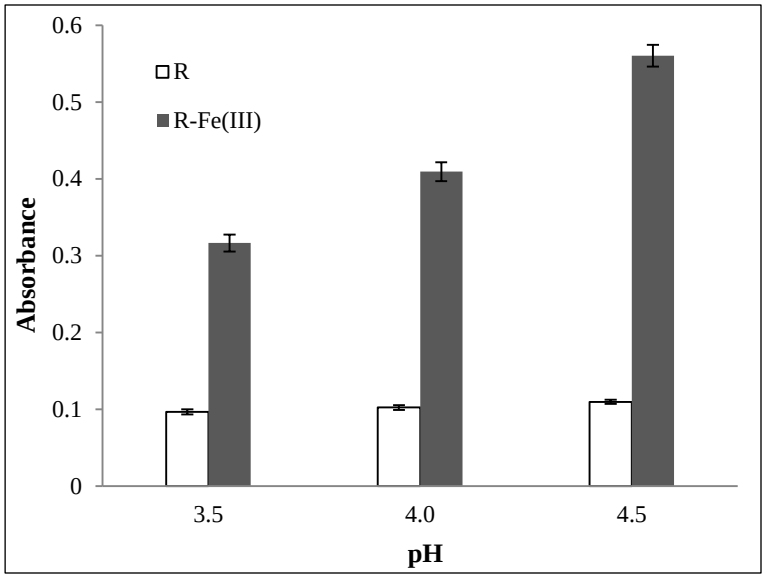


Figure 2. Effect of pH on the complexation of natural reagent with iron

The influence of extraction time on the extraction yield of phenolic compounds was investigated from 15, 30, 45 and 60 minutes (n=3). As shown in Figure 3, absorbance of the reagent and iron-reagent complex increased slightly with increasing extraction time from 15 to 30 minutes, and then remained constant with increasing extraction time from 30 to 60 minutes. This might be due to the excess total phenolic compounds in the extracts. Therefore, an extraction time of 30 minutes was selected as suitable.

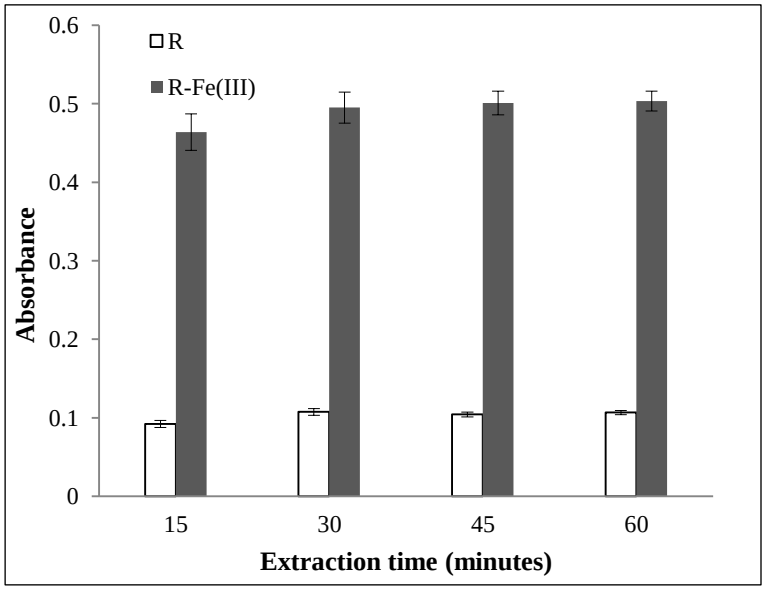


Figure 3. Effect of extraction time on the extraction yield of phenolic compounds

The amount of plant material related to the extraction yield was investigated by varying the weight of guava leaf powder from 3.0, 4.0, 5.0, and 6.0 g and extracting with 100 mL of deionized water (n=3). As shown in Figure 4,

the absorbance increased with increasing amounts of plant powder from 3.0 - 4.0 g, and then remained constant. The ratio of 5.0 g of plant material per 100 mL of water was selected for the extraction procedure.

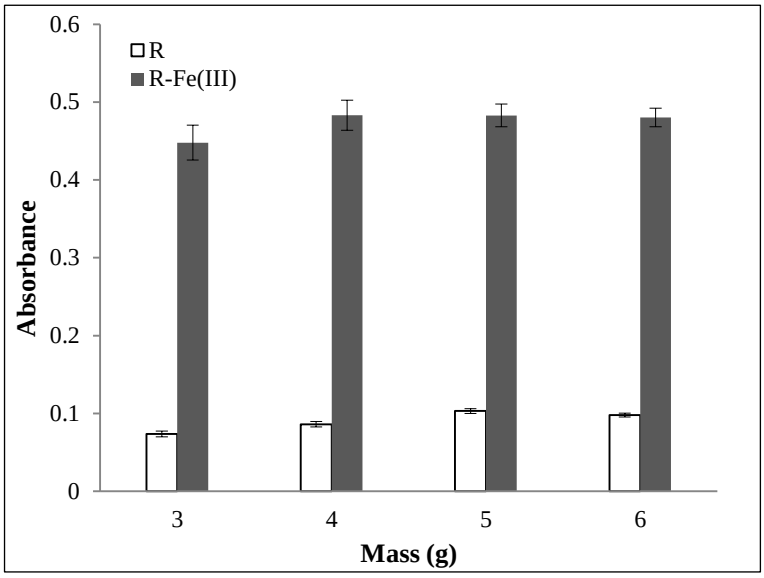


Figure 4. Effect of guava leaves mass on the extraction yield of phenolic compounds

To ensure the reproducibility of the various batches of natural reagent extracts for future use, the precision of absorbance of 10 batches of the extracts prepared independently was evaluated. The relative standard deviation (%RSD) for all 10 batches was 5.7% which is an acceptable range.

The stability of natural reagent and its complex were investigated. Absorbance of natural reagent with Fe(III) was recorded. A mixture of iron and freshly prepared extract was used for comparison. The signal of natural reagent did not show any loss in performance within 72 hours (3 days).

Analytical characteristics of the proposed micro-volume colorimetric method for iron

Analytical characteristics of the proposed colorimetric method were investigated using a microplate reader colorimeter at 562 nm. Under optimum extraction conditions as described above, standard calibration in the range of 1.0-10.0 mg L^{-1} was constructed by plotting absorbance against iron concentration. A linear calibration graph was obtained with calibration equation $y = 0.0527x + 0.1196$, $R^2 = 0.9974$. The limits of detection ($3\sigma/s$) and quantification ($10\sigma/s$) (where σ is the standard deviation of reagent blank (n=11) and s is the slope of the calibration curve) for iron were obtained at 0.30 and 1.0 mg L^{-1}, respectively. The relative standard deviation for seven replicate determinations of 2 mg L^{-1} and 4 mg L^{-1} were 2.6 and 2.1%, respectively.

The analytical performance of the proposed method with previous flow-based methods using other natural reagents such as fresh guava (*Psidium guajava* L.) leaves extract [14], green tea (*Camellia sinesis*) extract [15] *Phyllanthus emblica* L. extract [17] and *Smilax china* L. root extract [18] was summarized in Table 1. Although the proposed method was not as sensitive as some reported for other flow-based system, the sensitivity of this proposed method is enough to measure iron in pharmaceutical samples. The sampling rate of this method is comparable to those of previous flow-based system from its speed of simultaneously detection in 96 well of each microplate. Moreover, this method reduces contamination risk, performs on common and inexpensive equipment with a minimum of training. As compared to the fresh guava leaves extracts [14], the guava leaves extracts prepared from dried guava leaves powder could be a better alternative source of reagent because the dried plant powder can be stored for long time and its availability with homogeneity.

Table 1. The analytical characteristics of the colorimetric determination method for iron(III)

Method	Natural reagent	Linear Range (mg L^{-1})	LOD (mg L^{-1})	Sampling Rate (h^{-1})	Sample Volume (µL)	Ref.
Flow injection	Fresh guava (*Psidium guajava* L.) leaves extract	1 – 10	1	20	80[a]	[14]
Flow injection	Green tea (*Camellia sinesis*) extract	1.0 – 20.0	0.05	180	80[a]	[15]
Flow injection	*Phyllanthus emblica* L. extract	0.50 – 20.0	0.31	90	200[a]	[17]
Sequential injection	*Smilax china* L. root extract	1 - 8	0.05	12	150[b]	[18]
Microplate reader	Dried guava (*Psidium guajava* L.) leaves extract	1.0 – 10.0	0.30	>90	250[b]	This work

[a] sample volume only
[b] total analysis volume (sample+reagent+other solutions)

Effect of interfering species on the iron-natural reagent complex was investigated using the proposed method under optimum conditions. Various concentrations of foreign ions (Ca^{2+}, Mg^{2+}, Co^{2+}, Ni^{2+}, Cu^{2+}, Mn^{2+} and Cr^{3+}) were spiked into a standard solution of 5 mg L^{-1} Fe(III). An interfering concentration was considered as the value that caused signal variations higher than ±10%. Results showed that the system could tolerate spiked cations up to at least a 1:1 concentration ratio of iron to interfering cations. Higher interference ratios were not studied since these minerals are normally found in pharmaceutical formulations at lower amounts than iron compounds.

Application to pharmaceutical samples

The proposed method was employed for the determination of iron in pharmaceutical formulations in two different forms (ferrous fumarate and ferrous sulfate). Amounts of iron found in pharmaceutical samples after dissolution by standard method for analysis of iron in drugs [24] were compared with their label values and analyzed by FAAS. Results are presented in Table 2. Iron contents in all samples obtained from FAAS and proposed methods were determined in an acceptable range (90.0 – 110.0 %) of the labeled amounts. A *t*-test at 95% confidence limit, indicated that results obtained from both methods were in good agreement (t_{crit} = 2.26, t_{cal} = 1.07). Satisfactory recoveries in the range of 93-99% for all pharmaceutical samples were obtained. These results indicated that the proposed method was comparable to the reference method. This proposed method provides some advantages over the FAAS method including ease of operation, low cost of instrument, low chemical consumption, and high sample throughput.

Table 2. Determination of iron in pharmaceutical formulations (n = 3)

Sample[a]	Label Amount (mg Fe(II) tablet^{-1})	Reference Method		Proposed Method	
		Found (mg Fe(II) tablet^{-1})	% Label[b]	Found (mg Fe(II) tablet^{-1})	% Label[b]
F1	200	188 ± 2	94	198±3	99
F2	200	196 ± 7	98	201±11	101
F3	200	191 ± 7	96	203±1	102
F4	200	196 ± 2	98	198±1	100
F5	200	194 ± 2	97	195±2	98
F6	149	153 ± 2	103	156±2	105
F7	200	219 ± 4	110	213±2	106
S1	135	121 ± 2	90	122±3	90
S2	200	182 ± 6	91	180±7	90
S3	200	184 ± 5	92	188±7	94

[a]F1-F7 : ferrous fumarate, S1-S3 : ferrous sulfate
[b]% Label = [found / label value] x 100

Conclusion

A green, simple and reliable method based on natural reagent extracted from plant and micro-volume colorimetry at 562 nm was proposed for determination of iron. The crude aqueous extracts from the dried guava leaves can replace toxic chemical reagents for the quantitative analysis of iron content in pharmaceutical samples. The extraction procedure of dried guava leaves is simple and precise. One batch extraction of this natural reagent can be used for at least 3 days. The developed method provides low chemical usage, low cost of operation and high sample throughput. The satisfactory recoveries proved that the proposed method has high potential as a good alternative method for quality assurance of iron in pharmaceutical industry and low resource areas. In addition, the visual detection of this green approach trends to further development as a screening method for iron in ground water samples, which could be useful for developing countries.

Acknowledgement

This study was financially supported by the Faculty of Science, Mahasarakham University. The authors gratefully acknowledge TRF Distinguished Research Professor Award Grant (DPG608002) (K. Gaudian), the Mahasarakham University Development Fund and the Center of Excellence for Innovation in Chemistry (PERCH-CIC), Office of the Higher Education Commission, Ministry of Education. Additional support was received from the Center of Excellence for Innovation in Analytical Science and Technology (I-ANALY-ST), Chiang Mai University which was greatly appreciated. The authors wish to thank Ms. Pimpaka and Ms. Yonlada Karun for their invaluable assistance.

References

1. Clark, S.F. (2008). Iron deficiency anemia. *Nutrition in Clinical Practice*, 23: 128-141.
2. Killip, S., Bennett, J. M. and Chambers, M. D. (2007). Iron deficiency anemia. *American Family Physician*, 75: 671-678.
3. Beutler, E., Hoffbrand, A. V., and Cook, J. D. (2003). Iron deficiency and overload. Hematology, ASH Education Book. Americal Society of Hematology, Washington DC: pp. 40-61.
4. Zachariadis, G. A., Raidou, E. S., Themelis, D. G. and Stratis, J. A. (2002). Determination of mineral content of active dry yeast used in pharmaceutical formulations. *Journal of Pharmaceutical and Biomedical Analysis*, 28: 463-473.

5. Zachariadis, G. A. and Michos, C. E. (2007). Development of a slurry introduction method for multi-element analysis of antibiotics by inductively coupled plasma atomic emission spectrometry using various types of spray chamber and nebulizer configurations. *Journal of Pharmaceutical and Biomedical Analysis*, 43: 951-958.
6. Karpinska, J. and Kulikoska, M. (2002). Simultaneous determination of zinc(II), manganese(II) and iron(II) in pharmaceutical preparations. *Journal of Pharmaceutical and Biomedical Analysis*, 29: 153-158.
7. Zargba, S. and Hopkata, H. (1996). Spectrophotometric determination of Fe(II) in pharmaceutical multivitamin preparations by azo dye derivatives of pyrocatechol. *Journal of Pharmaceutical and Biomedical Analysis*, 14: 1351-1354.
8. Rybkowska, N., Koncki, R. and Strzelak, K. (2017). Optoelectronic iron detectors for pharmaceutical flow analysis. *Journal of Pharmaceutical and Biomedical Analysis*, 145: 504-508.
9. Vakh, C., Freze, E., Pochivalov, A., Evdokimova, E., Kamencev, M., Moskvin, L. and Butalov, A. (2015). Simultaneous determination of iron (II) and ascorbic acid in pharmaceutical based on flow sandwich technique. *Journal of Pharmacological and Toxicological Methods*, 73: 56-62.
10. van Standen, J. F., du Plessis, H. and Taljaard, R. E. (1997). Determination of iron(III) in pharmaceutical samples using dialysis in a sequential injection analysis system. *Analytica Chimica Acta*, 357: 141-149.
11. Mulaudzi, L. V., van Staden, J. F. and Stefan, R. I. (2002). On-line determination of iron(II) and iron(III) using a spectrophotometric sequential injection system. *Analytica Chimica Acta*, 467: 35-49.
12. Armenta, S., Garrigues, S. and de la Guardia, M. (2008). Green analytical chemistry. *Trends in Analytical Chemistry*, 27: 497-511.
13. Grudpan, K., Hartwell, S. K., Lapanantnoppakhun, S. and McKelvie, I. (2010). The case for the use of unrefined natural reagents in analytical chemistry—A green chemical perspective. *Analytical Methods*, 2: 1651-1661.
14. Settheeworrarit, T., Hartwell, S. K., Lapanatnoppakhun, S., Jakmunee, J., Christian, G. D. and Grudpan, K. (2005). Exploiting guava leaf extract as an alternative natural reagent for flow injection determination of iron. *Talanta*, 68: 262-267.
15. Pinyou, P., Hartwell, S.K., Lapanatnoppakhun, S., Jakmunee, J. and Grudpan, K. (2010). Flow injection determination of iron ions with green tea extracts as a natural chromogenic reagent. *Analytical Sciences*, 26: 619-623.
16. Grudpan, K., Hartwell, S. K., Wongwilai, W., Grudpan, S. and Lapanantnoppakhun, S. (2011). Exploiting green analytical procedures for acidity and iron assays employing flow analysis with simple natural reagent extracts. *Talanta*, 84: 1396-1400.
17. Jaikrajang, N., Kruanetr, S., Harding, D.J. and Rattanakit, P. (2018). A simple flow injection spectrophotometric procedure for iron(III) determination using *Phyllanthus embrica* Linn. as a natural reagent. *Spectrochimica Acta part A: Molecular and Biomolecular Spectroscopy*, 204: 726-734.
18. Ganranoo, L., Chokchaisiri, R. and Grudpan, K. (2019). Simple simultaneous determination of iron and manganese by sequential injection spectrophotometry using astilbin extracted from *Smilax china* L. root. *Talanta*, 191: 307-312.
19. Wu, J. W., Hsieh, C. L., Wang, H. Y. and Chen, H. Y. (2009). Inhibitory effects of guava (*Psidium guajava* L.) leaf extracts and its active compounds on the glycation process of protein. *Food Chemistry*, 113: 78-84.
20. Chen, H. Y., and Yen, G. C. (2007). Antioxidant activity and free radical scavenging capacity of extracts from guava (*Psidium guajava* L.) leaves. *Food Chemistry*, 101: 686-694.
21. Zhang, T., Liang, O. R., Qjan, H., Yuan, W. and Yao, W. R. (2006). Extraction and identification of phenolic compounds in acetone extract from guava leaf. *Journal of Food Science and Biotechnology*, 25: 104-108.
22. Cakar, S. and Ozacar, M. (2016). Fe-tannic acid complex dye as photo sensitizer for different morphological ZnO based DSSCs. *Spectrochimica Acta part A: Molecular and Biomolecular Spectroscopy*, 163: 79-88.
23. Official Methods of Analysis of AOAC International. (2005). Official Method 952.03, In section 26.1.37, 18th Edition, AOAC International, Gaithersberg, Maryland, USA.
24. Official Methods of Analysis of AOAC International. (1990). Official Method 977.30, 15th Edition, AOAC International, Gaithersberg, Maryland, USA.

Malaysian Journal of Analytical Sciences, Vol 23 No 4 (2019): 604 - 612
DOI: https://doi.org/10.17576/mjas-2019-2304-06

MALAYSIAN JOURNAL OF ANALYTICAL SCIENCES
Published by The Malaysian Analytical Sciences Society
ISSN 1394 - 2506

REMOVAL OF PARAQUAT HERBICIDE BY CETYLTRIMETHYL AMMONIUM BROMIDE MODIFIED PINEAPPLE LEAVES

(Penyingkiran Herbisid Parakuat oleh Daun Nanas yang Diubahsuai dengan Setiltrimetil Ammonium Bromida)

Nik Ahmad Nizam Nik Malek[1,2]*, Muhd Hafiz Jusoh[2], Auni Afiqah Kamaru[3]

[1]*Centre for Sustainable Nanomaterials (CSNano), Ibnu Sina Institute for Scientific and Industrial Research (ISI-ISIR)*
[2]*Department of Biosciences, Faculty of Science*
Universiti Teknologi Malaysia, 81310 UTM Sekudai, Johor, Malaysia
[3]*Geomatika University College,*
Prima Peninsula, Jalan Setiawangsa 11, Taman Setiawangsa, 54200 Kuala Lumpur, Malaysia

**Corresponding author: niknizam@utm.my*

Received: 19 August 2018; Accepted: 7 July 2019

Abstract

Paraquat herbicide is categorised under contaminants of emerging concern (CEC) that can cause serious environmental problem and toxic effects towards human and animals. Also, the decomposing of pineapple leaves by burning in the field could create environmental problems such as air pollution. Therefore, in the present study, the pineapple leaves powder (PLP) was utilised as a low-cost adsorbent to remove paraquat from aqueous solution. The adsorption of paraquat from aqueous solution by PLP and surfactant-modified PLP (SMPLP) was examined. A series of SMPLP was prepared by reacting PLP with different concentrations of cationic surfactant cetyltrimethyl ammonium bromide (CTAB) (0.5, 1.0, 2.5, and 4.0 mM). The PLP and SMPLP were characterised using Fourier transform infrared (FTIR) spectroscopy after the modification process with CTAB and after adsorption with paraquat. The results show no significant changes in the chemical structure of pineapple leaves after modification. The SMPLP exhibited higher adsorption affinity towards paraquat herbicide. The adsorption experiments of paraquat were carried out in a batch mode at room temperature. The effect of paraquat concentrations (2–20 mg/mL) on the adsorption capacity of PLP and SMPLP were investigated. The suitability of adsorbent was tested by fitting the adsorption data into Langmuir and Freundlich isotherm equilibrium models. The experimental adsorption data well fitted to Freundlich isotherm with multilayer adsorption capacity of 13.0 mg/g. The highest adsorption of paraquat was obtained by SMPLP treated with 2.5 mM CTAB while the lowest adsorption was obtained by PLP. As a conclusion, the utilisation of surfactant-modified pineapple leaves powder can become an alternative adsorbent for the removal of herbicide compound in aqueous solution.

Keywords: paraquat, pineapple leaves, surfactant, adsorption

Abstrak

Herbisid parakuat dikategorikan sebagai kemunculan bahan pencemar (CEC) yang boleh menyebabkan masalah pada alam sekitar dan memberikan kesan toksik terhadap manusia dan haiwan. Pada masa yang sama, pelupusan daun nanas melalui cara pembakaran boleh menyebabkan masalah kepada alam sekitar seperti pencemaran udara. Oleh yang demikian, dalam kajian ini serbuk daun nanas (PLP) telah digunakan sebagai bahan penjerap kos rendah untuk menyingkirkan parakuat dalam larutan akueus. Penjerapan parakuat dari larutan akueus oleh PLP dan PLP diubahsuai dengan surfaktan (SMPLP) telah dikaji. SMPLP dihasilkan melalui tindak balas PLP pada kepekatan surfaktan setiltrimetil ammonium bromida (CTAB) yang berbeza (0.5, 1.0, 2.5, dan 4.0 mM). PLP dan SMPLP telah dicirikan dengan menggunakan kaedah spektroskopi inframerah transformasi Fourier (FTIR) selepas proses pengubahsuaian dengan CTAB dan selepas proses penjerapan dengan parakuat. Keputusan FTIR menunjukkan tiada perubahan ketara pada struktur kimia daun nanas selepas pengubahsuaian. SMPLP menunjukkan keupayaan penjerapan yang tinggi terhadap herbisid parakuat yang bercas positif. Proses penjerapan secara berkelompok telah dijalankan

pada suhu bilik. Kesan terhadap keupayaan penjerapan PLP dan SMPLP pada kepekatan larutan parakuat (2–20 mg/mL) telah dikaji. Kesesuaian bahan penjerap yang digunakan telah diuji dengan menggunakan model Langmuir dan Freundlich. Data eksperimen berpadanan dengan model Freundlich dengan penjerapan berbilang lapis pada kapasiti 13.0 mg/g. Penjerapan tertinggi parakuat ialah dengan menggunakan SMPLP yang diubahsuai dengan 2.5 mM CTAB manakala PLP menunjukkan penjerapan yang terendah. Kesimpulannya, aplikasi daun nanas yang diubahsuai dengan surfaktan boleh dijadikan sebagai bahan penjerap alternatif untuk menyingkirkan herbisid dalam larutan akueus.

Kata kunci: parakuat, daun nanas, surfaktan, penjerapan

Introduction

Agriculture industry is the largest consumer that uses chemical pesticides to control various pests. About 85% of the world production of pesticide is used to reduce the population of pests [1]. Pesticides are defined as one of a few toxic substances that released deliberately into the environment to kill living organisms. Pesticides are not only related to insecticides, but also applicable to herbicides, fungicides, and various other substances used to control pests. One of the most widely used herbicides is paraquat (PQ) (1,10-dimethyl-4,40-bipyridinium chloride), also known as methyl viologen, which is effectively used against grasses and most broad-lead plant species [2]. However, the release of paraquat to the environment and its breakdown products could threaten life forms due to their toxic, carcinogenic, and mutagenic properties [3]. Therefore, several techniques have been used to reduce this problem such as degradation [4] and adsorption [5]. The adsorption method is preferable as this process is more efficient and economical compared to the other methods [5]. Besides, paraquat also is categorised under contaminants of emerging concern (CEC) because it can be detected in the flowing surface water and groundwater. This can bring adverse effects towards human life and environment. The chemical structure of paraquat as shown in Figure 1 reveals that it possesses positive charges from ammonium group and counter-balanced by chloride anions as well as aromatic rings.

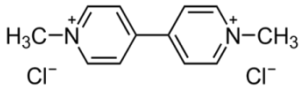


Figure 1. Chemical structure of paraquat (1,10-dimethyl-4,40-bipyridinium chloride)

Agricultural wastes are categorised as bio-based products which currently become popular among the researchers because it is considered as a part of green technology. The agriculture wastes such as pineapple leaves are considered as the other source of adsorbent due to its low operating cost, abundantly available and its regeneration capability [6]. Pineapple leaves in natural form possess a high tendency to remove cationic compounds rather than anionic compounds [7]. The modification of negatively charged adsorbent by cationic surfactant has been proven to be more efficient in increasing the adsorption affinity of biomass towards diverse contaminants [8]. Hence, in this research, the pineapple leaves were modified with cationic surfactant called cetyltrimethyl ammonium bromide (CTAB) to investigate the effect of different concentrations of surfactant in the adsorption capacity of pineapple leaves towards paraquat compound in water.

Materials and Methods

Preparation and characterisation of modified pineapple leaves

The pineapple leaves from Josapine type were provided by MARDI (Malaysian Agricultural Research and Development Institute) station in Pontian, Johor. The preparation of raw sample (UPLP) and its pre-treatment process were carried out based on previous work [8]. Four series of surfactant-modified pineapple leaf powder (SMPLP) were prepared by mixing the pre-treated pineapple leaf powder (PLP) with four different concentrations of CTAB aqueous solutions (0.5, 1.0, 2.5, and 4.0 mM). About 1000 mg of PLP was added with 100 mL CTAB solution and the mixture was stirred constantly for 15 minutes and the resulting SMPLP was filtered and dried at 90 °C overnight. After that, the dried SMPLP was ground into fine powder using pestle and mortar.

The amount of CTAB adsorbed onto the PLP was determined by calculating the differences in the remaining concentrations of CTAB in the solution before and after modification process. The procedure for the determination of CTAB in the solution involved the complexation of CTAB molecules by acid orange 7 in chloroform phase [9]. The samples were characterised using Fourier-transform infrared spectroscopy (FTIR) (Nicolet iS5 FT-IR Spectrometer, Thermo Fisher Scientific, USA) using attenuated total reflectance (ATR) method. The FTIR spectrum was recorded using OMNIC software in the range of 400 to 4000 cm^{-1}.

Adsorption of paraquat

The effect of the paraquat concentrations on the adsorption capacity of pineapple leaves was studied by adding different paraquat concentrations. The paraquat solution with the concentrations of 2, 5, 8, 10, and 20 mg/mL were prepared by diluting the stock solution (SP PARAQUAT 13%, Malaysia) in 100 mL volumetric flask. The fixed parameters were adsorbent dosage (250 mg), room temperature (24 °C), adsorption time (2 hours), and rate of stirring (200 rpm). The pH value of the paraquat solution was around 6.5 to 7.0. The removal test was performed by adding 250 mg of PLP and SMPLP samples with 25.0 mL of paraquat solution. The mixture was agitated at 200 rpm for 2 hours under room temperature and then it was separated by a single filtration through the Whatman filter paper (125 mm, pore size 11 µm). The concentration of paraquat in the filtrate solution was measured using a visible spectrophotometer (NANOCOLOR VIS, Macherey-Nagel) at $\lambda_{630\ nm}$. Each experiment was done in triplicate. The selected solid portion was dried in an oven and characterised using FTIR spectrophotometer. The calculation of the paraquat adsorption capacity from the solution on the adsorbent was calculated based on Eq. 1:

$$Adsorption\ capacity\ \left(\frac{mg}{g}\right), Q_0 = \frac{(C_0 - C_t)}{m}V \quad (1)$$

where C_0 is the initial paraquat concentration (mg/L), C_t is the residual concentration of the paraquat (mg/L) at different concentrations, V is volume (mL), and m is the adsorbent dose (mg).

Results and Discussion

Characterisation of samples

Figure 2 shows the amount of CTAB adsorbed on PLP with different initial concentrations of CTAB ($[CTAB]_{initial}$). This was done to observe the effect of different amounts of CTAB loading in their adsorption capacity towards paraquat. It is clear that the amount of CTAB adsorbed on PLP increased with the increased of $[CTAB]_{initial}$. These $[CTAB]_{initial}$ (0.5, 1.0, 2.5 and 4.0 mM) were selected based on the critical micelle concentration (CMC) of CTAB at around 1.0 mM. Therefore, at $[CTAB]_{initial}$ equal to 0.5 mM, the arrangement of CTAB molecules in the solution is in monomer and the micelles are formed at CTAB concentrations of 1.0 mM and above. In this experiment, the highest $[CTAB]_{initial}$ was 4.0 mM due to higher number of micelles in the solution and it affected the adsorption behaviour of CTAB molecules on the PLP surfaces. At a much higher concentration of more than the CMC of CTAB, the CTAB molecules will arrange in the form of aggregation and the CTAB molecules will adsorb on the surfaces via physical attachment and tend to release into the solution easily and eventually decrease its adsorption capacity. Furthermore, our previous study has proven that the modified PLP with CTAB at $[CTAB]_{initial}$ 4.0 mM showed the highest adsorption towards methylene blue and acid orange in aqueous solution [8]. The proposed mechanism of CTAB molecules adsorbed on PLP surfaces is given in the final section.

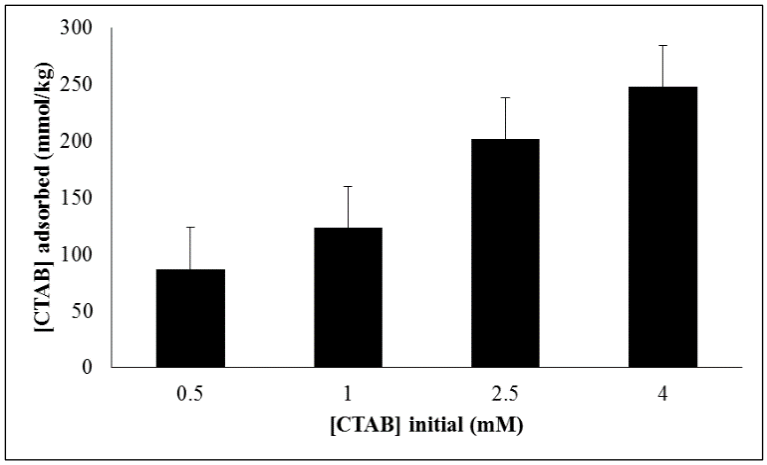


Figure 2. Amount of CTAB adsorbed onto pineapple leaf powder at different CTAB initial concentrations

Figure 3 shows the FTIR spectra for all of the samples to obtain information about the bonding presented in the PLP and also to observe the presence of CTAB molecules on the modified PLP. There will be higher amount of C–H bonds on the modified PLP with CTAB as the molecular structure of CTAB composes of 16 hydrocarbon (C–H) chain in its tail and they tend to form aggregate on the surfaces of PLP.

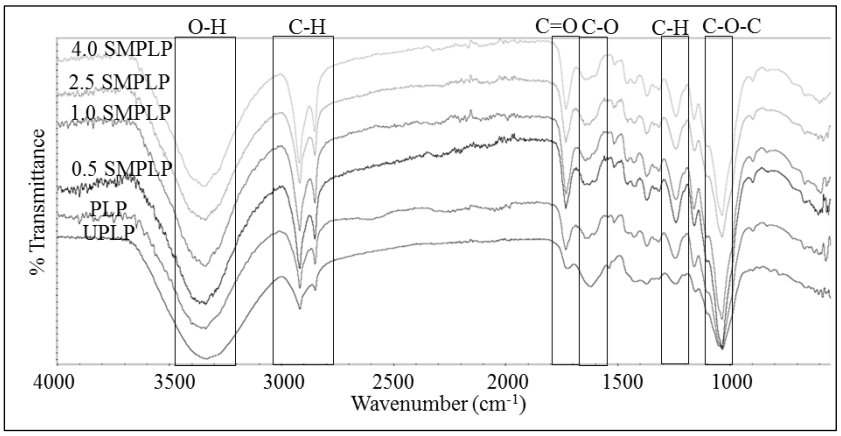


Figure 3. FTIR spectra of untreated PLP (UPLP), PLP, and SMPLP with different CTAB adsorbed

Based on Figure 3, strong broad peaks ranging from 3340 to 3350 cm^{-1} represent hydroxyl (O–H) vibration mode in cellulose and lignin structure [10] which could interact with each other through strong hydrogen bonding. The –OH stretching vibration is identical to the intermolecular and intramolecular hydrogen bond [11] of hydroxyl group at carbon number six in glucopyranose unit of cellulose component [12]. The strong and sharp band in the range of 1725 to 1732 cm^{-1} indicates carbonyl (C=O) stretching vibration mode representing acetyl or ester groups in hemicellulose [10] and ester linkage of lignin [11]. Furthermore, the bands at around 1625 to 1647 cm^{-1} represent carbon oxygen bonding (C–O–O) from the lignin aromatic C–C bond [13]. Furthermore, the peaks at 1420 to 1448 cm^{-1} are due to asymmetric carbon hydrogen bond ($–CH_2$) deformation in methyl and methylene groups of lignin and hemicellulose as well as the stretching of the benzene rings in the lignin structure [14]. The peak in the range of 1369 to 1373 cm^{-1} is attributed to the carbon hydrogen (C–H) deformation of cellulose and xylan while the peak between 1240 and 1243 cm^{-1} can be assigned as ether (C–O–C) bond of the cellulose chain or stretching of aryl group in lignin [11]. The shallow peaks in the range of 1150 to 1160 cm^{-1} can be assigned to the antisymmetric

ether (C–O–C) bridge pyranose rings cellulose [14, 15]. The overall FTIR spectra show that the important chemical nature and properties of pineapple leaves are composed of functional groups exist in cellulose, hemicellulose, and lignin [11, 13, 15].

The appearance of strong and sharp peaks at around 2900–2800 cm^{-1} indicates the presence of methyl (–C–H) stretching vibration from the CH_2 group of hemicellulose and cellulose which are also the main composition of PLP [14,15]. Besides that, the intensity of –C–H vibration peaks increased from PLP to SMPLP 4.0 is due to the increased in the aliphatic carbon content on SMPLP, indicating that the CTAB molecules are attached on the PLP surfaces [8]. This result is in accordance with that of Figure 2 where there is increased amount of CTAB molecules attached on PLP with higher $[CTAB]_{initial}$.

The results of FTIR spectroscopy especially at their fingerprint regions (below 1500 cm^{-1}) for each sample demonstrate that the chemical structure of the pineapple leaves remained unchanged after the pre-treatment process and surface modification. The PLP and SMPLP samples were then studied for their adsorption capacities towards herbicide paraquat solution. Figure 4 shows the adsorption capacity of the samples towards different concentrations of paraquat.

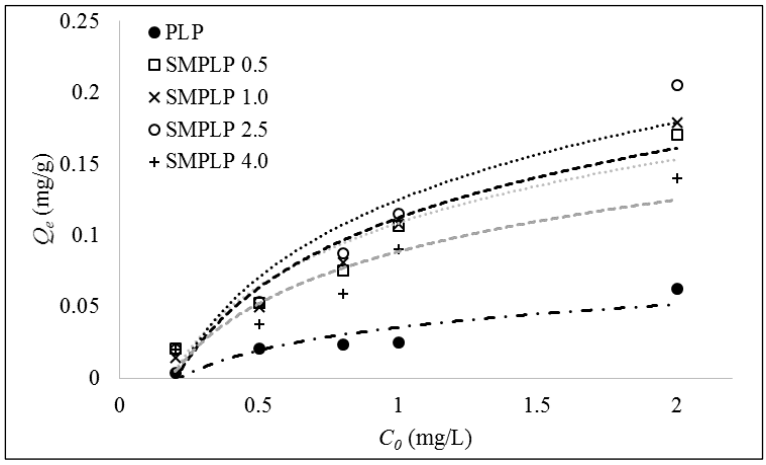


Figure 4. Adsorption capacity of PLP and SMPLP at different concentrations of paraquat

Figure 4 clearly shows that the SMPLP samples have higher adsorption capacity for paraquat compared to PLP and sample SMPLP 2.5 exhibited the highest adsorption of paraquat. The adsorption affinity of pineapple leaves towards paraquat compound followed this trend: SMPLP 2.5 > SMPLP 1.0 > SMPLP 0.5 > SMPLP 4.0 > PLP. Detailed mechanisms of paraquat adsorbed on PLP and SMPLP is discussed in the final section.

Adsorption of paraquat

The adsorption isotherm describes the distribution of adsorbates between liquid and solid phases and the behaviour of the adsorption system. The adsorption capacities of PLP and SMPLP towards paraquat were determined through isotherm studies. The data on adsorption capacity of paraquat were further analysed using Langmuir and Freundlich adsorption isotherm models. The Langmuir isotherm model is established based on the assumption that a monolayer adsorption occurs on the homogenous surface of adsorbent with constant adsorption energy and no transmigration or lateral interaction between adsorbates in the plane of the surface [16]. The Langmuir equation is given in Eq. 2:

$$\frac{x}{m} = \frac{bQ_0C_e}{1 + bC_e} \tag{2}$$

where *x* is the mass of adsorbates adsorbed (mg), *m* is the mass of adsorbent (g), C_e is the equilibrium concentration (mg/L), *b* is the Langmuir constant related to the affinity of the binding site, and Q_0 is the maximum adsorption at monolayer coverage (mg/g). Eq. 2 can be simplified if:

$$\frac{x}{m} = Q_e = \text{amount adsorbed at equilibrium (mg/g)} \tag{3}$$

Thus, the Eq. 2 can be linearized into:

$$\frac{1}{Q_e} = \frac{1}{Q_0} = \frac{1}{bQ_0C_e} \tag{4}$$

The plot of $\frac{1}{Q_e}$ against $\frac{1}{C_e}$ gives a straight-line graph with $\frac{1}{bQ_0}$ and $\frac{1}{Q_0}$ are slope and Y-intercept, respectively.

The Freundlich isotherm model is a nonlinear empirical equation developed based on the assumption that a monolayer adsorption occurs at heterogeneous surface of the adsorbent with inconsistent binding energy and unequal available active sites on the surface of adsorbent [17]. The Freundlich isotherm model is given in Eq. 5.:

$$\frac{x}{m} = q_e = KfC_e^{\frac{1}{n}} \tag{5}$$

where n is the favourability of the adsorption process and K_f is the maximum adsorption at monolayer coverage (mg/g). Eq. 5 can be linearized into:

$$log\frac{x}{m} = logq_e = logKf + \frac{1}{n}logC_e \tag{6}$$

The plot of $\log\frac{x}{m}$ or $\log q_e$ against $\log C_e$ gives a straight-line graph with $\frac{1}{n}$ and $\log kf$ are slope and Y-intercept, respectively. The values for adsorption isotherm parameters for both models are provided in Table 1.

Table 1. Fitted Langmuir and Freundlich parameters for paraquat adsorbed on PLP and SMPLP

Samples	**Langmuir isotherm model**			**Freundlich isotherm model**		
	Q_0 **(mg/g)**	b **(1/g)**	R^2	K_f **(mg/g)**	n **(1/g)**	R^2
PLP	0.027	0.568	0.951	33.744	0.830	0.928
SMPLP 0.5	1.645	0.064	0.999	10.425	1.076	0.992
SMPLP 1.0	0.199	0.347	0.989	10.322	0.904	0.983
SMPLP 2.5	1.095	0.091	0.999	13.004	0.969	0.997
SMPLP 4.0	0.260	0.402	0.975	12.634	0.463	0.980

The correlation coefficient (R^2) values for Freundlich isotherm indicate that this model fits all the experimental data better than the Langmuir isotherm model. The fitted adsorption data into Freundlich isotherm model describes the heterogeneous nature of PLP and SMPLP surfaces in which adsorption of paraquat onto both types of the adsorbents are assumed to have uniform adsorption activation energies [18] with no transmigration of paraquat molecules on the plane of the adsorbent surface. The Freundlich adsorption isotherm results also demonstrate the formation of multilayer coverage on the outer surfaces of PLP and SMPLP. Furthermore, this also rectifies the inconsistent values of Q_0 (Table 1) for each sample when the adsorption data were fitted with Langmuir isotherm equation particularly the Q_0 for SMPLP 0.5 is much higher than those for SMPLP 1.0 and SMPLP 2.5. The value of R^2 of less than 0.95 for PLP for Freundlich isotherm shows that the adsorption behaviour of PLP is different with

that of SMPLP as there is no additional compound (CTAB molecules) on the PLP surfaces. Detailed mechanism of paraquat adsorption on different concentrations of surfactant is explained in the next section.

The characterisation of the samples after adsorption of paraquat was performed using FTIR spectroscopy to determine the changes occurred in the chemical structure of pineapple leaves. The FTIR spectra after adsorption of paraquat by PLP and SMPLP are presented in Figure 5.

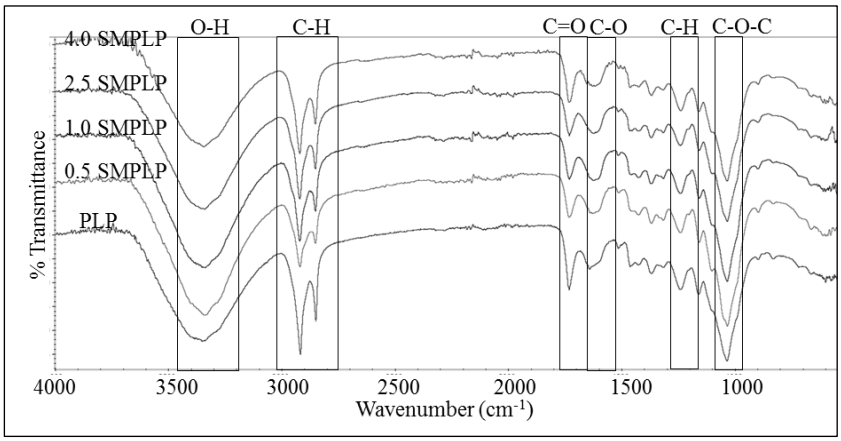


Figure 5. FTIR spectra of the samples after adsorption with paraquat

The appearance of strong sharp peaks at 2916 and 2850 cm^{-1} indicates the presence of methyl (–CH) stretching vibration from CH_2 group of hemicellulose and cellulose [10]. Additionally, another contribution that causes a high intensity of –C–H vibration peaks is due to the paraquat molecules because the paraquat structure consists many –C–H groups and causes the –C–H vibration peaks to be more intense. Although paraquat structure contains two aromatic rings, the peaks representing C=C or =CH did not appear in the FTIR spectra of the samples after the adsorption process may be due to the low amount of paraquat molecules that adsorbed on the sample. In addition, some of the peaks in the FTIR spectra overlapped with the same functional groups in the PLP as the PLP composed of several organic compounds. Importantly, the structure of the SMPLP sample after adsorption remains unchanged because paraquat molecules bound in between the surfactant layer on the surface of pineapple leaves. The adsorption also did not involve any changes on the major component of the pineapple leaves.

Proposed mechanism of adsorption

Figure 6 shows the proposed mechanism of CTAB adsorption on PLP and paraquat adsorption on SMPLP at (a) below the CMC level (0.5 mM), (b) near CMC, and (c) above CMC. At a lower CTAB concentration (0.93 mM and below), the CTAB molecules exist as monomers and form monolayer at the outer surface of PLP. The paraquat retained on the surface of the adsorbent via ion-exchange interaction and electrostatic forces while the interaction between paraquat molecules and hydrophobic tails involves hydrophobic interaction and van der Waals forces [19]. This resulted in the formation of surfactant monolayer on the surface of adsorbent and led to the lower adsorption capacity towards paraquat.

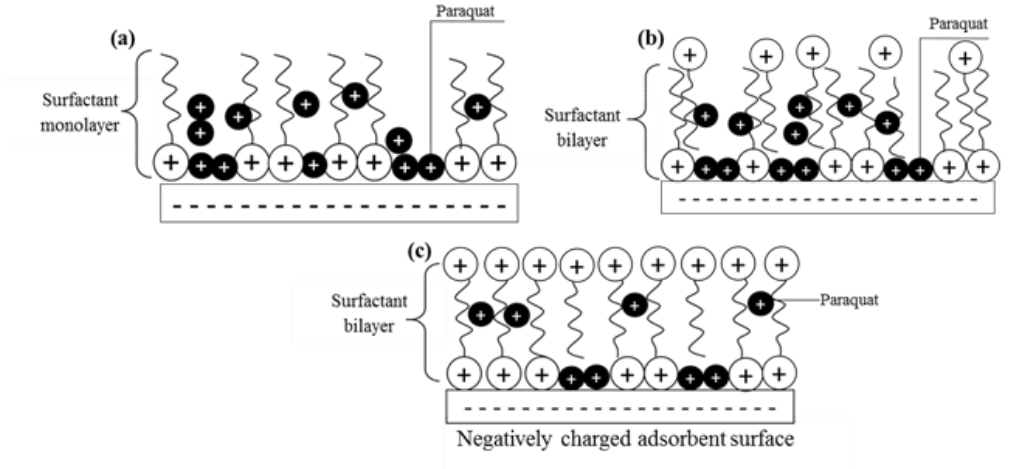


Figure 6. Proposed adsorption mechanism of CTAB and paraquat onto PLP for (a) SMPLP 0.5, (b) for SMPLP 1.0 and SMPLP 2.5, and (c) SMPLP 4.0

The surface of PLP which are not occupied by CTAB molecules possesses numerous hydroxyl groups of cellulose and lignin which gives the PLP surface its negative potential characteristics [8]. The negatively charged hydroxyl group acts as an active site to adsorb paraquat molecules with positively charged functional groups. For all SMPLP samples, some of the paraquat molecules are attached to hydrophobic tails of the surfactant. The molecules of paraquat are retained on the surface of pineapple leaves through ion-exchange mechanism or electrostatic force [19, 20, 21] while the interaction between paraquat molecules and hydrophobic tails involves hydrophobic interaction and van der Waals forces [19].

However, the adsorption mechanism of paraquat onto SMPLP 4.0 is different. At 4.0 mM, the CTAB molecules start to form bilayer formation at the outer surface of the adsorbent. From Figure 5(c), as the paraquat molecule is positively charged, it cannot bind to the positive hydrophilic head of CTAB molecules [22]. This resulted in the rejection of paraquat molecules towards the surfactant positive hydrophilic head. Moreover, the formation of the bilayer also hinders the paraquat molecules to penetrate the surface of PLP and thus reduced its adsorption capacity.

Conclusion

This study concludes the ability of pineapple leaves powder (PLP) in adsorbing CTAB surfactant and the CTAB adsorbed PLP enhanced the adsorption of paraquat in aqueous solution. The adsorption capacity of SMPLP towards paraquat also depended on the amount of CTAB adsorbed on the PLP where the highest adsorption was found for PLP adsorbed with 2.5 mM of CTAB. Therefore, the PLP modified CTAB could be used as an alternative adsorbent to remove paraquat herbicide released into the environment. Furthermore, the agricultural wastes modified with a suitable amount of surfactant can also be used to remove other organic contaminants in water.

Acknowledgement

This work was financially supported by the Universiti Teknologi Malaysia under the Research University Grant (Vot 18H87 and 08H01) and Ministry of Higher Education Malaysia.

References

1. Gilden, R. C., Huffling, K. and Sattler, B. (2010). Pesticides and health risks. *Journal of Obstetric, Gynecologic, and Neonatal Nursing*, 39(1): 103-110.
2. Posecion, N., Ostrea, E. and Bielawski, D. (2008). Quantitative determination of paraquat in meconium by sodium borohydride-nickel chloride chemical reduction and gas chromatography/mass spectrometry (GC/MS). *Journal of Chromatography B,* 862 (1-2): 93-99.

3. Huang, C. L., Lee, Y. C., Yang, Y. C., Kuo, T. Y. and Huang, N. K. (2012). Minocycline prevents paraquat-induced cell death through attenuating endoplasmic reticulum stress and mitochondrial dysfunction. *Toxicology Letters*, 209(3): 203-210.
4. Phuinthiang, P. and Kajitvichyanukul, P. (2019). Degradation of paraquat from contaminated water using green TiO_2 nanoparticles synthesized from *Coffea arabica* L. in photocatalytic process. *Water Science and Technology*, 79(5): 905-910.
5. Zbair, M., Anfar, Z., Ahsaine, H. A. and Khallok, H. (2019). Kinetics, equilibrium, statistical surface modeling and cost analysis of paraquat removal from aqueous solution using carbonated jujube seed. *RSC Advances*, 9(2): 1084-1094.
6. Chowdhury, S., Chakraborty, S. and Saha, P. (2011). Biosorption of basic green 4 from aqueous solution by *Ananas comosus* (pineapple) leaf powder. *Colloids and Surfaces B: Biointerfaces*, 84(2): 520-527.
7. Salleh, M. A. M., Mahmoud, D. K., Karim, W. A. W. A. and Idris, A. (2011). Cationic and anionic dye adsorption by agricultural solid wastes: A comprehensive review. *Desalination*, 280 (1–3): 1-13.
8. Kamaru, A. A., Sani, N. S. and Malek, N. A. N. N. (2016). Raw and surfactant-modified pineapple leaf as adsorbent for removal of methylene blue and methyl orange from aqueous solution. *Desalination and Water Treatment*, 57(40): 18836-18850.
9. Malek, N. A. N. N., Yusof, M. H. and Kamaru, A. A. (2019). Simultaneous action of surfactant modified sugarcane bagasse: adsorbent and antibacterial agent. *Malaysian Journal of Fundamental and Applied Sciences*, 15(1): 32-37.
10. Kassim, N. A., Mohamed, A. Z., Zainudin, E. S., Zakaria, S., Azman, S. K. Z. and Abdullah, H. H. (2018). Isolation and characterization of macerated cellulose from pineapple leaf. *BioResources*, 14(1): 1198-1209.
11. Nayan, N., Sharif, N., Razak, S., Wan Abdul Rahman, W. and Abd Majid, R. (2013). Effect of mercerization on the properties of paper produced from Malaysian pineapple leaf fibers. *International Journal of Engineering and Technology*, 13(4): 1-6.
12. Samal, R. and Ray, M. (1997). Effect of chemical modifications on FTIR spectra. II. Physicochemical behavior of pineapple leaf fiber (PALF). *Journal of Applied Polymer Scie*nce, 64(11): 2119-2125.
13. Banerjee, R., Chintagunta, A. D. and Ray, S. (2019). Laccase mediated delignification of pineapple leaf waste: An ecofriendly sustainable attempt towards valorization. *BMC Chemistry*, 13(1): 58-69.
14. Maniruzzaman, M., Rahman, M. A., Gafur, M. A., Fabritius, H. and Raabe, D. (2012). Modification of pineapple leaf fibers and graft copolymerization of acrylonitrile onto modified fibers. *Journal of Composite Materials*, 46(1): 79-90.
15. Weng, C. H. and Wu, Y. C. (2012). Potential low-cost biosorbent for copper removal: Pineapple leaf powder. *Journal of Environmental Engineering*, 138(3): 286-292.
16. Masel, R. I. (1996). Principles of adsorption and reaction on solid surfaces. John Wiley & Sons, Illinois: pp. 239-245
17. Jaroniec, M. (1975). Adsorption on heterogeneous surfaces: The exponential equation for the overall adsorption isotherm. *Surface Science*, 50(2): 553-564.
18. Mas, H. M. and Sathasivam, K. (2009). The removal of methyl red from aqueous solutions using banana pseudostem fibers. *American Journal of Applied Sciences*, 6(9): 1690-1700
19. Martins, D., Simões, M. and Melo, L. (2015). Adsorption of paraquat dichloride to kaolin particles and to mixtures of kaolin and hematite particles in aqueous suspensions. *Journal of Water Security*, 1(1): 25-36.
20. Han, R., Han, P., Cai, Z., Zhao, Z. and Tang, M. (2008). Kinetics and isotherms of neutral red adsorption on peanut husk. *Journal of Environmental Sciences*, 20(9): 1035-1041.
21. Janoš, P., Coskun, S., Pilařová, V. and Rejnek, J. (2009). Removal of basic (methylene blue) and acid (egacid orange) dyes from waters by sorption on chemically treated wood shavings. *Bioresource Technology*, 100(3): 1450-1453.
22. Paria, S. and Khilar, K. C. (2004). A review on experimental studies of surfactant adsorption at the hydrophilic solid - water interface. *Advances in Colloid and Interface Science*, 110(3): 75–95.

Malaysian Journal of Analytical Sciences, Vol 23 No 4 (2019): 613 - 624
DOI: https://doi.org/10.17576/mjas-2019-2304-07

MALAYSIAN JOURNAL OF ANALYTICAL SCIENCES
Published by The Malaysian Analytical Sciences Society
ISSN 1394 - 2506

INTERACTION STUDIES OF PUTATIVE CHEMICAL LIGANDS IN BINDING SITES OF THERMOSTABLE LIPASE FROM *Geobacillus zalihae* STRAIN T1

(Kajian Interaksi Ligan Kimia pada Tapak Pengikatan Lipase Termostabil daripada *Geobacillus zalihae* Stren T1)

Mohd Basyaruddin Abdul Rahman[1,2]* and Muhammad Alif Mohammad Latif [1,2,3]

[1]*Integrated Chemical BioPhysics Research*
[2]*Department of Chemistry, Faculty of Science*
[3]*Centre of Foundation Studies for Agricultural Science*
Universiti Putra Malaysia, 43400 UPM Serdang, Selangor, Malaysia

**Corresponding author: basya@upm.edu.my*

Received: 19 August 2018; Accepted: 3 July 2019

Abstract

Industrial biotechnology focusing on the usage of enzyme as the catalyst in many chemical reactions, however enzyme stability remains a major challenge. Enzyme can be modified *via* genetic or chemical methods by manipulating its structure. A potential biocatalyst based on lipase enzyme was designed by *in silico* approach. The enzyme-ligand interactions between selected chemical ligands and a thermostable lipase from *Geobacillus zalihae* strain T1 were studied by using molecular docking, AutoDock 3.0.5. The T1 lipase structure (PDB ID: 2DSN) was predicted to have 65 pockets in the structure, with nine of them have the potential binding sites for ligands based on their surface area, volume and number of residues. The characteristics of each selected binding site and chemical ligands were analyzed. Types of enzyme-ligand interactions involved in binding sites were determined and co-related with the final docked energies. All these discoveries may prove useful for designing novel binding sites, in particular as new biocatalyst.

Keywords: thermostable lipase, binding site, protein-ligand interaction, docking, biocatalyst

Abstrak

Industri bioteknologi memberi tumpuan kepada penggunaan enzim sebagai pemangkin dalam banyak tindak balas kimia, namun mengekalkan kestabilan enzim menjadi cabaran utama. Enzim boleh diubah melalui kaedah genetik atau kimia dengan memanipulasi struktur asasnya. Biokatalis yang berpotensi berdasarkan enzim lipase direka bentuk dengan menggunakan pendekatan berkomputer. Interaksi enzim-ligand antara ligan kimia dipilih dan lipase termostabil dari *Geobacillus zalihae* stren T1 telah dikaji dengan menggunakan pendokkan molekul, AutoDock 3.0.5. Struktur lipase T1 (PDB ID: 2DSN) diramalkan mempunyai 65 poket dalam struktur, dengan sembilan daripadanya mempunyai tapak pengikat yang berpotensi untuk ligan berdasarkan luas permukaan, jumlah dan bilangan residu. Ciri-ciri setiap tapak pengikat dan ligan kimia tersebut dipilih untuk dianalisis. Jenis-jenis interaksi enzim-ligan yang terlibat dalam tapak pengikat telah ditentukan dan berkait dengan tenaga berlabuh yang paling akhir. Semua penemuan ini terbukti bermanfaat bagi membentuk tapak mengikat novel, khususnya sebagai biokatalis yang baru.

Kata kunci: lipase termostabil, tapak pengikat, interaksi protein-ligan, pendokkan, biokatalis

Introduction

Lipases are water-soluble enzymes (EC 3.1.1.3) that catalyze the hydrolysis of ester bonds in triglycerides into free fatty acids and glycerol. Besides hydrolysis, lipases can catalyze esterification, transesterification and polyesterification reactions. Lipases are widely used in the production of cocoa butter substitutes, oleochemical products, detergents, surfactants, as well as the production of biodegradable polymers, lubricants and solvents [1]. Lipases from extreme thermophiles are special due to their inherent thermostability and resistance against chemical denaturants, such as extremely acidic and alkaline conditions, detergents, chaotropic reagents, organic solvents and protein inhibitors [2, 3]. They should be exploited extensively to maximize the potential and capability as industrial biocatalysts.

The thermoalkalophilic lipase (PDB ID: 2DSN) from *Geobacillus zalihae* strain T1 contains 388 amino acids. It has two metal ions, Ca^{2+} and Zn^{2+}, which are seldom found in bacterial lipases [4]. Sharing 30-35% homology with the Gram-positive *Staphylococcus* lipases [5], T1 lipase is classified under lipase family I.5 [6]. The *Geobacillus* lipase is larger in molecular size due to the presence of dimer interface and its structural zinc site [7]. Its metal binding site plays a major role in thermostability at elevated temperatures. Like P1 and L1 lipases (PDB ID: 1KU0 and 1JI3 respectively) [8, 9], there are conserved hydrophobic tryptophan residues around the zinc domain of the lipase [10]. Its active site is formed by Ser113, Asp317 and His358 [4]. The active site residues are covered by a long helix from residue 175 to 191. This area is not accessible by solvents, indicating that the T1 lipase structure is a closed conformation at room temperature [11].

Molecular modeling techniques are used to study macromolecular binding sites and predict their interactions with the bioactive conformers of ligands [12]. Previous research reported that a trypsin structure (PDB ID: 1AUJ) was successfully docked with ligands including 1,10-phenanthroline, ethanolamine, benzamidine, ethanol, propanol, 1,3-propandiol, phosphoethanolamine, *p*-aminobenzamidine, phenylacetic acid and phenylalanine at different pockets [13]. New binding pockets near the active site in peptide deformylase (PDF) was also discovered and explored to design potent inhibitors by using ZINC screening database and AutoDock software [14, 15]. Docking studies on lipase could provide further insight into the conformation and functional changes of lipase. To date, docking studies on T1 structure using AutoDock have not been reported. In this work, interactions between the pocket residues and docked ligands were investigated by exploring their binding modes.

Materials and Methods

Determination of pocket cavities of T1 lipase

The 3D coordinates of T1 lipase was sent to pocket and void Surfaces of Amino acid Residues (pvSOAR) (now known as pevoSOAR; http://sts.bioe.uic.edu/pevosoar/) [16, 17], a web server to determine the total pockets in the lipase and to search for macromolecular structures with high similarity in terms of atom coordination and surface pattern. The surface pattern of T1 lipase, which was then referred as 'pocket' in the selected surface database was compared, along with the surface patterns of the entire structure within the database [18]. Nine largest pockets defined from pvSOAR were then selected as possible binding sites of the protein structure.

Screening and selection of suitable chemical ligands for docking

Ten ligand structures were selected from Protein Data Bank (www.rcsb.org) based on their properties and functional groups such as amine, hydroxyl or both functional groups, to be used in the molecular docking stage. The ten ligands namely benzamidine (BEN), *p*-aminobenzamidine (PBZ), 1,10-phenanthroline (PHN), 1-propanol (POL), phenylacetic acid (PAC), 1,3-propandiol (PDO), ethanol (EOH), ethanolamine (ETA), *o*-phosphoethanolamine (PSE) and phenylalanine (PHE). Their structures are depicted in Table 1.

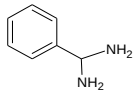
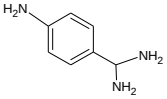
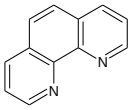
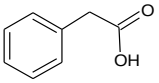
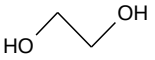
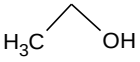
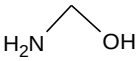
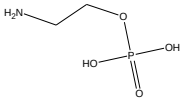
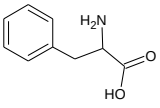
Preparation of T1 lipase and selected chemical ligands

After all the structures were obtained, T1lipase was protonated and solvated by using *protonate* and *addsol* tools in AutoDock 3.0.5 to generate a *pdbqt* file as the docking platform for selected ligands. Meanwhile, the selected chemical ligand structures were transferred into InsightII software for structural and force field correction procedures. The *ligands.mol2* file was generated for each selected ligand. This ligand.*mol2* files were transferred to AutoDock 3.0.5 and the *autotors* tool was used to determine their torsions. Lastly, *pdbqt* files were also generated for each ligand to be used in the molecular docking stage.

Docking of each ligand onto potential pocket cavities in T1 lipase structure

Each ligand structure was docked into the targeted potential binding sites using AutoDock 3.0.5, and the final docked energy of each successful docking was recorded. The grid map was sized at 60 x 60 x 60 with a grid point spacing of 0.375 Å. A total of 100 runs was performed for each ligand at different pockets. For each of the independent runs, up to 27,000 Lamarckian Genetic Algorithm (LGA) operations were generated on a single population of 50 individuals. The operator weights for crossover, mutation and elitism were 0.80, 0.02 and 1, respectively [19].

Table 1. Selected chemical ligands for molecular docking onto T1 lipase binding sites. The ligand selections were based on small molecules with amine or hydroxyl or both groups

Functional Group	**Name**	**PDB ID**	**Structure**
Amine	Benzamidine	BEN	
	p-aminobenzamidine	PBZ	
	1,10-phenanthroline	PHN	
Hydroxyl	1-propanol	POL	
	Phenylacetic acid	PAC	
	1,3-propandiol	PDO	
	Ethanol	EOH	
Amine and hydroxyl	Ethanolamine	ETA	
	o-phosphoethanolamine	PSE	
	Phenylalanine	PHE	

Results and Discussion

Structural studies of T1 lipase

A highly thermostable enzyme extracted from *Geobacillus zalihae strain* T1 was discovered by Abdul Rahman and co-researchers [4] and it's structural was simulated in detail [20]. As a thermophilic and alkaliphilic lipase, it can withstand denaturation at 65 ˚C and pH 9.0. Like other *Bacillus* lipases, an Ala replaces the first Gly residue in the Gly-Xaa-Ser-Xaa-Gly (Xaa refers to any amino acid) sequence, which is conserved among microbial and mammalian lipases. The three-dimensional structure of thermostable T1 lipase is displayed in Figure 1.

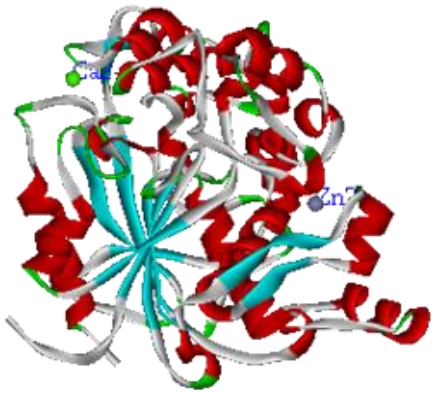


Figure 1. 3D lipase structure from *Geobacillus zalihae* Strain T1

The T1 lipase structure was uploaded onto pvSOAR and it predicted a total of 65 pockets in the structure. Querying the surface pattern of T1 lipase against the PDB database generated a list of macromolecule structures with high similarities to T1 lipase. Two structures with the highest similarities over 95% were lipases from *Bacillus stearothermophilus* P1 (1JI3) and *Bacillus stearothermophilus* L1 (1KU0) [8,9]. Like the T1 lipase, 1KU0 and 1JI3 structures also possess one each of Ca^{2+} and Zn^{2+} metal ions, which are not usually found in other lipases.

The nine largest pockets from T1 lipase were selected as the potential binding sites for ligands (Figure 2) and their surface area, volume and number of residues were analyzed. Pocket 65 was the largest pocket with the surface area of 296.1 $Å^2$, volume of 494.3 $Å^3$ and a total of 17 amino acids forming the concaved area. Pocket 64, the second largest pocket was formed by 12 amino acids and followed by pocket 63 with 14 amino acids. Although the number of amino acids in pocket 64 was fewer than pocket 63, pocket 64 had bigger volume at 335.9 $Å^3$ than pocket 63 at 187.8 $Å^3$. Pocket 59 was formed by 12 amino acids in which two residues, Ser113 and His358 were members of the catalytic triad [3,4]. Its surface area was 159.0 $Å^2$ and pocket volume was 144.6 $Å^3$. Both pockets 58 and 57 possessed 12 amino acid residues but the surface area and pocket volume of pocket 58 were much smaller than pocket 57. It might be due to the denser configuration of the amino acids formed in pocket 58 than in pocket 57.

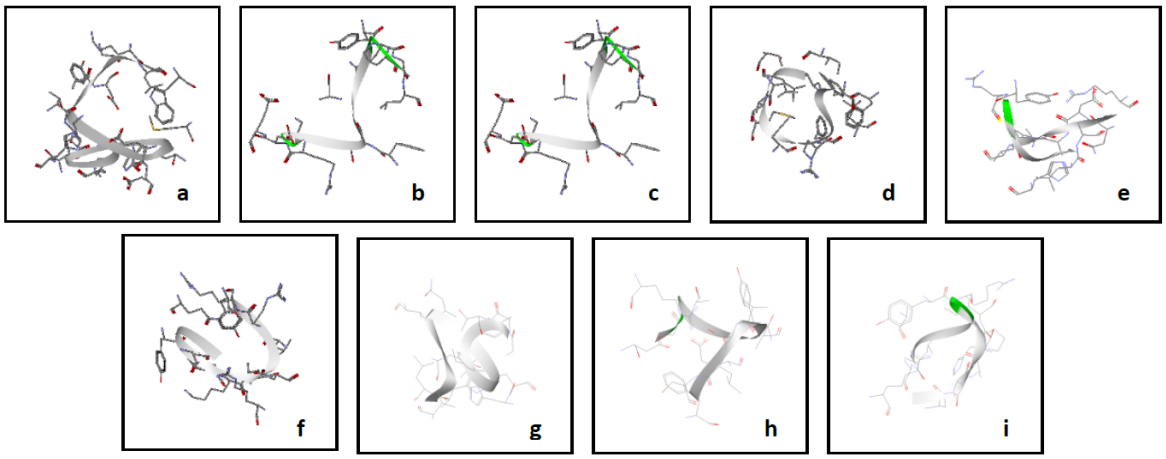


Figure 2. Nine potential binding sites in T1 lipase (2DSN). Each pocket was presented separately as secondary structure with stick display: (a) pocket 65 (the largest pocket) (b) pocket 64 (c) pocket 63 (d) pocket 62 (e) pocket 61 (f) pocket 60 (g) pocket 59 (h) pocket 58 and (i) pocket 57

Table 2 contains the number of amino acid residues in each selected binding site of thermostable T1 lipase structure. The amino acids with hydrophobic side groups are valine, leucine, isoleucine, methionine and phenylalanine while amino acids with hydrophilic side groups are asparagine, glutamic acid, glutamine, histidine, lysine, arginine and aspartic acid. These side groups play a vital role in ligand docking into potential binding sites.

Pocket 65 is a hydrophilic binding site due to the high number of hydrophilic residues on the pocket surface. It had eight amino acids with hydrophilic groups while only two amino acids contain hydrophobic groups. Pocket 64 was slightly hydrophilic due to the small difference of number of hydrophobic and hydrophilic groups. For pockets 63 and 62, both possessed seven hydrophilic amino acids, with two and three hydrophobic amino acids, respectively. These two pockets were highly hydrophilic.

Pocket 61 also showed more hydrophilic properties with six hydrophilic amino acid residues compared to two hydrophobic amino acid residues in the pocket. Pockets 65, 64, 63, 62 and 61 had hydrophilic properties, possibly due to their pocket positions, lying on the outer surface of the structure. Most folded proteins have a hydrophobic core in which the side chain stabilizes the folded state, and the charged or polar side chains are usually found on the solvent-exposed surface that interact with surrounding water molecules. It is generally accepted that minimizing the number of hydrophobic side chains exposed to water is the principal driving force behind the folding process [21, 22].

Pocket 60 was hydrophobic due to the presence of ten hydrophobic amino acid residues. The hydrophobic amino acids account for 76.92 % of the total residues. The hydrophobic surface of enzymes may increase the affinity with both the organic solvents and hydrophobic substrates [23]. Pocket 59 is considered hydrophobic as amino acid residues with hydrophobic groups outnumbered the hydrophilic groups. Pockets 58 and 57 possessed 5 amino acid residues each with hydrophobic groups but they were not highly hydrophobic due to the minor difference between the effects of hydrophobicity and hydrophilicity.

Table 2. List of the nine largest potential binding sites in T1 lipase (**2DSN**) by their residue constituents, volume and surface area

Pocket	Amino Acid Constituents	Number of Residues	Surface Area ($Å^2$)	Volume ($Å^3$)
65	S58, W60, H81, K84, H85, **M121**, S130, E132, E133, T237, D238, Y242, D243, G248, T251, **L252**, W255	17	296.1	494.3
64	G20, R21, E22, E23, **F49**, T50, A52, Q69, Y94, P95, G96, **L97**	12	181.7	335.9
63	H14, W19, G20, R21, E22, E23, **F27**, K28, Y29, W30, D36, E38, T50, **L51**	14	236.7	187.8
62	R92, Q202, Y204, D205, **F206**, K207, **L208**, D209, **L213**, R214, R215, Y224	12	183.6	157.0
61	A52, **V53**, W65, Q69, **V75**, Y77, G91, R92, Y94, K207, D209, Q210	12	194.3	165.5
60	**F16**, T168, **L170**, **V171**, **M173**, **F176**, R179, **F180**, **L183**, **L244**, **F290**, C295, **I319**	13	163.8	118.0
59	G15, **F16**, T17, Y29, H112, S113, **L183**, **V187**, **I319**, H358, **L359**, **I362**	12	159.0	144.6
58	D76, G78, A79, R89, E133, Y136, A137, **V142**, S143, **L144**, S145, **F148**	12	108.1	83
57	R4, N6, D7, A8, P9, **I10**, Y46, R47, H108, A380, **L383**, A384	12	123.3	109.9

*Amino acids in bolded form are hydrophobic type

All necessary information needed to identify the binding sites in T1 lipase were gathered and the locations of each of the selected binding sites were determined by using Accelrys Discover Studio 1.0 (DS Modeling 1.0) and UltraEdit. UltraEdit was applied in this study to edit the atomic information in the T1 lipase structural file for the construction of involved amino acid residues to form a binding site of T1 lipase.

Docking to the T1 lipase

Four ligands remark as POL, PHE, PDO and BEN were able to dock into pocket 65. PHE docked with the lowest final docked energy at -6.16 kcal/mol (Table 3). Four hydrogen bonds were established through hydrogen from amine and hydroxyl of PHE with carbonyl oxygen from THR237 and ASP243. BEN, like PHE with an aromatic ring and two amine groups, only managed to produce a final docked energy of 2.82 kcal/mol. Both ligands POL and PDO (Figure 3) docked with almost the same final docked energies, -4.04 and -3.99 kcal/mol, but lower than BEN. PHE formed a π-π stacking with TRP60 which explained the higher binding affinity of PHE towards pocket 65. Ligands containing hydroxyl group produce a lower final docked energy compared to ligands with an amine group.

It is worth noting that the hydroxyl groups are important as they form H-bonds with the residues of the receptor to increase the binding affinity [13, 24].

Table 3. **AutoDock** calculated final docked energy for each ligand bind to a binding site. The lowest final docked energy for each ligand determined the most favorable binding pocket.

Pocket	Docked Ligand	Final Docked Energy (kcal/mol)	Torsion
65	POL	-4.04	1
	PHE	-6.16	3
	PDO	-3.99	2
	BEN	-2.82	2
64	POL	-3.43	1
	PHE	-4.96	3
	PDO	-2.13	2
63	POL	-3.56	1
	PHE	-5.56	3
	PDO	-3.65	2
	BEN	-3.03	2
62	POL	-3.34	1
	PHE	-6.71	3
	PDO	-4.04	2
	BEN	-2.10	2
61	POL	-3.09	1
	PHE	-3.26	3
	PDO	-3.81	2
	BEN	-3.78	2
	ETA	-2.24	1
	EOH	-2.38	1
	PAC	-3.80	2
60	POL	-3.78	1
	PHE	-6.21	3
	PDO	-4.69	2
59	POL	-3.55	1
	PDO	-2.85	2
	BEN	-2.65	2
	ETA	-2.28	1
58	POL	-3.07	1
	PHE	-5.58	3
	PDO	-4.16	2
57	POL	-3.39	1
	PHE	-2.14	3

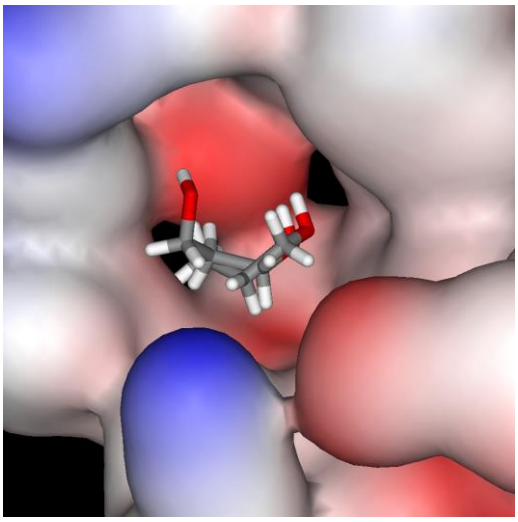


Figure 3. The hydroxyls of POL and PDO point to the surface area in pocket 65.

Ligands PHE, POL and PDO were docked into pocket 64. Ligand PHE produced the lowest final docked energy at -4.96 kcal/mol. There was 1 H-bond between carbonyl oxygen of PHE and hydrogen from primary amine of ARG21 (1.84 Å). A hydrogen bond (2.17 Å) was formed between hydroxyl hydrogen of POL and the nitrogen atom of the indole ring from TRP30. PDO formed 2 H-bonds with carbonyl oxygen from GLU38 (2.05 Å) and GLN39 (1.98 Å). The final docked energy of POL was lower than PDO due to the presence of hydrophobic interaction. Only GLN39 was involved in the hydrophobic interaction of PDO while POL had residues THR50, TRP30, LYS28 and ARG21 for the same type of interaction. PHE made the highest number of hydrophobic interactions when compared with PDO and POL (Figure 4).

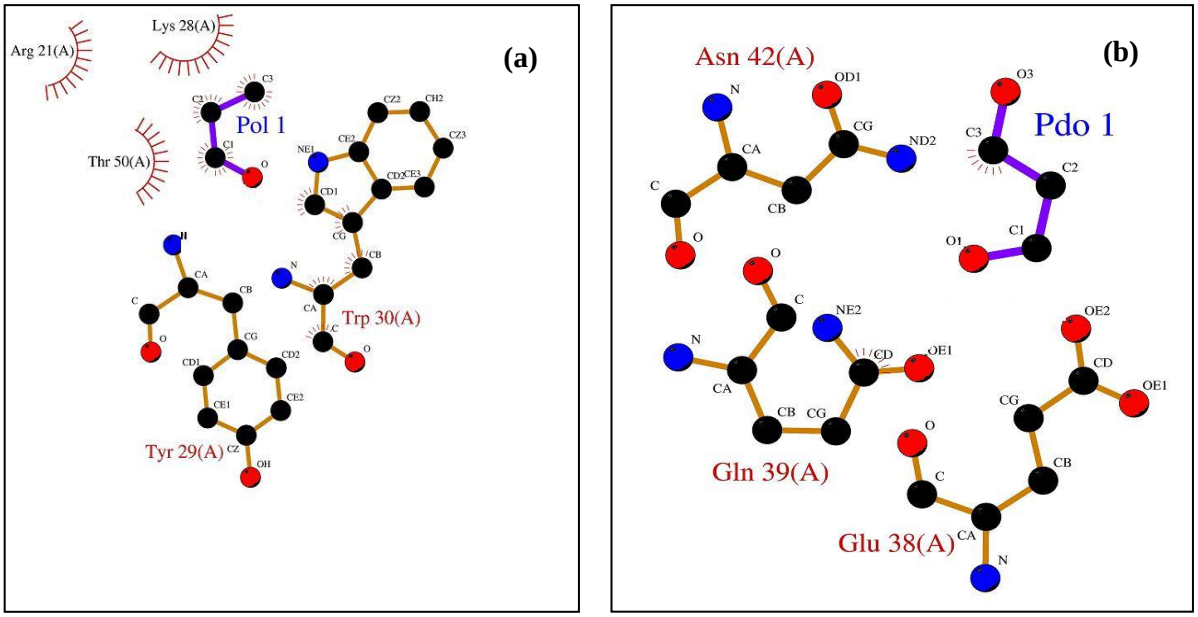


Figure 4. Hydrophobic interaction for ligand (a) POL and (b) PDO with their surrounding pocket residues in pocket 64

Four ligands were successfully docked into pocket 63. PHE led with the lowest final docked energy of -5.56 kcal/mol. Two H-bonds were formed between PHE and pocket residues. The first H-bond was formed between the hydroxyl hydrogen of PHE and the carbonyl oxygen of GLU22 (1.85 Å). The second H-bond was formed between the amine hydrogen of MET24 and the hydroxyl oxygen of PHE (2.28 Å). BEN produced the highest final docked energy among the four docked ligands at -3.03 kcal/mol. The amine hydrogen of BEN established a H-bond with the hydroxyl oxygen of SER201 (2.17 Å), showing again that ligands with –COO- or –CO- groups have better binding affinity than those with amine groups. The final docked energies of POL and PDO were similar because both ligands had the same number of hydrophobic interactions, despite the extra H bonding between PDO with pocket residues.

In pocket 62, PHE led the other 3 ligands (PDO, BEN and POL) with the lowest final docked energy at -6.71 kcal/mol, while BEN produced the highest final docked energy. PHE and POL made 3 H-bonds each while PDO and BEN had 1 H-bond each. Yet, the final docked energy of PDO was lower than POL. The numbers of hydrophobic interactions for both ligands were almost the same. Here, Van der Waals forces or London dispersion forces were considered to explain the differences of final docked energies. They are a class of intermolecular forces which arise from the polarization of molecules into dipoles or multipoles. The interaction distance for the van der Waals was within 4.00 Å. PDO had van der Waals interactions with 27 amino acid residues and only 18 residues for POL (Figure 5).

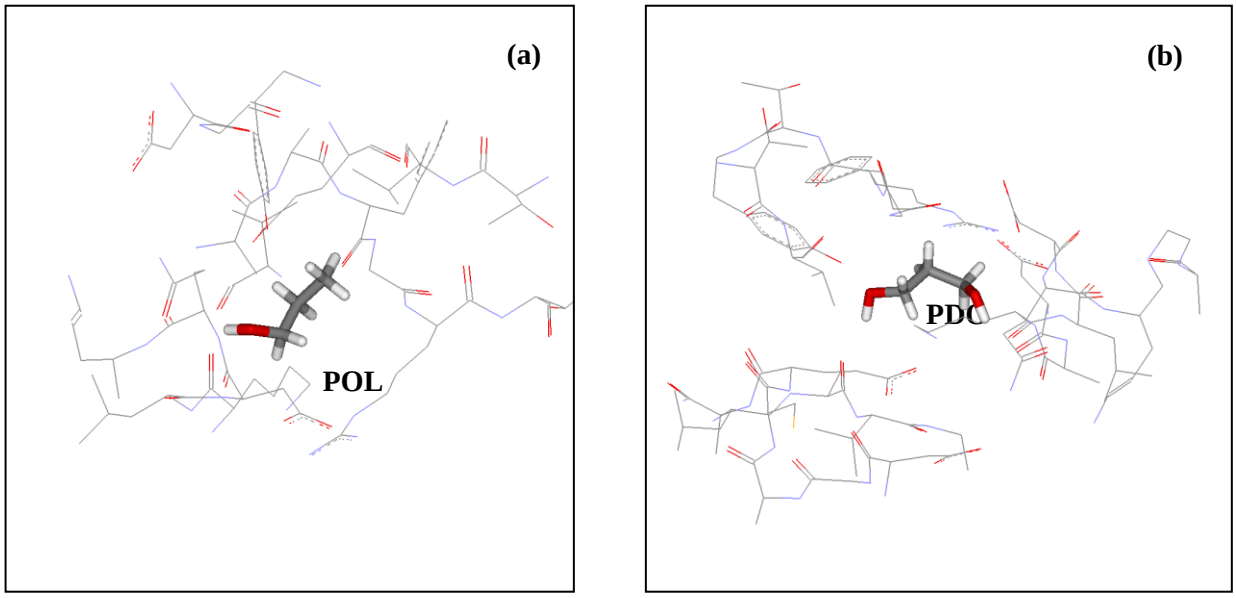


Figure 5. (a) POL had van der Waals interactions with 18 residues of pocket 62 while (b) PDO interacted with 27 pocket residues

Four ligands (PDO, BEN, PHE and POL) were successfully docked into pocket 61. The lowest final docked energy was scored by PDO at -3.81 kcal/mol which was slightly lower than BEN at -3.78 kcal/mol. Both PDO and BEN formed 3 hydrogen bonds each with pocket residues. Hydroxyl hydrogen from PDO bonded to the carbonyl oxygen groups of VAL171 (1.99 Å) and VAL174 (2.16 Å). An amine hydrogen of ARG241 also interacted with a carbonyl oxygen of PDO (1.98 Å). Meanwhile, the 3 H-bonds in BEN were from the amine hydrogen interactions with carbonyl oxygen groups of ASN172 (2.39 Å), MET173 (2.24 Å) and VAL174 (2.31 Å). The final docked energy of PHE was lower than POL, which might be due to the higher number of hydrophobic interactions between PHE and pocket residues although both ligands shared the same number of electrostatic interactions. The amine nitrogen of ARG241 made an electrostatic interaction with the hydroxyl oxygen of PDO at 2.80 Å while the amine nitrogen from PHE made the same interaction with the carbonyl oxygen of ASP182 at 3.20 Å. Electrostatic interactions

occur between opposite charged atoms, or a dipole or an induced dipole where charges on nuclei and electrons interact according to Coulomb's law.

PHE, PDO and POL ligands were successfully docked into pocket 60 with PHE producing the lowest final docked energy at -6.31 kcal/mol. PHE and PDO made 3 hydrogen bonds with the pocket residues while POL had only 2 hydrogen bonds. The reason of PHE having the lowest final docked energy might be due to the inferior number of hydrophobic interactions over the other 2 ligands. The 2 H-bonds from POL were found between its hydroxyl oxygen and the amine hydrogen of ARG92 (2.25 Å), and its hydroxyl hydrogen with the amine nitrogen of LEU208 (2.35 Å). The 3 H-bonds formed between PDO and pocket residues were hydroxyl hydrogen of PDO and carbonyl oxygen of ASP205 (1.74 Å), amine hydrogen of PHE206 and hydroxyl oxygen of PDO (1.83 Å), as well as hydroxyl hydrogen of PDO and carbonyl oxygen of ASP209 (1.69 Å). Both PDO and POL had the same number of hydrophobic and electrostatic interactions with pocket residues.

In pocket 59, the successfully docked ligands were POL, PDO and BEN. POL scored the lowest final docked energy at -3.55 kcal/mol. PDO had 3 hydrogen bonds while POL and BEN had 2 hydrogen bonds. PDO made H-bonds through its hydroxyl hydrogen with the carbonyl oxygens of ALA186 (1.99 Å) and ASN288 (1.69 Å), as well as its hydroxyl oxygen with the amine hydrogen of PHE290 (2.16 Å). However, POL had more hydrophobic interactions than PDO. The difference between the hydrophobic interactions of POL and PDO could compensate the lack of binding affinity with a single hydrogen bond only. Same reason could be applied to the difference of final docked energies between POL and BEN, although both ligands had the same number of hydrogen bonds with pocket residues.

Three ligands were able to dock into pocket 58 with PHE generating the lowest final docked energy at -5.58 kcal/mol. POL docked with highest final docked energy in pocket 58 at -3.07 kcal/mol and formed 2 hydrogen bonds with pocket residues. Both PHE and PDO had 3 hydrogen bonds each with pocket residues. For PDO, the distances of hydrogen bonds were 1.94 Å and 2.18 Å, between its hydroxyl hydrogen and the carbonyl oxygen of CYS6, THR74, respectively. Between amine hydrogen of ASP76 and hydroxyl oxygen of PDO, the H-bond distance was 1.68 Å Å. The higher number of hydrophobic and van der Waals interactions also contributed to the increase of the binding affinity of PHE, compared to PDO [25]. Lastly in pocket 57, the 2 docking ligands were POL and PHE. POL produced the lower final docked energy at -3.39 kcal/mol while PHE had -2.14 kcal/mol. Both POL and PHE formed 2 hydrogen bonds each with the pocket residues. But the binding affinity for POL was stronger due to a higher number of hydrophobic interactions (Figure 6).

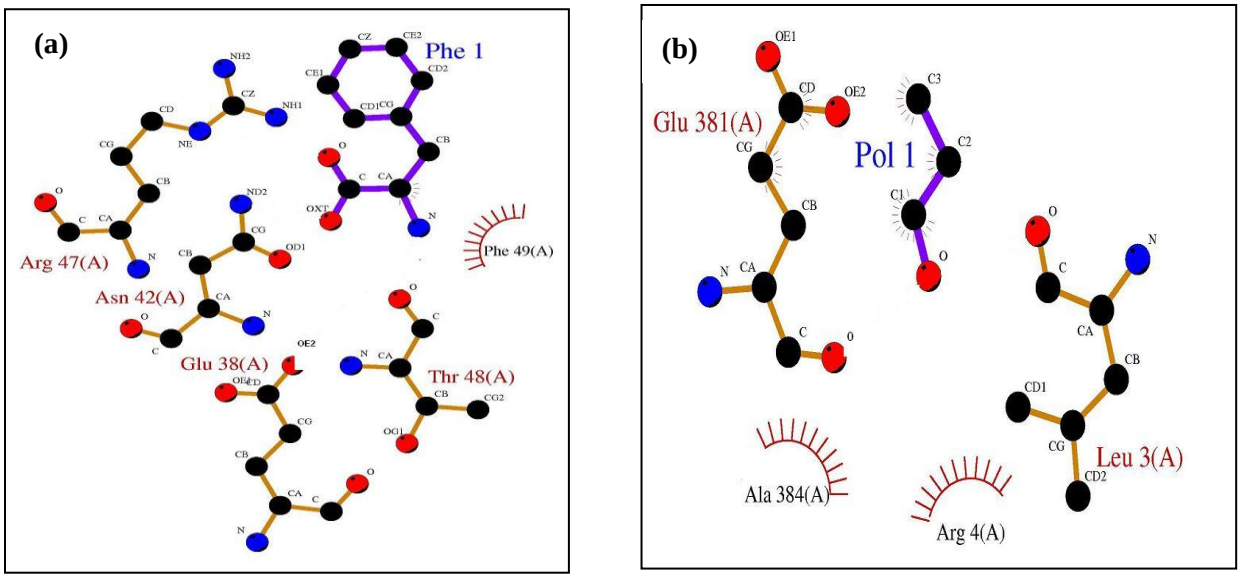


Figure 6. Hydrophobic contacts of ligands (a) POL and (b) PHE with surrounding residues in pocket 57

Conclusion

Selected binding sites of T1 lipase were investigated for ligand binding. The characteristics of each binding site and chemical ligand produced the latent information to determine the protein-ligand interactions. The binding modes of a series of chemical ligands with aromatic rings, amine and hydroxyl groups were explored using AutoDock software. Ligands PHE and BEN docked in the pockets with lowest final docked energy when compared to other selected ligands. Interactions like hydrogen bonds, electrostatic interactions, van der Waals and hydrophobic contacts played very important roles in the protein-ligand interaction studies. By employing *in silico* molecular docking, screening of putative ligands for possible interactions may enhance the discovery of novel semisynthetic enzymes and lead to new protein functions.

Acknowledgement

This work was supported by a grant from the Universiti Putra Malaysia, GP-IPB/2017/9581000.

References

1. Choudhury, P. and Bhunia, B. (2015). Industrial application of lipase: A review. *Biopharm Journal.* (2): 41-47.
2. Aliyu, S. and Md. Zahangir, A. (2015). Thermostable lipases: An overview of production, purification and characterization. *Biosciences Biotechnology Research Asia*, 11(3):1095-1107.
3. Abedi Karjiban, R., Abdul Rahman, M. B., Basri, M., Salleh, A. B., Jacobs, D. and Abdul Wahab, H. (2009). Molecular dynamics study of the structure, flexibility and dynamics of thermostable L1 lipase at high temperatures. *Protein Journal*, 28(1): 14-23.
4. Leow, T. C., Abdul Rahman, R. N. Z., Basri, M. and Salleh, A. B. (2004). High level expression of thermostable lipase from *Geobacillus* sp. strain T1. *Bioscience. Biotechnology and Biochemistry.* 68: 96-103.
5. Bertoldo, J. B., Razzera, G., Vernal, J., Brod, F. C., Arisi, A. C. and Terenzi, H. (2011). Structural stability of *Staphylococcus* xylosus lipase is modulated by Zn(II) ions. *Biochimica et Biophysica Acta 1814*, 9:1120-1126.
6. Jaeger, K. E., Dijkstra, B. W. and Reetz, M. T. (1999). Bacterial biocatalysts: molecular biology, three-dimensional structures, and biotechnological applications of lipases. *Annual Review of Microbiology.* 53: 315-351.
7. Timucin, E. and Sezerman, O. U. (2015). Zinc modulates self-assembly of *Bacillus thermocatenulatus* lipase. *Biochemistry.* 2015, 54(25): 3901-3910.
8. Tyndall, J. D. A., Sinchaikul, S., Forthergill-Gilmore, L. A., Taylor, P. and Walkinshaw, M. D. (2002) Crystal structure of a thermostable lipase from *bacillus stearothermophilus* P1. *Journal of Molecular Biology*, 323: 859-869.
9. Choi, W. C., Kim, M. H., Ro, H. S., Ryu, S. R., Oh. T. K. and Lee, J. K. (2005). Zinc in lipase L1 from *Geobacillus stearothermophillus* L1 and structural implications on thermal stability. *FEBS Letters*, 579 (16): 3461-3466.
10. Timucin, E., Cousido-Siah, A., Mitschler, A., Podjarny, A. and Sezerman, O. U. (2016). Probing the roles of two tryptophans surrounding the unique zinc coordination site in lipase family I.5. *Proteins: Structure Function and Bioinformatics*, 84(1): 129-142.
11. Abdul Rahman, M. Z., Salleh, A. B., Abdul Rahman, R. N. Z., Abdul Rahman, M. B., Basri, M. and Thean Chor, A. L. (2012). Unlocking the mystery behind the activation phenomenon of T1 lipase: A molecular dynamics simulations approach. *Protein Science* 21(8): 1210-1221.
12. Medina-Franco, J., Mendez-Lucio, O. and Martinez-Mayorga, K. (2014). Chapter one – the interplay between molecular modeling and cheminformatics to characterize protein-ligand and protein-protein interactions landscapes for drug discovery interactions. *Advances in Protein Chemistry and Structural Biology*, 96: 1-37.
13. Abdul Rahman, M. B., Misran, A., Basri, M., Abdul Rahman, R. N. Z., Salleh, A. B. and Abdul Wahab, H. (2005). Screening and docking chemical ligands onto pocket cavities of a protease for designing a biocatalyst. *Biocatalysis and Biotransformation*, 23: 211-216.
14. Chikhi, A. and Benseguemi, A. (2010). *In silico* study of the selective inhibition of bacteria peptide deformylases by several drugs. *Journal of Proteomics and Bioinformatics* 3: 061-065.
15. Gao, J., Liang, L., Zhu, Y., Qiu, S., Wang, T. and Zhang, L. (2016). Ligand and structural-based approaches for the identification of peptide deformylase inhibitors as antibacterial drugs. *International Journal of Molecular Science*, 17: 1141.

16. Binkowski, T. A., Freeman, P. and Liang, J. (2004). pvSOAR: detecting similar surface patterns of pocket and void surfaces of amino acid residues on proteins. *Nucleic Acids Research*, 32: W555-W558.
17. Binkowski, T. A., Adamian, L. and Liang, J. (2003). Inferring functional relationships of proteins from local sequence and spatial surface patterns. *Journal of Molecular Biology.* 332: 505-526.
18. Kumar, S. and Nussinov, R. (2002). Close-range electrostatic interactions in proteins. *ChemBioChem*. 23(7): 604-617.
19. Morris, G. M., Goodsell, D. S., Halliday, R. S., Huey, R., Hart, W. E., Belew, R. K. and Olson, A. J. (1998). Automated docking using a Lamarckian genetic algorithm and an empirical binding free energy function. *Journal of Computational Chemistry*, 18: 1639-1662.
20. Abdul Rahman, M. B., Karjiban, R. A., Salleh, A. B., Jacobs, D., Basri, M., Thean Chor, A. L., Abdul Wahab, H. and Abdul Rahman, R. N. Z. (2009). Deciphering the flexibility and dynamics *of Geobacillus zalihae* strain T1 lipase. *Protein and Peptide Letters*, 16(11):1460-1370.
21. Pace, C. N., Shirley, B. A., McNutt, M. and Gajiwala, K. (1996). Forces contributing to the conformational stability of proteins. *The FASEB Journal*, 10: 75-83.
22. Rose, G. D., Fleming, P. J., Banavar, J. R. and Maritan, A. (2006). A backbone-based theory of protein folding. *Proceedings of the National Academy of Sciences U.S.A*, 103(45): 16623-16633.
23. Sugimura, Y., Fukunaga, K., Matsuno, T., Nakao, K., Goto, M. and Nakashio, F. (2000). A study on the surface hydrophobicity of lipases. *Biochemical Engineering Journal*, 5: 123-128.
24. Abdul Rahman, M. B., Jaafar, A. H., Basri, M., Abdul Rahman, R. N. Z. and Salleh, A. B. (2014). Biomolecular design and receptor-ligand interaction of a potential industrial biocatalsyt: A thermostable thermolysin-phosphoethanolamine-Ca^{2+} protein complex. *Journal of Advanced Catalysis Science and Technology*, 2014: 1-5.
25. Panagiotis, L. K. and Alexandre M. J. J. B. (2013). On the binding affinity of macromolecular interactions: daring to ask why proteins interact. *Journal of The Royal Society Interface,*10: 20120835.

Malaysian Journal of Analytical Sciences, Vol 23 No 4 (2019): 625 - 636
DOI: https://doi.org/10.17576/mjas-2019-2304-08

MALAYSIAN JOURNAL OF ANALYTICAL SCIENCES
Published by The Malaysian Analytical Sciences Society
ISSN 1394 - 2506

ADSORPTION OF MALACHITE GREEN ONTO MODIFIED CHITOSAN–SULFURIC ACID BEADS: A PRELIMINARY STUDY

(Penjerapan Malakit Hijau ke atas Manik Kitosan-Asid Sulfurik Terubahsuai: Satu Kajian Awal)

Suhaila Mohd Yusoff[1], Wan Saime Wan Ngah[1], Faizatul Shimal Mehamod[2], Faiz Bukhari Mohd Suah[1]*

[1]*School of Chemical Sciences,*
Universiti Sains Malaysia, 11800 Minden, Pulau Pinang, Malaysia
[2]*School of Fundamental Science,*
Universiti Malaysia Terengganu, 21030 Kuala Nerus, Terengganu, Malaysia

**Corresponding author: fsuah@usm.my*

Received: 2 July 2018; Accepted: 9 July 2019

Abstract

The removal of malachite green (MG) from aqueous solutions by cross–linked chitosan–sulfuric acid (H_2SO_4) beads was investigated. Solubility and swelling tests were performed in order to determine the stability of the chitosan–H_2SO_4 beads in acidic solution, basic solution and distilled water. Different parameters affecting the adsorption capacity such as initial pH (pH 2-12), agitation period (10-60 minutes) and initial concentrations of MG (5-30 mg/L) were studied. In addition, the adsorption capacities of MG onto chitosan–H_2SO_4 beads were determined too. In order to describe adsorption isotherm of chitosan–H_2SO_4 beads, the sorption data were analyzed using linear form of Langmuir and Freundlich equation. It was found that Langmuir isotherm showed higher conformity than Freundlich isotherm (30.96>2.23). A kinetic study indicated that pseudo–second–order kinetic equation correlates well with the experimental data. FT–IR analysis established there was an interaction between MG and chitosan–H_2SO_4 beads. It can be concluded that chitosan–H_2SO_4 beads were favorable absorbers and could be used as alternate adsorbents for removal of MG in water treatment process.

Keywords: adsorption, chitosan–H_2SO_4 beads, isotherm, kinetics, malachite green

Abstrak

Penyingkiran malakit hijau (MG) daripada larutan akueus oleh manik kitosan-asid sulfurik (H_2SO_4) berangkai-silang telah dikaji. Ujian keterlarutan dan pengembangan dijalankan untuk menentukan kestabilan manik kitosan-H_2SO_4 di dalam larutan asid, larutan alkali dan air suling. Parameter berbeza yang mempengaruhi muatan penjerapan seperti pH awal (pH 2-12), tempoh putaran (10-60 minit) dan kepekatan awal MG (5-30 mg/L) dikaji. Sebagai tambahan, muatan penjerapan bagi MG terhadap kitosan-H_2SO_4 turut ditentukan. Bagi menentukan isoterma penjerapan manik kitosan-H_2SO_4, data penjerapan telah dianalisis menggunakan persamaan linear Langmuir dan Freundlich. Didapati isoterma Langmuir lebih sesuai berbanding isoterma Freundlich (30.96>2.23). Kajian kinetik menunjukkan persamaan tertib-pseudo-kedua berhubung baik dengan data kajian. Analisis FT-IR mengesahkan terdapat interaksi diantara MG dan manik kitosan-H_2SO_4. Dapat disimpulkan bahawa kitosan-H_2SO_4 adalah penjerap pilihan dan boleh digunakan sebagai penjerap alternatif bagi menyingkirkan MG dalam proses perawatan air.

Kata kunci: penjerapan, manik kitosan-H_2SO_4, isoterma, kinetik, malakit hijau

Introduction

Discharges of various types of waste product and the rapid growth of different chemical industries have become the main causes of environmental contamination and degradation to the country. Dyes, which are widely used in

different industries, can inhibit light penetration into water, retard photosynthetic activity, prevent the growth of biota and have a tendency to chelate metal ions. Dyes are classified according to their chemical properties and solubility. Dyes can be categorized as an acid dye, basic dye, direct dye, mordant dye, disperse dye, reactive dye and vat dye [1]. Basic dyes are the most commonly used in many industries and have become one of the main sources of severe water pollution. Malachite green (MG) is an example of a basic dye used to dye wool, silk, cotton and leather in textile industries and also as a strong anti-fungal, anti-bacterial and anti-parasitic agent in fish farming [1, 2]. Nowadays, MG is considered as a highly controversial compound due to its genotoxic and carcinogenic properties [3].

Adsorption has been found to be the most promising way to remove MG from wastewater because it uses low-cost adsorbents, which could be found in nature or are by-products [4]. Chitosan is one of the unindustrialized adsorption methods for the removal of dyes and heavy metal ions, even at low concentrations [5]. Chitosan is a type of natural polyaminosaccharide composed of poly(β-1–4)-2-amino-2-deoxy-D-glucopyranose and can be produced through deacetylation of chitin. Chitin is the second most abundant polymer in nature after cellulose that can be extracted from crustacean shells such as prawns, crabs and cell walls of fungi [6]. This nontoxic and biodegradable chitosan is an ideal adsorbent due to the presence of the amine ($–NH_2$) and hydroxyl (–OH) groups that serve as the adsorption sites for many adsorbates [7, 8].

In spite of chitosan's good adsorption capability, it also can be physically and chemically modified [9–11]. Accordingly, the physical modification of chitosan can provide support and increase the availability of the binding sites because the chitosan has low mechanical properties and low specific gravity [12, 13]. Therefore, efforts have been made to improve its chemical stabilities by cross-linking the chitosan to create a very stable and strong chitosan even in acidic and basic solutions.

Many studies have been reported for utilizing modified chitosan for application in MG removal, such as chitosan–ionic liquid beads [14], chitosan nanoparticles [15, 16], chitosan oligosaccharide [17], chitosan composite [18], chitosan–bentonite beads [19] and chitosan foam [20]. These approaches seem to be effective for removing MG but some improvement in existing methods is desirable. All of these modified chitosan's are difficult to prepare, time-consuming and unstable, especially the chitosan foam. Therefore, a simple approach has been taken in this study which is using a modified chitosan with sulfuric acid (H_2SO_4) to remove MG from an aqueous solution. The method to prepare this modified chitosan is relatively straightforward and not expensive.

In this preliminary study, chitosan–H_2SO_4 beads are used to remove MG dye in aqueous solution. The influences of initial pH, agitation time, adsorbent dosage and initial concentrations of MG on the adsorption process were studied. These are the basic parameters to determine the suitability and optimal conditions of the prepared cross-linked chitosan beads as an adsorbent. The pseudo-first-order and pseudo-second-order kinetics models were used to determine the adsorption rate during the adsorption process. The Langmuir and Freundlich isotherm models were used to evaluate the equilibrium adsorption capacity data for the adsorption of MG onto chitosan–H_2SO_4.

Materials and Methods

Materials

Samples of chitosan flakes (M.W. 100,000－150,000 g/mol) with a degree of deacetylation of 72.55% were supplied by Chito–Chem (M) Sdn. Bhd., Malaysia. MG was purchased from Fluka (Malaysia). Sodium hydroxide pellets, NaOH, hydrochloric acid 37.0%, HCl, acetic acid, CH_3COOH, were purchased from Sigma-Aldrich (Malaysia). All the reagents used throughout the experiments are analytical–reagent grade and used without any further purification. Distilled deionized water was used to prepare all solutions.

Preparations of chitosan beads and chitosan–H_2SO_4 beads

Chitosan beads were prepared by dissolving 2.0 g of chitosan flakes in 60 mL of 5% (v/v) acetic acid. The viscous solution was left overnight before dropping into 500 mL of 0.50 M NaOH solution using a dropper. The aqueous NaOH solution was under continuous stirring with the speed of 300 rpm. The chitosan hydrogel beads were allowed to immerse in 0.50 M NaOH solution for 15 minutes. Then, the formed chitosan beads were filtered with filter paper 2.5 µm of pore size (Whatman 42) and rinsed many times with distilled water. Eventually, the extensively washed

chitosan beads were then added into 100 mL of 0.50 M sulfuric acid solution and were stirred at 200 rpm for 24 hours at room temperature. After 24 hours the solution was filtered and the cross–linked beads were washed several times using distilled water. The chitosan–H_2SO_4 beads were allowed for drying. The beads were then ground using mortar and sieved to a constant size approximately (< 250 µm) before used. The structure of chitosan–H_2SO_4 beads before and after MG adsorption obtained was confirmed by a Perkin–Elmer FT–IR System 2000 Model spectrometer.

Solubility and swelling test of chitosan beads and chitosan–H_2SO_4 beads

The solubility of chitosan–H_2SO_4 beads was tested in 5% (v/v) acetic acid, 0.10 M NaOH and distilled water. Approximately 0.05 g of the beads was weighed and transferred into a 50 mL of these three solutions and were left stirring for 24 hours. After 24 hours, the solubility of the beads in these solutions was observed.

In the swelling test, both chitosan beads and chitosan–H_2SO_4 beads were studied. About 0.05 g of the beads was weighed and transferred into a glass tube with a diameter of 5 mm and a height of 100 mm. Three tubes were prepared. The level of the beads was marked before filling with 1 mL of 5 % (v/v) acetic acid, 0.10 M NaOH and distilled water. They were left for 24 h. After that, the height of the beads in all three solutions was calculated. The percentage swelling was calculated using the following equation:

$$S = \left(\frac{h_t - h_o}{h_o}\right) \times 100 \quad (1)$$

where, S is the percentage of swelling (%), h_t is the height of swollen beads or chitosan–H_2SO_4 beads at time t (cm), h_o is the initial height of chitosan beads or chitosan–H_2SO_4 beads (cm).

Batch adsorption experiments

A stock solution of 500 mg/L of MG was prepared freshly by dissolving approximately 0.25 g of MG in a 250 mL beaker with distilled water. The solution was transferred into a 500 mL volumetric flask. A series of experiments were conducted in 250 mL beaker using 0.05 g of chitosan–H_2SO_4 beads and left shaking for 30 minutes using Heidolph Unimax 1010 shaker. The absorbance of MG was obtained before and after adsorption at the maximum wavelength of 224 nm using a UV–Vis spectrophotometer (Perkin Elmer Lambda 35).

The effect of initial pH of the solution on the adsorption of MG onto chitosan–H_2SO_4 was performed in the pH range of 2-12. Six sets of 100 mL of MG solutions with concentration of 10 mg/L were prepared.

Adsorption equilibrium analysis was performed at optimum condition where the pH is 6 and the agitation time is 30 minutes for chitosan–H_2SO_4 beads. Isotherm studies were accomplished with a constant amount of chitosan–H_2SO_4 beads and varying the initial concentration of MG in the range of 0–70 mg/L. The adsorption capacity (q_e) at equilibrium was calculated using the following equation:

$$q_e = \frac{C_o - C_e}{m} v \quad (2)$$

where q_e is the adsorption capacity at equilibrium (mg/g), C_o is the initial concentration of MG (mg/L), C_e is the final concentration of MG (mg/L), v is the volume of MG (mL), m is the weight of the beads used (g). For batch kinetics studies of MG onto adsorbent was also studied. About 0.05 g of chitosan–H_2SO_4 beads were equilibrated at optimum condition. The beads and 10 mg/L of MG solutions were placed in 250 mL beakers and stirred continuously. The concentration of MG in solution was determined each time based on the differences of MG concentration in the solution before and after adsorption. Three replicates analyses have been done for each adsorption study and the average was reported.

In addition, several parameters were optimized too. Effect of adsorbent dosage (percentage removal) was calculated using the following expression:

$$\% \text{ Removal} = \frac{C_o - C_f}{C_o} \times 100 \quad (3)$$

where C_o is the initial concentration of MG (mg/L) and C_f is the final concentration of MG (mg/L).

Models for adsorption equilibrium isotherms used in this study were Langmuir and Freundlich isotherm models. Langmuir isotherm model used is applicable for monolayer sorption on to a surface with finite number of identical sites and is given by:

$$\frac{C_e}{q_e} = \frac{C_e}{Q} + \frac{1}{Qb} \quad (4)$$

where Q is the maximum adsorption at monolayer (mg/g), C_e is the equilibrium concentration of MG (mg/L), q_e is the amount of MG adsorbed per unit weight of chitosan–H_2SO_4 beads at equilibrium concentration (mg/g) and b is the Langmuir constant related to the affinity of binding sites (mL/mg) and is a measure of the energy of adsorption. A linearized plot of C_e/q_e against C_e gives Q and b.

Freundlich isotherm model is an empirical isotherm for non–ideal adsorption on heterogeneous surfaces as well as multilayer adsorption and is expressed as [21]:

$$\log q_e = \log K_F + \frac{1}{n} \log C_e \quad (5)$$

where K_F and n are Freundlich constant that indicates adsorption capacity (mg/g) and intensity, respectively. K_F and n can be obtained from linear plot of log q_e against log C_e.

The critical features of a Langmuir isotherm can be expressed in terms of dimensionless constant separation factor, R_L which can be expressed as:

$$R_L = \frac{1}{1 + bC_o} \quad (6)$$

where R_L is the separation factor parameter. C_o is the initial concentration (mg/L) and b is the Langmuir constant (L/mg).

Meanwhile adsorption kinetic models used in this study were pseudo–first–order and pseudo–second–order. The linear form of pseudo–first–order rate equation is expressed as Equation 7 [22]:

$$\log (q_e - q_t) = \log q_e - \frac{k_1}{2.303} t \quad (7)$$

where q_e and q_t (mg/g) are the amount of MG absorbed onto adsorbent at equilibrium and at time t (min), respectively and k_1 (min^{-1}) is the rate constant of pseudo–first–order adsorption. The straight-line plots of log (q_e–q_t) against t will yield the values of rate constant, k_1 and q_e from the slope and intercept, respectively.

The pseudo–second–order equation is based on the assumption that chemisorption is the rate determining step and is expressed as given by Equation 8 [23]:

$$\frac{t}{q_t} = \frac{1}{h} + \frac{t}{q_e} \quad (8)$$

where $h = k_2 q_e^2$ can be regarded as the initial adsorption rate (mg/g/min) as t approaches to zero, and k_2 (g/min/mg) is the rate constant of pseudo–second–order adsorption.

Results and Discussion

Solubility and swelling test of chitosan and chitosan–H_2SO_4 beads

Chitosan is known for its stability in acidic media. Therefore, physical and chemical alterations were carried out to increase the adsorption capacity and improve the stability of chitosan–H_2SO_4 beads. According to Ngah et al. [10], the primary group of amine causes the chitosan beads to have higher hydrophilicity triggering chitosan to be easily soluble in dilute acetic solution to yield a hydrogel. Based on Table 1, it can be seen that the chitosan beads were insoluble in both distilled water and alkaline solution but completely dissolved in acidic medium giving a viscous solution. The chitosan–H_2SO_4 beads were insoluble in all three media studied. This is due to the ionic cross-linking modification with sulfuric acid greatly reinforcing the chemical stability of chitosan in acidic solution. Both the chitosan beads and chitosan–H_2SO_4 beads do not dissolve in neutral and alkaline media because there is less H^+ ion present to protonate the amino group of chitosan. The insolubility of the chitosan–H_2SO_4 beads is important because it is the main indicator to determine the optimum pH for the adsorption process and as a sign that it can be used in all media.

Table 1. Solubility effect of chitosan beads and chitosan–H_2SO_4 beads

Adsorbent	Solubility Effect		
	5% (v/v) Acetic Acid	Distilled Water	0.1 M NaOH
Chitosan beads	Soluble	Insoluble	Insoluble
Chitosan–H_2SO_4 beads	Insoluble	Insoluble	Insoluble

The percentage of swelling is the most important to understand the crystalline nature of the adsorbent. From Table 2, the percentage of swelling of chitosan–H_2SO_4 beads was much lower than the percentage of swelling observed for chitosan beads. The swelling ability of chitosan–H_2SO_4 beads depended on the degree of cross-linking. The percentage of swelling will be much lower at a higher cross-linking density [11]. In this study, chitosan beads are soluble in acidic medium but have a higher percentage of swelling in neutral and alkaline medium. However, chitosan–H_2SO_4 beads show the highest percentage in both acidic and neutral medium but a lower percentage of swelling in alkaline medium. This proved that the reduction in the swelling percentage of chitosan can be attributed to ionic linkages formed between the protonated amine groups ($-NH_3^+$) of chitosan and SO_4^{2-} ions of sulfuric acid, which increased the chemical stability of the beads in acidic medium.

Table 2. Swelling behavior of chitosan beads and chitosan–H_2SO_4 beads in different medium

Adsorbent	Percentage of Swelling (%)		
	5% (v/v) Acetic Acid	Distilled Water	0.1 M NaOH
Chitosan beads	Soluble	164	104
Chitosan–H_2SO_4 beads	125	81.5	71

Effect of initial pH

Figure 1 shows the effect of different pH for the adsorption of MG onto chitosan–H_2SO_4 beads. It can be seen that dye adsorption was unfavorable at pH < 4. As the pH of the system decreased, the $–NH_2$ groups that surround the adsorbent surface are protonated. The number of negatively charged adsorbent sites decreased and the number of positively charged surface sites increased, which did not favor the adsorption of positively charged dye cations due to electrostatic repulsion. This would cause repulsion between the $–NH_3^+$ groups on the adsorbent surface and the $–N^+(CH_3)_2$ groups of MG. Lower adsorption of MG at acidic pH is due to the presence of excess H^+ ions competing with dye cations for the adsorption sites of chitosan–H_2SO_4 beads [12]. With the increase in pH, the number of H^+ ions decreased and the adsorbent surface carried more negative charge resulting in greater attraction between the adsorbent and the cationic form of the adsorbate. Therefore, pH 6 was chosen as the optimum condition for following adsorption experiments.

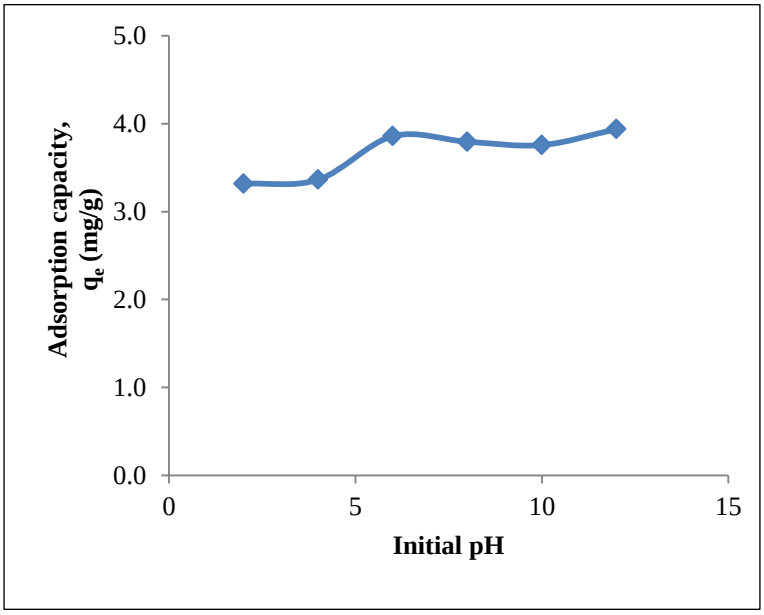


Figure 1. Effect of initial pH on the adsorption of MG onto chitosan–H_2SO_4 beads

Effect of adsorbent dosage

The effect of adsorbent dosage is illustrated in Figure 2. The percentage removal increases with the increasing adsorbent dosage from 8 to 17% for an adsorbent dosage of 0.01 g to 0.10 g. However, the adsorption capacity, which is the amount of MG adsorbed per unit weight decreased with increasing adsorbent dosage. Percentage removal is increased because the availability of adsorption surface is increased yet the decrease in adsorption capacity with increase adsorbent dosage is due to saturation of adsorption sites.

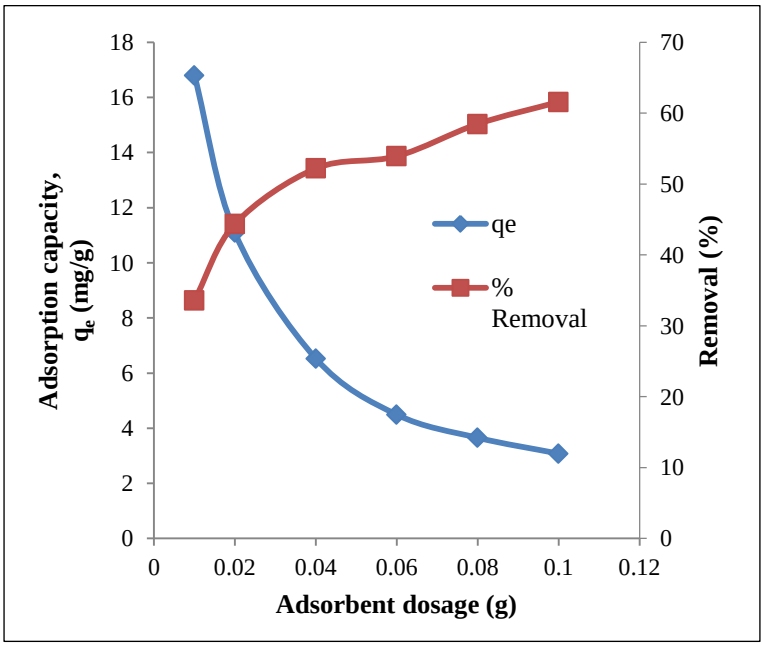


Figure 2. Effect of adsorbent dosage on the adsorption of MG onto chitosan–H_2SO_4 beads

Effect of agitation period

It is necessary to determine the optimum agitation period required for the adsorption of MG because it represented the time required for the adsorbate to reach an equilibrium state after contact with the adsorbent. The optimum period can be observed in Figure 3 by looking at a rapid adsorption capacity within the first 10 minutes, then a decrease before slowly becoming constant at 30 minutes. The initial rapid phase during the first 10 minutes was due to the availability of adsorption sites for the uptake of MG. Meanwhile, after 30 minutes the adsorption became constant because of the quick exhaustion of the adsorption sites [13]. As a result, the equilibrium time of 30 minutes was selected for additional studies.

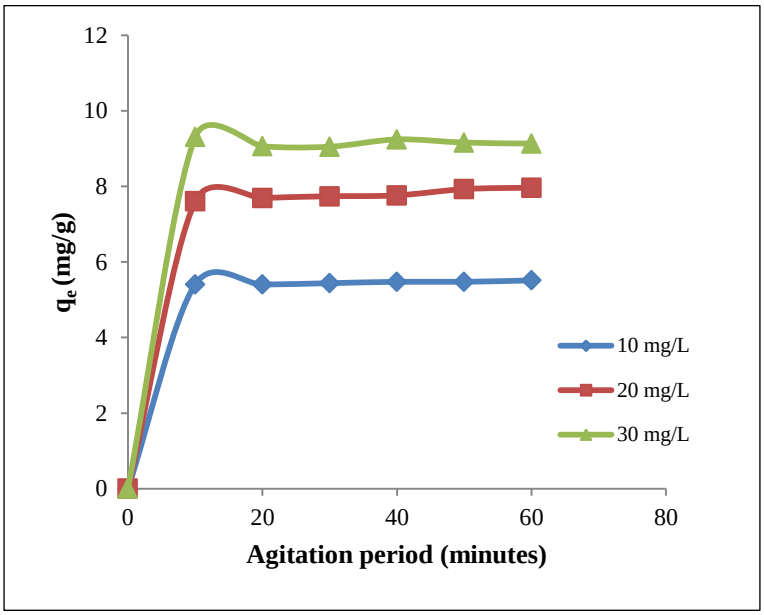


Figure 3. Effect of agitation time on the adsorption of MG onto chitosan–H_2SO_4 beads

Adsorption equilibrium isotherms

An adsorption isotherm is an expression that shows the relationship between the amounts of adsorbate adsorbed per unit weight of adsorbent (q_e, mg/g) and the concentration of adsorbate in the bulk solution (C_e, mg/L) at 300 K under equilibrium conditions. The Langmuir and Freundlich models are often used to describe equilibrium adsorption isotherms. The Langmuir isotherm usually indicates individual chemical adsorption (chemisorption) and reflects a relatively high affinity between adsorbate and the adsorbent within a low concentration range [1].

The Langmuir isotherm also assumes that the adsorbed layer is one molecule in thickness and that all adsorption sites have equal energies and enthalpies of adsorption. The linearized Langmuir and Freundlich models plot at 300 K are shown in Figures 4 and 5, respectively. Table 3 shows the obtained values for the Langmuir and Freundlich isotherms constants and coefficients of determination (R^2). Overall, the experimental data fitted well with the Langmuir isotherm model because the R^2 values were very high. This showed that chitosan–H_2SO_4 beads had homogeneous adsorption sites.

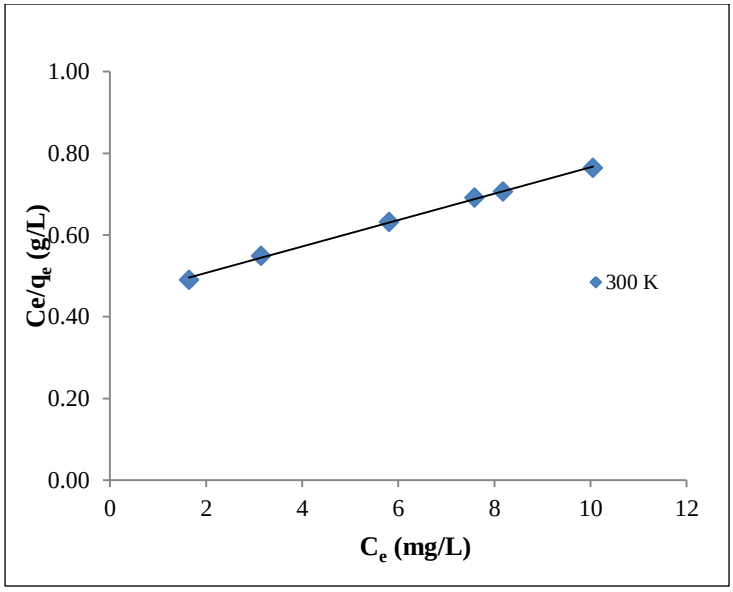


Figure 4. Linearized Langmuir adsorption isotherm of MG onto chitosan–H_2SO_4 beads

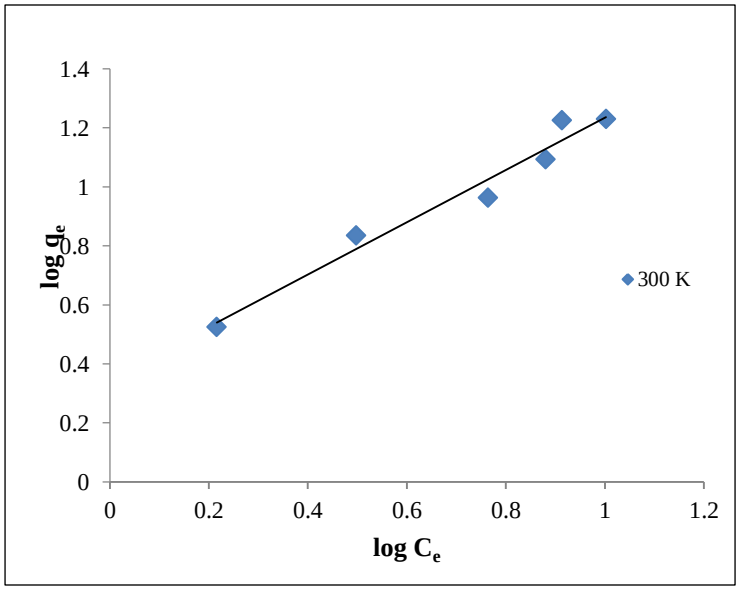


Figure 5. Linearized Freundlich adsorption isotherm of MG onto chitosan–H_2SO_4 beads

Table 3. Langmuir and Freundlich isotherm constants and correlation for the adsorption of MG onto chitosan–H_2SO_4 beads at 300 K

Langmuir			Freundlich		
Q (mg/g)	**b (L/mg)**	**R^2**	**K_f (mg/g)**	**n**	**R^2**
30.96	0.0730	0.9985	2.23	1.1287	0.9666

It has been stated that the effect of isotherm shape with a view to predicting if an adsorption system is 'favorable' or 'unfavorable'. It has been established that for favorable adsorption, $0 < R_L < 1$; unfavorable adsorption, $R_L > 1$; linear adsorption, $R_L = 1$; and irreversible adsorption process if $R_L = 0$. Based on Table 4, the R_L values are in the range of $0 < R_L < 1$, which reveals the adsorption of MG onto chitosan–H_2SO_4 beads is favorable.

Table 4. Values of R_L for initial concentrations range from 0 to 30 mg/L at 300 K

Initial Concentration of MG (mg/L)	**R_L value**
5	0.7326
10	0.5780
15	0.4773
20	0.4065
25	0.3540
30	0.3135

Adsorption kinetics

The kinetics of adsorption is applied to determine the adsorption rate of MG uptake on the beads. The most common kinetic models applied in adsorption studies are pseudo-first-order and pseudo-second-order. Figure 6 represents the pseudo-first-order kinetic plot for chitosan–H_2SO_4 beads.

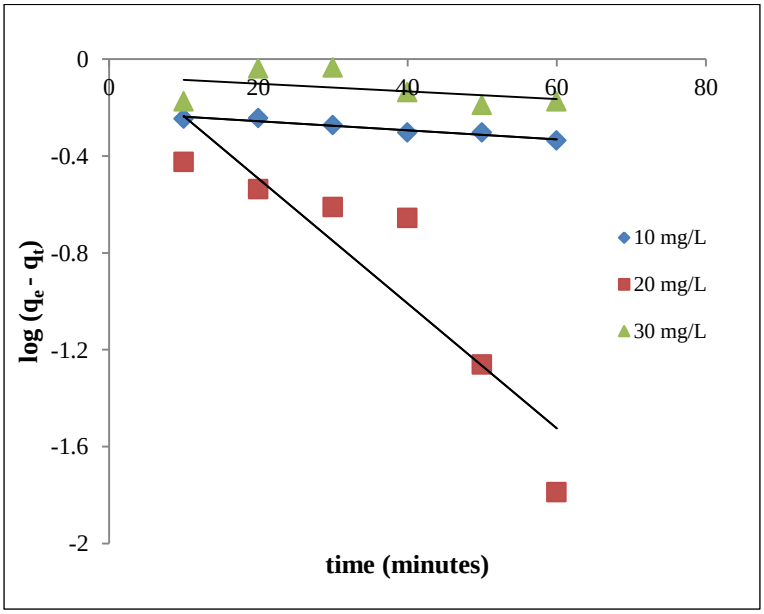


Figure 6. Plot of pseudo–first–order kinetic model for the adsorption of MG onto chitosan–H_2SO_4 beads

The straight-line plots of t/q_t against t were used to determine the rate constant, k_2 and coefficient of determination, R^2. Figure 7 represents the pseudo-second-order plot for chitosan–H_2SO_4 beads. The results of kinetic parameters of the pseudo-first-order and pseudo-second-order kinetic models for the adsorption of MG are given in Table 5. Based on the R^2 values shown in the table, it can be concluded that the pseudo-second-order kinetic model can be used to represent the adsorption behavior over the whole range of contact time. Moreover, the calculated adsorption

capacity ($q_{e, calc}$) values were in agreement with the experimental adsorption capacity ($q_{e, exp)}$ value. This showed that the uptake of MG onto chitosan–H_2SO_4 beads was rapid and favorable. The initial adsorption rate, h, of the pseudo-second-order kinetic model increased as concentrations increased. The large number of adsorption sites available on chitosan–H_2SO_4 beads might cause the rapid adsorption of MG at higher concentrations, possibly due to the increase in the driving force for mass transfer, and thus, allowing MG molecules to reach the adsorbent surface in a shorter period of time [24, 25].

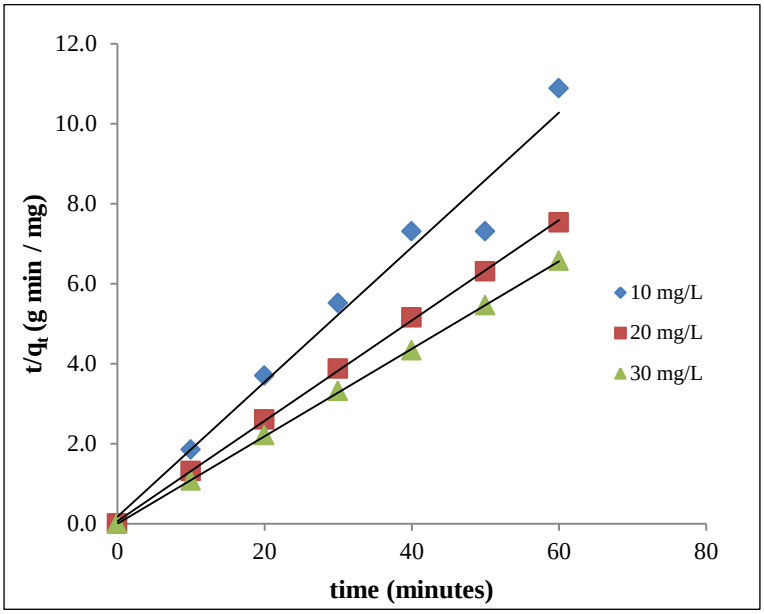


Figure 7. Plot of pseudo–second–order kinetic model for the adsorption of MG onto chitosan–H_2SO_4 beads

Table 5. Kinetic parameters for the adsorption of MG onto chitosan–H_2SO_4 beads based on pseudo–first–order and pseudo–second–order kinetic model

Concentration of MG (mg/L)	Pseudo–First–Order				Pseudo–Second–Order			
	$q_{e, exp}$ (mg/g)	k_1 (1/min)	R^2	$q_{e, calc}$ (mg/g)	k_2 (g/mg /min)	h (mg/g /min)	R^2	$q_{e, calc}$ (mg/g)
10	5.97	4.38×10^{-3}	0.9335	0.61	0.17	5.97	0.9716	5.93
20	7.98	5.94×10^{-2}	0.8227	1.06	0.25	16.10	0.9996	7.97
30	9.97	3.68×10^{-3}	0.1768	0.85	23.89	1999.74	0.9999	9.15

FT–IR analysis

The FTIR spectra obtained for chitosan beads and chitosan–H_2SO_4 beads before and after adsorption were shown in Figure 8. The broad peaks at 3428.58 cm^{-1} in chitosan beads can be assigned to stretching vibration of hydroxyl group and N–H groups found in chitosan. The adsorption band at 1655.12 cm^{-1} is the N–H bending in primary amine groups (–NH_2). Other major band observed at 1383.14 cm^{-1} represents C–N stretching vibration. After the cross–linking process, several changes were observed in the spectra obtained for chitosan–H_2SO_4 beads. The broad peak at 3428.58 cm^{-1}, shifted to 3423.52 cm^{-1} and eventually become broader. This showed that the –NH_2 groups in chitosan were protonated to –NH_3^+, as this broader band represented the stretching vibration of –NH_3^+. The adsorption bands at 1635.05 and 1532.64 cm^{-1} represented the bending vibration of –NH_3^+ groups. The involvement

of SO_4^{2-} ions in the cross–linking process was confirmed by the presence of the adsorption bands at 1191.64 cm^{-1} that represented the sulfo groups. The band observed at 1076.47 cm^{-1} also confirmed the presence of S=O stretching found in the SO_4^{2-} ions. This FTIR spectra proved that the formation of chitosan–H_2SO_4 beads was through the ionic interaction between the protonated amine groups ($–NH_3^+$) of chitosan and the SO_4^{2-} ions of sulfuric acid. The FTIR of chitosan–H_2SO_4 beads after adsorption showed there were no appearances of new bands. However, there were adsorption bands at 887.59 and 855.15 cm^{-1} represented $–NH_3^+$ rocking vibrations. These spectral changes shown that many amine groups were protonated to form $–NH_3^+$.

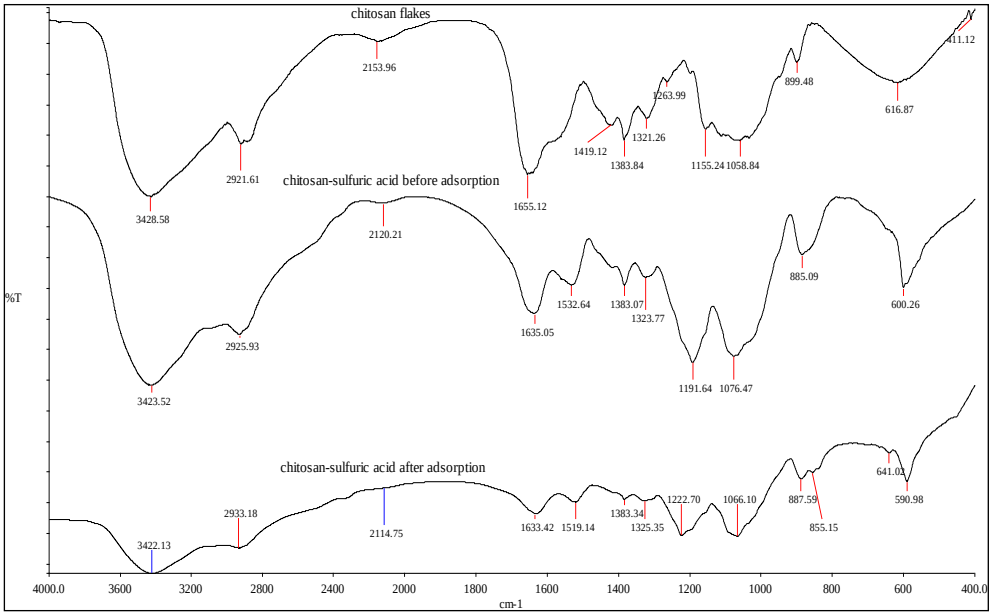


Figure 8. Infrared spectra for chitosan flakes and chitosan–H_2SO_4 before and after adsorption

Conclusion

This study demonstrated that chitosan–H_2SO_4 beads are a promising adsorbent for the removal of MG from aqueous solutions. Chitosan–H_2SO_4 beads show a lower percentage of swelling than chitosan beads. The adsorption isotherm could be well fitted by the Langmuir equation and the MG adsorption followed the pseudo-second-order equation. The interaction between MG and chitosan–H_2SO_4 beads was confirmed by FTIR spectroscopy. Hence, it can be concluded that chitosan–H_2SO_4 beads are effective adsorbents for the uptake of MG sorption studies. Based on these findings, the prepared chitosan–H_2SO_4 beads can be used to remove MG from the wastewater, which is currently being carried out. In addition, the chitosan–H_2SO_4 beads can also be prepared in membrane, microbead and nanoparticle forms. It is expected that the removal of MG shall be increased with the use of different physical shapes of the cross-linked chitosan–H_2SO_4.

Acknowledgement

Authors would like to thank Universiti Sains Malaysia for providing financial assistances through a bridging grant (304/PKIMIA/6316215) and a short-term grant (304/PKIMIA/6315197).

References

1. Zhou, Y., Lu, J., Zhou, Y. and Liu, Y. (2019). Recent advances for dyes removal using novel adsorbents: A review. *Environmental Pollution*, 252: 352-365.
2. Bekci, Z., Ozveri, C., Seki, Y. and Yurdakoc, K. (2008). Sorption of MG on chitosan beads. *Journal of Hazardous Materials*, 154: 254-261.

3. Yeoh, Y. L. and Mohd Suah, F. B. (2017). Extraction of malachite green from wastewater by using polymer inclusion membrane. *Journal of Environmental Chemical Engineering*, 5: 785-794.
4. Ngah, W. S. W., Fathinathan, F. and Yosop, N. A. (2011). Isotherm and kinetic studies on the adsorption of humic acid onto chitosan–H_2SO_4 beads. *Desalination*, 272: 293-300.
5. Ngah, W. S. W., Teong, L. C. and Hanafiah, M. A. K. M. (2011). Adsorption of dyes and heavy metal ions by chitosan composites: A review. *Carbohydrate Polymers*, 83: 1446-1456.
6. Ngah, W. S. W. and Isa, I. M. (1998). Comparison study of copper ion adsorption on chitosan Dowex A–1 and zeolite. *Journal of Applied Polymer Science*, 67: 1067-1070.
7. Muzzarelli, C., Stanic, V., Gobbi, L., Tossi, G. and Muzzarelli, R. A. A. (2004). Spray–drying of solutions containing chitosan together with polyuronans and characterization of the microspheres. *Carbohydrate Polymers*, 57: 73-82.
8. Chang, M. Y. and Juang, R. S. (2004). Adsorption of tannic acid, humic acid, and dyes from water using the composite of chitosan and activated clay. *Journal of Colloid Interface Science*, 278: 18-25.
9. Boddu, V. M., Abburi, K., Talbott, J. L. and Smith, E. D. (2003). Removal of hexavalent chromium from wastewater using a new composite chitosan biosorbent. *Environmental Science Technology*. 37: 4449-4456.
10. Ngah, W. S. W., Endud, C. S. and Mayanar, R. (2002). Removal of copper (II) ions from aqueous solution onto chitosan and cross–linked chitosan beads. *Reactive and Functional Polymers*, 50: 181-190.
11. Lee, S. T., Mi, F. L., Shen, Y. J. and Shyu, S. S. (2001). Equilibrium and kinetic studies of copper (II) ion uptake by chitosan–tripolyphosphate chelating resin. *Polymer*, 42: 1879-1892.
12. Hameed, B. H. and El–Khaiary, M. I. (2008). Batch removal of malachite green from aqueous solutions by adsorption on oil palm trunk fibre: Equilibrium isotherms and kinetic studies. *Journal of Hazardous Materials*, 154: 237-244.
13. El–Ashtoukhy, E. S. Z., Amin, N. K. and Abdelwahab, O. (2008). Removal of lead (II) and copper (II) from aqueous solution using pomegranate peel as a new adsorbent. *Desalination*, 223: 162-173.
14. Naseeruteen, F., Abdul Hamid, N. S. Mohd Suah, F. B., Wan Ngah, W. S. and Mehamod, F. S. (2018). Adsorption of malachite green from aqueous solution by using novel chitosan ionic liquid beads. *International Journal of Biological Macromolecules*, 107: 1270-1277.
15. Abou-Gamra, Z. M. and Ahmed, M. A. (2015). TiO_2 nanoparticles for removal of malachite green dye from waste water. *Advances in Chemical Engineering and Science*, 5: 373-388.
16. Wang, W. J., Cui, Q. Y., Qin, T. and Sun, H. H. (2018). Preparation of Fe_3O_4@SiO_2@ chitosan for the adsorption of malachite green. *IOP Conf. Series: Earth and Environmental Science*, 186: 012014.
17. Zhang, Y., Wan, H., Zhao, J. and Li, J. (2019). Biosorption of anionic and cationic dyes via raw and chitosan oligosaccharide-modified Huai Flos Chrysanthemum at different temperature. *RSC Advances*, 9: 11202-11211.
18. Arumugam, T. K., Krishnamoorty, P., Rajagopalan, N. R., Nanthini, S. and Vasudevan, D. (2019). Removal of malachite green from aqueous solutions using a modified chitosan composite. *International Journal of Biological Macromolecules*, 128: 655-664.
19. Ngah, W. S. W., Ariff, N. F. M., Hashim, A. and Hanafiah, M. A. K. M. (2010). Malachite green adsorption onto chitosan coated bentonite beads: Isotherms, kinetics and mechanism. *Clean–Soil Air Water*, 38: 394-400.
20. Li, X. X., li, J., Cai, L. Y., Li, T. T., Liu, X. F. and Li, J. R. (2016). Malachite green adsorption behavior of polyurethane/ chitosan foam. *Cellular Polymers*, 35: 1-17.
21. Gimbert, F., Morin–Crini, N., Renault, F., Badot, P. M. and Crini, G. (2008). Adsorption isotherm models for dye removal by cationized starch–based material in a single component system: Error analysis. *Journal of Hazardous Materials*, 157: 34-46.
22. Ho, Y. S. and McKay, G. (2000). The kinetics of sorption of divalent metal ions onto sphagnum moss peat. *Water Research*, 34: 735-742.
23. Ho, Y. S. and McKay, G. (1998). A comparison of chemisorption kinetic models applied to pollutant removal on various sorbents. *Process Safety and Environment Protection*, 76: 332-340.
24. Xu, X., Bai, B., Wang, H. and Suo, Y. (2017). Synthesis of human hair fiber-impregnated chitosan beads functionalized with citric acid for the adsorption of lysozyme. *RSC Advances*, 7: 6636-6647.
25. Pal, P. and Pal, A. (2017). Surfactant-modified chitosan beads for cadmium ion adsorption. *International Journal of Biological Macromolecules*, 104: 1548-1555.

Malaysian Journal of Analytical Sciences, Vol 23 No 4 (2019): 637 - 647
DOI: https://doi.org/10.17576/mjas-2019-2304-09

MALAYSIAN JOURNAL OF ANALYTICAL SCIENCES
Published by The Malaysian Analytical Sciences Society
ISSN 1394 - 2506

ANTIBACTERIAL AND ANTIOXIDANT ACTIVITIES OF EXTRACTS FROM *Calophyllum ferrugineum* AND *Calophyllum incrassatum*

(Aktiviti Antibakteria dan Antioksidan Terhadap Ekstrak daripada *Calophyllum ferrugineum* dan *Calophyllum incrassatum*)

Nurul Iman Aminudin[1]*, Farediah Ahmad[2], Muhammad Taher[3]

[1]*Department of Chemistry, Kulliyyah of Science,*
International Islamic University Malaysia, 25200 Kuantan, Pahang, Malaysia
[2]*Department of Chemistry, Faculty of Science,*
Universiti Teknologi Malaysia, 81310 Skudai, Johor, Malaysia
[3]*Department of Pharmaceutical Technology, Kulliyyah of Pharmacy,*
International Islamic University Malaysia, 25200 Kuantan, Pahang, Malaysia

**Corresponding author: nuruliman@iium.edu.my*

Received: 19 August 2018; Accepted: 23 June 2019

Abstract

Calophyllum is a pan-tropical genus belongs to the Guttiferae family and locally known in Malaysia as '*bintangor*'. There has been a continual interest to further investigate the phytochemistry of *Calophyllum sp* because this genus is a rich source of active secondary metabolites which shows anti-HIV, cytotoxicity and antimicrobial properties. In this study, antibacterial and antioxidant activities of barks and leaves of *C. ferrugineum* and *C. incrassatum* were investigated. Cold extraction method employing dichloromethane, ethyl acetate and methanol as solvent was performed. All extracts were tested for their total phenolic content and antioxidant activities by DPPH radical scavenging and Ferric Reducing Antioxidant Power (FRAP) assays. The methanol extract from the leaves of *C. ferrugineum* showed the highest TPC value at 122.08 mg GAE/g and the lowest DPPH SC_{50} value at 11.80 µg/mL. The methanol extract from the barks of *C. ferrugineum* was found to have the highest FRAP value among all extracts. The antibacterial activity of all extracts was tested using minimum inhibition concentration (MIC) test against *Bacillus subtilis, Staphylococcus aureus, Escheria coli* and *Pseudomonas aeruginosa*. Only the dichloromethane extract from bark of *C. ferrugineum* showed moderate MIC value against Gram positive bacteria, *B. subtilis* and *S. aureus* at 125 µg/mL.

Keywords: *Calophyllum, C. ferrugineum, C. incrassatum*, antioxidant, antibacterial

Abstrak

Calophyllum adalah genus pan-tropika di dalam keluarga Guttiferae dan dikenali secara tempatan di Malaysia sebagai *'bintangor'*. Terdapat minat berterusan untuk mengkaji lebih mendalam tentang fitokimia *Calophyllum sp* kerana genus ini adalah sumber yang kaya dengan metabolit sekunder aktif yang menunjukkan ciri-ciri anti-HIV, sitotoksiti dan antimikrob. Di dalam kajian ini, aktiviti antibakteria dan antioksidan kulit batang dan daun *C. ferrugineum* dan *C. incrassatum* telah dikaji. Kaedah pengekstrakan sejuk menggunakan diklorometana, etil asetat dan metanol sebagai pelarut telah dilakukan. Semua ekstrak telah diuji untuk kandungan total fenolik dan aktiviti antioksidan melalui cerakin pemerangkapan radikal DPPH dan kuasa antioksidan penurunan Ferik (FRAP). Ekstrak metanol daripada daun *C. ferrugineum* telah menunjukkan nilai TPC tertinggi pada 122.08 mg GAE/g dan nilai SC_{50} DPPH terendah pada 11.80 µg/mL. Ekstrak metanol daripada kulit batang *C. ferrugineum* telah menunjukkan nilai FRAP tertinggi antara semua ekstrak. Aktiviti antibakteria semua ekstrak telah diuji untuk kepekatan rencatan minimum (MIC) terhadap *Bacillus subtilis, Staphylococcus aureus, Escheria coli* dan *Pseudomonas aeruginosa*. Hanya ekstrak diklorometana kulit batang *C. ferrugineum* menunjukkan nilai MIC yang sederhana terhadap bakteria Gram positif, *B. subtilis* dan *S. aureus* pada 125 µg/mL.

Keywords: *Calophyllum, C. ferrugineum, C. incrassatum*, antioksidan, antibakteria

Introduction

Calophyllum is a pan-tropical genus that comprises approximately 180 – 200 species. It is the largest genus in the sub-family Calophylloideae and categorised under the Guttiferae family [1]. In Malaysia, *Calophyllum* is locally known as *'bintangor'*. This plant is used traditionally to treat malaria, bronchitis, gastric and hepatic disturbances pain, wound infections, inflammation, rheumatism, varicose, haemorrhoids, chronic ulcer and acts as diuretic [2]. Apart from medicinal values, *Calophyllum* is often used for decorative purposes such as furniture, parquet flooring, solid door and plywood due to their distinctive colours. The poisonous latex from the bark can also be used to numb fish and kill rats [3]. *Calophyllum* genus has been reported as a plant-rich source of phenolic compounds including xanthones, flavonoids and coumarins. Numerous researches had been conducted on common *Calophyllum* species such as *C. inophyllum* and *C. lanigerum* [4]. The discovery of a series of pyranocoumarins known as 'the calanolides' with strong anti-HIV properties from *C. lanigerum var. austrocoriaceum* [5] has elevated the phytochemical research of this species. This genus also produces chromanone carboxylic acids, terpenoids and phloroglucinol derivatives.

In continuation of phytochemicals and bioactivities studies on several *Calophyllum* species from Malaysia [6–9], the antioxidant and antibacterial activities of *C. ferrugineum* Ridley and *C. incrassatum* M. R. Henderson & Wyatt-Smith were investigated. *C. ferrugineum* is an evergreen tree distributed around Southeast Asia especially in Malaysia. It grows from 5 – 30 m and can be found in lowland or colline mixed dipterocarp forest. The bark is used to make walls and masts for house-building. It is also used as decoction by mothers three days after the childbirth. *C. incrassatum* is distributed in East Malaysia, Borneo and Sulawesi. This tree can grow up from 15 – 36 metres and is usually found in well-drained, mixed dipterocarp lowland forest or sometimes in swamp forest [1]. To date, there is no scientific report on the antioxidant and antibacterial activities for both species. Therefore, herein the authors report the evaluation of antioxidant and antibacterial activities of crude extracts from the barks and leaves of both species.

Materials and Methods

Chemicals and reagents

Folin-Ciocalteu's phenol, gallic acid, butylated hydroxyanisole (BHA) and butylated hydroxytoluene (BHT) were purchased from Sigma Aldrich. Ascorbic acid (AA) was purchased from Goodrich Chemical Enterprice (GCE) while 2,2-diphenyl-1-picrylhydrazyl (DPPH) was purchased from Fluka. 2,4,6-Tri(2-pyridyl)-S-triazine (TPTZ) was purchased from Merck while anhydrous sodium carbonate (Na_2CO_3), sodium acetate trihydrate ($CH_3COONa.3H_2O$), iron (III) chloride hexahydrate ($FeCl_3.6H_2O$) and hydrochloric acid (HCl) were obtained from Qrec. Nutrient agar (NA) and nutrient broth (NB) were purchased from Merck while streptomycin sulphate (SS) and 2-(4-iodophenyl)-3-(4-nitrophenyl)-5-phenyl-2*H*-tetrazolium (INT) were obtained from Sigma Aldrich. Sodium chloride (NaCl), tryptone, glycerol and H_2SO_4 (98%) were supplied by Qrec, yeast extract was obtained from Scharlau and Tween 80 was purchased from Fischerbrand.

Microorganism

The bacterial strains acquired were from the American Type Culture Collection (ATCC). The activities of the samples were screened against four strains, two Gram-positive bacteria, *Bacillus subtilis* (ATCC 6633), *Staphylococcus aureus* (ATCC 29737) and two Gram-negative bacteria, *Escherichia coli* (ATCC 10536) and *Pseudomonas aeruginosa* (ATCC 9027).

Plant material

Sample of *C. ferrugineum* Ridley (SK2587/14) was collected at Hutan Lenggong, Perak on 28 August 2014 while *C. incrassatum* M. R. Henderson & Wyatt-Smith (SK2612/14) was collected from Hutan Gunung Belumut, Kluang, Johor on 1 October 2014. Plant specimens of *C. ferrugineum* and *C. incrassatum* were deposited at Herbarium Universiti Putra Malaysia. All plant samples were identified by Dr Shamsul Khamis, a botanist from Universiti Kebangsaan Malaysia.

Extraction method

The dried and ground barks and leaves of *C. incrassatum* and *C. ferrugineum* were macerated sequentially with dichloromethane, ethyl acetate and methanol for 3 days at room temperature. The extracts were then filtered and similar extraction process was repeated twice. The extracts were then concentrated under reduced pressure by using rotary evaporator. All extracts were stored at 4°C for further use.

Antibacterial activity

The antibacterial activity of all extracts was tested quantitatively by evaluating their minimum inhibition concentration (MIC). Two *Gram* positive bacterial strains of *Bacillus subtilis* (ATCC 6633), *Staphylococcus aureus* (ATCC 29737) and two *Gram* negative bacterial strains of *Escheria coli* (ATCC 10536) and *Pseudomonas aeruginosa* (ATCC 9027) were chosen. The MIC was carried out by serial broth microdilution according to our previous reported method [7]. The sample stock solution (1000 µg/mL) was prepared in 5% DMSO in nutrient broth (NB) supplemented with 0.02% (v/v) Tween 80. Further twofold dilution with NB was performed to afford concentration of samples from 1000-7.81 µg/mL. 50 µL of bacteria inocula was dispensed in the 96-well microplate followed by 50 µL of sample solution. Streptomycin sulphate was employed as positive control in this assay. The microplates were pre-incubated for 24 hours at 37 ºC for *S. aureus*, *E. coli* and *P. aeruginosa* and 30 ºC *for B. subtilis*. 25 µL of *p*-iodonitrotetrazolium (INT) (0.2 mg/mL in sterile distilled water) solution was added to all wells and were pre-incubated for at least 30 minutes. Bacterial growth in the wells was indicated by the formation of reddish-pink color while clear well indicates inhibition of bacterial growth by the sample.

Antioxidant activity: Total phenolic content

The total phenolic content (TPC) of the extracts were determined by Folin-Ciocalteau's assay [10]. In brief, sample solution in MeOH (40 µL) with concentrations from 1000-7.81 µg/mL obtained from twofold dilution were mixed with Folin-Ciocalteau's reagent (20 µL) in the 96-well microplate and were incubated for 5 minutes at room temperature in a dark condition. Sodium carbonate (80 µL) was added to all wells followed by distilled water (60 µL). The mixture was kept in the dark for 90 minutes and the absorbances were recorded at 760 nm. A calibration graph of standard gallic acid at concentration 125-7.81 µg/mL versus absorbance was constructed. The total phenolic contents were expressed as mg gallic acid equivalent (GAE)/g of extract.

DPPH radical scavenging assay

2,2-Diphenyl-1-picrylhydrazyl (DPPH) radical scavenging assay of the extracts was carried out following the method by Kassim et al. [10]. In brief, DPPH reagent (30 µL) with final concentration of 300 µM was added to the samples (170 µL) with concentration ranging from 1000-7.81 µg/mL in MeOH obtained from twofold dilution. The reaction mixture was allowed to incubate in dark condition at room temperature for 30 minutes. The $DPPH_{blank}$ wells consisting of DPPH reagent and MeOH were reserved for each microplate. The absorbance for DPPH radical inhibition was measured at 517 nm. The radical scavenging effect was examined and compared with ascorbic acid (AA) and butylated hydroxytoluene (BHT) as the references. The percentage of DPPH radical scavenging inhibition was calculated by using the following formula;

$$\text{Scavenging Concentration (\%SC)} = [(A_{\text{DPPH blank}} - (A_{\text{Sample}} - A_{\text{blank sample}})] / A_{\text{DPPH blank}} \times 100\% \quad (1)$$

where $A_{\text{DPPH blank}}$ is the absorbance of DPPH reagent with MeOH, A_{sample} is the absorbance of sample solution with DPPH reagent and $A_{\text{blank sample}}$ is the absorbance of sample solution.

Ferric reducing antioxidant potential (FRAP) assay

Experiment was carried out following the method by Arriffin et al. [11]. FRAP reagent was freshly prepared, consist of stock solution with ratio 10:1:1 of acetate buffer (300 mM), TPTZ (10 mM) in HCl (40 mM) and $FeCl_3.6H_2O$ (20 mM) solutions. Sample (5 µL) with concentration of 1000-100 µg/mL, methanol (15 µL) and FRAP reagent (150 µL) were added to the 96-well microtiter plate. The absorbance was recorded after 10 minutes of incubation at 37 °C at 573 nm. A calibration graph of standard $FeSO_4.7H_2O$ solution with concentration of 1.0-0.1 mM vs absorbance was constructed. The FRAP activity of extracts was expressed as mM FRAP equivalent to $FeSO_4.7H_2O$

Statistical analysis

Three replicates of each sample were used for statistical analysis with values reported as mean ± SD. Standard curves were generated and calculation of the 50% inhibitory concentration (IC_{50}) values was done using GraphPad Prism for Windows (version 5.02) software. The Student's *t*-test was carried out using SPSS (version 22) software for comparison between treatment of samples and positive controls. Pearson's correlation coefficient was used to determine the correlation between two independent variables. A value of $p < 0.05$ was considered significantly different.

Results and Discussion

Antibacterial activity

The antibacterial activity of crude extracts from two *Calophyllum* species was tested against two Gram-positive bacteria, *B. subtilis* and *S. aureus* and two Gram-negative bacteria, *P. aeruginosa* and *E. coli* through MIC determination (Table 1). Streptomycin sulphate was employed as a positive control. According to Sousa et al., the antibacterial activity of MIC values of crude extracts over 1000 µg/mL is inactive, from 500 to 1000 µg/mL is weak, from 100 to 500 µg/mL is moderate and less than 100 µg/mL is considered good [12]. Rios and Recio also proposed that MIC values below 100 µg/mL for crude extracts are promising [13].

Table 1. Minimum Inhibition Concentration (MIC) of Extracts of *C. ferrugineum* and *C. İncrassatum*

***Calophyllum* Species**	**Part**	**Crude (Abbreviation)**	**Minimum Inhibition Concentration (MIC) (µg/mL)[a]**			
			Gram-positive		**Gram-negative**	
			B. s	***S. a***	***P. a***	***E. c***
Crude Extracts						
C. ferrugineum	B	CH_2Cl_2 (CFBD)	125	125	>1000	>1000
		EtOAc (CFBE)	500	1000	>1000	>1000
		MeOH (CFBM)	>1000	>1000	>1000	>1000
	L	CH_2Cl_2 (CFLD)	1000	>1000	1000	1000
		EtOAc (CFLE)	>1000	1000	500	>1000
		MeOH (CFLM)	>1000	>1000	>1000	>1000
C. incrassatum	B	CH_2Cl_2 (CIBD)	>1000	>1000	>1000	>1000
		EtOAc (CIBE)	>1000	>1000	>1000	>1000
		MeOH (CIBM)	>1000	>1000	>1000	1000
	L	CH_2Cl_2 (CILD)	1000	1000	>1000	>1000
		EtOAc (CILE)	1000	>1000	>1000	>1000
		MeOH (CILM)	>1000	>1000	>1000	>1000
SS[b]			1.56	50	6.25	0.78

[a] Data represent mean ± standard deviation of three replicate experiments; [b] Positive control; B: Barks; L: Leaves; *B. s*: *Bacillus subtilis*; *S. a*: *Staphylococcus aureus*; *P. a*: *Pseudomonas aeruginosa*; *E. c*: *Escherichia coli*; SS: Streptomycin Sulphate.

The dichloromethane extract from bark of *C. ferrugineum* showed moderate MIC value against Gram positive bacteria, *B. subtilis* and *S. aureus* at 125 µg/mL. It was suggested that high content of bark resins in the dichloromethane extracts of *C. ferrugineum* is responsible to the antibacterial activity. This justification is supported by the previous finding on the strong antimicrobial properties of the bark resins from *C. inophyllum* and *C. antillanum* [14]. Chromanone carboxylic acids compounds are presented as major compounds in the bark resin of *Calophyllum* species and these compounds are reported to have antibacterial activities. Previous report on the isolation of six chromanone acids from *C. brasiliense* also demonstrated a moderate-to-strong antibacterial activity especially to Gram-positive bacteria [15], thus supporting these findings. In contrast, the dichloromethane extract from bark of *C. incrassatum* showed inactive antibacterial activity against all strains. This result suggested that there

were no chromanone carboxylic acids types of compound present in the bark extract. The bark of *C. incrassatum* also did not contain resin, thus suggesting that no chromanone carboxylic acid can be isolated from this species. Meanwhile, the other crude extracts showed weak or inactive inhibition towards all bacterial strains tested.

Antioxidant activity

Spectrophotometric assay that involves the use of specific chromophore such as Folin-Ciocalteu (FC) reagent is commonly chosen, since it is simple and less time consuming as well as suitable for screening purposes. In general, yellow coloured FC reagent containing molybdenum, Mo^{6+} will reduce to Mo^{5+} in the presence of reducing agent in basic medium to form dark blue complex [16]. The standard calibration curve of gallic acid (Figure 1) was constructed to calculate the total phenolic content expressed as mg gallic acid equivalent (GAE) per gram of extract ($y = 0.0107x + 2.6402$, $R^2 = 0.9978$). In general, the MeOH extracts showed the highest TPC value followed by EtOAc extracts. It can be deduced from the trend that the TPC increased as the solvent polarity increased since the phenolic compounds normally constitutes in more polar extract. Meanwhile, all dichloromethane extracts tested were devoid to this assay and no phenolic content was detected.

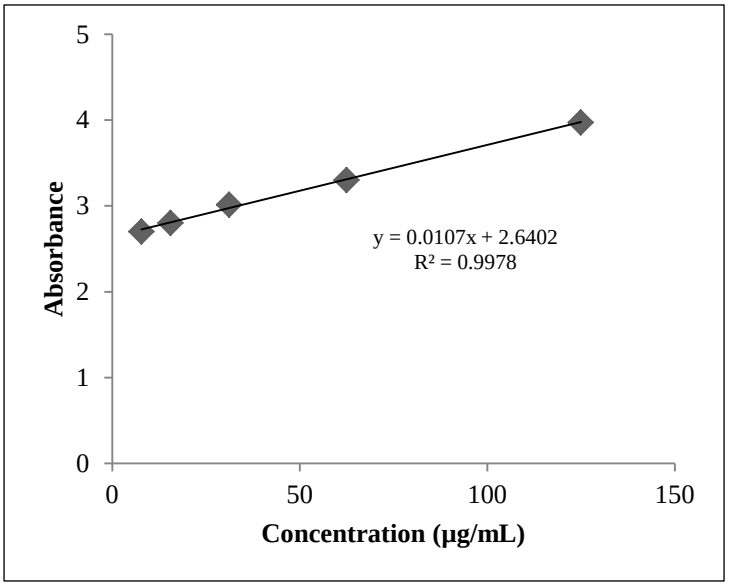


Figure 1. Gallic acid calibration curve

The methanol extract of leaves and barks of *C. ferrugineum* showed the highest TPC value at 122.08 mg GAE/g and 118.48 mg GAE/g, respectively. These TPC values were higher compared to the barks and leaves of *C. incrassatum* at 91.61 mg GAE/g and 45.68 mg GAE/g, respectively. A similar trend was also observed where ethyl acetate extracts from *C. ferrugineum* showed higher TPC values compared to *C. incrassatum*. These results suggested that *C. ferrugineum* is richer with phenolic constituents compared to *C. incrassatum*.

The concentration of sample needed to scavenge 50% of DPPH radical activity (SC_{50}) of the extracts is summarised in Table 2. All tested samples that showed ($P < 0.05$) were considered as statistically significant and different compared to ascorbic acid as the positive control. Blois had classified the antioxidant activity of the tested samples with the SC_{50} value as very strong ($SC_{50} < 50$ µg/mL), strong (50 µg/mL $< SC_{50} <$ 100 µg/mL), moderate (100 µg/mL $< SC_{50} <$ 150 µg/mL), weak (150 µg/mL $< SC_{50} <$ 200 µg/mL), very weak (200 µg/mL $< SC_{50} <$ 250 µg/mL) and inactive ($SC_{50} >$ 250 µg/mL) [17].

Table 2. TPC, DPPH SC_{50} and Pearson correlation coefficient values

***Calophyllum* Species**	**Part**	**Crude (Abbreviation)**	**Antioxidant Activity**		***r* coefficient**
			TPC (mg GAE/g)[a]	**DPPH SC_{50} (µg/mL)[a]**	
C. ferrugineum	B	CH_2Cl_2 (CFBD)	ND	> 1000	0.607
		EtOAc (CFBE)	84.09 ± 0.30*	26.72 ± 0.15***	0.810*
		MeOH (CFBM)	118.48 ± 0.01*	18.82 ± 0.38***	0.473
	L	CH_2Cl_2 (CFLD)	ND	> 1000	0.623
		EtOAc (CFLE)	75.68 ± 0.16*	18.70 ± 1.50**	0.893**
		MeOH (CFLM)	122.08 ± 0.04*	11.80 ± 1.03*	0.867**
C. incrassatum	B	CH_2Cl_2 (CIBD)	ND	> 1000	0.550
		EtOAc (CIBE)	18.29 ± 0.20*	49.90 ± 1.97***	0.800*
		MeOH (CIBM)	91.61 ± 0.01*	17.23 ± 1.21**	0.709*
	L	CH_2Cl_2 (CILD)	ND	> 1000	0.509
		EtOAc (CILE)	35.86 ± 0.01*	52.62 ± 1.38***	0.652
		MeOH (CILM)	45.68 ± 0.10*	53.33 ± 1.98**	0.612
AA[b]			NA	8.90 ± 0.27	NA
BHT[b]			NA	15.30 ± 0.63	NA

[a] Data represent mean ± standard deviation of three replicate experiments; [b] Positive control; B: Barks; L: Leaves; * $P < 0.05$, ** $P < 0.01$,*** $P < 0.001$; AA = Ascorbic acid; BHT: Butylated Hydroxytoluene; NA = Not Available.

All dichloromethane crude extracts displayed inactive DPPH radical scavenging activity with SC_{50} values of more than 1000 µg/mL. In contrast, all methanol and ethyl acetate extracts possessed significant DPPH radical scavenging activity in dose-dependent manner as depicted in Figure 2 and Figure 3, respectively. The methanol extract from the leaves of *C. ferrugineum* displayed the lowest SC_{50} value (11.80 µg/mL) compared to the positive control, butylated hydroxytoluene (BHT) (SC_{50} 15.30 µg/mL). In addition, the DPPH radical scavenging activities of methanol extracts from barks of *C. incrassatum* and barks of *C. ferrugineum*, as well as the ethyl acetate extract from the leaves of *C. ferrugineum* were comparable to BHT since their SC_{50} values lies in the range of 17.23 – 20.51 µg/mL. This shows that high TPC values of the methanol extracts are strongly associated with the present findings. Phenolic compounds that are rich in hydroxyl groups serve as a hydrogen donor to the radical thus act as good antioxidants.

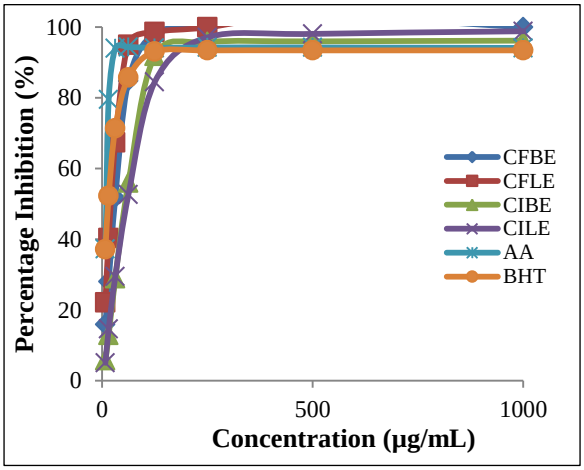


Figure 2. Percentage ınhibition of DPPH radical scavenging activity of EtOAc extracts

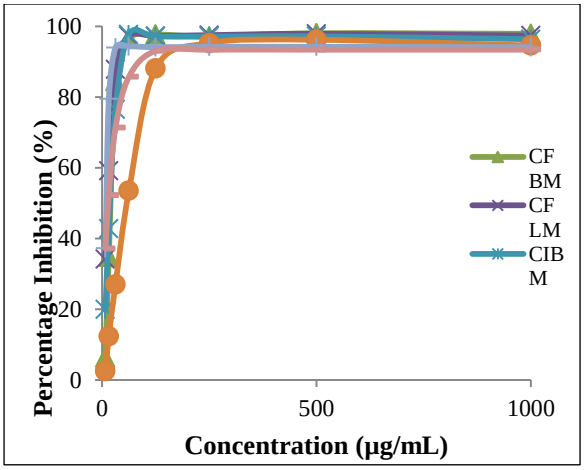


Figure 3. Percentage ınhibition of DPPH radical scavenging activity of MeOH extracts

The correlations between TPC and DPPH radical scavenging activity for each crude extract were evaluated using Pearson's correlation coefficient as tabulated in Table 1. In this study, the two variables were positively correlated with the *r* coefficient value in the range of 0.473 – 0.893. This indicates a positive correlation whereby high total phenolic content is proportional to strong DPPH radical scavenging activity. Previous work on the bioassay-guided fractionation of the methanol and ethanol extracts from several *Calophyllum* species that gave high DPPH radical scavenging activity led to the isolation phenolic compounds; flavonoids and xanthones [18,19].

Ferric Reducing Antioxidant Power (FRAP) involves the redox reaction between ferric (III) tripyridyltriazine complex and a reducing agent to form ferrous (II) tripyridyltriazine complex. The reduction process increases the absorbance value measured at 593 nm due to the colour changes from pale brown to intense blue [20]. The FRAP values were determined using standard calibration curve of standard $FeSO_4.7H_2O$ (y = 0.0005x + 0.0708, R^2 = 0.9992) as shown in Figure 4 and expressed as mM FRAP equivalent to $FeSO_4.7H_2O$.

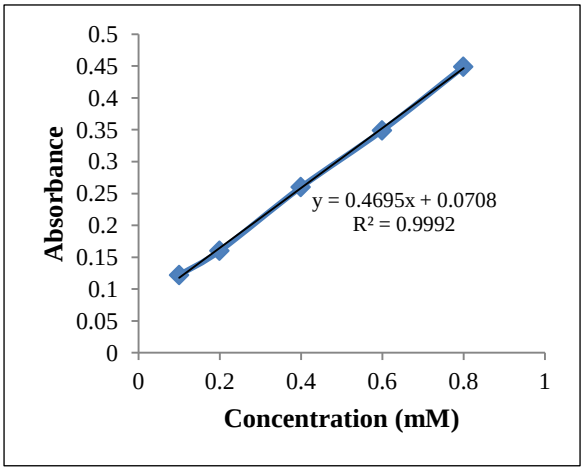


Figure 4. $FeSO_4.7H_2O$ standard calibration curve

The FRAP values of the crude extracts for the concentrations of 1.0, 0.8, 0.6, 0.4, 0.2 and 0.1 mM were summarised in Table 3. The trend for ferric ion reducing activities of the dichloromethane, ethyl acetate and methanol extracts from the barks and leaves of *C. incrassatum* and *C. ferrugineum* are illustrated in Figures 5-7, respectively. The

methanol extracts showed the highest reducing activities followed by ethyl acetate and dichloromethane extracts for all *Calophyllum* species. Similar trend was observed for the total phenolic content determination as discussed earlier. Thus, it can be deduced that high concentration of phenolic compounds in more polar extracts acts as reducing agent in this FRAP assay.

Table 3. FRAP equivalent of the extracts from *Calophyllum* species

***Calophyllum* Species**	**FRAP Equivalent to $FeSO_4.7H_2O$ (mM)[a]**					
	1.0	**0.8**	**0.6**	**0.4**	**0.2**	**0.1**
C. ferrugineum						
CFBD	0.24 ± 0.01 *	0.18 ± 0.02 *	0.16 ± 0.01 *	0.16 ± 0.02 *	0.12 ± 0.01 **	0.11 ± 0.01 **
CFBE	2.98 ± 0.65 **	1.98 ± 0.17 **	1.88 ± 0.79	1.13 ± 0.06 **	0.87 ± 0.21	0.37 ± 0.02 *
CFBM	3.72 ± 0.46 ***	2.74 ± 1.11	2.03± 0.63	1.41 ± 0.25 *	0.74 ± 0.19	0.40 ± 0.08
CFLD	0.37 ± 0.10	0.26 ± 0.02 *	0.20 ± 0.01 *	0.15 ± 0.01 *	0.13 ± 0.01 **	0.10 ± 0.01 **
CFLE	3.24 ± 1.04	1.24 ± 0.14 *	1.17 ± 0.42	0.68 ± 0.10	0.55 ± 0.05	0.22 ± 0.6 *
CFLM	2.57 ± 0.44 **	1.94 ± 0.72	1.37 ± 0.31	0.91 ± 0.12	0.72 ± 0.07	0.32 ± 0.03 *
C. incrassatum						
CIBD	0.23 ± 0.07 *	0.23 ± 0.02 *	0.16 ± 0.02 *	0.12 ± 0.01 *	0.07 ± 0.01 *	0.05 ± 0.01 **
CIBE	1.35 ± 0.04 **	1.15 ± 0.25	0.65 ± 0.09	0.40 ± 0.02	0.18 ± 0.02 *	0.09 ± 0.01 **
CIBM	3.23 ± 0.22 ***	2.44 ± 0.18 ***	2.00 ± 0.22 **	1.40 ± 0.03 ***	0.54 ± 0.04	0.20 ± 0.01 *
CILD	0.17 ± 0.05 *	0.11 ± 0.02 *	0.10 ± 0.02 *	0.10 ± 0.01 *	0.06 ± 0.01 **	0.05 ± 0.01 **
CILE	1.10 ± 0.27	0.62 ± 0.09	0.57 ± 0.11	0.39 ± 0.03	0.22 ± 0.02 *	0.14 ± 0.01 **
CILM	1.41 ± 0.29 *	0.98 ± 0.01	0.84 ± 0.09	0.57 ± 0.06	0.34 ± 0.04	0.22 ± 0.11 *
AA[b]	0.94 ± 0.24	0.29 ± 0.07	0.37 ± 0.09	0.17 ± 0.05	0.08 ± 0.01	0.07 ± 0.01
BHA[b]	1.30 ± 0.33	1.07 ± 0.14	0.83 ± 0.13	0.62 ± 0.11	0.33 ± 0.09	0.22 ± 0.06
BHT[b]	0.59 ± 0.21	0.36 ± 0.06	0.28 ± 0.05	0.21 ± 0.02	0.19 ± 0.04	0.09 ± 0.04

[a] Data represent mean ± standard deviation of three replicate experiments; [b] Positive control; AA = Ascorbic acid; BHT: Butylated Hydroxytoluene; BHA: Butylated Hydroxyanisole; * $P < 0.05$, ** $P < 0.01$,*** $P < 0.001$

The dichloromethane extract from the leaves of *C. ferrugineum* (CFLD) displayed the highest FRAP equivalent to $FeSO_4.7H_2O$ among all dichloromethane extracts followed by the bark extract of *C. ferrugineum* and *C. incrassatum* as shown in Figure 5. Meanwhile, the ethyl acetate extract from the bark of *C. ferrugineum* followed by ethyl acetate extract from the leaves of *C. ferrugineum*, ethyl acetate extract from the bark of *C. incrassatum* and ethyl acetate extract from leaves of *C. incrassatum* showed the FRAP equivalent to $FeSO_4.7H_2O$ in decreasing order (Figure 6). Moreover, the methanol extracts from bark of *C. ferrugineum*, bark of *C. incrassatum* and leaves of *C. ferrugineum* also depicted high FRAP equivalent to $FeSO_4.7H_2O$ among all methanol extracts displayed in Figure 7.

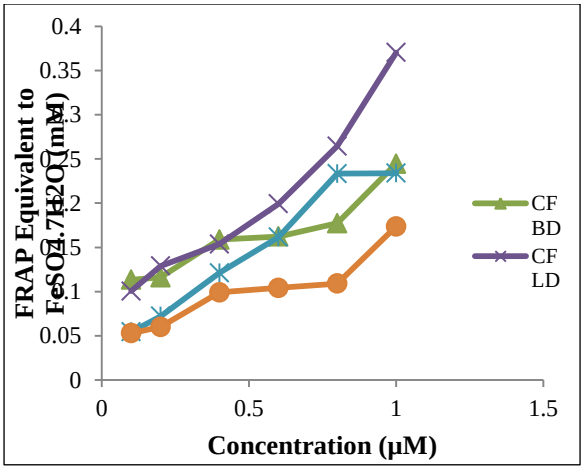


Figure 5. FRAP equivalent to $FeSO_4.7H_2O$ of dichloromethane extracts

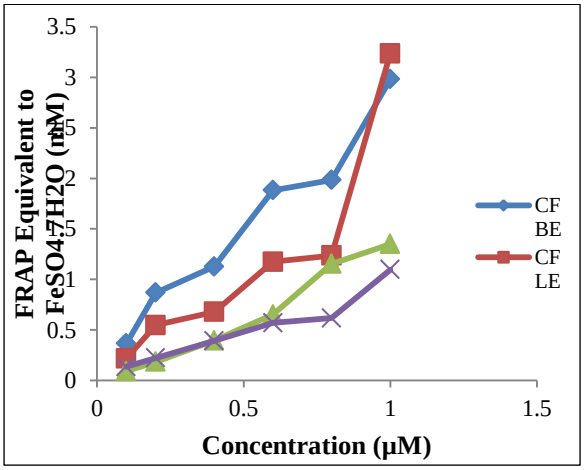


Figure 6. FRAP equivalent to $FeSO_4.7H_2O$ of ethyl acetate extracts

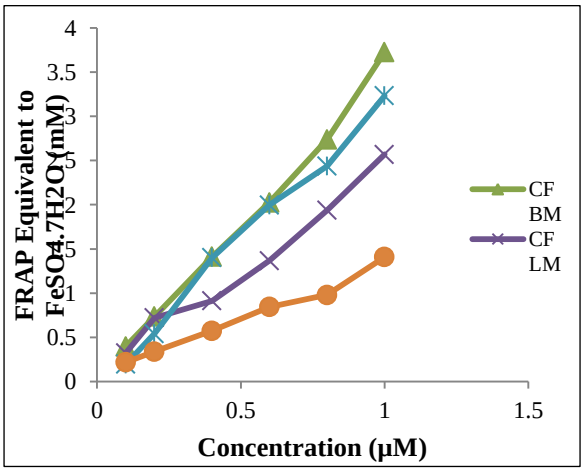


Figure 7. FRAP equivalent to $FeSO_4.7H_2O$ of methanol extracts

The antioxidant powers of CFBM, CFLM, CIBM, CFBE and CFLE extracts that showed highest FRAP equivalent to $FeSO_4.7H_2O$ with respect to their respective type of extracts were compared with antioxidant power of ascorbic acid (AA), butylated hydroxyanisole (BHA) and butylated hydroxytoluene (BHT) as the positive controls. From the graph (Figure 8), all extracts display higher FRAP equivalent to $FeSO_4.7H_2O$ compared to all positive controls. It justified their stronger antioxidant power compared to the positive controls. The CFBM extract was found to have the highest antioxidant power among all extracts followed by CIBM and CFBE.

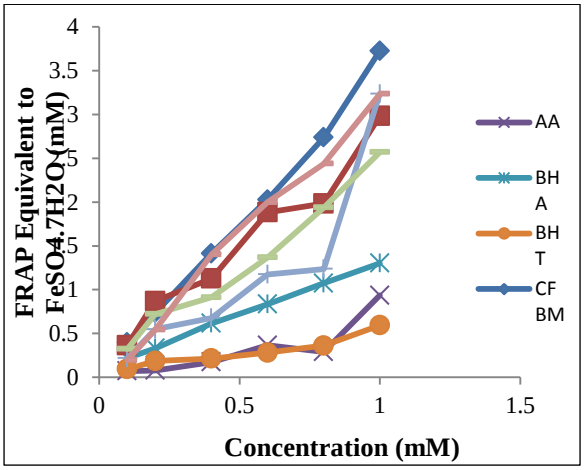


Figure 8. FRAP equivalent to $FeSO_4.7H_2O$ of selected extracts and positive controls

Conclusion

Based on the findings, both *Calophyllum* species showed a strong antioxidant activity especially from the methanol extracts, suggesting potent antioxidant agents may be isolated. Meanwhile, the dichloromethane extract from the bark of *C. ferrugineum* showed potent antibacterial activities selectively against the Gram-positive bacteria, suggesting it may serve as possible source for new antibacterial agents. Mode of antibacterial action of the extracts and isolated phytochemicals specifically against Gram-positive bacteria can be further studied.

References

1. Stevens, P. F. (1980). *Journal of the Arnold Arboretum*. USA: Harvard University. 117–424.
2. Alkhamaiseh, S. I., Taher, M. and Ahmad, F. (2011). The phytochemical contents and antimicrobial activities of Malaysian *Calophyllum Rubiginosum*. *American Journal of Applied Sciences*, 8: 201-205.
3. Kawamura, F., Muhamud, A., Hashim, R., Sulaiman, O. and Ohara, S. (2012). Two antifungal xanthones from the heartwood of *Calophyllum symingtonianum*. *Japan Agricultural Research Quarterly*, 46: 181-185.
4. Su, X. H., Zhang, M. L., Li, G. L., Huo, C. H., Gu, Y. C. and Shi, Q. W. (2008). Chemical constituents of the plants of the genus *Calophyllum. Chemistry & Biodiversity*, 5: 2579-2608.
5. Kashman, Y., Gustafson, K. R., Fuller, R. W., Cardellina, J. H., McMahon, J. B., Currens, M. J., Buckheit, R. W., Hughes, S. H., Cragg, G. M. and Boyd, M. R. (1992). The calanolides, A novel HIV-ınhibitory class of coumarin derivatives from the tropical rainforest tree, *Calophyllum lanigerum*. *Journal of Medicinal Chemistry*, 35: 2735-2743.
6. Aminudin, N. I., Ahmad, F., Taher, M., Zulkifli, R.M. (2015). α-Glucosidase and 15-Lipoxygenase inhibitory activities of phytochemicals from *Calophyllum symingtonianum*. *Natural Product Communications*, 10: 1585-1587.
7. Aminudin, N. I., Ahmad, F., Taher, M., Zulkifli, R.M. (2016). Cytotoxic and antibacterial evaluation of coumarins and chromanone acid from *Calophyllum symingtonianum. Journal of Applied Pharmaceutical Science*, 6: 23-27.

8. Aminudin, N. I., Ahmad, F., Taher, M. (2015). *In vitro* antioxidant, cholinesterase and tyrosinase inhibitory activities of *Calophyllum symingtonianum* and *Calophyllum depressinervosum* (Guttiferae). *Journal of Coastal Life Medicine*, 3: 126–131.
9. Aminudin, N. I., Ahmad, F., Taher, M., Zulkifli, R. M. (2016). Incrassamarin A–D: Four new 4-substituted coumarins from *Calophyllum incrassatum* and their biological activities. *Phytochemistry Letters*, 16: 287-293.
10. Kassim, N. K., Rahmani, M., Ismail, A., Sukari, M. A., Ee, G. C. L., Nasir, N. M. and Awang, K. (2013). Antioxidant activity-guided separation of coumarins and lignan from *Melicope glabra* (Rutaceae). *Food Chemistry*, 139: 87–92.
11. Arriffin, N. M., Jamil, S., Basar, N., Khamis, S., Abdullah, and A. and Lathiff, S. M. A. (2017). Phytochemical studies and antioxidant activities of *Artocarpus scortechinii* king. *Records of Natural Products*, 3: 299-303.
12. Sousa, R. M. F., Morais, S. A. L. D, Vieira, R. B. K., Napolitano, D. R., Guzman, V. B., Moraes, T. S., Cunha, L. C. S., Nascimento, E. A. D. and Oliveira, A. D. (2015). Chemical composition, cytotoxic, and antibacterial activity of the essential oil from *Eugenia calycina* cambess. leaves against oral bacteria. *Industrial Crops and Products*, 65: 71-78.
13. Ríos, J. L. and Recio, M. C. (2005). Medicinal plants and antimicrobial activity. *Journal of Ethnopharmacology*, 100: 80-84.
14. Cuesta-Rubio, O., Oubada, A., Bello, A., Maes, L., Cos, P. and Monzote, L. (2015). Antimicrobial assessment of resins from *Calophyllum antillanum* and *Calophyllum inophyllum*. *Phythotherapy Research*, 29: 1991-1994.
15. Cottiglia, F., Dhanapal, B., Sticher, O. and Heilmann, J. (2004). New chromanone acids with antibacterial activity from *Calophyllum brasiliense*. *Journal of Natural Products*, 67: 537-541.
16. Margraf, T., Karnopp, A. R., Rosso, N. D. and Granato, D. (2015). Comparison between Folin-Ciocalteu and Prussian Blue assays to estimate the total phenolic content of juices and teas using 96-well microplates. *Journal of Food Science*, 80: 2397-2403.
17. Blois, M. S. (1958). Antioxidant determinations by the use of a stable free radical. *Nature*, 181: 1199–1200.
18. Dharmaratne, H. R. W., Napagoda, M. T. and Tennakoon, S. B. (2009). Xanthones from roots of *Calophyllum thwaitesii* and their bioactivity. *Natural Product Research*, 23: 539-545.
19. Katrin, Elya, B., Mahamufrudho, A. and Rissyelly. (2014). Radical scavenging activity of extract, fraction and chemical compound from *Calophyllum sclerophyllum* vesq. stembark by using 1,1-Diphenyl-2-Picryl Hydrazil (DPPH). *International Journal of PharmTech Research*, 6: 396-402.
20. Cahnnarong, S., Jutiviboonsuk, A. and Korsanan, S. (2012). Total reducing antioxidant capacity of thai herbal aromatic powder (Ya-Hom) measured by FRAP assay. *Thai Pharmaceutical and Health Science Journal*, 7:111-114.

Malaysian Journal of Analytical Sciences, Vol 23 No 4 (2019): 648 - 653
DOI: https://doi.org/10.17576/mjas-2019-2304-10

MALAYSIAN JOURNAL OF ANALYTICAL SCIENCES
Published by The Malaysian Analytical Sciences Society
ISSN 1394 - 2506

HYDROSILYLATION OF ALDEHYDES CATALYZED BY DIETHYL 2-PYRIDYLPHOSPHONATE

(Hidrosililasi Aldehida Bermangkin Dietil 2-Piridilfosfonat)

Natsuhisa Oka[1,2]*, Kousuke Ito[1], Kaori Ando[1]*

[1]*Department of Chemistry and Biomolecular Science, Faculty of Engineering*
[2]*Center for Highly Advanced Integration of Nano and Life Sciences*
Gifu University, 1-1 Yanagido, Gifu 501-1193, Japan

**Corresponding authors: oka@gifu-u.ac.jp, ando@gifu-u.ac.jp*

Received: 31 March 2018; Accepted: 17 April 2019

Abstract

We studied the catalytic activity of diethyl pyridylphosphonates in the hydrosilylation of aldehydes using $HSiCl_3$ as a hydride source. Diethyl 2-pyridylphosphonate was found to be a good catalyst, while 2-pyridylthiophosphonate, 3- and 4-pyridylphosphonates, and phenylphosphonate showed much lower catalytic activity. The study shows that diethyl 2-pyridylphosphonate works as a bidentate Lewis base catalyst to activate $HSiCl_3$. A complete chemoselective hydrosilylation of benzaldehyde in the presence of acetophenone was also demonstrated.

Keywords: hydrosilylation, aldehyde, pyridyl, phosphonate, chemoselective

Abstrak

Kami mengkaji aktiviti pemangkinan dietil piridilfosfonat di dalam hidrosililasi aldehida telah dikaji dalam makalah ini menggunakan $HSiCl_3$ sebagai sumber hidrida. Dietil 2-piridilfosfonat didapati merupakan pemangkin yang baik sementara 2-piridiltiolfosfonat, 3- dan 4- piridilfosfonat, dan fenilfosfonat menunjukkan aktiviti pemangkinan yang lebih rendah. Kajian ini menunjukkan dietil 2-piridilfosfonat berfungsi sebagai pemangkin Lewis bes bidentat untuk mengaktifkan $HSiCl_3$. Satu hidrosililasi kemoselektif lengkap benzaldehida dengan kewujudan asetofenon juga telah dapat ditunjukkan dalam kajian ini.

Kata kunci: hidrosililasi, aldehida, piridil, fosfonat, kemoselektif

Introduction

Lewis base-catalyzed metal-free hydrosilylation is a useful alternative to the reduction using metal hydrides and transition metal-catalyzed hydrogenation. It is often used for the chemoselective reduction of aldehydes, ketones, and imines to the corresponding alcohols and amines in the presence of various functional groups which are susceptible to other kinds of reducing agents. Many kinds of Lewis base catalysts have been developed for this reaction so far [1-8]. However, there is still a need for the development of new catalysts with improved activity and selectivity.

In order to develop a new class of Lewis base catalyst, we focused on pyridylphosphonate derivatives [9]. A variety of Lewis base catalysts carrying pyridyl or P=O groups have been developed and applied to the hydrosilylation of aldehydes, ketones, and imines [10-18]. Both functional groups are usually used in combination with other kinds of coordinating groups such as carbonyl groups in the design of Lewis base catalysts. However, the combination of

pyridyl and P=O groups has been scarcely used and, to the best of our knowledge, pyridylphosphonates have not yet been studied for their catalytic activity. We have recently directed our efforts to the synthesis of 2-pyridylphosphonates and 2-pyridylphosphinates [19-20]. These compounds can be easily synthesized from low-cost starting materials, *H*-phosphonates and *N*-methoxypyridinium salts [9, 21-23] and thus can be cost-effective catalysts. In this study, we investigated the potential of diethyl 2-pyridylphosphonate and some relevant phosphonates as Lewis base catalysts in the hydrosilylation of aldehydes.

Materials and Methods

General information

Commercially available reagents were used without purification. Dry organic solvents were prepared by appropriate procedures prior to use. The other organic solvents were reagent grade and used as received. All reactions in dry solvents were carried out under argon. Analytical thin-layer chromatography (TLC) was performed on Merck TLC plates (No. 5715) precoated with silica gel 60 F_{254}. Column chromatography on silica gel was carried out using Kanto silica gel 60N (spherical, neutral, 63–210 μm). The ^{1}H (400 MHz) spectra were recorded on a JNM-ECS-400 spectrometer (JEOL). Diethyl 2-pyridylphosphonate **1a** [23], diethyl 2-pyridylthiophosphonate **1b** [24], diethyl 3-pyridylphosphonate **2** [25], and diethyl 4-pyridylphosphonate **3** [26] were synthesized according to the procedures reported in the literature.

General procedure for the hydrosilylation of aldehydes

An aldehyde (1.0 mmol) and $HSiCl_3$ (1.2 or 2.0 mmol) were added dropwise to a solution of **1a** (0.20 mmol) in dry CH_2Cl_2 (2.0 mL) under stirring at RT and stirring was continued for 20 hours. The mixture was then washed with a 1 M aqueous solution of HCl (10 mL). The aqueous layer was extracted with CH_2Cl_2 (5 × 10 mL). The organic layers were combined, dried over Na_2SO_4, filtered, and concentrated under reduced pressure. The residue was then purified by column chromatography on silica gel (hexane/ethyl acetate) to afford the corresponding alcohols in 27%–94% yield. Identities of the products were confirmed by comparison of ^{1}H NMR data with those of commercial samples.

Results and Discussion

Initially, we examined the hydrosilylation of benzaldehyde using $HSiCl_3$ and diethyl 2-pyridylphosphonate **1a** as a reducing agent and a catalyst, respectively (Figure 1 and Table 1). As shown in entries 1 and 2, benzaldehyde was completely reduced in the presence of 2 equiv. of $HSiCl_3$ and 20 mol% of **1a** in CH_2Cl_2 at RT within 20 h and benzyl alcohol was isolated in 70% yield. The reaction was also practically completed in $CHCl_3$, Et_2O, and toluene under the same conditions (entries 3–5). It was found that the reaction was slower in toluene than in CH_2Cl_2 by reducing the catalyst loading from 20 mol% to 10 mol% (entries 6, 7). Next, we used diethyl 2-pyridylthiophosphonate **1b**, diethyl 3-pyridylphosphonate **2**, diethyl 4-pyridylphosphonate **3**, diethyl phenylphosphonate **4**, and pyridine as catalysts in place of **1a** to investigate the structure–activity relationship of the catalyst (entries 8–13). The lower conversion of benzaldehyde (8%–47%) shows that these catalysts are much less effective than **1a** in this reaction. These results also indicate that **1a** promotes the reaction as a bidentate Lewis base catalyst which coordinates to the silicon atom of $HSiCl_3$ with its 2-pyridyl and P=O groups. The catalyst activity of **1b** is much lower (entry 8) because the coordination of the soft sulfur to the hard silicon of $HSiCl_3$ is weaker than that of the hard oxygen of **1a** [27,28]. Compounds **2** and **3** cannot work as bidentate Lewis bases due to their structural limitations. The low conversions by **4** and pyridine even with 40 mol% catalyst loading (entries 11–13) show that the pyridyl and phosphonate groups do not promote the reaction effectively when they work independently. It was also confirmed that the reaction did not proceed at all without catalyst (entry 14). Finally, the isolated yield of benzyl alcohol was improved from 70% to 80% as the amount of $HSiCl_3$ was reduced from 2.0 equiv. to 1.2 equiv. It is because the amount of polysiloxane produced by the hydrolysis of $HSiCl_3$ during aqueous workup was reduced and the isolation of the product became easier (entries 2 and 15).

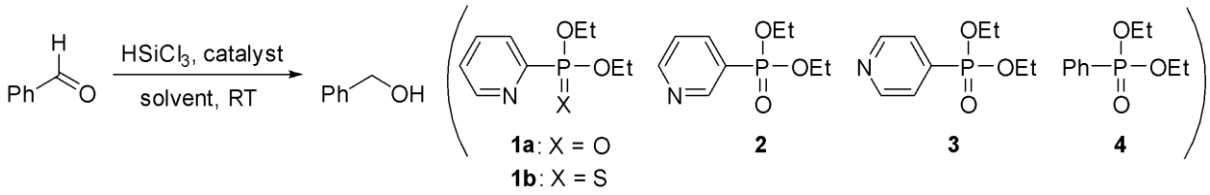


Figure 1. Hydrosilylation reaction of benzaldehyde

Table 1. Hydrosilylation of benzaldehyde

Entry	$HSiCl_3$ (equiv)	Catalyst (mol%)	Solvent	Time (hour)	Conversion (%)[a]	Isolated Yield (%)[b]
1	2.0	**1a** (20)	CH_2Cl_2	8	84	–
2	2.0	**1a** (20)	CH_2Cl_2	20	>99	70
3	2.0	**1a** (20)	$CHCl_3$	20	98	–
4	2.0	**1a** (20)	Et_2O	20	99	–
5	2.0	**1a** (20)	toluene	20	>99	–
6	2.0	**1a** (10)	CH_2Cl_2	20	98	–
7	2.0	**1a** (10)	toluene	20	52	–
8	2.0	**1b** (20)	CH_2Cl_2	20	19	–
9	2.0	**2** (20)	CH_2Cl_2	20	47	–
10	2.0	**3** (20)	CH_2Cl_2	20	25	–
11	2.0	**4** (40)	CH_2Cl_2	20	30	–
12	2.0	pyridine (40)	CH_2Cl_2	20	14	–
13	2.0	pyridine (20)	CH_2Cl_2	20	8	–
14	2.0	–	CH_2Cl_2	20	0	–
15	1.2	**1a** (20)	CH_2Cl_2	20	>99	80

[a] Determined by ^{1}H NMR. [b] Isolation was not attempted except for entries 2 and 15

The optimized conditions were then applied to several aromatic aldehydes, cinnamaldehyde, and cyclohexanecarboxaldehyde to examine the scope of substrates (Figure 2 and Table 2). As shown in entries 1–6, the aromatic aldehydes and cinnamaldehyde were completely converted into the corresponding alcohols, though some proportions of them were lost during purification procedures. The difficulty of isolation was partly due to the production of polysiloxane as described above and the reduction of the amount of $HSiCl_3$ from 2 equiv. to 1.2 equiv. greatly improved the isolated yield of *p*-chlorobenzaldehyde (entries 2, 3), though it did not improve the result with 1-naphthaldehyde (entries 4, 5). Contrary to the complete conversion of aromatic and α,β-unsaturated aldehydes, the reaction of cyclohexanecarboxaldehyde was not completed under the same conditions and the isolated yield of the desired alcohol was only 27% (entry 7).

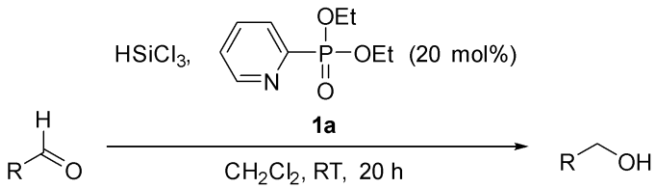


Figure 2. Hydrosilylation reaction of aldehydes

Table 2. Hydrosilylation of aldehydes

Entry	$HSiCl_3$ (equiv)	R	Conversion (%)[a]	Isolated Yield (%)
1	2.0	*p*-$MeOC_6H_4$	>99	50
2	2.0	*p*-ClC_6H_4	>99	62
3	1.2	*p*-ClC_6H_4	>99	94
4	2.0	1-naphthyl	>99	87
5	1.2	1-naphthyl	>99	83
6	2.0	(*E*)-PhCH=CH	>99	78
7	2.0	*c*-Hex	62	27

[a] Determined by ^{1}H NMR

Next, we investigated the hydrosilylation of acetophenone using **1a** as a catalyst (Figure 3 and Table 3). As expected from the result obtained with cyclohexanecarboxaldehyde, the hydrosilylation of acetophenone, which is less reactive than cyclohexanecarboxaldehyde, was very slow. Only 5% of acetophenone was converted into 1-phenylethanol under the conditions optimized for aldehydes (entry 1). The reaction was equally sluggish in $CHCl_3$ (entry 2) and toluene (entry 3) and promoted a little further in Et_2O (entry 4) and 1,4-dioxane (entry 5), though only up to 15%. The reaction did not occur when diethyl phenylphosphonate **4** was used as a catalyst in toluene (entry 6).

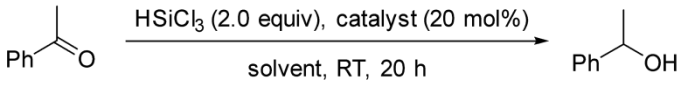


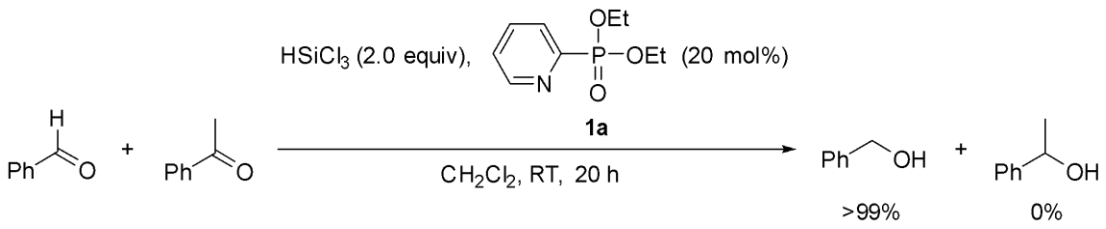
Figure 3. Hydrosilylation reaction of acetophenone

Table 3. Hydrosilylation of acetophenone

Entry	Catalyst	Solvent	Conversion (%)[A]
1	**1a**	CH_2Cl_2	5
2	**1a**	$CHCl_3$	4
3	**1a**	toluene	3
4	**1a**	Et_2O	11
5	**1a**	1,4-dioxane	15
6	**4**	toluene	0

[a] Determined by ^{1}H NMR

The marked difference in the reactivity of aldehydes and acetophenone suggested the possibility of chemoselective reduction of aldehydes over ketones. Therefore, we carried out the hydrosilylation of a 1:1 mixture of benzaldehyde and acetophenone in the presence of 20 mol% of **1a** (Scheme 1). As we expected, benzaldehyde was completely reduced to benzyl alcohol while acetophenone was recovered quantitatively. This result shows that **1a** will be useful for the chemoselective reduction of a formyl group over a keto group [29-31].



Scheme 1. Chemoselective hydrosilylation of benzaldehyde in the presence of acetophenone

Conclusion

In conclusion, we have found that diethyl 2-pyridylphosphonate works as an efficient catalyst for the hydrosilylation of aldehydes using $HSiCl_3$ as a reducing agent. A comparative study on the structure and activity of catalysts suggested that diethyl 2-pyridylphosphonate works as a bidentate Lewis base catalyst to activate $HSiCl_3$. The hydrosilylation was found to be completely chemoselective for an aldehyde over a ketone.

Acknowledgement

This research was partially supported by a Grant-in-Aid for Scientific Research on Innovative Areas "Advanced Molecular Transformations by Organocatalysts" from MEXT, Japan (Grant Number JP24105510).

References

1. Herrera, R. P. (2016). Organocatalytic transfer hydrogenation and hydrosilylation reactions. *Topics in Current Chemistry*, 374(29): 1-40.
2. Kocovsky, P. and Malkov, A. V. Edited by Vedejs, E. and Denmark, S. E. (2016). Lewis bases as catalysts in the reduction of imines and ketones with silanes (n → σ*). Lewis base catalysis in organic synthesis. Wiley-VCH, Germany: pp. 1077-1112.
3. Boyer, J., Corriu, R. J. P., Perz, R. and Reye, C. (1979). Catalyse heterogene en presence de sels et sans solvant: II. Hydrosilylation d'aldehydes et de cetones satures et α,β ethyleniques. *Journal of Organometallic Chemistry*, 172(2): 143-152.
4. Corriu, R. J. P., Perz, R. and Reye, C. (1983). Activation of silicon-hydrogen, silicon-oxygen, silicon-nitrogen bonds in heterogeneous phase: some new methods in organic synthesis. *Tetrahedron*, 39(6): 999-1009.
5. Fujita, M. and Hiyama, T. (1984). Highly diastereocontrolled reduction of ketones by means of hydrosilanes. practical synthesis of optically active 1,2-diols and 2-amino alcohols of threo or erythro configuration. *Journal of the American Chemical Society*, 106(16): 4629-4630.
6. Fujita, M. and Hiyama, T. (1988). Erythro-directive reduction of α-substituted alkanones by means of hydrosilanes in acidic media. *The Journal of Organic Chemistry*, 53(23): 5415-5421.
7. Kohra, S., Hayashida, H., Tominaga, Y. and Hosomi, A. (1988). Pentaco-ordinate organosilicon compounds in synthesis: Asymmetric reduction of carbonyl compounds with hydrosilanes catalyzed by chiral bases. *Tetrahedron Letters*, 29(1): 89-92.
8. Hojo, M., Fujii, A., Murakami, C., Aihara, H. and Hosomi, A. (1995). Divergent stereoselectivity in the reduction of α,β-epoxy ketones using hydridosilicates. *Tetrahedron Letters*, 36(4): 571-574.
9. Van der Jeught, S. and Stevens, C. V. (2009). Direct phosphonylation of aromatic azaheterocycles. *Chemical Reviews*, 109(6): 2672-2702.
10. Onomura, O., Kouchi, Y., Iwasaki, F. and Matsumura, Y. (2006). New organic activators for the enantioselective reduction of aromatic imines with trichlorosilane. *Tetrahedron Letters*, 47(22): 3751- 3754.
11. Onomura, O., Kirira, P. G., Tanaka, T., Tsukada, S., Matsumura, Y. and Demizu, Y. (2008). Diastereoselective arylation of l-proline derivatives at the 5-position. *Tetrahedron*, 64(32): 7498-7503.
12. Zheng, H., Deng, J., Lin, W. and Zhang, X. (2007). Enantioselective hydrosilylations of ketimines with trichlorosilane promoted by chiral *n*-picolinoylaminoalcohols. *Tetrahedron Letters*, 48(45): 7934-7937.
13. Zheng, H.-J., Chen, W.-B., Wu, Z.-J., Deng, J.-G., Lin, W.-Q., Yuan, W.-C. and Zhang, X.-M. (2008). Highly enantioselective synthesis of β-amino acid derivatives by the Lewis base catalyzed hydrosilylation of β-enamino esters. *Chemistry – A European Journal*, 14(32): 9864-9867.

14. Guizzetti, S., Benaglia, M. and Rossi, S. (2009). Highly stereoselective metal-free catalytic reduction of imines: an easy entry to enantiomerically pure amines and natural and unnatural α-amino esters. *Organic Letters*, 11(13): 2928-2931.
15. Xiao, Y.-C., Wang, C., Yao, Y., Sun, J. and Chen, Y.-C. (2011). Direct asymmetric hydrosilylation of indoles: combined Lewis base and Brønsted acid activation. *Angewandte Chemie International Edition*, 50(45): 10661-10664.
16. Malkov, A. V., Stewart-Liddon, A. J. P., McGeoch, G. D., Ramirez-López, P. and Kočovský, P. (2012). Catalyst development for organocatalytic hydrosilylation of aromatic ketones and ketimines. *Organic & Biomolecular Chemistry*, 10(25): 4864-4877.
17. Malkov, A. V., Liddon, A. J. S., Ramírez-López, P., Bendová, L., Haigh, D. and Kočovský, P. (2006). Remote chiral induction in the organocatalytic hydrosilylation of aromatic ketones and ketimines. *Angewandte Chemie International Edition*, 45(9): 1432-1435.
18. Bonsignore, M., Benaglia, M., Annunziata, R. and Celentano, G. (2011). New, readily available organocatalysts for the enantioselective reduction of α-imino- and β-imino esters. *Synlett*, (8): 1085- 1088.
19. Oka, N., Ito, K., Tomita, F. and Ando, K. (2012). Synthesis of 2-pyridylphosphinate and thiophosphinate derivatives by nucleophilic aromatic substitution of *n*-methoxypyridinium tosylates. *Chemistry Letters*, 41(12): 1630-1632.
20. Oka, N., Ori, K. and Ando, K. (2017). Synthesis of 2-pyridylthiophosphinic acids and 2-pyridylthiophosphonate monoesters via nucleophilic aromatic substitution. *Phosphorus, Sulfur, and Silicon and the Related Elements*, 192(4): 454-463.
21. Redmore, D. (1970). Phosphorus derivatives of nitrogen heterocycles. 2. pyridinephosphonic acid derivatives. *The Journal of Organic Chemistry*, 35(12): 4114-4117.
22. Chen, D., Martell, A. E., Motekaitis, R. J. and McManus, D. (1998). Syntheses and Fe(II)/Fe(III) equilibria of the new multidentate ligands pyridine-2-phosphonic-6-carboxylic acid and 2,6-pyridinediphosphonic acid for the use of their iron chelates as catalysts for the oxidation of H_2S to S_8 by air. *Canadian Journal of Chemistry*, 76(4): 445-451.
23. Johansson, T., Kers, A. and Stawinski, J. (2001). 2-pyridylphosphonates: A new type of modification for nucleotide analogues. *Tetrahedron Letters*, 42(11): 2217-2220.
24. Pitt, L. S., Large, G. B. and MacDonald, A. A. (1978). Insecticidal diethyl 2-pyridinethionophosphonate. German Offen., CAN: 89: 18370.
25. Hirao, T., Masunaga, T., Yamada, N., Ohshiro, Y. and Agawa, T. (1982). Palladium-catalyzed new carbon-phosphorus bond formation. *Bulletin of the Chemical Society of Japan.*, 55(3): 909-913.
26. Kalek, M., Jezowska, M. and Stawinski, J. (2009). Preparation of arylphosphonates by palladium(0)-catalyzed cross-coupling in the presence of acetate additives: Synthetic and mechanistic studies. *Advanced Synthesis & Catalysis*, 351(18): 3207-3216.
27. Brook, M. A. (2000). Atomic and molecular properties of silicon. silicon in organic, organometallic, and polymer chemistry. Wiley-Interscience, New York: pp. 27-38.
28. Theis, B., Metz, S., Burschka, C., Bertermann, R., Maisch, S. and Tacke, R. (2009). Neutral pentacoordinate silicon(iv) complexes with silicon-chalcogen (S, Se, Te) bonds. *Chemistry - A European Journal*, 15(30): 7329-7338.
29. Hosomi, A., Hayashida, H., Kohra, S. and Tominaga, Y. (1986). Pentaco-ordinate silicon compounds in synthesis: chemo- and stereo-selective reduction of carbonyl compounds using trialkoxy-substituted silanes and alkali metal alkoxides. *Journal of the Chemical Society, Chemical Communications*, (18): 1411-1412.
30. Kobayashi, S., Yasuda, M. and Hachiya, I. (1996). Trichlorosilane-dimethylformamide (Cl_3SiH-DMF) as an efficient reducing agent. reduction of aldehydes and imines and reductive amination of aldehydes under mild conditions using hypervalent hydridosilicates. *Chemistry Letters*, 25(5): 407-408.
31. Zhao, M., Xie, W. and Cui, C. (2014). Cesium carbonate catalyzed chemoselective hydrosilylation of aldehydes and ketones under solvent-free conditions. *Chemistry - A European Journal*, 20(30): 9259-9262.

Malaysian Journal of Analytical Sciences, Vol 23 No 4 (2019): 654 - 659
DOI: https://doi.org/10.17576/mjas-2019-2304-11

MALAYSIAN JOURNAL OF ANALYTICAL SCIENCES
Published by The Malaysian Analytical Sciences Society
ISSN 1394 - 2506

THE INTERACTION BETWEEN FIREFLY LUCIFERIN WITH G-QUADRUPLEX DNA AND CT-DNA

(Interaksi antara Lusiferin Kunang-Kunang bersama DNA G-Kuadrupleks dan CT-DNA)

Nurul Huda Abd Karim*, Roshatiara Shamsuddin, Aida Mastura Mohd Yussof, Nur Amirah Harunar Rashid

Centre for Advanced Materials and Renewable Resources, Faculty of Science and Technology
Universiti Kebangsaan Malaysia, 43600 UKM Bangi, Selangor, Malaysia

**Corresponding author: nurulhuda@ukm.edu.my*

Received: 31 March 2018; Accepted: 17 April 2019

Abstract

Firefly bioluminescence gives fascinating challenges and great interest for fundamental sciences. The luciferase enzyme which emits colour for firefly bioluminiscence has been intensively studied by chemists in various applications. Luciferin the substrate of luciferase, is also responsible for the characteristic of yellow light emission from many firefly species. In recent years, the binding of small molecules with DNA has been receiving great attention due to the potential of such binding to inhibit cancer cell growth. G-quadruplex DNA has been discovered as an interesting target since stabilizing its formation in telomere can inhibit the elongation of telomere in cancer cell where enzyme telomerase is 85% activated. Here, we investigate the binding properties between luciferin compound with G-quadruplex DNA. The binding interaction was studied using UV/Vis spectra and fluorescence. The results indicate that luciferin is more selective to stabilize G-quadruplex DNA with $K_b = 2.02 \pm 0.59 \times 10^5\ M^{-1}$ compared to CT-DNA.

Keywords: luciferin, bioluminescence, CT- DNA, G-quadruplex DNA

Abstrak

Kunang-kunang biopendarkilau memberikan cabaran yang menarik dan menyumbang kepentingan yang besar dalam bidang sains. Enzim lusiferase yang mengeluarkan pancaran warna bagi kunang-kunang biopendarkilau telah dikaji secara intensif oleh ahli kimia dalam pelbagai aplikasi. Lusiferin merupakan substrat bagi lusiferase yang bertanggungjawab untuk menghasilkan cahaya kekuningan daripada spesis kunang-kunang. Beberapa tahun kebelakangan ini, kajian pengikatan molekul kecil bersama DNA mula menarik perhatian kerana keupayaan pengikatannya dapat merencatkan tumbesaran sel kanser. DNA G-kuadrupleks dijadikan sebagai sasaran utama kerana kestabilan pembentukannnya dalam jujukan telomer dapat merencatkan pemanjangan sel kanser yang diaktifkan oleh 85% enzim telomerase. Melalui kajian ini, interaksi antara sebatian lusiferin dengan DNA G-kuadrupleks telah dikaji. Kajian pengikatan ini dianalisis menggunakan spektrum UV/ Vis dan pendarfluor. Hasil menunjukkan bahawa lusiferin lebih selektif berikat bersama DNA G-kuadrupleks dengan nilai pemalar pengikatan, $K_b = 2.02 \pm 0.59 \times 10^5\ M^{-1}$ berbanding CT-DNA.

Kata kunci: lusiferin, biopendarkilau, CT-DNA, DNA G-kuadrupleks

Introduction

Deoxyribonucleic acid (DNA) is as a double helical structure with its crucial role as genetic information storage. In the last several years, studies on the interaction between ligand and DNA have increased with improved instruments for DNA binding analysis. Many studies involving the interaction between DNA and small molecules, such as metal

complexes that act as metal-based drugs [1] were carried out due to its major role in the life process as cancer inhibitors [2]. Organic and inorganic molecules were reported to interact with DNA via three possible binding methods; (i) groove binding, where the small molecules interact with the grooves of the DNA chain, (ii) intercalative binding (π-π stacking), where the small molecules intercalate into the base pairs of DNA nucleotide base, (iii) electrostatic interaction, where the small molecules are adsorbed on the phosphates of DNA by electrostatic interaction [3,4]. DNA is an important target for several drugs [5]. Steroidal compounds are essential to life in many ways [6]. One of the example, anticancer drugs which are selectively interacting with DNA can inhibit the duplication or transcription of DNA [7]. In recent years, the search for suitable drug candidates, such as DNA G-quadruplex stabilization has led to the founding of several compounds including BRACO 19, TMPyP4 and 2,6-disubstituted anthraquinone, all of which have good binding constants between G-quadruplexes DNA and ligands.

Cancer cells have the ability to elongate the telomere due to the presence of a reverse transcriptase enzyme known as telomerase. Stabilization of telomeric G-quadruplex DNA can inhibit telomerase enzyme activity and finally lead to the cell cancer death [8]. G-quadruplexes DNA are planar G-quartet motifs which can be formed in guanine-rich DNA sequence like the telomeres. These structures interact with the inhibitor (ligands or complex) via π-π stacking, thereby stabilizing the G-quadruplex–inhibitor complex [9]. Suprisingly, many animals and plants in this world are bioluminiscent. Bioluminiscent mean the light emitted by living organisms results from oxidation of light-producing substance like luciferine by enzyme luciferase[10]. Firefly is a bioluminescent organism. The light emission by this organism results from the reaction between oxygen and an oxidizable substrate (a luciferin), and catalyzed by enzyme (a luciferase). The interaction between the luciferase (enzyme) and D-luciferin (LH_2) to generate light is generally proposed as equation 1 [11]:

$$E + LH_2 + ATPMg \leftrightarrow E\text{-}LH_2\text{-}AMP + O_2 \rightarrow OxL + light + AMP + CO_2 + Ppi \quad (1)$$

Usually the functions of bioluminescence are to warn or evade predators, to lure or detect prey and to communicate between members of the same species. The most interesting aspect of fireflies bioluminiscence is that it is applicable for various applications, such as in biomedical, pharmaceutical, bioanalytical, bioimaging applications[12], clinical and biochemical[13]. Although there are various applications regarding fireflies bioluminiscence, research on the interaction between luciferin (Figure 1) and DNA has not been yet reported. Thus, in this work, the interaction using UV/Vis and fluorescence spectroscopy was studied.

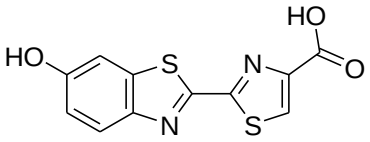


Figure 1. Chemical structure of D-luciferin

Materials and Methods

All chemicals (for compound and DNA titration) were purchased from Sigma-Aldrich. DNA binding experiments were carried out in Tris-KCl buffer at pH 7.4. pH measurements were carried out with PHM 210, while the UV/Vis absorption spectra were measured on a Shimadzu UV-1650 spectrophotometer using a 1 mL cuvette. Fluorescence spectra were measured using Perkin Elmer LS55 Luminescence Spectrophotometer.

Oligonucleotides preparation

The oligonucleotide, 22 bp human telomeric G-Quadruplex DNA (H-telo DNA), 5'-AGGGTTAGGGTTAGGGTTAGGG -3' was purchased from Sigma Aldrich. H-telo DNA was dissolved in 10 mM Tris-HCl/100 mM KCl (pH 7.4) buffer to yield a 1 mM solution. The oligonucleotide was annealed by heating it to 90 ºC for 5 min and then cooled to room temperature overnight. Duplex DNA, CT-DNA was also purchased from Sigma-Aldrich and dissolved overnight in a 10 mM Tris-HCl /100 mM KCl (pH7.4) buffer to yield 5 M solution.

The DNA concentration was determined from the band intensity at 260 nm with the molar extinction coefficient values for CT-DNA and H-Telo are 6600 M^{-1} cm^{-1} and 0.2285 mM^{-1} cm^{-1}, respectively.

Sample preparation
The luciferin compound was dissolved in a mixture of DMSO (95% by volume) and 10 mM Tris-HCl /100 mM KCl (pH 7.4) buffer to produce 5 mM stock solution. This solution was stored at -20°C and defrosted prior to use. Upon usage, the stock solution was thawed and diluted to 1 mM using DMSO. This was further diluted with a buffer to the appropriate concentrations.

UV/Vis titration studies procedure
The absorption titrations of the luciferin compound with H-Telo and CT-DNA were performed at room temperature. All experiments were repeated at least three times. The compound (30 μM) was titrated with concentrated solutions of DNA (0.39 mM Htelo G-Quadruplex DNA or 5 mM CT-DNA) 10 mM in Tris HCl/100 mM KCl buffer pH 7.4. The binding affinity between the compound and the DNA was determined with a constant concentration of compound. Absorbance values were recorded after each successive addition of DNA solution and equilibration (Figures 2 and 3). A 1 cm pathlength quartz cuvette was used to conduct the measurements. The percentage of hypochromicity was calculated according to equation 2:

$$\% \text{ hypochromicity} = [(\varepsilon \text{ free} - \varepsilon \text{ bound})/ \varepsilon \text{ free}] \times 100 \quad (2)$$

The intrinsic binding constant K_b of the ligand–DNA was determined according to equation 3:

$$D/\Delta\varepsilon ap = D/\Delta\varepsilon + 1/(\Delta\varepsilon \times K) \quad (3)$$

where the concentration of DNA is expressed in terms of base pairs (determined by measuring the absorption at 260 nm and the appropriate extinction coefficients), the apparent molar extinction coefficient εa =A observed/[Complex], Δεap = [εa - εf] and Δε = [εb -εf]. εb is the extinction coefficient of the DNA bound complex, and εf is the extinction coefficient of the free complex. From the plotted graph of [DNA]/(Δεap) versus [DNA], the y-intercept is equal to 1/ (Δεap × K) whereas the slope is equal to 1/Δεap. K is obtained by dividing the slope value by the y-intercept.

Emission titration procedure
Aliquots of a millimolar stock solution of DNA in Tris/KCl buffer (0–100 μM) were added to the solutions containing the test compounds (30 μM). The emission spectra were recorded at λ= 400–700 nm after equilibration for 1 min and the luminescence enhancement at λ max = 520 nm for luciferin was determined. Percentage of emission enhancement was determined for complex-H-telo DNA and complex-CT-DNA bindings, respectively.

Results and Discussion

UV-Vis titration study
Usually, compounds which bind with DNA through intercalation mode results in hypochromism and bathochromism (red shift). In weaker interaction, hypochromic or hyperchromic effect can only be observed without any change of shift in the spectrum [14, 15]. Generally, intercalative binding mode happens due to the strong interaction between molecules with DNA base pairs [4, 16]. Meanwhile, hyperchromism effect arises from the damage on DNA double helix structure or uncoiling of DNA helix structure, as well as different binding modes [17, 18]. Usually, compounds with an aromatic group bind with DNA via intercalation of an aromatic moeity [19].

The interaction between luciferin and G-Quadruplex DNA was identified through the changes in luciferin absorption spectra in the absence and presence of increasing DNA concentration. From the electronic absorption spectra of luciferin in Figure 2a and b, the titration of luciferin with G-Quadruplex DNA resulted in hypochomism (3%) and a slight red shift. This is the characteristics of intercalative binding mode between the compound to H-Telo G Quadruplex DNA [4, 20]. Luciferin has a binding constant K_b of $7.46 \pm 1.67 \times 10^5$ M^{-1} upon binding with G-Quadruplex DNA. The binding constant suggests that the interaction between luciferin and DNA is moderately intercalative mode.

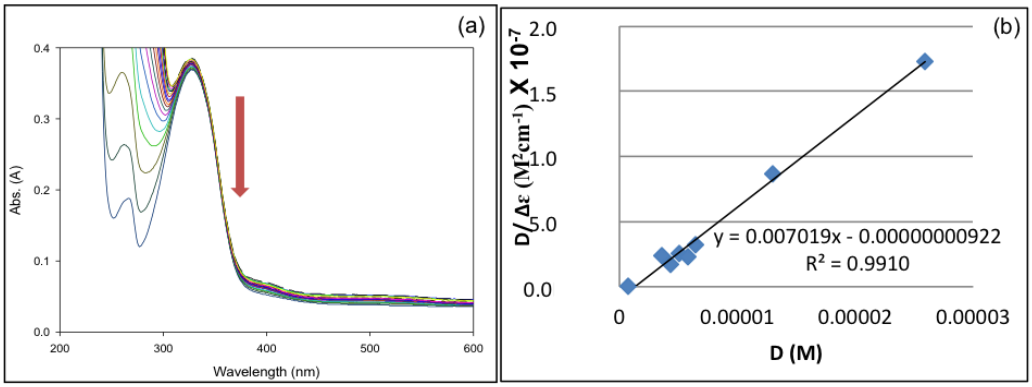


Figure 2. (a) Absorption spectral changes of luciferin (30 µM) in Tris/KCl buffer (pH 7.4) in the absence and presence of increasing concentration of H-Telo (0.328 mM - 0.39 mM); (b) The reciprocal plot that fits the absorbance data to obtain the binding constant

For comparison, the interaction between luciferin and duplex DNA, CT-DNA was identified through the changes in luciferin absorption spectra in the absence and presence of increasing concentration of CT-DNA. From the electronic absorption spectra of luciferin in Figure 3a and b, it was observed that the additional amount of DNA resulted in hypochromism (3%) at 331 nm, where a gradual decrease in molar absorptivity as well as a slight red shift (1.5 nm) occurred. The results confirmed the mode interacion between luciferin with ct-DNA is intercalation. Luciferin has a binding constant K_b = 2.02 ± 0.59 × 10^5 M^{-1} upon binding with CT-DNA. This type of shift and hypochromism have been associated with intercalative interaction mode with CT-DNA [21, 22]. These results suggest that luciferin shows higher binding affinity with G- Quadruplex DNA compared to CT- DNA.

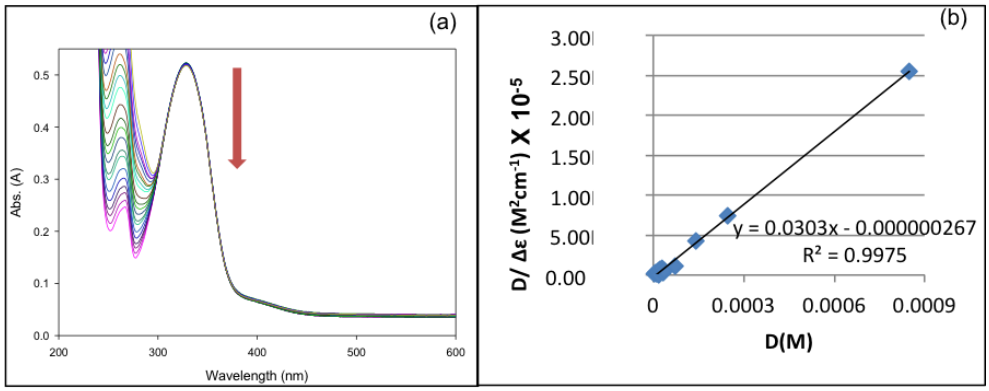


Figure 3. (a) Absorption spectral changes of luciferin (30 µM) in TRIS.HCl buffer (pH = 7.4) in the absence and presence of increasing concentration of CT-DNA (4 mM - 5 mM); (b) The reciprocal plot which fits the absorbance data to obtain the binding constant

Emission titration

The DNA-binding modes of luciferin compound were further monitored by emission titration using spectrofluorometer. It is well known that luciferin emits intense fluorescence since it has bioluminiscence character. Emission titration experiments were conducted to investigate whether their optical properties would change upon interaction with DNA (particularly G-quadruplex DNA). An increasing amount of G-quadruplex DNA and CT-DNA were added to luciferin solutions until saturation of compound emission was observed. The changes in intensity with increasing amounts of DNA are shown in Figure 4a and b.

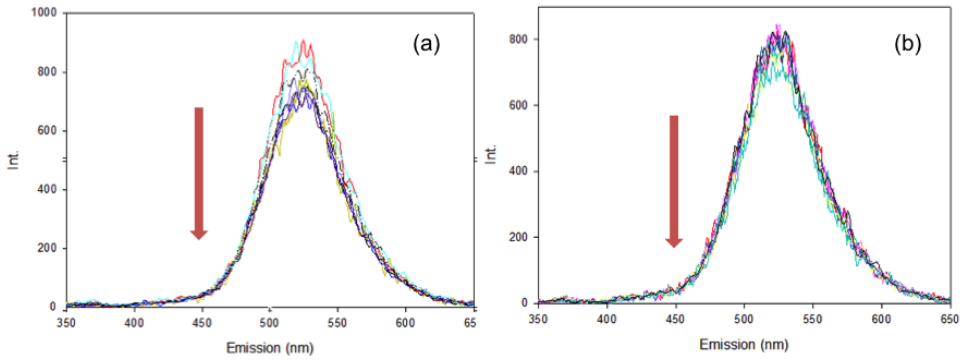


Figure 4. The emission spectra of luciferin compound (2 μM) in Tris/KCl buffer (pH 7.4) with increasing concentrations of (a) H-telo DNA (b) CT-DNA at 25 °C. The intensity of emission band of luciferin compound was reduced with increasing DNA concentration

The results of the emission titration of complexes showed that luciferin binds to both G-quadruplex and CT-DNA and decreased in emission intensity was observed. Increasing amount of G-quadruplex DNA and CT-DNA caused decrease in luciferin intensity by approximately 24% and 18%, respectively, which suggests that with regard to binding specificity, luciferin compound is not too selective of G-Quadruplex DNA.

Conclusion

DNA binding studies of luciferin were carried out using UV-Vis study and emission titration which suggested that luciferin bound moderately to G-quadruplex DNA with 4-fold selectivity over CT-DNA. However, 24-fold decrease in emission intensity was observed upon luciferin-G-quadruplex binding compared to 18-fold decrease in emission intensity observed for luciferin-CT-DNA binding. The results propose that luciferin as a promising candidate for further applications, namely as a DNA binder and an anticancer drug but not as fluorescence probe. Modification of luciferin compounds is suggested to improve G-quadruplex DNA binding ability.

Acknowledgement

The authors would like to acknowledge Ministry of Higher Education of Malaysia and Universiti Kebangsaan Malaysia for research grant LAUREATE 2013-002, FRGS/1/2016/STG01/UKM/02/1 dan GUP-2017-067.

References

1. Juan, C. G-R., Rodrigo, G-M., Fernando, C-G and Lena, R-A. (2013). Metal-based drug-DNA interactions. *Journal of Mexican Chemical Society*, 57: 245-259.
2. Xiaoyan, Z., Yong, W., Qianru, Z. and Zhousheng, Y. (2010). The interaction of taurine–salicylaldehyde Schiff base copper(II) complex with DNA and the determination of DNA using the complex as a fluorescence probe. *Spectrochimica Acta Part A*, 77: 1–5.
3. Janati Fard, F., Mashhadi Khoshkhoo, Z., Mirtabatabaei, H., Housaindokht, and Jalal, M. R. (2013). Synthesis, characterization and interaction of N, N0- dipyridoxyl(1,4-butanediamine) Co (III) salen complex with DNA and HAS. *Spectrochimica Acta Part A: Molecular and Biomolecular Spectroscopy*, 97: 74–82.
4. Dik-Lung, M., Daniel, S-H. C., Paul, L., Maria, H-T. K., and Chung-Hang, L. (2011). Molecular modeling of drug-DNA interactions: Virtual screening to structure-based design. *Biochimie*, 93: 1252-1266.
5. Ricci, C. G and Netz, P. A. (2009). Docking studies on DNA- ligand interactions: Building and application of a protocol to identify the binding mode. *Journal of Chemical Information and Modeling*, 49: 1925-1935.
6. Sultanat, Dar A. M, Rizvi, A. and Naseem, I. (2014). Synthesis, evaluation and docking studies of cholecalciferol derivative. *Oriental Journal Chemistry*, 30(3): 1-6.
7. Zhanguang, C., Yurui, P., Maohuai, C., Xi, C. and Guomin, Z. (2010). DNA as a target for anticancer compounds screening directly by resonance light scattering technique. *The Royal Society of Chemistry*, 135: 2653-2660.

8. Rahim S, Antony A, Lukose G, Mohanan K, Joe I. H and Joseyphus R. S. (2015). Synthesis, spectral characterization and computational studies of metal chelates of 4-n-(2-thienylidene)aminoantipyrine. *Oriental Journal Chemistry,* 31(4): 1-10.
9. Taetz, S., Murdter, T. E., Zappc, J., Boettcher, S., Baldes, C., Kleideiter, E., Piotrowska, K., Schaefer, U. F., Klotz, U., Lehr and C.-M. (2008). Decomposition of the telomere-targeting agent BRACO19 in physiological media results in products with decreased inhibitory potential. *International Journal of Pharmaceutics*, 357: 6-14.
10. Steven, H. D. H., Mark, A. M. and James, F. C. (2010). Bioluminescence in the Sea. *Annual Review of Marine Science*, 2: 443–493.
11. Fre´de´ric, B., Bernengo, J.-C., Min, K.-L. and Steghens, J.-P. (2000). Firefly luciferase generates two low-molecular-weight light-emitting species. *Biochemical and Biophysical Research Communications,* 270: 247-253.
12. João, V., Luís, P. da. S., Joaqui. and da Silva, C.G. E. (2012), Advances in the knowledge of light emission by firefly luciferin and oxyluciferin. *Journal of Photochemistry and Photobiology B: Biology*, 117: 33-39.
13. Takayuki, M., Hiroshi, O., Katsushi, A., Hiroaki, M. and Hidetoshi. (2010). Practical application of bioluminescence enzyme immunoassay using enhancer for firefly luciferine-luciferase bioluminescence. *The Journal of Biological and Chemical Luminiscence*, 26: 167-171.
14. Muhammad, S., Saqib, A. and Amin, B. (2013). Drug–DNA interactions and their study by UV–Visible, fluorescence spectroscopies and cyclic voltammetry. *Journal of Photochemistry and Photobiology B: Biology*, 124: 1–19.
15. Nahid, S., Somaye, M. and Robabeh A. (2011). DNA interaction studies of a new platinum (II) complex containing different aromatic dinitrogen ligands. *Bioinorganic Chemistry and Applications*, 2011: 1-8.
16. Xu-Jian, L., Qi-Pin, Q., Yan-Cheng, L. and Hong, L. (2012). Synthesis, antitumor activity and G-quadruplex DNA/ct-DNA binding properties of a cationic platinum (II) complex of 2-(4-nitro)-imidazole-[5, 6-f][1,10]-phenanthroline. Indian Journal of *Chemistry*, 53: 787-792.
17. Lingthoingambi, N., Singh, N. R. and Damayanti, M. (2011). DNA interaction and biological activities of Copper (II) complexes of alkylamidio-O-methylurea, *Journal of Chemical and Pharmaceutical Research*, 3(6): 187-194.
18. Nahid, S. and Somaye, M. (2012). Synthesis characterization and DNA interaction studies of a new zn (ii) complex containing different dinitrogen aromatic ligands. *Bioinorganic Chemistry and Applications*, 2012: 1-6.
19. Giampaolo, B., Alessio, T., Antonino, L., Anna, M. A., José, M. L., Natalia, B. and Bego˜na G. (2013). DNA-binding of nickel (II), copper (II) and zinc (II) complexes: Structure–affinity relationships. *Coordination Chemistry Reviews*, 2013: 1-15.
20. Shamsuddin, R., Sahudin, M. A., Hassan, N. H., and Abd Karim, N. H. (2017). Interaction of N, N'-Bis[4-[1-(2-hydroxyethoxy)]Salicylidene]-phenyldiamine-nickel(II) and copper(II) complexes with G-Quadruplex DNA. *Malaysian Journal of Analytical Sciences,* 21(3): 544-551.
21. Mariappan, M., Masahiko, S., Abhik, M. and Bhaskar, G. M. (2012). Synthesis, structure, DNA binding and photonuclease activity of a nickel(II) complex with a N,N-Bis(salicylidene)-9-(3,4-diaminophenyl)acridine ligand, *Inorganica Chimica Acta,* 390: 95-104.
22. Narayanaperumal, P. and Natarajan. P. (2013). DNA interaction and antimicrobial activity of novel tetradentate imino-oxalato mixed ligand metal complexes. *Inorganic Chemistry Communications*, 36: 45-50.

Malaysian Journal of Analytical Sciences, Vol 23 No 4 (2019): 660 - 666
DOI: https://doi.org/10.17576/mjas-2019-2304-12

MALAYSIAN JOURNAL OF ANALYTICAL SCIENCES
Published by The Malaysian Analytical Sciences Society
ISSN 1394 - 2506

RARE EARTH METAL DOPED CaO AS CATALYST FOR THE TRANSESTERIFICATION REACTION OF COOKING OIL

(Logam Nadir Bumi Dop CaO sebagai Mangkin untuk Tindak Balas Transesterifikasi Minyak Masak)

Wan Nur Aini Wan Mokhtar*, Mohd Rushashraaf Ramli, Muhammad 'Azim Jamaluddin, Suria Ramli

Centre for Advanced Materials and Renewable Resources, Faculty of Science and Technology, Universiti Kebangsaan Malaysia, 43600 UKM Bangi, Selangor, Malaysia

**Corresponding author: wannurainiwm@ukm.edu.my*

Received: 31 March 2018; Accepted: 17 April 2019

Abstract

Biodiesel has been introduced as an alternative fuel to replace the depletion of diesel oil and environmental pollution. Thus, the production of biodiesel is in demand and usually, conducted through base catalysed transesterification reaction towards the low grade cooking oil. In this research, bimetallic oxide cerium-calcium catalyst supported on activated carbon (AC) was prepared using impregnation method. Optimum catalytic parameter was observed with 30 wt.% of cerium loading on Ce/Ca/AC catalyst calcined at 500 °C and gave the highest free acid methyl ester (FAME) yield of 73.5% with fixed reaction conditions (65 °C, 1:18 wt.% oil to methanol ratio, 6 wt.% catalyst loading and 3 hours of reaction time). The enhanced activity of Ce/Ca/AC catalyst can be ascribed to the uniform needle-like morphology and well dispersion of the Ce-Ca on the support surface as indicated by FESEM images. XRD showed that the Ce/Ca/AC catalyst was in amorphous phase with BET surface area of 149.18 m^2/g. These results showed Ce/Ca/AC catalyst has promising potential to be used for production of FAME from low grade cooking oil.

Keywords: bimetallic oxide, Ce-Ca catalyst, cooking oil, transesterification, biodiesel

Abstrak

Biodiesel telah diperkenalkan sebagai bahan api alternatif bagi menggantikan pengurangan minyak diesel dan juga pencemaran alam sekitar. Oleh itu keperluan terhadap penggunaan biodiesel semakin meningkat, dan kebanyakan proses penghasilan biodiesel dilakukan melalui tindak balas transesterifikasi beralkali ke atas minyak masak bergred rendah. Melalui kajian ini, mangkin oksida dwilogam serium-kalsium berpenyokong karbon teraktif (AC) disediakan menggunakan kaedah pengisitepuan basah. Parameter optimum bagi mangkin dapat dilihat dengan kehadiran 30 wt.% kandungan serium dalam mangkin Ce/Ca/AC yang dikalsinkan pada suhu 500 °C, dan menghasilkan kadar penukaran asid bebas metil ester (FAME) sebanyak 73.5% dengan keadaan tindak balas tetap (65 °C, 1:18 wt.% nisbah minyak kepada metanol, 6 wt.% kuantiti mangkin dalam tempoh 3 jam tindak balas). Peningkatan aktiviti transesterifikasi adalah disebabkan oleh morfologi mangkin Ce-Ca yang berbentuk sepeti jarum dan sekata pada permukaan penyokong seperti yang ditunjukkan oleh imej FESEM. XRD pula menunjukkan bahawa mangkin Ce/Ca/AC berada di dalam fasa amorfus dengan luas permukaan BET sebanyak 149.18 m^2/g. Ini menunjukkan, mangkin Ce/Ca/AC adalah berpotensi untuk digunakan dalam pengeluaran FAME dari minyak masak bergred rendah.

Kata kunci: oksida dwilogam, mangkin Ce-Ca, minyak masak, transesterifikasi, biodiesel

Introduction

Concerns over the global oil price fluctuations, the depletion of natural fuel sources and the rising issues of climate pollution caused by greenhouse gas emissions have pushed for a transition to a better energy source. The government continues to update energy policies as an effort to ensure the efficiency and sustainability of national energy supplies, including replacing them with renewable energy sources [1, 2]. Biodiesel is seen as the best alternative fuel source in replacing petroleum-based diesel. Compared to diesel fuel, biodiesel is seen as environmentally friendly as it is free of sulfur and aromatic, making it non-toxic and biodegradable with lower emissions [3-5].

Almost all biodiesel is produced by base catalyzed transesterification as it is the most economical process since low temperatures are required, resulting in a high conversion yield. Furthermore, base catalyzed transesterification proceeds faster than acid catalyzed reaction [6, 7]. However, the costs of biodiesel production are still quite high in comparison to petroleum diesel. This is due to the use of homogenous catalyst in existing biodiesel production process. Homogeneous catalysts that commonly used such as sodium hydroxide (NaOH) or potassium hydroxide (KOH) causes saponification process and requires a lot of water to be separated from the product of the reaction [8]. Hence, studies on the use of solid-based or heterogeneous catalysts have been widely conducted to reduce the dependency towards homogeneous catalysts in the biodiesel production industry. Among the benefits in using the heterogeneous catalysts are no side effects that can pollute the environment apart from being easily isolated from the resulting biodiesel. Separated catalyst can then be reused in a continuous reactor in comparison to the homogeneous catalysts used in the batch reactor [9, 10].

Extensive studies of heterogeneous catalysts have been conducted for biodiesel synthesis over the last decade, including alkaline metals, transition metals, rare earth metals, amino acid-based polymers, and micro-promoted alkaline and silicon/aluminate mesoporous [11]. However, the use of dopant from transition metals group to base catalysts is still poorly utilized in the transesterification reaction. Among the heterogeneous catalysts, Ca-based catalysts are mostly mixed with MgO, BaO, La_2O_3, SnO_2 whereas less attention was paid on the potential rare earth metal as a dopant even though this metal oxide offers good performance [12]. Hence, this study will focus on the heterogeneous catalyst production from alkaline earth metals with added rare earth metal dopant through wet impregnation methods. The incorporation of cerium and calcium species into the functionalized activated carbon (AC) perhaps can enhance the interaction between catalyst particles and support. The catalytic performance of Ce/Ca/AC was then compared in the transesterification of low grade cooking oil.

Materials and Methods

Materials

Calcium nitrate tetrahydrate $Ca(NO_3)_2 \cdot 4H_2O$, cerium nitrate hexahydrate $Ce(NO_3)_3 \cdot 6H_2O$, hydrophosphoric acid (H_3PO_4), methanol and *n*-hexane were purchased from Merck. All chemicals and solvents were used without further purification. Low grade cooking oil and palm kernel shells were obtained from the local market.

Catalyst Preparation

The activated carbon was initially synthesized using chemical activation process. The palm kernel shells were pre-treated with H_3PO_4 for 20 hours followed by purification with distilled water till the solution adjusted to neutral pH. Before introducing metal precursors, the carbon support was functionalized at 200 °C calcination temperature. The activated carbon was then immersed in nitrate salts aqueous solution of calcium and cerium at various ratios (10 wt.%, 20 wt.% and 30 wt.%) and aging in the oven at 80-90 °C for 24 hours. Then, the samples were calcined at various temperatures of 500, 700 and 1000 °C for 5 hours using a ramp rate of 5 °C/min to eliminate all the metal precursor impurities.

Catalytic reaction and characterization

The transesterification reaction was carried out using batch-reflux reactor method. Approximately, 10 g of low grade cooking oil the calculated amount of Ce/Ca/AC catalyst and methanol were mixed and heating up to 65 °C for 3 hours of reaction time. The mixture was distilled to remove excess of methanol followed by centrifuged at 3000 rpm for 30 minutes to separate the FAME and glycerol. Catalytic activity performance for all the prepared catalysts were measured using GC-FID equipped with SP-2560 capillary column (100 m × 0.25 mm × 0.20 µm) to determine

the percentage FAME conversion of low grade cooking oil at fixed reaction conditions. The column temperature was programmed at 140°C for min and increased up to 240 °C for 15 minutes. meanwhile, the injector and detector temperatures were set up at 260 °C. The identified composition was compared with Supelco 37 component FAME mix standards.

The potential catalyst was characterized using X-ray diffraction (XRD) to identify the crystallography of Ce/Ca/AC while the specific surface area and pore distribution of the catalyst were determined by the Brunauer-Emmet-Teller (BET) using N_2 adsorption/desorption analyser. Field emission scanning electron microscopy (FESEM-EDX) to identify the morphology and elemental composition study.

Results and Discussion

Figure 1 shows the XRD pattern for all prepared Ce/Ca/AC catalysts after calcination at 500, 700 and 1000 °C. Overall, the XRD diffractogram of each calcination temperature presented the similar pattern, which was amorphous structure. The surface morphologies of Ce/Ca/AC catalysts at different calcination temperatures were examined by FESEM and shown in Figure 2. Overall, it could be seen that all the Ce/Ca/AC catalysts have a rough surface morphology, consisting of larger and smaller particle sizes, thus confirming the amorphous structure as mentioned by the previous XRD analysis. Figure 2(a) of Ce/Ca(30:70)/AC catalyst calcined at 500 °C showed the formation of smaller like-needle aggregated on the catalyst support. This characteristic should provide the spacious area for active site distribution on the catalyst surface. However, particle shape changed when the catalyst was calcined at 700 °C as shown in Figure 2(b). The catalyst was composed of coarse and non-uniform particles of different grain sizes, scattered on the catalyst surface. Reaching the calcination temperature to 1000 °C, the morphology structure of the catalyst altered and form more agglomeration and non-uniformly distributed on the surface of the catalyst. The dense packed surface at higher calcination temperature deteriorated the surface area as well as catalytic performance [13]. These changes were expected to have an effect on the transesterification reaction. The element composition of the Ce/Ca(30:70)/AC catalyst calcined at 500 °C was studied by EDX analysis (Figure 2(d)).

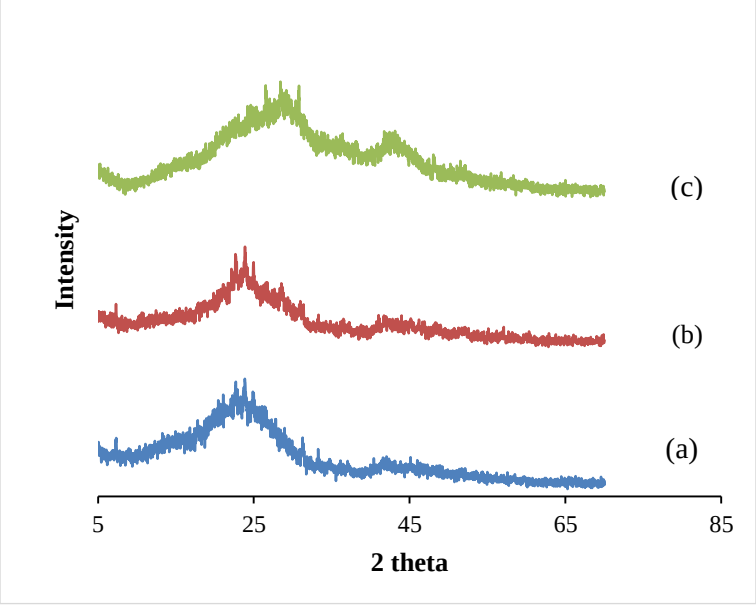


Figure 1. XRD diffractogram for Ca/Ce (30:70)/AC catalyst at calcination temperature of (a) 500 °C, (b) 700 °C and (c) 1000 °C

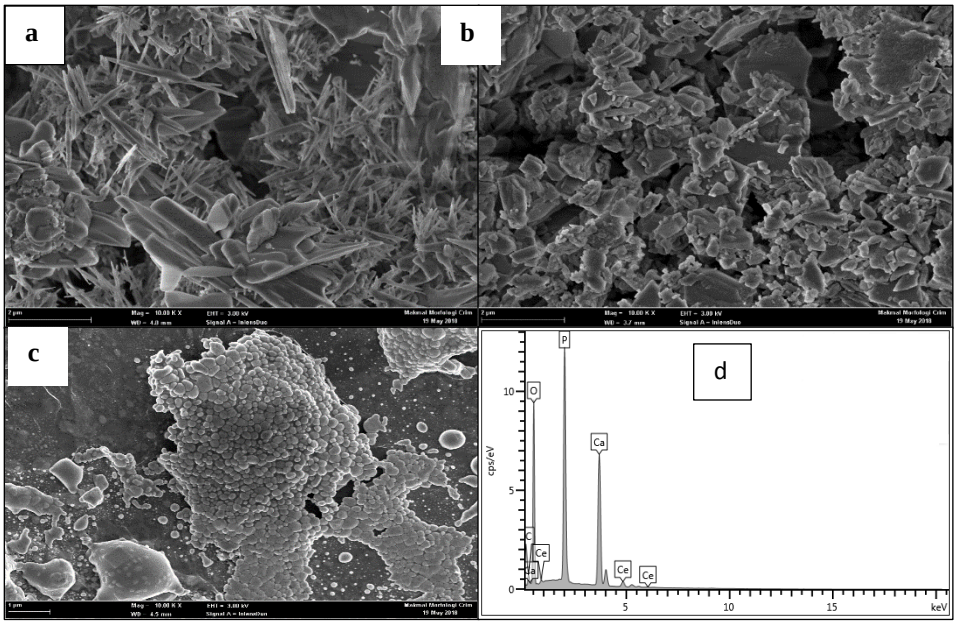


Figure 2. FESEM image for Ce/Ca (30:70)/AC catalysts calcined at (a) 500 °C, (b) 700 °C and (c) 1000 °C for 5 hours and (d) EDX result of Ce/Ca (30:70)/AC catalysts calcined at 500 °C

High performance catalysts are usually relied on materials with high surface area and associated with particle size below than 100 nm. The specific surface area (BET) and pore volumes of Ca/Ce (30:70)/AC catalysts are summarized in Table 1. The results of Ca/Ce (30:70)/AC showed gradually reduced of surface area and pore volume upon increasing of calcination temperature from 500 °C to 1000 °C while maintained the concentration of both Ce and Ca species. This observation might be due to the pore structure collapsed or most of the active site sitting on the bulk matrices instead of well-distributed on the catalyst surface.

Table 1. The specific surface area of Ce/Ca (30:70)/AC catalysts calcined at 500 °C, 700 °C and 1000 °C

Calcination T (°C)	**BET Surface area (m^2/g)**	**Pore Size (Å)**	**Pore Volume (cm^3/g)**
1000	70.28	19.13	0.034
700	127.65	19.74	0.063
500	149.18	20.16	0.082

Effect of cerium loading

Figure 3 illustrates the influence of cerium loading on Ca-based catalyst on the transesterification reaction. It was clearly observed that the triglyceride reduction was significantly increased as the cerium content of the catalyst increased from 10 wt.% to 30 wt.%, wherein more than 70% of FAME conversion was produced. These results, therefore, suggested the transesterification of low grade cooking oil was dependable on appropriate percentage of Ce/Ca ratio. In contrary, this ascending trend of transesterification activity was against the findings obtained by Kamal et al. [14] where the optimal transesterification was achieved with less than 20 wt.% of dopant loading. Increasing the amount of dopant gave no further performance towards transesterification reaction. They found that the excessive dopant loading caused agglomeration on catalyst surface and blocking the pores and the number of active sites.

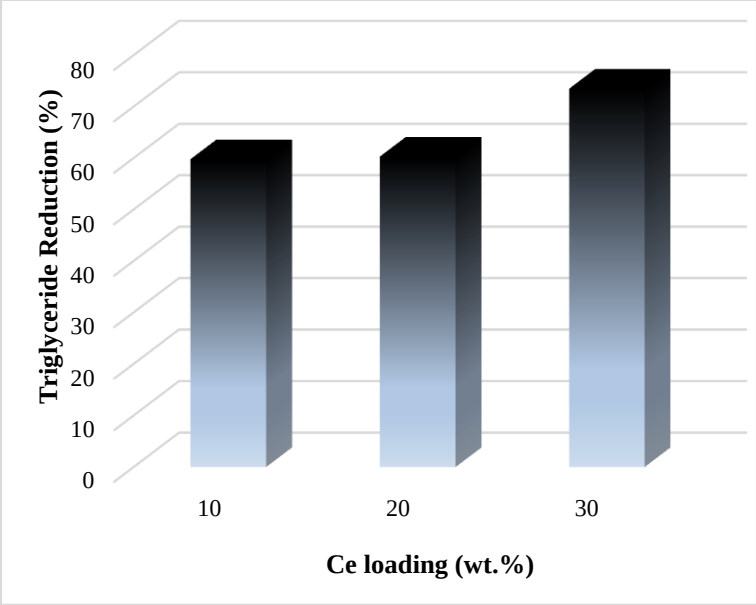


Figure 3. Effect of Ce loading of Ce/Ca/AC catalysts on the transesterification reaction

Effect of calcination temperature

Since calcination temperature affects the catalytic activity, the catalysts were calcined at different temperatures to determine the optimum calcination temperature for each based catalysts that could enhance the transesterification reaction. All the catalysts were calcined at different temperatures of 500, 700 and 1000 °C, while the cerium loading was varied at 10, 20 and 30 wt.%. Catalytic performances of all the catalysts were indicated in Table 2 which represented the percentage conversion of cooking oil at different calcination temperatures and various cerium loadings. At calcination temperature of 700 °C and 1000 °C, all catalysts showed low oil conversions. However, at lower calcination temperature of 500 ^{o}C, the oil conversion greatly increased for all catalysts. Among the prepared catalysts, the catalytic activity of Ce/Ca/AC catalysts calcined at 500 ^{o}C was the most promising catalyst for the transesterification reaction of low grade cooking oil to biodiesel compared to other catalysts. This might be due to the agglomeration of particles that occur on the surface of the catalyst during the calcination process, thus reducing the active sites of the catalyst [15].

Table 2. Effect of calcination temperature (CT) of Ce/Ca/AC catalyst on the transesterification reaction

	Triglyceride Reduction (%)		
Ce loading (wt.%)	**CT 500 °C**	**CT 700 °C**	**CT 1000 °C**
10	59.78	59.73	48.52
20	60.29	54.50	53.23
30	73.50	64.45	42.55

Effect of catalyst dosage

Catalyst dosage is another crucial factor that contribute to the higher conversion of FAME or biodiesel. From the previous findings, a variety of catalyst dosage affected the conversion percentage of biodiesel [16]. In this study, a range of 2 wt.% to 12 wt.% of Ce/Ca/AC catalyst was examined on the transesterification of low grade cooking oil. Based on the results, the ascending trend of triglyceride reduction or FAME conversion could be observed in Figure 4. The percentage yield from 2 wt. to 10 wt.% of FAME conversion was rapidly increased as catalyst provided more active sites for the transesterification reaction. 10 wt.% was considered as optimum catalyst dosage for reaching the

maximum conversion of FAME due to its possibility to contact more between solid catalyst and reactant during adsorption-desorption process. However, there was no increment when the catalyst dosage was beyond 10 wt.%, This was probably due to the catalyst reached its maximum catalyst loadings for the reaction and leaching effect start to occur.

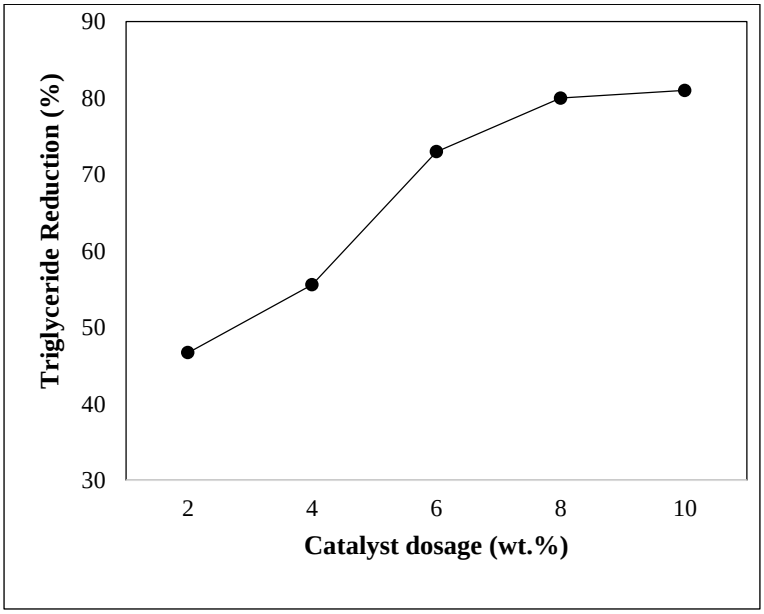


Figure 4. Effect of catalyst dosage on the reduction of triglyceride

Conclusion

As a conclusion, the optimum catalytic conditions for transesterification reaction was achieved with 30 wt.% of cerium on Ce/Ca/AC, calcined at 500 °C under the reaction conditions of 65 °C, 1:18 wt.% oil to methanol ratio, 6 wt.% catalyst loading and 3 hours of reaction time. Under these optimal conditions, almost 70% of FAME conversion was completed successfully. A high surface area of 149.18 m^2/g with needle-like shape and amorphous phase characteristics influenced the catalytic performance of Ce/Ca/AC towards transesterification reaction of low grade cooking oil.

Acknowledgement

The authors would like to acknowledge Universiti Kebangsaan Malaysia (UKM) for the financial support under Geran Galakan Penyelidik Muda (GGPM-2017-030).

References

1. Cai, Z. Z., Wang, Y., Teng, Y. L., Chong, K. M., Wang, J. W., Zhang, J. W. and Yang, D. P. (2015). A two-step biodiesel production process from waste cooking oil via recycling crude glycerol esterification catalyzed by alkali catalyst. *Fuel Processing Technology*, 137: 186-193.
2. Ezebor, F., Khairuddean, M., Abdullah, A. Z. and Boey, P. L. (2014). Esterification of oily-FFA and transesterification of high FFA waste oils using novel palm trunk and baggase-derived catalysts. *Energy Conversion and Management*, 88: 1143-1150.
3. Marinković, D. M., Stanković, M. V., Veličković, A. V., Avramović, J. M., Miladinović, M. R., Stamenković, O. O. and Jovanović, D. M. (2016). Calcium oxide as a promising heterogeneous catalyst for biodiesel production: Current state and perspectives. *Renewable and Sustainable Energy Reviews*, 56: 1387-1408.

4. Bankovic-Ilic, I., Miladinovic, M., Stamenkovic, O. and Veljkovic, V. (2017). Application of nano CaO-based catalysts in biodiesel synthesis. *Renewable & Sustainable Energy Reviews,* 72: 746-760.
5. Kesic, Z., Lukic, I., Zdujic, M., Mojovic, L. and Skala, D. (2016). Calcium oxide based catalysts for biodiesel production: A review. *Chemical Industry & Chemical Engineering*, 22(4): 391-408.
6. Kwong, T. L. and Yung, K. F. (2015). Heterogeneous alkaline earth metal–transition metal bimetallic catalysts for synthesis of biodiesel from low grade unrefined feedstock. *RSC Advances*, 5(102): 83748-83756.
7. Macala, G. S., Robertson, A. W., Johnson, C. L., Day, Z. B., Lewis, R. S., White, M. G. and Ford, P. C. (2008). Transesterification catalysts from iron doped hydrotalcite-like precursors: Solid bases for biodiesel production. *Catalysis Letters*, 122(3-4): 205-209.
8. Ullah, F., Dong, L., Bano, A., Peng, Q. and Huang, J. (2016). Current advances in catalysis toward sustainable biodiesel production. *Journal of the Energy Institute*, 89(2): 282-292.
9. Maneerung, T., Kawi, S., Dai, Y. and Wang, C.H. (2016). Sustainable biodiesel production via transesterification of waste cooking oil by using cao catalysts prepared from chicken manure. *Energy Conversion and Management,* 123: 487-497.
10. Marinković, D. M., Avramović, J. M., Stanković, M. V., Stamenković, O. S., Jovanović, D. M. and Veljković, V. B. (2017). Synthesis and characterization of spherically-shaped Cao/Γ-Al_2O_3 catalyst and its application in biodiesel production. *Energy Conversion and Management,* 144: 399-413.
11. Abeti, M., Wan Daud, W. M. A. and Aroua, M. K. (2009). Activity of solid catalysts for biodiesel production: A review. *Fuel Processing Technology,* 90(6): 770-777.
12. Warintorn T., Thawatchai M. and Sibudjing K., (2015). Highly active and durable Ca-doped Ce-SBA-15 catalyst for biodiesel production. *Energy*, 89: 946-956.
13. Abdullah, W. N. W., Azelee, W. A. W. A., Ali, R., Mokhtar, W. N. A. W. and Omar, M. F. (2017). Catalytic oxidative desulfurization technology of supported ceria based catalyst: Physicochemical and mechanistic studies. *Journal of Cleaner Production*, 162: 1455-1464.
14. Kamal, N. M., Bakar, W.A.W.A. and Ali, R. (2017). Catalytic optimization and physicochemical studies over Zn/Ca/Al_2O_3 catalyst for transesterification of low grade cooking oil. *Energy Conversion and Management,* 137: 113-120.
15. Rosid, S. J. M., Bakar, W. A. W. A. and Ali, R. (2015). Physicochemical study of supported cobalt–lanthanum oxide-based catalysts for Co_2/H_2 methanation reaction. *Clean Technologies and Environmental Policy*, 17(1): 257-264.
16. Wang, L. and Yang, J. (2007). Transesterification of soybean oil with Nano-MgO or not in supercritical and subcritical methanol. *Fuel*, 86: 328-333.

Malaysian Journal of Analytical Sciences, Vol 23 No 4 (2019): 667 - 676
DOI: https://doi.org/10.17576/mjas-2019-2304-13

MALAYSIAN JOURNAL OF ANALYTICAL SCIENCES
Published by The Malaysian Analytical Sciences Society
ISSN 1394 - 2506

UTILIZATION OF DEEP EUTECTIC SOLVENT (DES) AS POROGEN IN THE FABRICATION OF POLYMERIC MONOLITHIC CAPILLARY COLUMN

(Penggunaan Pelarut Eutektik Dalam (DES) Sebagai Porogen Dalam Fabrikasi Turus Kapilari Monolitik Polimerik)

Nabilah Suhaili[1], Lee Wah Lim[1]*, Takeuchi Toyohide[1], Rizafizah Othaman[2]

[1]Graduate School of Engineering, Faculty Engineering,
Gifu University, 1-1,Yanagido, Gifu-shi, 501-1193, Japan
[2]Faculty of Science and Technology,
Universiti Kebangsaan Malaysia, 43600 UKM Bangi, Selangor, Malaysia

**Corresponding author: lim@gifu-u.ac.jp*

Received: 31 April 2018; Accepted: 17 April 2019

Abstract

Deep eutectic solvents (DESs) from quaternary salts and hydrogen bond donors (HBDs) formation are widely known as an alternative for ionic liquid (IL) and commonly introduced in the synthesis of mesoporous materials. In this study, four types of choline chloride (ChCl) based DESs were prepared, and their utilization as porogens in fabricating methacrylate-based monolithic capillary columns was investigated. The selected DESs were prepared from different HBDs, including from organic acid (methacrylic acid MAA), alcohol (ethylene glycol EG), organic base (urea), and also combination of alcohol and organic base (EG and urea). This study found that the type of HBDs used have a crucial impact on the pore formation, and the results showed that DES A (ChCl:urea:EG) could effectively improve the structure of the monoliths and enhanced chromatographic separation for non-polar polycyclic aromatic hydrocarbons (PAHs). For repeatability evaluation using DES A in separation analysis, five PAHs achieved relative standard deviations (RSDs) of retention time in the range of 1.39 – 1.91%. Due to the lowest backpressure value (0.4 MPa) compared to other types of DESs, DES A that contained both HBDs from organic base and alcohol is believed to inherit both feature characteristics such as formation of through-pore and mesopore skeletal in monoliths column. A novel green stationary phase for separation of PAHs compounds was successfully synthesized using simple one-step polymerization with low cost and toxicity of DESs mixture as porogenic solvents instead of using traditional organic solvents.

Keywords: deep eutectic solvents, pore forming agent, monoliths, methacrylate, chromatography

Abstrak

Pelarut eutektik dalam (DESs) daripada pembentukan garam kuaternari dan penderma ikatan hidrogen (HBDs) dikenali secara meluas sebagai alternatif untuk cecair ionik dan biasanya diperkenalkan dalam pembuatan bahan mesoporos. Dalam kajian ini, empat jenis DESs berasaskan kolin klorida telah disediakan, dan penggunaannya sebagai porogen dalam fabrikasi turus kapilari monolit berasaskan metakrilat telah dikaji. DESs yang terpilih telah disediakan daripada HBDs yang berbeza, termasuklah daripada asid organik (asid metakrilik MAA), alkohol (etilena glikol EG), bes organik (urea) dan juga gabungan alkohol dan bes organik (EG dan urea). Kajian ini mendapati bahawa jenis HBDs yang digunakan memberikan impak penting ke atas pembentukkan liang dan hasil menunjukkan bahawa DES A (ChCl:urea:EG) boleh memperbaiki struktur monolit secara efektif dan memperbaiki pemisahan kromatografi hidrokarbon aromatik polisiklik (PAHs). Bagi ujian pengulangan menggunakan DES A dalam analisis pemisahan lima PAHs mencapai sisihan piawai relatif (RSDs) masa tahanan didalam lingkungan 1.39 – 1.91%. Disebabkan oleh nilai tekanan balik terendah (0.4 MPa) berbanding dengan jenis DESs lain, DES A yang mengandungi kedua-dua HBDs bes organik dan alkohol, dipercayai mewarisi kedua-dua ciri seperti pembentukan liang-liang dan rangka mesopor

dalam turus monolit. Fasa pegun hijau yang baru untuk pemisahan sebatian PAHs berjaya disintesis menggunakan pempolimeran satu langkah mudah dengan kos dan ketoksikan yang rendah campuran DESs sebagai pelarut porogenik daripada menggunakan larutan organik tradisional.

Kata kunci: pelarut eutektik dalam, agen pembentukan liang, monolit, metakrilat, kromatografi

Introduction

Due to increasing demand for green and sustainable analytical methods, many researchers have been using different attempts to improve and design environmentally friendly chemical processes and synthetic methodologies. Nowadays, preparation of porous polymer monolithic column aims to eliminate or reduce the use of hazardous and toxic chemicals at any stage of production in the industry or laboratory [1]. Organic solvents such as hexane, tetrahydrofuran, toluene, acetonitrile or methanol among the conventional solvents used as porogen due to dissolution ability, high boiling point and inertness. However, they are generally volatile, flammable, explosive and toxic for human beings, animals and plants. In addition, they also show acute and chronic toxicity, carcinogenicity, ecological toxicity and non-biodegradability [2]. To improve the protection of human health and the environment from the risks related with the use of hazardous organic solvents, substitution of these solvents with ones that show better Environmental, Health and Safety (EHS) properties are needed. One of the sustainable alternative solvents is deep eutectic solvents (DESs).

DESs have attracted considerable attention in the area of synthesis, electrochemistry, materials, biochemistry and separation [3-6] in recent years. Most type of DESs could be prepared handily, low volatility, high biodegradability and inexpensive. According to that, DESs have emerged as an interesting type of ionic liquid (IL) and have shown their usefulness as environmentally benign solvents and sustainable alternative to the conventional organic solvents in synthetic chemistry to increase efficiency of organic transformations [2]. Based on flexible structure of DESs which containing both an organic group and an anion, DESs might be a potential porogen and surfactant in the preparation of mesoporous polymer and siliceous materials. The application of DESs in preparation of mesoporous materials has been reported in several studies [7-10]. In 2016, Li et al. reported synthesis of mesoporous materials in choline chloride deep eutectic solvents by triblock copolymer-templated hydrothermal synthesis [8]. According to the research, DES-based mesoporous siliceous material with uniform pore structure and excellent stability were successfully produced. Herein, in this study, different types of DESs were used to investigate their effect on the porosity of the polymer monolith. To the best of our knowledge, it was the first time to use DESs as a porogen in preparation of methacrylate –based polymer monolithic column in capillary liquid chromatography (cLC).

There are some advantages of monolithic columns over packed columns, especially in capillary format, where the frits were absence. Also, due to the presence of macro-pores and meso-pores, lower backpressures were usually obtained and therefore higher flow rates could be applied. Based on the nature matrix chemistry, monolith columns can mainly be classified as organic polymer-based monolithic columns and silica-based monolithic columns [11]. Polymer-based monolithic columns have gained increasing attention in capillary liquid chromatography (cLC) and common capillary electro-chromatography (CEC) since they were first prepared in the early 1990s [12]. Polymer monoliths have feature that possess a large number of smaller pores, which furnishes them with a higher surface area thus leading to better separation efficiencies. Monolithic columns are often prepared by polymerization of functional monomers for generation of the chromatographic interaction sites, *via in situ* polymerization with a cross-linking agent, monomers and some porogens in a capillary tube [13].

The methacrylate polymers have received more attention than others in the diverse range of monolith materials. This can be accredited to their relatively ease of preparation, functionalization, and also ability to be fabricated with high degree of macro-porosity. Methacrylate is a term for any derivative of methacrylic acid, such as glycidyl methacrylate (GMA) and methyl methacrylate (MMA), which are common monomer precursors [14]. The epoxy group in GMA can be further modified and they have been processed successfully as the stationary for the separation of various compounds [15]. Due to the presence of carbonyl and ester bonds, methacrylates are moderately polar and in spite of the fact, they are popular and commonly used in reverse phase chromatography [14]. As a result of the mixed polar or non-polar groups and ease of preparation and functionalization, methacrylate

monoliths have been prepared for a number of different methods of chromatographic separation, such as ion exchange and hydrophilic interaction liquid chromatography (HILIC) [13].

Polycyclic aromatic hydrocarbons (PAHs) are organic compounds composed of two or more aromatic rings. PAHs are persistent, toxic and carcinogenic environmental pollutants and estimation of their toxicity can be challenging and time consuming due to the complexity of PAH-mixtures found in the environment. Due to that, the U.S Environmental Protection Agency (EPA) identified sixteen of PAHs as priority pollutants. Two common techniques are normally used to separate PAHs – gas chromatography (GC) and liquid chromatography (LC) [16]. In this study, separation and fractionation of five EPA's priority PAHs naphthalene, fluorene, anthracene, fluoranthene and pyrene were evaluated by methacrylate-based polymer monolith column in cLC.

The focus on this research is to synthesize a green methacrylate polymer monolith as stationary phase for cLC with emphasis on the two main goals of designing a monolith for LC application, i.e. optimizing the porous structure to allow the mobile phase to percolate through the monolithic bed by using DESs as a binary porogen with decanol and tailoring the surface chemistry to obtain the desired chromatographic separation of non-polar compounds polycyclic aromatic hydrocarbons (PAHs). The characterization of morphology and physical properties of the poly(GMA-PEGDMA) monolith capillary columns also have been investigated by using different types of DESs. Noteworthy to remember is that performance characteristics, such as stability, porosity and permeability, play a more important role in column performance in LC compared to CEC, because hydraulic pressure is used to drive the mobile phase. The main objective of this research is to synthesize a stationary phase for cLC which is green to environment by using simple step polymerization, low cost, low toxicity, and high efficiency for separation of non-polar compounds (PAHs).

Materials and Methods

Materials

Choline chloride (ChCl), 3-(trimethoxysilyl)-propylmethacrylate (γ-MAPS, 98%), poly(ethylene glycol) dimethacrylate (PEGDMA), methacrylic acid (MAA), 1-decanol, and ethylene glycol (EG) were purchased from Tokyo Chemical Industry (Tokyo, Japan). Anthracene, fluoranthene, fluorine, naphthalene, pyrene and urea were purchased from Nacalai Tesque Inc. (Kyoto, Japan). Glycidyl methacrylate (GMA, 95%), azobisisobutyronitrile (AIBN), acetonitrile (ACN, HPLC grade), methanol (MeOH, HPLC grade), acetone, 1 M hydrochloric acid and sulphuric acid were supplied by Wako Pure Chemical Industry, Ltd. (Japan). Bare fused silica capillary tubing (0.320 mm I.D., 0.450 mm O.D.) was supplied by GL Sciences Inc. (Tokyo, Japan).

The chromatographic measurements were carried out by using a cLC system that was constructed by an L.TEX 8301 Micro Feeder (LTEX, Corp., Tokyo, Japan) equipped with gas-tight syringe (0.5 mL; Ito, Fuji, Japan) as a pump, a model micro injection valve with an injection volume 0.2 μL (Upchurch Scientific, Oak Harbour, WA) as an injector, a 0.32 mm I.D. x 0.45 mm O.D. fused silica capillary column, a Model Detector UV-2075 (JASCO, Japan) and all data were collected by a CDS data processor (LASOFT, Chiba, Japan). Schematic diagram of a cLC laboratory-assembled instrumentation with a polymer monolithic column was shown in Figure 1. The morphology of the monolith was characterized by an SU-3500 scanning electron microscopy (SEM) purchased from Hitachi, Tokyo, Japan.

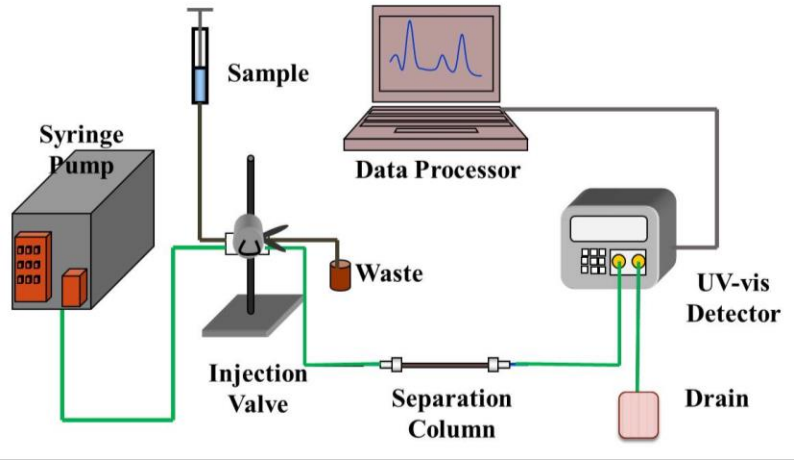


Figure 1. Schematic diagram of a capillary liquid chromatography (cLC) laboratory-assembled instrumentation with a polymer monolithic column

DESs preparation

The DESs were prepared by mixing the choline chloride (ChCl) as hydrogen bond acceptor (HBA) with the corresponding hydrogen bond donor (HBD) according to the molar ratio provided in Table 1. Four different types of DESs were used; DES A (ChCl: Urea: EG), DES B (ChCl: MAA), DES C (ChCl: EG), and DES D (ChCl: Urea). After weighing in the particular amounts of HBA and HBD in the 20 mL vial, the crimp cap was closed before the mixture was constantly stirred with a magnetic stirrer and heated at 80-90˚C until single clear liquid phase was formed [4]. The DESs were then stored in the desiccator prior used in this experiment as a binary porogen with decanol.

Preparation of poly(GMA-PEGDMA) monolithic capillary columns for PAHs

To obtain anchoring sites for the chemical grafting of the polymer at the inner wall of the capillary, the capillary was filled with 30% v/v of 3-trimethoxysilylpropyl methacrylate (γ-MAPS) in acetone after being rinsed with sodium hydroxide (NaOH), water, hydrochloric acid (HCl) for 45 min each. The silanization reaction was carried out in water bath at 60 ˚C for 24 hours and then capillary column washed and dried with acetone and nitrogen gas (N_2), respectively.

The poly(GMA-PEGDMA) monolith was prepared by one-step polymerization method, in which a polymerization mixture containing 12% v/v GMA, 20% v/v PEGDMA, 20% v/v DES and 45% v/v decanol as the binary porogenic solvents and 1% (w/v) AIBN (with respect to the total volume) as initiator was filled into a silanized capillary. After that, both ends of the capillary were sealed and it was placed in a water bath at 60 ˚C for 20 hours. The resulting monolith was carefully washed with acetonitrile (ACN) to eliminate the unreacted porogenic solvents and other soluble compounds [13].

For the preparation of poly(GMA-PEGDMA)-diol, the monolith capillary columns were flushed with 0.2 mol/L sulphuric acid (H_2SO_4) solution at room temperature for two hours to open the epoxide groups in order to form diols at the surface of the polymeric skeleton [17]. The resulting poly(GMA-PEGDMA)-diol monolith capillary column was then applied for determination and separation of non-polar compounds PAHs which are carcinogenic contaminants that produced as a by-product of combustion and normally found in drinking water, soils and sludge [16]. Five types of PAHs consist of 0.1% (w/v) of naphthalene, fluorine, anthracene, fluoranthene and pyrene were prepared for chromatographic separation.

Results and Discussion

DESs that were investigated in this experiment are based from the quaternary ammonium cation choline chloride (ChCl) which also known as cholinium cation. In comparison with imidazolium and pyridinium, this cation is nontoxic and has a comparatively low cost. It is classified as a pro-vitamin in Europe and is produced on the megaton scale as an animal feed supplement [4].

The selected DESs were prepared from different HBDs as shown in Table 1, and DES A with combination of choline chloride with urea and EG are first time reported and synthesized in this research. DESs are defined as combination of two or three safe and cheap components which are capable of self-association, through hydrogen bond interactions to form a eutectic mixture [18]. After heating at 80 °C for one hour and cool down to room temperature, the resulting molten salt were formed. By mixing ChCl with HBDs, a disruption on the crystalline structure of the quaternary ammonium salt was created which triggering a depression in the melting point and thus generating liquids at room temperature [18]. The cloudy formation of polymerization mixture of poly(GMA-PEGDMA) with DES B as porogen was observed and this result are believed due to its high viscosity compared to other types of DESs. Viscosity of binary eutectic mixture is essentially governed by hydrogen bonds, van der Waals and electrostatic interactions [2]. These types of DESs then are explored to determine their influence on the morphology and chromatographic performance of the poly(GMA-PEGDMA)-diol monolithic columns.

Table 1. The effects of four types of DESs on the performances of poly(GMA-PEGDMA)-diol monolithic columns

Column	DES (HBA : HBD)	Molar Ratio	Chromatographic Separation	Pressure (mPa)
DES A	ChCl : Urea : Ethylene Glycol	1 : 2 : 1	Good peak	0.4
DES B	ChCl : Methacrylic Acid	1 : 2	Peak overlapping	3.3
DES C	ChCl : Ethylene Glycol	1 : 2	Peak overlapping	1.5
DES D	ChCl : Urea	1 : 2	Peak overlapping	1.9

Characterization and evaluation of poly(GMA-PEGDMA) monolithic capillary columns

Morphological features of the poly(GMA-PEGDMA)-diol monolith were examined by scanning electron microscopy (SEM) at 250× and 1000× magnification.

Based on the wide-view images on Figure 2, a good monolith structure was formed on each type of the prepared columns and the monoliths were observed have attached tightly to the inner-wall of the capillary. The results indicated that the monoliths were covalently bonded to the capillary wall and this successful attachment was influenced by the pre-treatment step of the capillary column. Furthermore, it can be seen and observed from the SEM images, the monoliths and through-pores in the polymer skeletons are highly interconnected due to utilization of DES as porogen.

Li et al. has reported that the ChCl DESs with organic base-HBD (urea) and organic acid-HBD (acetic acid) interacted with PEG-PPG-PEG copolymer to shape the uniform mesoporous spheres [6]. The SEM images shown in Figure 2 proved this statement where the monolith materials synthesized with DES B (ChCl: MAA) and DES D (ChCl: urea) porogen, displays uniform mesoporous spheres with smaller interstitial porosity and skeletal structures. Furthermore, by using DES with alcohol-HBD (DES C) and organic base/alcohol-HBD (DES A) as porogen, larger micro-globular structures and larger number of through-pore skeletons were formed. The presence of through-pores and larger pores are very important in synthesis of monolith to prevent high backpressure during chromatographic separation and structural defects in the monolith, pump and tubing connection to cLC instrument [14]. Based on these results, it can be seen that different HBDs of DES may affect the particle morphologies of these mesoporous monolith formation and it can be concluded that, DES A (ChCl: urea: EG) that contained both organic base and alcohol HBDs are believed to inherit both feature characteristics such as through-pore and mesopore skeletal monoliths column.

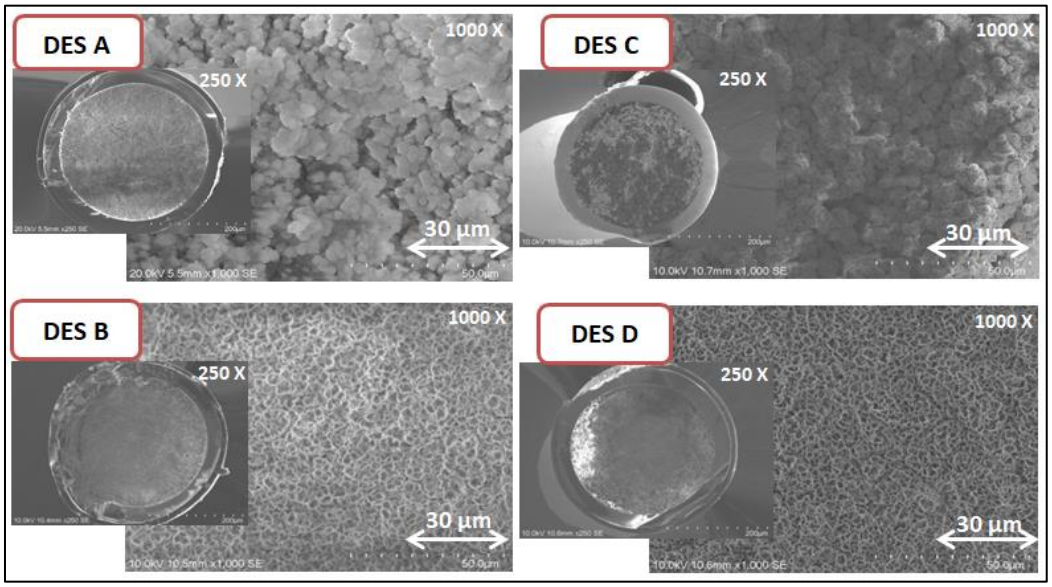


Figure 2. Wide-view (250×) and close-up-view (1000×) of scanning electron microscopy image of the poly(GMA-PEGDMA)-diol monolithic capillary columns with four types of DES; DES A (ChCl:urea:EG), DES B (ChCl:MAA), DES C (ChCl:EG), and DES D (ChCl:urea) respectively.

The poly(GMA-PEGDMA)-diol monolith was used in this experiment as stationary phase for the separation of non-polar compounds polycyclic aromatic hydrocarbons (PAHs). PAHs are consisted of fused aromatic rings, which are produced by incomplete combustion of carbon-containing fuels such as diesel and coal. Some of them are carcinogenic compounds and exist in a wide range of environmental matrices. Regarding to the toxic and carcinogenic properties of PAHs, the U.S Environmental Protection Agency (EPA) has identified sixteen of PAHs as priority pollutants and Figure 3 displays molecular structure of five out of sixteen EPA's priority pollutants of PAHs compounds that have been used in this experiment as analytes. These types of PAHs are highly hydrophobic, non-ionic and soluble in nonpolar organic solvents [19].

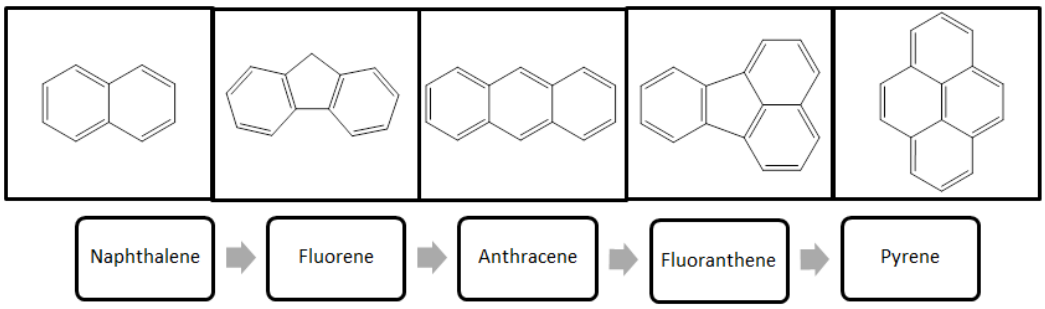


Figure 3. Molecular structure of 5 of the 16 EPA's priority PAHs and their elution order

Figure 4 shows four chromatograms of the prepared poly(GMA-PEGDMA)-diol monolith capillary columns by different types of DES as porogens on the separation of five typical PAHs with isocratic elution method. The diol groups at the surface of the polymer skeleton are expected to show separation ability towards polar compounds due to the specific interactions such as dipole–dipole and hydrogen bonding interactions [13]. acetonitrile mobile phase 70% that was used in this experiment is more polar than the stationary phase. Therefore, more polar compounds would theoretically migrate at higher rates through the column and elute first [16].

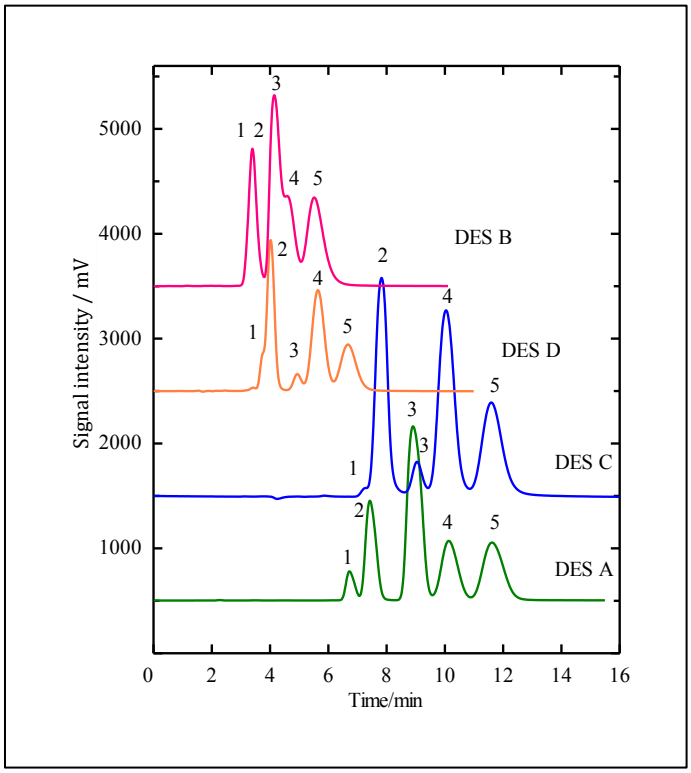


Figure 4. The effects of using four different types of DES as porogen on chromatographic separation of five types of PAHs. Poly(GMA-PEGDMA)-diol monolith column (100 x 0.32 mm I.D); Eluent, 70% acetonitrile (ACN); flow-rate, 3.0 µL/min; UV detection (λ), 254 nm; analytes, naphthalene (1), fluorene (2), anthracene (3), fluoranthene (4), pyrene (5) 0.1 % (w/v) each

PAHs were eluted in order of naphthalene, fluorene, anthracene, fluoranthene and pyrene according to their level of hydrophobicity in this experiment. When the elution process in reverse phase liquid chromatography (RP-LC) undergo either by isocratic condition or by gradient elution, the solute will be eluted in order of increasing molecular hydrophobicity [20]. Based on Pearlman et al., larger PAHs are generally more hydrophobic than the smaller ones [19]. Therefore, out of five PAHs used, the smaller 2-ringed naphthalene eluted first and pyrene that has larger four-ringed eluted last.

Furthermore, the chromatogram results show that different DESs may affect the chromatographic separation of non-polar compounds PAHs. By using DES C (ChCl: EG) as a porogen, only four clear sample peaks were appeared in chromatogram, while when using DES D (ChCl: urea), five peaks were appeared at short retention time but unable to be separated successfully. Interestingly, when using ternary DES A (ChCl: urea: EG), it can be observed from this chromatogram that five PAHs has been separated completely in reasonable retention time. The morphology of the monolithic column is an important parameter that can affect the efficiency of chromatographic separation. As

shown in Table 1, column DES A has the lowest back pressure (0.4 MPa) while column-DES B has the highest (3.3 MPa) when they were used at flow-rate 3 µL/min. The morphology shown in Figure 2 and the chromatography separation shown in the Figure 4 have proved that the DES A is the best porogen for the preparation of polymer monoliths column for the separations of PAHs in this experiment.

Reproducibility of poly(GMA-PEGDMA)-diol based DES A monolithic column

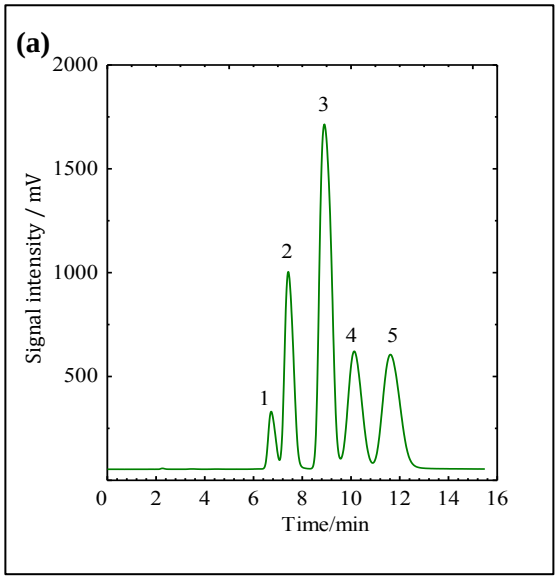
Due to the good results of poly(GMA-PEGDMA) based DES A monolithic column on surface morphology, lowest backpressure and good chromatographic separation, the column reproducibility was investigated further. The run-to-run repeatability of the retention time of PAH analytes was calculated under the same operating conditions for DES A-column. The relative standard deviations (RSDs) of the retention time of each PAHs used are shown in Table 2. The RSDs of the retention time for the four successive chromatographic runs under the optimum condition were in the 1.39% - 1.91% range. The RSD results for all five analytes PAHs were less than 2% and this showed that DES A-column had good repeatability.

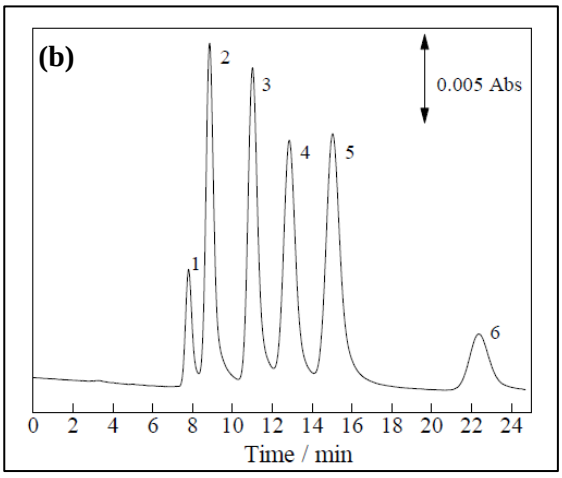
Table 2. Relative standard deviations (RSDs) of retention time (R_t) for four successive chromatographic runs under the optimum condition of DES A column

Peak	Naphthalene	Fluorene	Anthracene	Fluoranthene	Pyrene
R_t (min)	6.73	7.43	8.91	10.14	11.62
RSD (%)/(n=4)	1.41	1.39	1.53	1.72	1.91

Comparison on chromatographic separation between DES A and methanol as porogen

With the same polymerization mixture contents and porogen volume, comparison on chromatographic separation between utilization of DES 2 and methanol as porogen was evaluated and showed in in the following chromatogram (Figure 5). It was found that by replacing the traditional organic solvent (methanol) to the novel DES porogen (DES A), separation retention time and baseline separation were improved. This chromatogram shows that by using DES A (a) the chromatographic separation takes shorter retention time (13 minutes) while methanol (b) 18 minutes for separation of PAHs (reproduced from ref. [13] with permission).





Source: Linda et al. [13]

Figure 5. Chromatographic separation of PAHs using DES and methanol as porogen. Poly(GMA-PEGDMA)-diol monolith column, a) DES A, b) methanol (100 x 0.32 mm I.D); Eluent, 70% acetonitrile (ACN); flow-rate, 3.0 µL/min; UV detection (λ), 254 nm; analytes, naphthalene (1), fluorene (2), anthracene (3), fluoranthene (4), pyrene (5), benzo[a]pyrene (6), 0.1 % (w/v) each

Conclusion

It was found that, the type of HBD have a crucial impact on the pore formation, and the results showed that DES A (ChCl:urea:EG) with molar ratio 1:2:1 could effectively improve the structure of the monoliths and enhanced chromatographic separation for non-polar polycyclic aromatic hydrocarbons (PAHs) compare to other type of DESs. Based on the scanning electron microscopy (SEM) images of poly(GMA-PEGDMA) monolith columns, DES A porogen that contained both organic base and alcohol HBDs produced a monolith that inherited both feature characteristics such as through-pore and mesopore skeletal monoliths column. Furthermore, for repeatability evaluation of poly(GMA-PEGDMA)-diol for DES A-column, five PAHs achieved retention time relative standard deviations in the range of 1.39 – 1.91%. DES A-column also gives the lowest backpressure compare to other types of DESs with 0.4 MPa for PAHs separation. In comparison with methanol as porogen, chromatographic separation based on poly(GMA-PEGDMA)-DES A give better separation baseline and shorter retention time analysis. To the best of our knowledge, this is the first time that DESs were used as a porogen in the preparation of methacrylate-based polymer monolithic columns in cLC and for the first time DES A was synthesized. A novel green stationary phase for separation of PAHs compounds was synthesized successfully using simple step polymerization, low cost and toxicity of DESs mixture as porogenic solvents instead of traditional organic solvents.

Acknowledgement

The authors gratefully acknowledged the financial support from grant Gifu University, Japan and the facilities that was given to do this project. The acknowledgement also goes to Dr. Fusheng Li for his willingness to help in this research by making facilities available in River Basin Research Center, Gifu University.

References

1. Anastas, P. T. (1998). Green Chemistry: Theory and practice, J. Warner (Eds.). Oxford University Press, New York.
2. Khandelwal, S., Tailor, Y. K. and Kumar, M. (2016). Deep eutectic solvents (DESs) as eco-friendly and sustainable solvent/ catalyst systems in organic transformations. *Journal of Molecular Liquids*, 215: 345-386.
3. Durand, E., Lecomte, J. and Villeneuve, P. (2013). Deep eutectic solvents: Synthesis, application, and focus on lipase-catalyzed reactions. *European Journal of Lipid Science and Technology*, 115: 379.

4. Smith, E. L., Abbott, A. P. and Ryder, K. S. (2014). Deep eutectic solvents (DESs) and their applications. *Chemical Reviews*, 114: 11060-11082.
5. Garcia, G., Aparicio, S., Ullah, R. and Atilhan, M. (2015). Deep eutectic solvents: Physicochemical properties and gas separation applications. *Energy Fuel*, 29(4): 2616-2644.
6. Li, X., and Row, K. H. (2016). Development of deep eutectic solvents applied in extraction and separation. *Journal of Separation Science*, 39: 3505-3520.
7. Tang, B., and Row, K. H. (2015). Exploration of deep eutectic solvent-based mesoporous silica spheres as high-performance size exclusion chromatography packing materials. *Journal of Applied Polymer Science*, 2015: 44203.
8. Li, X., Lee, Y. R. and Row, K. H. (2016). Synthesis of mesoporous siliceous materials in choline chloride deep eutectic solvents and the application of these materials to high‐performance size exclusion chromatography. *Chromatographia*, 79: 375-382.
9. Zhang, L. S., Zhao, Q. L., Li, X. X., Li, X. X., Huang, Y. P. and Liu, Z. S. (2016). Green synthesis of mesoporous molecular sieve incorporated monoliths using room temperature ionic liquid and deep eutectic solvents. *Talanta*, 161: 660-667.
10. Zhang, J., Wu, T., Chen, S., Feng, P. and Bu, X. (2009). Versatile structure-directing roles of deep eutectic solvents and their implication in generating of porosity and open metal sites for gas storage. *Angewandte Chemie International Edition in English*, 48(19): 33486-3490.
11. Diaz-Bao, M., Barreiro, R., Miranda, J. M., Cepeda, A. and Regal, P. (2015). Recent advances and uses of monolithic columns for the analysis of residues and contaminants in food. *Chromatography*, 2: 79-95.
12. Tennikova, T. B., Belenkii, B. G. and Svec, F. (1990), High-performance membrane chromatography: A novel method of protein separation. *Journal of Liquid Chromatography*,13: 63-70.
13. Linda, R., Lim, L. W., Takeuchi, T. (2013). Methacrylate-based diol monolithic stationary phase for the separation of polar and non-polar compounds in capillary liquid chromatography. *Analytical Science*, 29: 631-635.
14. Groarke, R. J. and Brabazon, D. (2016). Methacrylate polymer monoliths for separation applications. *Materials*, 9(6): 446.
15. Dittmann, M. M., Masuch, K. and Rozing, G. (2000). Separation of basic solutes by reversed-phase capillary electrochromatography. *Journal of Chromatography, A*, 887: 209.
16. Sinioja, T. (2016). Development of a liquid chromatography method and fractionate EPA's 16 priority polycyclic aromatic hydrocarbons (PAHs). Project in Chemistry. Orebro University.
17. Wen, Y., and Feng, Y. Q. (2007). Preparation and evaluation of hydroxylated poly(glycidyl methacrylate-co-ethylene dimethacrylate) monolithic capillary for in-tube solid-phase microextraction coupled to high-performance liquid chromatography. *Journal of Chromatography A*, 1160: 90-98.
18. Liu, P., Hao, J. W., Mo, L. P., and Zhang, Z. H. (2015). Recent advances in the application of deep eutectic solvents as sustainable media as well as catalysts in organic reactions. *RSC Advances*, 5(60): 48675-48704.
19. Pearlman, R. S., Yalkowsky, S. H. and Banerjee, S. J. **(**1984). Water solubilities of polynuclear aromatic and heteroaromatic compounds. *Journal of Physical and Chemical Reference Data*, 13(2): 555-562.
20. Aguilar, M. I. (2004). HPLC of peptides and proteins methods and protocols: Reversed-phase high performance liquid chromatography. Springer: pp. 9-22.

Malaysian Journal of Analytical Sciences, Vol 23 No 4 (2019): 677 - 681
DOI: https://doi.org/10.17576/mjas-2019-2304-14

MALAYSIAN JOURNAL OF ANALYTICAL SCIENCES
Published by The Malaysian Analytical Sciences Society
ISSN 1394 - 2506

ISOLATION OF NEW ROTUNDONE FROM THE ROOTS OF *Croton hirtus* (EUPHORBIACEAE)

(Pemencilan Komponen Rotundona Terbaharu daripada Akar *Croton hirtus* (Euphorbiaceae))

Andi Rifki Rosandy [1], Anis Asmi Azman [1], Rozida Khalid[1], Rizafizah Othaman[1], Azwan Mat Lazim[1], Iqbal M. Choudary[2], Yana Maulana Syah[3], Jalifah Latip[1], Ikram M. Said[1], Muntaz Abu Bakar[1]*

[1]*Faculty of Science and Technology,*
Universiti Kebangsaan Malaysia, 43600 UKM Bangi, Selangor, Malaysia
[2]*Hussain Ebrahim Jamal Research Institute of Chemistry,*
University of Karachi, Karachi, 75270, Pakistan
[3]*Organic Chemistry Division, Faculty of Mathematics and Natural Sciences,*
Institut Teknologi Bandung, Jalan Ganesha 10, Bandung 40132, Indonesia

**Corresponding author: muntaz@ukm.edu.my*

Received: 31 March 2018; Accepted: 17 April 2019

Abstract

Croton is a genus of Euphorbiaceae which consists of approximately 1,300 species and are widely distributed in Asia, Africa and South America. Phytochemical study on the root of *Croton hirtus* has been conducted. The powder of the root of *C. hirtus* was extracted using the methanol solvent at room temperature for 24 hours and repeated three times. The crude extracts obtained were analysed using thin layer chromatography (TLC) then fractionated *via* vacuum column chromatography (VLC) and proceed the isolation using radial chromatography (RC) to get the pure compounds. The pure compounds obtained were elucidated by nuclear magnetic resonance (NMR), Fourier transform infrared (FT-IR) and mass spectroscopy to confirm their structures and from that analysis, the compounds were identified as two new compounds naming (+)5,14-dihydroxyrotundone-9-(2'-methybut-2'-enoate) (**1**) and (-)5,14-dihydroxyrotundane-9-benzoate (**2**) with total weight 135 mg and 145 mg respectively. This two compound were reported for this time on this genus.

Keywords: rotundone, euphorbiaceae, *Croton hirtus*

Abstrak

Croton merupakan genus dalam famili Euphorbiaceae yang mengandungi kira-kira 1,300 spesies dan taburannya meliputi Asia, Afrika dan Amerika Selatan. Kajian fitokimia ke atas akar *Croton hirtus* telah dijalankan. Serbuk akar *C. hirtus* diekstrak dengan menggunakan pelarut metanol pada suhu bilik selama 24 jam dan pengesktrakan diulang sebanyak tiga kali. Ekstrak mentah yang diperoleh dianalisis dengan menggunakan kromatografi lapisan nipis (KLN) kemudian difraksikan melalui kromatografi cecair vakum (KCV) dan pengasingan diteruskan dengan menggunakan kromatografi radial (KR) untuk mendapatkan sebatian tulen. Sebatian tulen yang diperoleh ditentukan oleh resonan magnetik nuklear (RMN), Inframerah transformasi Fourier (TFI) dan spektroskopi jisim untuk mengesahkan struktur mereka dan dari analisis itu, sebatian telah dikenal pasti sebagai dua sebatian baru yang diberi nama (+)5,14-dihidroksirotundona-9-(2'-metibut-2'-enoat) (**1**) and (-)5,14-dihidroksirotundana-9-benzoat (**2**) dengan jumlah berat masing-masing sebanyak 135 mg dan 145 mg. Kedua-dua sebatian ini dilaporkan buat kali pertama bagi genus ini.

Kata kunci: rotundona, euphorbiaceae, *Croton hirtus*

Introduction

Hairy croton or its scientific name *Croton hirtus* are a diverse and largest genus of ornamental plants with about 1,300 species that come from a family of Euphorbiaceae [1, 2]. Mostly, they can be found at Asia, Africa and some of it in North America [3]. Their species include shrubs, trees and herbs that distributed in tropical and subtropical region's ecosystems [4]. Saponins, terpenoids, steroids, phenols, tannins, alkaloids, flavonoids and anthroquinone are the bioactive secondary metabolites that rich in reddish or yellowish latex produced by croton species [5, 6]. Several species also contain aromatic compound, monoterpenoid, diterpenoid, sesquiterpenoids and shikimate – derived compounds due to its volatile oil constituents [7].

Previously, two new compounds from diterpenoid class, (-)5,8-dihydroxyjatrophan-3-one and (+)14,16,17-trihydroxykauran-1-on has been isolated from roots of same species, *Croton Hirtus* [8]. Asia, Africa and South America are among the countries that practiced used this species as their traditional medicine for many application [9, 10]. Biological and pharmacological activities of this genus species have been reported in the past study have played an important role to treat various diseases such as weight loss, anti-inflammatory, diabetes, hepatic disturbances, analgesic, gastrointestinal disturbances, cholesterol level, myorelaxant and cytotoxic [11, 12]. This paper describes NMR study of new rotundone from the roots of *Croton hirtus* species representative from Selangor, Malaysia.

Materials and Methods

The sample used in this research was the stem roots of *C. hirtus* which was collected from Tanjung Sepat, Banting, Selangor, Malaysia. Herbarium specimen of SM 461 was deposited at the Universiti Kebangsaan Malaysia Herbarium.

Extraction and isolation

Dried and ground roots of *C. hirtus* (415 g) were extracted with MeOH to give a dark green extract (18.25 g). The crude extract (18.25 g) was partitioned between $CHCl_3$ and water (1:1) after which the chloroform extract was further extracted with 10% *n*-hexane and 90% MeOH to give MeOH sub-extract. The sub-extract (3.52 g) was fractionated by using silica gel vacuum liquid chromatography eluted with increasing polarity of *n*-hexane-EtOAc to give ten fractions. The eluents that showed the same profile on thin layer chromatography (TLC) were combined to give four fractions (I-IV). Purification of fraction II (0.2027 g) was carried out using radial chromatography (RC) with silica gel plate of 1 mm thickness eluted with 60:40 *n*-hexane-EtOAc in 5% polarity increment to yield compound 1 (135 mg). Purification of fraction III (0.3163 g) was also carried out in a similar manner eluting with 1:1 *n*-hexane-EtOAc producing sub-fractions III^a-III^f. Sub-fraction (III^c= 0.0221 g) was further purified using RC with silica gel plate of **1** mm eluting with 30:70 *n*-hexane-EtOAc which resulted in the isolation of compound **2** (145 mg).

Analysis

The isolated compounds (**1** and **2**) were elucidated by means of Perkin-Elmer Lambda 35 UV-Vis (Waltham, MA, USA), Perkin-Elmer FT-IR (Waltham, MA, USA), Agilent Technologies GC-MS (Santa Clara, CA, USA) and one and two dimensioned nuclear NMR (Bruker, Billerica, MA, USA) spectroscopy. The proton NMR was recorded in 400 MHz while the carbon in 100 MHz. Chemical shift, δ, ppm recorded in $CDCl_3$.

Results and Discussion

(+)5,14-dihydroxyrotundone-9-(2'-methybut-2'-enoate**)** (**1**) was isolated as a clear needle crystal with molecular formula $C_{20}H_{32}O_4$, obtained by HR-CI–MS $[M+1]^+$ 337.2276 m/z, m.p. 123-125 $^{\circ}$C, and $[\alpha]_D^{25}$ +16.15 (*c* 1.30, $CHCl_3$). The IR spectra exhibited absorptions for hydroxyl groups (3347 cm^{-1}), cyclic aliphatic group (2958 and 2875 cm^{-1}), carbonyl group (1697 cm^{-1}) and double bond (1499 cm^{-1}).

The ^{13}C spectrum indicated the presence of 20 carbons consisting of four methyls, six methylenes, six methines and four quaternary carbons. The most highly deshielded signal at δ_C 168.1 (C-1`) integrated for carbon attributed to a carbonyl group, two signals for olefinic carbons at $\delta_C$ 128.8 (C-2`) and 137.3 (C-3`) are linked with two methyl carbons at $\delta_c$ 14.4 (C-4`) and 12.1 (C-5`), while the other five methine carbons at δ_c 59.8 (C-1), 49.1 (C-4), 44.4 (C-7), 76.5 (C-9) and 37.1 (C-11) belongs to five methylene carbons at δ_c 32.0 (C-2), 28.4 (C-3), 49.7 (C-6), 25.4 (C-8)

and 32.8 (C-2) are indicative of the aliphatic component of the cyclic system. The DBE value of $C_{20}H_{32}O_4$ is 5, indicating that the compound consists of two double bonds (one olefinics and one carbonyl) and three rings of aliphatic group. The ^{1}H-NMR spectrum showed 22 signals representing 32 protons. Twenty-two of the signals came from the three signals, four each from methyl group at H-4` (1.80, *d*, 7.0, 3H) and H-5` (1.84, *s*, 3H) bonded to an olefinic carbon at C-2` and C-3`, while the other two protons at H-13 (0.91, *d*, 6.6, 3H) and H-15 (0.89, *d*, 6.6, 3H) represent the two non- equivalent methyl protons in the cyclic aliphatic.

Furthermore, twelve signals at H-2 (2.03, *dd*, 14.0, 4.0, 1H & 1.42, *m*, 1H), H-3 (1.13, *m*, 1H & 1.89, *m*, 1H), H-6 (1.74, *d*, 7.0, 1H & 1.31, *m*, 1H), H-8 (2.20, *ddd*, 12.8, 12.4, 4.9, 1H & 1.75, *dd*, 12.8, 4.9, 1H), H-12 (1.50, *d*, 7.0, 1H & 1.22, *d*, 7.0, 1H) and H-14 (4.04, *d*, 11.0, 1H & 3.43, *d*, 11.0, 1H) represent the six non-equivalent methylene protons in the cyclic aliphatic while the other five signals at H-1 (1.46, *m*, 1H), 1.60, *m*, 1H), H-7 (0.79, *m*, 1H), H-9 (4.92, *dd*, 12.4, 4.9, 1H) and 1.15, *m*, 1H) represent the five methine protons (Figure 1).

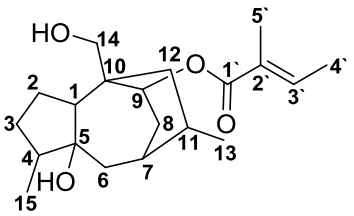


Figure 1. Chemical structure of **1**

The structure of the compound **1** was further confirmed using 2D NMR experiments including HMBC and COSY. From the HMBC experiments, the position of carbonyl carbon (C-1`) was proven by correlations of C-3` and C-9 toward C-1`. The proton H-15 in correlation with C-5 confirmed the position of this carbinol group bonded to C-5 and C-14 as branches to another one carbinol group. The H-H COSY experiment indicated that protons at δ_H 6.48 (1H, *dq*, *J*= 1.4, 7.0) and 1.80 (3H, *d*, *J*= 7.0) were related to each other and marked as olefinic (C-3`) and methyl protons at C-4`. Furthermore, correlation between saturated methines and methylenes protons was forming rotundone skeleton as main structure in this molecule (Figure 2).

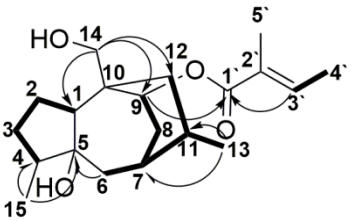


Figure 2. HMBC (→) and H-H Cosy (—) Correlation
Compound **1**

(-)5,14-dihidroxyrotundone-9-(2'-methylene-3'- hidroxybutanoate) (**2**) was isolated as pink olily and o.r. $[\alpha]_D^{25}$ - 27.14 (*c* 1.40, $CHCl_3$). The molecular formula is $C_{20}H_{32}O_5$, generated using HR-ESI-MS $[M + H]^+$ ion at m/z: 353.2217 (calc. for $C_{20}H_{32}O_5$ 353.2217). The FTIR spectral data displays broad absorbance peak at 3326 representing hydroxyl, 2985 and 2881 cm-1 representing the C-H (aliphatic cyclic). The presence of carbonyl group is characterized by absorbance bands, i.e. C=O stretch at 1716 cm^{-1} indicated that the carbonyl group linked with oxygen forming ester. Furthermore, Csp^2-H is characterized by absorbance at 1454-1401 cm^{-1}.

The ^{13}C spectrum contains 20 carbons consisting of three methyl, seven methylenes, six methines and four quaternary carbons. The most highly deshielded signals at δ_c 166.6 (C-1`) is attributed to carbonyl group linked with

another oxygen was formed ester group. Two signals of methine at δ_c 77.4 (C-9) provide information of the presence of a 2'-methylene-3'-hidroxybutanoate, while the other one (C-4) bind with an equivalent proton methyl (C-15). Carbons C-5, C-3` and C-14 represent the existence of carbinol groups in the molecule. The DBE value of $C_{20}H_{32}O_5$ is 5, indicating that the compound consists of two double bonds as carbonyl group and an olefinic group branch. Meanwhile, 23 proton signals representing 32 protons appeared in the ^{1}H-NMR spectrum. Twenty three of the signals came from the three signals, one each from a methyl group at H-4` (3H, 1.37, *d, J*= 6.3) bind with an oxymethine proton at H-3` (δ_H 4.96) are quartet, while an olefinic non-equivalent methylene protons at C-14. Furthermore, the other methine at δ_H 1.53 and 1.30 are multiplet, indicating it is adjacent to any carbons contain more than 4 total protons. The HMBC and H-H Cosy correlation of compound **2** show in Figure 3.

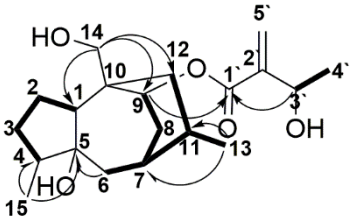


Figure 3. HMBC (→) and H-H Cosy (—) Correlation
Compound **2**

Conclusion

Two sesquiterpenoids; (+)5,14-dihydroxyrotundone-9-(2'-methybut-2'-enoate**)** (**1**) and (-)5,14-dihidroxyrotundone-9-(2'-methylene-3'- hidroxybutanoate) (**2**) were successfully isolated from the methanolic extract of *Croton hirtus*. To the best of our knowledge, this is the first report for both compounds from this species. Both of compounds can be used to carry out biological activities because this species was known as many useful in traditional medicine.

Acknowledgement

This research was funded by IRPA 09-02-0086-EA227, GGPM-2013-079 and FRGS/1/2014/SG01/UKM/02/5.

References

1. Berry, P. E., Hipp, A. L., Wurdack, K. J., Van Ee, B. and Riina R. (2005). Molecular phylogenetics of the giant genus Croton and tribe Crotoneae (Euphorbiaceae sensu stricto) using ITS and trnL-trnF DNA sequence data. *American Journal Botany*, 92: 1520-1534.
2. Berry, P. E., Van Ee, B. and Haber Elizabeth, A. (2011). Resolving the tangled identity of *Croton chrysodaphne* baill (Euphorbiaceae) in Madagascar. *Candollea*, 66: 113-118.
3. Webster, G. L. and Gillespie, L. (1994). Synopsis of the genera and suprageneric taxa of euphorbiaceae. *Annals Missouri Botanical Garden*, 81: 33-144.
4. Peixoto, R. N. S., Guilhon, G. M. S. P., Das Graças, B., Zoghbi, M., Araújo, I. S., Uetanabaro, A. P. T., Lourivaldo, S. S. and Brasil, D. D. S. B. (2013). Volatiles, a glutarimide alkaloid and antimicrobial effects of *Croton pullei* (Euphorbiaceae). *Molecules*, 18: 195-3205.
5. Da, Costa, Filho, L. O., de Moura, Silva, M. H., de Almeida-Cortez, J. S., da Silva, S. I, and Morais de Oliveira, A. F. (2012). Foliar cuticular n-alkane of some Croton species from Brazilian semiarid vegetation. *Biochemical Systematic Ecology*, 41: 13-15.
6. Sidney, G., De, L., Antônia, M. G. L. C., José, A. D. L., José M. M. N, Mariana, H. C. and Edilberto R. S. (2010). Fixed and volatile constituents of genus croton plants: *C. adenocalyx* baill - euphorbiaceae. *Review latinoamer química*, 38:133-144.
7. Suárez, A. I., Oropeza, M., Vásquez, L., Tillett, S. and Compagnone, R. S. (2011). Chemical composition of the essential oil of *Croton gossypiifolius* from Venezuela. *Natural Product Communication*s, 6(1): 97-99.
8. Rosandy, A. R., Azman, A. A., Khalid, R. M., Othaman, R., Lazim, A. M., Choudary, I. M., Syah, Y. M., Latip, J., Said. I. Md. and Bakar, M. A. (2018). New diterpenoids from the roots of *Croton hirtus* (Euphorbiaceae). *Malaysian Journal of Analytical Sciences*, 22(1): 64-71.

9. Nasib, A., Ali, K. and Khan, S. (2008). In vitro propagation of Croton *(Codiaeum varlegatum)*. *Journal Pakistan Botany*, 40: 99-104.
10. Júnior, F. E. B., De, Oliveira, D. R., Bento, E. B., Leite, L. H. I., Souza, D. O., Siebra, A. L. A., Sampaio, R. S., Martisn, A. O. P. B., Ramos, A. G. B., Tintino, S. R., Lacerda-Neto, L. J., Figueiredo, P. R. L., Oliveira, L. R., Rodrigues, C. K. S., Sales, V. S., Figueiredo, R. S. D. N., Nascimento, E. P., Monteiro, A. B., Costa, J. G. M., Coutinho, H. D. M,, Amaro, E. N., De Menezes, I. R. A. and Kerntopf, M. R. (2013). Antiulcerogenic activity of the hydroalcoholic extract of leaves of *Croton campestris* A. St.-Hill in rodents. *Evidence-based Complementary Alternative Medicine*, 2013: 1-10.
11. Salatino, A., Salatino, M. L. F. and Negri, G. (2007). Traditional uses, chemistry and pharmacology of Croton species (Euphorbiaceae). *Journal Brazil Chemistry Society*, 18: 11-33.
12. De Lima, S. G., Medeiros, L. B. P. and Cunha, C. N. L. C. (2012). Chemical composition of essential oils of *Croton hirtus* L'Her from Piauí (Brazil). *Journal Essential Oil Research*, 24: 371-376.

Malaysian Journal of Analytical Sciences, Vol 23 No 4 (2019): 682 - 689
DOI: https://doi.org/10.17576/mjas-2019-2304-15

MALAYSIAN JOURNAL OF ANALYTICAL SCIENCES
Published by The Malaysian Analytical Sciences Society
ISSN 1394 - 2506

PRELIMINARY INVESTIGATION OF LOW CURRENT FLASH SINTERING IN ZIRCONIA NANOPARTICLE COMPACT

(Kajian Awal Persinteran Kilat Arus Rendah dalam Nanopartikal Zirkonia Kompak)

Michiyuki Yoshida[1]*, Mitsuki Hada[1], Yutaka Shinoda[2], Osamu Sakurada[1], Fumihiro Wakai[2]

[1]Department of Chemistry and Biomolecular Science,
Gifu University, 1-1 Yanagido, Gifu-city 501-1193, Japan
[2]Laboratory for Materials and Structures,
Tokyo Institute of Technology, 4259 Nagatsuta Midori-ku Yokohama-city,226-8503, Japan

**Corresponding author: myoshida@gifu-u.ac.jp*

Received: 31 March 2018; Accepted: 17 April 2019

Abstract

Flash sintering is a newly developed technique to quickly densify conductive ceramics in the presence of an electric field. At a critical combination of field and temperature, densification takes place in a few seconds. In this paper, the feasibility of the densification in flash sintering with low current was investigated in the newly developed compact consisted of zirconia nanoparticles. Homogeneous microstructure with densely packing of nano-particles was successfully obtained by gel-casting of nano-suspension. The grain size and relative density of the sample flash sintered at 30 mA/mm^2 were 40.9 nm and 86.8%, respectively. The sample densified with limited grain growth in low current flash sintering. Although the full densification was not achieved in the present study, the effectiveness of the nanoparticle compact to reduce the current for the densification during flash sintering was shown by comparing the results reported in flash sintering with the coarser microstructure.

Keywords: zirconia, flash sintering, gel-casting

Abstrak

Pensinteran kilat merupakan satu teknik yang baru dibangunkan untuk mempercepatkan pemampatan seramik konduktif dalam kehadiran medan elektrik. Pada kombinasi kritikal antara medan dan suhu, densifikasi berlaku dalam beberapa saat. Dalam manuskrip ini, keberhasilan densifikasi dalam pensinteran kilat pada arus rendah telah dikaji dalam kompak yang baru dibangunkan terdiri daripada zirkonia nanopartikel. Struktur mikro homogen dengan pengisian padat partikel nano telah berjaya dihasilkan menggunakan acuan gel ampaian nano. Saiz butir dan ketumpatan relatif sampel bersinter pada 30 mA/mm^2 masing-masing adalah 40.9 nm dan 86.8%. Sampel telah dimampatkan dengan pertumbuhan butiran yang terhad di dalam arus pensinteran kilat yang rendah. Walaupun pemampatan penuh tidak dapat dicapai di dalam kajian ini, namun keberkesanan kompak nanopartikel untuk merendahkan aliran arus pemampatan ketika pensinteran kilat telah dapat dilihat dengan membandingkan hasil laporan pensinteran kilat ketika struktur mikro yang lebih besar dijalankan.

Kata kunci: zirkonia, pensinteran kilat, acuan gel

Introduction

Sintering refers to the process of firing and consolidating a body shaped from powder particle, and is originated from the fabrication of the pottery. During the sintering process, inter-particle pores in the green body are eliminated by atomic diffusion driven by capillary forces. A variety of sintering techniques, such as normal sintering, hot isostatic or uniaxial pressing has been applied in the production of ceramic materials. During the last

10–15 years, field assisted sintering (FAST) and microwave sintering have grown as a consequence of advantages including higher heating, cooling rates and lower sintering temperatures, compared with the traditional techniques. Quite recently, "Flash Sintering", as an extremely fast sintering method, has attracted much interest since it was first reported by Cologna et al. in 2010 [1]. In their original report, a DC electric field is applied to a sample (3 mol% Y_2O_3-stabilized ZrO_2) while it is heated in a conventional furnace and at a certain furnace temperature the densification takes place in a few seconds. Flash sintering has now been demonstrated with a wide range of different ceramics with submicron or micrometer scale microstructure [2-9].

One of the confirmed obstacles to achieve the industrialization of flash sintering is the homogeneous heating of the sample. In flash sintering, the final specimen temperature achieved, which can be expected to determine the extent of sintering, is controlled primarily by the limiting current in the power supply. However, too high a limiting current gives more scope for temperature gradients and catastrophic localization of the current[10]. For practical application of flash sintering, therefore, more sophisticated powder technology, which allow low currents to obtain the homogeneous heating of the sample. It is well known that the sinterability is expected to be improved for applying nanoparticles as a starting material. The green body consisted with nano-particles is expected to be densified by flash sintering with the homogeneous heating in low current.

Recently, our group successfully fabricated the densely packed green body by gel-casting of zirconia nano-suspension [11]. The initial compact prepared by the gel-casting in our study had the densely packed structure with a narrow pore size distribution. Almost fully dense sample with 99.5% of theoretical density was successfully obtained by the pressureless sintering at 1100 °C, which is 300 °C lower than that prepared by conventional process. In this work, the feasibility of the densification in flash sintering with low current was investigated in the newly developed zirconia nanoparticle compact.

Materials and Methods

In this study, the green body consisting of 3mol% yttria stabilized zirconia (3YSZ) nanoparticle was prepared by gel-casting. 3YSZ nano-suspension with the average particle size of 16 nm (MEL Chemicals Ltd., U.K.) was used as the starting material. The solids loading of the starting suspension measured by gravimetric analysis was 7.0 vol%. The as-received suspension with weak acidic pH of 2.7 was modified by adding tetra methyl ammonium hydroxide (Sigma-Aldrich, U.S.A) to pH 9.5 for the complete dissociation of citrate. Subsequently, 4.5 wt.% of triammonium citrate (99% purity, Kanto Chemical Co. Inc., Japan) was added as the dispersant. 0.6 wt.% of agarose (LM, Kanto Chemical Co. Inc., Japan) was added to the prepared suspension as the gelling agent. The zirconia suspension was heated before adding agarose and kept at a temperature of 80 °C in a closed vessel. The prepared suspension was casted to a plastic mold. After one week drying, the green body was calcined at the temperature of 650 °C for decomposing organic additions. The calcined sample with cylindrical shape was machined to have a dimension of φ4.5 mm×3.8mm for flash sintering.

The sample was sintered in a vertical split furnace fixed on a universal testing machine (AG-I, Shimadzu Co., Kyoto, Japan). The sample was initially heated in the furnace at a rate of 20 °C /min to 500 °C and then at 10 °C /min. A schematic illustration of the experimental setup for flash sintering is shown in Figure 1. Platinum electrodes on top and bottom of the sample ensured the application of the electrical field. These electrodes were maintained between alumina disks and specimen under a constant load of 10 N (~0.6 MPa). The constant electric field, E = 60 V cm^{-1} was applied by a commercial DC power source (ZX-400HN, Takasago Ltd, Kawasaki, Japan) from the start of heating. The current limit, at which the power supply switched from voltage control to current control, was set to 30 mA/mm^2, which was 4 times lower than the reported value of 120mA/mm^2 to reach the full densification in flash sintering with submicron microstructure [12]. The voltage across the Platinum electrodes and the current passing through the sample were measured using digital multimeters. After switching form voltage control to current control, the electric field was loaded on the sample for 10sec, and then the furnace was switched off to cool it down. Relative density of the flash sintered sample was calculated using Archimedes' method by taking 6.10 g/cm^3 as the theoretical density of tetragonal zirconia. Microstructure of the sample was observed from the fractured surfaces. The samples were coated with osmium and observed by scanning electron microscope (Model S4800, Hitachi Co., Japan). The equivalent circle diameter measured by the image analysis of SEM photographs was defined as the grain size.

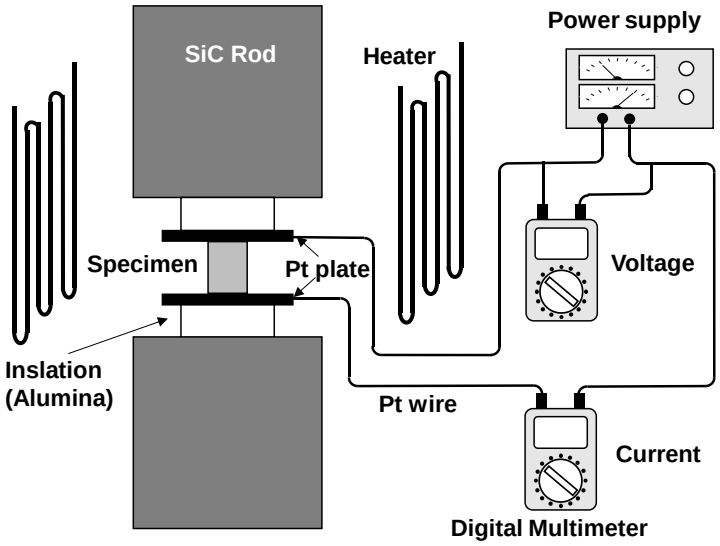


Figure 1. Schematic illustration of the experimental set up for flash sintering

Results and Discussion

Initial compact

The photograph of the gel-casted sample after drying is shown in Figure 2. After complete drying, no micro cracking and uniform shrinkage in a radial direction were observed. Figure 3 shows the FE-SEM micrograph for the fractured surface of the sample calcined at 650 °C. The grain size and relative density for the calcined sample were 28 nm and 52%, respectively. The calcined compact had a very narrow pore size distribution, and the average pore size was 15 nm. Homogeneous microstructure with densely packing of nano-particles was successfully obtained by slip-casting of nano-suspension.

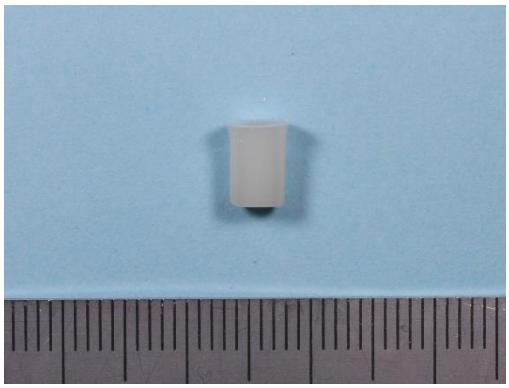


Figure 2. Photograph of the gel-casted sample

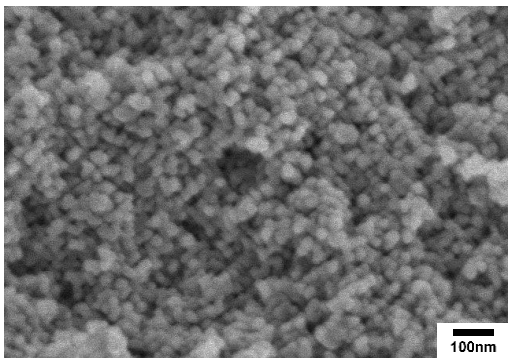


Figure 3. Fractured surface for the gel-casted sample calcined at 650 °C

General features of flash sintering

Current, voltage, resistance and power versus furnace temperature graphs during flash sintering are shown in Figure 4. The current rises slowly at first and then more rapidly until it reaches a pre-programmed limit (Figure 4(a)). The rapid increase in current at constant voltage shows that the specimen resistance was decreasing

throughout the process, as shown in Figure 4(c) so that the switch to current control results in a power spike (Figure 4(d)). These features demonstrate that the original results reported in the literature were successfully reproduced in this study. On the other hand, the observed width of the power spike in Figure 4(d) was about 150 sec, which was much longer than that reported in the literature (several seconds).

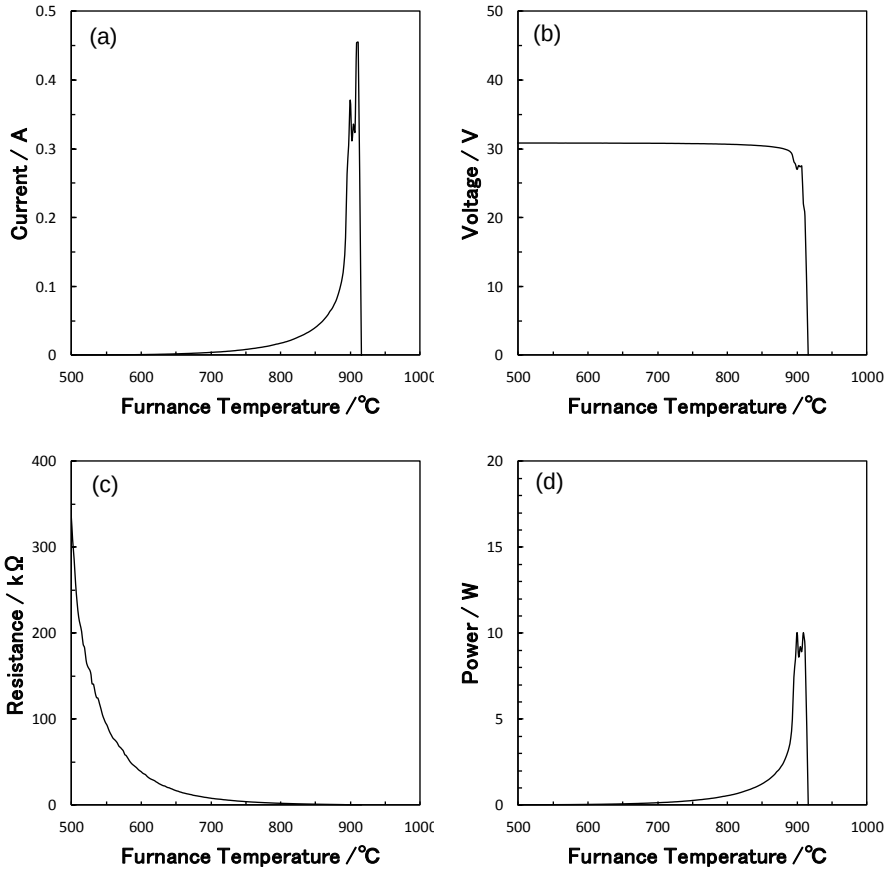


Figure 4. Current, voltage, resistance and power versus furnace temperature graphs during flash sintering

In the previous works, the connection between the electrodes and the specimen was made by inserting the electrodes through the holes in the specimens. This resulted in the improvement of the contact between the Pt and the specimen due to local melting/sintering around the contacts [13]. On the other hand, in this study, the contact between the electrodes and the sample was maintained by holding with SiC rods under a constant load of 10 N as shown in Figure 1. In this case, the rapid densification during flash sintering resulted in the poor contact between the electrode and the sample. This might cause an inhibiting effect on the runaway Joule heating and widen the width of the power spike in this study.

Specimen temperature and densification

The specimen temperature can rise considerably above the furnace temperature from Joule heating. We obtained an analytical estimate on the assumption of a uniform sample temperature, T_S, from the black body radiation model based on the Stefan-Boltzmann law [14]. According to this model, the sample temperature at steady state can be expressed as follows:

$$T_s = \left(T_0^4 + \frac{W}{A\varepsilon\sigma_s}\right)^{1/4} \quad (1)$$

where T_0 is the furnace temperature, W is the electrical power dissipated, A is the instantaneous surface area, ε is the emissivity and σ_s is Stefan–Boltzmann constant. The height of the specimens deduced from the displacement was used for calculating A in this case; it was assumed that the cross section of the specimen was constant during the test. The choice of emissivity is particularly problematic as it can be expected to vary with density during sintering as well as with surface roughness, wavelength and temperature. In this study, a value of 0.7 was chosen, based on the measurements of Tanaka et al. [15] on sintered zirconia. The relationship between the furnace temperature and the specimen temperatures calculated from eq. (1) are given in Figure 5(a). The dotted line in Figure 5(a) indicates the specimen temperature for no Joule heating, in which the specimen temperature is exactly same as the furnace temperature. The specimen temperature started to increase with Joule heating at around the furnace temperature of 600 °C, and then rapidly increased to reach 1270 °C at the furnace temperature of 880 °C. The displacement versus furnace temperature is shown in Figure 5(b), where the crosshead displacement was corrected with subtracting the thermal expansion of the SiC rods. The shrinkage of the specimen started to increase at the furnace temperature of 700 °C. The rapid densification was observed at the furnace temperature of 850 °C and was coincided with the rapid Joule heating of the sample apparently from Figure 5(a).

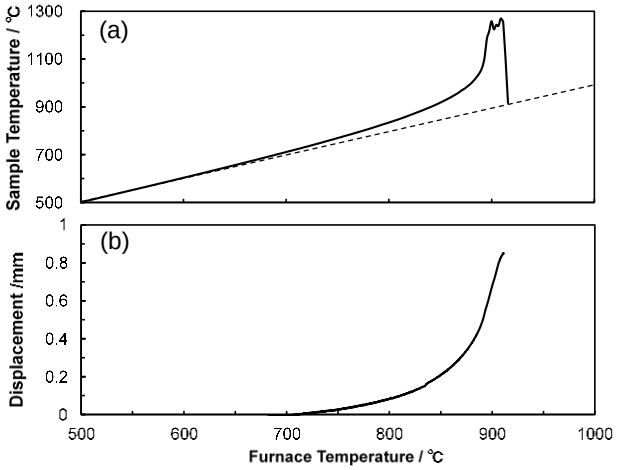


Figure 5. Sample temperature and displacement *vs* furnace temperature graphs during flash sintering

Microstructure

The micrograph for the fractured surface of the sample after flash sintering is shown in Figure 6. The grain size and relative density for the flash sintered sample were 40.9nm and 86.8%, respectively. In the case of the sample with submicron microstructure, the almost same density as in this study was obtained under the current of 60 mA/mm^2, which was twice as high as in this study [12]. This indicates that the nanoparticle compact reduces the current for the densification during flash sintering.

Average grain size is plotted as a function of density in Figure 7. For comparison, the results of normal sintering of gel casted sample [11], in which the samples were heated at the sintering temperatures for 2 hours, were also plotted in Figure 7. In normal sintering, the grain size increased with increasing the density. The hindered grain growth up to around 90% was shown in Figure 7. Subsequently, the exaggerated grain growth was observed at a density higher than 90% in which the relationship between grain size and relative density was parabolic. The transition from insignificant grain growth to rapid grain growth at around 90% density is believed to change from open to closed porosity, and this is the typical sintering behavior reported in the literature [16]. As shown in Figure 7, the result of flash sintered sample is in the region under a curve corresponding to the results of the normal sintering. This indicates that zirconia nanoparticle compact densified with limited grain growth in low current flash sintering.

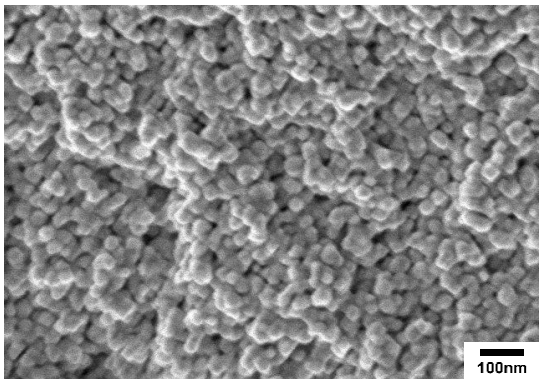


Figure 6. Fractured surface for the flash sintered sample at 30mA/mm^2

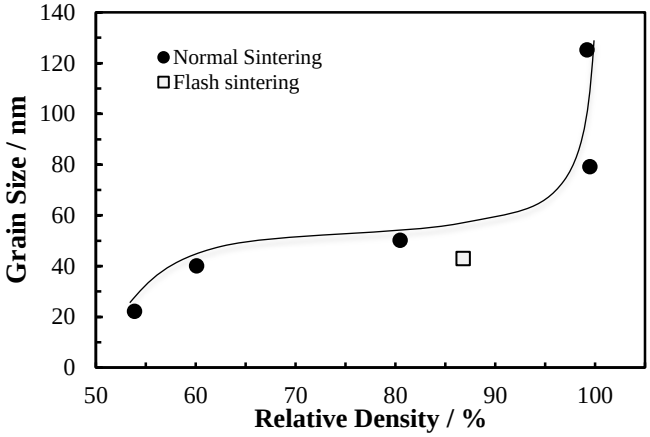


Figure 7. The relationship between relative density and grain size of the flash sintered sample. Results for normal sintered samples are plotted for comparison

The mechanisms responsible for flash sintering remain open to question [17, 18]. Recently, some researchers have shown that the power surge can be explained satisfactorily as thermal runaway resulting from the negative temperature coefficient of resistivity of most ceramics [10, 19, 20] whilst comparison with the sintering of powder compacts rapidly heated without an electric field suggests that the high densification rate may be at least in part a consequence of the fast heating in flash sintering [21]. Maximum heating rate observed in this study was 360 ◦C/min, which is 36 times higher than set up heating rate for the furnace, and comparable to that reported in the literature [21].

Although the full densification was not achieved, zirconia nanoparticle compact, obtained from gel-casting of nano-suspension, densified with the limited grain growth in low current flash sintering, and reduced the current for the densification during flash sintering. The optimization of the condition for the electrical loading, such as voltage and current set up in the power supply, is necessary to achieve the full densification of the nanoparticle compact.

Conclusion

In this study, we prepared the zirconia nanoparticle compact by gel-casting and demonstrated flash sintering. The conclusions obtained are summarized as follows: (1) Homogeneous microstructure with densely packing of nano-particles was successfully obtained by slip-casting of nano-suspension. The grain size and relative density of the

compact were 28nm and 52%, respectively. The sample had a very narrow pore size distribution with average pore size of 15nm, (2) While the original results reported in the literature were successfully reproduced in this study. the observed width of the power spike in this study was about 150 sec, which was longer than that reported in the literature (several seconds), (3) The grain size and relative density of the sample flash sintered at 30 mA/mm^2 were 40.9nm and 86.8%, respectively. The sample densified with limited grain growth in low current flash sintering. Although the full densification was not achieved in the present study, the effectiveness of the nanoparticle compacts to reduce the current for the densification during flash sintering was shown by comparing the result reported in flash sintering with the coarser microstructure.

Acknowledgement

This work was supported (in part) by the Collaborative Research Project of Materials and Structures Laboratory, Tokyo Institute of Technology.

References

1. Cologna, M., Rashkova, B. and Raj, R. (2010). Flash Sintering of Nanograin Zirconia in < 5 s at 850°C. *Journal of American Ceramic Society*, 93(11): 3556-3559.
2. Prette, A. L. G., Cologna, M., Sglavo, V. and Raj, R. (2011). Flash-sintering of Co_2MnO_4 spinel for solid oxide fuel cell applications. *Journal of Power Sources*, 196(4): 2061-2065.
3. Gaur, A. and Sglavo, V. M. (2014). Densification of $La0._6Sr_{0.4}Co_{0.2}Fe_{0.8}O_3$ ceramic by flash sintering at temperature less than 100 °C. *Journal of Material Sciences*, 49(18): 6321-6332.
4. Karakuscu, A., Cologna, M., Yarotski, D., Won, J., Francis, J. S. C., Raj, R. and Uberuaga, B. P. (2012). Defect structure of flash-sintered strontium titanate. *Journal of American Ceramic Society*, 95(8): 2531-2536.
5. Cologna, M., Francis, J. S. C. and Raj, R. (2011). Field assisted and flash sintering of alumina and its relationship to conductivity and MgO-doping. *Journal of European Ceramic Society*, 31(15): 2827-2837.
6. Muccillo, R. and Muccillo, E. N. S. (2014). Electric field-assisted flash sintering of tin dioxide. *Journal of European Ceramic Society*, 34(4): 915-923.
7. Zapata-Solvas, E., Bonilla, S., Wilshaw, P. R. and Todd, R. I. (2013). Preliminary investigation of flash sintering of SiC. *Journal of European Ceramic Society*, 33(13-14): 2811-2816.
8. Candelario, V. M., Moreno, R., Todd, R. I. and Ortiz, A. L. (2017). Liquid-phase assisted flash sintering of SiC from powder mixtures prepared by aqueous colloidal processing. *Journal of European Ceramic Society*, 37(2): 485-498.
9. Yoshida, H., Sakka, Y., Yamamoto, T., Lebrun, J. M. and Raj, R. (2014). Densification behaviour and microstructural development in undoped yttria prepared by flash-sintering. *Journal of European Ceramic Society*, 34(4): 991-1000.
10. Todd, R. I., Zapata-Solvas, E., Bonilla, R. S., Sneddon, T. and Wilshaw, P. R. (2015). Electrical characteristics of flash sintering: thermal runaway of Joule heating. *Journal of European Ceramic Society*, 35(6): 1865-1877.
11. Yoshida, M. Takeno, S. and Sakurada, O. (2016). Fabrication of translucent tetragonal zirconia by gelcasting of thin zirconia nano-slurry. *Journal of Ceramic Society of Japan*, 124(5): 500-505.
12. Francis, J. S. C. and Raj, R. (2013). Influence of the field and the current limit on flash sintering at isothermal furnace temperatures. *Journal of American Ceramic Society*, 96(9): 2754-2758.
13. Yoshida, M., Falco, S. and Todd. R. I. (2018). Measurement and modelling of electrical resistivity by four-terminal method during flash sintering of 3YSZ. *Journal of Ceramic Society of Japan*, 126(7): 579-590.
14. Raj, R. (2012). Joule heating during flash-sintering. *Journal of European Ceramic Society*, 32(10): 2293-2301.
15. Tanaka, H. Sawai, S., Morimoto, K. and Hisano, K. (2001). Measurement of spectral emissivity and thermal conductivity of zirconia by thermal radiation calorimetry. *Journal of Thermal Analytical Calorimetry*, 64(3): 867-72.
16. Mazaheri, C., Valefi, M., Hesabi, Z. R. and Sadrnezhaad, S. K. (2009). Two-step sintering of nanocrystalline $8Y_2O_3$ stabilized ZrO_2 synthesized by glycine nitrate process. *Ceramics International*, 35(1): 13-20.
17. Raj, R., Cologna, M., Francis, J. S. C. (2011). Influence of externally imposed and internally generated electrical fields on grain growth, diffusional creep, sintering and related phenomena in ceramics. *Journal of American Ceramic Society*, 94(7): 1941-1965.
18. Naik, K. S., Sglavo, V. M. and Raj, R. (2014). Flash sintering as a nucleation phenomenon and a model thereof. *Journal of European Ceramic Society*, 34(15): 4063-4067.

19. Zhang, Y. Y., Jung, J. I. and Luo, J. (2015). Thermal runaway, flash sintering and asymmetrical microstructural development of ZnO and ZnO–Bi_2O_3 under direct currents. *Acta Materialia*, 94: 87-100.
20. Bichaud, E., Chaix, J. M., Carry, C., Kleitz, M. and Steil, M. C. (2015). Flash sintering incubation in Al_2O_3/TZP composites. *Journal of European Ceramic Society*, 35(9): 2587-2592.
21. Ji, W., Parker, B., Falco, S., Zhang, J. Y., Fu, Z. Y. and Todd, R. I. (2017). Ultra-fast firing: Effect of heating rate on sintering of 3YSZ, with and without an electric field. *Journal of European Ceramic Society*, 37(6): 2547-2551.

Malaysian Journal of Analytical Sciences, Vol 23 No 4 (2019): 690 - 702
DOI: https://doi.org/10.17576/mjas-2019-2304-16

MALAYSIAN JOURNAL OF ANALYTICAL SCIENCES
Published by The Malaysian Analytical Sciences Society
ISSN 1394 - 2506

SYNTHESIS AND BINDING PROPERTIES OF TERT-BUTYL AMIDE MACROCYCLES FOR PSEUDOROTAXANES FORMATION

(Sintesis dan Sifat Pengikatan Makrosiklik Tetrabutil-Amida bagi Penghasilan Pseudorotazen)

Nurul Izzaty Hassan[1]* and Douglas Philp[2]

[1]Center for Advanced Material & Renewable Resources,
Faculty of Science and Technology
Universiti Kebangsaan Malaysia, 43600 UKM Bangi, Selangor, Malaysia
[2]Department of Chemistry,
Northwestern University, 2145 Sheridan Road, Evanston, IL 60208-3113, USA

**Corresponding author: drizz@ukm.edu.my*

Received: 31 March 2018; Accepted: 17 April 2019

Abstract

The tert-butyl amide macrocycle containing ethylene glycol moiety (cMDG) was constructed starting from 5-tert-butylisophthalic acid **1** which was activated to acid chloride derivative **2** using thionyl chloride in toluene. Further, the synthesis of the second macrocycle based on pyridine framework (cMP) was achieved in similar way before coupled to the diamine derivative **4**. Following that, the compound's electronic structure was calculated using simple molecular mechanics calculation to represent the preferable conformation of these macrocycles. In order to evaluate the influence of the benzene ring in the framework of both macrocycles to complex the guests, the following binding experiments were carried out with the synthesized maleimide **5** and CF_3 maleimide **6**. An equimolar mixture of macrocycle cMDG and maleimide **5** or **6** in $CdCl_3$ was prepared and analysed by ^1H and ^{19}F NMR spectroscopy, respectively. The similar binding experiments were then carried out with macrocycle cMP. The association constant, K_a for the complexation of pseudorotaxane [cMDG·5] and [cMP·5] were estimated to be 190 ± 20 M^{-1} and 160 ± 20 M^{-1}, respectively. On contrary, the association constant for the complexation of pseudorotaxane [cMDG·6] and [cMP·6] complexes were enhanced with a K_a value of 1000 ± 100 M^{-1} and 460 ± 50 M^{-1} at 25 °C in $CdCl_3$. In addition, the ^1H and ^{19}F NMR spectra of these macrocycles and maleimides showed complexes are in slow exchange on the ^1H NMR chemical shift timescale. This can be attributed to significant binding events of pseudorotaxane complexes, compare to the free species observed in isolation. In the case of slow exchange, the K_a was determined using the single-point method.

Keywords: macrocylic, ethylene glycol, pyridine, pseudorotaxane

Abstrak

Makrosiklik tetra-butil amida yang mengandungi moieti etilena glikol (cMDG) disintesis bermula dari pengaktifan asid 5-tetrabutilisoftalik **1** kepada sebatian asid klorida **2** menggunakan tionil klorida dalam pelarut toluena. Sebatian perantara ini kemudiannya ditambah kepada sebatian bis amina **3** untuk menghasilkan makrosiklik cMDG melalui sintesis pencairan tinggi. Selain itu, sintesis makrosiklik kedua berasaskan kerangka pyridina (cMP) turut dicapai melalui cara yang sama sebelum ditambah kepada sebatian terbitan diamina **4**. Berikutan itu, struktur elektronik makrosiklik dikira menggunakan pengiraan molekular mekanik asas bagi mendapatkan gambaran konformasi yang sesuai. Untuk menilai pengaruh gelang benzena dalam moeiti makrosiklik untuk pengkompleksan dengan tetamu, kajian pengikatan telah dijalankan menggunakan sebatian maleimida **5** dan CF_3 maleimida **6** yang telah disintesis terlebih dahulu. Satu campuran dengan kemolaran yang sama di antara makrosiklik cMDG dan maleimida **5** atau **6** dalam pelarut $CdCl_3$ disediakan dan dianalisa menggunakan ^1H dan ^{19}F RMN spektroskopi. Kajian pengikatan yang sama turut dijalankan menggunakan makrosiklik cMP. Nilai pemalar pengikatan, K_a bagi kompleks pseudorotazen [cMDG·5] dan [cMP·5] telah dianggarkan sebanyak 190 ± 20 M^{-1} dan 160 ± 20 M^{-1}, masing-masing. Sebaliknya, kekuatan pengikatan semakin meningkat bagi perkompleksan pseudorotazen [cMDG·6] dan [cMP·6] di mana nilai K_a yang

diperolehi ialah 1000 ± 100 M^{-1} dan 460 ± 50 M^{-1} pada 25 ° C dalam pelarut $CdCl_3$. Di samping itu, ^1H dan ^{19}F RMN spektra bagi sebatian makrosiklik dan maleimida menunjukkan kompleks dalam pertukaran lambat pada 1H NMR anjakan kimia. Ini boleh dikaitkan dengan proses pengikatan signifikan pada kompleks pseudorotazen berbanding sebatian yang tidak berikatan. Nilai K_a ditentukan menggunakan kaedah titik tunggal bagi kes pertukaran lambat.

Kata kunci: makrosikilik, etilena glikol, piridina, pseudorotazen

Introduction

A common retrosynthetic disconnection shared by generic [2]-rotaxane and [2]-catenane structures revolves around in the [2]-pseudorotaxane precursor, in which a linear molecule is threaded through a macrocyclic unit. Thus, they are similar to rotaxane structure with the exception that the linear molecule not terminated by the two bulky stoppers. Further modification of this precursor can possibly proceed in two ways, by virtue of (a) stoppering the end linear component with sufficient large groups, results in the formation of [2]-rotaxane or (b) macrocyclisation of the linear component to affords to [2]-catenane (Figure 1).

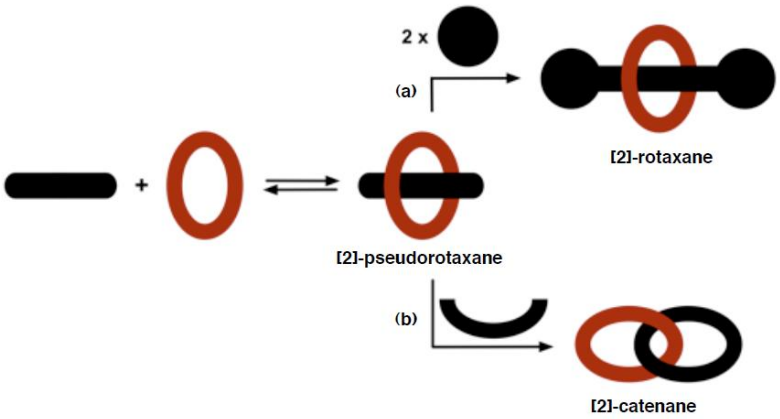


Figure 1. Graphical representation of the synthesis of (a) [2]-rotaxane by means of stoppering the linear component with two bulky end groups and (b) [2]-catenane by means of macrocyclisation of the linear component of the similar precursor

Prospective guests such as pyridone, urea and amide have been identified to probe as the binding components. Upon addition of a guest in the linear component and macrocycle with the complementary binding motifs, the equilibrium is established. The macrocycle is constantly being displaced from the binding site in the linear component, which resulted in two species, namely the [2]-pseudorotaxane complex and guest distinguishable in situ (Figure 2). The stability of the [2]-pseudorotaxane complex is defined by the association constants, K_a. The association constant relates to the affinity of the macrocycle to associate the binding site of the guest and can be varied by manipulating the temperature, based on the free energy Gibbs. In the case of low temperature, a substantial amount of the [2]-pseudorotaxane are obtained as a results of increase value of K_a [1]. A large association constant corresponds to a high equilibrium concentration of bound guest and hence more stable or tighter the preorganization of the [2]-pseudorotaxane complex. Undoubtedly, a high association constant of [2]-pseudorotaxane complex is mandatory to ensure a significant amount of rotaxane is synthesized.

An anion-directed pseudorotaxanes has been reported by Beer and co-workers [2]. The zwitterion comprised Crabtree-type pyridinium clef binding a chloride [3,4] with amide macrocycle results in the formation of a pseudorotaxane in acetone-d_6 with an association constant, K_a of 2400 M^{-1}. The pseudorotaxane is stabilized by chloride-NH hydrogen bonds, π-π stacking interaction and C-H···hydrogen bonds. A vast consideration has been given to the potential use of pseudorotaxanes in molecular devices [5] such as switches by means of external stimulus such as chemical [6], electrochemical [7] or photochemical [8].

One of the most important tasks in the formation of macrocycle is the key macrocyclisation step. In the absence of a suitable template, the synthesis of macrocyclic component employs the high-dilution conditions [9]. The high dilution approaches [10] have been used in a large number of macrocyclic syntheses. One rationale behind this strategy is that in dilute solution, the formation of the cyclic product by intramolecular reaction is more likely and thus faster than formation of a polymer, which requires a collision between two different starting reagents by means of intermolecular reaction. Furthermore, if the cyclisation is intrinsically faster than the rate of addition of the starting reagents, then the concentration of the reactants will always be small and not increase during the course of the reaction [11]. These approaches have been taken to assemble the macrocycle skeleton in this paper. A prototype amide-based macrocycle has been extensively [12-14] explored as the macrocyclic unit within our group and others. Nevertheless, the binding affinity shown in previous work [15] is moderate as a consequence of diminutive cavity and hence, decreasing the association constant, K_a in the [2]-pseudorotaxane complex. Herein, two tert-butyl amide-based macrocycles are proposed using high-dilution technique and analysed its binding properties with two respective guests. The existing complementary motif between hydrogen bond donor and acceptor are maintained in the new macrocycle framework.

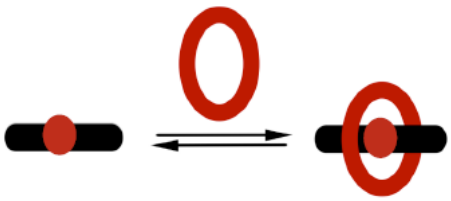


Figure 2. The reversible formation of the [2]-pseudorotaxane complex

Materials and Methods

Chemicals

5-tert-butylisophthalic acid, 4-(bromomethyl)benzonitrile, sodium hydride, diethylene glycol, thionyl chloride, trimethylamine, hydrochloric acid, potassium hydroxide, magnesium sulphate, BH_3·THF complex (1M solution in THF), 2,6-pyridine dimethanol,3,5-dimethylbenzoic acid, 4,4'-ethylene dianiline, sodium hydrogen carbonate, brine, maleic anhydride, zinc bromide, hexamethyldisilazone, 3,5-bis(trifluoromethyl)benzoyl chloride were purchased from ABCR GmbH & Co, Alfa-Aesar, Apollo Scientific Ltd., Avocado research Chemicals Ltd Fisher Scientific UK Ltd., Sigma-Aldrich company Ltd. or VWR International Ltd. and were used as received or otherwise purified by standard techniques where required. Most of non-aqueous reactions were carried out under an inert argon or nitrogen atmosphere with the inert gas passing through a bed of 4 Å molecular sieves and self-indicating silica gel. Brine refers to a saturated aqueous solution of sodium chloride. Anhydrous solvents were obtained under the following conditions, such as dry MeCN was distilled from calcium hydride in a recycling still, dry CH_2Cl_2 was obtained using a MBRAUN GmbH MB SPS-800 solvent purification system, which the solvent was dried by passage through filter columns and dispensed under an atmosphere of Ar or N_2 gas, $CdCl_3$ was neutralised over $CaCl_2$ filtered and stored over 4 Å activated molecular sieves and dry THF was distilled from sodium in a recycling still using benzophenone kethyl as indicator.

Chemical characterization

Analytical thin layer chromatography (TLC) analysis was performed on MACHEREY-NAGEL GmbH & Co, POLYGRAM® SIL G/UV254 plates, plastic backed 0.2 mm silica gel plates with fluorescent indicator. Developed plates were air-dried and visualized under UV lamp (λ_{max} 254 or 366 nm) or incubating with iodine on sand. Where necessary, thermal development after dipping in methanolic DNP and sulfuric acid solution and ninhydrin in *n*-butanol or a solution of aqueous potassium permanganate, was used to aid visualization. Flash Column chromatography and silica plugs were carried out on Apollo Scientific Ltd. Silica gel 40-63 micron or Silicycle

SiliaFash® P60 silica gel (230-400 mesh) eluting with solvents as supplied under a positive pressure of compressed air. Melting points were measured in open capillary tubes using an Electrothermal 9200 melting point apparatus and are uncorrected. Mass spectra were recorded on a Micromass GCT spectrometer for electron impact (EI) operating at 70 eV or chemical ionization (CI) using isobutane as the ionising gas. Electrospray ionisation spectra (ES) were performed on a Micromass LCT spectrometer operating in positive or negative mode from solutions of methanol, acetonitrile or water. *m/z* values are reported in Daltons and followed by their percentage abundance in parentheses.

General NMR spectroscopy procedures

^{1}H NMR spectra were recorded on a Bruker Avance 300 (300.1 MHz), a Bruker Avance II 400 (400.1 MHz), a Bruker Avance 500 (499.9 MHz) or a Varian UNITYplus 500 (500.1 MHz) spectrometer using the deuterated solvent as the lock and the residual spectra as the internal reference in all cases. The chemical shift information (δ_H) for each resonance signal is given in units of parts per million (ppm) relative to trimethylsilane (TMS) where δ_H TMS = 0.00. The number of protons (n) for a reported resonances signal are indicated from their integral value and their multiplicity are represented by the symbols s, d, t, q, m and br which denote singlet, doublet, triplet, quartet, multiplet and broad singlet, respectively. Their coupling constant (*J*) are determined by analysis using iNMR© (Version 3.6.3, Mestrelab Research, 2010) and quoted to the nearest 0.1 Hz. Identical coupling constants are averaged in each spectrum and also reported to the nearest 0.1 Hz. ^{13}C NMR spectra were recorded on a Bruker Avance 300 (75.5 MHz), a Bruker Avance II 400 (100.6 MHz) or a Bruker Avance 500 (125.7 MHz) spectrometer utilizing the DEPTQ pulse sequences with broadband proton decoupling using the deuterated solvents as the lock and the residual solvent as the internal reference in all cases. In the assignment of ^{13}C NMR spectra, the chemical shift information (δ_C) for each resonance signal are given in units of parts per million (ppm) relative to trimethylsilane (TMS) where δ_C TMS = 0.00. Mainly, the signals are singlets or unless stated, which their multiplicity is represented by the symbol d for doublet. ^{19}F NMR spectra were recorded using a Bruker Avance 300 (282.4 MHz), a Bruker Avance II 400 (376.5 MHz) or a Bruker Avance 500 (470.3 MHz) spectrometer using a broadband proton decoupling pulse sequence with the deuterated solvent as the internal lock. The chemical shift information (δ_F) for each resonance signal are given in units of parts per million (ppm) relative to CCl_3F where δ_F CCl_3F = 0.00. The analysis of ^{1}H, ^{13}C and ^{19}F spectra were carried out using iNMR© software (Version 3.6.3, Mestrelab Research, 2010).

Determination of binding constants

In the case of fast exchange (F) on the NMR chemical shift timescale between the complexed and uncomplexed species, the change in the observed chemical shift for discrete resonance is a weighted average between the bound and unbound species. The association constant, K_a was determined by NMR titration method using ^{1}H NMR spectroscopy at 298 K. The stock solutions and samples were made up in dry $CdCl_3$ using volumetric flask (accuracy ± 0.02 mL). In a typical ^{1}H NMR titration experiment, small aliquots of guest are added to a solution of host of known concentration and the NMR spectrum of the sample monitored as a function of guest concentration. Various atomic nuclei are often reported for their changes in chemical shift. The binding constant is extracted from the titration curve, which is the plot of changes in chemical shift against added guest concentration by fitting the curve using a non-linear curvefitting program. However, if the exchange of bound and unbound species is slow (S) on the NMR chemical shift timescale, then the association constant is estimated by simple integration of the ^{1}H and ^{19}F NMR resonances for bound and unbound host or guest, so called the single-point method.

Computational methods

All molecular mechanics calculations were performed on a Linux workstation using the OPLS2005 forcefield together with the GB/SA solvation model for chloroform as implemented in Macromodel (Version 9.8, Schrödinger Inc., 2010). Electronic structure calculations were carried out using MOPAC2009 running on a Linux cluster [16, 17].

5-*tert*-Butylisophthaloyl dichloride 2

5-*tert*-butylisophtalic acid **1** (2.0 g, 9.0 mmol) was suspended in toluene (45 mL) together with thionyl chloride (0.72 mL, 18.0 mmol) and refluxed at 80 °C for 18 h. An excess of thionyl chloride was distilled off by the azeotropic distillation with toluene to furnish dark yellow oil (2.28 g, 98%) as desired product. This product was used in the next step without further purification. ^{1}H NMR (300.1 MHz, $CdCl_3$) : δ_H 8.69 (1H, t, $^{4}J_{HH}$ 1.6 Hz; Ar*H*),

8.40 (2H, d, $^4J_{HH}$ 1.7 Hz; 2 × Ar*H*), 1.41 (9H, s; 3 × C*H*$_3$); ^{13}C NMR (75.5 MHz, $CdCl_3$) : δ_C 167.8 (*C*OCl), 154.1 (Ar*C*), 134.4 (Ar*C*), 134.2 (Ar*C*H), 131.8 (Ar*C*H), 35.5 (q*C*), 31.1 (*C*H$_3$); MS (ES^+) *m/z* 273.1 ([M+H]$^+$, 100), 477 (20).

(4,4'-(2,2'-Oxybis(ethane-2,1-diyl)bis(oxy))bis(methylene)bis(4,1-phenylene))dimethanamine 3
^{1}H NMR (300.1 MHz, $CdCl_3$): δ_H 7.31 (4H, d, $^3J_{HH}$ 8.2 Hz; 4 ×ArH), 7.26 (4H, d, $^3J_{HH}$ 8.2 Hz; 4 × ArH), 4.55 (4H, s; 2 × CH_2), 3.85 (4H, s; 2 × CH_2), 3.70 – 3.61 (8H, m; 4 × CH_2), 1.60 (4H, br s; 2 × NH_2); ^{13}C NMR (75.5 MHz, $CdCl_3$): δ_C 142.8 (ArC), 136.9 (ArCH), 128.2 (ArCH), 127.2 (ArC), 73.1 (CH_2), 70.8 (CH_2), 69.5 (CH_2), 46.4 (CH_2); MS (CI^+) m/z 105 (22), 119 (46), 120 (100), 328 (20), 345 ([M+H]$^+$, 12); HRMS (CI^+) m/z calculated for $C_{20}H_{29}N_2O_3$ [M+H]$^+$ 345.2178, found 345.2177.

(4,4'-Pyridine-2,6-diylbis(methylene))bis(oxy)bis(methylene)bis(4,1-phenylene))dimethanamine 4
^{1}H NMR (300.1 MHz, $CdCl_3$): δ_H 7.71 (1H, t, $^3J_{HH}$ 7.7 Hz; ArH), 7.39 (2H, d, ^{3}JHH 7.8 Hz; 2 × ArH), 7.36 (4H, d, $^3J_{HH}$ 8.2 Hz; 4 × ArH), 7.30 (4H, d, $^3J_{HH}$ 8.2 Hz; 4 × ArH), 4.66 (4H, s; 2 × CH_2), 4.63 (4H, s; 2 × CH_2), 3.87 (4H, s; 2 × CH_2), 1.46 (4H, br s; 2 × NH_2); ^{13}C NMR (75.5 MHz, $CdCl_3$): δ_C 158.1 (ArC), 143.1 (ArC), 137.4 (ArCH), 136.5 (ArC), 128.3 (ArCH), 127.3 (ArCH), 120.1 (ArCH), 73.2 (CH_2), 72.9 (CH_2), 46.5 (CH_2); MS (ES^+) m/z 374 (50), 378 ([M+H]$^+$, 100), 400 (47); HRMS (ES^+) m/z calculated for $C_{23}H_{27}N_3O_2Na$ [M+Na]$^+$ 400.2001, found 400.2005.

N-(4-(4-(2,5-Dioxo-2,5-dihydro-1H-pyrrol-1-yl)phenethyl)phenyl)-3,5- dimethylbenzamide 5
M.p. = 229.3 – 231.4 °C; ^{1}H NMR (400.1 MHz, $CdCl_3$): δ_H 7.81 (1H, s; NH), 7.57 – 7.54 (2H, m; 2 × ArH), 7.46 (2H, s; 2 × ArH), 7.29 – 7.27 (2H, m; 2 × ArH), 7.25 – 7.22 (2H, m; 2 × ArH), 7.19 – 7.17 (3H, m; 3 × ArH), 6.84 (2H, s; 2 × CH), 2.97 – 2.89 (4H, m; 2 × CH_2), 2.38 (6H, s; 2 × CH_3); ^{13}C NMR (100.6 MHz, $CdCl_3$): δ_C 169.8 (C=O), 166.1 (C=O), 141.8 (ArC), 138.6 (ArC), 137.7 (ArC), 136.2 (ArC), 135.2 (ArC), 134.3 (CH), 133.5 (ArCH), 129.4 (ArCH), 129.2 (ArC), 129.1 (ArCH), 126.1 (ArCH), 124.9 (ArCH), 120.4 (ArCH), 37.7 (CH_2), 37.3 (CH_2), 21.4 (CH_3); MS (ES^+) m/z 447 ([M+Na]$^+$, 75), 479 (100); HRMS (ES^+) m/z calculated for $C_{27}H_{24}N_2O_3Na$ [M+Na]$^+$ 447.1685, found 447.1674.

N-(4-(4-(2,5-Dioxo-2,5-dihydro-1H-pyrrol-1-yl)phenethyl)phenyl)-3,5- bis(trifluoromethyl)benzamide 6
M.p. = 249.5 – 251.3 °C; ^{1}H NMR (300.1 MHz, d_6-DMSO): δ_H 10.6 (1H, s; NH), 8.61 (2H, s; 2 × ArH), 8.36 (1H, s; ArH), 7.68 (2H, d, $^3J_{HH}$ 8.6 Hz; 2 × ArH), 7.34 (2H, d, $^3J_{HH}$ 8.5 Hz; 2 × ArH), 7.27 (2H, d, $^3J_{HH}$ 8.6 Hz; 2 × ArH), 7.22 (2H, d, $^3J_{HH}$ 8.5 Hz; 2 × ArH), 7.17 (2H, s; 2 × CH), 2.98 –2.87 (4H, m; 2 × CH_2); ^{13}C NMR (100.6 MHz, d_6-DMSO): δ_C 170.4 (C=O), 162.7 (C=O), 141.5 (ArC), 137.8 (ArC), 137.5 (ArC), 136.7 (ArC), 135.0 (CH), 130.8 (q, $^2J_{CF}$ 33.2 Hz, ArC), 129.3 (ArC), 128.7 (ArCH), 128.2 (ArCH), 128.1 (m; ArCH), 126.4 (ArCH), 124.7 (m; ArCH), 123.5 (q, $^1J_{CF}$ 276.6 Hz; CF_3), 120.2 (ArCH), 36.9 (CH_2),36.7 (CH_2); ^{19}F NMR (376.5 MHz, d_6-DMSO) : δ_F −61.7 ($ArCF_3$); MS (ES^-) m/z 531.1 ([M−H]$^-$, 100); HRMS (ES^-) m/z calculated for $C_{27}H_{17}N_2O_3F_6$ [M-H]$^-$ 531.1143, found 531.1140.

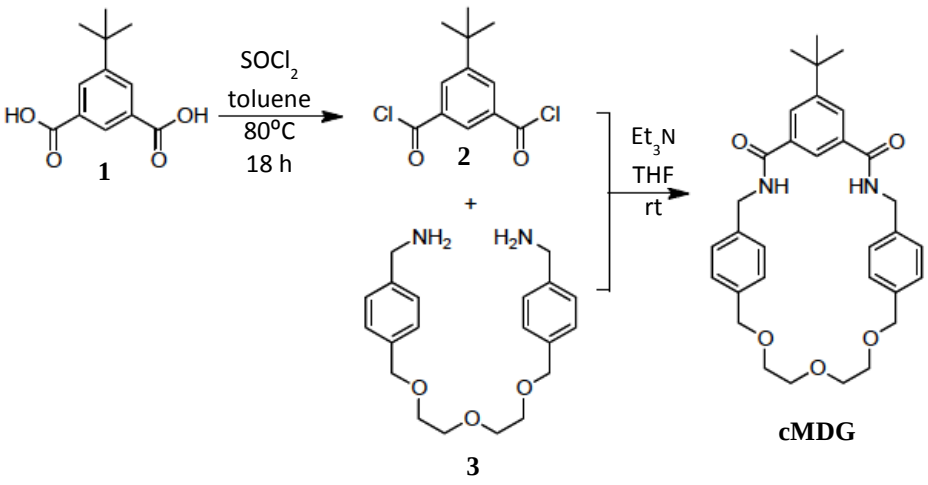
Macrocycle cMDG
A solution of amine derivative **3** (0.5 g, 1.45 mmol) and 5-tert-butylisophthaloyl dichloride **2** (0.38 g, 1.45 mmol) in dry THF (100 mL) were added simultaneously over 1 h to a solution of Et_3N (1.25 mL, 8.71 mmol) in dry THF (82 mL) and left stirred at ambient temperature under N_2 atmosphere for 3 days. The reaction mixture was concentrated by evaporation under reduced pressure and diluted with CH_2CI_2. The solution was then washed successively with 1M HCI and 1M KOH. The organic layers were dried with $MgSO_4$ and concentrated in vacuo. The residue was purified by column chromatography (Hexane:EtOAc, 1:1) to yield macrocycle cMDG as a colorless solid (81 mg, 11%). M.p. = 247.8 – 250.4 °C; ^{1}H NMR (400.1 MHz, $CdCI_3$): δ_H 8.10 (2H, d, $^3J_{HH}$ 1.5 Hz; 2 × NH), 7.53 (1H, br s; ArH), 7.30 (8H, s; 8 × ArH), 6.43 (2H, br s; 2 × ArH), 4.57 (4H, d, $^3J_{HH}$ 5.4 Hz; 2 × CH_2), 4.50 (4H, s; 2 × CH_2), 3.58 – 3.68 (8H, m; 4 × CH_2), 1.37 (9H, s; 3 × CH_3); ^{13}C NMR (75.5 MHz, $CDCI_3$): δ_C 167.3 (C=O), 153.2 (ArC), 137.8 (ArC), 137.4 (ArC), 134.7 (ArC), 128.8 (ArCH), 128.5 (ArCH), 128.4 (ArCH), 120.6 (ArCH), 73.1 (CH_2), 70.7 (CH_2), 69.6 (CH_2), 44.3 (CH_2), 35.3 (qC), 31.3 (CH_3); MS (ES^+) m/z 553.1 ([M+Na]$^+$, 100) 554.2 (30); HRMS (ES^+) m/z calculated for $C_{32}H_{38}N_2O_5Na$ [M+Na]$^+$ 553.2678, found 553.2664.

Macrocycle cMP

A solution of amine derivative **4** (0.6 g, 1.59 mmol) and 5-tert-butylisophthaloyl dichloride **2** (0.42 g, 1.59 mmol) in dry THF (100 mL) were added simultaneously over 2 h to a solution of Et_3N (1.3 mL, 9.36 mmol) in dry THF (95 mL) and left stirred at ambient temperature under N_2 atmosphere for 3 days. The reaction mixture was concentrated in vacuo and diluted with CH_2CI_2. The solution was then washed successively with 1M HCI and 1M KOH. The organic layers were dried with $MgSO_4$ and concentrated in vacuo. The residue was purified by column chromatography (Hexane:EtOAc, 1:1) to yield macrocycle cMP as a colorless solid (100 mg, 11%). M.p. = 256.3 – 258.9 °C; ^{1}H NMR (500.1 MHz, $CdCI_3$): δ_H 8.07 (2H, d, $^3J_{HH}$ 1.4 Hz; 2 × NH), 7.71 (1H, t, $^3J_{HH}$ 7.8 Hz; ArH), 7.57 (1H, s; ArH), 7.36 (2H, d, $^3J_{HH}$ 7.8 Hz; 2 × ArH), 7.31 (8H, s; 8 × ArH), 6.39 (2H, br s; 2 × ArH), 4.65 (4H, s; 2 × CH_2), 4.58 (4H, d, $^3J_{HH}$ 5.5 Hz; 2 × CH_2), 4.42 (4H, s; 2 × CH_2), 1.37 (9H, s; 3 × CH_3); ^{13}C NMR (100.6 MHz, $CdCI_3$): δ_C 167.3 (C=O), 157.4 (ArC), 152.9 (ArC), 137.6 (ArC), 137.3 (ArCH), 137.2 (ArC), 134.6 (ArC), 129.0 (ArCH), 128.7 (ArCH), 128.1 (ArCH), 120.8 (ArCH), 120.3 (ArCH), 72.2 (CH_2), 71.5 (CH_2), 44.3 (CH_2), 35.3 (q), 31.2 (CH_3); MS (ES^+) m/z 586.1 ($[M+Na]^+$, 100); HRMS (ES^+) m/z calculated for $C_{35}H_{37}N_3O_4Na$ $[M+Na]^+$ 586.2682, found 586.2684.

Results and Discussion

The *tert*-butyl macrocycle based on diethylene glycol (MDG) was constructed from 5-*tert*-butylisophthalic acid (**1**) which was activated to acid chloride derivatives (**2**) using thionyl chloride in toluene as outlined in literature [18]. The acyl chloride (**2**) was subsequently coupled to the bis amine compound (**3**) to give the macrocycle cMDG (11%) and outlined in Scheme 1. The synthesis of the analogous framework of the control macrocycle has been reported by others [19-22].



Scheme 1. Synthesis of macrocycle cMDG

Following this, we examined its calculated structure (Figure 3) to model the behavior of its structure. The opposite orientation of one of the carbonyl group in the upper fragment and the position of the diethylene glycol unit give rise to a bigger cavity in this new macrocycle.

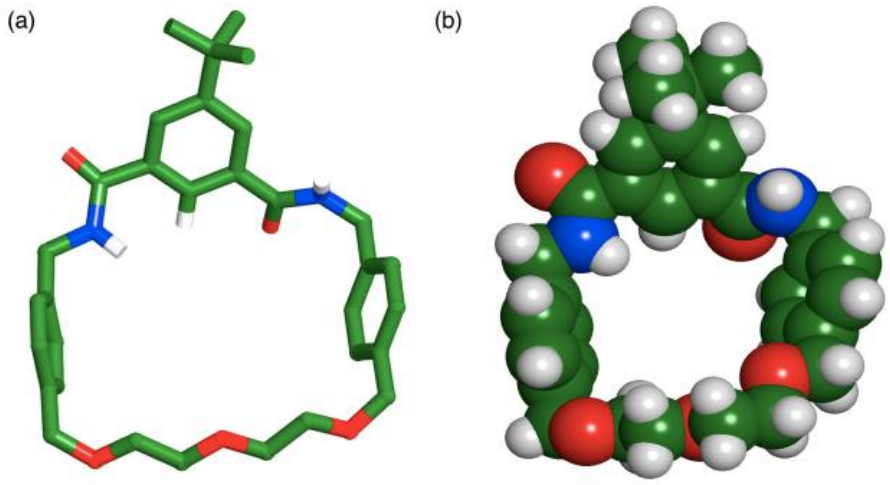
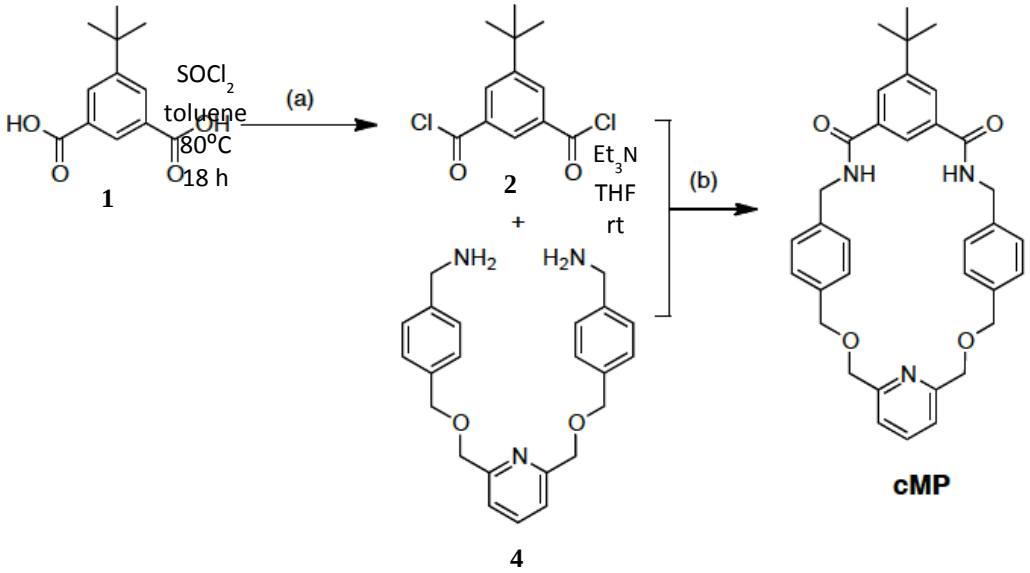


Figure 3. (a) Stick representation and (b) space filling model of the calculated structure (OPLS2005, GB/SA $CHCl_3$) of two preferable conformations for macrocycle cMDG. Carbon atoms are coloured green, oxygen atoms in red, nitrogen atoms in blue and hydrogen atoms in white (most hydrogen atoms have been removed for clarity)

Subsequently, the synthesis of the second *tert*-butyl macrocycle comprising pyridine moiety is encapsulated in Scheme 2. In similar way, treatment of the diacid (**1**) with thionyl chloride under dry conditions led to the formation of diacid dichloride (**2**), which then coupled to the diamine derivative (**4**), affording the macrocycle cMP in only 11% yield. Thus, using simple molecular mechanics calculation, we model the compound structure for macrocycle cMP (Figure 4). It is important to note that the yield of both cyclization step for macrocycle cMDG and cMP is significantly lower when the reactions were carried out in dichloromethane (4% yield). As might be expected, the possibility of the nucleophile attack in the amide bond formation step is relatively minimal in high dilution synthesis, but the use of the isophthaloyl building block further diminishes the efficiency of the ring closure step.



Scheme 2. Synthesis of control macrocycle cMP

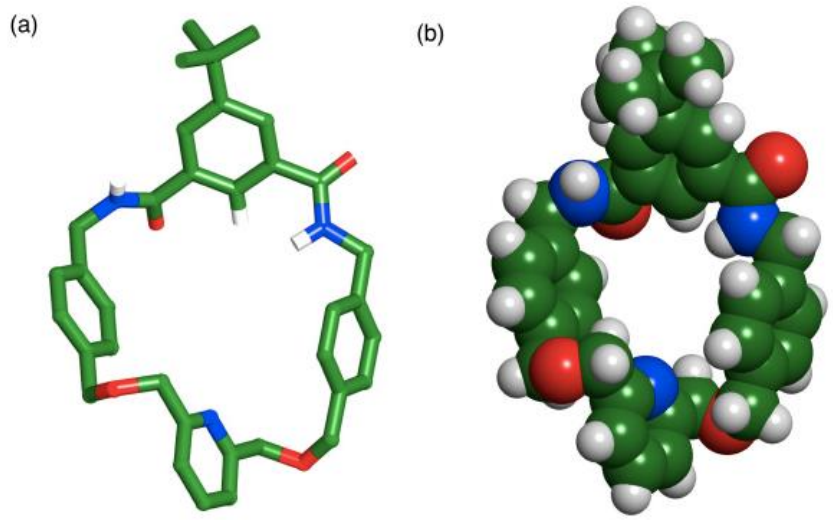


Figure 4. a) Stick representation and (b) space filling model of the calculated structure (OPLS2005, GB/SA CHCl3) of two preferable conformations for macrocycle cMDG. Carbon atoms are coloured green, oxygen atoms in red, nitrogen atoms in blue and hydrogen atoms in white (most hydrogen atoms have been removed for clarity)

Our preceding report [21] on the formation of amide macrocycle reveals the two hydrogen atoms of the amides and the electron pair of the pyridine nitrogen of the upper fragment of the macrocycle point into the interior of the macrocycle. In contrast to benzene, the electron density of the pyridine ring is not evenly distributed over the ring, reflecting the negative inductive effect of the nitrogen atom. For this reason, pyridine has a large dipole moment, which importantly influences the formation of the amide bond between the acid chloride and the amine. After the formation of the first amide bond, the other set of the acid chloride is in ideal position to aid the following nucleophilic attach and close the ring.

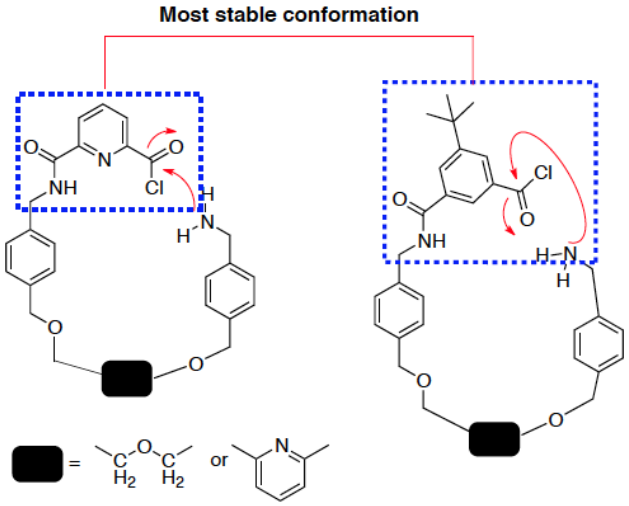
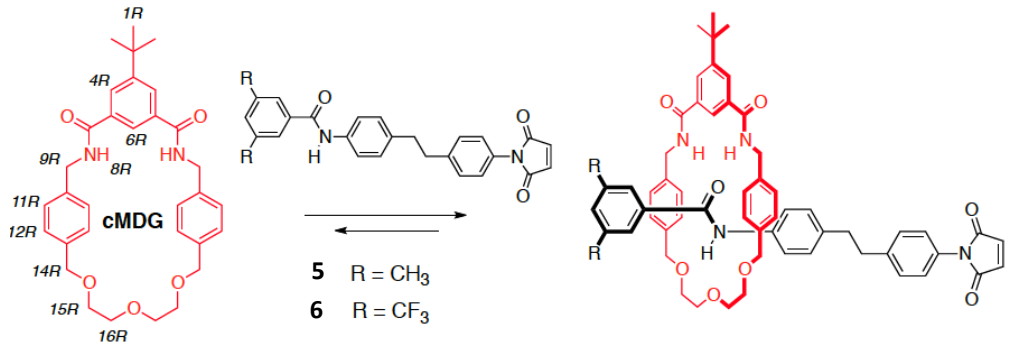


Figure 5. Possible nucleophilic acyl substitution for the ring closure for (a) macrocycle MDG or MP and (b) macrocycle cMDG or cMP

Additionally, the representation of the molecular structure for macrocycle cMDG (Figure 3) and cMP (Figure 4) reveals that their cavities are substantially larger than the parent macrocycles as a result of the absence of nitrogen atom in the upper fragment of their frameworks. The ability of these control macrocycles to complex with the potential guests is quantitatively tested in the following section.

Binding studies

Additional investigations must be conducted to evaluate the influence of the benzene ring in the framework of both control macrocycles in order to test its ability to complex the guests. In order to address this possibility, the following binding experiments were carried out with maleimide **5** and CF_3 maleimide **6**. An equimolar mixture of macrocycle cMDG and maleimide **5** in $CDCl_3$ was initially prepared and analysed by ^{1}H NMR spectroscopy. Some of the resonances of [cMDG□**5**] are rather broad at 25 °C with notable chemical shift changes, which corresponds to the pseudorotaxane formation (Figure 6a). The typical downfield shift (+1.15 ppm) of the NH macrocycle protons H8R, the upfield shift for the macrocycle phenylene protons, H11R and H12R (−0.57 ppm and −0.68 ppm) and the upfield shift for the macrocycle methylene protons H14R (−0.36 ppm) are noted. In addition, we recognized that the CH_3 resonance of maleimide **5** is separated into two sharp resonances, which corresponds to the unbound and bound state of maleimide **5**. This separation allows us to measure the association constant using the single-point method and we concluded that cMDG are capable of binding the maleimide **5** with a K_a value of 190 ± 20 M^{-1} at 25 °C in $CDCl_3$. An equimolar mixture of macrocycle cMDG and maleimide **6** in $CDCl_3$ was subsequently prepared. The 400.1 MHz ^{1}H NMR spectrum (Figure 6c) shows that the exchange resulting from the complexation and decomplexation rate of maleimide **6** is slow on the ^{1}H NMR chemical shift timescale and exhibits significant changes in chemical shifts upon the pseudorotaxane formation.



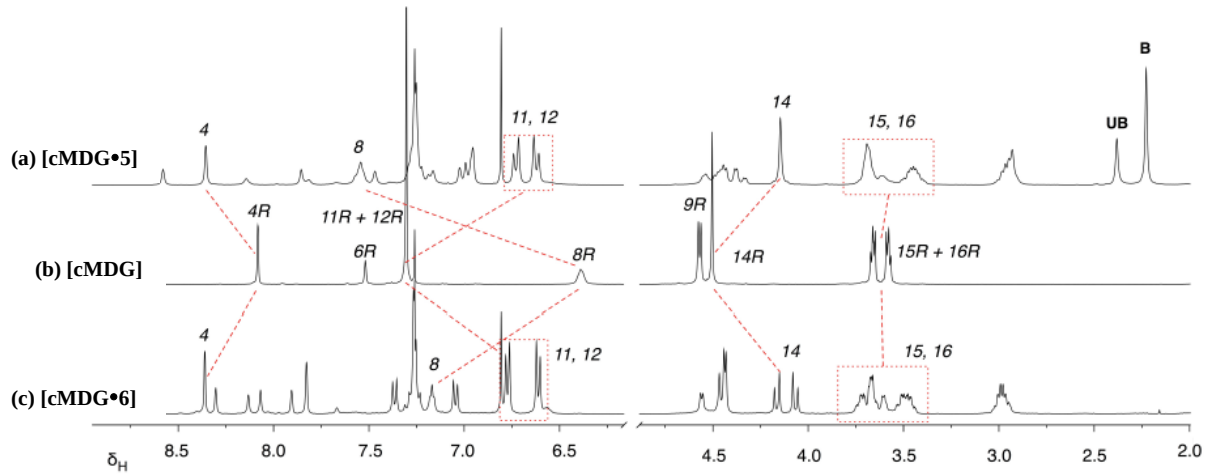


Figure 6. Partial 1H NMR spectra (300.1 MHz, 25 °C, $CDCl_3$, 20 mM) of (a) an equimolar mixture of macrocycle cMDG and maleimide **5** (b) macrocycle cMDG and (c) an equimolar mixture of macrocycle cMDG and maleimide **5**. R stands for ring component and in this case the macrocycle cMDG. Red dashed lines are shown to connect resonances for specific protons in bound and unbound states. UB stands for unbound species and B corresponds to bound species. ($\Delta\delta = \delta$unbound – δbound).

The resonance arising from the macrocycle NH protons, H8R, is again moved downfield (+0.78 ppm) as a result of the hydrogen bonding between these protons and the carbonyl group of the maleimide 110 and the characteristic upfield shifts of the macrocycle phenylene protons, H11R and H12R (−0.53 ppm and −0.69 ppm) residing in the shielding zone of an aromatic ring. Moreover, the macrocycle methylene protons H14R (singlet at δ_H 4.51 in the free macrocycle) give rise to an AB system at δ_H 4.12. From the ^{19}F NMR spectroscopy (376.5 MHz), the association constant for [cMDG•**6**] complex was estimated to be 1000 ± 100 M^{-1} at 25 °C in $CDCl_3$. The next step is to conduct the similar binding experiment in the presence of macrocycle cMP. An equimolar mixture of macrocycle cMP and maleimide **5** was prepared and analysed by ^1H NMR spectroscopy. The 300.1 MHz ^1H NMR spectrum, (Figure 7 a) shows that the [cMP•**5**] complex is near to a slow exchange process and a corresponding downfield shift of the macrocycle NH protons, H8R (+1.29 ppm) was noticed together with the upfield shifts of the macrocycle phenylene protons, H11R and H12R (−0.41 and −0.56 ppm, respectively). The association constant for the complexation of [cMDG•**5**] are determined similarly using the ^1H NMR single-point method and obtained a K_a value of 160 ± 20 M^{-1}. Binding experiment was performed next with maleimide **6**. The 400.1 MHz ^1H NMR spectrum of an equimolar mixture of macrocycle cMP and guest **6** in $CDCl_3$ (Figure 7 c) again displays a slow exchange process on the ^1H NMR chemical shift timescale. The resonances arising from NH8R is shifted downfield (+0.95 ppm), and the upfield shifts for both H11R and H12R (−0.49 and −0.56 ppm) are comparable with earlier observation in the presence of macrocycle cMDG. The macrocycle methylene protons resonances H9R, H14R and H15R are rendered magnetically inequivalent as a consequence of the unsymmetrical nature of maleimide **6**, leading to distinct complex patterns. The association constant for [cMP•**6**] complex was estimated to be 460 ± 50 M^{-1}.

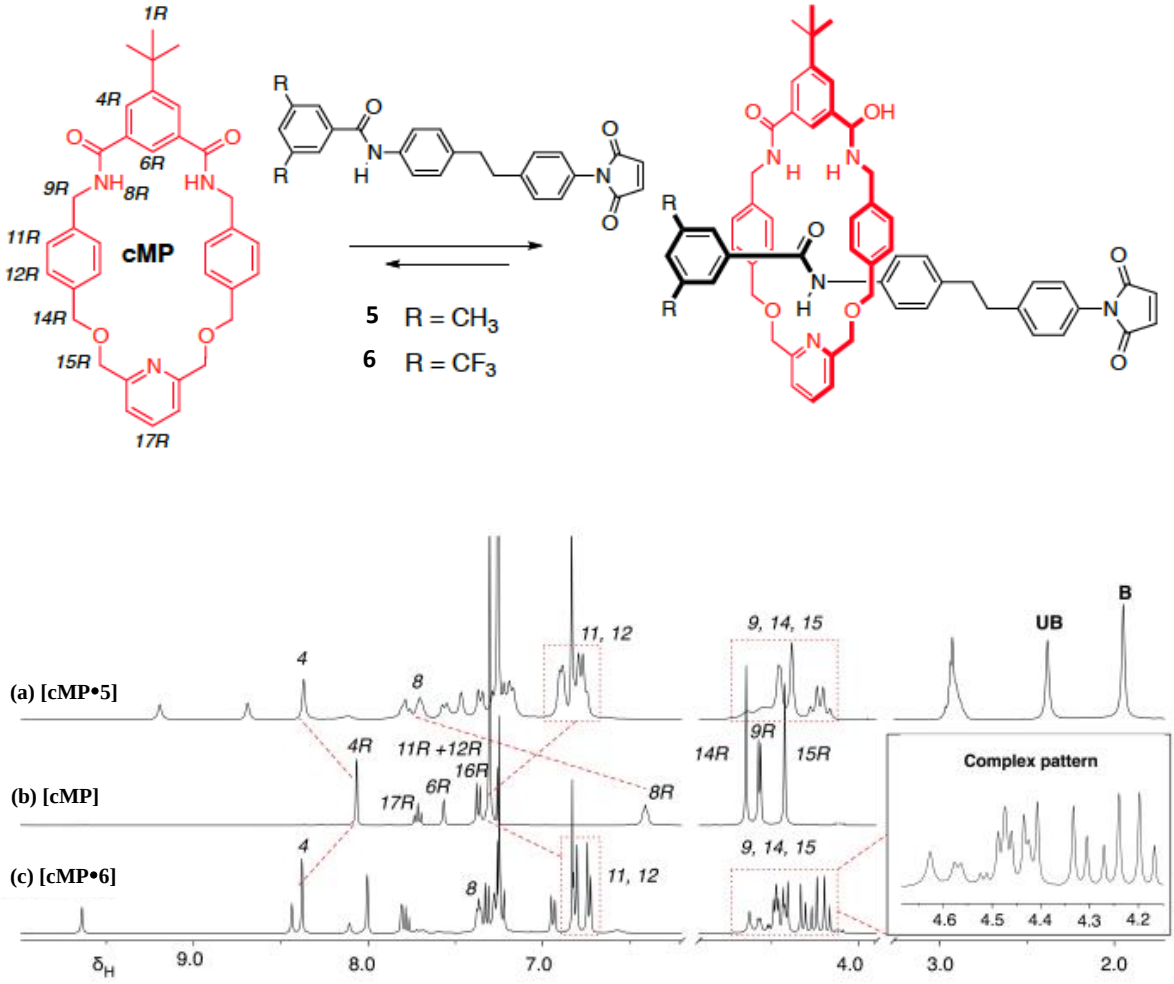
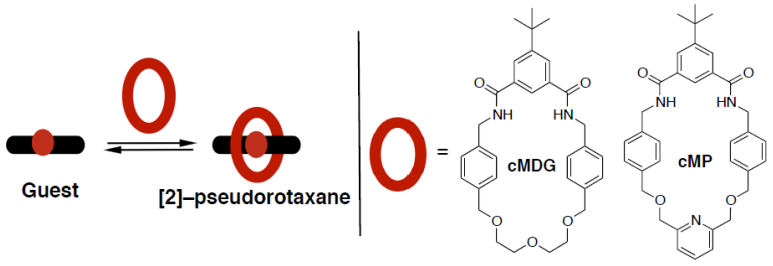


Figure 7. Partial ^{1}H NMR spectra (300.1 MHz, 25 °C, CDCl3, 20 mM) of (a) an equimolar mixture of macrocycle cMP and maleimide **5** (b) macrocycle cMP and (c) an equimolar mixture of macrocycle cMP and maleimide **6**. R stands for the ring component and in this case, the macrocycle cMP. Red dashed lines are shown to connect resonances for specific protons in bound and unbound states. UB stands for unbound species and B corresponds to bound species. ($\Delta\delta = \delta$unbound – δbound).

We realised that the association constant, K_a for [cMDG•**6**] complex is attributed to the lower fragments of the macrocycle participating in the binding event. We reasoned that the cavity of cMP is responsible for the insufficient preorganisation of maleimide **6** as a result of the loss of rigidity of the parent macrocycle MP containing pyridine moiety. In both pseudorotaxane assembly, the influence of rapid threading and dethreading process is evident and can be discerned from the NMR spectrum. The exchange between these processes were found slow on the ^{1}H NMR chemical shift timescale, yielding a spectrum containing two populated resonances corresponds with the relative amounts of each species, bound and unbound. The complex pattern from H9R, H14R and H15R are characteristics of the emergence of the pseudorotaxane species in solution. The outcomes for the binding experiments are summarized in Table 1.

Table 1. Binding assessments conducted with control macrocycle cMDG and cMP. The ^{1}H NMR spectrum of the macrocycle and guest showed complex is in slow exchange (S) that can be attributed to significant binding events, compared to the free species observed in isolation. In the case of slow exchange, the K_a was determined using the single-point method (#) either by ^{1}H NMR or ^{19}F NMR resonance (Relaxation time, d1 is 6 sec). The concentration used was 20 mM in $CDCl_3$ at 25 °C unless otherwise stated.



Maleimide Guest	K_a / M^{-1} (cMDG)	K_a / M^{-1} (cMP)
5	S#	S#
	K_a = 190 ± 20	K_a = 160 ± 20
6	S#	S#
	K_a = 1000 ± 100	K_a = 460 ± 50

Conclusion

The control macrocycles cMDG and cMP binds both maleimide **5** and **6** within the [2]-pseudorotaxanes assembly with a K_a value range from 160 – 1000 M^{-1}. The slow exchange process highlights the effect of the unsymmetrical nature of the maleimide component. A more complete evaluation on the effects of certain basic structural relationships on the abilities of the guest compound to thread the cavity of the macrocycle is currently being investigated.

Acknowledgement

The financial support for this work was provided by ESPRC (Grant EP/E017851/1) and GUP-2016-059. The authors acknowledge the School of Chemistry, University of St Andrews for providing facilities to carry out this research.

References

1. Hassan, N. I., del Amo, V., Calder, E. and Philp, D. (2011). Low temperature capture of pseudorotaxanes. *Organic Letters*, 13(3): 458-461.
2. Wisner, J. A., Beer, P. D. and Drew, M. G. B. (2011). A demonstration of anion templation and selectivity in pseudorotaxane formation. *Angewandte Chemie International Edition*, 40: 3606.
3. Kavallieratos, K., de Gala, S. R., Austin, D. J. and Crabtree, R. H. (1997). A readily available non-preorganized neutral acylic halide receptor with an unusual nonplanar binding conformation. *Journal of the American Chemical Society*, 119: 2325.
4. Kavallieratos, K., Bertao, C. M. and Crabtree, R. H. (1999). Hydrogen bonding in anion recognition: A family of versatile, non-preorganized neutral and acyclic receptors. *Journal of Organic Chemistry* 64: 1675.
5. Ashton, P. R., Ballardini, R., Balzani, V., Boyd, S. E., Credi, A., Gandolfi, M. T., Gomez-Lopez, M.; Iqbal, S., Philp, D., Preece, J. A., Prodi, L., Ricketts, H. G., Stoddart, J. F., Tolley, M. S., Venturi, M., White, A. J. P. and Williams, D. J. (1997). Simple mechanical molecular and supramolecular machines: photochemical and electrochemical control of switching processes. *Chemistry – a European Journal*, 3: 152.
6. Martinez-Diaz, M. V., Spencer, N. and Stoddart, J. F. (1997). The self-assembly of a switchable [2]rotaxane. *Angewandte Chemie International Edition*, 36: 1904.

7. Gaviña, P. and Sauvage, J.-P. (1997). Transition-metal template synthesis of a rotaxane incorporating two different coordinating units in its thread. *Tetrahedron Letters*, 38: 3521.
8. Mulder, A., Jukovic, A., Lucas, L. N., van Esch, J., Feringa, B. L., Huskens, J. and Reinhoudt, D. N. (2002). A dithienylethene-tethered beta-cyclodextrin dimer as a photoswitchable host. *Chemical Communications*, 75(22): 2734.
9. Illuminati, G. and Mandolini, L. (1998). Ring closure reactions of bifunctional chain molecules. *Accounts of Chemical Research* 14: 95.
10. Lindoy, L. F. (1989). The chemistry of macrocyclic ligand complexes. Cambridge University Press, England.
11. Steed, J. W. and Atwood, J. L. (2000). Supramolecular chemistry. John Wiley & Sons, Ltd, England.
12. Vidonne, A. and Philp, D. (2008). Integrating replication processes with mechanically interlocked molecular architectures, *Tetrahedron*, 64: 8464.
13. Alvarez-Pérez, M., Goldup, S. M., Leigh, D. A. and Slawin, A. M. Z. (2008). A chemically-driven molecular information ratchet. *Journal of the American Chemical Society*, 130: 1836.
14. Altieri, A., Aucagne, V., Carrillo, R., Clarkson, G. J., D'Souza, D. M., Dunnett, J. A., Leigh, D. A. and Mullen, K. M. (2011), Sulfur-containing amide-based [2]rotaxanes and molecular shuttles. *Chemical Science*, 2: 1922.
15. Vidonne, A., Kosikova, T. and Philp, D. (2016). Exploiting recognition-assembly and reactivity in [2]-rotaxane formation. *Chemical Science*, 7(4): 2592.
16. Stewart, J. J. P. (1989). Optimization of parameters for semiempirical methods II. Applications. *Journal of Computational Chemistry*, 10(2): 221.
17. Stewart, J. J. P. MOPAC (2009). Stewart Computational Chemistry, Colorado Springs, CO, USA Access from http://openmopacnet.
18. Ito, J. -I., Miyakawa, T. and Nishiyama, H. (2016). Carbon−carbon bond formation on a bis (oxazolinyl) phenyl− rhodium complex in a reduction and oxidative addition sequence. *Organometallics*, 25(22): 5216.
19. Berna, J., Brouwer, A. M., Fazio, S. M., Haraszkiewicz, N., Leigh, D. A. and Lennon, C. M. (2007). A rotaxane mimic of the photoactive yellow protein chromophore environment: effects of hydrogen bonding and mechanical interlocking on a coumarin amide derivative. *Chemical Communications*, 2007: 1910.
20. Leigh, D. A. and Thomson, A. R. (2006). Switchable dual binding mode molecular shuttle. *Organic Letters* 8(23): 5377.
21. Vickers, M. S. and Beer, P. D. (2007). Anion template assembly of mechanically interlocked structures. *Chemical Society Reviews*, 36: 211.
22. Sambrook, M. R., Beer, P. D., Wisner, J. A., Paul, R. L., Cowley, A. R., Szemes, F. and Drew, M. G. B. (2005). Anion-templated assembly of pseudorotaxanes: Importance of anion template, strength of ion-pair thread association, and macrocycle ring size. *Journal of the American Chemical Society*, 127: 2292.
23. Koulov, A. V., Mahoney, J. M. and Smith, B. D. (2003). Facilitated transport of sodium or potassium chloride across vesicle membranes using a ditopic salt-binding macrobicycle. *Organic and Biomolecular Chemistry*, 1: 27.
24. Vidonne, A. (2009). Exploiting recognition-assembly and reactivity in [2]-rotaxane formation. Thesis of PhD Degree, University of St. Andrews, Scotland.

Malaysian Journal of Analytical Sciences, Vol 23 No 4 (2019): 703 - 714
DOI: https://doi.org/10.17576/mjas-2019-2304-17

MALAYSIAN JOURNAL OF ANALYTICAL SCIENCES
Published by The Malaysian Analytical Sciences Society
ISSN 1394 - 2506

EFFECT OF PLASTICIZERS AND LITHIUM PERCHLORATE ON POLY(L-LACTIC ACID)-POLY(PROPYLENE GLYCOL) SOLID POLYMER ELECTROLYTE

(Kesan Pemplastik dan Litium Perklorat terhadap Elektrolit Polimer Pepejal Poli(L-Asid Laktik)-Poli(Propilena Glikol))

Siti Munirah Manap[1], Azizan Ahmad[1], Mohd Sani Sarjadi[2], Farah Hannan Anuar[1]*

[1]*Faculty of Science and Technology,*
Universiti Kebangsaan Malaysia, 43600 UKM Bangi, Selangor, Malaysia
[2]*Faculty of Science and Natural Resources,*
Universiti Malaysia Sabah, 88400 Kota Kinabalu, Sabah, Malaysia

**Corresponding author: farahhannan@ukm.edu.my*

Received: 31 March 2018; Accepted: 17 April 2019

Abstract

Solid polymer electrolyte (SPE) films were developed from poly(L-lactic acid)-poly(propylene glycol) (PLLA-PPG) with ethylene carbonate (EC) or propylene carbonate (PC) as plasticizer and lithium perchlorate ($LiClO_4$) salt using solution casting method. The conductivity behaviours of the samples prepared were studied by electron impedance spectroscopy (EIS). From the EIS analysis, PLLA-PPG with 30 wt.% of EC and 25 wt.% of $LiClO_4$ shows the highest conductivity value of 4.57×10^{-5} S cm^{-1} at room temperature. The attenuated total reflection-Fourier transform infrared spectroscopy (ATR-FTIR) confirm that there is chemical interaction between polymer host and lithium cation from lithium perchlorate. The shift of wavenumber for carbonyl (C=O) and ether (C-O-C) can be seen in ATR-FTIR spectrum. The crystallinity of PLLA was studied using X-ray diffraction (XRD) analysis. The absence of diffraction peaks corresponding to $LiClO_4$ in SPE, which indicates that $LiClO_4$ solvates well in the PLLA-PPG film. Thermal study by TGA indicated that PLLA-PPG SPE was thermally stable up to 270 ºC.

Keywords: poly(l-lactic acid), poly(propylene glycol), solid polymer electrolyte, plasticizer

Abstrak

Filem elektrolit polimer pepejal (EPP) dihasilkan daripada poli(L-asid laktid)-poli(propilena glikol) (PLLA-PPG) dengan etilena karbonat (EC) atau propilena karbonat (PC) sebagai pemplastik dan garam litium perkhlorat ($LiClO_4$) menggunakan kaedah pengacuanan larutan. Kekonduksian ionik bagi sampel yang disediakan dikaji menggunakan spektroskopi elektron impedan (EIS). Berdasarkan analisis EIS, PLLA-PPG dengan 30 bt.% EC dan 25 bt.% $LiClO_4$ menunjukkan nilai kekonduksian ionik tertinggi iaitu 4.587×10^{-5} S cm^{-1} pada suhu bilik. Spektroskopi inframerah transformasi Fourier (ATR-FTIR) memberi kepastian bahawa terdapat interaksi kimia di antara hos polimer dan kation litium daripada litium perklorat. Perubahan nombor gelombang pada kumpulan berfungsi karbonil (C=O) dan eter (C-O-C) dapat dilihat pada spektrum ATR-FTIR. Kehabluran PLLA dikaji menggunakan analisis pembelauan sinar-X (XRD). Kehilangan puncak $LiClO_4$ dalam EPP menunjukkan bahawa percampuran di antara garam $LiClO_4$ dan filem PLLA-PPG berlaku dengan baik. Analisis terma menunjukkan bahawa EPP PLLA-PPG adalah stabil secara terma sehingga suhu 270 ºC.

Kata kunci: poli(l-asid laktik), poli(propilena glikol), elektrolit polimer pepejal, pemplastik

Introduction

Solid polymer electrolyte (SPE) are a kind of solid state coordination compounds, consisting of a polymer host and a complexing lithium salt. Studies on SPE are more focused on the use of lithium ion batteries due to several advantages over liquid electrolytes, such as more stable, more flexible, spill proof and have a high resistance to heat [1]. Other advantages of SPE are wide operating temperature range, no vapour pressure, low volatility, ease of handling and manufacturing, high energy density and high ionic conductivity at ambient temperature. Study on SPE has been developed in order to improve its application in the production of electrochemical devices such as display, sensors, electrochemical window, super-capacitor, rechargeable battery and photoelectrochemical cell [2].

Poly(ethylene oxide) (PEO) and poly-ε-caprolactone (PCL) are the most common polymer used in SPE research. The research and development of SPE began when Wright found ion conductivity in a PEO-alkaline metal ion complex in 1975 [3]. The ionic conductivity of PEO-$LiCF_3SO_3$ with PEO molecular weight of 600000 g/mol and 15 wt.% $LiCF_3SO_3$ was 2.1×10^{-6} S cm^{-1}. The highest room temperature conductivity of 4.2×10^{-5} S cm^{-1} was achieved at 70:30 composition of PEO-ENR50 with the same wt.% of $LiCF_3SO_3$ [1]. Other than PEO, poly(ethylene glycol) (PEG) based SPE are also widely studied. The difference between PEO and PEG is PEG has molecular weight of less than 100000 g/mol, while PEO has molecular weight higher than 100000 g/mol. Based on Cha & Park, the best ionic conductivity of PEG with $LiClO_4$ has been determined to be 4.7×10^{-5} S cm^{-1}. The molecular weight of PEG used was 10000 g/mol while the O:Li ratio for PEG-LiClO complexes was 13:1 [4].

In particular, biodegradable polymer materials from renewable sources are of interest. The belief is that renewable biodegradable polymer materials will reduce the usage of polymer based on petroleum, thereby producing a positive effect to environment. Ng et al. used PCL which is a biodegradable polymer as a polymer host with lithium triflate and ethylene carbonate as a plasticizer to produce SPE [5]. The highest ionic conductivity of this SPE at room temperature is 3.48×10^{-4} S cm^{-1}. Another example of biodegradable polymer that also widely used in SPE research are cellulose and starch.

Since PEG is semi crystalline, it is challenging to get high ionic conductivity when using this polymer. In an approach report by Tan et al., PDLLA was copolymerized with PEG to improve the ionic conductivity. The resulted SPE with 25 wt.% of lithium iodide was found to achieve optimum ionic conductivity of 4.16×10^{-6} S cm^{-1} at room temperature [6]. In this study, PPG is used, which is an amorphous polyether and has T_g of - 60 to -75°C at molecular weight ranging from 150 g/mol to 4000 g/mol [7]. However, PPG by itself is not reliable to get a free standing SPE film, thus poly(L-lactic acid) (PLLA) was introduced to enhance the physical properties of SPE film. PLLA is a semi crystalline biodegradable polymer that has T_g of 60-70ºC and T_m of 170-180ºC [8].

The main purpose of this study is to develop SPE system using PLLA and PPG. Thus, in order to improve the ionic conductivity, plasticizer was introduced to increase the segmental motion of polymer backbone. Subsequently, it also can reduce crystallinity and increase amorphous phase of polymer host in order to promote ions mobility and generate higher ionic conductivity [9]. Ethylene carbonate (EC) is an effective plasticizer used in preparation of SPE. For example, Chew et al. used EC together with PLA to improve the ionic conductivity [10]. 35 wt.% of EC blended with PLA showed the highest ionic conductivity of 1.908×10^{-10} S cm^{-1}. In this study, SPE based on PLLA-PPG as the host polymer and lithium perchlorate ($LiClO_4$) as the charge carrier is expected to generate SPE with high ionic conductivity and better mechanical properties. The suitable type of plasticizer (EC or propylene carbonate (PC)) and the suitable wt.% of plasticizer to get the best ionic conductivity is investigated and presented in this finding.

Materials and Methods

Materials

Poly(L-lactic acid) (PLLA) was supplied by ESUN, China. Poly(propylene glycol) (PPG) with number average molecular weight, M_n of 4000, tin(II)2-ethylhexanoate ($Sn(Oct)_2$) (~95 %) catalyst and lithium perchlorate ($LiClO_4$) (≥98 %) salt were supplied by Sigma Aldrich (M) Sdn Bhd. 4,4'-Polymeric diphenylmethane diisocyanate (4,4'-PMDI) that act as chain extender was obtained from Behn Meyer. Ethylene carbonate (EC) and propylene carbonate (PC) were supplied by Fluka. Dichloromethane (DCM) and tetrahydrofuran (THF) were supplied by R&M Chemical. All chemicals were used as received.

Methods

In this work, three types of polymer electrolyte systems were prepared. The first system consists of PLLA-PPG system with the variation of plasticizer types; ethylene carbonate (EC) and propylene carbonate (PC)) with 0 and 15 wt.% of $LiClO_4$. For second system, PLLA-PPG system with different wt.% of EC were prepared. The third system consist of PLLA-PPG with 30 wt. % EC and 0, 5, 10, 15, 20, 25 and 30 wt.% of $LiClO_4$.The films were prepared using solution casting method. First, 30 wt.% of EC (0.6 g) and 0 wt.% of $LiClO_4$ (0 g) were dissolved in THF (15 mL) and stirred for 24 hours. In a second flask, PLLA (0.4 g) was dissolved in DCM (15 mL). The solution was stirred with magnetic bar. Then, PPG (1.6 g) was added into PLLA solution. After that, chain extender,4,4'-PMDI (163 µL) was added into the PLLA-PPG solution followed by catalyst, $Sn(Oct)_2$ (2.6 µL). The solution was stirred for 2 hours at room temperature. Then, the solution of EC and $LiClO_4$ were added to PLLA-PPG solution. The solution was stirred for 24 hours to achieve a homogenous mixture. Finally, the solution was casted in a Teflon petri dish (diameter = 10 cm) and left overnight in the fume hood at room temperature to make sure all the solvent evaporates. Residual solvents were further removed by vacuum for 24 hours. The film was peeled and stored in a desiccator until further use. This step was repeated using EC, PC and $LiClO_4$ of different amount as listed in Tables 1-3 for the three working systems.

Table 1. Variation of EC and PC with 0 and 15 wt.% of $LiClO_4$

PLLA-PPG + EC/PC	**wt. % of $LiClO_4$**
PLLA-PPG + 30 wt.% of EC	0
	15
PLLA-PPG + 30 wt.% of PC	0
	15

Table 2. Variation wt.% of EC with 15 wt.% of $LiClO_4$

PLLA-PPG + wt. % of EC	**wt. % of $LiClO_4$**
PLLA-PPG + 20	
PLLA-PPG + 25	15
PLLA-PPG + 30	
PLLA-PPG + 35	

Table 3. Variation wt.% of $LiClO_4$ with 30 wt.% of EC

PLLA-PPG + wt. % of EC	**wt. % of $LiClO_4$**
PLLA-PPG + 30	0
	5
	10
	15
	20
	25
	30

Characterization of polymer electrolyte films

ATR-FTIR analysis was conducted using Spectrum 400 Perkin Elmer GX Spectrometer. The prepared samples were analyzed with infrared ranged from the frequency of 4000 to 650 cm^{-1}. The ionic conductivity of synthesized polymer electrolyte was analysed using VersaSTAT 4 impedance analyser. The measurement was taken from frequency range of 0.1 to 1000000 Hz. The prepared SPE were cut and sandwiched between two stainless steel electrodes. The ionic conductivity, σ was calculated according to the equation $\sigma = [l/(R_b \cdot A)]$, where l represents the film thickness (cm), R_b is the bulk resistance while A is the effective contact area between electrode and the electrolyte (1.7671 cm^2). X-ray diffraction pattern of the prepared samples were analysed using Bruker D8-Advance diffractometer. Cu anode were used to study the diffraction pattern and the samples were scanned from diffraction angle, 2θ of 5° to 80° at scanning rate 0.025° s^{-1}. Thermal behaviour of the prepared samples was analysed using a Shimadzu TGA-50 instrument. The heating rate used was 10 °C/min, under nitrogen atmosphere and the range of measurement was started from room temperature up to 600 °C.

Results and Discussion

Polymer host synthesis

The polymer host, PLLA-PPG copolymer was synthesized through chain extension reaction by 4,4'-PMDI. The reaction is shown schematically in Figure 1. PLLA and PPG linear chains bear hydroxyl (-O-H) groups at both ends, whereas 4,4'-PMDI contains multiple isocyanate (-N-C=O) groups along the molecule. During the reaction, the O-H group from PLLA or PPG reacted with isocyanate group to form urethane bond. Repetitions of this reaction produces crosslinked polyester-polyether polyurethane where PLLA and PPG chains are connected randomly by PMDI crosslinker. The presence of new functional group urethane in the reaction product can be determined using ATR-FTIR analysis that will be presented at a later section of this paper.

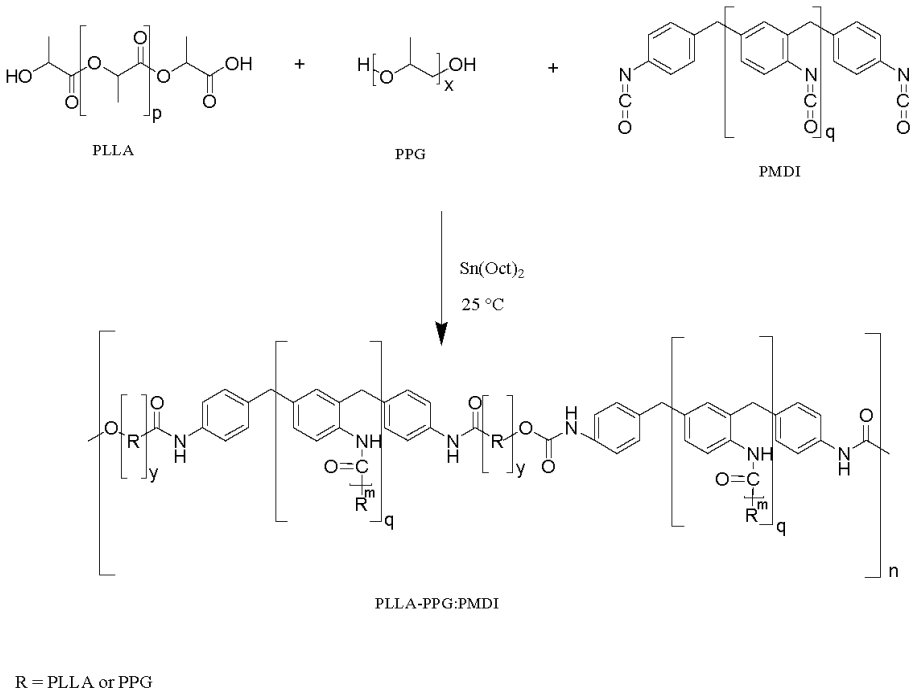


Figure 1. Reaction scheme between PLLA, PPG and PMDI

Ionic conductivity of PLLA-PPG SPE film with different plasticizer

Plasticizer was added to PLLA-PPG based polymer electrolyte to evaluate the ionic conductivity enhancement. $LiClO_4$ was chosen as dopant salt for all the system in this research. According to Rodrigues et al. $LiClO_4$ is a salt that is often used to produce SPE [1]. $LiClO_4$ salt is very stable at ambient moisture and less hygroscopic in

comparison to $LiCF_3SO_3$ salt [11, 12]. Ji et al. also used $LiClO_4$ salt in the production of SPE based PEO-b-PE [13]. The ionic conductivity of PLLA-PPG SPE without the addition of plasticizer is low even with 30 wt.% of $LiClO_4$, which is 9.96×10^{-6} S cm^{-1}. For this system, four types of film were produced. Ethylene carbonate (EC) and propylene carbonate (PC) were used to identify which plasticizer is the most suitable to produce SPE film with better ionic conductivity. EC and PC are widely used as plasticizer in SPE [14-18]. Based on the EIS analysis conducted (Table 4), the film with EC has better conductivity than PC which is 2.69×10^{-10} S cm^{-1} and 2.46×10^{-6} S cm^{-1} for 0 and 15 wt.% of $LiClO_4$. Therefore, EC is selected to be used in the production of these PLLA-PPG SPE films because it gives a better conductivity and physical properties. Pitawala et al. also used EC and PC in their study to prepare $(PEO)_9LiTf:Al_2O_3$ composite polymer electrolyte. The ionic conductivity of $(PEO)_9LiTf$ + 15 wt.% Al_2O_3 + 50 wt.% of EC is 4.98×10^{-5} S cm^{-1} whereas the ionic conductivity of $(PEO)_9LiTf$ + 15 wt.% Al_2O_3 + 50 wt.% of PC is 1.29×10^{-5} S cm^{-1}. The result of ionic conductivity from the study showed that the composite polymer electrolyte using EC has higher conductivity compared to PC [19].

Table 4. Ionic conductivity of PLLA-PPG SPE film with different plasticizer and wt. % $LiClO_4$

PLLA-PPG + 30 % EC/PC + 0 or 15 % $LiClO_4$	**Conductivity (S cm^{-1})**
PLLA-PPG + 30 % EC + 0 % $LiClO_4$	2.69×10^{-10}
PLLA-PPG + 30 % EC + 15 % $LiClO_4$	2.46×10^{-6}
PLLA-PPG + 30 % PC + 0 % $LiClO_4$	1.03×10^{-10}
PLLA-PPG + 30 % PC + 15 % $LiClO_4$	4.20×10^{-7}

Ionic conductivity of PLLA-PPG SPE film with different wt.% of EC

For the second system, the percentage of EC was reviewed to identify the most suitable wt.% of EC in the production of PLLA-PPG SPE film. Based on the EIS analysis conducted (Table 5), the highest ionic conductivity was at 30 wt.% of EC which is 2.80×10^{-6} S cm^{-1}. However, the ionic conductivity decreased after the optimum value at 30 wt.% of EC. Ibrahim et al. stated that an optimum composition is reached as the amount of plasticizer is increased, in which ion interactions between the solubilizing polymer and the plasticizer as such that ion mobility is maximized. A further increase in plasticizer content may eventually cause displacement of the host polymer by plasticizer molecules within the salt complexes and a decrease in ionic mobility eventually will contribute to decrease in ionic conductivity [18]. The similar observation was reported by Johan et al. which the highest conductivity of PEO-$LiCF_3SO_3$-EC system is obtained at 20 wt.% of EC, which is 8.12×10^{-5} S cm^{-1}. The conductivity decreases beyond 20 wt.% of EC [20].

Table 5. Ionic conductivity of PLLA-PPG SPE film with different wt.% of EC

PLLA-PPG + Variation wt. % of EC and 15 % $LiClO_4$	**Conductivity (S cm^{-1})**
PLLA-PPG + 20 % EC + 15 % $LiClO_4$	6.43×10^{-7}
PLLA-PPG + 25 % EC + 15 % $LiClO_4$	1.70×10^{-6}
PLLA-PPG + 30 % EC + 15 % $LiClO_4$	2.80×10^{-6}
PLLA-PPG + 35 % EC + 15 % $LiClO_4$	1.73×10^{-6}

Ionic conductivity of PLLA-PPG/EC and different wt. % of $LiClO_4$

For the third system, the concentration of EC was kept constant at 30 wt.% whereas the different wt.% of $LiClO_4$ are used. The ionic conductivity of the PLLA-PPG SPE film increased with wt.% of lithium perchlorate and reached an optimum value, 4.57×10^{-5} S cm^{-1}, at 25 wt.% of $LiClO_4$ (Figure 2). This optimum value signifies the maximum effective interaction between oxygen atoms and lithium cation in electrolyte system [6]. The ionic conductivity of PLA-PPG film is increased due to the increase in charge carrier as the number of free cations increases in the system. The presence of 25 wt.% of $LiClO_4$ increased the conductivity up to four magnitudes in comparison to

PLLA-PPG without $LiClO_4$ salt, which is 1.29×10^{-9} S cm^{-1}. Lithium salt loaded in the polymer system was dissociated into conducting species due to the presence of ether and ester oxygen atom in PPG and PLLA, respectively.

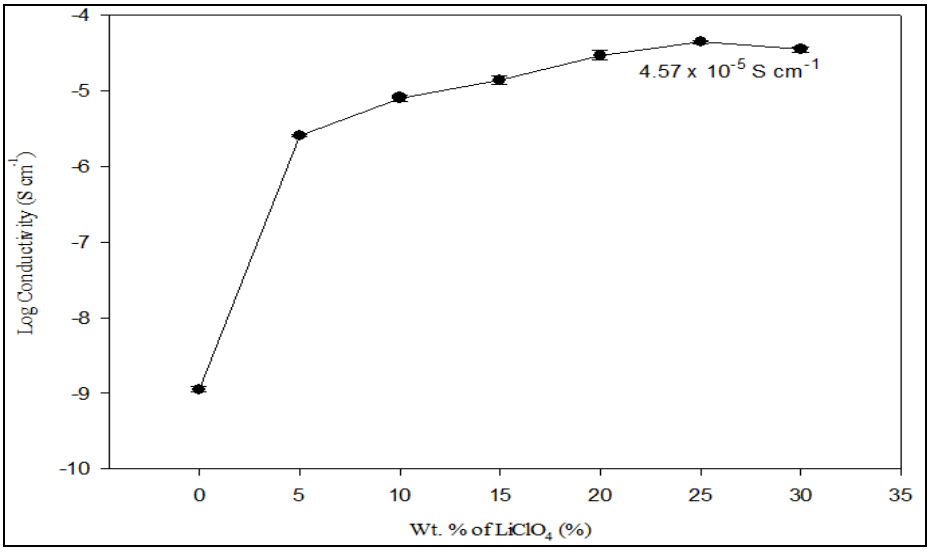


Figure 2. Variation of ionic conductivity of PLLA-PPG SPE film with 30 wt.% of EC and different wt.% of $LiClO_4$

Fourier transformed infrared analysis

In this study, FTIR spectroscopy has been used to confirm the coordination or the complexation of lithium salt with PLLA-PPG film. Oxygen atoms acted as an electron donor in the solid polymer electrolyte system. Lone pair electron of oxygen atom was donated to Li^+ from the dissociated lithium perchlorate and formed polymer-salt complex through dative bond. Figure 3 represents the FTIR spectra of PLLA-PPG film with 30% of EC and different wt.% of $LiClO_4$ salt at (a) 1850-1700 cm^{-1} and (b) 1120-1040 cm^{-1}. Table 6 showed that after $LiClO_4$ was added in PLLA-PPG system, the carbonyl band of EC shifted from 1806 cm^{-1} to lower wavenumber at 1801 cm^{-1} and carbonyl band of PLLA shifted from 1774 cm^{-1} to lower wavenumber at 1773 cm^{-1}. For C-O-C functional group, the stretching mode shifted to the left as the wt.% of $LiClO_4$ increased from 1072 to 1067 cm^{-1}. This shown that Li^+ interact more with PPG compared to PLLA.

The functional groups of PLLA-PPG film with 30% of EC and $LiClO_4$ (Table 7) can be described as: bands at around 3368-3590 cm^{-1} representing O-H from water or moisture; at around 2978-2970 cm^{-1} representing C-H stretching; at 1806 cm^{-1} representing C=O from EC; at 1774 cm^{-1} representing C=O from PLLA, at 1651 cm^{-1} representing C=O from urethane bond and 1074-1066 cm^{-1} representing C–O–C asymmetric stretching vibrations from PPG.

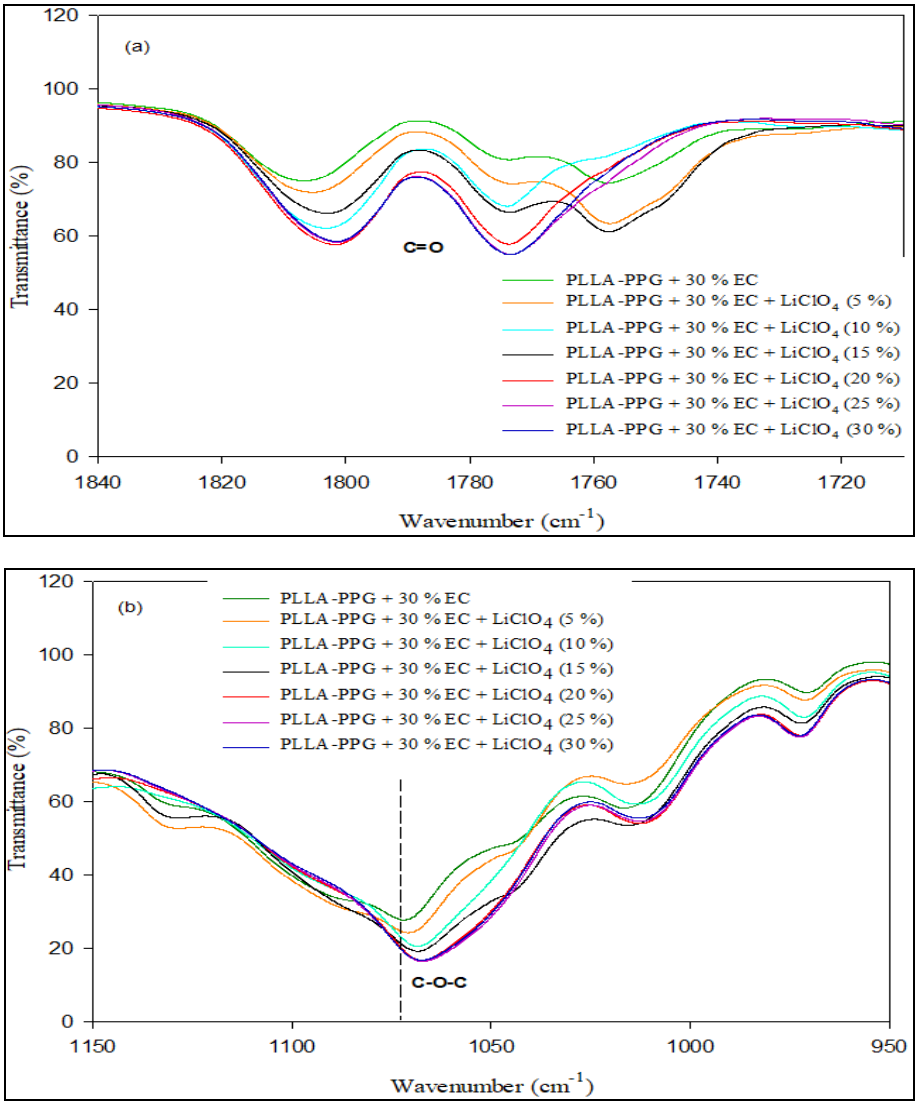


Figure 3. FTIR spectra of PLLA-PPG film with 30% of EC and different wt.% of $LiClO_4$ at (a) 1850-1700 cm^{-1} and (b) 1120-1040 cm^{-1}

Table 6. Wavenumber of functional group from PLLA-PPG SPE film with 30% of EC and $LiClO_4$ or without $LiClO_4$

Wt. % of $LiClO_4$	**C=O (EC) (cm^{-1})**	**C=O (ester) (cm^{-1})**	**C=O (urethane) (cm^{-1})**	**C-O-C (cm^{-1})**
Without $LiClO_4$	1806	1774	1651	1072
With $LiClO_4$	1801	1773	1651	1067

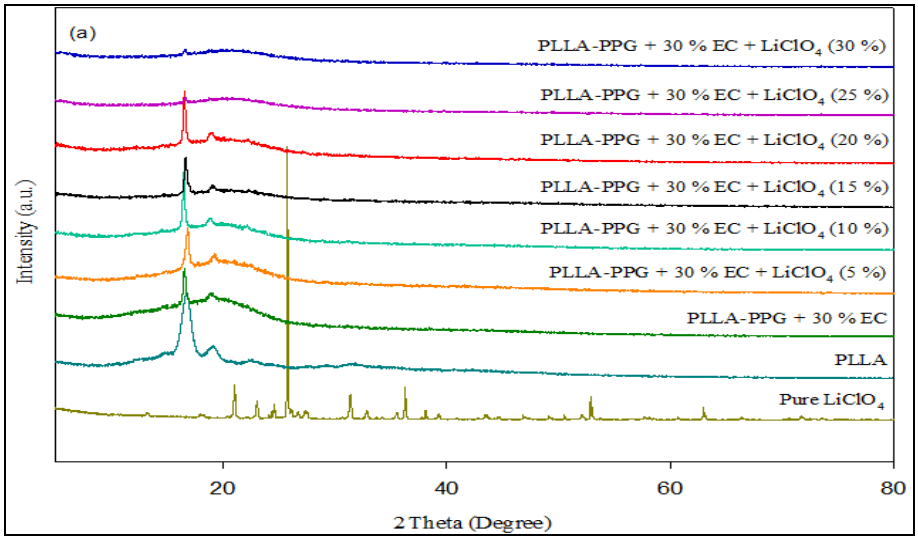
Table 7. Wavenumber of functional group from PLLA-PPG SPE film with 30% of EC and $LiClO_4$

Functional Group	**O-H**	**C-H**	**C=O (EC)**	**C=O (PLLA)**	**C=O (urethane)**	**C-O-C**
Wavenumber (cm^{-1})	3368-3590	2978-2970	1806	1774	1651	1074-1066

X-Ray diffraction analysis

X-Ray diffraction analysis was performed to study the structure and crystallization behaviour of the polymer-salt complexes. Figure 4 (a) shows the X-ray diffraction pattern of PLLA-PPG film with 30 wt.% of EC and different wt. % of lithium perchlorate in the range of 2θ = 5° to 80°. Pure PLA peaks appear at 16.6° and 18.9°. It reveals that the prominent peaks appear at 2θ values of 16.6° and 19.1° are representatives of PLLA since PPG are in amorphous phase. The PLLA crystalline peak remained exist even after the copolymerization reaction with PPG.

Pure $LiClO_4$ (Figure 4 (b)) shows high intense peak at 2θ = 21.1°, 23.1°, 25.7°, 31.4°,36.3°, 39.5° and 52.8°. From previous study, $LiClO_4$ was obtained at angles of 2θ = 21.1°, 23.2°, 31.3°, 35.7° and 39.3° [21]. The amorphous phase of PLLA-PPG film with 30 wt.% of EC increased with addition of $LiClO_4$. Meanwhile, the absence of diffraction peaks corresponding to $LiClO_4$ in $LiClO_4$ loaded SPE indicates that $LiClO_4$ solvates well in the PLLA-PPG film.



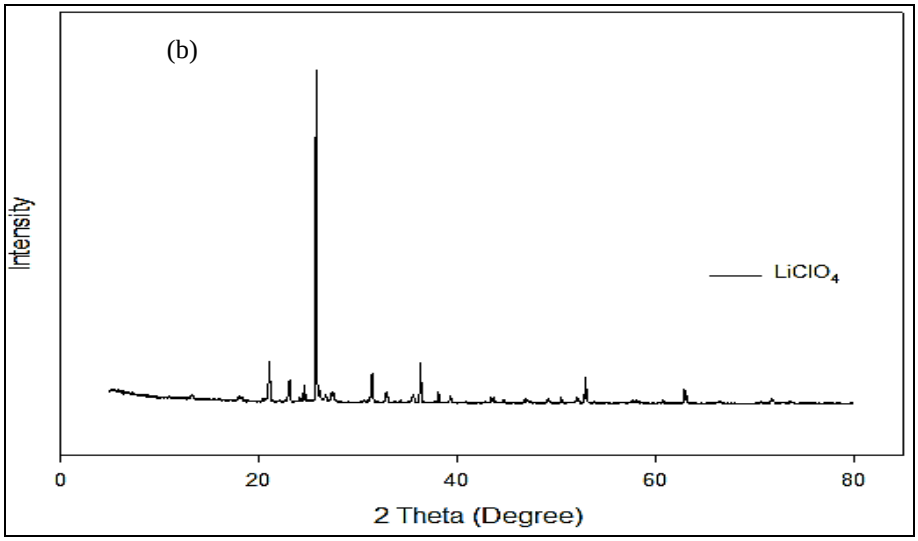


Figure 4. X-ray diffraction patterns of PLLA-PPG film with 30 wt.% of EC and different wt.% of $LiClO_4$ salt (a) and $LiClO_4$ salt (b)

Thermogravimetric analysis

Thermogravimetric analysis (TGA) has been used to investigate the thermal degradation, phase transition and crystallization of the polymers. The thermogravimetric curve for EC, PPG and PLLA was given in Figure 5. It is apparent that the EC start to decompose around 90 ºC while PPG only starts to decompose after 276 ºC. In addition, the weight of PLLA is almost constant up to 357 ºC. Above 357 ºC, PLLA start to decompose. EC, PPG and PLLA were observed to display a single step of decomposition. At temperature around 400 ºC, all sample were almost completely decomposed.

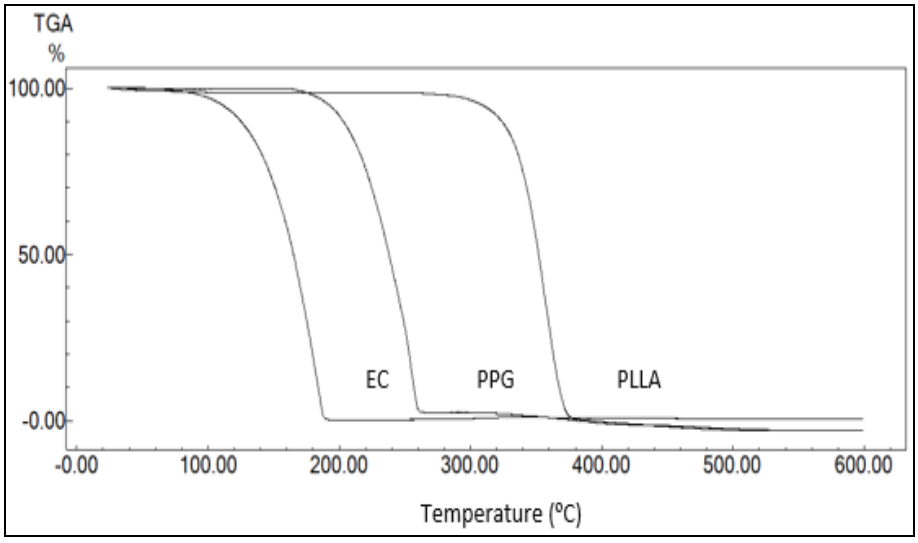


Figure 5. TGA thermogram of EC, PPG and PLLA

The TGA curve which contain 0, 15 and 30 wt.% of $LiClO_4$ in PLLA-PPG films with 30 wt.% of EC were illustrated in Figure 6(a). There were multi step decomposition from PLLA-PPG thin film with different wt.% of $LiClO_4$. The weight loss at around 100 ºC were caused by trapped moisture. There was no major weight loss for all the polymer electrolytes until around 270-280 °C and this suggested that the prepared SPE was thermally stable up to 270 °C. With the addition of salt, the thermal stability of material was reduced. This can be seen from the TGA curve for 0% sample, where major decomposition starts at 285 °C but after addition of salt, the major decomposition starts at around 265 to 270 ºC. $LiClO_4$ start to decompose at around 470 °C.

DTG thermogram from Figure 6 (b) shows that PLLA-PPG SPE with 30 wt.% of EC and without $LiClO_4$ salt was more stable compared to PLLA-PPG SPE with 30 wt.% of EC and $LiClO_4$ salt. The decomposition of all stage occurred more faster after the addition of $LiClO_4$ salt. This showed that the addition of $LiClO_4$ salt have decreased the decomposition temperature and lowered the thermal stability of SPE.

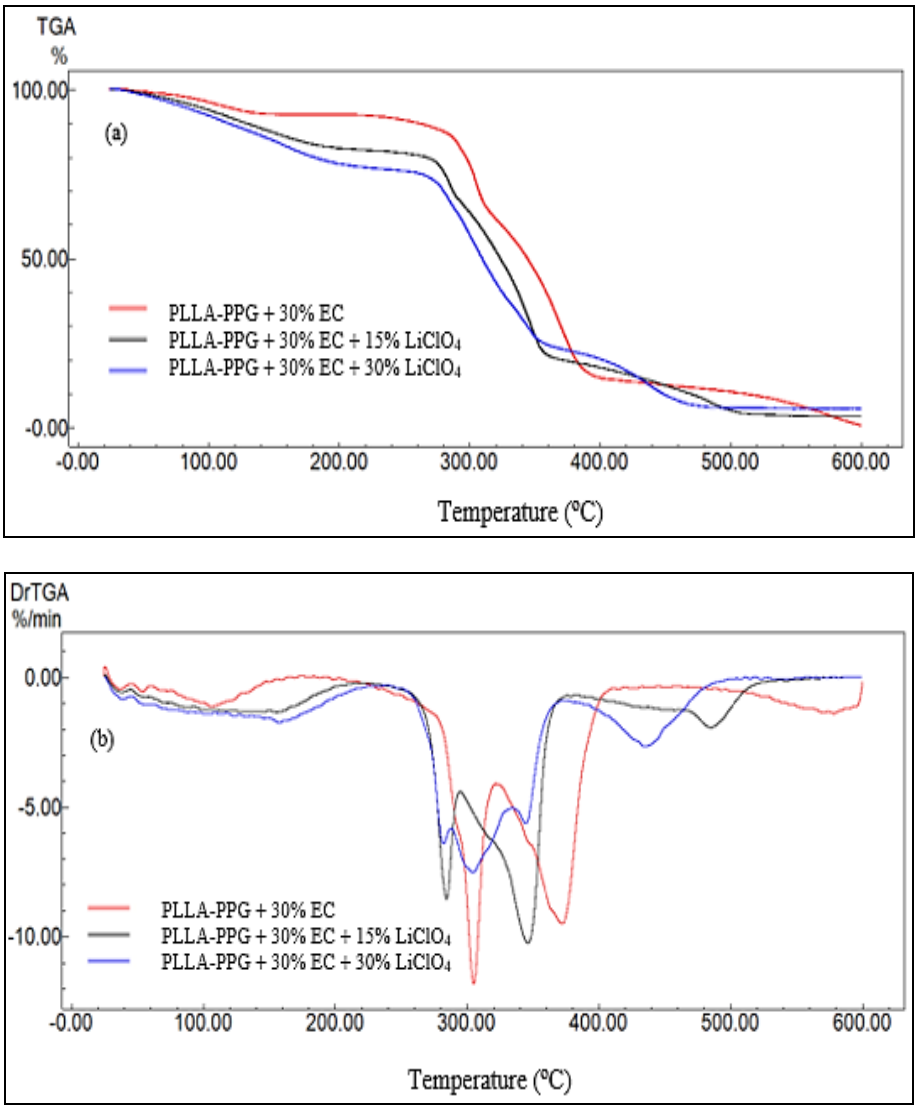


Figure 6. TGA (a) and DTG (b) thermogram of PLLA-PPG with 30 wt.% of EC and 0, 15 and 30 wt.% of $LiClO_4$

Conclusion

The solid polymer electrolyte PLLA-PPG with 30 wt. % of EC and different weight percent of $LiClO_4$ was successfully prepared by a solution casting method. The optimum ionic conductivity was estimated to be 4.57×10^{-5} S cm^{-1} at 25 wt.% of $LiClO_4$. Infrared analysis showed evidence for polymer-salt complex formation. Meanwhile, thermal analysis showed that the PLLA-PPG SPE film was stable up to 270 ºC. Lastly, XRD analysis proved that the crystallinity of the SPE film decreases with the addition of salt.

Acknowledgement

The authors would like to thank the Universiti Kebangsaan Malaysia (UKM) for providing analytical equipment used in this research. This work was supported by the Universiti Kebangsaan Malaysia and the Ministry of Higher Education under research grant numbers ERGS/1/2013/TK07/UKM/03/1 and GUP-2016-060.

References

1. Rodrigues, L. C., Silva, M. M. and Smith, M. J. (2012). Synthesis and characterization of amarphous poly(ethylene oxide)/poly(trimethylene carbonate) polymer blend electrolytes. *Electrochimica Acta,* 86: 339-345.
2. Noor, S. A. M., Ahmad, A., Rahman, M. Y. A and Talib, I. A. (2010b). Solid polymeric electrolyte of poly(ethylene)oxide-50% epoxidized natural rubber-lithium triflate (PEO-ENR50-$LiCF_3SO_3$). *Natural Science,* 3: 190-196.
3. Murata, K., Izuchi, S. and Yoshihisa, Y. (2000). An overview of the research and development of solid polymer electrolyte batteries. *Electrochimica Acta,* 45:1501-1508.
4. Cha, D. K. and Park, S. M. (1998). Electrochemical characterization of polyethylene glycols as solid polymer electrolytes. *Journal of Electroanalytical Chemistry,* 459: 135-144.
5. Ng, B. C., Wong, H. Y., Chew, K. W. and Osman, Z. (2011). Development and characterization of poly-ε-caprolactone-based polymer electrolyte for lithium rechargeable battery. *International Journal of Electrochemical Science,* 6: 4355-4364.
6. Tan, C. H., Ahmad, A. and Anuar F. H. (2014). Synthesis and characterization of polylactide-poly(ethylene glycol) block copolymer as solid polymer electrolyte. *Asian Journal of Chemistry,* 26: 230-236.
7. Piorkowska, E., Kulinski, Z., Galeski, A. and Masirek, R. (2006). Plasticization of semicrystalline poly(l-lactide) with poly(propylene glycol). *Polymer,* 47: 7178-7188.
8. Gupta, B., Revagade, N. and Hilborn, J. (2007). Poly(lactic acid) fiber: An overview. *Progress in Polymer Science,* 32: 455-482.
9. Su'ait, M. S., Ahmad, A., Badri, K. H., Mohamed, N. S., Rahman, M. Y. A., Ricardo, C. L. A. and Scardi, P. (2014). The potential of polyurethane bio-based solid polymer electrolyte for photoelectrochemical cell application. *International Journal of Hydrogen Energy,* 39: 3005-3017.
10. Chew, K. W., Ng, T. C. and How Z. H. (2013). Conductivity and microstructure study of PLA-based polymer electrolyte salted with lithium perchlorate, $LiClO_4$. *International Journal of Electrochemical Science,* 8: 6354-6364.
11. Ahmad, A., Rahman, M. Y. A., Harun, H., Su'ait, M. S. and Yarmo, M. A. (2012). Preparation and characterization of 49% poly(methyl methacrylate) grafted natural rubber (MG49)-stannum (IV) oxide (SnO_2)-lithium salt based composite polymer electrolyte. *International Journal of Electrochemical Science,* 7: 8309-8325.
12. Su'ait, M. S., Ahmad, A., Hamzah, H. and Rahman, M. Y. A. (2011). Effect of lithium salt concentrations on blended 49% poly(methyl methacrylate) grafted natural rubber and poly(methyl methacrylate) based solid polymer electrolyte. *Electrochimica Acta,* 57: 123-131.
13. Ji, J, K. and Zhong, W. H. (2011). Simultaneous improvement in ionic conductivity and mechanical properties of multi-functional block-copolymer modified solid polymer electrolytes for lithium ion batteries. *Journal of Power Sources,* 196: 10163-10168.
14. Isa, K. B. M., Othman, L. and Osman Z. (2011). Comparative studies on plasticized and unplasticized polyacrylonitrile (pan) polymer electrolytes containing lithium and sodium salts. *Sains Malaysiana,* 40: 695-700.

15. Pandey, K., Asthana, N., Dwivedi, M. M. and Chaturvedi, S. K. (2013). Effect of plasticizers on structural and dielectric behaviour of [PEO + $(NH_4)_2C_4H_8(COO)_2$] polymer electrolyte. *Journal of Polymers,* 2013: 752596.
16. Dash. S. and Ghosh. A. (2015). Ionic conductivity and dielectric permittivity of PEO-$LIClO_4$ solid polymer electrolyte plasticized with propylene carbonate. *AIP Advances* 5: 027125.
17. Pradhan, D. K., Choudhary, R. N. P., Samantaray, B. K., Karan, N. K. and Katiyar, R. S. (2007). Effect of plasticizer on structural and electrical properties of polymer nanocomposite electrolytes. *International Journal of Electrochemical Science,* 2: 861-871.
18. Ibrahim, S., Yasin, S. M. M., Ahmad, R. and Johan M. R. (2012). Effects of various ec plasticizer concentrations on salted PEO based solid polymer electrolytes. *International Journal of Plastic Technology*, 16(2): 125-135.
19. Pitawala, H. M. J. C., Dissanayake, M. A. K. L., Seneviratne, V. A., Mellander, B. -E. and Albinson I. (2008). Effect of plasticizers (EC or PC) on the ionic conductivity and thermal properties of the $(PEO)_9$LiTf: Al_2O_3 nanocomposite polymer electrolyte system. *Journal of Solid State Electrochemistry,* 12: 783-789.
20. Johan, M. R., Shy, O. H., Ibrahim, S., Yassin, S. M. M. and Hui, T. Y. (2011). Effects of Al_2O_3 nanofiller and EC plasticizer on the ionic conductivity enhancement of solid PEO-$LiCF_3SO_3$ solid polymer electrolyte. *Solid State Ionics,* 196: 41-47.
21. Lim, C. S., Teoh, K. H., Ng, H. M., Liew, C. W. and Ramesh, S. (2017). Ionic conductivity enhancement studies of composite polymer electrolyte based on poly(vinyl alcohol)-lithium perchlorate-titanium oxide. *Advanced Materials Letters,* 8(4): 465-471.

Malaysian Journal of Analytical Sciences, Vol 23 No 4 (2019):715 - 724
DOI: https://doi.org/10.17576/mjas-2019-2304-18

MALAYSIAN JOURNAL OF ANALYTICAL SCIENCES
Published by The Malaysian Analytical Sciences Society
ISSN 1394 - 2506

QUANTITATIVE ANALYSIS OF PHENOLICS CONTENT IN TWO ROSELLE VARIETIES (*Hibiscus sabdariffa*) BY HIGH PERFORMANCE LIQUID CHROMATOGRAPHY

(Analisis Kuantitatif bagi Sebatian Fenolik dalam Dua Varieti Roselle (*Hibiscus sabdariffa*) menggunakan Kromatografi Cecair Berprestasi Tinggi)

Siti Aishah Mohd Ali[1,2], Satirah Zainalabidin[3], Jalifah Latip[1]*

[1]*Chemistry Programme, Faculty of Science and Technology,*
Universiti Kebangsaan Malaysia, 43600 UKM Bangi, Selangor, Malaysia
[2]*Faculty of Science and Natural Resources,*
Universiti Malaysia Sabah, Jalan UMS, 88400 Kota Kinabalu, Sabah, Malaysia
[3]*School of Applied Health, Faculty of Health Sciences,*
Universiti Kebangsaan Malaysia, 50300 Kuala Lumpur, Malaysia

**Corresponding author: jalifah@ukm.edu.my*

Received: 31 March 2018; Accepted: 17 April 2019

Abstract

Phenolics content of two roselle varieties, *H. sabdariffa* var. UKMR-2 and *H. sabdariffa* var. UMKL-1 was determined based on high performance liquid chromatography method using a photodiode array detector (HPLC-PDA) with gradient elution. Roselle calyces were extracted with water *via* sonication (50 °C, 30 minutes). The chromatographic separation was carried out on Purospher STAR RP-18e LichroCART column (250 mm × 4.6 mm × 5 µm) and detection was carried out at three different wavelengths (265, 320 and 520 nm). The developed HPLC method provided high percentage of recovery (95 - 102%), good linearity at $R^2 > 0.99$, low limit of detection (LOD) and low limit of quantitation (LOQ). Two predominant anthocyanins were detected by HPLC-PDA in both *H. sabdariffa* varieties and were identified as delphinidin-3-*O*-sambubioside and cyanidin-3-*O*-sambubioside. In addition, chlorogenic acid, caffeic acid and ascorbic acid were also detected. High content of phenolics and ascorbic acid were detected in UKMR-2 as compared to UMKL-1, suggested this variety have high potential for commercial cultivation.

Keywords: anthocyanins, *Hibiscus sabdariffa*, HPLC-PDA

Abstrak

Kandungan fenolik bagi dua varieti rosel, *H. sabdariffa* var. UKMR-2 dan *H. sabdariffa* var. UMKL-1 ditentukan berdasarkan kaedah kromatografi cecair berprestasi tinggi menggunakan pengesan foto-diod (KCPT-PFD) dengan elusi kecerunan kekutuban. Kaliks rosel diekstrak dengan air secara sonikasi (50 °C, 30 minit). Pemisahan kromatografi dilakukan menggunakan turus Purospher STAR RP-18e LichroCART (250 mm × 4.6 mm × 5 µm) dan pengesanan dilakukan pada tiga panjang gelombang yang berbeza (265, 320 dan 520 nm). Kaedah KCPT yang dibangunkan mempunyai peratusan dapatan semula yang tinggi (95 - 102%), lineariti yang baik pada $R^2 > 0.99$ serta had pengesanan (LOD) dan kuantifikasi (LOQ) yang rendah. Dua sebatian antosianin dikesan oleh KCPT-PFD dalam kedua-dua varieti *H. sabdariffa* dan dikenal pasti sebagai delfinidin-3-*O*-sambubiosida dan sianidin-3-*O*-sambubiosida. Selain itu, asid klorogenik, asid kafeik dan asid askorbik juga berjaya dikesan. UKMR-2 dikesan mengandungi sebatian fenolik dan asid askorbik yang tinggi berbanding UMKL-1, mencadangkan varieti ini mempunyai potensi yang tinggi sebagai tanaman komersil.

Kata kunci: antosianin, *Hibiscus sabdariffa*, KCPT-PFD

Introduction

The species *Hibiscus sabdariffa*, popularly known as 'Asam Paya' or 'Asam Susur' in Malaysia, is a member of the Malvaceae family. This plant exhibits anti-oxidant, anti-cancer, anti-hypertensive, anti-hyperlipidemic, hepatoprotective and many other properties [1], being commonly consumed as beverages, jams and syrup, and used in folk medicine as diuretic, mild laxative, digestive, antiseptic, sedative, emollient of cardiac and nerve diseases [2, 3]. Roselle is rich in various bioactive compounds such as organic and phenolic acids, flavonoids, tannins and anthocyanins such as cyanidin-3-*O*-sambubioside and delphinidin-3-*O*-sambubioside, which are also responsible for the bright red colouration and antioxidant properties of calyces [4, 5]. *H. sabdariffa* var. UMKL-1 (also known as *Terengganu* variety) was launched in the early 1990s by Universiti Malaya (UM) for commercial cultivation purpose due to its high quality and calyx yield. In 2009, a new Malaysia roselle (mutant) var. UKMR-2 was released by Universiti Kebangsaan Malaysia (UKM). The new variety has special characteristics compared to their parent variety 'Arab' and other local varieties [6]. In general, var. UKMR-2 has a shorter life cycle, higher lodging resistance and produce higher yield of calyces per plant. The colour of roselle var. UKMR-2's calyces has deeper red color compared to var. UMKL-1 [6]. In general, red anthocyanin pigment colour is the reliable indicator to determine the maturity and quality of fruit.

Phenolics content have been widely investigated in various plants using different chromatographic techniques due to their nutritional potential and therapeutic value. Chemical verification using high performance liquid chromatography (HPLC) is the most popular and reliable technique among all chromatographic separation techniques for the separation of bioactive compound. HPLC has been reported in the identification and quantification of anthocyanins in roselle extract [7-8]. Sukwattanasinit et al. [7] and Bernal et al. [9] reported that delphinidin-3-sambubioside and cyanidin-3-sambubioside were two major anthocyanin compounds found in roselle dried calyces. Besides that, other anthocyanins (cyanidin-3-glucoside, delphinidin-3-glucoside), phenolic acid (chlorogenic acid, protocatechuic acid, hydroxycitric acid) and flavonoids (quercetin, kaempferol, gossypetin, hibiscetin, luteolin and its glycoside) have also been previously reported [5, 8-10].

Although the chemical composition of plants is largely determined by the genetic characteristics of the species, several factors can coordinate or change the rate of production such as various environmental factors [11], time collection [12] and the employment of different extraction methods [13]. Despite of the bioactive compounds and increasing demand of *H. sabdariffa* calyxes worldwide, little is known about chemical components such as phenolic constituents in different Malaysia roselle varieties. Hence, this paper aims to develop a simple analytical methodology to simultaneously identify and quantify phenolic content present in the calyx extracts of *H. sabdariffa* var. UKMR-2 and *H. sabdariffa* var. UMKL-1. The compound identification and quantification were carried out using high performance liquid chromatography with photodiode array detection (HPLC-PDA) with gradient elution.

Materials and Methods

Chemicals and standards

Formic acid and acetonitrile HPLC grade used for preparing mobile phases were purchased from Merck (Darmstadt, Germany) and Fisher Scientific (USA), respectively. The standard, ascorbic acid, chlorogenic acid, caffeic acid, delphinidin-3-*O*-sambubioside and cyanidin-3-*O*-sambubioside were purchased from Merck (Darmstadt, Germany) and Extrasynthese (Genay Cedex, France). Acetonitrile HPLC grade was degassed in an ultrasonic bath (Branson, USA) before using. As for vortex mixer, G560E Vortex-Genie 2 (Scientific Industries, Bohemia, NY, USA) was used. Distilled water was purified and deionized by EVOQua water system (Water Technologies, Fahrenberg, Germany).

Sample collection and preparation

Roselle var. UKMR-2 was collected from *Kompleks Rumah Tumbuhan* greenhouse, Universiti Kebangsaan Malaysia (UKM), Bangi at the end of December 2017, while for roselle var. UMKL-1 was purchased from HERBagus Sdn. Bhd. in Kepala Batas, Penang. The fresh calyces from each variety were washed with water, drained, followed by seed removal then air dried at room temperature. Dry calyces were ground into powder and the extraction was prepared according to the method described by Chumsri et al. [14]. Briefly, the extraction of dried calyces with water in a ratio of 1:10 conducted in a water bath at a constant temperature of 50 °C for 30 minutes.

Each extract was filtered with a piece of clean, sterile coarse cloth then filtrates were dried using Alpha 1-2 LDplus freeze dryer (Martin Christ, Germany). 10 mg of freeze-dried extracts from each variety were dissolved in 1 mL of 0.1% formic acid in water. Samples were sonicated for 5 minutes and filtered through a 0.45 µm PTFE membrane syringe filter (Gema Medical, Spain) and directly injected into the HPLC system.

High performance liquid chromatography with photodiode array detector

HPLC analyses were performed on the HPLC Waters e2695 separation module equipped with a degasser, an auto-sampler automatic injector and Waters 2998 Photodiode Array Detector at multiple wavelengths. HPLC experiments were conducted using Purospher STAR RP-18e LichroCART column (250 mm × 4.6 mm × 5 µm). HPLC-PDA separation and identification were carried out at a flow rate of 1 mL/min, injection volume 30 µL and 30 °C column oven temperature. 0.1% formic acid in water and 0.1% formic acid in acetonitrile were employed as mobile phases A and B, respectively, in gradient elution as follows: 10 - 15% B (0-15 minutes), 15 - 90% B (15-25 minutes), 90-10 % B (25-30 minutes) and 10% B (30-35 minutes). The chromatograms were monitored at 265, 320 and 520 nm. All compounds were determined by standard reference calibration curves and were expressed as mg per g dried weight. Linear correlation co-efficient were > 0.996 for each compound.

Method validation

The method was validated according to the International Conference on Harmonization, ICH guidelines [15]. The stock solution (1 mg/mL) of each standard (delphinidin-3-*O*-sambubioside, cyanidin-3-*O*-sambubioside, chlorogenic acid, caffeic acid and ascorbic acid) was diluted with 0.1% formic acid in water. Stock dilution was prepared using the same solvent into eight different concentrations ranges between 4.17 and 150 µg/mL. These standard solutions are kept at 4 °C before being analysed. The following validation characteristics were evaluated: Linearity, precision, accuracy and the limits of detection and quantification (LOD and LOQ). Linearity was determined by injecting 30 µL of the standard mixture in eight concentrations ranges from 4.17 to 150 µg/mL in triplicate. The calibration curves were obtained for each individual compound by plotting the peak area versus concentration. Regression analysis was performed in order to determine the linearity (R^2) of the calibration graphs. Precision was performed according to ICH guidelines that included repeatability and intermediate precision.

For repeatability (intra‐day assay precision), three concentrations of the standard compounds (25, 50 and 100 µg/mL) were injected in three replicates during the same day and under the same experimental conditions. The intermediate precision was performed by the same analyst using the same concentrations of marker compounds and injected in three different days in triplicates. The precision method was reported as a percentage of relative standard deviation (% RSD) of peak concentration and retention time. Limit of detection (LOD) and limit of quantification (LOQ) were calculated based on signal to noise (S/N) ratio through the slope and standard deviation (SD) method using the following formula; LOD = (3.3 × σ) / s and LOQ = (10 × σ) / s, where σ = SD of blank response and s = slope of the linear regression equations. The accuracy of an analytical method expresses the nearness between the expected value and the experimental value. The accuracy was analysed by calculating the average percentage of recoveries (% Recovery) for each standard at three different concentrations (25, 50 and 100 µg/mL). All standard solutions were carefully prepared and analysed (n = 3) by the proposed method in three non-consecutive days. The same solutions were used to calculate the precision. The recovery percentage of the experiment were analysed using formula in equation 1:

$$\% \text{ Recovery} = (\text{Recovered concentration} / \text{Injected concentration}) \times 100 \quad (1)$$

Results and Discussion

HPLC validation method

Validation method provides documented evidence, and a high degree of assurance that an analytical method employed for a specific test is suitable for its intended use. The regression equation with correlation equation (R^2), LOD and LOQ were showed in Table 1. All compounds showed good linearity with correlation equation (R^2) range from 0.9951 to 0.9992 and % RSD of < 2.0%. According to Anvisa [16], the minimum acceptable correlation coefficient is 0.990. The LOD was < 0.46 µg/mL and LOQ was < 1.39 µg/mL. LOD and LOQ values in this method showed good sensitivity that can be detected and quantified at a very low concentration (< 1.5 µg/mL).

Table 1. Linearity, correlation coefficient (R^2), LOD and LOQ of compounds

Compounds	Linearity Range (µg/mL)	Regression Equation	R^2 (*n*=3)	LOD (µg/mL)	LOQ (µg/mL)
Delphinidin 3-*O*-sambubioside	6.26 - 150	y = 36342x - 185574	0.9976	0.22	0.67
Cyanidin 3-*O*-sambubioside	6.26 - 150	y = 38423x - 162923	0.9951	0.46	1.39
Chlorogenic acid	4.17 - 100	y = 69202x - 89921	0.9991	0.04	0.13
Caffeic acid	4.17 - 100	y = 41593x - 13799	0.9992	0.08	0.26
Ascorbic acid	4.17 - 100	y = 3483.3x - 5052.3	0.9984	0.15	0.47

y = peak area; x = concentration (µg/mL); LOD = Limit of Detection; LOQ = Limit of Quantification; R^2 = Correlation equation

The RSD values for repeatability (intra‑day precision) were within the range of 0.21 - 1.83% for peak concentration and 0.01 - 0.46% for retention time. The RSD values for inter-day were in the range of 0.21 - 1.75% for peak concentration and 0.04 - 0.49% for retention time. These values for both intra-day and inter-day analyses were within the prescribed limits of the ICH guidelines (RSD < 2%). It is therefore the proposed method is precise and reproducible. Tables 2 and 3 showed the average percentage RSD values and average percentage recovery ± SD of the reference compounds. The results also showed a good accuracy between the experimental and theoretical values, which indicated the method is reliable and reproducible for quantitative determination of five compounds in roselle calyx extracts. Several HPLC quantification methods have been reported in roselle extracts [7-9, 17-18]. However, most of these methods are not properly validated. Moreover, the methods are either time consuming or require complex mobile phase, which will limit their application. Therefore, we herein presented an improved method for qualitative and quantitative evaluation of phenolic compounds and ascorbic acid with shorter run time, enhanced in reliability, efficiency and reproducibility.

Table 2. Repeatability analysis (intra‑day precision) of compounds

Compounds	Concentration (µg/mL)	Repeatability (Intra-Day Precision) (*n* = 3)			
		Mean ± SD (µg/mL)	% RSD	RT ± SD	% RSD
Delphinidin 3-*O*-sambubioside	25	23.98 ± 0.11	0.46	6.17 ± 0.03	0.42
	50	48.11 ± 0.20	0.42	6.13 ± 0.03	0.45
	100	100.46 ± 0.27	0.27	6.06 ± 0.02	0.34
Cyanidin 3-*O*-sambubioside	25	24.96 ± 0.46	1.83	9.10 ± 0.04	0.46
	50	47.65 ± 0.10	0.21	9.06 ± 0.04	0.46
	100	101.00 ± 1.27	1.26	9.00 ± 0.03	0.29
Chlorogenic acid	25	25.16 ± 0.06	0.25	11.57 ± 0.02	0.15
	50	48.81 ± 0.11	0.23	11.57 ± 0.04	0.33
	100	100.98 ± 0.22	0.22	11.57 ± 0.01	0.05
Caffeic acid	25	25.94 ± 0.14	0.53	15.55 ± 0.02	0.12
	50	47.17 ± 0.28	0.60	15.56 ± 0.04	0.28
	100	100.68 ± 0.22	0.22	15.56 ± 0.01	0.04
Ascorbic acid	25	24.09 ± 0.42	1.75	5.09 ± 0.00	0.05
	50	50.61 ± 0.68	1.35	5.08 ± 0.00	0.05
	100	101.76 ± 0.96	0.95	5.08 ± 0.00	0.01

SD=Standard deviation; % RSD=Percentage of relative standard deviation; RT=Retention time

Table 3. Accuracy and intermediate precision (inter‑day precision) data for the developed method

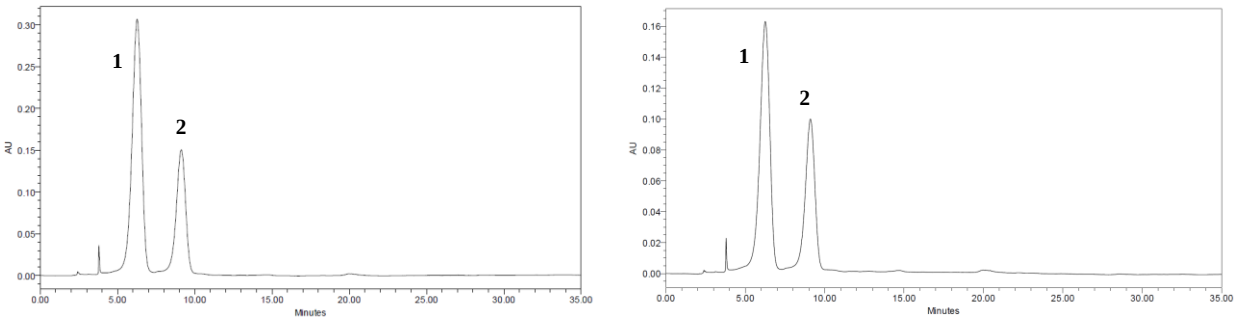
Compounds	Concentration (µg/mL)	Repeatability (Inter-Day Precision) (*n* = 3)				% Mean Recovery
		Mean ± SD (µg/mL)	% RSD	RT ± SD	% RSD	
Delphinidin 3-*O*-sambubioside	25	23.81 ± 0.17	0.70	6.32 ± 0.02	0.26	95.3
	50	48.08 ± 0.24	0.51	6.30 ± 0.03	0.49	96.2
	100	102.21 ± 1.38	1.35	6.29 ± 0.02	0.33	102.0
Cyanidin 3-*O*-sambubioside	25	25.22 ± 0.36	1.43	9.19 ± 0.02	0.20	100.9
	50	47.50 ± 0.26	0.54	9.17 ± 0.03	0.37	95.0
	100	101.67 ± 0.82	0.81	9.14 ± 0.03	0.30	101.7
Chlorogenic acid	25	25.37 ± 0.12	0.46	11.65 ± 0.02	0.19	101.5
	50	48.87 ± 0.11	0.23	11.65 ± 0.04	0.33	97.7
	100	101.02 ± 0.25	0.25	11.63 ± 0.02	0.19	101.0
Caffeic acid	25	26.01 ± 0.11	0.44	15.62 ± 0.02	0.11	104.0
	50	47.23 ± 0.17	0.36	15.61 ± 0.04	0.24	94.5
	100	100.72 ± 0.21	0.21	15.60 ± 0.02	0.13	100.7
Ascorbic acid	25	23.80 ± 0.12	0.51	5.10 ± 0.00	0.06	95.2
	50	50.04 ± 0.70	1.40	5.10 ± 0.01	0.14	100.1
	100	99.78 ± 1.74	1.75	5.09 ± 0.00	0.04	99.8

SD=Standard deviation; % RSD=Percentage of relative standard deviation; RT=Retention time

Identification and quantification of phenolic contents

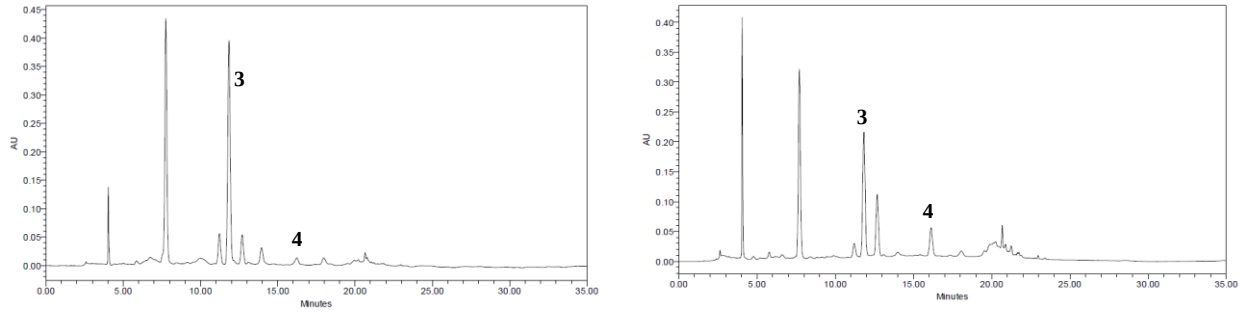
Measurements of phenolic content, especially on anthocyanins have long been utilized as an indicator to determine the quality and processing of roselle products. The methodology employed to determine the phenolic constituents by HPLC-PDA enables the separation and identification of five compounds as shown in Figure 1 - 3. In this study, phenolic compounds were identified and quantified based on their retention times, which were compared with the standard reference materials. Peaks were identified as; **1**. Delphinidin-3-*O*-sambubioside; **2**. Cyanidin-3-*O*-sambubioside; **3**. Chlorogenic acid; **4**. Caffeic acid; and **5**. Ascorbic acid. The phenolic and ascorbic acid content in the calyces of two roselle varieties is shown in Table 4. From the result, there are significant differences between compounds ($p < 0.05$) in different roselle varieties.

There are two main anthocyanins detected at 520 nm in both varieties of *H. sabdariffa* calyces with a retention time of 6.27 minutes and 7.81 minutes. The peaks were identified as delphinidin-3-*O*-sambubioside (**1**) and cyanidin-3-*O*-sambubioside (**2**). Anthocyanin production (based on the total amounts of anthocyanins) in UKMR-2 is 27.78 mg/g FDE, which almost three times higher than in the calyx of UMKL-1 (10.01 mg/g FDE). However, both varieties indicated delphinidin-3-*O*-sambubioside concentration was higher compared to cyanidin-3-*O*-sambubioside (Table 4). These findings agree with Bernal et al. [9] on Colombian *H. sabdariffa* L. and Kouakou et al. [8] on Côte d'Ivoire *H. sabdariffa* L. Delphinidin-3-sambubioside and cyanidin-3-sambubioside were identified as the major pigments with almost 70% of the anthocyanins in *H. sabdariffa* [19]. Delphinidin and cyanidin are known to contribute to the bioactive function because they have higher bioavailability as compared to the other anthocyanins [20].



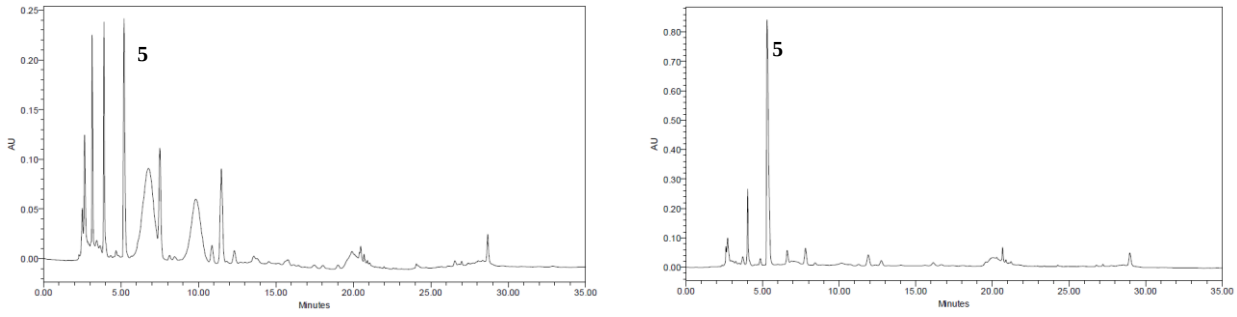
(a) (b)

Figure 1. HPLC-PDA profiles of phenolics in roselle calyces at 520 nm; (a) UKMR-2 and (b) UMKL-1. 1. Delphinidin-3-*O*-sambubioside; 2. Cyanidin-3-*O*-sambubioside



(a) (b)

Figure 2. HPLC-PDA profiles of phenolics in roselle calyces at 320 nm; (a) UKMR-2 and (b) UMKL-1. 3. Chlorogenic acid; 4. Caffeic acid



(a) (b)

Figure 3. HPLC-PDA profiles of ascorbic acid in roselle calyces at 265 nm; (a) UKMR-2 and (b) UMKL-1. 5. Ascorbic acid

Table 4. Concentrations of phenolics and ascorbic acid in two roselle varieties (UKMR-2 and UMKL-1)

Compound (peak)	Minutes	(mg/g FDE)		
		UKMR-2	UMKL-1	References
Delphinidin 3-O-sambubioside (**1**)	6.13 – 6.17	18.98 ± 5.11[a]	7.10 ± 0.02[b]	21.28 ± 0.05 [8]; 21.20 ± 2.16 [18]
Cyanidin 3-O-sambubioside (**2**)	9.05 – 9.10	8.80 ± 3.67[a]	2.91 ± 0.04[b]	17.11 ± 0.10 [8]; 5.17 ± 4.20 [18]
Chlorogenic acid (**3**)	11.54 – 11.57	5.11 ± 1.23[a]	4.06 ± 0.03[a]	2.70 ± 0.20 [23]
Caffeic acid (**4**)	15.52 – 15.56	0.76 ± 0.07[a]	1.58 ± 0.01[b]	2.98 ± 0.45 [18]
Ascorbic acid (**5**)	5.05 – 5.09	34.15 ± 13.23[a]	13.12 ± 1.07[a]	3.62 ± 2.14 [24]

Values represent the mean of three replicates ± standard deviation. Mean denoted by different letters in the same row indicate significant differences ($p < 0.05$). FDE, freeze-dried extract.

The results presented showed that the content of anthocyanins in both varieties is lower than previous findings. Kouakou et al. [8] reported that delphinidin-3-*O*-sambubioside and cyanidin-3-*O*-sambubioside contents in *H. sabdariffa* L. originated from Côte d'Ivoire is 21.38 mg/g DW and 17.11 mg/g DW respectively. The content and distribution of the anthocyanins in roselle are believed to be influenced by the fruit source, type of cultivation, the degree of fruit maturation, post-harvest storage condition, environmental conditions, genetic factors and the variety of the plant [13, 21, 22].

On the other hand, the analysis showed that only three non-anthocyanin compounds can be identified based on standard reference materials. At 320 nm, two peaks were identified as chlorogenic acid (**3**) and caffeic acid (**4**) with a retention time 11.91 and 16.29 min, respectively. Meanwhile, at 265 nm, only ascorbic acid (**5**) has been identified with a retention time of 5.39 min. The presence of all compounds is in agreement with previous reports on other *H. sabdariffa* varieties worldwide [8, 18, 23, 24]. UKMR-2 presented a higher diversity of phenolic compounds and ascorbic acid compared to UMKL-1. Figure 4 shows the structures of the identified compounds.

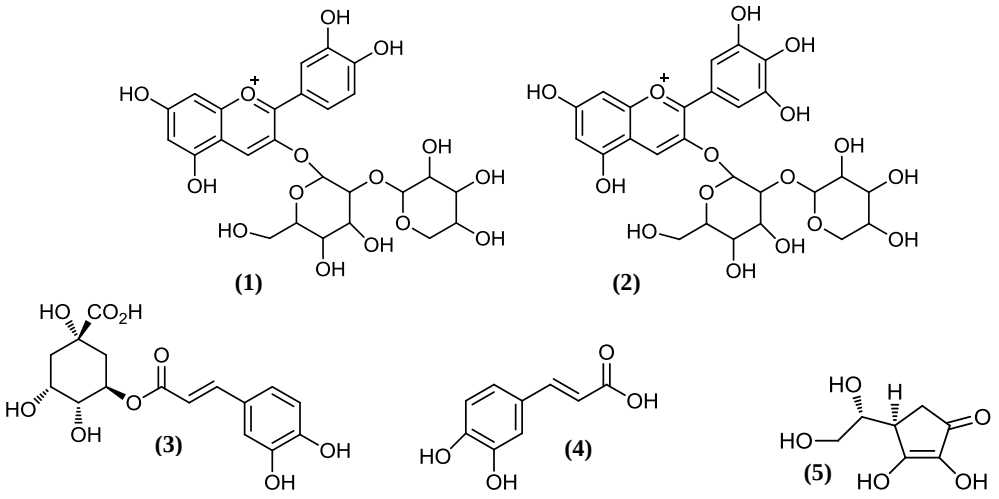


Figure 4. Proposed structures for the identified compounds in the *H. sabdariffa* water extract

A remarkable amount of ascorbic acid was found in UKMR-2 with 2.5-fold greater than in the calyces of UMKL-1. Ascorbic acid, a water-soluble vitamin is an essential nutrient in human diets and ubiquitous in fruits and vegetables. Due to the remarkable antioxidant and other biological properties of this compound, it is widely applied

in pharmaceutical and cosmetic industry [25]. The wide variation of ascorbic acid content in fruits and vegetables can be influenced by various factors such as genotype differences, pre-harvest climatic conditions, cultural practices, maturity and harvesting methods and post-harvest handling procedures [26, 27]. Due to its relatively high concentration especially in UKMR-2, ascorbic acid may contribute significantly to the antioxidant activity of roselle calyces. In addition, chlorogenic acid is reported to have potential protective effect on human health, in part by acting as an antioxidant through radical scavenging and metal chelation [28, 29]. The present study revealed a low amount of caffeic acid found in both calyces of *H. sabdariffa* varieties. Caffeic acid is one of the major hydroxycinnamic acid component and a well-known antioxidant, which boosts immunity, controls lipid levels in blood and anti-mutagenic. Caffeic acid is found mainly in the form of its ester (an immediate precursor of chlorogenic acid) in fruits, vegetables and herbs [30].

These results showed that the distribution of the phenolic and ascorbic acid compounds in both roselle varieties may depend on the genetic variety and growing techniques. This is likely due to different cultivation methods where UMKL-1 is grown at the farm in Kepala Batas, Penang, while UKMR-2 is grown in a nursery polyethene bag at the *Kompleks Rumah Tumbuhan* greenhouse, UKM. The two different cultivation methods (in terms of soil type, irrigation, fertilizer, weeding and spacing) can affect the production of secondary metabolites in roselle. Anthocyanin and phenolic contents are also directly related to the maturity degree as well as to the seasonal changes [31]. According to Khafaga and Koch [32], the acid content of the calyces increases during growth, but decreases when it reaches maturity or ripens. The acid content changes during maturity may be attributed to the anabolism and catabolism activities in calyx [33]. These results agree with several studies which report reductions of phenolic compounds during ripening [34-36]. Nevertheless, Raffo et al. [36] reported that the accumulation of some biologically active compounds was depended on different biosynthetic pathways and mechanisms of metabolic control.

Conclusion

A simple HPLC method was developed for quantitative analysis of major phenolics and ascorbic acid content in *H. sabdariffa* var. UKMR-2 and *H. sabdariffa* var. UMKL-1. The proposed HPLC method were validated and proved to be reliable. The HPLC-PDA profiles of the roselle water extract showed the presence of delphinidin-3-*O*-sambubioside, cyanidin-3-*O*-sambubioside, ascorbic acid, caffeic acid and chlorogenic acid. High content of phenolics and ascorbic acid detected in *H. sabdariffa* var. UKMR-2 suggested this variety may replace the current UMKL-1 variety for commercial cultivation.

Acknowledgement

This work was supported by NKEA Research Grant Scheme (NRGS) from Ministry of Agriculture (MoA) (NH1014D061). Financial assistance from the Ministry of Higher Education (MoHE) is kindly acknowledged for PhD scholarship. We indebted to the Centre for Research and Instrumentation Management (CRIM), UKM for the instrumentation facilities.

References

1. Padmaja, H., Sruthi, S. and Vangalaapati, M. (2014). Review on *Hibiscus sabdariffa* – A valuable herb. *International Journal of Pharmacy & Life Sciences,* 5(8): 3747-3752.
2. Fasoyiro, S.B., Babalola, S.O. and Owosibo T. (2005). Chemical composition and sensory quality of fruit-flavoured roselle (*Hibiscus sabdariffa*) drinks. *World Journal of Agricultural Sciences,* 1(2): 161-164.
3. Puro, K., Sunjukta, R., Samir, S., Ghatak, S., Shakuntala, I. and Sen, A. (2014). Medicinal uses of roselle plant (*Hibiscus sabdariffa* L.): A mini review. *Indian Journal of Hill Farming*, 27(1): 81-90.
4. Azza, A., Ferial, M. and Esmat, A. (2011). Physicochemical properties of natural pigments (anthocyanin) extracted from Roselle calyces (*Hibiscus sabdariffa). Journal of American Science*, 7(7): 445-456.
5. Obouayeba, A. P., Djyh, N. B., Diabate, S., Djaman, A. J., N'guessan, J. D., Kone, M. and Kouakou, T. H. (2014). Phytochemical and antioxidant activity of roselle (*Hibiscus sabdariffa* L.) petal extracts. *Research Journal of Pharmaceutical, Biological and Chemical Sciences*, 5(2): 1453-1465.
6. Osman, M., Golam, F., Saberi, S., Majid, N. A., Nagoor, N. H. and Zulqarnain. M. (2011). Morpho-agronomic analysis of three roselle (*Hibiscus sabdariffa* L.) mutants in tropical Malaysia. *Australian Journal of Crop Science,* 5(10):1150-1156.

7. Sukwattanasinit, T., Burana-osot, J. and Sotanaphun, U. (2007). Spectrophotometric method for quantitative determination of total anthocyanins and quality characteristics of roselle (*Hibiscus sabdariffa*). *Planta Medica,* 73: 1517-1522.
8. Kouakou, T. H., Konkon, N. G., Ayolie, K., Obouayeba, A. P., Abeda, Z. H. and Kone, M. (2015). Anthocyanin production in calyx and callus of roselle (*Hibiscus sabdariffa* L.) and its impact on antioxidant activity. *Journal of Pharmacognosy and Phytochemistry,* 4(3): 9-15.
9. Bernal, F. A., Orduz-Diaz, L. L. and Coy-Barrera, E. (2016). Application of FARAFAC and OPLS-DA analysis on HPLC fingerprints for the characterization of *Hibiscus sabdariffa* calyces. *Quimica Nova,* 39(2): 160-166.
10. Rodreguez-Medina, I.C., Debon, R.B., Molina, V.M., Villaverde, C.A., Joven, J., Menendez, J.A., Carretero, A.S. and Gutierrez, A.F. (2009). Direct characterization of aqueous extract of *Hibiscus sabdariffa* using HPLC with diode array detection coupled to ESI and ion trap MS. *Journal of Separation Science*, 32: 3441-3448.
11. Diniz, A. C. B., Astarita, L.V. and Santaré, E. R. (2007). Alterac¸ ão dos metabólitos secundáriosem plantas de *Hypericum perforatum* L. (Hypericaceae) submetidas à secagem eao congelamento. *Acta Botanica Brasilica*, 21, 443–450.
12. Gobbo-Neto, G. L. and Lopes, N. P. (2007). Plantas medicinais: fatores de influência noconteúdo de metabólitos secundários. *Quimica Nova,* 30, 374-381.
13. Naczk, M. and Shahidi, F. (2004). Extraction and analysis of phenolics in food. *Journal of Chromatography*, 1054: 95-111.
14. Chumsri, P., Airichote, A. and Itharat, A. (2008). Studies on the optimum conditions for the extraction and concentration of roselle (*Hibiscus sabdariffa* Linn.) extract. *Songklanakarin Journal of Science and Technology,* 30(1): 133-139.
15. Validation of analytical procedures: Text and methodology Q2 (R1). (2005). ICH Harmonised Tripartite Guideline, International Conference on Harmonization of Technical Requirements for Registration of Pharmaceuticals for Human Use. Access from http://www.ich.org/fileadmin/Public_Web_Site/ICH_Products/Guidelines/Quality/Q2_R1/Step4/Q2_R1_Guideline.pdf. [Access online 10 October 2017].
16. Anvisa (2003). Regulation-RE no. 899: Guide for validation of analytical and bioanalytical methods. National Health Surveillance Agency, Brazil. http://www.in.gov.br/imprensa/visualiza/index. [Access online 10 October 2017].
17. Chin, K. L., Zhen, J., Qi, Y., Chin, S. L., Breithaupt, M., Wu, Q. L., Simon, J., Henson, J. and Ferchaud, V. (2016). A comparative evaluation: Phytochemical composition and antioxidant capacity of three roselle (*Hibiscus sabdariffa* L.) accessions. *Acta Horticulturae,* 1125: 99-108.
18. Ifie, I., Ifie, B. E., Ibitoyed, D. O., Marshalla, L. J. and Williamson, G. (2018). Seasonal variation in *Hibiscus sabdariffa* (roselle) calyx phytochemical profile, soluble solids and α-glucosidase inhibition. *Food Chemistry,* 261: 164-168.
19. Amor, B. B. and Allaf, K. (2009). Impact of texturing using instant pressure drop treatment prior to solvent extraction of anthocyanins from Malaysian roselle (*Hibiscus sabdariffa*). *Food Chemistry* 115(3): 820-825.
20. Ichiyanagi, T., Shida, Y., Rahman, M. M., Hatano, Y. and Konishi, T. (2006). Bioavailability and tissue distribution of anthocyanins in bilberry (*Vaccinium myrtillus* L.) extract in rats. *Journal of Agriculture Food Chemistry,* 54: 6578–6587.
21. Deshmukh, S. R., Wadegaonkar, V. P., Bhagat, R. P. and Wadegaonkar, P. A. (2011). Tissue specific expression of anthraquinones, flavonoids and phenolics in leaf, fruit and root suspension cultures of Indian mulberry (*Morinda citrifola* L.). *Plant Omics Journal,* 4: 6-13.
22. Biswas, N., Balac, P., Narlakanti, S. K., Enamul Haque, M. D. and Mehedi Hassan, M. D. (2013). Identification of phenolic compounds in processed cranberries by HPLC method. *Journal of Nutrition and Food Science*, 3: 181.
23. Alarcon-Aguilar, F. J., Zamilpa, A., Perez-Garcia, M. D., Almanza-Perez, J. C., Romero-Nunez, E. and Campos-Sepulveda, E. A. (2007). Effect of *Hibiscus sabdariffa* on obesity in MSG mice. *Journal of Ethnopharmacology,* 114(1): 66-71.
24. Bamishaiye, E. I., Olayemi, F. F. and Bamishaiye, O. M. (2011). Effects of boiling time on mineral and vitamin C content of three varieties of *Hibiscus sabdriffa* drink in Nigeria. *World Journal of Agricultural Sciences,* 7(1): 62-67.

25. Prabhakar, B. and Pandita, N. (2010). Quantitative HPLC analysis of ascorbic acid and gallic acid in *Phyllanthus emblica*. *Journal of Analytical and Bioanalytical Techniques*, 1: 111.
26. Assis, S. A., Oliveira, O. M. M. F. and Lima, D. C. (2001). Activity of pectin methylesterase, pectin content and vitamin C in acerola fruit at various stages of fruit development. *Food Chemistry*, 74: 133-136.
27. Lee, J. K. and Kader, A. A. (2000). Pre-harvest and post-haverst factor influencing vitamin C content of horticultural crops. *Post-harvest Biology and Technology*, 20: 207-220.
28. Bouayed, J., Rammal, H., Dicko, A., Younos, C. and Soulimani, R. (2007). Chlorogenic acid, a polyphenol from *Prunus domestica* (Mirabelle), with coupled anxiolytic and antioxidant effects. *Journal of the Neurological Sciences*, 262: 77-84.
29. Lan, W. U. (2007). Effect of chlorogenic acid on antioxidant activity of *Flos lonicerae* extracts. *Journal of Zhejiang University Science*, 8(9): 673-679.
30. Seal, T. (2016). Quantitative HPLC analysis of phenolic acids, flavonoids and ascorbic acid in four different solvent extracts of two wild edible leaves, *Sonchus arvensis* and *Oenanthe linearis* of North-Eastern region in India. *Journal of Applied Pharmaceutical Science*, 6(2): 157-166.
31. Juliani, H. R., Welch, C. R., Wu, Q., Diouf, B., Malainy, D. and Simon, J. E. (2009). Chemistry and quality of Hibiscus (*Hibiscus sabdariffa*) for developing the natural-product industry in Senegal. *Journal of Food Science*, 74: S113.
32. Khafaga, E. R. and Koch, H. (1980). Stage of maturity and quality of roselle (*Hibiscus sabdariffa* L. var. *sabdariffa*) - Organic acids. *Angewandte Botanik*, 54: 287-293.
33. Hassanein, R. A., Khattab, H. K. I., EL-Bassiouny, H. M. S. and Sadak, M. S. (2005). Increasing the active constituents of sepals of roselle (*Hibiscus sabdariffa* L.) plant by applying gibberellic acid and benzyladenine. *Journal of Applied Sciences Research*, 1(2): 137-146.
34. Macheix, J. J., Fleuriet, A. and Billot, J. (1990). *Fruit Phenolic*. Boca Raton, CRC.
35. Buta, J. G. and Spaulding, D.W. (1997). Endogenous levels of phenolics in tomato fruit during growth and maturation. *Journal of Plant Growth Regulation*, 16: 43-46.
36. Raffo, A., Cherubino, L., Vincenzo, F., Ambrozino, P., Salucci, M., Gennaro, L., Bugianesi, R., Giuffrida, F. and Quaglia, G. (2002). Nutritional value of cherry tomatoes (*Lycopersicon esculentum* cv. Naomi F1) harvested at different ripening stages. *Journal of Agricultural and Food Chemistry*, 50: 6550-6556.

Malaysian Journal of Analytical Sciences, Vol 23 No 4 (2019): 725 - 735
DOI: https://doi.org/10.17576/mjas-2019-2304-19

MALAYSIAN JOURNAL OF ANALYTICAL SCIENCES
Published by The Malaysian Analytical Sciences Society
ISSN 1394 - 2506

SOLUTION CASTING EPOXIDIZED NATURAL RUBBER/POLY(VINYLIDINE FLUORIDE) MEMBRANE FOR PALM OIL EFFLUENT TREATMENT

(Pengacuanan Larutan Membran Getah Asli Terepoksida/Poli(Vinilidina Fluorida) untuk Rawatan Efluen Kilang Minyak Sawit)

Norliyana Mod, Farah Hannan Anuar, Rizafizah Othaman*

School of Chemical Sciences and Food Technology, Faculty of Science and Technology, Universiti Kebangsaan Malaysia, 43600 UKM Bangi, Selangor, Malaysia

**Corresponding author: rizafizah@ukm.edu.my*

Received: 31 March 2018; Accepted: 17 April 2019

Abstract

Poly(vinylidine fluoride) PVDF membrane is generally a chosen membrane for Palm Oil Mill Effluent (POME) treatment. The main focus is to make freestanding and robust PVDF based composite membranes with different ratio of epoxidized natural rubber (ENR) (ENR/PVDF: 0/100 wt.%, 20/80 wt.%, 40/60 wt.%, 60/40 wt.%, 80/20 wt.%, 100/0 wt.%) by solution casting method. Subsequently, these membranes were characterized using Fourier transform infrared spectroscopy (FTIR), differential scanning electron (DSC) and vapor pressure scanning electron microscope (VPSEM). The FTIR spectrums showed that ENR blended well with PVDF and the peak intensity followed the composition of the membranes. Meanwhile, the ENR and PVDF mixtures were miscible due to the formation of single peak glass transition temperature (T_g) as observed in DSC thermogram. Shifting in peaks of T_g suggested important interaction taking place between polymers. Surface morphology by SEM displayed the formation of random pores caused by the nature of PVDF polymer and phase inversion process. High composition of ENR caused a dense membrane and vice-versa while phase inversion contributed to the pores existences. The fluxes during POME treatment were lower than water fluxes. Higher flux was a sign of higher rejection which is efficient for separation of water and effluents. Thus, ENR/PVDF 40/60 wt.% has been selected as promising membranes to be applied for POME treatment.

Keywords: membrane, epoxidised natural rubber, poly(vinylidine fluoride)

Abstrak

Membran poli(vinilidina fluoride) PVDF umumnya adalah membran terpilih untuk rawatan efluen kilang minyak sawit (POME). Tumpuan adalah untuk membuat membran komposit berasaskan PVDF yyang fleksibel dan kuat dengan pelbagai nisbah ENR (ER/PVDF: 0/100 wt.%, 20/80 wt.%, 40/60 wt.%, 80/20 wt.%, 100/0 wt.%) dengan kaedah pengacuanan larutan. Selepas itu, membran ini dicirikan menggunakan spektroskopi inframerah transformasi Fourier (FTIR), kalorimeter imbasan pembeza (DSC), mikroskop elektron pengimbasan pelbagai tekanan (VPSEM). Spektrum FTIR menunjukkan bahawa ENR dicampur dengan baik dengan PVDF dan intensiti puncak mengikut komposisi membran. Sementara itu, ENR dan PVDF campuran adalah terlarut campur disebabkan oleh pembentukan puncak tunggal suhu peralihan kaca (T_g) sebagaimana yang berlaku di DSC termogram. Anjakan puncak T_g menandakan berlakunya interaksi antara polimer. Morfologi permukaan oleh SEM menunjukkan pembentukan liang yang rawak hasil daripada sifat polimer PVDF dan proses penyongsangan fasa. Komposisi ENR yang tinggi menyebabkan membran yang padat dan sebaliknya, manakala penyongsangan fasa menyebabkan pembentukan liang. Fluks semasa rawatan POME adalah lebih rendah daripada fluks air. Fluks tinggi adalah tanda penolakan yang lebih tinggi yang cekap untuk pemisahan air dan efluen. Oleh itu, ENR/PVDF 40/60 wt.% telah dipilih sebagai membran yang menyakinkan untuk digunakan bagi rawatan POME.

Kata kunci: membran, getah asli terepoksida, poli(vinilidina fluorida)

Introduction

Polymer composite is a process where two or more polymers are combined together using various methods such as internal mixture and solution casting. This combination can improve the properties of individual polymer at the end of processing. Membrane is one of the examples that can be made through the process of composite. It can be used as a selective barrier for various separation in industries such as for wastewater [1] and gas separation [2]. Membrane is a layer that allows permeation and selection of certain components in the fluid and it also has a porous support layer to provide mechanical strength of the membrane [3]. There are various methods that can be used for the preparation of membranes and in this study the method used is the phase inversion method. In all phase separation processes, a liquid polymer solution is precipitated into two phases: a solid, polymer-rich phase that forms the matrix of the membrane and a liquid, polymer-poor phase that forms the membrane pores [4].

Epoxidised natural rubber (ENR) is a modified natural rubber (NR) by addition of epoxide group in the chains *via* performic epoxidation process [5]. In most industries such as automotive, ENR-50 contains of 50 mol% epoxide group is used to react with other polar polymers. Thus, it will give more advantages for tensile strength, oil resistance, and fluid permeability [6]. ENR-50 also has been reported provides finer co-continuous structure and better mechanical properties than blend with ENR-25 [7]. ENR has good properties such as low glass transition temperature, T_g, good elasticity, and soft elastomer characteristics at room temperature [8]. Blending it with another polymer like poly(vinylidine fluoride) (PVDF) is believed will improve some properties blends and give good thermal stability to the polymer composite membrane. PVDF is a semi-crystalline polymer that contains crystalline and amorphous phases. Crystalline phase provides thermal stability, while amorphous phase has flexibility towards membranes. Phase of crystalline formed are named α (form II), β (form I), and γ (form III) [9]. Various ways can be used to control the crystallization, as such by using suitable temperature [10, 11], solvent [3], and addition of additives [12]. PVDF is easy to dissolve in many solvents, has chemical resistivity and thermal stability. PVDF is very high in modulus that makes it brittle to apply as it is.

However, PVDF is widely used in polymer industries as a membrane by combining with other polymers for example poly(methyl methacrylate) (PMMA) [13], poly(ethylene glycol) (PEG) [14], and poly(vinyl chloride) (PVC) [15]. PVDF has also been used for microfiltration (MF), ultrafiltration (UF), gas separation and pollutant removal from wastewater. Preparation of thermoplastic elastomer based on PVDF and ENR blends at 50/50 by weight with different type of ENR (i.e. ENR with 25 and 50 mol% epoxide) has been reported using melt blending method. The combination between thermoplastic and rubber produces thermoplastic rubber (TPR) composite that exhibits the properties of elastomeric materials with possibility of thermoplastic at the ambient temperature [7]. Moreover, preparation of PVDF membranes without support can be enhanced by the addition of ENR because ENR has elastic properties and can produce membranes that have durability and toughness [16]. There are many recent studies of composite membrane based ENR with various types of polymer for palm oil mill effluent (POME) treatment such as ENR/PVC/MCC [17] and ENR/PVC [18]. However to our best knowledge, the preparation of ENR/PVDF composite membrane for palm oil mill effluent (POME) treatment has not been reported yet.

POME is one of the effluents that contains high value of oil, chemical oxygen demand (COD), biological oxygen demand (BOD) and total suspended solid (TSS) which leads to water pollution [19]. As reported from Malaysian Palm Oil Board (MPOB), POME can be treated by ponding system, open tank digester and extended aeration system, and closed anaerobic system and land application system [20]. This system is less efficient to be used for nowadays because it takes large area for treatment, produce unpleasant smell, and it takes a long time to treat [20, 21]. So that, the membrane was introduced to replace this conventional system. Advantages of using membrane for fluid separation are minimum energy consumption, no addition of chemical is required and separation can be done continuously under controlled operation [22].

The focus of this study is to prepare ENR/PVDF composite membrane with various composition by using solution casting method and inversion method to generate pores in membranes. Then the effect of different compositions of ENR/PVDF on chemical, physical and properties of the membranes were studied. The composite membranes were

characterized using Fourier Transform Infrared spectroscopy (FTIR), Differential Scanning Electron (DSC), and Vapor Pressure Scanning Electron Microscope (VPSEM) before applying as the membranes for Palm Oil Mill Effluent (POME) treatment.

Materials and Methods

Raw materials

ENR with 50% mol of epoxidation level (ENR-50) (M_w = 640 000 g/mol) was obtained from Rubber Research Institute of Malaysia (RRIM). PVDF (M_w = 543 000 g/mol) was purchased from Sigma-Aldrich (M) Sdn. Bhd in powder formed. Tetrahydrofuran (THF) was purchased from Systerm Sdn. Bhd with purity 99.8%. *N*,*N*-dimethylacetamide (DMAC) was purchased from Merck with purity 99%. Distilled water was used as a coagulation bath for exchanging between solvent and non-solvent.

Membrane preparation

ENR/PVDF was prepared in different compositions (0/100 wt.%, 20/80 wt.%, 40/60 wt.%, 60/40 wt.%, 80/20 wt.%, 100/0 wt.%). ENR was swelled in THF for 24 hours and subsequently stirred until homogeneous. At the same time, PVDF was stirred in DMAC solution in a separate container until homogeneous. Then, the PVDF solution was poured into ENR solution and vigorously stirred. Once the membrane solution was homogeneous, the solution was degassed to eliminate the bubbles. Next, the solution was cast onto a glass plate with thickness of 0.15 mm using a casting knife. After casting, the solution was left to stand and the solvent evaporated into the air for 2 minutes before the sample was transferred to the coagulation bath. When the white solid membrane was formed, the sample was removed from coagulation bath and dried at ambient temperature. The average thickness of membrane after dried was about 0.05 mm.

Membrane characterization

Chemical characterization of ENR/PVDF membrane was performed by using Fourier transform infrared spectroscopy (FTIR). FTIR spectra were recorded by using Perkin Elmer (GX FTIR System) in wavelength between 4000 cm^{-1} to 400 cm^{-1}. FTIR characterization was conducted to analyze functional group that present in the membrane. The absorption band in the spectrum resulted from the change in energy caused by vibration of the molecules either stretching or bending.

Differential scanning calorimeter (DSC) is a thermal study that was used to characterize homogeneity of the sample *via* glass transition temperature (T_g). The DSC analyzer used was Mettler Toledo using STARe software. Samples were weighted between 6 – 9 mg with rate of heating 20 °C/min. Temperature used for cooling and heating was in the range of – 70 to 200 °C and the carrier gas was nitrogen gas.

Morphology of the membrane was studied by using variable pressure scanning electron microscope (VPSEM) with energy dispersion X-ray (EDX). The VPSEM model was ZEISS EVO MA 10 (UK) with EDAX APOLLO X (USA). The sample used for analyzing cross section was prepared by breaking the membrane after immersing in liquid nitrogen. Then, all the samples were sputter coated with gold before testing. Magnification for membrane surface sample is 5000 magnification, while for cross section is 1000 magnification.

Palm oil mill effluent (POME) treatment

Permeation test was done to study the flux of the membrane by using dead end stirred cell model HP4750. Membrane was cut into size of 49 mm in diameter and then tested under nitrogen gas at pressure of 0.5 bar at ambient temperature. POME sample from final discharge pond from Malaysian Palm Oil Board (MPOB) at Labu Negeri Sembilan was used in the experiment. The flux value can be calculated as equation 1 below [23]:

$$\text{Fluxs} = \frac{Q}{A\Delta T} \quad (1)$$

where Q (L) is the volume of permeate, A (m^2) is the active surface area of the membrane, and ΔT (h) is the time taken for permeation.

Chemical oxygen demand (COD) is measured by the amount of oxygen supplied by oxidizing agents such as

potassium dichromate used to decompose pollutants [24]. The percentage of COD removal can be calculated using equation 2 below where the pollutant sample is POME taken before and after treatment. Method 8000 (HACH standard method, DR 3900) is used to measure the value of COD content.

$$\text{Removal percentage of COD (\%)} = \frac{COD_0 - COD_f}{COD_0} \times 100 \quad (2)$$

where COD_0 is the initial COD value of POME before treatment and COD_f is final COD value POME after treatment.

The biological oxygen demand (BOD) is defined as the amount of oxygen required by the microorganism to decompose the organic matter found in the pollutants [24]. The treatment method used is APHA 2520 D [25]. The percentage of removal (%) can be calculated by taking pollutants samples (POME) before being treated and after treatment as shown in equation 3.

$$\text{Removal BOD (\%)} = \frac{BOD_0 - BOD_f}{BOD_0} \times 100 \quad (3)$$

where BOD_0 is initial BOD value for untreated POME and BOD_f is final BOD value for treated POME.

Results and Discussion

Functional group analysis

Figure 1 shows the FTIR spectrum for different ratio of ENR/PVDF membranes (0/100 wt.%, 20/80 wt.%, 40/60 wt.%, 60/40 wt.%, 80/20 wt.%, 100/0 wt.%). Peaks for pure ENR (100/0 wt.%) are 3498 cm^{-1}, 3022 cm^{-1}, 2960 cm^{-1}, 1664 cm^{-1}, 1452 cm^{-1}, 1379 cm^{-1}, 1252 cm^{-1} and 876 cm^{-1}. Meanwhile, peaks for pure PVDF (0/100 wt.%) are 2960 cm^{-1}, 1452 cm^{-1}, 1182 cm^{-1}, 1066 cm^{-1}, 876 cm^{-1} and 761 cm^{-1} can be attributed to CH_2 asymmetric, CH_2 wagging, C-C band, C-C-C asymmetrical stretching and C-F stretching, respectively. It can be seen that there are significant changes of peaks between IR spectrums of all ratios for ENR/PVDF membrane. Peak at 3498 cm^{-1} is correspond to the stretching of -OH group in the ENR. This peak was due to the ENR characteristic which tend to absorb water from surrounding [26].

In contrast, there are no peak of 3498 cm^{-1} when ENR/PVDF membranes 40/60 wt.% and 20/80 wt.% were used. This is due to PVDF hydrophobic properties, that indicated no absorbtion of water was occurred. Peak for ~3022 cm^{-1} was referred to =CH stretching from ENR and PVDF. This peak can be referred to the olefinic unsaturation for the pure ENR and other peaks also can be seen at 1664 cm^{-1}, while for PVDF due to the end chain of PVDF polymer. Stretching of C–H at peak 2960 cm^{-1} and bending of C–H at 1452 cm^{-1} referred to ENR and PVDF. However, the intensity of those peaks for PVDF is lower because of crystallization of PVDF [27]. Peaks at 1252 cm^{-1} and 876 cm^{-1} were obtained due to C-O stretching from epoxy group in ENR. Intensity peak at 876 cm^{-1} also present due to the PVDF crystallization [28]. Two strong peaks at 1182 cm^{-1} and 1066 cm^{-1} were referred to polyfluoroalkane group in PVDF. All the described peaks were proportional with the amount of ratio ENR and PVDF in the composite membranes. The lower the amount (wt.%) of PVDF used, the lower the intensity peak for polyfluoroalkane group, and the higher the amount of (wt.%) of ENR used, the bigger the intensity peak for –OH stretching group.

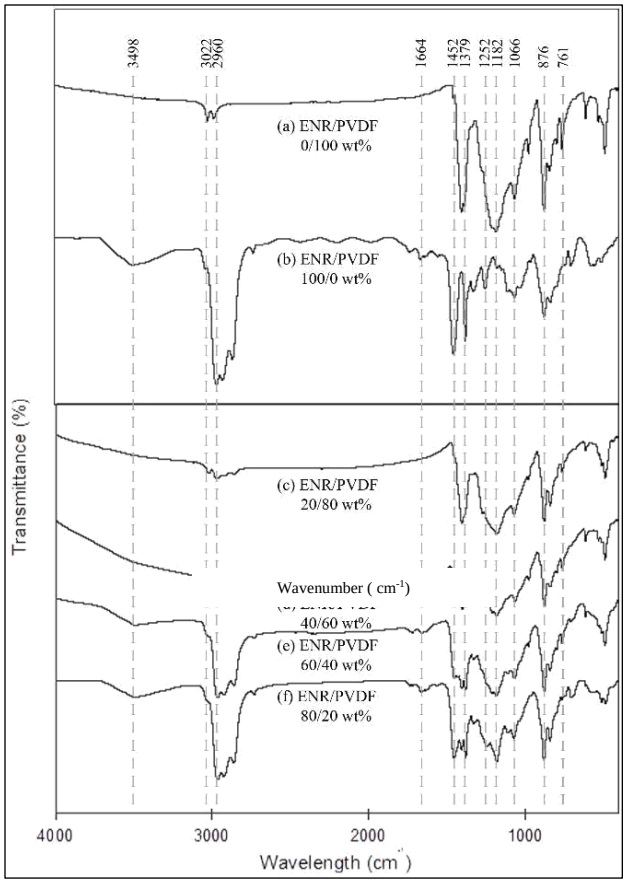


Figure 1. FTIR for ENR/PVDF membrane at different ratio of ENR/PVDF: (a) 0/100 wt.%; (b) 100/0 wt.%; (c) 20/80 wt.%; (d) 40/60 wt.%; (e) 60/40 wt.% and (f) 80/20 wt.%

Thermal properties

DSC is an analysis to study the homogeneity of the composite in terms of thermal stability. Homogeneity of the sample membrane from polymer or ENR mixing is very important for physical, rheology, and chemical properties of the sample. Single peak of T_g is an indicator for the miscibility of composite [29]. Figure 2 shows the DSC thermograms for ENR/PVDF membrane at different ratio and it can be seen that T_g appeared as a single peak for all ratios.

Additionally, shifting in peaks occurred when ratio of ENR increased due to the existence of interfacial adhesion between ENR and PVDF [7]. Based on the T_g values tabulated in Table 1, T_g for pure PVDF membrane was the lowest (-32.19 ^{0}C) because of the semi-crystalline property of PVDF. Meanwhile, T_g for pure ENR is higher (-19.67 ^{0}C) due to amorphous structure from ENR tends to absorb heat that has been supplied to become soft. T_g for all the composites were higher than the pure polymer. It implies that there was interaction between ENR and PVDF, which has resulted in a shifted and single peak to deduce the T_g value.

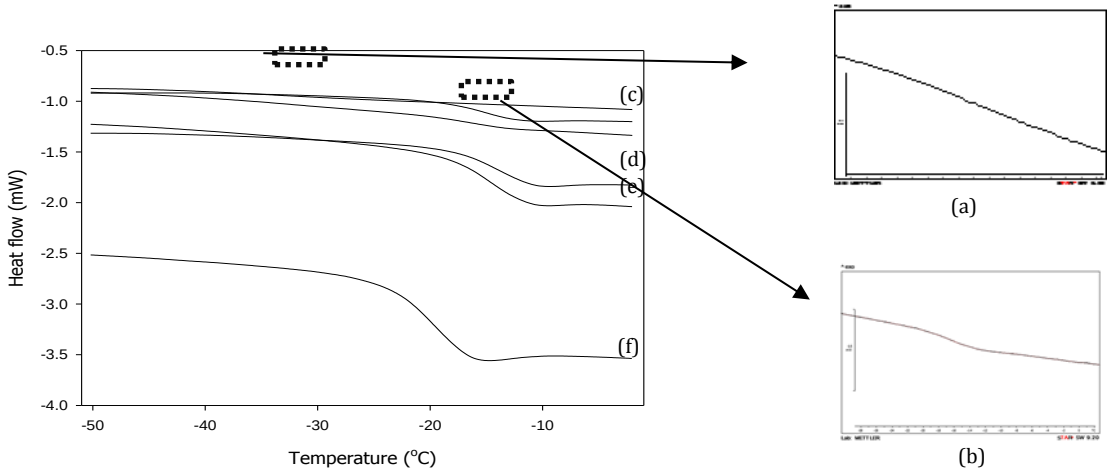


Figure 2. DSC thermograms for ENR/PVDF membranes at ratio (a) 0/100 wt.%; (b) 20/80 wt.% (c) 40/60 wt.% (d) 60/40 wt.% (e) 80/20 wt.% (f) 100/0 wt.%

Table 1. Glass transition (T_g) for ENR/PVDF membrane

ENR/PVDF (wt%)	T_g (°C)
0/100	-32.19
20/80	-16.19
40/60	-15.64
60/40	-14.03
80/20	-15.12
100/0	-19.67

Surface morphology

SEM micrograph for ENR/PVDF membranes with different ratio were shown in Figure 3. PVDF in nature is a porous membrane (Figure 3(a)) and ENR is a nonporous membrane (Figure 3(b)). The combination of these two polymers had produced composite membranes with random pores as can be seen from the micrographs. However as the amount of ENR increased, the pores size became smaller. This might due to the phase inversion, which is the exchange between solvents and non-solvents that induced pores [14]. Thus, choice of solvent for the membrane will affect the formation of pore [30]. When ENR predominant the membrane, it caused no pore formation on the surface as shown in Figure 3(f) for ENR/PVDF membrane at ratio 80/20 wt.%. In Figure 3(e) for ENR/PVDF membrane 60/40 wt.%, there was a layer of dense structure sandwiched between the porous layer (as shown in cross section), showing that the non-solvents did not reach some of the middle part of the membrane. This will affect the membrane porosity and permeability. In contrast, Figure 3(c) and Figure 3(d) shows that, 20/80 wt.% and 40/60 wt.% ENR/PVDF membranes relatively have good distribution of pores from surface to another surface and could be adopted as membrane.

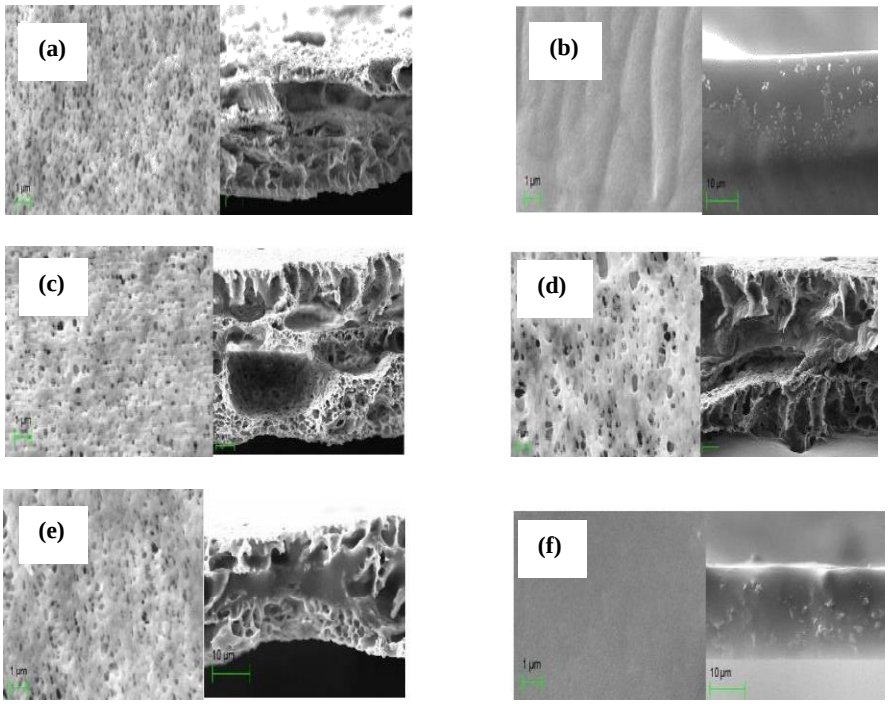


Figure 3. SEM micrograph for ENR/PVDF membrane free surface (5000 × magnification) and cross section (1000 × magnification): (a) 0/100 wt.% (b) 100/0 wt.% (c) 20/80 wt.% (d) 40/60 wt.% (e) 60/40 wt.% (f) 80/20 wt.%

Application of membrane

Flux is used to express the rate of permeates through membrane and were calculated by using equation 1. This permeation test is one of the important method for structural determination and membrane morphology. Formation of pores are very important for water to permeate through membrane especially for wastewater like POME. Figure 4 shows the water flux value for all ENR/PVDF membranes except for pure ENR membrane (100/0 wt.%). Since membrane ratio for 100/0 wt.% was a dense membrane without pore, thus water were unable to permeate through the membrane within the experimental conditions. ENR/PVDF 80/20 wt.% membrane showed the lowest flux since the membrane was still dense.The highest water flux was for ENR/PVDF 0/100 wt%, and followed closely by 60/40 wt.% composition.

In comparison, the fluxs for POME sample as shown in Figure 5 was lower than the water flux. Initially, the flux was higher but slowly reduced and maintained after some time. We reasoned that, the pores of the membrane was filled with suspended solid in POME to some extent. After a while, particles begin to block the pores causing the pore size to reduce, further decreased in the value of flux. Based on the results, ENR/PVDF 100/0 wt.% and 80/20 wt.% membranes could not be used for POME treatment since no water permeated. The trends of the fluxes were the same with water fluxes for respective membranes. The pure PVDF (0/100 wt.%) membrane has highest flux compare to other composition, but due to semi-crystalline properties of pure PVDF that have the lowest T_g values, ENR/PVDF membranes with mixing ratios 40/60 wt.% showed the possibility to be applied for POME treatment.

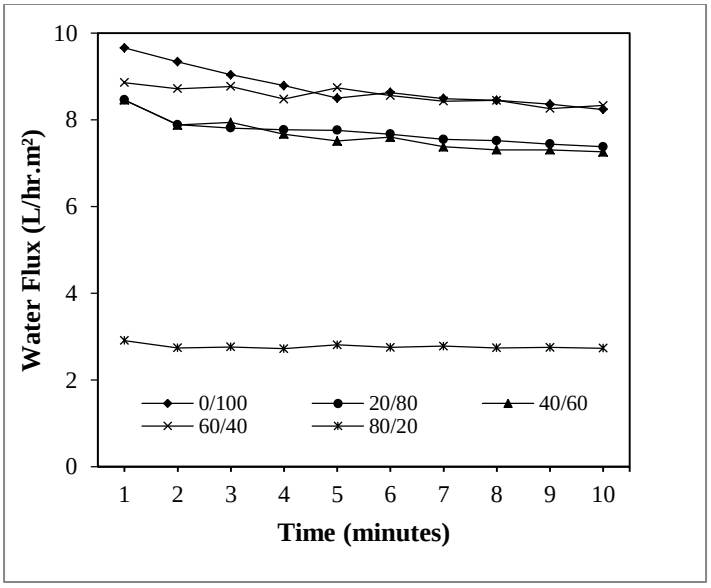


Figure 4. Water flux value for ENR/PVDF membranes

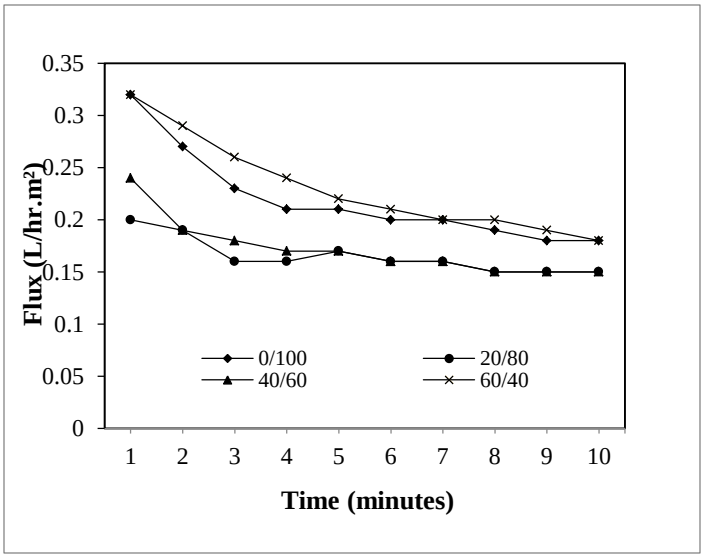


Figure 5. POME flux for ENR/PVDF membranes

A thick brownish liquid waste of POME that is viscous, slurry and has unpleasant odour can be seen in Figure 6(a). After permeation test is conducted, the appearance of POME liquid waste has been improved. As we can seen from Figure 6(b), the colour intensity of POME change to brighter colour, and the viscous concentration of POME is reduced and become less smelly. These sample was stored in cool place prior to following analysis. The level of COD and BOD for raw and treated POME has been analyzed from the first filtration cycle and ENR/PVDF membranes with composition 0/100 wt.%, 20/80 wt.%, 40/60 wt.% and 60/20 wt.% were used for this analysis. COD analysis test was conducted to quantify the amount of organic matter in the POME using an oxidizing agent. Initial COD value of POME is 18600 mg/L while BOD value is 1100 mg/L and as shown in Table 2, all the prepared membranes were successfully reduced COD and BOD level of POME. The declined in BOD value might

be due to the reduction of organic matter that gives blackish colour in POME sample. Membrane PVDF (0/100 wt.%) shows the highest removal percentage of both COD and BOD level by 93.6% and 80.5%, respectively. In addition, ratio 40/60 wt.% membrane give higher removal percentage than 20/80 wt.% due to morphology of membrane layer that more dense and better micropore distribution. As compared to the pure PVDF membrane, addition of ENR is believed to increase the denseness of membrane and enhance the durability and strength of membrane [16].

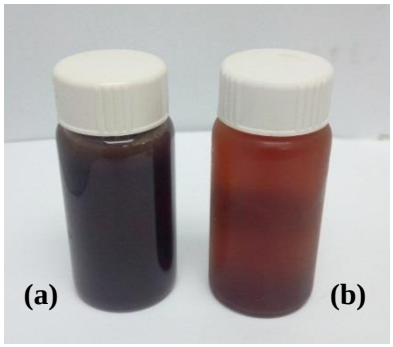


Figure 6. Observation on liquid waste POME (a) before and (b) after treatment

Table 2. Removal percentage (%) for COD and BOD of POME by ENR/PVDF membranes

ENR/PVDF (%wt)	Chemical Oxygen Demand (COD)			Biological Oxygen Demand (BOD)		
	Raw POME (mg/L)	Treated POME (mg/L)	Removal Percentage (%)	Raw POME (mg/L)	Treated POME (mg/L)	Removal Percentage (%)
0/100	18 600	1183	93.6	1100	215	80.5
20/80		1270	93.2		275	75.0
40/60		1212	93.5		235	78.6
60/40		1276	93.1		245	77.7

Conclusion

ENR/PVDF membranes with different ratio of ENR/PVDF (0/100 wt.%, 20/80 wt.%, 40/60 wt.%, 60/40 wt.%, 80/20 wt.%, 100/0 wt.%) were successfully prepared using solution casting method. FTIR detected the functional groups present for ENR and PVDF and the intensity of the peaks was proportional with the compositions. Analysis from DSC showed that there was single peak of T_g for each of sample and proved that ENR and PVDF composites were miscible. T_g of the composite membranes shifted from each single polymer showed the existence of interaction between ENR and PVDF. The membrane with smaller ENR composition displayed porous structure with random pores formed due to the PVDF nature and the solvents exchanged during phase inversion. It has been proven that these pores helped to increase the flux for water and during POME treatment. Thus, it can be concluded that the ENR/PVDF, 40/60 wt.% membranes will give higher rejection with slightly lower flux from permeation test to be able to separate water and other components in POME.

Acknowledgement

The authors gratefully acknowledged the financial support from grant ST-2017-008, Universiti Kebangsaan Malaysia (UKM), UKM-UCA International Joint Seminar on Science and Technology 2016, Fuel Cell Institute (SELFUEL) and Polymer Research Centre (PORCE) for the facilities that was given to do this project.

References

1. Medeiros, K. M., Araujo, E. M., Lira, H. L., Lima, D. F., Lima, C. A. P. (2017). Hybrid membranes of polyamide applied in treatment of waste water. *Material Research*, 20(2): 308-316.
2. Shilton, S. J., Ismail, A. F., Gough, P. J., Dunkin, I. R. and Gallivan, S. L. (1997). Molecular orientation and the performance of synthetic polymeric membranes for gas separation. *Polymer*, 38(9): 2215-2220.
3. Bottino, A., Camera-Rodab, G., Capannelli, G. and Munari, S. (1991). The formation of microporous polyvinylidene difluoride membranes by phase separation. *Journal of Membrane Science*, 57: l-20.
4. Baker, R. W. (2004). Membrane technology and applications, John Wiley & Sons, Ltd..
5. Yoksan, R. (2008). Epoxidized natural rubber for adhesive applications. *Kasetsart Journal (Natural Science)*, 42: 325-332.
6. Ismail, H. and Chia, H. H. (1998). The effects of multifunctional additive and epoxidation in silica filled natural rubber compounds. *Polymer Testing*, 17: 199-210.
7. Salaeh, S., Nakason, C., Boiteu, G. and Cassagnau, P. (2013). Co-continuous phase structure and properties of poly(vinylidene fluoride)/epoxidized natural rubber blends. *Advanced Materials Research*, 626: 71-74.
8. Chinnasa, P., Ponhan, W., Sarasee, P., Phoemphun, Y. and Swatsitang, E. (2016). Electrospun of epoxidized natural rubber with polyvinylpyrrolidone (PVP) composites membrane for PEMFC application. *Journal of Science & Technology,Ubon Ratchathani University*, 2016: 61-65.
9. Hasegawa, R., Takahashi, Y., Chatani, Y. and Tadokoro, H. (1972). Crystal structures of three crystalline forms of poly(vinylidine fluoride). *Polymer Journal*, 3(5): 600-610.
10. Salaeh, S., Boiteux, G., Gain, O., Cassagnau, P. and Nakason, C. (2014). Dynamic mechanical and dielectric properties of poly(vinylidene fluoride) and epoxidized natural rubber blends. *Advanced Materials Research*, 844: 97-100.
11. Tao, M., Liu, F., Ma, B. and Xue, L. (2013). Effect of solvent power on PVDF membrane polymorphism during phase inversion. *Desalination*, 316: 137-145.
12. Wang, X., Zhang, L., Sun, D., An, Q. and Chen, H. (2009). Formation mechanism and crystallization of poly(vinylidene fluoride) membrane via immersion precipitation method. *Desalination*, 236: 170-178
13. Cao, X., Ma, J., Shi, X. and Ren, Z. (2006). Effect of TiO_2 nanoparticle size on the performance of PVDF membrane. *Applied Surface Science*, 253: 2003-2010.
14. Freire, E., Bianchi, O., Monteiro, E. E. C., Nunes, R. C. R. and Forte, M. C. (2009). Processability of PVDF/PMMA blends studied by torque rheometry. *Materials Science and Engineering C*, 29: 657-661.
15. Wang, P., Tan, K. L., Kangb, E. T. and Neohb, K. G. (2002). Plasma-induced immobilization of poly(ethylene glycol) onto poly(vinylidene fluoride) microporous membrane. *Journal of Membrane Science*, 195: 103-114.
16. Abdullah, I. (2002). Strategi penyelidikan kimia getah asli. Bangi: Penerbit Universiti Kebangsaan Malaysia.
17. Alim, A. A. A., & Othaman, R. (2018). Epoxidized natural rubber/polyvinyl chloride/microcrystalline cellulose (ENR/PVC/MCC) composite membrane for palm oil mill effluent (POME) treatment. *Sains Malaysiana*, 47(7):1517-1525.
18. Shamsuddin, M. R., Abdullah, I., Othaman, R. (2013). Cellulose filled ENR/PVC membranes for palm oil effluent (POME) treatment. *AIP Conference Proceedings*, 1571: 897.
19. Igwe, J. C. and Onyegbado, C.C. (2007). A review of palm oil mill effluent (POME) water treatment. *Global Journal of Environmental Research* 1(2): 54-62.
20. Malaysia Palm Oil Board (MPOB) (2014). Access from http://www.mpob.gov.my/ms/info-sawit/alam-sekitar/520-achievements.
21. Chin, K. K., Lee, S. W. and Mohammad, H. H. (1996). A study of palm oil mill effluent treatment using a pond system. *Water Science Technology* 34(11): 119-123.
22. Yan, L., Honga, S., Li, M. L. and Li, Y. S. (2009). Application of the Al_2O_3–PVDF nanocomposite tubular ultrafiltration (UF) membrane for oily wastewater treatment and its antifouling research. *Separation and Purification Technology*, 66: 347-352.
23. Saljoughi, E., Sadrzadeh, M. and Mohammadi, T. (2009). Effect of preparation variables on morphology and pure water permeation flux through asymmetric cellulose acetate membranes. *Journal of Membrane Science*, 326: 627-634.
24. Kassim, M.A., Salim, M. R. and Othman, M. N. (1994). Rawatan kumbahan dalam iklim panas. Skudai: Universiti Teknologi Malaysia.

25. APHA (2005). Standard methods for the examination of water and wastewater. 21st edition American Public Health Association. Washington, DC.
26. Zurina, M., Ismail, H. and Bakar, A. A. (2004). Rice husk powder–filled polystyrene/styrene butadiene rubber blends. *Journal of Applied Polymer Science,* 92: 3320-3332.
27. Boccaccio, T., Bottino, A., Capannelli, G. and Piaggio, P. (2002). Characterization of PVDF membranes by vibrational spectroscopy. *Journal of Membrane Science,* 210: 315–329.
28. Ma, W., Yuan, H. and Wang, X. (2014). The effect of chain structures on the crystallization behavior and membrane formation of poly(vinylidene fluoride) copolymers. *Membranes* 4:243-256.
29. Bourara, H., Hadjout, S., Benabdelghani, Z. and Etxeberria, A. (2014). Miscibility and hydrogen bonding in blends of poly(4-vinylphenol)/poly(vinyl methyl ketone). *Polymers,* 6: 2752-2763.
30. Bottino, A., Capannelli, G., Munari, S. and Turturro, A. (1988). High performance ultrafiltration membranes cast from LiCI doped solutions. *Desalination,* 68: 167-177.

Malaysian Journal of Analytical Sciences, Vol 23 No 4 (2019): 736 - 747
DOI: https://doi.org/10.17576/mjas-2019-2304-20

MALAYSIAN JOURNAL OF ANALYTICAL SCIENCES
Published by The Malaysian Analytical Sciences Society
ISSN 1394 - 2506

ANALYSIS OF HEAVY METAL CONCENTRATIONS IN BALLAST WATER AND SEAWATER AT TANJUNG PELEPAS PORT

(Analisis Kandungan Kepekatan Logam Berat dalam Air Balast dan Air Laut di Pelabuhan Tanjung Pelepas)

Jacqueline Chong Kar Xin[1], Sharina Abu Hanifah[1,2]*, Nor Aishah Salleh[2], Normazida Rozi[1], Norfaizan Padli[2]

[1]*Centre for Advanced Materials and Renewable Resources, Faculty of Science and Technology*
[2]*Centre for Water Research and Analysis, Faculty of Science and Technology*
Universiti Kebangsaan Malaysia, 43600 UKM Bangi, Selangor, Malaysia

**Corresponding author: sharina@ukm.edu.my*

Received: 31 March 2018; Accepted: 17 April 2019

Abstract

Ballast water is water kept in the ballast tank of ships in order to increase its stability and balance during shipping. Although it helps in maintaining the ships' stability and safety, the exchange of ballast water causes the spreading of heavy metals present in the ballast tank to the surrounding seawater. Therefore, this research aims to investigate the spreading of heavy metals from ballast water taken from numerous countries and released at the Port Tanjung Pelepas. A comparison was done between seawater and ballast water samples using inductively coupled plasma optical emission spectrometer (ICP-OES) and the data were statistically analysed using Microsoft Excel. The results showed that Fe and Zn were detected at high concentrations in ballast water, while Fe was also highly concentrated in seawater. Besides that, this study found out that changes in weather is one of the factors that contribute to the differences in heavy metal concentrations in seawater.

Keywords: seawater, ballast water, heavy metals, statistical analysis

Abstrak

Air balast ialah air yang dibawa oleh sesebuah kapal dalam tangki balast untuk meningkatkan kestabilan dan keseimbangan semasa pelayaran. Akan tetapi, sistem pertukaran air balast juga akan menyebabkan kandungan logam berat dalam tangki balast tersebar kepada air persekitaran iaitu air laut. Oleh itu, kajian ini bertujuan untuk mengenalpasti penyebaran logam berat dalam air balast yang diambil dari pelbagai negara dan dilepaskan ke Pelabuhan Tanjung Pelepas. Perbandingan di antara sampel air persekitaran iaitu air laut dengan air balast telah dilakukan dengan menggunakan alat spektrometer pancaran plasma gandingan aruhan (ICP-OES) dan data yang diperoleh dianalisis secara statistik oleh Microsoft Excel. Hasil kajian menunjukkan bahawa Fe dan Zn dikesan mempunyai kepekatan paling tinggi dalam air balast manakala Fe pula mempunyai kepekatan paling tinggi dalam air laut. Selain itu, kajian ini juga mendapati bahawa perubahan cuaca merupakan salah satu faktor kepada perbezaan kepekatan logam berat air laut.

Kata kunci: air laut, air balast, logam berat, analisis statistik

Introduction

Malaysia is one of the countries that are rich with coastal areas and islands. These coastal areas have become potential areas for strong development. Rapid development does not only occur in land areas, but also in coastal areas and islands, particularly due to developments in the tourism, industry and agriculture sectors. Nevertheless, improper development planning has caused coastal areas to be exposed to pollution from heavy metals. This is a

serious matter as heavy metals contained in seawater cannot be easily removed and can consequently affect the quality of seawater as well as food chains, which will then affect human and aquatic life [1].

Heavy metals constitute of metallic elements that have a relative density of 5 times higher than water which density is 1 g/cm^3 [2]. Heavy metals are also considered as trace elements as they are only found in trace concentrations (less than 10 ppm). Heavy metals are one of the anthropogenic pollutants in water [3]. Its mean that the toxicity of heavy metals exposed to the environment is attributable to human activities such as industrial and agricultural activities. Indirectly, industrial activities such as burning coal at power plants, nuclear power plant operations and plastic manufacturing have released heavy metals to the environment. Not only manufacturing activities, agricultural activities also give an impact through the use of arsenic insecticides. Naturally, there are several types of heavy metals needed by aquatic life in seawater such as copper (Cu), zinc (Zn), iron (Fe), manganese (Mn) and nickel (Ni). However, there are also heavy metals that are not directly needed by aquatic life and can have toxic effects on aquatic ecosystems such as cadmium (Cd), mercury (Hg), lead (Pb) and arsenic (As) [4].

In addition, ballast water carried by ships in their ballast tanks to enhance stability and balance during navigation can also be a cause of seawater pollution as it contains thousands of aquatic species as well as heavy metals that are transferred into the ship and then discharged out into the seawater before the cargo is loaded. It is impossible to neglect the harmful consequence of the physiochemical parameters of ballast water, such as the presence of heavy metals which has an adverse effect on marine life [5]. The International Maritime Organization (IMO) is a United Nations (UN) organisation responsible for safeguarding shipping safety and preventing pollution from ships. Under the IMO, there is a committee responsible for the management of ballast water. The Marine Environment Protection Committee (MEPC) established in 2004 was assigned to set rules for ballast water exchange management systems. Ballast water exchange systems have the potential to spread dangerous organisms classified as Invasive Aquatic Species (IAS) such as cholera (*Vibrio cholerae*) and toxic algae that can kill various types of marine life. In addition, the ballast water exchange system can also cause the spread of heavy metals in ballast tanks from one area to another [6]. The presence of heavy metals in the sea will certainly endanger marine life and thus give a negative impact on humans through the intake of seafood in their daily diets [7].

Thus, the present study attempts to analyse the distribution of heavy metals in seawater in the coastal areas of Tanjung Pelepas Port (Johor Bahru, Malaysia) and its correlation with ballast water originating from various parts of the world and discharged in the port area. The study chooses to focus on this area as this location is surrounded by nearby villages, industries, and development activities. Moreover, it is Malaysia's largest port. Every day, ships release ballast water that may contain heavy metals directly to this coastal area. This may increase the existing concentration of heavy metals in the surrounding seawaters. Aquatic organisms living in the seawater may accumulate these heavy metals. Villagers living nearby also depend on this coastal area for their daily consumption. The heavy metal pollution problem can thus affect humans' health through the food chain. Thus, investigation on this area is important. The data collected will be compared with the heavy metal concentrations set by the Malaysia Marine Water Quality Criteria and Standard (IMWQS) in order to evaluate the degree of contamination in this area.

Materials and Methods

Study area

This study uses seawater samples taken from ships' ballast water and the seawater surrounding Tanjung Pelepas Port. Samples of seawater were taken from four different areas situated along the Tanjung Pelepas Port, Johor. In addition, eight samples of ballast water were also obtained. Sampling for seawater was performed twice, while sampling for ballast water was done once. The yellow marks in Figure 1 show the surrounding waters' sampling areas. Table 1 shows the locations of study stations for the surrounding water, and Table 2 shows the sampling information of ballast water taken from ships originating from eight different countries.



Figure 1. Sampling locations at the Tanjung Pelepas Port (Source: Google Maps)

Table 1. Location of research stations for seawater according to the coordinates and description of the location

Station	Coordinate	Description of Location
1	N 1°19'29.91" E 103°33'23.40"	Station is an entrance point for ships to the Tanjung Pelepas Port.
2	N 1°19'53.19" E 103°33'14.08"	Station 2 is located along the Tanjung Pelepas Port.
3	N 1°20'19.36" E 103°33'1.41"	Station 3 is also an area along the Tanjung Pelepas Port but it is near the end of the port area.
4	N 1°20'40.27" E 103°32'41.39"	Station 4 is adjacent to a mangrove swamp area with a distance of 100 m.

Table 2. Information regarding ballast water sampling

Ship	Ship Name	Type of Ship	Origin of the Ship	Location of Ballast Water Collection	Retention Time (days)	Sampling Section
1	*Maersk Warsaw*	Container Ship	Portugal	Sihanoukville, Cambodia	6	Manhole
2	*MSC London*	Container Ship	Panama	South of China Sea (Open Sea)	2	Manhole
3	*Areopolis*	Container Ship	Monrovia, Liberia	Arboleas, Spain	5	Manhole
4	*MSC New York*	Container Ship	Panama	Rotterdam	40	Manhole
5	*MV. Olympia*	Container Ship	Marshall Island	Yangon	3	Manhole
6	*Ever Loading*	Container Ship	London	Jeddah	6	Manhole

Table 2 (cont'd). Information regarding ballast water sampling

Ship	Ship Name	Type of Ship	Origin of the Ship	Location of Ballast Water Collection	Retention Time (days)	Sampling Section
7	*SM Qingdao*	Container Ship	Liberia	South Africa	14	Manhole
8	*Ever Laden*	Container Ship	Panama	Suez Canal	25	Manhole

Sample collection

Plastic sample bottles were used for sampling. Before sampling, all of the bottles were immersed in detergent for one night and then rinsed with tap water. Firstly, these bottles were rinsed with 10% nitric acid, followed by tap water and deionised water. 1 L of the surrounding water samples were taken from each area. This means that there were four 1 L sample bottles for each area. For ballast water, samples were taken from eight different ballast tanks of ships coming from overseas. For each ship, 500 mL of water sample was obtained. Samples of the surrounding waters and ballast water were taken at depths of two to three metres from the sea level.

Measurement of physical and chemical parameters

The physical and chemical parameters of seawater should be measured directly after received of samples. The physical parameter measured was temperature (˚C). For chemical parameters, pH, salinity, dissolved oxygen and conductivity were measured *in situ*. These parameters were measured using a multimeter tool.

Sample preservation and digestion

The samples were filtered under a vacuum filtration method using a 0.45 µm membrane acetate cellulose. After that, the samples were treated to obtain a pH of less than 2 by adding 3 mL of nitric acid (1 + 1) into the 1 L sample. After the samples were preserved with nitric acid, they were kept in a chiller room at 4 ˚C. The samples can be stored for about 6 months [8].

100 mL of sample was taken from each station and heated to a temperature range from 70 to 80 ˚C. The water samples were heated until the volume of water was reduced to between 20 to 25 mL. This heating procedure must be done in a condition where no boiling occurs. After heating, 5 mL of ambient water samples for each station were taken and diluted with 1% nitric acid to 50 mL using a volumetric flask. A ratio of 1:10 was used for the dilution. After discharge, samples were sent to ICP-OES for heavy metal analysis. All these processes were performed for the other surrounding water and water ballast samples [9].

Analysis of data

Two types of preserved samples were digested and diluted before they were delivered to the inductively coupled plasma optical plasma emission spectrometer (ICP-OES) to measure their heavy metal concentration. The data obtained were analysed using Microsoft Excel software. ANOVA was further used to check if the means of two or more groups were significantly different from each other.

Results and Discussion

Physical and chemical analysis of seawater and ballast water samples

For the first and second sampling of seawater (surrounding waters), the pH range was recorded from 7.50 to 8.11. Referring to Scientific America, the average pH for seawater is 8.10. According to Doney et al., the reduction in pH is due to the absorption of carbon dioxide by seawater which is also known as 'sea acidification' [10]. A temperature range from 29.80 to 31.80 ˚C was recorded when the sampling was performed. Conductivity values from 45.68 to 50.53 mS/m and salinity values from 26.55 to 29.22 g/L were measured. The level of dissolved oxygen obtained was from 2.45 to 3.77 mg/L. Dissolved oxygen is the amount of oxygen contained in seawater for aquatic life. Based on the Malaysia Standard Water Quality Criteria and Standards (IMWQS), the standards dissolved oxygen

determined for the port area should be 3 mg/L. However, the dissolved oxygen values of the first and second sampling did not reach the standard for seawater samples.

For ballast water sampling, a higher range of pH 2.00 to 6.89 was recorded. The pH values of the ballast water samples from all ships were lower than the pH values of the first and second seawater samples. This distinction may be due to the ships' water samples which came from foreign countries such as the Philippines, Africa and Cambodia. Therefore, their pH values were different than that of the Malaysian seawater because pH value depends on the activities carried out in the surrounding sea area. The temperature was recorded to range from 11.42 to 31.02 ˚C as sampling was carried out in the ship's ballast tank. The measured temperatures for all ballast water samples were also lower than the temperature of seawater at the Tanjung Pelepas Port as the ballast water was stored in ballast tanks within the range of 2 to 40 days. They have not been exposed to sunlight, thus causing the temperatures to decline.

On the other hand, seawater is out in the open and exposed to sunlight, thus its temperature was higher than the ballast water. The ballast water samples had also come from other countries which were likely experiencing winter, thus causing the ballast water's temperature to be lower. The levels of soluble oxygen measured ranged from 0.05 to 0.27 mg/L. The same explanation for temperature can also be applied to the value of dissolved oxygen in ballast water which was lower than the level of dissolved oxygen in the seawater taken at the port. Ballast water that is stored in closed ballast tank is not exposed to air like seawater. Additionally, the ballast water's conductivity was recorded ranging from 16.79 to 58.43 mS/m and the salinity ranged from 9.82 to 38.91 g/L. The conductivity and salinity values depend on weather and the fact that the ballast water samples had originated from overseas.

Analysis of heavy metal concentrations in seawater

Tables 3 and 4 show the levels of heavy metal concentrations that were detected in the first and second seawater samples, in which 11 types of heavy metals were studied. It was reported that it was raining on the second sampling day while the skies were sunny on the day of the first sampling. The difference in weather during sampling caused a difference in data between the two samples. Heavy metals such as Ag, Cr, Fe, Mn, Pb, Zn, Se and As showed higher concentrations in the first sampling compared to in the second sampling. Based on the study of relationship between season types and heavy metal concentrations of Lake Isikli in Turkey, they explained that heavy metal concentration decreases during rainy days as a result of a seawater dilution compared to seawater under hot weather [11]. In hot weather, the seawater temperature will increase and cause evaporation, thus increasing its heavy metal concentrations.

Table 3. Concentration of heavy metals during first sampling in seawater

Station	**Heavy Metal (mg/L)**										
	Ag	**Cd**	**Cr**	**Cu**	**Fe**	**Mn**	**Ni**	**Pb**	**Zn**	**Se**	**As**
1	0.011	*nd*	0.028	0.026	0.171	0.020	0.014	0.019	0.055	0.070	0.003
2	0.022	*nd*	0.029	*nd*	0.158	0.031	*nd*	0.013	0.029	0.079	0.006
3	0.001	*nd*	0.032	*nd*	*nd*	0.015	*nd*	0.011	0.035	0.074	0.003
4	*nd*	*nd*	0.028	*nd*	*nd*	0.012	*nd*	0.011	0.025	0.065	*nd*

nd means not detected

Table 4. Concentration of heavy metals during second sampling in seawater

Station	Heavy Metal (mg/L)										
	Ag	**Cd**	**Cr**	**Cu**	**Fe**	**Mn**	**Ni**	**Pb**	**Zn**	**Se**	**As**
1	0.008	*nd*	0.023	*nd*	0.038	0.009	*nd*	0.012	0.019	0.072	*nd*
2	0.010	*nd*	0.020	*nd*	0.024	0.008	*nd*	0.004	0.032	0.072	*nd*
3	0.004	*nd*	0.020	*nd*	0.027	0.008	*nd*	0.008	0.022	0.063	*nd*
4	0.005	*nd*	0.020	*nd*	0.027	0.008	*nd*	0.006	0.017	0.083	0.003

nd means not detected

Comparison of heavy metal concentrations in seawater between first and second sampling

A one-way ANOVA analysis was conducted to determine the significant differences between these two sampling due to weather differences occurring during the first and second sampling. The alpha value, α used for ANOVA analysis was 0.05. Results from ANOVA analysis for first and second sampling are summarised in Table 5.

Table 5. ANOVA analysis during the first and second sampling of seawater

Type of Heavy Metal	**Ag**	**Cd**	**Cr**	**Cu**	**Fe**	**Mn**	**Ni**	**Pb**	**Zn**	**Se**	**As**
Comparison between the 1st and 2nd sampling	-	*nd*	*	*nd*	-	*	*nd*	-	-	-	-

nd means not detected, * symbol means significant difference

The result of the ANOVA analysis shows that only heavy metals Cr and Mn showed significant differences between first and second sampling. The ANOVA analysis cannot be performed for Cd, Cu and Ni because their concentrations cannot be detected. For example, the concentrations of Cd cannot be detected for the first and second sampling, while for Cu and Ni, concentrations can only be detected from station 1 for the first sampling, while no data was obtained for all areas during the second sampling. Therefore, data comparison using ANOVA cannot be conducted. For the remaining heavy metals; Ag, Fe, Pb, Zn, Se and As, there were no significant differences observed.

Correlation analysis between physical and chemical parameters of heavy metal concentrations in seawater and ballast water samples

First sampling of seawater

Table 6 shows the correlation analysis performed to determine the relationship between the concentration of heavy metals and the physical and chemical parameters measured for the first sampling. A positive r value indicates that it is positively correlated. This means that if one of the value increases, the other value will also increase. A negative r value indicates that it is negatively correlated, which means that if one of the valueincrease, the other value decrease.

Based on Table 6, Ag has a significant and positive correlation with the other heavy metals i.e. Fe, Mn, As and Se because it has an r value that exceeds 0.70, but it also has a negative correlation with pH with an r value of -0.71. This means that if the concentration of Ag increases, then Fe, Mn, As and Se concentrations also increase, but the pH value will decrease. There was no r value calculated for Cd because no readings for Cd were detected from all four stations during the first sampling. Cr also gives a negative correlation with conductivity, while Cu shows a positive correlation with dissolved oxygen.

Fe shows a positive correlation with the temperature, conductivity and dissolved oxygen parameters. However, it

has a negative correlation with pH. Mn also shows a positive correlation with Se and As, but shares a negative correlation with pH. Furthermore, Ni also has positive correlations with Pb, Zn, conductivity and dissolved oxygen, while Pb shows positive correlations with Zn, temperature, conductivity and dissolved oxygen.

Table 6. Correlation analysis between physicochemical parameters and concentration of heavy metals during the first sampling of seawater

DO (mg/L)	Sal. (g/L)	Cond. (mS/m)	Temp. (˚C)	pH	As	Se	Zn	Pb	Ni	Mn	Fe	Cu	Cr	Ag	
0.55	-0.28	0.68	0.67	-0.71**	0.79*	0.72*	0.15	0.48	0.19	0.98*	0.88*	0.19	-0.42	1.00	**Ag**
-0.15	-0.65	-0.78**	-0.09	0.04	0.19	0.33	-0.26	-0.56	-0.53	-0.24	-0.61	-0.53	1.00		**Cr**
0.76*	-0.03	0.81*	0.62	-0.53	0.02	-0.25	0.95	0.95	1.00	0.03	0.62	1.00			**Cu**
0.78*	-0.21	0.94*	0.81*	-0.80**	0.62	0.44	0.56	0.83	0.62	0.79*	1.00				**Fe**
0.50	-0.39	0.53	0.65	-0.70**	0.87*	0.84*	0.03	0.34	0.03	1.00					**Mn**
0.76*	-0.03	0.81*	0.62	-0.53	0.02	-0.25	0.95*	0.95*	1.00						**Ni**
0.88*	-0.17	0.92*	0.79*	-0.73	0.30	0.03	0.92*	1.00							**Pb**
0.86*	-0.31	0.69	0.74*	-0.66	0.17	-0.09	1.00								**Zn**
0.42	-0.76**	0.09	0.60	-0.68	0.96*	1.00									**Se**
0.65	-0.80	0.32	0.79*	-0.85	1.00										**As**
-0.95	0.74*	-0.65	-0.99	1.00											**pH**
0.98*	-0.70	0.69	1.00												**Temp. (˚C)**
0.73*	0.04	1.00													**Cond. (mS/m)**
-0.62	1.00														**Sal. (g/L)**
1.00															**DO (mg/L)**

*Significant positive correlation has been shown
**Significant negative correlation has been shown

In addition, Zn shows positive correlation with the temperature and dissolved oxygen parameters, but Se has a negative correlation with salinity and As shows a significant correlation with temperature. Finally, pH shows a significant correlation with salinity. In addition, dissolved oxygen shows a positive correlation with temperature and conductivity.

Second sampling of seawater

Table 7 shows the correlation analysis performed to determine the relationships between the concentration of heavy metals and the physical and chemical parameters measured during the second sampling of seawater. From the table, Ag shows a positive correlation with dissolved oxygen, while the correlations between Cd, Cu and Ni with the other parameters cannot be determined as these three heavy metals cannot be detected in the second sampling. Cr shows positive correlations with Fe, Pb, salinity, dissolved oxygen, and especially with Mn because its r value is 1.00

(fully correlated). Fe shows positive correlations with Mn and Pb, while Mn shows positive correlations with Pb, salinity and dissolved oxygen. In addition, Se also shows a positive correlation with As, but has a negative correlation with temperature. As also shows negative correlations with all physical and chemical parameters, and ultimately, all parameters displayed positive correlations with each other.

Table 7. Correlation analysis between physicochemical parameters and concentration of heavy metals during the second sampling of seawater

DO (mg/L)	Sal. (g/L)	Cond. (mS/m)	Temp. (˚C)	pH	As	Se	Zn	Pb	Mn	Fe	Cr	Ag	
0.76*	0.64	0.59	0.62	0.54	-0.42	0.08	0.68	-0.16	0.30	0.08	0.30	1.00	**Ag**
0.78*	0.71*	0.69	0.44	0.68	-0.33	-0.04	-0.35	0.88*	1.00*	0.97*	1.00		**Cr**
0.62	0.57	0.56	0.29	0.55	-0.22	-0.03	-0.54	0.95*	0.97*	1.00			**Fe**
0.78*	0.71*	0.69	0.44	0.68	-0.33	-0.04	-0.35	0.88*	1.00				**Mn**
0.49	0.52	0.53	0.28	0.55	-0.29	-0.25	-0.60	1.00					**Pb**
0.32	0.36	0.36	0.60	0.34	-0.55	-0.34	1.00						**Zn**
-0.28	-0.53	-0.58	-0.70*	-0.64	0.86	100							**Se**
-0.71**	-0.87**	-0.89**	-0.97*	-0.91**	1.00								**As**
0.92*	0.99*	1.00*	0.96*	1.00									**pH**
0.85*	0.95*	0.95*	1.00										**Temp. (˚C)**
0.94*	1.00*	1.00											**Cond. (mS/m)**
0.96*	1.00												**Sal. (g/L)**
1.00													**DO (mg/L)**

*Significant positive correlation
** Significant negative correlation

Ballast water sampling

Table 8 shows the correlation analysis conducted to determine the relationship between the concentration of heavy metals and the physical and chemical parameters measured for the ballast water sampling. Based on Table 8, r values of 0.00 were obtained for Cd, As and Ni because these heavy metals cannot be detected in the ballast water. Fe has strong and positive correlations with Mn, Pb, Zn and dissolved oxygen, but has negative correlations with the pH, conductivity and salinity parameters. Mn also has the same relationship as Fe. Pb and Zn show positive correlations with Zn and dissolved oxygen, but show negative correlations with other parameters except temperature. Finally, the pH parameter shows positive correlations with salinity and conductivity, but is negatively correlated with dissolved oxygen.

Table 8. Correlation analysis between physiochemical parameters and heavy metal concentrations in ballast water

DO (mg/L)	Sal. (g/L)	Cond. (mS/m)	Temp. (˚C)	pH	As	Se	Zn	Pb	Mn	Fe	Cu	Cr	Ag	
0.39	-0.41	-0.42	0.25	-0.59	0.00	-0.35	0.59	0.66	0.55	0.58	-0.28	0.19	1.00	**Ag**
0.45	-0.34	-0.34	0.03	-0.35	0.00	0.48	0.14	0.25	0.14	0.25	0.50	1.00		**Cr**
0.23	-0.09	-0.08	0.20	0.15	0.00	0.58	-0.15	-0.09	-0.13	-0.08	1.00			**Cu**
0.85*	-0.93**	-0.94**	0.08	-0.97**	0.00	-0.37	0.99*	0.99*	0.99*	1.00				**Fe**
0.82*	-0.91**	-0.92**	0.06	-0.95**	0.00	-0.42	1.00*	0.98*	1.00					**Mn**
0.83*	-0.87**	-0.89**	0.04	-0.95**	0.00	-0.33	0.98*	1.00						**Pb**
0.81*	-0.92**	-0.93**	0.11	-0.96*	0.00	-0.46	1.00							**Zn**
-0.24	0.35	0.35	-0.57	0.38	0.00	1.00								**Se**
0.00	0.00	0.00	0.00	0.00	1.00									**As**
-0.80**	0.93*	0.94*	-0.10	1.00										**pH**
0.20	-0.24	-0.24	1.00											**Temp. (˚C)**
-0.81**	1.00	1.00												**Cond. (mS/m)**
-0.80**	1.00													**Sal. (g/L)**
1.00														**DO (mg/L)**

*Significant positive correlation
** Significant negative correlation

Comparison of heavy metal concentrations between the first sampling of seawater and ballast water

The concentration of heavy metals in the first and second sampling cannot be predicted in order to show comparison with ballast water samples due to the significant differences in the levels of Cr and Mn. Therefore, the first sampling which was obtained on a sunny day was compared with the ballast water sampling as shown in Table 9.

Table 9. ANOVA analysis for the first sampling of surrounding water and ballast water

Type of Heavy Metal	Ag	Cd	Cr	Cu	Fe	Mn	Ni	Pb	Zn	Se	As
Comparison between first sampling of seawater and ballast water sampling	-	*nd*	*	-	-	-	*nd*	-	-	-	*nd*

nd means not detected, * symbol means significant difference

Based on the results of the ANOVA analysis, it can be seen that only Cr shows a significant difference between the first sampling of seawater and ballast water. The concentrations of Cd for both sampling cannot be detected; therefore, the ANOVA test for Cd cannot be performed. As for Ni and As, their concentrations cannot be detected in

the ballast water sampling, thus the ANOVA test cannot be performed in comparison with seawater. There are no significant differences between both sampling for Ag, Cu, Fe, Mn, Pb, Zn and Se.

Concentration of heavy metals in ballast water

Table 10 shows the concentration of heavy metals for the ballast water samples which had originated from overseas. Eight types of ballast water samples were obtained in this study. Zn and Fe had the highest concentrations among the 11 types of heavy metals in all ballast water samples. The Malaysia Standard Water Quality Criteria and Standard (IMWQS) has set the standards for some heavy metals such as Cd, Cr, Cu, As, Pb and Zn.

Table 10. Heavy metal concentrations in ballast water

Ship	Heavy Metal (mg/L)										
	Ag	**Cd**	**Cr**	**Cu**	**Fe**	**Mn**	**Ni**	**Pb**	**Zn**	**Se**	**As**
1	0.000	*nd*	0.009	*nd*	0.173	0.009	*nd*	0.008	1.136	0.039	*nd*
2	0.003	*nd*	0.019	*nd*	0.058	*nd*	*nd*	0.007	0.036	0.051	*nd*
3	0.000	*nd*	0.019	0.002	0.176	0.004	*nd*	0.009	0.136	0.080	*nd*
4	0.015	*nd*	0.018	*nd*	0.037	*nd*	*nd*	0.010	0.085	0.054	*nd*
5	0.002	*nd*	0.021	0.021	0.139	0.001	*nd*	0.007	0.137	0.068	*nd*
6	0.000	*nd*	0.019	*nd*	0.014	0.000	*nd*	0.005	0.043	0.044	*nd*
7	0.014	*nd*	0.021	0.003	3.224	0.057	*nd*	0.035	9.067	0.040	*nd*
8	0.000	*nd*	0.022	0.025	0.270	0.004	*nd*	0.010	0.160	0.072	*nd*

nd means not detected

The first ship which ballast water had originated from Cambodia showed a Zn level of 1.136 mg/L and a Fe level of 0.173 mg/L. These two types of metals had the highest concentrations in all types of heavy metals studied, and Zn had exceeded the concentration level determined by the Malaysian standard of 100 ppb (0.100 mg/L). When the Zn concentration levels were compared between the ballast water sample and the surrounding seawaters at Tanjung Pelepas Port, the Zn concentration in the seawater was still at a safe level of less than 100 ppb for all four sampling stations. Ballast water from the second ship had originated from South China Sea (Open Sea). The Fe and Zn concentrations for the second ship were also lower than other ships at 0.058 mg/L (Fe) and 0.036 mg/L (Zn). However, Zn concentration did not exceed the prescribed limit set by the Malaysian government. One of the reasons is that this ballast water sample was taken from the open sea, unlike water taken from port areas which are home to many activities such as shipping and other industrial activities that may contribute to the increase in heavy metal concentration.

The third ship which originated from Spain also had high concentrations of Fe and Zn at 0.176 mg/L and 0.136 mg/L respectively. The concentration of Zn exceeded the standard set by the Malaysian government. However, the concentrations of Zn and Fe in the sample taken from the fourth ship which came from the Rotterdam Port, Netherland did not exceed the standard set by Malaysia. The concentrations of Zn and Cu in the sample from the fifth ship which came from Yangon Port, Myanmar had also exceeded the Malaysian standards. The standard set by the Malaysian government for Cu is 10 ppb, however 21 ppb of Cu was detected in the sample from the fifth ship.

In addition, the concentration of Fe in the sample from the sixth ship was lower compared to other ships at only 0.014 mg/L. However, the Zn and Se levels of the sample recorded the highest concentrations. However, the values recorded for the sample from the sixth ship still did not exceed the Malaysian standard level. The sample from the seventh ship which originated from South Africa had the highest concentrations of Zn and Fe among all ships that were studied. The concentrations of Zn and Fe were detected at 9.067 mg/L and 3.224 mg/L. Zn concentration far exceeded the standards set by the Malaysian government. Based on the current sampling observation, the ballast water sample from the seventh ship was the muddiest and dirtiest of all ballast water samples collected. Ballast water from the eighth ship which originated from the Suez Canal Port in Egypt contained Zn levels exceeding the

specified standard at a concentration of 0.160 mg/L, and its concentration of Fe was 0.270 mg/L. Cu was also present in the ballast water sample at a concentration of 0.025 mg/L. As for Cd, Ni and As, these heavy metals could not be traced in all ballast water samples. Cd was not found in all four stations for the first and second sampling of seawater. Ni and As could not be detected in some stations for both seawater sampling. The remaining heavy metals were still at a safe level as they did not exceed the specified standards.

Based on the concentration of detected heavy metals, Fe and Zn are the most detected metals in all ballast water samples. One of the factors of high Zn concentration is Zn has been widely used for corrosion protection in ships. Ballast water is seawater taken from the surrounding waters of a port and stored in a ballast tank made of iron. Thus, corrosion will occur due to the high level of salinity. During the ship building process, the surface of the ballast tank, cargo tank and other parts of the ship are coated with a Zn layer of nearly 120 μm thickness. This corrosion prevention method is a type of cathode protection where galvanization is done using Zn [12] Given that Zn is an important component of ships, therefore it explains why its concentration is one of the highest for heavy metals in ballast water.

The increase in Fe concentration levels of all samples may be due to the corrosion process. Corrosion occurs due to electrochemical processes where seawater which has ionic content attracts ions from other substances such as ion Fe^{2+} which may be withdrawn from the surface of the ballast tank. Seawater also has a high salinity level, and this will affect the conductivity of water. Then, Cl^- ions will enter the passive iron surface and try to pull ions inside the ballast tank by breaking the surface's passivity. The corrosion rate for iron in seawater is within the range of 0.1 to 0.3 mm/y, but it may increase to 2 to 4 mm/y if the seawater is contaminated with other corrosive materials. Thus, that may be the cause of high Fe concentrations in the collected seawater [13].

The first sampling (no rain occurring) was chosen to be compared to the ballast water samples because during a sunny day, dilution of seawater will not occur and affect the results. The concentrations of heavy metals such as Ag, Mn, Pb As and Se detected in the aquatic environment were higher due to the industrial activities happening around the port area. Cu and Ni can only be found at Station 1. Additionally, Fe, Pb, Zn and Cu concentrations were also high at Station 1. The concentration of Cu which was found only at Station 1 had exceeded the standards set by Malaysia. This may be due to ballast water discharge from ships entering the Tanjung Pelepas Port. Based on the information obtained during the sampling activity, ships release some ballast water before entering the port area because it helps stabilise the ship when anchored at port. Station 1 is an entry point into the port. The discharge of ballast water will cause heavy metals to spread from the ships' ballast water to Station 1 through natural phenomena such as high tide and low tide. The phenomena may contribute to the high concentration of some heavy metals at Station 1. Using this comparison, it is evident that Fe and Zn had the highest concentrations. As for the concentration of Pb that was higher in seawater than the ballast water, it was due to the smoke released by ships anchored at Tanjung Pelepas Port.

Furthermore, it can be seen that Zn and Cu were the two types of heavy metals that had exceeded the standards set by Malaysia in both seawater and ballast water. Zn and Cu are minerals required by the human body, but excessive amounts can cause health problems such as skin diseases and anaemia. The concentration of Fe was also very high in both types of samples, although it is not listed in the Malaysian standard. Fe is also an important element for the human body especially in the blood, but if it exceeds the limit, it will become a radical that is capable to do damage to human tissue cells. Based on the information collected during the sampling activity, a nearby area designated for fishing activity and mussel farming can be affected as the heavy metal content in both ballast water and seawater can be very hazardous and affect not only the water quality at the port but also the marine life and subsequently, humans through seafood consumption.

Conclusion

In conclusion, the weather factor can be one of the causes affecting the concentration of heavy metals in seawater. From the ANOVA analyses, it can be proved that the concentrations of Cr and Cd in both types of samples showed a significant difference. Furthermore, Fe showed the highest concentration of heavy metals in the aquatic environment. Fe and Zn showed highest concentrations in ballast water, thus have the potential to affect the water quality at Tanjung Pelepas Port through the ballast water release process. The cargo or container loading activities

carried out within the port area requires the discharge of ballast water before the process to ensure the stability of the ships. Through this process, the concentration of heavy metals in ballast water will be spread out to the port area. Therefore, this research has provides a feasible reference for future studies of onsite monitoring of water quality at the port and contribute to the idea in developed a simple, rapid and sensitive method for an onsite monitoring activity at the port such as sensor in order to control the release of heavy metals at the port area all around the world.

Acknowledgement

I would like to extend my appreciation to Universiti Kebangsaan Malaysia (UKM) Bangi, Selangor for providing the research grant GUP-2016-061 and GUP-2018-025. I would also like to thank the Marine Science UKM research group for their kind help in collecting the seawater and ballast water samples needed for this study.

References

1. Hsiang Tan, W., Tair, R., Aishah, S., Ali, M., Talibe, A., Sualin, F. and Payus, C. (2016). Distribution of heavy metals in seawater and surface sediment in coastal area of Tuaran, Sabah. *Transactions on Science and Technology*, 3(12): 114-122.
2. Tchounwou, P. B., Yedjou, C. G., Patlolla, A. K. and Sutton, D. J. (2012). Heavy metals toxicity and the environment. *National Institutes of Health Public Access*, 101: 133-164.
3. Naser, H. A. (2013). Assessment and management of heavy metal pollution in the marine environment of the Arabian Gulf: A review. *Marine Pollution Bulletin*, 72(1): 6–13.
4. Tavakoly Sany, S. B., Salleh, A., Rezayi, M., Saadati, N., Narimany, L. and Tehrani, G. M. (2013). Distribution and contamination of heavy metal in the coastal sediments of Port Klang, Selangor, Malaysia. *Water, Air, and Soil Pollution*, 224(4): 1476.
5. Nosrati-Ghods, N., Ghadiri, M. and Früh, W.-G. (2017). Management and environmental risk study of the physicochemical parameters of ballast water. *Marine Pollution Bulletin*, 114(1): 428–438.
6. International Maritime Organization. (2017). Ballast Water Management. Access from http://www.imo.org/en/OurWork/Environment/BallastWaterManagement/Pages/Default.aspx [Access online 10 October 2017]
7. Yunus, S. M., Hamzah, Z., Wood, A. K. and Ahmad. (2015). Assessment of heavy metals in seawater and fish tissues at Pulau Indah, Selangor, Malaysia. *AIP Conference Proceedings*, 1659: 050007.
8. Greenberg, A. E., Clesceri, L. S. and Eaton, A. D. (1992). Standard methods for the examination of water and wastewater. United States of America: American Public Health Association.
9. Noor, A. A. H., Farah, F. M. Z., Mohd, I. I. and Nik, A. N. A. (2015). Assessment of selected heavy metals in seawater and sediment at Klang coastal area Malaysia. *Malaysian Journal of Analytical Sciences*, 19(4): 730-738.
10. Doney, S. C., Fabry, V. J., Freely, R. A., Kleypas, J. A. (2009). Ocean acidification: The other CO_2 problem. *Annual Review of Marine Science*, 1(1): 169-192.
11. Tekin-özan, S. and Aktan, N. (2012). Relationship of heavy metals in water, sediment and tissues with total length, weight and seasons of *Cyprinus carpio* L., 1758 from Işikli Lake (Turkey). *Pakistan Journal of Zoology, 44*(5), 1405–1416.
12. BMT Defense Services (2009). The feasibility of a corrosion resistant ship. Access from https://www.bmtdsl.co.uk/media/1058725/BMTDSL-Corrosion-Resistant-Ship-Whitepaper.pdf[Access online 22 Mei 2018].
13. Aldez, B., Ramirez, J., Eliezer, A., Schorr, M., Ramos, R. and Salinas, R. (2016). Corrosion assessment of infrastructure assets in coastal seas. *Journal of Marine Engineering and Technology*, 15(3): 124-134.

Malaysian Journal of Analytical Sciences, Vol 23 No 4 (2019): 748 - 762
DOI: https://doi.org/10.17576/mjas-2019-2304-21

MALAYSIAN JOURNAL OF ANALYTICAL SCIENCES
Published by The Malaysian Analytical Sciences Society
ISSN 1394 - 2506

PSYCHROTOLERANT ACTINOBACTERIA *Barrientosiimonas humi* 39^T AS A SOURCE OF DIKETOPIPERAZINE

(Aktinobakteria Psikrotoleran *Barrientosiimonas humi* 39^T Sebagai Sumber Sebatian Diketopiperazin)

Andi Rifki Rosandy[1], Yeoh Chiann Ying[2], Cheah Yoke Kqueen[2], Muntaz Abu Bakar[1], Azira Muhamad[3], Rozida Mohd Khalid[1]*

[1]*School of Chemical Science and Food Technology, Faculty of Science and Technology*
Universiti Kebangsaan Malaysia, 43600 UKM Bangi, Selangor, Malaysia
[2]*Department of Biomedical Sciences, Faculty of Medicine and Health Sciences*
Universiti Putra Malaysia, 43400 Serdang, Selangor, Malaysia
[3]*Malaysia Genome Institute (MGI),*
National Institute of Biotechnology Malaysia (NIBM), Jalan Bangi, 43000 Kajang, Selangor, Malaysia

**Corresponding author: rozidakhalid@ukm.edu.my*

Received: 31 March 2018; Accepted: 17 April 2019

Abstract

Barrientosiimonas humi 39^T (*B. humi*) is a psychrotolerant actinobacteria from the family Dermacoccaceae, was first isolated from Antarctica. Five diketopiperazine derivatives: cyclo(-Pro-Val) (**1**), (-)-cyclo(-Pro-Tyr) (**2**), cyclo(-Pro-Phe) (**3**), (+)-cyclo(-Pro-Leu) (**4**), and L-tyrosine (**5**) were isolated from the crude extract of *B. humi*, and this is the first reported compounds isolated from *B. humi*. The crude extracts were obtained *via* liquid-liquid fractionation using ethyl acetate as the organic solvent. The compounds were isolated and purified using chromatographic methods such as vacuum liquid chromatography and radial chromatography. The chemical structures were elucidated by nuclear magnetic resonance (NMR) spectroscopy and mass spectrometry.

Keywords: *Barrientosiimonas humi* 39^T, diketopiperazine, *Dermacoccaceae*

Abstrak

Barrientosiimonas humi 39^T (*B. humi*) merupakan aktinobakteria psikrotoleran termasuk dalam famili Dermacoccaceae, asalnya dipencilkan dari Antartika. Lima terbitan diketopiperazin; siklo(-Pro-Val) (**1**), (-)-siklo(-Pro-Tir) (**2**), (-)-siklo(-Pro-Phe) (**3**), (+)-siklo(-Pro-Leu) (**4**) dan L-tirosina (**5**) diasingkan daripada ekstrak mentah *B. humi*, dan ini merupakan laporan pertama sebatian dipencilkan dari *B. humi.* Ekstrak mentah diperolehi melalui fraksi cecair-cecair menggunakan etil asetat sebagai pelarut. Sebatian-sebatian dipencilkan dan ditulenkan menggunakan kaedah kromatografi seperti kromatografi cecair vakum dan kromatografi jejari. Struktur kimia ditentukan menggunakan spektroskopi resonans magnetik nuklear (RMN) dan spektrometri jisim.

Kata kunci: *Barrientosiimonas humi* 39^T, diketopiperazine, *Dermacoccaceae*

Introduction

Psychrotolerant microorganisms are mostly present in the extremely cold environment [1, 2] but exhibit slower growth rates, as they automatically encounter number of growths limiting conditions such as reduced efficiency of

nutrient uptake, membrane disorders and decrease in the enzyme activity [3]. The psychrotolerants survive at low temperature due to their better nutritional adaptability [4] and have unique cold shock and cold acclimation proteins and enzymes [5]. In this century, actinobacteria derived from polar region have yielded an array of interesting new metabolites, genes, proteins, and other products with potential for commercial uses [6]. Polar actinobacteria often provide plentiful and diverse two bioactive alkaloids which are medicinally important such as nitrosporeusines A and nitrosporeusines B produced by *Streptomyces nitrosporeus* CQT14-24 [7].

The search for new and bioactive secondary metabolites is still going on, particularly from the extremophilic microorganisms. The psychrotolerant actinobacteria can be a good tool to explore the new bioactive metabolites of pharmaceutical importance due to uniqueness of their habitat and changes in the metabolic systems, amenable for their adaptation to extreme cold environmental conditions. The genus *Barrientosiimonas* (Bar.ri.en.to.si.i.mo′nas. N.L. n. Barrientosia Barrientos Island, an island in the Antarctic; L. fem. n. *monas* a unit, a monad; N.L. fem. n. *Barrientosiimonas* a bacterium isolated from Barrientos Island) was validly published early in the year 2013 with *Barrientosiimonas humi* 39^T (actinobacteria/gram-positive) as the type and only species [8]. *Barrientosiimonas humi* 39^T belongs to the family *Dermacoccaceae* [9] and was isolated from soil in Barrientos Island, Antarctica [8]. It is growth optimally at temperatures less than 15 °C and able to grow above 20 °C was called psychrotolerant [10]. So far, the chemical structures from *Barrientosiimonas humi* 39^T have not reported. The main objective of this paper is to describe the isolation and structure characterization from the ethyl acetate extract of *Barrientosiimonas humi* 39^T.

Materials and Methods

Biological materials

The *B. humi* 39^T was isolated from soil sampled at Barrientos Island (Antarctica) (62° 24′ 26.0″ S 59° 44′ 49.1″ W, 62° 24′ 24.4″ S 59° 44′ 44.2″ W and 62° 24′ 28.5″ S 59° 44′ 52.3″ W) during the XI Ecuadorian Antarctic Expedition in 2007. The cultural characteristics of strain 39^T were determined following growth on tap-water agar [11], solidified rich R medium [12] and ISP 2–7 [13] for 7 days at 28 °C. The culturing of *B. humi* 39^T was conducted in collaboration with the Department of Biomedical Sciences, UPM, Serdang Malaysia.

Cultivation of yeast

A single bacterial colony of *B. humi* 39^T will be inoculated into an Erlenmeyer flask (500 mL) containing 100 mL of actinomyces broth and incubated in an orbital shaker at 28 °C, 200 rpm for 72 hours. The seed culture (5%) will be then inoculated into Erlenmeyer flasks (1 L × 4) containing same media (300 mL × 4) and incubated at 28 °C with shaking at 200 rpm for 7 days [13, 14].

Extraction and isolation

The production culture was centrifuged (10,000 rpm, 4 °C, 5 minutes). The supernatant was extracted three times with ethyl acetate, and concentrated using a rotary evaporator. The EtOAc extract (300 mg) of *B. humi* 39^T was subjected to radial chromatography (RC) with 1 mm thickness silica gel on a round glass plate and eluted with the mixtures of $CHCl_3$ and MeOH with increasing polarity (started with $CHCl_3$/MeOH, 9 :1). The eluates showing the same profile on thin layer chromatography (TLC) were combined to give three fractions (I-III). Purification of fraction I (1-4) (29.7 mg) was carried out using RC with a silica gel plate of 0.5 mm thickness eluted with $CHCl_3$ and MeOH (9.2:0.8) in 5% polarity increment to yield compound **1** (1 mg).and **2** (1.5 mg). Purification of fraction III (5-7) (48.8 mg) was conducted utilizing another RC with silica gel plate of 0.5 mm thickness. Elution with $CHCl_3$ and MeOH (8.5:1.5) produced compounds **3** (1.5 mg), **4** (2 mg), and **5** (2 mg), respectively.

Results and Discussion

Characterization study

Cyclo(-Pro-Val) (**1**) is a needle crystal. m.p.: 218-219 °C. ESI-MS $[M + H]^+$ at *m/z* : 197. IR $\bar{\upsilon}_{max}$ (ATR) cm^{-1}: 3191, 2956, 1640, 1453, 1110, 922. ^1H NMR (DMSO, 700 MHz): δ_H 3.92 (*d, J* = 7 Hz, 1H, H-3), 7.93 (*br-s*, 1H, 4-NH), 4.11 (*t, J* = 7 Hz, 1H, H-6), 1.82 (*m*, 1H, H-7), 2.14 (*m*, 1H, H-7), 1.86 (*m*, 1H, H-8), 1.80 (*m*, 1H, H-8), 3.33 (*t, J* = 7 Hz, 1H, H-9), 3.38 (*t, J* = 7 Hz, 1H, H-9), 2.32 (*m*, 1H, H-10), 0.99 (*d, J* = 7 Hz, 3H, H-11), 0.83 (*d, J* = 7 Hz, 3H, H-12) ppm. NMR APT (DMSO,175 MHz): δ_C 165.8 (Cq-2), 59.9 (CH-3), 170.9 (Cq-5), 58.7 (CH-6), 28.3 (CH_2-7), 22.4 (CH_2-8), 45.1 (CH_2-9), 28.2 (CH-10), 18.7 (CH_3-11), 16.8 (CH_3-12) ppm.

(-)-Cyclo(-Pro-Tyr) (**2**) is a colorless amorphous solid. $[\alpha]_D^{20}$ -43.1 (c 0.14, ethanol). ESI-MS $[M + H]^+$ ion at *m/z* : 261. IR $\bar{\upsilon}_{max}$ (ATR) cm^{-1}: 3248, 2927, 2853, 1747, 1658, 1449, 1252, 1174, 1114, 1017, 858. ^1H NMR (CD_3OD, 700 MHz): δ_H 4.37 (*t, J* = 7 Hz, 1H, H-3), 7.65 (*br-s*, 1H, 4-NH), 4.05 (*t, J* = 7 Hz, 1H, H-6), 1.25 (*q, J*$_1$ = 7 Hz, 1H, H-7), 2.12 (*m*, 1H, H-7), 1.82 (m, 2H, H-8), 3.57 (*t, J* = 7 Hz, H-9), 3.36 (*t, J* = 7 Hz, H-9), 3.07 (*d, J* = 7 Hz, 2H, H-10), 7.06 (*d, J* = 7 Hz, 2H, H-2`/6`), 6.74 (*d, J* = 7 Hz, 2H, H-3`/5`), 9.15 (*br-s*, 1H, 4`-OH) ppm. NMR APT ($CD_3OD$, 175 MHz): $\delta_C$ 165.7 (Cq-2), 56.6 (CH-3), 169.6 (Cq-5), 58.7 (CH-6), 28.0 ($CH_2$-7), 21.4 ($CH_2$-8), 44.6 ($CH_2$-9), 36.3 ($CH_2$-10), 126.3 (Cq-1`), 130.7 (CH-2`/6`), 115.0 (CH-3`/5`), 156.1 (Cq-4`) ppm.

(-)-Cyclo(-Pro-Phe) (**3**) is a colorless solid. m.p.: 144-145 °C. $[\alpha]_D^{20}$-70.00 (*c* 0.02, MeOH). Turned to yellow with anisaldehyde/sulphuric acid. ESI-MS $[M + H]^+$ ion at *m/z* : 245. ^1H NMR (CD_3OD, 700 MHz): δ_H 4.38 (*t*, 7) 1H (H-3), 7.78 (*br-s*) 1H (4-NH), 4.06 (*t*, 7) 1H (H-6), 1.23 (*m*) 1H (H-7a), 2.11 (*m*) 1H (H-7b), 1.82 (*m*) 2H (H-8), 3.57 (*m*) 1H (H-9a), 3.37 (*m*) 1H (H-9b), 3.30 (*dd*, 7, 14) 1H (H-10a), 2.98 (*dd*, 7, 14) 1H (H-10b), 7.22 (*d*, 7) 2H (H-2`/6`), 7.27 (*t*, 7) 2H (H-3`/5`), 7.32 (*t*, 7) 1H (H-4`) ppm. NMR APT ($CD_3OD$, 175 MHz): $\delta_C$ 165.6 (Cq-2), 56.5 (CH-3), 169.4 (Cq-5), 58.7 (CH-6), 28.0 ($CH_2$-7), 21.3 ($CH_2$-8), 44.5 ($CH_2$-9), 38.9 ($CH_2$-10), 126.2 (Cq-1`), 130.4 (CH-2`/6`), 126.9 (CH-3`/5`), 128.1 (CH-4`) ppm.

(+)-Cyclo(-Pro-Leu) (**4**) is a white powder. $[\alpha]_D^{20}$ +28.1 (*c* 0.032, ethanol). ESI-MS $[M + H]^+$ ion at *m/z* : 211. IR $\bar{\upsilon}_{max}$ (ATR) cm^{-1}: 3222, 2958, 2930, 2872, 1686, 1676, 1426, 1302, 1275, 1235, 1157, 1102, 1032, 996-919. ^1H NMR (DMSO, 700 MHz): δ_H . 4.00 (*t, J* = 7 Hz, 1H, H-3), 7.99 (*br-s*, 1H, 4-NH), 4.18 (*t, J* = 7 Hz, 1H, H-6), 2.12 (*m*, 1H, H-7), 1.89 (*m*, 1H, H-7), 1.80 (*m*, 2H, H-8), 3.37 (*t, J* = 7 Hz, 1H, H-9), 3.36 (*t, J* = 7 Hz, 1H, H-9), 1.75 (*m*, 1H, H-10), 1.36 (*m*, 1H, H-10), 1.85 (*m*, 1H, H-11), 0.86 (*d, J* = 7 Hz, 3H, H-12), 0.85 (*d, J* = 7 Hz, 3H, H-13) ppm. NMR APT (DMSO, 175 MHz): δ_C 167.1 (Cq-2), 53.1 (CH-3), 171.1 (Cq-5), 58.9 (CH-6), 27.9 (CH_2-7), 22.9 (CH_2-8), 45.3 (CH_2-9), 38.1 (CH_2-10), 24.5 (CH-11), 23.2 (CH_3-12), 22.3 (CH_3-13) ppm.

L-Tyrosine (**5**) is a colorless amorphous solid. m.p.: 343-344 °C. ESI-MS $[M + H]^+$ at *m/z* 182. ^1H NMR (CD_3OD, 700 MHz): δ_H 6.84 (*d, J* = 7 Hz, 2H, H-2/6), 6.68 (*d, J* = 7 Hz, 2H, H-3/5), 9.23 (*br-s*, 1H, 4-OH), 2.51 (*d, J* = 7 Hz, H-7), 2.11 (*dd, J*$_1$ = 7 Hz, *J*$_2$ = 14 Hz, 1H, H-7), 3.85 (*t, J* = 7 Hz, 1H, H-8), 7.77 (*br-s*, 2H, 8-NH_2), 10.88 (*br-s*, 1H, 9-OH) ppm. NMR APT (CD_3OD, 175 MHz): δ_C 127.0 (Cq-1), 131.2 (CH-2/6), 115.5 (CH-3/5), 156.5 (CH-4), 39.3 (CH_2-7), 56.2 (CH_2-8), 166.7 (Cq-9) ppm.

Fraction I was applied to PF254 Gypsum (Merck 7749, size 0.040-0.063 mm) followed by TLC to afford compound **1** that turned to blue with chlorine/anisidine and violet when sprayed with anisaldehyde/sulphuric acid. The ^1H NMR (Figure 1) spectrum of **1** contained three methine proton signals; two methines δ_H 4.11 (H-6), 3.92 (H-3) were possibly connected to heteroatoms. A further methine signal was found at δ_H 2.32 (H-10) bind a geminal dimethyl proton at δ_C 18.7 (CH_3-11) and 16.8 (CH_3-12) (Figure 2). Additionally, three saturated non-equivalent methylenes signals at δ_H 1.82-2.14 (H-7), (H-7), 1.80-1.86 (H-8), and 3.33-3.38 (H-9) were attributed to a pyrrolidine ring. The ESI mass spectrum (Figure 3) showed molecular ion peaks at *m/z* ESI-MS $[M + H]^+$ which fixed the molecular weight as *m/z* 197. Compound **1** was found to have a molecular formula of $C_{10}H_{16}N_2O_2$ by LRESIMS. A search in the Anti-Base using all of the spectroscopic data above led to cyclo(-Pro-Val) (**1**) as a result. Cyclo(-Pro-Val) (**1**) was previously isolated from *Alternaria altenata* [12], *Aspergillus fumigatus* Brazilian strain [13] and *Pseudomonas aeruginosa* [14].

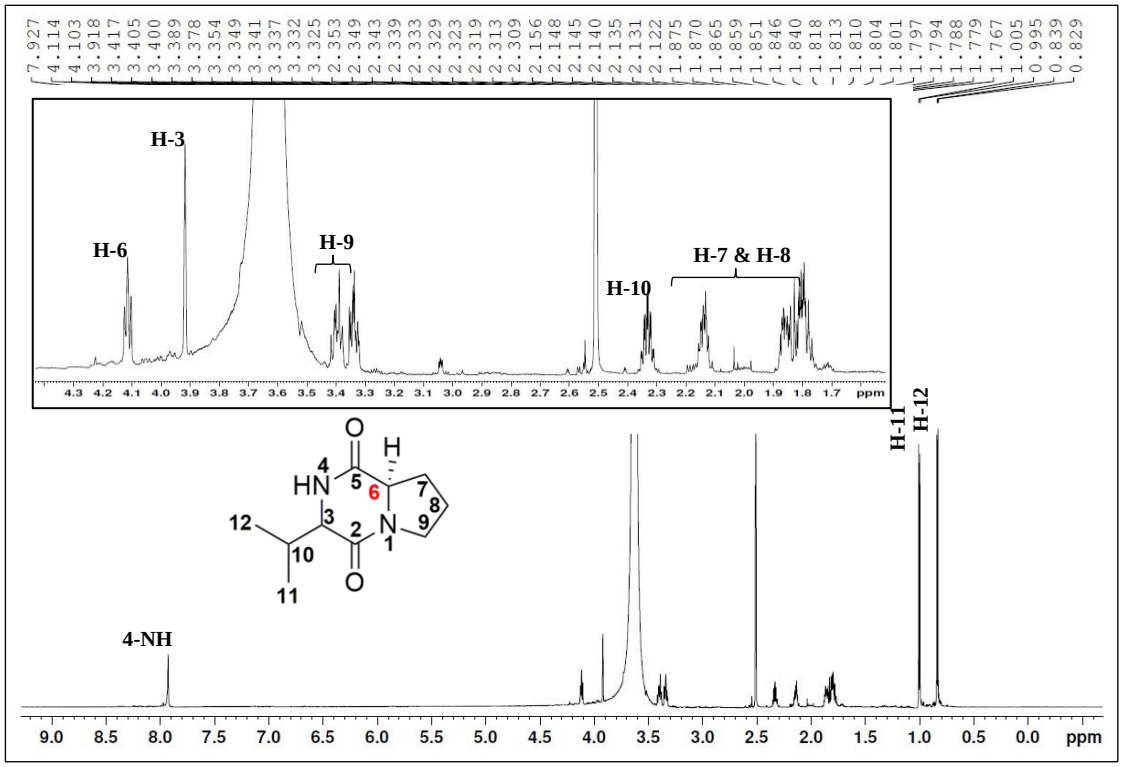


Figure 1. The ^{1}H-NMR (DMSO, 700 MHz) Spectrum of Cyclo(-Pro-Val) (**1**)

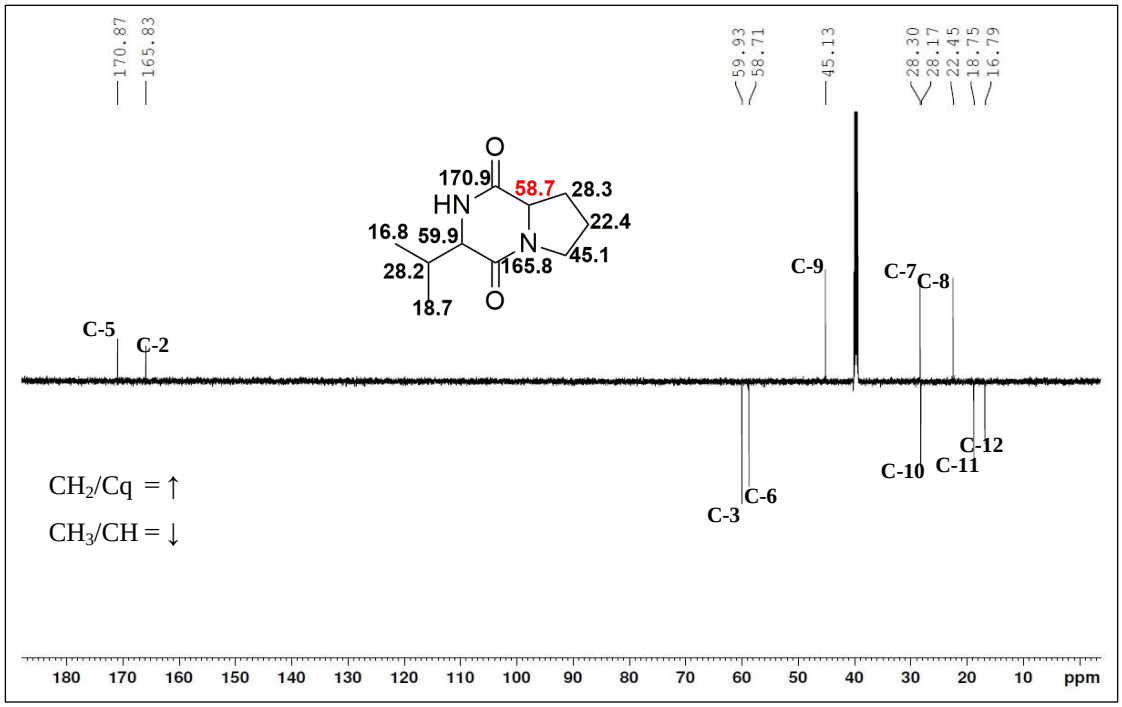


Figure 2. The ^{13}C NMR-APT (DMSO, 175 MHz) Spectrum of Cyclo(-Pro-Val) (**1**)

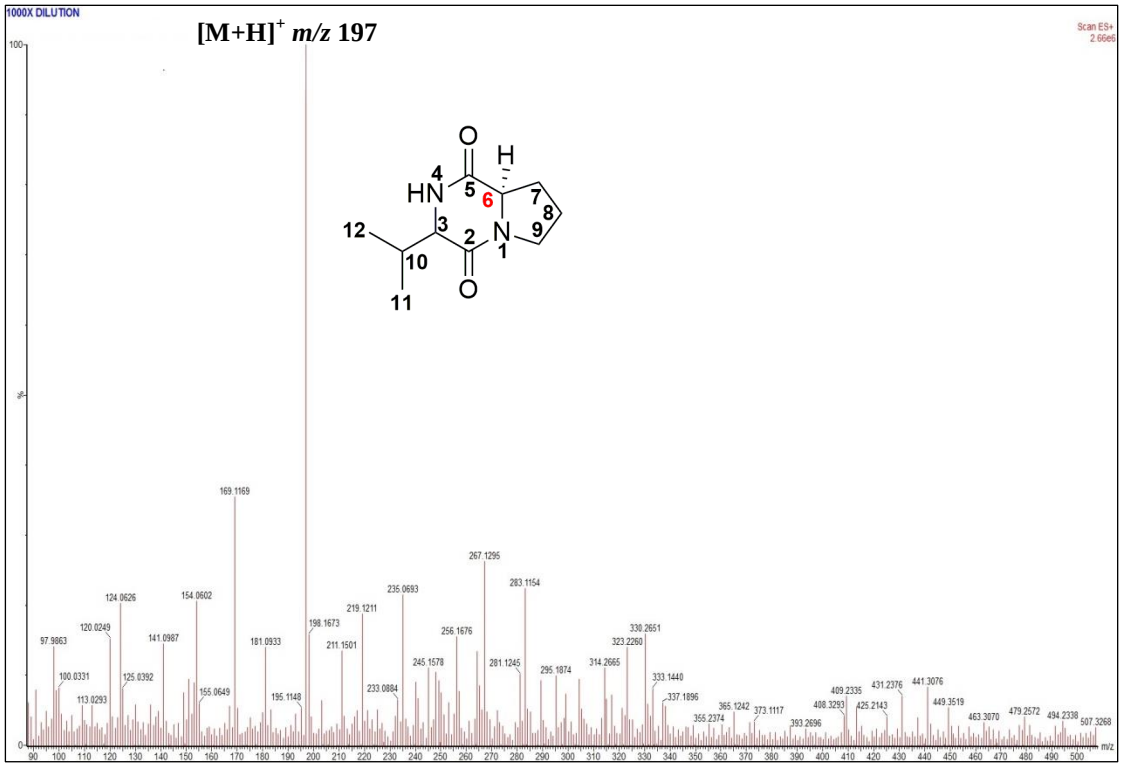


Figure 3. The LC-MS Spectrum of Cyclo(-Pro-Val) (**1**)

Compounds **2** was found in Fraction I as a UV absorbing spot, which stained to violet with sulphuric acid. The ^{1}H NMR and 13C NMR spectrum (Figure 4 and Figure 5) of Compound **2** showed two *ortho*-coupled signals at δ_H 7.05 (H-2', 6') and 6.79 (H-3', 5'), which illustrated as an AA'-BB' system of a 1,4-disubstituted aromatic ring, as well as two signals at δ_H 4.37 and 4.05 for two methines attached to electron withdrawing substituents. The spectrum proton of Compound **2** showed also two doublet of doublets for an ABX system of a methylene group at δ_H 3.46 and 2.79 (CH2-10), as well as three methylene multiplets (CH_2-7) (δ_H 2.33, 1.99) attached to a heteroatom and CH2-8, 9 (δ_H 2.01, 1.93, 3.63, 3.57). The ESI mass spectra (Figure 6) determined the molecular weight of Compound **2** as *m/z* 261 by (+)-ESI mode. The structure was further confirmed as cyclo(-Pro-Tyr) (**2**) was previously isolated from *Pseudomonas fluorescens* GcM5-1A [15], *Streptomyces* sp. H7372 and ML 1532 [16, 17], *Pseudomonas aeruginosa* [14] and *Lysobacter capsici* AZ78 [18].

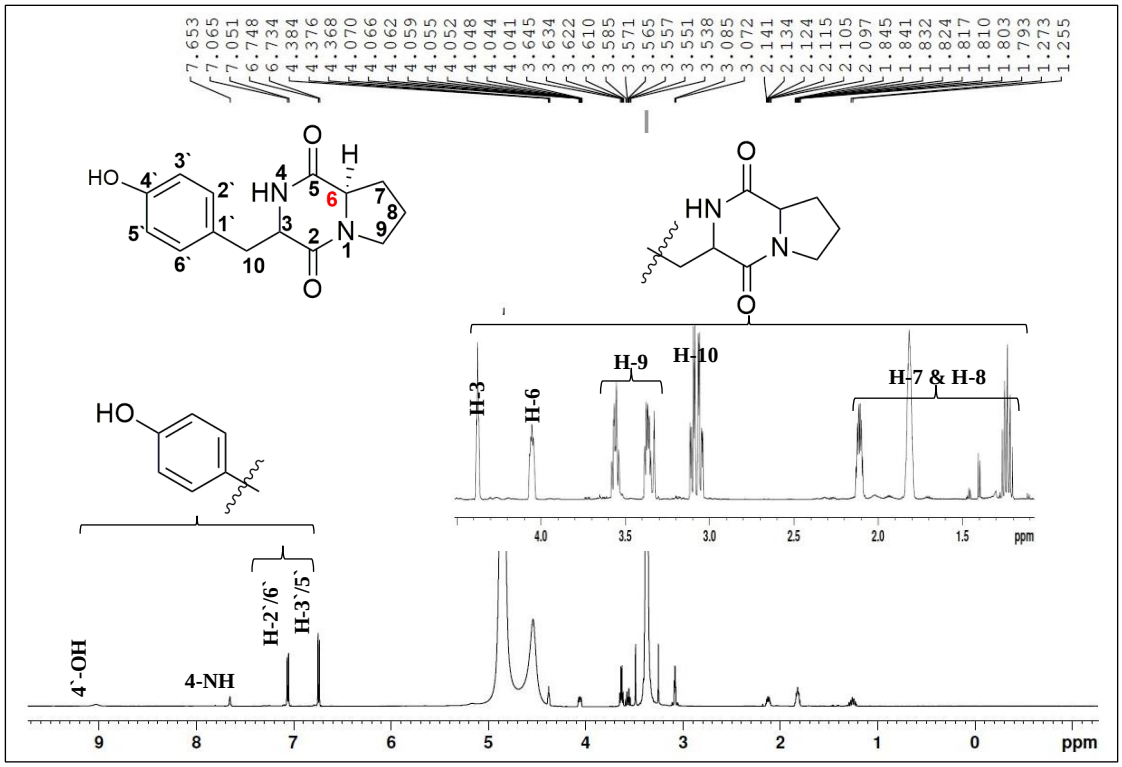


Figure 4. The ^{1}H-NMR (CD_3OD, 700 MHz) Spectrum of (-)Cyclo(-Pro-Tyr) (**2**)

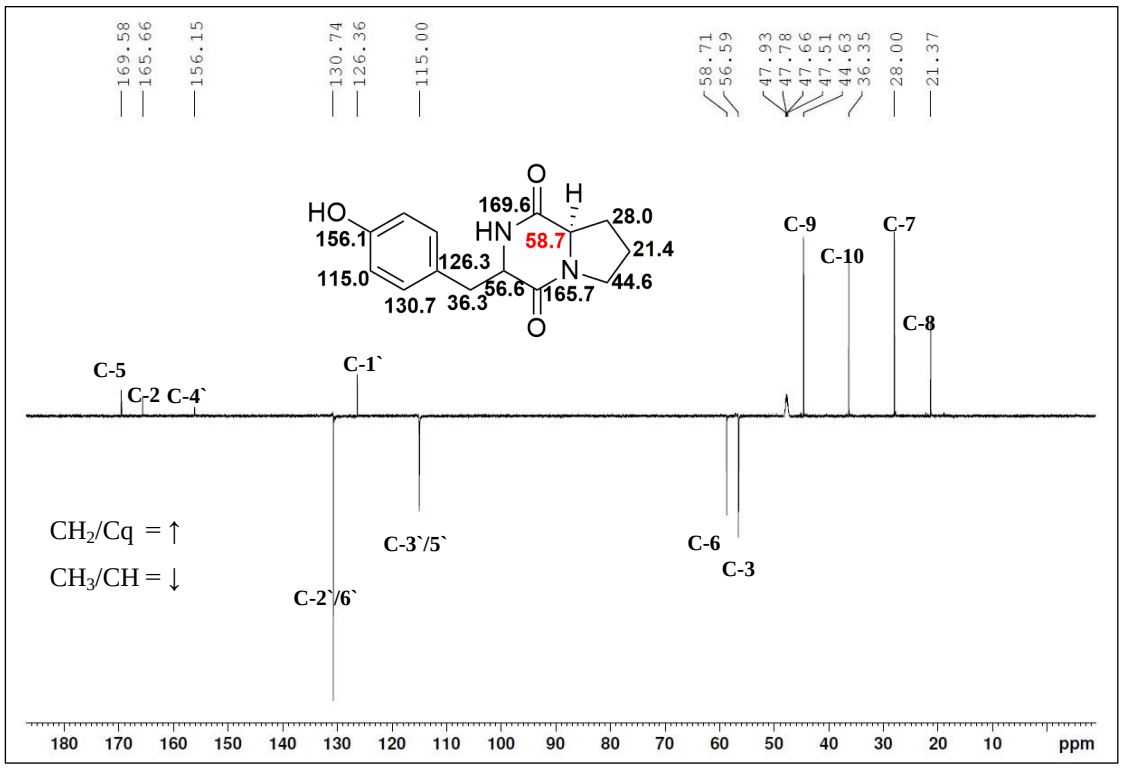


Figure 5. The NMR-APT(CD_3OD, 175 MHz) Spectrum of (-)Cyclo(-Pro-Tyr) (**2**)

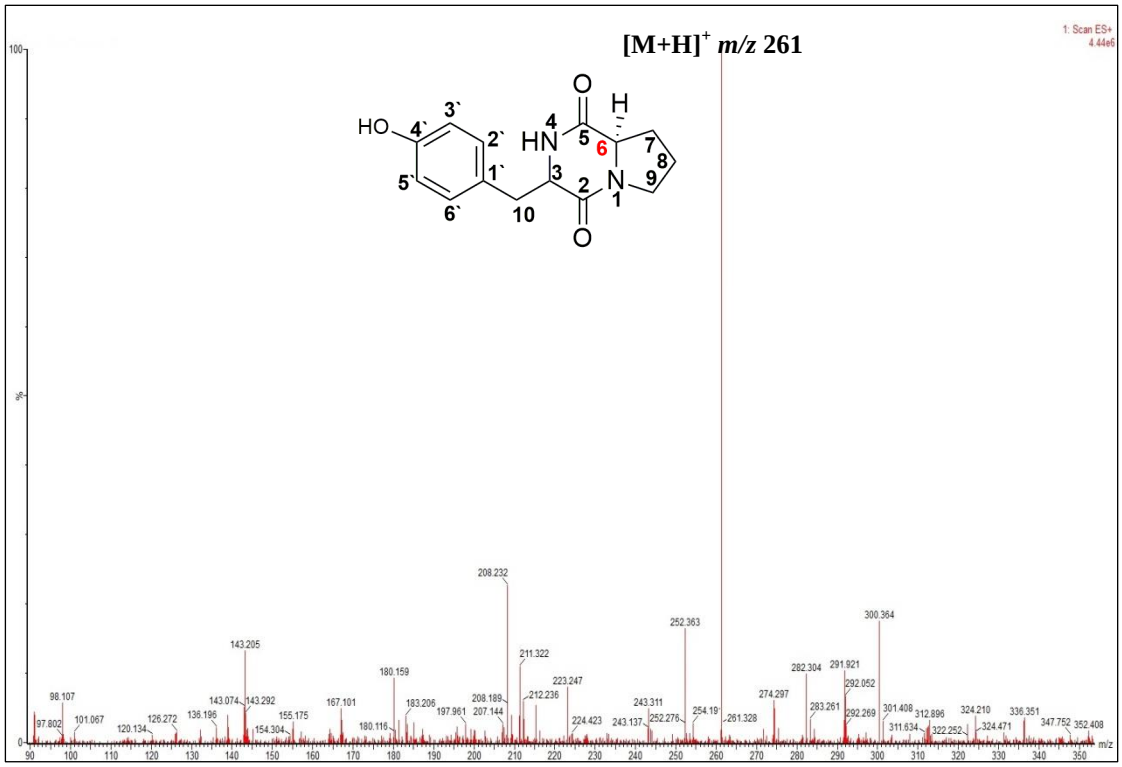


Figure 6. The LC-MS Spectrum of (-)Cyclo(-Pro-Tyr) (**2**)

Compounds **3** were found in Fraction III as a UV absorbing spot, which stained to violet with anisaldehyde/sulphuric acid. The ^{1}H NMR and ^{13}C NMR spectrum (Figure 7 and Figure 8) of compound **2** showed two ortho-coupled signals at δ_H 7.22 (H-2', 6') and 7.27 (H-3', 5'), which pointed to an AA'-BB' system of a 1,4-disubstituted aromatic ring, as well as two signals at δ_H 4.38 and 4.06 for two methines attached to electron withdrawing substituents. The spectrum proton of Compound **2** also depicted two doublet of doublets for an ABX system of a methylene group at δ_H 3.30 and 2.98 (CH_2-10), as well as three methylene multiplets (CH_2-7) (δ_H 1.23, 2.11) attached to a heteroatom and CH_2-8, 9 (δ_H 1.82, 3.57, 3.37). The ESI mass spectra (Figure 9) determined the molecular weight of Compound **3** as *m/z* 245 by (+)-ESI mode. The structure was further confirmed as (-)-cyclo(-Pro-Phe) (**3**) previously isolated from microbial *Streptomyces sudanensis*. A4.4 [19].

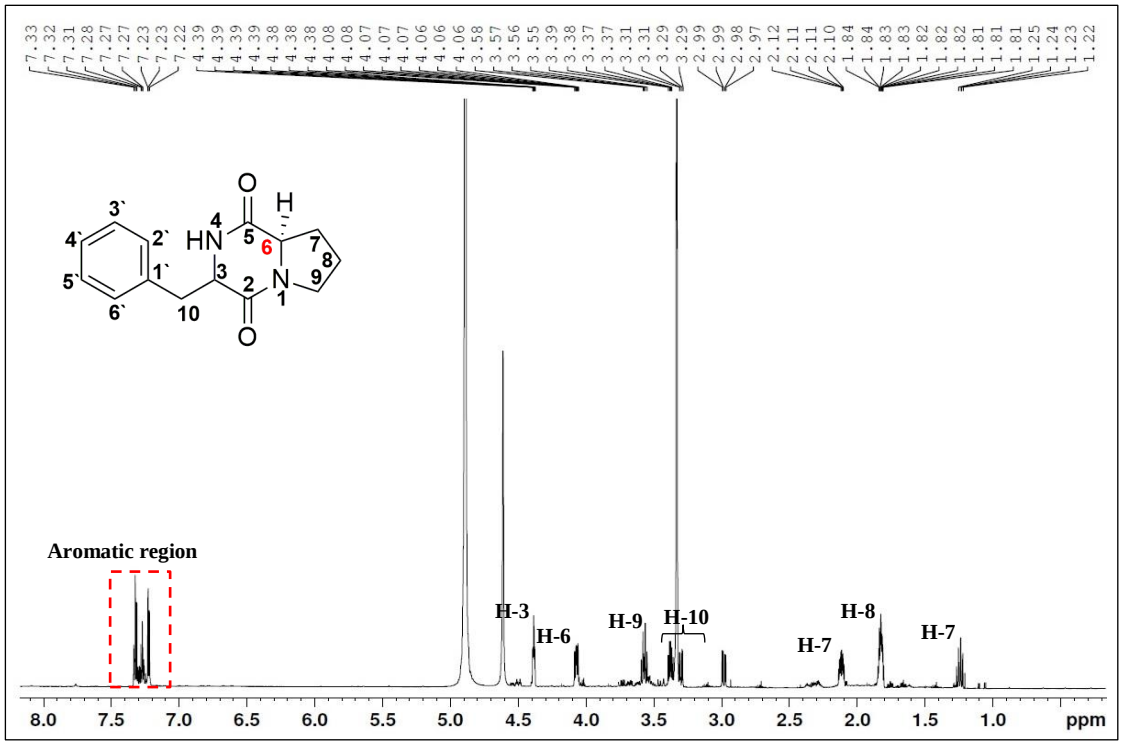


Figure 7. The ^{1}H-NMR (CD_3OD, 700 MHz) Spectrum of Cyclo(-Tyr-Phe) (**3**)

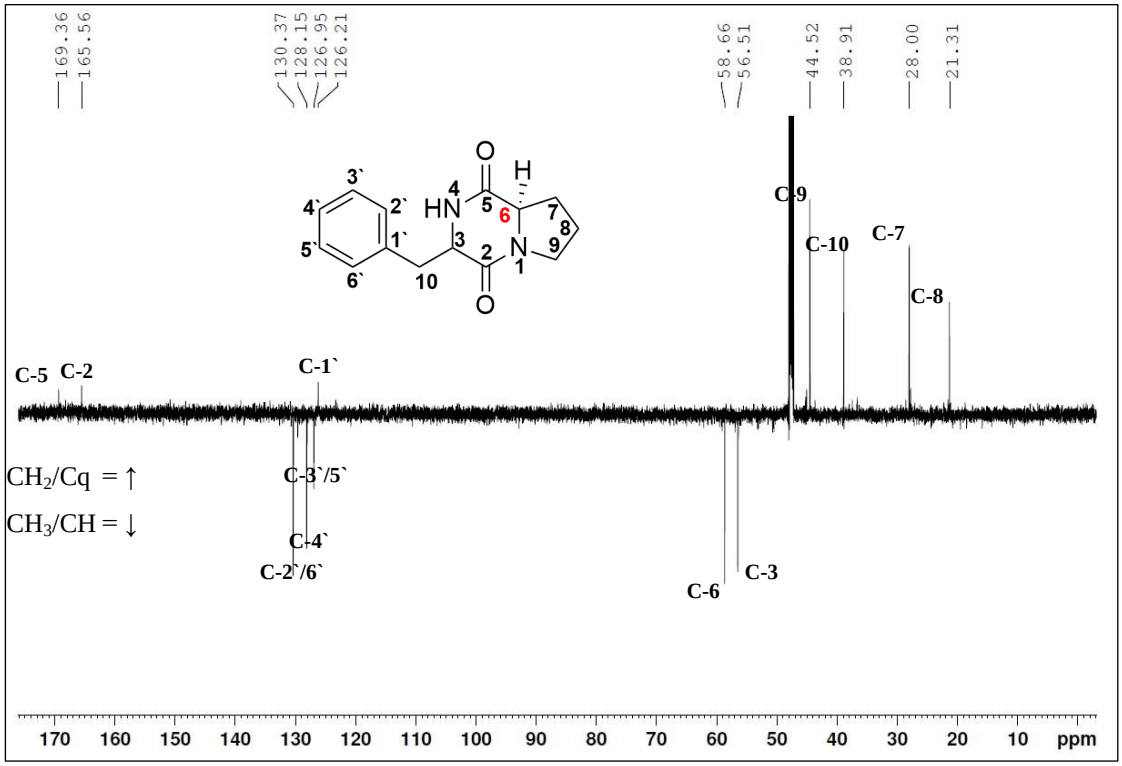


Figure 8. The NMR-APT (CD_3OD, 175 MHz) Spectrum of Cyclo(-Tyr-Asn) (**3**)

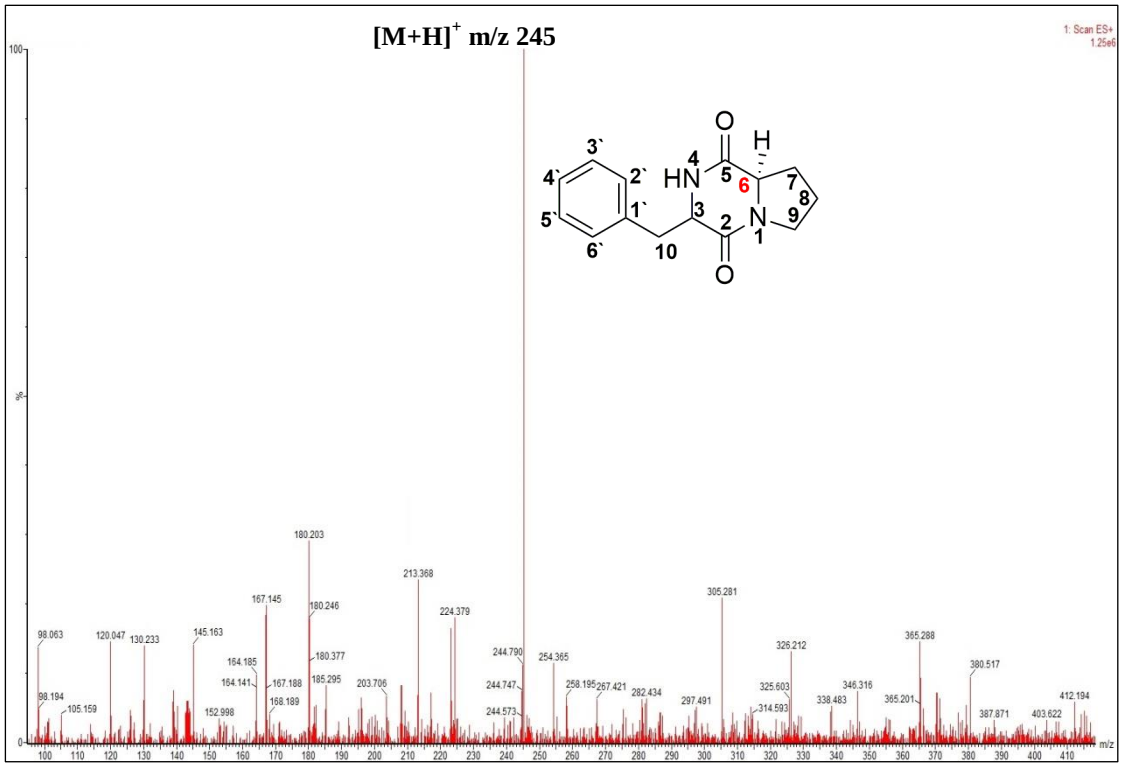


Figure 9. The LC-MS Spectrum of Cyclo(-Tyr-Phe) (**3**)

(+)-Cyclo(-Pro-Leu) (**4**), $[\alpha]_D^{20}$ +28.1 (*c* 0.032, ethanol), was isolated as a white amorphous material. The IR spectrum showed bands attributed to the aliphatic carbons (2958, 2930, 2872 cm^{-1}) and amide (1686, 1676 cm^{-1}) functional groups. ^{1}H NMR spectrum (Figure 10) of compound **4** indicated the presence of three methines at H-3, H-6 and H-11; four methylenes at H-7, H-8, H-9 and H-10; and two non-equivalents dimethyl at H-12 and H-13. NMR APT spectrum (Figure 11) exhibited the presence of 11 carbon signals corresponding to two methyls, four methylenes, three methines and two quaternary carbons. The observation of the quaternary carbons at δ_C 167.1 (C-2) and 171.1 (C-5) suggested that these carbon signals were due to the carbonyl carbon of the amide groups. The DBE value of four indicated that this compound was containing two double bonds and two cyclic aliphatic with molecular formula $C_{11}H_{18}N_2O_2$, supported by ESI–MS (Figure 12) $[M + H]^+$ *m/z* 211. The. (+)-Cyclo(Pro-Leu) previously isolated from the Gram-negative Proteobacteria of *Burkholderia cenocepacia* and *Serratia marcescens* [20], *Alternaria alternata* [12], the bacteria *Pseudoalteromonas* sp. [21] and *Vibrio alginolyticus* [22].

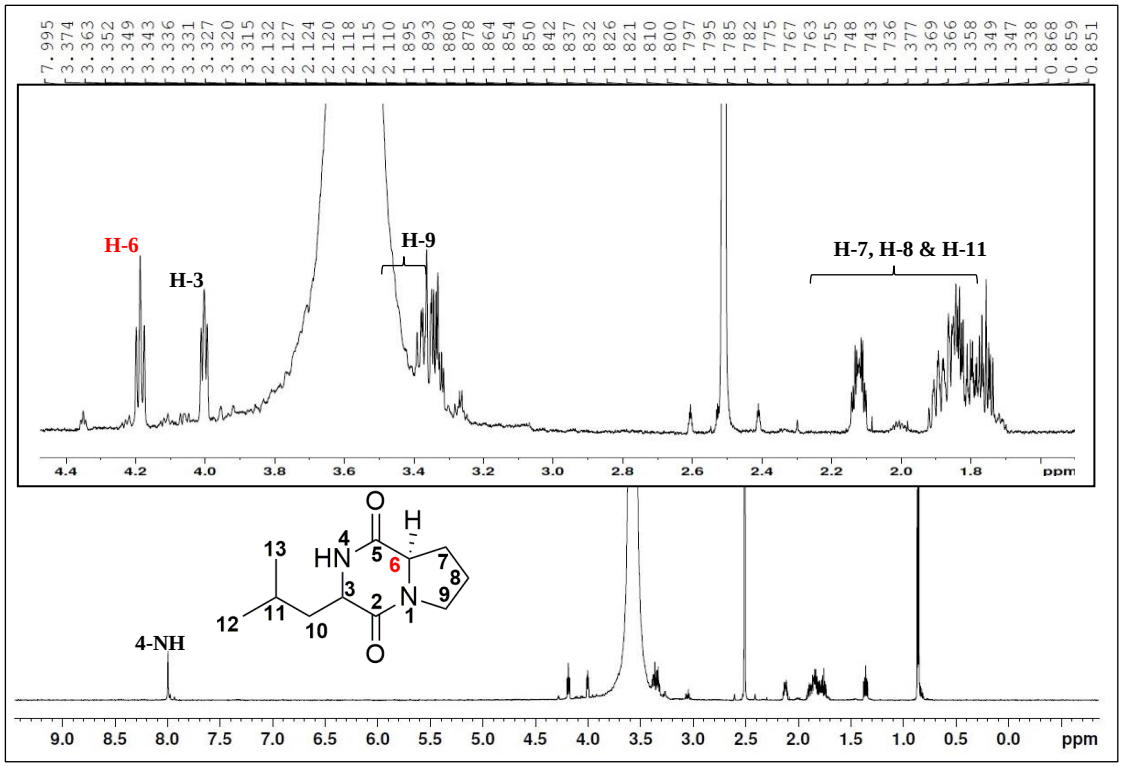


Figure 10. The ^{1}H-NMR (DMSO, 700 MHz) Spectrum of (+)Cyclo(-Tyr-Leu) (**4**)

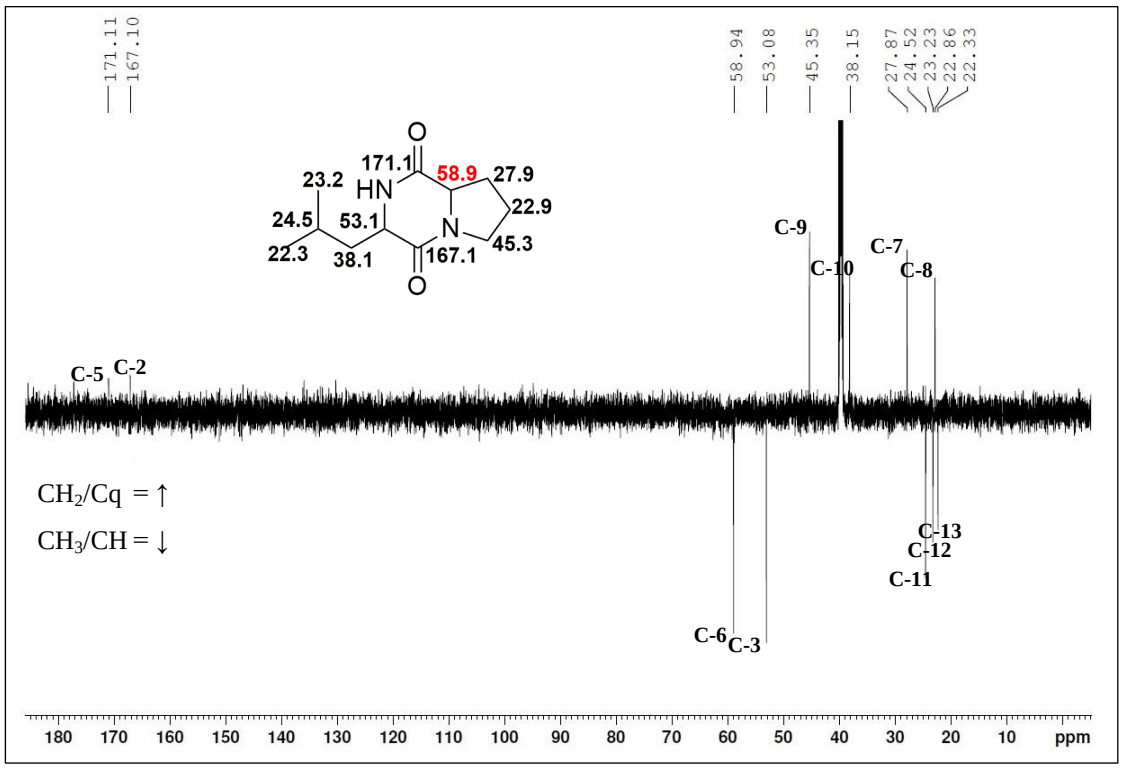


Figure 11. The NMR-APT (DMSO, 175 MHz) Spectrum of (+)Cyclo(-Tyr-Leu) (**4**)

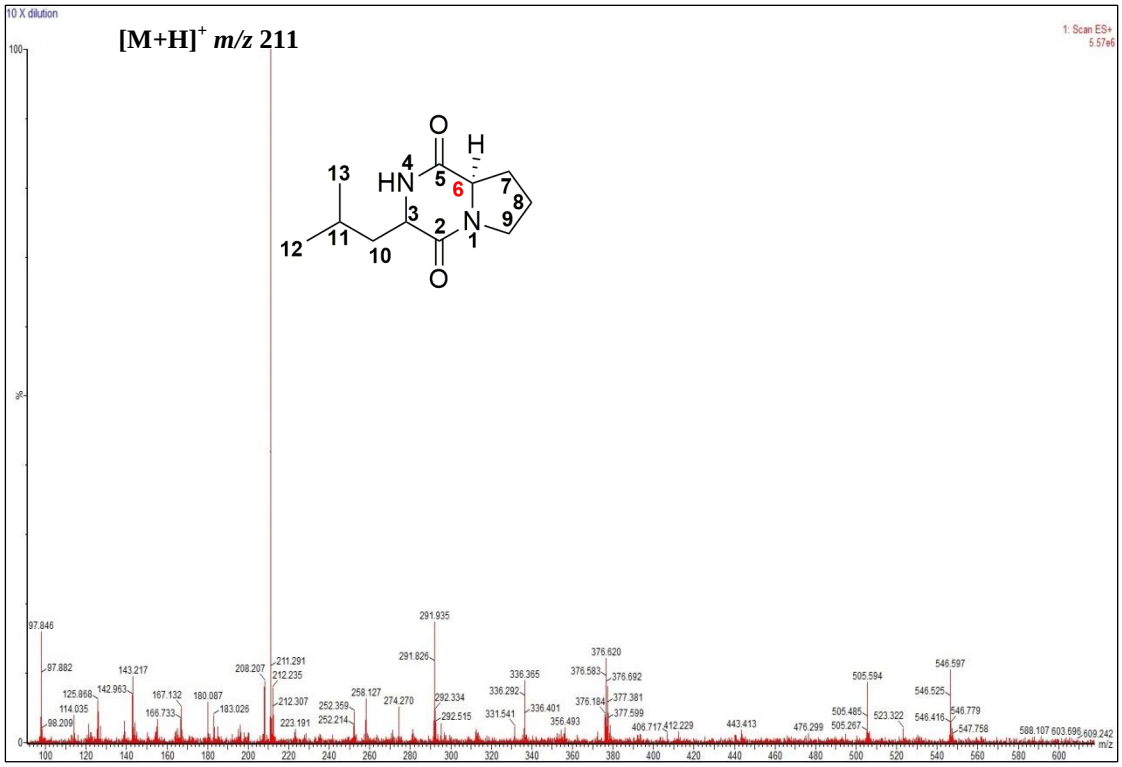


Figure 12. The LC-MS Spectrum of (+)Cyclo(-Tyr-Leu) (**4**)

Compound **5** was isolated as white amorphous from a UV absorbing zone in fraction III, which turned to violet with anisaldehyde reagent. The ^{1}H NMR spectrum (Figure 13) of compound **5** showed two *ortho*-coupled signals at δ_H 6.84 (H-2, 6) and 6.68 (H-3, 5), which pointed to an AA'-BB' system of a 1,4-disubstituted aromatic ring. In aliphatic region there was a methylene group at δ_H 2.11 and a methine at δ_H 3.85 ppm in the amino acid group. The NMR APT spectrum (Figure 14) exhibited seven carbon signals, among them the carbonyl signal of an amino acid derivative at δ_C 166.7 ppm and a methylene (C-7) as a link between amino acid with phenol. The ESI mass spectrum (Figure 15) indicated the peak at *m/z* 182 $[M + H]^+$ established the molecular formula as $C_9H_{11}NO_3$. A search in Anti-Base supported by ^{1}H, ^{13}C NMR, and MS spectroscopic data led to L-tyrosine (**5**) [23]. This compound previously isolated from bacteria *B. flavus* AJ-11955 [24] and *Klebsiella* sp. [25].

Out of five compounds, four are dipeptides with proline as one of its amino acid, and this is probably due to the nature of this microbe that can survive very low temperature. Some microbes were reported to produce higher amounts of L-proline at very low temperature as a cold adaptation mechanism [26, 27]. L-proline is a protectant stress agent that can moderate stability of cell membrane and control cell damage due to freeze-thaw mechanism during extreme low temperature [28, 29].

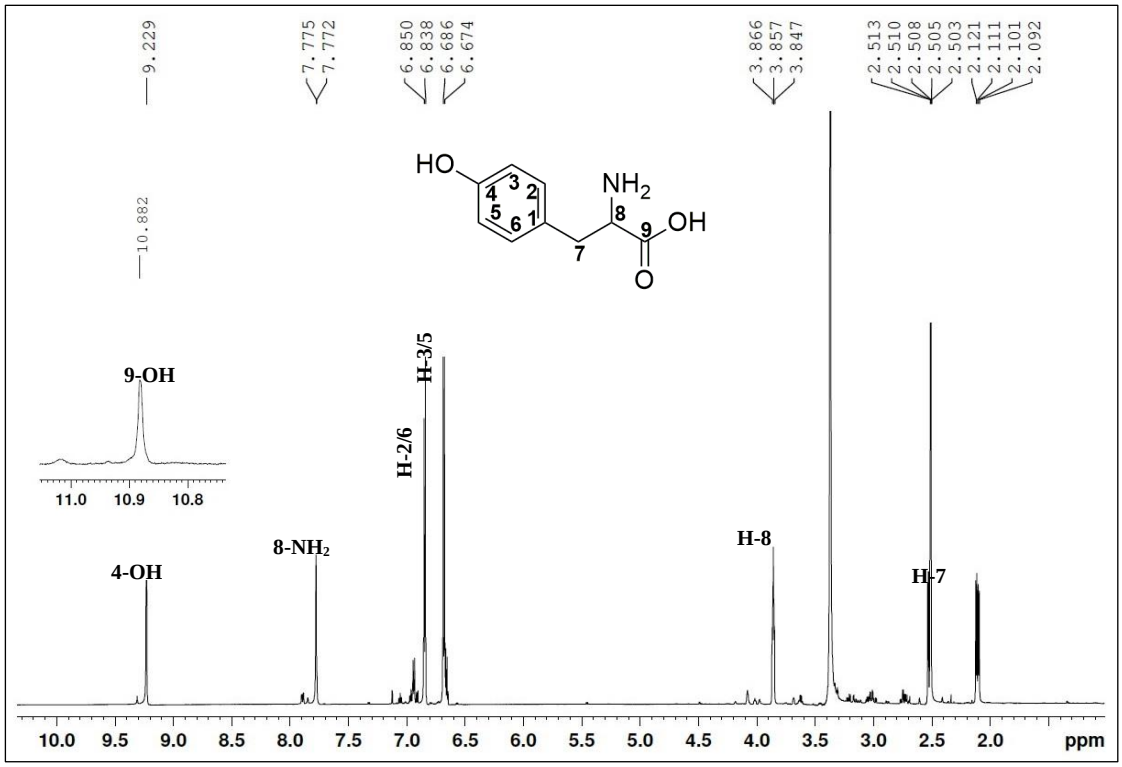


Figure 13. The ^{1}H-NMR (DMSO, 700 MHz) Spectrum of L-Tyrosine (**5**)

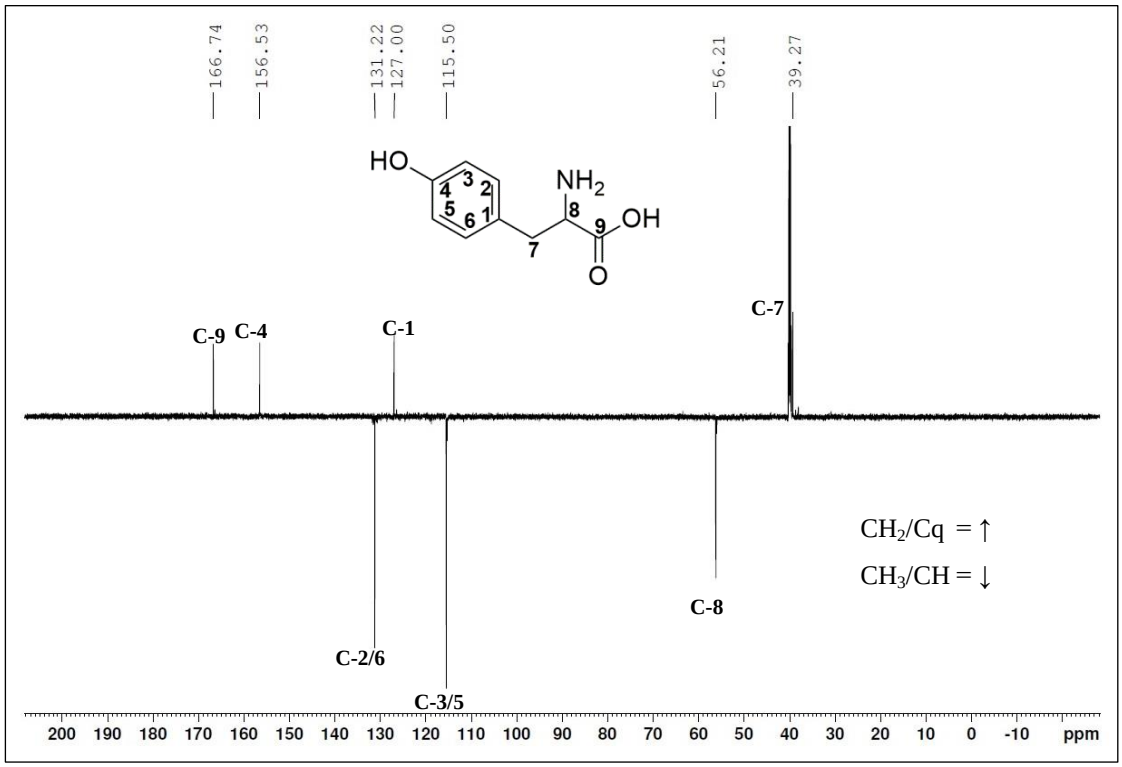


Figure 14. The NMR-APT (DMSO, 175MHz) Spectrum of L-Tyrosine (**5**)

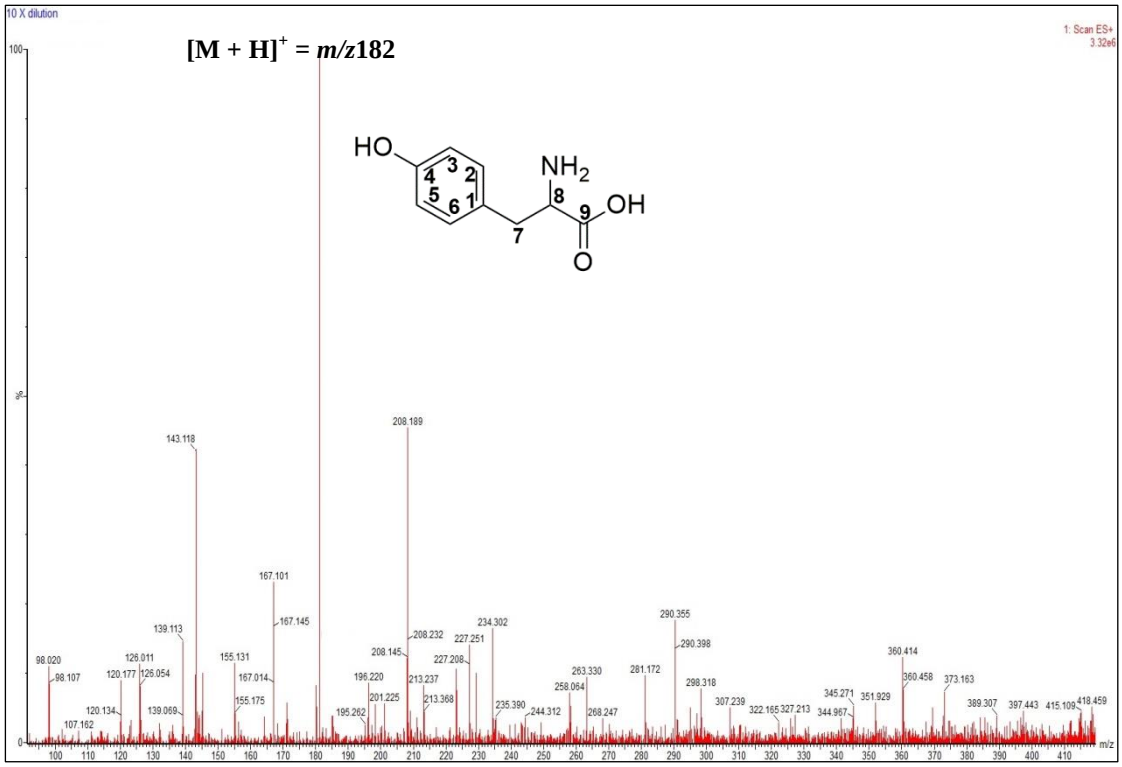


Figure 15. The LC-MS Spectrum of L-Tyrosine (**5**)

Conclusion

Five diketopiperazine derivatives namely cyclo(-Pro-Val) (**1**), (-)-cyclo(-Pro-Tyr) (**2**), (-)-cyclo(-Pro-Phe) (**3**), (+)-cyclo(-Pro-Leu) (**4**), and L-tyrosine (**5**) were isolated and reported for the first time from psychrotolerant actinobacteria *Barrientosiimonas* 39^T. These proline-based diketopiperazines probably act as modulators or molecules that play a part in cold-adaptation of psychrotolerant. All the compounds reported in the present study were not subjected to further bioactivity studies due to insufficient amounts.

Acknowledgement

We would like to thank the School of Chemical Sciences and Food Technology, Faculty of Science and Technology, Universiti Kebangsaan Malaysia (UKM); Malaysia Genome Institute (MGI) for providing research facilities. We would also like to express our gratitude to the Indonesia Endowment Fund for Education (LPDP), and Yayasan Penyelidikan Antartika Sultan Mizan for the financial support through the following research grant ST-2017-017.

References

1. Afzal, O., Kumar, S., Haider, M. R., Ali, M. R. and Kumar, R. (2015). A review on anticancer potential of bioactive heterocyclic quinoline. *European Journal of Medicinal Chemistry*, 97: 871-910.
2. Anderson, B., Smedsgaard, J. and Frisvad, J. C. (2004). *Penicillium expansum*: Consistent production of patulin, chaetoglobosins, and other secondary metabolites in culture and their natural occurrence in fruit products. *Journal of Agricultural and Food Chemistry*, 52: 2421-2428.
3. Ando, A., Nakamura, T., Murata, Y., Takagi, H. and Shima, J. (2007). Identification and classification of genes required for tolerance to freeze–thaw stress revealed by genome-wide screening of *Saccharomyces cerevisiae* deletion strains. *FEMS Yeast Research* 7: 244-253.

4. Antipova, T. V., Zhelifonova, V. P., Baskunov, B. P., Ozerskaya, S. M., Ivanushkina, N. E. and Kozlovsky, A. G. (2011). New producers of biologically active compounds-fungal strains of the genus *Penicillium* isolated from permafrost. *Applied Biochemistry and Microbiology*, 47(3): 288-292.
5. Araki, K. (1986). Tryptophan, phenylalanine, and tyrosine. In: Aida et al. (eds) Biotechnology of amino acid production. Kodansha/Elsevier; Tokyo: p. 247-256.
6. Archer, D. B., Connerton, I. F. and MacKenzie, D. A. (2008). Filamentous fungi for production of food additives and processing aids. *Advances in Biochemical Engineering/Biotechnology*, 111: 99-147.
7. Atlas, R. M. (1993). Handbook of microbiological media. Edited by L.C. Parks, CRC Press, Boca Raton.
8. Cheenpracha, S., Borris, R. P., Tran, T. T., Jee, J. M., Seow, H. F., Cheah, H. Y., Ho, C. C. and Chang, L. C. (2011). Three new amides from *Streptomyces* sp. H7372. Journal of the Brazilian Chemical Society, 22(2): 223-229.
9. Chen, C. and Dickman, M. B. (2005). Proline suppresses apoptosis in the fungal pathogen *Colletotrichum trifolii*. *Proceedings of the National Academy of Sciences*, 102(9): 3459-3464.
10. Cole, R. J. and Cox, R. H. (1981). Handbook of toxin fungal metabolites. Academic Press, New York.
11. De Pascale, D., De Santi, C., Fu, J. and Landfald, B. (2012). The microbial diversity of Polar environments is a fertile ground for bioprospecting. *Marine Genomics*, 8: 15-22.
12. Frisvad, J. C., Larsen, T. O., Dalsgaard, P. W., Seifert, K. A., Louis-Seize, G., Lyhne, E. K., Jarvis, B. B., Fettinger, J. C. and Overy, D. P. (2006). Four psychrotolerant species with high chemical diversity consistently producing cycloaspeptide A, *Penicillium jamesonlandense* sp. nov., *Penicillium ribium* sp. nov., *Penicillium soppii* and *Penicillium lanosum*. *International Journal of Systematic and Evolutionary Microbiology*, 56: 1427-1437.
13. Furtado, N. A. J. C., Pupo, M. T., Carvalho, I., Campo, V. L., Duarte, M. C. T., and Bastos, J. K. (2005). Diketopiperazines produced by an *Aspergillus fumigatus* Brazilian strain. Journal of the Brazilian Chemical Society, 16(6B): 1448-1453.
14. Gordon, R. E., Barnett, D. A., Handerhan, J. E. and Pang, C. (1974). *Nocardia coeliaca*, *Nocardia autotrophica*, and the nocardin strain. *International Journal of Systematic and Evolutionary Microbiology*, 24: 54-63.
15. Guo, Q., Guo, D., Zhao, B., Xu, J. and Li, R. (2007). Two cyclic dipeptides from *Pseudomonas fluorescens* GcM5-1A carried by the pine wood nematode and their toxicities to Japanese black pine suspension cells and seedlings in vitro. *Journal of Nematology*, 39(3): 243-247.
16. Hamza, A. A., Ali, H. A., Clark, B. R., Murphy, C. D. and Elobied, E. A. (2013). Cyclo (L-phenyl, L-prolyl). Diketopiperazines from a newly isolated *Streptomyces sudanensis*. A4.4. *Journal of Biotechnology and Pharmaceutical Research*, 4(1): 1-7.
17. Hagino, H. and Nakayama, K. (1973). L-Tyrosine production by analog-resistant mutants derived from a phenylalanine auxotroph of *Corynebacterium glutamicum*. *Agricultural and Biological Chemistry*, 37(9): 2013-2023.
18. Laatsch, H. (2010). AntiBase a data base for rapid dereplication and structure determination of microbial natural products. Wiley-VCH. Wein-heim. Germany.
19. Lee, L. H., Cheah, Y. K., Sidik, S. M., Xie, Q. Y., Tang, Y. L., Lin, H. P., Ab Mutalib, N. S. and Hong, K. (2013). *Barrientosiimonas humi* gen. nov., sp. nov., an actinobacterium of the family Dermacoccaceae. *International Journal of Systematic and Evolutionary Microbiology*, 63: 241 – 248.
20. Luis, S. M., Ballesteros, J. and Gutiérrez, M. (2011). Antibacterial constituents from the octocoral associated bacterium *Pseudoalteromonas* sp. Revista Latinoamericana de Química, 39: 1-2.
21. Macherla, V. R., Liu, J., Bellows, C., Teisan, S., Nicholson, B., Lam, K. S. and Potts, B. C. M. (2005). Glaciapyrroles A, B, and C, pyrrolosesquiterpenes from a *Streptomyces* sp. isolated from an Alaskan marine sediment. *Journal of Natural Products*, 68: 780-783.
22. Munekata, M. and Tamura, G. (1981). Selective inhibition of SV40-transformed cell growth by diketopiperazines Agricultural and Biological Chemistry, 45(11): 2613-2618.
23. Musetti, R., Polizzotto, R., Vecchione, A., Borselli, S., Zulini, L., D'Ambrosio , M., di Toppi, L. S. and Pertot, I. (2007). Antifungal activity of diketopiperazines extracted from *Alternaria alternata* against *Plasmopara viticola*: An ultrastructural study. *Micron*, 38: 643-650.

24. Puopolo, G., Cimmino, A., Palmieri, M. C., Giovannini, O., Evidente, A. and I. Pertot, I. (2014). *Lysobacter capsici* AZ78 produces cyclo(L-Pro-L-Tyr), a 2,5-diketopiperazine with toxic activity against sporangia of *Phytophthora infestans* and *Plasmopara viticola*. *Journal of Applied Microbiology*, 117: 1168-1180.
25. Ruckmani, A., Kaur, I., Schumann, P., Klenk, H. P. and Mayilraj, S. (2011). *Calidifontibacter indicus* gen. nov., sp. nov., a member of the family *Dermacoccaceae* isolated from a hot spring, and emended description of the family *Dermacoccaceae*. *International Journal of Systematic and Evolutionary Microbiology*, 61: 2419-2424.
26. Shirling, E. B. and Gottlieb, D. (1966). Methods for characterization of Streptomyces species. *International Journal of Systematic and Evolutionary Microbiology*, 16: 313-340.
27. Stierle, A. C., Cardellina, J. H. and Strobelt, G. A. (1988). Maculosin, a host-specific phytotoxin for spotted knapweed from *Alternaria Alternata*. *Proceedings of the National Academy of Sciences of the United States of America*, 85: 8008-8011.
28. Shiio, I. (1986). Tryptophan, phenylalanine, and tyrosine. In: Aida et al. (eds) Biotechnology of amino acid production. Kodansha/Elsevier; Tokyo, p. 188-206.
29. Takagi, H., Iwamoto, F. & Nakamori, S. (1997). Isolation of freeze-tolerant laboratory strains of *Saccharomyces cerevisiae* from prolineanalogue-resistant mutants. *Applied in Microbiology and Biotechnology* 47: 405-411.
30. Takagi, H. (2008). Proline as a stress protectant in yeast: physiological functions, metabolic regulations, and biotechnological applications. *Applied in Microbiology and Biotechnology* 81: 211-223.
31. Terao, Y., Nakamori, S. and Takagi, H. (2003). Gene dosage effect of L-proline biosynthetic enzymes on L-proline accumulation and freeze tolerance in *Saccharomyces cerevisiae*. *Applied and Environmental Microbiology* 69(11): 6527-6532.
32. Vasquez-Rivera, D., González, O., Guzmán-Rodríguez, J., Diaz-Pérez, A. L., Ochoa-Zarzosa, A., Lopez-Bucio, J., Meza-Carmen, V. and Campos-García, G. (2015). Cytotoxicity of cyclodipeptides from *Pseudomonas aeruginosa* PAO1 leads to apoptosis in human cancer cell lines. *BioMed Research International*, 2015: 1-9.
33. Yamada, K. and Komagata, K. (1972). Taxonomic studies on coryneform bacteria. IV. Morphological, cultural, biochemical, and physiological characteristics. *The Journal of General and Applied Microbiology*, 18: 399-416.
34. Yap, A. C., Kok-Gan Chan, K. G. and Choo, Y. M. (2016). Isolation and identification of metabolites from the Gram-negative proteobacteria of *Burkholderia cenocepacia* and *Serratia marcescens*. *Sains Malaysiana*, 45(7): 1073-1077.

Malaysian Journal of Analytical Sciences Vol 23 No 5 2019

		Page
1.	SYNTHESIS AND CHARACTERISATION OF 4-PROPOXYBENZALDEHYDE SUBSTITUTED HECK-SCHIFF BASE COMPOUND AS SPACER IN ELECTROCHEMICAL DNA SENSOR (Sintesis dan Pencirian Sebatian 4-Propoksibenzaldehid Gantian Heck-Schiff Bes sebagai Peruang dalam Sensor DNA Elektrokimia) *Norhafiefa Hassan and Hanis Mohd Yusoff*	763
2.	VISIBLE LIGHT DRIVEN PHOTOCATALYTIC DEGRADATION OF PARACETAMOL USING INCENSE ASH SUPPORTED ZnO NANOCOMPOSITES (Degradasi Paracetamol secara Pemangkinan Foto dengan Penggunaan Komposit Nano ZnO berasaskan Abu Kemenyan) *Pei Teng Lum, Keng Yuen Foo, Nor Azazi Zakaria*	771
3.	SURFACTANT-BOUND Fe_3O_4 NANOPARTICLES AS CATALYST SUPPORT: SYNTHESIS AND PHYSICOCHEMICAL PROPERTIES (Nanopartikel Fe_3O_4 Surfaktan Terikat Sebagai Sokongan Mangkin: Sintesis dan Ciri Fizikokimia) *Hassanain Hafiz Mohd Asnan, Siti Kamilah Che Soh, Wan Fatihah Khairunisa Wan Nor, Sabiqah Tuan Anuar, Uwaisulqarni M. Osman, Mohd Hasmizam Razali, Mohd Zul Helmi Rozaini, Mustaffa Shamsuddin*	781
4.	SPECTROSCOPIC STUDIES OF INCLUSION COMPLEX GLIPIZIDE AND β-CYCLODEXTRIN (Kajian Spektroskopik Kompleks Kemasukan Glipizida dan β-siklodekstrin) *Nurul Yani Rahim, Fatin Hamizah Samad, Asmaa' Mardhiah Rohisham*	789
5.	FILEM POLIMER SEBAGAI MATRIKS PEMEGUNAN PEWARNA CAMPURAN SEMULA JADI UNTUK SENSOR pH (Polymeric Films as Matrixes for the Immobilization of Mixed Natural Dyes for Optical pH Sensor) *Noor Azizah Ahmad, Lee Yook Heng, Sharina Abu Hanifah, Faridah Salam*	799
6.	APPLICATION OF DIRECT FLUORESCENCE-BASED LIVE/DEAD STAINING FOR ASSESSMENT OF ANTIFUNGAL ACTIVITY OF COCONUT OIL AGAINST *Candida albicans* (Aplikasi Pewarnaan Hidup/Mati Berasaskan Pendarfluor Langsung untuk Penilaian Aktiviti Antikulat Minyak Kelapa terhadap *Candida albicans*) *Nor Izzah Mukhtar, Zurainie Abllah, Azrul Naim Mohamad, Intan Azura Shahdan, Kamariah Long, Ummi Aqilah Haron*	812
7.	DURIAN SHELL HUSK EXTRACT ASSISTED SYNTHESIS OF COPPER OXIDES NANOPARTICLES FOR THE PHOTODEGRADATION OF PARACETAMOL (Ekstrak Sekam Kulit Durian Membantu Sintesis Nanozarah Tembaga Oksida Untuk Fotodegradasi Paracetamol) *Ahmad Masudi, Nurfatehah Wahyuny Che Jusoh, Zunika Bakri, Aishah Abdul Jalil, Roshafima Rasit Ali, Nur Farhana Jaafar*	818

8. SYNTHESIS OF PALLADIUM(II) DIIMINE COMPLEXES AND THE HYDROLYSIS OF α-DIIMINE LIGAND 828
(Sintesis Kompleks Diimina Palladium(II) dan Hidrolisis Ligan α-Diimina)
Suzie Hui Chin Kuan, Meng Guan Tay, Zhi-Qiang Liu

9. REMOVAL OF PHTHALATES IN AQUEOS SAMPLES USING NON-IONIC SILICONE SURFACTANT MEDIATED CLOUD POINT EXTRACTION VIA SPECTROPHOTOMETRY 839
(Penyingkiran Ftalat dalam Sampel Akues Menggunakan Teknik Pengekstrakan Titik Awan Surfaktan Silikon Tidak Berionik dengan Spektrofotometri)
Pei Wan Ooi, Muggundha Raoov Ramachandran, Noorfatimah Yahaya, Nik Nur Syazni Mohamed Kamal, Kasturi Gopal, Nor Aniisah Husin, Nur Nadhirah Mohamad Zain

10. THIOL MODIFIED AMPEROMETRIC IMMUNOSENSOR FOR BENZO[a]PYRENE DETECTION IN SURFACE RIVER WATER SAMPLES 849
(Immunosensor Amperometrik Diubahsuai Tiol untuk Pengesanan Benzo[a]pirina dalam Sampel Air Sungai Permukaan)
Noor Sheryna Jusoh, Tuan Fauzan Tuan Omar, Azrilawani Ahmad

11. THE EFFECT OF VANILLIN ON THE OXIDATIVE STABILITY OF PALM OLEIN 861
(Mengkaji Kesan Penambahan Vanilin terhadap Kestabilan Pengoksidaan Olein Sawit)
Fatin Nadzirah Mohd Azriyuddin, Mohammad Norazmi Ahmad, Muhammad Nor Omar, Erna Normaya Abdullah

12. AN ASSESSMENT OF FT-IR AND FT-NIR CAPABILITY IN SCREENING CRUDE PALM OIL AUTHENTICITY AND QUALITY COMBINED WITH CHEMOMETRICS 870
(Satu Penilaian Terhadap Kebolehan FT-IR Dan FT-NIR Untuk Menyaring Kesahihan dan Kualiti Minyak Sawit Mentah Digabung Dengan Kemometri)
Ng Jing Sheng, Widad Fadhullah, Mohd Omar Ab Kadir, Ainolsyakira Mohd Rodhi, Noor Hana Hanif Abu Bakar, Syahidah Akmal Muhammad

13. GLYCEROL DEGRADATION IN THE ABSENCE OF EXTERNAL HYDROGEN GAS BY USING WASTE EGGSHELL AS HETEROGENEOUS CATALYST 880
(Degradasi Gliserol Tanpa Kehadiran Hidrogen Luaran dengan Menggunakan Sisa Kulit Telur sebagai Mangkin Heterogen)
Mohamad Imran Firdaus Mhd Sawal, Ahmad Irfan Oslan, Muhammad Hazwan Muhamad Hatta, Noraini Hamzah, Norazzizi Nordin, Norsaliyana Jumali, Wan Zurina Samad

14. CHARACTERIZATION AND CATALYTIC ACTIVITY OF Os/BENTONITE CATALYST FOR HYDROGENOLYSIS OF GLYCEROL 892
(Pencirian dan Aktiviti Pemangkin Os/Bentonit untuk Tindak Balas Hidrogenolisis Gliserol)
Noraini Hamzah, Wan Zurina Samad, Nazrizawati Ahmad Tajuddin, Mohd Ambar Yarmo

15. EXTRACTION AND CHARACTERIZATION OF MICROFIBRILLATED AND NANOFIBRILLATED CELLULOSE FROM OFFICE PAPER WASTE 901
(Pengekstrakan dan Pencirian Mikrofibril dan Nanofibril Selulosa daripada Sisa Kertas Pejabat)
Siti Fatimah Md Hanafiah, Wan Hazman Danial, Mohd Armi Abu Samah, Wan Zurina Samad, Deny Susanti, Rosliza Mohd Salim, Zaiton Abdul Majid

Malaysian Journal of Analytical Sciences, Vol 23 No 5 (2019): 763 - 770
DOI: https://doi.org/10.17576/mjas-2019-2305-01

MALAYSIAN JOURNAL OF ANALYTICAL SCIENCES
Published by The Malaysian Analytical Sciences Society
ISSN 1394 - 2506

SYNTHESIS AND CHARACTERISATION OF 4-PROPOXYBENZALDEHYDE SUBSTITUTED HECK-SCHIFF BASE COMPOUND AS SPACER IN ELECTROCHEMICAL DNA SENSOR

(Sintesis dan Pencirian Sebatian 4-Propoksibenzaldehid Gantian Heck-Schiff Bes sebagai Peruang dalam Sensor DNA Elektrokimia)

Norhafiefa Hassan[1] and Hanis Mohd Yusoff[1,2]*

[1]*Faculty of Science and Marine Environment*
[2]*Advance Nano Materials (ANoMA) Research Group*
Faculty of Science and Marine Environment,
Universiti Malaysia Terengganu, 21030 Kuala Terengganu, Terengganu, Malaysia

**Corresponding author: hanismy@umt.edu.my*

Received: 27 May 2019; Accepted: 25 August 2019

Abstract

Schiff base compound produced from aromatic aldehydes and aromatic amines has been used in a wide range of applications in various fields, including pharmaceutical, life sciences and chemical science (e.g. inorganic and analytical chemistry). It has also been applied in optical and electrochemical sensors to enable the detection of enhanced selectivity and sensitivity of the sensors. These compounds give excellent prospects in sensor study. In this study, Schiff base compound derived from 4-(4-nitrostyryl) aniline and 4-(4-aminostyryl)benzonitrile with 4-propoxybenzaldehyde was synthesised using ethanol as the solvent. All compounds were characterised by using the Fourier transform infrared spectroscopy (FTIR), UV-Vis spectrophotometer and Nuclear Magnetic Resonance (NMR). FTIR showed the formation of C=N (imine) stretching vibrations within the range of 1604.36 – 1606.51 cm^{-1}. In UV-vis, π-π* electronic transition of the C=N in both compounds was observed within the peak range of 361-385 nm. Meanwhile in the ^{1}H NMR, the peak of CH=N (Imine) group was found at δ 8.32-8.34 ppm, whereas for ^{13}C NMR, the peaks were discovered at δ 158.72, δ 158.80 and 158.72 ppm. The application of the Schiff base as a linker in electrochemical DNA sensor (E-DNA) still has not been studied previously. In this study, two new Schiff base derivatives were synthesised and characterised due to its promising potential in sensors, which prompted its application as a future potential linker in electrochemical DNA sensor.

Keywords: Schiff base, synthesis, spacer, E-DNA sensor

Abstrak

Sebatian Schiff bes yang dihasilkan daripada aromatik aldehid dan aromatik amina telah digunakan dalam pelbagai aplikasi dalam pelbagai bidang termasuk farmaseutikal, sains hayat dan sains kimia termasuk kimia tak organik dan analisis kimia. Ia juga telah digunakan dalam sensor optik dan elektrokimia untuk membolehkan pengesanan meningkatkan pemilihan dan kepekaan sensor. Sebatian ini mungkin memberi prospek yang sangat baik dalam sensor. Sebatian Schiff bes yang diterbitkan daripada 4-(4-nitrostiril) anilina dan 4-(4-aminostiril) benzonitril dengan 4-propoksibenzaldehid disintesis menggunakan etanol sebagai pelarut. Kesemua sebatian telah dicirikan oleh spektroskopi inframerah transformasi Fourier (FTIR), UV-Vis spektrofotometer dan Resonans Magnet Nukleus (NMR). FTIR menunjukkan pembentukan C=N (imina) perengangan getaran pada julat 1604.36 – 1606.51 cm^{-1}. Dalam UV-Vis, peralihan elektron π-π* imina untuk kedua-dua sebatian diperhatikan pada julat puncak 361-385 nm. Sementara itu, puncak ^{1}H NMR untuk kumpulan CH=N (imina) telah dijumpai pada δ 8.32-8.34 ppm dan untuk ^{13}C NMR puncaknya telah dijumpai pada δ 158.80 dan 158.72 ppm. Aplikasi terbitan Schiff bes sebagai penyambung dalam sensor DNA elekrokimia (E-DNA) masih belum dikaji. Dalam kajian ini, dua terbitan Schiff bes yang baru telah disintesis

dan dicirikan kerana ia menjanjikan sensor yang mendorong kita untuk menggunakannya sebagai penyambung potensi masa depan dalam sensor DNA elektrokimia.

Kata kunci: Schiff bes, sintesis, pencirian, peruang, sensor E-DNA

Introduction

A Schiff base is a compound that consists of a carbon-nitrogen double bond, with the nitrogen connected to the aryl or alkyl group [1]. The reaction's name is taken after Hugo Schiff, the inventor [2]. It is produced *via* a condensation reaction between the primary amines and ketones or aldehydes under a specific condition [3]. The general formula for Schiff base is RHC=N-R1 (R, R1 = alkyl, aryl, cycloalkyl or heterocyclic groups), which is also known as anils, imines or azomethine. Previous research have shown that the presence of a lone pair of electrons in sp2 hybridised orbital of the nitrogen atom in the Schiff base plays an important role in chemical and biological applications [4].

Schiff base consisting of aryl substituent is more stable and easily synthesised compared to the Schiff base containing alkyl substituent. Furthermore, the Schiff base produced using an aliphatic aldehyde is unstable and readily undergoes polymerisation compared to those produced by aromatics, which are more stable and have an effective conjugation [5]. Schiff bases produced from aromatic aldehydes and aromatic amines have been used in a wide range of applications in various fields, including pharmaceutical, life sciences, and chemical science (e.g. inorganic and analytical chemistry)[2]. Aromatic aldehyde Schiff bases display an outstanding photoluminescence property due to the effect of the conjugation system. It has an excellent possibility in sensor, luminescent devices, and biological devices [6]. Besides, it can improve the selectivity and sensitivity detection of the sensor [7].

The identification and sequencing of DNA molecules have received much attention since Watson and Crick introduced the double helix structure of deoxyribonucleic acid (DNA) in 1953 [8]. The development method of DNA sensor has continued to grow due to possible applications in the field ranging from gene analysis, clinical diagnostics, forensic study and other medical applications [9]. There are many types of DNA biosensor, examples being electrochemical, optical, acoustic, and piezoelectric [10]. Among these, the electrochemical method provides promising benefits due to its simplicity, rapidness, relatively low cost and high sensitivity, which is suitable for the improvement of cheap and portable devices [9].

In electrochemical DNA (E-DNA) sensor, a recognition layer or known as spacer or linker is important to immobilise the DNA on an electrode and it may affect the detection [11]. The previous study has shown that alkanethiol is a common spacer used in the E-DNA sensor, for example, 3-mercapropionic acid (MPA), 11-mercaptoudecanoic acid (MUA) and 6-mercapto-1-hexanol (MCH) [12]. The aim of the study is to synthesise two Schiff bases consisting of 4-propoxybenzaldehyde substituted with three carbon length of the alkane chain, followed by chemical characterisation. The synthetic procedures for all synthesised compounds are shown in Scheme 1.

Materials and Methods

Materials and instrumentation

4-vinylaniline, 1-iodo-4-nitrobenzene, 4-iodobenzonitrile, palladium (II) chloride, trimethylamine, 4-hydroxybenzaldehyde, 1-bromopropane, potassium carbonate, potassium iodide, acetone, acetonitrile, hexane, ethyl acetate and ethanol were purchased from Merck, Sigma Aldrich, Acros Organic, Fisher Chemical and HmbG® Chemicals and used without further purification.

Infrared (IR) spectra of all synthesised compounds were recorded using Perkin Elmer 100 Fourier Transform Infrared Spectroscopy using potassium bromide (KBr) pellet within the range of 4000 – 450 cm^{-1}. The analysis of UV-Vis spectra was measured by double-beam Spectrophotometer Shimadzu UV-1800 in 1 cm^3 cuvette and acetonitrile as solvent. ^1H and ^{13}C nuclear magnetic resonance (NMR) spectra were determined by Bruker Avance II 400 spectrometer in deuterated chloroform ($CDCl_3$-d_6).

Synthesis of substituted amino stilbene (1): Synthesis of 4-(4-nitrostyryl) aniline (1a)

4-(4-nitrostyryl) aniline (1a) was synthesised *via* Heck-cross coupling method. 4-Vinyl aniline 90% (2.8 mmol) and 1-iodo-4-nitrobenzene (1.9 mmol) was dissolved in 4 ml of DMF and 3.5 ml trimethylamine, and then refluxed at 70-75 °C for 24 hours in the presence of $PdCl_2(PPh_3)_2$ (50 mg). The reaction was monitored by thin layer chromatography (TLC). The product was purified using column chromatography, by utilising hexane: ethyl acetate as an eluent. Red batter powder; Yield 257 mg, 53.3%; FTIR (KBr, υ cm^{-1}): 3463-3390 (N-H stretch), 3027 (aromatic C-H stretch), 1619, 1497 (aromatic C=C stretch), 1585 (alkene C=C stretch), 1340 (N=O nitro), 1181 (C-N stretch); ^{1}H NMR (400 MHz, $CDCl_3$, ppm) δ: 3.79 (S, 2H, NH_2), 6.84-7.09 (doublet-doublet, 2H, HC=CH), 6.11-8.12 (m,8H, CH, Ar). ^{13}C-NMR (400 MHz, $CDCl_3$, ppm) δ; 146.34 (Ar-C-NH_2), 145.14 (Ar-C-NO_2), 143.71, 132.46, 127.52, 123.14, 121.45, 114.12 (6 Ar-C), 125.23 (C=C); UV-Vis (Acetonitrile): λ_{max}=251 nm, 410 nm; MS: m/z 240 [M+.].

Synthesis of 4-(4-aminostyryl)benzonitrile (1b)

4-(4-aminostyryl)benzonitrile (1b) was synthesised *via* Heck-cross coupling method. 4-vinyl aniline 90% (2.18 mmol) and 4-aminobenzonitrile (3.27 mmol) was dissolved in 4 ml of DMF and 3.5 ml trimethylamine, and then refluxed at 70-75 °C for 24 hours in the presence of PdCl2(PPh3)2 (50 mg). The reaction was monitored by TLC. The product was purified using column chromatography, by utilising hexane: ethyl acetate as an eluent. Yellow powder; Yield 257 mg, 58%; FTIR (KBr, υ cm^{-1}): 3447-3369 (N-H stretch), 3033 (aromatic C-H stretch), 1618, 1439 (aromatic C=C stretch), 1594 (alkene C=C stretch), 2224 (C≡N), 1174 (C-N stretch); ^{1}H NMR (400 MHz, CDCl3, ppm) δ: 3.76 (2H, NH_2), 6.81- 7.05 (doublet-doublet, 2H, HC=CH), 6.61-7.52 (8H, CH, Ar). ^{13}C-NMR (400 MHz, $CDCl_3$, ppm) δ; 146.34 (Ar-C-NH_2), 118.25 (C≡N), 108.60-146.11 (6 Ar-C), 125.23 (C=C); UV-Vis (Acetonitrile): λ_{max}=252 nm, 357 nm; MS: m/z 240 [M+.].

Synthesis of 4-propoxybenzaldehyde (2*)*

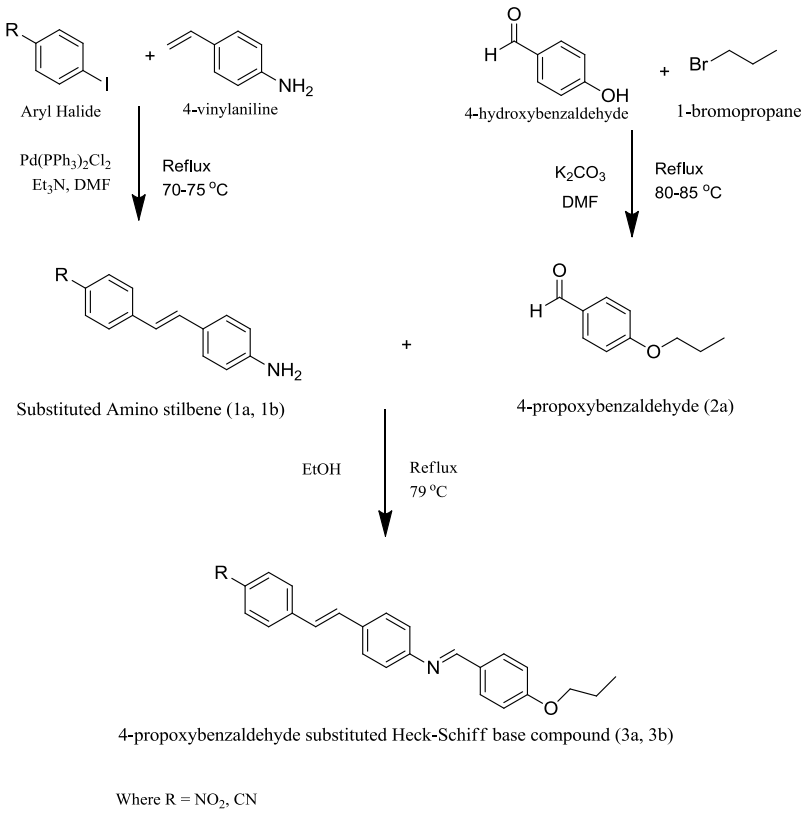
The formation of 4-propoxybenzaldehyde was synthesised *via* Williamson Ether synthesis. In this reaction, an equimolar mixture of 4-hydroxylbenzaldehyde and bromopropane was used. Firstly, 1.5 g of 4-hydroxylbenzaldehyde was stirred in 50 ml DMF at the temperature of 65 °C for 30 minutes in the presence of potassium carbonate, K_2CO_3,(1.6 g) and potassium iodide, KI, (1g). After that, bromoalkane was added into the mixture and was stirred continuously at 80-85 ºC for 24 hours. The mixture was next extracted using 50 ml of diethyl ether and washed with distilled water repeatedly to remove K_2CO_3, while the ether layer was washed with 25 ml of 5% NaOH to remove unreacted 4-hydroxybenzaldehyde. Repeated washes were done for the ether layer using distilled water until it became neutral at pH 7. Anhydrous $MgSO_4$ (1 g) was used to eliminate water contained in the solution. The diethyl ether was removed via rotary evaporator to obtain pure oily transparent pale-yellow liquids of 4-propoxybenzaldehyde. Light Yellow liquid; Yield 55%; FTIR (KBr, υ cm^{-1}): 3075 (aromatic C-H stretch), 2967-2828 (C-H stretch), 1693 (C=O), 1598, 1509 (aromatic C-H stretch), 1474 (CH_2 bend), 1428,1314 (CH_3 bend), 1254 (C-O stretch); ^{1}H NMR (400 MHz, $CDCl_3$, ppm) δ: 0.96 (m, 3H, CH_3), 1.76 (m, 2H, CH_2), 3.91 (m, 2H, CH_2), 6.89-7.74 (m,4H, CH, Ar), 9.78 (s, 1H, H-C=O). ^{13}C-NMR (400 MHz, $CDCl_3$, ppm) δ; 10.42, 22.41, 69.87 (CH_2-CH_2-CH_3), 114.75, 129.76, 131.97, 164.27 (Ar-C), 190.79 (C=O); UV-Vis (Acetonitrile): λ_{max}=218 nm, 274 nm; MS: m/z 164[M+].

Synthesis of Alkoxy substituted amino stilbene-Schiff base compound (3): 4-(4-((4-propoxybenzylidene)amino)styryl)benzonitrile anilines (3a)

Firstly, 157 mg of precursor 4-(4-nitrostyryl) aniline was fully dissolved in the ethanol and mixed with 0.1 ml 4-propoxybenzaldehyde. The mixture was refluxed at 79-80 °C for 2 hours and the solvent was reduced to half using a dean stalk. The reaction was monitored by thin layer chromatography (TLC). A precipitate was formed and recrystallised using acetonitrile. Yellow solid; Yield 51%; FTIR (KBr, υ cm^{-1}): 2969-2877 (C-H stretch), 1604 (C=N), 1584 (C=C alkene) , 1340 (N=O nitro), 1259 (C-N), 1164 (C-O stretch); ^{1}H NMR (400 MHz, $CDCl_3$, ppm) δ: 0.99 (m, 3H, CH_3), 1.77 (m, 2H, CH_2), 3.92 (m, 2H, CH_2), 6.91, 7.19, 7.51, 7.56, 7.77, 8.15 (d,12H, Ar), 7.05, 7.16 (doublet-doublet, 2H, HC=CH), 8.34 (s, 1H, HC=N). ^{13}C-NMR (400 MHz, $CDCl_3$, ppm) δ; 9.47, 21.49, 68.69 ($2CH_2$-CH_3), 113.73, 120.54, 123.15, 126.94, 127.84, 129.63, 131.86, 132.56, 143.00, 145.59, 151.76, 161.08 (Ar-C), 124.44, 125.70 (C=C), 158.80 (C=N); UV-Vis (Acetonitrile): λ_{max}=240 nm, 290 nm and 385 nm; MS: m/z 386 [M+.].

4-(4-((4-propoxybenzylidene)amino)styryl)benzonitrile anilines (3b)

139 mg of precursor 4-(4-aminostyryl)benzonitrile was fully dissolved in the ethanol and mixed with 0.1 ml 4-propoxybenzaldehyde. The mixture was refluxed for at 79-80 °C for 2 hours and the solvent was reduced to half using a dean stalk. The reaction was monitored by TLC and the precipitate formed was recrystallised using acetonitrile. Yellow solid; Yield 46 %; FTIR (KBr, υ cm^{-1}):3025 v(C-H) aromatic, 2967-2879 v(C-H), 2224 v(C≡N), 1604 v(C=N), 1584 v(C=C) alkene , 1249 v(C-N), 1164 v(C-O), 843 (C-H out of plane bend) ; ^{1}H NMR (400 MHz, $CDCl_3$, ppm) δ: 0.98 (3H, CH_3), 1.76, 3.91 (6H, CH_2), 6.90, 7.15, 7.47, 7.50, 7.54, 7.76 (12H, Ar), 6.98, 7.12 (doublet-doublet, 2H, HC=CH), 8.32 (1H, HC=N). ^{13}C-NMR (400 MHz, $CDCl_3$, ppm) δ; 9.47, 21.48, 68.67 ($2CH_2$-CH_3), 109.32, 113.72, 120.49, 126.81, 127.85, 129.61, 130.93, 131.46, 132.68, 140.95, 151.56, 161.04 (Ar-C), 124.44, 125.70 (C=C), 158.72 (C=N), 118.07 (C≡N) ; UV-Vis (Acetonitrile): λ_{max}=238 nm, 279 nm and 361 nm; MS: m/z 366 [M+].



Scheme 1: Synthesis procedures for 4-propoxybenzaldehyde substituted Heck-Schiff base compound

Results and Discussion

Fourier transform infrared spectroscopic analysis

The FTIR spectra of compounds 3a and 3b are presented in Figure 1. The spectra showed similar vibration types except for the main functional group of every compound. Based on the spectra, C-H stretching for aromatic for all compounds was observed around 3024.27 - 3025.13 cm^{-1} [13]. Meanwhile, C-H stretching for aliphatic appeared in the range of 2877.11 - 2969.09 cm^{-1}. For the imine group band, C=N, it was clearly observed at 1604.36 - 1606.51 cm^{-1} confirming the formation of Schiff base [14]. In addition, the absorption band of aliphatic alkene occurred within the range of 1582.82 - 1585.38 cm^{-1}. The FTIR spectrum of 3a shows the stretching of N=O (NO_2) asymmetric at the region ranging from 1509.23 - 1519.05 cm^{-1}. Furthermore, N=O **(**NO_2**)** symmetric was confirmed by the peak at the range between 1335.12 cm^{-1} - 1340.88 cm^{-1} [13]. Meanwhile, for spectrum 3b, the presence of the

cyano group in the compound was confirmed by the strong absorption peak at 2224.90 cm^{-1} that was assigned as C≡N stretching [15]. The C-O stretching for compounds 3a and 3b both was discovered at 1259.76 cm^{-1} and 1250.70 cm^{-1}, respectively [16].

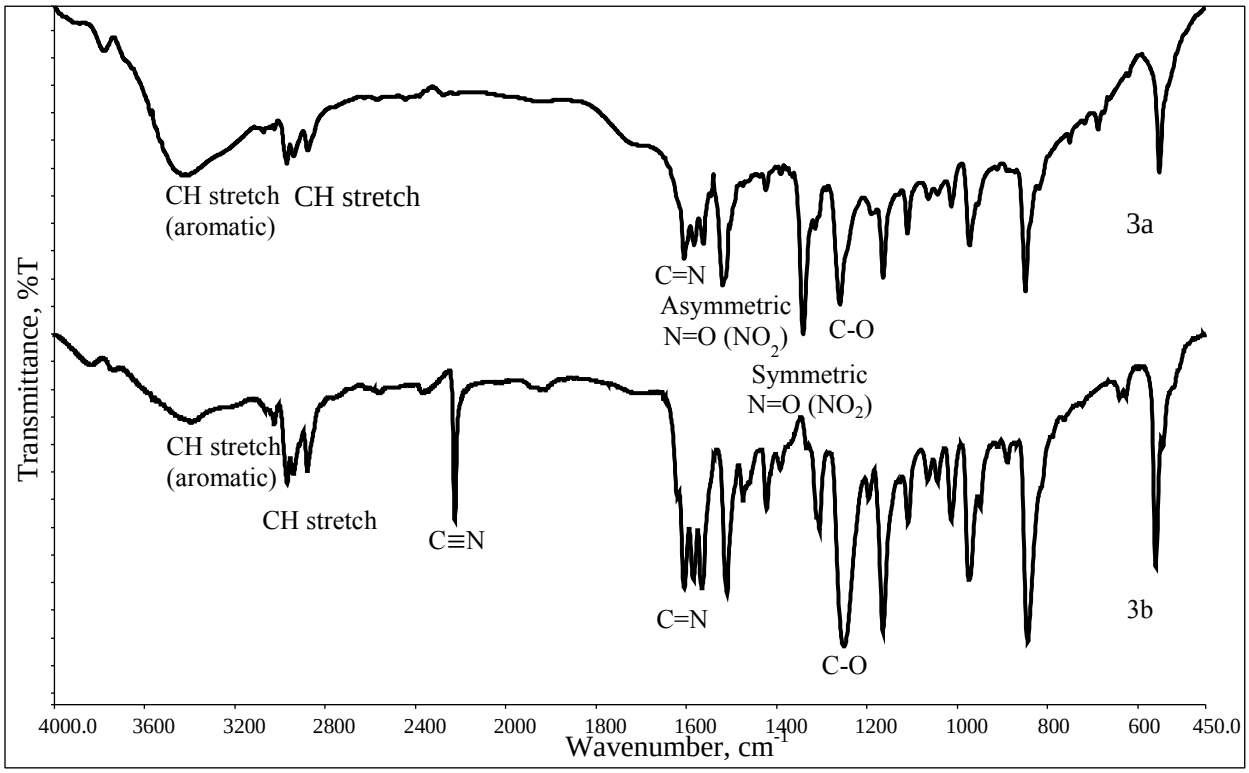


Figure 1. FTIR spectra of compounds 3a and 3b

Ultraviolet-visible (UV-vis) spectroscopy

The UV-Vis spectra of compounds 3a and 3b both are presented in Figure 2. The UV-vis spectroscopy analysis of compounds 3a-3b was done by using acetonitrile (1 x 10^{-5} M) as a solvent with a cut-off point at 190.0 nm. The electronic absorption band spectra of compound 3a and 3b showed three bands. The first two bands were indicated to transition π-π* of aromatic rings band at λ_{max} 240 nm and λ_{max} 290 nm [17]. The other peaks appeared at transition π-π* of azomethine band at λ_{max} 385 nm [18]. Meanwhile, the electronic band spectra for compound 3b showed three bands. The spectra showed the presence of π-π* electronic transition of C=C (aromatic) at the wavelength λ_{max} 238 nm and λ_{max} 279 nm. Additionally, the absorption appeared at 361 nm indicated to the transition of the azomethine band.

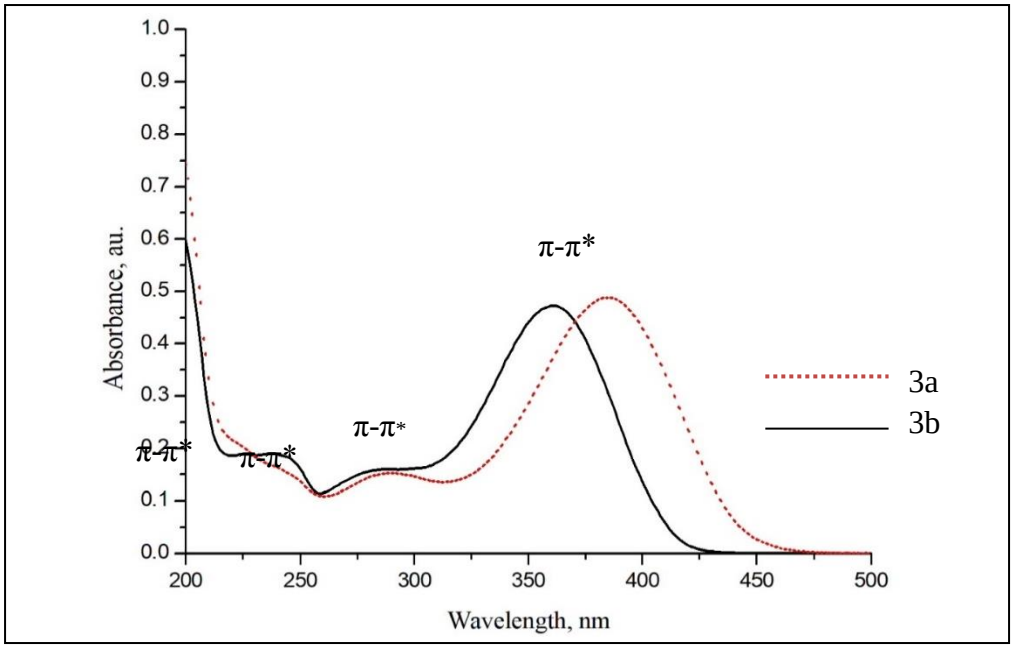


Figure 2: UV-vis spectra of compound 3a and 3b

^{1}H and ^{13}C nuclear magnetic resonance

^{1}H and ^{13}C nuclear magnetic resonance (NMR) analysis confirmed the identity of all synthesised Schiff bases in order to identify their structure. The azomethine group (CH=N) of synthesised compounds 3a and 3b both was discovered in the far downfield at δ 8.34 and 8.32 [18]. Furthermore, the ^{1}H NMR spectra data showed the presence of alky chain proton (C-H) observed at the upfield region within the range δ 1.76 to 3.92 ppm. Meanwhile, the signal moieties for the CH_3 of alkyl chain for compounds 3a and 3b were observed at 0.99 and 0.98, respectively. The aromatic protons of the benzene ring for all compounds resonated at region δ 6.90-8.15 ppm. In addition, the proton signal for the doublet-doublet of the vinyl bond was discovered around δ 6.98-7.16 ppm for all compounds [20].

Table 1. ^{1}H NMR spectral data of compounds 3a and 3b

Compound	CH_3	C-H (Alkyl chain)	C-H (Aromatic)	C=C (Alkene)	CH=N
3a	0.99	1.76, 3.92	6.91, 7.19, 7.50, 7.56, 7.77, 8.15	7.05, 7.16	8.34
3b	0.98	1.76, 3.91	6.90, 7.15, 7.47, 7.50, 7.54, 7.76	6.98, 7.12	8.32

Table 3.2 shows the ^{13}C NMR of compounds 3a and 3b both in $CDCl_3$ used as a complementary technique for approving the structure of the prepared Schiff bases. The resonance of the C-C alkyl chain was clearly observed at δ 9.46-68.67 ppm. For the aromatic ring, the resonance carbon was found at the range between δ 109.32-161.08 ppm. Furthermore, the carbon resonance for the (C=C) alkene of all compounds obviously appeared in the region δ 124.28-124.44 ppm and δ 125.70-125.73 ppm. The carbon NMR showed the chemical shift for the azomethine group (C=N) at δ 158.80 ppm and δ 158.72 ppm. In addition, for the 3b compound, the carbon resonance of C≡N was identified at δ 118.07 ppm.

Table 2. ^{13}C NMR spectral data of compounds 3a and 3b

Compound	C-C (Alkyl Chain)	C-C (Aromatic)	C=C (Alkene)	C=N (Imine)	C≡N
3a	9.46, 21.49, 68.68	113.73, 120.54, 123.15, 126.94, 127.84, 129.63, 131.86, 132.56, 143.00, 145.59, 151.76, 161.08	124.44, 125.70	158.80	-
3b	9.47, 21.48, 68.67	109.32, 113.72, 120.49, 126.81, 127.85, 129.61, 130.93, 131.46, 132.68, 140.95, 151.56, 161.04	124.28, 125.73	158.72	118.07

Conclusion

Two 4-propoxybenzaldehyde substituted Heck-Schiff bases: 3a and 3b were successfully synthesised by a condensation reaction between 4-(4-nitrostyryl) aniline and 4-(4-aminostyryl)benzonitrile with 4-propoxybenzaldehyde. All synthesised compounds were characterised by UV, FTIR, ^{1}H NMR, ^{13}C-NMR spectroscopies and mass spectrometry. The 4-propoxybenzaldehyde substituted the Heck-Schiff base compounds consisting of the aromatic substituent, which made the compounds more stable. These compounds are believed to yield a great prospect in sensors, as they could enhance the selectivity and sensitivity in sensor detection. In future work, the compounds should be applied as a potential linker in the E-DNA sensor for cancer detection to improve the sensor sensitivity. Besides, the compound is hoped to be an excellent linker as it consists of nitro and cyano functional groups and alkyl chain to chemically bind with a gold electrode and phosphate group in the DNA.

Acknowledgement

The authors would like to thank Universiti Malaysia Terengganu and Ministry of Higher Education (MOHE) for research grant FRGS vote number 59383 as financial support and the opportunity to be involved in this research.

References

1. Kumar, J., Rai, A. and Raj, V. (2017). A comprehensive review on the pharmacological activity of schiff base containing derivatives. *Organic & Medicinal Chemistry International Journal,* 1(3): 1-15.
2. Muzammil, K., Trivedi, P. and Khetani, D. (2015). Synthesis and characterization of schiff base m-nitro aniline and their complexes. *Research Journal of Chemical Sciences,* 5(5): 52-55.
3. Al Garawi, Z. S., Tomi, I. H. and Al-Daraji, A. H. (2012). Synthesis and characterization of new amino acid-schiff bases and studies their effects on the activity of ACP, PAP and NPA enzymes (In vitro). *E-Journal of Chemistry,* 9(2): 962-969.
4. Ashraf, M. A., Mahmood, K. and Wajid, A. (2011). Synthesis, characterization and biological activity of schiff bases. *2011 International Conference on Chemistry and Chemical Process,* 10: pp.1-7.
5. Chigurupati, S. (2015). Designing new vanillin schiff bases and their antibacterial studies. *Journal of Medical and Bioengineering,* 4(5): 363-366.
6. Wang, H., Qian, X. and Li, Jie. (2015). Synthesis and fluorescence properties of some aromatic schiff base compounds. *2nd International Conference on Green Materials and Environmental Engineering* (GMEE 2015): pp. 43-44.
7. Norhafiefa, H., Yusoff, H. M. and Rahamathullah, R. (2018). Synthesis and characterization of alkoxy substituted p-cyano stilbene schiff bases. In *IOP Conference Series: Materials Science and Engineering*, 440(1): p. 012016.
8. Liu, A., Wang, K., Weng, S., Lei, Y., Lin, L., Chen, W., Lin X. and Chen, Y. (2012). Development of electrochemical DNA biosensors. *Trends in Analytical Chemistry* 37: 101-111.
9. Jin, H., Wei, M. and Wang J. (2013). Electrochemical DNA biosensor based on the BDD nanograss array electrode. *Chemistry Central Journal,* 7(65): 1-6.
10. Junhui, Z., Hong, C. and Ruifu Y. (1997). DNA based biosensors. *Biotechnology Advances,* 15(1): 43-58.

11. Yusoff, H. M., Hassan, N. and Bulat, K. H. K. (2018). Computational study towards schiff base derivatives length as a potential recognition layer in electrochemical DNA sensor. In *IOP Conference Series: Materials Science and Engineering*, 440(1): p. 012009.
12. Hassan, N., Yusoff, H. M. and Shafawati, S. M. T. (2018). Synthesis and characterization of p-nitro stilbene schiff base as a potential linker in E-DNA. In *Proceedings of the 2018 8th International Conference on Biomedical Engineering and Technology*, pp. 103-107.
13. Sangeetha, K., Mathammal, R. and Prasad, L. G. (2016). Investigations on vibrational and optical properties of 4-chloro 2-nitroaniline for nonlinear optical applications. *Journal of Chemical and Pharmaceutical Sciences*, 9(1): 134-139.
14. Alsaygh, A., Al-Humaidi, J. and Al-Najjar, I. (2014). Synthesis of some new pyridine-2-yl-benzylidene-imines. *International Journal of Organic Chemistry*, 4:116-121.
15. Yusoff, H. M., Hassan, N. and Bulat, K. K. (2018). Theoretical and experimental approach towards p-cyano stilbene schiff base as a potential linker in E-DNA sensor. In *IOP Conference Series: Materials Science and Engineering*, 374(1): p. 012086.
16. Hasan, A., Abbas, A. and Akhtar, M. N. (2011). Synthesis, characterization and fluorescent property evaluation of 1, 3, 5-triaryl-2-pyrazolines. *Molecules*, 16(9): 7789-7802.
17. Issa, R. M., Khedr, A. M. and Rizk, H. (2008). ^{1}H NMR, IR and UV/VIS spectroscopic studies of some schiff bases derived from 2-aminobenzothiazole and 2-amino-3-hydroxypyridine. *Journal of the Chinese Chemical Society*, *55*(4): 875-884.
18. Iwan, A., Janeczek, H., Jarzabek, B., Domanski, M. and Rannou, P. (2009). Characterization, optical and thermal properties of new azomethines based on heptadecafluoroundecyloxy benzaldehyde. *Liquid Crystals*, 36(8): 873-883.
19. Issa, R. M., Khedr, A. M. and Rizk, H. F. (2005). UV–Vis, IR and ^{1}H NMR spectroscopic studies of some Schiff bases derivatives of 4-aminoantipyrine. *Spectrochimica Acta Part A: Molecular and Biomolecular Spectroscopy*, 62: 621-629.
20. Lampman, G. M., Kriz, G. S., Pavia, D. L. and Vyvyan, J. R. (2010). Spectroscopy. Brooks/Cole Publisher.

Malaysian Journal of Analytical Sciences, Vol 23 No 5 (2019): 771 - 780
DOI: https://doi.org/10.17576/mjas-2019-2305-02

MALAYSIAN JOURNAL OF ANALYTICAL SCIENCES
Published by The Malaysian Analytical Sciences Society
ISSN 1394 - 2506

VISIBLE LIGHT DRIVEN PHOTOCATALYTIC DEGRADATION OF PARACETAMOL USING INCENSE ASH SUPPORTED ZnO NANOCOMPOSITES

(Degradasi Paracetamol secara Pemangkinan Foto dengan Penggunaan Komposit Nano ZnO berasaskan Abu Kemenyan)

Pei Teng Lum*, Keng Yuen Foo, Nor Azazi Zakaria

River Engineering and Urban Drainage Research Centre (REDAC), Engineering Campus, Universiti Sains Malaysia,14300 Nibong Tebal, Penang, Malaysia

**Corresponding author: peiteng1013@gmail.com*

Received: 10 July 2019; Accepted: 3 September 2019

Abstract

In this work, the preparation of a newly synthesized incense ash (IA) supported zinc oxide (ZnO) nanocomposite has been attempted using a simple physical coating method. The physical and chemical properties of the nanocomposite were examined by using scanning electron microscopy (SEM), Fourier Transform Infrared Spectroscopy (FT-IR) and pore structural analysis. The photocatalytic activity was examined by performing the batch photocatalytic degradation of paracetamol (PCM). The preparation and experimental parameters including the ash impregnation ratio, catalyst loadings, initial PCM concentration and irradiation time were accessed. Morphological study revealed that highly porous structure of IA provides a suitable supporting surface area for the better deposition of ZnO to offer the enhanced adsorption and photodegradation reaction. A complete degradation with the high concentration of 50 mg/L was achieved within 3.5 hours. High stability of synthesized nanocomposite was demonstrated from the reusability test, with higher than 95% of removal even after five successive regeneration cycles. The present study provides an efficient photocatalytic degradation route by IA supported ZnO nanocomposite in PCM treatment, one of the emerging pollutants in wastewater effluents.

Keywords: incense ash, nanocomposites, paracetamol, photodegradation

Abstrak

Dalam kajian ini, penyediaan komposit nano zink oksida (ZnO) berasaskan abu kemenyan (IA) melalui teknik salutan fizikal telah dicuba. Ciri-ciri fizikal dan kimia komposit nano telah dikendalikan dengan menggunakan mikroskop imbasan elektron (SEM), Spektroskopi Infamerah Transformasi Fourier (FT-IR) dan analisis keliangan. Prestasi pemangkinan foto diuji dengan degradasi foto bagi paracetamol (PCM). Parameter penyediaan dan eksperimen termasuk nisbah jerap abu, dos pemangkin, kepekatan asal pewarna dan masa penyinaran telah dikaji. Kajian morfologi permukaan menunjukkan struktur IA yang berliang sesuai untuk dijadikan permukaan sokongan bagi pemendapan ZnO yang lebih lengkap dan menawarkan kecekapan tindak balas pemangkinan foto. Degradasi yang sempurna dengan kepekatan asal 50 mg/L dicapai dalam masa 3.5 jam. Ketahanan komposit nano ini yang tinggi telah ditunjukkan dari ujian penggunaan semula, dengan kecekapan degradasi foto yang melebihi 95% walaupun selepas lima kitaran penggunaannya. Kajian ini menzahirkan laluan degradasi pemangkinan foto yang cekap dengan penggunaan komposit nano ZnO berasaskan IA dalam perawatan PCM, salah satu bahan pencemar yang muncul dalam efluen air sisa.

Kata kunci: abu kemenyan, komposit nano, paracetamol, degradasi foto

Introduction

Paracetamol (PCM), chemically named as acetaminophen, 4-hydroxyacetamilide, 4- acetamidephenol or N-(4-hydroxyphenyl) acetamide, is a synthetic derivative of p-aminophenol with analgesic and antipyretic activity. It is an over-the-counter drug which most widely used for fever or pain relief worldwide. As the consequences of huge production and quantitative use of PCM, it is ubiquitous with a concentration up to 10 mg/L in the influents and effluents of wastewater treatment plants (WWTP), and in the range of 10 to 100 ng/L in surface water [1]. Besides, the presence of PCM has been recorded up to a concentration of 0.5 to 45 ng/L in drinking water and 4.1 to 73 ng/L in the freshwater river systems [2]. Untreated PCM is poorly biodegradable due to its complex molecular structure, and their chemically persistent.

To the best of our knowledge, despite there are no legally permissible limits for the existence of PCM in waste effluents, the effect of "chronic exposure to low dose" is still uncertain for human health, owing to findings have revealed that pharmaceuticals compounds are pharmacologically active and toxic in nature. They are genotoxicity, resistant to the microorganism, and long-term ingestion of these compounds through drinking water will lead to their bioaccumulation in bodies, potentially detrimental to human health [3]. For remediation, conventional WWTP consisted of the biological treatment process and physical-chemical process including adsorption, reverse osmosis, coagulation, flocculation, and filtration is inefficient to remove PCM completely, because these treatment techniques are not designed to treat these refractory micro-pollutants contaminated water. Predominantly, physical process sorely characterized by phase transfer of pollutants without degradation while biological treatment merely limited to biodegradable compounds containing wastewater [4].

Keeping in view above, the necessity of priority attention to identifying the reliable, efficient and eco-friendly techniques for the elimination of pharmaceuticals compounds is highlighted. In recent year, heterogeneous photocatalysis is gaining a considerable interest as a promising avenue in pharmaceuticals contaminants, owing to chemical stability, relatively low cost and non-toxicity [4]. It is characterized by the generation of reactive oxygen species (ROS), non-selectively to oxidize the recalcitrant contaminants through a complete mineralization into the carbon dioxide and water without producing secondary waste in the environment [5]. Among a variety of semiconductor photocatalyst, TiO_2 and ZnO are most widely used for the photocatalytic process in drugs contaminated water. Research on photodegradation of PCM have been studied using different doping contents and different morphologies of TiO_2 and ZnO. However, hitherto, there is a paucity of literature on the utilization of ash based photocatalyst on the photodegradation of PCM.

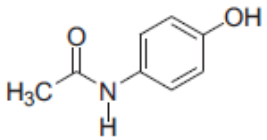
In the perspective, incense ash (IA), a waste by-product from incense burning, it is highly generated in Asian countries including Malaysia, Singapore, Thailand, China, Taiwan and Japan. Among Asian community, incense burning is not only a traditional practice for religious festivals in temples but also a long lasting daily practice in-house as paying respect to their ancestors [6]. In this case, daily generation of incense ash as longer time might contribute to the environmental problem if proper disposal is not implemented. It is noteworthy that many studies have been documented on the synthesis and photocatalytic activity of fly ash supported nanocomposite, in which ash is reported effective for the removal of certain pollutants [7]. Herein, a considerable interest is gained to develop a novel IA supported ZnO nanocomposite for the degradation of PCM. Morphological, functional and surface characterization were investigated. The effect of ash impregnation ratio, catalyst loadings, initial concentration and irradiation time on photocatalytic process were examined. The reusability of the prepared nanocomposite was also elucidated.

Materials and Methods

Model pollutants

Paracetamol (PCM), a pain relief drug was chosen as the model organic pollutant in this study. The chemical structure and physio-chemical properties of PCM are as given (Table 1). A standard stock solution with the concentration of 50 mg/L was prepared in deionized water. The working solutions were prepared by diluting the stock solution successively.

Table 1. Chemical structure and physiochemical properties of PCM

Compound	Chemical Structure	Molecular Weight (g mol^{-1})	p*Ka*	λ max (nm)
Paracetamol (PCM)		151.7	9.4	248.8

Preparation of photocatalytic nanocomposite

Incense ash (IA), a by-product of incense burning was chosen as the initial raw precursor. The collected IA was washed thoroughly with deionized water to remove adhering dirt particles, dried and sieved to the particles size of 250-500 µm. In the modification process, IA was basic functionalized with 1M of sodium hydroxide solution. The modified IA was rinsed with a copious amount of deionized water till a constant pH was acquired in the washing solution and dried at 80 ºC. The ZnO/IA nanocomposite was prepared by using a simple physical coating method. A requisite amount of ZnO pure powder were mixed thoroughly with modified IA in the impregnation ratio (ZnO: IA) of 1:1 to 1:5 kept in air-tight bottles for further analysis.

Characterization

Scanning Electron Microscopy (SEM, Zeiss Supra 35 VP, Germany) was performed to visualize the surface morphology. The surface functional groups were specified by Fourier Transform Infrared (FTIR) Spectroscopy (FTIR-2000, PerkinElmer) using KBr pellet method, in the scanning range of 4000–400 cm^{-1}. The surface physical properties of nanocomposites were specified by nitrogen adsorption–desorption isotherm at 77 K using an automatic Micromeritics ASAP 2020 volumetric adsorption analyzer. Prior to the gas adsorption measurement, the samples were degassed for 8 h at 573 K under a vacuum condition. The application of Brunauer-Emmett-Teller (BET) was applied to calculate the specific surface area, whereas the micropore surface area, external surface area, and micropore volume were accessed by using the t-plot method.

Photocatalytic study

The photocatalytic experiments were conducted in self-assembled photoreactor, consisting of a cylindrical flask equipped with four visible light sources, circulating water jackets and a cooling fan. In a typical test, a prefixed amount of photocatalyst was dispersed into 100 mL of PCM solution. Prior to irradiation, all mixture was stirred in darkness for 30 minutes to achieve adsorption-desorption equilibrium. Aliquots were withdrawn at a specific time for each experiment and filtered using a syringe filter (Nylon Millipore 0.25 µm) prior to analysis to minimize the interference of powdered catalyst with the analysis. The concentration of PCM solution was determined using UV-Vis spectrophotometer (UV-1800 Shimadzu, Japan) at 243 nm. The degradation efficiency of PCM can be expressed by the following equation:

$$\text{Degradation rate (\%)} = \frac{C_0 - C_t}{C_0} \times 100 \quad (1)$$

where C_0 and C_t referred to the initial concentration of PCM and at time *t*.

The effects of catalyst loading, initial concentration and irradiation time on the photocatalytic performances of PCM was evaluated. All the experimental run was conducted in duplicate and the average values were reported. The reusability test was conducted with five successive degradation cycles of PCM at the initial concentration of 10 mg/L under the optimized experimental condition. For each regeneration process, the nanocomposite was filtered, washed with deionized water till the constant pH acquired for the washing solution, and dried at 120 ºC for 1 hour. The regenerated nanocomposite was reutilized for the next consecutives degradation run.

Results and Discussion

Preparation of IA supported ZnO nanocomposite

The variation of photocatalytic performances of IA supported nanocomposite at different ash impregnation ratio were accessed, as presented in Figure 1. It can be clearly seen that the ZnO/IA nanocomposites exhibited a comparatively higher PCM degradation efficiency of 36% to 57%, as compared with the degradation rate of only 2.7% and 30% for the raw IA and pure ZnO, respectively. The result is mainly attributed to the principle of a kind of synergy was induced between IA and ZnO, introducing their bifunctional properties of adsorption and photocatalysis [8]. An increase of the availability of surface binding sites for the targeted PCM, induce a higher migration of adsorbed PCM to photoactive center of ZnO, as well as increase the rate of the photocatalytic process [9]. Another reason can be explained by IA improve the dispersion of nanocomposite in PCM solution and increase the photons reach the surface of the catalyst, in turn enhancing the utilization of visible light for photocatalysis [10].

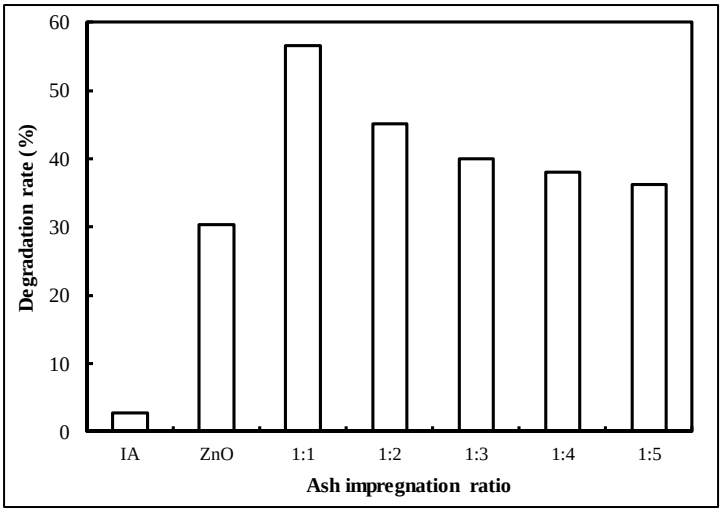


Figure 1. Effect of ash impregnation ratio (ZnO:IA) on the photodegradation of PCM (catalyst loading = 1.0 g/100 mL, C_0 = 50 mg/L; t = 60 minutes)

The removal of PCM was greatly enhanced with the addition of IA, however, the degradation efficiency was gradually decreased beyond the optimal impregnation ratio of 1:1. This observation can be assigned to an excessive loading of IA that turned unfavorable to the photocatalytic reaction, due to agglomeration of ash particles within the photocatalytic nanoparticles, which confine the path of the light from reaching to the ZnO photocatalyst. These phenomenon result in the lower formation of photo-induced electron-hole pairs and in turn inhibit the photocatalytic activity of the nanocomposite [11]. Therefore, the optimum ash impregnation ratio of 1:1 was applied for the further experiments.

Characterization

The surface morphology of IA, ZnO, ZnO/IA nanocomposite were visualized by the scanning electron micrographs (SEM), with a magnification of 500x, as displayed in Figure 2. Generally, the pristine ZnO (Figure 2a) exhibited a homogeneous surface, consisted of mainly a series of unique flower-like nanoparticles, with each nanoparticle were formed by a complex configuration of nanorods. Similar structure has been observed by Pant et al. [12] during the synthesis ZnO. The SEM image of raw IA exhibited a rough and highly porous structure, with the irregular distribution of spherical shaped particles. Conversely, the ZnO/IA nanocomposite revealed the dispersion of numerous clusters of ZnO derived nanoparticles over the spherical-shaped surface, to be filled inside the air holes of IA. This current finding indicates the successive deposition of ZnO nanoparticles onto the ash surface by using a simple physical coating technique. The morphological characterization has verified that these newly prepared nanocomposites are undoubtedly serve for a greater adsorptive and catalytic surface active site, to induce a higher generation of hydroxyl radicals in related to the absorption of greater photon energy, that in turn enhance the

synergistic adsorption from ash support and photocatalytic activity from photocatalyst for the effective degradation of PCM.

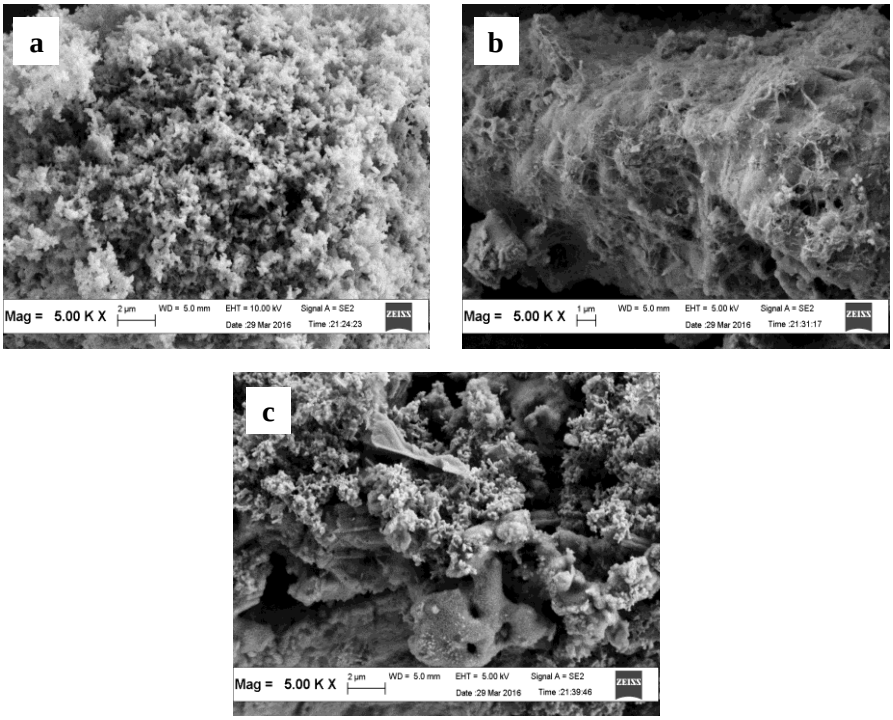


Figure 2. Scanning electron micrographs of (a) ZnO, (b) IA, and (c) ZnO/IA nanocomposite

The surface physical properties of IA, ZnO and ZnO/IA nanocomposite are given in Table 2. As shown in the table, the BET surface area, Langmuir surface area and total pore volume of ZnO and raw IA were obtained to be 5.78 m^2/g and 12.72 m^2/g; 7.51 m^2/g and16.15 m^2/g; 0.012 cm^3/g and 0.043 cm^3/g, respectively. As compared with ZnO and IA, ZnO/IA nanocomposite demonstrated an enhanced BET surface area, Langmuir surface area and total pore volume with 17.67 m^2/g, 21.54 m^2/g, and 0.046 cm^3/g, respectively. Notably, positive development was observed for the surface porosity of composite, suggesting that IA serves as an ideal absorbent to provide a larger surface area for the deposition of ZnO, as well as increases the surface area of whole matrix [13].

Table 2. Surface physical characteristics of ZnO, IA, and ZnO/IA nanocomposite

Properties	**ZnO**	**IA**	**ZnO/IA**
BET surface area (m^2/g)	5.78	12.72	17.67
Langmuir surface area (m^2/g)	7.51	16.15	21.54
External surface area (m^2/g)	6.31	12.30	16.64
Micropore surface area (m^2/g)	0.53	0.42	1.83
Total pore volume (cm^3/g)	0.012	0.043	0.046

The FTIR spectra of the ZnO, IA and ZnO/IA derived nanocomposite are presented in Figure 3, respectively. The broad band at 3446-3422 cm^{-1} is attributed to the stretching of O-H bonds. The region between 2924-2513 cm^{-1} is assigned to the stretching vibration of C-H bond. The signals at 1798 cm^{-1} is ascertained to the stretching vibration of C=O. The adsorption transmittance at 1427/1424 is ascribed to the symmetrical stretching of Si-O-Si bond,

whereas 1012-1008 cm^{-1}, 874 cm^{-1} and 480/475 cm^{-1} refer to the bending vibration of Si-O bond. The new peaks at 712 cm^{-1} on the FT-IR spectra of IA and ZnO/IA nanocomposite is pointing to the bending modes of COO-, indicating the presence of calcite ($CaCO_3$) [14]. On the other hand, the transmittance at 543/524 cm^{-1} and 439 cm^{-1} are denoted to the stretching vibration of Zn-O. The alteration between the IA and ZnO/IA nanocomposite, in terms of lower intensity and deconvolution of peaks has verified the homogeneous deposition of ZnO onto the surface of IA, *via* Van der Waals interaction over the matric surfaces [15]. Such interactions have been reported in the TiO_2-deposited fly ash derived nanocomposite [16].

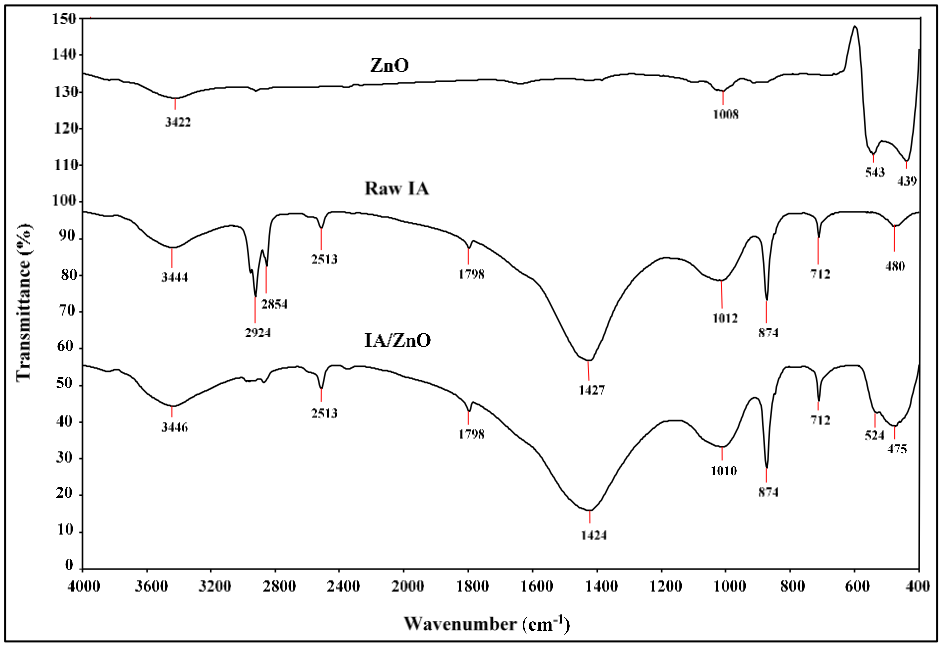


Figure 3. Fourier-Transform Infrared spectra of ZnO, IA, and ZnO/IA nanocomposite

Photocatalytic performances: Effect of catalyst loading

Catalyst loading is the major influencing parameter affecting the operation cost, and the feasibility for the large-scale practical applications. The effect of catalyst loading on the photocatalytic degradation of PCM was examined by varying the catalyst loading from 1.0 g/100 mL to 2.0 g/100 mL, as displayed in the Figure 4. Obviously, increasing the catalyst loading showed a decrement on the degradation process. The degradation efficiency of PCM decreased linearly from 57 % to 41%, with an increase of catalyst loading from 1.0 g/100 mL to 2.0 g/100 mL. At the optimal catalyst loading of 1.0 g/100 mL, the superior enhancement of PCM removal was achieved. The result is ascribed to the larger availability of surface absorption sites that favoring towards more PCM molecules adsorb on the catalyst surface [17]. As well, the higher number of surface catalytic sites at the optimal catalyst loading may contribute to the higher photons absorption to promote a greater formation of photogenerated hydroxyl radicals, in turn enhancing the photocatalytic reaction of PCM [18].

Beyond the catalyst loading of 1.0 g/100 mL, the rate of degradation decreased markedly and remained constant at approximately 42% as the catalyst amount further increased from 1.6 g/100 mL to 2.0 g/100 mL. Similar phenomenon was reported by Hu et al. [19] in the photodegradation of PCM by $BiVO_4$ catalyst. This finding is associated with the addition of excess catalyst above the saturation limit that might induce the dispersion of agglomerated catalyst particles, cripple the transparency of the PCM solution, which further reduce light penetration into the solution [20]. Consequently, a decrease of the number of photo-generated electron-hole pairs retard the degradation efficiency of PCM. This present study suggested a good balance between the catalyst loading with the tested pollutants should be well optimized to avoid superfluous catalyst usage.

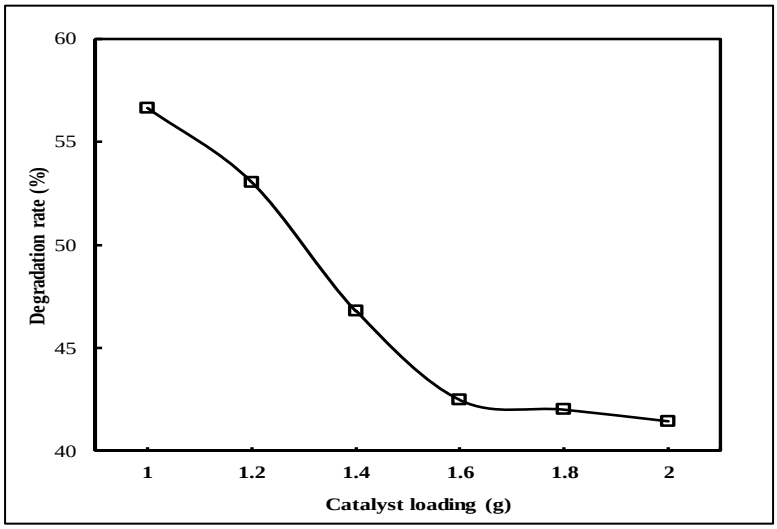


Figure 4. Effect of catalyst loading on the photodegradation of PCM (C_0 = 50 mg/L; t = 60 minutes)

Effect of initial concentration and irradiation time

The variation of PCM removal with respect to irradiation time, at the initial concentration of 10 mg/L to 50 mg/L under the optimized experimental conditions are depicted in Figure 5. In this study, increasing the initial concentration of PCM from 10 mg/L to 50 mg/L demonstrated a rising of irradiation time from 28 minutes to 210 minutes for the complete degradation of PCM. At lower concentration of PCM, the active sites on the catalyst surface are enough for the adsorption of PCM and water molecules to induce rapid oxidation process [18].

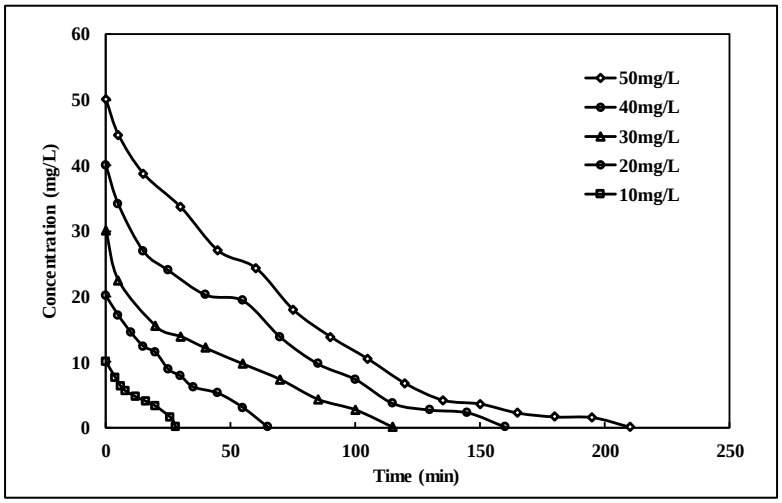


Figure 5. Plot of degradation of PCM as a function of initial concentrations and irradiation time

Conversely, additional PCM molecules that adsorbed onto the surface of the catalyst when the PCM were overloaded triggers to a saturation and deactivation of surface active. This phenomenon induces an ineffective action of hydroxyl radicals for the photocatalytic reaction. Additionally, a higher initial concentration decreases the degree of light transmission in aqueous solution. Lesser light activation and formation of reactive species radicals throughout the photodegradation process directly reduce the photocatalytic activity of the photocatalyst. In this case,

the photolysis of PCM molecules rather than the photocatalysis might take place [21]. As its consequences, the removal rate would be rapidly retarded as the initial concentration increased.

Reusability study

Catalytic stability is another essential parameter of the photocatalytic process for cost-effective and long-term practical application. The reusability of the newly synthesized ZnO/IA nanocomposite was examined by performing five consecutive cyclic experiments using PCM, as depicted in Figure 6. The result clearly demonstrated the extremely stable photocatalytic ability of these nanocomposites, with the high removal above 95% for PCM even after five successive cycles. No apparent loss of photocatalytic activity of the nanocomposite can be explained by the structural integrity of the heterostructure of the nanocomposite is maintained, it is not easily photo corroded and deactivated against the photodegradation process [22].

Moreover, it is deduced that IA could serve as the adsorptive support to immobilize the dispersion of ZnO onto the adsorbent surface, to protect against the destruction of the surface binding catalytic sites. This hybrid adsorptive and degradation surface active sites have contributed to both adsorptive force and the generation of photoinduced reactive species for the effective photodegradation reaction [23]. Nevertheless, further recovery resulted in a slight decrease of the photocatalytic activity, mainly related to the blockage of the surface binding active sites of the nanocomposites, and the possible leaching of the surface fragment of the catalyst after several successive adsorption and photocatalytic reaction [24].

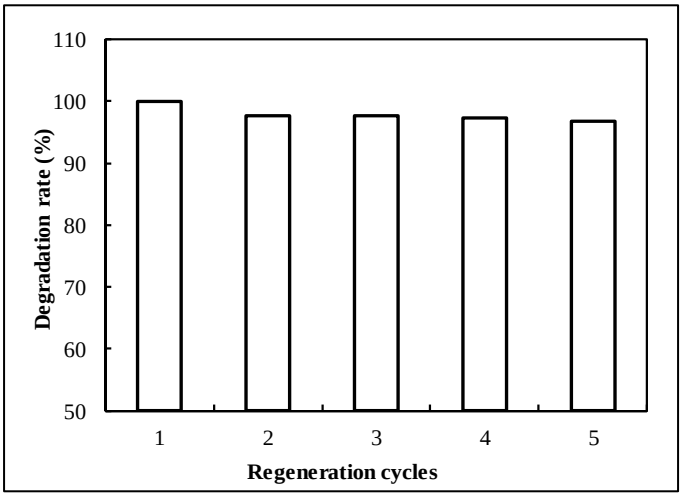


Figure 6. Reusability test of ZnO/IA nanocomposite for the photodegradation of PCM (catalyst loading = 1.0 g/100 mL, C_0 = 10 mg/L; t = 30 minutes)

Conclusion

This present study demonstrated that ZnO/IA nanocomposite have been successfully prepared, and it exhibited a good photocatalytic performance on the photodegradation of PCM under the optimized experimental conditions. The finding highlighted the alternative pathway and potentiality of incense ash to be a cost-effective supporting material for the preparation of a valuable photocatalytic nanocomposite. The synergistic effect of adsorption and photocatalysis from IA and ZnO, respectively, leading to an enhancement of the degradation of water contaminants. Therefore, several perspectives on the diverse applications for future research works are suggested. For the practicability, the photocatalytic activity of this newly prepared nanocomposite could be further examined for the on-site treatment of pharmaceutical effluents with multiple pollutants, instead of synthetic pharmaceuticals tested solution. Besides, the potential of other agricultural ash as the precursor for the preparation of low-cost photocatalyst could be explored.

Acknowledgement

The authors acknowledge the financial support provided by Universiti Sains Malaysia, under the USM Short Term grant scheme (Project No. 304/PREDAC/6315111).

References

1. Magureanu, M., Mandache, N. B. and Parvulescu, V. I. (2015). Degradation of pharmaceutical compounds in water by non-thermal plasma treatment. *Water Research*, 81: 124-136.
2. Gavrilescu, M., Demnerová, K., Aamand, J., Agathos, S. and Fava, F. (2015). Emerging pollutants in the environment: present and future challenges in biomonitoring, ecological risks and bioremediation. *New Biotechnology*, 32(1): 147-156.
3. Atanasov, A. G., Waltenberger, B., Pferschy-Wenzig, E.-M., Linder, T., Wawrosch, C., Uhrin, P., Temml, V., Wang, L., Schwaiger, S., Heiss, E. H., Rollinger, J. M., Schuster, D., Breuss, J. M., Bochkov, V., Mihovilovic, M. D., Kopp, B., Bauer, R., Dirsch, V. M. and Stuppner, H. (2015). Discovery and resupply of pharmacologically active plant-derived natural products: A review. *Biotechnology Advances*, 33(8): 1582-1614.
4. Mirzaei, A., Chen, Z., Haghighat, F., & Yerushalmi, L. (2016). Removal of pharmaceuticals and endocrine disrupting compounds from water by zinc oxide-based photocatalytic degradation: A review. *Sustainable Cities and Society*, 27: 407-418.
5. Kaur, A., Umar, A. and Kansal, S. K. (2016). Heterogeneous photocatalytic studies of analgesic and non-steroidal anti-inflammatory drugs. *Applied Catalysis A: General*, 510: 134-155.
6. Lung, S.-C. C. and Hu, S.-C. (2003). Generation rates and emission factors of particulate matter and particle-bound polycyclic aromatic hydrocarbons of incense sticks. *Chemosphere*, 50(5): 673-679.
7. Jarusiripot, C. (2014). Removal of reactive dye by adsorption over chemical pretreatment coal based bottom ash. *Procedia Chemistry*, 9: 121-130.
8. Ökte, A. N. and Karamanis, D. (2013). A novel photoresponsive ZnO-flyash nanocomposite for environmental and energy applications. *Applied Catalysis B: Environmental*, 142–143: 538-552.
9. Liu, S., Zhu, J., Yang, Q., Xu, P., Ge, J. and Guo, X. (2015). Preparation of SnO_2–TiO_2/fly ash cenospheres and its application in phenol degradation. *Photochemistry and Photobiology*, 91(6): 1302-1308.
10. Lv, J., Sheng, T., Su, L., Xu, G., Wang, D., Zheng, Z. and Wu, Y. (2013). N, S co-doped-TiO_2/fly ash beads composite material and visible light photocatalytic activity. *Applied Surface Science*, 284: 229-234.
11. Visa, M., Carcel, R. A., Andronic, L. and Duta, A. (2009). Advanced treatment of wastewater with methyl orange and heavy metals on TiO_2, fly ash and their mixtures. *Catalysis Today*, 144(1–2): 137-142.
12. Pant, H. R., Park, C. H., Pant, B., Tijing, L. D., Kim, H. Y. and Kim, C. S. (2012). Synthesis, characterization, and photocatalytic properties of ZnO nano-flower containing TiO_2 NPs. *Ceramics International*, 38(4): 2943-2950.
13. Kim, H. J., Joshi, M. K., Pant, H. R., Kim, J. H., Lee, E. and Kim, C. S. (2015). One-pot hydrothermal synthesis of multifunctional Ag/ZnO/fly ash nanocomposite. *Colloids and Surfaces A: Physicochemical and Engineering Aspects*, 469: 256-262.
14. Reig, F., Gimeno-Adelantado, J. V. and Moya Moreno, C. M. (2002). FTIR quantitative analysis of calcium carbonate (calcite) and silica (quartz) mixtures using the constant ratio method. Application to Geological Samples. *Talanta*, 58: 811-821.
15. Chai, B., Yan, J., Wang, C., Ren, Z. and Zhu, Y. (2017). Enhanced visible light photocatalytic degradation of Rhodamine B over phosphorus doped graphitic carbon nitride. *Applied Surface Science*, 391: 376-383.
16. Wang, B., Li, C., Pang, J., Qing, X., Zhai, J. and Li, Q. (2012). Novel polypyrrole-sensitized hollow TiO_2/fly ash cenospheres: Synthesis, characterization, and photocatalytic ability under visible light. *Applied Surface Science*, 258(24): 9989-9996.
17. Thejaswini, T. V. L., Prabhakaran, D. and Maheswari, M. A. (2016). Soft synthesis of Bi Doped and Bi–N co-doped TiO_2 nanocomposites: A comprehensive mechanistic approach towards visible light induced ultra-fast photocatalytic degradation of fabric dye pollutant. *Journal of Environmental Chemical Engineering*, 4(1): 1308-1321.
18. Mameri, Y., Debbache, N., Benacherine, M. E. M., Seraghni, N. and Sehili, T. (2016). Heterogeneous photodegradation of paracetamol using Goethite/H_2O_2 and Goethite/oxalic acid systems under artificial and natural light. *Journal of Photochemistry and Photobiology A: Chemistry*, 315: 129-137.

19. Hu, C., Xu, J., Zhu, Y., Chen, A., Bian, Z. and Wang, H. (2016). Morphological effect of $BiVO_4$ catalysts on degradation of aqueous paracetamol under visible light irradiation. *Environmental Science and Pollution Research*, 23(8):18421-18428.
20. Sheng, F., Zhu, X., Wang, W., Bai, H., Liu, J., Wang, P., Zhang, R., Han, L. and Mu, J. (2014). Synthesis of novel polyoxometalate $K_6ZrW_{11}O_{39}Sn{\cdot}12H_2O$ and photocatalytic degradation aqueous azo dye solutions with solar irradiation. *Journal of Molecular Catalysis A: Chemical*, 393: 232-239.
21. Soltani, R. D. C., Khataee, A. and Mashayekhi, M. (2016). Photocatalytic degradation of a textile dye in aqueous phase over ZnO nanoparticles embedded in biosilica nanobiostructure. *Desalination and Water Treatment*, 57(29): 13494-13504.
22. Malwal, D. and Gopinath, P. (2016). Enhanced photocatalytic activity of hierarchical three dimensional metal oxide@CuO nanostructures towards the degradation of Congo red dye under solar radiation. *Catalysis Science & Technology*, 6(12): 4458-4472.
23. Chatti, R., Rayalu, S. S., Dubey, N., Labhsetwar, N. and Devotta, S. (2007). Solar-based photoreduction of methyl orange using zeolite supported photocatalytic materials. *Solar Energy Materials and Solar Cells*, 91(2), 180-190.
24. Menon, S. G., Kulkarni, S. D., Choudhari, K. S. and Santhosh, C. (2016). Diffusion-controlled growth of $CuAl_2O_4$ nanoparticles: Effect of sintering and photodegradation of methyl orange. *Journal of Experimental Nanoscience*, 11(15), 1227-1241.

Malaysian Journal of Analytical Sciences, Vol 23 No 5 (2019): 781 - 788
DOI: https://doi.org/10.17576/mjas-2019-2305-03

MALAYSIAN JOURNAL OF ANALYTICAL SCIENCES
Published by The Malaysian Analytical Sciences Society
ISSN 1394 - 2506

SURFACTANT-BOUND Fe_3O_4 NANOPARTICLES AS CATALYST SUPPORT: SYNTHESIS AND PHYSICOCHEMICAL PROPERTIES

(Nanopartikel Fe_3O_4 Surfaktan Terikat Sebagai Sokongan Mangkin: Sintesis dan Ciri Fizikokimia)

Hassanain Hafiz Mohd Asnan[1], Siti Kamilah Che Soh[1]*, Wan Fatihah Khairunisa Wan Nor[1], Sabiqah Tuan Anuar[1], Uwaisulqarni M. Osman[1], Mohd Hasmizam Razali[1], Mohd Zul Helmi Rozaini[2], Mustaffa Shamsuddin[3]

[1]*Faculty of Science and Marine Environment*
[2]*Institute of Marine and Biotechnology*
Universiti Malaysia Terengganu, 21030 Kuala Nerus, Terengganu, Malaysia.
[3]*Department of Chemistry, Faculty of Science,*
Universiti Teknologi Malaysia, 81310 Skudai, Johor, Malaysia

**Corresponding author: sitikamilah@umt.edu.my*

Received: 10 June 2019; Accepted: 7 August 2019

Abstract

Magnetic nanoparticles are highly valuable solid support for the attachment of homogeneous inorganic catalyst and organocatalyst. In this study, surfactant-bound Fe_3O_4 nanoparticles were successfully synthesized *via* a co-precipitation method between $FeCl_3.6H_2O$ and $FeCl_2.4H_2O$, in which sodium dodecyl sulfate (SDS) was applied as a stabilizing agent. The use of surfactant was also to avoid the agglomeration process during the catalytic activity. Different techniques were employed to characterize the synthesized magnetic nanoparticles, such as Fourier Transform Infrared Spectroscopy (FTIR), Thermogravimetric Analysis (TGA), X-ray Diffraction (XRD), Field Emission Scanning Electron Microscopy/Electron Dispersive X-ray (FESEM/EDX), Vibrating Sample Magnetometer (VSM), and Brunauer–Emmett–Teller (BET) Surface Area Analysis. The specific surface area analysis of surfactant-bound Fe_3O_4 nanoparticles gave a higher value (117 m^2/g) with large pore volume (0.40 cm^3/g) compared to bare iron oxide. The VSM pattern demonstrates superparamagnetic properties of magnetic nanoparticles with saturation magnetization M_s, 53.98 emu/g. The analyses obtained recommended the surfactant-bound Fe_3O_4 nanoparticles potentially to be used as solid support for catalytic applications due to their unique properties, for example high surface area, superparamagnetism, and well-dispersed material.

Keywords: magnetite nanoparticles, catalyst support, heterogeneous catalysis

Abstrak

Nanopartikel magnet merupakan penyokong padu yang berharga untuk pengikatan mangkin homogen tak organik dan mangkin homogen organo. Dalam kajian ini, nanopartikel Fe_3O_4 surfaktan terikat berjaya disintesis melalui kaedah pemendakan bersama antara $FeCl_3.6H_2O$ dan $FeCl_2.4H_2O$, yang menggunakan natrium dodesil sulfat sebagai agen penstabilan. Penggunaan surfaktan juga untuk mengelak proses aglomerasi semasa aktiviti pemangkinan. Pelbagai teknik digunakan untuk pencirian nanopartikel magnet yang disintesis seperti Spektroskopi Inframerah Penjelmaan Fourier (FTIR), Analisis Gravimetri Terma (TGA), Pembelauan Sinar-X (XRD), Mikroskopi Elektron Pengimbasan Pancaran Medan/Sinar-X Sebaran Elektron (FESEM), Magnetometer Sampel Bergetar (VSM), dan Analisis Luas Permukaan Brunauer–Emmett–Teller(BET). Analisis luas permukaan khusus bagi nanopartikel Fe_3O_4 surfaktan terikat memberikan suatu nilai yang tinggi (117 m^2/g) dengan isi padu liang besar (0.40 cm^3/g) berbanding dengan oksida besi tanpa surfaktan. Pola VSM mempamerkan sifat superparamagnetik bagi nanopartikel magnetik dengan nilai pemagnetan tepu M_s, 53.98 emu/g. Analisis yang diperolehi mengesyorkan bahawa nanopartikel Fe_3O_4 surfaktan terikat berpotensi digunakan sebagai penyokong padu untuk aplikasi pemangkinan disebabkan oleh sifat-sifat uniknya seperti luas permukaan yang tinggi, superparamagnet dan sebagai bahan terserak yang baik.

Kata kunci: nanopartikel magnetit, sokongan mangkin, mangkin heterogen

Introduction

The use of magnetic nanoparticles as solid support materials is considered as a bridge between homogeneous and heterogeneous catalysts. Today, the development of iron oxide (Fe_3O_4) nanoparticles has led to the dramatic expansion of their applications by enabling environmentally-friendly and sustainable catalytic processes [1]. Having unique properties such as superparamagnetism, high surface area, low toxicity and economical, Fe_3O_4 nanoparticles possess numerous benefits for isolation and separation from desired mixtures using an external magnet [2,3]. Consequently, Fe_3O_4 nanoparticles are widely employed as solid support materials for homogeneous catalysts in the cross-coupling reactions [4].

Previous works reported that the synthesized Fe_3O_4 nanoparticles contributed to the spontaneous agglomeration in the catalytic system, which later became a critical problem [5]. Iron oxides have bare surface potential to agglomerate due to van der Waals forces, high energy surface, and strong magnetic attraction among particles [6,7]. The agglomeration of the nanoparticles may reduce the total exposed surface area of the catalyst as well as affect its magnetic properties [8,9]. Therefore, a modification for protection strategies has been made as a prerequisite to synthesise stable and effective catalyst support materials [5]. Hence, stabilizers such as surfactant were employed at the time of preparation. By coating and protecting the surface of Fe_3O_4 nanoparticles, the agglomeration and aggregation of the solid support materials could be reduced, and particle size could also be controlled in order to achieve compatibility and stability [10,11].

This study reported the synthesis and physicochemical properties of surfactant-bound Fe_3O_4 nanoparticles potentially used as solid support materials for homogeneous catalyst. The synthesized catalyst support was spectroscopically characterized by Fourier Transform Infrared Spectroscopy (FTIR), X-ray Diffraction (XRD), Thermogravimetric Analysis (TGA), Field Emission Scanning Electron Microscopy (FESEM), Vibrating Sample Magnetometer (VSM),and Brunauer–Emmett–Teller (BET) Surface Area Analysis.

Materials and Methods

Chemicals and reagents

Iron(III) chloride hexahydrate, iron(II) chloride tetrahydrate, and sodium dodecyl sulphate were purchased from Sigma Aldrich, USA. Aqueous ammonia and absolute ethanol were supplied from MERCK Chemical Co. All chemicals were used as received without any purification or any special precaution during the experimental procedure.

Characterization

The synthesized surfactant-bound Fe_3O_4 nanoparticles were successfully characterized using several spectroscopic and analytical techniques. The infrared spectrum of sample was collected on a Perkin Elmer 100 Fourier Transform Infrared Spectroscopy in the range of 4000-400 cm^{-1} by using potassium bromide (KBr) pellets. The thermal properties were investigated using Perkin Elmer TGA Analyser (Perkin Elmer Pyris 6 TGA) from 30 °C to 900 °C at the heating rate of 10 °C/min under nitrogen atmosphere. The XRD pattern was recorded on a Rigaku Miniflex II X-ray diffractometer with an X-ray of the Cu Kα radiation filtered by a Ni filter and had a wavelength of $\gamma = 1.54$. An estimation of particle size was performed using Scherrer equation:

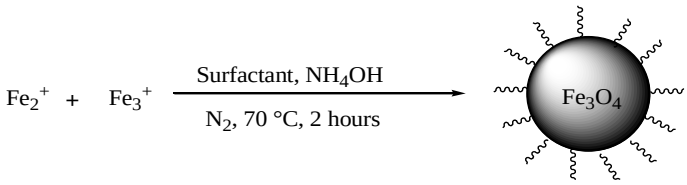
$$d = \frac{k\lambda}{(\beta \cos\theta)} \quad (1)$$

where d is the particle size; k is the Scherrer constant which is 0.9; λ is the wavelength (Cu Kα = 1.54); β is the full width at half maximum (FWHM); and θ is the corresponding Bragg diffraction. The surface area and pore size measurement were performed using Micromeritics ASAP 2020 instrument. The morphological structure was observed by JEOL JSM-6701F Field Emission Scanning Electron Microscope (FESEM) at a 10kV acceleration voltage with magnifications n of 50000x and 100000x attached with Electron Dispersive X-ray. The magnetization

analysis was performed using a Lake Shore vibrating sample magnetometer (VSM) 7404 model at room temperature.

Synthesis of Fe_3O_4 nanoparticles

The preparation of Fe_3O_4 nanoparticles was accomplished *via* modified co-precipitation method [12,13]. Equimolar amounts of $FeCl_2.4H_2O$ (1.0 g, 5.0 mmol) and $FeCl_3.6H_2O$ (2.6 g, 9.6 mmol) were mixed together in 100 mL of distilled water with vigorous stirring. The mixture was then treated with 100 mL of 0.5% SDS as a surfactant. An amount 10 mL of NH_4OH was added dropwise into the mixture. The reaction was heated at 70 °C for 2 hours under nitrogen atmosphere. The black precipitate was thoroughly washed with deionized water and ethanol until a neutral pH was reached. Finally, the product was separated from the reaction mixture and dried at 60 °C for 24 hours.



Scheme 1. Preparation of surfactant-bound Fe_3O_4 nanoparticles

Results and Discussion

Surfactant-bound Fe_3O_4 nanoparticles were successfully synthesized using a simple chemical co-precipitation method of Fe(II) and Fe(III) in alkaline pH under nitrogen atmosphere. This study provided physicochemical results of Fe_3O_4 nanoparticles by adding surfactants of sodium dodecyl sulfate (SDS) that could effectively prompt the formation of monodispersed nanoparticles [11]. This research was promising and produced favorable findings as compared to previous works, which were focused on synthesizing Fe_3O_4 nanoparticles without a surfactant [13]. The use of surfactants could give better control for the particle size distribution and represented better dispersibility [14] since SDS is an anionic surfactant that could also form complex with Fe^{2+} *via* ionic bonds [4]. The interaction occurred may lead to a strong ionic repulsion that could prevent close contact of the Fe_3O_4 nanoparticles [10] and become better catalyst support.

Figure 1 shows the FTIR spectra of surfactant-bound Fe_3O_4 nanoparticles and pristine Fe_3O_4 as well as pure SDS included for comparison. For both iron oxide samples, the analysis indicated absorption peaks at the range of 530 cm^{-1} - 593 cm^{-1} corresponding to the Fe-O vibration related to the magnetic phase [1,14]. For the SDS-Fe_3O_4 spectrum, the peak around 1224 cm^{-1} could be assigned for the characteristics of sulfate group SO_4^{2-} of SDS. The stretching vibration of S-O bond could be attributed by the peak of around 895 cm^{-1}, which confirmed that the surfactant was successfully immobilized on the synthesized iron oxides. These results are in close agreement with previous reported articles [15, 16].

The XRD pattern of Fe_3O_4 nanoparticles synthesized with SDS is shown in Figure 2. The red line pattern of bare Fe_3O_4 nanoparticles was also attached for comparison. Six characteristic peaks at 2θ: 30.1°, 35.4°, 43.1°, 53.4°, 57.0° and 62.6° were corresponding to the diffractions of (220), (311), (400), (422), (511), and (440) crystal planes of Fe_3O_4 with spinel structure [17]. The results obtained were in good agreement and matched well between the pattern of the standard Fe_3O_4 (JCPDS CARD NO. 19-629). Peak broadening observed was reflected by small-sized particles [18]. Taking into account, the synthesized catalyst support showed the normal and typical XRD pattern with no impurity peaks were detected in the sample [19]. The relative intensity of reflection peaks in the surfactant-bound Fe_3O_4 nanoparticles were dramatically decreased, promoting an interaction between the surfactant and iron oxide [20]. The approximate diameter of the surfactant-bound Fe_3O_4 using the Scherrer equation (Eqn. 1) was 6 nm, which was smaller than previously reported [13].

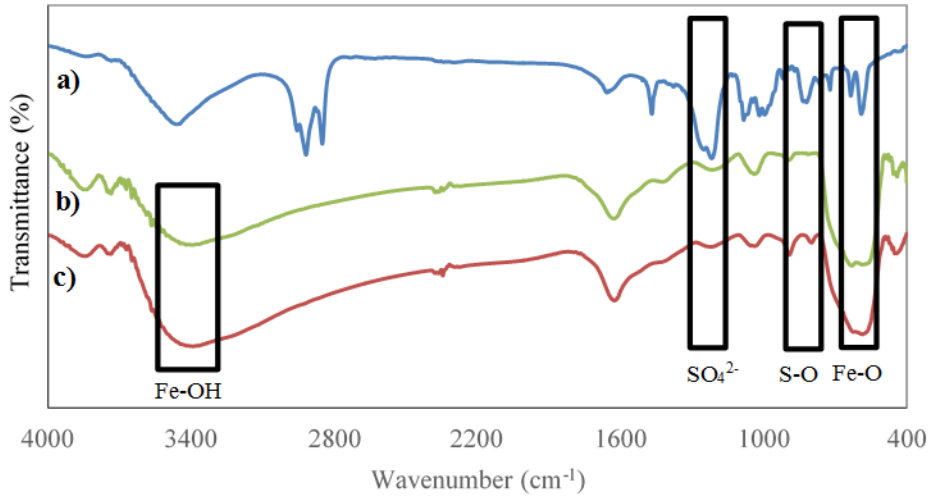


Figure 1. FT-IR spectrum of (a) pure SDS, (b) Fe_3O_4 nanoparticles, and (c) SDS-Fe_3O

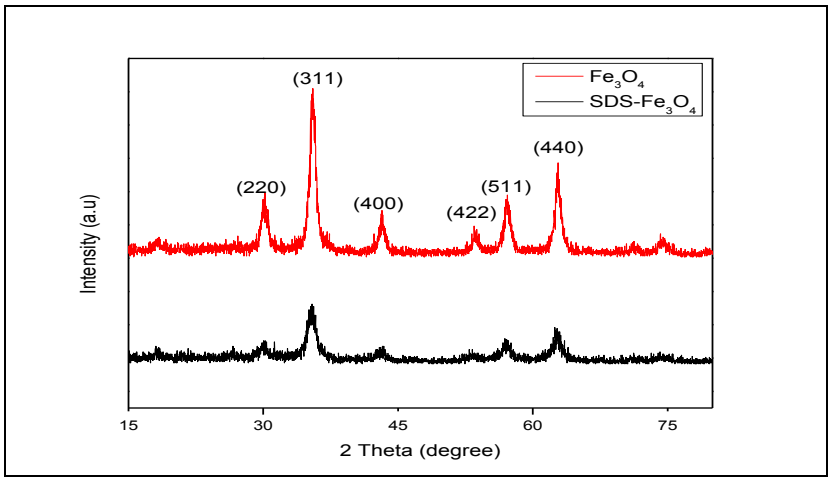


Figure 2. XRD patterns of bare Fe_3O_4 nanoparticles and surfactant-bound Fe_3O_4 nanoparticles

The morphology of synthesised catalyst support was obtained by using a Field Emission Scanning Electron Microscopy/Electron Dispersive X-ray (FESEM/EDX). As shown in Figure 3, the micrographs displayed that the surfactant-bound Fe_3O_4 nanoparticles were composed of small particles with nearly spherical shape [16]. The nanoparticles appeared as clustered together and loosely distributed which could prevent the agglomerations of the nanoparticles. The EDX spectrum clearly showing the appearance of surfactant-bound Fe_3O_4 nanoparticles by indicating Fe-O group of the element with the corresponding peaks of Na, S and C are the main constituents in the synthesized of magnetic nanoparticles.

The TGA curve of surfactant-bound Fe_3O_4 nanoparticles with SDS is shown in Figure 4. It can be seen that there is a slightly different thermal behavior as compared with bare Fe_3O_4 nanoparticles. The TGA result showed that the surfactant-bound Fe_3O_4 nanoparticles were stable up to 200 °C. The difference might originate from the presence of SDS coated on the surface of nanoparticles [16]. Three sharp weight losses were also observed in the TGA curve with a total loss of 6%. The initial weight loss occurred at the temperature range of 25 °C – 200 °C, which was possibly due to the removal of adsorbed water and/or solvent on the surface of nanoparticles [20,21]. The second

decomposition around 250 °C to 300 °C indicated SDS degradation in Fe_3O_4 nanoparticles with the percentage of mass loss about 3%. The third peak derived at 600 °C – 700 °C was attributed to the phase transition from Fe_3O_4 to FeO, because FeO was thermodynamically stable above 570 °C in the phase diagram of Fe-O system [22].

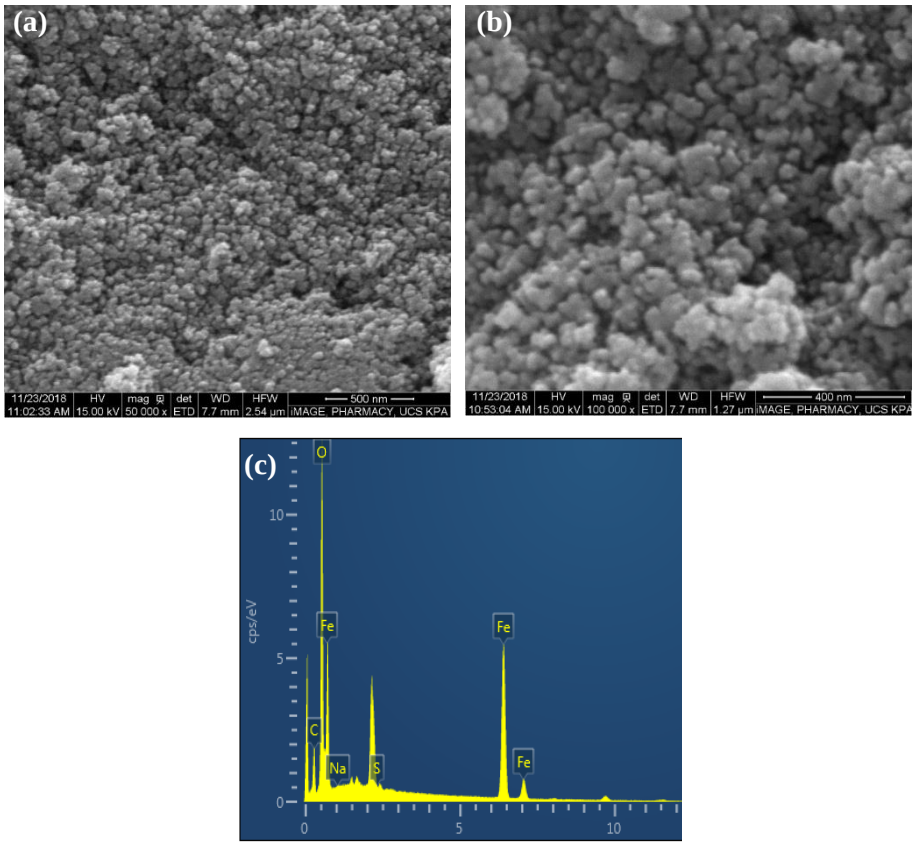


Figure 3. FESEM images of Fe_3O_4 nanoparticles with scale bar (a) 500 nm (b) 400 nm and (c) the EDX image of surfactant-bound Fe_3O_4 nanoparticles

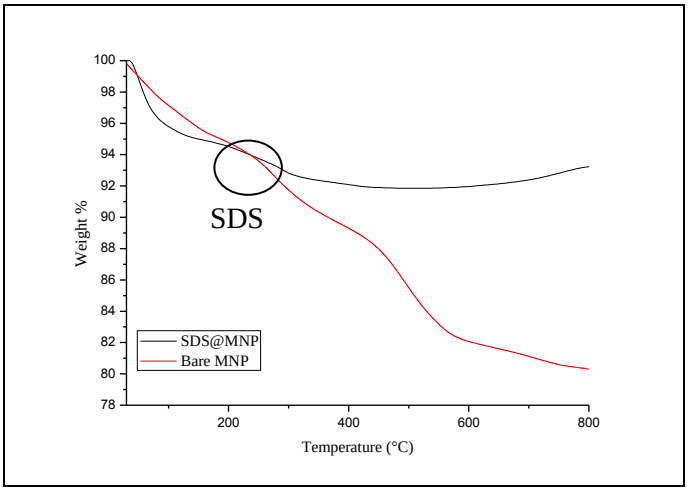


Figure 4. TGA curve of bare Fe_3O_4 nanoparticles and surfactant-bound Fe_3O_4 nanoparticles

The BET surface area and pore size measurements of the surfactant–bound and bare Fe_3O_4 nanoparticles are tabulated in Table 1. The addition of a stabiliser onto the magnetite nanoparticles gave a significant influence on the surface area and size. Surfactant-bound Fe_3O_4 nanoparticles were found to possess a higher surface area and pore volume as compared to bare magnetite nanoparticles at 117 m^2g^{-1} and 0.4 cm^3g^{-1}, respectively [13]. Gupta and co-workers reported that the synthesis of Fe_3O_4 nanoparticles without a surfactant had a tendency for agglomeration due to the hydrophobic bonds between the particles in the surface [23]. Hence, the magnetite nanoparticles existed in obviously large clusters. Consequently, surfactants play a vital role as stabilisers and particle protection from flocculation and agglomeration [10].

Table 1. BET results of Fe_3O_4

Sample	**Specific surface area (m^2/g)**	**Pore volume (cm^3/g)**
Fe_3O_4	94	0.3
SDS-Fe_3O_4	117	0.4

The magnetic properties of the synthesised surfactant-bound Fe_3O_4 (Figure 5) was examined by vibrating sampling magnetometer (VSM) at room temperature. The magnetisation curve of bare iron oxides was included for comparison. From the curve, it was confirmed that the synthesised Fe_3O_4 nanoparticles possessed nearly superparamagnetic behaviour. It was found that the saturation magnetisation value of the studied sample was 53. 98 emu/g, which was lower than that reported for pure Fe_3O_4 nanoparticles [14]. This can be explained as the introduction of non-magnetic materials (surfactants) on the synthesised compound leading to the diminution of magnetisation. Another factor that leads to the gradual decline in the saturation magnetisation value of the sample is that the surface is influenced by the reduced particle sizes, which caused the magnetic moments to be canted [15].

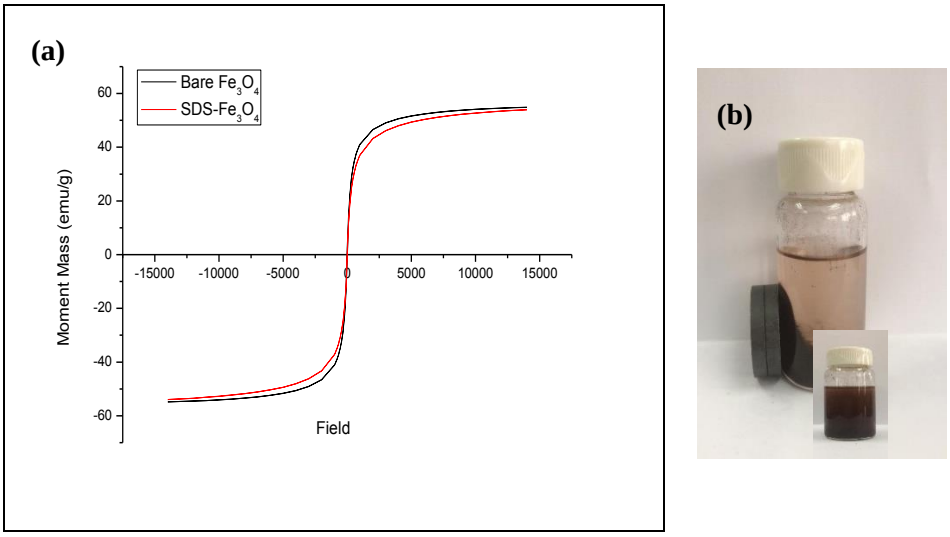


Figure 5. Magnetization curve of surfactant-bound Fe_3O_4 and bare Fe_3O_4 (a) and photograph of the magnetic separation of surfactant-bound Fe_3O_4 using an external magnetic field (b)

Conclusion

A recoverable surfactant-bound Fe_3O_4 nanoparticle as catalyst support was successfully synthesized *via* simple chemical co-precipitation method and the synthesized particles were characterized using several spectroscopic and

analytical techniques. The physicochemical properties of the surfactant-bound Fe_3O_4 nanoparticles as catalyst support showed promising properties for homogeneous catalyst. Thus, the nanoparticles obtained could be potentially used as catalyst support that could easily be separated by an external magnetic field.

Acknowledgement

The authors wish to thank the Ministry of Higher Education (FRGS) for funding under Grant No. 59456 and Universiti Malaysia Terengganu (UMT) for the use of research facilities.

References

1. Rezaei, G., Naghipour, A. and Fakhri, A. (2017). Catalytic performance studies of new Pd and Pt Schiff base complexes covalently immobilized on magnetite nanoparticles as the environmentally friendly and magnetically recoverable nanocatalyst in C–C cross coupling reactions. *Catalysis Letters*, 148(2): 732 - 744.
2. Dehghani, F., Sardarian, A. R. and Esmeilpour M. (2013). Salen complex of Cu(II) supported on superparamagnetic Fe_3O_4@SiO_2 nanoparticles: an efficient and recyclable catalyst for synthesis of 1- and 5-substituted 1H-tetrazoles. *Journal of Organometallic Chemistry*, 743: 87 - 96.
3. Rayati, S., Khodaei E., Jafarian M. and Wojtczak A. (2017). Mn-Schiff base complex supported on magnetic nanoparticles: synthesis, crystal structure, electrochemical properties and catalytic activities for oxidation of olefins and sulfides. *Polyhedron*, 133: 27 - 335.
4. Sydnes, M. O. (2017). The use of palladium on magnetic support as catalyst for Suzuki–Miyaura cross-coupling reactions. *Catalysts*, 7(1): 35.
5. Feng, X. and Lou, X. (2015). The effect of surfactants-bound magnetite (Fe_3O_4) on the photocatalytic properties of the heterogeneous magnetic zinc oxides nanoparticles. *Separation and Purification Technology*, 147: 266 - 275.
6. Ali A., Zafar H., Zia M., Haq I., Phull A. R., Ali J. S. and Hussain A. (2016). Synthesis, characterization, applications, and challenges of iron oxide nanoparticles. *Nanotechnology, Science and Applications*, 9: 49 - 67.
7. Yang Q., Dai Z., Yang K. and Li Y. (2015). Preparation of magnetic Fe_3O_4 microspheres using different surfactant and silica-coated magnetic particles. Atlantis Press, London: pp. 47 - 51.
8. Ng, K., Kok, K. and Ong, B. (2017). Facile synthesis of self-assembled cobalt oxide supported on iron oxide as the novel electrocatalyst for enhanced electrochemical water electrolysis. *ACS Applied Nano Materials*, 1(1): 401 - 409.
9. Sievers C., Noda Y., Qi L., Alburquerque E. M., Riuox R. M. and Scott S. L. (2018). Phenomena affecting catalytic reactions at solid-liquid interfaces. *ACS Catalytic*, 6 (12): 8286 - 8307.
10. Tan, W. L. and Bakar M. A. (2006). The effect of additives on the size of Fe_3O_4 particles. *Journal of Physical Sciences*, 17(2): 37 - 50.
11. Han, D., Yang, S., Yang, J., Zou, P., Kong, X., Yang, L. and Wang, D. (2016). Synthesis of Fe_3O_4 nanoparticles via chemical coprecipitation method: Modification of surface with sodium dodecyl sulfate and biocompatibility study. *Nanoscience and Nanotechnology Letters*, 8(4): 335 - 339.
12. Petcharoen, K. and Sirivat, A. (2012). Synthesis and characterization of magnetite nanoparticles *via* the chemical co-precipitation method. *Materials Science and Engineering*: *B*, 177 (5): 421 - 427.
13. Nor W. F. K. N., Soh S. K. C., Azmi A. A. A., Yusof M. S. M. and Shamsuddin M. (2017). Synthesis and physicochemical properties of magnetite nanoparticles (Fe_3O_4) as potential solid support for homogeneous catalysts. *Malaysian Journal of Analytical Sciences*, 2(5): 768 - 774.
14. Riva'i, I., Wulandari, I. O., Sulistyarti, H. and Sabarudin, A. (2018). Ex-situ synthesis of polyvinyl alcohol (PVA)-coated Fe_3O_4 nanoparticles by co precipitation-ultrasonication method. *IOP Conference Series: Materials Science and Engineering*, 299: 1 - 8.
15. Arévalo, P., Isasi, J., Caballero A.C., Marco, J. F. and Martín-Hernández, F. (2017). Magnetic and structural studies of Fe_3O_4 nanoparticles synthesized *via* co precipitation and dispersed in different surfactants. *Ceramics International*, 43(13): 10333 - 10340.
16. El-kharrag, R., Amin, A. and Griesh, Y. E. (2011). Synthesis and characterization of mesoporous sodium dodecyl sulfate-coated magnetite nanoparticles. *Journal of Ceramic Science and Technology*, 02(04): 203 - 210.

17. Liu, X., Kaminski, M. D., Guan, Y., Chen, H., Liu, H. and Rosengart, A. J. (2006). Preparation and characterization of hydrophobic superparamagnetic magnetite gel. *Journal of Magnetism and Magnetic Materials*, 306(2): 248 - 253.
18. Mascolo, M. C., Pei, Y. and Ring, T. A. (2013). Room temperature co-precipitation synthesis of magnetite nanoparticles in a large pH window with different bases. *Materials*, 6(12): 5549 - 5567.
19. Mürbe, J., Rechtenbach, A. and Töpfer, J. (2008). Synthesis and physical characterization of magnetite nanoparticles for biomedical applications. *Materials Chemistry and Physics*, 110(2-3): 426 - 433.
20. Dick, K., Dhanasekaran, T., Zhang, Z. and Meisel, D. (2002). Size-dependent melting of silica-encapsulated gold nanoparticles. *Journal of American Chemical Society*, 124(10): 2312 - 2317.
21. Villa, S., Riani, P., Locardi, F. and Canepa, F. (2016). Functionalization of Fe_3O_4 NPs by Silanization: Use of amine (APTES) and thiol (MPTMS) silanes and their physical characterization. *Materials*, 9(10): 826.
22. Mahdavi, M., Ahmad, M. B., Haron, M. J., Namvar, F., Nadi, B., Rahman, M. Z. and Amin, J. (2013). Synthesis, surface modification and characterisation of biocompatible magnetic iron oxide nanoparticles for biomedical applications. *Molecules*, 18(7): 7533 - 7548.
23. Gupta, A. K., and Gupta, M. (2005). Synthesis and surface engineering of iron oxide nanoparticles for biomedical applications. *Biomaterials*, 26(18): 3995 - 4021.

Malaysian Journal of Analytical Sciences, Vol 23 No 5 (2019): 789 - 798
DOI: https://doi.org/10.17576/mjas-2019-2305-04

MALAYSIAN JOURNAL OF ANALYTICAL SCIENCES
Published by The Malaysian Analytical Sciences Society
ISSN 1394 - 2506

SPECTROSCOPIC STUDIES OF INCLUSION COMPLEX GLIPIZIDE AND β-CYCLODEXTRIN

(Kajian Spektroskopik Kompleks Kemasukan Glipizida dan β-siklodekstrin)

Nurul Yani Rahim*, Fatin Hamizah Samad, Asmaa' Mardhiah Rohisham

School of Chemical Sciences,
Universiti Sains Malaysia,
11800 Gelugor, Pulau Pinang, Malaysia

**Corresponding author: nurulyanirahim@usm.my*

Received: 8 May 2019; Accepted: 3 September 2019

Abstract

The complex between hypoglycemic drug, glipizide, and β-cyclodextrin (β-CD) was prepared using the kneading method with aliquot addition of ethanol. The product was characterized using Fourier Transform Infrared (FTIR) spectrometer and Thermogravimetric Analysis (TGA). ^{1}H and NOESY Nuclear Magnetic Resonance (NMR) and UV-Vis spectroscopy were used to determine the interaction involved in the formation of inclusion complex β-CD/glipizide. ^{1}H and NOESY NMR results indicated that the hydrophobic interaction occurred between glipizide and β-CD. The formation constant values of complex β-CD/glipizide at pH 9 and 4 were close to each other. The stoichiometry ratio for the inclusion complex between β-CD with glipizide was 1:1.

Keywords: β-CD, antidiabetic drug, formation constant, cavity, kneading

Abstrak

Kompleks antara ubat hipoglisemia, glipizida, dan β-siklodekstrin (β-CD) telah disediakan dengan cara menguli bersama penambahan etanol alikuot. Produk ini dicirikan menggunakan spektrometer inframerah transformasi Fourier (FTIR) dan analisis termogravimetrik (TGA). Resonan Magnetik Nuklear (NMR) ^{1}H dan NOESY dan spektroskopi UV-Vis telah digunakan untuk menentukan interaksi yang terlibat dalam pembentukan kompleks kemasukan β-CD/glipizida. Hasil NMR ^{1}H dan NOESY menunjukkan bahawa interaksi hidrofobik berlaku antara glipizida dan β-CD. Nilai pemalar pembentukan kompleks β-CD/glipizida pada pH 9 dan 4 adalah lebih kurang sama. Nisbah stoikiometri untuk kompleks kemasukan antara β-CD dan glipizida ialah 1: 1

Kata kunci: β-CD, ubat antidiabetik, pemalar pembentukan, kaviti, menguli

Introduction

β-Cyclodextrins (β-CD) are cyclic oligosaccharides that contain seven units of glucose joined through α-1,4 linkage [1]. β-CD is produced from intramolecular transglycolation reaction from the degradation of starch by CD glucanotransferase(CGTase) enzyme. β-CD has a toroidal shape with a free hydroxyl group at two rims. β-CD is referred to as an all-purpose molecular container for organic, inorganic, organometallic, and metalloorganic compounds that may be neutral, cationic, anionic or even radical. The hydrophobic cavity inside of β-CD allows them to form inclusion complexes with hydrophobic compounds in aqueous environments [2]. The inclusion complex formation affects the physical, chemical, and biological properties of guest molecules. Moreover, it improves the application characteristics of guest molecules [3]. Based on various methods construct, β-CD has

received considerable attention in the pharmaceutical field for the past few years due to its extensive use in drug delivery processes [4-9]. Smart drug carriers can act as a new weapon for treating diseases. It is difficult to build up this kind of drug carrier by general synthetic chemistry due to its complex structure. However, the appearance of β-CD supramolecular self-assembly provides a fast, convenient, and flexible way to construct a biological simulative-responsive drug carrier.

Glipizide is a second-generation sulfonylurea hypoglycemic drug that can acutely lower the blood glucose level in humans by stimulating the release of insulin from the pancreas [10]. It is typically prescribed to treat non-insulin-dependent diabetes mellitus [11]. It is a whitish, odourless powder with pKa of 5.9 and belongs to Class II of the Biopharmaceutical Classification System (BCS). It is insoluble in water, and its dissolution is a rate-determining step in its absorption from the gastrointestinal fluids [12]. This is considered to be a main factor contributing to its very limited oral bioavailability, thus resulting in delayed absorption [11]. Several studies have been developed for the enhancement of the dissolution rate, solubility, and bioavailability of glipizide through inclusion complex formation [13-17].

Inclusion complexes are a type of complex in which one compound (the host) contains a cavity or spaces where another molecular entity (the guest) is located. This is with the consideration that no covalent bonding occurs between the host and the guest. The inclusion complexation of these host-guest systems occurs through various interactions such as hydrogen bonding, Van der Waals, and electrostatic or hydrophobic interactions. Previously, the improved bioavailability of glipizide complexed with β-CD and β-CD derivatives has been documented in several articles [13, 17, 18]. However, there is no information available on the study of interactions involved in the formation of complex between β-CD and glipizide. In this study, the inclusion complex of glipizide and β-CD was evaluated using spectroscopy techniques. The result provides information on the intermolecular interaction between glipizide and β-CD.

Materials and Methods

Materials

The present study utilized β-cyclodextrin ($C_{42}H_{70}O_{35}$), glipizide ($C_{21}H_{27}N_5O_4S$), ethanol (C_2H_6O), and methanol (CH_3OH). Ultra-pure water was used to dilute the solutions.

Characterization of samples

The formation of inclusion complexes was studied *via* an analysis of the peaks. Infrared (IR) absorption spectra were determined by using Perkin-Elmer 2000 system spectrometer in the range of 4000 cm^{-1} to 600 cm^{-1}. The thermal analysis was conducted through the Thermogravimetric Analysis (TGA) using Mettler Toledo TGA/SDTA 851E Thermogravimetric Analyzer. The analysis was done over the ambient temperature range of 30 °C to 920 °C in N_2 atmosphere to understand the weight loss profile for β-CD, glipizide, and β-CD/glipizide complex. The Bruker Avance spectrometer 500 MHz was used to determine ^1H NMR spectra of the β-CD, glipizide, and β-CD/glipizide complex by employing dimethyl sulfoxide-d_6 (DMSO-d_6) as a solvent. Absorption spectra measurements were carried out with Shimadzu UV2600 spectrometer in the range of 200 nm – 800 nm.

Preparations of β-CD/glipizide complex

The complex was prepared as previously reported using the kneading method. β-CD and glipizide were put in a ceramic mortar with a molar ratio of 1:1 and grounded with additional few drops of ethanol to form a homogeneous paste [19]. This process was continued for 30 minutes and the product was placed in a desiccator to the final mass.

Determination of the formation constant of β-CD/glipizide complex

The formation constant was determined as mention in the previous procedure [20]. In 10.0 mL of volumetric flask, 2.0 mL of 0.01 mM glipizide and 3.2 mL of 0.003 M of β-CD were added to form β-CD/glipizide solution. The solution was diluted using ultra-pure water to the mark. The absorption spectra of β-CD and glipizide were recorded against a reagent blank, which was prepared with the same reagent concentration but without the addition of glipizide. The absorption spectra of β-CD and glipizide alone were also recorded. The formation constant, K of β-CD and glipizide could be obtained from the slope of Benesi-Hildebrand plot that was generated using Eqs (1)

and (2). For the formation constant curve, the concentration of glipizide was held firmly at 0.01 mM, while the concentration of β-CD was varied (0.001, 0.002, 0.003, and 0.005 M).

$$\frac{1}{A-A_0} = \frac{1}{(A'-A_0)} + \frac{1}{K(A'-A_0)[\beta-CD]} \quad (1)$$

$$K=\frac{1}{Slope(A-A_0)} \quad (2)$$

where A_0 and A are the absorbance of the free guest and β-CD, respectively. $A^{'}$ is the absorbance at the maximum concentration of β-CD.

Results and Discussion

FT-IR

The FT-IR spectra and main frequencies of β-CD, glipizide, and complex of β-CD/glipizide are reported in Figures 1 (a)-(c) and Table 1, respectively. The frequencies for β-CD were observed at 3292.81 cm^{-1}, 2924.94 cm^{-1}, and 1152.37 cm^{-1}, which corresponded to the broad peaks of OH, CH_2, and -C-C, respectively. The spectrum of glipizide (Figure 1 (b)) showed absorption bands at 1687.51 cm^{-1} (for C=O stretching vibration), 1331.94 cm^{-1} (for -C-N stretching vibration), and 1484.95 cm^{-1} (for aromatic C=C groups stretching vibration).

In the spectrum of β-CD/glipizide complex (Figure 1 (c)), the frequencies of S=O (1157.21 cm^{-1}) for glipizide and C-O group (1334.23 cm^{-1}) disappeared, whereas the frequency of C-N, $-CH_3$, and -C=O shifted from 1331.94 cm^{-1} to 1332.52 cm^{-1}, 2944.00 cm^{-1} to 2927.26 cm^{-1} and 1687.51 cm^{-1} to 1689.38 cm^{-1} respectively. Besides, a broad hydroxyl band of pure β-CD at 3292.81 cm^{-1} was found to be narrowed in the spectrum of the β-CD/glipizide complex (Figure 1 (c)), which was a good indication of the formation of the inclusion complex. This is a common phenomenon observed by many researchers in synthesizing the inclusion complex between β-cyclodextrin as host and guest molecules [21-24]. The changes in the FT-IR spectrum of complex shown in Figure 1 (c) were due to the change of microenvironment with the formation of inclusion complex. Thus, the result of FT-IR spectroscopy indicated that the inclusion complex of glipizide with β-CD was formed.

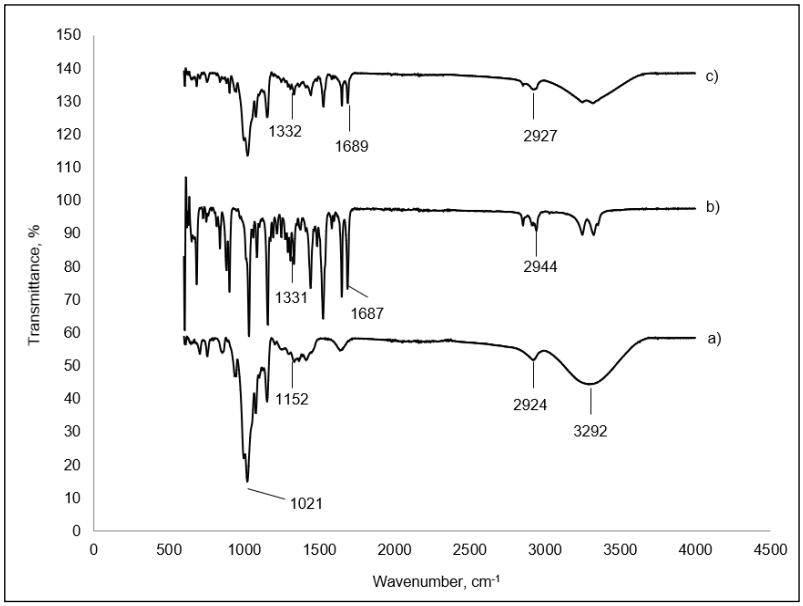


Figure 1. FTIR spectrums of a) β-CD b) glipizide c) β-CD/glipizide.

Table 1. Main FTIR frequencies for β-CD, glipizide and β-CD/glipizide

Wavenumber (cm^{-1})	**Assignments**	**β-CD**	**Glipizide**	**β-CD/glipizide**
3292.81	O-H stretch	√		
2944.00	C-H stretch		√	
2927.26				√
2924.94		√		
1689.38	C=O stretch			√
1687.51			√	
1484.95	C=C stretch		√	
1332.52	C-N stretch			√
1331.94			√	
1157.21	S=O		√	
1152.37	C-C	√		

Thermal analysis

TGA analyses were performed on the β-CD, glipizide, and β-CD/glipizide complex in the temperature range of 30 ^{o}C - 900 ^{o}C. Based on the thermogram shown in Figure 2, there was an initial loss of weight at temperature below 100 ^{o}C for β-CD, glipizide, and β-CD/glipizide complex due to the loss of water molecules. The weight losses of β-CD starting from 328.90 ^{o}C to 800 ^{o}C were attributed to the decomposition of β-CD, while glipizide started to decompose around 220 ^{o}C. The weight loss for β-CD/glipizide complex that occurred at the range of 210 ^{o}C - 400 ^{o}C could be related to the decomposition of organic moieties at the surface. The result showed that the β-CD/glipizide complex had the least pronounced weight loss than β-CD and glipizide. Apart from that, the high stability of β-CD/glipizide could be due to the strong hydrophobic interaction between β-CD and glipizide, which enabled this material to be used in high-temperature applications. The temperature of weight loss with detailed assignment is shown in Table 2.

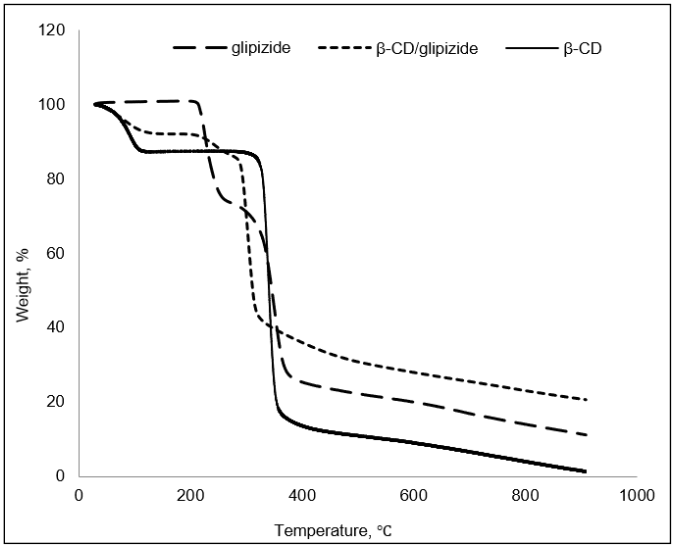


Figure 2. TGA for β-CD, glipizide and β-CD/glipizide

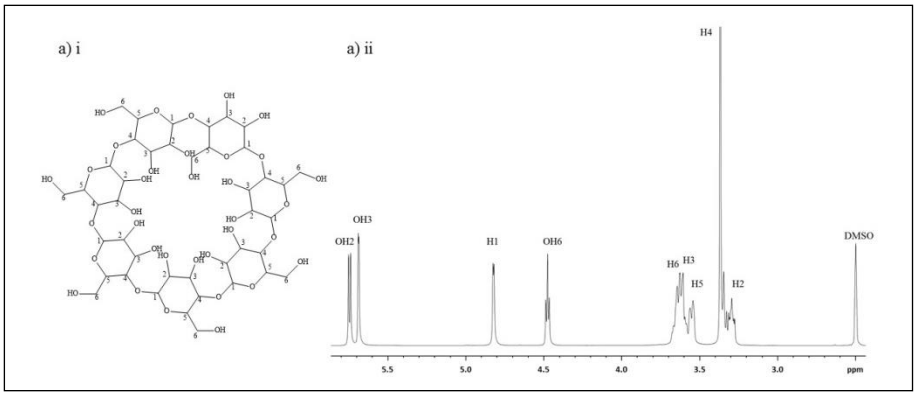
Table 2. The assignment for temperature of weight loss

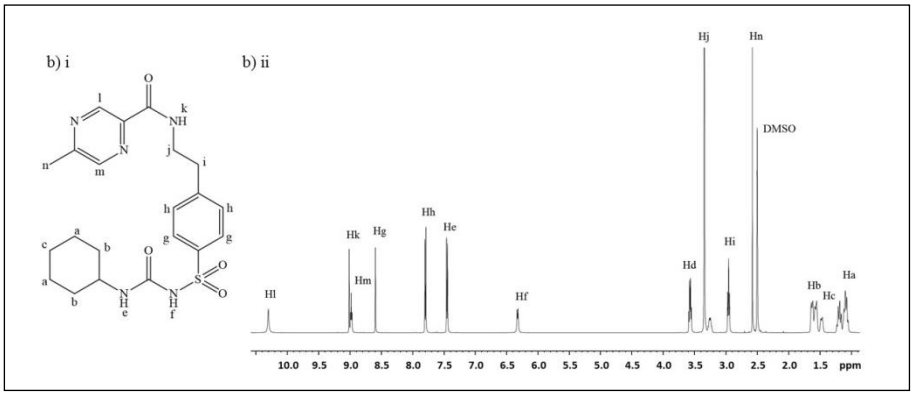
Samples	Region (°C)	Weight Loss (%)	Assignment
β-CD	<100	29.46	Water loss
	328.9-800	81.35	β-CD decomposition
glipizide	<100	29.52	Water loss
	220	96.96	Glipizide decomposition
β-CD/glipizide	<100	29.45	Water loss
	210-400	91.73	Glipizide decomposition

^{1}H NMR analysis

^{1}H NMR spectroscopy was introduced to study the inclusion complex formation. The deduced structures of β-CD and glipizide with the spectra of ^{1}HNMR are shown in Figure 3. Chemical shift (δ) variations provided evidence for the formation of inclusion complex. The values of chemical shifts obtained from ^{1}H NMR for each β-CD, glipizide, and β-CD/glipizide are listed in Table 3. The method relied on changes in chemical shift caused by the glipizide (guest) and β-CD (host) of one another. The difference in chemical shift for the protons of β-CD in the presence or absence of glipizide was defined as induced shift (Δδ). In this case, the induced shift was calculated using Eq 3:

$$\Delta\delta=\delta \text{ (complex)}-\delta \text{ (free)} \quad (3)$$





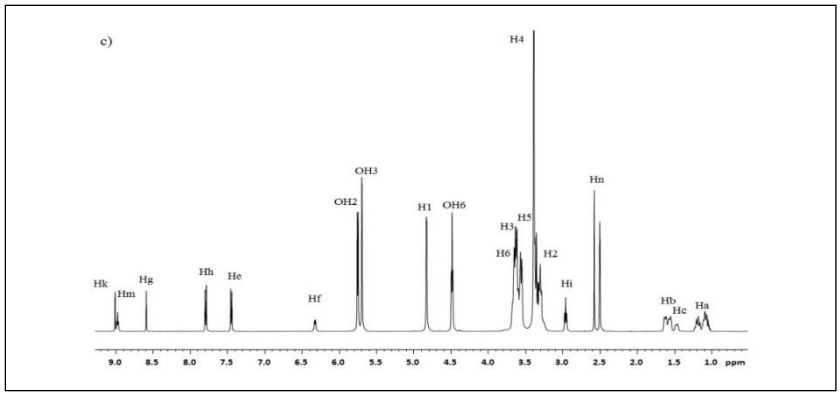


Figure 3. [1] H NMR spectra of a) β-CD, b) glipizide and c) β-CD/glipizide

Table 3. Chemical shift corresponding to β-CD and glipizide

Proton	β-Cyclodextrin δ	Glipizide δ	Inclusion Complex δ	Induced Shift Δδ
H1	4.826		4.829	0.003
H2	3.295		3.299	0.004
H3	3.606		3.610	0.004
H4	3.367		3.384	0.017
H5	3.542		3.563	0.021[a]
H6	3.643		3.629	-0.014
Ha		1.097	1.092	-0.005
Hb		1.554	1.551	-0.003
Hc		1.462	1.459	-0.003
Hd		3.565	-	-
He		7.461	7.458	-0.003
Hf		6.319	6.317	-0.002
Hg		8.597	8.593	-0.004
Hh		7.790	7.785	-0.005
Hi		2.961	2.958	-0.003
Hj		3.346	-	-
Hk		9.017	9.012	-0.005
Hl		10.307	-	-
Hm		8.983	8.978	-0.005
Hn		2.579	2.575	-0.004

[a] Values in bold refer to the highest induced shift of that particular proton

In the structure of β-CD (Figure 4), the protons H3 and H5 were located inside the cavity. Meanwhile, the other protons (H1, H2, and H4) were located at the exterior of the cavity. Normally, the inclusion of the non-polar region of an analyte into hydrophobic cavity would affect the inner protons of the glucose units of β-CD, which were H3 and H5 [19-20, 25]. For β-CD/glipizide complex, there was a significant shift at H5 (Table 3). However, there was

no significant change of chemical shift for H3. This revealed that there was a partial penetration of glipizide into the cavity of β-CD. 2D NMR, which is NOESY, was studied to obtain detailed information of the interaction involved. The cross peak (Figure 5) between Hm (proton of glipizide) and H5 (proton of β-CD) confirmed the aromatic moiety penetration of glipizide into the β-CD cavity.

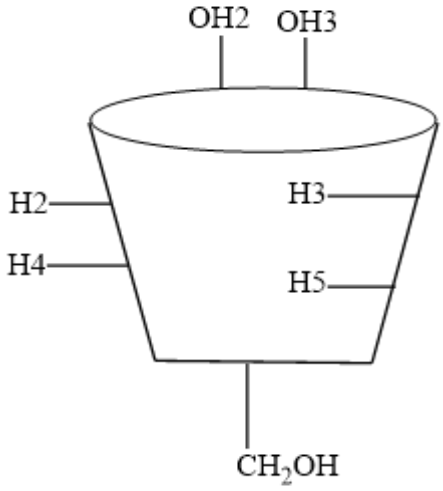


Figure 4. β-CD with proton numbering

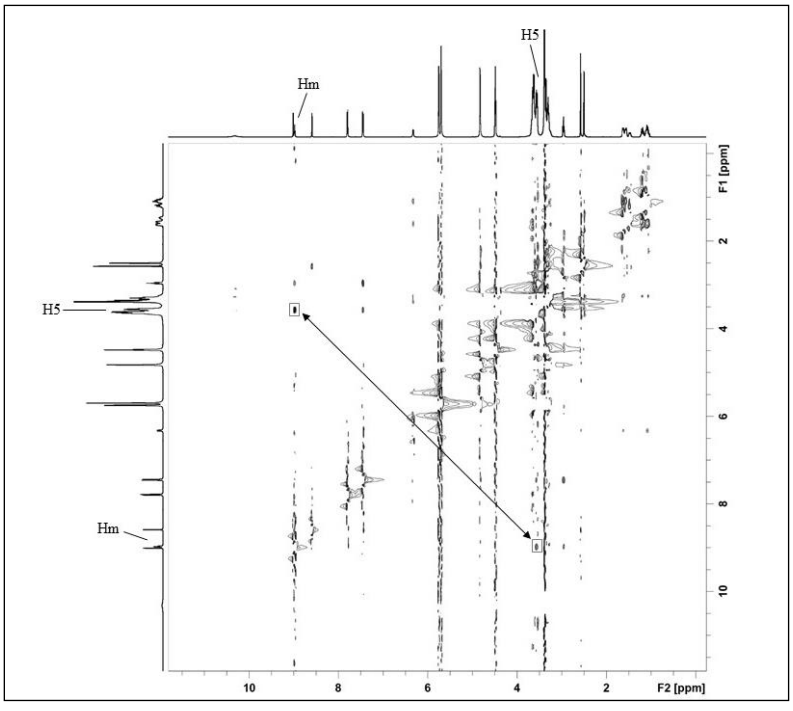


Figure 5. 2D NOESY spectra of complex β-CD/glipizide

UV-Vis

The stoichiometric ratios and formation constants describing the extent of formation of the complexes were obtained by measuring the changes in UV-Vis absorbance of the substrates, in the presence of increasing concentrations of β-CD. Figure 6 showed the absorbance increased by increasing the β-CD concentrations at pH 4 and pH 9. The absorption spectra of β-CD, glipizide, and β-CD/glipizide complexes are shown in Figure 7. The results indicated that β-CD/Glipizide had λ_{max} in the range of 250 nm – 300 nm. The absorbance of β-CD/glipizide complex underwent the hyperchromic effect, which increased the value of absorbance. The effect observed was due to π-π^* transition of dipole-dipole moments of aromatic ring. The formation constant, K values are shown in Table 4. The formation constant was carried out at two different pH values to find out whether the strength of binding between glipizide and β-CD was affected in acidic or basic condition. However, it was found that the binding strength was not affected in both acidic and basic conditions. The double reciprocal plot shown in Figure 8 clearly indicated that the stoichiometry ratio for the inclusion formation between glipizide and β-CD was 1:1.

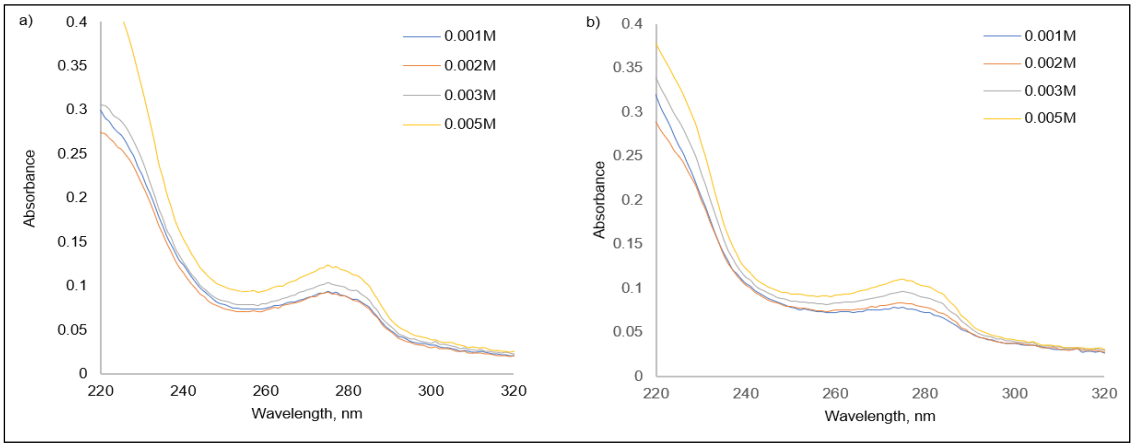


Figure 6. Absorption spectra of glipizide in the presence of increasing concentration of a) β-CD (0.001-0.005M) pH 4 and b) β-CD (0.001-0.005M) pH 9

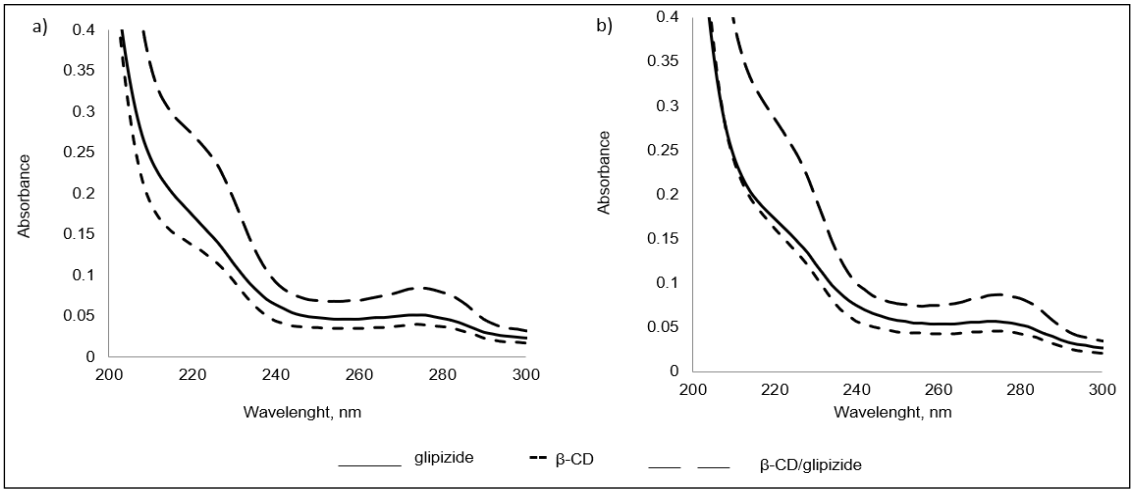


Figure 7. Absorption spectra of β-CD, Glipizide and β-CD/Glipizide at a) pH 4 and b) pH 9

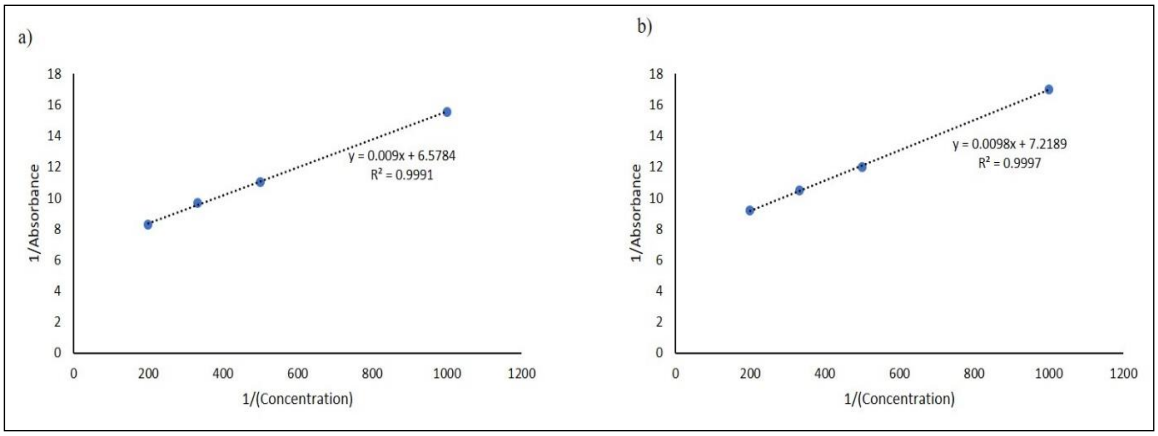


Figure 8. The double reciprocal plot of $\frac{1}{A}$ against $\frac{1}{[\beta-CD]}$ in a) pH 4 and b) pH 9

Table 4. Formation constant (K) values for β-CD/glipizide at differents pH

pH	Formation Constant, K
4	730.93
9	743.47

Conclusion

The inclusion complex between β-CD and glipizide was prepared using the kneading method and the determinations of formation constant were studied at pH 4 and 9. The results obtained from FT-IR and TGA proved that β-CD formed the inclusion complex with glipizide. From ^{1}H NMR determination, a large shift was observed at H5 proton of β-CD, proving the partial penetration of glipizide into the cavity of β-CD. This was strengthened by the cross-peak proton of aromatic glipizide with inner protons of β-CD from the NOESY experiment. β-CD/glipizide complex performed 1:1 host-guest interaction at pH 4 and 9 with apparent formation constants of 730.93 and 743.47, respectively, calculated from the Hildebrand-Benesi equation. This integrated experimental method revealed the molecular inclusion mechanism of β-CD with glipizide that would benefit the future formulation development of the drug carrier system.

Acknowledgement

Authors would like to seize this opportunity to express their gratitude to the Universiti Sains Malaysia for the Short-Term Grant (304/PKimia/6315106) and Ministry of Education for FRGS Grant (203.PKIMIA.6711641).

References

1. Bender, M. L. and Komiyama, M. (2012). Cyclodextrin chemistry. Springer Berlin Heidelberg, New York: pp. 2 – 3.
2. Abarca, R. L., Rodriguez, F. J., Guarda, A., Galotto, M. J. and Bruna, J. E. (2016). Characterization of beta-cyclodextrin inclusion complexes containing an essential oil component. *Food Chemistry*, 196: 968 – 975.
3. Zhu, X., Sun, J. and Wu, J. (2007). Study on the inclusion interactions of β-cyclodextrin and its derivative with dyes by spectrofluorimetry and its analytical application. *Talanta*, 72(1): 237 − 242.
4. de Paula, E., Cereda, C., Tofoli, G. R., Franz-Montan, M., Fraceto, L. F. and de Araújo, D. R. (2010). Drug delivery systems for local anesthetics. *Recent Patents on Drug Delivery & Formulation*, 4(1): 23 − 34.
5. Loftsson, T. and Duchene, D. (2007). Cyclodextrins and their pharmaceutical applications. *International Journal of Pharmaceutics*, 329(1-2): 1 − 11.

6. Machelart, A., Salzano, G., Li, X., Demars, A., Debrie, A. S., Menendez-Miranda, M., and Belhaouane, I. (2019). Intrinsic antibacterial activity of nanoparticles made of β-cyclodextrins potentiates their effect as drug nanocarriers against tuberculosis. *ACS Nano*, 13(4): 3992 − 4007.
7. Rasheed, A. (2008). Cyclodextrins as drug carrier molecule: A review. *Scientia Pharmaceutica*, 76(4): 567 − 598.
8. Crini, G., Fourmentin, S., Fenyvesi, E., Torri, G., Fourmentin, M. and Morin-Crini, N. (2018). Cyclodextrin fundamentals, reactivity and analysis. Springer Cham, Besancon: pp. 1 – 55.
9. Stella, V. J. and He, Q. (2008). Cyclodextrins. *Toxicologic Pathology*, 36(1): 30 − 42.
10. Bui, T. T., Ngo, D. Q., Tran, V. L., Nguyen, T. N. and Do, T. T. (2019). Acute and subacute toxic study on mice of glipizide synthesized in Vietnam. *Vietnam Journal of Science and Technology*, 57(1): 15 − 21.
11. Tan, B., Yang, A., Yuan, W., Li, Y., Jiang, L., Jiang, J., and Qiu, F. (2017). Simultaneous determination of glipizide and its four hydroxylated metabolites in human urine using LC–MS/MS and its application in urinary phenotype study. *Journal of Pharmaceutical and Biomedical Analysis*, 139: 179 − 186.
12. Nie, S., Zhang, S., Pan, W. and Liu, Y. (2011). In vitro and in vivo studies on the complexes of glipizide with water-soluble β-cyclodextrin–epichlorohydrin polymers. *Drug Development and Industrial Pharmacy*, 37(5): 606 − 612.
13. Huang, T., Zhao, Q., Su, Y. and Ouyang, D. (2018). Investigation of molecular aggregation mechanism of glipizide/cyclodextrin complexation by combined experimental and molecular modeling approaches. *Asian Journal of Pharmaceutical Sciences* (Article in Press).
14. Gan, Y., Pan, W., Wei, M. and Zhang, R. (2002). Cyclodextrin Complex Osmotic Tablet for Glipizide Delivery. *Drug Development and Industrial Pharmacy*, 28 (8): 1015 − 1021.
15. Chadha, R., Arora, P., Saini, A. and Jain, D. (2010). Inclusion parameters of pioglitazone hydrochloride and glipizide with β-cyclodextrin and its methyl derivative: Calorimetric and spectroscopic studies. *International Journal of Biological and Chemical Sciences*, 4(2): 258 − 273.
16. Ammar, H. O., Salama, H. A., Ghorab, M., El-Nahhas, S. A. and Elmotasem, H. (2006). A transdermal delivery system for glipizide. *Current Drug Delivery*, 33(3): 333 − 341.
17. Huang, H., Wu, Z., Qi, X., Zhang, H., Chen, Q., Xing, J., and Rui, Y. (2013). Compression-coated tablets of glipizide using hydroxypropylcellulose for zero-order release: in vitro and in vivo evaluation. *International Journal of Pharmaceutics*, 446(1-2): 211 − 218.
18. Gidwani, B. and Vyas, A. (2014). Synthesis, characterization and application of epichlorohydrin-β-cyclodextrin polymer. *Colloids and Surfaces B: Biointerfaces*, 114: 130 – 137.
19. Rahim, N. Y., Tay, K. S. and Mohamad, S. (2016). β-cyclodextrin functionalized ionic liquid as chiral stationary phase of high performance liquid chromatography for enantioseparation of β-blockers. *Journal of Inclusion Phenomena and Macrocyclic Chemistry*, 85(3-4): 303 − 315.
20. Rahim, N. Y., Tay, K. S. and Mohamad, S. (2016). Chromatographic and spectroscopic studies on β-cyclodextrin functionalized ionic liquid as chiral stationary phase: enantioseparation of favonoids. *Chromatographia*, 79(21-22): 1445 − 1455.
21. Li, N., Liu, J., Zhao, X., Gao, Y. A., Zheng, L., Zhang, J. and Yu, L. (2007). Complex formation of ionic liquid surfactant and β-cyclodextrin. *Colloids and Surfaces A: Physicochemical and Engineering Aspects*, 292(2-3): 196 − 201.
22. Li, W., Lu, B., Sheng, A., Yang, F. and Wang, Z. (2010). Spectroscopic and theoretical study on inclusion complexation of beta-cyclodextrin with permethrin. *Journal of Molecular Structure*, 981(1-3): 194 – 203.
23. Li, J., Ni, X., Zhou, Z. and Leong, K. W. (2003). Preparation and characterization of polypseudorotaxanes based on block-selected inclusion complexation between poly (propylene oxide)-poly (ethylene oxide)-poly (propylene oxide) triblock copolymers and α-cyclodextrin. *Journal of the American Chemical Society*, 125(7), 1788 − 1795.
24. Rusa, C. C., Luca, C. and Tonelli, A. E. (2001). Polymer-cyclodextrin inclusion compounds: Toward new aspects of their inclusion mechanism. *Macromolecules*, 34(5): 1318 − 1322.
25. Rahim, N. Y., Tay, K. S. and Mohamad, S. (2018). Chromatographic and spectroscopic studies on β-cyclodextrin functionalized ionic liquid as chiral stationary phase: enantioseparation of NSAIDs. *Adsorption Science & Technology*, 36(1-2): 130 − 148.

Malaysian Journal of Analytical Sciences, Vol 23 No 5 (2019): 799 - 811
DOI: https://doi.org/10.17576/mjas-2019-2305-05

MALAYSIAN JOURNAL OF ANALYTICAL SCIENCES
Published by The Malaysian Analytical Sciences Society
ISSN 1394 - 2506

FILEM POLIMER SEBAGAI MATRIKS PEMEGUNAN PEWARNA CAMPURAN SEMULA JADI UNTUK SENSOR pH

(Polymeric Films as Matrixes for the Immobilization of Mixed Natural Dyes for Optical pH Sensor)

Noor Azizah Ahmad[1,2], Lee Yook Heng[1]*, Sharina Abu Hanifah[1], Faridah Salam[2]

[1]*Fakulti Sains dan Teknologi,*
Universiti Kebangsaan Malaysia, 43600 Bangi, Selangor, Malaysia
[2]*Institut Penyelidikan dan Kemajuan Pertanian Malaysia,*
43400 Serdang, Selangor, Malaysia

**Corresponding author: yhl1000@ukm.edu.my*

Received: 7 July 2019; Accepted: 25 August 2019

Abstrak

Pencirian sensor pH yang berasaskan pemegunan pewarna campuran semula jadi daripada ekstrak tumbuhan *Clitoria* sp dan *Brassica* sp pada filem beberapa jenis polimer telah dilakukan. Matriks polimer yang telah dikaji ialah karagenan (ι- dan κ-), kanji jagung dan karboksil metil selulosa. Kesesuaian filem polimer dinilai dari segi keterlarutan polimer dalam air, serapan air oleh filem dan juga larut-resap bahan sensor terpegun daripada filem. Hasil kajian kesesuaian menunjukkan bahawa filem ι-karagenan adalah memenuhi ciri yang diperlukan sebagai filem sensor. Sensor pH yang dibina dengan filem ι-karagenan menunjukkan nilai sisihan piawai relatif (RSD) untuk ciri kebolehulangan dan kebolehasilan berada di bawah paras 5% pada nilai pH 4, 7 dan 12 yang diukur. Masa rangsangan yang diperlukan oleh filem sensor pH ini untuk bertindak balas dengan lengkap adalah 2 minit dalam tempoh perendaman. Filem sensor pH berasaskan ι-karagenan boleh disimpan pada suhu bilik selama 7 hari tanpa perubahan rangsangan (RSD 1.85%). Kestabilan foto bagi filem sensor pH selepas 12 minggu disimpan dalam suhu 4°C masih menunjukkan rangsangan yang stabil (RSD 1.63%). Kesan histerisis pada sensor pH juga didapati minimum dengan menggunakan filem ι-karagenan ini. Oleh yang demikian, kriteria yang terdapat pada filem ι-karagenan terpegun dengan pewarna campuran semula jadi menunjukkan ia berpotensi untuk digunakan sebagai sensor pH, khasnya dalam pemantauan kesegaran makanan semasa penyimpanan.

Kata kunci: sensor pH, antosianin, pewarna campuran semula jadi, ι-karagenan

Abstract

The characterization of pH sensors based on mixed natural dye from Clitoria sp and *Brassica* sp plant extracts on several types of polymers film have been performed. The polymer matrixes that have been studied were carrageenan (ι- and κ-), corn's starch and carboxyl methyl cellulose. The suitability of the polymer film is assessed in terms of water solubility, water absorption and leaching properties of the immobilized sensor material from the film. The study showed that ι-carrageenan film meets the required criteria as a sensor film. The pH sensor developed with the ι-carrageenan film shows the relative standard deviation (RSD) values are below 5% level of pH 4, 7 and 12 for repeatability and reproducibility properties. The response time of the pH sensor film for fully respond is 2 minutes during immersion period. The ι-carrageenan-based pH sensor film can be kept at room temperature for 7 days without response changes (RSD 1.85%). Photo stabilization of pH sensor film after 12 weeks stored at 4°C still shows stable response (RSD 1.63%). The hysteresis effect on the pH sensor was also found to be minimum by using this ι-carrageenan film. Therefore, the criterion found in the ι-carrageenan film immobilized with mixed natural dye indicates to be used as a potential pH sensor, especially in the monitoring of food freshness during storage.

Keywords: pH sensor, anthocyanin, mixed natural dye, ι-carrageenan

Pengenalan

Kajian tentang sensor pH telah mendapat perhatian ramai di kalangan penyelidik kerana kosnya yang rendah, bebas dari arus elektrik, selamat dan mungkin boleh digunakan sebagai pengesanan jarak jauh. Hisamato et al. [1] melaporkan bahawa sensor pH berpotensi untuk digunakan secara praktikal dalam analisis klinikal dan alam sekitar serta kawalan proses. Perubahan warna pada sensor pH bergantung kepada aktiviti ion hidronium (H_3O^+) dan ion hidrogen (H^+). Lazimnya sensor pH berasaskan penunjuk asid-bes dibangunkan melalui kaedah penjerapan pada permukaan bahan sokongan yang sesuai secara kimia [2] atau fizikal menerusi pemerangkapan pewarna dalam matrik polimer [3].

Kebanyakan sensor pH yang dibangunkan adalah berasaskan pewarna sintetik sensitif pH sama ada sebagai pewarna tunggal atau pewarna campuran. Antara perwarna sintetik tersebut termasuklah bromokresol hijau [4], bromotimol biru [5], metil merah [6], bromofenol biru [7] dan fenol merah [8]. Namun, dalam aplikasi makanan, penggunaan bahan kimia sintetik agak sukar untuk digunakan kerana berkemungkinan toksik dan boleh mendatangkan bahaya kepada kesihatan manusia. Secara umumnya penggunaan pewarna semula jadi mempunyai kelebihan yang jelas dari aspek kesan ketoksikan yang rendah, penyediaan yang mudah, boleh diperbaharui dan bebas daripada pencemaran. Pewarna semula jadi yang mengandungi antosianin berpotensi sebagai penunjuk pH kerana warnanya berubah dengan ketara pada nilai pH yang berbeza [9].

Penggunaan pewarna semula jadi yang mengandungi antosianin sebagai penunjuk sensitif pH telah dilaporkan dalam beberapa kajian sebelum ini. Kebanyakan sumber sebatian antosianin yang digunakan adalah daripada ekstrak kobis merah [10,11,12] dan ekstrak anggur [13,14], malahan ada juga penyelidik yang menggunakan sebatian antosianin komersil [15] dalam kajian mereka. Manakala Zhang et al. [9] telah menggunakan sebatian antosianin daripada ekstrak bunga *Bauhinia blakeana Dunn*. sebagai pewarna semula jadi. Walau bagaimanapun penggunaan ekstrak campuran tumbuhan daripada famili Leguminosae (*Clitoria* sp) dan Brassicaceae (*Brassica* sp) sebagai sumber antosianin belum pernah dilaporkan untuk digunakan sebagai pewarna bagi pembangunan sensor pH.

Sokongan pepejal atau matrik pemegun berperanan penting dalam menentukan kepekaan sesuatu sensor pH yang dibangunkan. Pelbagai bahan berasaskan biopolimer telah dilaporkan sebagai matrik pemegun sensor pH. Penggunaan beberapa biopolimer untuk pemegunan sebatian antosianin sebagai pewarna semula jadi sensitif pH juga telah dilaporkan seperti kanji jagung [16], selulosa nanofiber daripada bakteria [17], selulosa nanofiber daripada fabrik [10] dan kanji ubi kayu [13]. Bahan biopolimer seperti kitosan juga sering digunakan sebagai bahan pemegun sebatian antosianin di kalangan saintis [9,11,12,14,15]. Kajian ini adalah untuk mengenal pasti matrik polimer yang sesuai sebagai bahan pemegun yang terdiri daripada κ-karrageenan, ι-karrageenan, karboksil metil selulosa dan kanji jagung dalam menentukan keserasian ke atas ekstrak pewarna campuran semula jadi yang sensitif pH. Bahan polimer yang terpilih dicirikan bagi menentu kesesuaiannya sebagai satu bahan untuk sensor pH yang berfungsi.

Bahan dan Kaedah

Bahan kimia

Bahan kimia yang digunakan dalam kajian ini ialah asid hidroklorik (SYSTERM), asid sitrik, kalsium klorida (BDH CHEMICAL), natrium hidrogen fosfat, etanol dan natrium hidroksida (MERCK), ι-karagenan (SIGMA) serta ekstrak campuran daripada tumbuhan *Clitoria* sp dan *Brassica* sp. Bahan-bahan kimia ini digunakan terus tanpa penulenan lanjut.

Peralatan dan instrumentasi

Spektrofotometer Ultra Lembayung-Nampak, model Cary 100 Cons (Varian); pengisar pengadun, model MX-AC400 (Panasonic), penggoncang, model ZHWY-304 (Labwit), pengempar, model #7590 (Heraeus), vakum penyejat berputar, model Rotavapor R-3 (Buchi), vorteks (Velp) dan meter pH (Mettler Toledo).

Pengekstrakan pewarna semula jadi

Bunga *Clitoria* sp telah dipetik dari kawasan penanaman MARDI, Serdang. Kaedah pengekstrakan akueus telah dilakukan dengan menggunakan 40 g kelopak bunga di dalam 100 mL isipadu air suling. Kaedah pengekstrakan ini adalah merujuk kepada Kungsuwan et al. [18] dengan beberapa pengubahsuaian. Permulaan proses adalah dengan merendamkan kelopak bunga di dalam air suling selama 30 minit. Kemudian, rendaman ini (air bersama kelopak bunga) dimasukkan ke dalam pengisar pengadun dan dikisar selama 30 saat. Sementara itu, *Brassica* sp dibeli dari pasar tempatan di Kajang, Malaysia. Kaedah pengekstrakan yang digunakan merujuk kepada Devarayan dan Kim [10, 19] dengan beberapa pengubahsuaian. Daun sampel dipotong menjadi kepingan kecil dan dihancurkan menggunakan pengisar. Pengekstrakan dilakukan dengan merendamkan 50 g kobis merah yang telah hancur di dalam 100 mL pelarut etanol berkepekatan 80%. Setelah itu, digoncang secara berterusan selama 12 jam dengan kelajuan 150 rpm pada suhu bilik dalam keadaan gelap. Kemudian, kedua-dua sampel dituras secara berasingan dengan kain kasa (berukuran 30 × 22 cm^2) untuk mengeluarkan partikel bersaiz besar bagi menghasilkan ekstrak mentah *Clitoria* sp dan *Brassica* sp. Hasil turasan ini diempar pada kelajuan 8000 rpm selama 10 minit untuk memisahkan partikel halus yang terampai. Seterusnya, proses pemekatan dilakukan ke atas ekstrak mentah sebanyak 5 kali dengan menggunakan alat vakum penyejat berputar pada suhu 50°C. Ekstrak pekat ini disimpan pada suhu -19°C sehingga digunakan. Pewarna campuran disediakan dengan mencampurkan kedua-dua ekstrak pekat ini pada nisbah 1:1 (isipadu/isipadu) dan dihomogenkan selama 3 minit.

Penyediaan larutan penimbal

Larutan penimbal pH 4, 7 dan pH 12 disediakan mengikut kaedah Devarayan dan Kim [10] pada suhu bilik. Percampuran bahan kimia antara asid sitrik dan natrium hidrogen fosfat untuk pH 4 dan pH 7. Manakala garam natrium hidroksida dan asid hidroklorik digunakan untuk penyediaan larutan penimbal pH 12.

Penyediaan filem untuk pemegunan pewarna campuran semula jadi

Setiap filem disediakan dengan melarutkan perlahan-lahan 2 g serbuk polimer (karboksil metil selulosa, κ-karagenan, ι-karagenan dan kanji jagung) di dalam 100 mL air suling dan dikacau hingga homogen di atas plat pemanas. Kemudian suhu larutan dinaikkan sehingga 80-90°C dan dibiarkan selama 10 minit bagi memastikan proses pengelatinan berlaku dengan lengkap. Setelah itu, sebanyak 0.73 mg/L jumlah kandungan antosianin dimasukkan ke dalam larutan dan diaduk sehingga sekata. Seterusnya larutan tersebut dituangkan ke dalam piring petri (25 g) dan dikeringkan di dalam ketuhar pada suhu 37±1°C selama 18-24 jam. Filem yang telah kering disimpan dalam desikator untuk dianalisa.

Penyediaan filem sensor pH

Filem untuk sensor pH disediakan dengan melarutkan 2 g serbuk ι-karagenan secara perlahan-lahan ke dalam air suling di bawah pengadukan berterusan sehingga larut sepenuhnya. Setelah itu, 1 mL larutan kalsium klorida berkepekatan 1.0 M (kepekatan telah dioptimumkan) dimasukkan dan dikacau selama 10 minit. Suhu larutan dinaikkan sehingga 80°C dan dibiarkan selama 10 minit untuk penyeragaman percampuran berlaku. Kemudian, ekstrak pewarna pekat yang mengandungi antosianin daripada campuran tumbuhan *Clitoria* sp dan *Brassica* sp dimasukkan ke dalam larutan dan pengadukkan dilakukan sehingga sekata. Seterusnya larutan tersebut dituangkan sebanyak 25 g secara tepat ke dalam setiap piring petri untuk menghasilkan ketebalan filem yang seragam. Pengeringan dilakukan dengan menggunakan ketuhar pada suhu 37±1°C selama 18-24 jam. Filem yang telah kering disimpan dalam desikator sehingga dianalisa.

Analisis larut resap pewarna terpegun

Analisis larut resap dilakukan dengan merendamkan filem polimer terpegun pewarna campuran semula jadi (berukuran 2 × 3 cm^2) ke dalam 80 mL air ternyahion mengikut kaedah yang digunakan oleh Yew dan Heng [20] dengan pengubahsuaian. Kemudian, larutan tersebut diambil setiap 10 minit untuk direkod bacaan serapan. Prosedur ini dilakukan untuk tempoh 60 minit masa rendaman. Bacaan serapan larutan diambil pada panjang gelombang 625 nm dengan menggunakan Spektrofotometer Ultra Lembayung-Nampak. Analisis diulangi sebanyak 3 kali.

Analisis keterlarutan air

Peratus keterlarutan air bagi filem yang terpegun pewarna campuran semula jadi dan $CaCl_2$ pada kepekatan 0-1.4 M ditentukan mengikut kaedah yang diterangkan oleh Romero-Bastida et al. [21]. Kepingan filem berukuran 2 × 3 cm^2

disimpan dalam desikator (0% RH) selama 7 hari. Setiap filem ditimbang sehingga 4 titik perpuluhan (0.0001 g) yang terdekat dan dimasukkan ke dalam 80 mL air ternyahion. Kemudian digoncang secara berterusan selama 1 jam pada suhu bilik (25°C). Seterusnya, kepingan baki filem ditapis melalui kertas turas (Whatman No. 1), diikuti dengan pengeringan dalam ketuhar pada suhu 60°C sehingga mendapat bacaan berat tetap. Analisis diulangi sebanyak 3 kali dan peratusan jumlah bahan larut (% keterlarutan) telah dikira mengikut persamaan di bawah:

$$\% \text{ Ketelarutan filem} = \frac{(\text{berat kering awal} - \text{berat kering akhir})}{\text{berat kering awal}} \times 100 \quad (1)$$

Analisis serapan air

Analisis serapan air dijalankan secara merendam kepingan filem sensor pH di dalam 30 mL air ternyahion. Selepas 5 minit perendaman, filem tersebut dikeluarkan dan titisan air pada permukaannya dikeringkan dengan kertas turas. Seterusnya berat filem ditimbang dengan menggunakan penimbang elektronik. Langkah ini diulangi untuk tempoh selama 60 minit. Peratus berat air yang terserap di dalam filem ditentukan mengikut pengiraan oleh Hadi dan Idayu [22] seperti berikut:

$$\text{Peratusan penyerapan air (\%)} = [\{W_t - W_0\} / W_0] \times 100 \quad (2)$$

di mana W_t adalah berat filem pada masa t dan W_0 adalah berat awal filem. Analisis ini dijalankan sebanyak 3 kali untuk mengurangkan kesilapan dan dilaporkan sebagai nilai purata.

Kebolehulangan

Analisis kebolehulangan dilakukan dengan merujuk kaedah yang digunakan oleh Zhang et al. [9]. Sensor pH dicelup ke dalam larutan penimbal pH 4 selama lebih kurang 0.5 minit dan kemudian spektrum serapan diambil pada julat panjang gelombang 380-800 nm. Langkah yang sama diulangi menggunakan larutan penimbal pH dan filem yang baru bagi setiap kali pengukuran dilakukan sehingga mendapat bacaan dari 5 filem yang berbeza. Keseluruhan tatacara ini diulangi semula untuk larutan penimbal pH 7 dan pH 12. Peratus RSD dikira berdasarkan formula persamaan 3 berikut:

$$\text{RSD (\%)} = (\text{Sisihan piawai} / \text{nilai purata}) \times 100 \quad (3)$$

Kebolehasilan

Analisis kebolehasilan sensor pH dilakukan dengan merujuk kepada kaedah yang ditunjukkan oleh Zhang et al. [9] di mana filem sensor dicelupkan ke dalam larutan penimbal pH 4 selama lebih kurang 0.5 minit dan kemudian spektrum serapan diambil pada julat panjang gelombang 380 - 800 nm. Selepas pengukuran serapan dalam larutan penimbal pH selesai dilakukan, filem tersebut dicelup ke dalam air ternyahion bagi memastikan ianya bersih daripada larutan penimbal yang terdahulu sebelum pengukuran serapan dilakukan dalam pH larutan penimbal berikutnya. Langkah-langkah ini diulangi sehingga mendapat bacaan untuk 5 pengukuran menggunakan filem sensor yang sama. Seterusnya, keseluruhan tatacara ini diulangi semula untuk larutan penimbal pH 7 dan pH 12. Peratus RSD dikira berdasarkan formula persamaan 3.

Masa rangsangan

Analisis masa rangsangan dijalankan untuk menentukan masa yang diperlukan bagi larutan penimbal pH (4, 7 dan 12) bertindak balas lengkap dengan sensor pH, mengikut kaedah yang ditunjukkan oleh Zhang et al. [9] dengan pengubahsuaian dilakukan ke atas sela masa. Bacaan serapan direkodkan pada sela masa 0, 0.5, 1.0, 1.5, 2.0, 5, 10, 15, 20 dan 25 minit. Serapan diambil pada panjang gelombang 530 nm. Kaedah yang sama digunakan untuk larutan penimbal pH 7 dan pH 12. Analisis ini diulangi sebanyak 3 kali bagi mendapatkan nilai yang lebih tepat.

Kestabilan foto

Kajian kestabilanfoto dijalankan mengikut kaedah yang digunakan oleh Rosmawani et al. [23] dengan pengubahsuaian dilakukan ke atas keadaan penyimpanan. Kajian ini melibatkan penyimpanan sensor pH pada tiga keadaan berbeza iaitu dalam persekitaran suhu bilik, persekitaran suhu bilik yang gelap (dibalut) dan pada suhu

dingin yang persekitaran gelap (dibalut) untuk satu tempoh tertentu. Seterusnya, data serapan diambil pada panjang gelombang maksimum 615 nm bagi mendapatkan nilai RSD. Peratus RSD dikira berdasarkan formula persamaan 3.

Kesan histerisis

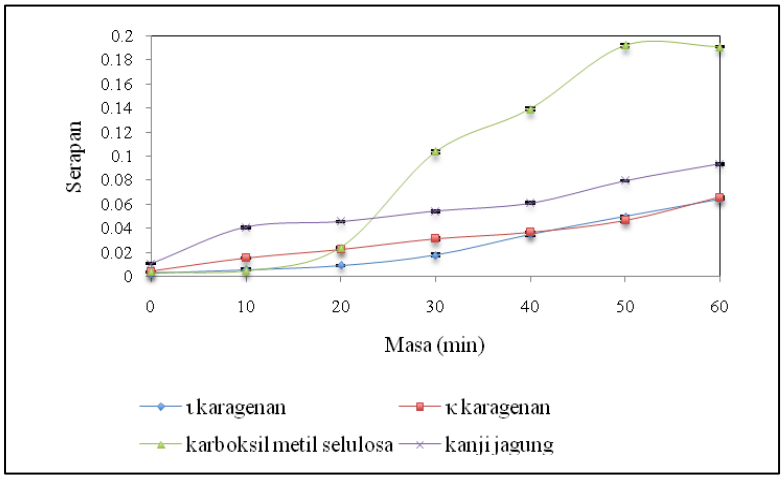
Kajian ini dilakukan untuk melihat kepekaan atau kecekapan filem sensor pH dalam menghasilkan isyarat rangsangan yang sama apabila dicelup ke dalam larutan penimbal pH 2-10 (asid kepada alkali) dan daripada pH 10-2 (alkali kepada asid). Kaedah kajian dijalankan seperti yang digunakan oleh Rosmawani et al. [23]. Kajian ini dilakukan sebanyak 3 kali dengan menggunakan 3 filem yang berbeza bagi mendapatkan nilai purata dan sisihan piawai.

Keputusan dan Perbincangan

Analisis larut resap bahan pemegun

Keputusan analisis larut resap untuk empat filem (κ-karagenan, ι-karagenan, karboksil metil selulosa dan kanji jagung) yang dicampurkan dengan pewarna campuran semula jadi ditunjukkan dalam Rajah 1. Hasil kajian menunjukkan larut resap berlaku ke atas semua filem yang dianalisa selama 60 minit dengan bacaan serapan maksimum pada panjang gelombang 625 nm. Walau bagaimanapun filem daripada polimer karagenan menampilkan kadar larut resap yang lebih rendah berbanding dengan filem daripada karboksil metil selulosa dan kanji jagung. Umumnya diketahui bahawa karagenan merupakan polimer anionik bercas negatif melalui kehadiran kumpulan sulfat pada struktur molekul yang wujud secara berulangan. Manakala antosianin yang terkandung dalam pewarna semula jadi ini pula adalah wujud sebagai bentuk kationik dalam larutan berair (akueus). Oleh yang demikian, kadar perembesan warna yang perlahan untuk filem karagenan adalah dipercayai hasil daripada interaksi secara elektrostatik antara karagenan anionik dengan pewarna semula jadi yang bersifat kationik. Hasil penemuan ini disetujui dengan laporan oleh Soedlak [24] terhadap penggunaan pewarna metilena biru yang bersifat kationik ke atas hidrokoloid karagenan.

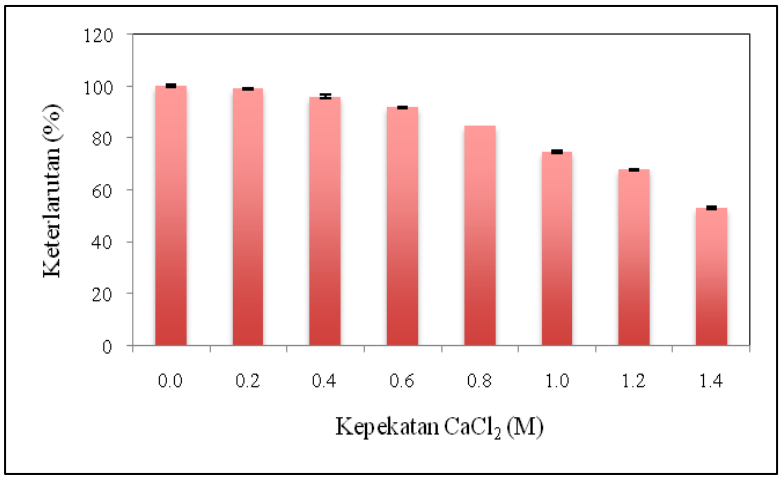
Keputusan kajian juga menunjukkan bahawa kadar larut resap untuk filem ι-karagenan lebih perlahan berbanding dengan κ-karagenan (Rajah 1). Ini dijelaskan dengan perbezaan bilangan kandungan kumpulan sulfat yang terdapat pada struktur polimer karagenan. Lazimnya κ-karagenan dan ι-karagenan yang diperoleh secara komersil mengandungi 22 dan 32% (berat/berat) kumpulan sulfat setiapnya walaupun berbeza-beza mengikut spesies dan kelompok rumpai laut [25]. Menurut Soedlak [24], jumlah bilangan kumpulan sulfat (anion) yang terdapat pada karbohidrat adalah penting dalam interaksi dengan pewarna kationik di mana aktiviti pengikatan berkadar terus dengan nilai peratusan kehadiran kumpulan sulfat. Berdasarkan keputusan analisis larut resap ini, polimer ι-karagenan dipilih sebagai bahan pemegun untuk pencirian selanjutnya.



Rajah 1. Kesan larut resap pewarna daripada matrik pemegun yang berbeza

Kesan kepekatan $CaCl_2$ terhadap keterlarutan air filem ι-karagenan

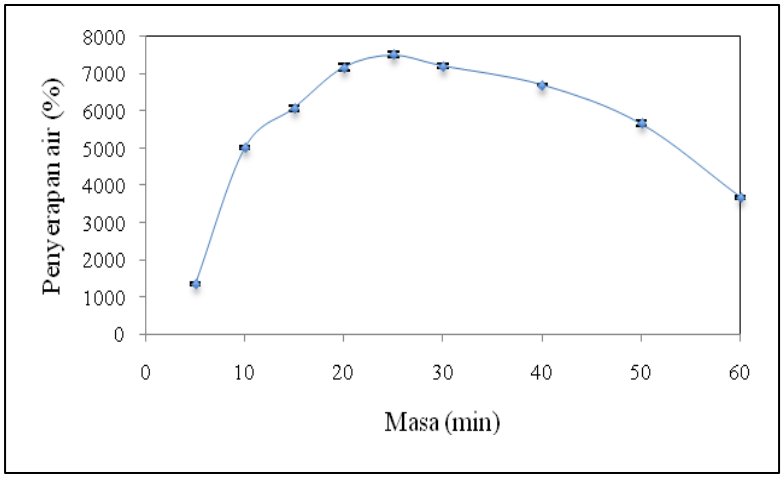
Oleh kerana polimer ι-karagenan merupakan polisakarida bersifat hidrofilik, maka ciri keterlarutannya perlu diatasi bagi memastikan filem ini berupaya berfungsi sebagai sensor pH yang baik apabila digunakan semasa aplikasi pada sampel sebenar. Tako et al. [26] melaporkan bahawa penambahan ion kalsium (Ca^{2+}) ke atas polimer ι-karagenan menyebabkan berlakunya pengegelan (*gelation*). Pengegelan ialah proses peningkatan kelikatan larutan yang terhasil disebabkan peranan kation yang meningkatkan pembentukan ikatan silang dalam jaringan karagenan [26]. Kesan kepekatan larutan $CaCl_2$ terhadap peratusan keterlarutan filem ι-karagenan digambarkan dalam Rajah 2. Keputusan kajian menunjukkan bahawa nilai peratusan keterlarutan menurun dengan pertambahan kepekatan larutan $CaCl_2$. Ini mencadangkan bahawa kehadiran Ca^{2+} dalam kuantiti yang banyak berupaya berinteraksi dengan semua kumpulan sulfat yang terdapat pada polimer ι-karagenan, membentuk jambatan yang memungkinkan molekul air sukar untuk menembusi matrik filem. Kalsium merupakan kation dwivalen yang mampu membentuk jambatan intra-molekul antara kumpulan sulfat dengan anhidro-D-galaktosa dan residu D-galaktosa pada ι-karagenan. Jambatan antara molekul yang terhasil dengan Ca^{2+} menyebabkan larutan karagenan membentuk struktur kuarterner pada suhu sejuk [27].



Rajah 2. Kesan kepekatan $CaCl_2$ terhadap peritus keterlarutan

Kajian serapan air filem sensor pH

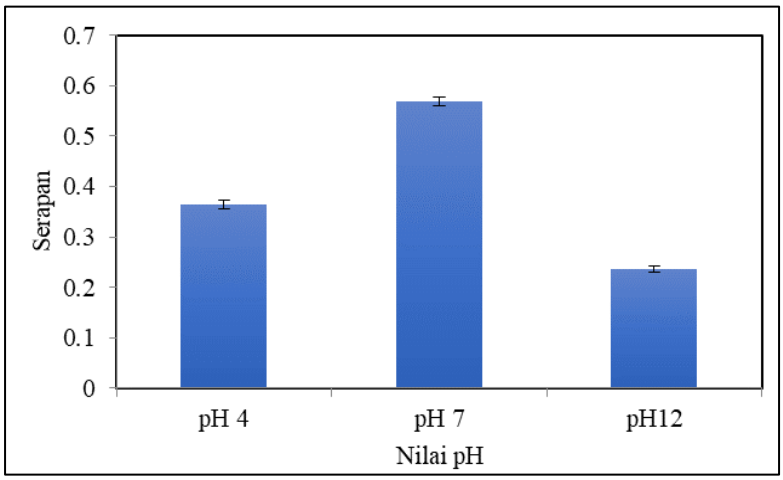
Rajah 3 menampilkan peratusan serapan air bagi filem sensor pH meningkat dengan masa rendaman pada suhu ambien. Nilai serapan air didapati maksima selepas 25 minit masa rendaman. Fenomena ini disebabkan bahan pemegun yang terdiri daripada polimer ι-karagenan adalah bersifat hidrofilik, menjadikan filem sensor pH berupaya memegang sejumlah besar air dalam strukturnya dengan kehadiran air yang banyak [28]. Walau bagaimanapun peratusan serapan air didapati mula berkurangan pada minit ke 30 dan terus berkurangan selepas 60 minit rendaman. Ini disebabkan struktur filem sensor pH didapati mula pecah dan seterusnya mengalami penyusutan berat. Menurut Carabeo [28], tahap serapan air adalah bergantung kepada muatan air yang boleh dipegang oleh polimer tersebut. Sementara penemuan oleh Subhas dan Pathik [29] pula mendapati bahawa secara semula jadinya polisakarida mempunyai sifat mekanikal yang lemah. Oleh itu perendaman filem sensor pH pada tempoh tertentu dalam kuantiti air yang banyak menyebabkan strukturnya pecah dan terurai.



Rajah 3. Kajian serapan air bagi filem sensor pH pada sela masa yang ditetapkan

Kebolehulangan sensor pH

Kebolehulangan sensor pH dikaji menggunakan larutan penimbal pH 4, pH 7 dan pH 12. Hasil kajian yang diperolehi ditunjukkan dalam Rajah 4 dengan pengukuran pada panjang gelombang 530 nm. Nilai RSD untuk kebolehulangan pada pH 4, pH 7 dan pH 12 adalah masing-masingnya 2.26%, 1.64% dan 2.85%. Kesemua nilai RSD yang diperolehi ini boleh dikatakan rendah dan diterima kerana berada di bawah paras 5%. Ini menunjukkan bahawa sensor pH yang dibangunkan ini mempunyai taburan pewarna campuran semula jadi dan ketebalan filem yang sekata memandangkan pengukuran dilakukan pada titik yang berlainan kerana menggunakan filem yang berbeza. Makote dan Collinson [30] memperoleh nilai RSD sebanyak 5% untuk analisis kebolehulangan dan kebolehasilan ke atas pewarna kresol merah dan bromokresol hijau yang terpegun di dalam filem dan mengklafikasikan sebagai baik.

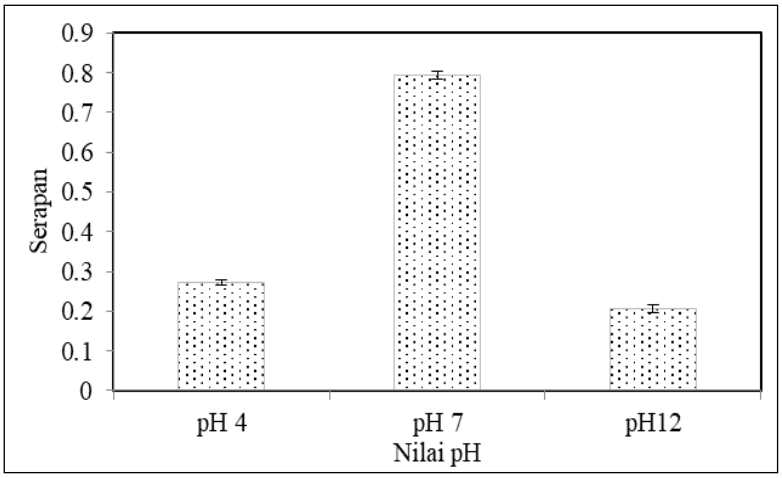


Rajah 4. Kajian kebolehulangan sensor pH berasaskan pewarna campuran semula jadi terpegun dalam filem ι-karagenan pada panjang gelombang 530 nm (n=5)

Kebolehasilan sensor pH

Analisis kebolehasilan bagi filem sensor pH merujuk kepada pengukuran yang dilakukan secara berterusan menggunakan filem yang sama dalam larutan penimbal pH 4, pH 7 dan pH 12. Nilai RSD bagi kebolehasilan untuk pH 4, pH 7 dan pH 12 adalah masing-masingnya 2.47%, 1.25% dan 3.28% (Rajah 5). Keputusan kajian mendapati

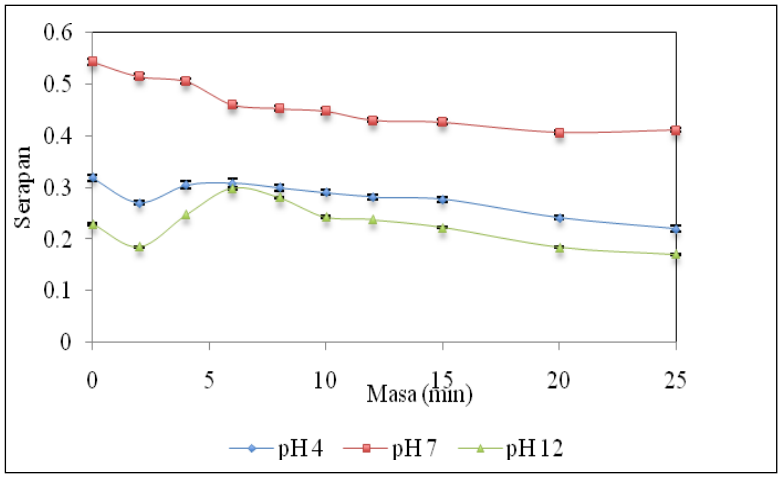
nilai RSD kebolehasilan adalah lebih tinggi daripada kebolehulangan dan secara tidak langsung menunjukkan bahawa sifat kebolehulangan sensor pH yang difabrikasi adalah lebih baik berbanding sifat kebolehasilan. Pemerhatian kajian juga mendapati sensor pH mengalami pengembangan atau pembengkakan apabila dicelup dalam larutan penimbal secara berulangan. Faktor ini diyakini menjadi penyebab utama kepada perbezaan rangsangan yang diperolehi semasa pengukuran serapan untuk kajian kebolehasilan kerana ketebalan sensor pH tidak sekata. Menurut Grant dan Glass [31], ketebalan filem serta saiz liang yang berlainan menyebabkan kesukaran untuk mendapatkan nilai RSD yang lebih kecil. Walau bagaimanapun semua nilai RSD untuk kebolehasilan yang dicatat adalah di bawah paras 5% dan masih diterima.



Rajah 5. Kajian kebolehasilan sensor pH berasaskan pewarna campuran semula jadi terpegun dalam filem ι-karagenan pada panjang gelombang 530 nm (n=5)

Masa rangsangan sensor pH

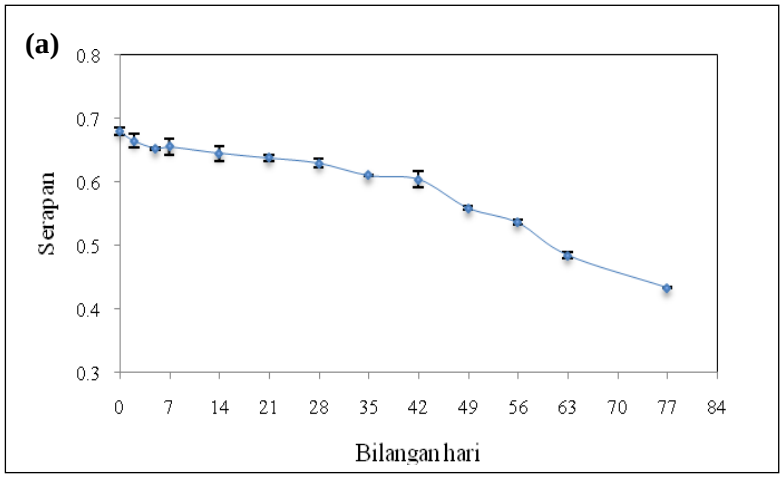
Kajian masa rangsangan dijalankan untuk menentukan masa yang diperlukan bagi filem sensor pH bertindak balas lengkap dengan larutan penimbal pH. Ujikaji dijalankan terhadap pH 4, pH 7 dan pH 12 yang mewakili keadaan asid, neutral dan bes. Rajah 6 memperlihatkan sensor pH yang direndam di dalam ketiga-tiga larutan penimbal pH mengalami perubahan warna selepas 2 minit tempoh rendaman. Nilai serapan sensor pH menjadi hampir malar selepas 6 minit perendaman dalam pH 4 dan pH 7, manakala terus menyusut untuk pH 12. Secara keseluruhannya, keamatan serapan menurun dengan tempoh perendaman, namun pH 7 menunjukkan nilai serapan lebih tinggi berbanding dengan pH 4 dan pH 12. Ini menunjukkan sensor pH yang dibangun lebih stabil pada keadaan neutral. Penemuan ini selaras dengan keputusan yang diperolehi Zhang et al. [9] ke atas filem kitosan yang digabungkan dengan pewarna semula jadi daripada ekstrak *Bauhinia blakeana Dunn*. Warna sensor pH adalah ungu gelap dalam larutan penimbal pH 4 dan bertukar kepada biru dalam pH 7, manakala dalam larutan penimbal pH 12 filem menjadi warna kehijauan.

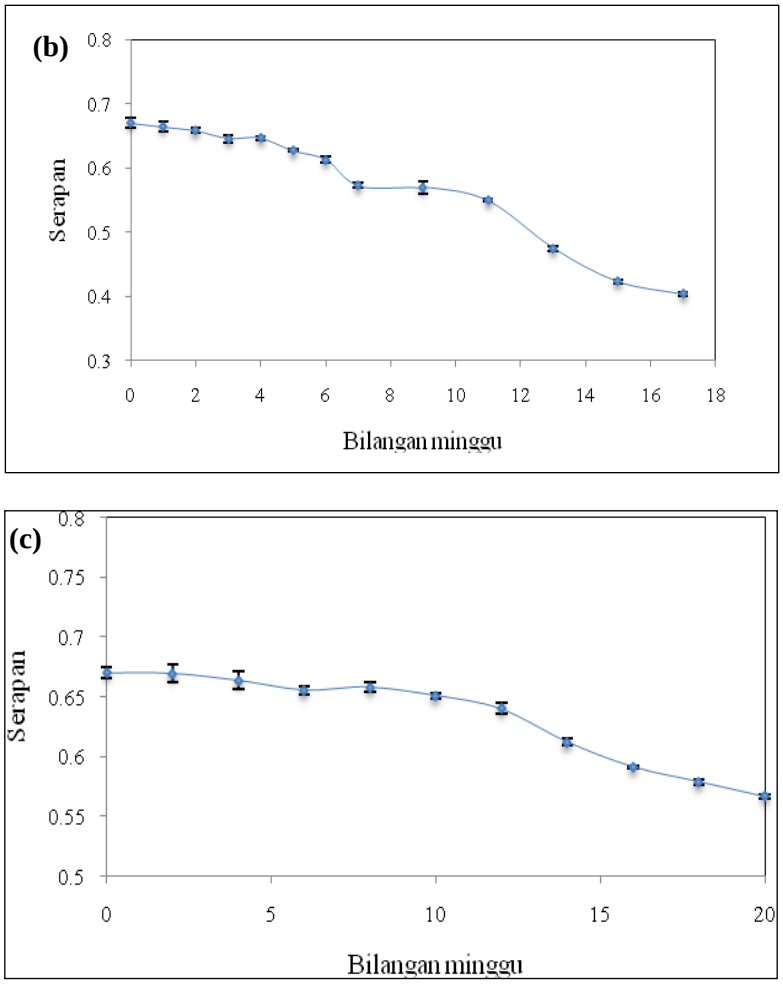


Rajah 6. Kesan masa rangsangan sensor pH berasaskan pewarna campuran semula jadi terpegun dalam filem ι-karagenan pada panjang gelombang 530 nm

Kestabilan foto sensor pH

Kajian kestabilan foto dilakukan pada tiga keadaan berbeza iaitu persekitaran suhu bilik, persekitaran suhu bilik dan gelap (dibalut) serta suhu 4°C dalam keadaan gelap (dibalut) untuk satu tempoh tertentu. Tiga keadaan ini dipilih untuk mengkaji kestabilan sensor pH terhadap pengaruh cahaya dan suhu. Keputusan menunjukkan nilai serapan menurun dengan ketara mengikut tempoh penyimpanan. Nilai RSD serapan berubah masing-masing sebanyak 12.55%, 7.01% dan 1.63% untuk penyimpanan pada tiga keadaan berbeza selama 77 hari (suhu bilik dan suhu bilik + gelap) dan 12 minggu (4°C + gelap) seperti yang ditunjukkan dalam Rajah 7 (a-c). Nilai RSD yang diperolehi untuk penyimpanan selama 17 minggu pada suhu bilik dan gelap adalah sebanyak 15.86% (Rajah 7b) manakala 6.04% untuk sensor pH yang disimpan selama 20 minggu pada suhu 4°C dan gelap (Rajah 7c). Namun begitu, penyimpanan pada suhu bilik dan gelap mencatatkan nilai RSD sebanyak 1.65% untuk tempoh 4 minggu pertama (Rajah 7b) dan masih stabil untuk kegunaan sebagai penunjuk kesegaran makanan berbungkus.





Rajah 7. Kestabilan foto bagi sensor pH (serapan pada panjang gelombang 615 nm) berasaskan pewarna campuran semula jadi terpegun dalam filem ι-karagenan pada (a) suhu bilik, (b) suhu bilik dan keadaan gelap dan (c) suhu 4°C dan keadaan gelap

Walau bagaimanapun, untuk tempoh yang terbaik dari segi penyimpanan, nilai RSD bagi sensor pH yang stabil (paling kecil) boleh diperoleh daripada tempoh penyimpanan pada suhu bilik adalah sekitar 1.85% yang disimpan selama 7 hari (Rajah 7a). Nilai RSD yang kecil juga diperoleh daripada penyimpanan pada suhu 4°C dan gelap selama 12 minggu pertama (Jadual 1). Oleh yang demikian, sensor pH ini masih boleh digunakan untuk memantau kesegaran makanan berbungkus pada suhu bilik untuk tempoh penyimpanan yang singkat.

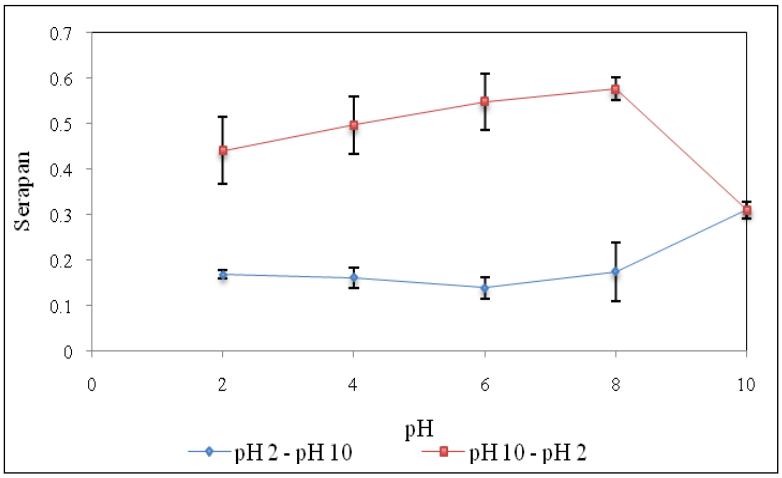
Jadual 1. Data kestabilan foto (serapan pada 615 nm) filem sensor pH disimpan pada suhu berbeza dan gelap (dibalut) dalam tempoh terpilih

Keadaan Kajian	**Tempoh Paling Stabil**	**Nilai Serapan Purata**	**Sisihan Piawai**	**% RSD**
Suhu bilik	0-7 hari	0.66	0.01	1.85
Suhu bilik dan gelap	0-4 minggu	0.58	0.01	1.65
Suhu 4°C dan gelap	0-12 minggu	0.66	0.01	1.63

Menurut Giusti dan Wrolstad [32], degradasi antosianin berlaku dengan kadar yang cepat pada suhu lebih tinggi disebabkan oleh hidrolisis pada struktur 3-glukosida, yang memberi kesan ke atas kestabilan sebatian antosianin. Selain dari itu, hidrolisis pada gelang pirilium akan menghasilkan struktur kimia antosianin berbentuk kalkon iaitu gelang ketiga pada struktur tunggal terbuka yang menyebabkan warna berubah. Sadilova et al. [33] menyatakan bahawa pada suhu rendah, degradasi berlaku lebih perlahan berbanding suhu tinggi, menunjukkan masa dan suhu mempunyai pengaruh yang kuat terhadap kestabilan antosianin. Penemuan yang sama dilaporkan oleh Liu et al. [34] ke atas kestabilan foto sensor pH berasaskan pemegunan fenol merah dalam membran poli- vinil alkohol yang mendapati nilai serapan menurun dengan ketara apabila dibandingkan antara 15 hari pertama dan hari yang ke-90 penyimpanan. Hasil penemuan yang dilaporkan oleh Rosmawani et al. [23] menunjukkan bahawa filem hibrid sol-gel/kitosan melamin yang terpegun dengan reagen kurkumin mempunyai nilai RSD sebanyak 3.69% untuk tempoh kajian kestabilan foto selama 3 minggu. Penurunan nilai serapan yang ketara pada filem yang disimpan pada persekitaran suhu bilik tanpa dibalut mungkin disebabkan degradasi berlaku ke atas sebatian antosianin. Menururt Jaakola [35], cahaya adalah penting untuk biosintesis antosianin, namun pada masa yang sama ia juga mempercepat kemerosotan atau degradasi pigmen. Antosianin yang terdedah kepada cahaya menyebabkan kandungannya lebih rendah dan kuantiti kehilangannya berkadar terus dengan masa pendedahan.

Kesan histerisis sensor pH

Rajah 8 merumuskan bahawa sensor pH ini menunjukkan kesan histerisis apabila dicelup ke dalam larutan penimbal pH 2 hingga pH 10 dan berbalik kepada pH 2. Nilai keamatan rangsangan yang dihasilkan tidak sama apabila melalui kitaran mengikut tertib pH 2-10-2. Ini bermaksud sensor pH yang dibina bersifat tidak berbalik dan tidak boleh digunakan semula pada ukuran pH mengikut urutan asid-alkali-asid. Sifat tidak berbalik ini penting untuk fabrikasi sensor pH di peringkat aplikasi dalam menentukan kesegaran produk makanan berbungkus. Ciri ini diperlukan kerana, sekiranya sensor pH telah menunjukkan rangsangan ke atas metabolit kerosakan makanan pada keadaan alkali atau asid, maka ianya tidak berpatah balik apabila berlaku gangguan kadar tindak balas.



Rajah 8. Kesan histerisis sensor pH berasaskan pewarna campuran semula jadi terpegun dalam filem ι-karagenan pada panjang gelombang 615 nm (n=3)

Kesimpulan

Polimer ι-karagenan dipilih sebagai bahan pemegun untuk pewarna campuran semula jadi peka pH berdasarkan kecenderungan minima yang ditunjukkan dalam analisis larut resap. Penambahan ion kalsium (Ca^{2+}) menyebabkan peratusan keterlarutan air bagi filem ι-karagenan menurun. Pencirian sensor pH melalui kajian kebolehulangan dan kebolehasilan mendapati nilai RSD yang dihasilkan berada di bawah paras 5%. Masa rangsangan yang diambil untuk menunjukkan perubahan warna adalah selepas 2 minit. Filem sensor pH menunjukkan ciri kestabilan foto yang baik untuk tempoh penyimpanan selama 12 minggu pada suhu 4°C dalam keadaan gelap. Namun begitu, filem

sensor yang disimpan pada suhu bilik sahaja masih didapati stabil sehingga 7 hari. Kesan histerisis diperhatikan apabila sensor pH digunakan untuk mengukur pH dalam kitaran asid-bes-asid. Berdasarkan pencapaian positif melalui kajian pencirian yang ditunjukkan oleh filem ι-karagenan terpegun dengan pewarna campuran semula jadi ini, maka penemuan ini berpotensi dikembangkan untuk pembangunan sensor pH optik. Sensor ini boleh diaplikasi dalam sistem pembungkusan pintar untuk mengesan metabolit kerosakan makanan berbungkus berasaskan perubahan pH.

Penghargaan

Penyelidik merakamkan ucapan terima kasih untuk sokongan kewangan daripada Dana Geran Penyelidikan GP-5179-2019.

Rujukan

1. Hisamato, H., Tsubuku, M., Enomoto, T., Watanabe, K., Kawaguchi, H., Koike, Y. and Suzuki, K. (1996). Theory and practice of rapid flow-through analysis based on optode detection and its application to pH measurement as a model case. *Analytical Chemistry*, 68: 3871.
2. Glenn, S. J., Gullum, B. M., Nair, R. B., Nivens, D. A., Murphy, C. J. and Angel, S. M. (2001). Lifetime-based fiber-optic water sensor using a luminescent complex in a lithium-treated Nafion^{TM} membrane. *Analytica Chimica Acta*, 448: 1-8.
3. Sotomayor, P. T., RaimundoJr, I. M., Zarbin, A. J. G, Rohwedder, J. J. R. and Alves, O. L. (2001). Construction and evaluation of an optical pH sensor based on polyaniline-porous Vycor glass nanocomposite. *Sensors and Actuators B: Chemical*, 74: 157-162.
4. Pacquit, A., Frisby, J., Diamond, D., Lau, K. T., Farrell, A. and Quilty, B. (2007). Development of a smart packaging for the monitoring of fish spoilage. *Food Chemistry*, 102(2): 466-470.
5. Nopwinyuwong, A., Trevanich, S. and Suppakul, P. (2010). Development of a novel colorimetric indicator label for monitoring freshness of intermediate-moisture dessert spoilage. *Talanta*, 81(3): 1126-1132.
6. Kuswandi, B. and Nurfawaidi, A. (2017). On-package dual sensors label based on pH indicators for real-time monitoring of beef freshness. *Food Control*, 82: 91-100.
7. Kuswandi, B., Maryska, C., Jayus, Abdullah, A. and Heng, L. Y. (2013). Real time on-package freshness indicator for guavas packaging. J*ournal of Food Measurement and Characterization*, 6: 1-4.
8. Rukchon, C., Nopwinyuwong, A., Trevanich, S., Jinkarn, T. and Suppakul, P. (2014). Development of a food spoilage indicator for monitoring freshness of skinless chicken breast. *Talanta*, 130: 547-554.
9. Zhang, X., Lu, S., and Chen, X. (2014). A visual pH sensing film using natural dyes from Bauhinia blakeana Dunn. *Sensors and Actuators B: Chemical*, 198: 268-273.
10. Devarayan, K. and Kim, B. S. (2015). Reversible and universal pH sensing cellulose nanofibers for health monitor. *Sensors and Actuators B: Chemical*, 209: 281-286.
11. Pereira Jr, V. A., de Arruda, I. N. Q. and Stefani, R. (2015). Active chitosan/PVA films with anthocyanins from *Brassica oleraceae* (red cabbage) as time–temperature indicators for application in intelligent food packaging. *Food Hydrocolloids*, 43: 180-188.
12. Silva-Pereira, M. C., Teixeira, J. A., Pereira-Júnior, V. A. and Stefani, R. (2015). Chitosan/corn starch blend films with extract from *Brassica oleraceae* (red cabbage) as a visual indicator of fish deterioration. *Food Science and Technology*, 61(1): 258-262.
13. Golasz, L. B., Silva, J. D. and Silva, S. B. D. (2013). Film with anthocyanins as an indicator of chilled pork deterioration. *Food Science and Technology (Campinas)*, 33: 155-162.
14. Yoshida, C. M. P., Maciel, V. B. V., Mendonca, M. E. V. and Franco, T. T. (2014). Chitosan biobased and intelligent films: Monitoring pH variations. *Food Science and Technology*, 55: 83-89.
15. Maciel, V. B. V., Yoshida, C. M. P. and Franco, T. T. (2012). Development of a prototype of a colourimetric temperature indicator for monitoring food quality. *Journal of Food Engineering*, 111: 21-27.
16. Prietto, L., Mirapalhete, T. C., Pinto, V. Z., Hoffmann, J. F., Vanier, N. L., Lim, L. T., Guerra Dias, A. R. and Zavareze, E. D. (2017). pH-sensitive films containing anthocyanins extracted from black bean seed coat and red cabbage. *LWT-Food Science and Technology*, 80: 492-500.
17. Pourjavaher, S., Almasi, H., Meshkini, S., Pirsa, S. and Parandi, E. (2017). Development of a colorimetric pH indicator based on bacterial cellulose nanofibers and red cabbage (*Brassica oleraceae*) extract. *Carbohydrate Polymers*,156: 193-201.

18. Kungsuwan, K., Sing, K., Phetkao, S. and Utama-ang, N. (2014). Effect of pH and anthocyanin concentration on colour and antioxidant activity of *Clitoria ternatea* extract. *Journal of Food and Applied Bioscience*, 2(1): 31-46.
19. Lapornik, B., Prošek, M. and Wondra, A. G. (2005). Comparison of extracts prepared from plant by-products using different solvents and extraction time. *Journal of Food Engineering*, 71: 214-22.
20. Yew, P. L. and Heng, L. Y. (2014). A reflectometric ion sensor for potassium based on acrylic microspheres. *Sensors and Actuators B: Chemical*, 191: 719-726.
21. Romero-Bastida, C. A., Bello-Pérez, L. A., García, M. A., Martino, M. N., Solorza-Feria, J. and Zaritzky, N. E. (2005). Physicochemical and microstructural characterization of films prepared by thermal and cold gelatinization from non-conventional sources of starches. *Carbohydrate Polymers*, 60 (2): 235-244.
22. Hadi, H. and Idayu, I. M. (2013). Modification and swelling kinetic study of kappa-carrageenan-based hydrogel for controlled release study. *Journal of Chinese Institute Chemical Engineers*, 44: 182-191.
23. Rosmawani, M., Musa, A. and Jamaluddin, M. D. (2007). Potensi kurkumin sebagai penunjuk pH semula jadi untuk pembangunan sensor optik pH. *Malaysian Journal of Analytical Sciences*, 11(2): 351-360.
24. Soedlak, H. S. (1994). Colorimetric determination of carrageenans and other anionic hydrocolloids with methylene blue. *Analytical Chemistry*, 66: 4514-4518.
25. De Ruiter, G. A. and Rudolph, B. (1997). Carrageenan biotechnology. *Trends Food Science Technology*, 8: 389-395.
26. Tako, M., Nakamura, S. and Kohda, Y. (1987). Indicative evidence for a conformational transition in ι-carrageenan. *Carbohydrate Research*, 161: 247-253.
27. Thrimawithana, T. R., Young, S., Dunstanb, D. E. and Alany, R. G. (2010). Texture and rheological characterization of kapa and iota carrageenan in the presence of counter ions. *Carbohydrate Polymers*, 82: 69-77.
28. Carabeo, M. M. C. (2005). Swelling capacity of different polyvinyl alcohol and ι- carrageenan blend films. A Thesis Report, Mapúa Institute of Technology, Philippines.
29. Subhas, C. S. and Pathik, M. S. (2014). Edible polymers: challenges and opportunities. *Journal of Polymers*, 2014: 1-13.
30. Makote, R. and Collinson, M. M. (1999). Organically modified silicate films for stable pH sensors. *Analytica Chimica Acta*, 394: 195-200.
31. Grant, S.A. and Glass, R. S. (1997). A sol-gel based fiber optic sensor for local blood pH measurements. *Sensors and Actuators B*, 45: 35-42.
32. Giusti, M. M. and Wrolstad, R. E. (2001). Anthocyanins: characterization and measurement of anthocyanins by uv-visible spectroscopy. In: Wrolstad, R., Ed., Current Protocols in Food Analytical Chemistry. John Wiley & Sons, Inc., New York: F1.2.1-F1.2.13.
33. Sadilova, E., Stintzing, F. C. and Carle, R. (2006). Thermal degradation of acylated and nonacylated anthocyanins. *Journal of Food Science*, 71: 504-512.
34. Liu, Z., Luo, F. and Chen, T. (2005). Phenol red immobilized PVA membrane for an optical pH sensor with two determination ranges and long-term stability. *Sensors and Actuators B*, 107: 311-316.
35. Jaakola, L. (2013). New insights into the regulation of anthocyanin biosynthesis in fruits. *Trends in Plant Science*, 18(9): 477-483.

Malaysian Journal of Analytical Sciences, Vol 23 No 5 (2019): 812 - 817
DOI: https://doi.org/10.17576/mjas-2019-2305-06

MALAYSIAN JOURNAL OF ANALYTICAL SCIENCES
Published by The Malaysian Analytical Sciences Society
ISSN 1394 - 2506

APPLICATION OF DIRECT FLUORESCENCE-BASED LIVE/DEAD STAINING FOR ASSESSMENT OF ANTIFUNGAL ACTIVITY OF COCONUT OIL AGAINST *Candida albicans*

(Aplikasi Pewarnaan Hidup/Mati Berasaskan Pendarfluor Langsung untuk Penilaian Aktiviti Antikulat Minyak Kelapa terhadap *Candida albicans*)

Nor Izzah Mukhtar[1], Zurainie Abllah[2]*, Azrul Naim Mohamad[1], Intan Azura Shahdan[3], Kamariah Long[4], Ummi Aqilah Haron[1]

[1]*Department of Biotechnology, Kulliyyah of Science*
[2]*Department of Pediatric Dentistry and Dental Public Health, Kulliyyah of Dentistry*
[3]*Department of Biomedical Sciences, Kulliyyah of Allied Health Sciences*
International Islamic University Malaysia, 25200 Kuantan, Pahang, Malaysia
[4]*Biotechnology Research Centre,*
MARDI Headquarters, Serdang, P.O. Box 12301, 50774 Kuala Lumpur, Malaysia

**Corresponding author: drzura@iium.edu.my*

Received: 16 January 2019; Accepted: 3 August 2019

Abstract

Candida albicans is one of the common causes for oral candidiasis worldwide. The proliferation of antifungal-resistant *C. albicans* has become a major concern. This study was carried out to evaluate activated virgin coconut oil (AVCO) and crude extract of virgin coconut oil (VCO) as new antifungal agents for treatment of oral candidiasis. *C. albicans* viability was determined using LIVE/DEAD bacterial viability kit. *C. albicans* cells were grown in yeast peptone dextrose (YPD) broth overnight. The fungus was treated with AVCO and VCO at the concentration of minimum fungicidal concentration (MFC) of 6.24 mg/mL and incubated for three different time points (1, 2, and 3 h). To evaluate the viability of *C. albicans*, SYTO 9 and propidium iodide (PI) staining were used and the cells were observed using fluorescence microscopy. *C. albicans* treated with AVCO showed more dead cells compared to cells treated with VCO. The data indicate that exposure of *C. albicans* to AVCO was the most inhibitory to its growth ($p < 0.01$).

Keywords: LIVE/DEAD staining, `antifungal activity, *Candida albicans*, virgin coconut oil

Abstrak

Candida albicans ialah salah satu penyebab kepada kandidiasis mulut di seluruh dunia. Malahan, pembiakan *C. albicans* rintang antikulat semakin mendapat perhatian. Kajian ini dijalankan untuk menilai kesan-kesan minyak kelapa dara teraktif (AVCO) dan ekstrak minyak kelapa dara (VCO) dalam pencarian agen antikulat yang baharu untuk rawatan kandidiasis mulut. Kebolehhidupan sel *C. albicans* ditentukan dengan penggunaan kit daya kebolehhidupan bakteria HIDUP/MATI. *C. albicans* dibiakkan semalaman di dalam kultur cecair yis pepton dekstrosa (YDP). Kulat tersebut dirawat dengan minyak kelapa teraktif dan ekstrak minyak kelapa dara pada kepekatan fungisidal minimum (MFC) sebanyak 6.24 mg/mL dan dieramkan pada tiga masa yang berbeza (1, 2, dan 3 jam). Untuk menilai kebolehhidupan *C. albicans*, pewarnaan SYTO 9 dan propidium iodida digunakan dan sel dilihat dengan menggunakan mikroskop pendarfluor. *C. albicans* yang telah dirawat dengan minyak kelapa dara teraktif menunjukkan lebih banyak sel yang mati berbanding sel yang dirawat dengan ekstrak minyak kelapa dara. Data menunjukkan minyak kelapa dara teraktif adalah paling berkesan untuk menghalang pembiakan *C. albicans* ($p < 0.01$).

Kata kunci: pewarnaan HIDUP/MATI, aktiviti rintang kulat, *C. albicans*, minyak kelapa dara

Introduction

Candida albicans is an opportunistic fungal species in the oral cavity where it can become pathogenic under several circumstances like weakened immune system or damaged mucosal barriers, leading to mucous membrane infections [1–7]. Occasionally, candida infection may cause superficial infections such as oral candidiasis which can disseminate to other organs, causing systemic infections that can be fatal [8, 9]. Generally, oral candidiasis occurs in immunocompromised people such as HIV-positive patients, transplant recipients, patients with lymphoma, drug abusers, and pregnant women [10–11].

Despite having numerous types of antifungal agents to treat oral candidiasis, current antifungal treatments are ineffective due to increased antifungal resistance, which contributes to fungal growth causing oral candidiasis [12, 13]. *C. albicans* has been shown to develop resistance against amphotericin B and fluconazole [14–16]. The low success rate in treating candidiasis also is due to the biofilm growth not only on host tissues, but also on dental devices and prosthesis [16, 17]. Therefore, an alternative antifungal therapy is necessary to combat candidiasis. The major constituents of activated virgin coconut oil (AVCO) are medium-chain fatty acids (C_6 to C_{14}), which are widely known for their antifungal and antibacterial activities.

Over the years, virgin coconut oil (VCO) has been stated to have a broad spectrum of antimicrobial/antifungal activity against Gram-positive bacteria, e.g. *Staphylococcus aureus*, *Streptococcus pyogenes*, and *Listeria monocytogenes*; Gram-negative bacteria, e.g. *Vibrio cholerae* and *Escherichia coli*; and fungi, e.g. *Candida krusei*, *Pityrosporum ovale*, and *Candida albicans* [18]. Recent reports have shown that AVCO has greater antimicrobial activity against mycobacterium and some viruses [19, 20]. The major constituents of activated virgin coconut oil are medium-chain fatty acids (C_6 to C_{14}), which are widely known for their antifungal and bactericidal activities [21–22]. Considering the potential antifungal effect of AVCO, this study investigated the viability of *C. albicans* against AVCO with the aid of live/dead viability kit.

Materials and Methods

Preparation of VCO and source of AVCO

Coconuts were bought from Taman Pertanian Agroteknologi MARDI, Cherating, Kuantan. The endosperm of the coconut was made into a viscous slurry and was squeezed through a cheesecloth until all the creamy milk was obtained. The creamy coconut milk was left at room temperature for at least 48 h. The coconut milk formed three layers after fermentation. The second layer was the VCO. It was gently scooped out, centrifuged to remove coconut residue, and kept at room temperature in a dark bottle. AVCO (100% purity) was bought from MARDI (UPM, Selangor, Malaysia).

Growth and maintenance of *Candida albicans*

Candida albicans (strain MYA 4901) was obtained from American Type Culture Collection (ATCC), subculture from freezer stocks at 4 °C onto yeast extract peptone dextrose (YPD) agar plates and incubated at 36 °C overnight to generate *C. albicans* yeast used for the experiments.

Culture conditions and preparation of fungal suspensions

Preparations for fungal suspensions were done according to the LIVE/DEAD BacLight Bacterial Viability Kit L7012 (Invitrogen, Carlsbad, CA, USA) manual that has been previously used for *C. albicans* by Vasconceles et al. [7]. Briefly, 30 mL culture of *C. albicans* was grown from a single colony in nutrient YPD broth and incubated at 36 ℃ for 12 hours. Reading of optical density of the broth culture was taken using a spectrophotometer at 600 nm by a microplate reader and was adjusted to 1×10^7 cell/mL (OD_{600} ~0.38) [13]. The culture then was concentrated by centrifugation at 10,000 × *g* for 15 minutes. The supernatant was removed and the pellet was suspended in 2 mL of 0.85% NaCl. Each mL of this suspension was added to tubes containing 10 mL of 0.85% NaCl, 10 mL of 70% ethanol, 10 mL of AVCO, and 10 mL of VCO. All samples were incubated at room temperature for 1 hour and were pelleted by centrifugation at 10,000 × *g* for 15 minutes. After centrifugation, the supernatant was discarded and all pellets were resuspended in 10 mL of 0.85% NaCl. The optical density of a 200 µL aliquot of the fungal suspensions was determined in 96-well plates at 600 nm.

Staining fungi in suspension with SYTO 9 and propidium iodide (PI)

Cell viability was assessed using SYTO 9 and propidium iodide (PI) included in the LIVE/DEAD BacLight Bacterial Viability Kit, as per manufacturer's directions. Equal volumes of SYTO 9 and PI in a microfuge tube were combined and mixed thoroughly. Three microlitres of the dye was added for each mL of the suspension. The suspension was mixed thoroughly and incubated at room temperature in the dark for 15 minutes. Then, 15 µL of the stained suspension was trapped between a slide and an 18-mm^2 coverslip. The suspension was observed under a fluorescence microscope equipped with filter sets FITC (excitation wavelength: 467–498 nm, emission wavelength: 513–556 nm) and TRITC (excitation wavelength: 540–580 nm, emission filter: 600–660 nm). The viability of yeast cells was visualized by using fluorescence microscopy (Nikon Eclipse T*i*, Japan) at a resolution of 1280 × 960. Cells with intact membranes appeared green, whereas cells with compromised membranes appeared red.

Calculations for live and dead cells

To determine the number of cells, five sides of the slide covered with cover slid were chosen. The stained cells were counted manually for live and dead cells separately using ImageJ software (https://imagej.nih.gov/ij/). The following formula was used to calculate the percentage of dead cells.

$$\frac{Total\ number\ of\ dead\ cells}{Total\ number\ of\ cells} \times 100\% \quad (1)$$

Statistical analysis

Data were analysed statistically by one-way ANOVA and Tukey's test to evaluate the mean difference with standard deviation (mean ± standard deviation) between the control and the test groups and the level of significance was compared at $p < 0.01$. All experimental results were triplicated.

Results and Discussion

The results on cell quantification of *C. albicans* treated with AVCO and VCO for three different periods of exposure (1, 2, and 3 hours) by fluorescence microscopy are shown in Table 1. The average value of the three exposure times of the viable cells of the negative control (saline) and crude extract of VCO was similar with no significant statistical difference between them ($p < 0.01$). In contrast, the result assays showed that AVCO efficiently reduced cell viability like the positive control ($p < 0.01$) after 2 hours incubation period. No significant changes between three different incubation periods were seen after treating *C. albicans* with AVCO or VCO (Table 1).

This research utilised the minimal fungicidal concentration of AVCO and VCO to assess the viability of *C. albicans*. Generally, antifungal agents target various part of fungal cells such as cell walls, nuclei, membranes, and microtubules. An increase in plasma membrane permeability is associated with the disturbance of intracellular electrochemical gradient. The viability test for fungal cells by using the combination of SYTO 9 and PI is suitable for the present study because they stain tissues regardless of cell morphology [6]. The change in membrane integrity of *C. albicans* was evaluated using PI where the dye penetrates and fluoresces the damaged membrane of the cell.

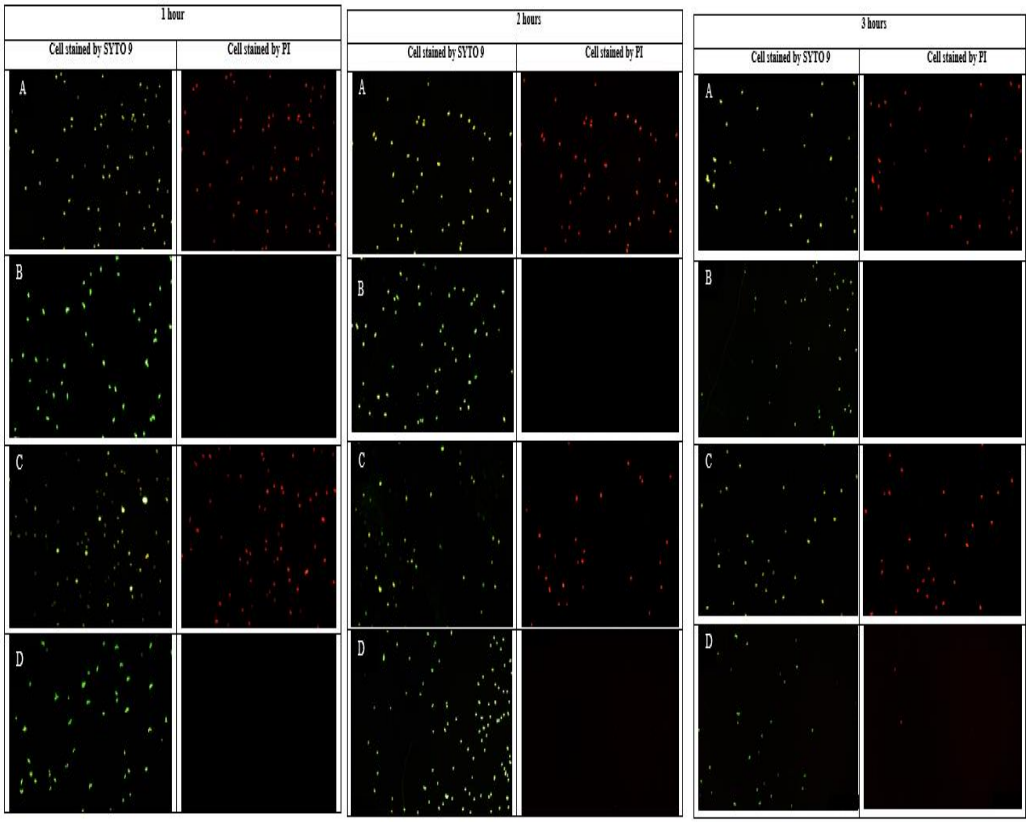
Our finding is consistent with a recent report that showed AVCO having a significant antifungal activity with an MFC value of 6.24 mg/mL and a *p*-value of less than 0.01 compared to the crude extract of VCO, which did not show any major activity against *C. albicans* [24]. The mechanism of action of AVCO is related to the solubilisation of the cell membrane that causes the cells to be lysed, which is indicated by the permeation of PI on the cell membrane after exposure to AVCO. SYTO 9 penetrates intact membranes of viable cells and sometimes stains non-viable cells and appears green/yellow. Meanwhile, PI only stains dead cells and appears red.

Table 1. Number of dead cells and percentage distribution of dead cells after staining

Sample	Exposure Time (h)	Non-Viable Cells (%)
AVCO	1	91.00 ± 8.06^{a}
	2	92.42 ± 0.57^{a}
	3	97.68 ± 0.62^{a}
VCO	1	0.46 ± 0.12^{b}
	2	1.67 ± 1.48^{b}
	3	1.90 ± 0.99^{b}
PC	1	100.00 ± 0.00^{a}
	2	99.59 ± 0.42^{a}
	3	99.70 ± 0.53^{a}
NC	1	0.00 ± 0.00^{b}
	2	1.49 ± 0.30^{b}
	3	0.00 ± 0.00^{b}

Note. Mean values ± SD are shown. Positive control was ethanol (PC), negative control was saline (NC), VCO is virgin coconut oil, AVCO is activated virgin coconut oil. Statistical significance of data was evaluated using one-way ANOVA. The level of statistical significance was set at $p < 0.01$. Mean ± SD values in the same exposure time (h) group with no superscript in common differ significantly ($p < 0.01$). The abbreviations next to the mean ± SD values indicate from which groups the relevant group differs significantly (a = $p < 0.01$), (b = $p > 0.01$).

The fungicidal activity of AVCO was comparable to the positive control (70% ethanol) at 2 and 3 hours of incubation period (Figure 1). AVCO had higher antifungal activity against *C. albicans* compared to VCO (Table 1 and Figure 1). LIVE/DEAD staining executed on fungal suspensions from control, VCO, or AVCO treatments exhibited a change in membrane permeability as measured by PI. AVCO inhibited the growth of *C. albicans* and caused all fungal cells to transform immediately from green (live) to red (dead). The uniqueness of AVCO is due to the presence of significant amount of medium chain fatty acids (MCFA) through enzymatic hydrolysis process which can act as antifungal agent. Lauric acid is the major constituent of MCFA of AVCO [21–24]. Our findings suggest that AVCO exerts its potent fungicidal activity by inhibiting cell wall integrity of *C. albicans*. Meanwhile, fungal growth was not inhibited by the crude extract of VCO. AVCO significantly disrupted the cell membrane with its MCFA.



Note. Scale bars represent 100 µm. Viable and non-viable fungi were stained with SYTO 9 and appeared green. Non-viable fungi were stained with propidium iodide and appeared red.

Figure 1. *C. albicans* were exposed to (A) ethanol, (B) normal saline, (C) AVCO, and (D) VCO for 1, 2, and 3 hours incubation

Conclusion

AVCO has a great potential to be consumed as a new antifungal treatment against oral candidiasis. Such measure may serve to decrease the colonisation of the fungus in patients and reduce the cases of hospital-acquired oral candidiasis. A limited analysis has been shown in this *in vitro* study. Thus, further investigation of AVCO and its compositions should be undertaken to study their impact on *C. albicans*.

Acknowledgement

This study was funded by the Fundamental Research Grant Scheme (FRGS16-0202-0519). We would also like to express our gratitude to Dr. Kamariah Long from MARDI for her assistance in obtaining AVCO.

References

1. Chanda, W., Joseph, T. P., Wang, W., Padhiar, A. A. and Zhong, M. (2017). The potential management of oral candidiasis using anti-biofilm therapies. *Medical Hypotheses*, 106: 15 - 18.
2. Gow, N. A., and Hube, B. (2012). Importance of the *Candida albicans* cell wall during commensalism and infection. *Current Opinion in Microbiology*, 15 (4): 406 - 412.
3. Katiraee, F., Khalaj, V., Khosravi, A., and Hajiabdolbaghi, M. (2014). Sequences type analysis of *candida albicans* isolates from iranian human immunodeficiency virus infected patients with oral candidiasis. *Acta Medica Iranica*, 52(3): 187 - 191.
4. Millsop, J.W. and Fazel, N. (2016). Oral candidiasis. *Clinics in Dermatology*, 34(4): 487 - 494.

5. Perlroth, J., Choi, B. and Spellberg, B. (2007). Nosocomial fungal infections: Epidemiology, diagnosis, and treatment. *Medical Mycology*, 45(4): 321 – 346.
6. Silva, S., Henriques, M., Hayes, A., Oliveira, R., Azeredo, J., and Williams, D. W. (2011). *Candida glabrata* and *Candida albicans* co-infection of an *in vitro* oral epithelium. *Journal of Oral Pathology & Medicine*, 40(5): 421 - 427.
7. Vasconceles, L. C., Sampaio, F. C., dos Reis Albuquerque, A. J. and Souza Vasconcelos, L. C. (2014). Cell viability of *candida albicans* against the antifungal activity of thymol. *Brazilian Dental Journal*, 25 (4): 227 - 281.
8. Kong, E. F., Kucarikova, S., Dijck, P. V., Peters, B.M., Shirtliff, M. E. and Jabra-Rizk, M. A. (2015). Clinical implications of oral candidiasis: host tissue damage and disseminated bacterial disease. *Infection and Immunity*, 83(2): 604 - 613.
9. Pfaller, M. A. and Diakema, D. J. (2007). Epidemiology of invasive candidiasis: A persistent public health problem. *Clinical Microbiology Reviews*, 20(1): 133 - 163.
10. Fidel, P. L. (2011). *Candida*-host interactions in HIV disease: Implications for oropharyngeal candidiasis. *Advances in Dental Research*, 23(1): 45 - 49.
11. Lyu, X., Zhao, C., Yan, Z., and Hua, H. (2016). Efficacy of nystatin for the treatment of oral candidiasis: A systematic review and meta-analysis. *Drug Design, Development and Therapy*, 10: 1161 - 1171.
12. Dhanasekaran, D., Vinothini, K., Latha, S., Thajuddin, N. and Paneerselyam, A. (2014). Human dental biofilm: screening, characterization, *in vitro* biofilm formation and antifungal resistance of *Candida spp. The Saudi Journal for Dental Research*, 5(1): 55 - 70.
13. Mosci, P., Gabrielli, E., Luciano, E., Perito, S., Cassone, A., Pericolini, E., and Vecchiarelli, A. (2014). Involvement of IL-17A in preventing the development of deep-seated candidiasis from oropharyngeal infection. *Microbes and Infection*, 16(8): 678 - 689.
14. He, M., Du, M., Fan, M. and Bian, Z. (2007). *In vitro* activity of eugenol against *Candida albicans* biofilms. *Mycopathologia*, 163: 137 - 143.
15. Ilyas, M. and Sharma, A. (2017). Cutaneous fungal infections in solid organ transplant recipients. *Transplantation Reviews*, 31(3): 158 - 165.
16. Jin, Y., Zhang, T., Samaranayake, Y. H., Fang, H. H. P., Yip, H. K., and Samaranayake, L. P. (2005). The use of new probes and stains for improved assessment of cell viability and extracellular polymeric substances in *Candida albicans* biofilms. *Mycopathologia*, 159(3): 353 - 360.
17. Rasteiro, V. M. C., Costa, A. C. B. P., Araujo, C. F., Barros, P. P., Rossoni, R. D., Anbinder, A. L., Jorge, A. O. C. and Junquiera, J. C. (2014). Essential oil of *Melaleuca alternifolia* for the treatment of oral candidiasis induced in an immunosuppressed mouse model. *BMC Complementary and Alternative Medicine*, 14: 489 - 499.
18. Schelenz, S., Abdallah, S., Gray, G., Stubbings, H., Gow, I., Baker, P. and Hunter P. R. (2011). Epidemiology of oral yeast colonization and infection in patients with haematological malignancies, head neck and solid tumors. *Journal of Oral Pathology Medicine*, 40: 83 - 89.
19. Thompson III, G. R., Patel, P. K., Kirkpatrick, W. R., Westbrook, S. D., Berg, D., Erlandsen, J., Redding, S. W. and Patterson, T. F. (2010). Oropharyngeal Candidiasis in the Era of Antiretroviral Therapy. *Oral Surgery, Oral Medicine, Oral Pathology, Oral Radiology, and Endodontology*, 109 (4): 488 - 495.
20. Williams D. W., Kuriyama T., Silva, S., Malic, S. and Lewis, M. A. O. (2011). *Candida* biofilms and Oral candidosis: Treatment and prevention. *Periodontology 2000*, 55: 250-265.
21. Lima, E. B. C., Sousa, C. N. S., Meneses, L. N., Ximenes, N. C., Júnior, S., Vasconcelos, G. S., Lima, N. B., Patocinio, M. C., Macedo., D. and Vasconcelos, S. M. M. (2015). *Cocos nucifera* (*L.*) (*Arecaceae*): A phytochemical and pharmacological review. *Brazilian Journal of Medical and Biological Research*, 48(11): 953 - 964.
22. Long K. Modified coconut oils with broad antimicrobial spectrum. Malaysian Granted Patent MY140578-A. 2009. https://patents.google.com/patent/WO2007067028A1. [Access online 26 November 2017].
23. Soo-Peng, K., Harun, D., Mat-Amin, M. and Long, K. (2016). Enhanced virgin coconut oil (EVCO) as natural postmilking teat germicide to control environmental mastitis pathogens. *International Journal of Biotechnology for Wellness Industries*, 5: 128 - 134.
24. Haron, U. A., Abllah, Z. and Nasir, N. A. M. M. (2018). The comparative antimicrobial effect of activated virgin coconut oil (AVCO) and virgin coconut oil (VCO) against dental caries-related pathogens. *Advances in Health Science Research*, 8: 312 - 317.

Malaysian Journal of Analytical Sciences, Vol 23 No 5 (2019): 818 - 827
DOI: https://doi.org/10.17576/mjas-2019-2305-07

MALAYSIAN JOURNAL OF ANALYTICAL SCIENCES
Published by The Malaysian Analytical Sciences Society
ISSN 1394 - 2506

DURIAN SHELL HUSK EXTRACT ASSISTED SYNTHESIS OF COPPER OXIDES NANOPARTICLES FOR THE PHOTODEGRADATION OF PARACETAMOL

(Ekstrak Sekam Kulit Durian Membantu Sintesis Nanozarah Tembaga Oksida Untuk Fotodegradasi Paracetamol)

Ahmad Masudi[1], Nurfatehah Wahyuny Che Jusoh[1,2]*, Zunika Bakri[1], Aishah Abdul Jalil[2,3], Roshafima Rasit Ali [1,2], Nur Farhana Jaafar[4]

[1]*Department of Chemical Process Engineering, Malaysia-Japan International Institute of Technology (MJIIT), Universiti Teknologi Malaysia Kuala Lumpur, Jalan Sultan Yahya Petra, 54100 Kuala Lumpur, Malaysia*
[2]*Center of Hydrogen Energy, Institute of Future Energy*
[3]*School of Chemical and Energy Engineering, Faculty of Engineering Universiti Teknologi Malaysia, 81310 UTM Johor Bahru, Johor, Malaysia*
[4]*School of Chemical Sciences, Universiti Sains Malaysia, 11800 USM Penang, Malaysia*

**Corresponding author: nurfatehah@utm.my*

Received: 13 February 2019; Accepted: 20 September 2019

Abstract

A series of copper oxide (CuO) nanoparticles catalysts were prepared *via* electrochemical method. The addition of different concentrations of Durian Shell Husk (DSH) extract in the electrolyte system was evaluated for degradation of paracetamol under visible light irradiation. The catalysts were characterized by using X-ray diffraction (XRD), Fourier Transform Infrared (FTIR) and Scanning Electron Microscopy (SEM). The characterization data showed that the different sizes of CuO were obtained when the amount of DSH extract added into the electrolyte system were varied. The crystallite size of CuO prepared with DSH was decreased from 40 nm to 29 nm, which showed the role of DSH extract as a capping agent. The particle sizes reduction caused a significant increment towards paracetamol degradation. The initial degradation rate was increased from 2.67×10^{-2} to 7.28×10^{-2} mg/L.min. From this study, the optimum condition was noticed for CuO that was prepared by using 0.06 mg/L of DSH extract at a paracetamol initial concentration of 10 mg/L (pH 9) by using 0.1 g/L catalyst. Finally, the result could contribute to the production of copper oxide with ideal sizes using abundant agriculture waste extract for the removal of paracetamol in wastewater.

Keywords: electrochemical, copper oxide, durian shell husk, paracetamol

Abstrak

Satu siri pemangkin nanozarah tembaga oksida (CuO) telah disediakan melalui kaedah elektrokimia. Penambahan pelbagai kepekatan ekstrak sekam kulit durian (DSH) dalam sistem elektrolit telah dinilai untuk degradasi paracetamol di bawah sinar cahaya boleh lihat. Pemangkin telah dicirikan menggunakan pembelauan sinar-X (XRD), spektroskopi inframerah transformasi Fourier (FTIR) and mikroskopi imbasan elektron (SEM). Data pencirian menunjukkan bahawa pelbagai saiz CuO diperoleh apabila jumlah ekstrak DSH yang ditambah di dalam sistem elektrolit telah diubah-ubah. Saiz kristal CuO yang disediakan menggunakan DSH menurun dari 40 nm ke 29 nm, yang mana menunjukkan peranan ekstrak DSH sebagai ejen pelekatan. Pengurangan saiz zarah ini menyebabkan kenaikan ketara terhadap degradasi paracetamol. Kadar degradasi awal meningkat daripada 2.67×10^{-2} kepada 7.28×10^{-2} mg/L.min. Daripada kajian ini, keadaan optimum telah dikenalpasti untuk CuO yang disediakan menggunakan 0.06 mg/L ekstrak DSH pada kepekatan awal paracetamol 10 mg/L (pH 9) dengan menggunakan

0.1 g/L pemangkin. Akhirnya, hasil kajian ini dapat menyumbang kepada penghasilan tembaga oksida dengan saiz yang ideal menggunakan ekstrak sisa buangan pertanian untuk penyingkiran paracetamol dalam air sisa.

Kata kunci: elektrokimia, tembaga oksida, sekam kulit durian, paracetamol

Introduction

The pharmaceutical market in Malaysia increases 9.5% annually, which is double than average of the Asia Pacific region. The market is still predicted to grow from $ 2.3 billion in 2015 to $ 3.6 billion in 2020. The increasing demand of drugs will be followed by large municipal and discharge waste which is hazardous to the environment. Paracetamol (PCT) is the largest analgesic and antipyretic drug without prescription worldwide. PCT was detected 0.033-0.071 µg/L at water surface in Korea [1], 0.22-6.8 µg/L at treated water in Spain [2] and 0.01-0.07 µg/L in surface and sewage water in Malaysia [3]. Therefore, it was proven that the conventional technology still needs some advancements.

Advanced Oxidation Process (AOPs) is one of promising method to degrade emerging pollutants. This technology is based on massive reaction between organic radicals with pollutants. The radical compounds were produced from heterogeneous catalyst (for example, TiO_2 and ZnO) which activates after exposure to external light such as ultraviolet, visible or solar light. The common photocatalysts are TiO_2 and ZnO [4]. However, these catalysts mainly absorp UV light and consume extensive energy [5, 6]. CuO is p-type semiconductor which has the potential to become a photocatalyst with low band gap energy in the range of 1.2 eV -1.8 eV and active under visible or fluorescent lamp [7, 8]. There are many approaches reported for synthesis of CuO, such as precipitation [9], sol-gel [10] and solution combustion method [11]. However, these methods require an extremely controlled set-up including high temperature or a long reaction time to obtain the CuO. Therefore, it is necessary to find a simple and rapid method for synthesis. Electrochemical method seems to be a potential method due to its effectiveness, facile experimental set-up and can also be operated at ambient temperature and pressure [12]. However, from the previous study, an expensive ionic liquid are usually used as a synthesis media in electrochemical method [13].

Hence, it is crucial to find a low cost material as an alternative media. To date, the synthesis of CuO nanoparticles by using plant extract has received great attention due to the expanding need in environmentally friendly technologies in material synthesis. Plant extracts are basically enriched in polysaccharide compound that acts as a stabilizing agent in the synthesis of CuO [14]. However, the synthesis of CuO nanoparticles using plant extract through electrochemical method is still rare since most of the studies used precipitation and sol gel method. Therefore, this study aims to synthesize CuO nanoparticles via electrochemical method by using durian shell husk (DSH) extract as a media. The DSH extract contains polysaccharides which act as capping agent and stabilizer during the synthesis. As compared to ionic liquid, the DSH extract also has other advantages, such as cost effective and environmentally friendly. The synthesized CuO nanoparticles were then analysed by X-ray diffraction (XRD), Fourier Transform Infrared (FTIR) and Scanning Electron Microscopy (SEM). Next, the photocatalytic activity of the CuO nanoparticles was studied towards the degradation of paracetamol (PCT).

Materials and Methods

Preparation of copper oxides assisted by DSH

An open electrolysis cell consisted of copper plate electrode (2x2 cm^2) and platinum plate electrode (2x2 cm^2) were placed in parallel each other. 10 mL of solution containing different amounts of DSH extract (0 mg/L, 0.02 mg/L, 0.06 mg/L and 0.1 mg/L) were added to the solution at a constant stir (150 rpm). The solution also comprised of 0.1 M of tetraethyl ammonium perchlorate (TEAP) as the supporting electrolyte. The electrolysis was conducted at 0°C and ambient pressure with constant current density (120 mA/cm^2) . After electrolysis, the mixture was dried overnight at 60 °C and calcined at 550 °C for 2 hours. The catalyst was donated as CuO_x (x= 0, 0.02, 0.06 and 0.1 mg/L of DSH extract).

Characterization

Catalyst crystallinity structure was evaluated by using X-ray diffraction (XRD, D8 Advance Bruker X-ray diffractometer). Meanwhile the chemical functional groups in catalyst were identified by Fourier Transformation

Infrared (FTIR, Perkin Elmer Spectrum GX FTIR spectrometer). Finally, the catalyst morphologies were observed with Scanning Electron Microscopy (SEM, JEOL JSM-6300).

Photodegradation test

PCT degradation was tested under visible light irradiation (36 watts). Before exposure to the visible light, a certain amount of catalyst was added into 100 mL of PCT solution in dark condition and was continuously stirred. This procedure was conducted to achieve equilibrium between the PCT solution and catalyst. The solution was exposed to the visible light radiation for another 1 hour. Then, 1.5 mL of solution was taken periodically for every 10 minutes and degradation of PCT was analyzed by using a UV-Vis spectrometer (Shimadzu UV-2600) at maximum wavelength of 245 nm.

Results and Discussion

Catalyst characterization

Crystallinity and purity of copper oxides (CuO) nanoparticles were confirmed with X-ray diffraction (XRD). Based on the XRD pattern as presented in Figure 1, the diffraction peaks appeared at 33°, 35°, 39°, 49°, 53°, 57°, 62°, 68° and 75°. These peaks correspond to monoclinic CuO and match with JCPDS no.5-661 [15]. The crystallite sizes (D) of CuO_0, $CuO_{0.02}$, $CuO_{0.06}$ and $CuO_{0.1}$ from Debye Scherrer equation were 40.74, 40.73, 29.6370 and 29.6371 nm respectively. From this result, its was obvious that the various DSH concentrations affected the CuO particle size. As reported by Song et al, the particle size of the synthesized gold nanoparticles was decreased at a high concentration of *Magnolia kobus* plant extract [16]. At low concentration, the gold nanoparticles were hexagonal or triangular in shape, but changed to spherical at high concentration. In this present study, at low concentration of DSH (0.02 mg/L), the amount of DSH might not be enough to cover all the Cu^{2+} ions, and thus could not act as a good capping agent. However, the crystallinity of CuO nanoparticles increased while using 0.06 mg/L, followed by significant reduction in particle size. Meanwhile, the particle size was almost the same at a higher concentration of DSH (0.1 mg/L). The concentration of plant extract needed to be optimized since its did not only affect the particle size, but also the morphology catalyst as reported in literature [17].

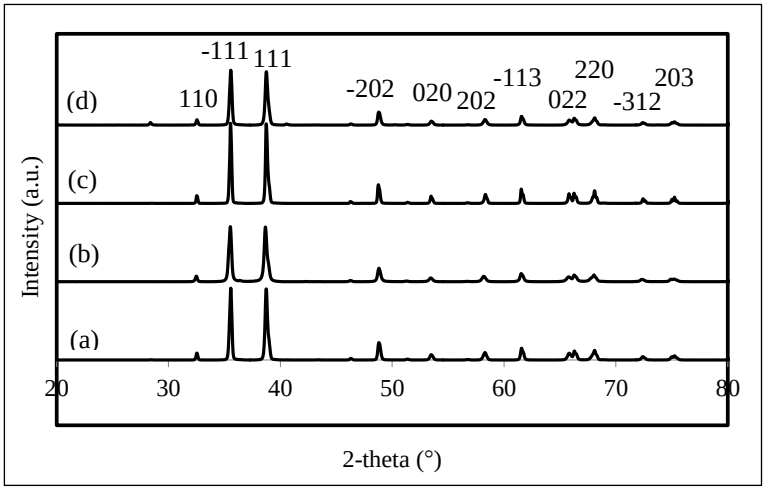


Figure 1. XRD patterns of (a) CuO_0 (b) $CuO_{0.02}$ (c) $CuO_{0.06}$ (d) $CuO_{0.1}$

The functional groups of raw DSH and series of CuO were determined by using FTIR spectroscopy to verify the formation mechanism of the catalyst. FTIR spectra of DSH in Figure2(a) shows four major spectra at 3323 cm^{-1}, 1732 cm^{-1}, 1610 cm^{-1} and 1033 cm^{-1}. The peak at 3323 cm^{-1} corresponded to stretching of –OH group of macromolecular association. Meanwhile, the peaks at 1732 cm^{-1} and 1610 cm^{-1} were contributed from the carbonyl group and –OH stretching from H_2O. The band around 1033 cm^{-1} referred to the C-O band of polysaccharide group. In CuO catalyst series, there was no observed DSH peak due to the removal of DSH after calcination at 550 °C. In

these catalysts, a new intense peak appeared at 560 cm^{-1}, which corresponded to the Cu-O stretching bond, had proven the existence of CuO nanoparticles [18].

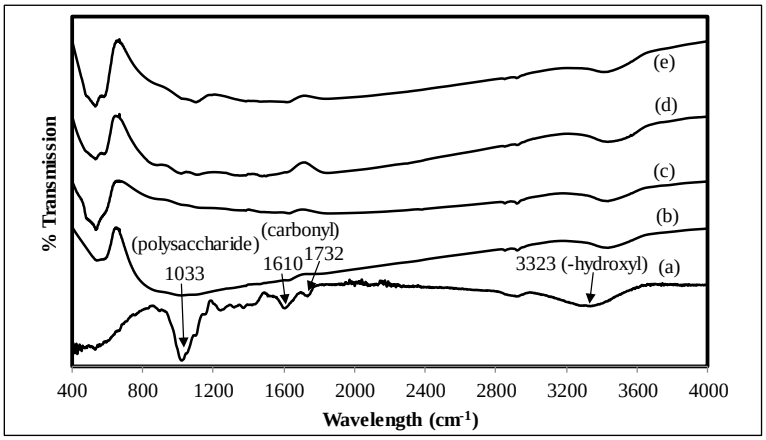


Figure 2. FTIR result for (a) DSH (b)CuO_0 (c) $CuO_{0.02}$ (d) $CuO_{0.06}$ (e) $CuO_{0.1}$

The CuO morphology was spherical shaped as presented by the SEM result in Figure 3. The SEM result had convinced that $CuO_{0.06}$ is much smaller than CuO_0 which proved that DSH is good stabilizer. A study by Naika et al. also obtained the spherical shape of CuO using *Gloriosa superba* L plant extract which dominantly contained the alkaloid compound [19].

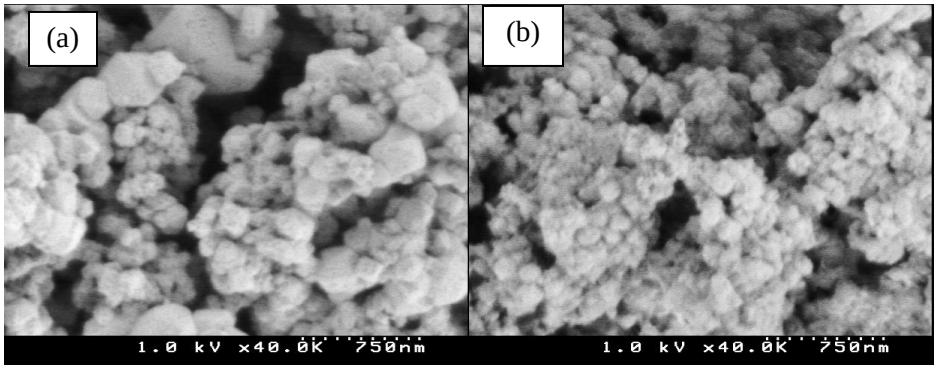


Figure 3. SEM result for (a) CuO_0 (b) $CuO_{0.06}$

Photodegradation test

The series of synthesized CuO nanoparticles were tested for paracetamol degradation. Several parameters were studied to obtain the optimum condition.

Effect of pH

Initial pH solution affected the interaction between pollutants and catalyst (Figure 4). The point of zero charge (PZC) of CuO and PCT were at 7.9 and 9.2, respectively [20-22]. At lower pH than pH_{PZC}, the molecules became positively charged and became negative charged at higher pH than pH_{PZC}. In pH 5 and 7, both CuO and PCT were in positively charged, which would lead to repulsion with each other. Meanwhile, the degradation rate increased at pH 9 due to the attractive interaction between the negatively charged CuO and positively charged PCT. However, the reaction rate decreased again as both CuO and PCT were negatively charged.

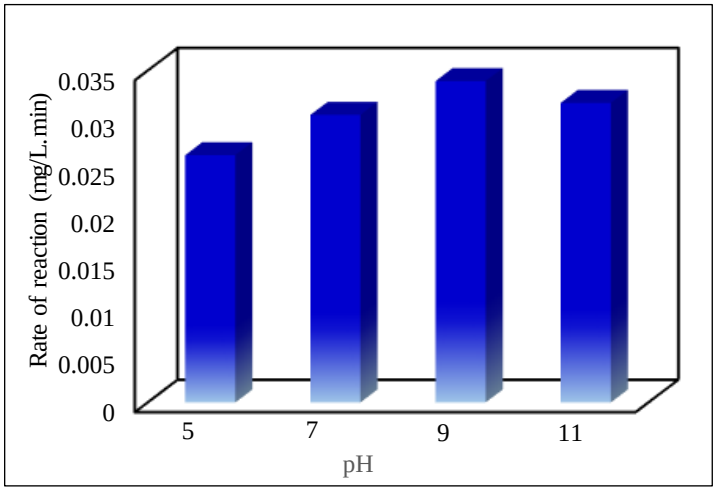


Figure 4. The effect of initial pH for PCT degradation

Effect of catalyst dosage

The rate of photocatalytic degradation was also influenced by catalyst dosage. Figure 5 display the effect of catalyst dosage from 0.1 to 1 g/L for PCT degradation. The rate of reaction was slightly increased at catalyst dosage of 0.1 to 0.5 g/L. Then, the rate of reaction increased drastically by using catalyst dosage of 1 g/L. The increase in degradation rate with increasing catalyst dosage was due to the increase in the number of active sites and active radicals in the solution. A similar result was also observed in another copper-based catalyst to degrade the PCT [23]. The degradation efficiency increased from 38.6% to 90% when the catalyst dosage increased from 0.1 to 0.3 g/L. This phenomenon occurs due to increase in active sites when the catalyst dosage was increased.

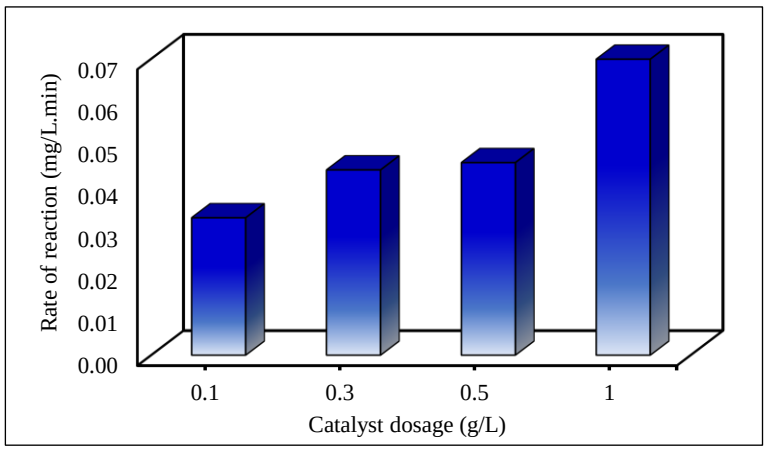


Figure 5. The effect of catalyst dosage

Effect of DSH concentration

DSH is one of potential stabilizers in nanoparticle formation. As reported, the concentration of plant extract had differentiated the particle size of nanoparticle [24]. This study was conducted at different concentrations of DSH extract which were 0, 0.02, 0.06 and 0.1 mg/L. Figure 6 shows the different catalytic activities of the catalysts for PCT degradation. It was observed that the highest reaction rate was obtained with CuO prepared by using 0.06 mg/L of DSH extract. The introduction of 0.02 mg/L DSH showed only little improvement on its catalytic activity as compared to without DSH extract. At low concentration, DSH may not covered all the CuO nuclei, which then

caused the large particle size was confirm with XRD. The particle size of CuO decreased significantly after the addition of 0.06 mg/L DSH and it was also highly crystalline indicating a complete covering of CuO nuclei. However, the particle size increased again after the insertion of 0.1 mg/L DSH. This phenomenon may be assigned to the agglomeration of DSH extract which hindered CuO nuclei stabilization.

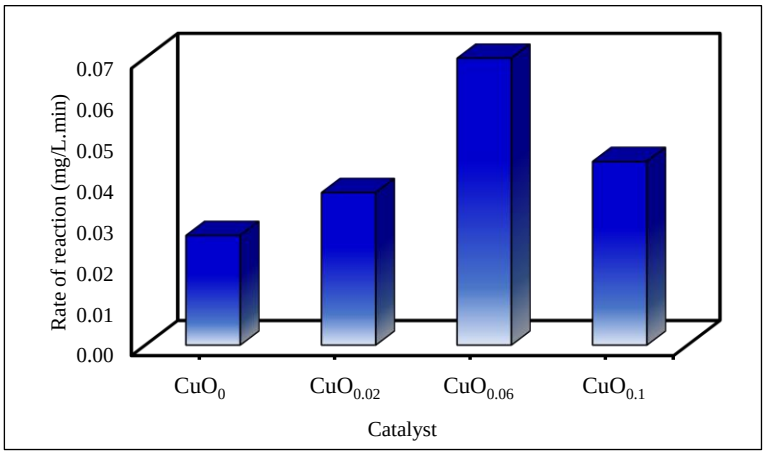


Figure 6. The effect of DSH concentration

Effect of reaction temperature

Figure 7 demonstrates the effect of reaction temperature for PCT degradation. In this study, the effect of temperature was carried out at 30, 40 and 50 °C. It was observed that the degradation rate at 30 °C was much higher than at 40 and 50 °C. The highest degradation rate was 6.99 x 10^{-2} mg/L.min. Therefore, the degradation of PCT was considered as an exothermic reaction with unnecessary high temperature condition is needed. This gives an advantage to this reaction as the other copper catalyst is commonly an endothermic reaction which requires an extensive energy [25]. Then, by using the degradation constant and temperature, activation energy (Ea, J/mol) can be estimated by using Arrhenius equation as presented in equation (1),

$$\ln k_{app} = \left(\frac{-Ea}{R}\ \frac{1}{T}\right) + \ln A \quad (1)$$

This equation consisted of R as the gas constant (8.314 J.K/mol) where k_{app} and A are as apparent rate constant and frequency factor, respectively. This plot exhibited high R^2 (0.9995) with activation energy of 101 kJ/mol, as presented in inset Figure 7. This activation energy was lower than other copper catalyst as reported in literature [25]. With lower activation energy, the reaction time was faster, and the energy consumption can be reduced.

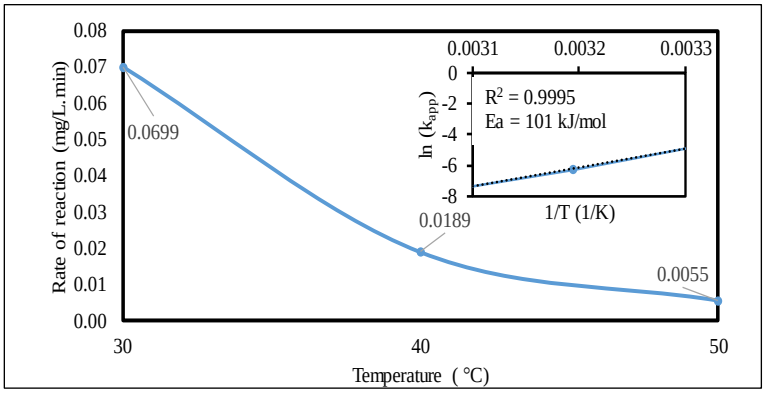


Figure 7. Effect of reaction temperature

Effect of initial concentration

The Initial concentration of pollutant is essential in a degradation studies, especially for industrial application. This study showed that reaction rate increased from 0.0407 to 0.122 mg/(L.min), when increasing the PCT concentration from 5 to 20 mg/L. The reaction rate decreased to 0.0170 mg/(L.min) at higher initial concentration of 30 mg/L. From this result, its was obvious that CuO nanoparticles were efficient until 20 mg/L of PCT as presented in Table 1. At higher concentration than 20 mg/L, the turbidity of solution hindered the light penetration, and then decreased degradation rate significantly.

Table 1. Effect of initial concentration of PCT

Concentration of PCT (mg/L)	Rate of Reaction (mg/L.min)
5	0.04
10	0.08
20	0.12
30	0.02

Propose mechanism for CuO formation and PCT degradation

The possible mechanism for CuO formation was proposed according to the characterization results and literature as shown in Figure 9. The electrolysis at anode and cathode involved the following reactions (2-3):

$$\text{Anode} \quad : Cu \rightarrow Cu^{2+} + 2e^- \tag{2}$$

$$\text{Cathode} \quad : 2H_2O + 2e^- \rightarrow 2H_2 + 2OH^- \tag{3}$$

The copper plate was oxidized to generate copper cations (Cu^{2+}) and released electrons at the anode. As reported, DSH is rich with polysaccharide compound. The presence of polysaccharide in electrolyte formed a complex compound with Cu^{2+} to form Cu[polysaccharide]$^{2+}$. This Cu[polysaccharide]$^{2+}$ then played an important role in the formation of CuO nuclei. The polysaccharide reacted as a capping agent as well as a stabilizer which controlled the growth of CuO nuclei. Therefore, as observed in XRD, the particles size of synthesized CuO in the presence of DSH extract was much smaller than in the absence of DSH extract. Since the electrochemical synthesis was conducted in open air, part of oxygen could be dissolved and formed a highly crystalline CuO [26]. Meanwhile at the cathode, the generated electrons reacted with the hydroxyl group from electrolyte to form hydrogen gas on the electrode surface.

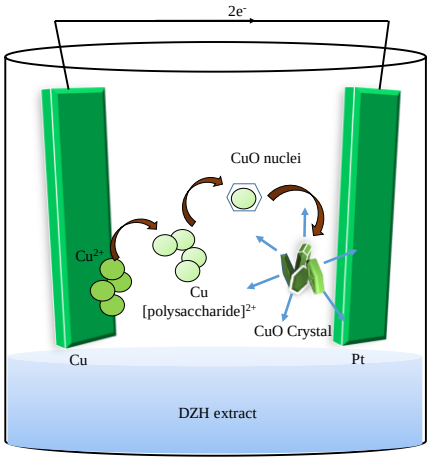


Figure 9. Propose mechanism for CuO nanoparticles formation

PCT degradation was initiated by the reaction between free electron from Cu oxidation and oxygen to produce $O_2 \cdot^-$. Then, the O_2^- will react with hydrogen ion (H^+) from water to produce ·OH with HOO· as the intermediate reaction. Meanwhile, the holes in VB were positive enough to oxidize water or OH^- on the copper surface to produce hydroxyl radicals (·OH). Therefore, ·OH would react with PCT and produce degradation product. The degradation product mainly consists of carbocyclic acid which further decreases the pH value after reaction [27]. The proposed degradation is presented in Figure 10.

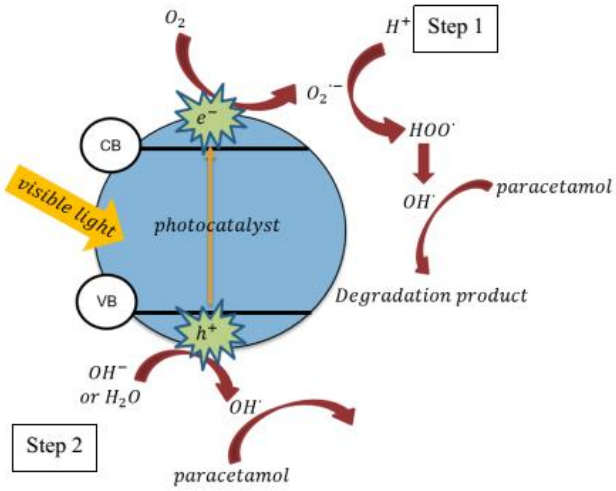


Figure 10. Propose PCT degradation

Conclusion

Pure copper oxide (CuO) nanoparticles were successfully prepared by using electrochemical method. CuO was spherical in shape and the particles sized was highly affected by the durian shell husk (DSH) concentration. The particle size decreased drastically from 40 nm to 29 nm in the presence of optimum DSH content. The photodegradation rate of paracetamol (PCT) by using CuO in the presence of DSH increased by more than twice as compared to in the absence of DSH. The optimum condition for PCT degradation was obtained by using 1 g/L of $CuO_{0.06}$ in pH 9 at 30 °C to degrade 20 mg/L of PCT with the highest degradation rate of 0.1222 mg/L.min. These findings suggested that DSH extract was remarkably important for an efficient nanoparticle's synthesis and PCT degradation. For future prospect, the combination of CuO with a catalyst support or other metal oxides will be a great contribution to enhance the photocatalytic activity and stability of the catalyst.

Acknowledgement

The authors would like to express appreciation for the financial support by the Fundamental Research Grant Scheme from Ministry of Higher Eduacation (Grant No. 5F031), Research University Grant (Grant No. 19H37) and MJIIT Incentive Scheme (Ahmad Masudi) form MJIIT UTM.

References

1. Gómez, M. J., Martínez Bueno, M. J., Lacorte, S., Fernández-Alba, A. R. and Agüera. A. (2007). Pilot survey monitoring pharmaceuticals and related compounds in a sewage treatment plant located on the Mediterranean coast. *Chemosphere*, 66(6): 993-1002.
2. Kim, S. D., Cho, J., Kim, I. S., Vanderford, B. J. and Snyder. S. A. (2007) Occurrence and removal of pharmaceuticals and endocrine disruptors in South Korean surface, drinking, and waste waters. *Water Research*, 41(5):1013-1021.

3. Al-Odaini, N. A., Zakaria, M. P., Yaziz, M. I. and Surif. S. (2010). Multi-residue analytical method for human pharmaceuticals and synthetic hormones in river water and sewage effluents by solid-phase extraction and liquid chromatography–tandem mass spectrometry. *Journal of Chromatography A*, 1217(44): 6791-6806.
4. Sidik, D. A. B., Hairom, N. H. H., Zainuri, N. Z., Desa, A. L., Misdan, N., Yusof, N., Ong, C. B., Mohammad, A. W. and Aripen. N. S. M. (2018). Photocatalytic degradation of industrial dye wastewater using zinc oxide-polyvinylpyrrolidone nanoparticles. *Malaysian Journal of Analytical Sciences*, 22(4): 693-701.
5. Vaiano, V., Sacco, O. and Matarangolo, M. (2018). Photocatalytic degradation of paracetamol under UV irradiation using TiO_2-graphite composites. *Catalysis Today*, 315: 230-236.
6. Jusoh, N.W.C., Jalil, A. A., Triwahyono, S., Karim, A. H., Salleh, N. F., Annuar, N. H. R., Jaafar, N. F., Firmansyah, M. L., Mukti, R. R. and Ali, M.W. (2015). Structural rearrangement of mesostructured silica nanoparticles incorporated with ZnO catalyst and its photoactivity: Effect of alkaline aqueous electrolyte concentration. *Applied Surface Science*, 330: 10-19.
7. Mazumder, N. A. and Rano. R. (2018). Synthesis and characterization of fly ash modified copper oxide (FA/CuO) for photocatalytic degradation of methyl orange dye. *Materials Today: Proceeding*, 5: 2281-2286.
8. An, J. and Zhou. Q. (2012). Degradation of some typical pharmaceuticals and personal care products with copper-plating iron doped Cu_2O under visible light irradiation. *Journal of Environmental Sciences,* 24(5): 827-833.
9. Phiwdang, K., Suphankij, S., Mekprasart, W. and Pecharapa. W. (2013). Synthesis of CuO nanoparticles by precipitation method using different precursors. *Energy Procedia*, 34: 740-745.
10. Kayani, Z. N., Ali, Y., Kiran, F., Batool, I., Butt, M. Z., Umer, M., Riaz, S. and Naseem. S. (2015). Fabrication of copper oxide nanoparticles by sol-gel route. *Materials Today: Proceedings*, 2(10): 5446-5449.
11. Dong, C., Xing, X., Chen, N., Liu, X. and Wang, Y. (2016). Biomorphic synthesis of hollow CuO fibers for low-ppm-level n -propanol detection via a facile solution combustion method. *Sensors and Actuators B: Chemical*, 230: 1-8.
12. Sapawe, N., Jalil, A. A., Triwahyono, S., Sah, R. N. R. A., Jusoh, N. W. C., Hairom, N. H. H. and Efendi, J. (2013). Electrochemical strategy for grown ZnO nanoparticles deposited onto HY zeolite with enhanced photodecolorization of methylene blue: Effect of the formation of SiOZn bonds. *Applied Catalysis A: General*, 456: 144-158.
13. Jusoh, R., Jalil, A. A., Triwahyono, S., Idris, A., Haron, S., Sapawe, N., Jaafar, N. F. and Jusoh, N. W. C. (2014). Synthesis of reverse micelle α-FeOOH nanoparticles in ionic liquid as an only electrolyte: Inhibition of electron–hole pair recombination for efficient photoactivity. *Applied Catalysis A: General*, 469: 33-44.
14. Chutrakulwong, F. and Thamaphat, K. (2014). Durian peeling extract mediated green synthesis of silver nanoparticles. *Advanced Materials Research*, 875-877: 18-22.
15. Raghav, R., Aggarwal, P. and Srivastava. S. (2015). Tailoring oxides of copper-Cu_2O and CuO nanoparticles and evaluation of organic dyes degradation. *AIP conference proceeding*, 1724: 020078-1-020078-5.
16. Song, J.Y., Jang, H. K. and Kim. B. S. (2009). Biological synthesis of gold nanoparticles using *Magnolia kobus* and *Diopyros kaki* leaf extracts. *Process Biochemistry*, 44(10): 1133-1138.
17. Mittal, A. K., Chisti, Y. and Banerjee, U. C. (2013). Synthesis of metallic nanoparticles using plant extracts. *Biotechnology Advances*, 31: 346-356.
18. Srivastava, R., Anu Prathap, M. U. and Kore. R. (2011). Morphologically controlled synthesis of copper oxides and their catalytic applications in the synthesis of propargylamine and oxidative degradation of methylene blue. *Colloids and Surfaces A: Physicochemical and Engineering Aspects*, 392(1): 271-282.
19. Suresh, D., Kumar, D., Nagabhushana, H., Nagaraju, G. Manjunath, K., Naika, H. R. and Lingaraju, K. (2014). Green synthesis of CuO nanoparticles using *Gloriosa superba* L. extract and their antibacterial activity. *Journal of Taibah University for Science*, 9(1): 7-12.
20. Guedes, M., Ferreira, J. M. F. and Ferro. A. C. (2009). A study on the aqueous dispersion mechanism of CuO powders using Tiron. *Journal of Colloid and Interface Science*, 330(1): 119-124.
21. Mestre, A.S., Bexiga, A. S., Proença, M., Andrade, M., Pinto, M. L., Matos, I., Fonseca, I. M. and Carvalho, A. P. (2011). Activated carbons from sisal waste by chemical activation with K_2CO_3: Kinetics of paracetamol and ibuprofen removal from aqueous solution. *Bioresource Technology*, 102(17): 8253-8260.
22. Bernal, V., Erto, A., Giraldo, L. and Moreno-Piraján, C. J. (2017). Effect of Solution pH on the Adsorption of paracetamol on chemically modified activated carbons. *Molecules*, 22(7): 1032.

23. Zhang, Y., Zhang, Q. and Hong. J. (2017). Sulfate radical degradation of acetaminophen by novel iron–copper bimetallic oxidation catalyzed by persulfate: Mechanism and degradation pathways. *Applied Surface Science*, 422: 443-451.
24. Dubey, S.P., M. Lahtinen, and M. Sillanpää. (2010). Green synthesis and characterizations of silver and gold nanoparticles using leaf extract of Rosa rugosa. *Colloids and Surfaces A: Physicochemical and Engineering Aspects*, 364(1-3): 34-41.
25. Shen, Y., Zhang, Z.and Xiao, K. (2015). Evaluation of cobalt oxide, copper oxide and their solid solutions as heterogeneous catalysts for Fenton-degradation of dye pollutants. *RSC Advances*, 5(111): 91846-91854.
26. Jaafar, N. F., Jalil, A. A., Triwahyono, S., Efendi, J., Mukti, R. R., Jusoh, R., Jusoh, N. W. C., Karim, A. H., Salleh, N. F. M. and Suendo, V. (2015). Direct in situ activation of Ag^0 nanoparticles in synthesis of Ag/TiO_2 and its photoactivity. *Applied Surface Science*, 338: 75-84.
27. Moctezuma, E., Leyva, E., Aguilar, C. A., Luna, R. A. and Montalvo, C. (2012). Photocatalytic degradation of paracetamol: Intermediates and total reaction mechanism. *Journal of Hazardous Materials*, 243: 130-138.

Malaysian Journal of Analytical Sciences, Vol 23 No 5 (2019): 828 - 838
DOI: https://doi.org/10.17576/mjas-2019-2305-08

MALAYSIAN JOURNAL OF ANALYTICAL SCIENCES
Published by The Malaysian Analytical Sciences Society
ISSN 1394 - 2506

SYNTHESIS OF PALLADIUM(II) DIIMINE COMPLEXES AND THE HYDROLYSIS OF α-DIIMINE LIGAND

(Sintesis Kompleks Diimina Palladium(II) dan Hidrolisis Ligan α-Diimina)

Suzie Hui Chin Kuan[1]*, Meng Guan Tay[1], Zhi-Qiang Liu[2]

[1]*Faculty of Resource Science and Technology,*
Universiti Malaysia Sarawak, 94300 Kota Samarahan, Malaysia
[2]*State Key Lab of Crystal Materials,*
Shandong University, 27 Shanda South Road, Jinan, 250100, China

**Corresponding author: suzie_kuan0807@hotmail.com*

Received: 23 May 2019; Accepted: 28 August 2019

Abstract

The reactions of dichlorobis(acetonitrile)palladium(II) precursors with 1,4-diaza-1,3-butadienes (α-diimine) give rise to the products (1,4-bis(4-methoxyphenyl)-1,4-diaza-1,3-butadiene)dichloropalladium(II) (**2a)** and (1,4-bis(4-methylphenyl)-1,4-diaza-1,3-butadiene)dichloropalladium(II) (**2b**), as deduced from elemental analysis, FTIR, and UV-Vis. Both complexes are soluble in dimethylformamide and single crystals were collected for an X-ray crystallographic study. Based on the crystallographic data, complex **2a** is crystalized in a monoclinic system with $P2_1/c$ space group. The Pd-N bond lengths for Pd01-N004 and Pd01-N005 are 2.045(2) and 2.033(2) Å, respectively. Surprisingly, when complex **2b** dissolved in dimethylformamide, 4-methylaniline was produced from the hydrolysis of the α-diimine ligand **1b,** therefore *trans*-dichloridobis(4-methylaniline-κN)-palladium(II) (**2c**) was formed as confirmed, by crystallographic data. Complex **2c** is crystallized in a triclinic system with P $2_1/b$ $2_1/c$ $2_1/a$ (Pbca) space group. The bond lengths of Pd-N are 2.050(3) Å and Pd-Cl is 2.318(8) Å. There are weak intermolecular N-H···Cl hydrogen bonds, that are responsible for the packing of the molecules in formation.

Keywords: 1,4-diaza-1,3-butadienes, palladium diimine complex, X-ray crystal, hydrolysis, hydrogen bonds

Abstrak

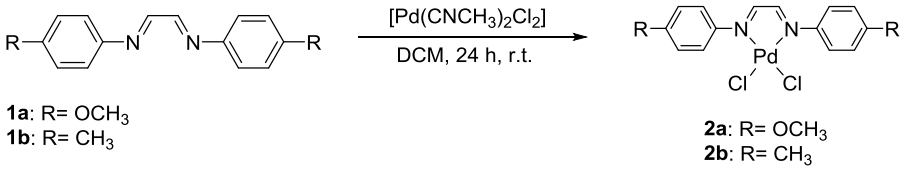
Tindak balas diklorobis(asetonitril)palladium(II) prakursor dengan 1,4-diaza-1,3-butadiena menghasilkan produk sebagai (1,4-bis(4-metoksifenil)-1,4-diaza-1,3-butadiena)dikloropalladium(II) atau 4-bis(4-metilfenil)-1,4-diaza-1,3-butadiena)dikloro palladium(II) yang disimpulkan daripada analisis unsur, FTIR, dan UV-Vis. Kedua-dua kompleks ini larut dalam dimetilformamida dan hablur tunggal telah dikumpulkan untuk kajian kristalografi sinar-X. Berdasarkan data kristalografi, kompleks **2a** menghablur dalam sistem monoklinik dengan kumpulan ruang P21/c. Panjang ikatan Pd-N ialah 2.045 (2) untuk Pd01-N004 dan 2.033 (2) Å untuk Pd01-N005. Walau bagaimanapun, apabila kompleks **2b** larut dalam dimetilformamida, 4-metilanilina telah dihasilkan dari hidrolisis ligan α-diimine **1b**, oleh itu, *trans*-dikloroidobis(4-metilanilina-κN)-palladium(II) **(2c**) telah terbentuk seperti yang dibuktikan oleh data hablur. Kompleks **2c** menghablur dalam sistem triklinik dengan kumpulan ruang P 21/b 21/c 21/a (Pbca). Panjang ikatan Pd-N ialah 2.050 (3) Å dan Pd-Cl ialah 2.318 (8) Å. Terdapat ikatan intermolekul yang lemah N-H···Cl yang bertanggungjawab untuk pemadatan molekul.

Kata kunci: 1,4-diaza-1,3-butadiena, kompleks diimina palladium, hablur sinar-X, hidrolisis, ikatan hidrogen

Introduction

The coordination chemistry of α-diimines, also known as 1,4-diaza-1,3-butadiene (R-DAB) compounds has been of substantial interest, over the past few decades due to the compounds displaying both flexibilities in their coordination mode to a metal centre, and their interesting electronic properties [1]. From the aspect of coordination chemistry, α-diimines are bidentate nitrogen donor ligands which have been widely used as ancillary ligands in metal complex formation, giving complexes with five-membered chelate rings [1, 2]. In addition, the double bond in the C=N bonds and the lone pair electrons on the nitrogen atoms allow the diimine molecule to act both as σ-donor and π-acceptor ligand in a coordination complex. Therefore, the versatility of this class of compounds has given rise to a number of applications in the fields of organic and organometallic synthesis and catalysis [3-7]. However, diimine compounds with an electron acceptor, are difficult to synthesize because of the insufficient basicity of amine attack to the carbonyl group to form imine bond. In addition, these types of compounds were often unstable and easily hydrolysed back to the amine. In this research, we observed that hydrolysis happened to palladium(II) diimine complexes, despite the diimine ligand being with an electron donor group substituent.

Hence, we report the synthesis of two palladium diimine complexes, through the reaction of R-DAB ligands with dichlorobis(acetonitrile)palladium(II), $[PdCl_2(CNMe)_2]$ precursors as shown in Scheme 1. Apart from showing the molecular structure of palladium diimine complex **2a**, the molecular structure of hydrolysed complex **2c** is also discussed in this paper.



Scheme 1. Synthesis of palladium diimine complexes

Materials and Methods

All of the synthetic reactions were conducted at room temperature. Palladium(II) chloride ($PdCl_2$) was purchased from Precious Metal Online, as the starting materials for the synthesis of $[PdCl_2(CNMe)_2]$ precursors. All chemicals used for the reaction were purchased from Fluka, Aldrich and Acros-organic. Unless otherwise stated, the chemicals and solvents were used without further purification. All NMR spectra were recorded on a JEOL 500 MHz FT-NMR spectrometer with appropriate deuterated solvent (DMSO-d_6: 2.50 ppm) and tetramethylsilane was used as the internal standard. The absorption spectra of the synthesized compounds were recorded on a Jasco V-630 Ultraviolet spectrophotometer in the range of 200–800 nm. Elemental analyses for carbon, hydrogen, nitrogen percentages in the synthesized compounds and complexes were carried out with Flashea 1112 Series CHN Elemental Analyzer.

Fourier-transform infrared spectroscopy (FT-IR) was recorded, in a KBr disc, using Thermo Scientific Nicolet iS10 Fourier-Transform Infrared Spectrophotometer, with the wavelength range from 400 to 4000 cm^{-1}. X-ray measurements for palladium(II) diimine complexes were performed on a Bruker D8 Venture diffractometer equipped with PHOTON II CPAD detector and IμS 3.0 Microfocus source of Cu Kα radiation source. The frame integration was performed using the program SAINT [8]. The structure was solved by a direct method provided by the program package SHELXTL-97 and refined a full matrix least square against F2 for all data [9]. All non-hydrogen atoms were refined anisotropically. All hydrogen atoms were introduced at idealized positions and were allowed to refine isotropically.

Preparation of R-DAB compounds

The R-DAB compounds, 1,4-bis(4-methoxyphenyl)-1,4-diaza-1,3-butadiene, **1a** and 1,4-bis(4-methylphenyl)-1,4-diaza-1,3-butadiene, **1b** were synthesized according to the procedure mentioned in previous paper [10].

Preparation of palladium complexes: Preparation of [1,4-bis(4-methoxyphenyl)-1,4-diaza-1,3-butadiene] dichloropalladium(II) (2a)

$[PdCl_2(CNMe)_2]$ precursor (0.19 mmol, 0.050 g) was transferred to a conical flask followed by addition of compound **1a** (0.19 mmol, 0.052 g) and 20 mL of dichloromethane. The mixture was stirred at room temperature for 24 hours yielding the product as a red precipitate, isolated by filtration, washed several times with cold dichloromethane and dried *in vacuo*. X-ray quality crystal was grown by slow evaporation of a DMF solution. Yield: 0.075 g, 88%. ^{1}H NMR (500 MHz, DMSO-d_6, δ, ppm): 8.46 (s, 2H, HC=N), 7.42 (d, 4H, J = 9 Hz, H_{Ar}), 7.00 (d, 4H, J = 9 Hz, H_{Ar}), 3.80 (s, 6H, OCH_3). ^{13}C NMR (125 MHz, DMSO-d_6, δ, ppm): 159.3, 157.6, 142.5, 123.2, 114.6, 55.6. IR (KBr, cm^{-1}): 2986(w), 2929(w), 1601(s), 1499(s), 1303(m), 1252(s), 540(m). UV-VIS (CH_2Cl_2 λmax /nm): 271, 319, 467, 499 and 534 nm. Anal. Calcd for $C_{16}H_{16}O_2N_2PdCl_2$: C, 43.12; H, 3.62; N, 6.29; Found: C, 43.06; H, 3.82; N, 6.21%.

Preparation of [1,4-bis(4-methylphenyl)-1,4-diaza-1,3-butadiene]dichloropalladium(II) (2b)

A similar procedure to the synthesis of **2a** was adopted. Yellow solid was obtained by reacting $[PdCl_2(CNMe)_2]$ precursor (0.23 mmol, 0.060 g) with compound **1b** (0.23 mmol, 0.055 g). Yield: 0.088 g, 92%.^{1}H NMR (500 MHz, DMSO-d_6, δ, ppm): 8.44 (s, 2H, HC=N), 7.30 (d, 4H, J = 8 Hz, H_{Ar}), 7.26 (d, 4H, J = 8 Hz, H_{Ar}), 2.34 (s, 6H, CH_3). ^{13}C NMR (125 MHz, DMSO-d_6, δ, ppm): 159.1, 147.2, 137.6, 129.9, 121.5, 20.7. IR (KBr, cm^{-1}): 3046(w), 2982(w), 1603(s), 1499(s), 1301(m), 530(m). UV-VIS (CH_2Cl_2 λmax /nm): 294, 371, 400 and 506 nm. Anal. Calcd for $C_{16}H_{16}N_2PdCl_2$: C, 46.46; H, 3.90; N, 6.77; Found: C, 46.16; H, 3.95; N, 6.72%.

Preparation of *trans*-dichloridobis(4-methylaniline-κN)-palladium(II) (2c)

Complex **2c** was obtained accidently from the recrystallization of complex **2b** *via* slow evaporation of DMF solution. The light orange crystal obtained was suitable for X-ray crystallography and discovered the formation of complex **2c**. In order to fully characterize complex **2c**, this complex was prepared accordingly to literature procedure [11] with slightly modification. $[PdCl_2(CNMe)_2]$ precursor (0.078 g, 0.30 mmol) was transferred to a conical flask followed by addition of 4-methylaniline (0.064 g, 0.60 mmol) and 15 mL of dichloromethane. The solution was stirred at room temperature and rapid formation of an orange yellow precipitate corresponding to **2c** was observed. The stirring was continued for 24 hours and then the orange yellow solid was isolated by filtration, washed with cold dichloromethane (3 × 2 mL) and dried *in vacuo*. X-ray quality crystal was grown by slow evaporation of a THF solution. Yield: 0.105 g, 89%. IR (KBr, cm^{-1}): 3281(s), 3205(s), 3120(m), 3035(w), 2915(w), 2859(w), 1593(w), 1570(m), 1511(s), 1379(w), 1217(m), 1117(s), 814(s), 742(m), 559(w). Anal. Calcd for $C_{14}H_{18}Cl_2N_2Pd$: C, 42.94; H, 4.63; N, 7.15; Found: C, 42.82; H, 4.56; N, 7.12%.

Results and Discussion

The palladium precursor, $[PdCl_2(CNMe)_2]$ was synthesized according to the literature procedure for the corresponding benzonitrile complexes [12]. The synthesis of palladium complexes **2a** and **2b** was conducted by reacting R-DAB ligands with the precursor complex, in DCM for 24 h (Scheme 1). The palladium diimine complexes were fully characterized using spectroscopic techniques and the molecular structures were determined using X-ray diffraction analysis.

The palladium(II) diimine complexes **2a** and **2b** were stable at room temperature in solid state, without observing any significant changes after being left in the air for a long period of time. However, the complex is unstable in the solution state, especially in DMSO. When a small amount of complex **2a** was dissolved in deuterated DMSO, the colour of the sample changed from red to orange in a few minutes. It was suspected that complex **2a,** underwent dissociation in DMSO solution, whereby the Pd-N bond was broken and the diimine compound **1a** was reformed. This was observed when we attempted to perform the NMR analysis for complexes **2a** and **2b** in DMSO-d_6, whereby a residual precipitate of $PdCl_2$ was found at the bottom of NMR tube. Consequently, no chemical shift was observed in the NMR spectra of complexes **2a-2b** as compared to the free ligands. Meanwhile, the NMR spectrum of complex **2c** displays a mixture of complex **2c** and 4-methylaniline, which was then hydrolysed from the diimine ligand **1b**. This can be supported by a literature study, whereby the successful formation of complex **2c** can only be characterized by solid state NMR spectroscopy, that produced spectra showing hydrogen and carbon peaks compatible with the proposed structure [11]. Despite the NMR spectroscopy not providing convincing evidence for

the formation of palladium complexes, the spectroscopic data from IR and UV have provided evidence for the changes, after the complexation reactions. In addition, further evidence for the successful formation of palladium diimine complexes was shown in the CHN analysis (Table 1) whereby the differences in percentages of carbon, hydrogen and nitrogen were less than ±0.4% indicating that the complexes **2a-2c** were pure.

Table 1. Analytical data for complexes **2a-2c**

Complex	Formula	Physical Appearance	Yield (%)	Observed (Calculated) C%	H%	N%
2a	$C_{16}H_{16}Cl_2N_2O_2Pd$	Red crystal	88	43.06 (43.12)	3.82 (3.62)	6.21 (6.29)
2b	$C_{16}H_{16}Cl_2N_2Pd$	Yellow solid	92	46.16 (46.46)	3.95 (3.90)	6.72 (6.77)
2c	$C_{14}H_{18}Cl_2N_2Pd$	Light orange crystal	89	42.82 (42.94)	4.56 (4.63)	7.12 (7.15)

Spectroscopy analysis of palladium complexes: FTIR analysis

The formation of the palladium diimine complexes **2a** and **2b** were supported by IR spectra as shown in Figures 1 and 2, respectively. In the IR spectra of the free R-DAB compounds, the C=N stretching vibration of imine group is located at 1607 cm^{-1} [10]. After complexation, the ν(C=N) stretching band was shifted to lower frequencies at 1600 cm^{-1} proving the presence of back bonding from the Pd metal centre to the π*orbitals of the diazadiene moiety. This shifting reveals the binding of imine nitrogen to the palladium metal centre was successfully formed. In addition, the ν(C-N) stretching vibration was also shifted to lower frequency at 1303 cm^{-1} which further support the participation of nitrogen atom in the complex formation. Besides, a new IR band is also observed at 540 cm^{-1} in the fingerprint region which is assigned to Pd-N bond [13].

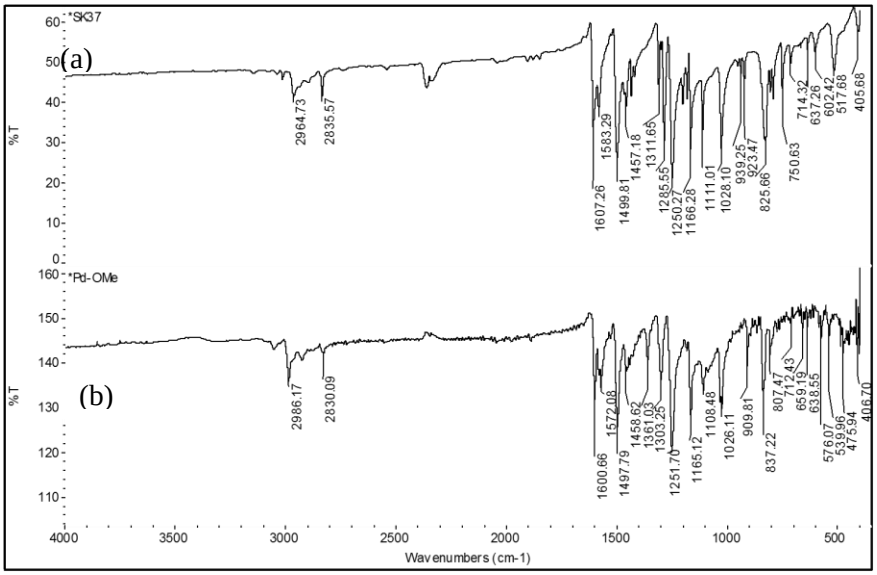


Figure 1. IR spectra of (a) R-DAB compound **1a** and (b) palladium diimine complex **2a**

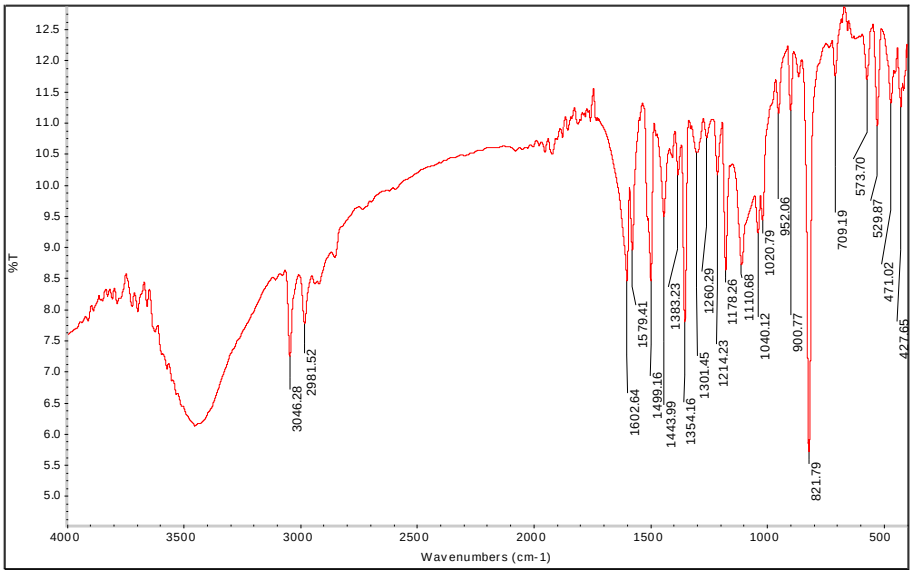


Figure 2. IR spectrum of palladium diimine complex **2b**

Based on the IR spectrum of complex **2c** (Figure 3), there is no sharp band observed in the range of 1630 cm^{-1} to 1600 cm^{-1} which corresponds to the -C=N- stretching vibration [14]. The absence of this signal proves that complex **2b** might undergo dissociation during recrystallization to form the diimine compound **1b**, and subsequently change to the parent amine. The presence of amine can be indicated by the occurrence of two N-H absorption bands at 3280 cm^{-1} and 3204 cm^{-1}. Moreover, a new band was also observed at 559 cm^{-1} in the fingerprint region which is assigned to Pd-N bond [13].

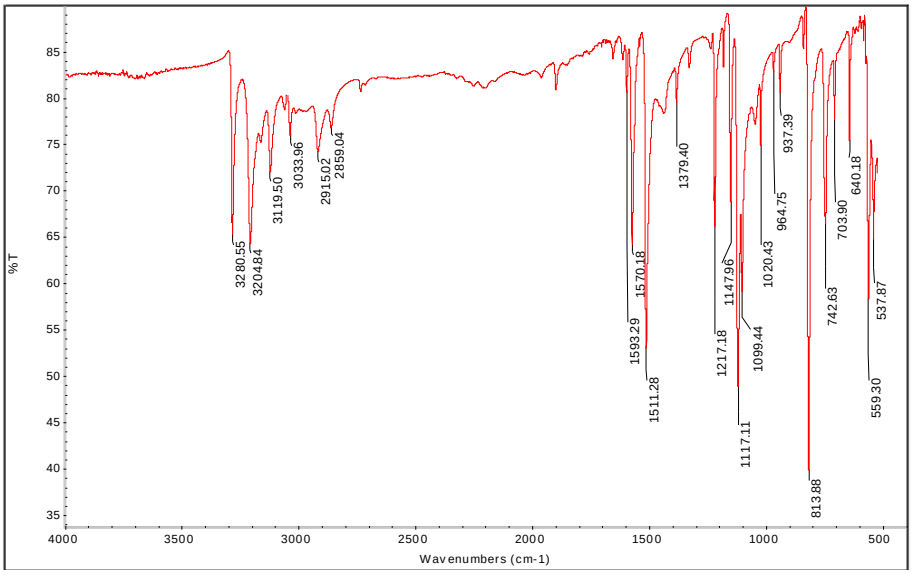


Figure 3. IR spectrum of complex **2c**

UV-Vis

The UV-Visible spectra of palladium(II) complexes **2a-2b**, were recorded in DCM solution at room temperature, at the wavelength of 240–800 nm. The important absorption peaks of compounds **1a-1b** and complexes **2a-2c** are

summarized in Table 2. In the UV-Visible spectrum of complex **2a** (Figure 4), five absorption peaks are observed at 271, 319, 467, 499 and 534 nm. The bands that appear at 271 nm are assigned to intra-ligand transition in the complex, indicating the π to π* transitions, due to the presence of benzene ring. In addition, the transition appeared at 319 nm, which is assigned to n to π* transition due to the presence of imine C=N bond [15]. In the visible region of the square planar palladium complexes, three spin-allowed d-d transitions were considered [16]. These transitions are corresponding to the transitions $^1A_{1g}\rightarrow{}^1A_{2g}$ at 467 nm, $^1A_{1g}\rightarrow{}^1B_{1g}$ at 499 nm and $^1A_{1g}\rightarrow 1E_g$ at 534 nm [17]. The UV-Visible spectrum of complex **2b** is similar to complex **2a**, except that there is lack of one band observed in the visible region due to the presence of very intense charge transfer band covering this band. Hence, only the band $^1A_{1g}\rightarrow{}^1B_{1g}$ at 400 nm, and $^1A_{1g}\rightarrow{}^1E_g$ at 506 nm are clearly observed.

Table 2. The UV-Vis data of compounds **1a-1b** and **2a-c**

Compounds	**Type of Transitions**				
	π→π*	**n→π***	***d-d***		
			$^1A_{1g}\rightarrow{}^1A_{2g}$	$^1A_{1g}\rightarrow{}^1B_{1g}$	$^1A_{1g}\rightarrow 1E_g$
1a	241, 294	373			
2a	217	319	467	499	534
1b	285	349			
2b	294	371		400	506

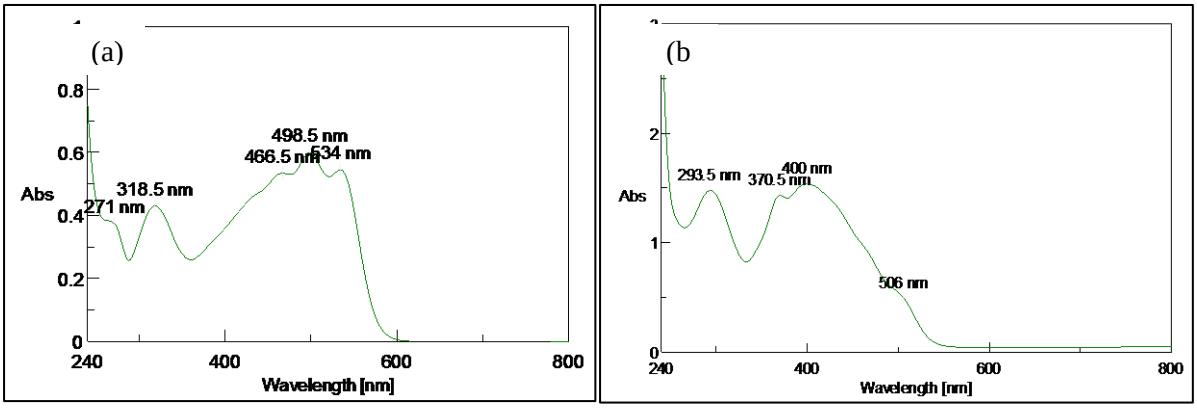


Figure 4. UV-visible spectra of (a) complex **2a** and (b) complex **2b**

Molecular structures of palladium complexes

Red crystal of complex **2a** and light orange crystal of complex **2c** were obtained, *via* slow evaporation of a DMF solution at ambient conditions. Both complexes have been structurally characterized by X-ray crystallography and the ORTEP diagram of both complexes, are shown in Figures 5 and 6. The main crystallographic parameters are tabulated in Table 3 and the selected bond lengths as well as bond angles are tabulated in Tables 4 and 5, respectively.

The X-ray crystallographic analysis of complex **2a**, reveals that the palladium metal centre coordinates with two azomethine nitrogen atoms of the R-DAB ligand in a *cis* configuration, forming a stable five-membered ring complex. Meanwhile, two chlorine atoms occupy the *trans* site of the azomethine nitrogen atoms. The Pd-N bond lengths are 2.045(2) and 2.033(2) Å, respectively, which is in the typical range for palladium α-diimine complexes [18]. The C00D-C00C bond length is 1.447(4) Å, which is slightly shorter than a standard C-C single bond length (1.54 Å) [19] due to the electron delocalization in the Pd five-membered ring. Complex **2a**, crystallized in a

monoclinic system with $P2_1/c$ space group. The bond angles of N004-Pd01-Cl02 and Cl03-Pd01-N005 were found to be 95.01(6)° and 94.27(6)° and revealed complex **2a** is in a distorted square planar geometry. The sum of internal angles of the chelating ring with the value of 539.31° indicates all of the five atoms of the chelating ring are in one plane [20].

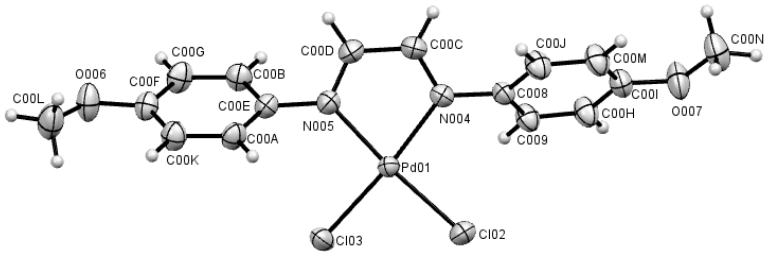


Figure 5. Molecular structure of complex **2a** with the thermal ellipsoids plotted at 50% probability

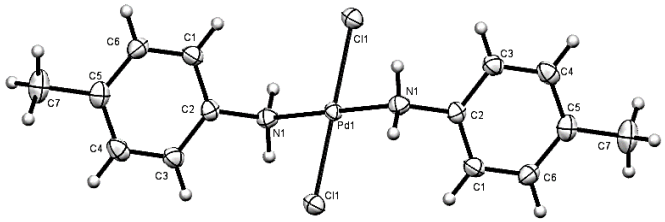


Figure 6. Molecular structure of complex **2c** with the thermal ellipsoids plotted at 50% probability

Table 3. Summary of crystal data and structure refinement parameters of complex **2a** and **2c**

Compound	**2a**	**2c**
Empirical formula	$C_{16}H_{16}Cl_2N_2O_2Pd$	$C_{14}H_{18}Cl_2N_2Pd$
Formula weight	445.61	391.60
Temperature (K)	298(2)	173(2)
Radiation, λ (Å)	Cu $_{K\alpha}$ 1.54178	Cu $_{K\alpha}$ 1.54184
Crystal system	Monoclinic	Orthorhombic
Space group	$P2_1/c$	Pbca
a (Å)	13.1291(3)	6.0261(10)
b (Å)	9.5829(2)	18.7585(4)
c (Å)	13.7811(3)	13.2455(3)
α (°)	90.00	90.00
β (°)	102.7720(10)	90.00
γ (°)	90.00	90.00
Volume ($Å^3$)	1690.97(6)	1497.28(5)
Z	4	4
ρc_{alcd} (g cm^{-3})	1.750	1.737
Absorption coefficient (mm^{-1})	11.847	13.170

Table 3 (cont'd). Summary of crystal data and structure refinement parameters of complex **2a** and **2c**

Compound	**2a**	**2c**
F(000)	888	784
Theta range for data collection (º)	3.29 to 72.44	5.740 to 76.069
Reflections collected	9901	4280
Independent reflections	3315	1343
Data / Restraints / Parameters	9901/ 0 / 210	4280 / 0 / 89
Goodness-of-fit on F^2	1.289	1.083
Final R indices [I>2σ(I)]	*R*1= 0.0207	*R*1 = 0.0402
	*wR*2= 0.0676	*wR*2 = 0.1103
R indices (all data)	*R*1= 0.0225	*R*1=0.0436
	*wR*2= 0.0699	*wR*2=0.1133
Maximum/minimum residual electron density (e $Å^{-3}$)	0.487/ -0.597	1.446/-0.855

Table 4. Selected bond lengths (Å) and angles (°) of complex **2a**

Bond Lengths (Å)		**Bond Angles (°)**	
Pd01-N004	2.045(2)	Cl03-Pd01-Cl02	90.58(2)
Pd01-N005	2.033(2)	N004-Pd01-Cl02	95.01(6)
Pd01-Cl02	2.2901(6)	N004-Pd01-Cl03	173.99(6)
Pd01-Cl03	2.2726(6)	N005-Pd01-Cl02	175.10(6)
C00C-C00D	1.447(4)	N005-Pd01-Cl03	94.27(6)
C00C-N004	1.283(3)	N005-Pd01-N004	80.18(8)
C00D-N005	1.288(3)		

Table 5. Selected bond lengths (Å) and angles (°) of complex **2c**

Bond Lengths (Å)		**Bond Angles (°)**	
Pd1-Cl1	2.318(8)	Cl1-Pd1-Cl1	180.0
Pd1-Cl1	2.318(8)	N1-Pd1-Cl1	88.64(9)
Pd1-N1	2.050(3)	N1-Pd1-Cl1	91.36(9)
Pd1-N1	2.050(3)	N1-Pd1-Cl1	88.64(9)
N1-C2	1.455(5)	N1-Pd1-Cl1	91.36(9)
		N1-Pd1-N1	180.0

Initially, we expected to obtain a similar structure of complexes **2a** and **2b** from the crystallographic analysis, but surprisingly, the complex **2b** was converted to **2c**, which is another structure, as shown in Figure 6 called *trans*-dichloridobis(4-methylaniline-κN)-palladium(II). This shows the imine (C=N) bond in complex **2b**, underwent hydrolysis and reformed the parent amine (R-NH_2) compound, when it was dissolved in DMF.

The X-ray crystallographic analysis of complex **2c** reveals a square planar geometry (Figure 5). The bond lengths of Pd1-N1 [2.050(3) Å] and Pd1-Cl1 [2.318(8) Å] are comparable with values found in [$PdCl_2(C_6H_5NH_2)_2$] [20]. The longer bond length of Pd-Cl than Pd-N bond indicates that the primary amine ($PhNH_2$) exerts stronger *trans*-effect, than the Cl atom due to its strong σ-donor nature. The crystal structure displays weak intermolecular N-H···Cl hydrogen bonding (Figure 7) [21].

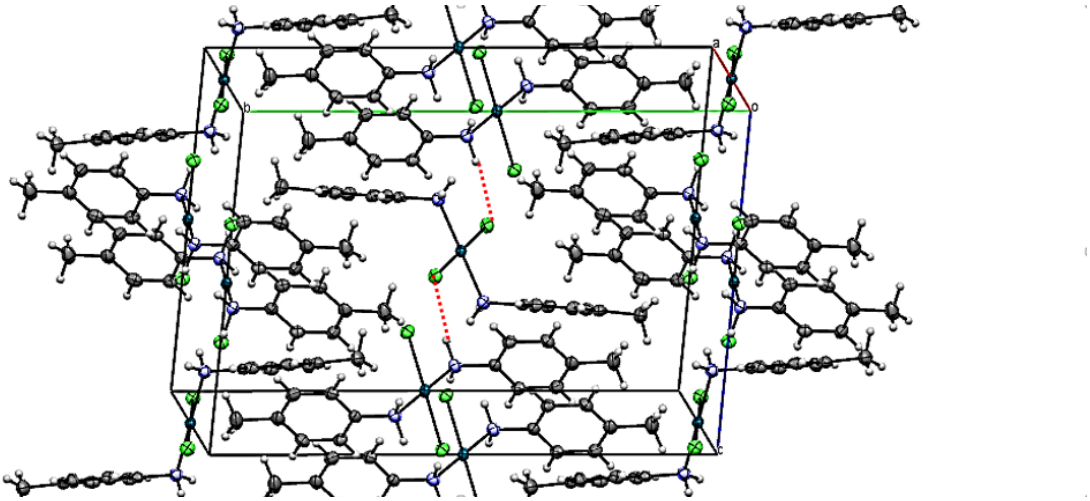
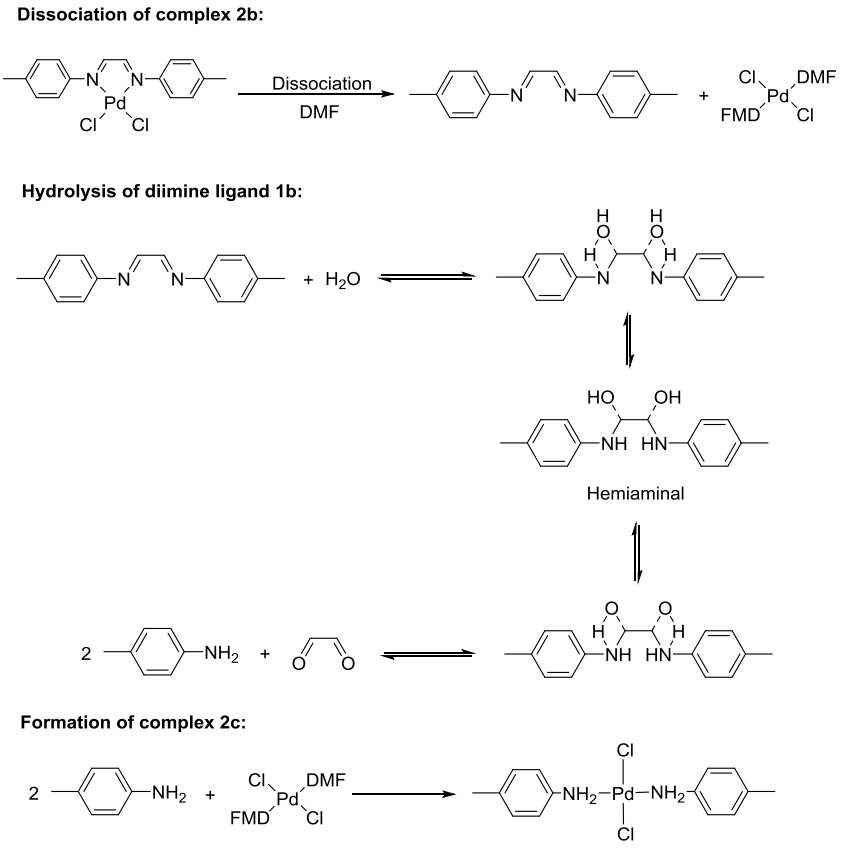


Figure 7. Crystal packing and view of the extensive hydrogen bonding (dashed lines) of complex **2c**

Mechanism of hydrolysis

A general mechanism is postulated (Scheme 2), to explain the formation of complex **2c** from **2b**. During the recrystallization of the palladium(II) diimine complex **2b**, the dissociation of ligand **1b** from the complex **2b** probably occurred, and subsequently led to the hydrolysis of diimine ligand **1b** to its starting materials, 4-methylaniline and glyoxal. In the subsequent step, the amino nitrogen atom of 4-methylaniline binds to the palladium metal to give a molecular complex **2c**. The mechanism for the hydrolysis reaction of diimine ligand **1b** involves three steps, namely: (i) formation of a hemiaminal intermediate; (ii) transferring the hydrogen atom bonded oxygen atom, to a nitrogen atom; and (iii) dissociation of the hemiaminal to give glyoxal and 4-methylaniline.



Scheme 2. Postulated mechanisms for the formation of complex **2c**

Conclusion

In conclusion, two palladium diimine complexes (**2a-2b**) using R-DAB ligands with $[PdCl_2(CNMe)_2]$ precursors were successfully synthesized. Complex **2b** was believed to be dissociated in DMF, to form diimine compound **1b** and subsequently hydrolysed to 4-methylaniline. The coordination of 4-methylaniline with $PdCl_2$ has led to the formation of *trans*-dichloridobis(4-methylaniline-κN)-palladium(II), **2c**. Both complexes were structurally characterized by X-ray crystallography.

Supplementary data

CCDC 1945836 and 1945837 contain the supplementary crystallographic data of complexes **2a** and **2c**, respectively. These data can be obtained free of charge from the Cambridge Crystallographic Data Centre via www.ccdc.cam.ac.uk/data_request/cif.

Acknowledgement

The authors would like to thank MyRA Special Grant Scheme [F07/SpGS/1549/2017] for financial support to the project.

References

1. Koten, G. V. and Vrieze, K. (1982). 1,4-diaza-1,3-butadiene (α-Diimine) ligands: Their coordination modes and the reactivity of their metal complexes. *Advances in Organometallic Chemistry*, 21(1): 151-239.
2. Bazargan, M., Mirzaei, M., Franconetti, A. and Frontera, A. (2019). On the preferences of five-membered chelate rings: Insights from the cambridge structural database and theoretical calculations. *Dalton Transactions*, 48(17): 5476-5490.

3. Sui, X., Hong, C., Pang, W. and Chen, C. (2017). Unsymmetrical α-diimine palladium catalysts and their properties in olefin (co)polymerization. *Materials Chemistry Frontiers*, 1(5): 967-972.
4. Fang, J., Sui, X., Li, Y. and Chen, C. (2018). Synthesis of polyolefin elastomers from unsymmetrical α-diimine nickel catalyzed olefin polymerization. *Polymer Chemistry*, 9(30): 4143-4149.
5. Saraiva, M. S., Nunes, C. D., Félix, V., Ribeiro, A. P. C., de Castro, C. N. and Calhorda, M. J. (2018). Molybdenum(II) complexes with α-diimines: Catalytic activity in organic and ionic liquid solvents. *European Journal of Inorganic Chemistry*, 35: 3922-3932.
6. Gomes, C. S. B., Gomes, P. T. and Duarte, M. T. (2014). α-diimine transition-metal complexes: Mechanochemistry − a new synthetic approach. *Journal of Organometallic Chemistry*, 760: 101–107.
7. Merino, E., Poli, E., Díaz, U. and Brunel, D. (2012). Synthesis and characterization of new ruthenium N-heterocyclic carbene Hoveyda II-type complexes. Study of reactivity in ring closing metathesis reactions. *Dalton Transactions*, 41(36): 10913-10918.
8. Siemens, SMART and SAINT. (1996). Siemens analytical X-ray instruments Inc., Madison, Wisconsin, USA.
9. Sheldrick, G. M. (1997). SHELXS-97, Program for crystal structure determination. University of Göttingen: Germany.
10. Tay, M. G., Chia, Y. Y., Kuan, S. H. C. and Phan, T. P. (2019). The formation of dinuclear trichloro‑bridged and mononuclear ruthenium complexes from the reactions of dichlorotris(p-tolylphosphine)ruthenium(II) with diazabutadiene ligands. *Transition Metal Chemistry*, 44(3): 293-301.
11. Grirrane, A., Garcia, H., and Álvarez, E. (2013). Isolation and X-ray characterization of palladium-N complexes in the guanylation of aromatic amines. Mechanistic implications. *Beilstein Journal of Organic Chemistry*, 9: 1455-1462.
12. Doyle, J. R., Slade, P. E., Jonassen, H. B. and Rhoda, R. N. (1960). Metal-diolefin coordination compounds. *Inorganic Syntheses*, 6(1): 216-219.
13. Budakoti, A., Abid, M. and Azam, A. (2006). Synthesis and antiamoebic activity of new 1-*N*-substituted thiocarbamoyl-3,5-diphenyl-2-pyrazoline derivatives and their Pd(II) complexes. *European Journal of Medicinal Chemistry*, 41(1): 63-70.
14. Kaya, Y., Yilmaz, V. and Buyukgungor, O. (2016). Synthesis, spectroscopic, structural and quantum chemical studies of a new imine oxime and its palladium(II) complex: Hydrolysis mechanism. *Molecules*, 21(1): 52.
15. Osowole, A. A. (2012). Synthesis, spectroscopic characterization, in-vitro antibacterial and anti-proliferative activities of some metal (II) complexes of 3,4-dihydronaphthalen-1(2h) one Schiff base. *Experimental Clinical Sciences International Online Journal*, 11: 338-345.
16. Das, S. and Pal, S. (2004). Cyclopalladated complexes with N-(benzoyl)-N'-(2,4-dimethoxybenzylidene)hydrazine: syntheses, characterization and structural studies. *Journal of Organometallic Chemistry*, 689(2): 352-360.
17. Takjoo, R., Takjoo, R., Yazdanbakhsh, M., Aghaei kaju, A. and Chen, Y. (2010). Mixed ligand palladium(ii) complex with ns-bidentates-allyldithiocarbazate Schiff base: Synthesis, spectral characterization, crystal structure and decoding intermolecular interactions with Hirshfeld surface analysis. *Chinese Journal of Chemistry*, 28(2): 221-228.
18. Zou, W. and Chen, C. (2016). Influence of backbone substituents on the ethylene (co)polymerization properties of α-diimine Pd(II) and Ni(II) catalysts. *Organometallics*, 35(11): 1794-1801.
19. Chandrasekaran, P., Greene, A. F., Lillich, K., Capone, S., Mague, J. T., DeBeer, S. and Donahue, J. P. (2014). A structural and spectroscopic investigation of octahedral platinum bis(dithiolene)phosphine complexes: Platinum dithiolene internal redox chemistry induced by phosphine association. *Inorganic Chemistry*, 53(17): 9192-9205.
20. Zhou, J., Sun, H., Harms, K. and Sundermeyer, J. (2008). Synthesis and X-ray crystal structures of acenaphthenequinone-based α-diimine palladium complexes and a novel V-shape tripalladium cluster. *Zeitschrift für anorganische und allgemeine Chemie*, 634(9): 1517-1521.
21. Chen, Y. B., Li, Z. J., Qin, Y. Y., Kang, Y., Wu, L. and Yao, Y. G. (2002). Synthesis and crystal structure of dichlorodianiline palladium(II)($C_6H_5NH_2)_2PdCl_2$. *Chinese Journal of Structural Chemistry*, 21(5): 530-532.

Malaysian Journal of Analytical Sciences, Vol 23 No 5 (2019): 839 - 848
DOI: https://doi.org/10.17576/mjas-2019-2305-09

MALAYSIAN JOURNAL OF ANALYTICAL SCIENCES
Published by The Malaysian Analytical Sciences Society
ISSN 1394 - 2506

REMOVAL OF PHTHALATES IN AQUEOS SAMPLES USING NON-IONIC SILICONE SURFACTANT MEDIATED CLOUD POINT EXTRACTION VIA SPECTROPHOTOMETRY

(Penyingkiran Ftalat dalam Sampel Akues Menggunakan Teknik Pengekstrakan Titik Awan Surfaktan Silikon Tidak Berionik dengan Spektrofotometri)

Pei Wan Ooi[1], Muggundha Raoov Ramachandran[2], Noorfatimah Yahaya[1], Nik Nur Syazni Mohamed Kamal[1], Kasturi Gopal[1], Nor Aniisah Husin[1], Nur Nadhirah Mohamad Zain[1]*

[1]*Integrative Medicine Cluster, Advanced Medical and Dental Institute, Universiti Sains Malaysia, 13200 Kepala Batas, Penang, Malaysia*
[2]*Department of Chemistry, Faculty of Science, Universiti Malaya, 50603 Kuala Lumpur, Malaysia*

**Corresponding author: nurnadhirah@usm.my*

Received: 16 April 2019; Accepted: 29 July 2019

Abstract

Removal of phthalates in environmental compartments become crucial in recent years due to the growing global concern about the health effects of phthalates. In this study, a greener method based on cloud point extraction procedure was developed for the removal of selected phthalates in environmental samples using non-ionic silicone surfactant (DC193C). The parameters affecting the extraction efficiency, such as the surfactant concentration, salt types, salt concentration, temperature and incubation time were evaluated and optimized. Good linearity with correlation coefficients (R^2) in the range of 0.9963 – 0.9988 for all calibration curves was obtained. The proposed method was applied in removing the diethhylhexyl phthalate and dibutyl phthalate in river water samples under optimized conditions with satisfactory recoveries in the range of 82 – 98%.

Keywords: cloud point extraction, non-ionic silicone surfactant, phthalates, spectrophotometry

Abstrak

Penyingkiran ftalat dalam alam sekitar menjadi satu isu yang penting kebelakangan ini disebabkan peningkatan kesedaran global mengenai kesan-kesan ftalat terhadap kesihatan. Dalam kajian ini, satu teknik pengekstrakan titik awan yang lebih mesra alam telah dibangunkan untuk penyingkiran ftalat tertentu daripada sampel alam sekitar dengan menggunakan surfaktan silikon tidak berionik (DC193C). Faktor-faktor yang mempengaruhi kecekapan pengekstrakan seperti kepekatan surfaktan, jenis garam, kepekatan garam, suhu dan masa keseimbangan telah dikaji dan dioptimumkan. Kelinearan baik dengan pekali korelasi (R^2) dalam julat 0.9963 – 0.9988 telah dicapai untuk semua lengkung tara. Kaedah yang dicadangkan telah digunakan untuk penyingkiran dietilheksil ftalat dan dibutil ftalat dalam sampel alam sekitar yang telah dipilih di bawah keadaan yang optimum dengan perolehan semula yang memuaskan dalam julat 82 – 98 %.

Kata kunci: pengekstrakan titik awan, surfaktan silikon tidak berionik, ftalat, spektrofotometri

Introduction

Phthalates, also known as phthalic acid esters, are a class of chemical compounds used widely in industrial and domestic applications to increase the flexibility and durability of the product [1]. Phthalates are esters manufactured

through reaction of phthalic anhydride with oxo alcohol through esterification which occurs in two successive steps: (1) the formation of monoester by alcoholysis of phthalic acid, and (2) the conversion of the monoester to the di-ester [2]. Since the chemical and physical properties of the individual phthalates depend on the functional group, the types of phthalates added to the products are determined by their function and properties [3]. Phthalates are not covalently attached, therefore significant amount have leached into the environmental compartment during the process of their production, usage and disposal, mainly via natural and anthropogenic combustion processes [4].

Despite their short half-lives in the human body, phthalates are found to be capable of causing adverse effects and are toxic to many species including protozoans, fishes and invertebrates due to the intensive and continuous release of these pollutants into the environments [5, 6]. The United State Environmental Protection Agency (USEPA) has included an initial list of chemicals, which include phthalates, into a program under the Toxic Substances Control Act (TSCA) [7]. Among all the phthalates used worldwide, diethylhexyl phthalate (DEHP) is the one that causes most concern since DEHP is the most commonly produced and used. It is reported that more than two million tons of DEHP has been produced worldwide [2]. Even though no criterion have been set for saltwater aquatic life, the water quality criteria for dibutyl phthalate (DBP) and DEHP are determined to be 5 mgL^{-1} and 10 mgL^{-1} respectively by USEPA for protection of human health [8].

In order to monitor these contaminants in the environment, many extraction methods have been employed. Among the traditional liquid-liquid extraction (LLE) methods, cloud point extraction (CPE) requires a very small amount of relatively nonflammable and nonvolatile surfactant that is environmentally-friendly. Another important merit is that no analytes is lost because it is unnessary to evaporate the solvents. CPE is a technique that use surfactant and manipulate temperature to induce formation of micellar environment [9]. Surfactants consists of amphiphilic molecules that assemble in various shapes, which then self-organize to form micelle when the concentration of the surfactant is above critical micellar concentration (CMC). When the surfactant solution was heated to cloud point temperature (CPT), the solution will become turbid and separate into two immiscible phases; surfactant rich phase (small volume) and aqueous phase (bulk amount). This method is based on the principle of decreasing solubility of the surfactant in the water at certain temperature, thus separation into two phases [10].

Well-known previous non-ionic surfactants, such as Triton X and PONPE series, have a high background absorbance in the ultraviolet region, due to the presence of an aromatic moiety in their structure. Using a surfactant without ultraviolet absorbance signals is considered to be the best way to avoid the absorbance interference. Silicone surfactant has gained attention since it is not only endowed with the common features of conventional non-ionic surfactants but also posseses some unique properties. It is reported that silicone surfactants are known to be equally surface active in both water and non-aqueous solvents besides their ability to remain as liquid even with high molecular weights [11]. Non-ionic silicone DC193C surfactant, which is also referred to as polyethylene glycol (PEG), PEG-12 Dimethicone and polydimethylsiloxane copolymer polyols, has a wide range of applications in personal care products as well as in automotive and household cleaning products. Even though this surfactant is yet to be fully studied for its application in CPE, this surfactant has the potential to be a green alternative as their safety to human and environmental friendly has been recognized [12]. In this study, the main objectives is to develop a new approach of CPE method by using non-ionic silicone surfactant DC193C for removing DBP and DEHP in water samples. The developed method was then applied on selected river water samples around industrial areas for the removal of selected phthalates.

Materials and Methods

Instrumentation

A Perkin Elmer Precisely, Model Lambda 25 UV-Vis spectrophotometer (Massachusetts, U.S.) was used for the measurement of selected DBP and DEHP. A Memmert water bath (Schwabach, Germany) was used to maintain the desired temperature.

Chemicals and reagents

Dow Corning DC193C, also known as polyethylene glycol (PEG) silicone, was supplied by Ingredients Plus, (Selangor, Malaysia). The values of *x*, *y* and molecular weight of this compound was available from the manufacturer. Triton X-114 was supplied from Sigma Aldrich (St. Louis, MO, USA). Triton X-100 was obtained

from R&M Chemicals (Essex, UK). Surfactant sodium dodecyl sulphate (SDS) was purchased from Fisher Chemical (Pittsburgh, USA). Tween-80 and Tween-20 were purchased from Fisher Chemical (Pittsburgh, USA). Tween-80 and Tween-20 were purchased from Merck (Darmstadt, Germany). Dibutyl phthalate (molecular weight: 278.34 g/mol, λ_{max}: 230 nm) was purchased from Sigma Aldrich (St. Louis, MO, USA; 99% purity) while diethylhexyl phthalate (molecular weight: 390.56 g/mol, λ_{max}: 228 nm) was purchased from Dr Ehrenstorfer GmBH (Augsburg, Germany; 98.5% purity). Figure 1 shows the absorption of the UV-Vis spectra for DBP and DEHP. Stock solutions of each phthalates (1000 ppm) were prepared in methanol. Working solution were prepared daily by appropriate dilution of the stock solutions with deionized water. Potassium hydroxide (KOH), potassium chloride (KCl), sodium chloride (NaCl), sodium nitrate (Na_2NO_3) and sodium sulphate (Na_2SO_4) (QRec, Malaysia) were prepared by dissolving an appropriate amount in deionized water.

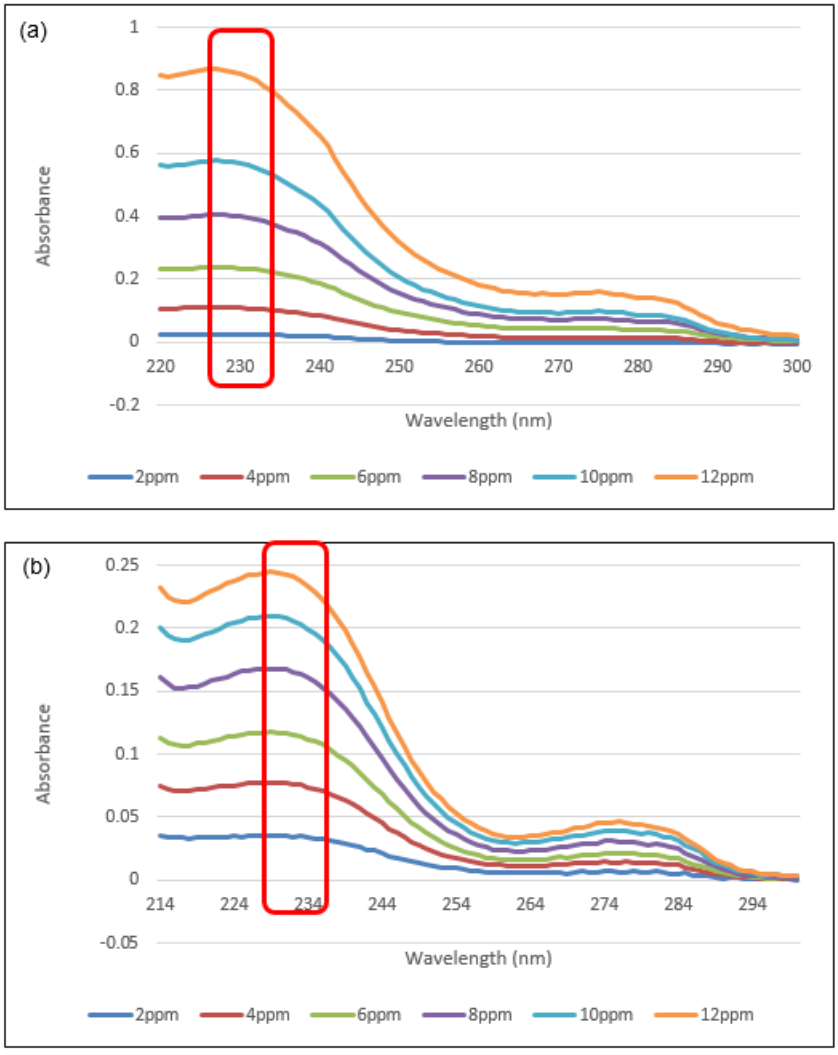


Figure 1. Absorption of the UV-Vis spectra for (a) DEHP and (b) DBP

Cloud point extraction

An aliquot of 1.0 mL of sample containing the analyte (10 ppm), 1.0 mL of surfactant DC 193C (0.1% v/v) and 0.5 mL of 1.5 M of Na_2SO_4 were mixed and sonicated for 6 minutes in a glass centrifuge tube. Then, the phase separation was induced by heating the content in a water bath at 50 °C for 20 minutes. Surfactant rich phase was at

the top layer and aqueous phase was at the bottom after two phases were formed. The surfactant rich phase was then separated by using a syringe needle for minimizing the possibility of cross contaminating the analyte. After that, the surfactant rich phase was diluted 5-fold with deionized water to reduce its viscosity and to make the final volume feasible to be transferred into the optical cell to be measured at respective maximum absorption. Three replicate experimental data (n=3) was collected in each optimization. Standard solutions containing 5, 50 and 300 µg L^{-1} of DEHP and DBP were added to a real water samples for the recovery test, respectively.

Sample collection

Water samples (1L) were taken and collected in Duran® bottles from five selected rivers in industrial area in Penang, Malaysia, namely Sungai Derhaka Juru (5.3500° N, 100.4167° E), Sungai Juru (5.3333° N, 100.4000° E), Sungai Nibong Kecil (5.3422°, 100.3028° E), Sungai Ara (5.44187° N, 100.3167° E) and Sungai Perai (5.3833° N, 100.3833°E). Prior to analysis, the water samples were first filtered using a 0.45 µm nylon membrane filter to remove any suspended particulate materials and then stored at 4 °C before extraction.

Results and Discussion

Optimization of parameters in CPE

The influential factors that affect the extraction efficiency in CPE such as temperature, incubation time, type of salt and concentration of salt used have been optimized in this study. The extraction efficiency was calculated using Eq. (1):

$$\text{Extraction efficiency, (\%)} = \frac{C_S V_S}{C_0 V_0} \times 100\% \quad (1)$$

where C_S represents the phthalates concentration in the surfactant rich phase volume V_S; C_0 represents the phthalates concentration in the initial sample-surfactant mixture of volume V_0.

Screening of surfactant types

Six types of non-ionic surfactants such as Triton X-114, Triton X-100, sodium dodecyl sulphate (SDS), Tween 80, Tween 20 and DC193C were compared. In this study, non-ionic silicone DC193C was chosen as CPE surfactant due to its non-toxic, non-flammable and greener properties as compared to Triton X series and Tween series surfactants used previously in CPE [13, 14]. Triton surfactants are found to have aromatic chromophore that will interfere with the ultraviolet absorbance or fluorescence signals [15] while Tween surfactants are well known for their high viscosity [16]. The absorbance spectrum of different types of surfactant was shown in Figure 2.

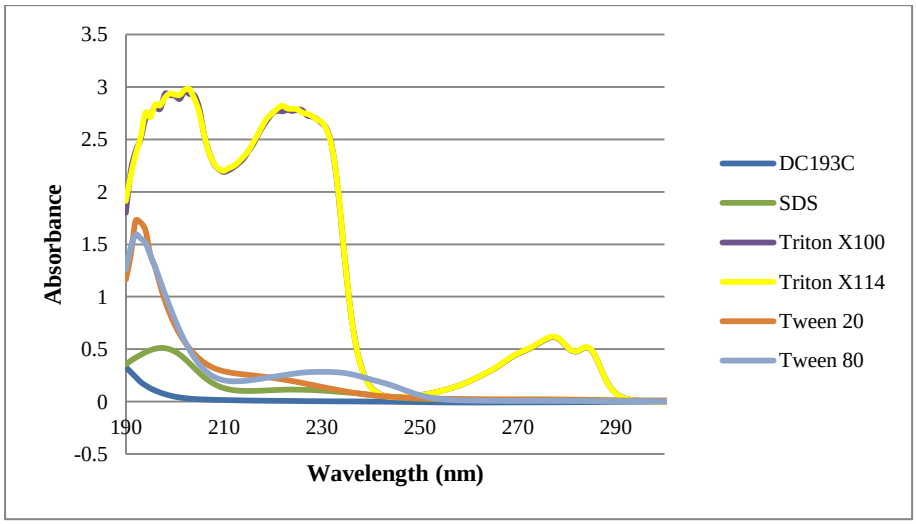


Figure 2. Absorbance spectrum of different types of surfactants

Effect of surfactant concentration

Surfactants are amphiphilic molecules that can interact with both polar and non-polar groups in the surrounding environment. The molecules undergo self-assembly and form well defined aggregates, known as micelles, when the concentration reaches CMC [17]. Since the concentration of surfactant plays important role in formation of micelles, 0.1% v/v to 1.0% v/v of non-ionic silicone DC193C surfactant were studied to select suitable surfactant concentration. Based on Figure 3, the extraction efficiency slightly increased as the concentration of surfactant increased. However, there was no significant difference on the extraction efficiency in the range of surfactant concentration studied. Since CPE is a greener method, minimum concentration of surfactant used was desired in this study to obtain maximum extraction of selected phthalates. Thus, since 0.1% v/v of DC193C was able to obtain more than 75% of recovery, 0.1% v/v was selected in this part as an approach for an optimal consumption of raw materials, solvents and energy.

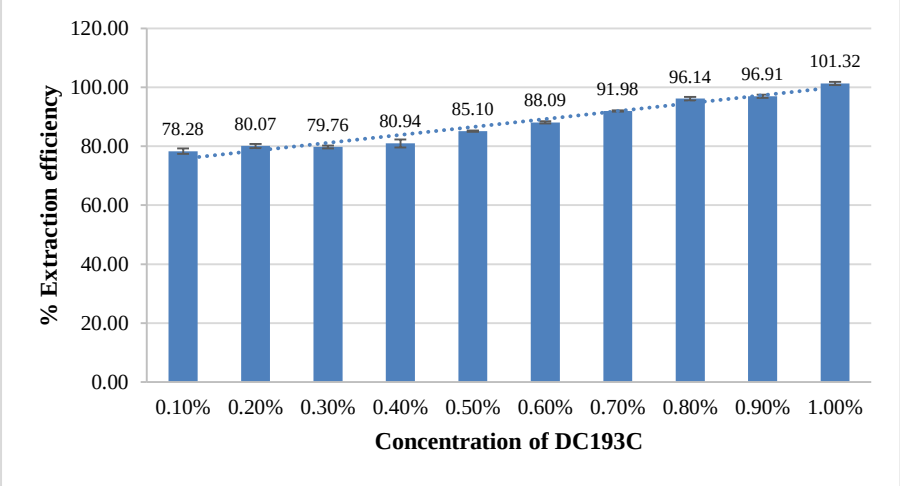


Figure 3. Effect of concentration of DC193C on extraction efficiency of DBP in CPE. Condition: 10 ppm of phthalates, 1.5 mol L^{-1} of Na_2SO_4 at 50 °C

Effect of temperature and incubation time

Cloud point temperature (CPT) is another important characteristic for non-ionic surfactants whereby the surfactants will be separated into two phases at this point temperature. Increasing the temperature will reduce the interaction between the surfactant and water through breakdown of the hydrogen bonds between the water molecules and the hydrophilic part of surfactant [18]. The clouding process is also ascribed as the efficient and effective dehydration of hydrophilic portion of micelles at higher temperature condition [19]. As a result, the external layer of the rapidly increasing number of micelles can be dehydrated with the approach of CPT and the mixture can be separated into phases. Non-ionic silicone DC193C surfactant used in this study has a high cloud point temperature, which is approximate 87 °C [12]. However, adding salt to the surfactant micellar solution can decrease the CPT and facilitates the separation of the two phases by altering the density of the bulk aqueous phase. Thus, different temperatures were studied in this part of experiment starting from room temperature, 25 °C to 80 °C. Figure 4(a) shows the extraction efficiency for both DEHP and DBP increased as the temperature increased from 25 °C to 50 °C and yet started to decrease when the temperature was above 50 °C. Non-ionic silicone surfactant appears moderately more hydrophobic at higher temperatures owing to an equilibrium shift that favours dehydration of the ether oxygens. This leads to an increase in the number concentration of micelles. Hence, the solubilization capability of the micellar solution increases with temperature leading to increase in the DBP and DEHP extraction. Unfortunately, elevated temperature may lead to decomposition of the analytes even though raising of temperature may improve the interaction between surfactant molecules and analytes [20].

Incubation time is another parameter optimized in the CPE since employment of shortest equilibration time is one of the compromise between efficient separation of phases and completion of extraction [21]. The shortest incubation

time with high extraction efficiency is preferable in CPE [22]. Thus, the study was carried out in the range from 5 to 30 minutes at 50 ^{o}C as shown in Figure 4(b). Based on the result, the extraction efficiency increased as the incubation time increased to 20 minutes and decreased when the incubation time continued to increase. Hence, 20 minutes at 50 ^{o}C was chosen as an incubation time for both analytes since this is the lowest possible temperature and shortest incubation time with higher extraction efficiency.

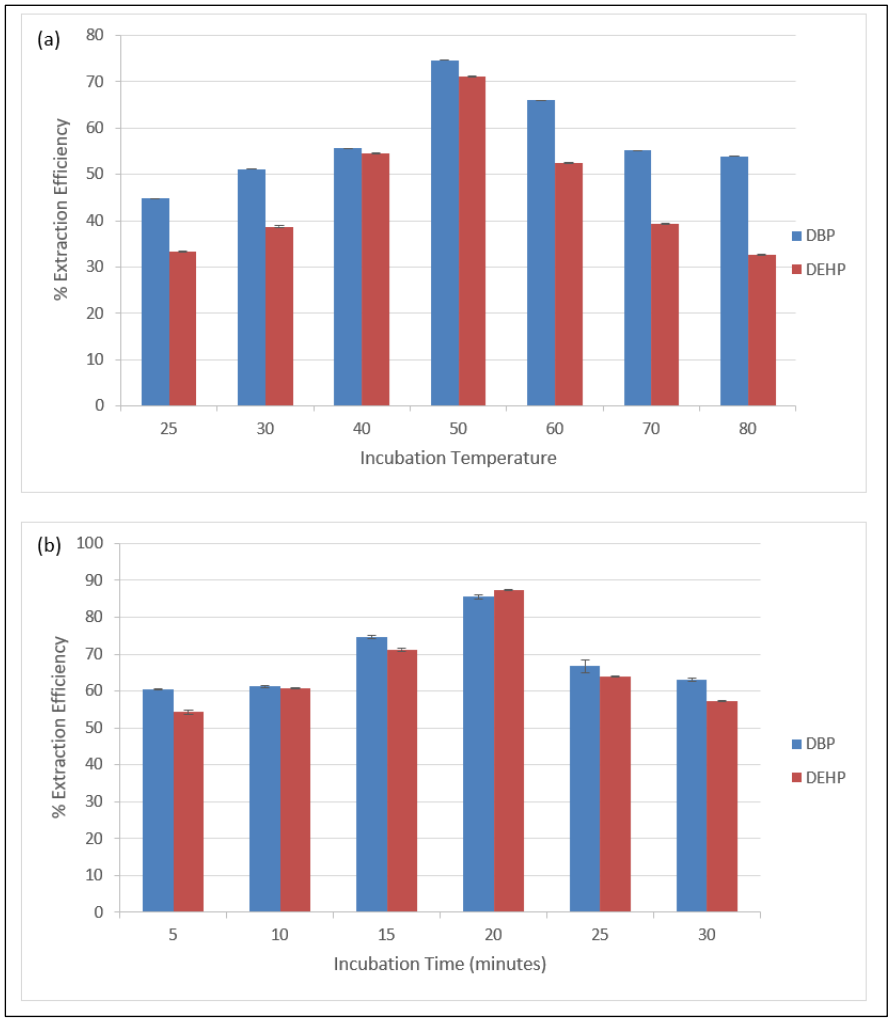


Figure 4. Effect of (a) temperature and (b) incubation time on extraction efficiency of phthalates in CPE. Condition (a): 10 mg L^{-1} of phthalates, 0.1 %v/v of DC193C, 1.5 mol L^{-1} of Na_2SO_4. Condition (b): 10 mg L^{-1} of phthalates, 0.1 %v/v of DC193C, 1.5 mol L^{-1} of Na_2SO_4 at 50 ^{o}C

Effect of salt types

Generally, CPE can be carried out without additives. However, the addition of salt to the solution may influence the extraction process. In the case of most non-ionic surfactants, the presence of salt may facilitate phase separation since it increases the density of the aqueous phase. Available electrolytes can also change the CPT of non-ionic surfactants [10]. This is because salt will decrease the solubility of surfactant in water and can alter the CPT and facilitate the separation of two phases by altering the density of the bulk aqueous phase [23]. This will then lead to the easier formation of two phases, which are surfactant rich phase and aqueous phase. Based on Table 1, only sodium sulphate (Na_2SO_4) helped in transferring the selected phthalates and formed surfactant rich phase while there

is no phase formation when other salts were employed. This finding is in agreement with other study which also reported that Na_2SO_4 salt may enhance the solubility of analytes in the surfactant rich phase through increasing the size of the micelles and aggregation number [24]. Enhanced solubility will result in higher extraction efficiency since there will be lesser water in the surfactant rich phase. The enhanced solubility is due to the ability of kosmotropic ions such as carbonate (CO_3^{2-}) and sulphate (SO_4^{2-}) in interacting with water molecules [25]. The unique characteristics of sodium sulphate which is comprised of Na^+ cation and SO_4^{2-} anion play some roles [26]. Na^+ cation is found to have the ability to reduce the cloud point temperature while SO_4^{2-} anion can speed up the dehydration of the micelle since it is a polyvalent ion.

Table 1. Effect of Salt (% Extraction efficiency ± RSD)

Salts	Dibutyl Phthalate (DBP)	Diethylhexyl Phthalate (DEHP)
Na_2NO_3	No phase formation	No phase formation
KCl	No phase formation	No phase formation
NaCl	No phase formation	No phase formation
KOH	No phase formation	No phase formation
Na_2SO_4	83.64 ± 0.21	87.83 ± 0.41

Effect of salt concentration

Ghasemi and Kaykhaii reported that salt concentration can change the ionic strength of the sample solution which then helped in reducing the cloud point [13]. Thus, different concentration of Na_2SO_4, ranging from 0.5 M to 3.0 M, were studied. However, phase separation did not occur when 0.5 M and 1.0 M of salt were employed (not shown in Figure 5). Based on the result obtained, 1.5 M of salt gave the greatest extraction efficiency among all concentrations. However, the percentage of recovery decreased as the concentration of salt employed increased. This result agreed with other study [27] which reported on the usage of calcium chloride to facilitate the extraction of congo red. The addition of excessive Na_2SO_4 (> 1.5 M) to the micellar solution will lead to very low CPT and, thus, render the formation of unwanted and very viscous surfactant rich phase [28]. Therefore, 1.5 M has been chosen as the concentration of salt to be employed for this study. Figure 6 shows the proposed mechanism between non-ionic silicone surfactant of DC193C and DBP.

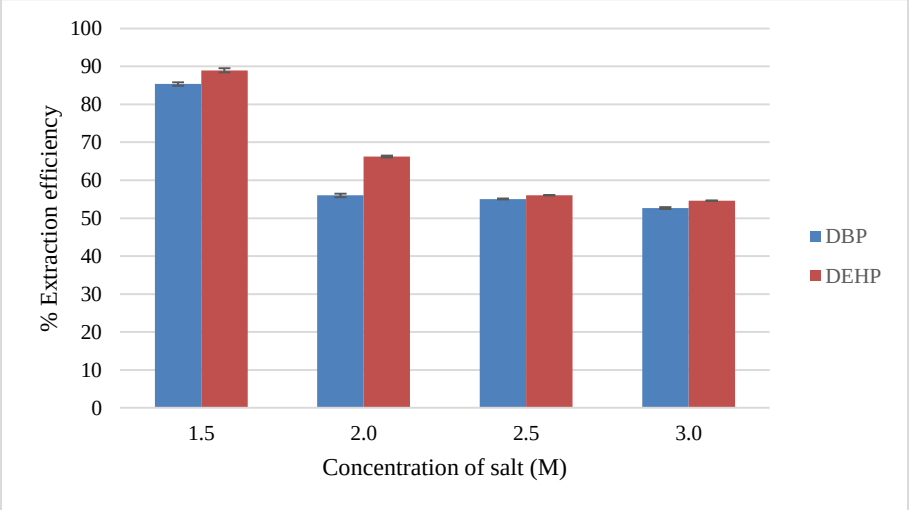


Figure 5. Effect of salt concentration on extraction efficiency of phthalates in CPE. Condition: 10 mg L^{-1} of phthalates, 0.1 %v/v of DC193C, 50 ^oC

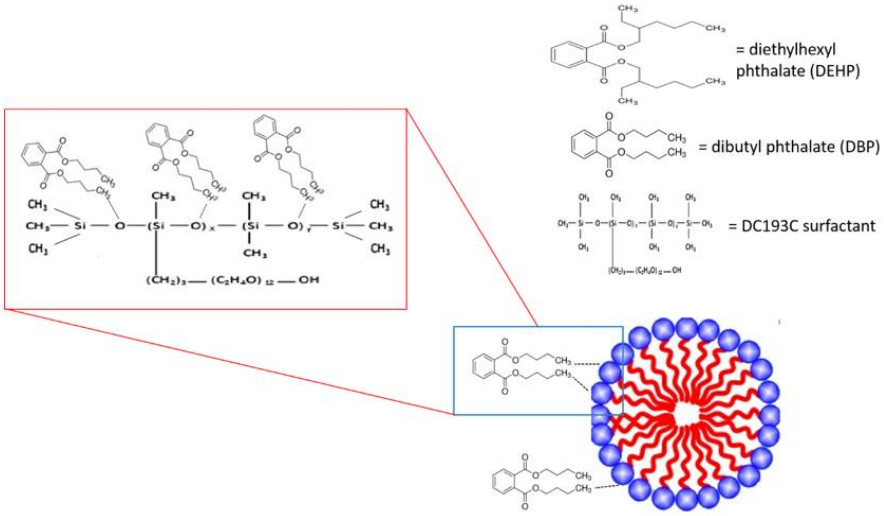


Figure 6. Proposed mechanism between non-ionic silicone surfactant and DBP

Method validation

Under the optimized conditions, the calibration graphs were constructed by plotting the absorbance signal against the concentrations of each analyte according to the general procedure for the CPE. The measurement of each analyte spectrophotometrically at the respective absorption maxima against a reagent blank were prepared under similar conditions. The calibration data are summarized in Table 2.

Table 2. Method validation of spectrophotometric of phthalates species using CPE

Analytes	Linear Equation	Linear Range ($\mu g\ L^{-1}$)	R^2
DEHP	y = 0.0001 x + 0.0065	1 – 500	0.9963
DBP	y = 0.0002 x + 0.0029	1 – 500	0.9988

Application in real samples

The calibration graphs in the range of 1 – 500 $\mu g\ L^{-1}$ were constructed by plotting the absorbance signal against the concentration of each phthalate sample according to the general procedure under the optimized conditions. The developed method was applied to evaluate its feasibility by spiking each phthalate to the water sample. The results were summarized in Table 3 and the recoveries for all phthalates were calculated to be in the range of 82 – 98%. Therefore, the method can be considered as a reliable method for the removal of phthalates in water samples.

Table 3. Recovery of phthalates species in spiked environmental waters

Analytes	Added (μg L^{-1})	% Recovery (% RSD, *n*=3)				
		Sungai Derhaka Juru	Sungai Juru	Sungai Nibong Kecil	Sungai Ara	Sungai Perai
DEHP	5	83 (7.18)	94 (8.65)	84 (10.39)	82 (10.16)	94 (2.74)
	50	86 (1.96)	96 (2.22)	91 (7.18)	91 (6.41)	93 (6.45)
	300	87 (2.22)	92 (0.87)	98 (1.28)	82 (2.45)	98 (1.30)
DBP	5	83 (4.51)	85 (4.91)	88 (4.46)	85 (6.11)	91 (5.09)
	50	85 (0.96)	85 (1.68)	87 (1.90)	83 (2.56)	84 (4.96)
	300	94 (2.18)	86 (2.12)	88 (0.87)	83 (0.50)	91 (0.79)

Conclusion

The non-ionic surfactant-based polyethylene glycol silicone has been demonstrated to be useful in the extraction of DBP and DEHP from water samples. Under the optimized conditions (1 mL of 0.1% v/v DC193C surfactant; 1.5 mol L^{-1} of Na_2SO_4; 50 ^oC of incubation temperature and 20 minutes of incubation time), the extraction efficiency for both phthalates were in the satisfactory range of 82% to 98% with relative standard deviation (RSD) value less than 10.39%. The proposed CPE is an easy, safe and inexpensive methodology for the extraction of DBP and DEHP from water samples using non-ionic silicone surfactant. Therefore, the DC193C non-ionic silicone surfactant as an extractant in the CPE has a great potential to be explored for removing contaminants and pollutants from water samples due to their unique structure molecules that could entrap hydrophobic and as well as hydrophilic substances.

Acknowledgement

The authors gratefully acknowledge Universiti Sains Malaysia and the Ministry of Education Malaysia for financial support through the Bridging Grant (304.CIPPT.6316266) and Fundamental Research Grant Scheme (FRGS: 203.CIPPT.6711661). The authors also acknowledge the Advanced Medical and Dental Institute, Universiti Sains Malaysia for the facilities provided.

References

1. Pérez-Outeiral, J., Millán, E. and Garcia-Arrona, R. (2016). Determination of phthalates in food simulants and liquid samples using ultrasound-assisted dispersive liquid–liquid microextraction followed by solidification of floating organic drop. *Food Control*, 62: 171-177.
2. Mariana, M., Feiteiro, J., Verde, I., and Cairrao, E. (2016). The effects of phthalates in the cardiovascular and reproductive systems: A review. *Environment International*, 94: 758-776.
3. Chen, B. and Zhang, L. (2013). An easy and sensitive analytical method of determination of phthalate esters in children's toys by UPLCMS/MS. *Polymer Testing*, 32(4): 681-685.
4. Zhang, L., Dong, L., Ren, L., Shi, S., Zhou, L., Zhang, T., and Huang, Y. (2012). Concentration and source identification of polycyclic aromatic hydrocarbons and phthalic acid esters in the surface water of the Yangtze River Delta, China. *Journal of Environmental Sciences*, 24(2): 335-342.
5. Chen, X., Xu, S., Tan, T., Lee, S. T., Cheng, S. H., Lee, F. W. F., and Ho, K. C. (2014). Toxicity and estrogenic endocrine disrupting activity of phthalates and their mixtures. *International Journal of Environmental Research and Public Health*, 11(3): 3156-3168.
6. Koch, H. M. and Calafat, A. M. (2009). Human body burdens of chemicals used in plastic manufacture. *Philosophical Transactions of the Royal Society B: Biological Sciences*, 364(1526): 2063-2078.
7. Schecter, A., Lorber, M., Guo, Y., Wu, Q., Yun, S. H., Kannan, K., and Cheng, D. (2013). Phthalate concentrations and dietary exposure from food purchased in New York State. *Environmental Health Perspectives*, 121(4): 473.

8. Regulations, U.S.E.P.A. (1980). Ambient water quality criteria for Phthalate Esters. 1980: The Division.
9. Souza, V.S., Teixeira, L.S. and Bezerra, M.A. (2016). Application of multivariate designs in the development of a method for vanadium determination in natural waters by HR-CS GF AAS after cloud-point extraction. *Microchemical Journal*, 129: 318-324.
10. Santalad, A., Burakham, R., Srijaranai, S., Srijaranai, S., and Deming, R. L. (2012). Role of different salts on cloud-point extraction of isoprocarb and promecarb insecticides followed by high-performance liquid chromatography. *Journal of Chromatographic Science*, 50(6): 523-530.
11. Soni, S., Panjabi, S. and Sastry, N. (2011). Effect of non-electrolyte additives on micellization and clouding behavior of silicone surfactant in aqueous solutions. *Colloids and Surfaces A: Physicochemical and Engineering Aspects*, 377(1): 205-211.
12. Bingjia, Y., Li, Y., Qiong, H., & Shigendo, A. (2007). Cloud point extraction of polycyclic aromatic hydrocarbons in aqueous solution with silicone surfactants. *Chinese Journal of Chemical Engineering*, 15(4): 468-473.
13. Ghasemi, E. and Kaykhaii, M. (2016). Application of micro-cloud point extraction for spectrophotometric determination of malachite green, crystal violet and rhodamine B in aqueous samples. *Spectrochimica Acta Part A: Molecular and Biomolecular Spectroscopy*, 164: 93-97.
14. Zain, N., Abu Bakar, N. and Mohamad, S. (2016). Study of removal of phenol species by adsorption on non-ionic silicon surfactant after cloud point extraction methodology. *Desalination and Water Treatment*, 57(8): 3532-3543.
15. Zain, N., Bakar, N. A., Mohamad, S., and Saleh, N. M. (2014). Optimization of a greener method for removal phenol species by cloud point extraction and spectrophotometry. *Spectrochimica Acta Part A: Molecular and Biomolecular Spectroscopy*, 118: 1121-1128.
16. Hollis, G.L. (2007). Surfactants Europa. Royal Society of Chemistry Publishing.
17. Salem, J. K., El-Nahhal, I. M., Najri, B. A., and Hammad, T. M. (2016). Utilization of surface Plasmon resonance band of silver nanoparticles for determination of critical micelle concentration of cationic surfactants. *Chemical Physics Letters*, 664: 154-158.
18. Ren, Y., Zhao, B., Chang, Q., and Yao, X. (2011). QSPR modeling of nonionic surfactant cloud points: An update. *Journal of Colloid and Interface Science*, 358(1): 202-207.
19. Samaddar, P. and Sen, K. (2014). Cloud point extraction: A sustainable method of elemental preconcentration and speciation. *Journal of Industrial and Engineering Chemistry*, 20(4): 1209-1219.
20. Tang, X., Zhu, D., Huai, W., Zhang, W., Fu, C., Xie, X., and Fan, H. (2017). Simultaneous extraction and separation of flavonoids and alkaloids from *Crotalaria sessiliflora* L. by microwave-assisted cloud-point extraction. *Separation and Purification Technology*, 175: 266-273.
21. Pirdadeh-Beiranvand, M., Afkhami, A. and Madrakian, T. (2017). Cloud point-magnetic dispersive solid phase extraction for the spectrofluorometric determination of citaloperam. *Journal of Molecular Liquids*, 241: 43-48.
22. Yang, X., Li, G., Yang, X., Jia, Z., and Luo, N. (2015). Determination of manganese in environmental samples by UV-Vis after cloud point extraction. *2nd International Conference on Green Materials and Environmental Engineering*, 2015: 91-94.
23. Sato, N., Mori, M. and Itabashi, H. (2013). Cloud point extraction of Cu (II) using a mixture of triton X-100 and dithizone with a salting-out effect and its application to visual determination. *Talanta*, 2013. 117: 376-381.
24. Purkait, M., DasGupta, S. and De, S. (2006). Performance of TX-100 and TX-114 for the separation of chrysoidine dye using cloud point extraction. *Journal of Hazardous Materials*, 137(2): 827-835.
25. Hunger, J., Neueder, R., Buchner, R., and Apelblat, A. (2013). A conductance study of guanidinium chloride, thiocyanate, sulfate, and carbonate in dilute aqueous solutions: ion-association and carbonate hydrolysis effects. *The Journal of Physical Chemistry B*, 117(2): 615-622.
26. Purkait, M., DasGupta, S. and De, S. (2009). Determination of thermodynamic parameters for the cloud point extraction of different dyes using TX-100 and TX-114. *Desalination*, 244(1-3): 130-138.
27. Purkait, M. K., Vijay, S. S., DasGupta, S., and De, S. (2004). Separation of congo red by surfactant mediated cloud point extraction. *Dyes and Pigments*, 63(2): 151-159.
28. Wang, L., Jiang, G.-B., Cai, Y.-Q., He, B., Wang, Y.-W., and Shen, D.-Z. (2007). Cloud point extraction coupled with HPLC-UV for the determination of phthalate esters in environmental water samples. *Journal of Environmental Sciences*, 19(7): 874-878.

Malaysian Journal of Analytical Sciences, Vol 23 No 5 (2019): 849 - 860
DOI: https://doi.org/10.17576/mjas-2019-2305-10

MALAYSIAN JOURNAL OF ANALYTICAL SCIENCES
Published by The Malaysian Analytical Sciences Society
ISSN 1394 - 2506

THIOL MODIFIED AMPEROMETRIC IMMUNOSENSOR FOR BENZO[a]PYRENE DETECTION IN SURFACE RIVER WATER SAMPLES

(Immunosensor Amperometrik Diubahsuai Tiol untuk Pengesanan Benzo[a]pirina dalam Sampel Air Sungai Permukaan)

Noor Sheryna Jusoh, Tuan Fauzan Tuan Omar, Azrilawani Ahmad*

Faculty of Science and Marine Environment,
Universiti Malaysia Terengganu, 21030 Kuala Nerus, Terengganu, Malaysia

**Corresponding author: azrilawani.ahmad@umt.edu.my*

Received: 27 May 2019; Accepted: 28 August 2019

Abstract

An amperometric immunosensor for the determination of benzo[a]pyrene (BaP) in surface river water samples was developed using screen-printed gold electrodes (SPGEs). The SPGE was modified with 11-mercaptoundecanoic acid (11-MUA) and immobilised the biomolecules on SPGE by applying an indirect competitive enzyme-linked immunosorbent assay (ELISA). The sensitivity of the competitive assay on bare and modified electrodes was compared electrochemically by conducting an amperometric measurement at 300 mV. The limit of detection (LOD) recorded for the bare SPGE was 0.26 mg/L and that for the modified SPGE was 0.01 mg/L. The lower LOD value proved the better sensitivity of the biosensor in the presence of 11-MUA. The recovery study carried out for water samples showed good recovery, ranging from 97%–114%. The improved biosensor method was tested using real water samples collected from Semerak River, Kelantan. An amperometric detection of real water samples showed no BaP for all the sampling stations. The developed immunosensor was then compared with a gas chromatography-flame ionisation detector (GC-FID); the corresponding results revealed that the developed amperometric immunosensor showed higher sensitivity than the GC-FID in the determination of BaP in environmental water.

Keywords: amperometric measurement, enzyme-linked immunosorbent assay, benzo(a)pyrene, gas chromatography-flame ionisation detector

Abstrak

Imunosensor amperometrik untuk penentuan benzo[a]pirina (BaP) dalam sampel air sungai permukaan dibangunkan menggunakan elektrod emas skrin tercetak (SPGE). SPGE telah diubahsuai dengan asid 11-merkaptoundekanoik (11-MUA) dan pemegunan biomolekul pada SPGE dengan menggunakan asai imunojerapan berpaut enzim berpesaingan tak langsung (ELISA). Kepekaan ujian kompetitif pada elektrod kosong dan diubahsuai telah dibandingkan secara elektrokimia dengan menjalankan pengukuran amperometrik pada 300 mV. Had pengesanan (LOD) yang direkodkan untuk SPGE kosong adalah 0.26 mg / L dan bagi SPGE diubah suai adalah 0.01 mg / L. LOD rendah membuktikan kepekaan biosensor yang lebih baik dengan kehadiran 11-MUA. Kajian perolehan semula yang dijalankan untuk sampel air menunjukkan perolehan semula yang baik, dari 97%-114%. Kaedah biosensor yang lebih baik telah diuji menggunakan sampel air sebenar yang diambil dari Sungai Semerak, Kelantan. Pengesanan amperometrik sampel air sebenar menunjukkan tiada BaP untuk semua stesen pensampelan. Imunosensor yang dibangunkan kemudiannya dibandingkan dengan kromatografi gas pengesan nyala pengionan (GC-FID); keputusan mendedahkan bahawa imunosensor amperometrik yang dibangunkan menunjukkan kepekaan yang lebih tinggi berbanding teknik kromatografi untuk penentuan BaP dalam air alam sekitar.

Kata kunci: pengukuran amperometrik, asai imunojerapan berpaut enzim, benzo[a]pirina, kromatografi gas pengesan nyala pengionan

Introduction

An immunosensor is an affinity-based biosensor designed to detect the direct binding of an antibody or an antigen [1]. The biological reactions on the surface of an electrode can be detected by a transducer and are converted into physical signals. The development of immunosensors for determining polycyclic aromatic hydrocarbon (PAH) compounds in water samples has attracted considerable attention from researchers in many fields, and several latest studies have reported an improved performance of these biosensors [2, 3]. Sun et al. successfully designed a whole-cell bioreporter to detect naphthalene in natural water and soil samples [4]. Interestingly, the designed sensor was only selective towards naphthalene, which made it highly sensitive for a real sample analysis. Further, cell-based biosensors are capable of distinguishing cell complex responses for environmental monitoring, particularly in PAH assessments [5]. In a different study, the researchers utilised a biorecognition element combined with a fluorescence sensor and reported a rapid and sensitive detection of fluorene in water samples [6]. Because of their selectivity, sensitivity, reliability, ease of handling, and short analysis time, and because they do not require the pre-treatment of samples, immunosensors have the potential to replace conventional methods such as gas chromatography-flame ionisation detectors (GC-FIDs) as alternative detection systems.

A screen-printed electrode (SPE) is made from the deposition of several layers of special inks on an inert solid substrate. The production of disposable SPE has gained considerable attention from researchers and SPE manufacturing companies. Many companies put an extra effort in designing and developing an applicable SPE, such as the printing media (inks) and substrates. Such enhancement in designing is done to minimise the volume of samples and to particularly improve the sensing performance of SPE [7]. SPGE consists of a gold working electrode. In particular, the application of SPGE in analytical measurement is increasing, because of the high conductance of gold as compared to that of carbon. However, because of the high cost of production and as a new product, not many studies have utilised SPGE. Thus, at the beginning of the production of SPGE, electrochemical characterisation was conducted to test the performance of SPGE [8, 9]. Gold has been well known to provide excellent sensing performance in the monitoring of mercury [7]. Other applications of SPGE include those related to heavy metals [10], organophosphorus [11], medicine [12, 13], and DNA [14].

The modification of an electrode's surface can provide a good attachment site for the immobilisation of biomolecules. This modification is important for enhancing the performance of the electrode, and the process varies for different applications. Thus far, researchers have developed and found more efficient and selective sensing materials. An amperometric biosensor was developed by Hatefi-Mehjardi to determine carbaryl in fruit juice samples using 3-MPA on a polycrystalline gold electrode, where the 3-MPA-modified gold electrode showed a considerable decrease in the current reading [15]. In a different approach, Sherdevani and Poubeyram developed a method for DNA determination by immobilizing Zr(IV) on a gold electrode using 3-MPA-modified electrode [16]. Othman and co-workers constructed a dithizone-PVC membrane that is used as an ionophore reagent material for a chemically modified silver (Ag) electrode to determine the metal ions in an aqueous solution [17].

Amperometry is a form of voltammetry where current is measured as a function of time, while applying a constant potential. It is a technique which is vastly applied in chemical sensors, because of its considerable sensitivity and selectivity. An electrochemical method is commonly paired with bioassays to improve the selectivity and sensitivity of compound detection. For example, an amperometric immunosensor has been developed to detect phenanthrene in river water and tap water [18]. An indirect competitive assay is combined with an amperometric measurement to provide a sensitive detection of the target analyte. Another research includes the modification of a gold electrode before conducting an amperometric immunosensor measurement for naphthalene detection [19]. The developed immunosensor was highly sensitive, stable, and regenerative towards the target analyte.

Among the 16 listed priority compounds, BaP has predominantly attracted the most attention from researchers. Previous studies have reported that BaP was normally utilised in carcinogenic tests in animals using various carcinogenicity bioassays. The results from these studies showed that BaP actively produced tumours in every experimented animal, including the presence of physical defects in new born animals. Fortunately, these effects were not observed in humans. The recent research conducted by Li et al. utilised a fluorescence immunoassay for determining BaP in an aqueous solution [20]. The results exhibited that the assay was highly sensitive and selective towards BaP in low concentration. An approach by Beloglazova et al. utilised both polymer and monoclonal

antibodies for developing an electrochemical biosensor for BaP detection in river water [21]. This study proved that the immobilisation of a biorecognition element on the electrode surface provided more sensitive and selective results towards BaP than a polymer. In a different study, Li et al. successfully established a rapid and sensitive immunosensor for evaluating 3–5-ring PAHs, including BaP, pyrene, phenanthrene, anthracene, and chrysene [22]. The 10-minutes analysis revealed that the developed monoclonal antibody was more sensitive in determining 3–5-ring PAHs than the commercially available monoclonal antibodies. The modification of electrodes for electrochemical immunosensor development was conducted and examined with respect to BaP, resulting in a low detection limit with high stability and good reproducibility [23].

The selectiveness of an electrochemical immunoassay is contributed by the enzyme label used, which can exhibit a higher catalytic activity toward the substrate. In this study, an alkaline phosphatase (AP) enzyme label was selected with 4-aminophenyl phosphate (4-APP) as the corresponding substrate. In the presence of AP, 4-APP was hydrolysed to produce an electroactive product, 4-aminophenol (4-AP) (Figure 1). At 300 mV, 4-AP was oxidised by losing two electrons, resulting in the catalytic conversion of 4-AP into 4-quinone imine (4-QI) [24].

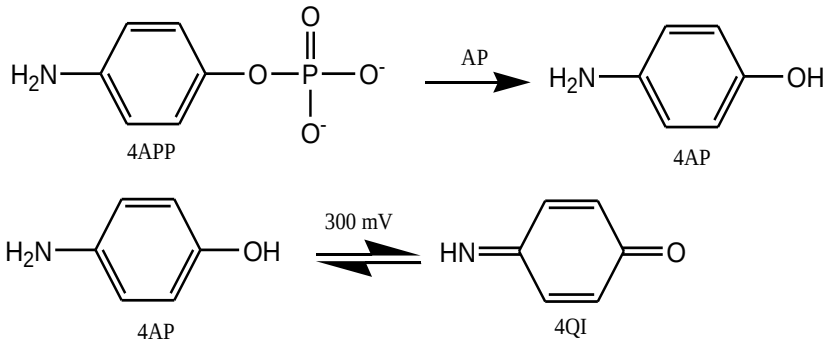


Figure 1. Catalytic activity of AP with 4-APP to produce 4-AP, which then oxidised into 4-QI at 300 mV.

The objective of this research was to develop an amperometric immunosensor by modifying SPGE to enhance the performance of the sensor. The presence of BaP in the surface river water sample was tested using the developed amperometric immunosensor detection.

Materials and Methods

Materials and reagents

Sulphuric acid, hydrogen peroxide, absolute ethanol, anhydrous sodium sulphate, and nitric acid were purchased from R&M, UK. N-hydroxysuccinimide (NHS), acenaphthylene, and fluorene were purchased from Aldrich, Japan. Diethanolamine (DEA), Tween 20, phenanthrene, naphthalene, acenaphthene, dichloromethane (DCM), methanol (MeOH), and ethyl acetate (EtAc) were purchased from Merck, Germany. Goat anti-mouse IgG AP and mouse monoclonal antibody (4D5) were purchased from Santa Cruz Biotechnology, USA. 11-MUA and 4-APP were purchased from Sigma-Aldrich, Switzerland. Bovine serum albumin (BSA), BaP, and phosphate buffer saline (PBS) were purchased from Sigma, USA. Pyrene (Acros Organics, USA), fluoranthene (Aldrich, China), N-(3-dimethylaminopropyl)-N'-etylcarbodiimide hydrochloride (EDC) (Sigma-Aldrich, Japan), hexane (for liquid chromatography, Fisher Scientific), and tris(hydroxymethyl)aminomethane (Tris) (Sigma-Aldrich, USA) were purchased for the experiment. All the reagents were of analytical grade or better.

Instrumentation

A mini incubator (VWR, China) was used to incubate samples at 37°C. SPGE (DRPC220BT) was purchased from DropSens, Spain. An Autolab PGSTAT30 (Metrohm, Switzerland) instrument was used for the amperometric measurement. A ProPlus instrument was used to test the physicochemical parameters (temperature, pressure, dissolved oxygen, conductivity, salinity, and pH) of the water at each sampling point. A chromatographic analysis of all the samples was carried out using GC-FID Q2010Plus (Shimadzu, Japan).

River water collection

Water sampling was conducted at Semerak River in Tok Bali, Kelantan, Malaysia. The sampling was carried out in January 2016. Five sampling points were selected along the Semerak River (Figure 2). Table 1 lists the coordinates for each sampling point.

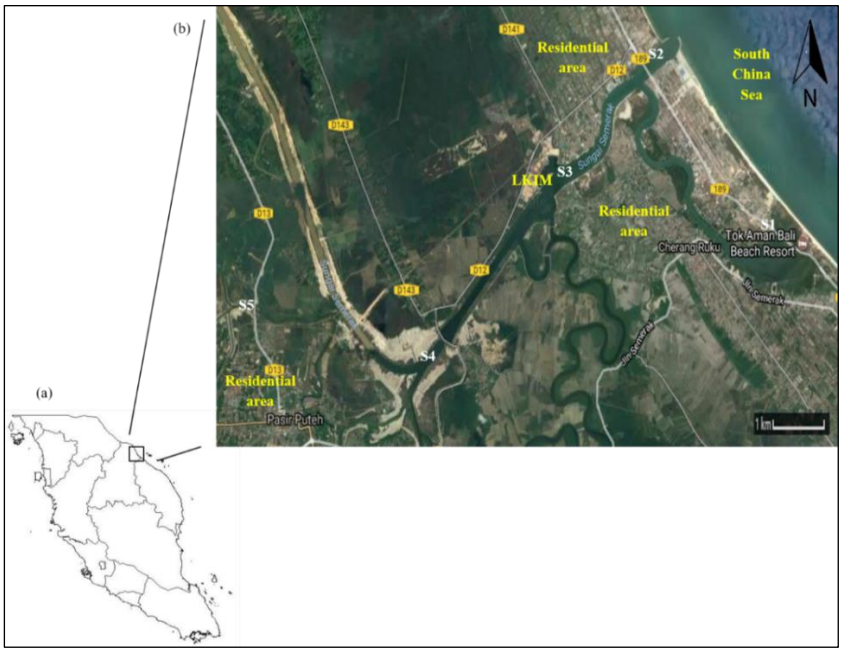


Figure 2. Map of (a) peninsular Malaysia and (b) sampling stations along Semerak River, Kelantan.

Table 1. Coordinates and brief description of all sampling stations.

Station	Coordinates		Description
	Latitude	Longitude	
1	5.865733	102.5061	Lagoon of the river, a popular spot for clam searching
2	5.896389	102.4821	Nearest to the sea, a recreation place
3	5.877756	102.4616	Near Lembaga Kemajuan Ikan Malaysia, a boat parking site
4	5.845452	102.4326	Near border that separates salty and fresh water
5	5.853874	102.3990	Near residential area

All the water samples were collected using grab sampling. In all, three 500-mL bottles (glass) of water samples were taken at each point. Approximately, 1 mL of 2-M nitric acid was added into the water samples for preservation. Then, the bottles were wrapped with aluminium foil and stored in an ice box. The bottles were then transferred into a 4 °C chiller for storage until further analysis.

Water extraction (Disk extraction)

Water samples were extracted using disk extraction following US EPA Method 525.2 [25]. The solid-phase extraction disk (Empore C_{18}) was inserted into the filler apparatus. The disk was then washed with 5 mL of DCM, half of the solvent was pulled, and the disk was soaked for 1 minute before pulling out the remaining solvent. The disk was pre-wetted with 5 mL of MeOH, half of the solvent was pulled, and the disk was soaked for 1 minute before pulling out the remaining solvent, leaving a thin layer of MeOH on the disk. Deionised water (5 mL) was used to rinse the disk and mostly pulled out, leaving a thin layer of deionised water on the disk.

In each water sample, 2.5 mL of MeOH was added and mixed well. Approximately 100 µL of a 100-mg/L BaP standard was added into the sample for the recovery studies. The water sample was then added into the reservoir, and full vacuum was applied. The disk was dried by maintaining the vacuum for 10 minutes. The filtration top was removed, and a collection tube was inserted to the filtration top to contain the eluant.

Next, 5 mL of EtAc was added to the sample bottle, rinsed thoroughly and allowed to settle at the bottom of the bottle, and then transferred to the disk. The sides of the filtration reservoir were rinsed with a pipette. Half of the solvent was pulled out, and the disk was allowed to soak for 1 minutes before drawing the remaining solvent. This step was repeated using DCM. With a pipette, the filtration reservoir was rinsed twice with 3-mL portions of 1:1 EtAc: DCM. The solvent was pulled into the collector tube. The eluant was then poured through the drying tube containing 3 g of anhydrous sodium sulphate. The drying tube and the anhydrous sodium sulphate were rinsed twice with 3-mL portions of 1:1 EtAc: DCM. All the extracts and washings were collected and were concentrated to 0.5–1 mL by using a hot plate at 50 °C. The concentrated extract was stored at 4 °C before the analysis.

Electrode modification

SPGE was cleaned using a piranha solution (mixture of 3 mL of 1.5-M sulphuric acid and 1 mL of 30% hydrogen peroxide) for 2 minutes and then rinsed with deionised water. The cleaned SPGE was modified with 5-mM 11-MUA in an ethanolic solution for 20 hours. The modified SPGE was rinsed with absolute ethanol to remove any unbound 11-MUA and then air-dried at room temperature. Next, the 11-MUA-modified SPGE was activated with a 50-mM EDC and 50-mM NHS solution for 6 h [26].

Preparation of buffers

Buffer solutions and substrates were freshly prepared prior to the assay. For the blocking solution, 0.3029 g (50 mM) of Tris was dissolved in deionised water, and then, the solution was used to dissolve 0.5 g of BSA (1% in Tris buffer) (pH 7.4). For the washing buffer, 0.3029 g (50 mM) of Tris was dissolved in deionised water. The Tris solution (50 µL) was pipetted out and replaced with 50 µL of Tween-20 (pH 7.4).

Immobilisation of biomolecules

Biomolecules were immobilised on the modified SPGE by applying indirect competitive ELISA (Figure 3). The gold working electrode was coated with 5 µL of a bovine serum albumin-phenanthrene (BSA-PHEN) coating conjugate (n=3) and then incubated for 1 hour at 37 °C. After incubation, the electrode was washed with 20 µL of the washing buffer. Five (5) µL of the blocking buffer was added onto the electrode and incubated again for 1 hour at 37 °C. Thereafter, the electrode was washed again. Serial dilutions of BaP standards were mixed with the 4D5 monoclonal antibody (diluted in PBS) and were left for 15 min to react. The mixture was prepared at a concentration two times higher than the desired concentration. Then, 5 µL of each solution was added onto the electrode and incubated at 37 °C for 1 hour. After washing, 5 µL of the AP labelled antibody (diluted in PBS) was added and allowed to react at 37 °C for 1 hour. After 1 hour, the electrode was washed and stored at 4 °C prior to the amperometric measurement. The indirect competitive assay was repeated with seven other PAH compounds, namely acenaphthene, acenaphthylene, pyrene, phenanthrene, naphthalene, fluorene, and fluoranthene, for the cross-reactivity study [27].

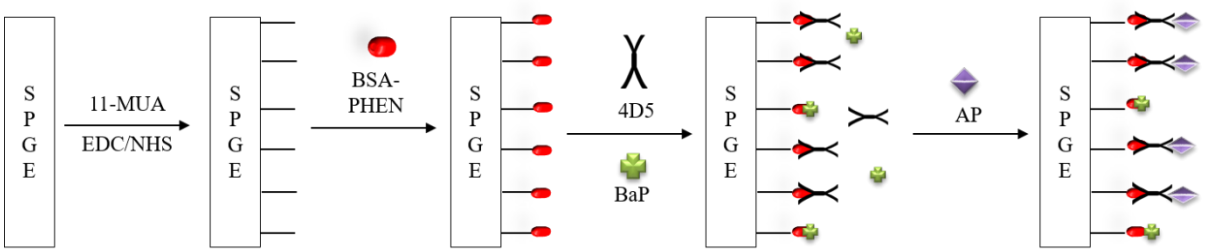


Figure 3. Modification and immobilisation of biomolecules on SPGE

Amperometric measurement

Amperometric detection was carried out in 8 mL of a 1-M DEA buffer (pH 9.5) with 4-APP as the substrate. The measurement was set to 80 s, and a potential of 300 mV was applied. At 60 s, 78.4 µL of 4-APP was injected into the DEA buffer. The peak current produced after the injection of 4-APP was recorded.

Chromatographic analysis with GC-FID

A chromatographic analysis was carried out using GC-FID Q2010Plus (Shimadzu, Japan) equipped with an auto injector. All the BaP standards and water samples were analysed using the same parameters. A BPX5 column (30.0 m × 0.025 µm × 0.2 mm ID) with the column temperature range from 40 – 300°C was used. The gases involved in the analysis included helium gas (carrier gas, 3 mL/min), nitrogen gas (make-up gas, 30 mL/min), hydrogen gas (40 mL/min), and compressed air (400 mL/min). The measurement took 37 minutes for every sample to finish. Hexane was selected as the mobile phase solvent.

Results and Discussion

River water sampling

All the data of the water parameters at each station are recorded in Table 2. Station 1, Station 2, and Station 3 recorded high salinity, which proved that salty water was collected from the sampling points. In contrast, low salinity was measured at Station 4 and Station 5, which were located in the freshwater area. In terms of pH, compared with Station 1, Station 2, and Station 4, Station 3 and Station 5 recorded slightly acidic water because of the nature of the sampling site. The presence of many boats at Station 3 and the location of Station 5, which was near to a residential area, contributed to the faintly low pH values.

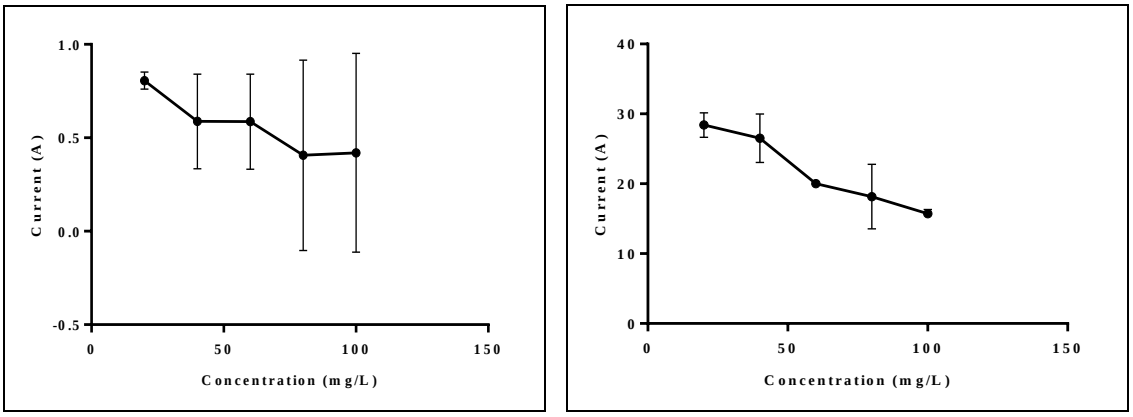
Table 2. River water parameters of all sampling stations

Station	Station 1	Station 2	Station 3	Station 4	Station 5
Temperature (°C)	30.2	28	28	27.8	27.4
Pressure (mmHg)	763.9	762.9	762.8	762.7	762.4
Dissolved Oxygen (%L)	66.1	83.8	63.6	52.4	66.3
Dissolved Oxygen (mg/L)	4.55	6.33	4.81	3.99	5.01
Specific Conductance (µS/cm)	20507	8386	9671	119.4	44.1
Salinity (ppt)	12.7	4.65	5.44	0.05	0.02
pH	7.25	7.52	6.6	7.26	6.53
pH (mV)	−66.4	−80.4	−31.5	−65.4	−27.6

Amperometric detection

The amperometric measurement for a competitive assay was carried out by comparing the electrochemical performance of the bare and the modified SPGE. Figure 4 shows that the current reading of the assay with the modified SPGE was significantly higher than that in the case of the bare SPGE. The presence of 11-MUA increased

the sensitivity of the assay, where a lower IC_{50} value was recorded (Table 3). In addition, the LOD and limit of quantification (LOQ) values for the modified electrode were lower than those for the bare electrode. This implied that the 11-MUA-modified SPGE gave strong binding sites for biomolecules compared with the bare SPGE. The obtained LOD values were higher than those reported in the study conducted by Ahmad and Moore using an integrated electrode [28]; however, the application of SPGE was far more cost effective. In addition, the immunosensor developed in this study was highly stable for real sample determination.



(a) bare electrode (b) 11-MUA-modified electrode

Figure 4. Indirect competitive assay of (a) bare and (b) modified SPGE at potential of 300 mV in 1-M DEA buffer (pH 9.5)

Table 3. Comparison of competitive assay between bare and modified SPGE

SPGE	LOD (mg/L)	LOQ (mg/L)	IC_{50} (mg/L)	Linear Range (mg/L)	R^2
Bare	0.26	0.79	39.39	20-40	0.8642
Modified	0.01	0.04	11.85	40-60	0.9530

Measurement with river water samples

The amperometric detection of BaP in the river water samples was conducted, and the results were tabulated in Table 4. All the sampling sites had a strong contribution as BaP sources, as they were near a residential area and there were fishing and boating activities along the river. However, there was no BaP detected in the river water samples. This was attributed to the fact that no BaP was found despite all the fishing and boating activities. The other reason was the very low concentration of BaP in the river water samples, which could not be detected by the developed biosensor. The water samples were spiked with 20-mg/L BaP, and all the samples showed good recovery from 97% to 114%.

Table 4. Recovery studies of spiked river water samples using amperometric detection

Station	Added: 20 mg/L	
	Found (mg/L)	Recovery (%)
1	19.46	97.3
2	22.93	114.7
3	22.41	112.1
4	22.75	113.7
5	22.47	112.3

Stability study of coated electrode

The stability of the coated SPGE was studied by comparing the amperometric measurements of the electrode for seven days at two different storage temperatures. The coated electrodes were stored in 1-M DEA buffer (pH 9.5) at 4°C and −20 °C. As recorded in Figure 5, 4 °C displayed a higher current reading than −20 °C, for all the measured days. The higher current reading represented the greater stability of the assay, where the enzymatic cleavage was measured [24]. However, a drastic decline in the current reading was observed on Day 2 and Day 3 for 4 °C and −20 °C, respectively. This was attributed to the fact that the isoenzymes of AP were considerably unstable, resulting in a reduction in stability, particularly when stored at −20 °C [29, 30]. However, the stable enzymatic reaction of AP was recorded to be better at the refrigerated temperature (4 °C–9 °C), and 4 °C was the best storage temperature to store the AP-related samples [31]. This study showed that the coated SPGE was not suitable for reuse.

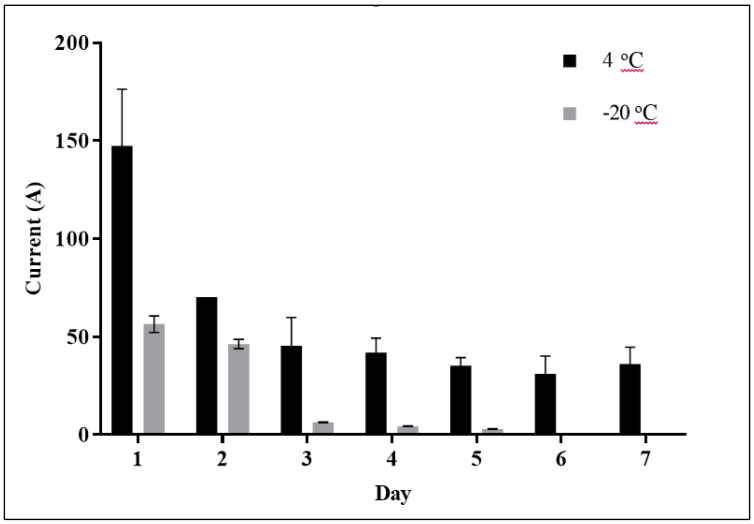


Figure 5. Stability of coated SPGE at different storage temperatures in 1-M DEA buffer (pH 9.5)

Cross-reactivity study

The cross-reactivity of seven PAH compounds against BaP was measured, and the results are displayed in Table 5. A low IC_{50} value was recorded for BaP, which proved the sensitivity of the assay toward the BaP detection. Even though pyrene has one benzene ring less than BaP, it showed the highest cross-reactivity because of the similar structure arrangement. Fluorene recorded the lowest cross-reactivity with BaP because of the significant difference in their molecular structures.

Table 5. Cross-reactivities of seven PAH compounds against BaP for amperometric measurement

PAH Compounds	IC_{50} (mg/L)	Cross-Reactivity (%)
Benzo(a)pyrene	11.9	100.0
Acenaphthene	111.6	10.7
Acenaphthylene	80.6	14.8
Pyrene	12.4	95.9
Phenanthrene	197.6	6.0
Naphthalene	66.1	18.0
Fluorene	242.3	4.9
Fluoranthene	181.5	6.6

Chromatography analysis

Serial dilutions of the BaP standard ranging from 10 mg/L to 50 mg/L were analysed using a gas chromatography-flame ionisation detector (GC-FID). The GC-FID chromatograms of the standards are shown in Figure 6. A complete single measurement of the sample took 37 minutes. At 27.50 minutes, a clear BaP peak was detected for all the standards. The peak area of each standard was recorded, and the calibration curve was plotted as shown in Figure 7. The LOD, LOQ, and linear range recorded were 10.24 mg/L, 31.04 mg/L, and 10 mg/L–30 mg/L, respectively.

The results of the analysis conducted using GC-FID showed that no BaP peak was observed in all the river water samples at 25–30 minutes. Even though a few peaks were detected, the peaks were not considerable and might be attributed to the column background noise. Further, the GC-FID analysis revealed that no BaP was found in all the water samples, even though some potential sources of BaP were present along all the sampling sites for examples at Station 1, which is the main route for boats from and to the sea, as well as Station 3, which is the parking site for those boats.

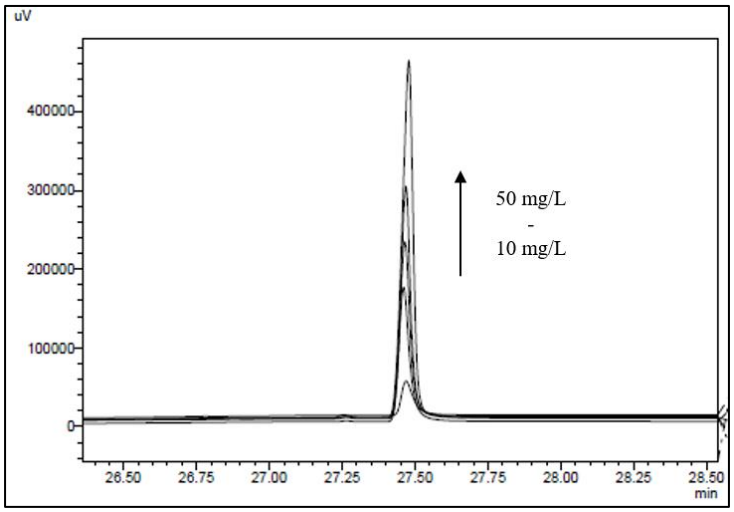


Figure 6. Chromatogram of BaP peaks of 10 mg/L–50 mg/L BaP standards recorded at 27.50 minutes

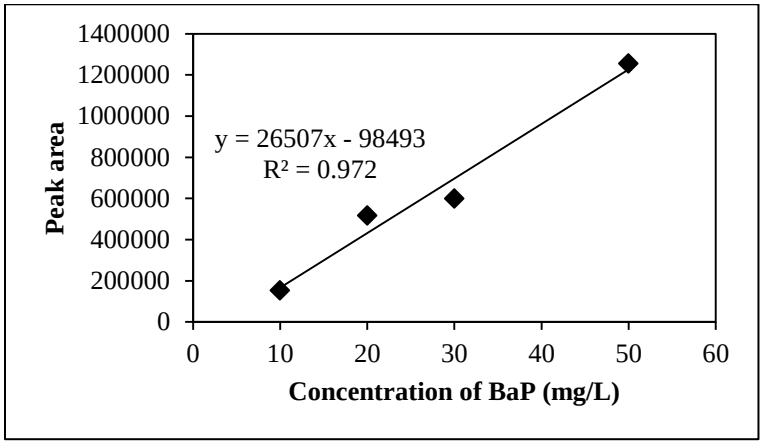


Figure 7. Calibration curve of BaP standards using GC-FID analysis

A recovery study was conducted by spiking 100 mg/L of BaP in the river water samples. The recovery results are depicted in Table 6. Overall, the samples showed good recoveries in the range of 80%–120 %. The low recovery for the solid phase extraction was contributed by the analyte lost during the extraction process and the weak solvent used for the elution of the analyte [32]. Three main issues must be considered while measuring PAHs in water samples: (i) low solubility of PAH compounds, which is below the detection limit of the analytical instruments, (ii) commonly combined with other materials to form aggregates of colloidal particles, and (iii) sample loss due to absorption to glassware containers [33]. Thus, special precaution has been taken in order to limit the disadvantages of the solid phase extraction.

Table 6. Recovery studies for river water samples spiked with 100 mg/L of BaP

Station	**Added: 100 mg/L**	
	Found (mg/L)	**Recovery (%)**
1	112.12	112.1
2	99.43	99.4
3	86.54	86.5
4	81.83	81.8
5	95.20	95.2

Comparison of developed method with GC-FID

Table 7 shows the comparison of all the detection methods. Overall, the modified electrode showed better results than the bare electrode and the chromatographic measurements. This was attributed to the presence of 11-MUA, which enhanced the performance of the sensor. A high LOD value was recorded for chromatographic detection because of the low instrument precision.

Table 7. Comparison between electrochemical and chromatographic measurements

Measurement	**LOD (mg/L)**	**LOQ (mg/L)**	**IC_{50} (mg/L)**	**Linear Range (mg/L)**	**R^2**
Electrochemical					
Bare	0.26	0.79	48.3	20–40	0.8642
Modified	0.01	0.04	11.9	40–60	0.9530
Chromatographic	10.24	31.04	3.72	10–30	0.9881

Conclusion

An ideal biosensor is a device with high stability and reproducibility while maintaining its sensitivity for a long period of time. The main challenge for the development of biosensor devices is to achieve these characteristics. In this research, an immunosensor was successfully developed by modifying SPGE with 11-MUA and immobilising biomolecules. The developed enzyme-based biosensor using SPGE provided good sensitivity and selectivity towards BaP detection in water samples. Even though this method was not as precise as the chromatographic technique, amperometric detection offers wide opportunities for further improvements in electrochemical detection. Besides the commonly used chromatographic technique, this developed biosensor method can be applied as an alternative because of its operational cost efficiency.

Further improvement in immunosensors should be considered by implementing the current trends in biosensors such as genetic engineering of biomolecules and incorporation of nanomaterials on electrodes. The genetic engineering of enzymes has been developed to enhance the efficiency, sensitivity, and selectivity of the enzymes

toward the target analytes. Carbon-based nanomaterials such as graphene, fullerene, and carbon nanotubes have been applied in electrochemical biosensors because of their excellent electrochemical properties and high stability. Metal nanomaterials such as metal oxides and nanocomposites are preferred in electrode modification, as they provide an ideal environment for the immobilisation of biomolecules.

Acknowledgements

The authors would like to acknowledge the financial support received from Ministry of Higher Education, Malaysia for Research Acculturation Grant Scheme (RAGS 57093) and Fundamental Research Grant Scheme (FRGS 59487), and Universiti Malaysia Terengganu for providing laboratory facilities and instrumentation.

References

1. Moina, C. and Ybarra, G. (2012). Fundamentals and applications of immunosensors: Advances in Immunoassay Technology. Croatia: InTech. pp. 65 – 80.
2. Behera, B. K., Das, A., Sarkar, D. J., Weerathunge, P., Parida, P. K., Das, B. K., Thavamani, P., Ramanathan, R. and Bansal, V. (2018). Polycyclic aromatic hydrocarbons (PAHs) in inland aquatic ecosystems: Perils and remedies through biosensors and bioremediation. *Environmental Pollution*, 241: 212 – 233.
3. Nsibande, S. A., Montaseri, H. and Forbes, P. B. C. (2019). Advances in the application of nanomaterial-based sensors for detection of polycyclic aromatic hydrocarbons in aquatic systems. *Trends in Analytical Chemistry*, 115: 52 – 69.
4. Sun, Y., Zhao, X., Zhang, D., Ding, A., Chen, C., Huang, W.E. and Zhang, H. (2017). New naphthalene whole-cell bioreporter for measuring and assessing naphthalene in polycyclic aromatic hydrocarbons contaminated site. *Chemosphere*, 186: 510 – 518.
5. Ahmad, A. and Moore, E. J. (2009). Comparison of cell-based biosensors with traditional analytical techniques for cytotoxicity monitoring and screening of polycyclic aromatic hydrocarbons in the environment. *Analytical Letters*, 42: 1 – 28.
6. Qiao, B., Li, Y., Hu, P., Sun, Y., Si, Z., Lu, S., Ren, H., Liu, Z., Zhang, Y. and Zhou, Y. (2018). EuNPs-MAb fluorescent probe based immunochromatographic strip for rapid and sensitive detection of fluorene. *Sensors and Actuators B: Chemical*, 262: 221 – 227.
7. Hayat, A. and Marty, J.L. (2014). Disposable screen-printed electrochemical sensors: Tools for environmental monitoring. *Sensors*, 14: 10432 – 10453.
8. Bernalte, E., Marín-Sánchez, C., Pinilla-Gil, E. and Brett, C.M.A. (2013). Characterisation of screen-printed gold and gold nanoparticle-modified carbon sensors by electrochemical impedance spectroscopy. *Journal of Electroanalytical Chemistry*, 709: 70 – 76.
9. García-González, R., Fernández-Abedul, M.T., Pernía, A. and Costa-García, A. (2008). Electrochemical characterization of different screen-printed gold electrodes. *Electrochimica Acta*, 53(8): 3242 – 3249.
10. Wan, H., Sun, Q., Li, H., Sun, F., Hu, N. and Wang, P. (2015). Screen-printed gold electrode with gold nanoparticles modification for simultaneous electrochemical determination of lead and copper. *Sensors and Actuators B: Chemical*, 209: 336 – 342.
11. Arduini, F., Guidone, S., Amine, A., Palleschi, G. and Moscone, D. (2013). Acetylcholinesterase biosensor based on self-assembled monolayer-modified gold-screen printed electrodes for organophosphorus insecticide detection. *Sensors & Actuators: B. Chemical*, 179: 201 – 208.
12. Cordeiro, T. A. R., Goncalves, M. V. C., Franco, D. L., Reis, A. B., Martins, H. R. and Ferreira, L. F. (2019). Label-free electrochemical impedance immunosensor based on modified screen-printed gold electrodes for the diagnosis of canine visceral leishmaniasis. *Talanta*, 195: 327 – 332.
13. Pandey, P., Pandey, A. and Shukla, N. K. (2018). Screen printed gold electrode with cysteamine and single walled carbon nanotubes for the recognition of prostate specific antigen. *Materials Today: Proceedings*, 5: 15311 – 15318.
14. Malecka, K., Stachyra, A., Góra-Sochacka, A., Sirko, A., Zagórski-Ostoja, W., Radecka, H. and Radecki, J. (2016). Electrochemical genosensor based on disc and screen printed gold electrodes for detection of specific DNA and RNA sequences derived from Avian Influenza Virus H5N1. *Sensors and Actuators B: Chemical*, 224: 290 – 297.
15. Hatefi-Mehrjardi, A. (2013). Bienzyme-self assembled monolayer on gold electrode: An amperometric biosensor for carbaryl determination. *Electrochimica Acta*, 114: 394 – 402.

16. Shervedani, R.K. and Pourbeyram, S. (2010) Electrochemical determination of calf thymus DNA on Zn(IV) immobilized on gold-mercapropropionic-acid self-assembeled monolayer. *Bioelectrochemistry*, 77 (2): 100 – 105.
17. Othman, M. A. F., Ahmad, A. and Zuki, H. M. (2016). Dithizone modified electrode for the determination of metals ion in aqueous solution. *Malaysian Journal of Analytical Sciences*, 20(1): 197 – 204.
18. Fahnrich, K. A., Pravda, M. and Guilbault, G. G. (2003). Disposable amperometric immunosensor for the detection of polycyclic aromatic hydrocarbons (PAHs) using screen-printed electrodes. *Biosensors and Bioelectronics*, 18: 73 – 82.
19. Zhang, Y. and Zhuang, H. S. (2010). Amperometric immunosensor based on layer-by-layer assembly of thiourea and nano-gold particles on gold electrode for determination of naphthalene. *Chinese Journal of Analytical Chemistry*, 38(2): 153 – 157.
20. Li, T., Choi, Y. H., Shin, Y. B., Kim, H. J. and Kim, M. G. (2016). A fluorescence enhancement-based label-free homogeneous immunoassay of benzo[a]pyrene (BaP) in aqueous solutions. *Chemosphere*, 150: 407 – 413.
21. Beloglazova, N. V., Lenain, P., Rycke, E. D., Goryacheva, I. Y., Knopp, D. and Saeger, S. D. (2018). Capacitive sensor for detection of benzo(a)pyrene in water. *Talanta*, 190: 219 – 225.
22. Li, X., Kaattari, S. L., Vogelbein, M. A., Vadas, G. G. and Unger, M. A. (2016). A highly sensitive monoclonal antibody based biosensor for quantifying 3-5 ring polycyclic aromatic hydrocarbons (PAHs) in aqueous environmental samples. *Sensing and Bio-Sensing Research*, 7: 115 – 120.
23. Wang, C., Lin, M., Liu, Y. and Lei, H. (2011). A dendritic nanosilica-functionalized electrochemical immunosensor with sensitive enhancement for the rapid screening of benzo[a]pyrene. *Electrochimica Acta*, 56: 1988 – 1994.
24. Ronkainen-Matsuno, N. J., Thomas, J. H., Halsall, H. B. and Heineman, W. R. (2002). Electrochemical immunoassay moving into the fast lane. *Trends in Analytical Chemistry*, 21(4): 213 – 225.
25. USEPA (1995). Method 525.2: Determination of Organic Compounds in Drinking Water by Liquid-Solid Extraction and Capillary Column Gas Chromatography/Mass Spectrometry, Revision 2.0. Cincinnati, OH: USA.
26. Jusoh, N. S., Azmi, A. A. and Ahmad, A. (2017). Enzyme-linked immunosorbent assay (ELISA)-based-sensor for determination of benzo[a]pyrene in river water using screen-printed gold electrode. *Malaysian Journal of Analytical Science*, 21(3): 518 – 526.
27. Ahmad, A., Lee, P. K. and Jusoh, N. S. (2016). A comparative study of thiols self-assembled monolayers on gold electrode. *Middle-East Journal of Scientific Research*, 24 (6): 2152 – 2158.
28. Ahmad, A. and Moore, E. J. (2012). Electrochemical immunosensor modified with self-assembled monolayer of 11-mercaptoundecanoic acid on gold electrodes for detection of benzo[a]pyrene. *Analyst*, 137: 5839 – 5944.
29. Heins, M., Heil, W. and Withold, W. (1995). Storage of serum or whole blood samples: Effects of time and temperature on 22 serum analytes. *European Journal of Clinical Chemistry Clinical Biochemistry*, 33 (4): 231 – 238.
30. Cray, C., Rodriguez, M., Zaias, J. and Altman, N. H. (2009). Effects of storage temperature and time on clinical biochemical parameters from rat serum. *Journal of the American Association for Laboratory Animal Science*, 48 (2): 202 – 204.
31. Divya, P. D. and Jayavardhanan, K. K. (2010). Effect of temperature and storage time on Hepatobiliary enzyme activities in Goat serum. *Veterinary World*, 3(6): 277 – 279.
32. Cosby, C. N., Troiano, N. W. and Kacena, M. A. (2008). The effects of storage conditions on the preservation of enzymatic activity in bone. *Journal of Histotechnology*, 31(4): 169 – 173.
33. McGowin, A. E. (2006). Polycyclic aromatic hydrocarbons: Chromatographic analysis of the environment. CRC Press, Florida. pp. 555 – 616.

Malaysian Journal of Analytical Sciences, Vol 23 No 5 (2019): 861 - 869
DOI: https://doi.org/10.17576/mjas-2019-2305-11

MALAYSIAN JOURNAL OF ANALYTICAL SCIENCES
Published by The Malaysian Analytical Sciences Society
ISSN 1394 - 2506

THE EFFECT OF VANILLIN ON THE OXIDATIVE STABILITY OF PALM OLEIN

(Mengkaji Kesan Penambahan Vanilin terhadap Kestabilan Pengoksidaan Olein Sawit)

Fatin Nadzirah Mohd Azriyuddin, Mohammad Norazmi Ahmad, Muhammad Nor Omar, Erna Normaya Abdullah*

Experimental and Theoretical Research Laboratory,
Department of Chemistry, Kulliyyah of Science,
International Islamic University Malaysia, 25200 Kuantan, Pahang, Malaysia

**Corresponding author: ernanormaya@iium.edu.my*

Received: 16 January 2019; Accepted: 25 August 2019

Abstract

The existence of unsaturated fatty acids in palm olein contributes to the oil's degree unsaturation and reduces the oil's oxidative stability when it is exposed to atmospheric oxygen and heat. The purpose of this research was to study the effect of vanillin on improving the oxidative stability of palm olein. 1% of vanillin was incorporated into palm olein and the sample was heated at 90 °C in an oven for 200 hours. Samples were collected at 0 hours, 50 hours, 100 hours, 150 hours and 200 hours heating prior to analysis using a thermal oxidative stability test including iodine value test, peroxide value test, Fourier transform infrared (FTIR) spectroscopy and thermogravimetric analysis (TGA). The results obtained were compared with the result of palm olein without antioxidant (blank). The results showed that the presence of vanillin in palm olein reduced the autoxidation process and increased the oxidative stability of palm olein by 16.10%, 46.51% and 25.00% based on the peroxide value, absorbance of the infrared spectrum and thermogravimetric sample's weight gain per cent, respectively.

Keywords: oxidation, oxidative stability, palm olein, vanillin

Abstrak

Kewujudan asid lemak tak tepu dalam olein sawit menyumbang kepada darjah ketaktepuan minyak dan mengurangkan kestabilan pengoksidaan minyak apabila terdedah kepada oksigen dan haba atmosfera. Kajian ini bertujuan mengkaji kesan penambahan vanilin dalam meningkatkan kestabilan pengoksidaan olein sawit. Sampel olein sawit yang mengandungi 1% vanilin dipanaskan pada suhu 90 °C selama 200 jam. Sampel pada masa 0 jam, 50 jam, 100 jam, 150 jam dan 200 jam setelah dipanaskan telah dianalisis melalui ujian kestabilan pengoksidaan termal iaitu ujian nilai peroksida, spektroskopi inframerah transformasi Fourier (FTIR) dan analisis termogravimetri (TGA). Keputusan yang diperoleh dibandingkan dengan olein sawit tanpa antioksida. Hasil menunjukkan kehadiran vanilin dalam olein sawit mengurangkan proses pengautooksidaan dan meningkatkan kestabilan pengoksidaan olein sawit sebanyak 16.10%, 46.51% dan 25.00%, masing-masing berdasarkan nilai peroksida, keserapan pada spektrum inframerah dan peratus peningkatan berat sampel termogravimetri.

Kata kunci: pengoksidaan, kestabilan pengoksidaan, olein sawit, vanillin

Introduction

The oxidative stability of oil gives an indication of the oil's resistance to oxidation during processing and storage [1]. It is one of the important measures to determine the shelf life and quality of the oil. The oxidative stability of fats, oils and lipid-based foods will be affected by the presence of catalytic systems such as light, heat, enzymes, metals, metalloproteins and microorganisms [2, 3]. The catalytic system will act as an initiator that leads to the

oxidation process, resulting in the formation of low-molecular-weight off-flavour compounds that cause the oil to be rancid. Being used in daily life as an ingredient in food preparation and cooking, palm oil may have been subjected to high-temperature cooking such as in deep-fat frying. During this process, oxygen that existed in the deep-fat frying will react with the oil through thermal oxidation and leads to the formation of off-flavour, toxic and hazardous compounds that contribute to the degradation of palm oil and a decrease in its oxidative stability [4]. Thermal oxidation has a similar chemical mechanism to autoxidation [3, 4]. It proceeds via a free radical chain reaction that will be accelerated at a higher temperature for which the mechanism is shown in equation 1 below [1]:

Initiation	RH	$\rightarrow$	R• + H•		
Propagation	R• + $^3O_2$	$\rightarrow$	ROO•	(peroxide formation)	
	ROO• + RH	$\rightarrow$	ROOH + R•	(hydroperoxide formation)	
Termination	ROO• + R•	$\rightarrow$	ROOR		
	R• + R•	$\rightarrow$	RR		(1)

Autoxidation of oil requires the fatty acids and acylglycerols to be in radical forms [1]. In the presence of an initiator such as heat, the unsaturated lipid molecules lose a hydrogen atom and produce lipid alkyl radicals [3]. The lipid alkyl radicals react with atmospheric oxygen, $^3O_2$, and produce lipid peroxy radicals, which act as the chain carriers of a rapidly progressing reaction by attacking a new lipid molecule, leading to the formation of lipid hydroperoxides [1, 3]. Oxygen availability and temperature will determine the rate of formation of the lipid peroxy radicals and lipid hydroperoxides [1]. The primary oxidation products, lipid hydroperoxides, are stable at room temperature [1]. Nevertheless, at an elevated temperature or in the presence of metal, the lipid hydroperoxides will be broken down into alkoxy radicals, which will then form secondary oxidation products such as aldehydes, ketones, acids, esters, alcohols and low-molecular-weight hydrocarbons on further reaction [1]. Palm oil is composed of mixtures of triacylglycerols (TAGs) as the main constituent where each of the glycerol molecules is esterified with three fatty acids [5, 6]. The major components of fatty acids present in palm oil are palmitic acid (16:0), oleic acid (18:1) and linoleic acid (18:2) [5]. To protect these fatty acids from being oxidized by free radicals, vitamin E, which is a major antioxidant in palm oil, plays an important role [5–7]. However, it was shown that the vitamin E in edible palm olein could be decomposed during a high-heat cooking process such as deep-fat frying [7]. Prior to this, the incorporation of another type of natural antioxidant in palm olein is really important to improve the oxidative stability of the oil towards oxidation processes, thus enhancing the nutritional value, organoleptic properties and sensory quality of the oil.

In this study, vanillin, with the IUPAC name of 4-hydroxy-3-methoxybenzaldehyde, which is the main component of natural vanilla that can be extracted from beans or pods of a tropical climbing orchid called *Vanilla planifolia*, *Vanilla tahitensis* or *Vanilla pompona* [8–12] was added to palm olein to slow down the oil's degradation and to increase its oxidative stability. Instead of synthetic antioxidants such as butylated hydroxyanisole (BHA), butylated hydroxytoluene (BHT), propyl gallate (PG) and *tert*-butylhydroquinone (TBHQ) that have an adverse effect on human health, a naturally occurring antioxidant is preferable to be used as an antioxidant in palm olein because it is non-toxic and readily accepted by the body [13, 14]. The aims of this research were to study the effect of vanillin on the oxidative stability of palm olein using peroxide value test and thermogravimetric analysis (TGA) in an oxygen atmosphere and to characterize the oxidative stability of palm olein using Fourier transform infrared (FTIR) spectroscopy.

Materials and Methods

Chemicals

The chemicals used in this study include vanillin (QReC), cyclohexane (Merck), Wijs solution (QReC), acetic acid (Bendosen), chloroform (R&M), sodium thiosulfate (Bendosen), palm olein, starch (QReC) and distilled water.

Sample preparation

1% of vanillin was added to 50 g of palm olein using a weight to weight ratio. The palm olein that contained vanillin (POV) was pre-heated to 90 °C while stirring to dissolve the vanillin. Palm olein without the addition of vanillin (PO) was used as the reference. The samples of PO and POV were then heated at 90 °C in an oven. Samples were collected at 0, 50, 100, 150 and 200 hours heating for analysis.

Starch indicator preparation
0.5 g of starch was mixed with enough cold water to make a thin paste, followed by the addition of 50 mL of boiling distilled water. The solution was stirred using a magnetic stirrer to dissolve the starch with rotation of speed 300 rpm. The starch solution was prepared each time before each analysis to ensure the effectiveness of the starch solution as an indicator.

Peroxide value (PV) test
30 mL of acetic acid–chloroform solution in the ratio of 3:2 was added to 5.0 g of sample in an Erlenmeyer flask. The flask was shaken to dissolve the sample. Then, 0.5 mL of saturated potassium iodide solution was added. The solution was shaken again for 1 minute before the addition of 30 mL distilled water. The solution was titrated with 0.1 N sodium thiosulfate solution until the yellow colour of the solution faded. 10 drops of starch indicator were added to the solution and the titration was continued until the blue colour of the solution disappeared. The test was done in triplicate to avoid any error that occurred during the titration. The above steps of the PV test were repeated for the blank determination without the presence of PO and POV. The PV was calculated using equation 2 below [15]:

$$\text{PV } (m_{equiv} \text{ peroxide/1000 g oil}) = \frac{(S-B) \times N \times 1000}{W} \quad (2)$$

S = volume of sodium thiosulfate used for sample's titration, mL; B = volume of sodium thiosulfate used for blank's titration, mL; N = normality of sodium thiosulfate, N; W = weight of sample used, g. Tukey's test was used in validating the significant effect of adding vanillin to the PO based on the PV test.

Fourier transform infrared (FTIR) spectroscopy
The oil sample was also characterized using an FTIR spectrometer (Perkin Elmer FTIR Frontier 96255) to determine the functional groups of compounds present in the sample, specifically the primary oxidation product. The characterization was done using the potassium bromide, KBr pellet method. First, the KBr pellet was prepared. The oil sample was then thoroughly spread on the prepared KBr pellet. The spectrum of the sample was recorded from 4000 cm^{-1} to 400 cm^{-1}. The FTIR characterization was conducted at each selected time for each sample of PO and POV [16, 17].

Thermogravimetric analysis in an oxygen atmosphere
The analysis was performed using a Hitachi STA7200 model TGA-DSC instrument. First, POV was prepared and weighed in an alumina cell. The cell was placed in the furnace at room temperature. After 2 minutes, the temperature of the furnace was increased from 30 °C to 70 °C. The sample was continuously heated from 70 °C to 210 °C with the temperature increment of 2 °C per minute. The sample was purged with oxygen at a rate of 50 cm^3 per minute during the analysis. The steps were repeated for the sample of PO [18].

Results and Discussion

Peroxide value test
The PV test was performed to determine the hydroperoxide concentration in the oil samples. This is one of the most common methods used to indicate the initial stages of oxidation [19]. The PV of the original palm olein was directly proportional to the hours of heating [20]. The longer the oil is heated, the greater the number of hydroperoxides generated as a result of oxidation of the unsaturated fatty acids in the sample. Figure 1 shows the variation of PV with different times of heating for both PO and POV, while Table 1 shows the PV of PO and POV after heating at 90 °C for different selected times.

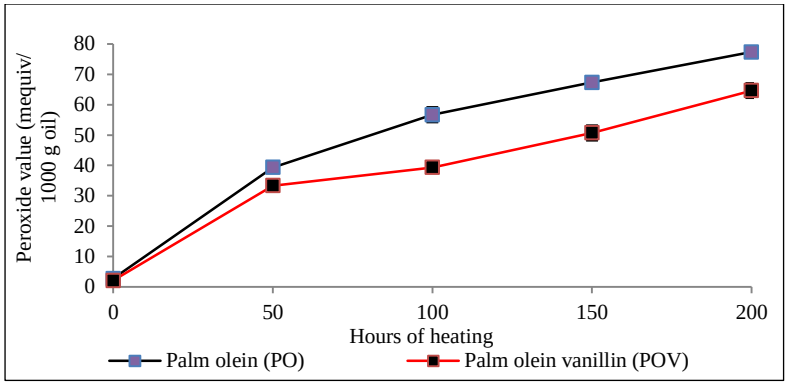


Figure 1. Variation of PV with different times of heating for PO and POV

Table 1. The PV of PO and POV after heating at 90 °C for different selected times

Hours of Heating	PV (mequiv peroxide/1000 g oil)				
	0 hours	50 hours	100 hours	150 hours	200 hours
PO	2.73 ± 0.94	39.35 ± 1.63	56.69 ± 2.49	67.31 ± 1.65	77.32 ± 1.65
POV	2.07 ± 0.94	33.34 ± 1.63	39.34 ± 1.63	50.69 ± 2.51	64.65 ± 2.49

The initial PV of PO at 0 hours was 2.73 mequiv peroxide/1000 g oil compared with the initial PV of POV, which was 2.07 mequiv peroxide/1000 g oil. The initial PV of PO was slightly higher than the initial PV of POV because the PO sample had been oxidized. Hydroperoxide had already started to form in PO although the sample was not yet thermally treated at 0 hours. The PV increased to 39.35 mequiv peroxide/1000 g oil, 56.69 mequiv peroxide/1000 g oil, 67.31 mequiv peroxide/1000 g oil and 77.32 mequiv peroxide/1000 g oil at 50 hours, 100 hours, 150 hours and 200 hours, respectively for PO and rose to 33.34 mequiv peroxide/1000 g oil at 50 hours, 39.34 mequiv peroxide/1000 g oil at 100 hours, 50.69 mequiv peroxide/1000 g oil at 150 hours and finally to 64.65 mequiv peroxide/1000 g oil at 200 hours for POV. The oxidation of PO and POV increased their PV due to the generation of primary oxidation product, hydroperoxide, as a result of heating in the presence of atmospheric oxygen. From 0 hours to 50 hours, the PV showed a relatively small difference between PO and POV and when the time passed from 50 hours to 200 hours, the PV of POV started to deviate to a smaller extent than the PO, as can be seen in Table 2 and Figure 2. The addition of vanillin to palm olein has a significant effect ($p \leq 0.05$) in reducing the rate of oxidation as well as the formation of hydroperoxide in the sample, which led to a lower PV. Vanillin efficiently worked as an antioxidant. It acted as a hydrogen donor to the free radicals that formed during the autoxidation, which by this way could prevent the radicals from attacking a new lipid molecule that resulted in generation of more hydroperoxide. The incorporation of vanillin into palm olein reduced the hydroperoxide formation by 16.10%, while the remaining 83.89% of the oil was being oxidized.

Table 2. PO's and POV's absorbance in between the region of 3600 and 3250 cm^{-1} for every selected hours of heating

Hours of Heating	Absorbance				
	0 hour	50 hours	100 hours	150 hours	200 hours
PO	0.04	0.06	0.09	0.18	0.23
POV	0.03	0.04	0.06	0.10	0.13

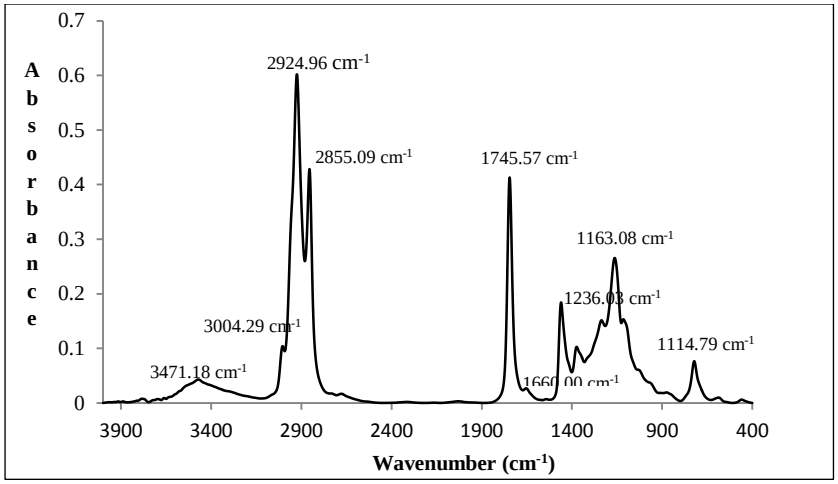


Figure 2. The assigned functional groups of the infrared spectrum of palm olein incorporated with vanillin, before heating (0 hours)

Fourier transform infrared spectroscopy (FTIR) analysis

Palmitic acid (16:0), oleic acid (18:1) and linoleic acid (18:2) contributed in a large proportion in the composition of palm olein. All of these fatty acids consisted of O–H, C=C, C=O, C–O, aliphatic C–H and olefinic C–H functional groups in their structure. The differences among these fatty acids are in the length of the carbon chain and also the number of double bonds that are present in the compound. As for vanillin, the functional groups that exist in the compound include O–H, C=C, C=O, C–O, aliphatic C–H and olefinic C–H. The expected functional groups mentioned above could be confirmed using FTIR spectroscopy. Figure 2 shows the assigned functional groups of the infrared (IR) spectrum of palm olein incorporated with vanillin at 0 hours, before heat was applied. From the spectrum, there was IR absorption of the O–H stretching vibration at frequency 3471.18 cm^{-1} [21, 22] due to the presence of the carboxylic acid functional group in the fatty acids chain and phenolic O–H group in vanillin. The C=C stretching vibration absorbed at frequency 1660.00 cm^{-1} [23] due to the presence of unsaturated fatty acids and the aromatic ring of vanillin, C=O stretching vibration at frequency 1745.57 cm^{-1} arose from the existence of the carboxylic acid functional group in the fatty acid's chain and the aldehyde functional group in vanillin and C–O stretching vibration at frequency 1236.03 cm^{-1}, 1163.08 cm^{-1} and 1114.79 cm^{-1} [22] were due to the presence of the carboxylic acid functional group in the fatty acid's chain, phenolic O–H group and ether functional group in vanillin. There were also peaks that existed at the frequencies 2924.96 cm^{-1} and 2855.09 cm^{-1}, indicating the functional group of aliphatic C–H stretching vibration. The olefinic C–H stretching vibration functional group gave rise to the band at frequency 3004.29 cm^{-1} [24]. Both the aliphatic and olefinic C–H stretching vibration functional groups exist in the structure of free fatty acids and vanillin.

Although infrared spectroscopy was able to analyse most of the functional groups of the oxidation products formed, however, in this research, the use of this technique has focussed on the detection of primary oxidation products of hydroperoxides and the changes that occurred specifically in the band in the region of 3600–3250 cm^{-1}. Figure 3 shows the infrared spectrum of PO and POV from 0 hours to 200 hours of heating in the region of the O–H stretching vibration (3600–3250 cm^{-1}), indicating the presence of hydroperoxides. Based on the figure, the peak intensity of O–H stretching vibration for the sample of PO was higher than that of POV for every selected time of heating. This was due to the antioxidant activity of vanillin in the POV sample, which retards the formation of hydroperoxide during the oxidation process. The concentration of hydroperoxide in the sample increased with the increase in the time of heating because the heat that is applied acted as an initiator for the oxidation reaction and will be accompanied by an increase in the absorbance in the infrared spectrum because the peak intensity is directly proportional to the concentration of the respective functional groups, as stated by the Beer–Lambert law equation, $A = \varepsilon bc$ [22]. The hydroperoxide band shifted towards a smaller wavenumber and became more intense, broader and wider [22–24].

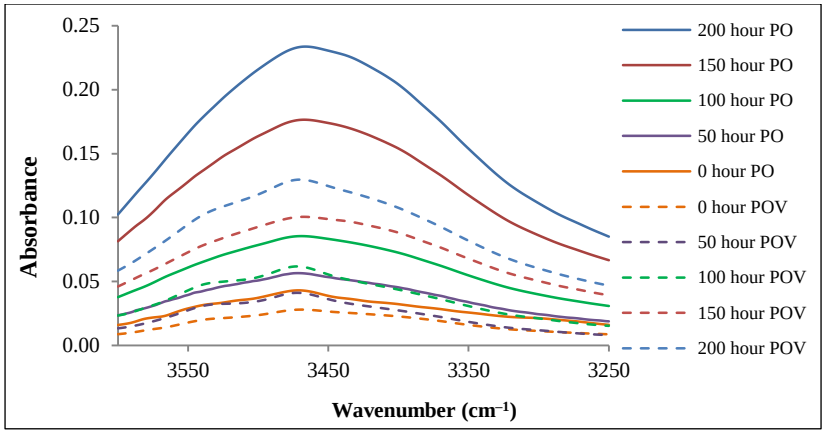


Figure 3. Palm olein (PO) and palm olein vanillin (POV) spectra from 0 hours to 200 hours of heating in the region of the O–H stretching vibration (3600–3250 cm^{-1}), indicating the presence of hydroperoxides

The tabulated absorbance of the O–H stretching vibration in the region 3600–3250 cm^{-1} is shown in Table 2 and the increasing trend of the absorbance throughout the heating can be seen in Figure 4. The absorbance of the O–H stretching vibration of PO increased from 0.04 at 0 hours to 0.06, 0.09, 0.18 and 0.23 at 50 hours, 100 hours, 150 hours and 200 hours, respectively. The initial absorbance of the O–H stretching vibration of POV was 0.03 at 0 hours, slightly lower than the PO due to the low concentration of hydroperoxide present in POV in the initial state. The value increased to 0.04 at 50 hours, 0.06 at 100 hours, 0.10 at 150 hours and finally to 0.13 at 200 hours for POV. Only a small difference could be observed in the absorbance values of PO and POV from 0 hours to 100 hours. However, a significant difference in the absorbance values between these two samples can be seen from 100 hours to 200 hours. The absence of vanillin in the PO sample encouraged the oxidation reaction and the formation of hydroperoxide, especially at elevated temperature. The large amount of hydroperoxide produced in PO sharply increased the intensity of absorption of the O–H stretching vibration between 100 hours and 200 hours of heating. The presence of vanillin in PO successfully inhibited the formation of hydroperoxide by 46.51%. The results obtained from this FTIR spectroscopic analysis correlated to the results of the PV test.

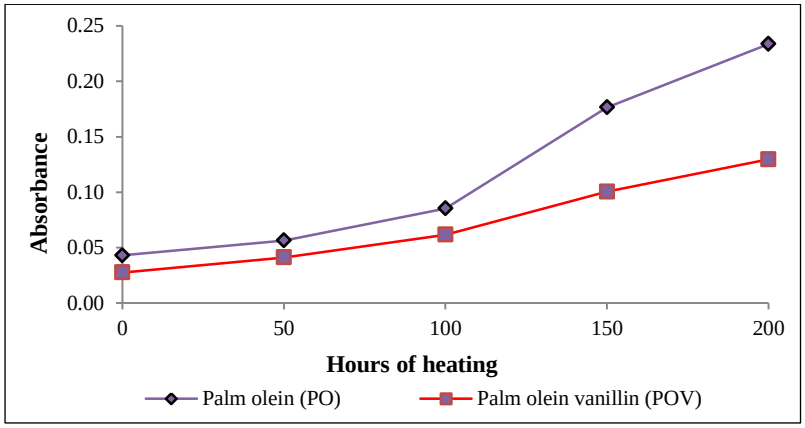


Figure 4. Variation of absorbance with different times of heating for PO and POV

Thermogravimetric analysis

Figures 5 and 6 show the thermogravimetric (TG) curves of PO and POV, respectively, whereas Table 4 shows the initiation (T_i) and final (T_f) oxidation temperatures of PO and POV. T_i is the temperature at which the oxidation rate increases quickly while T_f is the point at which the sample gains maximum weight [25]. The increase in temperature

after T_f results in a loss of the sample's weight until the run is completed [25].

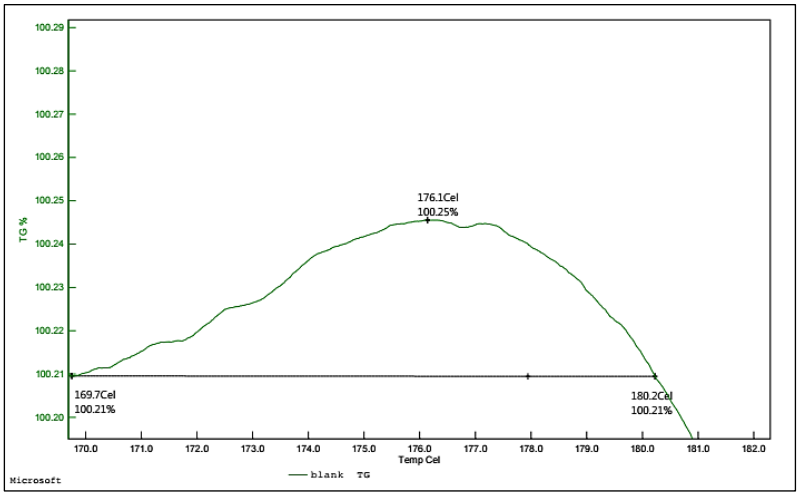


Figure 5. The thermogravimetric curve of PO

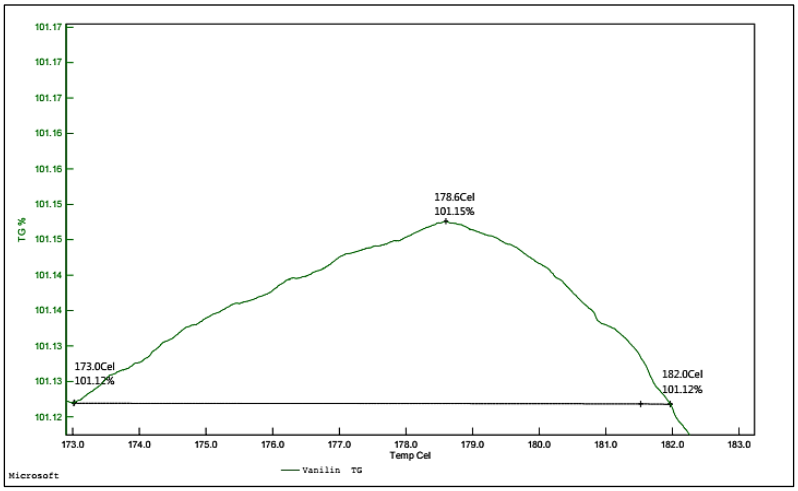


Figure 6. The thermogravimetric curve of POV

Table 4. The initial and final oxidation temperature (T_i and T_f) of PO and POV

Sample	T_i (°C)	T_f (°C)	Sample's Weight Gained, Δ (%)
PO	169.7	176.1	0.04
POV	173.0	178.6	0.03

Based on Figures 5 and 6, it can be seen that the PO sample started to be oxidized at a lower temperature than POV because there was no antioxidant in the PO sample that could help in delaying the oxidation process. The absence of natural antioxidant contributed to the difference in T_i [26]. The T_i of PO was 169.7 °C and the T_i of POV was 173.0 °C. The heat and oxygen that are present during the analysis acted as an initiator for the oxidation reactions of

PO and POV. The TG curve of PO increased until it reached T_f of 176.1 °C and the TG curve of POV increased to the T_f of 178.6 °C due to the gain in the sample's weight because of the formation of hydroperoxides from the oxygen uptake at the beginning of oxidation [26, 27]. The weight increased from 100.21% to 100.25% for PO and from 101.12% to 101.15% for POV with the samples' weight gained percentages of 0.04% and 0.03%, respectively. This showed that the maximum number of hydroperoxides was formed in PO at a lower T_f than in POV. The TG curves started to drop after T_f because the hydroperoxides previously formed were degraded into secondary oxidation products that were volatile [26, 27]. The volatility of the secondary oxidation products reduced the mass of PO and POV samples until the end of the analysis. The existence of vanillin in PO effectively increased the oxidative stability of PO and successfully reduced the deterioration of PO due to oxidation by 25.00% according to the TGA.

Conclusion

It can be concluded that vanillin, a naturally occurring antioxidant, inhibited the autoxidation process and increased the oxidative stability of PO by 16.10%, 46.51% and 25.00% based on the PV, absorbance of the infrared spectrum and the sample's weight gain per cent, respectively. Vanillin can be incorporated into PO as an alternative to a synthetic antioxidant. It is recommended that the incorporation of another antioxidant into PO be tested in the future to identify the antioxidant that has the optimum activity to improve the oil's oxidative stability. Other than that, vanillin could also be used as an antioxidant in other vegetable oils because it has the ability to slow down the oxidation process of oil due to the presence of the phenolic O–H group that it possesses. This condition enables the compound to act as a hydrogen donor to retard the free radical chain reaction during the initial stages of oxidation.

Acknowledgement

The authors are thankful to the International Islamic University Malaysia for supporting this research through the IRF19-014-0014.

References

1. Choe, E. and Min, D. B. (2006). Mechanisms and factors for edible oil oxidation. *Comprehensive Reviews in Food Science and Food Safety*, 5: 169-186.
2. Pimpa, B., Kanjanasopa, D. and Boonlam, S. (2009). Effect of addition of antioxidants on the oxidative stability of refined bleached and deodorized palm olein. *Kasetsart Journal (Natural Science)*, 43: 370-377.
3. Shahidi, F. and Zhong, Y. (2010). Lipid oxidation and improving the oxidative stability. *Chemical Society Reviews*, 39: 4067-4079.
4. Choe, E. and Min, D. B. (2007). Chemistry of deep-fat frying oils. *Journal of Food Science*, 72(5): 77-86.
5. Koushki, M., Nahidi, M. and Cheraghali, F. (2015). Physico-chemical properties, fatty acid profile and nutrition in palm oil. *Journal of Paramedical Sciences*, 6(3): 117-134.
6. Sundram, K., Sambanthamurthi, R. and Tan, Y. A. (2003). Palm fruit chemistry and nutrition. *Asia Pacific Journal of Clinical Nutrition*, 12(3): 355-362.
7. Kuppithayanant, N., Hosap, P. and Chinnawong, N. (2014). The effect of heating on vitamin E decomposition in edible palm oil. *International Journal of Environmental and Rural Development*, 2014: 121-125.
8. Mourtzinos, I., Konteles, S., Kalogeropoulos, N. and Karathanos, V. T. (2009). Thermal oxidation of vanillin affects its antioxidant and antimicrobial properties. *Food Chemistry*, 114(3): 791-797.
9. Walton, N. J., Mayer, M. J. and Narbad, A. (2003). Vanillin. *Phytochemistry*, 63: 505-515.
10. Tai, A., Sawano T., Yazama, F. and Ito, H. (2011). Evaluation of antioxidant activity of vanillin by using multiple antioxidant assays. *Biochimica et Biophysica Acta*, 1810(2): 170-177.
11. Kumar, S. S., Priyadarsini, K. I. and Sainis, K. B. (2002). Free radical scavenging activity of vanillin and *o*-vanillin using 1,1-diphenyl-2-picrylhydrazyl (DPPH) radical. *Redox Report*, 7(1): 35-40.
12. Sinha, A. K., Sharma, U. K. and Sharma, N. (2008). A comprehensive review on vanilla flavor: Extraction, isolation and quantification of vanillin and others constituents. *International Journal of Food Sciences and Nutrition*, 59(4): 299-326.
13. Bera, D., Lahiri, D. and Nag, A. (2006). Studies on a natural antioxidant for stabilization of edible oil and comparison with synthetic antioxidants. *Journal of Food Engineering*, 74: 542-545.
14. Taghvaei, M. and Jafari, S. M. (2015). Application and stability of natural antioxidants in edible oils in order to substitute synthetic additives. *Journal of Food Science and Technology*, 52(3): 1272-1282.

15. American Oil Chemists' Society (1993). Iodine value of fats and oils, cyclohexane method: Official recommended practice Cd 1b-87, revised 1990. In *Official Methods and Recommended Practices of the American Oil Chemists' Society* (3rd ed.). Champaign: AOCS Press.

16. American Oil Chemists' Society (1997). Peroxide value: Method Cd 8-53. In D. Firestone (Ed.), *Official Methods and Recommended Practices of the American Oil Chemists' Society*, (4th ed.). Champaign: AOCS Press.
17. Liang, P., Chen, C., Zhao, S., Ge, F., Liu, D., Liu, B., Fan, Q., Han, B. and Xiong, X. (2013). Application of Fourier transform infrared spectroscopy for the oxidation and peroxide value evaluation in virgin walnut oil. *Journal of* Spectroscopy, 2013: 1-5.
18. Liang, P., Wang, H., Chen, C., Ge, F., Liu, D., Li, S., Han, B., Xiong, X. and Zhao, S. (2013). The use of Fourier transform infrared spectroscopy for quantification of adulteration in virgin walnut oil. *Journal of Spectroscopy*, 2013: 1-6.
19. Guillen, M. D. and Cabo, N. (1997). Infrared Spectroscopy in the study of edible oils and fats. *Journal of the Science of Food and Agriculture*, 75: 1-11.
20. Ghazali, Z., Nik, W. B. W., Bulat, K. H. K., Ani, F. N. and Xian, L. F. (2006). The effect of light on the oxidative stability of palm olein. *International Conference on Natural Resources Engineering and Technology*, 2006: 631-637.
21. Guillen, M. D. and Goicoechea, E. (2007). Detection of primary and secondary oxidation products by Fourier transform infrared spectroscopy (FTIR) and ^{1}H nuclear magnetic resonance (NMR) in sunflower oil during storage. *Journal of Agricultural and Food Chemistry*, 55: 10729-10736.
22. Guillen, M. D. and Cabo, N. (2002). Fourier transform infrared spectra data versus peroxide and anisidine values to determine oxidative stability of edible oils. *Food Chemistry*, 77: 503-510.
23. Guillen, M. D. and Cabo, N. (2000). Some of the most significant changes in the Fourier transform infrared spectra of edible oils under oxidative conditions. *Journal of the Science of Food and Agriculture*, 80: 2028-2036.
24. Goburdhun, D., Laulloo, S. B. J. and Musruck, R. (2001). Evaluation of soy bean oil quality during conventional frying by FT-IR and some chemical indexes. *International Journal of Food Sciences and Nutrition*, 52: 31-42.
25. Coni, E., Podesta, E. and Catone, T. (2004). Oxidizability of different vegetables oils evaluated by thermogravimetric analysis. *Thermochimica Acta*, 418: 11-15.
26. Gao, F. and Birch, J. (2015). Oxidative stability, thermal decomposition and oxidation onset prediction of carrot, flax, hemp and canola seed oils in relation to oil composition and positional distribution of fatty acids. *European Journal of Lipid Science and Technology*, 117: 1-11.
27. Jayadas, N. H. (2008). Evaluation of the oxidative properties of vegetable oils as base stocks for industrial lubricants using spectroscopic and thermogravimetric analyses. *Journal of Synthetic Lubrication*, 25: 105-113.

Malaysian Journal of Analytical Sciences, Vol 23 No 5 (2019): 870 - 879
DOI: https://doi.org/10.17576/mjas-2019-2305-12

MALAYSIAN JOURNAL OF ANALYTICAL SCIENCES
Published by The Malaysian Analytical Sciences Society
ISSN 1394 - 2506

AN ASSESSMENT OF FT-IR AND FT-NIR CAPABILITY IN SCREENING CRUDE PALM OIL AUTHENTICITY AND QUALITY COMBINED WITH CHEMOMETRICS

(Satu Penilaian Terhadap Kebolehan FT-IR Dan FT-NIR Untuk Menyaring Kesahihan dan Kualiti Minyak Sawit Mentah Digabung Dengan Kemometri)

Ng Jing Sheng[1], Widad Fadhullah[1,2], Mohd Omar Ab Kadir[1], Ainolsyakira Mohd Rodhi[3], Noor Hana Hanif Abu Bakar[4], Syahidah Akmal Muhammad[1,3]*

[1]*Environmental Technology Division, School of Industrial Technology, Universiti Sains Malaysia, 11800 USM, Penang, Malaysia*
[2]*Environmental and Occupational Health Program, School of Health Sciences, Health Campus, Universiti Sains Malaysia, 16150 USM, Kubang Kerian, Kelantan, Malaysia.*
[3]*Analytical Biochemistry Research Centre*
[4]*School of Chemical Sciences*
Universiti Sains Malaysia, 11800 USM, Penang, Malaysia

**Corresponding author: syahidah.muhammad@usm.my*

Received: 16 January 2019; Accepted: 26 August 2019

Abstract

This study was conducted to assess the authenticity and evaluate the quality of palm oil with the aid of mid-infrared and near-infrared spectroscopy. Experiments were carried out to imitate the effect of frying in food service industry, therefore crude palm oil (CPO) samples were fried with different meat products (beef, mutton, fish, pork) at varying frequency of 3, 10, 20 and 30 times. Then the used frying oils were mixed with fresh and authentic CPO at different proportions, 5, 10, 20 and 30 (m/m %). Discriminant analysis on the infrared spectrum was carried out and the analysis was based on two class classification, which is to separate between 2 classes of samples. The results showed that the analysis with mid-IR spectrum successfully classified the adulterated oil samples from the authentic CPO with 2 misclassifications of adulterated oil into the authentic group out of 66 samples. The performance index of this model was 95.1 based on the Mahanalobis distance. The success rate of authentication was 96.7% for the mid-IR spectrum. However, the NIR spectrum analysis showed different results from the mid-IR as 11 adulterated samples out of 66 samples showed false positive result. The performance index of this model was 85.7 and the success rate of authentication was 83.3%. On the other hand, for the work on the classification of oil quality using mid-IR, the success rate was only 42.4% with the performance index of 73.4. Additionally, the NIR model for oil quality discrimination had 36.4% of success rate with a performance index of 56.4. The evaluation of oil quality based on the frequency of frying was not very successful and further work will be carried out. Overall, the authentication of palm oil was quite successful, but the evaluation of the quality of palm oil did not achieve our current objective. These rapid screening techniques, which are mid-infrared and near infrared spectroscopy have been proven to be useful for the authentication of edible palm oil but the evaluation of quality has to be further improved.

Keywords: crude palm oil, authenticity, mid-infrared, near-infrared, discriminant analysis

Abstrak

Kajian ini telah dijalankan untuk menilai kesahihan dan kualiti minyak sawit dengan bantuan spektroskopi inframerah-tengah dan hampir. Eksperimen dijalankan dengan menggoreng minyak sawit mentah (CPO) dengan beberapa jenis produk daging

haiwan (daging lembu, kambing, ikan dan khinzir) bertujuan untuk meniru kesan menggoreng makanan dalam industri perkhidmatan makanan, dengan kekerapan yang berbeza iaitu 3, 10, 20 dan 30 kali. Minyak goreng tersebut kemudian telah dicampur dengan minyak sawit mentah dengan peratusan berbeza iaitu 5, 10, 20 dan 30 (m/m %). Selepas itu, spektrum inframerah telah digunakan untuk menjalankan analisis diskriminan dengan menggunakan kemometrik. Analisis diskriminan ini merupakan analisis berasaskan 2 kelas, dan analisis ini berkeupayaan untuk membezakan 2 kelas yang berbeza. Keputusan menunjukkan bahawa analisis specktrum inframerah-tengah telah berjaya mengasingkan minyak goreng terpakai daripada minyak tulen dengan hanya 2 pengelasan salah daripada 66 sampel. Indeks prestasi untuk model ini ialah 95.1 berdasarkan jarak Mahalonobis. Kadar berjaya bagi model ini ialah 96.7%. Seterusnya, model spektrum inframerah-hampir menunjukkan keputusan yang berbeza daripada inframerah-tengah kerana terdapat 11 sampel daripada 66 sampel telah diklasifikasi sebagai positif palsu. Indeks prestasi untuk model ini merupakan 85.7 dan kadar berjaya untuk klasifikasi kesahihan minyak ialah 83.3%. Manakala, dalam bahagian penilaian kualiti minyak menggunakan inframerah-tengah, kadar berjaya hanya 42.4% dengan indeks prestasi sebanyak 73.4. Seterusnya, penilaian kualiti minyak goreng dengan menggunakan model inframerah-hampir menunjukkan kadar berjaya sebanyak 36.4% dan indeks prestasi serendah 56.4. Penilaian kualiti minyak goreng berdasarkan kekerapan menggoreng adalah kurang berjaya dan kajian lebih lanjut akan dijalankan pada masa yang akan datang. Secara keseluruhannya, pengesahan kesahihan minyak sawit adalah berjaya tetapi penilaian kualiti minyak masih tidak dapat mengecapi objektif kajian ini. Teknik pemeriksaaan pantas ini, iaitu spektroskopi inframerah-tengah dan hampir telah dibuktikan berkesan untuk pengesahan kesahihan minyak sawit tetapi penilaian kualiti masih memerlukan penambahbaikan.

Kata kunci: minyak sawit mentah, kesahihan, inframerah-tengah, inframerah-hampir, analisis diskriminan

Introduction

Malaysia is one of the major producers of palm oil. In 2015, the price of crude palm oil peaked at MYR 2294/tonne and a total export of 25.37 million tonnes of crude palm oil was recorded [1]. Crude palm oil can be classified into two groups, which are palm kernel oil from the kernel and crude palm oil from the mesocarp. The palm kernel oil is rich in lauric and myristic acids while crude palm oil is rich in palmitic acid, though both of them mainly consist of triglyceride. Palm oil plays a crucial role in many consumer products. The consumer palm oil products available in the market such as cooking oil are used to meet our daily needs for example in food preparation. In Malaysia, frying during food preparation is very popular. This method enhances the taste and crispiness of food and requires a relatively short time for food preparation. However, frying at high temperature will cause changes in the chemical properties and structure of fatty acid which may cause harmful effects to consumers. Therefore, it is not suitable to reuse used frying oil for consumption purposes as the oil had lost its value for cooking. Hence it would lead to unimaginable repercussion if the waste oils were reprocessed and consumed by consumers. It is also unethical for manufacturers to adulterate brand new palm oil products with used frying oil for the sake of making more profits. When an oil of cheaper value is added to another oil with higher value illegally, the practice is considered as adulteration [2].

The quality of palm oil is determined by a few parameters such as free fatty acid content, peroxide value, moisture and impurities. In Malaysia, Malaysia Palm Oil Board (MPOB) is the government agency responsible for developing national objectives and policies for the palm oil industry to ensure their well-being. The determination of oil quality can be done via distinct types of wet chemistry methods, for instance, mass spectrometry, High Performance Liquid Chromatography (HPLC) and gas chromatography techniques [3, 4]. These methods are time consuming, required skilled technicians and the disposal of reagents need to be done cautiously [5]. Nevertheless, in this 21st century, speed and efficiency matter the most. The methods mentioned above are time consuming and involve a lot of laboratory procedures, solvents and glassware [6]. It may not be suitable to send those suspicious samples for further investigation without a proper indicator which might end up wasting resources and money if the samples turn out to be genuine.

Hence, the use of a rapid screening technique can be useful to red-flag a suspected sample, remove it from the shelf or any other stage in the supply chain before proceeding to confirmation analyses for quality and authenticity test. A screening technique is very useful to prevent a suspected sample from reaching a customer, to avoid a brand controversy and safeguard consumer's trust. An option for this kind of screening technique is vibrational spectroscopy. The advancement in vibrational spectroscopy in terms of measurement speed and the minimal disposal of waste has gained popularity in research, control and industrial laboratories [7]. Specifically, mid-infrared (MIR) and near-infrared (NIR) techniques are the common implementations in research work related to

food application, pharmaceutical industry and others. In contrast to conventional analytical methods, for example, wet lab analysis and chromatography technique which involve chemical reagents and separation of components, these techniques are advantageous in terms of their rapid scanning instrumental nature, high resolution and wide wavelength number interval covered by infrared radiation [7].

Near infrared spectroscopy is a fast and non-destructive technique that provides multi-constituent analysis to virtually any matrix [8]. Meanwhile, the mid-infrared is more frequently used for qualitative work which include the identification of functional groups and molecular characterization [9]. The relative easiness to operate and nearly without complex samples preparation have made mid-infrared technique a favorable option [10]. Mid-infrared spectroscopy equipped with attenuated total reflectance (ATR) crystal enables the minimal sample preparation to obtain spectral information and can be done within a relatively short time. Moreover, the ATR-FTIR is able to perform quantitative studies involving solid and liquid samples. Recent studies have shown that the adulteration of different types of edible oil could be detected with mid-infrared technique [6, 11, 12] and near infrared technique [13-15]. Given the complexity of the infrared spectra, chemometric software has been developed to support the statistical analysis. Hence, the objective of this study is to assess the capability of FT-IR and FT-NIR in screening the authenticity and quality of crude palm oil combined with chemometric analysis.

Materials and Methods

Sampling

The sample used in this study was fresh and authentic crude palm oil (CPO) obtained from Malaysia Palm oil Board (MPOB) northern region branch, located in Penang, Malaysia. This MPOB branch received CPO directly from palm oil mills under their purview, thus ensuring the authenticity of these CPO samples.

Sample preparation

Prior to sending CPO samples to MPOB, the palm oil mills extracted the CPO using mechanical extraction process. Once samples were received in our laboratory, they were subsequently stored in the fridge at 4 °C prior to simulation test.

Simulation test

In this study, simulation test was designed to produce CPO which has similar properties to the used frying oil. Therefore, 10 mL of CPO was fried with different meat products (lard, fish, beef, lamb) which were purchased from local markets and had been cut into approximately 0.5×1 cm (width x length). Each type of meat was fried at different frequencies, 3, 10, 20, 30 times in which the meat cube was fried twice before being discarded. The time interval for each frying was 1 minute. This process was to simulate the frying process done in the food service industry, where the oil was repeatedly fried with food. Nevertheless, this experiment was done on a small scale; thus, to reduce the losses of oil through evaporation, the frying interval for the meat had to be short (Σ1 minute) and the meat was fried twice to ensure that the meat was thoroughly cooked.

Adulteration of oil

The used frying oil produced was allowed to cool to room temperature, then mixed with fresh and authentic CPO at different proportions of 5, 10, 20 and 30 (weight/weight) (m/m %). All the samples were kept separately in 15 mL polypropylene containers and refrigerated at 4°C prior to spectroscopic analyses.

Spectra acquisition of oil samples: Fourier transform-infrared spectroscopy

Spectra was obtained with PerkinElmer Frontier MIR spectrometer equipped with an optical system with KBr beam splitter with the best resolution at 0.4 cm^{-1} coupled to the universal attenuated total reflectance (UATR) adapter. The configuration of the recording of spectra was 4 cm^{-1} resolution, 32 scan, transmission mode at the range of 4000 cm^{-1} to 600 cm^{-1} [16] and recorded using Spectrum® software. A drop of oil sample, coming from different sample populations, where one population represents the fresh and authentic oil samples and the other represents used oils that were fried with different meats spiked into fresh and authentic CPO to become our adulterated sample population, was placed on the ATR surface. A spectrum of each run was obtained and recorded. The surface of the ATR was then cleansed with wipes and ethanol before proceeding to the next sample scan.

Fourier transform-near infrared spectroscopy

Thermo Scientific Nicolet™ iS™5N Near infrared spectrometer with heated transmission accessory was used to obtain spectra of the oil samples in the wavenumber range of 10000 cm^{-1} to 4000 cm^{-1}. The detector used in this instrument was Deuterated Triglycine Sulfate (DTGS), KBr beam splitter, and white light source. The instrument software and data processor is TQ Analyst 10. Blank spectrum was first collected against the background in absorbance mode. The oil samples were filled up in a quartz cuvette (10 mm x 10 mm x 50 mm) and the spectrum was obtained and saved in absorbance mode at a resolution of 4 cm^{-1}, after 32 scans. The heated transmission accessory was used to maintain the temperature of the sample at 40 °C because the sample transparency decreased with temperature drop thus affecting the spectrum obtained. Cleaning of the cuvette was done each time before a new scan was performed by washing the cuvette with 5% Decon solution and ethanol. The spectrum in absorbance mode was converted to the first derivative with the help of Thermo Scientific TQ Analyst® 10 software. The purpose of pre-processing of spectrum was to remove the scattering and pathlength effect on the spectra and ease the process of identifying the most vital factor that contributes to the variability.

Statistical analysis was done with Thermo Scientific TQ Analyst 10. This software package was designed for spectroscopic application, namely, mid-infrared and near infrared. The technique used in this study was discriminant analysis (DA), which classifies the unknown samples to the closest group of known samples. Both the MIR and NIR spectra underwent the analysis using TQ Analyst 10. The spectra were divided into 2 sets, which were the calibration set and the validation set. The ratio of calibration set to validation set was 7:3 [10], which is the ratio commonly used to establish the calibration and validation set. In total, there were 66 samples, where 47 and 19 samples made up the calibration and validation set, respectively. Out of the 66 samples, 64 samples were adulterated samples and 2 samples were fresh and authentic samples. The calibration set was constructed based on the characteristics of known group of samples (authentic and used frying oil) while the validation set was used to determine if the samples in this set could be correctly classified.

Results and Discussion

Authentication of CPO: Fourier transform-infrared spectroscopy

Peaks were detected at wavenumber of 2922 cm^{-1} (C-H stretching (asymmetrical)), 2853 cm^{-1} (C-H stretching (symmetrical)), 1744 cm^{-1} (C=O stretching), 1417 cm^{-1} (C-H rocking), 1377 cm^{-1} (C-H bending (symmetrical)), 1160 cm^{-1} and 1116 cm^{-1} (C-H and C-O stretching and bending) as well as 721 cm^{-1} (C-H rocking (overlapping)). Figure 1 shows the stack up of multiple spectrum in an overlay view. The spectra demonstrated a very similar profile to other adulterated CPOs and the differences were almost impossible to be differentiated without the magnification of the peak positioned at 1744 cm^{-1} (Figure 1). This is surprising considering the fact that other works have reported changes in several peaks such as at 3012 cm^{-1} which is being attributed to C-H stretching of cis double bond. A previous study [17] also showed a significant decrease in the intensity of the same peak due to the breakage of the cis double bond, as a result of extensive heating and oxygen uptake effect. In this work, as the oil was fried with different meat products at different time interval, the intensity of the peak at 1744 cm^{-1} underwent slight changes which could be picked up by chemometric analysis. The inset in Figure 1 shows the stack up of this peak from multiple spectrums in an overlay view.

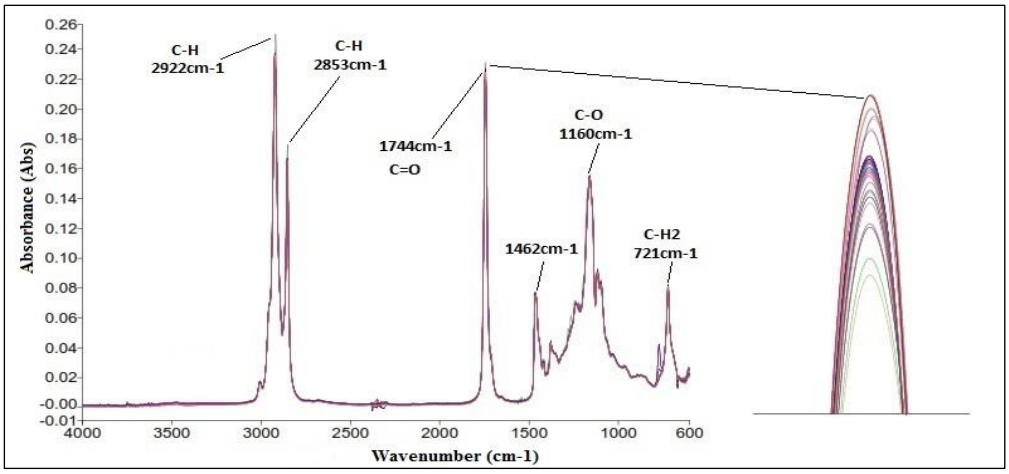


Figure 1. The FT-IR spectra of typical used frying oil. [Inset: Magnification of peak at wavenumber 1744 cm^{-1}]

Fourier transform-near infrared spectroscopy

Figure 2 shows the NIR spectra of used frying oil in the range of 10000 cm^{-1} to 4000 cm^{-1}. From the spectra, significant absorption bands which are observed at around 8135 cm^{-1} (C-H stretching second overtone), 7231 cm^{-1}, 7130 cm^{-1} and 7058 cm^{-1} are related to the hydroxyl group stretching in first overtone. The absorption band at 5959 cm^{-1} is assigned to the first overtone of C-H stretching vibration. The small peak around 5330 cm^{-1} to 5303 cm^{-1} is attributed to the C=O stretching second overtone. The absorption bands at 4798 cm^{-1} (C-H stretching absorption (terminal double bond cis-unsaturation)) and 4550 cm^{-1} (combination of C-H asymmetric stretching in C=C stretching vibration) were also detected. From observation, it was found that the spectra had an extensive overlapping of bands in the overtones and combination region. Therefore, chemometric analysis is an integral part which ensures that the spectroscopic data makes sense due to its power to detect the slightest differences in each sample spectrum obtained by the NIR instrument. The first derivative was applied to the spectra to remove the effect of scattering and noise in the spectra.

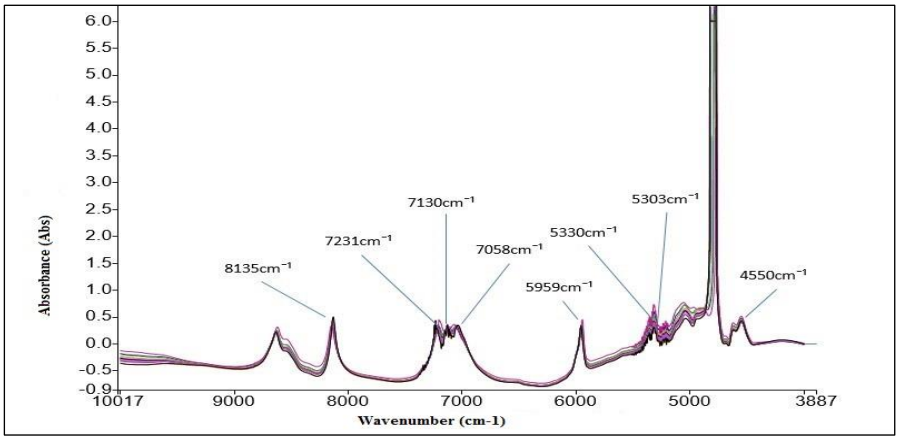


Figure 2. FT-NIR spectra overlay of typical used frying oil

Discriminant analysis (DA) of spectroscopic data for authenticity screening

The discriminant analysis (DA) in the TQ Analyst 10 was adopted using a similar mathematical algorithm as Soft Independent Modelling of Class Analogy (SIMCA). It was needed to classify the authentic oil samples from that of the adulterated oil samples based on selected region or fingerprints. The region of 3934 to 669 cm^{-1} was used to

perform the analysis and different class distribution was calculated for each class, in this case, the authentic and adulterated oil spectra. This discriminant model was set with the confidence level of 95% and the maximum number principal component was 10 by default. Basically, our model was designed to pull the adulterated CPO to the y-axis and away from the x-axis. The higher the concentration of adulteration, the closer they are to the y-axis. On the other hand, the lower the concentration of adulteration, the closer they are to the x-axis.

Fourier transform-infrared spectroscopy

In Figure 3, results show that only two samples were misclassified, whereby the two adulterated samples in the calibration set were classified as authentic. It can be observed from Figure 3 that the authentic samples (triangle) cannot be clearly distinguished from the adulterated samples. Nevertheless, the calculated Mahanolobis distance value of majority of the samples was above 0.7 from the authentic class which implied that the authentic samples could be differentiated from the adulterated samples. The calibration model had a performance index score of 95.1 based on the calculated Mahanolobis distance while the model had explained 99% of the variation. This model could differentiate most of the adulterated samples from the authentic samples with some exception, even though from the visual inspection of the Cooman plot, there is no distinguishable class that can be observed from the result of analysis. The Mahalanobis distance was useful to classify unknown samples into different groups of known measured samples. The rate of successful classification was 96.7% and this rate is comparable to a previous study [18].

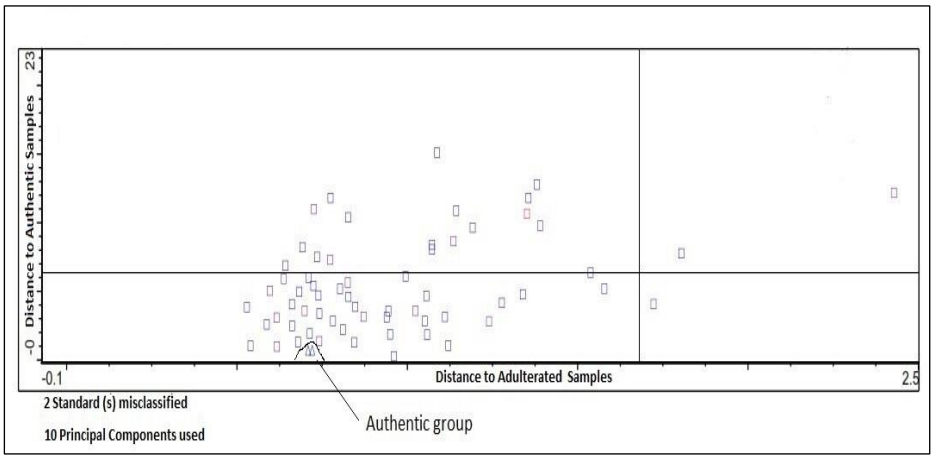


Figure 3. Cooman plot of discriminant analysis of FT-IR (3934 cm^{-1} to 669 cm^{-1}). The squares represent the calibration set of adulterated samples. The triangles represent the authentic CPO. Blue colour represents calibration set. Black colour represents validation set

Fourier transform-near infrared spectroscopy

Figure 2 shows that NIR spectra consists of broad and overlapping peaks which happened to be the overtone of the fundamental absorption bands. Hence, the spectra had undergone pre-processing of spectrum so that the overlapping peaks could be revealed, and the differences could be picked up by the chemometric analysis. The NIR spectra were treated with the first derivative before the spectral information undergone DA analysis. Discriminant analysis was carried out between 9879 cm^{-1} to 5000 cm^{-1} of NIR spectra of Figure 2. The Cooman plot derived from this analysis is presented in Figure 4. The choice of region is due to the fact that a peak where the absorbance exceeded the detection limit existed in the region of 5000 to 4000 cm^{-1}. Hence inclusion of this result would affect the result of the analysis. The outcome of the analysis showed that from a total of 64 samples, 11 adulterated samples were misclassified as authentic samples. The percentage of successful classification was 83.3%.

This model had explained 99% variation of the samples analysed. The 11 misclassified samples consisted of 1 sample adulterated with fish frying oil (10 times,20%), pork frying oil (30 times, 5% and 30 times,10%), mutton frying oil (3 times, 5%, 3 times, 20%, 3 times, 30%, 10 times, 5%, 10 times, 10%, 10 times, 20%, 30 times, 5%, 30 times, 20%). The small number of repetitive frying could be the possible cause of this false positive result. The time interval of frying process was also too short to give a significant impact on the composition of the CPO. Besides, the low percentage of adulteration could also contribute to the misclassification. Previous work has shown that the performance of NIR analysis in the authentication of vegetable oil was lower in comparison to FT-IR and FT-Raman as NIR is more commonly used for quantitative study due to its broad and overlapping spectrum [18].

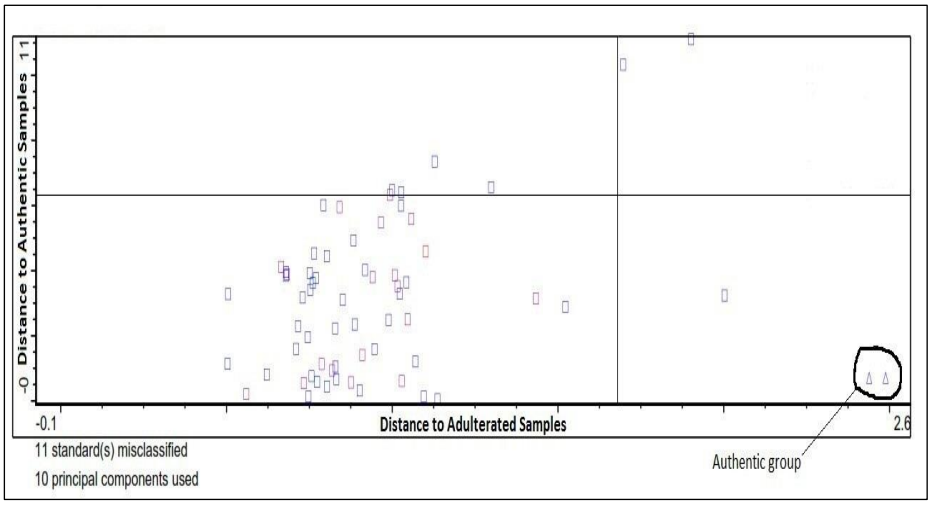


Figure 4. Cooman plot of discriminant analysis of FT-NIR (9879 cm^{-1}-4119 cm^{-1}). The squares represent the calibration set of adulterated samples. The triangles represent the authentic CPO. Blue colour represents calibration set. Black colour represents validation set

Discriminant analysis (DA) of spectroscopic data for quality screening

The discriminant analysis used to assess the spectroscopic data for quality screening of CPO adopted a similar approach to the one used in the discriminant analysis of spectroscopic data for authenticity screening. The MIR model had a misclassification of 38 samples with performance index of 73.4. The success rate of classification was 42.4%. Meanwhile, the model built based on the NIR spectra had misclassified 42 samples into the wrong categories with performance index of 56.4. The Cooman plot of these models is shown in Figure 5 and Figure 6. These two models are considered unsuccessful as the samples could not be correctly classified into their categories. A previous study [19] has shown that the authenticity and evaluation of used oil can be completely distinguished. Hence it might be possible that the short time interval of frying as well as the low temperature used may have caused the indistinguishable results.

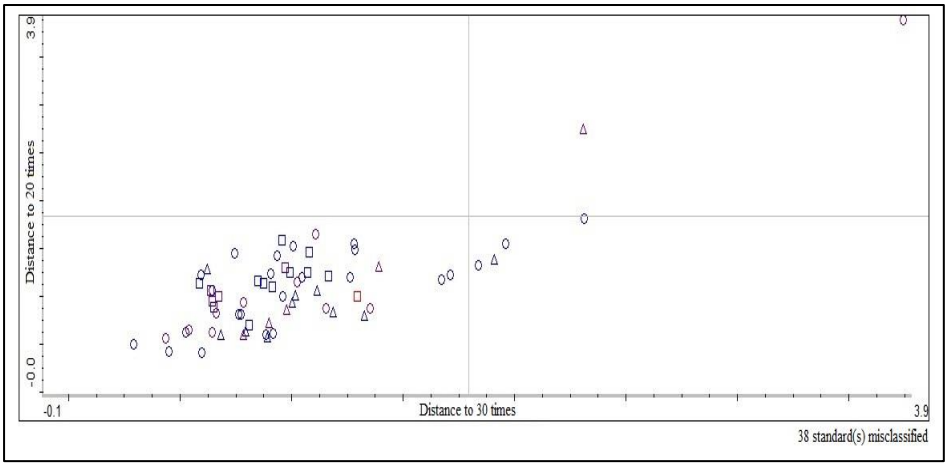


Figure 5. Cooman plot of discriminant analysis of FT-IR (3934 cm^{-1} to 669 cm^{-1}). The squares represent the oil samples of 30 times frying. The triangles represent the oil samples of 20 times frying. The circles represent the other oil samples (10 times, 5 times and authentic)

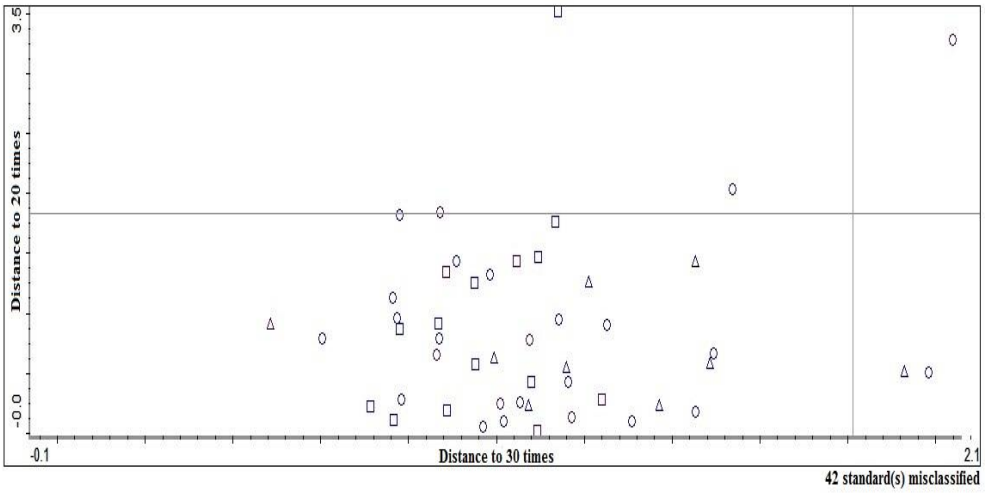


Figure 6. Cooman plot of discriminant analysis of FT-NIR (9879 cm^{-1}- 4119 cm^{-1}). The squares represent the oil samples of 30 times frying. The triangles represent the oil samples of 20 times frying. The circles represent the other oil samples (10 times, 5 times and authentic)

Conclusion

Mid-Infrared and near-infrared spectroscopy combined with chemometrics were assessed to screen for authenticity and quality of CPO. The techniques were successful for authenticity screening with 96.7% correct classification on FT-IR and 83.3% correct classification on FT-NIR, whilst for quality screening, they were not satisfactory with only 42.4% and 36% of successful classification on both FT-IR and FT-NIR. The time taken for the infrared spectrum to be obtained was roughly 3 min for FT-IR and merely 30 s for FT-NIR. This work demonstrated the rapidness, non-destructive, and minimal sample preparation for the screening to take place. These techniques could help to identify the adulteration of edible palm oil which is considered unfit for human consumption. Nevertheless, a lot of improvements can be made to increase the reliability of this classification model for this spectroscopy techniques to be employable for the authenticity and quality screening of edible palm oil in the future.

Acknowledgement

The authors would like to extend their deepest gratitude to the International Atomic Energy Agency (IAEA) for the funding obtained under Coordinated Research Project (CRP) G42007/D52040 with grant number: USM 304/PTEKIND/650887/I111. The authors would also like to appreciate the additional financial assistance given by Universiti Sains Malaysia under the USM bridging grant (304/PTEKIND/6316075). Lastly, the authors are grateful to Nexus Analytic Sdn. Bhd. for the usage of Thermo NIR (Thermo Scientific Nicolet™ iS™5N) for the NIR work.

References

1. Malaysia Palm Oil Board. (2015). Overview of the Malaysia Oil Palm Industry 2015. http://palmoilis.mpob.gov.my/index.php/overview-of-industry/408-overview-of-industry-2015. Access online 30/10/2017.
2. Nunes, C. A. (2014). Vibrational spectroscopy and chemometrics to assess authenticity, adulteration and intrinsic quality parameters of edible oils and fats. *Food Research International*, 60: 255-261.
3. Park, Y. W., Chang, P.-S. and Lee, J. (2010). Application of triacylglycerol and fatty acid analyses to discriminate blended sesame oil with soybean oil. *Food Chemistry*, 123(2): 377-383.
4. Lerma-García, M. J., Herrero-Martínez, J. M., Ramis-Ramos, G. and Simó-Alfonso, E. F. (2008). Evaluation of the quality of olive oil using fatty acid profiles by direct infusion electrospray ionization mass spectrometry. *Food Chemistry*, 107(3): 1307-1313.
5. Bertran, E., Blanco, M., Coello, J., Iturriaga, H., Maspoch, S. and Montoliu, I. (1999). Determination of olive oil free fatty acid by Fourier transform infrared spectroscopy. *Journal of the American Oil Chemists' Society*, 76(5): 611-616.
6. Yang, H., Irudayaraj, J. and Paradkar, M. M. (2005). Discriminant analysis of edible oils and fats by FTIR, FT-NIR and FT-Raman spectroscopy. *Food Chemistry*, 93(1): 25-32.
7. Moros, J., Garrigues, S. and Guardia, M. D. l. (2010). Vibrational spectroscopy provides a green tool for multi-component analysis. *TrAC Trends in Analytical Chemistry*, 29(7): 578-591.
8. Reich, G. (2005). Near-infrared spectroscopy and imaging: Basic principles and pharmaceutical applications. *Advanced Drug Delivery Reviews*, 57(8): 1109-1143.
9. van de Voort, F. R., Ghetler, A., García-González, D. L. and Li, Y. D. (2008). Perspectives on quantitative Mid-FTIR spectroscopy in relation to edible oil and lubricant analysis: Evolution and Integration of analytical methodologies. *Food Analytical Methods*, 1(3): 153-163.
10. Maggio, R. M., Kaufman, T. S., Carlo, M. D., Cerretani, L., Bendini, A., Cichelli, A. and Compagnone, D. (2009). Monitoring of fatty acid composition in virgin olive oil by Fourier transformed infrared spectroscopy coupled with partial least squares. *Food Chemistry*, 114(4): 1549-1554.
11. Rohman, A., Che Man, Y. B., Hashim, P. and Ismail, A. (2011). FTIR spectroscopy combined with chemometrics for analysis of lard adulteration in some vegetable oils Espectroscopia FTIR combinada con quimiometría para el análisis de adulteración con grasa de cerdo de aceites vegetales. *CyTA - Journal of Food*, 9(2): 96-101.
12. Rohman, A., Che Man, Y. B., Ismail, A. and Hashim, P. (2010). Application of FTIR Spectroscopy for the determination of virgin coconut oil in binary mixtures with olive oil and palm oil. *Journal of the American Oil Chemists' Society*, *87*(6): 601-606.
13. Wang, L., Lee, F. S. C., Wang, X. and He, Y. (2006). Feasibility study of quantifying and discriminating soybean oil adulteration in camellia oils by attenuated total reflectance MIR and fiber optic diffuse reflectance NIR. *Food Chemistry*, *95*(3): 529-536.
14. Basri, K. N., Hussain, M. N., Bakar, J., Sharif, Z., Khir, M. F. A. and Zoolfakar, A. S. (2017). Classification and quantification of palm oil adulteration via portable NIR spectroscopy. *Spectrochimica Acta Part A: Molecular and Biomolecular Spectroscopy*, 173: 335-342.
15. Blanco, M. and Pagès, J. (2002). Classification and quantitation of finishing oils by near infrared spectroscopy. *Analytica Chimica Acta*, 463(2): 295-303.
16. Che Man, Y. B., Syahariza, Z. A., Mirghani, M. E. S., Jinap, S. and Bakar, J. (2005). Analysis of potential lard adulteration in chocolate and chocolate products using Fourier transform infrared spectroscopy. *Food Chemistry*, 90(4): 815-819.

17. Goburdhun, D., Jhaumeer-Laulloo, S. B., Musruck, R. (2001). Evaluation of soybean oil quality during conventional frying by FTIR and some chemical indexes. *International Journal of Food Sciences and Nutrition*, *52*(1): 31-42.
18. Yang, H. and Irudayaraj, J. (2001). Comparison of near-infrared, fourier transform-infrared, and fourier transform-raman methods for determining olive pomace oil adulteration in extra virgin olive oil. *Journal of the American Oil Chemists' Society*, 78(9): 889.
19. Innawong, B., Mallikarjunan, P., Irudayaraj, J. and Marcy, J. E. (2004). The determination of frying oil quality using Fourier transform infrared attenuated total reflectance. *LWT - Food Science and Technology*, 37(1): 23-28.

Malaysian Journal of Analytical Sciences, Vol 23 No 5 (2019): 880 - 891
DOI: https://doi.org/10.17576/mjas-2019-2305-13

MALAYSIAN JOURNAL OF ANALYTICAL SCIENCES
Published by The Malaysian Analytical Sciences Society
ISSN 1394 - 2506

GLYCEROL DEGRADATION IN THE ABSENCE OF EXTERNAL HYDROGEN GAS BY USING WASTE EGGSHELL AS HETEROGENEOUS CATALYST

(Degradasi Gliserol Tanpa Kehadiran Hidrogen Luaran dengan Menggunakan Sisa Kulit Telur sebagai Mangkin Heterogen)

Mohamad Imran Firdaus Mhd Sawal[1], Ahmad Irfan Oslan[1], Muhammad Hazwan Muhamad Hatta[1], Noraini Hamzah[2], Norazzizi Nordin[3], Norsaliyana Jumali[1], Wan Zurina Samad[1]*

[1]*Department of Chemistry, Kulliyyah of Science,*
International Islamic University Malaysia, Bandar Indera Mahkota, 25200 Kuantan, Pahang, Malaysia
[2]*Faculty of Applied Sciences,*
Universiti Teknologi MARA, 40450 Shah Alam, Selangor, Malaysia
[3]*School of Chemical Sciences,*
Universiti Sains Malaysia, 11800 Minden, Pulau Pinang, Malaysia

**Corresponding author: wzurina@iium.edu.my*

Received: 16 January 2019; Accepted: 29 July 2019

Abstract

The demand of biodiesel production nowadays is increasing every day. However, the booming of biodiesel demand resulted in the increase of glycerol production as a major by-product. Although glycerol could serve in various industries, the demand and usage are still limited. Therefore, an alternative method was proposed in this research in order to convert glycerol into more value-added chemicals such as methanol (MeOH), propanol (1-PrOH), and 1,2-propanediol (1,2-PDO) through a new low cost and simple approach which is the reflux technique in the absence of external hydrogen gas. Due to the concern of global food waste issues, calcium oxide (CaO) catalyst derived from waste eggshells is utilized as a possible heterogeneous catalyst. This preliminary research studied the influence of reaction temperature and reaction time whereas catalyst weight and glycerol concentration were fixed as independent variables. Overall, the three chemicals were successfully synthesized with different optimum conditions. The formation of 1,2-PDO is more preferred at lower temperature (130 °C and 5 hours) with glycerol conversion and selectivity of 53.70% and 64.76%, respectively. However, the formation of MeOH and 1-PrOH are preferred at higher temperature. The formation of 1-PrOH (170 °C and 5 hours) resulted in glycerol conversion and selectivity of 81.64% and 70.85%, respectively. Meanwhile, the best condition in the formation of MeOH is at 190 °C and 7 hours reaction time with glycerol conversion and selectivity of 65.8 % and 46.44%, respectively.

Keywords: glycerol, degradation, external hydrogen, waste eggshell, heterogeneous catalyst

Abstrak

Permintaan pengeluaran biodiesel semakin meningkat setiap hari. Fungsi biodiesel itu sendiri sebagai bahan api alternatif untuk menggantikan penggunaan bahan api fosil adalah salah satu teknik terbaik untuk mengurangkan pembebasan gas karbon dioksida (CO_2) yang dikeluarkan di atmosfera. Walau bagaimanapun, permintaan biodiesel yang tinggi menyebabkan peningkatan penghasilan gliserol sebagai produk sampingan utama. Walaupun gliserol boleh digunakan dalam pelbagai industri, permintaan dan penggunaannya masih terhad. Oleh itu, satu alternatif telah diambil dalam penyelidikan ini untuk menukar gliserol menjadi bahan kimia yang lebih bernilai seperti metanol (MeOH), propanol (PrOH) dan 1,2-propanediol (1,2-PDO) melalui pendekatan baharu yang lebih murah dan lebih mudah iaitu dengan menggunakan teknik refluks. Penukaran gliserol juga dilakukan tanpa kehadiran gas hidrogen luaran. Dengan mengambil kira mengenai isu kenaikan sisa makanan global, mangkin

kalsium oksida (CaO) yang diperoleh daripada sisa kulit telur telah digunakan sebagai mangkin heterogen. Penyelidikan awal ini bertumpu mengkaji parameter pengaruh suhu tindak balas dan masa tindak balas, manakala berat mangkin dan kepekatan gliserol dijadikan sebagai pemboleh ubah tidak bersandar. Secara keseluruhan, ketiga-tiga bahan kimia telah berjaya disintesis dengan keadaan optimum yang berbeza. Pembentukan 1,2-PDO lebih baik pada suhu yang rendah (130 °C dan 5 jam) dengan penukaran gliserol dan selektiviti pada 53.70% dan 64.76%. Walau bagaimanapun, penghasilan MeOH dan 1-PrOH lebih baik pada suhu yang lebih tinggi. Penghasilan 1-PrOH (170 °C dan 5 jam) mencatatkan penukaran gliserol pada 81.64% dan selektiviti pada 70.85%. Sementara itu, keadaan terbaik dalam pembentukan metanol adalah pada 190 °C, dan masa reaksi 7 jam dengan penukaran gliserol pada 65.87% dan selektiviti produk masing-masing 46.44%.

Kata kunci: gliserol, degradasi, hidrogen luaran, sisa kulit telur, mangkin heterogen

Introduction

Recently, glycerol or also known as 1,2,3-propanetriol is used globally. For example, in food production, glycerol is used to produce sweeteners, humectants and solvents. Glycerol is also used in skin protection, cosmetic and pharmaceutical products. In medical and skin protection, glycerol is used to increase smoothness and also acts as a moisturizer [1]. The main activity that generates glycerol is biodiesel production. The increase in the production of biodiesel generates more glycerol as a major by-product. Biodiesel is one of the biofuels that can be used to replace fossil fuels as a source of energy because biodiesel produces less emission of hydrocarbons, particulate matters, and carbon monoxide, as well as has excellent lubricant properties. Other than that, biodiesel can be used in cosmetics, tobacco, cellulose firms, and paper industries [2-4]. In fact, glycerol is also primarily derived from animal fats and vegetable oils. To note, one mole of glycerol is produced for every three moles of biodiesel produced. It is estimated that glycerol contributes to approximately 10% as a by-product in biodiesel production [5]. It is reported by Anand and Saxena [6] that, on average, 5-10 gallons of crude glycerol are produced for every 100 gallons of biodiesel produced. From the projection on the world biodiesel market based on previous statistical data, it is estimated that approximately 4 billion gallons of crude glycerol will be produced in 2016 [6, 7]. Although glycerol could serve in various industries, the drawbacks still occur as the demand for glycerol is still limited, thus, there is abundance of glycerol in nature. The price of glycerol will be affected due to the excessive amount of glycerol produced, as well as the difficulties and high cost of glycerol refinery processes [8]. Apart from that, the excess of glycerol in nature can bring harm to the environment as glycerol is very hard to be disposed in the environment [8, 9]. Referring to these drawbacks, an approach is taken in order to convert glycerol to more valuable chemicals through catalytic activity.

For catalytic approach, calcium oxide (CaO) basic heterogeneous catalyst derived from waste chicken eggshells is chosen due to the availability in obtaining eggshells around us. Generally, eggshells consist of mainly calcium carbonate ($CaCO_3$), amino acid groups such as methionine (Met), alanine (Ala), and histidine (His), and a small amount of sodium (Na), magnesium (Mg), and potassium (K) [10]. Eggshells are available from any places such as markets, restaurants, and poultry farms. Besides, the price of eggshells is also reasonable and affordable, and eggshells are harmless to the environment [11]. Despite that, waste eggshells are also categorized in food waste, which, can be considered as one of the green catalysts. Furthermore, waste eggshell derived catalysts can be classified as safe, inhibit high catalytic activity, cheap and known as renewable resources [12].

There are a lot of methods involving chemical reactions in glycerol conversion. For example, glyceric acid, acrolein and methanol can be obtained from oxidation, dehydration, and hydrogenation processes, respectively [13]. However, these reactions occur in extreme conditions and mostly require stainless steel reactors particularly batch and flow reactors. For instance, previous researchers [13] stated that, studies conducted using supercritical process require extreme temperature ranges (676–726.85 °C), high pressure (24-27 MPa) and also the use of CO/CO_2 gaseous for reactions and separation. Thus, the current study is conducted to propose a new and low cost method under a mild condition and without the presence of a reactor to perform glycerol conversion, which is through a simple reflux method. Basically, reflux technique involves the condensation of vapor and the energy that accelerates the reaction, which is supplied by thermal heating [14]. Although this technique is widely used in industries and laboratories, its usage in catalytic conversion is still limited, primarily in glycerol conversion. Commonly, reflux technique is regularly used to synthesize and control various nanostructures, nanocatalyst materials, and its particle size [15]. By applying this method, no external hydrogen is needed during the conversion and it can be done in the

laboratory scale. Currently, CaO as a solid base catalyst has been studied in many processes, especially in biodiesel production [16], synthesis of dimethyl carbonate (DMC), and synthesis of syngas [13, 17, 18]. Meanwhile, for glycerol conversion, to the best of the author's knowledge, only glycerol conversion to lactic acid has been reported [19]. Therefore, this research might be the starting point in converting glycerol to more value-added products, which are methanol, 1-propanol and 1,2-propanediol.

MeOH, 1-PrOH, and 1,2- PDO have a lot of functions. For example, 1,2-PDO or also known as propylene glycol, is a non-toxic chemical mainly used in liquid detergents, pharmaceuticals, cosmetics, tobacco products, fragrances, flavours and humectants [3]. Another function of 1,2-PDO is this diol is the main component in the production of resins, polyesters and polyurethanes [20]. It is extensively used as a monomer for polyester resins, as an antifreeze agent, in liquid detergents, paints, cosmetics, food and others [5]. Meanwhile, MeOH and 1-PrOH can be used as a major chemical intermediates in a wide range of utilities [13]. They are also important as alternatives for transportation fuels, polymers, paintings and alcohols [4].

The present study focus on the preliminary investigation of the conversion of glycerol by eco-friendly CaO catalyst derived from waste chicken eggshells as a promising solid base catalyst. The used of a simple, reactorless and low cost reflux technique in the absence of external hydrogen has been attempted. To the best of our knowledge, these approaches still have limited resources and reliability, thus need to be investigated. Suitable operating parameters under two dependent variables which are reaction temperature and reaction time are also studied respectively.

Materials and Methods

List of chemicals

The experiment was carried out by using refined glycerol from Sigma Aldrich, paraffin oil (for oil bath), 1,4-butanediol (as an internal standard for gas chromatography-flame ionization detector (GC-FID), and distilled water. The chemicals were reagent grade and used without further purification.

Catalyst preparation

The method used was adapted from previous researchers with slightly modification [21]. Chicken eggshells (approximately 1-2 kg) obtained from nearby restaurants were washed thoroughly by distilled water and repeatedly three times in order to eliminate any impurities. After that, the eggshells were boiled at 100 °C by using a water bath to kill any bacteria and microorganisms. Then, the eggshells were dried at the temperature range of 100 to 110 °C in an oven overnight. Next, the dried eggshells were ground by using a blender (domestic Pensonic small-scale grinder) to fine and random size powder. Lastly, the powder was calcined at 900 °C in a furnace for approximately 120 minutes to produce the final as-prepared CaO catalyst powder.

General Procedure of Glycerol Conversion

In order to prepare 20 wt.% of glycerol feedstock, 4.0 g of glycerol was added to 20 mL of distilled water and stirred until a homogeneous solution was formed. Then, 1.0 g of CaO catalyst was added. The amount of catalyst was fixed for each reaction. The conversion of glycerol was carried out by using a 50 mL of round bottom flask, a hot plate, a digital thermometer, an Allihn condenser, and a magnetic stirrer. Figure 1 shows the set-up for the reflux apparatus used. The dependent variables used in this conversion were reaction temperature (130, 150, 170, and 190 °C) and reaction time (1, 3, 5, and 7 hours). These parameter ranges were chosen by considering the average minimum and maximum conditions of glycerol conversion reaction conditions used in previous studies [13, 20, 22, 23].

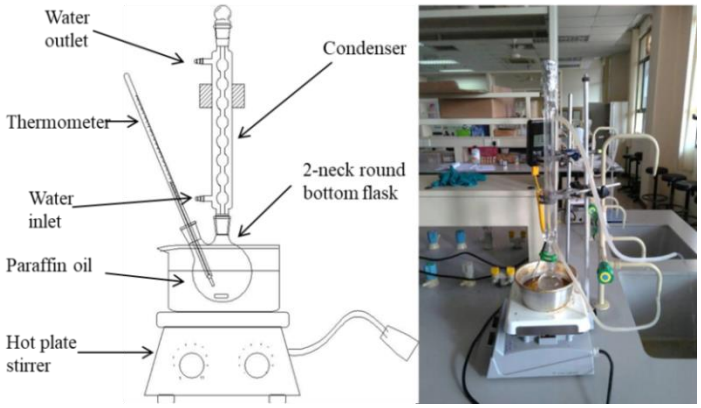


Figure 1. The set-up of reflux apparatus for glycerol conversion

Instrumentation

The instrumentation can be divided into catalyst characterization and product characterization (i.e. catalytic activity). For catalyst characterization, surface morphology study was conducted using scanning electron microscope (SEM) technique (Carl Zeiss brand, evo50 model). For elemental composition characterization, the analyses were conducted using energy dispersive X-ray (EDX), and CHNS/O analysis using Perkin-Elmer Series II, 2400 instrument. In order to identify the functional groups of the prepared CaO catalyst, the characterization was performed using the Fourier-transform infrared (FTIR) spectroscopy from Perkin-Elmer (96255) with the wavelength from 4000 to 500 cm^{-1}.

Meanwhile, for product characterization, the instruments used were gas chromatography-mass spectroscopy (GC-MS) by Clarus 680GC and GC-FID from Agilent Technologies (model 7890A). A similar column was used for both GC-MS and GC-FID (HP-INNOWAX) with the specifications of 30 m length, 0.250 mm diameter, and 0.50 µm inner diameter. For oven temperature, the initial temperature was set at 45 °C for 3 minutes before it was increased to 240 °C at a rate of 5 °C/min. Ramping time was constant at 240 °C for 5 min using splitless injection. The overall time required for one sample was 47 minutes and the maximum temperature of the oven was 260 °C.

Solid-phase micro extraction method (SPME) was used to determine conversion of products. For SPME, polyacrylate fiber was used with the thickness of 85 µm. The fiber was withdrawn from the syringe and soaked in the sample vial for 5 minutes with stirring for the extraction of conversion product. Then, the fiber was removed from the vial and inserted to the GC inlet and left for 10 minutes. Lastly, the fiber was removed and washed by using distilled water at 100 °C for 30 minutes to remove previous extraction products and the same steps were repeated for other product samples.

Results and Discussion

Catalyst characterization

For surface morphology analysis using SEM, both samples of non-calcined and calcined eggshell (CaO) catalyst were characterized. It is inferred that both non-calcined and calcined catalysts have irregular shape comprises spherical and flake shapes with various sizes in the range of 0.4 to 2.0 µm, and it is also supported by previous researchers [21, 24]. It can also be observed that the catalysts possessed porous surfaces as it could be clearly seen from the existence of pores as shown in Figure 2.

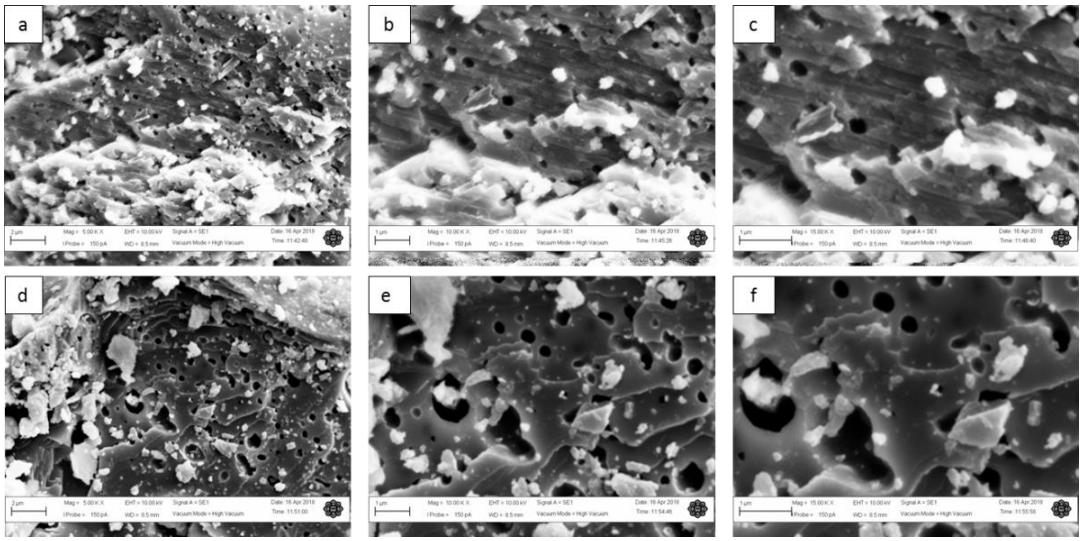


Figure 2. SEM images of non-calcined catalyst at different magnification (a) 5.00 kx (b) 10.00 kx and (c) 15.00 kx and SEM images of calcined catalyst at different magnification (d) 5.00 kx (e) 10.00 kx and (f) 15.00 kx

However, based on the images shown in Figure 2, the biggest difference between both non-calcined ($CaCO_3$) and calcined eggshells (CaO) catalysts is the calcined eggshell catalyst has high apparent porosities. In fact, it is obviously observed that there is an increasing of pore diameter from non-calcined to calcined samples. It is measured that the pore diameter in non-calcined samples has an average diameter of 0.3 µm, whereas for calcined samples the average diameter is 1.4 µm. The enlarged pores after calcination might be due to heating process expanded and activated the pores. Thus, more active areas for reaction are available. Other than that, it is also due to the decomposition of $CaCO_3$ to CO_2 during calcination. Therefore, the larger contact area is a result of a large number of pits and pores distributed over the entire eggshell surface [21]. The higher the contact surface area, the more reaction could occur at active sites of the catalyst. Other than that, physically, it is observed that the number of pores and pore diameters of calcined eggshells (CaO) are higher compared to non-calcined eggshells.

Next, for elemental analysis, the result of EDX analysis is supported with the CHNO/S analysis. From the EDX results, it is shown that in non-calcined eggshells ($CaCO_3$) in Figure 3(a), carbon (C) element shows higher peaks than calcium (Ca) and oxygen (O) elements, whereas for calcined eggshells in Figure 3(b), O element shows the higher peaks than C and Ca. It is clearly demonstrated that thermal degradation occurred during calcination process. The full results of elemental composition (%) for both techniques are summarized in Table 1 and Table 2.

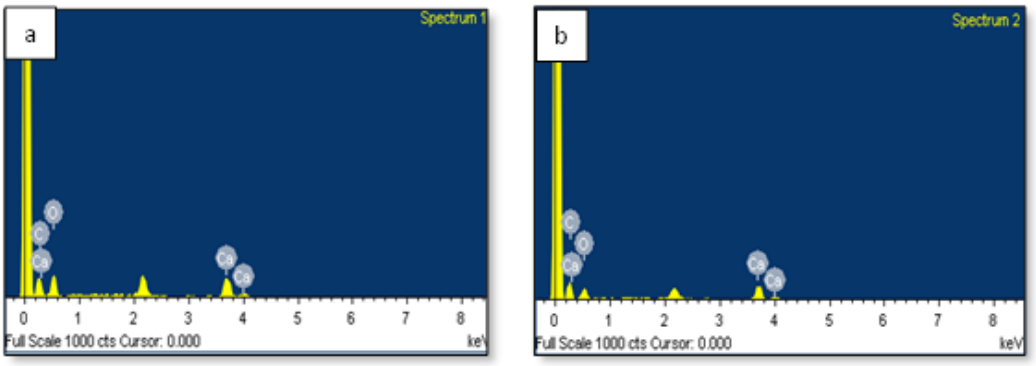


Figure 3. EDX spectrum for (a) non-calcined ($CaCO_3$) and (b) calcined (CaO) eggshells

Table 1. Percentage compositions for non-calcined ($CaCO_3$) and calcined eggshells (CaO) by using EDX technique

Sample	Element (atomic %)		
	Carbon (C)	Oxygen (O)	Calcium (Ca)
Non-calcined ($CaCO_3$)	43.74	36.75	19.52
Calcined catalyst (CaO)	34.99	46.50	18.51

Table 2. Results of compositional analysis using CHNSO technique

Run/Sample Details		Element Composition (%)				
Run	Weight (g)	Carbon	Hydrogen	Nitrogen	Sulphur	Oxygen
Non-Calcined eggshells ($CaCO_3$)	1.909	9.274	0.030	3.163	-0.118	87.651
Calcined catalyst (CaO)	1.940	6.692	0.186	2.201	-0.105	91.026

However, the percentage for Ca remain unchanged in both non-calcined ($CaCO_3$) and calcined samples (CaO), which suggests that the metal cluster bonded strongly in the catalyst system. In order to support the elemental analysis and to assure the existence of other important element in the samples, further composition analysis was then carried out and supported with CHNS/O analysis as shown in Table 2.

Table 2 present the percentage C, H, N, S, and O elements. Again, the reduction of C percentage from non-calcined eggshells (9.274%) to calcined eggshells (6.692%) shows the occurrence of decarbonation process. However, the percentage for H increased significantly from 0.0030% to 0.186%, which shows the impurities originated from sample preparation. This is because the O in CaO adsorbed water vapor from the surrounding to form calcium hydroxide ($Ca(OH)_2$). The presence of nitrogen is also noticeable. It is due to the presence of amino acids such as methionine (Met), alanine (Ala), histidine (His), and others in the membrane of eggshells [10]. Furthermore, it is also noticed that the percentage of N in CaO catalyst (calcined) is lower compared to non-calcined eggshells. The suggested reason is some nitrogen has been oxidized in the calcination process to produce NO_2.

FTIR analysis was conducted for further determination of any changes in the functional groups between non-calcined catalyst ($CaCO_3$) and calcined CaO catalyst samples. Figure 4 shows the overlaid of FTIR spectra for non-calcined eggshells ($CaCO_3$) and calcined eggshells (CaO). From the spectra, both samples have quite similar peaks at specific bands. However, there is a new significant peak at 3641 cm^{-1} in the CaO catalyst spectrum. This peak is attributed to the hydroxide (OH) in $Ca(OH)_2$ due to the adsorption of water by CaO [21]. Therefore, that peak could confirm the existence of Ca-O phase. Next, a similar band also existed for both spectra of non-calcined eggshells and calcined eggshells at 712.30 cm^{-1} in which the band corresponds to Ca-O bond. For non-calcined eggshells, well-defined IR bands at 1401.35 cm^{-1} and 872.66 cm^{-1} indicated asymmetric C-O bond in stretching mode for CO_3^{2-} molecules [21]. Besides, the peaks at 2972, 2878, 2516, and 1795 cm^{-1} are due to amines and amides present in eggshells [25]. Furthermore, the Figure 4 also shows the spectrum of calcined CaO. A similar range of peak is noticeable for CaO catalyst (calcined) at 1405.37 cm^{-1} and 872.43 cm^{-1} for asymmetric C-O bond in stretching mode.

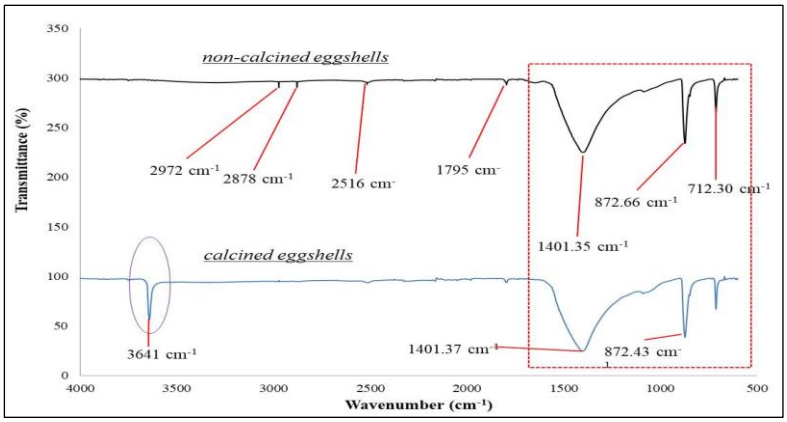


Figure 4. FTIR spectra for non-calcined eggshells and calcined CaO catalyst

Catalytic activity (Glycerol conversion)

Catalytic activity for CaO catalyst (calcined eggshell) at 130 °C

The percentage of conversion at 130 °C is quite constant from 1 to 5 hours with the highest conversion of 69.03% recorded at 7 hours (Figure 5). Selectivity towards MeOH shows a constant trend around 19.27% to 22.77% from 1 h to 7 hours. Unlike MeOH, the selectivity to 1-PrOH and 1,2-PDO increased and decreased throughout 7 hours reaction time. For 1-PrOH, the selectivity at 1 hour is quite high (50.39%) before it decreased steeply to 15.97% at 5 hours. However, the selectivity of 1-PrOH increased significantly again to 68.93% at 7 hours. Meanwhile, for 1,2-PDO, it started with low selectivity at 26.84% during 1 hour before increased significantly to 64.76% after 5 hours of reaction time. Then, the selectivity of 1,2 PDO dropped very steeply to only 10.76% at 7 hours.

For the highest total yield, it could be seen that 1-PrOH has the highest values of 47.58% at 7 hours since it has the highest percentage of glycerol and selectivity of the product. The lowest total yield is 7.43% for 1,2-PDO at 7 hours.

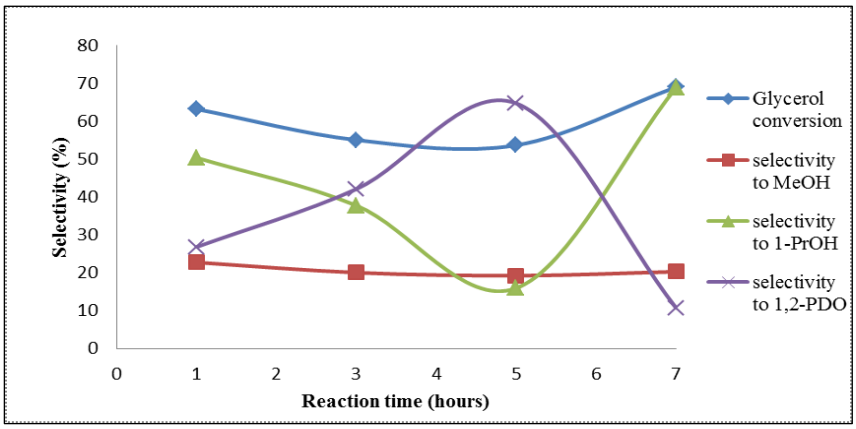


Figure 5. Catalytic profile effect of reaction time at 130 °C

The decrease in selectivity and total yield of 1-PrOH from 1 to 5 hours of reaction time is due to the high formation of 1,2-PDO at that time. It is also noticed that the conversion to 1,2-PDO is only active at 130 °C, then, for the rest of experimental temperatures, the conversion to 1,2-PDO is low and remained constant. The optimum period for C-O at glycerol to split in order to form 1,2-PDO is 5 hours. However, longer reaction time would make more another C-O at 1,2-PDO to be broken, which explains the increase of the percentage of 1-PrOH at 7 hours. Besides, at lower temperature, the kinetic energy for collision to occur is low, hence only one C-O bond at glycerol molecule is able

to be removed. The percentage of selectivity and MeOH yield seemed to be constant throughout 7 hours. It shows that the temperature of 130 °C is not suitable for breaking C-C bond at glycerol composition. Overall, the conversion at 130 °C is suitable for the formation of 1,2-PDO at shorter reaction time (1 to 5 hours) and 1-PrOH (longer than 5 hours).

Catalytic activity for CaO catalyst (calcined eggshells) at 150 °C

At 150 °C, different patterns can be seen for glycerol conversion, selectivity and yield percentage for each product (Figure 6). It is observed that glycerol conversion increased as reaction time increased. The highest percentage of glycerol conversion is at 7 hours (73.91%). However, there is a little drop in glycerol conversion at 3 hours from 69.61% to 59.91% which might be due to experimental error. Errors such as rate of stirring, rate of water flow (for cooling system), and catalysts attached to the wall of round-bottom flask might occur while conducting experiment. Therefore, some deviated data are obtained. Besides, at this temperature, the selectivity and total yield towards 1-PrOH are the highest compared to MeOH and 1,2-PDO. The highest selectivity of 1-PrOH is at 7 hours with 77.51% and the lowest is at 3 hours.

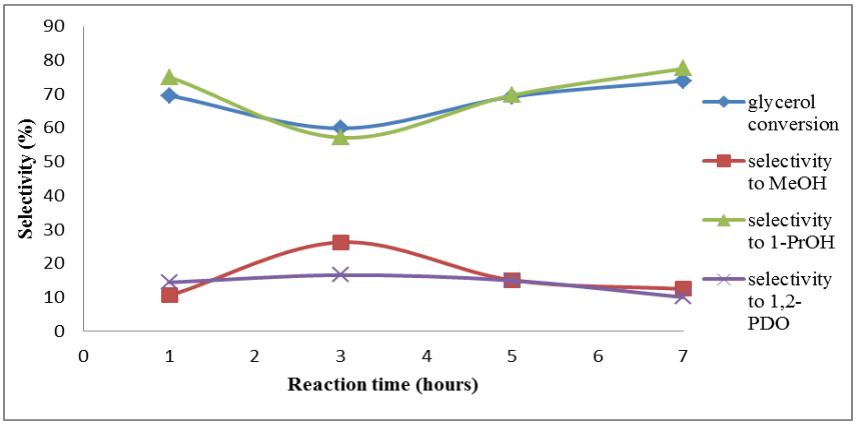


Figure 6. Catalytic profile effect of reaction time at 150 °C

Overall, Figure 6 shows that glycerol conversion at 150 °C is higher compared to 130 °C. The selectivity and total yield of 1-PrOH also increased. This is because the energy supply to break C-O bond at glycerol was sufficient to form 1-PrOH. The formation of 1,2-PDO is also lower at 150 °C compared to 130 °C. This is probably because most of 1,2-PDO have successfully converted to 1-PrOH. The selectivity and total MeOH yield at 150 °C are quite similar with 130 °C. It shows that there is still noticeable MeOH present from the reaction, yet the formation is not significant at this reaction temperature in which the chemical reaction still focuses on 1-PrOH (C-OH bond breaking).

Catalytic activity for CaO catalyst (calcined eggshell) at 170 °C

Next, the conversion was conducted at 170 °C. It can clearly be seen that 1-PrOH is still a major product formed at this reaction temperature (Figure 7). There are still traces of MeOH and 1,2-PDO left throughout 7 hours reaction time. It is clearly observed that MeOH showed an increasing pattern at this temperature. The highest percentage of glycerol conversion is recorded at 5 hours with 81.64% followed by 3, 1, and 7 hours with the conversion of 69.57%, 61.43%, and 54.67%, respectively. Throughout the first 5 hours of reaction, the conversion seemed to increase, probably due to enough time for a reaction to occur for glycerol to be adsorbed on the surface of catalyst to release a product. However, at 7 hours reaction time, the conversion percentage dropped because at this temperature, the reaction might focus on product formation rather than bond breaking. The conversion of glycerol at 5 hours for this temperature is the best conversion achieved among all the conversion in this study. Therefore, it can be concluded that reaction temperature of 170 °C and 5 hours reaction time are the optimum conditions.

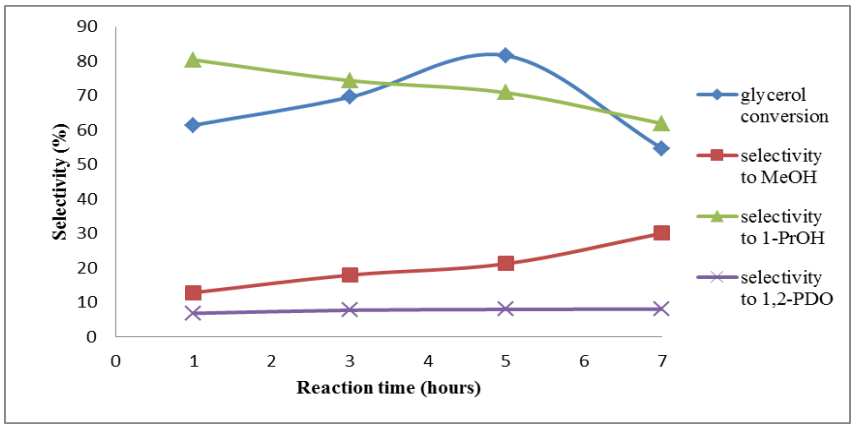


Figure 7. Catalytic profile effect of reaction time at 170 °C

From Figure 7, it can be clearly seen that the reaction is no more selective to 1,2-PDO compared to at 130 °C, and the selectivity maintained from 1 to 7 hours. Meanwhile, the selectivity of 1-PrOH dropped from 80.35% at 1 hour to 61.9 % at 7 hours whereas the product selectivity of MeOH increased by time. An almost similar pattern is also observed for yield percentage, except the value of 1–PrOH increased slightly at 7 hours. The best reason is probably because a large number of 1,2-PDO have converted to 1- PrOH before converting to MeOH. This is because higher temperature and longer time give enough energy to degrade the product by splitting either C-O bond for 1,2-PDO or C-C bond for 1-PrOH in the formation of MeOH. The increase in temperature also allows more frequent collision between glycerol particles. This collision would give enough energy to be used in breaking the C-C bond to form MeOH. Thus, the higher temperature is very suitable for bond dissociation from three carbons to only one carbon.

Catalytic activity for CaO catalyst (calcined eggshells) at 190 °C

The last conversion was conducted at 190 °C. A similar trend of result for each product at 170 °C can be clearly seen (Figure 8). Glycerol conversion still shows an increasing trend as reaction time increased from 1 to7 hours. However, the average glycerol conversion at 190 °C is slightly lower compared to at 170 °C. The best conversion is recorded at 7 hours (65.87 %) followed by 5 hours (58.89 %), 3 hours (57.44 %) and the least is at 1 hour (53.77 %). Following the pattern throughout 7 hours, the conversion seemed to increase probably due to enough time for a reaction to occur and for glycerol to be adsorbed on the surface of catalyst to release a product. Besides, increasing the temperature would give more energy for glycerol particles to collide with each other to break and form new bonds in order to produce new products.

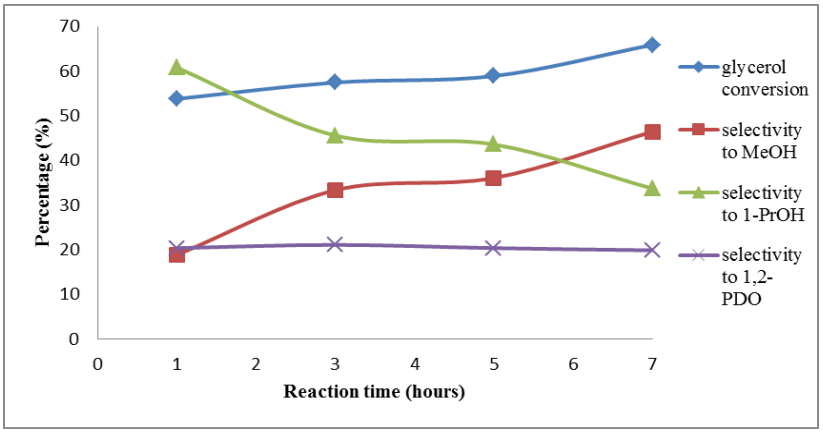


Figure 8. Catalytic profile effect of reaction time at 190 °C

Referring to Figure 8, the selectivity of 1,2-PDO dropped slightly from 1 h to 7 hours from 20.37% to 19.87%, respectively. Meanwhile, the selectivity of 1-PrOH decreased significantly from 60.76% at 1 hour to 33.69% at 7 hours. However, the product selectivity of MeOH increased gradually from 18.87% at 1 hour to 46.44% at 7 hours. For 1,2-PDO, the selectivity towards this product is the lowest compared to MeOH and 1-PrOH. The range of reduction of 1,2-PDO is between 20.37% at 1 hour and 19.87% at 7 hours. Similar pattern is also shown in the percentage yield for every product throughout 7 hours of reaction. Comparable to reaction temperature of 170 °C, higher temperature and longer time give enough energy to degrade the product by splitting either C-O bond for 1,2-PDO and 1-PrOH, and C-C bond in the formation of MeOH. The decline of 1-PrOH and 1,2-PDO is noticed as major conversion into MeOH.

Comparison of the reactions in the presence and absence of catalyst at optimum conditions

The comparison of the reactions with and without catalyst was investigated to observe the efficiency of using the catalyst. The optimum condition for both reactions was identified. For the reaction without catalyst under hydrogenolysis, the optimum condition is at 170 °C, 7 hours and 20 wt.% glycerol concentration. Meanwhile, for this experiment, the best optimum condition for glycerol conversion by using CaO as the catalyst is at 170 °C, 5 hours and 20 wt.% glycerol concentration. The data obtained are shown in Table 3.

Table 3. Catalytic activity result for reactions with and without catalyst

Condition	Glycerol Conversion (%)	Selectivity (%)			Total Yield (%)		
		MeOH	1-PrOH	1,2-PDO	MeOH	1-PrOH	1,2-PDO
Without catalyst	45.64	3.89	16.01	80.10	1.78	7.31	36.56
With catalyst	81.64	7.95	70.85	21.20	6.49	57.84	17.31

Based on the data in Table 3, it is clearly seen that the use of catalyst almost doubled the conversion of glycerol from 45.64% to 81.64% for reactions without and with catalyst, respectively. For selectivity towards products, it can be noticed that the reaction with catalyst produced products with a lower number of carbon and oxygen. For example, in this experiment, the production of MeOH and 1-PrOH is higher in the reaction with catalyst compared to the reaction without catalyst. However, 1,2-PDO shows a different trend. It can be clearly seen that the conversion to 1,2-PDO is higher in the reaction without catalyst compared to the reaction with catalyst.

The reason for the results of both reactions is because; the use of a catalyst could provide an alternative route for the reaction with lower activation energy (Ea) of the reactant. Thus, the reaction could appear more efficiently in order to convert glycerol to more value-added chemicals. This is because, by lowering the Ea, there would be more successful collisions from particles, which generated enough energy for bond dissociation of C-C and C-O to occur. Hence, the percentage conversion and selectivity to MeOH and 1-PrOH are higher in the reaction with catalyst compared to the reaction without catalyst. The CaO catalyst is known to have basic sites that consist of Ca^{2+} and O^{2-}. Therefore, it is suggested that the surface of O^{2-} would extract H^+ from H_2O in order to form hydroxide ions (OH^-). Next, OH^- would extract H^+ and then remove one hydroxyl group from glycerol to form 1,2-PDO. The same process would be repeated in order to form 1-PrOH from 1,2-PDO.

Comparison of the reactions for all reaction temperatures

Next, the comparison of the reactions for all reaction temperatures (130, 150, 170 and 190 °C) in this study was carried out. Figure 9 illustrates the results for different temperatures towards glycerol conversion. Based on Figure 9, temperature plays an important role in glycerol conversion. Higher conversion could occur at higher temperature. This is because temperature induces the collision between particles in glycerol to collide faster and more frequently. As a result, more products could be formed by breaking the bonds in glycerol structure as sufficient kinetic energy is supplied due to increasing temperature. However, at 190 °C, the reaction is lower because at that temperature, the reaction is more focused on product formation rather than breaking the bond in glycerol.

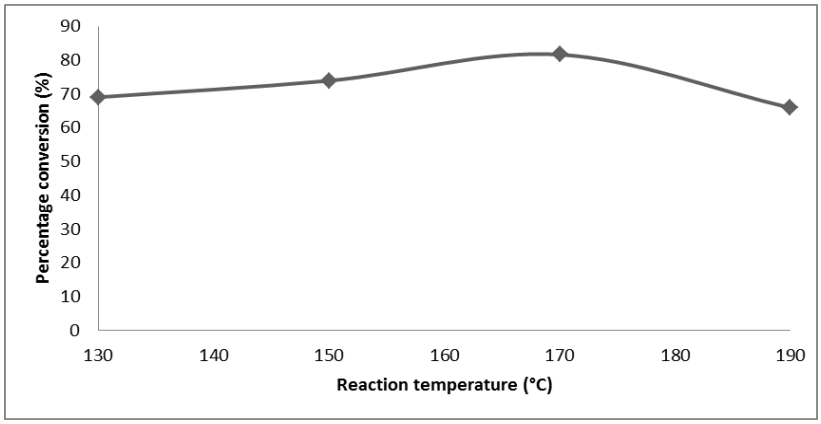


Figure 9. Effect of reaction temperature on glycerol conversion

Conclusion

Generally, CaO as a catalyst from waste chicken eggshells has been prepared. Based on the results obtained, CaO catalyst gives a positive result in hydrogenolysis of glycerol. The formation of 1,2-PDO is more preferred at lower temperature, whereby the selectivity and yield percentage are considerably higher compared to 1-PrOH and MeOH. The highest formation of 1,2-PDO is at 130 °C in 5 hours. The conversion is 53.70% with selectivity of 64.76% and total percentage yield of 34.78%. However, the formation of MeOH and 1-PrOH are preferred at higher temperature. The best condition for 1-PrOH is at 170 °C and 5 hours reaction time. The glycerol conversion is 81.64% with product selectivity of 70.85% and total percentage yield of 57.84%. Meanwhile, at 190 °C and 7 hours reaction time, the glycerol conversion and selectivity of MeOH are 65.87% and 46.44%, respectively. The catalyst used can also be considered very useful since three products can be formed in each reaction, whether at low or high temperature. Therefore, the use of eggshells as a catalyst in the industrial sector is possibly good due to its properties and activity in forming more value-added products. This preliminary study has proved that, glycerol conversion can be successfully conducted through a reactorless method which is by reflux technique. No external hydrogen gas is utilized in this study and it could open up a new interest in glycerol conversion study. This study will be expanded in the future by the utilization of other reaction parameters, such as catalyst weight, glycerol concentration, and recyclability test.

Acknowledgement

This research was supported by the grant of RIGS16-304-0468. The authors would also like to acknowledge the Ministry of Education Malaysia (Higher Education) and Dr Norsaliyana Jumali for the financial support under the grant of FRGS17-016.

References

1. Qadariyah, L., Mahfud., Sumarno., Mahmudah, S., Wahyudiono., Sasaki. M. and Goto M. (2011). Degradation of glycerol using hydrothermal process. *Bioresource Technology*, 102: 9267 - 9271.
2. Johnson, D. T. and Taconi, K. A. (2007). The glycerin glut: options for the value-added conversion of crude glycerol resulting from biodiesel production. *Environmental Progress & Sustainable Energy*, 26(4): 338-348.
3. Nanda, M. R., Yuan, Z., Shui, H. and Xu, C. (2017). Selective hydrogenolysis of glycerol and crude glycerol (a by-product or waste stream from the biodiesel industry) to 1,2-propanediol over B_2O_3 promoted Cu/Al_2O_3 catalysts. *Catalysts*, 7(7): 196.
4. Nanda, M. R., Yuan, Z., Qin, W. and Xu, C. (2016). Recent advancements in catalytic conversion of glycerol into propylene glycol: A review. *Catalysis Review*, 58(3): 309 - 336.
5. Samad, W. Z., Salleh, M. M., Shafiee, A. and Yarmo, M. A. (2011). Structural, optical and electrical properties of fluorine doped tin oxide thin films deposited using inkjet printing technique. *Sains Malaysiana*, 40(3): 251 - 257.

6. Anand, P. and Saxena, R. K. (2012). A comparative study of solvent-assisted pretreatment of biodiesel derived crude glycerol on growth and 1,3-propanediol production from *Citrobacter freundii*. *New Biotechnology*, 29(2): 199 - 205.
7. Yang, F., Hanna, M. A. and Sun, R. (2012). Value-added uses for crude glycerol–A byproduct of biodiesel production. *Biotechnology for Biofuels*, 5(1): 13.
8. Quispe, C. A. G., Coronado, C. J. R. and Carvalho, J. A. J. (2013). Glycerol: production, consumption, prices, characterization and new trends in combustion. *Renewable and Sustainable Energy Reviews*, 27: 475 - 493.
9. Da Silva, G. P. D., Mack, M. and Contiero, J. (2009). Glycerol: A promising and abundant carbon source for industrial microbiology. *Biotechnology Advances*, 27: 30 - 39.
10. Nakano, T., Ikawa, N. I. and Ozimek, L. (2003). Chemical composition of chicken eggshell and shell membranes. *Poultry Science*, 82(3): 510 - 514.
11. Buasri, A., Chaiyut, N., Loryuenyong, V., Worawanitchaphong, P. and Trongyong, S. (2013). Calcium oxide derived from waste shells of mussel, cockle, and scallop as the heterogeneous catalyst for biodiesel production. *The Scientist World Journal*, 2013: 1 - 7.
12. Verma, P., Sharma, M. P. and Dwivedi, G. (2016). Impact of alcohol on biodiesel production and properties. *Renewable and Sustainable Energy Reviews*, 56: 319 - 333.
13. Haider, M. H., Dummer, N. F., Knight, D. W., Jenkins, R. L., Howard, M., Moulijn, J., Taylor, S. T. and Hutchings, G. J. (2015). Efficient green methanol synthesis from glycerol. *Nature Chemistry*, 7 (12): 1028.
14. Henry, Z. K. (1992). Distillation design. McGraw Hill, United State of America: pp. 2 - 3.
15. Aditha, S. K., Kurdekar, A. D., Chunduri, L. A. A., Patnaik, S. and Kamisetti, V. (2016). Aqueous based reflux method for green synthesis of nanostructures: Application in CZTS synthesis. *MethodsX*, 3: 35 - 42.
16. Hassan, S. T. and Nageswara, R. L. (2018). Utilization of modified eggshells as a solid catalyst for the conversion of waste cooking oil to biodiesel. *Austin Chemical Engineering*, 5(1): 1 - 8.
17. Praikaew, W., Kiatkittipong, W., Kiatkittipong, K., Laosiripojana, N., Viriya-empikul, N., Boonyasuwat, S., Aiouache, F., Najdanovic, V. and Assabumrungrat, S. (2018). Synthesis of glycerol carbonate from dimethyl carbonate and glycerol using CaO derived from eggshells. *MATEC Web of Conferences*, 192(03045): 1 – 4.
18. Renita, A., Chowdhury, P. P., Sultana, P., Phukan, P. and Hannan, A. (2016). Utilization of waste eggshells for production of renewable catalyst for transesterification. *International Journal of Pharmacy and Pharmaceutical Sciences*, 8(7): 143 -146.
19. Chen, L., Ren, S. and Ye, X. P. (2014). Lactic acid production from glycerol using CaO as solid base catalyst. *Fuel Processing Technology*, 120: 40 - 47.
20. Feng, J., Zhang, Y., Xiong, W., Ding, H. and He B. (2016). Hydrogenolysis of glycerol to 1,2-propanediol and ethylene glycol over Ru-Co/ZrO_2 catalysts. *Catalysts*, 6(4): 51.
21. Mosaddegh, E. and Hassankhani, A. (2014). Preparation and characterization of nano-CaO based on eggshell waste: novel and green catalytic approach to highly efficient synthesis of pyrano [4, 3-b] pyrans. *Chinese Journal of Catalysis*, 35(3): 351 - 356.
22. Maris, E. P. and Davis, R. J. (2007). Hydrogenolysis of glycerol over carbon-supported Ru and Pt catalysts. *Journal of Catalysis*, 249(2): 328 - 337.
23. Samad, W. Z., Goto, M., Kanda, H., Wahyudiono., Nordin, N., Liew, K. H., Yarmo, M. A. and Yusop, M. R. (2017). Fluorine-doped tin oxide catalyst for glycerol conversion to methanol in sub-critical water. *The Journal of Supercritical Fluids*, 120: 366 - 378.
24. Borhade, A. V., Uphade, B. K. and Gadhave, A. G. (2016). Calcinized eggshell: An environmentally benign green catalyst for synthesis of 2-arylbenzothiazole derivatives. *Research on Chemical Intermediates*, 42(7): 6301 - 6311.
25. Tsai, W. T., Yang, J. M., Lai, C. W., Cheng, Y. H., Lin, C. C. and Yeh, C. W. (2006). Characterization and adsorption properties of eggshells and eggshell membrane. *Bioresource technology*, 97(3): 488 - 493.

Malaysian Journal of Analytical Sciences, Vol 23 No 5 (2019): 892 - 900
DOI: https://doi.org/10.17576/mjas-2019-2305-14

MALAYSIAN JOURNAL OF ANALYTICAL SCIENCES
Published by The Malaysian Analytical Sciences Society
ISSN 1394 - 2506

CHARACTERIZATION AND CATALYTIC ACTIVITY OF Os/BENTONITE CATALYST FOR HYDROGENOLYSIS OF GLYCEROL

(Pencirian dan Aktiviti Pemangkin Os/Bentonit untuk Tindak Balas Hidrogenolisis Gliserol)

Noraini Hamzah[1]*, Wan Zurina Samad[2], Nazrizawati Ahmad Tajuddin[3], Mohd Ambar Yarmo[4]

[1]*School of Chemistry and Environment, Faculty of Applied Sciences, Universiti Teknologi MARA, 40450 Shah Alam, Selangor, Malaysia*
[2]*Department of Chemistry, Kulliyah of Sciences, International Islamic University Malaysia, 25200 Kuantan, Pahang, Malaysia*
[3]*Department of Chemistry, Universiti Teknologi MARA, Perak Branch, Tapah Campus, 35400 Tapah, Perak, Malaysia*
[4]*School of Chemical Science and Food Technology, Faculty of Science and Technology, Universiti Kebangsaan Malaysia, 43600 UKM Bangi, Selangor, Malaysia*

**Corresponding author: pnoraini@salam.uitm.edu.my*

Received: 13 September 2018; Accepted: 29 July 2019

Abstract

In this study, osmium catalysts (Os/Bentonite, Os/TiO_2) and ruthenium catalysts (Ru/Bentonite, Ru/TiO_2) with 5% wt/wt metal loading were prepared using impregnation method and applied to convert glycerol, a renewable feedstock, to value-added chemical, 1,2-propanediol. Among these catalysts, the bentonite supported Os catalyst showed high performance with conversion and selectivity to 1,2-propanediol which were 63.3% and 82.7%, respectively. Catalytic performances of these catalysts were evaluated in glycerol hydrogenolysis using stainless steel autoclave reactor equipped with a magnetic stirrer at 150 °C, hydrogen pressure 20 - 40 bar for 7 hours reaction. The effect of glycerol concentration and reaction temperature were investigated to obtain optimum conditions due to glycerol conversion and products selectivity greatly depend on these factors. Experimental results show that hydrogenolysis of glycerol at 160 °C reaction temperature and 5% glycerol concentration gives a conversion of glycerol up to 100.0% with 82.9% selectivity of 1,2-propandiol. This study showed that bentonite which is cheap and abundant clay is potentially a good catalyst support material. The Os/bentonite catalyst was characterized by Temperature Programmed Reduction (TPR), nitrogen adsorption-desorption analysis (BET), Temperature Programmed Desorption-Ammonia(TPD-NH_3) for obtaining some physicochemical properties of the catalysts.

Keywords: osmium, bentonite, glycerol hydrogenolysis, 1,2-propanediol

Abstrak

Dalam kajian ini, pemangkin osmium (Os/bentonit, Os/TiO_2) dan pemangkin ruthenium (Ru/bentonite, Ru/TiO_2) dengan muatan logam 5% wt/wt disediakan dengan menggunakan kaedah impregnasi dan diaplikasikan kepada penukaran gliserol yang merupakan bahan mentah yang boleh diperbaharui kepada bahan kimia yang bernilai tinggi iaitu 1,2-propanadiol. Antara pemangkin yang dikaji, Os berpenyokong bentonit menunjukkan sifat pemangkin yang baik dengan nilai peratus penukaran dan pemilihan masing-masing adalah 63.3% dan 82.7%. Aktiviti pemangkin diuji dalam tindak balas hidrogenolisi gliserol menggunakan reaktor autoklaf tahan karat yang dilengkapi dengan pengacau magnetik pada suhu 150 ^{0}C, tekanan hidrogen 20-40 bar selama 7 jam. Kesan kepekatan gliserol dan suhu tindak balas didapati memberi kesan signifikasi terhadap peratus penukaran gliserol dan pemilihan produk. Keputusan kajian menunjukkan bahawa keadaan optimum pada suhu 160 ^{0}C dan kepekatan gliserol 5% (wt/wt) memberikan penukaran gliserol sehingga 90.0% dengan peratus pemilihan terhadap 1,2-propanadiol 82.9%. Kajian ini menunjukkan bahawa bentonit yang merupakan tanah liat murah dan mudah didapati adalah berpotensi digunakan sebagai penyokong mangkin. Pemangkin Os/bentonit dicirikan menggunakan suhu pemprograman

penurunan (TPR), analisis jerapan-nyahjerapan nitrogen (BET), suhu pemprograman nyahjerapan ammonia (TPD-NH3) bagi mendapatkan maklumat mengenai sifat fizikal dan kimia pemangkin.

Kata kunci: osmium, bentonit, hidrogenolisis gliserol, 1,2-propanadiol

Introduction

Catalytic conversion of renewable biomass resources, as feedstocks for the chemical industry, becomes more and more important because of the worldwide and serious energy and environment problems [1]. Transesterification of triglycerides with methanol in the presence of basic or acidic catalysts produced biodiesel that consists of fatty acid methyl esters. Production of every 9 kg biodiesel, about 1 kg of the crude glycerol by-product is also formed [2].

Nowadays, biodiesel derived from vegetable oils and animal fats has received considerable attention. The recent rapid development of biodiesel processes has caused some concern over the oversupply of glycerol. The glycerol market will likely to be saturated because of limited utilization of glycerol at the present time [3]. It is known that glycerol can be catalytically converted into functionalized and value-added chemical *via* a variety of reaction routes such as oxidation, hydrogenolysis, dehydration, pyrolysis, steam reforming, etherification, esterification, oligomerization and polymerization [4]. The hydrogenolysis of glycerol produces 1,2-propanediol (1,2-PDO) and ethylene glycol (EG) as a major product with a 4% annual market growth [5]. Typical uses of 1,2-propanediol are in unsaturated polyester resins, functional fluids, pharmaceuticals, cosmetics, paints, etc [6]. Therefore, the new usages of glycerol are being quested widely.

Several review papers [7-15] have reported on different catalyst systems, including supported transition metal catalyst such as Rh, Ni, Ru, Pt, Pt-Ru and Cu catalyst, for the hydrogenolysis of glycerol. Tomishige and co-workers developed Ru-solid acid bifunctional catalyst system for the hydrogenolysis of glycerol. However, the highest selectivity to 1,2-PDO achieved was 82% with 40% conversion of glycerol [16-19]. Besides that, Lahr et al. [20] have also investigated the effect of sulphur addition to Ru/C catalyst, in which the selectivity to 1,2-PDO increased linearly with sulphur loading. It is clear that from the literature Pt and Ru catalyst exhibited higher activity among the noble catalysts for the hydrogenolysis of glycerol, but Ru leads to C-C bond cleavage forming undesirable byproducts such as ethylene glycol and propanol while Pt catalyst gives higher selectivity to lactate [20].

1,2-PDO formation *via* glycerol hydrogenolysis involves selective cleavage of a C-O bond without breaking the C-C bond. Furthermore, bentonite is potentially a good and cheap catalyst support material. For the example, previous study prepared novel solid acid catalyst, bentonite supported polytrifluoromethanesulfosilaxane and used in the Friedel-Crafts acylation of ferrocene and gave 70% yield of aliphatic acyl ferrocene [11]. Natural clay minerals known as bentonite are a type of environmentally benign material. Bentonite (BEN) is a clay consisting predominantly of montmorillonite with a layered structure, large surface areas and cation exchange capacity. The special properties of bentonite make it a valuable material for a wide range of applications such as catalysis, pharmaceuticals, cosmetics, environment and agriculture [12].

Effective catalysts which work under mild conditions are required in the hydrogenolysis of glycerol to produce propanediols. Therefore, we aimed to develop new supported metal catalyst which is osmium supported on bentonite that will exhibit good catalytic performance and do not require any promoter for the glycerol hydrogenolysis. Until today, no documented paper reported on the performance of Os/bentonite catalyst for glycerol hydrogenolysis. In our preliminary study, Os/bentonite exhibited good activity, which is glycerol conversion was achieved at 63.3% with 82.7% selectivity to 1,2-PDO under a mild condition at 150 °C , 2MPa initial hydrogen pressure for 7 hours reaction time. The catalyst was characterized for its physiochemical properties based on which the observed activity results have been discussed. Effect of various reaction parameters on conversion of glycerol and selectivity to 1,2-PDO has also been reported for the Os/bentonite catalyst.

Materials and Methods

Materials

Glycerol (99.9%) and ruthenium trichloride, $RuCl_3$ precussor and TiO_2 used as support were purchased from Sigma-Aldrich. The clay mineral used in this work is a calcium-rich bentonite (CaB) was obtained as a powder from PT Superintending Company of Indonesia also used as support. The bulk chemical analysis of bentonite (mass%) is SiO_2, 64.15; TiO_2, 0.47; CrO_3, 0.003; Al_2O_3, 0.70; Fe_2O_3, 0.10; MgO, 0.70; CaO, 0.03; Na_2O, 0.20; K_2O, 0.50 and loss on ignition (LOI), 22.61.

Catalyst preparation

All supported catalysts with 5% metal loading were prepared by impregnation method. Titania, TiO_2 (anatase >99%, Aldrich) and bentonite (Aldrich) were used as the support material. Both of supports were calcined in air at 300 °C for 24 hours before used to remove moisture and impurities. The precursor used for Os and Ru were $OsCl_3$ and $RuCl_3$, respectively. For preparation with a nominal metal loading of 5 wt%, 100 mg of precursor catalyst was dissolved in acetone and stirred at room temperature for 15 minutes. This resulting solution was poured into the support (1800 mg) and sonicated for 60 minutes. The catalysts were then dried in an oven at 60 °C during 12 hours. In the next step, the catalyst was calcined in N_2 flow at 200 °C for 2 hours and further reduced with a hydrogen stream at 200 °C for 2 hours. Then the catalyst was used directly for hydrogenolysis without any further treatment.

Catalyst characterization

The surface area of the supported metal catalyst was measured using the BET method (N_2 adsorption) with a Gemini apparatus (Micromeritics Instrument Corporation). The reduction characterizations of the catalyst were studied by a temperature programmed reduction(TPR) using the same apparatus and pretreatment method for the CO pulse chemisorption-TPD measurements. After pretreatment, the temperature was raised from 30 ^{0}C to 600 ^{0}C at a rate of 10 ^{0}C/min in a 10% H_2/He flows (30 cm^3/min). The acidity properties of the catalyst were measured by a temperature-programmed desorption ammonia (TPD-NH_3). The sample was heated in a helium flow at 150 ^{0}C for 30 minutes. After a cooling temperature of 70 ^{0}C, the sample was exposed to ammonia and flushed with a 50 mL/min helium for 60 minutes. The TPD measurement was carried out with a heating rate 10 ^{0}C/min up to 750 ^{0}C under a flowing helium (50 mL/min). The desorption of ammonia was monitored by a thermal conductivity detector (TCD).

Hydrogenolysis of glycerol

The catalytic hydrogenolysis reactions were carried out in a 50 mL stainless-steel autoclave, PARR reactor equipped with an electronic temperature controller and a mechanical stirrer. The reaction was normally conducted under the following standard conditions: 150 ^{0}C temperature, 20 bar initial hydrogen pressure, 1.0 g catalyst weight, 23 ml of 20 wt.% aqueous solution of glycerol, 7 hours reaction time and at constant stirring speed.

The hydrogenolysis reaction sequence was as follows: loading of the reactor with an aqueous solution of glycerol and the appropriate amount of catalyst. Then the reactor was flushed three times with N_2 in order to remove oxygen gas and pressurized with H_2 to 20 bar. The mixture of glycerol and the catalyst was heated up to 150 ^{0}C at constant stirring speed and maintained for 7 hours.

Product characterization

After the reaction, the reactor was cooled at room temperature and the liquid phase products were separated from the catalyst by centrifuge at 4000 rpm for 15 minutes then filtered. These products were analysed using a gas chromatograph (GC-Hewlett Packard Model 6890N) equipped with a flame ionization detector (FID). The GC column used was a DB-WAX capillary column (30 m x 0.32 mm x 0.5 mm) manufactured by Agilent Technologies. Solutions of n-butanol and 1,4- butanediol with known amounts of internal standards were used for quantification of various glycerol-derived compounds in the product. The conversion of glycerol, the selectivity of propanediol, ethylene glycerol and other products (propanol (1,2), ethanol and methanol) were the factors used to evaluate the catalyst performance. The conversion and selectivityof glycerol are calculated as the following equations:

$$\text{Conversion}(\%) = \frac{\text{amount of glycerol (g)}}{\text{total amounts of glycerol in the feed (g)}} \text{ x } 100\% \quad (1)$$

$$\text{Selectivity (\%)} = \frac{amount\ of\ product\ produced\ (g)}{amount\ of\ glycerol\ converted\ (g)} \text{ x } 100\% \quad (2)$$

Only selectivities to 1,2-propanediol (1,2-PDO) and ethylene glycol (EG) were discussed in this study in view of their commercial important and relatively large amounts detected in the products.

Results and Discussion

Effect of support

Figure 1 shows the performances of Ru and Os metal catalyst prepared with different supports. The amounts of Ru and Os metal catalysts were kept the same. All the catalysts were evaluated at a reaction condition of 150 °C, 20 bar initial hydrogen pressure and 7 hours reaction time. In this study, we only focused on 1,2-propanediol and ethylene glycol since these products produced as a major in hydrogenolysis glycerol. In term of conversion, these results revealed that bentonite supported catalysts were most active than TiO_2 supported catalysts. Such results indicate that the nature of support has a strong effect on the performance of the tested catalyst. When we make a comparison between the catalytic activity and BET result, it seems that bentonite support with the highest surface area is more suitable for hydrogenolysis glycerol. Between two bentonite supported catalysts, the result clearly shows that Ru/bentonite exhibited the highest activity with glycerol conversion reached to 79.6%. In contrast, Os/bentonite catalyst only gave 63.3% conversion. This result was not significant with EDX analysis because Os metal dispersed more (3.49%) than Ru metal (2.81%). Therefore we make the conclusion that metal dispersion seems to be unrelated with the activity of the catalysts.

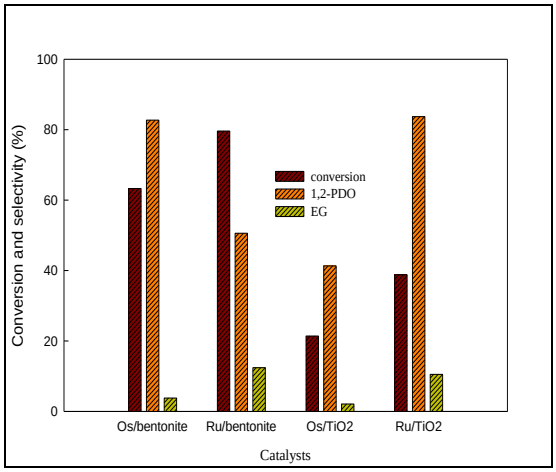


Figure 1. Performance of Ru and Os catalysts on different supports

On the other hand, selectivity to 1,2-propanediol is most predominate over Os/bentonite and Ru/TiO_2 with 82.7% and 83.7% selectivity, respectively. However, as we mentioned earlier activity of Os/bentonite catalyst was double compared to Ru/TiO_2. Therefore, from these screening, we conclude that Os/bentonite catalyst was the best catalyst in glycerol hydrogenolysis due to highest selectivity (82.7%) with the conversion of glycerol 63.3% at mild reaction condition of 150 °C, 20-40 bar hydrogen pressure for 7 hours. Normally, hydrogenolysis of glycerol was conducted at higher temperature and pressure [21, 22]. For further study, Os/bentonite catalyst was selected to optimize two parameters namely are glycerol concentration and reaction time.

Effect of glycerol concentration

In order to achieve maximum productivity of 1,2-PDO, the effect of aqueous glycerol concentration on the conversion wal also studied. Figure 2 shows that the conversion of glycerol decreased from 100% to 58.1% with an increase in glycerol concentration up to 20 wt.%. This is because the limiting number of catalyst active sites was

available since the catalyst concentration was constant. A similar observation was reported by another researcher [23]. For further study, we choose concentration 5 wt(%) glycerol rather than 1 wt(%) glycerol due to practically practice. There was not the much different effect of glycerol concentration on the selectivity pattern of 1,2-PDO and EG.

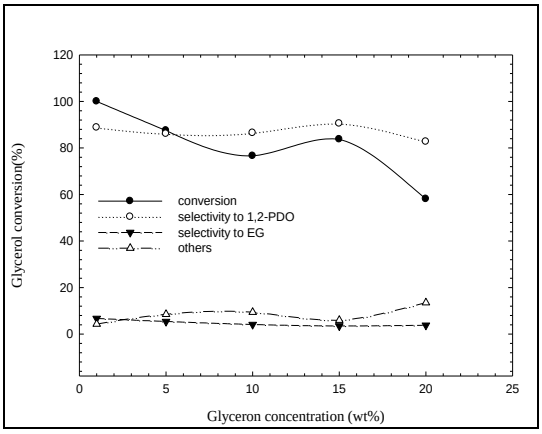


Figure 2. Effect of glycerol concentration. Reaction conditions : 20-30 bar H_2 pressure, 1.0g catalyst, 150 °C (423 K), 7 hours

Effect of reaction temperature

Figure 3 shows the influence of reaction temperature on conversion and selectivity pattern in 5 wt(%) glycerol hydrogenolysis over Os/bentonite catalyst. Glycerol conversion increased from 45.6% to 100% with an increase in temperature from 120 °C to 160 °C. Maximum conversion of 100% was obtained at 160 °C however, selectivity to 1,2-PDO decreased slightly from 100% to 83.7%, correspondingly increasing the selectivity to others from 0% to 11.7%. This result indicates that at higher temperature favoured degradation products due to excessive hydrogenation of 1,2-PDO to propanol. Interestingly, there was insignifigant effect of reaction temperature on selectivity to EG. It seems that Os/bentonite catalyst was highly selective to 1,2-PDO. Os/bentonite was a new catalyst which is favoured to C-O cleavage without the addition of any promoter. Furthermore, Os/bentonite catalyst gave 100% conversion with 83.7% selectivity to 1,2-PDO at a shorter time (7 hours). Until today, none catalyst was reported can perform 100% conversion at 160°C, 20 bar initial H_2 pressure for 7 hours reaction time.

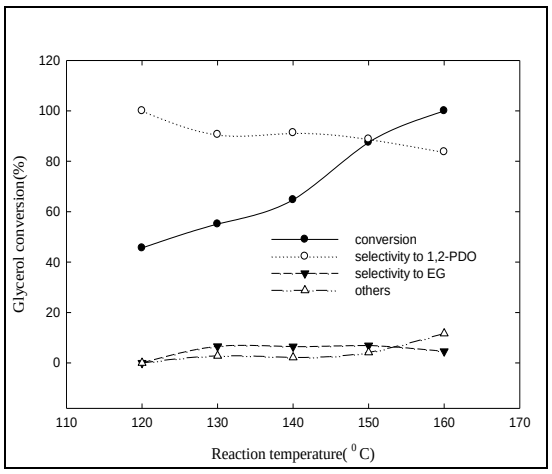


Figure 3. Effect of reaction temperature. Reaction conditons : 5 wt(%) glycerol aqueous solution (20 g) 20-30 bar H_2 pressure, 1.0g catalyst, 7 hours

Catalyst characterization: BET surface area

The BET surface area, pore volume and pore diameter of osmium supported catalysts are summarized in Table 1. Os/Al_2O_3 and Os/SiO_2 have the highest surface area followed by Os/bentonite and Os/TiO_2. The result shows that Os supported on bentonite and TiO_2 have a low BET surface area which are not contributed to the good performance of the catalyst in hydrogenolysis of glycerol. Similar result was reported that surface is not the main factor for the performance of the catalyst [20]. The good catalytic of Os/bentonite might be due to the amount of acidity in the catalyst and TPD-NH_3 analysis was done to confirm this property.

Table 1. Physical parameter of support and supported catalysts

Catalyst	S_{BET} (m^2/g)	d_{pore} (m^2/g)	V_{pore} (cm^3/g)
Os/TiO_2	8.0	0.038	26
Os/Al_2O_3	142	0.239	7
Os/SiO_2	130	0.834	26
Os/bentonite	8.2	1.800	0.0009

TPR analysis

Redox properties of Os/bentonite catalyst at different loading was measured using H_2-TPR analysis and the profiles are shown in Figure 4. A small peak observed at temperature of 230 °C for bentonite support, might be due to reduction of oxide species on the surface of the bentonite support [24]. This TPR profile shows that reduction of oxide osmium occurred at a temperature around 140 ^{0}C. It was found that the intensity of the peak becomes obvious with increasing metal loading of Os metal from 0.01 wt(%) to 5.0 wt(%). This result indicated that Os/bentonite catalyst could be easily reduced at a reaction temperature of 150 ^{0}C and provided good active site for the hydrogenolysis of glycerol. Percentange of glycerol conversion was increased with increasing of metal loading of Os/bentonite in hydrogenolysis of glycerol. It was found that best conversion was obtained at metal loading of 5 wt(%) with 70%. This might be due to more active site are available to convert glycerol into 1,2-propanediol.

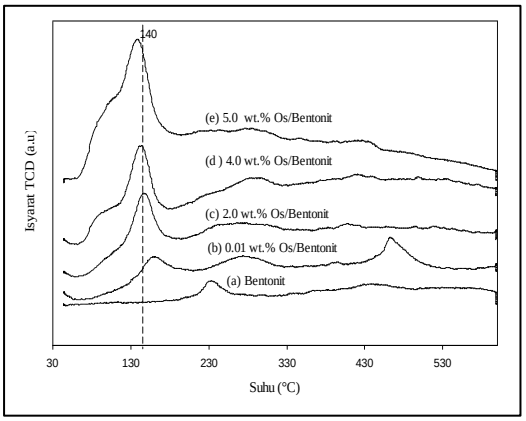


Figure 4. TPR analysis of Os/bentonite at different metal loading

TPD-NH_3 analysis

The acidity of the catalysts was quantified by the integration of the desorption curves for TPD-NH_3. The areas under the curves were considered as proportional to the number of moles of gas desorbed from the surface. The maximum temperature on the curves was designated as T_{max}. The TPD profiles of the osmium supported on the different

support were shown in Figure 5. The TPD-NH_3 analysis result indicated that Os/bentonite catalyst has stong acid site because desorption of ammonia occurred at temperature above 400^{0}C with total acidity of 117.45 mmol NH_3 per gram catalyst.

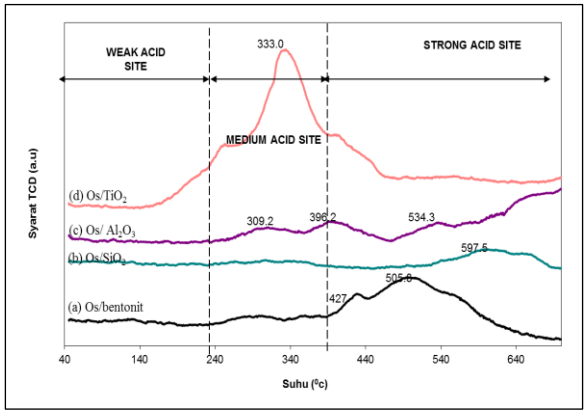


Figure 5. TPD-NH_3 analysis of Os/bentonite at different support

The total acidity of supported Os catalyst was listed in Table 2. The acidity strength was characterized by the temperature of the desorption peak, meanwhile, the number of acidic sites was measured by the amount of ammonia desorbed [9]. Os/ TiO_2 catalyst has high total acidity (254.87 mmol of NH_3/ g catalyst), however, this catalyst did not perform well in glycerol hydrogenolysis due to acid site medium. This result shows that hydrogenolysis of glycerol need the optimum strong acid site to convert glycerol into 1,2-propanediol.

Table 2. TPD-NH_3 analysis of Os supported at the different support

Catalyst	**Total Acidity (mmol of NH_3/g Catalyst)**
Os/TiO_2	254.87
Os/Al_2O_3	53.93
Os/SiO_2	102.55
Os/bentonite	117.45

Conclusion

Os/bentonite catalyst exhibits good performance for catalyzing the hydrogenolysis of aqueous glycerol to produce 1,2-PDO at mild reaction condition. 100% conversion of glycerol and 82.9% selectivity of 1,2-PDO could be achieved when using 5 wt.% aqueous glycerol at 160 °C, 20-40 bar hydrogen pressure, 7 hours. The characterization results suggested that the high surface area is not the main factor that contributed good catalytic of the catalyst.

Acknowledgement

The authors would like to acknowledge the Research Management Centre (RMC), Ministry of Education (MOE) and Universiti Teknologi MARA (UiTM) to finance the project under BESTARI fund (600-IRMI/DANA 5/3 BESTARI (050/2017))

References

1. Huang, Z., Cui, F., Kang, H., Chen, J. and Xia, C. (2009). Characterization and catalytic properties of the CuO/SiO_2 catalysts prepared by precipitation-gel method in the hydrogenolysis of glycerol to 1,2-propanediol: effect of residual sodium. *Applied Catalysis A: General*, 366(2): 288-298.
2. Vasiliadou, E. S., Heracleous, E., Vasalos, I. A. and Lemonidou, A. A. (2009). Ru-based catalysts for glycerol hydrogenolysis-effect of support and metal precursor. *Applied Catalysis B: Environmental,* 92 (1-2): 90-99.
3. Feng, J., Fu, H., Wang, J., Li, R., Chen, H. and Li, X. (2008). Hydrogenolysis of glycerol to glycols over ruthenium catalysts: Effect of support and catalyst reduction temperature. *Journal of Catalysis Communications*, 9(6): 1458-1464.
4. Jiang, T., Zhou, Y., Liang, S., Liu, H. and Han, B. (2009). Hydrogenolysis of glycerol catalyzed by Ru-Cu bimetallic catalysts supported on clay with the aid of ionic liquids. *Green Chemistry*, 11(7): 1000-1006.
5. Chaminand, J., Djakovitch, L., Gallezot, P., Marion, P., Pinel, C. and Rosierb, C. (2004). Glycerol hydrogenolysis on heterogeneous catalysts. *Green Chemistry*, 6: 359-361.
6. Maris, E. P., Ketchie, W. C., Murayama, M. and Davis, R. J. (2007). Glycerol hydrogenolysis on carbon-supported Pt-Ru and Au-Ru bimetallic catalysts. *Journal of Catalysis*, 251(2): 281-294.
7. Shinmi, Y., Koso, S., Kubota, T., Nakagawa, Y. and Tomishige, K. (2010). Modification of Rh/SiO_2 catalyst for the hydrogenolysis of glycerol in water. *Applied Catalysis B: Environmental*, 94(3-4): 318-326.
8. Wang, S. and Liu, H. (2007). Selective hydrogenolysis of glycerol to propylene glycol on Cu-ZnO catalysts. *Catalysis Letters*, 117(1-2): 62-67.
9. Yu, W., Zhao, J., Ma, H., Miao, H., Song, Q. and Xu, J. (2010). Aqueous hydrogenolysis of glycerol over Ni-Ce/Ac catalyst: Promoting effect of Ce on catalytic performance. *Applied Catalysis A: General*, 383(1-2): 73-78.
10. Zheng, J., Zhu, W. C., Ma, C. X., Jia, M. J., Wang, Z. L., Hou, Y. H. and Zhang, W. X. (2009). Hydrogenolysis of glycerol to 1,2-propanediol over Cu/SiO_2 catalysts prepared by ion-exchange method. *Polish Journal of Chemistry*, 83(7): 1379-1387.
11. Zhou, J., Zhang, J., Guo, X., Mao, J. and Zhang, S. (2012). Ag/Al_2O_3 for glycerol hydrogenolysis to 1,2-propanediol: activity, selectivity and deactivation. *Green Chemistry*, 14(1): 156-163.
12. Basit, A., Suzana, Y., Armando T. Q., Ruzaimah, N. M. K., Yoshifumi S., Muhammad A., Tetsuya K. (2016). Pretreatment and bentonite-based catalyzed conversion of palm-rubber seed oil blends to biodiesel. *Procedia Engineering*, (148): 501-507.
13. Banu, M., Sivasanker, S., Sankaranarayanan, T. M. and Venuvanalingam, P. (2011). Hydrogenolysis of sorbitol over Ni and Pt loaded on nay. *Catalysis Communications*, 12(7): 673-677.
14. Kwak, B. K., Park, D. S., Yun, Y. S. and Yi, J. (2012). Preparation and characterization of nanocrytalline $CuAl_2O_4$ spinel catalysts by sol-gel method for the hydrogenolysis of glycerol. *Catalyst Communications*, 24: 90-95.
15. Montassier, C., Ménézo, J. C., Hoang, L. C., Renaud, C. and Barbier, J. (1991). Aqueous polyol conversions on ruthenium and on sulfur-modified ruthenium. *Journal of Molecular Catalysis*, 70(1): 99-110.
16. Shinmi, Y., Koso, S., Kubota, T., Nakagawa, Y. and Tomishige, K. (2010). Modification of Rh/SiO_2 catalyst for the hydrogenolysis of glycerol in water. *Applied Catalysis B: Environmental*, 94(3-4): 318-326.
17. Miyazawa, T., Koso, S., Kunimori, K. and Tomishige, K. (2007). Development of a Ru/C catalyst for glycerol hydrogenolysis in combination with an ion-exchange resin. *Journal of Applied Catalysis A: General*, 318: 244-251.
18. Miyazawa, T., Kunimori, K. and Tomishige, K. (2006). Glycerol hydrogenolysis in the aqueous solution under hydrogen over Ru/C^+ an ion-exchange resin and its reaction mechanism. *Journal of Catalysis*, 240(240): 213-221.
19. Maris, E. P. and Davis, R. J. (2007). Hydrogenolysis of glycerol over carbon-supported Ru and Pt catalysts. *Journal of Catalysis*, 249(2): 328-337.
20. Lahr, D. G. and Shanks, B. H. (2003). Kinetic analysis of the hydrogenolysis of lower polyhydric alcohols: Glycerol to glycols. *Industrial and Engineering Chemistry Research*, 42(22): 5467-5472.
21. Zheng, J., Zhu, W., Ma, C., Hou, Y., Zhang, W. and Wang, Z. (2010). Hydrogenolysis of glycerol to 1,2-propanediol on the high dispersed Sba-15 supported copper catalyst prepared by the ion-exchange method. *Reaction Kinetics, Mechanisms and Catalysis*, 99(2): 455-462.

22. Zhou, Z., Li, X., Zeng, T., Hong, W., Cheng, Z. and Yuan, W. (2010). Kinetics of hydrogenolysis of glycerol to propylene glycol over Cu-ZnO-Al_2O_3 catalysts. *Chinese Journal of Chemical Engineering*, 18(3): 384-390.
23. Ma, L., He, D. and Li, Z. (2008). Promoting effect of rhenium on catalytic performance of Ru catalysts in hydrogenolysis of glycerol to propanediol. *Catalysis Communications*, 9(15): 2489-2495.
24. Jiménez-Morales, I., Vila, F., Mariscal, R. and Jiménez-López, A. (2012). Hydrogenolysis of glycerol to obtain 1,2-propanediol on Ce-promoted Ni/Sba-15 catalysts. *Applied Catalysis B: Environmental*, 117-118(1): 253-259.

Malaysian Journal of Analytical Sciences, Vol 23 No 5 (2019): 901 - 913
DOI: https://doi.org/10.17576/mjas-2019-2305-15

MALAYSIAN JOURNAL OF ANALYTICAL SCIENCES
Published by The Malaysian Analytical Sciences Society
ISSN 1394 - 2506

EXTRACTION AND CHARACTERIZATION OF MICROFIBRILLATED AND NANOFIBRILLATED CELLULOSE FROM OFFICE PAPER WASTE

(Pengekstrakan dan Pencirian Mikrofibril dan Nanofibril Selulosa daripada Sisa Kertas Pejabat)

Siti Fatimah Md Hanafiah[1], Wan Hazman Danial[1]*, Mohd Armi Abu Samah[1], Wan Zurina Samad[1], Deny Susanti[1], Rosliza Mohd Salim[1], Zaiton Abdul Majid[2]

[1]*Department of Chemistry, Kulliyyah of Science,*
International Islamic University Malaysia, 25200 Kuantan, Pahang, Malaysia
[2]*Department of Chemistry, Faculty of Science,*
Universiti Teknologi Malaysia, 81310 UTM Johor Bahru, Johor, Malaysia

**Corresponding author: whazman@iium.edu.my*

Received: 16 January 2019; Accepted: 14 August 2019

Abstract

The tremendous increase in papermaking and cellulose production, both of which are sourced from wood pulp, has resulted in the severe exploitation of trees, thereby leading to environmental problems, including deforestation. Besides, the reduction of paper usage is not on the horizon. Thus, when it comes to the environmental issue, the extraction of cellulose from paper waste can be an alternative initiative to mitigate the negative impact of deforestation *via* the reuse of paper waste. In this study, the extraction of cellulose microfibres and nanofibres was achieved through the use of office paper waste as the source material. Alkali and bleaching treatments were employed for the extraction of cellulose fibres, followed by acid hydrolysis under controlled conditions for the isolation of the cellulose nanofibres. The alkali treatment was carried out using various concentrations of 2%, 4%, 8% and 16% of sodium hydroxide (NaOH) solution, while the bleaching treatment was carried out using sodium hypochlorite (NaClO) solution. The extraction of nano-fibrillated cellulose was achieved by means of acid hydrolysis with various concentrations of 5%, 15%, 30% and 60% sulphuric acid (H_2SO_4) under controlled conditions. The structural and functional groups were analysed using attenuated total reflection Fourier transform infra-red (ATR-FTIR) imaging, while a morphological analysis was performed using optical microscopy and transmission electron microscopy (TEM). The FTIR analysis indicated that the lignin, ink, fillers and other components had been removed after the alkali and bleaching treatments. The imaging analysis using an optical microscope showed that the extracted cellulose had a fibrous and rod-like structure, while the TEM images showed that the extracted cellulose ranged from micro to nano size down to ~20-30 nm depending on the concentration of acid used. The extraction of either micro-fibrillated or nano-fibrillated cellulose from office paper waste in this work might pave the way towards the alternative reuse of office paper waste for the production and application of cellulose materials.

Keywords: cellulose, microfibrillated, nanofibrillated, office paper waste

Abstrak

Peningkatan besar dalam penghasilan kertas dan selulosa, di mana kedua-dua sumber berasal dari pulpa kayu telah menyebabkan eksploitasi hutan yang teruk membawa masalah alam sekitar, iaitu penebangan hutan. Selain itu, pengurangan penggunaan kertas agak tidak seimbang. Oleh itu, berhubung dengan isu alam sekitar, pengambilan selulosa dari sisa kertas boleh menjadi inisiatif alternatif untuk mengurangkan kesan negatif melalui kitar semula sisa kertas. Dalam kajian ini, pengekstrakan selulosa mikrofibril dan nanofibril telah dicapai menggunakan bahan buangan kertas sebagai sumber. Rawatan alkali dan pelunturan digunakan untuk pengestrakan serat selulosa diikuti oleh kaedah hidrolisis asid yang terkawal untuk pengasingan selulosa nanofibril. Rawatan alkali dijalankan menggunakan pelbagai kepekatan 2%, 4%, 8% dan 16% natrium hidroksida (NaOH) manakala rawatan pelunturan dilakukan dengan menggunakan larutan natrium hipoklorit (NaClO). Pengekstrakan selulosa

nanofibril dicapai dengan menggunakan kaedah hidrolisis asid yang terkawal dengan pelbagai kepekatan 5%, 15%, 30% dan 60% asid sulfurik (H_2SO_4). Analisa kumpulan struktur dan fungsi dianalisis dengan menggunakan pantulan keseluruhan dikecilkan spektroskopi infra-merah transformasi Fourier (ATR-FTIR) manakala pengimejan dan analisis morfologi diperiksa menggunakan mikroskop optik dan mikroskop elektron transmisi (TEM). Analisis FTIR menunjukkan lignin, dakwat, pengisi dan komponen lain dikeluarkan selepas rawatan alkali dan pelunturan. Analisa pengimejan menggunakan mikroskop optik menunjukkan struktur berserat dan rod seperti selulosa dapat diekstrak manakala imej TEM menunjukkan saiz selulosa yang diekstrak dari mikro ke saiz nano hingga ~20-30 nm bergantung kepada kepekatan asid yang digunakan. Pengekstrakan selulosa microfibril atau nanofibril dari sisa kertas pejabat dalam kajian ini mungkin membuka jalan ke arah penggunaan semula sisa kertas pejabat dalam pengeluaran dan aplikasi bahan selulosa.

Kata kunci: selulosa, microfibril, nanofibril, sisa kertas pejabat

Introduction

Cellulose is an organic polymer consisting of high-molecular weight β-glucopyranose rings, as the repeating unit structure, which is covalently linked together by β-1-4 glucosidic bonds [1]. Besides being commonly used in the production of paperboard and paper [2], cellulose is also used in various applications such as in biomedical materials, nanocomposites, reinforcing fillers in polymers, drugs, rubber, gas barrier films and optically transparent functional materials [3]. Cellulose is being used in a wide range of applications due to its geometrical characteristics and mechanical properties [3]. It can be extracted from various sources including wood pulp, cotton, ramie, sisal, pineapple leaves, and mengkuang leaves, which are all mainly sourced from plants or trees [4]. However, some of these source materials may not be readily accessible. Alternatively, paper waste, which contains an abundance of cellulosic components, is easily accessible and readily available.

Paper is being used throughout the world, and its consumption is not limited to workplaces, schools, universities, and industries. Millions of tons of paper are being produced each year (and the amount is increasing yearly), and the reduction of paper usage is not on the horizon. As a consequence, there is currently paper pollution due to paper waste. In fact, millions of tons of solid municipal waste are composed of paper waste. Paper waste keeps increasing and is flooding landfills. Nowadays, the generation of waste, especially paper waste, is increasing tremendously, and is contributing to health problems and continuous harm to the land [5] due to the additional hazard of toxic inks, dyes and polymers. Besides, the huge increase in papermaking and cellulose production, both of which are sourced from wood pulp, has also resulted in the severe exploitation of trees, leading to environmental problems, including deforestation. Thus, when it comes to environmental issues, an initiative such as the utilization of paper waste to lower the rising negative impact would be significant. Thus, this work addressed the idea and effort to utilize paper waste for the extraction of cellulose to mitigate the impact of waste generation as well as deforestation.

In this research, micro-fibrillated and nano-fibrillated cellulose were extracted from office paper waste. The method of extraction was carried out using several stages of treatments, including alkali treatment with various concentrations of sodium hydroxide (NaOH) solution, and bleaching treatment with sodium hypochlorite (NaClO) solution. The extraction process was followed by acid hydrolysis with various acid concentrations to investigate the effect of the removal of the amorphous region of the cellulose on the cellulose dimension. The extracted cellulose was analysed using attenuated total reflection Fourier transform infra-red (ATR FT-IR) spectroscopy, optical microscopy and transmission electron microscopy (TEM). It is worth mentioning that the cellulose extracted in this work was produced by means of a top-down approach, and thus, the identification of the presence of cellulose was reliable, as generally discussed in the literature.

Materials and Methods

Pre-treatment

Office paper, consisting of printed and non-printed papers, was used to represent the office paper waste. About 25 g of office paper waste was cut into small pieces. The cut paper was then boiled for 1 hour. Then, the paper was mechanically ground into slurry using a blender (Khind) and filtered and rinsed several times with distilled water [4] in order to partially disperse the fibrous materials prior to the next treatment. Then, the slurry was boiled again for about 1 hour to remove any excess dirt. The boiled paper was then filtered and rinsed with distilled water and

dried in an oven at about 80 ^{o}C for 2 hours. Next, the raw and pre-treated samples were analysed using ATR-FTIR spectroscopy and observed under an optical microscope.

Alkali treatment

Sodium hydroxide solution, NaOH (Merck), was used for the alkali treatment. The slurry prepared from the previous pre-treatment was treated with NaOH to remove inks, fillers (*i.e*. kaolin, talc, calcium carbonate and TiO_2) [6], and hemicellulose from the office paper matrix [4]. Besides, this treatment disrupted the hydrogen bonds [6] between the different cellulose chains prior to the next treatment. As shown in Table 1, the treatment was carried out under reflux at 100 ^{o}C for 90 minutes with a paper to NaOH solution ratio of 1:20 (w/v), and involved various concentrations of 2 wt.%, 4 wt.%, 8 wt.%, and 16 wt.% of NaOH solution. The mixture was then filtered through a filter paper, and the filtrate was washed with distilled water until a neutral pH was reached. The samples were dried in an oven for 2 hours at 50^{o}C. Next, the samples were analysed using ATR-FTIR spectroscopy, and were observed under an optical microscope to compare their sizes.

Table 1. Alkali treatments' parameters

Part of Office Waste Paper	**Concentration of NaOH (wt.%)**				**Temperature (^{o}C)**	**Time (minutes)**
Printed	2	4	8	16	100	90
Non- printed	2	4	8	16	100	90

Bleaching treatment

The samples were chosen according to the optimum concentration of NaOH for the treatment, which was based on the FT-IR analysis results of the composition of the cellulose. The samples were then treated with sodium hypochlorite, NaClO (R&M Chemicals), in order to remove any lignin [4]. The concentration of the NaClO solution was fixed at 2 wt.%. The mixture was then filtered and washed with distilled water until a neutral pH was achieved. Then, the samples were analysed using ATR-FTIR spectroscopy, and were compared to pure cellulose (Sigma-Aldrich) as a reference. An optical microscope was used to observe and investigate the size of the cellulose fibres after the bleaching treatment.

Acid hydrolysis

The treatment continued with acid hydrolysis using sulphuric acid, H_2SO_4 (QreC) to investigate the effects of acid treatment on the cellulose structure. The acid treatment was expected to result in the production of nano-sized cellulose *via* the removal of the amorphous region of the cellulose. The cellulose was mixed with different concentrations of 5 wt.%, 15 wt.%, 30 wt.%,and 60 wt.% of H_2SO_4 solution for 20 minutes (see Table 2) under reflux at 100^{o}C. Then, the mixture was diluted with distilled water to remove the spent acid, and it was stored for about 1 day to allow the deposit to settle at the bottom of the beaker, with the water being changed five times. The samples were then dialysed in a dialysis membrane to neutralize the suspension, during which time, the water was changed about five times. The samples were then analysed using optical microscopy and transmission electron microscopy for the imaging and morphological analysis.

Table 2. Acid hydrolysis treatments' parameters

Part of Office Waste Paper	**Concentration of H_2SO_4 (wt.%)**				**Temperature (^{o}C)**	**Time (minutes)**
Printed	5	15	30	60	100	20
Non- printed	5	15	30	60	100	20

Optical microscopy

Optical microscopy (Leica) was used to observe the morphology (dimensions, size and structure) of the extracted cellulose after each chemical treatment. Only a few drops of cellulose suspension were required to be placed on the microscope slide for the observation process. The average size and diameter of the fibres were recorded using ImageJ software.

Transmission electron microscopy

Since a high-magnification imaging analysis could not be achieved *via* optical microscopy, a detailed structural analysis of the cellulose extracted from the office paper waste was carried out using transmission electron microscopy (TEM) (Zeiss). The cellulose samples extracted after the acid hydrolysis treatment using 5 wt.%, 30 wt.% and 60 wt.% of acid were compared and analysed using TEM. The cellulose suspension was deposited on the TEM grid and dried before the analysis. The diameter of the observed cellulose fibres was recorded using ImageJ software.

Results and Discussion

The ATR-FTIR spectra of the raw office paper waste (printed), and alkali-treated office paper waste using 2%, 4%, 8% and 16% NaOH are shown in Figure 1. The C-O-C glycoside ether band and C-C ring breathing band observed at ~1105 cm^{-1} and ~1160 cm^{-1}, respectively for the printed raw office paper waste spectrum in Figure 1a indicated the presence of cellulose [4]. The presence of the C-O-C pyranose ring skeletal vibration of the cellulose band could also be observed around ~1027 [7]. The band observed at ~2899 $cm^{-1}$was assigned to the C-H stretching vibration band, which represents the general organic content [4]. Besides, the observed band at ~3333 cm^{-1} referred to the O-H stretching vibration, indicating the presence of hydrogen bonds in the samples. There were two types of hydrogen bonding, one located at 3285 cm^{-1} (attributed to the intermolecular hydrogen bond) and the other at 3335cm^{-1} (attributed to the intramolecular hydrogen bond) [8]. On the other hand, the hemicellulose band, which can usually be found around ~1735 cm^{-1}, was assigned to the C=O band from acetyl stretching [4]. However, in the raw office paper waste spectrum, no sign of hemicelluloses could be observed. This indicated the absence of hemicellulose in the raw office paper waste that was used, and it was expected that the hemicellulose had been removed previously during the papermaking process.

.

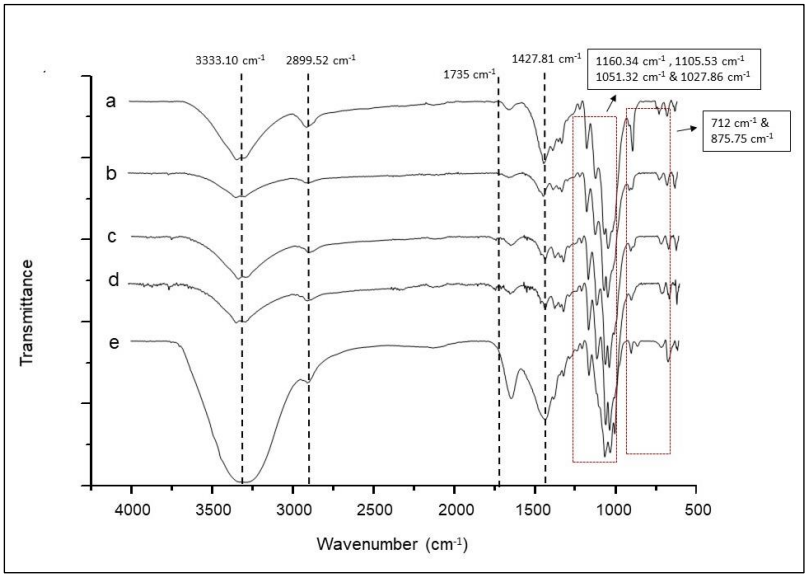


Figure 1. FT-IR spectra for printed (a) raw office paper waste, and alkali treated office paper waste using b) 2% NaOH, c) 4% NaOH, d) 8% NaOH, and e) 16% NaOH

The C=C in-plane aromatic vibration band, which could be observed at 1427 cm^{-1},indicated the presence of lignin in the raw office paper waste, while the band located around ~1263 cm^{-1},was assigned to the C-O-C stretching from the ether linkage in lignin [4]. The band at 875.75 cm^{-1} indicated the presence of calcite in relation to the symmetric C-O stretching of calcite, while the band located at ~712 cm^{-1} referred to the O-C-O bending mode of calcite [6], which were both ascribed to the presence of fillers or calcite used in the papermaking process. The pre-treatment process (where the samples were boiled and ground) was carried out in order to remove foreign substances, but the cellulose, calcite and lignin remained intact in the sample. The alkaline treatment using various concentrations of 2%, 4%, 8% and 16% of sodium hydroxide was carried out in order to investigate the suitable and optimum concentration of sodium hydroxide for the extraction of cellulose. The FTIR spectrum for each concentration can be observed in Figures 1 b-e, respectively. It can be seen that the bands assigned for the lignin, fillers and calcite were considerably decreased after the treatment with 2% sodium hydroxide. However, the bands remained similar at sodium hydroxide concentrations of 4%, 8% and 16%. This indicated that a concentration of 4% of NaOH was sufficient and could be considered as a suitable and optimum concentration for the alkaline treatment.

The ATR-FTIR spectra of the non-printed raw office paper waste and alkali-treated office paper waste using various concentrations of NaOH are shown in Figure 2. The observed bands around 1106.21 cm^{-1}, 1160.82 cm^{-1}, 1028.67 $cm^{-1}$and 1052.22 cm^{-1} in Figure 2a (non-printed raw office paper waste) indicated the presence of cellulose, as was similarly observed in the printed raw office paper waste spectrum (see Figure 1a). The band located at 2898.47 cm^{-1} corresponded to the C-H stretching vibrations of the alkyl groups in the aliphatic bonds, while the 3333.10 cm^{-1} band that was attributed to the O-H band was mainly due to the cellulose-hydrogen bonding. However, the C-H band in the non-printed raw office paper waste spectrum was lower compared to the printed raw office paper spectrum (see Figure 1a) due to the presence of aliphatic groups associated with the ink components [6].

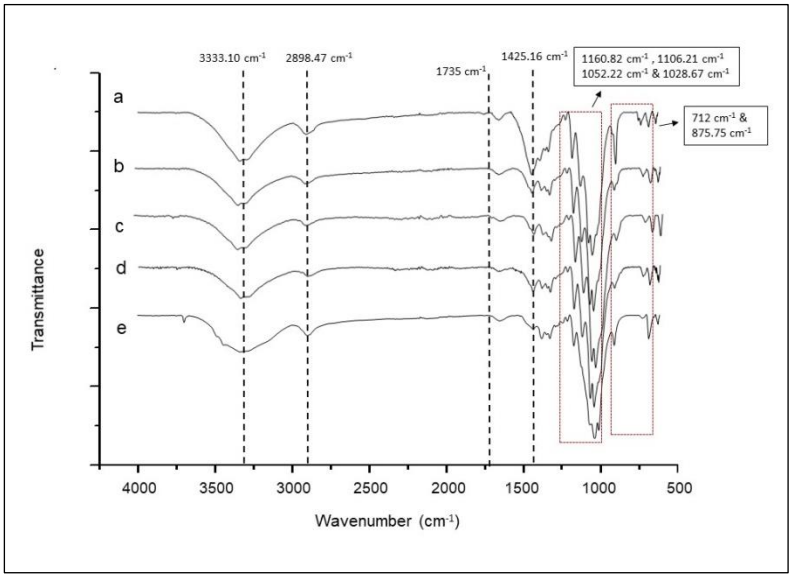


Figure 2. FT-IR spectra for non-printed, (a) raw office paper waste, and alkali treated office paper waste using b) 2% NaOH, c) 4% NaOH, d) 8% NaOH, and e) 16% NaOH

Similar to the printed raw paper, the absence of a hemicellulose band around ~1735 cm^{-1} indicated that there was no hemicellulose present in the sample. The band at 1425.16 cm^{-1} showed the presence of lignin in the raw office paper waste, while the band around 1300-1375 cm^{-1} corresponded to the S=O band and N-H band, both of which were ascribed to the presence of ink compounds. The band at 875.75 $cm^{-}1$, which was assigned to the presence of calcite, could also be observed in the non-printed raw office paper waste. The ATR-FTIR spectra after the alkali treatment using 2%, 4%, 8% and 16% of NaOH can be seen in Figures 2 b-e, respectively. Similar to the printed paper waste spectra, the bands representing lignin, ink compounds and fillers (calcite) were markedly reduced after the treatment

with 2% sodium hydroxide. Thus, it could be concluded that the sodium hydroxide concentration of 4% was the optimum concentration to be used for the alkali treatment of the non-printed office paper waste.

Figures 3b and 3d show that the bands at 1109.96cm^{-1}, 1161.14cm^{-1}, 1031.08cm^{-1} and 1054.75cm^{-1} remained in the spectrum that corresponded to the existence of cellulose [6]. Moreover, the band at 2899.34 cm^{-1} represented the C-H band, while the band at 3333.10 cm^{-1} corresponded to the O-H band, similar with the pure cellulose (reference) spectrum. The band at 1428.21cm^{-1}, which was assigned to lignin, decreased slightly after the bleaching treatment.

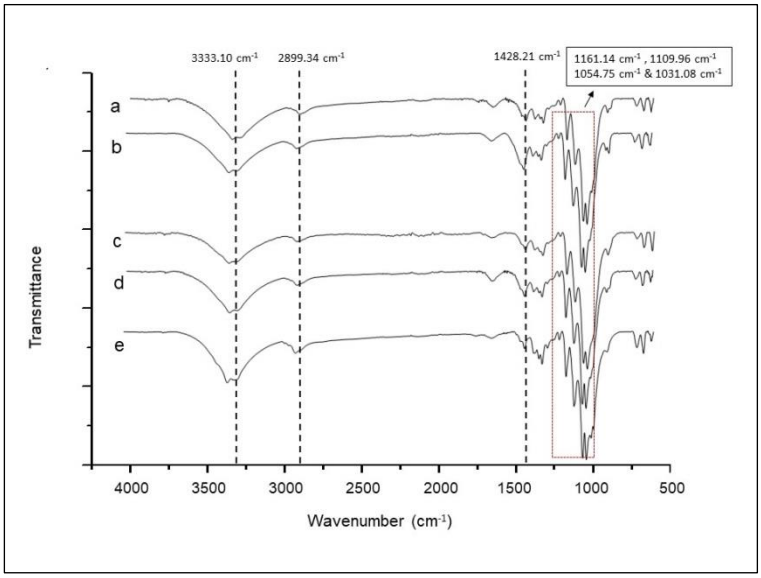


Figure 3. FT-IR spectra of office paper waste treated with a) 4% NaOH (printed), b) NaCIO (printed), c) 4% NaOH (non-printed), d) NaCIO (non-printed) and e) pure cellulose standard

In conclusion, the raw office paper waste contained cellulose, lignin, calcite, and other organic contents, such as sulfone, amine groups and filler or ink components. The difference between the printed and non-printed paper was that the ink intensity at 2899.52 cm^{-1} was more noticeable for the printed paper. Originally, the alkali treatment was aimed at the removal of hemicellulose. However, it was found that no hemicellulose was present in the paper, since it was processed paper, in which hemicellulose had been removed during the papermaking process. Based on the FTIR analysis, the treatment reduced the intensity of the lignin and calcite bands and removed the organic contents and ink components. The sodium hydroxide concentration of 4% was found to be the optimum concentration for the alkali treatment as a higher concentration would have resulted in a processing cost. It was also expected that some of the lignin would have already been dissolved during the alkali treatment due to the alkali-sensitive linkages formed by the lignin [9].

Morphology analysis using optical microscope

Figure 4 shows the image of the cellulose structure of the printed raw paper and the non-printed raw paper waste, and the cellulose structures of the printed and non-printed paper after the pre-treatment process.

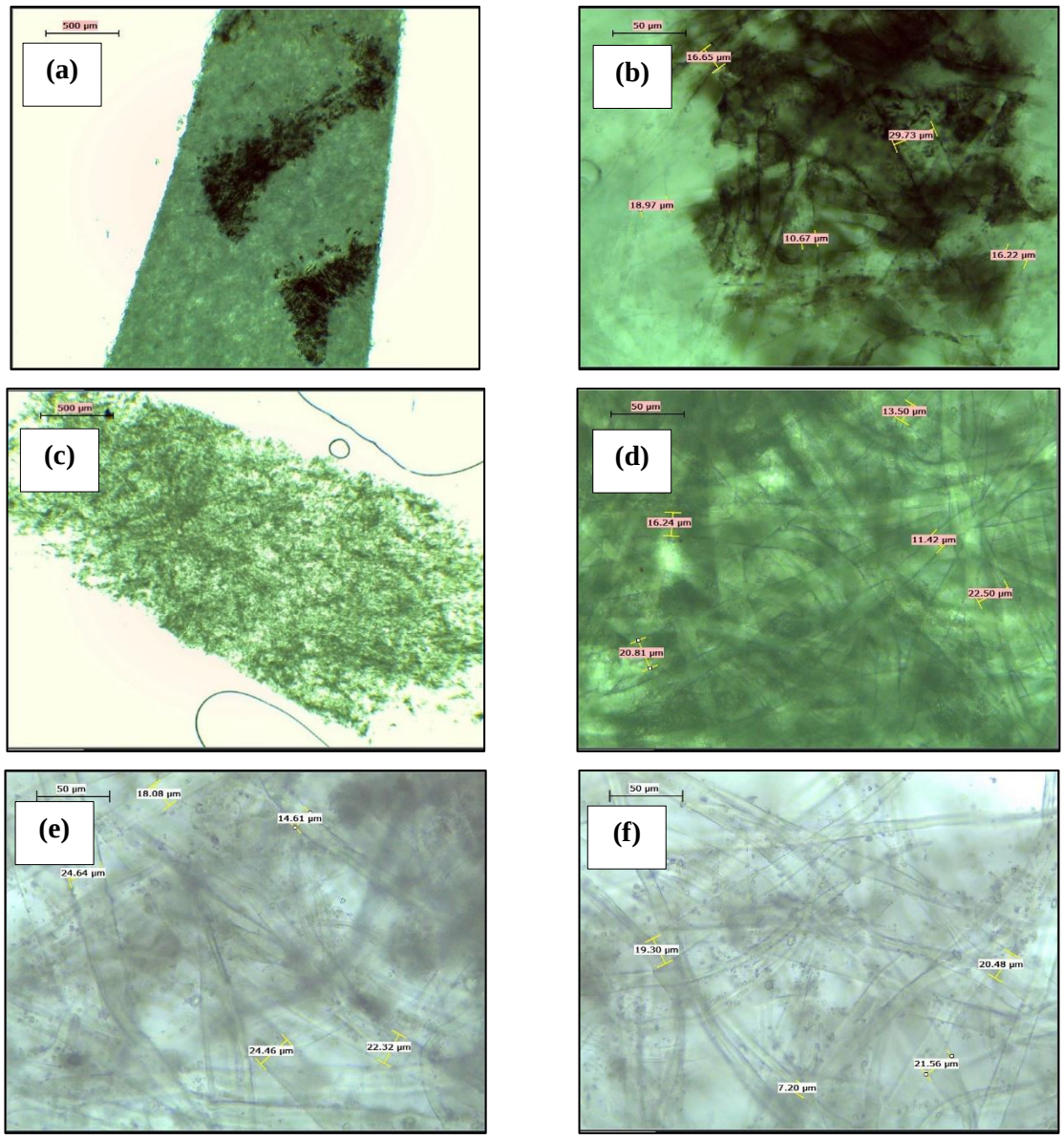


Figure 4. Optical microscope images of (a) Printed raw paper at 4x magnification, (b) Printed raw paper at 40x magnification, (c) Non-printed raw paper at 4x magnification, (d) Non-printed raw paper at 40x magnification, (e) Pre-treatment (printed) at 40x magnification, (f) Pre-treatment (non-printed) at 40x magnification

Figure 4 shows that the cellulose extracted from the office paper waste after all the treatments had a fibrous, rod-like structure, with some of the fibres being arranged longitudinally and attached to each other by hydrogen bonds [4]. The printed raw paper is shown in Figures 4a and 4b, where the black ink could be clearly observed on the fibres. No ink could be observed on the fibres shown in Figures 4c and 4d, which represented the non-printed raw paper. The fibrous structure of the cellulose could be clearly observed in the optical images. After the pre-treatment process, the cellulose fibres came apart loosely due to the boiling and grinding processes, as shown in Figures 4e and 4f. The ink components on the fibres of the printed paper had also been partially removed after the pre-treatment process prior to the alkali treatment.

The optical images of the cellulose fibres for the printed office paper and alkali-treated office paper using various concentrations of sodium hydroxide are shown in Figure 5. Figures 5a-d show the images of the cellulose fibres after being treated with 2%, 4%, 8% and 16% NaOH, respectively. At a NaOH concentration of 4% and above, no significant differences could be observed between the cellulose fibres, despite the use of a higher concentration of alkali (16% NaOH) for the treatment. This further supported the finding that a sodium hydroxide concentration of 4% is sufficient and optimum for the alkali treatment. However, at a NaOH concentration of 2%, the cellulose fibres still looked closely packed, which suggested the expected ineffectiveness of the 2% NaOH treatment due to the stronger hydrogen bonding remaining between the adjacent fibres. Thus, a concentration of 4% NaOH is a suitable and optimum concentration for the alkali treatment and cellulose extraction.

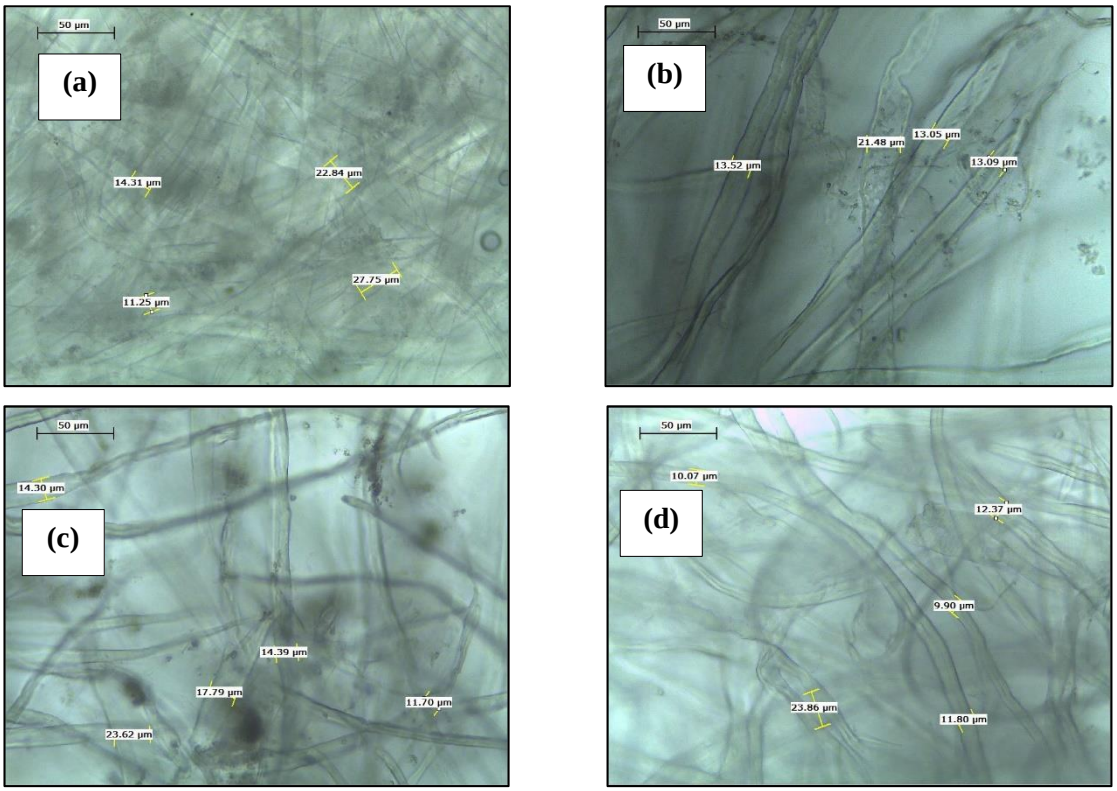


Figure 5. Optical microscope images of printed office paper after alkaline treatment using (a) 2% NaOH, (b) 4% NaOH, (c) 8% NaOH, and (d) 16% NaOH (all at 40x magnification)

Figure 6 shows the image of the cellulose fibres of the non-printed paper, and of the non-printed paper after the treatment with various concentrations of alkali. Figures 6a, 6b, 6c and 6d indicate the images of the cellulose fibres after having been treated with 2%, 4%, 8% and 16% NaOH, respectively. The cellulose fibres of the non-printed paper were similar, and no significant differences could be observed when compared to the printed paper fibres shown in Figure 5.

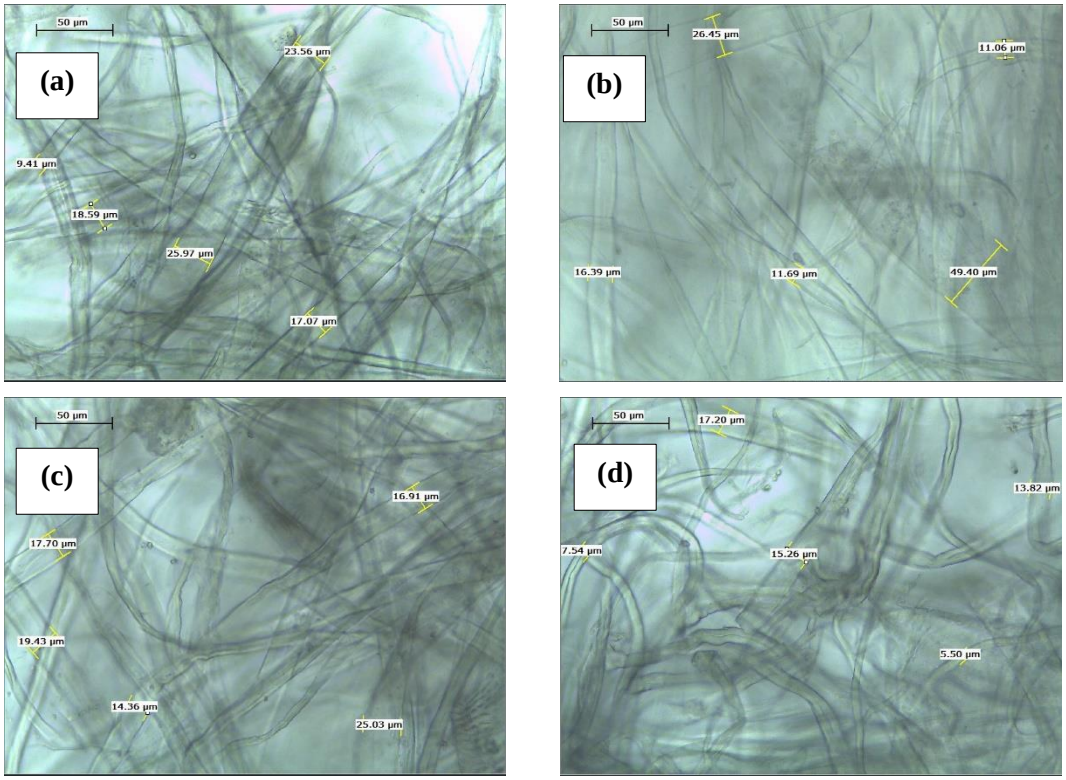


Figure 6. Optical microscope images of non-printed paper after alkaline treatment using (a) 2% NaOH, (b) 4% NaOH, (c) 8% NaOH, and (d) 16% NaOH (all at 40x magnification)

The optical images of the cellulose fibres for the printed and non-printed office paper after the bleaching treatment are shown in Figures 7a and 7b, respectively. The individual cellulose fibres could be clearly observed, and the individual fibres were separated from each other following the bleaching treatment. The bleaching treatment was aimed at removing any undesirable components such as lignin, and to loosen the interactions between the adjacent fibres, leaving behind the cellulose fibres.

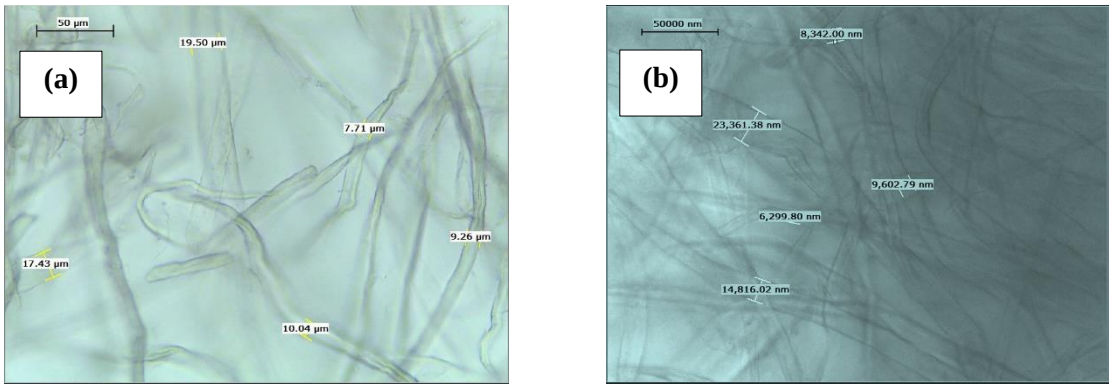


Figure 7. Optical microscope images of paper after bleaching treatment with NaClO (a) printed paper (b) Non-printed paper (both at 40x magnification)

The acid hydrolysis treatment was aimed at breaking the strong hydrogen bonds between the cellulose fibres and to reduce the micro-sized cellulose to nano-scale by removing the amorphous structure of the cellulose. Figure 8 clearly indicates that the size of the cellulose was reduced as the concentration of acid used was increased. The higher the concentration of acid, the smaller the diameter of the cellulose. Unfortunately, for an acid concentration of 60%, the cellulose could no longer be observed through the use of an optical microscope, and instead, a transmission electron microscope (TEM) had to be used for the analysis to allow a precise examination of the nano-sized cellulose to be made.

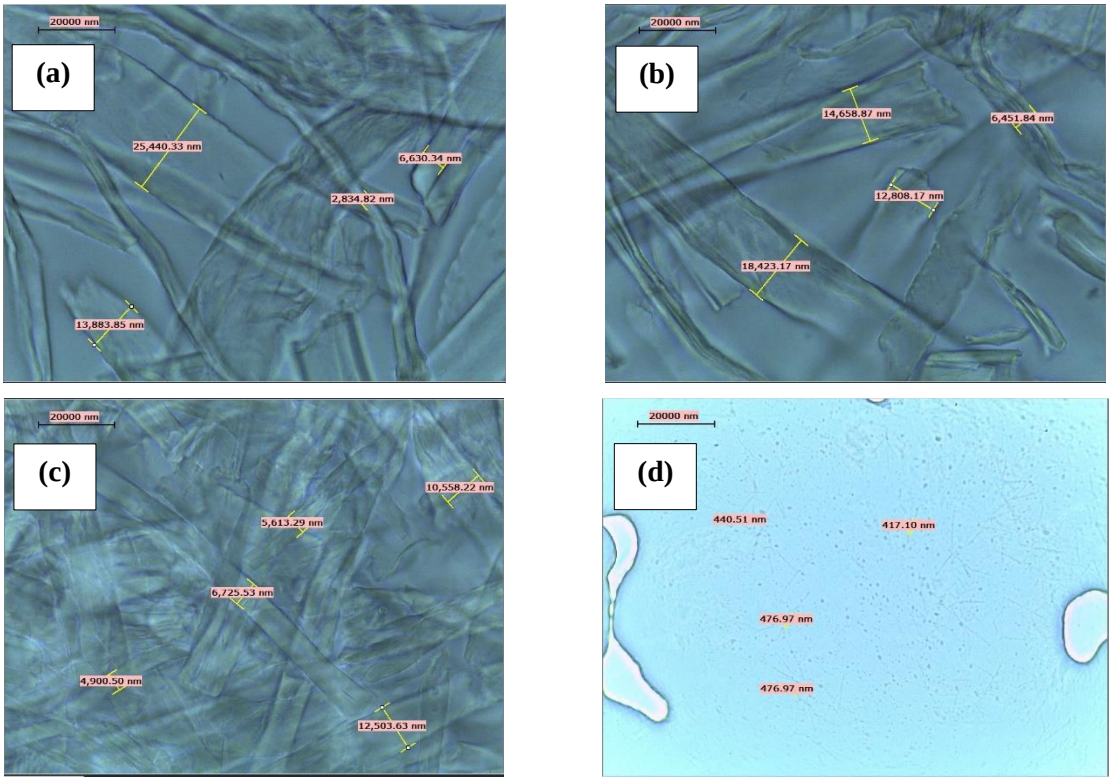


Figure 8. Optical microscope images of the samples after acid hydrolysis treatment using (a) 5%, (b) 15%, (c) 30%, and (d) 60% sulphuric acid (all at 100x magnification)

Table 3 shows the trend in the sizes using an optical microscope for the analysis of raw office waste paper until the acid hydrolysis treatment. From the results, the diameter of the fibres in the raw paper samples until the NaClO treatment remained unchanged at around 12-16 μm. Then, the size of the cellulose changed after the treatment with acid, and this varied according to the concentration of the acid used. The higher the concentration of acid, the smaller the diameter of the fibres. The diameter of the cellulose fibres after treatment with 5% and 15% acid showed no significant difference as compared to the size after the bleaching treatment. However, the size was reduced significantly following treatment with acid concentrations of 30% and 60%.

Table 3. Average diameter of cellulose fibres for printed and non-printed paper for all stages of treatments

Printed Paper	**Average Diameter (µm)**	**Non- Printed Paper**	**Average Diameter (µm)**
Raw paper	16.32	Raw paper	16.02
Pre-treatment paper	16.82	Pre-treatment paper	14.81
NaOH 2 %	15.52	NaOH 2 %	13.83
NaOH 4 %	14.72	NaOH 4 %	13.35
NaOH 8 %	13.15	NaOH 8 %	12.57
NaOH 16 %	11.81	NaOH 16 %	11.28
After Treatment with 4% NaOH			
NaCIO	12.38	NaCIO	11.56
Acid 5 %	13.96	N.C	None
Acid 15 %	12.54	N.C	None
Acid 30 %	9.91	N.C	None
Acid 60 %	5.87	N.C	None

*N.C = Not Conducted

TEM analysis: Nano scale of cellulose

Figure 9 shows the morphology of cellulose samples after acid hydrolysis treatment with different concentrations. All samples were observed using transmission electron microscope (TEM).

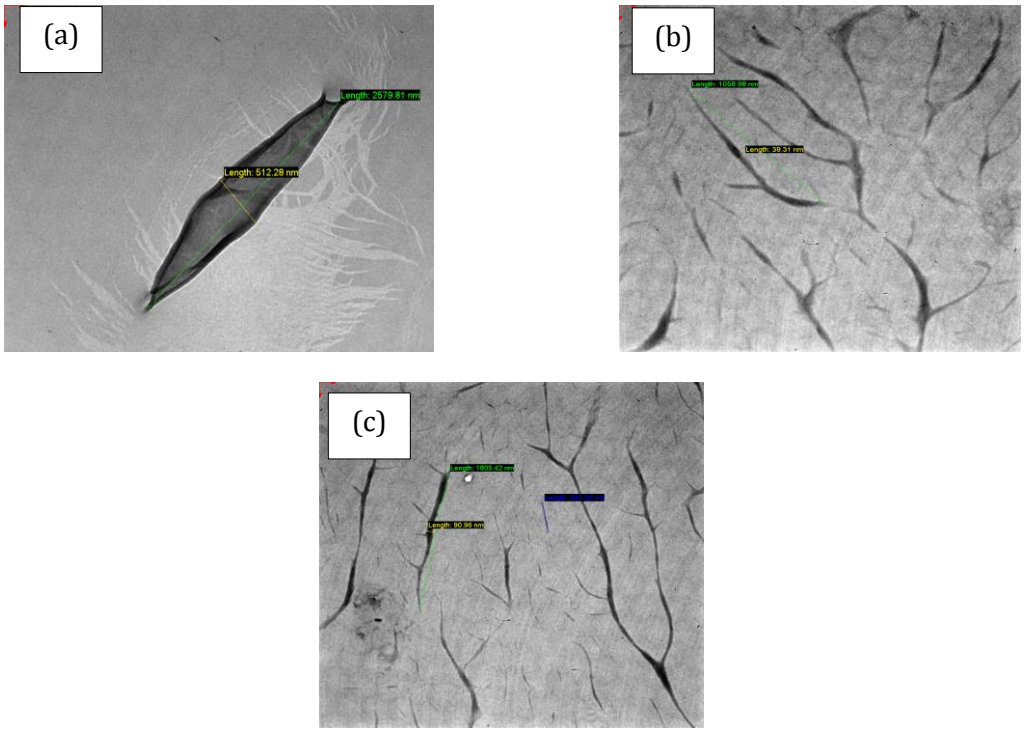


Figure 9. TEM images after acid hydrolysis treatment using (a) 5% acid at 10kx magnification, (b) 30% acid at 20kx magnification and (c) 60% acid at 10kx magnification.

Table 4 indicates the average diameter of the cellulose fibres after treatment with various concentrations of acid. The acid treatment was expected to affect the size of the cellulose fibres to nano-scale, based on a previous study [6]. TEM was used in this analysis due to the high magnification required for the imaging analysis, which could not be achieved previously using an optical microscope. Until the bleaching treatment, the size and morphology of the cellulose fibres could still be observed using an optical microscope. After the acid hydrolysis treatment, a TEM analysis was much more reliable, and was recommended for the detailed imaging of the nano-sized cellulose.

Table 4. Size comparison on average diameter using TEM and optical microscopy

Acid Concentration (%)	**TEM: Average Diameter (nm)**	**(OM) Average Diameter (µm)**
5	512.28	13.96
30	30.89	9.91
60	25.62	5.87

Figure 9 shows the fibrous structure of the cellulose that was extracted from the office paper waste after all the treatments until the acid hydrolysis, which was the last stage of the treatment. Table 4 shows that the diameter of the cellulose fibres varied depending on the concentration of acid used. The higher the concentration of acid used, the smaller the diameter of the cellulose fibres that were obtained after the treatment. The average diameters of the cellulose fibres obtained using acid concentrations of 5%, 30% and 60% were 512 nm, 30 nm and 25 nm, respectively. The average diameter of the CNCs obtained using 60% acid concentration is slightly lower than the value of ~33 nm for CNCs obtained from office waste reported by Orue et. al. [6]. However, the value is higher as compared to the average value of 17nm reported for CNCs extracted from wood pulps [10]. Unlike the alkali and bleaching treatments, the acid hydrolysis process allowed the production of nano-fibrillated cellulose to a certain extent, depending on the technique or process applied. This was due to the removal of the amorphous region in the cellulose fibres that was susceptible to the acid treatment. In this study, the treatment produced nano-sized cellulose fibres, but in a small fraction, throughout the cellulose sample. Some of the micro-sized fibres were mixed with a fraction of the nano-sized cellulose fibres, thereby explaining the co-mixture of both micro-fibrillated and nano-fibrillated cellulose in the samples.

Conclusion

Micro-fibrillated and nano-fibrillated cellulose were obtained from office paper waste by subjecting the paper to an alkaline treatment (with sodium hydroxide solution, NaOH), bleaching treatment (with sodium hypochlorite solution, NaCIO) and acid hydrolysis treatment (with sulphuric acid, H_2SO_4). Cellulose was successfully extracted from the office paper waste as the FT-IR analysis indicated that lignin, ink and other components had been removed and reduced after the alkali and bleaching treatments. The spectrum of the treated office paper waste was similar to that of pure cellulose, thereby indicating that cellulose can be obtained from office paper waste. The analysis revealed that a sodium hydroxide concentration of 4% is an adequate and optimum concentration of alkali to be used for the extraction of cellulose from office paper waste. The morphology of the cellulose in the paper waste showed that it had a fibrous, long and rod-like structure. On the other hand, the size of the cellulose decreased as the concentration of acid used was increased, thereby suggesting that acid hydrolysis treatment is required for the production of nano-sized cellulose. The results showed that the extracted cellulose had sizes ranging from micro- to nano-scale, which was around ~20-30 nm. Further research on the extraction of nanocellulose from office paper waste, such as the reaction time and temperature, should be pursued and optimized since this work only focused on its extraction using different concentrations of NaOH in order to reuse and mitigate environmental issues concerning waste paper.

Acknowledgement

This study was supported by the Fundamental Research Grant Scheme (FRGS19-015-0623), Ministry of Education, Malaysia and International Islamic University Malaysia.

References

1. Nguyen, S. T., Feng, J., Li Ai, T. T., Hoang, N., Vincent Tan, B. C. and Duong Hai, M. (2013). Cellulose aerogel from paper waste for crude oil spill cleaning. *Industrial & Engineering Chemistry Research*, 52: 18386-18391.
2. Riyad, A. S. M. (2014). Scenario of paper waste recycling and reuse practices in Khulna City of Bangladesh. *International Journal of Scientific & Engineering Research*, 5(3): 705-711.
3. Chirayil, C. J., Mathew, L., and Thomas, S. (2014). Review recent research in nanocellulose preparation from different lignocellulosic fibers. *Review Advance Materials Science*, 37: 20-28.
4. Danial, W. H., Majid, Z. A., Mohd Muhid, M. N., Triwahyono, S., Bakar, M. B., and Ramli, Z. (2015). The reuse of wastepaper for the extraction of cellulose nanocrystals. *Carbohydrate Polymers*, 118: 165-169.
5. Jannatun, N. I., and Zulhabri, I. (2014). Sustainable construction waste management strategic implementation model. *WSEAS TRANSACTIONS on Environment and Development*, 10: 48-58.
6. Orue, A., Santamaria-Echart, A., Eceiza, A., Pena-Rodriguez, C. and Arbelaiz, A. (2017). Office waste paper as cellulose nanocrystal source. *Journal of Applied Polymer Science*, 134: 45257.
7. Nguyen, H. D., Mai, T. T. T., Nguyen, N. B., Dang, T. D., Le, M. L. P., Dang, T.T., and Tran, V. M., (2013). A novel method for preparing microfibrillated cellulose from bamboo fibers. *Advanced in Natural Sciences: Nanoscience and Nanotechnology*, 4: 1-9.
8. Hathama, R. H., and Muna, H. S. (2014). Novel method for extraction of cellulose from agricultural and industrial wastes. *Chemical Technology an Indian Journal*, 9(4): 148-153.
9. Cherian, B. M., Leão, A. L., de Souza, S. F., Thomas, S., Pothan, L. A., and Kottaisamy, M. (2010). Isolation of nanocellulose from pineapple leaf fibres by steam explosion. *Carbohydrate Polymers*, 81: 720-725.
10. Dong, H., Strawhecker, K. E., Snyder, J. F., Orlicki, J. A., Reiner, R. S., and Rudie, A. W. (2012). Cellulose nanocrystals as a reinforcing material for electrospunpoly(methyl methacrylate) fibers: Formation, properties and nanomechanical characterization. *Carbohydrate Polymers*, 87: 2488-2495.

Malaysian Journal of Analytical Sciences Vol 23 No 6 2019

Articles 7 - 18 are selected papers from the "Tropical Ocean and Marine Science International Symposium (TOMSY2018), 30 - 31 October 2018 at Universiti Malaysia Terengganu; organized by Institute of Oceanography and Environment, Universiti Malaysia Terengganu

Guest Editor: Suhaimi Suratman

Page

1. ANTIBACTERIAL PROPERTIES OF CHITOSAN EDIBLE FILMS INCORPORATED WITH MUSK LIME EXTRACTS FOR THE PRESERVATION OF SQUIDS (Sifat Antibakteria Filem Kitosan Boleh Dimakan Yang Ditambah Dengan Ekstrak Limau Kasturi Bagi Pengawetan Sotong) 914
Choong Kah Wai, Tee Yee Bond, Nyam Kar Lin, Pui Liew Phing

2. ADSORPTION STUDY ON THE REMOVAL OF COPPER IONS FROM AQUEOUS SOLUTION USING SODIUM HYDROXIDE-MODIFIED Carica papaya PEELS (Kajian Penjerapan Dalam Penyingkiran Ion Kuprum Dari Larutan Akueus Menggunakan Kulit Carica papaya Yang Dimodifikasikan Dengan Sodium Hidroksida) 926
Muhammad Shahrain Shuhaimen, Erna Normaya Abdulah, Rosliza Mohd Salim, Mohd Armi Abu Samah, Muhammad Nor Omar, Mohammad Norazmi Ahmad

3. PREPARATION AND CHARACTERISATION OF HYDROXYAPATITE EXTRACTED FROM FISH SCALE WASTE FOR THE REMOVAL OF GALLIC ACID AS INHIBITOR IN BIOFUEL PRODUCTION (Penyediaan dan Perincian Hidroksiapatit yang Diekstrak daripada Sisa Sisik Ikan untuk Penyingkiran Asid Galik sebagai Perencat dalam Pemprosesan Bahan Api Bio) 938
Nurul Fakhriah Ismail, Sofiah Hamzah, Nurul Ashraf Razali, Wan Mohd Hafizuddin Wan Yussof, Nora'aini Ali, Abdul Wahab Mohammad

4. CHEMICAL CONSTITUENTS AND ANTIOXIDANT POTENTIALS OF SEVEN PHILIPPINE MOSSES (Juzuk Kimia dan Potensi Antioksidan bagi Tujuh Lumut Filipina) 950
Mary Stephanie S. Carranza, Virgilio C. Linis, Consolacion Y. Ragasa, Maria Carmen S. Tan

5. ANALYSIS OF VOLATILE COMPOUNDS OF SPICES GROWN IN BANYUMAS DISTRICT, JAWA TENGAH, INDONESIA USING SOLID PHASE MICROEXTRACTION-GAS CHROMATOGRAPHY MASS SPECTROMETRY (Analisis Sebatian Meruap bagi Rempah yang Tumbuh di Daerah Banyumas, Jawa Tengah, Indonesia Menggunakan Pengekstrakan Mikro Fasa Pepejal-Kromatografi Gas Spektrometri Jisim) 963
Fajar Hardoyono, Kikin Windhani, Herman Sambodo, Hary Pudjianto

6. RADIOACTIVITY OF ^{210}Po IN GREEN MUSSELS (*Perna viridis*) AT THE WEST COAST OF JOHORE STRAITS, MALAYSIA (Radioaktiviti ^{210}Po dalam Kupang (*Perna viridis*) di Pantai Barat Selat Johor, Malaysia) 980
Mei Peng Lim and Che Abd Rahim Mohamed

7. MODIFICATION OF GOLD SCREEN PRINTED ELECTRODE FOR THE DETECTION OF TOXIC DOMOIC ACID 991
(Pengubahsuaian Elektrod Cetakan Skrin Emas bagi Pengesanan Asid Domoik Toksik)
Hafiza Mohamed Zuki, Norhidayah Mohd Nasri, Fatin Nabilah Muhamad, Noor Sheryna Jusoh, Azrilawani Ahmad, Marinah Mohd Ariffin

8. SOURCES AND COMPOSITION OF POLYCYCLIC AROMATIC HYDROCARBONS IN THE RIVER AND ESTUARIAL SEDIMENT ALONG THE VICINITY OF KUALA KEDAH, MALAYSIA 1001
(Sumber dan Komposisi Hidrokarbon Aromatik Polisiklik dalam Sedimen Sungai dan Muara di Sepanjang Persekitaran Kuala Kedah, Malaysia)
Terence Ricky Chiu and Masni Mohd Ali

9. PALEOPRODUCTIVITY VARIATION IN TERENGGANU OFFSHORE DURING HOLOCENE BASED ON TOTAL ORGANIC CARBON AND $CaCO_3$ RECORDS 1009
(Variasi Paleoproduktiviti di Luar Pesisir Pantai Terengganu Ketika Holosen Berdasarkan Rekod Jumlah Karbon Organik dan $CaCO_3$)
Erick Naim, Hasrizal Shaari, Mohd Fadzil Akhir

10. THE COMBINED EFFECT OF ZINC AND pH ON GROWTH RATE AND CHLOROPHYLL CONTENT OF BROWN SEAWEED, *Padina boryana* 1018
(Kesan Gabungan Zink dan pH ke Atas Kadar Pertumbuhan dan Kandungan Klorofil Rumpai Laut Perang, *Padina boryana*)
Nabeela Ali Nasser Al-Awlaqi, Noor Azhar Mohamed Shazili, Nurulnadia Mohd Yusoff

11. DISTRIBUTION OF NUTRIENTS CONCENTRATION IN THE UPWELLING AREA OFF THE EAST COAST OF PENINSULAR MALAYSIA DURING THE SOUTHWEST MONSOON 1030
(Taburan Kepekatan Nutrien di Kawasan Julang Air di Pantai Timur Semenanjung Malaysia Semasa Monsun Barat Daya)
Azyyati Abdul Aziz, Suhaimi Suratman, Poh Heng Kok, Mohd Fadzil Akhir

12. DISTRIBUTION OF DISSOLVED ALUMINIUM (dAl) IN SEAWATER AT PULAU PERHENTIAN, TERENGGANU 1044
(Taburan Aluminium Terlarut (dAl) di dalam Air Laut di Pulau Perhentian, Terengganu)
Khairul Nizam Mohamed, Edriana Godon, Shamsuddin Johan, Fairuza Shaheera Jaafar

13. RARE EARTH ELEMENTS DISTRIBUTION CHARACTERISTICS IN DISSOLVED AND PARTICULATE FRACTION, AND IN SEDIMENT OF BRUNEI BAY, BORNEO 1054
(Ciri-Ciri Taburan Unsur Nadir Bumi dalam Fraksi Terlarut dan Partikulat, dan Sedimen di Teluk Brunei, Borneo)
Noor Azhar Mohd Shazili, Adiana Ghazali, Joseph Bidai

14. SETTLEMENT RATE OF FOULING SERPULID *Ficopomatus* cf. *uschakovi* PILLAI, 1960 ON ARTIFICIAL STRUCTURE AT SETIU WETLANDS, TERENGGANU, MALAYSIA 1067
(Kadar Penempatan Petumbuhan Serpulid *Ficopomatus* cf. *uschakovi* Pillai, 1960 pada Struktur Tiruan di Tanah Bencah Setiu, Terengganu, Malaysia)
Noor Shahida Rosli, Nurulafifah Yahya, Izwandy Idris, Zainudin Bachok

15. DISTRIBUTION AND BEHAVIOR OF NUTRIENTS IN BESUT RIVER ESTUARY, TERENGGANU, MALAYSIA 1077
(Taburan dan Perlakuan Nutrien di Muara Sungai Besut, Terengganu, Malaysia)
Fatin Adlina Md Nasir, Suhaimi Suratman, Dung Quang Le

16. TEMPORAL VARIABILITY OF PHYTOPLANKTON BIOMASS IN RELATION TO SALINITY AND NUTRIENTS IN A SHALLOW COASTAL LAGOON 1090
(Kepelbagaian Temporal Biojisim Fitoplankton Berdasarkan Kemasinan dan Nutrien di Lagun Pesisir Pantai yang Cetek)
Zuraini Zainol and Mohd Fadzil Akhir

17. DISTRIBUTION OF PHYTOPLANKTON IN KUANTAN PORT, MALAYSIA DURING NORTHEAST MONSOON SEASON 1107
(Taburan Fitoplankton di Pelabuhan Kuantan, Malaysia Semasa Musim Monsun Timur Laut)
Amir Safwan Hamzah, Normawaty Mohammad-Noor, Aimimuliani Adam, Zuhairi Ahmad

18. DISTRIBUTION AND SOURCES OF POLYCYCLIC AROMATIC HYDROCARBONS IN COASTAL SURFACE SEDIMENTS OFF TERENGGANU 1120
(Taburan dan Sumber Hidrokarbon Polisiklik Aromatik dalam Sedimen Permukaan Pesisir Pantai Terengganu)
Mohd Mursyid Mohd Sanip, Muhammad Fais Fadzil, Suhaimi Suratman, Shahirah Rozmi, Norhayati Mohd Tahir

Malaysian Journal of Analytical Sciences, Vol 23 No 6 (2019): 914 - 925
DOI: https://doi.org/10.17576/mjas-2019-2306-01

MALAYSIAN JOURNAL OF ANALYTICAL SCIENCES
Published by The Malaysian Analytical Sciences Society
ISSN 1394 - 2506

ANTIBACTERIAL PROPERTIES OF CHITOSAN EDIBLE FILMS INCORPORATED WITH MUSK LIME EXTRACTS FOR THE PRESERVATION OF SQUIDS

(Sifat Antibakteria Filem Kitosan Boleh Dimakan Yang Ditambah Dengan Ekstrak Limau Kasturi Bagi Pengawetan Sotong)

Choong Kah Wai[1], Tee Yee Bond[2], Nyam Kar Lin[1], Pui Liew Phing[1]*

[1]*Department of Food Science and Nutrition, Faculty of Applied Sciences, UCSI University, 56000 Cheras, Kuala Lumpur, Malaysia*
[2]*Centre for Pre-University Studies, Stella Maris International School, Lorong Setiabistari 2, Medan Damansara, 50490 Kuala Lumpur, Malaysia.*

[*]*Corresponding author: puilp@ucsiuniversity.edu.my*

Received: 30 May 2019; Accepted: 3 November 2019

Abstract

The chitosan (CH) films incorporated with different concentrations (1% to 5%) of musk lime extracts (MLE) were investigated for physical, mechanical, chemical, and antibacterial properties. Storage test on squids' shelf-life was also conducted. The addition of MLE into CH film had increased the inhibition zones against gram-negative bacteria, *Pseudomonas aeruginosa* and *Vibrio parahaemolyticus*. It also reduced the moisture content, water solubility, tensile strength and elongation at break. Films with higher concentration of MLE had higher intensity in opacity and appeared more greenish. From the Fourier transforms infrared (FTIR) spectra, the addition of 4% and 5% of MLE in CH films shifted the -CH_3 stretching at peak 2921 cm^{-1} and the signal of the hydrophilic representative zones (-OH and –NH stretch, amide II and carboxyl group) were slightly reduced at 3200 cm^{-1}, 1570 cm^{-1} and 1400 cm^{-1}, respectively. The FTIR results did not suggest any cross-linkage between the MLE and CH. At 4 °C storage condition, wrapping the squids with MLE incorporated films had prolonged their shelf-life from 5 days to 15 days compared to wrapping with neat CH film.

Keywords: edible film, shelf-life, antibacterial properties, chitosan, musk lime

Abstrak

Filem kitosan (CH) yang ditambah dengan ekstrak limau kasturi (MLE) dalam kepekatan yang berbeza (1% hingga 5%) telah disiasat untuk sifat fizikal, mekanikal, kimia, dan antibakteria. Ujian hayat makanan ke atas sotong juga dijalankan. Penambahan MLE ke dalam filem CH telah meningkatkan zon perencatan terhadap bakteria gram-negatif, *Pseudomonas aeruginosa* dan *Vibrio parahaemolyticus*. Ia juga mengurangkan kandungan kelembapan, keterlarutan air, kekuatan tegangan dan pemanjangan. Filem dengan kepekatan MLE yang lebih tinggi mempunyai intensiti yang lebih tinggi dalam kelegapan dan kelihatan lebih hijau. Spektrum inframerah transformasi Fourier (FTIR) menunjukan bahawa penambahan 4% dan 5% MLE menyebabkan peralihan regangan -CH_3 di puncak 2921 cm^{-1} dan isyarat wakil zon hidrofilik (-OH dan -NH, amida II dan kumpulan karboksil) dikurangkan sedikit masing-masing pada 3200 cm^{-1}, 1570 cm^{-1} dan 1400 cm^{-1}. Keputusan FTIR tidak menunjukkan sebarang hubungan silang antara MLE dan CH. Pada suhu penyimpanan 4 °C, pembungkusan sotong dengan filem yang ditambah dengan MLE didapati menambah jangka hayat sotong dari 5 hari kepada 15 hari, jika dibandingan dengan filem CH yang dibalut dengan kemas.

Kata kunci: filem yang boleh dimakan, jangka hayat, sifat antibakteria, kitosan, limau kasturi

Introduction

Food packaging had been designed as a medium of transportation and containment for food products since the 19th centuries [1]. There is an increase in demand for eco-friendlier and safer packaging materials, mainly for those free from chemical preservatives and packaging with natural antimicrobial compounds [2]. Several technologies were utilized in packaging to prevent food from microbial and chemical hazards. These include active, intelligent and edible packaging catered to various of food products such as oxygen scavengers for high lipid food, gas-sensing devices as indicator for the maturity of fruits and quince seed film with thymol and oregano essential oil to pack fish products [3, 4].

Among the technologies, edible packaging is one of the most practical and useful packaging technologies [5]. There is a great potential for edible spices packaging to be applied on meat products by improving their flavor, nutritional value and shelf-life [6]. Some studies had showed the use of chitosan film as an effective medium to deliver bioactive compounds into food components [7, 8]. Compared to the traditional method of marinating with spices, the delivery of bioactive components was not as efficient because of the direct interaction and thus, oxidation of bioactive components with food samples [9]. Muppalla et al. [10] reported that the addition of clove essential oil (2%) into carboxymethyl cellulose films and wrapped onto chicken meat could extend its shelf-life from 4 days to 12 days. Emiroğlu et al. [11] reported that the wrapping of beef patties with soy edible film incorporated with 5% of thyme and oregano essential oil reduced the growth of coliforms such as *Escherichia coli* and *Pseudomonas spp*.

Musk lime is one of the most frequently used spices and fruits in Southeast Asia [12]. Its pulp was generally used as flavouring in food and beverages for steaks, desserts and drinks [13]. Although the seeds and peels contained nutritious components such as unsaturated fatty acid and other bioactive compound, they were not fully utilized by the industries [14, 15]. To our best knowledge, there had not been any studies done on the use of extracts from the musk lime (seeds, peels and pulps) in edible films.

Squids had relatively short shelf-life due to high contents of amino acids [16]. Even in ice storage at 0 °C, the squids were reported for rejection and spoilage at around 10 days to 14 days [17, 18]. The present work developed chitosan edible films with the addition of various concentrations musk lime extracts (seeds, peels and pulps). They were studied in terms of physical, mechanical, chemical and antibacterial properties. Then, an optimized film was used to wrap around the squids and a storage test was done. This was with the aim to possibly increase the shelf-life of the squids.

Materials and Methods

Materials

Musk and squids (*Loligo spp*.) were purchased from local hypermarket, namely Pasar Segar, Pandan Jaya, Selangor, Malaysia. Chitosan powder and Tween-80 emulsifier were of food grade, while chemicals and reagent-grade were of analytical grade and purchased from Chemolab Sdn. Bhd., Selangor, Malaysia.

Preparation and extraction of spices

The musk limes were washed with distilled water and the stems were removed from fruits. They were sliced and hand-squeezed to partially remove the juice. The peels, seeds and pulps were placed on aluminium foils and subjected to overnight heating at 50 °C with a convection oven. The dried spices (peels, seeds and pulps) were ground into fine powder particles using a grinder (Sharp, Japan). The extraction of MLE was conducted as described by Weerakkody et al. [19] with modifications. About 100 g of ground spices was added into 1000 mL of 95% ethanol in a 2 L beaker. The solution was stirred overnight at 25 °C using a magnetic stirrer (Labmart, Korea) with the top of the beaker covered. Then, the solution was filtered with Whatman No.3 filter paper with the aid of a vacuum filter (Millipore, USA). A rotary evaporator (Büchi, Switzerland) was used to evaporate the filtrates at 45 °C in vacuum until there was no more condensation of wastes in the waste collector. The extracts were kept at 4 °C in sterile universal bottles until further use.

Preparation of film

The film samples were prepared according to Remya et al. [8] with modifications. Chitosan (CH) solution (1.5%, w/v) was prepared by dissolving 1.5 g of CH powder in 100 mL 1% acetic acid by stirring overnight. The CH solution was filtered using vacuum filter with Whatman No.3 filter paper to remove suspended particles. About 25 mL of the CH filtrate was poured into a 50 mL beaker. CH film without MLE will be the control in the characterization tests. For CH films with MLE, they were prepared with the addition of 1.0, 2.0, 3.0, 4.0 and 5.0% v/v of the CH solution, respectively. Glycerol as plasticizer (0.5% v/v of CH solution) and Tween-80 as emulsifier (0.05% v/v of CH solution) were also then added. The solution was homogenized using a homogenizer (Daihan Scientific, Korea) at 9,000 rpm for 3 minutes. 25 mL of the homogenous solution was casted onto a 90 mm x 15 mm Petri dish and dried in a convection oven at 40 °C for 24 hours. The dried film was manually peeled using a spatula and stored in a desiccator until further analyses. The samples were labelled as 'CH + 0% MLE' to 'CH + 5% MLE'.

Physical properties of films: Moisture content

The sample was cut into 2 x 2 cm and stored in a desiccator for a day. It was weighed for initial mass and subjected to convection oven heating at 105 °C for 6 hours until a constant weight was achieved (final weight) [20]. The moisture content was reported in average of triplicate with standard deviation. It was calculated by:

$$Moisture\ content = \frac{M_i - M_f}{M_i} \times 100\% \quad (1)$$

where M_i stands for initial mass sample and M_f stands for final mass of dried sample.

Water solubility

The water solubility test was determined according to Zaman et al. [21]. After the determination of moisture content, the dried film was immersed in excess distilled water (50 mL) for 24 hours. Then, the sample was taken out and blotted dry with filter paper, followed by weighing (final weight). The water solubility was reported in average of triplicate with standard deviation. It was calculated by:

$$Water\ solubility = \frac{M_f - M_i}{M_f} \times 100 \quad (2)$$

where M_i stands for initial mass dried sample and M_f stands for final mass of immersed sample.

Color

The sample's color was determined using a colorimeter33 (Hunterlab, USA) as conducted in the work of Zaman et al. [21]. A circular sample with 64 mm diameter was cut and placed in ColorFlex sample cup after standardization with white and black plates. The color of the film was expressed as L*(lightness-darkness), a* (red-green) and b* (yellow-blue) values. The results were reported in average of triplicate with standard deviation. The following equation was used to calculate the index of ΔE to identify the total color differences between each sample:

$$\Delta E = \sqrt{(L^* - L)^2 + (a^* - a)^2 (b^* - b)^2} \quad (3)$$

where L*, a* and b*are the color values of the musk lime film samples and L, a and b are the color parameters of thewhite standard tile.

Mechanical properties of films

The thickness of film was measured using a micrometer. For each sample, three measurements were taken from different location on the film selected randomly and reported as average readings with standard deviations. Tensile strength and elongation at break were determined according to Remya et al. [8] with slight modifications using a tensile testing machine (Lloyd Instrument, UK). The films were cut into 20 x 50 mm rectangular strip and held parallel by the grip with a separation of 30 mm. The speed that pulled apart was set to be 20 mm/min. The results were reported in triplicates with standard deviations.

Chemical properties of films

FTIR spectra of ML films and CH films were analyzed using FTIR spectroscopy (Thermo Fisher Scientific, Nicolet iS5FT-IR spectrometer, Waltham, MA, USA) according to Hoque et al. [22]. All spectra were collected nder 20 scans in transmittance mode from 4000 cm^{-1} to 600 cm^{-1} at a resolution of 4 cm^{-1} against background spectrum recorded from empty cell at 25 °C.

Antibacterial properties of films

The antibacterial properties of samples were evaluated according to Velu et al. [23] with slight modifications. An overnight pre-cultured of *Pseudomonas aeruginosa* and *Vibrio parahaemolyticus* was separately suspended into 10 mL of nutrient broth and 10 mL of 3% NaCl nutrient broth respectively. The turbidity of bacterial suspensions was adjusted to 0.5 Mcfarland standard. A bacterial suspension (100 µL) was inoculated on Mueller-Hilton Agar (MHA) and swabbed evenly on MHA plate by sterile swabs under aseptic condition.

The edible film discs (6.5 mm) were punched and placed onto the pre-inoculated MHA plate using sterile forcep and gently pressed on it. Streptomycin (10 mg/mL) and ampicillin (20 mg/mL) was used as positive control for *Pseudomonas aeruginosa* and *Vibrio parahaemolyticus*, respectively. Negative control was prepared by impregnating 20 µL of 95% ethanol on 6.5 mm sterile paper disc (Whatman filter paper No.3) and dried for 20 minutes in laminar flow. The plates were incubated for 24 hours at 37 °C. The total diameter of inhibition zone was measured by a ruler and reported in millimeter (mm). The results were reported in triplicates with standard deviations.

Storage test of squids

The pre-treatment of squids was carried out according to Kumar et al. [24]. The squids were washed with potable water to remove debris or dirt. Then, the squid pens, viscera, tentacles, eyes and beaks were removed. The squid mantles were used for the present work. They were cut for 10 g into pieces with 3 cm x 3 cm and kept at 4°C in chiller prior to experiment.

The pH test was carried out according to Tantasuttikul et al. [25] with slight modifications. The buffer solutions of pH 4, 7 and 10 were calibrated before conducting the test. The squid mantles were placed into the stomacher bag and mixed with 90 mL sterile distilled water and homogenized by a stomacher (LGC Scientific Sdn Bhd, Malaysia) for two minutes. The film was peeled and not homogenized with the squid mantles. The pH reading was taken using a digital pH meter (EUTech Instruments, Singapore) and performed in duplicates and reported in average with standard deviation.

The total plate count was carried out according to Remya et al. [8]. 10 g of squid mantles were mixed with 90 mL of 0.1% sterile peptone water in stomacher bag and homogenized under a stomacher for 2 minutes. The film was peeled and not homogenized with the squid mantles. A suitable of serial dilution ranges was prepared in each of universal bottles to enumerate the colonies in the range of 30 to 300. Each serial dilution was inoculated for 100 µL on Plate Count Agar using spread plate technique and incubated at 37 °C for 24 hours.

The colonies counts were converted into logarithms from the number of colony forming units (cfu/g). The control (without film wrapping) and 4% musk lime film wraps were conducted at each interval. Measurements in duplicates were taken at intervals of 0, 3, 6, 9, 12, 14 and 16 days.

Statistical analysis

One-way ANOVA with the Tukey test was carried out to determine the significant differences among the films with different MLE concentrations. All the significant differences were set as 95% interval ($p < 0.05$). Paired-t test was conducted to analyze the significant difference in terms of total plate count and pH reading between two different batches of squids (without wrapping and with MLE film wrapping).

Results and Discussion

Physical properties of films

The moisture contents of the film samples were shown in Table 1. The gradual addition of (MLE) had led to a significant decrease of moisture content. The addition of MLE could have reduced the water evaporation rate from the film. The addition of MLE had occupied the spaces in between of chitosan polymer network [26]. As a result, the initial polymer network volume was altered and this caused lesser water was entrapped in between the network [27].

Table 1. Moisture content and water solubility on different concentration of musk lime extracts incorporated with chitosan film

% MLE in Chitosan Film	Moisture Content (%)	Water Solubility (%)
0	24.70 ± 1.80^{a}	58.60 ± 2.16^{a}
1	24.41 ± 1.32^{a}	31.80 ± 3.50^{b}
2	19.22 ± 0.56^{b}	31.25 ± 1.14^{b}
3	18.07 ± 1.47^{b}	23.11 ± 1.65^{c}
4	17.94 ± 2.04^{b}	12.67 ± 2.46^{d}
5	15.27 ± 1.13^{c}	9.15 ± 0.96^{e}

MLE = Musk lime extracts, CH = Chitosan. Values were expressed as triplicate in mean ± standard deviation. a–e different superscripts within the same column indicate significant differences between formulations ($p < 0.05$).

Water solubility was studied to test the samples' resistance against water [28]. As reported in Table 1, the water solubility significantly decreased as the concentration of MLE increased. This seemed to reduce the hydrophilicity of the CH film. The water solubility of a material is related to its water binding capacity [29]. The hydrophilicity of film was reduced due to the addition of hydrophobic components in MLE which includes the fatty acids and polyphenolic compounds [15]. The antioxidant extracts could have limited the polysaccharide-water interactions by reducing its availability to form hydrogen bonds with water molecules [30].

The color parameters of all the film samples were shown in Table 2. The ΔE showed a gradual increasing trend from the increasing addition of MLE into films. This denoted the degree color changes. From the L*, a* and b* parameters, the increasing concentration of MLE in the samples lowered the transparency, reddish and yellowish attributes. Concurrently, it increased the opacity, greenness and blueness of the films as shown in Figure 1. The MLE extracted in the present work was dark green in color. The color attributes from MLE were from pigments such as flavonoids (hesperidin and narginin), carotenoids, chlorophyll and others [31].

Table 2. Parameter of color in different concentration of musk lime extracts incorporated with chitosan film

% MLE in Chitosan Film	L*	a*	b*	ΔE
0	31.11 ± 0.24^{a}	-0.78 ± 0.07^{a}	4.71 ± 0.04^{a}	62.80 ± 0.24^{a}
1	41.38 ± 0.01^{b}	7.38 ± 0.01^{b}	36.01 ± 0.04^{b}	63.30 ± 0.01^{b}
2	33.92 ± 0.11^{c}	12.33 ± 0.02^{c}	24.44 ± 0.07^{c}	65.51 ± 0.11^{c}
3	28.67 ± 0.01^{d}	9.93 ± 0.01^{d}	17.77 ± 0.01^{d}	67.04 ± 0.01^{d}
4	24.82 ± 0.02^{e}	4.56 ± 0.06^{e}	5.18 ± 0.07^{e}	69.05 ± 0.02^{e}
5	21.93 ± 0.03^{f}	1.51 ± 0.02^{f}	0.89 ± 0.01^{f}	71.88 ± 0.02^{f}

MLE = Musk lime extracts, CH = Chitosan. Values were expressed as triplicate in mean ± standard deviation. a–d different superscripts within the same column indicate significant differences between formulations ($p < 0.05$).



Figure 1. Appearances of chitosan-based films incorporated with different concentrations (0%, 3% and 5% from left to right) of musk lime extracts

Mechanical properties of films

The thicknesses, tensile strength (TS) and elongation at break (EB) of all the samples were reported in Table 3. The addition of MLE in the CH film significantly reduced the TS and EB, with 'CH + 5% MLE' reported the lowest TS and EB at 3.03 MPa and 15.02%. The decrease of EB may be due to the decrease of moisture content in the films. Hosseini et al. [32] reported that higher moisture contents in the films resulted in higher elasticity and extensibility. From the present work, the CH film with increased MLE concentrations significantly reduced its moisture content.

There were studies which reported similar influence in the tensile properties in films from the addition of various extracts. Rubilar et al. [27] reported a decrease in the chitosan film's TS (43 MPa to 22.56 MPa) and EB (28% to 10.9%) with the increasing concentration of grape seed extracts. Bourtoom [33] reported that the addition of 50% palm oil in rich starch-chitosan film reduced its TS (12.91 MPa to 9.91 MPa) and EB (24.28% to 18.99%). The addition of 4% oleic acid in chitosan film also significantly reduced the TS (17 MPa to 11 MPa) and EB (12% to 7.4%).

Table 3. Thickness and mechanical properties on different concentration of musk lime extracts incorporated with chitosan film

% MLE in Chitosan Film	Thickness (mm)	Tensile Strength (MPa)	Elongation at Break (%)
0	0.057 ± 0.011^{a}	11.36 ± 0.27^{a}	30.27 ± 1.81^{a}
1	0.117 ± 0.026^{b}	7.51 ± 1.23^{b}	22.13 ± 1.87^{b}
2	0.126 ± 0.194^{b}	6.42 ± 0.47^{bc}	19.47 ± 1.29^{b}
3	0.151 ± 0.024^{b}	4.52 ± 0.51^{c}	19.03 ± 0.40^{b}
4	0.181 ± 0.013^{c}	4.14 ± 0.41^{c}	19.33 ± 1.20^{bc}
5	0.219 ± 0.025^{d}	3.03 ± 0.17^{c}	15.02 ± 0.65^{c}

MLE = Musk lime extracts, CH = Chitosan. Values were expressed as triplicate in mean ± standard deviation. a–d different superscripts within the same column indicate significant differences between formulations ($p < 0.05$)

Chemical properties of films

The Fourier-transform infrared spectroscopy (FTIR) study was done to analyze the interaction between the chitosan-based film and MLE. All distinctive peaks from all film samples were shown in Figure 2. In general, all chitosan films showed similar pattern with main absorption peaks at around 3280 cm^{-1}, 2900 cm^{-1}, 1570 cm^{-1}, 1400 cm^{-1}, 1150 cm^{-1} and 1000 cm^{-1}. These wavenumbers were found in several studies on pure chitosan film [34-36].

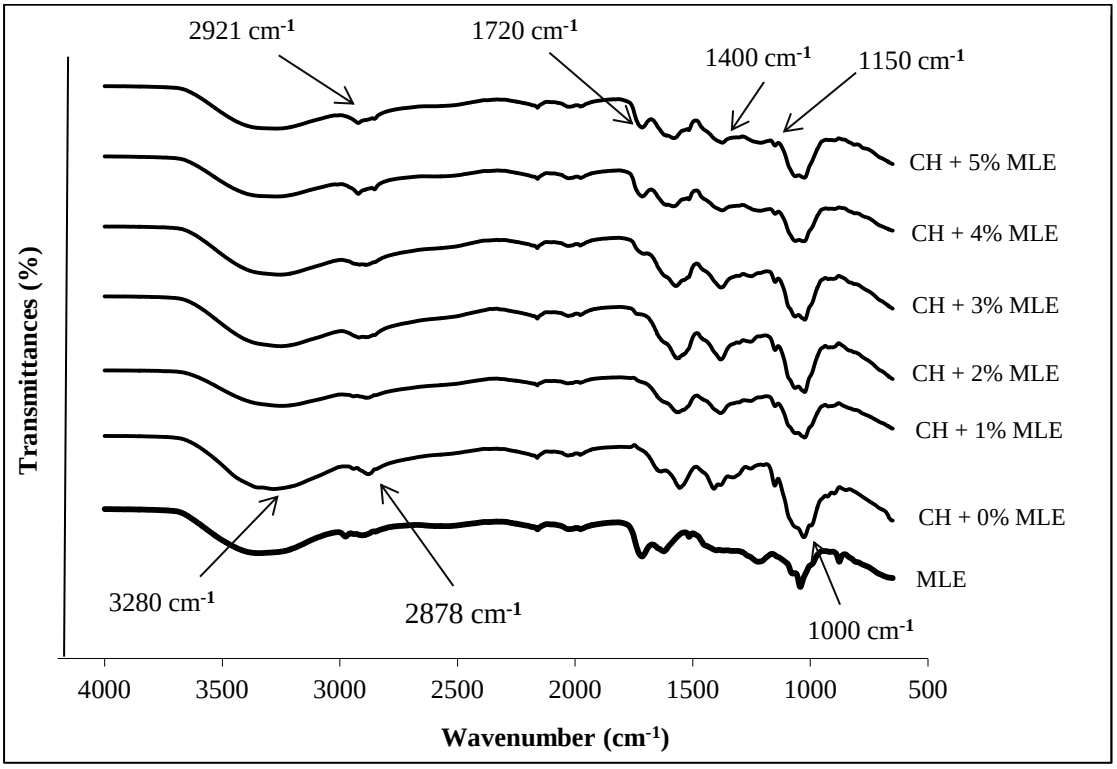


Figure 2. FTIR spectra of all types of films and musk lime extracts

The absorption peaks in the area around 3200 cm^{-1} to 3300 cm^{-1} belonged to the stretching of O-H and N-H bonds [37]. Absorption area of 2800 cm^{-1} to 2900 cm^{-1} corresponded to $–CH_3$ stretching, while 1550 to 1590 cm^{-1} and 1400 cm^{-1} were denoted as amide II (C-N and –NH stretching) and carboxylic group (–COO-), respectively [35]. 1000 cm^{-1} and 1150 cm^{-1} was expected to be carbonyl group (C-O) [34]. Interestingly, the absorption peak at 1720 cm^{-1} became more obvious from 3% to 5% of MLE in the samples. This absorption peak was similarly found in the spectrum of MLE. It could be from the polyphenolic compounds which consisted of C=O bonding [26, 38].

Compared to 'CH + 0% MLE' sample, there was a shift of absorption peaks from wavenumber 2878 cm^{-1} to 2921 cm^{-1} in 'CH + 4% MLE' and 'CH + 5% MLE' samples. This showed a hydrophobicity interaction within the CH film samples [38]. As there was no improvement in tensile strengths from the addition of MLE into the CH films, thus, it is indicative that there was no cross-linkages between them. This phenomenon was similarly reported by Yuan et al. [39] in the development of chitosan film added with carvacrol and pomegranate peel extracts. Reportedly, it was due to the insufficient of interactions between the chitosan and the polyphenolic compound.

Antibacterial properties of films

The antibacterial activities of chitosan films with different concentrations of MLE were shown in Table 4. While MLE and chitosan respectively exhibited inhibition towards *Pseudomonas aeruginosa* (PA) and *Vibrio parahaemolyticus* (VP), the increasing addition of MLE into the chitosan-based films further improved them with the highest inhibition zone against PA and VP at 8.32 mm and 9.88 mm, respectively. Note that there was no significant difference ($p > 0.05$) of inhibition activities between the addition of 4% and 5% of MLE into the films. Thus, 'CH + 4% MLE' was considered as the optimum sample for further storage test with squids.

Table 4. Antibacterial activity of musk lime extracts incorporated with chitosan film on main strains of bacteria found in squid

Total Diameter Inhibition Zone (mm) Including Film (6.5mm)		
Type of Films	***Pseudomonas aeruginosa***	***Vibrio parahaemolyticus***
CH + 0% MLE	6.78 ± 0.24^{a}	6.97 ± 0.15^{a}
CH + 1% MLE	7.03 ± 0.02^{a}	7.03 ± 0.14^{a}
CH + 2% MLE	7.13 ± 0.17^{ab}	7.13 ± 0.27^{a}
CH + 3% MLE	7.33 ± 0.19^{b}	9.00 ± 0.24^{b}
CH + 4% MLE	8.07 ± 0.26^{c}	9.28 ± 0.62^{c}
CH + 5% MLE	8.32 ± 0.22^{c}	9.88 ± 0.82^{c}

MLE = Musk lime extracts, CH = Chitosan. Values were expressed as triplicate in mean ± standard deviation. a–c different superscripts within the same column indicate significant differences between formulations ($p < 0.05$).

The active sites of chitosan molecules had diffused and slowed the microbes. It was evidenced by Allwin et al. [40] which obtained 14 mm of inhibition zone for PA due to its active amino residues. Chaiyakosa et al. [41] reported the use of chitosan to reduce VP in shrimp. The antibacterial effect of chitosan could be due to the interruption of cell wall by electrostatic force generated from cationic group of protonated amino group (NH_3^+) with negative residue of bacteria cell wall.

The low pH or acidity of MLE used in the films may have inhibited the growth of PA and VP because they grow optimally at neutral pH [42]. It was reported that the citric acid extracted from musk limes fruits inhibited the growth of Vibrio *spp*. [43]. The flavonoid in citrus fruits such as naringin in musk the limes was proven to inhibit PA [44-45].

Storage test of squids

The trends of squids' pH without wrapping (control) and with 'CH + 4% MLE' wrapping throughout 16 days were shown in Figure 3. The present work recorded the squid's initial pH as 6.6, which was in par with other works [46]. Without the film, the squid's pH gradually increased to 7.5, which is just slightly above the neutral pH- a favorable pH for common microbes to develop. In contrary with the wrapping, the squid's pH was in the acidic range with pH 3 at Day 3 and 5.6 at Day 16. Pairing with the TPC results from the storage test, it was notable that the acidic condition contributed by the MLE in the wrapping had slowed down the growth of microbes. The gradual increase in pH value with storage time was due to the presence of cathepsin and alkalinizing bacteria from the squids [47]. This caused the accumulation of alkaline compounds such as ammonia and trimethylamine.

The trends of the TPC of squid samples without wrapping (control) and with 'CH + 4% MLE' wrapping throughout 16 days were shown in Figure 4. The initial TPC of both samples were at log 4.55, which was in par with that reported by other works [48, 49]. While both samples gradually increased in the TPC with time, it was markedly reduced with the wrapping of 'CH + 4% MLE', denoting a hindrance in the growth of microbes.

The maximum acceptable microbial counts limit was at log 6.0 [48]. A food is considered unsafe for consumption when the TPC is more than log 6.0. Based on this limit as shown in Figure 4, the shelf-life of the squid was extended from five days to fifteen days when it is wrapped with the film sample. This marked extension was due to the antibacterial properties of the film as discussed above.

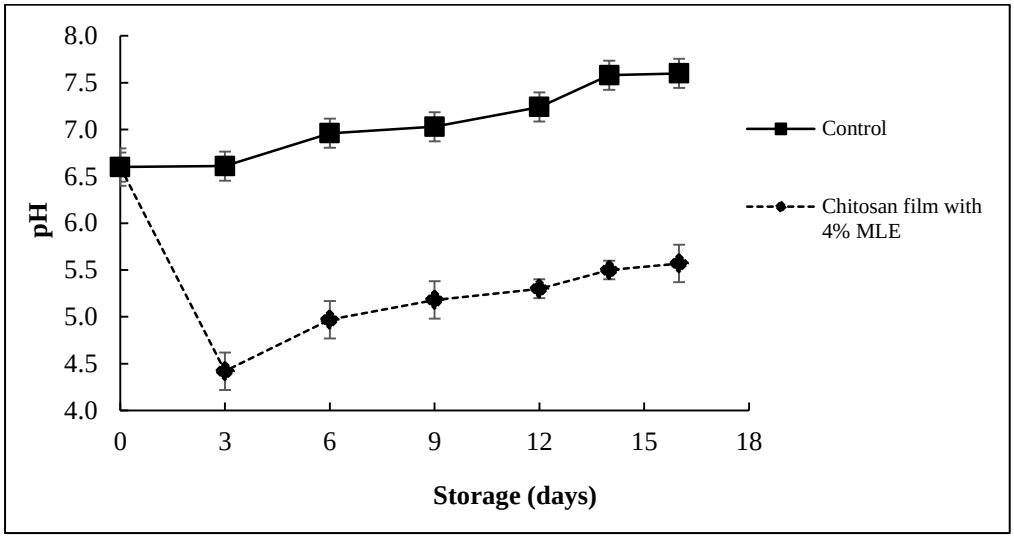


Figure 3. The changes of squids' pH with and without 'CH + 4% MLE' wrapping throughout the storage period

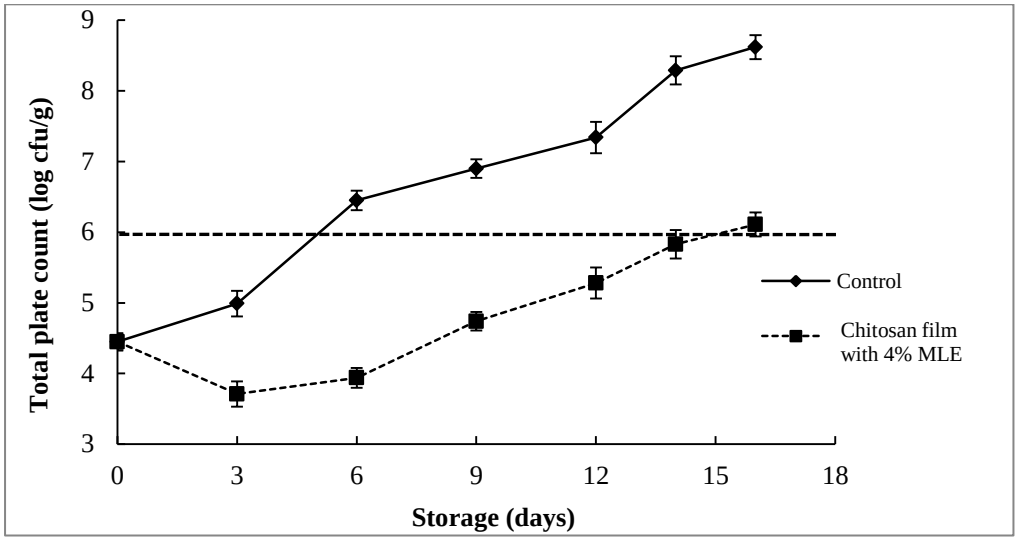


Figure 4. Changes of TPC in log (CFU/mL) with and without 'CH + 4% MLE' wrapping throughout the storage period

Conclusion

The present work had developed a chitosan-based edible film, incorporated with musk lime extracts. From the tests done, it is conclusive that the higher concentration of musk lime extract in chitosan film would result in increased antibacterial properties, thickness and total color changes. Concurrently, it reduced the moisture content, water solubility and tensile properties. At optimized concentration of 4% of MLE added in the chitosan-based film, it effectively extended the shelf-life of squid in the 4°C storage. In a nutshell, MLE has the potential to be used as a safe alternative additive into film materials for shelf-life extension of food its antibacterial properties. It is suggested that other physical analysis of the film such as water vapor permeability, oxygen permeability and scanning electron microscope to be explored in future research.

Acknowledgement

The authors acknowledge the UCSI University (Malaysia) for providing financial support for the research project under the UCSI University Pioneer Scientist Fund (Proj-In-FAS-056).

References

1. Robertson, G. L. (2005). Food packaging: principles and practice. CRC press.
2. Giatrakou, V. I. and Savvaidis, I. N. (2012). Bioactive packaging technologies with chitosan as a natural preservative agent for extended shelf-life food products. In Modified atmosphere and active packaging technologies. CRC Press, Florida: pp. 708-753.
3. Jouki, M., Yazdi, F. T., Mortazavi, S. A., Koocheki, A. and Khazaei, N. (2014). Effect of quince seed mucilage edible films incorporated with oregano or thyme essential oil on shelf life extension of refrigerated rainbow trout fillets. *International Journal of Food Microbiology*, 174: 88 - 97.
4. Restuccia, D., Spizzirri, U. G., Parisi, O. I., Cirillo, G., Curcio, M., Iemma, F., Puoci, F., Vinci, G. and Picci, N. (2010). New EU regulation aspects and global market of active and intelligent packaging for food industry applications. *Food Control*, 21(11): 1425 - 1435.
5. Embuscado, M. E. and Huber, K. C. (2008). Edible films and coatings: Why, what, and how. Springer, New York: pp.1 - 25.
6. Saremnezhad, S., Azizi, M. H., Barzegar, M., Abbasi, S. and Ahmadi, E. (2011). Properties of a new edible film made of faba bean protein isolate. *Journal of Agricultural Science and Technology*, 13(2): 181 - 192.
7. Mastromatteo, M., Danza, A., Conte, A., Muratore, G. and Del Nobile, M. A. (2010). Shelf life of ready to use peeled shrimps as affected by thymol essential oil and modified atmosphere packaging. *International Journal of Food Microbiology*, 144(2): 250 - 256.
8. Remya, S., Mohan, C. O., Bindu, J., Sivaraman, G. K., Venkateshwarlu, G. and Ravishankar, C. N. (2016). Effect of chitosan based active packaging film on the keeping quality of chilled stored barracuda fish. *Journal of Food Science and Technology*, 53(1): 685 - 693.
9. Quintavalla, S. and Vicini, L. (2002). Antimicrobial food packaging in meat industry. *Meat Science*, 62(3): 373 - 380.
10. Muppalla, S. R., Kanatt, S. R., Chawla, S. P. and Sharma, A. (2014). Carboxymethyl cellulose–polyvinyl alcohol films with clove oil for active packaging of ground chicken meat. *Food Packaging and Shelf Life*, 2(2): 51 - 58.
11. Emiroğlu, Z. K., Yemiş, G. P., Coşkun, B. K. and Candoğan, K. (2010). Antimicrobial activity of soy edible films incorporated with thyme and oregano essential oils on fresh ground beef patties. *Meat Science*, 86 (2): 283 - 288.
12. Lim, T. K. (2012). Citrus x microcarpa. Springer, Netherlands: pp. 865 - 870.
13. Beh, L. K., Zakaria, Z., Beh, B. K., Ho, W. Y., Yeap, S. K. and Alitheen, N. B. M. (2012). Comparison of total phenolic content and antioxidant activities of freeze-dried commercial and fresh fruit juices. *Journal of Medicinal Plants Research*, 6(48): 5857 - 5862.
14. Chen, H. C., Peng, L. W., Sheu, M. J., Lin, L. Y., Chiang, H. M., Wu, C. T., Wu, C.S. and Chen, Y. C. (2013). Effects of hot water treatment on the essential oils of calamondin. *Journal of Food and Drug Analysis*, 21(4): 363 - 368.
15. Manaf, Y. N., Osman, A., Lai, O. M., Long, K. and Ghazali, H. M. (2008). Characterisation of musk lime (*Citrusmicrocarpa*) seed oil. *Journal of the Science of Food and Agriculture*, 88(4): 676 - 683.
16. Paarup, T., Sanchez, J. A., Moral, A., Christensen, H., Bisgaard, M. and Gram, L. (2002). Sensory, chemical and bacteriological changes during storage of iced squid (*Todaropsis eblanae*). *Journal of Applied Microbiology*, 92(5): 941 - 950.
17. Lapa-Guimarães, J., de Felício, P. E. and Guzmán, E. S. C. (2005). Chemical and microbial analyses of squid muscle (*Loligo Plei*) during storage in ice. *Food Chemistry*, 91(3): 477 - 483.
18. Vaz-Pires, P., Seixas, P., Mota, M., Lapa-Guimarães, J., Pickova, J., Lindo, A. and Silva, T. (2008). Sensory, microbiological, physical and chemical properties of cuttlefish (*Sepia Officinalis*) and broadtail shortfin squid (*Illex coindetii*) stored in ice. *LWT-Food Science and Technology*, 41(9): 1655 - 1664.
19. Weerakkody, N. S., Caffin, N., Turner, M. S. and Dykes, G. A. (2010). In vitro antimicrobial activity of less-utilized spice and herb extracts against selected food-borne bacteria. *Food Control*, 21(10): 1408 - 1414.

20. Association of Analytical Chemists (1995). Official methods of analysis of AOAC international.
21. Zaman, N. B. K., Lin, N. K. and Phing, P. L. (2018). Chitosan film incorporated with *Garcinia Atroviridis* for the packaging of indian mackerel (*Rastrelliger kanagurta*). *Ciência e Agrotecnologia*, 42(6): 666 - 675.
22. Hoque, M. S., Benjakul, S. and Prodpran, T. (2011). Properties of film from cuttlefish (*Sepia pharaonis*) skin gelatin incorporated with cinnamon, clove and star anise extracts. *Food Hydrocolloids*, 25(5): 1085 - 1097.
23. Velu, S., Abu Bakar, F., Mahyudin, N. A., Saari, N. and Zaman, M. Z. (2014). In vitro antimicrobial activity of musk lime, key lime and lemon extracts against food related pathogenic and spoilage bacteria. *International Food Research Journal*, 21(1): 379 - 386.
24. Kumar, V., Sukumar, D. and Muruganantham, M. (2015). Microbial quality of frozen squid (*Sepioteuthis lessoniana*, Lesson 1830) treated with food grade commercial chemicals. *Indian Journal of Animal Research*, 49(5): 736 - 741.
25. Tantasuttikul, A., Kijroongrojana, K. and Benjakul, S. (2011). Quality indices of squid (*Photololigo duvaucelii*) and cuttlefish (*Sepia aculeata*) stored in ice. *Journal of Aquatic Food Product Technology*, 20 (2): 129 - 147.
26. Siripatrawan, U. and Harte, B. R. (2010). Physical properties and antioxidant activity of an active film from chitosan incorporated with green tea extract. *Food Hydrocolloids*, 24(8): 770 - 775.
27. Rubilar, J. F., Cruz, R. M., Silva, H. D., Vicente, A. A., Khmelinskii, I. and Vieira, M. C. (2013). Physico-mechanical properties of chitosan films with carvacrol and grape seed extract. *Journal of Food Engineering*, 115(4): 466 - 474.
28. Cano, A., Cháfer, M., Chiralt, A. and González-Martínez, C. (2016). Physical and antimicrobial properties of starch-PVA blend films as affected by the incorporation of natural antimicrobial agents. *Foods*, 5 (1): 3.
29. Ojagh, S. M., Rezaei, M., Razavi, S. H. and Hosseini, S. M. H. (2010). Effect of chitosan coatings enriched with cinnamon oil on the quality of refrigerated rainbow trout. *Food Chemistry*, 120(1): 193 - 198.
30. Gómez-Guillén, M. C., Ihl, M., Bifani, V., Silva, A. M. D. O. E. and Montero, P. (2007). Edible films made from tuna-fish gelatin with antioxidant extracts of two different murta ecotypes leaves (*Ugni molinae Turcz*). *Food Hydrocolloids*, 21(7): 1133 - 1143.
31. Asif, M. (2014). Brief information related to potential therapeutic tendencies of citrus plants. *International Journal of Biological Research*, 2(2): 116 - 120.
32. Hosseini, M. H., Razavi, S. H. and Mousavi, M. A. (2009). Antimicrobial, physical and mechanical properties of chitosan-based films incorporated with thyme, clove and cinnamon essential oils. *Journal of Food Processing and Preservation*, 33(6): 727 - 743.
33. Bourtoom, T. (2008). Edible films and coatings: characteristics and properties. *International Food Research Journal*, 15(3): 237 - 248.
34. Pelissari, F. M., Grossmann, M. V., Yamashita, F. and Pineda, E. A. G. (2009). Antimicrobial, mechanical, and barrier properties of cassava starch− chitosan films incorporated with oregano essential oil. *Journal of Agricultural and Food Chemistry*, 57(16): 7499 - 7504.
35. Pranoto, Y., Rakshit, S. K. and Salokhe, V. M. (2005). Enhancing antimicrobial activity of chitosan films by incorporating garlic oil, potassium sorbate and nisin. *LWT-Food Science and Technology*, 38(8): 859 - 865.
36. Xuan, X. T., Fan, Y. F., Ling, J. G., Hu, Y. Q., Liu, D. H., Chen, S. G., Ye, X.Q. and Ding, T. (2017). Preservation of squid by slightly acidic electrolyzed water ice. *Food Control*, 73: 1483 - 1489.
37. Xu, Y. X., Kim, K. M., Hanna, M. A. and Nag, D. (2005). Chitosan–starch composite film: Preparation and characterization. *Industrial Crops and Products*, 21(2): 185 - 192.
38. Tongnuanchan, P., Benjakul, S. and Prodpran, T. (2012). Properties and antioxidant activity of fish skin gelatin film incorporated with citrus essential oils. *Food Chemistry*, 134(3): 1571 - 1579.
39. Yuan, G., Lv, H., Yang, B., Chen, X. and Sun, H. (2015). Physical properties, antioxidant and antimicrobial activity of chitosan films containing carvacrol and pomegranate peel extract. *Molecules*, 20(6): 11034 - 11045.
40. Allwin, S. J., Jeyasanta, K. I. and Patterson, J. (2015). Extraction of chitosan from white shrimp (*Litopenaeus vannamei*) processing waste and examination of its bioactive potentials. *Advances in Biological Research*, 9(6): 389 - 396.
41. Chaiyakosa, S., Charernjiratragul, W., Umsakul, K. and Vuddhakul, V. (2007). Comparing the efficiency of chitosan with chlorine for reducing *Vibrio parahaemolyticus* in Shrimp. *Food control*, 18(9): 1031 - 1035.
42. Kirbaşlar, F. G., Tavman, A., Dülger, B. and Türker, G. (2009). Antimicrobial activity of turkish citrus peel oils. *Pakistan Journal of Botany*, 41(6): 3207-3212.

43. Musa, N., Wei, L. S., Seng, C. T., Wee, W. and Leong, L. K. (2008). Potential of edible plants as remedies of systemic bacterial disease infection in cultured fish. *Global Journal of Pharmacology*, 2(2): 31 - 36.
44. Wang, Y. C., Chuang, Y. C. and Hsu, H. W. (2008). The flavonoid, carotenoid and pectin content in peels of citrus cultivated in Taiwan. *Food Chemistry*, 106(1): 277 - 284.
45. Vandeputte, O. M., Kiendrebeogo, M., Rasamiravaka, T., Stevigny, C., Duez, P., Rajaonson, S., Diallo, B., Mol, A., Baucher, M. and El Jaziri, M. (2011). The flavanone naringenin reduces the production of quorum sensing-controlled virulence factors in *Pseudomonas aeruginosa* PAO1. *Microbiology*, 157(7): 2120 - 2132.
46. Márquez-Ríos, E., Morán-Palacio, E. F., Lugo-Sánchez, M. E., Ocano-Higuera, V. M. and Pacheco-Aguilar, R. (2007). Postmortem biochemical behavior of giant squid (*Dosidicus gigas*) mantle muscle stored in ice and its relation with quality parameters. *Journal of Food Science*, 72(7): 356 - 362.
47. Wang, J. J., Lin, T., Li, J. B., Liao, C., Pan, Y. J. and Zhao, Y. (2014). Effect of acidic electrolyzed water ice on quality of shrimp in dark condition. *Food Control*, 35(1): 207 - 212.
48. Tomac, A. and Yeannes, M. I. (2012). Gamma radiation effect on quality changes in vacuum-packed squid (*Illex argentinus*) mantle rings during refrigerated (4 - 5° C) storage. *International Journal of Food Science and Technology*, 47(7): 1550 -1557.
49. Zaragozá, P., Fuentes, A., Ruiz-Rico, M., Vivancos, J. L., Fernández-Segovia, I., Ros-Lis, J. V., Barat, J.M. and Martínez-Máñez, R. (2015). Development of a colorimetric sensor array for squid spoilage assessment. *Food Chemistry*, 175: 315 - 321.

Malaysian Journal of Analytical Sciences, Vol 23 No 6 (2019): 926 - 937
DOI: https://doi.org/10.17576/mjas-2019-2306-02

MALAYSIAN JOURNAL OF ANALYTICAL SCIENCES
Published by The Malaysian Analytical Sciences Society
ISSN 1394 - 2506

ADSORPTION STUDY ON THE REMOVAL OF COPPER IONS FROM AQUEOUS SOLUTION USING SODIUM HYDROXIDE-MODIFIED *Carica papaya* PEELS

(Kajian Penjerapan Dalam Penyingkiran Ion Kuprum Dari Larutan Akueus Menggunakan Kulit *Carica papaya* Yang Dimodifikasikan Dengan Sodium Hidroksida)

Muhammad Shahrain Shuhaimen[1], Erna Normaya Abdulah,[1] Rosliza Mohd Salim[2], Mohd Armi Abu Samah[2], Muhammad Nor Omar[3], Mohammad Norazmi Ahmad[1]*

[1]*Experimental and Theoretical Research Laboratory, Department of Chemistry, Kulliyyah of Science*
[2]*Department of Chemistry, Kulliyyah of Science*
[3]*Department of Biotechnology, Kulliyyah of Science*
International Islamic University of Malaysia, 25200 Kuantan, Pahang, Malaysia

**Corresponding author: mnorazmi85@gmail.com*

Received: 1 August 2018; Accepted: 10 November 2019

Abstract

Recently, environment contamination by heavy metals has gained much attention due to the significant impact on public health. Heavy metals such as copper are non-biodegradable pollutants and they are very difficult to eliminate naturally from the environment. Therefore, this study was conducted to deal with the removal copper from an aqueous solution using a highly efficient, environmentally friendly adsorbent from *Carica papaya* peels (CPP) prepared by chemical treatment of NaOH modification. The effects of adsorbent mass, pH of the aqueous solution, and contact time were studied in batch experiments. The optimum parameters for the removal of copper (79%) are 0.9 g, pH = 3, and 45 minutes. Scanning electron microscopy (SEM) and Fourier transform infrared spectroscopy (FT-IR) were employed to validate the efficiencies of the adsorbents towards copper. FT-IR analysis showed that carboxyl and hydroxyl functional groups were involved in the adsorption of copper ions. As a conclusion, the chemical-treated CPP can be utilized as a potential biosorbent for copper removal from aqueous solutions.

Keywords: *Carica papaya* peels, adsorbent, heavy metal

Abstrak

Sejak kebelakangan ini, pencemaran alam sekitar berpunca dari logam berat telah mendapat banyak perhatian berikutan kesannya yang signifikan terhadap kesihatan awam. Logam berat seperti kuprum adalah bahan pencemar tidak boleh diurai dan ianya sangat sukar untuk disingkirkan secara semula jadi dari alam sekitar. Oleh itu, kajian ini dijalankan untuk menangani penyingkiran tembaga daripada larutan akueus menggunakan penjerap yang berkesan dan mesra alam dari kulit *Carica papaya* (CPP) yang dihasilkan melalui pengolahan secara kimia menggunakan NaOH. Kesan jisim penjerap, pH larutan akueus, dan masa hubungan dikaji dalam eksperimen ini. Parameter optima keberkesanan penjerap untuk menyingkirkan kuprum (79%) adalah pada 0.9 g jisim penjerap, pH = 3, dan 45 minit masa pengeraman. Pengimbas mikroskop elektron (SEM) dan Fourier spektroskopi inframerah Fourier (FT-IR) digunakan untuk mengesahkan kecekapan penjerap untuk menjerap kuprum. Analisis FT-IR menunjukkan bahawa kumpulan berfungsi karboksil dan hidroksil adalah terlibat dalam penjerapan ion kuprum. Sebagai kesimpulan, CPP yang dirawat dengan kimia boleh digunakan sebagai penjerap yang berpotensi untuk penyingkiran kuprum daripada larutan akueus.

Kata kunci: kulit *Carica papaya*, penjerap, dan logam berat

Introduction

Wastewater discharged by industrialization and urbanization into the water stream is a great concern to the world as it is detrimental to living organisms. This is because wastewater contains toxic metals (poisonous soluble metal ions) that may be fatal at high concentration and cannot be degraded easily [1, 2]. Copper (Cu) is one example of a toxic metal that could be discharged from electrical, construction, and household pipes. The two oxidation states of Cu, cuprous (Cu^{+}) and cupric (Cu^{2+}) ions, can form complexes with oxygen-containing ligands and partial covalent bonding with nitrogen- and sulphur-containing cores that can affect the structure and function of biomolecules, to which long-term overexposure can cause health problems [3].

Thus, a safe and effective treatment of wastewater containing toxic metal ions is always a challenge to industrialists and environmentalists. Previously, conventional technologies (ion exchange, chemical precipitation, reverse osmosis, and membrane separation) have been employed to remediate toxic metals pollution [4, 5] However, these are limited by technical (high level of expertise and generation of noxious chemical sludge) and economic (high capital and operational cost) issues [6, 7]. Furthermore, conventional adsorbents have low adsorption capacity and cannot be reused. Therefore, nowadays researchers are looking for other potential and effective materials for toxic metals' removal. Currently, agricultural by-products adsorbents have gained wide attention because of their abundant availability, low cost, renewability, biodegradability, higher efficiency and good reusability [8]. Furthermore, they have a large number of hydroxyl functional groups and a porous structure that are important to bind and complex with the toxic metal ions [3, 9, 10].

In this study, we developed a highly efficient and environmentally friendly adsorbent prepared by chemical modification of *Carica papaya* peels with sodium hydroxide (NaOH). *Carica papaya* was chosen because it is rich with hydroxyl functional groups [11, 12] and easily available in Malaysia (ranked second in the world for exported *Carica papaya*) [13]. The optimization of parameters, namely adsorbent mass, pH, and contact time for adsorption of Cu, was carried out using atomic absorption spectroscopy (AAS). Characterization was performed using scanning electron microscopy (SEM) and Fourier transform infrared spectroscopy (FT-IR) to understand further the physical and chemical properties, respectively.

Materials and Methods

Reagents

Sodium hydroxide (NaOH, ≥98%,), hydrochloric acid (HCl, 35-37%) and copper standard solution (1000 mg/L) were purchased from Sigma-Aldrich (Missouri, USA). Potassium bromide (KBr) was purchased from Merck KGaA (Germany). All reagents were of analytical grade. All experiments were done using ultrapure deionized distilled water (Sartorius Stedim, France).

Preparations of adsorbents

Carica papaya peels (CPP) used were obtained from the local fruit market (Malaysia). Prior to the experiments, the adsorbents were washed, dried, and chemically-treated by soaking completely in 0.1 M NaOH solution in stirred at an ambient temperature of 28 ± 1 °C for 1 hour. Adsorbents were dried in an oven (Memmert GmbH, Germany), at 60 °C for 48 hours. Dried adsorbents were finely ground in a Waring blender and sieved in an automatic siever (Endecotts Limited, London) of size No. 40 (ASTM E11:01) for uniformity in particle size and total surface area across the adsorbents. Untreated adsorbents were also prepared as a control.

Procedures for adsorption of Cu^{2+}

The adsorption of metal ions on the adsorbents was studied by mixing a known mass of adsorbent into 200 mL of 10 mg/L metal adsorbate solution and agitating at 200 rpm speed, at an ambient temperature of 28 ± 1 °C for 1 hour on a magnetic plate stirrer (Wisd Laboratory Instruments, Germany). The experiments were conducted for Cu ions with various parameters such as the adsorbent mass (0.1, 0.3, 0.5, 0.7 and 0.9 g), the pH of the aqueous solution (pH 1, 3, 5, 7 and 9) and the contact time of adsorption (0, 15, 30, 45 and 60 minutes). The pH of the aqueous solutions was adjusted with either 0.1 M NaOH or HCl. The solution was then filtered using Whatman filter paper, Grade 1 (GE Healthcare, Illinois, USA), into a 15 mL Falcon centrifuge tube to filter off solid adsorbents from the metal

adsorbate solution. The metal adsorbate solution filtrate was analysed using AAS (PerkinElmer, Germany) to measure the remaining metal adsorbate concentration and calculate the percentage removal as in Eq. (1).

$$\text{Percentage removal } (\%) = \frac{(C_0 - C_t)}{C_0} \times 100\,, \quad (1)$$

where C_0 is the initial (t = 0 min) liquid-phase concentration of metal adsorbate solution (mg/L) and C_t is the liquid-phase concentration of adsorbate solution at any time t (mg/L).

Characterisation of adsorbents

The surface morphology of the adsorbents between the NaOH-treated and untreated CPP, as well as after the adsorption of copper was analysed using a scanning electron microscope (SEM) (Carl Zeiss Microscopy GmbH, Germany). About 1–2 mg of adsorbent samples were sprinkled on an adhesive tape attached on a knob, and then coated with conductive gold by fitting the knobs into the sputter coater (Leica Microsystems, Singapore) operated in vacuum (10^{-2}–10^{-1} mbar) for 2 hours, followed by a gold-coating process (of thickness 15–20 nm) for 60 s at 45 mA. The samples were then analysed with SEM operated at 10 kV. The functional groups present in these adsorbents were characterised using Fourier Transform Infrared Spectroscopy (FT-IR) (PerkinElmer, Germany) in the mid-infra-red region, 400–4000 cm^{-1}. A blank KBr disc was prepared from KBr powder as the background control. Then, 1–2 mg of the adsorbent powders was mixed together with 300–350 mg KBr powder to produce the sample disc using a hydraulic press for analysis.

Results and Discussion

The effect of adsorbent mass

CPP was ground and sieved to a size of less than 425 μm (No. 40 by ASTM E11:01) for uniformity in particle size and total surface area across the adsorbents. It was established that the smaller the size of the adsorbents, the higher the percentage removal of metal adsorbates [5, 14, 15]. The relationship between adsorbent size and percentage removal is explained by the shell adsorption mechanism which explains the preference of natural organic matter to adsorb on the exterior surface of the adsorbent particles instead of penetrating through it [16]. The increase in the percentage removal is due to the increase in the effective total surface area of the same mass of adsorbents and shortened diffusion path as the size of the adsorbents gets smaller [15, 17]. The smaller adsorbent size also makes the internal pore structure more accessible to the penetration of adsorbates and the large effective surface area provides an increasing number of binding sites [15, 17].

Figure 1 shows the percentage removal of Cu metal ions in aqueous solution between untreated and treated adsorbents. The results show that the sorption is initially fast and then slowed until equilibrium was reached. Cu percentage removal was constant at 0.7 g of untreated adsorbent but for treated adsorbents did not reach a constant value. The increase in percentage removal was due to the enhancement of mass of adsorbents, which increases the total surface area that is exposed to the adsorbate solution, generally allowing more metal adsorbate to be adsorbed onto the adsorbent surface. When the percentage removal graph was horizontal at equilibrium, this shows that all of the binding sites had been taken, leaving behind adsorbates that were impossible or difficult to interact with the adsorption sites (which explains the remaining percentage of unremoved metal adsorbate).

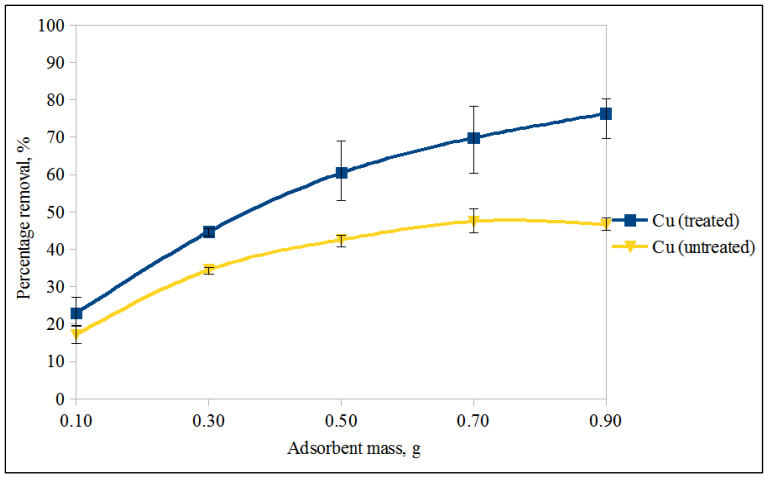


Figure 1. Percentage removal of Cu in aqueous solution (10 mg/L, 200 mL) by varying adsorbent mass of treated and untreated CPP adsorbent (0.1-0.9 g, 200 rpm)

Distinctively, treated adsorbents showed improved percentage removal over untreated adsorbents for Cu removal throughout the adsorbent mass range. Cu adsorbates' adsorption was enhanced from 47% using untreated adsorbents to 76% using the NaOH-treated adsorbents (at a mass of 0.9 g). Ong et al. reported that the introduction of a strong base (such as NaOH in this experiment) to the adsorbents modifies the surface properties of the adsorbent, besides enhancing the solubility and the ionization degree of the metal ions, which would improve the adsorption density [18]. As used in this study, Chong and Thoe reported that 0.1 M NaOH concentration is the optimum concentration that gives the best adsorption of heavy metals onto the adsorbents [19]. This is attributed to the partial solubilisation of lignin and soluble organic components in the adsorbents that have exposed more adsorption sites for the binding of heavy metals [19]. NaOH also removes tannins and de-esterifies, resulting in more active binding sites, which increases the adsorbents' capacity to adsorb metal adsorbates [5]. The 0.1 M NaOH concentration was also utilised in various previous studies [21–24]. In NaOH-treated adsorbents, the total surface negative charge is increased significantly (contributed by the hydroxyl ions in the NaOH solution) and thus encouraging positively charged metal ions such as Cu^{2+} to be adsorbed on the adsorbent [8]. NaOH solution reacts with the functional groups on the adsorbent as characterised by Eq. (2) and Eq. (3) [20]. Therefore, NaOH chemical-modification treatment on the adsorbents was chosen for this experiment to be compared with the untreated adsorbents.

$$ROH + NaOH = RO^{-}Na^{+} + H_2O \quad (2)$$

$$2RO^{-}Na^{+} + M^{2+} = R_2O_2M + 2Na^{+} \quad (3)$$

where R is the functional group on the adsorbent surface and M^{2+} is the metal ion in aqueous solution.

Effect of pH

Figure 2 illustrates the percentage removal of Cu ions in aqueous solution using treated adsorbents by varying the pH of the aqueous solution. The pH can affect both the surface charge of the adsorbents and solubility of metal ions. The point of zero charge (pH_{pzc}) of the functional groups on an adsorbent is the pH at which the groups have no net potential charge (zero charge). The zero charge of the adsorbents may be influenced by the pH of the solution. If the pH of the solution is below pH_{pzc} of a functional group, the group will be protonated by H^{+} ions; in contrast, if the pH is above the pH_{pzc}, the group will be deprotonated instead [7, 11]. For effective adsorption of metal ions, the ionic state of the functional groups on the adsorbents that are involved in adsorption should be in an anionic state (negatively charged) because the metal ions are cations (positively charged) and hence an interaction between them can occur. The change in the charges of the functional groups due to the change of surrounding pH can be generalised by Eq. (4), where R is the functional group on the adsorbent surface.

In general, the percentage removal of Cu was the lowest at pH 1, at 17%. This shows that at pH 1, adsorption on the surface of the adsorbent materials occurs at the most inefficient rate [6, 10, 18]. At lower pH, the carboxyl and phenolic hydroxyl functional groups of the adsorbents exist as their neutral or protonated conformations. The neutral structures, –COOH and –OH, respectively, have no net charge and thus prevent adsorption of any Cu^{2+} ions. These functional groups may also exist in the protonated state of $–CO_2H_2^+$ and $–OH_2^+$, respectively, which repulses same-charged species [25, 26]. Besides, Cu^{2+} ions have to compete with the free excess H^+ ions at low pH for any available adsorption sites. As the pH value increases, the carboxylic group on the adsorbent surface will be deprotonated to become $–COO^-$ followed by deprotonation of phenolic hydroxyl to $–O^-$. Deprotonation of various functional groups on the CPP surface, each with its own pH_{pzc}, formed negatively charged groups that encourage binding to the metal ions. The percentage removal trend showed a sharp increase from pH 1 to reaching the peak at pH between 3 and 5, followed by a sharp decline at higher pH. The deprotonated carboxylic and phenolic hydroxyl groups which are polar functional groups help in metal binding [5]. The percentage removal of Cu was at its highest value, 75%, at pH 3. This is characterised in Eq. (5) as the hydrolysis of Cu^{2+} ions.

$$–RH_2^+ (<pH_{pzc}) \rightleftharpoons –RH (pH_{pzc}) \rightleftharpoons –R^- (>pH_{pzc}) \quad (4)$$

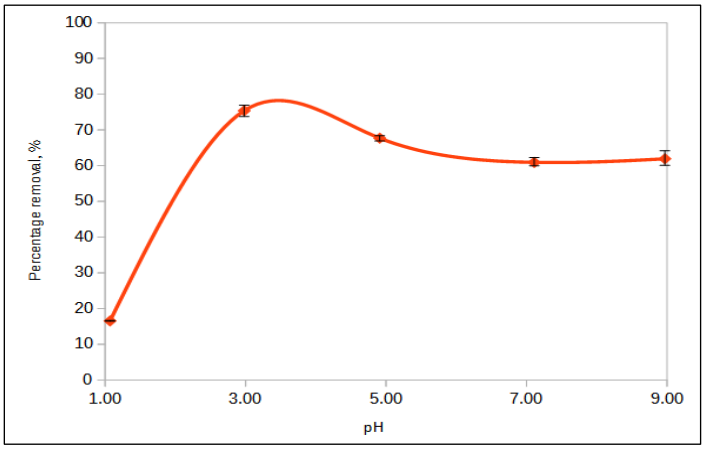


Figure 2. Percentage removal of Cu in aqueous solution (10 mg/L, 100 mL) by varying the pH of the aqueous solution (pH 1-9, 200 rpm, 1 h) using 0.9 g of treated CPP adsorbent

Although the deprotonation of the adsorption sites would increase the attraction of metal cations to the sites, the rising concentration of hydroxyl ions (from the formation of anionic hydroxides) at higher pH changes the ionization degree of the metal ions, and thus hinders their ability to adhere to the adsorption sites on the adsorbents, which explains the decline in percentage removal after the peak pH values [6]. This is characterised in Eq. (5) as the hydrolysis of Cu^{2+} ions.

$$Cu(aq)^{2+} + 2H_2O \rightleftharpoons CuOH^+ + H^+ + H_2O \rightleftharpoons Cu(OH)_2 + 2H^+ \quad (5)$$

Cu^{2+} is the dominant species below pH 6.0, which is involved in adsorption [27]. It was reported that $Cu(OH)^+$ begins to be formed around pH 4 to 5 and $Cu(OH)_2$ is precipitated at pH higher than 6 and therefore not completely removed *via* adsorption [12]. These hydroxyl ions interact with the metal ions to form hydroxide precipitates, which results in the reduction of free metal ions aside from the hydrolysis of metallic ions [6, 7, 18]. The increase in copper precipitation at higher pH causes the percentage removal to appear to flatten between pH 7.0 and 9.0 instead of drastically declining to the level similar to when the pH was 1.0. Cu^{2+} ions, which are detectable by AAS, are only dominant up to pH 7.5 [28]. At pH 6 to 8, Cu^{2+} ions will be hydrolysed, which will result in the formation of

$CuOH^+$ and $Cu(OH)_2$ hydrolysed forms at higher pH [29]. At pH near to 10 and above, the dominant species existing in the solution are $Cu(OH)_2$, $Cu(OH)_3^-$, and $Cu(OH)_4^{2-}$ [30].

Effect of contact time

Figure 3 shows the percentage removal of Cu at various contact times. There was a rapid increase in the percentage removal of Cu during the first 15 minutes of the experiment. The significant increase during the initial duration is because all of the adsorbent surfaces have not taken up any metal adsorbates, and therefore, a large surface area of the adsorbents is readily available and exposed for the adsorption of metal adsorbates to take place [7]. As adsorption of metal adsorbates on the surface of the adsorbents becomes saturated with time, fewer and limited spaces on the adsorbent surface are accessible for new adsorption to take place. The adsorption gradually flattens up to equilibrium at 45 minutes onwards, after which no significant additional removal was observed. At equilibrium, the adsorption rate is equal to the desorption rate. The highest percentage removal for Cu removal achieved at equilibrium (at minute 45) is 79%. A similar trend was also recorded in previous literature [6], where the adsorption flattens at an equilibrium.

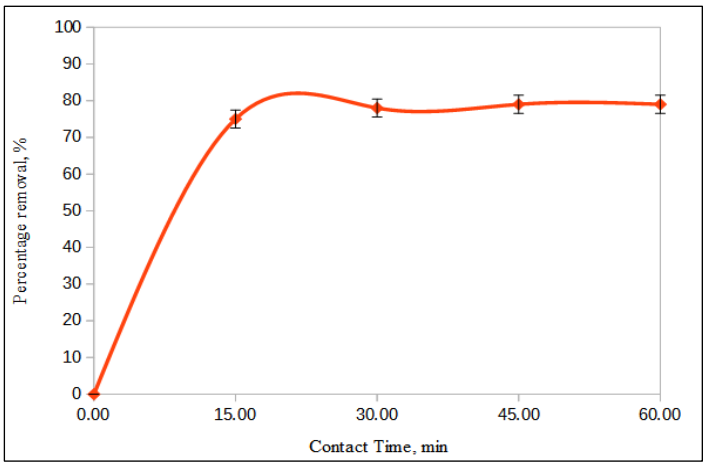


Figure 3. Percentage removal of Cu in aqueous solution (100 mL, 10 mg/mL) at various contact time intervals (0-60 minutes) using 0.9 g of treated CPP, adsorbents (pH 3, 200 rpm)

SEM analysis of adsorbents

It was observed that porous cavities did not exist in the untreated adsorbents in Figure 4, but the surface structure of NaOH-treated adsorbents in Figure 5 appeared to have porous cavities. The porous structure was also observed in previous literature on NaOH-treated adsorbents [31–33]. NaOH acts as an activating agent for the adsorbent, enlarging the pore size on the surface resulting from reduction and oxidative modifications [34]. A theory proposed by Pezoti et al. is that the reactions between active intermediates in the NaOH solution and the carbon surface of the adsorbent will cause the evolution of H_2, CO_2 and CO, and subsequently lead to the development of porosity [34]. The reactions are given in Eq. (6), Eq. (7) and Eq. (8) [34].

$$6NaOH + 2C \rightarrow 2Na + 2Na_2CO_3 + 3H_2 \uparrow \quad (6)$$

$$Na_2CO_3 \rightarrow Na_2O + CO_2 \uparrow \quad (7)$$

$$2Na + CO_2 \rightarrow Na_2O + CO \uparrow \quad (8)$$

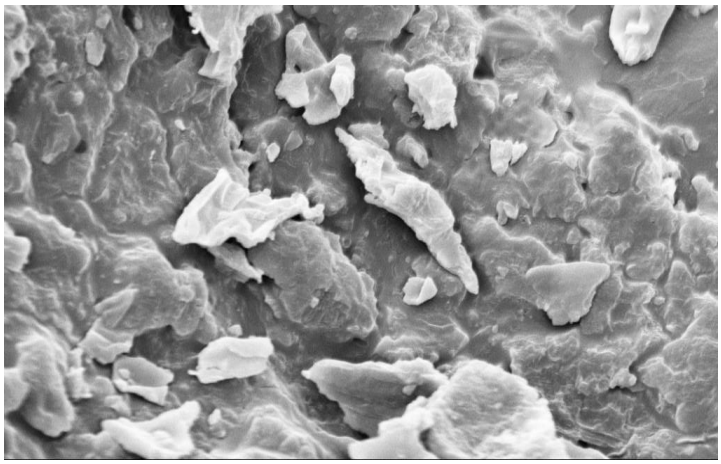


Figure 4. SEM micrograph of untreated CPP adsorbents at 2000x magnification (operating at 10 kV)

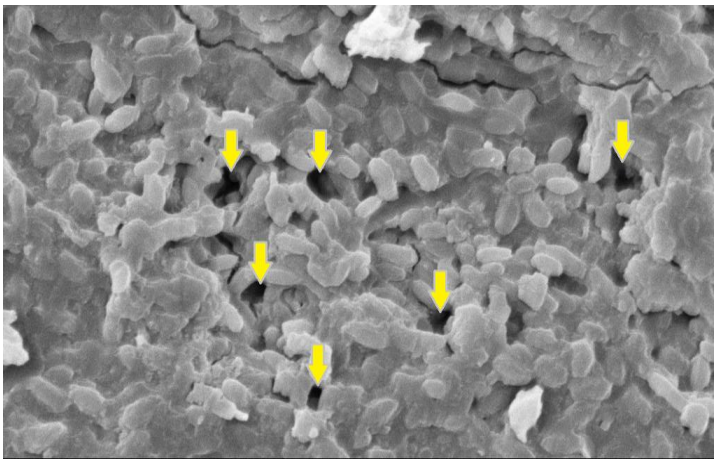


Figure 5. SEM micrograph of treated CPP adsorbents at 3500x magnification (operating at 10 kV). The arrows show the appearance of pores on the surface structure of treated adsorbents

These porous cavities provide an increased specific surface area available for penetration of metal adsorbates through the pores, allowing interactions with the surface functional groups and therefore increasing its adsorption capacity [35]. This porous structure provides more ligands for metal ion binding. Alkaline activation of adsorbents also allows the hydrolysis of surface functional groups to carboxylate ion ($–COO^-$) and alcohol (–OH) groups, which promotes cationic adsorption [35]. Figure 6 shows the adsorption of Cu ions on the surface structure of the treated adsorbents.

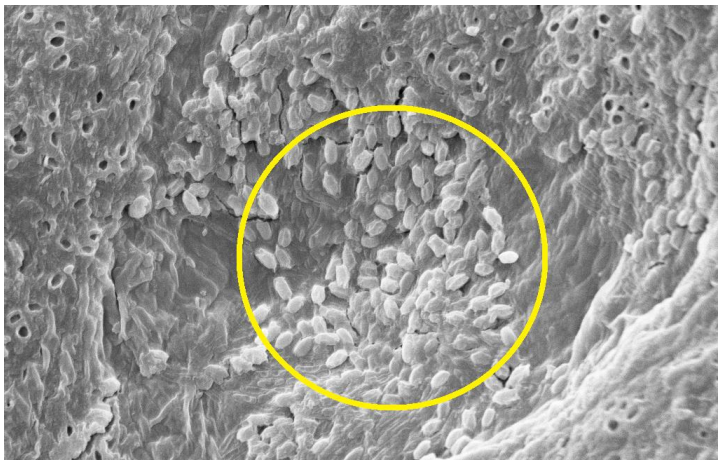


Figure 6. SEM micrograph of treated CPP adsorbents with adsorbed Cu ions at 2000x magnification (operating at 10 kV). The circle shows the presence of oviform Cu ions on the adsorbent surface

FT-IR analysis of adsorbents

Spectral characteristics of the adsorbents are recorded in Table 1. In general, for both treated and untreated adsorbents' spectra, the wavenumber range 3500–3200 cm^{-1} shows the broad absorption band of O–H stretching (can be assigned to alcohols, carboxylic acids and phenols). Two strong sharp absorptions of C–H stretching were present at wavenumbers in the range 2900–2850 cm^{-1} and 2850–2800 cm^{-1} that can be assigned to alkanes and carboxylic acids, which can be associated with the C–H stretching of the methyl sp^3 substituent. The wavenumber range 1750–1730 cm^{-1} displays a medium absorption of C=O stretching that can be assigned to the carbonyl functional group, from carboxylic acids or their esters. Another strong sharp absorption is visible in the wavenumber range 1680-1600 cm^{-1}, signifying the C=C stretching of alkenes. In the fingerprint region, two medium sharp absorptions were observed in the wavenumber range 1450–1375 cm^{-1} indicating the presence of $–CH_3$ symmetric bending. Various medium intensity peaks were observed in the wavenumber range 1300–1000 cm^{-1} and 950–690 cm^{-1} representing, respectively, C–O stretching and aromatic C–H group, out-of-plane bending. Major shifts were observed between the untreated and NaOH-treated adsorbents. The 3377 cm^{-1} peak in untreated adsorbents shifted to 3395 cm^{-1} in treated adsorbents, the 1413 cm^{-1} peak shifted to 1425 cm^{-1} and the 1105 cm^{-1} peak shifted to 1152 cm^{-1}. Other shifts apart from those mentioned are small. These visible shifts to a higher wavenumber are associated with a stronger bond that resulted in the formation of gases as demonstrated in Eqs. (6 – 8) as the result of NaOH solution interactions with the functional groups on the adsorbent [34].

Comparing before and after the metal adsorptions, the wavenumber shifts indicated the location at which the metal ions formed bonds. Cu ions interact with the –OH group region on the adsorbent as illustrated by the wavenumber shifts from 3395 cm^{-1} (before adsorption) to 3421 cm^{-1}. Another major shift is in the C=O stretching region where the wavenumber shifted from 1732 cm^{-1} before the adsorption to 1726 cm^{-1} after metal adsorptions for Cu ions, suggesting the formation of hydrogen bonding with hydroxyl oxygen (HO–C=O) [34]. Previous literature also showed that the shift in –OH, C–H bending, –C=O stretching vibration and –C=O functional groups spectra were caused by metal adsorption [35,37,38]. Figure 7 further characterises the spectral features of the adsorbents.

Table 1. FT-IR spectral characteristic of CPP adsorbents

Region	Wavelength Range (cm^{-1})	Before Adsorption		After Adsorption Cu	Assignment
		Untreated	Treated		
A	3500-3200	3377	3395	3421	H-bonded O–H group
B					C–H sp^3 stretching
	3000-2850	2925	2923	2922	(Alkanes)
	2900-2800	2859	2856	2859	(Aldehyde)
C	1750-1730	1732	1732	1726	C=O stretching (Ester)
D	1680-1600	1640	1639	1639	C=C alkenes
E	1450-1375	1413	1425	1426	$–CH_3$ symmetric bending
		1378	1378	1378	
F	1300-1000	1329	1329	1329	C–O stretching
		1248	1248	1248	
		1105	1152	1154	
		1060	1060	1060	
G	950-690	900	900	900	C–H aromatics, out-of-plane bending

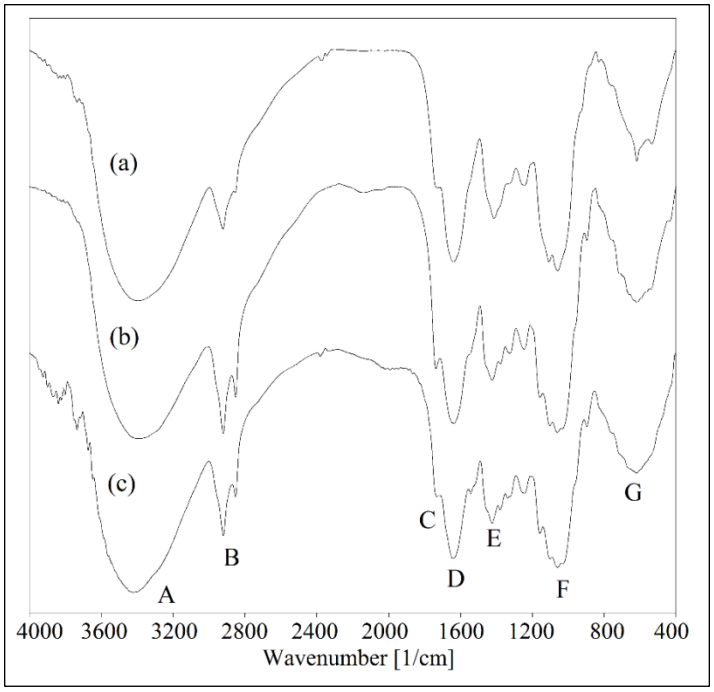


Figure 7. FT-IR spectra of (a) untreated adsorbents, (b) NaOH-treated adsorbents and (c) Cu-loaded adsorbents. Labels A to G are the peak regions, denoted in Table 1.

In *Carica papaya*, lignin and cellulose are the major constituents of its peel, which is embedded with polar functional groups including alcohols, aldehydes, ketones, carboxylic acids, ethers, and prominent phenolics (such as ferulic acid, caffeic acid and rutin) in the peel and carotenoids (such as lycopene) in the seeds, which are capable of binding to toxic metal ions via electron pair donation to form complexes [6, 11, 12].

Conclusion

A biosorbent was successfully produced from *Carica papaya* peels (CPP), by NaOH-treated modification, and was tested of its adsorption potential on the removal of Cu ions from an aqueous solution. The effects of adsorbent mass, pH and contact time were studied in batch experiments and the optimum value of adsorbent mass, pH of the aqueous solution, and contact time for Cu removal are 0.9 g, pH = 3, and 45 minutes, respectively. The optimum percentage removal of Cu ions obtained was 79%. The results from SEM and FT-IR further validate the efficiency of the CPP adsorbent in removing Cu from aqueous solution. FT-IR analysis showed that carboxyl and hydroxyl functional groups were involved in the adsorption of copper ions. It is suggested for future investigations to study on the combinations of different adsorbent sources into a singular composite material to test the synergistic effects they have on the adsorption of hazardous heavy metals. It is hoped that studies as these could be taken up by the industries to further investigates, manufacture and commercialize a practical biosorbent materials that can be utilized in the industrial and household sectors.

Acknowledgement

The project was funded by the International Islamic University Malaysia (Grant No. IRF 19-014-0014).

References

1. Drinking-water Quality Committee. (2011). Guidelines for Drinking-water Quality. Geneva: World Health Organization.
2. Othman, N., Asharuddin, S. M., and Rahman, M. F. H. A. (2013). An overview of fruit waste as sustainable adsorbent for heavy metal removal. *Applied Mechanics and Materials*, 389: 29 – 35.
3. Environmental Health Criteria 200 (1998). Copper. Geneva: World Health Organization.
4. Krishna, R. H., and Swamy, A. V. V. S. (2012). Physico-chemical key parameters, Langmuir and Freundlich isotherm and lagergren rate constant studies on the removal of divalent nickel from the aqueous solutions onto powder of calcined brick. *International Journal of Engineering Research and Development*, 4(1): 29 – 38.
5. Mathew, B. B., Jaishankar, M., Biju, V. G., and Beeregowda, K. N. (2016). Role of bioadsorbents in reducing toxic metals. *Journal of Toxicology*, 2016: 4369604.
6. Hadi, N. A., Rohaizar, N. A., and Sien, W. C. (2011). Removal of Cu(II) from water by adsorption on papaya seed. *Asian Transactions on Engineering*, 1(5): 49 – 55.
7. Abas, S. N. A., Ismail, M. H. S., Kamal, M. L., and Izhar, S. (2013). Adsorption process of heavy metals by low-cost adsorbent: A review. *World Applied Sciences Journal*, 28(11): 1518 – 1530.
8. Kyzas, G. Z., and Kostoglou, M. (2014). Green adsorbents for wastewaters: A critical review. *Materials*, 7(1): 333 – 364.
9. Saka, C., Şahin, O., and Kucuk, M. M. (2012). Applications on agricultural and forest waste adsorbents for the removal of lead (II) from contaminated waters. *International Journal of Environmental Science and Technology*, 9(2): 379 – 394.
10. Kanyal, M., and Bhatt, A. A. (2015). Removal of heavy metals from water (Cu and Pb) using household waste as an adsorbent. *International Biodeterioration and Biodegradation*, 6(1): 269 – 275.
11. Ghani, N. T. G., and El-Chaghaby, G. A. (2014). Biosorption for metal ions removal from aqueous solutions: A review of recent studies. *International Journal of Latest Research in Science and technology*, 3(1): 24 – 42.
12. Nasuha, N., Zurainan, H. Z., Maarof, H. I., Zubir, N. A., and Amri, N. (2011). Effect of cationic and anionic dye adsorption from aqueous solution by using chemically modified papaya seed. *International Conference on Environmental Science and Engineering*, 8: 50 – 54.
13. Hameed, B. H. (2009). Evaluation of papaya seeds as a novel non-conventional low-cost adsorbent for removal of methylene blue. *Journal of Hazardous Materials*, 162(2): 939 – 944.
14. Mondal, P., Majumder, C. B., and Mohanty, B. (2008). Effects of adsorbent dose, its particle size and initial arsenic concentration on the removal of arsenic, iron and manganese from simulated ground water by Fe^{3+} impregnated activated carbon. *Journal of Hazardous Materials*, 150: 695 – 702.

15. Stankovic, M. N., Krstic, N. S., Mitrovic J. Z., Najdanovic S. M., Petrovic, M. M., Bojic, D. V. and Bojic, A. L. (2016). Biosorption of copper(II) ions by methyl-sulfonated *Lagenaria vulgaris* shell: Kinetic, thermodynamic and desorption studies. *New Journal of Chemistry*, 40(3): 2126 – 2134.
16. Matsui, Y., Yoshida, T., Nakao, S., Knappe, D. R. U., and Matsushita, T. (2012). Characteristics of competitive adsorption between 2-methylisoborneol and natural organic matter on superfine and conventionally sized powdered activated carbons. *Water Research*, 26: 4741 – 4749.
17. Shafiq, M., Alazba, A. A., and Amin, M. T. (2018). Removal of heavy metals from wastewater date palm as a biosorbent: a comparative review. *Sains Malaysiana*, 47: 35 – 49.
18. Ong, S. T., Yip, S. P., Keng, P. S., Lee, S. L., and Hung, Y. T. (2012). Papaya (*Carica papaya*) seed as a low-cost sorbent for zinc removal. *African Journal of Agricultural Research*, 7(5): 810 – 819.
19. Chong, H. L. H., and Thoe, J. M. L. (2018). Impact of sodium hydroxide concentration and reaction time on the modification of empty fruit bunch for heavy metal adsorption. *ASM Science Journal*, 11(2): 164 – 170.
20. Argun, M. E., and Dursun, S. (2007). Activation of pine bark surface with NaOH for lead removal. *Journal of International Environmental Application and Science*, 2(1 -2): 5 – 10.
21. Afroze, S., Sen, T. K., and Ang, H. M. (2016). Adsorption removal of Zinc (II) from aqueous phase by raw and base modified *Eucalyptus sheathiana* Bark: Kinetics, mechanism and equilibrium study. *Process Safety and Environment Protection*, 102: 336 – 352.
22. Khokhar, A., Siddique, Z., and Misbah. (2015). Removal of heavy metal ions by chemically treated *Melia azedarach L.* leaves. *Journal of Environmental Chemical Engineering*, 3: 944 – 952.
23. Feng, N. C., Guo, X. Y., Liang, S. (2010). Enhanced Cu(II) adsorption by orange peel modified with sodium hydroxide. *Transactions of Nonferrous Metals Society of China*, 20: 146 – 152.
24. Hu, C., Li, J., Zhou, Y., Li, M., Xue, F., and Li, H. (2009). Enhanced removal of methylene blue from aqueous solution by pummelo peel pretreated with sodium hydroxide. *Journal of Health Science*. 55(4): 619 – 624.
25. Al-Degs, Y., El-Barghouthi, M. I., El-Sheikh, A., and Walker, G. (2008). Effect of solution pH, ionic strength, and temperature on adsorption behavior of reactive dyes on activated carbon. *Dyes and Pigments*, 77: 16 – 23.
26. Cismesia, A. P., Nicholls, G. R., and Polfer, N. C. (2016). Amine vs. carboxylic acid protonation in ortho-, meta-, and para-aminobenzoic acid: An IRMPD spectroscopy study. *Journal of Molecular Spectroscopy*, 332: 79 – 85.
27. Hossain, M. A., Ngo, H. H., Guo, W. S., and Nguyen, T. V. (2012). Removal of copper from water by adsorption onto banana peel as bioadsorbent. *International Journal of GEOMATE*, 2(2): 227 – 234.
28. Albrecht, T. W. J., Addai-Mensah, J., and Fornasiero, D. (2011). Effect of pH, concentration and temperature on copper and zinc hydroxide formation/precipitation in solution. In proceedings of CHEMECA 2011 – Engineering a Better World, Sydney, New South Wales, September 18–21: 2100 – 2110.
29. Torapava, N. (2011). Hydration, solvation and hydrolysis of multicharged metal ions. Thesis of PhD Degree. Uppsala: Swedish University of Agricultural Sciences.
30. Wang, X., and Wang, C. (2016). Chitosan-poly(vinyl alcohol)/attapulgite nanocomposites for copper(II) ions removal: pH dependence and adsorption mechanisms. *Colloids and Surfaces A: Physicochemical and Engineering Aspects*, 500: 186 – 194.
31. Nasuha, N., and Hameed, B. H. (2011). Effect of cationic and anionic dye adsorption from aqueous solution by using chemically modified papaya seed. *Chemical Engineering Journal*, 166(2): 783 – 786.
32. Chowdhury, S., Mishra, R., Saha, P., and Kushwa, P. (2011). Adsorption thermodynamics, kinetics and isosteric heat of adsorption of malachite green onto chemically modified rice husk. *Desalination*, 265(1): 159 – 168.
33. Pua, F. L., Sajab, M. S., Chia, C. H., Zakaria, S., Rahman, I. A., and Sali, M. S. (2013). Alkaline-treated cocoa pod husk as adsorbent for removing methylene blue from aqueous solutions. *Journal of Environmental Chemical Engineering*, 1(3): 460 – 465.
34. Pezoti, O., Cazetta, A. L., Bedin, K. C., Souza, L. S., Martins, A. C., Silva, T. L., and Almeida, V. C. (2016). NaOH-activated carbon of high surface area produced from guava seeds as a high-efficiency adsorbent for amoxicillin removal: Kinetic, isotherm and thermodynamic studies. *Chemical Engineering Journal*, 288: 778 – 788.
35. Lalhruaitluanga, H., Jayaram, K., Prasad, M. N. V., and Kumar, K. K. (2010). Lead (II) adsorption from aqueous solutions by raw and activated charcoals of *Melocanna baccifera* Roxburgh (bamboo) - A comparative study. *Journal of Hazardous Materials*, 175(1): 311 – 318.

36. Nie, B., Stutzman, J., and Xie, A. (2005). A vibrational spectral maker for probing the hydrogen-bonding status of protonated Asp and Glu residues. *Biophysical Journal*, 88(4): 2833 – 2847.
37. Iqbal, M., Saeed, A., and Zafar, S. I. (2009). FTIR spectrophotometry, kinetics and adsorption isotherms modeling, ion exchange, and EDX analysis for understanding the mechanism of Cd^{2+} and Pb^{2+} removal by mango peel waste. *Journal of Hazardous Materials*, 164 (1): 161 – 171.
38. Gilbert, U. A., Emmanuel, I. U., Adebanjo, A. A., and Olalere, G. A. (2011). Biosorptive removal of Pb^{2+} and Cd^{2+} onto novel biosorbent: defatted *Carica papaya* seeds. *Biomass & Bioenergy*, 35(7): 2517 – 2525.

Malaysian Journal of Analytical Sciences, Vol 23 No 6 (2019): 938 - 949
DOI: https://doi.org/10.17576/mjas-2019-2306-03

MALAYSIAN JOURNAL OF ANALYTICAL SCIENCES
Published by The Malaysian Analytical Sciences Society
ISSN 1394 - 2506

PREPARATION AND CHARACTERISATION OF HYDROXYAPATITE EXTRACTED FROM FISH SCALE WASTE FOR THE REMOVAL OF GALLIC ACID AS INHIBITOR IN BIOFUEL PRODUCTION

(Penyediaan dan Perincian Hidroksiapatit yang Diekstrak daripada Sisa Sisik Ikan untuk Penyingkiran Asid Galik sebagai Perencat dalam Pemprosesan Bahan Api Bio)

Nurul Fakhriah Ismail[1], Sofiah Hamzah[1]*, Nurul Ashraf Razali[1], Wan Mohd Hafizuddin Wan Yussof[2], Nora'aini Ali[1], Abdul Wahab Mohammad[3]

[1]*Faculty of Ocean Engineering Technology and Informatics, Universiti Malaysia Terengganu, 21300 Kuala Nerus, Terengganu, Malaysia*
[2]*Faculty of Chemical and Natural Resources Engineering, Universiti Malaysia Pahang, Lebuhraya Tun Razak, 26300 Kuantan, Pahang, Malaysia*
[3]*Faculty of Engineering and Built Environment, Universiti Kebangsaan Malaysia, 43600 UKM Bangi, Selangor, Malaysia*

**Corresponding author: sofiah@umt.edu.my*

Received: 13 December 2018; Accepted: 20 October 2019

Abstract

Acid pre-treatment of lignocellulosic waste to produce fermentable sugar for the production of bioethanol and biofuel has created phenolic compounds, aliphatic acid, and furfural. These compounds are recognised as inhibitors in the fermentation process, which could reduce the final product yield. This is a preliminary study that is focused on the potential of hydroxyapatite (HAp) extracted from fish scale for the removal of phenolic compounds (gallic acid was used as a model solution). HAp was extracted *via* a modified enzymatic hydrolysis at various temperatures (500 °C, 600 °C, 700 °C, 800 °C, 900 °C, 1,000 °C) and calcined for 4 hours. The extracted HAp was characterised using Fourier transform infrared spectroscopy (FTIR), X-ray diffraction (XRD), and scanning electron microscope (SEM). Batch adsorption was conducted to select the best adsorbent and to study the effects of initial concentration, time, dosage, and temperature. The results showed gallic acid removal of 78.9% in 100 mg/L of initial gallic acid concentration, which were adhered by HAp800. This adsorption process fit the Freundlich isotherm (r^2 = 0.9951) better than to Langmuir isotherm. The kinetics of adsorption most fitted the pseudo-second order (0.996).

Keywords: batch adsorption, Langmuir, Freundlich, first-order, Pseudo-second order

Abstrak

Pra-rawatan asid terhadap sisa lignoselulosa untuk menghasilkan gula boleh tapai dalam penghasilan bioetanol dan bahan api bio telah menghasilkan sebatian fenolik, asid alifatik, dan furfural. Sebatian ini dikenal pasti sebagai perencat dalam proses penapaian yang akan mengurangkan hasil akhir produk. Kajian awal ini adalah bertujuan untuk mengkaji potensi hidroksiapatit (HAp) yang diekstrak daripada sisik ikan untuk menyingkirkan sebatian fenolik (asid galik digunakan sebagai model larutan). HAp diekstrak melalui proses hidrolisis enzimatik yang diubahsuai pada suhu yang berbeza (500 °C, 600 °C, 700 °C, 800 °C, 900 °C, 1000 °C) dan dikalsin selama 4 jam. HAp yang diekstrak telah dianalisis menggunakan spektroskopi inframerah transformasi Fourier (FTIR), pembiasan sinar-X (XRD), dan mikroskop elektron pengimbas (SEM). Penjerapan kelompok dilakukan untuk memilih penjerap terbaik dan untuk mengkaji kesan kepekatan awal sampel, masa penjerapan, dos penjerap, dan suhu penjerapan. Hasil kajian menunjukkan sebanyak 78.9% asid galik berjaya disingkirkan dalam 100 mg/L kepekatan awal asid galik yang dijerap oleh HAp800. Proses penjerapan ini isoterma dan kinetik HAp800 dan HAp/Chi berpadanan lebih baik

dengan isoterma Freundlich (r^2 = 0.9951) berbanding dengan isoterma Langmuir. Kinetik penjerapan lebih berpadanan dengan pseudo tertib kedua (0.996).

Kata kunci: penjerapan kelompok, Langmuir, Freundlich, kinetik tertib pertama, kinetik pseudo tertib kedua

Introduction

The world's fossil energy reserves will be depleted within a few decades and the environmental issues are causing major concerns and forcing authorities to find alternative sources of energy. Concern over the adverse economic effect of the depleting energy sources, namely, oil, gas, and coal, has driven the production of biofuel and bioethanol from biomass waste as substitutes. The lignocellulosic hydrolysate of biomass waste (plant-based) consists of fermentable sugar. The fermentation process will produce biofuel and bioethanol *via* anaerobic degradation [1]. However, undesirable compounds, such as phenolic compound, aliphatic acid, and furfural will also be produced due to the extreme condition during acid hydrolysis [2]. As an inhibitor, phenolic compounds will remain unconverted during the process, which would lead to a higher reduction of hydrogen yield, as oppose to other inhibitors [3]. Phenolic compounds will inhibit the process and lead to phenolic-protein precipitation [4]. Thus, several methods have been introduced to overcome this situation, including biological, chemical, and physical methods [5]. Biological methods are rather complicated because enzymes and bacterial strains would be involved. These methods are also ineffective because they are expensive and time consuming. Physical and chemical adsorptions that use adsorbents are the simplest method to remove inhibitors. Natural materials can be utilised as adsorbents, such as activated carbon, chitosan, and biosorbents for the adsorption of organic matters, such as gallic acid and salicylic acid [6]. Gallic acid is a form of phenolic compound that can be found in plant hydrolysate. This study will focus on the adsorption of gallic acid using hydroxyapatite (HAp).

Hydroxyapatite ($Ca_5(PO_4)_3OH$) or calcium phosphate apatite is the main component in hard tissues, such as scales, shells, bones, and teeth [7] and it is abundantly present in nature. HAp has many applications in the biomedical fields for the reconstruction of human bones, as bone implants, dental paste, and bone cement [8]. HAp is chemically stable in a physiological environment, has high biocompatibility, and induces specific biological activity [7]. These traits are suitable for the chromatographic separation of polypeptides and proteins [9]. A recent study employed HAp to remove heavy metals in soil and water [8] and it is widely used in dye removal processes [10]. Zou et al. reported the successful removal of heavy metal ions, including Hg^{2+}, Pb^{2+}, and Zn^{2+} using hydroxyapatite with different morphologies [11]. Alumina-hydroxyapatite composites were also employed for phenol removal in which the hydroxyapatite was extracted from phosphate [12].

Indeed, various methods have been developed to extract natural HAp due to the high cost of commercially available HAp. The extraction of HAp from its natural sources must be taken into consideration. Fish processing industries produce approximately 50% of waste [13], which consists of 4% of fish scales. HAp from fish scales can be synthesised via alkaline hydrolysis [13], enzymatic hydrolysis [14], and hydrothermal hydrolysis [15] methods. Good quality HAp was successfully extracted from biomass, such as shells, animal bones, and fish scales [8]. The present work has extended the findings in the previous study by extracting HAp from fish scales *via* enzymatic hydrolysis for phenolic acid removal.

Materials and Methods

Material

Fish scales (500 g) were collected from local markets around Kuala Terengganu. Protease enzyme from Bacillus complex (Protamex®) and commercial hydroxyapatite were purchased from Sigma-Aldrich. Gallic acid monohydrate ($C_7H_6O_5$) (molecular weight = 170 g/mol) was purchased from ACS reagent. All chemicals are of analytical grades.

Hydroxyapatite sample extraction

Fish scales were collected and washed several times using tap water to remove flesh, gills, and other impurities. Then, the fish scales were dried in static air at 80 °C for 24 hours. The dried fish scales were boiled for 3 hours, while being stirred at 450 rpm using an overhead stirrer. The fish scales were filtered and washed using distilled water. Next, the boiled fish scales were dried at 80 °C for 24 hours. Then, the fish scales were ground into powder

using an analytical mill (IKA A11 basic analytical mill) and the resulting powder was treated with 1% of Protamex® solution for 3 hours in an optimum controlled temperature (40 °C) at pH 9. Next, the mixture was washed with distilled water and centrifuged. The white precipitate that formed was dried at 80 °C for 24 hours and left to cool down to room temperature. The resulting HAp was calcined at different temperatures of 500 °C (HAp500), 600 °C (HAp600), 700 °C (HAp700), 800 °C (HAp800), 900 °C (HAp900), and 1,000 °C (HAp1000) for 4 hours.

Characterisation of HAp

The morphology of the synthesised HAp was studied using a scanning electron microscope (SEM) (JEOL JSM 5410 & JSM 5300, Japan). The samples were first prepared by coating them with gold. Then, the FTIR IRTracer-100 from Shimadzu was used to study the surface functionalities of HAp. The spectra were collected at a range of 4,000 to 400 cm^{-1} with a resolution of 4 cm^{-1}. HAp samples were prepared using the potassium bromide (KBr) pellet method. The crystallographic phases were studied using a Rigaku Mini Flex II desktop X-Ray diffractometer employing 18 kW CuKα radiation, with 45 kV of voltage, current of 40 mA, and λ at 1.5406 Å. Data were collected from 2θ = 20°–80°. Then, the collected data were analysed using search-match software and compared with the powder diffraction data (PDF no-796940).

Batch adsorption study

A model of the phenolic compound was prepared by mixing gallic acid monohydrate and deionised water as solvent. Batch adsorption was conducted at the initial concentration of 50–100 mg/L with different HAp dosages from 1 to 25 g/L. These adsorption reactions were conducted at 10 °C to 60 °C. The samples were shaken for 30 to 480 minutes in an incubator shaker that was set at 240 rpm. Then, the HAp was filtered using Whatman™ 1002-125 filter paper with pore size of 8 µm. The final concentration of gallic acid was quantified using blue Prussian method. The experimental work was repeated three times to ensure the reproducibility of the experimental data. The percentage removal (R_t) of gallic acid at any given time was calculated using the following Eq. (1):

$$R_t = \left(\frac{C_0 - C_t}{C_0}\right) \text{x } 100 \quad (1)$$

where C_0 is the initial concentration of gallic acid (mg/L) and C_t is the concentration of gallic acid at the specific time [9].

The adsorption capacity was calculated using the following Eq. (2):

$$Q_e = V\frac{(C_0 - C_t)}{m} \quad (2)$$

where Q_e is the amount of gallic acid adsorbed at equilibrium (mg/g), V is the volume of gallic acid (L), and m is the mass of adsorbents (g).

Analysis of adsorption isotherm

Langmuir and Freundlich isotherm models were used to analyse the adsorption behaviour of the adsorption process. A comparison between these isotherms is important to develop the equation that will accurately represent the results [16]. These models describe the adsorption based on different assumptions. Langmuir isotherm assumes that the adsorption is homogenous and monolayer, with no interaction between the adsorbed molecules [17].The linear Langmuir equation is presented by the following Eq. (3):

$$\frac{C_e}{Q_e} = \frac{1}{q_m K_L} + \frac{1}{q_m} C_e \quad (3)$$

where C_e is the gallic acid concentration at equilibrium (mg/L), Q_e is the amount of gallic acid adsorbed at equilibrium (mg/g) calculated from Eq. (2), K_L is Langmuir isotherm constant (L/mg), and q_m is the maximum amount of gallic acid adsorbed per unit weight of adsorbent (mg/g) [13]. On the other hand, Freundlich isotherm was developed to recover the constraints of Langmuir isotherm. Freundlich model is an empirical model that is valid

for heterogeneity, which takes into account the multisite adsorption that might exist between the adsorbate molecules [18]. The Freundlich equation and its linear term are presented by the following Eqs. (4) and (5), respectively:

$$Q_e = K_F C_e^{1/n} \tag{4}$$

$$\ln Q_e = \ln K_F + \frac{1}{n} C_e \tag{5}$$

where Q_e is the amount of gallic acid adsorbed at equilibrium (mg/g) calculated from Eq. (2), C_e is the gallic acid concentration at equilibrium (mg/L), K_F is Freundlich isotherm constant (L/mg), and n is the empirical parameter related to the intensity of adsorption, which varies with the heterogeneity of the material. When n values are in the range of $0.1 < 1/n < 1$, the adsorption process is favourable [19].

Kinetic analysis of adsorption

Kinetic analysis of adsorption is a theoretical study that describes the adsorption rate constant of adsorbate to adsorbent, as well as explains the possible reaction mechanisms related to the adsorption [20]. Thus, it is a critical analysis for selecting optimum condition parameters, especially in designing and modelling the process [19]. In this batch adsorption, three mostly used kinetic analyses (first-order, pseudo-second order, and intraparticle diffusion) were applied to the experimental data. First-order kinetic model is mainly used for the adsorption of solute from a liquid solution [13]. The equation is shown by Eq. (6):

$$\frac{1}{q_t} = \frac{K_1}{q_1}\frac{1}{t} + \frac{1}{q_1} \tag{6}$$

where q_1 and q_t are the amounts of gallic acid adsorbed on adsorbent at equilibrium (mg/g) and at various times (t), respectively. K_1 is the rate constant (min^{-1}) of the first-order model for the adsorption process. The graph of $1/qt$ against $1/t$ was plotted. The values of K_1 and q_1 were calculated from the slope and y-intercept, respectively. The pseudo-second order model is usually used to describe the sorption capacity of the solid phase [17]. This model assumes that chemisorption is the main process of the adsorption [21]. Another assumption by this kinetics model is that the removal of solute from the solution could be due to physiochemical interaction with surface adsorption, which is the rate limiting step [20]. The pseudo-second order model is expressed by the following Eq. (7) [22]:

$$\frac{t}{q_t} = \frac{1}{K_2 (q_2)^2} + \frac{t}{q_2} \tag{7}$$

where q_2 is the maximum adsorption capacity (mg/g) for the pseudo-second order adsorption, q_t is the amount of phenol (mg/g) at time t (min), and K_2 is the rate constant of the pseudo-second order adsorption (g/(mg.min)). Values of K_2 and q_2 were calculated from the plot of t/qt against t.

Another kinetic model applied in this study was the intraparticle diffusion model. The equation is expressed by the following Eq. (8):

$$q_t = K_3 t^{1/2} + C \tag{8}$$

where q_t is the amount of gallic acid adsorbed (mg/g) at time t (min), C is the intercept, and K_3 is the intraparticle diffusion rate constant (mg/(g.min$^{1/2}$)). Values of K_3 and C were calculated from the plot of q_t against $t^{(1/2)}$ [16]. According to this model, the graph of q_t versus $t^{(1/2)}$ should be linear or multi-linear if the intraparticle diffusion is involved in the overall adsorption mechanism [23].

Results and Discussion

Characterisation study: Fourier transform infrared

The FTIR analysis was conducted to identify the surface functionalities of HAp samples that were calcined at 500 °C to 1,000 °C. The spectra of HAp prepared in-house were compared with commercial HAp, as shown in Figure 1. The peak appearing at 3431 to 3560 cm^{-1} confirmed the presence of hydroxyl group (OH^-), which indicates that water was adsorbed onto the surface of HAp [13]. Peaks detected at 1436 - 1649 cm^{-1} describe the presence of the carbonate group (CO_3^{2-}). The source of carbonate may originate from CO_2 in atmosphere [24] or it may be from the HAp itself. The stretching bands of OH^- and CO_3^{2-} have decreased with increasing calcination temperature. This condition can be explained by loses of water adsorbed and by decarbonation process (releasing of the CO_3^{2-} group) to calcium oxide [13]. The high intensity of the peak at 978 cm^{-1} to 1093 cm^{-1} suggests the presence of phosphate stretching. The spectrum also shows a strong bend at 550 cm^{-1} to 650 cm^{-1} (phosphate bending).

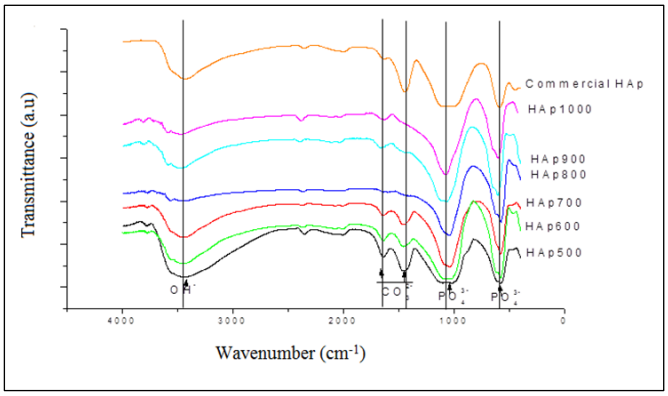


Figure 1. FTIR spectra of commercial HAp and HAp samples prepared in-house, calcined at 500 °C to 1,000 °C

X-ray diffraction

The crystalline phase and intermolecular distances of the HAp was analysed using the wide angle X-ray diffraction (XRD) [22]. The XRD patterns of HAp samples calcined at different temperatures are presented in Figure 2. The XRD patterns show that the peak intensities are improved with increasing calcination temperature. HAp sample calcined at 500 °C shows low crystallinity compared to HAp samples that were calcined at > 800 °C. This change indicates that the HAp sample contains a large amount of organics [25]. The sharp peaks also indicate the crystallinity of the substance, in which the crystallinity of HAp increases with increasing calcination temperature.

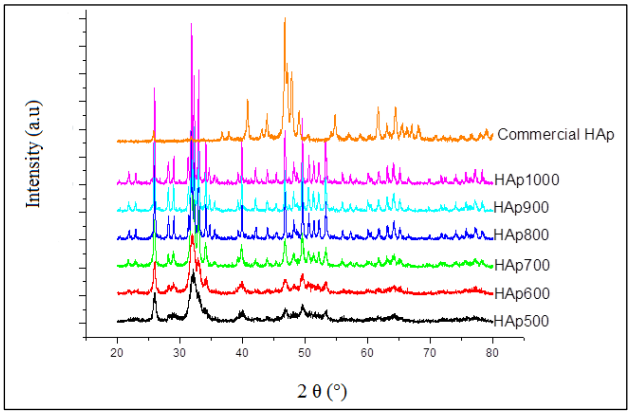


Figure 2. XRD patterns of commercial HAp and HAp samples prepared in-house, calcined from 500 °C to 1,000 °C

Scanning electron microscope

The following Fig. 3 shows the SEM micrographs of HAp samples calcined between 500 °C and 1,000 °C. The morphology of HAp samples extracted from fish scales *via* enzymatic extraction shows irregular shapes and a wide range of particle size distribution.

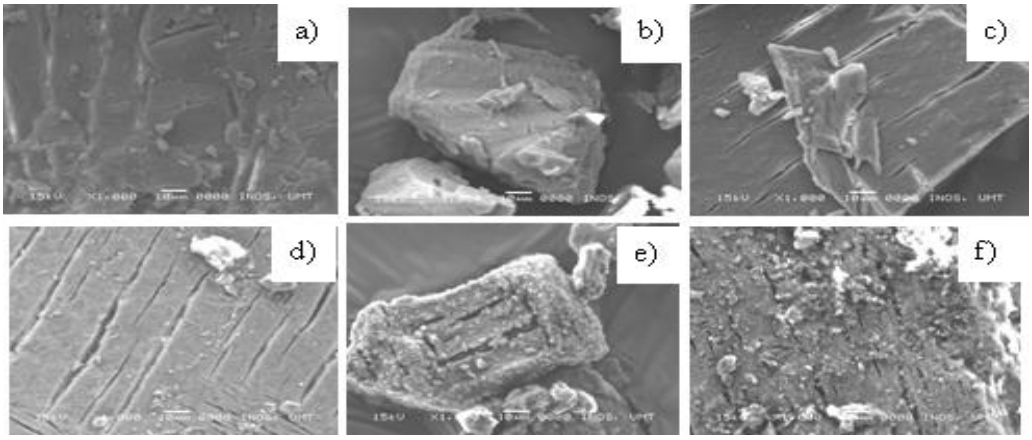


Figure 3. Surface morphology (a) HAp500, (b) HAp600, (c) HAp700, (d) HAp800, (e) HAp900, (f) HAp1000. Magnification is 1000x

Evaluation performance of HAp for gallic acid removal: Effect of calcination temperature of HAp

Different calcination temperatures could influence the properties and performance of the synthesised HAp. Batch adsorption experiments were conducted to determine gallic acid adsorption by each HAp sample, as shown in Figure 4.

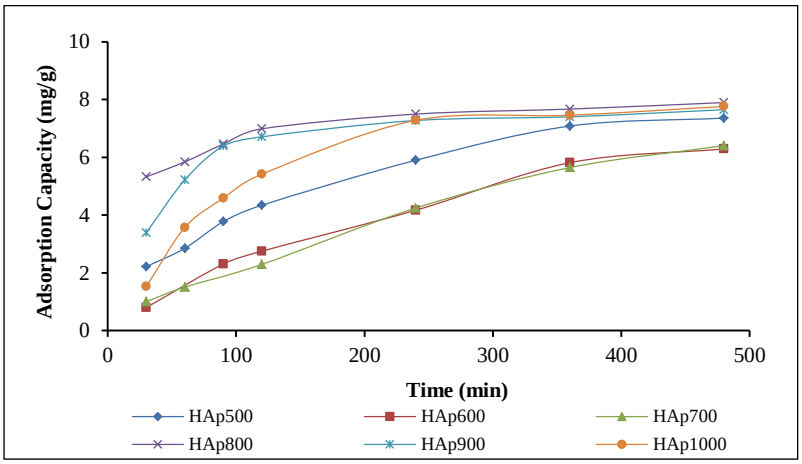


Figure 4. Adsorption capacity of gallic acid by HAp samples produced at different calcination temperatures

Generally, each adsorbent behaved similarly, in which the adsorption process took place in two stages during the kinetic process. The adsorption at the first stage occurred rapidly and became constant in the second stage upon reaching equilibrium. However, HAp samples calcined at higher temperatures (800 °C and above) reached equilibrium at 240 minutes, which was faster than HAp500, HAp600, and HAp700. This experiment showed that HAp800 has the highest adsorption capacity, and thus, was selected for used in the consecutive experiment.

Effect of initial concentration and adsorption isotherm

Langmuir and Freundlich isotherms are commonly used to compare and analyse the behaviour of the isotherm mechanisms. The adsorption process was tested with different initial concentrations of gallic acid solution, from 50 to 100 mg/L using HAp800. The percentage of gallic acid removal had decreased with the increasing initial concentration of gallic acid. In general, the ratio of active sites on HAp for the adsorption to take place and the number of solutes were decreasing with the increasing initial concentration of gallic acid. This situation was due to the higher driving force between the concentration gradient adhered by the high initial concentration and the low initial concentration [25]. The graphs for both Langmuir and Freundlich isotherms were plotted according to Eqs. (3) and (5), respectively, as shown in Figure 5. A summary of isotherm constants is presented in Table 2. Freundlich isotherm fit the experimental data better, with correlation value of $r^2 = 0.995$, in contrast to Langmuir isotherm ($r^2 = 0.876$). The same isotherm was reported in the adsorption of phenolic compounds using activated carbon [26]. This finding also proves that heterogeneous adsorption had occurred, in which the multisite adsorption process was not limited by monolayer formation.

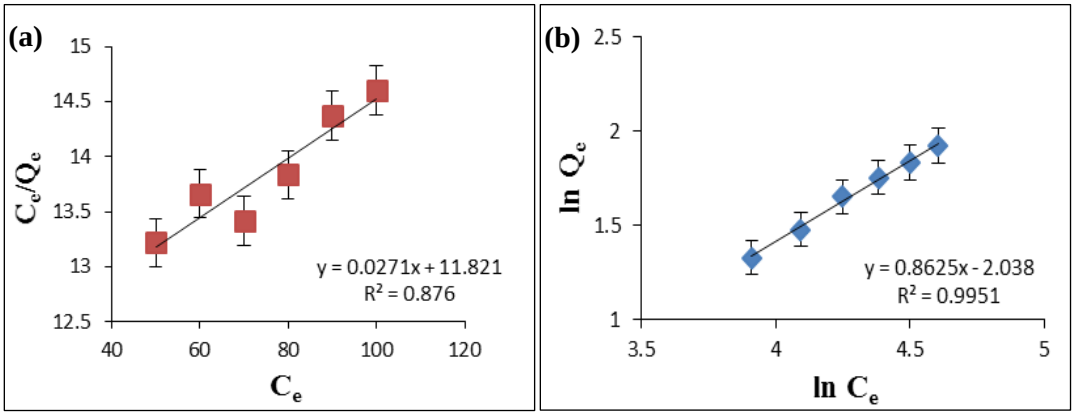


Figure 5. The plotted graphs (a) Langmuir isotherm and (b) Freundlich isotherm for gallic acid adsorption with HAp800 at 60 °C and shaken at 240 rpm

The Freundlich graph shows that the slope value is considerably high (0.862), indicating the high heterogeneity of the adsorbent surface [13]. According to Table 1, the value of n is within $0.1 < 1/n < 1$, which shows that the adsorption is favourable. On the other hand, when the n value is more than 1, this indicates the occurrence of a physical adsorption [16].

Table 1. Langmuir and Freundlich isotherm constants for gallic acid adsorption by HAp800 at 60 °C and shaken at 240 rpm

Langmuir Isotherm		**Freundlich Isotherm**	
r^2	0.876	r^2	0.9951
K_L	2.2925×10^{-3} L/mg	K_F	0.130 (mg/g(L/mg)$^{1/n}$)
q_m	36.90mg/g	$\frac{1}{n}$	0.8625

Effect of time and kinetic analysis

The adsorption was conducted at different time intervals. Gallic acid removal was the highest (78.9%) at 480 minutes upon the introduction of 10 g/L of HAp800 and initial concentration of gallic acid solution of 100 mg/L (Figure 6). The figure shows a sharp increase from minute 30 to 120. The percentage of gallic acid removal showed

a slight increase from 120 to 240 minutes, which became stagnant until 480 minutes. Based on this observation, the equilibrium constant is concluded to be achievable at 240 minutes (74.98%).

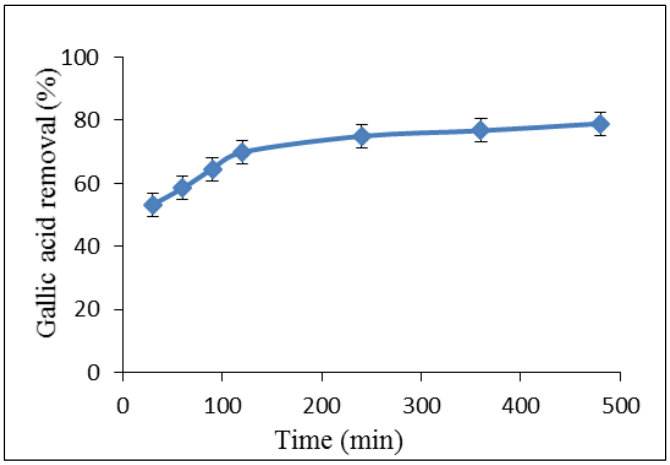


Figure 6. Removal of gallic acid at different reaction times, with initial concentration of 100 mg/L, HAp dosage of 10 g/L, temperature at 60 °C, and shaken at 240 rpm

The experimental data on the effect of time on the percentage of gallic acid removal were used to study the three kinetic adsorption theories: (1) first-order; (2) pseudo-second order kinetic; and (3) intraparticle diffusion. These data are plotted in Figure 7 and the kinetic constant analysis is summarised in Table 2. Both first-order and pseudo-second order models showed good applicability with high values of r^2 of 0.923 and 0.999, respectively. However, the pseudo-second order model fit better with the experimental results since its value of r^2 (0.996) was much closer to unity than the r^2 value of the first-order (r^2 = 0.932) (the results showed the same behaviour, regardless of the adsorption condition). The graph for the intraparticle diffusion model was plotted with two linear lines. According to Cagnon et al., the first linear plot represents the limitation of adsorption by external diffusion, while the last plot represents the final equilibrium [17]. The final equilibrium usually occurs due to the decreased solute concentration in the aqueous solution. According to Figure 7, the adsorption of gallic acid on HAp is predominantly (within 120 min) on the first linear plot. Thus, this adsorption was concluded to be a surface adsorption (external diffusion).

Table 2. Kinetic parameters for the first-order, pseudo-second order, and intraparticle diffusion of gallic acid in the presence of HAp800, with initial concentration of 100 mg/L, temperature at 60 °C and shaken at 240 rpm

	First-order	**Pseudo-Second Order**	**Intraparticle Diffusion**
r^2	0.9236	0.9996	0.8556
k	15.77/min	0.046 g/(mg.min)	0.1316 g/(mg/min$^{1/2}$)
q_e	7.867 mg/g	8.203 mg/g	-
C	-	-	5.0137

Gallic acid adsorption on HAp was assumed to follow the pseudo-second order theory. However, in the capacity of equilibrium adsorption, the first-order model (7.867 mg/g) was closer to the experimental q_e (7.498 mg/g) compared to the pseudo-second order model (8.203 mg/g). The adsorption data were further analysed for the kinetic process using the pseudo-second order kinetic theory.

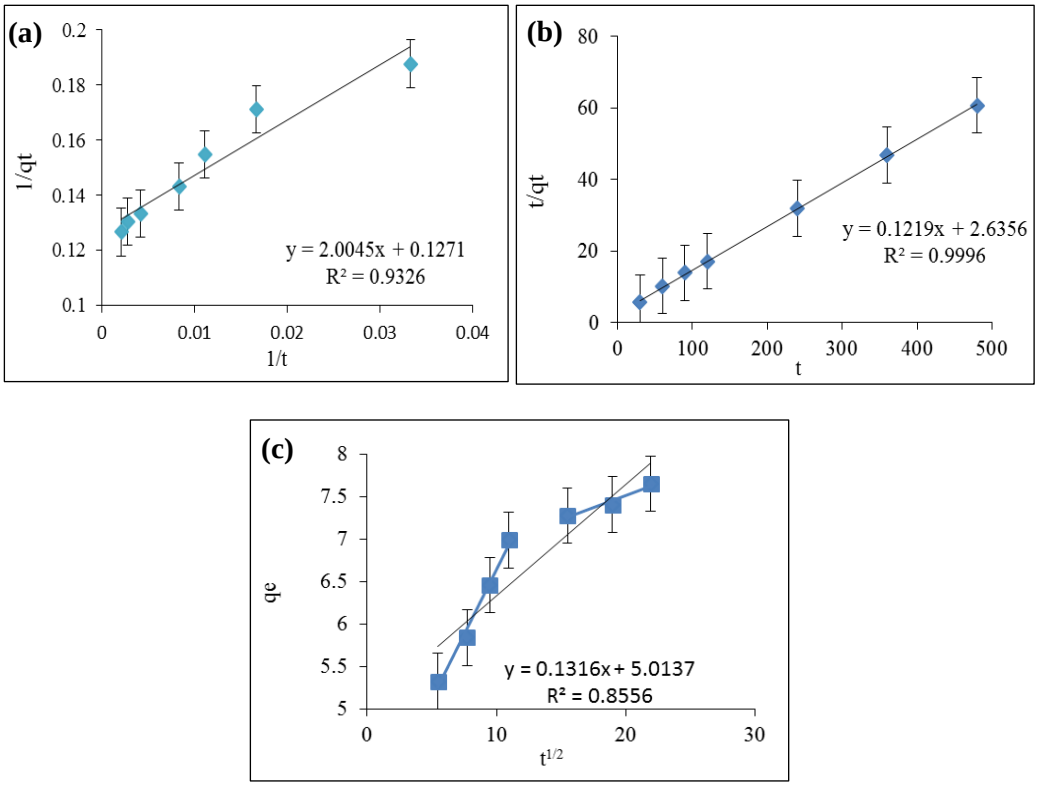


Figure 7. The plotted graphs of (a) first-order kinetic, (b) pseudo-second order kinetic and (c) intraparticle diffusion of gallic acid in the presence of HAp800 and initial concentration of 100 mg/L, temperature at 60 °C and shaken at 240 rpm

Next, the kinetics analysis was conducted by varying the initial concentrations of gallic acid (50–100 mg/L), which were applied on the pseudo-second order model. The adsorption was conducted for 30 to 480 minutes. The maximum adsorption capacity is increased with increasing initial concentration, as shown in Table 3. The experimental work demonstrated that the highest rate constant (0.0109 g/(mg/min)) was achieved from the reaction with initial gallic acid concentration of 50 mg/L. A possible explanation was that the equilibrium adsorption was achieved faster in low initial concentrations. Further analysis showed that during the first 120 minutes, the range of the kinetic constant was double than during the consecutive time. This was due to the abundance of active sites during the earlier time. The number of active sites was decreased over time, leading to a slower adsorption process [26].

Table 3. Pseudo-second order kinetic parameters for different gallic acid concentrations in the presence of HAp800: dosage of 10 g/L, temperature at 60 °C, and shaken at 240 rpm

Initial Concentration (mg/L)	r^2	k **g/(mg/min)**	q_e **(mg/g)**
50	0.9985	0.01090	3.923
60	0.9996	0.00880	4.589
70	0.9981	0.00646	5.593
80	0.9975	0.00573	6.357
90	0.9974	0.00375	7.380
100	0.9977	0.00312	8.347

Effect of dosage

The effect of dosage on the adsorption process was analysed by adding 1, 5, 10, 15, 20, and 25 g/L of HAp to 100 mg/L of gallic acid. According to the graph shown in Figure 8, the percentage of gallic acid removal is increased with increasing HAp dosage, from 1 to 10 g/L. Nonetheless, higher dosage of HAp had shown only a slight increase in the percentage of gallic acid removal. A possible explanation would be that the number of adsorption sites had increased with the increasing HAp dosage. Thus, more active sites were available for the adsorption reaction to take place [17]. In this case, the equilibrium constant was achieved upon the introduction of 10 g/L of HAp dosage, with 79.80% of gallic acid removed. These results were compared to the findings in a previous work. Lin et al. reported that only 28.32% of phenol was removed in the presence of 4 g/L of hydroxyapatite nanopowders, with other similar parameters [12]. On the other hand, the increasing HAp dosage had resulted in the decrease of adsorption capacity. This is because the occupied adsorption site per gram of adsorbent was decreased in high adsorbent dosage. In order to overcome this situation, the initial concentration of gallic acid needs to be increased. In some cases, high dosage is inefficient for the adsorption reaction to take place, which leads to clumps of adsorbents. Thus, it is crucial to study the optimum dosage.

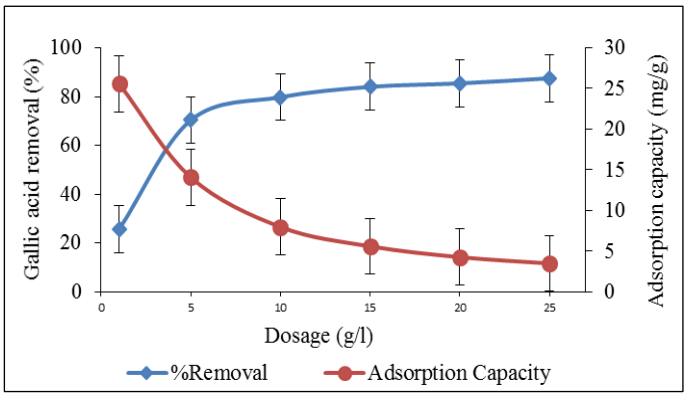


Figure 8. Percentage of removal and adsorption capacity at different HAp dosages. Initial gallic acid concentration = 100 mg/L, temperature = 60 °C, and time = 240 minutes

Effect of temperature

The adsorption reaction was conducted between 10 °C and 60 °C. The adsorption capacity was increased with increasing reaction temperature, as shown in Figure 9. These results indicated that the adsorption reaction had underwent an endothermic process [21]. In addition, these results indicated that the mobility of gallic acid molecules in the solution had increased with increasing temperature.

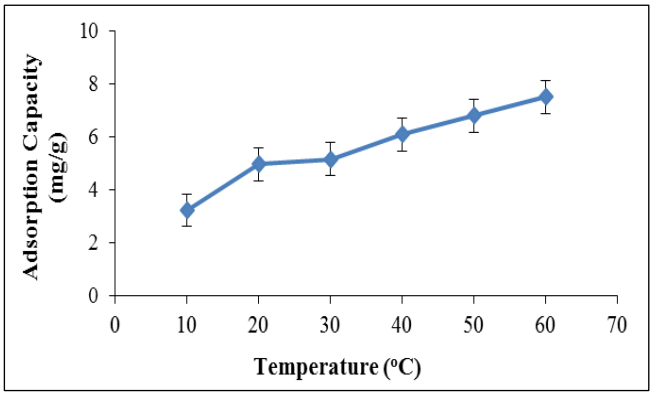


Figure 9. The effect of reaction temperature on the adsorption capacity of HAp800. Initial gallic acid conentration = 100 mg/L, HAp dosage = 10 g/L, time = 240 minutes

Conclusion

HAp was successfully extracted from fish scales using the enzymatic extraction method. HAp samples that were calcined between 500 °C to 1,000 °C employed herein were able to adsorb gallic acid. The percentage of gallic acid removal was the highest (78.9%) at 480 minutes upon the introduction of 10 g/L of HAp800 and the initial concentration of gallic acid solution was 100 mg/L. This adsorption was best fitted with Freundlich isotherm and pseudo-second order kinetics. Thus, this study concludes that this was a heterogeneous process, with multisite adsorption. Meanwhile, the absorption reaction was found to be endothermic.

Acknowledgement

The authors gratefully acknowledge the Ministry of Higher Education Malaysia for the financial support (LRGS Vot no: 53194) and the Central Laboratory of Universiti Malaysia Terengganu for providing equipment and support.

References

1. Prasad, R. K., Chatterjee, S., Mazumder, P. B., Gupta, S. K., Sharma, S., Vairale, M. G. and Gupta, D. K. (2019). Bioethanol production from waste lignocelluloses: A review on microbial degradation potential. *Chemosphere*, 231: 588–606.
2. Lee, J. W., Trinh, L. T. P. and Lee, H. J. (2014). Removal of inhibitors from a hydrolysate of lignocellulosic biomass using electrodialysis. *Separation and Purification Technology*, 122: 242–247.
3. Lin, R., Cheng, J., Ding, L., Song, W., Zhou, J. and Cen, K. (2015). Inhibitory effects of furan derivatives and phenolic compounds on dark hydrogen fermentation. *Bioresource Technology*, 196: 250–255.
4. Kim, Y., Ximenes, E., Mosier, N. S. and Ladisch, M. R. (2011). Enzyme and microbial technology soluble inhibitors/deactivators of cellulase enzymes from lignocellulosic biomass. *Enzyme and Microbial Technology*, 48: 408–415.
5. Palmqvist, E. and Hahn-Hargedal, B. (2000). Fermentation of lignocellulosic hydrolysates I : Inhibition and detoxification. *Bioresource Technology*, 74(1): 17–24.
6. Han, F., Xu, C., Sun, W. Z., Yu, S. T. and Xian, M. (2017). Effective removal of salicylic and gallic acids from single component and impurity-containing systems using an isatin-modified adsorption resin. *RSC Advances*, 7: 23164–23175.
7. Chavan, P. N., Bahir, M. M., Mene, R. U., Mahabole, M. P. and Khairnar, R. S. (2010). Study of nanobiomaterial hydroxyapatite in simulated body fluid: Formation and growth of apatite. *Materials Science and Engineering B: Solid-State Materials for Advanced Technology*, 168(1): 224–230.
8. Piccirillo, C., Pullar, R. C., Tobaldi, D. M., L. Castro, P. M. and E. Pintado, M. M. (2014). Hydroxyapatite and chloroapatite derived from sardine by-products. *Ceramics International*, 40: 13231–13240.
9. Elliott, J. C., Wilson, R. M. and Dowker, S. E. P. (2002). Apatite structures. *Advances in X-Ray Analysis*, 45: 172–181.
10. Nguyen, V. C. and Pho, Q. H. (2014). Preparation of chitosan coated magnetic hydroxyapatite nanoparticles and application for adsorption of reactive blue 19 and Ni^{2+} ions. *The Scientific World Journal*, 2014: 1–9.
11. Zou, X., Zhao, Y. and Zhang, Z. (2019). Preparation of hydroxyapatite nanostructures with different morphologies and adsorption behavior on seven heavy metals ions. *Journal of Contaminant Hydrology*, 226: 103538.
12. Bouiahya, K., Es-saidi, I., El Bekkali, C., Laghzizil, A., Robert, D., Nunzi, J. M. and Saoiabi, A. (2019). Synthesis and properties of alumina-hydroxyapatite composites from natural phosphate for phenol removal from water. *Colloids and Interface Science Communications*, 31: 100188.
13. Kongsri, S., Janpradit, K., Buapa, K., Techawongstien, S. and Chanthai, S. (2013). Nanocrystalline hydroxyapatite from fish scale waste: Preparation, characterization and application for selenium adsorption in aqueous solution. *Chemical Engineering Journal*, 215–216: 522–532.
14. Huang, Y., Hsiao, P. and Chai, H. (2011). Hydroxyapatite extracted from fish scale: Effects on MG63 osteoblast-like cells. *Ceramics International*, 37(6): 1825–1831.
15. Parhi, P., Ramanan, A. and Ray, A. (2006). Hydrothermal synthesis of nanocrystalline powders of alkaline-earth hydroxyapatites, $A_{10}(PO_4)_6OH)_2$ (A=Ca, Sr and Ba). *Journal of Material Sciences*, 41: 1455–1458.

16. Lin, K., Pan, J., Chen, Y., Cheng, R. and Xu, X. (2009). Study the adsorption of phenol from aqueous solution on hydroxyapatite nanopowders. *Journal of Hazardous Materials*, 161(1): 231–240.
17. B Cagnon, B., Chedeville, O., Cherrier, J. F., Caqueret, V. and Porte, C. (2011). Evolution of adsorption kinetics and isotherms of gallic acid on an activated carbon oxidized by ozone: Comparison to the raw material. *Journal of the Taiwan Institute of Chemical Engineers*, 42: 996–1003.
18. Anbia, M., Mohammadi, N. and Mohammadi, K. (2010). Fast and efficient mesoporous adsorbents for the separation of toxic compounds from aqueous media. *Journal of Hazardous Materials*, 176, 965–972.
19. Rengaraj, S., Yeon, J., Kim, Y., Jung, Y., Ha, Y. and Kim, W. (2007). Adsorption characteristics of Cu (II) onto ion exchange resins 252H and 1500H: Kinetics, isotherms and error analysis. *Journal of Hazardous Materials*, 143: 469–477.
20. Robati, D. (2013). Pseudo-second-order kinetic equations for modeling adsorption systems for removal of lead ions using multi-walled carbon nanotube. *Journal of Nanostructure in Chemistry*, 3: 55.
21. Abdelwahab, O. and Amin, N. K. (2013). Adsorption of phenol from aqueous solutions by *Luffa cylindrica* fibers: Kinetics, isotherm and thermodynamic studies. *Egyptian Journal of Aquatic Research*, 39: 215–223.
22. Azmi, N. A. I., Zainudin, N. F., Ali, U. F. M. and Senusi, F. (2015). Adsorption kinetics on basic red 46 removal using *Cerbera odollam* activated carbon. *Journal of Engineering Science and Technology*, 10: 82–91.
23. Smiciklas, I., Dimović, I. and Mitrić, M. (2006). Removal of Co^{2+} from aqueous solutions by hydroxyapatite. *Water Research*, 40(12): 2267–2274.
24. Salimi, M. N., Bridson, R. H., Grover, L. M. and Leeke, G. A. (2012). Effect of processing conditions on the formation of hydroxyapatite nanoparticles. *Powder Technology*, 218: 109–118.
25. Yusof, S. R. M., Zahri, N. A. M., Koay, Y. S., Nourouzi, M. M., Chuah, L. A. and Choong, T. S. Y. (2015). Removal of fluoride using modified kenaf as adsorbent. *Journal of Engineering Science and Technology*, 10: 11–22.
26. Anbia, M. and Ghaffari, A. (2009). Adsorption of phenolic compounds from aqueous solutions using carbon nanoporous adsorbent coated with polymer. *Applied Surface Science*, 255: 9487–9492.

Malaysian Journal of Analytical Sciences, Vol 23 No 6 (2019): 950 - 962
DOI: https://doi.org/10.17576/mjas-2019-2306-04

MALAYSIAN JOURNAL OF ANALYTICAL SCIENCES
Published by The Malaysian Analytical Sciences Society
ISSN 1394 - 2506

CHEMICAL CONSTITUENTS AND ANTIOXIDANT POTENTIALS OF SEVEN PHILIPPINE MOSSES

(Juzuk Kimia dan Potensi Antioksidan bagi Tujuh Lumut Filipina)

Mary Stephanie S. Carranza[1], Virgilio C. Linis[2], Consolacion Y. Ragasa[1,3], Maria Carmen S. Tan[1]*

[1]*Chemistry Department,*
De La Salle University, 2401 Taft Avenue, Manila 1004, Philippines
[2]*Biology Department,*
De La Salle Araneta University, 303 Victoneta Avenue, Potrero Malabon City 1475, Philippines
[3]*Chemistry Department,*
De La Salle University Science & Technology, Complex Leandro V. Locsin Campus, Biñan City, Laguna 4024, Philippines

**Corresponding author: maria.carmen.tan@dlsu.edu.ph*

Received: 23 May 2019; Accepted: 1 October 2019

Abstract

Seven species of Philippine mosses, namely *Calyptothecium ramosii* Broth., *Gymnostomum recurvirostum* Hedw., *Hypnum plumiforme* Wilson, *Leucobryum scalare* Müll.Hal. ex M.Fleisch., *Meteoriopsis reclinata* (Müll.Hal.) M.Fleisch., *Mitthyridium undulatum* (Dozy & Molk.) H.Rob. and *Pelekium boniamum* (Besch) were examined in this study. The mosses were analyzed using a gas chromatography equipped with a mass spectrometer (GC-EI-MS) and an energy dispersive X-ray fluorescence spectrometer (EDX) to substantiate their possible usage as dietary supplements. EDX results displayed that calcium was the major mineral found in all the moss samples (1.199% to 11.427%). The free radical scavenging activity of the dried dichloromethane moss extracts was highest for *G. recurvirostum* indicative of the lowest IC_{50} concentration at 0.236 mg/mL followed by *C. ramosii* at 0.306 mg/mL and *P. boniamum* at 0.315 mg/mL. *M. undulatum* (IC_{50} = 1.360 mg/mL) and *M. reclinata* (IC_{50} = 1.544 mg/mL) had moderate antioxidant activity, whereas, *L. scalare* (IC_{50} = 2.120 mg/mL) and *H. plumiforme* (IC_{50} = 2.213 mg/mL) had minimal free radical scavenging potential. The possible antioxidant capabilities of each respective bryophyte were correlated to the presence of the following major constituents from GC-EI-MS investigation: in *P. boniamum*, α-cadinol, (9.11%), caryophyllene (6.39%) and (-)-spathulenol (5.52%); in *G. recurvirostum*, pentanoic acid, 2,2,4-trimethyl-3-carboxyisopropyl, isobutyl ester (56.26%), caryophyllenyl alcohol (5.96%) and α-cadinene (5.88%); in *C. ramosii*, phytol (17.86%), and phytol acetate (14.03%). 7,9-di-tert-butyl-1-oxaspiro (4,5) deca-6,9-diene-2,8-dione (9.59%), and 4,8,12,16-tetramethylheptadecan-4-olide (6.11%). Apart from *H. plumiforme*, all the samples contained considerable concentrations of n-hexadecanoic acid (range from 3.76% to 29.03%).

Keywords: bryophyte, free radical scavenging activity, gas chromatography - mass spectrometry, energy dispersive x-ray fluorescence spectroscopy

Abstract

Tujuh spesis lumut Filipina iaitu *Calyptothecium ramosii* Broth., *Gymnostomum recurvirostum* Hedw., *Hypnum plumiforme* Wilson, *Leucobryum scalare* Müll.Hal. ex M.Fleisch., *Meteoriopsis reclinata* (Müll.Hal.) M.Fleisch., *Mitthyridium undulatum* (Dozy & Molk.) H.Rob. dan *Pelekium boniamum* (Besch) telah diuji dalam kajian ini. Lumut telah dianalisa menggunakan kromatografi gas dilengkapi spectrometer jisim (GC-EI-MS) dan spektrometer pendaflour tenaga serakan sinar-X (EDX) untuk melihat potensi digunakan sebagai makanan tambahan. Keputusan EDX menunjukkan kalsium merupakan mineral utama yang dijumpai dalam semua sampel lumut (1.199% to 11.427%). Aktiviti pemerangkapan radikal bebas melalui ekstrak lumut menggunakan diklorometana telah memberikan *G. recurvirostum* hasil paling tinggi pada kepekatan IC_{50} iaitu 0.236 mg/mL diikuti *C. ramosii* pada 0.306 mg/mL and *P. boniamum* pada 0.315 mg/mL. *M. undulatum* (IC_{50} = 1.360 mg/mL) dan *M.*

reclinata (IC_{50} = 1.544 mg/mL) menghasilkan aktiviti antioksidan yang sederhana, manakala *L. scalare* (IC_{50} = 2.120 mg/mL) dan *H. plumiforme* (IC_{50} = 2.213 mg/mL) mempunyai potensi pemerangkapan radikal bebas yang minumum. Keupayaan antioksidan setiap briofit adalah dikaitkan dengan kehadiran juzuk utama iaitu hasil analisa GC-EI-MS seperti di dalam *P. boniamum*, mengandungi α-kadinol, (9.11%), kariofilena (6.39%) dan (-)-spathulenol (5.52%); di dalam *G. recurvirostum* seperti asid pentanoik, 2,2,4-trimetil-3-karboisopropil, isobutil ester (56.26%), kariofilenil alkohol (5.96%) dan α-kadinena (5.88%), di dalam *C. ramosii*, fitol (17.86%), fitol asetat (14.03%). 7,9-di-tert-butil-1-oksaspiro (4,5) deka-6,9-diena-2,8-dion (9.59%), dan 4,8,12,16-tetrametillheptadekan-4-olida (6.11%). Selain dari *H. plumiforme*, semua sampel mengandungi kepekatan asid n-heksadekanoik (julat dari 3.76% hingga 29.03%).

Keywords: briofit, aktiviti pemerangkapan radikal bebas, kromatografi gas-spektrometri jisim, spektroskopi pendaflour tenaga serakan sinar-X

Introduction

There has not been much research done on non-vascular plants, particularly on mosses which belong to the division Bryophyta [1], primarily because moss samples are usually small and are considered insignificant [2]. Traditionally, Native Americans are known to have used mosses as concoctions for treating tuberculosis, pneumonia, neurasthenia, wounds and burns [3, 4]. Large mosses such as *Polytrichum commune* Hedw. have been confirmed to have antimicrobial activity on several bacteria strains (*Bacillus cereus* Frankland & Frankland 1887, *Pseudomonas aeruginosa* (Schröter 1872) Migula 1900, *Staphylococcus aureus* Rosenbach 1884, and *Escherichia coli* (Migula 1895) Castellani and Chalmers 1919) by exhibiting inhibition zone diameters which varied from 9 to 15 mm [5]. Other mosses such as *Sphagnum magellanicum* Brid., *Dicranum polysetum* Sw., *Pleurozium schreberi* (Brid.) Mitt.) displayed high antiproliferative activity (0.9–5 μg/mL) on rat glioma cells [5]. Some work has been specifically done on the use of mosses as biomonitors to short-term responses and antioxidant fluctuations due to heavy metal damage [6]. For instance, allelochemicals (phytoalexins in rice) momilactone A and B have been isolated from *Hypnum plumiforme* Wilson [7]. Short–term responses of H_2O_2 concentration have been found to increase in the presence of Pb and Ni induced stress in *H. plumiforme* [8]. LC-ToF-MS analysis of ethanolic moss extracts, on the other hand, revealed that the most abundant constituents are fatty acids (329–1707 mg/100 g dry moss), sterols (632–2130 mg/100 g dry moss), and amino acids (590–3266 mg/100 g dry moss) [5].

In this study, seven Philippine mosses specifically *Calyptothecium ramosii* Broth. (**CR**), *Gymnostomum recurvirostum* Hedw. (**GR**), *Hypnum plumiforme* Wilson (**HP**), *Leucobryum scalare* Müll.Hal. ex M.Fleisch. (**LS**), *Meteoriopsis reclinata* (Müll.Hal.) M.Fleisch. (**MR**), *Mitthyridium undulatum* (Dozy & Molk.) H.Rob. (**MA**), and *Pelekium boniamum* (Besch.) (**PB**) were gathered from several localities in Central Luzon Region, Philippines and were selected for investigation. Furthermore, all these mosses are essentially extra-Philippine species occurring throughout Southeast Asia and none are endemics.

Chemical characterization of the seven moss species was achieved using gas chromatograph in tandem with a mass spectrometer (GC-EI-MS) and energy dispersive X-ray spectroscopy (EDX) technique. Free radical scavenging capacity was ascertained in the dichloromethane extracts from these mosses. To the best of our knowledge, this is the first reported study using this methodology of antioxidant activity on the aforementioned crude bryophyte extracts and chemical analyses of the samples.

Materials and Methods

The mat or aerial portion taken from each moss samples was pulverized into a powdered biomass. The powder was used for the stipulated analytical techniques to characterize the aforementioned mosses gathered from Central Luzon Region, Philippines.

Solvent extraction

Each moss sample was grounded followed by soaking 3.0 grams of the powdered biomass in 20 mL of dichloromethane (DCM) for three hours. Extracts were filtered and then dried under nitrogen for one hour. The crude extracts from **PB** (0.4 mg), **HP** (0.5 mg), **GR** (0.3 mg), **LS** (0.5 mg), **MR** (0.4 mg), **CR** (0.4 mg) and **MA** (0.3 mg**)** were dissolved in one millilitre of dichloromethane for subsequent GC-EI-MS analyses.

GC-EI-MS parameters

Crude extracts from DCM soaked moss samples were analysed by gas chromatography – electron ionization - mass spectrometry analysis. An Agilent GC MS 7890B with a HP-5 ms (5% phenyl methyl siloxane) ultra-inert column (30 m x 250 mm x 0.25 mm) with ultra-high purity grade helium as a gas carrier was used for the analysis of the volatile constituents. The flow rate of the helium gas was set at 1.0587 mL/min, pressure was made to be at 9.4889 psi, with an average velocity of 37.862 cm/sec and hold time of 1.3206 minute. The initial setpoint temperature was at 70 ^{o}C. The program was as followed: first ramp was set at 2 ^{o}C /min to 135 ^{o}C and held for 10 minutes, second ramp had a rate of 4 ^{o}C/min to 220 ^{o}C and held for 10 minutes, and finally, the last ramp had a rate of 3.5 ^{o}C/min to 270 ^{o}C and held for 37 minutes. The heatmap was generated from the software XLSTAT v. 2015.1.

Compound identification was done using the NIST library v. 2.0 and peak areas were processed from the resultant total ion chromatograms as total correlation maximum percentage. The resultant data was confirmed by the comparison of the compounds according to their elution order with their relative retention indices on a non-polar stationary phase. The retention indices were computed for all of the volatile constituents' utilizing a homologous series of n-alkanes. All tests were performed in triplicates and data (retention time) were shown as mean ± SEM.

Free radical scavenging assay

The free radical scavenging activity of moss extracts was carried out using a modified DPPH assay protocol by Jose Prieto [9]. Powdered moss samples (15 g) were incubated in 20 mL of dichloromethane (DCM) for three hours. Extracts were filtered and then dried under nitrogen for one hour. The crude extracts from **PB** (4.0 mg), **HP** (4.0 mg), **GR** (3.6 mg), **LS** (6.9 mg), **MR** (5.7 mg), **CR** (4.8 mg) and **MA** (6.40 mg**)** were dissolved in 4.5 mL of methanol for DPPH analyses.

A 0.2 mM DPPH solution was prepared by diluting 3.94 mg of 1, 1-diphenyl-2-picrylhydrazyl (DPPH) in 50 mL of methanol in a volumetric flask. A stock solution for each moss was prepared at 4 mg of crude extract in one mL of methanol. The blank was made to be 1 mL of this solution in addition to 1 mL of methanol. 1 mL of the 4 mg/mL stock was added to a 10 mL test tube along with one mL of the 0.2 mM DPPH solution. A total of eight concentrations from 17.5 to 0.27 mg/mL were made by serial dilution. The absorbances were read at 515 nm (UV-VIS Shimadzu 2900) after samples were incubated at room temperature for 30 minutes. Statistical analyses and graphs were done using GraphPad Prism 7.01 (GraphPad Software, Inc.). Results were considered significant at $p < 0.05$. The IC_{50} value of the sample, or the concentration of the sample which can inhibit 50% of the DPPH free radicals, was determined by calculating the percent DPPH scavenging effect which was calculated by the following formula in equation 1;

$$\text{DPPH scavenging effect (\%) or Percent inhibition} = (A_o - A_1/ A_o) \times 100 \quad (1)$$

Results and Discussion

GC-MS analysis revealed a total of 56 compounds determined from the seven species of mosses as seen in Table 1 and 2 and Figure 1 and 2, respectively. In **PB**, 11 constituents were found which were primarily composed of (3) sesquiterpenes, (3) alcohols, (2) compounds with diverse functional groups, (1) saturated fatty acid, (1) hydrocarbon and an ester. In another moss, **HP**, a total of 9 constituents were found to consist of (4) sesquiterpene alcohols, (3) diverse functional groups, (1) sesquiterpene and (1) steroid alcohol. **GR**, on the other hand, had a total of 7 constituents and these were (2) sesquiterpene alcohols, (2) diverse functional groups, (1) saturated fatty acid, (1) sesquiterpene and (1) hydrocarbon. In **LS**, 8 constituents were found and these are (2) diverse functional groups, (2) alcohols, (1) sesquiterpene, (1) ester, (1) saturated fatty acid and (1) ketone while in **MR**, 11 constituents were found and these are the (4) saturated fatty acids, (2) alcohols, (1) aldehyde, (1) diverse functional group, (1) ester, (1) polyunsaturated fatty acid and (1) hydrocarbon. Meanwhile, **CR** was found to contain 7 constituents, and these were (2) esters, (1) diterpenoid, (1) diverse functional group, (1) saturated fatty acid, (1) alcohol and (1) hydrocarbon. Lastly, moss **MA** was found to contain only three primary constituents: (1) diverse functional group, (1) saturated fatty acid and (1) alcohol.

All seven mosses were observed to contain compounds exhibiting wide range of structures. Most notable were the sesquiterpenes and compounds with diverse functional groups which were found to primarily constitute the

composition of the samples. In **PB**, for instance, saturated fatty acids such as palmitic acid (16.28%) and formic acid, the 3,7,11-trimethyl-1,6,10-dodecatrien-3-yl ester (9.29%), phytol (9.12%), and a sesquiterpenoid alcohol, alpha-cadinol, (9.11%) were its major components. Interestingly, □-cadinol was also observed to be one of the four major components of the essential oil derived from Strawberry guava (*Psidium cattleyanum* Sabine) from Southern Brazil which exhibited high anti-microbial activity against gram-negative and gram-positive bacterium strains [10]. Two compounds classified to have diverse functional groups, pentanoic acid, 2,2,4-trimethyl-3-carboxyisopropyl, isobutyl ester and methyl retinoate were discovered to have the highest intensity values for **HP** at 28.69% and 21.16%, respectively. Methyl retinoate, which was also found in the Brazilian green bee propolis, has been linked to have a positive correlation with the anti-oxidant capacity linked to the extensive conjugated pi-electron system which through donation of electrons can oxidize radical species [11].

The moss **GR**, on the other hand, was identified to contain bioactive compounds naphthalene, 1,2,3,5,6,8a-hexahydro-4,7-dimethyl-1-(1-methylethyl)-, (1S-cis)- (5.88%) and caryophyllenyl alcohol (5.96%). Naphthalene, 1,2,3,5,6,8a-hexahydro-4,7-dimethyl-1-(1-methylethyl)-, (1S-cis)-, also known as beta-cadinene, was reported to be a component of the commonly used basil (*Ocimum basilicum* L.). This essential oil is largely known for its anti-oxidant properties [12]. Similar to **HP**, **LS** also contained pentanoic acid, 2,2,4-trimethyl-3-carboxyisopropyl, isobutyl ester (56.26%) and n-hexadecanoic acid (13.37%). **MR** was established to contain squalene (45.26%) and n-hexadecanoic acid (16.21%) while the major constituents of **CR** were found to be composed of the saturated fatty acid, n-hexadecanoic acid (29.03%) and squalene (18.81%). Likewise, n-hexadecanoic acid (15.83%) was detected in moss **MA**.

Table 1. The chemical constituents of **PB**, **HP**, and **GR** moss extracts

Constituent	**RT (minute)**	**RI[a]**	**% Peak Area**	**Compound Class**
Pelekium bonl amum, PB				
Caryophyllene	18.67	1425	6.39	bicyclic sesquiterpene
1H-Cyclopenta[1,3]cyclopropa[1,2]benzene, octahydro-7-methyl-3-methylene-4-(1-methylethyl)-, [3aS-(3aα,3bβ,4β,7α	20.2	1488	5.52	diverse functional groups
Naphthalene, 1,2,3,4,4a,5,6,8a-octahydro-7-methyl-4-methylene-1-(1-methylethyl)-, (1α,4aβ,8aα)-	21.2	1528	4.97	bicyclic sesquiterpene
(-)-Spathulenol	22.51	1581	5.52	tricyclic sesquiterpene
Pentanoic acid, 2,2,4-trimethyl-3-carboxyisopropyl, isobutyl ester	22.9	1600	8.85	diverse functional groups
Formic acid, 3,7,11-trimethyl-1,6,10-dodecatrien-3-yl ester	24.05	1650	9.29	terpene ester
α-Cadinol	24.25	1659	9.11	sesquiterpenoid alcohol
Heptadecane, 8-methyl-	26.07	1747	6.88	Hydrocarbon
4,4,8-Trimethyltricyclo[6.3.1.0(1,5)]dodecane-2,9-diol	28.88	1883	1.27	polycyclic diol
n-Hexadecanoic acid	30.56	1966	16.82	saturated fatty acid

Table 1 (cont'd). The chemical constituents of **PB**, **HP**, and **GR** moss extracts

Constituent	**RT (minute)**	**RI[a]**	**% Peak Area**	**Compound Class**
Hypnum plumaeforme, HP				
Phytol	33.33	2058	9.12	diterpene alcohol
Naphthalene, 1,2,3,5,6,8a-hexahydro-4,7-dimethyl-1-(1-methylethyl)-, (1S-cis)-	21.63	1572	3.57	diverse functional groups
(-)-Spathulenol	22.55	1616	5.18	tricyclic sesquiterpene alcohol
Globulol	22.99	1630	3.82	tricyclic hydroazulene sesquiterpene
Pentanoic acid, 2,2,4-trimethyl-3-carboxyisopropyl, isobutyl ester	22.9	1627	28.69	diverse functional groups
Cubenol	23.65	1652	5.55	sesquiterpene alcohol
.tau.-Muurolol	23.96	1662	8.59	sesquiterpene alcohol
α-Cadinol	24.25	1671	14.83	sesquiterpene alcohol
β-Sitosterol	36.84	3017	8.98	steroid alcohol
Rectinoic acid, methyl ester	42.75	3351	21.16	diverse functional groups
Gymnostomum recurvirostum, GR				
Naphthalene, 1,2,3,5,6,8a-hexahydro-4,7-dimethyl-1-(1-methylethyl)-, (1S-cis)-	21.20	1547	5.88	sesquiterpene
Caryophyllenyl alcohol	22.33	1583	5.96	sesquiterpene alcohol
Pentanoic acid, 2,2,4-trimethyl-3-carboxyisopropyl, isobutyl ester	22.89	1601	56.26	diverse functional groups
α-Cadinol	24.24	1661	5.83	sesquiterpene alcohol
7,9-Di-tert-butyl-1-oxaspiro(4,5)deca-6,9-diene-2,8-dione	29.73	1923	2.45	diverse functional groups
n-Hexadecanoic acid	30.47	1961	3.76	saturated fatty acid
Squalene	44.59	2832	13.37	triterpene

[a] Retention Index (HP-5ms column), [b] Compounds listed in order of elution from a HP-5ms column

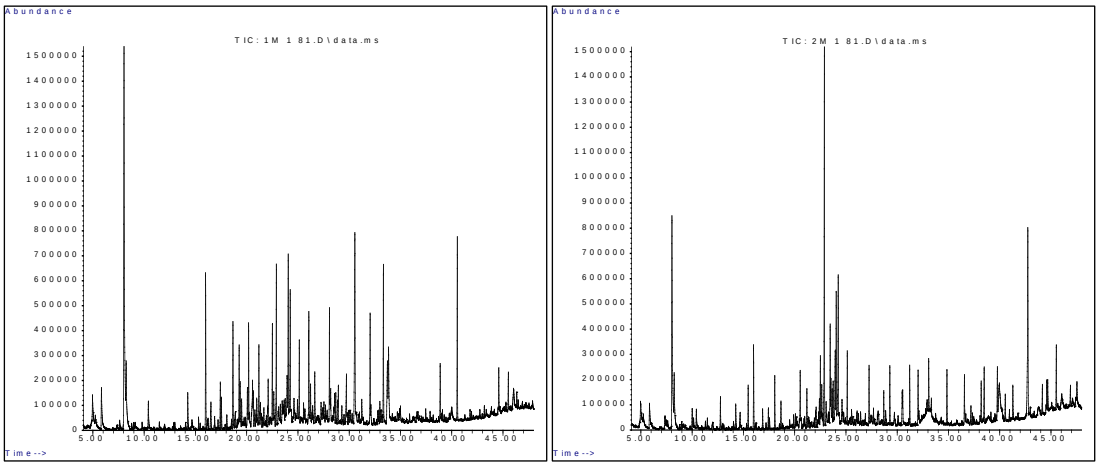
Table 2. The chemical constituents of **LS**, **MR**, and **CR** moss extracts

Constituent	**RT (minute)**	**RI[a]**	**% Peak Area**	**Compound Class**
Leucobryum scalore, LS				
Naphthalene, 1,2,3,5,6,8a-hexahydro-4,7-dimethyl-1-(1-methylethyl)-, (1S-cis)-	21.20	1519	5.88	sesquiterpene
Caryophyllenyl alcohol	22.33	1551	5.96	sesquiterpenoid alcohol
Pentanoic acid, 2,2,4-trimethyl-3-carboxyisopropyl, isobutyl ester	22.89	1567	56.26	diester
α-Cadinol	24.24	1618	5.83	sesquiterpenoid alcohol
2-Butyloxycarbonyloxy-1,1,10-trimethyl-6,9-epidioxydecalin	29.73	1653	2.45	diverse functional groups
2-Pentadecanone, 6,10,14-trimethyl-	30.47	1846	3.76	aliphatic ketone
7,9-Di-tert-butyl-1-oxaspiro(4,5)deca-6,9-diene-2,8-dione	40.54	1922	6.12	diverse functional groups
n-Hexadecanoic acid	44.59	1961	13.37	saturated fatty acid
Meteoriopsis reclinate, MR				
Nonanal	10.16	1105	10.88	aldehyde
Nonanoic acid	14.83	1276	6.78	saturated fatty acid
3,7,11,15-Tetramethyl-2-hexadecen-1-ol	28.09	1840	2.64	polyprenol
Pentadecanoic acid	28.37	1854	2.33	saturated fatty acid
7,9-Di-tert-butyl-1-oxaspiro(4,5)deca-6,9-diene-2,8-dione	29.74	1922	1.59	diverse functional groups
n-Hexadecanoic acid	30.58	1966	16.21	saturated fatty acid
Arachidonic acid	32.06	2044	3.10	polyunsaturated fatty acid
Phytol	33.35	2114	4.11	diterpene alcohol
9,12-Octadecadienoic acid (Z,Z)-	33.74	2136	4.66	saturated fatty acid
4,8,12,16-Tetramethylheptadecan-4-olide	37.48	2355	2.44	aliphatic lactone
Squalene	46.38	2961	45.26	triterpene

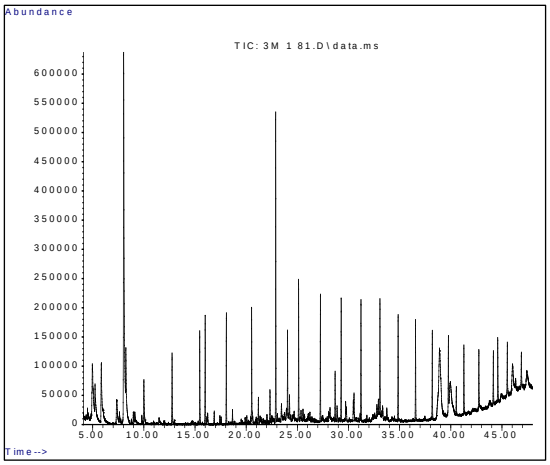
Table 2 (cont'd). The chemical constituents of **LS**, **MR**, and **CR** moss extracts

Constituent	**RT (minute)**	**RI[a]**	**% Peak Area**	**Compound Class**
Calyptotheciom ramosii, CR				
Phytol acetate	28.088	1839	14.03	diterpene ester
7,9-Di-tert-butyl-1-oxaspiro(4,5)deca-6,9-diene-2,8-dione	29.75	1922	4.57	diverse functional group
Oxacycloheptadec-8-en-2-one, (8Z)	30.008	1936	9.59	cyclic ester
n-Hexadecanoic acid	30.577	1965	29.03	saturated fatty acid
Phytol	33.3525	2114	17.86	diterpene alcohol
4,8,12,16-Tetramethylheptadecan-4-olide	37.4895	2355	6.11	diterpenoid
Squalene	44.6135	2831	18.81	triterpene
Mitthydridium andulatum, MA				
Benzoic acid, 2,4-dihydroxy-3,6-dimethyl-, methyl ester	25.4237	1712	12.89	diverse functional groups
n-Hexadecanoic acid	30.561	1964	15.83	saturated fatty acid
Phytol	33.359	2114	12.13	diterpene alcohol

[a] Retention Index (HP-5ms column), [b] Compounds listed in order of elution from a HP-5ms column

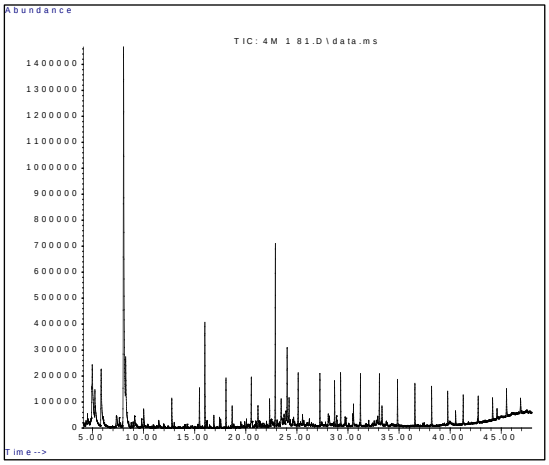


(PB) **(HP)**

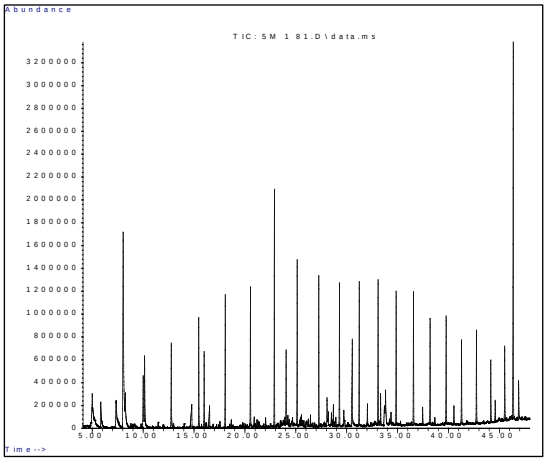


(GR)

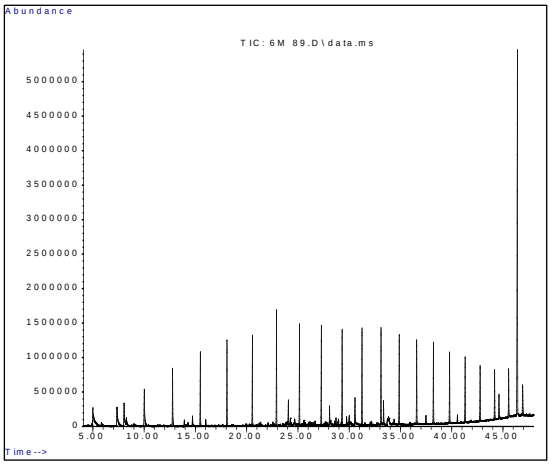
Figure 1. Total ion chromatogram of DCM extracts of dried **PB**, **HP** and **GR** with n-alkanes



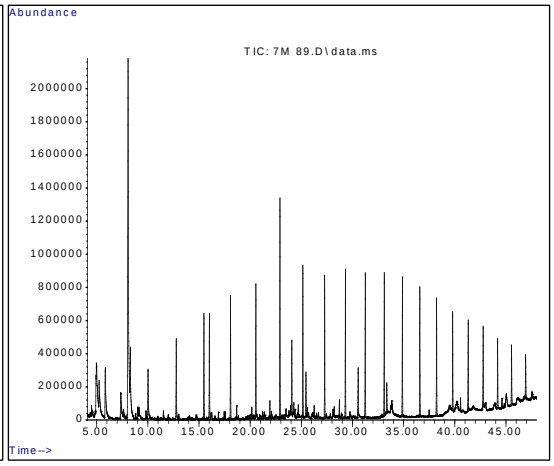
(LS)



(MR)



(CR)



(MA)

Figure 2. Total ion chromatogram of DCM extracts of dried **MR**, **CR**, and **MA** with n-alkanes

Elemental composition by energy dispersive X-ray spectroscopy analysis

Dehydrated samples from the seven mosses were subjected to elemental analysis using energy dispersive X-ray spectrometry (Shimadzu EDX-7000) in 10mm Mylar cups. Table 3, Figure 3 and 4 shows the chemical compositions of the adsorbents in elemental percentage (<ppm). For all species, $C_6H_{10}O_5$ (polydextrose units) were found to be dominant in the biomass ranging from ~51% to ~96%. Tukey's post hoc multiple analyses showed significant differences in silicon concentration in **GR** *vs.* **LS**, **CR**, **MR**, and **MA**. Multiple comparisons in $C_6H_{10}O_5$ displayed disparate differences in **GR** *vs.* **PB**, **HP**, **LS**, **MR**, **CR**, and **MA**. The moss **GR** was found to be the most unique as it contained elements, Ir (0.003%) and V (0.045%), which are not detected in the other samples.

Hierarchical clustering has been utilized to interpret data through calculating the distance matrices of data objects and then merging objects that are close to each other to form sub-clusters [13]. The heatmap (Figure 3) demonstrated a pattern in element composition between **LS** and **MA** and were found comparable to **HP** and **MR**. **PB** and **CR**, on the other hand, were grouped in one cluster due to the shared intensity in percent element composition of the elements Cl, K, Br, P, S and Sr. In addition, **PB** and **CR** were within the same range of percent polydextrose units present at 89.597% and 92.353%, respectively. Furthermore, the heatmap proved the distinguishable characteristic of **GR** which was found to contain a significantly larger amount of the same elements detected in the other moss samples. **GR** was grouped in its own cluster and was also found to contain the lowest amount of cellulose (at 51.987%) among the other elements detected including Ca (11.427%), Si (19.361%), Fe (5.995%), Al (6.589%), Mg (2.903%) and Ti (0.561%).

Table 3. Elemental analysis (EDX) of mosses

	PB	**HP**	**GR**	**LS**	**MR**	**CR**	**MA**
Analyte	**Elemental %**						
Ca	4.497	1.856	11.427	1.192	6.518	2.780	1.994
Si	1.923	2.032	19.361	1.007	0.282	1.212	0.437
K	1.504	0.458	0.419	0.534	0.622	0.717	0.718
Fe	0.675	0.575	5.995	0.354	0.043	0.138	0.118
S	0.606	0.195	0.440	0.161	0.433	0.878	0.556
Al	0.471	1.965	6.589	0.533	0	0.252	0.421
P	0.400	0.181	0	0.041	0.193	0.513	0.077
Cl	0.244	0.110	0	0.082	0.117	0.152	0.117
Ti	0.033	0.072	0.561	0.031	0	0.017	0.011
Mn	0.013	0.017	0.147	0.009	0.010	0.016	0.007
Mg	0	0	2.903	0.329	0.805	0.743	0.434
Zn	0.013	0.013	0.016	0.004	0.011	0.022	0.005
Sr	0.013	0.009	0.014	0	0.012	0.014	0.007
Cu	0.007	0.006	0.065	0.005	0.007	0.006	0.005
Br	0.003	0.001	0.001	0.001	0	0.002	0.002
Cr	0.002	0.002	0.026	0.003	0.002	0.002	0
Ir	0	0	0.003	0	0	0.001	0
V	0	0	0.045	0	0	0	0
$C_6H_{10}O_5$	89.597	92.507	51.987	95.7123	90.945	92.353	95.090

Elevated percentages of calcium (Ca) in all of moss samples indicated that each moss species metabolized a high consumption of mineral nutrients absorbed from the substrates as demonstrated by Figure 3. It has been reported that calcium ingestion in healthy elderly women are beneficial in the normalization of lipid profiles, glucose metabolism, and reduction in blood pressure [14, 15].

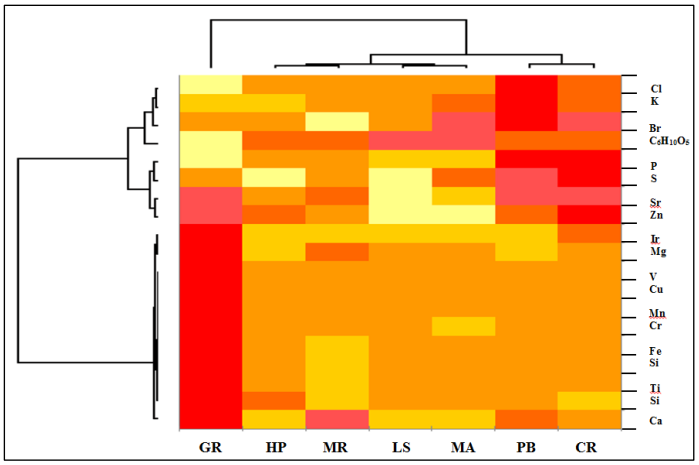
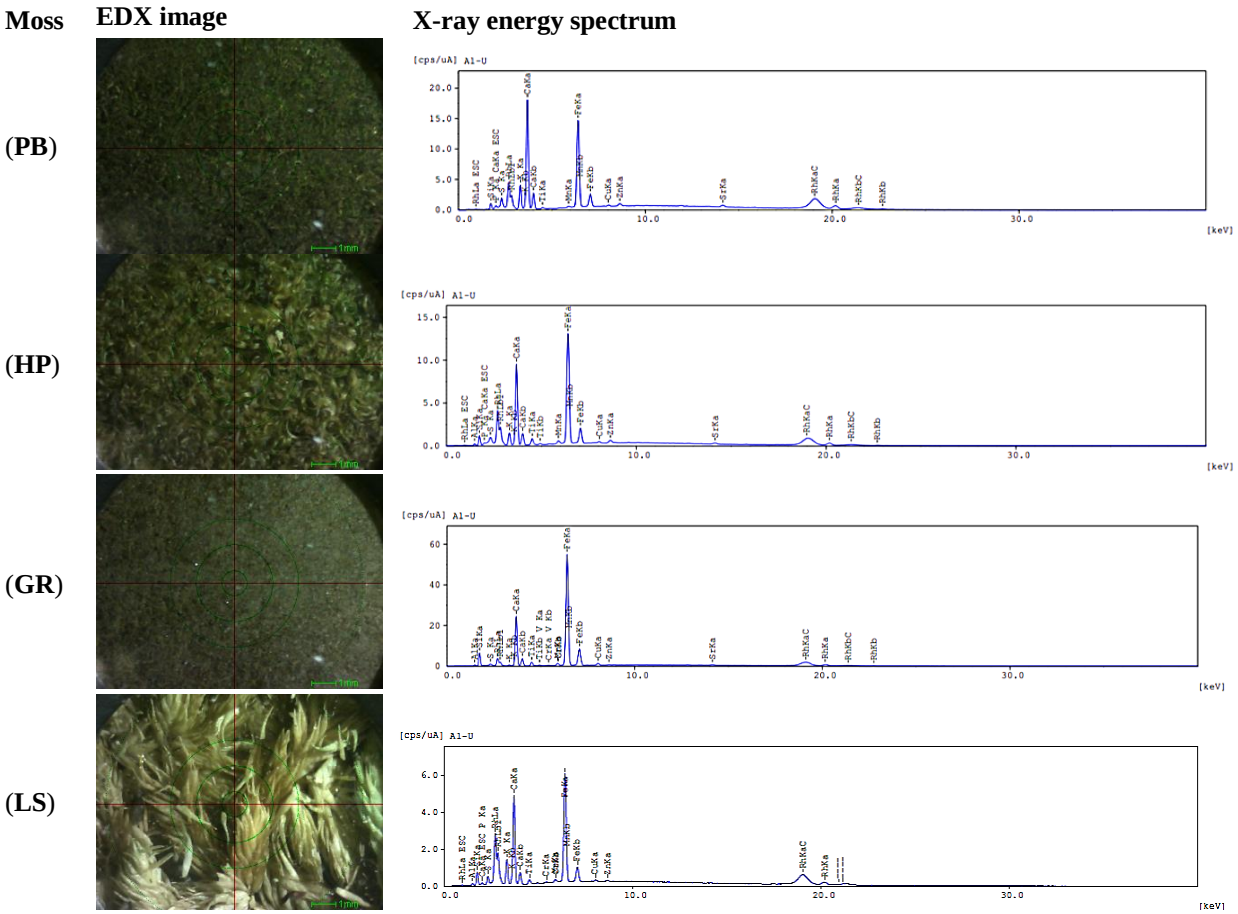


Figure 3. A hierarchically clustered heat map of the element analyses inherent in mosses.



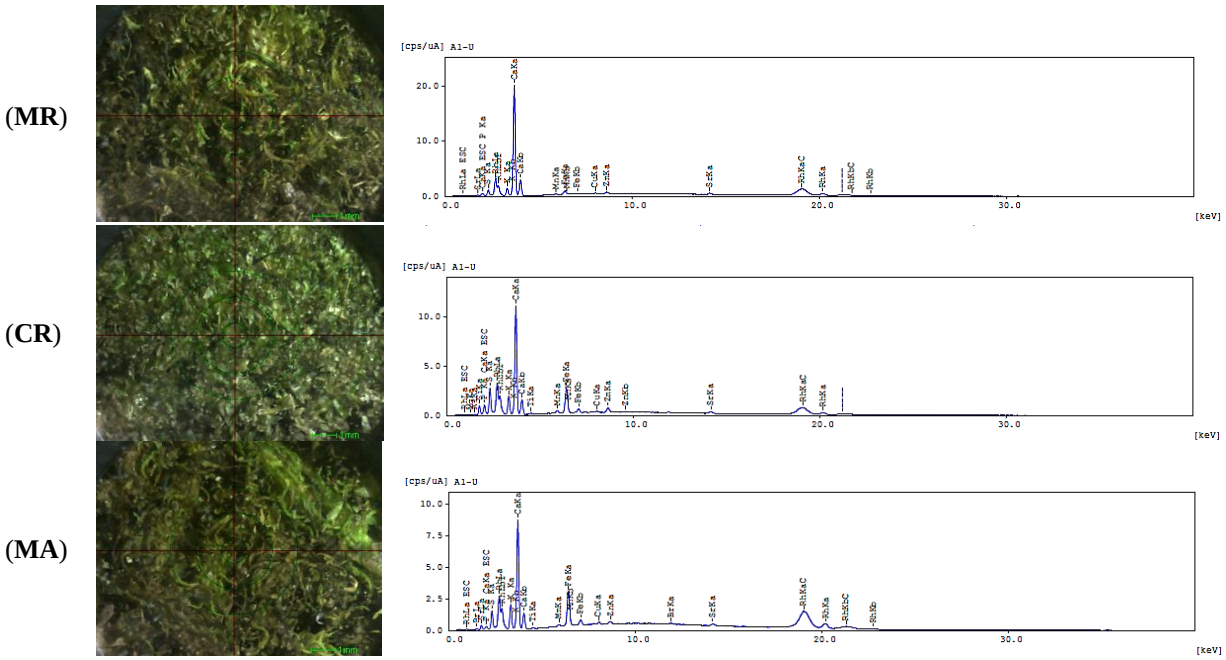


Figure 4. EDX image and X-ray energy spectrum of **PB**, **HP**, **GR**, **LS**, **MR**, **CR**, and **MA**

Free radical scavenging activity

DCM extracts of the mosses were tested for their free radical scavenging activity as seen in Figure 5. The inhibitory activity of the mosses was found to vary in range starting with **GR** demonstrating the lowest IC_{50} at 0.236 mg/mL followed by **CR** at 0.306 mg/mL and then **PB** at 0.315 mg/mL. **MA** and **MR** both have moderate antioxidant activity exhibiting IC_{50} = 1.360 mg/mL and 1.554 mg/mL, respectively while **LS** and **HP** exhibited the highest half maximum inhibitory concentration values at 2.120 mg/mL and 2.213 mg/mL respectively. The IC_{50} value of all seven mosses was found to be primarily constituted by oxygenated sesquiterpenes which was also observed to exhibit high anti-oxidant activity. Even at low concentrations, these low-weight, volatile molecules were capable of either reducing or preventing oxidative damage caused by the production of reactive oxygen species [16]. These free radicals are typically produced in the intracellular compartments as by-products of the plant cell biochemistry. **GR**, which displayed the lowest IC_{50} value, was composed primarily of γ-cadinene or naphthalene, 1,2,3,5,6,8a-hexahydro-4,7-dimethyl-1-(1-methylethyl)-, (1S-cis)- (Peak area: 5.88%). This compound, also known as beta-cadinene, was found to be a component in the most commonly used basil, *Ocimum basilicum* L. The essential oil is largely known for its anti-oxidant properties [12].

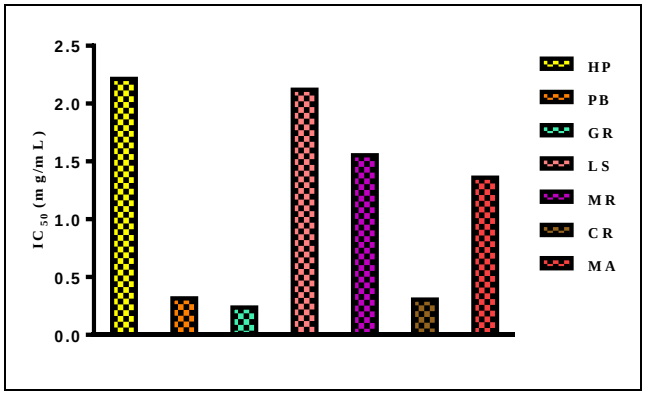


Figure 5. DPPH assay IC_{50} values of mosses

Conclusion

The focus of this study was to ascertain if mosses **PB**, **HP**, **GR**, **LS**, **MR**, **CR**, and **MA** could possess nutritive values based on chemical characterization and free radical scavenging assay. Among these seven mosses, **GR**, **PB**, and **CR** exhibited exceptionally low half maximal inhibitory potential against free radicals (IC_{50} less than 0.032 mg/mL). The half maximum inhibitory concentrations of **GR** (*G. recurvirostum*), **PB** (*P. boniamum*), and **CR** (*C. ramosii*) were better than the accepted values of other medicinal plants [17]. In all the seven moss species analysed in this study, $C_6H_{10}O_5$ were found to be the most dominant component ranging from ~51% to ~96% followed by calcium content which ranged from 1.199% to 11.427%. The following were the bioactive constituents found among the seven mosses analysed: **PB**, α-cadinol, caryophyllene and (-)-spathulenol; **GR**, pentanoic acid, 2,2,4-trimethyl-3-carboxyisopropyl, isobutyl ester, caryophyllenyl alcohol, and β-cadinene; **LS** predominately comprised of pentanoic acid, 2,2,4-trimethyl-3- carboxyisopropyl, isobutyl ester (56.26%) and n-hexadecanoic acid (13.37%); and **CR**, 4,8,12,16-tetramethylheptadecan-4-olide, 7,9-di-tert-butyl-1-oxaspiro (4,5) deca-6,9-diene-2,8-dione, phytol, and phytol acetate. The pharmacognosy of these mosses could be linked to the capabilities of each in the quenching of free radicals and could add to the furtherance of the utilization of these plants as pharma supplements. Future research should be directed towards the application of these moss extracts on diseases associated with oxidative stress or injury such as atherosclerosis, diabetes, and cancer.

Acknowledgement

A research grant, project number 10 IR 2TAY16-3TAY17 from De La Salle University Science Foundation through the University Research Coordination Office, is gratefully acknowledged.

References

1. Goffinet, B. and Buck, W. R. (2004). Molecular systematics of bryophytes. Missouri Botanical Garden Press, Illinois: pp. 205-239.
2. Dey, A. and Mukherjee, A. (2015). Therapeutic potential of bryophytes and derived compounds against cancer. *Journal of Acute Disease*, 4(3): 236-248.
3. Singh, M., Govindarajan, R., Nath, V., Rawat, A. K. S. and Mehrotra, S. (2006). Antimicrobial, wound healing and antioxidant activity of *Plagiochasma appendiculatum* Lehm. et Lind. *Journal of Ethnopharmacology*, 107: 67-72.
4. Saboljevic, A., Sokovic, M., Glamočlija, J., Čirič, A., Vujičic, M., Pejin, B. and Saboljevic, M. (2010). Comparison of extract bio-activities of in-situ and *in vitro* grown selected bryophyte species. *African Journal of Microbiology*, 4: 808-812.
5. Klavina, L., Springe, G., Nikolajeva, V., Martsinkevich, I., Nakurte, I., Dzabijeva, D. and Steinberga, I. (2015). Chemical composition analysis, antimicrobial activity and cytotoxicity screening of moss extracts (moss phytochemistry). *Molecules*, 20: 17221-17243.
6. Sun, S.-Q., He, M., Cao, T., Zhang, Y. C. and Han, W. (2008). Response mechanisms of antioxidants in bryophyte (*Hypnum plumiforme*) under the stress of single or combined Pb and/or Ni. *Environmental Monitoring and Assessment*, 149: 291-302.
7. Nozaki, H., Hayashi, K., Nishimura, N., Kawaide, H., Matsuo, A. and Takaoka, D. (2007). Momilactone A and B as allelochemicals from moss *Hypnum plumiforme*: First occurrence in bryophytes. *Bioscience Biotechnology Biochemistry*, 71(12): 3127-3130.
8. Sun, S.-Q., He, M., Cao, T., Yusuyin, Y., Han, W. and Li, J. L. (2010). Antioxidative responses related to H_2O_2 depletion in *Hypnum plumiforme* under the combined stress induced by Pb and Ni. *Environmental Monitoring and Assessment*, 163(1-4): 303-312.
9. Blois, M. S. (1958). Antioxidant determinations by the use of a stable free radical. *Nature*, 29: 1199-1200.
10. Scur, M. C., Pinto, F. G. S., Pandini, J. A., Costa, W. F., Leite, C. W. and Temponi, L. G. (2016). Antimicrobial and antioxidant activity of essential oil and different plant extracts of *Psidium cattleyanum* Sabine. *Brazilian Journal of Biology*, 76(1): 101-108.
11. Bittencourt, M. L. F., Ribeiro, P. R., Franco, R. L. P., Hilhorst, H. W. M., de Castro, R. D. and Fernandez, L.G. (2015). Metabolite profiling, antioxidant and antibacterial activities of Brazilian propolis: Use of correlation and multivariate analyses to identify potential bioactive compounds. *Food Research International*, 76(2015): 449-457.

12. Chávez-Gonzáles, M. L., Rodríguez-Herrera, R. and Aguilar, C. N. (2016). Essential oils: A natural alternative to combat antibiotics resistance antibiotic resistance in mechanisms and new antimicrobial approaches in antibiotic resistance. Academic Press, Massachusetts: pp. 227–237.
13. Moon, J. Y., Jung, H. J., Moon, M. H., Chung, B. C. and Choi, M. H. (2009). Heat-map visualization of gas chromatography-mass spectrometry based quantitative signatures on steroid metabolism. *Journal of American Society Mass Spectrometry*, 20(9):1626-1637.
14. Reid, I. R., Horne, A., Mason, B., Ames, R., Bava, U. and Gamble, G. D. (2005). Effects of calcium supplementation on body weight and blood pressure in normal older women: a randomized controlled trial. *Journal of Clinical Endocrinology Metabolism*, 90: 3824-3829.
15. Reid, I. R., Mason, B., Horne, A., Ames, R., Clearwater, J., Bava, U., Orr-Walker, B., Wu, F., Evans, M. C. and Gamble, G. D. (2002). Effects of calcium supplementation on serum lipid concentration on serum lipid concentrations in normal older women: a randomized controlled trial. *American Journal of Medicine*, 112: 343-347.
16. Khan, N., Afaq, F. and Mukhtar, H. (2008). Cancer chemoprevention through dietary antioxidants: Progress and promise. *Antioxidant Redox Signal*, 10: 475-510.
17. Pourmorad, F., Hosseinimehr, S. J. and Shahabimajd, N. (2006). Antioxidant activity, phenol and flavonoid contents of some selected Iranian medicinal plants. *African Journal of Biotechnology*, 5(11): 1142-1145.

Malaysian Journal of Analytical Sciences, Vol 23 No 6 (2019): 963 - 979
DOI: https://doi.org/10.17576/mjas-2019-2306-05

MALAYSIAN JOURNAL OF ANALYTICAL SCIENCES
Published by The Malaysian Analytical Sciences Society
ISSN 1394 - 2506

ANALYSIS OF VOLATILE COMPOUNDS OF SPICES GROWN IN BANYUMAS DISTRICT, JAWA TENGAH, INDONESIA USING SOLID PHASE MICROEXTRACTION-GAS CHROMATOGRAPHY MASS SPECTROMETRY

(Analisis Sebatian Meruap bagi Rempah yang Tumbuh di Daerah Banyumas, Jawa Tengah, Indonesia Menggunakan Pengekstrakan Mikro Fasa Pepejal-Kromatografi Gas Spektrometri Jisim)

Fajar Hardoyono[1]*, KikinWindhani[2], Herman Sambodo[2], Hary Pudjianto[2]

[1]*Laboratory of Physics, Faculty of Islamic Education and Teaching Sciences, Institut Agama Islam Negeri Purwokerto, Jalan A. Yani 40 A, Purwokerto, Indonesia*
[2]*Department of Economics and Development Studies, Faculty of Economics and Business, Universitas Jenderal Soedirman, Jalan HR. Bunyamin 708, Purwokerto, Indonesia*

**Corresponding author: hardoyono@iainpurwokerto.ac.id*

Received: 14 October 2018; Accepted: 31 October 2019

Abstract

Indonesia is well-known as one of high-quality spices producers in the world. Some of the spices products from Indonesia show high economic value in the European market due to their taste, flavour, and deliciousness. The quality of Indonesian spices was contributed by specific volatile constituents identified in the essential oils. This paper investigated major volatile constituents from seven types of spice grown in Banyumas District, Jawa Tengah, i.e. pepper, nutmeg, cinnamon, clove, chilli pepper, ginger, and turmeric. For experiment, 5 kg of each spice was collected from the farm surrounding Banyumas District, Jawa Tengah. Specific parts of these materials were selected. Pepper, nutmeg, and cloves used the seeds; ginger and turmeric used the rhizomes; while cinnamon used the bark. Each spice was prepared separately through these procedures: (1) slicing the spices; (2) drying the spices in a drying cabinet for 24 hours at 40 °C; (3) grinding the dried spices to powder for 5 minutes at 2500 rpm. For solid phase microextraction-gas chromatography mass spectrometry (SPME-GC/MS) analysis, 200 mg of spice powder was put in a vial glass. The fibre extracted volatile compounds of spice. Mass spectrometry detector identified the volatile compounds based on molecularly mass of molecules. Data tabulation of seven SPME-GC/MS chromatograms identified 69 volatile compounds in seven types of spice. Major volatile compounds dominant in pepper were caryophyllene and δ-limonene. Myristicin, methyl-eugenol, terpinene-4-ol, and asarone were major compounds in nutmeg. Cinnamon and clove were dominated by cinnamaldehyde and γ-muurolene, respectively. β-elemene and α-muurolene were identified as major compounds in chilli pepper. Meanwhile, ginger and turmeric were dominated by sesquiphellandrene and ar-tumerone, respectively. Some major compounds identified in these spices were bioactive and efficacious for human health as anticancer, antioxidant, and antitumor.

Keywords: Indonesian spices, volatile compounds, solid phase microextraction-gas chromatography mass spectrometry

Abstrak

Indonesia terkenal dengan produk rempah berkualiti tinggi. Beberapa produk rempah dari Indonesia menunjukkan nilai ekonomi yang tinggi di pasar Eropha kerana rasa, aroma dan kelazatannya. Kualiti rempah Indonesia disebabkan oleh juzuk sebatian meruap yang dikenalpasti di dalam minyak pati. Kajian ini menyiasat sebatian meruap utama pada 7 jenis rempah Indonesia yang tumbuh di daerah Banyumas, iaitu lada hitam, buah pala, kayu manis, cengkih, cili, halia dan kunyit. Untuk penelitian, setiap 5 kg rempah diperoleh dari kebun di sekitar daerah Banyumas, Jawa Tengah. Bahagian khusus dari bahan mentah dipilih

untuk eksperimen. Untuk lada hitam, buah pala, dan cengkih menggunakan biji, halia dan kunyit menggunakan rhizom, manakala kayu manis menggunakan pelepah. Selanjutnya, setiap rempah disiapkan untuk analisa pengekstrakan mikro fasa pepejal-kromatografi gas spektrometri jisim (SPME-GC/MS) melalui prosedur berikut: (1) Pengirisan rempah; (2) pengeringan rempah selama 24 jam pada suhu 40 °C; (3) Penggilingan rempah kering menjadi serbuk selama 5 minit pada kelajuan 2500 rpm. Bagi analisa pengekstrakan mikro fasa pepejal-kromatografi gas spektrometri jisim SPME-GC/MS, 10 mg serbuk rempah diletakkan di dalam vial kaca. Spektrometer jisim mengenalpasti sebatian meruap berdasarkan berat molekul. Olahan data kromatogram SPME-GC/MS merekodkan 60 sebatian meruap pada 7 jenis rempah Indonesia. Sebatian utama bagi lada hitam ialah kariofelena dan δ-limonena. Miristisin, metil-eugenol, terpinen-4-ol dan asaron merupakan sebatian utama bagi buah pala. Kayu manis dan cengkih, masing -masing mengandungi sinamaldehid dan γ-muurolena. β-elemene dan α-muurolene dikenalpasti sebagai sebatian utama bagi sampel cili. Manakala, halia dan kunyit masing-masing mengandungi seskuifelandrena dan ar-tumeron. Semua sebatian yang dikenalpasti pada rempah ini bersifat bioaktif dan berkhasiat bagi kesihatan manusia sebagai antikanser, antioksidan, dan antitumor.

Kata kunci: rempah Indonesia, sebatian meruap, pengekstrakan mikro fasa pepejal-kromatografi gas spektrometri jisim

Introduction

Indonesia is well known as one of the spices producing countries in the world. High quality of spices from Indonesia has invited European countries for hunting spices in the Indonesian archipelago. In ancient time, the history of Indonesian civilization through Srivijayan and Majapahit Empire corresponded with spice trade [1]. The colonialism in Indonesia since the 15th century by the Portuguese, British, and Dutch Indies was also stimulated by the volition for dominating and controlling spice trade in the European market [2, 3].

In the modern era, spices are still the prime commodities of agro-industry that supporting income for the Indonesian government [4]. The total national income obtained from exporting spice products reaches more than US $801 million. The eight top highest values of exported Indonesian spice products in 2015 were pepper (US $535.37 million), nutmeg (US $106.97 million), cinnamon (US $100.55 million), clove (US$46.36 million), dried chilli (US $22.11 million), vanilla (US $16.55 million), ginger (US $12.25 million), and turmeric (US $10.23 million). The majority of these products are exported to the European market [5]. Even though there are some other spice producing countries including India, Madagascar, and Comoros, the European market still prefers Indonesian spice products than those of other countries [6]. In 2012, Indonesia was the biggest supplier of turmeric and cinnamon. The contribution of turmeric and cinnamon from Indonesia in the European market was almost 78% and 63%, respectively. Moreover, the market share of clove commodities from Indonesia has contributed 21% to the European market. These cases indicated that the quality of clove and other spices grown in Indonesia is unique, tasteful, and preferred by the customer.

Spice commodities have been well-known as the tasteful and aromatic agro-industry products. Delicious taste and spicy aroma in spice commodities promise worth the price of these products. On the other hand, the composition of volatile organic compounds is worth the flavour and the taste of spices. Different composition of major compounds generates different odour description in some spices. Commonly, spices odour exhibits a warm, sweet, bitter, and spicy taste with a slightly pungent mouth [7]. Spices widely grow in some regions in the world, e.g. Central America, Mexico, India, Iran, Africa, Mediterranean countries, Europe, Africa, China, and Southeast Asian countries. Some spices, e.g. pepper, nutmeg, cinnamon, clove, chilli pepper, vanilla, ginger, and turmeric are well-grown in Indonesia, China, India, Thailand, Brazil, and Madagascar, Central America, and other countries [8]. Commonly, the composition of volatile organic compounds also depends on the growing location of these plants. The similar spice grown in the different regions has a different composition of volatile compounds, flavour, and taste. Indonesia is well-known as one of the aromatic and tasteful spices producing countries in the world. These main spices commodities exported to the overseas are pepper, nutmeg, cinnamon, clove, chilli pepper, vanilla, ginger, and turmeric. Based on the data from Food and Agriculture Organization (FAO), Indonesia is the largest producer of vanilla and clove, and also the second-largest producer of pepper and nutmeg [5]. The growing location of these spice commodities is widely spreading in almost all Indonesian archipelagos, especially in Sumatera, Maluku, Sulawesi, and Papua [1]. The total production of these spices commodities from Indonesia was almost 216,000 tons in 2014 [5].

Previous research reported the composition of volatile organic compound of some spices as follows pepper [9, 10], nutmeg [11, 12], cinnamon [13, 14], clove [15, 16], chilli pepper [17, 18], ginger [19, 20] and turmeric [21, 22]. However, the previous articles that especially reported the identification of chemical constituents of Indonesian spices were still rare in International Journal. Some of them were reported by [23, 24, 25]. Dupuy et al. [23] that described the composition of the volatile compound of Indonesian nutmeg essential oil based on gas chromatography and chemometric analysis of mid-infra-red. Amelia et al. [24] reported the volatile composition of Indonesian clove bud essential oil grown in Java and Manado. Meanwhile Retnowati et al. [25] investigated the chemical constituents of the essential oil of white turmeric (zedoary) from Indonesia and its toxicity toward *Artemia salina lench*. Other Indonesian spices, i.e. pepper, cinnamon, chilli pepper, ginger and also turmeric have not been reported yet in the paper.

Indonesia as one of the biggest producing spice commodities in the world must take care of the quality of the spices as the raw material of food flavouring, herbal drink, and herbal medicine. Investigation of chemical compounds of the main Indonesia spices grown in Indonesia is necessarily conducted. Based on previous references, the composition of chemical compounds in the spices essential oil was commonly identified using chromatographic techniques and non-chromatographic techniques. The most common chromatographic techniques for identification of volatile compounds in ginger used solid-phase micro-extraction gas chromatography/mass spectroscopy (SPME-GC/MS) [17, 26] thin layer chromatography (TLC) [27] and high-performance liquid chromatography (HPLC) [28, 29]. In addition, Fourier transforms infrared spectroscopy (FTIR) [30] and electronic noses [31] were also used as common techniques of non-chromatographic used for identifying chemical components in spice essential oils.

SPME-GC/MS is a technique of quantitative analysis most commonly used for identifying the composition of the chemical compound for spices in the solid phase. The employing of this instrument has been used for identifying the chemical composition of pepper [32] cinnamon [33], ginger [34], and chilli pepper [17, 35]. SPME-GC/MS is equipped with fibres for extracting the volatile organic compound of the solid sample and mass spectroscopy detector for calculating molecular mass. This instrument is also possible for obtaining information on the name of identified chemical compounds and their quantities rapidly in a solid phase [36]. The aim of this study is to identify the composition of the volatile organic compound of the main spice commodities grown in Indonesia and also estimate the odour profile and the efficaciousness of spices for health. In the experiment, seven types of spice, i.e. pepper, nutmeg, cinnamon, clove, chilli pepper, ginger, and turmeric were analysed using solid phase micro-extraction gas chromatography-mass spectrometry (SPME-GC/MS). The identification of major compounds in the spices was conducted by analysing the chromatogram obtained from GC/MS. Based on the quantity of volatile compounds identified in spices, the aroma profile and the potency of spices can be estimated.

Materials and Methods

Materials

We used seven types of spice grown in Indonesia, i.e. pepper (*Piper nigrum*), nutmeg (*Myristica fragrans*), cinnamon (*Cinnamomum verum*), clove (*Syzygium aromaticum*), chilli pepper (*Capsicum frutescens*), ginger (*Zingiber officinale*), and turmeric (*Curcuma longa*). Five kg of raw material were taken out for each type of spice. These raw materials were collected from seven different farms, surrounding Banyumas district, Jawa Tengah, Indonesia from February 2017 until April 2017. The locations of farms for collecting the materials were presented in Table 1. The part of the spices that yielded a strong aroma is used as a sample. Pepper, nutmeg, and clove were taken part of the seeds. Ginger and turmeric were taken part of the rhizome, while cinnamon was taken part of the bark. We selected only fresh, wet, tasteful and aromatic spices for obtaining the optimum concentration of the essential oil in these materials.

Table 1. List of location for obtaining sample of seven types of spice grown in Indonesia

Date of collection	Variety	Location	Latitude Longitude	Altitude (m)	Weight (kg)
February 2, 2017	Pepper (*Pipper nigrum*)	Cingebul village, surrounding Lumbir, Banyumas district, Jawa Tengah	S: 7.458248 E: 108.913593	580	1.20
February 10, 2017	Nutmeg (*Myristica fragrans*)	Kemawi village, surrounding Somagede, Banyumas district, Jawa Tengah	S: 7.536195 E: 109.366314	760	2.45
March 3, 2017	Cinnamon (*Cinnamomum verum*)	Krajan village, surrounding Pekuncen, Banyumas district, Jawa Tengah	S: 7.335283 E: 109.083641	860	3.50
March 15, 2017	Clove (*Syzygium aromaticum*)	Klinting, surrounding Somagede, Banyumas district, Jawa Tengah	S: 7.543079 E: 109.334887	765	2.10
March 27, 2017	Chilli pepper (*Capsicum frutescens*)	Kemutug lor village, surrounding Baturaden, Banyumas district, Jawa Tengah	S: 7.293833 E: 109.228711	760	3.50
April 8, 2017	Ginger *(Zingiber officinale var officinale*)	Karang gondang , Sambirata village, surrounding Cilongok, Banyumas district, Jawa Tengah	S: 7.313662 E: 109.147474	580	10.80
April 21, 2017	Turmeric (*Curcuma longa*)	Gunung lurah village, surrounding Cilongok, Banyumas district, Jawa Tengah	S: 7.379301 E: 109.151232	410	2.50

Preparation of sample

All spices collected from the farm were washed using water to remove the soil which adhered to the surface of the spices. After finishing the washing process, the spices were dried in a drying cabinet for 24 hours at 40 °C. For ginger, turmeric, and cinnamon these materials were sliced before dried in drying cabinet. The slicing dimension was set up at 1 cm x 1 cm x 0.1 mm. The spices were grinded to powder using a blender machine (Philips, Netherlands) for 5 minutes at 2500 rpm. Thus, the powder was kept in a-100 mL glass bottle and put in a storage box at 25 °C. The procedure of sample preparation of the spices was conducted separately to avoid cross-contamination of odour and volatile organic compounds among spices.

SPME-GC/MS instrument

SPME-GC/MS analyses were carried out using Shimadzu GC/MS-QP-2010 (Kyoto, Japan), equipped with auto-sampler Agilent 7683b and MSD Agilent 5975C mass spectroscopy. GC/MS was coupled to QP 2010 SE mass spectrometer (Compaq-Pro Linear data system, class 5 K software). It was equipped with Agilent- DB-1 column (30m x 0.25mm i.d. x 0.2µm film thickness Crossband R 100% dimethylpolysiloxane). A manual SPME holder, a type of fibre (65 µm-blue hub plain, polydimethylsiloxane/divinyl-benzene (PDMS/DVB)) and 10 mL vials from Supelco (Bellefonte, USA) were used for the extraction procedures.

Identification of volatile compound with SPME-GC/MS

The fibres were conditioned for 10 minutes at 250 °C in the GC/MS injector before SPME-GC/MS analysis. Two hundred mg of spice powder was put in a 10-mL of the vial. The fibre coating was embedded into the headspace to determine temperature and time value set in the experiment. The temperature was set at 50 ºC while incubation and extraction time were set 5 minutes and 10 minutes, respectively. The fibre containing the extracted volatile compounds of ginger was injected into GC/MS. The direct injection of helium was used as the carrier gas in the split mode. Injector and detector temperature were maintained at temperature between 200 ºC and 280 ºC. The measurement of each spice sample using GC/MS equipped with auto-sampler was set for about 60 minutes. The temperature of the column was programmed initially at 70 ºC and then increased at 250 ºC for 10 minutes (at a rate of 18 °C min^{-1}). Mass conditions were followed: ionization voltage, 70 eV; ion source temperature, 200 °C; full scan mode in the 30-450 amu mass ranges with 0.2 s $scan^{-1}$ velocities. The identification of compounds was identified by using NIST 08 database (NIST mass spectral database, PC Version 2008). The total ion current from GC/MS spectra was used to calculate the relative percentages of separated compounds by a computerized integrator. This procedure of SPME-GC/MS analysis was similar for all spices samples and it was replicated three times for each type of spice. Thus, the average quantity of volatile compounds from three times measurement was used for data tabulation.

Results and Discussion

Composition of volatile constituents

The chromatograms obtained from SPME-GC/MS analyses of seven types of spice are shown in Figures 1-3. Moreover, data tabulation of major volatile compounds of them is presented in Table 2. Pepper, the first variety of Indonesian main spices was dominated by caryophyllene and δ-limonene. The abundances of these compounds in pepper were 45.10% and 26.11%, respectively (Table 2). Other lower quantities of major compounds identified in pepper were: caryophyllene oxide (5.10%), 3-carene (4.12%), α-caryophyllene (3.55%), β-pinene (2.76%), tetracyclo [6.3.2.0(2,5).0(1,8)] tridecan-9-ol, 4,4-dimethyl] (1.97%), β-myrcene (1.90%), δ-elemene (1.71%), δ-cadinene (1.67%), spathulenol (1.47%), and aroma dendrene (1.16%).

Caryophyllene, the largest quantity of volatile compounds identified in pepper was a member of the class of compounds known as sesquiterpene. Previous research reported that the odour description of caryophellene was spicy, woody and cider wood odour [8]. Consequently, the presence of caryophellene that was more than 45% contributed to appearing the spicy taste in pepper. Moreover, this compound has potency for the human as antimicrobial [37, 38]. Furthermore, the taste of sour and lemon-like in pepper was contributed by δ-limonene [8]. Based on previous studies this compound was efficacious as antibacterial [39], antitumor [40], and anticancer [41]. Other chemical compounds identified in lower quantities in pepper were caryophyllene oxide (5.10%) and 3-carene (4.12%). Caryophyllene oxide is categorized as a cannabinoid. It is a metabolite of β-caryophyllene, which is an essential oil found in *C. sativa* and other plants [42]. These bioactive compounds have potency as an anti-inflammatory [43]. While 3-carene, is a bicyclic monoterpene, contributed a sweet and pungent turpentine-like odour [44, 45].

The composition of volatile compounds identified in nutmeg was dominated by myristicin (24.55%), methyl-eugenol (21.24%), terpinen-4-ol, and asaron (14.20%) (Table 2). The myristicin, the largest quantity identified in the nutmeg is a phenylpropane. This compound is commonly found in the essential oil of nutmeg, parsley, and dill that contributes to spicy odour [45]. Myristicin has been investigated as a bioactive compound used for antioxidant and anticancer [46, 47]. Methyl-eugenol was also identified almost as same as concentration to myristicin. This compound was well-known as allylveratrol. In the nutmeg essential oil, this compound has a delicate clove-carnation odour with a bitter and burning taste [44]. It also had bioactive properties like antioxidant, antibacterial, antifungal, and bioinsecticide [48, 49]. Furthermore, terpinen-4-ol, the third major compound identified in nutmeg, contributed to sweet, and citrus green with the fruity character [44]. This bioactive compound has potency as antioxidant [50], antifungal [51], antibacterial [52], and antiviral [53].

Four major compounds were identified in cinnamon, i.e. cinnamaldehyde (65.38%), copaene (8.02%), α-bergamotene (7.95%), and α-bisabolene (5.13%) ((Table 2). Other lower quantities of volatile compounds identified in cinnamon were: β-bisabolene, δ-cadiene (2.71%), eugenol (1.80%) and β-cadiene (1.02%).

Cinnamaldehyde, a flavonoid, was identified as the highest quantity compound in cinnamon. Due to appear significantly, this compound contributes to the specific odour and flavour in cinnamon [44]. This compound has potency as antimicrobial properties [54]. Besides the cinnamaldehyde, the copaene and α-bergamotene appeared also in the cinnamon. Even these compounds appeared around 8%, the copaene and α-bergamotene contributed to woody type odour, respectively. Other volatile compounds identified in the cinnamon were α-bisabolene and β-bisabolene. These two compounds are isomers and sesquiterpenes. The total quantity of these compounds in the cinnamon was around 5.13% and contributed to a pleasant, warm, sweet-spicy-balsamic odour [44]. Based on the previous investigation, β-bisabolene was exhibited cytotoxicity in breast cancer cell lines, and also antitumor agent [55, 56].

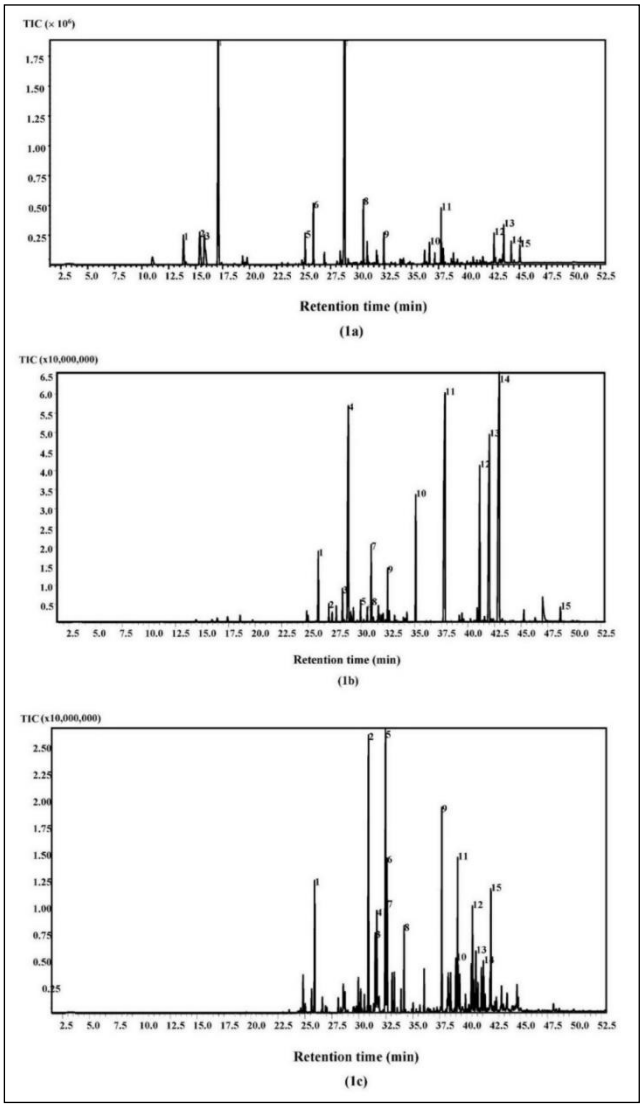


Figure 1. SPME-GC/MS chromatogram of the spices grown: (1a) pepper, (1b) nutmeg, (1c) cinnamon

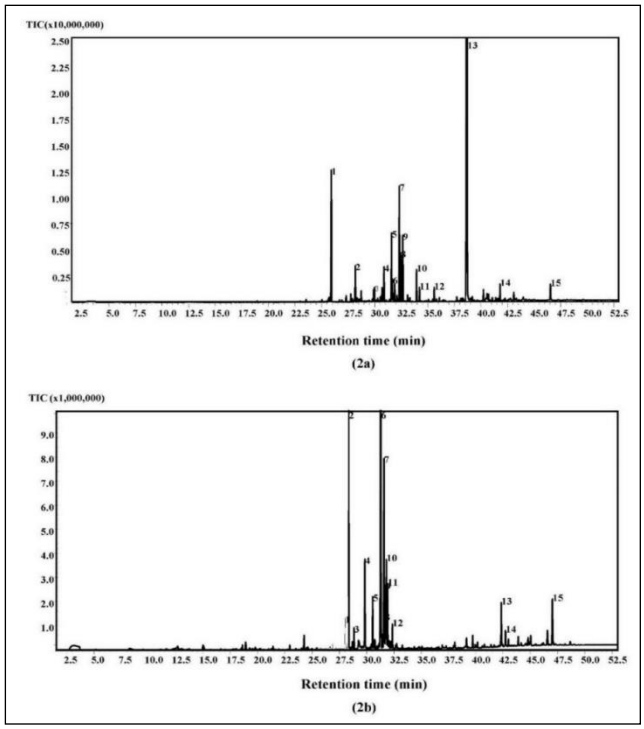


Figure 2. SPME-GC/MS chromatogram of the spices: (2a) clove, (2b) chilli pepper

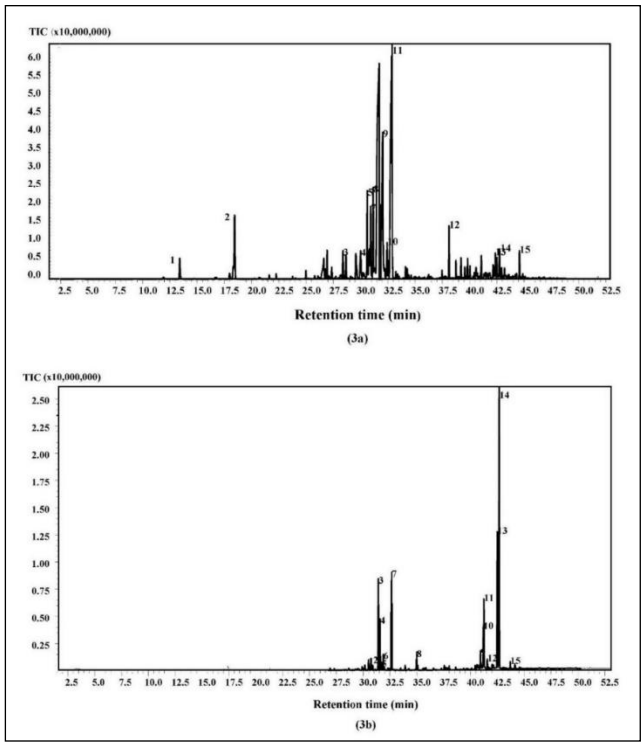


Figure 3. SPME-GC/MS chromatogram of dried spices grown in Banyumas District, Jawa Tengah, Indonesia: (3a) ginger, and (3b) turmeric

Table 2. List of major volatile organic compound in the spices

Compound Name	Concentration of TIC (%)						
	Pepper	Nutmeg	Cinnamon	Clove	Chilli	Ginger	Turmeric
2-methoxycinnamaldehyde	-	-	0.87	-	-	-	-
3-carene	4.12	-	-	-	-	-	-
α-terpineol	-	3.28	-	-	-	-	-
α-bergamotene	-	1.14	7.95	-	-	-	-
α-bisabolene	-	-	5.13	-	-	-	-
α-bisabolol	-	-	0.71	-	-	-	-
α-bulsenene	-	-	-	-	1.01	-	-
α-cadinol	-	-	-	10.28	-	-	-
α-caryophyllene	3.55	0.45	-	-	-	-	-
α-eudesmol	-	-	-	-	1.88	-	-
α-farnesene	-	-	-	-	-	14.01	1.55
α-muurolene	-	-	-	4.56	27.83	-	-
α-selenine	-	-	-	-	20.37	-	-
α-terpineol	-	-	-	-	-	3.88	-
Aromadendrene	1.16	-	0.62	-	-	-	-
Artemisia ketone	-	-	-	-	-	-	4.37
Ar-tumerone	-	-	-	-	-	-	32.46
Asarone	-	14.20	-	-	-	-	-
Benzene, 1,3,5-trimethoxy-	-	-	-	4.76	-	-	-
Benzene, 1-methoxy-4-(1-propenyl)-	-	-	-	-	-	-	-
β-bisabolene	-	-	-	-	-	-	6.02
β-cadinene	-	-	1.02	-	-	-	-
β-elemene	-	-	-	-	31.55	2.03	-
β-eudesmol	-	-	-	-	-	1.91	-
β-farnesene	-	0.57	-	-	-	-	-
β-himachalene	-	-	-	-	-	3.73	1.10
β-myrcene	1.90	-	-	-	-	-	-
β-pinene	2.76	-	-	-	-	-	-
β-selenine	-	-	-	-	3.44	-	-
Borneol	-	-	-	-	-	5.79	-
Calamenene	-	-	0.69	4.13	-	-	-
Camphene	-	-	-	-	-	1.44	-
Caryophyllene	45.10	-	-	-	-	-	-
Caryophyllene oxide	5.10	-	-	-	-	-	-
Cedrene	-	-	-	7.68	-	-	-
Cinnamaldehyde	-	-	65.38	-	-	-	-
Citral	-	-	-	-	-	5.10	-
Copaene	3.38	2.88	8.02	6.56	-	-	-
Curcumene	-	-	-	2.42	-	-	17.16
Curlone	-	-	-	-	-	-	14.40
Cyclopentanecarboxylic acid, 3-isopropylidene-, bornyl ester	-	-	-	-	-	-	0.73
Dehydronerolidol	-	-	-	-	-	1.72	0.85
δ-cadinene	1.67	1.86	2.71	17.15	-	-	-
δ-elemene	1.71	-	-	-	-	-	-
δ-limonene	26.11	-	-	-	-	-	-

Table 2 (cont'd). List of major volatile organic compound in the spices

Compound Name	Concentration of TIC (%)						
	Pepper	Nutmeg	Cinnamon	Clove	Chilli	Ginger	Turmeric
Eucalyptol	-	-	-	-	-	4.97	-
Eugenol	-	-	1.80	2.39	-	-	1.02
γ-muurolene	-	-	-	30.94	-	1.89	-
Globulol	-	-	-	-	-	2.40	-
Humulene	-	-	-	-	4.93	-	-
Isolongifolene, 4,5-dehydro-	-	-	-	-	4.61	-	-
Juniper-camphor	-	-	-	-	0.69	-	-
Linalool	-	0.54	-	-	-	-	-
Methyleugenol	-	21.24	-	9.13	-	-	-
Methylisoeugenol	-	8.03	-	-	-	-	-
m-Toluic acid, tridec-2-ynyl ester	-	-	-	-	-	-	0.95
Myristicine	-	24.55	-	-	-	-	-
Nerolidol	-	-	-	-	-	3.02	-
Phenol, 2,6-dimethoxy-4-(2-propenyl)-	-	0.68	-	-	-	-	-
p-Menthane, 2,3-dibromo-8-phenyl-	-	-	-	-	-	-	1.74
Safrole	-	4.99	-	-	-	-	-
Selinadiene	-	-	-	-	2.72	-	-
(-)-spathulenol	1.47	-	-	-	-	-	-
β-sesquiphellandrene	-	-	-	-	-	48.11	-
Terpinen-4-ol	-	-	-	-	-	-	-
Tetracyclo[6.3.2.0(2,5).0(1,8)]tridecan-9-ol, 4,4-dimethyl-	1.97	-	-	-	-	-	-
Tumerone	-	-	-	-	-	-	8.89
Xenitorin A	-	-	-	-	3.49	-	-
Zingiberene	-	-	-	-	-	-	9.78

The clove is mainly used for the cigarette industry as well as for food flavouring and seasoning. SPME-GC/MS analysis of clove identified four major compounds, i.e. γ-muurolene (30.94%), δ-cadinene (17.15%), α-cadinol (10.28%), methyl-eugenol (9.13%), cedrene (7.68%), and copaene (6.56%) (see Table 2). Other compounds identified less than 5% were: α-muurolene (4.56%), curcumene (2.42%), and eugenol (2.39%). A compound of γ-muurolene was identified as the largest quantity in the clove that contributes woody type odour [44]. The compound of δ-cadinene appeared in appreciable content, contributed to herbal-type odour [44]; Previous studies showed that efficaciousness of this compound as anti-insecticide for eradicating of malaria, dengue, and filariasis mosquitoes [57], inhibited the growth of ovarian cancer [58], antifungal [59] and antibacterial [60]. The methyl-eugenol was also identified in the clove. This compound was well-known as allylveratrol. Similar to the nutmeg essential oil, this compound has a delicate clove-carnation odour with a bitter and burning taste [44]. It also had bioactive properties such as antioxidant, antibacterial, antifungal, and bioinsecticide [48, 49]. Meanwhile, the cedrene, identified in clove was a sesquiterpene that had cedar wood-like odour.

The SPME-GC/MS analysis of chilli pepper showed that this spice contained four volatile compounds, i.e. β-elemene (31.55%), α-muurolene (27.83%), α-bulsenene (1.01%), and α-selenine (20.37%). Other volatile compounds identified less than 5% were: humulen-(v1) (4.93%), Isolongifolene, 4,5-dehydro- (4.61%), xenitorin A (3.49%), β-selenine (3.44%), selenadiene (2.72%), α-eudesmol (1.88%) (see Table 2). β-elemene, the largest quantity in the chilli pepper is a sesquiterpene that has a floral odour. Previous research reported that the β-elemene has been used as medicinal plants due to efficacious as anticancer [61], antioxidant [62], antitumor [63] and anti-proliferative agent [64]. The α-muurolene was also identified in the chilli pepper as well as in the clove. The α-bulnesene and α-selinene, the other major compounds identified in the chilli pepper contributed to floral odour, respectively.

Ginger was one of the well-known herbal medicines used by people for hundreds of years. In Indonesia, ginger is usually used for spice, food flavouring, or beverages. The pharmaceutical industry in Indonesia has also utilized ginger as the raw material for producing herbal drink and herbal medicine. SPME-GC/MS analysis identified four major volatile compounds in ginger, i.e. sesquiphellandrene (48.11%), α-farnesene (14.01%), borneol (5.79%), and citral (5.10%). Other compounds identified less than 5% in ginger were: eucalyptol (4.97%), α-terpineol (3.88%), β-himachalene (3.73%), nerolidol (3.02%), globulol (2.40%), β-elemene (2.03%), β-eudesmol (1.91%), γ-muurolene (1.89%), dehydronerolidol (1.72%) and camphene (1.44%) (Table 2). Sesquiphellandrene was identified as the largest quantity in ginger. The sesquiphellandrene was a sesquiterpene that had herbal type odour. The previous study showed the efficaciousness of this compound as an anticancer [21]. Furthermore, α-farnesene, a sesquiterpene, was also identified in ginger. This compound releases green apple odour, and also has potency for antioxidant [65]. In addition, other chemical compounds identified in lower quantities were borneol and neral. Borneol is a bicyclic organic compound and a terpene derivative. This compound has a camphor-like odour and burning taste somewhat reminiscent of mint [44] and also has potency as anti-influenza virus [66] and antidepressant [67]. Meanwhile, citral has a spicy, fruity odour with a woody and balsamic odour. This compound has potency as antimicrobial, antioxidant, and antitumor [68].

The turmeric has been widely used in Indonesia mainly for food colouring, herbal beverages, and herbal medicines. SPME-GCMS analysis of turmeric identified five major volatile compounds, i.e. ar-turmerone (32.46%), curcumene (17.16%), curlone (14.40%), tumerone (8.89%), and β-bisabolene (6.02%) (Table 2). Other volatile compounds identified less than 5% were: artemisia ketone (4.37%), p-Menthane, 2, 3,-dibromo-8-phenyl- (1.74%), α-farnesene (1.55%). β-himachalene (1.10%), and eugenol (1.02%). Ar-turmerone, a sesquiterpene, identified as the most abundant in turmeric. Ar-turmerone has isomeric to turmerone. The total quantity of ar-turmerone and its isomer in turmeric essential oil was around 39%. The specific odour and taste of the turmeric were contributed by ar-turmerone [8]. This compound was also efficacious for human health as antitumor [69], antimicrobe [70], antiplatelet [71], and anti-venom [72]. The curcumene, another major compound in turmeric, contributed to yellow-bright colour in turmeric essential oil. This compound release turmeric-like odour, efficacious as antitoxic for malaria, chikungunya, and St. Louis encephalitis mosquito vectors [73]. Furthermore, curlone and zingiberene also appeared in turmeric essential oil even the quantity of them was not as much as ar-turmerone and curcumene. Curlone was commonly found in turmeric essential oils besides ar-turmerone and turmerone, while zingiberene was commonly identified as one of the major compounds in ginger. α-zingiberene has been reported as a bioactive compound that is efficacious for anti-aggregate, anticancer, anti-inflammatory, and antioxidant [46, 47].

Estimation of odour profile and the potency of spices for human based on the quantity of compounds

Burdock [44] has been investigated odour profile of pure organic volatile compounds. Several references also investigated the efficaciousness of volatile compounds of phytomedicine for human health. Both of them are presented simultaneously in Table 3. In this study, we estimate the odour profile of spices by looking through the number of volatile compounds in Table 2. Pepper and nutmeg have combination of woody, spicy and clove-like odour. The presence of caryophyllene in large quantity (45.10%) contributes for appearing strong woody, spicy and clove-like odour in pepper. Meanwhile, myristicine identified 24.55% contributes for moderate woody, spicy and clove-like odour in nutmeg.

Table 3. Odour description and efficaciousness of bioactive compound in spices based on previous research

Spice Name	Major Compound	Odour Description [44]	Benefit for Human Health
Pepper	caryophyllene	woody-spicy, dry, clove-like aroma	antimicrobial [37, 38]
	δ-limonene	citrus	antibacterial , antitumour, anticancer [39, 40]
Nutmeg	myristicine	woody-spicy [45]	antioxidant [46], anticancer [47]
	methyl-eugenol	clove-like	antifungal [48], bioinsecticide [49].
Cinnamon	cinnamaldehyde	spicy, cinnamons odour	antimicrobial [54]
	copaene	woody	-
	α-bergamotene	woody	-
	α-bisabolene	balsamic spicy floral	anticancer [55], antitumour [56].
Clove	δ-cadinene	woody-longifolone	antimalarial, dengue and filariasis mosquitoes [57], anti- ovarian cancer [58], antifungal[59], and antibacterial [60].
	γ-muurolene	woody	-
	methyl-eugenol	clove-like	antioxidant, antibacterial, antifungal [48], and bioinsecticide [49].
	cedrene	ceder wood-like	-
	copaene	-	-
	α-cadinol	herbal-type	-
Chilli pepper	β-elemene	floral-type	anticancer [61], antioxidant [62], antitumour[63], anti-proliferative agent [64].
	α-muurolene	woody-type	-
	α-bulnesene	floral	-
	α-selenine	amber	-
Ginger	sesquiphellandrene	herbal-type	anticancer [21]
	α-farnesene	green apple odour	antioxidant [65]
	borneol	camphor-like odour	anti-influenza virus [66], antidepressant [67]
	citral	spicy odour	antimicrobial, antioxidant, and antitumor [68]
Turmeric	ar-turmerone	spicy woody	antitumour[69], antimicrobial [70], antiplatelet [71], and anti-venom [72]
	curcumene	herbal-type	antimalarial, anti-chikungunya, and anti- St. Louis encephalitis mosquito [73].
	curlone	-	
	zingiberene	spicy	anti-aggregate, anticancer [46], anti-inflammatory, and antioxidant [47]
	tumerone	spicy woody	-
	β-bisabolene	balsamic spicy floral	-

Cinnamon, clove, chilli pepper, ginger, and turmeric have also specific odour, respectively. The strong odour of cinnamon is contributed by cinnamaldehyde in appreciable quantity (65.38%). The combination of γ-muurolene and δ-cadinene that appear 48.09% contribute strong woody odour in clove. Moreover, chilli pepper yields strong floral and moderate green apple combined by woody odour due to the presence of β-elemene and α-muurolene, respectively. In addition, sesquiphellandrene identified 48.11% in ginger contributes to strong herbal type odour. Strong spicy combined with moderate herbal-type released in turmeric was contributed by ar-turmerone, tumerone, curcumene, and zingiberene.

We also predict the level potency of spices for human health and presented in Table 4. The level potency of spice for human health is not analysed based on empirical data obtained from an experiment involving efficaciousness measurement of bioactive compounds in spices for human metabolism. Nevertheless, it is estimated by looking

through previous studies that investigated spice potency for human health and presented in Figure 4. Thus, the level of efficaciousness of spice is also estimated by looking through the number of bioactive compounds identified in the spices listed in Table 2. Based on data in Table 2 and Table 3 it can be estimated that pepper and cinnamon have high potency for antimicrobial due to the presence of caryophyllene and cinnamaldehyde in large amount, respectively. Pepper is also predicted moderately efficacious as anti-bacteria, anticancer, and antitumor existence of δ-limonene. The presence of 24.55% of myristicine in nutmeg renders it has high potency for anti-bacteria, antioxidant, antifungal, antiviral, and bio-insecticides at moderate level. Chilli pepper is moderately efficacious for antitumor, anticancer, antioxidant, anti-proliferative agent due to the presence of β-elemene for 31.55%. Ginger is predicted highly efficacious as anticancer due to the presence large amount of β-sesquiphellandrene, it was also moderately effectual as antioxidant due to the presence 14.01% of α-farnesene. Meanwhile, compound of ar-turmerone identified 32.46% in turmeric render it highly potent as antimicrobial, antitumor, antiplatelet, and antivenom. In addition, Curcuma in turmeric contributes as bio-insecticides in moderate potency.

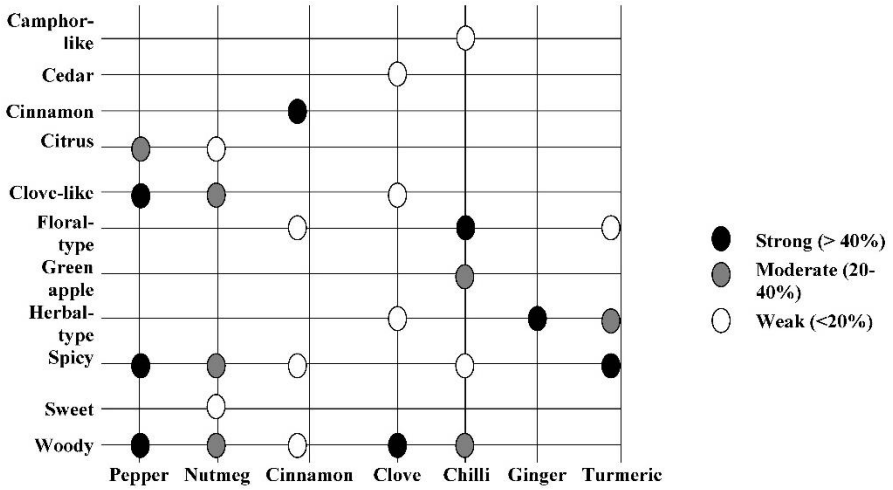


Figure 4. Odour profile estimation released from the spices grown by looking through the quantity of volatile compounds and compared them to reference

Table 4. Potency estimation of spices for human health by looking through the quantity of volatile compounds and compared them to previous studies

Potency	Pepper	Nutmeg	Cinnamon	Clove	Chilli	Ginger	Turmeric
Antibacterial	▲	▲		□			
Anticancer	▲		□		▲	■	□
Antidepressant						□	
Antifungal		▲					
Anti-inflammatory	□						□
Antimicrobial	■		■				■
Antioxidant		▲		□	▲	▲	□
Anti-platelet							■
Anti-proliferative agent					▲		
Antitumour	▲				▲	□	■
Antivenom							■
Antiviral		▲				□	
Bioinsecticide		▲		□			▲

■ Strong; presence of volatile compound was more than 40%
▲ Moderate; presence of volatile compound was 20% up to 40%
□ Weak; presence of volatile compound was less than 20%

Conclusion

Seven types of spice grown in Banyumas District, Jawa Tengah, Indonesia have been analysed using SPME-GC/MS. Based on mass spectroscopy analysis, 69 compounds were identified from the spices. Caryophyllene and δ-limonene dominated in pepper. Myristicin, methyl-eugenol, terpinen-4-ol and asaron were highly abundant in nutmeg. Cinnamon and clove were dominated by cinnamaldehyde and γ-muurolene, respectively. Moreover, β-elemene and α-muurolene were identified as major compounds in chilli pepper. Meanwhile, ginger and turmeric were dominated by sesquiphellandrene and ar-tumerone, respectively. By looking through the quantity of bioactive compound identified in GC/MS experiment, then compare it to previous studies that investigated the efficaciousness of spice for human health, it can be estimated that pepper and cinnamon were highly efficacious as antimicrobe, whereas ginger and turmeric were highly potent as anti-tumour. In addition, turmeric has high potency as anticancer, antiplatelet, and antivenom. Based on analysis of these potencies, it is necessary to change the habit and cultivation culture of local farmers in Indonesia for cultivating these herbal medicines for phytomedicine utilization and or raw material supplier for the pharmaceutical industry. This policy also increases the economic value and benefit of Indonesian spices for local people in the future.

Acknowledgment

This work was fully funded by the project of "Penelitian Kompetensi 2017, BLU Universitas Jenderal Soedirman Purwokerto". The authors are thankful to SPME-GC/MS technician from the Laboratory of Organic Chemistry, Faculty of Mathematics and Natural Science, Universitas Gadjah Mada, Yogyakarta, Indonesia who have conducted SPME-GC/MS analysis for seven types of spice.

References

1. Hannigan, T. A. (2015). Brief history of Indonesia, sultans, spices, and tsunamis: the incredible story of southeast asia largest nation. Tuttle Publishing, Vermont. pp: 50-55.
2. Drakeley, S. (2005). The history of Indonesia. Greenwood Press, Connecticut. pp: 23-37.
3. Ricklefs, M.C. (2001). A history of modern Indonesia since c. 1200. Palgrave, London. pp: 26-30.
4. Gerard, F. and Ruf, F. (2001). Agriculture in crisis: People, Commodities and Natural Resources in Indonesia, 1996-2000. Curzon Press, Richmond. pp.384-395
5. Ardiyanti, S.T. (2018). Potency of Indonesian Spices Exported Products. Leaflet Publishing of Agency for the Assessment and Development of Trade, Ministry of Trade Republic of Indonesia, 2018. Retrieved from http://bppp.kemendag.go.id/leaflet_artikel_perdagangan/view/MjI%3D. [Accessed online 26 January 2018].
6. CBI Ministry of Foreign Affair (2018). Market Insight for Indonesian Spices. Tailored market intelligence: EU market insights for Indonesian spices). Retrieved from https://www.cbi.eu/ sites/default/files/ market_information/researches/tailored-information-indonesian-spices-eu-market-insights-indonesia-europe-spices-herbs-2013.pdf. [Accessed online 26 January 2018].
7. Raghavan, S. (2007). Handbook of spices, seasoning, and flavorings. CRC Press, New York. pp: 36-38.
8. Peter, K.V. (2004). Handbook of herbs and spices. CRC Press, New York. pp: 14-15.
9. Yu, G.-W., Cheng, Q., Nie, J., Wang, P., Wang, X.-J., Li, Z.-G. and Lee, M.-R. (2001). DES-based microwave hydro-distillation coupled with GC-MS for analysis of essential oil from black pepper (*Piper nigrum*) and white pepper. *Analytical Methods*, 9(48): 6777-6784.
10. Marques, A. M., Fingolo, C. E. and Kaplan, M. A. C. (2017). HSCCC separation and enantiomeric distribution of key volatile constituents of *Piper claussenianum* (Miq.) C. DC. (*Piperaceae*). *Food and Chemical Toxicology*, 109: 1111-1117.
11. Muchtaridi, Subarnas, A., Apriantono, A. and Mustarichie, R. (2010). Identification of compounds in the essential oil of nutmeg seeds (*Myristica fragrans* Houtt.) that inhibit locomotor activity in mice. *International Journal of Molecular Sciences*, 11: 4771-4781.
12. Verma, R. S., Padalia, R. C. and Chauhan, A. (2012). Fragrant volatile oil composition of nutmeg geranium (*Pelargonium fragrans Willd.*) from India. *Natural Product Research*, 27(8): 761-766.
13. Malsawmtluangia, L., Nautiyala, B. P., Hazarikaa, T., Chauhan, R. S. and Tavac, A. (2016). Essential oil composition of bark and leaves of *Cinammoum verum Bertch* from Mizoram, North East India. *Journal of Essential Oil Research*, 28 (6): 551-556.

14. Sandner, D., Krings, U. and Berger, R. G. (2017). Volatiles from *Cinnamomum cassia* buds. *Zeitschrift fur Naturforschung*, C. 73(1): 67-75.
15. Kasai, H., Shirao, M. and Ikegami-Kawai, M. (2016). Analysis of volatile compounds of clove (*syzygium aromaticum*) buds as influenced by growth phase and investigation of antioxidant activity of clove extracts. *Flavour Fragrance Journal*, 31: 178-184.
16. El-Mesallamy, L. A. M. D., El-Gerby, M., Abd El Azim, M. H. M, and Awad, A. (2012). Antioxidant, antimicrobial activities and volatile constituents of clove flower buds oil. *Journal of Essential Oil Bearing Plants*, 15(6), 900-907.
17. Patel, K., Ruiz, C., Calderon, R., Marcelo, M. and Rojas, R. (2016). Characterisation of volatile profiles in 50 native Peruvian chili pepper using solid phase microextraction–gas chromatography mass spectrometry (SPME–GCMS). *Food Research International*, 89(1): 471-475.
18. Gurnani, N., Gupta, M., Mehta, D. and Mehta, B. K. (2016). Chemical composition, total phenolic and flavonoid contents, and *in vitro* antimicrobial and antioxidant activities of crude extracts from red chilli seeds (*Capsicum frutescens L.*). *Journal of Taibah University for Science*, 10: 462–470.
19. Toure, A. and Xiaomin, Z. (2007). Gas chromatographic analysis of volatile components of Guinean and Chinese ginger oils (*Zingiber officinale*) extracted by steam distillation. *Journal of Agronomy*, 6**:** 350-355.
20. Mesomo, M. C., Corazza, M. L., Ndiaye, P. M. and Santa, O. R. D. (2013). Supercritical CO_2 extracts and essential oil of ginger (*Zingiber officinale R.*): Chemical composition and antibacterial activity. *The Journal of Supercritical Fluids*, 80: 44-49.
21. Tyagi, A. K., Pasad, S., Yuan, W., Li, S. and Aggarwal, B. B. (2015). Identification of a novel compound (β-sesquiphellandrene) from turmeric (*Curcuma longa*) with anticancer potential: Comparison with curcumin. *Investigational New Drugs*, 33(6), 1175:1186.
22. Xiang, H., Zhang, L., Yang, Z., Chen, F., Zheng, X. and Liu, X. (2017). Chemical compositions, anti-oxidative, antimicrobial, anti-inflammatory and antitumor activities of *Curcuma aromatic Salisb.* essential oils. *Industrial Crops and Products*, 108: 6-16.
23. Dupuy, N., Molinet, J., Mehl, F., Nanlohy, F., Le Dreau, Y. and Kister, J. (2013). Chemometric analysis of mid infrared and gas chromatography data of Indonesian nutmeg essential oils. *Industrial Crops and Products*, 43: 596–601.
24. Amelia, B., Saepudin, E., Cahyana, A. H., Rahayu, D. U., Sulistiyoningrum, A. S. and Haib, J. (2017). GC-MS analysis of clove (*syzygium aromaticum*) bud essential oil from Java and Manado. *AIP Conference Proceedings*, 1862: 030082.
25. Retnowati, R., Rahman, M. F. and Yulia, D. (2014). Chemical constituents of the essential oils of white turmeric (*Curcuma zedoaria* (Christm.) Roscoe) from Indonesia and its toxicity toward *artemia salina leach*. *Journal of Essential Oil Bearing Plants*, 17 (3): 393-396.
26. Jelen, H. and Gracka, A. (2015). Analysis of black pepper volatiles by solid phase micro extraction–gas chromatography: A comparison of terpenes profiles with hydrodistillation. *Journal of Chromatography A*, 1418: 200-209.
27. O'Shea, S. K., Riesen, D. V. and Ross, L. L. (2012). Isolation and analysis of essential oils from spices. *Journal of Chemical Education*, 89(5): 665–668.
28. Bag, A. and Chattopadhyay, R. R. (2015). Evaluation of synergistic antibacterial and antioxidant efficacy of essential oils of spices and herbs in combination. *PLoS ONE*, 10(7): 1-17.
29. Damašius, J., Venskutonis, P. R., Kaškonienėb, V. and Maruškab, A. (2014). Fast screening of the main phenolic acids with antioxidant properties in common spices using on-line HPLC/UV/DPPH radical scavenging assay. *Analytical Methods*, 6(8): 2774-2779.
30. Gad, H. A. and Bouzabata, A. (2017). Application of chemometrics in quality control of turmeric (*Curcuma longa*) based on ultra-violet, Fourier transform-infrared and ^{1}H NMR spectroscopy. *Food Chemistry*, 237: 857-864.
31. Liu, H., Zeng, F. K., Wang, Q. H., Wu, H. S. and Tan, L. H. (2013). Studies on the chemical and flavor qualities of white pepper (*Piper nigrum L.*) derived from five new genotypes. *European Food Research and Technology*, 237: 245–251.
32. Junior, S. B., Tavares, A. M., Filho, J. T., Zini, C. A. and Godoy, H. T. (2012). Analysis of the volatile compounds of Brazilian chilli peppers (*Capsicum spp.*) at two stages of maturity by solid phase micro-extraction and gas chromatography-mass spectrometry. *Food Research International*, 48(1): 98-107.

33. Golmohammad, F., Eikani, M. H., and Maymandi, H. M. (2012). Cinnamon bark volatile oils separation and determination using solid-phase extraction and gas chromatography. *Procedia Engineering*, 42: 247 – 260.
34. Shao, Y. L., Marriott, P., Shellie, R. and Hugel, H. (2003). Solid-phase micro-extraction comprehensive two-dimensional gas chromatography of ginger (*Zingiber officinale*) volatiles. *Flavour and Fragrance Journal*, 18: 5-12.
35. Aziz, K., Hayaloglu, A. A. and Atasoy, A. F. (2017). Evaluation of the volatile compounds of fresh ripened *Capsicum annuum* and its spice pepper (dried red pepper flakes and isot). LWT - *Food Science and Technology*, 84: 842-850.
36. McMaster, M. C., 2016. GC/MS: A Practical User's Guide. John Wiley and Sons, New York. pp. 9-10
37. Sabulal, B., Dan, M., John J, A., Kurup, R., Pradep, N.S., Valsama, R. K. and George, V. (2006). Caryophyllene-rich rhizome oil of *Zingibernimmonii* from South India: Chemical characterization and antimicrobial activity, *Phytochemistry*, 67: 2469-2473.
38. Myszka, K., Schmidt, M. T., Majcher, M., Juzwa, W. and Czaczyk, K. (2017). β-Caryophyllene-rich pepper essential oils suppress spoilage activity of *Pseudomonas* fluorescens KM06 in fresh-cut lettuce. *LWT - Food Science and Technology*, 83:118-126.
39. Montironi, I. D., Cariddi, L. N. and Reinoso, E. B. (2016). Evaluation of the antimicrobial efficacy of *Minthostachysverticillata* essential oil and limonene against *Streptococcus uberis* strains isolated from bovine mastitis. *Revista Argentina de Microbiología*, 48(3): 210-216.
40. Vandresen, F., Falzirolli, H., Batista, S. A. A., da Silva-Giardini, A. P. B., de Oliveira, D. N., Catharino, R. R., Ruiz, A. L. T. G., de Carvalho, J. E., Foglio, M. A. and da Silva, C.C. (2014). Novel R-(þ)-limonene-based thiosemicarbazones and their antitumor activity against human tumor cell lines. *European Journal of Medicinal Chemistry*, 79: 110-116.
41. Chen, J. J., Lu, M., Jing, Y. and Dong, J. (2006). The synthesis of L-carvone and limonene derivatives with increased antiproliferative effect and activation of ERK pathway in prostate cancer cells. *Bioorganic and Medicinal Chemistry*, 14: 6539-6547.
42. Gertsch, J., Leonti, M. and Raduner, S. (2008). β-caryophyllene is a dietary cannabinoid. *Proceeding National Academy Science USA*, 105(26): 9099-9104.
43. Chavan, M. J., Wakte, P. S. and Shinde, D. B. (2010). Analgesic and anti-inflammatory activity of caryophyllene oxide from *Annonasquamosa* L. bark. *Phytomedicine*, 17:149-151.
44. Burdock, G. (2010*).* Fenaroli's Handbook of Flavor Ingredients. CRC Press, Florida, pp. 201-230.
45. Teranishi, R., Wick, E. L., and Horstein, I. (1999). Flavor chemistry thirty years of progress. Kluwer Academic/Plenum Publisher, New York. pp. 301-302.
46. Rahman, N., Xin, T. B., Kamilah, H. and Arifin, F. (2018). Effects of osmotic dehydration treatment on volatile compound (Myristicin) content and antioxidants property of nutmeg (*Myristica fragrans*) pericarp. *Journal of Food Science and Technology*, 55(1): 183-189.
47. Martins, C., Doran, C., Silva, I. C., Miranda, C., Rueff, J. and Rodrigues, A. S. (2014). Myristicin from nutmeg induces apoptosis *via* the mitochondrial pathway and down regulates genes of the DNA damage response pathways in human leukaemia K562 cells. *Chemico-Biological Interactions*, 218: 1-9.
48. Siddique, S., Parveen, Z., Bareen, F. E., Chaudhary, M. N., Mazhar, S. and Nawaz, S. (2017). The essential oil of *Melaleuca armillaris* (*Sol. ex Gaertn.*) Sm. leaves from Pakistan: A potential source of eugenol methyl ether. *Industrial Crops and Products*, 109: 912-917.
49. Xu, H., Zheng, X., Yang, Y., Tian, J., Lu, Y., Tan, K., Heong, K. and Lu, Z. (2015). Methyl eugenol bioactivities as a new potential botanical insecticide against major insect pests and their natural enemies on rice (Orizasativa). *Crop Protection*, 72: 144-149.
50. Souza, C. F., Baldissera, M. D., de L. Silva, L., Geihs, M. A. and Baldisserotto, B. (2018). Is monoterpene terpinen-4-ol the compound responsible for the anesthetic and antioxidant activity of *melaleuca alternifolia* essential oil (tea tree oil) in silver catfish? *Aquaculture*, 486: 217-233.
51. Brilhante, R. S. N., Caetano, E. P., de Lima, R. A. C., de Farias Marques, F. J., Castel-Branco, D. C. M., de Melo, C. V. S., Guedes, G. M., de Olievera, J. S., de Camargo, Z. P., Moriera, J. L. B., Monteiro, A. J., Bandeira, T. P. G., Cordeiro, R., Rocha, M. F. G. and Sidrim, J. J. C. (2016). Terpinen-4-ol, tyrosol, and -lapachone as potential antifungals against dimorphic fungi. *Brazilian Journal of Microbiology*, 47: 917-924.

52. Baldissera, M. D., Grando, T. H., Souza, C. F., Gressier, L. T., Stefani, L. M., da Silva, A. S. and Monteiro, S. G. (2016). In vitro and in vivo action of terpinen-4-ol, γ-terpinene, and α-terpinene against *Trypanosomaevansi*. *Experimental Parasitology*, 162: 43-48.
53. Govindarajan, M., Mohan, R. and Giovanni, B. (2016). Delta-cadinene, calarene and delta-4-carene from *Kadsura heteroclita* essential oil as novel larvicides against malaria, dengue and filariasis mosquitoes. *Combatorial Chemistry and High Throughput*, 19(7): 565-571.
54. Muller, J., Quesada, A. C., Martinez, C.G. and Chiralt, A. (2017). Antimicrobial properties and release of cinnamaldehyde in bilayer films based on polylactic acid (PLA) and starc. *European Polymer Journal*, 96: 316-325.
55. Yeo, S. K. Ali, A. Y., Hayward, O. A., Turnham, D., Jackson, T., Bowen, I. D. and Clarkson, R. (2016). β-Bisabolene, a sesquiterpene from the essential oil extract of opoponax (*Commiphoraguidottii*), exhibits cytotoxicity in breast cancer cell lines. *Phototherapy Research*, 30: 418-425.
56. Rodrigues, A. C. B. C., Bomfim, L. M., Neves, S. P., Menezes, L. R. A., Dias, R. B., Soares, M. B. P., Prata, A. P. N., Rocha, C. A. G., Costa, E. V. and Berezza, D. P. (2015). Antitumor properties of the essential oil from the leaves of *Duguetia gardneriana. Planta Medica*, 81(10): 798-803.
57. Govindarajan, M., Rajeswari, M., Hoti, S. L. and Benelli, G. (2016). Larvicidal potential of carvacrol and terpinen-4-ol from the essential oil of *Origanum vulgare* (Lamiaceae) against *Anopheles stephensi*, *Anopheles subpictus*, *Culexquinque fasciatus* and *Culex tritaeniorhynchus* (Diptera: Culicidae). *Research in Veterinary Science*, 104: 77-82.
58. Hui, L. M., Zhao, G. D. and Zhao, J. J. (2015). Delta-cadinene inhibits the growth of ovarian cancer cells via caspase-dependent apoptosis and cell cycle arrest. *International Journal of Clinical and Experimental Pathology*, 8(6): 6046-6056.
59. Kundu, A., Saha, S., Walia, S., Shakil, N. A., Kumar, J. and Annapurna, K. (2013). Cadinene sesquiterpenes from *Eupatorium adenophorum* and their antifungal activity. *Journal of Environmental Science and Health Part B: Pesticides Food Contaminants and Agricultural Wastes*, 48(6): 516-522.
60. Perez-Lopes, A., Cirio, A. T., Ravas-Galindo, V. M., Aranda, R. S. and de Torres, N.W. (2011). Activity against *Streptococcus pneumoniae* of the essential oil and delta-cadinene isolated from *Schinus molle* fruit. *Journal of Essential Oil Research*, 23 (5): 25-28.
61. Chang, Z., Gao, M., Zhang, W., Song, L., Jia, Y. and Qin, Y. (2017). β-Elemene attenuates atherosclerosis in apolipoprotein e-deficient mice via restoring no levels and alleviating oxidative stress. *Surgical Oncology*, 26(4): 333-337.
62. Ji-Chao, C., Wen-Li, D., Ren-Ren, B. A. I., He-Quan, Y., Xiao-Ming, W., Jing, S. and Jin-Yu, X. (2015). Synthesis of 13-β-elemene ester derivatives and evaluation of their antioxidant activity in human umbilical vein endothelial cells. *Chinese Journal of Natural Medicines*, 13(8): 618-627.
63. Qin, Y., Guo, Y., Wei, W., Wang, B., Jin, H., Sun, J., Qi, X., Ren, S. and Zuo, Y. (2012). Anti-tumor effect of β-elemene in murine hepatocellular carcinoma cell line H22 depends on the level of c-Met down regulation. *Biomedicine and Preventive Nutrition*, 2(2): 91-98.
64. Sun, Y., Liu, G., Zhang, Y., Zhu, H., Ren, Y. and Shen, Y. (2009). Synthesis and in vitro anti-proliferative activity of β-elemene mono substituted derivatives in hela cells mediated through arrest of cell cycle at the G1 phase. *Bioorganic and Medicinal Chemistry*, 17(3): 1118-1124.
65. Yazdani, D., Arzani, K., Mostofi, Y. and Shekarchi, M. (2011). α-farnesene and antioxidative enzyme systems in Asian pear (*Pyrusserotina Rehd.*) fruit. *Postharvest Biology and Technology*, 59(3): 227-231.
66. Sokolova, A. S., Yarofaya, O. I, Semenova, M. D., Shtro, A. A., Orshanskaya, R., Zarubaev, V.V. and Salakhudinov, N. F. (2017). Synthesis and in vitro study of novel borneol derivatives as potent inhibitors of the influenza a virus. *Medical Chemistry Communication*, 8(5): 960-963.
67. Huo, T., Li, X. and Peng, C. (2017). Borneol enhances the antidepressant effects of asiaticoside by promoting its distribution into the brain. *Neuroscience Letters*, 646: 56-61.
68. Shi, C., Zhao, X., Zonghui, L., Chen, X., Guo, N. and Rizeng, M. (2016). Antimicrobial, antioxidant, and antitumor activity of epsilon-poly-l-lysine and citral, alone or in combination. *Food & Nutrition Research*, 60: 1-8.
69. Kim, D., Suh, Y., Lee, H. and Lee, Y. (2012). Immune activation and antitumor response of ar-turmerone on P388D1 lymphoblast cell implanted tumors. *International Journal of Molecular Medicine*, 29: 386-392.

70. Lee, H. S. (2006). Antimicrobial properties of turmeric (*Curcuma longa L.*) rhizome-derived ar-turmerone and curcumin. *Food Science and Biotechnology*, 15(4): 559-563.
71. Lee, H. S. (2006). Antiplatelet property of *Curcuma longa L*. rhizome-derived ar-turmerone. *Bioresource Technology*, 97(12): 1372-1376.
72. Fereira, L. A. F., Henriques, O. B., Andreoni, Vital, G. R. F., Campos, M. M. C., Habermehl, G. G. and de Moraes, V. L. G. (1992). Antivenom and biological effects of ar-turmerone isolated from *Curcuma longa (zingiberaceae). Toxicon*, 30(10): 1211-1218.
73. AlShelby, M. M., AlQahtani, F. S., Govindarajan, M., Gopinanth, K., Vijayan, P. and Benelli, G. (2017). Toxicity of ar-curcumene and epi-β-bisabolol from hedychiumlarsenii (*Zingiberaceae*) essential oil on malaria, chikungunya and St. Louis encephalitis mosquito vectors. *Ecotoxicology and Environmental Safety*, 137: 149-157.

Malaysian Journal of Analytical Sciences, Vol 23 No 6 (2019): 980 - 990
DOI: https://doi.org/10.17576/mjas-2019-2306-06

MALAYSIAN JOURNAL OF ANALYTICAL SCIENCES
Published by The Malaysian Analytical Sciences Society
ISSN 1394 - 2506

RADIOACTIVITY OF ^{210}Po IN GREEN MUSSELS (*Perna viridis*) AT THE WEST COAST OF JOHORE STRAITS, MALAYSIA

(Radioaktiviti ^{210}Po dalam Kupang (*Perna viridis*) di Pantai Barat Selat Johor, Malaysia)

Mei Peng Lim and Che Abd Rahim Mohamed*

School of Environmental and Natural Resource Sciences,
Faculty of Science and Technology,
Universiti Kebangsaan Malaysia, 43600 UKM Bangi, Selangor, Malaysia

**Corresponding author: carmohd@ukm.edu.my*

Received: 19 August 2019; Accepted: 11 November 2019

Abstract

Johor Straits is one of the most polluted coastal areas in the southern part of Peninsular Malaysia and sampling of green mussels in various sizes and locations (e.g., cultured, wild and local market) was conducted to investigate its ability to accumulate ^{210}Po into their organs. Levels of ^{210}Po varied according to the organ and origin of the organisms, where the level of activity in the stomach and tissues ranged from 64.51 ± 3.47 Bq kg^{-1} dry weight to 520.26 ± 27.25 Bq kg^{-1} dry weight and 25.44 ± 1.25 Bq kg^{-1} dry weight to 154.28 ± 5.62 Bq kg^{-1} dry weight, respectively. Green mussels from the wild contained the highest mean activity of ^{210}Po as 406.35 ± 14.10 Bq kg^{-1} dry weight in the stomach and 79.33 ± 0.87 Bq kg^{-1} dry weight in tissue because of contaminations from the industrial and domestic effluent discharges directly into the sampling locations. The activity levels were also relatively higher than other marine organisms from different areas in Malaysia as well as worldwide values. Therefore, it is assumed that green mussels might be a radiation risk to seafood consumers from the Johor Straits, since the radiation dose of ^{210}Po exceeds permitted levels by the USEPA.

Keywords: radioactivity, green mussel, seafood, radiation, contamination

Abstrak

Selat Johor adalah kawasan pinggir pantai yang tercemar di bahagian Selatan Semenanjung Malaysia dan pensampelan kupang dalam pelbagai saiz dan lokasi (contoh seperti ternak, liar dan pasaran tempatan) dilakukan untuk memeriksa keupayaan akumulasi ^{210}Po ke dalam organnya. Aras ^{210}Po adalah berbeza bergantung kepada jenis organ dan lokasi asal organisma tersebut, julat aras aktiviti dalam perut dan tisu masing-masing dari 64.51 ± 3.47 Bq kg^{-1} berat kering hingga 520.26 ± 27.25 Bq kg^{-1} berat kering dan 25.44 ± 1.25 Bq kg^{-1} berat kering hingga 154.28 ± 5.62 Bq kg^{-1} berat kering. Kupang liar mengandungi aktiviti purata ^{210}Po tertinggi iaitu 406.35 ± 14.10 Bq kg^{-1} berat kering dalam perut dan 79.33 ± 0.87 Bq kg^{-1} berat kering dalam tisu kerana bahan buangan pencemaran daripada industri dan domestik dikeluarkan terus ke kawasan pensampelan kerang. Aras aktiviti umumnya adalah tinggi berbanding dengan organisma marin yang lain diperolehi dari kawasan berlainan di Malaysia begitu juga nilai aktiviti peringkat dunia. Oleh itu, boleh dianggap bahawa kupang mungkin menjadi risiko radiasi kepada pengguna makanan laut dari Selat Johor, kerana dos radiasi ^{210}Po melebihi tahap yang dibenarkan oleh USEPA.

Kata kunci: radioaktiviti, kupang, makanan laut, radiasi, pencemaran

Introduction

The safety of seafood consumption garners serious attention in tandem with increased global preference for seafood [1]. Apart from the problems caused by the use of antibiotics, radioactivity levels in seafood are also a concern of

seafood consumers. This fear seems to have worsened after the Fukushima Daiichi nuclear disaster in Japan in 2011. However, the presence of radionuclides in the marine environment could be from cosmogenic and primordial sources as well as from anthropogenic activities. Marine organisms become contaminated when radioactive materials are absorbed from surrounding waters and are accumulated in their body; this can be transferred to humans via the food chain [2-6]. Several studies on ^{210}Po and other natural radionuclides in marine organisms in Malaysian coastal waters have been conducted by other researchers [7-10]. However, studies on ^{210}Pb in the west coast of Johor Straits in marine organisms are limited.

The Straits of Johor is located in the southern part of Peninsular Malaysia where the west and east part of the straits is separated by a causeway built in 1924. The water body has been blocked and water in the strait cannot flow freely between the southern South China Sea or the Straits of Malacca. Heavy pollution occurs in both the water column and sediment from massive toxic elements deposited from the surrounding inland regions (i.e., Johor, Malaysia and Singapore). Since the west coast of Johor Strait is famous for the production of green mussels, this study was conducted to investigate levels of the natural radionuclide ^{210}Po as a bio-indicator of environmental pollution.

The production of green mussel in the Straits of Johor is also famous because of the availability of spat fall. This study would clearly reveal the impacts of urbanization from both sides i.e., Malaysia and Singapore, and their contribution to the increased natural radioactivity levels in the coastal area. Furthermore, the existence of natural radionuclide contaminants in seafood might indicate its potential impact on human health through consumption. The relationship between ^{210}Po and marine organisms has been widely investigated because it is one of the most important sources of internal radiation for most organisms that emit alpha radiation [11-13]. Thus, this study investigates the activity of ^{210}Po levels in green mussels from the west coast of Johor Straits, Malaysia as an *in-situ* bio-indicator.

Materials and Methods

Sampling was conducted on 25th March 2014 and 1st June 2014 in the west coast of the Johor Straits, Malaysia, indicated as culture farm station (ST02, ST03, ST07, ST08, ST09), wild station (ST04, ST05, ST06) and market station (ST01) (Figure 1). Samples collected were from culture farms (n=35), wild caught (n=21) and market bought (n=7). Shell lengths and widths of the green mussels were also measured immediately after sampling. The radiochemical separation method was used to estimate ^{210}Po in the samples [6]. The green mussels were dissected with a knife to obtain the stomach and soft tissue, and these were oven dried at 60°C. About 0.5 g of dried sample was taken and a known activity of ^{209}Po (12.17 dpm/mL) was added as a yield tracer. The samples were then digested with 15 mL of nitric acid and peroxide acid. The solution was filtered and gently evaporated to 2 mL as near dryness.

The sample was dissolved in 0.5 M hydrochloric acid and 1.0 g of ascorbic acid to reduce Fe (III), and ^{210}Po was spontaneously deposited on brightly polished silver discs (2 cm diameter) for a period of 1 to 2 hours at a temperature of 70-90 °C. The discs were counted for ^{210}Po activities with Alpha Spectrometry along a silicon-surface barrier detector by Canberra immediately after deposition process. The recovery yield varied from 65% to 90%. Depositions of ^{210}Po were carried out within two months of sampling and the calculation of ^{210}Po activities involved the date of sampling. Then, to ensure the quality of the methodology, ^{210}Po was estimated with a certified reference material IAEA-134 (Cockle flesh).

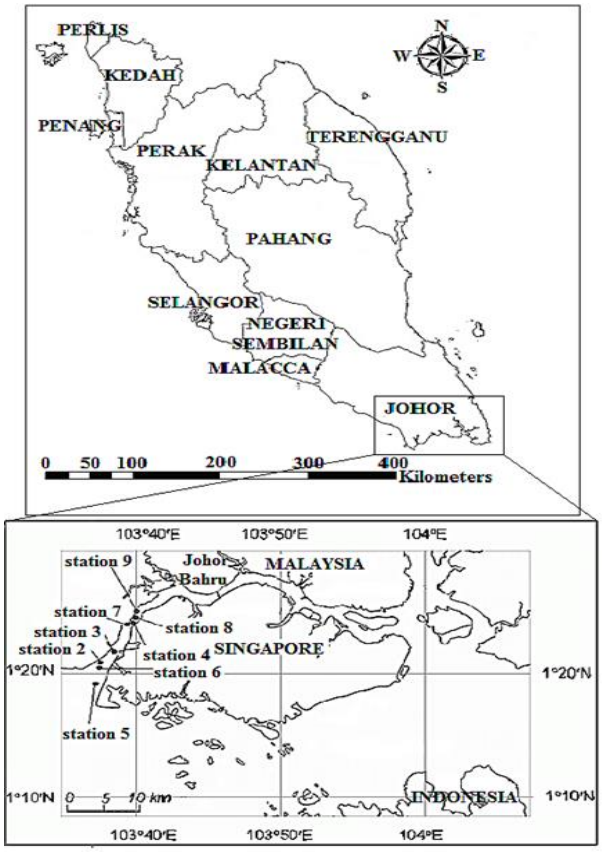


Figure 1. Sampling stations in the west coast of Johore Straits, Malaysia

Results and Discussion

^{210}Po activity concentrations in the green mussels

^{210}Po activity concentrations in green mussels of dry and wet samples varied between sampling locations (Table 1). A comparison of ^{210}Po activity concentrations between the stomach and tissue of the green mussels showed that the stomachs have a remarkably higher average activity concentration of ^{210}Po 168 ± 5.43 Bq/kg in dry weight, indicative of its nature as filter feeder organisms. The results shown in this study are also similar to a previous study done by Waska et al. [14]. Upon dissection of green mussels for radioactivity analysis, the stomach accounted for the highest activity. The statistical correlations between wet and dry weight of tissues found a positive correlation $y = 4.98x + 0.03$; $R^2 = 0.827$ (Figure 2, where y and x represent wet and dry weight in gram, respectively), and in general the body weight is inversely related to body fluid content as filter feeding processes [15, 16]. The contents of natural polonium in the body of green mussels are positively proportionate with feeding habit in the *in-situ* environment [17]. The content of natural polonium in mussels' tissue from the wild samples are higher than the cultured or local market samples because the sampling stations ST04, ST05 and ST06 are near/at the domestic discharge. However, the culture area is usually far from pollution sources and harvests for local market consumption with the sequence of contents of natural polonium in edible tissues are as follows: wild > culture > local market.

Table 1. ^{210}Po activity concentrations in the stomach and tissue of green mussel

Location	Station	Sample	Length (mm)	Wide (mm)	Stomach		Tissue		Po-210 in Dry Sample		Po-210 in Wet Sample	
					Wet (g)	Dry (g)	Wet (g)	Dry (g)	Stomach (Bq/kg)	Tissue (Bq/kg)	Stomach (Bq/kg)	Tissue (Bq/kg)
Local Market	ST 01 (n = 7)	1	96.20	39.65	2.41	0.45	8.88	1.47	64.51 ±3.47	43.49 ±1.94	12.08 ±0.65	7.21 ±0.32
		2	73.25	32.20	0.88	0.20	4.11	0.50	78.64 ±4.89	50.56 ±2.68	18.39 ±1.14	6.22 ±0.33
		3	71.20	36.10	1.41	0.28	4.94	0.87	78.22 ±4.50	39.73 ±2.02	15.56 ±0.89	7.05 ±0.36
		4	66.60	31.60	0.98	0.206	2.528	0.69	80.23 ±5.08	27.81 ±1.68	16.84 ±1.07	7.66 ±0.46
		5	80.45	35.90	1.63	0.27	5.41	0.78	69.72 ±3.98	42.86 ±2.19	11.71 ±0.67	6.21 ±0.32
		6	69.35	34.10	1.40	0.27	3.18	0.51	62.26 ±3.72	42.63 ±2.48	12.02 ±0.72	6.90 ±0.40
		7	95.65	38.15	2.14	0.39	5.99	1.10	70.00 ±3.70	46.72 ±2.00	12.81 ±0.68	8.64 ±0.37
Culture	ST 02 (n =7)	1	66.60	35.10	1.00	0.29	2.80	0.70	131.44 ±6.13	57.57 ±2.83	38.52 ±1.80	14.36 ±0.71
		2	69.20	34.15	0.84	0.25	3.33	0.80	154.61 ±7.45	63.00 ±2.68	47.73 ±2.30	15.15 ±0.64
		3	71.85	33.30	0.92	0.24	3.83	0.91	150.81 ±6.99	58.37 ±2.58	40.47 ±1.88	13.87 ±0.61
		4	75.90	35.60	1.57	0.41	4.53	1.14	110.56 ±4.94	46.59 ±2.09	29.25 ±1.31	11.82 ±0.53
		5	76.65	38.10	1.60	0.36	5.13	1.18	106.03 ±4.90	37.70 ±1.68	23.98 ±1.11	8.68 ±0.39
		6	76.10	34.40	1.11	0.27	4.29	1.04	128.97 ±6.33	60.53 ±2.64	31.54 ±1.55	14.71 ±0.64
		7	70.40	31.10	0.94	0.24	3.22	0.759	152.52 ±7.18	55.22 ±2.62	39.35 ±1.85	13.00 ±0.62
	ST 03 (n = 7)	1	70.25	29.25	1.03	0.28	4.17	1.07	124.96 ±5.52	45.95 ±1.92	34.68 ±1.53	11.83 ±0.49
		2	70.60	27.20	0.84	0.23	5.12	1.26	142.16 ±6.44	51.74 ±2.05	38.75 ±1.76	12.82 ±0.51
		3	64.20	29.45	0.82	0.23	3.32	0.84	117.19 ±5.74	45.22 ±2.05	33.11 ±1.62	11.53 ±0.52
		4	67.10	29.90	0.73	0.21	3.27	0.89	156.10 ±6.90	51.31 ±2.15	46.56 ±2.06	14.07 ±0.59
		5	66.40	31.30	0.95	0.27	3.62	0.94	125.05 ±5.86	50.39 ±2.12	36.00 ±1.69	13.11 ±0.55
		6	64.20	31.40	0.92	0.27	3.32	0.90	120.60 ±5.41	59.84 ±2.54	35.87 ±1.61	16.27 ±0.69
		7	67.40	30.00	0.97	0.26	3.27	0.82	124.29 ±5.76	46.01 ±2.20	34.33 ±1.59	11.54 ±0.55

Table 1 (cont'd). ^{210}Po activity concentrations in the stomach and tissue of green mussel

Location	Station	Sample	Length (mm)	Wide (mm)	Stomach		Tissue		Po-210 in Dry Sample		Po-210 in Wet Sample	
					Wet (g)	Dry (g)	Wet (g)	Dry (g)	Stomach (Bq/kg)	Tissue (Bq/kg)	Stomach (Bq/kg)	Tissue (Bq/kg)
Wild	ST 04 (n = 7)	1	61.4	30.30	1.34	0.23	2.23	0.48	176.27 ±7.78	50.52 ±2.65	30.38 ±1.34	11.01 ±0.58
		2	63.00	28.50	0.63	0.15	2.19	0.50	251.79 ±10.98	54.88 ±2.89	62.46 ±2.72	12.60 ±0.66
		3	72.00	32.40	1.66	0.25	2.64	0.62	139.32± 6.67	46.02 ±2.44	21.73 ±1.04	10.98 ±0.58
		4	69.60	30.50	0.73	0.19	3.54	0.80	178.49 ±8.72	32.38 ±1.63	45.93 ±2.24	7.39 ±0.37
		5	69.60	31.30	1.20	0.25	2.67	0.60	156.99 ±7.19	41.94 ±2.28	33.94 ±1.55	9.44 ±0.51
		6	60.30	31.40	0.71	0.17	1.40	0.35	266.83 ±11.76	67.11 ±3.71	64.84 ±2.86	16.96 ±0.94
		7	60.50	35.90	0.53	0.128	2.11	0.46	333.41 ±14.94	29.88 ± 1.83	80.48 ±3.61	6.54 ±0.40
	ST 05 (n = 7)	1	40.30	26.30	0.15	0.04	1.21	0.24	520.36 ±27.25	102.41 ±5.21	157.59 ±8.25	20.90 ±1.06
		2	58.20	31.60	0.45	0.12	2.35	0.50	413.32 ±16.72	123.46 ±4.60	112.78 ±4.56	26.77 ±1.00
		3	60.50	32.70	0.41	0.11	2.77	0.62	492.71 ±19.97	154.28 ±5.62	138.52 ±5.61	34.70 ±1.26
		4	48.00	21.60	0.16	0.04	0.91	0.19	480.79 ±25.34	139.79 ±6.93	129.82 ±6.84	29.17 ±1.45
		5	49.65	24.10	0.21	0.06	1.48	0.35	384.17 ±18.96	72.99 ±3.64	118.79 ±5.86	17.30 ±0.86
		6	47.60	25.00	0.21	0.07	1.12	0.22	372.07 ±18.05	143.28 ±6.84	122.03 ±5.92	28.80 ±1.37
		7	53.30	32.10	0.31	0.06	1.05	0.21	457.32 ±22.89	143.53 ±6.64	93.16 ±4.66	29.23 ±1.35
	ST 06 (n = 7)	1	60.00	30.50	1.20	0.24	3.11	0.54	199.11 ±9.33	70.51 ±3.5	40.48 1±.90	12.33 ±0.61
		2	61.60	29.40	1.05	0.21	3.34	0.58	172.29 ±8.32	55.46 ±2.93	34.38 ±1.66	9.66 ±0.51
		3	60.30	29.10	1.06	0.22	2.80	0.53	224.13 ±10.38	70.89 ±3.45	46.99 ±2.18	13.47 ±0.65
		4	66.10	30.70	1.21	0.25	3.96	0.72	188.89 ±8.95	56.95 ±2.85	39.93 ±1.89	10.43 ±0.52
		5	66.30	29.40	1.11	0.23	3.90	0.70	196.22 ±9.13	65.95 ±3.10	42.11 ±1.96	11.98 ±0.56
		6	64.20	27.40	0.86	0.17	2.68	0.47	269.57 ±13.04	79.22 ±4.03	53.98 ±2.61	13.95 ±0.71
		7	63.8	29.10	0.83	0.16	3.52	0.62	252.12 ±12.79	64.52 ±3.08	49.89 ±2.53	11.42 ±0.55

Table 1 (cont'd). ^{210}Po activity concentrations in the stomach and tissue of green mussel

Location	Station	Sample	Length (mm)	Wide (mm)	Stomach		Tissue		Po-210 in Dry Sample		Po-210 in Wet Sample	
					Wet (g)	Dry (g)	Wet (g)	Dry (g)	Stomach (Bq/kg)	Tissue (Bq/kg)	Stomach (Bq/kg)	Tissue (Bq/kg)
Culture	ST 07	1	78.30	32.2	2.05	0.44	6.50	1.09	101.35 ±4.78	38.15 ±1.78	22.24 ±1.05	5.03 ±0.30
		2	78.30	32.45	1.66	0.36	8.38	1.61	88.19 ±4.32	42.02 ±1.79	19.37 ±0.95	7.95 ±0.41
		3	82.80	38.30	1.80	0.36	7.61	1.37	114.51 ±5.39	30.67 ±1.41	23.01 ±1.08	6.43 ±0.36
		4	73.00	32.40	1.88	0.42	8.08	1.49	84.14 ±4.17	25.44 ±1.25	18.79 ±0.93	6.10 ±0.35
		5	81.20	34.40	1.78	0.37	6.71	1.16	130.84 ±6.03	35.24 ±1.64	27.60 ±1.27	6.87 ±0.38
		6	75.00	35.50	1.69	0.38	6.65	1.28	106.18 ±5.09	34.76 ±1.63	24.26 ±1.16	5.54 ±0.30
		7	73.00	30.00	1.69	0.36	7.43	1.21	98.44 ±4.67	25.50 ±1.25	21.15 ±1.00	8.40 ±0.43
	ST 08	1	59.10	26.40	1.14	0.27	3.54	0.65	92.78 ±4.92	27.10 ±1.64	22.13 ±1.17	5.03 ±0.30
		2	62.10	26.10	1.48	0.32	3.72	0.64	86.33 ±4.42	45.73 ±2.35	18.98 ±0.97	7.95 ±0.41
		3	58.30	28.10	0.83	0.18	3.32	0.59	156.13 ±8.11	36.05 ±2.00	34.82 ±1.81	6.43 ±0.36
		4	59.90	26.60	1.16	0.22	3.33	0.56	106.06 ±5.74	36.23 ±2.08	20.55 ±1.11	6.10 ±0.35
		5	56.10	25.00	1.08	0.23	3.22	0.50	97.35 ±5.35	43.47 ±2.41	20.60 ±1.13	6.87 ±0.38
		6	57.10	25.00	1.04	0.23	3.89	0.70	80.35 ±4.75	30.65 ±1.66	18.13 ±1.07	5.54 ±0.30
		7	60.50	30.50	1.35	0.28	3.04	0.72	69.99 ±4.10	35.07 ±1.79	14.57 ±0.85	8.40 ±0.43
	ST 09	1	62.20	27.10	1.25	0.29	3.37	0.97	81.07 ±4.28	36.17 ±1.63	19.13 ±1.01	10.49 ±0.47
		2	69.10	34.00	1.53	0.33	5.15	1.30	90.36 ±4.27	25.73 ±1.23	19.97 ±0.94	6.49 ±0.31
		3	70.90	31.40	1.38	0.29	5.59	1.06	102.83 ±4.82	38.79 ±1.66	22.18 ±1.04	7.37 ±0.32
		4	72.20	34.10	1.31	0.29	5.85	1.07	115.13 ±5.46	30.64 ±1.40	25.57 ±1.21	5.62 ±0.26
		5	69.40	30.00	1.33	0.31	4.51	0.80	93.62 ±4.59	32.90 ±1.68	21.78 ±1.07	5.87 ±0.30
		6	68.10	30.50	1.31	0.31	5.03	1.01	108.21 ±5.07	31.78 ±1.53	26.10 ±1.22	6.38 ±0.31
		7	65.50	34.40	1.20	0.26	4.28	0.78	105.32 ±5.18	36.91 ±1.74	23.50 ±1.16	6.73 ±0.32
Average activity of ^{210}Po at wild area (ST 04, ST 05 & ST 06)									291.72 ±13.77	79.33 ±3.80	72.39 ±3.42	16.43 ±0.79
Average activity of ^{210}Po at culture area (ST 02, ST 03, ST 07, ST 08 & ST 09)									112.98 ±5.64	41.38 ±1.93	27.84 ±1.34	9.27 ±0.44
Average activity of ^{210}Po at local market area (ST 01)									71.94 ±4.19	41.97 ±2.14	14.20 ±0.83	7.13 ±0.37

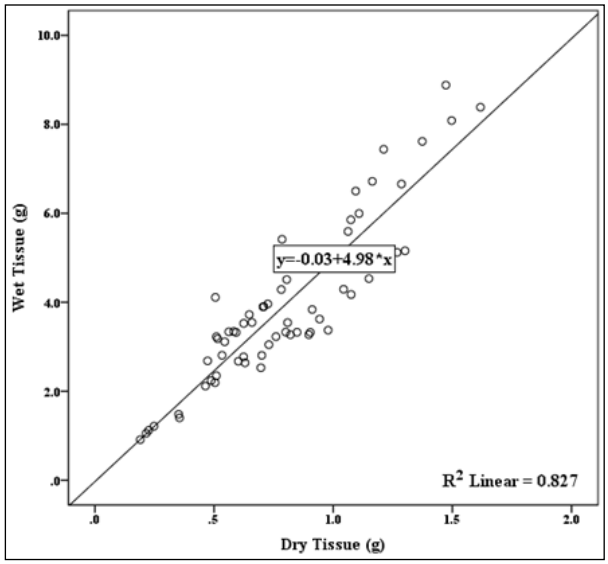


Figure 2. Correlation between wet and dry weight (g) of tissue of green mussels.

The distribution of natural radionuclide e.g., ^{210}Po will accumulate in the stomach and edible tissue body of green mussels. According to the International Commission on Radiological Protection (ICRP), ingested food will first accumulate into the stomach followed by the small intestine (SI) and 50% of the total activity concentration in the SI will be transferred with nutrition into the blood and will be distributed to other tissue parts [18]. The greater amount of radioactive materials remaining in the stomach with the greater chances of absorption of radionuclides occurred into the stomach. Thus, green mussel stomachs play the main role in absorption and digestion of this contaminant [19, 20]. Therefore, if the mussels' stomachs possess more than 36% of natural polonium before absorption in other organs, then the consumption of green mussel stomachs should not be recommended (Table 1).

^{210}Po activity concentrations vary in green mussels regardless of the origin of the samples obtained (Table 1). Although Carvalho and Fowler [21] showed that most dissolved ^{210}Po in water is absorbed by the outer surface of the organism instead of incorporation in internal tissues, this study found higher ^{210}Po concentration activity in the stomach which might be because of the filter feeding habits of green mussels.

Green mussels' diet

Radionuclide concentrations of ^{210}Po are consistently found in green mussels, though the strength of that concentration varies with sample stations (Table 1). Generally, green mussels obtained from wild locations showed higher mean ^{210}Po levels in the stomach (291.72 ± 13.77 Bq/kg) and tissue (79.33 ±3.80 Bq/kg) compared to samples taken from mussel culture sites and the local market, where the wild green mussels sampled were smaller than both cultured and local market samples. Moreover, the wild mussels were attached to the sub-strata such as on rock and pillars, and because of its attachment in a higher position than the low tide, it stops feeding due to limited water flow. But the cultured mussels maintained the status of physico-chemical parameters and timely food supply for effective muscle growth. Variations in size have also influenced activity concentrations of ^{210}Po in green mussels. If bioaccumulation and bioconcentration of contaminants occur in one individual, then the level of contaminants will eventually increase as the individual grows. However, this study found that the accumulation of radionuclides is size-dependent and similar results were reported by Theng et al [7], where juvenile green mussels tend to have more frequent feeding rates in order to recoup growth and a faster metabolism rate compared to adult green mussels. This is indicated in the higher accumulation levels of ^{210}Po in wild samples.

Therefore, precautions should be taken in the consumption of green mussels from the Straits of Johor due to the slightly higher risks of radiation as the levels found in the study are higher than the permitted levels recommended by the USEPA; an estimated effective radiation dose of ^{210}Po between 2.61 to 11.54 mSv/year. However, radionuclide content in terms of food safety has not been thoroughly studied. This study determined a negative statistical correlation between the concentration of natural polonium and shell length of green mussels, $y = -7.59x + 6.76E^2$; $R^2 = 0.424$ (Figure 3A); ^{210}Po activity concentrations (Bq/kg) in dry tissue vs. green mussels length (mm) as $y = -1.57x + 1.59E^2$; $R^2 = 0.269$ (Figure 3B); ^{210}Po activity concentrations (Bq/kg) in wet stomach vs. green mussels length (mm) as $y = -2.22x + 1.9E^2$; $R^2 = 0.433$ (Figure 3C); and ^{210}Po activity concentrations (Bq/kg) in wet tissue vs. green mussels length (mm) as $y = -0.34x + 34.24$; $R^2 = 0.265$ (Figure 3D) [where y and x represents ^{210}Po activity (Bg/kg) and length of shell mussels (mm), respectively]. It has been shown that ^{210}Po activity concentrations decrease with an increase in shell length. Hence the findings suggest that seafood consumers should select large shells for consumption rather than small shells so as to be less exposed to ^{210}Po radiation.

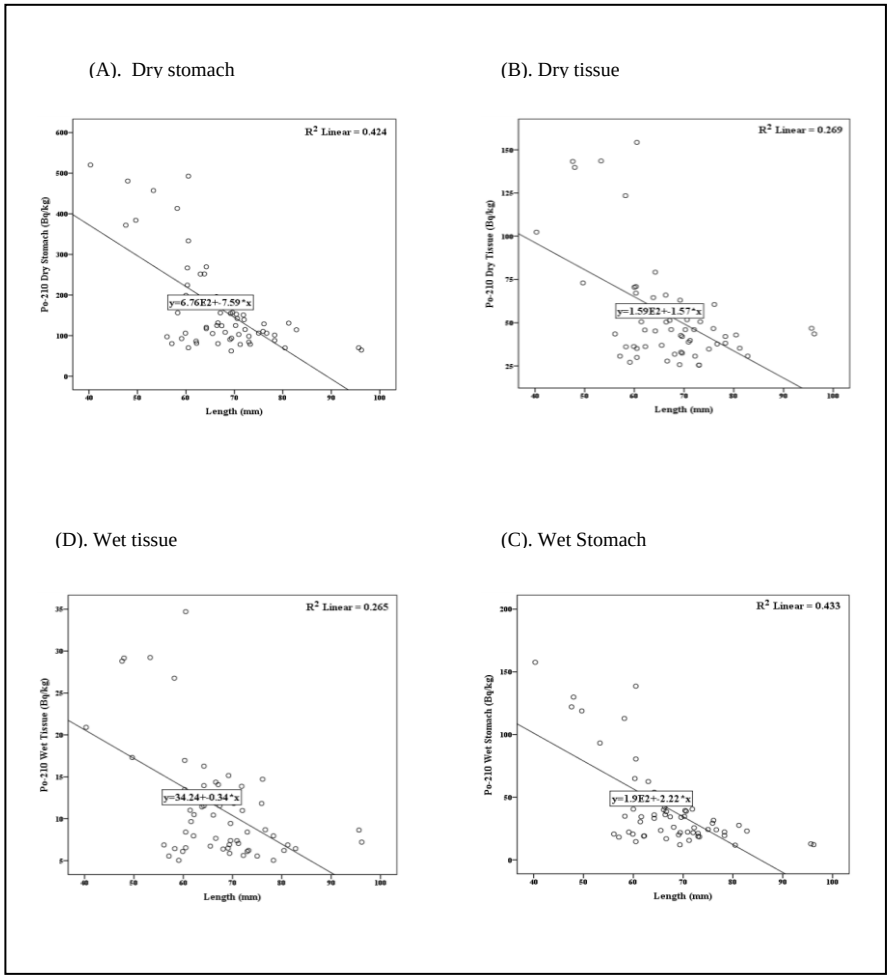


Figure 3. Correlation between mussel length (mm) and ^{210}Po activity concentrations (Bq/kg) in various organs obtained during this study

Risk assessment on the ^{210}Po contaminant

The samples collected have been classified into several classes and the activities of both ^{210}Po are shown in Table 2. Samples of wild origin have the highest activity distribution of ^{210}Po (mean: 310.48 ± 8.49 Bq kg^{-1} dry weight). The results have shown a remarkable decreasing trend in radioactivity as size increases. However, an inconsistent trend

was noticed for the cultured samples. Furthermore it has been proven that radionuclide activity decreases as soft body tissue increases [22].

Table 2. Average activities of ^{210}Po in samples collected from different origin

Origin	Range Size (mm)	^{210}Po Activity (Bq kg^{-1} dry weight)
Market	Class 1 (60-80 mm)	109.77 ± 3.38 (n = 4)
	Class 2 (>80.1 mm)	107.35 ± 2.88 (n = 3)
	Mean	108.56 ± 3.13
Culture	Class 1 (50-60 mm)	124.76 ± 3.87 (n = 5)
	Class 2 (60.1-65 mm)	122.00 ± 3.43 (n = 5)
	Class 3 (65.1-71 mm)	150.26 ± 3.91 (n = 13)
	Class 4 (71.1-80mm)	138.73 ± 3.49 (n = 10)
	Class 5 (>81 mm)	144.71 ± 3.62 (n = 2)
	Mean	136.09 ± 3.66
Wild	Class 1 (40-50 mm)	466.25 ± 14.03 (n = 4)
	Class 2 (50-60 mm)	406.04 ± 10.61 (n = 3)
	Class 3 (60.1-65 mm)	307.22 ± 7.79 (n = 9)
	Class 4 (65-70 mm)	211.49 ± 5.48 (n = 4)
	Class 5 (>70 mm)	161.42 ± 4.55 (n = 1)
	Mean	310.48 ± 8.49

The daily intake of ^{210}Po in green mussels based on green mussel consumption and ^{210}Po accumulation in the human body are calculated with the equation (1):

$$\text{Daily intake (mBq day}^{-1}\text{ person}^{-1}\text{)} = AC \times AP \times 0.4 / (MP \times 365) \quad (1)$$

where AC is the average concentration (Bq kg^{-1} dry weight); AP is green mussel production (2384.97 metric tonnes) reported by the Department of Fisheries Malaysia [23], whereas 0.4 represents the edible portion of green mussels; MP is the Malaysia population (29.3 million) at the time the survey was conducted by Department of Statistics, Malaysia [24]; and 365 specifies the days in a year As seen in the calculations shown below (Table 3), the daily intake of ^{210}Po ranges from 9.70 – 29.12 m Bq day^{-1} person^{-1} regardless of the origin of the green mussels consumed.

Table 3. Estimation of daily intake, CED and cancer risk

Nuclide	Origin	Daily intake (mBq day^{-1} person^{-1})	CED (mSv year^{-1})	Cancer Risk	
				Lifetime Mortality Risk	Lifetime Morbidity Risk
^{210}Po	Market	9.70	2.61	1.17 x 10^{-5}	1.61 x 10^{-5}
	Culture	12.40	3.34	1.50 x 10^{-5}	2.06 x 10^{-5}
	Wild	29.12	7.83	3.52 x 10^{-5}	4.83 x 10^{-5}

The committed effective dose (CED) of ^{210}Po in green mussels can be calculated by the following equation (2):

$$\text{CED (mSv year}^{-1}\text{)} = A \times B \times C \quad (2)$$

A is the igestion dose conversion factor (^{210}Po: 1.2 x 10^{-3} mSv Bq^{-1}; [25]); B is green mussel consumption per year (20.1 kg year^{-1}) as provided by Statisitics of Agro Food [26]; and C is the average concentration (Bq kg^{-1} dry

weight). The annual effective dose via the ingestion of green mussels is shown to be very high for ^{210}Po (2.61 – 7.83 m Sv year^{-1}), and exceeds the safe limit recommended by ICRP (1 mSv year^{-1} ^{210}Po; [27]).

The cancer risk related with lifetime mortality risk and lifetime morbidity risk can be calculated with the provided equation (3):

$$R = r \times I \quad (3)$$

r is the cancer risk coefficient where ^{210}Po is 4.44 x 10^{-8} risk Bq^{-1} and 6.09 x 10^{-8} risk Bq^{-1} for the lifetime mortality risk and lifetime morbidity risk respectively [28]; and I is the average lifetime intake of ^{210}Po. It can be derived from the multiplication of daily intake with time (365); and Malaysian average life expectancy at birth (74.55) by Department of Statistics, Malaysia [24]. The highest average mortality and morbidity risk taken for ^{210}Po are 3.52 x 10^{-5} and 4.83 x 10^{-5} per individual, respectively. In the opinion of US-EPA, risk values below 1 x 10^{-6} are insignificant. Attention should be given to risk calculations ranging between 1 x 10^{-6} – 1 x 10^{-4} as the risk calculation approaches baseline limits and a plan to remedy the situation needs to be framed [29].

In view of the assessments of risk discussed above, wild green mussels may result in some degree of health problems. This study has shown that smaller-sized green mussels are more likely to exceed suggested safety limits. In addition, most green mussels in the local markets are from both wild and cultured sources. Hence, oversight to sensure a minimum the marketable size of green mussels would minimise radioactivity exposure to the human body.

Conclusion

^{210}Po activity concentrations vary in green mussel body parts (e.g., stomach and tissues) and also vary between the organism's source (e.g. wild, cultured or market). Samples from the wild showed the highest concentrations of natural polonium activity because it received direct contaminants from industrial and domestic discharges. Moreover, ^{210}Po levels in wild organisms in the Johor Strait were relatively higher than other marine organisms in different areas of Malaysia as well as higher compared to worldwide values. Therefore, it is presumed that consumers of green mussels from the Straits of Johor probably have radiation risks exceeding those recommended by the USEPA. Despite the fact that mortality and morbidity risk were in acceptable range and no serious health problem will be caused, frequent consumption of green mussels is not recommended. Further analysis of pollutants (e.g., ^{210}Po) in green mussels at the Johor Strait needs to continue especially with regards to human consumption of those mussels.

Acknowledgement

The authors would like to thank the laboratory staff of the Faculty of Science and Technology, Universiti Kebangsaan Malaysia and others for helping during this study. Acknowledgement is also extended to the Ministry of Science, Technology and Innovation (Grant no. 04-01-02-SF0801) and the Ministry of Higher Education, Malaysia (KPT.P.(S)400-7/2/29-4(65)) for providing the grants to conduct this research project.

References

1. Worland, J. (2017). The lingering effects of fukushima on fish. 2016. Retrieved from Time Inc. http://time.com/4241443/fukushima-disaster-food-safety/ [Access date 15 September 2017].
2. Alonso-Hernandez, C., Diaz-Asencio, M., Munos-Caravaca, A., Suarez-Morell, E. and Avila-Moreno, R. (2002). ^{137}Cs and ^{210}Po dose assessment from marine food in Cienfuegos Bay (Cuba). *Journal of Environmental Radioactivity*, 61(2): 203-11.
3. Bustamante, P., Germain, P., Leclerc, G. and Miram, P. (2002). Concentration & distribution of Po-210 in the tissues of the scallop *Chlamys varia* & the mussel *Mytilus edulis* from the coast of Charente-Maritime (France). *Marine Pollution Bulletin*, 44(10): 997-1002.
4. Al-Masri, M. S., Nashawati, A., Amin,Y. and Al-Akell, B. (2004). Determination of Po-210 in tea, mate and their infusions and its annual intake by Syrians. *Journal of Radioanalytical and Nuclear Chemistry*, 260(1): 27-34.

5. Carvalho, F. P. (2011). Polonium (^{210}Po) and lead (^{210}Pb) in marine organisms and their transfer in marine food chains. *Journal of Environmental Radioactivity*, 102(5): 462-72.
6. Alam, L. and Mohamed, C. A. R. (2011). Natural radionuclide of Po-210 in the edible seafood affected by coal-fired power plant industry in Kapar coastal area of Malaysia. *Environmental Health*, 10(1):43.
7. Theng, T., Ahmad, Z. and Mohamed, C. A. R. (2004). Activity concentrations of ^{210}Po in the soft parts of cockle (*Anadara granosa*) at Kuala Selangor, Malaysia. *Journal of Radioanalytical and Nuclear Chemistry*, 262(2): 485-488.
8. Zakaria, N., Sarimin, A. S., Sabuti, A. A. and Mohamed, C. A. R. (2013). Assessment activity of ^{210}Po and ^{210}Pb in the edible tissues of cultured seabass (*Lates calcarifer*) at Peninsular Malaysia. *EnvironmentAsia*, 6(1): 66-73.
9. Ariffin, N. A. N. and Mohamed, C. A. R. (2014). Natural isotope radium in marine biota at Kapar, Klang coastal area. *Malaysian Journal of Analytical Sciences*, 18(1): 127-139.
10. Zakri, N. and Mohamed, C. A. R. (2016). Po-210 as an Indicator of Safe Radiation Levels in Cockles (*Anadara granosa*) in Peninsular Malaysia. *EnvironmentAsia*, 9(1): 99-106.
11. Carvalho, F (1988). ^{210}Po in marine organisms: a wide range of natural radiation dose domains. *Radiation Protection Dosimetry*, 24(1-4):113-117.
12. Cherry, R. and Heyraud, M. (1982). Evidence of high natural radiation doses in certain mid-water oceanic organisms. *Science*, 218(4567):54-56.
13. McDonald, P., Baxter, M., and Scott, E. (1996). Technological enhancement of natural radionuclides in the marine environment. *Journal of Environmental Radioactivity*, 32(1-2):67-90.
14. Waska, H., Kim, S., Kim, G., Kang, M. R. and Kim, G. B. (2008). Distribution patterns of chalcogens (S, Se, Te, and ^{210}Po) in various tissues of a squid, *Todarodes pacificus*. *Science of The Total Environment*, 392(2): 218-224.
15. Bayne, B. L. (1976). Marine mussels: their ecology and physiology, (Vol. 10): Cambridge University Press.
16. Jørgensen, C. B. (1996). Bivalve filter feeding revisited. Marine Ecology Progress Series, pp. 287-302.
17. Preiss, N., Mélières, M-A, and Pourchet, M. (1996). A compilation of data on lead 210 concentration in surface air and fluxes at the air-surface and water-sediment interfaces. *Journal of Geophysical Research*: *Atmospheres*, 101(D22):28847-28862
18. ICRP (1979). Limits for intakes of radionuclides by workers. Pergamon Press, New York, ICRP Publication 30.
19. Gosling, E. (2008). Bivalve molluscs: Biology, ecology and culture. Oxford, Blackwell.
20. Hawkins, A., Bayne, B., and Clarke, K. (1983). Coordinated rhythms of digestion, absorption and excretion in *Mytilus edulis* (Bivalvia: Mollusca). *Marine Biology*, 74(1): 41-48.
21. Carvalho, F. P, and Fowler, S. W. (1994). A double-tracer technique to determine the relative importance of water and food as sources of polonium-210 to marine prawns and fish. *Marine Ecology Progress Series*, 251-264.
22. Carvalho, F. P., Oliveira, J. M., Alberto, G. and Vives, I. and Batlle, J. (2010). Allometric relationships of ^{210}Po and ^{210}Pb in mussels and their application to environmental monitoring. *Marine Pollution Bulletin* 60(10): 1734-1742.
23. Department of Fisheries Malaysia (2012). The fisheries statistics of year. Retrieved from http:// www.dof.gov.my/web/guest/perangkaan-perikanan-tahunan-2012 [Access date 30 June 2014].
24. Department of Statistics (2012). Social Statistics Bulletin Malaysia 2012. Retrieved from https://www.dosm.gov.my/v1/portal/download_Labour/files/BPS/Buletin_Perangkaan_Sosial2012.pdf?
25. ICRP (1996). Age-dependent doses to the members of the public from intake of radionuclides. Compilation of Ingestion and Inhalation Coefficients 72.
26. Department of Statistics (2012). Abridged Life Tables 2009-2011. Retrieved from https://www.dosm.gov.my/v1/index.php
27. ICRP (2007). Recommendations of International Commission on Radiological Protection ICRP Publication 103. Annals ICRP 2007(37): 2-4.
28. Environmental Protection Agency (1988). Limiting values of radionuclide intake and air concentration and dose conversion factors for inhalation, submersion and ingestion. Oal Ridge National Laboratory, Oask Ridge, TN; US, EPA, Washington, DC. Federal Guidance report No. 11, EPA-520/1-88-020.
29. Environmental Protection Agency (1991). Role of the baseline risk assessment in superfund remedy selection decisions. US Environmental Protection Agency, Washington DC.

Malaysian Journal of Analytical Sciences, Vol 23 No 6 (2019): 991 - 1000
DOI: https://doi.org/10.17576/mjas-2019-2306-07

MALAYSIAN JOURNAL OF ANALYTICAL SCIENCES
Published by The Malaysian Analytical Sciences Society
ISSN 1394 - 2506

MODIFICATION OF GOLD SCREEN PRINTED ELECTRODE FOR THE DETECTION OF TOXIC DOMOIC ACID

(Pengubahsuaian Elektrod Cetakan Skrin Emas bagi Pengesanan Asid Domoik Toksik)

Hafiza Mohamed Zuki*, Norhidayah Mohd Nasri, Fatin Nabilah Muhamad, Noor Sheryna Jusoh, Azrilawani Ahmad, Marinah Mohd Ariffin

Faculty of Science and Marine Environment,
Universiti Malaysia Terengganu, 21030 Kuala Nerus, Terengganu, Malaysia

**Corresponding author: hafiza@umt.edu.my*

Received: 30 October 2018; Accepted: 26 September 2019

Abstract

Entrapped ninhydrin in polyvinylchloride (PVC) film is directly immobilized on the surface of gold screen printed electrodes (Au-SPE). Ninhydrin acts as a potential reagent for the detection of toxic Domoic Acid (DA) on the modified Au-SPE sensing system. The modified Au-SPE was characterized using cyclic voltammetry (CV), where the electrochemical behavior of ninhydrin-DA on modified Au-SPE surface was investigated in the potential range of -0.6 V to +0.85 V at a 50 mVs^{-1} scan rate, in the presence of 10 mM potassium ferricyanide in 0.1 M potassium chloride (KCl). Good responses were observed for ninhydrin-DA redox reactions with a linear relationship forming between peak currents and concentrations. The obtained limit of detection (LOD) for the sensing system was 7.64 x 10^{-5} M. The developed sensing system of modified Au-SPE exhibited excellent reproducibility with RSD obtained between 0.8% to 1.2%.

Keywords: domoic acid, ninhydrin, modified gold screen printed electrode, cyclic voltammetry

Abstrak

Ninhidrin yang diperangkap dalam lapisan filem polivinilklorida (PVC) dipegunkan secara langsung pada permukaan elektrod cetakan skrin emas (Au-SPE). Ninhidrin bertindak sebagai reagen yang berpotensi untuk mengesan asid domoik (DA) toksik diatas sistem pengesan Au-SPE yang diubahsuai. Au-SPE yang diubahsuai dicirikan dengan menggunakan voltametri kitaran (CV) di mana sifat elektrokimia ninhidrin-DA pada permukaan Au-SPE yang diubahsuai telah dikaji dalam julat keupayaan antara -0.6 hingga +0.85 V pada kadar imbasan 50 mVs^{-1} dalam kehadiran 10 mM kalium ferisianida dalam 0.1 M kalium klorida (KCl). Rangsangan yang baik telah dicerap bagi tindak balas redoks ninhidrin-DA dengan hubungan linear diperoleh antara arus puncak dan kepekatan. Had pengesanan (LODs) yang diperolehi bagi system pengesan adalah 7.64 x 10^{-5} M. Sistem pengesan Au-SPE diubahsuai yang dibangunkan, mempamerkan kebolehulangan yang sangat baik dengan julat nilai RSD diperolehi antara 0.8% hingga 1.2%.

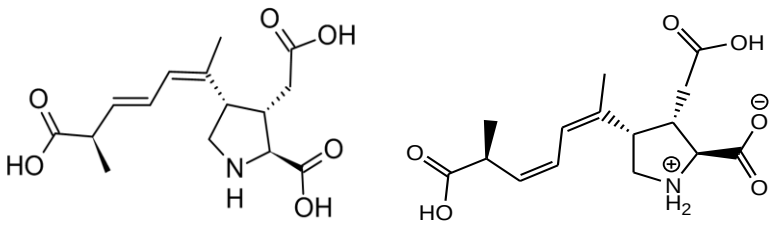
Kata kunci: asid domoik, ninhidrin, elektrod cetakan skrin emas, voltametri kitaran

Introduction

Marine toxins, also known as phycotoxins, are potent organic compounds harbored by almost 100 different species of diatoms and dinoflagellates species [1]. Toxicosis in human, other mammals, birds and fishes from marine phycotoxin producers can occur *via* direct contact, inhalation, or ingestion of toxigenic organisms. Shellfish poisoning threats in humans occur by ingestion, after passage of the toxins through food chains to shellfish [2]. This shellfish poisoning threat is greatly affecting human health as the reported poisoning cases by consumption of

shellfish seafood have increased significantly around the globe [3]. There are seven different types of identified seafood poisoning, which are based on the specific toxins or chemicals that are responsible for different specific and nonspecific symptoms. Those types are; Diarrheic Shellfish Poisoning (DSP), Paralytic Shellfish Poisoning (PSP), Amnesic Shellfish Poisoning (ASP), Neurologic Shellfish Poisoning (NSP), Azaspiracid Shellfish Poisoning (AZP), Ciguatera Fish Poisoning (CFP) and puffer fish poisoning [2].

ASP or domoic acid (DA) poisoning is caused by a potent neurotoxin water-soluble acidic amino acid (Figure 1a) and its derivatives. Humans affected by ASP could experience nausea, vomiting, abdominal cramps, temporary memory loss as well as death [2]. However, DA had been used in Japan as an anthelmintic drug back in 1958 [4]. DA was originally isolated from diatoms of red microalgae species known as *Pseudo-nitzschia* [5] and *Chondria armata* [6]. The first reported DA poisoning was observed in Prince Edward Island, Canada, in 1987, causing illnesses in over 143 individuals and deaths in about 4, after the consumption of DA contaminated mussels [7]. In 1991, the outbreak of DA poisoning produced by a related diatom *Pseudo-nitzschia australis* caused the deaths of more than 100 brown pelicans (*Pelecanus occidentalis*) and cormorants (*Phalacrocorax penicillatus*) that consumed the anchovies which had consumed the toxic diatom in Monterey Bay, California [8]. Several cases of DA poisoning were discovered in different animals such as crabs, anchovies, sardines, seabirds and sea lions between the years 1990 and 1998 [8]. Since the occurrence of these incidents, global awareness of DA has been raised and its producing sources have been identified. Up until now, many occurrence of ASP toxins (DA) in coastal waters have been recorded around the globe in places such as Iceland [9], Angola [10], Belgium [11], Great Britain [12], France [13], Scotland [14], China [15], Argentina [16] as well as in South East Asia [17] and Malaysia [18]. Additionally, recent publications have identified potential DA producers in Malaysian waters such as in Johor [19] and Malacca [20].



(a) (b)

Figure 1. Structure of domoic acid (a) normal structure and (b) zwitterionic form

DA's toxicity can be explained by its structural similarity with the excitatory neurotransmitters of glutamic and kainic acids. Due to the stronger receptor affinity of DA which is more potent than kainic and glutamic acid, DA binds predominately to N-methyl-D-aspartate (NMDA), kainite and α-amino-3-hydroxy-5-methyl-4-isoxazolepropionic acid (AMPA) receptors [21], causing excitotoxic effects towards these receptors, where the damaged receptors are unable to control the excessive influx of Ca^{2+} and Na^{+} into neurons [22, 23]. The normal impulse balance is disturbed, which eventually kills the nerve cell [24]. The affected neurons are mainly located in the hippocampus, an area in the brain which is responsible for learning and memory processing. Thus, DA poisoning may lead to neurological distortions including seizures and other uncontrolled movements, brain lesions and permanent memory loss.

At present, chromatographic techniques have been widely used for the detection of marine toxins [2, 25, 26]. Although chromatography is one of the best techniques for domoic acid detection, it requires expensive equipment, trained personnel, sophisticated methods of preparation of samples and is time consuming. In this research, an electrochemical approach of detecting DA was attempted using immobilized ninhydrin in PVC film coated on the surface of working electrodes of Au-SPE. Chemically, ninhydrin reacts with primary amino acids to produce both hydrindantin [27] and Ruhemann's purple [7] (Figure 2), which is a reliable method to detect amino acids in samples. However, DA is a secondary amino acid, in which the reaction with ninhydrin is almost impossible.

Fortunately, besides its neutral molecular structure, DA also possesses a zwitterionic form (Figure 1b), which provides additional hydrogen and nitrogen at physiological pH [28, 29], which suggests that the optimum condition for a DA-ninhydrin interaction would give a yellow colored product. The interactions between DA and ninhydrin on the modified Au-SPE were measured using cyclic voltammetry (CV) responses. CV is widely known for its ability to detect target analytes in low concentrations. This study is important as it supports the need of developing an electrochemical sensor using modified electrodes for monitoring DA in seafood markets, in order to prevent the potential ASP outbreak in Malaysia.

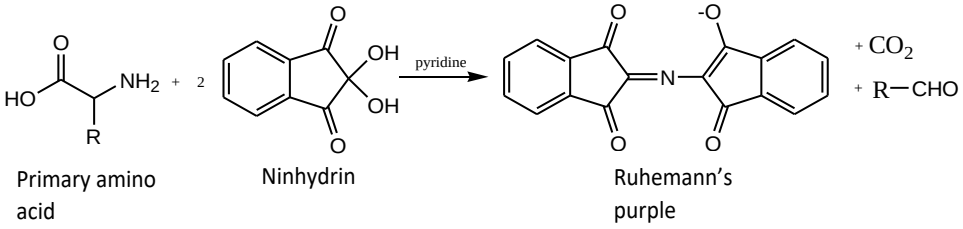


Figure 2. Standard reactions of ninhydrin with primary amino acids

Materials and Methods

Domoic acid, sodium tetraphenyl borate, tetrahydrofuran and tributyl phosphate were purchased from Merck, Germany. Polyvinylchloride was purchased from Sigma-Aldrich, Italy. Ninhydrin was purchased from R&M, UK. All reagents used were of analytical grade.

Instrumentation

Au-SPE was purchased from DropSens, Spain. A mini Potensiostat (Metrohm, Switzerland) was used for electrochemical cyclic voltammetry measurement. Cable connectors (DropSens, Spain) were used to connect the instrument and the electrode. The surface morphology of screen-printed gold electrode (SPGE) was investigated using a Scanning Electron Microscope (SEM) JSM-6360 JEOL, from Japan.

Preparation of thin film cocktail

10 µL of 5 mM ninhydrin, 1.5 g of sodium tetraphenyl borate, 1.2 g of polyvinyl chloride and 2.4 g of tributyl phosphate were mixed with 20 mL of tetrahydrofuran. The mixture was stirred for one hour to make sure it was completely dissolved.

Electrode modification

1 µL of ninhydrin-PVC film cocktail was spread on the working electrode surface of Au-SPE. The modified Au-SPE was dried in an oven at 50 °C for 1 hour and left overnight at room temperature before use.

Cyclic voltammetry measurement

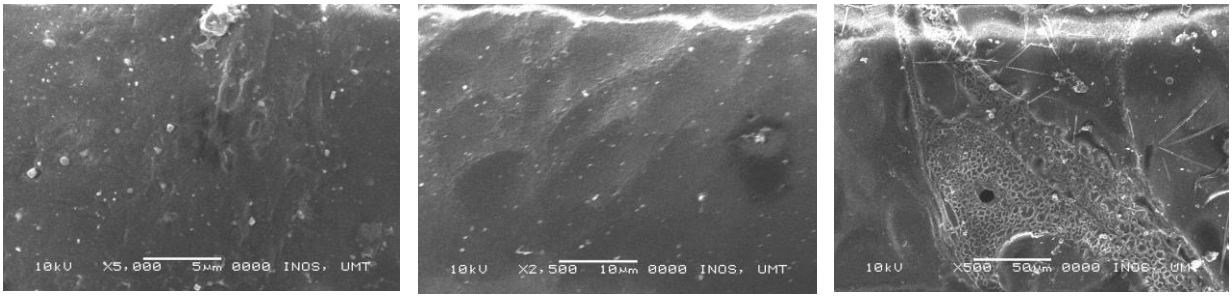
CV measurements were carried out at a scan rate of 50 mV/s at a potential range of -0.6 V to 0.85 V in the presence of 10 mM potassium ferricyanide in 0.1 M KCl.

Results and Discussion

Scanning electron microscope

The surface morphology of bare and modified Au-SPEs was investigated using SEM at different levels of magnifications (Figure 3). At 5000 times magnification, aggregates of different sizes and forms were clearly observed on the surface of modified ninhydrin-Au-SPE, as a result of the stacking of ninhydrin in the PVC film. The smooth surface of bare Au-SPE changed to rumples after the immobilization of PVC film containing ninhydrin.

Bare Au-SPE



Modified Au-SPE

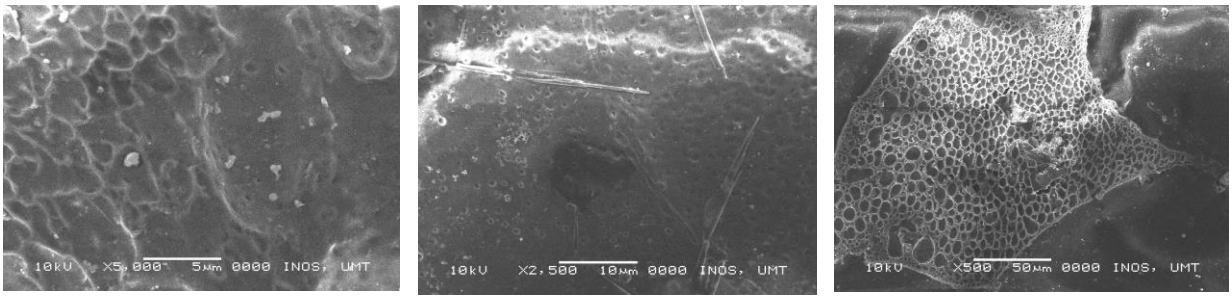


Figure 3. SEM images of bare and modified Au-SPE at different magnifications

Cyclic voltammetry test

The electrochemical characterization of modified Au-SPE was done using a cyclic voltammetry (CV) technique, where the electrochemical behavior of ninhydrin-DA on modified Au-SPE surface was investigated as discussed in the following subsection.

Bare electrode versus modified Au electrode

The performance of bare electrode and modified Au-SPEs was compared using a 10 mM potassium ferricyanide in 0.1 M KCl electrolyte solution with a scan rate of 50 mV/s. The electron-transfer kinetic of ferricyanide redox couple was greatly decreased for modified Au-SPE (Figure 4). The blocking of access of ferricyanide redox couple to the gold electrode is due to the present of a coated ninhydrin-PVC membrane on the Au-SPE.

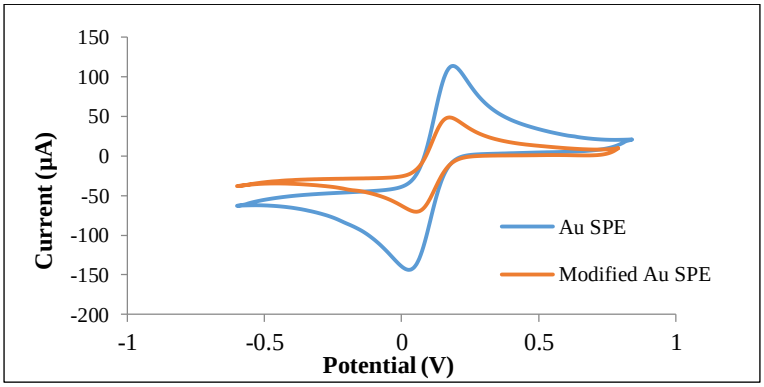


Figure 4. Voltammograms of bare and modified Au-SPEs at scan rate of 50 mV/s in 10 mM potassium ferricyanide in 0.1 M KCl

Effect of scan rate

The electrochemical behavior of a species generated at the modified Au-SPE can be studied using a scan rate analysis of cyclic voltammetry [30]. The diffusion behavior of DA was investigated by conducting CV with different scan rates ranging from 50-100 mV/s, in 0.3 M DA solution containing 10 mM potassium ferricyanide in 0.1 M KCl. From the results obtained, the peak currents recorded were directly proportional to the scan rate (Figure 5). High peak currents obtained at higher scan rates and low peak current obtained at lower scan rates were measured due to fast and slow redox reactions on the electrode surface.

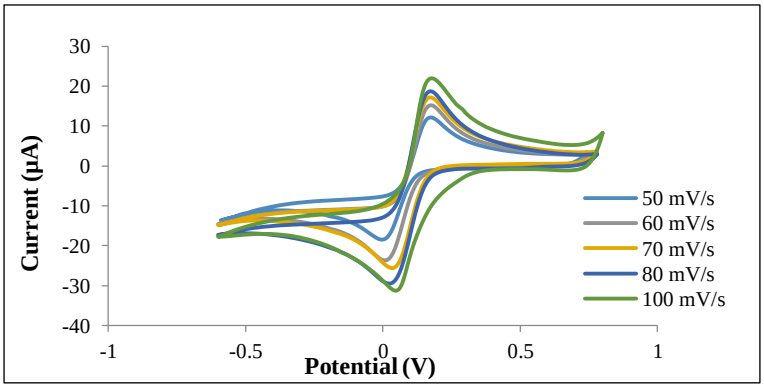


Figure 5. Voltammogram of different scan rates in 10 mM potassium ferricyanide in 0.1 M KCl

Table 1 displays the peak potential separation (ΔE_p) and peak current ratio (I_p) of different scan rates. The values of ΔE_p and I_p indicate that the electron transfer process was irreversible. The recorded ΔE_p values of all scan rates exceeded both the theoretical (59 mV) and quasi-reversible values (120 mV) [31]. A relationship between the peak current densities (i_p) and the square root of scan rate $(v)^{1/2}$ was determined by the Randles-Sevcik equation, which shows a linear relationship. The values of correlation coefficient (R^2) of anodic peak (0.9624) and cathodic peak (0.8825) confirm that the electrochemical system of the DA with modified electrode was under the diffusion control process [32].

Table 1. Peak potential separation and peak current ratio values of different scan rates

Scan Rate (mV/s)	E_0 (mV)	ΔE_p (mV)	I_c (µA)	I_a (µA)	I_p	$v^{1/2}$
50	90	180	18	19	0.95	7.07
60	95	170	22	25	0.88	7.75
70	105	150	26	27	0.96	8.37
80	100	160	28	32	0.88	8.94
100	115	130	31	32	0.97	10.00

Effect of coating time

The influence of coating time of PVC film on Au SPE was examined in 10 mM potassium ferricyanide in 0.1 M KCl in presence of 10 µM ninhydrin. As shown in Figure 6, the electrochemical measurement shows a direct perpendicular trend between the peak current and coating time. Maximum peak current was recorded at 2 hours, which indicates that the film was firmly attached on the Au-SPE.

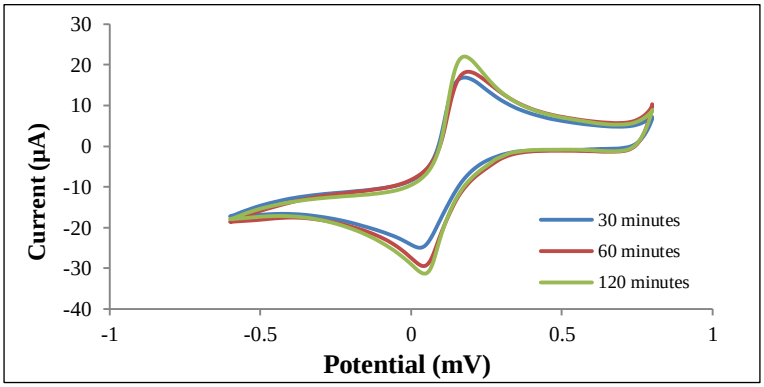


Figure 6. Voltammograms of different immobilisation time in 10 mM potassium ferricyanide in 0.1 M KCl. Scan rate: 50 mV/s

Sensing response

Diffusion of DA through the PVC film allowed the reaction of DA with immobilized ninhydrin inside the film. Reaction of zwitterionic DA with ninhydrin resulted in the oxidation of DA and reduction of ninhydrin, which showed a yellow color formation of the film. In Figure 7 and Figure 8, by progressively increasing the amount of DA, a steady increase in current reading was observed. This shows that the sensing response towards DA, of the immobilized ninhydrin on the surface of the modified Au-SPE electrode, was successfully developed.

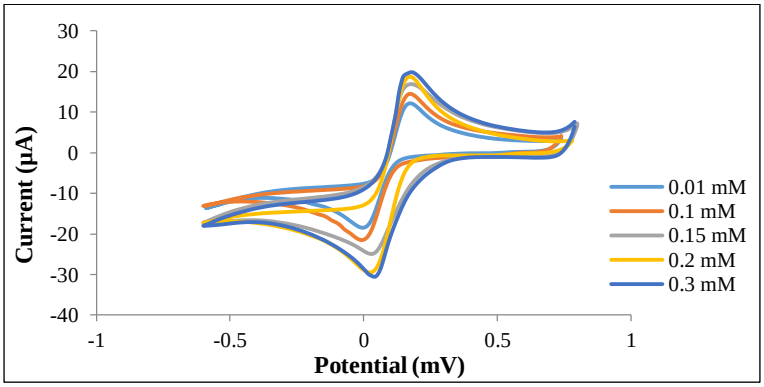


Figure 7. Voltammogram of different concentration of DA in 10 mM potassium ferricyanide in 0.1 M KCl. Scan rate: 50 mV/s

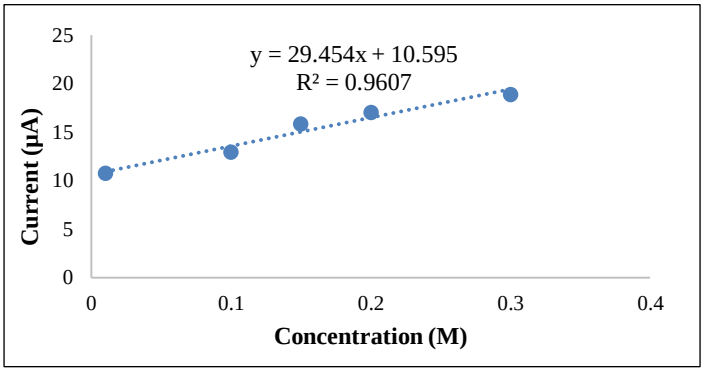


Figure 8. Calibration plot for different concentration of DA in 10 mM potassium ferricyanide in 0.1 M KCl. Scan rate: 50 mV/s

The sensitivity of the modified Au-SPE towards DA was determined by calculating the limit of detection (LOD) of the sensing responses. Table 2 shows the value of LOD calculated from the sensing responses of DA analysis (anodic response). An LOD value of 7.64 x 10^{-5} M shows that the modified sensing system is relatively sensitive where it can measure concentrations of DA as low as 10^{-5} M.

Table 2. Reaction response of DA analysis

Standard Deviation, σ	Slope, s	LOD (M)
0.75	29.45	7.64 x 10^{-5}

Reproducibility

Reproducibility is defined as the closeness of agreement between independent results, obtained from the same method, on identical test materials, but under different conditions [33]. In this study, the purpose of the reproducibility test was to examine the capability of every single modified AU-SPE prepared, in providing similar responses towards 0.1 mM DA in each test. Figure 9 shows the reproducibility of modified Au-SPE prepared in two batches. Both batches were able to produce almost uniform modified AU-SPEs that can sense DA with very low relative standard deviations (RSD) in each batch. The RSD values calculated were 0.88 % and 1.15% for films in batch 1 and films in batch 2 respectively. However, the difference in current readings between batches (1 and 2) indicate that the uniformity of the modified AU-SPE preparation in different batch conditions is still difficult to achieve. Several factors, such as film thickness and coated surface areas resulting from the preparation techniques, need to be improved in order to achieve the reproducibility of the modified AU-SPE.

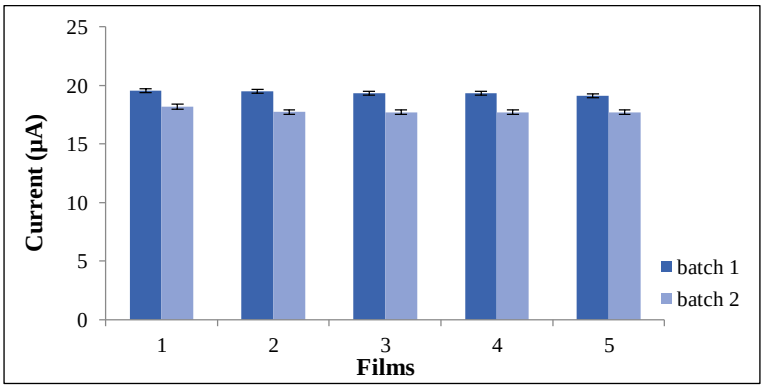


Figure 9. Reproducibility of modified Au-SPE with DA

Stability

The stability of modified Au-SPE was studied in 10 mM potassium ferricyanide in 0.1 M KCl, at a scan rate of 50 mV/s. The purpose of the stability test is to examine the capability of each single modified AU-SPE prepared, to be used repetitively in measuring responses towards DA. In this study, 20 repetitive measurements of DA were conducted daily for 20 days using the same modified Au-SPE. Figure 10 shows that the response signal had slightly increased from its initial response over the testing period with a calculated RSD value of 7.47%, thus indicating that the modified Au-SPE is still not stable to be used repetitively. However, since the modified Au-SPEs are reproducible, it is suitable for the electrode to be used as a one-off electrode.

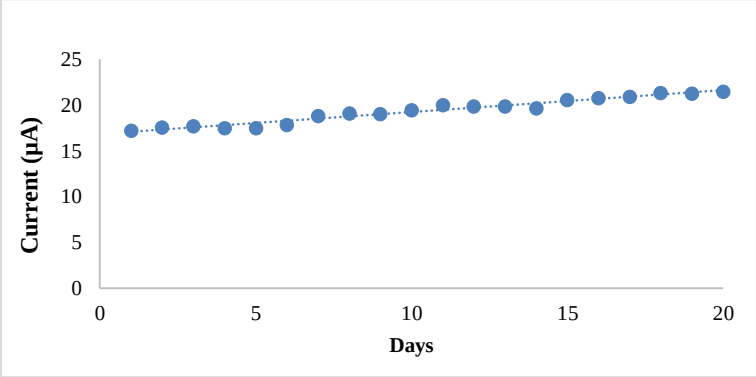


Figure 10. Stability of modified Au-SPE in 10 mM potassium ferricyanide (in 0.1 M KCl) for 20 days. Scan rate: 50 mV/s

Conclusion

A modified Au-SPE for the detection of DA was successfully developed by immobilizing a ninhydrin reagent into a thin film of PVC coated onto the surface of Au-SPE working electrode. The modified Au-SPE was capable of sensing DA by exhibiting irreversible electrochemical signals in a potential ranging from -0.6 to +0.85 V. The sensing system of the modified electrode showed excellent electrochemical characteristics with a good detection limit, efficient reproducibility and suitability to be used as one-off sensor. Further modifications can be studied in order to develop its stability. An active electrochemical interaction shows that the combination of ninhydrin and Au-SPE promises to be a simpler and easier detection method with reliable results.

Acknowledgement

The authors would like to acknowledge the Ministry of Education Malaysia through Fundamental Research Grant Scheme of FRGS/1/2015/ST04/UMT/02/1 (FRGS 59409) and Universiti Malaysia Terengganu for providing support, laboratory facilities and instrumentation.

References

1. Rodriguez, I., Vieytes, M.R. and Alfonso A. (2017). Analytical challenges for regulated marine toxins: Detection methods. *Current Opinion in Food Science*, 18: 29-36.
2. Campas, M., Prieto-Simon, B. and Marty, J-L. (2007). Biosensors to detect marine toxins: Assessing food safety. *Talanta, 72*: 884-895.
3. Nicolas, J., Hoogenboom, R. L. A. P., Hendriksen, P. J. M., Bodero, M., Bovee, T. F. H., Rietjens, I. M. C. M. and Gerssen, A. (2017). Marine biotoxins and associated outbreaks following seafood consumption: Prevention and surveillance in the 21st century. *Global Food Security*, 15: 11-21.
4. Saeed, A. F., Awan, S. A., Ling, S., Wang, R. and Wang, S. (2017). Domoic acid: Attributes, exposure risks, innovative detection techniques and therapeutics. *Algal Research*, 24: 97-110.

5. Bates, S. S., Garrison, D. L. and Horner, R. A. (2008). Bloom dynamics and physiology of domoic acid producing *Pseudo-nitzschia* species, *Physiological Ecology of Harmful Algal Blooms*, Springer-Verlag, Heidelberg: pp. 267-292.
6. Jiang, S., Kuwano, K., Ishikawa, N., Yano, M., Takatani, T. and Arakawa, O. (2014). Production of domoic acid by laboratory culture of the red alga Chondria armata. *Toxicon,* 92: 1-5.
7. Friedman, M. (2004). Applications of the ninhydrin reaction for analysis of amino acids, peptides, and proteins to agricultural and biomedical sciences. *Journal of Agriculture and Food Chemistry,* 52: 385-406.
8. Mos, L. (2001). Domoic acid: A fascinating marine toxin. *Environmental Toxicology and Pharmacology*, 9: 79-85.
9. Jamesa, K. J., Gillman, M., Amandi, M. F., Lopez-Rivera, A., Puente, P. F., Lehane, M., Mitrovic, S. and Furey, A. (2005). Amnesic shellfish poisoning toxins in bivalve molluscs in Ireland. *Toxicon,* 46: 852-858.
10. Blanco, J., Livramento, F. and Rangel, I. M. (2010). Amnesic shellfish poisoning (ASP) toxins in plankton and molluscs from Luanda Bay, Angola. *Toxicon,* 55: 541-546.
11. Anjelkovic, M., Vandevijvere, S., Klaveren, J. V., Oyen, H. V. and Loco, J. V. (2012). Exposure to domoic acid through shellfish consumption in Belgium. *Environment International*, 49: 115-119.
12. Johnson, S., Harrison, K. and Turner, A. D. (2016). Application of rapid test kits for the determination of amnesic shellfish poisoning in bivalve molluscs from Great Britain. *Toxicon,* 117: 76-83.
13. Thorel, M., Claquin, P., Schapira, M., Gendre, R. L., Riou, P., Goux, D., Roy, B. L., Raimbault, V., Deton-Cabanillas, A. F., Bazin, P., Kientz-Bouchart, V. and Fauchot, J. (2017). Nutrient ratios influence variability in *Pseudo-nitzschia* species diversity and particulate domoic acid production in the Bay of Seine (France). *Harmful Algae,* 68: 192-205.
14. Bresnan, E., Fryer, R. J., Fraser, S., Smith, N., Stobo, L., Brown, N. and Turrell, E. (2017). The relationship between *Pseudo-nitzschia* (Peragallo) and domoic acid in Scottish shellfish. *Harmful Algae,* 63: 193-202.
15. Li, Y., Huang, C. X., Xu, G. S., Lundholmc, N., Teng, S. T., Wue, H. and Tan, Z. (2017). *Pseudo-nitzschia simulans* sp. nov. (Bacillariophyceae), the first domoic acid producer from Chinese waters. *Harmful Algae*, 67: 119-130.
16. D'Agostinoa, V. C., Degratia, M., Sastrec, V., Santinellic, N., Krockd, B., Krohnd, T., Dansa, S. L. and Hoffmeyer, M. S. (2017). Domoic acid in a marine pelagic food web: Exposure of southern right whales *Eubalaena australis* to domoic acid on the Península Valdés calving ground, Argentina. *Harmful Algae,* 68: 248-257.
17. Romero, M. L. J., Kotaki, Y., Lundholm, N., Thoha, H., Ogawa, H., Relox, J. R., Terada, R., Takeda, S., Takata, Y., Haraguchi, K., Endo, T., Lim, P. T., Kodama, M. and Fukuyo, Y. (2011). Unique amnesic shellfish toxin composition found in the South East Asian diatom *Nitzschia navis-varingica*. *Harmful Algae*, 10: 456-462.
18. Tan, S. N., Teng, S. T., Lim, H. C., Kotaki, Y., Bates, S. S., Leaw, P. C. and Lim, P. T. (2016). Diatom *Nitszia navis-varingica* (Bacillariophyceae) and its domoic acid production from the mangrove environments of Malaysia. *Harmful Algae*, 60: 139-149.
19. Suriyanti, S. N. P. and Usup, G. (2015). First report of the toxigenic *Nitszia navis-varingica* (Bacillariophyceae) isolated from Tebrau Strait, Johor, Malaysia. *Toxicon,* 108: 257-263.
20. Teng, S. T., Lim, H. C., Lim, P. T., Dao, B. H., Bates, S. S. and Leaw, C. P. (2014). *Peudo-nitszia kodamae* sp. nov. (Bacillariophyceae), a toxigenic species from the Strait of Malacca. *Harmful Algae*, 34: 17-28.
21. Lefebvre, K. A. and Robertson, A. (2010). Domoic acid and human exposure risks: A review. *Toxicon,* 56: 218-230.
22. Tasker, R. A. R., Perry, M. A., Doucette, T. A. and Ryan, C. L. (2005). NMDA receptor involvement in the effects of low dose domoic acid in neotanal rats. *Amino Acids,* 28: 193-196.
23. Zabaglo, K., Chrapusta, E., Bober, B., Kaminski, A., Adamski, M. and Bialczyk, J. (2016). Environmental roles and biological activity of domoic acid: A review. *Algal Research,* 13: 94-101.
24. Costa, L. G., Giordano, G. and Faustman, E. M. (2010). Domoic acid as a developmental neurotoxin. *NeuroToxicology,* 31: 409-423.
25. Mohd Syaifudin A. R., Jayasundera K. P. and Mukhopadhyay S. C. (2009). A low cost novel sensing system for detection of dangerous marine biotoxins in seafood. *Sensors and Actuators B: Chemical*, 137: 67-75.

26. Lotierzo M., Henry O. Y. F., Piletsky S., Tothill I., Cullen D., Kania M., Hock B. and Turner A. P. F. (2004). Surface plasmon resonance sensor for domoic acid based on grafted imprinted polymer. *Biosensors & Bioelectronics*, 20: 145-152.
27. Anantharaman, S., Padmarajaiah, N., Al-Tayar, N. G. S. and Shrestha, A. K. (2017). Ninhydrin-sodium molybdate chromogenic analytical probe for the assay of amino acids and proteins. *Spectrochimica Acta Part A: Molecular and Biomolecular Spectroscopy*, 173: 897-903.
28. Djaoued, Y., Balaji, S. and Priya, S. (2007). Non-resonance micro-Raman spectroscopic studies on crystalline domoic acid and its aqueous solutions. *Spectrochimica Acta Part A,* 67: 1362-1369.
29. Kimura, O., Kotaki, Y., Hamaue, N., Haraguchi, K. and Endo, T. (2011). Transcellular transport of domoic acid across intestinal Caco-2 cell monolayers. *Food and Chemical Toxicology*, 49: 2167 – 2171.
30. Othman, M. A. F., Othman, A. A. and Zuki H. M. (2016). Dithizone modified silver electrode for the determination of metal ions in aqueous solution. *Malaysian Journal of Analytical Sciences,* 20(1): 197-204
31. Scholz, F. (2009). *Electroanalytical Methods*. (2nd edition). Berlin: Springer German.
32. Dossi, C., Monticelli, D., Pozzi, A. and Recchia, S. (2016). Exploiting chemistry to improve performance of sceen-printed, bismuth film electrodes (SP-BiFE). *Biosensors,* 6(3): 38.
33. Pellizzari, E., Lohr, K., Blatecky, A. and Creel, D. (2017). Reproducibility: A primer on semantics and implications for research. New Castle: RTI Press.

Malaysian Journal of Analytical Sciences, Vol 23 No 6 (2019): 1001 - 1008
DOI: https://doi.org/10.17576/mjas-2019-2306-08

MALAYSIAN JOURNAL OF ANALYTICAL SCIENCES
Published by The Malaysian Analytical Sciences Society
ISSN 1394 - 2506

SOURCES AND COMPOSITION OF POLYCYCLIC AROMATIC HYDROCARBONS IN THE RIVER AND ESTUARIAL SEDIMENT ALONG THE VICINITY OF KUALA KEDAH, MALAYSIA

(Sumber dan Komposisi Hidrokarbon Aromatik Polisiklik dalam Sedimen Sungai dan Muara di Sepanjang Persekitaran Kuala Kedah, Malaysia)

Terence Ricky Chiu[1] and Masni Mohd Ali[1,2]*

[1]*School of Environmental and Natural Resource Sciences, Faculty of Science and Technology, Universiti Kebangsaan Malaysia, 43600 UKM Bangi, Selangor, Malaysia*
[2]*Institute of Oceanography and Environment, Universiti Malaysia Terengganu, 21030 Kuala Nerus, Terengganu, Malaysia*

**Corresponding author: masni@ukm.edu.my*

Received: 30 October 2018; Accepted: 26 September 2019

Abstract

Sixteen surface sediment samples were taken along the vicinity of Kuala Kedah, especially the Kedah River and estuary areas. The surface sediments taken were identified and quantified by gas chromatography coupled with mass spectrometry (GC-MS). The knowledge and information gained from the study show that the concentration of individual Polycyclic Aromatic Hydrocarbon (PAH) compounds was known to be between 1.09 ng/g to 59.01 ng/g dry weight sediment. The river mouth sampling point was found to have the highest total PAHs concentration of 226.03 ng/g sediment dry weight. On the contrary, the S2 sampling point was found to have the lowest concentration of total PAHs with 7.20 ng/g sediment dry weight. Among all the incorporated sampling points, the highest number of an individual compound of PAHs found was that of benzo[ghi]perylene. On the other hand, acenaphthylene, which is another individual compound of PAHs, showed the lowest concentration. Apart from the estimation of the total and individual PAHs concentrations, the molecular indices and the Low Molecular Weight (LMW)/High Molecular Weight (HMW) of phenanthrene/anthracene and fluoranthene/pyrene were analyzed in this study to establish whether the sediment sources were pyrolytic or pyrogenic based. Lastly, based on the study of the sources of the PAHs, it was established that the study site's sources consisted of mixed PAHs sources with a dominance of pyrogenic sources of fossil fuel combustion, vehicle engine combustion, open wood combustion and charcoal combustion; which were the main causes that contributed towards the diversity of sources in the sediments along the vicinity of Kuala Kedah river and estuary areas.

Keywords: PAHs, surface sediments, molecular indices, pyrogenic, pyrolytic

Abstrak

Enam belas sampel sedimen permukaan telah diambil di sekitar kawasan Kuala Kedah terutama di kawasan sungai dan muara. Sedimen permukaan yang di ambil ditentu dan dikuantifikasi oleh kromatografi gas-spektrometri jisim (GC-MS). Maklumat yang diperoleh daripada kajian menunjukkan bahawa kepekatan individu sebatian HAP adalah antara 1.09 ng/g hingga 59.01 ng/g berat kering sedimen. Kawasan persampelan di muara sungai didapati mempunyai jumlah kepekatan tertinggi HAP iaitu 226.03 ng/g berat kering sedimen. Sebaliknya, titik pensampelan S2 mempunyai kepekatan HAP terendah dengan 7.20 ng/g berat kering sedimen. Bilangan tertinggi individu HAP yang dijumpai adalah benzo[ghi]perilena untuk keseluruhan titik pensampelan. Sebaliknya, asenaftilena menunjukkan kepekatan yang paling rendah. Selain daripada anggaran jumlah dan kepekatan individu PAH, indeks molekul fenantrena/antrasena, benzo[a]antrasena/krisena, fluoranthena/pirena dan berat molekul rendah (BMR)/berat molekul tinggi (BMT) juga dianalisis dalam kajian ini untuk menentukan sama ada sumber sedimen adalah pirolitik atau pirogenik. Akhir sekali, berdasarkan penemuan sumber-sumber HAP, terbukti bahawa sumber di kawasan kajian

adalah sumber bercampur yang didominasi oleh sumber pirogenik oleh pembakaran bahan bakar fosil, pembakaran enjin kenderaan, pembakaran kayu terbuka dan pembakaran arang adalah penyebab yang menyumbang ke arah kepelbagaian sumber di sedimen di sepanjang kawasan sekitaran dan sungai muara Kuala Kedah.

Kata kunci: HAP, sedimen permukaan, indeks molekular, pirogenik, pirolitik

Introduction

Polycyclic Aromatic Hydrocarbons (PAHs) are pollutants of marine coastal sediments [1]. The US EPA Priority and European Union Pollutant List have included polycyclic aromatic hydrocarbons (PAHs) because they represent the major group of compounds that are carcinogenic, mutagenic and teratogenic [2, 3]. Petrogenic and pyrolytic are the most widely known anthropogenic sources and are usually widely distributed in marine environments [1]. Additionally, a lower molecular weight friction characterizes petrogenic pollution while the higher molecular weight of PAHs characterizes pyrolytic pollution [1]. Many studies have demonstrated that the sources of PAHs can be distinguished by the ratio of low molecular weight (LMW) PAHs to high molecular weight (HMW) PAHs [4-7].

In Malaysia, the marine environment is rapidly being exposed to threats from spills and grease contaminations [7, 8]. Previous studies that investigated the concentrations of PAHs around Malaysia, found PAHs that ranged from the lowest value of 2.1 ng/g in the Straits of Malacca near Port Dickson to the highest value of 1689 ng/g in the east coastal sea around Kelantan, Besut and Terengganu rivers [6, 7, 9]. Kuala Kedah's estuary faces outwards towards the Straits of Malacca, which is the main route for large ships travelling from the east to the west or vice versa. Hence, the objectives of this study are to determine the characteristics and possible sources of PAH compounds in Sungai Kedah, Kuala Kedah, Malaysia. Kuala Kedah is a district and parliamentary constituency in Kota Setar District, Kedah, Malaysia. It is a fishing port, located at the mouth of the Kedah River, and serves as a terminus for ferries to the tourist island of Langkawi. It is home to a fort, Kota Kuala Kedah, which was built in 1770.

Materials and Methods

Study area

A total of sixteen sampling stations were established along the Kedah River from Kuala Kedah, Kedah to the area near the capital city of Alor Setar, Kedah (Figure 1 and Table 1). Surface sediment was collected from each of these sampling stations using a PONAR grab. All the samples were then preserved in pre-cleaned glass jars. All the samples were frozen at 4 °C prior to analysis.

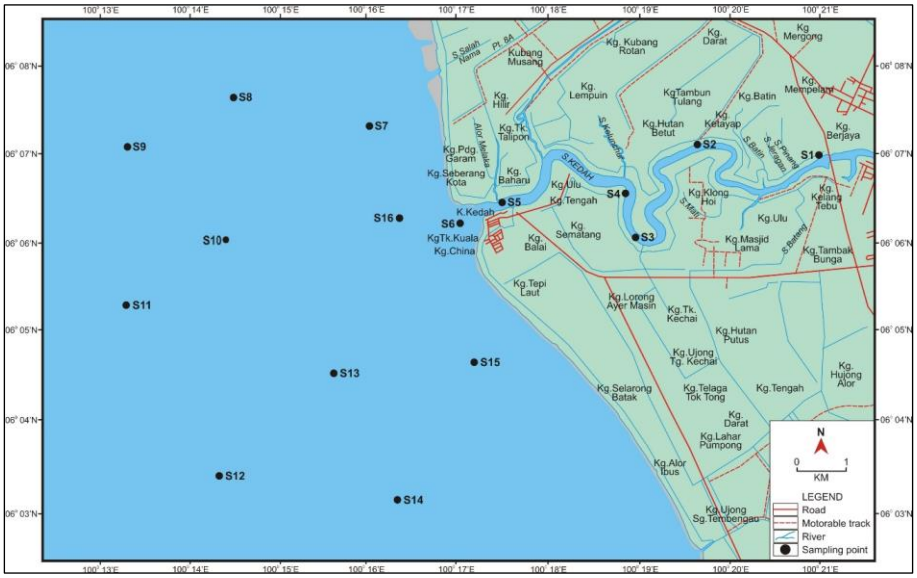


Figure 1. Sampling stations at the study area

Table 1. Description of sampling stations around Kuala Kedah, Kedah

Station	Descriptions of Sampling Stations	Depth of Water Column (m)	Latitude (N)	Longitude (E)
1	Residential Area	5.8	06º 7.007’	100º20.876’
2	Residential Area	3.6	06º 7.154’	100º19.687’
3	Residential Area	2.8	06º 6.043’	100º18.958’
4	Residential Area	4.9	06º 6.659’	100º18.708’
5	Residential Area	4.7	06º 6.529’	100º17.580’
6	River Mouth (Jetty Area)	3.0	06º 6.382’	100º17.123’
7	Coastal Area	0.8	06º 7.385’	100º16.019’
8	Open Sea	6.6	06º 7.657’	100º14.546’
9	Open Sea	11.6	06º 7.094’	100º 13.313’
10	Open Sea	2.4	06º 5.686’	100º 14.802’
11	Open Sea	13.7	06º 5.239’	100º 13.323’
12	Open Sea	12.1	06º 3.413’	100º 14.378’
13	Open Sea	4.7	06º 4.521’	100º 15.764’
14	Open Sea	8.5	06º 3.121’	100º 16.486’
15	Coastal Area	2.6	06º 4.681’	100º 17.278’
16	River Mouth	1.7	06º 6.043’	100º18.958’

PAHs extraction

A total of 20 g of sediment sample was taken from each station and mixed with sodium anhydrous to eliminate the water content. The dried sample was put into a thimble extractor (30 mm x 150 mm) and extracted with dichloromethane for about 10 hours. About 250 mL of dichloromethane was put into a round bottom flask and was heated to 60 ^{o}C using a heater. After 10 hours, the extract was evaporated to near dryness by using a rotary evaporator. The residue was later diluted with dichloromethane and was transferred into a 5 mL vial. This residue is known as the Total Extractable Lipid (TEL). The TEL extracts were divided through two stages of silica gel column chromatography. The concentrated sample was then transferred into the silica gel column and washed with 2 mL (0.4 mL, 0.3 mL, 0.3 mL, 0.5 mL and 0.5 mL) hexane/dichloromethane (3:1), subsequently followed by 18 mL hexane/dichloromethane (3:1).

Hydrocarbons that ranged from n-alkanes to PAHs were then collected into a conical flask. Eluent from the first step chromatography was then concentrated by the rotary evaporator, and the PAH fraction was collected with 14 mL mixture of hexane/dichloromethane (3:1). The PAH fraction was labeled and stored in the freezer for further analysis. The PAH sample was then transferred to a 1 mL vial and injected to determine the concentration of PAH compounds. It then underwent the process of nitrogen blowdown evaporation and was refilled with distilled n-hexane prior to injection into the GC-MS (GC, 6890N coupled with 5975C MSD, Agilent, USA). The carrier gas used was helium at a fixed rate of 1 mL/min with a pressure of 158 kpa. An HP-5 fused silica capillary column (30 m × 0.25 mm i.d. and 0.25 um thickness) was used to separate the compounds in split-less mode at 270 °C. It was found that the GC temperature gradient was at 40 °C, then had increased at 8 °C/min to 150 °C, then at 5 °C/min to 310 °C, and finally had held for about 10 minutes. The GC-MS operating conditions were 70eV ionization potential with an MS source at 230 °C for 1.4 scans/sec, and an electron multiplier at 1400 V with the dwell time set to 40 sec. The interface temperature was 280 °C, while the injector temperature was maintained at 250 °C. The 18 PAHs were quantified based on their retention time and the ion m/z ratio of the native standard PAHs.

Quality control and assurance

To confidently confirm the precision of the sample analyses, several pre-detection steps were applied. Firstly, any cross-contamination that might have happened during the research was eradicated. This simultaneously involved the processing of blank and environmental samples. The validation of PAH peaks was determined based on the compatibility of the retention time of each and the abundance of quantification ions of individual PAHs with the 18 PAHs mixture, coupled with the surrogate standard. Apart from that, 5 points of external standard calibration curves (L20950018AL, Dr. Ehrenstorfer GmbH, Germany) were conducted in the range of 0.1 ppm-1.0 ppm, with a correlation coefficient higher than 0.990. The method detection limit (MDL) was also obtained to ensure the limit detection for each PAH. The MDL for naphthalene, acenaphthene, fluorene, phenanthrene, anthracene, fluoranthene, pyrene, benzo[k]fluoranthene, benzo[e] pyrene, indeno[1,2,3-cd]pyrene and benzo[ghi]perylene were 0.72, 1.22, 0.06, 2.08, 1.17, 1.05, 0.88, 1.11, 1.12, 1.17 and 0.72, respectively. The recoveries for phenanthrene and chrysene were 68.66% and 87.00%, respectively.

Results and Discussion

Composition of PAHs

Concentration of individual compounds ranged from 1.09 ng/g to 59.01 ng/g dry weight sediment as seen in Tables 2 and 3. The highest total PAH concentration was detected in S6, which was 226.03 ng/g dry weight sediment; while the lowest concentration was detected in S3, which was 7.20 ng/g dry weight sediment. This is because S6 is located at the river's estuary where all the sediments are transported *via* the river, which flows to the sea and as such the sediments are deposited here. Based on Figure 2, it was also observed that the total concentration of PAHs was lower in the residential areas in S1, S2, S3, S4 and S5, with the concentration value ranging from 7.20 ng/g-39.35 ng/g, compared to the jetty areas and the open sea, where the concentration value ranged from 13.91 ng/g-226.04 ng/g. This result is supported by Claudine et al. [10], who reported in their findings that PAHs in the residential areas are often lower than the jetty areas, which usually experience a high traffic of water vehicle activities.

Table 2. The concentration of individual PAHs found in sediment samples of Kuala Kedah

Compounds	**Concentrations (ng/g)**							
	S1	**S2**	**S3**	**S4**	**S5**	**S6**	**S7**	**S8**
Naphthalene	1.9	1.59	ND	2.49	5.92	4.27	1.12	2.26
Acenaphthene	ND	ND	ND	ND	2.18	2.08	ND	ND
Fluorene	1.26	ND	ND	1.14	3.55	3.73	ND	ND
Phenanthrene	5.83	4.05	4.78	5.39	9.55	10.56	2.59	4.40
Anthracene	ND	4.67	ND	6.21	11.01	1.52	2.99	ND
Fluoranthene	1.83	ND	1.14	1.32	2.75	20.81	1.83	3.99
Pyrene	1.46	ND	1.28	1.26	3.03	23.19	3.14	6.59
Benzo[k]fluoranthene	ND	ND	ND	ND	ND	39.4	ND	ND
Benzo[e]pyrene	3.23	1.21	ND	ND	ND	12.5	ND	ND
Indeno[1,2,3-cd]pyrene	ND	ND	ND	ND	ND	59.01	ND	ND
Benzo[ghi]perylene	ND	ND	ND	ND	1.36	48.96	1.69	3.41
a) Total PAHs	15.51	11.52	7.2	17.81	39.35	226.03	13.91	20.64
b) Total LMW PAHs	9.12	8.72	7.2	14.19	26.33	56.09	10.56	14.98
c) Total HMW PAHs	3.23	1.21	ND	ND	1.36	159.86	1.77	3.41
LMW/HMW	2.82	7.19	ND	ND	19.31	0.35	5.96	4.39

a) Total PAHs ranging from naphthalene to benzo[ghi]perylene,
b) Total of penanthrene, anthracene, fluorenthene and pyrene,
c) Total of benzo[k]fluoranthene, indeno-1,2,2-cd]pyrene, benzo[g,h,i]perylene, ND is not detected

Table 3. The concentration of individual PAHs found in sediment samples of Kuala Kedah

Compounds	Concentrations (ng/g)							
	S9	S10	S11	S12	S13	S14	S15	S16
Naphthalene	3.97	4.93	8.21	7.64	2.84	4.27	3.97	1.09
Acenaphthene	1.32	2.55	2.59	2.82	ND	1.91	1.72	ND
Fluorene	ND	1.78	2.64	2.11	1.13	2.03	1.65	ND
Phenanthrene	5.01	8.04	12.36	6.49	6.28	10.21	7.18	3.46
Anthracene	5.78	9.27	ND	ND	7.24	11.77	8.28	3.99
Fluoranthene	ND	3.91	4.51	3.35	1.91	2.73	1.44	1.79
Pyrene	5.29	5.73	8.41	4.26	2.56	3.34	1.55	3.79
Benzo[k]fluoranthene	ND	ND	1.25	1.26	ND	ND	ND	27.17
Benzo[e]pyrene	ND	ND	ND	ND	ND	ND	ND	ND
Indeno[1,2,3-cd]pyrene	ND	ND	1.34	ND	ND	ND	ND	14.51
Benzo[ghi]perylene	ND	3.38	5.24	15.59	15.17	13.28	6.23	75.83
a) Total PAHs	22.03	39.6	46.55	43.79	37.13	49.55	32.02	131.63
b) Total LMW PAHs	16.08	26.96	25.28	14.11	17.98	28.06	18.45	13.03
c) Total HMW PAHs	ND	3.38	7.83	17.11	15.17	13.28	6.23	117.51
LMW/HMW	ND	7.97	3.23	0.82	1.18	2.11	2.96	0.11

a) Total PAHs ranging from naphthalene to benzo[ghi]perylene,
b) Total of penanthrene, anthracene, fluorenthene and pyrene,
c) Total of benzo[k]fluoranthene, indeno-1,2,2-cd]pyrene, benzo[g,h,i]perylene,
ND is not detected

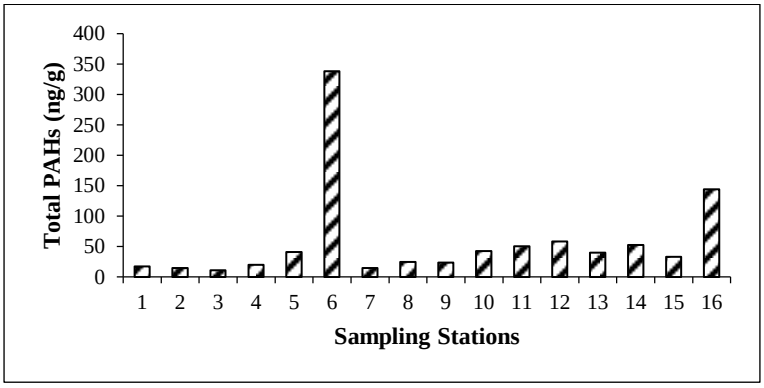


Figure 2. Total PAHs concentration (ng/g) for all sampling stations in Kuala Kedah

According to Baumard et al. [11], the four pollution levels based on total PAHs can be defined as: 0 ng/g-100 ng/g PAHs in the sediment which is classified as low, 100 ng/g-1000 ng/g classified as being moderate, 1000 ng/g-5000 ng/g classified as high, and a concentration of >5000 ng/g, which is classified as very high. Based on these levels, the range concentration of PAHs detected in the area of research in Kedah River can be considered as being in the low to moderately polluted range (11.16 ng/g-338.04 ng/g). The surface sediment samples from these sampling points were dominated by benzo[ghi]perylene and phenanthrene, with the values of 25% and 14% respectively (Figure 3). The lowest occurring compound was benzo[e]pyrene, with a total occurrence of 2% and a total concentration of 16.94 ng/g dry weight sediment.

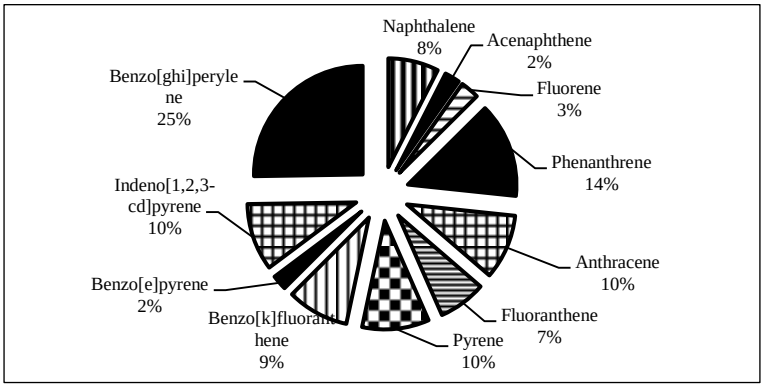


Figure 3. Percentage of individual compounds of PAHs found in Kuala Kedah sediment samples

Molecular ratio index

Figure 4 illustrates the general molecular index of fluoranthene/pyrene against phenanthrene/anthracene. Molecular ratios of Phenanthrene/Anthracene and Fluoranthene/Pyrene were determined in order to differentiate between PAHs of dissimilar origin, where the Phenanthrene/Anthracene ratio is temperature-dependent and consists of approximately 3 of the emissions from the combustion of various fuels [12]. Phenanthere/Anthracene ratios of less than10 are related to the combustion processes, while values more than 10 are derived from petroleum sources or are diagenetic [11]. From our research, S1 indicated a petroleum source while S3, S8, S11 and S12 indicated mixed sources, while other stations indicated combustion sources, which makes pyrolytic source the dominant source based on this ratio. LMW/HMW ratios greater than 1 indicate dominance of petrogenic inputs, and LMW/HMW lesser than 1 indicate pyrogenic inputs [13, 14]. Figure 5, on the other hand, shows that for the Low Molecular Weight (LMW)/High Molecular Weight (HMW) index, the stations that obtained values less than 1 (pyrolytic) are S3, S4, S6, S9, S12 and S16, while the rest attained values of more than 1 (petrogenic). Low molecular PAHs can be observed in Table 2, which comprise of 2-3 fused aromatic benzene rings, compared to high molecular weight of PAHs with 4-6 fused aromatic benzene rings, which suggest that the source of sediment is petrogenic [3, 15]. Based on all the molecular ratio indices used, it can be clearly seen that the major sources of PAHs in the sediment were mixed sources, which were dominated by both petrogenic and pyrolytic sources.

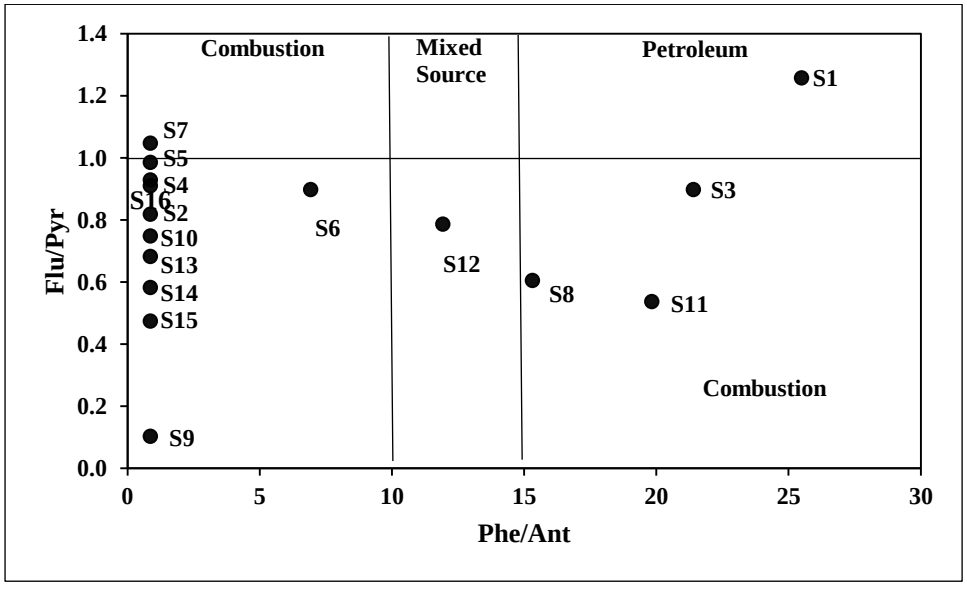


Figure 4. Fluoranthene/Pyrene against Phenanthrene/Anthracene molecular index

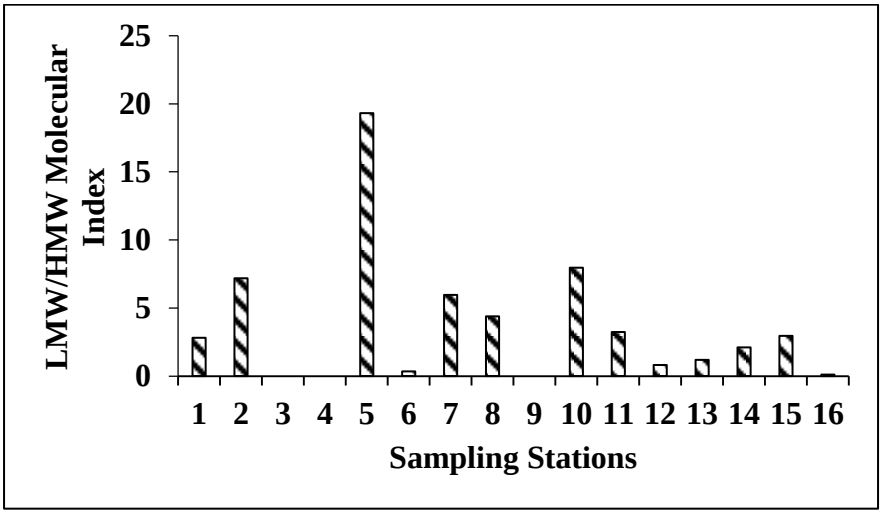


Figure 5. LMW/HMW molecular index

A pyrolytic source is a source that originates from anthropogenic contamination, coming from the combustion of trees, woods, vehicle's engine as well as organic combustion [15]. The sampling locations along the river of Sungai Kedah which originated from the Alor Setar area to the Kuala Kedah area, are primarily residential areas. However, there is also an industrial area known as *Kawasan Perusahaan* Mergong Barrage that could have contributed to the combustion source in the sediment. Apart from that, the road system network that circulates around Kuala Kedah and the Alor Setar area also caters to a significant number of vehicles that emit petroleum combustions to the atmosphere. These can be deposited into the water column and form the sediments at the bottom [17, 18]. A petrogenic source is that which originates from petroleum contamination sources [19].

Conclusion

The total concentrations of all the PAHs in this study ranged from 7.02 ng/g to 226.03 ng/g, which can be categorized under low to moderate pollution levels [11]. Based on the molecular index calculations of Fluoranthene/Pyrene, Phenanthere/Anthracene and LMW/HMW, the PAH concentrations and their possible sources found in this study mostly originated from PAH contaminations that were caused by the combustion of trees, woods, vehicle engine combustions and organic combustions.

Acknowledgement

The authors would like to thank the Ministry of Science, Technology and Innovation of Malaysia (MOSTI) and Universiti Kebangsaan Malaysia for the E-science Fund 04-01-02-SF0698 and DPP-2014-162 research grants.

References

1. Luca, G. D., Furesi, A., Micera, G., Panzanelli, A., Piu, P. C., Pilo, M. I., Spano, N. and Sanna, G. (2005). Nature, distribution and origin of polycyclic aromatic hydrocarbons (PAHs) in the sediments of Olbia harbor (Northern Sardinia, Italy). *Marine Pollution Bulletin*, 50: 1223-1232.
2. Chiu, W. C. and Chih, F. C. (2011). Distribution, origin, and potential toxicology significance of polycyclic aromatic hydrocarbon (PAHs) in sediments of Kaohsiung Harbor, Taiwan. *Marine Pollution Bulletin* 63: 417-423.
3. Qiao, M. W., Huang, S., Wang, D. and Wang, Z. (2006). Composition, sources, and potential toxicological significance of PAHs in the surface sediments of the Meiliang Bay, Taihu Lake, China. *Environmental International*, 32: 28-33.
4. Keshavarzifard, M., Zakaria, M. P. and Hwai, T. S. (2017). Bioavailability of polycyclic aromatic hydrocarbons (PAHs) to short neck clam (*Paphia undulata*) from sediment matrices in mudflat areas of West coast of Peninsular Malaysia. *Environmental Geochemistry and Health*, 39(3): 591-610.

5. Vaezzadeh, V., Zakaria, M. P., Mustafa, S., Ibrahim, Z. Z., Shau-Hwai, A. T. and Keshavarzifard, M. (2015). Source type evaluation of polycyclic aromatic hydrocarbons (PAHs) in surface sediments from the Muar River and Pulau Merambong, Peninsular Malaysia. *Environmental Forensics*, 16: 135-142.
6. Sakari, M., Zakaria, M. P., Lajis, N., Mohamed, C. A. R., Chandru, K. and Sahpoury. (2011). Polycyclic aromatic hydrocarbons and hopane in Malacca coastal water: 130 years of evidence for their land-based sources. *Environmental Forensics*, 12: 1-16.
7. Zakaria, M. P., Takada, H., Tsutsumi, S., Ohno, K., Yamada, J., Kuono, E. and Ku Mata, H. (2002). Distribution of polycyclic aromatic hydrocarbons (PAHs) in rivers and estuaries in Malaysia: A widespread input of petrogenic PAHs. *Environmental Science and Technology*, 36: 1907-1918.
8. Mohd Tahir, N., Rani Abdullah, A., Tong, S. L. and Wang, C. W. (1999). Oil and grease pollution in Malaysian coastal waters: current status and future considerations. In: Assessment and monitoring of marine system. Universiti Putra Malaysia Terengganu, Kuala Terengganu, Malaysia: pp. 115-123.
9. Sakari M., Zakaria, P. and Lajis, N. H. (2008). Distribution, characterisation and origins of polycyclic aromatic hydrocarbons (PAHs) in major rivers from the east coast of Peninsular Malaysia. *Coastal Marine Science Journal*, 32(1): 9-18.
10. Claudine, N., Rialet, P., Laura, P. Q., Henrik, K. and Anders R. (2011). Polycyclic aromatic hydrocarbons (PAHs) in soil and sediment from industrial, residential, and agricultural areas in central South Africa: An initial assessment. *Soil and Sediment Contamination: An International Journal*, 20: 199-204.
11. Baumard, P., Budzinski, H., Michon, Q., Garrigues, P., Burgeot, T. and Bellocq, J. (2008). Origin and bioavailability of PAHs in the Mediterranean Sea from mussel and sediment records. *Estuarine, Coastal and Shelf Science*, 47: 77-90.
12. Gscwend, P. M. and Hites, R. A. (1981). Fluxes of polycyclic aromatic hydrocarbons to marine and lacustrine sediments in the northeastern United States. *Geochimica et Cosmochima Acta*, 45: 2359-2367.
13. Magi, E., Bianco, R., Ianni, C. and Carro, M. D. (2002). Distribution of polycyclic aromatic hydrocarbons in the sediments of the Adriatic Sea. *Environmental Pollution*, 119: 91-98.
14. Soclo, H. H., Garrigues, P. and Ewald, M. (2000). Origin of polycyclic aromatic hydrocarbons (PAHs) in coastal marine sediments: Case studies in Cotonou (Benin) and Aquataine (France) areas. *Marine Pollution Bulletin*, 40 (5): 387-396.
15. Sanders, M., Sivetsen, S. and Scott, G. (2002). Origin and distribution of polycyclic aromatic hydrocarbons in surficial sediments from the Savannah River. *Archives of Environmental Contamination and Toxicology*, 43: 438-448.
16. Yunker, M. B., Macdonald, R. W, Vingarzan, R., Mitchell, R. H, Goyette, D. and Sylvestre, S. (2002). PAHs in the Fraser river basin: a critical appraisal of PAH ratios as indicators of PAH source and composition. *Organic Geochemistry*, 33: 489-515.
17. Luo, X. S., Yu, S., Zhu, Y. G. and Li, X. D. (2011). Trace metal contamination in urban soils of China. *Science of the Total Environment*, 421-422: 17-30.
18. Harrison, R. M., Smith, D. J. T., Pio, C. A. and Castro, L. M. (1996). Source apportionment of atmospheric polycyclic aromatic hydrocarbons collected from an urban location in Birmingham, UK. *Environmental Science & Technology*, 30(3): 825-832.
19. Zhang, J., Cai, L. Z., Yuan, D. X. and Chen, M. (2004). Distribution and sources of polynuclear aromatic hydrocarbons in mangrove surficial sediments of deep bay, China. *Marine Pollution Bulletin*, 49: 479-486.

Malaysian Journal of Analytical Sciences, Vol 23 No 6 (2019): 1009 - 1017
DOI: https://doi.org/10.17576/mjas-2019-2306-09

MALAYSIAN JOURNAL OF ANALYTICAL SCIENCES
Published by The Malaysian Analytical Sciences Society
ISSN 1394 - 2506

PALEOPRODUCTIVITY VARIATION IN TERENGGANU OFFSHORE DURING HOLOCENE BASED ON TOTAL ORGANIC CARBON AND $CaCO_3$ RECORDS

(Variasi Paleoproduktiviti di Luar Pesisir Pantai Terengganu Ketika Holosen Berdasarkan Rekod Jumlah Karbon Organik dan $CaCO_3$)

Erick Naim[1], Hasrizal Shaari[1,2]*, Mohd Fadzil Akhir[1]

[1]*Institute of Oceanography and Environment*
[2]*Faculty of Science and Marine Environment*
Universiti Malaysia Terengganu, 21030 Kuala Nerus, Terengganu, Malaysia.

**Corresponding author: riz@umt.edu.my*

Received: 30 October 2018; Accepted: 26 September 2019

Abstract

In this study, a sediment core (TER16-GC13C) length 180 cm was sampled in the offshore area of Terengganu, southern South China Sea (SSCS) with RV Discovery to establish the paleoproductivity records during the Holocene. The concentrations of total organic carbon (TOC) and calcium carbonate ($CaCO_3$) were analyzed by using a Shimadzu TOC Analyzer. The age model was established from carbon-14 data of the intact shells (*Anadara* sp., *Mactra* sp., *Meiocardia* sp., *Pecten* sp.) found within the sediment core. The time frame of the analyzed sediment core sample covered the Northgrippian (~7840 cal yr BP). Average TOC value was 0.23±0.07% with a decreasing trend towards Meghalayan. $CaCO_3$ content ranged from 3.38% to 12.05% with an average of 6.95±2.05% with an increasing trend towards Meghalayan. We suggested that TOC and $CaCO_3$ represent the organic and carbonate-based organisms, respectively. This scenario suggested that a change in community structure had occurred in the study site in which organic (calcareous) organism population had remained low (increased) from Northgrippian towards Meghalayan. This work is the first attempt in reconstructing paleoproductivity records in Malaysian waters.

Keywords: paleoproductivity, total organic carbon, calcium carbonate, Holocene, southern South China Sea

Abstrak

Dalam kajian ini, teras sedimen (TER16-GC13C) sepanjang 180 cm telah disampel di kawasan luar pesisir pantai Terengganu, selatan Laut China Selatan (SSCS) dengan RV Discovery untuk menyediakan rekod-rekod paleoproduktiviti ketika Holosen. Kandungan jumlah karbon organik (TOC) dan kalsium karbonat ($CaCO_3$) telah dianalisa menggunakan penganalisa TOC Shimadzu. Model usia telah dihasilkan daripada data karbon-14 cengkerang sempurna (*Anadara* sp., *Mactra* sp., *Meiocardia* sp., *Pecten* sp.) yang dijumpai di dalam teras sedimen. Jangka usia teras sedimen yang dikaji meliputi tempoh Northgrippian (~7840 cal yr BP). Nilai purata TOC adalah 0.23±0.07% dengan pola pengurangan ke arah Meghalayan. Kandungan $CaCO_3$ berjulat daripada 3.38% hingga 12.05% dengan purata 6.95±2.05%, dan meningkat ke arah Meghalayan. Kami berpendapat bahawa TOC dan $CaCO_3$ mewakili organisma-organisma berasaskan organik dan karbonat secara relatifnya. Senario ini menggambarkan suatu perubahan dalam struktur komuniti telah berlaku di kawasan kajian di mana populasi organisma organik (karbonat) kekal rendah (meningkat) dari Northgrippian menuju Meghalayan. Kajian ini merupakan percubaan pertama dalam pembinaan semula rekod-rekod paleoproduktiviti di perairan Malaysia.

Kata kunci: paleoproduktiviti, jumlah karbon organik, kalsium karbonat, Holosen, selatan Laut China Selatan

Introduction

Paleoproductivity reconstruction provides insights into the past fertility of an area of interest with focus on the primary producers. Over time, many approaches have been developed to measure ocean paleoproductivity, including the utilization of total organic carbon (TOC) [1-3] and calcium carbonate ($CaCO_3$) as reliable proxies [4] which were used in this study. It is very important that the paleoproductivity of an area of interest is assessed by using more than one proxy because each proxy is subjected to multiple influencing factors and has varying sensitivities which may change temporally and spatially [5-7]. This argument was introduced by Averyt and Paytan [6] who reported conflicting results among proxies studied in a common core.

TOC ($CaCO_3$) is derived from the organic (carbonate) remains of primary producers which have accumulated on the seabed over time. Microscopic calcareous organisms i.e. coccolithophores (algae) and foraminifera which live in the water column, form their shells from $CaCO_3$ [8]. Wang and Lin [9] stated that the major factors controlling the proxies are surface water productivity and/or sediment preservation, on top of other influencing aspects. Additionally, despite being influenced by a number of factors, TOC in sediment is mainly governed by three master variables which are the input, the preservation, and the dilution of organic matter, with the latter two influenced by sedimentation rate [10]. Despite being preserved in only a small portion from the initial amount, the total amount of organic carbon preserved in sediment is still a reliable proxy of palaeoceanographic and paleoenvironmental conditions [11].

Both biogenic proxies were used to reconstruct the surface ocean productivity in the past at the study area in Terengganu water. To date, no published data is available on the past surface productivity of Malaysian waters. The focus area is generally relatively poor in productivity as compared to main fishing grounds (e.g. west coasts of South America and Africa). Here we present the records of TOC and $CaCO_3$ over the last 7840 cal yr BP from a sediment core recovered from the southern South China Sea (SCS), specifically from an area which was part of the landmass known as Sundaland before being flooded during the early Holocene sea level transgression which took place between 11650 yr BP and 7000 yr BP [12, 13]. This research aims to seek knowledge on the site productivity status during Holocene, filling in the research gap as well as providing a baseline for future studies in the region.

Materials and Methods

Study area

The SCS is one of the largest marginal basins in the Pacific Ocean, encompassing an area of 3.5×10^6 km^2 [14] and subjected to northeast monsoons and southwest monsoons, with the former having stronger influence over the region in terms of precipitation (Figure 1). The study area is located within the shallow Sunda shelf at the SSCS.

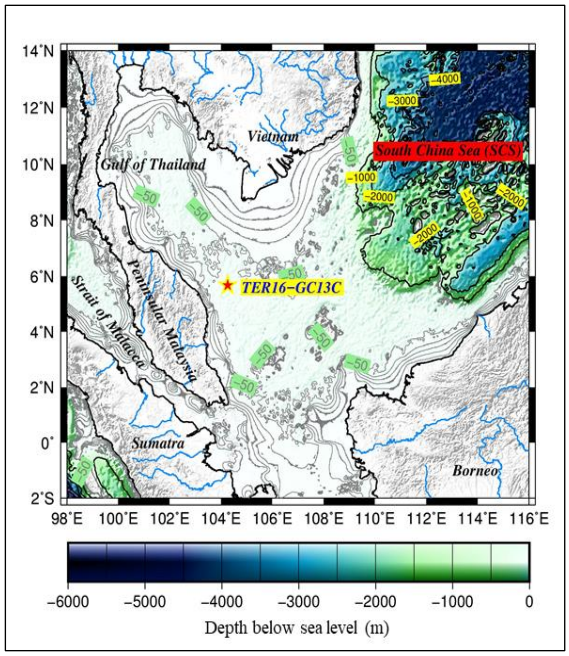


Figure 1. Bathymetric map of South China Sea showing core sampling location on the Sunda Shelf

Sample collection and preservation

A 180 cm marine sediment core (TER16-GC13C) was retrieved at ~70 nautical miles (5°39.993 N, 104°15.632 E, 73 m water depth) from the Kuala Terengganu coastline in 2016, on board of a Universiti Malaysia Terengganu (UMT) research vessel, RV Discovery, by using gravity corer (Figure 1). The collected sediment core was brought back to the laboratory for subsampling. The sediment core was sliced at 2 cm intervals, bringing a total of 90 samples. The subsampled sediments were frozen at -20 °C for 24 hours before being freeze-dried for 3 days and stored in clean labelled containers to prevent possible contamination. Samples for TOC/$CaCO_3$ analysis were powdered and homogenized using an agate mortar, and sifted through a sieve with 150 µm mesh size. Meanwhile, samples for particle size analysis and radiocarbons were kept in clean containers without powdering and homogenizing.

Laboratory analysis: Total carbon analysis

Sediment samples were analyzed for total carbon (TC) and inorganic carbon (IC) contents using Shimadzu TOC Analyzer with an accompanying Shimadzu Solid Sample Module SSM-5000A. Ceramic sample boats and glass wool used in the analysis were combusted at 400 °C for 4 hours. For TC analysis, 10 mg of the homogenized sample was combusted at 900 °C. For IC analysis, 10 mg of homogenized sample was digested using 60% phosphoric acid at 200 °C. For the purpose of quality control, standard research materials (glucose and sodium carbonate for TC and IC analysis) were analyzed at every analysis session in which 100% recovery was achieved. The TOC values were obtained by subtracting the IC value from the TC value. $CaCO_3$ values were obtained by multiplying IC values with 8.33 (the ratio of molecular mass of $CaCO_3$ to carbon, 100/12), with the assumption that all inorganic carbon is pure calcite.

Grain size analysis

Grain size analysis was performed following the procedure in [15] with some modifications. About 2 g of dried sample was weighed in clean plastic containers. 10 drops of undiluted hydrogen peroxide were added into the samples, followed by 5 mL of 20% sodium hexametaphosphate. Distilled water was then added to the volume and the samples were left to stand for 24 hours. Next, the samples were analyzed using Malvern Mastersizer 2000™ laser diffraction particle size analyzer.

AMS ^{14}Carbon analysis

Sediment core age was determined using accelerated mass spectrometry (AMS) radiocarbon dating facility available at International Chemical Analysis (ICA), Miami, U.S. Age samples composed of intact shells of *Anadara* sp., *Mactra* sp., *Meiocardia* sp. and *Pecten* sp. were picked at corresponding depths as shown in Table 1. The shells were identified based on references from the Natural History Museum, Rotterdam [16]. The age model was plotted using the data of ^{14}C age calendar against core depth (Figure 2). Due to the lack of intact carbonate shell samples, the age model could only be established between the depth of 32 and 168 cm covering ~ 76% of total core length. The calibrated ages were calculated by using the Calib 7.1 calibration program based on Marine13 calibration curve and 2 sigma calibrations [17] with delta-R -15±38. The sediment ages refer to the calibrated year Before Present (cal yr BP).

Table 1. TER16-GC13C radiocarbon dating samples

Depth (cm)	Dated shell genus
32	*Pecten*
44.5	*Meiocardia*
77	*Anadara*
101	*Mactra*
155	*Anadara*
168	*Mactra*

Results and Discussion

Age models and sedimentation rate

The six point of AMS^{14}C dates for TER16-GC13C range from 2560 to 7370 yr BP (Table 2 and Figure 2). The AMS^{14}C dates of TER16-GC13C provide age controls for the stratigraphic interval between 32 and 168 cm depth of the core. The calibrated AMS^{14}C age model reveals that the mean sedimentation rate of TER16-GC13C occurred at 0.05 cm yr^{-1} since 7840 cal yr BP.

Table 2. TER16-GC13C radiocarbon age estimates. The calibrated age ranges reported following Reimer et al. [17]

Depth (cm)	AMS ^{14}C age (yr BP)	2σ age (cal yr BP) (Calib 7.1)
32	2560	2232
44.5	3920	3922
77	6310	6791
101	6610	7133
155	6980	7492
168	7370	7840

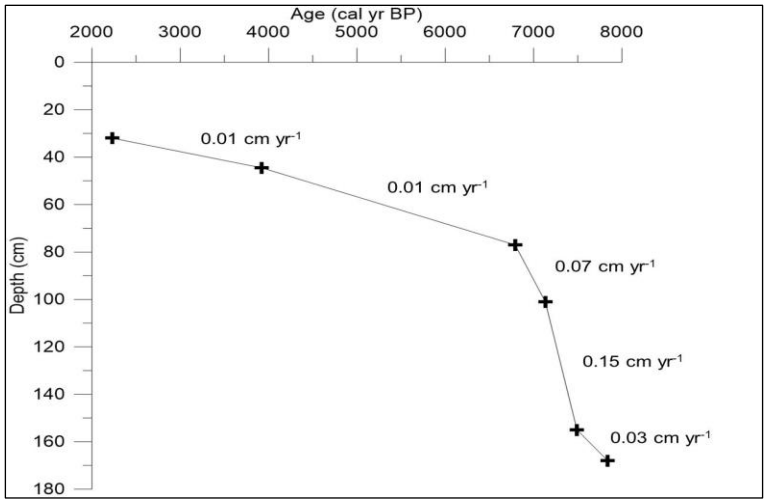


Figure 2. Age model of TER16-GC13C with corresponding sedimentation rates

TOC, $CaCO_3$ and mean grain size

The vertical profiles of TOC, $CaCO_3$ content and mean grain sizes for core TER16-GC13C are shown in Figure 3. The TOC concentration varied from 0.11% and 0.39% with mean values of 0.23 ± 0.07%. The highest and lowest concentration of TOC for the studied core was recorded at 93 cm and 111 cm. However, the variation of TOC content across the core is small, as determined by the very low standard deviation. Therefore, we interpret the TOC signal as being low (<0.4%) with insignificant fluctuations. The values of $CaCO_3$ varied from 3.38% to 12.05%, with an average value of 6.95 ± 2.05%. The concentrations of $CaCO_3$ in sediment cores increased towards the core top. High values of $CaCO_3$ were recorded at the top section of the sediment core (0 cm to 52 cm). The mean grain size ranged from 3.87 phi to 7.63 phi, with an average value of 6.18 phi, indicating an increase in grain size towards the core top (Figure 3c).

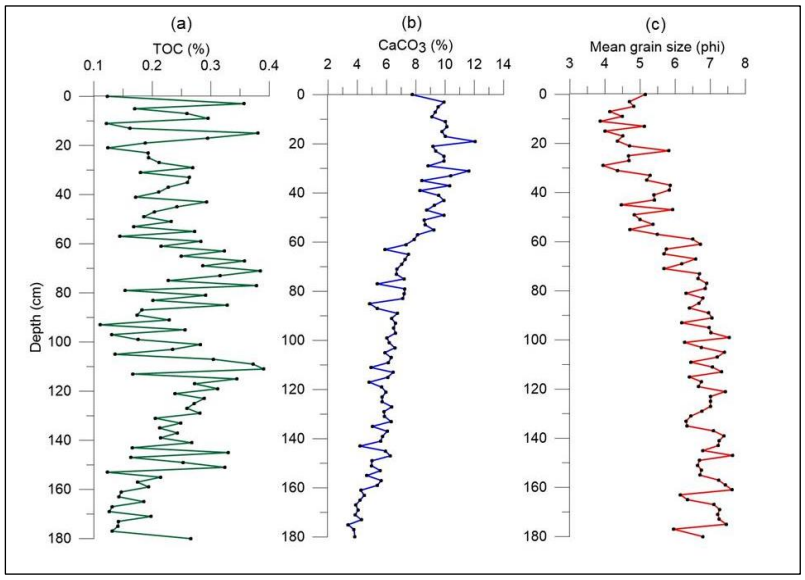


Figure 3. Vertical profiles of TOC content, $CaCO_3$ content and mean grain size of core TER16-GC13C

Pearson's correlation indicates that there is no significant relationship between TOC and grain size, implying that grain size had no appreciable influence on TOC concentration in sediment (Table 3). Meanwhile, there is a strong negative correlation between $CaCO_3$ and grain size (Table 3 and Figure 4).

Table 3. Pearson's correlation coefficient between proxies

	$CaCO_3$	**Grain Size**
TOC	-0.0035(p=0.9776)	-0.1072 (p=0.3841)
$CaCO_3$		**-0.5955 (p=8.4726E-08)**

Note: Bold type designates significant negative correlations at the significance level of 0.05

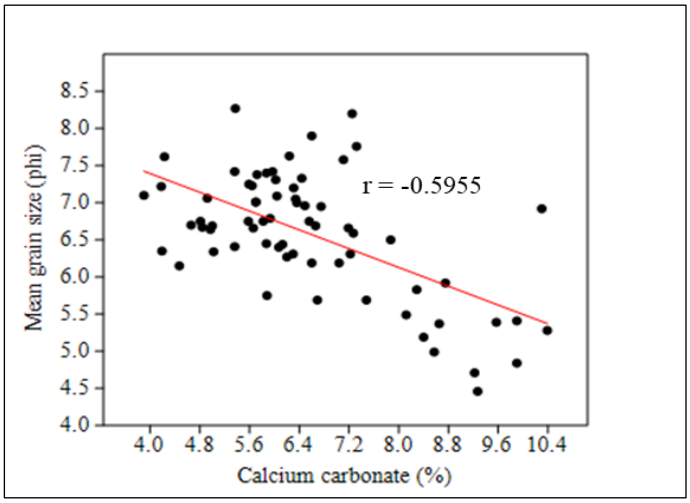


Figure 4. Scatterplot of $CaCO_3$ against mean grain size

Holocene sedimentation rate

Based on the age model, the average sedimentation rate of TER16-GC13C was 0.06 cm yr^{-1} (Figure 2). The sedimentation rate in this study was relatively lower compared to the ^{210}Pb excess age estimation from short sediment core of EC02 (0.34 cm yr^{-1}) and EC03 (0.38 cm yr^{-1}) in the East Coast of Peninsular Malaysia, which was established by Mohamed et al. [18]. The difference can be attributed to the distance of sampling locations from the shoreline. Szmytkiewicz and Zalewska [19] stated that shorter distances of core location to the source of sediment lead to high accumulation rate of sediment. The locations of core EC02 and EC03 are closer to the terrestrial area compared to core TER16-GC13C. TER16-GC13C sedimentation rate was relatively lower at 0.07 cm yr^{-1} – 0.15 cm yr^{-1}, which covers the age between 2560 and 7370 yr BP. Sedimentation rate decreased to 0.01 cm yr^{-1} between 6310 and 3190 yr BP. The sea level rise which flooded the region during Holocene deglaciation caused the study area to be at a further distance than the new land-sea border, limiting sediment sources from the terrestrial environment [19]. This is the reason why the sedimentation rate is relatively lower at the upper part than bottom part of the sediment core.

Paleoproductivity variability

The concentration of TOC in marine sediment cores is widely used as a proxy for surface water paleoproductivity; high (low) TOC value is linked to high (low) paleoproductivity [20-23]. However, this study reveals that it is inaccurate to generally deduce the paleoproductivity record based solely on the TOC content. The value of $CaCO_3$ content had been steadily increasing since the last 7840 cal yr BP (Figure 5b), implying higher carbonate

production, while TOC content remained low (Figure 5a). This finding is consistent with the previous finding that the primary productivity of poor nutrient surface water in the ocean was dominated by carbonate-based primary producer [5]. The production of organic matter by primary producers converts CO_2 into organic matter while $CaCO_3$ production in the ocean photic zone counteracts by releasing CO_2 [5].

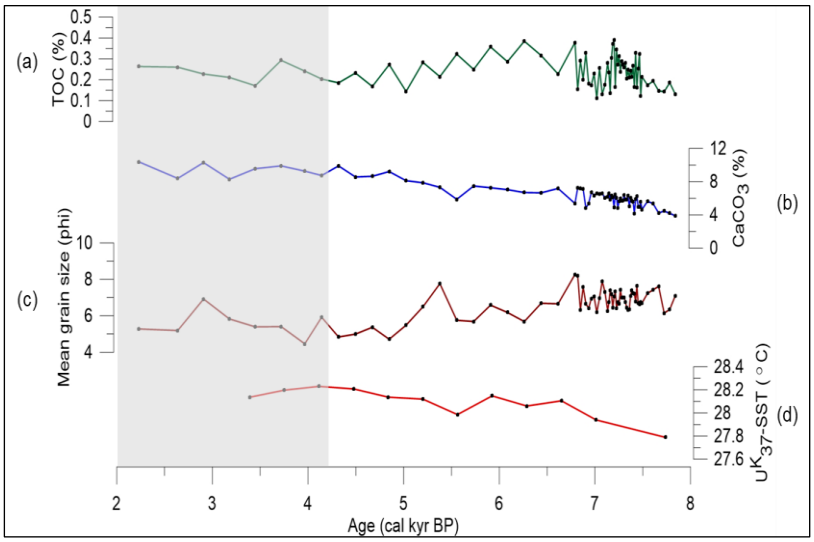


Figure 5. Profiles of (a) TOC content, (b) $CaCO_3$ content, (c) mean sediment grain size and (d) U^K_{37}-SST during the last 7840 cal yr BP. U^K_{37}-SST from core 18287-3 was supplied by Kienast et al. [23]. Shaded region marks Meghalayan while unshaded region represents Northgrippian

In high productivity areas, the surplus in organic matter supply to marine sediment results in high production of metabolic CO_2 [24]. The excess CO_2 contributes to higher carbonate ions (CO_3^{2-}), which increases the dissolution of $CaCO_3$ by binding with calcium ion (Ca^{2+}) in sediment. The low TOC content observed from the study area helped promote the preservation of $CaCO_3$ in sediment as low CO_2 was produced from the degradation of organic matter.

The similarity in trend and the strong negative correlation between $CaCO_3$ content and mean grain size (Figure 5c) might be caused by the contribution of $CaCO_3$ to the coarser fraction of sediment. Similar phenomenon was also reported by Wang and Lin [9] in which the downcore content of coarse fraction mimicked the $CaCO_3$ content. This finding can be inferred to the increase in $CaCO_3$ rain from the photic zone.

The Holocene sea surface temperature (SST) of SCS reported by Kienast et al. [23] (Figure 5d) shows that the SST trend is synchronous with the increasing trend of $CaCO_3$. This is in agreement with Rühlemann et al. [5] which stated that higher SST promotes primary productivity, and in this case, it is carbonate-based primary productivity. We postulate that the poor nutrient surface water in Terengganu offshore inhibited organic-based primary productivity and therefore, the increase in SST did not cause an increase in primary productivity magnitude. The results of this study also suggest that the community structure in the surrounding area had changed from organic- to calcareous-based producers.

Comparison with regional studies

This study generally reported relatively low TOC and $CaCO_3$ contents as compared to other studies in the region (Table 4) and therefore has lower paleoproductivity signal. It is important to note the time scale of the core used in different studies. Previous studies listed in Table 4 are related to cyclic glaciation-deglaciation events while our study was not influenced by similar events due to a shorter temporal resolution.

Table 4. A comparison of TOC and $CaCO_3$ concentration with the other studies

	Site	TOC (%)	$CaCO_3$ (%)	Temporal Resolution
This study	Terengganu waters	0.11 - 0.39	3.38 - 12.05	Holocene (Northgrippian – Meghalayan)
Black et al. [25]	Japan Sea	0.16 - 6.36	0 - 44.29	Pliocene - Holocene
	East China Sea	0.10 - 2.85	0.70 - 42.84	Middle Pleistocene - Holocene
Shiau et al. [26]	SSCS	0.2 - 1.6	~20 - 50	Middle Pleistocene - Holocene
Wang and Lin [9]	Nansha area, SSCS	Generally <0.5	6.03 - 59.02	Miocene - Holocene

Conclusion

The paleoproductivity of the study site was justified with regards to TOC and $CaCO_3$ content. The TOC content decreased from Northgrippian to Meghalayan. The $CaCO_3$ content increased with time and showed parallelism with the increasing trends of SST. Primary producer community structure might have changed during the Holocene, which resulted in more calcareous-based primary producers during Meghalayan, and the population is expected to further increase based on current trend. This study is limited on both spatial and temporal aspects and therefore, future studies using cores from multiple sites and longer cores are recommended.

Acknowledgement

This project was funded by the Higher Institute Centre of Excellence (HICoE) Grant (Vote No. 66928) awarded to Institute of Oceanography and Environment (INOS), Universiti Malaysia Terengganu and Fundamental Research Grant Scheme (FRGS/1/2015/WAB09/UMT/02/1) provided by Ministry of Education Malaysia. The authors are grateful to INOCEM Research Station, Kuliyyah of Science, International Islamic University Malaysia, for granting access to Malvern Mastersizer 2000™.

References

1. Müller, P. J. and Suess, E. (1979). Productivity, sedimentation rate, and sedimentary organic matter in the oceans-I. Organic carbon preservation. *Deep Sea Research Part A, Oceanographic Research Papers*, 26(12): 1347-1362.
2. Canfield, D. E. (1994). Factors influencing organic carbon preservation in marine sediments. *Chemical Geology*, 114: 315-329.
3. Zonneveld, K. A. F., Versteegh, G. J. M., Kasten, S., Eglinton, T. I., Emeis, K. C., Huguet, C., Koch, B. P., de Lange, G. J., Middelburg, J. J., Mollenhauer, G., Prahl, F. G., Rethemeyer, J. and Wakeham, S. G. (2010). Selective preservation of organic matter in marine environments; processes and impact on the sedimentary record. *Biogeosciences*, 7: 483-511.
4. Rühlemann, C., Frank, M., Hale, W., Mangini, A., Mulitza, S., Müller, P. J. and Wefer, G. (1996). Late quaternary productivity changes in the western equatorial Atlantic: Evidence from ^{230}Th-normalized carbonate and organic carbon accumulation rates. *Marine Geology*, 135: 127-152.
5. Rühlemann, C., Muller, P. J. and Schneider, R. R. (1999). Organic carbon and carbonate as paleoproductivity proxies: Examples from high and low productivity areas of the tropical Atlantic. In 1999, *Use of Proxies in Paleoceanography: Examples from the South Atlantic* (Fischer, G. and Wefer, G. (eds), Springer-Verlag Berlin Heidelberg, pp. 315-344.
6. Averyt, K. B. and Paytan, A. (2004). A comparison of multiple proxies for export production in the equatorial Pacific, *Paleoceanography*, 19: PA4003.
7. Anderson, R. F. and Winckler, G. (2005). Problems with paleoproductivity proxies. *Paleoceanography*, 20: PA3012.
8. Su, X., Liu, C., Beaufort, L., Tian, J. and Huang, E. (2013). Late quaternary coccolith records in the South China Sea and East Asian monsoon dynamics. *Global and Planetary Change*, 11: 88-96.

9. Wang, L. W. and Lin, H. L. (2004). Data report: Carbonate and organic carbon contents of sediments from Sites 1143 and 1146 in the South China Sea. In: Prell, W. L., Wang, P., Blum, P., Rea, D. K., and Clemens, S. C. (Eds.), *ODP Proceedings, Scientific Results*, 184: 1-9.
10. Tyson, R. V. (2001). Sedimentation rate, dilution, preservation and total organic carbon: some results of a modelling study. *Organic Geochemistry*, 32: 333-339.
11. Meyers, P. A. and Eadie, B. J. (1993). Sources, degradation and recycling of organic matter associated with sinking particles in Lake Michigan. *Organic Geochemistry*, 20(1): 47-56.
12. Sathiamurthy, E. and Voris, H. K. (2006). Maps of Holocene sea level transgression and submerged lakes on the Sunda shelf. *The Natural History Journal of Chulalongkorn University*, Supplement 2: 1-44.
13. Smith, D. E., Harrison, S., Firth, C. R. and Jordan, J. T. (2011). The early Holocene sea level rise. *Quaternary Science Reviews*, 30: 1846-1860.
14. Tamburini, F., Adatte, T., Föllmi, K., Bernasconi, S. M. and Steinmann, P. (2003). Investigating the history of East Asian monsoon and climate during the last glacial-interglacial period (0-140 000 years): Mineralogy and geochemistry of ODP Sites 1143 and 1144, South China Sea. *Marine Geology*, 201: 147-168.
15. Kamaruzzaman, B. Y., Ong, M. C., Noor Azhar, M. S., Shahbudin, S., and Jalal, K. C. A. (2008). Geochemistry of sediment in the major estuarine mangrove forest of Terengganu region, Malaysia. *American Journal of Applied Sciences*, 5(12): 1707-1712.
16. Natural History Museum Rotterdam (2018). Collection database. Retrieved from http://www.marinespecies.org/nmr [Accessed online March 2018].
17. Reimer, P., Bard, E., Bayliss, A., Beck, J., Blackwell, P. and Ramsey, C. (2013). IntCal13 and Marine13 radiocarbon age calibration curves 0–50,000 Years cal BP. *Radiocarbon*, 55(4): 1869-1887.
18. Mohamed, C. A. R., Mahmood, Z. U. W. and Ahmad, Z. (2008). Recent sedimentation of sediments in the coastal waters Peninsular Malaysia. *Pollution Research*, 27(1): 27-36.
19. Szmytkiewicz, A. and Zalewska, T. (2014). Sediment deposition and accumulation rates determined by sediment trap and ^{210}Pb isotope methods in the Outer Puck Bay (Baltic Sea). *Oceanologia*, 56(1): 85-106.
20. Reichart, G. J., den Dulk, M.,Visser, H. J., Van der Weijden, C. H. and Zachariasse, W. J. (1997). A 225 kyr record of dust supply, paleoproductivity and the oxygen minimum zone from the Murray ridge (Northern Arabian Sea), *Palaeogeography Palaeoclimatology Palaeoecology*, 134(1-4): 149-169.
21. Schulz, H., von Rad, U. and Erlenkeuser, H. (1998). Correlation between Arabian Sea and Greenland climate oscillations of the past 110,000 years. *Letters to Nature*, 393: 54-57.
22. von Rad, U., Schaaf., M., Michels, K. H., Schulz, H., Berger, W. H. and Sirocko, F. (1999). A 5000-yr Record of climate change in varved sediments from the oxygen minimum zone off Pakistan, Northeastern Arabian Sea. *Quaternary Research*, 51: 39-53.
23. Kienast, A. M., Steinke, S., Stattegger, K., Calvert, S. E., Tto, S. and Chandra, S. (2001). Synchronous Tropical South China Sea SST change and Greenland warming during deglaciation. *Science*, 291(5511): 2132-2134.
24. Meyers, P. A. and Robinson, R. S. (2001). Data report: Carbonate and organic carbon contents of sediments from Site 1087, Southern Cape Basin. *In* Wefer, G., Berger, W. H., and Richter, C. (Eds.), *Proceedings of the Ocean Drilling Program, Scientific Results,* 175: 1-11.
25. Black, H. D., Anderson, W. T. and Alvarez Zarikian, C.A. (2018). Data report: organic matter, carbonate, and stable isotope stratigraphy from IODP Expedition 346 Sites U1426, U1427, and U1429. *In* Tada, R., Murray, R.W., Alvarez Zarikian, C.A., and the Expedition 346 Scientists (Eds.), *Proceedings of the Integrated Ocean Drilling Program*, 346: 1-9.
26. Shiau, L. J., Yu, P. Sen, Wei, K. Y., Yamamoto, M., Lee, T. Q., Yu, E. F., Fang, T. and Chen, M. T. (2008). Sea surface temperature, productivity, and terrestrial flux variations of the southeastern South China Sea over the past 800000 years (IMAGES MD972142). *Terrestrial, Atmospheric and Oceanic Sciences*, 19(4): 363-376.

Malaysian Journal of Analytical Sciences, Vol 23 No 6 (2019): 1018 - 1029
DOI: https://doi.org/10.17576/mjas-2019-2306-10

MALAYSIAN JOURNAL OF ANALYTICAL SCIENCES
Published by The Malaysian Analytical Sciences Society
ISSN 1394 - 2506

THE COMBINED EFFECT OF ZINC AND pH ON GROWTH RATE AND CHLOROPHYLL CONTENT OF BROWN SEAWEED, *Padina boryana*

(Kesan Gabungan Zink dan pH ke Atas Kadar Pertumbuhan dan Kandungan Klorofil Rumpai Laut Perang, *Padina boryana)*

Nabeela Ali Nasser Al-Awlaqi[1]*, Noor Azhar Mohamed Shazili[1], Nurulnadia Mohd Yusoff[2]

[1]*Institute of Oceanography and Environment*
[2]*Faculty of Science and Marine Environment*
Universiti Malaysia Terengganu, 21030 Kuala Nerus, Terengganu, Malaysia

**Corresponding author: Nabeela.awlaqi@gmail.com*

Received: 30 October 2018; Accepted: 26 September 2019

Abstract

Brown seaweed, *Padina boryana* is found along the coast of Terengganu, Malaysia and may serve as a potential heavy metal biomonitor in the coastal zones. To better understand the impact of heavy metal pollution on *P. boryana* at varying seawater pH levels, the combined effect of zinc (Zn) and pH on its growth rate and chlorophyll content was investigated in laboratory exposures. After exposure for 21 days in a mixed treatment of 6 pH variations (4 to 9) and three Zn concentrations (30, 150, 300 ppb), maximum growth rate was observed in controlled treatments at pH 8 with no added Zn, whereas treatments at pH 4 and 9 showed negative growth rates after 18 days. The growth rate and chlorophyll content of *P. boryana* decreased significantly with an increase in Zn concentration. At pH 6, 7 and 8, *P. boryana* showed significant decreases ($p < 0.05$) in growth rates and chlorophyll content in all concentrations of Zn compared with control plants (no Zn). At pH of 6.0 and below, controls were also affected with significantly reduced growth rates and chlorophyll contents while Zn treated seaweed showed significant effects compared to these controls. The effect of pH and Zn on all measured factors was obvious on Day 6 onwards, whereas the interaction effect between them was significant on chlorophyll content throughout the experiment. From Day 9 onwards, the growth rate and chlorophyll content showed significant correlation among each other.

Keywords: brown seaweed, *Padina boryana*, zinc, pH, growth

Abstrak

Rumpai laut Perang, *Padina boryana* ditemui di sepanjang pantai Terengganu, Malaysia dan boleh menjadi biopemantau logam berat yang berpotensi di kawasan pantai. Untuk lebih memahami kesan pencemaran logam berat terhadap *P. boryana* pada pH air laut yang berbeza, kesan gabungan zink (Zn) dan pH terhadap kadar pertumbuhan dan kandungan klorofil telah disiasat dalam makmal. Selepas pendedahan selama 21 hari dalam rawatan campuran 6 variasi pH (4 hingga 9) dan tiga kepekatan Zn (30, 150, 300 ppb), kadar pertumbuhan maksimum diperhatikan dalam rawatan kawalan pada pH 8 tanpa tambahan Zn, manakala rawatan di pH 4 dan 9 menunjukkan kadar pertumbuhan negatif selepas 18 hari. Kadar pertumbuhan, kandungan klorofil *P. boryana* menurun dengan ketara dengan peningkatan kepekatan Zn. Pada pH 6, 7 dan 8, *P. boryana* menunjukkan penurunan ketara ($p < 0.05$) dalam kadar pertumbuhan, kandungan klorofil dalam semua kepekatan Zn berbanding dengan rawatan kawalan (tiada Zn). Pada pH 6.0 dan ke bawah, rumpai laut dalam rawatan kawalan juga terjejas dengan kadar pertumbuhan dan kandungan klorofil yang merosot manakala rumpai laut yang didedah kepada Zn menunjukkan kesan yang lebih ketara berbanding dengan rawatan kawalan. Kesan pH dan Zn terhadap semua faktor yang diukur adalah jelas pada hari ke-6 dan seterusnya, manakala kesan interaksi di antara mereka adalah signifikan terhadap kandungan klorofil di sepanjang eksperimen. Pada hari ke-9 dan seterusnya, kadar pertumbuhan dan kandungan klorofil menunjukkan korelasi yang signifikan antara satu sama lain.

Kata kunci: rumpai laut perang, *Padina boryana*, zink, pH, pertumbuhan

Introduction

With the advent of technology and industrialization, heavy metal pollution has become a pressing problem worldwide. Among the most common pollutants found in industrial effluents are zinc (Zn), lead (Pb), copper (Cu), cadmium (Cd) and nickel (Ni) [1]. Although some such as Zn and Cu are essential trace elements that are needed for human health, the concentrations of these naturally occurring elements are rising rapidly due to anthropogenic activities, including mining and shipping activities. Zn in particular could cause serious health problems on overexposure. Severe exposure to Zn could cause pancreatic damage, arteriosclerosis and respiratory disorders [2]. Additionally, the concentration of Zn could be bio-magnified up the food chain when it is absorbed by primary producers such as microalgae and macroalgae, and travels from fish to humans.

It has been proven that instead of directly measuring water samples, the use of bioindicators to assess marine pollution, particularly metal contamination in water columns, is more economical, in which high-sensitivity methods required for water analysis are not required and seasonal or spatial fluctuations in concentrations could be integrated [3]. Marine seaweeds have been used as bioindicators due to their various benefits and suitability, including their accessibility, presence at locations that are prone to pollution such as estuaries and coastal zones, and their benthic and hardy nature [3]. However, different seaweed species are known to exhibit different responses to varying Zn concentrations, with brown seaweeds of the genus *Padina* and *Sargassum* and the red seaweed *Spyridia* being more tolerant than green seaweed *Ulva* and *Enteromorpha* [4]. In a more detailed study, Sheng et al. [1] also reported that brown seaweeds (*Padina* sp. and *Sargassum* sp.) exhibited better metal removal abilities compared to green seaweed (*Ulva* sp.) and red seaweed (*Gracillaria* sp.), with both uptake capacity and affinity constants of *Padina* sp. and *Sargassum* sp. following the order Pb > Cu > Zn > Cd > Ni and Pb > Cu > Cd > Ni > Zn, respectively. Additionally, the release of heavy metals, including Zn, into water bodies is affected by pH, with increasing concentrations of metal released as pH is decreased [5]. As reported by Adams and Sanders [5], the threshold release pH for Zn-loaded sludge into water bodies is 5.8. However, no literature has reported on the combined effect of Zn and pH on the growth of *P. boryana*.

pH plays a crucial role in the growth of seaweed. Hence it has an impact on biochemical process of marine organisms [6]. It affects this growth in different ways such as alteration in the distribution of carbon dioxide species, availability of carbon [7] and, availability of trace metals and essential nutrients [8]. High pH levels can cause direct physiological changes [9].

As a native seaweed species in the coastal zones of Terengganu, Malaysia, *P. boryana* is found abundantly in shallow waters. The heavy metal contents of *P. boryana* from the coastal waters of the Gulf of Aden [10], the Persian Gulf [11] and the Suez Gulf [12] were previously assessed. The level of heavy metals, especially Zn, exceeded the maximum level allowed according to the Malaysian Food Act of 1983 in the tissue of oysters from Setiu Lagoon, Terengganu [13] whereas its level is still acceptable in several fish species from Mengabang Telipot and Paka estuary, Terengganu [14,15]. However, the specific effect of heavy metals on the growth of *P. boryana* is still unclear. Thus, the objective of the present study is to assess the combined effect of Zn and pH on growth rate and chlorophyll content of brown seaweed, *P. boryana*.

Materials and Methods

Sampling

Wild brown seaweed *P. boryana* were collected by hand in a depth of 0.5 m during low tide at Kuala Abang (N 4° 51'6.49'' E 103° 24' 11.36'') off the coast of Terengganu, Malaysia (Figure 1). Samples were identified to the species level based on the taxonomic key provided by Geraldino et al. [16]. All collected seaweeds were of the same size (within the range of 8 cm from top to bottom) and had a normal healthy appearance, i.e. normal and evenly distributed green coloration. Only samples from clear distinct patches were collected to avoid collecting samples from the same individuals [17]. The collected samples were transported to the laboratory in 50 L seawater containers within 2 hours of collection. Studies have shown that due to several factors such as variability in growth rates, the analysis of different plant parts, plant age and collection location's habitat, seaweeds collected from the

same site might differ in their metal absorption properties [3, 18, 19]. Thus, to minimize such variations, only seaweeds of the same size and growth stage were collected from the same shore levels (habitat) at the same site.
The water quality parameters were recorded during each field trip [20]. Briefly, during each sampling trip, measurements of temperature, salinity, pH, total dissolved solids (TDS), and dissolved oxygen (DO) were taken using YSI, 556 MPS (YSI Inc, Ohio, USA).

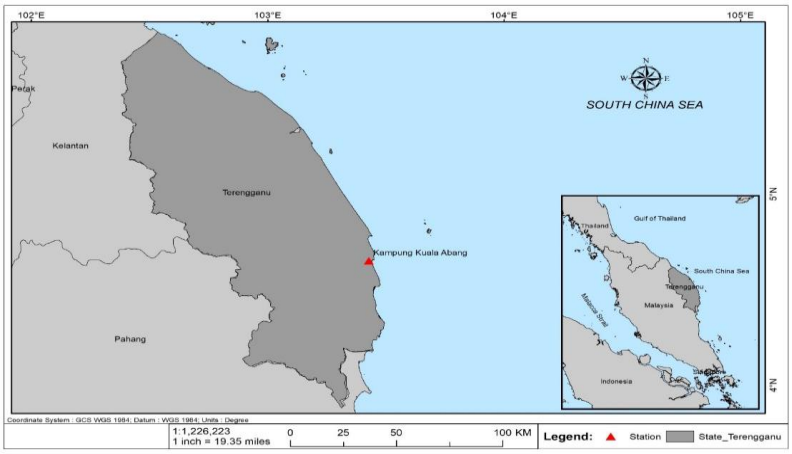


Figure 1. Map illustrating the Terengganu coast and the location of sample collection

Experimental setup
All samples were divided into sixty 1 L transparent aquarium tanks with each tank holding approximately 14 g of thalli, i.e. holdfast, stipe and blades. The shared culture parameters were: artificial seawater with water salinity of 33 ppt, room temperature, photoperiod of 12/12 hours dark/light (illumination of 120 µmol photons $m^{-2}s^{-1}$) [21, 22]. The cultures were continuous aeration (supplied with sterilized dry air (97%) and CO_2 (97:3, % v/v) [21]. Samples were cultured in six pH levels, i.e. pH 4, 5, 6, 7, 8 and 9. pH was adjusted by the addition of HNO_3 or KOH. Furthermore, there were three varying Zn concentrations ((30, 150 and 300 ppb (there concentrations are 10, 50 and 100 times, the measured Zn concentration in seawater from the study sites 2.96±1.57 µg L^{-1})) within each pH level. Each treatment was conducted in triplicate and a treatment without addition of Zn was considered as control. Zn was prepared from zinc sulphate heptahydrate ($ZnSO_4.7H_2O$). Seawater renewal was conducted every three days. The whole experiment was carried out for a period of 21 days [23].

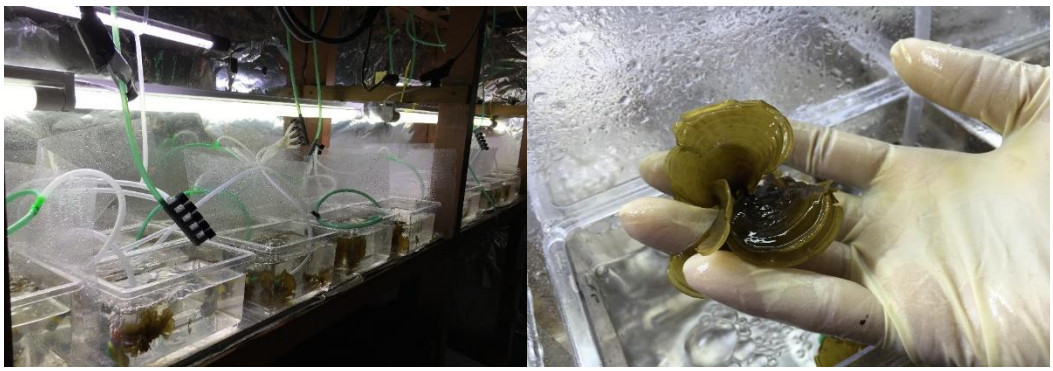


Figure 2. Experimental setup of *P. boryana* treatments

Growth rate, chlorophyll content and photosynthesis activity

The weight of each thallus was recorded every three days [23]. Prior to weighing, the samples were gently blotted using filter papers to remove excess water retained on their surfaces. The calculation of growth rate is as follows:

$$Growth\,rate\ (\%) = 100 \times \frac{ln\frac{W_t}{W_0}}{t} \quad (1)$$

where W_0 is the initial biomass (mg) and W_t is the biomass (mg) after t days [23, 24].

Chlorophyll content was determined based on the method of Liu et al. [25]. Briefly, the chlorophyll levels of *P. boryana* were determined by taking six readings for each leaf using a Chlorophyll Meter SPAD-502 (Minolta Corporation, NJ, USA), and the average value for treatment was used in the following equation 2:

$$Y = 0.996X - 1.52$$

where Y is the chlorophyll concentration and X is the SPAD-502 chlorophyll readings (µg cm^{-2}).

Statistical analysis

All statistical analyses were conducted using SPSS version 23. All data was tested for normality. Two-way analysis of variance (ANOVA) was used to test for any significant differences among treatments. To understand the effect of pH and Zn concentrations on three different dependent factors (growth rate and chlorophyll content) at any given time interval, general linear model was used. Post-hoc Tukey's test was carried out if significant differences among treatments were observed. Pearson's correlation was used to determine if growth rate and chlorophyll content correlate among each other at different time intervals.

Results and Discussion

Growth rate and chlorophyll content comparison based on pH: Treatment at pH 4

The introduction of Zn in treatment at pH 4 had significant effects on all measured parameters. The growth rate of *P. boryana* decreased with increasing Zn concentration (Figure 3a). As for chlorophyll concentration, treatments with 150 ppb and 300 ppb Zn were lower than that of 30 ppb Zn and control groups, starting day 9 onwards (Figure 3b).

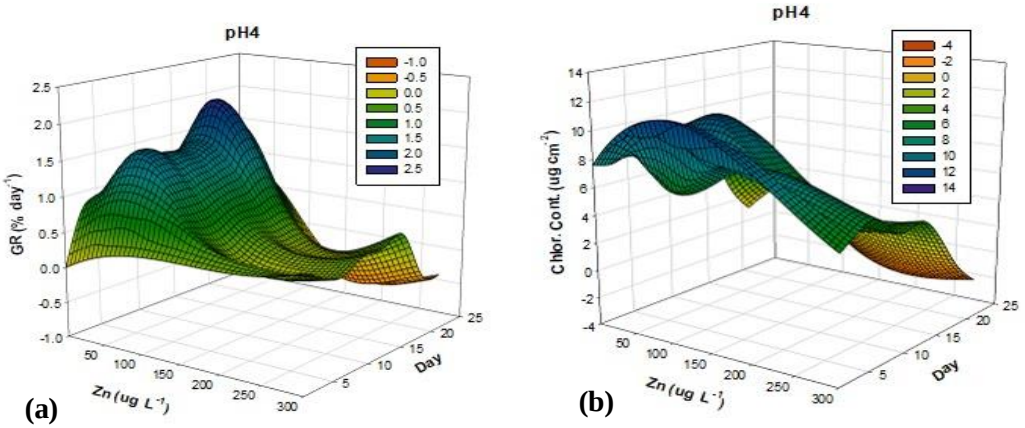


Figure 3. The (a) growth rate (GR, %), and (b) chlorophyll content of *P. boryana* cultured for 21 days at pH 4

Treatment at pH 5

At pH 5, the growth rate of *P. boryana* in all treatments and control showed positive values, with control showing the highest growth rate, followed by Zn with increasing concentrations (Figure 4a). The pattern of chlorophyll content which was observed in treatments at pH 5, was similar to those in pH 4, where *P. boryana* cultured in Zn with 30 ppb and control were of higher chlorophyll contents compared to those cultured in Zn with 150 ppb and 300 ppb, starting from day 6 onwards (Figure 4b).

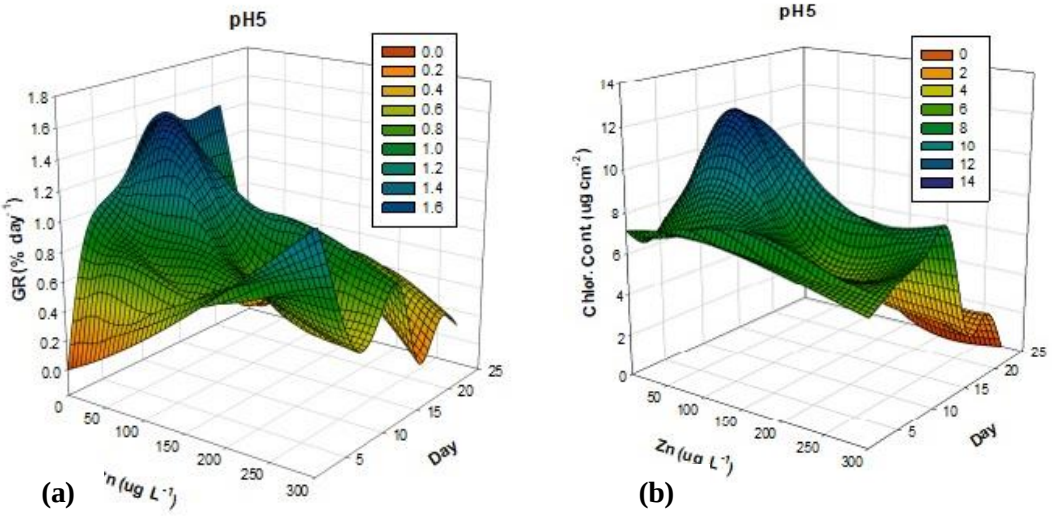


Figure 4. The (a) growth rate (GR, %), and (b) chlorophyll content of *P. boryana* cultured for 21 days at pH 5

Treatment at pH 6

At pH 6, only the growth rate of the control showed increasing values, whereas that of treatments with various concentrations of Zn increased slightly until half of the culture period and decreased towards the end, with decreasing growth rate values with increasing Zn concentrations (Figure 5a). The chlorophyll content was well above 5 µg cm^{-2} for all treatments, except treatments with 150 ppb and 300 ppb Zn which dropped below 5 µg cm^{-2} after 18 days (Figure 5b).

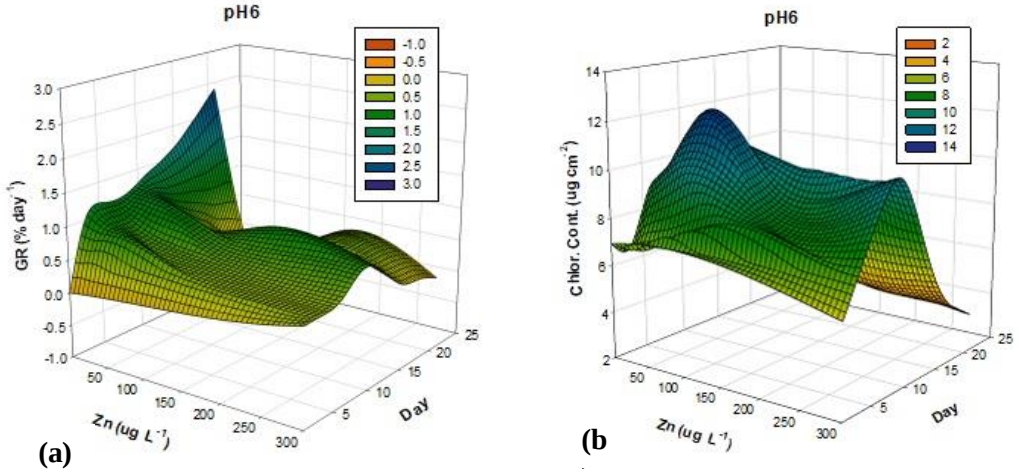


Figure 5. The (a) growth rate (GR, %), and (b) chlorophyll content of *P. boryana* cultured for 21 days at pH 6

Treatment at pH 7

The growth rates of *P. boryana* in treatments at pH 7 showed similar trends as those in pH 6, with only the control exhibiting a positive increase in growth rate (Figure 6a). The chlorophyll content values were the highest in control at the end of the experiment, whereas treatments showed decreasing values in chlorophyll content values with increasing Zn concentrations (Figure 6b).

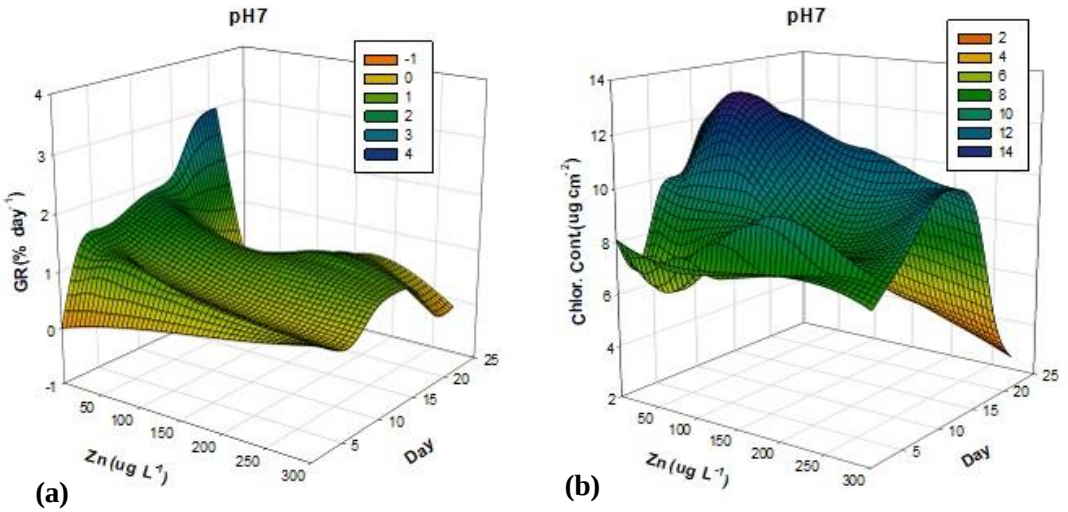


Figure 6. The (a) growth rate (GR, %), and (b) chlorophyll content of *P. boryana* cultured for 21 days at pH 7

Treatment at pH 8

The growth rates, and chlorophyll content values in treatments at pH 8 were similar to that of pH 7, with chlorophyll content production significantly reduced from Day 6 onwards (Figure 7).

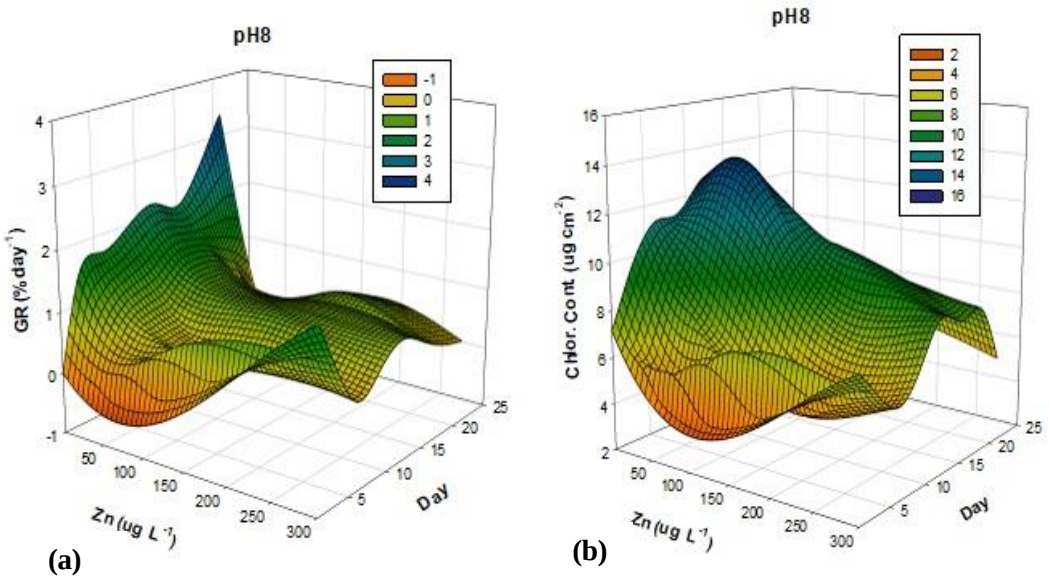
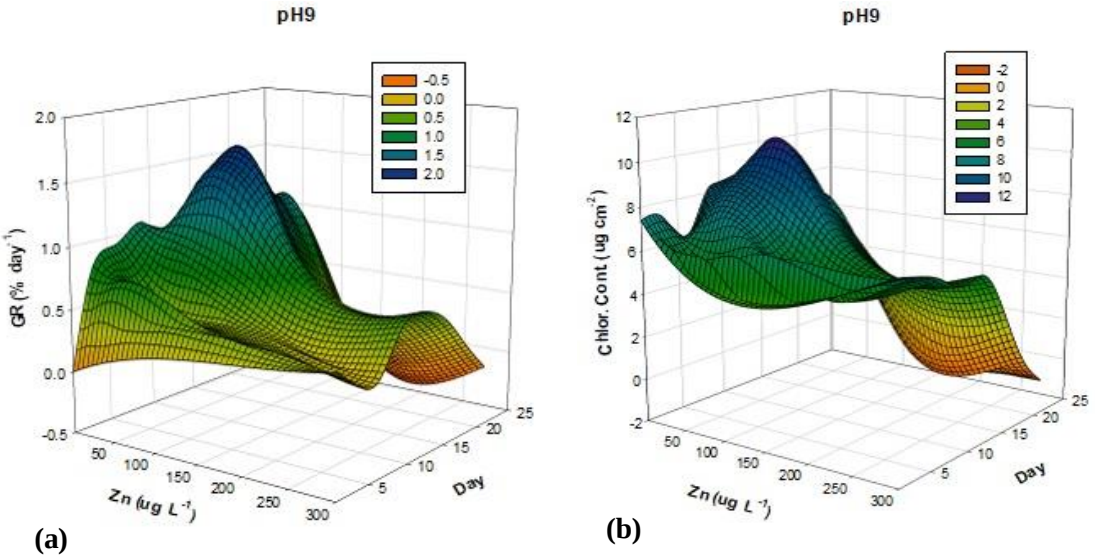


Figure 7. The (a) growth rate (GR, %), and (b) chlorophyll content of *P. boryana* cultured for 21 days at pH 8

Treatment at pH 9

Significant decreases in values of growth rate (Figure 8a) were observed in treatments with 150 ppb and 300 ppb Zn from Day 6 onwards. Chlorophyll content reduced significantly from Day 9 onwards in treatments with 300 ppb Zn (Figure 8b).



(a) (b)

Figure 8. The (a) growth rate (GR, %), and (b) chlorophyll content of *P. boryana* cultured for 21 days at pH 9

Combined effect of Zn and pH

At 3 days of exposure, pH and Zn had no significant effect on the growth rate, but both influenced the chlorophyll content of *P. boryana*, and their interaction effect was also significant (Table 1). Zn at concentration of 150 ppb and pH between 4-7 showed significantly higher chlorophyll content (Figure 9).

Table 1. The General linear model analysis of pH and Zn concentration on two dependent factors (growth rate and chlorophyll content). Significance level was at $p < 0.05$.

	Growth Rate and Chlorophyll Content	**Day 3**	**Day 6**	**Day 9**	**Day 12**	**Day 15**	**Day 18**	**Day 21**
		***P* value**						
pH	Growth rate	0.570	0.001	0.001	0.001	0.001	0.001	0.001
	Chlorophyll content	0.001	0.001	0.001	0.001	0.001	0.001	0.001
Zn	Growth rate	0.915	0.117	0.001	0.001	0.001	0.001	0.001
	Chlorophyll content	0.001	0.001	0.001	0.001	0.001	0.001	0.001
pH × Zn	Growth rate	0.885	0.693	0.558	0.048	0.001	0.001	0.015
	Chlorophyll content	0.001	0.001	0.001	0.001	0.001	0.001	0.001

On Day 6, pH and Zn significantly affected all dependent factors except Zn on growth rate. The interaction effect of pH × Zn was significant in influencing the chlorophyll content (Table 1). Growth rate of *P. boryana* increased to a maximum at 8 before dropping drastically to its lowest at pH 9. Similarly, low chlorophyll content was recorded at pH 9, although it peaked at pH 7. Lowest Zn concentration of 30 ppb showed the highest chlorophyll content (Figure 9).

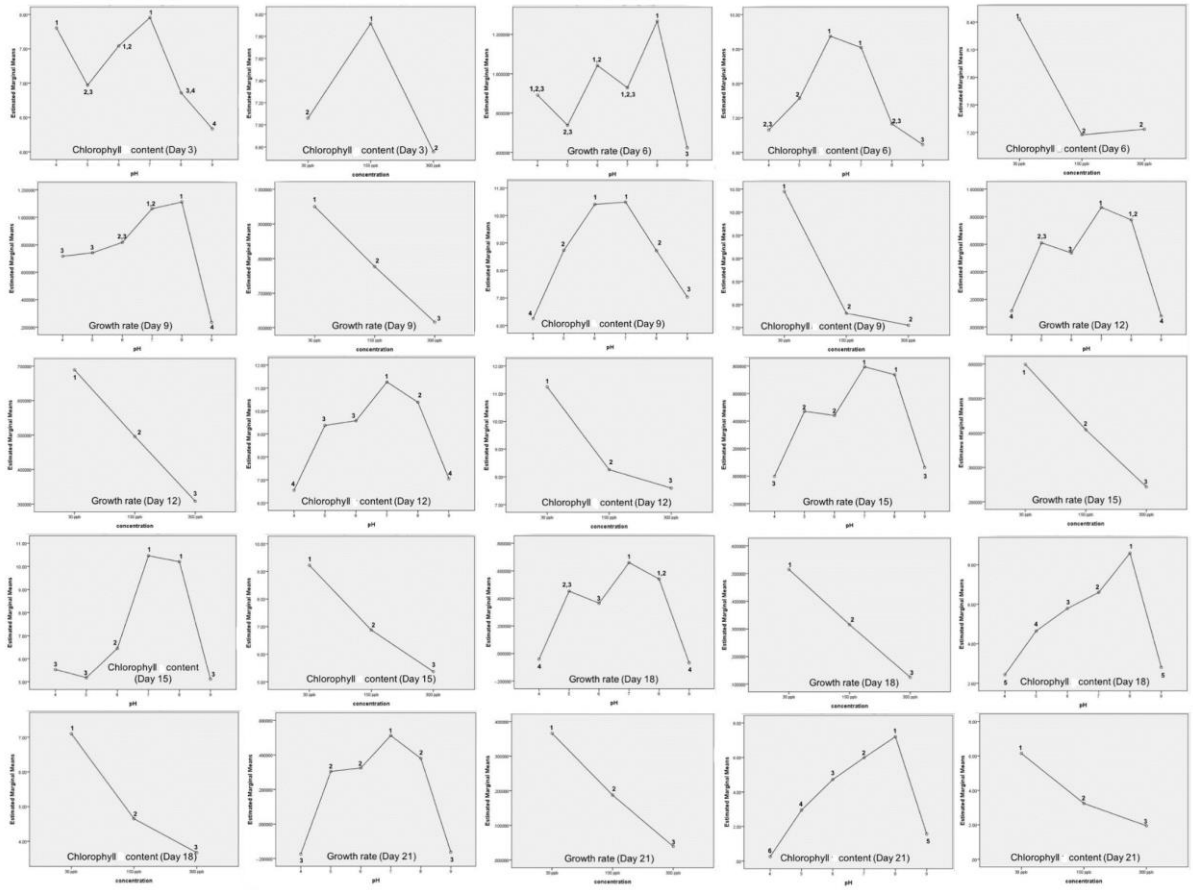


Figure 9. The effect of pH and Zn concentration on the estimated marginal means of growth rate and chlorophyll content at different day period. Different numberings on one figure indicates significant difference ($p < 0.05$)

From Day 9 onwards, the effect of pH and Zn concentrations on the growth rate and chlorophyll content of *P. boryana* were almost similar: pH and Zn concentrations significantly affected all two dependent factors (Table 1). Similarly, the interaction between pH and Zn had affected the growth rate and the chlorophyll content of *P. boryana* on Day 12 onwards. Overall, pH 8 and Zn concentration of 50 ppb were the best conditions for *P. boryana's* growth, as measured by growth rate and chlorophyll content (Figure 9).

Correlation among growth rate and chlorophyll content

At 3 days' post exposure to a combination of various pH and Zn concentration treatments, no significant correlation was found among growth rate and chlorophyll content of *P. boryana* (all $p > 0.05$). On Day 6, chlorophyll content and growth rate were significantly correlated ($r = 0.51$, $p < 0.001$). On Day 9 onwards, growth rate and chlorophyll content showed significant correlation among each other (all $p < 0.05$).

Overall, results in this study showed that the growth rate, and chlorophyll content of *P. boryana* decreased significantly with the increase in Zn concentration and at increasing acidity levels (pH 6, 5 and 4), as well as at a high pH level (pH 9). The detrimental effects of lower pH on *P. boryana* are expected as decrease in water pH is known to adversely affect the growth, development and reproduction of seaweeds. For example, red seaweed *Gracilaria secundata* and *Kappaphycus alvarezii* exhibited bell-shaped growth curves from pH 7.0 to 9.0 which peaked at 8.2, and from pH 6.0 to 9.0 which peaked at 8.4, respectively [26, 27]. Similarly, higher growth rates were

observed in juvenile coralline alga *Arthrocardia corymbose* maintained under pH 8.05 compared to those under pH 7.65 [28]. Also, Roleda et al. [29] reported that lowered pH (7.59-7.60) significantly reduced the germination process of giant kelp *Macrocystis pyrifera.*

The pH range for most seaweed cultures is recommended to be in between 7 and 9, although the optimum range is narrowly between 8.2-8.7 [27]. Normal seawater is of slightly alkaline nature, with a pH of approximately 8.07, of which a huge portion (91%) is made up of total dissolved inorganic carbon, and the rest are carbonate ions (8%) and dissolved CO_2 (1%) [29]. Any fluctuation in the pH of seawater may disrupt the equilibrium of the carbonate system and alter the percentage of inorganic carbon species, thereby negatively affecting the growth of carbon-depending photosynthetic seaweeds [30]. At pH above 8.5, the photosynthetic activity of seaweeds was reported to decline rapidly due to the reduction in dissolved CO_2 and carbonate ions' concentrations [31]. This explains the zero growth of *P. boryana* in both treatments of pH 4 and 9 after 18 days, as these extreme pHs disrupted their normal physiological and growth processes. Such zero growth was also reported in the adult algae *A. corymbose* maintained at lower pH 7.65 [28].

The growth rates of *P. boryana* were adversely affected when they were exposed to Zn from 30 to 300 ppb at all pH levels, except in treatments with 30 ppb Zn which showed slightly stimulated algal growth at pH 4 and pH 9. The feasibility of *P. boryana* to survive and in treatments with varying Zn concentrations and pH levels are expected as they are the more tolerant seaweed species compared to others [4]. Their higher tolerant characteristics towards adverse conditions might be contributed to the high polysaccharide content in their cell walls. Using analytical electron microscopy techniques, Amado Filho et al. [32] found that Zn was present as dense granules along cell walls but absent in the cytoplasm, indicating that cell walls play a major role in the Zn accumulation in *Padina* sp. In addition to this, Zn deficiency is known to reduce the chlorophyll content and adversely affect plant growth, whereas an excess in Zn concentration could be toxic to plant and damage the plant's metabolism [33]. Thus, the reduced performance in terms of growth rates and chlorophyll content when *P. boryana* was exposed to increasing concentrations of Zn suggests that Zn might alter the permeability of the cell membrane, leading to a sharp reduction in potassium and sodium content of the cell. This eventually inhibits photosynthesis and nitrogen fixation, and ultimately affects cell multiplication. The adverse effects of increasing Zn concentration on the growth rate were also reported in another important bio-monitor species, the microalgae [34].

The combined effect of pH and Zn on chlorophyll content of *P. boryana* was highlighted in the results of our study, where significant interaction effect of pH and Zn on chlorophyll content was observed throughout the 21-days treatment period (Table 2). Additionally, the growth rate of *P. boryana* was also affected by the interaction effect between pH and Zn from Day 12 onwards. Thus, when heavy metal accumulation is high (resulting in acidic pH), the growth rate and chlorophyll content of *P. boryana* will be greatly affected, with a greater effect observed at lower pH and/or higher heavy metal concentrations [18, 31]. Apart from pH, it is well known that correlation also exists among heavy metals. For example, Fe concentrations in seaweeds of Marsa-Matrouh beaches, Egyptian Mediterranean Sea were positively correlated with Cu and Pb, but negatively correlated between Cu and Ni, Pb and Zn [35].

The ability of the cells to accumulate Zn is important since algae are a major vector for transferring the metal from the abiotic environment into food webs. In the natural environment, red algae exhibit higher Zn accumulation properties compared to green and brown algae [3]. The variation among species of Rhodophyta, however, was large [3]. As shown in another brown seaweed species, *Laminaria digitata*, once Zn is absorbed from the aquatic environment, it shows little tendency to be lost from the plant [35]. Additionally, it was reported that the growing region above the stipe of *L. digitata* exhibited significantly higher Zn absorption compared to the more distal part of the lamina (slower growing region) [36]. Furthermore, Munda [37] showed that the accumulation of heavy metals is higher in vegetative parts of the thalli than in receptacles of brown seaweed *Fucus spiralis*. Thus, although this study showed that the increasing concentration of Zn negatively affects the growth and chlorophyll content of *P. boryana*, future studies on the retention of accumulated Zn and the different absorption capabilities of various plant parts and growth stages are recommended, if *P. boryana* is to be used in heavy metal biomonitoring in Terengganu coastal waters.

Conclusion

This study provides useful data on Zn tolerance and effect of Zn on the growth and chlorophyll content of *P. boryana*, a seaweed species that could serve as a suitable bioindicator along the coasts of Terengganu. While the adverse effects of extreme pH and high Zn concentrations is observed, the ability of *P. boryana* to survive these treatments highlights the sturdiness of this species and its potential in future heavy metal biomonitoring. Additional research regarding the effect of other heavy metals on the growth of *P. boryana* is recommended to better understand its metal accumulation ability and coping mechanism towards various heavy metal exposures. Future research should also look into the effect of pH fluctuations on the growth of *P. boryana*, as ocean acidification is a growing concern, especially in coastal zones.

Acknowledgement

This study was supported by the Ministry of Education Higher Institution Centre of Excellence Grant (Vote No. 66928). We would like to thank the staff of the Institute of Tropical Aquaculture (AKUATROP), Universiti Malaysia Terengganu for technical support provided throughout the study.

References

1. Sheng, P. X., Ting, Y.-P., Chen, J. P. and Hong, L. (2004). Sorption of lead, copper, cadmium, zinc and nickel by marine algal biomass: characterization of biosorptive capacity and investigation of mechanisms. *Journal of Colloid and Interface Science*, 275: 131-141.
2. Plum, L. M., Rink, L. and Haase, H. (2010). The essential toxin: Impact of Zinc on human health. *International Journal of Environmental Research and Public Health*, 7(4): 1342-1365.
3. Stengel, D. B., Macken, A., Morrison, L. and Morley, N. (2004). Zinc concentrations in marine macroalgae and a lichen from western Ireland in relation to phylogenetic grouping, habitat and morphology. *Marine Pollution Bulletin*, 48: 902-909.
4. Amado Filho, G. M., Karez, C. S., Andrade, L. R., Yoneshigue-Valentin, Y. and Pfeiffer, W. C. (1997). Effects on growth and accumulation of zinc in six seaweed species. *Ecotoxicology and Environmental Safety*, 37: 223-228.
5. Adams, T. Mc. and Sanders, J. R. (1984). The effect of pH on the release to solution of zinc, copper and nickel from metal-loaded sewage sludges. *Environmental Pollution Series B, Chemical and Physical*, 8(2): 85 – 99.
6. Visviki, I. and Palladino, J. (2001). Growth and cytology of *Chlamydomonas acidophila* under acidic stress. *Bulletin of Environmental Contamination and Toxicology*, 66(5): 623-630.
7. Fabry, V. J., Seibel, B. A., Feely, R. A. and Orr, J. C. (2008). Impacts of ocean acidification on marine fauna and ecosystem processes. *ICES Journal of Marine Science*, 65(3): 414-432.
8. Gensemer, R. W., Smith, R. E. and Duthie, H. C. (1993). Comparative effects of pH and aluminum on silica-limited growth and nutrient uptake in *Aastrionella ralfsii var americana* (Bacillariophyceae) 1. *Journal of Phycology*, 29(1): 36-44.
9. Hansen, P. J. (2002). Effect of high pH on the growth and survival of marine phytoplankton: implications for species succession. *Aquatic Microbial Ecology*, 28(3): 279-288.
10. Al-Shwafi, N. A. and Rushdi, A. I. (2008). Heavy metal concentrations in marine green, brown, and red seaweeds from coastal waters of Yemen, the Gulf of Aden. *Environmental Geology*, 55(3): 653-660.
11. Faedeh, A., Hossein, R. and Hossein, Z. (2013). Metal concentrations in *Padina* species and associated sediment from Nayband Bay and Bostaneh Port, Northern Coast of the Persian Gulf, Iran. *Journal of the Persian Gulf*, 4(11): 17-24.
12. Mohamedein, L. I., El-Moselhy, K., Diab, A. A. and Tolba, M. R. (1999). Levels of some heavy metals in coastal water, sediment and the Limpet *Patella sp.* from the northern part of the Suez Gulf (Suez Bay). *Egyptian Journal of Aquatic Research*, 3(2): 69-84.
13. Azlisham, M., Vedamanikam, V. J. and Shazili, N. A. M. (2009). Concentrations of cadmium, manganese, copper, zinc, and lead in the tissues of the oyster (*Crassostrea iredalei*) obtained from Setiu Lagoon, Terengganu, Malaysia. *Toxicological and Environmental Chemistry*, 91(2): 251-258.
14. Kamaruzzaman, Y., Ong, M. C. and Jalal, K. C. A. (2008). Levels of copper, zinc and lead in fishes of Mengabang Telipot River, Terengganu, Malaysia. *Journal of Biological Sciences*, 8(7): 1181-1186.

15. Kamaruzzaman, Y., Zaleha, K., Ong, M. C. and Willison, K. (2007). Copper and zinc in three dominant brackish water fish species from Paka estuary, Terengganu, Malaysia. *Malaysian Journal of Science*, 26(2): 65 – 70.
16. Geraldino, P. J. L., Liao, L. M. and Boo, S. M. (2005). Morphological study of the marine algal genus *Padina* (Dictyotales, Phaephyceae) from Southern Philippines: 3 species new to Philippines. *Algae*, 20(2): 99-112.
17. Wichachucherd, B., Prathep, A. and Zuccarello, G. C. (2014). Phylogeography of *Padina boryana* (Dictyotales, Phaeophyceae) around the Thai-Malay Peninsula. *European Journal of Phycology*, 49(3): 313-323.
18. Bryan, G. W. and Hummerstone, L. G. (1973). Brown seaweeds as an indicator of heavy metals in estuaries in southwest England. *Journal of the Marine Biological Association of the United Kingdom*, 53: 705-720.
19. Stengel, D. B. and Dring, M. J. (2000). Copper and iron concentrations in *Ascophyllum nodosum* (Fucales, Phaeophyta) from different sites in Ireland and after culture experiments in relation to thallus age and epiphytism. *Journal of Experimental Marine Biology and Ecology*, 246: 145-161.
20. Qadir, A., Malik, R. N. and Husain, S. Z. (2008). Spatio-temporal variations in water quality of Nullah Aik-tributary of the river Chenab, Pakistan. *Environmental Monitoring and Assessment*, 140(1-3), 43-59.
21. El-Sheekh, M. M., El-Naggar, A. H., Osman, M. E. H. and El-Mazaly, E. (2003). Effect of cobalt on growth, pigments and the photosynthetic electron transport in *Monoraphidium minutum* and *Nitzchia perminuta*. *Brazilian Journal of Plant Physiology*, 15(3): 159-166.
22. Zou, D. (2005). Effects of elevated atmospheric CO_2 on growth, photosynthesis and nitrogen metabolism in the economic brown seaweed, *Hizikia fusiforme* (Sargassaceae, Phaeophyta). *Aquaculture*, 250(3-4): 726-735.
23. Mamboya, F., Pratap, H., Mtolera, M. and Björk, M. (2007). Accumulation of copper and zinc and their effects on growth and maximum quantum yield of the brown macroalga *Padina gymnospora*. *Western Indian Ocean Journal of Marine Science*, 6(1): 17-28.
24. Nielsen, M. M., Bruhn, A., Rasmussen, M. B., Olesen, B., Larsen, M. M. and Møller, H. B. (2012). Cultivation of Ulva lactuca with manure for simultaneous bioremediation and biomass production. *Journal of Applied Phycology*, 24(3): 449-458.
25. Liu, M., Liu, X., Li, M., Fang, M. and Chi, W. (2010). Neural-network model for estimating leaf chlorophyll concentration in rice under stress from heavy metals using four spectral indices. *Biosystems Engineering*, 106(3): 223-233.
26. Lignel, A. and Pedersén, M. (1989). Effects of pH and inorganic carbon concentration on growth of *Gracilaria secundata*. *British Phycological Journal*, 24: 83-89.
27. Tee, M. Z., Yong, Y. S., Rodrigues, K. F. and Yong, W. T. L. (2015). Growth rate analysis and protein identification of *Kappaphycus alvarezii* (Rhodophyta, Gigartinales) under pH induced stress culture. *Aquaculture Reports*, 2: 112-116.
28. Roleda, M. Y., Cornwall, C. E., Feng, Y., McGraw, C. M., Smith, A. M. and Hurd, C. L. (2015). Effect of ocean acidification and pH fluctuations on the growth and development of coralline algal recruits, and an associated benthic algal assemblage. *PLoS ONE*, 10(10): e0140394.
29. Roleda, M. Y., Morris, J. N., McGraw, C. M. and Hurd, C. L. (2012). Ocean acidification and seaweed reproduction: increased CO_2 ameliorates the negative effect of lowered pH on meiospore germination in the giant kelp *Macrocystis pyrifera* (Laminariales, Phaeophyceae). *Global Change Biology*, 18(3): 854-864.
30. Cornwall, C. E., Hepburn, C. D., Pritchard, D., Currie, K. I., McGraw, C. M., Hunter, K. A. and Hurd, C. L. (2012). Carbon-use strategies in macroalgae: differential responses to lowered pH and implications for ocean acidification. *Journal of Phycology*, 48: 137-144.
31. Menéndez, M., Martinez, M. and Comin, F. A. (2001). A comparative study of the effect of pH and inorganic carbon resources on the photosynthesis of three floating macroalgae species of a Mediterranean coastal lagoon. *Journal of Experimental Marine Biology and Ecology*, 256: 123-136.
32. Amado Filho, G. M., Karez, C. S., Pfeiffer, W. C., Yoneshigue-Valentin, Y. and Farina, M. (1996). Accumulation, effects on growth, and localization of zinc in *Padina gymnospora* (Dictyotales, Phaeophyceae). *Hydrobiologia*, 326/327: 451-456.
33. Radić, S., Babića, M., Škobićb, D., Roje, V. and Pevalek-Kozina, B. (2010). Ecotoxicological effects of aluminum and zinc on growth and antioxidants in *Lemna minor* L. *Ecotoxicology and Environmental Safety*, 73: 336-342.

34. Ouyang, H. L., Kong, X. Z., He, W., Qin, N., He, Q. S., Wang, Y., Wang, R. and Xu, F. L. (2012). Effects of five heavy metals at sub-lethal concentrations on the growth and photosynthesis of *Chlorella vulgaris. Chinese Science Bulletin*, 57(25): 3363-3370.
35. Khaled, A., Hessein, A., Abdel-Halim, A. M. and Morsy, F. M. (2014). Distribution of heavy metals in seaweeds collected along Marsa-Matrouh beaches, Egyptian Mediterranean Sea. *The Egyptian Journal of Aquatic Research*, 40(4): 363-371.
36. Bryan, G. W. (1969). The absorption of zinc and other metals by the brown seaweed *Laminaria digitata*. *Journal of the Marine Biological Association of the United Kingdom*, 49: 225-243.
37. Munda, I. M. (1986). Differences in heavy metals accumulation between vegetative parts of thalli and receptacles in *Fucus spiralis* L. *Botanica Marina*, 29(4): 341-350.

Malaysian Journal of Analytical Sciences, Vol 23 No 6 (2019): 1030 - 1043
DOI: https://doi.org/10.17576/mjas-2019-2306-11

MALAYSIAN JOURNAL OF ANALYTICAL SCIENCES
Published by The Malaysian Analytical Sciences Society
ISSN 1394 - 2506

DISTRIBUTION OF NUTRIENTS CONCENTRATION IN THE UPWELLING AREA OFF THE EAST COAST OF PENINSULAR MALAYSIA DURING THE SOUTHWEST MONSOON

(Taburan Kepekatan Nutrien di Kawasan Julang Air di Pantai Timur Semenanjung Malaysia Semasa Monsun Barat Daya)

Azyyati Abdul Aziz[1], Suhaimi Suratman[1,2]*, Poh Heng Kok[1], Mohd Fadzil Akhir[1]

[1]*Institute of Oceanography and Environment*
[2]*Institute of Tropical Biodiversity and Sustainable Development*
Universiti Malaysia Terengganu, 21030 Kuala Nerus, Terengganu, Malaysia

**Corresponding author: miman@umt.edu.my*

Received: 30 October 2018; Accepted: 26 September 2019

Abstract

An oceanographic survey was conducted with RV Discovery at the east coast of Peninsular Malaysia (ECPM) (i.e. Kelantan and Terengganu) facing the South China Sea during the southwest monsoon in July 2017, to understand the variations in the distribution of phosphate, silicate, dissolved organic carbon (DOC), and chlorophyll-a (chl-a) in response to coastal upwelling events. Seawater samples were collected from five transects, consisting of 27 sampling stations within the area from 4.0ºN - 6.5ºN and 102.3ºE - 106.0ºE. The data collection was organized into horizontal and vertical distributions. Physico-chemical parameters like temperature and salinity were also studied. We found that the horizontal distribution of phosphate and chl-a was significantly higher in the coastal area as compared to the offshore area. An irregular distribution pattern of DOC and silicate was also observed. Additionally, higher concentrations of phosphate, silicate, DOC and chl-a were observed at the northern area (nearby Gulf of Thailand) as compared to the southern area. It is possible that the northern area received a high input of nutrients from the Gulf of Thailand. Generally, the vertical distributions of nutrients show a tendency to be lower in surface water areas and increase towards deep water areas. An upwelling event was observed in Terengganu waters as a sudden decrease in temperature (from 29.85 to 24.89 ºC) was found at 4.0ºN -5.0ºN here, as compared to other areas in the ECPM. The results from this study can be used in comparisons as there is no baseline of nutrient concentrations available for this area at the moment.

Keyword: phosphate, silicate, dissolved organic carbon, upwelling, vertical and horizontal distribution, southwest monsoon

Abstrak

Kajian oseanografi telah dijalankan dengan RV Discovery di Pantai Timur Semenanjung Malaysia (ECPM) (iaitu Kelantan dan Terengganu) yang menghadap ke Laut China Selatan semasa monsun barat daya pada bulan Julai 2017 untuk memahami taburan variasi fosfat, silikat, karbon organik terlarut (DOC) dan klorofil-a (chl-a) yang bertindak balas terhadap julang air pantai. Sampel-sampel air laut diambil dari lima transek yang terdiri daripada 27 stesen pensampelan yang merangkumi kawasan dari 4.0 - 6.5 ºN dan 102.3 -106.0 ºE. Himpunan data telah disusun secara taburan mendatar dan menegak. Parameter fiziko-kimia seperti suhu dan saliniti turut dikaji. Kami mendapati taburan mendatar fosfat dan klorofil-a adalah secara signifikan lebih tinggi di kawasan pantai berbanding kawasan luar pesisir, dan diperhatikan corak taburan tidak teratur untuk DOC dan silikat. Di samping itu, kepekatan fosfat, silikat, DOC dan chl-a adalah tinggi di kawasan utara (berhampiran Teluk Thailand) berbanding dengan kawasan selatan. Adalah kemungkinan kawasan utara menerima kemasukan nutrien yang tinggi dari Teluk Thailand. Umumnya, taburan nutrien di permukaan air secara menegak menunjukkan kecenderungan untuk menurun dan meningkat ke arah air dalam. Julang air diperhatikan di perairan Terengganu apabila terdapatnya penurunan suhu secara mendadak (dari 29.85

hingga 24.89 ºC) yang ditemui di 4.0-5.0 ºN berbanding dengan kawasan lain di ECPM. Hasil dari kajian ini boleh digunakan sebagai perbandingan kerana setakat ini tiada kepekatan dasar mengenai nutrien di kawasan ini.

Kata kunci: fosfat, silikat, karbon organik terlarut, julang air, taburan menegak dan mendatar, monsun barat daya

Introduction

The east coast of Peninsular Malaysia (ECPM) is situated in the southwestern part of the South China Sea (SCS) and it lies within the shallow continental shelf of the Sunda shelf. The SCS is one of the largest semi-enclosed marginal seas in the tropical northwest Pacific Ocean, with a total area of about 3.8 million km^2 and an average depth of about 200 m. The SCS is regulated by the East Asian monsoon [1]. In boreal winter, north-easterly winds prevail over the SCS (termed as northeast monsoon), whereas in boreal summer, the prevailing winds reverse their courses into south-westerly (termed as southwest monsoon) [2, 3]. The prevailing winds during the southwest monsoon with the north-south orientation of the coastline induced offshore Ekman transport, thus being favourable for upwelling along the ECPM [4, 5]. The upwelling area along the ECPM was represented by an elongated cooler water spread, from the southern tip of Johor until Dungun, between June to September during the southwest monsoon [4-6]. This cooler upwelling water deviated offshore at about 5°N and continued to flow north-eastward before joining the cooler upwelling water in the Vietnamese coast [6].

Nutrients are the essential elements which strongly influence primary production in aquatic environments. Nitrogen (N), phosphorus (P) and silicon (Si) are examples of elements that play a key role in marine primary productivity [7, 8]. Nitrogen and phosphorus have been the subject of much research due to their major impact on net primary productivity and as a limiting nutrient in the marine environment. Previous studies in East China [9] and South China Sea [10] have shown that nitrogen had short supply for phytoplankton growth. Meanwhile, phosphorus occasionally replaces nitrogen as the limiting nutrient in marine environments such as in the North Sea [11] and the Mediterranean Sea [12]. However, the study on Si has received little attention, even though this nutrient is also important as the potential limiting nutrient for diatomaceous algae [13, 14]. As nutrients strongly influence phytoplankton growth and have an indirect impact on food web dynamics, the study of variations in nutrient distributions is important for understanding this marine ecosystem.

The distributions of nutrients in the ocean in response to upwelling events is a well-known phenomenon in oceanography [15, 16] and the nutrients have also been used as tracers for upwelling identification in the continental shelf [17]. Upwelling is a term used to describe a natural process in the marine environment involving the transport of cold and nutrient-rich water from the deeper layer to replace the warm and nutrient-depleted surface water [18, 19]. Upwelling usually possesses a significant impact on fishery production since it sustains a higher level of primary productivity. The information on nutrients in the upwelling system of the ECPM is still poorly understood due to the lack of nutrient data for vertical distribution. Zainol & Akhir [20] did find that the nutrient and chlorophyll-a (chl-a) concentration was slightly higher during upwelling, but their study only focuses on surface water at the ECPM coast. Coastal upwelling is a well-known phenomenon to induce a higher concentration of nutrients in the surface water, and hence it often results in the increase of biological productivity [21, 22]. These nutrient waters are considered as ‘new’ nutrients and they can be recycled within the water column [23]. This greatly enhances phytoplankton biomass and also contributes ~11% to global new production [24]. However, coastal upwelling waters do not necessarily contain higher nutrients or chlorophyll-a, as the upwelling events have different consequences on the environment depending on physical processes, ecosystem types and basin scale [25]**.** For example, in Makassar, Indonesia [26], southern Taiwan Strait [27], and Nanwan Bay, Taiwan [28], they found low concentrations of nutrients during the upwelling event.

This study is the first attempt to understand both, the chemical and the physical interaction based on in-situ data from the ECPM upwelling region. The main aim of this study was to investigate the distribution of nutrients, focusing on phosphate, silicate and dissolved organic carbon (DOC), and also to relate this to phytoplankton biomass and to understand the relationship between physical governing factors of the upwelling and nutrients availability.

Materials and Methods

Oceanographic sampling

A cruise survey with RV Discovery was carried out between 4/7/2017 and 8/7/2017 during the southwest monsoon. The sampling area is at the east coast of Peninsular Malaysia (Kelantan and Terengganu). The area spans from approximately 4.0ºN – 6.5ºN to 102.3ºE -106.0ºE. Sampling activities were organized into five transects covering 27 stations which range from near coast to about 290 km offshore (Figure 1). At each sampling station, surface water samples (~ 0.5 m) were collected for horizontal distribution. Vertical distribution at a different depth was performed only at two transects (Transects A and D). Transect A is located at the Kelantan waters and transect D was within a smaller area of reported upwelling activity (104ºE - 105ºE, out to 100 km from the coast) in Terengganu waters [6]. For both transects, water samples were collected from the depths of 0.5, 5, 10, 20, 30, 45 and 60 m (depending on the bottom depth). For both surface and vertical water, samples were collected using a Niskin bottle (20 L). Vertical distributions of temperature and salinity were measured by calibrated Sea-Bird conductivity-temperature-depth (CTD). The samples for phosphate, DOC, and chl-a analyses were filtered onboard, through pre-combusted (5 hours at 450 ºC) and pre-weighed Whatman GF/F filters (nominal pore size 0.7 µm), while samples for silicate were filtered through a cellulose membrane filter. The filtered samples were stored in acid-washed polyethylene bottles and frozen at –20 °C until analysis. Filter paper for chlorophyll-a was folded, wrapped in foil squares and immediately preserved in the dark under low temperature and returned to the laboratory for analysis.

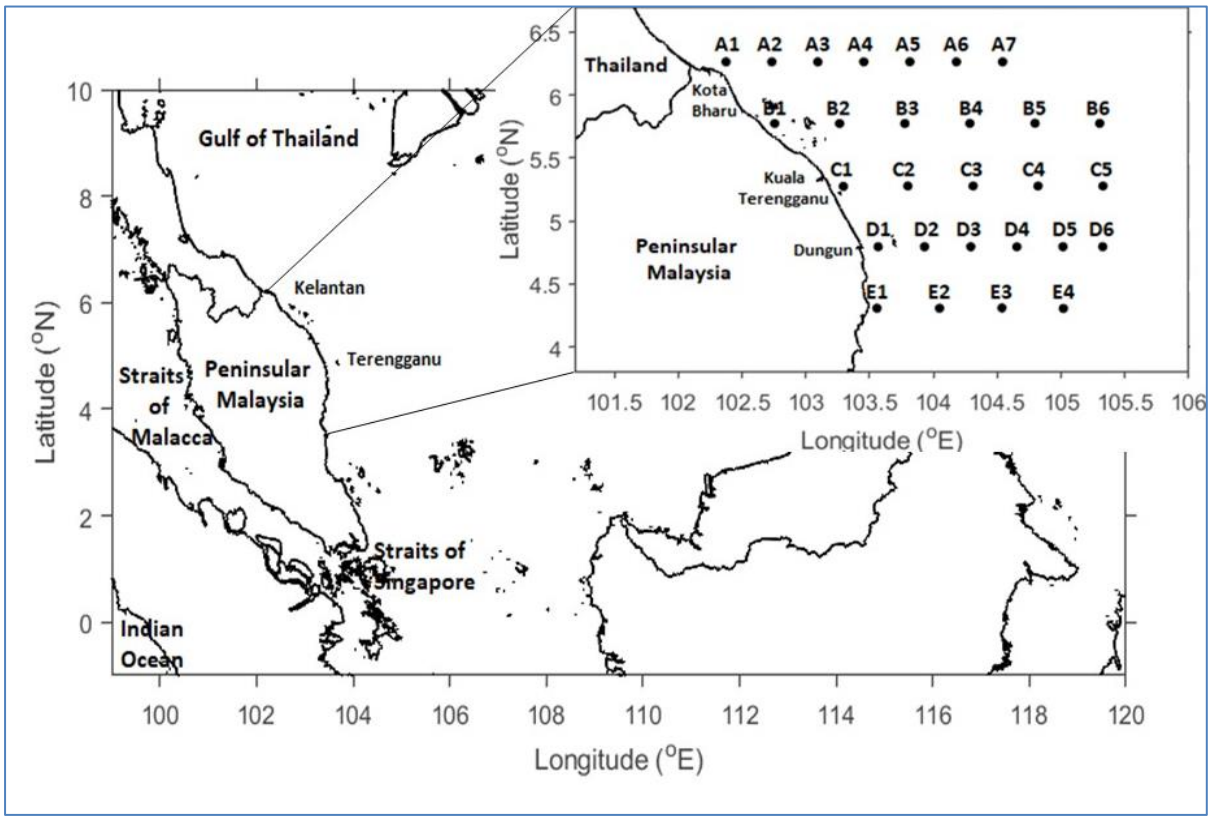


Figure 1. Map of the study area. Transect and stations are shown in the inset

Upwelling signature (Ekman transport)

Average wind data at 10 m height with a resolution of 0.125° × 0.125° within the period of study were obtained from the European Centre for Medium-range Weather Forecast (ECMWF) Interim Reanalysis (ERA-Interim) (https://www.ecmwf.int) and further analysis were conducted to obtain Ekman transport, as such, to provide knowledge on the upwelling-driven mechanism. The Ekman transport are calculated by the mean of:

$$Q_x = \frac{\rho_a C_d (W_x{}^2 + W_y{}^2)^{1/2} W_x}{\rho_w f} \quad (1)$$

$$Q_y = -\frac{\rho_a C_d (W_x{}^2 + W_y{}^2)^{1/2} W_y}{\rho_w f} \quad (2)$$

where ρ_a is the density of air (1.22 kg m^{-3}), C_d is the dimensionless drag coefficient (1.3×10^{-3}), W is the wind speed at 10m height, ρ_w is the density of seawater (1025 kg m^{-3}), $f = 2\Omega sin\theta$ is the Coriolis parameter, where Ω is the Earth's angular velocity (7.292×10^{-5} rad s^{-1}), θ is the latitude, x and y subscripts are zonal and meridional components, respectively.

Laboratory analysis of phosphate, silicate, DOC and chlorophyll-a

Dissolved phosphate and silicate were analysed based on standard colorimetric methods described by EPA [29] using a SmartChem 200 discrete autoanalyzer (AMS Alliance) and detected spectrophotometrically as a colored complex. DOC analyses were made by high temperature catalytic oxidation (HTCO) using a Shimadzu TOC-L analyser (furnace temperature: 680 ± 10 ºC, catalyst: 0.5% Pt/Al_2O_3) coupled to a non-dispersive infrared (NDIR) detector for CO_2 analysis arising from DOC oxidation [30, 31]. Before analysis, acidification and sparging of samples was carried out to eliminate inorganic C by adding 10% HCl to a sample and sparged with high purity N_2 to eliminate all inorganic C. DOC concentration was determined by subtracting system blank area from the average peak area and dividing by the slope of the calibration curve [32]. The certified reference material (CRM) of deep seawater from the Sargasso Sea was obtained from the Hansell's laboratory, University of Miami, in order to monitor analytical accuracy. The DOC concentrations obtained for the CRM were between 45-52 µM (mean 47 ± 3 µM, n=8) after blank correction, close to the agreed value of the CRM (43-44 µM). The chl-a was determined using a Shimadzu 1201 spectrophotometer after 20-24 hours extraction into 90% acetone following Parsons et al. [33] method and calculated according to Jeffrey and Humphrey [34].

Results and Discussion

Horizontal distribution

The horizontal distributions of temperature, salinity, phosphate, silicate, DOC and chl-a in Kelantan and Terengganu waters are shown in Figure 2. The surface temperature is typically warm with very slight variation between 29.39 ºC and 30.70 ºC (mean 30.00 ± 0.29 ºC) (Figure 2a). The surface salinity ranged from 29.68 psu to 33.39 psu (mean 32.95 ± 0.76 psu) with lower salinity found in the northern compared to the southern area (Figure 2b). Among the nutrients measured, DOC recorded higher concentrations, ranging from 1.55 µM to 14.22 µM (mean 11.33 ± 2.44 µM) (Figure 2e), followed by silicate and phosphate where the concentration varied from 0.57 µM to 15.90 µM (mean 4.83 ± 3.80 µM) (Figure 2d) and 0.03 µM to 0.32 µM (mean 0.14 ± 0.08 µM) (Figure 2c), respectively. Additionally, the chl-a concentration in the study area varied from 0.01 μgL^{-1} to 0.14 μgL^{-1} (mean 0.06 ± 0.03 μgL^{-1}).

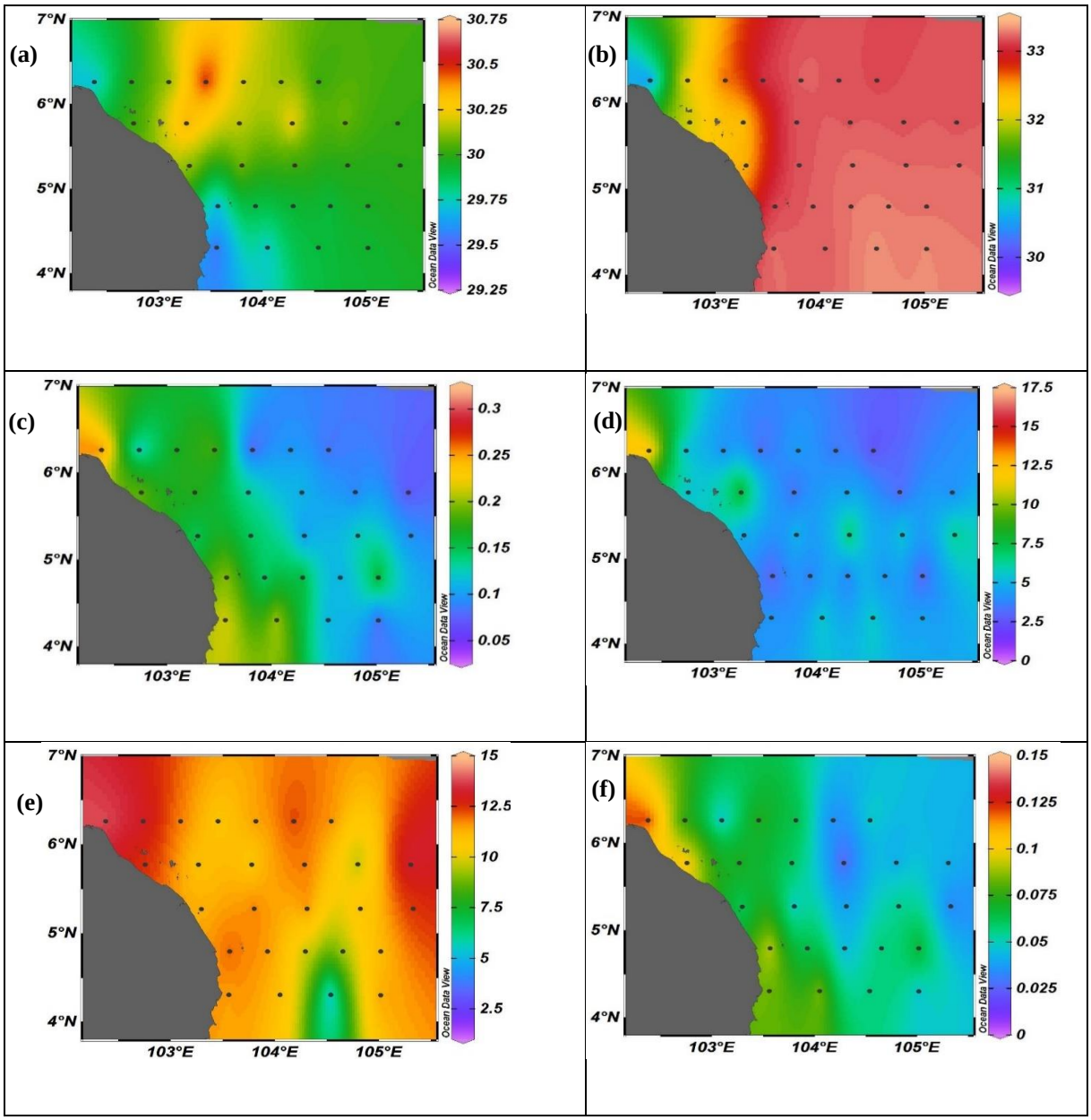


Figure 2. The horizontal distribution of (a) temperature (ºC); (b) salinity (psu); (c) phosphate (µM); (d) silicate (µM); (e) DOC (µM); (f) chl-a (µgL^{-1}) along Kelantan and Terengganu waters

In general, the observed nutrients demonstrated a higher concentration in the northern area and were identified associated with low salinity waters (6 – 6.5 latitude), probably attributed to the higher input from Kelantan River and/ or Gulf of Thailand (GoT), associated with the effluent from untreated domestic sewage, industrial activities and agriculture activities. The distribution of surface phosphate was somewhat similar to chl-a (Figures 2(c) and 2(f)), especially in the southern part until about 5°N. This pattern may be due to two possible reasons; (a) chl-a distribution was influenced by phosphate, where chl-a was found to be strongly correlated with phosphate (Figure 3 (R^2=0.4457; R=0.6676)) as compared to silicate (R^2=0.0554; R=0.2353) and DOC (R^2=0.008; R=0.089). The result

implying that phosphate is an important nutrient regulating the phytoplankton biomass, (b) higher phosphate and chl-a also appears in the area that was categorised with cooler water and high salinity, which was located at transect D near Dungun. This is probably due to the presence of coastal upwelling in this particular area. The coastal upwelling eventually transports high phosphate concentrations from the deeper layer (i.e. indicated by cool and high salinity water) to the surface, which encourages the phytoplankton growth, concurrently leading to the high chl-a concentrations.

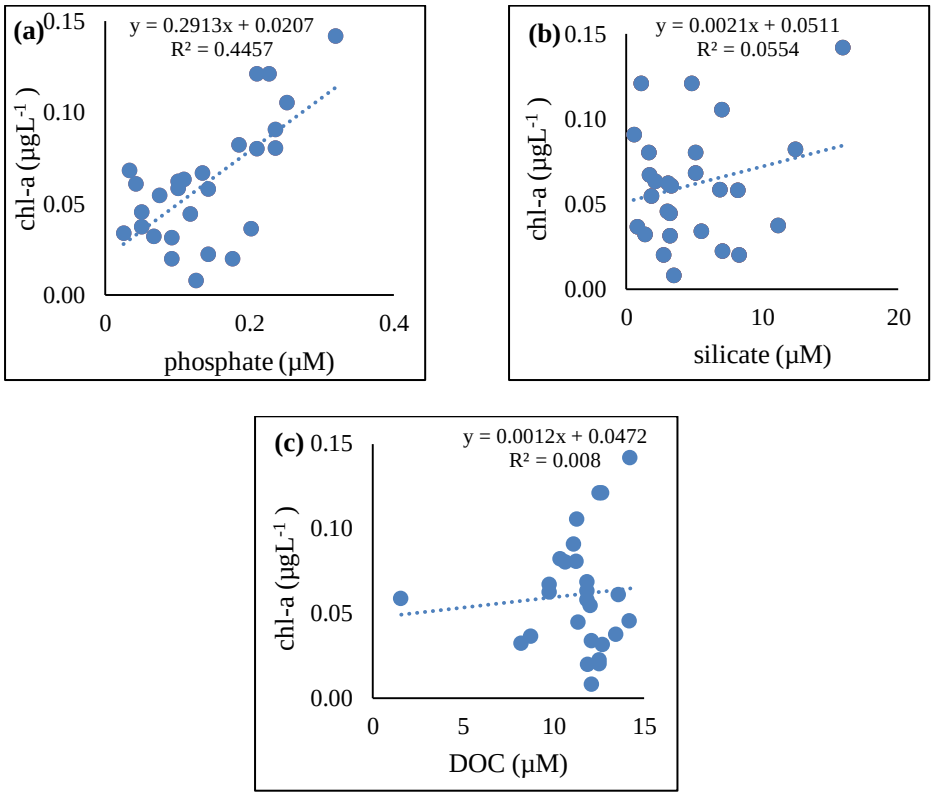


Figure 3. The relationship between chl-a and phosphate (a) silicate (b) and DOC (c) for horizontal distribution

Evidence of upwelling

The Ekman transport was calculated based on the surface wind data obtained from the ECMWF (Figure 4). Based on the figure, there is an evident of upwelling occurred along the ECPM as observed by previous studies [4-6]. The upwelling was driven by offshore Ekman transport that was roughly perpendicular to the coastline in the Terengganu waters from the southern part up to until about 5°N. Consequently, the coastal water was pushed away from the coast and replaced by the underneath cooler and saltier waters in the inshore region (Figure 2a and 2b). A contradictory situation occurred at the north of 5°N, where the Ekman transport in this region was orientated roughly parallel to the coast, which was less favourable for upwelling and hence pronounced slightly warmer and fresher water. Additionally, this region (i.e. north of 5°N) is located near to the GoT where it was predominantly influenced by the riverine runoff that carried warmer and fresher waters [6].

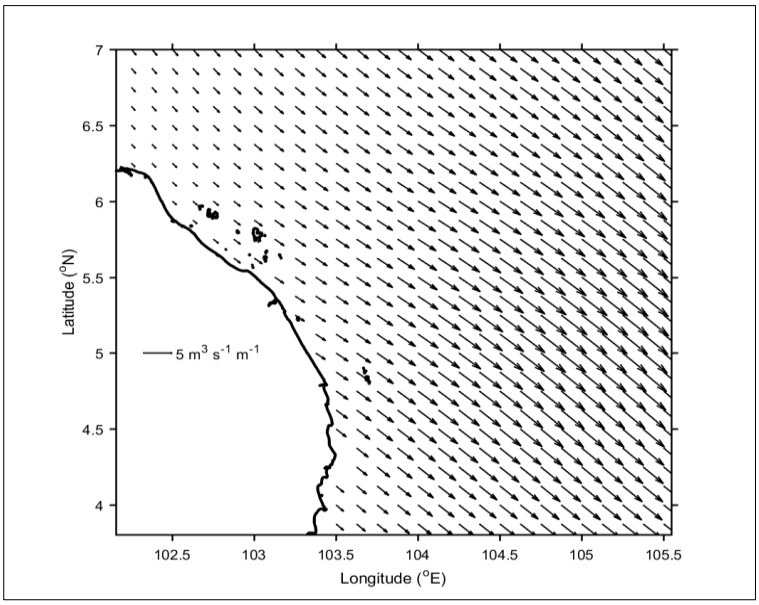
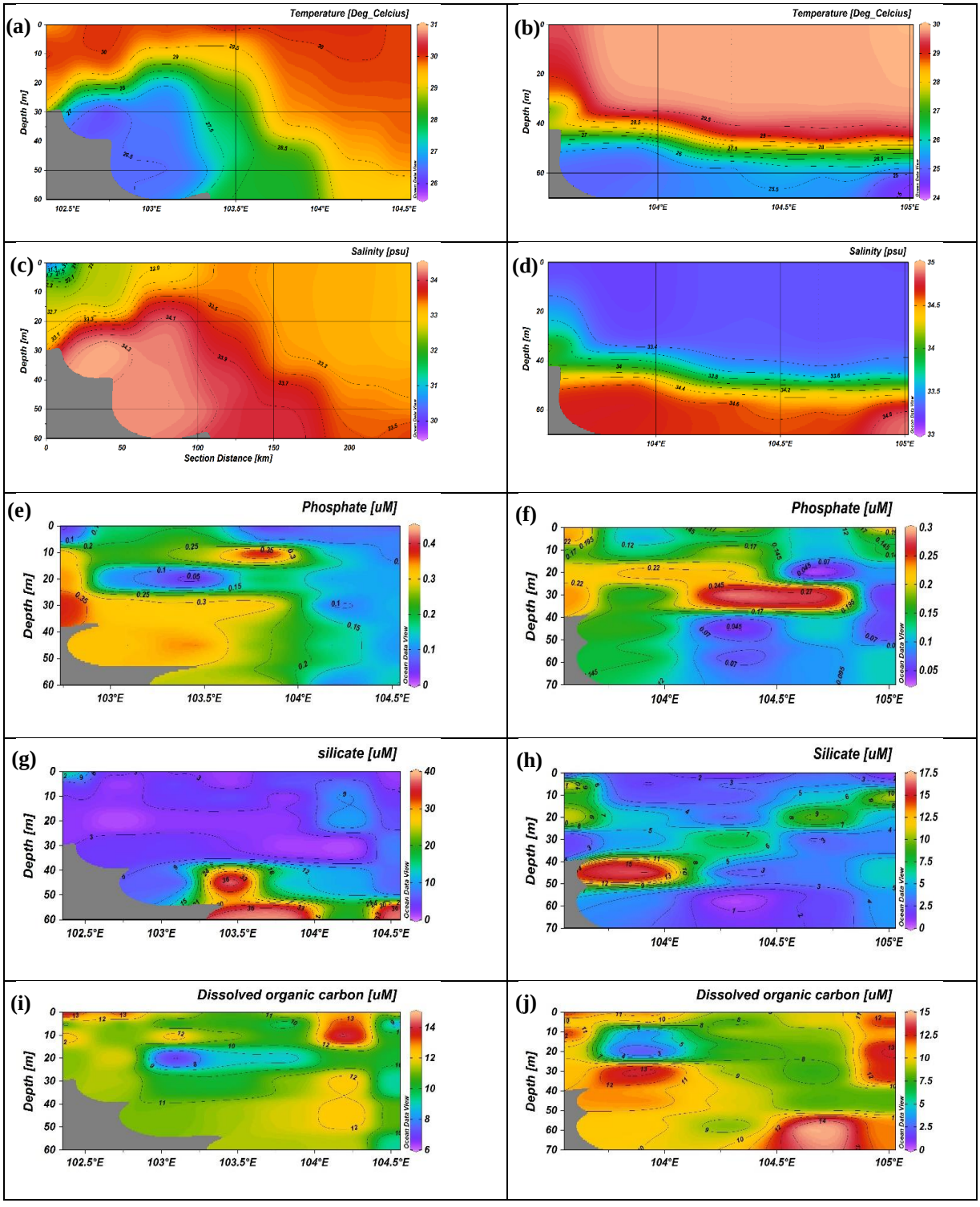


Figure 4. Ekman transport ($m^3 s^{-1} m^{-1}$) along the Terengganu and Kelantan waters

Vertical distribution

The two vertical profiles (transects A and D) for temperature, salinity, phosphate, silicate, DOC and chl-a are illustrated in Figure 5. Both transects showed variation in their spatial distribution in the water column. In transect A, the temperature ranged from 25.91 °C to 30.70 °C, with an average of 29.07 ± 1.19 ºC. Besides this, isotherm of 29.5 °C was shoaled until 10 m in the region of 103°E, and it bent downward as it approached the coast (Figure 5a). The salinity recorded was from 29.6 psu to 34.5 psu (33.38 ± 0.59 psu). The isohaline of 32.5 psu displayed the similar onshore shoaling tendency with the isotherm. There was a freshwater lens with warmer water (> 30 °C) and fresher water (31.1 psu – 33.3 psu) located at above 10 m into Transect A, which showed a typical feature of riverine outflow from the GoT as discussed in the previous section (horizontal distribution).This feature was also observed by Kok et al. [6], where freshwater lens had played an important role to restrict the water underneath from reaching the surface. Moreover, this region was less favourable for upwelling since the Ekman transport was roughly parallel to the coast (Figure 4), which also explained why the underneath water did not reach the surface.

Nutrients and chl-a in Transect A varied remarkably from the surface to the bottom. The vertical profile of phosphate (0.03 µM to 0.45 µM (mean 0.20 ± 0.12 µM)) in Figure 5e shows that the concentrations are fairly enriched in the area near the coast and depleted in areas beyond the continental shelf. The phenomenon of high phosphate concentration in the coastal area in Transect A indicates that the riverine input from Kelantan River estuary or GoT is the main source for phosphate. This is further supported by less saline water observed (Figure 5c) in the area as evidence of the riverine plume. In contrast to the pattern of phosphate, the vertical profiles of silicate (Figure 5g) displayed a maximum concentration close to the bottom, followed by a rapid decrease towards the surface, with concentrations varying between 1.07 µM to 39.00 µM (mean 7.32 ± 9.57 µM). In the case of DOC, there was no clear trend; DOC fluctuated with a concentration in the range of 6.80 µM to 14.30 µM (mean 11.01 ± 1.57 µM). The trend of chl-a (Figure 5k) was similar, with highest concentrations at the bottom water areas, especially at the middle of the transect. The chl-a concentrations in Transect A were in the range of 0.01 μgL^{-1} to 0.63 μgL^{-1} (mean 0.16 ± 0.16 μgL^{-1}).


(a)
Temperature [Deg_Celcius]
Depth [m]
102.5°E
103°E
103.5°E
104°E
104.5°E
(b)
Temperature [Deg_Celcius]
Depth [m]
104°E
104.5°E
105°E
(c)
Salinity [psu]
Depth [m]
Section Distance [km]
(d)
Salinity [psu]
Depth [m]
104°E
104.5°E
105°E
(e)
Phosphate [uM]
Depth [m]
103°E
103.5°E
104°E
104.5°E
(f)
Phosphate [uM]
Depth [m]
104°E
104.5°E
105°E
(g)
silicate [uM]
Depth [m]
102.5°E
103°E
103.5°E
104°E
104.5°E
(h)
Silicate [uM]
Depth [m]
104°E
104.5°E
105°E
(i)
Dissolved organic carbon [uM]
Depth [m]
102.5°E
103°E
103.5°E
104°E
104.5°E
(j)
Dissolved organic carbon [uM]
Depth [m]
104°E
104.5°E
105°E

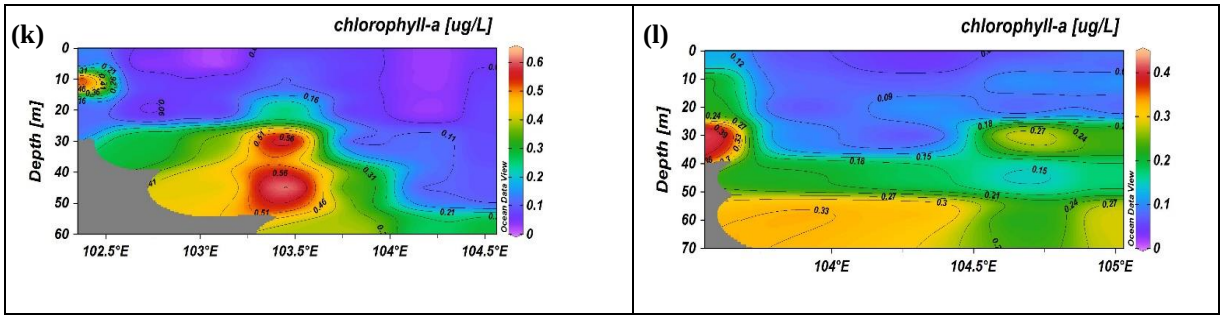


Figure 5. Cross-sectional for transect A; (a) temperature (c) salinity (e) phosphate (g) silicate (i) DOC (k) chl-a and transect D; (b) temperature (d) salinity (f) phosphate (h) silicate (j) DOC (l) chl-a

For Transect D, the temperature varied from 24.95 ºC to 29.95 ºC, with an average of 28.85 ± 1.64 ºC, where the isotherm of 29.5 °C was shoaled towards the coast and surface, which typically showed the classical sign of upwelling. Astonishingly, cross-sectional distribution of salinity (33.22 psu - 34.91 psu (mean 33.59 ± 0.51 psu)) showed that the isohaline of 33.4 psu was only shoaled until about 13 m, which was probably due to the sparse spatial coverage or due to the small amount of freshwater discharge from the Dungun River, which was indicated by the freshwater lens floating between surface and 30 m into the region between the coastal area and 104.2°E, which restricted isohaline from reaching the surface. Both features of abnormal temperature and salinity in this transect indicate the existence of coastal upwelling in this study area. With the exception of DOC, nutrient concentrations decreased with distance for all depths, with high concentrations at the coastal and low concentrations at offshore stations. The results are consistent with the observation at the horizontal water distribution. Concentration of phosphate ranged from 0.025 µM to 0.294 µM (mean 0.149 ± 0.07 µM). A maximum was found between 30 m and 40 m depth in the region between 104.2°E and 104.8°E and was not rigidly predictable. In contrast, silicate recorded the highest concentration at 40 m to 50 m, with a wide range of 0.35 µM to 16.79 µM, with a mean of 4.75 µM ± 3.90 µM. For DOC, patchy trends of high and low concentrations were found in this transect with values ranging from 1.81 µM to 14.91 µM (mean 9.83 ± 2.83 µM). Additionally, concentrations of chl-a in this transect were found to vary between 0.03 μgL^{-1} and 0.40 μgL^{-1} (mean 0.15 ± 0.10 μgL^{-1}).

The relationship between nutrients and chl-a is presented in Figure 6. For both transects, no correlation occurred between nutrients and chl-a. Supposedly, high nutrients are expected to increase the phytoplankton growth (i.e. high chl-a concentration) and *vice versa* [35-37]. Polat and Terbiyik [31] found that chl-a increased with increasing nitrate and silicate, and enhanced phytoplankton growth in the North-eastern Mediterranean Sea. Similarly, chl-a concentrations were strongly associated with the high silicate concentrations in in the southwest of East China Sea, where high chl-a concentrations were observed at the area that contained high concentrations of silicate, and these resulted in diatoms or chain-forming phytoplankton capable of more rapid growth [36, 37]. However, this was not observed in the present study, probably due to the consumption or exhaustion of nutrients for the growth of phytoplankton. This is consistent with Kang et al. [38], who found that nutrients in the deeper water were quickly absorbed by phytoplankton and caused nutrient concentrations to rapidly decrease.

The nutrient distributions in this present study during the upwelling event might, not be so obvious as compared to the typical coastal upwelling systems such as Oregon upwelling [39], Peru upwelling [40] and California upwelling [41] which recorded high concentrations of nutrients and chl-a. It is difficult to explain as this is a unique phenomenon and it is rarely found, because upwelling had been synonymous with triggering nutrients to the surface layer. In this study, there was an increase in nutrients, especially phosphate near the shore of Transect D (Dungun), which corresponds with lower temperature (27.0 ^{o}C - 29.5 ^{o}C) and high salinity (33.4 psu - 34.0 psu). Higher concentrations of chl-a (0.2 μgL^{-1} - 0.4 μgL^{-1}) were also recorded at this particular section. Kok et al. [6] revealed that upwelling intensity increased from June and reached its peak in August before declining in September. Thus,

the present study suggests that the low strength of the upwelling could be due to the sampling period which was carried out in early July 2017, as this period was considered as a preliminary stage of upwelling.

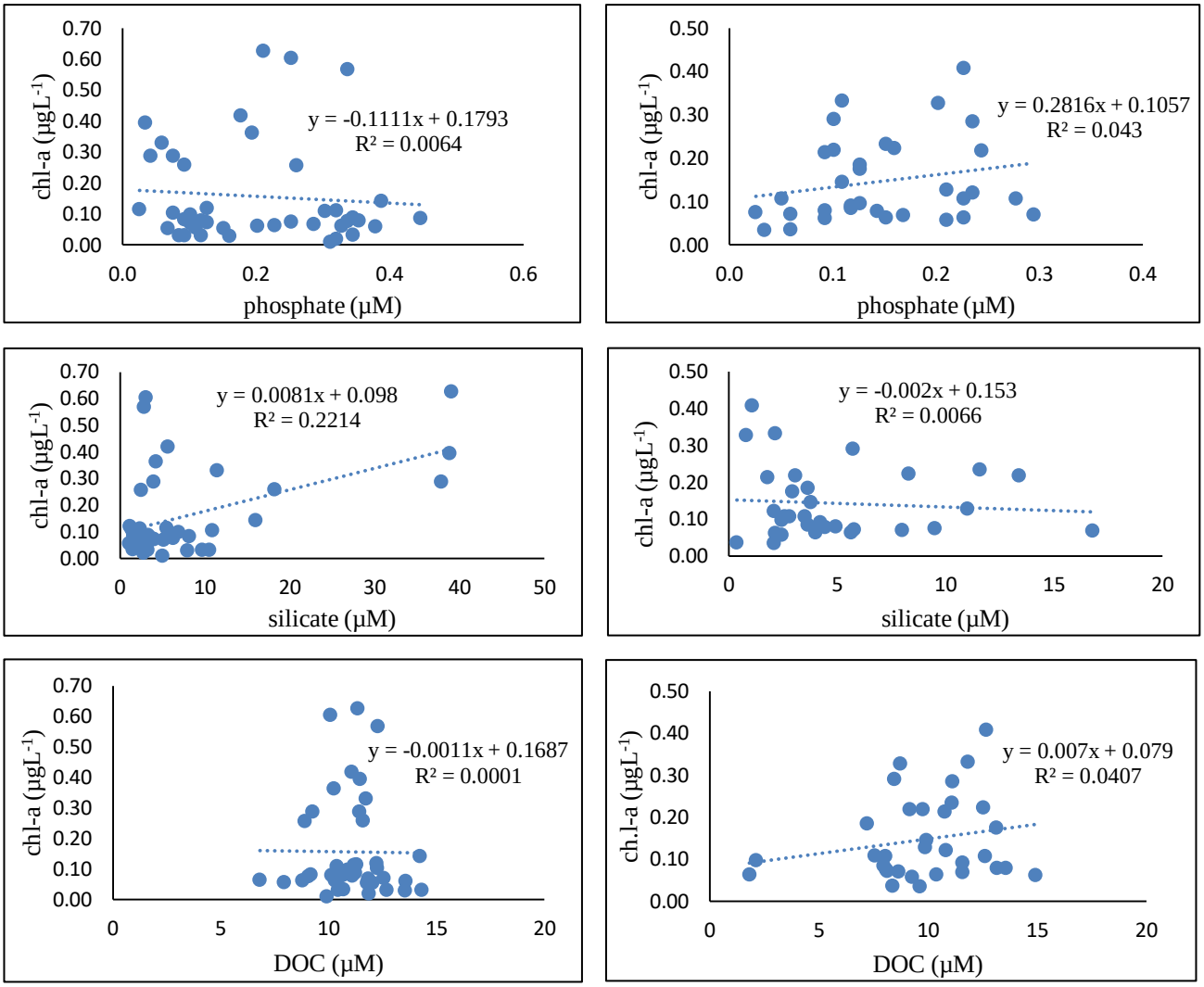


Figure 6. The relationship between chl-a and nutrients for vertical distribution

It is important to compare the nutrients and chl-a concentrations obtained in the present study with other upwelling systems nearby the ECPM. The nutrients and chl-a information for these upwelling areas are listed in Table 1. No comparisons could be made for DOC concentrations as other studies did not measure this parameter. In general, phosphate concentrations in the study area were 2 to 3 times lower than other upwelling regions. Meanwhile, apart from the Vietnamese coast, silicate concentration in this present study was also recorded to be lower as compared to other upwelling regions nearby. This is probably due to the consumption of nutrients by phytoplankton during the early stages of the upwelling event, thereby leading to low levels of the nutrients. The chl-a values were relatively low in comparison to values reported by others, but slightly higher than those found in Southern Makassar Strait, Indonesia [26]. The strong intensity of upwelling events could be the reason that contributes to the high nutrients

and chl-a in the Vietnamese coast [42], Changjiang [43] and East China Sea [44]. For example, Dipper et al. [42] found that the clockwise rotation and stretching deformation-induced upwelling due to the circulation pattern, were the main causes that contributed to the maximum chl-a and nutrient concentrations in the Vietnamese coast.

Table 1. Comparison of nutrients and chl-a among coastal upwelling system

Upwelling region	**Phosphate (µM)**	**Silicate (µM)**	**Chl-a (μgL^{-1})**	**Reference**
Vietnamese coast, Vietnam	0.0-1.4	0.0-24.7	0.0-1.6	[42]
Changjiang, China	0.4-1.4	15-100	0.1-19.5	[43]
East China Sea, China	0.2-0.8	2-50	n.a	[44]
Southern Taiwan Strait, Taiwan	<0.5	n.a	1-8.51	[27]
Southern Makassar Strait, Indonesia	0.001-1.89	0.157-54.53	0.1-0.44	[26]
ECPM	0.03 - 0.45	0.35 - 39.00	0.01-0.63	Present study

n.a = not available

Additionally, the deeper water in the East China Sea is able to uplift until about a depth of around 10 m, and tends to bring up high nutrient-rich water to the surface, hence contributing to the high phytoplankton biomass [44]. Despite low nutrient values, the Southern Taiwan Strait [27] contained higher chl-a concentration as compared to this present study. Hu et al. [27] indicated that upwelling events did not always bring the high concentration of nutrients, and suggested that the high rate of phytoplankton growth was due to suitable conditions during the upwelling process, such as the suitability of N/P ratio, temperature and light intensity. Similarly, Rosdiana et al. [26] also found out about the low nutrient events with high chl-a during upwelling and suggested that the phytoplankton biomass controlled nutrients in this short term. Thus, there were several different factors that controlled nutrients and chl-a in the upwelling region, depending on biological and physical processes, ecosystem types and basin scale.

Conclusion

Horizontal surface distribution has demonstrated that the concentrations of nutrients were higher at the coastal waters in comparison to offshore areas, which indicates that the freshwater inputs are the major sources of nutrients in the coastal areas. Additionally, water from the GoT also played a major role as a contributor of nutrients to the northern part of the ECPM. Vertical profiling showed the normal condition, where high concentrations of nutrients were recorded in the deeper layer compared to the surface water. An upwelling event which was characterised by cool and high salinity water at the surface occurred near Dungun. However, nutrients did not follow the same trend in response to coastal upwelling events i.e. high concentrations that were supposedly recorded at the surface water. This is probably due to the weak upwelling intensity which was unable to draw up nutrients from the deeper layer to the surface layer, while the sampling was performed during the early stages of the upwelling event. The data obtained was based on a single sampling with a limited number of stations, and depth profiling, to reveal the distribution of nutrients during the coastal upwelling event. However, this data is expected to provide preliminary results about physicals, chemicals and phytoplankton biomass during the early upwelling event.

Acknowledgements

This work was supported by the Higher Institution Centre of Excellence (HICoE) Research Grant (Vote No. 66928) and National Scientific Cruise Expedition (Vote No. 53209) awarded to the Institute of Oceanography and Environment, Universiti Malaysia Terengganu.

References

1. Wyrtki, K. (1961). Physical oceanography of the Southeast Asian waters. In: NAGA report Vol. 2. University of *California, La Jolla:* pp. 195.
2. Morgan, J. R. and Valencia, M. J. (1983). The natural environmental setting. In: Morgan, J. R. and Valencia, M.J. (Eds.), Atlas for Marine Policy in Southeast Asian Seas. University of California Press, California: pp. 4-17.
3. Taira, K., Saadon, M. N. B., Kitagawa, S. and Yanagi, T. (1996). Observation of temperature and velocity in the coastal water off Kuala Terengganu, Malaysia. *Journal of Oceanography*, 52: 251–257.
4. Akhir, M. F., Daryabor, F., Husain, M. L., Tangang, F. and Qiao, F. (2015). Evidence of upwelling along Peninsular Malaysia during southwest monsoon. *Open Journal of Marine Science*, 5: 273–279.
5. Kok, P. H., Fadzil, M., Akhir, M., Tangang, F. and Husain, M. L. (2017). Spatiotemporal trends in the southwest monsoon wind-driven upwelling in the southwestern part of the South China Sea. *PLos ONE*, 12(2): e0171979.
6. Kok, P. H., Akhir, M. F. and Tangang, F. T. (2015). Thermal frontal zone along the east coast of Peninsular Malaysia. *Continental Shelf Research*, 110: 1-15.
7. Suratman, S., Weston, K., Greenwood, N., Sivyer, D. B., Pearce, D. J. and Jickells, T. (2010). High frequency measurements of dissolved inorganic and organic nutrients using instrumented moorings in the southern and central North Sea. *Estuarine, Coastal and Shelf Science*, 87(4): 631-639.
8. Nausch, M. and Nausch, G. (2011). Dissolved phosphorus in the Baltic Sea - occurrence and relevance. *Journal of Marine Systems*, 87(1): 37-46.
9. Chen, Y. L. L., Chen, H. Y., Gong, G. C., Lin, Y. H., Jan, S. and Takahashi, M. (2004). Phytoplankton production during a summer coastal upwelling in the East China Sea. *Continental Shelf Research*, 24(12):1321-1338.
10. Lee Chen, Y. (2005). Spatial and seasonal variations of nitrate-based new production and primary production in the South China Sea. *Deep Sea Research Part I*, 52(2): 319-340.
11. Riegman, R., Colijn, F., Malschaert, J. F. P., Kloosterhuis, H. T. and Cadée, G. C. (1990). Assessment of growth rate limiting nutrients in the North Sea by the use of nutrient-uptake kinetics. *Netherlands Journal of Sea Research*, 26(1): 53-60.
12. Thingstad, T. F. and Rassoulzadegan, F. (1995). Nutrient limitations, microbial food webs, and biological C-pumps: Suggested interactions in a P-limited Mediterranean. *Marine Ecology Progress Series*, 117(1-3), 299-306.
13. Suratman, S. and Mohd Tahir, N. (2012). Concentrations of silicate compounds in surface water of Setiu Wetland: a preliminary study. *Journal of Sustainability Science and Management*, 7(2): 128-130.
14. Trommer, G., Leynaert, A., Klein, C., Naegelen, A. and Beker, B. (2013). Phytoplankton phosphorus limitation in a north Atlantic coastal ecosystem not predicted by nutrient load. *Journal of Plankton Research*, 35(6): 1207-1219.
15. D'Croz, L. and O'Dea, A. (2007). Variability in upwelling along the pacific shelf of Panama and implications for the distribution of nutrients and chlorophyll. *Estuarine, Coastal and Shelf Science*, 73(1–2): 325-340.
16. Cravo, A., Relvas, P., Cardeira, S. and Rita, F. (2013). Nutrient and chlorophyll a transports during an upwelling event in the NW margin of the Gulf of Cadiz. *Journal of Marine Systems*, 128: 208-221.
17. Braga, E. S., Chiozzini, V. C., Berbel, G. B. B., Maluf, J. C. C., Aguiar, V. M. C., Charo, M., Molina, D., Romero, S. I. and Eichler, B. B. (2008). Nutrient distributions over the southwestern south Atlantic continental shelf from Mar del Plata (Argentina) to Itajaí (Brazil): winter–summer aspects. *Continental Shelf Research*, 28(13): 1649-1661.
18. Lehmann, A. and Myrberg, K. (2008). Upwelling in the Baltic Sea - A review. *Journal of Marine Systems*, 74: S3-12.
19. Mann, K. H. and Lazier, J. R. N. (2006). Dynamics of marine ecosystems (3rd ed.). Massachusetts: Blackwell Publishing, pp. 163-215.
20. Zainol, Z. and Akhir, M. F. (2016). Coastal upwelling at Terengganu and Pahang coastal waters: Interaction of hydrography, current circulation and phytoplankton biomass. *Jurnal Teknologi*, 78(8): 11-27.

21. Duarte, C., R., Prego, R., López-López, S., Aguirre-Bahena, F. and Ospina-Alvarez, N. (2013). Annual patterns of nutrients and chlorophyll in a subtropical coastal lagoon under the upwelling influence (SW of Baja-California Peninsula). *Estuarine, Coastal and Shelf Science*, 120: 54-63.
22. Tremblay, J.-É., Raimbault, P., Garcia, N., Lansard, B., Babin, M. and Gagnon, J. (2014). Impact of river discharge, upwelling and vertical mixing on the nutrient loading and productivity of the Canadian Beaufort Shelf. *Biogeosciences*, 10(10): 16675-16712
23. Benavides, M., Santana-Falcón, Y., Wasmund, N. and Arístegui, J. (2014). Microbial uptake and regeneration of inorganic nitrogen off the coastal Namibian upwelling system. *Journal of Marine Systems*, 140: 123-129.
24. Clark, D. R., Miller, P. I., Malcolm, E., Woodward, S. and Rees, A. P. (2011). Inorganic nitrogen assimilation and regeneration in the coastal upwelling region of the Iberian Peninsula. *Limnology and Oceanography*, 56(3): 1689-1702.
25. Fuchs, R., Pinazo, C., Douillet, P., Fraysse, M., Grenz, C., Mangin, A. and Dupouy, C. (2013). Modelling ocean-lagoon interaction during upwelling processes in the South West of New Caledonia. *Estuarine, Coastal and Shelf Science*, 135: 5-17.
26. Rosdiana, A., Prartono, T., Atmadipoera, A.S. and Zuraida, R. (2017). Nutrient and chlorophyll-a distribution in Makassar upwelling region: From MAJAFLOX CRUISE 2015 A. IOP Conference Series. *Earth and Environmental Science*, 9(1): 3-10.
27. Hu, J., Lan, W., Huang, B., Chiang, K. P. and Hong, H. (2015). Low nutrient and high chlorophyll a coastal upwelling system – A case study in the southern Taiwan Strait. *Estuarine, Coastal and Shelf Science*, 166: 170-177.
28. Chen, C. T. A., Wang, B. J. and Hsing, L. Y. (2004). Upwelling and degree of nutrient consumption in Nanwan Bay, southern Taiwan. *Journal of Marine Science and Technology*, 12(5): 442-447.
29. Environment Protection Agency (1993). Method 365.1, revision 2.0: Determination of phosphorus by semi-automated colorimetry.
30. Suzuki, Y. and Sugimura, Y. (1988). A high-temperature catalytic oxidation method for the determination of non-volatile dissolved organic carbon in seawater by direct injection of a liquid sample. *Marine Chemistry*, 24: 105-131.
31. Cauwet, G. (1994). HTCO method for dissolved organic carbon analysis in seawater: influence of catalyst on blank estimation. *Marine Chemistry*, 47(1): 55-64.
32. Thomas, C., Cauwet, G. and Minster, J.-F. (1995). Dissolved organic carbon in the equatorial Atlantic Ocean. *Marine Chemistry*, 49(2–3): 155-169.
33. Parsons, T. R., Maita, T. and Lalli, C. M. (1984). Plant pigment. In: A manual of chemical and biological method for seawater analysis. Oxford: Pergamon Press: pp. 173.
34. Jeffrey, S. W. and Humphrey, G. F. (1975). New spectrophotometric equations for determining chlorophylls a, b, c1 and c2 in higher plants, algae and natural phytoplankton. *Biochemie und Physiologie der Pflanzen*, 167: 191-194.
35. Polat, S. and Terbiyik, T. (2013). Variations of planktonic chlorophyll- a in relation to environmental factors in a Mediterranean coastal system (Iskenderun Bay, Northeastern Mediterranean Sea). *Sains Malaysiana*, 42(10): 1493-1499.
36. Fu, D., Huang, Z., Zhang, Y., Pan, D., Ding, Y., Liu, D., Zhang, Y., Mao, Z. and Chen, J. (2015). Factors affecting spring bloom in the South of Cheju Island in the East China Sea. *Acta Oceanologica Sinica*, 34(3): 51-58.
37. Zhang, Y., Huang, Z., Fu, D., Tsou, J. Y., Jiang, T., Liang, X. S. and Lu, X. (2018). Monitoring of chlorophyll-a and sea surface silicate concentrations in the south part of Cheju Island in the East China sea using MODIS data. *International Journal of Applied Earth Observation and Geoinformation*, 67: 173-178.
38. Kang, J., Chen, X. and Zhang, M. (2014). The distribution of chlorophyll a and its influencing factors in different regions of the Bering Sea. *Acta Oceanologica Sinica*, 33(6): 112-119.
39. Geen, V. A., Takesue, R. K., Goddard, J., Takahashi, T., Barth, J. A. and Smith, R. L. (2000). Carbon and nutrient dynamics during coastal upwelling off Cape Blanco, Oregon. *Deep-Sea Research II*, 47: 975-1002.
40. Silva, N., Rojas, N. and Fedele, A. (2009). Water masses in the Humboldt current system: Properties, distribution, and the nitrate deficit as a chemical water mass tracer for equatorial subsurface water off Chile. *Deep-Sea Research II: Topical Studies in Oceanography*, 56(16): 992-1008.

41. Pennington, J. T. and Chavez, F. P. (2000). Seasonal fluctuations of temperature, salinity, nitrate, chlorophyll and primary production at station H3/M1 over 1989-1996 in Monterey Bay, California. *Deep Sea Research II*, 47: 947-973.
42. Dippner, J. W., Nguyen, K. V., Hein, H., Ohde, T. and Loick, N. (2007). Monsoon-induced upwelling off the Vietnamese coast. *Ocean Dynamics*, 57(1): 46-62.
43. Pei, S., Shen, Z. and Laws, E. A. (2009). Nutrient dynamics in the upwelling area of Changjiang (Yangtze River) estuary. *Journal of Coastal Research*, 253: 569-580.
44. Wang, B. and Wang, X. (2007). Chemical hydrography of coastal upwelling in the East China Sea. *Chinese Journal of Oceanology and Limnology*, 25(1): 16-26.

Malaysian Journal of Analytical Sciences, Vol 23 No 6 (2019): 1044 - 1053
DOI: https://doi.org/10.17576/mjas-2019-2306-12

MALAYSIAN JOURNAL OF ANALYTICAL SCIENCES
Published by The Malaysian Analytical Sciences Society
ISSN 1394 - 2506

DISTRIBUTION OF DISSOLVED ALUMINIUM (dAl) IN SEAWATER AT PULAU PERHENTIAN, TERENGGANU

(Taburan Aluminium Terlarut (dAl) di dalam Air Laut di Pulau Perhentian, Terengganu)

Khairul Nizam Mohamed[1,2]*, Edriana Godon[1], Shamsuddin Johan[1,2], Fairuza Shaheera Jaafar[1]

[1]*Department of Environmental Sciences, Faculty of Environmental Studies*
[2]*Environmental Forensic Research Unit, Faculty of Environmental Studies*
Universiti Putra Malaysia, 43400 UPM Serdang, Selangor, Malaysia.

**Corresponding author: k_nizam@upm.edu.my*

Received: 30 October 2018; Accepted: 26 September 2019

Abstract

The distribution of dissolved aluminum (dAl) was determined in seawater collected from Pulau Perhentian in November 2015 and April 2016, in order to identify a possible effect of the Northeast monsoon on dAl. Seawater sample profiles were collected at five different stations at 4-5 different depths. The concentration of dAl was determined directly by using cathodic stripping voltammetry on the hanging mercury drop electrode. This method was optimized in order to fit the determination of dAl concentration in seawater at this study area. During the measurements in November 2015, the concentration of dAl was found to be between 31.1 µg/L and 98.7 µg/L at that surface layer, and was found to be increasing with depth. On the other hand, the concentration ranged between 30.9 µg/L and 167.3 µg/L at surface layer and decreased with depth in April 2016. This indicates that the distribution of dAl throughout the water column was different between the two periods. It suggests that there was a possible source of Al from the surface sediment due to the high current turbulence during the Northeast monsoon season in this area, as mentioned by previous studies.

Keywords: dissolved aluminium, seawater, biological uptake, atmospheric input, monsoon

Abstrak

Taburan aluminium terlarut (dAl) telah ditentukan di dalam air laut yang diperolehi dari Pulau Perhentian pada November 2015 dan April 2016 bagi menentukan kebarangkalian kesan Monsun Timur laut ke atas dAl. Sampel air laut secara turus telah diambil di lima stesen yang berbeza pada 4-5 kedalaman yang berbeza. Kandungan kepekatannya telah ditentukan secara terus dengan menggunakan kaedah pelucutan voltametri pada hujung elektrod merkuri. Kaedah ini telah dioptimumkan bagi menentuukur kandungan kepekatan dAl di dalam air laut di kawasan ini. Kandungan kepekatan dAl adalah julat diantara 31.1-98.7 µg/L pada lapisan permukaan dan ianya meningkat dengan kedalaman air pada November 2015. Di sebaliknya pula, kandungan kepekatannya adalah diantara 30.9-167.3 µg/L pada lapisan permukaan dan berkurang dengan kedalaman air pada April 2016. Ini menunjukkan bahawa, taburan dAl di sepanjang turus air adalah berbeza di antara kedua-dua masa tersebut. Ini mencadangkan bahawa kemugkinan sumber Al adalah dari permukaan sedimen yang disebabkan oleh arus pergolakan yang tinggi semasa musim monsun Timur laut di kawasan ini, sepertimana yang telah dicadangkan sebelum ini.

Kata kunci: aluminium terlarut, air laut, pengambilan secara biologi, input atmosfera, monsun

Introduction

Aluminum (Al) is the third most abundant element in the earth's crust, and its hydrolysis states of $Al(OH)^{4-}$ and $Al(OH)_3^0$ are the dominant species in seawater (pH 8). Since Al is a particle-reactive element similar to Thorium

(Th) and Ferum (Fe), its concentration is low due to its ready removal from seawater. According to previous studies [1, 2], the behavior of Al in high-productivity coastal regions is not well characterized. Investigation of the sources of both dissolved and particulate Al in coastal waters is needed in order to understand their biogeochemistry process and for gaining an insight into the behavior of these Al fractions, in both surface waters and at depths.

Al is the best illustration of a trace metal with a scavenged-type distribution in the oceans. The major external input of aluminum is from the partial dissolution of atmospheric dust delivered to the surface ocean [1]. Trace metals are able to penetrate the food web in oceans through the direct intake of water or uptake by marine organisms [2]. According to Riley and Roth [3], dissolved aluminum (dAl) is an important tracer of atmospheric dust input in the oceans. The global pattern of atmospheric dust deposition is therefore a crucial component in models of global biogeochemical cycles, such as the global carbon cycle, which in turn, has a direct bearing on constraining future monsoon scenarios. In seawater, Al only exists in nanomolar concentrations [4]. The low concentration of dissolved Al in the oceans is the result of multiple biogeochemical processes.

Because of the low concentrations of dAl in seawater and the presence of a matrix of major ions such as Ca^{2+}, Mg^{2+}, Na^{+}, and Cl^{-}, at concentrations of six or seven orders of magnitude greater than the dAl concentrations, a method that provides for the removal of the seawater matrix and increases the concentration of the analyte such as dAl is highly desirable [5]. Furthermore, dAl concentrations in surface waters of the open ocean can provide reliable estimates of atmospheric dust fluxes in the world's oceans [6]. This relationship between dAl concentrations and atmospheric dust deposition is of interest in a time when global estimates of the delivery of bio-limiting elements such as iron via dust deposition to global surface waters are greatly needed. Thus, the ability to accurately measure dAl in seawater is very valuable, and therefore significant interest has been shown in understanding the marine biogeochemistry of Al in oceanic waters.

In Malaysia, most of the current trace metal studies focus on sediments and freshwater [7-11]. The latest study of Al in seawater was by Godon and Mohamed [12], that studied the distribution of dissolved Fe, Cu and Al at Pulau Perhentian, Terengganu by using pre-concentrate of seawater on Chelex-100 resin and Inductive Couple Plasma-Mass Spectrometry (ICP-MS) as detector. However, this method requires complex and expensive analytical equipment, thereby limiting their potential application. Therefore, a lack of data on dissolved Al in seawater samples might be due to the analytical method, where the sample itself (seawater) has a high metric and contains higher salt levels, which is something that is challenging to analyze directly. Therefore, a direct analysis of dissolved Al in seawater is needed in order to increase our understanding of its biogeochemistry cycle in our coastal water regions.

This study was proposed to determine levels of dissolved Al in seawater by optimizing the electrochemistry method. Due to the high salt content, this technique can be conducted directly in seawater, as the pre-concentration is performed, and followed by a potential scan towards more negative potentials which helps in determining the cathodic (reductive) currents. The measurement will be done by using cathodic stripping voltammetry (CSV) preceded by adsorptive collection of complex ions with 1,2-dihydroxyanthraquinone-3-sulphonic acid (DASA), on the hanging mercury drop electrode. This method is based on the measurement of current response as a function of the potential applied to a voltammetric cell.

Pulau Perhentian, Terengganu is located on the southern side of the South China Sea and exposed to both the atmospheric and oceanic impacts of the monsoon. This region is strongly affected by severe weather during the northeast monsoon from November to March [13]. During this event, the near coastal areas of the continental shelves tend to have high concentrations of chlorophyll and phytoplankton [14]. The possible effect of Malaysia's climate to dAl distribution in this area is high because the monsoon brings heavy rain and wind which change considerably in strength owing to variations in the distribution of atmospheric pressure. Determination of dAl is needed in this area in order to understand the possible influence of the Northeast monsoon event on dust deposition, which links the nutrient sources to the surface water. Thus, we are conducting this study by measuring dAl and particulate Al through-out the water column at a few selected stations. Therefore, the objective of this study is to determine the concentration of dAl in seawater profiles during pre-monsoon and post-monsoon seasons.

Materials and Methods

Seawater samples (1 L) were collected at 5 different stations (Figure 1) in November 2015 and April 2016 at Pulau Perhentian, Terengganu. The profile samples were taken at 4-5 depths (depending on the water depth) at each station by using van dorm water sampler. *In-situ* parameters such as dissolved oxygen, pH, salinity, turbidity and conductivity were measured in each water sample by using YSI Pro Plus. Filtration on seawater sample was carried out through 0.45µM Whatman® glass microfiber (25 mm diameter, grade GF/F, Sigma- Aldrich, Buchs, Switzerland) fitted with a peristaltic pump, forcing the seawater from the bottle samplers. Samples for dAl analyses were acidified to pH 2 using ultra clean HCl (Romil UHP grade), and stored in Low Density Polyethylene (LDPE) bottles (Nalgene) which had been cleaned according to a standard protocol [15].

For the dAl concentration in seawater samples, we applied an adsorptive stripping voltammetry measurement by using 3,4-dihydroxy-2-anthraquinonsulfonic acid Na-salt (DASA) solution and N, N-bis-(2-hydroxyethyl)-2-aminoethansulfonic acid (BES) as a buffer [16]. A Metrohm Model VA 797 automated hanging mercury drop electrode (HDME) (Figure 2) was used throughout the analysis. The reference electrode was Ag/AgCl, saturated AgCl,

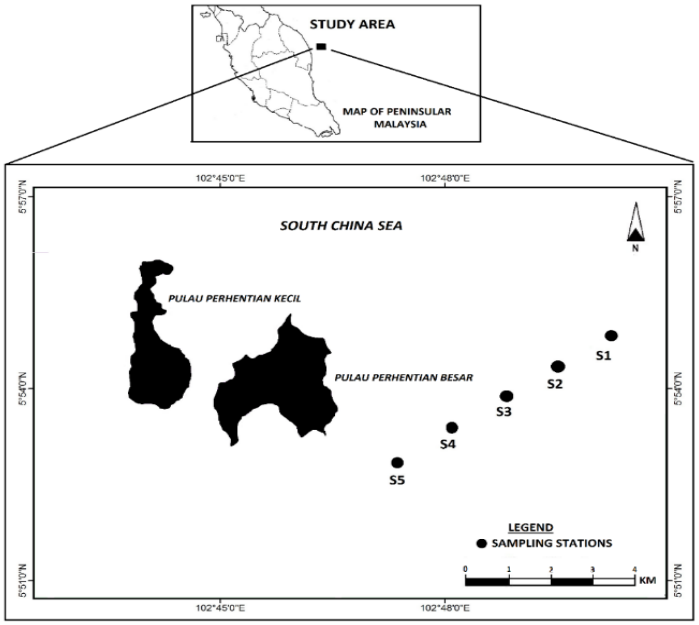


Figure 1. Location of our sampling stations at Pulau Perhentian, Terengganu, Malaysia during sampling activity in November 2015 and April 2016

A seawater sample (10 mL, pH 2) was pipetted into the voltammetry cell and its pH was adjusted to normal seawater pH by adding ammonium hydroxide. A 10 µL of the BES pH buffer was added, followed by a DASA stock solution at final concentration of 10^{-5} M. After deaeration of the solution with inert gas (99.999% pure nitrogen) for 5 minutes, the stirrer was started, and the potentiostat was set to -0.9 V. A new mercury drop was then extruded, which signified the beginning of the adsorption time. The stirrer was stopped after 60 s, and 10 s was allowed for the solution to become quiescent. The differential-pulse cathodic-stripping scan was then started, at a rate of 20 mVs^{-1}, with a pulse height of 25 mV and a pulse time of 0.1 s. The aluminium- DASA complex peak appeared at –0.3 V in the seawater sample (Figure 3). The aluminum concentration in the sample was then evaluated from a repeated measurement after adding standard Al, twice.

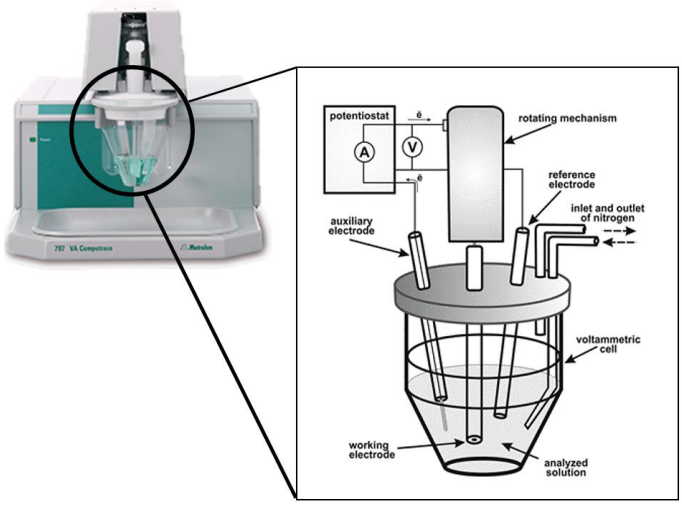


Figure 2. The voltammetry Metrohm Model VA 797 instrument used in dissolved aluminum (dAl) in seawater by using hanging mercury drop electrode (HMDE) as working electrode 1 M KCl, with a platinum wire as the counter electrode. The drop surface area of the HDME was 0.45 mm^2. A rotating PTFE rod was used to stir the solutions during the deposition step

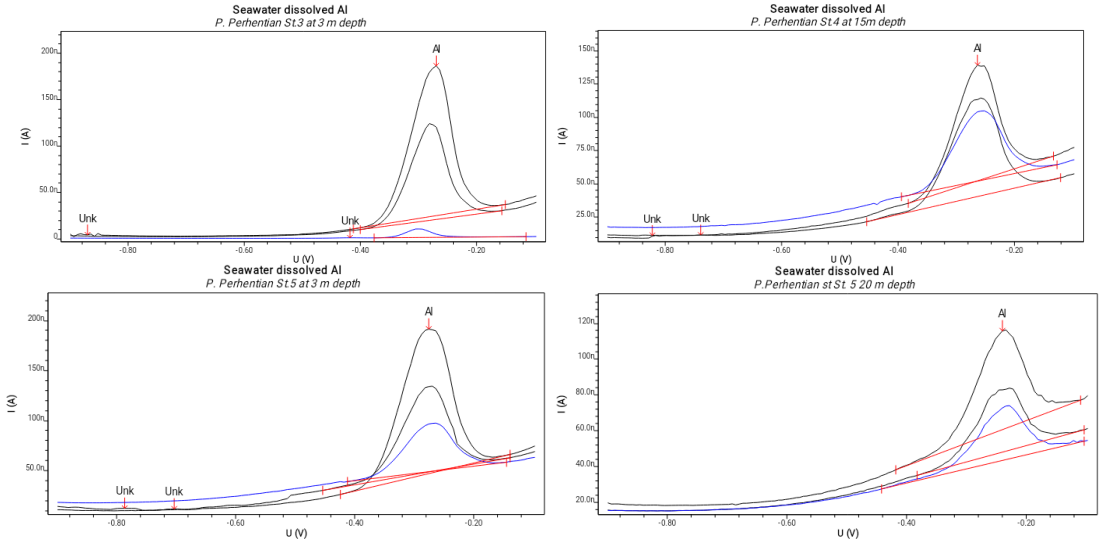


Figure 3. Voltammogram of Al peak under differential pulse mode from seawater sample from St. 3, St. 4 and St.5 at Pulau Perhentian, Terengganu. Voltammetric parameters: deposition time 120 s; deposition potential -1.1 V and start potential -0.15 V

Data for dAl was compared between both sampling periods (November 2015 and April 2016) in order to identify the possible influence of Northeast monsoon on dAl distribution on the surface and throughout the water column. Our sampling during November 2015 and April 2016 was represented as pre-monsoon and post-monsoon events, respectively.

Results nd Discussion

The concentrations of dAl in seawater were determined by cathodic stripping voltammetry, preceded by adsorptive collection of complex ions with 1,2-dihydroxyanthraquinone-3-sulphonic acid (DASA) on the hanging mercury drop electrode. Complexation of aluminium by DASA is rapid and no waiting period or heating of the sample is required. Optimal conditions are achieved with a DASA concentration of 10^{-5} M, a solution pH of 7.1-7.3 and an adsorption potential of -0.3 V (Figure 2). The limit of detection is 1 nM aluminium for an adsorption time of 45 s. The total time needed, including 5 minutes deaeration and a standard addition, is 10-15 minutes per sample. No serious interferences were found, and hence we did not need to apply U.V. irradiation on our samples as recommended by Van den Berg et al. [16] for samples containing high levels of organic materials.

Our station was located at the south-east part of Pulau Perhentian, Terengganu which faces the South China Sea (Figure 1) in a transect line. Each station was located approximately 2.0 km away from another station, in order to identify the possible changes between stations. Table 1 below shows the physical parameters at each station during our sampling in April 2016.

Our data for in-situ parameters were plot throughout the column at each station, as shown in Figure 4 below. For temperature, the warmer seawater was recorded in November 2015 from surface to the bottom layer (Figure 2). It was between 29.8^{o}C - 29.9^{o}C during November 2015 and 29.3^{o}C - 29.4^{o}C during April 2016 at St. 1 (Table 1). The low-temperature value during April 2016 might have been due to the strong land sea breeze and precipitation, as suggested by Govindasamy [17]. We also recorded a higher conductivity condition at St. 1, St. 2 and St. 3 during April 2016 throughout the water column. It was between 22.9 mS/cm - 48.3 mS/cm during November 2015, and between 62.3 mS/cm - 63.4 mS/cm during April 2016 (Table 1) at St. 1.

The range of pH throughout the water column was 8.2-8.3 (Table 1, Figure 4) and 8.0–8.5 (Table 3, Figure 4a) during November 2015 and April 2016, respectively. This indicated that the pH throughout the water column in our study area had remained alkaline during both sampling occurrences. The difference in pH values during both the sampling periods was attributed to factors like removal of CO_2 by photosynthesis through bicarbonate degradation, reduction in salinity and temperature and decomposition of organic matter [18]. A slightly constant pH was recorded during November 2015, compared to April 2016 (Figure 4).

The seawater salinity throughout our study area during November 2015 was slightly low and generally consistent (31.0-32.0 ppt) (Table 1, Figure 4), as compared to the salinity during April 2016 (37.1-39.0 ppt) (Table 1, Figure 4). This could suggest that there was an input of saline water from the South China Sea, resulting from the Northeast monsoon.

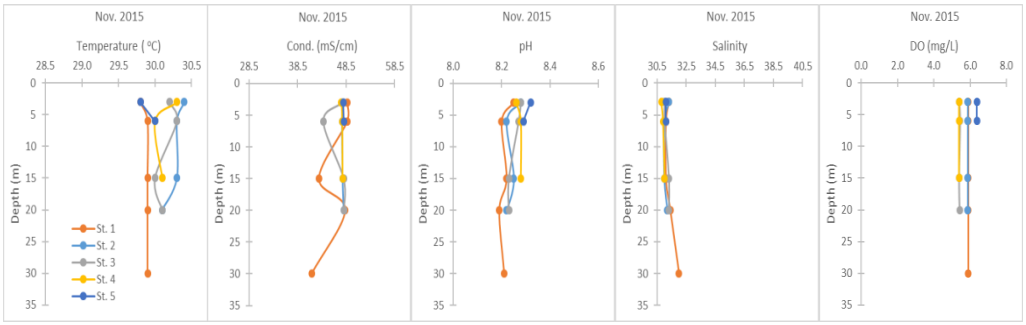
During the Northeast monsoon in 2016, a strong El Niño episode had occurred. This episode was among the top 3 strongest episodes since 1979. The duration of this monsoon was longer than usual, in agreement with the finding that monsoons generally last longer during El Niño episodes. It happened in line with a very strong El Niño episode [29]. The wind data from February 2016 review showed pressure level at 850-hPa, indicating a stronger than normal northerly flow over South China Sea, Indochina and Borneo, which converged over the southern South China Sea, Indian Ocean, and the southern Sarawak [29]. Interestingly, a high tide phenomenon also occurred during this month at the Peninsular East Coast, as reported by the Malaysian Meteorological Department and the local news. This condition would contribute to the significantly high readings on all the in-situ parameters on April 2016.

The distribution of dissolved oxygen was observed to be more consistent during November 2015, as compared to April 2016. The range of dissolved oxygen was 5.4 mg/L - 5.9 mg/L (Table 1, Figure 4) and 3.7 mg/L - 6.3 mg/L (Table 1, Figure 4) during November 2015 and April 2016, respectively. In aquatic systems, oxygenation results from an imbalance between the process of photosynthesis, degradation of organic matter [19], and physicochemical properties of water [10, 20].

Table 1. Physical parameters observed at stations during our sampling in November 2015 and April 2016 at Pulau Perhentian, Terengganu

Station (Depth) Coordinate	Sample Depth (m)	Temp. (°C)		Cond. (mS/cm)		pH		Salinity (ppt)		DO (mg/L)		dAl conc. (µg/L)	
		Nov. 15	Apr. 16	Nov. 15	Apr. 16	Nov. 15	Apr. 16	Nov. 15	Apr. 16	Nov. 15	Apr. 16	Nov. 15	Apr. 16
1 (45.0 m)	3	29.8	29.4	28.7	63.4	8.3	8.4	31.3	38.4	5.9	6.3	98.7±0.4	74.1±0.2
N 05º 54.791'	6	29.9	29.3	28.7	63.4	8.2	8.4	31.1	38.7	5.9	5.7	152.6±1.2	55.0±0.1
E 102º 50.563'	15	29.9	29.3	22.9	63.5	8.2	8.5	31.1	38.4	5.9	5.0	150.9±0.6	39.0±0.5
	20	29.9	29.4	48.3	63.2	8.2	8.3	31.4	38.5	5.9	3.7	208.4±0.9	40.7±0.0
	30	29.9	29.3	31.4	62.3	8.2	8.3	32.0	38.5	5.9	5.5	123.3±0.8	68.6±0.8
2 (40.2m)	3	30.4	30.1	47.9	63.0	8.3	8.2	31.3	38.5	5.9	5.0	92.4±0.4	32.7±0.2
N 05º 54.207'	6	30.3	30.2	47.7	63.5	8.2	8.4	31.0	38.3	5.9	3.5	117.5±0.4	23.0±0.2
E 102º 50.477'	15	30.3	29.9	47.8	63.3	8.3	8.3	31.0	39.0	5.9	3.8	256.3±2.9	13.1±0.5
	20	30.1	29.3	48.0	62.4	8.2	8.3	31.2	37.4	5.9	4.3	80.7±1.2	39.0±0.0
	30		28.9		62.1		8.5		38.3		4.4		22.0±0.4
3 (36.5m)	3	30.2	29.7	47.8	63.5	8.3	8.0	31.0	38.5	5.4	4.3	88.0±1.8	167.3±1.0
N 05º 53.410'	6	30.3	29.6	43.8	63.4	8.3	8.3	31.0	38.4	5.4	4.9	43.4±0.2	150.2±1.7
E 102º 49.525'	15	30.0	29.6	48.0	63.4	8.2	8.4	31.3	38.5	5.4	4.5	59.4±1.0	77.7±1.4
	20	30.1	29.7	48.0	63.3	8.2	8.4	31.3	38.5	5.4	4.5	112.1±0.6	34.0±0.0
	30		29.2		62.6		8.5		38.4		4.6		52.4±0.7
4 (33.30m)	3	33.3	29.9	47.5	63.5	8.3	8.3	30.8	38.5	5.4	6.1	16.2±0.4	50.8±0.3
N 05º 53.227'	6	33.0	29.9	47.7	63.3	8.3	8.5	30.9	38.3	5.4	4.6	22.7±0.1	47.4±0.3
E 102º 48.344'	15	33.1	30.0	47.8	63.0	8.3	8.4	31.0	38.2	5.4	4.7	23.5±0.2	65.6±0.8
	20		29.5		62.5		8.1		38.2		4.4		114.9±0.6
5 (29.1m)	3	29.8	30.1	47.9	63.3	8.3	8.2	31.1	38.4	6.4	4.4	31.1±0.5	31.0±0.3
N 05º 52.746'	6	29.0	30.0	48.0	63.3	8.3	8.5	31.1	38.4	6.4	5.8	32.4±0.8	31.7±0.0
E 102º 47.048'	15		29.7		63.4		8.4		38.5		4.5		37.2±0.2
	20		29.8		63.3		8.2		38.5		5.3		59.4±0.7

Based on our present *in-situ* data, it could be suggested that the water column condition at our study area was warmer and slightly stable (less turbulence) during November 2015, as compared to its condition in April 2016, probably due to the Northeast monsoon event, as suggested by Godon and Mohamed [12].



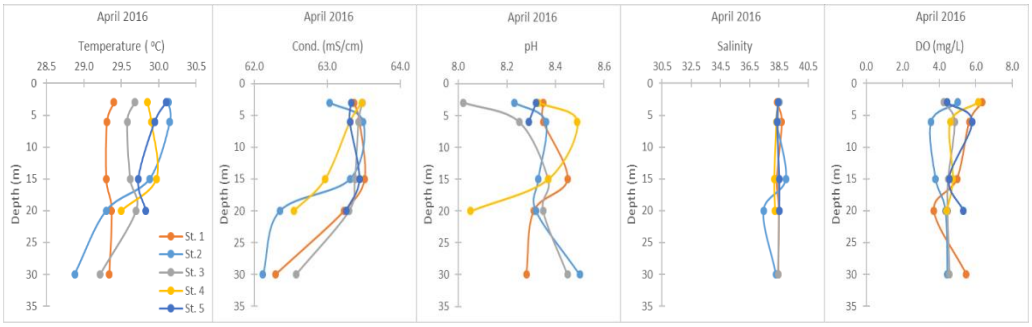


Figure 4. *In-situ* parameter recorded during our sampling activities at Pulau Perhentian, Terengganu in November 2015 and April 2016

Dissolved Aluminium (dAl) distribution

The concentration of dAl was measured throughout the water column at our study area. The concentrations of dAl during November 2015 and April 2016 are shown in Table 1.

During November 2015, dAl ranged between 31.1 µg/L - 98.7 µg/L at the surface layer (3-meters depth) (Table 1) before it was observed to increase with depth at most of the stations (Figure 5). Its concentration was between 59.4 µg/L - 256.3 µg/L at 15-meter depth (Table 1). On the other hand, dAl concentration ranged between 30.9 µg/L - 167.3 µg/L at the surface (Table 1) and 13.1 µg/L - 77.7 µg/L at 15-meter depth (Table 1) respectively, in April 2016. This shows that the distribution of dAl throughout the water column between both sampling periods differed significantly ($p>0.05$). During November 2015, its distribution depleted at the surface and increased with depth until the middle layer. On the other hand, its distribution was higher at surface and decreased with depth during April 2016 (Figure 5).

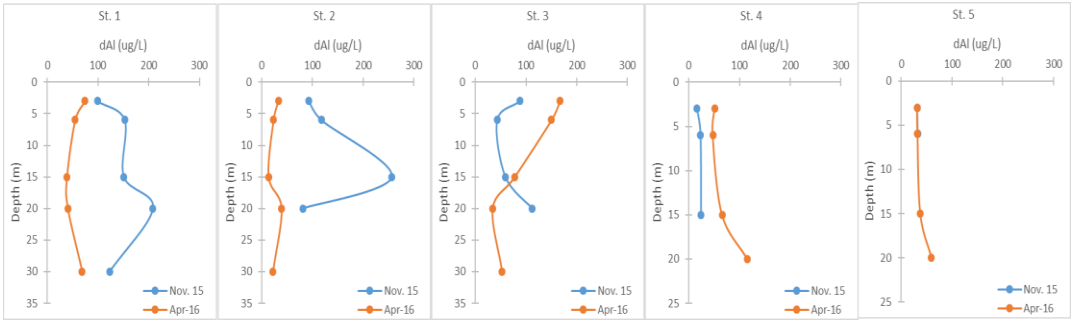


Figure 5. Distribution of dissolved aluminium (dAl) throughout the column at each station at Pulau Perhentian, Terengganu in November 2015 and April 2016

The distribution of dAl was higher in November 2015 as compared to April 2016, throughout the water column at St. 1 and St. 2 (Figure 5). The dAl concentration in November 2015 was about 1.3-19.5 times higher than that in April 2016 at these stations (St. 1 and St. 2). The highest concentration of dAl at 15 m depth (St. 2) during November (Figure 5) was an outlier due to it being unaffected by any in-situ parameters. On the other hand, a significantly different ($p>0.05$) distribution was recorded at St. 4 and St. 5, where its concentration was higher in April 2016 compared to that in November 2015. The concentration of dAl was about 0.3-3.3 times higher in April 2016. This indicated that a possibly huge input of Al, probably from surface sediment, had enriched its dissolved concentration throughout the water columns at St. 1 and St. 2 (Figure 5) in November 2015.

The increasing concentration of trace metals was due to the high current turbulence during the Northeast monsoon season (October-March), which led to a resuspension of surface sediment. A strong current velocity had released

some metals from suspended particulate matter in the water column [8]. However, this input of Al from bottom sediments was less at stations near to the island, resulting in the low and slightly constant dAl concentrations throughout the water columns at St. 4 and St. 5 (Figure 5). According to Hydes [21], dAl is supplied from rivers and the atmosphere to the ocean surface. However, because riverine dAl is rapidly removed within estuaries, its signal in the ocean surface transported by advection-diffusion processes from coastal areas cannot be recognized. Based on our present data, there was a small difference in concentration of dAl at the surface layer (3 m depth) during both periods (Figure 5). There might have been less input from the partial dissolution of Al from atmospheric mineral dust into this area, which indicated that dissolution of aerosol aluminum was a less important source of dAl to these waters.

Our present data was in line with our previous study at the area [12]. During the previous study (October 2014 and April 2015), we also recorded a similar distribution pattern of dAl throughout the water column (Figure 6). The concentration of dAl at the surface layer was low, and at a wider range in the middle depth regions, during October 2014. However, during April 2015 (Figure 6), its concentration was higher at surface layer and slightly constant in the middle depth. This could be the cause of the additional input of dAl into surface layer during April, and different distributions of dAl throughout the water columns during both sampling periods.

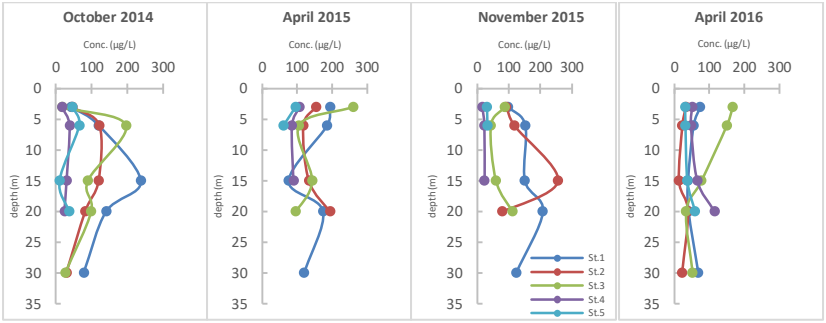


Figure 6. Distribution of dAl throughout water column at our study area during November 2015 and April 2016. The distribution of dAl during October 2014 and April 2015 [12]

A low concentration of dAl at the surface layer and high concentration in the middle of the water column during November 2015 (Figure 6) is due to the active biological uptake by phytoplankton at surface layer and remineralization in deeper layer. Biological processes in the coastal ocean can remove dAl. Plankton incorporate significant quantities of aluminum into biological tissue [3, 22-25]. Previously, it was suggested that the dAl concentration in the oceans is controlled by biological activity and the aluminum cycles in the oceans are linked through the activity of diatoms [26]. Lewin [27] suggested that Al and Fe are necessary for the formation of diatom frustules because the adsorption of these cations onto the silica frustules renders them resistant to dissolution. According to the current study by Ramjam and Mohamed [28], they discovered that about 70% of the population was composed of phytoplankton and 30% of zooplankton. The phytoplankton composition mostly consisted of diatoms, followed by cyanobacteria and dinoflagellates. This suggests that during this period in our study area, the dAl was taken up from near-surface waters by diatoms during growth, and was then returned to the solution as dead organisms which decayed and sank through the water columns.

The highest dAl concentration was recorded at St. 3 (167.3 µg/L; Table 1) at the surface layer during April 2016. This station is far away from the island, compared to St. 4 and St. 5 (Figure 1), which have dAl concentrations of 50.8 µg/L and 30.9 µg/L at the surface (Table 1), respectively. Interestingly, the highest dAl concentration was also recorded at the same station previously in April 2015 [12]. Based on *in-situ* parameters, St. 3 had a lower pH during April 2016 (pH=8.0, Table 1). According to Paquin [2], Al can exist as organic complexes in natural waters and it is thought to be dominated largely by the dissolved inorganic hydrolysis species $Al(OH)_2^+$, $Al(OH)_3^0$, and $Al(OH)_4^-$. However, at pH 8.2, that Al exists entirely in complexes with hydroxide ion, OH^-, forming the hydrolysis species. At low pH (< 4) it is dominated by the free Al^{3+} ion. At higher pH (≥ 7), the Al speciation is thought to be

dominated by Al $(OH)_4^-$ or aqueous $Al(OH)_3^0$ [30]. This indicates that pH plays an important role in dAl speciation distribution, and this might be an explanation for the highest dAl concentration at our St. 3.

Conclusion

Our present data on dAl distribution has suggested that there is a certain biological processes that occurs in the surface water to remove dAl from the water column. An active biological uptake of dAl by phytoplankton (diatoms) takes place during pre-monsoon seasons (November 2015) in the surface layer. This dAl is then returned to the water column in a deeper layer by the remineralization process. However, during post-monsoon seasons (April 2016), an additional input of Al from surface sediments results in the enrichment of the concentration of dAl in surface water. This indicates the influence of Northeast monsoons, which had resulted in high current turbulences and resuspension of surface sediments, which played an important role in the Al biogeochemistry distribution at Pulau Perhentian. However, further studies on dissolved Al and its speciation are needed to gain better information on its bioavailability to the primary producer in this region during both seasons.

Acknowledgment

Special thanks to Department of Marine Park Malaysia, Ministry of Natural Resources and Environment, and Department of Environmental Sciences, Faculty of Environmental Studies, Universiti Putra Malaysia, for assistance given during the analysis. This study was funded by the Ministry of Higher Education (07-02-14-1533FR).

References

1. Bruland K. W. and Lohan M. C. (2003). Controls of trace metals in seawater. Pergamon, *Oxford*. 23-47.
2. Paquin, P. R., Santore, R. C., Wu, K. B., Kavvadas, C. D. and Di Toro, D. M. (2003). The biotic ligand model: A model of the acute toxicity of metals to aquatic life. *Environment Science Policy*, 3: 175-182.
3. Riley, J. P. and Roth, I. (1971). The distribution of trace elements in species of phytoplankton grown in culture. *Journal of Marine Biological Association U.K.*, 51: 63-72.
4. Middag, R., De Baar, H. J. W., Laan, P. and Bakker, K. (2009). Dissolved aluminium and the silicon cycle in the Arctic Ocean. *Marine Chemistry*, 115 (3–4): 176-195.
5. Matthew P. M., Diane, M. M., Steven, C. C. and Mark W. W. (2009). A model of degradation and production of three pools of dissolved organic matter in an alpine lake. *Limnology and Oceanography*, 54(6): 2213-2227.
6. Measures, C. I. and Vink, S. (2000). The use of dissolved aluminum in surface waters to estimate dust deposition to ocean. *Global Biogeochemical Cycles*, 14(1): 317-327.
7. Koh, M. K., Suratman, S. and Mohd Tahir, N. (2015). Dissolved and suspended particulate metals in Setiu River Basin, Terengganu. *Sains Malaysiana*, 44(7): 957-964.
8. Adiana, G., Shazili, N.A.M., Marinah, M.A. and Bidai, J. (2013). Effects of northeast monsoon on trace metal distribution in the South China Sea of Peninsular Malaysia. *Environmental, Monitoring and Assessment*, 186: 421-431.
9. Yap, C. K., Chee, M. W., Shamarina, S., Edward, F. B., Chew, W. and Tan, S. G. (2011). Assessment of surface water quality in the Malaysian coastal waters by using multivariate analyses. *Sains Malaysiana*, 40(10): 1053-1064.
10. Ahmad, A. K., Musrifah, L. and Othman, M. S. (2009). Water quality and heavy metal concentrations in sediment of Sungai Kelantan, Kelantan, Malaysia: A Baseline study. *Sains Malaysiana*, 38(4): 435-442.
11. Yusof, N., Haraguchi, A., Hassan, M. A., Othman, M. R., Wakisaka, M. and Shirai, Y. (2009). Measuring organic carbon, nutrients and heavy metals in rivers receiving leachate from controlled and uncontrolled municipal solid waste (MSW) landfills. *Waste Management*, 29: 2666-2680.
12. Godon, E. and Mohamed, K. N. (2016). Distribution of dissolved Fe, Al and Cu at Perhentian Island, Terengganu. In-house Seminar of the Chemical Oceanography Laboratory, *Issue 1*, Vol. II: pp. 12-18.
13. Lim, J. T. and Azizan, A. S. (2004). Weather and Climate of Malaysia. University of Malaya Press.
14. Stewart C. R. (2008). Proline accumulation: Biochemical aspects. In: Paleg LG, Aspinall D (Eds), *Physiology and Biochemistry of Drought Resistance in Plants*. 243-251.
15. Achterberg, E. P. and Braungardt, C. (2001). Stripping voltammetry for the determination of trace metal speciation and in-situ measurements of trace metal distributions in marine waters. *Analytical Chemical Acta*, 400: 381-397.

16. Van den Berg, C. M. G., Buckley, P. J. M., Huang, Z. Q. and Nimmo, M. (1986). An electrochemical study of the speciation of copper, zinc and iron in two estuaries in England. *Estuarine and Shelf Science*, 22: 479-486.
17. Govindasamy, C., Kannan, L. and Azariah, J. (2000). Seasonal variation in physico- chemical properties and primary production in the coastal water biotopes of Coromandel Coast, India. *Journal Environment Biology*, 21: 1-7.
18. Rajasegar, M., Srinivasan, M. and Rajaram, R. (2003). Phytoplankton diversity associated with the shrimp farm development in Vellar estuary, south India. *Seaweed Research*, 22: 125-131.
19. Granier, A., Biron, P. and Lemoine, D. (2000). Water balance, transpiration and canopy conductance in two beech stands. *Agricultural and Forest Meteorology*, 100: 291-308.
20. Aston, S. R. (1980). Evaluation of the chemical forms of plutonium in seawater. *Marine Chemistry*, 8: 319-325.
21. Hydes, D. J. (1989). Seasonal variation in dissolved aluminium concentrations in coastal waters and biological limitation of the export of the riverine input of aluminium to the deep sea. *Continental Shelf Research*, 9: 919 - 929.
22. Martin, J. H. and Knauer, G. A. (1973). The elemental composition of plankton. *Geochimica Cosmochimica Acta*, 37: 1639-1653.
23. Bostrom, K., Burman, B., Ponter, C., Brandlof, S. and Alm, B. (1978). Geochemistry, minerology, and origin of the sediments in the Gulf of Bothnia. *Finnish Marine Research*, 224: 8-36.
24. Collier, R. and Edmond, J. (1984). The trace element geochemistry of marine biogenic particulate matter. *Progress in Oceanography*, 13: 113-199.
25. Noriki, S., Ishimori, N, Harada, K. and Tsunogai, S. (1985). Removal of trace metals from sea water during phytoplankton bloom as studied with sediment traps in Funka bay, Japan. *Marine Chemistry*, 17: 75-89.
26. Mackenzie, F. T., Stoffyn, M. and Wollast, R. (1978). Aluminum in seawater: control by biological activity. *Science*, 199: 680-682.
27. Lewin, J. C. (1961). The dissolution rate of silica from diatom walls. *Geochimica Cosmochimica Acta*, 21: 182-195.
28. Ramjam, J. and Mohamed, K. N. (2017). Determination of dissolved nutrients at Pulau Redang, Terengganu. Thesis of Bachelor in Environmental Science and Technology, Universiti Putra Malaysia.
29. Sang, Y. W., Adam, M. K. M., Fakaruddin, F. J., Saleh, F. Z., Chang, N. K., Yunus, F. and Abdullah, M. H. (2016). Review of The November 2015 – March 2016 Northeast Monsoon in Malaysia. *Malaysian Meteorological Department*, *MOSTI Research Publication* 4/2016
30. Turner, D. R., Whitfield, M. and Dickson, A. G. (1981). The equilibrium speciation of dissolved components in freshwater and seawater at 25 ºC and 1 atm pressure. *Geochimica Cosmochimica Acta*, 45: 855-881.

Malaysian Journal of Analytical Sciences, Vol 23 No 6 (2019): 1054 - 1066
DOI: https://doi.org/10.17576/mjas-2019-2306-13

MALAYSIAN JOURNAL OF ANALYTICAL SCIENCES
Published by The Malaysian Analytical Sciences Society
ISSN 1394 - 2506

RARE EARTH ELEMENTS DISTRIBUTION CHARACTERISTICS IN DISSOLVED AND PARTICULATE FRACTION, AND IN SEDIMENT OF BRUNEI BAY, BORNEO

(Ciri-Ciri Taburan Unsur Nadir Bumi dalam Fraksi Terlarut dan Partikulat, dan Sedimen di Teluk Brunei, Borneo)

Noor Azhar Mohd Shazili[1]*, Adiana Ghazali[2], Joseph Bidai[1]

[1]*Institute of Oceanography and Environment*
[2]*Faculty of Science and Marine Environment*
Universiti Malaysia Terengganu, 21030 Kuala Nerus, Terengganu, Malaysia

**Corresponding author: nazhar@umt.edu.my*

Received: 30 October 2018 ; Accepted: 26 September 2019

Abstract

The rare earth element (REE) concentrations in the Bay of Brunei were measured in the riverine, main bay area and the South China Sea. The abundance of REE in dissolved, particulate and sediment decreased from light REE (LREE) > medium REE (MREE) > heavy REE (HREE). The ΣREE concentrations were higher in January 2014 as compared to July 2013 in river and estuary sampling sites in all matrices, but more so in the particulate fraction. LREE was found to be highly enriched over HREE in sediment with La/Yb of 22.3 in July 2013 and 14.9 in January 2014. LREE enrichment occurred to a lesser degree in particulate fraction in seawater with La/Yb in the range of 11.7 to 12.8 in July 2013 and 8.4 to 10.6 in January 2014. In the dissolved fraction, LREE was enriched in July 2013 with La/Yb of 3.3 – 3.5 but in January 2014, during the wet Northeast Monsoon season, LREE was depleted with La/Yb of 0.48 in bottom water and 0.74 in surface water. Enhanced scavenging by the higher SPM content entering the bay during the wet season is thought to be the cause of the removal of LREE from the dissolved fraction.

Keywords: rare earth element, dissolved, particulate, sediment, La/Yb

Abstrak

Kepekatan unsur nadir bumi (REE) di Teluk Brunei diukur di kawasan sungai, kawasan teluk dan Laut China Selatan. Kepekatan REE dalam bentuk terlarut, partikulat dan sedimen berkurang dari REE ringan (LREE)> REE sederhana berat (MREE)> REE berat (HREE). Kepekatan ΣREE lebih tinggi pada bulan Januari 2014 berbanding pada bulan Julai 2013 di kawasan sungai dan muara di dalam semua jenis sampel tetapi lebih banyak lagi dalam pecahan partikulat. Didapati LREE sangat diperkaya dengan HREE dalam sedimen dengan La/Yb bernilai 22.3 pada bulan Julai 2013 dan 14.9 pada Januari 2014. Pengkayaan LREE berkurangan di dalam fraksi partikulat di dalam air laut dengan La/Yb bernilai antara 11.7 hingga 12.8 pada bulan Julai 2013 dan 8.4 hingga 10.6 pada bulan Januari 2014. Dalam fraksi terlarut, LREE diperkayakan pada Julai 2013 dengan La/Yb bernilai dari 3.3 - 3.5 tetapi pada Januari 2014, semasa musim Monson Timur Laut yang berkadar hujan yang tinggi, LREE rendah dengan nilai La/Yb 0.48 di air dasar dan 0.74 di permukaan air. Peningkatan penyingkiran oleh kandungan SPM yang lebih tinggi yang memasuki teluk semasa musim hujan dicadangkan sebagai penyebab penyingkiran LREE dari fraksi terlarut.

Kata kunci: unsur nadir bumi, terlarut, partikulat, sedimen, La/Yb

Introduction

The concentrations of rare earth elements (REEs) in seawater and sediment, and comparisons of their dissolved and particulate fractions, may be useful in pollution studies of other elements due to their strong binding to particulates and sediment. As they are tightly correlated with trace metals in sediments, changes in the relative proportions of metals to REEs may indicate anthropogenic influence. The heavy rare earth elements (HREEs) are strongly complex and more stable in solution form, thus facilitating comparisons between the proportions of light rare earth elements (LREEs) and HREEs as another tool for understanding the chemistry of REEs in seawater.

Comparisons of chondrite normalized data may reveal fractionation changes between the different environmental media as a result of variation in physico-chemical characteristics in the aquatic environment. Very little information is available in the context of the Malaysian marine environment. However, REEs have been studied in the freshwater environment of the Terengganu River basin by Sultan and Shazili [1]. Comparison of REEs in Kenyir Lake, Terengganu River and Terengganu River estuary found that the total dissolved solids dominantly control the distribution of dissolved REEs, since it was observed that the concentration of dissolved REEs systematically increased with distance from the upstream towards the downstream. Rezaee et al. [2] has carried out research on REEs in the marine surface sediment off Malaysian waters. The chondrite-normalized REEs show that the sedimentation pattern along Malaysian waters signify the anthropogenic activities as well as the natural processes. Another study carried out by Rezaee et al. [3] found that the chondrite-normalized REEs show the enrichment of LREEs and flat depletion of HREEs in the Malaysian marine sediment.

The Brunei Bay environment is rather complex, with many rivers supplying freshwater from pristine as well as agriculturally and urban developed regions in Sarawak, Sabah and Brunei; and possible anthropogenic sources of metals and REEs from a port, and industrial activities on Labuan Island. In this study, the concentrations of REEs in seawater dissolved (<0.45μm), in particulate fractions and in sediment were measured in Brunei Bay, with the objective of determining the extent of variations in REE concentrations and fractionation between the different fractions during the dry season in July 2013 and during the wet Northeast Monsoon season in January 2014.

Materials and Methods

Five sampling trips were carried out in the period of 10^{th} – 12^{th} May 2013, 26^{th} June 2013 – 2^{nd} July 2013, 10^{th} – 12^{th} October 2013, 7^{th} – 18^{th} January 2014 and 4^{th} – 7^{th} April 2014. Samples were collected at both coastal and transect stations during July 2013 and January 2014. For May 2013, October 2013 and April 2014, the samples were collected at coastal stations only. The investigated area extended from Menumbuk to Limbang of the Malaysian coastline. Seventeen coastal stations were selected along the Brunei Bay coastline and riverine (Figure 1), nine stations were selected surrounding the Labuan Island, noted as Labuan stations, and twenty-two stations were selected in a grid remarked as the transect stations. Water samples were collected at both surface and bottom waters at all transect stations, whilst at the coastal stations, the samples were collected at the surface water column only.

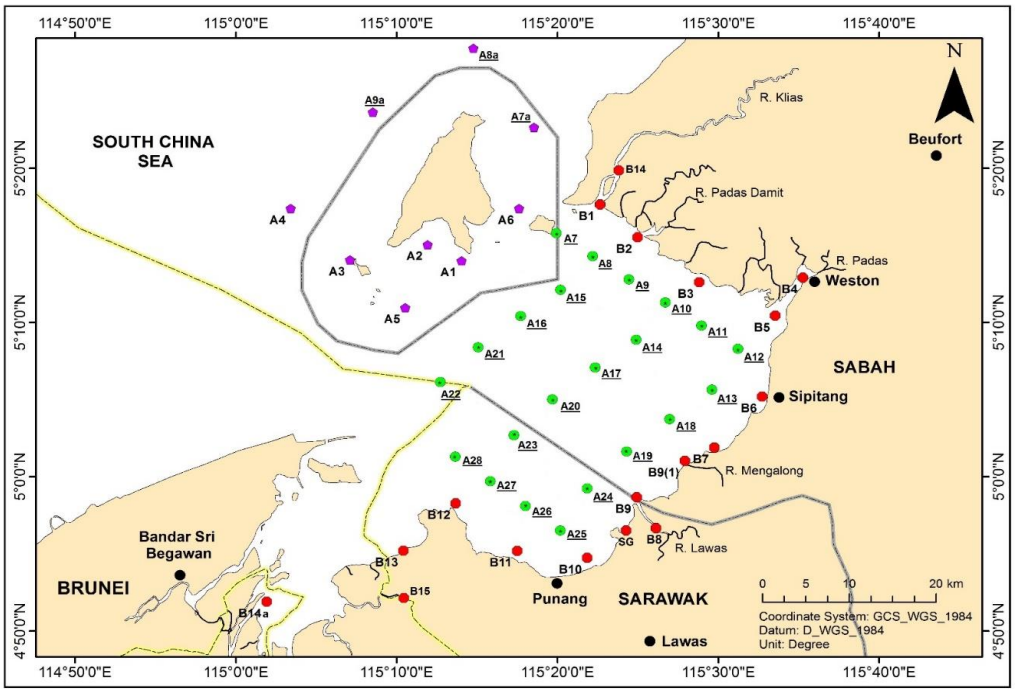


Figure 1. Map of the sampling locations of Brunei Bay, Borneo

Laboratory preparation

All equipment for sampling and sample preparation was thoroughly cleaned with dilute nitric acid and rinsed with ultrapure water before use. Chelex-100 column was prepared using Chelex-100 (sodium form, mesh size of 100-200, powder form, Bio-Rad Laboratories). Polytetrafluoroethylene (PTFE) columns containing Chelex-100 resin were prepared for REE pre-concentration. 50 mL of 2.5 M nitric acid was passed through the column to rinse out all contaminants, followed by 50 mL of deionized water to remove the excess nitric acid. Ammonia solution (50 mL 2M) was then passed through the column, followed by 50 mL of deionized water. Finally, the column was buffered with 20 mL of 1M ammonium acetate (pH 5.3) buffer that had been previously purified using Chelex-100 resin [4, 5]. Solvents, deionized water, buffer, eluent and samples were forced through the column using a peristaltic pump (Masterflex L/S Variable-Speeds Digital Drives) and C-Flex tubing (L/S 14) at a flow rate of 2 mL/min [6]. All procedures were carried out in a Class-100 laminar flow hood to ensure the process is free from contamination. Concentrations of the REEs were measured by an Inductively Coupled Plasma Mass Spectrometer (ICPMS - Perkin Elmer Elan 9000) in a Class-1000 clean room with a Class 100 hood under which the ICPMS was sited.

Sample collection

Duplicate water samples were collected by hand for surface samples and Niskin water sampler for bottom water, and placed in acid washed polyethylene (PE) bottles. The samples were filtered through a 0.45 µm PTFE membrane under a modified closed laminar flow hood equipped with a Class-100 air purifier on the same day. The water samples were then preserved with 2 mL of 65% nitric acid and sealed individually inside PE bags. Suspended particulate matter retained on the PTFE membrane (particulate fraction) was stored inside an acid washed PE container and sealed inside a PE zip lock bag individually. Both samples were kept at low temperature for transportation to the laboratory. Surface sediment was collected using a Ponar grab. The top 5 cm of the sediment was sampled using a plastic scoop. Samples were sealed inside a double layer of PE zip lock bags, kept at low temperature prior to the transportation to the laboratory and kept frozen in a freezer at the laboratory. Water quality parameters including suspended particulate matter were measured with a multiparameter water quality meter (YSI).

Sample treatment and analysis
All procedures in the laboratory were carried out under a Class-100 laminar flow hood in order to prevent contamination.

Dissolved REEs in water sample
Pre-concentration of elements is frequently required owing to their inherent low level in the water samples. Additionally, elements pre-concentration also functions to remove the high concentration of alkali and alkaline earth metal ions in seawater that interferes in the instrumental analysis [7]. Chelex-100 chelating resin was used to pre-concentrate the REEs which were in the "exchangeable fraction" [8, 9]. Chelex-100 operational efficiency is well defined; based on the contact time of the resin with the sample, resin volume as well as sample flow rate can be measured [8, 10].

The REEs pre-concentration procedure was carried out under a Class-100 laminar flow hood to avoid contamination. Filtered water samples were adjusted to pH 5.3, and a total of 200 mL of water sample was passed through a Chelex-100 column at a flow rate of 2 mL/min. Columns were washed with 25 mL of ammonium acetate (previously cleaned by Chelex-100 resin) to remove the saline matrix [11, 12] The elements were finally eluted with 10 mL of 2M nitric acid with a flow rate of 2 mL/min and kept in 15 mL centrifuge tubes at 4°C before analysis using ICP-MS was conducted. This pre-concentration step resulted in a concentration factor of 20 times the initial amount. Blanks were measured to check for metal contamination.

Particulate REEs in water sample
All procedures were done under a Class-100 laminar flow hood to minimise contamination. Suspended particulate matter retained by 0.45 µm PTFE membrane filter was dried to constant weight under Class-100 laminar flow hood. Afterwards, the PTFE filter membrane was digested with 1.5 mL of mixed acids (nitric acid, hydrochloric acid and hydrofluoric acid in the ratio 3:3:1). The mixture was then digested in a closed Teflon bomb under oven heating for 7 hours at a temperature of 120°C and left to cool to room temperature [7, 13]. The sample volume was made up to 10 mL with deionized water. Blanks were measured to check for elemental contamination. Digested samples were kept in centrifuge tubes at 4°C before conducting ICP-MS measurements.

REEs in sediment sample
The method used to digest sediment samples was adopted from [14, 15]. Sediment samples were dried at 60 °C under oven heating. The dried sediments were then crushed mildly using a pestle and mortar. Approximately 0.05g of the bulk sediment was weighed in a Teflon bomb vessel and 1.5 mL of mixed acids (nitric acid, hydrochloric acid and hydrofluoric acid in the ratio 3:3:2) were added. The mixture was digested under oven heating for 7 hours at a temperature of 120 °C, then left to cool until room temperature. The sample volume was made up to 10 mL with deionized water. Blanks were measured to check for metal contamination. Digested samples were kept in centrifuge tubes at 4 °C before analysis using ICP-MS was done.

Accuracy and precision
The internal standard method was applied to validate the REEs in dissolved, particulate and surface sediment samples using 5 ppb and 10 ppb of Multi-elements Calibration Standard 2, 10 µg/mL (17 elements in 5% nitric acid). Chelex-100 column blanks were carried out by using 200 mL of deionized water as the water sample, followed by the same steps as for water samples for dissolved metal analysis. The particulate metal blanks were prepared by digesting clean PTFE membrane filters without any sediment sample. Sediment blanks consisted of acid digestion in the PTFE vessels without sediment. Besides assessing the quality control, blanks were used to determine the limit of detection [16]. Good recoveries were achieved for REEs in the dissolved (95.8 ± 4.11% for 5ppb; 94.5 ± 4.47% for 10 ppb) and particulate fraction (97.8 ± 3.64% for 5 ppb; 96.6 ± 4.16% for 10 ppb) and sediment (96.1 ± 3.63% for 5 ppb; 97.8 ± 3.86% for 10 ppb). The detection limits ranged from 0.2 ng/L for Tm to 2.2 ng/L for La in the dissolved fraction. In the particulate fraction, detection limits ranged from 0.16 µg/kg for Tm to 48 µg/kg for La, and in sediment, from 1.0 µg/kg for Tm to 40.9 µg/kg for La.

Results and Discussion

Dissolved rare earth elements

The average, standard deviation, minimum and maximum data of dissolved REEs are recorded in Table 4. The highest dissolved elements found in May 2013 water samples were Cerium (Ce), Praseodymium (Pr), Neodymium (Nd), Samarium (Sm), Europium (Eu), Gadolinium (Gd), Terbium (Tb), Dysprosium (Dy), Erbium (Er) and Ytterbium (Yb). Dissolved Holmium (Ho), Thulium (Tm) and Lutetium (Lu) were higher in the surface water of January 2014 while dissolved La concentration was highest in July 2013 in the bottom waters (Figure 2). Dissolved Sm, Eu, Gd, Tb, Dy, Ho, Er, Tm, Yb and Lu concentrations were lowest in October 2013 while dissolved La, Ce, Pr and Nd concentrations were lowest in bottom waters in January 2014 (Figure 2).

Table 4. Mean, standard deviation and range (in parentheses) concentration of dissolved REEs and Al for the different sampling periods (µg/L)

Element (µg/L)	July 2013 surface	July 2013 bottom	January 2014 surface	January 2014 bottom
La	0.127 ± 0.112 (0.039 - 0.692)	0.186 ± 0.191 (0.035 - 0.972)	0.060 ± 0.119 (0.013 - 0.831)	0.027 ± 0.008 (0.017 - 0.052)
Ce	0.102 ± 0.068 (0.043 - 0.452)	0.125 ± 0.123 (0.035 - 0.618)	0.093 ± 0.133 (0.014 - 0.827)	0.038 ± 0.017 (0.023 - 0.100)
Pr	0.097 ± 0.213 (0.020 - 1.352)	0.074 ± 0.121 (0.025 - 0.677)	0.051 ± 0.112 (0.012 - 0.788)	0.020 ± 0.006 (0.012 - 0.036)
Nd	0.462 ± 1.246 (0.079 - 7.821)	0.255 ± 0.201 (0.099 - 0.970)	0.119 ± 0.140 (0.028 - 0.950)	0.068 ± 0.015 (0.034 - 0.104)
Sm	0.075 ± 0.031 (0.009 - 0.135)	0.087 ± 0.141 (0.013 - 0.797)	0.115 ± 0.140 (0.054 - 1.041)	0.082 ± 0.014 (0.055 - 0.110)
Eu	0.054 ± 0.020 (0.019 - 0.119)	0.071 ± 0.139 (0.022 - 0.776)	0.059 ± 0.136 (0.017 - 0.964)	0.033 ± 0.009 (0.016 - 0.051)
Gd	0.199 ± 0.588 (0.016 - 3.699)	0.109 ± 0.122 (0.034 - 0.651)	0.103 ± 0.132 (0.038 - 0.965)	0.071 ± 0.017 (0.041 - 0.110)
Tb	0.045 ± 0.022 (0.018 - 0.116)	0.059 ± 0.141 (0.018 - 0.776)	0.058 ± 0.144 (0.017 - 1.018)	0.027 ± 0.005 (0.015 - 0.037)
Dy	0.040 ± 0.037 (0.001 - 0.209)	0.054 ± 0.116 (0.001 - 0.640)	0.081 ± 0.118 (0.023 - 0.861)	0.051 ± 0.014 (0.021 - 0.078)
Ho	0.006 ± 0.004 (0.001 - 0.019)	0.008 ± 0.026 (0.000 - 0.141)	0.017 ± 0.043 (0.004 - 0.302)	0.009 ± 0.002 (0.006 - 0.013)
Er	0.052 ± 0.021 (0.014 - 0.103)	0.063 ± 0.119 (0.001 - 0.666)	0.078 ± 0.143 (0.028 - 1.032)	0.053 ± 0.010 (0.036 - 0.079)
Tm	0.004 ± 0.002 (0.001 - 0.010)	0.005 ± 0.013 (0.001 - 0.072)	0.013 ± 0.034 (0.003 - 0.238)	0.006 ± 0.001 (0.003 - 0.009)
Yb	0.038 ± 0.028 (0.000 - 0.118)	0.053 ± 0.127 (0.000 - 0.697)	0.081 ± 0.140 (0.016 - 1.008)	0.056 ± 0.014 (0.029 - 0.092)
Lu	0.003 ± 0.002 (0.000 - 0.009)	0.004 ± 0.014 (0.001 - 0.076)	0.010 ± 0.028 (0.002 - 0.197)	0.004 ± 0.001 (0.001 - 0.006)
Al	10.4 ± 10.4 (0.122 - 36.6)	10.6 ± 21.8 (0.124 - 115)	110 ± 446 (24.7 - 3132)	26.4 ± 10.3 (19.3 – 76.9)

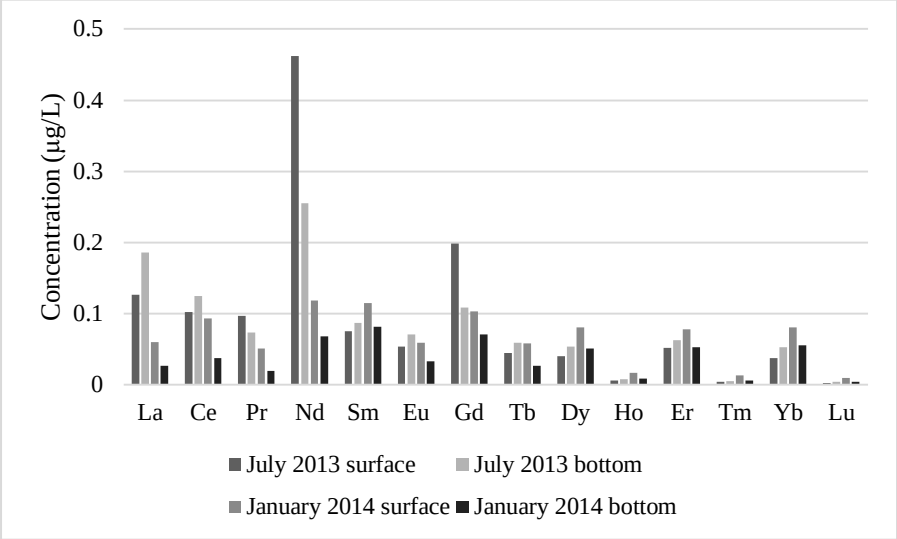


Figure 2. The average concentration of dissolved REEs in Brunei Bay

Particulate rare earth elements

Particulate Ce, Pr, Nd, Sm, Eu, Gd, Tb, Dy, Ho, Er, Tm, Yb and Lu were highest in average concentrations in October 2013, while particulate La was the only element recorded with the highest average concentration in surface water in January 2014 (Figure 3). This finding is likely influenced by the northeast monsoon period since significant correlation ($p < 0.05$) of the above mentioned REEs with high concentration of suspended particulate matter and acidic water pH was observed. During the northeast monsoon, the western region of Borneo Island receives heavy rainfall [17, 18]. Such occurrence leads to a flushing out of a high load of suspended particulate matter into the sea, which reduced the water pH value. The average, standard deviation, minimum and maximum concentration of particulate REEs are recorded in Table 5. Overall, bottom water samples in July 2013 had the lowest average concentrations of all particulate REEs (La, Ce, Pr, Nd, Sm, Eu, Gd, Tb, Dy, Ho, Er, Tm, Yb and Lu) as compared to other sampling periods.

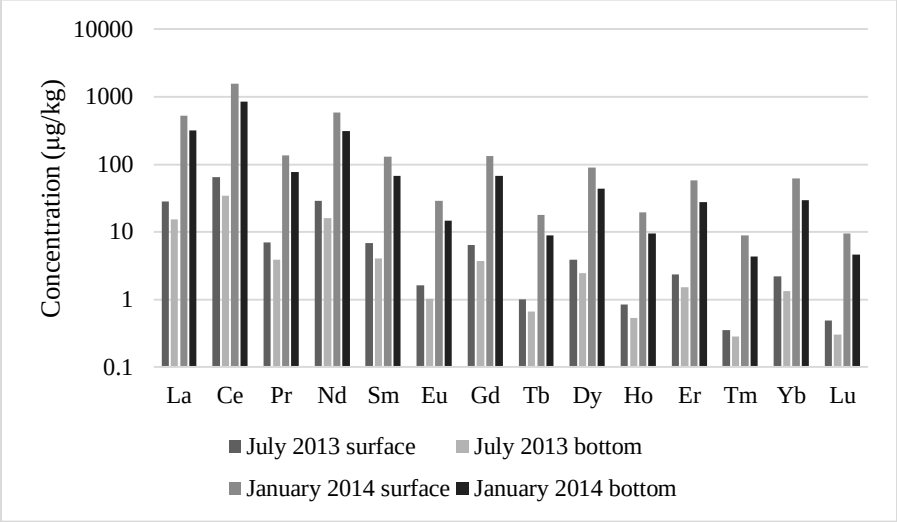


Figure 3. The average concentration of particulate REEs in Brunei Bay

Table 5. Mean, standard deviation and range (in parentheses) concentration of particulate REEs and Al for the different sampling periods (µg/g)

Element (µg/kg)	July 2013 Surface	July 2013 Bottom	January 2014 Surface	January 2014 Bottom
La	28.0 ± 40.9 (2.35 - 187)	15.5 ± 11.1 (3.09 - 106)	527 ± 414 (72.2 - 2100)	315 ± 222 (57.4 - 1060)
Ce	64.5 ± 94.4 (4.82 - 404)	34.1 ± 26.0 (7.35 - 245)	1556 ± 1348 (135 - 4612)	850 ± 920 (106 - 4328)
Pr	7.06 ± 10.5 (0.585 - 47.8)	3.85 ± 2.73 (0.945 - 27.3)	137 ± 109 (13.8 - 388)	76.8 ± 66.7 (10.8 - 296)
Nd	28.7 ± 43.5 (1.66 - 201)	16.1 ± 11.0 (2.78 - 112)	582 ± 486 (55.2 - 1944)	311 ± 267 (44.1 - 1264)
Sm	6.89 ± 9.26 (1.25 - 40.6)	4.08 ± 2.29 (0.97 - 22.9)	129 ± 106 (12.9 - 374)	67.4 ± 61.7 (8.64 - 253)
Eu	1.62 ± 2.08 (0.220 - 8.99)	1.02 ± 0.556 (0.245 - 4.71)	28.8 ± 23.4 (2.74 - 82.9)	14.7 ± 13.2 (1.86 - 57.2)
Gd	6.37 ± 8.78 (0.983 - 38.4)	3.68 ± 2.18 (0.947 - 19.5)	132 ± 107 (18.2 - 389)	66.9 ± 60.8 (9.71 - 262)
Tb	1.00 ± 1.16 (0.222 - 5.04)	0.661 ± 0.317 (0.181 - 2.53)	17.8 ± 14.3 (2.73 - 51.8)	8.86 ± 7.89 (1.58 - 36.4)
Dy	3.86 ± 5.29 (0.161 - 25.0)	2.44 ± 1.32 (0.570 - 11.7)	90.3 ± 76.7 (13.1 - 285)	43.8 ± 41.1 (6.19 - 189)
Ho	0.847 ± 0.98 (0.155 - 4.74)	0.536 ± 0.267 (0.153 - 2.31)	19.7 ± 16.8 (2.86 - 63.8)	9.55 ± 8.76 (1.66 - 41.1)
Er	2.33 ± 2.80 (0.364 - 12.1)	1.53 ± 0.846 (0.367 - 6.76)	57.7 ± 51.1 (7.90 - 196)	27.6 ± 26.0 (4.56 - 122)
Tm	0.352 ± 0.391 (0.030 - 2.13)	0.282 ± 0.130 (0.054 - 0.940)	8.98 ± 7.92 (1.27 - 31.1)	4.36 ± 4.09 (0.728 - 19.4)
Yb	2.18 ± 2.61 (0.255 - 12.4)	1.32 ± 0.818 (0.177 - 6.25)	62.5 ± 57.2 (7.29 - 227)	29.7 ± 29.2 (3.79 - 136)
Lu	0.490 ± 0.546 (0.092 - 2.87)	0.304 ± 0.177 (0.081 - 0.989)	9.50 ± 8.65 (1.36 - 34.0)	4.59 ± 4.43 (0.561 - 20.9)
Al	362 ± 529 (31.4 - 2249)	202 ± 157 (56.0 - 737)	6915 ± 8220 (211 - 19732)	1858 ± 2889 (210 - 14211)

Rare earth elements in surface sediment

The average, standard deviation, minimum and maximum data of REEs in surface sediment are recorded in Table 6. Similar to the dissolved and particulate REEs, the distribution of the highest and lowest REEs in surface sediment was more consistent as compared to metals in surface sediment samples. Overall, the highest average concentration of REEs (including La, Ce, Pr, Nd, Sm, Eu, Gd, Tb, Dy, Ho, Er, Tm, Yb and Lu) was found in the October 2013 samples.

Surface sediment samples during April 2014 recorded the lowest in average values of La, Ce, Pr, Nd, Sm, Eu, Gd, Tb, Dy, Ho and Er, while Tm, Yb and Lu were lowest in May 2013 (Figure 4). This finding is influenced by the southwest monsoon period, since significant correlation ($p<0.05$) of the above mentioned REEs with lowest concentration of suspended particulate matter was observed. During the southwest monsoon, the western region of

Borneo Island experiences relatively drier weather [17, 18]. Such occurrence leads to a significantly low load of suspended particulate matter flushed out into the sea.

Table 6. Mean, standard deviation and range (in parentheses) concentration of REEs (µg/g) and Al (%) in surface sediment from all sampling sites

Element (µg/g)	**July 2013**	**January 2014**
La	11.7 ± 5.01 (3.61 - 20.3)	15.6 ± 13.9 (0.133 - 42.8)
Ce	25.5 ± 10.4 (7.47 - 42.5)	41.2 ± 33.9 (0.006 - 106)
Pr	2.91 ± 1.14 (0.829 - 4.73)	4.17 ± 3.50 (0.006 - 10.9)
Nd	11.7 ± 4.45 (3.30 - 18.7)	17.0 ± 14.2 (0.025 - 45.0)
Sm	2.34 ± 0.868 (0.639 - 3.65)	3.40 ± 2.74 (0.006 - 8.97)
Eu	0.502 ± 0.190 (0.142 - 0.782)	0.746 ± 0.567 (0.003 - 1.88)
Gd	2.38 ± 0.881 (0.685 - 3.90)	3.55 ± 2.86 (0.008 - 9.02)
Tb	0.264 ± 0.093 (0.080 - 0.404)	0.392 ± 0.301 (0.000 - 0.990)
Dy	1.32 ± 0.447 (0.422 - 2.04)	2.11 ± 1.57 (0.002 - 5.27)
Ho	0.229 ± 0.076 (0.077 - 0.365)	0.390 ± 0.289 (0.000 - 0.958)
Er	0.614 ± 0.205 (0.200 - 0.953)	1.11 ± 0.834 (0.003 - 2.76)
Tm	0.082 ± 0.026 (0.030 - 0.131)	0.160 ± 0.120 (0.001 - 0.395)
Yb	0.520 ± 0.165 (0.178 - 0.792)	1.05 ± 0.788 (0.001 - 2.47)
Lu	0.075 ± 0.024 (0.028 - 0.114)	0.152 ± 0.117 (0.000 - 0.380)
Al (%)	3.72 ± 2.04 (0.440 – 6.08)	4.01 ± 2.33 (0.004 – 7.72)

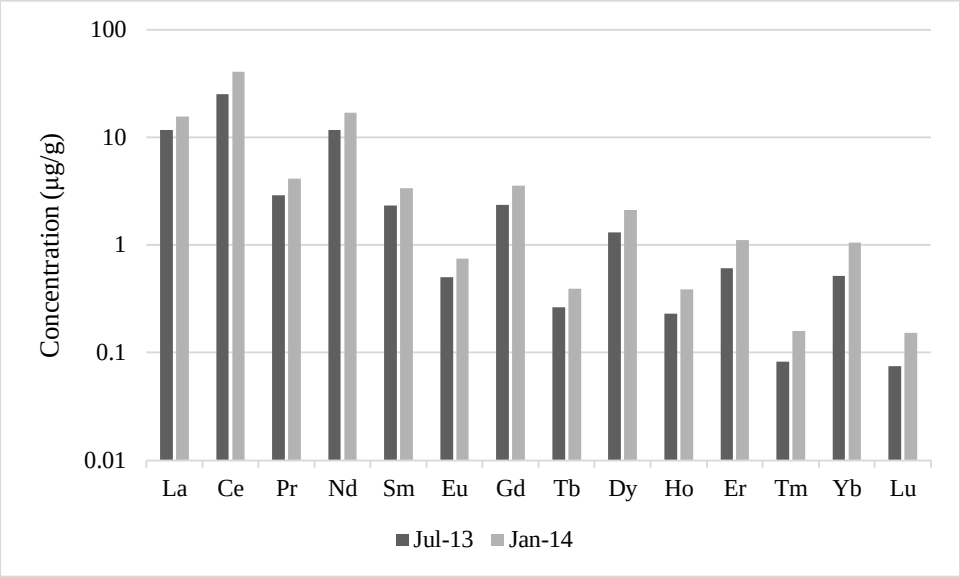


Figure 4. The average concentration of REEs in the surface sediment of Brunei Bay

Rare earth elements (REE) can be used to define the source of contaminants [19] by determining the origin of metals that are closely related to water-sediment interaction, and as geochemical tracers of flow paths of water in water bodies [20]. The partitioning of the aqueous and solid fractions REEs is influenced by pH, temperature, redox as well as selective ligand-complexation of dissolved REE ions in water [21-26].

The average concentration of REEs in Brunei Bay samples are shown in Table 7. The abundance order of REEs in dissolved, particulate and surface sediment decreased from light REE (LREE) > medium REE (MREE) > heavy REE (HREE). Overall, the concentration of LREEs was higher than HREEs for all sampling periods, probably due to high adsorption of LREEs onto clay particles, while HREEs remain dominant in solution. This finding is similar to the findings discovered in the sediment of Yellow Sea, Yangtze River, Florida Bay as well as in the estuarine sediment of east coast of India [27-30]. ΣREE concentration were higher in January 2014 than in July 2013 in river and estuary sampling sites, and especially so in particulate fraction from all sampling sites (Table 7). The majority of the REEs during January 2014 were in the LREE fraction in river, estuary and bay particulate matter while in particulates from the South China Sea off Labuan Island, a significantly lesser number of REEs were in the LREE fraction.

ΣLREE is highly enriched over ΣHREE in sediment and in particulates in July 2013 compared to January 2014 particularly in riverine stations (Table 7), but the difference is less for estuarine, the bay and South China Sea stations. In the dissolved fraction ΣLREE:ΣHREE ratios in the bay area were generally similar to South China Sea stations during both sampling periods.

The La/Yb anomaly is usually applied to determine the ratio between LREE and HREE. Specifically, La/Yb was 22.3 in July 2013 and in January 2014 La/Yb was 14.9 in sediment in riverine stations. In particulate fraction, in surface and bottom water of the bay, La/Yb ranged from 11.7 to 12.8 for July 2013, and from 8.4 to 10.6 in January 2014. A La/Yb of 3.3-3.5 in dissolved fraction in July 2013 indicates much lower enrichment in the dissolved fraction compared to particulate fraction and sediment (Table 9). LREE enrichment relative to HREE has been similarly measured in the Terengganu River Basin, Terengganu [1]. High LREE in the surface sediment results from the high affinity of REE to bind with carbonates. This finding is similar to those found in the surface marine sediment of Malaysian coasts [2, 3, 31].

Table 7. The average concentration of REE in Brunei Bay, Borneo

Sampling period		Dissolved (µg/L)				Particulate (µg/g)				Surface Sediment (µg/g)			
		R	E	B	S	R	E	B	S	R	E	B	S
July 2013	ΣREE	722	1252	904	403	588	538	76	19	48	90	62	18
	ΣLREE	569	1081	803	298	553	506	69	16	46	84	58	17
	ΣMREE	152	346	204	99	48	41	7.05	2.09	2.85	7.00	4.66	1.33
	ΣHREE	153	171	102	105	35	33	6.79	2.32	2.04	5.66	3.24	1.01
	ΣLREE/ ΣHREE	3.7	6.3	2.8	2.8	15.8	15.3	10.2	6.9	22.5	14.8	17.9	15.4
January 2014	ΣREE	806	1800	434	395	5940	7877	2586	560	129	111	92	3.86
	ΣLREE	631	1215	289	263	5443	7230	2388	513	120	103	87	3.53
	ΣMREE	201	543	136	117	466	640	206	48	9.97	8.54	6.76	0.42
	ΣHREE	175	585	146	132	497	647	198	47	8.63	7.48	5.11	0.33
	ΣLREE/ ΣHREE	3.6	2.1	2.0	2.0	11.0	11.2	12.1	10.9	13.9	13.8	17.0	10.7

Note: R - River stations, E - Estuary stations, B - Bay stations, S - South China Sea stations

ΣREE, ΣLREE and ΣHREE concentrations increased by up to ten times in the particulate fraction in January 2014. Interestingly LREE was seen depleted in January 2014 with ratios of La/Yb of 0.48 in bottom water and 0.74 in surface water, although this is not obvious from the ΣLREE: ΣHREE ratio (Table 7). This depletion in LREE indicates dilution by freshwater during the Monsoon rains in January. It also indicates that different chemistries between bottom and surface waters play a significant role in the REE distribution in the dissolved and particulate fraction and in sediment. According to Suhaila and Jemain [17], the northeast monsoon typically sets in over the South China Sea in early November, lasting till early March, which brings in heavy rainfall to the east coast of Peninsular Malaysia and western Sarawak [18].

Normalization of Sm to Nd (Table 8) results in similar Sm/Nd ratios of 0.16-0.34 in the three sample types during July 2013 and January 2014, except for January 2014 where Sm/Nd were close to 1.0 (0.97-1.21). The ratios of Nd/La are close to 1.0 (0.97-1.10) for particulate fraction and sediment in July 2013 and January 2014, whereas Nd is significantly enriched relative to La in the dissolved fraction for both sampling periods. A similar pattern is observed for Er/La with ratios of 0.05-0.11 for particulate fraction and sediment, and significant enrichment of Er over La during January 2014 with ratios of 1.3-1.96.

The SPM concentration in Brunei Bay was highest (32.1 ± 104 mgL^{-1}) in surface water during January 2014 (Table 9), and thus scavenging capacity and dilution by fresh SPM resulted in lower La/Yb in dissolved and particulate fraction compared to the drier conditions in July 2013 (Table 8). Water quality parameters (Table 9) during these two sampling periods showed only a slightly lower pH during January 2014, but a marked reduction in dissolved oxygen was recorded in the surface waters of Brunei Bay. Thus, **Σ**LREE is relatively enriched in the dissolved fraction than in particulate fraction and in sediment, with enrichment in sediment > particulate fraction > dissolved fraction.

In the wet northeast Monsoon season (January 2014 samples) a significantly different pattern in REE distribution is generally observed in the dissolved fraction, particularly with regards to La/Yb, Sm/Nd and Er/La ratios (Table 8). The ratios of Sm/Nd, Nd/La and Er/La in the particulate fraction are similar to values in sediment, indicating that there is no fractionation of REEs in the mineralised form. However, REE ratios in the dissolved fraction differ substantially between the July and January sampling periods, indicating leaching from land sources or increased

scavenging (La/Yb). Ratio of La/Yb is significantly reduced in the dissolved fraction in January 2014, indicating enhanced scavenging of light REEs together with dilution by the higher SPM content (Table 9) from terrigenous sources, as evidenced by the 19-fold increase in Al concentration in particulates (Table 5).

Table 8. REE ratios in Brunei Bay in dissolved and particulate forms and in sediment for the July 2013 and January 2014

		July 2013		January 2014	
		Surface	**Bottom**	**Surface**	**Bottom**
La/Yb	Dissolved	3.34	3.51	0.74	0.48
	Particulate	12.8	11.7	8.43	10.6
	Sediment	22.5		14.8	
$(La/Yb)_{diss}/(La/Yb)_{part}$		0.26	0.30	0.09	0.04
Sm/Nd	Dissolved	0.16	0.34	0.96	1.21
	Particulate	0.24	0.25	0.22	0.22
	Sediment	0.20		0.20	
Nd/La	Dissolved	3.63	1.37	1.98	2.5
	Particulate	1.02	1.04	1.10	0.98
	Sediment	1.00		1.09	
Er/La	Dissolved	0.41	0.33	1.3	1.96
	Particulate	0.08	0.10	0.11	0.09
	Sediment	0.05		0.07	

Comparison of relative REE concentrations in the dissolved phase with those in the suspended particulate matter phase by $(La/Yb)_{dissolved}$:$(La/Yb)_{particulate}$ result in ratios of 0.26 and 0.3, respectively, during the dry season, and 0.09 and 0.04, respectively, in the wet season, indicating the strong influence of riverine input in Brunei Bay on REE chemistry. These values are typical of tropical rivers and indicate relative enrichments of heavy REEs in the suspended load from the formation of carbonate complexes favoured in river water of pH = 8 [32].

Table 9. Mean, standard deviation and range (in parentheses) of water physical parameters of Brunei Bay

Sampling Period	**pH**	**DO (mg/L)**	**Salinity (ppt)**	**Temperature (°C)**	**SPM (mg/L)**
July 2013 (surface)	8.17 ± 0.33 (7.24 - 8.42)	6.05 ± 0.54 (4.72 - 6.95)	26.8 ± 6.97 (0.38 - 31.3)	30.4 ± 0.95 (27.8 - 32.0)	14.8 ± 27 (0.67 - 166)
July 2013 (bottom)	8.17 ± 0.19 (7.89 - 8.39)	3.51 ± 2.03 (0.21 - 5.71)	32.8 ± 0.85 (30.3 - 33.9)	29.6 ± 0.84 (27.6 - 30.8)	11.3 ± 7.68 (4.50 - 45.0)
January 2014 (surface)	7.85 ± 0.54 (6.04 - 8.18)	4.88 ± 1.16 (0.65 - 8.47)	23.2 ± 9.12 (0.03 - 30.7)	28.7 ± 1.57 (24.6 - 30.6)	32.1 ± 104 (4.50 - 679)
January 2014 (bottom)	8.04 ± 0.07 (7.88 - 8.12)	3.68 ± 0.91 (1.32 - 4.69)	33.9 ± 0.78 (31.9 - 34.6)	28.9 ± 0.38 (28.4 - 29.7)	9.69 ± 7.25 (4.50 - 38.3)

Conclusion

Rare earth element concentrations in particulate and sediment fractions showed some differences between the sampling period of July in the dry season and of January in the wet season. However, the dissolved fraction showed similar distributions of ΣLREE:ΣHREE during both sampling periods. Light over heavy REE as determined by La/Yb ratios is significantly reduced in the dissolved fraction in January 2014, indicating enhanced scavenging of light REEs together with dilution by the higher SPM content from terrigenous sources during the wet season.

Acknowledgements

This study is supported by the Ministry of Education (MOE) Higher Institution Centre of Excellence (HICoE) Research Grant No. 66928. The authors express their appreciation for the support of INOS staff in the sampling work in Brunei Bay.

References

1. Sultan, K. and Shazili, N. A. M. (2009). Rare earth elements in tropical surface water, soil and sediments of the Terengganu River Basin, Malaysia. *Journal of Rare Earths*, 27(6): 1072-1078.
2. Rezaee, K., Saion, E. B., Wood, A. K. and Abdi, M. R. (2010). Rare earth elements determination and distribution patterns in surface marine sediments of the South China Sea by INAA, Malaysia. *Journal Radioanalytical and Nuclear Chemistry*, 283:823-829.
3. Rezaee, S. K. E., Elias, S. B., Wood, A. K. and Reza, A. M. (2009). Rare earth elements distribution in marine sediments of Malaysia coasts. *Journal of Rare Earths*, 27: 1066-1071.
4. Guéguen, C., Belin, C., Thomas, B. A., Monna, F., Favager, P.-Y. and Dominik, J. (1999). The effect of freshwater UV-irradiation prior to resin preconcentration of trace metals. *Analytica Chimica Acta*, 386: 155-159.
5. Long, S. E. and Martin, T. D. (2008). Determination of trace elements in marine waters by on-line chelation preconcentration and inductively coupled plasma-mass spectrometry: Method 200-10. In: *Asean Marine Water Quality – Management Guidelines and Monitoring Manual*, pp 201 – 213. Australian Marine Science and Technology Ltd (AMSAT).
6. William, W. H. T. (2008). Distribution of dissolved and particulate trace metals in Terengganu River estuary. Universiti Malaysia Terengganu, Malaysia. MSc Thesis.
7. Adiana G., Shazili N. A. M., Marinah M. A. and Bidai J. (2014). Effects of northeast monsoon on trace metal distribution in the South China Sea off Peninsular Malaysia. *Environmental Monitoring and Assessment*, 186: 421-431.
8. Beck, A. J., Cochran, J. K. and Sañudo-Wilhelmy, S. A. (2010). The distribution and speciation of dissolved trace metals in a shallow subterranean estuary. *Marine Chemistry*, 121:145-156.
9. Beck, A. J. and Sañudo-Wilhelmy, S. A. (2007). Impact of water temperature and dissolved oxygen on copper cycling in an urban estuary. *Environmental Science Technology*, 41: 6103-6108.
10. Bowles, K. C., Apte, S. C., Batley, G. E., Hales, L.T. and Rogers, N. J. (2006). A rapid chelex column method for the determination of metal speciation in natural waters. *Analytica Chimica Acta*, 558: 237-245.
11. Abbasse, G., Ouddane, B. and Fischer, J. C. (2002). Determination of total and labile fraction of metals in seawater using solid phase extraction and inductively coupled plasma atomic emission spectrometry (ICP-AES). *Journal of Analytical Atomic Spectrometry*, 17(10): 1354-1358.
12. Scoullos, M., Sakellari, A., Giannopoulou, K., Paraskevopoulou, V. and Dassenakis, M. (2007). Dissolved and particulate trace metal levels in the Saronikos Gulf, Greece, in 2004. The impact of the primary Wastewater Treatment Plant of Psittalia. *Desalination*, 210: 98-109.
13. Wells, M. L., Smith, G. J. and Bruland, K. W. (2000). The distribution of colloidal and particulate bioactive metals in Narragansett Bay, RI. *Marine Chemistry*, 71: 143-163.
14. Bidai J., Adiana G. and Shazili N.A.M (2016). Particle sizes effect of the elements in the South China Sea sediment off Pahang coastal during the Northeast monsoon (pre-) and the Southwest monsoon (post-) periods. *Environmental Earth Sciences*, 75: 614-625.

15. Morford, J. L., Russell, A. D. and Emerson, S. (2001). Trace metal evidence for changes in the redox environment associated with the transition from terrigenous clay to diatomaceous sediment, Saanich Inlet, BC. *Marine Geology*, 174: 355-369.
16. Miller, J. C. and Miller, J. N. (1993). Statistics for analytical chemistry, pp 11-120. Ellis Horwood PTR Prentice Hall, New York.
17. Suhaila, J. and Jemain, A. A. (2009). Investigating the impacts of adjoining wet days on the distribution of daily rainfall amounts in Peninsular Malaysia. *Journal of Hydrology*, 368: 17-25.
18. Goswami, B. N. (2005). South asian summer monsoon: an overview. In: The Global Monsoon System: Research and Forecast (Report No.: WMO/TD No. 1266) Report of the International Committee of the Third International Workshop on Monsoons (IWM-III), ed. Chang, C.-P., Wang, B. and Lau, N.-C. G., pp 47-71. Secretariat of the World Meteorological Organization, Geneva, Switzerland.
19. Zhu, Y., Itoh, A., Fujimori, E., Umemura, T. and Haraguchi, H. (2006). Determination of rare earth elements in seawater by ICP-MS after preconcentration with a chelating resin-packed minicolumn. *Journal of Alloys and Compounds*, 408-412: 985-988.
20. Verplanck, P. L. (2013). Partitioning of rare earth elements between dissolved and colloidal phases. *Procedia Earth and Planetary Science*, 7: 867-870.
21. Leleyter, L., Rousseau, C., Biree, L. and Baraud, F. (2012). Comparison of EDTA, HCl and sequential extraction procedures, for selected metals (Cu, Mn, Pb, Zn), in soils, riverine and marine sediments. *Journal of Geochemical Exploration*, 116-117: 51-59.
22. Okonkwo, J. O. and Mothiba, M. (2005). Physico-chemical characteristics and pollution levels of heavy metals in the rivers in Thohoyandou, South Africa. *Journal of Hydrology*, 308: 122-127.
23. Filgueiras, A. V., Lavilla, I. and Bendicho, C. (2004). Evaluation of distribution, mobility and binding behavior of heavy metals in surficial sediments of Louro River (Galicia, Spain) using chemometris analysis: a case study. *Science of the Total Environment*, 330: 115-129.
24. Michalke, B. (2003). Element speciation definitions, analytical methodology, and some examples. *Ecotoxicology and Environmental Safety*, 56: 122-139.
25. Tokalıoğlu, Ş. and Kartal, Ş. (2002). Atomic absorption spectrometric determination of heavy metal contents of soils around different highways in Turkey and statistical interpretation of the data. *Journal of Trace and Microprobe Techniques*, 20(1): 127-140.
26. Sokolowski, A., Wolowicz, M. and Hummel, H. (2001). Distribution of dissolved and labile particulate trace metals in the overlying bottom water in the Vistula River Plume (Southern Baltic Sea). *Marine Pollution Bulletin*, 42(10): 967-980.
27. Xu, Z., Lim, D., Choi, J., Yang, S and Jung, H. (2009). Rare earth elements in bottom sediments of major rivers around the Yellow Sea: implications for sediment provenance. *Geo-Mar. Letter*, 29: 291-300.
28. Caccia, V. G. and Milero, J. F. (2007). Distribution of yttrium and rare earths in Florida Bay sediments. *Marine Chemistry*, 104:171-185.
29. Yang, S. Y., Jung, H. S., Choi, M. S. and Li, C. X. (2002). The rare earth element compositions of the Changjiang (Yangtze) and Huanghe (Yellow) river sediments. *Earth Planet Science Letter*, 201:407-419.
30. Ramesh, R., Ramanathan, A. L., James, R. A., Subramaniam, V., Jacobson, S. B. and Holland, H. D. (1999). Rare earth elements and heavy metal distribution in estuarine sediments of east coast of India. *Hydrobiologia*, 397: 89-99.
31. Ashraf, A., Saion, E., Gharibshahi, E., Kamari, H. M., Kong, Y. C., Hamzah, M. S. and Elias, M. S. (2016). Rare earth elements in core marine sediments of coastal East Malaysia by instrumental neutron activation analysis. *Applied Radiation and Isotopes*, 107: 17-23.
32. Goldstein, S. J. and Jacobsen, S. B. (1988). Rare earth elements in river waters. *Earth and Planetary Science Letters*, 89: 35-47.

Malaysian Journal of Analytical Sciences, Vol 23 No 6 (2019): 1067 - 1076
DOI: https://doi.org/10.17576/mjas-2019-2306-14

MALAYSIAN JOURNAL OF ANALYTICAL SCIENCES
Published by The Malaysian Analytical Sciences Society
ISSN 1394 - 2506

SETTLEMENT RATE OF FOULING SERPULID *Ficopomatus* cf. *uschakovi* PILLAI, 1960 ON ARTIFICIAL STRUCTURE AT SETIU WETLANDS, TERENGGANU, MALAYSIA

(Kadar Penempatan Petumbuhan Serpulid *Ficopomatus* cf. *uschakovi* Pillai, 1960 pada Struktur Tiruan di Tanah Bencah Setiu, Terengganu, Malaysia)

Noor Shahida Rosli[1], Nurulafifah Yahya[1], Izwandy Idris[1,2], Zainudin Bachok[1]*

[1]*Institute of Oceanography and Environment,*
[2]*South China Sea Repository and Reference Centre, Institute of Oceanography and Environment,*
Universiti Malaysia Terengganu, 21030 Kuala Nerus, Terengganu, Malaysia

**Corresponding author: zainudinb@umt.edu.my*

Received: 30 October 2018; Accepted: 26 September 2019

Abstract

Fouling polychaetes from genus *Ficopomatus* are known to have adverse impacts on human activities through fouling on man-made structures such as ship hulls, seawater intake pipes and aquaculture platforms. Various studies on fouling patterns of the fouling species have been done worldwide, as some of the species are estuarine invaders, which have become pests to the environment. This study was conducted to determine the spatial and temporal distribution of the *Ficopomatus* cf. *uschakovi* settlement and their relationship with environmental parameters in Setiu Wetlands. A monthly assessment was conducted at three stations for 14 months from May 2017 until July 2018. A frame consisting of three replicates of perspex plate (14 x 10 cm) was placed randomly at each station and collected for assessment every month. All *F.* cf. *uschakovi* tubes on the front and back of the plate were counted. Physico-chemical parameters collected included temperature (^{o}C), salinity (ppt), pH and dissolved oxygen (mg/L) of the water column. The results showed the larval attachments were spatially and temporally variable. A higher density of *F.* cf. *uschakovi* tubes was recorded at the station with protected area and orientation. The settlement rate of *F.* cf. *uschakovi* was low, at only 0.044 individuals.dm^{-2}/sampling month. It was further found out that the distribution and occurrence of *F.* cf. *uschakovi* tubes in Setiu Wetlands was affected by the environmental parameters, particularly, temperature, salinity and pH of the water column.

Keywords: fouling polychaete, Serpulidae, *Ficopomatus*, larval settlement, Setiu Wetlands

Abstrak

Petumbuhan poliket dari genus *Ficopomatus* diketahui memberi kesan buruk terhadap aktiviti manusia melalui petumbuhan pada struktur buatan manusia seperti badan kapal, paip pengambilan air laut dan pelantar akuakultur. Pelbagai kajian mengenai corak petumbuhan bagi spesies ini telah dilakukan di seluruh dunia, kerana sesetengah spesies adalah penceroboh muara, sehingga menjadi perosak kepada alam sekitar. Kajian ini dijalankan untuk menentukan taburan tempat dan masa bagi penempatan *Ficopomatus* cf. *uschakovi* dan hubungannya dengan parameter sekitar di Tanah Bencah Setiu. Penilaian bulanan dilakukan pada tiga stesen selama 14 bulan dari Mei 2017 hingga Julai 2018. Bingkai yang terdiri daripada tiga replikasi plat perspeks (14 x 10 cm) diletakkan secara rawak di setiap stesen dan dikumpulkan untuk penilaian setiap bulan. Kesemua tiub *F.* cf. *uschakovi* di bahagian depan dan belakang plat dikira. Parameter fiziko-kimia yang dikumpulkan ialah suhu (^{o}C), saliniti (ppt), pH dan oksigen terlarut (mg/L). Hasilnya menunjukkan penempatan larva berubah-ubah mengikut lokasi dan tempoh masa. Ketumpatan tiub *F.* cf. *uschakovi* yang tinggi dicatatkan di stesen yang berkawasan dan berorientasi terlindung. Kadar penempatan *F.* cf. *uschakovi* adalah rendah, iaitu hanya 0.044 individu.dm^{-2}/bulan pensampelan. Penemuan seterusnya mendapati bahawa taburan

dan kehadiran tiub *F.* cf. *uschakovi* di Tanah Bencah Setiu dipengaruhi oleh parameter sekitar, terutamanya, suhu, kemasinan, oksigen terlarut dan pH turus air.

Kata kunci: petumbuhan poliket, Serpulidae, *Ficopomatus*, penempatan larva, Tanah Bencah Setiu

Introduction

Fouling is an undesirable accumulation of unwanted organisms (e.g., microorganisms, plants, algae and animals) on submerged structures that happens all over the world [1-3]. Several examples of fouling communities are algae, ascidians, crustaceans, hydroids, molluscs, sea anemones, sponges as well as polychaetes [4]. Fouling polychaete can be tubeworms (family Sabellidae and Serpulidae) or burrowers (family Spionidae and Terebellidae), but the most important components of the fouling polychaete community globally are the serpulids [4-7].

Serpulids are distributed globally in tropical, subtropical and temperate areas around the world, mainly in the intertidal zone whereby they can also be found attached on mangrove plants [8]. Serpulids are sessile and filter feeder polychaete that have protandric hermaphroditism, broadcast spawning and have a lifespan of one to five years [5]. Past studies had discovered that the serpulids prefer an enclosed area with turbid waters, rich in organic matter and weak water currents [9]. Besides this, temperature and salinity are factors that affect the reproduction and settlement of serpulids. Serpulids are also known as ecosystem engineers as they can; 1) improve water quality with their high rate of ingestion and particle clearance; 2) act as efficient suspension feeders as they eat suspended detritus and phytoplankton; 3) act as reef builders, where many associated organisms live together, hence causing an increase in biodiversity and abundance of the affected areas; and 4) help in bio-erosion [9, 10].

Research on fouling serpulids has been done worldwide, as some of the species are global estuarine invaders, including genus *Ficopomatus* Southern, 1921 [11]. *Ficopomatus* are euryhaline species and are the only brackish water serpulids that are classified under the subfamily Serpulinae. They are capable of building large, reef-like colonies that can have strong ecological and economic impacts [12]. For example, they can foul on man-made structures, aquaculture structures and seawater intake pipes. This fouling behaviour increases drag on the vessels, decrease structure stability and durability, thereby reducing water flow, oxygen supply, food intake and waste removal of cultured species [4, 5]. In an ecological aspect, *Ficopomatus* are capable of invading areas outside of their original geographical distribution via vessels, which contribute to the alteration of the composition and function of benthic communities [4, 9]. For instance, *Ficopomatus enigmaticus* (Fauvel, 1923) is originally described from Caen Canal (northwestern France), but was recorded worldwide in temperate and subtropical waters. However, the information about the ecological and economic effects of this genus in the world is still scarce because they are small in size and hence are often overlooked or ignored [4].

The Setiu Wetlands are in a semi-enclosed area and are complex wetlands located in the east coast of Peninsular Malaysia, within the southern South China Sea region (sSCS) [13]. The wetland belongs to the Terengganu state under the District of Setiu, covering 23,000 ha of land and 880 ha of water body [14]. It consists of nine types of interconnected ecosystems which include seas, beaches, mudflats, lagoons, estuaries, rivers, mangrove forests, islands and coastal forests [15]. Each of these are characterised by unique yet intricate physical environments that support their biological entities [14]. Cage cultures are one of the main activities in Setiu Wetlands. However, the accumulation of fouling organisms (oyster, barnacle, tubeworms, etc.) on the cage cultures is the main constraint to such activities, as it reduces the effectiveness of the cages.

In Malaysia, the fouling serpulids are not well known, and, to date there are only a few records about serpulids that occur in Malaysian waters [16]. In the Setiu Wetlands, *F.* cf. *uschakovi* can be found attached on the mangrove plants such as on the root of *Rhizophora apiculata*, on the bark of *Nypa fruticans*, on oysters clump as well as on the cage culture activities. Therefore, this study aims to determine the spatial and temporal distribution of *Ficopomatus* cf. *uschakovi* settlements and to investigate the effect of environmental parameters on their settlements in Setiu Wetlands. Hence, this study will improve on the existing fouling polychaete information and hence provide a better understanding of this group in Malaysia. The output from this study could be used as baseline data for the aquaculture industry, for future investigations on environmental changes in this area and as a reference for wetland management activities.

Materials and Methods

Study area

Monthly field sampling was conducted from May 2017 to July 2018 (14 months) during low tide, at three stations (Figure 1) which were chosen in order to represent the range of activities within the study area (Table 1). The physical water quality parameters (temperature, salinity, pH and dissolved oxygen) were measured in situ using a water quality multi-parameter instrument, either a Hydrolab Quanta (Multiprobe System) or a YSI meter.

Experimental method and sampling

A frame consisting of smooth sides of white perspex (14 x 10 cm) with three replicates (n=3) was attached randomly on a floating raft at each station and was submerged 0.2 m below the estuary surface water, following [9] slight modifications (Figure 2). Each perspex was labelled at the front (facing outside the raft) and back (facing inside the raft) sides. Each plate was photographed from the front and the back using a digital camera (Canon IXUS 175). Then, the photographed plates were removed and placed in containers filled with *in situ* water and aerated. New plates were placed and left for a month after each assessment time.

Laboratory analysis

In the laboratory, both sides (front and back) of each plate were observed. All *F.* cf. *uschakovi* tubes present were counted and preserved in 80% ethanol. The density is determined as a total number of individual(s) per decimeter^2 (No. of individuals.dm^{-2}) (1 dm = 100 cm). The settlement rate for *F.* cf. *uschakovi* was calculated using the formula based from [7]:

$$\text{Settlement rate} = \frac{\text{Mean density (Individuals.dm}^{-2})}{\text{Total no. of sampling months}} \quad (1)$$

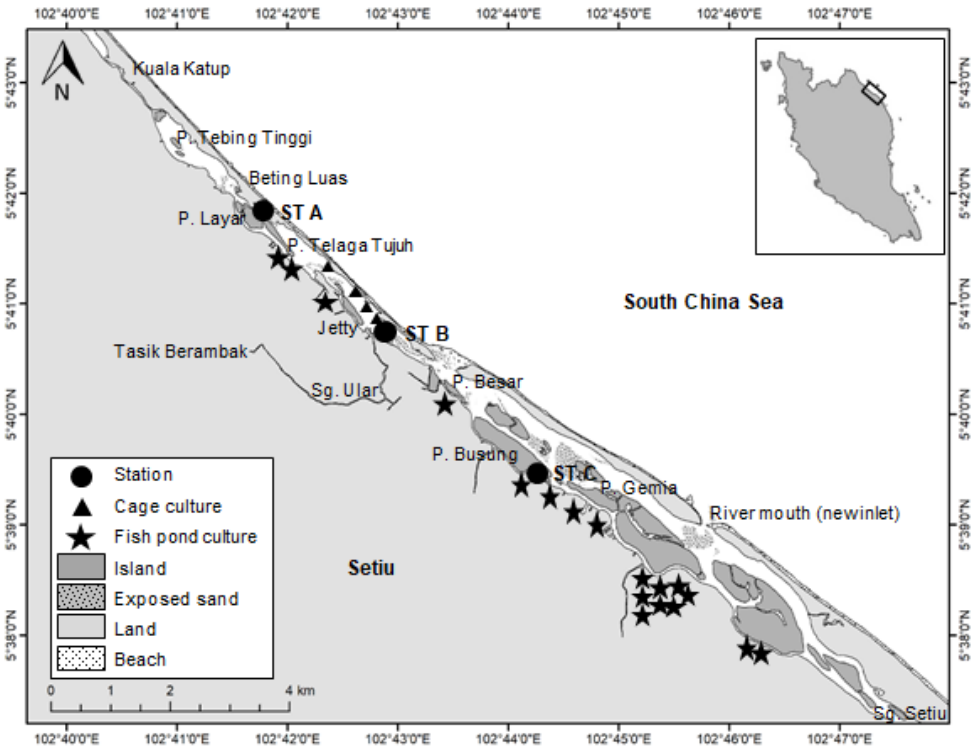


Figure 1. The locations of sampling station at Setiu Wetlands

Table 1. Description of the sampling stations

Station	Coordinate		Site Description
	Latitude (N)	Longitude (E)	
A	5°41' 50.40"	102°41' 42.20"	Northern part of the lagoon. Lack of human activity.
B	5°40' 46.44"	102°42' 50.58"	Middle part of the lagoon. Center of human activities such as boat landing, aquaculture, and seafood-based food production [13]
C	5°39' 25.68"	102°44' 20.70"	Southern part of the lagoon. Sheltered area with small scale fishponds and abandoned cage cultures

Statistical analyses

Calculations on significant differences in the mean of biological parameters (e.g. density of *F.* cf. *uschakovi*) and physico-chemical parameters (temperature, salinity, DO, pH) among stations and sampling periods were performed using SPSS (Statistic Package for Social Science) version 22. For the data that failed to meet the assumptions of analysis of variance (ANOVA), the Kruskal Wallis test was used. If the one-way ANOVA showed a significant result, a post hoc test was conducted for a pairwise comparison. For all tests, a criterion of $p < 0.05$ was used to determine statistical significance. The PCA analysis was conducted to determine the factor that affected the distribution of *F.* cf. *uschakovi*.

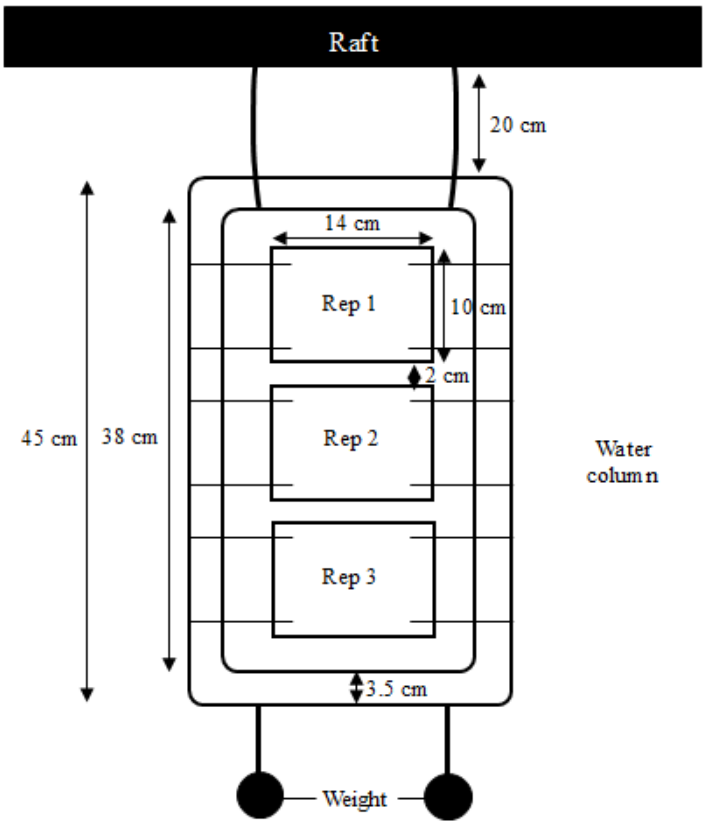


Figure 2. Diagram of a single experimental frame attached on a raft consists of 3 perspex plates

Results and Discussion

In the present study, mean temperature, salinity, DO, and pH exhibited approximately a similar pattern at all sampling stations throughout the study period (Figure 3). The Kruskal Wallis test showed that all the parameters did not differ significantly ($p > 0.05$) between sampling stations. The mean temperatures observed ranged between 28 ^{o}C and 33 ^{o}C. The range of water Salinity was between 2 ppt and 31 ppt (Figure 3). High mean salinity was recorded at ST C due to its location near the river mouth which contributes more seawater. The lowest salinity values were recorded during December 2017 (2 to 4 ppt), which was because of the influence of rainfall during the sampling activities. The salinity values saw a reduction from October until February because of the northeast monsoon that dominates the sSCS region from November to March every year, which results in strong northeasterly monsoon wind stress and heavy rainfall [17].

The mean DO concentrations ranged from 2.6 mg/L to 11.9 mg/L (Figure 3), which were lower compared to Suratman et al. [13]. This was probably due to the location of the station, which is in an area where a large scale of palm oil plantation activity takes place, upstream of the Sungai Ular (Figure 1). The use of fertilisers at this plantation increased the runoff of nutrients, thus increasing the phytoplankton growth, followed by the decomposition processes when the phytoplankton died, resulting in low DO in the water column [13, 18]. Moreover, it was probably due to the aquaculture activities in the area. A decrease of the DO concentration can also be as a result of the respiration of the farm fish and other aquatic organisms inside the caged area of the water column [19]. Besides that, low DO at ST C was probably also caused by the input of domestic wastes from the town of Penarik, located upstream of Sungai Setiu. While for pH, the values ranged between 5.6 and 8.1 (Figure 3). Generally, there was no consistent trend of high or low pH values at the different stations, with water pH being similar throughout the sampling period for all stations.

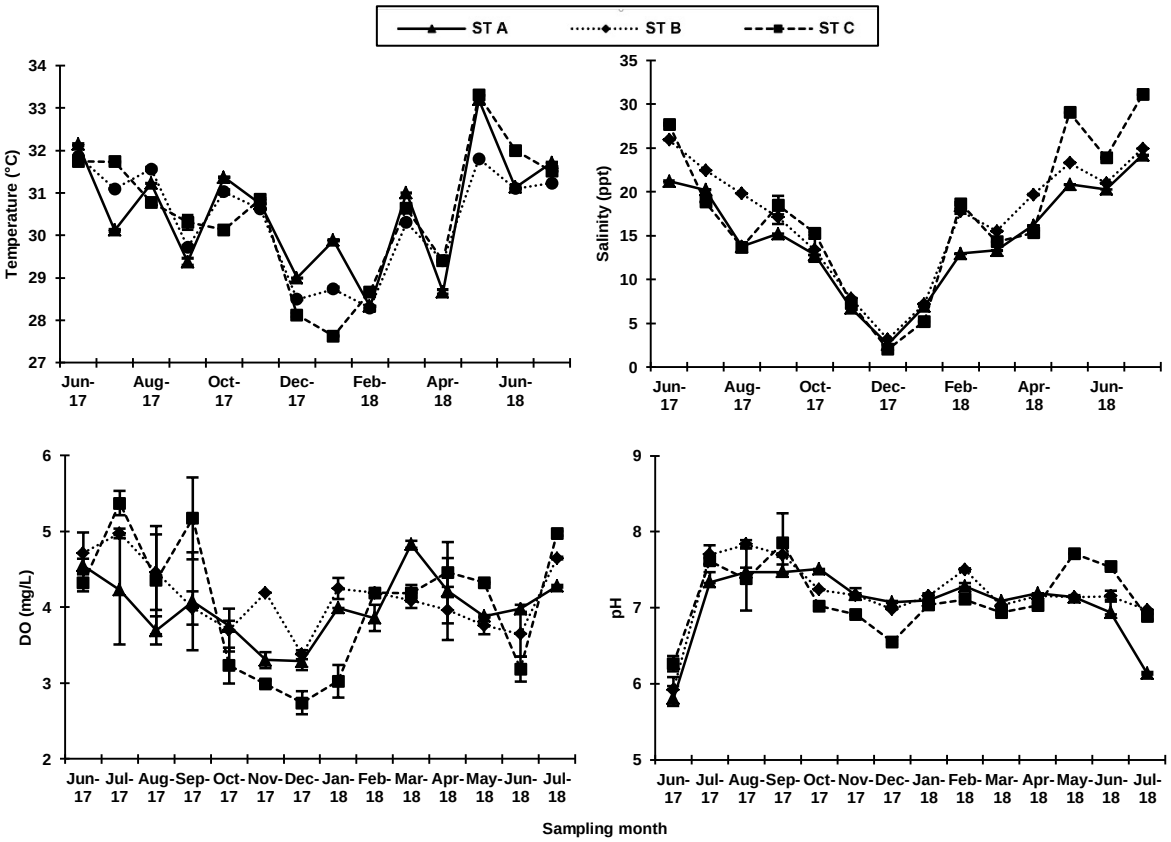


Figure 3. Variation of mean temperature, salinity, DO and pH at station A, B, and C of Setiu Wetlands

Mean density of *F.* cf. *uschakovi* tube (individuals/dm^2) attached on the plate is shown in Figure 4. The Kruskal Wallis test showed that the mean density of the front and back side of the plate did not differ significantly ($p > 0.05$) between sampling stations. A wide variation of *F.* cf. *uschakovi* density was found throughout the study period. A high density of *F.* cf. *uschakovi* tubes was recorded on the back side of the plate which was in a protected orientation compared to the front side. *F.* cf. *uschakovi* tubes were observed at all stations only in August 2017 (front), December 2017 (back) and January 2018 (back). ST C had a higher occurrence of *F.* cf. *uschakovi* tubes throughout the sampling months while ST A had the lowest occurrence. The finding shows that *F.* cf. *uschakovi* tubes preferred an area that was sheltered (ST C) and in protected orientation (back). Dittmann et al. [9] believed that salinity is one of the factors that affect the *F. enigmaticus* larval settlements. However, despite the low salinity during the monsoon (October – February), there was a high settlement of *F.* cf. *uschakovi* tubes in Setiu Wetlands. A previous study [20] showed that the current velocity in Setiu Wetlands ranges from 0.04 m sec^{-1} to 0.88 m sec^{-1} from November to February, which is very low. It might have been the reason for high settlements of *F.* cf. *uschakovi* tubes, as the tubes did not get easily detached from the plate and hence were not carried away by the currents.

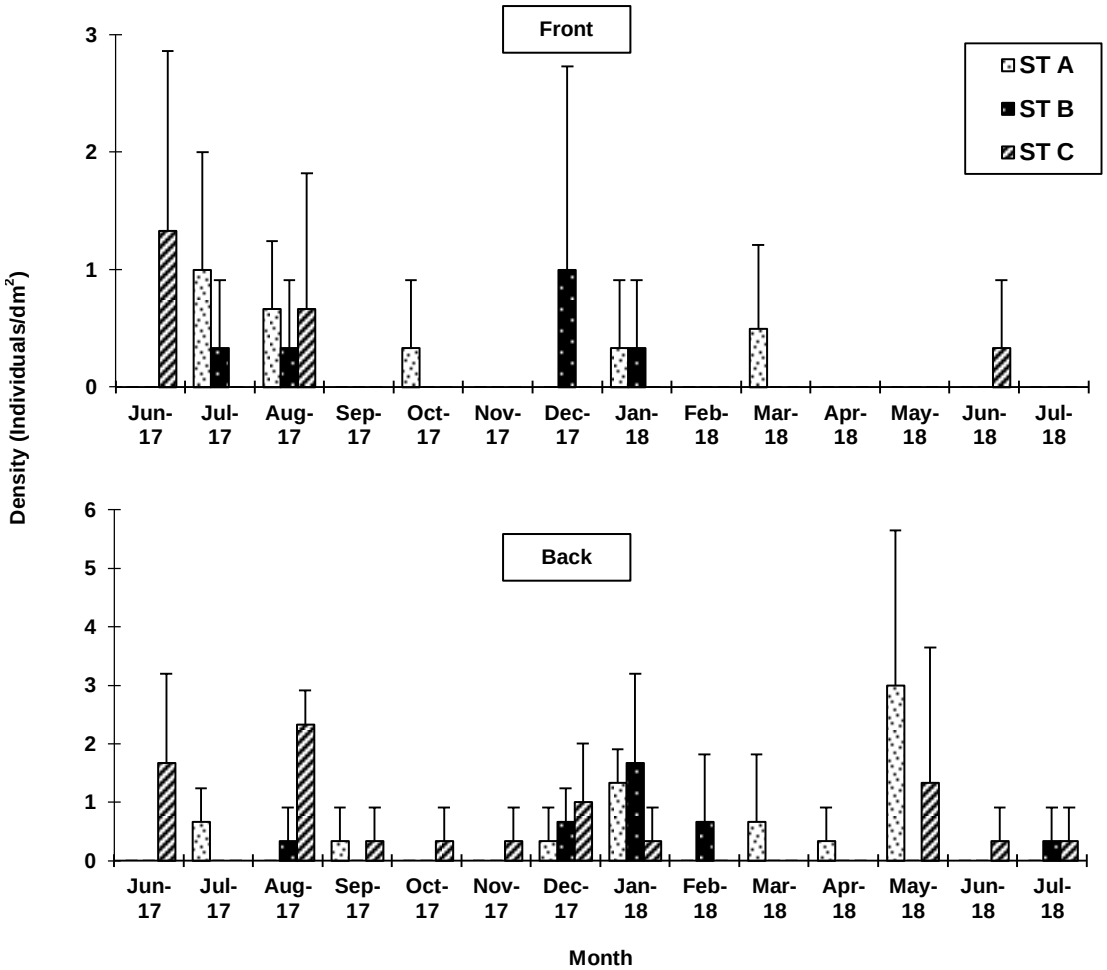


Figure 4. Colonisation pattern of *F.* cf. *uschakovi* on three perspex plates (mean ± standard deviation) submerged at station A, B and C of Setiu Wetlands

Settlement rates of *F.* cf. *uschakovi* tubes (individuals.dm^{-2}/month) at each sampling station throughout the sampling months are shown in Table 2 and Figure 5. Overall, the back side of the plate had a high settlement rate as compared to the front side, except for July 2017 (Figure 5). These results correlated with the mean density shown in Figure 4. An analysis of ST C showed that this area had the highest settlement rate of *F.* cf. *uschakovi* tubes (0.090 individuals.dm^{-2}/sampling month) for the back side of the plate compared to other stations. However, the settlement rate for the front side of the plate was almost similar for all three stations, which was within a range of 0.020 – 0.027 individuals.dm^{-2}/sampling month. This study had also found that the settlement rate of *F.* cf. *uschakovi* tubes was 0.044 individuals.dm^{-2}/sampling month, which generally considered to be low.

Table 2. Settlement rate of *F.* cf. *uschakovi* tube (individuals.dm^{-2}/sampling month) at each sampling station for 14 months from Jun 2017 until July 2018

Station	Plate Position	*F.* cf. *uschakovi* Settlement Rate (individuals.dm^{-2}/sampling month)
A	Front	0.027
	Back	0.067
B	Front	0.020
	Back	0.037
C	Front	0.023
	Back	0.090
Mean total		0.044

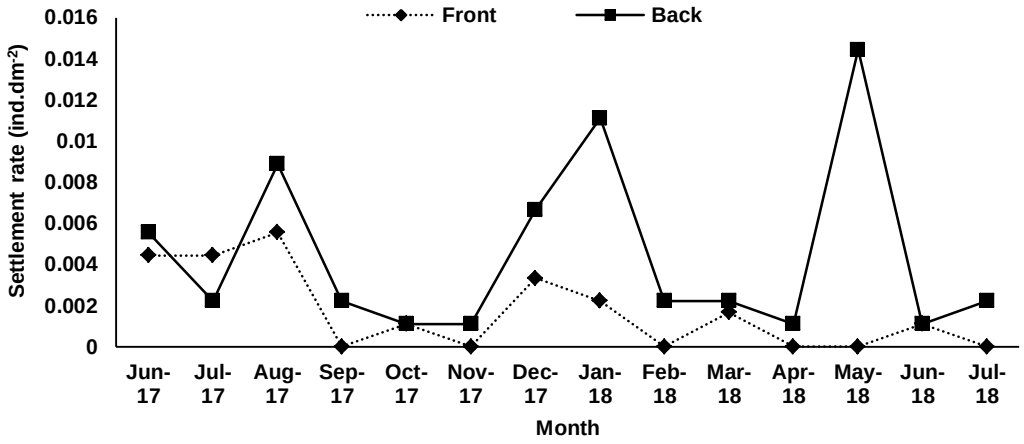


Figure 5. Settlement rate of *F.* cf. *uschakovi* tube (individuals.dm^{-2}/sampling month) on front and back of perspex plate for 14 months from Jun 2017 until July 2018

PCA analyses show that three factors can be extracted based on total eigenvalue more than 1 (Table 3), where all the factors had less than 50% of cumulative of variance (rotation sums of squared loadings). The total variance explained by the three-factor solution is 77.289%, which can be considered high. Each of the three factors explains a portion of the total variance and can be categorised as PC1 (32.829%), PC2 (23.923%) and PC3 (20.537%). Based on the rotated component matrix (Table 4, Figure 5), PC1 consists of temperature and salinity, PC2 consists of mean density (front & back), while PC3 consists of mean density (front & back) and pH. This finding shows that the distribution and settlement rate of *F.* cf. *uschakovi* tubes in Setiu Wetlands was affected by environmental parameters, particularly, the temperature, salinity and pH of the water column. Although Sateesh and Wesley [21]

said that the hydrobiological parameters are not a critical factor in a tropical coast, the occurrence and breeding periods of marine organisms largely depend on environmental fluctuations, particularly those involving temperature and salinity [22].

Table 3. Summary of Principal Component Analysis (PCA)

Component	Initial Eigenvalues			Rotation Sums of Squared Loadings		
	Total	% of Variance	Cumulative %	Total	% of Variance	Cumulative %
1	1.673	33.454	33.454	1.641	32.829	32.829
2	1.190	23.802	57.256	1.196	23.923	56.752
3	1.002	20.033	77.289	1.027	20.537	77.289
4	0.777	15.535	92.824			
5	0.359	7.176	100.00			

Table 4. Rotated component matrix

Variables	Component		
	1	2	3
Mean Density (Front)		0.755	0.270
Mean Density (Back)		0.790	-0.224
Temperature	0.900		
pH			0.948
Salinity	0.905		

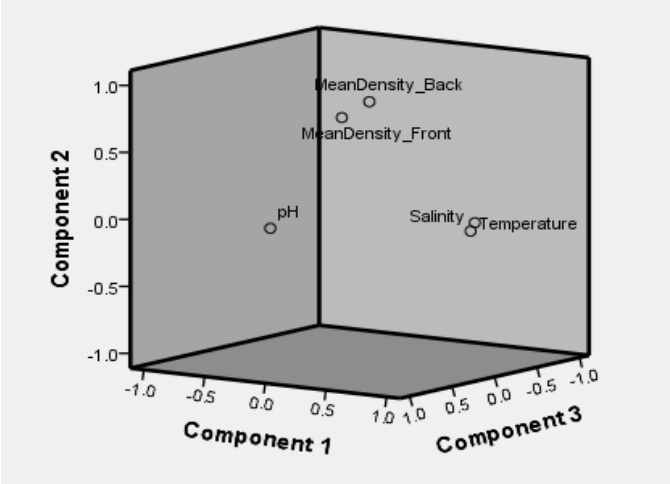


Figure 5. Component plot of five factors measured over sampling period

Conclusion

Ficopomatus cf. *uschakovi* larval attachments were found to be spatially and temporally variable. A higher density of *F.* cf. *uschakovi* tubes was recorded at the station with sheltered and in protected orientation. The settlement rate of *F.* cf. *uschakovi* was low, only 0.04 individuals.dm^{-2}/month. The distribution and settlement rate of *F.* cf.

uschakovi tubes in Setiu Wetlands was affected by environmental parameters, particularly, the temperature, salinity and pH of the water column. The information obtained from this study provides significant baseline information for sustainable wetland management ecosystem of Setiu Wetlands. However, yearly monitoring of *F.* cf. *uschakovi* distribution and settlement rate in Setiu Wetlands should be conducted. Further research on settlement cues for antifouling measures is needed for better understanding of this tubeworm in Malaysian waters.

Acknowledgement

This study was funded by research grants of Higher Institution Centre of Excellence (HICoE) Vote No. 66928 and Fundamental Research Grant Scheme (FRGS) Vote No. 59455, Ministry of Education Malaysia. We greatly appreciate colleagues, the local communities, especially Kamaruddin (boatman) and Azmi (owner of cage culture) who assisted us during the sampling activities, and staffs of Institute of Oceanography and Environment (INOS), Universiti Malaysia Terengganu, for their assistance.

References

1. Dürr, S. and Thomason, J. C. (2010). Biofouling. Blackwell Publishing Ltd, United Kingdom: pp. 1-429.
2. International Maritime Organization (2017). Biofouling. http://www.imo.org/en/OurWork /Environment/Biofouling/Pages/ default.aspx. [Access online 25 October 2017].
3. Swami, B. S. and Udhayakumar, M. (2010). Seasonal influence on settlement, distribution and diversity of fouling organisms at Mumbai harbor. Indian Journal of Marine Science, 39(1): 57-67.
4. Bloecher, N., Olsen, Y. and Guenther, J. (2013). Variability of biofouling communities of fish cage nets: A 1-year field study at a Norwegian salmon farm. Aquaculture, 416: 302-309.
5. Bastida-Zavala, J. R., McCann, L. D., Keppel, E. and Ruiz, M. (2017). The fouling serpulids (Polychaeta: Serpulidae) from United States coastal waters: An overview. European Journal of Taxonomy. 344: 1-76.
6. Lewis, J. A. (1982). A guide to the principal marine fouling organisms with particular reference to Cockburn Sound. W.A. Report for the Department of Defence Support, Defence Science and Technology Organisation, Melbourne, Victoria. pp. 1-28.
7. Madin, J. (2010). Biofouling and short-term dynamics on fish cage netting in relation to fish rearing and environmental factors. Thesis of Doctor of Philosophy, University of Malaya.
8. Bastida-Zavala, J. R. and Garcia-Madrigal, S. (2012). First record in the Tropical Eastern Pacific of the exotic species *Ficopomatus uschakovi* (Polychaeta, Serpulidae). ZooKeys, 238: 45-55.
9. Dittmann, S., Rolston, A., Benger, S. N. and Kupriyanova, E. K. (2009). Habitat requirements, distribution and colonisation of the tubeworm *Ficopomatus enigmaticus* in the Lower Lakes and Coorong. Report for the South Australian Murray-Darling Basin Natural Resources Management Board, Adelaide: pp. 1-99.
10. Kupriyanova, E. K. and Dittmann, S. (2008). Literature review on the reef-building serpulid polychaete *Ficopomatus enigmaticus* (Fauvel, 1923: *Mercierella enigmatica*): distribution, ecology, reproduction, control. School of Biological Sciences, Flinders University, Adelaide. pp. 1-35.
11. Styan, C. A., McCluskey, C. F., Sun, Y. and Kupriyanova, E. K. (2017). Cryptic sympatric species across the Australian range of the global estuarine invader *Ficopomatus enigmaticus* (Fauvel, 1923) (Serpulidae, Annelida). Aquatic Invasions, 12(1): 53-65.
12. Hove, H. A. and Kupriyanova, E. K. (2009). Taxonomy of Serpulidae (Annelida, Polychaeta): The state of affairs. Zootaxa, 2009: 1-126.
13. Suratman, S., Hussein, A. N. A. R., Mohd Tahir, N, Latif, M. T., Mostapa, R. and Weston, K. (2016). Seasonal and spatial variability of selected surface water quality parameters in Setiu Wetlands, Terengganu, Malaysia. Sains Malaysiana, 45(4): 551-558.
14. Salim, J. M., Mohamad, F. and Shahrudin, R. (2015). Setiu: More than a wetland. In: Setiu Wetlands: Species, Ecosystems and Livelihoods. Penerbit Universiti Malaysia Terengganu, Kuala Terengganu: pp. 87-100.
15. Yaacob, R., Bachok, Z., Yahya, M. H., Saidin, A. A. and Ibrahim, S. (2006). Habitat status and management issues of Setiu Wetlands and Merang coastal areas, east coast of Peninsular Malaysia. In: KUSTEM 5th Annual Seminar on Sustainability Science and Management, Terengganu: pp. 501-507.
16. Rosli, N. S. and Bachok, Z. (2016). Diversity of Polychaeta (Annelida) in the continental shelf of southern South China Sea. Middle-East Journal of Scientific Research, 24(6): 2086 – 2092.
17. Akhir, M. F. (2014). Review of current circulation studies in the southern South China Sea. Journal of Sustainability Science and Management, 9(2): 21-30.

18. Sullivan, A. B., Snyder, D. M, and Rounds, S. A. (2010). Controls on biochemical oxygen demand in the upper Klamath River, Oregon. Chemical Geology, 269: 12-21.
19. Sidik, M. J., Un-Nabi, M. R. and Hoque, M. A. (2008). Distribution of phytoplankton community in relation to environmental parameters in cage culture area of Sepanggar Bay, Sabah, Malaysia. Estuarine, Coastal and Shelf Science, 80: 251-260.
20. Norzilah, A., Ahmad, M. F., Tofany, N., Yaacob, R. and Muslim, A. M. (2016). Hydrodynamics modelling at Setiu Wetland, Terengganu. Journal of Environmental Science and Technology, 9: 437-445.
21. Sateesh, S. and Wesley, S. G. (2011). Influence submersion season on the development of test panel biofouling communities in a tropical coast. Estuarine, Coastal and Shelf Science, 94: 155-163.
22. Sahu, G., Achary, M. S., Satpathy, K. K., Mohanty, A. K., Biswas, S. and Prasad, W. V. R. (2011). Studies on the settlement and succession of macrofouling organisms in the Kalpakkam coastal waters, southeast coast of India. Indian Journal of Geo-Marine Sciences, 40(6): 747-761.

Malaysian Journal of Analytical Sciences, Vol 23 No 6 (2019): 1077 - 1089
DOI: https://doi.org/10.17576/mjas-2019-2306-15

MALAYSIAN JOURNAL OF ANALYTICAL SCIENCES
Published by The Malaysian Analytical Sciences Society
ISSN 1394 - 2506

DISTRIBUTION AND BEHAVIOR OF NUTRIENTS IN BESUT RIVER ESTUARY, TERENGGANU, MALAYSIA

(Taburan dan Perlakuan Nutrien di Muara Sungai Besut, Terengganu, Malaysia)

Fatin Adlina Md Nasir[1], Suhaimi Suratman[1]*, Dung Quang Le[2]

[1]*Institute of Oceanography and Environment,*
Universiti Malaysia Terengganu,
21030 Kuala Nerus, Terengganu, Malaysia.
[2]*Health and Safety, Group Health, Safety, Security and Environment,*
Tower 1, PETRONAS Twin Towers, Kuala Lumpur City Centre,
50088 Kuala Lumpur, Malaysia.

**Corresponding author: miman@umt.edu.my*

Received: 30 October 2018; Accepted: 26 September 2019

Abstract

This study was designed to determine the distribution and behaviour of nitrogen-, phosphorus- and silicon- based nutrients, chlorophyll-a and physical parameters in the Besut River estuary area (southern water of South China Sea). Surface water samples at a depth of 1 meter were collected using a Van Dorn sampler along the salinity gradient. All nutrients behaved in a non-conservative manner in the study area. The concentrations of nitrite, ammonia, dissolved inorganic phosphate, total dissolved phosphate, silicate, total dissolved silicate and total particulate silicate showed positive deviation from the theoretical dilution line. Their concentrations ranged from 3.02 µM - 12.75 µM (mean 0.137 ± 0.137 µM), 0.45 µM - 5.21 µM (mean 2.80 ± 1.40 µM), 0.02 µM - 0.75 µM (mean 0.32 ± 0.17 µM), 0.05 µM - 0.98 µM (mean 0.54 ± 0.23 µM), 0.03 µM - 10.32 µM (mean 3.61 ± 2.10 µM), 0.01 µM - 5.27 µM (mean 2.66 ± 1.01 µM) and 0 µM - 6.30 µM (mean 2.90 ± 1.29 µM), respectively. In contrast, the concentrations of nitrate, total dissolved nitrogen and total particulate phosphate were found to be in the negative deviation region, with concentrations ranging from 3.02 µM to 12.75 µM (mean 6.65 ± 1.27 µM), 4.54 µM to 15.83 µM (mean 9.28 ± 2.16 µM) and 0.06 µM to 2.26 µM (mean 0.65 ± 0.32 µM), respectively. Based on the Redfield molar ratio, dissolved inorganic phosphate was the nutrient limiting factor for phytoplankton growth in this estuary.

Keywords: nutrients, surface water, distribution, behaviour, Besut River estuary

Abstrak

Tujuan kajian ini dijalankan adalah untuk menentukan taburan dan perlakuan sebatian berasaskan nitrogen, fosforus dan silikon, klorofil-a dan parameter fizikal di muara Sungai Besut (bahagian selatan Laut China Selatan). Sampel air telah diambil dengan menggunakan pensampel Van Dorn pada kedalaman 1 meter di bawah permukaan air pada saliniti yang berbeza. Kesemua sebatian nutrien berkelakuan tak konservatif di muara sungai ini. Kepekatan nitrit, ammonia, fosfat takorganik terlarut, jumlah terlarut fosfat, silikat dan jumlah terlarut silikat menunjukkan sisihan positif daripada garisan pencairan teori di mana kepekatan masing-masing berada berjulat dari 3.02 µM - 12.75 µM (purata 0.137 ± 0.137 µM), 0.45 µM - 5.21 µM (purata 2.80 ± 1.40 µM), 0.02 µM - 0.75 µM (purata 0.32 ± 0.17 µM), 0.05 µM - 0.98 µM (purata 0.54 ± 0.23 µM), 0.03 µM - 10.32 µM (purata 3.71 ± 2.13 µM), 0.01 µM - 5.27 µM (purata 2.66 ± 1.01 µM) dan 0 µM - 6.30 µM (purata 2.90 ± 1.29 µM). Walau bagaimanapun, nitrat, jumlah nitrogen terlarut, jumlah partikulat nitrogen dan jumlah partikulat fosfat masing-masing berada dalam kawasan sisihan negatif dengan kepekatan di antara 3.02 µM hingga 12.75 µM (purata 6.65 ± 1.27 µM), 4.54 µM hingga 15.83 µM (purata 9.28 ± 2.16 µM) dan 0.06 µM hingga 2.26 µM (purata 0.65 ± 0.32 µM). Berdasarkan nisbah molar Redfield, fosfat takorganik terlarut, adalah nutrien penghad untuk pertumbuhan fitoplankton di muara ini.

Kata kunci: nutrien, air permukaan, taburan, perlakuan, muara Sungai Besut

Introduction

Estuarine environments are among the most productive on earth, creating more organic matter each year than comparably sized areas of forests, grasslands or agricultural lands [1]. It is a zone of high biological productivity compared to rivers and oceans, as it controls the quantity of nutrient input from river to reach the ocean [2]. According to Wan Omar et al. [3], an estuary receives continuous mixed inflow from both sea and fresh water, which is influenced by high tides and low tides. This causes the estuary to receive nutrients from land-based points and nonpoint sources, atmospheric and groundwater inputs, where each source contributes different amount of specific nutrients, which varies their proportional ratio to that of other nutrients in that source [4]. Nutrients such as nitrogen (nitrate, nitrite and ammonia), phosphate and silicate are used as a benchmark to indicate the water quality of estuaries and whether the water bodies can maintain their designated uses or not.

However, the rapid population growth is upsetting the natural balance of estuarine ecosystems and threatening their integrity [5], as it has increased the demand for fertilizer use, sewage output, untreated effluents from industries, runoff from agriculture land and use of freshwater [4]. According to Patricia et al. [4], this condition could lead to eutrophication, landscape changes, invasive species, and alterations to hydrology, overfishing and climate change. Eutrophication is a major type of water pollution where excessive richness of nutrients in water encourages algae growth, causing algae to bloom over the water surface [6]. Due to recent rapid industrial and agricultural developments, there are many tropical rivers in Southeast Asia that have suffered serious eutrophication [7], as estuaries receive substantial amounts of anthropogenic inputs from both point and non-point upstream sources of pollution from industrialization and urbanization activities [2].

A previous study by Smith [8] revealed that nitrogen and phosphorus are chosen as the limiting factors that help control the biological activity such as phytoplankton growth in marine systems. It is believed that nitrogen availability limits the net organic production in marine ecosystems, and that phosphorus availability limits the net organic production in freshwater ecosystems [8]. During the transportation from the freshwater i.e. river to the estuary and coastal area, the nutrients can behave either conservatively or non-conservatively, depending upon environmental conditions such as precipitation, change in river flow and biological activities [9].

In Malaysia, many studies on the distribution of nutrients and impacts of human activities on water quality have been done in many locations such as on Merbuk River estuary [10], Selangor River estuary [11], and Kuala Sibuti river estuary [12]. However, their behaviour in the estuaries during the mixing process between the fresh and saline waters is not well documented. This study focuses on the determination of the distribution and behaviour of nitrogen (N)-, phosphorus (P)- and silicon (Si)- based nutrients, chlorophyll-a (chl-a) content and physical parameters in Besut River estuary.

Materials and Methods

The Besut river estuary is located on the east coast part of Peninsular Malaysia, an area of tropical climate, which is strongly influenced by the Northeast (NE) monsoon from November to February and Southwest (SW) monsoon from March to September. The NE monsoon brings heavy rain and strong wind, affecting the estuary physically and chemically; while SW monsoon is known as the dry season. There are few rivers that flow into the Besut River such as, Pelagat River, Jertih River, Tenang River, Angga River, Peda River, La River and Keriuk River. All constitutes in Besut River then flow to the coastal area of the South China Sea.

The early objective of this study was to know the effect of monsoon season on the distribution and behaviour of nutrients and the related parameters, but due to bad weather and heavy rainfall in the wet season, we only managed to get samples in the dry season. Samplings were carried out three times on 1/4/2003, 31/5/2003 and 27/8/2003, at 17 sampling stations along the salinity gradient in the Besut River estuary as shown in Figure 1. No fixed stations were sampled in this estuary as the main objective was to know the distribution and behaviour of the parameters measured and this is based on the concentration at different salinity regions [9]. The sampling started at the

freshwater area (station 1) and ended at coastal area (station 17). Water samples were collected at the surface water at about ~0.5 m depth using a Van Dorn Sampler, and stored in acid-washed high-density polyethylene (HDPE) bottles. The bottles then were kept in an ice chest during the sampling trip. The physical parameters were measured in situ using YSI Multiparameter Data Logger, which had been calibrated before the sampling. The parameters measured were salinity, temperature, dissolved oxygen (DO), pH and redox potential.

Water samples that were to be used for the determination of dissolved inorganic and organic nutrients were filtered through pre-combusted (450 ˚C) Whatman GF/F glass fibre filters using a vacuum pump. The filtration was carried out under low vacuum (<50 mm Hg) to avoid rupture of the filter, which would have resulted in the loss of dissolved organic nutrients. After that, all filtered and unfiltered water samples were stored frozen in HDPE bottles at -20 ˚C before analysis. The nutrients of dissolved and particulate forms were analysed using the standard colorimetric method [13], while the chlorophyll-a was determined spectrophotometrically [14]. In brief, the determination of nitrite, nitrate, ammonia, DIP and DISi was based on azo dye method, cadmium reduction column method, indophenol method, ascorbic acid method and molybdenum method, respectively. In order to know the concentration of total dissolved (TDN, TDP and TDSi) and particulate (TPP and TPSi) nutrients, water samples were persulphate wet digested so as to change the organic nutrients to inorganic form and analysed subsequently [13]. Concentrations of TPN were not presented due to data loss.

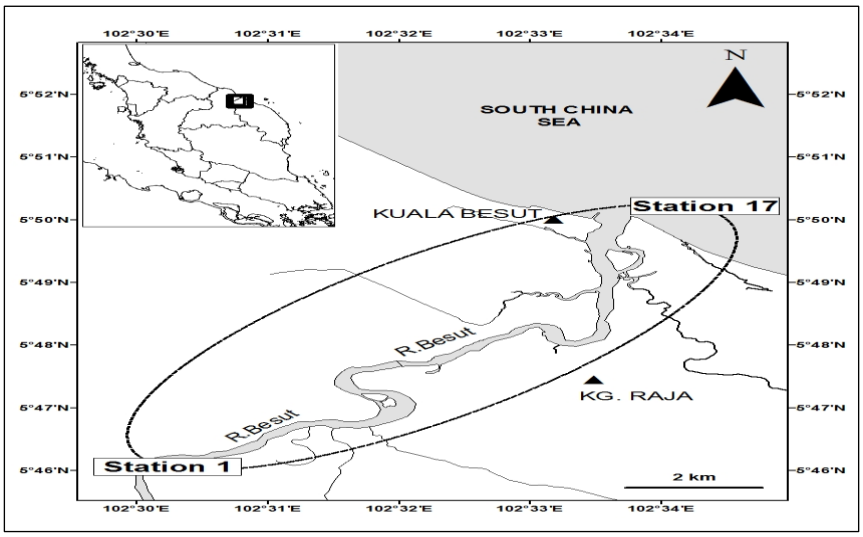


Figure 1. Location of sampling stations in Besut River estuary

Results and Discussion

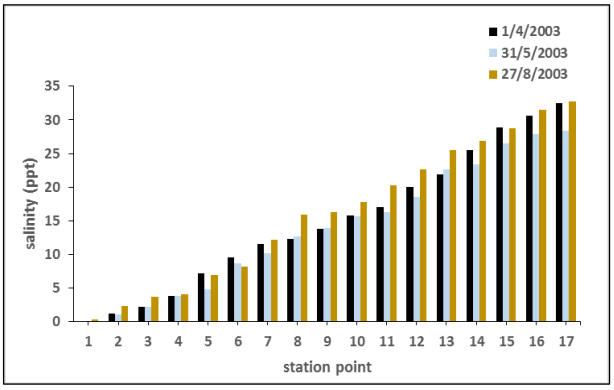
Physical parameters

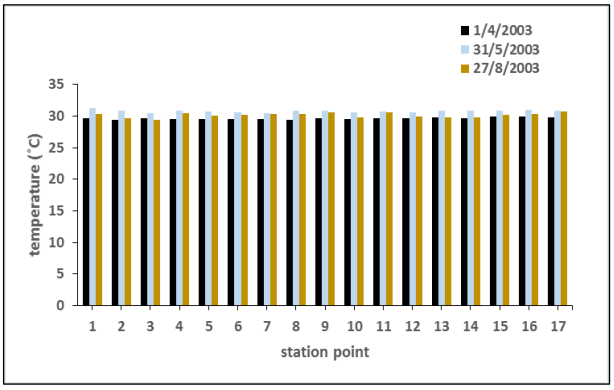
The physical parameters at different stations within the Besut River estuary are shown in Figure 2. Based on the ANOVA test, the salinity levels showed no significant differences among the dates ($p > 0.05$) and station points ($p > 0.05$). The data showed that the salinity levels increased in going from the freshwater to the coastal area due to the intrusion of more saline water with high salt content as compared to the low salt content at freshwater area. Salinity of an estuary is influenced by depth, daily tides and the volume of fresh water flowing into the estuary [15]. It can also be affected by rainfall loading, which can dilute the saline water, and evaporation, which leads to concentrated salt formation [16]. In this study, the values of salinity between the three samplings were not different as the samplings were performed at the same tide conditions and the same dry season.

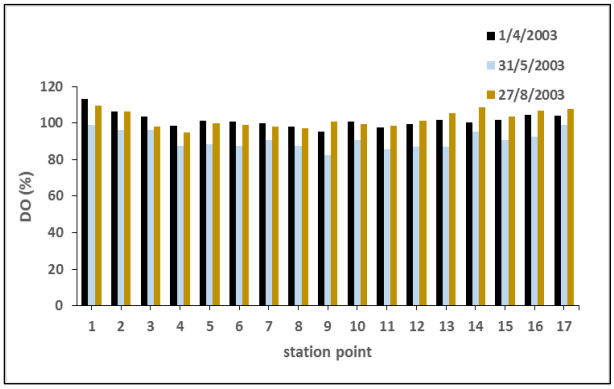
The water temperature was in the range of 29.81 ˚C to 30.47 ˚C (mean 30.19 ± 0.61 ˚C). There were no significant differences between sampling dates ($p > 0.05$) and sampling points ($p > 0.05$) based on the ANOVA test. The water temperature showed constant values for every sampling location, as the sampling was carried out during the daytime in the dry season.

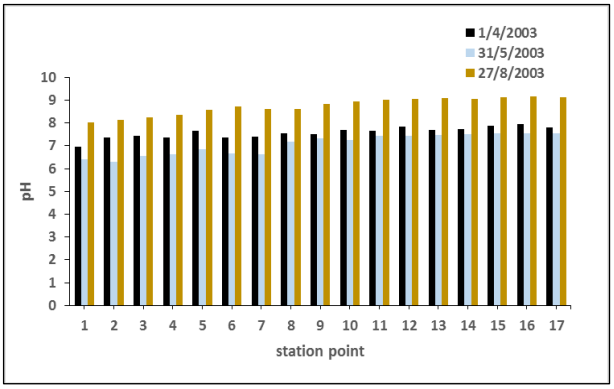
Based on the ANOVA analysis, the DO concentrations showed that there were no significant differences among the dates of sampling ($p > 0.05$) and sampling points ($p > 0.05$). The DO concentrations varied from 92.87% to 107.17% (mean 98.12 ± 6.63%), where relatively higher concentrations were detected at the freshwater region, and the lowest concentrations were detected at the coastal area. This is because, as the salinity of water increases, the solubility of oxygen in water decreases [17]. DO also has a negative correlation to the water temperature, where, the amount of oxygen dissolved in water decreases as the temperature increases [10]. However, this trend is not observed in this study as the temperature values were almost constant.

The values of pH were in the range of 7.13 to 8.21 (mean 7.80 ± 0.87). It showed no significant differences among the dates ($p > 0.05$) and sampling points ($p > 0.05$) based on the ANOVA test. The pH values had shown no variation throughout the sampling locations, due to the mixing of fresh and sea water, especially in the estuary as there was turbulence during the mixing. Generally, streams and rivers transport large quantities of dissolved and particulate constituents, which consist largely of humic materials, which are acidic in nature [10]. The average pH of seawater is typically around 8.2 [18].









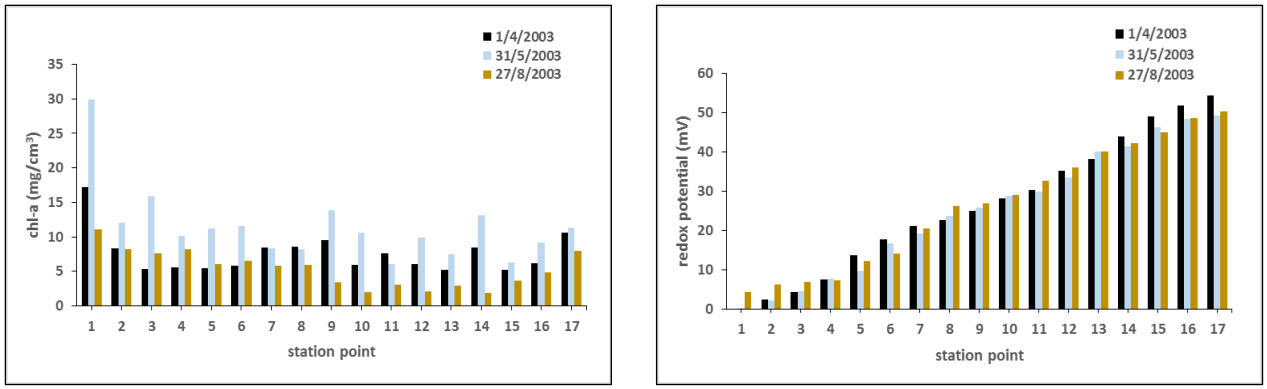


Figure 2. Variations of physical parameters at Besut River estuary

Therefore, the mixture of freshwater with low pH values and saltwater with high pH values causes the increase of pH values at the estuary. This occurs almost constantly due to turbulence mixing.

The chl-a concentration was recorded in the range of 5.05 mg/cm^3 to 19.40 mg/cm^3 (mean 8.16 ± 3.40 mg/cm^3). Based on the ANOVA test, the distribution of chl-a showed a significant difference ($p < 0.05$) between sampling stations but no difference ($p > 0.05$) between sampling dates. Relatively, higher chl-a concentration was found at the upstream area. This may be due to high nutrients at this area, as the nutrients such as nitrate and phosphate are known as the required nutrients for reproduction and growth of phytoplankton in an estuarine environment [19].

Based on the ANOVA analysis, the redox potential values showed that there were no significant differences among the dates of sampling ($p > 0.05$) and sampling points ($p > 0.05$). Redox potentials were found in the range from 1.55 mV to 51.25 mV (mean 25.91 ± 1.54 mV). The highest redox potential value was recorded at the coastal area, while the lowest value was recorded at the freshwater area. It showed that the redox potential values increased with the increasing salinity of water. The greater the salt contents, the higher the redox potential values.

Nutrients distribution

Figures 3, 4 and 5 shows the distribution of N-, P- and Si- based nutrients in the Besut River estuary, respectively. From the figure, it can be seen that Total Dissolved Nitrogen (TDN) recorded the highest concentration, ranging from 4.54 µM to 15.83 µM (mean 9.28 ± 2.16 µM), followed by nitrate, ammonia, and nitrite with the values of 3.02 µM - 12.75 µM (mean 6.65 ± 1.27 µM), 0.45 µM - 5.21 µM (mean 2.80 ± 1.40 µM) and 0.01 µM - 0.18 µM (mean 0.101 ± 0.023 µM), respectively. Among the P-based nutrients, Total Particulate Phosphate (TPP) was found to be the highest, ranging between 0.06 µM to 2.26 µM (mean 0.65 ± 0.33 µM), followed by Total Dissolved Phosphate (TDP) and Dissolved Inorganic Phosphate (DIP), with values of 0.05 µM to 0.98 µM (mean 0.54 ± 0.23 µM) and 0.02 µM to 0.75 µM (mean 0.32 ± 0.17 µM), respectively. Meanwhile for Si-based nutrients, Dissolved Inorganic Silicate (DISi) showed the highest concentration, ranging between 0.03 µM and 10.32 µM (mean 3.61 ± 2.10 µM). This was followed by Total Particulate Silicate (TPSi) and Total Dissolved Silicate (TDSi), with values of 0 µM to 6.30 µM (mean 2.90 ± 1.29 µM) and 0.01 µM to 5.27 µM (mean 2.66 ± 1.01 µM), respectively. TDSi concentration for third sampling was not included because the values were significantly lower than those in other sampling occasions due to sample loss during the analysis.

In general, the distributions of nutrients were fluctuated, where most of the nutrient compounds were found to increase towards the estuary area and decrease when reaching the coastal area. The mixing between fresh and seawater in the estuary will create water turbulence, and this process tends to release the nutrients from the resuspension of bottom sediment to the surface water. Differently from the middle estuary, the lower part of the estuary was strongly influenced by sea water, which then would dilute and lower the concentrations of nutrients in this lower part. These phenomena which recorded high nutrient concentrations due to the water turbulence and mixing in estuary, coincide with the results for many other estuaries [20-22].

However, unlike other nutrient compounds, the concentration of TPP showed a different trend, where it was lowest at the freshwater region and highest at the coastal area. This may suggest that the coastal area is the main contributor of TPP in the Besut River estuary, especially during the flood tides. A previous study in Humber estuary reported that TPP was found to be the highest at low salinity due to flocculation, and phosphate being trapped in the sediment of the estuary [23]. However, this condition was not observed in this study as the highest concentration of TPP was found at the highest salinity.

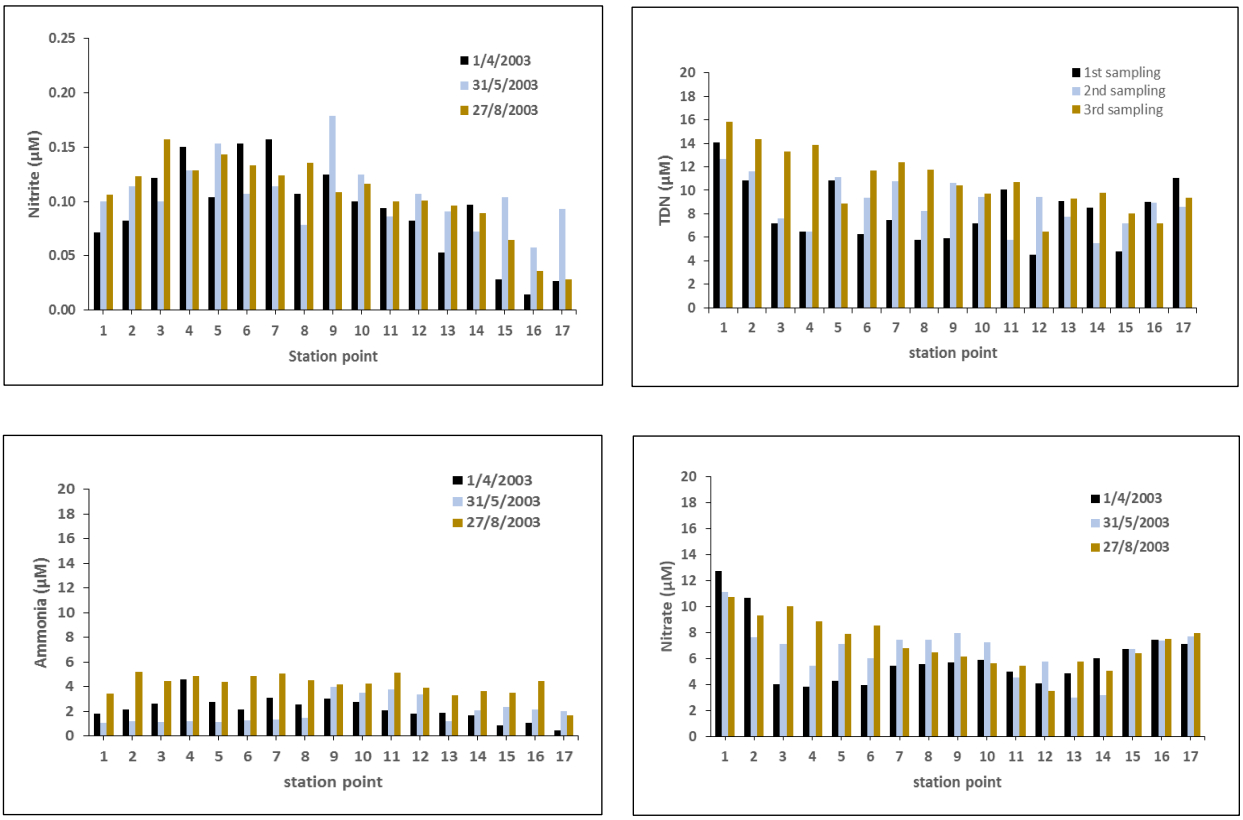
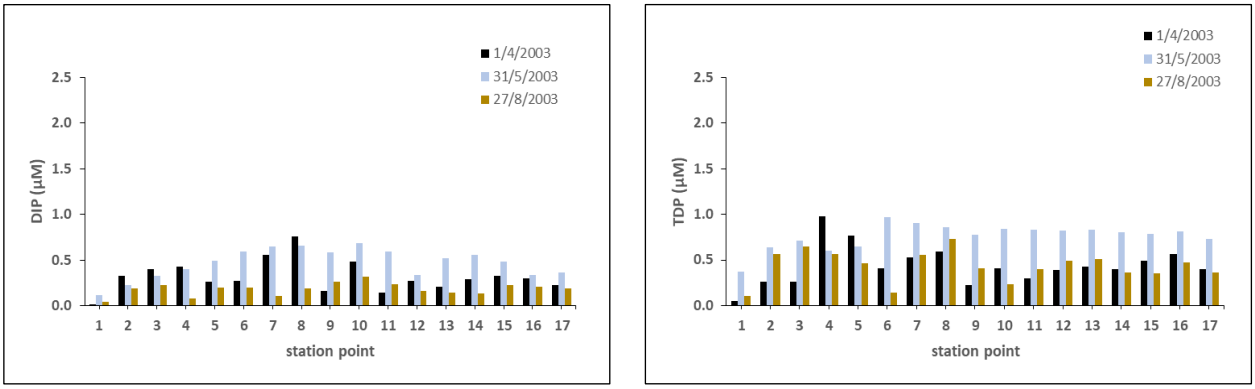


Figure 3. Variations of N-based nutrient concentration in Besut River estuary



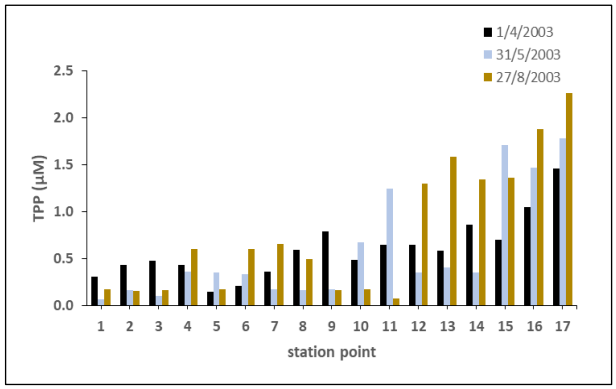


Figure 4. Variations of P-based nutrient concentrations in Besut River estuary

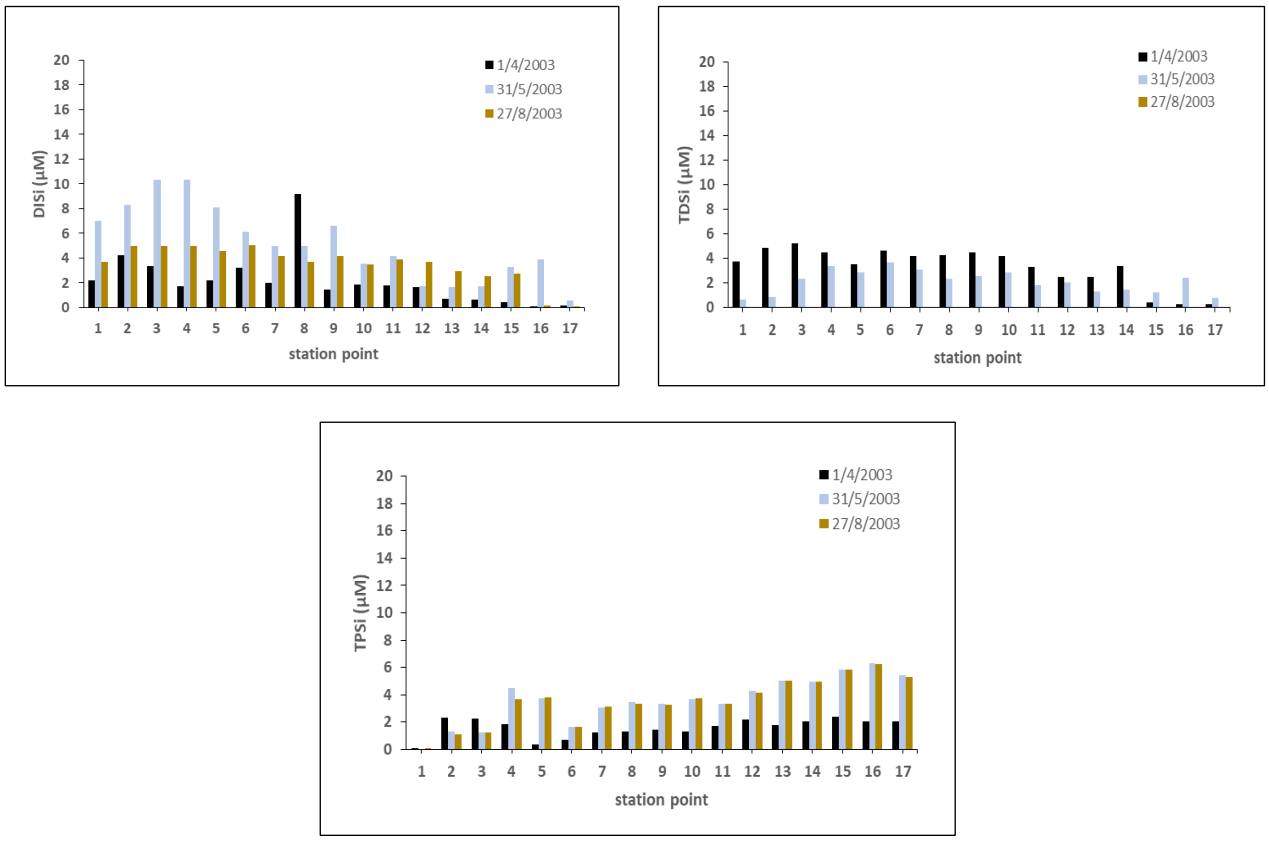


Figure 5. Variations of Si-based nutrient concentrations in Besut River estuary

In this study, the main activity of the residents around the estuary is from agricultural-related activities. High loading of anthropogenic nutrients such as the discharges of untreated domestic sewage from the urban and rural areas, and agricultural run-off, where fertilizer residues which contain high ammonium are leached out into the upstream of the river, could increase the nutrient concentrations. Suratman et al. [11] previously reported that human activities like industrial and agricultural activities would increase the concentration of N-based nutrients in the Selangor River, while Mohd Tahir et al. [24] also found that untreated effluent discharges caused the high

concentration of N-based nutrients at the Paka River. It is believed that most of the sewage waste in the Besut town was discharged into the river as there was no proper waste management.

Data obtained from this study was compared with other areas (Tables 1, 2 and 3). In general, the Besut River estuary recorded lower concentrations of most nutrients compared to other estuaries, except in the case of nitrate. This is because, although there was less anthropogenic disturbance around the estuary, there were the agriculture-related activities at the upstream of the river system and boat activities within the estuary. Merbok [10] and Kuala Sibuti River estuaries [12] were also reported to have similar ranges of concentration values of inorganic nutrients, especially ammonia. Merbok River estuary is a mangrove estuary and the main source of nutrients was from the domestic wastewater discharges [10], while the Kuala Sibuti estuary is bordered by pristine mangrove forests and hence there are no major anthropogenic activities there [12]. Studies carried out by Suratman et al. [25] and Salum [26] at the Terengganu River estuary revealed that the concentrations of most nutrients were higher due the presence of the breakwater at the end of the estuary. Thus, nutrients were trapped in the Terengganu River estuary and were not able to be flushed out into the open sea. Meanwhile, unlike other estuaries, the Selangor River estuary showed the highest concentration of nutrients, as most of the area was occupied by agriculture, most of which were oil palm and rubber estates [11].

Table 1. Comparison of N-based nutrients (μM) within selected area in Malaysia river estuary

Estuary	Nitrate	Nitrite	Ammonia	TDN
Besut River (Present study)	3.02-12.75	0.01-0.18	0.45-5.21	4.54-15.83
Merbok River [10]	0.05-0.21	0.10-0.19	0.10-1.18	NA
Selangor River [11]	7.71-56.79	0.05-2.13	0.36-17.00	18.93-75.07
Kuala Sibuti River [12]	0.40-3.53	NA	0.06-1.24	NA
Terengganu River [26]	0.30-4.70	0.002-0.39	1.00-35.40	3.20-40.60

NA: not available

Table 2. Comparison of P-based nutrients (μM) within selected area in Malaysia river estuary

Estuary	DIP	TDP	TPP
Besut River (Present study)	0.02-0.75	0.05-0.98	0.06-2.26
Merbok River [10]	0.06-0.08	NA	NA
Selangor River [11]	0.07-0.32	0.14-0.46	NA
Kuala Sibuti River [12]	0.01-1.92	NA	NA
Terengganu River [26]	0.38-2.83	0.38-3.20	0.50-3.34

NA: not available

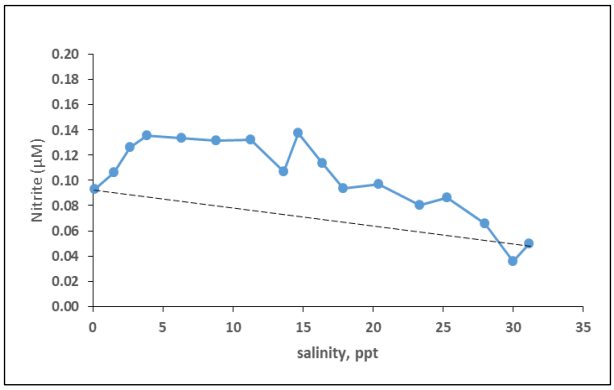
Table 3. Comparison of Si-based nutrients (μM) within selected area in Malaysia river estuary

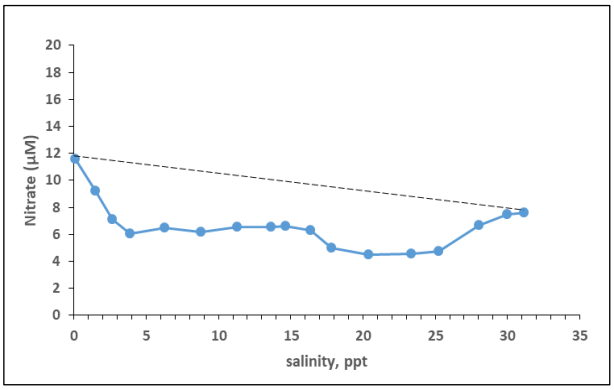
Estuary	DISi	TDSi	TPSi
Besut River (Present study)	0.03-10.32	0.01-5.27	0-6.30
Merbok River [10]	NA	NA	NA
Selangor River [11]	NA	NA	NA
Kuala Sibuti River [12]	NA	NA	NA
Terengganu River [26]	20.28-324.4	33.72-375.0	43.14-488.50

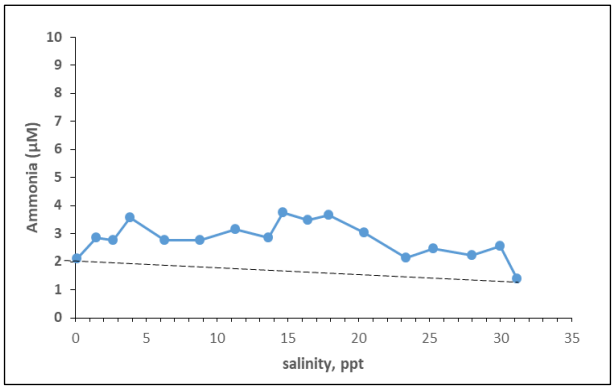
NA: not available

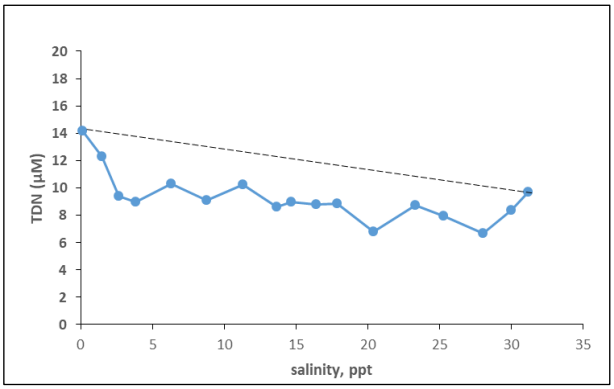
Behaviour of nutrients

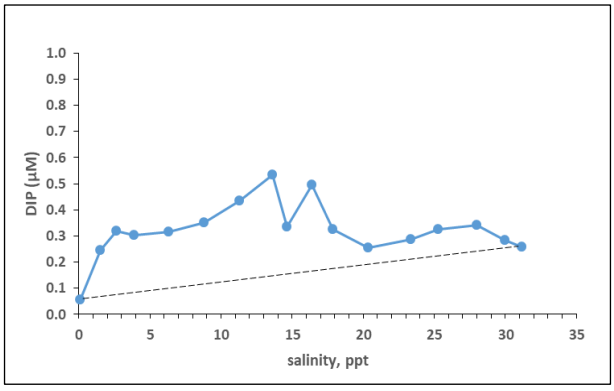
All nutrients behaved in a non-conservative manner in this study during the mixing between saline and freshwater (Figure 6). Nitrite, ammonia, DIP, TDP, DISi, TDSi and TPSi showed an addition manner, whilst nitrate, TDN and TPP showed a removal trend. A previous study by Nilva et al. [24] reported that the nutrient behaviours in an estuary are greatly influenced by the changes of pH, turbidity and ecosystem metabolism during the estuarine mixing between fresh and saltwater's, other than tidal variations. There are also several processes which affect the behaviour of nutrients in an estuary, such as, precipitation, adsorption and desorption, biological assimilation and denitrification, and organic matter degradation and excretion [27].

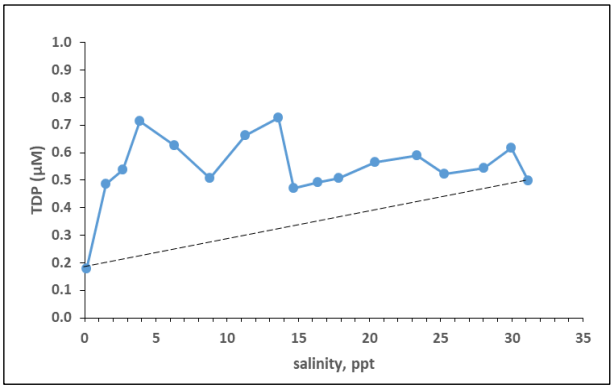












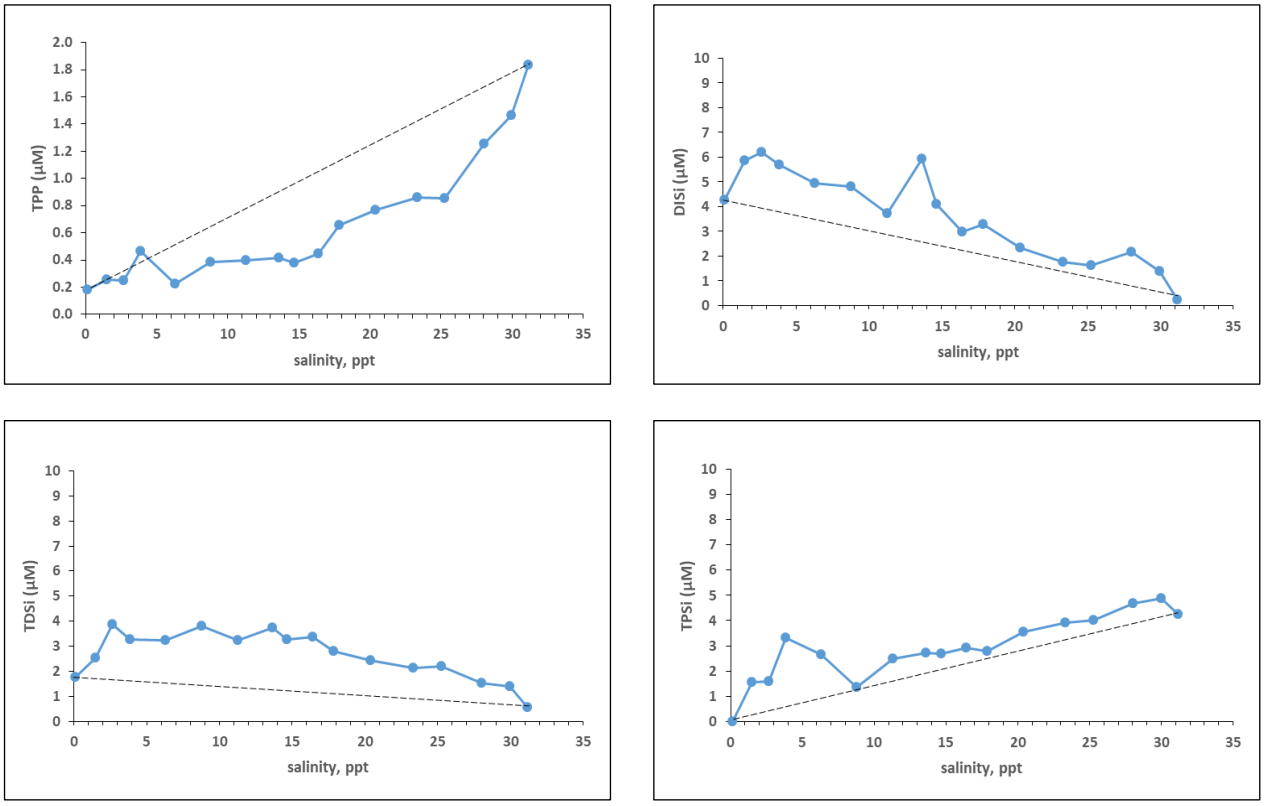


Figure 6. Distribution of nutrients across salinity gradients during the estuarine mixing

The additional source of nutrients could probably relate to the input of organic matter and nutrients from anthropogenic activities such as agricultural run-off, which flowed into the low and middle salinity regions of the Besut River estuary. This was similar to the studies done in the Selangor River estuary [11] and the Terengganu River estuary [25], where nutrients were observed to behave non-conservatively with an addition of N-based nutrient compounds, due to anthropogenic activities such as direct disposal of domestic sewage and runoff from urban areas, and tourism in Kuala Terengganu. Chemical processes such as oxidation of ammonia, reduction of nitrate, recycling of nitrogen and bacterial decomposition also contributed to the additional trend during estuarine mixing [28]. In this study, the addition of ammonia could be due to the denitrification process inside the estuary, as the removal of nitrate occurred in parallel with the increment of ammonia and nitrite. Resuspension of bottom sediment could also account for the additional source of nutrients into surface water, as the previous study in Severn estuary, UK, revealed that the higher input of nutrients were influenced by the resuspension from estuary bed [29].

The denitrification process could be a major influence for nitrate removal during estuarine mixing. This was because, the non-conservative additional of nitrite and ammonia, occurred simultaneously with the nitrate removal as shown in the mixing diagram above. In the nitrogen cycle, denitrification may occur under low oxygen conditions and lead to the rapid conversion of nitrate (oxides form) to ammonia and nitrite under anoxic conditions [30]. The findings of the present study showed the same pattern in which low concentration nitrate lead to a high ammonia concentration with low DO concentration. According to Suratman et al. [25], the denitrification process has been proven and cited widely as an efficient mechanism for nitrate removal during estuarine mixing such as in Cachoeira River estuary in Brazil [30] and Elbe River estuary in Germany [31].

TPP which also showed a removal trend during the estuarine mixing, might be influenced by the desorption process, where phosphorus absorbed particles in low salinity water but released it on reaching highly saline water, due to the density of water. The previous study done in Elbe estuary [28] also observed the same pattern, where low concentrations of phosphate absorbed the riverine particulate matter until it became saturated. Later, the particles were discharged on reaching the coastal area, as the salinity increased, which reduced the particles' solubility effects.

N:P ratio

The relationship between nitrogen (nitrate + nitrite + ammonia) and DIP was obtained by calculating the ratio of mean dissolved inorganic N:P as in Table 4. Redfield ratio suggests that the nutrient limiting factor for phytoplankton growth in marine is 16:1 (based on molecular concentrations) [32]. Large differences from 16 at low N:P ratios can be an indication of a potential nitrogen limitation, and at high N:P ratios, the potential phosphorus limitation is the primary production of phytoplankton. From Table 4, it can be seen that the N:P ratio was higher than 16:1, thus indicating that P was the limiting factor in the Besut River estuary. This finding was similar to the findings of other freshwater environments such as Setiu River [33], where phytoplankton growth was also be controlled by P-based nutrients.

Table 4. Ratio of mean nitrogen to mean phosphate (N:P)

Station	Nitrogen (µM)	Phosphate (µM)	N:P ratio
1	13.74	0.06	241:1
2	12.18	0.25	50:1
3	9.96	0.32	31:1
4	9.78	0.30	32:1
5	9.36	0.32	30:1
6	9.09	0.35	26:1
7	9.86	0.44	23:1
8	9.50	0.53	18:1
9	10.50	0.34	31:1
10	9.87	0.49	20:1
11	8.76	0.33	27:1
12	7.59	0.25	30:1
13	6.76	0.29	24:1
14	7.31	0.33	22:1
15	8.94	0.34	26:1
16	10.09	0.28	36:1
17	9.05	0.26	35:1

Conclusion

In general, the nutrient parameters were higher at the upstream and middle of the estuary than at the coastal areas. This shows that the concentration of nutrients was controlled by the freshwater input and surface runoff from the anthropogenic activities within the area. Comparisons with other study areas revealed that the nutrient concentrations in the Besut River estuary were among the lowest due to low anthropogenic activities. The mixing pattern obtained in this study revealed that all the nutrients behaved non-conservatively i.e. the estuary acted as a source for nitrite, ammonia, DIP, TDP, DISi, TDSi and TPSi and a sink for nitrate, TDN and TPP. This study also provides the information that the growth of phytoplankton in the Besut River estuary was controlled by P-based nutrients.

Acknowledgements

This work was partly supported by the Higher Institution Centre of Excellence (HICoE) research grant (Vote no. 66928) awarded to the Institute of Oceanography and Environment, Universiti Malaysia Terengganu. We are grateful for the helpful comments on the manuscript from anonymous reviewers.

References

1. Pereira-Filho, J., Schettini, C.A.F., Rorig, L. and Siegle, E. (2001). Intertidal variation and net transport of dissolved inorganic nutrients, POC and chlorophyll a in the Camboriu river estuary, Brazil. *Estuarine, Coastal and Shelf Science*, 53: 249-257.
2. Jickells, T. D., Weston, K., Fernand, L. and Parker, E. R. (2004). Nitrogen cycling in the southern North Sea: consequences for total nitrogen transport. *Estuarine, Coastal and Shelf Science*, 59: 559-573.
3. Wan Omar, W. M., Rahmah, S., Lim, C. C., Lee, W. P., Fatema, K. and Mat Isa, M. (2016). Effects of tidal events on the composition and distribution of phytoplankton in Merbok river estuary Kedah, Malaysia. *Tropical Ecology*, 57: 213-229.
4. Patricia, M. G., Christopher, J. M., Walter, B. David, F., Cynthia, H. and Jonathan, S. (2010). Nutrients in estuaries. *National Estuarine Experts Workgroup*, 2005-2007.
5. Huang, X. P., Huang, L. M. and Yue, W. Z. (2003). The characteristics of nutrients and eutrophication in the Pearl River estuary, South China. *Marine Pollution Bulletin*, 47: 30-36.
6. Chen, Y., Liu, R., Sun, C., Zhang, P., Feng, C. and Shen, Z. (2012). Spatial and temporal variations in nitrogen and phosphorus nutrients in the Yangtze River Estuary. *Marine Pollution Bulletin*, 64: 2083-2089.
7. Kawasaki, N., Kushairi, M. R. M., Nagao, N., Yusoff, F., Imai, A. and Kohzu. A. (2016). Seasonal changes of nutrient distributions along Selangor River, Malaysia. *International Journal of Advances in Chemical Engineering and Biological Sciences*, 7(2): 113-116.
8. Smith, S. V. (1984). Phosphorus versus nitrogen limitation in the marine environment. *Limnology and Oceanography*, 29(6): 1149-1160.
9. Liss, P. S. (1967). Conservative and non-conservative behaviour of dissolved constituents during estuarine mixing. In: Estuarine Chemistry. Burton, J.D. and Liss, P.S.(eds.). Academic Press, London: pp. 229.
10. Kaniz, F., Wan Omar, W. M. and Mat Isa, M. (2014). Spatial and temporal variation of physico-chemical parameters in the Merbok Estuary, Kedah, Malaysia. *Tropical Life Sciences Research*, 25(2): 1-19.
11. Suratman, S., Mohd Tahir, N. and Tong, S.L. (1996). Tidal variations of some physico-chemical and nutrient parameters in Selangor River estuary. *Malaysian Journal Analytical Sciences*, 2(2): 317-326.
12. Saifullah, A. S. M., Mustafa Kamal, A. H., Idris, M. H., Rajaee, A. H. and Ismail, J. (2014). Seasonal variation of water characteristics in Kuala Sibuti River estuary in Miri, Sarawak, Malaysia. *Malaysian Journal of Science*, 33(1): 9-22.
13. Grasshoff, K., Ehrhardt, M. and Kremling, K. (1983). Methods of seawater analysis. 2nd edition. Weinheim: Verlag *Chernie.*
14. Parsons, T. R., Maita, T. and Lalli, C. M. (1984). Plant pigment. A manual of chemical and biological method for seawater analysis. Oxford: pp. 173.
15. Nursuhayat, A. S., Yusoff, F. M. and Shariff, M. (2013). Spatial and temporal distribution of phytoplankton in Perak Estuary, Malaysia, during monsoon season. *Journal of Fisheries and Aquatic Science*, 8: 480-493.
16. Savenije, H. H. G. (2005). Salinity and tides in alluvial estuaries. 1st edition. Elsevier: pp. 1-50.
17. Satpathy, K. K., Mohanty, A. K., Sahu, G., Sarkar, S. K., Natesan, U., Venkatesan, R. and Prasad, M.V.R. (2010). Variations of physiochemical properties in Kalpakkam coastal waters, east coast of India, during southwest to northeast monsoon transition period. *Environmental Monitoring and Assessment*, 171(1-4): 411-24.
18. Santana-Casiano, J. M. and González-Dávila, M. (2010). pH decrease and effects on the chemistry of seawater. In book Oceans and the Atmospheric Carbon Content, Springer: pp. 95-114.
19. Spatharis, S., Tsirtsis, G., Danielidis, D.B., Chi T. D. and Mouillot, D. (2007). Effects of pulsed nutrient inputs on phytoplankton assemblage structure and blooms in an enclosed coastal area. *Estuarine Coastal and Shelf Science*, 73: 807-815.

20. Pereira-Filho, J., Schettini, C. A. F., Rorig, L. and Siegle, E. (2001). Intratidal variation and net transport of dissolved inorganic nutrients, POC and chlorophyll a in the Camboriu River estuary, Brazil. *Estuarine, Coastal and Shelf Science*, 53: 249-257.
21. Davies, O. A. and Ugwumba, O. A. (2013). Tidal influence on nutrients status and phytoplankton population of Okpoka Creek, Upper Bonny Estuary, Nigeria. *Journal of Marine Biology*, 2013: 1-16.
22. Suratman, S., Abdul Aziz, A., Mohd Tahir, N. and Hin Lee, L. (2018). Distribution and behavior of nitrogen compounds in the surface water of Sungai Terengganu estuary, southern waters of South China Sea, Malaysia. *Sains Malaysiana*, 47(4): 651-659.
23. Prastka, K. E. and Malcolm, S. J. (1994). Particulate phosphorus in the Humber estuary. *Netherlands Journal of Aquatic Ecology*, 28(3-4): 397-403.
24. Mohd Tahir, N., Suratman, S., Awang, M. and Ang, K. T. (2004). Studies on nitrogen-based nutrients of Paka River system, Terengganu. *Proceeding in KUSTEM Annual Seminar on Sustainability Science and Management*, 407-411.
25. Suratman, S., Abdul Aziz, A., Mohd Tahir, N. and Lee, H. L. (2018). Distribution and behaviour of nitrogen compounds in the surface water of the Sungai Terengganu Estuary, Southern Waters of South China Sea, Malaysia. *Sains Malaysiana*, 47: 651-659.
26. Salum, S. S. (2015). Distribution and behaviour of phosphate- and silicate-based nutrients with respect to tidal variations in the surface water of the Terengganu River estuary. *Thesis of degree of Master of Science. Universiti Malaysia Terengganu*, pp. 78-86.
27. Nilva, B., Ana-Paula, C. R., Ilene, M. A., Luiz, C. C. J., Bastiaan, A. K. and Wilson, M. (2016). Nutrient behaviour in a highly-eutrophicated tropical estuarine system. *Acta Limnologica Brasiliensia*, 28: 21.
28. Mansor, M., Mohammad-Zafrizal, M., Nur-Fadhilah, M., Khairun, Y. and Wan-Maznah, W. O. (2012). Temporal and spatial variations in fish assemblage structures in relation to the physicochemical parameters of the Merbok Estuary, Kedah. *Journal of Natural Sciences Research*, 2(7): 110-127.
29. Kadiri, M., Bockelmann-Evans, B. and Rauen, W. B. (2014). Assessing the susceptibility of two UK estuaries to nutrient enrichment. *Continental Shelf Research*, 88: 151-160.
30. Silva, M. A. M., Souza, M. F. L. and Abreu, P. C. (2015). Spatial and temporal variation of dissolved inorganic nutrients and chlorophyll-a in a tropical estuary in Northeastern Brazil: dynamics of nutrient removal. *Brazilian Journal of Oceanography*, 63(1): 1-15.
31. Dahnke, K., Bahlmann, E. and Emeis, K. (2008). A nitrate sink in estuaries? An assessment by means of stable nitrate isotopes in the Elbe estuary. *Limnology and Oceanography*, 53: 1504-1511.
32. Redfield, A.C. (1958). The biological control of chemical factors in the environment. *American Scientist*, 46(3): 205-221.
33. Suratman, S., Mohd Tahir, N. and Suriyati, S. (2004). Dissolved nutrients and chlorophyll a status of the Setiu River, Terengganu, Malaysia. *Bulletin of Environmental Contamination and Toxicology*, 73: 1094-1100.

Malaysian Journal of Analytical Sciences, Vol 23 No 6 (2019): 1090 - 1106
DOI: https://doi.org/10.17576/mjas-2019-2306-16

MALAYSIAN JOURNAL OF ANALYTICAL SCIENCES
Published by The Malaysian Analytical Sciences Society
ISSN 1394 - 2506

TEMPORAL VARIABILITY OF PHYTOPLANKTON BIOMASS IN RELATION TO SALINITY AND NUTRIENTS IN A SHALLOW COASTAL LAGOON

(Kepelbagaian Temporal Biojisim Fitoplankton Berdasarkan Kemasinan dan Nutrien di Lagun Pesisir Pantai yang Cetek)

Zuraini Zainol and Mohd Fadzil Akhir*

Institute of Oceanography and Environment,
Universiti Malaysia Terengganu, 21030 Kuala Nerus, Terengganu, Malaysia.

**Corresponding author: mfadzil@umt.edu.my*

Received: 30 October 2018; Accepted: 26 September 2019

Abstract

With agriculture and aquaculture activities in proximity, the unique feature of Setiu Lagoon, which is an almost closed system and connected to the coastal sea with only one inlet leaves a huge question on how this ecosystem maintains its productivity under restricted conditions. In this study, results of three field samplings carried out during the southwest monsoon (August 2017), wet period of northeast monsoon (December 2017), and dry period of northeast monsoon (February 2018) are used to examine the differences in phytoplankton biomass in relation to salinity and nutrients under different monsoonal settings. These samplings are representative of typical conditions existing during a dry season (southwest monsoon) and a rainy one (northeast monsoon). In the lagoon, the most determinant factor affecting the phytoplankton biomass distribution is the freshwater intrusion, strengthened by increased rainfall amount and strong flow that brings along nutrients from land resulting in higher chlorophyll *a* concentrations. As per classification of Malaysia Marine Water Quality Criteria and Standard (MWQCS), mean nutrient concentrations at the study area were in Classes 1 and 2, which are suitable for local aquaculture activities. However, conservation actions must also be in line with the economic development.

Keywords: salinity, tidal, freshwater intrusion, nutrients, chlorophyll *a*, shallow coastal lagoon

Abstrak

Dengan dikelilingi dengan aktiviti akuakultur dan pertanian di kawasan terdekat, persekitaran unik Lagun Setiu - yang merupakan sebuah sistem yang hampir tertutup dan hanya mempunyai satu muara yang menghubungkan lagun dengan laut - meninggalkan satu persoalan yang besar tentang bagaimanakah ekosistem ini mengekalkan produktiviti dalam keadaan yang terbatas. Dalam kajian ini, hasil kajian melalui tiga pensampelan lapangan yang dijalankan sewaktu monsun barat daya (Ogos 2017), musim hujan monsun timur laut (Disember 2017), dan musim kering monsun timur laut (Februari 2018) digunakan untuk mengkaji perubahan biojisim fitoplankton berdasarkan kemasinan dan nutrien di bawah pengaruh monsun yang berbeza. Pensampelan ini mewakili keadaan biasa yang wujud semasa musim kering (monsun barat daya) dan musim hujan (monsun timur laut). Di dalam lagun ini, kemasukan air tawar yang dipengaruhi oleh pertambahan air hujan dan nutrien dari daratan yang dibawa oleh aliran air yang kuat merupakan faktor yang paling mempengaruhi penghasilan biojisim fitoplankton yang tinggi. Merujuk kepada Kriteria dan Piawaian Kualiti Air Marin, Malaysia (MWQCS), purata kepekatan nutrien di kawasan kajian berada di dalam Kelas 1 dan 2, yang sesuai untuk aktiviti akuakultur tempatan. Walaubagaimanapun, usaha pemuliharaan juga haruslah seiring dengan perkembangan ekonomi.

Kata kunci: kemasinan, pasang surut, kemasukan air tawar, nutrien, klorofil *a*, lagun pesisir pantai yang cetek

Introduction

Occupying approximately 13% of the world's coastal area, coastal lagoons are known as shallow water bodies with an average depth of less than 2m and are connected to the ocean by one or more inlets [1]. Generally, the ecology of a coastal lagoon is highly variable, depending on its prevalent physical and chemical environment [2]. Within this shallow transitional water system, seasonal changes in phytoplankton biomass are believed to be under the influence of site-specific hydrological characteristics such as river discharge and salinity [3]. A coastal lagoon normally has limited points of water exchange, which make them a good shelter for the accumulation of nutrients [4]. Furthermore, due to this unique coastal feature, it is believed that coastal lagoons are able to promote effective use and recycling of nutrient inputs, which contribute to high levels of primary production [1].

Despite being shallow in depth, a coastal lagoon that has close proximity to land is more vulnerable to anthropogenic activities such as enhanced input of nutrients that stimulate primary producers growth [3]. This sheltered ecosystem also provides a variety of goods and services to fisheries, aquaculture, tourism, and other sectors, at local, regional, and national levels [5]. Moreover, despite its role in supporting a rich biodiversity of aquatic plants and animals [6], a coastal lagoon, which is composed of a mixture of brackish and sea water, also serves as a buffer zone for storage of nutrients and fluxes originating from adjacent continental drainage to the marine environment [7].

Setiu Lagoon has received significant attention since the 1990's due to its unique habitat, which consists of sizable array of biological diversities [8]. Somehow, Setiu Lagoon had experienced shoreline changes in 2015 due to the continuous action of wind, current, and nearshore waves, especially during the northeast monsoon [9], which led to the closing of the old inlet and the opening of a new inlet as shown in Figure 1. To the best of our knowledge, as of now, almost all previous studies on Setiu Lagoon such as Ong et al. [10], Suratman and Latif [11], and Bakar et al. [12] are focused on the old inlet, which was closed naturally in 2015 (Figure 1). No prior study has acknowledged the interaction between the localised physical properties and nutrients in shaping the productivity in Setiu Lagoon at the current inlet. In this regard, the present work aims to understand the hydrodynamics, the distribution of nutrients and chlorophyll *a* (a proxy for phytoplankton biomass [13]) within the study area, and further uncover the mechanisms that shape the dynamics in this unique shallow coastal lagoon.

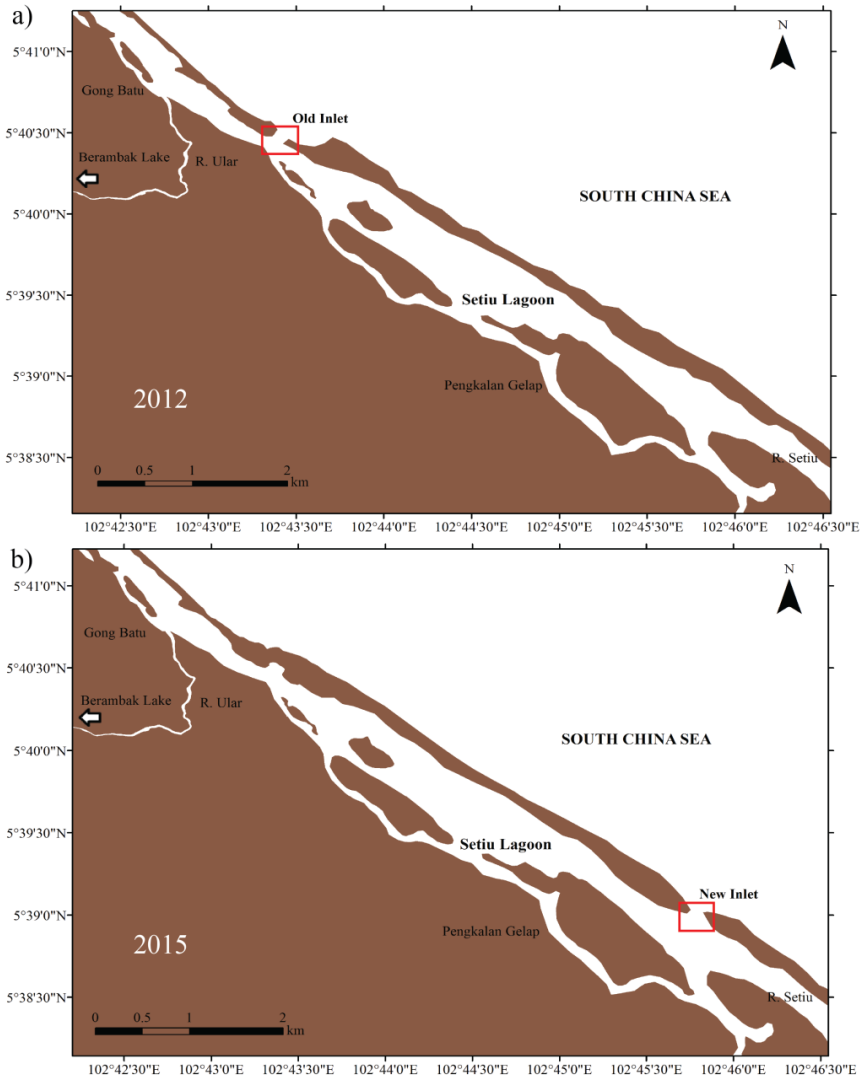


Figure 1. The coastline changes observed in Setiu Lagoon during (a) 2012 and (b) 2015. Strong seasonal wind, wave, and current in the study area has resulted in the closing of the old inlet and the opening of the new inlet, which is located approximately 4 km away from each other

Materials and Methods

Description of the study area

Setiu Lagoon is situated within the Setiu Wetland area, which is approximately 23,000 hectares in size and extends from 5° 35' N to 5° 45' N latitude and 102° 41' E to 102° 49' E longitude. This lagoon is a shallow basin with a depth of 0.5 – 3.0 m, with a dependent tidal state [14]. With a mean spring tide of 1.8 m and a tidal range that rarely exceeds 2 m, the Setiu Lagoon is classified as a low mesotidal coastal type [15]. Its main source of freshwater comes from the Setiu River that flows directly into the lagoon (Figure 2). Meanwhile, another freshwater input comes from the natural lake (Berambak Lake), which is connected to the lagoon through the Ular River (Figure 2). The upstream activities are dominated by agriculture, mainly the palm oil plantations and aquaculture activities, which dominate the area within the wetland [8]. Since Setiu Lagoon is located in the South China Sea (SCS) region, it is therefore subjected to alternating southwest (May – September) and northeast monsoons (November – March). Salinity within the lagoon varies between 0 – 30 psu, where a higher salinity condition is restricted to the region

closer to the inlet [16]. Somehow, during the northeast monsoon, river discharges as a result of heavy rainfall restricts the extension of the salt wedge at the study area [17].

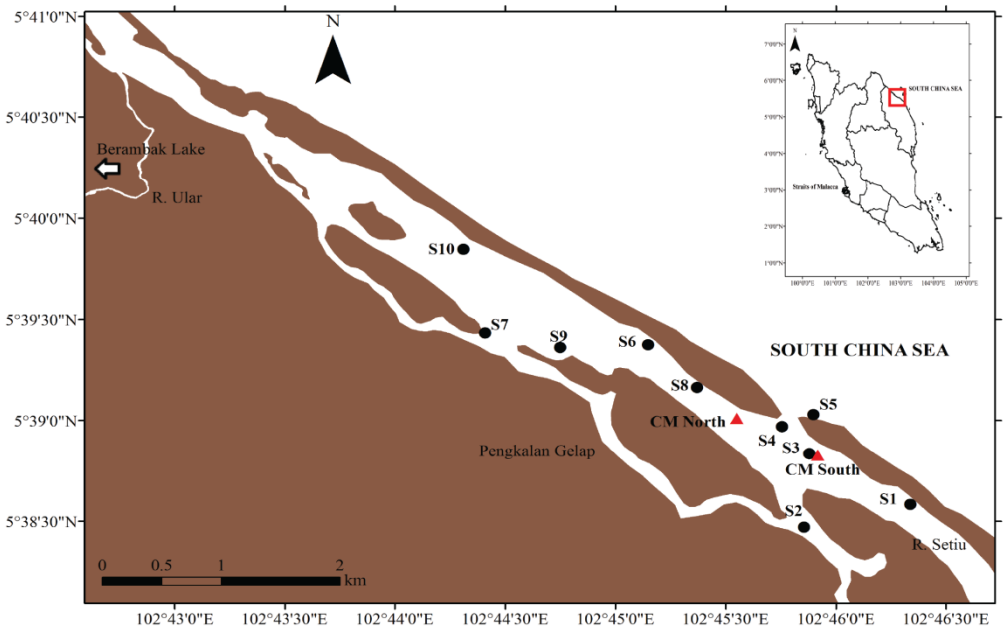


Figure 2. Location of the study site (red box), which faces the South China Sea. The main freshwater input in the study area comes from Setiu River, while another source of freshwater comes from Ular River. The dot indicate the stations for salinity data and water samples collection meanwhile the triangle indicate the stations for current meters deployment

Sampling procedure

The first field sampling was carried out from 7th to 8th of August 2017, which represented the southwest monsoon. A total of 7 stations (S1 – S7) were set up for the purpose of salinity, chlorophyll *a*, and nutrient analysis in August 2017. Another station (S8) was added in the salinity characteristic analysis during August 2017. The second and third research sampling was carried out from 27th to 28th December 2017 and 12th to 13th February 2018, which represented the wet and dry periods of the northeast monsoon, respectively. In December 2017 and February 2018, S9 and S10 were added as sampling stations to capture the interaction between seawater and freshwater. The total of number of sampling stations was increased to 10 stations (Figure 2). Unfortunately, there was no data available for S3 and S5 during December 2017 and for S2, S3, and S5 during February 2018, due to shallow water that made it difficult to access the stations. In terms of tidal circulation, the spring tide occurred during 7 – 8 August 2017, with a tidal range of 1.4 m for both days. Neap tide occurred during 27 – 28 December 2017 and 12 – 13 February 2018. During 27 and 28 December 2017, the tidal range was 0.8 m and 0.7 m, respectively. On the other hand, during 12 and 13 February 2018, the tidal range was 1.2 m and 1.4 m, respectively.

Salinity data (indirectly through water conductivity) was taken from the SonTek CastAway Conductivity, Temperature, and Depth (CTD) profiler. The flow conditions were estimated from the moored data of two units of Valeport Model 308 at CM North and CM South (Figure 2). Hourly water level data was obtained from the tide tables provided by the National Hydrographic Centre, Malaysia. Water samples for nutrients and chlorophyll *a* analysis were collected at 0.5 m depth using a Van-Dorn water sampler. Samples collected were filtered through pre-combusted Sartorius Stedim glass fibre GF/F filter papers (47 mm diameter, nominal pore size 0.7 µm) using a vacuum pump. The filter papers for chlorophyll a analysis were rolled and kept in a 15 mL centrifuge tube, and were then wrapped with aluminium foil and stored in a freezer until they were returned to laboratory, to prevent pigments degradation. Meanwhile, filtered water samples for nutrient analysis were transferred into 250 mL acid-

washed high density polyethylene (HDPE) bottles and stored in a freezer until further analysis. Concentrations of chlorophyll *a* were analysed using a UV-VIS Spectrophotometer with an adopted procedure from the American Public Health Association (APHA), 2005 method [18]. Laboratory analyses for nitrate, phosphate, ammonium, and silicate were conducted using Westco SmartChem 200 Discrete Analyser (AMS-Alliance) with U.S. Environmental Protection Agency (EPA) methods [19].

Results and Discussion

Salinity in the lagoon

The hourly flows during the study period of August 2017 can be seen in Figure 3a. It can be observed that the flows were characterised by strong hourly irregularities. At the north of the inlet, the daily flow oscillated between 0 – 389 m^3/s with an average flow of 215 m^3/s. Meanwhile, at the south of the inlet, the average flow was 302 m^3/s with minimum and maximum daily values of 0.4 m^3/s and 667 m^3/s, respectively. To identify the influencing factor that shapes the flow within the lagoon, the daily flow is compared with the water level data (Figure 3b). The figure clearly shows that the highest peaks of the flows occurred during the high tide, which indicated a strong seawater inflow. Interestingly, there were few peaks observed during the ebbing, which indicated a presence of small river discharges into the lagoon. In Setiu Lagoon, the penetration of seawater, with an average value of 32.4 psu during the high tide of August 2017, had reached S7, which was located approximately 2.5 km away from the inlet (Figure 4a). This condition agreed well with strong seawater inflow at the north (average flow of 303 m^3/s) and south (average flow of 494 m^3/s) of the inlet during the period where data collection was made (0920 – 1000 hours; Figure 3a). During the low tide of August 2017, slightly saline water (average of 31.0 psu) was observed at stations closer to the inlet (S4 – S6 and S8), while less saline water (average of 25.4 psu) was observed at stations away from the inlet (Figure 4b). This was expected since river discharge is a common feature during low tides [20]. Furthermore, as mentioned earlier, small river discharges were observed at both north and south of the inlet during data collection (1510 – 1610 hours), with average flows of 330 m^3/s and 452 m^3/s respectively (Figure 3a). The presence of this river discharge is believed to have been the causative factor that prevented the salt water intrusion into stations further away from the inlet (S1, S2, and S7; Figure 4b).

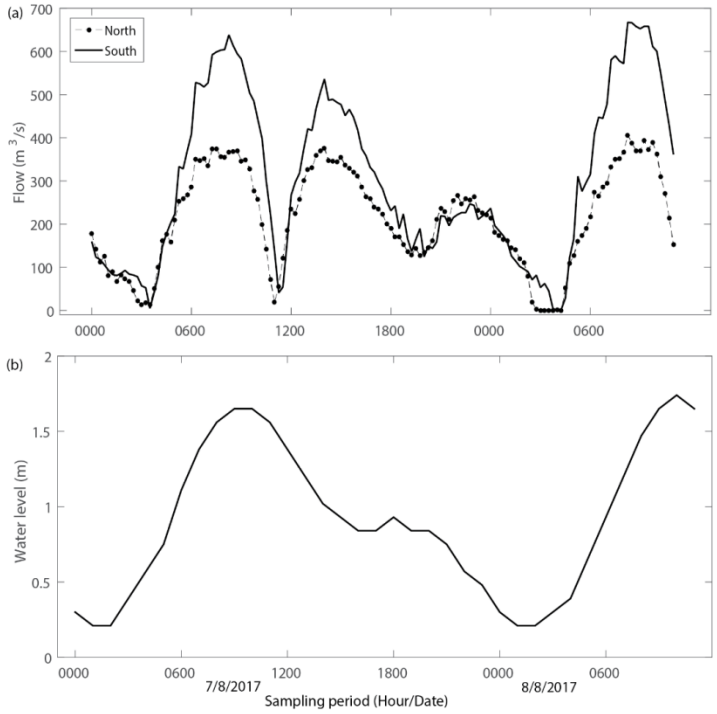


Figure 3. (a) Hourly flow at the north and south of inlet and (b) water level at Setiu Lagoon during 7-8 August 2017

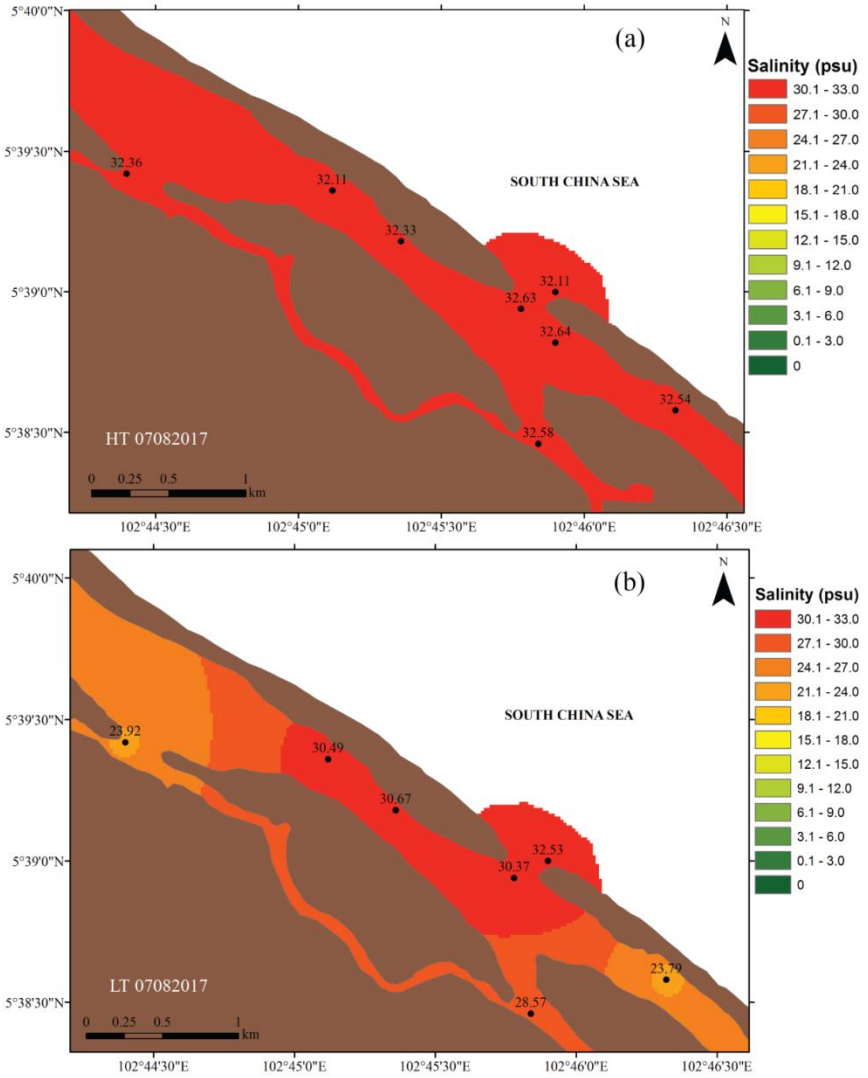


Figure 4. Salinity distribution in Setiu Lagoon during (a) high and (b) low tides on 7 August 2017

During the second field sampling exercise, surface salinity distribution in Setiu Lagoon on December 2017 was plotted in Figure 5. An average flow rate of 144 m^3/s (north) and 238 m^3/s (south) was recorded during the second visit (Figure 6a). As it can be observed, freshwater flooded the whole study area with an average salinity of 8.8 psu during the high tide (Figure 5a) and 12.9 psu during the low tide (Figure 5b). This was possible due to two main reasons - river discharge and increase in rainfall amount. Comparing the flow rates with water level data (Figure 6b) clearly demonstrated the influence of river discharges from both sources (Setiu and Ular Rivers). During the low tide of the visiting period (0930 – 1010 hours), average critical flux of 242 m^3/s (north) and 369 m^3/s (south) was recorded, compared to average flux of 27 m^3/s (north) and 135 m^3/s (south) during high tide (1530 – 1605 hours), indicating that large river discharges do not allow the penetration of seawater into the lagoon. The record of daily rainfall amounts in Setiu, obtained from the Department of Irrigation and Drainage, Terengganu (Table 1), also proved the increased amount of freshwater input during December 2017, where the average daily rainfall amount within a 3-day visiting period was 42.2 mm/day compared to 17.0 mm/day during February 2018 and 0.0 mm/day during August 2017.

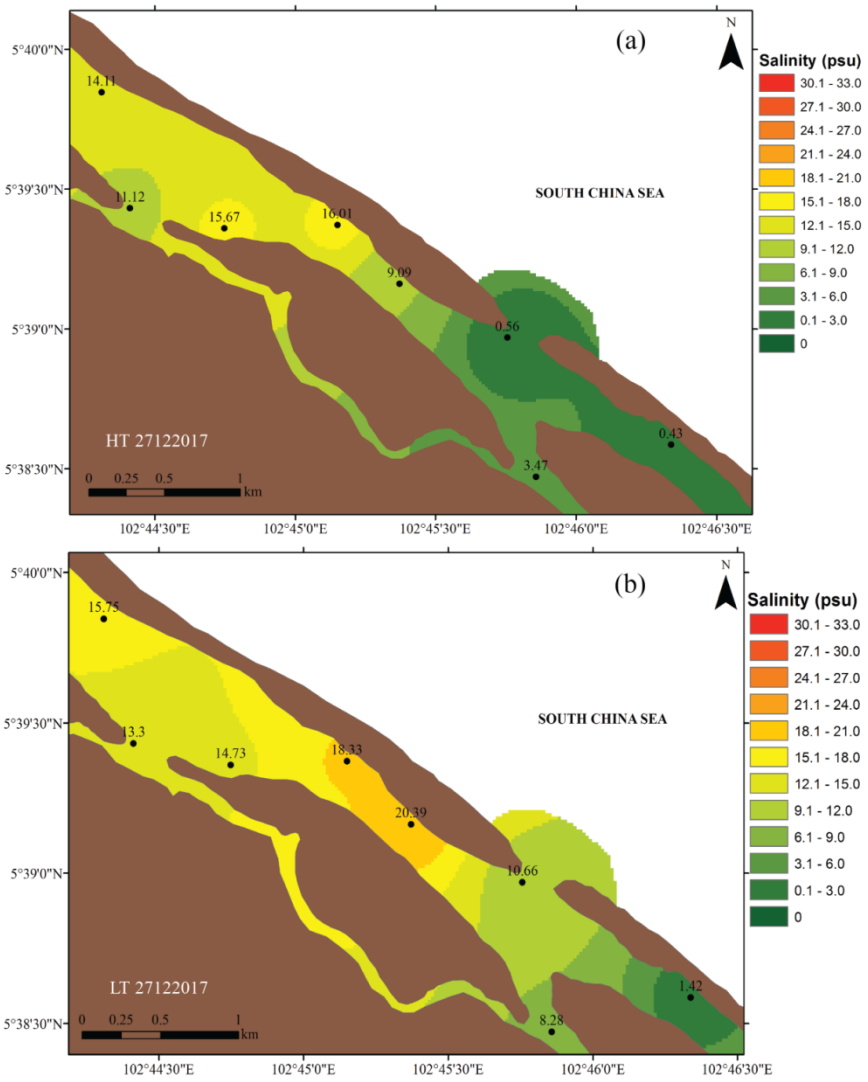


Figure 5. Salinity distribution in Setiu Lagoon during (a) high and (b) low tides on 27 December 2017

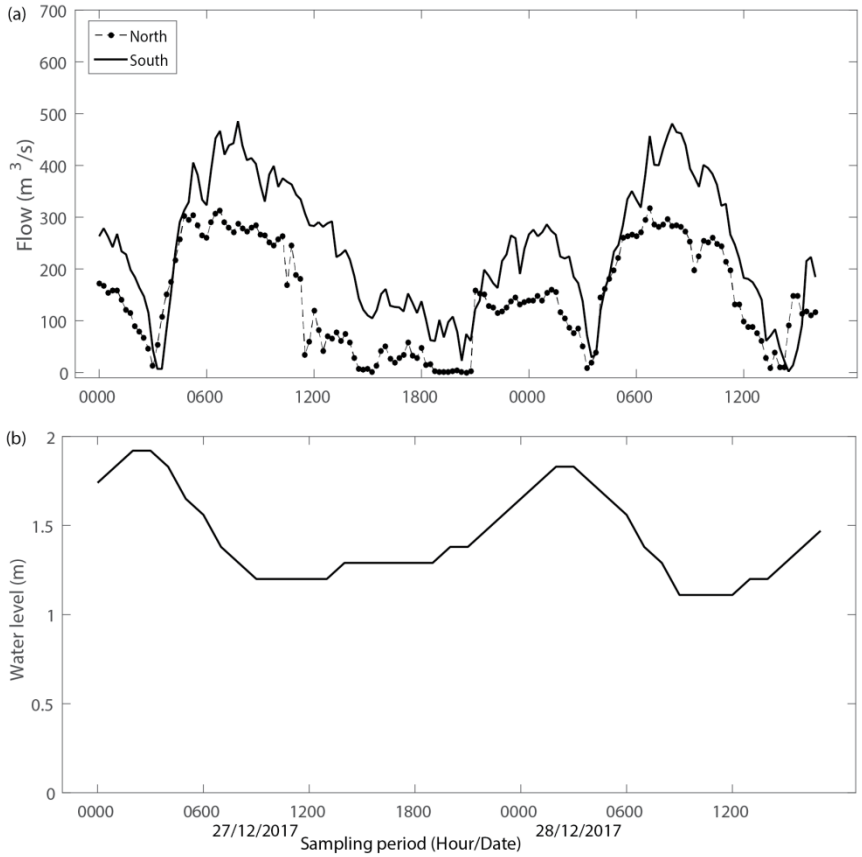


Figure 6. (a) Hourly flow at the north and south of inlet and (b) water level at Setiu Lagoon during 27-28 December 2017

Table 1. 3-days average daily rainfall amount during visiting period

Date	**3-Days Average Rainfall Amount (mm/day)**
6 – 8 Aug 2017	0.0
26 – 28 Dec 2017	42.2
11 – 13 Feb 2018	17.0

During the third field sampling (February 2018), as the northeast monsoon started to reduce in strength, slightly saline water (29.0 psu) as a result of seawater intrusion, began to dominate the southern area of the study site during high tide, while the effects of river discharge were slightly reduced (Figure 7a). However, on the northern part of the study area, the domination of freshwater was still prominent (22.2 psu). Through the observation of the flow rate at the north (Figure 8a), it was discovered that the flow rate was almost constant throughout the study period within a range of 15 – 193 m^3/s, with an average value of 125 m^3/s. The only possible reason for this condition was the siltation process, where accretion occurred at the river mouth, which resulted in the accumulation of sand and the formation of a sand spit during the sampling period, that lead to the narrow waterway at the north. A previous study by Kasawani et al. [9] showed that the movement of sediments such as accretion is a general phenomenon in Setiu Lagoon, especially during the northeast monsoon due to wave action. During low tide, the salinity was slightly

fresher, which was believed to be associated with the presence of a small amount of freshwater intrusion, as the documented rainfall amount in that particular period was 2.0 mm.

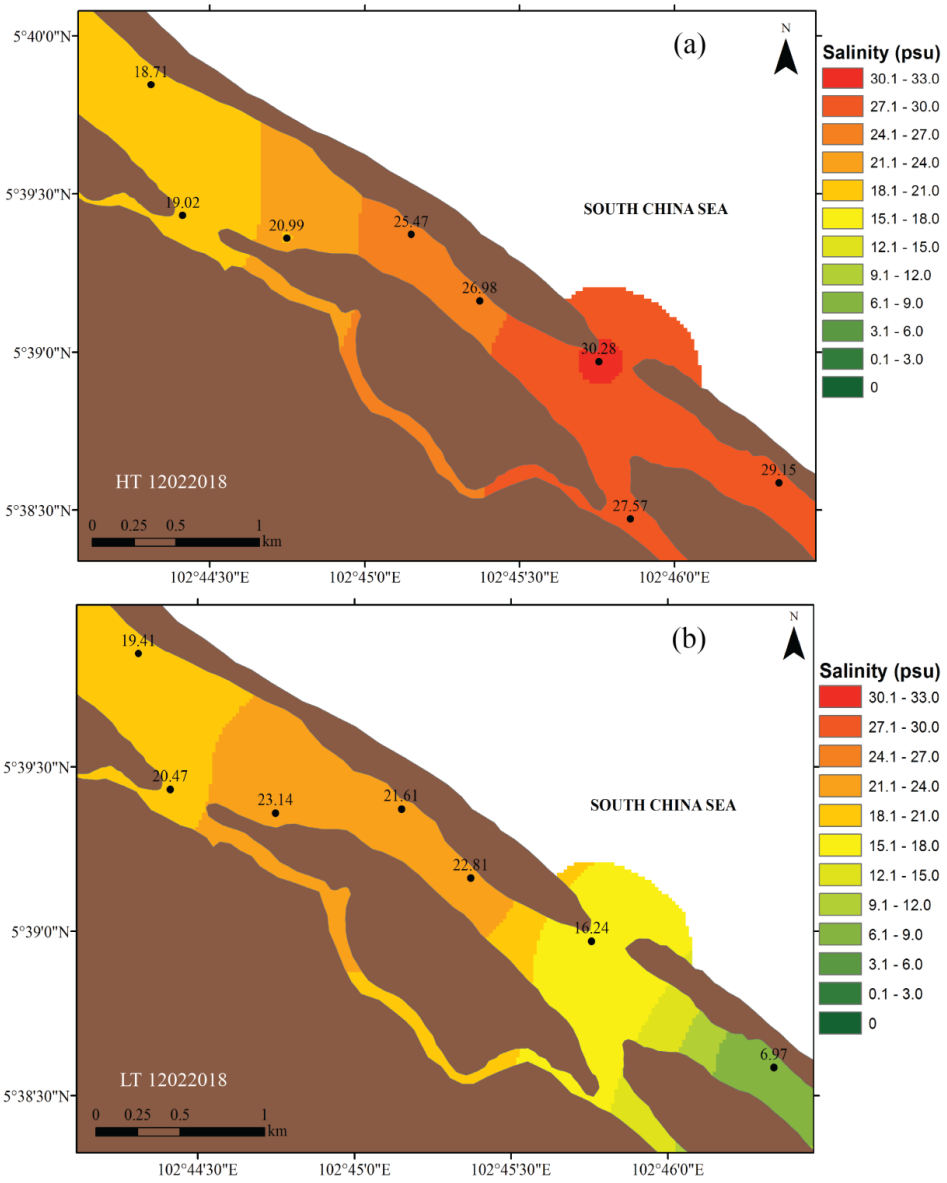


Figure 7. Salinity distribution in Setiu Lagoon during (a) high and (b) low tides on 12 February 2018

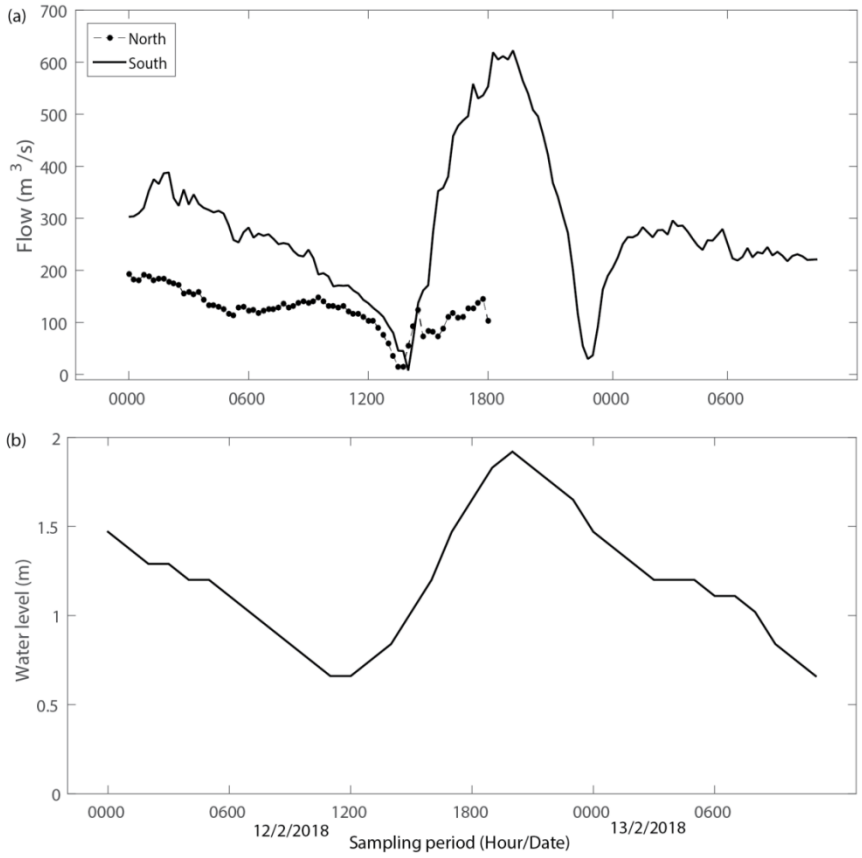


Figure 8. (a) Hourly flow at the north and south of inlet and (b) water level at Setiu Lagoon during 12-13 February 2018

Nutrients in the lagoon

The concentrations of nitrate, phosphate, ammonium, and silicate during southwest monsoon (August 2017), wet period of northeast monsoon (December 2017), and dry period of northeast monsoon (February 2018) are shown in Table 2. Surface nutrients were relatively high during the low tide compared to the high tide, which suggested that the major input of nutrients in Setiu Lagoon originated from the freshwater region. A similar observation was obtained by Bakar et al. [12], where mostly the lowest nutrient concentrations were found around the high tide, and the highest concentrations were found at the low tide, due to the increased nutrient input from inland river runoff. Inter-seasonally, higher surface nutrients were observed during the wet period of the northeast monsoon (December 2017) compared to the dry period of the northeast monsoon (February 2018) and the southwest monsoon (August 2017). This strengthens the fact that the main source of nutrients was coming from the land runoff, which flows into the lagoon through the rivers. Increased rainfall amount during the northeast monsoon, especially in December 2017 as documented in Table 1, is believed to be the main reason resulting in the supply of large river discharge, which brought along nutrients from land into the lagoon.

Few studies have acknowledged heavy rainfalls as the responsible factor that leads to the wash out of large amounts of terrestrial organic matter into the rivers, resulting in increased nutrient input in the lagoon [21, 22, 23]. Furthermore, higher nutrient concentrations observed during the northeast monsoon compared to the southwest monsoon, were also believed to be associated with the unique feature of Setiu Lagoon, which is characterised to be a closed system with only an inlet that connects this area to the sea. Therefore, this unique feature may have caused high amounts of nutrients to be flushed from rivers and to be concentrated in the lagoon, since the water movement and exchange flow was restricted [24]. In an evaluation with the Malaysia Marine Water Quality Criteria and Standards (MWQCS; Table 3), the mean concentrations of ammonium (42 µg/L) and nitrate (30 µg/L) in Setiu Lagoon were found to be in Class 2, which represents suitability for marine life, fisheries, coral reefs, recreational activities, and mariculture. On the other hand, the mean phosphate concentration (5 µg/L) in this study was found to be in Class 1, which represents areas that are for preservation, marine protected areas, and marine parks (Table 3).

Table 2. Mean (±SD) of surface nutrient concentrations during the study

Parameter	Tidal range	August 2017	December 2017	February 2018
Nitrate (µg/L)	HT	11.26 ± 6.99	38.16 ± 17.88	14.82 ± 10.95
	LT	26.27 ± 19.12	55.19 ± 34.76	35.34 ± 26.58
Phosphate (µg/L)	HT	4.01 ± 1.38	3.51 ± 1.67	4.62 ± 2.12
	LT	3.46 ± 1.91	6.09 ± 2.18	9.46 ± 7.00
Ammonium (µg/L)	HT	34.76 ± 13.59	52.00 ±17.82	10.47 ± 5.33
	LT	66.50 ± 40.43	62.71 ± 24.23	23.96 ± 16.60
Silicate (µg/L)	HT	646.80 ± 391.43	1519.34 ± 693.23	1493.67 ± 546.56
	LT	1804.05 ± 571.04	2312.44 ± 446.94	2927.94 ± 1978.15

Table 3. Marine Water Quality Criteria and Standard (MWQCS) for Malaysia

Parameter (µg/L)	Class			
	1	2	3	E
Ammonia	35	70	320	70
Nitrate	10	60	1000	60
Phosphate	5	75	670	75
Beneficial uses				
Class 1	Preservation, marine protected area, marine parks			
Class 2	Marine life, fisheries, coral reefs, recreational, and mariculture			
Class 3	Ports, oil & gas fields			
Class E	Mangroves, estuarine & river-mouth water			

Phytoplankton biomass in the lagoon

Chlorophyll *a* is an indicator of biological activity, whose surface concentrations during August 2017, December 2017, and February 2018 are presented in Figures 9 – 11. During August 2017, the chlorophyll *a* concentration during the high tide was slightly low, with an average value of 0.63 mg/L compared to the concentrations during the low tide (average value of 0.78 mg/L; Figure 9). A similar observation was made by Shamsudin and Ambak [25], where a lower rate of photosynthetic values were documented at Sungai Ibai Estuary, Terengganu during high tide compared to low tide. Besides this, Krumme et al. [21] suggested that sufficient light and reduced current flow during spring tides enhanced phytoplankton activity, especially during late ebb tides in the afternoon. This statement

coincided well with the timing of our first field sampling (1510 – 1610 hours), where the flows were slightly slow (Figure 3a) and high solar radiation was observed.

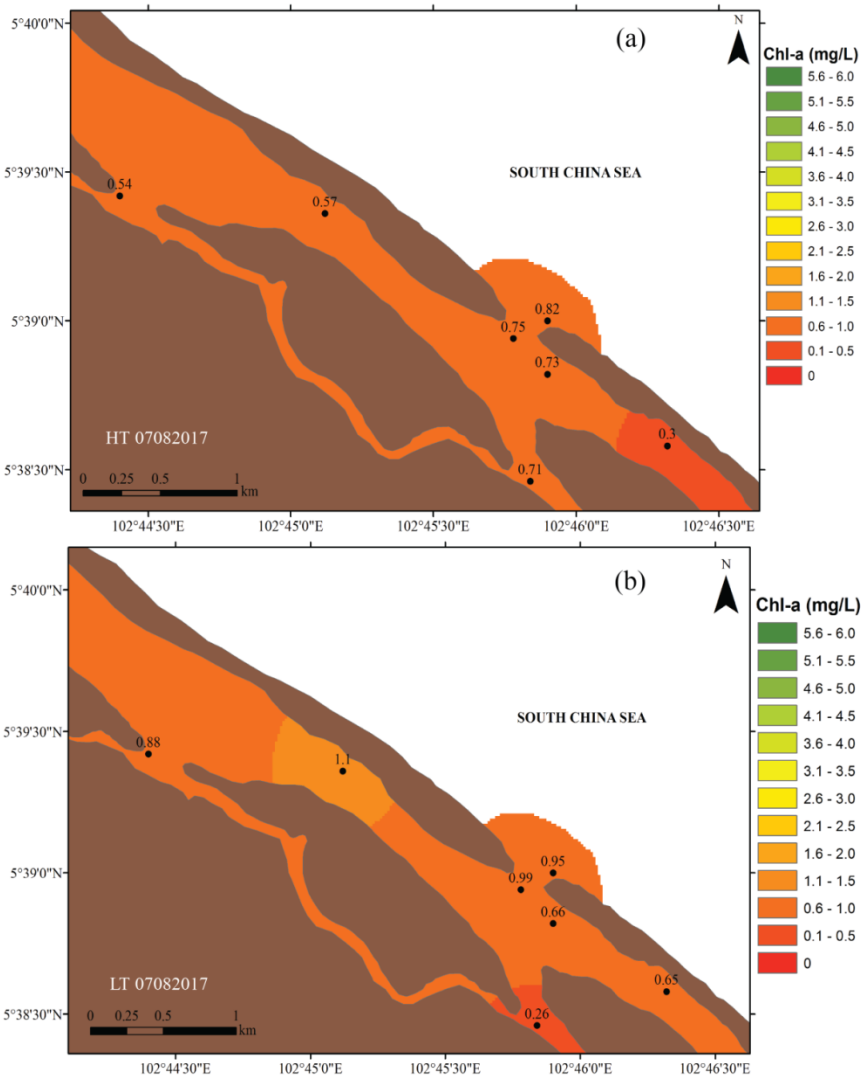


Figure 9. Chlorophyll *a* distribution in Setiu Lagoon during (a) high and (b) low tides on 7 August 2017

During December 2017, chlorophyll *a* concentrations were highly variable during the high tide, ranging from 0.38 – 3.85 mg/L, while during the low tide it was within the range of 0.19 – 1.31 mg/L (Figure 10). This shows that the concentrations of chlorophyll *a* during the high tide were generally high compared to the low tide, with an average difference of 1.06 mg/L. During the low tide, it was believed that freshwater outflow from the rivers had lead to the dilution of the chlorophyll *a* concentrations during the sampling trip (0930 – 1010 hours), as documented in the flow rate of the lagoon (Figure 6a). On top of that, the chlorophyll *a* distribution pattern during February 2018 was relatable to December 2017, where the concentrations during the high tide (average of 2.75 mg/L) were slightly high than those during the low tide (average of 1.83 mg/L; Figure 11). Low chlorophyll *a* concentrations as a result of the dilution factor were also observed in the Merbok Estuary, Kedah, Malaysia, where increased water mixing and tidal flushing diminished the bloom, resulting in low phytoplankton biomass [26].

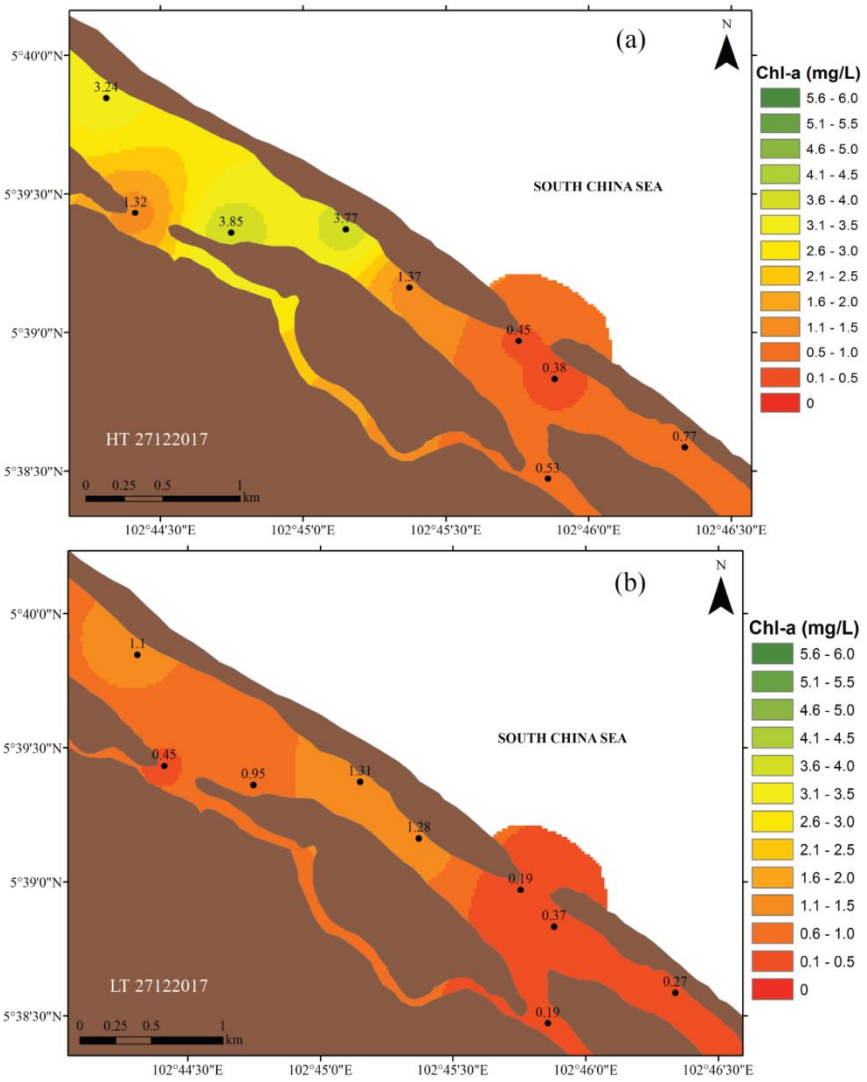


Figure 10. Chlorophyll *a* distribution in Setiu Lagoon during (a) high and (b) low tides on 27 December 2017

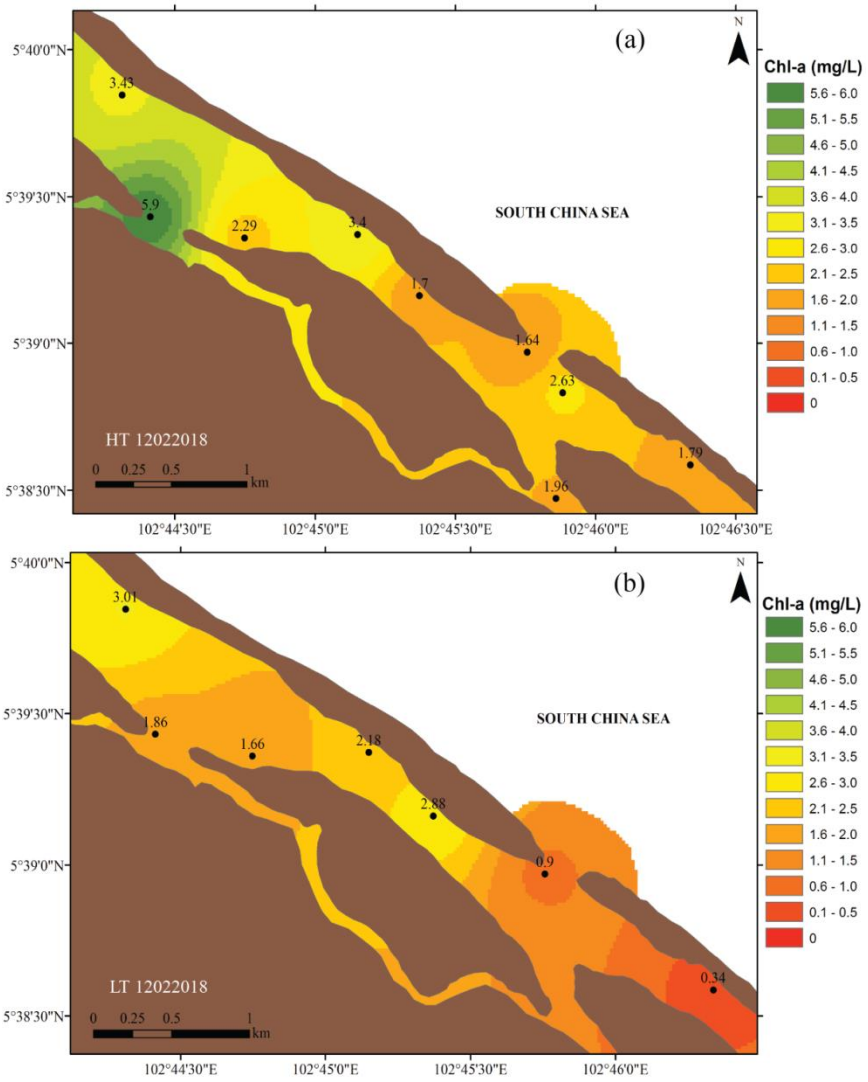


Figure 11. Chlorophyll *a* distribution in Setiu Lagoon during (a) high and (b) low tides on 12 February 2018

To confirm the main influencing parameter affecting the phytoplankton biomass in Setiu Lagoon, the R^2 was calculated and tabulated in Table 4. During the high tide of August 2017, only nitrate showed slightly significant correlation with chlorophyll *a* (R^2 = 0.397). On the other hand, during the low tide of the same day, chlorophyll *a* was significantly correlated with nitrate and ammonium, with R^2 of 0.336 and 0.386 respectively. During the high tide of December 2017, a strong positive correlation was noted between chlorophyll *a* with salinity (R^2 = 0.837) and ammonium (R^2 = 0.657). Meanwhile, during the low tide, chlorophyll *a* was positively and significantly correlated to salinity (R^2 = 0.714) and phosphate (R^2 = 0.689). In February 2018, chlorophyll *a* was significantly correlated to salinity (R^2 = 0.557) and nitrate (R^2 = 0.370) during the high tide. During the low tide, chlorophyll *a* showed a strong postive correlation with all parameters.

Table 4. Correlation matrix (R^2) for surface water quality parameters in Setiu Lagoon

Parameter		Chlorophyll *a* Concentrations					
		August 2017		December 2017		February 2018	
		HT	LT	HT	LT	HT	LT
Salinity	HT	0.005		0.837		0.557	
	LT		0.110		0.714		0.576
Nitrate	HT	0.397		0.202		0.370	
	LT		0.336		0.068		0.704
Phosphate	HT	0.093		0.104		0.036	
	LT		0.002		0.689		0.336
Ammonium	HT	0.061		0.657		0.125	
	LT		0.386		0.261		0.872
Silicate	HT	0.022		0.261		0.130	
	LT		0.212		0.200		0.652

Our study showed that the wet season freshwater flows of the northeast monsoon (December 2017) resulted in significantly high phytoplankton biomass. Therefore, it is believed that the phytoplankton in the study area are affected by the duration and magnitude of the freshwater flow and the nutrients supply. For example, despite having low salinities, the chlorophyll *a* concentrations in the study area were the highest during December 2017, which indicate that the high nutrients supply, which was as a result of heavy rainfall enhanced the phytoplankton growth [21]. Furthermore, a previous study by Suratman et al. [24] inferred that in Setiu Lagoon, large freshwater inputs as a results of heavy rainfall flushed the nutrients from land, which is surrounded by palm oil plantation and aquaculture activities.

Conclusion

Setiu Lagoon is a shallow, almost closed and tidally dominated system with a significant nutrient input from aquaculture and agriculture activities. The salinity, chlorophyll *a*, and nutrients varied between high and low tidal cycles. Patterns were site-specific and altered by freshwater discharges. Less saline water with high nutrients entered the lagoon through the rivers during the ebb tides. Somehow, increased rainfall manifested through the daily rainfall amount and strong flow, increased the freshwater discharges into the lagoon, which blocked the penetration of seawater. Furthermore, increased rainfall amount was also the causative factor that shaped the dynamics of the lagoon during the northeast monsoon. Large freshwater discharges into the lagoon as a result of heavy rainfall, brought along nutrients from terrestrial areas, which resulted in a high concentration of nutrients that enhanced the phytoplankton biomass. Referring to the Malaysia MWQCS scale, nutrients in Setiu Lagoon are classified under Classes 1 and 2, suggesting that aquaculture activities and conservation actions should take place concurrently.

Acknowledgement

The authors wish to thank the staff, especially Mr Roslan Latif and Mr Afifi Johari, from the Institute of Oceanography and Environment (INOS), Universiti Malaysia Terengganu, for their contribution in data collections of this research. This research was supported by the Tuanku Canselor Scholarship (BTC), Universiti Malaysia Terengganu and Higher Institution Centre of Excellence (HICoE) grant vote no. 66928 awarded to INOS.

References

1. de Brito Jr., A. N., Fragoso Jr., C. R. and Larson, M. (2018). Tidal exchange in a choked coastal lagoon: A study of Mundaú Lagoon in northeastern Brazil. *Regional Studies in Marine Science*, 17: 133-142.
2. Hemraj, D. A., Hossain, M. A., Ye, Q., Qin, J. G. and Leterme, S. C. (2017). Plankton bioindicators of environmental conditions in coastal lagoons. *Estuarine, Coastal and Shelf Science*, 184: 102-114.

3. Haraguchi, L., Carstensen, J., Abreu, P. C. and Odebrecht, C. (2015). Long-term changes of the phytoplankton community and biomass in the subtropical shallow Patos Lagoon Estuary, Brazil. *Estuarine, Coastal and Shelf Science*, 162: 76-87.
4. Brito, A. C., Newton, A., Tett, P. and Fernandes, T. F. (2012). How will shallow coastal lagoons respond to climate change? A modelling investigation. *Estuarine, Coastal and Shelf Science*, 112: 98-104.
5. Pagano, M., Rodier, M., Guillaumot, C., Thomas, Y. and Henry, K. (2017). Ocean-lagoon water and plankton exchanges in a semi-closed pearl farming atoll lagoon (Ahe, Tuamotu archipelago, French Polynesia). *Estuarine, Coastal and Shelf Science*, 191: 60-73.
6. Mahanty, M. M., Mohanty, P. K., Pattnaik, A. K., Panda, U. S., Pradhan, S. and Samal, R. N. (2016). Hydrodynamics, temperature/salinity variability and residence time in the Chilika lagoon during dry and wet period: Measurement and modeling. *Continental Shelf Research*, 125: 28-43.
7. Panda, U. S., Mahanty, M. M., Ranga Rao, V., Patra, S. and Mishra, P. (2015). Hydrodynamics and water quality in Chilika Lagoon-A modelling approach. *Procedia Engineering*, 116: 639-646.
8. Suratman, S., Tahir, N. M. and Latif, M. T. (2012). A preliminary study of total petrogenic hydrocarbon distribution in Setiu Wetland, southern South China Sea (Malaysia). *Bulletin of Environmental Contamination and Toxicology*, 88: 755-758.
9. Kasawani, I., Kim Asbiyallah Shah, A., Sulong, I., Mohd Hasmadi, I. and Kamaruzaman, J. (2010). Coastal change detection using GIS in Setiu Lagoon, Terengganu, Malaysia. *Journal of GIS Trends*, 1(1): 20-26.
10. Ong, M. C., Kamaruzzaman, B. Y. and Joseph, B. (2009). Geochemical studies of Setiu lagoon, Terengganu, Malaysia. *Malaysian Journal of Science*, 28(2), 217-222.
11. Suratman, S. and Latif, M. T. (2015). Reassessment of nutrient status in Setiu Wetland, Terengganu, Malaysia. *Asian Journal of Chemistry*, 27(1), 239–242.
12. Bakar, N. H. A., Jusoh, A., Ahmad, M. F., Noor, M. J. M. M. and Norzilah, A. (2016). A spatial nutrient distribution due to seabass aquaculture activities at Setiu, Terengganu, Malaysia. *Journal of Fisheries and Aquatic Science*, 11: 332-348.
13. Zainol, Z. and Akhir, M. F. (2016). Coastal upwelling at Terengganu and Pahang coastal waters: Interaction of hydrography, current circulation and phytoplankton biomass. *Jurnal Teknologi*, 78(8), 11-27.
14. Culver, S. J., Leorri, E., Mallinson, D. J., Corbett, D. R. and Shazili, N. A. M. (2015). Recent coastal evolution and sea-level rise, Setiu Wetland, Peninsular Malaysia. *Palaeogeography, Palaeoclimatology, Palaeoecology*, 417: 406-421.
15. Yaacob, R. and Mustapa, M. Z. (2010). Grain-size distribution and subsurface mapping at the Setiu wetlands, Setiu, Terengganu. *Environmental Earth Sciences*, 60: 975-984.
16. Culver, S. J., Leorri, E., Corbett, D. R., Mallinson, D. J., Shazili, N. A. M., Mohammad, M. N. and Yaacob, R. (2013). Infaunal mangrove swamp foraminifera in the Setiu Wetland, Terengganu Malaysia. *Journal of Foraminiferal Research*, 43(3): 262-279.
17. Culver, S. J., Mallinson, D. J., Corbett, D. R., Leorri, E., Rouf, A. A., Shazili, N. A. M. and Parham, P. R. (2012). Distribution of foraminifera in the Setiu estuary and lagoon, Terengganu, Malaysia. *The Journal of Foraminiferal Research*, 42(2): 109-133.
18. APHA (2005). *Standard Methods for the Examinations of Water and Wastewater* (20th ed.). New York: American Public Health Association.
19. U.S. Environmental Protection Agency. (1993). Methods for chemical analysis of water and wastes. Cincinnati, Ohio.
20. Garrison, T. (2010). Oceanography: An invitation to marine science (7th edition). Yolanda Cossio.
21. Krumme, U., Herbeck, L. S. and Wang, T. (2012). Tide- and rainfall-induced variations of physical and chemical parameters in a mangrove-depleted estuary of East Hainan (South China Sea). *Marine Environmental Research*, 82: 28-39.
22. Cervantes-Duarte, R., Prego, R., López-López, S., Aguirre-Bahena, F. and Ospina-Alvarez, N. (2013). Annual patterns of nutrients and chlorophyll in a subtropical coastal lagoon under the upwelling influence (SW of Baja-California Peninsula). *Estuarine, Coastal and Shelf Science*, 120: 54-63.
23. Suratman, S. and Aziz, A. A. (2017). Spatial and seasonal variations of organic carbon-based nutrients in Setiu Wetland , Malaysia. *Sains Malaysiana*, 46(6): 859-865.

24. Suratman, S., Hussein, A. N. A. R., Mohd Tahir, N., Latif, M. T., Mostapa, R. and Weston, K. (2016). Seasonal and spatial variability of selected surface water quality parameters in Setiu Wetland, Terengganu, Malaysia. *Sains Malaysiana*, 45(4): 551-558.
25. Shamsudin, L. and Ambak, M. A. (1983). The diurnal variation in photosynthetic values, inorganic nutrient contents and other environmental factors within a tidal cycle of Sungai Ibai, Trengganu. *Pertanika*, 6(2): 39-44.
26. Wan Maznah, W. O., Rahmah, S., Chiew, C. L., Wang, P. L., Fatema, K. and Isa, M. (2016). Effects of tidal events on the water quality in the Merbok Estuary, Kedah, Malaysia. *Tropical Ecology*, 57(2): 213-229.

Malaysian Journal of Analytical Sciences, Vol 23 No 6 (2019): 1107 - 1119
DOI: https://doi.org/10.17576/mjas-2019-2306-17

MALAYSIAN JOURNAL OF ANALYTICAL SCIENCES
Published by The Malaysian Analytical Sciences Society
ISSN 1394 - 2506

DISTRIBUTION OF PHYTOPLANKTON IN KUANTAN PORT, MALAYSIA DURING NORTHEAST MONSOON SEASON

(Taburan Fitoplankton di Pelabuhan Kuantan, Malaysia Semasa Musim Monsun Timur Laut)

Amir Safwan Hamzah, Normawaty Mohammad-Noor, Aimimuliani Adam*, Zuhairi Ahmad

Department of Marine Science, Kulliyah of Science,
International Islamic University Malaysia, 25200 Kuantan, Pahang, Malaysia.

**Corresponding author: aimiadam@iium.edu.my*

Received: 30 October 2018; Accepted: 26 September 2019

Abstract

Harmful algal bloom (HAB) is a proliferation of phytoplankton that can produce bio toxins and cause harm to human health, as well as the environment and the organisms associated with it. The first case of HAB in Kuantan Port was recorded in November 2013, followed by another outbreak in August 2014. This study aims to investigate the phytoplankton distribution and dispersal in the Kuantan Port during the Northeast monsoon season in order to identify the extent of the spread of HAB, should such an event occur again. Phytoplankton samples were taken at Kuantan Port from three levels of depth (surface, middle, and bottom) at every hour during a period of 24 hours. Samples were preserved in Lugol's iodine. Chemical properties such as phosphorus, nitrate, nitrite, and ammonia were also taken during each sampling. Phytoplankton samples were counted and identified up to genus level. Simulation of phytoplankton dispersal in Kuantan Port was conducted using the program MIKE 21. RMSE error was conducted to improve accuracy between ADCP data and simulated data, and was found to be within acceptable range. The MIKE 21 simulation showed that the algal bloom would remain inside the port and would not spread out to the sea. Thirty-seven taxa of phytoplankton were identified. Phytoplankton concentrations ranged from 124 cells/L to 775 cells/L. TSS value ranged from 0.0110 mg/L to 0.0345 mg/L. Phosphorus concentration ranged from 0.075 mg/L PO_4 to 3.82 mg/L PO_4. Nitrate concentration ranged from 1.05 mg/L NO_3^-N to 2.45 mg/L NO_3^-N. Nitrite concentration ranged from 0.0040 mg/L NO_2^-N to 0.0095 mg/L NO_2^-N. Ammonia concentration ranged from 0.045 mg/L NH_3^-N to 0.140 mg/L NH_3^-N. A positive correlation was found between phytoplankton abundance and nutrient concentration of phosphorus, nitrate and ammonia, with a slightly negative correlation for nitrite. This study recorded the presence of several HAB species such as *Dinophysissp*, *Noctillucasp*, and *Prorocentrum sp*. The presence of these species further indicates that several safety measures need to be considered to safeguard public health, particularly in the coastal waters of Pahang.

Keywords: phytoplankton, harmful algal bloom, Northeast monsoon, Kuantan Port, simulation

Abstrak

Mekar alga berbahaya (HAB) adalah perkembangan fitoplankton yang boleh menghasilkan biotoksin dan menyebabkan kemudaratan kepada kesihatan manusia, serta alam sekitar dan organisma yang berkaitan dengannya. Kes pertama mekar alga berbahaya di Pelabuhan Kuantan telah direkodkan pada November 2013, diikuti dengan wabak lain pada bulan Ogos 2014. Kajian ini bertujuan untuk menyiasat taburan dan penyebaran fitoplankton di Pelabuhan Kuantan semasa musim monsun Timur Laut untuk mengenal pasti sejauh mana HAB dapat tersebar sekiranya berlaku kejadian seperti itu lagi. Sampel fitoplankton diambil di Pelabuhan Kuantan dari tiga tahap ke dalaman (permukaan, tengah, dan bawah) dari setiap jam dalam tempoh 24 jam. Sampel dipelihara dalam iodin Lugol. Sifat kimia seperti fosforus, nitrat, nitrit, dan ammonia juga diambil untuk pensampelan. Sampel fitoplankton dikira dan dikenalpasti sehingga tahap genus. Simulasi penyebaran fitoplankton di Pelabuhan Kuantan dijalankan dengan menggunakan program MIKE 21. Ralat punca kuasa dua telah dijalankan untuk memastikan data antara ADCP dan simulasi adalah tepat, dan didapati jumlahnya dalam nilai berpatutan. Simulasi menunjukkan bahawa mekar alga akan berada di dalam Pelabuhan Kuantan dan tidak akan merebak kepada perairan persekitaran. Tiga puluh tujuh taksonomi

fitoplankton telah dikenalpasti. Kepekatan fitoplankton berkisar dari 124 sel/L hingga 775 sel/L. Nilai TSS adalah dari 0.0110 mg/L kepada 0.0345 mg/L. Kepekatan fosforus berkisar dari 0.075 mg/L PO_4 kepada 3.82 mg/L PO_4. Kepekatan nitrat adalah dari 1.05 mg/L NO_3^-N hingga 2.45 mg/L NO_3^-N. Kepekatan nitrit adalah dari 0.0040 mg/L NO_2^-N hingga 0.0095 mg/L NO_2^-N. Kepekatan ammonia adalah dari 0.045 mg/L NH_3^-N hingga 0.140 mg/L NH_3^-N. Korelasi positif telah didapati antara kelopak fitoplankton dan kepekatan fosforus, nitrat dan ammonia, serta korelasi negatif untuk nitrit. Kajian ini mencatatkan kehadiran beberapa spesies mekar alga berbahaya seperti *Dinophysissp*, *Noctillucasp*, dan *Prorocentrum sp*. Kehadiran spesies ini terus menunjukkan bahawa beberapa langkah keselamatan perlu dipertimbangkan untuk melindungi kesihatan awam, khususnya di perairan pantai Pahang.

Kata kunci: fitoplankton, mekar alga berbahaya, monsun timur laut, Pelabuhan Kuantan, simulasi

Introduction

Phytoplankton, also known as microalgae, are free floating unicellular, filamentous and colonial autotrophic organisms that grow in aquatic environments, whose movement is more or less dependent on water currents [1]. According to Sze [2], phytoplankton swim and move with the water flow, but they cannot move against the ocean current as their size is small and they have insufficient energy. Most phytoplankton are buoyant and float in the upper part of the ocean, where sunlight penetrates the water. Phytoplankton also require inorganic nutrients such as nitrates, phosphates, and sulfur which they convert into proteins, fats, and carbohydrates.

A rapid increase or accumulation of phytoplankton population is known as algal blooms. Certain algal blooms, particularly ones caused by dinoflagellates, are known as harmful algal blooms (HAB), due to the threat and danger that they pose to humans and marine species alike. HAB species are capable of generating potent toxins that can influence the well-being of humans through the consumption of contaminated shellfish and/or fish, or through water and aerosol exposure [3]. In addition to their harmful effects on humans, these toxins also contribute to the death of fishes and shellfishes, as well as marine mammals, birds, and other animals that depend on the marine food web [4, 5].

One way of predicting the dispersal of algal blooms is through hydrodynamics. Hydrodynamics is the study of the movement of liquid, and in oceanic studies this usually revolves around wind stress and tidal stress. A high wind and tidal stress will cause the phytoplankton to be dispersed and spread out due to the shear strain and active movement of water, reducing the chances of causing a bloom due to them being dispersed. On the other hand, a low wind and tidal stress would allow the water to stabilize, and the phytoplankton to be less spread out. On another note, wind movements can also cause the phytoplankton to travel towards the direction the wind is blowing, either because of the wind directly pushing them or because of the shift in nutrients from the wind breeze, causing the phytoplankton to naturally follow suit [6]. Changes in these hydrodynamic patterns can be linked to different monsoon seasons.

The monsoon system in Malaysia is characterized by two monsoon regimes, which are, the Northeast monsoon, lasting from November to March, and the Southwest monsoon, lasting from May to October. During the Northeast monsoon, the area in the east coast of Peninsular Malaysia normally receives a large amount of rainfall [7], along with strong northeastern winds.

The purpose of this study is to investigate the phytoplankton and nutrient distribution and dispersal in the Kuantan Port during the Northeast monsoon season. With this, we can predict the period where harmful algal blooms are most likely to happen via hydrodynamic simulation, and take precautionary steps to mitigate the bloom. Kuantan Port has been chosen as the location of the study due to the port acting like a semi-enclosed body of water, while also being connected to the South China Sea. Furthermore, ships that dock at Kuantan Port may also introduce phytoplankton species that are not native to the area from their ballast water discharge. A study conducted by Mohammad-Noor et al. [8] has also shown that the Kuantan Port has a history of HAB outbreaks, which confirms the presence of HAB species. Mohammad-Noor et al. [8] also discovered that in the 12 month period of sampling, the HAB species *A. tamiyavanichii*was found to be most abundant during September 2014, which was during the Northeast monsoon season. This study also investigates the correlation between phytoplankton count and nutrients (phosphorus, nitrate, ammonia and nitrite) during Northeast monsoon in Kuantan Port.

Materials and Methods

Study area

This study was conducted at Kuantan Port (Latitude 3°58'N, Longitude 103° 26'E), Pahang, which is about 25 km to the north of Kuantan city. This port is a multipurpose port which offers container handling and one of the longest free storage periods in Malaysia. Previously run by the Kuantan Port Authority, the busy port was privatized in 1988 and is currently operated by Kuantan Port Consortium Sdn Bhd. Samples were taken on the 1st of February 2017, starting at 12.00 pm until 11.00 am of the 2nd of February 2017.

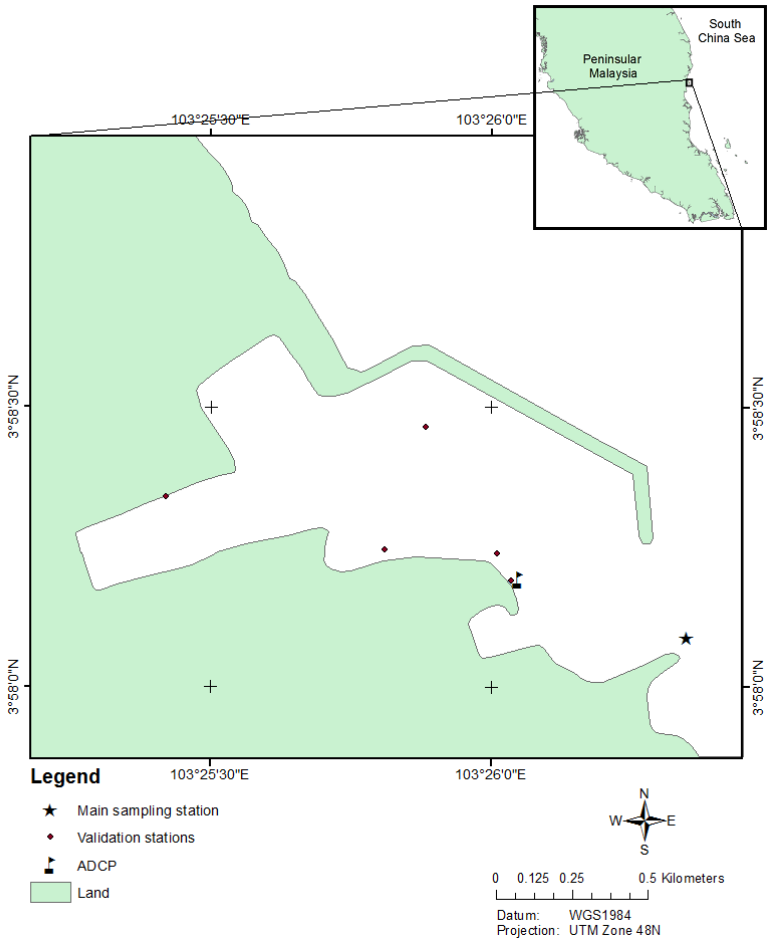


Figure 1. Map of the study area

Sample collection

Water samples were collected from the main station, which is located at the model boundary (Figure 1) in an hourly interval for up to 24 hours, at coordinates 3° 58.090'N 103° 26.353'E, starting from 12:00 pm on 1st February until 12:00 pm on 2nd February. An acoustic Doppler current profiler was also deployed at the same time at coordinates 3° 58.265'N 103° 26.120'E to record the current speed and direction. Samples were also taken from validation stations located inside the port at random intervals.

Water samples were collected at three different depths (surface, middle, and bottom) using a 5 L Niskin water sampler. Average water depth of Kuantan Port was found to be at 15 meters below surface. Samples for identification and counting were immediately preserved in Lugol's iodine for phytoplankton identification and

quantification. For nutrient analysis, 1 L of water sample was collected for each depth. An extra 1 L of water sample was collected on the surface depth for chlorophyll-a analysis. The water samples were then filtered using Whatman Glass Microfiber filters with a diameter of 47 mm before further analysis was conducted. The filters were collected and stored for TSS analysis.

Phytoplankton analysis

Phytoplankton samples that were preserved in Lugol's iodine were transferred into measuring cylinders for a sedimentation process until the concentration of samples was approximately 50 mL. Samples were then observed under a Leica DME Light Microscope under 100x magnification using a Sedgewick Rafter Counting Cell Chamber. The counting procedure was done twice for each sample. Phytoplankton samples were identified up to the genus level based on Tomas [9] and Omura et al. [10].

Nutrient analysis

Nutrient analysis was conducted via colorimetry using the HACH DR900 Multiparameter Portable Colorimeter and its corresponding powder pillow reagents. Phosphorus was analyzed with PhosVer® 3 reagent powder pillows using HACH method 8048. Nitrate was analyzed with NitraVer® 5 reagent powder pillows using HACH method 8171. Ammonia was analyzed using HACH nitrogen-ammonia reagent set using HACH method 8155. Nitrite was analyzed with NitriVer® 3 reagent powder pillows using HACH method 8507.

Total suspended solid analysis

The filters used for total suspended solids (TSS) analysis had been labeled and dried overnight in a Memmert laboratory oven at a temperature of 103 ^{o}C. After that, each filter was weighed using an AND HR-200 Digital Analytical Balance. Then, each of the filters was used to filter the water samples. Following that, the filters are again dried overnight at a temperature of 103 ^{o}C, and were weighed again. TSS was calculated using the following formula in equation 1:

$$\text{TSS (mg/L)} = \frac{(\text{final weight of filter} - \text{initial weight of filter})}{\text{volume of sample filtered}} \quad (1)$$

Simulation

Simulation was conducted using the program MIKE 21 with the purpose of predicting the spread of algal bloom in Kuantan Port. The point of origin for the a mulated data for surface elevation, current speed and current direction were compared with the data obtained from the ADCP device with RMSE error for higher accuracy. The phytoplankton dispersal simulation was set to the following parameters:

- Minimum plankton weight of 0.25 µg [11],
- Doubling time, the period of time required for phytoplankton to double in value, set to 1 day [12],
- Sinking rate, the estimated rate for phytoplankton to settle down in the water column, set to 1 m/day [13], and
- Death rate, the life expectancy of the simulated phytoplankton, set to 5 days.

Secondary data such as tide data, bathymetry data and wind data for Kuantan Port were obtained through external sites and programs. Tide data was obtained using the program ADMIRALTY Total Tide. Bathymetry data was obtained from the website General Bathymetric Chart of the Oceans (GEBCO). Wind data was obtained from the website Iowa Environmental Mesonet. RMSE error with data obtained from ADCP was calculated to increase the accuracy of the model.

Data analysis

Significant tests for phytoplankton abundance and nutrient concentration between depths were carried out using PAST (Paleontological Statistic), with one way ANOVA for parametric data and Kruskal-Wallis for nonparametric data. Pearson correlation test between phytoplankton abundance and nutrient concentration was also conducted.

Results and Discussion

A total of thirty-seven phytoplankton genera were identified during the study period. Most of these genera belonged to Diatoms (24 genera), followed by Dinoflagellates (12 genera) and blue-green algae (1 genus).

Table 1 shows the list of all thirty-seven phytoplankton genera found in Kuantan Port. The most dominant genus found was *Thalassionema* spp (67.48%), followed by *Nitzchia* spp (17.43%), *Coscinodiscus* spp (16.72%), and *Chaetoceros* spp (6.21%). Study conducted by Mohammad-Noor et al. [14] in Kuantan coastal waters had also encountered a high abundance of diatoms. Several potential harmful species were identified in this study, such as *Prorocentrummicans*, *Dinophysis* spp., and *Chaetoceros* spp.

Table 1. Phytoplankton genera recorded in Kuantan Port during sampling

Phytoplankton Genus	
Thalassionema (Thalassionemataceae)	*Nitzschia (Basillariaceae)*
Coscinodiscus (Coscinodiscaceae)	*Chaetoceros (Chaetocerotaceae)*
Ditylum (Lithodesmiaceae)	*Odontella (Eupodiscaceae)*
Pleurosigma (Naviculaceae)	*Amphiprora (Amphipleuraceae)*
Amphora (Catenulaceae)	*Prorocentrum (Prorocentraceae)*
Bacteriastrum (Chaetocerotaceae)	*Detonula (Thalassiosiraceae)*
Ceratium (Ceratiaceae)	*Protoperidinium (Protoperidinaceae)*
Pyrocystis (Pyrocystaceae)	*Dinophysis (Dinophysaceae)*
Gonyaulax (Gonyaulacaceae)	*Hemiaulus (Hemiaulaceae)*
Guinardia (Rhizosoleniaceae)	*Rhizosolenia (Rhizosoleniaceae)*
Lauderia (Thalassiosiraceae)	*Dictyocha (Dictyochophyceae)*
Noctilluca (Noctilucaceae)	*Skeletonema (Thalassiosiraceae)*
Asteromphalus (Coscinodiscophyceae)	*Histoines (Dinophysaceae)*
Meauniera (Naviculaceae)	*Gyrodinium (Gymnodiniaceae)*
Thalassiosira (Thalassiosiraceae)	*Podolampas (Podolampadaceae)*
Stephanopyxis (Melosiraceae)	*Nematodinium (Warnowiaceae)*
Planktoniella (Thalassiosiraceae)	*Dactyliosolen (Rhizosoleniaceae)*
Asterionellopsis (Fragilariaceae)	*Cochlodinium (Gymnodiniaceae)*
Corethron (Leptocylindraceae)	

Figure 2 shows that the total highest amount of phytoplankton individuals observed according to depth is the middle area, at 8504 cells L^{-1}, while the lowest is the surface area at 5426 cells L^{-1}. Likewise, the total highest amount of phytoplankton individuals observed according to time is at 13:00 at 1365 cells L^{-1}, while the lowest is at 14:00 at 679 cells L^{-1}.

The difference of phytoplankton abundance across each water depth is not statistically significant ($p > 0.05$). This means that the water column is homogenous and well-mixed, most likely due to the port itself being quite shallow compared to the open ocean.

This simulation model was validated by simulating the surface elevation, current speed and current direction of the sampling period. The data obtained between modeled and measured flows were compared, and RMSE error was calculated to increase the accuracy of the model (Table 2). All RMSE values were found to be within the acceptable limits.

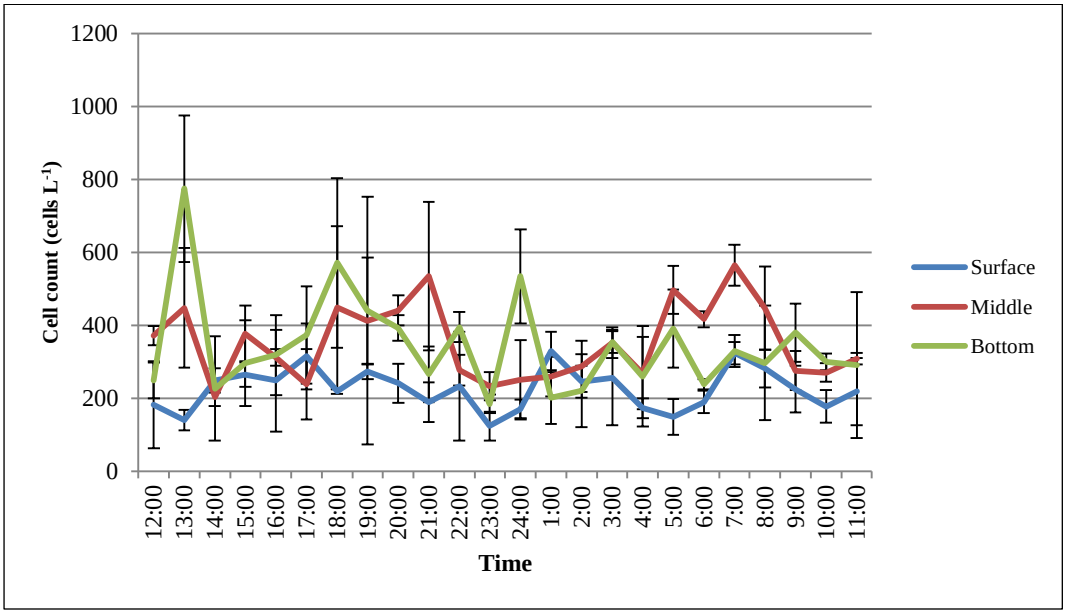


Figure 2. Phytoplankton abundance (cells L^{-1}) obtained over sampling time

Table 2. RMSE error calculation for surface elevation, current speed and current direction for Northeast monsoon

Measurement	RMSE %	JPS Limit
Surface elevation	5.10%	≤10%
Current speed	7.14%	≤20%
Current direction	18.44%	≤20%

Figure 3 and Figure 4 show the distribution of phytoplankton during low tide and high tide. Figure 3 shows that the phytoplankton distribution is higher in the port during low tide. However, Figure 4 shows that phytoplankton distribution is much more concentrated at the port mouth, and surpasses even the highest count of phytoplankton inside the port during low tide. The reasoning behind this is that during high tide, water from the open ocean flows inside the port, bringing in a high amount of phytoplankton from the sea along with it, which remain around the port mouth. During low tide, the seawater does not flow very well due to lower surface elevation, causing the phytoplankton count inside the port to become higher, relative to the area near the port mouth. The lack of significant phytoplankton abundance across each depth also shows that the phytoplankton abundance is not affected by the water column, and instead is more affected by the current movement. The results of phytoplankton dispersal simulation in Kuantan Port suggest that should an algal bloom ever occur in Kuantan Port, the bloom will remain inside the port and will not spread out to the open ocean (Figures 5 and 6).

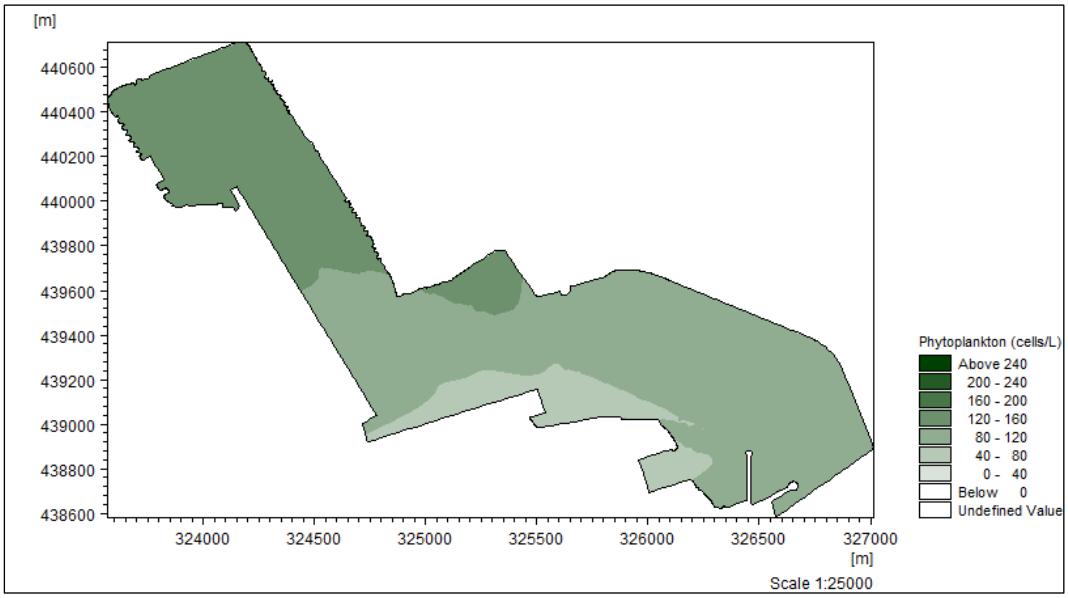


Figure 3. Phytoplankton abundance (cells) observed during low tide in Kuantan Port

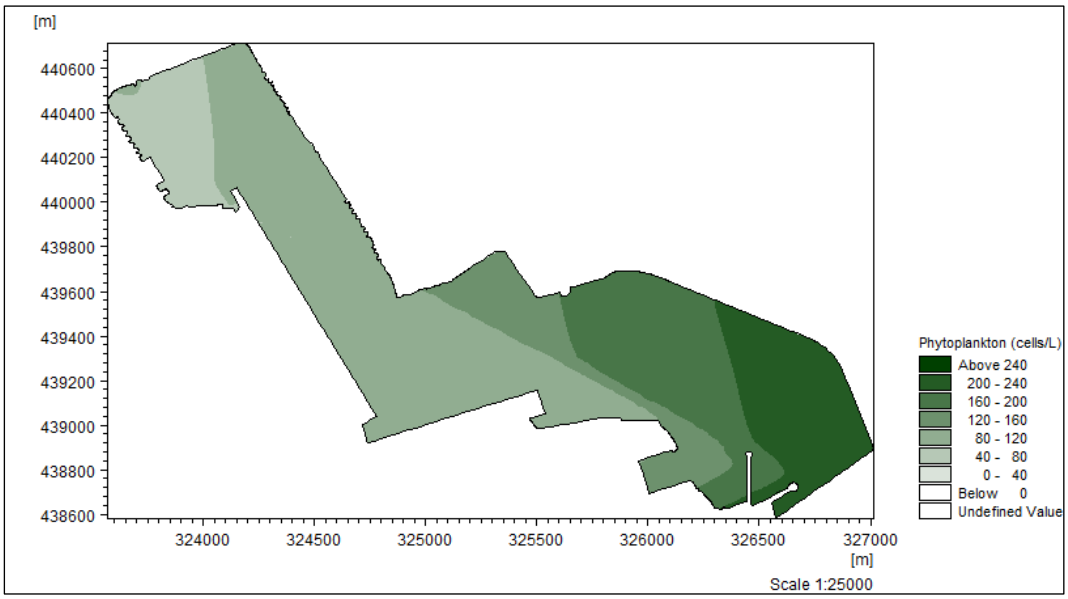


Figure 4. Phytoplankton abundance (cells) observed during high tide in Kuantan Port

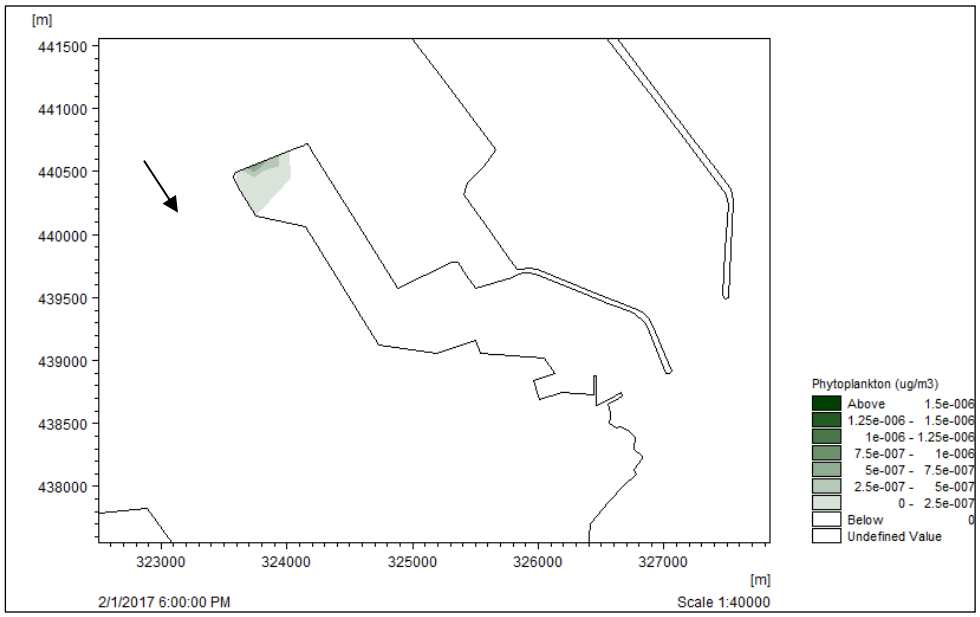


Figure 5. Simulation of phytoplankton dispersal (µg/m³) observed during low tide in Kuantan Port

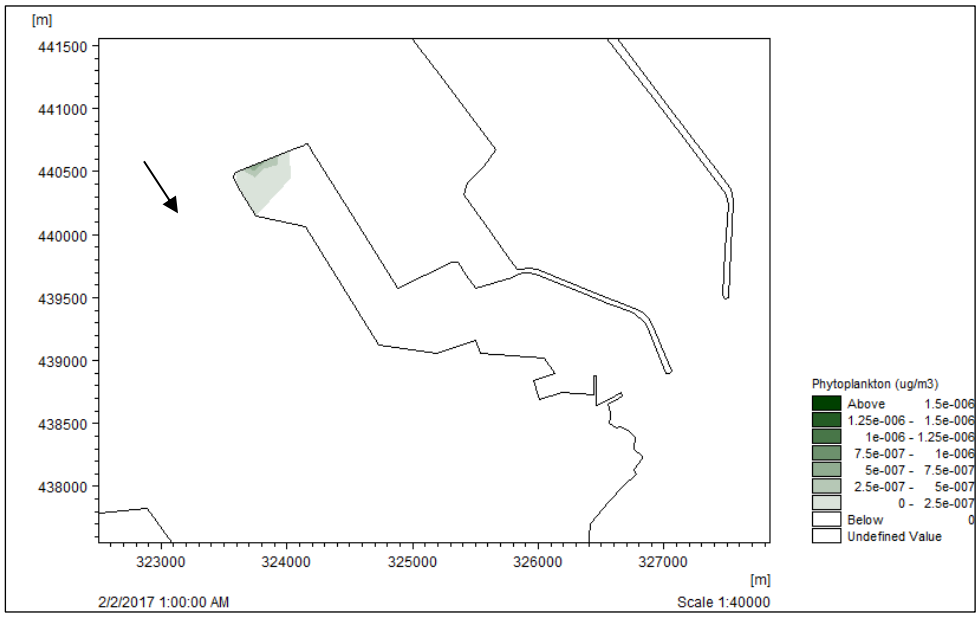


Figure 6. Simulation of phytoplankton dispersal (µg/m³) during high tide in Kuantan Port

For phosphorus, the difference in phosphorus concentrations across each depth was not found to be statistically significant ($p > 0.05$). This means that the water column was homogenous and well-mixed, most likely due to the port itself being quite shallow compared to the open ocean. However, phosphorus concentration across different sampling times (Figure 7) was statistically significant ($p < 0.05$). There were no significant differences in the interaction between depth and sampling time.

Based on the Pearson test with count which returns a value of 0.054, there is a positive correlation between phytoplankton abundance and phosphorus. According to Jalal et al. [15], phosphorus is considered to be the most significant among other nutrients responsible for eutrophication, as it is the primary initiating factor.

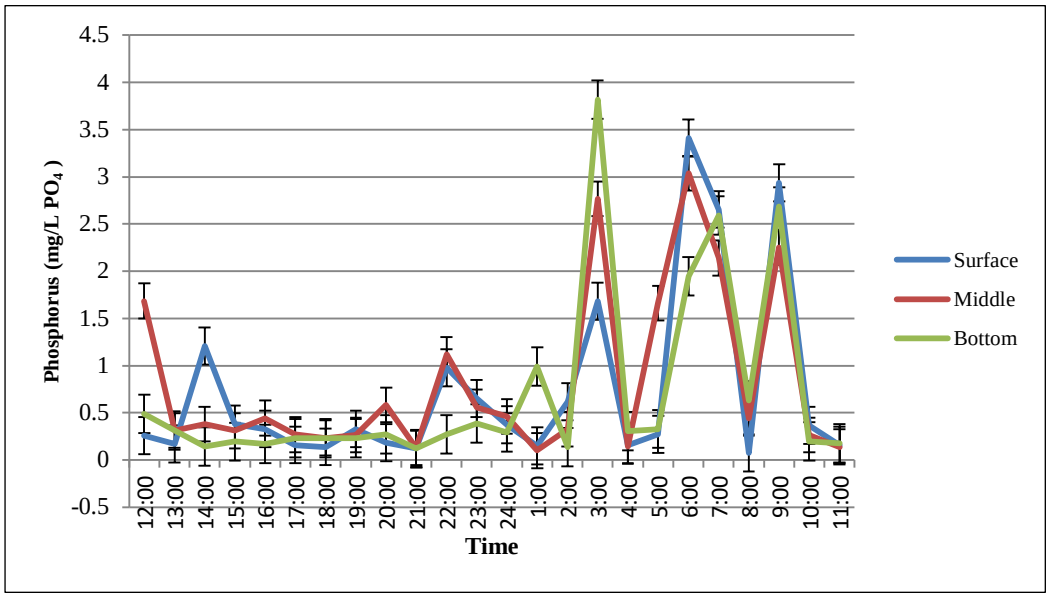


Figure 7. Phosphorus content in Kuantan Port over time for each depth

The nitrate concentration across each water depth was not found to be statistically significant ($p > 0.05$). This means that the water column was homogenous and well-mixed, most likely due to the port itself being quite shallow compared to the open sea. However, nitrate concentration across different sampling times (Figure 8) was statistically significant ($p < 0.05$). There were also significant differences in the interaction between depth and sampling time.

Pearson test with count returns a value of 0.014, indicating positive correlation between phytoplankton abundance and nitrates. According to Jalal et al. [15], an abundance of nitrates in combination with phosphorus will stimulate the excessive growth of algae.

The ammonia concentration across each water depth was not statistically significant ($p > 0.05$). This means that the water column was homogenous and well-mixed, most likely due to the port itself being quite shallow compared to the open ocean. However, ammonia concentration across different sampling times (Figure 9) was statistically significant ($p < 0.05$). There were no significant differences in the interaction between depth and sampling time. Pearson test with count returns a value of 0.233, which indicates positive correlation between phytoplankton abundance and ammonia. According to Jalal et al. [15], an abundance of ammonia will stimulate the growth of algae and can result in algal blooms.

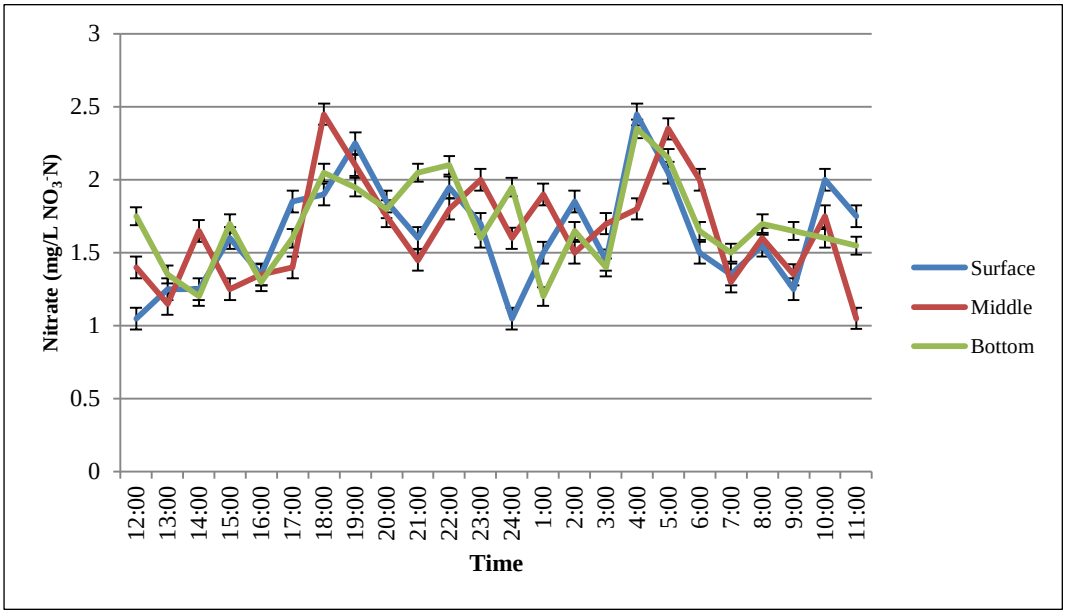


Figure 8. Nitrate content in Kuantan Port over time for each depth

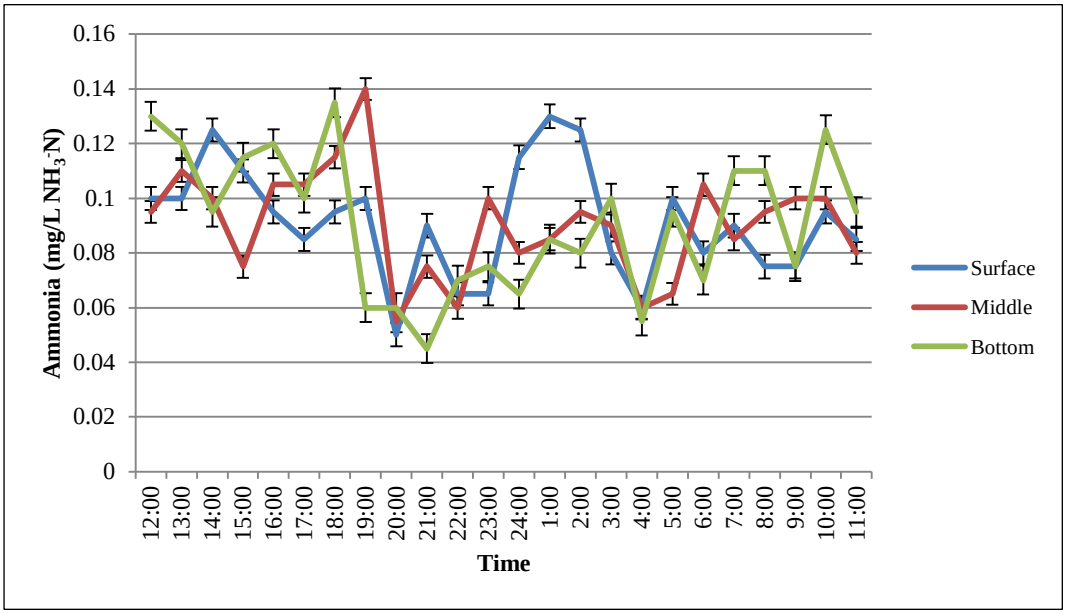


Figure 9. Ammonia content in Kuantan Port over time for each depth

The nitrite concentration across each water depth (Figure 10) was statistically significant ($p < 0.05$). Nitrite concentration across different sampling times was found to be statistically significant as well ($p < 0.05$). There were also significant differences in the interaction between depth and sampling time. This means that the water column was not homogenous and well-mixed for nitrite. A likely explanation is that the nitrate analysis method was not sensitive enough, leading to a large difference in the number of nitrite concentration between water depths.

Pearson test with count returns a value of -0.007, which indicates a slight negative correlation between phytoplankton abundance and nitrites. This is highly likely due to the fact that nitrifying microorganisms usually thrive at depths where phytoplankton are light-limited [16], and Kuantan Port's shallow water ensures that the phytoplankton receive enough sunlight.

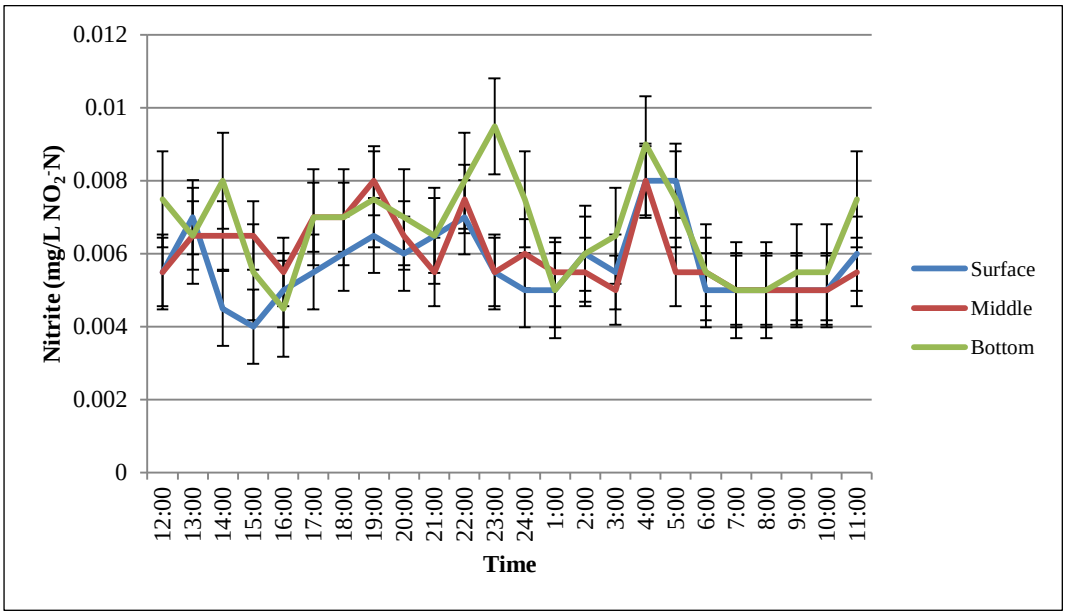


Figure 10. Nitrite content in Kuantan Port over time for each depth

The highest amount of TSS value obtained (Figure 11) was 0.0345 mg/L, which was for the sample taken at 23:00 at the bottom layer. According to Jalal et al. [15], even a TSS value of 0.044 g is still favorable for aquatic life, which means that the Kuantan Port is very favorable for phytoplankton. Pearson test conducted between total suspended solids and phytoplankton count returns a value of 0.207, which indicates positive correlation between phytoplankton abundance and total suspended solids.

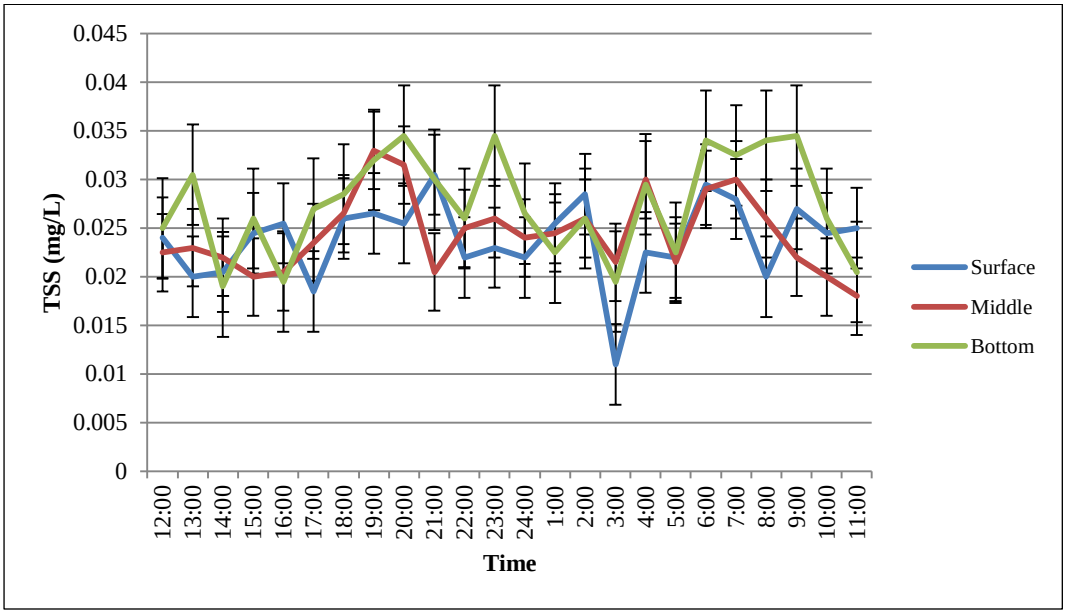


Figure 11. Total suspended solids in Kuantan Port over time for each depth

Conclusion

This research confirms the existence of harmful algal bloom species in Kuantan Port. Results also confirm that phytoplankton counts have a positive correlation with phosphorus, nitrate and ammonia, showing that these nutrients can influence phytoplankton density in Kuantan Port during Northeast monsoon. Based on the MIKE 21 simulated model, the algal bloom will remain inside the Kuantan Port and will not spread out to the open sea during Northeast monsoon. It is strongly suggested that the previous occurrence of HAB in Kuantan Port was not caused by a native species. Instead, it could have possibly been caused by a foreign HAB species being introduced into the port via ballast water from international ships. It is also possible that human activities surrounding Kuantan Port may have contributed towards the algal bloom.

Acknowledgement

This study was conducted under RIGS 16-105-0269 and RIGS 16-102-0266 of International Islamic University Malaysia Kuantan, Malaysia.

References

1. Millman, M., Cherrier, C. and Ramstack, J. (2005). The seasonal succession of the phytoplankton community in Ada Hayden Lake, North Basin, Ames, Iowa. Limnology Laboratory, Iowa State University, Ames Iowa.
2. Sze, P. (1998). Biology of the Algae. 3rd Edition. McGraw Hill Inc, USA.
3. Van Dolah, F. M. (2000). Diversity of Marine and Freshwater Algal Toxins. In: Botana L., editor. Seafood Toxicology: Pharmacology, Physiology and Detection. Marcel Dekker, New York: pp. 19-43
4. Scholin, C.A., Gulland, F., Doucette, G.J., Benson, S., Busman, M., Chavez, F.P. and Van Dolah, F.M. (2000). Mortality of sea lions among the central California coast linked to a toxic diatom bloom. *Nature*, 430: 80-84.
5. Flewelling, L. J., Naar, J. P., Abbott, J. P., Baden, D. G., Barros, N. B., Bossart, G. D. and Landsberg, J.H. (2005). Brevetoxicosis: red tides and marine mammal mortalities. *Nature*, 435: 755-756.
6. Buranapratheprat, A., Yanagi, T., Niemann, K.O., Matsumura, S. and Sojisuporn, P. (2008). Surface chlorophyll-a dynamics in the upper Gulf of Thailand revealed by a coupled hydrodynamic-ecosystem model. *Journal of Oceanography*, 64: 639.

7. Yoshida, T., Toda, T., Yusoff, F. M. and Othman, B. H. R. (2006). Seasonal variation of zooplankton community in the coastal waters of the Straits of Malacca. *Coastal Mar Sci*, 30: 320-327.
8. Mohammad-Noor, N., Adam, A., Lim, P.T., Leaw, C.P., Lau, W.L.S., Liow, G.R., Muhammad-Bunnori, N., Hamdan, N., Md-Nor, A., Kemat, N. and Muniandi, D. (2018). First report of paralytic shellfish poisoning (PSP) caused by *Alexandrium tamiyavanichii* in Kuantan Port, Pahang, East Coast of Malaysia. *Phycological Research*, 66: 37-44.
9. Tomas, C. R. (1997). Identifying marine phytoplankton. Florida Marine Research Institute, Florida.
10. Omura, T., Iwataki, M., Borja, V.M., Takayama, H. and Fukuyo, Y. (2012). Marine phytoplankton of the Western Pacific. Kohseisha Kouseikaku, Japan.
11. González, E. J. and Tundisi, J. G. (2008). Size and dry weight of main zooplankton species in Bariri reservoir (SP, Brazil). *Brazilian Journal of Biology*, 68(1): 69-75.
12. Laws, E. A. (2013). Evaluation of in situ phytoplankton growth rates: a synthesis of data from varied approaches. *Annual Review of Marine Science,* 5:247-268.
13. Peperzak, L., Colijn, F., Koeman, R., Gieskes, W. W. C and Joordens, J. C. A. (2003). Phytoplankton siking rates in the Rhine region of freshwater influence. *Journal of Plankton Research*, 25(4): 365-383.
14. Mohammad-Noor, N., Harun, S. N. R., Mat Lazim, Z., Mukai, Y., Mohammad, N. T. and Saad, S. (2013). Diversity of phytoplankton in coastal water of Kuantan, Pahang, Malaysia. *Malaysian Journal of Analytical Sciences*, 32(1): 29-37.
15. Jalal, K. C. A., Akbar John, B. Hassan I. Sheikh, Shahbudin S., and Nor Hafiza, Y. A. A. (2017). Study on physiochemical parameters and distribution of phytoplankton in Kuantan Estuary, Pahang. *Environment and Ecosystem Science*, 1(1):8-12.
16. Zakem, E. J., Al-Haj, A., Church, M. J., Dijken, G. L., Dutkiewicz, S., Foster, S. Q. and Follows, M. J. (2018). Ecological control of nitrite in the upper ocean. *Nature communications*, 9(1): 1206.

Malaysian Journal of Analytical Sciences, Vol 23 No 6 (2019): 1120 - 1132
DOI: https://doi.org/10.17576/mjas-2019-2306-18

MALAYSIAN JOURNAL OF ANALYTICAL SCIENCES
Published by The Malaysian Analytical Sciences Society
ISSN 1394 - 2506

DISTRIBUTION AND SOURCES OF POLYCYCLIC AROMATIC HYDROCARBONS IN COASTAL SURFACE SEDIMENTS OFF TERENGGANU

(Taburan dan Sumber Hidrokarbon Polisiklik Aromatik dalam Sedimen Permukaan Pesisir Pantai Terengganu)

Mohd Mursyid Mohd Sanip[1], Muhammad Fais Fadzil[1], Suhaimi Suratman[1], Shahirah Rozmi[2], Norhayati Mohd Tahir[2]*

[1]*Institute of Oceanography and Environment*
[2]*Faculty of Science and Marine Environment*
Universiti Malaysia Terengganu, 21030 Kuala Nerus, Terengganu, Malaysia

**Corresponding author: hayati@umt.edu.my*

Received: 30 October 2018; Accepted: 26 September 2019

Abstract

PAHs (Polycyclic Aromatic Hydrocarbons) are a group of pollutants that are of concern in the marine environment. This study determines the distribution and sources of PAHs in surface sediments of the Terengganu coast. Sediments from sixteen stations along the Terengganu coast were collected using Smith Mclntyre grab. PAHs in the sediment samples were extracted using the ultra-sonication method, with dichloromethane (DCM): methanol (MeOH) (3:1 v/v) as solvent. After cleaning up using the saponification technique, the nonpolar component was fractionated using a silica column; and the PAH compounds were eluted using DCM: hexane (1:1 v/v) mixture. Nineteen PAH compounds were determined using a Shimadzu gas chromatography which was fitted with a mass spectrometer detector (Shimadzu GC-2010 Plus). The total concentration of PAHs detected ranged between 20-790 ng/g. Calculation of several molecular ratios for PAHs such as Anthracene/ (Anthracene+Phenanthrene) (Ant/(Ant+Phe)), Phenanthrene/Anthracene (Phe/Ant), Benzo(a)anthracene/Chrysene (BaA/Chr), (Benzo(a)anthracene/(Benzo(a)anthracene+Chrysene)) (BaA/(BaA+Chr)), and low molecular weight/high molecular weight of PAHs (LMW/HMW), yielded values ranging from 0.10–0.97, 0.03-9.40, 0.13-51.4, 0.12-0.98, and 0.03-1.26, respectively. These values suggested that the PAHs found in the surface sediments of the study area mainly originated from pyrolytic sources. The level of PAH contamination in the sediments was between low to moderate. Retene was also detected throughout the study area, indicating a minor contribution of biogenic PAHs to the sediment.

Keywords: surface sediments, polycyclic aromatic hydrocarbons, east coast Peninsular Malaysia, pyrolytic sources, PAHs diagnostic ratios

Abstrak

PAH (Hidrokarbon Aromatik Polisiklik) adalah salah satu pencemaran yang menjadi kerisauan pada alam marin. Tujuan kajian ini adalah untuk mengkaji taburan dan sumber PAH di sedimen persisir pantai Terengganu. Sampel sedimen dari 16 stesen sepanjang persisir pantai Terengganu telah diambil dengan menggunakan pencakup Smith Mclntyre. PAHs dari sedimen diekstrak melalui teknik ultra sonikasi, dengan mengunakan diklorometana (DCM): metanol (MeOH) (3:1 v/v) sebagai pelarut. Selepas pembersihan melalui teknik saponifikasi, komponen yang tak berkutub telah dipisahkan dengan mengunakan turus silika; PAH telah dialirkan keluar dengan pelarut DCM: heksana (1:1 v/v). Sebanyak 19 sebatian PAH telah ditentukan dengan menggunakan Shimadzu kromatografi gas disuaipadankan bersama pengesan spektrometer jisim (Shimadzu GC-2010 Plus). Jumlah kepekatan PAH yang dikesan adalah dalam lingkungan 20-790 ng/g. Beberapa nisbah molekul bagi PAH seperti Antracena/(Antracena+Fenantrena) (Ant/(Ant+Phe)), Fenantrena/Antracena (Phe/Ant), Benzo(a)antracena/Chrysene (BaA/Chr),

(Benzo(a)antracena/(Benzo(a)antracena+Chrysene)) (BaA/(BaA+Chr)), dan berat molekul rendah/berat molekul tinggi bagi PAH (LMW/HMW) telah dikira. Nilai nisbah yang dikira masing-masing adalah 0.10–0.97, 0.03-9.40, 0.13-51.4, 0.12-0.98, dan 0.03-1.26 menyarankan PAH yang dijumpai pada sedimen permukaan di kawasan kajian adalah berasal dari sumber pirolitik. Kadar pencemaran PAH dalam sedimen permukaan adalah di antara rendah dan sederhana. Retene turut dikesan di seluruh kawasan kajian menunjukkan terdapat sumbangan kecil PAH biogenik kepada sedimen.

Kata kunci: sedimen permukaan, polisiklik aromatik hidrokarbon, pantai timur Semenanjung Malaysia, sumber pirolitik, nisbah diagnostik PAH

Introduction

PAHs are a group of anthropogenic pollutants that are widely distributed in the environment. Their presence is of concern because many of these PAHs have carcinogenic and mutagenic properties [1]. In the marine ecosystem itself, PAH contaminants may cause long-term adverse effects to the marine life [2]. PAHs in the marine ecosystem generally can be classified into two major sources, viz. natural, also known as biogenic, and anthropogenic sources [1]. Biogenic PAHs such as Retene and Perylene naturally exist at low concentrations in water and sediments. The sources of natural PAHs may come from the biosynthesis processes of marine organisms, terrestrial plant waxes, and through diagenesis transformations of organic matter (after deposited in sediment) into PAHs [3, 4]. On the other hand, the anthropogenic PAHs are introduced into the marine ecosystem through human activities such as domestic and industrial wastewater discharges, oil exploration, and harbor activities. In aquatic environments, due to the hydrophobic characteristics of PAHs, these compounds are rapidly deposited in sediment as a final sink [1, 3]

The sources of anthropogenic PAHs in the environment can be classified according to their formation mechanism, as petrogenic or pyrolytic sources. The petrogenic sources are mainly derived from unburned fossil fuel or crude oil itself, whereas the pyrolytic PAHs are formed through incomplete combustion of organic matter (e.g. wood, coal, petroleum) [4, 5]. In order to distinguish the differences between PAH origins and sources, previous researchers have used several molecular diagnostic ratios to identify PAHs derived from petrogenic and pyrolytic sources. Yunker et al. [6] proposed several diagnostic ratios; among the proposed ratios were Anthracene/(Anthracene+Phenanthrene) (Ant/(Ant+Phe)), Phenanthrene/Anthracene (Phe/Ant), (Benzo(a)anthracene/(Benzo(a) +Chrysene)) (BaA/(BaA+Chr)), and Benzo(a)anthracene/Chrysene (BaA/Chr). Other researchers [3-5, 7, 8] also used similar ratios to determine sources of PAHs formed in their sediments. Additionally, Lukman [5], Mohd Tahir et al. [3] and Topal [4] used the ratio value of low molecular weight/high molecular weight PAHs (LMW/HMW) to differentiate between petrogenic and pyrolytic sources. These diagnostic ratios and their proposed values are listed in Table 1.

Table 1. PAHs diagnostic ratios

Ratio	Petrogenic	Mixed	Pyrolytic	References
Ant/(Ant+Phe)	<0.1		>0.1	[6]
Phe/Ant	>10		<10	[6,7]
BaA/(BaA+Chr)	<0.2	0.2-0.35	>0.35	[3,5,6]
BaA/Chr	<1		>1	[6,8]
LMW/HMW	>1		<1	[3-5]

Ant: Anthracene, Phe: Phenanthrene, BaA: Benzo(a)anthracene,
Chr: Chrysene, LMW/HMW: PAHs with 2-3 rings relative to PAHs with 4-6 rings

The Terengganu coast is located in the east coast of Peninsular Malaysia. Main human activities that might contribute to the presence of PAHs in the area are operational discharge from fishing vessels, tourist boats and ferries activities plying between the mainland and several nearby islands (Pulau Tenggol, Pulau Kapas, Pulau Redang, and Pulau Perhentian), oil and gas exploration, and other maritime activities. Furthermore, human activities

on land such as fuel combustion (vehicle-powered by diesel or gasoline fuel), forest or grass burning, and surface runoff from urban areas also tend to contribute PAHs into the marine ecosystem. Studies on PAH contaminations at the Terengganu coast are still limited. Elias et al. [2] reported on the contamination of PAHs in the surface sediment of east coast of peninsular Malaysia. The concentration of total PAHs in the surface sediment of Kuala Terengganu and Kuala Dungun coast are 270 ng/g and 290 ng/g, respectively.

Mohd Tahir et al. [9] had reported on the distribution and sources of PAHs in sediment cores from the Southern Terengganu coast, covering an area from Dungun to Kemaman coast. The concentration of total PAHs from the sediment cores that were collected during May and September 2007 ranged from 6.01 ng/g - 20.2 ng/g and 4.89 ng/g - 34.7 ng/g, respectively. Likewise, Chiu et al. [10] had reported on the distribution of PAHs in surface sediments of the Pulau Kapas area. The reported concentration of total PAHs from 12 stations ranged from 43 ng/g - 336 ng/g. These three studies suggested that the Terengganu coast is contaminated with a large number of pyrolytic PAH sources [2, 9, 10]. This present study, on the other hand, focuses on a wider area covering the whole coast of Terengganu state, starting from near the coast to approximately 100 km towards offshore. The main objective of this study is to fill the data gap for future references on the monitoring of our coastal environments, specifically on natural and anthropogenic PAHs off the Terengganu coast.

Materials and Methods

Study area

Sampling was carried out during 6th-13th May 2014 using the RV Discovery. Sixteen sampling sites (station 1-16) were selected along the Terengganu coast, covering an area from Bachok (Tok Bali) to Kemaman (Kerteh) (Figure 1). The coordinates of the stations are shown in Table 2. Water depth was generally shallow near the shore and deeper offshore, with depths ranging from 15.6 m to 59.8 m. Surficial samples were collected using a Smith Mc-Intyre grab sampler. Sediment samples were then transferred into a pre-cleaned aluminum foil container (pre-rinsed with hexane) using a stainless-steel spatula, refrigerated at -20 ºC, and then transported to the laboratory.

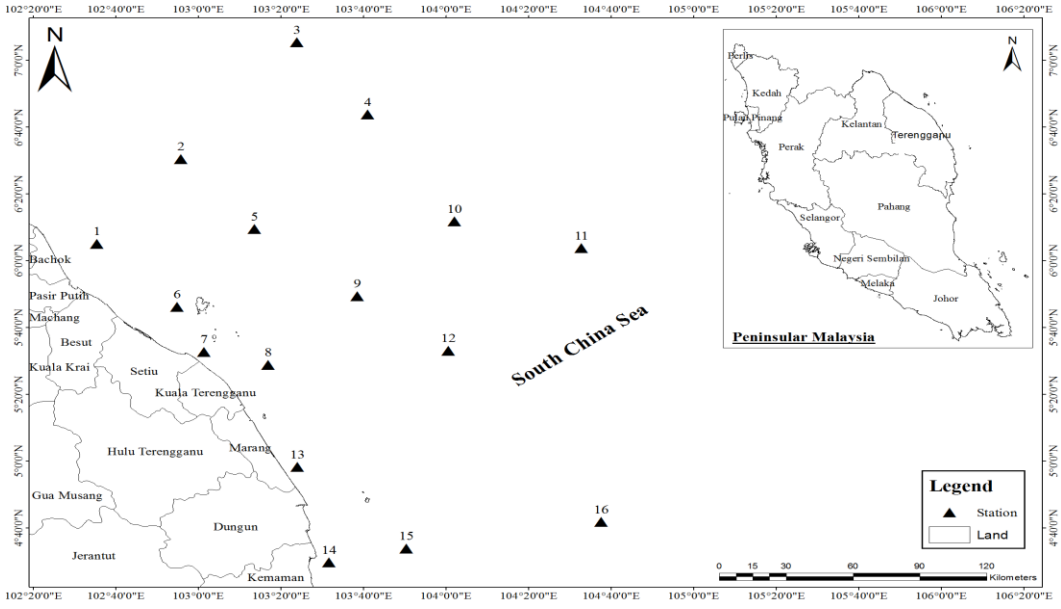


Figure 1. Sampling stations at Terengganu coast

Table 2. Coordinates and water depth of chosen sampling stations at Terengganu coast

Station	Latitude (DD)	Longitude (DD)	Water Depth (m)
1	6.083790000	102.5906830	22.2
2	6.505767000	102.9297950	59.8
3	7.088330000	103.3979570	55.5
4	6.727781000	103.6850770	43.6
5	6.157149000	103.2265030	55.2
6	5.769532000	102.9150040	15.6
7	5.544715000	103.0227370	25.0
8	5.479661000	103.2829690	33.6
9	5.822548000	103.6430020	39.1
10	6.194689000	104.0337520	54.3
11	6.061839000	104.5462690	55.5
12	5.550546000	104.0094080	48.4
13	4.970750000	103.4006389	31.4
14	4.494508333	103.5289111	16.5
15	4.563722222	103.8404917	31.0
16	4.696044444	104.6261278	45.5

Sample pre-treatment

The sediment samples were freeze-dried and then sieved using a 500 µm sieve. Analysis was carried out on the fraction <500 µm [11].

Extraction and fractionation

After freeze-drying, 20 g of sediments was extracted using the ultra-sonication method with dichloromethane (DCM): methanol (MeOH) (3:1 v/v) as solvent. Before extraction, internal standards Phenanthrene-d_{10} and Perylene-d_{12}, were spiked into the sediment samples for recovery assessment [11]. The extracts were concentrated to about 3 mL using a rotary evaporator (at temperature <35 °C) then cleaned up using the saponification technique (isolation of polar and non-polar compounds) [12]. The non-polar component was concentrated to about 1 mL and fractionated into sub fractions on a silica column (5% deactivated using deionized water). Alkanes (fraction 1) was eluted using 3.5 mL of hexane, followed by PAHs (fraction 2) using 4 mL of 10% DCM in hexane and 3 mL of 50% DCM in hexane. Only the PAHs fraction was analyzed in this study.

A total of 19 PAHs were analysed in this study. The sum of these compounds is reported as total PAHs (∑PAH). Out of the 19 compounds analysed, 16 of them are classified as priority PAH pollutants by the United States Environmental Protection Agency (USEPA), based on their most harmful characteristics and their existence in the environment [11]. These 16 PAHs are; Naphthalene (Nap), Acenaphtylene (Acp), Acenaphtene (Ace), Fluorene (Flo), Phenanthrene (Phe), Anthracene (Ant), Fluoranthene (Fla), Pyrene (Pyr), Benzo*(a)*anthracene (BaA), Chrysene (Chr), Benzo*(b)*fluoranthene (BbF), Benzo*(k)*fluoranthene (BkF), Benzo*(a)*pyrene (BaP), Indeno*(1,2,3–cd)*pyrene (IcP), Dibenzo*(a,h)*anthracene (DaA) and Benzo*(g,h,i)*perylene (BgP). The sum of these 16 PAHs is denoted as $\sum PAH_{16}$. The other three PAHs that were analysed were Retene (Retene), Perylene (Pery) and Benzo(e)pyrene (BeP).

Gas chromatography-mass spectroscopy analysis

The identification and quantification of PAHs was carried out using Shimadzu GC-2010 Plus. The GC-MS operating conditions were as follows: SGE BP5MS fused silica capillary column (29.7 m length x 0.32 mm internal

diameter, 0.25 µm filmed thicknesses); injection temperature was set at 290 ˚C using splitless mode; the column temperature for the analysis was programmed as follows: hold for 1 minute at 50 ˚C; 60 ˚C – 290 ˚C at 5 ˚C/min; maintained at 290 ˚C for 15 minutes; GC-MS interface was set to 300 ˚C; helium gas was used as the carrier gas at a constant pressure of 500 kPa with a column flow rate of 1.19 mL/min. The identification and quantification of PAHs was based on ion fragmentation, and retention time compared to the external PAHs standard [13].

Recovery and limit of detection

The recovery of the internal standards, Phenanthrene-d_{10} and Perylene-d_{12}, ranged from 70% - 81% and 85% - 96%, with an average value of 72% and 92%, respectively. The sample was then corrected for analytical loss [11]. The ranges for Limit of Detection (LOD) and Limit of Quantitation (LOQ) in this study were 0.01 ng/g - 0.23 ng/g and 0.03 ng/g - 0.76 ng/g, respectively.

Results and Discussion

Total PAHs (ΣPAH) detected in this study is shown in Figure 2 and Table 3. The ΣPAH detected ranged between 20.0 ng/g and 790 ng/g, with an average concentration 131 ng/g. The highest ΣPAH detected was at station 14 and station 7, with values of 790 ng/g and 541 ng/g, respectively. Both stations were located in the coastal area that could potentially receive PAH sources from the nearest river mouth; Sungai Kerteh and Sungai Merang, respectively. On the other hand, station 11 recorded the lowest ΣPAH at 20.0 ng/g. It is located farthest from the coast (offshore). According to Baumard et al. [14], the level of PAHs pollution is considered low if the value of sum PAHs concentration < 100 ng/g, and moderate if the concentration < 1000 ng/g. Tolosa et al. [7] also used these criteria to evaluate the level of PAHs pollution. Using the criteria proposed by Baumard et al [14], the level of PAHs contamination in the surface sediment of the Terengganu coast can be concluded to be between low and moderate. This finding is consistent with the findings reported by earlier researchers in the Terengganu coast [2, 9, 10].

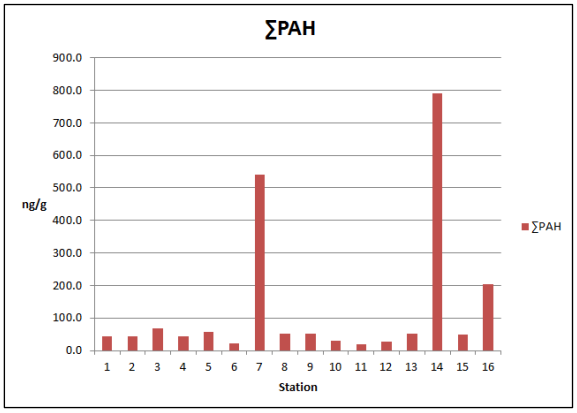


Figure 2. Concentration and distribution of ΣPAH with station

The composition of PAHs in sediments may reveal the sources from which these PAHs were derived [15, 16]. Higher concentrations of low molecular weight (LMW) PAHs (2- and 3-ring compounds) such as Nap, Acp, Ace, Flo, Phe, and Ant most commonly occur in sample matrices contaminated with petrogenic sources. On the other hand, PAHs originating from pyrolytic sources often contain elevated concentrations of high molecular weight (HMW) PAHs (4- to 6-ring compounds) such as Fla, Pyr, BaA, Chr, BbF, BkF, BaP, IcP, DaA, and BgP [17]. Figure 3 shows the distribution of a PAH compound according to the number of benzene rings in its molecular structure. In this study, the distributions of PAH compounds was found to vary with station. While a majority of the stations showed an abundance of HMW PAHs (4- to 6-rings), only stations 3, 8, and 11 showed the abundance of LMW PAHs (3-rings). The overall order of abundance of PAHs detected in the sediments was 6 rings> 5 rings> 3 rings> 4 rings. The abundance of total HMW PAH compounds detected in the majority of the stations suggested that there were significant inputs of pyrolytic sources in the Terengganu coast.

The calculated values of selected diagnostic ratios are shown in Table 3. In the case of LMW/HMW ratio, values obtained ranged from 0.03-1.26. LMH/HMW <1 has been suggested as an input from pyrolytic sources, whereas ratio values >1 are derived from petrogenic sources [3-5]. In this study, the majority of the sampling area showed the input of the pyrolytic PAH sources (Figure 4). Only stations 8 and 11 indicated a slight petrogenic PAH contamination, with the ratio values of 1.21 and 1.26, respectively.

Table 3. Concentration level PAHs (ng/g), sum (ng/g), and selected diagnostic ratios

	PAH Compounds	Station									
		1	2	3	4	5	6	7	8	9	10
LMW	Napthalene (Nap)	3.14	6.41	9.30	6.69	2.67	5.12	6.82	3.78	5.07	2.30
	Acenaphthene (Ace)	1.14	0.34	0.89	0.61	0.29	0.10	0.11	0.63	4.07	**BDL**
	Acenaphthylene (Acp)	0.75	2.16	2.36	**BDL**	0.22	1.02	0.074	0.72	**BDL**	0.52
	Fluorene (Flo)	0.42	1.20	0.53	0.22	0.20	0.40	0.52	0.83	**BDL**	0.35
	Phenanthrene (Phe)	2.91	1.21	5.83	4.15	0.75	1.64	4.83	0.62	4.94	0.53
	Anthracene (Ant)	1.12	2.97	3.79	1.68	0.43	0.28	1.05	20.8	1.25	0.28
	Retene (Retene)	1.63	6.65	2.95	1.25	16.7	1.58	3.99	0.74	13.7	1.51
HMW	Fluoranthen (Fla)	0.38	0.96	1.14	0.80	0.26	0.17	43.0	0.34	2.69	0.59
	Pyrene (Pyr)	1.53	1.23	4.20	6.35	0.69	0.62	0.54	2.75	0.30	0.61
	Benzo(a)anthracene (BaA)	0.26	0.24	1.80	1.12	1.02	0.86	9.46	0.03	0.04	0.47
	Chrysene (Chr)	0.98	0.35	1.94	0.30	1.02	0.01	3.93	0.16	0.32	0.38
	Benzo(b)fluoranthene (BbF)	13.3	1.59	5.43	**ND**	2.34	**ND**	43.5	8.27	1.28	2.13
	Benzo(k)fluoranthene (BkF)	1.55	0.69	1.92	2.76	1.88	**ND**	39.8	0.95	0.86	6.28
	Benzo(e)pyrene (BeP)	0.34	0.08	3.03	0.44	2.27	**ND**	106	0.06	1.25	2.52
	Benzo(a)pyrene (BaP)	1.45	2.27	2.47	6.46	3.07	**ND**	53.6	0.89	0.94	0.98
	Perylene (Pery)	0.80	1.01	13.0	1.76	15.1	3.53	97.0	0.09	0.85	4.58
	Indeno(1,2,3-cd)pyrene (IcP)	1.11	9.15	4.63	8.04	7.96	2.96	35.2	7.37	9.51	2.67
	Dibenzo(a,h)anthracene (DaA)	5.93	3.86	0.68	1.19	1.42	2.89	31.2	**ND**	1.59	2.25
	Benzo(g,h,i)perylene (BgP)	4.91	2.30	2.82	**ND**	**ND**	**ND**	59.9	1.63	2.88	1.39
	∑PAH	43.7	44.7	68.7	43.8	58.3	21.2	541	50.7	51.6	30.4
	LMW	9.48	14.3	22.7	13.4	4.59	8.56	13.4	27.4	15.3	4.00
	HMW	32.6	23.7	43.1	29.2	37.0	11.1	523	22.6	22.5	24.9
PAHs Indices	LMW/HMW	0.29	0.60	0.52	0.45	0.12	0.77	0.03	1.21	0.68	0.16
	Phe/Ant	2.59	0.40	1.54	2.47	1.76	5.70	4.62	0.03	3.96	1.87
	Ant/(Ant+Phe)	0.27	0.71	0.39	0.28	0.36	0.14	0.17	0.97	0.20	0.34
	BaA/Chr	0.26	0.69	0.92	3.73	1.00	51.4	2.41	0.20	0.13	1.25
	BaA/(BaA+Chr)	0.21	0.40	0.48	0.78	0.49	0.98	0.70	0.17	0.11	0.55

BDL= below detection limit; ND = not detected; Phe/Ant = Phenanthrene/Anthracene;
Ant/(Ant+Phe) = Anthracene/(Anthracene+Phenanthrene); BaA/Chr = Benzo(a)anthracene/Chrysene;
BaA/(BaA+Chr) = (Benzo(a)anthracene/(Benzo(a)anthracene+Chrysene));
LMW/HMW = low molecular weight/high molecular weight

Table 3 (cont'd). Concentration level PAHs (ng/g), sum (ng/g), and selected diagnostic ratios

	PAH Compounds	Station					
		11	12	13	14	15	16
LMW	Napthalene (Nap)	5.12	4.42	4.39	6.29	5.14	6.64
	Acenaphthene (Ace)	3.56	1.64	5.44	0.35	0.16	1.28
	Acenaphthylene (Acp)	1.38	1.69	3.82	10.8	1.06	2.10
	Fluorene (Flo)	0.21	0.11	1.02	31.9	8.46	4.46
	Phenanthrene (Phe)	0.66	0.61	0.96	3.12	1.19	0.80
	Anthracene (Ant)	0.07	1.32	1.88	2.36	2.62	4.69
	Retene (Retene)	0.23	3.84	1.11	3.35	0.64	5.42
HMW	Fluoranthen (Fla)	0.56	0.36	0.31	0.47	0.49	0.14
	Pyrene (Pyr)	2.94	1.28	1.62	0.95	22.3	7.73
	Benzo(a)anthracene (BaA)	0.17	0.85	0.59	9.17	0.04	7.62
	Chrysene (Chr)	0.21	0.29	2.42	2.47	0.17	5.66
	Benzo(b)fluoranthene (BbF)	0.71	3.47	2.34	670	1.23	4.13
	Benzo(k)fluoranthene (BkF)	1.27	1.41	1.07	12.3	**ND**	14.1
	Benzo(e)pyrene (BeP)	0.72	0.81	1.01	2.18	0.05	6.60
	Benzo(a)pyrene (BaP)	0.46	1.14	0.34	10.4	**ND**	31.2
	Perylene (Pery)	1.30	0.03	**ND**	4.57	0.01	27.8
	Indeno(1,2,3-cd)pyrene (IcP)	0.30	3.39	19.8	5.21	1.29	30.7
	Dibenzo(a,h)anthracene (DaA)	**ND**	0.14	**ND**	6.63	2.37	26.2
	Benzo(g,h,i)perylene (BgP)	0.04	1.57	2.39	7.20	2.43	16.9
	∑PAH	20.0	28.4	50.6	790	49.7	204
	LMW	11.0	9.79	17.5	54.8	18.6	20.0
	HMW	8.71	14.8	32.0	731	30.4	179
PAHs Indices	LMW/HMW	1.26	0.66	0.54	0.07	0.61	0.11
	Phe/Ant	9.40	0.46	0.51	1.32	0.45	0.17
	Ant/(Ant+Phe)	0.09	0.68	0.66	0.43	0.68	0.85
	BaA/Chr	0.81	2.91	0.24	3.71	0.24	1.35
	BaA/(BaA+Chr)	0.45	0.74	0.19	0.78	0.19	0.57

BDL= below detection limit; ND = not detected; Phe/Ant = Phenanthrene/Anthracene;
Ant/(Ant+Phe) = Anthracene/(Anthracene+Phenanthrene);
BaA/Chr = Benzo(a)anthracene/Chrysene;
BaA/(BaA+Chr)= (Benzo(a)anthracene/(Benzo(a)anthracene+Chrysene));
LMW/HMW = low molecular weight/high molecular weight

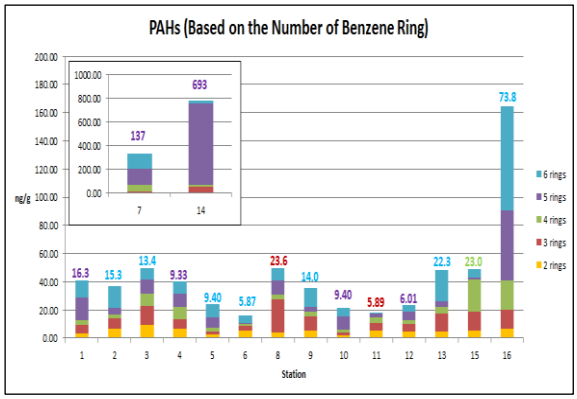


Figure 3. The relative abundance of PAHs compounds with station (based on the number of benzene ring)

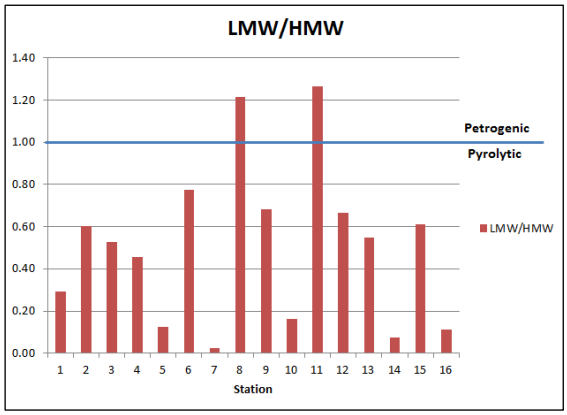


Figure 4. Distribution of LMW/HMW ratio with station

The diagnostic ratios of Ant/(Ant+Phe) (Figure 5) and Phen/Ant (Figure 6) found in this study ranged from 0.10-0.97 and 0.03-9.40, respectively. The Ant/(Ant+Phe) values being > 0.1 imply pyrolytic sources, whereas values < 0.1 imply petrogenic sources [6]. On the other hand, the diagnostic ratio of Phen/Ant being < 10 implies pyrolytic sources, whereas values of >10 are a characteristic of petrogenic sources [7]. The results from Ant/(Ant+Phe) and Phen/Ant diagnostic ratios suggest that the PAHs in all sampling areas were derived from pyrolytic sources.

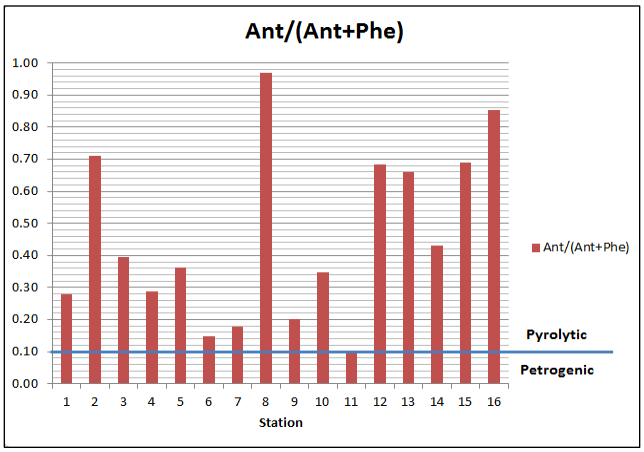


Figure 5. Distribution of Ant/(Ant/Phe) ratio with station

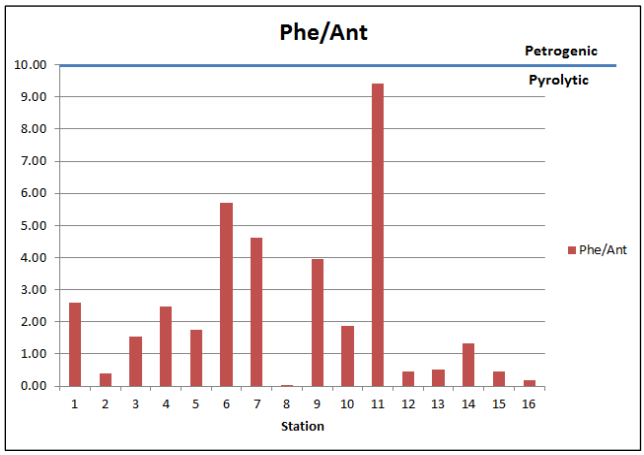


Figure 6. Distribution of Phe/Ant ratio with station

The calculated isomer pairs ratios of BaA/Chr and BaA/(BaA+Chr) ranged between 0.13-51.4 and 0.12-0.98, respectively. The BaA/Chr diagnostic ratio value was also used to suggest the origin of PAH sources; petrogenic <1 and pyrolytic >1[8]. On the other hand, BaA/(BaA+Chr) ratios were used to narrow down the sources into the following three categories [5]. The ratio implies pyrolytic sources if the value is > 0.35, while a value of < 0.2 implies petrogenic sources. However, a value ranging from 0.2 to 0.35 is indicative of a mixture of petrogenic and pyrolytic sources. Results from the BaA/Chr diagnostic ratios (Figure 7) showed that half of the study areas (station 1, 2, 3, 8, 9, 11, 13 and 15) were contaminated with significant amounts of petrogenic sources, while the other half (station 4,5,6,7,10,12,14 and 16) were contaminated with pyrolytic sources. In the case of BaA/(BaA+Chr) ratio (Figure 8), values at station 1 (0.21), 13 (0.20) and 15 (0.20) suggested a mixture of petrogenic and pyrolytic sources, values at station 8 (0.17) and 9 (0.12) suggested petrogenic sources, and values at the remaining stations suggested that the PAH compounds were mainly derived from pyrolytic sources.

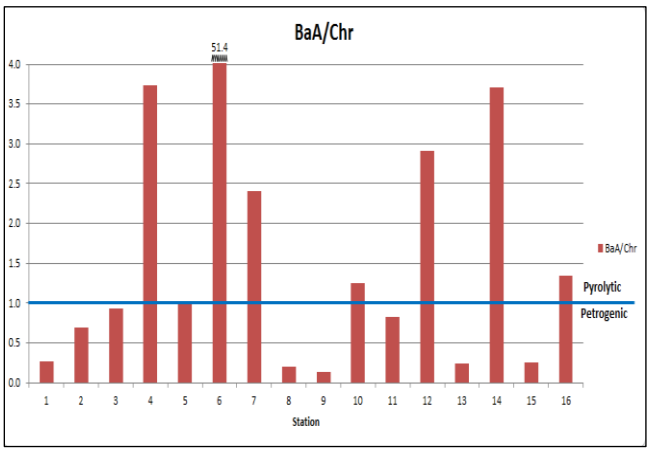


Figure 7. Distribution of BaA/Chr ratio with station

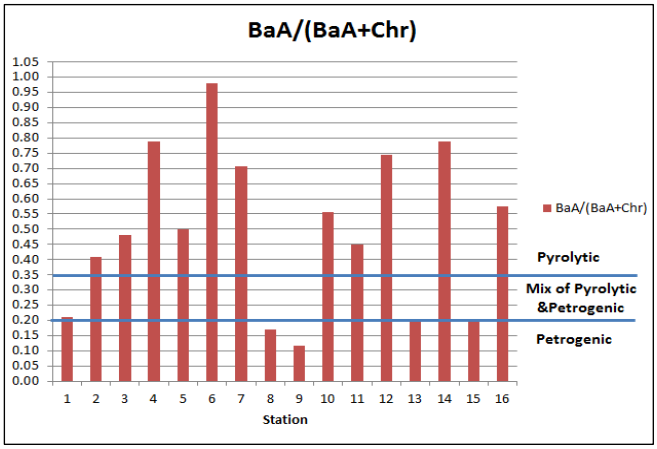


Figure 8. Distribution of BaA/(BaA+Chr) ratio with station

The presence of PAH compounds, Retene (m/z 234) and Perlyene (m/z 252) has often been associated with the natural (biogenic or diagenetic) PAH sources [7]. Retene is a PAH compound that consists of a 3-benzene ring structure and acts as a PAH biomarker for terrestrial plants. On the other hand, Perylene is a compound that can also be related to the pyrolytic sources. In this study, all of the sampling sites show the presence of Retene ranging from 0.24 ng/g to16.7 ng/g (Figure 9). With exception of station 13, Perylene was detected in all stations with concentrations ranging from 0.01 ng/g to 97.01 ng/g (Figure 10). According to Bakhtiari et al. [18], the percentage ratio of Perylene to ΣPAH_{16} is considered as pyrolytic if the value ranges from 1% to 4% and biogenic if the value is > 4%. In this study, the percentage of Perylene to ΣPAH_{16} ranged from 0.03% to 62.2%. Most of the stations indicated contamination from pyrolytic sources. With the exception of stations 3,4,5,6,7,10, and 11, which indicated that the Perylene was derived from biogenic sources, other remaining stations indicated that the Perylene contamination was from pyrolytic sources. Tolosa et al. [7] suggested another ratio to evaluate the sources of Perylene in marine sediments. This ratio is the percentage of Perylene to the sum of pentacyclic aromatic isomers (PAI) (BbF, BkF, BeP, BaP, Pery) (%Pery/PAI). A %Pery/PAI > 20% would indicate a diagenetically derived Pery, whereas a value < 20% would indicate a pyrolytically derived Pery. In this study, the values of %Pery/PAI ranged from 0.39% to 100%. Most of the stations indicate the pyrolytic sources of Pery, except for stations 3,4,5,6,7,10, and 11. This finding is consistent with the conclusion drawn from the percentage ratio of Perylene to ΣPAH_{16}.

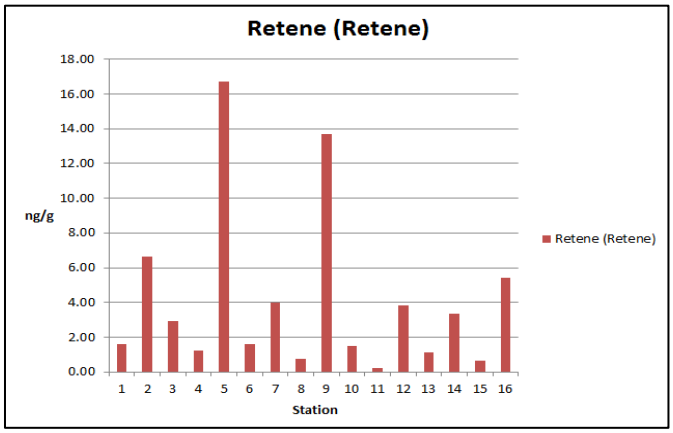


Figure 9. Concentration and distribution of Retene with station

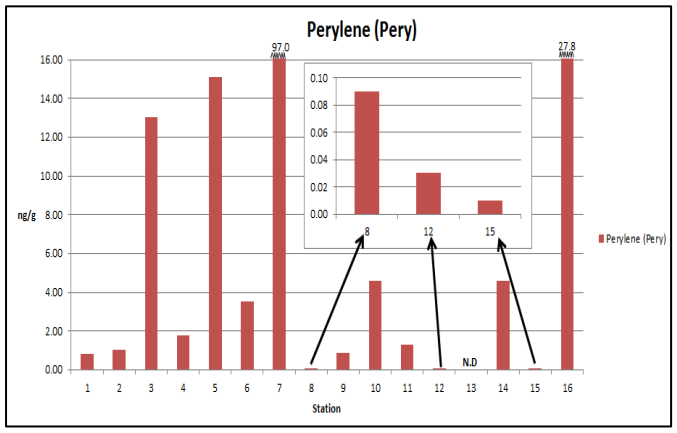


Figure 10. Concentration and distribution of with station

Overall result from the selected PAHs diagnostic ratios suggested the dominance of pyrolytic PAH sources over the petrogenic sources in sediments of the Terengganu coast. According to Abdel-Shafy et al. [1] the pyrolytic PAHs are formed when organic substances are exposed to high temperature combustion under insufficient oxygen conditions which created an incomplete combustion process. The dominance of pyrolytic PAHs the in Terengganu coast sediment, suggested that these PAH compounds were derived from human activities. Maritime activities such as fishing boats, oil and gas exploration and production and shipping industries were main possible contributors to the presence of PAHs in the study area. Human activities on land such as incomplete combustion of wood in forest fires and fireplaces, and incomplete combustion of fuels in vehicular engines, could also contribute PAHs to the marine environment through atmospheric deposition and/or riverine discharge of urban run-offs. Thus, it is not surprising that station 7 (Merang) and 14 (Kemaman), which are located in the vicinity of a jetty and a port, showed the highest ΣPAH concentration in this study.

Conclusion

The ΣPAH concentration found in this study ranged from 20-790 ng/g, with a mean concentration of 131 ng/g. Evaluation of selected PAH diagnostic ratios suggested that pyrolysis was the main source of the 16 USEPA priority pollutant PAHs, with minor contributions from petrogenic sources. Evaluation of Pery indices suggested that, depending on stations, Pery was derived from either pyrolytic or biogenic sources. On the hand, the presence of Retene in all stations, albeit in minor amounts, clearly indicated the important contribution of biogenic PAHs to the marine environment.

Acknowledgement

Financial support from INOS (UMT) through a HICoE research grant vote no. 66928 and the use of facilities at the UMT Central Laboratory is kindly acknowledged. Inputs from Dr. T. F.T. Omar, Ms. Pang Swee Yun and Mr. Mohd Fathi Azmi on some aspects of this research are kindly acknowledged.

References

1. Abdel-Shafy, H. I. and Mansour, M. S. (2016). A review on polycyclic aromatic hydrocarbons: source, environmental impact, effect on human health and remediation. *Egyptian Journal of Petroleum*, 25(1): 107-123.
2. Elias, M. S., Wood, A. K., Hashim, Z., Siong, W. B., Hamzah, M. S., Rahman, S. A. and Talib, A. (2007). Polycyclic aromatic hydrocarbon (PAH) contamination in the sediments of East Coast Peninsular Malaysia. *Malaysian Journal of Analytical Sciences*, 11(1): 70-75.
3. Tahir, M. N., Fadzil, F. M., Ariffin, J. Maarop, I. H. and Wood, H. K. A. (2011). Sources of polycylic aromatic hydrocarbons in mangrove sediments of Pulau Cik Wan Dagang, Kemaman. *Journal of Sustainability Science and Management*, 6: 98-106.
4. Topal, T. (2011) Investigation of extraction methodologies for quantitative determination of polycyclic aromatic hydrocarbons in sediments. Thesis Degree of Doctor Philosophy, Middle East Technical University.
5. Lukman, M. (2010). Distribution and sources of polycyclic aromatic hydrocarbons in sediments, suspended particulate matter and waters from the Siak River system, estuary and coastal area of Sumatra, Indonesia. Thesis Degree of Doctor Philosophy, Universität Bremen, Bremen.
6. Yunker, M. B., Macdonald, R. W., Vingarzan, R., Mitchell, R. H., Goyette, D. and Sylvestre, S. (2002). PAHs in the Fraser River basin: A critical appraisal of PAH ratios as indicators of PAH source and composition. *Organic Geochemistry*, 33: 489-515.
7. Tolosa, I., Mora, S. D., Sheikholeslami, M. R., Villeneuve, J. P., Bartocci, J., Cattini, C. (2004) Aliphatic and aromatic hydrocarbons in coastal Caspian Sea sediments. *Marine Pollution Bulletin*, 48: 44-60.
8. Sulej, A. M., Polkowska, Ż. and Namieśnik, J. (2011). Contamination of runoff water at Gdańsk Airport (Poland) by polycyclic aromatic hydrocarbons (PAHs) and polychlorinated biphenyls (PCBs). *Sensors*, 11(12): 11901-11920.
9. Tahir, N. M., Pang, S. Y., Hii, Y. S. and Simoneit, B. R. (2014). Distribution and sources of perylene and other polycyclic aromatic hydrocarbons (PAHs) in South China Sea sediments off Southern Terengganu Coast, Malaysia. In: From Sources to Solution. Springer, Singapore: pp. 463-467.
10. Chiu, T. R., Nanyan, N. F. M. and Ali, M. M. (2015). Distribution of polycyclic aromatic hydrocarbons (PAHs) in surface sediments of Kapas Island, Terengganu, Malaysia. *Procedia Environmental Sciences*, 30: 162-167.
11. United Nations Environment Programme (UNEP). (1992) Determination of petroleum hydrocarbons in sediments. Reference Methods for Marine Pollution Studies No. 20.
12. Tolosa, I. and de Mora, S. (2004). Isolation of neutral and acidic lipid biomarker classes for compound-specific-carbon isotope analysis by means of solvent extraction and normal-phase high-performance liquid chromatography. *Journal of Chromatography A*, 1045(1-2): 71-84.
13. Tan. H. S. (2012) Extractable organic compound in smoke particulate matter from burning of three tropical wood species. Thesis of Master Degree, Universiti Malaysia Terengganu, Terengganu, Malaysia.
14. Baumard, P., Budzinski, H., Michon, Q., Garrigues, P., Burgeot, T. and Bellocq, J. (1998). Origin and bioavailability of PAHs in the Mediterranean Sea from mussel and sediment records. *Estuarine, Coastal and Shelf Science*, 47(1): 77-90.

15. Simpson, C. D., Harrington, C. F., Cullen, W. R., Bright, D. A. and Reimer, K. J. (1998). Polycyclic aromatic hydrocarbon contamination in marine sediments near Kitimat, British Columbia. *Environmental Science & Technology*, 32(21): 3266-3272.
16. Yan, W., Chi, J., Wang, Z., Huang, W. and Zhang, G. (2009). Spatial and temporal distribution of polycyclic aromatic hydrocarbons (PAHs) in sediments from Daya Bay, South China. *Environmental Pollution*, 157(6): 1823-1830.
17. La Nafie, N., Asmawati, M. R. and Arief, A. (2016). Distribution of polycyclic aromatic hydrocarbons (PAHs) in sediments of Losari Beach and adjacent areas, South Sulawesi, Indonesia. *International Journal of Applied Chemistry*, 12(4): 675-682.
18. Bakhtiari, A. R., Zakaria, M. P., Yaziz, M. I., Lajis, M. N. H., Bi, X. and Rahim, M. C. A. (2009). Vertical distribution and source identification of polycyclic aromatic hydrocarbons in anoxic sediment cores of Chini Lake, Malaysia: perylene as indicator of land plant-derived hydrocarbons. *Applied Geochemistry*, 24(9): 1777-1787.